PAC

Proceedings of the

2003 Particle Accelerator Conference

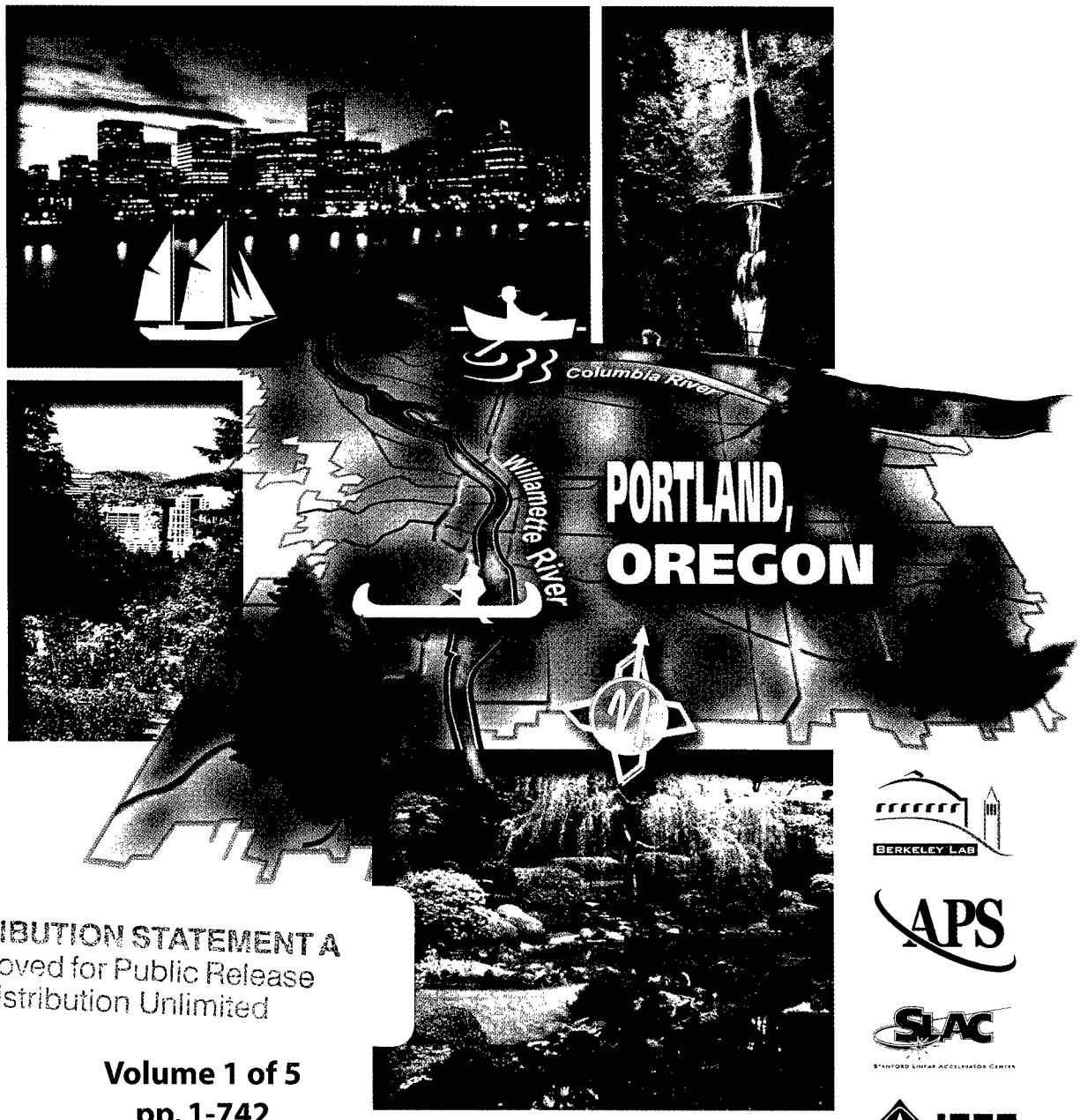

DISTRIBUTION STATEMENT A
Approved for Public Release
Distribution Unlimited

Volume 1 of 5
pp. 1-742

BERKELEY LAB

APS

SLAC
STANFORD LINEAR ACCELERATOR CENTER

IEEE

REPORT DOCUMENTATION PAGE

Form Approved OMB No. 0704-0188

Public reporting burden for this collection of information is estimated to average 1 hour per response, including the time for reviewing instructions, searching existing data sources, gathering and maintaining the data needed, and completing and reviewing the collection of information. Send comments regarding this burden estimate or any other aspect of this collection of information, including suggestions for reducing this burden, to Washington Headquarters Services, Directorate for Information Operations and Reports, 1215 Jefferson Davis Highway, Suite 1204, Arlington, VA 22202-4302, and to the Office of Management and Budget, Paperwork Reduction Project (0704-0188), Washington, DC 20503.

1. AGENCY USE ONLY (*Leave Blank*)	2. REPORT DATE	3. REPORT TYPE AND DATES COVERED
		Final

4. TITLE AND SUBTITLE
2003 Particle Accelerator Conference
Vol. 1

5. FUNDING NUMBERS
G

6. AUTHORS
variou

7. PERFORMING ORGANIZATION NAME(S) AND ADDRESS(ES)
IEEE
445 Hoes Lane, PO Box 1331
Piscataway, NJ 08855-1331

8. PERFORMING ORGANIZATION REPORT NUMBER

9. SPONSORING / MONITORING AGENCY NAME(S) AND ADDRESS(ES)
Office of Naval Research
Ballston Centre Tower One
800 North Quincy Street
Arlington, VA 22217-5660

10. SPONSORING / MONITORING AGENCY REPORT NUMBER
N00014-04-1-0417

11. SUPPLEMENTARY NOTES

12a. DISTRIBUTION / AVAILABILITY STATEMENT
DISTRIBUTION STATEMENT A
Approved for Public Release
Distribution Unlimited

12b. DISTRIBUTION CODE

13. ABSTRACT (*Maximum 200 words*)

The twentieth biennial Particle Accelerator Conference on Accelerator Science and Technology was held May 12 – 16, 2003 at the Hilton Hotel in Portland, Oregon. The Stanford Linear Accelerator Center and the Lawrence Berkeley National Laboratory organized PAC 2003, and it was held under the auspices of the Nuclear and Plasma Sciences Society of the Institute of Electrical and Electronics Engineers and the Division of Physics of Beams of the American Physical Society. The attendance was 1025 registrants from 21 countries. The Program Committee was co-chaired by Alan Jackson and Ed Lee. The program they arranged had opening and closing plenary sessions that covered the most important accomplishments, opportunities, and applications of accelerators. During the remainder of the conference there were parallel sessions with oral and poster presentations. In addition, there was an industrial exhibit during the first three days. The Proceedings present a total of 1154 papers from the invited, contributed orals, and poster sessions.

14. SUBJECT TERMS
Particle Accelerators and Colliders, Beam Dynamics, Magnets, RF Systems, Synchrotron radiation sources, Free Electron Lasers, Energy Recovery Linacs, Instabilities, Feedback Instrumentation, Pulsed Power, High Intensity Beams, Accelerator Applications, Advanced Accelerators.

15. NUMBER OF PAGES
3571

16. PRICE CODE

17. SECURITY CLASSIFICATION OF REPORT	18. SECURITY CLASSIFICATION OF THIS PAGE	19. SECURITY CLASSIFICATION OF ABSTRACT	20. LIMITATION OF ABSTRACT
Unclassified	**Unclassified**	**Unclassified**	

NSN 7540-01-280-5500

Standard Form 298 (Rev. 2-89)
Prescribed by ANSI Std. Z39-1
298-102

PAC 2003

PROCEEDINGS OF THE 2003 PARTICLE ACCELERATOR CONFERENCE

Portland, Oregon U.S.A.
May 12-16, 2003

Joe Chew, Peter Lucas, and Sara Webber, editors

Volume 1 of 5

Organized by
Stanford Linear Accelerator Center
Lawrence Berkeley National Laboratory

Held under the joint auspices of
Institute of Electrical and Electronics Engineers
(Nuclear and Plasma Sciences Society)
American Physical Society
(Division of Physics of Beams)

Sponsored by
U.S. Department of Energy
Office of Naval Research
National Science Foundation

20040311 168

ACKNOWLEDGEMENTS

Cover Design: Terry Anderson

Photographs: Edmund Keene Photographers

Funding for these proceedings was provided under DOE Grant No. DE-FG03-01ER41233 by the following U.S. Department of Energy offices:

- Office of High Energy and Nuclear Physics
- Office of Basic Energy Sciences
- Office of Fusion Energy Sciences

This work related to Department of Navy grant N00014-03-1-0417 issued by the Office of Naval Research. The United States Government has a royalty-free license throughout the world in all copyrightable material contained herein.

Funding for student and postdoctoral associate travel to attend the conference was provided by National Science Foundation Grant No. PHY-0225358.

Proceedings of the 2003 Particle Accelerator Conference

Copyright and Reprint Permission: Abstracting is permitted with credit to the source. Libraries are permitted to photocopy beyond the limit of U.S. copyright law for private use of patrons those articles in this volume that carry a code at the bottom of the first page, provided the per-copy fee indicated in the code is paid through Copyright Clearance Center, 222 Rosewood Drive, Danvers, MA 01923. For other copying, reprint, or republication permission, write to IEEE Copyrights Manager, IEEE Operations Center, 445 Hoes Lane, P.O. Box 1331, Piscataway, NJ 08855-1331. All Rights reserved. Copyright ©2003 by the Institute of Electrical and Electronics Engineers, Inc.

IEEE Catalog Number: 03CH37423

ISBN: 0-7803-7738-9

Library of Congress: 88-647453

Additional copies of this publication are available from
IEEE Operations Center
445 Hoes Lane
Piscataway, NJ 08855-1331 USA
+1 800 678 IEEE
+1 732 981 9667 (FAX)
email: customer.service@ieee.org

The 2003 Particle Accelerator Conference

The twentieth biennial Particle Accelerator Conference on Accelerator Science and Technology was held May 12–16, 2003 at the Hilton Hotel in Portland, Oregon. The Stanford Linear Accelerator Center and the Lawrence Berkeley National Laboratory organized PAC 2003, and it was held under the auspices of the Nuclear and Plasma Sciences Society of the Institute of Electrical and Electronics Engineers and the Division of Physics of Beams of the American Physical Society. The attendance was 1025 registrants from 21 countries. These Proceedings present 195 papers from the nearly 225 invited and contributed orals, as well as 925 papers from the poster sessions.

The primary purpose of Particle Accelerator Conferences is to provide a forum for communication and exchange of ideas among accelerator scientists and engineers. This purpose was well served at PAC 2003 by the program of invited and contributed papers and through the informal interactions made possible by the hospitality and ambience of the Hilton Hotel and Portland.

The Program Committee was co-chaired by Alan Jackson and Ed Lee. The program they arranged had opening and closing plenary sessions that covered the most important accomplishments, opportunities, and applications of accelerators. During the remainder of the conference there were parallel sessions with oral and poster presentations. In addition, there was an industrial exhibit during the first three days.

The social program began on Sunday evening with a reception for conference participants. The banquet, which was on Thursday evening, featured the jazz of the Leonard Webb Quartet.

There was a special session Wednesday afternoon for presentations by some of the award winners honored at the conference. This was followed by an enjoyable awards ceremony and reception sponsored by the IEEE Nuclear and Plasma Sciences Society and the APS Division of Physics of Beams. The honorees were:

APS Robert R. Wilson Prize
Helen T. Edwards (Fermilab)

IEEE/NPSS Particle Accelerator Science and Technology Awards
Stephen Milton (Argonne National Laboratory)
Keith Symon (University of Wisconsin)

IEEE/NPSS Early Achievement Award
Simon Cooke (Naval Research Laboratory & SAIC)

APS Award for Outstanding Doctoral Thesis Research in Beam Physics
David Pritzkau (Big Bear Networks, Inc., & SLAC)

U.S. Particle Accelerator School Prize for Achievement in Accelerator Physics and Technology
Martin Reiser (University of Maryland)
Sami Tantawi (SLAC)

APS Fellowships

Stephen Benson (TJNAF)
Yu-Jiuan Chen (LLNL)
Ralph Fiorito (Catholic Univ. of America)
Alan Jackson (LBNL)
Stephen Milton (Argonne Nat'l Lab)
Nikolai Mokhov (Fermilab)
Donald Prosnitz (US Dept. of Justice)

In addition, the winners of the student travel awards sponsored by the National Science Foundation, the IEEE NPSS, and the APS DPB were recognized.

PAC 2003 was a success because of the efforts of many people. Maura Chatwell and Adrienne Higashi coordinated the conference and handled all the arrangements. Joy Kono and Anna Smith provided essential support for the program, and Sara Webber was invaluable in producing these proceedings. I would like to give my thanks to them and to the other members of the Local Organizing Committee, the JACoW Editorial Staff, the Proceedings Staff, the Computing and Networking Staff, and the Registration Staff. Their hard work, dedication, and congeniality made PAC 2003 a pleasant and rewarding experience.

Bob Siemann
Chair, 2003 Particle Accelerator Conference

LOCAL ORGANIZING COMMITTEE

Robert Siemann, SLAC, Conference Chair
Maura Chatwell, SLAC, Conference Coordinator
Adrienne Higashi, SLAC, Conference Coordination & Industrial Exhibits
Laurie Escudero, SLAC, Finance
James Spencer, SLAC, Travel Awards
Terry Anderson, SLAC, Graphics
Ruth McDunn, SLAC, WWW Support
Sara Webber, FNAL, Editorial Support
Stephanie Santo, SLAC, Satellite Meetings
Edward Lee, LBNL, Program Co-Chair
Alan Jackson, LBNL, Program Co-Chair
Joe Chew, LBNL, Proceedings and Computing
Joy Kono, LBNL, Program Administrator
Anna Smith, LBNL, Program Support
Kathleen Weber, LBNL, Program Support
Vik Bhatia, LBNL, Database Management
Matt Arena, FNAL, Database Management
Hannah Siemann, Conference Support

JACoW EDITORIAL STAFF

Matt Arena, FNAL
Jan Chrin, PSI
Martin Comyn, TRIUMF
Cathy Eyberger, ANL
Charlie Horak, ORNL
Allison Lavis, FNAL
Lief Liljeby, MSL
Peter Lucas, FNAL
Michaela Marx, DESY
Christine Petit-Jean-Genaz, CERN
Jeff Patton, ORNL
John Poole, CERN
Alicia Seifrid, FNAL
Toshiya Tanabe, RIKEN
Sara Webber, FNAL

PROCEEDINGS OFFICE STAFF

Kymba A'Hearn, LBNL
Martha Condon, LBNL
Cathy Vanecek, LBNL

COMPUTING AND NETWORKING STAFF

John Christman, LBNL
Tom Gallant, LBNL

REGISTRATION STAFF

Linda Ahlf, SLAC
Nicole Brown-Sinkler, TJNAF
John Escudero, SLAC
Vickee Flynn, SLAC
Myra Fultz, ORNL
Donna Gilchrist, TJNAF
Ann Jordan, ORNL
Lori Lane, ORNL
Kathy Rosenbalm, ORNL
Lorraine Stanford, LANL

PAC2003 ORGANIZING COMMITTEE

Robert Siemann, SLAC, Chair

W. A. Barletta, LBNL
I. Ben-Zvi, BNL
B. Brown, NPSS, FNAL
J. Cary, Colorado
S. Chattopadhyay, TJNAF
Y. Cho, ANL
L. Costrell, NIST
M. K. Craddock, TRIUMF, UBC
G. Dugan, Cornell
D. A. Finley, FNAL
N. Holtkamp, ORNL
A. Jackson, LBNL
G. P. Jackson, HBAR Tech
R. Kustom, ANL
J. L. Laclare, Saclay
Won Namkung, POSTECH
P. O'Shea, Maryland
N. Phinney, SLAC
C. W. Roberson, ONR
R. Ruth, DPB, SLAC
S. O. Schriber, LANL
B. Strauss, DOE
D. F. Sutter, DOE
A. Todd, AES
W. T. Weng, BNL

PAC2003 PROGRAM COMMITTEE

Alan Jackson & Edward Lee, LBNL, Co-Chairs

C. Adolphsen, SLAC
W. Barletta, LBNL
J. Barnard, LLNL
S. Biedron, ANL, MaxLab
E. Blackmore, TRIUMF
D. Bruhwiler, Tech-X
G. Caporaso, LLNL
C. Celata, LBNL
Y. Chen, LLNL
Y. Cho, ORNL
P. Debenham, DOE
G. Decker, ANL
M. deJong, Saskatoon
G. Dugan, Cornell
G. Dutto, TRIUMF
P. Emma, SLAC
D. Finley, FNAL
K. Flöttmann, DESY
J. Galambos, ORNL
E. Gluskin, ANL
J. Haines, ORNL
K. Harkay, ANL
S. Henderson, ORNL
I. Hofmann, GSI
A. Hutton, TJNAF
G. Jackson, HBAR-Tech
T. Katsouleas, USC
R. Kishek, Maryland
G. Krafft, TJNAF
F. Krawczyk, LANL
S. Kurokawa, KEK
V. Lebedev, FNAL
W. McDowell, ANL
S. Mishra, FNAL
G. Neil, TJNAF
P. O'Shea, Maryland
R. Pasquinelli, FNAL
S. Peggs, BNL
M. Plum, LANL
M. Poole, Daresbury Lab
T. Raubenheimer, SLAC
A. Regan, LANL
L. Rivkin, PSI
D. Rubin, Cornell
F. Ruggiero, CERN
R. Ruth, SLAC, Vice-Chair
R. Ryne, LBNL
J. Seeman, SLAC
T. Shea, ORNL
K. Shepard, ANL
J. Sherman, LANL
C. Sinclair, Cornell
C. Steier, LBNL
M. Stockli, ORNL
B. Strauss, DOE
D. Sutter, DOE
N. Toge, KEK
J. Tompkins, FNAL
W. Waldron, LBNL
P. Wanderer, BNL
J. Weis, BNL
Y. Yamazaki, JAERI
R. York, MSU

EDITOR'S NOTE

The 1150-paper Proceedings that you are reading was the work of many hands. As the nominal conference editor, I am deeply aware of how much I owe to others, so besides the people named by conference chair Bob Siemann, I would like to particularly thank my editorial team.

Sara Webber not only brought diligence and skill to our editorial and publication functions *per se* but also proved to be an invaluable reservoir of the PAC 2001 knowledge base, advising and training us on paper reception, the final planning meeting of the Program Committee, and other key behind-the-scenes tasks. She moved on to another assignment after the end of our conference but continues to give us key assistance at the culmination of the editorial process. Her Fermilab colleague and PAC 2001 co-editor Peter Lucas stepped forward to lead the large effort involved in turning so many manuscripts into well-organized and professional-looking books and CDs, with assistance through the summer from Alison Lavis and Alicia Seifrid. Sara and Peter have truly been my co-editors in this endeavor, which it has been my good fortune to "lead" by figuring out where they were going and attempting to keep up.

The conference also owes a tremendous debt of gratitude to their fellow members of the Joint Accelerator Conferences Website group (JACoW, described at http://accelconf.web.cern.ch/AccelConf/index.html). For several years now, JACoW has promulgated standards, provided common resources, and hosted online proceedings for several of the major particle-accelerator conferences. What's more, a dozen or so members of this worldwide group travel to each conference – no small favor on the part of either themselves or their home institutions. Their services let us perform most of the editing (by which we primarily mean compliance checking and format normalization rather than language editing) and a fair bit of the quality assurance in real time. Editing *during* the conference is by far the best approach, since most problems are minor and can be either resolved by consultation with the author or easily remedied using the bank of computers provided.

The JACoW editors bring us vast experience in both the subject matter and the technical aspects of turning out papers of uniform and high-quality appearance—a considerable task, as the manuscripts originated in either of two very different programs, Word and LaTeX, on any of several combinations of hardware and operating system, and then pass through two or three other programs before completion. Working with these people has been not only a fine professional experience but also a pleasure.

So besides Sara and Peter, thanks are due to Jan Chrin (PSI); Martin Comyn (TRIUMF); Cathy Eyberger (Argonne); Charlie Horak (Oak Ridge), my successor for PAC 2005; Leif Liljeby (MSL); Michaela Marx (DESY); Christine Petit-Jean-Genaz and John Poole (CERN); and Toshiya Tanabe (RIKEN). I benefitted greatly from the help, appreciated the lengths they went to in order to provide it, and hope to reciprocate in future JACoW endeavors.

JACoW provides technical services too, notably including an interactive database for accepting and managing abstracts and manuscripts. This database in its present form is largely the work of Matt Arena at Fermilab (who has meanwhile been developing its next-generation replacement) and was operated by Vik Bhatia and his staff at Berkeley Lab. Jeff Patton of Oak Ridge, who will be handling the database at PAC 2005, studied the operation and discovered a talent for editing as well.

Data connections between the conference venue and the manuscript and registration servers at the sponsoring laboratories (hundreds of miles away in our case) are crucial to these conferences. Fortunately, on the other end of my walkie-talkie was network engineer John Christman. He came with years of expertise; a van-load of everything we knew we'd need and a few things we ended up being glad he'd brought anyway; and complete unflappability when we needed more cables than originally planned or had to isolate a faulty piece of someone else's equipment in parts of a hotel even Arthur Hailey wouldn't know about. In the user area, Tom Gallant, along with Matt, put a friendly face on technical competence, helping hundreds of people through the trials of performing difficult tasks on unfamiliar computers.

Alice Ramirez of LBNL's Technical and Electronic Information Department gave me timely expertise in art and layout, just as she has on so many projects over the years.

Finally, no list of unsung heroes of the program side of the conference would be complete without the administrative staff at the venue and back home at Berkeley, who showed such a combination of efficiency and courtesy throughout the planning and execution phases: Kymba A'Hearn, Martha Condon, Kathleen Erickson-Weber, Anna Smith, and Cathy Vanecek, under the leadership of program-committee administrator Joy Kono. Even at those moments when it must have seemed like keeping a pile of leaves organized in a tornado, they not only did a good job but took it all in stride.

Thanks, good work, and 'til next time, everyone.

Joe Chew
Editor, PAC 2003

EXHIBITORS

ACCEL Instruments GmbH
AccelSoft Inc.
ACQIRIS
Advanced Energy Systems, Inc.
Advanced Ferrite Technology Inc.
Alpha Scientific Electronics
Amuneal Manufacturing Corporation
AS&E High Energy Systems Division
Bergoz Instrumentation
Bodycote Alphabraze
Burle Industries, Inc.
Ceramic Magnetics
Claflin Associates Inc.
CPI Inc.
Danfysik A/S
Diversified Technologies, Inc.
e2v Technologies
Energen, Inc.
FMB Feinwerk- und Messtechnik GmbH
GMW Associates
HeatWave Labs Inc.
Holton Machinery Ltd
Icarus Research, Inc.
IE Power Inc.
Imtech Vonk B.V.
Instrumentation Technologies d.o.o.
L-3 Electron Devices
Mega Industries, LLC.
Meyer Tool & Mfg., Inc.
Mission Research Corporation
Pearson Electronics, Inc.
PMB
SAES Getters USA, Inc.
SDMS
SIGMAPHI
Simulation Technology & Applied Research, Inc.
STI Optronics Inc
Struck Innovative Systeme GmbH
Thales Components Corporation
Toshiba Corporation
UMA
Wah Chang
Wang NMR Inc.

ATTENDEES

Editor's Note: This information was drawn from the registration database. Many attendees gave what seemed to be home addresses. Therefore, to err on the side of safety with regard to privacy, we omit mailing addresses and give only institutional affiliations. E-mail addresses, also, are as specified in the database; some people gave group addresses or the address of an assistant, and a few gave the address of the laboratory or university where they were working at the time rather than of their home institution. Especially as time goes on, we suggest that you use Web directories or search engines to double-check the addresses. –jc

A

Dan Tyler Abell, Tech-X, dabell@txcorp.com
Wolfgang Ackermann, Darmstadt University of Technology, ackermann@temf.tu-darmstadt.de
Andreas Adelmann, Lawrence Berkeley National Laboratory, AAAdelmann@lbl.gov
Jelili Adeniyi, DOMECO NIG Ltd., chibodoman@hotmail.com
Chris Adolphsen, Stanford Linear Accelerator Center, star@slac.stanford.edu
Larry Ahle, Lawrence Livermore National Laboratory, larahle@yahoo.com
Kazunork Akai, KEK, kazunori.akai@kek.jp
Ronald A. Akre, Stanford Linear Accelerator Center, akre@slac.stanford.edu
Alexander Aleksandrov, Oak Ridge National Laboratory, sasha@ornl.gov
James G. Alessi, Brookhaven National Laboratory, alessi@bnl.gov
Christopher Allen, Los Alamos National Laboratory, ckallen@lanl.gov
Matthew Allen, Stanford Linear Accelerator Center, mattmar@pacbell.net
Trent Allison, Thomas Jefferson National Accelerator Facility, allison@jlab.org
Asu Alp, Argonne National Laboratory, asualp@aps.anl.gov
James Amundson, Fermi National Accelerator Laboratory, spentz@fnal.gov
Wolfgang Anders, BESSY, anders@bessy.de
Scott Anderson, Lawrence Livermore National Laboratory, anderson131@llnl.gov
Gerard Andonian, UCLA, gerard@physics.ucla.edu
Maria Elena Angoletta, CERN, Maria.Elena.Angoletta@cern.ch
Tsuyoshi Aoki, SPring-8, aoki@spring8.or.jp
Saeed Assadi, Oak Ridge National Laboratory, saeed@sns.gov
Ralph W Assmann, CERN, ralph.assmann@cern.ch
Patrick Audebert, LULI, patrick.audebert@polytechnique.fr
Mark Augustine, Thomas Jefferson National Accelerator Facility, Augustin@jlab.org

B

Nicoleta Baboi, Stanford Linear Accelerator Center, nicoleta@slac.stanford.edu
Raymond H. Backman, Mega Industries, LLC., rbackman@megaind.com
Sorin Badea, Brookhaven National Laboratory
Mei Bai, Brookhaven National Laboratory, mbai@bnl.gov
Roger Bailey, CERN, roger.bailey@cern.ch
Rene Bakker, Sincrotrone Trieste, rene.bakker@elettra.trieste.it
Vladimir Balakin, INP, balakin@vlepp.serpukhov.su
Valeri Balbekov, Fermi National Accelerator Laboratory, balbekov@fnal.gov
Pascal Balleyguier, CEA, pascal.balleyguier@cea.fr
Laura Bandura, Synchrotron SOLEIL
Roger Bangerter, Lawrence Berkeley National Laboratory, rogerob@sbcglobal.net
Samer Banna, Technion - Department of Electrical Engineering - Technion -IIT, samer@tx.technion.ac.il
Kenneth Baptiste, Lawrence Berkeley National Laboratory
Nikolai Barov, Northern Illinois University, barov@nicadd.niu.edu

Buz Barstow, Cornell University, Wilson Laboratory, RLF2@Cornell.edu
Yuri Batygin, Stanford Linear Accelerator Center, batygin@slac.stanford.edu
Ivan Bazarov, Cornell University, ib38@cornell.edu
Kevin Beard, Thomas Jefferson National Accelerator Facility, beard@jlab.org
Jurgen Bedau, Bruker BioSpin GmbH, jb@bruker.de
Mahdia Belgroune, Synchrotron Soleil, mahdia.belgroune@synchrotron-soleil.fr
Giulia Bellodi, CCLRC, Rutherford Appleton Laboratory, c.prior@rl.ac.uk
Sergey Belomestnykh, sab@lns.cornell.edu
Chris Beltran, Los Alamos National Laboratory, cbeltran@lanl.gov
Gabriele Benedetti, INFN-LNF, gabriele.benedetti@lnf.infn.it
Stephen Benson, Thomas Jefferson National Accelerator Facility, felman@jlab.org
Ilan Ben-Zvi, Brookhaven National Laboratory, ilan@bnl.gov
Wilhelmus Berden, FOM "Rijnhuizen," berden@rijnh.nl
J. Scott Berg, Brookhaven National Laboratory, jsberg@bnl.gov
Steve Berg, Argonne National Laboratory, sberg@aps.anl.gov
William Berg, Argonne National Laboratory, berg@aps.anl.gov
Santiago Bernal, University of Maryland. lsjan@glue.umd.edu
Rene Bertholom, Thales Components Corporation
Fred E. Bertrand, Oak Ridge National Laboratory, feb@ornl.gov
Patrick Bertrand, GANIL, bertrand@ganil.fr
Chandra Bhat, Fermi National Accelerator Laboratory, cbhat@fnal.gov
Ronak Bhatt, MIT PSFC, ronak@mit.edu
Maria E. Biagini, INFN, biagini@lnf.infn.it
George Biallas, Thomas Jefferson National Accelerator Facility, biallas@jlab.org
Sandra Biedron, Argonne National Laboratory, sandra.biedron@maxlab.lu.se
Frank Bieniosek, Lawrence Berkeley National Laboratory, fmbieniosek@lbl.gov
Michael G. Billing, Cornell University, Wilson Laboratory, RLF2@Cornell.edu
Caterina Biscari, INFN-LNF, caterina.biscari@lnf.infn.it
Kip Bishofberger, UCLA, kipster@physics.ucla.edu
Joseph Bisognano, Univ. of Wisconsin Synchrotron Radiation Center, jbisognano@src.wisc.edu
Ewart Blackmore, TRIUMF, ewb@triumf.ca
Klaus Blasche, GSI, k.blasche@gsi.de
Michael Blaskiewicz, Brookhaven National Laboratory, mmb@bnl.gov
Barbara Blind, Los Alamos National Laboratory, bblind@lanl.gov
Henry Blosser, National Superconducting Cyclotron Laboratory/MSU, mcintyre@nscl.msu.edu
Hans Bluem, Advanced Energy Systems, Bluem@grump.com
Carlo Bocchetta, Sincrotrone Trieste, carlo.bocchetta@elettra.trieste.it
Michael Boege, Paul Scherrer Institute, vera.loehle@psi.ch
S. Alex Bogacz, Thomas Jefferson National Accelerator Facility, bogacz@jlab.org
Heinz Bohlen, CPI, Inc., heinz.bohlen@cpii.com
Courtlandt Bohn, Northern Illinois University, clbohn@fnal.gov
Nikolai V. Bondarenco, Kharkov Institute for Physics & Technology, bon@kipt.kharkov.ua
Valerie Bookwalter, Thomas Jefferson National Accelerator Facility, bookwalt@jlab.org
Frédérick Bordry, CERN, frederick.bordry@cern.ch
Robert A. Bosch, Synchrotron Radiation Center, bosch@src.wisc.edu
James R. Boyce, Thomas Jefferson National Accelerator Facility, boyce@jlab.org
Joseph Bradley, Los Alamos National Laboratory
Branislav Brajuskovic, Argonne National Laboratory, bran@aps.anl.gov
Hans-H. Braun, CERN, Hans.Braun@cern.ch
Enrico Bravin, CERN, enrico.bravin@cern.ch
J. Michael Brennan, Brookhaven National Laboratory, brennan@bnl.gov
Pierre Bricault, TRIUMF, bricault@triumf.ca
Debbie Brodbar, American Physical Society, debbie@aps.org
Daniel Broemmelsiek, Fermi National Accelerator Laboratory, broemmel@fnal.gov

William Broste, Bechtel Nevada, b3@wytbear.com
Bruce Brown, Fermi National Accelerator Laboratory, bcbrown@fnal.gov
Kevin Brown, Brookhaven National Laboratory, kbrown@bnl.gov
Winthrop Brown, Lawrence Livermore National Laboratory, brown179@llnl.gov
Donald Bruno, Brookhaven National Laboratory, bruno@bnl.gov
James Buchmiller, EDS,, jbuchmil@mailaps.org
Daniele Bulfone, Sincrotrone Trieste, daniele.bulfone@elettra.trieste.it
Nathan Bultman, Los Alamos National Laboratory, nbultman@lanl.gov
Helmut Burkhardt, CERN, Helmut.Burkhardt@cern.ch
Andrew Burrill, Brookhaven National Laboratory
Philip Burrows, Queen Mary, University of London, p.burrows@qmul.ac.uk
Yuri Bylinsky, TRIUMF
John Byrd, Lawrence Berkeley National Laboratory, JMByrd@lbl.gov
Warren Byrne, Lawrence Berkeley National Laboratory, webyrne@lbl.gov

C

Yunhai Cai, Stanford Linear Accelerator, yunhai@slac.stanford.edu
Ofelia Capatina, CERN
George Caporaso, Lawrence Livermore National Laboratory, caporaso1@llnl.gov
Martinis Carlo, University of Milan, carlo.demartinis@mi.infn.it
Bruce E. Carlsten, Los Alamos National Laboratory, bcarlsten@lanl.gov
Jean-Paul Carneiro, DESY, carneiro@mail.desy.de
John R. Cary, University of Colorado, Department of Physics, cary@colorado.edu
Jeff Casey, Diversified Technologies
Pedro Castro-Garcia, DESY, pedro.castro@desy.de
Christine Celata, Lawrence Berkeley National Laboratory
Edwin Chacon-Golcher, Los Alamos National Laboratory, LANSCE-2, edcg@lanl.gov
Yong-Chul Chae, Argonne National Laboratory, chae@aps.anl.gov
Mark Champion, Oak Ridge National Laboratory, championms@sns.gov
Kwokchi Chan, Los Alamos National Laboratory, kcchan@lanl.gov
Mabel Chan, SAES Getters/USA Inc.
Cheng-Hsiang Chang, NSRRC, chang@srrc.gov.tw
Jui-Chi Chang, NSRRC, jcchang@srrc.gov.tw
Yu-Chiu Chao, Thomas Jefferson National Accelerator Facility
Elena Chapochnikova, CERN
Anthony Chargin, Lawrence Livermore National Laboratory, chargina@sns.gov
Swapan Chattopadhyay, Thomas Jefferson National Accelerator Facility, swapan@jlab.org
Joel Chavanne, ESRF
Chiping Chen, MIT, chenc@psfc.mit.edu
Dezhi Chen, Fermi National Accelerator Laboratory, meiqin@fnal.gov
Yu-Jiuan Chen, Lawrence Berkeley National Laboratory, chen6@llnl.gov
Harry Cheung, Fermi National Accelerator Laboratory, cheung@fnal.gov
Pavel Chevtsov, Thomas Jefferson National Accelerator Facility, chevtsov@jlab.org
Luisa Chiesa, Lawrence Berkeley National Laboratory, lchiesa@lbl.gov
Yong Ho Chin, yongho.chin@kek.jp
Yanglai Cho, Argonne National Laboratory, yc@aps.anl.gov
Vinod Chohan, CERN
Ping-Jung Chou, NSRRC, pjchou@srrc.gov.tw
Weiren Chou, Fermi National Accelerator Laboratory,
Myung-hwan Chun, Pohang Accelerator Laboratory, mhchun@postech.ac.kr
Chinwha Chung, Pohang Accelerator Laboratory, cwchung@postech.edu
Gianluigi Ciovati, Thomas Jefferson National Accelerator Facility
Ray Claflin, Claflin Associates Inc., ray@888claflin.com

James Clarke, Daresbury Laboratory, j.a.clarke@dl.ac.uk
M. Clarke-Gayther, CCLRC, Rutherford Appleton Laboratory, m.a.clarke-gayther@rl.ac.uk
Chris Clayton, UCLA, cclayton6@yahoo.com
David Cline, UCLA
Ronald Cohen, Lawrence Livermore National Laboratory
Eric R. Colby, Stanford Linear Accelerator Center, ecolby@slac.stanford.edu
Patrick Colestock, Los Alamos National Laboratory, colestoc@lanl.gov
Manoel Conde, Argonne National Laboratory, conde@anl.gov
Linda Coney, Columbia University, lconey@fnal.gov
Simon Cooke, Naval Research Laboratory, simon.cooke@nrl.navy.mil
William J. Corbett, Stanford Linear Accelerator Center, corbett@slac.stanford.edu
John N. Corlett, Lawrence Berkeley National Laboratory, jncorlett@lbl.gov
Alexander Cours, Argonne National Laboratory, cours@aps.anl.gov
Sarah Cousineau, Oak Ridge National Laboratory, scousine@ornl.gov
Thomas Cowan, University of Nevada-Reno, kari@physics.unr.edu
Graham Cox, CCLRC, Daresbury Laboratory, g.cox@dl.ac.uk
Michael Craddock, TRIUMF, craddock@triumf.ca
James Crittenden, LEPP, Cornell University, Wilson Laboratory, RLF2@Cornell.edu
Yupeng Cui, University of Maryland, lsjan@glue.umd.edu
Karen Cummings, Los Alamos National Laboratory, kcummings@lanl.gov
Eileen Cunningham, Meyer Tool & Manufacturing, Inc., ek.cunningham@worldnet.att.net

D

Leslie Dallin, Canadian Light Source, les.dallin@cls.usask.ca
Giove Dario, INFN, giove@mi.infn.it
Ronald Davidson, Princeton University, rdavidson@pppl.gov
Harold Davis, Los Alamos National Laboratory, davis@lanl.gov
Joseph De Long, Brookhaven National Laboratory
Carlo De Martinis, University of Milan, carlo.demartinis@mi.infn.it
Stefano De Santis, Lawrence Berkeley National Laboratory, sdesantis@lbl.gov
Christian Debbaut, ANI, acdebbaut@aol.com
Philip Debenham, DOE, phil.debenham@science.doe.gov
Franz-Josef Decker, Stanford Linear Accelerator Center, Decker@SLAC.Stanford.edu
Glenn Decker, Argonne National Laboratory
John DeFord, Simulation Technology & Applied Research, Inc., john.deford@staarinc.com
Bernd Dehning, CERN, Bernd.dehning@cern.ch
Jean Delayen, Thomas Jefferson National Accelerator Facility, Bernd.dehning@cern.ch
Theo Demma, University of Sannio, tdemma@unisannio.it
Patric Den Hartog, Argonne National Laboratory
Suzhi Deng, University of Southern California, sdeng@usc.edu
Yarolslav Serg Derbenev, Thomas Jefferson National Accelerator Facility, derbenev@jlab.org
Vladimir Derenchuk, Indiana University, Bloomington Campus, East@iucf.indiana.edu
Arnaud Devred, CEA/Saclay
Shashi Dewan, IE Power Inc., iepower@iepower.com
Nicholas P. Di Monte, Argonne National Laboratory, npd@aps.anl.gov
Richard W. Dickson, Thomas Jefferson National Accelerator Facility, dickson@jlab.org
Steven Dierker, Brookhaven National Laboratory, dierker@bnl.gov
Daniel Dietderich, Lawrence Berkeley National Laboratory, drdietderich@lbl.gov
Dimitre Dimitrov, Tech-X Corporation, lwr@txcorp.com
Steffen Doebert, Stanford Linear Accelerator Center, doebert@slac.stanford.edu
Donald Dohan, Argonne Nationial Laboratory, dohan@aps.anl.gov
Valery Dolgashev, Stanford Linear Accelerator Center, dolgash@slac.stanford.edu
Lawrence Donley, Argonne National Laboratory, ldonley@anl.gov

Jeffrey Dooling, Argonne National Laboratory, jcdooling@anl.gov
Lawrence Doolittle, Lawrence Berkeley National Laboratory
David H. Dowell, Stanford Linear Accelerator Center, dowell@slac.stanford.edu
Michael Downer, University of Texas, Department of Physics, downer@physics.utexas.edu
Henry Downs, Dielectric, henry.downs@dielectric.spx.com
Adnan Doyuran, Brookhaven National Laboratory
Alessandro Drago, INFN-LNF, alessandro.drago@lnf.infn.it
Alex Dragt, University of Maryland, rdahms@physics.umd.edu
Angelika Drees, Brookhaven National Laboratory, drees@bnl.gov
Alexander Drozhdin, Fermi National Accelerator Laboratory
Laurent Ducimetiere, CERN, l.ducimetiere@cern.ch
Gerald F. Dugan, Cornell University, gfd1@cornell.edu
Jonathan Duke, RAL, CCLRC, j.p.duke@rl.ac.uk
Alexander Durkin, Moscow Radiotechnical Institute, apdurkin@mtu-net.ru
John E. Dusatko, Stanford Linear Accelerator Center, jedu@slac.stanford.edu
Gerardo Dutto, TRIUMF, dutto@triumf.ca
Roger Dwinell, Lawrence Berkeley National Laboratory, rddwinell@lbl.gov
Douglas M. Dykes, CCLRC, Daresbury Laboratory, d.m.dykes@dl.ac.uk

E

Marvin Eberhardt, CPI, Inc., linda.dilorenzo@eimac.cpii.com
Donald A. Edwards, Fermi National Accelerator Laboratory, edwards@fnal.gov
Philip Efthimion, Princeton University, pefthimion@pppl.gov
Dieter Einfeld, SESAME / UNESCO, einfeld@iss.fzk.de
Carl Ekdahl, Los Alamos National Laboratory
Louis Emery, Argonne National Laboratory, emery@aps.anl.gov
Stephan Emhofer, LMU Muenchen, Stephan.Emhofer@CERN.CH
Paul Emma, Stanford Linear Accelerator Center, Emma@SLAC.Stanford.edu
Kuninori Endo, KEK, endohome@yahoo.co.jp
Robert England, UCLA, england@physics.ucla.edu
Robert Ennis, American Magnetics, Inc., bob@americanmagnetics.com
Deborah Errede, University of Illinois, derrede@uiuc.edu
Lyndon Evans, CERN, SPS Division, lyn.evans@cern.ch
Shmuel Eylon, Lawrence Berkeley National Laboratory

F

Tai-ching Fan, NSRRC, fantc@srrc.gov.tw
Jyan-Min Fang, Columbia University, fang@beamer8.physics.yale.edu
Manouchehr Farkhondeh, MIT-Bates, manouch@mit.edu
Richard Farnsworth, Major Projects Victoria, garry.seaborne@mpv.vic.gov.au
Stephane Fartoukh, CERN, stephane.fartoukh@cern.ch
Andy Faltens, Lawrence Berkeley National Laboratory
Anthony Favale, Advanced Energy Systems, ajfavale@optonline.net
Michael Fazio, Los Alamos National Laboratory, mfazio@lanl.gov
Max Febvre, CERCA, max.febvre@framatome-anp.com
Alexei Fedotov, Brookhaven National Laboratory
Mikhail Fedurin, Louisiana State University/CAMD, evstev@lsu.edu
Jorg Feikes, BESSY
Benedict Feinberg, Lawrence Berkeley National Laboratory, B_Feinberg@lbl.gov
Donald W. Feldman, University of Maryland, dfeldman@sprynet.com
Robin Ferdinand, CEA/Saclay
Patrick Ferguson, Calabazas Creek Research, mdsfer@netvista.net

Paolo Ferracin, Lawrence Berkeley National Laboratory, pferracin@lbl.gov
Massimo Ferrario, INFN-LNF, Massimo.Ferrario@lnf.infn.it
Ted Fieguth, Stanford Linear Accelerator Center, fieguth@slac.stanford.edu
David A. Finley, Fermi National Accelerator Laboratory, finley@fnal.gov
Paul Finman, LCF Enterprises, pfinman@lcfamps.com
Ralph Fiorito, University of Maryland, LSJAN@glue.umd.edu
Wolfram Fischer, Brookhaven National Laboratory
Alan Fisher, Stanford Linear Accelerator Center, afisher@slac.stanford.edu
Daniel H. Fitzgerald, Los Alamos National Laboratory, fitzg@lanl.gov
Jacob Flanz, Massachusetts General Hospital, nflan1@aol.com
Raymond P. Fliller III, Brookhaven National Laboratory, Collider Accelerator Dept., rfliller@bnl.gov
Kenneth Fong, TRIUMF
George Foster, Fermi National Accelerator Laboratory, gwf@fnal.gov
Randall Fowkes, Stanford Linear Accelerator Center, wrfowkes@packbell.net
John D. Fox, Stanford Linear Accelerator Center, jdfox@slac.stanford.edu
Bernhard Franzke, GSI
Arne Freyberger, Thomas Jefferson National Accelerator Facility
Alex Friedman, Lawrence Livermore National Laboratory, Lawrence Berkeley National Laboratory, af@llnl.gov
Dennis Friesel, Indiana University, IU Cyclotron Facility
Pedro Frigola, UCLA, frigola@stout.physics.ucla.edu
Josef C. Frisch, Stanford Linear Accelerator Center, frisch@slac.stanford.edu
Hans Frischholz, CERN, hans.frischholz@cern.ch
Gwenael Fubiani, Lawrence Berkeley National Laboratory, gjfubiani@lbl.gov
Yasuo Fukui, Stanford Linear Accelerator Center, fukui@slac.stanford.edu
Warren Funk, Thomas Jefferson National Accelerator Facility, lwfunk@jlab.org
Miguel Furman, Lawrence Berkeley National Laboratory, mafurman@lbl.gov

G

Wei Gai, Argonne National Laboratory, wg@hep.anl.gov
Juan Gallardo, Brookhaven National Laboratory
Santo Gammino, INFN-LNS, gammino@lns.infn.it
Robert W. Garnett, Los Alamos National Laboratory, rgarnett@lanl.gov
Roland Garoby, CERN, Roland.Garoby@cern.ch
Alper Garren, UCLA, AAGarren@lbl.gov
Carmeron Geddes, Lawrence Berkeley National Laboratory, cgrgeddes@lbl.gov
Rongli Geng, Cornell University, Wilson Laboratory, RLF2@Cornell.edu
Ali Ghalam, University of Southern California, feizzarr@usc.edu
Andrea Ghigo, INFN, andrea.ghigo@lnf.infn.it
Rodolfo E. Giacone, University of Colorado, Center for Integrated Plasma Studies, rgia@colorado.edu
George Gillespie, AccelSoft Inc., accelsoft@ghga.com
J. Douglas Gilpatrick, Los Alamos National Laboratory
Massimo Giovannozzi, CERN, massimo.giovannozzi@cern.ch
Mark Gisi, Amuneal Manufacturing, markg@amuneal.com
Hank Glass, Fermi National Accelerator Laboratory, glass@fnal.gov
Robert Gluckstern, University of Maryland, rdahms@physics.umd.edu
Efim Gluskin, Argonne National Laboratory, gluskin@aps.anl.gov
Steven Gold, Naval Research Laboratory, higgs@nrl.navy.mil
Ivan Gonin, Fermi National Accelerator Laboratory, gonin@fnal.gov
Carl Goodzeit, clhjm@attbi.com
Daniel Gordon, Naval Research Laboratory, dfgordon@sarkomand.com
Dmitry Gorelov, National Superconducting Cyclotron Laboratory/MSU, box@nscl.msu.edu

Steve Gottschalk, STI Optronics, nancyh@stioptronics.com
Harvey Gould, Lawrence Berkeley National Laboratory, gould@lbl.gov
Krishnaswamy Gounder, Fermi National Accelerator Laboratory
Stephen Gourlay, Lawrence Berkeley National Laboratory, sagourlay@lbl.gov
William Graves, MIT, wsgraves@mit.edu
Zipora Greenwald, Cornell University, Wilson Laboratory, RLF2@Cornell.edu
Christiana Grenoble, Thomas Jefferson National Accelerator Facility
Terry Grimm, National Superconducting Cyclotron Laboratory/MSU, mcintyre@nscl.msu.edu
Larry Grisham, Princeton Plasma Physics Laboratory, ccummings@pppl.gov
David Grote, Lawrence Berkeley National Laboratory, dpgrote@lbl.gov
Daniel Grubb, Northern Illinois University, grubb@math.niu.edu
Peter Gruber, CERN, peter.gruber@cern.ch
Vincenzo Guidi, University of Ferrara and INFN, guidi@fe.infn.it
Kim Gunther, Heatwave Labs, Inc.

H

Edwin G. Haas, Brookhaven National Laboratory, haas@bnl.gov
Irving Haber, University of Maryland, mpasztal@glue.umd.edu
Bahman Hafizi, Icarus Research, Inc., solcat9@aol.com
Harald Hahn, Brookhaven National Laboratory
Jacob Haimson, Haimson Research Corporation, haimson@aol.com
Jang Min Han, KAERI, jmhan1@kaeri.re.kr
Samy Hanna, Siemens Medical Solutions, samy.hanna@siemens.com
Robert Hardekopf, Los Alamos National Laboratory, hardekopf@lanl.gov
David J. Harding, Fermi National Accelerator Laboratory, harding@fnal.gov
Katherine Harkay, Argonne National Laboratory, harkay@aps.anl.gov
John R. Harris, University of Maryland, Energy Research Facility, harrisjr@wam.umd.edu
Frederic Hartemann, Lawrence Livermore National Laboratory, hartemann1@llnl.gov
Donald Hartill, Cornell University, Wilson Laboratory, RLF2@Cornell.edu
Walter Hartung, National Superconducting Cyclotron Laboratory/MSU, hartung@nscl.msu.edu
Leigh H. Harwood, Thomas Jefferson National Accelerator Facility, harwood@jlab.org
Helmut Haseroth, CERN, helmut.haseroth@cern.ch
Barry Hawkins, UMA Engineering
Antti S. Heikkila, CERN, Geneva 23, antti.heikkila@cern.ch
Richard Helms, Cornell University, Wilson Laboratory, helms@lepp.cornell.edu
Stuart D. Henderson, Oak Ridge National Laboratory, shenderson@sns.gov
Enrique Henestroza, Lawrence Berkeley National Laboratory
Joerg Herrmann, DESY, joerg.herrmann@desy.de
Mark Hess, MIT, mhess@psfc.mit.edu
Robert O. Hettel, Stanford Linear Accelerator Center, hettel@slac.stanford.edu
Tom Hiatt, Thomas Jefferson National Accelerator Facility
James Hinkson, Lawrence Berkeley National Laboratory, jhinkson@aol.com
Jay Hirshfield, Omega-P, Inc., jay@omega-p.com
Ching-Hung Ho, Siemens Medical Solutions USA, Inc., ching-hung.ho@siemens.com
Jon Hock, Brookhaven National Laboratory
Georg Hoffstaetter, RLF2@Cornell.edu
Ingo Hofmann, GSI, RLF2@Cornell.edu
Mark J. Hogan, Stanford Linear Accelerator Center, hogan@slac.stanford.edu
Stephen Holmes, Fermi National Accelerator Laboratory
Norbert Holtkamp, Oak Ridge National Laboratory, holtkamp@ornl.gov
Katja Honkavaara, DESY, katja.honkavaara@desy.de
Douglas Horan, Argonne National Laboratory, horan@aps.anl.gov
Michael Hourican, CERN, michael.hourican@cern.ch

Hsiao-Chaun Hseuh, Brookhaven National Laboratory
Chengkun Huang, UCLA, huangck@ee.ucla.edu
Haixin Huang, Brookhaven National Laboratory
Yongzhang Huang, Axcelis Technology, youngzhang.huang@axcelis.com
Richard Hubbard, Naval Research Laboratory, higgs@nrl.navy.mil
Markus Huening, Fermi National Accelerator Laboratory
Thomas Hughes, Mission Research Corporation, lindmc@mrcabq.com
Stanley Humphries, Field Precision, humphries@fieldp.com
Patrick Hurh, Fermi National Accelerator Laboratory
Erhard Huttel, FZK/ANKA, huttel@anka.fzk.de
Andrew M. Hutton, Thomas Jefferson National Accelerator Facility, andrew@jlab.org
Woon Ha Hwang, Pohang Accelerator Laboratory, hohwang@postech.ac.kr

I

Susumu Igarashi, KEK, grubb@math.niu.edu
Ubaldo Iriso Ariz, Brookhaven National Laboratory, ubaldo@bnl.gov
Peter Ivanov, Fermi National Accelerator Laboratory
Valentin Ivanov, Stanford Linear Accelerator Center, ivanov@slac.stanford.edu
Robert Ives, CCR, Inc., rlives@calcreek.com
Yoshitaka Iwasaki, Saga Synchrotron Light Source, iwasaki@saga-ls.jp

J

Alan Jackson, Lawrence Berkeley National Laboratory
Gerald P. Jackson, Hbar Technologies, LLC, gjackson@hbartech.com
Jorn Jacob, ESRF,
Ken Jacobs, Univ. of Wisconsin Synchrotron Radiation Center, kjacobs@src.wisc.edu
Eberhard Jaeschke, BESSY
Andrew Jason, Los Alamos National Laboratory, ajason@lanl.gov
Chris Jensen, Fermi National Accelerator Laboratory
Kevin Jensen, Naval Research Laboratory, kljensen@ieee.org
Dong-o Jeon, Oak Ridge National Laboratory, jeond@ornl.gov
Jose Miguel Jimenez, CERN
Paul Jines, Louisiana State University/CAMD, cdboyet@lsu.edu
Lihui Jinlh, University of Kansas, University of Kansas, Physics & Astronomy Dept., jinlh@ku.edu
Brant Johnson, Brookhaven National Laboratory, brant@bnl.gov
Devon Johnson, UCLA, dkjohnso@ucla.edu
Erik Johnson, Brookhaven National Laboratory, erik@bnl.gov
Phillip Johnson, University of Maryland, rdahms@physics.umd.edu
Rolland Johnson, Muons, Inc., roljohn@aol.com
John Johnstone, Fermi National Accelerator Laboratory
Frederick Jones, TRIUMF
James Jones, CCLRC, Daresbury Laboratory, j.k.jones@dl.ac.uk
Roger M. Jones, Stanford Linear Accelerator Center, rmj@slac.stanford.edu
Theodore Jones, Naval Research Laboratory, ted.jones@nrl.navy.mil
William Jones, Indiana University Cyclotron Facility, jonesw@indiana.edu
Kevin Jordan, Thomas Jefferson National Accelerator Facility, jordan@jlab.org
Chad Joshi, Energen, Inc., chad@energeninc.com
Chan Joshi, UCLA, joshi@ee.ucla.edu
Jin-Young Jung, Lawrence Berkeley National Laboratory

K

Andreas Kabel, Stanford Linear Accelerator Center, andreas.kabel@slac.stanford.edu
Igor Kaganovich, Plasma Physics Laboratory, Princeton University, ikaganov@pppl.gov
Stephen Kahn, Stanford Linear Accelerator Center
Anders Källberg, Manne Siegbahn Laboratory, kallberg@msi.se
Juris Kalnins, Lawrence Berkeley National Laboratory, JGKalnins@lbl.gov
Dobrin Kaltchev, TRIUMF
Alex Kanareykin, Stanford Linear Accelerator Center
Heung-Sik Kang, Pohang Accelerator Laboratory, hskang@postech.ac.kr
Vadim Kashikhin, Fermi National Accelerator Laboratory, vadim@fnal.gov
Vladimir Kashikhin, Fermi National Accelerator Laboratory, johnz@fnal.gov
Tom Katsouleas, University of Southern California, katsoule@usc.edu
Roderich Keller, Lawrence Berkeley National Laboratory, r_keller@lbl.gov
Michael P Kelly, Argonne National Laboratory, kelly@phy.anl.gov
Michael Kempkes, Diversified Technologies
Roberto Kersevan, European Synchrotron Radiation Facility
Amit Kesar, MIT, kesar@psfc.mit.edu
Dr. Oliver Kester, Sektion Physik, LMU München, oliver.kester@physik.uni-muenchen.de
Timergali Khabiboulline, Fermi National Accelerator Laboratory, khabibul@fnal.gov
Arsen Khachatryan, University of Twente, f.a.vangoor@tn.utwente.nl
Shaukat Khan, BESSY, khan@mail.bessy.de
Igor Khodak, Kharkov Institute for Physics & Technology, khiv@kipt.kharkov.ua
Farzad Kialashaki, Meggitt Safety Systems Inc., fkialashaki@safetysystem.com
Eun-San Kim, Pohang Accelerator Laboratory, eskim1@postech.ac.kr
Guang-Hoon Kim, KERI, ghkim@keri.re.kr
Jin Cheol Kim, Pohang Accelerator Laboratory, jckim@postech.ac.kr
Kye Ryung Kim, KAERI, kimkr@kaeri.re.kr
Mun Gyung Kim, Pohang Accelerator Laboratory, nsh@postech.ac.kr
Sang-ho Kim, Oak Ridge National Laboratory, kimsh@ornl.gov
Suk Hong Kim, Argonne National Laboratory, shkim@aps.anl.gov
Yujong Kim, DESY, yujong.kim@desy.de
Wayne Kimura, STI Optronics, Inc.
Harold Kirk, Brookhaven National Laboratory, nspk@lanl.gov
Matthias Kirsch, Struck Innovative Systeme GmbH
David L. Kitterman, Sandia National Laboratories, dlkitte@sandia.gov
Hans-Udo Klein, ACCEL Instruments GmbH, lohmar@accel.de
Jens Knobloch, BESSY GmbH, knobloch@bessy.de
Mojca Kodric, Instrumentation Technologies, rok@i-tech.si
Andrei Kolomiets, ITEP, kolomiets@vitep1.itep.ru
Richard Konecny, Argonne National Laboratory, rsk@hep.anl.gov
Isak Konkashbaev, Argonne National Laboratory, isak@anl.gov
Stephen Korbly, MIT, skorbly@psfc.mit.edu
Sergey Korenev, Steris Corporation, Sergey@korenev.com
Shane, Koscielniak, TRIUMF
Kunio Koseki, KEK, koseki@bnl.gov
Dieter Kraemer, BESSY, kraemer@bessy.de
George Krafczyk, Fermi National Accelerator Laboratory
Mikhail Krasilnikov, DESY, kras@ifh.de
Anatoly Krasnykh, Stanford Linear Accelerator Center, krasnykh@slac.stanford.edu
Patrick Krejcik, Stanford Linear Accelerator Center, pkr@slac.stanford.edu
Detlef Krischel, ACCEL Instruments GmbH
Norio Kudo, Waseda University, easy-going@suou.waseda.jp
Kai-Uwe Kuehnel, Institut für Angewandte Physik, k.kuehnel@iap.uni-frankfurt.de
Masayuki Kumada, NIRS/JST, kumada@ama.po-jp.com

Changhor Kuo, NSRRC, chkuo@srrc.gov.tw
Sergey S. Kurennoy, Los Alamos National Laboratory, kurennoy@lanl.gov
Ryunosuke Kuroda, Waseda University, rkuroda@aoni.waseda.jp
John Kurzydlo, Toshiba, john.kurzydlo@taec.toshiba.com
Peter Kuske, BESSY
Robert Kustom, Argonne National Laboratory, rlk@aps.anl.gov
Joe Kwan, Lawrence Berkeley National Laboratory
Slawomir Kwiatkowski, Lawrence Berkeley National Laboratory, skwiatkowskr@lbl.gov
Hyeok Jung Kwon, KAERI, hjkwon@kaeri.re.kr

L

J. B. Lafon, Euro Industries, jblafon@euro-industries.net
Jean-Michel Lagniel, CEA-DAM
Glen Lambertson, Lawrence Berkeley National Laboratory, grlambertson@lbl.gov
Robert Lambiase, Brookhaven National Laboratory
Mike Lamont, CERN, Mike.Lamont@cern.ch
Jean-Luc Lancelot, SIGMAPHI, contact@sigmaphi.fr
Michael LaPointe, Omega-P, Inc., lapointe@omega-p.com
Jacques Laskar, Observatoire de Paris, laskar@imcce.fr
Thomas Lau, Darmstadt University of Technology, lau@temf.tu-darmstadt.de
Robin J. Lauckner, CERN, Robin.Lauckner@cern.ch
Matthew Lawrence, Holton Machinery Ltd.
Robert Laxdal, TRIUMF, lax@triumf.ca
Valeri Lebedev, Fermi National Accelerator Laboratory
Gregory LeBlanc, MAX-Laboratory
Paul Lebrun, Fermi National Accelerator Laboratory, spanacek@fnal.gov
Ed Lee, Lawrence Berkeley National Laboratory, eplee@lbl.gov
Jinhyung Lee, Center for Integrated Plasma Studies, University of Colorado, jinhyung@colorado.edu
Peter Lee, University of Wisconsin-Madison, lee@engr.wisc.edu
Shyh Yuan Lee, Indiana University, shylee@indiana.edu
Soon-Hong Lee, Argonne National Laboratory
Yong Lee, Brookhaven National Laboratory, yylee@bnl.gov
Wim Leemans, Lawrence Berkeley National Laboratory, WPLeemans@lbl.gov
Ulf Lehnert, FZ Rossendorf - ELBE, U.Lehnert@fz-rossendorf.de
Daniela Leitner, Lawrence Berkeley National Laboratory, dleitner@lbl.gov
Sergio Lemaitre, GE Medical Systems, Sergio.Lemaitre@med.ge.com
Stephan Lenci, Communications and Power Ind., steve.lenci@cpii.com
Frank Lenkszus, Argonne National Laboratory, frl@aps.anl.gov
John Leopold, RAFAEL, johnl@rafael.co.il
Eliane Lessner, Argonne National Laboratory, esl@phy.anl.gov
Marie Paule Level, Synchrotron Soleil, marie-paule.level@synchrotron-soleil.fr
John Lewellen, Argonne National Laboratory, lewellen@aps.anl.gov
Greg E. Leyh, Stanford Linear Accelerator Center, leyh@slac.stanford.edu
Derun Li, Lawrence Berkeley National Laboratory, DLi@lbl.gov
Jingyi Li, FEL Lab, Duke University, jing@fel.duke.edu
Nanyang Li, Stanford Linear Accelerator Center, nanyang@slac.stanford.edu
Rui Li, Thomas Jefferson National Accelerator Facility
Yanxia Li, CPI, Inc., linda.dilorenzo@eimac.cpii.com
Yuelin Li, Argonne National Laboratory, ylli@aps.anl.gov
Yulin Li, Cornell University, Wilson Laboratory, RLF2@Cornell.edu
Zenghai Li, Stanford Linear Accelerator Center, lizh@slac.stanford.edu
Steven Lidia, University of Californiasmlidia@lbl.gov

Holger Liebermann, Institut für Angewandte Physik, Liebermann@iap.uni-frankfurt.de
Alan Lietzke, Lawrence Berkeley National Laboratory, aflietzke@lbl.gov
Robert Lill, Argonne National Laboratory, Blill@aps.anl.gov
Jae Lim, UCLA, jlim90095@yahoo.com
Cecile Limborg, Stanford Linear Accelerator Center, limborg@slac.stanford.edu
Ming-Chyuan Lin, NSRRC, chyuan@srrc.gov.tw
Trevor Linnecar, CERN, trevor.linnecar@cern.ch
Vladimir Litvinenko, Duke University, vl@phy.duke.edu
Jian-Fei Liu, Los Alamos National Laboratory, JFLiu@lanl.gov
Yuan Liu, Oak Ridge National Laboratory, yliu@ornl.gov
Agusta S. Loftsdottir, Lawrence Berkeley National Laboratory, ALoftsdottir@lbl.gov
Alessandra M. Lombardi, CERN, Alessandra.Lombardi@cern.ch
Henrik Loos, Brookhaven National Laboratory, loos@bnl.gov
Mauricio Lopes, Instituto de Fisica, Universidade de Sao Paulo, mllopes@if.usp.br
C. M. Loring Jr., marsh.l@rcn.com
Wei Lu, UCLA, luwei@ucla.edu
Alex Lumpkin, Argonne National Laboratory, lumpkin@aps.anl.gov
Steven Lund, Lawrence Berkeley National Laboratory, smlund@lbl.gov
Yan Luo, DULY Research Inc.
John Lyles, Los Alamos National Laboratory, jtml@lanl.gov

M

Pierre Maccioni, CERCA, pierre.maccioni@framatome-anp.com
Robert J. Macek, Los Alamos National Laboratory, rjmacek@earthlink.net
William Mackay, Brookhaven National Laboratory
Sunao Maebara, JAERI, sumaebara@aol.com
Takaaki Maekawa, Mitsubishi Electric, takaaki.maekawa@meppi.mea.com
Ernest I. Malamud, Fermi National Accelerator Laboratory, malamud@foothill.net
Jerome Malenfant, American Physical Society, jm@aps.org
Nikolay Malitsky, Brookhaven National Laboratory
Django Manglunki, CERN, django@cern.ch
Alberto Marchionni, Fermi National Accelerator Laboratory
Eric Margoto, Thales Electron Devices, eric.margoto@thales-electrondevices.com
Frank Marhauser, BESSY GmbH, marhauser@bessy.de
Ioannis Marneris, Brookhaven National Laboratory
Sergio Rodrigo Marques, LNLS, pedro@lnls.br
Kenneth Marsh, UCLA, kamarsh@ucla.edu
Michael Martens, Fermi National Accelerator Laboratory
Felix Marti, National Superconducting Cyclotron Laboratory/MSU, mcintyre@nscl.msu.edu
Marcos Martins, Instituto de Fisica, Universidade de Sao Paulo, martins@if.usp.br
Brian Martlew, CCLRC, Rutherford Appleton Laboratory, b.g.martlew@dl.ac.uk
Giovanni Mazzitelli, INFN-LNF, giovanni.mazzitelli@lnf.infn.it
James McCarrick, Lawrence Livermore National Laboratory, mccarrick1@llnl.gov
Michael McCarthy, Oak Ridge National Laboratory, mm1897@aol.com
Rodney McCrady, Los Alamos National Laboratory,
Trent McCuistian, Los Alamos National Laboratory, trentmc@lanl.gov
Kirk T. McDonald, Princeton University, kirkmcd@princeton.edu
Peter A. McIntosh, Stanford Linear Accelerator Center, pmi@slac.stanford.edu
Ian McNulty, Argonne National Laboratory, mcnulty@aps.anl.gov
Evgeny A. Medvedko, Stanford Linear Accelerator Center, medvedko@slac.stanford.edu
Larry Megugorac, Bodycote Thermal Processing, lmegugorac@bodycote-na.com
Alfred Meidinger, Betchel Nevada, US DOE, NNSA
Robert Meller, Cornell University, Wilson Laboratory, RLF2@Cornell.edu

Robert Merl, Los Alamos National Laboratory
Nikolitsa Merminga, Thomas Jefferson National Accelerator Facility
Wolfhard Merz, DESY, wolfhard.merz@desy.de
Stuart Metcalfe, Stanford Linear Accelerator Center, sjm@slac.stanford.edu
Alexander Mikhailichenko, RLF2@Cornell.edu
Stepan Mikhailov, Duke University, smikhail@fel.duke.edu
Catia Milardi, INFN-LNF, catia.milardi@lnf.infn.it
Stephen Milton, Argonne National Laboratory, APS, milton@aps.anl.gov
Andrey Mishin, AS&E High Energy Systems Division
Chandra Shekhar Mishra, Fermi National Accelerator Laboratory, rbecker@fnal.gov
Takako Miura, KEK, takako.miura@kek.jp
Tsukasa Miyajima, KEK, tsukasa.miyajima@kek.jp
Michele Modena, CERN
Nikolai Mokhov, Fermi National Accelerator Laboratory
Arthur Molvik, Lawrence Livermore National Laboratory, molvik1@llnl.gov
Christoph Montag, Brookhaven National Laboratory
Mel Month, Brookhaven National Laboratory
Elizabeth R. Moog, Argonne National Laboratory, moog@aps.anl.gov
Craig Moore, Fermi National Accelerator Laboratory
Ronald Moore, Fermi National Accelerator Laboratory
Warren B. Mori, UCLA, Mori@physics.ucla.edu
Alban Mosnier, CEA/Saclay
Andrew Moss, Daresbury Laboratory, a.j.moss@dl.ac.uk
C. Thomas Mottershead, Los Alamos National Laboratory, mottershead@lanl.gov
Michael Mouat, TRIUMF
Anke-Susanne Mueller, Institute for Synchrotron Radiation - ANKA, Anke-Susanne.Mueller@iss.fzk.de
Wolfgang Franz Otto Mueller, Darmstadt University of Technology, mueller@temf.tu-darmstadt.de
Patric Muggli, University of Southern California, muggli@usc.edu
James Murphy, Brookhaven National Laboratory
Pietro Musumeci, UCLA, musumeci@physics.ucla.edu

N

Kazuhisa Nakajima, KEK, nakajima@post.kek.jp
Norio Nakamura, University of Tokyo, nakamura@issp.u-tokyo.ac.jp
Sang Hoon Nam, Pohang Accelerator Laboratory, gto@postech.ac.kr
Won Namkung, Pohang University of Science and Technology, namkung@postech.ac.kr
Olivier Napoly, CEA/Saclay
Ritesh Narang, UCLA, EE Dept., ritesh@ucla.edu
Boaz Nash, Stanford Linear Accelerator Center, bnash@slac.stanford.edu
Subrata Nath, Los Alamos National Laboratory, subratanath@att.net
George Neil, Thomas Jefferson National Accelerator Facility, neil@jlab.org
Jeffrey Neilson, CCR,Inc., jeff@calcreek.com
Janice L. Nelson, Stanford Linear Accelerator Center, jnelson@slac.stanford.edu
Tony Nelson, Wah Chang
Jonathan G. Neumann, University of Maryland, neumann@glue.umd.edu
David Newsham, DULY Research Inc.
Oleg Nezhevenko, Omega-P, Inc., nezhev@omega-p.com
Chet Nieter, University of Colorado, CIPS, candace.nichols@colorado.edu
Hiroshi Nishimura, RIKEN, H_Nishimura@lbl.gov
Robert J. Noble, Stanford Linear Accelerator Center, noble@slac.stanford.edu
James Norem, Argonne National Laboratory, norem@anl.gov
Alexander Novokhatski, Stanford Linear Accelerator Center, novo@slac.stanford.edu

O

Caolionn L. O'Connell, caolionn@stanford.edu
Hiroshi Ogawa, AIST, ogawa.h@aist.go.jp
Hideaki Ohgaki, Institute of Advanced Energy, Kyoto University, ohgaki@iae.kyoto-u.ac.jp
Kazuhito Ohmi, KEK, ohmi@post.kek.jp
Norihtio Ohuchi, KEK, norihito.ohuchi@kek.jp
David Olsen, Oak Ridge National Laboratory, olsendk@ornl.gov
Kenneth Olsen, DOE Consultant, kenolsen7@aol.com
Yukiyoshi Onishi, KEK, yukiyoshi.onishi@kek.jp
Michael Oothoudt, Los Alamos National Laboratory
Will Oren, Thomas Jefferson National Accelerator Facility, oren@jlab.org
Yushiro Osamu, Toshiba
Petr Ostroumov, Argonne National Laboratory, ostroumov@phy.anl.gov
Klaus Ott, BESSY, ott@bessy.de
Thomas Owens, UT-Battelle, owenstl@sns.gov
Joseph Ozelis, Thomas Jefferson National Accelerator Facility

P

Hasan Padamsee, Cornell University, hsp3@cornell.edu
Carlo Pagani, INFN & DESY, carlo.pagani@mi.infn.it
Chien-Ih Pai, Brookhaven National Laboratory
Renato Paktar
Mark Palmer, Cornell University, Wilson Laboratory, RLF2@Cornell.edu
Yannis Papaphilippou, ESRF
Richard Pardo, Argonne National Laboratory, pardo@phy.anl.gov
Doug Parent, CPI, Inc., doug.parent@cpii-us.com
Jang Ho Park, Pohang Accelerator Laboratory, wpjho@postech.ac.kr
Stanley Pasky, Argonne National Laboratory
Ralph Pasquinelli, Fermi National Accelerator Laboratory
Marco Pedrozzi, Paul Scherrer Institute, vera.loehle@psi.ch
Stephen Peggs, Brookhaven National Laboratory
Michael Peiniger, ACCEL Instruments GmbH, peiniger@accel.de
Michael Pekeler, ACCEL Instruments GmbH, pekeler@accel.de
Thomas Pelaia, Oak Ridge National Laboratory
William Pellico, Fermi National Accelerator Laboratory
Gerald Peters, US Department of Energy, jerry.peters@science.doe.gov
Larry Phillips, Thomas Jefferson National Accelerator Facility
Nan Phinney, Stanford Linear Accelerator Center, nan@slac.stanford.edu
Nicolas Pichoff, CEA/Saclay
Christian Piel, ACCEL Instruments GmbH, piel@accel.de
Fulvia Pilat, Brookhaven National Laboratory
Chandra Pillai, Los Alamos National Laboratory
Phillippe Piot, Fermi National Accelerator Laboratory
Eugeniusz Plawski, Institute for Nuclear Studies in Swierk, plawski@ipj.gov.pl
Tomasz Plawski, Thomas Jefferson National Accelerator Facility
Mark Plesko, Cosylab, Ltd., mark.plesko@cosylab.com
Tomas Plettner, Stanford University, Department of Applied Physics, tplettne@stanford.edu
Michael Plum, Los Alamos National Laboratory, plum@lanl.gov
Holger J. Podlech, Institut für Angewandte Physik, h.podlech@iap.uni-frankfurt.de
Boris Podobedov, Brookhaven National Laboratory
Roger L. Poirier, TRIUMF, rogerlpoirier@netscape.net
Montserrat Pont, Institute for Synchrotron Radiation - ANKA, pont@iss.fzk.de
Michael Poole, Daresbury Laboratory, m.w.poole@dl.ac.uk

John Power, Argonne National Laboratory, jpower@lanl.gov
Eduard Pozdeyev, National Superconducting Cyclotron Laboratory/MSU, box@nscl.msu.edu
Joseph Preble, Thomas Jefferson National Accelerator Facility
Eric Prebys, Fermi National Accelerator Laboratory
Soren Prestemon, Lawrence Berkeley National Laboratory
Hywel Price, CCLRC, Rutherford Appleton Laboratory, h.g.price@dl.ac.uk
Vernon G. Price, Stanford Linear Accelerator Center, v.price@ieee.org
Benjamin Prichard, SAIC, beeryb@saic.com
Christopher Prior, CCLRC, Rutherford Appleton Laboratory, c.prior@rl.ac.uk
Veronique Probyn, e2v Technologies, veronique.probyn@e2Vtechnologies.com
Lionel Prost, Lawrence Berkeley National Laboratory, LRProst@lbl,gov
Vadim Ptitsyn, Brookhaven National Laboratory,

Q

Bao Liang Qian, MIT, blqian@psfc.mit.edu
Ji Qiang, Lawrence Berkeley National Laboratory
Peter Quigley, Cornell University, Wilson Laboratory, RLF2@Cornell.edu
Bryan Quinn, University of Maryland, lsjan@glue.umd.edu

R

James Rank, Brookhaven National Laboratory
Triveni Rao, triveni@bnl.gov
Yi-Nong Rao, TRIUMF
Deepak Raparia, Brookhaven National Laboratory
Alessandro Ratti, Lawrence Berkeley National Laboratory
Ulrich Ratzinger, Institut für Angewandte Physik, U.Ratzinger@iap.uni-frankfurt.de
Michael Read, Calabazas Creek Research, mike@calcreek.com
William A. Reass, Los Alamos National Laboratory, wreass@lanl.gov
Stefano Redaelli, CERN , University of Lausanne (UNIL), Stefano.Redaelli@cern.ch
Charles Reece, Thomas Jefferson National Accelerator Facility
Jeffrey Reed, Pearson Electronics, Inc., jeffreed@pearsonelectronics.com
Daniel Rees, Los Alamos National Laboratory,
Amy Regan, Los Alamos National Laboratory
Sven Reiche, UCLA, reiche@stout.physics.ucla.edu
Martin Reiser, University of Maryland, mreiser@unb.edu
Douglas B. Remsen Jr, General Atomics Energy Products, remsen@gat.com
Timothy J. Renk, Sandia National Laboratories, tjrenk@sandia.gov
Ximenes Rocha Resende, LNLS, gislaine@lnls.br
Seung J. Rhee, Stanford University, rhees@stanford.edu
David Rice, Cornell University, Wilson Laboratory, RLF2@Cornell.edu
Thomas C. Ries, TRIUMF, trrt@triumf.ca
Robert Rimmer, Thomas Jefferson National Accelerator Facility
Leonid Rivkin, Paul Scherrer Institute, Leonid.Rivkin@psi.ch
Chuck Roberson, Office of Naval Research, robersc@onr.navy.mil
David S. Robin, Lawrence Berkeley National Laboratory, dsrobin@lbl.gov
Dennis Robinson, Diversified Technologies, Inc., robinson@divtecs.com
Kem Robinson, Lawrence Berkeley National Laboratory, kerobinson@lbl.gov
Claus Rode, Thomas Jefferson National Accelerator Facility
Jose Alberto Rodriguez, National Superconducting Cyclotron Laboratory/MSU,
box@nscl.msu.edu
Frederico Roncarolo, CERN
Annick Ropert, ESRF

David V. Rose, Mission Research Corporation, drose@mrcabq.com
James Rose, Brookhaven National Laboratory
Thomas Roser, Brookhaven National Laboratory
Marc C. Ross, Stanford Linear Accelerator Center, mcrec@slac.stanford.edu
Carlo Rossi, CERN, carlo.rossi@cern.ch
Lucio Rossi, CERN
Robert Rossmanith, Research Center Karlsruhe, rossmanith@anka.fzk.de
Gary Rouleau, Los Alamos National Laboratory, Grouleau@lanl.gov
Prabir Roy, Lawrence Berkeley National Laboratory
David Rubin, Cornell University, Wilson Laboratory, RLF2@Cornell.edu
Roman Ruegg, TRIUMF
Alessandro Ruggiero, Brookhaven National Laboratory
Hartmut Ruhl, University of Nevada-Reno, karilevin@yahoo.com
Giovanni Rumolo, ESRF
Ronald Rumrill, Alpha Scientific Electronics, nrumrill@alphascientific.com
Brian Rusnak, Lawrence Livermore National Laboratory, rusnak1@llnl.gov
Robert Russell, AFT Inc., BobK4ew@aol.com
Steven J. Russell, Los Alamos National Laboratory, srussell@lanl.gov
Thomas Russo, Brookhaven National Laboratory, trusso@bnl.gov
William Rust, Thomas Jefferson National Accelerator Facility, rust@jlab.org
Ronald D. Ruth, Stanford Linear Accelerator Center, rruth@slac.stanford.edu
Robert Rutherford, BURLE Industries, Inc., burlepwm@burle.com
Lawrence Rybarcyk, Los Alamos National Laboratory
Robert Ryne, Lawrence Berkeley National Laboratory, rdryne@lbl.gov

S

Roberto Saban, CERN
David Sagan, Cornell University, Wilson Laboratory, RLF2@Cornell.edu
Richard C. Sah, Siemens Medical Solutions, richard.sah@sms.siemens.com
Kenji Saito, KEK, ksaito@post.kek.jp
Vadim Sajaev, Argonne National Laboratory, sajaev@aps.anl.gov
Izumi Sakai, KEK, izumi.sakai@kek.jp
Ned Saleh, University of Michigan,
Paul Sampson, Brookhaven National Laboratory, petway@bnl.gov
Shigemi Sasaki, Argonne National Laboratory, sasaki@aps.anl.gov
Yoichi Sato, Oak Ridge National Laboratory, satoy@ornl.gov
Todd Satogata, Brookhaven National Laboratory, satogata@bnl.gov
Andreas Christof Sauer, Institut für Angewandte Physik, a.sauer@iap.uni-frankfurt.de
Xavier Sauge, SDMS, sauge@sdms.fr
Aleksandr Saverskiy, AS&E High Energy Systems Division, asaverskiy@as-e.com
Masaru Sawamura, JAERI, sawamura@popsvr.tokai.jaeri.go.jp
Walther Scandale, CERN, Switzerland,
Thomas Scarvie, Lawrence Berkeley National Laboratory, tom_scarvie@lbl.gov
Levi Schachter, Technion - IIT, levi@ee.technion.ac.il
George E. Schaller, Ceramic Magnetics, GScha12195@cs.com
Stuart Schaller, Los Alamos National Laboratory
Alwin Schempp, Institut für Angewandte Physik, a.schempp@em.uni-frankfurt.de
Thomas Schilcher, Paul Scherrer Institute
Holger Schlarb, DESY, holgers@slac.stanford.edu
Bjoern S Schmekel, Cornell University, bss28@cornell.edu
Pierre Schmelzbach, Paul Scherrer Institute, vera.loehle@psi.ch
John F Schmerge, Stanford Linear Accelerator Center, schmerge@slac.stanford.edu
Hermann Schmickler, CERN, Hermann.Schmickler@cern.ch

Frank Schmidt, CERN, frank.schmidt@cern.ch
Roland Schmidt, Siemens Medical Solutions, roland.schmidt@siemens.com
Paul Schmor, TRIUMF
Uwe Schneck, FMB Feinwerk- und Messtechnik GmbH, U.Schneck@fmb-berlin.de
Dieter H. Schneider, Lawrence Livermore National Laboratory, schneider2@llnl.gov
Russell Schonberg, AS&E High Energy Systems Division, srcruss@aol.com
Dale Schrage, Los Alamos National Laboratory
Ulrich Schramm, ulrich.schramm@physik.uni-muenchen.de
Siegfried Schreiber, DESY, siegfried.schreiber@desy.de
Stan Schriber, National Superconducting Cyclotron Laboratory/MSU, schriber@nscl.msu.edu
Chris M. Sears, Stanford University, cmsears@stanford.edu
Norihiro Sei, AIST, sei.n@aist.go.jp
Peter Seidl, Lawrence Berkeley National Laboratory
Jacek Sekutowicz, Thomas Jefferson National Accelerator Facility
Sergey Seletskiy, Fermi National Accelerator Laboratory
Tanaji Sen, Fermi National Accelerator Laboratory
Luca Serafini, INFN-Milan, luca.serafini@mi.infn.it
Nick Sereno, Argonne National Laboratory
Andrei Seryi, Stanford Linear Accelerator Center, seryi@slac.stanford.edu
Stefan Setzer, Darmstadt University of Technology, setzer@temf.tu-darmstadt.de
Timur Shaftan, Brookhaven National Laboratory
Charles Shank, Lawrence Berkeley National Laboratory
Michael Shapiro, MIT, 25 Arnold Ter., shapiro@psfc.mit.edu
Sergey Sharamentov, Argonne National Laboratory, sharamentov@phy.anl.gov
William M. Sharp, Lawrence Livermore National Laboratory, wmsharp@lbl.gov
Yuri M. Shatunov, Budker Institute of Nuclear Physics, shatunov@inp.nsk.su
Sergey V. Shchelkunov, Columbia University, shchelkunov@bnl.gov
Thomas J. Shea, Oak Ridge National Laboratory, shea@sns.gov
Ron Sheldrake, e2v Technologies
Valery Shemelin, Cornell University, Wilson Laboratory, RLF2@Cornell.edu
Kenneth Shepard, Argonne National Laboratory, kwshepard@anl.gov
Joseph Sherman, Los Alamos National Laboratory, LANSCE-2, jsherman@lanl.gov
Brad Sherrill, National Superconducting Cyclotron Laboratory/MSU, mcintyre@nscl.msu.edu
Jicong Shi, University of Kansas, jshi@ku.edu
Michelle Shinn, Thomas Jefferson National Accelerator Facility, shinn@jlab.org
Tsumoru Shintake, RIKEN, shintake@spring8.or.jp
Masazumi Shoji, SPring-8/Japan, shoji@spring8.or.jp
Deming Shu, Argonne National Laboratory
R. Coles Sibley III, Oak Ridge National Laboratory, sibley@sns.gov
Ioannis Sideris, Northern Illinois University, sideris@nicadd.niu.edu
Robert H. Siemann, Stanford Linear Accelerator Center, siemann@slac.stanford.edu
David F. Simmons, Los Alamos National Laboratory, dsimmons@lanl.gov
Nikolaos Simos, Brookhaven National Laboratory, simos@bnl.gov
Stefan Simrock, DESY, stefan.simrock@desy.de
Charles K. Sinclair, Cornell University, cks26@cornell.edu
Om Vir Singh, Argonne National Laboratory,
John Smedley, Brookhaven National Laboratory, smedley@bnl.gov
Alexei Smirnov, DULY Research Inc.
Evgenya Smirnova, MIT, smirnova@mit.edu
Jeff Smith, Cornell University, Wilson Laboratory, RLF2@Cornell.edu
Kevin S. Smith, Brookhaven National Laboratory, ksmith@bnl.gov
Terry Smith, Argonne National Laboratory, tls@aps.anl.gov
Younguk Sohn, Pohang Accelerator Laboratory, cwchung@postech.edu
Robert Soliday, Argonne National Laboratory

Nikolay Solyak, Fermi National Accelerator Laboratory, solyak@fnal.gov
Liqun Song, Calabazas Creek Research, purobi@calcreek.com
Kiran Sonnad, University of Colorado, sonnad@colorado.edu
Kouichi Soutome, SPring-8, soutome@spring8.or.jp
Cherrill M. Spencer, Stanford Linear Accelerator Center, cherrill@slac.stanford.edu
James E. Spencer, Stanford Linear Accelerator Center, jus@slac.stanford.edu
Panagiotis Spentzouris, Fermi National Accelerator Laboratory, spentz@fnal.gov
Thomas Spickermann, Los Alamos National Laboratory, spickermann@lanl.gov
Peter Spiller, GSI, k.blasche@gsi.de
John Staples, Lawrence Berkeley National Laboratory, staples@lbl.gov
Edward Startsev, Plasma Physics Laboratory, estarts@pppl.gov
Christoph A. Steier, Lawrence Berkeley National Laboratory, CSteier@lbl.gov
James Steimel, Fermi National Accelerator Laboratory
Werner Stein, Lawrence Livermore National Laboratory, stein1@llnl.gov
Frank Stephan, DESY Zeuthen, frank.stephan@desy.de
Dale Stevenson, ACQIRIS, d.stevenson@acqiris.com
Glen Stinson, TRIUMF
Martin Stockli, Oak Ridge National Laboratory, stocklimp@yahoo.com
Peter H. Stoltz, Tech-X Corporation, pstoltz@attbi.com
Gregory Stover, Lawrence Berkeley National Laboratory
Jim Strait, Fermi National Accelerator Laboratory, mbruce@fnal.gov
Bruce P. Strauss, U.S. Department of Energy, bruce.strauss@science.doe.gov
Gennady Stupakov, Stanford Linear Accelerator Center, stupakov@slac.stanford.edu
Yusuke Suetsugu, KEK, yusuke.suetsugu@kek.jp
Steve Suhring, Thomas Jefferson National Accelerator Facility, suhring@jlab.org
Hyyong Suk, KERI, hysuk@keri.re.kr
Victor P. Suller, Daresbury Laboratory CCLRC, v.suller@dl.ac.uk
Michael K. Sullivan, sullivan@slac.stanford.edu
Yin-e Sun, University of Chicago, yinesun@uchicago.edu
Chieh Sung, UCLA, jaysung@seas.ucla.edu
David F. Sutter, U.S. Department of Energy, hep-tech@science.doe.gov
Tsuyoshi Suwada, KEK, tsuyoshi.suwada@kek.jp
Michele Svandrlik, Sincrotrone Trieste, michele.svandrlik@elettra.trieste.it
Michael Sweeney, L-3 Electron Devices, mike.sweeney@L-3com.com
Donald Swenson, Linac Systems, LLC, DASwenson@aol.com
Keith R. Symon, University of Wisconsin-Madison, krsymon@facstaff.wisc.edu
Hans-Arno Synal, EPAC'04, synal@phys.ethz.ch

T

Chiu-Ting Tai, Energen, Inc., chowyee@energeninc.com
Toshiki Tajima, JAERI Kansai, tajima@apr.jaeri.go.jp
Harunori Takeda, Los Alamos National Laboratory, htakeda@lanl.gov
Seishi Takeda, KEK & JSPS, seishi.takeda@kek.jp
Richard Talman, Cornell University, Newman Laboratory, talman@lns62.lns.cornell.edu
Cheng-Yang Tan, Fermi National Accelerator Laboratory
Hirofumi Tanaka, Mitsubishi Electric Corp., Tanaka.Hirofumi@wrc.melco.co.jp
Yasunori Tanimoto, KEK, yasunori.tanimoto@kek.jp
Sami Tantawi, Stanford Linear Accelerator Center, US, tantawi@slac.stanford.edu
Thomas Taylor, CERN, AT Division, Tom.Taylor@cern.ch
Frank Tecker, CERN, tecker@cern.ch
Patrice Tekian, PMB, patrice.tekian@pmb-mt.com
Soren Williams Telfer, UCLA, telfer@physics.ucla.edu
Richard Temkin, MIT, temkin@psfc.mit.edu

Alexander (Sasha) Temnykh, Cornell University, Wilson Laboratory, RLF2@Cornell.edu
Lee C. Teng, Argonne National Laboratory, teng@aps.anl.gov
Christopher D. Tennant, Thomas Jefferson National Accelerator Facility, tennant@jlab.org
Steven Tepikian, Brookhaven National Laboratory,
Andrei G. Terebilo, Stanford Linear Accelerator Center, terebilo@ssrl.slac.stanford.edu
Dmitry Teytelman, Stanford Linear Accelerator Center, dim@slac.stanford.edu
Jan Thibus, Institut für Angewandte Physik, thibus@stud.uni-frankfurt.de
Carsten Thoma, Mission Research Corporation, lindmc@mrcabq.com
Robert J. Thomas, IEEE, bobthomas97068@yahoo.com
Matthew Thompson, UCLA, mct@physics.ucla.edu
William Thur, Lawrence Berkeley National Laboratory
Maury Tigner, Cornell University, mt52@cornell.edu
Sergei, Tochitsky, UCLA, sergei12@ucla.edu
Alan Todd, Advanced Energy Systems, alan_todd@mail.aesys.net
Raimund Toelle, Forschungszentrum Juelich, r.toelle@fz-juelich.de
Takio Tomimasu, Saga Synchrotron Light Source, tomimasu@sweet.ocn.ne.jp
John Tompkins, Fermi National Accelerator Laboratory, jct@fnal.gov
Kota Torikai, KEK, strategy@meteor.nucl.kyushu-u.ac.jp
Theodor Tortschanoff, CERN
Nathan Towne, Brookhaven National Laboratory
Hiroyuki Toyokawa, Thomas Jefferson National Accelerator Facility, hiroyuki@jlab.org
Emil Trakhtenberg, Argonne National Laboratory
Gil Travish, UCLA, travish@physics.ucla.edu
Dejan Trbojevic
Todd Treado, CPI, todd.treado@bmd.cpii.com
Aaron M. Tremaine, Lawrence Livermore National Laboratory, tremaine1@llnl.gov
Dieter Trines, DESY, Dieter.Trines@desy.de
Christoph Tschalaer, MIT, Laboratory for Nuclear Science
Nicholaos Tsoupas, Brookhaven National Laboratory
Koji Tsumaki, SPring-8/JASRI, tsumaki@spring8.or.jp
Joseph Tuozzolo, Brookhaven National Laboratory, Building 911B, Upton, NY, 11973-5000, US,

U

Mitsuru Uesaka, University of Tokyo, uesaka@utnl.jp
Didier Uriot, CEA Saclay

V

Cristina Vaccarezza, INFN-LNF, Cristina.Vaccarezza@lnf.infn.it
Robert Valdiviez, Los Alamos National Laboratory, valdiviez@lanl.gov
Agust Valfells, University of Maryland, lsjan@glue.umd.edu
Ton van de Water, Imtech Vonk B.V., wtr@vonk-systems.nl
Jan van der Laan, MIT-Bates, janvdl@mit.edu
Fred van Goor, University of Twente
Jeroen van Tilborg, Lawrence Berkeley National Laboratory
Iouri Vanenkov, CERN
Vincenzo Variale, INFN-Bari, v_variale@hotmail.com
Gueorgui V. Velev, velev@fnal.gov
Raymond Veness, CERN, Raymond.Veness@cern.ch
Marco Venturini, Lawrence Berkeley National Laboratory, mventurini@lbl.gov
Vadim Veshcherevich, Cornell University, vgv@lns.cornell.edu
Kurt Vetter, Brookhaven National Laboratory, vetter@bnl.gov
Guidi Vincenzo, INFN-Bari

Nikolai Vinogradov, Argonne National Laboratory, vinogradov@phy.anl.gov
Bernard Visentin, CEA/Saclay
Arnold E. Vlieks, Stanford Linear Accelerator Center, aev@slac.stanford.edu
Hanspeter Vogel, ACCEL Instruments GmbH, vogel@accel.de
James T. Volk, Fermi National Accelerator Laboratory, volk@fnal.gov
Leonid Vorobiev, National Superconducting Cyclotron Laboratory/MSU, box@nscl.msu.edu

W

Yoshio Wada, Hiroshima University, fourty@hiroshima-u.ac.jp
Masayoshi Wake, KEK, wake@post.kek.jp
Pete E. Wakeland, Sandia National Laboratories, pewakel@sandia.gov
Geoff Waldschmidt, Argonne National Laboratory, waldschm@aps.anl.gov
Ian Walker, GMW Associates, ian@gmw.com
Nicholas J. Walker, DESY, nicholas.walker@desy.de
Richard Walker, Diamond Light Source Limited, e.l.a.medlock@diamond.ac.uk
Peter Walstrom, Los Alamos National Laboratory
Mark Walter, University of Maryland, lsjan@glue.umd.edu
Dieter Walz, Stanford Linear Accelerator Center, dwalz@slac.stanford.edu
Weishi Wan, Lawrence Berkeley National Laboratory
Peter Wanderer, Brookhaven National Laboratory, wanderer@bnl.gov
Changbiao Wang, Yale University, cbwang@beamer6.physics.yale.edu
Chun-xi Wang, Argonne National Laboratory, wangcx@aps.anl.gov
Fuhua Wang, MIT Bates, fwang@mit.edu
Haipeng Wang, Thomas Jefferson National Accelerator Facility
Min Huey Wang, NSRRC, mhwang@srrc.gov.tw
Sou Tien Wang, Wang NMR, 550 N. Canyons Parkway, wangnmr@yahoo.com
Tai-Sen Wang, Los Alamos National Laboratory, twang@lanl.gov
Tong Wang, Thomas Jefferson National Accelerator Facility, tong@jlab.org
Xijie Wang, Brookhaven National Laboratory, xwang@bnl.gov
Yanshan Wang, Louisiana State University/CAMD, wangysh@lsu.edu
Thomas Wangler, Los Alamos National Laboratory
Robert L. Warnock, Stanford Linear Accelerator Center, warnock@slac.stanford.edu
Robert Webber, Fermi National Accelerator Laboratory
Jonah Weber, Lawrence Berkeley National Laboratory
Jie Wei, Brookhaven National Laboratory
Udo Weinrich, GSI, u.weinrich@gsi.de
Hans Weise, DESY, hans.weise@desy.de
Dale R. Welch, Mission Research Corporation, drwelch@mrcabq.com
Jim Welch, Stanford Linear Accelerator Center
Carsten P. Welsch, MPI Heidelberg, carsten.welsch@mpi-hd.mpg.de
Robert F. Welton, ORNL/SNS/UT-Battelle, welton@sns.gov
Mark W. Wendel, Oak Ridge National Laboratory, wendelmw@ornl.gov
Wu-Tsung Weng, Brookhaven National Laboratory
Christopher Wesselborg, American Physical Society, chrisw@aps.org
Glen Westenskow, Lawrence Livermore National Laboratory, gw@llnl.gov
Glen White, Queen Mary, University of London, g.white@qmul.ac.uk
Karen S. White, Thomas Jefferson National Accelerator Facility, karen@jlab.org
Marion White, Spallation Neutron Source, mwhite@sns.gov
Kenneth Whitham, Siemens Medical Solutions, ken.whitham@siemens.com
Marjorie Widmeyer, Stanford Linear Accelerator Center, widmeyer@slac.stanford.edu
Ferdinand Willeke, DESY
Erich H. Willen, Brookhaven National Laboratory, Pwillen@bnl.gov
Ernest Williams, Oak Ridge National Laboratory, smithdl@ornl.gov

Katherine Wilson, Thomas Jefferson National Accelerator Facility
Kenneth Wilson, PHPK Technologies Incorporated, info@phpk.com
Perry Wilson, Stanford Linear Accelerator Center, pwilson@slac.stanford.edu
Mark Wiseman, Thomas Jefferson National Accelerator Facility
Walter Wittmer, CERN and University of Technology Graz, Austria, walter.wittmer@cern.ch
Andrzej Wolski, Lawrence Berkeley National Laboratory, awolski@lbl.gov
Edward Wright, CPI, Inc., ed.wright@cpii.com
Genfa Wu, Thomas Jefferson National Accelerator Facility
Juhao Wu, Stanford Linear Accelerator Center, jhwu@SLAC.Stanford.EDU
Xiaoyu Wu, National Superconducting Cyclotron Laboratory/MSU, xwu@nscl.msu.edu
Ying Wu, Duke University, wu@fel.duke.edu
Walter U. Wuensch, walter.wuensch@cern.ch
Godehard Wustefeld, BESSY

X

Meiqin Xiao, Fermi National Accelerator Laboratory

Y

Torun Yagmur, Illinois Institute of Technology, torun@iit.edu
Vitaly Yakimenko, Brookhaven National Laboratory
Vyacheslav Yakovlev, Omega-P, Inc., slava@omega-p.com
Akiyoshi Yamamoto, IHI, 20-13, akiyoshi_yamamoto@ihi.co.jp
Yoshishige Yamazaki, JAERI, yoshishige.yamazaki@kek.jp
Xi Yang, Fermi National Accelerator Lab, rwill9955@hotmail.com
Atsunori Yano, Toshiba Corporation, atsunori.yano@toshiba.co.jp
Chihyuan Yao, Argonne National Laboratory, cyao@aps.anl.gov
Yan Yin, YY Labs, Inc., yanyin@YYLabs.com
Rodney Yoder, UCLA, yoder@physics.ucla.edu
Richard York, National Superconducting Cyclotron Laboratory/MSU, mcintyre@nscl.msu.edu
Iwashita Yoshihisa, Kyoto University, iwashita@kyticr.kuicr.kyoto-u.ac.jp
Andrew Young, Stanford Linear Accelerator Center, ayoung@slac.stanford.edu
Lloyd Young, Los Alamos National Laboratory, lyoung@lanl.gov
David Yu, DULY Research, Inc.
Simon Yu, Lawrence Berkeley National Laboratory
Byung Yunn, Thomas Jefferson National Accelerator Facility
Zikri Yusof, Argonne National Laboratory, HEP Division, yusof@hep.anl.gov

Z

Vladimir Zadorozhny, Institution of Cybernetics NAN Ukraine, zvf@compuserv.com.ua
Igor Zagorodnov, Darmstadt University of Technology, zagor@temf.tu-darmstadt.de
Valeriy V. Zakutin, Kharkov Institute for Physics & Technology, zakutin@kipt.kharkov.ua
Alex Zaltsman, Brookhaven National Laboratory
James Zaroda, LARCAN USA, jzaroda@larcan.com
Al Zeller, National Superconducting Cyclotron Laboratory/MSU, Department of Physics and Astronomy, jzaroda@larcan.com
Shou-Yuan Zhang, Brookhaven National Laboratory
Wu Zhang, Brookhaven National Laboratory
Xiaolong Zhang, Fermi National Accelerator Lab
Yan Zhang, Oak Ridge National Laboratory
Yuhong Zhang, Thomas Jefferson National Accelerator Facility
Yongxiang Zhao, Brookhaven National Laboratory

Feng Zhou, Brookhaven National Laboratory, zhouf@bnl.gov
Jing Zhou, MIT, jea_zhou@mit.edu
Frank Zimmermann, CERN, frank.zimmermann@cern.ch
Holger Zimmermann, Institut für Angewandte Physik, ho.zimmermann@iap.uni-frankfurt.de
Michael S. Zisman, Lawrence Berkeley National Laboratory, mszisman@lbl.gov
Alexander Zlobin, Fermi National Accelerator Laboratory, zlobin@fnal.gov
Bruno Zotter, CERN, bruno.zotter@cern.ch
Yun Zou, University of Maryland, Institute for Research in Electronics and Applied Physics, yunzou@glue.umd.edu
Townsend Zwart, MIT, Zwart@rocko.mit.edu

Opening Plenary

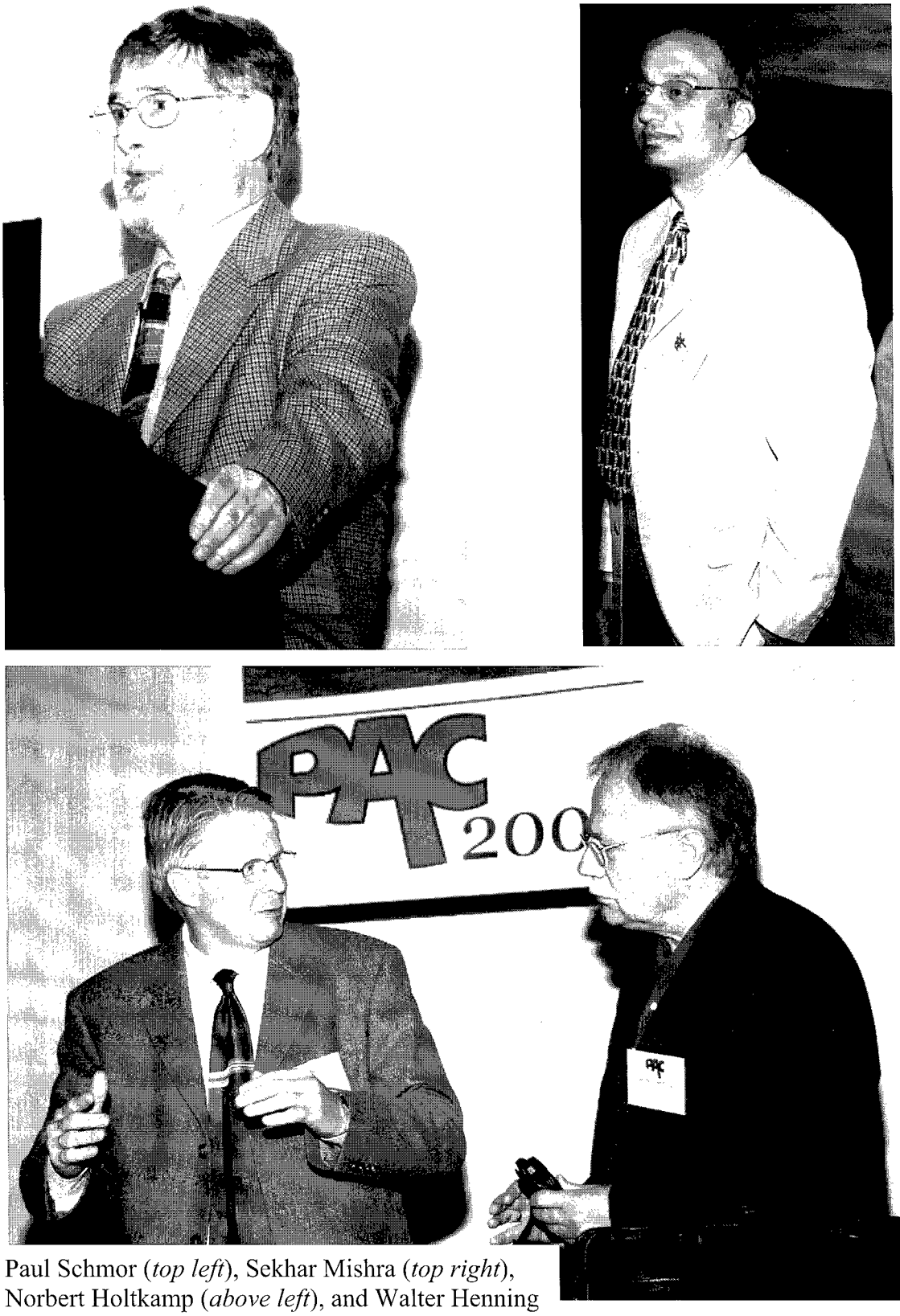

Paul Schmor (*top left*), Sekhar Mishra (*top right*), Norbert Holtkamp (*above left*), and Walter Henning (*above right*) open the conference in plenary session on Monday morning.

Awards Banquet

Edwards: "For her pivotal achievement and critical contribution as the leader in the design, construction, commission, and operation of the Tevatron and for her continued contributions to the development of high gradient super-conducting linear accelerators as well as bright and intense electron sources."

Left: Award presenter Alex Dragt looks on as Helen Edwards prepares to give her talk upon receiving the Robert R. Wilson Prize. It is awarded by the American Physical Society to recognize and encourage outstanding achievement in the physics of particle accelerators. The prize is sponsored by the APS Division of Physics of Beams and Division of Particles and Fields, and by the friends of R.R. Wilson.

Below: Ed Hoffman presents Stephen Milton (*below left*) and Keith Symon with the Particle Accelerator Science and Technology Award. PAC gives the award on behalf of the IEEE Nuclear and Plasma Sciences Society, sponsor of the award. Two awards are given to recognize outstanding contributions to the development of particle accelerator technology.

Symon (below, at left): *"For many fundamental accelerator concepts which include invention of Fixed Field Alternating Gradient Accelerators (FFAG), most notably incorporated into spiral sector cyclotrons; for defining a formalism describing motion under the influence of RF as required for stacking and other particle manipulations; and for techniques for analyzing collective instabilities."*

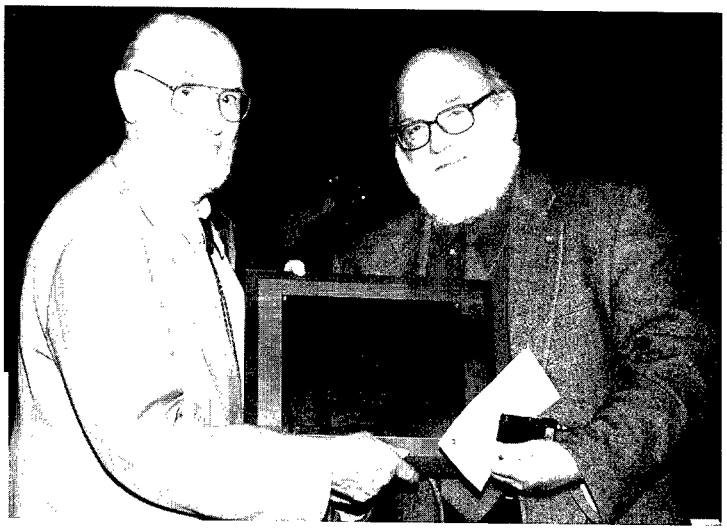

Milton (above, at left): *"For contributions to coherent radiation sources, especially his leading role in achieving saturated operation at visible and ultraviolet wavelengths in a self-amplified spontaneous emission free-electron laser."*

APS Award for Outstanding Doctoral Thesis Research in Beam Physics

Alex Dragt (*below right*) congratulates David Pritzkau for doctoral thesis research of outstanding quality and achievement in beam physics and engineering. The award was established in 1990 by the APS Division of Physics of Beams and is supported by Brookhaven Science Associates and Universities Research Association.

"For an experimental study of the effects of surface heating due to high-power pulsed RF. The experiment established a limit on maximum surface magnetic field and through it one limit on achievable accelerating gradient."

U.S. Particle Accelerator School Prize for Achievement in Accelerator Physics and Technology

The US Particle Accelerator School honors individuals by recognizing their outstanding achievements over the full range of accelerator physics and technology. The awards are made possible by donations from the Brookhaven Science Associates, Southeastern Universities Research Association, the Universities Research Association, and John Wiley and Sons Publishers. This year S.Y. Lee of Indiana University presented the award to Sami Tantawi and Martin Reiser.

Sami Tantawi (*center*)
"For his contribution to the theory and technology of rf components for the production and distribution of very high peak rf power, with particular application to pulse compression systems for high-gradient linear colliders."

Martin Reiser
"For his seminal contributions on the physics of high intensity beams, and for his life-long accomplishments in technology, research, community leadership, and education in the physics of beams."

Newly Elected Fellows of the American Physical Society

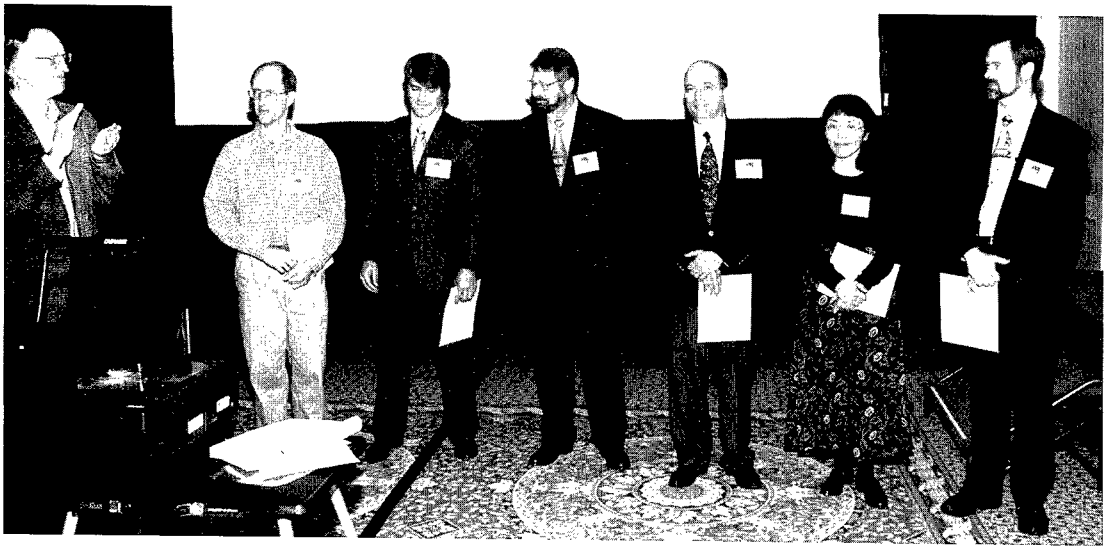

Presenter Alex Dragt *(far left)* welcomes the newly elected Fellows. From left to right:

Nikolai V. Mokhov, Fermi National Accelerator Laboratory
"For critical contributions to the understanding of the interaction of high energy particle beams with materials."

Stephen Val Milton, Argonne National Laboratory
"For the development of 3rd and 4th generation light sources including the first demonstration of saturation of self-amplified spontaneous emission (SASE) in the visible and ultraviolet wavelengths."

Alan Jackson, Lawrence Berkeley National Laboratory
"For pioneering work in the development and construction of 3rd generation synchrotron radiation sources."

Ralph Bruno Fiorito, Catholic University of America
"For pioneering contributions to the understanding and application of transition radiation, diffraction radiation, and parametric x-radiation."

Yu-Jiuan Chen, Lawrence Livermore National Laboratory
"For revolutionizing the achievable beam quality of linear induction accelerators and advancing the state-of-the-art of flash x-ray radiographic technology."

Stephen Vincent Benson, Thomas Jefferson National Accelerator Facility
"For critical contributions to the development of free-electron lasers, including the first demonstration of lasing at harmonics and of multi-kilowatt lasing with an energy recovered linac."

Donald Prosnitz, United States Department of Justice (not depicted)
"For major contributions to physics and society spanning fundamental physics research to national security and law enforcement technologies, including pioneering technical contributions to the development of Free Electron Lasers."

Student Travel Awards

The National Science Foundation, APS/DPB and IEEE/NPSS sponsored grants to help worthy students defray their travel costs. The APS/DPB and IEEE/NPSS grants were awarded in honor of two people who have made many contributions to the accelerator community. The DPB grants honor Mel Month for his dedication to students and education, and the NPSS grants honor Lou Costrell for his nurturing of the Particle Accelerator Conferences. The awards included a complimentary one-year student membership in the sponsoring professional society.

Award Presenters

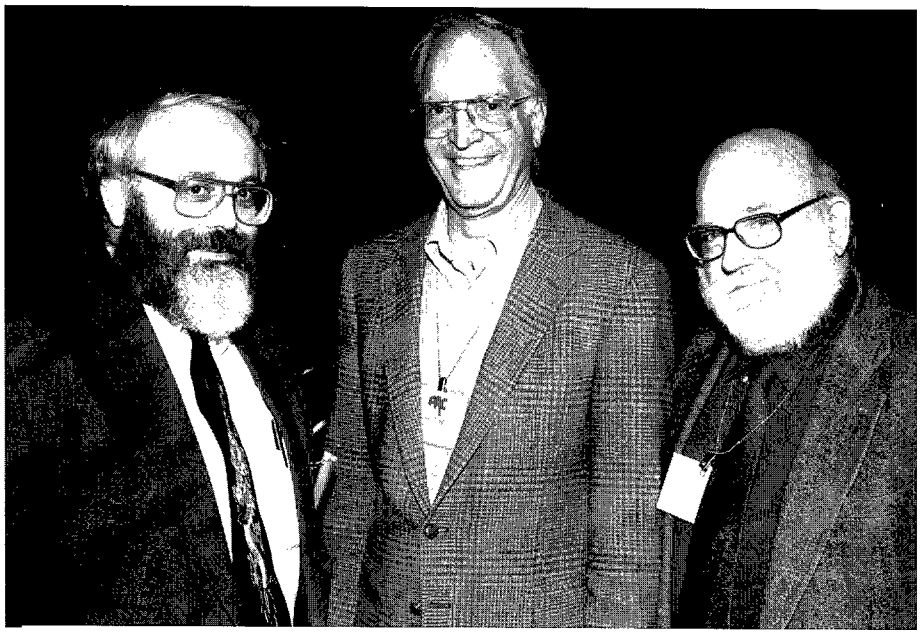

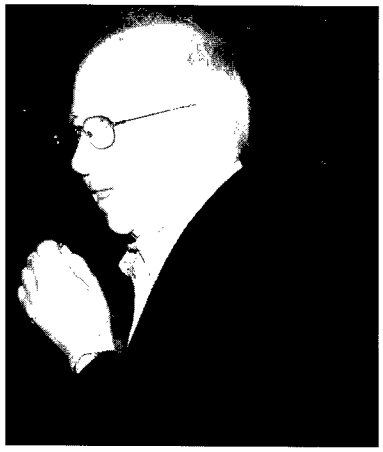

Bruce Brown, Alex Dragt, Ed Hofmann *(together, left to right)*, and Matt Allen were the masters of ceremonies at the awards banquet.

Conference Banquet and Reception

The Leonard Webb Quartet (sax, bass, drums, piano) at the banquet.

Conference officials and visiting dignitaries were among the head-table guests.

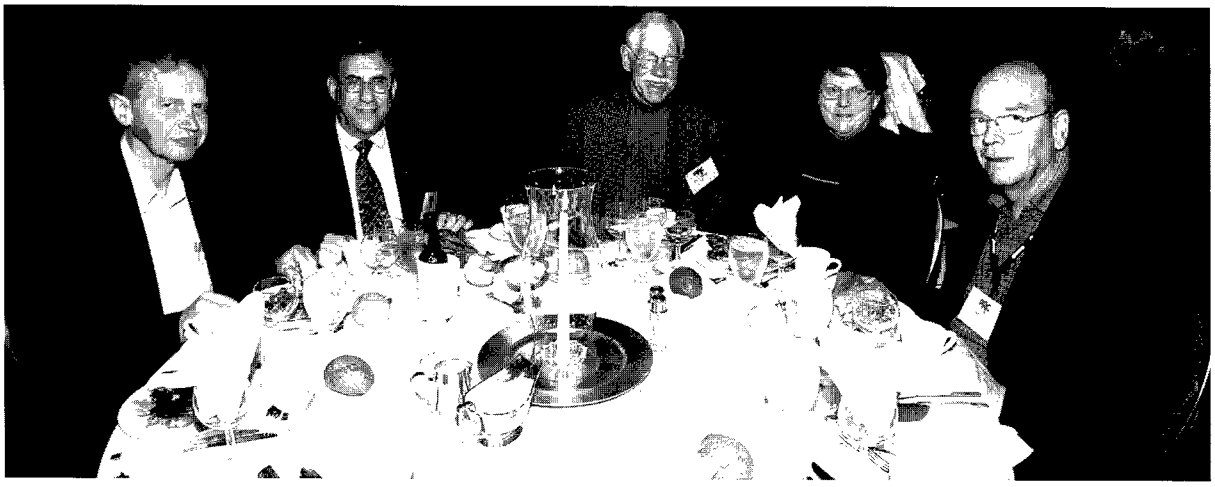

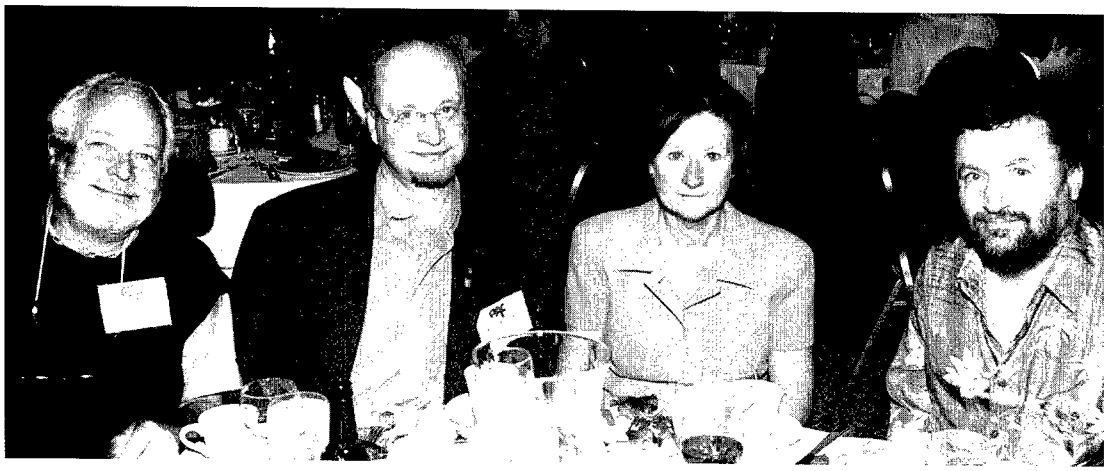

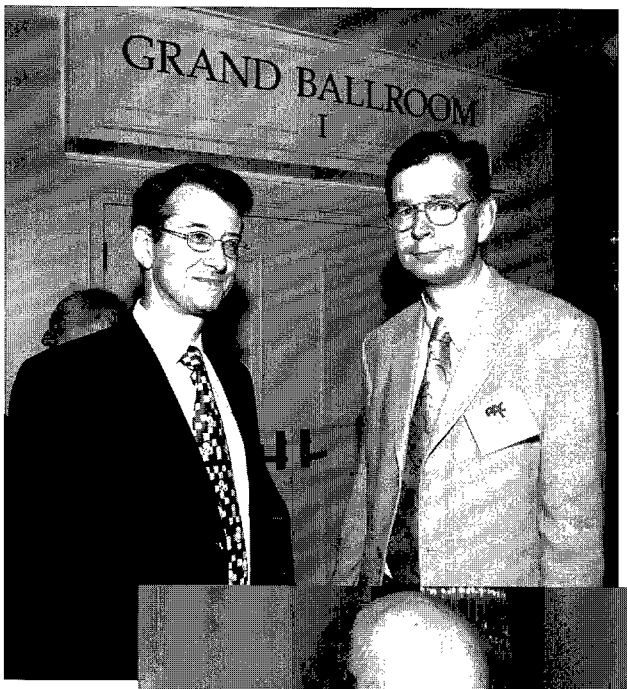
GRAND BALLROOM
I

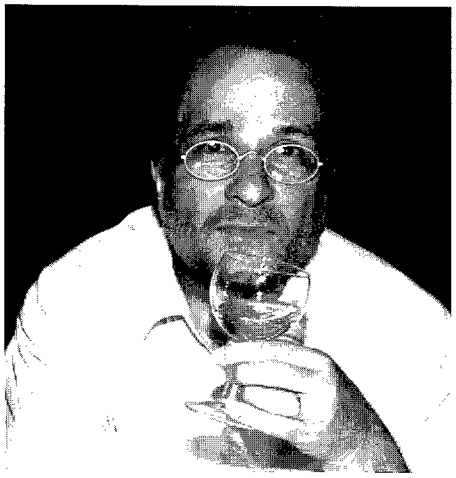

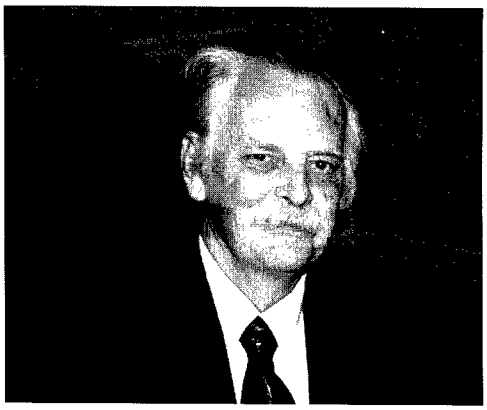

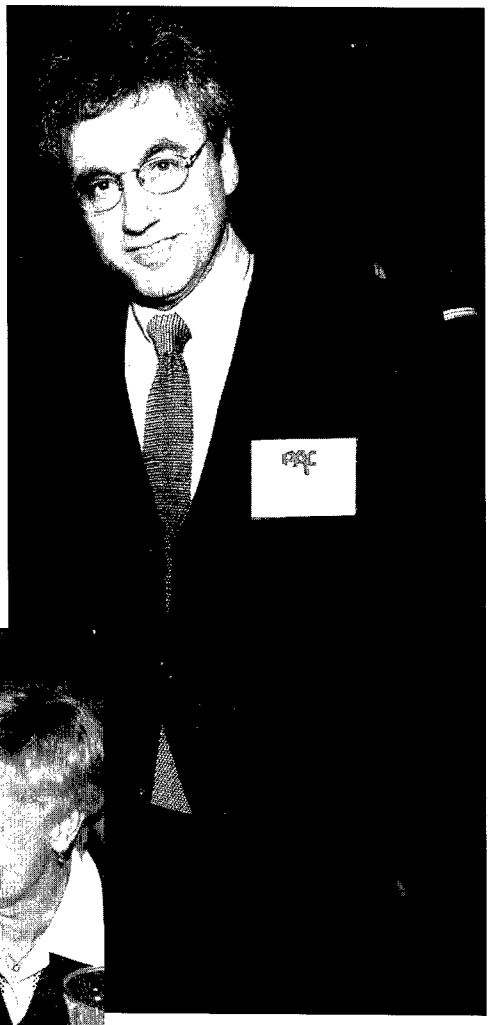

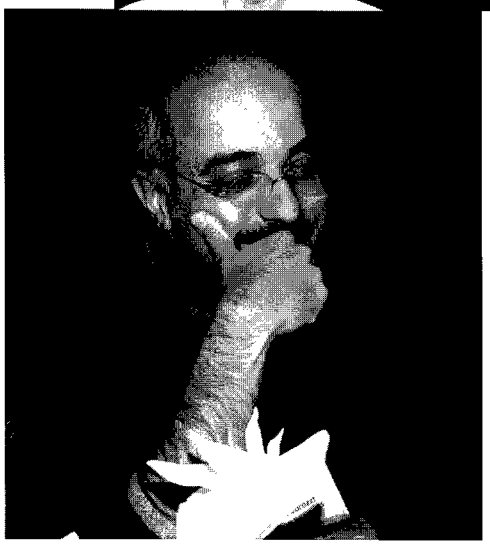

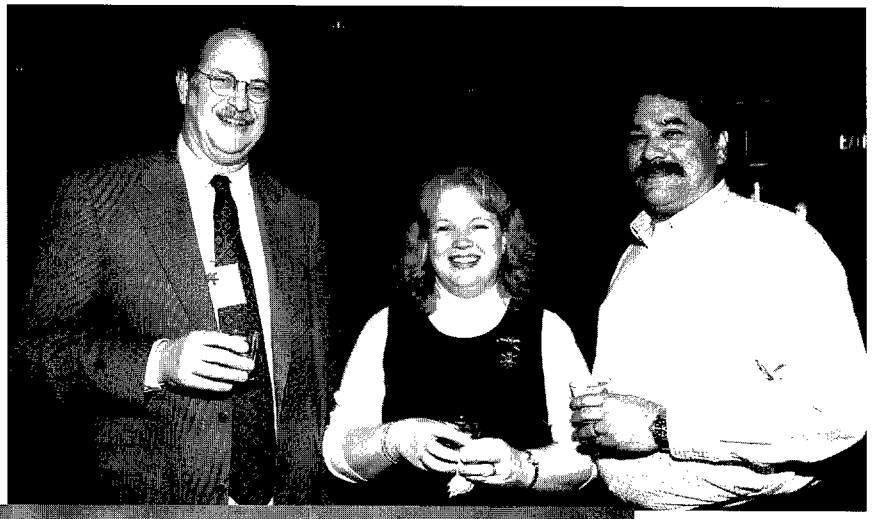

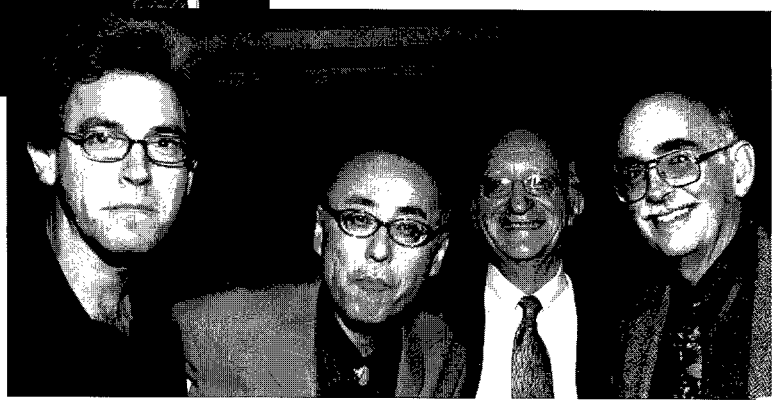

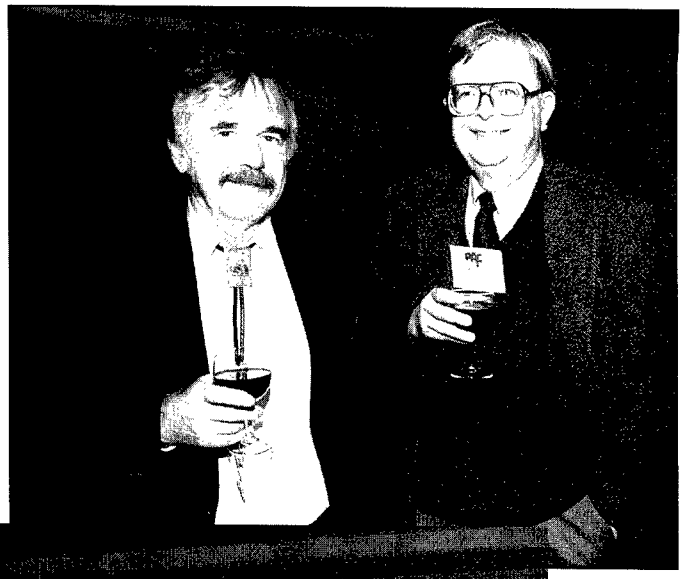

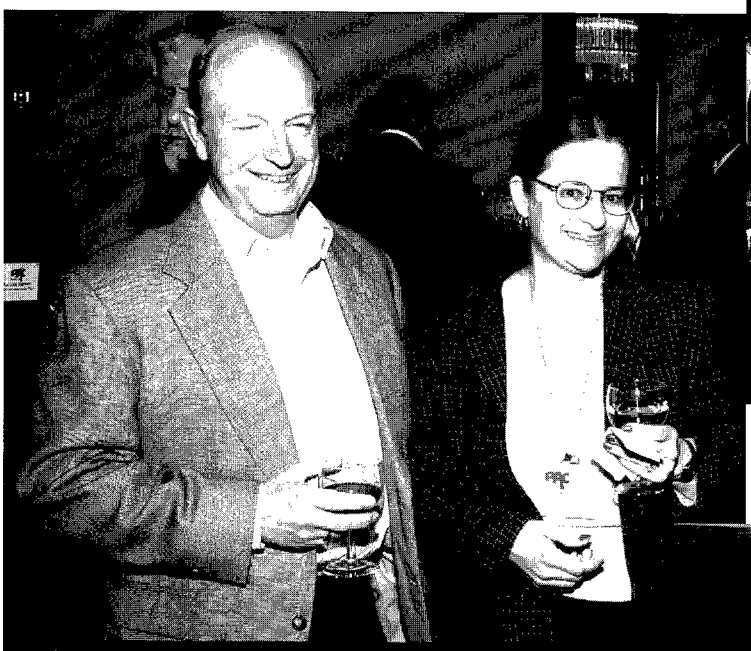

RESTROOMS
TELEPHONES
COAT ROOM

Volume 1

High Luminosity Operation of the Fermilab Accelerator Complex
C.S. Mishra (FNAL) 1

Recently Commissioned and Future RNB Facilities
P. Schmor (TRIUMF) 6

Status of the Spallation Neutron Source
N. Holtkamp (ORNL) 11

The Future GSI Facility: Beams of Ions and Antiprotons
W. Henning (Gesellschaft fËr Schwerionenforschung mbH) 16

Beam Physics at LHC
L.R. Evans (CERN) 19

RHIC Status and Plans
T. Roser (BNL) 24

Beam Physics at Tevatron Complex
V.A. Lebedev (FNAL) 29

New Aspects of Beam-Beam Interactions in Hadron Colliders
T. Sen (FNAL) 34

R&D towards Cooling of the RHIC Collider
I. Ben-Zvi, J.M. Brennan, A. Burrill, R. Calaga, X. Chang, M. Christoph, G. Citver, A. Fedotov, H. Hahn, M. Harrison, A. Hershcovitch, A. Jain, J. Kewisch, W.W. MacKay, G. McIntyre, D. Pate, S. Peggs, J. Rank, T. Roser, J. Scaduto, T. Srinivasan-Rao, D. Trbojevic, D. Wang, A. Zaltsman, Y. Zhao (BNL) 39

Towards a New LHC Interaction Region Design for a Luminosity Upgrade
J.B. Strait, M. Lamm, P. Limon, N.V. Mokhov, T. Sen, A.V. Zlobin (FNAL), R. Gupta, M. Harrison, S. Peggs, F. Pilat (BNL), O.S. BrËning, A. Devred, R. Ostojic, L. Rossi, F. Ruggiero, T. Taylor, H. ten Kate (CERN), S. Caspi, S.A. Gourlay, G. Sabbi (LBNL) 42

Designing and Building a Collimation System for the High-Intensity LHC Beam
R. Assmann, O. Aberle, M. Brugger, L. Bruno, H. Burkhardt, E. Chiaveri, B. Dehning, A. Ferrari, B. Goddard, J.-B. Jeanneret, V. Kain, M. Lamont, F. Ruggiero, R. Schmidt, P. Sievers, J. Uythoven, V. Vlachoudis, L. Vos, J. Wenninger (CERN), I. Baishev (Institute of High Energy Physics, Protvino), D. Kaltchev (TRIUMF) 45

Effects of RF Noise on Longitudinal Emittance Growth in the Tevatron
J. Steimel, I. Gonin, T. Khabiboulline, V.A. Lebedev, J. Reid, G. Romanov, V. Shiltsev, A.V. Tollestrup (FNAL) 48

Polarized Proton Acceleration at the Brookhaven AGS and RHIC
H. Huang, L. Ahrens, J. Alessi, M. Bai, J. Beebe-Wang, S. Brarvar, J.M. Brennan, K.A. Brown, A. Drees, W. Fischer, C. Gardner, J. Glenn, A.U. Luccio, W.W. MacKay, C. Montag, F. Pilat, V. Ptitsyn, T. Roser, T. Satogata, S. Tepikian, D. Trbojevic, N. Tsoupas, A. Zelenski, K. Zeno, S.Y. Zhang, J. van Zeijts (BNL), H. Spinka, D. Underwood (ANL), I. Alekseev, D. Svirida (Institute for Theoretical and Experimental Physics), G. Bunce, O. Jinnochi (RIKEN Accelerator Research Facility), G. Igo, J. Wood (University of California, Los Angeles) 51

RHIC Pressure Rise and Electron Cloud
S.Y. Zhang, M. Bai, M. Blaskiewicz, P. Cameron, A. Drees, W. Fischer, D. Gassner, J. Gullotta, P. He, H. Hseuh, H. Huang, U. Iriso-Ariz, R.C. Lee, W.W. MacKay, B. Oerter, V. Ponnaiyan, V. Ptitsyn, T. Roser, T. Satogata, L. Smart, D. Trbojevic, K. Zeno (BNL) 54

Tune Shift Compensation Using the Tevatron Electron Lens
K. Bishofberger (University of California, Los Angeles), G. Kuznetsov, V. Shiltsev, X.L. Zhang (FNAL) 57

25 Years of Technical Advances in RFQ Accelerators
L.M. Young (LANL) 60

Commissioning of the Spallation Neutron Source front End Systems
A. Aleksandrov (ORNL) 65

Heavy Ion Fusion Sources
D.P. Grote (LLNL), J. Kwan (LBNL) 70

H⁻ Surface Converter Source Development at Los Alamos
G. Rouleau, E. Chacon-Golcher, E. Geros, E.G. Jacobson, B.J. Meyer, B.A. Prichard Jr., J. Sherman, J.E. Stelzer, R.R. Stevens Jr. (LANL) 73

Very High Voltage Photoemission Electron Guns
C.K. Sinclair (Cornell University) 76

Advanced ECR Sources for Highly Charged Ions
S. Gammino, L. Ando, L. Celona, G. Ciavola (INFN), A. Girard, D. Hitz, G. Melin (CEA Grenoble) 81

Commissioning of the Superconducting ECR Ion Source VENUS
D. Leitner, S.R. Abbott, R.D. Dwinell, M.A. Leitner, C.M. Lyneis, C. Taylor (LBNL) 86

Design of an EBIS for RHIC
J. Alessi, E. Beebe, D. Graham, A. Kponou, A. Pikin, K. Prelec, J. Ritter, V. Zajic (BNL) 89

Design, Construction and Status of an All Niobium Superconducting Photoinjector at BNL
T. Srinivasan-Rao, I. Ben-Zvi, A. Burrill, G. Citver, A. Hershcovitch, D. Pate, A. Reuter, J. Scaduto, Q. Zhao, Y. Zhao (BNL), H. Bluem, M. Cole, A. Favale, J.W. Rathke, T.J. Schultheiss (Advanced Energy Systems), J. Delayen, P. Kneisel (Thomas Jefferson National Accelerator Facility) 92

Generation of High Brightness X-Rays with the PLEIADES Thomsen X-Ray Source
W. Brown, S.G. Anderson, C.P.J. Barty, J.K. Crane, R.R. Cross, D.N. Fittinghoff, F. Hartemann, J. Kuba, G.P. LeSage, D.R. Slaughter, P.T. Springer, A.M. Tremaine (LLNL), D.J. Gibson (University of California, Davis), J.B. Rosenzweig (University of California, Los Angeles) 95

Focusing and Neutralization of Intense Beams
S.S. Yu, A. Anders, F.M. Bieniosek, S. Eylon, E. Henestroza, P.K. Roy, D. Shuman, W. Waldron (LBNL), W.M. Sharp (LLNL), D.V. Rose, D.R. Welch (Mission Research Corporation), P. Efthimion, E. Gilson (Plasma Physics Laboratory, Princeton University) 98

Theory and Observations of Microbunching Instability in Electron Machines
G.V. Stupakov (SLAC) 102

Beam Dynamics in the Spallation Neutron Source Linac
D. Jeon (ORNL) 107

Storage of Crystalline Ion Beams
U. Schramm, M. Bussmann, D. Habs, T. Schaetz (Sektion Physik der LMU MËnchen) 112

Computational Studies of Collective Beam Dynamics in High Intensity Rings
J. Holmes, S. Cousineau, V. Danilov, S. Henderson, A. Shishlo (ORNL), A. Fedotov (BNL) 117

Effect of Stimulated and Thermal Desorption in DARHT-2
T. Hughes (Mission Research Corporation), H. Davis (LANL) 120

Beam-Beam Interaction, Electron Cloud, and Intrabeam Scattering for Proton Super-Bunches
F. Zimmermann, F. Ruggiero (CERN), Y. Papaphilippou (European Synchrotron Radiation Facility), G. Rumolo (Gesellschaft fËr Schwerionenforschung mbH) 123

A New Analysis of Intrabeam Scattering
B. Nash, K. Bane, A. Chao, J. Wu (SLAC) 126

Nonlinear Resonance Benchmarking Experiment at the CERN Proton Synchrotron
I. Hofmann, G. Franchetti (Gesellschaft fËr Schwerionenforschung mbH), M. Giovannozzi, E. M_tral, M. Martini (CERN) 129

Stray-Electron Accumulation and Effects in HIF Accelerators
R. Cohen, A. Friedman, S.M. Lund, A.W. Molvik (LLNL), M. Furman, J.-L. Vay (LBNL), P. Stoltz (Tech-X Corporation) 132

Observation of Strong-Strong and Other Beam-Beam Effects in RHIC
W. Fischer, M. Blaskiewicz, J.M. Brennan, P. Cameron, R. Connolly, C. Montag, S. Peggs, V. Ptitsyn, S. Tepikian, D. Trbojevic, J. van Zeijts (BNL) 135

Progress Report on the Small Isochronous Ring Project at NSCL
E. Pozdeyev, R. Fontus, D. Lawton, F. Marti, J. Rodriguez, D. Sanderson, R. York, A. Zeller, R. Zink (National Superconducting Cyclotron Laboratory) 138

The LHC Superconducting Magnets
L. Rossi (CERN) 141

High Field Accelerator Magnets Beyond LHC
A. Devred (CEA and CERN) 146

Advances in Superconducting Strand for Accelerator Magnet Application
Peter J. Lee, David C. Larbalestier (Applied Superconductivity Center, University of Wisconsin-Madison) 151

Novel Insertion Devices
E.R. Moog (ANL) 156

Radiation Resistant Magnet R&D at the NSCL
A. Zeller, J.C. DeKamp (National Superconducting Cyclotron Laboratory) 161

Performance Summary of the Helical Magnets for RHIC
E. Willen, M. Anerella, J. Escallier, G. Ganetis, A. Ghosh, R. Gupta, M. Harrison, A. Jain, W.W. MacKay, A. Marone, J. Muratore, S. Plate, R. Thomas, P. Wanderer, K.C. Wu (BNL), M. Okamura (RIKEN Accelerator Research Facility) 164

Production and Testing Considerations for CESR-c Wiggler Magnets
D. Rice, S. Chapman, R. Gallagher, Y. He, J. Kandaswamy, V. Medjidzade, A. Mikhailichenko, N.B. Mistry, T. Moore, S. Richichi, K. Smolenski, A. Temnykh, W. Trask (Cornell University) 167

Magnetic Field Measurements of the Nb_3Sn Common Coil Dipole RD3c
L. Chiesa, S. Caspi, D.R. Dietderich, P. Ferracin, S.A. Gourlay, R.R. Hafalia, A.F. Lietzke, A.D. McInturff, G. Sabbi, R.M. Scanlan (LBNL) 170

Controlling Field Quality in Magnet Production
W. Scandale, L. Bottura, A. Devred, V. Remondino, S. Sanfilippo, E. Todesco, C. Vollinger, E. Wildner (CERN) 173

Energy Recovery Linacs Light Sources: an Overview
J.B. Murphy (BNL) 176

FEL Oscillators
G.R. Neil (Thomas Jefferson National Accelerator Facility) 181

A Recirculating Linac-Based Facility for Ultrafast X-Ray Science
J. Corlett, W.A. Barletta, S. De Santis, L. Doolittle, W. Fawley, M.A. Green, P. Heimann, S. Leone, D. Li, S.M. Lidia, A. Ratti, K. Robinson, R. Schoenlein, J. Staples, W. Wan, R.P. Wells, A. Wolski, A. Zholents (LBNL), M. Placidi (CERN), W. Pirkl (Consultant), S.-H. Wang (Indiana University), F. Parmigiani (Sincrotrone Trieste), R.A. Rimmer (Thomas Jefferson National Accelerator Facility) 186

4GLS - a New Type of Fourth Generation Light Source Facility

M.W. Poole, S.L. Bennett, N. Bliss, M.A. Bowler, J.A. Clarke, D.M. Dykes, R.C. Farrow, C. Gerth, D.J. Holder, M.A. MacDonald, B. Muratori, H.L. Owen, F.M. Quinn, E.A. Seddon, S.L. Smith, V.P. Suller, N.R. Thompson (Daresbury Laboratory), I.N. Ross (Rutherford Appleton Laboratory), B.W.J. McNeil (University of Strathclyde) 189

The Cornell ERL Prototype Project

C.K. Sinclair, B. Barstow, I. Bazarov, S. Belomestnykh, D. Bilderback, S. Gruner, G.H. Hoffstaetter, M. Liepe, H. Padamsee, D. Sagan, V. Shemelin, R. Talman, M. Tigner, V. Veshcherevich (Cornell University), G.A. Kraft, L. Merminga (Thomas Jefferson National Accelerator Facility) 192

CEBAF Energy Recovery Experiment

A. Bogacz, K. Beard, J. Bengtsson, C. Butler, Y. Chao, S. Chattopadhyay, H. Dong, D. Douglas, A. Freyberger, A. Guerra, R. Hicks, A. Hofler, C. Hovater, A. Hutton, R. Lauze, L. Merminga, T. Plawski, Y. Roblin, M. Spata, C. Tennant, M. Tiefenback (Thomas Jefferson National Accelerator Facility), A. Bernard (Friedrich-Alexander University), H. Toyokawa (National Institute of Advanced Industrial Science and Technology) 195

Steps Towards X-Ray Sources Based on Linac-Driven Free-Electron Lasers

P. Castro (DESY) 198

Computation of FEL Processes

S. Riche (University of California, Los Angeles) 203

Applications of the Cancellation Effect in the CSR Studies

R. Li (Thomas Jefferson National Accelerator Facility) 208

Pulse Length Control in an X-Ray FEL by Using Wakefields

S. Reiche, C. Pellegrini (University of California, Los Angeles), P. Emma (SLAC) 211

FERMI@ELETTRA: the Single-Pass Free-Electron Laser for the VUV and Soft X-Ray Spectral Range at Elettra

R.J. Bakker, C.J. Bocchetta, P. Craievich, G. D'Auria, M. Danailov, G. De Ninno, S. Di Mitri, B. Diviacco, M. Ferianis, V. Smaluk, L. Tosi, V. Verzilov (Sincrotrone Trieste) 214

Saturation of the NSLS DUV-FEL at BNL

A. Doyuran, L. DiMauro, R. Heese, E. Johnson, S. Krinsky, H. Loos, J.B. Murphy, G. Rakowsky, J. Rose, T. Shaftan, B. Sheehy, Y. Shen, J. Skaritka, X.J. Wang, Z. Wu, L.H. Yu (BNL), W.S. Graves (MIT-Bates) 217

The Canadian Light Source

L. Dallin, I. Blomqvist, D. Lowe, M. Silzer, M. de Jong (Canadian Light Source) 220

Superbend Upgrade at the Advanced Light Source

D. Robin (LBNL) 224

Progress Report on the Construction of SOLEIL

M.-P. Level, P. Brunelle, R. Chaput, A. Da˜l, J.-C. Denard, J.-M. Filhol, C. Herbeaux, A. Loulergue, P. Marchand, O. Marcouill_, J.L. Marlats, A. Nadji, L. Nadolski, R. Nagaoka, M.A. Tordeux (SOLEIL) 229

Progress with the Diamond Light Source Project

R.P. Walker (Diamond Light Source Ltd.) 232

SPEAR 3 Upgrade Project: The Final Year

R. Hettel, R. Akre, S. Allison, P. Bellomo, R. Boyce, L. Cadapan, R. Cassel, B. Choi, W. Corbett, D. Dell'Orco, T. Elioff, I. Evans, R. Fuller, A. Hill, D. Keeley, N. Kurita, J. Langton, G.E. Leyh, C.G. Limborg, D. MacNair, D. Martin, P. McIntosh, E. Medvedko, C.-K. Ng, I. Nzeadibe, J. Olsen, M. Ortega, C. Pappas, S. Park, T. Rabedeau, H. Rarback, A. Ringwall, P. Rodriguez, J. Safranek, H. Schwartz, B. Scott, J. Sebek, S. Smith, T. Straumann, T. Tanabe, A. Terebilo, A. Trautwein, C. Wermelskirchen, M. Widmeyer, R. Yotam, K. Zuo (SLAC) 235

SESAME, 2.5 GeV Synchrotron Light Source for the Middle East Region
D. Einfeld, E. Al-Dmour (UNESCO), R.H. Sarraf (Al-Balqua Applied University Alt-Salt), H. Hashemi, H. Hassanzadegan (DESY), S. Varnasery (Daresbury Laboratory), M. Attal, K. Tavakoli (LURE), H. Tarawneh (MAX-Lab), A. Aladwan, B. Kalantari (Swiss Light Source) 238

NSLS Upgrade Concept
B. Podobedov, J.M. Ablett, L. Berman, R. Biscardi, G.L. Carr, B. Casey, S. Dierker, A. Doyuran, R. Heese, S. Hulbert, E. Johnson, C.C. Kao, S.L. Kramer, H. Loos, J.B. Murphy, R. Pindak, S. Pjerov, J. Rose, T. Shaftan, B. Sheehy, P. Siddons, N. Towne, J.M. Wang, X.J. Wang, L.H. Yu (BNL) 241

Single-Particle Beam Dynamics in BOOMERANG
A. Jackson (Australian Synchrotron Project), H. Nishimura (LBNL) 244

Advanced Photon Source Booster Synchrotron Low-Emittance Lattice Commissioning Results
N.S. Sereno, M. Borland, H. Shang (ANL) 247

Generation of High-Energy Synchrotron Radiation with a 10-T Superconducting Wiggler Installed in the SPring-8 Storage Ring
K. Soutome, S. Dat_, H. Ego, T. Fukui, M. Hara, N. Hosoda, Y. Kawashima, M. Kodera, N. Kumagai, T. Magome, M. Masaki, T. Masuda, S. Matsui, T. Nakamura, T. Noda, Y. Ohashi, T. Ohshima, M. Oishi, H. Saeki, S. Sasaki, J. Schimizu, M. Shoji, S. Takano, M. Takao, T. Takashima, H. Takebe, K. Tamura, H. Tanaka, Y. Taniuchi, K. Tsumaki, H. Yonehara, T. Yorita, C. Zhang (SPring-8), A. Batrakov, G. Karpov, G. Kulipanov, M. Kuzin, N. Mezentsev, V. Shkaruba, A. Skrinsky (BINP) 250

In-Vacuum Undulators at ESRF
J. Chavanne, C. Penel, B. Plan, F. Revol (European Synchrotron Radiation Facility) 253

Possible Long-Term Improvements to the Advanced Photon Source
L. Emery, M. Borland (ANL) 256

Simulation Tools for High Intensity Rings
S. Cousineau (ORNL) 259

Multipacting Simulations for Superconducting Cavities and RF Coupler Waveguides
R.L. Geng (Cornell University) 264

CASCADE - An Advanced Computational Tool for Waveguide Component and Window Design
L. Ives, J. Neilson, W. Vogler (Calabazas Creek Research, Inc.) 269

Towards the UAL Open Source Project
N. Malitsky, M. Blaskiewicz, R. Calaga, R. Fliller III, A.U. Luccio, T. Satogata, R. Talman, J. Wei (BNL) 272

Simulation Using Initial 4D Beam Particle Distributions Synthesized from Experimental Data
A. Friedman, D.P. Grote (LLNL), F.M. Bieniosek, C.M. Celata, L.R. Prost, P.A. Seidl (LBNL) 275

Remote Operations in a Global Accelerator Network
S. Peggs, T. Satogata (BNL), D. Rice (Cornell University), D. Agarwal (LBNL) 278

Integration of Orbit Control with Real-Time Feedback
F. Lenkszus, M. Borland, L. Emery, H. Shang, O. Singh, R. Soliday (ANL) 283

Control Systems on Low Cost Computers
E.L. Williams Jr., Greg S. Lawson (ORNL) 288

Integrating Control Systems to Beam Dynamics Applications with CORBA
M. BÅge, J. Chrin (Paul Scherrer Institut) 291

Measuring and Matching Transport Optics at Jefferson Lab
Y. Chao (Thomas Jefferson National Accelerator Facility) 294

Formation and Dissipation of the Electron Cloud
M. Furman (LBNL) 297

Electron Cloud Effects in Present and Future High Intensity Hadron Machines
M. Baskiewicz (BNL) 302

Electron Cloud Studies and Analyses at SPS for LHC-Type Beams
J.M. Jimenez, G. Arduini, V. Baglin, P. Collier, G. Ferioli, H. Henrist, N. Hilleret, B. Jenninger, L. Jensen, J.M. Laurent, A. Rossi, K. Weiss, F. Zimmermann (CERN) 307

Initial Experimental Studies of Electron Accumulation in a Heavy-Ion Beam
A.W. Molvik, R. Cohen, A. Friedman, S.M. Lund (LLNL), D. Baca, F.M. Bieniosek, M. Furman, E.P. Lee, L.R. Prost, P.A. Seidl, J.-L. Vay (LBNL), A. Sakumi (RIRF and CERN) 312

Simulation Study of Electron Cloud Multipacting in Straight Sections of PEP-II
A. Novokhatski, J. Seeman (SLAC) 315

Survey of Digital Feedback Systems in High Current Storage Rings
D. Teytelman (SLAC) 318

Bunch-by-Bunch Digital Dampers for the Fermilab Main Injector and Recycler
G.W. Foster, S. Hansen, D. Nicklaus, W. Schappert, A. Semenov, D. Wildman (FNAL), W. Ashmanskas (University of Chicago and ANL) 323

Calculations and Observations of the Longitudinal Instability Caused by the Ferrite Inductors at the Los Alamos Proton Storage Ring (PSR)
C. Beltran (Indiana University), A. Browman, R.J. Macek (LANL) 326

Microbunching and Beam Break-up in DUV FEL Accelerator
T. Shaftan, L. Carr, H. Loos, B. Sheehy (BNL), W.S. Graves (MIT Plasma Science and Fusion Center), Z. Huang, C.G. Limborg (SLAC) 329

Tools to Predict Beam Breakup in Recirculating Linacs
K. Beard, L. Merminga, B. Yunn (Thomas Jefferson National Accelerator Facility) 332

Future Plans for e^+e^- Factories
C. Biscari (INFN) 335

Interaction Region Upgrades of e^+e^- B-Factories
M. Sullivan (SLAC) 340

Recent Developments in Designs for e^+e^- Colliders
K. Ohmi (KEK) 345

Buildup of Electron Cloud with Different Bunch Pattern in the Presence of Solenoid Field
Y. Cai, M. Pivi (SLAC), M. Furman (LBNL) 350

Study of Beam-Beam Interactions with/without Crossing Angle
K. Ohmi, K. Oide, M. Tawada (KEK) 353

High Intensity Issues for Super B-Factories
K. Akai (KEK) 356

R&D Toward Neutrino Factories and Muon Colliders
M. Zisman (LBNL) 361

100 Bunch DAÏNE Operation
A. Drago, D. Alesini, G. Benedetti, M. Biagini, C. Biscari, R. Boni, M. Boscolo, A. Clozza, G. Delle Monache, G. Di Pirro, A. Gallo, A. Ghigo, S. Guiducci, F. Marcellini, G. Mazzitelli, C. Milardi, L. Pellegrino, M.A. Preger, P. Raimondi, R. Ricci, C. Sanelli, M. Serio, F. Sgamma, A. Stecchi, A. Stella, C. Vaccarezza, M. Vescovi, M. Zobov (INFN) 366

Study of Beam-Beam Effects in HERA with Self-Consistent Beam-Beam Simulation
J. Shi, L. Jin (University of Kansas), G.H. Hoffstaetter (Cornell University) 369

Electron-Ion Collisions at RHIC Using a High Intensity Self-Polarizing Electron Ring
V. Ptitsyn, J. Kewisch, B. Parker, S. Peggs, D. Trbojevic (BNL), D.E. Berkaev, I.A. Koop, A.V. Otboev, Yu.M. Shatunov (BINP), D.P. Barber (DESY), C. Tschalaer, F. Wang, J.B. van der Laan (MIT-Bates) 372

Investigation of the Flat-Beam Model of the Beam-Beam Interaction
B.S. Schmekel, G.H. Hoffstaetter, J.T. Rogers (Cornell University) 375

Frequency Map Analysis and Particle Accelerators
J. Laskar (BDL) 378

Resonances and Beam Loss in High Intensity Rings
A. Fedotov (BNL) 383

Adiabatic Beam Trapping in Stable Islands of Transverse Phase Space: Measurement Results at CERN Proton Synchrotron
M. Giovannozzi, R. Cappi, E. M_tral, G. M_tral, M. Martini, R. Steerenberg (CERN), A.-S. MËller (Forschungszentrum Karlsruhe) 388

Nonlinear Dynamics in the Duke Storage Ring with FEL Wigglers
Y.K. Wu, J. Li, V. Litvinenko, S.F. Mikhailov (Duke University) 391

Stochastic Cooling Studies in RHIC
M. Blaskiewicz, J.M. Brennan, P. Cameron, J. Wei (BNL) 394

Accelerator Physics Challenges of the FS-Slicing Upgrade at the ALS
C. Steier, E. Forest, L. Nadolski, H. Nishimura, D. Robin, W. Wan, Y. Wu, A. Zholents (LBNL) 397

Heavy-Ion Beam Dynamics in the Rare Isotope Accelerator Facility
P.N. Ostroumov (ANL) 400

Spin Dynamics in AGS and RHIC
W.W. MacKay, L. Ahrens, M. Bai, K.A. Brown, E.D. Courant, J. Glenn, H. Huang, A.U. Luccio, V. Ptitsyn, T. Roser, T. Satogata, S. Tepikian, N. Tsoupas, A. Zelenski (BNL) 405

Beam Dynamics in a Storage Ring for Neutral (Polar) Molecules
G.R. Lambertson (LBNL) 410

Muon Acceleration in FFAG Rings
E. Keil (FNAL), A.M. Sessler (LBNL) 414

Transverse Impedance Distribution Measurements Using Response Matrix Fit Method at APS
V. Sajaev (ANL) 417

Femto-seconds Electron Beam Diffraction Using Photocathode RF Gun
X.J. Wang, Z. Wu (BNL), H. Ihee (University of Chicago) 420

Commissioning of the SPPS Linac Bunch Compressor
P. Krejcik, F.-J. Decker, P. Emma, K. Hacker, L. Hendrickson, C.L. O'Connell, H. Schlarb, H. Smith, M. Stanek (SLAC) 423

Beam Transport Experiments over Half-Turn at the University of Maryland Electron Ring (UMER)
S. Bernal, B. Beaudoin, Y. Cui, D. Feldman, R. Feldman, M. Glanzer, T. Godlove, I. Haber, J. Harris, M. Holloway, Y. Huo, R.A. Kishek, D. Lamb, W.-T. Lee, H. Li, P.G. O'Shea, B. Quinn, M. Reiser, A. Valfells, M. Walter, M. Wilson, R. Yun, Y. Zou (University of Maryland) 426

Neutrino Beam Facilities and Projects
W.T. Weng, M. Diwan (BNL) 429

Storage Rings for Fast Cooling of Antiproton and Radioactive Ion Beams
B. Franzke, K. Beckert, P. Beller, A. Dolinskii, P. HËlsmann, F. Nolden, C. Peschke, M. Steck (Gesellschaft fËr Schwerionenforschung mbH) 434

High Power Targets for ISOL Radioactive Ion Beam Facility
P. Bricault, M. Dombsky, P. Schmor (TRIUMF), A. Dowling (University of Victoria) 439

Transmission of Muons in an Alternating Gradient Funneling System
F. Meot, F. Lemuet (CE Saclay), B. Autin, A. Verdier (CERN) 444

RF Superconductivity: Enabling Technology for the Future
H. Edwards (FNAL) 447

MURA Days
K.R. Symon (University of Wisconsin) 452

SNS Cryomodule Performance
J. Preble, I. Campisi, E. Daly, G.K. Davis, J. Delayen, M. Drury, C. Grenoble, J. Hogan, L. King, P. Kneisel, J. Mammosser, T. Powers, M. Stirbet, H. Wang, T. Whitlatch, M. Wiseman (Thomas Jefferson National Accelerator Facility) 457

Development of Electropolishing Technology for Superconducting Cavities
K. Saito (KEK) 462

Cold- and Beam Test of the First Prototypes of the Superstructure for the TESLA Collider
J. Sekutowicz, C. Albrecht, V. Ayvazyan, T. BËttner, R. Bandelmann, P. Castro, S. Choroba, J. Eschke, B. Faatz, A. GÅssel, K. Honkavaara, B. Horst, J. Iversen, K. Jensch, H. Kaiser, R. Kammering, D. Kostin, G. Kreps, R. Lange, J. Lorkiewicz, W.-D. MÅller, A. Matheisen, H.-B. Peters, D. Proch, K. Rehlich, D. Reschke, H. Schlarb, S. Schreiber, S. Simrock, W. Singer, X. Singer, K. Twarowski, G. Weichert, M. Wendt, G. Wojtkiewicz, K. Zapfe (DESY), M. Liepe (Cornell University), M. HËening (FNAL), M. Ferrario, C. Pagani (INFN), E. Plawski (Institute for Nuclear Studies, Poland), N. Baboi (SLAC), H. Chen, C. Tang, H. Wenhui, S. Zheng (Tsinghua University, Beijing) 467

First Demonstration of Microphonic Control of a Superconducting Cavity with a Fast Piezoelectric Tuner
S. Simrock, G. Petrosyan (DESY), S. Andreoli, A. Facco, R. Paparella, V. Zviagintsev (INFN) 470

RF Power Generation in LHC
H. Frischholz, O. Brunner, D. Valuch (CERN) 473

Operation of the RHIC RF Systems
J.M. Brennan, M. Blaskiewicz, J. DeLong, W. Fischer, T. Hayes, K.S. Smith, A. Zaltsman (BNL) 476

Status of the GLC X-Band Power Source R&D
Y.H. Chin (KEK) 479

High Power Tests of a Multimode X-Band RF Distribution System
S.G. Tantawi, C.D. Nantista (SLAC) 482

Progress on the C-Band Accelerator for the SPring-8 Compact SASE Source
T. Shintake, Y.H. Baba, T. Bizen, Z. Chao, H. Ego, T. Hara, T. Inagaki, T. Ishikawa, Y. Kawashima, H. Kitamura, T. Kudo, X. Marechal, S. Matsui, K. Onoe, K. Saino, T. Seike, K. Sezaki, S. Takahashi, T. Takashima, K. Takeshita, K. Tamasaku, T. Tanaka, K. Togawa (SPring-8), H. Matsumoto, Y. Takasu, S. Takeda, M. Yoshida (KEK) 487

High Power Testing of X-Band Dielectric-Loaded Accelerating Structures
J.G. Power, W. Gai, C. Jing, R. Konecny, W. Liu (ANL), A.K. Kinkead (LET Corporation), S.H. Gold (Naval Research Laboratory) 492

A Demonstration of High-Gradient Acceleration
W. Wuensch, C. Achard, H. Braun, S. DÅbert, I. Syratchev, M. Taborelli, I. Wilson (CERN) 495

The Spallation Neutron Source Diagnostics: Initial Integration and Commissioning Progress Report
S. Assadi (ORNL) 498

Laser-Based Profile Monitor for Electron Beams
M.C. Ross (SLAC) 503

Electron Cloud Diagnostics in Use at the Los Alamos PSR
R.J. Macek, M. Borden, A. Browman, D. Fitzgerald, T.S. Wang, T. Zaugg (LANL), K. Harkay, R.A. Rosenberg (ANL) 508

Longitudinal Space-Charge Effects in a Retarding Field Energy Analyzer
Y. Zou, Y. Cui, I. Haber, P.G. O'Shea, M. Reiser (University of Maryland) 511

Longitudinal Emittance Measurements in the Fermilab Recycler Ring
C.M. Bhat, J.P. Marriner (FNAL) 514

Chirped-Laser Based Electron Bunch Length Monitor
G. Berden, G. Knippels, D. Oepts, A.F.G. van der Meer (FELIX, FOM-Rijnhuizen), J.L. Shen (Capital Normal University), I. Wilke (Rensselaer Polytechnic Institute), W.A. Gillespie, S.P. Jamison, A.M. MacLeod, X. Yan (University of Abertay Dundee) 519

RHIC Third Generation PLL Tune System
P. Cameron, J. Cupolo, W. Dawson, C. Degen, A. DellaPenna, M. Kesselman, A. Marusic, J. Mead, C. Schultheiss, R. Sikora, K. Vetter, J. van Zeijts (BNL) 524

Self-Consistent, Unbiased Exclusion Methods of Emittance Analysis
M.P. Stockli, R.F. Welton (ORNL), R. Keller (LBNL) 527

Electron-Beam Size Measurement with a Beam Profile Monitor Using Fresnel Zone Plates
N. Nakamura, K. Iida, H.R. Sakai, K. Shinoe, H. Takaki (Institute for Solid State Physics, University of Tokyo), H. Hayano, Y. Kamiya, M. Nomura (KEK), T. Koseki (RIKEN Accelerator Research Facility), N. Aoki, K. Nakayama (Toshiba Corporation), Y. Amemiya (University of Tokyo) 530

Development of a New Beam-Energy-Spread Monitor Using Multi-Stripline Electrodes
T. Suwada, K. Furukawa, M. Satoh (KEK) 533

The High Current Transport Experiment for Heavy Ion Inertial Fusion
P.A. Seidl, D. Baca, F.M. Bieniosek, C.M. Celata, A. Faltens, L.R. Prost, G. Sabbi, W. Waldron (LBNL), R. Cohen, A. Friedman, S.M. Lund, A.W. Molvik (LLNL), I. Haber (University of Maryland) 536

Emittance Measurements with a Pulsed Power Photo-Injector
J. Smedley, T. Srinivasan-Rao, T. Tsang (BNL), K. Batchelor, J.P. Farrell (Brookhaven Technology Group) 541

A 50 kV Solid State Multipulse Kicker Modulator
P. Walstrom (LANL), E.G. Cook (LLNL) 544

Solid-State Pulsed Power Systems for the Next Linear Collider
M.P.J. Gaudreau, J.A. Casey, T. Hawkey, M.A. Kempkes, J.M. Mulvaney, I.S. Roth (Diversified Technologies, Inc.) 547

Design, Development, and Construction of SNS Extraction Fast Kicker System
W. Zhang, R.F. Lambiase, Y.-Y. Lee, R. Lockey, J. Mi, T. Nehring, C. Pai, J. Sandberg, N. Tsoupas, J. Tuozzolo, D. Warburton, J. Wei (BNL), R. Cutler, K. Rust (ORNL) 550

Design, Status, and First Operations of the Spallation Neutron Source Polyphase Resonant Converter Modulator System
W.A. Reass, S.E. Apgar, D. Baca, D.L. Borovina, J. Bradley III, J.D. Doss, J.M. Gonzales, R.F. Gribble, T. Hardek, M.T. Lynch, D.E. Rees, P.J. Tallerico, P.G. Trujillo (LANL), D.E. Anderson, D.A. Heidenreich, J.D. Hicks, V.N. Leontiev (ORNL) 553

First Beam at DARHT-II

C. Ekdahl, E.O. Abeyta, L. Caudill, K.C.D. Chan, D. Dalmas, S. Eversole, R. Gallegos, J. Harrison, M. Holzscheiter, E. Jacquez, J. Johnson, B.T. McCuistian, N. Montoya, K. Nielsen, D. Oro, L. Rodriguez, P. Rodriguez, M. Sanchez, M. Schauer, D. Simmons, H.V. Smith, J. Studebaker, G. Sullivan, C. Swinney, R. Temple (LANL), H. Bender, W. Broste, C. Carlson, G. Durtschi, D. Frayer, D. Johnson, K. Jones, A. Meidinger, K. Moy, R. Sturgess, C.Y. Tom (Bechtel Nevada), S. Eylon, W. Fawley, E. Henestroza, S.S. Yu (LBNL), Y.-J. Chen, T. Houck (LLNL), T. Hughes, C. Mostrom (Mission Research Corporation) 558

Electron Beam/Converter Target Interactions in Radiographic Accelerators

J. McCarrick, G. Caporaso, F. Chambers, Y.-J. Chen, S. Falabella, F. Goldin, G. Guethlein, D. Ho, R. Richardson, J. Weir (LLNL) 563

R&D Works on 1MHz Power Modulator for Induction Synchrotron

K. Koseki (The Graduate University for Advanced Studies), Y. Arakida, S. Igarashi, S. Inagaki, J. Kishiro, E. Nakamura, H. Sato, Y. Shimosaki, M. Shirakata, K. Takayama, K. Torikai, T. Toyama, M. Wake (KEK) 568

Spallation Neutron Source Ring -- Status, Challenges, Issues, and Perspectives

J. Wei, Y.-Y. Lee, D. Raparia, J. Sandberg, J. Tuozzolo, W.T. Weng (BNL) 571

The JAERI-KEK Joint Project for the High-Intensity Proton Accelerator, J-PARC

Y. Yamazaki (Japan Atomic Energy Research Institute) 576

Status of Low and Intermediate Velocity Superconducting Accelerating Structures

K.W. Shepard (ANL) 581

Upgrading CEBAF to 12 GeV

L. Harwood (Thomas Jefferson National Accelerator Facility) 586

The GSI Synchrotron Facility Proposal for Acceleration of High Intensity Ion and Proton Beams

P. Spiller, K. Blasche, O. Boine-Frankenheim, G. Franchetti, B. Franczak, I. Hofmann, P. Huelsmann, K. Kaspar, A. Krȩmer, G. Moritz, E. Mustafin, H. Reich-Sprenger, P. Schuett (Gesellschaft fËr Schwerionenforschung mbH) 589

Observations of Electrons in the Intense Pulse Neutron Source (IPNS) Rapid Cycling Synchrotron (RCS)

J.C. Dooling, F.R. Brumwell, W.S. Czyz, K. Harkay, M.K. Lien, G.E. McMichael (ANL) 592

SPIRAL2 : A High Intensity Deuteron and Ion Linear Accelerator for Exotic Beam Production

A. Mosnier (CEA Dapnia) 595

COSY-SCL, the Superconducting Injector Linac for COSY

R. Toelle, U. Bechstedt, N. Bongers, J. Dietrich, R. Eichhorn, F.M. Esser, O. Felden, R. Gebel, K. Henn, H. Jungwirth, A. Lehrach, R. Maier, U. Pfister, D. Prasuhn, P.v. Rossen, A. Schnase, H. Schneider, Y. Senichev, R. Stassen, H. Stockhorst, E. Zaplatin (Forschungszentrum Juelich), A. Schempp (Institut fur Angewandte Physik) 598

The ISAC-II Upgrade at TRIUMF - Progress and Developments

R.E. Laxdal, G. Clark, G. Dutto, K. Fong, A. Mitra, Z.H. Peng, R. Poirier, W. Rawnsley, T. Ries, I. Sekachev, G. Stanford (TRIUMF) 601

2 MW Upgrade of the Fermilab Main Injector

W. Chou (FNAL) 604

Machine Protection Strategies for High Power Accelerators

C. Sibley (ORNL) 607

Vacuum System for High Power Lepton Rings

Y. Suetsugu (KEK) 612

Thin Diamond Films for SNS H⁻ Injection Stripping

R.W. Shaw, R. Cutler, A.D. Herr (ORNL), Y.-Y. Lee, C.J. Liaw (BNL), C.S. Feigerle (University of Tennessee) 617

Vacuum Pumping Study of Titanium-Zirconium-Vanadium Thin Films
Y. Li, S. Ho (Cornell University) 620

A New Kind of Beam Pipe for Rapid Cycling Proton Synchrotrons
Z. Tang, A. Chen, W. Chou (FNAL) 623

Accelerator Availability and Reliability Issues
S. Suhring (Thomas Jefferson National Accelerator Facility) 625

Low-Conductivity Water Systems for Accelerators
R. Dortwegt (ANL) 630

Accelerator Magnet Plugging by Metal Oxides: A Theoretical Investigation, Remediation and Preliminary Results
W.W. Rust (Thomas Jefferson National Accelerator Facility) 635

Safety Critical Monitoring for Prompt Radiation Hazards
L. Moritz, J. Drozdoff, G. Dutto, F. Mammarella, M. Mouat, R. Ruegg (TRIUMF) 638

Comprehensive Electro-Magnetic, Thermal, and Structural Finite Element Analysis of the Lithium Collection Lens at the FNAL Antiproton Source
P. Hurh, J. Morgan, S. Tariq (FNAL) 641

Inertial Sensor Development for Active Vibration Stabilization
J. Frisch, E. Doyle, L. Eriksson, L. Hendrickson, T. Himel, T. Markiewicz, R. Partridge (SLAC) 644

Report from the International Linear Collider Technical Review Committee
G.A. Loew (SLAC) 647

Damping Ring Designs and Issues
A. Wolski (LBNL), W. Decking (DESY) 652

Damping Ring to Interaction Point Beam Transport Issues
N. Walker (DESY), D. Schulte (CERN), A. Wolski (LBNL), A. Seryi, P. Tenenbaum, M. Woodley (SLAC) 657

Effects of Dynamic Misalignments and Feedback Performance on Luminosity Stability in Linear Colliders
A. Seryi, L. Hendrickson, T.O. Raubenheimer, P. Tenenbaum, M. Woodley (SLAC), D. Schulte (CERN) 662

Colliding Nanobeams in CLIC with Magnets Stabilized to the Sub-nm Level
S. Redaelli, R. Assmann, W. Coosemans, G. Guignard, D. Schulte, I. Wilson, F. Zimmermann (CERN) 665

Normal-Conducting RF Structure Test Facilities and Results
C. Adolphsen (SLAC) 668

Superconducting RF Structures - Test Facilities and Results
H. Weise (DESY) 673

Reliability Issues for Linear Colliders
N. Phinney, C. Adolphsen, M.C. Ross (SLAC) 678

The JLC/NLC Baseline Design
P. Tenenbaum (SLAC) 681

Bunch Frequency Multiplication in the CLIC Test Facility CTF3
F. Tecker, R. Corsini, L. Rinolfi (CERN), C. Biscari, A. Ghigo, M.A. Preger (INFN), P. Royer (Universit_ de Lausanne, Switzerland), A. Ferrari (Uppsala University, Sweden) 684

Feedback on Nanosecond Timescales (FONT): Results from First Beam Tests at the NLCTA at SLAC
P.N. Burrows (Queen Mary College, University of London) 687

Treating Patients with the NPTC Accelerator Based Proton Treatment Facility
J. Flanz, T. Delaney, H. Kooy, S. Rosenthal, U. Titt (Massachusetts General Hospital) 690

HICAT- The German Hospital-Based Light Ion Cancer Therapy Project
H. Eickhoff, R. BЄr, A. Dolinskii, Th. Haberer, B. Schlitt, P. Spiller, U. Weinrich (Gesellschaft fËr Schwerionenforschung mbH) 694

Status of the Midwest Proton Radiotherapy Institute
D.L. Friesel, V. Anferov, J. Collins, W.P. Jones, J. Katuin, S.B. Klein, A.N. Schreuder (Indiana University) 699

Design and Operation of a Proton Microscope for Radiography at 800 MeV
T. Mottershead, D. Barlow, B. Blind, G. Hogan, A. Jason, F. Merrill, K. Morley, C. Morris, A. Saunders, R. Valdiviez (LANL) 702

Antimatter Driven Sail for Deep Space Missions
G. Jackson, S. Howe (Hbar Technologies, LLC) 705

Facilities for Industrial Customers at the Daresbury Synchrotron Radiation Source (SRS)
E. Towns-Andrews, E.J. MacLean (Daresbury Laboratory) 708

Gamma-Ray Computerized Tomography Using 10 MeV Laser-Compton Photon Beam
H. Toyokawa, T. Mikado, H. Ogawa, N. Sei, K. Yamada, M. Yasumoto (National Institute of Advanced Industrial Science and Technology), H. Ohgaki (Kyoto University), N. Aoki, N. Kobayashi (Toshiba Corporation) 713

Simulation of Accelerated Electron Spectra in Laser Wakefield Accelerators
R.F. Hubbard, D.F. Gordon, T. Jones, J.R. Pe¿ano, P. Sprangle, A. Ting (Naval Research Laboratory), B. Hafizi, A. Zigler (Icarus Research, Inc.), D. Kaganovich (LET Corporation) 716

All-Optical Beamlet Train Generation
J.R. Cary, R. Giacone, C. Nieter (University of Colorado at Boulder), E. Esarey, G. Fubiani, W.P. Leemans (LBNL), D.L. Bruhwiler (Tech-X Corporation) 719

Scaling Laws of a Dielectric Optical Accelerator
S. Banna, A. Mizrahi, L. SchЄchter (Technion - Israel Institute of Technlology), E. Colby, M. Javanmard, R.J. Noble, R.H. Siemann (SLAC), R. Byer, B. Cowan, T. Plettner (Stanford University) 722

Selected Advanced Acceleration Concepts
J.L. Hirshfield (Omega-P, Inc. and Yale University) 725

Dielectric Bragg Accelerator
R.H. Siemann (SLAC), R. Byer (Stanford University), A. Mizrahi, L. SchЄchter (Technion - Israel Institute of Technlology) 728

Positron Beam Propagation in a Meter Long Plasma Channel
T.C. Katsouleas, P. Muggli (University of Southern California), F.-J. Decker, M.J. Hogan, R. Iverson, C.L. O'Connell, P. Raimondi, R.H. Siemann, D. Walz (SLAC), B.E. Blue, C. Clayton, C. Joshi, K.A. Marsh, W.B. Mori (University of California, Los Angeles) 731

Simulation of Ionization Effects for High-Density Positron Drivers in Future Plasma Wakefield Experiments
D.L. Bruhwiler, J.R. Cary, D.A. Dimitrov (Tech-X Corporation), E. Esarey, W.P. Leemans (LBNL) 734

Technology Options for Linear Colliders
G. Dugan (Cornell University) 737

Volume 2

RHIC Power Supplies: Lessons Learned From the 1999 - 2001 RHIC Runs
D. Bruno, W. Eng, G. Ganetis, R.F. Lambiase, W. Louie, J. Sandberg, C. Schultheiss (BNL) 743

Booster Main Magnet Power Supply Improvements for NASA Space Radiation Laboratory at BNL
I. Marneris, K.A. Brown, J. Glenn, A. Mc Nerney, J. Morris, J. Sandberg, S. Savatteri (BNL) 746

Light Triggered Thyristor Crowbar for Klystron Protection Application
W. Merz, J.-P. Jensen (DESY) 749

Improving Power Supply Performance for Duke Storage Ring
Y.K. Wu, S. Hartman, V. Litvinenko, S.F. Mikhailov, P. Morcombe, O. Oakeley, I. Pinayev, V.G. Popov, P. Wallace, P. Wang (Duke University) 752

Compensation of Load Fluctuation of Power Supply System for Large Accelerator using SMES
H. Sato, S. Igarashi, M. Muto, T. Shintomi (KEK), K. Furukawa, T. Ise (Osaka University) 755

Test Results on Capacitor Commutation Charging Type of Resonant Power Supply for Synchrotron Ring Magnets
S. Dong, C. Yao, Y. Zhang (National Synchrotron Radiation Lab) 758

High Resolution Analog / Digital Power Supply Controller
E. Medvedko, R. Hettel, G.E. Leyh, J. Olsen, S. Smith, T. Straumann, C. Wermelskirchen (SLAC) 761

Modification and Implementation of the Correction Bipolar Power Supply of the Storage Ring
L. Chen-Yao, Y.-C. Chien, J. Chiou, C.H. Kuo (Synchrotron Radiation Research Center) 764

Increasing Output Current Stability of Power Supply with Component Replacement
Kuo-Bin Liu, Y.-C. Chien, C.-S. Fann (Synchrotron Radiation Research Center) 767

1400A,+/-900V Peak Pulse Switch Mode Power Supplies for SNS Injection Kickers
S. Dewan (Digital Predictive Systems Inc.), W. Eng, R.F. Lambiase, J. Sandberg (BNL), R. Holmes (IE Power Inc.), K. Rust (ORNL), J. Zeng (University of Toronto) 770

FLUKA Simulations of the Loss of the Stored Electron Beam at BESSY
K. Ott (BESSY) 773

The Shielding Design of the Metrology Light Source (MLS)
K. Ott (BESSY) 776

Further Experience with the SLC Permanent Magnetic (PM) Multipoles
J. Spencer, S. Mao, C.M. Spencer (SLAC) 779

Radiation Measurement around a 10-T Superconducting Wiggler at SPring-8
M. Shoji, N. Kumagai, T. Magome, T. Ohshima, M. Oishi, S. Sasaki, K. Soutome, J. Tada, T. Takagi, M. Takao, K. Tsumaki, H. Yonehara, T. Yorita (SPring-8), Y. Asano (Japan Atomic Energy Research Institute) 782

Improvement of RHIC Warm Beam Vacuum for High Intensity Operation
H. Hseuh, P. He, R.C. Lee, M. Mapes, L. Smart, D. Weiss, S.Y. Zhang (BNL) 785

Outgassing and Surface Properties of TiN Coated SNS Ring Vacuum Chambers
H. Hseuh, P. He, M. Mapes, R. Todd (BNL), N. Hilleret (CERN) 788

Pressure Distribution Simulation for SNS Ring Vacuum Systems
H. Hseuh, P. He, R. Todd (BNL) 791

Electron Detectors for Vacuum Pressure Rise Diagnostics at RHIC
U. Iriso-Ariz, A. Drees, W. Fischer, D. Gassner, O. Gould, J. Gullotta, R.C. Lee, V. Ponnaiyan, D. Trbojevic, K. Zeno, S.Y. Zhang (BNL) 794

Electron Cloud and Pressure Rise Simulations for RHIC
U. Iriso-Ariz, M. Blaskiewicz, A. Drees, W. Fischer, S. Peggs, D. Trbojevic (BNL) 797

Development of Movable Mask with Reduced-HOM Design for KEKB
K. Shibata, T. Kageyama, Y. Suetsugu (KEK) 800

Development of Winged HOM Damper for Movable Mask in KEKB
Y. Suetsugu, T. Kageyama, K. Shibata, Y. Takeuchi (KEK) 803

Conceptual Design of Vacuum System for Super KEKB
Y. Suetsugu, K. Kanazawa, K. Shibata (KEK) 806

Vacuum Systems Renewal for the PF-AR Upgrade
Y. Tanimoto, Y. Hori, T. Nogami, T. Uchiyama (KEK) 809

Re-Circulating Linac Vacuum System
R.P. Wells, J. Corlett, A. Zholents (LBNL) 812

Improvment of the Storage Ring UHV System of NSRL
Y. Wang, L. Fan, C.Y. Guan, D.M. Jing, J.P. Wang, W. Wei, G. Wu, F.Y. Zhao (National Synchrotron Radiation Lab) 815

Adsorption Study of Al_2O_3 Coating on the Pulse Septum Magnet Surface
H. Zhang, Y.J. Pei (National Synchrotron Radiation Lab) 818

Vacuum Commissioning for the SWLS Absorber Inside a Kicker-Chamber at TLS Storage Ring
G.Y. Hsiung, J.R. Chen, S.N. Hsu, C.S. Hwang, K.C. Kuan (Synchrotron Radiation Research Center) 821

Insertion Device Vacuum Chamber for the Linac Coherent Light Source
Soon-Hong Lee, P. Den Hartog, E. Trakhtenberg (ANL) 824

Advanced Photon Source Booster Synchrotron Subharmonic RF Capture Design
N.S. Sereno (ANL) 827

New Insertion Device Vacuum Chambers at the Advanced Photon Source
E. Trakhtenberg, B. Brajuskovic, P. Den Hartog, G. Wiemerslage (ANL) 830

Dual Canted Undulators at the Advanced Photon Source
P. Den Hartog, G. Decker, L. Emery (ANL) 833

Layout of a Femtosecond X-Ray Source at BESSY II
S. Khan, H.-J. B€cker, J. Bahrdt, H.A. DËrr, V. DËrr, W. Eberhardt, A. Gaupp, K. Holldack, E. Jaeschke, D. Kr€mer, H.-C. Mertins, W.B Peatman, T. Quast, G. Reichardt, M. Scheer, F. Senf, G. WËstefeld (BESSY), I. Hertel, F. Noack, W. Sandner, I. Will, N. Zhavoronkov (Max-Born-Institute) 836

Coherent Synchrotron Radiation Experiments at BESSY II
K. Holldack, P. Kuske, G. WËstefeld (BESSY), H.-W. Hubers (Deutsches Zentrum fur Luft-und Raumfahrt (DLR)) 839

Lattice Options for a 5 GeV Light Source at Cornell
I. Bazarov, G.H. Hoffstaetter (Cornell University) 842

Lifetime Reduction due to Insertion Devices at BESSYII
J. Feikes (Cornell University), G. WËstefeld (BESSY) 845

A Lattice for a 5GeV ERL in the CESR Tunnel
G.H. Hoffstaetter, I. Bazarov, D. Sagan, R. Talman (Cornell University) 848

Chromaticity Measurements in the ESRF Booster
Y. Papaphilippou, G. Chazot, J.M. Koch, E. Plouviez, J.L. Revol, A. Ropert (European Synchrotron Radiation Facility) 851

Operation and Recent Developments of the ESRF

J.L. Revol, P. Berkvens, J.C. Biasci, J. Chavanne, P. Duru, P. Elleaume, L. Farvacque, T. Guenzel, L. Hardy, J. Jacob, R. Kersevan, G. Naylor, Y. Papaphilippou, E. Plouviez, A. Ropert, K. Scheidt (European Synchrotron Radiation Facility) 854

The Lattice Design of the Super SOR Light Source

K. Harada, Y. Kobayashi (KEK), N. Nakamura, H.R. Sakai, H. Takaki (Institute for Solid State Physics, University of Tokyo), T. Koseki (RIKEN Accelerator Research Facility) 857

Present Status of Photon Factory Advanced Ring

T. Miyajima, K. Ebihara, E. Ezura, H. Fukuma, K. Haga, K. Harada, Y. Hori, T. Ieiri, S. Isagawa, T. Kasuga, T. Katoh, H. Kawata, M. Kikuchi, M. Kobayashi, Y. Kobayashi, K. Kudo, Y. Minagawa, T. Mitsuhashi, S. Nagahashi, T.T. Nakamura, H. Nakanishi, T. Nogami, T. Obina, Y. Ohsawa, Y. Onishi, M. Ono, T. Ozaki, Y. Sakamoto, S. Sakanaka, M. Sato, M. Satoh, T. Shioya, M. Suetake, R. Sugahara, M. Tadano, T. Takahashi, S. Takasaki, Y. Takeuchi, Y. Tanimoto, M. Tejima, K. Tsuchiya, T. Uchiyama, A. Ueda, K. Umemori, N. Yamamoto, S. Yamamoto, S. Yoshimoto, M. Yoshioka (KEK), T. Fujita (Hiroshima University) 860

A Model for Producing Stable, Broadband Terahertz Coherent Synchrotron Radiation in Storage Rings

J. Byrd, A. Loftsdottir, M.C. Martin, F. Sannibale, M. Venturini (LBNL) 863

Collective Effects Analysis for the Berkeley Femtosource

S. De Santis, J. Corlett, A. Wolski, A. Zholents (LBNL) 866

Noise Reduction Efforts for the Infrared Beamline at the Advanced Light Source

T. Scarvie, N. Andresen, K. Baptiste, J. Byrd, M. Chin, M.C. Martin, W. McKinney, C. Steier (LBNL) 869

Longitudinal Phase Space Control in the Berkeley Femtosecond X-Ray Light Source LUX

A. Zholents (LBNL) 872

Newly Developed Injection Mode of Pohang Light Source

M.G. Kim, J. Choi, J.Y. Huang, E.S. Park (Pohang Accelerator Laboratory) 875

First Operational Results of the 3rd Harmonic Super Conducting Cavities in SLS and ELETTRA

M. Pedrozzi, W. Gloor (Paul Scherrer Institut), P. Bosland, P. Bredy, S. Chel, G. Devanz (CE Saclay), O. Aberle, E. Chiaveri, R. Losito, S. Marque (CERN), A. Anghel (EPFL - CRPP), P. Marchand (SOLEIL), P. Craievich, A. Fabris, C. Pasotti, G. Penco, M. Svandrlik (Sincrotrone Trieste) 878

Beam-Performance Improvement of the SPring-8 Storage Ring

H. Ohkuma, S. Dat_, N. Kumagai, M. Masaki, T. Nakamura, T. Ohshima, K. Soutome, S. Takano, M. Takao, K. Tamura, H. Tanaka (SPring-8) 881

Magnet-Related Failure Experiences at the SPring-8 Storage Ring

K. Tsumaki, N. Kumagai, S. Matsui, M. Ohishi, H. Yonehara (SPring-8), T. Tateishi, Y. Torii (Kobeluko Kaken, Ltd.) 884

Commissioning Low Emittance Beam at Aladdin

K.D. Jacobs, R.A. Bosch, D.E. Eisert, M. Fisher, M.A. Green, R.G. Keil, K.J. Kleman, R.A. Legg, J.P. Stott, W. Trzeciak (Synchrotron Radiation Center, University of Wisconsin) 887

Coupling Correction Study at NSRRC

C.C. Kuo, H.P. Chang, K.T. Hsu, G.H. Luo, H.J. Tsai, D.J. Wang, M.H. Wang (Synchrotron Radiation Research Center), G. Portmann, J. Safranek (SLAC) 890

Studies of Beam Lifetime at ANKA

E. Huttel, I. Birkel, A.-S. MËller, F. Perez, M. Pont (Forschungszentrum Karlsruhe) 893

Refined Tracking Procedure for the SOLEIL Energy Acceptance Calculations

A. Nadji, M. Belgroune, P. Brunelle, L. Nadolski (SOLEIL) 896

Field Error Compensation and Thermal Beam Load in a Superconductive Undulator
R. Rossmanith, S. Chouhan, S. Strohmer (Forschungszentrum Karlsruhe), D. Doelling, A. Geisler, A. Hobl, S. Kubsky (ACCEL Instruments GmbH) 899

The Saga Synchrotron Light Source in 2003
T. Tomimasu, Y. Iwasaki, S. Koda (Saga Synchrotron Light Source), H. Ohgaki (Kyoto University), H. Toyokawa, M. Yasumoto (National Institute of Advanced Industrial Science and Technology), Y. Hashiguchi, T. Kitsuka, Y. Ochiai, Y. Yamatsu (Saga Prefectural Government) 902

Temporal Characteristics of a SASE FEL
Y. Li, Z. Huang, K.-J. Kim, J.W. Lewellen, S.V. Milton, V. Sajaev (ANL) 905

Beam-Based Undulator Field Characterization and Correction at DUV-FEL
H. Loos, T. Shaftan (BNL) 908

Electron Bunch Shape Measurements at the TTF-FEL
S. Schreiber, Ch. Gerth, K. Honkavaara (DESY), P. Piot (FNAL) 911

Start to End Simulations for the SPARX Proposal
M. Ferrario, M. Biagini, M. Boscolo, E. Chiadroni, V. Fusco, S. Guiducci, L. Serafini, B. Spataro, C. Vaccarezza, M. Zobov (INFN), R. Bartolini, G. Dattoli, L. Giannessi, L. Mezi, M. Quattromini, C. Ronsivalle (Ente Nazionale per le Nuove Tecnologie l'Energia e l'Ambiente), P. Emma (SLAC), J.B. Rosenzweig (University of California, Los Angeles) 914

Crystal Undulator as a Novel Compact Source of Radiation
V. Guidi, S. Bellucci, S. Bini, G. Giannini (INFN), V.M. Biryukov, G.I. Britvich, Y. Chesnokov, V.I. Kotov, V.A. Maisheev, V.A. Pikalov (Institute of High Energy Physics, Protvino), Yu.M. Ivanov, A.A. Petrunin, V.V. Skorobogatov (Petersburg Nuclear Physics Instituite), C. Malagu, G. Martinelli, M. Stefancich, D. Vincenzi (University of Ferrara), F. Tombolini (University of Rome) 917

Photoinjector RF Cavity Design for High Power CW FEL
R.L. Wood, S. Kurennoy, D.L. Schrage, L.M. Young (LANL), V. Christina, J.W. Rathke, T.J. Schultheiss (Advanced Energy Systems) 920

Simulation Studies of an XUV/Soft X-Ray Harmonic-Cascade FEL for the Proposed LBNL Recirculating Linac
W. Fawley, W.A. Barletta, J. Corlett, A. Zholents (LBNL) 923

Limitations of Electron Beam Conditioning for Free-Electron Lasers
P. Emma, G.V. Stupakov (SLAC) 926

Throughput and Noise of the Aladdin Infrared Beamline
R.A. Bosch, M.A. Green, R.W.C. Hansen, K.D. Jacobs, R.L. Julian, K.J. Kleman (Synchrotron Radiation Center, University of Wisconsin) 929

Periodic Ion Channel Laser
R.A. Bosch (Synchrotron Radiation Center, University of Wisconsin) 932

Beam-Frame Calculation of Free-Electron Laser Gain
R.A. Bosch (Synchrotron Radiation Center, University of Wisconsin) 935

Sub-Picosecond, High Flux, Thomson X-Ray Sources at Jefferson Lab's High Power FEL
J.R. Boyce, D. Douglas, H. Toyokawa (Thomas Jefferson National Accelerator Facility), W. Brown, F. Hartemann (LLNL) 938

Image Charge Undulator: Theoretical Model and Technical Issues
Y. Zhang, J.R. Boyce, Y. Derbenev, R. Li (Thomas Jefferson National Accelerator Facility) 941

Design and Status of the VISA II Experiment

G. Andonian, R. Agustsson, A. Murokh, C. Pellegrini, S. Reiche, J.B. Rosenzweig, G. Travish (University of California, Los Angeles), M. Babzien, I. Ben-Zvi, V. Yakimenko (BNL), L. Palumbo, C. Vicario (University of Rome) 944

The FEL Program at the PEGASUS Injector

S. Reiche, G. Andonian, P. Frigola, J.B. Rosenzweig, S. Telfer, G. Travish (University of California, Los Angeles) 947

A Numerical Model of Electron Beam Shot Noise

B.W.J. McNeil, G.R.M. Robb (University of Strathclyde), M.W. Poole (Daresbury Laboratory) 950

An Improved 1-D Model for Ultra High Power Radiation Pulse Propagation in the Helical Wiggler Free Electron Laser

B.W.J. McNeil, G.R.M. Robb (University of Strathclyde), M.W. Poole (Daresbury Laboratory) 953

Design Study for the RF Photoinjector for the MIT Bates X-Ray Laser Project

M. Farkhondeh, W.S. Graves, R. Milner, C. Tschalaer, F. Wang, A. Zolfaghari, T. Zwart, J.B. van der Laan (MIT-Bates) 956

X-Ray Laser Seeding for Short Pulses and Narrow Bandwidth

W.S. Graves, M. Farkhondeh, F.X. Kaertner, R. Milner, C. Tschalaer, F. Wang, A. Zolfaghari, T. Zwart, J.B. van der Laan (MIT-Bates), D.E. Moncton (ANL), W. Fawley (LBNL) 959

On the Realistic Gain Estimation of the CSR Microbunching Instability in Bunch Compressors

Y. Kim (DESY), Y. Kim, D. Son (CHEP, Kyungpook National University), H. Kitamura (RIKEN Harima Institute in SPring-8), T. Shintake (SPring-8) 962

Tolerances of the TTF-2 First Bunch Compressor

Y. Kim, K. Floettmann (DESY), Y. Kim, D. Son (CHEP, Kyungpook National University), H. Kitamura (RIKEN Harima Institute in SPring-8), P. Emma (SLAC), T. Shintake (SPring-8) 965

Coherent Harmonic Generation Experiment on Hefei Synchrotron Radiation Source

J.Y. Liu, C.Z. Diao, D.H. He, Q.K. Jia, G. Li, H.L. Xu, P.F. Zhang, S.C. Zhang (University of Science and Technology of China) 968

Numerical Study of Coherent Harmonic Generation in the VUV on the NIJI-IV FEL

H. Ogawa, T. Mikado, N. Sei, K. Yamada, M. Yasumoto (National Institute of Advanced Industrial Science and Technology) 971

Measured Performance of the Free Electron Lasers and Electron Beam in the Compact Storage Ring NIJI-IV

N. Sei, T. Mikado, H. Ogawa, H. Toyokawa, K. Yamada, M. Yasumoto (National Institute of Advanced Industrial Science and Technology) 974

High-Power Electron Beam Injectors for 100 kW Free-Electron Lasers

A. Todd, H. Bluem, V. Christina, M. Cole, J.W. Rathke, T.J. Schultheiss (Advanced Energy Systems), P. Colestock, J.P. Kelley, S. Kurennoy, D. Nguyen, S. Russell, D.L. Schrage, R.L. Wood, L.M. Young (LANL), I. Campisi, E. Daly, D. Douglas, G.R. Neil, J. Preble, R.A. Rimmer, C.H. Rode, J. Sekutowicz, T. Whitlatch, M. Wiseman (Thomas Jefferson National Accelerator Facility) 977

The MIT Bates X-Ray Laser Project

T. Zwart, M. Farkhondeh, W.S. Graves, F.X. Kaertner, R. Milner, D.E. Moncton, C. Tschalaer, F. Wang, A. Zolfaghari, J.B. van der Laan (MIT-Bates) 980

The Mucool Test Area Linac Experimental Facility at Fermilab

D. Errede (University of Illinois), R. Alber, A. Bross, M. Foley, S. Geer, C. Johnstone, N.V. Mokhov, B. Norris, M. Popovic, I.L. Rakhno, K. Vaziri (FNAL), E. Black (Illinois Institute of Technology), M.A.C. Cummings (Northern Illinois University) 983

Creating Microbeams and Nanobeams by Channeling in Micro- and Nano-Structures
V.M. Biryukov, Y. Chesnokov (Institute of High Energy Physics, Protvino), W. Scandale (CERN), S. Bellucci, V. Guidi (INFN) 986

A Neutron Source Facility for Neutron Cross-Section Measurements on Radioactive Targets at RIA
L. Ahle, R. Berio, L. Bernstein, B. Rusnak (LLNL) 989

Determination of Low Level RF Control Requirements for Superconducting Cavities from Microphonics Measurements
J. Delayen, L. Harwood (Thomas Jefferson National Accelerator Facility) 992

An Axial Injection System for the ORIC
G.D. Alton, B.A. Tatum, Y. Zhang (ORNL) 995

Initial Performance of a 6 GHz "Volume" ECR Ion Source
Y. Liu, G.D. Alton, J.M. Cole, F.W. Meyer, G.D. Mills, C.A. Reed, C.L. Williams (ORNL), H. Bilheux (University of Versailles) 998

The Electric Field Distribution in a Spiral Inflector for Cyclotron Injection Applications
Y. Zhang, G.D. Alton (ORNL) 1001

An RFQ Injection System for the HRIBF
Y. Zhang, P.E. Mueller (ORNL) 1004

Microwave Radiation Stimulated by Atom or Ion Beams
V. Grishin (Scobeltsyn Institute of Nuclear Physics of Moscow Lomonosov State University) 1007

Effective Source of Sharp Focused Electromagnetic Radiation of Electrons with Moderate Relativistic Energy
V. Grishin, S. Likhachev (Scobeltsyn Institute of Nuclear Physics of Moscow Lomonosov State University) 1010

Effects of Propagation for High Power CW Electron Beam in Air
S. Korenev (STERIS Corporation), I. Korenev (Northern Illinois University) 1013

The Concept of Beam Lines from Rhodotron for Radiation Technologies
S. Korenev (STERIS Corporation) 1015

Mechanical Analysis of the Prototype Undulator for the Linac Coherent Light Source
B. Brajuskovic, P. Den Hartog, E. Trakhtenberg (ANL) 1017

Development of a Short-Period Superconducting Undulator
S.H. Kim, R.J. Dejus, C. Doose, R.L. Kustom, E.R. Moog, M. Petra, K.M. Thompson (ANL) 1020

A Magnetic Field Model for Wigglers and Undulators
D. Sagan, J. Crittenden, D.L. Rubin (Cornell University), E. Forest (KEK) 1023

Vibrating Wire and Flipping Coil Magnetic Measurement of a CESR-c 7-Pole Wiggler Magnet
A. Temnykh (Cornell University) 1026

Status of the DIAMOND Insertion Devices
J.A. Clarke, N. Bliss, D.G. Clarke, F.E. Hannon, C. Hill, A.A. Muir, D.J. Scott (Daresbury Laboratory), V. Francis (Rutherford Appleton Laboratory) 1029

Design and Evaluation of a Short Period Nb_3Sn Superconducting Undulator Prototype
S. Prestemon, D.R. Dietderich, S.A. Gourlay, P. Heimann, S. Marks, G. Sabbi, R.M. Scanlan, R. Schlueter (LBNL), B. Wahrer, B. Wang (Wang NMR) 1032

Harmonic Contents of and Detailed Study on a High-Gain Harmonic Generation Free Electron Laser
J. Wu (SLAC) 1035

Calculation of the Coherent Synchrotron Radiation Impedance from a Wiggler
J. Wu, T.O. Raubenheimer, G.V. Stupakov (SLAC) 1038

Design of a Revolving Helical Staggered Undulator
C.H. Chang, T.C. Fan, C.S. Hwang, G.H. Luo, Ch. Wang (Synchrotron Radiation Research Center) 1041

Operational Experience of the Insertion Devices and Expectation of the Future Superconducting Wigglers at NSRRC
H.P. Chang, C.H. Chang, J. Chen, K.T. Hsu, C.S. Hwang, C.H. Kou, C.C. Kuo, G.H. Lou (Synchrotron Radiation Research Center) 1044

Magnetic Field Measurement on Superconducting Multipole Wiggler with Narrow Duct
T.C. Fan, C.H. Chang, M.H. Huang, C.S. Hwang, F.Y. Lin (Synchrotron Radiation Research Center) 1047

Commissioning of Two New Insertion Devices at ELETTRA
D. Zangrando, S. Di Mitri, B. Diviacco, C. Knapic, L. Tosi (Sincrotrone Trieste) 1050

CAMD Low Beta Configuration for 7 Tesla Wiggler
M. Fedurin, B. Craft, G. Vignola (Center for Advanced Microstructures and Devices) 1053

Period Length Optimization for the LNLS Undulator
X.R. Resende (LaboratÂrio Nacional de Luz S°ncrotron, Brazil) 1056

Studies on Sextupole Components Generated by Eddy Currents in the Rapid Cycling Medical Synchrotron
J. Cardona, D. Abell, S. Peggs (BNL) 1059

Status of the Integrated RFQ-Drifttube-Combination for the Medicine-Synchrotron in Heidelberg
A. Bechtold, U. Ratzinger, A. Schempp (Institut fur Angewandte Physik), B. Schlitt (Gesellschaft fËr Schwerionenforschung mbH) 1062

Potential Alternate Beam Source for Proton Therapy
W.P. Jones, D.L. Friesel, S.Y. Lee (Indiana University) 1065

Proton Therapy Treatment Room Controls Using a Linux Control System
J. Katuin (Indiana University) 1068

Development of High Field Dipole and High Current Pulse Power Supply for Compact Proton Synchrotron
K. Endo, K. Egawa, Z. Fang (KEK), M. Mizobata, A. Teramoto (Mitsubishi Corporation) 1071

RF Cavities and Power Amplifier for the Compact Proton Synchrotron
Z. Fang, K. Egawa, K. Endo (KEK), I.I. Averboukh (BINP), T. Hirashima (Denki Kogyo Co., Aikou-gun, Japan) 1074

Application of Statistical Process Control (SPC) in the Manufacturing of Medical Accelerators
S.M. Hanna (SIEMENS MEDICAL SOLUTIONS) 1077

Radiation-Acoustic Monitoring of Therapeutic Beam
G.F. Popov, A.I. Kalinichenko, V.T. Lazurik, V.V. Tovstiak (Kharkiv National University) 1080

Closing in on the Final Design of the BESSY-FEL
D. KrÉmer (BESSY) 1083

Analysis of the HOM Damping with Modulated Beam in the First Prototype of Superstructure
P. Castro, A. GÅssel, S. Schreiber, M. Wendt (DESY), G. Devanz (CE Saclay), N. Baboi (SLAC), J. Sekutowicz (Thomas Jefferson National Accelerator Facility) 1086

Operation of the LEP CW Klystrons in Pulsed Mode
D. Valuch (CERN) 1089

Ferrite Evaluation for AHF Proton Synchrotrons
J.T.M. Lyles (LANSCE), F. Bridges, L.J. Rybarcyk (LANL) 1092

The SNS Linac High Power RF System Design, Status, and Results
D.E. Rees, J. Bradley III, K. Cummings, T. Hardek, M.T. Lynch, W. Roybal, P.J. Tallerico (LANL) 1095

JLAB High Efficiency Klystron Baseline Design for 12 GeV Upgrade
H. Wang, J. Delayen, L. Harwood, C. Hovater, R. Nelson (Thomas Jefferson National Accelerator Facility) 1098

Analytical Design of a Waveguide Iris/Stub Tuning Coupler to an Overcoupled Superconducting Cavity
H. Wang (Thomas Jefferson National Accelerator Facility) 1101

HOM Damping Performance of JLAB SL21 Cryomodule
H. Wang, K. Beard, I. Campisi, J. Mammosser, J. Preble, R.A. Rimmer (Thomas Jefferson National Accelerator Facility), C. Thomas-Madec (SOLEIL) 1104

On Creation of a Cathode Unit for the X-Band Klystron
A.N. Dovbnya, N.I. Aizatsky, V.N. Boriskin, M.A. Krasnogolovets, V.A. Kushnir, V.A. Mitrochenko, N.G. Reshetnyak, Yu.Ya. Volkolupov, V.V. Zakutin (NSC KIPT) 1107

Design of an X-band, 50Mw, Multiple Beam Klystron
L. Ives, P. Ferguson, D. Marsden, G. Miram, M. Mizuhara, L. Song (Calabazas Creek Research, Inc.) 1110

Development of Improved Cathodes for High Power RF Sources
L. Ives, G. Miram, M. Mizuhara, M.E. Read (Calabazas Creek Research, Inc.), P. Borchard, L. Falce (Consultant), K. Gunther (HeatWave Laboratories, Inc.) 1113

Development of Multiple Beam Guns for High Power RF Sources
L. Ives, G. Miram, M. Mizuhara, M.E. Read (Calabazas Creek Research, Inc.), P. Borchard, L. Falce (Consultant), K. Gunther (HeatWave Laboratories, Inc.) 1116

10 MW, 91 GHz Gyroklystron for High Freqency Accelerator Research
L. Ives, D. Marsden, M. Mizuhara, J. Neilson, M.E. Read, T. Robinson (Calabazas Creek Research, Inc.), B. Hogan, W. Lawson (University of Maryland) 1119

Development of an 805-MHz, 550 kW Pulsed Klystron for the Spallation Neutron Source
S. Lenci, E. Eisen, B. Stockwell (Communications and Power Industries, Inc.) 1122

Design and Test of a 100MW X-Band TE01 Window
J. Neilson, L. Ives (Calabazas Creek Research, Inc.), S.G. Tantawi (SLAC) 1125

Development of a Multi-Megawatt Circulator for X-Band
J. Neilson, L. Ives (Calabazas Creek Research, Inc.), S.G. Tantawi (SLAC) 1127

Performance of X-Band Pulsed Magnicon Amplifier
O.A. Nezhevenko, V.P. Yakovlev (Omega-P, Inc.), E.V. Kozyrev (BINP), A.K. Kinkead (LET Corporation), A.W. Fliflet, S.H. Gold (Naval Research Laboratory), J.L. Hirshfield (Omega-P, Inc. and Yale University) 1128

34 GHz, 45 MW Pulsed Magnicon: First Results
O.A. Nezhevenko, M.A. LaPointe, V.P. Yakovlev (Omega-P, Inc.), J.L. Hirshfield (Omega-P, Inc. and Yale University) 1131

Equilibrium Transport of Sheet Electron Beams in Solenoidal Focusing Fields
R. Pakter (Universidade Federal do Rio Grande do Sul) 1134

Gridded Sheet Beam Gun for a Sheet Beam Klystron
M.E. Read, L. Ives, G. Miram (Calabazas Creek Research, Inc.), V. Ivanov, A. Krasnykh (SLAC) 1137

A Magnetron Injection Gun with Inverted Geometry for an 80 MW Gyroklystron
M.E. Read, L. Ives, G. Miram (Calabazas Creek Research, Inc.), V. Granatstein, W. Lawson, G. Nusinovich (University of Maryland) 1140

Development of a 19KW, CW, L-Band Klystron for the Continuous Electron Beam Accelerator Facility
M.E. Read, L. Ives, G. Miram, A. Mizuhara, L. Song (Calabazas Creek Research, Inc.) 1142

Development of a 10-MW, L-Band, Multiple-Beam Klystron for TESLA
E. Wright, A. Balkcum, H. Bohlen, M. Cattelino, L. Cox, M. Cusick, F. Friedlander, B. Stockwell, L. Zitelli (Communications and Power Industries, Inc.) 1144

First High-Power Experiments on a Two-Channel X-Band Active RF Pulse Compressor
A.L. Vikharev (Institute of Applied Physics and Omega P., Inc.), A.M. Gorbachev, V.A. Isaev, O. A. Ivanov, S. V. Kuzikov (Institute of Applied Physics and Omega-P, Inc.), A.K. Kinkead (LET Corporation), S.H. Gold (Naval Research Laboratory), O.A. Nezhevenko (Omega-P, Inc.), J.L. Hirshfield (Omega-P, Inc. and Yale University) 1147

Active RF Pulse Compressor with a Ferroelectric Switch
V.P. Yakovlev, O.A. Nezhevenko (Omega-P, Inc.), J.L. Hirshfield (Omega-P, Inc. and Yale University) 1150

PBG Cavities for Single-Beam and Multi-Beam Electron Devices
D. Yu, D. Newsham, A.V. Smirnov (DULY Research Inc.) 1153

Construction and Testing of a 21 GHz Ceramic Based Power Extractor
D. Yu, D. Newsham, A.V. Smirnov (DULY Research Inc.), W. Gai, R. Konecny, W. Liu (ANL), H. Braun, G. Carron, S. DÅbert, L. Thorndahl, I. Wilson, W. Wuensch (CERN) 1156

Using Ferrite as a Fast Switch for Improving Rise Time of IPNS Extraction Kicker
L.I. Donley, J.C. Dooling, G.E. McMichael (ANL) 1159

The LHC Injection Kicker Magnet
L. Ducimetiere, N. Garrel (CERN), M.J. Barnes, G.D. Wait (TRIUMF) 1162

Switching Power Supply for the PFL Kicker Magnet
H. Sato, S. Igarashi, T. Kawakubo, S. Murasugi, E. Nakamura, S. Yamanaka (KEK), T. Hatano, N. Shimizu (NGK Insulators, Ltd.), A. Tokuchi (Nichicon Corporation) 1165

Accelerated Neutron-Induced Failure Tests of 3300-V IGBTs for the Spallation Neutron Source Accelerator
D.L. Borovina, J. Bradley III, T. Hardek, M.T. Lynch, M. Pieck, R.S. Przeklasa, W.A. Reass, D.E. Rees, S.C. Ruggles, B.E. Takala, P.J. Tallerico, S.A. Wender (LANL) 1168

Electrical Breakdown Studies with Mycalex Insulators
W. Waldron, S. Eylon, W. Greenway, E. Henestroza, S.S. Yu (LBNL) 1171

A Critical Analysis of IGBT Geometries, with the Intention of Mitigating Undesirable Destruction Caused by Fault Scenarios of an Adverse Nature
G.E. Leyh (SLAC) 1174

Fast Ferrite Tuner Operation on a 352-MHz Single-Cell RF Cavity at the Advanced Photon Source
D. Horan, E. Cherbak (ANL) 1177

Mechanisms Limiting High Gradient RF Cavities
J. Norem, A. Hassanein, I. Konkashbaev (ANL) 1180

Dark Current and X Ray Measurements of an 805 MHz Pillbox Cavity
J. Norem (ANL), P. Gruber (CERN), A. Bross, S. Geer, A. Moretti, Z. Qian (FNAL), D.M. Kaplan, Y. Torun (Illinois Institute of Technology), D. Li, M. Zisman (LBNL), R.A. Rimmer (Thomas Jefferson National Accelerator Facility) 1183

HOM Damped NC Passive Harmonic Cavities at BESSY
W. Anders, P. Kuske (BESSY) 1186

Impedance Measurements of a HOM-Damped Low Power Model Cavity
F. Marhauser, E. Weihreter (BESSY), C. Weber (Technical University, Berlin) 1189

Radio-Frequency Control System for the DUVFEL
J. Rose, A. Doyuran, W.S. Graves, H. Loos, T. Shaftan, B. Sheehy, Z. Wu (BNL) 1192

Progress in the Development of High Level RF for the SNS Ring
A. Zaltsman, M. Blaskiewicz, J.M. Brennan, J. Brodowski, J. Butler, M. Meth, F. Severino, K.S. Smith, R. Spitz (BNL) 1195

Buncher Cavity for ERL
V. Veshcherevich, S. Belomestnykh (Cornell University) 1198

Input Coupler for ERL Injector Cavities
V. Veshcherevich, I. Bazarov, S. Belomestnykh, M. Liepe, H. Padamsee, V. Shemelin (Cornell University) 1201

Linearization of the Fermilab Recycler High Level RF
J. Dey, S. Dris, T. Kubicki, J. Reid (FNAL) 1204

Coupler Design for NLC/JLC Accelerting Structures
I. Gonin, D. Finley, T. Khabiboulline, N. Solyak (FNAL) 1207

Development of X-Band Accelerating Structures at Fermilab
N. Solyak, T. Arkan, C. Boffo, E. Borissov, H. Carter, D. Finley, I. Gonin, T. Khabiboulline, G. Romanov, B. Smith (FNAL) 1210

Development of the Third Harmonic Cavity at Fermilab
N. Solyak, H. Edwards, M. Foley, I. Gonin, T. Khabiboulline, D. Mitchell, J. Reid, L. Simmons (FNAL) 1213

Multi-Harmonic RF Control System for J-PARC RCS
F. Tamura, M. Yamamoto (Japan Atomic Energy Research Institute), A. Schnase (Forschungszentrum Juelich), C. Ohmori, A. Takagi, T. Uesugi, M. Yoshii (KEK) 1216

Design of 20MeV DTL for PEFP
Y.S. Cho, B.H. Choi, J.H. Jang, H.J. Kwon, M.Y. Park (Korea Atomic Energy Research Institute) 1219

RF Power Delivery System Design and Its Component Characterization for PEFP DTL
H.J. Kwon, Y.S. Cho, B.H. Choi, J.M. Han, K.K. Jeong (Korea Atomic Energy Research Institute) 1222

R & D Status of C-Band Accelerating Unit for SuperKEKB
T. Kamitani, T. Suwada (KEK) 1225

Improvements in the RF System for the Photon Factory Advanced Ring (PF-AR)
S. Sakanaka, K. Ebihara, E. Ezura, S. Isagawa, T. Kasuga, H. Nakanishi, M. Ono, M. Suetake, T. Takahashi, K. Umemori, S. Yoshimoto (KEK) 1228

Radio Frequency Acceleration System for 150MeV FFAG
A. Takagi, Y. Mori, J. Nakano, M. Sugaya, T. Uesugi (KEK) 1231

Direct-Cooling MA Cavity for J-PARC Synchrotrons
T. Uesugi, Y. Mori, C. Ohmori, A. Takagi, M. Yoshii (KEK), A. Schnase (Forschungszentrum Juelich), F. Tamura, M. Yamamoto (Japan Atomic Energy Research Institute) 1234

High Power Testing of the 402.5 MHz and 805 MHz RF Windows for the Spallation Neutron Source Accelerator
K. Cummings, J.M. De Baca, J. Harrison, M. Rodrigiuez, P.A. Torrez, D.K. Warner (LANL) 1237

HOM Dampers for ALS Storage Ring RF Cavities
S. Kwiatkowski, K. Baptiste, J. Byrd, J. Julian, R. Low, L. Lyn, D. Plate (LBNL) 1240

A 201 MHz RF Cavity Design with Non-Stressed and Pre-Curved Be Windows for Muon Cooling Channels
D. Li, A. Ladran, J. Staples, S. Virostek, M. Zisman (LBNL), W. Lau, S. Yang (Oxford University), R.A. Rimmer (Thomas Jefferson National Accelerator Facility) 1243

RF Tests of an 805 MHz Pillbox Cavity at Lab G of Fermilab
D. Li, J. Corlett, R. MacGill, M. Zisman (LBNL), J. Norem (ANL), A. Moretti, Z. Qian, J. Wallig, V. Wu (FNAL), Y. Torun (Illinois Institute of Technology), R.A. Rimmer (Thomas Jefferson National Accelerator Facility) 1246

Deflecting RF Cavity Design for a Recirculating Linac Based Facility for Ultrafast X-Ray Science
D. Li, J. Corlett (LBNL) 1249

RF Power Detector/Monitor Upgrade for the 500MHz Systems at the ALS
K. Baptiste (LBNL) 1252

Theoretical Analysis of Overmoded Dielectric Photonic Band Gap Structures for Accelerator Applications
M.A. Shapiro, C. Chen, E.I. Smirnova, R.J. Temkin (MIT Plasma Science and Fusion Center) 1255

An 11 GHz Photonic Band Gap Accelerator Structure with Wakefield Suppression
E.I. Smirnova, C. Chen, M.A. Shapiro, R.J. Temkin (MIT Plasma Science and Fusion Center) 1258

Transverse Impedance Bench Measurements in NLC/JLC Accelerating Structures
N. Baboi, G. Bowden, R.M. Jones, J.R. Lewandowski, S.G. Tantawi (SLAC) 1261

Status of X-band Standing Wave Structure Studies at SLAC
V.A. Dolgashev, C. Adolphsen, G. Bowden, D.L. Burke, R.M. Jones, J.R. Lewandowski, Z. Li, R. Loewen, R.H. Miller, C.-K. Ng, C. Pearson, R.D. Ruth, S.G. Tantawi, J.W. Wang, P. Wilson (SLAC) 1264

High Magnetic Fields in Couplers of X-Band Accelerating Structures
V.A. Dolgashev (SLAC) 1267

Circuit and Scattering Matrix Analysis of the Wire Measurement Method of Beam Impedance in Accelerating Structures
R.M. Jones, N. Baboi, S.G. Tantawi (SLAC), N.M. Kroll (University of California, San Diego) 1270

An Automated 476 MHz RF Cavity Processing Facility at SLAC
P. McIntosh, A. Hill, H. Schwarz (SLAC) 1273

Novel Accelerator Structure Couplers
C.D. Nantista, V.A. Dolgashev, S.G. Tantawi (SLAC) 1276

Use of Acoustic Emission to Diagnose Breakdown in Accelerator RF Structures
M.C. Ross, J. Frisch, K. Jobe, F. Le Pimpec, D. McCormick, J. Nelson, T. Smith (SLAC) 1279

Gradient Limitation in Accelerating Structures Imposed by Surface Melting
P. Wilson (SLAC) 1282

TRIUMF ISAC RF System Improvements after 2 Years of Operational Experience
I. Bylinsky, Z. Ang, S. Fang, K. Fong, R. Kumaran, J. Lu, R. Poirier (TRIUMF) 1285

RF Acceleration System at HIRFL-CSR Main Ring
W. Zhang, Z. Xu, X. Yang, W. Zhan, H. Zhao (Institute of Modern Physics) 1288

Microphonics Measurements in SRF Cavities for RIA
M.P. Kelly, J.D. Fuerst, M. Kedzie, S.I. Sharamentov, K.W. Shepard (ANL), J. Delayen (Thomas Jefferson National Accelerator Facility) 1291

Superconducting 345 MHz Two-Spoke Cavity for RIA
K.W. Shepard, J.D. Fuerst, M. Kedzie, M.P. Kelly (ANL), E. Peterson (Advanced Energy Systems) 1294

Superconducting Intermediate-Velocity Cavity Development for RIA
K.W. Shepard, J.D. Fuerst, M. Kedzie, M.P. Kelly (ANL) 1297

Design of a Superconducting Linac Cavity for High-Current Energy Recovery Linac Operation
D. Wang, I. Ben-Zvi, X. Chang, J. Kewisch, C. Montag, Y. Zhao (BNL), J. Sekutowicz (DESY), C. Pagani, P. Pierini (INFN) 1300

Experimental Results on 700 MHz Multicell Superconducting Cavity for Proton Linac
B. Visentin, A. Aspart, D. Braud, J.P. Charrier, Y. Gasser, E. Jacques, J.P. Poupeau, D. Roudier, P. Sahuquet, F. Simoens (CE Saclay), J.L. Biarrotte, S. Blivet, S. Bousson, T. Junquera, H. Saugnac, Ph. Szott (Institut de Physique Nucl_aire d'Orsay) 1303

Using Passive Superconducting Cavities for Bunch Shortening in CESR
S. Belomestnykh, R. Kaplan, J. Reilly, J. Sikora, V. Veshcherevich (Cornell University) 1306

First RF Test at 4.2K of a 200MHz Superconducting Nb-Cu Cavity
R.L. Geng, P. Barnes, D. Hartill, H. Padamsee, J. Sears (Cornell University), S. Calatroni, E. Chiaveri, R. Losito, H. Preis (CERN) 1309

A 1500MHz Niobium Cavity Made of Electropolished Half-Cells
R.L. Geng, A. Crawford, G. Eremeev, H. Padamsee, J. Sears (Cornell University) 1312

An Optimized Shape Cavity for TESLA: Concept and Fabrication
R.L. Geng, J. Kirchgessner, H. Padamsee, J. Sears, V. Shemelin (Cornell University) 1314

Overview of the Cornell ERL Injector Cryomodule
M. Liepe, B. Barstow, I. Bazarov, S. Belomestnykh, R.L. Geng, H. Padamsee, V. Shemelin, C.K. Sinclair, K. Smolenski, M. Tigner, V. Veshcherevich (Cornell University) 1317

First Studies for a Low Temperature Higher-Order-Mode Absorber for the Cornell ERL Prototype
M. Liepe, B. Barstow, H. Padamsee (Cornell University) 1320

New Possibilities for Superconducting Cavity Testing at Cornell University
M. Liepe, P. Barnes, I. Bazarov, S. Belomestnykh, R.L. Geng, H. Padamsee, J. Sears (Cornell University), J. Knobloch (BESSY) 1323

Microphonic Detuning in the 500 MHz Superconducting CESR Cavities
M. Liepe, S. Belomestnykh (Cornell University) 1326

RF Parameter and Field Stability Requirements for the Cornell ERL Prototype
M. Liepe, S. Belomestnykh (Cornell University) 1329

Successful Beam Test of the HOM Free Superconducting SOLEIL Cavity Prototype at the ESRF
J. Jacob, D. Boilot (European Synchrotron Radiation Facility), P. Bosland, P. Bredy, S. Chel (CE Saclay), E. Chiaveri, R. Losito (CERN), J.-M. Filhol, M.-P. Level, P. Marchand, C. Thomas-Madec (SOLEIL) 1332

Higher Order Mode Investigation of Superconducting CH Structures and Status of the CH Prototype Cavity
H. Podlech, H. Deitinghoff, H. Klein, H. Liebermann, U. Ratzinger, A. Sauer, X. Yan (Institut fur Angewandte Physik) 1335

High Power RF Tests on Input Couplers for 972MHz Superconducting Cavities in the J-PARC Project
E. Kako, S. Noguchi, T. Shishido (KEK), H. Asano, E. Chishiro, M. Matsuoka, H. Suzuki, M. Yamazaki (Japan Atomic Energy Research Institute) 1338

Results of Two LANL Beta = 0.175, 350-MHz, 2-Gap Spoke Cavities
T. Tajima, R.L. Edwards, R. Gentzlinger, F.L. Krawczyk, J.E. Ledford, J.-F. Liu, D.I. Montoya, R.J. Roybal, D.L. Schrage, A.H. Shapiro (LANL), G. Corniani (E. Zanon, S.P.A.), D. Barni, A. Bosotti, C. Pagani (INFN) 1341

Q Disease on 350-MHz Spoke Cavities
T. Tajima, R.L. Edwards, F.L. Krawczyk, J.-F. Liu, D.L. Schrage, A.H. Shapiro (LANL) 1344

Update on RF System Studies and VCX Fast Tuner Work for the RIA Driver Linac
B. Rusnak, S. Shen (LLNL) 1347

Cryomodule Design for the Rare Isotope Accelerator
T. Grimm, W. Hartung, M. Johnson, R. York (National Superconducting Cyclotron Laboratory), P. Kneisel, L. Turlington (Thomas Jefferson National Accelerator Facility) 1350

Experimental Study of a 322 MHz v/c=0.28 Niobium Spoke Cavity
T. Grimm, J. Bierwagen, S. Bricker, C. Compton, W. Hartung, F. Marti, R. York (National Superconducting Cyclotron Laboratory) 1353

X-Ray Tomography of Superconducting RF Cavities
T. Grimm, W. Hartung, S.E. Musser (National Superconducting Cyclotron Laboratory) 1356

Mechanical Properties, Microstructure, and Texture of Electron Beam Butt Welds in High Purity Niobium
T. Grimm, C. Compton (National Superconducting Cyclotron Laboratory), T.R. Bieler, H. Jiang (MSU) 1359

Status Report on Multi-Cell Superconducting Cavity Development for Medium-Velocity Beams
W. Hartung, C. Compton, T. Grimm, R. York (National Superconducting Cyclotron Laboratory), G. Ciovati, P. Kneisel (Thomas Jefferson National Accelerator Facility) 1362

Simulation of Quench Dynamics in SRF Cavities under Pulsed Operation
S.-H. Kim (ORNL) 1365

The Numerical Analysis of Higher-Order Modes for Superconducting RF Cavity at SRRC
P.J. Chou (Synchrotron Radiation Research Center) 1368

Effects of Material Properties on Resonance Frequency of a CESR-III Type 500 MHz SRF Cavity
M.C. Lin, L.H. Chang, G.H. Luo, Ch. Wang (Synchrotron Radiation Research Center), M.K. Yeh (National Tsing-Hua University) 1371

Preliminary Studies of Electric and Magnetic Field Effects in Superconducting Niobium Cavities
G. Ciovati, P. Kneisel, G. Myneni, J. Sekutowicz (Thomas Jefferson National Accelerator Facility), A. Brinkmann, W. Singer (DESY), J. Halbritter (Forschungszentrum Karlsruhe) 1374

Improved Prototype Cryomodule for the CEBAF 12 GeV Upgrade
E. Daly, I. Campisi, J. Henry, W.R. Hicks, J. Hogan, P. Kneisel, D. Machie, C. Reece, T. Rothgeb, J. Sekutowicz, K. Smith, T. Whitlatch, K.M. Wilson, M. Wiseman (Thomas Jefferson National Accelerator Facility) 1377

Lorentz Detuning of Superconducting Cavities with Unbalanced Field Profiles
J. Delayen (Thomas Jefferson National Accelerator Facility) 1380

Piezoelectric Tuner Compensation of Lorentz Detuning in Superconducting Cavities
J. Delayen, G.K. Davis (Thomas Jefferson National Accelerator Facility) 1383

Investigation into the Effectiveness of the JLAB High Pressure Rinsing System
J. Mammosser, T. Rothgeb, T. Wang, A.T. Wu (Thomas Jefferson National Accelerator Facility) 1386

Towards Strongly HOM-Damped Multi-Cell RF Cavities
R.A. Rimmer, H. Wang, G. Wu (Thomas Jefferson National Accelerator Facility), D. Li (LBNL) 1389

Active HOMs Excitation in the First Prototype of Superstructure
J. Sekutowicz, A. GÅssel, G. Kreps (DESY), S. Zheng (Tsinghua University, Beijing) 1392

Cavities for JLAB's 12 GeV Upgrade
J. Sekutowicz, G. Ciovati, P. Kneisel, G. Wu (Thomas Jefferson National Accelerator Facility), A. Brinkmann (DESY), R. Parodi (INFN), W. Hartung (MSU), S. Zheng (Tsinghua University, Beijing) 1395

Field Emission Studies from Nb Surfaces Relevant to SRF Cavities
T. Wang, C. Reece, R. Sundelin (Thomas Jefferson National Accelerator Facility) 1398

Niobium Thin Film Properties Affected by Deposition Energy during Vacuum Depostion
G. Wu, L. Phillips, R. Sundelin, A.-M. Valente (Thomas Jefferson National Accelerator Facility) 1401

RF Control System for ISAC II Superconducting Cavities
K. Fong, S. Fang, M. Laverty (TRIUMF), Q. Zheng (Institute of Modern Physics) 1404

Magnetostrictive Tuners for SRF Cavities
C.H. Joshi, A. Mavanur, C.-Y. Tai (Energen, Inc.), T. Grimm (National Superconducting Cyclotron Laboratory) .. 1407

Fabrication, Test and First Operation of Superconducting Accelerator Modules for Storage Rings
M. Pekeler, S. Bauer, M. Peiniger, H. Vogel, P. vom Stein (ACCEL Instruments GmbH), S. Belomestnykh, H. Padamsee, P. Quigley, J. Sears (Cornell University) 1410

Beam Photography: A Technique for Imaging Dark Currents
P. Gruber (CERN), Y. Torun (Illinois Institute of Technology) 1413

Rebuilding WR-340 and WR-284 Waveguide Switches to Meet Higher Power at the Advanced Photon Source
S. Berg, D. Bromberek, J. Gagliano, G. Goeppner, A. Grelick, A. Nassiri, T.L. Smith (ANL) 1416

Conducting Research and Operator Training While Maintaining Top-up Reliability Using the Advanced Photon Source Linear Accelerator
S. Pasky, R. Soliday (ANL) 1419

Bidirectional Coupler Optimization in WR284-Type Waveguide
T.L. Smith, S. Berg, A. Grelick, G. Waldschmidt (ANL) 1422

Calibration of RHIC Electron Detector
P. He, D. Gassner, J. Gullotta, H. Hseuh, D. Trbojevic, S.Y. Zhang (BNL) 1425

Integration of the Beam Scraper and Primary Collimator in the SNS Ring
H. Ludewig, J. Browdowski, D. Davino, C. Longo, B. Mullany, D. Raparia, N. Simos, J. Touzzolo (BNL), N. Catalan-Lasheras (CERN), S. Cousineau (ORNL) 1428

Vibration Studies on a Superconducting RHIC Interaction Region Quadrupole Triplet
C. Montag, G. Ganetis, L. Jia, W. Louie (BNL) 1431

Mechanical Dynamic Analysis of the LHC Arc Cryo-Magnets
O. Capatina, K. Artoos, N. Bourcey, O. Calvet, C. Hauviller (CERN) 1434

Digital Cryogenic Control System for Superconducting RF Cavities in CESR
P. Quigley, S. Belomestnykh, R. Kaplan (Cornell University) 1437

Autopsy Results of Failed Lithium Collection Lenses at the FNAL Antiproton Source
P. Hurh, A. Leveling (FNAL) 1440

The Design of a Diffusion Bonded High Gradient Collection Lens for the FNAL Antiproton Source
P. Hurh, J. Morgan, R. Schultz (FNAL) 1443

Beamline Design for Particle Production Experiment, E907, at FNAL
C. Johnstone, C. Brown, D. Carey, M. Kostin, R. Raja (FNAL), E. Hartouni (LLNL) 1446

Volume 3

Lithium Collection Lens Filling Process for Fermilab Antiproton Source
R. Schultz, P. Hurh (FNAL) 1449

Li Material Testing- Fermilab Antiproton Source Lithium Collection Lens
S. Tariq, K. Ammigan, P. Hurh, R. Schultz (FNAL), P. Liu, J. Shang (University of Illinois) 1452

Beam Study with RF Choppers in the MEBT of the J-PARC Proton Linac
T. Kato, M. Ikegami (KEK), S. Fu, S. Wang (Institute of High Energy Physics, Beijing) 1455

Spallation Neutron Source High-Power RF Transmitter Design for High Availability, Ease of Installation and Cost Containment
J. Bradley III, T. Hardek, M.T. Lynch, D.E. Rees, W. Roybal, P.J. Tallerico (LANL) 1458

Completion of CCL Hot Model for SNS-Linac R&D Program
R. Hardekopf, J. Bernardin, J. Billen, N. Bultman, W. Fox, T. Hardek, S. Hopkins, S. Nath, D. Rej, P.J. Tallerico, L.M. Young (LANL) 1461

Operational Performance of the SNS LLRF Interim System
A. Ratti, L. Doolittle, M. Monroy (LBNL), M. Champion, H. Ma (ORNL) 1464

Beam Dump Window Design for the Spallation Neutron Source
S. Henderson, A. DeCarlo, S.-H. Kim, G. Murdoch, K. Potter, T. Roseberry (ORNL), J. Rank, D. Raparia (BNL) .. 1467

Status of Timing System and Its Upgrade for the PLS Storage Ring
M.H. Chun, Y.J. Han, H.S. Kang, D.T. Kim, S.H. Nam, B.R. Park, J.S. Yang (Pohang Accelerator Laboratory) 1470

Slow-Wave Electrode Structures for the ESS 2.5 MeV Fast Chopper
M.A. Clarke-Gayther (Rutherford Appleton Laboratory) 1473

Electrical Power and Grounding Systems Study and Improvement at TLS
J.C. Chang, J.R. Chen, K.C. Kuo, S.C. Lei, Y.C. Lin (Synchrotron Radiation Research Center) 1476

De-Ionized Cooling Water System Study and Improvement at TLS
J.C. Chang, J.R. Chen, Y.C. Chung, C.Y. Liu, Z.D. Tsai (Synchrotron Radiation Research Center) 1479

Air Temperature Control Improvement for the Storage Ring Tunnel
J.C. Chang, J.R. Chen, C.Y. Liu (Synchrotron Radiation Research Center) 1482

Machine Protection for High Average Current Linacs
K. Jordan, T. Allison, J. Coleman, R. Evans, A. Grippo (Thomas Jefferson National Accelerator Facility) 1485

A Mechanical Tuner for the ISAC-II Quarter Wave Superconducting Cavities
R.E. Laxdal, K. Fong, S. Koscielniak, T. Ries, G. Stanford (TRIUMF) 1488

The Jefferson Lab Quality Assurance Program for the SNS Superconducting Linac Accelerator Project
J.P. Ozelis (Thomas Jefferson National Accelerator Facility) 1491

Utilization of Integrated Process Control, Data Capture, and Data Analysis in Construction of Accelerator Systems.
J.P. Ozelis, V. Bookwalter, B. Madre, C. Reece (Thomas Jefferson National Accelerator Facility) 1494

Study of Coherent Radiation from an Electron Beam Prebunched at the Photocathode
J. Neumann, D. Demske, R. Fiorito, P.G. O'Shea (University of Maryland), G.L. Carr, H. Loos, T. Shaftan, B. Sheehy, Z. Wu (BNL) 1497

A Solid-State Transmitter for the Argonne Advanced Photon Source
I.S. Roth, J.A. Casey, M.P.J. Gaudreau, T. Hawkey, M.A. Kempkes, J.M. Mulvaney, J.E. Petry (Diversified Technologies, Inc.) 1500

Fermilab Booster Beam Collimation and Shielding
N.V. Mokhov, A. Drozhdin, P.H. Kasper, J.R. Lackey, E.J. Prebys, R.C. Webber (FNAL) 1503

Basis for the Reliability Analysis of the Proton Linac for an ADS Program
D. Sertore, D. Barni, P. Michelato, L. Monaco, M. Novati, C. Pagani, R. Paulon, P. Pierini (INFN), L. Burgazzi (Ente Nazionale per le Nuove Tecnologie l'Energia e l'Ambiente) 1506

Beam Commissioning of the J-PARC Linac Medium Energy Beam Transport at KEK
M. Ikegami, S. Anami, S. Arai, J. Chiba, S. Fukuda, Y. Fukui, Z. Igarashi, K. Ikegami, E. Kadokura, N. Kamikubota, T. Kato, M. Kawamura, J. Kishiro, H. Kobayashi, C. Kubota, F. Naito, K. Nigorikawa, S. Noguchi, M. Okada, E. Takasaki, H. Tanaka, A. Ueno, S. Yamaguchi, K. Yoshino (KEK), S. Fu, S. Wang (Institute of High Energy Physics, Beijing), K. Hasegawa, T. Ito, T. Kobayashi, Y. Kondo, Y. Yamazaki, H. Yoshikawa (Japan Atomic Energy Research Institute), J. Qiang, R.D. Ryne (LBNL) 1509

H^- Painting Injection System for the J-PARC 3GeV High Intensity Proton Synchrotron
I. Sakai, Y. Arakida, Y. Irie, T. Kawakubo, S. Machida, I. Sugai, Y. Takeda (KEK), F. Noda, K. Shigaki, T. Shimada, T. Takayanagi, Y. Watanabe, K. Yamamoto (Japan Atomic Energy Research Institute), Y. Ishi (MELCO, Kobe, Japan) 1512

Particle-Beam Behavior in the SNS Linac with Simulated and Reconstructed Beams
S. Nath, J. Billen, J. Stovall, H. Takeda, L.M. Young (LANL), D. Jeon (ORNL), K. Crandall (TechSource, Inc.) 1515

Particle-in-Cell Simulations of the High Current Experiment
C.M. Celata, F.M. Bieniosek, L.R. Prost, P.A. Seidl (LBNL), A. Friedman, D.P. Grote (LLNL) 1518

Design Choices for the Integrated Beam Experiment (IBX)
M.A. Leitner, C.M. Celata, E.P. Lee, B.G. Logan, G. Sabbi, W. Waldron (LBNL), J.J. Barnard (LLNL) 1521

Beam in Gap Measurements at the SNS Front-End
A. Aleksandrov, S. Assadi, W. Blokland, C. Deibele, W. Grice, J. Pogge (ORNL) 1524

ISIS Megawatt Upgrade Plans
C.R. Prior, D.J. Adams, C.P. Bailey, D.W.J. Bellenger, G. Bellodi, J.R.J. Bennett, I.S.K. Gardner, F. Gerigk, J.W. Gray, W.A. Morris, G.H. Rees, J.V. Trotman, C.M. Warsop (Rutherford Appleton Laboratory) 1527

Improvements for the Third Generation Plasma Wakefield Experiment E-164 at SLAC
C.D. Barnes, F.-J. Decker, P. Emma, M.J. Hogan, P. Iverson, P. Krejcik, C.L. O'Connell, R.H. Siemann, D. Walz (SLAC), B.E. Blue, C. Clayton, C. Huang, D. Johnson, C. Joshi, K.A. Marsh, W.B. Mori (University of California, Los Angeles), S. Deng, T.C. Katsouleas, P. Muggli, E. Oz (University of Southern California) 1530

A Slab-Symmetric Dielectric-Loaded Structure for High-Gradient Acceleration at THz
R. Yoder, J.B. Rosenzweig (University of California, Los Angeles) 1533

A Lie Transform Perturbation Scheme for Hamiltonian Averaging in Self Consistent Systems
K.G. Sonnad (University of Colorado at Boulder), J.R. Cary (Center for Integrated Plasma Studies) 1536

Beam Test of a CW Microtron with a 500 MHz RF Cavity for Industrial Applications
H. Tanaka, T.H. Kim, Y. Makita, A. Maruyama, S. Nakamura, T. Nakanishi, Y. Pu, C. Tsukishima, S. Yamamoto (Mitsubishi Corporation) 1539

Commissioning Results of Slow Extraction of Heavy Ions from the AGS Booster
K.A. Brown, L. Ahrens, S. Bellavia, S. Binello, B. Brelsford, D. Du Mont, W. Eng, C. Gardner, D. Gassner, J. Glenn, L. Hammons, J. Hock, L. Hoff, E. Hutchinson, J. Jamilkowski, N. Kling, Y. Kotlyar, A. Krishock, R. Lockey, M. Mapes, I. Marneris, G. Marr, A. Mc Nerney, A. Meyer, J. Morris, C. Naylor, S. Nemesure, D. Phillips, A. Rusek, J. Ryan, T. Shrey, L. Snydstrup, N. Tsoupas, B. VanKuik, S. Zahariou-Cohen, K. Zeno (BNL) 1542

Status of Slow Extraction of High Intensity Protons from Brookhaven's AGS
K.A. Brown, L. Ahrens, J.M. Brennan, J. Glenn, T. Roser, T. Russo, K.S. Smith, N. Tsoupas, K. Zeno (BNL) 1545

LHC Pilot Bunches from the CERN PS Booster
M. Benedikt (CERN) 1548

An 8-GeV Synchrotron-Based Proton Driver
W. Chou (FNAL) 1551

A New Antiproton Beam Transfer Scheme without Coalescing
W. Chou, J. Griffin, J.A. MacLachlan, S. Werkema (FNAL) 1554

Optics of a Proton Driver
L. Michelotti, W. Chou, A. Drozhdin, N. Gelfand, C. Johnstone (FNAL), G.H. Rees (Rutherford Appleton Laboratory), D. Ritson (Stanford University), A.A. Garren (University of California, Los Angeles), S. Ohnuma (University of Hawaii) 1557

Applying Virtual Prototyping to the Innovative Design of Low Energy Accelerators
M. Fan, D. Chen, Shiqui Li, Y. Xiong, T. Yu (HuaZhong University of Science and Technology) 1560

First Tests of a CW RFQ Injector for the IUCF Cyclotrons
V.P. Derenchuk, V. Anferov, D.L. Friesel, W.P. Jones (Indiana University), R.W. Hamm (AccSys Technology Inc.), J. Staples (LBNL) 1563

Longitudinal Tracking Studies for the AHF Booster Synchrotron
L.J. Rybarcyk (LANL) 1566

The Commissioning Plan for the Spallation Neutron Source Ring and Transport Lines
S. Henderson, S. Assadi, S. Cousineau, V. Danilov, G. Dodson, J. Galambos, J. Holmes, K. Reece, T.J. Shea (ORNL), M. Blaskiewicz, Y.-Y. Lee, Y. Papaphilippou, D. Raparia, J. Wei (BNL) 1569

Exploration of Beam Fault Scenarios for the Spallation Neutron Source Target
S. Henderson, S. Cousineau, V. Danilov, J. Holmes, T. McManamy (ORNL), A. Fedotov, Y.-Y. Lee, D. Raparia, J. Wei (BNL) 1572

Superstructures for High Current FEL Application
J. Sekutowicz, K. Beard, P. Kneisel, G. Wu (Thomas Jefferson National Accelerator Facility), C. Thomas (French Atomic Energy Commission), S. Zheng (Tsinghua University, Beijing) 1575

Investigation of Space Charge Effect in TRIUMF Injection Beamline
R. Baartman, Y.-N. Rao (TRIUMF) 1578

Feasibility Studies for a Radioactive-Ion Storage Ring
M.K. Craddock, D. Kaltchev (TRIUMF) 1581

The TRIUMF 500 MeV Cyclotron: Present Operation and Intensity Upgrade
G. Dutto, R. Baartman, P. Bricault, I. Bylinsky, M. Dombsky, R.E. Laxdal, R. Poirier, Y.-N. Rao, L. Root, R. Ruegg, P. Schmor, M. Stenning, G. Stinson (TRIUMF) 1584

Fermilab Booster Orbit Correction
L. Coney, J. Monroe (Columbia University), W.A. Pellico, E.J. Prebys (FNAL) 1587

CRYRING Progress: Weak Beams, Rare Ions and Ordering
A. K_llberg, G. Andler, L. Bagge, M. BjÅrkhage, M. Blom, H. Danared, P. LÅfgren, A. Pa_l, K.-G. Rensfelt, A. Simonsson, F. ˜sterdahl, M. af Ugglas (Manne Siegbahn Laboratory) 1590

Design of a Racetrack Microtron to Operate Outside the Phase Stability Region
M.N. Martins, P.B. Rios, J. Takahashi (Instituto de Fisica da Universidade de Sao Paulo), L.A.A. Terremoto (Instituto de Pesquisas Energeticas e Nucleares) 1593

Beam Transport System for the IFUSP Microtron
M.N. Martins, M.L. Lopes, P.B. Rios, J. Takahashi (Instituto de Fisica da Universidade de Sao Paulo) 1596

Insights in the Physics of the Dynamic Detuning in SRF Cavities and its Active Compensation
M. Doleans, S.-H. Kim (ORNL) 1599

Contruction of User Facilities for the Proton Beam Utilization of PEFP (Proton Engineering Frontier Project)
K.R. Kim, B.H. Choi, H.R. Lee, K.Y. Nam, B.S. Park (Korea Atomic Energy Research Institute) 1602

The Bunching System Based on the Evanescent Oscillations
S.A. Perezhogin, M.I. Ayzatsky, E.Z. Biller, N.G. Golovko, K. Kramarenko, V.A. Kushnir, V.V. Mitrochenko (NSC KIPT) 1605

Pulsed Electron Accelerator for Radiation Technologies
S. Korenev (STERIS Corporation) 1608

The Real-Time System of Electron Beam Dose Measurements for Industrial Accelerators
S. Korenev (STERIS Corporation), I. Korenev (Northern Illinois University) 1611

Target for Production of X-Rays
S. Korenev (STERIS Corporation) 1614

Simulation Tool for Scanning X-Ray Beams Irradiator
G.F. Popov, V.M. Lazurik, V.T. Lazurik, Yu.V. Rogov (Kharkiv National University) 1616

Radiation Processing of Composites for Orthopaedic Implants
G.F. Popov, A. Avilov, V. Deryuga, N. Popova, V. Rudychev (Kharkiv National University) 1619

Design Studies of an Electrostatic Storage Ring
C.P. Welsch, J. Ullrich (Max-Planck-Institut fuer Kernphysik), H. Schmidt-BÅcking (Institut fuer Kernphysik), C. GlÉÙner, K.-U. Kuehnel, A. Schempp (Institut fur Angewandte Physik) 1622

Up-Graded RHIC Injection Kicker System
H. Hahn, W. Fischer, Y.K. Semertzidis, D. Warburton (BNL) 1625

Super-Invar as a Target for Pulsed High-Intensity Proton Beams
H. Kirk, H. Ludewig, L. Mausner, N. Simos, P. Thieberger, R.J. Weggel (BNL), K.T. McDonald (Princeton University) 1628

A High-Field Pulsed Solenoid Magnet for Liquid Metal Target Studies
H. Kirk, M. Iarocci, J. Scaduto, R.J. Weggel (BNL), G. Mulholland (Applied Cryogenics Technology), P. Titus (MIT Plasma Science and Fusion Center), K.T. McDonald (Princeton University) 1631

Moving Solid Metallic Targets for Pion Production in the Muon Collider / Neutrino Factory Project
P. Thieberger, H. Kirk, R.J. Weggel (BNL), K.T. McDonald (Princeton University) 1634

Injection Acceleration and Extraction of High Intensity Proton Beam for the "Neutrino Facility" Project at BNL
N. Tsoupas, J. Alessi, D. Barton, G. Ganetis, A. Jain, Y.-Y. Lee, I. Marneris, W. Meng, D. Raparia, T. Roser, A.G. Ruggiero, J. Tuozzolo, P. Wanderer, W.T. Weng (BNL) 1637

Advancement of the RHIC Beam Abort Kicker System
W. Zhang, L. Ahrens, J. Mi, B. Oerter, J. Sandberg, D. Warburton (BNL) 1640

Final Results on the CERN PS Electrostatic Septa Consolidation Program
J. Borburgh, M. Hourican, A. Prost (CERN) 1643

LHC Beam Dumping System: Extraction Channel Layout and Acceptance
B. Goddard, M. Gyr, J. Uythoven, R. Veness, W. Weterings (CERN) 1646

Performance of Antiproton Injection and Extraction Transfer Lines of the Recycler Ring at Fermilab
A. Marchionni, T.G. Anderson, G.W. Foster, C. Gattuso, M. Hu, D. Johnson, C. Johnstone, C.S. Mishra, A.R. Oleck, H. Piekarz, M. Syphers, M.J. Yang (FNAL) 1649

Initial Operation of the Fermilab MiniBooNE Beamline
C. Moore, J. Anderson Jr., R. Ducar, R. Ford, T. Kobilarcik, E.J. Prebys, A. Russell, R. Stefanski (FNAL), J. Monroe (Columbia University) 1652

Highly Efficient Crystal Deflector for Channeling Extraction of a Proton Beam from Accelerators
V. Guidi (INFN), W. Scandale (CERN), V.M. Biryukov, Y. Chesnokov, V.I. Kotov (Institute of High Energy Physics, Protvino), C. Malagu, G. Martinelli, M. Stefancich, D. Vincenzi (University of Ferrara) 1655

DAÏNE Beam Test Facility Commissioning
G. Mazzitelli, A. Ghigo, M.A. Preger, F. Sannibale, P. Valente, G. Vignola (INFN) 1658

Fabrication of MEBT Chopper for the Spallation Neutron Source
R. Hardekopf, S. Kurennoy, J. Power, R.J. Roybal, D.L. Schrage (LANL), S. Collins, R. Sherwood (Directed Energy, Inc.) 1661

The Mechanical Design of a Proton Microscope for Radiography at 800 MeV
R. Valdiviez, D. Barlow, B. Blind, C. Espinoza, J. Gomez, A. Jason, T. Mottershead, F. Sigler (LANL) 1664

Ionization Cross-Sections in Ion-Atom Collisions for High Energy Ion Beams
I.D. Kaganovich (Princeton University), R.C. Davidson, E.A. Startsev (Plasma Physics Laboratory, Princeton University) 1667

A Proposal for an Additional Beamline to the TRIUMF ISAC Facility
G. Stinson, P. Bricault (TRIUMF) 1670

Electro-Mechanical Design for Injection in the University of Maryland Electron Ring
M. Walter, S. Bernal, T. Godlove, I. Haber, R.A. Kishek, H. Li, P.G. O'Shea, B. Quinn, M. Reiser, A. Valfells, Y. Zou (University of Maryland) 1673

Beam Optics Design on a New Injection Scheme for the University of Maryland Electron Ring (UMER)
H. Li, S. Bernal, T. Godlove, R.A. Kishek, P.G. O'Shea, M. Reiser, M. Walter (University of Maryland) 1676

Beam Extraction of the POP FFAG with a Massless Septum
Y. Yonemura, T. Adachi, M. Aiba, S. Machida, Y. Mori, A. Muto, J. Nakano, C. Ohmori, I. Sakai, Y. Sato, M. Sugaya, A. Takagi, R. Ueno, T. Uesugi, A. Yamazaki, T. Yokoi, M. Yoshimoto, Y. Yuasa (KEK), K. Koba (FNAL), M. Matoba (Kyushu University) 1679

Heavy Ion Beams in the LHC
J.M. Jowett, J.-B. Jeanneret, K. Schindl (CERN) 1682

Abort Gap Studies and Cleaning during RHIC Heavy Ion Operation
A. Drees, L. Ahrens, R. Fliller III, W. Fu, G. Heppner (BNL), V. Kain (CERN) 1685

Results from Vernier Scans at RHIC during the PP Run 2001-2002
A. Drees, B. Fox, Z. Xu (BNL), H. Huang (Yale University) 1688

New Results from Crystal Collimation at RHIC
R. Fliller III, A. Drees, D. Gassner, L. Hammons, G. McIntyre, S. Peggs, D. Trbojevic (BNL), V.M. Biryukov, Y. Chesnokov, V. Terekov (Institute of High Energy Physics, Protvino) 1691

Commissioning of a First-Order Transition Jump in RHIC
J. Kewisch, C. Montag (BNL) 1694

Commissioning Spin Rotators in RHIC
W.W. MacKay, L. Ahrens, M. Bai, E.D. Courant, W. Fischer, H. Huang, A.U. Luccio, C. Montag, F. Pilat, V. Ptitsyn, T. Roser, T. Satogata, D. Trbojevic, J. van Zeijts (BNL) 1697

Design of a Fast Chromaticity Jump in RHIC
C. Montag, D. Bruno, G. Ganetis, J. Kewisch, W. Louie (BNL) 1700

Nonlinear Effects in the RHIC Interaction Regions: Measurement and Correction
F. Pilat, S. Binello, P. Cameron, V. Ptitsyn (BNL) 1703

Commissioning of RHIC Deuteron-Gold Collisions
T. Satogata, L. Ahrens, M. Bai, J. Beebe-Wang, M. Blaskiewicz, J.M. Brennan, K.A. Brown, D. Bruno, P. Cameron, J. Cardona, R. Connolly, A. Drees, W. Fischer, R. Fliller III, G. Ganetis, C. Gardner, J. Glenn, H. Hahn, T. Hayes, H. Huang, U. Iriso-Ariz, W.W. MacKay, A. Marusic, R. Michnoff, C. Montag, F. Pilat, V. Ptitsyn, R. Roser, K.S. Smith, S. Tepikian, D. Trbojevic, N. Tsoupas, S.Y. Zhang, J. van Zeijts (BNL) 1706

Concept Design of the Target/Horn System for the BNL Neutrino Oscillation Experiment
N. Simos, A. Carroll, M. Diwan, S.A. Kahn, H. Kirk, H. Ludewig, D. Raparia, W.T. Weng (BNL), K.T. McDonald (Princeton University), G. Evangelakis (University of Ioannina) 1709

High Luminosity Ù*=0.5m RHIC Insertions
S. Tepikian, H. Huang, W.W. MacKay, F. Pilat, V. Ptitsyn, T. Satogata, D. Trbojevic, J. van Zeijts (BNL) 1712

The RHIC Injector Accelerator Configurations, and Performance for the RHIC 2003 Au-d Physics Run
L. Ahrens, J. Alessi, J. Benjamin, M. Blaskiewicz, J.M. Brennan, K.A. Brown, C. Carlson, T. D'Ottavio, J. DeLong, B. Frak, C. Gardner, J. Glenn, M. Harvey, T. Hayes, H. Hseuh, P. Ingrassia, D. Lowenstein, W.W. MacKay, G. Marr, J. Morris, T. Roser, T. Satogata, G. Smith, K.S. Smith, D. Steski, P. Thieberger, N. Tsoupas, K. Zeno, S.Y. Zhang (BNL) 1715

The LHC Proton Beam in the CERN SPS: an Update
G. Arduini, P. Baudrenghien, T. Bohl, P. Collier, K. Cornelis, W. HÅfle, T. Linnecar, E. Shaposhnikova, J. Tuckmantel, J. Wenninger (CERN) 1718

Protection Devices in the Transfer Lines to the LHC
H. Burkhardt, B. Goddard, V. Mertens (CERN) 1721

PS 13.3-20 MHz RF Systems for LHC
M. Morvillo, R. Garoby, D. Grier, M. Haase, A. Krusche, P. Maesen, M. Paoluzzi, C. Rossi (CERN) 1724

Present Understanding of Electron Cloud Effects in the Large Hadron Collider
F. Zimmermann, G. Arduini, V. Baglin, E. Benedetto, R. Cimino, P. Collier, I. Collins, K. Cornelis, B. Henrist, N. Hilleret, B. Jenninger, J.M. Jimenez, A. Rossi, F. Ruggiero, G. Rumolo, D. Schulte (CERN) 1727

Analysis of the b2 Correction in the Tevatron
P. Bauer, G. Annala, J. DiMarco, R. Hanft, D. Harding, M. Lamm, M. Martens, P. Schlabach, D. Still, M. Tartaglia, J. Tompkins, G. Velev, M. Xiao (FNAL), L. Bottura, F. Zimmermann (CERN) 1730

Beam Loss and Backgrounds in the CDF and D0 Detectors due to Nuclear Elastic Beam-Gas Scattering
A. Drozhdin, V.A. Lebedev, N.V. Mokhov, L.Y. Nicolas, S.I. Striganov, A.V. Tollestrup (FNAL) 1733

Slip Stacking Experiments at Fermilab Main Injector
K. Koba, B. Barnes, T. Berenc, B. Chase, I. Kourbanis, J.A. MacLachlan, K. Meisner, J. Steimel (FNAL) 1736

Observations on the Luminosity Lifetimes and Emittance Growth Rates at the Tevatron
P. Lebrun, V.A. Lebedev, V. Shiltsev, J. Slaughter (FNAL) 1739

Accelerator Related Backgrounds in the LHC Forward Detectors
N.V. Mokhov, A. Drozhdin, I.L. Rakhno (FNAL), D. Macina (CERN) 1742

Mitigation of Effects of Beam-Induced Energy Deposition in the LHC High-Luminosity Interaction Regions
N.V. Mokhov, J.S. Kerby, I.L. Rakhno, J.B. Strait (FNAL) 1745

Energy Deposition Limits in a Nb_3Sn Separation Dipole in Front of the LHC High-Luminosity Inner Triplet
N.V. Mokhov, V.V. Kashikhin, I.L. Rakhno, J.B. Strait, S. Yadav, A.V. Zlobin (FNAL), R. Gupta, M. Harrison (BNL), O.S. BrËning, R. Ruggiero (CERN) 1748

Longitudinal Bunch Dynamics in the Tevatron
R. Moore, V. Balbekov, A. Jansson, V.A. Lebedev, K.Y. Ng, V. Shiltsev, C.Y. Tan (FNAL) 1751

Beam Losses at Injection Energy and during Acceleration in the Tevatron
T. Sen, P. Lebrun, R. Moore, V. Shiltsev, M. Syphers, X.L. Zhang (FNAL), W. Fischer (BNL), F. Schmidt, F. Zimmermann (CERN) 1754

Experimental Studies of Beam-Beam Effects in the Tevatron
T. Sen, Y. Alexahin, V. Shiltsev, M. Xiao, X.L. Zhang (FNAL), F. Schmidt, F. Zimmermann (CERN) 1757

Theoretical Studies of Beam-Beam Effects in the Tevatron at Collision Energy
T. Sen, B. Erdelyi, M. Xiao (FNAL) 1760

Tevatron Run II Luminosity, Emittance and Collision Point Size
J. Slaughter, J. Estrada, K. Genser, A. Jansson, P. Lebrun, J.C. Yun (FNAL), S. Lai (University of Toronto) 1763

Correction Magnets for the Fermilab Recycler Ring
J.T. Volk, G.W. Foster, C. Gattuso, H. Glass, D. Johnson, C.S. Mishra, M.J. Yang (FNAL) 1766

Antiproton Acceleration in the Fermilab Main Injector Using 2.5 MHz (H=28) and 53 MHz (H=588) RF Systems
V. Wu, C.M. Bhat, B. Chase, J. Dey, J.A. MacLachlan, K. Meisner, J. Reid (FNAL) 1769

Tevatron Beam-Beam Simulations at Injection Energy
M. Xiao, B. Erdelyi, T. Sen (FNAL) 1772

Simulations of Octupole Compensation for Head-Tail Instability at the Tevatron
M. Xiao, T. Sen (FNAL), F. Schmidts (CERN) 1775

The Special Applications of Tevatron Electron Lens in Collider Operation
X.L. Zhang, V. Shiltsev (FNAL), F. Zimmermann (CERN), K. Bishofberger (University of California, Los Angeles) 1778

Upgrades of the Tevatron Electron Lens
X.L. Zhang, J. Crisp, J. Fitzgerald, G. Kuznetsov, M. Olson, H. Pfeffer, G. Saewert, A. Semenov, V. Shiltsev, N. Solyak, D. Wildman (FNAL), M. Tiunov (BINP), E. Kashtanov, S. Kozub, V. Sytnik, L. Tkachenko (Institute of High Energy Physics, Protvino), K. Bishofberger (University of California, Los Angeles) 1781

Design Study of 1 MHz Induction Cavity for Induction Synchrotron
K. Torikai, Y. Arakida, S. Inagaki, J. Kishiro, K. Koseki, E. Nakamura, K. Takayama, T. Toyama, M. Wake (KEK), K. Ishibashi (Kyushu University) 1784

Progress in Designing a Muon Cooling Ring with Lithium Lenses
Y. Fukui, D. Cline, A.A. Garren (University of California, Los Angeles), H. Kirk (BNL) 1787

Longitudinal Bunch Rotation Scheme in a Muon Cooling Ring
Y. Fukui (University of California, Los Angeles) 1790

Gaseous Hydrogen for Muon Beam Cooling
R.P. Johnson, R.E. Hartline (Muons, Inc.), C. Ankenbrandt, M. Kuchnir, A. Moretti, M. Popovic (FNAL), M. Alsharo'a, E. Black, D.M. Kaplan (Illinois Institute of Technology) 1792

MICE: The International Muon Ionization Cooling Experiment
Y. Torun (Illinois Institute of Technology) 1795

Muon Cooling Research and Development
M.A.C. Cummings (Northern Illinois University), D.M. Kaplan (Illinois Institute of Technology) 1798

Bench Measurements of Low Frequency Transverse Impedance
A. Mostacci (University of Rome), U. Iriso-Ariz (BNL), F. Caspers, L. Vos (CERN) 1801

A Very Fast Ramping Muon Synchrotron for a Neutrino Factory
D.J. Summers (University of Mississippi), J.S. Berg, R.B. Palmer (BNL), A.A. Garren (University of California, Los Angeles) 1804

A POP Experiment Scenario of Induction Synchrotron at the KEK 12GeV-PS
K. Takayama, Y. Arakida, S. Igarashi, D. Iwashita, J. Kishiro, K. Koseki, E. Nakamura, M. Sakuda, H. Sato, Y. Shimosaki, M. Shirakata, K. Torikai, T. Toyama, M. Wake (KEK), K. Horioka, M. Shiho (Tokyo Institute of Technology) 1807

New RF Design for 11.4GHz Dielectric Loaded Accelerator
W. Gai, C. Jing, R. Konecny, W. Liu, J.G. Power (ANL) 1810

A Compact Wakefield Measurement Facility
J.G. Power, W. Gai, K.-J. Kim, J.W. Lewellen, S.V. Milton, J. Simpson, H. Wang (ANL), H. Carter, D. Finley (FNAL) 1813

FFAG Lattice for Muon Acceleration with Distributed RF
D. Trbojevic, J.S. Berg, M. Blaskiewicz, E.D. Courant (BNL), R. Palmer (CERN), A.A. Garren (LBNL) 1816

Proposal for a Pre-Bunched Laser Wakefield Acceleration Experiment at the BNL DUV-FEL Facility
X.J. Wang, B. Sheehy, Z. Wu (BNL), W. Gai (ANL), A. Ting (Naval Research Laboratory) 1819

Characteristics of Gradient Undulator
A. Mikhailichenko (Cornell University) 1822

Short X and Gamma Production with Swept Laser Bunch
A. Mikhailichenko (Cornell University) 1825

Damping Ring for Generation of Positroniums and Investigation of Fermi-Degeneration in Moving Beams
A. Mikhailichenko (Cornell University) 1828

Longitudinal Dynamics in an FFAG Accelerator under Conditions of Rapid Acceleration and Fixed, High RF
C. Johnstone (FNAL), S. Koscielniak (TRIUMF) 1831

The Integration of Liquid and Solid Muon Absorbers into a Focusing Magnet of a Muon Cooling Channel
M.A. Green (LBNL), R.B. Palmer (BNL), E. Black, M.A. Cummings, D.M. Kaplan (Illinois Institute of Technology), S. Ishimoto (KEK), J.H. Cobb, W. Lau, S. Yang (Oxford University) 1834

Lattices for Milli-eV Neutral Molecules
H. Nishimura, H. Gould, J.G. Kalnins, G.R. Lambertson (LBNL) 1837

Shaping of Pulses in Optical Grating-Based Laser Systems for Optimal Control of Electrons in Laser Plasma Wake-Field Accelerator
C. Toth, J. Faure, C.G.R. Geddes, W.P. Leemans, J. van Tilborg (LBNL) 1840

A Fundamental Theorem on Particle Acceleration
M. Xie (LBNL) 1843

Particle-In-Cell Simulations of Optical Injectors for Plasma Accelerators
D.F. Gordon, R.F. Hubbard, T. Jones, P. Sprangle, A. Ting (Naval Research Laboratory), B. Hafizi (Icarus Research, Inc.) 1846

A Simulation for Electron Trapping and Acceleration in Parabolic Density Profile and Ongoing Experimental Plan
J.U. Kim, N. Hafz, C. Kim, G.H. Kim, H.J. Lee, H. Suk (Korea Electrotechnology Research Institute) 1849

Self-Injection of Electrons from Evolution of Wake Wave
C. Kim, I.S. Ko (Pohang Accelerator Laboratory), G.H. Kim, J.U. Kim, H.J. Lee, H. Suk (Korea Electrotechnology Research Institute) 1852

Photonic Crystal Laser Accelerator Structures
B. Cowan, M. Javanmard, R.H. Siemann (SLAC) 1855

The ORION Facility
R.J. Noble, E. Colby, D.T. Palmer, R.H. Siemann, D. Walz (SLAC), R. Byer (Stanford University), C. Joshi, W.B. Mori, J.B. Rosenzweig (University of California, Los Angeles), T.C. Katsouleas (University of Southern California) 1858

Miniaturization Techniques for Accelerators
J. Spencer (SLAC), J. Mansell (Intellite Inc), W. Ha, T. Plettner, J. Wisdom (Stanford University) 1861

Plasma Wakefield Acceleration of an Intense Positron Beam: Correlation Between Time-Resolved and Time-Integrated Diagnostics
B.E. Blue, C. Clayton, C. Huang, C. Joshi, K.A. Marsh, W.B. Mori (University of California, Los Angeles), F.-J. Decker, M.J. Hogan, R. Iverson, C.L. O'Connell, R.H. Siemann, D. Walz (SLAC), T.C. Katsouleas, P. Muggli (University of Southern California) 1864

Status of the Inverse Free Electron Laser Experiment at the Neptune Laboratory
P. Musumeci, C. Pellegrini, J.B. Rosenzweig, S. Totchisky, G. Travish, R. Yoder (University of California, Los Angeles), S. Tolmachev, A. Varfolomeev, A. Varfolomeev, Jr., T. Yarovoi (RRC Kurchatov Institute) 1867

The UCLA/NICADD Plasma Density Transition Trapping Experiment
M.C. Thompson, W. Lu, W.B. Mori, J.B. Rosenzweig, G. Travish (University of California, Los Angeles), N. Barov (Northern Illinois University) 1870

Acceleration of Injected Electrons in a Laser Beatwave Experiment
S.Ya. Tochitsky, C. Clayton, C.V. Filip, C. Joshi, K.A. Marsh, P. Musumeci, R. Narang, C. Pellegrini, J.B. Rosenzweig, R. Yoder (University of California, Los Angeles) 1873

A Proposal to Experimentally Demonstrate a Novel Regime of Electron Vacuum Acceleration by Using a Tightly Focused Laser Beam
F. Zhou, D. Cline, L. Shao (University of California, Los Angeles), H.K. Ho (Fudan University) 1876

Surface Roughness Effect on a Moving Bunch
S. Banna, L. Schєchter (Technion - Israel Institute of Technlology), R.H. Siemann (SLAC) 1879

Numerical Study of Interference between Transition Radiation and Cerenkov Wake Field Radiation in a Planar Dielectric Structure
J.-M. Fang, T.C. Marshall (Columbia University), V.P. Tarakanov (ITES, RAS), J.L. Hirshfield (Omega-P, Inc. and Yale University) 1882

Generation of Single Pulse Particle Beams in a Plasma Channel by Laser Injection in Laser Wakefield Accelerators
R. Giacone, J.R. Cary, C. Nieter (University of Colorado at Boulder), E. Esarey, G. Fubiani, W.P. Leemans, C.B. Schroeder (LBNL) 1885

A Method for Tuning Dielectric Loaded Accelerating Structures
A. Kanareykin (Euclid Concepts LLC), W. Gai, J.G. Power (ANL), E. Nenasheva (Ceramics Ltd., St. Petersburg), S. Karmanenko, I. Sheinman (St. Petersburg Electrical Engineering University) 1888

A Tunable Dielectric Structure with Built in Transverse Mode Suppression
A. Kanareykin (Euclid Concepts LLC), A. Altmark, I. Sheinman (St. Petersburg Electrical Engineering University) 1891

Transformer Ratio Enhancement Experiment
A. Kanareykin (Euclid Concepts LLC), W. Gai, J.G. Power (ANL), E. Nenasheva (Ceramics Ltd., St. Petersburg), A. Altmark (St. Petersburg Electrical Engineering University) 1894

A Double-Layered, Planar Dielectric Loaded Accelerating Structure
A. Kanareykin (Euclid Concepts LLC), A. Altmark, I. Sheinman (St. Petersburg Electrical Engineering University) 1897

Generation of an Ultra-Short Relativistic-Electron-Bunch by a Laser Wakefield
A.G. Khachatryan, K.-J. Boller, F.A. van Goor (University of Twente) 1900

Charged Particle Interaction with a Chirped Electromagnetic Pulse
A.G. Khachatryan, K.-J. Boller, F.A. van Goor (University of Twente) 1903

Laser Wakefield Acceleration Experiment at KERI
G.H. Kim, C. Kim, J.U. Kim, H.J. Lee, H. Suk (Korea Electrotechnology Research Institute) 1906

STELLA-II: Demonstration of Monoenergetic Laser Acceleration
W.D. Kimura, L.P. Campbell, C.E. Dilley, S.C. Gottschalk, D.C. Quimby (STI Optronics, Inc.), M. Babzien, I. Ben-Zvi, J.C. Gallardo, K.P. Kusche, I.V. Pogorelsky, J. Skaritka, V. Yakimenko (BNL), R.H. Pantell (Stanford University), D. Cline, F. Zhou (University of California, Los Angeles), L.C. Steinhauer (University of Washington) 1909

Electron Acceleration by Laser Wakefields in Tapered Plasma Densities
H. Suk, C. Kim, G.H. Kim, J.U. Kim, H.J. Lee (Korea Electrotechnology Research Institute) 1912

Focusing of 28.5 GeV Electron and Positron Beams in Meter-Long Plasmas
P. Muggli (University of Southern California) 1915

VORPAL: A Computational Tool for the Study of Advanced Accelerator Concepts
C. Nieter, J.R. Cary (University of Colorado at Boulder) 1918

Towards Realizing Optical Injection of Electrons in Resonantly Excited Plasma Wakefields
N. Saleh, S. Chen, W. Theobald, D. Umstadter, C. Widjaja, V. Yanovsky, P. Zhang (University of Michigan) 1921

Experimental and Numerical Studies of Dielectric Wake Field Acceleration Devices
S.V. Shchelkunov, J.-M. Fang, T.C. Marshall (Columbia University), J.L. Hirshfield (Omega-P, Inc. and Yale University) 1924

Multicavity Proton Cyclotron Accelerator
C. Wang (Yale University), V.P. Yakovlev (Omega-P, Inc.), J.L. Hirshfield (Omega-P, Inc. and Yale University) ... 1927

Stability of Electron Orbits in the Strong Wake Fields Generated by a Train of FSEC Bunches
C. Wang (Yale University), T.C. Marshall (Columbia University), J.L. Hirshfield (Omega-P, Inc. and Yale University) 1930

Modeling of Beam-Ionized Sources for Plasma Accelerators
S. Deng, O. Erdem, T.C. Katsouleas, P. Muggli (University of Southern California), C.D. Barnes, F.-J. Decker, P. Emma, M.J. Hogan, R. Iverson, P. Krejcik, C.L. O'Connell, R.H. Siemann, D. Walz (SLAC), C. Clayton, C. Huang, D. Johnson, C. Joshi, W. Lu, K.A. Marsh, W.B. Mori (University of California, Los Angeles) .. 1933

Magnetic Design of a Superconducting AGS Snake
R. Gupta, A.U. Luccio, W.W. MacKay, G. Morgan, K. Power, T. Roser, E. Willen (BNL), M. Okamura (RIKEN Accelerator Research Facility) 1936

Engineering of the AGS Snake Coil Assembly
M. Anerella, R. Gupta, P. Kovach, A. Marone, S. Plate, K. Power, J. Schmalzle, E. Willen (BNL) 1939

Status of the LHC Main Dipole Pre-Series Production
M. Modena, M. Bajko, M. Cornelis, G. De Rijk, P. Fessia, J. Miles, P. Pugnat, J. Rinn, F. Savary, A. Siemko, E. Todesco, J. Vlogaert (CERN) 1942

The LHC Test String 2: Results from Run 2

R. Saban, E. Blanco-Vinuela, F. Bordry, L. Bottura, D. Bozzini, C. Calzas-Rodriguez, E. Carlier, R. Denz, V. Granata, R. Herzog, Q. King, D. Milani, B. Puccio, F. Rodriguez-Mateos, R. Schmidt, L. Serio, F. Tegenfeldt, H. Thiesen, R. van Weelderen (CERN) 1945

Performance of the First LHC Main Quadrupoles Made in Industry

T. Tortschanoff, K.-M. Schirm, W. Venturini-Delsolaro (CERN), R. Burgmer, H.-U. Klein, D. Krischel, B. Schellong, P. Schmidt, T. Stephani (ACCEL Instruments GmbH), M. Durante, M. Peyrot, J.-M. Rifflet, F. Simon (CE Saclay) 1948

Influence of Azimuthal Coil Size on Skew Multipoles in the LHC Dipoles

I. Vanenkov, C. Vollinger (CERN) 1951

Design Considerations for the CESR-c Wiggler Magnets

J. Crittenden, A. Mikhailichenko, A. Temnykh (Cornell University) 1954

Short Period SC Undulator

A. Mikhailichenko (Cornell University) 1957

Improvements in SC Wiggler Performance

A. Mikhailichenko (Cornell University) 1960

To the Radiation of Particles in a Solenoid

A. Mikhailichenko (Cornell University), E. Bessonov (Moscow FIAN) 1963

Conceptual Design of Large-Bore Superconducting Quadrupoles with Active Magnetic Shielding for the AHF

V.S. Kashikhin, G. Ambrosio, N. Andreev, S. Bhashyam, V.V. Kashikhin, T. Peterson, J. Tompkins, A.V. Zlobin (FNAL), A. Jason, J.P. Kelley, P. Walstrom (LANL) 1966

Field Quality of the LHC Inner Triplet Quadrupoles being Fabricated at Fermilab

G. Velev, R. Bossert, R. Carcagno, J. Carson, D. Chichili, J. DiMarco, S. Feher, H. Glass, V.V. Kashikhin, J.S. Kerby, M. Lamm, T. Nicol, A. Norbrega, D. Orris, T. Page, T. Peterson, R. Rabehl, P. Schlabach, J.B. Strait, C. Sylvester, M. Tartaglia, J. Tompkins, S. Yadav, A.V. Zlobin (FNAL) 1969

Measurements of Field Decay and Snapback Effect on Tevatron Dipole Magnets

G. Velev, G. Annala, P. Bauer, R. Carcagno, J. DiMarco, H. Glass, R. Hanft, R. Kephart, M. Lamm, M. Martens, P. Schlabach, M. Tartaglia, J. Tompkins (FNAL) 1972

Aperture Limitations for 2nd Generation Nb_3Sn LHC IR Quadrupoles

A.V. Zlobin, V.V. Kashikhin, J.B. Strait (FNAL) 1975

Status of LHC Low-Beta Quadrupole Magnets, MQXA, at KEK

N. Ohuchi, Y. Ajima, N. Higashi, M. Iida, N. Kimura, T. Nakamoto, T. Ogitsu, H. Ohhata, T. Shintomi, S. Sugawara, K. Sugita, K. Tanaka, A. Terashima, K. Tsuchiya, A. Yamamoto (KEK), T. Fujii, E. Hashiguchi, T. Kanahara, S. Murai, W. Odajima, T. Orikasa (Toshiba Corporation) 1978

Force Free Design of Super-Ferric Beam Line Magnet

M. Wake, H. Sato, K. Takayama (KEK), H. Piekarz, R. Yamada (FNAL) 1981

Field Quality Analysis of a Second Generation IR Quadrupole for the LHC

P. Ferracin, S. Caspi, L. Chiesa, D.R. Dietderich, S.A. Gourlay, R.R. Hafalia, A.F. Lietzke, A.D. McInturff, G. Sabbi, R.M. Scanlan (LBNL) 1984

Superconducting Solenoids for the MICE Channel

M.A. Green (LBNL), R.B. Palmer (BNL), J.M. Rey (CE Saclay), P. Fabbricatore, S. Farinon (INFN), G. Barr (Oxford University), D.E. Baynham, J.H. Rockford (Rutherford Appleton Laboratory) 1987

Superconducting Focusing Quadrupoles for Heavy Ion Fusion Experiments
G. Sabbi, A. Faltens, M.A. Leitner, A.F. Lietzke, P.A. Seidl (LBNL), R.B. Meinke (Advanced Magnet Lab, Inc.), J.J. Barnard, S.M. Lund, N. Martovetsky (LLNL), C. Gung, J. Minervini, A. Radovinsky, J. Schultz (MIT Plasma Science and Fusion Center) 1990

The Strongest Permanent Dipole Magnet
M. Kumada (National Institute of Radiological Sciences (NIRS)), Y. Iwashita (Kyoto University), M. Aoki, E. Sugiyama (Sumitomo Special Metal Co.,Ltd.) 1993

Superconducting Double-Helix Accelerator Magnets
R.B. Meinke, M.J. Ball, C.L. Goodzeit (Advanced Magnet Lab, Inc.) 1996

Measurements of Beam Driven Hydrodynamic Turbulence
J. Norem (ANL), E. Black (Illinois Institute of Technology), L. Bandura, M.A.C. Cummings (Northern Illinois University), D. Errede (University of Illinois) 1999

Muon Cooling in the RFOFO Ring Cooler
R.C. Fernow, J.S. Berg, J.C. Gallardo, R.B. Palmer (BNL) 2002

Layout and Optics for the RHIC Electron Cooler
J. Kewisch, I. Ben-Zvi, X. Chang, C. Montag, D. Wang (BNL) 2005

Muon Storage Rings for 6D Phase-Space Cooling
H. Kirk (BNL), D. Cline, Y. Fukui, A.A. Garren (University of California, Los Angeles) 2008

Effect of Solenoid Field Errors on Electron Beam Temperatures in the RHIC Electron Cooler
C. Montag, J. Kewisch (BNL) 2011

Lithium Lenses Based Muon Cooling Channel
V. Balbekov (FNAL) 2014

Investigation and Simulation of Muon Cooling Rings with Tilted Solenoids
V. Balbekov (FNAL) 2017

Commissioning of the Fermilab Electron Cooler Prototype Beam Line
S. Nagaitsev, A. Burov, K. Carlson, B. Kramper, T. Kroc, J. Leibfritz, M. McGee, G. Saewert, C.W. Schmidt, A. Shemyakin, A. Warner (FNAL), V. Tupikov (BINP), S. Seletsky (University of Rochester) 2020

Analysis of a Grid Window Structure for RF Cavities in a Muon Cooling Channel
A. Ladran, D. Li, J. Staples, S. Virostek, M. Zisman (LBNL), A. Moretti (FNAL), R.A. Rimmer (Thomas Jefferson National Accelerator Facility) 2023

Longitudinal Cooling of a Strongly Magnetized Electron Plasma
Jinhyung Lee, J.R. Cary (University of Colorado at Boulder) 2026

The Advanced Photon Source Injector Test Stand: Phase Two
S. Berg, T. Barsz, D. Briddick, M. Givens, G. Goeppner, A. Grelick, W. Jansma, J.W. Lewellen, A. Lopez, M. Martens, W. Michalek, S. Wesling (ANL) 2029

A New High Intensity Electron Beam for Wakefield Acceleration Studies
M.E. Conde, W. Gai, C. Jing, R. Konecny, W. Liu, J.G. Power, H. Wang, Z. Yusof (ANL) 2032

Energy-Spread Compensation of a Thermionic-Cathode RF Gun
J.W. Lewellen (ANL) 2035

A Flexible Injector Test Stand Design
J.W. Lewellen, K. Beczek, S. Berg, D. Briddick, R. Dortwegt, M. Givens, A. Grelick, A. Nassiri, S. Pasky, T.L. Smith (ANL) 2038

Ultrashort Electron Bunches with Low Longitudinal Emittance in Multi-Cell Superconducting RF Guns
V.N. Volkov (BINP) 2041

Generation of Sub-Picosecond Electron Bunches in Superconducting RF Photocathode Injector
V.N. Volkov (BINP) 2044

Tests of Niobium Cathode for the Superconducting Radio Frequency Gun
Q. Zhao, T. Srinivasan-Rao (BNL), M. Cole (Advanced Energy Systems) 2047

The Analysis of the Cross-Talk in a RF Gun Superconducting Cavity
Y. Zhao (BNL), M. Cole (Advanced Energy Systems) 2050

Simulation of High Charge Extraction from the ELSA RF Photo-Injector
P. Balleyguier, Ph. Guimbal (French Atomic Energy Commission) 2053

Emittance Growth Study Using 3DE Code for the ERL Injector Cavities with Various Coupler Configurations
Z. Greenwald, D.L. Rubin (Cornell University) 2056

Dipole-Mode-Free and Kick-Free 2-Cell Cavity for the SC ERL Injector
V. Shemelin, S. Belomestnykh, R.L. Geng, M. Liepe, H. Padamsee (Cornell University) 2059

High Brightness, High Current Injector Design for the Cornell ERL Prototype
C.K. Sinclair, I. Bazarov (Cornell University) 2062

Emittance Growth due to the Field Asymmetry in the TTF RF Gun
J.-P. Carneiro (DESY) 2065

Experimental Studies of RF Breakdowns in the Coupler of the TTF RF Gun
J.-P. Carneiro, S. Schreiber (DESY), D. Edwards, I. Gonin (FNAL) 2068

On the Photocathodes Used at the TTF Photoinjector
S. Schreiber (DESY), P. Michelato, L. Monaco, D. Sertore (INFN) 2071

Measurement of the Beam Energy Spread in the TTF Photo-injector
M. HËening (FNAL), H. Schlarb (DESY) 2074

Beam Dynamics Studies for the SPARC Project
M. Ferrario, M. Biagini, M. Boscolo, V. Fusco, S. Guiducci, M. Migliorati, L. Serafini, C. Vaccarezza (INFN), R. Bartolini, L. Giannessi, M. Quattromini, C. Ronsivalle (Ente Nazionale per le Nuove Tecnologie l'Energia e l'Ambiente), C.G. Limborg (SLAC) 2077

Study and Design of Room Temperature Cavities for an RF Compressor Prototype
D. Giove, D. Alesini, F. Alessandria, A. Bacci, C. De Martinis, M. Ferrario, A. Gallo, F. Marcellini, M. Mauri, L. Serafini (INFN) 2080

RF Surface Resistance of Copper-on-Beryllium at Cryogenic Temperatures Measured by a 22-GHz Demountable Cavity
J.-F. Liu, F.L. Frawczyk, S. Kurennoy, D.L. Schrage, A.H. Shapiro, T. Tajima, R.L. Wood (LANL) 2083

An Injector for the Proposed Berkeley Ultrafast X-Ray Light Source
S.M. Lidia, J. Corlett, J. Pusina, J. Staples, A. Zholents (LBNL) 2086

Emittance Compensation Studies of Photoinjector Beams with Angular Momentum
S.M. Lidia (LBNL) 2089

The LBNL Femtosource 10 kHz Photoinjector
J. Staples, S.M. Lidia, S. Virostek (LBNL), R.A. Rimmer (Thomas Jefferson National Accelerator Facility) 2092

Initial Testing of a Field Symmetrized Dual Feed 2 MeV 17 GHz RF Gun
A.S. Kesar, S. Korbly, I. Mastovsky, R.J. Temkin (MIT Plasma Science and Fusion Center), J. Haimson, B. Mecklenburg (Haimson Research Corporation) 2095

Current Nanopulse Generation in RF Electron Gun with Metal-Dielectric Cathode
I.V. Khodak, M.I. Ayzatsky, V.A. Kushnir, V.V. Mitrochenko, V.F. Zhiglo (NSC KIPT) 2098

An Electron Source for a Laser Accelerator
E. Colby, C.D. Barnes, C.M. Sears (SLAC) 2101

Analysis of Slice Emittance Measurements for the SLAC Gun Test Facility
D. Dowell, P.R. Bolton, J. Clendenin, S. Gierman, C.G. Limborg, B.F. Murphy, J.F. Schmerge (SLAC) 2104

Experimental Measurements of the ORION Photoinjector Drive Laser Oscillator Subsystem
D.T. Palmer, R. Akre (SLAC) 2107

Status of the UCLA PEGASUS Laboratory
G. Andonian, P. Frigola, S. Reiche, J.B. Rosenzweig, S. Telfer, G. Travish (University of California, Los Angeles) 2110

The UCLA Pegasus Plane-Wave Transformer Photoinjector
G. Travish, G. Andonian, P. Frigola, S. Reiche, J.B. Rosenzweig, S. Telfer (University of California, Los Angeles) 2112

Experimental Characterization of the Electron Source at the Photo Injector Test Facity at DESY Zeuthen
M. Krasilnikov, K. Abrahamyan, J. B€hr, I. Bohnet, J.-P. Carneiro, K. Floettmann, U. Gensch, H.J. Grabosch, J.H. Han, V. Miltchev, A. Oppelt, B. Petrossyan, J. Rossbach, S. Schreiber, F. Stephan (DESY), M.v. Hartrott, E. Jaeschke, D. Kr€mer (BESSY), D. Lipka (DESY Zeuthen), P. Michelato, C. Pagani, D. Sertore (INFN), I. Tsakov (INRNE Sofia), H. Redlin, W. Sandner, R. Schumann, I. Will (Max-Born-Institute), R. Cee, S. Setzer, T. Weiland (Technische U. Darmstadt) 2114

Velocity Bunching Experiment at the Neptune Laboratory
P. Musumeci, J.B. Rosenzweig, R. Yoder (University of California, Los Angeles) 2117

An Integrated Traveling-Wave Photoinjector
S. Telfer (Xgamma Corporation and UCLA) 2120

Wedge-Shaped, Large-Aperture, Dipole Magnet Design for the Jefferson Lab FEL Upgrade
D. Yu, Y. Luo, D. Newsham, A.V. Smirnov (DULY Research Inc.), G. Biallas (Thomas Jefferson National Accelerator Facility) 2123

Parmela Simulations of a PWT Photoinjector
D. Yu, Y. Luo, D. Newsham (DULY Research Inc.), J. Clendenin (SLAC) 2126

Development of a Polarized Electron Gun Based on an S-Band PWT Photoinjector
D. Yu, Y. Luo, D. Newsham, A.V. Smirnov (DULY Research Inc.), J. Clendenin, D. Schultz (SLAC) 2129

Design of a DC/RF Photoelectron Gun
D. Yu, Y. Luo, D. Newsham, A.V. Smirnov, J. Yu (DULY Research Inc.), J.W. Lewellen (ANL), J. Smedley, T. Srinivasan-Rao (BNL), A. Zholents (LBNL) 2132

Short Multipole Magnet Designs for JLAB FEL Upgrade
D. Yu, Y. Luo, D. Newsham, A.V. Smirnov (DULY Research Inc.), G. Biallas, R. Wines (Thomas Jefferson National Accelerator Facility) 2135

Building a Family of Corrector Magnets for SNS Facility
S.V. Badea, J. Alduino, N. Tsoupas, J. Tuozzolo (BNL) 2138

Design of an Ultra High Vacuum Compatible Copper Septum Magnet
M. Mapes, N. Tsoupas (BNL) 2141

Mechanical Design of a Ferrite-Based Injection Kicker for SNS Accumulator Ring
C. Pai, N. Catalan-Lasheras, W. Eng, H. Hseuh, R.F. Lambiase, Y.-Y. Lee, W. Meng, J. Sandberg, S. Tepikian, J. Tuozzolo (BNL) 2144

Mechanical Design of Fast Extraction Kicker and PFN for SNS Accumulator Ring
C. Pai, D. Davino, H. Hahn, H. Hseuh, Y.-Y. Lee, W. Meng, J. Mi, J. Sandberg, N. Tsoupas, J. Tuozzolo, D. Warburton, W. Zhang (BNL) 2147

Design Considerations for a Lambertson Septum Magnet for the Spallation Neutron Source
J. Rank, Y.-Y. Lee, K. Malm, G. Miglionico, D. Raparia, N. Tsoupas, J. Tuozzolo (BNL) 2150

Magnetic Field Calculations for a Large Aperture Narrow Quadrupole
N. Tsoupas, J. Jackson, Y.-Y. Lee, D. Raparia, J. Wei (BNL) 2153

Design and Manufacturing of SNS Accumulator Ring and Transport System D.C. Magnets
J. Tuozzolo, J. Alduino, S.V. Badea, J. Brodowski, G. Mahler, D. Raparia, S. Seberg (BNL) 2156

Volume 4

Final Test Results for the SNS Ring Dipoles

P. Wanderer, J. Jackson, A. Jain, Y.-Y. Lee, W. Meng, Y. Papaphilippou, C. Spataro, S. Tepikian, N. Tsoupas, J. Wei (BNL) 2159

Initial Test of a Fast-Ramped Superconducting Model Dipole for GSI's Proposed SIS200 Accelerator

P. Wanderer, M. Anerella, G. Ganetis, A. Ghosh, P. Joshi, A. Marone, J. Muratore, J. Schmalzle, R. Soika, R. Thomas (BNL), W. Hassenzahl (Advanced Energy Analysis, Inc.), M.N. Wilson (Consultant), J. Kaugerts, G. Moritz (Gesellschaft fËr Schwerionenforschung mbH) 2162

Beam Based Measurements of Hysteresis Effects in Fermilab Main Injector Magnets

B.C. Brown, D.P. Capista (FNAL) 2165

A New Lambertson Magnet for the FNAL 400 MeV Linac

J.-F. Ostiguy, H. Glass, D. Harding, J.R. Lackey, W. Robothom (FNAL) 2168

Pulse Octupole Magnet System at the Photon Factory Storage Ring

T. Miyajima, Y. Kobayashi, S. Nagahashi (KEK) 2171

SPEAR3 Gradient Dipole Core Fabrication

N. Li, R. Boyce, D. Dell'Orco, D. Ernst (SLAC), X. Wang, N. Xu (Institute of High Energy Physics, Beijing), J. Tanabe (SPEAR3 Project Consultant) 2174

Cost Based Failure Modes and Effects Analysis (FMEA) for Systems of Accelerator Magnets

C.M. Spencer (SLAC), S.J. Rhee (Stanford University) 2177

Permanent Magnets for Radiation Damage Studies

J. Spencer (SLAC), J.T. Volk (FNAL) 2180

Magnetic Measurement of the 10 kW, IR FEL 180 Degree Dipole

K. Baggett, G. Biallas, D. Bullard, J. Dail, D. Douglas, T. Hiatt, M. McCrea (Thomas Jefferson National Accelerator Facility) 2183

Magnetic Modeling vs. Measurements of the Dipoles for the JLAB KW Free Electron Laser Upgrade

G. Biallas, K. Baggett, D. Douglas, T. Hiatt, R. Wines (Thomas Jefferson National Accelerator Facility), V. Christina, J.W. Rathke, T.J. Schultheiss (Advanced Energy Systems), Y. Luo, D. Newsham, A.V. Smirnov, D. Yu (DULY Research Inc.) 2186

Magnetic Measurement of the 10 kW, IR FEL Dipole Magnets

T. Hiatt, K. Baggett, M. Beck, G. Biallas, D. Douglas, K. Sullivan, C. Tennant (Thomas Jefferson National Accelerator Facility) 2189

An Adjustable Permanent Magnet Quadrupole Final Focus System for Low Energy Experiments

J. Lim, P. Frigola, J.B. Rosenzweig, S. Telfer, G. Travish (University of California, Los Angeles), W. Brown, A.M. Tremaine (LLNL) 2192

Canadian Light Source Magnets

L. Dallin, D. Lowe, J. Swirsky (Canadian Light Source) 2195

Permanent Magnet Quadrupole for Final Focus for Linear Collider

Y. Iwashita, T. Mihara (Kyoto University), E. Antokhin (BINP), M. Kumada (National Institute of Radiological Sciences (NIRS)), M. Aoki (Sumitomo Special Metal Co.,Ltd.) 2198

A Switching Magnet for the IFUSP Microtron

M.N. Martins, R.R. Lima, M.L. Lopes, A.A. Malafronte, U. Schnitter, J. Takahashi (Instituto de Fisica da Universidade de Sao Paulo) 2201

Measuring Beta Function and Phase Advance in RHIC with an AC Dipole

M. Bai, S. Peggs, T. Roser, T. Satogata, D. Trbojevic (BNL) 2204

Measurement of Linear Coupling Resonance in RHIC
M. Bai, F. Pilat, T. Satogata (BNL), F. Schmidt, R. Tom_s (CERN), R. Calaga (State University of New York) 2207

Linear Model for Non-Isosceles Absorbers
J.S. Berg (BNL) 2210

Linear Design of Combined-Function Ionization Cooling Lattices
J.S. Berg, H. Kirk (BNL), A.A. Garren (University of California, Los Angeles) 2213

Design of FFAGs Based on a FODO Lattice
J.S. Berg (BNL), C. Johnstone (FNAL) 2216

End Field Effects in Bend-Only Cooling Lattices
J.S. Berg, H. Kirk (BNL), A.A. Garren (University of California, Los Angeles) 2219

Linear Coupling Correction with N-Turn Maps
W. Fischer (BNL) 2222

On-Line Monitoring of the Linear Coupling Resonances for the LHC
S. Fartoukh, N. Catalan-Lasheras, J.P. Koutchouk (CERN) 2225

Measurement of Sextupolar Resonance Driving Terms in RHIC
R. Tom_s, F. Schmidt (CERN), W. Fischer (BNL) 2228

Completion of the Sextupole Driving Terms Measurement at the SPS
R. Tom_s, M. Hayes, F. Schmidt (CERN) 2231

A Technique to Measure Chromaticity Based on the Harmonic Analysis of a Longitudinally Kicked Beam
R. Tom_s (University de Valencia), G. Rumolo (Gesellschaft fËr Schwerionenforschung mbH) 2234

Correcting the LHC Beta* at Collision
W. Wittmer, A. Verdier, F. Zimmermann (CERN) 2237

2002 Nonlinear Optics Measurements and Modelling for the CERN SPS
F. Zimmermann, G. Arduini, R. Tom_s (CERN), N. Iida (KEK), A. Faus-Golfe (University de Valencia) 2240

Slow Ground Motion Modelling of DIAMOND
J.K. Jones (Daresbury Laboratory) 2243

Impact of Narrow Gap Undulators on the Advanced Light Source
D. Robin, C. Steier, W. Wan, A. Wolski (LBNL) 2246

ID Modeling at the ALS
D. Robin, H. Nishimura, C. Steier, W. Wan (LBNL), Y.K. Wu (Duke University), E. Forest (KEK) 2249

Maxwell-Lorentz Equations in General Frenet-Serret Coordinates
A.C. Kabel (SLAC) 2252

Global Beam Based Alignment Method
A. Terebilo (SLAC) 2255

Generation of Femtosecond Electron Bunches and Hard-X-Rays by Ultra-Intense Laser Wake Field Acceleration in a Gas Jet
M. Uesaka, T. Hosokai (University of Tokyo), K. Kinoshita, A. Zhidkov (National Institute of Radiological Sciences (NIRS)) 2258

Feedforward Correction of the Pulsed Circularly Polarizing Undulator at the Advanced Photon Source
O. Makarov, B. Deriy, L. Emery, S. Sasaki, R. Soliday, I. Vasserman (ANL) 2261

A Thin Beryllium Injection Window for CESR-c
Y. Li (Cornell University) 2264

Diagnosis of Optical Errors with a Precision BPM System at CESR
M.A. Palmer, D.L. Rubin, D. Sagan, J.C. Smith (Cornell University) 2267

Power Supply Performance Monitoring and Analysis Using Operation Data
J. Li, S. Hartman, Y.K. Wu (Duke University) 2270

Status of the Booster Synchrotron for Duke FEL Storage Ring
S.F. Mikhailov, M. Busch, M. Emamian, S. Hartman, V. Litvinenko, I. Pinayev, V.G. Popov, G. Swift, P. Wallace, Y.K. Wu (Duke University), N. Gavrilov, Yu. Matveev, D. Shvedov, N. Vinokurov, P. Vobly (BINP) 2273

Challenges for Magnetic Design of a Compact Booster Fed by Single Power Supply
S.F. Mikhailov (Duke University) 2276

Feasibility Study of a 2 GeV Lepton Collider at DAFNE
G. Benedetti, D. Alesini, M. Biagini, C. Biscari, R. Boni, M. Boscolo, A. Clozza, G. Delle Monache, G. Di Pirro, A. Drago, A. Gallo, A. Ghigo, S. Guiducci, M. Incurvati, C. Ligi, F. Marcellini, G. Mazzitelli, C. Milardi, L. Pellegrino, M.A. Preger, P. Raimondi, R. Ricci, C. Sanelli, M. Serio, F. Sgamma, A. Stecchi, A. Stella, C. Vaccarezza, M. Vescovi, M. Zobov (INFN) 2279

Bunch Pattern By-3 in PEP-II
F.-J. Decker, A. Kulikov, M. Sullivan (SLAC) 2282

Injection Related Background due to the Transverse Feedback
F.-J. Decker, R. Akre, A. Fisher, R. Iverson, M. Weaver (SLAC) 2285

Lattice with Smaller Momentum Compaction Factor for PEP-II High Energy Ring
Y. Nosochkov, Y. Cai, M. Donald (SLAC) 2288

Tracking Simulations Near Half-Integer Resonance at PEP-II
Y. Nosochkov, Y. Cai (SLAC) 2291

RF Heating and Temperature Oscillations due to a Small Gap in a PEP-II Vacuum Chamber
A. Novokhatski, J. Seeman, M. Sullivan (SLAC) 2294

Progress of the PEP-II B-Factory
J. Seeman, M. Browne, Y. Cai, W. Colocho, F.-J. Decker, M. Donald, S. Ecklund, R. Erickson, A. Fisher, J. Fox, S. Heifets, R. Iverson, W. Kozanecki, P. Krejcik, A. Kulikov, A. Novokhatski, P. Schuh, H. Schwarz, M. Stanek, M. Sullivan, D. Teytelman, J.L. Turner, U. Wienands, Y. Yan, J. Yocky (SLAC), M. Biagini (INFN), M. Zisman (LBNL) 2297

Design Studies for a 10^{36} Super-B-Factory
J. Seeman, Y. Cai, F.-J. Decker, S. Ecklund, A. Fisher, J. Fox, S. Heifets, Y. Nosochkov, A. Novokhatski, M. Sullivan, D. Teytelman, U. Wienands, Y. Yan (SLAC), M. Biagini (INFN) 2300

Improvements in Aladdin Bend Magnet Stability by Reduction of Leakage Currents
D.J. Wallace, M. Fisher, K.D. Jacobs, G. Rogers, L. Rowley, M. Thikim, W. Trzeciak (Synchrotron Radiation Center, University of Wisconsin) 2303

Longitudinal Single-Bunch Instabilities for Different Operation Energies at ELETTRA
G. De Ninno, M. Danailov, B. Diviacco, F. Iazzourene, E. Karantzoulis, M. Marsi, L. Tosi, M. Trovà (Sincrotrone Trieste) 2306

Injection and FEL Lasing with Front End Open at ELETTRA
G. De Ninno, K. Casarin, F. Iazzourene, E. Karantzoulis, L. Tosi, G. Tromba, A. Vascotto (Sincrotrone Trieste) ... 2309

Initial Studies of Longitudinal Dynamics on UMER
A. Valfells, B. Beaudoin, S. Bernal, A. Diep, I. Haber, J. Harris, Y. Huo, P.G. O'Shea, B. Quinn, M. Reiser, M. Walter (University of Maryland) 2312

Nonlinear Optimization of a Low Emittance CLIC Damping Ring Lattice
M. Korostelev, F. Zimmermann (CERN) 2315

Status of the MAX-III Storage Ring
G. LeBlanc, A. Andersson, M. Demirkan, M. Eriksson, L.-J. Lindgren, H. Tarawneh, S. Werin (MAX-Lab), B. Anderberg (AMACC, Sweden) 2318

MAX 4, a 3 GeV Light Source
G. LeBlanc, A. Andersson, M. Bergqvist, M. Eriksson, L.-J. Lindgren, L. Malmgren, H. Tarawneh, E. Wall_n, S. Werin (MAX-Lab), B. Anderberg (AMACC, Sweden), JÅrgen Larsson (Lund University) 2321

Bates South Hall Ring Commissioning for Internal Target Experiments
J.B. van der Laan, D. Cheever, M. Farkhondeh, W.A. Franklin, E. Ihloff, S. Krause, L. Longcoy, C. Tschalaer, E. Tsentalovich, F. Wang, A. Zolfaghari, T. Zwart (MIT-Bates) 2324

Connection-Oriented Relational Database of the APS Control System Hardware
D.A. Dohan, N.D. Arnold (ANL) 2327

Use of a General-Purpose Optimization Module in Accelerator Control
L. Emery, M. Borland, H. Shang (ANL) 2330

An Operator Training Facility at the Advanced Photon Source
J.W. Lewellen, S. Pasky (ANL) 2333

All Digital IQ Servo-System for CERN Linacs
A. Rohlev, R. Garoby, J. Serrano (CERN) 2336

Pulsed NMR Magnetometers for CESR
R.E. Meller, D. Hartill (Cornell University) 2339

Requirements for RF Control of TTF II FEL User Facility
V. Ayvazyan, K. Rehlich, S. Simrock (DESY) 2342

Antiproton Stacking and Un-stacking in the Fermilab Recycler Ring
C.M. Bhat (FNAL) 2345

Gated Current Integrator for the Beam in the RR Barrier Buckets
C.M. Bhat, A. Cadorna, J. Crisp, B. Fellenz (FNAL) 2348

Improvement of Photon Factory Advanced Ring Control System
T. Obina, A. Akiyama, T. Katoh, T. Kawamoto, I. Komada, K. Kudo, S. Nagahashi, T.T. Nakamura, J. Odagiri, Y. Takeuchi, N. Yamamoto (KEK) 2351

The LANSCE RICE Control System Upgrade
S. Schaller, E. Bjorklund, M. Burns, G. Carr, J. Faucett, D. Hayden, M. Lusk, R. Merl, M. Oothoudt, J. Potter, J. Reynolds, D. Romero, F. Shelley, Jr. (LANL) 2354

The Upgrade of HLS Linac Control System
G. Liu, X. Bao, L. Chen, C. Li, W. Li, J.P. Wang (National Synchrotron Radiation Lab), J. Li (Duke University) ... 2357

Application Programming Structure and Physics Applications
C. Chu, J. Galambos, W.-D. Klotz, T.A. Pelaia, A. Shishlo (ORNL), D. Ottavio (BNL), C.K. Allen, C.A. McChesney, N. Pattengale (LANL) 2360

SNS Global Database Use in Application Programming
J. Galambos, C. Chu, E. Danilova, J. Patton, T.A. Pelaia, A. Shishlo (ORNL), W.-D. Klotz (European Synchrotron Radiation Facility) 2363

The EPICS Based Virtual Accelerator - Concept and Implementation
A. Shishlo, P. Chu, J. Galambos, T.A. Pelaia (ORNL) 2366

Accelerator Control Middle Layer
A. Terebilo, J. Corbett, G. Portmann (SLAC) 2369

Simulated Commissioning of SPEAR 3 Storage Ring
A. Terebilo, J. Corbett, D. Keeley, G. Portmann (SLAC) 2372

A New Real-Time Operating System and Python Scripting on Aladdin
D.E. Eisert, R.A. Bosch, K.D. Jacobs, K.J. Kleman, J.P. Stott (Synchrotron Radiation Center, University of Wisconsin) 2373

Control System for the Superconducting Insertion Devices of NSRRC
K.T. Hsu, C.K. Chang, J. Chen, S.-Y. Hsu, K.H. Hu, C.S. Hwang, C.H. Kuo, Demi Lee (Synchrotron Radiation Research Center) 2376

Low Level RF System for Jefferson Lab Cryomodule Test Facility
T. Plawski, T. Allison, J. Delayen, C. Hovater, T. Powers (Thomas Jefferson National Accelerator Facility) 2379

PLC and Linux Based Control System for the CAMD Linac
P. Jines, E. Anzalone, B. Craft, A. Crappell, M. Fedurin, T. Miller, M. Smith, Y. Wang, T. Zhao (Center for Advanced Microstructures and Devices) 2382

Cross Platform SCA Component using C++ Builder and Kylix
H. Nishimura, J.L. McDonald, C. Timossi (LBNL) 2385

Design of Control System for SAGA Synchrotron Light Source
H. Ohgaki (Kyoto University), K. Kudo, H. Toyokawa (National Institute of Advanced Industrial Science and Technology), Y. Iwasaki, S. Koda, T. Tomimasu (Saga Synchrotron Light Source) 2387

SNS Ring and Transport System Magnet Acceptance and Installation Preparation
S. Tepikian, R. Anderson, M. Hemmer, H. Hseuh, J. Jackson, A. Jain, F. Karl, Y.-Y. Lee, W. McGahern, D. Raparia, R. Savage, J. Tuozzolo, P. Wanderer, J. Wei (BNL) 2390

Laser-Based Alignment System for the J-PARC Linac
M. Ikegami, Y. Higashi, T. Kato, H. Tanaka, K. Yoshino (KEK) 2393

A Model of ATL Ground Motion for Storage Rings
A. Wolski (LBNL), N. Walker (DESY) 2396

Design and Operation of the Cryostat for the CESR-c Superconducting Wiggler Magnets
Y. He, G. Codner, R.D. Ehrlich, Y. Li, V. Medjidzade, A. Mikhailichenko, N.B. Mistry, E. Nordberg, D. Rice, D. Sabol, E.N. Smith, K. Smolenski, D. Widger (Cornell University) 2399

The Pilot-Runs of the Helium Cryogenic System for the TLS Superconducting Cavity
F.Z. Hsiao, J.C. Chang, S.H. Chang, J.R. Chen, T.C. King, H.C. Li, M.C. Lin, Ch. Wang (Synchrotron Radiation Research Center) 2402

Design of Cryogenic System for Several Super-Conducting Modules at National Synchrotron Radiation Research Center
T.C. King, J.C. Chang, S.H. Chang, J.R. Chen, F.Z. Hsiao, H.C. Li (Synchrotron Radiation Research Center) 2405

Techniques for Synchronization of X-Ray Pulses to the Pump Laser in an Ultrafast X-Ray Facility
J. Corlett, L. Doolittle, R. Schoenlein, J. Staples, R. Wilcox, A. Zholents (LBNL) 2408

Bunch Purity Evolution during APS Storage Ring Top-up Operations
A.H. Lumpkin, T. Toellner, B.X. Yang, C.Y. Yao (ANL) 2411

The Feasibility of OTR Imaging of High-Intensity Proton Beams at FNAL
A.H. Lumpkin (ANL), V. Scarpine (FNAL) 2414

Recent Characterizations of Electron Beams from the APS Linac
A.H. Lumpkin, W.J. Berg, M. Borland, J.W. Lewellen (ANL) 2417

Initial CTR-Based Bunch Length Measurements of Linac Beams Following the APS Bunch Compressor
A.H. Lumpkin, W.J. Berg, M. Borland, J.W. Lewellen, N.S. Sereno (ANL) 2420

X-Ray Imaging of the APS Storage Ring Beam Stability Effects: from the Alaskan Earthquake to Undulator Field Changes
A.H. Lumpkin, L. Emery, B.X. Yang, C.Y. Yao (ANL) 2423

Super-Conducting Resonator as Beam Induced Signal Pickup
R.C. Pardo, B.E. Clifft, P.N. Ostroumov, S.I. Sharamentov, G.P. Zinkann (ANL) 2426

Beam Position Monitor Systems for the SNS LINAC
J. Power, L. Day, M.A. Plum, M. Stettler (LANL) 2429

Split Scattering Effects in a Well Aligned Pepper Pot
J.G. Power (ANL) 2432

Advanced Photon Source Booster Synchrotron Beam Position Monitor Upgrade and Applications
N.S. Sereno, F. Lenkszus, Robert M. Lill (ANL) 2435

Tune System Applications at the APS
C.Y. Yao, L. Emery, K. Harkay (ANL) 2438

AGS Booster Beam Position, Tune, and Longitudinal Profile Data Acquisition System
K.A. Brown, L. Ahrens, F. Severino, K.S. Smith, M. Wilinski (BNL) 2441

Spallation Neutron Source Ring Diagnostics
P. Cameron, J. Brodowski, P. Cerniglia, R. Connolly, J. Cupolo, C. Dawson, C. Degen, A. DellaPenna, D. Gassner, R. Gonzalez, M. Grau, J. Gullotta, L. Hoff, A. Huhn, M. Kesselman, C.J. Liaw, J. Mead, R. Sikora, G. Smith, K. Vetter, M. Wilinski (BNL), M.A. Plum (LANL), S. Assadi, W. Blokland, C. Diebele, D. Purcell, T.J. Shea (ORNL), R.L. Witkover (TechSource, Inc.) 2444

Spallation Neutron Source Beam Loss Monitor System
D. Gassner, P. Cameron, C. Mi (BNL), R.L. Witkover (TechSource, Inc.) 2447

Design and Testing of the New Ion Chamber Loss Monitor for SNS
D. Gassner (BNL), R.L. Witkover (TechSource, Inc.) 2450

Beam Current Monitor Calibrator for the Spallation Neutron Source
M. Kesselman, C. Dawson, G. Smith (BNL) 2453

Electro-Optic Longitudinal Electron Beam Diagnostic at SDL
H. Loos, A. Doyuran, J.B. Murphy, J. Rose, T. Shaftan, B. Sheehy, Y. Shen, J. Skaritka, X.J. Wang, Z. Wu, L.H. Yu (BNL) 2455

A High Dynamic-Range Beam Position Measurement System for ELSA-2
P. Balleyguier, D. Deslandes, Ph. Guimbal (French Atomic Energy Commission), H. Borrion (University College) 2458

Upgrades to the Digital Receiver-based Low-Intensity Beam Diagnostics for CERN AD.
M.E. Angoletta, D. Belohrad, L. Bojtar, A. Findlay, M. Ludwig, F. Pedersen (CERN), O. Marqversen (TERMA A/S, Radar Systems) 2461

OTR Studies for the High Charge CTF3 Beam
T. Lefevre, E. Bravin (CERN), C. Vermare (French Atomic Energy Commission) 2464

Measurement of Beam Position Using Highly-Damped Accelerating Structures
J. Prochnow, E. Jensen, W. Wuensch (CERN) 2467

Cavity Mode Related Wire Breaking of the SPS Wire Scanners and Loss Measurements of Wire Materials
F. Roncarolo, F. Caspers, B. Dehning, E. Jensen, J. Koopman, J.F. Malo (CERN) 2470

System Level Implementation of Beam Position Monitors with Local Data Processing Capability for the Cornell Electron Storage Ring
M.A. Palmer, J. Dobbins, B.Y. Rock, C.R. Strohman (Cornell University), J.R. Moffitt (The College of Wooster) ...2473

Design of OTR Beam Profile Monitors for the TESLA Test Facility, Phase 2 (TTF2)
K. Honkavaara, A. Brenger, R. Fischer, D. NÅlle, K. Rehlich (DESY), L. Cacciotti, M. Castellano, L. Catani, A. Cianchi, G. Di Pirro, M. Raparelli, R. Sorchetti (INFN) ...2476

BPM and Orbit Correction Systems at the Duke Storage Ring
Y.K. Wu, J. Li, V. Litvinenko, P. Wang (Duke University) ...2479

A Physics Based Control System for the Duke Storage Ring
Y.K. Wu, S. Hartman, S.F. Mikhailov (Duke University) ...2482

The SNS Linac Wire Scanner System
M.A. Plum, W. Christensen, R.E. Meyer Sr., C.R. Rose (LANL) ...2485

Performance of a Beam Monitor in the Fermilab Tevatron Using Synchrotron Light
H.W.K. Cheung, A. Hahn, A. Xiao (FNAL) ...2488

Measurement of Proton and Anti-proton Intensities in the Tevatron Collider
S. Pordes, J. Crisp, B. Fellenz, R. Flora, A. Hahn, T.S. Meyer, A.V. Tollestrup (FNAL), W. Blokland (ORNL) ...2491

Digital Down Conversion Technology for Tevatron Beam Line Tuner at FNAL
W. Schappert, E. Lorman, V. Scarpine (FNAL), M.C. Ross, J. Sebek, T. Straumann (SLAC) ...2494

Measurements of the Longitudinal and Transverse Beam Loss at the Tevatron
A.V. Tollestrup, M.E. Binkley, B.M. Hanna, V.A. Lebedev, R. Moore, V. Shiltsev, R. Tesarek, R. Vidal (FNAL) ...2497

Study of a Low Impedance Beam Position Monitor for Short Bunches
D. Alesini, B. Spataro, C. Vaccarezza (INFN), C. D'Alessio, A. Mostacci, L. Palumbo (University of Rome) ...2500

Improved SR Extraction Chamber for KEKB LER SR Monitor
J.W. Flanagan, S. Hiramatsu, H. Ikeda, K. Kanazawa, T. Mitsuhashi (KEK) ...2503

Construction of SR Monitor for Photon Factory Advanced Ring
T. Mitsuhashi, M. Tadano (KEK) ...2506

Beam Position Measurement Using Linac Microstructure at the KEK Booster Synchrotron
T. Miura, Y. Irie, Y. Sato, H. Someya (KEK) ...2509

Beam Position Measurements at Los Alamos: Isotope Production Facility and Switchyard Kicker Upgrade
J.D. Gilpatrick, D. Barr, D. Martinez, J.F. O'Hara, R.B. Shurter, M. Stettler (LANL) ...2512

A Multiwire Proportional Chamber System for Monitoring Low Momentum Beam in Accelerators
R. Merl, F. Gallegos, C. Pillai, B.J. Sanchez, F. Shelley, A. Steck (LANL) ...2515

High Speed Epics Data Acquisition and Processing on One VME Board
R. Merl, F. Gallegos, C. Pillai, F. Shelley (LANL) ...2518

Halo Measurements of the Extracted Beam at the Los Alamos Proton Storage Ring
T. Zaugg, M. Borden, A. Browman, D. Fitzgerald, R.J. Macek, R. McCrady, T. Spickermann (LANL) ...2521

Beam Imaging Diagnostics for Heavy Ion Beam Fusion Experiments
F.M. Bieniosek, W. Ghiorso, L.R. Prost (LBNL) ...2524

A Second Beam-Diagnostic Beamline for the Advanced Light Source
F. Sannibale, D. Baum, N. Kelez, T. Scarvie (LBNL), K. Holldack (BESSY) ...2527

Development of a Longitudinal Density Monitor for Storage Rings
W. Turner, J.-F. Beche, J. Byrd, P. Datte, S. De Santis, P. Denes, M. Placidi, A. Ratti, V. Riot, R. Schoenlein, M. Zolotorev (LBNL) 2530

DARHT-II Energy Analyzer
A.C. Paul, S. Hawkins, J. McCarrick, J. Sullivan, J.A. Watson, G. Westenskow (LLNL), W. Nexsen (Johnston Controls), S. Eylon, T.J. Fessenden (LBNL) 2533

Progress on a Smith-Purcell Radiation Bunch Length Diagnostic
S. Korbly, A.S. Kesar, M.A. Shapiro, R.J. Temkin (MIT Plasma Science and Fusion Center) 2536

Beam Diagnostic System for High Intensity Proton Linac at KAERI
S.J. Park, Y.S. Bae, J.Y. Huang, W.H. Hwang, S.H. Nam, J.H. Park (Pohang Accelerator Laboratory), Y.S. Cho, B.H. Choi, J.M. Han, S.H. Han (Korea Atomic Energy Research Institute) 2539

Improved Results from the Gas Scattering Energy Spectrometer on the ISIS RFQ Test Stand
J.P. Duke, D.J.S. Findlay, A.P. Letchford, J. Thomason (Rutherford Appleton Laboratory) 2542

Very High Resolution RF Cavity BPM
M.C. Ross, J. Frisch, L. Hendrickson, D. McCormick (SLAC), V. Vogel (BINP), H. Hayano, J. Urakawa (KEK) ... 2545

RF Cavity BPM's as Beam Angle and Beam Correlation Monitors
M.C. Ross, J. Frisch, D. McCormick (SLAC), H. Hayano (KEK) 2548

Bunched Beam Cleaning System of SPring-8 Booster Synchrotron
T. Aoki, K. Fukami, N. Hosoda, T. Ohshima, M. Shoji, K. Tamura, H. Yonehara (SPring-8) 2551

Beam Position Monitoring System for the 1.5 GeV Transport Line of NSRRC
K.H. Hu, J. Chen, K.T. Hsu, C.H. Kuo, Demi Lee, C.J. Wang (Synchrotron Radiation Research Center) 2554

Functionality of the Digital Beam Position Monitor Test-Bed in NSRRC
C.H. Kuo, J. Chen, K.T. Hsu, K.H. Hu (Synchrotron Radiation Research Center) 2557

Synchrotron Light Interferometer at Jefferson Lab
P. Chevtsov, A. Freyberger, R. Hicks (Thomas Jefferson National Accelerator Facility), J.-C. Denard (SOLEIL) .. 2560

Development of a BPM Lock-in Diagnostic System
R. Dickson (Thomas Jefferson National Accelerator Facility) 2563

Large Dynamic Range Beam Profile Measurements
A. Freyberger (Thomas Jefferson National Accelerator Facility) 2565

Tunneling Ionization Bunch Length Monitor for the Ultrarelativistic Compressed Electron Beams
A. Murokh (University of California, Los Angeles) 2568

Design and Testing of a Fast Beam Position Monitor
B. Quinn, B. Beaudoin, S. Bernal, A. Diep, M. Glanzer, J. Harris, M. Holloway, D. Lamb, W.-T. Lee, P.G. O'Shea, M. Quirus, M. Reiser, A. Valfells, M. Walter, R. Yun (University of Maryland) 2571

Time Resolved Emittance Measurement in the University of Maryland Electron Ring
M. Walter, S. Bernal, I. Haber, R.A. Kishek, D. Lamb, H. Li, P.G. O'Shea, B. Quinn, M. Reiser, M. Snowel, A. Valfells (University of Maryland) 2574

Alignment of Components at the University of Maryland Electron Ring
M. Walter, S. Bernal, A. Diep, M. Glanzer, I. Haber, J. Harris, R.A. Kishek, D. Lamb, W.-T. Lee, H. Li, P.G. O'Shea, B. Quinn, M. Quirus, M. Reiser, A. Valfells (University of Maryland) 2577

Emittance Measurement by Using Duo Image Pattern of Cherenkov Radiation
J. Chen, Y. Ding, S. Quan, B. Zhang, K. Zhao (Peking University), R. Geng, A. Gu (Princeton University) 2580

Filling Pattern Measurement in the LNLS Storage Ring
S.R. Marques, H.J. Onisto, P.F. Tavares (LaboratÂrio Nacional de Luz S°ncrotron, Brazil) 2583

Multichannel Single-Shot Transient Signal Measurements with an Optical Fiber Recirculating Delay Line Loop
Y. Yin, A. Chen, G. Chen, X.Z. Wang, W. Zhang (YY Labs, Inc.) 2586

Compensation of Nonlinear Resonances in the Presence of Space Charge
A. Fedotov, G. Parzen (BNL) 2589

Application of Envelope Instability to High-Intensity Rings
A. Fedotov (BNL), I. Hofmann (Gesellschaft fËr Schwerionenforschung mbH), H. Okamoto (Hiroshima University), R.L. Gluckstern (University of Maryland) 2592

Spill Structure in Intense Beams
J. Glenn, M. Blaskiewicz, K.A. Brown, E. Raka, J. Ryan (BNL) 2595

Electron-Cloud Mitigation in the Spallation Neutron Source Ring
J. Wei, M. Blaskiewicz, J. Brodowski, P. Cameron, D. Davino, A. Fedotov, P. He, H. Hseuh, Y.-Y. Lee, H. Ludewig, W. Meng, D. Raparia, J. Tuozzolo, S.Y. Zhang (BNL), N. Catalan-Lasheras (CERN), R.J. Macek (LANL), M. Furman (LBNL), A. Aleksandrov, S. Cousineau, V. Danilov, S. Henderson (ORNL), M. Pivi (SLAC) 2598

On Emittance Evolution in the Extraction System of High-Current Electron and Ion Sources
J.-M. Lagniel, P. Balleyguier, D. Guilhem, J.-L. Lemaire, N. Pichoff, M. Prom_ (French Atomic Energy Commission) 2601

Resistive-Wall Wake for Non-Ultrarelativistic Beams
F. Zimmermann (CERN), K. Oide (KEK) 2604

Effects of Space Charge on Decoherence in Ion Beams
G. Rumolo, O. Boine-Frankenheim, I. Hofmann, Y. Liu (Gesellschaft fËr Schwerionenforschung mbH), A. Al-Khateeb (Yarmouk University) 2607

Space Charge Effects during the Injection Period of the KEK PS Main Ring
S. Igarashi, T. Miura, E. Nakamura, Y. Shimosaki, M. Shirakata, K. Takayama, T. Toyama (KEK) 2610

Challenge of Benchmarking Simulation Codes for the LANL Beam-Halo Experiment
T.P. Wangler, R.W. Garnett, W.P. Lysenko (LANL), J. Qiang (LBNL) 2613

High Brightness Potassium Ion Gun for the HIF Neutralized Transport Experiment (NTX)
S. Eylon, E. Henestroza, P.K. Roy, S.S. Yu (LBNL) 2616

Final Focus System for High Intensity Beams
E. Henestroza, F.M. Bieniosek, S. Eylon, P.K. Roy, S.S. Yu (LBNL) 2619

Neutralized Transport of High Intensity Beams
E. Henestroza, A. Anders, S. Eylon, P.K. Roy, W. Sharp, S.S. Yu (LBNL), D.V. Rose, D.R. Welch (Mission Research Corporation), P. Efthimion, E. Gilson (Plasma Physics Laboratory, Princeton University) 2622

Non-Intercepting Diagnostic for the HIF Neutralized Transport Experiment
P.K. Roy, S. Eylon, R. Hannink, E. Henestroza, J. Ludvig, D. Shuman, S.S. Yu (LBNL) 2625

Magnetic Lattice for the HIF Neutralized Transport Experiment (NTX)
D. Shuman, S. Eylon, E. Henestroza, P.K. Roy, W. Waldron, S.S. Yu (LBNL), T. Houck (LLNL) 2628

Analytical Study of Envelope Modes for a Fully Depressed Beam in Solenoidal and Quadrupole Periodic Transport Channels
S.M. Lund (LLNL), B. Bukh (LBNL) 2631

Influence of Conducting Plate Boundary Conditions on the RMS Envelope Equations Describing Intense Ion Beam Transport
S.M. Lund (LLNL), B. Bukh (LBNL) 2634

Realistic Modeling of Chamber Transport for Heavy-Ion Fusion
W.M. Sharp, D.A. Callahan, D.P. Grote, M. Tabak (LLNL), E. Henestroza, S.S. Yu (LBNL), D.V. Rose, D.R. Welch (Mission Research Corporation), P.F. Peterson (University of California, Berkeley) 2637

Reverted Resonant "Wakefield"
E.S. Masunov (MEPhI), A.V. Smirnov (DULY Research Inc.) 2640

Three-Dimensional Modeling of Intense Bunched Beams in RF Accelerators and Sources
R. Bhatt, C. Chen, M. Hess (MIT Plasma Science and Fusion Center) 2643

Beam Halo Formation and Loss Induced by Image-Charge Effects in a Small-Aperture Alternating-Gradient Focusing System
J. Zhou, C. Chen, B.L. Qian (MIT Plasma Science and Fusion Center), S. Eylon, E. Henestroza, S.S. Yu (LBNL) ... 2646

Initial Experimental Results of the Small Isochronous Ring (SIR)
J. Rodriguez, F. Marti, E. Pozdeyev (National Superconducting Cyclotron Laboratory) 2649

SNS Linac Commissioning - Transverse Matching
D. Jeon (ORNL), J. Stovall (LANL) 2652

Recent Results from the Paul Trap Simulator Experiment
H. Qin, R.C. Davidson, P. Efthimion, E. Gilson, R. Majeski (Plasma Physics Laboratory, Princeton University) ... 2655

Drift Compression and Final Focus of Intense Heavy Ion Beam
H. Qin, R.C. Davidson (Plasma Physics Laboratory, Princeton University), E.P. Lee (LBNL), J.J. Barnard (LLNL) 2658

RF Plasma Source for Heavy Ion Beam Charge Neutralization
P. Efthimion, R.C. Davidson, E. Gilson, L. Grisham (Plasma Physics Laboratory, Princeton University), B.G. Logan, S.S. Yu (LBNL) 2661

Simulating Accelerator Structure Operation at High Power
V. Ivanov, C. Adolphsen, N. Folwell, L. Ge, A. Guetz, K. Ko, Z. Li, C.-K. Ng, J.W. Wang, M. Wolf (SLAC), M. Weiner (Harvey Mudd College), G. Schussmann (University of California, Davis) 2664

A Modified QuadScan Technique for Emittance Measurement of Space Charge Dominated Beams
C.G. Limborg, S. Gierman (SLAC), J.G. Power (ANL) 2667

Calculation of the Maximum Stored Beam Current Considering the Phase Noise of a Generator RF Signal
L.H. Chang, M.C. Lin, G.H. Luo, Ch. Wang (Synchrotron Radiation Research Center) 2670

Space-Charge-Dominated Phenomena in the UMER Source Region
I. Haber, S. Bernal, R.A. Kishek, P.G. O'Shea, B. Quinn, M. Reiser, Y. Zou (University of Maryland), J.-L. Vay (LBNL), A. Friedman, D.P. Grote (LLNL) 2673

Large Diffuse Halos in Time-Dependent Space-Charge Potentials with Colored Noise
C.L. Bohn (Northern Illinois University and Fermilab), I.V. Sideris (Northern Illinois University) 2676

Main Regularities of Particle Redistribution in Space Charge-Dominated Beam Transport and Bunching
B.I. Bondarev, A.P. Durkin (Moscow Radiotechnical Institute) 2679

Angular Momentum Measurement of the FNPL Electron Beam
Y. Sun, K.-J. Kim (University of Chicago), K. Desler, D. Edwards, H. Edwards, M. HËening, P. Piot, J. Santucci (FNAL), S.-H. Wang (Indiana University), S.M. Lidia (LBNL), N. Barov, D. Mihalcea (Northern Illinois University), R. Tikhoplav (University of Rochester) 2682

Multiple Beam Interaction Studies in Heavy Ion Fusion
D.R. Welch, D.V. Rose (Mission Research Corporation), S.S. Yu (LBNL), C.L. Olson (Sandia National Laboratories) 2685

Observation of Coherent Microwave Transition Radiation in the APS Linac
G. Decker, X. Sun (ANL) 2688

RHIC Transverse Injection Damping
A. Drees, P. Cameron, R. Michnoff, C. Montag, M. Wilinski (BNL) 2691

RHIC Electron Detector Signal Processing Design
J. Gullotta, D. Gassner, D. Trbojevic, S.Y. Zhang (BNL) 2694

Multi-Million-Turn Beam Position Monitors for RHIC
T. Satogata, P. Cameron, P. Cerniglia, J. Cupolo, C. Dawson, C. Degen, J. Mead, K. Vetter (BNL) 2697

Waveguide Mode Reflectometry for Obstacle Detection in the LHC Beam Pipe Including Signal Attenuation
T. Kroyer, F. Caspers (CERN) 2700

Tune Measurement Methods of the Tevatron
C.Y. Tan, P. Lebrun, X.L. Zhang (FNAL) 2703

The SNS Laser Profile Monitor Design and Implementation
S. Assadi, A. Aleksandrov, W. Blokland, A. DeCarlo, C. Deibele, P. Gibson, W. Grice, M. Hechler, T. Hunter, J. Kelly, P. Ladd, G. Murdoch, J. Pogge, K. Potter, D. Purcell, T.J. Shea, D. Stout (ORNL) 2706

Design of an Optical Diffraction Radiation Beam Size Monitor at SLAC FFTB
Y. Fukui, D. Cline, F. Zhou (University of California, Los Angeles), M. Tobiyama, J. Urakawa (KEK), P.R. Bolton, M.C. Ross (SLAC), R. Hamatsu, P.V. Karataev, T. Muto (Tokyo Metropolitan University), A.S. Aryshev, G.A. Naumenko, A.P. Potylitsyn (Tomsk Polytechnic University) 2709

Measurement of Electron Beam Divergence Using OTR-ODR Interferometry
R. Fiorito, P.G. O'Shea, A.G. Shkvarunets (University of Maryland) 2712

A New Tool for Beam-Life Research at HLS Storage Ring
Yuxiong Li, Juexin Li, W. Li, Zuping Liu (National Synchrotron Radiation Lab) 2715

New Design of the TESLA Interaction Region with l* = 5 m
J. Payet, O. Napoly (CE Saclay) 2718

Optimum Choice of RF Frequency for Two Beam Linear Colliders
H. Braun, D. Schulte (CERN) 2721

Progress in the Design of a Damped and Tapered Accelerating Structure for CLIC
J.-Y. Raguin, I. Wilson, W. Wuensch (CERN) 2724

Main Linac Emittance Growth and Luminosity in Future Linear Colliders
D. Schulte (CERN) 2727

Bunch-to-Bunch Energy Stability Test of the Nb Prototypes of the TESLA Superstructure
H. Schlarb, V. Ayvazyan, P. Castro, R. Kammering, S. Schreiber, J. Sekutowicz, S. Simrock, M. Wendt (DESY), M. HËening (FNAL), M. Ferrario (INFN) 2730

Intra-Bunch-Train Luminosity Optimisation for the TESLA Linear Collider
N. Walker (DESY), D. Schulte (CERN), G.R. White (Queen Mary College, University of London) 2733

Simulations of the Static Tuning for the TESLA Linear Collider
N. Walker (DESY), D. Schulte (CERN) 2736

Comparison of the TESLA, NLC and CLIC Beam-Collimation System Performance
A. Drozhdin, N.V. Mokhov (FNAL), W. Kozanecki, O. Napoly (CE Saclay), D. Schulte, F. Zimmermann (CERN), N. Walker (DESY), G. Blair (Royal Holloway College), L. Keller, T. Markiewicz, T. Maruyama, T.O. Raubenheimer, A. Seryi, P. Tenenbaum, M. Woodley (SLAC) 2739

CTF3 Prototypes: Design, Tests and Measurements
A. Ghigo, D. Alesini, C. Biscari, R. Boni, A. Clozza, G. Delle Monache, A. Drago, A. Gallo, F. Marcellini, C. Milardi, C. Sanelli, M. Serio, F. Sgamma, A. Stecchi, A. Stella, M. Zobov (INFN), R. Corsini, L. Rinolfi (CERN) 2742

Harmonic Cavities for the NLC Damping Rings
A. Wolski, S. De Santis (LBNL) 2745

Study of Near-Field Vibration Sources for the NLC Linac Components
F. Asiri, F. Le Pimpec, A. Seryi (SLAC) 2748

Capture and Polarization of Positrons in a Proposed NLC Polarized Positron Source
Y.K. Batygin, J.C. Sheppard (SLAC) 2751

A Test of NLC-Type Beam Loading in the SLAC Linac
F.-J. Decker, T.O. Raubenheimer, A. Seryi, J.L. Turner, M. Woods, J. Yocky (SLAC) 2754

Implementation of Dynamic Misalignments and Luminosity Stabilization
L. Hendrickson, T. Himel, T.O. Raubenheimer, A. Seryi, P. Tenenbaum, M. Woodley (SLAC), D. Schulte (CERN) 2757

Optimized Wakefield Suppression & Emittance Dilution-Imposed Alignment Tolerances in X-Band Accelerating Structures for the JLC/NLC
R.M. Jones, Z. Li, R.H. Miller, T.O. Raubenheimer (SLAC) 2760

Energy Dispersion Compensation and Beam Loading in X-Band Linacs for the JLC/NLC
R.M. Jones, C. Adolphsen, V.A. Dolgashev, R.H. Miller, J.W. Wang (SLAC) 2763

A Recipe for Linear Collider Final Focus System Design
A. Seryi, M. Woodley (SLAC), P. Raimondi (INFN) 2766

Long Term Stability Study at FNAL and SLAC Using BINP Developed Hydrostatic Level System
A. Seryi, R. Ruland (SLAC), A. Chupyra, A. Erokhin, M. Kondaurov, A. Medvedko, V. Parkhomchuk, E. Shubin, S. Singatulin (BINP), J. Lach, D. Plant, V. Shiltsev (FNAL), A. Kuznetsov (Novosibirsk State University) 2769

Wigglers and Single-Particle Dynamics in the NLC Damping Rings
M. Venturini, A. Wolski (LBNL), A. Dragt (University of Maryland) 2772

A Lattice with Larger Momentum Compaction for the NLC Main Damping Rings
M. Woodley, T.O. Raubenheimer, J. Wu (SLAC), A. Wolski (LBNL) 2775

Feedback on Nanosecond Timescales: Fast Feedback Simulations
G.R. White (Queen Mary College, University of London) 2778

Form-Factor for a Target Used for Positron Generation with Undulator Radiation Conversion
A. Mikhailichenko (Cornell University) 2781

Pulsed Undulator to Test Polarized Positron Production at SLAC
A. Mikhailichenko (Cornell University) 2784

The Technical Realisation of RF Kickers for CLIC Test Facility CTF3
E. Plawski, A. Kucharczyk, S. Kulinski (Institute for Nuclear Studies, Poland) 2787

Development of Room Temperature Accelerating Structures for the RIA
N.E. Vinogradov, P.N. Ostroumov, E. Rotela, S.I. Sharamentov, S. Sharma, G.P. Zinkann (ANL), J.W. Rathke, T.J. Schultheiss (Advanced Energy Systems), D.L. Schrage (LANL) 2790

AGS Upgrade to 1-MW with a Super-Conducting Linac Injector
A.G. Ruggiero, J. Alessi, D. Raparia, T. Roser, W.T. Weng (BNL) 2793

Study of a 10-MW Continuous Spallation Neutron Source
A.G. Ruggiero, H. Ludewig, S. Shapiro (BNL) 2796

Results of the IPHI Drift Tube Linac's Hot Model CW Tests
P.-E. Bernaudin, G. Congretel (CE Saclay), P. Balleyguier (French Atomic Energy Commission), A. Fontenille, E. Froidefond, M. Fruneau, D. Marchand, M. Planet, J.-C. Ravel (LPSC Grenoble) 2799

Beam Dynamics Studies in SPIRAL II Linac
R. Duperrier, D. Uriot (CE Saclay), N. Pichoff (French Atomic Energy Commission), P. Bertrand, B. Bru, A. Savalle, F. Varenne (Grand Accelerateur National d'Ions Lourds), J.L. Biarrotte (Institut de Physique Nucl_aire d'Orsay), J.-M. De Conto, E. Froidefond (LPSC Grenoble) 2802

Instabilities Study and Implications for the RIA Project
R. Duperrier (CE Saclay), D. Gorelov (National Superconducting Cyclotron Laboratory) 2805

A SCRF Linac as a FEL Driver and Storage Ring Injector
J. Rose, J.B. Murphy, B. Podobedov, T. Shaftan, B. Sheehy, X.J. Wang, L.H. Yu (BNL) 2808

Beam Dynamic Calculations for the Superconducting COSY Injector Linac
A. Lehrach, H. Jungwirth, R. Maier, R. Toelle (Forschungszentrum Juelich) 2811

Debuncher Developing for H and D Beams Injection into COSY Ring
Y. Senichev, R. Maier, R. Stassen, R. Toelle, N. Vasyukhin (Forschungszentrum Juelich) 2814

The RFQ-Injector for COSY-SCL
K.-U. Kuehnel, A. Schempp (Institut fur Angewandte Physik), A. Schnase, R. Toelle (Forschungszentrum Juelich), C.P. Welsch (Max-Planck-Institut fuer Kernphysik) 2817

Design of a Superconducting CH-Cavity for Low- and Medium Beta Ion and Proton Acceleration
H. Liebermann, H. Podlech, U. Ratzinger, A. Sauer (Institut fur Angewandte Physik) 2820

The Frankfurt Funneling Experiment
J. Thibus, I. Mueller, N. Mueller, A. Schempp, H. Zimmermann (Institut fur Angewandte Physik) 2823

Cold-Model Tests of an Annular Coupled Structure for Upgrade of a J-PARC Linac
H. Ao (Japan Atomic Energy Research Institute), V. Paramonov (Institute for Nuclear Research, Moscow), N. Hayashizaki (Tokyo Institute of Technology) 2826

Low Power Test of RFQ Mock-up Modules at 175MHz for IFMIF Project
S. Maebara, T. Imai, T. Morishita, M. Sugimoto, H. Takeuchi (Japan Atomic Energy Research Institute), M. Saigusa, S. Sazawa (Ibaraki University) 2829

Development of a Low-Energy Proton Accelerator System for the Proton Engineering Frontier Project (PEFP)
J.M. Han, Y.S. Cho, B.H. Choi, S.H. Han, J.H. Jang, K.K. Jeong, Y.J. Kim, H.J. Kwon, H.H. Lee, J.H. Na, M.Y. Park, K.T. Seol (Korea Atomic Energy Research Institute) 2832

Volume 5

Tuning of the RF Field of the DTL for the J-PARC
F. Naito, M. Ikegami, T. Kato, E. Takasaki, H. Tanaka (KEK), T. Ito (Japan Atomic Energy Research Institute)....2835

High-Gradient Tests on S-Band 2m-Long Accelerating Structures for KEKB Injector Linac
Y. Igarashi (The Graduate University for Advanced Studies), A. Enomoto, Y. Higashi, K. Kakihara, S. Ohsawa, T. Oogoe, S. Yamaguchi (KEK), H. Hanaki, T. Taniuchi, H. Tomizawa (SPring-8) 2838

Mechanical Design of the Drift-Tube Linac (DTL) for the Spallation Neutron Source
T. Ilg, S. Ellis, W. Fox, R. Gentzlinger, R. Martineau, L. Rowton, J. Sims (LANL), G. Johnson (ORNL)....2841

Fabrication and Tuning of the SNS CCL Hot Model
N. Bultman, J. Billen, Z. Chen, M. Collier, D. Richards, L.M. Young (LANL)....2844

RIA Fragmentation Line Beam Dump
W. Stein (LLNL)....2847

Analysis of a Multi-Spoke Option for the RIA Driver Linac
D. Gorelov, T. Grimm, W. Hartung, F. Marti, X. Wu, R. York (National Superconducting Cyclotron Laboratory)..2849

Numerical Design and Optimization of Cooling System for 2 MeV Traveling Wave Accelerator
L. Shen, L. Cao, Shaoqing Li, Xiaoguang Li, J. Yao (University of Science and Technology of China), D. Jiang, Y.J. Pei (National Synchrotron Radiation Lab) 2852

Impact of Cavity RF Field Phase and Amplitude Control Uncertainties on the SNS Linac
D. Jeon (ORNL), J. Stovall, H. Takeda (LANL), K. Crandall (TechSource, Inc.) 2855

The Low Level RF System for 100MV Proton Linac of KOMAC
I.H. Yu, M.H. Chun, K.M. Ha, Y.J. Han, W.H. Hwang, H.S. Kang, D.T. Kim, S.C. Kim, S.H. Nam, J.S. Yang (Pohang Accelerator Laboratory), Y.S. Cho, J.M. Han, H.J. Kwon, K.T. Seol (Korea Atomic Energy Research Institute) 2857

Status of the Production Electropolishing System at JLAB
J. Mammosser, J. Delayen, J. Gordon, L. Phillips, A.-M. Valente, T. Wang, A.T. Wu (Thomas Jefferson National Accelerator Facility), J. Saunders (ORNL) 2860

Gradient Optimization for SC CW Accelerators
W.J. Schneider, P. Kneisel, C.H. Rode (Thomas Jefferson National Accelerator Facility)....2863

Mechanical Cavity Design for 100MV Upgrade Cryomodule
K.M. Wilson, E. Daly, J. Henry, J. Hogan, D. Machie, J. Sekutowicz, T. Whitlatch (Thomas Jefferson National Accelerator Facility)....2866

Commissioning-Results of the REX-ISOLDE Linac
S. Emhofer, F. Ames, J. Cederkєll, D. Habs, O. Kester, K. Rudolph (Sektion Physik der LMU MËnchen), T. Sieber (CERN) 2869

An Energy Upgrade of the REX-ISOLDE Linac
O. Kester, H. Bongers, W. Carli, S. Emhofer, D. Habs, K. Rudolph, T. Sieber (Sektion Physik der LMU MËnchen) 2872

Front End Design of the RIA Driver Linac
A.A. Kolomiets (Institute for Theoretical and Experimental Physics), V.N. Aseev, P.N. Ostroumov, R.C. Pardo (ANL) 2875

High Power Electron S-band Linac for Industrial Purposes
V.A. Kushnir, M.I. Ayzatsky, E.Z. Biller, V.N. Boriskin, A.N. Dovbnya, V.V. Mitrochenko (NSC KIPT), V.I. Beloglasov, N.V. Demidov, L.K. Myakushko, T.F. Nikitina, V.A. Popenko, G.D. Pugachev, G.D. Repikhov, L.V. Reprintzev, V.A. Shendrik, D.L. Stepin, G.E. Tarasov, Yu.D. Tur, V.L. Uvarov (Kharkov Institute of Physics and Technology) 2878

Pulsed Heating Experiments at 34 GHz
O.A. Nezhevenko, V.P. Yakovlev (Omega-P, Inc.), J.L. Hirshfield (Omega-P, Inc. and Yale University), G.V. Serdobintsev (Yale University) 2881

The Vacuum Systems for PEFP Linac
M.Y. Park, Y.S. Cho, J.M. Han, J.H. Jang, K.K. Jeong, Y.J. Kim, H.J. Kwon (Korea Atomic Energy Research Institute) 2884

Series Production of Copper and Niobium Cavities for the Spallation Neutron Source
M. Pekeler, S. Bauer, K. Dunkel, B. Griep, C. Piel, H. Vogel, P. vom Stein (ACCEL Instruments GmbH) 2887

Continued Development of the RFI Linac Structure
D.A. Swenson, K.R. Crandall, F.W. Guy, W.J. Starling (Linac Systems) 2889

Upgrades of Linac System at CAMD
Y. Wang, M. Fedurin, P. Jines, T. Miller, T. Zhao (Center for Advanced Microstructures and Devices) 2892

Linear Coupling of RMS Emittances
L.C. Teng (ANL) 2895

Proposal of Partial Siberian Snake based on Helical Magnets for AGS
Yu.M. Shatunov, I.A. Koop, A.V. Otboev, E.A. Perevedentsev, P.Yu. Shatunov (BINP) 2898

Action and Phase Analysis to Determine Sextupole Errors in RHIC and the SPS
J. Cardona, S. Peggs, T. Satogata (BNL), R. Tom_s (CERN) 2901

Beam Diffusion Measurements at RHIC
R. Fliller III, A. Drees, D. Gassner, G. McIntyre, S. Peggs, D. Trbojevic (BNL) 2904

Measurement of the Nonlinear Momentum Compaction Factor in RHIC
C. Montag (BNL) 2907

Adiabatic Capture of Charged Particles in Stable Islands: a Novel Approach to Multi-Turn Extraction
M. Giovannozzi, R. Cappi (CERN) 2910

Optics Studies for the CERN Proton Synchrotron: Linear and Nonlinear Modelling Using Beam Based Measurements
M. Giovannozzi, R. Cappi, E. M_tral, G. M_tral, M. Martini, R. Steerenberg (CERN), A.-S. MËller (Forschungszentrum Karlsruhe) 2913

Measurements of Transverse Space-Charge Effects in the CERN Proton Synchrotron
E. M_tral, M. Giovannozzi, G. M_tral, M. Martini, R. Steerenberg (CERN) 2916

Beam-Based BPM Alignment
R. Talman, N. Malitsky (BNL) 2919

Barrier RF Stacking at Fermilab
W. Chou, J. Griffin, K.Y. Ng, D. Wildman (FNAL), H. Zheng (California Institute of Technology), A. Takagi (KEK) 2922

Fermilab Booster Modeling and Space Charge Study
W. Chou, A. Drozhdin, P. Lucas, J.-F. Ostiguy (FNAL) 2925

Ion Production and Tune Shift in the Recycler Ring
K. Gounder, J.P. Marriner, C.S. Mishra (FNAL) 2928

Analysis and Measurements of Emittance Dilution from Vacuum Windows in the Fermilab Recycler Transfer Lines
C. Johnstone, C. Gattuso, D. Johnson, M. Syphers (FNAL), K. Paul (University of Illinois) 2931

Automatic Beamline Correction
T. Kobilarcik, J. DeVoy, C. Moore (FNAL) 2934

Increasing the Intensity of the Fermilab Booster
E.J. Prebys, C. Ankenbrandt, W. Chou, A. Drozhdin, P.H. Kasper, J.R. Lackey, N.V. Mokhov, W.A. Pellico, R. Tomlin, R.C. Webber (FNAL) 2936

Space Charge in the FNAL Booster: Experiment and Modeling
P. Spentzouris, J. Amundson (FNAL) 2939

End-to-End Simulations of a Superconducting Deuteron CH-DTL for IFMIF
A. Sauer, H. Deitinghoff, H. Klein, H. Liebermann, H. Podlech, U. Ratzinger, R. Tiede (Institut fur Angewandte Physik) 2942

Developments in Linear and Non-Linear DAFNE Lattice
C. Milardi, G. Benedetti, M. Biagini, C. Biscari, M. Boscolo, S. Guiducci, M.A. Preger, P. Raimondi, C. Vaccarezza, M. Zobov (INFN) 2945

Jitter Control and Scraping in the 12-View AHF HEBT
B. Blind, A. Jason (LANL) 2948

The Use of Electric Multipole Lenses for Bending and Focusing Polar Molecules, with Application to the Design of a Rotational-State Separator
J.G. Kalnins (LBNL) 2951

Space-Charge Driven Emittance Growth in a 3D Mismatched Anisotropic Beam
J. Qiang, R.D. Ryne (LBNL), I. Hofmann (Gesellschaft fËr Schwerionenforschung mbH) 2954

Pulse Compression Via Velocity Bunching with the LLNL Thomson X-Ray Source Photoinjector
S.G. Anderson, W. Brown, A.M. Tremaine (LLNL), P. Musumeci, J.B. Rosenzweig (University of California, Los Angeles) 2957

Eliminating the Spot Dilution due to Kicker Switching in DARHT-II
Y.-J. Chen, F. Chambers, A.C. Paul, J.A. Watson, J. Weir (LLNL) 2960

RF Focusing Methods for Heavy Ions in Low Energy Accelerators
E.S. Masunov, S.M. Polozov (MEPhI), P.N. Ostroumov, N.E. Vinogradov (ANL) 2963

Image-Charge Effects on the Envelope Dynamics of an Unbunched Intense Charged-Particle Beam
B.L. Qian, C. Chen, J. Zhou (MIT Plasma Science and Fusion Center) 2966

Random-Regular Accelerating Structures
K. Kramarenko, M.I. Ayzatsky (NSC KIPT) 2969

The Beam Dynamics Studies of Combined Misalignments and RF Errors for RIA
X. Wu, D. Gorelov, T. Grimm, W. Hartung, F. Marti, R. York (National Superconducting Cyclotron Laboratory) 2972

Plasma Neutralization Models for Intense Ion Beam Transport in Plasma
I.D. Kaganovich, S. O'Rourke (Princeton University), E.P. Lee (LBNL), R.C. Davidson, E.A. Startsev (Plasma Physics Laboratory, Princeton University) 2975

Intense Sheet Beam Stability Properties for Uniform Phase-Space Density
E.A. Startsev, R.C. Davidson (Plasma Physics Laboratory, Princeton University) 2978

RF Modes in the PEP-II Shielded Vertex Bellows
A. Novokhatski, S. Weathersby (SLAC) 2981

Characteristics of Pulse Compression in Laser Pulse Amplification by Stimulated Raman Backscattering
J.B. Kim (KERI and POSTECH), H.J. Lee, H. Suk (Korea Electrotechnology Research Institute), I.S. Ko (Pohang Accelerator Laboratory) 2984

Effect of Preplasmas on High-Energy Ion Generation by an Intense Laser Pulse Irradiated on Overdense Plasmas
H.J. Lee, C. Kim, G.H. Kim, J.U. Kim, H. Suk (Korea Electrotechnology Research Institute), J.B. Kim (KERI and POSTECH) 2987

New Regions of Stability for Periodically Focused Particle Beams
R. Pakter, J.S. Moraes, F.B. Rizzato (Universidade Federal do Rio Grande do Sul) 2990

Coupling Impedances for Corrugated Beam Pipes from Impedance Boundary Conditions
S. Petracca, Th. Demma (University of Sannio and INFN) 2993

The Gaussian Approximation for a Purely Inductive Wake Function
S. Petracca, Th. Demma (University of Sannio and INFN), K. Hirata (The Graduate University for Advanced Studies) 2996

Electromagnetic Fields in the Toroidal Region of LHC-Like Rings
S. Petracca, Th. Demma (University of Sannio and INFN) 2999

Non-Coulomb Perturbations Influence on Beam Dynamics in Extended Accelerating/Focusing Channels
B.I. Bondarev, A.P. Durkin (Moscow Radiotechnical Institute) 3002

Acceleration and Self-Focused Particle Beam Drivers
V. Zadorozhny (Institute of Cybernetics, Ukraine), Z. Parsa (BNL) 3005

Vertical Coupling Impedance of the APS Storage Ring
Y.-C. Chae, K. Harkay, X. Sun (ANL) 3008

Horizontal Coupling Impedance of the APS Storage Ring
Y.-C. Chae, K. Harkay, X. Sun (ANL) 3011

Longitudinal Coupling Impedance of the APS Storage Ring
Y.-C. Chae, K. Harkay, X. Sun (ANL) 3014

The Impedance Database and its Application to the APS Storage Ring
Y.-C. Chae (ANL) 3017

Bunch Length Measurements at BESSY
P. Kuske, M. Abo-Bakr, W. Anders, G. WËstefeld (BESSY) 3020

Coherent Emission of Synchrotron Radiation and Longitudinal Instabilities
P. Kuske, M. Abo-Bakr, J. Feikes, K. Holldack, G. WËstefeld (BESSY) 3023

Transverse Instabilities in RHIC
M. Blaskiewicz, J.M. Brennan, P. Cameron, C. Dawson, C. Degen, K. Drees, W. Fischer, E. Koropsak, R. Michnoff, C. Montag, T. Roser, T. Satogata (BNL), N. Catalan-Lasheras (CERN) 3026

Longitudinal Solitons in RHIC
M. Blaskiewicz, J.M. Brennan, P. Cameron, W. Fischer, J. Wei (BNL), A. Luque, H. Schamel (University of Bayreuth) 3029

Effects of Space Charge and Nonlinearities on Collective Instabilities of a Long Bunch
A. Fedotov, J. Wei (BNL), V. Danilov (ORNL) 3032

Coupling Impedance Measurements of the SNS RF Cavity and Extraction Kicker Magnet
H. Hahn, M. Blaskiewicz, D. Davino (BNL) 3035

The Electron Cloud Instability of the LHC Beam in the CERN SPS
G. Arduini, K. Cornelis, W. HÅfle, G. Rumolo, F. Zimmermann (CERN) 3038

Investigation of Space Charge Effects in the SPS
H. Burkhardt, G. Rumolo, F. Zimmermann (CERN) 3041

Coherent Tune Shifts Measured with Few Bunches in the SPS and Comparison with Resistive Wall Theory
H. Burkhardt, A. Koschik, G. Rumolo, F. Zimmermann, B. Zotter (CERN) 3044

Longitudinal Microwave Instability in Lepton Bunches
E. M_tral (CERN) 3047

Nominal Longitudinal Parameters for the LHC Beam in the CERN SPS
E. Shaposhnikova, P. Baudrenghien, T. Bohl, T. Linnecar, J. Tuckmantel (CERN) 3050

Transverse 'Monopole' Instability Driven by an Electron Cloud?
F. Zimmermann, E. Benedetto, D. Schulte (CERN), Y. Papaphilippou (European Synchrotron Radiation Facility), G. Rumolo (Gesellschaft fËr Schwerionenforschung mbH), K. Ohmi (KEK) 3053

Simulation Study of Coupled-Bunch Instabilities due to Resistive Wall, Ions, or Electron Cloud
F. Zimmermann (CERN), H. Fukuma, K. Ohmi, Y. Ohnishi, S.S. Win (KEK) 3056

Instability Threshold Currents vs. Energy in CESR
M. Billing, J. Sikora (Cornell University) 3059

Head-Tail Instability at Tevatron
P.M. Ivanov, G. Annala, A. Burov, V.A. Lebedev, E. Lorman, V. Ranjbar, V. Scarpine, V. Shiltsev (FNAL) 3062

Impedances of Tevatron Separators
K.Y. Ng (FNAL) 3065

A 1.7 GHz Waveguide Schottky Detector System
R.J. Pasquinelli, E. Cullerton, D. Peterson, P. Seifrid, J. Steimel, D. Sun, D. Tinsley (FNAL) 3068

The Tevatron Bunch by Bunch Longitudinal Dampers
C.Y. Tan, J. Steimel (FNAL) 3071

The Tevatron Transverse Dampers
C.Y. Tan, J. Steimel (FNAL) 3074

Bunch Lengthening Recently Observed at PF-AR
T. Ieiri, T. Kasuga, Y. Minagawa, T. Obina (KEK), T. Fujita (Hiroshima University) 3077

Transverse Sawtooth Instability Observed in Photon Factory Advanced Ring
Y. Minagawa, T. Ieiri, T. Kasuga, T. Obina (KEK), T. Fujita (Hiroshima University) 3080

Study of ep Instability for a Coasting Proton Beam in Circular Accelerators
K. Ohmi, M. Tomizawa, T. Toyama (KEK) 3083

An Experimental Study of Microwave Stability near Transition in the PSR
P. Colestock, C. Beltran, A. Browman, J.D. Gilpatrick, R.J. Macek, R. McCrady, F. Neri, L.J. Rybarcyk, T. Spickermann (LANL), M. Schulze (General Atomics) 3086

Status of the Experimental Studies of the Electron Cloud at the Los Alamos Proton Storage Ring
R.J. Macek, M. Borden, A. Browman, D. Fitzgerald, R. McCrady, T. Spickermann, T. Zaugg (LANL) 3089

A Three-Dimensional Kinetic Theory of Continuous-Beam Stability
T.S. Wang (LANL) 3092

A Numerical Study of Bunched Beam Transverse Electron-Proton Instability Based on the Centroid Model
T.S. Wang (LANL) 3095

RF Impedance Measurements on the DARHT-II Accelerator Intercell Assembly
W. Fawley, S. Eylon (LBNL), R. Briggs (Science Applications International Corporation) 3098

The Stabilization of Budker-Chirikov Instability by the Spread of Longitudinal Velocities
Yu.Ya. Golub (Moscow Radiotechnical Institute) 3101

New Vortices in Axisymmetric Inhomogeneous Beams
Yu.Ya. Golub (Moscow Radiotechnical Institute) 3103

Beam Instabilities at the PLS Storage Ring
E.-S. Kim (Pohang Accelerator Laboratory) 3105

Simulations on Wakefield Effects in the Electron Beam at the 2.5 GeV PLS Linac
E.-S. Kim, H. Heo, S.H. Nam (Pohang Accelerator Laboratory) 3108

Design Considerations for SASE-FEL at PLS
E.-S. Kim (Pohang Accelerator Laboratory) 3111

Operational Performance in 2.5 GeV Full Energy Injection at PLS
E.-S. Kim, Y.J. Han, S.-H. Jeong, M.G. Kim, S.C. Kim, S.-S. Park, J.-H. Seo (Pohang Accelerator Laboratory) 3114

Instability Driven by Wall Impedance in Intense Charged Particle Beams
R.C. Davidson, H. Qin (Plasma Physics Laboratory, Princeton University), G. Shvets (Illinois Institute of Technology) 3117

Delta-f Simulation Studies of the Ion-Electron Two-Stream Instability in IBX
H. Qin, R.C. Davidson, E.A. Startsev (Plasma Physics Laboratory, Princeton University) 3120

Kinetic Studies of Temperature Anisotropy Instability in Intense Charged Particle Beams
E.A. Startsev, R.C. Davidson, H. Qin (Plasma Physics Laboratory, Princeton University) 3123

Measurement of the Longitudinal Wakefield in the SLAC Linac for Extremely Short Bunches
K. Bane, F.-J. Decker, P. Emma, L. Hendrickson, P. Krejcik, C.L. O'Connell, H. Schlarb, J. Welch, M. Woodley (SLAC) 3126

Measurements of Transverse Emittance Growth due to Coherent Synchrotron Radiation in the SLAC SPPS Bunch Compressor Chicane
P. Emma, F.-J. Decker, P. Krejcik, C.L. O'Connell, M. Woodley (SLAC), H. Schlarb, F. Stulle (DESY) 3129

Single-Mode Coherent Synchrotron Radiation Instability
S. Heifets, G.V. Stupakov (SLAC) 3132

Nonlinear Regime of a Single-Mode CSR Instability
S. Heifets, G.V. Stupakov (SLAC) 3135

Effects of Linac Wakefield on CSR Microbunching in the Linac Coherent Light Source
Z. Huang, P. Emma (SLAC), M. Borland, K.-J. Kim (ANL) 3138

An Over-Damped Cavity Longitudinal Kicker for the PEP-II LER
P. McIntosh, R. Akre, D. Anderson, S. DeBarger, M. Dormiani, J. Fox, K. Jobe, H. Schwarz, D. Teytelman, U. Wienands, A. Young (SLAC), F. Marcellini (INFN), M. Tobiyama (KEK) 3141

Evolving Bunch and Retardation in the Impedance Formalism
R. Warnock (SLAC), M. Venturini (LBNL) 3144

Robinson Modes at Aladdin
R.A. Bosch, J.J. Bisognano, K.J. Kleman (Synchrotron Radiation Center, University of Wisconsin) 3147

The Effects of Temperature Variation on Electron Beams with RF Voltage Modulation
P.J. Chou, M.H. Wang (Synchrotron Radiation Research Center), S.Y. Lee (Indiana University) 3150

A Fast Method to Estimate the Gain of the Microbunch Instability in a Bunch Compressor
S. Reiche, J.B. Rosenzweig (University of California, Los Angeles) 3153

Experimental Study of Energy Spread in a Space-Charge Dominated Electron Beam
Y. Cui, I. Haber, R.A. Kishek, P.G. O'Shea, M. Reiser, A. Valfells, Y. Zou (University of Maryland) 3156

Alternative Bunch Formation for the Tevatron Collider
G. Jackson (Hbar Technologies, LLC) 3159

Longitudinal Emittance Growth in the Fermilab Booster Synchrotron
G. Jackson (Hbar Technologies, LLC) 3162

Two-Stream Studies for Heavy Ion Beam Propagation in a Reactor Chamber
D.R. Welch, T.C. Genoni, D.V. Rose (Mission Research Corporation), C.L. Olson (Sandia National Laboratories) 3165

Simulated Growth Rates for Single-Bunch Instabilities Driven by a Resistive Impedance
N. Towne (BNL) 3168

Analytical and Time-Domain Computations of Single-Bunch Loss-Factor in a Planar Structure
D. Yu, A.V. Smirnov (DULY Research Inc.) 3171

Simulation of Beam-Electron Cloud Interactions in Circular Accelerators Using Plasma Models
A.Z. Ghalam, T.C. Katsouleas (University of Southern California), V. Decyk, C. Huang, W.B. Mori (University of California, Los Angeles) 3174

Booster's Coupled Bunch Damper Upgrade
W.A. Pellico, D. Wildman (FNAL) 3177

Beam Dynamics Simulations for the Fermilab Recycler Ring Barrier Buckets
C.M. Bhat, J.A. MacLachlan, J.P. Marriner (FNAL), H. Kang (Stanford University) 3180

Studies of a Generalized Beam-Induced Multipacting Resonance Condition
K. Harkay, R.A. Rosenberg (ANL), L. Loiacono (Loyola University) 3183

Simulation of Magnetized Beams
D. Wang, I. Ben-Zvi, X. Chang, J. Kewisch, C. Montag (BNL), F. Zhou (University of California, Los Angeles) 3186

Probing the Non-Linear Dynamics of the ESRF Storage Ring with Experimental Frequency Maps
Y. Papaphilippou, L. Farvacque, A. Ropert (European Synchrotron Radiation Facility), J. Laskar (BDL, Paris) 3189

Non-Linear Longitudinal Beam Dynamics with Harmonic RF Systems for Bunch Lengthening
V. Serriere, J. Jacob (European Synchrotron Radiation Facility) 3192

Synergia: A Hybrid, Parallel Beam Dynamics Code with 3D Space Charge
J. Amundson, P. Spentzouris (FNAL) 3195

Flat Beam Production in Low Energy Injectors
S.-H. Wang (Indiana University), J. Corlett, S.M. Lidia, J. Staples, A. Zholents (LBNL) 3198

Low Emittance Optics at the Photon Factory
K. Harada, M. Izawa, Y. Kobayashi, T. Obina, A. Ueda (KEK) 3201

Injection Performance with a Traveling Wave Kicker Magnet System at the Photon Factory Storage Ring
Y. Kobayashi, T. Mitsuhashi, A. Ueda (KEK) 3204

Measurement of the Transverse Quadrupole-Mode Frequencies of an Electron Bunch in the KEK Photon Factory Storage Ring
S. Sakanaka, T. Mitsuhashi, T. Obina (KEK) 3207

Simulation Results of Corkscrew Motion in DARHT-II
K.C.D. Chan, C. Ekdahl (LANL), Y.-J. Chen (LLNL), T. Hughes (Mission Research Corporation) 3210

Coupling Correction and Beam Dynamics at Ultralow Vertical Emittance in the ALS
C. Steier, D. Robin, A. Wolski (LBNL), G. Portmann, J. Safranek (SLAC) 3213

Comparison of PARMELA Simulations with Longitudinal Emittance Measurements at the SLAC Gun Test Facility
C.G. Limborg, P.R. Bolton, J. Clendenin, D. Dowell, S. Gierman, B.F. Murphy, J.F. Schmerge (SLAC) 3216

Recent Electron-Cloud Simulation Results for the Main Damping Rings of the NLC and TESLA Linear Colliders
M. Pivi, T.O. Raubenheimer (SLAC), M. Furman (LBNL) 3219

Mitigation of the Electron-Cloud Effect in the PSR and SNS Proton Storage Rings by Tailoring the Bunch Profile
M. Pivi (SLAC), M. Furman (LBNL) 3222

Derivation of FEL Gain Using Wakefield Approach
G.V. Stupakov, S. Krinsky (SLAC) 3225

Coherent Synchrotron Radiation Effects in the Electron Cooler for RHIC
J. Wu (SLAC), D. Wang (BNL), F. Zhou (University of California, Los Angeles) 3228

Impact of the Wiggler Coherent Synchrotron Radiation Impedance on the Beam Instability
J. Wu, Z. Huang, T.O. Raubenheimer, G.V. Stupakov (SLAC) 3231

Electron Beam Motion Observed in Infrared Synchrotron Radiation at NSRRC
D.S. Hung, C.I. Chen, C.H. Kuo, Y.C. Lo (Synchrotron Radiation Research Center) 3234

Experimental Measurements of 2-Dimensional Nonlinear Resonances
T.S. Ueng, J. Chen, K.T. Hsu, K.H. Hu, C.H. Kuo (Synchrotron Radiation Research Center) 3237

First Experimental Test of Emittance Measurement Using the Quadrupole-Mode Transfer Function
M.H. Wang (Synchrotron Radiation Research Center), S.Y. Lee, Y. Sato (Indiana University) 3240

Beam Characterization in the CEBAF-ER Experiment
C. Tennant, Y. Chao, D. Douglas, A. Freyberger, M. Tiefenback (Thomas Jefferson National Accelerator Facility) 3243

A Beam Breakup Instability in a Recirculating Linac Caused by a Quadrupole Mode
B. Yunn (Thomas Jefferson National Accelerator Facility) 3246

The Short-Range Transverse Wakefields in TESLA Accelerating Structure
I. Zagorodnov, T. Weiland (Technische U. Darmstadt) 3249

Calculation of Collimator Wakefields
I. Zagorodnov, T. Weiland (Technische U. Darmstadt), K. Bane (SLAC) 3252

Focusing Horn System for the BNL Very Long Baseline Neutrino Oscillation Experiment
S.A. Kahn, A. Carroll, M. Diwan, J.C. Gallardo, H. Kirk, C. Scarlett, N. Simos, B. Viren, W. Zhang (BNL) 3255

Beam Shaping and Compression Scheme for the UCLA Neptune Laboratory
R.J. England, P. Musumeci, J.B. Rosenzweig, R. Yoder (University of California, Los Angeles) 3258

Detection of Wake Field Using Test-Bunch Method at Photon Factory Advanced Ring
T. Fujita (Hiroshima University), T. Kasuga, Y. Minagawa, T. Obina (KEK) 3261

Bunch Transverse Emittance Increases in Electron Storage Rings
J. Gao (Laboratoire de L'Accelerateur Lineaire [LAL]) 3264

Analytical Estimation of Dynamic Apertures Limited by the Wigglers in Storage Rings
J. Gao (Laboratoire de L'Accelerateur Lineaire [LAL]) 3267

Lattice Design of Saga Synchrotron Light Source
Y. Iwasaki, S. Koda, T. Tomimasu (Saga Synchrotron Light Source), H. Ohgaki (Kyoto University), H. Toyokawa, M. Yasumoto (National Institute of Advanced Industrial Science and Technology), Y. Hashiguchi, T. Kitsuka, Y. Ochiai, Y. Yamatsu (Saga Prefectural Government) 3270

Linear and Nonlinear Optics Studies in the ANKA Storage Ring
A.-S. MËller, I. Birkel, E. Huttel, F. Perez, M. Pont, R. Rossmanith (Forschungszentrum Karlsruhe) 3273

Beam Size and Bunch Length Measurements at the ANKA Storage Ring
F. Perez, I. Birkel, E. Huttel, A.-S. MËller, M. Pont (Forschungszentrum Karlsruhe) 3276

Single-Bunch Injection System for the LNLS Booster Injector
P.F. Tavares, S.R. Marques, H.J. Onisto (LaboratÂrio Nacional de Luz S°ncrotron, Brazil) 3279

Polarized H⁻ Ion Source Performance During the 2003 RHIC Run
J. Alessi, B. Briscoe, O. Gould, A. Kponou, Vincent LoDestro, D. Raparia, J. Ritter, A. Zelenski (BNL), V. Klenov, S. Kokhanovski, V. Zubets (Institute for Nuclear Research, Moscow) 3282

The SPARC Project: A High Brightness Electron Beam Source at LNF to Drive a SASE-FEL Experiment
L. Palumbo, A. Cianchi, A. D'Angelo, R. Di Salvo, A. Fantini, D. Moricciani, C. Schaerf (University of Rome), R. Bartolini, F. Ciocci, G. Dattoli, A. Doria, F. Flora, G.P. Gallerano, L. Giannessi, E. Giovenale, G. Messina, L. Mezi, P.L. Ottaviani, L. Picardi, M. Quattromini, A. Renieri, C. Ronsivalle (Ente Nazionale per le Nuove Tecnologie l'Energia e l'Ambiente), D. Alesini, F. Alessandria, A. Bacci, S. Bertolucci, M. Biagini, C. Biscari, R. Boni, I. Boscolo, M. Boscolo, F. Broggi, M. Castellano, L. Catani, E. Chiadroni, S. Cialdi, A. Clozza, C. De Martinis, G. Di Pirro, A. Drago, A. Esposito, M. Ferrario, V. Fusco, A. Gallo, F.S. Gamma, A. Ghigo, D. Giove, S. Guiducci, M. Incurvati, D. Levi, C. Ligi, F. Marcellini, C. Maroli, M. Mattioli, G. Medici, C. Milardi, L. Pellegrino, V. Petrillo, M.A. Preger, P. Raimondi, R. Ricci, M. Rom¬, C. Sanelli, L. Serafini, M. Serio, B. Spataro, A. Stecchi, A. Stella, S. Tazzari, F. Tazzioli, C. Vaccarezza, M. Vescovi, C. Vicario, M. Zobov (INFN), J.B. Rosenzweig (University of California, Los Angeles) 3285

A Simulation Study of the JLC Positron Source
T. Kamitani, Y. Ohnishi (KEK), S. Kashiwagi (Waseda University) 3288

Diffusion of Alkali Species in Porous Tungsten Substrates Used in Contact-Ionization Sources
E. Chacon-Golcher (LANL), J. Kwan (LBNL), E.C. Morse (University of California, Berkeley) 3291

Fabrication of Large Diameter Alumino-Silicate K^+ Sources
D. Baca, J. Kwan, J.K. Wu (LBNL), E. Chacon-Golcher (LANL) 3294

Beam Optics of a 10-cm Diameter High Current Heavy Ion Diode
J. Kwan, F.M. Bieniosek, J.-L. Vay (LBNL), E. Halaxa, G. Westenskow (LLNL), I. Haber (University of Maryland) 3297

Characterization of an RF-Driven Plasma Ion Source for Heavy Ion Fusion
G. Westenskow, E. Halaxa, R.P. Hall (LLNL), J. Kwan (LBNL) 3300

Stability of Electron Beam Parameters in Sources with Cold Secondary-Emission Cathodes
A.N. Dovbnya, N.I. Aizatsky, V.N. Boriskin, M.A. Krasnogolovets, V.A. Kushnir, V.A. Mitrochenko, N.G. Reshetnyak, Yu.Ya. Volkolupov, V.V. Zakutin (NSC KIPT) 3303

Development and Status of the SNS Ion Source
R.F. Welton, S.N. Murray, M.P. Stockli (ORNL), R. Keller (LBNL) 3306

Proof-of-Concept Experiments for Negative Ion Driver Beams for Heavy Ion Fusion
L. Grisham (Plasma Physics Laboratory, Princeton University), S.K. Hahto, S.T. Hahto, J. Kwan, K.N. Leung (LBNL) 3309

3D Modeling Activity for Novel High Power Electron Guns at SLAC
A. Krasnykh, V. Ivanov, G. Scheitrum, D. Sprehn (SLAC), L. Ives, G. Miram (Calabazas Creek Research, Inc.).....3312

An Improved Version of TOPAZ 3D
A. Krasnykh, V. Ivanov, G. Scheitrum (SLAC), A. Jensen (Oregon Institute of Technology).....3315

First Test of the Charge State Breeder BRIC
V. Variale, V. Valentino (INFN), P. Bak, Y. Boimelshtein, P. Logatchov, B. Skarbo, M. Tiunov (BINP), A. Boggia, G. Brautti, T. Clauser, A. Raino (Dipartimento di Fisica di Bari and INFN).....3318

Design and Operation of Pegasus Thermionic Cathode
P. Frigola, G. Andonian, S. Reiche, J.B. Rosenzweig, S. Telfer, G. Travish (University of California, Los Angeles).....3321

Development of Dispenser Photocathodes for RF Photoinjectors
D. Feldman, P.G. O'Shea, M. Virgo (University of Maryland), K.L. Jensen (Naval Research Laboratory).....3323

The Research on the Carbon Nano Tube Cathode
A. Yamamoto, N. Kaneko, H. Nakai, T. Nakashizu (Ishikawajima-Harima Heavy Industries Co.,Ltd.), M. Ikeda, S. Ohsawa, T. Sugimura (KEK).....3326

Crystal-Based Spin Analyzer for Fast Neutron Beams
N. Bondarenco, N. Shul'ga (Kharkov Institute of Physics and Technology).....3329

Pulsed HV Electron Gun with Thermionic Cathode for the Soft X-Ray FEL Project at SPring-8
K. Togawa, K. Onoe, T. Shintake (SPring-8), H. Baba (RIKEN Harima Institute in SPring-8), T. Ishizuka (Sumitomo Heavy Industries).....3332

Ion and Neutral Beam Generation by 1TW, 50fs Laser Irradiation of Thin Foils
Y. Wada, T. Kubota, A. Ogata (Hiroshima University).....3335

Topology for a DSP Based Beam Control System in the AGS Booster
J. DeLong, J.M. Brennan, T. Hayes, Tuong N. Le, K.S. Smith (BNL).....3338

A Bunch to Bucket Phase Detector Using Digital Receiver Technology
J. DeLong, J.M. Brennan, T. Hayes, Tuong N. Le, K.S. Smith (BNL).....3341

Progress on the SNS Ring LLRF Control System
K.S. Smith, M. Blaskiewicz, J.M. Brennan, J. DeLong, F. Heistermann, A. Zaltsman (BNL), T.L. Owens (ORNL)..3344

A New Digital Control System for CESR-c and the Cornell ERL
M. Liepe, S. Belomestnykh, J. Dobbins, R. Kaplan, C.R. Strohman (Cornell University).....3347

Longitudinal Damping System with Two Transverse Kickers
A. Mikhailichenko (Cornell University).....3350

53 MHz Feedforward Beam Loading Compensation in the Fermilab Main Injector
J. Dey, I. Kourbanis, J. Reid, J. Steimel (FNAL).....3353

2.5 MHz Feedforward Beam Loading Compensation in the Fermilab Main Injector
J. Dey, I. Kourbanis, J. Steimel (FNAL).....3356

Tune and Coupling Drift Compensation during the Tevatron Injection Porch
M. Martens, G. Annala, P. Bauer (FNAL).....3359

Beam Loading Compensation for Slip Stacking
J. Steimel, T. Berenc, C. Rivetta (FNAL).....3362

Analysis of the Feedback System Used to Damp Longitudinal Quadrupole-Mode Bunch Oscillations
S. Sakanaka, T. Obina (KEK).....3365

Two-Bunch Orbit Correction Using the Wake Field Kick
M. Satoh, K. Furukawa, M. Kikuchi, H. Koiso, Y. Ogawa, T. Suwada (KEK) 3368

Newly Designed Field Control Module for the SNS
A. Regan, K. Kasemir, S. Kwon, J. Power, M. Prokop, H. Shoaee, M. Stettler (LANL), C. Swanson (Alpha Cad, Inc.), L. Doolittle, A. Ratti (LBNL), M. Champion (ORNL) 3371

Commissioning Results of the Fast Orbit Feedback at the ALS
C. Steier, A. Biocca, E. Domning, S. Jacobson, G. Portmann, T. Scarvie, E. Williams (LBNL) 3374

The Spallation Neutron Source Accelerator Low Level RF Control System
M. Champion, M. Crofford, H. Ma, M. Piller (ORNL), K. Kasemir, S. Kwon, J. Power, M. Prokop, A. Regan, H. Shoaee, M. Stettler, D. Thomson (LANL), S. De Santis, L. Doolittle, M. Monroy, A. Ratti (LBNL) 3377

Control of Heavily-Beam-Loaded SNS-Ring Cavities
T.L. Owens (ORNL), K.S. Smith, A. Zaltsman (BNL) 3380

Analysis of Slow Orbit Movement in PLS Storage Ring
H.S. Kang, J. Choi, Y.J. Han, H.J. Park (Pohang Accelerator Laboratory) 3383

Commissioning of the Fast Orbit Feedback at SLS
M. Boege, B. Keil, T. Schilcher, V. Schlott (Paul Scherrer Institut) 3386

Low-Mode Coupled Bunch Feedback Channel for PEP-II
J. Fox, L. Beckman, N. Hassanpour, L. Sapozhnikov, D. Teytelman (SLAC) 3389

Upgrading the Orbit Feedback System in the Taiwan Light Source
C.H. Kuo, J. Chen, K.T. Hsu, K.H. Hu (Synchrotron Radiation Research Center) 3392

Operation of the Digital Multi-Bunch Feedback Systems at ELETTRA
D. Bulfone, V. Forchi', M. Lonza, L. Zambon (Sincrotrone Trieste), M. Dehler (Paul Scherrer Institut) 3395

Strong-Strong Simulation of Beam-Beam Interaction for Round Beams
A. Valishev, E.A. Perevedentsev (BINP), K. Ohmi (KEK) 3398

Macroparticle Simulations of Antiproton Lifetime at 150 GeV in the Tevatron
J. Qiang, R.D. Ryne (LBNL), T. Sen, M. Xiao (FNAL) 3401

Parallel Computation of Beam-Beam Interactions Including Longitudinal Motion
F.W. Jones (TRIUMF), W. Herr (CERN) 3404

Measurement and Application of Betatron Modes with MIA
C.X. Wang (ANL) 3407

Spatial-Temporal Modes Observed in the APS Storage Ring Using MIA
C.X. Wang (ANL) 3410

FFAGs for Muon Acceleration
J.S. Berg, S.A. Kahn, R.B. Palmer, D. Trbojevic (BNL), C. Johnstone, E. Keil (FNAL), M. Aiba, S. Machida, Y. Mori, T. Ogitsu, C. Ohmori (KEK), A.M. Sessler (LBNL), S. Koscielniak (TRIUMF) 3413

Beam Dump Optics for the Spallation Neutron Source
D. Raparia, Y.-Y. Lee, J. Wei (BNL), S. Henderson (ORNL) 3416

Beam Scrubbing Strategy for Electron-Cloud Suppression in the Spallation Neutron Source Ring
S.Y. Zhang, M. Blaskiewicz, H. Hseuh, J. Wei (BNL), R.J. Macek (LANL) 3419

The AGS Electrostatic Septum
J. Hock, K.A. Brown, J. Glenn, T. Russo (BNL) 3422

Beam Based Characterization of a New 7-Pole Superconducting Wiggler at CESR
A. Temnykh, J. Crittenden, D. Rice, D.L. Rubin (Cornell University) 3425

Status of the Cooler Synchrotron COSY-Juelich
D. Prasuhn, U. Bechstedt, J. Dietrich, R. Gebel, K. Henn, A. Lehrach, B. Lorentz, R. Maier, A. Schnase, H. Schneider, R. Stassen, H.J. Stein, H. Stockhorst, R. Toelle (Forschungszentrum Juelich) 3428

Fermilab Recycler Stochastic Cooling Commissioning and Performance
D. Broemmelsiek, R.J. Pasquinelli (FNAL) 3431

Time Evolution of Beam Current in the Recycler Ring
K. Gounder, J.P. Marriner, C.S. Mishra (FNAL) 3434

Residual Gas Pressure Profile in the Recycler Ring
K. Gounder, T.G. Anderson, J.P. Marriner, C.S. Mishra (FNAL) 3437

Lattice Function Measurements of Fermilab Recycler Ring
M.J. Yang, A. Marchionni, C.S. Mishra (FNAL) 3440

Linac Optics Optimization for Energy Recovery Linacs
R. Nagai, R. Hajima, N. Kikuzawa, E.J. Minehara, N. Nishimori, M. Sawamura (Japan Atomic Energy Research Institute) 3443

Performance and Upgrade of the JAERI ERL-FEL
M. Sawamura, R. Hajima, N. Kikuzawa, E.J. Minehara, R. Nagai, N. Nishimori (Japan Atomic Energy Research Institute) 3446

Cost Estimation of an Energy Recovery Linac Light Source
M. Sawamura, R. Hajima, N. Kikuzawa, E.J. Minehara, R. Nagai, N. Nishimori (Japan Atomic Energy Research Institute) 3449

Status of 150MeV FFAG Synchrotron
T. Yokoi, S. Machida, Y. Mori, A. Muto, J. Nakano, C. Ohmori, I. Sakai, Y. Sato, A. Takagi, T. Uesugi, A. Yamazaki, M. Yoshii, M. Yoshimoto, Y. Yuasa (KEK), M. Matoba, Y. Yonemura (Kyushu University), M. Aiba, M. Sugaya (University of Tokyo) 3452

Stripper Foil Temperatures and Electron Emission at the Los Alamos Proton Storage Ring
T. Spickermann, M. Borden, A. Browman, D. Fitzgerald, R.J. Macek, R. McCrady, T. Zaugg (LANL) 3455

Testing and Commissioning of the ALS Adjustable, Hysteresis-Free Chicane Magnet
J.Y. Jung, S. Marks, R. Schlueter (LBNL) 3458

SDDS-Based Software Tools for Accelerator Design
L. Emery, M. Borland, H. Shang, R. Soliday (ANL) 3461

Application of Model-Independent Analysis Using the SDDS Toolkit
L. Emery (ANL) 3464

Beam Dynamics Optimization in the Rare Isotope Accelerator Driver Linac
Eliane S. Lessner, P.N. Ostroumov (ANL) 3467

New Features in the SDDS-Compliant EPICS Toolkit
H. Shang, M. Borland, L. Emery, R. Soliday (ANL) 3470

New Features in the SDDS Toolkit
R. Soliday, M. Borland, L. Emery, H. Shang (ANL) 3473

Use of a Simple Storage Ring Simulation for Development of Enhanced Orbit Correction Software
R. Soliday, M. Borland, L. Emery, H. Shang (ANL) 3476

Evaluation of the Horizontal to Vertical Transverse Impedance Ratio for LHC Beam Screen Using a 2D Electrostatic Code
U. Iriso-Ariz (BNL), F. Caspers (CERN), A. Mostacci (University of Rome) 3479

Configurable UAL-Based Modeling Engine for Online Accelerator Studies
N. Malitsky, T. Satogata (BNL), R. Talman (Cornell University) 3482

A Comparison of Several Lattice Tools for Computation of Orbit Functions of an Accelerator
D. Trbojevic, J.S. Berg, E.D. Courant (BNL), R. Talman (Cornell University), A.A. Garren (LBNL) 3485

LIONS_LINAC: A New Particle in Cell Code for Linacs
P. Bertrand (Grand Accelerateur National d'Ions Lourds) 3488

New Implement in TraceWIN/PARTRAN Codes: Integration in External Field Map
N. Pichoff (French Atomic Energy Commission), D. Uriot (CE Saclay) 3491

Tools for Predicting Cleaning Efficiency in the LHC
R. Assmann, M. Brugger, M. Hayes, J.-B. Jeanneret, F. Schmidt (CERN), I. Baichev (Institute of High Energy Physics, Protvino), D. Kaltchev (TRIUMF) 3494

MAD-X -- An Upgrade from MAD8
F. Schmidt, H. Grote (CERN) 3497

Recent Improvements to the ASTRA Particle Tracking Code
S.M. Lidia (LBNL), K. Floettmann (DESY), P. Piot (FNAL) 3500

PyORBIT: A Python Shell for ORBIT
J.-F. Ostiguy (FNAL), J. Holmes (ORNL) 3503

A Framework Design for a Cyclotron Virtual Control Platform Based on Object-Oriented Methodology
B. Qin, D. Chen, M. Fan, X. Jian, Y. Xiong, T. Yu (HuaZhong University of Science and Technology) 3506

Modeling and Beam Dynamic Visualization in Cyclotron Virtual Prototyping
X. Jian, D. Chen, M. Fan, B. Qin, Y. Xiong, T. Yu (HuaZhong University of Science and Technology) 3509

Self-Consistent 3D PIC Code for the Modeling of High Brightness Beams
L. Serafini, A. Bacci, C. Maroli, V. Petrillo (INFN) 3512

RF Coupler for High-Power CW FEL Photoinjector
S. Kurennoy, L.M. Young (LANL) 3515

Recent Improvements in the PARMILA Code
H. Takeda, J. Billen (LANL) 3518

The Particle Tracking Code PARMELA
L.M. Young, J. Billen (LANL) 3521

PARSEC: Parallel Self-Consistent 3D Electron-Cloud Simulation in Arbitrary External Fields
A. Adelmann, M. Furman (LBNL) 3524

A Modular On-line Simulator for Model Reference Control of Charged Particle Beams
C.K. Allen, C.A. McChesney (LANL), C. Chu, J. Galambos, T.A. Pelaia, A. Shishlo (ORNL), W.-D. Klotz (ORNL and ESRF), N.D. Pattengale (Sandia National Laboratories) 3527

Monte-Carlo Simulation Module for LIDOS.RFQ.Designer Code
I.V. Shumakov, B.I. Bondarev, A.P. Durkin, Yu.D. Ivanov, S.V. Vinogradov (Moscow Radiotechnical Institute) 3530

Template Potentials Technique with Fully-Parameterized Field Solver for High-Current Beams Simulation
L.G. Vorobiev, R. York (National Superconducting Cyclotron Laboratory) 3533

On-Line Model of the SNS Medium Energy Beam Transport Line
A. Aleksandrov (ORNL), V. Alexandrov (Branch of INP, Protvino) 3536

Particle Tracking and Bunch Population in TraFiC4 2.0
A.C. Kabel (SLAC) 3539

A Parallel Code for Lifetime Simulations in Hadron Storage Rings in the Presence of Parasitic Weak-Strong Beam-Beam Interactions
A.C. Kabel, Y. Cai (SLAC), B. Erdelyi, T. Sen, M. Xiao (FNAL) 3542

Parallel Simulation Algorithms for the Three-Dimensional Strong-Strong Beam-Beam Interaction
A.C. Kabel (SLAC) 3545

Code Comparison for Simulations of Photo-Injectors
C.G. Limborg, Y.K. Batygin (SLAC), J.-P. Carneiro, K. Floettmann (DESY), L. Giannessi, M. Quattromini (Ente Nazionale per le Nuove Tecnologie l'Energia e l'Ambiente), M. Boscolo, M. Ferrario, V. Fusco, C. Ronsivalle (INFN) 3548

Simulation of Particle Dynamics in Accelerators Using the Ensemble Model
W. Ackermann, W. Beinhauer, H.-D. Graef, M. Krasilnikov, A. Richter, T. Weiland (Technische U. Darmstadt) 3551

Periodic Boundary Conditions in the Parallel Eigensolver OM3P: Application of the Inexact Lanczos Process to Hermitian Systems
J.F. DeFord, B. Held (Simulation Technology & Applied Research, Inc.) 3554

Simulation Tools for High-Intensity Radiographic Diodes
S. Humphries (Field Precision), J. McCarrick, T. Orzechowski (LLNL) 3557

Development of 3D Finite-Element Charged-Particle Code with Adaptive Meshing
L. Ives, T. Bui, W. Vogler (Calabazas Creek Research, Inc.), D. Datta, M. Shephard (Rensselaer Polytechnic Institute) 3560

Conformal Modelling of Space-Charge-Limited Emission from Curved Boundaries in Particle Simulations
E. Gjonaj, T. Lau, T. Weiland (Technische U. Darmstadt) 3563

Simulation of Dark Currents in a FEL RF-Gun
S. Setzer, W. Ackermann, T. Weiland (Technische U. Darmstadt), M. Krasilnikov (DESY) 3566

Investigation of Dark Currents in the S-DALINAC Superconducting Cavity
S. Setzer, M. Gopych, H.-D. Graef, U. Laier, M. Platz, A. Richter, A. Stascheck, S. Wazlawik, T. Weiland (Technische U. Darmstadt) 3569

HIGH LUMINOSITY OPERATION OF THE FERMILAB ACCELERATOR COMPLEX*

S. Mishra#, Fermilab, Batavia, IL 60510, USA

Abstract

Run-II at Fermilab is progressing steadily. In the Run-II scheme, 36 antiproton bunches collide with 36 proton bunches at the CDF and D0 interaction regions in the Tevatron at 980 GeV per beam. The current status and performance of the Fermilab Accelerator complex is reviewed. The plan for Run-II, accelerator upgrades and integration of the Recycler in the accelerator chain will be presented.

INTRODUCTION

The Fermilab is the highest energy colliding beam accelerator in the world. It will remain so till the turn-on of the LHC. The accelerator complex is running with the new Main Injector and upgraded proton source that consists of the Linac and Booster, an upgraded Antiproton source, and the Tevatron. The commissioning of the Recycler continues. The collider physics program is making steady progress with two upgraded detectors and increasing luminosity. This paper will give a brief introduction to the accelerator complex and, present the performance, issues and upgrade plans for the accelerators. We will also present the collider performance and exciting physics results from the two experiments.

ACCELERATOR COMPLEX

Figure 1 shows the schematic view of the Fermilab accelerator complex with the newly commissioned Main Injector and Recycler. The proton production cycle starts at the Crockoft-Walton. The Crockoft-Walton accelerates H^- ions to 750 KeV and injects them into the Linac. The linac accelerates the H^- ions to 400 MeV. The H^- ions are stripped and injected into the Booster. Protons are accelerated in the Booster to 8.9 GeV/c in 33 msec and transferred to Main Injector using an 8.9 GeV/c transfer line built using permanent magnets. In the Main Injector the protons are accelerated from 8.9 GeV/c to 120 GeV/c in 1.5 sec and sent to the pbar production target. For Tevatron operation the Main Injector accelerates 5-7 bunches of protons to 150 GeV/c, coalesces them into one bunch, and transfers the bunch to the Tevatron.

At present, Main Injector accelerates about $5x10^{12}$ protons to 120 GeV/c every 2.4 sec and extracts it to a nickel production target. A lithium lens operating at 760 Tesla/meter downstream of the antiproton production target focuses $85x10^6$ antiprotons at 8.9 GeV/c. These antiprotons are collected, stored and stochastically cooled in the Debuncher and Accumulator (using the stacking lattice). When stack reaches somewhere between 100-150e10 anti-protons and the Tevatron is ready for the next store, the 8.9 GeV/c antiprotons are extracted from the Accumulator (using the shot lattice), and injected in to the Main Injector. The Main Injector accelerates the antiprotons to 150 GeV using the 53 MHz rf system, coalesces them, and transfers them to the Tevatron.

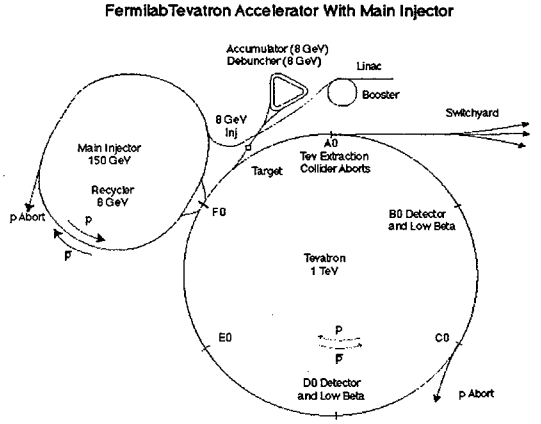

Figure 1. Schematic layout of the Fermilab Accelerator complex.

The Tevatron accelerates both protons and antiprotons from 150 GeV to 980 GeV on helical orbits and collides them at the B0 and D0 interaction regions.

Major changes to accelerator between Run-I and Run-II are: a) Rapid cycling Main Injector replaced Main Ring, b) Antiproton source and Tevatron were upgraded to handle higher intensity, c) the number of proton and pbar bunches have been increased from 6 to 36, with a crossing time of 396 nsec, d) the Tevatron collision energy has increased from 1.8 TeV to 1.96 TeV, and e) The Recycler a new permanent magnet 8.9 GeV/c storage ring for antiproton accumulation was added and is now being commissioned.

PROTON SOURCE

The Proton Source is made up of the Crockoft-Walton, Linac, and Booster. The performance of these accelerators is excellent and the Booster is accelerating higher intensity proton beams to 8.9 GeV/c for Run-II and the MiniBooNE experiment [1]. Figure 2 show the intensity and beam loss plot for the 33 msec Booster acceleration cycle. There is a loss of beam in first few msec at the injection energy and early in the acceleration cycle. This loss is attributed to space charge effects, momentum spread and lattice issues. There is a small loss of beam at transition energy as shown by an increase in the loss monitor readings (red curve in Figure 2).

Linac and Booster are routinely delivering 250k pulses in 24 hours with an average repetition rate of 3 Hz and

0-7803-7738-9/03/$17.00 © 2003 IEEE

peak rate of 5 Hz. The total intensity delivered is being limited by losses, which lead to activation in the Booster tunnel. Booster delivers 4-5e16 protons per hour to users.

Physics issues that are being addressed includes a) the space charge effect at injection, b) emittance preservation through the ramp, and c) better understanding of the injection lattice.

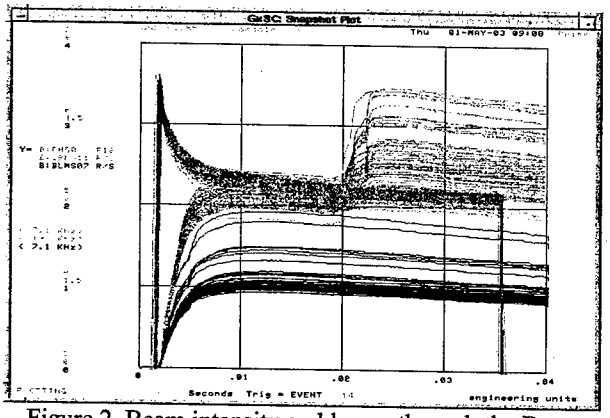

Figure 2. Beam intensity and losses through the Booster acceleration cycle. Green line is proton intensity, blue and red are loss monitor readings.

The optics of the Booster is significantly perturbed by the edge focusing of the injection and extraction orbit bumps [2]. There is a sizable dispersion error at injection in the Booster. It has been calculated and measured that the injection "Or-Bump" and the "dog-leg" around the extraction septum is contributing to this error.

Increasing the proton intensity and reducing the loss of beam in the Booster tunnel is the main emphasis of the Proton Source Department. Several projects including a) Longitudinal Dampers, b) transition jump system, c) ramped corrector to control the orbit and improve aperture, d) ramp monitor program, and e) larger aperture RF cavities.

MAIN INJECTOR

The Main Injector was commissioned in 1999 and has been supporting the Fermilab physics program since that time. Main Injector has achieved most of its design goals and the main emphasis continues to be on improving the quality of beam [3]. Recent development includes a) lattice matching between injection and extraction lines to Main Injector to preserve emittances, b) beam loading compensation for proton coalescing, c) multi-batch beam loading compensation for antiproton coalescing, d) R&D on a longitudinal damper to reduce the longitudinal emittance growth in the Main Injector, e) development of transverse dampers for injection and high intensity operation, f) development of a 2.5 MHz acceleration scheme for Recycler antiproton acceleration, g) an upgraded BPM system and h) development of slip stacking to increase the proton flux on the antiproton production target. Main Injector runs more than 95% efficient for pbar production and has delivered in excess of 5.25e12 proton per pulse to the antiproton production target. The Main Injector cycle time for antiproton production is 1.46 sec.

Protons and antiprotons are accelerated in the Main Injector to 150 GeV to fill The Tevatron for collider operation. In the process of proton acceleration, 5-7 bunches of protons are injected from Booster to the Main Injector in 53 MHz buckets. The Main Injector accelerates these bunches using the 53 MHz rf system to 150 GeV. At 150 GeV the bunches are rotated by turning off the 53 MHz rf cavities and captured by 2.5 MHz rf cavities to form a single high intensity coalesced bunch. Then the 53 MHz rf is turned on and the beam is transferred to the Tevatron. This process is 85-92% efficient, with a bunch intensity of 250-330e9/bunch and the longitudinal emittance is 2.2-3.2 eV-sec for 5-7 bunch operation. We routinely run the 7 bunch operation to meet the intensity demand of the Tevatron due to the poor injection and acceleration efficiency of the Tevatron. The longitudinal emittance of the proton beam is about 30% higher than the Run-II goal, because of instabilities and the 7 bunches coalescing instead of 5 to meet the intensity demand.

The antiproton acceleration process in the Main Injector is similar to the proton process, except in this mode 4 batches of antiprotons (396 nsec apart) are injected from the Accumulator. One of the recent improvements in the Main Injector for the antiproton acceleration has been the implementation of multi-batch beam loading compensation. Figure 3 shows the longitudinal emittance of the antiprotons as a function of batch number for several stores. The emittance is larger for the higher bunch numbers due to beam loading. Figure 4 shows the same after the beam loading compensation has been commissioned. The average injected longitudinal emittance of the antiproton bunches is 1.5 eV-Sec. There is a small growth during the acceleration process. As expected the coalescing process increases the longitudinal emittance by about a factor of 2 to an average value of about 2.7 eV-Sec. The Run-II design goal of 2 eV-Sec was set assuming use of the Recycler and 2.5 MHz acceleration. The 2.5 MHz acceleration process in the Main Injector from 8 GeV through transition energy to 27 GeV is designed to replaces the coalescing process. The

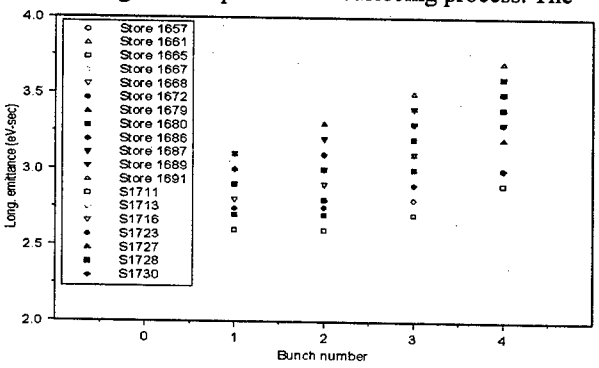

Figure 3. Longitudinal emittance of the antiproton as a function of bunch number with out beam loading compensation.

average coalescing efficiency of the pbar acceleration and coalescing through the Main Injector exceeds 85%. There is a small transverse emittance growth of less than 2 pi mm-mr (95% normalized) in the Main Injector from injection to 150 GeV. The transverse emittance of the proton and antiproton beams in the Main Injector at 150 GeV is similar to Run-II design goals.

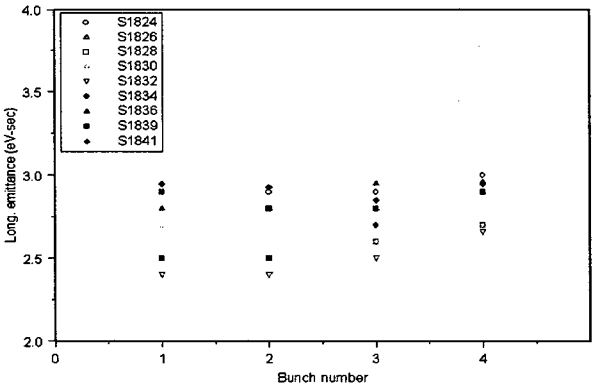

Figure 4. Longitudinal emittance of the antiproton as function of bunch number with beam loading compensation.

ANTIPROTON SOURCE

The Antiproton source was upgraded in association with the Main Injector project to increase the stacking rate to 18-20e10 antiprotons/hour [4]. A peak stacking rate of 13.5e10 antiprotons/hour and an average stacking rate of about 8e10/hr have been achieved. The peak stacking rate is limited by the stochastic cooling, but the average stacking rate problem could be alleviated by storing antiprotons in the Recycler. One of the major problems with the antiproton source was the larger than expected transverse emittances of the cooled antiproton. Figure 5 shows the transverse emittance of the beam in Run-I and Run-II as a function of stack size. The typical horizontal emittance of a 1e12 antiproton stack was 17π mm-mr as compared to the design goal of 8. The larger emittance was due to an increased Intra-beam scattering (IBS) (60%) caused by a change in the Accumulator lattice and trapped ions (40%).

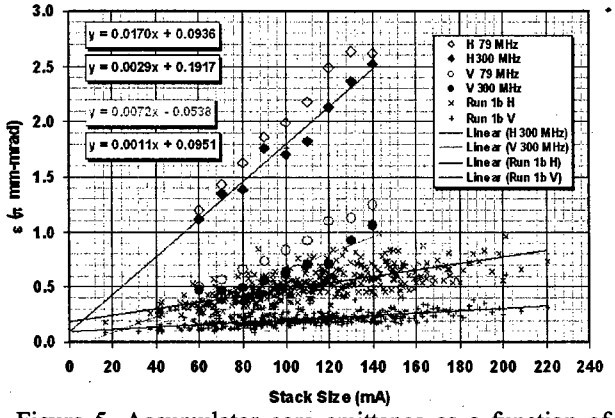

Figure 5. Accumulator core emittance as a function of stack size. These are unnormalized 95% emittances.

This large emittance problem was solved by a) better transverse stochastic cooling of the Accumulator core, and b) dual lattice operation of the Accumulator. The bandwidth of the stochastic cooling system was increased by a factor of two and the center frequency of the bean was increased by a factor of 1.5. Six new cooling systems and four new ultra-high vacuum tanks were built, installed and commissioned in less than 8 months. The dual lattice operation has a "fast stacking" lattice ($\eta = 0.012$) for pbar production and a "shot" lattice ($\eta = 0.022$) for Tevatron injection. During the shot setup for collider operation the Accumulator lattice is ramped with a cooled antiproton beam at the core orbit from fast stacking lattice to shot lattice. The shot lattice reduces the IBS heating by a factor of 2.5 and increases the cooling rate by a factor of 2 by increasing the mixing due to the change in η. Figure 6 shows the improvement in the emittance after these upgrade. These upgrades resulted in a factor of 2-3 reduction in core transverse emittance and a 40% increase in the collider luminosity.

The main Antiproton source R&D efforts are towards increasing the stacking rate. The R&D includes a) Debuncher momentum cooling improvements, b) a transverse Debuncher Notch Filter, c) commission core momentum stacktail compensation legs, d) implementing core momentum spreading during stacking, e) a stacktail notch filter upgrade, f) Improved transverse compensation of the stacktail, g) a reduction of Main Injector Longitudinal emittance, and h) an improvement of the AP2/Debuncher aperture

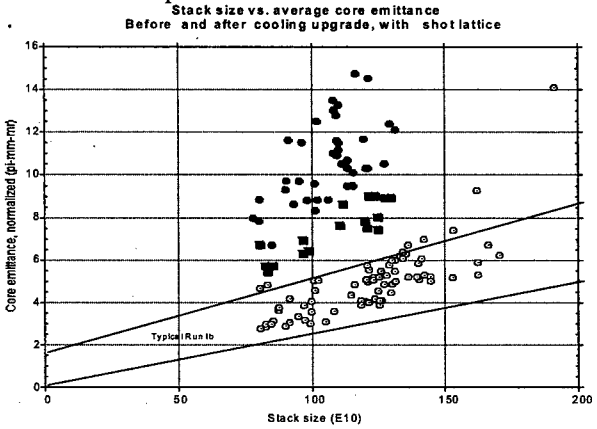

Figure 6. Average core emittance vs. Stack size. Green before upgrade, red after cooling upgrade and purple after shot lattice. (95% normalize emittance).

TEVATRON

The Tevatron has been making considerable progress in understanding the physics issues related to the delivery of higher luminosity [5]. It has been successful in utilizing the progress made in the upstream accelerator intensity and emittances and converted it to higher luminosity. Although a factor of two below the Run-II goals, the Tevatron is typically running with a factor of two higher peak luminosity than Run-I. This situation is due to

fundamental physics limitations, which are new compared to Run-I, such as larger beam-beam effects, instabilities and poor lifetime. We are running with higher number of bunches 36 x 36 as compared to 6 x 6. There are several limitations in understanding and solving these issues, including poor BPM, unstable Tevatron Lattice due to alignment and orbit motion and lack of beam study time.

Figure 7 shows typical beam intensities for a Tevatron collider fill. We observe a loss of proton beam at injection, open of helix and poor lifetime at 150 GeV. The pbar beam, although 1/10 the intensity of the protons, has

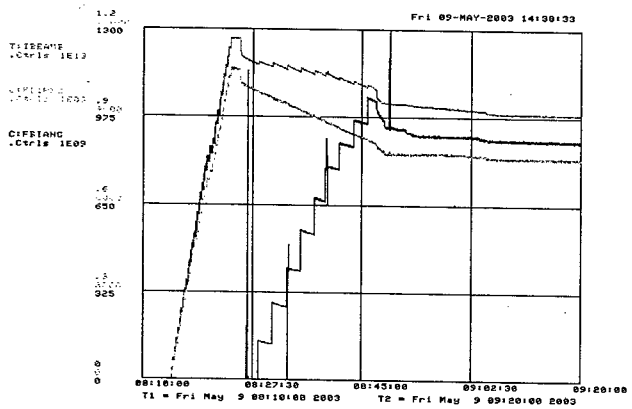

Figure 7. Typical Tevatron fill intensity and losses. Green is the total proton intensity, sky blue is the bunched proton beam intensity and blue is the bunched antiproton.

a poor lifetime due to larger beam growth at injection into the Tevatron and the stronger beam-beam effect. About 10% of the bunched beam is lost during the ramp and squeeze for collision.

Several controlled beam studies have been performed to study and improve the performance of the Tevatron. These improvements include a) tune, coupling and chromaticity compensation at 150 GeV through collision, b) orbit smoothing, c) a longitudinal damper to stop σ_s blowup during store, d) a transverse damper to improve 150 GeV lifetime, and e) general tuning of the machine.

The beam-beam effect is one of the main contributions to the poor lifetime of the pbar beam in the Tevatron. Several observations indicated that a smaller pbar beam size yields a better pbar lifetime at 150 GeV and that an antiproton only store has a better lifetime. During the Jan 03 shutdown the Lambertson at the C0 region was replaced with Main Injector dipoles to increase the helix separation and to reduce the impedance of the Tevatron. We are also investigating the possibility of improving diagnostic in the Tevatron (new BPMs electronics, Schottky etc.), including improvements in hardware and understanding systematic errors. Several study groups have been formed to systematically study Tevatron beam dynamics.

RECYCLER

The Recycler is designed to store and cool antiprotons at 8.9 GeV/c. It was built using permanent magnet technology, but during the commissioning period ramped dipole correctors were added. In its first phase, the Recycler was designed to store 2e12 antiproton by frequent transfer of antiprotons from the Accumulator to the Recycler. The Accumulator stacking rate decreases as the stack size in the Accumulator increases. The plan is to transfer antiprotons from the Accumulator to the Recycler every 2-3 hours to keep the stacking rate high. The design goal of the Recycler Ring is to have 2e12 antiprotons stacked with 100 hours of lifetime using stochastic cooling. At a later date, the Recycler cooling will be upgraded with electron cooling.

The Recycler Ring has made considerable commissioning progress over last two years [6]. Fig. 8 shows the stacking of antiprotons in the Recycler Ring with total efficiency of 75%. The best lifetime achieved for pbars is 180 hours. The lifetime has a small dependence on the stack size in the Recycler: lifetime= -0.44x(Stack Size)+183. We have the mechanisms in place to transfer pbars from the Accumulator to the Recycler, cool the pbar in the Recycler, extract and bunch the pbars in 2.5 Mhz bunches from the Recycler, transfer the pbar bunches to the Main Injector, accelerate the pbars in the Main Injector to 150 GeV, and transfer them to the Tevatron.

The Recycler needs improvements in its performance before it can be integrated into the Accelerator complex. Some of the issues are a) injection and circulating efficiency for proton and pbar is about 90-95%, b) emittance growth is about a factor of 2 larger than the design value, c) the longitudinal emittance is effected by the Main Injector ramp and is larger than the design goal, d) the Recycler orbit is not well established due to lack of a working BPM, e) cooling and RF manipulations needs further optimization.

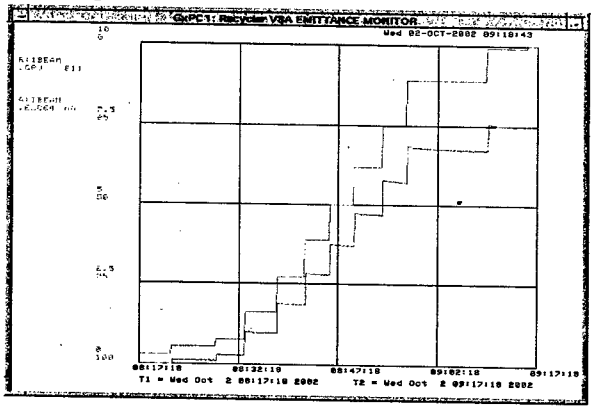

Figure 8. Stacking of pbar in the Recycler. Blue in the pbar intensity in the Accumulator and Green in the Recycler intensity. The scale of Blue is reversed.

A significant fraction of Recycler beam transverse emittance growth is vacuum related. A plan is in place to improve the Recycler vacuum by doubling the number of ion pumps, baking the Recycler to a higher temperature and fixing small leaks, which may be present around the ring. The ramped correctors will be used to reduce the effect of the Main Injector ramp on the Recycler. Initial

tests already show positive results. The Recycler BPM electronics are being upgraded using digital electronics. It is expected that with the upgrade and integration plans that are already in place the Recycler will perform as described in its initial design report.

COLLIDER PERFORMANCE

In the last one year the luminosity of the Tevatron collider has improved by more than a factor of 3. The collider luminosity is within a factor of two of the Main Injector design. Every improvement in luminosity of the complex has been associated with a specific modification to the accelerators. These included a) Accumulator cooling and shot lattice (40%), b) Accumulator to Main Injector lattice match and antiproton emittance at Tevatron injection (20%), c) antiproton coalescing improvement in the Main Injector (15%), d) Improved antiproton and proton efficiency through Tevatron low beta (10% each), and e) larger antiproton stack (10%). Most of the luminosity increase is due to increasing the number of antiprotons at low beta. Figure 9 shows the total number of antiproton to low beta as a function of shot number.

The current antiproton production rate is sufficient to support a luminosity in the 6-8e31 $cm^{-2}sec^{-1}$ range. The protons at low beta are 95% of the goal. Although antiproton efficiency has improved from 32% to 70%, the antiprotons are still only 70% of the goal. The primary outstanding issues towards achieving higher luminosity are a) emittance preservation from Tevatron injection to acceleration in Tevatron, b) proton and antiproton lifetime and acceleration efficiency in the Tevatron and c) Tevatron beam dynamics which is adversely effected by beam-beam effects, lattice, alignment and coupling. A variety of hardware projects are currently underway dealing with these issues. An upgrade plan is being developed to improve the luminosity even further.

Figure 10 shows the weekly peak luminosity as a function of week number and peak luminosity as a 10x running average. The luminosity has been increasing steadily since the beginning of Run-II. At the time of this talk the Accelerator complex has delivered in excess of 220 pb^{-1} to each detector since the beginning of the run.

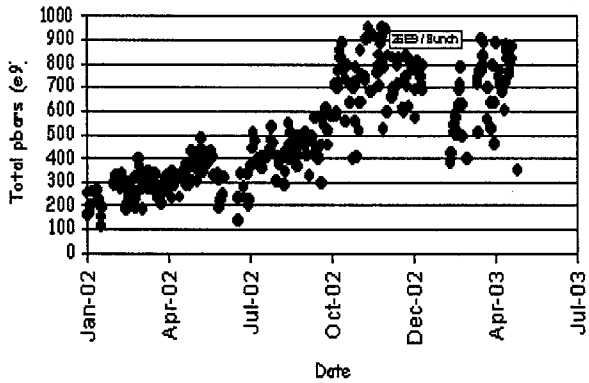

Figure 9. Total number of antiproton at low beta.

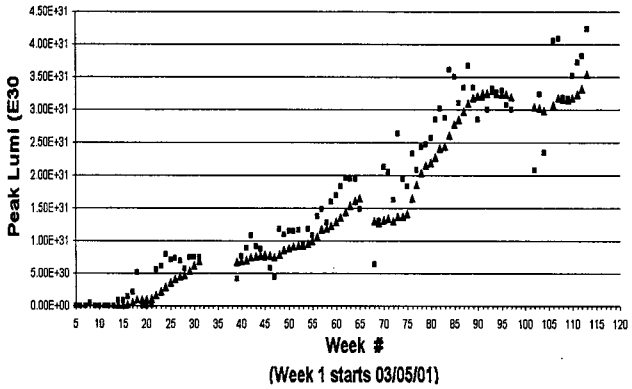

Figure 10. Peak Luminosity as a function of week. Blue is the peak luminosity of the week and green the 10 shot running average.

The goal of the collider program for FY03 is to deliver 200 pb-1, with a peak luminosity of 10 pb-1 per week by the end of FY2003.

SUMMARY

The Fermilab collider program at 1.96 TeV is well underway with exciting physics results from both the collider detectors. The collider is running with in a factor of two of the Run-II designed luminosity with the new Main Injector. There are several hardware upgrade projects underway to improve the luminosity. We are interleaving accelerator studies and operations to further improve the luminosity. The Recycler Ring commissioning has progressed well and the machine is close to being ready for integration into the accelerator complex after a shutdown to improve vacuum and instrumentation.

ACKNOWLEDGEMENT

I will like to thank the following for helping me prepare this talk by providing their talks and discussing the details of their view of accelerator complex with me; Elliot McCory, Dave Johnson, Elvin Harm, Mike Martin and Steve Holmes. I will also like to thank John Marrier for his valuable comments on the talk and paper.

REFERENCES

[1] E. McCory, talk at AAC : http://www-bd.fnal.gov/aac/ Fermilab, Feb 2003.
[2] W. Chou et al. 'Fermilab Booster Modeling and Space Charge studies.', PAC2003 Proceeding, Portland.
[3] D. Johnson, talk at AAC http://www-bd.fnal.gov/acc/ Feb 2003, Fermilab.
[4] E. Harm, talk at AAC. Feb 2003, Fermilab.
[5] M. Matrin, talk at AAC, Feb 2003, Fermilab.
[6] S. Mishra, talk at AAC, Feb 2003, Fermilab.

*Work supported by the US department of energy under contract DE-AC02-76CH003
#Email: Mishra@fnal.gov

RECENTLY COMMISSIONED AND FUTURE RNB FACILITIES

Paul Schmor, TRIUMF, 4004 Wesbrook Mall, Vancouver, BC, Canada, V6T 2A3

Abstract

There is a worldwide interest in fundamental and applied scientific research with exotic nuclear beams in order to improve our understanding of the nature of matter and of the evolution of matter in the universe. The nuclear physics working group of the OECD Megascience Forum concluded in 1999 that "A new generation of high-intensity RNB facilities of each of the two basic types, ISOL (Isotope Separator On Line) and In-Flight, should be built on a regional basis. Interested governments are encouraged to undertake the necessary decisions within the next few years, and the facilities themselves should become operational in five to ten years." [1] This interest has led to the design and development of a number of new facilities to increase both the variety and the number of exotic ions. This paper reviews and compares recently commissioned and proposed facilities.

INTRODUCTION

There is wide range of interest, for scientific as well as for applied research, involving the use of radioactive ion beams (RIB). Several recent studies have documented the scientific case. [2,3,4,5] In nuclear physics, the motivation is centered around improving our under-standing of the origin of the elements in the cosmos, our understanding of the nature of nucleonic material and exploring the physics beyond the standard model. Much of our recent understanding of condensed matter has involved the use of microscopic magnetic probes. Radioactive nuclei can be very sensitive magnetic probes. Radioisotopes with high specific activity are of interest for biomedical R&D. Radioactive nuclei have been successfully used as diagnostics to study and improve the wear characteristics of materials. Finally programs such as the accelerator based transmutation of waste (ATW) and science based stewardship program (SBSS) require certain improved cross sections in order to enhance the accuracy of their models.

The two approaches for producing radioactive ion beams (RIBs) are complementary. The ISOL approach uses gammas, neutrons, protons or other light ions impinging on a thick target. Interactions with the target nuclei produce exotic nuclei that diffuse out of the hot target and by effusion to an ionizer where the isotopes are extracted and formed into a beam of tens of eV. The isotopic distribution and intensities depend on the target material, its chemistry, target dimensions, isotope half-lives and target temperatures. The extracted beams are of high quality but generally contain a variety of isotopes and desired isotopes can be separated by high-resolution mass-separators. The radioactive ion beams are either stopped for experimental observation or accelerated to higher energies. The diffusion and effusion processes inherently limit the exotic beams to those having half-lives greater than 10 ms.

The IF (in-flight or projectile fragmentation) approach uses an energetic heavy ion beam impinging on a thin target. The heavy ion beam fragments and the fast exotic beam that come out of the thin target are separated by an ion optical system. The energetic fragments are independent of the target chemistry, depend on the energy of the incident beam but are generally greater than 25 MeV/nucleon. A high acceptance separator is required to capture a significant fraction of the exotic beam because of the angular scattering and the momentum spread from the target. Consequently the separator has limited mass resolution. However the approach is inherently fast and half-lives of the order of microseconds can be captured.

Numerous facilities are operating, being upgraded, under construction or in the proposal stage. This activity reflects the emphasis placed on the need for such facilities by the OECD working group.[1] A list of facilities, albeit partial, is given in table 1. The status is listed as C (under construction), U (an upgrade), O (operating) and P (proposed).

Table 1: A list of RIB Facilities

NAME	LOCATION	TYPE	STATUS
BRNBF	CHINA	ISOL	C
CRC	BELGIUM	ISOL	O
DUBNA	RUSSIA	IF	O
EURISOL	EU	ISOL	P
EXCYT	LNS/ITALY	ISOL	C
GSI	GERMANY	ISOL	O,U
HOLIFIELD	ORNL, USA	ISOL	O
IMP	CHINA	IF	O
ISAC I	CANADA	ISOL	O
ISAC II	CANADA	ISOL	C
ISOLDE	CERN/EU	ISOL	O
MAFF	GERMANY	ISOL	C
NSCL/MSU	USA	IF	O
PNPI	RUSSIA	ISOL	O
RCNP	JAPAN	IF	O
RIA	USA	ISOL/IF	P
RIKEN	JAPAN	IF	C
RMS/JAERI	JAPAN	ISOL	C
SPIRAL	FRANCE	ISOL	O
SISSE/LISE	FRANCE	IF	O
VECC	INDIA	ISOL	P

These proceedings contain details of the recent status and plans of a number of the listed facilities. In what follows is a personally selected list of characteristics of ma-

0-7803-7738-9/03/$17.00 © 2003 IEEE

jor accomplishments at some of these facilities to give the reader an impression of where the RNB developments are heading. RIB intensities are much lower than the stable beam intensities at conventional accelerator facilities. However since the RIB flux is proportional to the intensity of the driver beam that is used to create the RIB, the driver technology is state of the art and is a key element in the facility development. As the driver current increases so do the challenges in developing the high power targets needed to create the RIBs and the remote handling to deal with the maintenance of these targets with high levels of residual activation.

IN-FLIGHT FACILITIES

MSU/NSCL

The K500 and K800 cyclotrons have been modified to operate in a coupled mode. Intense heavy ion beams are initially accelerated in the K500 cyclotron, extracted, transported to and injected into the K800 cyclotron where a foil strips off most of the remaining electrons. The nearly bare nuclei are then further accelerated in the K800, extracted and transported through a fragment production target. More recently the A1900 projectile fragment separator has been completed and commissioned.[6] The separator uses twenty-four superconducting quadrupole magnets. Compared to the previous A1200 spectrometer the acceptance has increased from 2-4% to over 90%. The design specifications for the ECR and coupled -cyclotron system predict a peak beam power of 5 kW in the A=40 region at the target, well above the ability of the present fragment target. Target development on a novel new target capable of dealing with these beam powers has begun.[7]

GSI

RIB related research, using both the ISOL and IF techniques, has been an important part of the scientific program at GSI for many years. Recently there has been approval, with some restrictions, of a major facility upgrade that when completed is predicted to increase the secondary RIB intensity by a factor of 10^4.[8] The increase is the result of a number of factors. New fast ramped superconducting synchrotron drivers will permit the heavy ion intensities to increase by a factor of 10^2 and the energy to increase by a factor of 15. Finally a larger acceptance fragment separator (super FRS) replaces the FRS. Again a more robust target is needed to handle the increase in beam power.[9]

RIKEN RIBF

Riken has been providing intense light ion beams for the production of RIBs by projectile fragmentation at energies of 100 MeV/u since 1990. Driver intensities have increased with the installation of a new 18 GHz ECR ion source, a variable frequency RFQ linac and a charge state multiplier. A major upgrade to the radioisotope facility at RIKEN is now under construction.[10] The upgraded facility requires three new cyclotrons, the fRC (fixed energy ring cyclotron), IRC (intermediate stage ring cyclotron) and SRC (superconducting ring cyclotron). It also includes the installation of a new larger acceptance fragment separator (BigRIPS). Beam experiments with this new facility are scheduled to begin in 2007.[11] When finished it will be capable of accelerating elements up to A=40 to 400 MeV/u decreasing to 350 MeV/u for uranium. Currents will be limited to about 1 pμA for the lighter elements by the radiation shielding and slightly less than 1 pμA for the heavier elements. Plans call for the facility to include an ISOL type production target as well.

ISOL FACILITIES

CRC Louvain la Neuve

The cyclotrons at Louvain la Neuve have been used to carry out a great deal of the pioneering effort in developing beams for nuclear astrophysics using a high intensity 30 MeV proton driver. Recently a K=44 cyclotron specially designed to meet the specific requirements of mass separation and high transmission for nuclear astrophysics has been brought into operation. This new accelerator has delivered a beam of ^{19}Ne with an intensity around 5 x 10^9 particles/sec in the energy range 7.5 to 9.5 MeV.

HRIBF ORNL

The Holifield radioactive ion beam facility uses the ORIC cyclotron as a driver and the tandem as a post accelerator. This combination requires the formation of negative ions. Target development here has led to the use of HfO_2 fiber targets that have been shown to have excellent isotopic release and thermal properties. Recently the scientific program has expanded by creating neutron rich beams from proton-induced fission using approximately 10 μm thick uranium carbide deposited onto carbon fibers.[12] Plans have been developed to construct a second high-voltage platform that would contain a target system capable of being used at higher driver powers. Plans also include the possible replacement of the ORIC cyclotron with a higher intensity and higher energy driver in the future.

SPIRAL GANIL

The GANIL RIB program began with the production of exotic beams using the in-flight projectile method with the high-intensity heavy-ion beams in the energy range 50 to 100 MeV/u from the cyclotron drivers. More recently SPIRAL (Système de Production d'Ions Radioactifs avec Accélération en Ligne) has come into operation. The exotics are created by the ISOL method, ionized in an ECR ion source and accelerated with a K=265 cyclotron (CIME) to energies between 1.7 and 25 MeV/u. The development of high power targets and a remote handling system to deal with the high level of induced radioactivity have been key elements in the success. Unlike ISOL targets at light ion facilities where spallation or proton-induced fission is major mechanism for the creation of

exotic isotopes, here with heavy ions the primary production mechanism in the target is projectile fragmentation. The energy deposition profile by these heavy ions has required the development of special targets. The targets consist of a series of spatially separated carbon disks capable of handling up to 6 kW of beam power and operating at temperatures of 2300 K.[13] A detailed study has developed a conceptual design for SPIRAL2. In the initial stage the driver would be a 5 mA, 40 MV deuteron (q/A=1/2) and 1 mA (q/A=1/3) linac. This would permit the creation of exotic beams by fission either through neutrons or by direct bombardment.[14]

ISOLDE CERN

ISOLDE has been producing RIBs using the ISOL technique for over 30 years, initially with 600 MeV protons from the synchrocyclotron (SC), next with 1 GeV protons from the booster synchrotron that has recently been upgraded to provide 1.4 GeV protons. With these changes has come a change in beam structure from nearly DC to pulsed with high peak currents averaging to about 2μA. The inherent thermal cycling from the pulsed operation impacts the ideal target temperature regime and hence the target performance and lifetime. Recent ion source developments using lasers and resonant laser ionization have greatly improved the mass selectivity and efficiently ionized many elements of the periodic table. The facility has been designed so that two independent target stations can be used to provide independent RIBs to two different experimental stations. Recently experiments have started with accelerated beams using the REX-ISOLDE facility. Key elements in this new facility have been the RIB post accelerators, the charge booster comprised of a cooler, Penning trap and EBIS. The optimum energy range in now 0.8 to 2.2 MeV/u but work has begun on changes to upgrade the maximum energy to 3.1 MeV/u. An additional upgrade to 4.2 MeV/u is planned. Encouraging tests have recently been carried out with two-step targets where the proton beam impacts a neutron-producing target and the neutrons are used to produce the exotic nuclei in a uranium target. The result is a significant suppression of the spallation and fragmentation products and only a slight decrease in the neutron rich fission products. The lifetime of the target should be considerably longer than with direct proton bombardment targets. CERN is examining a high-intensity superconducting linac (SPL). This linac could be configured with existing tunnels to feed the ISOLDE targets.[15]

MAFF MUNICH

MAFF (Munich accelerator for fission fragments) has been designed for operation at the new high-flux Munich research reactor facility FRM-II. The reactor has recently been completed and licensed to begin operation. MAFF will provide intense beams of neutron rich isotopes at energies of 30 keV that will be further accelerated to energies from 3.7 to 5.9 MeV/u. MAFF creates the radioactive isotopes by the thermal-neutron-induced fission of uranium targets. The high neutron flux and large cross-sections for fission result in large yields of neutron rich fission products. Following the production target, MAFF includes ion sources, beam transport and a mass separator and is similar to other existing ISOL facilities. Initial RIB experiments at MAFF are anticipated in about two years. Post acceleration similar to REX-ISOLDE is foreseen.[16]

ISAC TRIUMF

The ISAC facility at TRIUMF uses energetic protons from the 500 MeV cyclotron driver to produce exotic elements by the ISOL technique. The shielding, cooling and remote-handling have been designed to be compatible with 50 kW (100 μA at 500 MeV) proton beam impinging a thick uranium target. The first RIB experiment began using a radioactive potassium beam in 1998. An active scientific program with low energy beams has been formulated around a neutral atom trap, a low temperature nuclear orientation setup, a β-NMR facility capable of providing a variety of polarized exotic beams, a modified Chalk River 8π spectrometer and various general-purpose stations. Recently a precision instrument based on an EBIT (electron beam ion trap) to measure exotic masses precisely has been funded. A little more than two years after the first RIB, accelerated exotic beams became available for nuclear astrophysics experiments. The accelerators were designed to meet the basic nuclear astrophysics requirements and provide continuously variable energy beams from 0.15 to 1.5 MeV/u for masses up to A=30. They consist of a cw 8m long RFQ linac and a five-tank cw IH DTL.

An important issue continues to be the development of targets that can reliably withstand the high powers in the driver beam. Target development has resulted in target lifetimes that now exceed an integrated proton dose of $5x10^{20}$.[17] Routine proton beam power delivered to the target has gradually increased from the 1 kW in 1998 to 20 kW today. The full 50 kW was successfully tested on a prototype target. A thermal surface-ionization, ion-source has been the RIB production source up until now, but an ECR ionizer is being commissioned and a resonant laser ion source is being tested on a test bed. Video surveillance, remotely operated cranes and remote manipulators in a heavily-shielded hot-cell are needed to deal with the high levels of residual activity experienced during target changes. Radiation induced diffusion enhances the yields of short-lived activity from the target as the proton current is increased. ISAC is being upgraded to provide higher energies and a broader range of masses in the ISAC II project with an ECR charge state booster and a superconducting linac to provide energies of 6.5 MeV/u for masses up to A=150.[18] Initial operation of this new post accelerator will begin in 2005 at a maximum energy of 4.3 MeV/u. Full energy operation is scheduled to begin in 2007. High power target development has not been compatible with efficient beam delivery to experiments. Consequently a plan to build a dedicated full power target development station is being proposed. The H^- cyclotron is versatile and can accommodate an additional 100 μA

extracted beam.[19] The beam would be taken to an expanded target hall. Existing nuclear ventilation and remote handling equipment would be used. The technology would be similar to the presently operating target stations. It is anticipated that this facility would be complete by 2008. In the future this facility could be used to provide independent RIBs simultaneously to two experiments from a single driver. A study has proposed using a storage ring to use the exotic isotopes more efficiently or to further accelerate the RIBs. [20]

RIA

RIA (rare isotope accelerator) is a new generation facility being planned in the US for basic research in nuclear physics. The facility proposes to use a unique cw driver accelerator that will lead to unprecedented yields of radioactive beams using both the ISOL and in-flight projectile fragmentation methods.[21] The proposed driver is a cw superconducting linac capable of accelerating all elements from protons to uranium through a maximum 1.4 GV potential. Beam power throughout the mass range is 400 kW. The final energy varies from 900 MeV for protons through to 400 MeV/u for uranium. In order to achieve the design beam power for the heavier elements with current technology the driver accelerator takes advantage of the large phase space acceptance of the independently phased superconducting resonators to capture and accelerate multiple charge states from the ECR and subsequent strippers. R&D on key elements of the proposed driver is being funded at a number of universities and national laboratories. This includes work on the ECR, the various types of superconducting structures required to cover the large range of β, high power stripper technology and the high power targets.[22,23] A windowless liquid lithium target is proposed for the in-flight fragmentation target.[24] A large acceptance fragment separator can be used in conjunction with energy degraders and a gas catcher to efficiently provide intense, low-emittance, radioactive ion beams suitable for stopped beam experiments or injection into a post accelerator.[25] The proposal also includes a second high-resolution, high-purity fragment separator. Traditional ISOL type targets using radiation-handling technology developed for ISAC are also proposed using direct proton irradiation as well as two-step neutron-induced fission. The proposed post-accelerator for RIB acceleration is designed for cw operation to accelerate singly-charged ions with masses up to 240 from the ion source energy to energies above the coulomb barrier.[26]

EURISOL

The European ISOL community is preparing the specifications for a next generation ISOL facility. The proposed driver would provide up to 5 MW of proton beams at 1 GeV and be upgradeable to 2 GeV.. The driver should also be capable of accelerating intense beams of other light ions. The proposal also includes the possibility of a supplementary electron machine that would be used for producing fission products. The RIB post accelerators would cover the ranges from 0.2 to 1 and 5 to 10 MeV/u with the possibility of achieving 100 MeV/u for A<80 decreasing to 20 MeV/u for A=200. [5,27]

SUMMARY

The scientific justification for exotic beams has been clearly made. There is a need to expand both the intensity and the range of exotic species. Laboratories in Asia, Europe and North America are actively pursuing technological solutions to meet the requirements. These new facilities are complex and costly. Intense stable beams from high-energy accelerators are required. Targets capable of handling the available powers are a challenge. Satisfying the legitimate safety concerns of the general public and licensing agencies is a challenge in these facilities that are designed to create and release activity easily. As the facility cost becomes significant, it has become important to find cost effective ways of providing the exotic beams to users. It is essential to find techniques that permit multiple simultaneous users.

REFERENCES

[1] The OECD Megascience Forum, Report from the Working Group on Nuclear Physics, OECD, Paris, France, 1999.

[2] Opportunities in Nuclear Science, A Long Range Plan for the Next Decade, The DOE/NSF Nuclear Science Advisory Committee, April 2002

[3] Scientific Opportunities with Fast Fragmentation Beams from the Rare Isotope Accelerator, NSCL, Michigan State University, March 2000.

[4] To the heart of matter, Report of the Canadian Subatomic Physics five year planning committee, June 2001.

[5] The Physics Case for EURISOL, Report of the key experiments task force, December 2002 Draft, http://www.ganil.fr/eurisol/Final_Report/A-Physics-Case-20-Dec-02.pdf.

[6] D. J. Morrisey et. al., Nuclear Instruments and Methods B, Volume 204, (2003), p. 90.

[7] J. A. Nolen et. al., Nuclear Instruments and Methods B, Volume 204, (2003), p. 298.

[8] Walter Henning, "SIS 100/200 System and Planned Research", these proceedings paper MOPL004

[9] N. A. Tahir et. al., Nuclear Instruments and Methods B, Volume 204, (2003), p. 282

[10] T. Motobayashi, Nuclear Instruments and Methods B, Volume 204, (2003), p. 736.

[11] Toshiyuki Kubo, Nuclear Instruments and Methods B, Volume 204, (2003), p. 97.

[12] D. W. Stracener, Nuclear Instruments and Methods B, Volume 204, (2003), p. 42.

[13] Antonio C. C. Villari et. al., Nuclear Instruments and Methods B, Volume 204, (2003), p. 31.

[14] Alban Mosnier, "SPIRAL2: A High Intensity Deuteron and Ion Linear Accelerator for Exotic Beam Production" these proceedings paper ROPA008

[15] Mats Lindroos et. al., Nuclear Instruments and Methods B, Volume 204, (2003), p. 730.
[16] D. Habs et. al., Nuclear Instruments and Methods B, Volume 204, (2003), p. 739.
[17] Pierre Bricault, "High Power Targets for ISOL Radioactive Ion Beam Facility", these proceedings paper WOAD003
[18] Robert Laxdal et. al., "The ISAC-II Upgrade at TRIUMF – Progresss and Developments, these proceedings paper ROPA010.
[19] Glen Stinson et. al., "A Proposal for an additional Beamline to the TRIUMF ISAC Facility", these proceedings paper TPPB024.
[20] Michael Craddock et. al., "Feasibility Studies of a Storage Ring for radioactive ions", these proceedings paper TPPE015
[21] Bradley Sherrill, "Overview of Radioactive Ion Accelerators, these proceedings paper ROPA004
[22] Ken Shepard, these proceedings, "Status of Low and Intermediate velocity Superconducting Accelerating Structures", these proceedings paper ROPA003
[23] Daniela Leitner et. al., "Commissioning of the Superconducting ECR Ion Source VENUS"' these proceedings paper MOPB008.
[24] J. A. Nolen et. al., Nuclear Instruments and Methods B, Volume 204, (2003), p. 298.
[25] Guy Savard, Nuclear Instruments and Methods B, Volume 204, (2003), p. 582.
[26] P. N. Ostroumov, Nuclear Instruments and Methods B, Volume 204, (2003), p. 433.
[27] The Driver Accelerator for EURISOL, Report of the Driver Accelerator Group, December 5, 2002. http://www.ganil.fr/eurisol/Final_Report/B-DriverReport-600dpi-5-Dec-02.pdf

STATUS OF THE SNS* PROJECT

N. Holtkamp, ORNL, Oak Ridge, TN 37820, USA

Abstract

The Spallation Neutron Source (SNS) [1,2] is a second-generation pulsed neutron source under construction at Oak Ridge National Laboratory. SNS is funded by the U.S. Department of Energy's Office of Basic Energy Sciences and is dedicated to the study of the structure and dynamics of materials by neutron scattering. A partnership of six national laboratories (ANL, BNL, JLab, LANL, LBNL, and ORNL) is responsible for the design and construction of the various subsystems. The facility will begin operation in 2006 and will deliver a 1.0-GeV, 1.4-MW proton beam with a pulse length of approximately 700 nanoseconds to a liquid mercury target. The expertise of the different laboratories has been exploited to enhance the delivered beam power by almost an order of magnitude compared to existing neutron facilities. The achievable neutron-scattering performance will exceed present sources by more than a factor of 20 to 100. To achieve such a big step, the subsystems require substantial improvements compared with existing accelerators. The challenges, the status of the project, and potential upgrades are presented here.

INTRODUCTION

The Spallation Neutron Source (SNS) [1, 2], authorized for construction in fiscal year 1999, is 63% complete. The accelerator, Central Laboratory and Office Building (which includes the central control room), Center for Nanophase Material Sciences (CNMS), and the Joint Institute for Neutron Science (JINS) are shown in Fig. 1, together with an artistic overlay of the facilities on top of a photo of the actual construction site. JINS will be operated in conjunction with the University of Tennessee in support of the users program. CNMS is one out of five nanophase science centers under construction in the United States.

Currently, all of the SNS accelerator-associated buildings and tunnels are completed and are ready for accelerator component installation. The goal for SNS is to deliver a proton beam of up to 1.4-MW beam power to a mercury target for neutron spallation. In a recent proposal, even higher beam power operation, following moderate upgrade proposals, was discussed [3]. The site layout (Fig. 1) has possible future upgrades incorporated, for example, the second target station (shown shaded) and

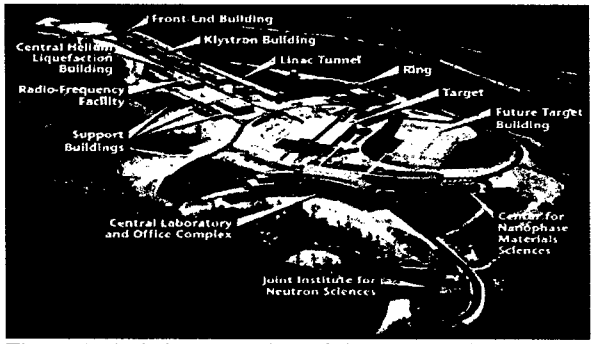

Figure 1: Artist's conception of the SNS facility overlaid on a early site photo of the Chestnut Ridge construction site at ORNL.

space next to the radio-frequency (RF) building for a superconducting RF (SRF) facility that will be needed to maintain the existing cryomodules, as well as to develop and build new ones at a rate consistent with a two-year upgrade schedule. Empty spaces in the tunnel allow for installation of an additional nine cryomodules to increase the energy to more than 1.3 GeV. The accelerator systems, basically a full-energy injector linac and an accumulator ring, operate at a repetition rate of 60 Hz and an average current of 1.6 mA. The accelerator systems consist of a negative hydrogen (H^-) RF volume source capable of delivering more than 50 mA of peak current, a low-energy beam transport (LEBT) housing a first-stage beam chopper, a 4-vane RF quadrupole (RFQ) for acceleration up to 2.5 MeV, a medium-energy beam transport (MEBT) housing and a second-stage chopper, a 6-tank drift-tube linac (DTL) up to 87 MeV, a 4-module coupled-cavity linac (CCL) up to 186 MeV, an SRF linac with 11 medium-β cryomodules (up to 379 MeV) and 12 high-β cryomodules (up to 1000 MeV), a high-energy beam transport (HEBT) for diagnostics and collimation, and an accumulator ring for compressing the 1-GeV, 1-ms pulse to »700 ns for delivery onto the target through a ring-to-target beam transport (RTBT) beam line. Neutrons are produced by spallation in the mercury target, and their energy is moderated to useable levels by supercritical hydrogen and water moderators. The basic parameters of the facility are summarized in Table 1.

The simultaneous performance goals of 1.4 MW of proton beam power and ultimately having more than 90% facility availability place significant operational-reliability demands on the technical and conventional systems. Hands-on maintenance capability, made possible by low activation in the accelerator, is key, and requires maintaining beam loss of < 1 W/m. Figure 2 is a schematic layout of the different linac structures as a function of beam energy.

*SNS is a partnership of six U.S. national laboratories: Argonne National Laboratory (ANL), Brookhaven National Laboratory (BNL), Thomas Jefferson National Accelerator Facility (JLab), Los Alamos National Laboratory (LANL), Lawrence Berkeley National Laboratory (LBNL), and Oak Ridge National Laboratory (ORNL). SNS is managed by UT-Battelle, LLC, under contract DE-AC05-00OR22725 for the U.S. Department of Energy.

0-7803-7738-9/03/$17.00 © 2003 IEEE

Table 1: Summary of SNS Facility Parameters

Parameter	Value	Unit
Proton beam energy on target	1.0	GeV
Proton beam current on target	1.4	mA
Proton beam power on target	1.4	MW
Pulse repetition rate	60	Hz
Beam macropulse duty factor	6	%
H- peak current from front end	>38	mA
Average current per macropulse	26	mA
Chopper beam-on duty factor	68	%
Linac length, incl. front end	335	m
Ring circumference	248	m
Ring fill time	1	ms
Ring extraction gap	250	ns
Protons per pulse on target	1.5×10^{14}	
Liquid mercury target	18 tons	1 m^3
Number of moderators	4	
Minimum initial instruments	8	

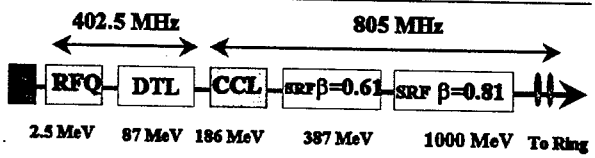

Figure 2: Schematic layout of the linac structures as a function of beam energy.

ACCELERATOR SYSTEMS

Front-End System (FES) (LBNL)

The FES, shown schematically in Fig. 3 (top left), consists of a multicusp, volume-production, cesium-enhanced, RF-driven, H- ion source; an electrostatic LEBT; a 4-vane RFQ with π-mode stabilizers that accelerates the 65-keV beam from the ion source to 2.5 MeV; beam-chopping systems; and a beam-transport, rebunching, and matching section (MEBT). Current-, profile-, and position-monitoring diagnostics are incorporated into the FES. Primary beam chopping is performed by the LEBT, with final chopping in the MEBT. Large beam eccentricity in the MEBT leads to nonlinear space charge forces that can lead to halo in the CCL; thus, collimation is necessary to prevent losses. Collimation is performed in the MEBT, reducing halo at the CCL by 97%. Collimator locations are shown in Fig. 3 (bottom).

FES commissioning at LBNL was performed in May 2002 by a multilaboratory team led by LBNL. A peak beam current of more than 50 mA was produced at low duty factor, and a 25-mA beam was produced at 6% duty factor. In December 2002, these results were reproduced with a fully integrated system at the SNS site (Fig. 4). The MEBT rms output emittance was ε_x ~ 0.3 π mm mrad / ε_y ~0.27 π mm mrad at 25 mA, meeting the SNS requirement within measurement accuracy.

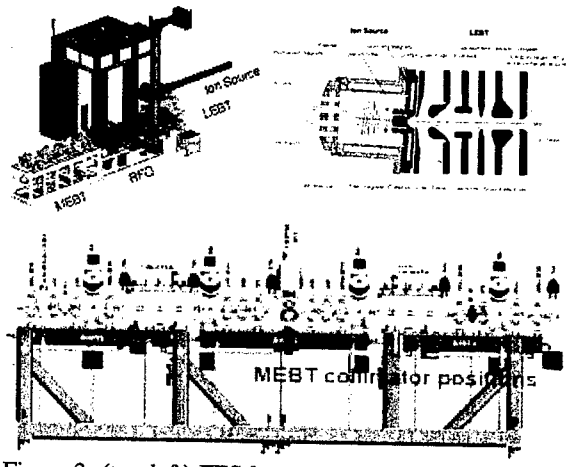

Figure 3: (top left) FES layout, (top right) H- ion source, and (bottom) MEBT collimator locations.

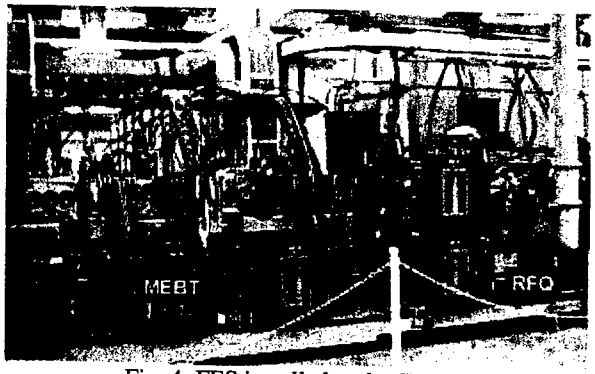

Fig. 4. FES installed at the SNS site.

Normal-Conducting Linac (LANL) and High-Power RF Systems

Downstream of the MEBT, beam is accelerated to 87 MeV by a 216-cell, six-tank DTL, provided by LANL. Each DTL tank is driven by a 402.5-MHz, 2.5-MW (peak power) klystron. Permanent magnet quadrupoles, beam position monitors, current monitors, and steering dipoles are integrated into the drift tubes. Diagnostic sections are between each tank. The third of the six DTL tanks was installed and operated in May 2003. Fig. 5 shows a photograph of the DTL, and the inset shows the drift tubes. DTL 3 conditioned up to full field in less then 24 hours and achieved 40% of its design average power within 48 hours.

The CCL, operating at 805 MHz and powered by four 5-MW (peak) klystrons, accelerates the beam to 186 MeV. The CCL has four modules with a total of 384 cells and is made of oxygen-free copper. A CCL hot-model prototype, including a bridge coupler, was successfully power tested at LANL.

The high-power RF systems design of the linac is finished, and klystron deliveries are in full swing. Klystrons to be installed in the ~330-m-long klystron gallery include 7+4 (installed + spares) 402.5-MHz, 2.5-MW; 4+5 805.0-MHz, 5-MW; and 81+20 805.0-MHz,

0.55-MW klystrons. The klystrons are powered by 13 high-voltage converter modulators (HVCMs), which were specifically developed for SNS (Fig. 6). Extremely high-power density and efficient high AC-to-DC high-voltage conversion are the main features. High-frequency (20-kHz) switching using IGBT technology and newly developed boost transformers allow for a very compact design that saves investment cost as well as real estate. The HVCMs typically operate at 11-MW peak power and ~1-MW average power, feeding between 2 CCL and 12 superconducting linac (SCL) klystrons. Integrated into the design are rectifiers and transformers, control racks, and SCR regulators.

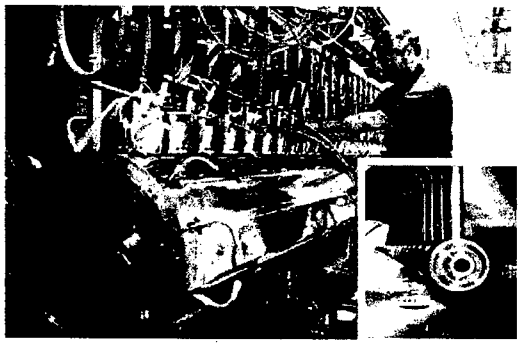

Figure 5: DTL tank 3 in the tunnel during final installation. Tank 3 contains 33 DTs.

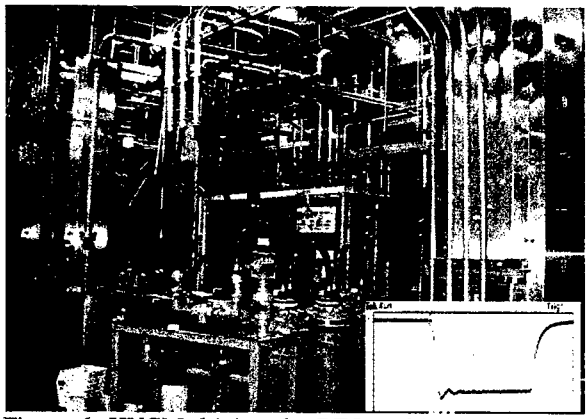

Figure 6: HVCM driving the RFQ and DTL 1 klystron (402.5 MHz, 2.5 MW) installed in the klystron gallery. The graph shows the flat top of a full 1.3-ms-long pulse.

SRF Linac (JLab)

SNS will be the first large-scale superconducting proton linac that provides high beam power. Advantages offered by the superconducting structures, as well as progress over the last decade in reliably achieving high-performance accelerating structures, led to the design choice. The most prominent arguments for an SCL are large aperture, operational flexibility, high gradient, less real estate, lower operating costs, small wakefields, excellent vacuum, and very high efficiency.

The velocity of the H^- ions within the SCL varies from β=0.55-0.87. The most economic approach (balancing the number of different types of cells versus the accelerating efficiency) is a two-cavity geometry with β=0.61 and β=0.81. Some design parameters for both types are listed in Table 2. Beam is accelerated from 186 to 387 MeV by 11 cryomodules (CMs) with 3 medium-β (β = 0.61) cavities each and to 1 GeV by 12 CMs with 4 high-β (β = 0.81) cavities each, or a total of 81 cavities.

Table 2: Some Cavity Design Parameters

Parameter	β=0.61	β=0.81	Unit
No. of cells	6	6	
E_{peak}	27.5	35.0	MV/m
E_{peak}/E_{acc}	2.71	2.19	
B_{peak}/E_{peak}	2.10	2.14	mT/(MV/m)
Cell:cell cplng	1.61	1.61	%
Q at 2.1 K	$>5 \times 10^9$	$>5 \times 10^9$	
Active length	0.682	0.906	m

Fig. 7 shows the surface, on-axis, and effective accelerating fields for both cavity geometries, as a function of the velocity (β) of the particles. Particle tracking shows that there is almost no emittance growth in the SRF linac.

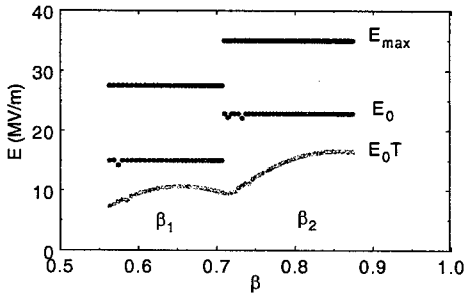

Figure 7: Surface (E_{max}), on-axis (E_0), and effective accelerating (E_0T) fields for both optimized cavity geometries, as a function of particle beta.

The SRF cavities are manufactured by industry out of high-purity RRR 250 niobium sheets. They are then shipped to JLab for surface treatment, where they are subjected to standard cycles of buffered chemical polishing, high-pressure ultrapure water rinsing, and vacuum degassing, after which they are RF-power tested in a radiation-shielded vertical Dewar. Electropolishing, a technique that has been demonstrated to further improve surface gradients, will be applied to the high β cavities to guarantee good performance. The gradient performance achieved with a total of 14 medium-β cavities and 1 electropolished high-β cavity is shown is Fig. 8. So far, all medium-β cavities have exceeded the specification during cw testing, some of them by more than 50%. The first electropolished high-β cavity shows a gradient of 21 MeV/m, compared with a 16.5-MeV/m specification.

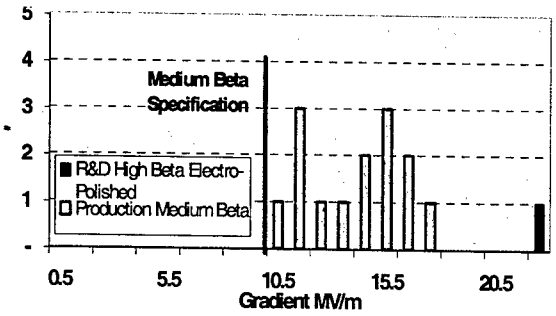

Figure 8: Performance of cavities in the medium β cryomodule at the design Q_0 of 5×10^9. Also shown is the first electropolished high β cavity.

Three medium-β and four high-β cavities in their helium vessels are connected together, and RF couplers, HOM couplers, field probes, and gate valves are installed, forming a cavity string. All couplers, all medium-β CMs, and 2 out of the 12 high-β CMs have been or will be tested in a dedicated test stand at JLab before installation in the tunnel. The first production cryomodule is shown in Fig. 9 in its assembly area. This CM, as well as the prototype, performed well in initial testing, giving confidence to proceed with mass production.

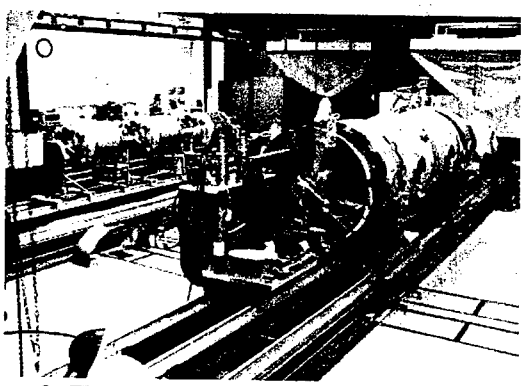

Figure 9: The first production medium-β cryomodule in the assembly area. A second string of cavities can be seen in the background.

Because SNS is a pulsed accelerator, compensation of Lorentz force detuning effects is a concern. The RF system has adequate margin to accommodate 470 Hz of detuning, but the real detuning depends on cavity stiffness, and decisions had to be made before cavity production started. Fast piezoelectric tuners are installed on all cavities to further reduce power requirements for resonance control. Test results indicate that these tuners are unnecessary at baseline gradients as the detuning is below 470 Hz and that the piezo tuners are able to reduce detuning even further by a factor of three.

It is critical that particulates not be introduced into the SRF cavities, as the resulting field emission would severely degrade their performance. A nonintercepting beam profile diagnostic, the laser wire, is being developed and tested. A laser scanned through the H- ion beam strips off electrons, which are collected and sampled. The position of the laser versus electron intensity can replicate the transverse and longitudinal profile (up to single bunch resolution) and down to the 10^{-4} resolution level, as shown in Fig. 10.

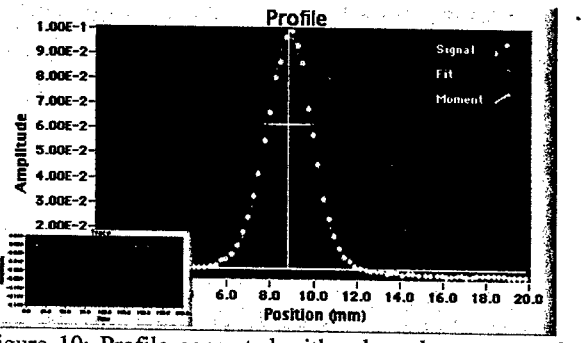

Figure 10: Profile generated with a laser beam scanned across the H- ion beam. The electron collector current is shown in the lower left corner. This system will be used throughout the SCL.

Helium to cool the SRF linac is provided by the central helium liquefier (CHL), major parameters of which are listed in Table 3. Gas flows from two pairs of warm screw compressors, through oil removal, a coalescer-demister, and charcoal filters. It is then piped to the 4.5 K cold box where a standard liquefier cycle sends helium through cryogenic transfer lines to the cryomodules.

Table 3: Refrigeration Parameters

32 CMs	Primary	Secondary	Shield
Temp. (K)	2.10	5.0	35-55
Pressure (bar)	0.041,3	3.0	4.0-3.0
Static load	850 W	5.0 g/sec	6125 W
Dynamic load	600 W	2.5 g/sec	0 W
Capacity	2,850 W	15 g/sec	8300 W
Margin	100%	100%	35%

Joule Thompson valves on the cryomodules produce 2.1 K, 0.041 bar liquid helium for cavity cooling and 4.5 K helium for fundamental power coupler lead cooling. Cooling boil-off goes to four cold compressors capable of 120 g/s steady state, recompressing the stream to 1.05 bar and 30 K for counter-flow cooling in the 4.5 K cold box. Transfer line and CHL installation are under way, and commissioning of the CHL will begin at the end of this calendar year.

Accumulator Ring (BNL)

The 1-ms-long linac pulse is compressed to a single 695 ns bunch in the accumulator ring through multiturn, charge-exchange injection. To minimize space-charge effects, transverse phase-space painting is used to increase the total beam emittance to 240 π mm mrad, thereby reducing the space-charge tuneshift to ~0.15. The resulting halo is removed by a two-stage collimation system. A 1-MHz RF system maintains a clean beam gap

that is longer than the extraction kicker rise time. After accumulation, the extraction kicker directs the beam into the RTBT line that takes it to the target. Major ring parameters are listed in Table 4.

Table 4: Major Parameters of the Ring

No of injected turns	1060	
Revolution frequency	1.058	MHz
Filling fraction	68	%
Transvrs emittance 99%	240	π mm mr
Transvrs acceptance	480	π mm mr
Space charge tune shift	0.15	$\Delta Q_{x,y}$
Ring peak current	52	A
HEBT/RTBT Length	170/150	m
Circumference	248	m
RTBT transvrs acceptance	480	π mm mr
Beam size @ tgt (H × V)	200 × 70	mm × mm

A variety of technical issues that come with high-intensity operation of the accumulator have been addressed in the meantime to further ensure operation of up to 2 MW at 1 GeV. To control the e-p instability, solenoidal coils have been added to certain areas of the vacuum chamber and special electron collectors have been included in the present stripping area, while coating of the interior vacuum chamber with titanium nitride continues. At the same time, a research and development (R&D) program to develop higher power stripping foils based on a diamond substrate is under way and will be reported on this conference. Dynamic detuning of the RF system has been demonstrated, and kicker rise and fall times are consistent with the design specifications. Meanwhile, installation of the HEBT beam line and ring tunnel components has started and is making good progress.

Controls

Controls for the SNS complex are distributed among the partner labs but are coordinated at ORNL. SNS relies on an EPICS control system and does make use of a distributed network between partner labs. Also integrated into EPICS are the controls for the utilities and the power distribution systems, which were developed by a commercial vendor that worked on the SNS software platform.

TARGET AND INSTRUMENTS

The SNS target consists of 1 m^3 of liquid mercury that weighs ~18 tons. The mercury circulates constantly to aid the target system's ability to survive the tremendous thermo-mechanical shocks resulting from the pulsed beam energy of ~20 kJ/pulse. Evidence of cavitation-induced pitting in the steel has been investigated in detail in a dedicated R&D program over the last 12 months, and several ways to mitigate these effects are under way. Test data show that at ~1 MW the present design will sustain the effect for at least two weeks. Construction of the target conventional facilities is proceeding apace. Many of the major components are now on site, and target installation has begun.

Selection of SNS instruments is based on scientific merit, and a peer-review body provides advice in that regard. So far, 16 instruments have been approved, 5 of which are funded within the SNS project: a high-resolution backscattering spectrometer; vertical surface (magnetism) reflectometer; horizontal surface (liquids) reflectometer; extended Q-range, small-angle diffractometer; and a third-generation powder diffractometer. Three additional instruments are funded by instrument development teams: a wide-angle thermal chopper spectrometer, cold neutron chopper spectrometer with 10- to 100-μeV resolution, and an engineering materials diffractometer. Funding is being sought for the remaining approved instruments: a high-pressure diffractometer, disordered materials diffractometer, fundamental physics beam line, high-resolution thermal chopper spectrometer, and a single-crystal diffractometer.

CONCLUSIONS

SNS construction is proceeding rapidly. At the time of this conference, the total project is 62% complete. More than 1.3 million cubic yards of earth have been excavated, the accelerator tunnels and buildings have been turned over for component installation, and support buildings are progressing well. SNS is on schedule to be completed, within budget, in June 2006. Three million person-hours of work have taken place without a lost-time injury. Up-to-date information about SNS can be found on our web site [1]. Many SNS papers from other accelerator conferences, as well as this one, can be found using the JACOW web site and its excellent search engine [5] (an apology for the incomplete citation, but a complete list would go beyond the available framework of this article). Many of the developments mentioned here are reported in detail in other papers submitted to this conference, and consulting those papers is encouraged.

ACKNOWLEDGMENTS

This paper is presented on behalf of all our SNS colleagues whether they are members of the partner labs or are among the many friends and colleagues worldwide who collaborate with us on this project. We gratefully acknowledge their contributions, whether intellectual or practical, as their efforts have been crucial to SNS.

REFERENCES

[1] SNS web site: www.sns.gov.

[2] NSNS Collaboration, *NSNS Conceptual Design Report*, NSNS-CDR-2/V1, Martin Marietta Energy Systems, Inc., Oak Ridge Natl. Lab., Oak Ridge, Tenn., 1997.

[3] G. Richmond and S. Sinha, *BESAC Subcommittee Workshop Report on 20 Year Basic Energy Sciences Facility Roadmap*, Feb. 22-24, 2003.

[4] Y. Cho et al., *Preliminary Design Report: Superconducting Radio Frequency Linac for the Spallation Neutron Source*, SNS-SRF-99-101, Lockheed Martin Energy Systems, Inc., Oak Ridge Natl. Lab., Oak Ridge, Tenn., Dec. 20, 1999.

[5] Joint Accelerator Conference Web site (JACoW): accelconf.web.cern.ch/AccelConf.

THE FUTURE GSI FACILITY: BEAMS OF IONS AND ANTIPROTONS

Walter F. Henning, GSI Darmstadt, Germany

Abstract

A brief description is given of the conceptual layout, technical aspects and overall performance characteristics, some R&D, and the main research areas of the future international facility for beams of ions and antiprotons to be constructed at the GSI Laboratory.

INTRODUCTION

With strong participation from its users and the international science community, GSI over the past few years has developed plans [1] for a major new international accelerator facility, using the present GSI system as an injector (Figure 1). Following an evaluation of the proposal by the Wissenschaftsrat, the science advisory committee to the German federal government, and its recommendation to construct the facility [2], the government has recently given approval for construction under two conditions: that a technical plan be developed for staged construction, and that 25% of the total cost come from international partners [3].

The central goals for the new facility are to substantially increase the intensities of ion beams, their energy, and to provide secondary beams with unique characteristics: intense beams of short-lived nuclei up to 1-2 GeV per nucleon and energetic, high-quality beams of antiprotons, both with the options for storage, beam cooling and in-ring experimentation.

FACILITY DESCRIPTION

The intensity of 'low-energy' ion beams, i.e. beams around 1-2 GeV per nucleon, will be increased by two to three orders of magnitude over present (two orders in space charge limit, up to three orders over actual present performance). This will be achieved by increasing the cycling rate of the injector, the present synchrotron SIS18, by a factor ten. A second factor arises from reducing the charge state of, for example, uranium beams from 73 to around 25. Since the space charge limit enters quadratically with charge state, this gives close to a second factor of ten.

The most important consequence of this will be the increase in secondary beam intensities, i.e. beams of short-lived nuclei ('radioactive beams') by three to four orders of magnitude. This comes from the fact that in addition to the primary intensity increase, collection efficiency and storage of secondary beams will be substantially improved.

Ion beams of high charge-state and thus higher energy, up to 30-35 GeV per nucleon for medium to heavy masses, will also become available at substantially increased intensities over present facilities.

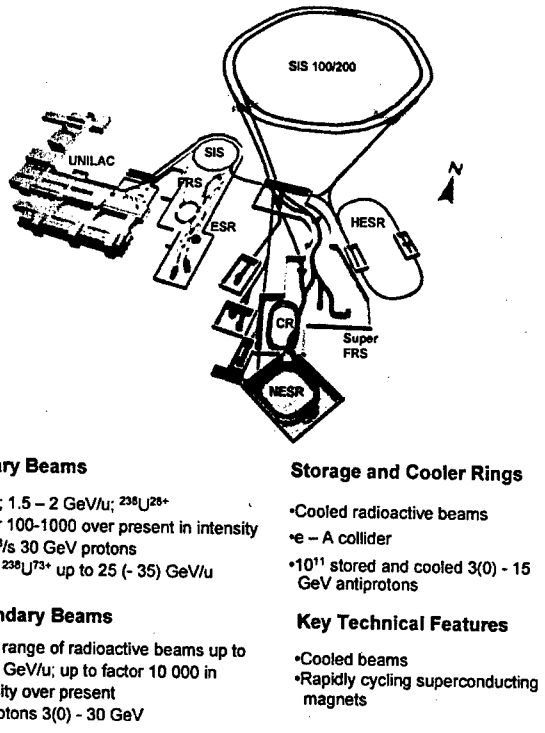

Figure 1: The existing GSI facility (left) with the linear accelerator UNILAC, the heavy-ion synchrotron SIS18, the fragment separator FRS and the experiment storage ring ESR; and the new project (right) with the double-ring synchrotron SIS100/200, the high-energy storage ring HESR, the collector ring CR, the new experiment storage ring NESR, the super-conducting fragment separator Super-FRS and several experimental stations. The present UNILAC/SIS18 complex serves as injector for the new double-ring synchrotron.

An important new development at GSI will be the availability of high-energy, high-quality antiproton beams over a broad range of beam energies, from thermal energies up to 15 GeV.

A characteristic feature of the new facility is the broad usage of storage and beam-cooler rings (see Figure 1). Stochastic and electron-beam cooling are widely used, together with internal targets, which open a range of new opportunities for high-resolution and precision experiments. In particular electron-beam cooling, originally developed to raise luminosities in proton-proton [4] and proton-antiproton collider rings [5] (but never really used at colliders pushing the energy frontier simply because the needed electron-beam energies and powers were out of reach) have proven to be superb tools for beam handling and beam improvements at the low-

0-7803-7738-9/03/$17.00 © 2003 IEEE

energy antiproton and proton rings, and most recently at ion storage rings in particular the high-energy ion storage ring ESR at GSI [6].

Beam cooling, storage-ring beam handling schemes, and in-ring experimentation are key features of the new facility. Some of these aspects, and in addition research and development into rapidly-cycling superconducting magnets and vacuum issues at very high beam currents, are discussed in other presentations to this conference [7,8].

The research program proposed for the future facility is broad and covers several areas of study into the structure of matter. It emphasizes the regime of the strong force (quarks, nucleons, nuclei, and quark and nuclear matter), but also has strong components into matter-ion interactions at the material science level, in particular in plasma physics and in atomic physics with highly stripped relativistic ions.

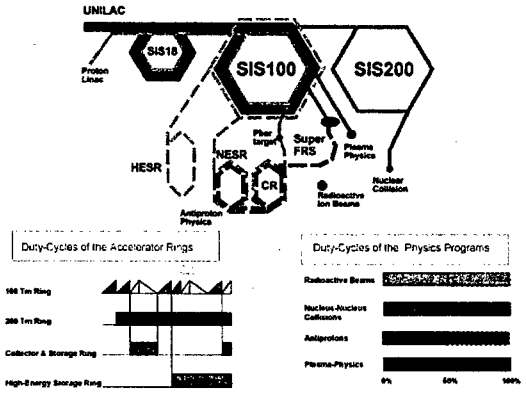

Figure 2: Schematic illustration of the highly efficient parallel operation at the new facility. In the example shown, all four different scientific programs are served in parallel: A proton beam (orange), accelerated in SIS100, produces antiprotons (orange dashed) in the antiproton target-station, which are then collected, accumulated and cooled in the CR/NESR storage-ring combination, injected and accelerated in SIS100, and then transferred to the HESR for in-ring experiments. In parallel, i.e. during the fraction of the SIS100 super-cycle not needed for the protons, a primary ion beam (blue) is accelerated in SIS100 and slowly extracted to the Super-FRS to produce radioactive secondary beams (blue dashed) for fixed target experiments. (Alternatively the radioactive beams could be sent to the CR and NESR instead of the antiprotons after fast extraction from SIS 100). In addition, every 10-100 seconds a high-energy heavy-ion beam (red) is accelerated in SIS100/200 and slowly extracted for nuclear collision experiments; these experiments require a lower beam intensity than the maximum possible from the accelerator. Moreover, intense beam pulses (green) are provided every few minutes for plasma physics experiments that require very low repetition rates.

The reasons for the broad research program are basically twofold: first, the methods and goals of the science exploring the (microscopic) structure of matter are often similar at the different levels of the hierarchy, and thus relate to each other in a synergetic way.

Second, though, to achieve the challenging goals in beam intensity and overall accelerator performance asked for by today's research programs, large (and very costly) facilities need to be built (including the present project). It seems prudent simply from considerations of the cost/benefit ratio that such major facilities can serve several science fields or research communities simultaneously. The present facility, due to the wide use of rings and the resulting intrinsic cycling times and storing possibilities, leans itself well to a highly parallel and multiple use. This is illustrated in Figure 2.

THE RESEARCH PROGRAM

An overview of the various research programs, grouped into five categories, is listed in Table 1. It is discussed in detail in the Conceptual Design Report [1] and at various workshops. Here we only repeat some overarching aspects that, to a certain extent, connect the different research areas.

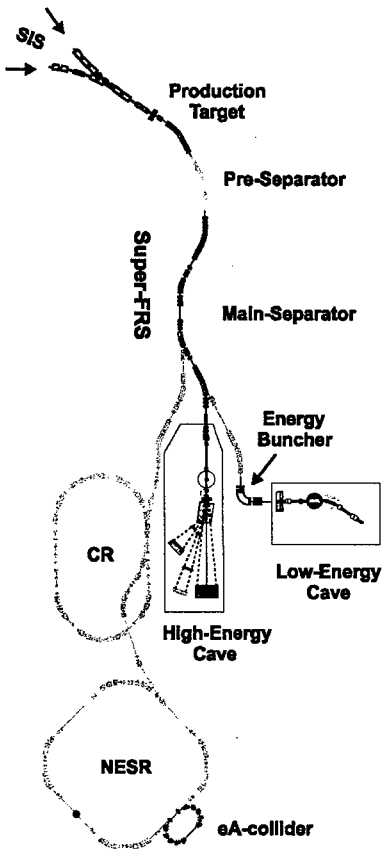

Figure 3: Schematic layout of the proposed Super-FRS exotic nuclear beams facility shown to scale. The three main branches of experimental areas are indicated.

The first goal is to achieve a comprehensive and quantitative understanding of all aspects of matter that are governed by the strong force. Matter at the level of nuclei, nucleons, quarks and gluons is governed by the strong interaction and is often referred to as hadronic matter.

The research goal of the present facility thus encompasses all aspects of hadronic matter, including the investigation of fundamental symmetries and interactions that are relevant for this regime.

The second goal addresses many-body aspects of matter. The many-body aspects play an important and often decisive role at all levels of the hierarchical structure of matter. They govern the behavior of matter as it appears in our physical world.

These two broad science aspects, the structure and dynamics of hadronic matter and the complexity of the physical many-body system, transcend and determine the more specific research programs listed in Table 1.

Table 1: Summary of research areas at the GSI future facility

Research Areas	**Exemplary Topics**	**Facility Aspects**
Structure and Dynamics of Nuclei	Nucleonic matter Nuclear astrophysics Fundamental symmetries	Radioactive Beams
Hadron Structure and Quark-Gluon Dynamics	Non-perturbative QCD Quark-gluon degrees of freedom Confinement and chiral symmetry	Antiprotons
Nuclear Matter and the Quark-Gluon Plasma	Nuclear phase diagram Compressed nuclear/strange matter Deconfinement and chiral symmetry	Relativistic Heavy-Ion Beams
Physics of Dense Plasmas and Bulk Matter	Properties of high-density plasmas Phase transitions and equation of state Laser - ion interaction with and in plasmas	Bunch Compression
Ultra High EM-Fields and Applications	QED and critical fields Ion - laser interaction Ion - matter interaction	Highly-stripped relativistic ions/ Petawatt Laser

The program summarized in Table I builds on the accelerator parameters but also forefront experimental equipment. Examples are shown in Figure 3 for the research with beams of short-lived nuclei (radioactive beams); and in Figure 4 for the High Energy Storage Ring (HESR) and the internal-target PANDA detector, for in-ring experimentation with cooled, high-quality energetic antiproton beams at energies covering the charmed quark region. More information is again found in [1].

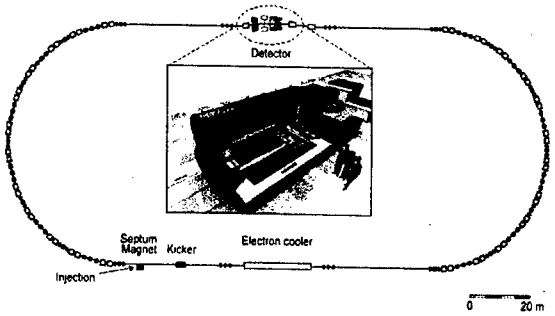

Figure 4: View of the HESR and the PANDA Detector.

REFERENCES

[1] An International Accelerator Facility for Beams of Ions and Antiprotons; Conceptual Design Report, 11/2001; http://www.gsi.de/GSI-Future/cdr/; this report is also available on CD. Mail to press@gsi.de to request a copy.

[2] Press release 24/2002, www.wissenschaftsrat.de/

[3] Press release, 5.2.03, www.bmbf.de/presse01/799

[4] G.I. Budker, Atomnaja Energia, 22, p. 346, 1967

[5] G.I. Budker, Ya.S. Derbenev, N.S. Dikansky , V.I. Kudelainen, I.N. Meshkov, V.V. Parkhomchuk, D.V. Pestrikov, B.N. Sukhina, A.N. Skrinsky, IEEE Trans. Nucl. Sci. NS-22,2093-7(1975)

[6] Contributions to the "11th International Advanced ICFA Beam Dynamics Workshop on Beam Cooling and Instability Damping", Moscow, 1997, Nucl. Instr. Meth. 391,1 (1997). For a recent review on present and future applications of beam cooling see: Contributions to "Rare Isotope Physics at Storage Rings" - An International Workshop Organized by GSI and RIKEN, Hirschegg, Austria, 2002; the presentations given at that Workshop are available on CD. Mail to press@gsi.de to request a copy.

[7] P. Spiller, contribution to this conference.

[8] B. Franzke, contribution to this conference.

BEAM PHYSICS AT LHC

L.R. Evans, CERN, Geneva, Switzerland

Abstract

The design of the Large Hadron Collider incorporates the accumulated knowledge obtained from previous generations of hadron colliders. Among the well known effects limiting machine performance are intrabeam scattering, the beam-beam interaction and stability against collective motion. Simulations and recent experiments in the SPS have shown that the electron cloud effect observed in the B-factories will be present both in the LHC and in its injector. All of these phenomena are discussed together with the measure taken in the machine design to overcome them.

INTRODUCTION

The Large Hadron Collider, now under construction at CERN will provide proton-proton collisions with a centre-of-mass energy of 14 TeV and an unprecedented luminosity of 10^{34} cm^{-1} s^{-2}. In order to achieve this it must operate with more than 2800 bunches per beam and a very high intensity. The stored energy per beam at design energy is 350 MJ. The machine will also operate for heavy (Pb) ion physics at a luminosity of 10^{27} cm^{-1} s^{-2}.

Many accelerator physics issues must be taken into consideration in the machine design. The first is a sound and flexible optics, robust against inevitable lattice perturbations and able to cater for changes in layout demanded by hardware builders and particle physicists. The interaction of the beam with its immediate environment and with the other beam can produce many undesirable effects. Incoherent single particle effects include the beam-beam interaction due to the influence of the electromagnetic field of one beam on the particles in the other, and intrabeam scattering, multiple Coulomb scattering between the particles in the same beam. Collective effects include single bunch instabilities driven by short range wakefields and coupled bunch effects due to the large number of bunches and small separation. Since the unavoidable imperfections in superconducting magnets produce non-linear field errors, the issue of dynamic aperture, the maximum useful betatron amplitude of particles over a long time duration, is also of fundamental importance.

The 25 ns bunch spacing can give rise to a new effect, now known to be a limiting factor in the B-factories. Electrons, produced by synchrotron radiation or by ionisation of rest gas, can be accelerated to the walls of the vacuum chamber, producing secondaries which can themselves be accelerated by following bunches. This can give rise to a rapid build-up in the "electron cloud" and is a source of heat deposition into the cryogenic system, emittance blow-up and even instability

MACHINE LAYOUT

The basic layout mirrors that of LEP, with eight long straight sections, each approximately 500 m in length available for experimental insertions or utilities. Two high luminosity insertions are located at diametrically opposite straight sections, Point 1 (ATLAS) and Point 5 (CMS). A third experiment, optimised for heavy ion collisions (ALICE) will be located at Point 2. A fourth experiment (LHCb) will be located at Point 8. The two detectors at Points 1 and 5 require a substantial amount of new civil engineering infrastructure, whilst the other two will be integrated into existing LEP caverns. The beams cross from one ring to the other only at these four locations. Points 2 and 8 also contain the injection systems for the 450 GeV/c beams provided by the SPS.

The other four long straight sections do not have beam crossings. Points 3 and 7 are practically identical and are used for collimation of the beam halo in order to minimise the background in the experiments as well as the beam loss in the cryogenic parts of the machine. Consequently they only contain classical warm magnets robust against the inevitable beam loss and secondary shower from the collimators. Point 4 contains the 400 MHz RF systems which are independent for the two beams, where the beam separation must be increased from 194 mm in the regular arcs to 420 mm in order to provide the transverse space needed. Finally, Point 6 contains the beam abort system, where the two beams are extracted using a combination of fast pulsed magnets and steel septa and transported to the external beam dumps.

OPTICS

The regular arc cell is 106.9 m in length and contains six dipoles, each of 14.3 m magnetic length. The lattice quadrupoles, 3.1 m in length, are integrated into "short straight sections" containing a combined orbit correction dipole and chromaticity sextupole and space for another short corrector, either a trim quadrupole, skew quadrupole or octupole, depending on its position in the lattice. The dipoles and quadrupoles are powered independently, with different gradients in the two quadrupole apertures allowing a tune split of up to ten units in order to render the machine insensitive to linear coupling.

The four collision insertions have a similar layout. Moving out from the interaction point (IP), one first encounters the inner triplet. The distance from the IP to the first element of the triplet is 23 m, with the IP at Point 8 displaced longitudinally by 11.25 m with respect to the centre of the experimental hall due to the asymmetric geometry of the LHCb detector. After the triplet, the beams are separated. In the high luminosity insertions 1 and 5 the separation dipoles are not superconducting due to the very high particle flux from

0-7803-7738-9/03/$17.00 © 2003 IEEE

the IP. In the other two insertions they must be superconducting due to the restricted longitudinal space available because of the presence of the injection systems.

The long straight section terminates with a twin aperture dipole to bring the beams into the two magnetic channels and a set of four independently powered matching quadrupoles. Between the long straight section and the regular arc there is a dispersion suppressor approximately 171 m long, where the dispersion function is matched to that of the arc. The first three quadrupoles in the dispersion suppressor are also independently powered in order to increase flexibility.

In addition to the normal lattice correctors for chromaticity and orbit control, a number of different multipole correctors are included to compensate for field imperfections and to control instabilities. All dipoles contain a sextupole spool piece to correct for persistent current effects and residual sextupole errors. Half of the dipoles also contain a ganged octupole and decapole corrector to compensate unwanted field harmonics. In about half of the main quadrupole cold masses, octupoles are included to provide Landau damping against transverse instabilities. The inner triplets contain their own corrector packs in order to correct multipole errors locally in the very sensitive regions where the beta function is very large in collision.

ACCELERATOR PHYSICS ISSUES

The Beam-Beam Interaction

The beam-beam interaction is an inevitable consequence of bringing the beams into collision. The particle trajectories in one beam are perturbed by the electromagnetic field of the other beam. This non-linear interaction excites betatron resonances and also produces a variation of tune with amplitude, generating a tune spread in the beams which makes it more difficult to steer clear of these resonances.

Experience in the SPS has shown that the beam lifetime is strongly reduced when particles straddle resonances of order less than 12. The tune footprint, the image of the beam in the tune diagram, must therefore be small enough to fit in between these resonances. The LHC working point can safely be placed close to the diagonal between 3rd and 10th order resonances provided the tune footprint stays below 0.01. The value of the beam-beam parameter of .0034 with two insertions illuminated is very close to that achieved routinely in the SPS collider.

Due to the small (25 ns) bunch separation and crossing angle, the effect of long-range beam-beam interactions must also be taken into consideration. It has been shown that the most optimum situation is obtained by alternating the crossing angle between horizontal and vertical in adjacent collision points. In the initial commissioning phase of the LHC, it is foreseen to have a 75 ns bunch separation available. This minimises the effect of long-range interactions and will also eliminate the electron cloud effects mentioned below.

Intrabeam Scattering

Intrabeam scattering, or multiple Coulomb scattering between particles in the same bunch, can give rise to a redistribution of the energy of oscillation between the different degrees of freedom. Roughly speaking, the bunch can be thought of as a relativistic gas which is not in thermal equilibrium. Due to the Lorenz contraction, the longitudinal phase plane is much "colder" than the transverse planes, so a transfer of energy takes place between betatron and synchrotron motions. This should result in slow damping of transverse emittance and increase in energy spread. However, due to the dispersion, there is a heating term in the radial phase plane that dominates the damping term. Intrabeam scattering therefore results in an increase in radial emittance that can rapidly degrade the luminosity unless remedial action is taken. The transverse emittance growth can be strongly reduced by diluting the 6-dimensional phase space density by artificially increasing the longitudinal emittance. In the LHC, the emittance will be increased from its injection value of 1 to 2.5 eV.s at collision energy. This fixes the maximum RF voltage of 16 MV per beam in order to give sufficient bucket area.

Dynamic Aperture and Field Quality

The beam-beam interaction generates resonances due to the non-linear nature of the beam-beam force and can limit the available aperture during collision. However, superconducting magnets also have non-linear field errors coming from many sources including persistent currents, small errors in coil geometry and redistribution of current between the strands during ramping. These errors are dominant at the injection field level where the beam must survive for many minutes. The dynamic aperture is defined as the maximum stable amplitude of oscillation in the presence of these errors combined with other effects such as tune ripple and closed orbit distortion.

At the present time the only quantitative ways to investigate the dynamic aperture is by computer simulation and by experiments on existing machines. For the LHC, a computer farm has been dedicated to this activity, where particles are tracked through sample machines where the non-linearities are statistically distributed, for up to 10^6 turns. These results are used to define limits for multipole field components in the main magnets.

During production, magnet field quality is continuously monitored directly at the factory as soon as the coils are collared. This allows errors in fabrication (for example, missing shims) to be detected and corrected at an early stage. It also allows trends in field quality and magnetic length to be continuously monitored and corrected much earlier than results are available from cold tests of assembled dipoles would allow.

Figure 1 shows the measured sextupole component in the main dipole for the first 80 collared coils [1] (160 apertures) produced in three firms. Early dipoles showed b3 to be substantially out of the tolerance band.

After nine dipoles, it was decided to make a downward correction of b3 by small modifications of the wedges in the coil cross section. This correction fed through after dipole number 30. The new cross section has a lower sextupole component which is on the upper edge of the tolerance band due to the fact that the b3 drifted slightly upwards after the correction was computed. This geometry is perfectly acceptable from the point of view of dynamic aperture and will be maintained for the whole of the first octant of dipoles in order not to introduce too much spread in b3. It will be possible to introduce a correction in the second octant by changing slightly the thickness of the mid-plane insulation although a final decision has not yet been taken. The main interest in a last correction is to increase the margin for further possible upward drift in b3 which may make the chromaticity correction more difficult.

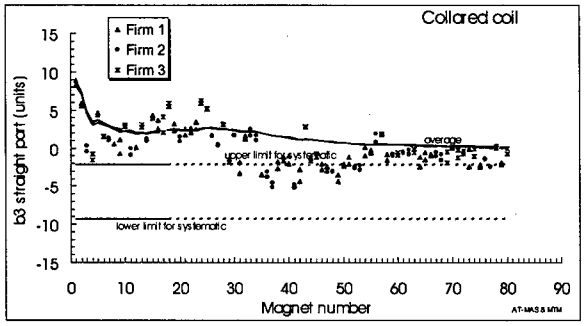

Figure 1: Sextupole component of the collared coils of 80 dipoles.

Field quality is also measured on the cold test benches up to nominal field, where other important effects such as snapback and dynamic behaviour of multipoles can be studied. Solid warm-cold correlations have also been established for the most important multipoles, validating the procedure of computing corrections on the collared coils, where data is available many months before the cold measurements are performed.

Collective Effects

Collective effects can be broadly separated into single bunch effects, where bunch instability is driven through the short range wakefields generated by the interaction of the beam with its environment, and multibunch instabilities generated by the long range wakefields .

The most common of the single bunch instabilities is the transverse slow head-tail instability. This can be suppressed for the rigid dipole mode m=0 by operating the machine with a small positive chromaticity. Another instability driven by the broadband impedance is caused by coupling between transverse modes and is potentially much more dangerous since it cannot be suppressed in this way. However, this instability, unlike the head-tail, shows a threshold behaviour, which occurs at about twice the nominal beam current for the LHC. The longitudinal equivalent of the transverse mode-coupling instability is known as the microwave instability. Due to the very low coupling impedance, the threshold for onset of this instability is also well above the nominal bunch current.

The most important multibunch effect in the LHC is the transverse resistive wall instability. Its growth rate is proportional to the square root of the resistivity of the beam pipe and to the inverse cube of its radius. The instability exhibits no threshold behaviour but its growth rate can be reduced by coating the inside of the beam screen with a 50 μm layer of copper and cooling it to below 20 K where its resistivity is further reduced. The e-folding time for the most dangerous mode at a frequency of a few kHz then exceeds 100 turns, which can easily be damped with an active feedback system.

Collective effects are not only important in the LHC. The injector chain, which includes the PS and SPS must deliver stable beams with well defined characteristics. In particular, before 2002, the beam in the SPS exhibited a strong microwave instability due to its large coupling impedance. An intensive programme of impedance reduction has been implemented, removing all obsolete equipment from the ring, damping essential equipment like kickers and septa and smoothing vacuum chamber discontinuities with sleeves. The results [2] have been quite spectacular. Figure 2 shows the bunch length as a function of intensity on the injection plateau before and after the impedance reduction. The data after the intervention is consistent with inductive wall bunch lengthening, emittance is preserved. Figure 3 shows the quadrupole mode frequency shift as a function of intensity. The improved quality of the data is immediately apparent. From this data, the impedance (Z/n) is estimated to be about 5 ohms, approximately a factor of 3 reduction.

The result is that stable beam can be maintained at nominal intensity with an emittance of less than 0.7 eV.s which, with the 7 MV available in the SPS at 200 MHz, will allow clean transfer and capture by the LHC 400 MHz system without the need for the sub-harmonic capture cavities originally foreseen.

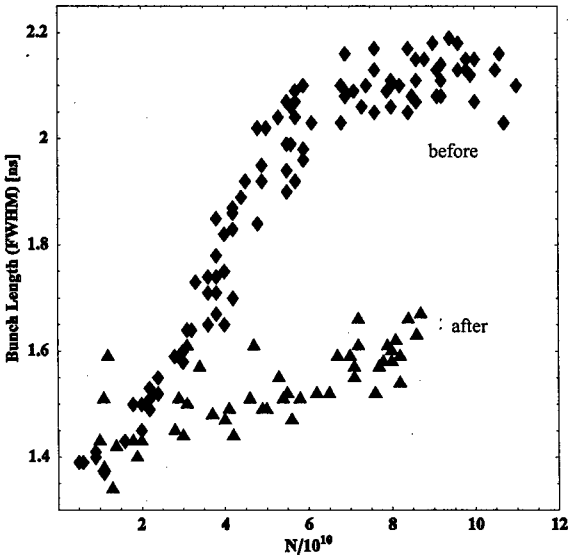

Figure 2: Bunch length as a function of intensity in the SPS before and after the impedance reduction.

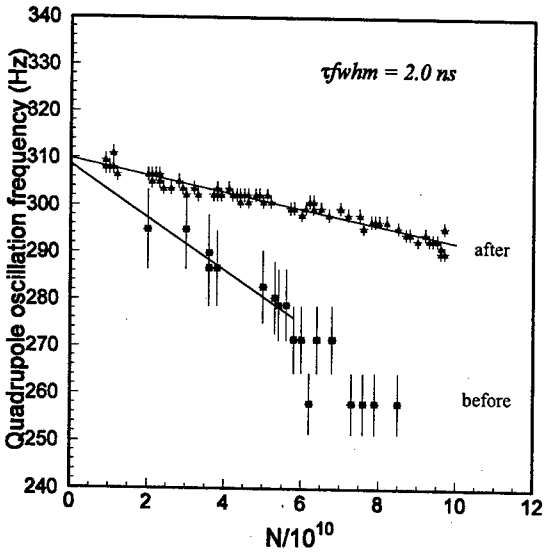

Figure 3: Coherent frequency shift of the longitudinal quadrupole mode in the SPS before and after the impedance reduction.

VACUUM

The high intensity beams in the LHC will deposit heat into the cryogenic surface surrounding the beam through a number of effects, including image currents (up to about 0.8 W/m) and synchrotron radiation (0.6 W/m). These heat loads cannot be taken at 1.9 K and will be intercepted by a beam screen fitted inside the magnet cold bore and cooled by circulation of supercritical helium between 5 K and 20 K. Gas desorbed by the synchrotron radiation cannot be efficiently cryo-pumped by the screen at this high temperature. In order to avoid a catastrophic pressure rise, the screen is punched with small holes over about 2% of its surface so that the cold bore of the magnets at 1.9 K can pump away the gas while being protected from the heat source. Heat can also be produced by inelastic scattering of protons with the residual gas molecules. This cannot be intercepted by the screen and must be transported away by the superfluid helium.

Another effect that can result in considerable heat input into the cryogenic system and vacuum degradation is due to beam induced multipactoring by the electric field of successive bunches as first observed [3] in the ISR. It arises through a resonant motion of secondary electrons bouncing back and forth between the walls of the beam screen. If the secondary electron yield is sufficiently large, this can lead to an exponential build-up, stimulating gas desorption and heating of the beam screen. This effect is known to limit the performance of the B-factories and has received much attention in recent years. It has now been clearly observed in the SPS for LHC beam conditions [4]. As the electron bombardment of the surface proceeds, it has a conditioning effect, reducing the secondary electron yield and cleaning the surface of the chamber.

Recent experiments at the SPS have clearly demonstrated this cleaning effect. Figure 4 shows a measurement of the vacuum pressure during a four day "scrubbing" run. A reduction of 4 orders of magnitude over the scrubbing period can be observed. This is accompanied by a reduction of the secondary emission coefficient of the surface (see Fig. 5).

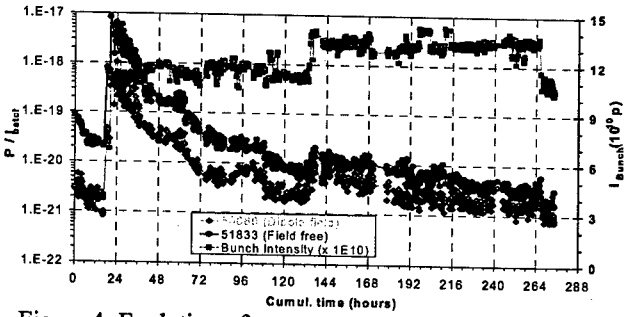

Figure 4: Evolution of vacuum pressure with time during the SPS "scrubbing" run.

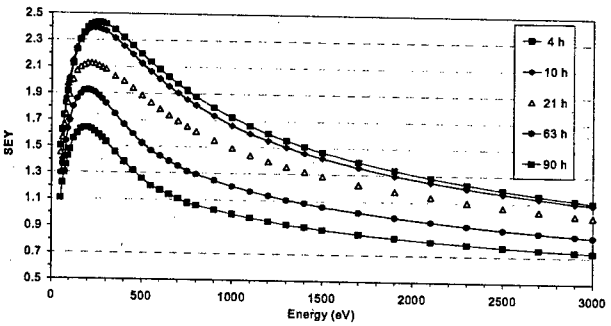

Figure 5: Reduction of the secondary emission yield on the SPS vacuum chamber during the scrubbing process.

Experimental results have been compared with multiparticle simulation of the process [5]. For example, in a dipole field the simulation code predicts that the electron bombardment should be concentrated in two stripes on the top and bottom of the vacuum chamber where the separation varies linearly with bunch intensity. Figure 6 shows a measurement of this effect in the SPS together with the most recent simulation results.

The scrubbing of the SPS vacuum chamber, together with the impedance reduction programme previously mentioned has allowed the SPS to accelerate the full LHC beam to 450 GeV. Further experiments are planned to investigate the efficiency of the scrubbing process on cold surfaces similar to the situation in the LHC itself.

In the warm regions of the LHC, the electron cloud effect can be suppressed by coating the chamber with a new non-evaporable getter (NEG) material developed at CERN [6]. This material (TiZrV) can be activated at 200° C, a temperature lower than for conventional getters. Once activated, the secondary electron yield is very low and, as shown in SPS experiments, the electron cloud effect is suppressed. These chambers also contribute to the production of ultra high vacuum due to their ability to pump gas.

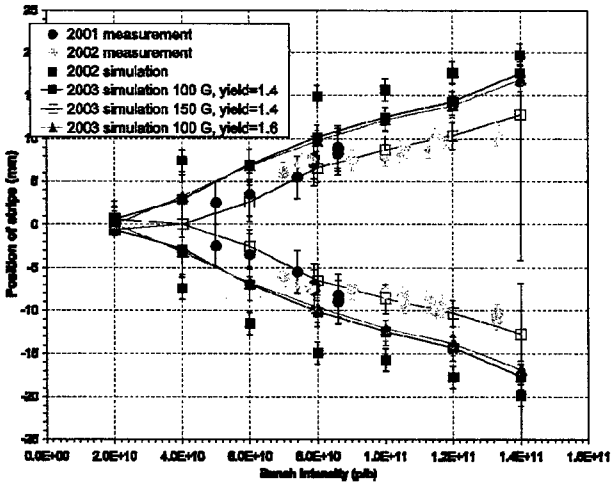

Figure 6: Distance between the two strips as a function of intensity compared with simulation results.

OPERATION WITH PB IONS

In addition to high-luminosity proton-proton collisions, the LHC must provide Pb-Pb ion collisions with a luminosity of up to 10^{27} cm^{-1} s^{-1}. This poses a number of special problems. The PS injector chain must be supplemented by an intermediate accumulation and cooling ring in order to achieve the Pb ion beam of the required brightness. This will be achieved by converting the existing low energy antiproton ring (LEAR) with additional strong electron cooling.

Another problem is that a very large cross section is predicted (~ 300 barns) for electron capture by pair production [7]. This process removes particles from the beams, reducing the luminosity lifetime and may affect the quench behaviour of superconducting magnets of unfavourable locations. The effect is under careful study.

CONCLUSIONS

From the point of view of accelerator physics, the LHC machine design rests on a sound base, with a great deal of accumulated knowledge from previous projects to guide the choice of parameters and the steps needed to combat undesirable effects. The most serious new phenomenon revealed is the electron cloud effect, where experiments and simulations have led to a good understanding of how it will be overcome in the LHC.

ACKNOWLEDGEMENTS

I would like to acknowledge the outstanding work of the LHC team on the machine design and the continuing efforts in understanding performance limitations.

REFERENCES

[1] E. Todesco, et al., "Controlling field quality in magnet production", Proceedings of the LHC Performance Workshop, Chamonix XII, Chamonix (2003), p. 104.

[2] T. Bohl, T. Linnecar and E. Shaposhnikova, "Impedance reduction in the CERN SPS as seen from longitudinal beam measurements", EPAC'02, Paris (2002), p. 1446.

[3] O. Gröbner, "Bunched induced multipacting", 10th Int. Conf. on High-Energy Accelerators, Protvino (1977).

[4] M. Jimenez, et al., "Electron cloud studies and analyses at SPS for LHC type beams", these proceedings.

[5] F. Zimmermann, "A simulation study of electron-cloud instability and beam-induced multipacting in the LHC", CERN LHC Project Report 95 (1997).

[6] C. Benvenuti, et al., "Vacuum properties of TiZrV non-evaporable getter films", Vacuum, Vol. 60, (January 2001), p. 57.

[7] J. Jowett, et al., "Heavy ion beams in the LHC", these proceedings.

RHIC STATUS AND PLANS*

Thomas Roser
Brookhaven National Laboratory, Upton, New York 11793-5000, USA

Abstract

RHIC is the first hadron accelerator and collider consisting of two independent rings. It is designed to operate over a wide range of beam energies and with particle species ranging from polarized protons to heavy ions. Machine operation and performance will be reviewed that includes gold-on-gold collisions at design beam energy (100 GeV/u), first high energy polarized proton-proton collisions (100 GeV on 100 GeV) as well as first asymmetric operation of RHIC to produce deuteron-on-gold collisions. Plans for future luminostiy upgrades will also be presented.

THE RHIC FACILITY

With its two independent rings RHIC is a highly flexible collider of hadron beams ranging from colliding intense beams of polarized protons to colliding fully stripped gold ions. The collision of 100 GeV/nucleon gold ions probes the conditions of the early universe by producing extreme conditions where quarks and gluon are predicted to form a quark-gluon plasma - new state of matter.

The RHIC polarized proton collider will open up the completely unique physics opportunities of studying spin effects in hadronic reactions at high-luminosity high-energy proton-proton collisions. It will allow study of the spin structure of the proton, in particular the degree of polarization of the gluons and anti-quarks, and also verification of the many well-documented expectations of spin effects in perturbative QCD and parity violation in W and Z production. The RHIC center-of-mass energy range of 200 to 500 GeV is ideal in the sense that it is high enough for perturbative QCD to be applicable and low enough so that the typical momentum fraction of the valence quarks is about 0.1 or larger. This guarantees significant levels of parton polarization.

During its first three years of operation RHIC has already operated close to design parameters for gold-gold collisions[1], had a very successful operating period of deuteron-gold collisions with both beams at the same energy per nucleon but, of course, different rigidity, and two short but very successful running periods with polarized protons. RHIC was operating for all of these runs with beam energies of 100 GeV/nucleon - the gold beam design energy.

GOLD-GOLD OPERATION

Fig. 1 shows the layout of RHIC and the three injector accelerators Tandem, Booster and AGS. The gold ions

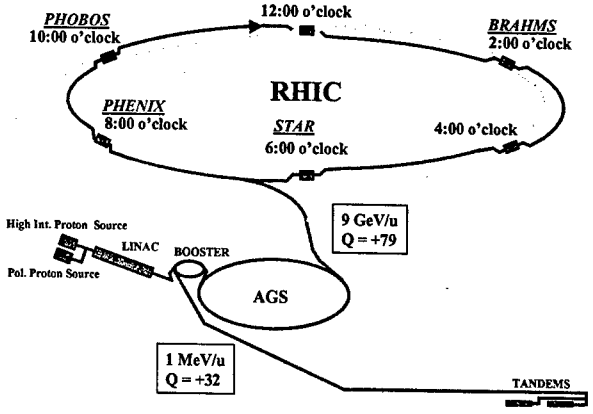

Figure 1: Layout of RHIC and the injector accelerators. The gold ions are stepwise ionized as they are accelerated to RHIC injection energy.

are stepwise ionized as they are accelerated to RHIC injection energy, at which point they are fully ionized. The performance of the injector[2] is summarized in Table 1. The Tandem Van de Graaff accelerates Au^{-1} from a sputter source to about 1 MeV/nucleon. The 530 ms long beam pulse is stripped to Au^{+32} and injected into the Booster using horizontal and vertical phase space painting. After acceleration to about 100 MeV/nucleon the beam is stripped to Au^{+77} and transferred to the AGS where it is accelerated to the RHIC injection kinetic energy of 8.6 GeV/nucleon. In the AGS the beam bunches from the Booster are merged to reach the required intensity of about 1×10^9 Au ion per bunch at a longitudinal emittance of 0.3 eVs/nucleon. The final stripping to bare Au^{+79} occurs on the way to RHIC.

RHIC is the first super-conducting, slow ramping accelerator that crosses transition energy during acceleration. At transition energy the spreads of the particle revolution frequency stemming from the spread in velocity and spread in path length cancel exactly and all particles maintain their relative position for a long time. Interaction between parti-

Table 1: RHIC injector performance

Location	RHIC bunch intensity	Efficiency
Tandem	5.4×10^9	
Booster Injection	2.9×10^9	54%
Booster Extraction	2.4×10^9	83%
AGS Injection	1.2×10^9	50%
AGS Extraction	1.1×10^9	92%
Total		20%

* Work performed under Contract Number DE-AC02-98CH10886 with the auspices of the U.S. Department of Energy

0-7803-7738-9/03/$17.00 © 2003 IEEE

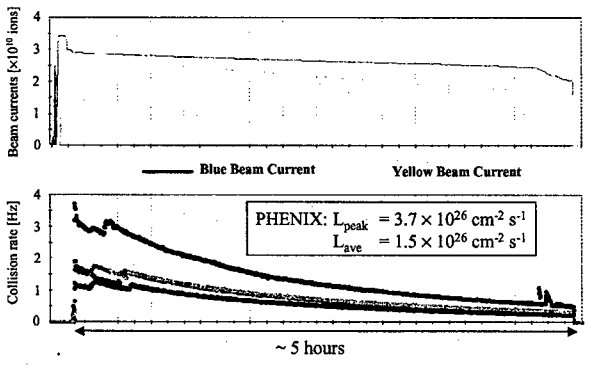

Figure 2: Evolution of the collision rate at the four RHIC detectors during a typical store. The intensity drop at the end of the store is due to the removal of the beam in the abort gap.

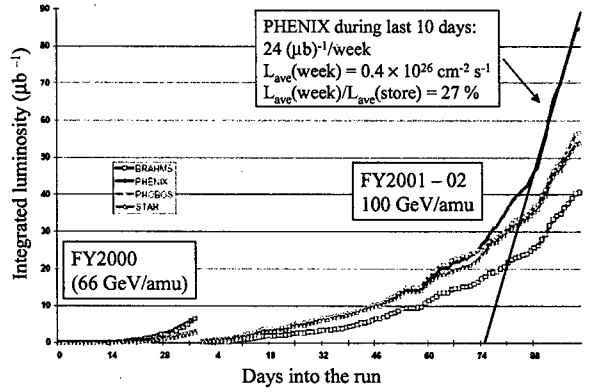

Figure 3: Integrated luminosity of the four RHIC experiments.

cles can then cause instabilities. With pulsed quadrupole power supplies the transition energy is changed quickly during acceleration to effectively jump across it. The dispersion distortion required to change the transition energy is local and the betatron tune shift is corrected in a zero-dispersion region[3]. This scheme allows for up to 1 GeV change in transition energy with very little lattice distortion.

The two RHIC rings, labelled blue and yellow, are intersecting at six interaction regions (IR), four of which are occupied by the collider experiments BRAHMS, STAR, PHENIX and PHOBOS. All IRs can operate at a betastar between 2 and 10 m. In two interaction regions (STAR and PHENIX) the quality of the triplet quadrupoles allows further reduction of betastar to 1 m. During this run betastar was 10 m at injection energy for all IRs and was then squeezed during the acceleration cycle to 1 m for PHENIX, 2 m for the other experiments and 10 m in the remaining two IRs. A typical acceleration cycle consists of filling the blue ring with 56 bunches in groups of 4 bunches, filling the yellow ring in the same way and then simultaneous acceleration of both beams to storage energy. During acceleration the beams are separated vertically by about 10 mm in the interaction regions to avoid beam losses from the two beams colliding.

Typical stores lasted about 5 hours. Fig. 2 shows the evolution of the collision rate in the four experiments during a typical store. After optimizing longitudinal and transverse steering the initial observed luminosity at PHENIX was about $3.7 \times 10^{26}\ cm^{-2}\ s^{-1}$ with an average luminosity over the 5 hour store of $1.5 \times 10^{26}\ cm^{-2}\ s^{-1}$, which is close to the design average luminosity . This corresponds to an initial normalized 95% beam emittance of about $15\pi\ \mu m$ growing to about $30\pi\ \mu m$ at the end of the store. The beam loss and transverse emittance growth during the store is mainly caused by intra-beam scattering, which is particularly important for the fully stripped, highly charged gold beams[4].

The collision rate was measured using identical Zero Degree Calorimeters (ZDC) at all four interaction regions. The ZDC counters detect at least one neutron on each side from mutual Coulomb and nuclear dissociation with a total cross section of about 10 barns[5]. The overall average luminosity for PHENIX during the last 10 days of the run was $0.4 \times 10^{26}\ cm^{-2}\ s^{-1}$ which gives an effective running efficiency of 27%. The integrated luminosity over the run is shown in Fig. 3 and exceeded 80 $(\mu b)^{-1}$ for PHENIX.

The gold beam intensity were limited mainly by vacuum break-downs in the room temperature sections of the RHIC rings[6][7]. Possible explanations for this process include gas desorption from halo scrapping and/or electron multipacting driven by the gold beam bunches. Gas desorption and electron production is very large for gold ions striking the vacuum chamber at a glancing angle. The situation can be greatly improved by baking all room temperature sections to a residual gas pressure of less than 10^{-10} Torr.

The bunch intensity was also limited by a very fast single bunch transverse instability, shown in Fig. 4, that develops near transition where the chromaticity needs to cross zero. It could be stabilized using octupoles. This instability has a growth rate faster than the synchrotron period and is similar to a beam break-up instability[9].

DEUTERON GOLD OPERATION

During the last running period RHIC was operating for the first time with asymmetric collisions[10]. Colliding 100 GeV/nucleon deuteron beam with 100 GeV/nucleon gold beam will not produce a quark-gluon plasma and therefore serves as an important comparison measurement to the gold-gold collisions. The rigidity of the two beams is different by about 20%, which results in different deflection angles in the beam-combining dipoles on either side of the interaction region as shown in Fig. 5. This requires a non-zero angle at the collision point, which slightly reduces the available aperture.

The injection energy into RHIC was also the same for both beams requiring the injector to produce beams with different rigidity. With same energy beams throughout

the acceleration cycle in RHIC the effect of beam collisions could be minimized. Typical bunch intensity of the deuteron beam was about 1.2×10^{11} with emittances of about 12 $\pi\mu m$ [norm., 95%] and 0.3 eVs/nucleon. The gold beam parameters were similar to the gold-gold operation described above. The high intensity deuteron beams required careful adjustment of the chromaticity, especially around transition, to avoid transverse instabilities. A peak luminosity of $6.2 \times 10^{28}\ cm^{-2}\ s^{-1}$ and store-averaged luminosity of $2.8 \times 10^{28}\ cm^{-2}\ s^{-1}$ was reached at the IRs with the 2 m betastar.

POLARIZED PROTON COLLISIONS

Fig. 8 shows the lay-out of the Brookhaven accelerator complex highlighting the components required for polarized beam acceleration[11][12]. The new 'Optically Pumped Polarized Ion Source'[13] is producing 10^{12} polarized protons per pulse. A single source pulse is captured into a single bunch, which is ample beam intensity to reach the nominal RHIC bunch intensity of 2×10^{11} polarized protons.

In the AGS a 5% solenoidal partial snake that rotates the spin by 9° is sufficient to avoid depolarization from imperfection resonances up to the required RHIC transfer energy of about 25 GeV. Full spin flip at the four strong intrinsic resonances can be achieved with a strong artificial rf spin resonance excited coherently for the whole beam by driving large coherent vertical betatron oscillations. The remaining polarization loss in the AGS is caused by coupling resonances and weak intrinsic resonances. Faster acceleration rate and a future, much stronger partial Snake should eliminate depolarization in the AGS.

The full Siberian snakes (two for each ring) and the spin rotators (four for each collider experiment) for RHIC each

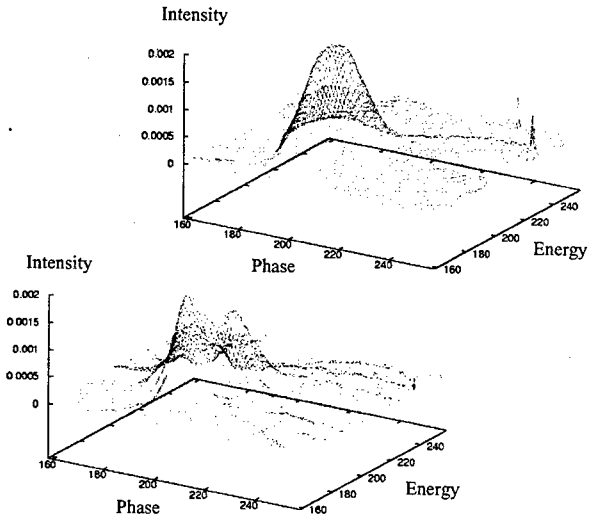

Figure 4: Tomographic reconstruction of a gold bunch before (top) and after a fast transverse instability[8].

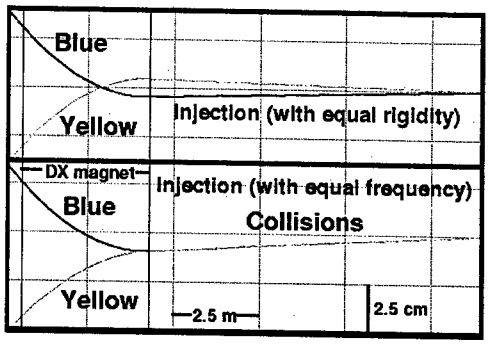

Figure 5: Orbits of the gold and deuteron beams through the beam-combining dipole that is located on either side of the IR. The top figure shows the initial geometry at injection with equal beam rigidities. The bottom figure shows the collision geometry with equal beam energies. Equal energy was later also used at injection to avoid beam loss from beam-beam induced tune modulations.

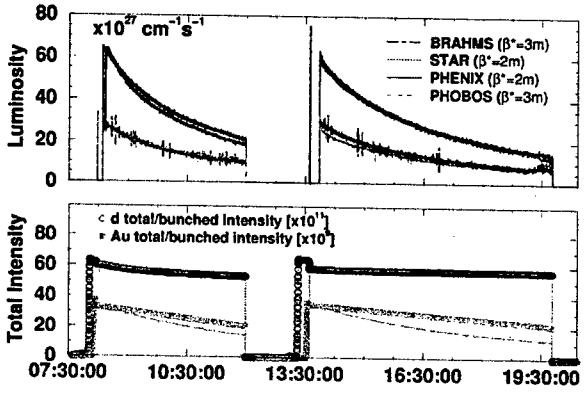

Figure 6: Evolution of the luminosity and beam intensities at the four RHIC detectors during two typical deuterium-gold stores.

consist of four 2.4 m long, 4 T helical dipole magnet modules each having a full 360° helical twist. The 9 cm diameter bore of the helical magnets can accommodate 3 cm orbit excursions at injection. Fig. 7 shows the orbit and spin trajectory through a RHIC snake. The super-conducting helical dipoles were constructed at BNL using thin cable placed into helical grooves that have been milled into a thick-walled aluminum cylinder[14].

In addition to maintaining polarization, the accurate measurement of the beam polarization is of great importance. Very small angle elastic scattering in the Coulomb-Nuclear interference region offers the possibility for an analyzing reaction with a high figure-of-merit which is not expected to be strongly energy dependent[15]. For polarized beam commissioning in RHIC an ultra-thin carbon ribbon was used as an internal target, and the recoil carbon nuclei were detected to measure both vertical and radial polarization components. The detection of the recoil carbon with silicon detectors using both energy and time-of-flight in-

formation showed excellent particle identification. It was demonstrated that this polarimeter can be used to monitor polarization of high energy proton beams in an almost non-destructive manner and that the carbon fiber target could be scanned through the circulating beam to measure polarization profiles. In the future a polarized gas jet will be installed as an internal target for small angle proton-proton scattering which will allow the absolute calibration of the beam polarization to better than 5 %.

During the first polarized proton collider run in RHIC from Dec. 2001 to Jan. 2002 polarized beams were successfully accelerated to 100 GeV and stored and collided with a peak luminosity of about 1.5×10^{30} cm^{-2} s^{-1}. The beam polarization at the AGS was only about 30% mainly due to the fact that a back-up AGS main power supply had to be used with a much reduced ramp rate that amplified the effect of the depolarizing resonances. However, essentially all beam polarization was preserved during acceleration and beam storage in RHIC. Fig. 9 shows circulating beam current and measured asymmetries of two typical stores. The analyzing power at 100 GeV for the RHIC polarimeters is not known but expected to be similar to the value at injection energy. Under this assumption the polarization at store was typically about 25 %. To preserve beam polarization in RHIC during acceleration and storage the vertical betatron tune had to be maintained between 0.220 and 0.235 and the orbit had to corrected to better than 1 mm rms. This is in good agreement with the predictions from spin tracking calculations.

More than 20 years after Y. Derbenev and A. Kodratenko[16] made their proposal to use local spin rotators to stabilize polarized beams in high energy rings, it has now been demonstrated that their concept is working flawlessly even in the presence of strong spin resonances at high energy.

For the second polarized proton run all eight spin rotators were installed to allow for longitudinal polarization at both PHENIX and STAR[17]. With the nominal acceleration rate the polarization at the AGS was about 45 %. Polarization of up to 35% was reached at 100 GeV and longitudinal polarization was produced at the PHENIX IR. At the store energy of 100 GeV the betastar was squeezed from 10 m to 1 m at STAR and PHENIX and 3 m at BRAHMS and PHOBOS. The peak luminosity with 1 m betastar was about 3×10^{30} cm^{-2} s^{-1} with 55 bunches in each ring with a bunch intensity of 0.5×10^{11} and a 95% normalized emittance of about 12 $\pi\mu m$. Note that the beam-beam tune shift parameter under these conditions is about 0.003 for each IR or 0.012 for four IRs with colliding beam[18].

Operation at full collision energy of $\sqrt{s} = 500$ GeV is planned for the future with a luminosity of up to 2×10^{32} cm^{-2} s^{-1}.

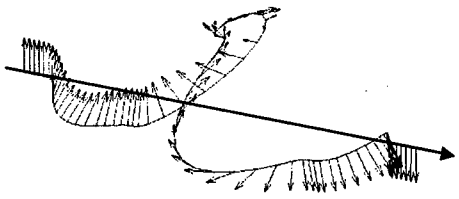

Figure 7: Orbit and spin tracking through the four helical magnets of a Siberian Snake at = 25. The spin tracking shows the reversal of the vertical polarization.

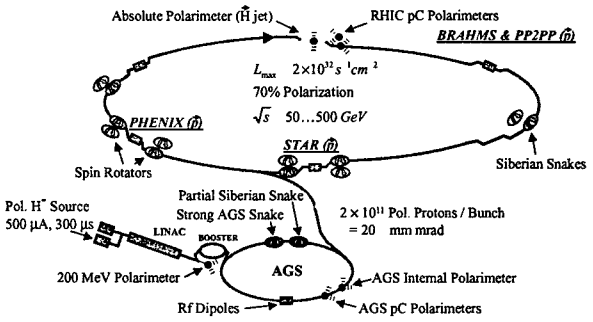

Figure 8: Layout and design parameters for the Brookhaven polarized proton collider. The eight spin rotators and the absolute polarimeter were not installed for this run.

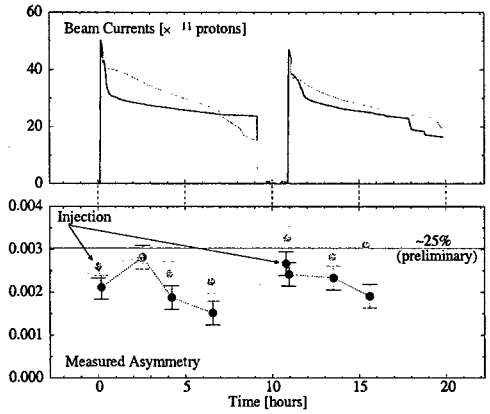

Figure 9: Circulating beam and measured asymmetry in the blue and yellow RHIC ring (blue(dark) and yellow(light) lines and symbols, respectively) for two typical stores.

RHIC UPGRADE PLANS

An initial upgrade of the RHIC luminosity for heavy ion operation by a factor of four beyond design (2×10^{26} cm^{-2} s^{-1}) can be achieved by doubling the number of bunches to 110 (100 ns bunch spacing) and reducing betastar from 2 m to 1 m. As described above this has already partially been achieved although further progress is required in controlling vacuum break-downs before routine operation with 100 ns bunch spacing is possible.

Even further upgrade of the luminosity requires that the emittance growth from intra-beam scattering is reduced or

eliminated. The growth of the beam size due to intra-beam scattering can be overcome by cooling the beams with a high intensity cold electron beam[19]. To cool the 100 GeV/n gold beam with 10^9 ions per bunch in RHIC a 54 MeV electron beam with an average current of about 100 mA is required. In this case the charge of each electron bunch is about equal to the charge of the ion bunch. The high beam power of about 5 MW of the electron beam makes it necessary to recover the beam energy by decelerating it in the super-conducting linac as has been successfully demonstrated at JLab with a 50 MeV, 5 mA electron beam.

Table 2 shows the parameters for future RHIC luminosity upgrades for the first stage without electron cooling and then with electron cooling. Electron cooling has the most dramatic effect on the luminosity of gold collisions. However, it also improves operation with polarized protons due to the lower beam emittance.

Electron cooling of the high energy, heavy ion beams in RHIC extends beyond presently operating electron cooling facilities in several regards: the use of bunched electron beam accelerated by a linear accelerator, beam cooling during collider operation, and the use of a highly magnetized, angular momentum-dominated electron beam to avoid recombination of e^- and Au^{79+}.

An R&D program has started to develop the critical items of the RHIC electron cooling system. The high-brightness, high-current electron source consists of a rf photo-cathode gun operating at 700 MHz capable of providing 2.5 MeV and about 100 mA current. A 700 MHz super-conducting cavity for the energy-recovering linac will be developed that is capable of accelerating the high intensity electron beam without causing beam-breakup. The feasibility of a long, highly uniform super-conducting solenoid for the electron cooling section will be demonstrated with a prototype.

Table 2: RHIC luminosity upgrade with electron cooling.

Gold-gold	w/o e-cool.	with e-cool.
Beam energy [GeV/n]	100	100
Emittance (95%) $[\pi\mu m]$	$15 \rightarrow 40$	$15 \rightarrow 3$
Beta function at IR [m]	1.0	$1.0 \rightarrow 0.5$
Number of bunches	112	112
Bunch population $[10^9]$	1	$1 \rightarrow 0.3$
Beam-beam param. per IR	0.0016	0.004
Peak lum. $[10^{26} cm^{-2} s^{-1}]$	32	90
Ave. lum. $[10^{26} cm^{-2} s^{-1}]$	8	70
Proton-proton:		
Beam energy [GeV]	250	250
Emittance (95%) $[\pi\mu m]$	20	12
Beta function at IR [m]	1.0	0.5
Number of bunches	112	112
Bunch population $[10^{11}]$	2	2
Beam-beam param. per IR	0.007	0.012
Lum. $[10^{32} cm^{-2} s^{-1}]$	2.4	8.0

A low emittance cooled gold beam in RHIC will also be essential for a future electron ion collider at RHIC. A high current 10 GeV polarized electron beam would be collided with the 100 GeV/n cooled gold beam or the 250 GeV polarized proton beam a RHIC interaction region with luminosities of $5 \times 10^{30}\ cm^{-2}\ s^{-1}$ (eAu) and $0.5 \times 10^{33}\ cm^{-2}\ s^{-1}$ (ep).

ACKNOWLEDGMENT

The highly successful commissioning and early operation of RHIC was made possible by the excellent and dedicated RHIC design, construction, and commissioning team.

REFERENCES

[1] F. Pilat, "RHIC Status and Plans", proceedings of EPAC2002.

[2] L. Ahrens et al., "The RHIC Injector Accelerators Configurations and Performance for the RHIC 2003 Au-d Physics Run", TPPB047, these proceedings.

[3] J. Kewisch and C. Montag, "Commissioning of a First-Order Transition Jump in RHIC", TPPB035, these proceedings.

[4] W. Fischer et al., "Intra-beam Scattering Measurements in RHIC", proceedings of EPAC2002.

[5] A. Drees and N. Kling, "Luminosity Monitoring at RHIC with Various Species", TPPB031, these proceedings.

[6] S.Y. Zhang et al., "RHIC Pressure Rise and Electron Cloud", MOPA010, these proceedings.

[7] S.Y. Zhang et al., "RHIC Run-away Type Pressure Rise", TPPB046, these proceedings.

[8] C. Montag et al., "Longitudinal Phase-Space Tomography in RHIC", proceedings of EPAC2002.

[9] M. Blaskiewicz et al., "Transverse Instabilities in RHIC", RPPB007, these proceedings.

[10] T. Satogata et al., "Commissioning of RHIC Deuteron-Gold Collisions", TPPB043, these proceedings.

[11] H. Huang et al., "Polarized Proton Operations in the AGS and RHIC", MOPA009, these proceedings.

[12] W. W. MacKay et al., "Spin Dynamics in AGS and RHIC", WOAB008, these proceedings.

[13] A.N. Zelenski et al., 'Optically-Pumped Polarized H- ION Sources for RHIC and HERA Colliders', proceedings of PAC99.

[14] E. Willen et al., "Construction of helical dipoles for RHIC", proceedings of PAC99.

[15] J. Tojo et al., Phys. Rev. Lett. 89, 052302 (2002).

[16] Ya.S. Derbenev and A.M. Kondratenko, Part. Accel. 8, 115 (1978).

[17] W. W. MacKay et al., "Commissioning Spin Rotators in RHIC", TPPB038, these proceedings.

[18] W. Fischer et al., "Observation of Strong-Strong and Other Beam-Beam Effects in RHIC", TOAA011, these proceedings.

[19] I. Ben-Zvi et al., "R&D Towards Cooling of the RHIC Collider", MOPA005, these proceedings.

BEAM PHYSICS AT TEVATRON COMPLEX*

Valeri Lebedev#, FNAL, Batavia, IL 60510, USA

Abstract

The challenge of achieving the Tevatron Run II luminosity goal of $3\cdot10^{32}$ $cm^{-2}s^{-1}$ requires high level of engineering and machine operation, good and reliable diagnostics, and clear understanding of the underlying accelerator physics. Recent history demonstrated steady increase of the Tevatron luminosity, which was supported by each of the three listed above items. This report reviews major developments in the accelerator physics, which contributed in the Run II luminosity growth. Present limitations of the luminosity and projections of further luminosity growth are also discussed.

INTRODUCTION

The commissioning of Tevatron Run II began in the spring of 2001 with the first luminosity seen in June. By the year end the luminosity was in the range of $(5\text{-}10)\cdot10^{30}$ $cm^{-2}s^{-1}$. Although the luminosity growth was significantly slower than expected, steady growth of luminosity has been demonstrated during last two years with the peak luminosity of $42\cdot10^{30}$ $cm^{-2}s^{-1}$ achieved in April 2003. This luminosity growth would not be possible without deep insight into the accelerator physics problems, which have restricted the machine operation. Important contributions came from (1) optics correction in transfer lines, (2) improvements of helical beam separation in Tevatron [1], (3) introduction of dual lattice operation in Accumulator to suppress intrabeam scattering (IBS), (4) feedforward compensation of beam loading in Main Injector, (5) correction of injection errors for antiproton transfers from MI to Tevatron, (6) understanding transverse instability in Tevatron with subsequent transverse impedance reduction [2], and (7) active damping of instabilities in Tevatron [3,4]. Although understanding of longitudinal undamped oscillations in Tevatron [5] not contribute directly to the luminosity growth it has been critical for planning Run II upgrades. Several interesting accelerator physics problems encountered in Run II commissioning are considered in this report.

1 IBS IN ACCUMULATOR

Accumulator [6] stacks antiprotons with an average accumulation rate of $\sim10^{11}$ per hour, so that after 20 hours the stack of $\sim2\cdot10^{12}$ antiprotons can be accumulated. The total number of antiprotons along with the longitudinal and transverse emittances are the major parameters which determine the collider luminosity. At the beginning of 2002, once the antiproton source was successfully commissioned, it became clear that there is a strong heating of horizontal degree of freedom in Accumulator. That caused the horizontal emittance to be significantly higher than in Run I (see Figure 1).

The source of the problem was found to be the upgrade of machine optics, which caused an increase in IBS heating. The optics upgrade was aimed to increase the antiproton production [7]. That required an increase of frequency band for stochastic cooling systems with subsequent decrease of the slip factor η to prevent the bad mixing. Although the betatron tunes were changed insignificantly the IBS heating rate was strongly increased.

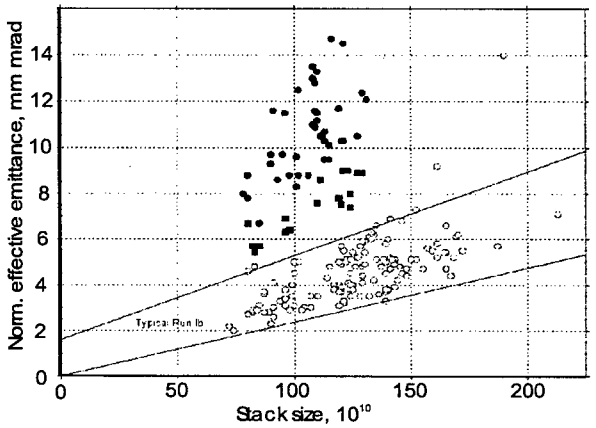

Figure 1: Dependences of antiproton normalized effective emittance, $(\varepsilon_x + \varepsilon_y)/2$, on beam current (100 mA = 10^{12}) before upgrades (•), after the stochastic cooling upgrade (▪), and after both the cooling and optics upgrades were implemented (o). Each dot corresponds to one collider shot. Lines present emittance boundaries for Run Ib.

Typically, in Accumulator, the longitudinal velocity spread in the beam frame is much smaller than the transverse ones, and the transverse emittance growth is dominated by excitation of betatron motion due to energy changes at collisions. That significantly simplifies formulas. If $k_{\|}=2.2\sigma_p/(\gamma\theta_{\perp})\le0.15$ the IBS growth rates are:

$$\frac{d}{dt}\begin{bmatrix}\sigma_p^2\\ \varepsilon_x\\ \varepsilon_y\end{bmatrix}\approx\frac{r_p^{\,2}cN}{4\gamma^3\beta^3C}\left\langle\frac{\sqrt{2\pi}L_C}{\sigma_x\sigma_y\theta_{\perp}}\begin{bmatrix}2\left(1-k_{\|}\right)\\ A_x\left(1-\kappa\right)\\ A_x\kappa\end{bmatrix}\right\rangle_s . \qquad (1)$$

Here r_p and c are the proton classical radius and the speed of light, γ and β are the relativistic factors, C is the ring circumference, N is the number of particles, σ_p is the rms relative momentum spread, σ_x, σ_y, θ_x, and θ_y are the rms sizes and the local angular spreads, κ is the x-y coupling parameter, $\theta_{\perp}=\sqrt{\theta_x^{\,2}+\theta_y^{\,2}}$, $\langle\,\rangle_s$ denotes averaging over the ring, L_C is the Coulomb logarithm ($L_C\approx20$),

$$A_x=\frac{D_x^{\,2}+\left(D_x'\beta_x+\alpha_xD_x\right)^2}{\beta_x}, \qquad (2)$$

β_x and α_x are the horizontal beta- and alpha-functions, and

*Work supported by the Universities Research Assos., Inc., under contract DE-AC02-76CH03000 with the U.S. Dept. of Energy.
#val@fnal.gov

0-7803-7738-9/03/$17.00 © 2003 IEEE

D_x and D_x' are the dispersion and its derivative.

Usually ring optics is sufficiently smooth, and the second term in Eq. (2) can be neglected. However, in the case of Accumulator optics upgrade, average value of A_x is well above the value corresponding to the smooth lattice approximation and 2.5 times higher the value before the upgrade. That caused strong amplification of horizontal emittance growth. To reduce the IBS we introduced dual lattice operation. The stacking is performed at the stacking lattice, which has been designed for fast stacking but has strong heating due to IBS. After stacking is completed the machine optics is retuned to the "shot" lattice (similar to the Run I lattice), which has the same tunes but smaller IBS heating, and therefore is more suitable for the final cooling. After about 20 minutes cooling, the beam is ready for extraction.

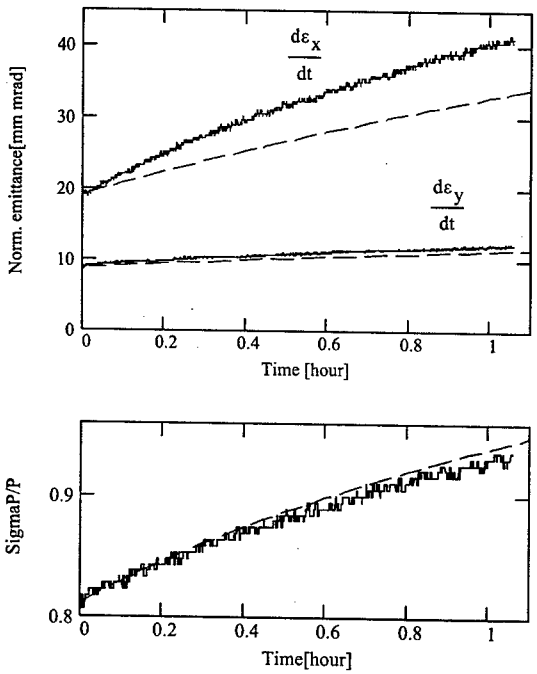

Figure 2: Measured (solid lines) and calculated (dashed lines) normalized 95% emittances (top) and energy spread (bottom) for antiproton current of 105 mA in Accumulator, $\kappa = 0.1$ is used in the simulations.

Figure 2 presents computed and measured emittances of antiproton beam for stacking lattice with cooling turned off. There is good agreement between theory and measurements for the energy spread and the vertical emittance but it is not as good for horizontal emittance. However good agreement was found in the case of proton beam. The difference is caused by additional heating from the self-stabilized two-beam instability due to small amount of ions stored in the beam. The instability appears at antiproton currents above ~30 mA. The emittance growth related to multiple collisions with the residual gas is sufficiently large and was taken into account in the simulations.

The described optics manipulations together with the core cooling upgrade were introduced after the 2002 summer shutdown and allowed us to achieve the antiproton beam emittances required for Run II.

2 SINGLE AND MULTIPLE SCATTERING

There are a few applications in the Tevatron complex for which simultaneous consideration of multiple and single Coulomb scattering is important.

The first one is associated with separation of different heating mechanisms contributing to transverse emittance growth in Tevatron. The three basic sources of the beam heating are IBS, multiple scattering on the residual gas and the noise in magnets, kickers, etc. While the first one can be easily separated due to strong dependence on the beam parameters, the effects of the other two look very similar. Nevertheless, there is a fundamental difference between them. In distinguish from the noise the beam interaction with residual gas, additionally to diffusion, creates non-gaussian tails due to single scattering. Approach developed in Ref. [8] uses an integro-differential equation to describe the evolution of the distribution in a linear focusing field. The equation correctly treats both single and multiple scattering and can be written in the following form

$$\frac{\partial f}{\partial t} - \lambda \frac{\partial}{\partial I}(If) = \int_0^\infty W(I,I')\left(f(I',t) - f(I,t)\right)dI' \quad , \quad (3)$$

where the kernel is

$$W(I,I') = \frac{D\left(I + I' + I_{\min}/2\right)}{L_C\left((I-I')^2 + (I+I')I_{\min} + {I_{\min}}^2/4\right)^{3/2}} \quad , (4)$$

λ is the damping decrement (if cooling is present), D is the diffusion coefficient, $L_C = \ln\left(\sqrt{I_{\max}/I_{\min}}\right)$ is the Coulomb logarithm, $I_{\min}$ and $I_{\max}$ are the minimum and maximum actions.

The following experiment was performed to measure the emittance growth rate and to separate contributions of noise and gas scattering. A low intensity beam was injected into Tevatron. The beam was debunched (to reduce IBS) and scraped in both planes to a known size. The scrapers were then removed, and the beam was left alone for 1 hour. To measure resulting distribution we scraped the beam vertically while measuring the beam current as function of scraper position. Good agreement between the measurements and numerical solution of Eq. (3) ($\lambda = 0$) has been found. Both the emittance growth in the core (5 mm mrad/hour) and the tail population were described well by the model. That means that in the case of small intensity beam, when IBS is negligible, gas scattering is a major source of the beam heating and there is no visible heating could be associated with noise. Last year vacuum improvements yielded some reduction of the beam heating due to gas scattering and reduced background in CDF and D0 detectors.

The second example is related to the beam lifetime computations in Recycler where the beam emittances and machine acceptances are quite close. Solving Eq. (3) with

zero boundary condition at the machine acceptance we found the dependence of the rms beam size and the beam lifetime as functions of time for different cooling decrements. After some time the system comes into equilibrium, where the shape of distribution function does not depend on time, and the intensity decays exponentially with the decay time τ_∞. We define the lifetime correction factor, K, as a ratio of τ_∞ at given equilibrium emittance (determined by cooling decrement) to the lifetime of zero-emittance beam (determined by the single scattering only). Figure 3 presents K as a function of ratio of the rms equilibrium emittance to the machine acceptance. Without cooling the rms beam emittance reaches its maximum of ≈0.391, where the lifetime is ≈40 times worse than for a point-like beam. Although, the model described above was developed for a one-dimensional case, when the aperture is limited in one plane only, the results presented in Figure 3 can be used for the lifetime correction factor of two-dimensional case if the emittances and the acceptances in both planes are equal.

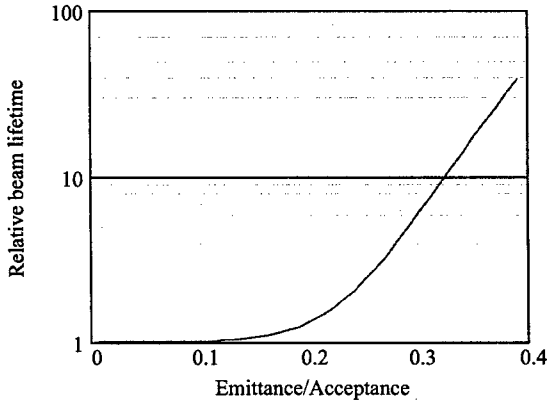

Figure 3: Dependence of the lifetime correction factor, K, on the ratio of the rms emittance to the machine acceptance.

The last example of this section is related to the evolution of longitudinal distribution in Tevatron governed by IBS. In this case the non-linearity of potential well changes the kernel in Eq. (3) to [9]:

$$\tilde{W}(E,E') = \frac{B\omega_0\omega\omega'}{(E-E')^2} \begin{cases} \frac{1}{2\omega} + \frac{I}{E'-E} & , \quad E' \geq E + \delta E, \\ \frac{1}{2\omega'} + \frac{I'}{E-E'} & , \quad E' \leq E - \delta E. \end{cases} \tag{5}$$

Here ω_0 is the frequency of small amplitude motion, E is the energy, $I = (1/2\pi)\oint p dx$ and $\omega = \partial E / \partial I$ are the action and the frequency. Similar to Eq. (4) the divergence in Eq. (5) at $E \approx E'$ need to be confined for the energy difference below $\delta E \sim \omega_0 I_{min}$. Eq. (5) reduces to Eq. (4) for linear motion. For the sinusoidal potential of longitudinal motion the energy is,

$$E = p^2/2 + \omega_0{}^2(1 - \cos(x)) \ . \tag{6}$$

Evolution of the longitudinal bunch profile in time obtained by numerical solution of Eq. (3) with kernel of Eq. (5) is presented in Figure 4. The initial distribution function has no tails, because before acceleration the particle distribution fits into 4 eV s bucket size, while after acceleration the bucket size is 10 eV s. Therefore the initial particle loss occurs due to the single scattering only, later, however, the tail population grows and diffusion loss begins to dominate. In distinguish from the standard (local) diffusion the large non-gaussian tails are created from the very beginning. For a point-like beam the lifetime is determined by single scattering and is equal to $\tau_0 = 4L_C / D$. The lifetime decreases with beam expansion and, when the beam size achieves its maximum rms size of ≈0.931 rad, the lifetime reaches its asymptotic value of $\tau_0 \approx 0.741/D$.

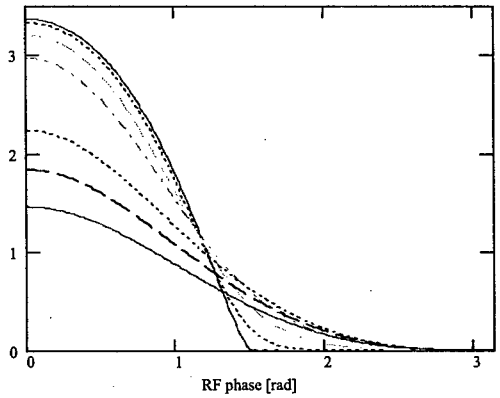

Figure 4: Numerical simulation of the longitudinal bunch profile evolution during the store in Tevatron.

3 LUMINOSITY EVOLUTION

Numerous factors affect the Tevatron luminosity and its evolution in time. Each store is different and because of finite instrumentation accuracy it is practically impossible to state what was different or what came wrong for every particular store. Nevertheless the luminosity evolution is similar for most of the stores. It is driven by some basic processes, which are not very sensitive to the details of distribution function, and therefore the luminosity evolution can be described by comparatively simple parametric model. The model takes into account the major beam heating and particle loss mechanisms. They are (1) the emittance growth and the particle loss due to scattering on the residual gas, (2) the particle loss and the emittance growth due to scattering in IPs, (3) the transverse and longitudinal emittance growth due to IBS, (4) the bunch lengthening due to RF noise, and (5) the particle loss from the bucket due to heating of longitudinal degree of freedom [10]. If the collider tunes are correctly set and the beam intensity is not too high the beam-beam effects are not very important and the model describes the observed dynamics of beam parameters and the luminosity comparatively well.

Figure 5 presents measured and computed luminosity for the Store 2138 (Jan.05.2003). The only free parameters used in the model were the residual gas pressure of

$1.2 \cdot 10^{-9}$ Torr of molecular nitrogen equivalent at room temperature, the x-y coupling parameter $\kappa = 0.45$, and the spectral density of RF phase noise of 50 $\mu rad^2/Hz$. They correspond to the gas scattering lifetime of 380 hours, and the bunch lengthening due to RF noise of $2.2 \cdot 10^{-3}$ $rad^2/hour$. RF phase noise was measured directly [11] and agrees with the fit to the model within the measurement accuracy (factor of 2). The computed proton and antiproton intensities are close to the measured ones as can be seen in Figure 6. It has been critical to use the described above model for non-local diffusion in longitudinal direction to achieve such a good agreement

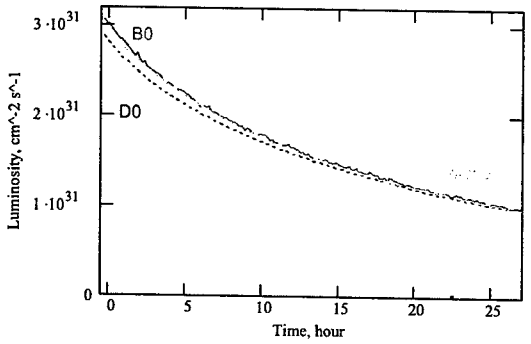

Figure 5: Dependence of luminosity on time for Store 2138; solid and dotted lines - luminosity measured by CDF and D0 detectors, dashed line – model prediction.

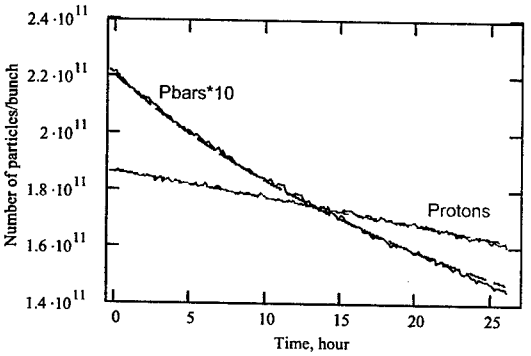

Figure 6: Dependence of intensities for proton and antiproton beams on time for Store 2138; solid lines – measurements, dashed lines - model prediction.

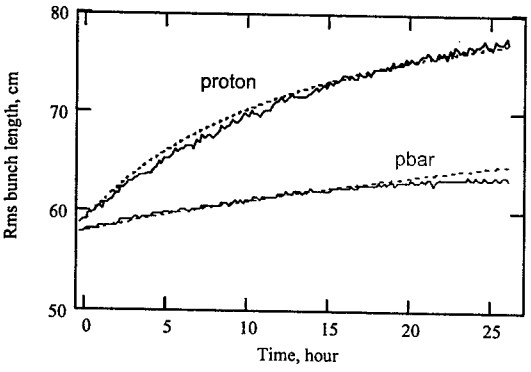

Figure 7: Dependence of bunch lengths for proton and antiproton beams on time for Store 2138; solid lines – measurements, dashed lines - model prediction.

The major mechanism for loss of antiprotons is the luminosity loss. The cross-section of 70 mbarn is used for proton-antiproton scattering in the IP. The proton bunch lengthening (see Figure 7) is mainly driven by IBS, while for low intensity antiproton beam the RF phase noise usually dominates. Figure 8 presents a comparison of measured and computed antiproton emittances versus time. The emittances were measured with synchrotron light monitors [12]. The obtained values were corrected for diffraction to match them with the effective emittance computed from the luminosity and the emittance measurements performed with flying wires at the beginning and the end of the store. At the beginning of the store, the vertical emittance grows significantly faster than the model prediction. Our present belief is that it is related to an amplification of diffusion by the beam-beam effects.

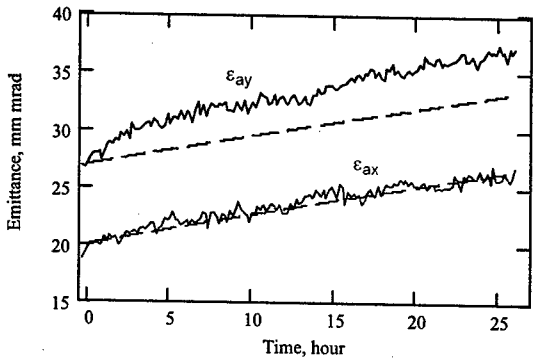

Figure 8: Dependence of horizontal and vertical antiproton beam emittances on time for Store 2138; solid lines – measurements, dashed lines - model prediction.

The store 2138 discussed above has moderate discrepancies with the model, and can be considered a regular store. Most of our stores are influenced more by the beam-beam interaction, but fortunately it weakly affects the luminosity decay and the luminosity integral. Figures 9 and 10 present measured and computed parameters for Store 2328 (Mar.20.2003). The same vacuum and RF phase noise were used in the model. Unlike Store 2138, both the proton and antiproton beam intensities decay faster and the proton bunch length grows significantly slower than the model predicts [12,13]. The most probable cause of such misbehavior is small, uncontrolled store-to-store tune variation causing a loss of dynamic stability for particles at large synchrotron amplitudes with subsequent particle loss and reduction of bunch lengthening.

The results presented above show that the beam-beam interactions certainly affect the luminosity decay. However this effect is sufficiently small. Thus, the developed model, with some reservations, can be used to analyze the luminosity dynamics for the final Run II parameters. Table 1 presents parameters for one of our best stores (Store 2328), typical collider parameters in April 2003 and projections for the final Run II parameters. Evidently, in order to increase the luminosity by a factor of 7.2 times we need to quadruple the number of antiprotons extracted from the stack. The remaining factor of 1.8 should result from the improvements in the antiproton transport and

Tevatron. Three major contributions are an increase of the proton intensity by ~30%, an improvement of coalescing in MI, and improvements of antiproton transport efficiency (from the antiproton stack to the collisions in Tevatron). Two last items are expected to increase the transfer efficiency from ~60% to ~80%. The chosen proton intensity, $2.7 \cdot 10^{11}$ per bunch, corresponds to the linear head-on tune shift of 0.01 for each of two IPs. This is the maximum tune shift achieved in Run Ib with 6×6 bunch operation. We choose the maximum antiproton intensity to be half of the proton intensity. Further increase of antiproton intensity is limited by antiproton production.

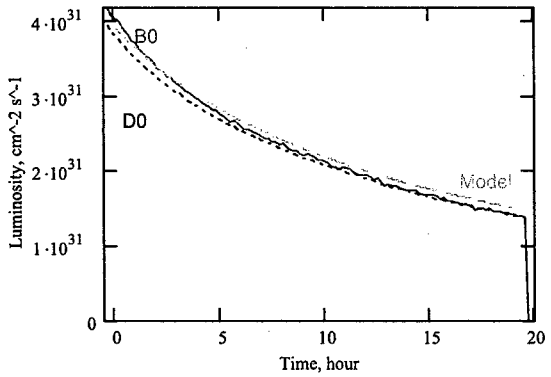

Figure 9: Dependence of luminosity on time for Store 2328; solid and dotted lines - luminosity measured by CDF and D0 detectors, dashed line – model prediction.

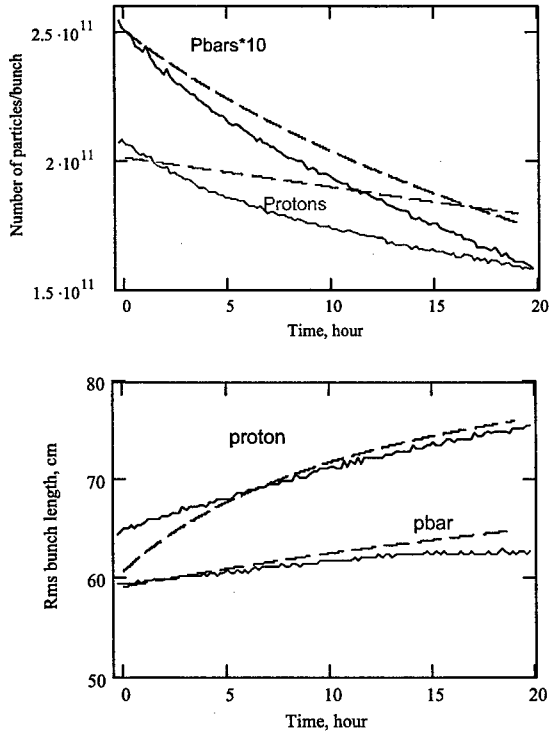

Figure 10: Dependence of intensities (top) and bunch lengths (bottom) for proton and antiproton beams on time for Store 2328; solid lines – measurements, dashed lines - model prediction.

Due to reduction of luminosity lifetime with growth of peak luminosity, the average luminosity grows slower than the peak luminosity. After all Run II upgrades are introduced the luminosity integral is estimated to be ~2.5 fb^{-1}/year.

Table 1: Present and final Run II parameters

	Store 2328	Typical Apr.03	Final Run II
Protons, 10^{10} / bunch	20.7	20	27
Pbars, 10^{10}/ bunch	2.54	2.2	13.5
Norm. 95% proton emittances, $\varepsilon_x/\varepsilon_y$, mm mrad	~14/24	~15/25	20/20
Norm. 95% pbar emittances, $\varepsilon_x/\varepsilon_y$, mm mrad	~15/24	~16/25	20/20
Proton bunch length, cm	65	62	50
Pbar bunch length, cm	59	58	50
Initial luminosity, 10^{30} $cm^{-2}s^{-1}$	40.5	35	290
Initial luminosity lifetime, hour	11	12	7.1
Store duration, hour	19	20	15.2
Lumin. integral per store, pb^{-1}	1.71	1.2	8.65

The work reported in this paper is the result of expertise, ingenuity and dedication of a large number of people in Fermilab. The author wishes to acknowledge their excellent results, and is grateful for the contribution received.

REFERENCES

[1] Yu. Alexahin et al.., "Tevatron Lattice Upgrades," these proceedings.
[2] P. Ivanov et al., "Head-Tail Instability at Tevatron," these proceedings.
[3] C.Y. Tan, J. Steimel, "The Tevatron Bunch by Bunch Longitudinal Dampers," these proceedings.
[4] C. Y. Tan, J. Steimel, "The Tevatron Coupled Bunch Mode Transverse Dampers," these proceedings.
[5] R. Moore et al., "Longitudinal Bunch Dynamics in the Tevatron," these proceedings.
[6] J. Peoples, "Antiproton source", Physics of particle accelerators - AIP conf. Proc. 184, 1988, p.1846.
[7] Run II handbook, FNAL, 1998.
[8] V. Lebedev and S. Nagaitsev, Proc. of EPAC 2002, Paris, France, June 4-10, 2002. p. 1362-1364.
[9] A. Burov, Private communications, 2003.
[10] FNAL report for the summer 2003 DoE review, FNAL, 2003.
[11] J. Steimel et al., "Effects of RF noise on the longitudinal emit. growth in Tevatron," these proceedings.
[12] H.W.K.Cheung et al., "Performance of a Beam Monitor in the Fermilab Tevatron Using Synchrotron Light," these proceedings.
[13] A. Tollestrup et al., "Measurements of the longitudinal and transverse beam loss at the Tevatron," these proceedings.
[14] P. Lebrun et al., "Observations on the Luminosity Lifetimes, emittance growth factors and Intra-Beam Scattering at the Tevatron," these proceedings.

NEW ASPECTS OF BEAM-BEAM PHENOMENA IN HADRON COLLIDERS

T. Sen *, FNAL, Batavia, IL 60510, USA

Abstract

Long-range beam-beam interactions in Run II at the Tevatron are the dominant sources of beam loss and lifetime limitations of anti-protons, especially at injection energy. The main focus of the talk will be observations of the long-range effects during Run II and theoretical understanding of these effects.

INTRODUCTION

The Tevatron is currently delivering luminosities close to 4×10^{31} cm^{-2} sec^{-1} to the CDF and D0 experiments. In a record store on May 2nd, 2003, (average initial luminosity = 4.2×10^{31} cm^{-2}sec^{-1}), the average bunch intensities at the start of collisions were $N_p = 1.96 \times 10^{11}$, $N_{\bar{p}} = 0.25 \times 10^{11}$. These are to be compared with design values for Run II of 2.7×10^{11} and 1.35×10^{11} for protons and anti-protons respectively. Beam-beam effects have generally been more severe on the anti-protons but with increasing anti-proton intensity, their effects on protons are also increasing. I will review the beam-beam effects at various stages of the operational cycle of the Tevatron.

After 36 bunches of protons are injected and placed on the proton helix, anti-protons are injected four bunches at a time. After all bunches are injected, acceleration to top energy takes about 85 seconds. After reaching flat top, the optics around the interaction regions (IRs) is changed to lower β^* from 1.6 m to 0.35 m at B0 and D0 and the beams are brought into collision. During a high energy physics store each bunch experiences two head-on collisions with bunches in the opposing beam and seventy long-range interactions. At all other stages, each bunch experiences only long-range interactions - seventy two in all.

THEORETICAL ANALYSIS OF BEAM-BEAM INTERACTIONS

Beam-beam forces change the linear and nonlinear dynamics of particles in fundamental ways. The long-range beam-beam force has in general both quadrupolar and skew-quadrupolar components. The magnitude of the tune and coupling shift depends on the beam separation but also on the amplitude of the particle experiencing the force. Since there is dispersion at the locations of the long-range interactions in the Tevatron, the separation between the test particle and the other beam and therefore the tune shift depends on the momentum deviation of the particle. An amplitude dependent tune shift implies that the chromaticity

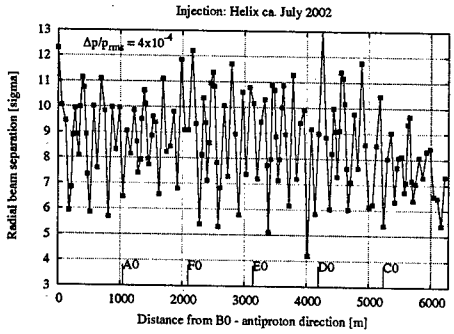

Figure 1: Beam separations at all the parasitics at 150 GeV with the design value for the proton momentum spread and the present injection helix.

shift is also amplitude dependent. These amplitude dependences introduce the familiar tune footprint but also coupling and chromaticity footprints within a bunch.

Theoretical expressions have been developed for the amplitude dependent tune shifts, chromaticities and coupling for arbitrary aspect ratios [1] because the proton beam is not round at most of the long-range interactions. Some conclusions are easily drawn however from the round beam case. At large distances, both the tune shift and the coupling fall as $1/d^2$ while the chromaticity falls off more rapidly as $1/d^3$. The tune shift for round beams vanishes if the plane of the helix is at 45°. Minimizing the chromaticity requires the plane of the helix to be either at 30° or vertical. The coupling vanishes if the separation is either in the horizontal or the vertical plane. Since each of these parameters has a different dependence on the helix angle, it is not possible to minimize them simultaneously with a choice of the angle.

Each anti-proton bunch sees a different sequence of long-range interactions with different optics functions. This leads to a significant spread of tune shifts, coupling and chromaticities between the bunches. Thus the working point for example cannot be optimized for all bunches at once. Due to the amplitude dependence of these quantities, the spread within a bunch can be comparable to the spread between the bunches.

Injection Energy

There are 138 different locations of parasitic interactions around the ring. Figure 1 shows the beam separations with the present helix and assuming the design value of $(\Delta p/p)_{rms}$. The smallest separation is about 4σ close to D0 but there is a large variation between 5-12 σ at most of the other parasitics. At most parasitics the beta func-

* tsen@fnal.gov

0-7803-7738-9/03/$17.00 © 2003 IEEE

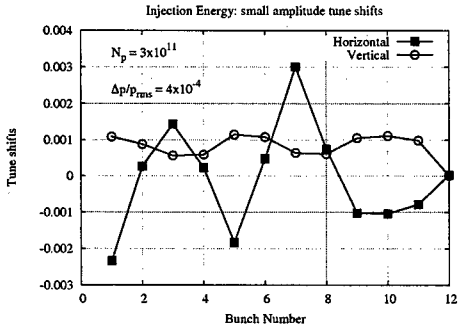

Figure 2: Beam-beam induced tune shifts of anti-protons at small amplitude, bunch by bunch.

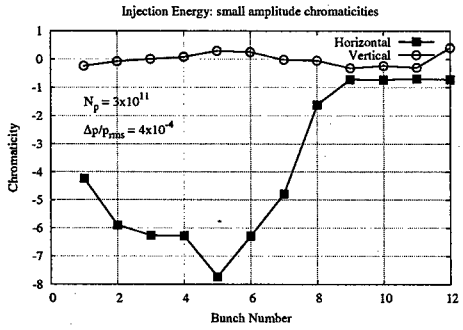

Figure 3: Beam-beam induced chromaticity at small amplitude, bunch by bunch (150 GeV).

tions are larger in the horizontal plane. This asymmetry in the beta functions is reflected in parameters like the tune shifts.

Figure 2 shows the small amplitude tune shifts of the anti-protons, bunch by bunch. The tune footprint at large amplitudes however is determined by the machine nonlinearities which change the sign of the detuning.

The beam-beam induced global coupling at small amplitude is of the same magnitude as the lattice induced global coupling. Figure 3 shows the small amplitude chromaticity. The large spread in chromaticity could make some bunches more sensitive to synchro-betatron resonances and to coherent instabilities at high anti-proton intensities. Bunch 12 suffers the least changes to its tune, coupling and chromaticity from the beam-beam interactions at injection.

Resonance driving terms have been calculated from a nonlinear map, first with only the lattice nonlinearities and second with the lattice and the beam-beam nonlinearities for anti-proton bunch 1. The lattice nonlinearities include the correction sextupoles and the error fields in the magnets. These terms were evaluated along the diagonal at an amplitude of 2σ, and the largest resonance strength was normalized to 1. The resonance condition is $p\nu_x + q\nu_y =$ integer. Fourth order resonances are driven strongly by the lattice, the largest of these being the difference (2,-2) resonance. Addition of the beam-beam effects shows that they dominate the lattice resonances, as seen in Figure 4

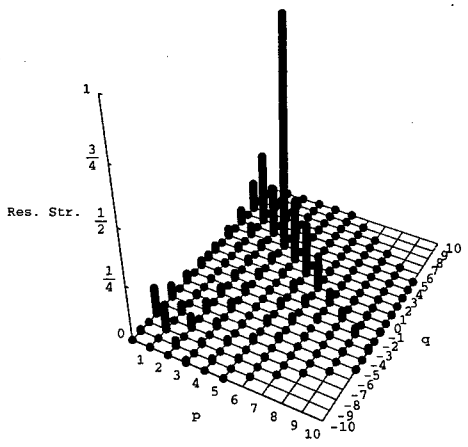

Figure 4: Resonance strengths at injection at an amplitude of 2σ with lattice and beam-beam nonlinearities.

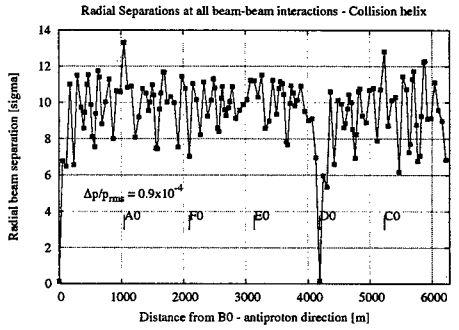

Figure 5: Beam separations at all the parasitics at 980 GeV with expected values for the proton momentum spread.

which has a completely different resonance pattern. The beam-beam fields drive the seventh order resonances, the strongest at this amplitude being the (3, 4) resonance.

The large energy spread at injection makes synchro-betatron resonances also important. Calculations [2] show that at present chromaticities and energy spreads, the synchrotron sidebands of some betatron resonances are wide enough to overlap which may lead to faster diffusion. A smaller energy spread at injection would therefore increase the dynamic aperture at injection.

Collision

The smallest separations at the parasitic collisions occur at the ones immediately upstream and downstream of the head-on collisions at B0 and D0. Figure 5 shows the beam separations around the ring. The beta functions at these four parasitics are also the largest. Consequently the tune shifts and resonance driving terms (for example) contain the largest contributions from these parasitics amongst all the parasitics.

The bunch by bunch variation in tunes is quite different from the variation at injection [cf. Figure 2]. Only the

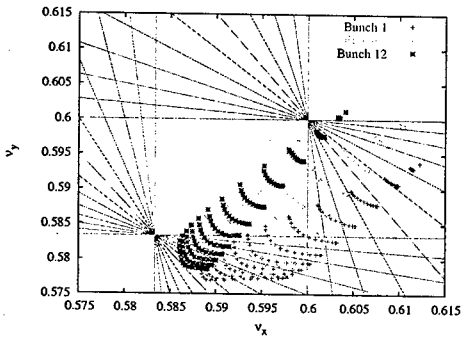

Figure 6: Tune footprints of bunches 1, 6 and 12 superposed on the 5th and 12th order sum resonances.

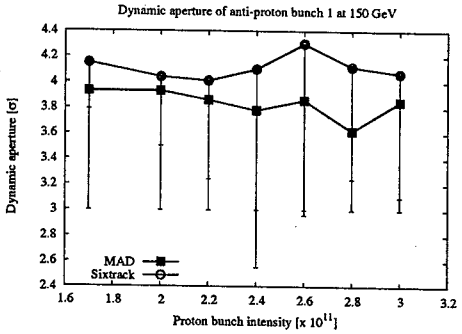

Figure 7: Dynamic aperture after 10^6 turns of anti-proton bunch 1 vs proton intensity at injection. The average value (over all angles in coordinate space) along with one-sided error bars to represent the minimum value at each intensity are shown.

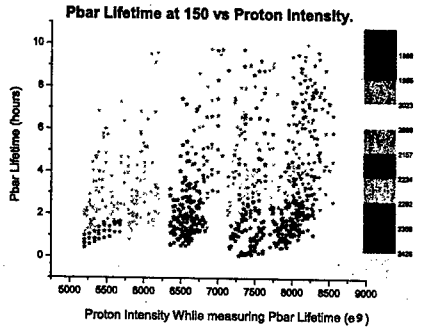

Figure 8: Lifetime of anti-proton bunches vs proton intensities in several recent stores.

head (bunch 1) and the tail (bunch 12) of the train have tune shifts significantly different from the others. Bunch 1 does not suffer the first parasitic upstream (where β_y is large) of the IPs and bunch 12 misses the first parasitic downstream (where β_x is large) of the IPs. Figure 6 shows the tune footprint (up to 6σ) of these bunches and that of bunch 6 which is representative of all the other bunches. The extent of the footprint is largely determined by the head-on collisions for all bunches. The beam-beam induced coupling at small amplitudes is smaller than at injection. The beam-beam induced chromaticity (both the variation over the bunches and the magnitude) is larger than at injection.

The head-on collisions create the strongest nonlinear fields but drive only even order resonances, mainly the 12th order resonances. The effects of these resonances is considerably weakened (by two orders of magnitude at some amplitudes) as a consequence of phase averaging [1]. However with increasing chromaticity the number of synchrotron sidebands with significant width increases as well which increases the effective width of the resonances. The long-range interactions drive the odd order 5th and 7th order resonances. The relatively large chromaticity generated by these interactions create synchrotron sidebands of these resonances which overlap at relatively small amplitudes.

A nonlinear Taylor map has been used to calculate the resonances with both lattice and beam-beam nonlinearities. As at injection, we find that at an amplitude of $2\sigma_p$, the 7th and 5th order resonances driven by the beam-beam dominate. The largest of these are the (3, 4) and (3, 2) resonances. Compared to injection, there are now many more resonances of comparable strength but the strengths themselves are smaller.

SIMULATIONS AND EXPERIMENTS

Injection

The beam-beam interactions have a strong influence on the anti-proton lifetime at 150 GeV. During a study in September 2002 with only anti-protons injected into the Tevatron, the lifetimes at 150 GeV varied between 10-25 hours compared to lifetimes of 1-10 hours in stores. The losses during acceleration were also small about 2%, compared to typical losses around 10% in stores.

The dynamic aperture of a few anti-proton bunches at 150 GeV has been calculated with extensive simulations. The nonlinearities in the model include the measured multipoles in the magnets, the chromaticity and feed-down sextupoles together with the beam-beam interactions. The results from two different codes, MAD and Sixtrack, typically agree to within 15%. Tracking results show for example that the dynamic aperture with beam-beam interactions drops by about $3\sigma_p$ compared to the case without beam-beam interactions. Figure 7 shows a plot of the average dynamic aperture (after 10^6 turns or 2 seconds in the Tevatron) as a function of the proton bunch intensity. The averaging is done over several initial angles of the particles in physical space. This plot predicts that the dynamic aperture at 150 GeV is about $3\sigma_p$ and nearly independent of the proton intensities over this range.

Figure 8 shows the lifetime of anti-protons at 150 GeV as a function of proton intensity over several recent stores. The lifetimes of most bunches varies between 2-10 hours under typical conditions but is observed to be relatively independent of the proton intensities obtained so far - in

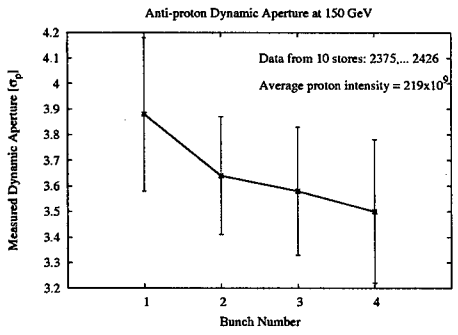

Figure 9: Dynamic aperture of the first four anti-proton bunches at injection calculated from the measured drop in emittance in 10 recent stores. The error bars represent the variation over the stores.

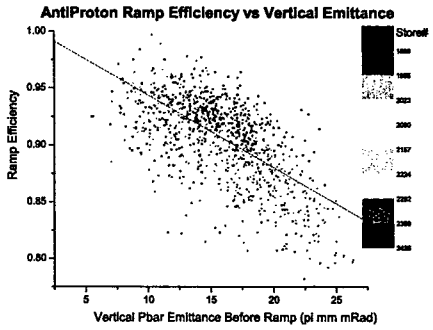

Figure 11: Anti-proton ramp efficiency vs anti-proton vertical emittance in several recent stores.

agreement with the result expected from Figure 7. In several recent stores, the emittance of the anti-protons was observed to decrease with time after injection. An example is seen in Figure 10. We consider the first four bunches injected since their emittances are measured 10 time with the flying wires before acceleration. The dynamic aperture was calculated from the asymptotic emittance for 10 recent stores where there was an observed emittance reduction. The dynamic apertures, shown in Figure 9, are in good agreement with the simulation results in Figure 7.

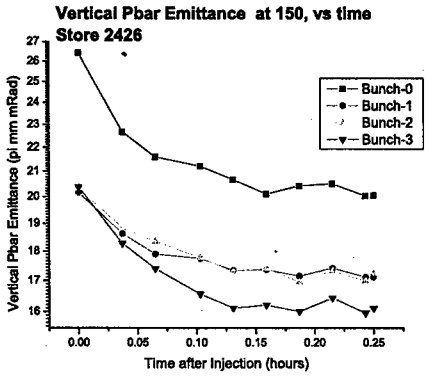

Figure 10: Drop in vertical emittance of the first four anti-proton bunches after injection in a recent store. The asymptotic emittance of each bunch is a measure of its dynamic aperture.

Vertical dampers were recently re-commissioned at injection. The vertical chromaticity can now be dropped from 8 to 4 units while keeping the protons stable. At this lower chromaticity we have not observed the sharp drop in anti-proton emittance during injection. The dynamic aperture has therefore increased from the value shown in Figure 9.

A. Kabel at SLAC has developed a six-dimensional code called PlibB for lifetime simulations. An interesting prediction from one of his simulations is a significant increase in the lifetime when the vertical chromaticity is reduced below 4 units. Another parallel code called BeamBeam3D has been developed by J. Qiang at SLAC. As with Kabel's code, the only nonlinearities included so far are those due to the beam-beam interactions. Lifetimes from simulations using this code can be in the range of 1-2 hrs if the physical aperture is small enough. Further development will include the nonlinearities of the magnets.

Ramp and squeeze

A significant fraction of proton losses during the ramp occur in the first 20 seconds while the bucket area is shrinking. Dedicated studies have shown that the proton losses are determined by the longitudinal emittance and the quality of coalescing in the Main Injector. Beam-beam effects on protons during the ramp do not appear to be significant until now. Anti-proton losses during the ramp were measured to be $\sim$2% during a dedicated anti-proton only store in September 2002. However during regular stores with protons present, anti-proton losses averaged around 11% in March 2003. These losses occur during the entire ramp.

The beam separations (in scaled units) are kept constant from 150 GeV to 500 GeV by increasing the separator voltages proportionally to $\sqrt{E}$. At higher energies there is not enough separator strength to maintain constant separations so the beam separations fall by about 30% during the second half of the ramp. Mitigating the beam-beam driven loss requires an increase in the beam separations during the entire ramp with a different combination of separators.

The anti-proton loss during the ramp is also well correlated with the anti-proton vertical emittance, as seen in Figure 11. Reducing the emittance blow-up while injecting anti-protons in the Tevatron onto the anti-proton helix would therefore also reduce the loss during the ramp. The longitudinal emittance does not appear to have much influence on the anti-proton losses during the ramp.

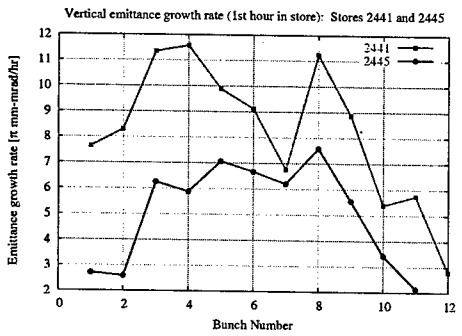

Figure 12: Bunch by bunch vertical emittance growth rates at the beginning of two recent stores. Lowering the vertical tune by 0.001 helped lower the growth rate in Store 2445.

Collision

Extensive dynamic aperture and other tracking calculations at collision optics and Run II design parameters lead to several conclusions. For example, the head-on interactions largely determine the tune footprint but they have very little influence on the dynamic aperture. Of the seventy long-range interactions, the four interactions nearest to the two IPs are the most important in determining the DA but the synchro-betatron resonances driven by the other long-range interactions are important. These calculations also predict that the DA will drop by about 1σ from present intensities ($N_p \sim 210 \times 10^9$) to design intensity ($N_p = 270 \times 10^9$). Analysis of data shows that at present the anti-proton lifetime during stores is not strongly influenced by the beam-beam effects.

In several dedicated studies we have explored the possibility of improving the anti-proton lifetime by changing the collision helix. In the first set of studies (done in August and September of 2002), the helix size in the short arc (between B0 and D0 in the proton direction) was changed. This changed the separation at two of the four parasitics nearest the IPs. Opening the helix vertically seemed to improve the lifetime in the experiment. In subsequent stores the helix was increased vertically by 8% in the short arc but no significant improvement of anti-proton lifetimes was observed. Opening the helix horizontally in the short arc at the start of a few stores did not also show much improvement in the lifetime.

More recently in a study done on March 21, 2003, at the end of a store, the helix was changed in the entire ring and in both planes simultaneously. Losses stayed nearly the same when the helix was opened by 20%. On decreasing the helix size, the losses in both beams decreased at first - perhaps due to the beams moving away from the collimators in the long arc. When the helix was was reduced by more than 80%, losses climbed - a combination of beam-beam effects and tunes changing with the helix size. The experimental results from increasing the helix size at collision have therefore been somewhat mixed so far.

Emittance growth at the start of a store has occasionally been a concern. In most of these cases the anti-proton emittance growth rate was large at the start, then dropped with falling beam intensities. This emittance growth is strongly bunch dependent; typically bunches 1 and 12 have lower growth rates than the others. Small changes to the tune usually suffice to lower the growth rate. Figure 12 shows an example from two recent stores. In Store 2441 the growth rate was large for most bunches. In Store 2445 lowering the vertical tune by 0.001 reduced the growth significantly. Even with the lower growth rate there are differences amongst bunches due to the differences in bunch tunes. More details about experimental beam-beam studies can be found in a companion paper [3].

SUMMARY

We summarize the status of beam-beam effects in the Tevatron. At injection energy they limit the anti-proton lifetime to under 10 hrs but have not influenced proton lifetimes much. During the ramp anti-proton losses (and perhaps emittance growth) are largely due to beam-beam effects. Occasional proton losses, large enough to quench the Tevatron, during the final cogging and squeeze are attributed to beam-beam effects. Proton losses during luminosity are occasionally much higher than observed during machine studies with only protons of similar intensities. Lifetimes of both anti-protons and protons at collision however are largely determined by luminosity with a comparable contribution from residual gas scattering to the proton lifetime.

We are vigorously pursuing several ways of reducing beam-beam limitations at all stages. New helical solutions that increase the separations are being developed and tested using the present set of electrostatic separators. There are also plans to install additional separators around the IPs to increase the separations at the nearest parasitics. Other planned measures include (a) Improving the alignment in the Tevatron, (b) Injecting beams with smaller emittances, (c) Operating with lower chromaticities, (d) Testing different bunch patterns, (e) Improving the IR optics, (f) Searching for better working points, (g) Active compensation of beam-beam effects with the Tevatron electron lens [4] and perhaps in tandem, compensation with current carrying wires.

REFERENCES

[1] T. Sen, B. Erdelyi, M. Xiao, *Theoretical studies of beam-beam effects in the Tevatron at collision energy*, these proceedings.

[2] Y. Alexahin, *Beam-beam effects at injection*, http://www-bdnew.fnal.gov/beam-physics-studies/Notes/2002/bb_SBR_at_inj.pdf

[3] X.L. Zhang et al., *Experimental studies of beam-beam effects at the Tevatron*, this conference

[4] K. Bishofberger, this conference

R&D TOWARDS COOLING OF THE RHIC COLLIDER*

Ilan Ben-Zvi†, Joseph Brennan, Andrew Burrill, Rama Calaga, Xiangyun Chang, Gregory Citver, Harald Hahn, Michael Harrison, Ady Hershcovitch, Animesh Jain, Christoph Montag, Alexei Fedotov, Joerg Kewisch, William Mackay, Gary McIntyre, David Pate, Stephen Peggs, Jim Rank, Thomas Roser, Joseph Scaduto, Triveni Srinivasan-Rao, Dejan Trbojevic, Dong Wang, Alex Zaltsman, Yongxiang Zhao,
C-AD, Brookhaven National Laboratory Upton NY 11973 USA

Abstract

We introduce the R&D program for electron-cooling of the Relativistic Heavy Ion Collider (RHIC). This electron cooler is designed to cool 100 GeV/nucleon bunched-beam ion collider at storage energy using 54 MeV electrons. The electron source will be an RF photocathode gun. The accelerator will be a superconducting energy recovery linac. The frequency of the accelerator is set at 703.75 MHz. The maximum bunch frequency is 28.15 MHz, with bunch charge of 10 nC. The R&D program has the following components: The photoinjector, the superconducting linac, start-to-end beam dynamics with magnetized electrons, electron cooling calculations and development of a large superconducting solenoid.

INTRODUCTION

The Collider-Accelerator Department (C-AD) at Brookhaven National Laboratory is operating the Relativistic Heavy Ion Collider (RHIC), which includes the dual-ring, 3.834 km circumference superconducting collider and the venerable AGS as the last part of the RHIC injection chain.

CAD is planning on a luminosity upgrade of the machine. One important component of the luminosity upgrade is electron cooling of RHIC. In addition, electron cooling is essential for eRHIC, a future electron-ion collider. This project has a number of new features as electron coolers go: It will cool use 54 MeV electrons; it will be the first attempt to cool a collider at storage-energy; and it will be the first cooler to use a bunched beam and a linear RF accelerator as the electron source.

The linac will be superconducting with energy recovery. The electron source will be a photocathode gun. The project is carried out by the Collider-Accelerator Department at BNL in collaboration with the Budker Institute of Nuclear Physics [1] and Jefferson National Accelerator Facility.

The parameters of the electron beam for the RHIC electron cooler are: Bunch charge 10 nC, average current 94mA (RHIC) or 280mA (eRHIC), energy up to 54 MeV, rms normalized emittance 50 μm, energy spread 0.02%.

* Under contract with the United States Department of Energy, Contract Number DE-AC02-98CH10886
†ilan@bnl.gov

We simulated the performance of the cooler with the computer code Simcool [2]. Figure 1 shows the performance of the cooler for a proton beam at a few energies.

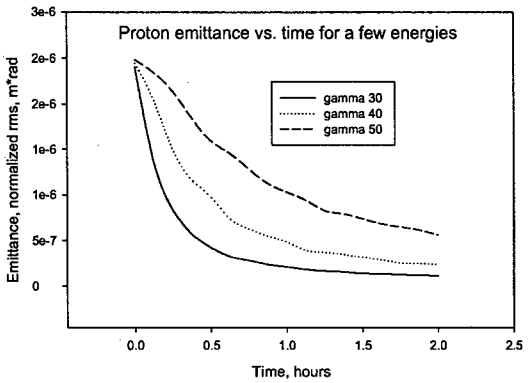

Figure 1. Cooling proton beams at RHIC.

The two RHIC rings would require two coolers operating simultaneously. In the following, we will describe the ongoing R&D program aimed at reducing the risks associated with a construction of this novel device.

ELECTRON GUN

We will produce the electron beam with a CW photoinjector (laser photocathode RF gun). The cathode of the gun will be immersed in a magnetic field to produce a 'magnetized' electron beam.

Photocathode development

We plan on using CsK_2Sb (cesium potassium antimonite) cathodes. These cathodes exhibit a very high quantum efficiency of over 5% for green light [3]. This material is sensitive to contaminants and we have initiated a research program to study the deposition and lifetime issues for various vacuum qualities. The UHV deposition system is shown in Figure 2. The rightmost chamber is the deposition chamber, the middle one is a storage chamber and the one on the left is a test chamber. A manipulator arm allows the transfer of targets between chambers.

0-7803-7738-9/03/$17.00 © 2003 IEEE

Laser development

We will use a highly efficient, diode-pumped, solid-state laser at a wavelength of 1064nm, where commercially available oscillators can provide continuous mode-locked operation with 10's of watts. we need an efficient method to convert the light to 532nm as well as reduce the pulse repetition frequency from about 80 to 100 MHz to 9.4 or 28 MHz. We are investigating a resonant multi-pass cavity. The IR pulse stream passes once through the bowtie cavity, the 2nd harmonic at 532nm is trapped for a number of turns in the cavity and is coherently converted with high efficiency.

CW photoinjector development

We adopt the design of the Los-Alamos / Advanced Energy Systems of a 2.5 cell, 700 MHz normal-conducting photoinjector. The device will be powered by a 1 MW CW klystron and produce about 2.5 MeV beam at over 100 mA. Figure 4 shows an outline of the photoinjector with the calculated electric field distribution.

SUPERCONDUCTING LINAC

Following some initial acceleration to about 2.5 MeV the beam will be injected into a 703.75 MHz superconducting Energy Recovery Linac (ERL). Each linac cavity has 5 cells with aperture of 19 cm diameter. We plan to intercept the Higher-Order Mode (HOM) power by ferrite absorbers located in the beam pipe at room temperature [4]. Following the initial 20 cm beam-pipe at 19 cm diameter (serving to block the fundamental mode), the beam pipe is enlarged to 24 cm diameter in order to conduct the HOMs. For the TE11 mode, the enlarged pipe (24cm) has a cutoff frequency of 732 MHz, which is below all HOMs.

This structure has been simulated by MAFIA. Figure 5 shows some electric field patterns of HOMs with the lowest frequencies. HOM with higher frequencies will be less important. Table 1 shows the external Q, which measures how much power drains to the beam pipe and will be absorbed by the ferrite. Most modes couple extremely well to the ferrite with the exception of three TM modes clustered between 952 to 964 MHz. A separate coupler will drain these modes.

We investigated the Beam Break-Up (BBU) of the new cavity [4] using the computer simulation code TDBBU developed in Jefferson Lab. We simulated an ERL with a circumference of 251 RF wavelengths, about 108 meters. The bunch repetition rate was fixed at 9.4 MHz. Simple transverse optics was assumed as the design of the cavity and transport is still underway. R/Q and Q values of major HOMs with ferrite HOM absorbers were calculated by MAFIA. The preliminary results are shown in Figure 5. The threshold current can exceed 1000 mA for a reasonable distribution of frequencies of the HOMs of 0.001 rms.

MAGNETIZED BEAM TRANSPORT

Figure 6 is a schematic layout of the RHIC high-energy cooler [5]. There are a few straight sections in RHIC where the electron cooler may be introduced. We are considering a placement next to IP4 of RHIC, in the straight section between Q3 and Q4, which can accept about 30 m long solenoids. The electron accelerators will reside outside the RHIC tunnel.

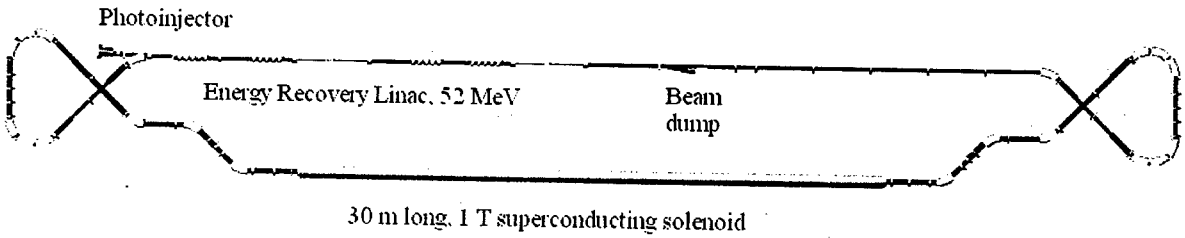

Figure 6. Schematic layout of the high-energy cooler.

The lattice can debunch the beam in order to reduce the space-charge interaction of the electron and ion beams or to reduce the energy spread of the electron beam. The beam transport has to obey certain rules in order to preserve the magnetization of the beam in the transport with discontinuous magnetic field. Emerging from the long cooling solenoid, the electron beam will be separated from the ion beam, rebunched (to match the linac acceptance) and decelerated to recover its energy. We dump the beam at about 2.5 MeV.

Merging the low energy and high-energy beams at the entrance of the linac uses two weak dipoles with a Stabenov Solenoid. The linac design assumes the use of 3rd harmonic cavities for additional control of the longitudinal phase space.

We propose to use two solenoids with opposing fields in the cooling section to eliminate coupling in the ion beam. A quadrupole matching section between the solenoids maintains magnetization.

A start to end simulation with PARMELA for non-magnetized beam shows energy spread of 8×10^{-5} in the

cooling solenoid and a normalized emittance of 24 microns rms to 10 nC bunches. For a magnetized beam the simulation, a transverse temperature of 100 eV is seen past the linac and 1500 eV inside the cooling solenoid. Part of the temperature growth in the linac is due to a conflict between emittance correction and magnetized beam transport. We have ideas on how to resolve that. A simplification of the debunching section can lead to additional reduction of temperature.

SUPERCONDUCTING SOLENOID

For high electron temperature, the influence of the magnet field is very significant, and for a temperature approaching 1000 eV, it is necessary to use a solenoid magnet field of about 1T. The required precision is of the order of the ions' angular spread, $\Delta\theta$. In our case $\Delta\theta$ is about 10^{-5}. Cooling simulations show that we require a solenoid error below 8×10^{-6}.

The superconducting solenoid for electron cooling in RHIC is designed for a 1 T field, with ample quench margin. The total available space for solenoids is approximately 26 meters. Naturally, we would like to use a very long solenoid to increase the cooling rate. In order to facilitate production, testing and installation, we plan to construct the solenoid in two sections of 13 meters each. We chose a rectangular conductor of 2.4 mm x 1.6 mm cross section to achieve good field quality, as well as a reasonable inductance. The desired field of 1 T is obtained at ~1kA with a two layer coil. The conductor has a rather large copper to superconductor ratio of 7:1 for simple quench protection, and still provides about 90% quench margin. Thus, the solenoid can be operated at significantly above 1 T, if needed. Figure 7 shows a transverse cross section of the solenoid.

The solenoid must meet very stringent field quality requirements. We anticipate that typical construction tolerances will not achieve the desired field quality. Consequently, the solenoid will also have concentric arrays of ~150mm long vertical and horizontal dipole correctors to compensate for any transverse components. These dipole correctors will be built using inexpensive printed circuit coils [6] and will provide corrections of up to 10^{-3} T with a maximum operating current of 2 A. We intend to develop a measurement system, using a mirror and magnetic needle, similar to that used at other laboratories [7].

COOLING RATE SOFTWARE

We simulated the performance of the cooler with the computer code Simcool [2] for the beam parameters provided in the introduction. Figure 8 shows the performance of eRHIC for a gold beam with and without cooling, for a constant beam-beam parameter of 0.005 in two IPs with β^*=1m. The disintegration cross section σ_{tot}=212 barns limits the integrated luminosity through rapid particle loss at the highest luminosity. After 5 hours of operation most of the beam has disintegrated, and the luminosity is maintained only through the cooling. The loss of particles and constant beam-beam parameter leads to a decline in the luminosity.

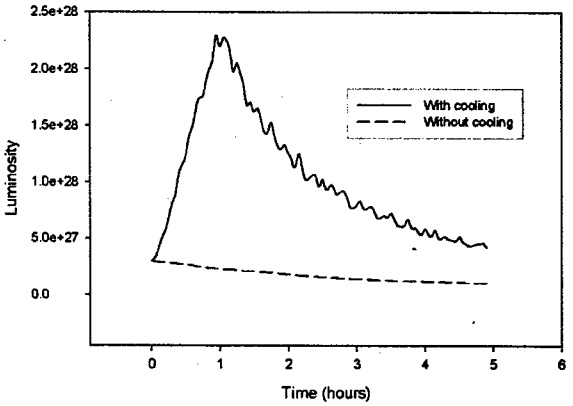

Figure 8. Luminosity of gold collisions in RHIC.

In order to complement Simcool and provide new capabilities in the code, BNL is collaborating with JINR Dubna on the code Betacool [8]. The new capabilities will include arbitrary distribution functions, improved IBS model bunched beams and more.

Analytical electron cooling calculations are not precise for this problem. BNL is collaborating with Tech-X [9] on a new code. Coulomb collisions between electrons and fully-ionized Au ions will be simulated from first principles. The charged particles are advanced using a fourth-order Hermite predictor-corrector algorithm, which has been shown in galactic dynamics simulations to tolerate the orders of magnitude variations in time step that are required to correctly resolve close binary collisions. The goal is to simulate the friction and diffusion coefficients for single ions passing once through the interaction region, as a function of the initial ion position and velocity.

REFERENCES

[1] V.V. Parkhomchuk and I. Ben-Zvi, BNL Collider-Accelerator report C-A/AP/47, 2001.

[2] The code Simcool was written by Vasily Parkhomchuk (BINP) with some modifications by Ilan Ben-Zvi (BNL).

[3] D. H. Dowell et al., Appl. Phys. Lett. **63** (15), 2035 (1993)

[4] D. Wang et al., Proc. PAC'03, Portland, Oregon. USA 2003.

[5] J. Kewisch et al., Proc. PAC'03, Portland, Oregon. USA 2003.

[6] W.W. Zhang, et al., PRST-AB **3**, 122401 (2000)

[7] C. Crawford et al., Proc. PAC99, pp 3321-3.

[8] I.N. Meshkov, et al., Proc. Beam Cooling and Related Topics, Bad Honnef, Germany, 2001

[9] D.L. Bruhwiler, et al., Proc. PAC'03, Portland, Oregon USA 2003.

TOWARDS A NEW LHC INTERACTON REGION DESIGN FOR A LUMINOSITY UPGRADE

J. Strait[+], M. Lamm, P. Limon, N.V. Mokhov, T. Sen, A.V. Zlobin, FNAL*, Batavia, IL, USA
O. Brüning, R. Ostojic, L. Rossi, F. Ruggiero, T. Taylor, H. ten Kate, CERN, Geneva, Switzerland
A. Devred, CEA/Saclay, Gif-sur-Yvette, France and CERN, Geneva, Switzerland
R. Gupta, M. Harrison, S. Peggs, F. Pilat, BNL*, Upton, NY, USA
S. Caspi, S. Gourlay, G. Sabbi, LBNL*, Berkeley, CA, USA

Abstract

After the LHC operates for several years at nominal parameters, it will be necessary to upgrade it for higher luminosity. Replacing the low-β insertions with a higher performance design based on advanced superconducting magnets is one of the most straightforward steps in this direction. Preliminary studies show that, with magnet technology that is expected to be developed by early in the next decade, a factor of 2 to 5 reduction in β^* could be achieved with new insertions, as part of an upgrade aimed at a factor of 10 luminosity increase. In this paper we survey several possible second generation LHC interaction regions designs, which address the expected limitations on LHC performance imposed by the baseline insertions.

INTRODUCTION

Although initial operation of the LHC is several years away, studies have begun for upgrades to extend its performance [1,2]. A luminosity upgrade towards 10^{35} cm^{-2} s^{-1} will be desired by the middle of the next decade after the LHC has operated for several years at its nominal parameters. The baseline LHC already pushes the limits of the state-of-the-art, and an extended R&D program will be needed to ensure that the new technologies required for the upgrade, especially advanced superconducting magnets, are ready. In this paper we discuss several possible new interaction region (IR) designs which address potential limitations in the baseline LHC, and indicate the R&D that must be done to aim towards higher luminosity.

IR LAYOUTS

Three major factors drive the designs of new IRs: minimizing β^*, minimizing the effects of long-range parasitic beam-beam interactions, and the large radiation power due to the *pp* collisions (9 kW/beam at 10^{35} cm^{-2} s^{-1}) directed towards the IRs. The first two point towards maximizing the magnet apertures and minimizing their distances to the IP, and the solutions to the third must be considered in every configuration.

Figures 1-5 show five sample IR layouts that address these issues in different ways and to different extents. The main parameters of these IRs are summarized in Table 1, which shows the distance from the IP to the first quadrupole, the quadrupole coil aperture (D_{quad}), the minimum β^* achievable consistent with physical aperture requirements, β_{max} for β^*_{min}, and the strength (B_{D1}), length (L_{D1}), and coil aperture (D_{D1}) of the first dipole.

Preliminary studies [3] suggest that with increases in J_c of Nb_3Sn that are expected within the next 3-5 years, it may be possible to build quadrupoles with apertures up to 110 mm that operate, with 20% margin, at the same 200 T/m as in the baseline IRs. This gradient with this aperture requires a 4-layer coil with outer radius sufficiently large to preclude its use in a dual-bore geometry with 194 mm spacing. In this study, we take 100 mm as an upper bound on the quadrupole aperture in a dual-bore magnet.

The minimum β^* is set by the maximum possible beam size in the IR quadrupoles at β_{max}. The required physical aperture in the baseline quadrupole triplet is estimated in Eqn. (5) in [1] as 1.1 x (7.5 + 2 x 9)σ_{max} + 2 x 8.6 mm, where σ_{max} is the maximum rms beam size, 7.5σ is the minimum beam separation, 9σ is the required envelope about each beam, the factor 1.1 accounts for 20% β-beating, and 8.6 mm is the sum of mechanical tolerance and orbit errors. For beams passing on axis, the factor of 7.5σ is dropped, and for off-axis orbits in the separation dipoles, the 7.5σ term is replaced by the actual orbit offset. In determining β_{max} and β^*_{min}, the physical aperture is assumed to be 15 mm smaller than the coil diameter.

The field strength of the first dipole is given for the case of zero horizontal crossing angle. Generally the field is lower for non-zero crossing angles, as shown in the figures. The dipole coil diameter is computed according to the formulation above.

The simplest IR upgrade (Fig. 1) replaces the existing inner triplet with quadrupoles of the same strength and length, but larger aperture. A factor of 3 reduction in β^* is possible, if all other parameters are held constant. However, other than using a shorter D1, this change doesn't reduce the number of parasitic collisions. If the beam

Table 1: IR Parameters

	Baseline	Fig. 1	Fig. 2	Fig. 3	Fig. 4	Fig. 5
IP to Q1 (m)	23	23	52.8	42.5	34	23
D_{quad} (mm)	70	110	100	100	100	100
β^*_{min} (cm)	50	16	26	19	15	10
β_{max} (km)	5	15	23	23	23	23
B_{D1} (T)	2.75	15.3	15	14.6	14.5	14.3
L_{D1} (m)	9.45	1.5	10	12	6	9
D_{D1} (mm)	80	110	135	165	75	105

*Work supported by the United States Department of Energy.
[+]strait@fnal.gov

0-7803-7738-9/03/$17.00 © 2003 IEEE

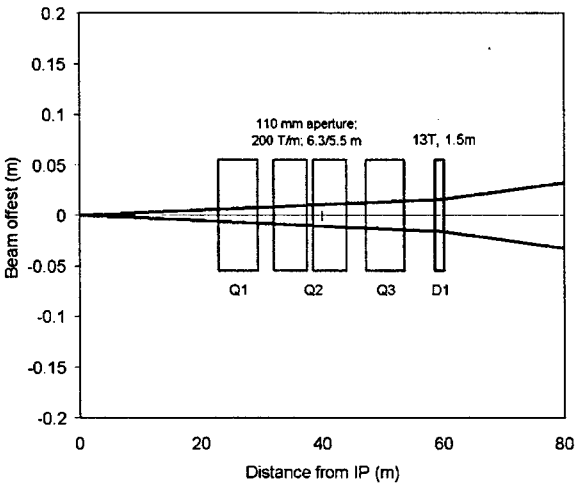

Figure 1: Quadrupole-first IR.

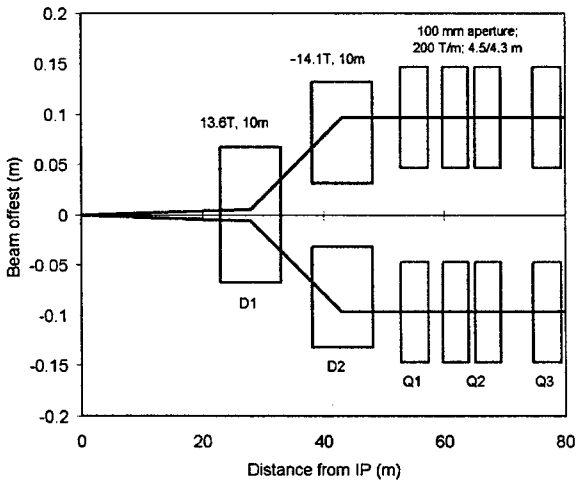

Figure 2: Dipoles-first IR.

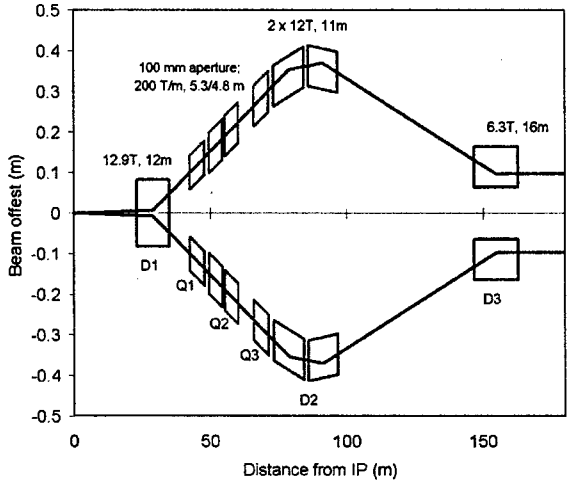

Figure 3: IR with quads between the separation dipoles.

current is increased to increase luminosity, then it is likely that the crossing angle will have to be increased, forcing an increase in β^* to stay within the physical aperture.

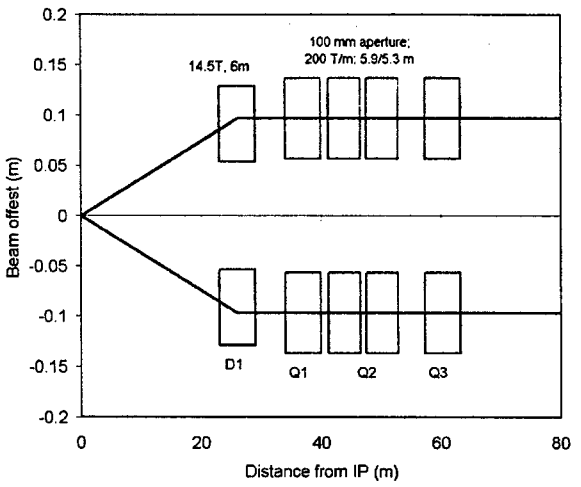

Figure 4: Dipole-first IR with large crossing angle.

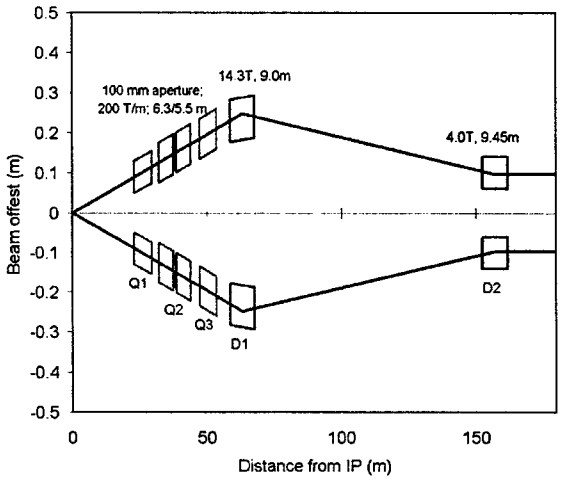

Figure 5: Quadrupole-first IR with large crossing angle.

Placing the separation dipoles between the IP and the quadrupoles (Fig. 2) reduces the number of parasitic collisions by more than a factor of three. Also, correction of quadrupole field errors is more robust, since the beams pass through the quadrupoles on axis and independent correction elements can be used for each beam. However, the quadrupoles are considerably farther from the IP, increasing β_{max} for a given β^*. The D1 also suffers very large energy deposition from collision debris, since the majority of the forward charged particles will be swept into it by the large magnetic field [4]. An added challenge is to maintain good field quality in the D2 with strong coupling between the two close, high-field apertures.

To maintain the benefits of the dipole-first layout, but reduce β_{max}, the quadrupoles could be placed *between* the separation dipoles (Fig. 3), requiring dual-bore quadrupoles with non-parallel axes. The D2 and D3 restore the beams to a 194 mm spacing at the same distance as in the baseline. This layout allows a smaller β^* than in Fig. 2, but the D1 is in the same radiation environment, and the feasibility of the non-parallel axis magnets and of dispersion suppression in this geometry have not been studied.

The IRs in Figs. 1-3 assume that the crossing angle θ_c is as small as possible, consistent with maintaining >9σ beam separation at all parasitic collisions. This is the solution if beam intensity is limited by factors other than the beam-beam effect. If the intensity can be increased to the beam-beam limit, then the luminosity is increased by increasing θ_c and lengthening the bunches (including the "superbunch" option) [1,5]. This allows us to consider two large crossing angle layouts, shown in Figs. 4 and 5.

The first has a twin-aperture dipole first, then conventional dual-bore quadrupoles. The beam separation and the distance to the IP set $\theta_c = \pm 3.7$ mrad. The β_{min} is as small as in Fig. 1. But this layout is practical only if the beam current can be increased sufficiently (or crab cavities are used to rotate the bunches). The aperture through which the outgoing beam passes is subject to similar radiation heating as the D1 in Figs. 2 and 3. In fact, the situation is more challenging since the forward going neutral particles may impinge on the magnet, if the aperture is not sufficient to allow them to pass through the magnet.

The layout in Fig. 5 aims non-parallel axis twin-aperture quadrupoles directly at the IP. With the same optics as in Fig. 1 but in a dual-bore geometry, β^* as small as 10 cm may be possible. As with Fig. 4, this is practical only if the beam current can be increased enough. As with Fig. 3, the non-parallel axis configuration must be studied for feasibility. And the first dipole is subject to similar radiation heating as the D1 in Fig 4.

DISCUSSION

The IR layouts presented here for a possible LHC luminosity upgrade are very preliminary, and much work remains to show that the estimated reductions in β^*, which are based on simple scaling rules for aperture and beam-beam separation requirements, can be achieved when all constraints and realistic conditions are included.

Other accelerator systems must be upgraded if the reduction in β^* is to translate into a corresponding increase in luminosity. If bunch intensity is limited below the beam-beam limit, then the bunches must be shortened to limit the luminosity loss due the crossing angle form factor. The required RF voltage grows as β^* decreases, and it may or may not be feasible to take full advantage of $\beta^* <$ 25 cm. Alternatively, crab cavities could rotate the bunches so they collide head-on in a transversely moving coordinate system. However, any imperfections in bunch manipulation will result in a transverse emittance blow-up. To allow the bunch intensity to be increased to the beam-beam limit at larger crossing angles, many factors, some of which will be known only with operating experience, must be addressed. For example, the collimation or beam dump systems may need to be upgraded, or unexpected beam instabilities may need to be dealt with. A substantial new RF system would be required if the superbunch option were to be implemented.

The choice of IR layout for the luminosity upgrade will depend on developing an understanding of the LHC beams and which factors limit the luminosity. For example, the extent to which the parasitic collisions limit the performance will only be fully understood after experience with LHC beams. Successful development of proposed systems for compensating the beam-beam effect could affect the choice of IR layout. Finally, the upgrade scheme may be affected by the capabilities of the experiments, for example with regard to bunch structure.

Many questions specific to the IR magnet system must be addressed by vigorous R&D. A few examples are:

- What is the maximum D_{quad} for G>200 T/m?
- What is the maximum D_{quad} in a dual-bore quadrupole with 194 mm spacing?
- Can dipoles be made to operate as high as 15 T in the extreme radiation environment at very high luminosity?
- How can the many kW of beam power be removed from the cryogenic magnets for a tolerable cost?
- Are non-parallel axis dual-bore quadrupoles feasible?
- What dispersion suppression scheme works in this case?
- Can good field quality be maintained over the full operating range in very high field, dual-bore dipoles with parallel field directions?
- Can triplet errors be adequately corrected given the very large β-functions?

Some of these questions can be answered by design studies, but most will require extended hardware R&D.

CONCLUSIONS

A new IR design will be a key element in an LHC upgrade aimed at raising the luminosity by up to an order of magnitude. Several possible IR layouts exist which offer the possibility of reducing β^* by up to a factor of five below the baseline value, and of reducing the number of long-range beam-beam collisions. Extensive R&D must be done on superconducting magnets and other accelerator systems to determine if these ideas are feasible and to develop the technology to allow their implementation on the time scale required by the LHC physics program. Because the systems for the upgraded LHC must go well beyond the current state of the art, this R&D must start. Ultimately the performance of the baseline LHC, together with the results of this R&D, will determine which of these IR designs will best serve to raise the luminosity.

REFERENCES

[1] O. Brüning, et al., LHC Luminosity and Energy Upgrade: A Feasibility Study, LHC Project Report 626, December 2002.

[2] T. Taylor, Superconducting Magnets for a Super LHC, EPAC 2002, Paris, France, p.129.

[3] A.V. Zlobin, et al., Aperture Limitations for 2nd Generation Nb_3Sn LHC IR Quadrupoles, PAC 2003, Portland, OR.

[4] N.V. Mokhov, et al., Energy Deposition Limits in a Nb_3Sn Separation Dipole in Front of the LHC High-Luminosity Inner Triplet, PAC 2003, Portland, OR.

[5] F. Zimmermann, et al., Beam-Beam Interaction, Electron Cloud, and Intrabeam Scattering for Proton Super-Bunches, presented at PAC2003, Portland, OR.

DESIGNING AND BUILDING A COLLIMATION SYSTEM FOR THE HIGH-INTENSITY LHC BEAM

R. Aßmann, O. Aberle, M. Brugger, L. Bruno, H. Burkhardt, E. Chiaveri, B. Dehning, A. Ferrari, B. Goddard, J.B. Jeanneret, M. Jimenez, V. Kain, M. Lamont, F. Ruggiero, R. Schmidt, P. Sievers, J. Uythoven, V. Vlachoudis, L. Vos, J. Wenninger, CERN, Geneva, Switzerland,
I. Baishev, IHEP, Protvino, Russia, D. Kaltchev, TRIUMF, Canada

Abstract

The Large Hadron Collider (LHC) will collide proton beams at 14 TeV c.m. with unprecedented stored intensities. The transverse energy density in the beam will be about three orders of magnitude larger than previously handled in the Tevatron or in HERA, if compared at the locations of the betatron collimators. In particular, the population in the beam halo is much above the quench level of the superconducting magnets. Two LHC insertions are dedicated to collimation with the design goals of preventing magnet quenches in regular operation and preventing damage to accelerator components in case of irregular beam loss. We discuss the challenges for designing and building a collimation system that withstands the high power LHC beam and provides the required high cleaning efficiency. Plans for future work are outlined.

INTRODUCTION

Each of the two LHC [1] rings will store 2808 bunches, each bunch populated with $1.1 \cdot 10^{11}$ protons at energies of up to 7 TeV (nominal design parameters). The stored energy amounts to 350 MJ, two orders of magnitude beyond the achievements in the Tevatron or HERA. Comparing transverse energy densities, LHC advances the state of the art by even three orders of magnitude, from 1 MJ/mm^2 to 1 GJ/mm^2. At the same time the superconducting magnets in the LHC would quench if small amounts of energy (on the level of 30 mJ/cm^{-3}, induced by a local transient loss of 4×10^7 protons) are deposited into the superconducting magnet coils [2].

Any significant beam loss into the cold aperture must be avoided. However, beam losses cannot be completely avoided. A so-called "primary beam halo" will continuously be filled by various beam dynamics processes and the beam current lifetime will be finite [3]. The handling of the high intensity LHC beams and the associated high loss rates of protons requires a powerful collimation system with the following functionality:

1. Efficient cleaning of the beam halo.
2. Tuning of the halo-induced experimental backgrounds.
3. Passive protection of the machine aperture.

In addition the integrity of the system must be maintained during regular and irregular operational conditions. The challenges for designing and building an appropriate system are discussed.

DESIGN CONSTRAINTS

The collimation system must fulfil a number of important design constraints, which are listed below for proton operation. Similar constraints must be fulfilled for operation with ions.

Beam loss rates Regular LHC operation is assumed to include short periods of reduced beam lifetime. At 7 TeV the collimation system should accept losses of $4.1 \cdot 10^{11}$ p/s (0.2 h lifetime) for 10 s or $0.8 \cdot 10^{11}$ p/s (1 h lifetime) continuously.

Cleaning efficiency Assuming the above beam loss rates, the expected quench levels and nominal intensity, the required local cleaning inefficiency is calculated to be $2 \cdot 10^{-5}$ m^{-1} [4]. The local inefficiency is defined as the inefficiency (number of halo protons reaching $\geq 10\sigma$ per impacting primary proton) divided by the length over which losses are spread (e.g. 50 m).

Number of collimators and phase advance requirements The above mentioned goal for cleaning inefficiency can only be achieved with a cleaning system that has at least two stages with collimators put at special phase advance locations [5, 6]. Momentum and betatron cleaning must be performed separately. Cleaning systems based on aluminium and copper jaws have been integrated into the LHC layout and optics. The jaw materials and lengths are being reviewed and the IR3 and IR7 insertions must be adapted to the final design choices. In the old design 7 collimators per beam (1 primary and 6 secondaries) provide momentum cleaning in IR3 and 20 collimators per beam (4 primaries and 16 secondaries) provide betatron cleaning in IR7. The goal inefficiency is achieved. Some additional absorbers are required to capture the proton induced showers in the cleaning insertions. An eventual opening of collimator gaps would require additional collimators at the experimental insertions.

Beta functions in cleaning insertions Ideally, beta functions should be large at the collimators in order to alleviate the consequences if some bunches impact on the jaw. However, the available space in the warm cleaning insertions limits the beta functions to values of 50 m to 350 m (IR7) [6]. Corresponding transverse beam sizes are small, from 160 μm to 420 μm at 7 TeV.

0-7803-7738-9/03/$17.00 © 2003 IEEE

Collimator gaps The available LHC physical aperture is about 10 σ both at injection (limited in arcs) and at 7 TeV (limited at triplets). The primary and secondary collimators must then be closed to nominally 6 σ and 7 σ, respectively, for providing the required cleaning inefficiency at 10 σ. The corresponding collimator full gaps at 7 TeV are small (2.2 - 4.4 mm). It is noted that there is some flexibility in the collimator settings [7].

Operational and mechanical tolerances The relevant tolerances derive directly from the difference in settings between primary and secondary collimators ($1\sigma \approx 200\mu$m), as well as from the impact parameter at the secondary collimators (average impact parameter is 200 μm). Tolerances are a fraction of these values. For example, the tolerances for transient orbit movements and transient beta beat were determined to be 0.6 σ and 8%, respectively. Tolerances were estimated for jaw surface flatness ($\sim 25\mu$m), reproducibility of jaw settings (20μm), step size in jaw movements ($\sim 10\mu$m, $\sim 15\mu$rad) and knowledge in collimator gap 50μm. Some trade-off between different tolerances is possible.

Impedance The collimators can produce significant transverse resistive impedance due to the small gaps at 7 TeV (impedance scales inversely proportional to the third power of gap size). At nominal beam intensity, the LHC octupoles provide Landau damping of the rigid dipole modes for a total collimator impedance of up to 110 MΩ/m, to be compared with an impedance of 100 MΩ/m generated by the rest of the ring.

Shock beam impact In case of irregular beam dumps several bunches can be deflected on a collimator jaw. Any jaw can be hit, because the primary collimators only cover one phase space location and the overall LHC tune should be allowed to vary. The collimator hardware should withstand beam impact during irregular dumps. The expected maximum beam impact was calculated to be about 20 bunches [8]. Recently this value was reduced to about 8 bunches, due to a substantial improvement in the dump re-trigger time. The presently ongoing material studies still use as input the now pessimistic, old scenario.

Reliability and maintenance The lost protons will activate the installations in the cleaning insertions leading to maximal dose rates of up to several mSv/h at direct accessible hot-spots, e.g. shielding or downstream magnets. The collimator jaws may reach higher values. The expected dose rates depend strongly on the collimation layout, the materials chosen, the cooling time as well as the exact location in the insertion. However, human interventions such as maintenance nearby highly activated installations must be restricted to the absolute minimum, hence collimators and belonging equipment must be designed for maximum reliability. Detailed studies are ongoing.

Vacuum aspects The collimators must be bakeable and outgassing rates must remain acceptable. For example, for a graphite collimator this imposes special heat treatment, careful outbaking, and a maximum jaw temperature of 50°C, to be assured by collimator cooling. Graphite dust is believed to be uncritical. The magnitude of a local electron cloud and its possible effects are being studied and outgassing measurements are being performed.

The design of the collimation hardware should address these constraints in a consistent way, even though some constraints support conflicting preferences.

MATERIAL STUDIES

The previously foreseen collimation system for the LHC relies on aluminium and copper jaws, as used in LEP. These choices do not allow collimator survival e.g. during irregular dumps. If about 10^{-5} of the stored 7 TeV beam intensity is lost in a single turn on one copper collimator damage can occur. The losses during irregular dumps are more than two orders of magnitude above this damage threshold.

Energy Deposition in Various Materials

The expected beam impact distribution for irregular dumps [8] was used to calculate the energy deposition versus jaw length in various materials (see also [9]). FLUKA [10] was used to perform a full shower study. The predicted peak temperature rise is shown in Fig.1. It is seen how the shower develops along the length of the jaw. The length of secondary jaws, as required for achieving the desired cleaning efficiency, varies between 0.5 m for copper and 1.0 m for graphite or beryllium. The temperature rise for these lengths is large, ruling out high Z materials for the bulk of the collimator jaws as well as for thin coatings on jaws made of low Z material. Shorter primary jaws (a few cm to 20 cm) are less critical. As possible candidate materials graphite and beryllium are retained.

Other FLUKA studies have been performed (required thickness of graphite layer, injection impacts) and some others are under preparation (fiber-reinforced graphite, copper doped graphite, ions, slow losses in 200 nm surface layer, energy deposition downstream of jaw, input for electron cloud estimate).

Fatigue and Stress Analysis

The FLUKA results are used in the ANSYS program to predict stresses. The static stresses were calculated for fine-grain graphite and beryllium (for the 7 TeV irregular dump). It was found that static stresses for graphite are about a factor of 2 and for beryllium about a factor of 5 beyond the engineering tolerance. Dynamic stresses usually further increase the stress values by a factor of 2. Detailed dynamical calculations are being done. In addition, ANSYS calculations are planned for fiber-reinforced graphite, copper doped graphite, ions and injection cases.

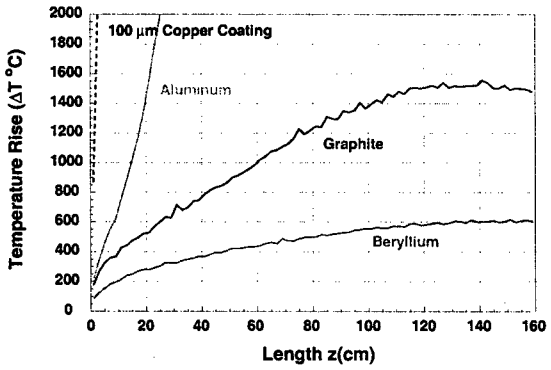

Figure 1: Temperature increase (peak) from 20°C versus collimator length for different materials. Input is the proton impact distribution from an irregular dump at 7 TeV (single-module pre-trigger with a 1.3 μs re-trigger time). Approximately 20 bunches impact on the jaw face.

The ANSYS results allow selecting the material with the best mechanical properties for LHC collimation. It is too early for any final conclusions, however, graphite looks most promising. Taking into account the recent factor 2.5 reduction in beam impact (improved dump re-trigger time) and 2 times higher stresses in a dynamic calculation, it is seen that fine-grain graphite is less than a factor of two away from the design target. The graphite jaws would survive most irregular dumps at nominal intensity and would have appropriate robustness for running during the first years of the LHC where the total intensity will be limited to 50% of the nominal. It is hoped that fiber-reinforced graphite will show even better mechanical resistance.

Impedance

The transverse resistive impedance was evaluated for the collimators, assuming nominal gaps at 7 TeV, nominal intensity, and different materials. Large impedance was found, ranging from 100 MΩ/m for copper jaws to 1050 MΩ/m for graphite jaws. While the copper-based solution is acceptable for impedance and unacceptable for robustness, the graphite-based solution is almost acceptable for robustness but unacceptable for impedance. A full beryllium-based system has insufficient robustness. A solution with graphite jaws in the horizontal plane (the dump sweep is horizontal) and beryllium jaws elsewhere would allow to reduce the impedance to about 300 MΩ/m. This is still unacceptably large and in addition the use of beryllium would introduce additional safety concerns. The conflicting requirements prevent a straight-forward solution.

More elaborate solutions are being investigated. For example, a graphite-based collimation system might have acceptable impedance with a collimation strategy, where secondary collimators are opened to $\sim 10\ \sigma$. Possibilities to achieve this without constraining the LHC performance are under study. It is also investigated whether copper doped graphite has a lower impedance and good robustness.

SUMMARY AND OUTLOOK

The design challenges for the LHC collimation system have been reviewed, giving a list of specific constraints. Possible jaw materials are being studied with the goal of building collimators that can survive the expected conditions during LHC operation, including irregular dump actions. This would avoid the use of more elaborate and possibly more expensive concepts like "consumable" or "renewable" collimators. At present no appropriate jaw material could be identified. Graphite is very promising in terms of robustness but generates unacceptably high transverse resistive impedance. The use of a graphite-based collimation system would require a different collimation strategy that uses larger gaps. This is being studied but would require additional collimators close to the experimental interaction points. In addition hybrid solutions (graphite/copper, graphite/beryllium) and more advanced materials (copper doped graphite) are being investigated. Concepts of "consumable" or "repairable" jaws are considered with still lower priority.

The mechanical design of the collimator tanks, the jaws themselves, the cooling, etc is being addressed in parallel to the material studies. Once a material has been selected and the mechanical layout has been chosen, a prototype will be built for April 2004. After successful prototype testing the production of about 66 collimators and additional spares will be started. The collimators would be installed in 2006 and be ready in time for LHC commissioning in 2007.

Collimation for the LHC is a difficult task offering many interesting challenges. The commissioning, operation, and understanding of the system will be an opportunity to learn about handling of high-intensity proton beams in a completely new regime.

REFERENCES

[1] The Large Hadron Collider, CERN/AC/95-05(LHC), 1995.

[2] J.B. Jeanneret, D. Leroy, L. Oberli, T. Trenkler. LHC Project Report 44 (1996).

[3] R. Assmann, F. Schmidt, F. Zimmermann, M.P. Zorzano. LHC-PROJECT-REPORT-592. EPAC02.

[4] R. Assmann et al. LHC-PROJECT-REPORT-599. EPAC02.

[5] J.B. Jeanneret, Phys. Rev. ST Accel. and Beams, **1**, 081001, December 1998.

[6] D. Kaltchev et al., PAC99, CERN LHC Project Report 305, 1999.

[7] R. Assmann. Proc. Chamonix 2003. CERN-AB-2003-008 ADM.

[8] R. Assmann, B. Goddard, E. Vossenberg, E. Weisse. LHC-PROJECT-NOTE-293 (2002).

[9] P. Sievers et al. Proc. Chamonix 2003. CERN-AB-2003-008 ADM.

[10] A. Fasso, A. Ferrari, J. Ranft, P.R. Sala. Proc. of the Int. Conf. Monte-Carlo 2000, Lisbon, Portugal, Oct. 23-26, 2000, p. 955, Springer-Verlag Berlin Heidelberg (2001).

EFFECTS OF RF NOISE ON LONGITUDINAL EMITTANCE GROWTH IN THE TEVATRON*

J. Steimel, V. Lebedev, I. Gonin, T. Khabibouline, J. Reid, G. Romanov, V. Shiltsev, A. Tollestrup,
FNAL, Batavia, IL 60510, USA

Abstract

Phase and amplitude noises in the Tevatron RF system and the intrabeam scattering (IBS) produce longitudinal emittance growth with consecutive particle loss from the RF buckets. That causes a decrease of the luminosity and an increase of the background in particle detectors during the store. The report presents experimental measurements of RF system noise and the effect on the longitudinal emittance growth. There is a satisfactory agreement between measured noise spectral densities and observed emittance growth. For high bunch intensities, IBS plays an important role and has been taken into account. The sources of noises and plans for further system improvements are discussed.

INTRODUCTION

One of the major upgrades to the Fermilab Tevatron between Run I and Run II was the increase in the number of colliding bunches by a factor of 6. The total proton intensity was also increased by about the same factor (currently 4.7). In the course of the early commissioning process, the Tevatron would quench every time that 980 GeV beam was aborted with high intensity. Abort kicker timing was inspected and optimized, but the quenches continued.

The quenches are due to beam that has wandered into the abort gap. Measurements show that a line density of somewhere between 3e9 and 9e9 protons distributed around the ring is enough to quench the superconducting magnets on abort. This beam is difficult to measure directly, because its low intensity is below the resolution of the Tevatron DC beam monitors. Only indirect measurements verified the presence of beam in the abort gap until recently. The Tevatron electron lens (TEL) was reconfigured to act as fast pulse kicker in the beam abort gap [1]. The pulse rate was configured to resonate with the betatron tune of the beam to kick beam out of the abort gap. When the lens is activated during a store, there is a sharp loss measured by the DC beam detectors but no effect on luminosity. By turning the lens on and off for different time periods, one could verify DC beam in the abort gap and measure its rate of accumulation.

With confirmation from the electron lens that DC beam was accumulating in the abort gap, we attempted to locate the mechanism for the accumulation. Beam is obviously leaking from the RF bucket, but the mechanism was not obvious. The analysis of the problem has focused on two different mechanisms: intrabeam scattering [2] and noise in the accelerating cavities. The rest of this paper focuses on the experiments and analysis of noise sources in the accelerating system.

* Work supported by the Universities Research Assoc., Inc., under contract DE-AC02-76CH03000 with the U.S. Dept. of Energy.

RF NOISE SOURCES

A catalogue of possible sources of noise in the RF system was created in order to trace down possible DC beam generators. Each potential source was measured for noise amplitude, and its possible effect on the beam was analyzed.

Longitudinal Dynamics of RF Noise

In order for beam to spill out of the bucket because of RF noise, there must be beam close to the edge of the bucket separatrix. Beam at high energy in the Tevatron does not fill the bucket initially after the ramp, but the longitudinal emittance increases until the bucket is full. DC beam generation begins when the bucket is full. We assume that the same process that generates DC beam also causes the longitudinal emittance growth. Since we could not measure DC beam directly initially, we measured longitudinal emittance growth to determine the effect that

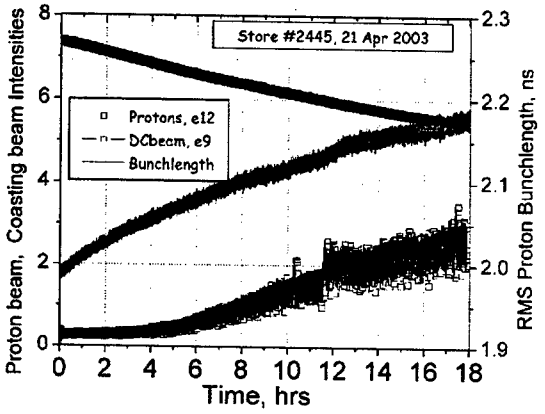

Figure 1: Longitudinal emittance growth and DC beam accumulation vs. time in Tevatron store at 980 GeV.

noise has on beam. The formula for bunch length (σ_ϕ in rms radians) growth in the presence of RF phase noise spectral density ($P_{\phi RF}$ in rms rad^2/Hz) is given in equation (1) where f_s is the synchrotron frequency in Hz [2].

$$\frac{d(\sigma_\phi^2)}{dt} = 2\pi f_s^2 P_{\phi RF}(f_s) \qquad (1)$$

RF Reference Measurements

The first test was to insure that there was not a considerable amount of noise contaminating the reference signal. Measurement of the reference signal using a spectrum analyzer revealed that even the 60Hz spurs were 90dB below the carrier and the noise floor was more than 100dB below the carrier.

RF Cavity Measurements

With the knowledge that the damaging source of RF noise was downstream of the reference, the eight individual cavities were inspected closely. The phase modulation spectrum of each cavity was measured using a phase detector between each accelerating voltage gap monitor and the reference. All of the cavities exhibited a peak in the modulation amplitude from 32-38 Hz, even without beam in the Tevatron. This frequency corresponds to the synchrotron frequency of the Tevatron at 980 GeV.

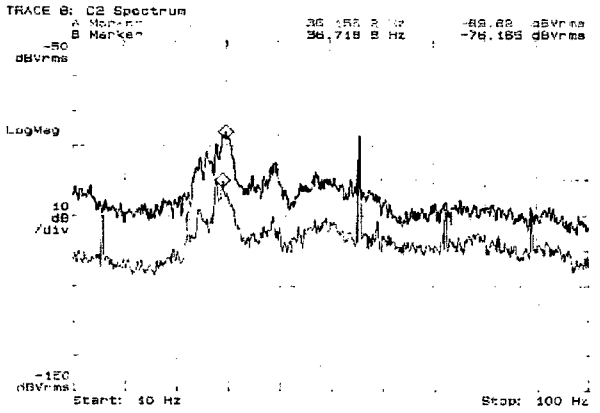

Figure 2: Spectrum of the output of the RF reference to global station fanback phase detector. Top trace is with local station feedback disabled on 3 cavities and bottom trace is with feedback enabled.

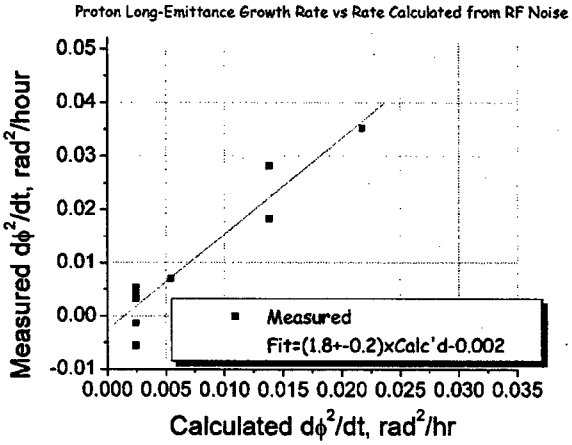

Figure 3: Plot comparing the measured longitudinal emittance growth rate to the emittance growth rate calculated based on the total spectral density of phase noise measured at the synchrotron frequency.

A phase feedback system at each station maintains proper phasing between the gap monitor and reference drive for low frequencies. The gain of this feedback loop was varied for different combinations of cavities. The emmitance growth rate was measured for each gain setting and compared to the noise power measured at the cavities. The intercept of the plot at zero measured cavity noise is very close to the origin. This reveals that the cavity noise is the dominant mechanism for longitudinal emittance growth in the Tevatron at high field.

MECHANICAL MOTION

With data showing that the source of RF noise was somewhere in the cavity system, the next step involved trying to find the specific source. Because the frequency of the modulation is so low and did not correspond to any harmonics of the power cycle, there were suspicions that the cause of the modulation was due to cavity vibrations.

Mechanical Simulations

The central electrode in Tevatron accelerating cavity actually is a pretty long tube beam with rigid supports and links in the middle of it. Such a cantilever beam usually can be a good oscillator (like a piece of tuning fork). A solid model of the central electrode design has been built and a simulation of mechanical vibrations has been performed. The simulated frequencies of mechanical vibrations in a case of copper central electrode are in a close agreement with the measured RF and acoustic noise frequencies. For us it has been a first indication that the central electrode mechanical vibrations may be a cause of RFnoise.

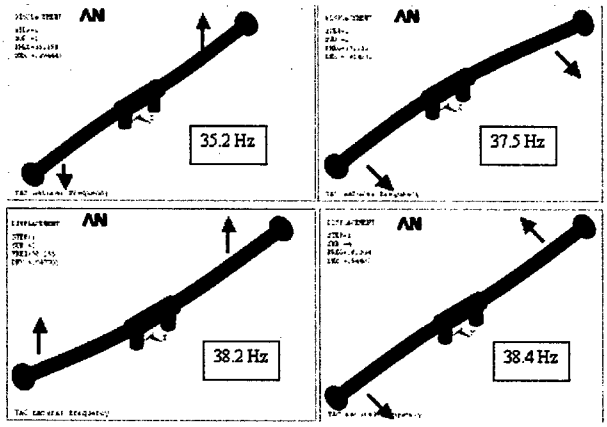

Figure 4: The modes of the central electrode mechanical vibrations.

Effects of Vibrations on RF Noise

A cavity with bent central electrode has been simulated to estimate amplitude of the central electrode vibrations and vibration's influence on RF parameters. Only a half of cavity without transmission line was simulated to increase accuracy of calculations. The curvature of central electrode axis is a regular arc. It seems to be a good enough approximation of small real sinusoidal deformations of electrode during vibrations. Only

horizontal deformations have been considered because pick-up electrodes are in horizontal plane and sensitive to these deformations.

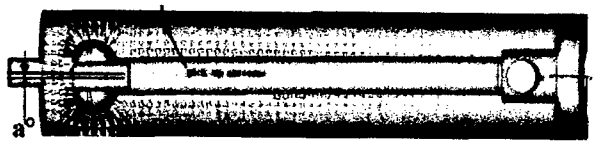

Figure 5: A cavity with bent central electrode.

From the RF noise point of view two cavity parameters are important: 1) modulation of resonant frequency of cavity that produces amplitude and phase modulation of accelerating field, and 2) electric field level modulation in pick-up electrode area. The latter has nothing to do directly with particle acceleration, but it is very important as the only signal for the feedback systems. Equation (2) shows the empirical relationship between resonant frequency shift and electrode bend angle.

$$\Delta f = a\theta^2 \qquad (2)$$

Modulation of cavity resonant frequency produces modulation of phase and amplitude of electromagnetic field oscillations. The sensitivity of resonant frequency to the central electrode bend is low around zero bend point and resonant frequency modulation does not seem to be a problem in a case of perfect axial symmetrical cavity. But the central electrodes can have "natural" bends in any plane that could occur during manufacturing and installation. An estimation for phase shift enhanced by initial permanent central electrode bend is given in (3), where Θ is an initial bend angle, θ is a small bend deviation the initial bend angle. Q is the cavity quality factor, and "a" is the empirically determined factor from equation (2). For the Tevatron cavities this value was calculated to be 79 kHz/degree^2.

$$\varphi \approx \frac{2Q(2a\Theta\theta + a\theta^2)}{f} \qquad (3)$$

Amplitude modulation due to the field level variation at pick-up electrode area seems to be predominant at normal operating conditions. Amplitude modulation is transformed into phase modulation in a phase feedback loop, because even an ideal linear phase-lock loop system can generate phase noise responding to amplitude modulation of input signals.

Measurements of Vibrations

Four geophones were installed at opposite ends of a Tevatron test cavity, two in the horizontal plane and two in the vertical plane. The spectrum measured from the sensors on the test cavity, with water pumps and heaters on, match the noise spectrum measured on the operating cavities. The experiment was repeated with water pumps and water heaters disabled, and the 37Hz modulation was significantly reduced. Measurements of vibrations on the operating cavities revealed the same relationship between the modulation and the water pumps. Thus, the water pumps act as the drive for the cavity mechanical resonance.

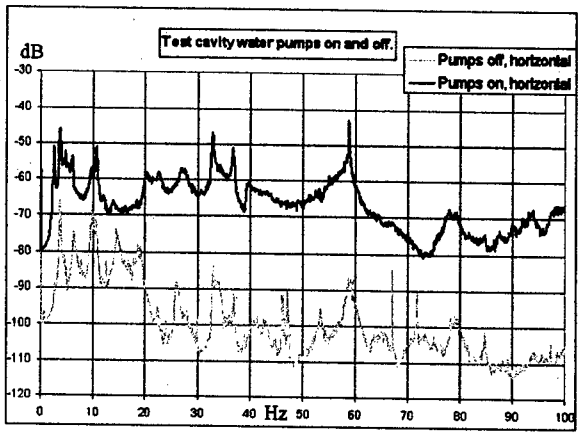

Figure 6: Comparison of mechanical vibration spectra with and without water pumps.

CONCLUSIONS

There is very strong evidence that the mechanical vibrations of the Tevatron RF cavities cause longitudinal emittance growth and accumulate DC beam. We plan to try methods to decrease vibrations during the collider operation:

- Remove sources of mechanical vibrations. For example, insulate water heaters from cavities mechanically.
- Use two pickup antennae from the cavity and combine these signals to reduce amplitude modulation due to cavity warping.
- Implement direct RF feedback around each individual station.

REFERENCES

[1] X. Zhang, et al, "The Special Applications of Tevatron Electron Lens in Collider Operation," PAC '03, these proceedings.

[2] V. Lebedev, "Beam Physics at Tevatron," PAC'03, these proceedings

POLARIZED PROTON ACCELERATION AT THE BROOKHAVEN AGS AND RHIC*

H.Huang[1], L. Ahrens [1], J.G. Alessi [1], I. Alekseev [2], M. Bai [1], J. Beebe-Wang[1], S. Brarvar[1], M. Brennan[1], K.A. Brown[1], G. Bunce[3], A. Drees[1], W. Fisher[1], C. Gardner[1],W. Glenn[1], G. Igo[4], O. Jinnochi[3], A.U. Luccio[1], W. MacKay[1], C. Montag[1], F. Pilat[1], V. Ptytsin[1], T. Roser[1], T. Satogata[1], H. Spinka[5], D. Svirida[2], S. Tepikian[1], D. Trbojevic[1], N. Tsoupas[1], D. Underwood[5], J. van Zeijts[1], J. Wood[4], A. Zelenski[1], K. Zeno[1], S.Y. Zhang[1]
(1) Brookhaven National Laboratory, Upton, NY 11973, USA
(2) ITEP, 117259, Moscow, Russia
(3) RIKEN BNL Research Center, Upton, NY 11973, USA
(4) Physics Department, UCLA, Los Angeles, CA 90095, USA
(5) Argonne National Laboratory, 9700 Cass Ave., Argonne, IL 60493, USA

Abstract

Polarized proton beam has been accelerated and stored at 100GeV in Relativistic Heavy Ion Collider (RHIC) to study spin effects in the hadronic reactions. The essential equipment includes four Siberian snakes and eight spin rotators in two RHIC rings, a partial snake in the AGS, fast relative polarimeters, and ac dipoles in the AGS and RHIC. This paper summarizes the performance of RHIC as a polarized proton collider and of AGS as the injector to RHIC.

INTRODUCTION

In a perfect planar synchrotron with vertically oriented guiding magnetic field, the spin vector of a proton beam precesses around the vertical axis $G\gamma$ times per orbital revolution, where $G = (g-2)/2 = 1.7928$ is the gyromagnetic anomaly of the proton, and γ is the Lorentz factor. The number of precessions per revolution is called the spin tune ν_{sp} and is equal to $G\gamma$ in this case.

In general, a spin resonance is located at

$$\nu_{sp} = G\gamma = k \pm l\nu_y \pm m\nu_x \pm n\nu_{syn}, \qquad (1)$$

where k, l, m and n are integers, ν_x and ν_y are horizontal and vertical betatron tunes, and ν_{syn} is the tune of the synchrotron oscillation. There are three main types of depolarizing resonances: imperfection resonances at $\nu_{sp} = k$, intrinsic resonances at $\nu_{sp} = l \pm \nu_y$ and coupling resonances at $\nu_{sp} = n \pm \nu_x$.

When a polarized beam is uniformly accelerated through an isolated spin resonance, the final polarization P_f is related to the initial polarization P_i by the Froissart-Stora formula[2]

$$P_f = (2e^{-\pi|\epsilon_k|^2/2\alpha} - 1)P_i, \qquad (2)$$

where α is the rate of change of spin tune per radian of the orbit angle due to acceleration: $\alpha = \frac{d(G\gamma)}{d\theta}$, and θ is the orbital angle in the synchrotron. In the AGS, a few weak intrinsic resonances were not corrected with any scheme. The final polarization were affected by the value of α.

* Work performed under Contract Number DE-AC02-98CH10886 with the auspicies of the US Deparment of Energy.

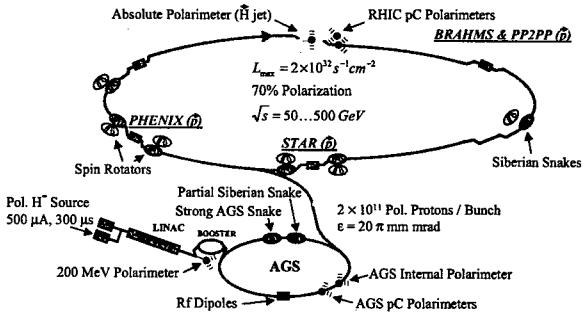

Figure 1: The Brookhaven polarized proton facility complex, which includes the OPPIS source, 200 MeV LINAC, the AGS Booster, the AGS, and RHIC.

For a ring with a partial snake with strength s, the spin tune ν_{sp} is given by

$$\cos\pi\nu_{sp} = \cos\frac{s\pi}{2}\cos G\gamma\pi, \qquad (3)$$

where $s = 1$ would correspond to a full snake which rotates the spin by 180°. When s=1, the spin tune is always 1/2 and energy independent. Thus, all imperfection, intrinsic and coupling resonance conditions can be avoided. However, when the spin resonance strength is large, a new class of spin-depolarizing resonance can occur. These resonances, due to coherent higher-order spin-perturbing kicks, are called snake resonances [3] and located at

$\Delta\nu_y = \frac{k\pm\nu_{sp}}{n}$, where $\Delta\nu_y$ is the fractional part of vertical betatron tune, n and k are integers, and n is called the Snake resonance order.

POLARIZED PROTONS IN THE AGS

The Brookhaven polarized proton facility complex is shown schematically in Fig.1. The polarized H^- beam from the optically pumped polarized ion source (OPPIS) was accelerated through the 200 MeV LINAC. The OPPIS source produced 10^{12} polarized protons per pulse with

0-7803-7738-9/03/$17.00 © 2003 IEEE

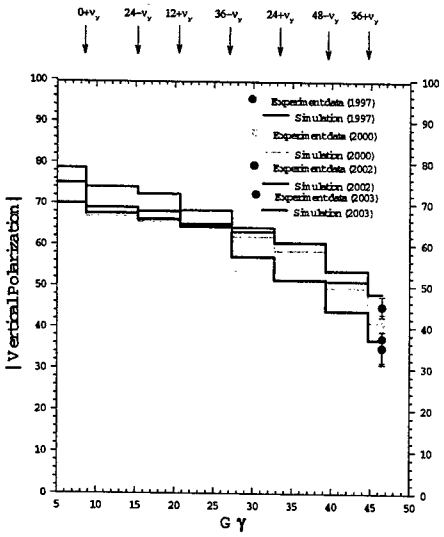

Figure 2: Measured AGS polarization vs. simulation for various years.

70-75% polarization. The beam was then strip-injected and accelerated in the AGS Booster up to 2.5 GeV or $G\gamma = 4.7$.

At the AGS, a 5% partial Siberian snake that rotates the spin by 9° is sufficient to avoid depolarization from imperfection resonances up to the required RHIC transfer energy [4]. Full spin flip at the four strong intrinsic resonances can be achieved with a strong artificial rf spin resonance excited coherently for the whole beam by firing an ac dipole [5]. The remaining polarization loss in the AGS is caused by coupling resonances and weak resonances. The polarized proton beam was accelerated up to $G\gamma = 46.5$ or 24.3 GeV. Since the intrinsic and coupling resonance strength is dependent on transverse emittance, it is very important to maintain emittance as small as possible. The beam was scraped in three dimension in the Booster: both transverse dimensions and longitudinal dimension. The longitudinal scraping is to meet the RHIC requirement of 0.5 eV-s longitudinal emittance. The beam intensity varied between 0.5 -0.7$\times 10^{11}$ protons per fill. The polarization level at the AGS extraction energy was about 40-45%. A future, much stronger partial snake should eliminate depolarization in the AGS [6].

A new polarimeter based on proton carbon elastic scattering in the Coulomb Nuclear Interference (CNI) region has been installed in AGS to measure polarization fast and reliably. The polarimeter consists of ultra-thin carbon targets(5 μg/cm^2 and 600 μm wide) and two silicon detectors. Fig. 3 shows the layout of the AGS CNI polarimeter. The electronics has to be designed and installed carefully to live with the noisy environment of AGS ring. One advantage of this new polarimeter is to measure polarization during acceleration. Fig. 4 shows such a ramp measurement compared with expected polarization. The analyzing power for CNI process is expected to be largely independent of energy for energy above a few GeV. These data show that other process might have mixed in and analyzing power is not a constant in this energy region.

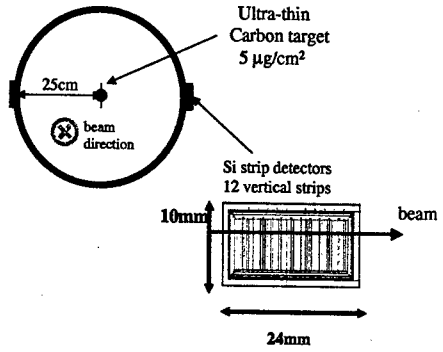

Figure 3: The layout of the AGS CNI polarimeter. The two Si strip detectors measure left-right asymmetry of recoil carbons at 90 degree recoil angle.

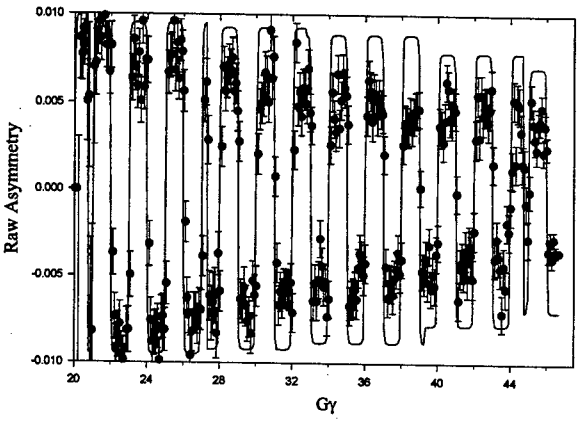

Figure 4: The measured asymmetry between $G\gamma = 20$ to 46.5. The 5% partial snake flips spin at every integer of $G\gamma$.

POLARIZED PROTONS IN RHIC

The basic construction unit for RHIC snake is a superconducting helical magnet producing a 4T dipole filed that rotates 360° in a length of 2.4 meters. These magnets are assembled in group of four to build four Siberian snakes (two for each ring) for RHIC. With two snakes in each ring, the stable spin direction is vertical in RHIC and independent of beam energy.

The second RHIC polarized proton run of nine weeks are still going on. Spin Rotators are required at the IRs used by PHENIX and STAR to allow measurements of spin effects with longitudinally polarized protons. The spin rotators rotate the polarization from the vertical direction into the horizontal plane on one side of the IR and restore it to the vertical direction on the other side. Eight spin rotators have

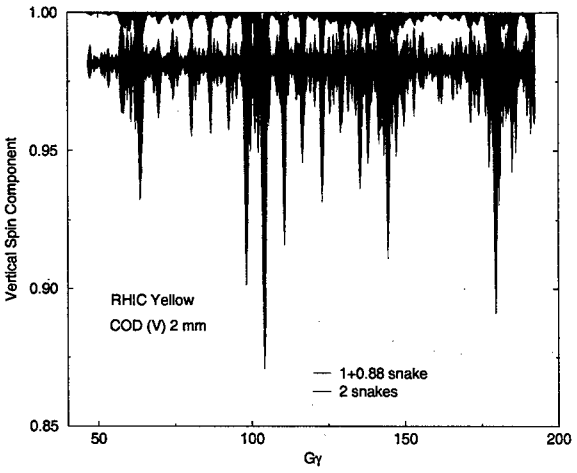

Figure 5: A single particle spin tracking for Yellow ring with two snakes and 1.88 snake scenarios. For the 1.88 snake case, the stable spin direction is not vertical.

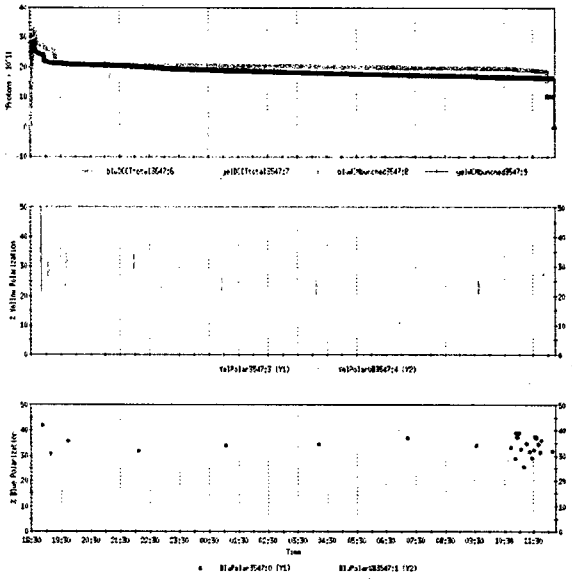

Figure 6: Beam intensity (top) and measured polarization in the Blue (bottom) and Yellow (middle) rings for a typical store.

been installed in the RHIC after last run. 60 bunches pattern was used in each ring (55 filled, 5 empty for an abort gap). The beam emittance was about 12 π mm-mrad in both transverse planes. The beam was injected into RHIC with 10 m * lattice and accelerated up to 100 GeV without beta-squeeze. * was then squeezed down to 1 m and 3 m at various IRs. A separate rotator ramp brings spin to longitudinal at IR 8 [7]. The set at IR 6 will be commissioned soon. The total intensity of 3.3×10^{12} and peak luminosity of about 4.5×10^{30} $cm^{-2}s^{-1}$ have been achieved.

The fractional betatron tune space ranged between 0.215 and 0.23 for the horizontal tune and between 0.225 to 0.24 for the vertical. The vertical betatron tune was chosen to avoid 3/14 snake resonance. Close attention was also paid to the orbit, since the imperfection resonance strength is proportional to the rms orbit error.

In the middle of operation, one helical magnet unit failed due to defects of coils. With the rest units, we decided to run this snake as a 88% partial snake while keeping the angles between the two snakes as 90°. The polarization in Yellow was recovered with the new configuration although it is more sensitive to tune value and orbit errors. Simulation shown in Fig. 5 confirms this. In general, the polarization level was not as good as Blue ring.

Although the analyzing power at 100 GeV for the RHIC polarimeter is unknown, it is expected to be similar at injection energy. Under this assumption the polarization measured at store was typically about 30-35%, while injection polarization is consistently about 40%. One example is shown in Fig.6. The loss of polarization is likely in the beta squeeze part of the ramp.

CHALLENGES AHEAD

The real time tune control system has been tested successfully for a few RHIC fills along the up ramp. But it needs work to be operational. It is essential to have the tune control system operational to control betatron tunes along the ramp. In RHIC the primary source of coupling comes from quadrupole rolls in the triplet quadrupoles at the six interaction regions. In addition, a small longitudinal field is introduced by each helical dipole snake. The decoupling was done fairly well at injection and flattop. However, problems during the ramp persisted since a dynamic correction technique has yet to be implemented.

There are also intensity limitation due to vacuum pressure rise for 110 bunch of 10^{11}. Some beam study has been done to fight this problem [8]. Another limitation we are facing is beam-beam tune shift limit [9]. The beam-beam tune shift is about 0.012 for four IRs. We have to live with operation close to the beam-beam tune shift limit.

To reach the desired 70% polarization in RHIC, a new strong partial snake in the AGS, higher polarization from the source, and good control of RHIC orbit and tunes are needed.

REFERENCES

[1] Ya.S. Derbenev and A.M. Kondratenko, Part. Accel. **8**, 115 (1978).

[2] M. Froissart and R. Stora, Nucl. Instrum. Meth. **7**, 297(1960).

[3] S.Y. Lee and S. Tepikian, Phys. Rev. Lett. **56**, 1635 (1986).

[4] H. Huang, *et al.*, Phys. Rev. Lett. **73**, 2982 (1994).

[5] M. Bai, *et al.*, Phys. Rev. Lett. **80**, 4673 (1998).

[6] H. Huang,*et al.*, proceedings of SPIN2002.

[7] W. MacKay, *et al.*, these proceedings.

[8] S.Y Zhang, *et al.*, these proceedings.

[9] W. Fisher, *et al.*, these proceedings.

RHIC PRESSURE RISE AND ELECTRON CLOUD*

S.Y. Zhang, M. Bai, M. Blaskiewicz, P. Cameron, A. Drees, W. Fischer, D. Gassner, J. Gullotta, P. He, H.C. Hseuh, H. Huang, U. Iriso-Ariz, R. Lee, W.W. MacKay, B. Oerter, V. Ptitsyn, V. Ponnaiyan, T. Roser, T. Satogata, L. Smart, D. Trbojevic, K. Zeno, BNL

Abstract

In RHIC high intensity operation, two types of pressure rise are currently of concern. The first type is at the beam injection, which seems to be caused by the electron multipacting, and the second is the one at the beam transition, where the electron cloud is not the dominant cause. The first type of pressure rise is limiting the beam intensity and the second type might affect the experiments background for very high total beam intensity. In this article, the pressure rises at RHIC are described, and preliminary study results are reported. Some of the unsettled issues and questions are raised, and possible counter measures are discussed.

INTRODUCTION

In very successful RHIC operations since 2001 [1], two types of pressure rise have shown up, which are of concern for current and future operations, with the increasing beam intensity.

First one is the pressure rise at beam injection, which is very sensitive to bunch intensity and bunch spacing, and tends to approach a saturation for a given beam. Currently, this type of pressure rise is limiting the gold beam bunch intensity of 55-bunch injection at slightly below the design, and it is also preventing the 110-bunch operation with high intensity.

Second type of pressure rise is at beam transition, which is somewhat quasi-exponentially proportional to the total beam intensity, but not sensitive to the bunch intensity and bunch spacing. This pressure rise is not currently limiting the beam intensity. However, in the deuteron-gold beam operation this year, it had caused high background at some of the detectors, and hence hampers further luminisity improvement.

There are several peculiar features of the RHIC pressure rise and electron cloud. For example, bunch spacing in the RHIC is much longer than the ones elsewhere the electron multipacting had been observed. It is suspected that the beam halo scraping at the long straight beam chambers may have produced enough positive ions to help electrons survive the long bunch gap, and hence makes electron multipacting possible. Also higher than usual beam ion gas desorption rate is needed to explain the pressure rise observation, which might be again related to halo grazing angle scraping.

For the counter measures, we have tried and been studying several options, such as baking of the chamber, beam scrubbing, solenoids, and NEG coating.

*Work performed under Contract Number DE-AC02-98CH 10886 with the auspices of the US Department of Energy

PRESSURE RISE AT INJECTION

In the 2001-2003 RHIC runs, pressure rise at the high intensity beam injection has often occurred in the warm straight sections, which are in total about 1,300 m in both rings, over the machine circumference of 3,834 m. Usually the pressure rise takes place in part, not all, of the warm sections, with various pressure rise level [2].

This type of pressure rise has limited the gold beam bunch intensity at 9×10^8 ions per bunch for the 55-bunch mode, just below the design of 10^9 ions per bunch. The pressure rise was very sensitive to the bunch spacing, therefore, for the 110-bunch injection, the situation was much worse, and hence this mode was not operational with acceptable bunch intensity. These are illustrated in Fig.1, where the beam intensity and pressure rise are shown for both 55-bunch (216 ns bunch spacing) and 110-bunch (108 ns bunch spacing) mode.

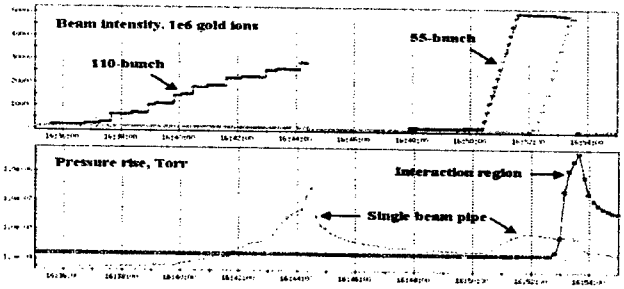

Fig.1. Pressure rise of 55-bunch injection caused valve close in an interaction region. The pressure rise was much higher at a single beam straight for 110-bunch injection.

Longer straights can have lower intensity threshold of the pressure rise. In Fig.2, it is shown that the intensity threshold at single beam straight section, 34 m long, is a little more than half of that at the interaction region, 20 m.

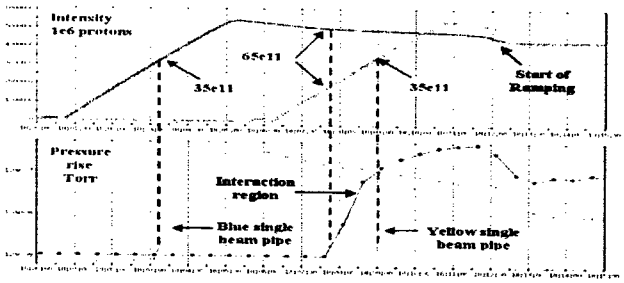

Fig.2. Pressure rise of 55-bunch fill with intensity of 10^{11} protons per bunch. Intensity threshold at both blue and yellow straight sections were 35×10^{11} protons, and it was 65×10^{11} at the interaction straight section.

0-7803-7738-9/03/$17.00 © 2003 IEEE

Electron cloud seems to be responsible for this type of pressure rise [3-5]. The on-set of the electron multipacting and the strength of the electron signal were in coincidence with the pressure rise. In Fig.3, the peak electron signal with 41 bunches injected into RHIC is shown to compare with the pressure rise. Meanwhile, a solenoid around the electron detector was set off, and on with various strength. The pressure rise is correlated with the electron signal. Also both pressure rise and electron signal were reduced by the solenoid field.

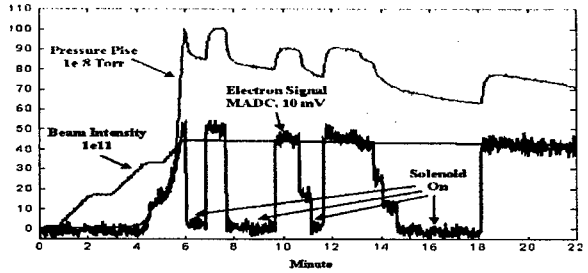

Fig.3. Beam intensity, pressure and the amplitude of electron signal. Solenoid was set off and on, which covers 4 m in the straight section of 34 m long.

In Fig.4, the electron signals observed at a scope are shown with the solenoid off, and on at 27 and 5 Gauss.

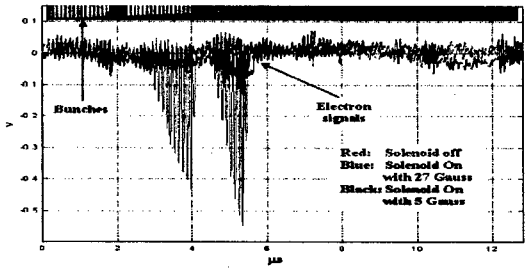

Fig.4. Electron multipacting in a beam injection with gaps, note the gaps re-set the multipacting. The electron signal is reduced when weak solenoid fields applied.

PRESSURE RISE AT TRANSITION

In the 2003 deuteron-gold (d-Au) run, a new type of pressure rise was observed, which was peaked at the transition, and gradually reduced afterwards. Two features of this pressure rise are of concern. The first is that this pressure rise comprises large mass gases molecule desorption, and the pressure rise takes more than 10 hours to settle down. Therefore, the beam-gas induced detector background might affect experiment data taking. The second feature is that the magnitude of this pressure rise can be approximated as quasi-exponentially proportional to the total beam intensity.

In Fig.5, the peak transition pressure rise at 3 of 6 interaction regions, i.e. IR2, IR10 and IR12, of total 74 high intensity ramps in the d-Au run are plotted against the total beam charge intensity in a 10^9 gold ion normalized unit. Data include both 55-bunch and 110-bunch ramps, showing that this pressure rise is not sensitive to bunch spacing. Both deuteron and gold beams are accounted in same way, provided the charges are the same, showing that there is no Z^2 and/or other ion charge effects .

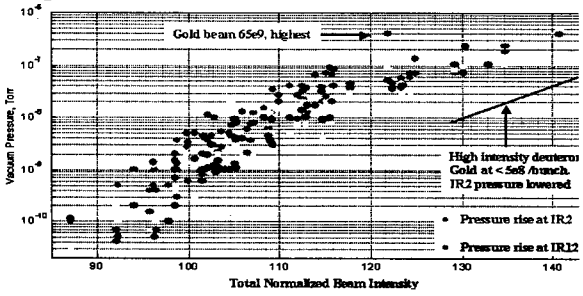

Fig.5. Peak pressure rise of 3 interaction regions at the transition, against total beam intensity. Above total intensity unit of 130, the deuteron beam intensity was higher than gold.

The dominant driving force of this type of pressure rise is probably the beam halo scraping at the chamber wall, with very shallow grazing angle. There is no beam loss correlated with the pressure rise, but at the grazing angle scraping, the gas desorption rate could be very high for high energy ions.

At store, bunches are re-bucketed to the 200 MHz storage RF cavities from the 28 MHz acceleration ones. Re-bucketing shortens bunch length to 5 ns, about the same as that at the transition. Since the beam transverse size is smaller than the one at the transition, the beam potential is higher, yet no pressure rise was observed at the re-bucketing. In Fig.6, the pressure rise, the beam potential and beam momentum spread are shown in time. The bunch potential is calculated using $V_{pot} = IZ_0/(2\pi(0.5 + \ln(b/a)))$, where I is the peak current, $Z_0 = 377\Omega$ is the impedance of free space, b and a are chamber and beam radii, respectively. Bunch intensity of 5×10^8 gold ions is used in calculation. Note that the largest beam momentum spread is at the transition, which may cause some halo scraping.

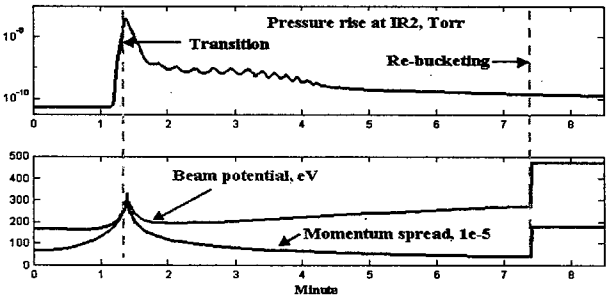

Fig.6. Transition pressure rise at the interaction region IR2. Beam momentum spread is highest at the transition, and the beam potential is highest at the re-bucketing.

Transition pressure rise existed in previous Au-Au run, but it was largely ignored, because of the small amplitude. The total intensity then was 80 units, and from Fig.5 it can be seen that below 90 units this effect cannot be identified clearly. The mechanism is not fully understood yet, however, the possibility that this pressure rise becomes a problem in the next Au-Au run cannot be overlooked.

QUESTIONS AND DISCUSSION

The RHIC electron multipacting may take place at the bunch spacing as long as 216 ns. As a comparison, with the similar chamber, comparable bunch intensity and shorter bunch, CERN SPS used 50 ns instead of 25 ns bunch spacing, the electron signal was significantly reduced, and LHC type beam could be injected [6].

Assuming that the beam halo scraping at the long straight beam pipe produces enough positive ions to help the secondary electrons survive the long bunch gap, and hence to make the electron multipacting possible, then several other observations at RHIC might be explained.

- The threshold at the long straight sections is lower than that at shorter sections, as shown in Fig.2.
- A less than 1 mm radial steering increased pressure rise from 5×10^{-9} to 4×10^{-8} *Torr* in some location.
- Smaller transverse beam size at the straight sections improved pressure rise.
- RHIC pressure rise was not distributed evenly in the warm sections. For gold run, it was in fact only taking place in a few locations, and locations may shift.

Experimental data for ion gas desorption rate at the glancing angle scraping was only available recently for low energy ions [7,8]. On the other hand, observation in RHIC operations may have already provided some clue. Both in last Au-Au run, and the recent d-Au run, beam loss induced pressure rise seems showing that the high energy ion gas desorption rate could be very large. In Fig.7, pressure rises of a gold beam fill at two locations are compared with the beam loss monitor data. Assuming that all the lost ions were dissipated at the location Yi2, the gold ion gas desorption rate is about 1.5×10^{7} of N_2-equivalent molecules. Note that less then 10×10^{9} gold ions lost before the beam dump.

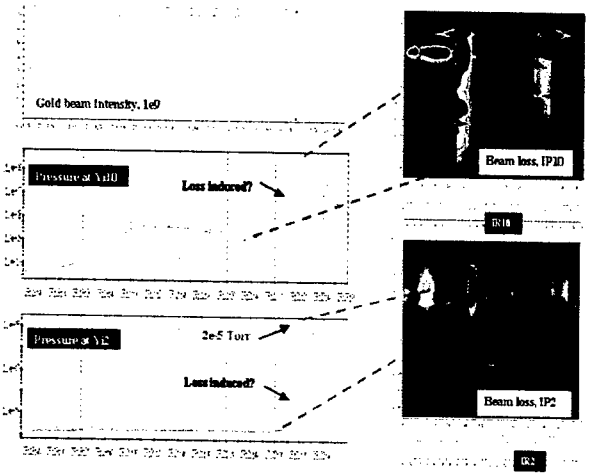

Fig.7. Beam intensity, beam loss induced pressure rises, and the corresponding beam losses at two locations, single beam straight sections Yi10 and Yi2. Note that the pressure rises at Yi2 by 5 orders of magnitude to 2×10^{-5} *Torr*

This argument may provide a plausible explanation for what happened at the transition pressure rise, for even shallower incident angle. The conclusion is, however, still to be reached. Some studies are necessary to clear this out.

It is possible that electron multipacting took a part in the beam loss induced pressure rise. Because of the positive ions produced by sputtering, the usual space charge force, which confines the electron density, might be reduced, and hence the electron saturation level is raised. However, electron desorption is probably not dominant here. It was observed that strong solenoid field at an interaction region (housed the STAR detector) was effective for the pressure rise at the injection, but had no effect on the transition pressure rise.

COUNTER MEASURES

Currently, several counter measures for the pressure rise are undertaken, or under studying at the RHIC.

- Vacuum chamber baking. In last shutdown, additional 40% of the warm chambers were in-situ baked. In this run, the pressure rise is in general improved in these locations, but not eliminated.
- Solenoid. It has been observed that the solenoid is effective in suppressing the electron multipacting. Since the RHIC pressure rise takes place only in straight sections, solenoid can be applied. However, it will not be effective for the transition pressure rise.
- Beam scrubbing [9]. It has been planned for a study at the RHIC. Since the RHIC pressure rise is very unevenly distributed in the ring, therefore, a complete scrubbing of the ring will be very difficult.
- Beam injection with gaps. It has been shown in a study that beam gaps can be used to reduce the pressure rise. This will be useful in the future operation.
- NEG (Non-evaporable getter) coating [10]. The NEG coating reduces not only the secondary electron yield, but also the electron and ion gas desorption rates. Therefore, it may improve both types of pressure rise at the RHIC, i.e., pressure rise at the injection, and at the transition. NEG coating also provides linear pumping, hence may improve experiment background due to beam-gas. A section test for the NEG coating is under consideration, and potential problems such as aging, activation, etc. are under studying.

REFERENCES

[1]. T.Roser, these proceedings.
[2]. H.C. Hseuh et al, these proceedings.
[3]. U. Irish-Ariz et al, these proceedings.
[4]. J. Gullotta et al, these proceedings.
[5]. P. He et al, these proceedings.
[6]. J.M. Jimenez, Chamonix XI, CERN, 2001.
[7]. S.Y. Zhang and L.A. Ahrens, PAC1999, p.3294, New York, 1999.
[8]. E. Mahner et al, PRST-AB, Volume 6, 013201, 2003.
[9]. J.M. Jimenez, Mini-Workshop on SPS Scrubbing Run, CERN, 2002.
[10]. C. Benvenuti, PAC 2001, p.602, Chicago, 2001.

TUNE-SHIFT COMPENSATION USING THE TEVATRON ELECTRON LENS

K. Bishofberger; University of California, Los Angeles
G. Kuznetsov, V. Shiltsev, X. Zhang; Fermi National Accelerator Laboratory

Abstract

The Tevatron Electron Lens was originally designed to alleviate the tune shift and spread induced in Tevatron antiproton bunches from interactions with the proton bunches. We report recent developments and successful results of such tune-shift compensation. Lifetime measurements are central to our data and the basis of our analysis. Future goals and possible uses for the lens are also discussed.

INTRODUCTION TO THE TEVATRON ELECTRON LENS

A description of the Tevatron Electron Lens (TEL) has been described in several previous articles, including a detailed motivation for tune-shift compensation of the Tevatron's beam-beam interaction during Run II [1,2]. Antiproton bunches in the Tevatron suffer a tune shift due to their interaction with proton bunches at the collision points. In addition, parasitic crossings (long-range interaction points) and nonlinear fields cause a spreading of a bunch's tune. These two effects create a large, unwieldy tune footprint that encourages emittance growth and low average luminosity [3].

Overview of the TEL

The TEL consists of an electron gun placed in a solenoid that directs the low-energy electron beam along the field lines. A second, superconducting solenoid bends the beam along the path of the antiprotons, and a third bends the electrons back out where they are collected [4]. Figure 1 illustrates most of the hardware, with a rendering of the electron beam interacting with the antiproton bunches while avoiding the protons. The central magnet is two meters long, and beam position monitors (BPMs) are located near both ends to ensure that the electrons and antiprotons are collinear along the entire magnet length [5].

The goal of the TEL is to provide a radial space-charge force on the antiprotons during every pass that is opposite the tune shift caused by the protons. Adjusting the electron-beam current for each bunch will allow the space-charge force to mimic the linear forces caused by the protons. Creating nonlinear fields to decrease the tune spread within individual bunches is also being addressed [6].

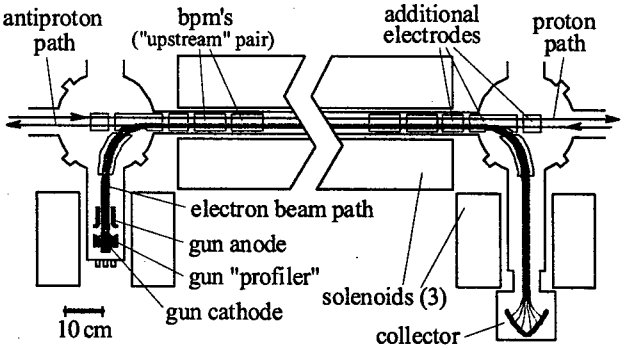

Figure 1: An approximate CAD drawing of the TEL apparatus. The electron beam as drawn interacts with the antiprotons.

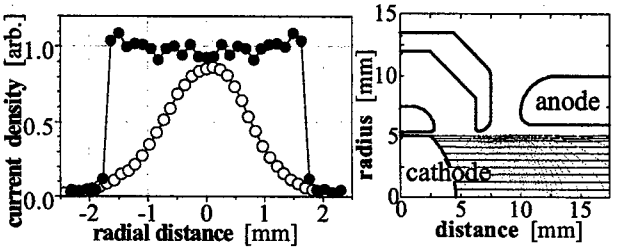

Figure 2: Comparison of the beam profiles of the "flattop gun" and "Gaussian gun" and a cross section of the latter.

The changing of the gun

At the beginning of the current year, the electron gun was replaced with one of a different geometry. The initial gun had a large measured perveance (possibly as high as 5.6 μP) and a flat transverse current distribution, both in accordance with its design goals. The "flattop" beam profile, illustrated in Figure 2, produced nicely linear focusing forces on the immersed antiproton bunches. However, the steep edges on the sides created extremely nonlinear forces on antiprotons with large betatron amplitudes. These forces excited oscillations until the antiprotons were lost.

This unfortunate effect spurred the design of a new gun with a very smooth, almost Gaussian-shaped profile. The perveance is only 1.8 μP, but the central current density is about the same than that of the "flattop gun." Figure 2 also shows a cross-section of the "Gaussian gun" and its current profile, and more description of the changes can be found in another publication [5].

0-7803-7738-9/03/$17.00 © 2003 IEEE

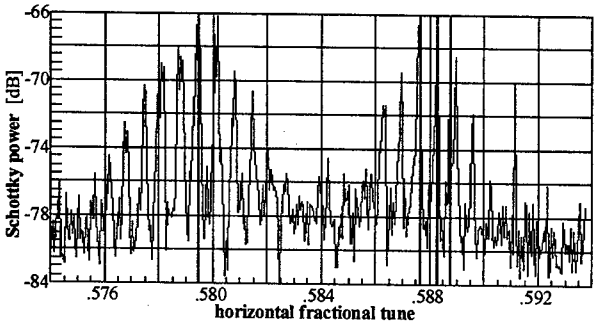

Figure 3: Schottky spectra while one bunch is tune-shifted.

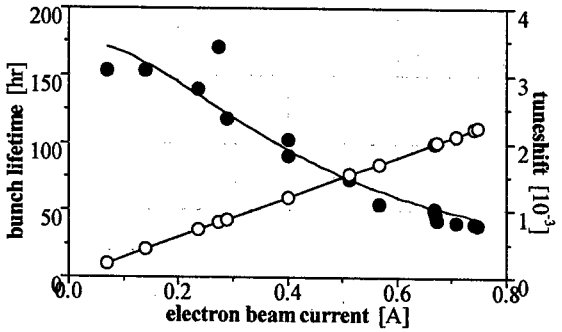

Figure 4: Tune shift (open circles) and lifetime (closed circles) depend on beam current.

Schottky detectors in the Tevatron are used to measure the tunes of the bunches. During one test of the lens, three proton bunches (without antiprotons) were injected into the Tevatron, and the observed (fractional) horizontal tune of all three bunches was 0.5795. Then the lens was pulsed such that it only intercepted one of the three bunches. The two spectra that were associated with the other two bunches remained unaltered, but the tune of the third shifted by 0.0082 to 0.5877, and its spectra appeared quite stable. Figure 3 shows the resulting spectra; the two untouched bunches produced the set of peaks on the left, and only after turning the TEL on did the third bunch produce the set on the right.

Changing the electron-beam current changes the observed tune shift and the losses of bunch particles. Figure 4 illustrates the nearly linearly increasing tune shift (open circles).

EFFECTS ON BUNCH LIFETIME

During most Tevatron operations, the antiproton and proton emittances have been larger than expected, especially toward the end of stores. Due to this, the "flattop gun" always reduced bunch lifetime. The "Gaussian gun," however, was able to preserve the original lifetime of a bunch. Figure 4 shows how increasing the peak current from the latter gun decreased the observed lifetime; nevertheless, these values rival the typical lifetimes for the Tevatron and corroborate our belief that a smoother profile preserves the bunch emittance.

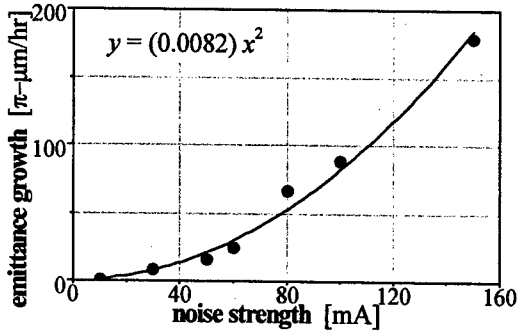

Figure 5: Emittance growth scales with the square of current fluctuations.

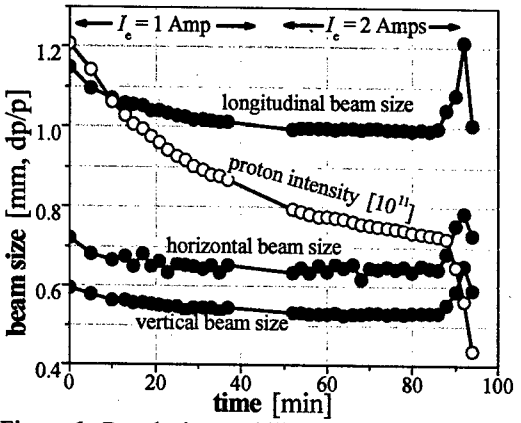

Figure 6: Bunch sizes stabilize after TEL collimates them.

Another cause of bunch blowup could be turn-by-turn fluctuations of the electron beam current. During typical studies, these fluctuations were found to be approximately 0.1%. In order to assess the effect of , measurements of purposefully large current fluctuations were taken. Figure 5 presents this data, where 0.1% corresponds to less than 1 mA and therefore about 0.01 π-μm/hr emittance growth.

TEL as a soft collimator

An interesting application of the "flattop gun" is to slowly eliminate bunch particles with large betatron amplitudes, thereby leaving a lower-emittance bunch. Figure 6 shows the size of a particular bunch while it was collimated in this manner. One amp of electron-beam current was applied initially. Many particles were quickly lost, decreasing the beam size; however, the loss rate began to level off because the remaining core bunch was stable. To confirm our understanding, the beam current was doubled to two amps, but the beam size was still secure.

Also shown is the bunch intensity (open circles) in units of 10^{11} particles, and the linear attrition rate indicates that there was a uniform, slow diffusion of particles in phase space, which caused a small amount of continuous losses.

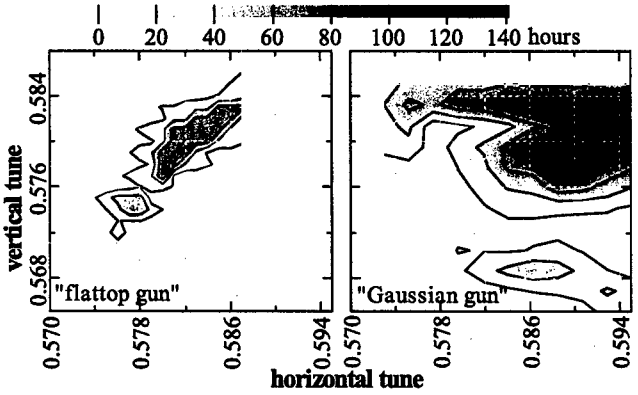

Figure 7: Working-point scans for the "flattop gun" and the "Gaussian gun."

At the very end of the study, the electron beam was misaligned purposefully. The bunch, now passing through the highly nonlinear beam edge, quickly gained emittance and lost particles.

Dependence on working point

Figure 7 supplies cogent evidence that a smoother beam profile can preserve the bunch lifetime. Two working-point scans (measuring lifetime at various horizontal and vertical tunes) were conducted: the first with the "flattop gun," the second with the "Gaussian gun." While the two scans did not cover the exact same regions of tune space, most of the scans overlap each other. The plots have identical boundaries and color scales, and contours are drawn every 20 hours. The "flattop gun" could not surpass eighty hours, and its highest lifetimes were confined to a small diagonal region. On the other hand, the "Gaussian gun" offered decent lifetimes over a much broader area and sometimes exceeded 120 hours. Again, these values are indistinguishable from typical Tevatron lifetimes. The tune shift in both scans was set to about 0.004.

FUTURE GOALS

The TEL has a number of ongoing projects and upgrades under development. For the past 18 months, the lens has been needed to clean the abort gap of residual particles. Recent tests have pulsed the lens for this cleaning operation in addition to tune-shift compensation [5].

Improvements to the TEL

Currently we have additional solenoids that will be installed in the bends; at the same time, the gun and collector will be moved so that the beam needs only to bend about 53 degrees, instead of the current 90 degrees. These changes will stabilize current-dependent position changes and facilitate a larger beam diameter without scraping along the beam pipe.

The goal of extracting more current from the "Gaussian" gun requires more voltage pulsed to the anode. A new pulse modulator will do this and hopefully provide quicker rise and fall times. In addition, the pulse-to-pulse fluctuations will hopefully be decreased further with a different design.

Ongoing work on a better BPM system has shown promising results. These BPMs have a significantly smaller frequency and intensity dependence than the previous model, and our hope is to install them within this year.

Lastly, new solenoids for an entire new lens are currently being fabricated.

Other uses for the TEL

The proton bunches in typical Tevatron stores suffer more beam-beam effects than expected, and the sheer number of protons makes their losses as problematic as the antiprotons. There are proposals to perform tune-shift compensation on protons instead [7].

Another source of emittance blowup in the Tevatron is a head-tail instability in proton bunches while the Tevatron is at low energy. An idea of stabilizing the effects of collective oscillations with the lens should alleviate this problem.

Integrating tune-shift compensation with Run II operations is our highest priority, but the number of other ideas by which the TEL can be useful to the Run II program is always increasing. Intense discussion of incorporating at least one into the LHC design and other accelerators is another tribute to our ongoing success.

ACKNOWLEDGEMENTS

The number of people involved with the TEL has evolved and increased over the past few years. Appreciation goes to A. Semenov, D. Wildman, D. Wolff, and M. Olson, all of who have contributed considerable efforts. In particular, N. Solyak, G. Saewert, and H. Pfeffer never wavered in trying to solve problems on any aspect of the lens, and their passion for turning the lens into a well-understood, reliable machine has been a blessing.

REFERENCES

[1] K. Bishofberger, *et al.*, Advanced Accelerator Concepts Workshop '02, pp. 821-9.
[2] V. Shiltsev, *et al.*, PAC '01, pp. 154, 8.
[3] T. Sen, *et al.*, this conference.
[4] K. Bishofberger, *et al.*, PAC '01, pp. 2076-8.
[5] X. Zhang, *et al.*, this conference.
[6] V. Shiltsev, *et al.*, Physical Review Special Topics □ Accelerators and Beams, v. 2, pp. 071001.1□21. 1999.
[7] V. Shiltsev, *et al.*, Beam-Beam Workshop '03, Brookhaven National Laboratory, 2003.

25 YEARS OF TECHNICAL ADVANCES IN RFQ ACCELERATORS*

Lloyd Young, Los Alamos National Laboratory, Los Alamos, New Mexico 87545 USA

Abstract

The radio frequency quadrupole (RFQ) accelerator began as "The ion linear accelerator with space-uniform strong focusing" conceived by I. M. Kapchinskii and V. A. Teplyakov[1]. In 1979, R. H. Stokes, K. R. Crandall, J. E. Stovall and D. A. Swenson[2] gave this concept the name RFQ. Shortly after Valentine's Day in 1980 a telegram was sent to I. M. Kapchinskii. It stated, "The RFQ is alive and well at the Los Alamos Scientific Laboratory". Thus begins a very informative story of the early history of the development of the RFQ[3]. By 1983, at least 15 laboratories throughout the world were working on various RFQ designs. H. Klein wrote an excellent review of a number of different RFQ structures[4]. In the early years, there were many types of geometry considered for the RFQ, but only a few types have survived. The two cavity geometries now used in almost all RFQs are the 4-vane and 4-rod structures. The 4-vane structure is the most popular because its operating frequency range (80 to ~500 MHz) is suitable for light ions. Heavy ions require low frequencies (below 200 MHz). Because the 4-rod structure has smaller transverse dimensions than a 4-vane RFQ at the same frequency, the 4-rod RFQ is often preferred for these applications. This paper will describe how the RFQ accelerates and focuses the beam. The paper also discusses some of the important technical advances in designing and building RFQs.

RFQ DESCRIPTION

The RFQ has 4 electrodes with alternating RF voltage impressed on them. The dominant characteristic of the electric field is that of a quadrupole shown in Figure 1. A beam of ions traveling down the axis of an RFQ, with a cross section similar to that shown in Figure 1, sees alternating focusing and defocusing electric quadrupole fields. Because the fields oscillate at the frequency of the RF, and are spatially continuous along the axis of the RFQ, the focusing force does not depend on the velocity of the ions. By modulating the radius of the pole tips, a longitudinal electric field can be obtained with the same energy ion beam while bunching and accelerating. Figure 2 defines some of the typical parameters that describe the geometry of the RFQ pole tips. Beta "β" is the velocity of the ions in units of "c," the speed of light, and "λ" is the free space wavelength of the RF Frequency. The modulation factor is "m" and "a" is the minimum distance from the pole tip to the RFQ axis. The gap voltage between adjacent vanes is "V". It is apparent from looking at Figure 2 that the voltage on the axis is tending toward +V/2 at the position indicated with "a". Not shown

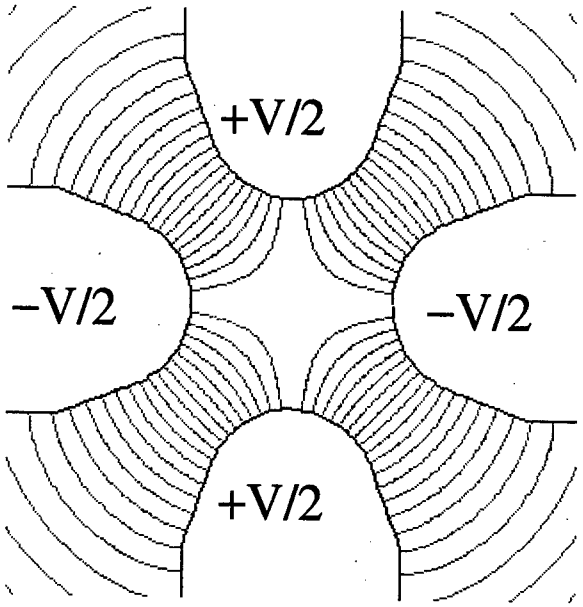

Figure 1: Electric field lines in a RFQ.

in figure 2 are the horizontal vanes that have their minimum distance from the axis of "a" where the vertical vanes are "ma" from the axis. Figure 3 shows how the horizontal vanes are offset from the vertical vanes by one cell length. The voltage on axis at the position marked "ma" is tending toward −V/2. Thus there is a longitudinal electric field on axis that peaks half way between "a" and "ma" in Figure 2. The "unit cell" in the RFQ is defined in Figure 2 by βλ/2.

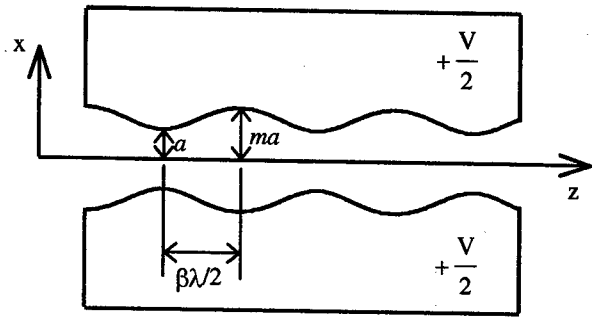

Figure 2: RFQ pole-tip geometry. This figure shows the two opposing vertical electrodes that have the same voltage +V/2. The modulations of the -V/2 horizontal electrodes are shifted by βλ/2 in Z. The length of a unit cell is βλ/2. The modulation is defined as "m".

* Work supported by the US DOE.

0-7803-7738-9/03/$17.00 © 2003 IEEE

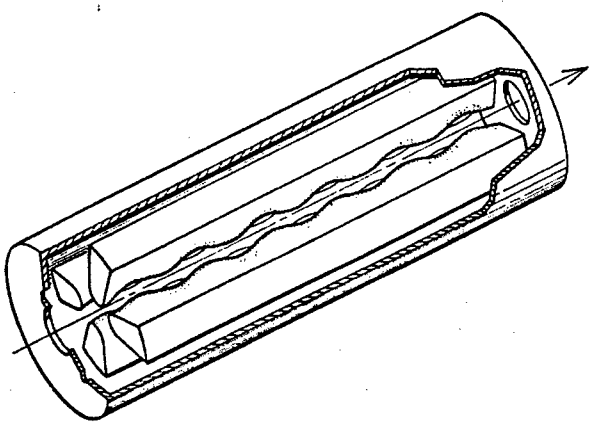

Figure 3: Illustration of modulated vanes in a RFQ showing how the modulation of the horizontal vanes is offset one unit cell from the vertical vanes.

PARMTEQ

Almost as important as the invention of the RFQ was the development of the computer code Parmteq that simulates the beam in the RFQ. K. Crandall modified a version of Parmila and called it Parmteq (phase and Radial Motion in Transverse Electric Quadrupoles)[5]. Parmteq performed the basic functions of designing an RFQ. It generated a physical description of the RFQ, then generated an input particle distribution, and transported the beam through the RFQ. Parmteq also generated output distributions and graphical representations of the beam. This code and local variations were used at most laboratories through out the world and became a standard reference for RFQ simulation.

THE FIRST RFQ

In April-May of 1975 a 4-rod RFQ was started up at the Institute of High-Energy Physics in the USSR[6]. This RFQ operated at 148.5 MHz. The maximum accelerated proton beam current was 140 mA at 1.97 MeV. The normalized emittance was less than 2.5 micron (for 85% of the particles). The pulse length was 10 μsec at 25 Hz.

THE POP EXPERIMENT

The first successful test of a 4-vane RFQ occurred in 1980[7] with the proof of principle (POP) experiment at Los Alamos. A picture of the POP RFQ appears in Figure 4. This RFQ had several features that are still used in modern 4-vane RFQs. The desired operating mode is the TE_{210}. This means the fields are transverse electric (TE). The (21) means that in cross section the fields are quadrupole. The zero (0) means no variation in fields along the axis. In this RFQ, to make the fields uniform the vanes have an undercut on the vane ends. These undercuts are just visible in Figure 3. The end plates in POP had small button tuners opposite the ends of the vane tips. These tuners were used to fine-tune the field flatness. The magnetic field in the TE mode is longitudinal and the

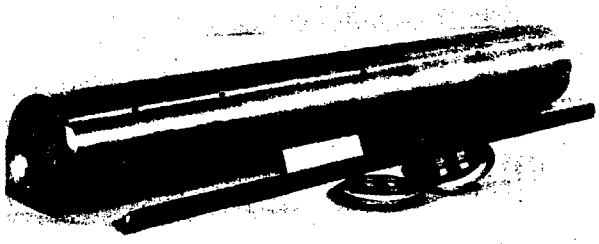

Figure 4: A picture of the POP RFQ experiment.

flux, which alternates direction in adjacent quadrants, must have a way to turn around at the ends of the RFQ. Without the undercuts, the end pieces would short out the electric field and the electric fields would be zero at the ends. Then the lowest frequency quadrupole mode would be a TE_{211} mode. This type of structure will also support the TE_{11n} modes (where n=0, 1, 2, ...) also known as dipole modes. The frequencies of the dipole modes are not too much different from the quadrupole modes.

Beam dynamics issues

The RFQ can take an intense DC beam from an ion source, bunch it, and accelerate the beam to high enough energy to be accelerated by a conventional linac. Therefore, the RFQ must accept beam from a beam line that has static focusing. Whereas the focusing in the RFQ is time varying. The section of the RFQ that accepts the injected beam is called the radial matching section (RMS). The aperture at the leading end of the RMS is quite large and slowly decreases in a prescribed manner[7,8] to the aperture of the next section. The RMS is typically 2 to 5 $\beta\lambda$ long. As the beam traverses the RMS the RF time varying focusing increases slowly, conditioning the beam to the time varying focusing channel of the RFQ. With the code TRACE2D[9] a beam from a static transports system can be matched to the RFQ with a RMS. The next section in the RFQ is called the "shaper". In the shaper the modulation "m" starts at 1.0 and increases linearly with z, the position along the axis. The synchronous phase at the start of the shaper is –90 degrees and it also increases linearly with z. The designer can chose the length, final modulation, and final synchronous phase so that the beam distribution has the appropriate shape for the next section which Kapchinskii called the "gentle buncher." In the "gentle buncher" two conditions are imposed: the average length of the bunch is held constant and the small amplitude longitudinal frequency is held constant. These conditions determine "m" and the synchronous phase in the "gentle buncher." The RFQ designer picks the final energy and final synchronous phase of the "gentle buncher." The last section is the accelerator, where in early designs the modulation "m" increases to a maximum practical value of about 2, and the synchronous phase was held constant. The length of the accelerator section depends on the required final energy. These beam-dynamics design philosophies are common to both 4-rod and 4-vane RFQ's.

DIPOLE SUPPRESION

The 4-vane RFQ has pole tips with a gap of only a few mm between the adjacent tips. Under these circumstances the frequency separation between the TE_{21n} and TE_{11n} modes becomes quite small. Depending on the length of the structure, one of the TE_{11n} modes may be very nearly degenerate with the TE_{210} mode. Small perturbations can cause these modes to mix with the TE_{210} mode and distort the fields. On the POP RFQ it was thought that direct excitation from the drive frequency could also excite the nearby TE11n modes and distort the fields. It was for this reason that a coaxial manifold was used to feed RF power to the POP RFQ and several other early RFQs[10,11,12]. Resonant coupling loops were used to transfer power from the coax manifold to the four quadrants of the RFQ providing symmetric power to drive the TE_{210} mode but with negligible coupling to TE_{11n} modes.

Vane coupling rings

The first effective technique used to eliminate the effect of these TE11n modes occurred at Berkeley[13] with the invention of the vane coupling rings (VCR). Vane coupling rings short opposite vanes to each other through holes in the adjacent vanes, effectively raising the frequency of the TE_{11n} modes well above the desired TE_{210} mode. These rings, although simple, had some problems associated with them. Mechanically, they were hard to implement, and electrically, parasitic capacitance associated with the VCR's caused dips in the electric field strength. The increased capacitance also lowered the frequency of the TE_{210} mode. Therefore, the use of coupling rings as dipole suppressors was brief.

Stabilizing loops

In 1990, two new methods of suppressing dipole modes were introduced. The π-mode stabilizing loop (PISL)[14] and the loop-coupled TEM lines[15]. PISLs were used in at least two RFQs: A 432-MHz, 3-MeV RFQ for the Japanese Hadron Project[15] and the 402.5-MHz, 2.5-MeV RFQ for the Spallation Neutron Source (SNS)[16]. In the RFQ for SNS, the PISLs raised the frequency of the lowest dipole mode to about 35 MHz above the quadrupole mode and lowered the quadrupole mode by 11 MHz. Topologically, the PISL is similar to the VCRs and, therefore, they also increase the capacitance or reduce the inductance. Because the PISL's are not so close to the vane tips, no significant dips in the electric quadrupole fields occur. The loop-coupled TEM lines were never used.

Dipole tuning posts

The RFQ for the beam experiment aboard a rocket (BEAR)[17] used dipole suppressors similar to that suggested by Vretenar[18]. These stabilizers were mounted on the end of the quadrants such that they did not effect the tuning of the quadrupole modes, but could lower the frequency of the dipole modes. The advantage these stabilizers had were the ease of installation and virtually no effect on the frequency of the quadrupole mode. The stabilizers only changed the frequency of the dipole modes, so one could adjust them to move the frequency of the dipole mode several MHz from the quadrupole mode. The dipole suppressors, coupled with tuners along the outer wall of the BEAR RFQ resulted in electric quadrupole field strength within a few percent of the design. This type of dipole suppressors has been used on a number of RFQs: the ground test accelerator (GTA)[19], the RFQ for the superconducting super collider (SSCL)[20], the continuous wave deuterium demonstrator (CWDD)[21], and the low-energy demonstration accelerator (LEDA)[22,23]

RFQ BEAM DYNAMICS CODES

PARMTEQ was the first of the RFQ beam-dynamics codes. A number of variations of the code were developed at various laboratories during the early years, but PARMTEQ was the standard with which the other codes were compared. PARMETQ used the two-term potential[2] to calculate the fields for the beam dynamics simulation. In the mid 1980s the code RFQTRAK was being developed at Chalk River[24], This code used higher order multipoles calculated by the code RFQCOEF[25] and used a 3D finite element method to calculate the effects of space charge and image charge. The first use of PARMTEQM, a modified version of PARMTEQ that use the first 8 terms of the RFQ potential, was on the design of the RFQ for SSCL[20]. This RFQ was first designed with PARMTEQ, but it had a much lower injection energy (35 keV) than previous RFQs. A PARMTEQM simulation showed that in this design the transmission was unacceptably low. PARMTEQM was used to redesign the SSCL RFQ and the transmission increased to ~90% for the design current. Simulations of the LEDA RFQ with PARMTEQM and RFQTRAK agreed very well[23].

The newest RFQ simulation codes use the finite difference method to solve for the 3D fields. TOUTATIS[26,27] was used to simulate the LEDA RFQ and the results agreed very well with PARMTEQM and with RFQTRAK, However, there was a very subtle difference in the output distribution. The output distribution from TOUTATIS, when used in simulations of the halo experiment, agreed quite well with the experiment[28]. The distribution from PARMTEQM apparently had fewer particles that ended up in the halo[29]. LIDOIS[30,31] is a package of codes that can optimize the design of the RFQ, then simulate the beam dynamics with fields calculated with the real vane shape.

RESONANTLY COUPLED RFQ

The 8-meter-long LEDA RFQ is comprised of four 2-meter-long RFQ segments resonantly coupled together. The operating mode is the zero mode, meaning all 4 sections are resonating in phase. Figure 5 shows a picture of this RFQ on the tuning table. The idea of resonantly coupling short RFQ together was first expressed in 1990[32]. A 8-meter-long model was built to verify the

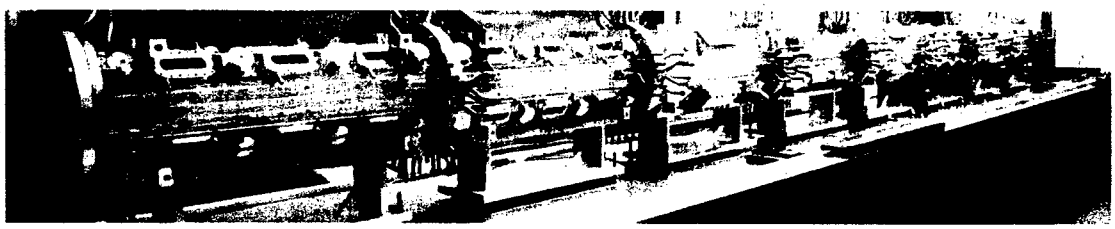

Figure 5: Eight-meter-long RFQ in the tuning laboratory. Adjustable slug tuners can be seen in this picture.

theory[33]. After the successful operation of the LEDA RFQ[34] at least two more Coupled RFQs are being built. The 5 MeV IPHI RFQ is being built at CEA-Scalay[35] and the 5 MeV TRASCO RFQ at INFN-LNL Italy[36]. A 3.5-MeV, 5.7-meter-long coupled RFQ with two sections is being studied in China[37]. In Korea, a 350-MHz, 3-MeV, cw RFQ with two sections coupled together has been built[38].

REFERENCES

[1] I. M. Kapchinskii and V. A. Teplyakov, Prib, Tekh. Eksp. No. 2 (1970) p. 19.

[2] R. H. Stokes, K. R. Crandall, J. E. Stovall and D. A. Swenson, "RF Quadrupole Beam Dynamics," IEEE Trans. NS-26 (1979) p. 3469.

[3] J. T. Ahearne, "RFQ IS ALIVE AND WELL...," Atom, Vol. 17, No. 4 July/August 1980 p. 2-9.

[4] H. Klein, "Development of the Different RFQ Accelerating Structures and Operation Experience," IEEE Trams. Nuc. Sci. 30 (4) (1983), p. 3313-3322.

[5] K.R. Crandall, R. H. Stokes, and T. P. Wangler, "RF Quadrupole Beam Dynamics Design Studies," Proc. 1979 Linear Accelerator Conference, Montauk, NY, BNL-51134, p. 205.

[6] B. M. Gorshkov, S. A. Ilevskii, G. M. Kolomenskii, S. P. Kuznetsov, N. N. Kutorga, A. P. Mal'tsev, K. G. Mirzoev, V. B. Stepanov, V. A. Teplyakov, and I. M. Shalashov, Sov. Phys. Tech. Phys. 22 (11) (Nov. 1977).

[7] R. W. Hamm, K. R. Crandall, L. D. Hansborough, J. M. Potter, G. W. Rodenz, R. H. Stokes, J. E. Stovall, D. A. Swenson, T. P. Wangler, C. W. Fuller, M. D. Machalek, R. A. Jameson, E. A. Knapp, and S. W. Williams, Proc. International Conference on Low Energy Ion Beams 2, University of Bath (April 1980) p. 54.

[8] K. R. Crandall, "RFQ Radial Matching Sections and Fringe Fields," Proc. 1984 Linac Conference, Gesellschaft für Schwerionenforschung, Darmstadt report GSI-84-11 (September 1984)

[9] K. R. Crandall, D. P. Rusthoi, "TRACE: An Interactive Beam-Transport Code," Los Alamos National Laboratory report LA-10235-MS (January 1985)

[10] C. W. Fuller, S. W. Williams, and J.M. Potter, "Mechanical Design Considerations in the FMIT RFQ Development," 1979 Linear Accelerator Conference, Montauk, NY (September 9-14, 1979) p. 401-404

[11] J. M. Potter, "An RF Power Manifold for the Radio Frequency Quadrupole Linear Accelerator" 1979 Linear Accelerator Conference, Montauk, NY, (September 9-14, 1979) p. 138-143

[12] R. H. Stokes, T. P. Wangler, and K. R. Crandall, "The Radio-Frequency Quadrupole – a New Linear Accelerator" Proc. 1981 Particle Accelerator Conference, Washington D. C. (March 11-13, 1981)

[13] P. Howard and H. Lancaster, "Vane Coupling Rings, A Simpler Technique for Stabilizing a Four-Vane Radio Frequency Quadrupole Structure," Proc. 7th Conf. on Applications of Accelerators in Research and Industry, Denton, Texas (November 1982).

[14] A. Uneo, Y. Mori, A. Takagi, C. Kubota and Y. Yamazaki, "The π-Mode Stabilizing Loop For Four-Vane Type RFQs," Proc. 1990 Linear Accelerator Conf., LANL report, LA-12004-C 329 (1990)

[15] A. Ueno, S. Fujimura, Y. Yamashita, M. Tanaka, C. Kubota, K. Yoshino, Y. Morozumi, M. Kawamura, K. Kudo, M. Ono, S. Anami, Z. Igarashi, E. Takasaki, A. Takagi and Y. Yamazaki, "Beam Test of the Pre-Injector and the 3-MeV H^- RFQ With a New Field Stabilizer PISL," Proc. XVIII International Linac Conference, Geneva, CH (August 1996) p. 293-297.

[16] A. Ratti, R. DiGennaro, R. A. Gough, M. Hoff, R. Keller, K. Kennedy, R. MacGill, J. Staples, S. Virostek, R. Yourd, "The Design of a High Current, High Duty Factor RFQ for the SNS," Proc. European Particle Accelerator Conference, Vienna, Austria (June 2000) p. 495-497.

[17] D. Schrage, L. Young, B. Campbell, J. H. Billen, J. Stovall, F. Martinez, W. Clarck, G. Bolme, S. Gibbs, D. King, P. O'Shea, and T. Butler, "BEAR RFQ-Beam Experiment Aboard a Rocket," Proc. Tenth International Conference on the Application of Accelerators in Research and Industry, Denton, TX (November 7-9, 1988) p. 949-953.

[18] M. Vretenar, Proc. of the First Workshop on INFN Eliosatron Project, Erice, Sicily (Plenum, New York, 1986) p. 271.

[19] K. F. Johnson, O. R. Sander, W. H. Atkins, G. O. Bolme, S. Brown, R. Connolly, R. Garnett, J. D. Gilpatrick, F. W. Guy, W. B. Ingalls, C. Little, R. A. Lohsen, S. Lloyd, G. Neuschaefer, J. Power, K. Saadatmand, D. P. Sandoval, R. R. Stevens, Jr. G. Vaughn, E. A. Wadlinger, R. Weiss, and V. Yuan, "Commissioning of the Ground Test Accelerator RFQ," Proc. 1992 Linear Accelerator Conference, AECL Research, Chalk River Laboratories Report, AECL-10728 (1992) p. 64-66.

[20] T. S. Bhatia, J. H. Billen, A Cucchetti, F. W. Guy, G. Neuschaefer, L. M. Young, "Beam Dynamics Design of an RFQ for the SSC Laboratory," Proc. 1991 IEEE Particle Accelerator Conference, San Francisco, CA (May 6-9, 1991) p. 1884-1886.

[21] A. M. M. Todd, M. P. S. Nightingale, T. J. Yule and the CWDD team, "The Continuous Wave Deuterium Demonstrator (CWDD) Design and Status," Proc. 1993 Particle Accelerator Conference, IEEE catalog Number: 93CH3279-7, Washington, D. C. (May 17-20, 1993) p. 1777-1779.

[22] D. Schrage, L. Young, P. Roybal, A. Naranjo, D. Baca, W. Clark, F. Martinez, H. Haagenstad, J. Mitchell, D. Montoya, A. Rendon, F. Krawczyk, T. Davis, D. Casillas, A. Gonzales, G. Gonzales, S. Hidalgo, E. Kettering, G. Leeches, B. Ormond, R. Reinert, O. Smith, J. Tafoya, "CW RFQ Fabrication and Engineering," Proc. LINAC98, Chicago (August 24-28, 1998) p. 679-683.

[23] L. M. Young, L. J. Rybarcyk, J. D. Schneider, M. E. Schulze, and H. V. Smith, "High Power Operations of LEDA," Proc. LINAC2000 Monterey, CA (August 21-25, 2000) p. 336-340.

[24] N. J. Diserens, "Investigation of the Effects of Space Charge and Image Charge Forces on Beam Loss in an RF Quadrupole," Proc. 1984 Linear Accelerator Conference, Seeheim, Germany (May 7-11, 1984) p. 91-93.

[25] N. J. Diserens, "RFQCOEF, A Package For Extracting The Harmonic Coefficients for the Potential Function in an RF Quadrupole Cell," Proc. 1984 Linear Accelerator Conference, Seeheim, Germany (May 7-11, 1984) p. 324-326.

[26] R. Duperrier, "Intense Beam Dynamics in RFQ Linacs," PhD thesis n° 6194, University of Orsay, Orsay (July 2000).

[27] R. Duperrier, R. Ferdinand, J-M. Lagniel, N. Pichoff, "Toutatis, The Cea-Saclay RFQ Code," Proc. XX International Linac Conference, Monterey, CA (August 21 - 25, 2000) p. 839-841.

[28] C. K. Allen, K. C. D. Chan, P. L. Colestock, R. W. Garnett, J. D. Gilpatrick, W. P. Lysenko, J. D. Schneider, R. L. Sheffield, H. V. Smith, T. P. Wangler, J. Qiang, K. R. Crandall, M. E. Schulze, "Experimental Study of Proton Beam Halo in Mismatched Beams," Proc. XXI International Linac Conference, Gyeongju, Korea (August 19-23, 2002).

[29] W.P. Lysenko , J.D. Gilpatrick, J. Qiang, L.J. Rybarcyk, R.D. Ryne , J.D. Schneider, H.V. Smith, L.M. Young, M.E. Schulze, "Characterizing Proton Beam of 6.7 MeV Leda RFQ by Fitting Wire-Scanner Profiles to 3-D Nonlinear Simulations," Proc. 2001 Particle Accelerator Conference, Chicago, IL (June 18-22, 2001) p. 3051-3053.

[30] B. Bondarev, A. Durkin, Y. Ivanov, I. Shumakov, S. Vinogradov, A. Ovsyannikov, D. Ovsyannikov, "The Lidos.Rfq.Designer," Proc 2001 Particle Accelerator Conference, Chicago, IL (June 18-22, 2001) p. 2947-2949.

[31] B.I. Bondarev, A.P. Durkin, S.V. Vinogradov , I.V. Shumakov,"New Tasks and New Codes for RFQ Beam Simulation," Proc. XX International Linac Conference, Monterey, CA (August 21-25, 2000) p. 830-832.

[32] M. J. Browman, L. M. Young, "Coupled Radio-Frequency Quadrupoles as Compensated Structures," Proc. 1990 Linear Accelerator Conference, Los Alamos National Laboratory report LA-12004-C Albuquerque, NM (September 10-14, 1990) p. 70-72.

[33] L. M. Young, "An 8-Meter-Long Coupled Cavity RFQ Linac," Proc. 1994 International Linac Conference, Tsukuba, Japan (August 21-26, 1994) p. 178-180.

[34] L. M. Young, "Operations of the Leda Resonantly Coupled RFQ," Proc. 2001 Particle Accelerator Conference, Chicago, IL (June 18-22, 2001) p. 309-313.

[35] R. Ferdinand, P-Y. Beauvais, R. Duperrier, A. France, J. Gaiffier, J-M. Lagniel, M. Painchault, F. Simoens, P. Balleyguier, "Status Report on the 5 Mev IPHI RFQ," Proc. XX International Linac Conference, Monterey, CA (August 21-25, 2000) p. 551-553.

[36] A. Palmieri, M. Comunian, J. Esposito, A. Pisent, G. V. Lamanna, "Study and Design for TRASCO RFQ High Power Coupler," Proc. XXI International Linac Conference, Gyeongju, Korea (August 19-23, 2002).

[37] S. Fu, S. Fang, J. Li, Z. Luo, H. Ouyang, J. Qiao, W. Xu, T. Xu, Z. Zhang, X. Guan, J. Fang, Z. Guo, "R&D Status of a 3.5MeV RFQ Accelerator for ADS Study in China," Proc. XXI International Linac Conference, Gyeongju, Korea (August 19-23, 2002)

[38] B. H. Choi, P. K. Joo, K. R. Kim, J. Y. Kim, J. H. Lee, J. M. Han, Y. S. Cho, H. J. Kwon, "High Power Proton Linac Program In Korea," Proc. XXI International Linac Conference Gyeongju, Korea (August 19-23, 2002).

COMMISSIONING OF THE SPALLATION NEUTRON SOURCE FRONT END SYSTEMS*

A. Aleksandrov, Spallation Neutron Source, ORNL, Oak Ridge, TN 37830 USA
for the SNS collaboration

Abstract

The Front-End (FE) for the Spallation Neutron Source (SNS) accelerator system is a 2.5-MeV linac injector consisting of the following major subsystems, the rf-driven H- ion source, the electrostatic Low Energy Beam Transport line, a 402.5 MHz RFQ, the Medium Energy Beam Transport line, a beam chopper system and a suite of diagnostic devices. After construction and initial commissioning at LBNL the Front End was shipped to Oak Ridge in the summer of 2002, installed at the SNS site and re-commissioned. This paper provides an overview of the major design features and the experimental results obtained during the final commissioning of the Front End Systems. Performance of the various subsystems will be described, and the final beam output performance will be summarized.

INTRODUCTION

The SNS accelerator systems are comprehensively discussed elsewhere [1]. They are designed to deliver intense proton beam pulses to the spallation target at 60Hz repetition frequency with average beam power of 1.44MW.

The front-end for the SNS accelerator systems is a 2.5MeV injector consisting of the following major subsystems: the rf-driven H- source, the electrostatic low energy beam transport line (LEBT), a 402.5MHz RFQ, the medium energy beam transport line (MEBT), a beam chopper system and a suite of diagnostic devices [2,7]. The beam line is shown schematically in Fig.1. The front-end is required to produce a 38mA beam of 2.5MeV energy at 6% duty factor. The 1ms long H- macro-pulses are chopped at the revolution frequency of the accumulator ring into mini-pulses of 645ns duration with 300ns gaps. Beam chopping is performed by two separate chopper systems located in the LEBT and MEBT, respectively. The LEBT chopper removes most of the beam charge during the mini-pulse gaps, and the MEBT chopper further cleans the gap and reduces the rise and fall time of the mini-pulse to 10ns. The main design parameters for the SNS front-end are listed in Table 1. After construction and initial commissioning at LBNL [3] the front-end systems were shipped to Oak Ridge in the summer of 2002, installed at the SNS site (Fig. 2) and re-commissioned. In spite of the fact the required beam parameters were achieved during commissioning of the front-end at Berkeley, an extensive re-commissioning program was carried out to prepare the front-end for delivering beam to the linac at its permanent location. A commissioning period of two months was allocated, limited by installation activities. As a result, the main commissioning goals were achieved at a reduced duty factor of ~.1% after 46 days of intense work.

Table 1. Parameters of the SNS front-end system

Output beam energy	2.5 MeV
Peak current	38mA
Transverse emittance (norm.)	$<.3\ \pi$ mm mrad
Longitudinal emittance	< .15 MeV degree
Pulse width	1ms
Repetition rate	60Hz
Chopping frequency	1MHz
Chopping extinction ratio	$< 10^{-4}$

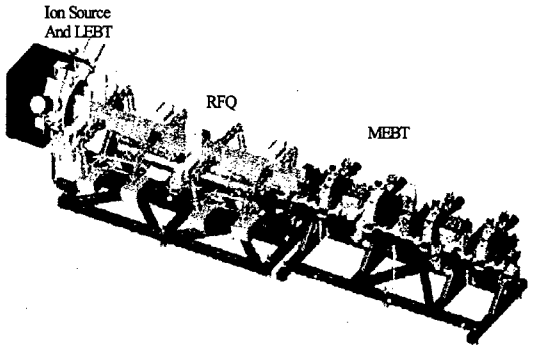

Figure 1. Schematic view of the SNS front-end systems

Figure 2. Front-end systems at the SNS site

* SNS is managed by UT-Battelle, LLC, under contract DE-AC05-00OR22725 for the U.S. Department of Energy. SNS is a partnership of six national laboratories: Argonne, Brookhaven, Jefferson, Lawrence Berkeley, Los Alamos and Oak Ridge.

0-7803-7738-9/03/$17.00 © 2003 IEEE

ION SOURCE AND LEBT PERFORMANCE

Details of the ion source and LEBT design can be found in [4]. General performance of the ion source during commissioning is summarized in Fig.3, where operational current is shown for each day of commissioning. Since there is no beam diagnostics in the ion source or LEBT, the beam current is measured in the MEBT after the RFQ. A maximum current of 51mA was achieved in last days of commissioning, significantly exceeding the base line requirement of 38mA. Continuous 24/7 operation of the ion source revealed several mechanical weaknesses in the LEBT design. These issues together with the remediation plan are described in [5].

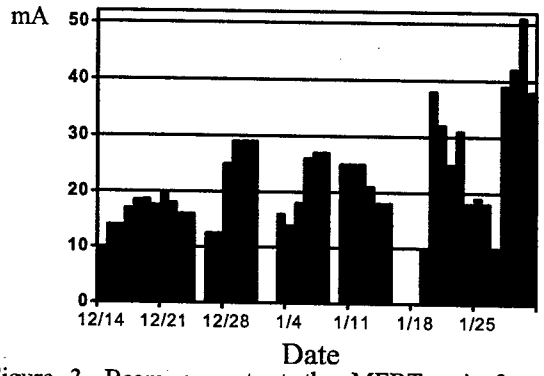

Figure 3. Beam current at the MEBT exit for each commissioning day

RFQ PERFORMANCE

The design of the 3.72-m long 4-vane RFQ with π-mode stabilizers is described in detail elsewhere [6]. It operates at 402.5MHz and accelerates H- beam from 65kV to 2.5MeV.

The RFQ was conditioned to full nominal RF gradient at 6% duty factor, and the field flatness is within ±1% peak.

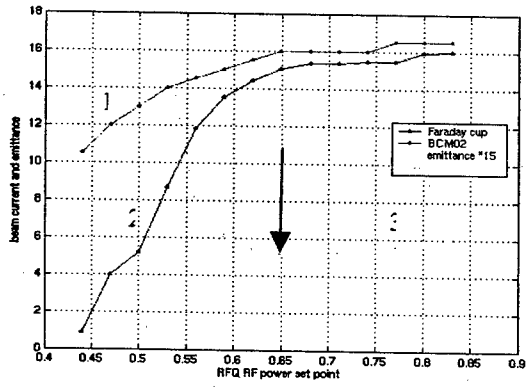

Figure 4. Beam current at the RFQ exit (1), beam current at MEBT exit (2) and transverse emittance at MEBT exit (3) vs. RFQ field. The correct set point is indicated by the arrow.

The only tunable parameter for RFQ is RF power. We used measurements of the RFQ transmission vs. RF power in order to establish the nominal set point. Since we couldn't measure the beam current injected into the RFQ from the LEBT, the absolute value of the RFQ transmission couldn't be calculated. Instead we compared measured data with PARMTEQ simulations and derived the set point and actual transmission from the model. The correct choice of RF power set point was later confirmed by transverse emittance measurement at the MEBT exit. The transverse emittance reaches a minimum when RF power is set in accordance with the transmission scan as shown in Fig. 4.

MEBT PERFORMANCE

The MEBT is a complex beam transport line [7] shown schematically in Fig. 5. It matches the beam from the RFQ through the MEBT chopper system and into the drift-tube linac. Fourteen quadrupole magnets and four rebuncher cavities provide transverse and longitudinal focusing. The MEBT is equipped with a suite of beam diagnostics including two beam current monitors (BCM), six beam position and phase monitors (BPM) installed within quadrupole magnets, five dual- plane wire scanners (WS) and slit/collector-type emittance device at the MEBT exit. Detailed description of the diagnostics is given in [2].

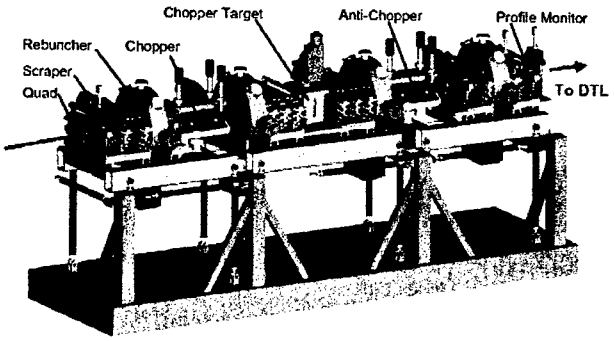

Figure 5. MEBT schematic layout

Transmission through the MEBT

The beam trajectory had to be corrected using dipole correctors in order to establish optimal transmission through the MEBT. After correction beam losses in the MEBT are below the measurement accuracy of the BCMs as illustrated by Fig. 6. In this picture beam current pulse at the MEBT exit is shown on top of the beam pulse at the MEBT entrance. The only visible beam losses are on the trailing edge of the pulse where the RF field in the RFQ decays to below nominal value and a low energy tail develops in the beam energy distribution. Low energy particles are able to reach the first BCM but are lost in the MEBT before reaching the second BCM.

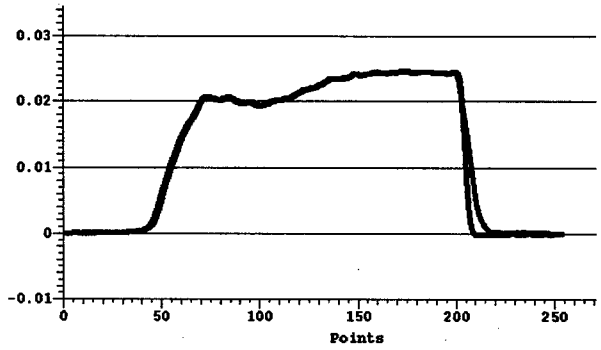

Figure 6. Snapshot of the BCM screen. Beam current pulse at MEBT exit (blue) on top of beam current pulse at MEBT entrance (red), for a 75 μsec pulse.

Transverse emittance

A slit/collector type emittance device was installed at the MEBT exit for transverse emittance measurements. It allowed measurements in one plane (vertical or horizontal). In order to switch to another plane vacuum had to be broken and the device physically rotated, therefore no simultaneous measurements in both directions were obtained. Typical emittance scan plots are shown in Figs. 7, 8.

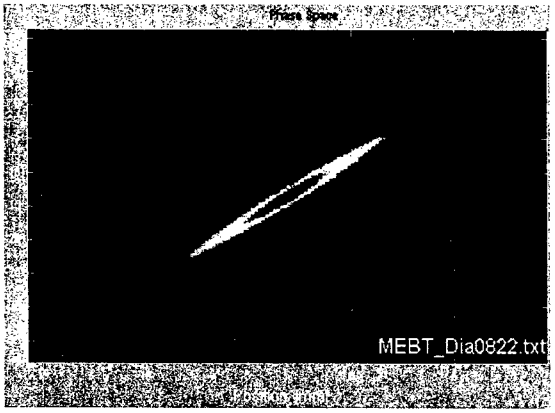

Figure 7. Vertical emittance scan. The normalized emittance $\varepsilon = .3\ \pi$ mm·mrad at I = 38mA.

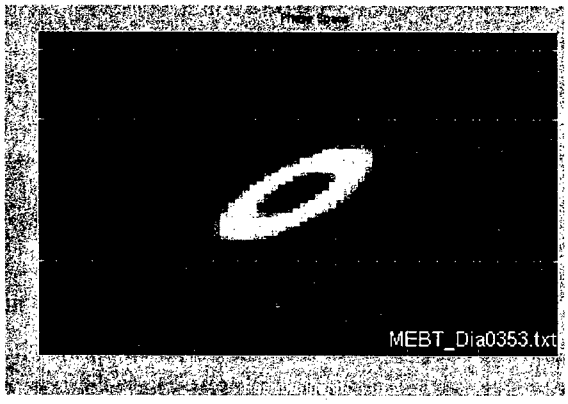

Figure 8. Horizontal emittance scan. The normalized emittance $\varepsilon = .24\ \pi$ mm·mrad at I = 32mA.

The horizontal emittance scan in Fig. 8 clearly shows S-shape distortion caused by non-linear space charge forces and non-linear transverse focusing in the rebuncher cavities. Even in the presence of the emittance growth due to non-linearity, the r.m.s. emittance values satisfy the requirements in a wide range of beam currents as illustrated in Fig.9, where output r.m.s. emittance is plotted vs. beam current. Figure 10 shows the dependence of the r.m.s. emittance on beam current within one pulse. Both plots demonstrate the weak dependence of output emittance upon beam current.

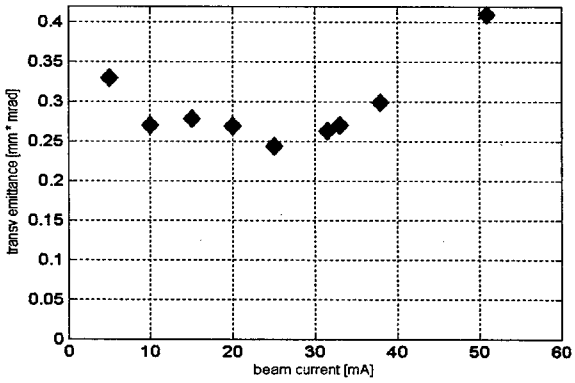

Figure 9. Transverse r.m.s. emittance vs. beam current.

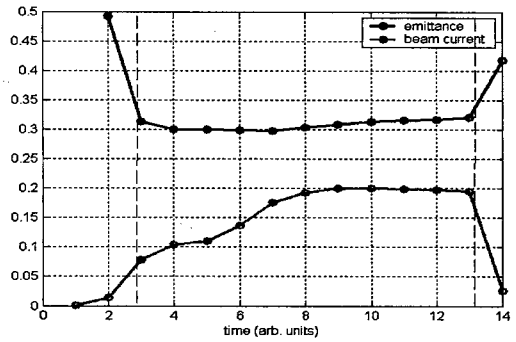

Figure 10. Transverse r.m.s. emittance (upper trace) and peak beam current (lower trace) vs. time within one beam pulse.

Transverse beam envelope

The transverse beam dynamics were compared with model predictions as illustrated in Fig. 10, where the r.m.s beam size measured using wire scanners is compared with PARMILA simulations. Measured profiles agree with simulations within 5%, limited by the accuracy of the wire scanners.

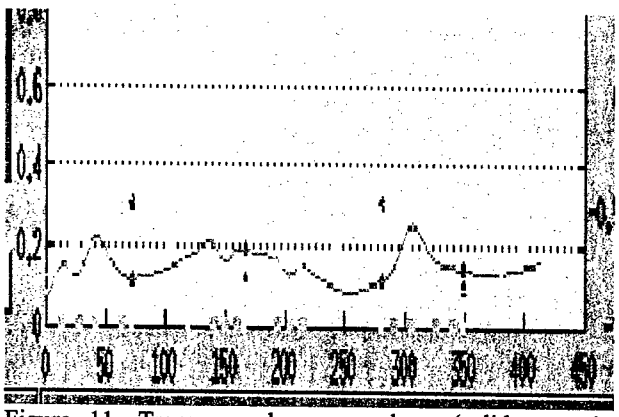

Figure 11. Transverse beam envelope (solid curves) calculated using PARMILA simulation and beam size measured with wire scanners (dots)

CHOPPING

The 1ms long H- macro-pulses have to be chopped at the revolution frequency of the accumulator ring into mini-pulses of 645ns duration with 300ns gaps. Beam chopping is performed by two separate chopper systems located in the LEBT and MEBT, respectively. The LEBT chopper removes most of the beam charge during the mini-pulse gaps, and the MEBT chopper further cleans the gap and reduces rise and fall time of the mini-pulse to 10ns.

LEBT chopper

The last lens in the LEBT is split into four quadrants to allow for electrostatic chopping using the RFQ entrance flange as a chopper target. The lens segments are pulsed with bipolar signals up to ±3kV supplied by commercial solid state active switches. Chopped beam pattern measured at the MEBT beam dump is shown in Fig. 12.

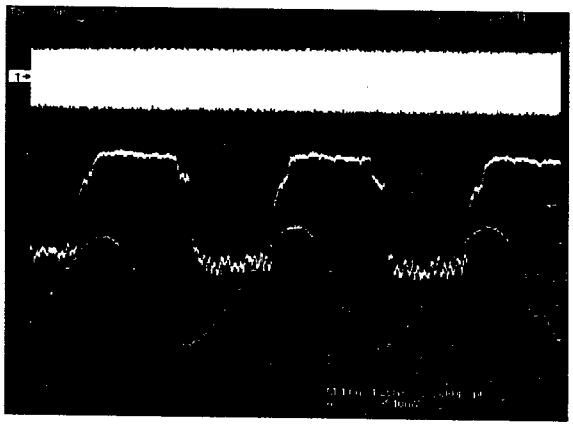

Figure 12. Oscilloscope snapshot of the beam current modulated by the LEBT chopper (meander trace).

The measured beam extinction ratio after the LEBT chopper is below the design specification of 1% at the nominal chopper voltage of 3kV. The dependence of the extinction ratio upon LEBT chopper voltage is shown in Fig. 13.

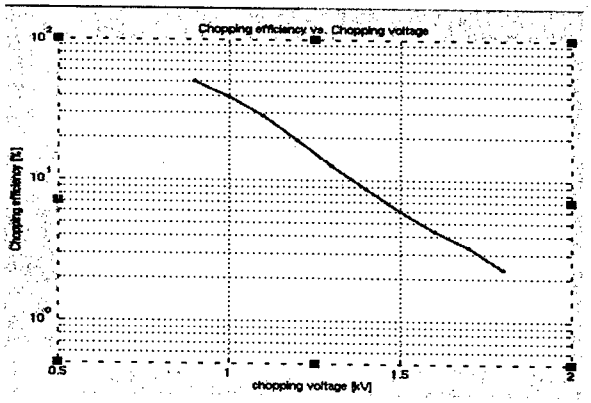

Figure 13. Beam extinction ratio after the LEBT chopper vs. chopper voltage

MEBT chopper

The LEBT chopper system is complemented by a traveling-wave chopper in the MEBT that provides faster rise and fall times to 10ns and further attenuates the beam in the gap to a level of 10-4 [7]. We were unable to test the MEBT chopper with beam due to a failure of the commercial high voltage switches feeding the chopper deflector. Nevertheless, a laser based system capable of measuring rise/fall time with 5ns resolution and beam extinction ratio with 10-4 resolution was installed and tested. Details can be found in [8].

LONGITUDINAL MEASUREMENTS

There are no baseline diagnostics for direct measurements of longitudinal parameters of the beam within a micro-bunch. The only measurements of micro-pulse temporal profile could be carried out 2m downstream of the MEBT using an experimental wide bandwidth Faraday cup [2]. With nominal settings of the rebuncher cavities in the MEBT, the beam would be completely debunched after 2m drift, therefore longitudinal focusing was retuned to achieve a minimum micro-bunch length at the Faraday cup. The measured temporal profile is shown in Fig.14.

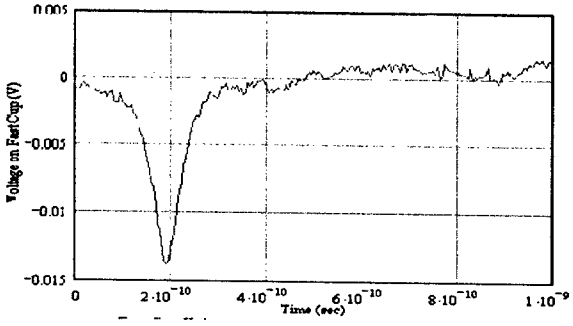

Figure 14. Oscilloscope snapshot of a temporal micro-bunch profile.

An upper limit for longitudinal emittance can be obtained from the minimum micro-bunch length using the following estimation:

$$\varepsilon \leq \frac{d \cdot D}{L},$$

where d is bunch length at the waist, D is the bunch length at the focusing element, L is the distance from the focusing element to the waist. The bunch length D in the last rebuncher cavity is unknown, but as the bunch has to be in the linear part of the bunching field, we can use an estimate of $D \leq \lambda/4$, where λ is wavelength of the bunching RF. This rough estimate gives an upper limit of .25 MeV·degree for the longitudinal emittance at the MEBT exit, which is twice larger than the design value. More precise measurements will be done after the DTL linac where longitudinal diagnostics are available.

HIGH POWER BEAM TEST

The final commissioning task was to reach the nominal beam duty factor of 6%, which corresponds to a 1ms pulse width at 60Hz. Pulse width of 1ms at the MEBT exit is shown in Fig. 15. At 10Hz repetition rate, the high voltage converter modulator failed and due to along repair time, the high power test was terminated. It should be noted that full power operation was demonstrated during initial commissioning at Berkeley.

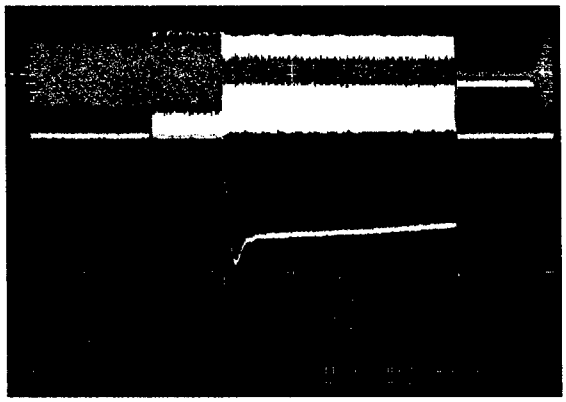

Figure 15. Oscilloscope snapshot of 1ms pulse width at the MEBT beam stop.

CONCLUSION

The FES was shipped to Oak Ridge and installed at the SNS site in the summer of 2002. Extensive re-commissioning at ORNL was performed in a two-month period ending January 31, 2003. A number of technical systems were new to the ORNL FES installation, namely the high-power RF, low-level RF and controls systems, and therefore were commissioned for the first time at ORNL. The Front-end re-commissioning was an important milestone for the SNS project as it demonstrates the first accelerated beam on the SNS site and also marks the beginning of the 2 ½ year phased commissioning program of the accelerator systems.

The primary beam parameter goals of peak current and transverse emittance were both achieved. The maximum beam current achieved at the MEBT output was 51 mA , far exceeding the design specification of 38 mA. Transverse normalized emittances at the MEBT output, measured in a variety of beam conditions, were less than the baseline specification of 0.3 π mm-mrad. The design extinction ratio of the LEBT chopper of 1% was demonstrated, as shown in Fig. 4. The MEBT chopper system, designed to achieve an extinction ratio of 10^{-4}, was not tested due to hardware difficulties.

The main beam parameter goals were achieved at reduced duty factor, typically 0.05-0.1%, limited administratively by hardware concerns. A maximum duty factor of 0.5% was achieved with full 1 msec pulse length but reduced repetition rate. The nominal 6% repetition rate was achieved during the FES commissioning at LBNL.

In addition, two novel diagnostic systems were successfully tested. A laser-based diagnostic capable of performing both transverse profile measurements and Beam-In-Gap measurements was successfully deployed and tested. A dynamic range of 10^4 in beam intensity was measured. Additionally, a prototype Fast Faraday Cup was tested and used to measure a bunch length of 140 psec at the MEBT output.

Following the completion of Front-End commissioning, two of the six Drift Tube Linac tanks will be installed in spring 2003, with commissioning studies of the Front-End and the first DTL tank beginning in the summer of 2003.

REFERENCES

[1] N. Holtkamp. 'Status of the Spallation Neutron Source', Procs. of this conference, PAC2003

[2] S. Assadi, 'The Spallation Neutron Source Diagnostics', Procs. of this conference, PAC2003

[3] R. Keller, et al., 'Commissioning of the SNS Front-End Systems at Berkeley Lab', EPAC 2002, Paris

[4] R. Keller, et. al, 'Design, Operational Experiences and Beam Results Obtained with the SNS H- Ion Source and LEBT at Berkeley Lab', Proc. 9th International Symposium on the Production and Neutralization of Negative Ions and Beams, Saclay (2002).

[5] R. Welton et al., 'The Development and Status of the SNS Ion Source', Procs. of this conference, PAC2003

[6] A. Ratti, et al., 'The design of a high current, high duty factor RFQ for the SNS', Proc. EPAC 2000, 495-497

[7] J. Staples et al.,'Design of the SNS MEBT', Proc. XX-th International Linac Conference, Monterey, CA USA, August 2000

[8] A. Aleksandrov, et al., 'Beam in Gap measurements at the SNS Front-End', Procs. of this conference, PAC2003

HEAVY ION FUSION SOURCES*

D. P. Grote, G. Westenskow, LLNL, Livermore, CA, USA
J. Kwan, LBNL, Berkeley, CA, USA

Abstract

In Heavy-Fusion and in other applications, there is a need for high brightness sources with both high current and low emittance. The traditional design with a single monolithic source, while very successful, has significant constraints on it when going to higher currents. With the Child-Langmuir current-density limit, geometric aberration limits, and voltage breakdown limits, the area of the source becomes a high power of the current, A~I^8/3. We are examining a multi-beamlet source, avoiding the constraints by having many beamlets each with low current and small area. The beamlets are created and initially accelerated separately and then merged to form a single beam. This design offers a number of potential advantages over a monolithic source, such as a smaller transverse footprint, more control over the shaping and aiming of the beam, and more flexibility in the choice of ion sources. A potential drawback, however, is the emittance that results from the merging of the beamlets. We have designed injectors using simulation that have acceptably low emittance and are beginning to examine them experimentally.

MULTIBEAMLET INJECTOR

A requirement of heavy ion fusion (HIF) is a source the produces a beam with high brightness --- having both high current and low emittance. Traditionally in the HIF program, the sources that have been used are monolithic, solid, hot plate sources. While these have performed quite successfully over the years, they do have limitations. They have poor scaling when going to higher currents and have limited lifetimes before the ions are depleted. Going to multiple beamlets circumvents the scaling problem at high current and allows use of a plasma source which does not have the problem of ion depletion. The multibeamlet injector concept has been extensively studied, with a focus on understanding and minimizing the emittance growth[1]. As part of that work, a procedure for designing a multibeamlet injector was laid out and several examples given. In this paper, that work is extended, using an improved layout of the beamlets and further examining some details.

HIGH CURRENT SCALING

When going to higher currents, the single beam injectors do not scale well. Taking into consideration the space-charge limited current density given by the Child-Langmuir relation, voltage breakdown limits, and limits on the geometry to minimize aberrations, the source radius varies as a high power of the current and the current density varies inversely with the current[1]. The poor scaling can be circumvented by using multiple beamlets --- each beamlet has a low current and avoids the poor scaling. Fixing the total area of the source (the sum of the area of the beamlets), the current density becomes proportional to the total current. The inherent emittance of an injected beam from the temperature of the emitter varies as the square root of the product of the temperature and the beam area. Since the total area of the beamlet source can be much smaller than the area of a single source, the temperature of the emitter can be higher for a multibeamlet injector. This allows use of plasma type sources, which have higher operating temperatures than solid sources.

INJECTOR DESIGN

The design of the injector consists of a pre-accelerator column where the beamlets are accelerated independently, followed by a merging region where the beamlets are merged and further accelerated. The pre-accelerator column consists of a diode followed by a series of apertures plates. The plates act both to accelerate the beamlets with a net voltage drop along the column, and to focus it transversely via a series Einzel lenses. The plates also isolate the beamlets from each other, shielding them from the space-charge fields of their neighbors.

When the beamlets leave the last plate, they begin to interact and merge. A conservation of energy argument can be made, which leads to the conversion to emittance of the "extra" space-charge energy of the beamlet configuration, as compared to a uniform beam. This gives the result that the higher the energy at which the beamlets are merged, the lower the emittance. This must be balanced however with other limits, such as the decreasing focusing strength of the Einzel lenses at higher energies. In the merging region, further acceleration of the beam can be done to bring it up to the required energy for the transport lattice.

One important feature of the multibeamlet injector is that the beamlets can be aimed so that the merged beamlet is exactly matched to the transport lattice as it enters it. This removes the need of a separate matching section. Flexibility is gained by allowing the first quadrupole of the lattice to be of partial length. The merged beam can then be matched to any part of the beam envelope in the lattice.

The system must be designed as a whole. The two fundamental parameters are the number of beamlets and the energy at which they merge. Given constraints on the design, such as material strength of the aperture plates

*This work performed under the auspices of the U.S Department of Energy by University of California, Lawrence Livermore and Lawrence Berkeley National Laboratories under contracts No. W-7405-Eng-48 and DE-AC03-76SF00098.

0-7803-7738-9/03/$17.00 © 2003 IEEE

(How close can the holes be to each other?) and construction errors, and the desire to minimize the emittance of the merged beam, the rest of the design falls into place.

APERTURE PLATE DESIGN

The shape of the aperture plates is critical to having the beamlets propagate through the pre-accelerator column to the merging region. It is desirable, for robustness, to the the beamlets propagate in a straight line through the column. For this to happen, since the plates supply an accelerating field, the path of the beamlets must be normal to the surface of the plates. The convergence angles of the individual beamlets is set to increase linearly relative to the transverse position. This is to match the linear variation of the transverse velocity relative to transverse position for particles propagating in an alternating gradient focusing lattice.

The beamlets are aimed to match into the elliptical beam of an alternating gradient focusing lattice. Therefore, the focal points in the two transverse planes are not the same --- the focus is astigmatic. The convergence angles of the beamlets, x' and y', can be written

$$x' = xa'/a$$
$$y' = yb'/b$$

where x and y are the transverse location of the beamlets at some z longitudinal location where the size and convergence of the out edge of the beamlets is given by a, b, a', and b'. No surface has been found which exactly meets these requirement. However, an approximate surface can be constructed.

Given the linear variation of the beamlet convergence angle, in order for the beamlet path to be normal to the surface, the intersection of the surface with any z-x or z-y plane must be circular. Furthermore, the circles in all of the z-x planes must be concentric with each other, and likewise for the z-y plane. The centers of the circles in the z-x and z-y planes will be different. This leads to a method of construction of the surface whereby the intersection with the z-x plane at y=0 is fixed, and then for each point in that circle, a circle is generated in the z-y plane that the point lies in. Similarly the intersection can be fixed in a z-y plane. This method produces surfaces described by the following equations, depending on which plane the intersection is fixed.

$$(z-z_b)^2 = \left[z_a - z_b - \sqrt{(z_0 - z_a)^2 - x^2} \right]^2 - y^2$$

$$(z-z_a)^2 = \left[z_b - z_a - \sqrt{(z_0 - z_b)^2 - y^2} \right]^2 - x^2$$

The z_a and z_b are the center of the circles in the x and y planes respectively, and z_0 is the location of the surface where it intersects the axis, x=y=0. Neither of these surfaces are exactly normal to the beamlet path. However, given the design parameters, where z_a and z_b are much greater than the transverse positions, the error is small. Given a transverse size of the order of 5 cm and radii of order 1 m, the error (as measured by the differences in the two surfaces) is of the order of several microns, less than typical machining tolerances. To make the errors symmetric, the actual surface used is the average of the two surfaces.

OPTIMAL BEAMLET ARRANGEMENT

In order to minimize the emittance of the merged beam, the beamlets must be packed as close to each other as possible. Hexagonal dense pack should be ideal. In the previous study[1], an arrangement similar to close pack was used, where the beamlets were laid out on ellipses instead of hexagons, that had the advantage of having a smooth edge. It was thought that having the smooth edge was more important than a slightly denser pack. It has since been determined that a dense pack is optimal, producing the lowest emittance, even with a more ragged beam edge. The beamlets are packed with uniform spacing and only those within a proscribed ellipse are used. In some cases, removing beamlets on the outermost corners can further reduce the emittance. See Figure 1 for an example layout.

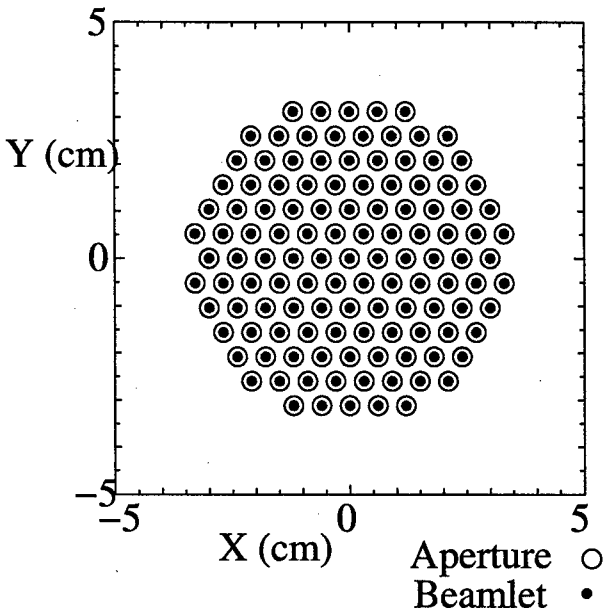

Figure 1: Example arrangement of beamlets with hexagonal packing and outermost corners removed.

Another issue effecting the merged emittance is the ellipticity of the arrangement. With an elliptical arrangement of beamlets, the emittances of the merged beam in the two transverse planes are significantly different. The emittance in the plane of the major radius of the ellipse is greater. After propagating some distance ,however, the emittances equilibrate. There is a concern, though, that the initially different emittances could potentially lead to halo or other other problems. Therefore, a circular arrangement of beamlets was adopted. The resulting emittances where significantly less

different, though still not the same since the convergence angles of the beamlets in the two planes still differ. In this case, the length of the first quadrupole of the lattice was varied in order to get an exact match. Typically the length is just over half the normal length. See Figure 2 which shows the envelopes for an example case.

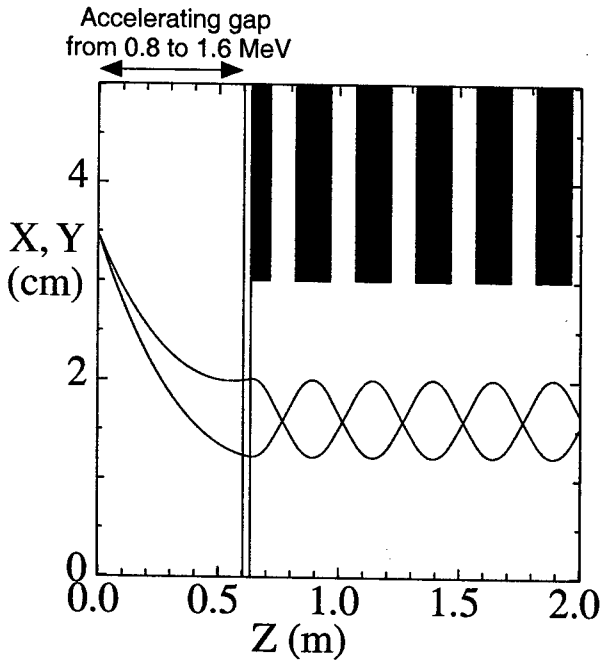

Figure 2: Envelopes for an example case, starting with a round arrangement of beamlets for the merge.

OPTIMIZED DESIGNS

Table 1: Parameters of optimized pre-accelerator columns

Beamlet Spacing (mm)	# Beamlets	Merge Energy (MeV)	Normalized Emittance (π-mm-mrad)
6	121	1.2	0.80
		0.8	0.86
	199	1.2	0.70
		0.8	0.76
5	121	1.2	0.60
		0.8	0.62
	199	1.2	0.51
		0.8	0.55

Using the hexagonal packing and an overall circular extent, optimized designs were created for differing number of beamlets, and values of merging energy and beamlet separation. Table 1 gives the resulting emittances obtained. An approximately 20% reduction in emittance was found by switching to hexagonal packing, a small but not insignificant difference. Going to a more tightly packed arrangement with less material between the apertures could potentially lead to further improves. The caveats though are that the plates may not be stable enough, the smaller aperture separation leads to sharper corners which may reduce the voltage holding, and the plates supply less shielding so the beamlets will interact more before exiting the column.

A further refinement of the design is spreading out evenly the pre-accelerator column plates. This should simplify construction and alignment. This leads to somewhat less flexibility in optimizing the beamlet focusing resulting in a small increase in emittance. The increase is of the order of a few percent. Figure 3 shows the beamlet envelope in the pre-accelerator column for the case with 121 beamlets, merging at 0.8 MeV and with 5 mm between beamlets.

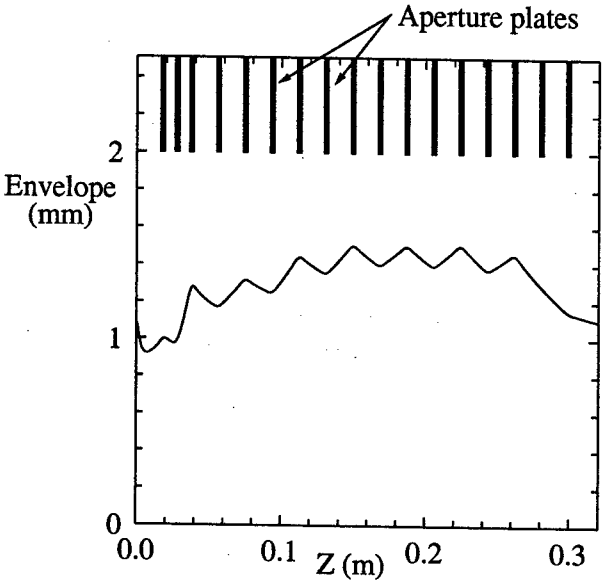

Figure 3: The beamlet envelope in the pre-accelerator column for the optimized case with 121 beamlets, merging at 0.8 MeV and with 5 mm between beamlets.

CONCLUSIONS

The single beam sources that have traditionally been used for heavy-ion fusion experiments and driver design have proven successful but have limitations, such as poor scaling in the source size at higher currents. To circumvent the poor scaling, many small beamlets are used and are merged. Designs of merging multi-beamlet injectors have been done that meet the requirements for example transport lattice, including a low emittance. The next step is experimental validation, which is in progress.

REFERENCES

[1] D. P. Grote, Enrique Henestroza, and Joe W. Kwan, Phys Rev ST AB, January 8, 2003.

H⁻ SURFACE CONVERTER SOURCE DEVELOPMENT AT LOS ALAMOS*

Gary Rouleau, Edwin Chacon-Golcher, Ernest Geros, E. G. Jacobson, B. J. Meyer,
Benjamin A. Prichard, Jr., Joseph Sherman, J. E. Stelzer, and Ralph R. Stevens, Jr.
Los Alamos National Lab, Los Alamos, NM87545

Abstract

Production of H⁻ ions by the surface conversion process is being pursued at the Los Alamos Neutron Science Center (LANSCE) as part of an upgrade project to provide higher currents and enhanced flexibility for injecting a 800 MeV H⁻ beam into the proton storage ring (PSR). An eventual goal of 40-mA H⁻ current at 80 keV beam energy with 0.13 πmm-mrad (1rms normalized) emittance at 12% duty factor (120 Hz, 1ms) is desired. To attain this goal, two types of surface converter sources are being investigated in which H⁻ ions are extracted either radially or axially through a line-cusp magnetic field. The radial source produces 18 mA H⁻ in a 28-day run cycle for LANSCE production while the axial source has been developed to the desired 40 mA current. However, an emittance growth of factor 2-3 accompanied the increased axial source current. The axial source development program includes electron suppression, increased beam current, and 80-keV beam emittance measurements. The current understanding of the emittance growth mechanism will be discussed.

INTRODUCTION

The LANSCE upgrade project[1] goal is to attain 200 μA average current at a spallation neutron source target. The PSR[2] compresses an approximate 1ms H⁻ source macropulse to 250 ns. PSR beam instabilities[3] have been observed in the beam compression process. Both the higher current LANSCE facility request and PSR tuning flexibility would benefit from a higher current H⁻ source. For these reasons a higher current H⁻ surface converter source was developed for LANSCE in collaboration with the Lawrence Berkeley National Lab (LBNL). This collaboration produced a six-filament axial source[4] which produced the required 40-mA H⁻ current, and a higher-perveance accel column.[5] A factor 2-3 emittance growth, however, was discovered while testing the 80-keV axial source at LANSCE.[6] The surface conversion process has been used at LANSCE to provide reliable H⁻ beam operations since 1985.[7] The present LANSCE production source produces 18-mA H⁻, at 12 % duty factor (120 Hz, 1ms), 80-keV beam energy, and 28 day lifetime.

EXPERIMENTAL RESULTS

An ion source test stand (ISTS), which has the same functionality as the 80-keV LANSCE production injector, has been built at Los Alamos.[8] Measurements reported here on the axial source were carried out on the ISTS. Figure 1 shows a PBGUNS[9] scale drawing of the prototype axial H⁻ source electrodes used in the LANSCE testing. The primary H⁻ production mechanism is the

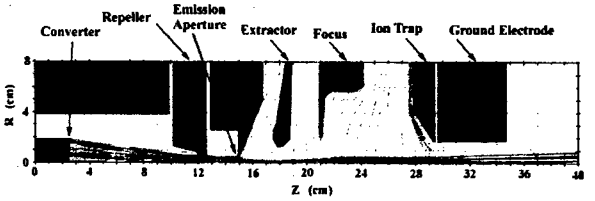

Fig. 1. PBGUNS trajectory simulations for the prototype axial H⁻ source used in these measurements.

formation of H⁻ ions on the converter surface that are self-extracted by the -250 to -300V converter voltage. The electron suppressor, composed of electric and magnetic fields, is located in the repeller electrode. The emission aperture is 2.3 cm downstream from the repeller. For results reported here the emission aperture had radii = R_{em} = 0.5 and 0.8cm. Different magnetic field configurations for the repeller, including line cusp, solenoid ring, and undulator (opposing dipole), have been investigated to optimize the 80 keV e/H- ratios. The measured e/H⁻ ratios

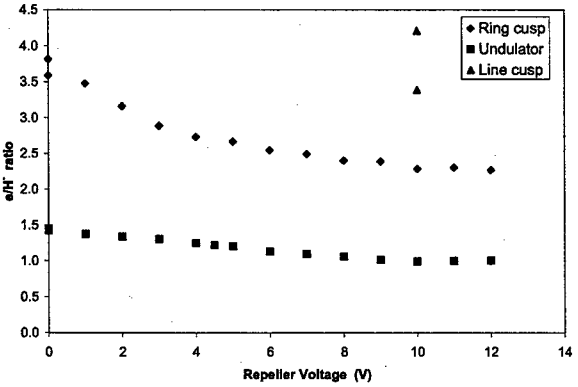

Fig. 2. The measured e/H⁻ ratios for three different repeller magnet configurations.

are shown in Fig. 2 as a function of the repeller electrode voltage. These measurements were made for an H⁻ beam current, I_b, equal to 33-mA extracted from the source with R_{em} = 0.8cm. The electron to H⁻ ratios are calculated by the formula e/H⁻ = $(I_{reg} - I_b)/I_b$ where I_{reg} equals the total pulsed current delivered by the 80-kV regulator circuit.[10] At repeller voltage of +10 V, the e/H⁻ = 1.1, 2.3, and 4 for the undulator, ring cusp, and line cusp magnets, respectively. Many measurements were made on the e/H⁻

*Work supported by NNSA/DP through the U.S. DOE under contract W-7405-ENG-36.

0-7803-7738-9/03/$17.00 © 2003 IEEE

ratio for the line cusp, and the two points for the line cusp in Fig. 2 are representative of the spread for different source tunes. There is a clear preference for the undulator magnetic field for electron suppression.

Figure 3 shows the measured H^- current as a function of discharge power, P_d, for the source equipped with R_{em} = 0.8cm. P_d is the product of the discharge voltage and current. The H^- current is measured in a current transformer after the beam passes through a low-energy beam transport solenoid magnet, thus nearly eliminating the remaining co-extracted electron current. The discharge voltage varies from –140 to –190V in these measurements. The H^- current, considering the data scatter, has a weak dependence on the magnetic filter arrangement in the repeller electrode. The 40-mA current level is reached most efficiently (less discharge power) in the order of line cusp, undulator, and then the ring cusp magnets. Another feature seen in Fig. 3 is an approximate dependence of extracted H^- current on the square root of the discharge power. For comparison to the data an empirical curve showing $I_b(mA) = 10(\sqrt{P_d(kW)})$ is shown.

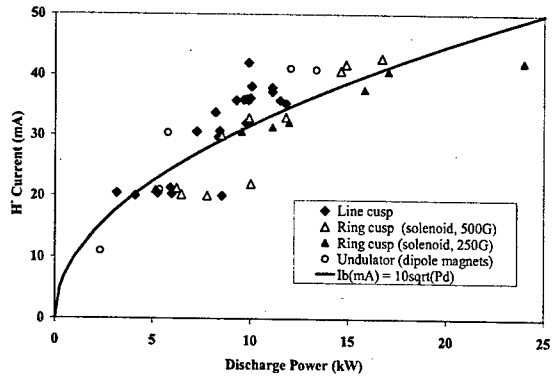

Figure 3. Measured H^- current as a function of the discharge power. R_{em} = 0.8cm in these measurements.

The I_b vs P_d data for the axial source with the R_{em} = 0.5cm emission aperture is shown in Fig. 4. Here the filled triangle and open circle symbols are H^- currents measured at two different H_2 gas flows with the converter voltage varying between –230 and –270V. The undulator repeller magnet configuration is used in acquiring the Fig. 4 data. An approximate square root dependence of I_b on P_d is again observed. The empirical square root dependence is shown by the equation $I_b(mA) = 3.47\sqrt{P_d(kW)}$. The filled square and open diamond symbols show that significant H^- currents are extracted for the measured P_d when the external converter power supply is switched off. This result is suggestive that production mechanisms other than surface production at the converter are significant in the axial source and apparently increase with discharge power.

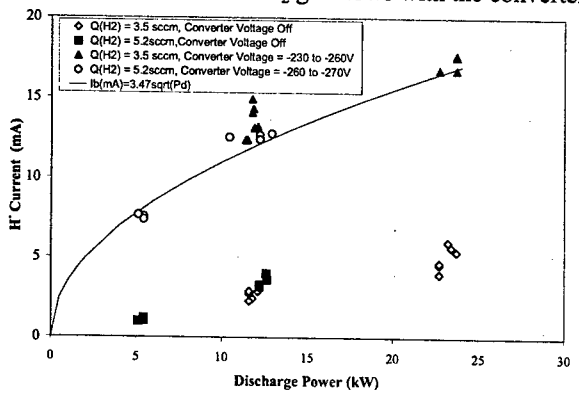

Figure 4. Plot of the measured H^- currents vs discharge power for R_{em} = 0.5cm.

A selection of emittance measurements for the 80-keV beams with R_{em} = 0.5 and 0.8cm are shown in Fig. 5.

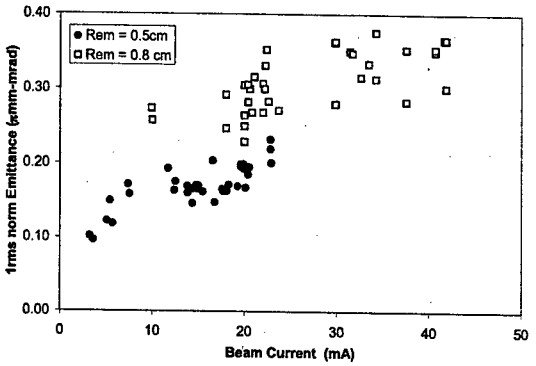

Figure 5. Summary of normalized emittances measured on the axial surface converter H^- source.

The total lab emittance was extracted from the phase-space scans with the area calculated for 98% of the beam, $\varepsilon_{tot}(98\%)$. These total lab emittances are then converted in low ion energy limit to 1rms normalized ($\varepsilon_{1rms,n}$) by the equation $\varepsilon_{1rms,n} = \beta^*\varepsilon_{tot}(98\%)/7$, where β is the relativistic velocity factor for 80-keV H^- ions and the factor 7 is applied to convert the 98% beam fraction to 1rms beam fraction.[6] On this $1\varepsilon_{rms,n}$ emittance scale, the present LANSCE accelerator emittance request is in the range of 0.13 – 0.15 (πmm-mrad). Measurements made by LANSCE operations team[11] confirm that the 750 keV transport would have to be rebuilt to accommodate the larger emittances associated with the R_{em} = 0.5cm and 0.8cm apertures reported in Fig. 5.

DISCUSSION

The admittance limit for the R_{em} = 0.5cm and 0.8cm emission apertures are calculated to be 0.10 and 0.14 (πmm-mrad) ($1\varepsilon_{rms,n}$). These admittances are calculated on the basis of uniform H^- beam illumination[12] of the repeller and emission apertures from the converter surface at converter voltages (typically –250 to -300V). Such a diagram, constructed at the emission aperture, is shown in Fig. 6 for the axial source geometry shown in Fig. 2 where R_{em} = 0.5cm. The discrete points contained within the admittance diagram are phase-space predictions derived from the PBGUNS code.[9] These admittances are a reasonable expectation of the beam emittance, and is found to be true (cf measured emittances at low beam currents reported in Fig. 5). A proposed interpretation for

the emittance growth observed between the admittance limits and the higher-current emittances observed in Fig. 5 is that two beams corresponding to directed H^- ion energies characteristic of converter (≈300eV) and plasma sheath (≈12eV) energies appear simultaneously at the plasma meniscus. Such a mixed species beam has previously been observed in magnetron H^- sources[13] which have similar geometric construction to the present H^- surface converter source.

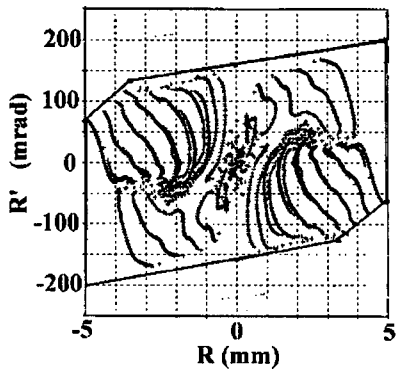

Fig. 6. Admittance diagram for the surface converter source geometry shown in Fig. 2.

Further evidence for a mixed species beam is shown in Fig. 4 where significant H^- currents are observed with the converter voltage turned off. A PBGUNS model was made for extraction of mixed species beam from a plasma. The $1\varepsilon_{rms,n}$ emittance results are shown in the ordinate of Fig. 7. The abscissa contains the percent of 12eV species compared to 300eV species. The prediction

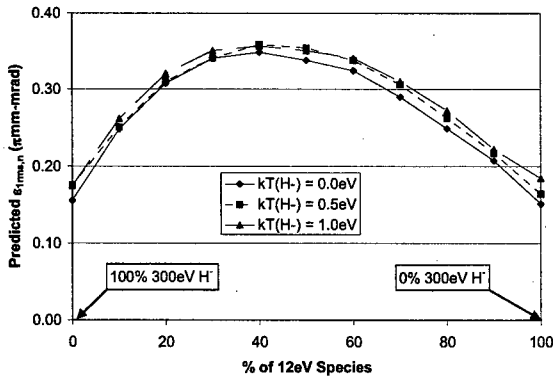

Fig. 7. PBGUNS model for emittance predictions of extraction of mixed-energy H^- from a plasma source.

at the limit of pure surface converter (left) is in agreement with admittance expectations. However, predictions are that admixture of 10% of a 12eV component give a rapid rise in predicted emittance. The mechanism for emittance growth proposed here is one of mismatch[14], not of increased H^- ion temperature. Figure 7 shows predictions for the three ion temperatures of 0.0, 0.5, and 1.0 eV in a Maxwellian model, and their influence on the predicted emittance is small compared to the mismatch mechanism. The emittance growth model predictions are in the 2 – 2.5 range, about the same as the measured emittance growths shown in Fig. 5. Thus, a reasonable physical picture for the experimentally observed emittance growths is the simultaneous extraction of 250 to 300 eV surface converter produced and order 12 eV volume or anode produced ions. The results from Fig. 4 show evidence that a two-component beam increases as discharge power increases, just as emittance (Fig. 5) increases with beam current, or equivalently P_d.

REFERENCES

[1] The LANL SPSS Project, LAUR-98-4172(1998).
[2] D. H. Fitzgerald, et. al., Proc. of the 1999 Particle Accelerator Conf., (New York) IEEE Catalog No. 99CB36366, 518(1999).
[3] R. J. Macek, et. al., Proc. of the 2001 Particle Accelerator Conf., (Chicago) IEEE Catalog No. 01CH37268C, 688(2001).
[4] S. Hoekstra, K. N. Leung, R. Thomae, and B. Prichard, Proc. of the 2000 European Particle Accelerator Conf., (Vienna, Austria), 1604(2000).
[5] R. Keller, J. M. Verbeke, P. Scott, M. Wilcox, L. Wu, and N. Zahir, Proc. of the 1999 Particle Accelerator Conf., (New York)IEEE Catalog No. 99CB36366, 1926(1999).
[6] Benjamin A. Prichard, Jr., and Ralph R. Stevens, Jr., "Status of the SPSS H^- Ion Source Development Program", Los Alamos Unclassified Report, LA-UR-02-547, (2002).
[7] R. L. York, Ralph R. Stevens, Jr., R. A. DeHaven, J. R. McConnell, E. P. Chamberlin, and R. Kandarian, Nucl. Instrum and Meth. In Phys. Res. B10/11, 891(1985).
[8] W. B. Ingalls, et. al., Proc. of the 1999 Particle Accelerator Conf., (New York)IEEE Catalog No. 99 CB36366, 1923(1999).
[9] J. E. Boers, Proc. of the 1995 Particle Accelerator Conf., IEEE Catalog No. 95CH35843, 2312(1995).
[10] E. G. Jacobson, R. L. Haffner, W. B. Ingalls, B. J. Meyer, and J. E. Stelzer, Proc. of the XIX International Linac Conf., (Chicago, IL)ANL-98/28,621(1998).
[11] Rodney C. McCrady, Mark S. Gulley, and Andrew Browman, LANSCE-6 Technical Report LANSCE-6-01-88-TR, LA-UR-01-6005, (2001).
[12] Paul Allison, Proc. of the Fourth International Symposium on the Production and Neutralization of Negative Ions and Beams, (Brookhaven, NY), AIP Conf. Proc. No. 158, 465(1986).
[13] G. E. Derevyankin and V. G. Dudnikov, Proc. of the Third International Symposium on the Production and Neutralization of Negative Ions and Beams, (Brookhaven, NY), AIP Conf. Proc. No. 111, 376(1983).
[14] J. Guyard and M. Weiss, Proc. of the 1976 Linear Accelerator Conf., (Chalk River, Ontario, Canada), AECL-5677, 254(1976).

VERY HIGH VOLTAGE PHOTOEMISSION ELECTRON GUNS*

Charles K. Sinclair#, Cornell University, Ithaca, NY 14853, USA

Abstract

There are a growing number of applications for CW electron accelerators, many requiring high average current and small transverse and longitudinal emittances. Very high voltage DC electron guns with photoemission cathodes are a natural choice for generating the beams for these machines. High average current applications require high quantum efficiency photocathodes at practical wavelengths. The necessary lasers are state-of-the-art systems that must be considered in choosing a photocathode. Field emission from the electrode structures limits the operating voltage and cathode field gradient in these guns. The photocathode operational lifetime is limited by the gun vacuum and by ion back bombardment. Recent developments in areas as diverse as vacuum technology, CW lasers with RF time structure, and the reduction of field emission from large area electrodes show promise for the development of a new generation of DC photoemission electron guns, operating at very high voltage and cathode field strengths well above those obtainable in the past. These developments, and various designs for very high voltage photoemission electron guns, will be reviewed.

INTRODUCTION

The successful demonstration of beam energy recovery at the Jefferson Laboratory IRFEL [1], coupled with the excellent performance of superconducting RF cavities at high accelerating gradient [2], has led to a number of ideas and proposals for CW electron accelerators for electron cooling [3], the production of synchrotron radiation [4], and linac-ring versions of a future electron-ion collider [5]. These machines all require high average current CW electron sources, frequently with demanding specifications on transverse and longitudinal emittances.

DC electron guns with photoemission cathodes are a natural choice for such applications. While RF guns operating at very high accelerating gradients are the current choice for delivering high charge electron bunches at low duty factor, their maximum accelerating gradient in CW operation is significantly lower [6]. Recent developments in the reduction of field emission from large area electrodes offer the possibility of operating DC guns with cathode field gradients comparable to those practical in CW RF guns [7].

High average current operation requires high quantum efficiency photocathodes, which are notoriously sensitive to the vacuum environment. Compared with RF guns, DC guns offer distinct advantages for the production of excellent vacuum. In DC guns, there are few restrictions on vacuum chamber geometry or the location and size of ports, and many choices for wall materials. They operate at ambient temperature without cooling. Electron-optically, they have no time varying fields, and easily incorporate transverse focusing at the cathode.

To date, DC photoemission guns have employed GaAs photocathodes, and are used primarily for the production of low average currents of polarized electrons. Operating voltages have been modest, typically about 100 kV. The Jefferson Lab IRFEL gun is a significant exception to these statements. This gun has operated at ~ 320 kV, delivering 5 mA of average current at bunch repetition rates of ~ 75 MHz [8]. It is presently being upgraded to operate at 500 kV and 10 mA average current.

High average current, high brightness CW electron injectors will require significant R&D before they are realized. The technology choice between high voltage DC photoemission guns, normal conducting RF guns, and superconducting RF guns is a matter of current debate. In the sections below, we present information on the current issues and state-of-the-art with DC guns, and indicate where future improvements might lead.

FIELD EMISSION

Field emission is the principal effect limiting the operating voltage and electrode field strength in DC electron guns. It is the source of undesirable phenomena, such as charging of ceramic insulators, localized melting in areas struck by field emitted electrons, and vacuum degradation from both heating and electron stimulated desorption (ESD). These problems can lead to voltage breakdown of the cathode-anode gap, electrode surface damage, and punch through of the ceramic insulator.

In a gun with a Pierce electrode to provide focusing, the peak field on the electrode is two to three times higher than the field on the cathode. Electrodes are generally made from stainless steel. At field strengths approaching 10 MV/m field emission currents typically become unacceptable, and conservative gun designs limit electrode fields to values below this level. The strong dependence of field emission on field strength means that one does not have to reduce the field too greatly.

Many researchers have empirically explored field emission and its reduction by various surface treatments. These studies have usually been made on small area samples with small gaps over relatively short periods of time, making it difficult to apply a "good" experimental result to the real conditions in a high voltage gun. A test chamber was constructed at Jefferson Lab to study large area electrodes with moderate gaps. The electrodes had a uniform field area of 116 cm^2. Voltages to 125 kV were applied to several mm gaps during eight hour tests. We demonstrated a dramatic reduction in field emission from samples coated with ~ 500 nm of silicon dioxide. Two samples showed field emission below 1.5 pA/cm^2 at 30 MV/m, and undetectable emission below 22 MV/m [7].

*Work supported by Cornell University
#cks26@cornell.edu

0-7803-7738-9/03/$17.00 © 2003 IEEE

CERAMIC INSULATORS FOR HIGH VOLTAGE HOLDOFF

A ceramic insulator isolates the high voltage applied to the cathode electrode and its support structure. Field emission originating at the ceramic-metal-vacuum triple junction is a well-understood cause of internal surface flashover, and is controlled by reducing the field on the junction with electrostatic shields. The external ceramic surface is usually fluted to inhibit flashover.

Charging caused by small field emission currents is a serious problem due to the exceptionally high ceramic bulk resistivity. Various ways of overcoming this problem have been developed. An insulator comprised of a series of ceramic rings separated by appropriately shaped metal electrodes can prevent field-emitted electrons from striking the ceramic. The electrodes are joined with external resistors to grade the potential uniformly [9]. Coatings with suitable sheet resistance have been used. More recently, ion implantation has been shown to produce a stable uniform sheet resistance on the surface of a ceramic [10]. While difficult to adapt to a large ceramic, this is an otherwise attractive solution. A sheet resistance of 50 to 100 Gohm/square is appropriate. The ideal solution may be to develop a ceramic with a stable homogeneous bulk resistivity of about 70 Gohm-cm. The temperature dependence of these high resistivities must not allow thermal runaway. Finally, the "inverted" gun design, described below, avoids the problem of field-emitted electrons striking the ceramic.

PHOTOCATHODE CHOICES

For any laser illuminated linear photoemitter, the photocurrent is given in terms of the laser wavelength and power and the cathode quantum efficiency by:

$$i(mA) = \frac{\lambda(nm)}{124} \bullet P_{laser}(W) \bullet Q.E.(\%)$$

This expression gives the minimum product of laser power and quantum efficiency to produce the current, since it assumes every electron and laser photon is used. If, for example, photons are lost in shaping the laser beam temporally or spatially, a higher raw laser power is required.

There are three families of practical high quantum efficiency photoemitters. These are alkali antimonides, alkali tellurides, and III-V semiconductors. All are p-type semiconductors. The first two have positive electron affinity (PEA), while the III-V semiconductors have negative electron affinity (NEA). In the PEA case, the bottom of the conduction band in the bulk material lies below the vacuum level outside the cathode, while in the NEA case, the conduction band minimum lies above the external vacuum level. This difference has important consequences for the cathode thermal emittance. Table 1 gives the operating parameters of typical photocathodes from each of the three high quantum efficiency families.

Table 1. Typical Cathode Operating Characteristics

Typical Cathode	Operating Wavelength (nm)	P x Q.E. to produce a 1 A current (Watt-%)
K_2CsSb	527	235
KCsTe	266	466
GaAs (Cs,F)	780	159

Photoemission from these cathodes is described by the "three step" model. These steps are (a) photon absorption in the bulk cathode material; (b) electron diffusion to the cathode surface; and (c) electron emission through the surface potential barrier. Since the semiconductors are p-type, their conduction band is empty. The incident light is absorbed by valence band electrons, which are promoted to the conduction band. Electrons in the conduction band experience electron-phonon collisions, in which they lose energy and change direction as they diffuse toward the cathode surface. This energy loss continues until the electron reaches the conduction band minimum, where it remains until it is either emitted or recombines.

In a PEA cathode, electrons at the conduction band minimum are energetically prevented from being emitted, unlike in the NEA case. Electrons excited to the conduction band in NEA materials are likely to thermalize at the band minimum before they are emitted if the exciting photon energy is not too great. The emitted electrons thus originate from a population with an effective temperature close to the physical temperature of the cathode, resulting in a very low thermal emittance. This is in direct contrast to PEA emitters. Several emittance measurements of the beams from NEA GaAs photoemitters have confirmed the low thermal emittance, down to temperatures of 77 K [11].

Optical absorption in the antimonides and tellurides is very much greater than in the III-V materials, leading them to have a much faster temporal response, since the electrons have a much shorter distance to diffuse to reach the cathode surface. III-V photocathodes can support electron pulses no shorter than about 20 - 40 ps, while the antimonide and telluride cathodes support ps or shorter duration pulses.

LASER SYSTEMS

Lasers with RF time structure are required to produce a beam bunched at the photocathode, for subsequent acceleration in an RF linac. The time structure is generally produced in an actively mode-locked laser. At high repetition rates, the laser cavity length becomes impractically short, and in this case harmonic mode-locking may be used [12].

A convenient method of harmonic mode-locking was demonstrated at Jefferson Lab. Light from an RF gain-switched diode laser was injected into a Ti:sapphire laser cavity. The RF was derived from the accelerator master oscillator. This scheme has produced >2 W average power pulse trains stably locked to the accelerator RF at rates between ~200 MHz and 3 GHz [13]. The fundamental wavelength of Ti:sapphire lasers is well matched to GaAs photocathodes. Ti:sapphire lasers

operating at much higher power levels have been developed, and a version of this system operating at ~ 10 W appears feasible [14].

Alkali antimonide and telluride photocathodes require shorter wavelength illumination, presently provided by frequency doubling or quadrupling Nd:YAG or Nd:YLF lasers, or frequency doubling or tripling Ti:sapphire lasers. Quantum efficiencies of 10% or greater have been prepared on cathodes of each type in Table 1, implying that average optical powers of ~ 2-5 W are necessary to generate 100 mA average current. In practice, one needs optical power well above this minimum, to accommodate degradation of the quantum efficiency with beam delivery. This laser power requirement is far more challenging at shorter wavelengths, when the inefficiencies of frequency multiplication are included. The use of alkali telluride photocathodes at high average current appears particularly daunting in this regard.

PHOTOCATHODE LIFETIME AND VACUUM ISSUES

Nothing happens during photoemission that degrades the quantum efficiency of a photocathode. However, all high quantum yield photocathodes are chemically reactive, and are degraded by chemically active gas species in the vacuum. For example, exposures to a small fraction of a Langmuir of H_2O or CO_2 can significantly degrade quantum efficiency. Photocathodes may also be damaged by ion back bombardment, independent of the gas species forming the ion. Thus, for long photocathode operational lifetimes, both the partial pressures of reactive gas species and the absolute pressure must be very low.

If the photocathode lifetime is long with no high voltage applied to the gun, one can be confident that harmful residual gases are not present. Static photocathode lifetimes of thousands of hours have been demonstrated at many laboratories and with all three photocathode types. At Jefferson Lab, one GaAs cathode showed no measurable loss of quantum efficiency on a cathode exposed to the static vacuum for several months, corresponding to a 1/e lifetime over 20,000 hours.

Field-emitted electrons may be a source of residual gases through ESD, and thus shorten the cathode life when high voltage is applied to the gun. While measurements of cathode lifetime with high voltage applied but no illumination have not been made for extended times, information on this point can be had by observing the lifetime at low average beam current. For most guns constructed to date, ESD from field-emitted electrons has not caused significant quantum efficiency degradation. This situation may prove different in DC guns operating at very high electric fields.

Electrons originating at the cathode and striking downstream vacuum chamber walls can generate a significant gas load. This was observed in the Jefferson Lab polarized guns, and was traced to electrons originating from very large radius on the cathode, near the junction between the cathode and the focusing (i.e. Pierce) electrode. Electrons from this region receive a substantial transverse kick from the locally large transverse fields, and follow extreme trajectories that ultimately strike beam tube walls. Deadening the quantum efficiency at large radius cured this problem, and resulted in lifetime improvements of factors of a thousand or more [15].

When all reactive gases are eliminated, ion back bombardment remains as a source of photocathode degradation. This mechanism has a clear signature, since the photocathode typically has an active area much larger than the illuminated area. In such circumstances, and with focusing at the cathode, electrons originating from off-center on the cathode follow trajectories that move toward the electrostatic axis of the gun. The ions produced, however, are accelerated directly back to the cathode with very little transverse displacement. Thus, the ions damage only regions of the cathode radially inside the electron emission point, along a line joining the emission point and the electrostatic center of the cathode. This damage signature has been clearly observed in several DC guns. While the details of the ion damage mechanisms are not clear, the solution is to reduce the vacuum pressure.

When ion back bombardment is the cathode lifetime limiting phenomenon, the cathode life is better expressed in terms of the charge delivered per unit illuminated area, rather than in clock hours or charge delivered. The best GaAs cathode lifetime reported to date is a 1/e degradation of the quantum efficiency from the delivery of 2×10^5 C/cm^2. It is important to note that III-V cathodes are bulk materials with a monatomic surface dipole layer, while the alkali antimonide and telluride cathodes are stoichiometric compounds. Thus, the response of these cathodes to ion back bombardment may be quite different.

In a DC gun with no ESD gas load, outgassing is the source of residual gas. This can be greatly reduced by the use of non-evaporable getter coatings sputtered on the chamber walls [16]. These coatings have very low outgassing, very high pumping speed for chemically active gases, very low ESD, and act as a diffusion barrier to gases permeating through the chamber walls.

LOAD LOCKS AND GUN DESIGNS

No high quantum efficiency cathode can be transferred through air without being destroyed, and it seems unlikely that a suitably inert atmospheric pressure environment can be established to allow such transfers without degradation. Attempts to prepare protective coatings on photocathodes have been made, but to date all have caused a loss in the quantum efficiency to levels unsuited for high average current use [17]. Thus, it is necessary to either prepare cathodes in situ in the electron guns, or transfer them under vacuum from a separate preparation chamber, using a load lock.

Three reasons are generally given in support of using a load lock system. These are that with a load lock (a) it is

possible to have multiple cathodes prepared, ready for transfer into the gun; (b) the gun vacuum, once established, is never disturbed by cathode exchanges; and (c) there is no risk of contamination of high field electrode surfaces with alkali metals.

The first two of these reasons are weakened somewhat by operating experience with the Jefferson Lab polarized sources. Very long cathode lifetimes, ease of repeatedly cleaning and re-activating cathodes to their original quantum efficiency, and demonstrably excellent vacuum conditions were all reliably obtained in guns with no load lock. However, contamination of high field strength electrode surfaces with even tiny amounts of alkali metals could easily lead to unacceptably high levels of field emission, particularly in guns designed to operate at high field strength, and is reason enough to use a load lock. No doubt all future very high voltage DC photoemission guns will employ load locks.

The simplest gun design involves no load lock. An example is shown in figure 1. This gun, designed to operate at 500 kV for the Jefferson Lab IRFEL, has a GaAs wafer mounted on a long cathode "stalk". Installation of the cathode stalk involves breaking the gun vacuum. Following a vacuum bakeout after cathode installation, the cathode is activated by the introduction of cesium through the anode aperture. In practice, though the gun could be processed to full voltage before the

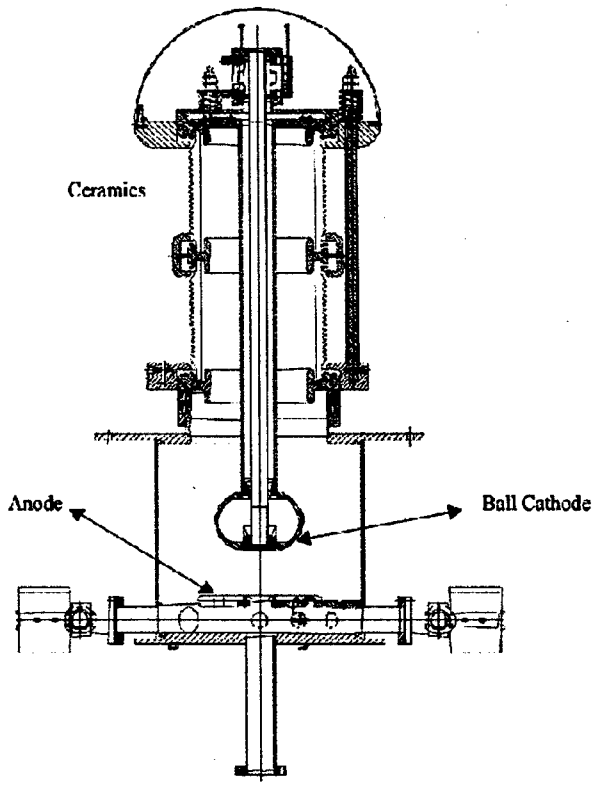

Figure 1. The 500 kV gun at the JLab IRFEL

cathode was activated, after activation field emission was excessive above 320-335 kV. The gun did operate reliably for extended periods of time and multiple cathode activations at this reduced voltage [8].

As there is significant space available within the large cathode electrode, this gun has been redesigned to allow the cathode to be activated while retracted completely within this electrode, greatly reducing the likelihood of cesium contamination on the high field surfaces. A shutter blocks the aperture in the cathode electrode during high voltage processing. These changes are expected to allow the gun to reach its 500 kV design voltage, and will soon be tested.

The simplest implementation of a load lock places the entire cathode preparation chamber and load lock transfer mechanism at cathode potential. This solution was adopted for the SLC polarized source, which operated at 120 kV [18]. It becomes increasingly awkward to implement as the operating voltage is increased. In a design developed at Mainz, the cathode was moved into the cathode-anode gap, allowing cathode preparation and transfer mechanisms to be mounted at ground potential [19]. There are concerns that the edges of the cathode electrode could become a source of field emission in a very high voltage gun of this design.

Another way to locate the cathode preparation and transfer mechanism at ground potential is to use a second ceramic insulator between cathode potential and ground. Cathode transfer takes place along the axis of this second insulator. This solution was developed by Novosibirsk for the 100 kV NIKHEF polarized source [20], and has been adopted for a 200 kV gun built at Nagoya [21]. At high voltages, the transfer distance can become quite long.

A clever scheme known as the "inverted" gun was developed at SLAC, and shown in figure 2 [22]. The cathode electrode is supported within the gun chamber on ceramic rods, with the cathode preparation and transfer mechanisms at ground. High voltage is brought in through the bore of one of the rods, but could also be delivered through a separate feedthrough. In this design, field emitted electrons cannot reach the ceramic rods. The

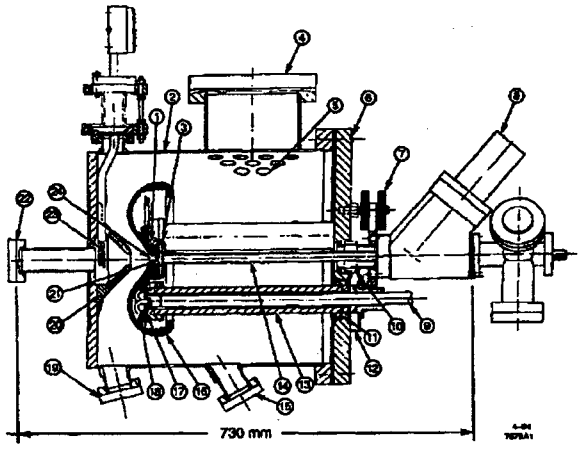

Figure 2. The inverted gun developed at SLAC

SLAC gun was designed to reach 200 kV, and operated there, though with very high levels of field emission, which were not understood.

Another load lock gun design has been developed at Jefferson Lab. The cathode electrode is a hollow cylinder, isolated by a conventional ceramic, as shown in figure 3 [23]. The cathode is introduced through one end of this cylinder and secured into its operating location at the other end. This design incorporated an atomic hydrogen cleaning chamber, allowing a cathode sample to be cleaned prior to being moved into the preparation chamber. With this system, a cathode sample has been taken from the laboratory environment to beam delivery in several hours.

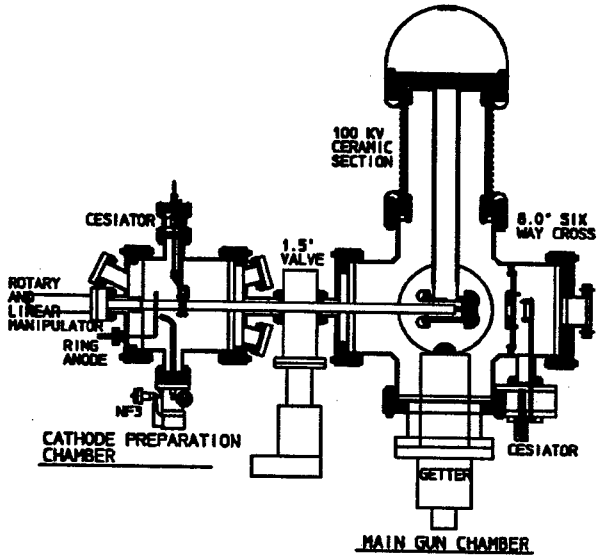

Figure 3. The JLab load-locked gun design

CONCLUSIONS

Very high voltage photoemission electron guns may well be able to meet the requirements for a number of currently envisioned CW electron accelerators. Methods for dramatically reducing the field emission from large area electrodes set the stage for operating such guns with electrode field strengths of 20 MV/m or more. Ion implantation, the development of ceramics with appropriate bulk restivities, insulator designs incorporating internal protective rings, or the use of the inverted gun design can eliminate the problem of ceramic charging from even small field emission currents. Various load-locked gun designs operating reliably and breakdown free at voltages above 500 kV and at cathode field strengths above 10 MV/m now seem within reach.

For high average current operation, only high quantum efficiency photocathodes can be considered. Of the three families of such photocathodes, the alkali antimonides and tellurides have been used in RF guns, while NEA GaAs cathodes have been used in DC guns. In the GaAs cathode/DC gun case, the cathode operational lifetime is limited by ion back bombardment. The best 1/e lifetime reported to date is 2 x 10^5 C/cm^2. The lifetime of the alkali antimonide and telluride cathodes may well be better than GaAs in a DC gun. The ion back bombardment lifetime may be improved by reducing the total vacuum pressure, which appears practical using NEG coatings in the gun vacuum chamber.

Lasers with the necessary RF time structure pose a challenge for high average current operation. The GaAs cathode offers an advantage, as the fundamental wavelength of a Ti:sapphire laser is suitable. Alkali antimonide cathodes require frequency doubled Nd or Ti lasers, while the tellurides require frequency quadrupled Nd, or frequency tripled Ti lasers, and thus require more fundamental laser power to overcome the inefficiency of frequency multiplication. Fundamental frequency or harmonic mode-locked Nd or Ti lasers delivering 10 W of optical power with suitable RF time structure are well within reach.

NEA GaAs offers a significantly lower thermal emittance per unit illuminated area, compared to PEA cathodes, while PEA cathodes offer far shorter pulse durations. In a DC gun followed by a buncher, the long pulse from NEA GaAs may not be a significant drawback. Based on all these considerations, we plan to construct a 500 to 750 kV gun with a NEA GaAs cathode to provide a 1300 MHz train of 77 pC bunches – 100 ma average current – for the Cornell/JLab ERL prototype [4].

REFERENCES

[1] G. R. Neil et al., Phys. Rev. Letters **84**, 662 (2000).
[2] B. Aune et al., Phys. Rev. ST-AB **3**, 092001 (2000).
[3] V. Parkhomchuk and I. Ben-Zvi, ref. 47 at http://www.agsrhichome.bnl.gov/ap_notes/cad_ap_index.html
[4] CHESS Technical Memo 01-003, available at http://erl.chess.cornell.edu/papers/ERL_Study.pdf
[5] L. Merminga et al., EPAC 2002, p. 203
[6] R. A. Rimmer et al., EPAC 2002, p. 1801
[7] C. K. Sinclair et al., PAC 2001, p. 610.
[8] T. Siggins et al., NIM A **475**, 549 (2001)
[9] J. Haimson, IEEE Trans. Nucl. Sci. **NS-22**, 1354 (1975)
[10] S. Anders et al., PAC 1993, p. 1390
[11] B. M. Dunham et al., PAC 1995, p. 1030; D. A. Orlov et al., Appl. Phys. Letters **78**, 2721 (2001)
[12] M. F. Becker et al., IEEE J. QE, **8**, 687 (1972).
[13] C. Hovater and M. Poelker, NIM A **418**, 280 (1998)
[14] W. J. Wadsworth et al., Appl. Opt. **38**, 6904 (1999)
[15] C. K. Sinclair, PAC 1999, p. 65; K. Aulenbacher, private communication.
[16] C. Benvenuti et al., JVST A **16**, 148 (1998), Y. Li and S. Ho, these proceedings.
[17] A. Breskin et al., Appl. Phys. Letters **69**, 1008 (1996).
[18] R. Alley et al., NIM A **365**, 1 (1995).
[19] K. Aulenbacher et al., NIM A **391**, 498 (1997).
[20] C. W. de Jager et al., AIP Conf. Proc. No. 421, p. 483 (1997).
[21] M. Yamamoto et al., LINAC 2002, to be published.
[22] M. Breidenbach et al., NIM A **350**, 1 (1994).
[23] W. J. Schneider et al., PAC 1999, p. 1991

ADVANCED ECR SOURCES FOR HIGHLY CHARGED IONS

S. Gammino, G. Ciavola, L. Celona, L. Andò
Istituto Nazionale di Fisica Nucleare-Laboratori Nazionali del Sud, Via S. Sofia 44, 95123 Catania, ITALY

D. Hitz, A. Girard, G. Melin
CEA Grenoble, Département de Recherche Fondamentale sur la Matière Condensée
Service des Basses Températures, 17 Rue des Martyrs, 38054 Grenoble Cedex 9, FRANCE

Abstract

New technologies for next generation Electron Cyclotron Resonance Ion Sources (ECRIS) are under development in many laboratories in the world, in order to achieve higher charge states and higher currents, especially for heavy ion beams. In particular, in the last few years the efforts have been concentrated on the coupling of high power high frequency microwaves (e.g. 10 kW, 28 GHz), on the study and the development of complex magnetic systems for an adequate plasma confinement, on the design of extractors able to minimize the emittance of heavy ion beams at high current level (tens of milliamperes).

The first injection of a high power (6 kW) of a 28 GHz wave in a B-min ECRIS was achieved in the SERSE superconducting source at INFN-LNS, Catania in 2000. High currents of ions were produced, both in pulsed and dc modes. Since then, other relevant improvements in the ECR source technology have been carried out. The talk will describe the major developments of ECRIS science and technology in Europe, Asia and US.

The conceptual design of a high magnetic field superconducting ECR ion source, named GyroSerse will be also described. This multipurpose ECR ion source aims to:

- the production of very high charge states of heavy ion beams (i.e. up to 1 eμA of U^{60+} and 5 pμA of light ions up to Ar^{16+} in cw mode).
- the production of high current of highly charged ions both in cw and pulsed mode such as 1 emA of Xe^{20+} beams or 0.3 emA of U^{30+} beams in dc mode and 6 emA of U^{28+} in pulsed mode (with a pulse duration of 200 μs).

For injection into the accelerator, all these beams should fulfill the following requirements: energy from 2.5 to 5.0 keV/nucleon, emittance lower than 200 π mm.mrad and high reliability.

1 INTRODUCTION

The future accelerators need ion beams with higher charge state and higher current. This demand will be met by the 'third generation' Electron Cyclotron Resonance Ion Sources' (ECRIS) which will make use of increased plasma density by means of higher magnetic field and of higher microwave frequency, thus boosting the performance of nowadays ECRIS operating at the frequency of 14 and 18 GHz. The possibility to obtain confining fields exceeding 4 Tesla, by means of special design of NbTi superconducting magnets, open the way to a new operational domain, at the typical frequencies of gyrotrons, above 28 GHz, with plasma densities never achieved before in ECRIS (10^{13} cm^{-3} and higher).

A similar ECR ion source is useful for any accelerator facility based on a linac or a cyclotron, and particularly relevant is the gain for the future accelerator facilities (LHC and GSI in Europe and RIA in US) which needs currents of a few hundreds eμA or even thousands [1, 2, 3].

Even if relevant improvements were obtained by some conventional ECRIS in the recent past, the highest performance from ECRIS can be obtained only at higher frequencies and with higher confining fields, so that the B-minimum trap must be realized with superconducting magnets.

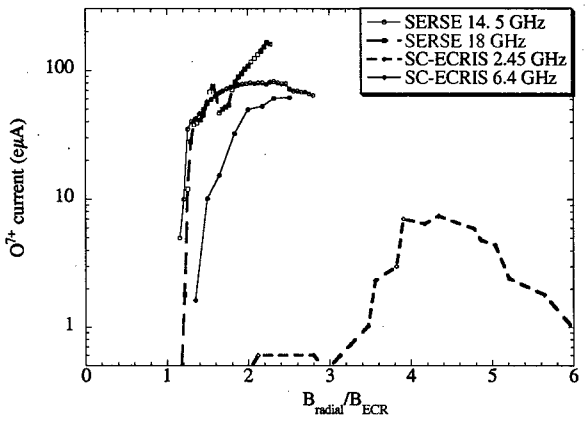

Figure 1: The comparison of ECRIS performance at different frequency versus the magnetic field.

2 EXPERIENCE AT LOWER FREQUENCIES

A large number of experiments have permitted to establish the rules that link the ion source performance to magnetic field strength and shape as well as to the frequency [4]. In particular systematic tests have been carried out with two superconducting magnets ECRIS, at

0-7803-7738-9/03/$17.00 © 2003 IEEE

MSU-NSCL in 1993-95 [5,6] and at INFN-LNS in 1998-99 [7], in order to validate the scaling laws and the High B mode concept. The results of these tests are summarized by Fig. 1, which shows the beam currents as a function of the radial confinement for frequencies between 2.45 and 18 GHz. Already in 1995 we proposed [8] some rules which an efficient ECRIS must follow to produce intense beams of medium and high charge states and that have been recently defined as the ECRIS standard model [9].

3 PIONEERING 28 GHZ OPERATIONS AND STATE OF THE ART OF ECRIS

In 1994, at INFN-LNS a design study of an ECRIS operating at 28 GHz was carried out. This project was suspended because the technology needed to the construction of a 3T hexapole was not available at that time. In 1995 the proposal of another fully superconducting magnets 28 GHz ECRIS, called VENUS, was presented from LBNL, with a lower magnetic field, according to the existing technology [10]. The construction of the source started in 1997 and its first plasma was obtained on May 2002 at 18 GHz [11].

In the meantime at INFN-LNS, after the successful exploitation of the SERSE source at 14 and 18 GHz and the validation of the High B mode concept, the GyroSERSE project was reconsidered, even because the possibility to obtain fields above 3 T became realistic.

In order to define the best parameters for the design of 3rd generation ECRIS, experiments have been performed with SERSE, coupled to a 28 GHz gyrotron-based generator [12,13,14]. It was the first time that this high frequency has been launched into a minimum-B structure and the first part of tests was devoted to the study of the RF coupling to the plasma, in order to achieve the cutoff density and the maximum electron temperature at the same time.

For the tests of SERSE at 28 GHz, a 10kW gyrotron was available, but only 2 to 4 kW were used in cw mode. The maximum power launched into SERSE was limited by the plasma chamber cooling power which was originally calculated for a maximum RF power of 2.5 kW at 18 GHz. In the afterglow mode, 6.5 kW have been launched at 10 Hz repetition rate (maximum duty cycle was 50%).

Even if the performance at 28 GHz were limited by the RF power, as well as by the poor magnetic confinement (the last closed iso-B surface being $B_{last} \approx 1.5\ B_{ECR}$) and by the low extraction voltage (26 kV maximum), the 28 GHz operations permitted to get currents exceeding half mA for Xe ions with charge states up to 25^+, as well as some eμA of charge states between 38^+ and 42^+, results which have been never obtained by any other source.

The full set of results at 28 GHz, complementary to the ones in fig. 1, are reported in refs. [12,13,14]. The experiments performed at 18 and 28 GHz gave more detailed rules for the magnetic confinement:

a) the last closed surface must be $B_{last} \approx 2\ B_{ECR}$, i.e. the so called High B mode [4, 10], customary used by the Caprice source [16];

b) the radial magnetic field value at the plasma chamber wall must be $B_{rad} \geq 2.2\ B_{ECR}$;

c) the axial magnetic field value at injection must be at least $B_{inj} \approx 3B_{ECR}$;

d) the axial magnetic field value at extraction must be about $B_{ext} \approx B_{rad}$;

e) the axial magnetic field value at minimum must be in the range $0.30 < B_{min}/B_{rad} < 0.45$.

The ideal ECRIS should have the highest frequency as possible to reach the highest electron density as possible (cutoff density is about proportional to the square of the frequency) and its magnetic field should obey to all these rules.

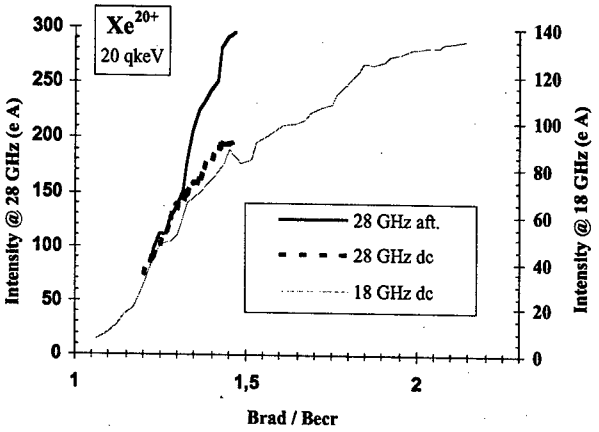

Figure 2 : Effect of the radial magnetic field on Xe^{20+} current [13].

The radial confinement had a major influence in the beam production for medium and high charge states as well, thus confirming the ECRIS standard model even at 28 GHz. Fig. 2 presents Xe^{20+} current increase with the radial mirror ratio (B_{rad} / B_{ECR}) at 18 GHz and 28 GHz. The left Y-axis scale is obtained from the right Y- axis scale by multiplying it for the square of the frequency ratio; then one can notice the remarkable superimposition of both curves in dc mode. Being the technological limit for the SERSE radial magnetic field 1.45 T, one can easily extrapolate that a further 75% gain is possible with a higher magnetic field, while keeping the other parameters constant. Additionally, a higher extraction voltage increases the extracted currents according to the $V^{3/2}$ law [13,14]. Therefore we concluded that a SERSE-type source scaled for 28 GHz operations can be the ideal source for high charge states and high current beam production.

Some other innovative sources have been commissioned or built more recently. In particular the liquid-He-free RAMSES 18 GHz ECRIS with hybrid magnets have given good results at RIKEN, Tokyo, already almost as good as the previous room temperature 18 GHz source. The source is shown in fig. 3. The

superconducting set of coils permits to get an axial magnetic field of 3 T and the NdFeB hexapole produce a radial field of 1.2 T at the plasma chamber wall radius. As reference for high current production, about 2 emA in dc mode of Ar^{8+} are produced at RIKEN [17].

However, because of the cost of superconducting ion sources, source development could be achieved on room temperature devices. The room temperature GTS source at CEA Grenoble [18,19] represents an extreme application of conventional techniques and it features the interesting possibility to inject 10, 14, 18 and 29 GHz microwave at the same time in the plasma chamber, that will permit to deepen the knowledge of the ECRIS science and technology. In single frequency operation (18 GHz) beam current above 1 mA of Ar^{8+} has been obtained and world record intensities have been broken for higher charge states like 420 μA of Ar^{11+}, 110 μA of Ar^{14+} . On the other hand, 2.1 μA of Ar^{17+} have been produced (two sources only are able to produce such high currents of H-like Argon, i.e. the superconducting SERSE source at INFN-LNS and the conventional AECR-U source at LBNL [20]). Beam intensities given by GTS confirm the necessity for any ECRIS to be operated with a confinement as presented in paragraph 3. With a reasonable extrapolation up to 28 GHz, one can think in reaching the 1 mA level for Ar^{12+}.

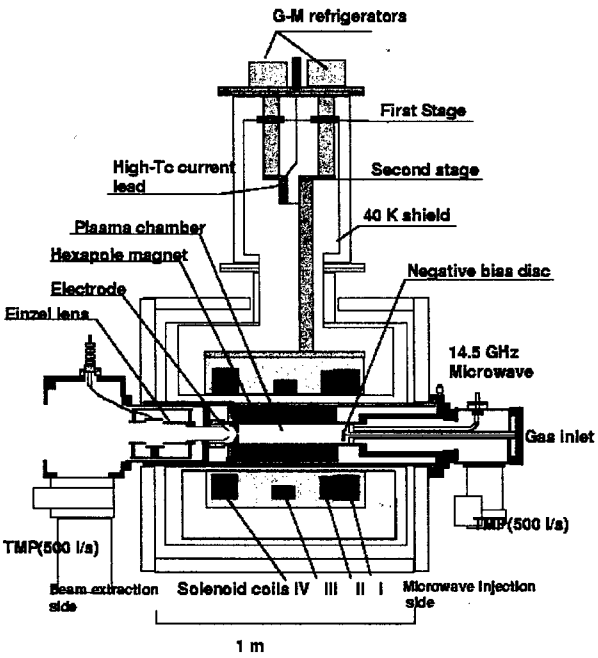

Figure 2: The RAMSES 18 GHz ECR ion source.

This summary of the ECRIS technology state of the art is certainly not exhaustive and more developments in the ECRIS field are under way but are not considered here for limits of space. More information can be found in [21].

It is worth mentioning in the next pages three appealing source designs based on fully superconducting magnets, as the SECRAL source of IMP, Lanzhou, the VENUS source of LBNL, Berkeley, and the GyroSERSE source.

4 SECRAL

The SECRAL source (fig. 4) has an innovative magnet design, which realizes a B-minimum trap by means of an hexapole external to the three solenoids, i.e. the contrary of what is usually done in any ECRIS. In this way the magnetic field is not so high as for VENUS and GyroSERSE design, and a much more compact source can be built, with a plasma chamber of 125 mm diameter and a total length of the source of the order of 1 m only.

The maximum radial field at the plasma chamber wall is expected to reach 2 T, which is almost the optimum field for 28 GHz operations.

The source construction is now under way and the magnets will be ready in summer 2003. As it is the case for VENUS, a preliminary series of tests at lower frequency will be carried out. More details on the SECRAL source are available in [22].

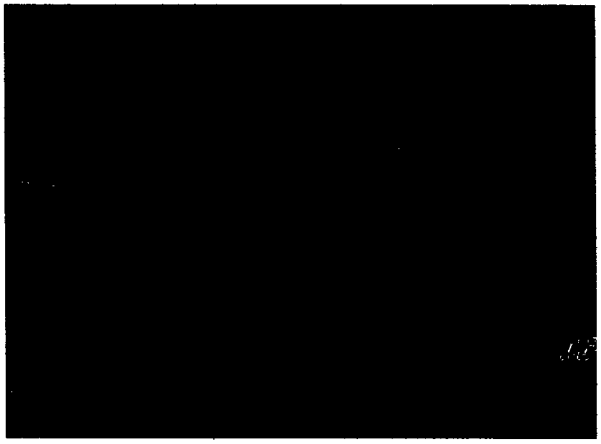

Figure 4 – The innovative design of the SECRAL source magnets at IMP, Lanzhou.

5 VENUS

VENUS source at the Lawrence Berkeley National Laboratory (fig. 5) is the first 3rd generation ECRIS to be completed. At this moment it is operating at 18 GHz, but it is able to operate in High B mode even at 28 GHz. Because of its excellent magnetic trap design, VENUS is deemed to get the leading role in the ECRIS field for the coming years and it is expected to fulfil the largest part of the requirements of the RIA project [3,9].

Some relevant improvements to the existing ECRIS technology were made to obtain large beams.

The plasma chamber has been designed to be able to handle 15 kW of RF power and inner surface is not round, as it presents cut-out at the location of plasma flutes. This original feature can improve the capability to withstand a large RF power which is needed to get the best results.

Special attention has been paid to the design of an adequate beam transport system, able to handle intense

beams. The experience of SERSE tests at 28 GHz has put in evidence the need to minimize the emittance growth and the solution chosen by the LBNL group is effective. A detailed description of the VENUS design and its state of the art is presented in ref. [23].

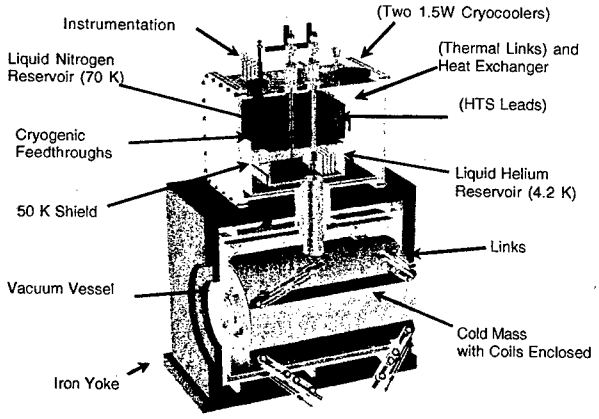

Figure 5 – An artistic view of the VENUS source.

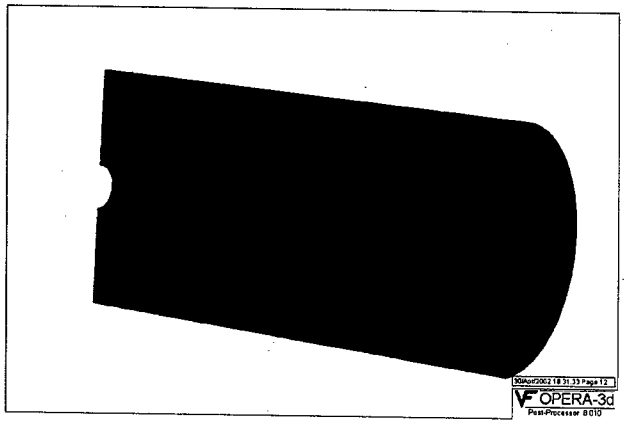

Figure 6: The OPERA-3D model of the GyroSERSE magnetic system.

6 GYROSERSE

The GyroSERSE project [24,25] was completed in 2001 and it was approved for funding in 2002-04. Unfortunately the construction was stopped because of budget limitations at INFN. Anyway further developments (study of the beamline, stray fields, etc.) continued, as there is a strong interest to install a 3rd generation ECRIS at LNS.

The main features of the magnet design of the GyroSERSE source and the comparison with the ones of SERSE, SECRAL and VENUS are given in tab. 1. Fig. 6 shows a model of the magnetic system, with the solenoids and the hexapole surrounded by an iron yoke and followed by the focusing solenoid which is the first element of the beamline. The mechanical constraints have obliged to choose a well larger inner bore than for SERSE, because of the boundary conditions for the hexapole. The plasma chamber inner diameter is 180 mm, 50 mm larger than the one of SERSE, and total volume will be doubled with respect to that source.

The B-mod lines in the plasma chamber features a value of the last closed surface of about 3 T. Then the magnetic field will permit to operate in High B mode, i.e. with a mirror ratio greater than 2, at any frequency between 28 and 37 GHz.

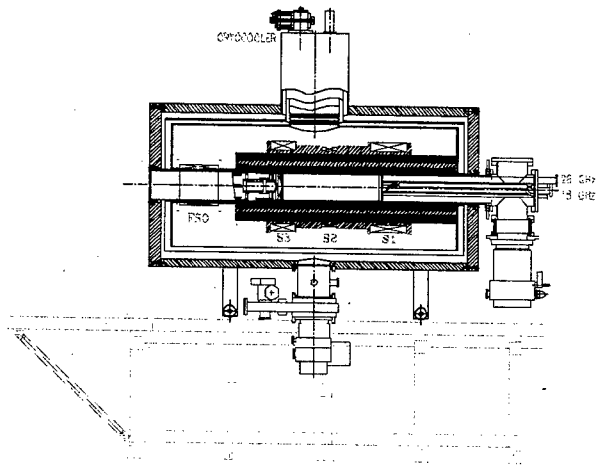

Figure 7: A sketch of the GyroSERSE source.

The coils of the magnetic system will be wound from NbTi superconducting composites and cooled by immersion in a liquid helium bath. The electrical connection to the power supply at room temperature will be made by high critical temperature superconducting currents leads.

The use of two cryocoolers will permit to operate the cryostat without external supply of liquid helium. The mechanical design is aimed to reliable operations at 50 kV extraction voltage and to the achievement of vacuum pressure of 10^{-8} mbar. In fig. 7 the sketch of the GyroSERSE is presented.

The 28 GHz RF coupling to the plasma will follow the guidelines of the one used for the SERSE 28 GHz experiment line [13] and a similar 28 GHz 10 kW gyrotron (TE_{02} output mode) will be used.

One of the major difference between the existing ECRIS and the 3rd generation ECRIS consists of the need to get rid of the space charge effects. By increasing the RF frequency heating from 18 GHz to 28 GHz, one had to face with extracted beams in the range of tens mA, which lead to larger emittances. Then the extraction voltage should be at least 40 kV to avoid the beam blowup due to space charge forces. A standard triode topology was chosen for GyroSERSE because of its simplicity, but a larger voltage and a smaller gap are considered. The calculated emittance ranges between 120 and 200π mm mrad at 40 kV extraction voltage. An extraction voltage higher than 40 kV may further decrease the emittance.

The different design options and the preliminary beamline simulations are described in more details in ref. [26].

More information on the GyroSERSE source design can be found in [24,25].

7 CONCLUSIONS

In the next three or four years a significant increase in the ECRIS performance is expected, as soon as the VENUS and SECRAL sources will be operating at 28 GHz.

In general, the trend to higher currents of multiply charged ions is expected to steadily continue. As an increase of one order of magnitude per decade was obtained over last twenty years, we are confident that multi-mA production can be possible by the end of this decade. As for the highest charge states, up to now achievable by Laser Ion source (with poor reproducibility and bad emittance) and by Electron Beam Ion Sources (with low currents), we expect that technology improvements can allow to increase the competition, with the production of intense dc beams with good emittance and reproducibility, up to 60^+ charge state and even more.

8 ACKNOWLEDGEMENTS

We acknowledge the support of the European Community – Access to Research Infrastructure action of the Improving Human Potential Programme, contract HPRI-1999-50014.

9 REFERENCES

[1] N. Angert et al., Proc. of the 14th Workshop on ECR ion sources, Geneve, (1999) 220
[2] P. Spiller et al, these proceedings
[3] B. Sherrill, these proceedings
[4] S. Gammino, G. Ciavola, Plasma Sources Science & Technology 5 (1996) 19
[5] S. Gammino et al., Rev. Sci. Instr. 67 (1), (1996) 155
[6] S. Gammino, et al., Rev. Sci. Instr. 67(12), (1996) 4109
[7] S. Gammino et al., Rev. Sci. Instr. 70(9), (1999) 3577
[8] S. Gammino G. Ciavola, Proc. 14th Int. Conf. on Cyclotrons & Appl., Capetown, (1995), 377
[9] C. Lyneis, 2nd RIA workshop, Argonne (2002), unpublished
[10] C. Lyneis, Z. Xie, Proc. of the 12th Workshop on ECR ion sources, Tokyo, (1995) 119
[11] M. Leitner et al., Proc. of the 15th Workshop on ECR ion sources, Jyvaskyla, (2002) 29
[12] D. Hitz et al., Proc. Workshop on "Production of Intense Beams of Highly charged ions", Catania (2000), Italian Phys. Soc. vol. 72, 13.
[13] S. Gammino et al., Rev. Sci. Instr., 72 (11), (2001) 4090
[14] D. Hitz et al., Rev. Sci. Instr. 73 (2), (2002), 509
[15] G. Ciavola, S. Gammino, Rev. Sci. Instr. 63(4), (1992) 2881
[16] B. Jacquot, M. Pontonnier, Nuc. Inst. Meth. A287 (1990) 341
[17] T. Nakagawa et al., Proc. of the 15th Workshop on ECR ion sources, Jyvaskyla, (2002) 25
[18] D. Hitz, D. Cormier, J.M. Mathonnet, Proc. of the 8th European Particle Accelerator Conference, Paris (2002) 1718
[19] D. Hitz et al., Proc. of the 15th Workshop on ECR ion sources, Jyvaskyla, (2002) 53
[20] Z. Xie, C. Lyneis, Proc. of the 13th Workshop on ECR ion sources, College Station, (1997) 16
[21] Proc. of the 15th Workshop on ECR ion sources, Jyvaskyla, (2002), editors J. Arje, H. Koivisto and P. Suominen
[22] H. Zhao et al., Proc. of the 15th Workshop on ECR ion sources, Jyvaskyla, (2002) 42
[23] D. Leitner et al., these proceedings
[24] L. Celona, et al., Proc. Workshop on "Production of Intense Beams of Highly charged ions", Catania (2000), Italian Phys. Soc. vol. 72, 157
[25] S. Gammino et al., Proc. of the 15th Workshop on ECR ion sources, Jyvaskyla, (2002) 19
[26] G. Ciavola et al., Nucl. Instr. & Meth. B 204 (2003) 410

Table 1: Comparison between the main parameters of SERSE, SECRAL, VENUS and GyroSERSE.

	SERSE	SECRAL	VENUS	GyroSERSE
Frequency	14 GHz +18 GHz	18 – 28 GHz	18-28 GHz	28-37 GHz
Maximum RF power P_{max}	2 kW + 2 kW	10 kW	10 kW	10 kW
B_{radial}	1.55 T	2.0 T	2.0 T	3 T
B_1 (injection)	2.7 T	4.0 T	4.0 T	4.5 T
B_2(extraction)	1.6 T	2.0 T	3.0 T	3.5 T
$\phi_{chamber}$	130 mm	126 mm	140 to 152 mm	180 mm
$L_{chamber}$	550 mm	804 mm	1030 mm	700 mm
$\phi_{cryostat}$	1000 mm	900 mm	1060*970 mm	1000 mm
$L_{cryostat}$	1310 mm	1000 mm	1070 mm	2150 mm
V_{extr}	20 kV (25 max)	40 kV	30 kV	40-50 kV
LHe consumption	~4l/h (100 l/day)	1 l/h	0	0

COMMISSIONING OF THE SUPERCONDUCTING ECR ION SOURCE VENUS *

D. Leitner**, S.R. Abbott, R.D. Dwinell, M. Leitner, C. Taylor, C.M. Lyneis,
LBNL, CA 94720, USA

Abstract

VENUS (Versatile ECR ion source for NUclear Science) is a next generation superconducting ECR ion source, designed to produce high current, high charge state ions for the 88-Inch Cyclotron at the Lawrence Berkeley National Laboratory. VENUS also serves as the prototype ion source for the RIA (Rare Isotope Accelerator) front end. The magnetic confinement configuration consists of three superconducting axial coils and six superconducting radial coils in a sextupole configuration. The nominal design fields of the axial magnets are 4T at injection and 3T at extraction; the nominal radial design field strength at the plasma chamber wall is 2T, making VENUS the world most powerful ECR plasma confinement structure. The magnetic field strength has been designed for optimum operation at 28 GHz. The four-year VENUS project has recently achieved two major milestones: The first plasma was ignited in June, the first mass-analyzed high charge state ion beam was extracted in September of 2002. The paper describes the ongoing commissioning. Initial results including first emittance measurements are presented.

VENUS ECR ION SOURCE

The goal of the VENUS ECR ion source project as the RIA R&D injector is the production of 200e A of U^{30+}, a high current medium charge state beam. On the other hand, as an injector ion source for the 88-Inch Cyclotron the design objective is the production of 5e A of U^{48+}, a low current, very high charge state beam. To achieve those ambitious goals, the VENUS ECR ion source has been designed for optimum operation at 28 GHz. This frequency choice has several design consequences. To achieve the required magnetic confinement, superconducting magnets have to be used. The size of the superconducting magnet structure implies a relatively large plasma volume. Consequently, high power 28 GHz microwave coupling becomes necessary to achieve sufficient plasma heating power densities. Finally, the extraction of the high current, multi-species ion beam out of the ion source plasma in the presence of a high magnetic field is a challenging task, and VENUS will provide an essential database for the design of future ECR high current injector systems.

Fig. 1 shows the mechanical layout of the ECR ion source. The mechanical design is described in detail elsewhere [1]. The water-cooling of the ion source is sufficient to allow continuous operation at 15 kW microwave input power.

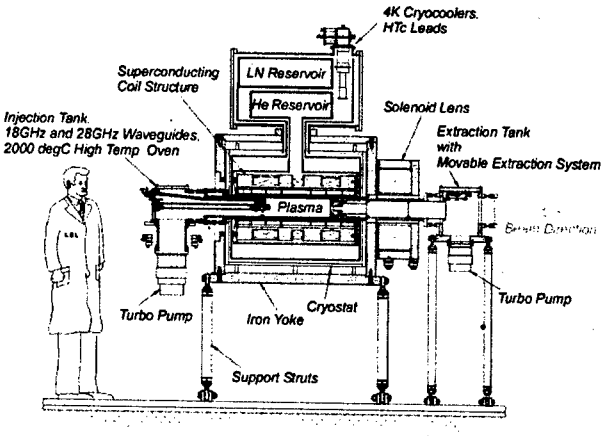

Figure 1: Mechanical layout of the VENUS ion source and cryogenic system.

The design and development of the superconducting magnets are described in [1,2]. The sextupole coils are wound around a pole with iron in the center, which enhances the peak field about 10%. The superconducting sextupole coils experience strong forces in the axial field of the solenoids. Therefore, a new clamping scheme utilizing liquid metal filled bladders was developed to prevent any movement of the energized coils [2]. During commissioning of the superconducting magnets, the sextupole reached 110% of its design field after a few training quenches (2.4T) with the solenoids operating at their design fields, 4T at injection and 3T at extraction respectively.

The cryogenic system for VENUS has been designed to operate at 4.2° K with two cryocoolers each providing up to 45 W of cooling power at 50° K and 1.5 W at 4° K in a closed loop mode without further helium transfers. During the acceptance test in September 2001, the cryostat failed to meet design specifications. The heat leak exceeded the design goal of 1.5 W and was measured to be about 3 W, which is at the limit of the two croycoolers' capacity. Furthermore the heat exchanger, which couples the LHe Reservoir to the two 1.5 W cryocoolers did not function properly, making it necessary to frequently transfer liquid helium. Thorough analysis of the original heat exchanger showed, that the thermal resistance of the flexible copper link was too high to efficiently transfer heat from the helium reservoir to the cryocoolers. Therefore, a new design approach was developed. Sets of fins machined from blocks of high conductivity copper are mounted directly on each cryocooler head and act as helium vapor

* This work was supported by the Director, Office of Energy Research, Office of High Energy and Nuclear Physics, Nuclear Physics Division of the U.S. Department of Energy under Contract DE AC03-76SF00098.
** DLeitner@lbl.gov ; http://ecrgroup.lbl.gov

0-7803-7738-9/03/$17.00 © 2003 IEEE

condensers. A tube was installed to transfer helium vapor from the reservoir to the condensers. There the vapor condenses, and the liquid helium returns to the reservoir through a second tube [3].

The two cryocoolers now provide sufficient cooling power for 18 GHz operation [3]. For 28 GHz operation, the expected x-ray flux will add to the heat load of the cryostat. Therefore, we are currently constructing a cryostat extension with an additional (third) cryocooler.

Beam Transport System

The low energy ion beam transport system shown in Fig. 2 consists of a moveable accel-decel extraction system (operating at voltages up to 30 kV), a solenoid lens, and a large gap, 90 degree double focusing analyzing magnet [4, 5]. The beam transport system was designed for high current, high charge state extraction. Therefore, to minimize beam blow up due to space charge, the extracted ion beam is directly matched into the analyzing magnet. In this kind of arrangement, a single solenoid lens is used to adjust the divergence of the beam going into the magnet. The beam diameter cannot be adjusted independently at the same time with only a single solenoid lens. Consequently, a large gap (18 cm) magnet was chosen to accommodate the ion beam size at high intensities [1].

After the mass analyzing section, a two-axis emittance scanner has been installed. In order to measure the actual ion source emittance instead of the magnet acceptance, 100% ion beam transmission with minimal aberrations through the analyzing section is essential.

In the early commissioning phase, during which total currents between 1 and 5 emA have been extracted, ion beam transmissions of 80 to 100% have been measured. Systematic emittance measurements are being carefully compared to the beam transport simulations. These studies will improve the theoretical understanding of the multi-ion species beam transport and will provide guidance for the design of future high current ECR injector systems.

FIRST COMMISSIONING RESULTS

The first plasma was ignited in June, the first mass-analyzed high charge state ion beam was extracted in September of 2002. Several technical challenges were solved during the first commissioning months. A PLC (programmable logic controller) based external regulation

	AECR-U 10+14 GHz	SERSE 14 GHz	SERSE 14+18 GHz	VENUS 18 GHz
O^{6+}	570	430	540	810
O^{7+}	300	225	225	220
Ar^{11+}	270	260	260	290
Ar^{12+}	192	200	200	180

Table 1 First VENUS commissioning results compared to best performance data from the AECR-U and the SERSE [7] ion sources at the given frequencies. The VENUS ion source has not been tested for very high charge state production.

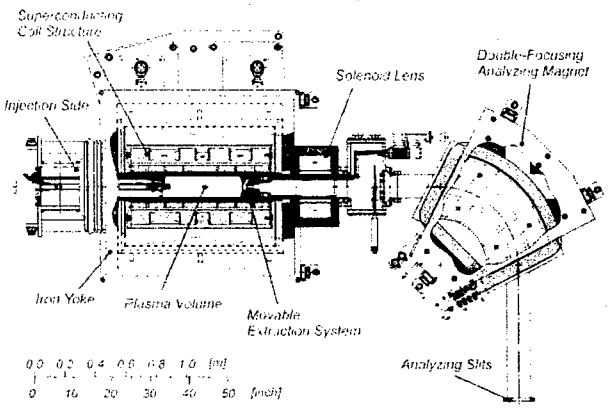

Figure 2: Mechanical layout of the beam transport system for VENUS.

loop for the superconducting magnet power supplies was developed. It allows ramping of the magnets in a reasonable time and stabilizes the magnets at the requested currents without fast oscillations, which can cause quenches. In addition, a new quartz HV break was developed for reliable 18 GHz microwave operation up to 2 kW. Holes were drilled into the waveguide inside the ion source vacuum chamber for better pumping in this long waveguide section to suppress a parasitic ECR discharge found in initial tests.

The vacuum system design, which uses only UHV compatible components and metal seals, is optimized for good plasma chamber pumping. Therefore, after initial operation with plasma, the base pressure is excellent (injection chamber low 10^{-8} mbar, extraction chamber low 10^{-9} mbar). So far, oxygen and argon gases have been used in the tests. Heavy ion beam production for very high charge states and metal ion beam production will be started this summer. Some preliminary results are presented in Table 1.

Venus has a plasma volume of about 9 liters, which is large compared to the AECR-U [6]. The microwave power density used in the AECR-U at peak performance is 1700 W/liter in double frequency mode and about 1000 W/liter in single frequency mode. A total power of 10 kW will be required to achieve an equivalent power density in VENUS. Once the 28 GHz gyrotron has been installed at the end of this year, this power density will be available.

Fig. 3 shows the analyzed O^{6+} current in e A as a function of 18 GHz microwave power. The current increases almost linearly with power, demonstrating that more rf power is needed to reach optimum performance.

In Fig. 4 the analyzed O^{6+} and O^{7+} current is plotted as a function of the radial field. For reference, the ratio of the radial field to the electron cyclotron resonance field (radial mirror ratio, B_{rad}/B_{ecr}) for 18 GHz is also shown. The current values peak at a radial mirror ratio of about 2, similar to the radial mirror ratio for maximum performance observed in SERSE at 14.5 GHz [8]. For 28 GHz operation, this maximum would be at 2 to 2.2T sextupole field. Therefore, the confinement of VENUS

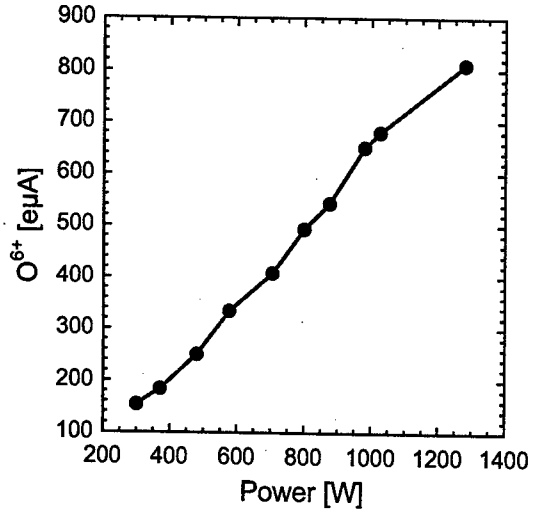

Figure 3: Analyzed O^{6+} current in dependence of the coupled RF power.

should be sufficient to achieve maximum performance at 28 GHz.

Systematic emittance studies with argon have begun recently, and first results are presented in Fig. 5. The 1-rms normalized emittance values for different argon charge states are plotted. Several charge states have been measured for various ion source and tuning conditions (rf power, plasma stability, extraction matching and ion optics). The different values are graphed to show the spread in measured emittance values.

The theoretical minimum emittance caused by the ion source axial magnetic field at the extraction is also plotted in this graph. The strong axial ion source magnetic field at the extraction induces a beam rotation that leads to emittance growth as described in [5]. There is a good agreement between the measured data and the predicted values. This suggests that the extraction system is well matched to the extracted ion beam current. On the other

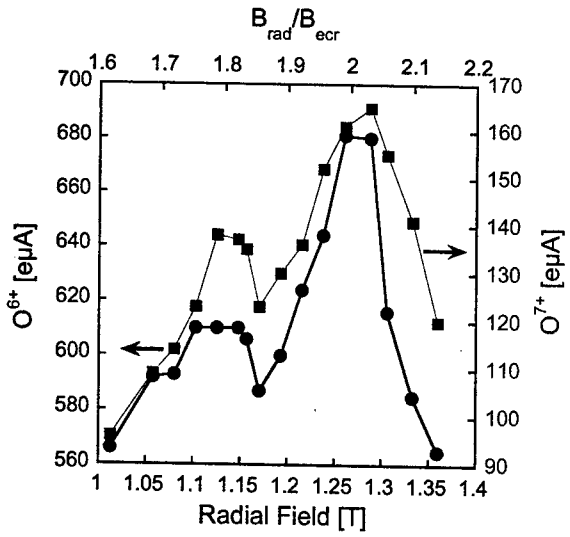

Figure 4: O^{6+} and O^{7+} ion beam intensity versus the radial magnetic plasma confinement field.

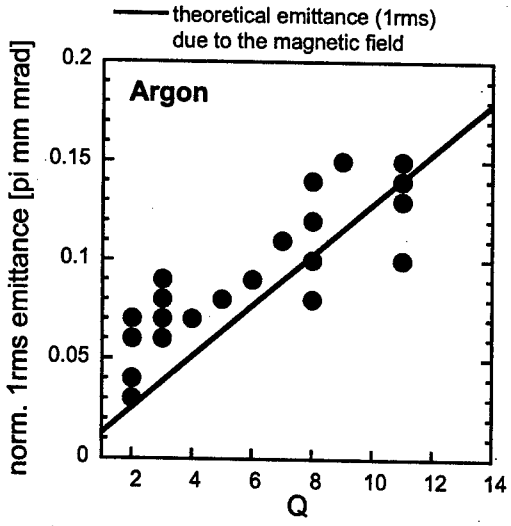

Figure 5: Measured emittance values for different charge states of argon in comparison with the predicted [5] theoretical minimum values due to the magnetic field.

hand, these measurements differ from previously measured emittance values at the AECR-U ion source [9], in which the emittance values decline for the higher charge states. It may be that the VENUS source tuning is not yet optimized for very high charge state production, in which higher charge states are extracted closer to the beam axis [5].

REFERENCES

[1] M.A. Leitner, C.M. Lyneis, D. Wutte, C.E. Taylor and S.R. Abbott, Physica Scripta, T92, 171-173, 2001

[2] C. E. Taylor, S. Caspi, M. Leitner, S. Lundgren, C. Lyneis, D. Wutte, S.T. Wang, J.Y. Chen, Magnet System for an ECR Ion Source, IEEE Transactions on Applied Superconductivity, 2000, 10(1), p. 224

[3] M.A. Leitner, D. Leitner, S. R. Abbott, C. E. Taylor, C. M. Lyneis, Proc. of 15th international workshop on ECR ion source, University of Jyväskylä, Finland June 12-14, 2002

[4] M.A. Leitner, C.M. Lyneis, D. Wutte, C.E. Taylor and S.R. Abbott, Proc. of 15th international workshop on ECR ion source, University of Jyväskylä, Finland June 12-14, 2002

[5] M.A. Leitner, C.M. Lyneis, D. Wutte, C.E. Taylor and S.R. Abbott, Proceedings of the Particle Accelerator Conference (PAC'01), Chicago, 2001

[6] D. Xie, C. M. Lyneis, Proc. of 13th international workshop on ECR ion source, Texas A&M, USA, 1997

[7] S. Gammino, G. Ciavola, L. Castro, F. Chines, S. Marletta, Rev. Sci. Instrum. 70, 3577 (1999)

[8] D. Hitz, A. Girard, G. Melin, S. Gammino, G, Ciavola, L. Celona, Proc. of 15th international workshop on ECR ion source, University of Jyväskylä, Finland June 12-14, 2002

[9] D. Wutte, M.A. Leitner and C.M. Lyneis, Physica Scripta, T92, 247-249, 2001

DESIGN OF AN EBIS FOR RHIC*

J. G. Alessi, E. Beebe, D. Graham, A. Kponou, A. Pikin, K. Prelec, J. Ritter, V. Zajic
BNL, Upton, NY 11973, USA

Abstract

An Electron Beam Ion Source (EBIS) can be used to produce beams of high charge state heavy ions, and is an excellent choice for injection into a synchrotron, since short pulses of high intensity can be produced for single- or few-turn injection into the ring. As a result of successful experiments on a test EBIS at BNL, we are now confident that an EBIS meeting RHIC requirements can be built. This EBIS would be part of a new linac-based preinjector which would serve as a modern alternative to the existing Tandem preinjectors, offering improvements in performance and operational simplicity. The BNL test EBIS, which is a ½ trap-length prototype of the RHIC EBIS, has produced > 10^9 ions per pulse of Au^{32+}, in 10-20 microsecond pulses, and has exceeded our design goals. Performance of the test EBIS is summarized and the design of the RHIC EBIS presented.

INTRODUCTION

The present preinjector for heavy ions for AGS/RHIC uses the Tandem Van de Graaff, built around 1970. In fact, the required gold beam intensities for RHIC could only be met with a Tandem until the recent success in EBIS development at Brookhaven. An alternative to the Tandem can now be an Electron Beam Ion Source (EBIS), followed by a Radiofrequency Quadrupole (RFQ) accelerator, and a short Linac. This new preinjector offers improvements in both performance and operational simplicity. While the Tandem has proven to be reliable, quite a few systems are becoming obsolete, and would have to be replaced to maintain reliable long term operation for RHIC. The RFQ and linac are a simpler, modern, more robust technology, which will require less maintenance. Since the EBIS produces directly the high charge state desired for Booster injection, two stripping stages can be eliminated, with the accompanying intensity and energy spread variations as foils age and then break, often over a time scale of only a couple hours at highest intensities. The 860 m long transport line from Tandem to the Booster would be replaced by a line of ~ 30 m. The EBIS will inject full intensity over only 1-4 turns, as compared to 30-40 from Tandem, so injection will be much easier. Finally, the EBIS is capable of producing any ion species, while the Tandem is limited to those starting as negative ions.

The performance required for an EBIS meeting RHIC requirements is shown in Table 1. Also shown in the Table is the present performance of the prototype EBIS which is now in operation at BNL.

Table 1: EBIS parameters

Parameter	RHIC EBIS	EBTS (achieved)
e-beam current	10 A	10 A
e-beam energy	20 keV	20 keV
e-beam density	~ 575 A/cm^2	> 575 A/cm^2
Ion trap length	1.5 m	0.7 m (solenoid limit)
Trap capacity (charges)	11 x 10^{11}	5.1 x 10^{11} (10A)
Yield, charges	5.5 x 10^{11} (Au, 10A)	3.4 x 10^{11} (Au, 8 A)
Pulse length	≤ 40 μs	20 μs
Yield Au^{32+}	3.4 x 10^9 ions/pulse	> 1.5 x 10^9 ions/pulse

PERFORMANCE OF THE EBIS TEST STAND

The construction and previous results on the EBIS test stand (EBTS) have been presented [1-3]. EBTS is a ~half length version of the RHIC EBIS, capable of operating at the full 10 A electron current. With a trap half the length of the final EBIS, we have consistently exceeded our goal of half the ion yield required for RHIC. While we have demonstrated low loss operation at 10 A electron beam, we are typically operating at 7-8 A due to some trap power supply limits. Ion injection of low charge gold ions from a low energy vacuum arc ion source (LEVA) [4] and subsequent extraction of high charge state Au has been demonstrated with electron beams up to 8A. Gold spectra with dominant charge state 34+ and total ion charge of 55 nC measured on a current transformer at the EBIS exit has been obtained after a 30 ms confinement period. This corresponds to ~85% of the theoretical ion trap capacity, and exceeds our goal of 50% neutralization. Time-of-flight spectra indicate that 20% of the gold charge is concentrated in charge state 34+. The collected ion charge is proportional to the electron current and the gold charge state scales with the electron current density.

In addition to a high resolution time of flight spectrometer, we have recently installed large aperture gridded electrodes which can accept and sample the full extracted ion beam, which is then measured on a downstream Faraday cup, allowing a low resolution time-of-flight measurement of the full output current. A sample spectrum is shown in Figure 1, where one can see the gold charge states, and low mass peaks coming from ionization of background gas. This served to verify the large fraction of gold ions in the extracted ion pulse.

*Work performed under Contract Number DE-AC02-98CH10886 with the auspices of the US Department of Energy.

0-7803-7738-9/03/$17.00 © 2003 IEEE

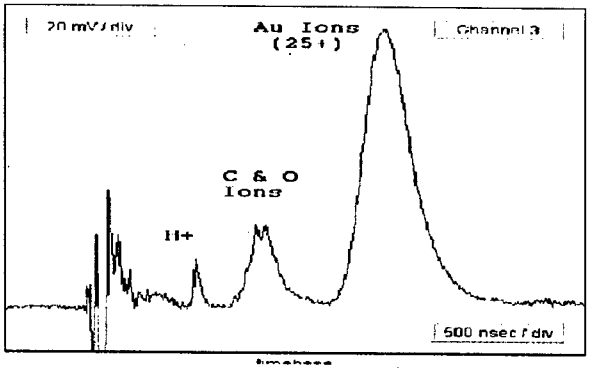

Figure 1: Course time-of-flight measurement of the total output. Ie=7A, 10 ms confinement, ~83% Au ions, peaked at 25^{+}. (Noise from the chopper voltage pulse is to left of the H peak).

Another recent improvement has been the addition of an extra solenoid coil between the electron gun and the EBIS trap region. This allows one to increase the magnetic field, and thus the compression of the electron beam, at the entrance to the early drift tubes, resulting in a reduction in beam loss on these electrodes from the 10^{-4} level to $< 10^{-5}$.

EBTS performance represents more than an order of magnitude improvement over past EBIS sources. At the same time, operation has been very reproducible and stable. Some of the key features of this EBIS are the following:

- A novel electron gun design [5]. It uses a convex LaB_6 cathode, and the resultant beam, with low rotational velocity, is less sensitive to acceleration and deceleration common in an EBIS.
- A warm bore, unshielded superconducting solenoid for the main trap region. With no cryopumping in the trap region surfaces, we are less sensitive to beam losses in the trap.
- Careful vacuum separation of the trap region from the electron gun and electron collector regions.
- Large bore (32mm) drift tubes have been used, compared to the 3-9mm tubes typical for an EBIS. This helps with pumping in the warm bore and reduces loading (desorption) effects. It also reduces the requirements on alignment, and with the electron beam far from drift tube gaps lessens RF coupling.
- The use of auxiliary (warm) solenoids, one near the electron gun and one in the transition region at the entrance of the electron collector. This allows the gun and collector, which are both sources of vacuum degradation, to be located far from the ionization region, thereby accommodating differential pumping stages. This also allows additional control of the electron beam launching, compression, and collection. In addition EBTS makes use of many transverse magnet coils for steering corrections from the electron gun to the collector.
- Since the desired charge state can be reached in 10's of milliseconds, while the time between pulses is 100's of milliseconds, the electron beam is pulsed to reduce the average power on the electron collector.
- Very versatile controls allow one to easily apply a time dependent potential distribution to the ion trap [6]. The controller coordinates the application of all time dependent voltages and timing references associated with the ion source, with a time resolution of 1 μs. At present, to simplify the user interface, the software limits the distribution to 10 EBIS subcycles or "plateaus" and 10 ramps between the plateaus. The analog functions are used to control drift tube power supplies, ramping and pulsing of the electron gun voltages, and ramping of the electron gun solenoidal field.

DESIGN OF AN EBIS FOR RHIC

Parameters for the RHIC EBIS are the following:

Output (single charge state): 1.1×10^{11} charges
Ion output (Au^{32+}): 3.4×10^{9} particles/pulse
Pulse width: 10 - 40 μS
Max rep rate: 10 Hz
Beam current (single charge state): 1.7-0.42 mA
Output energy: 8.5 keV/amu
Output emittance: 0.35 π mm mrad, norm, 90%

Our experience so far in the operation of the EBTS has confirmed the validity of our approach to the design of the RHIC EBIS. The primary difference in the RHIC EBIS is the doubling of the trap length to double the ion output. Other new features we plan to incorporate into the final EBIS will be made in order to make the final EBIS more robust. A schematic of the RHIC EBIS is shown in Fig. 2. Presented below is our present concept for several key EBIS components.

Superconducting Solenoid

In order to increase the trap region length from 71 cm to 150 cm, the solenoid length will be increased from 100 cm to 200 cm. The field will remain at 5 T, but the bore diameter will be increased from 155 mm to 204 mm, in order to facilitate pumping in the longer trap region.

Electron Gun

The existing electron gun can generate an electron current of 10 A for 1000 hours, with an emission density of 13.5 A/cm^2 for 10 A electron beam. While the existing unit meets the RHIC EBIS requirements, to have a more comfortable safety factor and a reserve for a possible future increase of the ion beam intensity, it would be advantageous to have an electron gun which is capable of generating an electron beam with a current of ~15 A. To be able to extract an electron current in excess of 10A while at the same time increasing the lifetime of the gun, we plan to test a cathode unit based on IrCe rather than the present LaB_6. Published results of tests of IrCe cathodes show that even for an emission density as high as 30 A/cm^2 the lifetime is several thousands hours – much longer than we now have. In collaboration with the

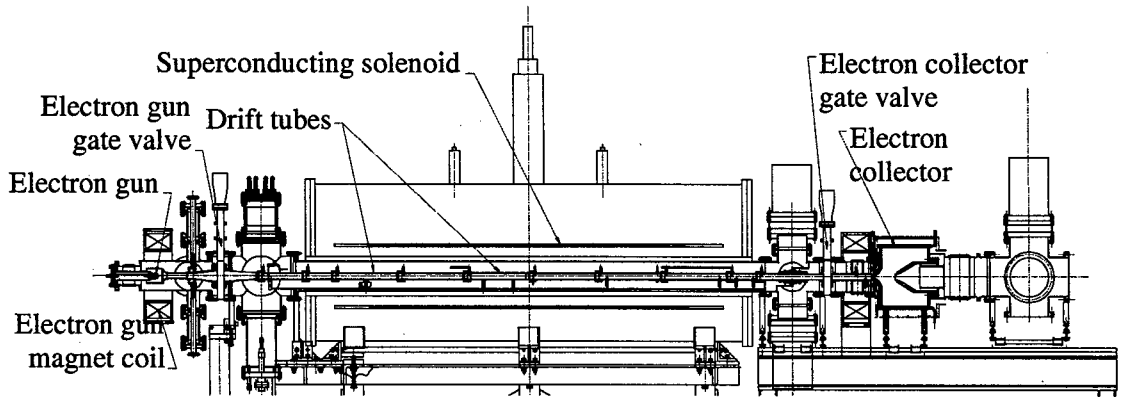

Figure 2: Schematic of the RHIC EBIS

Budker Institute of Nuclear Physics (BINP), a test of such a cathode on EBTS is planned for the near future.

Electron Collector

The main improvement in the new electron collector (EC) for the RHIC EBIS is an increase in its capacity to dissipate power, compared with the existing EC on the EBTS. The new EC will be designed to dissipate a power of 230 kW, higher than our expected load of 100 kW. To reduce the maximum power density on the surface-water interface, the longitudinal distribution of the electron beam on this surface will be made more homogeneous than in the existing EC by optimizing the shape of the magnetic field. The total area of the cylindrical water-cooled surface of the EC will also be increased; with the new collector having an inner diameter of 30 cm and a length of 24 cm. Unlike in the EBTS, the outer surface of the new EC will be exposed to atmosphere. This concept allows us to practically eliminate any probability of water leaks into the vacuum volume, because no water-cooling tubes will be in the vacuum.

Vacuum

Ion confinement times as long as 100 ms may have to be used to reach some charge states of interest. The background pressure in the trap region should be low enough that one does not produce a significant number of ions from the background gas. One can tolerate a residual gas pressure P=1x10^{-9} Torr, since one then estimates that less than 20% of accumulated ions in a trap will be background gas ions. The pressure in the regions with high outgassing rate (electron gun and electron collector) can be higher than in the ionization region, provided there is efficient vacuum separation between the sections. Unlike in EBTS, the central region containing the ion trap will be preserved from venting to atmosphere during maintenance or upgrade operations with electron gun and electron collector by separating it from these regions with gate valves. In addition, there will beincreased vacuum conductivity between the middle part of the central chamber and the ends where pumps are located, due to the increase in diameter of the central chamber from our present 4" to 6". The use of non-evaporable getters (NEG) in the region of the ion trap is also being considered.

Seeding the EBIS Trap

The primary means of seeding the trap of the RHIC EBIS will be injection and trapping of singly charged ions from an external ion source. This technique has been used very successfully on other EBISs, as well as on EBTS, and allows one to produce a very narrow charge state distribution. The requirements of the external source are relatively modest, needing currents of only about 100 μA.

CONCLUSION

The RHIC EBIS design will be very similar to the present EBTS operating at BNL. No significant improvement in performance is required, other than the straightforward scaling of ion output with an increase in trap length. Beyond this, changes to the EBTS design, which was a device built to demonstrate feasibility, will make the RHIC EBIS an "operational" device, i.e. simplier to maintain, and more reliable due to increased engineering margins on components.

ACKNOWLEDGEMENTS

We would like to acknowledge the help of many colleagues in this EBIS development. The electron beam development has progressed via a strong collaboration with G. Kuznetsov and M. Tiunov, from Novosibirsk. Excellent technical assistance has been provided by D. McCafferty, B. Schoepfer, D. Cattaneo, and D. Boeje. R. Lockey and O. Gould have provided engineering support. Valuable physics discussions with L. Liljeby and A. Hershcovitch are gratefully acknowledged.

REFERENCES

[1] A. Pikin et al., EBIS/T-2000, AIP Conf. Proceedings 572 (2001) 3.
[2] E.N. Beebe et al., Rev. Sci. Instr., 73, (2002) 699.
[3] A. Pikin et al., Proc. EPAC 2002, p. 1732.
[4] I.G. Brown et al., Rev. Sci. Instrum. 65, (1994) 1260.
[5] A. Kponou, E. Beebe, A. Pikin, G. Kuznetsov, M. Batazova, M.Tiunov, Rev. Sci. Instr. 69, (1998) 1121.
[6] E. Beebe et al., Proc. EPAC 2002, p. 1688.

DESIGN, CONSTRUCTION AND STATUS OF ALL NIOBIUM SUPERCONDUCTING PHOTOINJECTOR AT BNL

T. Srinivasan-Rao, I. Ben-Zvi, A. Burrill, G. Citver, A. Hershcovitch, D. Pate, A. Reuter, J. Scaduto, Q. Zhao, Y. Zhao, BNL, Upton, NY

J. Delayen, P. Kneisel, TJNAF, Newport News, VA

H. Bluem, M. Cole, A. Favale, J. Rathke, T. Schultheiss, Advanced Energy Systems, Medford, NY

Abstract

We present here the design and construction of an all niobium superconducting RF injector to generate high average current, high brightness electron beam. A ½ cell superconducting cavity has been designed, built, and tested. A cryostat has been built to cool the cavity to ~2 K. The RF system can deliver up to 500 W at 1.3 GHz to the cavity. A mode-locked Nd:YVO_4 laser, operating at 266 nm with 0.15 W average power, phase locked to the RF, will irradiate a laser cleaned Nb surface at the back wall of the cavity. Description of critical components and their status are presented in the paper. Based on DC measurements, QE of up to 10^{-4} can be expected from such cavity

INTRODUCTION

In recent years, there had been considerable interest in developing high average current, high brightness electron beams both for accelerator and photon source applications. With its low power requirements a superconducting RF (SCRF) photoinjector is an ideal electron source for these applications. However, the low quantum efficiency of Nb and the short lifetime and complicated design associated with alkali cathodes have slowed the implementation of this scheme. Recently, it has been shown that the QE of Nb can be improved significantly by laser cleaning it in vacuum [1]. A feasibility study to incorporate this technique in the surface preparation of SCRF injector and generate high average current electron beam was undertaken and the results are presented in the following sections.

SIMULATIONS

A schematic of the cavity, cryostat and electron beam transport are shown in Figure 1.

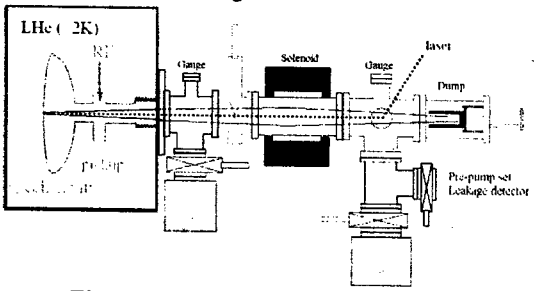

Figure 1: Schematic of the beam transport

The laser is reflected by an off axis metallic mirror into the beam line to irradiate the cathode. The electron beam generated by the laser is transported through a solenoid to the Faraday cup at the end of the beam line. The beam envelope simulated using PARMELA is shown in Figure 2. The energy and longitudinal and transverse emittances of a electron bunch with 1 pC charge from 1 mm spot size and 6 ps duration, measured at the exit of the gun is shown in Figure 3 for different launch phases

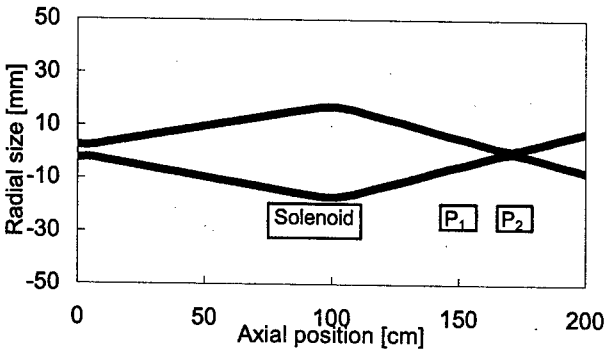

Figure 2: Beam envelope simulation using PARMELA Q=1pC, R_0,rms=1.2mm, E_{max}=45MV/m, f0=40deg, Bz=750Gs

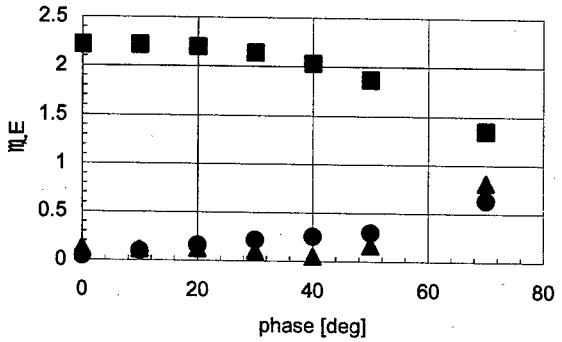

Figure 3: PARMELA simulation of longitudinal beam emittance (●) in KeV Degree, transverse emittance (▲) in mm.mrad and energy (■) in MeV at different injection phase. Q=1pC, R=1.2mm(Gaussian), t=6ps, E_{max}=45MV/m

COMPONENTS DESCRIPTION

The critical components of the system are the cavity, cryostat, RF system, solenoid, photocathode and laser. Specifications of each are given in the following sections

RF Cavity:

The superconducting gun is a 1.3 GHz, single cell Nb cavity as shown in Figure 4. It is essentially one-half of an elliptical cell terminated by an end wall. The end wall has a domed shape for added stiffness, but no external stiffeners. The cavity was hydro formed from sheet RRR250 Nb and EB welded. The niobium cavity wall thickness is sized to 3.5 mm to operate with a 15 psi pressure load on the outside of the cavity and vacuum on the inside, pass 1 watt of laser power and the RF surface thermal load through its thickness while maintaining superconducting temperatures. For this proof of principle test no cavity tuner was included. Due to the use of an end wall in the cavity, both the cavity drive port and the pickup port are on the same side of the cavity. This leads to serious cross talk during room temperature measurements, which are discussed elsewhere in these proceedings [2]. Fortunately, this problem will diminish when cool down to superconducting status.

Figure 4: Photograph of ½ cell Nb cavity

Earlier concepts for the cavity utilized a reentrant nose to increase the field at the cathode, thereby increasing the QE, and the current. This proved counterproductive. The effect due to the radial E fields forces the beam spot size at the cathode to be reduced if the beam quality is to be maintained. The reduced beam size causes the power density from the laser to increase. Thermal simulations show that with the reentrant nose, the limit on allowable laser power density actually causes a reduction in the laser power and hence the total beam current.

RF System

The niobium cavity is expected to have an internal Q of about 7×10^9 in 2K superconducting status. With maximum beam current the beam loaded Q is 1×10^8. The RF system is designed to have an external Q around 10^8. It will excite the cavity to a maximum gradient of 45 MV/m. The system consists of a 500W CW amplifier from PRO-COMM. The LLRF system will operate as a PLL (phase locked loop) so that its frequency will catch up with the resonant frequency of the cavity. This frequency will be divided 16 times to trigger the laser for synchronization.

Laser:

The photocathode driving laser is a commercial frequency quadrupled mode-locked Nd:YVO_4 laser operating at 266 nm with an average power of 150 mW and pulse duration of ~6 ps. Figure 5 shows the autocorrelator trace of the 2.3 eV beam from this laser, while Figure 6 shows the UV beam profile. This UV beam is reflected by a vacuum metal mirror custom dielectric-coated for 266 nm, positioned off axis in the beam line to illuminate the cavity nearly at normal incidence. The thickness of the dielectric layer is small enough to avoid charge build up yet maintain the high reflectivity. This mirror could be externally manipulated for irradiating the center of the rear surface of the cavity. Since the power density of this laser is not high enough for laser cleaning the cavity in a reasonably short time, an excimer laser will be used to irradiate the cathode surface at normal incidence for the surface preparation.

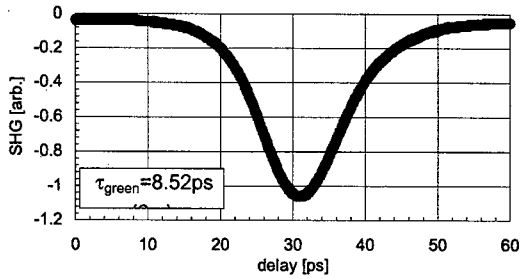

Figure 5: Autocorrelation signal of 532 nm radiation from the laser. In the absence of saturation, the UV pulse duration is expected to be 6 ps

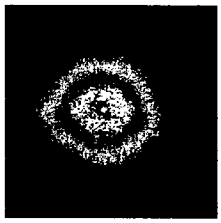

Figure 6: UV laser beam profile. 1/e diameter is 1 mm

Photocathode:

Surface preparation of the Nb surface is critical to maintain high QE. Laser cleaning of either chemically etched or electro polished Nb can be increased by two orders of magnitude by irradiating with high intensity UV laser. Figure 7 shows the increase in the QE of a BCP Nb when irradiated with a laser beam of energy density ~ 3 mJ/mm^2, pulse duration of 20 ns and photon energy of 5 eV. Detailed information on laser cleaning is discussed elsewhere in these proceedings [3].

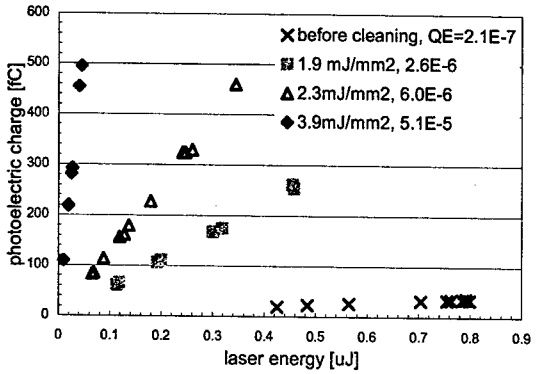

Figure 7: Electron yield of BCP sample as a function of 266 nm laser energy for different 248 nm cleaning energies. The QE of (♦) is $5^* 10^{-5}$

Solenoid:

The solenoid is designed to focus the electron beam so that all the electrons can be collected in the Faraday cup or focused onto beam profile monitors placed at locations P1 and P2 in Figure 2 for emittance measurement. The measured field distribution along the beam axis and its dependence on the solenoid current are shown in Figures 8 and 9 respectively.

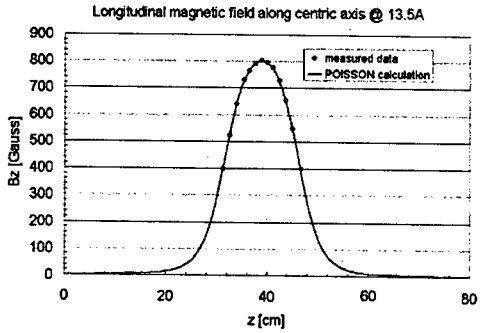

Figure 8: Longitudinal magnetic field along the center line@ 13.5 A

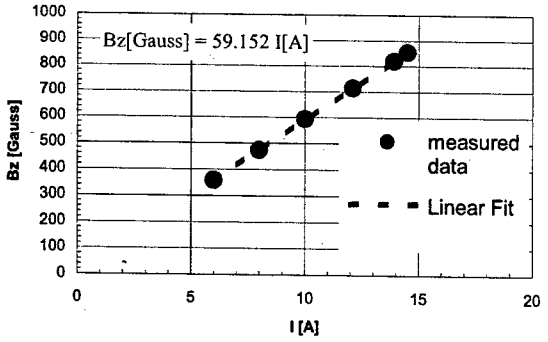

Figure 9: Measured longitudinal magnetic field as a function of solenoid current

Cryostat and Cryogenic System:

The major components of the system include the cryostat, LHe and LN2 storage dewars, mechanical vacuum pumps, cryogenic and recovery piping, vacuum piping, valving, instrumentation and controls. The cryostat consists of a stainless steel vacuum chamber, a stainless steel liquid nitrogen vessel, and a stainless steel liquid helium vessel with about 40 layers of super insulation wrapped around the nitrogen shield and LHe helium vessel. The cryostat is designed to hold about 60 liters of LHe to run experiment at 2K, while pumped down, for about 8 hours. The cryostat equipped with sensors to monitor inside pressure, temperatures of LHe, cavity, LN2 shield, bellow connecting inner and outer vessels. Three temperature sensors installed at the same elevation over LHe on RF cables and in He gas space. Two level probes are to measure level of LHe at 4.2K and 2K and one - level of LN2. Proportional control valve installed between cryostat and vacuum pump is designed to maintain automatically a required cavity temperature. G-10 sleeves put on RF cables are to utilize boil-off He flow to cool the RF cables ad exemplum gas-cooled current leads. The cryostat general arrangement and the cryostat top cover configuration are shown below in figure 10.

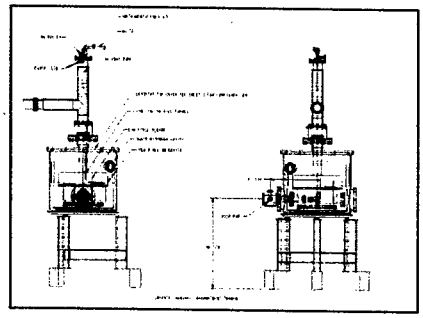

Figure 10: Section view of the cryostat

Status:

The cavity has been cooled down to 4K. The frequency and the Q of the superconducting cavity have been measured to be 1.3 GHz and 10^7. The electron beam transport has been installed. The low level RF system has been designed, built and is being tested. The laser has been characterized and the transport system is being built.

This research is supported by the U.S. Department of Energy under Contract No. DE-AC02-98CH10886, DE-AC02-98CH10886DOE, and SBIR grant DE-FG02-99ER82724.

REFERENCES

[1] M. Cole, et al., "Development of a Novel SC RF photocathode electron gun", LINAC'2000, p 116

[2] Y. Zhao, M. Cole, "The analysis of the cross-talk in a RF gun superconducting cavity", PAC03 paper WPAB009.

[3] Q. Zhao, T. Srinivasan-Rao, M. Cole, "Tests of Niobium Cathode for the Superconducting Radio Frequency Gun," PAC03 paper WPAB008.

GENERATION OF HIGH BRIGHTNESS X-RAYS WITH THE PLEIADES THOMSON X-RAY SOURCE

W.J. Brown, S.G. Anderson, C.P.J. Barty, J.K. Crane, R.R. Cross, D.N. Fittinghoff, F.V. Hartemann, J. Kuba, G.P. Le Sage, D.R. Slaughter, P.T. Springer, A.M. Tremaine, LLNL, Livermore, CA
J.B. Rosenzweig, UCLA, Los Angeles, CA
D.J. Gibson, UCD, Department of Applied Science, Livermore, CA

Abstract

The use of short laser pulses to generate high peak intensity, ultra-short x-ray pulses enables exciting new experimental capabilities, such as femtosecond pump-probe experiments used to temporally resolve material structural dynamics on atomic time scales. PLEIADES (Picosecond Laser Electron InterAction for the Dynamic Evaluation of Structures) is a next generation Thomson scattering x-ray source being developed at Lawrence Livermore National Laboratory (LLNL). Ultra-fast picosecond x-rays (10-200 keV) are generated by colliding an energetic electron beam (20-100 MeV) with a high intensity, sub-ps, 800 nm laser pulse. The peak brightness of the source is expected to exceed 10^{20} photons/s/0.1% bandwidth/mm^2/mrad^2. Simulations of the electron beam production, transport, and final focus are presented. Electron beam measurements, including emittance and final focus spot size are also presented and compared to simulation results. Measurements of x-ray production are also reported and compared to theoretical calculations.

1 INTRODUCTION

PLEIADES (Picosecond Laser Electron InterAction for the Dynamic Evaluation of Structures) is a next generation Thomson scattering x-ray source being developed at Lawrence Livermore National Laboratory (LLNL). Ultra-fast ps x-rays (10-200 keV) are generated by colliding an energetic electron beam (20-100 MeV) with a high intensity, sub-ps, 800 nm laser pulse. Generation of sub-ps pulses of hard x-rays (30 keV) has previously been demonstrated at the LBNL Advanced Light Source injector linac, with x-ray beam fluxes of 10^5 photons per pulse [1]. The LLNL source is expected to achieve fluxes between 10^7 – 10^8 photons for pulse durations of 100 fs to 5 ps using interaction geometries ranging from 90° (side-on collision) to 180° (head-on collision). In this paper, we describe the first production of x-rays using Thomson scattering at the LLNL facility.

2 EXPERIMENT LAYOUT

The PLEIADES facility consists of a Ti-Sapphire laser system capable of producing bandwidth limited laser pulses of 50 fs with up to 500 mJ of energy at 800 nm, an S-band photo-cathode RF gun, and a 100 MeV linac consisting of 4, 2.5-meter-long accelerator sections. The RF gun, which is driven by a picosecond, 300 μJ, UV laser that is synchronized to the interaction drive laser, is designed to produce up to 1 nC of charge at 5 MeV [2]. The accelerator is then used to accelerate the electron beam to energies ranging from 20-100 MeV.

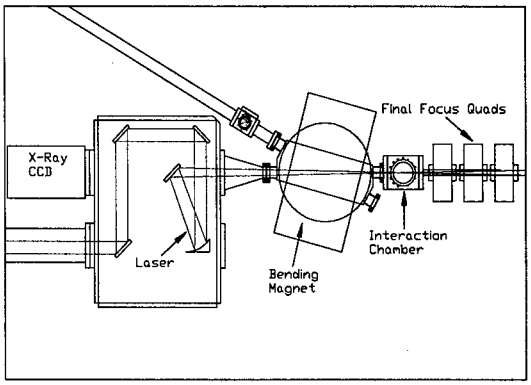

Figure 1: Interaction Geometry

A schematic of the interaction region is shown in Fig. 1. To maximize x-ray flux while minimizing effects of timing jitter, the laser incidence angle is 180 degrees with respect to electron beam direction, though a 90 degree interaction geometry will also be possible in future experiments. The focal length between the final focus quadrupole triplet and the interaction region is 10 cm to allow for maximum focus strength and minimum electron bunch spot size. A 30-degree dipole magnet is used to bend the electron bunch out of the x-ray beam path following the interaction. An off-axis, 1.5 m focal length parabolic mirror is used to focus the laser, which, assuming a diffraction limited spot, should reach a minimum spot size of about 15 μm FWHM at the interaction point. Currently, a fused-silica flat mirror is placed in the x-ray beam path to serve as the final steering optic for the laser, though there are plans to replace this with a beryllium flat, which will be more transparent to the x-ray beam. The interaction chamber also serves as a diagnostic chamber used for imaging and streak camera analysis of the laser and electron bunches. The x-rays have been measured with a 16 bit CCD array fiber coupled to a cesium iodide scintillator.

3 ELECTRON BEAM SIMULATIONS

The electron beamline has been fully modeled, from the S-band photo-cathode RF gun to the interaction point

0-7803-7738-9/03/$17.00 © 2003 IEEE

using the Los Alamos particle dynamics code, PARMELA, and the electrostatic and electromagnetic field solvers: POISSON and SUPERFISH. These include simulations of emittance compensation between the RF gun and the first linac section, velocity compression of the bunch through the first linac section, and the acceleration and optimization of the beam energy spread and emittance during transport through the subsequent accelerator sections.

Two modes of linac operation have been investigated through simulation. The first is when the electron beam is accelerated on crest through the accelerator. In this case, the minimum electron bunch length is about 6 ps FWHM (2.5 ps rms). The second mode of operation employs velocity compression, in which the beam is injected into the first linac section near the zero crossing of the accelerating field in order to provide an energy chirp to the beam. This results in longitudinal compression of the accelerated bunch. The second accelerator section is then used to accelerate the beam from about 10 MeV to about 35 MeV. The third and fourth sections can then be used to either remove a large portion of the energy spread induced by the velocity compression process, or to simply accelerate the beam further, depending on the final beam energy desired. Fig. 2 shows the evolution of several of the beam characteristics determined from PARMELA simulations for the case of a 0.5 nC bunch where velocity compression is implemented. At the exit of the accelerator, the electron beam normalized rms emittance is about 3.5 mm-mrad, the rms bunch length is 0.7 ps, and the rms energy spread is 0.5 %. While it is possible to compress further, this bunch length was chosen to minimize emittance growth resulting from the compression process, while maximizing x-ray yield from the Thomson scattering interaction. In this particular case, the final beam energy is 35 MeV, though larger energies are possible with similar results.

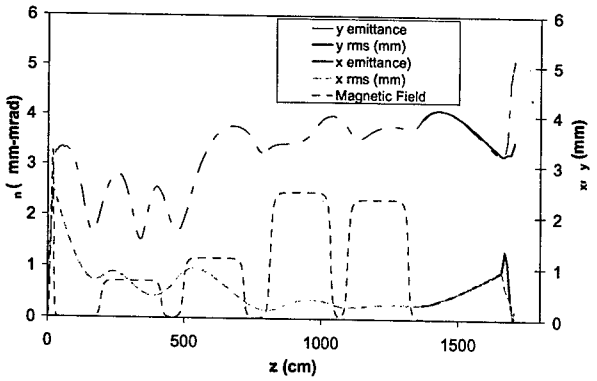

Figure 2: PARMELA simulation of electron beam production from the RF gun to the final focus. Emittance and spot size are plotted vs z position from the RF gun cathode.

The electrons are transported 3 meters from the accelerator exit and focused with a high gradient quadrupole triplet. The triplet is about 50 cm long, and the focal length is about 10 cm. The maximum field gradient in the quadrupole magnets is 15 T/m. Final focus simulations were performed using PARMELA and Trace-3D, and have indicated that a spot size of abut 30 μm FWHM (12 μm rms) should be obtainable at the focus.

4 EXPECTED X-RAY PRODUCTION

The expected x-ray production was calculated by integrating the emission probability per unit time, dN_x/dt, given by

$$\frac{dN_x}{dt} t = \sigma c \; 1 \quad \mathbf{v} \; \mathbf{k} \iiint n_\gamma \; \mathbf{x},t \; n_e \; \mathbf{x},t \; d^3x, \qquad (1)$$

where N_x is the total number of x-rays produced, n (**x**,t) is the laser photon density, n_e(**x**,t) is the electron density, is total Thomson cross section, **v** is the velocity of the electron beam, and **k** is the wave number of the laser pulse. The calculations were performed for a 300 mJ, 300 fs laser pulse in conjunction with the PARMELA output in place of n_e(**x**,t). n (**x**,t) was assumed to have a Gaussian profile in the transverse and longitudinal dimensions, and the Rayleigh range of the laser focus was determined assuming a 2 X diffraction limited focus. For the electron beam parameters determined from the simulation shown in Fig. 2, the peak x-ray energy is 30 keV, and the peak x-ray flux was found to be about 6 x 10^{19} photons/s with an integrated photon yield of about 10^8. In addition, a 3-D frequency domain code [3] was used to calculate the expected spectral bandwidth to be about 10% on axis, with a peak spectral brightness of about 10^{20} photons/s/0.1% bandwidth/mm^2/mrad^2.

5 BEAM MEASUREMENTS

To date, electron bunches with up to 700 pC of charge have been produced with up to 200 μJ of UV laser energy incident on the gun photo-cathode. The beam has been transported through the linac and accelerated up to 60 MeV without velocity compression. Quad scan emittance measurements have been performed for 300 pC, 60 MeV bunches, yielding a normalized rms emittance of 9 mm-mrad. The rms energy spread has been measured to be 0.2%. Improvements in emittance are expected after planned improvements in the UV drive laser uniformity and optimization of the electron beam transport.

Both the electron beam and the interaction drive laser have been imaged by placing a metal cube in the interaction chamber to send OTR light from the electron beam and laser light into the same camera. Using a CCD camera, the electron beam spot sized has been measured to be about 70 μm rms, while the laser spot size has been measured to be about 30 μm. This is about twice the optimized spot size determined from PARMELA simulations, based on the measured beam emittance. Further optimization of the final focus quads should help reduce the measured spot size.

The synchronization between the laser and electron bunches has been characterized with a streak camera. A schematic of the measurement, as well as the streak camera image is shown in Fig. 3, indicating good temporal overlap of the two bunches. The jitter has been measured to be within the resolution of the streak camera (about 2 ps), which is in agreement with indirect timing jitter measurements performed by mixing wakefields produced by the electron bunch with a frequency multiplied photo-diode signal from the laser oscillator.

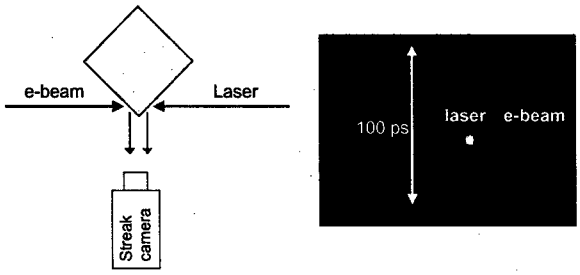

Figure 3: E-beam to laser synchronization measurement.

6 X-RAY PRODUCTION

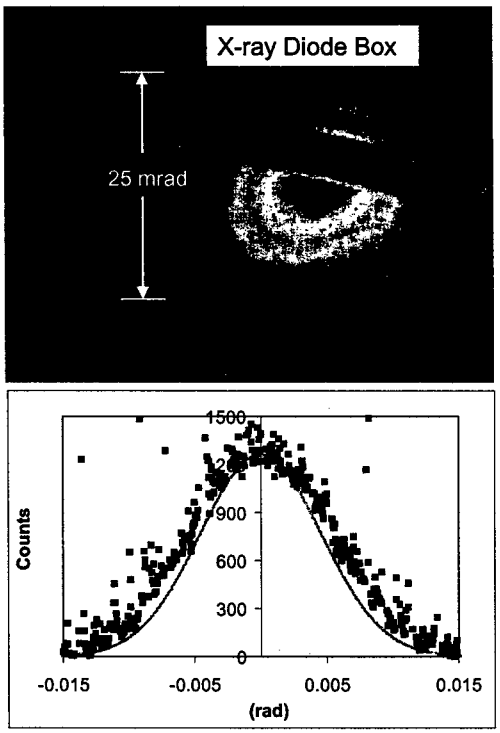

Figure 4: Measurement of X-ray beam profile. Top: CCD image. Bottom: Line-out intensity profile: measurement (dots), theory (line).

First light of the PLEIADES Thomson x-ray source was achieved in January, 2003. Figure 4 shows the measured beam profile taken with the x-ray CCD camera. The electron beam energy in this case was 54 MeV, and the bunch charge was about 250 pC. The laser energy delivered at the interaction was about 40 mJ. The image is integrated over 1200 shots. The estimated average photon count per shot is about 5 x 10^4, and the peak photon energy is about 70 keV. The theoretical intensity profile (shown in the bottom half of Fig. 4) agrees well with the measured profile. The theoretical curve includes the broadening effects from the measured beam emittance and the narrowing effects derived from the spectral dependence of the transmission coefficient of the laser turning mirror.

Dramatic improvements of the per shot x-ray dose are expected after improvements in the electron beam final focus optics, maximization of the IR drive laser energy delivered to the interaction region, and reduction of electron beam emittance through the optimization of both the photocathode drive laser uniformity and the electron beam transport. These improvements will allow for the realization of final focus spot sizes as small as 10 μm rms, and the production of up to 10^8 x-ray photons per collision.

7 CONCLUSIONS

The PLEIADES Thomson X-ray source is a unique, high peak brightness x-ray source that will be useful for ultra-fast imaging applications to temporally resolve material structural dynamics on atomic time scales. Electron beam transport and x-ray production simulations have been performed to completely model the theoretical source performance. To date, 0.3 nC, 54 MeV bunches have been focused to 70 μm rms spot sized and collided with a 40 mJ, 30 μm laser pulse to produce 70 keV x-rays. Optimization of the experiment will include increasing the laser energy delivered to the interaction region to about 300 mJ, and decreasing the electron beam emittance to less the 5 mm-mrad rms. This will enable the achievement of a 10 μm spot size at the interaction and the production of 10^8 x-ray photons per pulse. Once optimization is complete, PLEIADES should achieve a peak x-ray brightness approaching 10^{20} photons/s/0.1% bandwidth/mm^2/mrad^2.

8 ACKNOWLEDGEMENTS

This work was performed under the auspices of the U.S. Department of Energy by the University of California, Lawrence Livermore National Laboratory under contract No. W-7405-Eng-48.

9 REFERENCES

[1] R.W. Schoelein, et. al., *Science* **274**, 236 (1996).
[2] S.G. Anderson, J.B. Rosenzweig, G.P. LeSage, J. Crane, Proceedings of the 2001 Particle Accelerator Conference (Cat. No.01CH37268), p.2260-2 (2001).
[3] F.V. Hartemann, et. al., Physical Review E, vol.64, (no.1), p.016501/1-26. (2001).

FOCUSING AND NEUTRALIZATION OF INTENSE BEAMS

Simon S. Yu, Andre Anders, F.M. Bieniosek, Shmuel Eylon, Enrique Henestroza, Prabir Roy, Derek Shuman, William Waldron *LBNL* , William Sharp *LLNL* , Dave Rose, Dale Welch *Mission Research Corporation* , Philip Efthimion, Eric Gilson *Princeton Plasma Physics Laboratory*

Abstract

In heavy ion inertial confinement fusion systems, intense beams of ions must be transported from the exit of the final focus magnet system through the target chamber to hit millimeter spot sizes on the target. Effective plasma neutralization of intense ion beams through the target chamber is essential for the viability of an economically competitive heavy ion fusion power plant. The physics of neutralized drift has been studied extensively with PIC simulations. To provide quantitative comparisons of theoretical predictions with experiment, the Heavy Ion Fusion Virtual National Laboratory has completed the construction and has begun experimentation with the NTX (Neutralized Transport Experiment) as shown in Figure 1. The experiment consists of 3 phases, each with physics issues of its own. Phase 1 is designed to generate a very high brightness potassium beam with variable perveance, using a beam aperturing technique. Phase 2 consists of magnetic transport through four pulsed quadrupoles. Here, beam tuning as well as the effects of phase space dilution through higher order nonlinear fields must be understood. In Phase 3, a converging ion beam at the exit of the magnetic section is transported through a drift section with plasma sources for beam neutralization, and the final spot size is measured under various conditions of neutralization. In this paper, we present first results from all 3 phases of the experiment.

INTRODUCTION

In the quest for heavy ion fusion (HIF) the desire for compact cost-effective driver has led us to consider beams with low kinetic energy and high current. [1] The final focusing of the beams with strong space-change self-forces is particularly challenging. The target and chamber requirements are such that after the last focusing magnet, each beam must drift through several meters of target chamber and chamber-magnet interface regions to converge on a millimeter-sized spot. [2] Space-change blowup of the beam can be avoided if a plasma could be introduced into the drift region to neutralize the repulsive self-forces. The mainline HIF chamber with thick liquid walls has an equilibrium vapor of a millitorr. Heavy ion impact ionization of the background is a natural source of plasma. Once the target gets hot (~100eV), photons are emitted and the region around the target will be populated

*Supported by the Office of Energy Research, US DOE, at LBNL & LLNL, contract numbers DE-AC03-76SF00098 and W-7405-Eng-48.

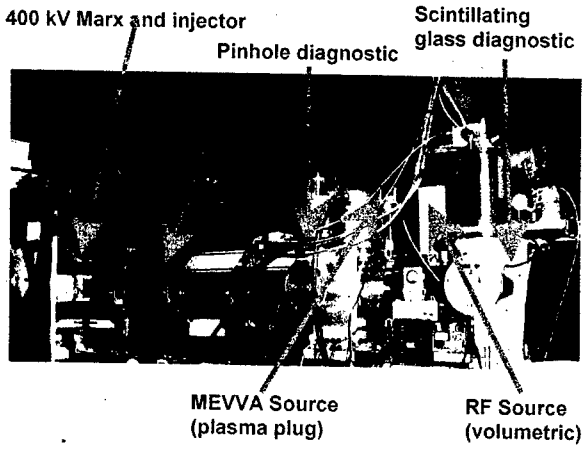

Figure 1: Neutralized Transport Experiment (NTX).

with a volume plasma from photo-ionization of the background gas. While the introduction of plasma into the interior of the chamber is difficult, it is straightforward to inject a "plasma plug" at the entrance to the chamber. [3] The plasma plug provides a reservoir from which electrons are dragged along as the ion beam leaves the plug and enters the chamber. The mechanisms of neutralization with beam-initiated ionization of background gas, volume plasma, and plasma plug are quite different. Simulations with the 3-D electromagnetic code LSP show that the cumulative effect of all 3 sources of plasma will provide enough neutralization of the ion beams to meet the mm spot size requirement. [4]

Even if the neutralization is 100% effective, the beam will not be able to hit the small spot unless the emittance after the magnetic final focusing system is sufficiently small. Indeed there are higher order nonlinearities in the final focusing system, which are known to cause emittance growth. Chromatic and geometric aberrations for highly space-charge dominated beams are areas of active ongoing research [5].

In this paper we report on an experiment to study the neutralization physics and emittance growth in the magnet final focus system. The Neutralized Transport Experiment (NTX) uses singly charged potassium ions of up to 400kV and 80mA. The relevance of a low energy low current experiment is determined by a key parameter, the beam perveance Q, defined as

$$Q = \frac{e\lambda}{4\pi\varepsilon_0 T}$$

0-7803-7738-9/03/$17.00 © 2003 IEEE

where λ is the line charge density, and

$$T=\frac{1}{2}Mv^2$$

is the kinetic energy of the heavy ion. From simulations and theory, it has been shown that the essential physics of the magnetic aberrations as well as much of the neutralization processes are determined by the perveance. [6] Since the perveance is the ratio of the potential energy to the kinetic energy of the beam, we can access driver-relevant physics with low energy beams as long as the experimental perveance values are driver-relevant. NTX addresses final focus physics in the $Q\sim10^{-3}$ range in contrast to previous experiments in the $Q\sim10^{-5}$ range [7].

INJECTOR

The NTX injector [8] is required to have variable perveance in order to study final transport and neutralization dynamics when perveance is changed. The injector must have low emittance $(\varepsilon_N \le 0.1\pi mm-mr)$ in order to provide a sensitive probe of magnetic high-order aberrations, and residual fields from incomplete neutralization. Beam aperturing is a technique we deployed to achieve the dual purpose of variable perveance and low emittance.

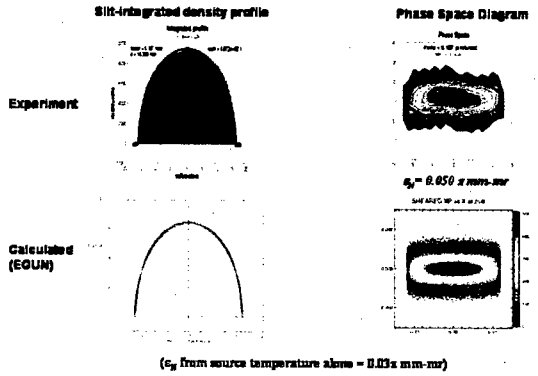

Figure 2: A High brightness apertured beam (300kV, 25 mA, 2 cm aperture).

In the NTX gun, a 1" hot alumina silicate source produces up to 80 mA of singly charged potassium ions at 400 keV from a conventional 12 cm diode with Pierce electrodes at the source. Immediately downstream of the diode is an aperture plate with a variable hole size sandwiched axially between 2 cylinders, which can hold several kV of negative potential (bias). The purpose of the cylinders is to serve as an electron trap, which confines electrons produced at the aperture plate locally, and to inhibit unwanted beam neutralization away from the aperture. In the ion source characterization phase of the experiment, a diagnostic station downstream of the aperture assembly measures the current with a Faraday cup and measures the line-integrated beam profile and emittance at injection with a slit/slit-cup set up. When the bias potential is turned off, electron neutralization leads to enhanced current density on-axis and highly non-uniform beam profile. However, when a bias potential of 2 to 3kV is turned on, a uniform beam profile is obtained. The unapertured beam current follows a Child-Langmuir Law reaching 80mA at 400kV. With a 2cm diameter aperture; the current is reduced by approximately one half. A 1cm diameter aperture reduces the current to 1/4 of the 2cm aperture value.

Most of the detailed experiments were performed with the 2cm aperture where the current is 25mA at 300kV. The line-integrated beam profile is parabolic, indicative of a uniform beam profile, and the normalized edge emittance is measured to be 0.05 π-mm-mr, which is less than a factor of 2 above the source temperature imposed value. The beam size, density, and emittance are in good agreement with EGUN predictions as shown in Figure 2. [8]

MAGNETIC LATTICE

The second phase of NTX consists of magnetic transport with 4 pulsed quadrupoles [9] enclosing a thin-wall stainless steel tube approximately 26 cm in diameter. The half-lattice period is 60 cm. Figure 3 shows the beam going through large excursions of up to 10 cm in the magnetic lattice to reach an exit condition of 2 cm radius and 20 mr convergence in both the x and y planes. This is the desired entrance condition for the final neutralized drift experiment.

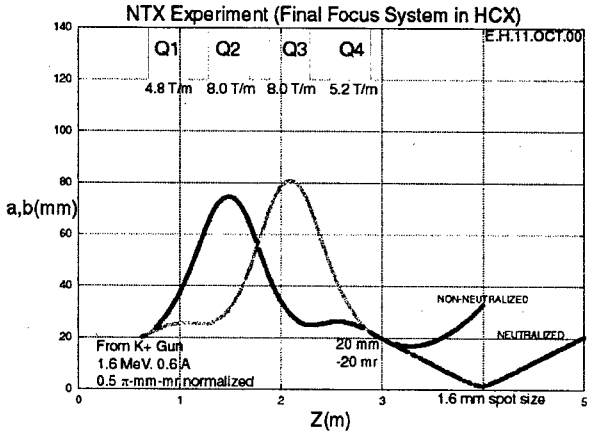

Figure 3: Final focus lattice for neutralized drift.

The pulsed magnets [10] were fabricated in-house, and the conductors were arranged to minimize unwanted higher order multipoles. Fields were measured with accurate 3-way B dot probes, and the agreement with ANSYS code calculations was excellent as shown in Figure 4.

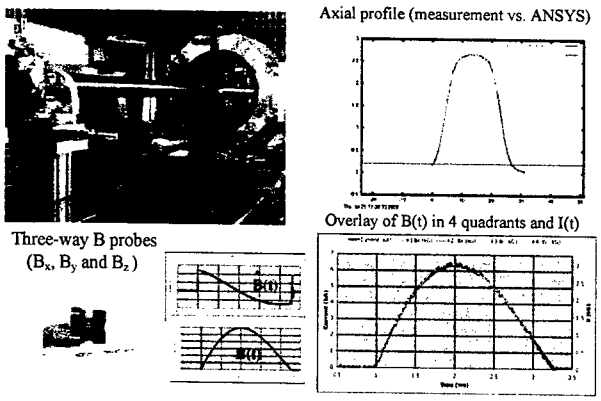

Figure 4: Magnetic field measurement.

The beam size and angle at lattice exit were quite sensitive to small changes in quad fields and/or beam energy. These changes were measured optically, and found to be in excellent agreement with predictions of WARP3D, a 3-D particle-in-cell code for space charge dominated beam transport. [9] In Figure 5 we show the variations with beam energy (in steps of 3%) of the measured beam image (bottom row) against WARP3D simulations (top row).

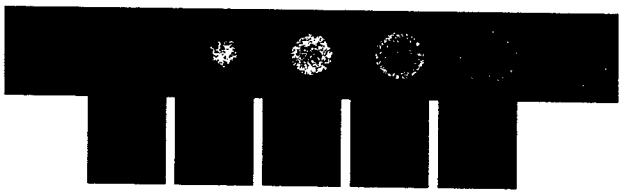

Figure 5: Numerical results and camera images of beam profiles as function of energy.

NEUTRALIZED DRIFT

The neutralized drift experiment [11], the third phase of NTX, is performed in a one-meter long pipe installed at the exit of the four-pulsed-quadrupole section. Two sources of plasma were injected at the upstream and downstream end of the 3" diameter pipe.

The upstream source is a MEVVA source [12] consisting of two metal vapor arcs that provide plasma pulses of $\sim 10^{10}/cm^3$ injected from two opposite holes on the side of the 3" beam pipe. The plasma is not expected to be spatially uniform, and has a pulse-to- pulse jitter of 10%. This source serves as a plasma plug from which the ion beam would extract electrons for neutralized drift downstream. Theory predicts that as long as the plasma density is much higher that the beam density (which is the case in our experiment), beam neutralization is insensitive to spatial inhomogeneities or small pulse-to-pulse variations. [3]

In the downstream end of the drift section is an RF plasma source [13], which produces a comparable plasma density of up to $10^{10}/cm^3$. The RF plasma source is very stable from pulse-to-pulse. It is operated in a pulsed mode where short puffs of Argon gas are injected into the beam region where ionization by the RF source takes place. By varying the duration and timing of the gas puff, and by varying the power of the RF source, both the plasma density as well as the gas density can be independently controlled. The evolution of the gas and plasma densities was well characterized prior to installation into the NTX beamline.

The Langmuir probe measurements of plasma density profile were also extended to the MEVVA source. The purpose of the RF source downstream is to simulate the volume plasma from photo-ionization in a target chamber, as well as the gas effects in a vapor-filled thick-liquid-wall chamber. The MEVVA source and the RF source parameters are varied during the course of the neutralization drift experiments.

The first drift experiment was conducted with both plasma sources turned off. A large 2cm radius beam was measured at the exit of the 1-meter drift, consistent with the predicted vacuum solution. It should be noted that this solution was obtained only after measures to minimize wall emission of electrons were implemented. With the MEVVA source turned on, the spot size was significantly reduced. The spot size continued to decrease as we tuned on the RF source and gas effects respectively. It should be pointed out that the interpretation of these results were somewhat complicated by electrons emitted from the target scintillator plate, and by an associated upstream bias potential which was independently controlled. See Figure 6.

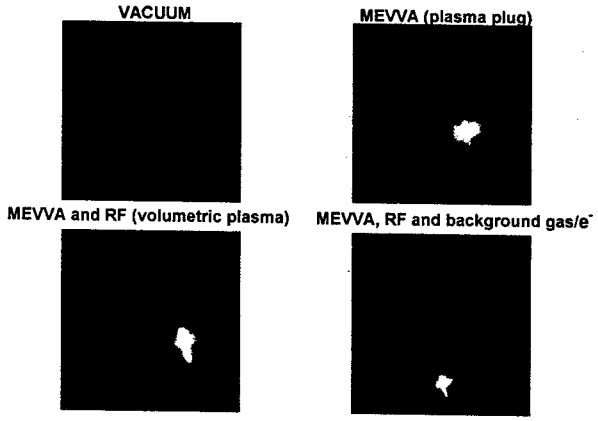

Figure 6: Spot size dependence on neutralization mechanism. Image box size is 4cm × 4 cm squares.

While the first results are qualitatively consistent with theoretical expectations, quantitative comparisons with simulation results require much more work.

The first step toward quantitative comparison is a much better characterization of the 4-D phase space of the incoming ion beam. The final spot size at target is very

sensitive to beam emittance and details of the beam phase space. We measured the transverse 4-D phase space with a movable pinhole inserted at the entry plane to the drift section, i.e., at the exit of the magnetic lattice. The image from the pinhole was measured at the focal point. If the beam had zero emittance such a measurement would yield an identical spot at the same location as the pinhole is moved around to sample different parts of the entering beam. In reality, we measure large aberrations, particularly at the beam edge, consistent with the prediction of geometric aberrations through the magnetic lattice. Superposition of all these images provides a measurement of the purely ballistic beam. At the same time, they provide information of the full 4-D phase space at entrance. [11]

CONCLUSIONS

In the future, we expect to continue detailed comparisons of LSP simulations with measurements. In this regard, a new diagnostic under development, a non-intercepting electron-beam diagnostic [14] to measure the beam electric field profile with and without plasma), will provide much more detailed information of the neutralization dynamics throughout the path of the converging ion beam. While the experimental investigation of the final focusing of high perveance ion beams is still ongoing, the results, both theoretical and experimental have given us a much better understanding of both magnetic final transport as well as neutralized drift. In the process of these investigations, we have developed diagnostics and made measurements to a level of detail hitherto unattained, and the comparisons between theory and experiments are quite encouraging.

REFERENCES

[1] W.R. Meier, R.O. Bangerter and A. Faltens, *Nucl. Instrum. Methods Phys. Res. A*, **415**, 249(1998).

[2] S.S. Yu et al., "A Robust Point Design for a Heavy Ion Fusion Reactor, " to be published *Fusion Sci. and Tech.* (2003).

[3] D. R. Welch, D. V. Rose, W. M. Sharp, and S. S. Yu, "Effects of Pre-Neutralization on Heavy-Ion-Fusion Chamber Transport, " to be published in Proc. 2002 Heavy Ion Fusion Symposium, Moscow, Russia, 27 - 31 May 2002.

[4] W. M. Sharp, D. A. Callahan-Miller, D. P. Grote, M. Tabak, E. Henestroza, S. S. Yu, D. V. Rose, D. R. Welch, and P. F. Peterson, "Realistic Modeling of Chamber Transport for Heavy-Ion Fusion," Proc. PAC '03, WPPG022.

[5] D. Neuffer, "Geometric aberrations in final focusing for heavy ion fusion", Proc. HIF Workshop, ANL, Sept. 19-26, 1978, ANL-79-41.

[6] C.L. Olson, "Chamber Transport", Proc. 13th Int. Symposium on HIF, San Diego, Cal., March 13-17, 2000, p. 118.

[7] S.A. MacLaren, et al., "Results from the scaled final focus experiment", Proc. 13th Int. Symposium on HIF, San Diego, Cal., March 13-17, 2000, p. 126.

[8] S. Eylon et al., "High brightness potassium source for the HIF neutralized transport experiment", Proc. PAC '03, WPPG012.

[9] E. Henestroza et al., "Final Focus System for High Intensity Beams", Proc. PAC '03, WPPG013.

[10] D. Shuman et al., "Magnetic lattice for the HIF neutralized transport experiment", Proc. PAC '03, WPPG017.

[11] E. Henestroza et al., "Neutralized Transport of High Intensity Beams", Proc. PAC '03, WPPG014.

[12] R.A. MacGill, et al., "Streaming metal plasma generation by vacuum arc plasma guns", *Rev. of Sci. Inst.*, Vol. **69**, No. 2, 801(1998).

[13] P. Efthimion, R. Davidson, E. Glison, L. Grisham, "ECR Source for Heavy Ion Beam Charge Neutralization", Proc. PAC '03, WPPG030.

[14] P.K. Roy et al., "Non-intercepting Diagnostics for the HIF Neutralized Transport Experiment", Proc. PAC '03, WPPG016.

THEORY AND OBSERVATIONS OF MICROBUNCHING INSTABILITY IN ELECTRON MACHINES

G. Stupakov
Stanford Linear Accelerator Center, Stanford University, Stanford, CA 94309

INTRODUCTION

Over the last years there have been several reports of quasiperiodic bursts of coherent synchrotron radiation (CSR) in electron rings in the microwave and far-infrared range. The observations were made on synchrotron radiation light sources which include the Sinchrotron Ultraviolet Radiation Facility SURF II [1], VUV ring at the National Synchrotron Light Source at BNL [2,3], second generation light source MAX-I [4], BESSY II [5], and the Advanced Light Source at the Berkeley National Laboratory [6]. General features of those observations can be summarized as follows. Above a threshold current, there is a strongly increased radiation of the beam in the range of wavelengths shorter than the bunch length, $\lambda < \sigma_z$. At large currents, this radiation is observed as a sequence of random bursts. In the bursting regime, intensity of the radiation scales approximately as square of the number of particles in the bunch, indicating a coherent nature of the phenomenon.

It is generally accepted that the source of this radiation is related to the microbunching of the beam arising from development of a microwave instability. The impedance that causes the instability may be due to geometric wake fields from the vacuum chamber, especially in the rings with long bunches [1, 2]. However, according to diffraction model [7], the longitudinal impedance falls off with the frequency as $\omega^{-1/2}$ and cannot account for the instability at the wavelengths of order of a fraction of a millimeter. It has long been known that the synchrotron radiation itself generates a collective force [8] which, if the beam current is large enough, can alter the dynamics of the beam. The impedance associated with the synchrotron radiation increases with the frequency as $\omega^{1/3}$. A possible instability due to this force has been pointed out in Refs. [9, 10].

Typically in rings, the coherent synchrotron radiation at wavelengths of order of σ_z is suppressed due to the shielding effect of conducting walls of the vacuum chamber [11]. However, the wavelengths shorter than σ_z may not be shielded, and this allows to develop a simple theory of the CSR instability which assumes a coasting beam approximation and uses a CSR wake as the only source of the instability [12].

CSR – REVIEW OF THEORY

In application to the CSR instability, we are interested in the synchrotron radiation at wavelengths of the order of a size of microbunches, with a frequency ω typically well below the critical frequency for the synchrotron radiation. For an ultrarelativistic particle with the Lorentz factor $\gamma \gg 1$, in this range of frequencies, the spectrum of the radiation $dP/d\omega$ (per unit length of path) can be written as

$$\frac{dP}{d\omega} = \frac{3^{1/6}}{\pi}\Gamma\left(\frac{2}{3}\right)\left(\frac{\omega}{\omega_H}\right)^{1/3}\frac{e^2\omega_H}{c^2}, \qquad (1)$$

where $\omega_H = eB/\gamma mc$, with B the magnetic field, e the electron charge, m the electron mass, c the speed of light, and Γ the gamma-function. The characteristic angular spread θ of the radiation with reduced wavelength λ (where $\lambda = c/\omega = 1/k$) is of order of $\theta \sim (\lambda/R)^{1/3}$, where R is the bending radius, $R = c/\omega_H$. Another important characteristic of the radiation is the formation length l_f: $l_f \sim \lambda/\theta^2 \sim (\lambda R^2)^{1/3}$—this is the length after which the electromagnetic field of the particle moving in a circular orbit "disconnects" from the source and freely propagates away. In a vacuum chamber with perfectly conducting walls, whether this "disconnection" actually occurs depends on another parameter, often called the "transverse coherence size", $l_\perp$. An estimate for $l_\perp$ is: $l_\perp \sim l_f\theta \sim \lambda/\theta \sim (\lambda^2 R)^{1/3}$. One of physical meanings of $l_\perp$ is that it is equal to the minimal spot size to which the radiation can be focused. Another meaning of this parameter is that it defines a scale for radiation coherence in the transverse direction. Electrons in a transverse cross section of a bunch of size $\sigma_\perp$ would radiate coherently only if $\sigma_\perp \lesssim l_\perp$. We emphasize here that both parameters, $l_\perp$ and l_f, are functions of frequency, with the scalings $l_\perp \propto \omega^{-3/2}$ and $l_f \propto \omega^{-1/2}$.

Closely related to the transverse coherence size is the shielding of the radiation by conducting walls: if the walls are closer than $l_\perp$ to the beam, the field lines during circular motion close onto the conducting walls, rather than disconnect from the charge. This means that the radiation at the frequencies where $l_\perp \gtrsim a$, where a is the pipe radius, is suppressed, or shielded.

For a bunch with N electrons, the radiation of each electron interferes with others. Assuming full transverse coherence (a one dimensional model of the beam), the total radiation of the bunch is [13]:

$$\left.\frac{dP}{d\omega}\right|_{\text{bunch}} = \frac{dP}{d\omega}N\left(1 + N|\hat{f}(\omega)|^2\right), \qquad (2)$$

where $\hat{f}(\omega) = \int_{-\infty}^{\infty} dz f(z) e^{i\omega z/c}$ is the Fourier transform of the longitudinal distribution function of the beam $f(z)$ (normalized by $\int_{-\infty}^{\infty} f(z)dz = 1$). The first term on the right hand side of Eq. (2) is due to incoherent, and the

0-7803-7738-9/03/$17.00 © 2003 IEEE

second one – to coherent radiation. For a smooth distribution function (e.g., Gaussian, with rms bunch length σ_z), the Fourier image $\hat{f}(\omega)$ vanishes for $\lambda \lesssim \sigma_z$, and the radiation is incoherent. However, beam density modulation with $\lambda \lesssim \sigma_z$ would contribute to $\hat{f}(c/\lambda)$ and result in coherent radiation, if the amplitude of the perturbation is such that $|\hat{f}(c/\lambda)| \gtrsim N^{-1/2}$.

RADIATION REACTION FORCE—CSR WAKE FIELD

The collective force acting on the beam due to its coherent synchrotron radiation is described in terms of the so called CSR longitudinal wake [8, 14, 15]. For an ultra-relativistic particle, in one-dimensional approximation, this wake (per unit length of path) is given by the following formula:

$$w(z) = -\frac{2}{3^{4/3} R^{2/3} z^{4/3}} \,. \qquad (3)$$

The wake is valid for distances z such that $R \gg z \gg R/\gamma^3$—a general behavior of the wake function including also distances $z \sim R/\gamma^3$ is shown in Fig. 1. The wake is

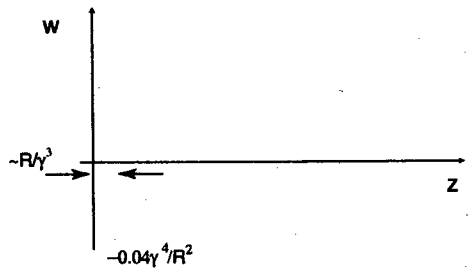

Figure 1: CSR wake as a function of distance. A simple formula (3) is applicable for not very short distances, to the right of the minimum of the wake. The wake reaches minimum at $z \sim R/\gamma^3$, with the minimum value of $-0.04\gamma^4/R^2$.

localized in front of the particle in contrast to "traditional" wakes in accelerator physics which trail the source charge [7]. This is explained by the fact that the charge follows a circular orbit and the radiation propagates along chords getting ahead of the source. The wake given by Eq. (3) has a strong singularity at $z \to 0$. In calculations, this singularity is eliminated by integration by parts and using the fact that the area under the curve $w(z)$ is equal to zero.

A simple wake Eq. (3) assumes a small transverse beam size [15], $\sigma_\perp \lesssim l_\perp \sim (\lambda^2 R)^{1/3}$, and neglects the shielding effect of the conducting walls. It is valid only for long enough magnets, $l_{\rm magnet} \gg l_f$, when transient effects at the entrance to and exit from the magnet can be neglected. A detailed study of transient effects in a short magnet can be found in Refs. [16, 17].

Using the wake field Eq. (3) one can calculate the CSR longitudinal impedance Z:

$$Z(k) = \frac{1}{c}\int_0^\infty dz w(z) e^{-ikz} = \frac{2}{3^{1/3}}\Gamma\left(\frac{2}{3}\right) e^{i\pi/6} \frac{k^{1/3}}{cR^{2/3}} \,. \qquad (4)$$

The real part of this impedance is related to the spectrum of the energy loss of a charge due to radiation: $dP/d\omega = (e^2/\pi)\mathrm{Re}Z$, see Eq. (1). Plots of a CSR wake for a Gaussian bunch can be found in Refs. [14, 15].

CSR INSTABILITY

Due to the CSR wake, an initial small density perturbation δn induces energy modulation in the beam δE. A finite momentum compaction factor of the ring converts δE into a density modulation. At the same time, the energy spread of the beam tends to smear out the initial density perturbation. Under certain conditions, which depend on the beam current, energy spread, and the wavelength of the modulation, the process can lead to an exponential growth of the perturbation.

A quantitative description of the instability can be obtained if we assume that the wavelength of the perturbation is much shorter than the bunch length, $\lambda \ll \sigma_z$, and use a coasting beam approximation. In this case, the dispersion relation for the frequency ω is given by the Keil-Schnell formula [18]:

$$\frac{inr_0c^2Z(k)}{\gamma}\int_{-\infty}^{\infty}\frac{d\delta\,(df/d\delta)}{\omega + ck\eta\delta} = 1 \,, \qquad (5)$$

where n is the number of particles per unit length, η is the momentum compaction factor of the ring, $r_0 = e^2/mc^2$, $Z(k)$ is the CSR impedance given by Eq. (4), $f(\delta)$ is the energy distribution function normalized so that $\int f(\delta)d\delta = 1$. To take into account straight sections in the ring, where $R = \infty$ and there is no CSR wake, Z is replaced with a weighted impedance: $Z \to ZR/\langle R\rangle$, where $\langle R\rangle = C/2\pi$. The plot of $\mathrm{Re}\,\omega$ and $\mathrm{Im}\,\omega$ calculated from Eq. (5) for a Gaussian energy distribution with an rms relative energy spread δ_0, and $\eta > 0$ is shown in Fig. 2. It is convenient to introduce the dimensionless parameter Λ:

$$\Lambda = \frac{1}{|\eta|\gamma\delta_0^2}\frac{I}{I_A}\frac{R}{\langle R\rangle} \,, \qquad (6)$$

where $I_A = mc^3/e = 17.5$ kA is the Alfven current. The maximum growth rate is reached at $kR = 0.68\Lambda^{3/2}$ and is equal to $(\mathrm{Im}\,\omega)_{\max} = 0.43\Lambda^{3/2}c\eta\delta_0/R$.

Three colored areas in this plot refer to stability regions in the parameter space. In the green area 1, the beam is stable because $\mathrm{Im}\omega < 0$ due to Landau damping. This region corresponds to high frequencies, $kR > 2.0\Lambda^{3/2}$. In the yellow region 2, where $k \lesssim R^{1/2}/a^{3/2}$ (a is the transverse size of the vacuum chamber), the instability is suppressed by shielding of the radiation. Finally, at even lower

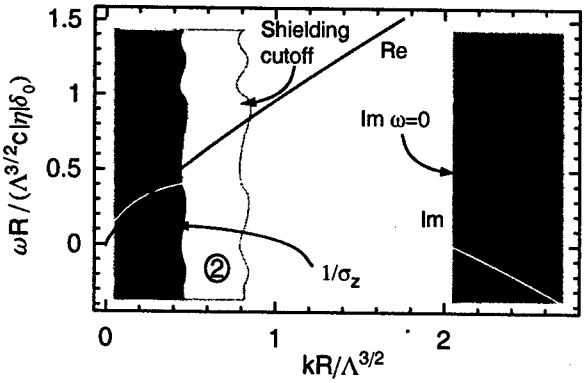

Figure 2: Plot of real (blue) and imaginary (red) parts of frequency ω as functions of k for positive η. Normalization of the frequency ω and the wavenumber k on the axes involves the parameter Λ defined by Eq. (6).

frequencies, in the blue area 3, the wavelength of the instability exceeds the bunch length and the coasting beam theory breaks down. The wavy lines between stability regions indicate fuzziness of the transition boundaries in our model.

In table 1, accelerator and beam parameters are presented for four existing rings, where the theory predicts CSR instability. The parameter I_b is the bunch current

Ring	ALS	VUV	LER KEKB
E (GeV)	1.5	0.81	3.4
η	$1.41 \cdot 10^{-3}$	$2.35 \cdot 10^{-2}$	$1 \cdot 10^{-4}$
δ_0	$7.1 \cdot 10^{-4}$	$5.0 \cdot 10^{-4}$	$7 \cdot 10^{-4}$
$\langle R \rangle$ (m)	31.3	8.11	480
R (m)	4	1.91	16.3
a (cm)	2	2.1	2.5
I_b (mA)	30	400	1
σ_z (cm)	0.7	4.7	1
$\lambda_{\rm sh}$ (cm)	0.14	0.2	0.1
$\lambda_{\rm th}$ (cm)	$4.7 \cdot 10^{-3}$	0.02	0.015

Table 1: Numerical Estimates for LER PEP-II, ALS, VUV and LER KEK-B rings

in the ring. Calculated in two last rows of the table are the reduced wavelength $\lambda_{\rm sh} = a^{3/2}R^{-1/2}$ for the shielding cutoff, and the instability threshold $\lambda_{\rm th} = 0.5R\Lambda^{-3/2}$. The beam is unstable for perturbations with the wavelengths between $2\pi\lambda_{\rm th}$ and $2\pi\lambda_{\rm sh}$.

There are several effects that are neglected in the simple theory described above. First, a zero transverse emittance of the beam was assumed. Second, the synchrotron damping γ_d due to incoherent radiation was neglected which makes the growth rate of the instability somewhat smaller, $\mathrm{Im}\,\omega \to \mathrm{Im}\,\omega - \gamma_d$ [19]. Finally, the retardation effects were neglected which is valid if the formation time for the radiation is smaller than the instability growth time, $t_f \sim l_f/c \ll 1/\mathrm{Im}\omega$. In most cases characteristic for modern rings, those effects are relatively minor.

NONLINEAR REGIME

After initial exponential growth, described by a linear theory, the instability comes into a nonlinear regime. Study of the nonlinear regime requires numerical simulation. Such simulations have been carried out in Ref. [20] where the authors numerically solved the Vlasov-Fokker-Planck equation, including CSR shielding with parallel plates, damping and quantum fluctuations due incoherent radiation.

The results of the numerical simulation can be described as follows. Initially, there are microstructures in the bunch of very small amplitude, giving small Fourier components with short wavelengths. Above a current threshold these Fourier components build up exponentially in agreement with linear theory described above. There is a corresponding burst of radiation, but it is limited in duration by a quick smoothing of the phase space distribution. Continued exponential growth is prevented by the intrinsic nonlinearity of self-consistent many-particle dynamics, which also contributes to phase space smoothing through quick generation of a relatively large spectrum of Fourier modes. Within one or two synchrotron periods the microstructures have almost disappeared, the overall bunch length has increased, and the burst of coherent radiation is finished. Next, radiation damping and diffusion from the usual incoherent radiation gradually reduce the bunch length and energy spread, restoring the conditions for instability and another burst, after a time somewhat smaller than the damping time. The computed bunch length shows fast oscillations typical of a quadrupole mode, while the envelope of those oscillations shows a sawtooth or relaxation pattern similar to the experimentally observed patterns.

COMPARISON WITH EXPERIMENT

A detailed comparison of the theory with observations has been carried out in the experiment at the Advanced Light Source (ALS), a 1.9 GeV electron storage ring [6]. The authors presented experimental evidence indicating that the instability thresholds predicted by the microbunching model correspond to the observed thresholds for the CSR bursts. For different electron beam energies and bunch lengths, the instability threshold was measured at 94 GHz by microwave detector, and by Si bolometer (up to $\lambda = 100$ μm).

It was observed that above a threshold single bunch current, bursts of signal appear. As the current increases, the burst signals increase in both amplitude and frequency. The polarization of the radiation was measured to be entirely in the plane of the electron beam orbit, consistent with the expected polarization level of greater than 99.5%. At the highest single bunch current, the bursts appear almost continuously. The plot of measured threshold current as a function of beam energy is shown in Fig. 3. A good agreement with the theory was found for two different wavelengths of the microbunching.

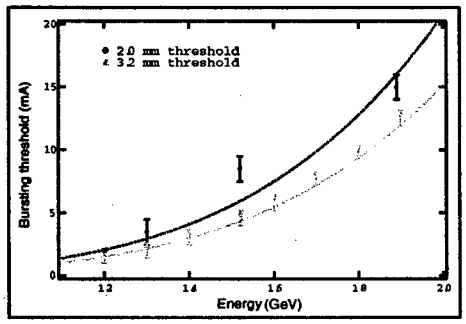

Figure 3: Plot of threshold current as a function of beam energy at two wavelengths: $\lambda = 2$ mm (blue dots), and $\lambda = 3.2$ mm (red triangles) [from Ref. [6]]. Solid lines are theoretical predictions for the thresholds obtained from Eq. (5).

RINGS WITH WIGGLERS

In the damping ring of the Next Linear Collider [21], there will be long magnetic wigglers which introduce an additional contribution to the radiation impedance. The analysis of the CSR instability in such a ring requires knowledge of the impedance of the synchrotron radiation in the wiggler. Based on the earlier study of the coherent radiation from a wiggler [22], in Ref. [23], a steady-state wake averaged over the wiggler period has be derived for the case $K^2/2 \gg 1$ (where K is the wiggler parameter) and $\gamma \gg 1$. The most interesting from the point of view of instability is a low-frequency part of the impedance, given by the following formula (per unit length of path):

$$Z_{\rm wiggler}(\omega) \approx \frac{Z_0 \omega}{4c}\left[1 - \frac{2i}{\pi}\log\frac{\omega}{\omega_*}\right], \qquad (7)$$

where $\omega_* = 4\gamma^2 c k_w/K^2$ and $Z_0 = 377$ Ohm. Eq. (7) is valid for $\omega \ll \omega_*$.

Results of the analysis of CSR instability in the NLC ring, taking into account the wiggler CSR impedance can be found in Ref. [24].

DISCRETE MODES NEAR SHIELDING THRESHOLD

There are several reasons why the simple theory of CSR microbunching instability developed in Ref. [12] is not applicable near that shielding threshold, $\lambda \sim a^{3/2}/R^{1/2}$. The most important one is that CSR does not have continuous spectrum here, and the modes that can interact with the beam, are discrete. The discreteness of the spectrum has been demonstrated in early papers [25, 26] for toroids of rectangular cross section. A more recent analysis of the shielded CSR impedance [27] extends the previous treatment of the problem and deals with arbitrary shapes of the toroid cross section.

Each synchronous mode in the toroid is characterized by frequency ω_n, a loss factor κ_n (per unit length), and a group velocity $v_{g,n}$. The wake associated with the n-th mode is

$$w_n(z) = 2\kappa_n \cos\left(\frac{\omega_n}{c} z\right).$$

This wake, for lowest modes, propagates behind the particle. Calculation of ω_n, κ_n, and $v_{g,n}$, in the general case of arbitrary cross section requires numerical solution of two coupled partial differential equations [27]. For a toroid of round cross section of radius a, the lowest mode has been found to have the frequency $\omega_1 = 2.12cR^{1/2}a^{-3/2}$, the loss factor $\kappa_1 = 2.11a^{-2}$ and the group velocity $1 - v_{g,1}/c = 1.1a/R$.

Near the shielding threshold, the CSR instability should be treated as an interaction of the beam with single modes, [28]. When the wavelength of the mode is smaller than the bunch length, one can still use the coasting beam approximation, but one cannot neglect retardation effects. Assuming an ideal toroidal chamber with a constant cross section (no straight sections in the ring), it turns out that the theory of single-mode instability [28] parallels that of SASE FEL (see, e.g., [29]). It gives the maximum growth rate of the instability for nth mode equal $\sqrt{3}\rho_n\omega_n/2$ where

$$\rho_n = \left[\frac{I}{I_A}\frac{c^2\eta\kappa}{\omega_n^2\gamma}\left(1 - \frac{v_{g,n}}{c}\right)\right]^{1/3} \qquad (8)$$

is an analog of the Pierce parameter in FELs.

Nonlinear regime of the instability in this approximations has been studied in Refs. [28,30]

BUNCH COMPRESSOR

Microbunching due to CSR induced instability has been also identified in computer simulations as a potential danger in bunch compressors [31], where the energy spread in the beam is extremely small.

The basic mechanism of the instability is the same as in rings, with an additional complication due to the energy chirp in the beam [32–34]. As a result of the instability, an initial density perturbation in the beam with amplitude n_1 and a wavelength λ, after passage through the compressor, will be amplified to amplitude n_2. The ratio $G = n_2/n_1$ is called the gain factor; it is a function of λ. Note, that the wavelength of the perturbation after compression is smaller than the initial wavelength by a factor of compression ratio. Unstable wavelengths observed in simulations can be very short—of order of few microns. It was found that both the transverse emittance of the beam and its energy spread have a strong stabilizing effect at short wavelengths.

Calculation of the gain factor for combined effect of both LCLS bunch compressors was carried out in Ref. [35], and is shown in Fig. 4. The solid line corresponds to the rms energy spread $\delta_{\rm rms} = 3 \cdot 10^{-6}$ and the dash line shows the case $\delta_{\rm rms} = 3 \cdot 10^{-5}$. The lines are calculated from the theory, and squares and triangles are numerical simulations which show a good agreement between the two approaches. Note that with a small energy spread, the maximum amplification approaches 10, at wavelengths about 80 microns

(after compression, this wavelength reduces to about 2 microns). Increase of the energy spread by ten times strongly suppresses the gain at short wavelength.

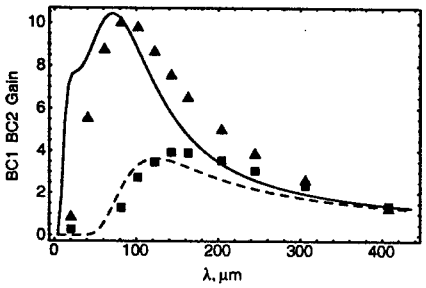

Figure 4: Gain factor for two LCLS bunch compressors as a function of wavelength λ of perturbations before compression (from Ref. [35]).

CONCLUSION

Coherent synchrotron radiation in electron and positron machines introduces a universal source of impedance which may become dominant source of the wake at high frequency where geometric and resistive wall impedances become small. Unless the wall shielding effect suppresses the CSR, its impedance remains even in a smooth vacuum chamber with perfectly conducting walls, and can drive a microwave instability of the beam.

Over the last several years, there has been a remarkable progress, both theoretically and experimentally, in our understanding of this microbunching instability and related coherent synchrotron radiation in rings. The existing theory predicts thresholds for the instability, and computer simulations show nonlinear evolution of the unstable state. These theoretical results are in good agreement with experimental observations.

Another practically important area of application of the CSR theory is bunch compressors, where amplification of an initial density perturbation can lead to the emittance growth of the compressed beam. Detailed studies and simulations of microbunching resulted in improved design of compressors, with a deleterious effect of CSR suppressed to a tolerable level.

REFERENCES

[1] U. Arp et al., Phys. Rev. ST Accel. Beams **4**, 054401 (2001).

[2] G. L. Carr et al., NIM, Sec. A **463**, 387 (2001).

[3] B. Podobedov et al., in *Proc. of the PAC 2001* , (2001).

[4] A. Andersson, M. S. Johnson, and B. Nelander, Opt. Eng. **39**(12), 3099 (2000).

[5] M. Abo-Bakr et al., Phys. Rev. Lett. **88**, 254801 (2002).

[6] J. Byrd et al., Phys. Rev. Lett. **89**, 224801 (2002).

[7] A. W. Chao, *Physics of Collective Beam Instabilities in High Energy Accelerators* (Wiley, New York, 1993).

[8] L. V. Iogansen and M. S. Rabinovich, Sov. Phys. JETP **37**, 83 (1960).

[9] R. L. Warnock and K. Bane, in *Proc. of PAC 1995*, (1996).

[10] J.-M. Wang, Phys. Rev. **E58**, 984 (1998).

[11] J. S. Nordvick and D. S. Saxon, Phys. Rev. **96**, 180 (1954).

[12] S. Heifets and Stupakov G. V., Phys. Rev. ST Accel. Beams **5**, 054402 (2002).

[13] A. W. Chao and M. Tigner, *Handbook of Accelerator Physics and Engineering* (2002), 2nd ed.

[14] J. B. Murphy, S. Krinsky, and R. L. Gluckstern, in *Proc. of PAC 1995* (1996).

[15] Y. S. Derbenev et al., DESY FEL Report TESLA-FEL 95-05, (1995).

[16] E. L. Saldin, E. A. Schneidmiller, and M. V. Yurkov, NIM, Sec. A **398**, 373 (1997).

[17] Stupakov G. and Emma P., in *Proc. of EPAC 2002*, (2002).

[18] J.-L. Laclare, in *Proc. CERN Accelerator School* (1985), no. 85-19 in CERN Yellow Report, pp. 377–414.

[19] S. Heifets and G. Stupakov, Report SLAC-PUB-8803, SLAC (Mar 2001).

[20] M. Venturini and R. Warnock, Phys. Rev. Lett. **89**, 224802 (2002).

[21] A. Wolski, *NLC damping rings*, URL: http://awolski.lbl.gov /nlcdrlattice/default.htm.

[22] E. L. Saldin, E. A. Schneidmiller, and M. V. Yurkov, NIM, Sec. A **417**, 158 (1998).

[23] J. Wu, T. Raubenheimer, and G. Stupakov, Phys. Rev. ST Accel. Beams **6**, 040701 (2003); this Proceedings.

[24] J. Wu, T. Raubenheimer, and G. Stupakov, Report SLAC-PUB-9629, SLAC (2003); this Proceedings.

[25] R. L. Warnock and P. Morton, Part. Accel. **25**, 113 (1990).

[26] K.-Y. Ng, Part. Accel **25**, 153 (1990).

[27] G. V. Stupakov and I. A. Kotelnikov, Phys. Rev. ST Accel. Beams **6**, 034401 (2003).

[28] S. Heifets and G. Stupakov, Report SLAC-PUB-9627, SLAC (2003); this Proceedings.

[29] R. Gluckstern, S. Krinsky, and H. Okamoto, Phys. Rev. **E47**, 4412 (1993).

[30] S. Heifets, Report SLAC-PUB-9626, SLAC (2003).

[31] M. Borland, Phys. Rev. ST Accel. Beams **4**, 070701 (2001); NIM **A483**, 268 (2002).

[32] S. Heifets, Stupakov G. V., and Krinsky S., Phys. Rev. ST Accel. Beams **5**, 064401 (2002).

[33] E. L. Saldin, E. A. Schneidmiller, and M. V. Yurkov, NIM **A490**, 1 (2002).

[34] Z. Huang and K.-J. Kim, Phys. Rev. ST Accel. Beams **5**, 074401 (2002).

[35] Z. Huang et al., Report SLAC-PUB-9538, SLAC (2002).

BEAM DYNAMICS IN THE SPALLATION NEUTRON SOURCE LINAC*

D. Jeon# representing the SNS Project, Oak Ridge, Tennessee, USA

Abstract

Being an 1.44MW machine, the beam loss requirement on the SNS linac is less than 1W/m and controlling halo particle generation is of great importance. Beam dynamics aspects of the SNS linac design are presented considering various halo generation mechanisms. A halo generation mechanism in the non-periodic lattices such as the SNS linac MEBT (Medium-Energy Beam-Transport between RFQ and DTL) is reported. We find that the nonlinear space charge force resulting from large transverse beam eccentricity ~2:1 in the ~1.6-m-long MEBT chopper section is responsible for halo formation [1]. The proposed mitigation measures are modifying the MEBT optics and introducing adjustable collimators in the MEBT. The transient beam behavior of the LEBT and MEBT choppers is also studied for the fate of partially chopped beams.

INTRODUCTION

The SNS (Spallation Neutron Source) accelerator system is designed to accelerate intense proton beams to energy of 1-GeV, delivering more than 1.4 MW (upgradeable to 2 MW) of beam power to the neutron production target [2]. The peak current in the linac is 38mA and the macropulse average current is 26mA. The SNS linac has the following structure; ion source, LEBT (Low-Energy Beam-Transport), RFQ (Radio-Frequency Quadrupole), MEBT (Medium-Energy Beam-Transport), DTL (Drift Tube Linac), CCL (Coupled Cavity Linac), and SCL (SuperConducting Linac). A primary concern is potential damage and radio activation of accelerator components resulting from uncontrolled beam losses. A major source of loss is beam halo that intercepts the bore of the linac.

First, beam dynamics aspects of the SNS linac design are presented. A new halo mechanism and its mitigation scheme are presented. The transient beam behavior of the LEBT and MEBT choppers is also presented, which shows significant emittance growth.

BEAM DYNAMICS DESIGN

Aspects of the SNS linac design have been reported [3]. The following lists the conditions imposed to avoid or minimize halo generation:

- Avoid envelope instabilities by keeping zero current phase advance below 90°.
- Minimizing space charge coupling resonance crossing.
- Making phase advance per unit length continuous for current independence.

* SNS is managed by UT-Battelle, LLC, under contract DE-AC05-00OR22725 for the U.S. Department of Energy.
#jeond@ornl.gov

We selected focusing lattice parameters to avoid envelope instabilities throughout the linac. The zero current phase advance per period σ_{ot} and σ_{ol} never exceeds 90° as in Fig. 1. We avoid the 1:1 parametric resonance by adjusting quadrupole gradients so that σ_{ot} and σ_{ol} do not cross except in the DTL tank 1 and CCL module 4 where matching considerations take precedence.

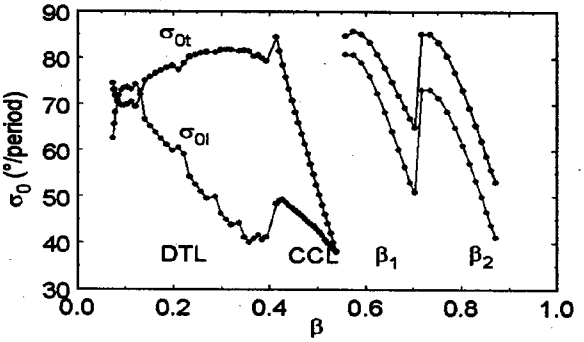

Figure 1: Phase advance is below 90° and resonance crossing is minimized.

Figure 2 is a resonance chart for the nominal SNS design parameter, which includes a 52mA beam current and an emittance ratio $\varepsilon_z/\varepsilon_x$ of 1.2. The contoured peaks identify space charge coupling resonances. The shaded contours indicate the expected rates of emittance growth with 5% being the lowest value plotted. The two peaks on the left side represent weak coupling resonances that take a long time to develop (3:1 and 2:1). This indicates that space charge coupling resonance poses little risk for the current SNS linac design. Vertical axis is tune depression and horizontal axis is the tune ratio between transverse and longitudinal dimension.

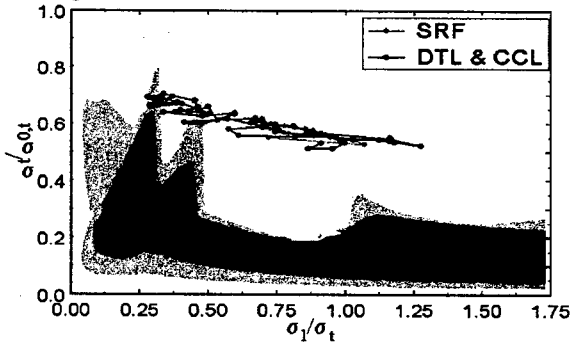

Figure 2: The SNS linac tune trajectory on the resonance chart.

We make k_{ot} and k_{ol}, the phase advance per unit length continuous across all lattice transitions as shown in Fig. 3. This design feature minimizes the potential for

mismatches and helps assure a current independent design.

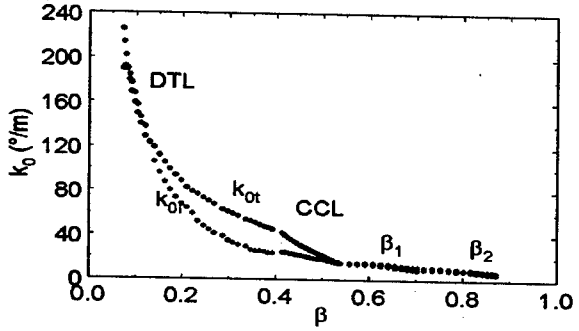

Figure 3: Phase advance per unit length is continuous.

HALO GENERATION MECHANISM

Beam dynamics simulations of the SNS linac show that the beam halo develops at low energy, but some halo particles survive acceleration to higher energies before being lost primarily on the CCL bore as shown in Fig. 4. This particle loss at higher energies results in radio activation of the CCL. In order to find ways to mitigate this halo related beam loss, we conducted studies to identify the sources and mechanism of halo formation. It turns out that the MEBT is the largest contributor to FE halo generation in the SNS linac [1].

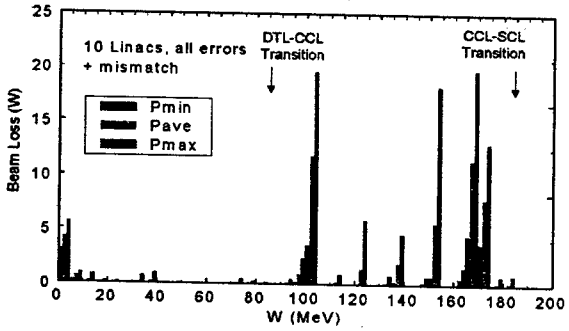

Figure 4: Beam loss along the SNS linac.

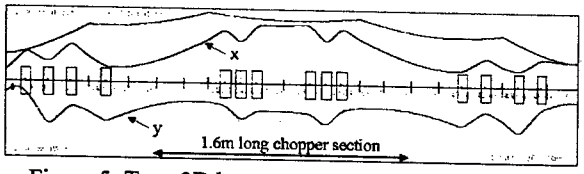

Figure 5: Trace3D beam envelope profiles of MEBT.

To better understand MEBT optics, the horizontal (x curve) and vertical (y curve) envelope profiles of the sqrt(5) * rms beam size in the MEBT are plotted in Fig. 5. The top curve is longitudinal envelope profile. The beam is squeezed vertically to clear the vertical deflection plates of both the chopper and anti-chopper and relaxed horizontally. This arrangement is necessary to have 90° zero-current betatron phase advance between the chopper box and the chopper target in the middle, and between the chopper target and the anti-chopper box as well. However, this 1.6-m-long chopper section with a large beam eccentricity is the source of halo formation.

Figure 6 shows the electric field (in arbitrary unit) on top of real space projections of beam distribution at the chopper target (in the middle of the MEBT) where the beam eccentricity is ~2:1. The beam is wide in x and narrow in y. The Ex becomes nonlinear beyond x=0.5 cm, which is well inside the core. This means that the outer part of core with |x| > 0.5 cm (marked as "potential halo") is subject to nonlinear space charge force and their phase advance is quite different from the inner part of the core seeing linear space charge force. The phase advance difference over the 1.6-m chopper section leads to severe beam distortion in horizontal phase space. In the case of Ey, only small fraction of halo particles sees nonlinear space charge force. This is why the tail develops mainly in x phase space by the end of the MEBT.

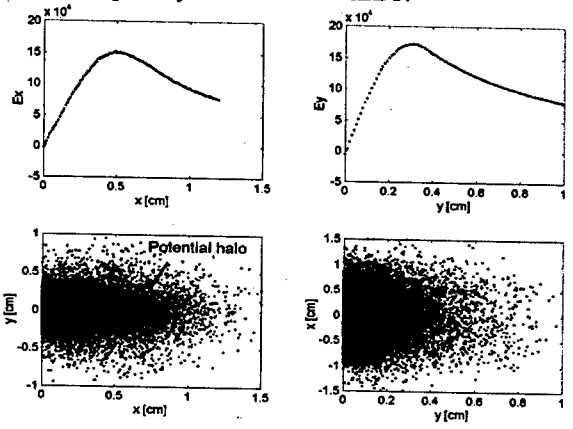

Figure 6: Plots of E field and real space projections of beam distribution. The unit of E field is arbitrary. x rms beam size is 3.40mm and y rms beam size 1.71 mm.

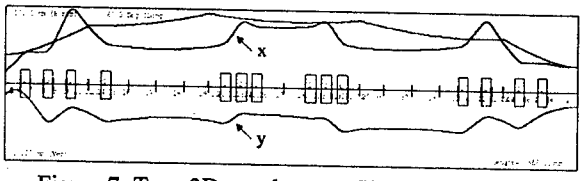

Figure 7: Trace3D envelope profiles of round beam optics.

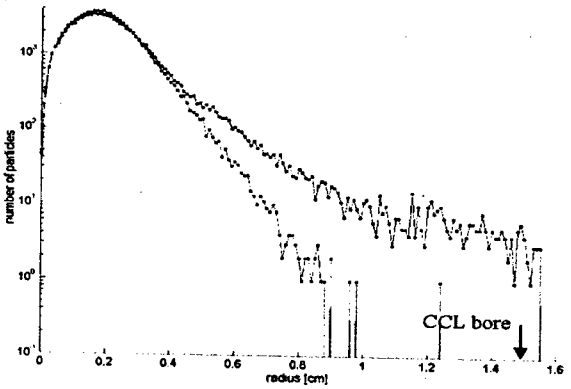

Figure 8: radial beam profile at 171MeV before (the blue curve, baseline case) and after the MEBT optics change alone (the red curve).

To suppress halo formation induced by large transverse beam eccentricity, the optics of lattices should make the beam as round as possible. For the purpose of studying, we modified the entire MEBT optics to reduce beam eccentricity as shown in Fig. 7 (compare with Fig. 5).

Making the beam round indeed suppresses the halo formation as shown in Fig. 8 that depicts the beam profiles at 171 MeV before and after optics modification. However, modification of the entire MEBT optics is not viable to facilitate the beam chopping for ring injection. At least the first half of the MEBT should not be modified, while the second half can be modified.

HALO MITIGATION SCHEME

A hybrid scheme is adopted for halo mitigation that is a combination of alternative MEBT optics and adjustable collimators at the MEBT chopper target.

Alternative MEBT optics

In an alternative design, the upstream half of MEBT optics is preserved while the downstream half of MEBT optics is modified for round beam. The resulting beam cross section is more circular as shown in Fig. 9. Now, the anti-chopper no longer restores a partially chopped portion of the beam to its original (on-axis) position in phase space, if indeed that were desirable. Also, the beam now has a larger vertical extent and approaches the anti-chopper plates as designed.

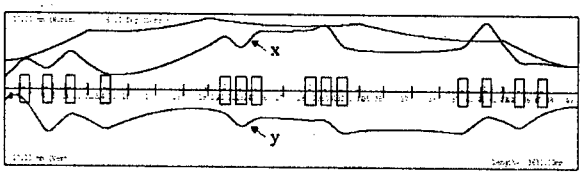

Figure 9: The proposed alternative MEBT optics.

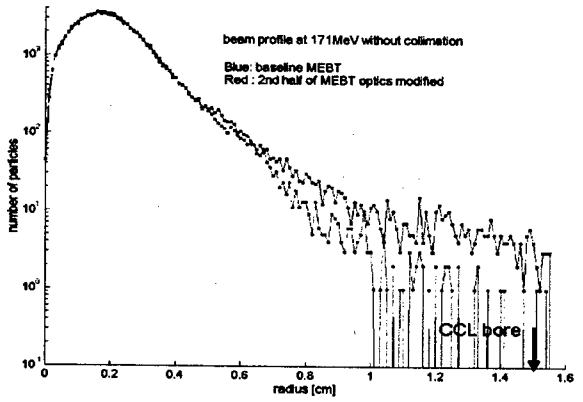

Figure 10: Radial beam distribution at 171MeV for the baseline MEBT optics without collimation (the blue curve) and for the alternative MEBT optics without collimation (the red). 87% of the beam tail with r > 9 mm is removed just due to optics change.

This simple modification to the optics alone reduces the formation of transverse tails substantially and improves the beam quality in the downstream linac. Figure 10 shows that 87% of the beam tails with r > 9 mm at 171MeV is removed (compared with the blue curve).

MEBT scraping

There are only a few places where collimators will fit in the MEBT. One convenient place is at the chopper target. Figure 11 shows the layout of the MEBT with the chopper target and anti-chopper box indicated by arrows. A pair of adjustable horizontal collimators would be installed in the chopper target box (at the red arrow). The chopper target itself is located above the mid-plane to intercept beam that is deflected upward. Collimators mounted on horizontal actuators will not interfere with the function of the target.

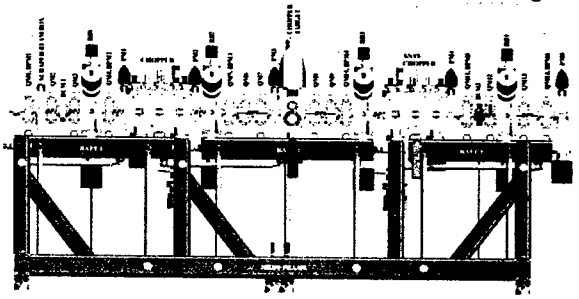

Figure 11: Schematic layout of MEBT indicating the location of adjustable collimators.

This assembly is shown schematically in Fig. 12. This collimator implementation has the advantage that it is readily adjustable to accommodate the actual beam conditions, which are expected to vary with different operating conditions such as beam current, ion-source performance, LEBT, RFQ, and MEBT tuning. The other advantage is that the proposed collimators can be cooled easily. The adjustable collimators are designed to scrape up to about 20% of beam power when they are made of Carbon/Carbon composite [4].

Figure 12: Schematic drawing of adjustable collimators and the chopper target.

Figure 13 shows the radial beam distribution at 171 MeV resulting from this hybrid solution, which combines the alternative MEBT optics and the MEBT scraping at the chopper target. 97% of the halo with r > 9 mm is removed compared with the baseline case (in blue). Even for the increased peak current of 54mA rather than 38mA, there is also an enough safety margin even for this case.

With the adopted mitigation scheme, we expect to reduce uncontrolled beam loss associated with halo to a manageable level.

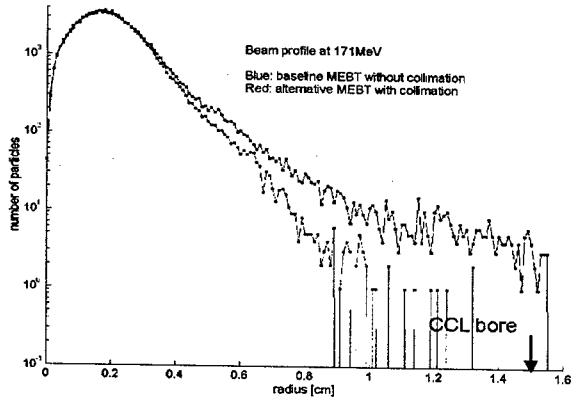

Figure 13: Radial beam profile at 171MeV for the adopted hybrid scheme mitigating halo (red curve).

TRANSIENT BEAM BEHAVIOR

Detailed analysis of transient beam behavior of LEBT and MEBT choppers was performed [5]. The beam duty factor of the SNS linac is 6%: 1-ms macropulses at 60 Hz. The chopping breaks each macropulse into 1060 minipulses separated by 300-ns gaps for ring extraction, thus passing 68% of the beam as illustrated in Fig. 14.

Chopping is done in two stages: LEBT chopper and MEBT chopper. The LEBT chopper deflects the beam into the RFQ, and the MEBT chopper deflects beam vertically onto the chopper target. Because of the several-ns rise and fall time of the chopper voltage, the edges of the beam gap are "contaminated" with partially chopped micropulses whose destiny is of interest.

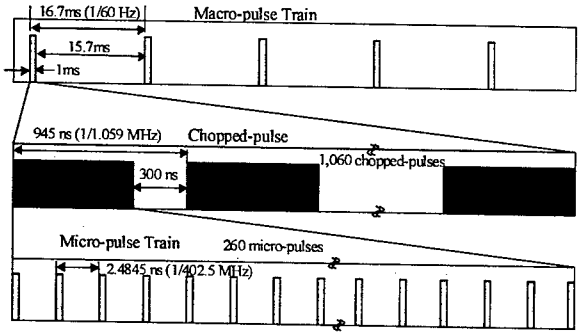

Figure 14. Time structure of the SNS beam-pulses.

LEBT chopper

The LEBT chopper is a segmented Einzel lens as shown at left in Fig. 15. This segmented electrode is just upstream of the grounded entrance aperture of the RFQ at far right in the figure.

Collectively, the four chopper electrodes operate at -40 kV to focus the beam into the RFQ. By superimposing ±2 kV on opposing segment pairs we can arrange to deflect the beam toward 45°, 135°, 225°, or 315°. During a 300-ns chopping gap, the electrodes maintain a constant orientation. For a voltage rise and fall time of 25 ns, up to 20 micropulses in each gap may experience only partial deflection. Operating in the chopping mode breaks axial symmetry the of LEBT fields. For our beam simulation studies, we transport the beam through the 3-D fields of the LEBT.

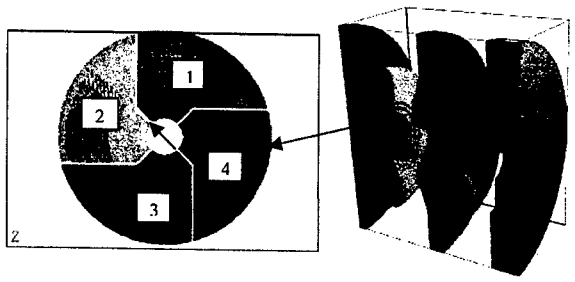

Figure 15: LEBT chopper configuration.

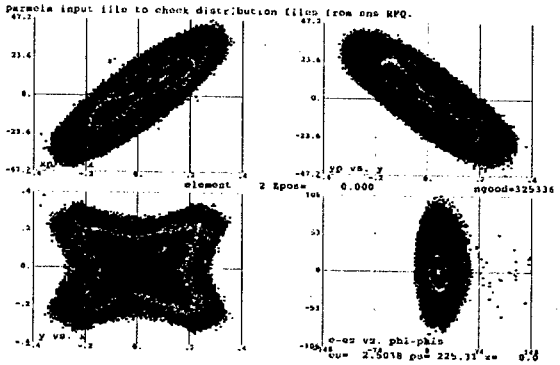

Figure 16: Superimposed phase-space distributions at the RFQ-exit for 4 partially LEBT-chopped beams.

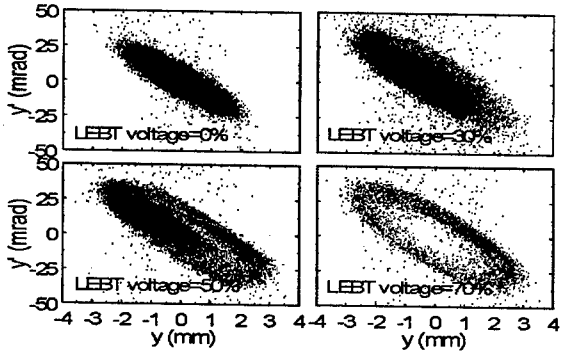

Figure 17: Phase space (y-y') projections at the RFQ exit for different LEBT voltages.

With the chopper off, the beam arrives "matched" at the RFQ entrance. When the LEBT chopper is on, the beam enters the RFQ off-axis and off-angle. This off axis beam results in significant emittance growth at its exit as shown in Fig. 16.

Figure 17 shows the evolution of the y-y' phase space of this beam at the RFQ exit during the LEBT voltage ramp at 0%, 30%, 50% and 70% of maximum deflection into the first quadrant. Blue dots represent particles that have survived the RFQ. During the ramp, we see about ten-fold increase in emittance and the y-y' projection

transforms to a hollow ellipse. Red dots represent the particles at the RFQ output that survived the MEBT chopper at its full voltage and appear at the entrance to the DTL. These particles represent potential contamination of the edges of the chopper gap.

MEBT chopper

Figure 18 shows the y-y' emittance at the DTL entrance for four voltages of MEBT acting alone. The asymmetry of the unchopped beam reflects the missing 1% removed by the chopper target. During the MEBT transient, the beam entering the linac nominally remains within the phase space defined by the matched beam. However, even at full chopper voltage ~16 μA (peak) enters the linac, which fails to meet the gap-current goal, when MEBT chopper acting alone. Nonetheless, the remnant of the beam is well within the acceptance of the SNS linac.

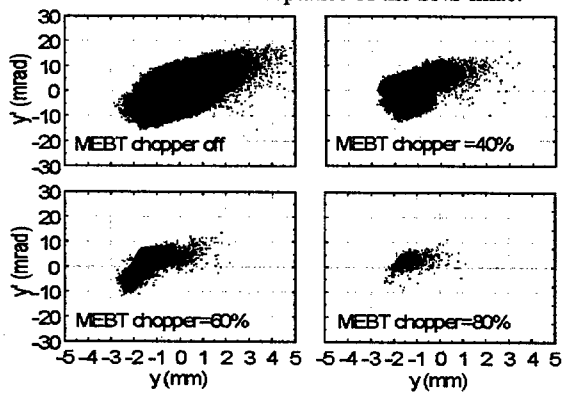

Figure 18: Particle coordinates (y-y') at the DTL input for various MEBT chopper voltage when acting alone.

We consider four different chopper-timing sequences that are illustrated in Fig. 19. The left-hand column shows the relative timing between the LEBT chopper (in red) and the MEBT chopper (in blue) and the voltage ramps of the two choppers. The middle column shows the corresponding current in individual micropulses at the entrance to the DTL, assuming a linear relationship between voltage and beam current chopped. The right-hand column shows the current intercepted on the MEBT-chopper target during the turn-on transient. Table 1 summarizes the relative virtues of the four options in Fig. 18. To test the linear model we simulated the performance for option 1 using 10^6 macroparticles.

Option 3 is most attractive because it minimizes the potential beam loss in the linac while easily meeting the chopper-target power limitations. Partially chopped beam lost at or near the DTL entrance corresponds to less than 0.1 W, meeting the beam-loss limit of 1 W/m. With both choppers at full voltage, only ~31 nA peak current (1.2x 10^{-5}) enters the DTL, easily meeting the gap cleanliness requirement of 10^{-4}.

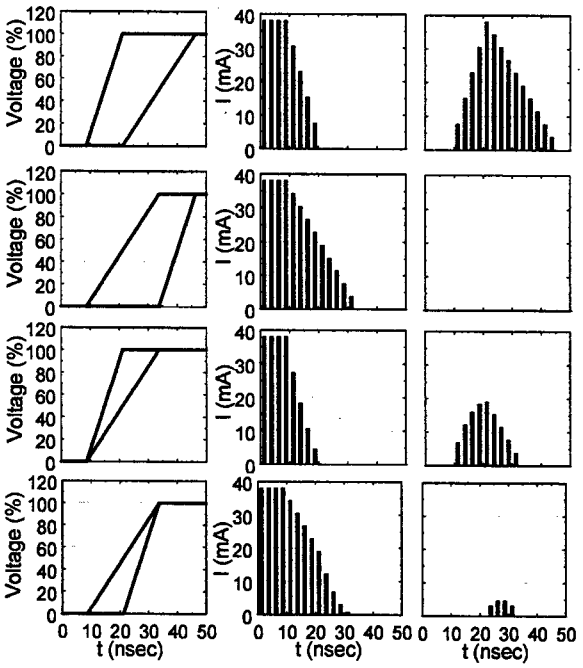

Figure 19: Chopper timing options showing LEBT and MEBT voltage ramps, micropulse current in the falling edge of the chopper gap and micropulse current on the chopper target.

Table 1: Linear model predictions and simulation.

chopper timing option	average linac current during transient	average MEBT target power dissipation
	(μA)	(W)
1	24	226
2	54	0
3	19	87
4	49	12
simulation	16	208

REFERENCES

[1] D. Jeon et al, Phys. Rev. ST Accel. Beams **5**, 094201 (2002).

[2] J. Wei et al, Proceedings of the 2001 Part. Accel. Conf. (Chicago, 2001), p. 319.

[3] J. Stovall et al, Proceedings of the 2001 Part. Accel. Conf. (Chicago, 2001), p. 446.

[4] Private communication with S. Kim: Carbon/Carbon is considered developed for the fusion reactor is. See http://www.toyotanso.com.

[5] S. Nath et al, Proceedings of the 2002 LINAC Conf. (Gyongju, S. Korea, 2002), p. 319.

STORAGE OF CRYSTALLINE ION BEAMS *

U. Schramm †, T. Schätz ‡, M. Bussmann, D. Habs
Sektion Physik, LMU Munich, D-85748 Garching, Germany

Abstract

Recently, the phase transition of a low-energy $^{24}Mg^{+}$ ion beam into the Coulomb-ordered 'crystalline' state could be realized in the rf quadrupole storage ring PALLAS at the LMU Munich. Thereby, an increase of the phase space density of the beam, subjected to longitudinal laser cooling, by about six orders of magnitude was observed. In this paper, we focus on the systematic experimental investigation of the role of the focusing conditions and of bending shear in the storage ring on the attainment of crystalline beams of different crystal structure.

CRYSTALLINE BEAMS

Almost two decades after the first discussion of the 'crystallization' [1, 2, 3, 4] of stored ion beams into a Coulomb-ordered state, this phase transition could recently be realized in the table-top rf quadrupole storage ring PALLAS (PAul Laser CooLing Acceleration System) for coasting [5, 6, 7] and for bunched ion beams [8, 9]. The phase transition of a space-charge dominated ion beam to the 'crystalline' state can occur when the mutual Coulomb-energy of the ions overcomes their mean kinetic energy by about two orders of magnitude [1, 7]. As typical inter-ion distances of stored singly charged ions amount to of the order of 10 μm, beam temperatures in the range of mK are required. This temperature range can be reached with laser cooling [10] provided that heating mechanisms as intra-beam scattering (IBS) [11, 12] in the emittance-dominated 'gaseous' regime are sufficiently reduced. This can be achieved either by a strong dilution of the ion beam, as demonstrated by experiments on electron-cooled heavy ion beams [13, 14, 15] and on laser-cooled $^{9}Be^{+}$ beams [16], or by minimizing modulations of the beam envelope, which has been realized with PALLAS.

The crystalline state of an ion beam represents the state of ultimate brilliance in the sense that for given focusing strength and ion current, ultimate phase space densities are reached [5]. Moreover, crystalline beams were found to be rather insensitive to the strong heating mechanisms (IBS) omnipresent in the non-crystalline regime [5, 6]. As these mechanisms rely on dissipative Coulomb collisions, they are strongly suppressed in the crystalline regime [2, 11, 12, 17]. Even without further cooling, no significant emittance growth was experienced for crystalline beams for typically 10^6 focusing periods [5, 18].

Yet, the inevitable modulation of the beam envelope in the alternating fields of a storage ring and velocity dependent shear forces have been predicted to complicate the maintenance of crystalline structures larger than a one-dimensional (1D) string of ions [2, 17, 19]. In this paper, the focusing conditions for which crystalline beams are attainable in PALLAS are therefore discussed as a function of the ion beam velocity. Another issue is that longitudinal laser cooling itself, due to the randomness of photon scattering, may cause transverse instabilities of crystalline beams [18], as this effect has been proposed [20] to have hindered the crystallization of dilute ion beams in the storage rings ASTRID (Aarhus) and TSR (Heidelberg) [16].

EXPERIMENTAL TECHNIQUES

A sketch of the low-energy table-top rf quadrupole storage ring PALLAS [21] is given in Fig. 1.

Experimental Setup

For the transverse confinement and simultaneous bending of a low-energy $^{24}Mg^{+}$ ion beam, an rf voltage U_{rf} of several 100 V is applied between the quadrupole ring electrodes, depicted in Fig. 1, at a frequency $\Omega = 2\pi \times 6.3$ MHz. The alternating quadrupole field leads to a bound periodic motion of the stored particles at the secular frequency $\omega_{sec} = q\Omega/\sqrt{8}$ superimposed by a fast quiver motion (micro-motion) at the driving frequency Ω, where $q = 2eU_{rf}/(m\Omega^2 r_0^2)$ denotes the stability parameter of the underlying Mathieu differential equation, e and m stand for the charge and mass of the $^{24}Mg^{+}$ ions, $r_0 = 2.5$ mm for the aperture radius of the quadrupole channel.

Similar to the more common case of an ion storage ring consisting of a periodic lattice of bending and focusing magnets, the transverse confinement of the ion beam in the rf quadrupole storage ring PALLAS can be characterized by the period length of the confining force and the corresponding transverse ion motion. The number of focusing sections per revolution, the periodicity P, corresponds to the number of rf cycles per revolution $P = \Omega/\omega_{rev} = \Omega R/v$ and the number of transverse betatron oscillations, the storage ring tune Q, to the number of secular oscillations in the rf field $Q = \omega_{sec}/\omega_{rev} = \omega_{sec}R/v$. Notably, both quantities become velocity dependent in contrast to the case of magnetic confinement. For a typical beam velocity of $v = 2800$ m/s, the periodicity amounts to $P \approx 800$. Although the absolute focusing strength of the rf electric focusing is comparatively strong in PALLAS ($\omega_{sec} = 2\pi \times 390$ kHz for $Q = 50$), the phase advance per lattice cell $2\pi \times Q/P$ and thus the envelope modulation of the beam remains moderate.

After the loading of the ring with a cloud of ions [6], the resonant light pressure of the continuously tuned co-

* supported by DFG (HA-1101/8) and MLL
† email: ulrich.schramm@physik.uni-muenchen.de
‡ present address: NIST Boulder, USA

0-7803-7738-9/03/$17.00 © 2003 IEEE

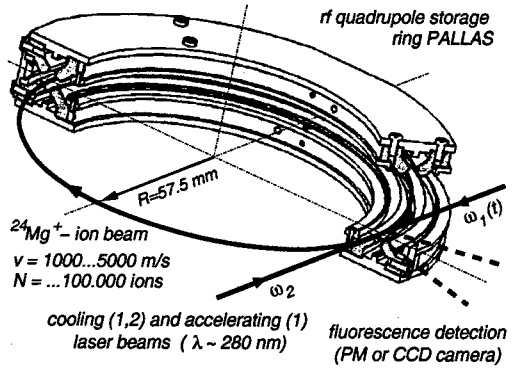

Figure 1: Schematic view of the table-top rf quadrupole storage ring PALLAS. The design orbit of the ion beam is defined by concentric ring electrodes in quadrupole geometry (aperture radius $r_0 = 2.5\,\mathrm{mm}$). Two counter-propagating laser beams are overlapped tangentially with the ion orbit.

propagating laser beam (frequency $\omega_1(t)$) is used to accelerate a non-crystalline $^{24}Mg^+$ ion ensemble to a beam velocity v defined by the fixed frequency ω_2 of the counter-propagating laser beam, as sketched at the bottom of Fig. 2 and described in [5, 6]. The *longitudinal* velocity spread of the ion beam is efficiently reduced by the friction force, resulting from the combination of both accelerating and decelerating forces. No direct damping of the *transverse* ion motion is applied which therefore has to rely on the coupling of the transverse to the longitudinal motion by the inter-particle Coulomb interaction.

Ion Beam Crystallization

The fluorescence signal emitted by a non-crystalline beam ($q = 0.2$) as a function of the relative detuning $\Delta\omega_1(t)$ of the co-propagating laser beam (and thus of the beam velocity v) is shown in Fig. 2. The behaviour drastically changes when the focusing strength is raised and the coupling between the ions is enhanced (grey curve at $q = 0.31$). The signal first increases corresponding to the cooling of the initially non-crystalline beam. Then, at $\Delta\omega_1(t) \approx -25\,\Gamma/2$, the signal decreases and subsequently rises to a sharp peak. At last, the rate drops off when the forces of the two laser beams compensate ($\Delta\omega_1(t) \equiv 0$). For the ion current discussed here, this signature of the 'dip' in the fluorescence signal is characteristic for the phase transition to a crystalline beam. It can be understood as a vanishing of the rf heating (IBS) in the gaseous regime which else caused the broadening of the velocity spread. With slightly reduced rf heating the phase transition sets in earlier. The characteristic 'dip' cannot be resolved any more (black curve at $q = 0.31$).

The phase transition to the crystalline beam is further pinpointed by the sudden decrease of the transverse beam size to the size of a linear string of ions [5, 6], demonstrated with the images inserted in Fig. 2.

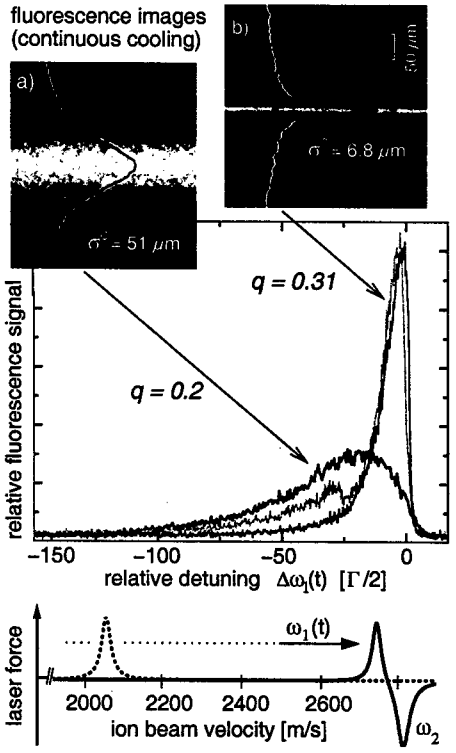

Figure 2: Fluorescence signal of an ion beam ($N = 18,000$) as a function of the relative detuning $\Delta\omega_1(t)$ of the co-propagating laser beam in terms of half the natural transition line width $\Gamma = 2\pi \times 42.7\,\mathrm{MHz}$. In this non-stationary cooling regime, used also for the acceleration of the ions as sketched below, the laser frequency $\omega_1(t)$ is tuned at a typical rate of about $50\,\Gamma/\mathrm{s}$. With an increase of the focusing strength ($q = 0.2 \rightarrow 0.31$) the phase transition is induced. The signal changes markedly as described in the text and further displayed in the inserted fluorescence images, recorded at constant detuning.

Properties of Ion Crystals

The structure of crystalline ion beams was first studied in MD simulations [22] and observed in experiments with elongated *stationary* ion crystals in ring-shaped [23, 5, 7] and linear [24] rf quadrupole traps. It was found to uniquely depend on the dimensionless linear density $\lambda = N/(2\pi R) \times a_{ws}$ expressed in terms of the Wigner-Seitz radius $a_{ws} = [1/(4\pi\varepsilon_0) \times 3e^2/(2m\omega_{sec}^2)]^{1/3}$ to account for the dominant influence of the charge neutralizing confining potential on the average ion density. The structure develops with rising λ from a string of ions for $\lambda < 0.71$ over a zig-zag band into three-dimensional helical structures, as later illustrated with Fig. 4. Also dynamic properties of the ion crystal as the plasma frequency $\omega_p = \sqrt{2}\omega_{sec}$ are determined by the focusing conditions.

The state of the stored ion ensemble is characterized by the plasma parameter $\Gamma_p = 1/(4\pi\varepsilon_0) \times e^2/(a_{ws}\,kT)$ the

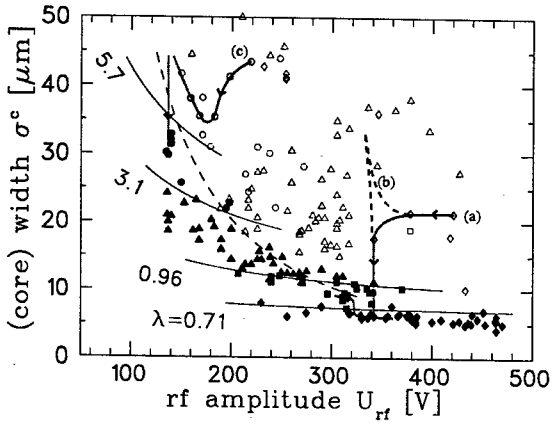

Figure 3: Correlation of the absolute width of stored ion beams (not corrected for the spatial resolution of the imaging system of about 5 μm) and the applied rf voltage. Crystalline beams are depicted as filled (black), non-crystalline beams as open (grey) symbols. For crystalline beams, the solid contour lines of constant linear density λ separate regions of different crystal structure. At the dashed line, the energy contained in the driven transverse motion equalizes the melting temperature of crystalline beams. The grey lines illustrate transition paths (marked a,b,c) from the non-crystalline to the crystalline state (constant N).

ratio of the energy of the mutual Coulomb repulsion to the thermal energy. Large three-dimensional ensembles are expected to be in the crystalline state for $\Gamma_p > 178$ while surface dominated ensembles like ion beams may require higher values [26]. For the case of the sample crystalline beam presented above, the linear string ($\lambda \approx 0.4$), the velocity spread and thus the plasma parameter was measured [5] to $\Gamma_p > 500$, well within the crystalline regime.

SYSTEMATIC STUDIES

In Fig. 3, the transverse width σ^c of crystalline (filled symbols) and non-crystalline beams (open symbols) of different particle numbers N is plotted against the applied rf voltage U_{rf}. The phase transition from the non-crystalline to the crystalline state can be followed for two typical cases (grey lines). In (a), a reduction of the focusing strength, which was initially chosen rather high for the preparation of the beam, lead to a reduction of the rf heating of the gaseous beam and thus to a reduction of the transverse width down to the point where the crystallization occurred for a given cooling strength. Especially for beams of low linear density, the focusing strength had to be at first reduced to a point where the width of the beam expanded in order to reduce rf heating. A quick increase in the focusing strength, increasing the coupling between the longitudinal and the transverse motion, then lead to the crystallization of the beam (b), similar to the sample situation discussed above [5]. Both phases are possible for identical focusing conditions (hysteresis).

With the use of the relation $\sigma^c/a_{ws} \propto \sqrt{\lambda}$ (solid) contour lines are drawn for the threshold values of constant linear density [23]. In this way, the classification of the crystalline beams (filled symbols only) relies on the determination of the width of the beam σ^c and of the rf voltage U_{rf} [6], both of which are known to better than $\pm 5\%$ The alternative classification, based on the ion number N, is expressed by the different symbols.

Focusing requirements

Crystalline beams were observed to occur only in a curved band in the $(U_{rf} - \sigma^c)$ diagram (filled symbols in Fig. 3 [6]). Although the time-averaged focusing force is exactly canceled by the space charge force of a crystalline beam, the constituent ions are forced to oscillate in the transverse plane because of the discrete (or in this case time-dependent) periodic focusing [27]. Following Schiffer [17], an apparent temperature can be assigned to the spread of this transverse motion

$$3kT^f_{app} \approx \left(\frac{\Delta\sigma^c}{\sigma^c}\right)^2 \left(\frac{\sigma^c}{R}\right)^2 \frac{Q^4 m v^2}{2P^2} \approx \frac{e^2}{4\pi\varepsilon_0\, a_{ws}} \frac{\pi^2}{6} \frac{\lambda Q^2}{P^2} \,. \quad (1)$$

This relation can be rewritten for an apparent plasma parameter $\Gamma^f_{app} \propto 1/(U_{rf}^{5/3}\sigma^c)^2 \propto (P/Q)^2/\lambda$.

The curvature of the band in Fig. 3 follows the dashed line, which is based on the argument that the apparent temperature equalizes the melting temperature, or that $\Gamma^f_{app} \approx 180$. Yet, it has to be emphasized that this driven periodic transverse motion in the quadrupole potential should not be automatically regarded as random or thermal motion. It was shown in simulations [19, 28] as well as in experiments [5, 18, 14] that the energy transfer from the periodic to the random motion is strongly suppressed compared to a non-crystalline ensemble. Thus, crossing this line does not immediately lead to the melting of a crystalline beam. On the other hand, for beams which are not sufficiently cold the coupling of collective motion into random motion is expected to increase and to hinder the crystallization.

The same curved bands of stability dominate the graphs in Fig. 4. In these $(\lambda - Q)$ diagrams, upper and lower limits of the focusing strength can be distinguished. The *lower* focusing limit appears to be rather constant for 3D beams but considerably raises for the lower dimensional crystalline beams. This effect is believed to be due to the specific cooling scheme, based on direct longitudinal laser cooling. Below the limiting focusing strength the ion density and thus the coupling between the transverse and the longitudinal degrees of freedom becomes too low to provide sufficient sympathetic transverse cooling. Thus, the tendency was to raise the focusing strength in order to increase the coupling up to the point where the depth of the transverse modulation of the crystalline beam sets the upper limit.

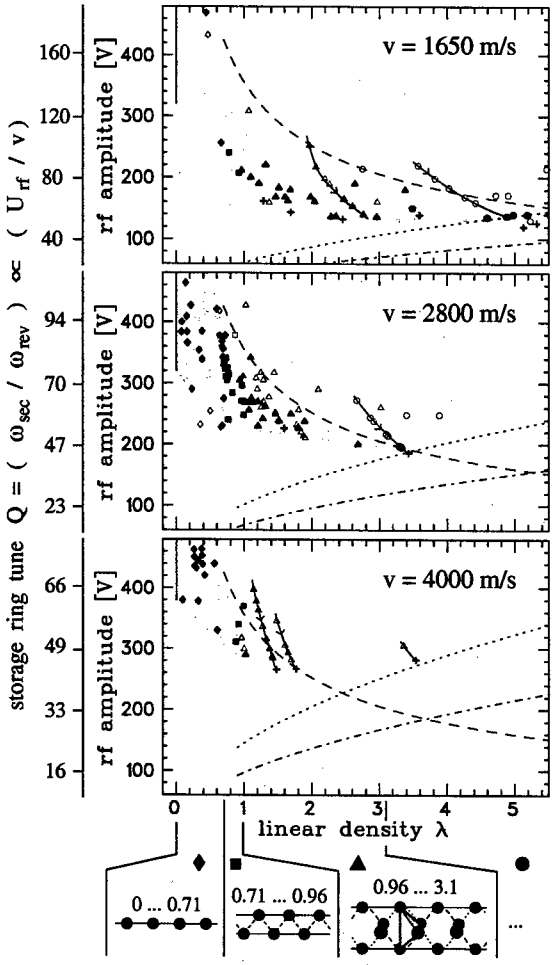

Figure 4: The focusing conditions for which crystalline ion beams of different linear density λ and thus of different structure (as illustrated below) were attainable in PALLAS are illustrated (grey shaded area) for three beam velocities. In each of the three graphs, the dashed line corresponds to the one in Fig. 3, the dotted and dash-dotted lines indicate the increasing influence of bending shear with rising velocity as explained in the text. Few solid lines indicate paths from the non-crystalline to the crystalline state or to beam losses (crosses), respectively.

This *upper* limiting focusing strength lies more than a factor of three below the value at which an excitation of bulk modes of the 3D crystalline beam is expected to occur. Their characteristic frequency is close to the plasma frequency $\omega_p = \sqrt{2}\,\omega_{sec}$ [25]. To avoid an excitation of such bulk modes in the oscillating fields of the storage ring, the lowest possible side-band of the driving frequency $(\Omega - \omega_p)$ has to exceed twice the eigen-frequency ω_p or $\Omega > 2\,\omega_p$, which translates into the often discussed maintenance criterion $P > 2\sqrt{2}\,Q$ [17, 12]. This criterion is always fulfilled in PALLAS, where $P = \sqrt{8}\,Q/q$ and $q < 0.9$ for a sinusoidal rf driving voltage, but difficult to meet in the existing heavy ion storage rings like TSR with $(Q = 2.8, P = 2)$.

The above criterion is not restricted to crystalline beams but part of a more general approach to envelope instabilities of space-charge dominated beams. There, the latter condition corresponds to the first half-integer stop band (Mathieu instability) or, in other words, to the condition that the phase advance per lattice cell (or per rf period) must not exceed $2\pi/2\sqrt{2}$ [29, 30]. For emittance dominated (non-crystalline) beams, the phase advance per unit cell has to remain below $\pi/2$ [29, 30]. This criterion is important for the generation of crystalline beams starting from the gaseous phase and independent from the treatment of heating due to intra-beam scattering.

Bending shear

In addition to the previous presentation, the focusing conditions are now discussed for the three different beam velocities, depicted in the three separate graphs of Fig. 4. Obviously, crystalline beams of higher linear density could only be attained for the lowest beam velocity of $v = 1650\,\mathrm{ms}^{-1}$. For higher beam velocities, and especially for $v = 4000\,\mathrm{ms}^{-1}$, the beams were lost when the focusing strength was decreased into a region where crystalline beams had been attainable at lower velocities. Surprisingly, the lower focusing limit for the highest linear densities seems to appear at a tune of $Q \approx 45$ independent from the beam velocity.

Continuous bending of a crystalline beam extending into the horizontal plane ($\lambda > 1$) implies that the beam has to propagate with constant angular velocity to maintain its crystalline order [2, 17, 19]. The consequence of cooling the beam to constant linear velocity was illustrated by Schiffer [17] assigning an apparent temperature T^s_{app} to the mean centrifugal energy spread of the beam

$$3k_B T^s_{app} \approx \left(\frac{\sigma^c}{R}\right)^2 \frac{mv^2}{2} \approx \frac{e^2}{4\pi\varepsilon_0\, a_{ws}} \frac{4\pi^2}{9} \frac{\lambda}{Q^2}\ , \quad (2)$$

which can be related to an apparent plasma parameter as $\Gamma^s_{app} \approx 0.7\,Q^2/\lambda$. When the beam is laser-cooled to constant linear velocity, this energy spread is fully transferred into random motion. This condition translates into the lower limit of the focusing strength as a function of the linear density, that is indicated by the dash-dotted lines in Fig. 4. It rises with increasing beam velocity in the same way as the experimental observations. This agreement is emphasized by the dotted lines which result from a multiplication of the latter limit by a factor of 1.5. The factor could be interpreted as taking into account only the transverse degrees of freedom in Eq. 2. It seems that, at present, bending shear prohibits the attainment of large crystalline structures already above velocities of around 2500 m/s in PALLAS.

However, to a certain degree, an already existing crystalline beam has been expected to withstand the bending due to its natural shear elasticity, characterized by the secular frequency ω_{sec} divided by λ [2, 17]. In this model,

the condition for a crystalline beam to resist bending shear becomes $Q > \lambda$, as the characteristic frequency (ω_{sec}/λ) has to remain higher than the driving revolution frequency ω_{rev}. Thus, no evidence for this 'stiff beam limit' has been found in the present experiments.

Cooling the ion beam to constant angular velocity could help to unambiguously decipher the role of bending shear in the observed velocity dependence of the lower focusing limit. Due to the comparatively low ion velocity in PALLAS, this cooling scheme could be accomplished by merging the ion and laser beams inside a segmented drift tube similar to the method, realized earlier for the measurement of the longitudinal velocity spread [5]. In the fringe field of a segmented drift tube, the change in ion energy slightly depends on the displacement from the ideal ion orbit so that constant angular velocity can be transformed into constant linear velocity and vice-versa. The ion beam can be cooled to constant linear velocity locally inside the drift tube and propagate at constant angular velocity outside.

CONCLUSIONS

Crystalline ion beams of different structure were attained starting from non-crystalline beams, which were subjected to longitudinal laser cooling. Integer-tune stop-bands had to be crossed when the secular motion was frozen out. Promisingly, no effect of this forbidden crossing of resonances was experienced. For the specific laser cooling scheme, the coupling between transverse and longitudinal motion came out to be crucial especially for the lower-dimensional beams and to require higher focusing strength. Direct transverse cooling - tough non-trivial to achieve [31] - should improve this situation [7].

The coupling of the driven transverse motion into thermal motion seems to set an upper limit ($Q \propto \sqrt{\lambda}$) to the applicable confinement strength. This limit was observed to be about a factor of three lower than the established maintenance criterion $P > 2\sqrt{2}\,Q$, a fact that further raises the demands on the 'smoothness' of the lattice of a high-energy storage ring.

With cooling to linear velocity, bending shear gains importance with increasing beam radius. The first experimental findings, that the attainment of large crystalline beams becomes more difficult (or even impossible) with rising ion beam velocity agrees with simple models ($Q \propto 1/\sqrt{\lambda}$). Scaling the present result according to Eq. 2, storage rings of several 100 m radius (and considerably high tune) are required to maintain helical structures at about $v/c \approx 0.1$ unless a method for cooling to constant angular velocity can be found.

More generally, bunched beam laser cooling will be the method of choice for the anticipated attainment of dense crystalline ion strings at relativistic energies, as the huge Doppler-shift only allows for counter-propagating laser and ion beams. A test experiment is currently prepared for the ESR of GSI, where a beam of Li-like C^{3+} ions at a velocity of $v/c = 0.47$ will be subjected to a combination of transverse electron and longitudinal laser cooling. With the operation of larger heavy ion synchrotrons (SIS 300 at GSI), laser cooling of Li-like ions of the order of uranium becomes possible with fascinating possibilities for the forward scattering of laser light into the keV range. On the other hand, the application of refined cooling techniques could strongly enhance the luminosity of radioactive beam colliders, presently under discussion.

REFERENCES

[1] J.P. Schiffer and P. Kienle, Z. Phys. A **321**, 181 (1985).

[2] J.P. Schiffer and A. Rahman, Z. Phys. A **331** 71 (1988).

[3] For an overview, see D. Habs and R. Grimm, Ann. Rev. Nucl. Part. Sci. **45**, 391 (1995) and refs. in [5, 7].

[4] *Crystalline Beams and Related Issues*, D.M. Maletic and A.G. Ruggiero (eds.), World Scientific, Singapore, (1996).

[5] T. Schätz, et al., Nature **412**, 717 (2001).

[6] U. Schramm, et al., Phys. Rev. E **66** 036501 (2002).

[7] U. Schramm, et al., Plasma Phys. Control. Fusion **44**, B375 (2002).

[8] U. Schramm, et al., Phys. Rev. Lett. **87**, 184801 (2001).

[9] U. Schramm, et al., Physics Scripta (at press 2003) and M. Bussmann, et al., J. Phys. A, (at press 5/2003).

[10] S. Schröder et al., Phys. Rev. Lett. **64**, 2901 (1990) and J.S. Hangst, et al., Phys. Rev. Lett. **67**, 1238 (1991).

[11] Q. Spreiter, et al., Nucl. Instr. Meth. A **364**, 239 (1995) and M. Seurer, et al., Hyp. Int. **99**, 253 (1996).

[12] J. Wei, et al., in [4], p 229 (1996).

[13] M. Steck, et al., Phys. Rev. Lett. **77**, 3803 (1996).

[14] M. Steck, Proc. PAC 2001 (Chicago, USA) TOAA002 (2001) and M. Steck, et al., J. Phys. B **36**, 991 (2003).

[15] H. Danared, et al., Phys. Rev. Lett. **88**, 174801 (2002).

[16] U. Eisenbarth, et al., Hyp. Int. **127**, 223 (2000).

[17] J.P. Schiffer, in [4], p 217 (1996).

[18] U. Schramm, et al., J. Phys. B **36**, 561 (2003).

[19] J. Wei, et al., Phys. Rev. Lett. **80**, 2606 (1998).

[20] N. Madsen, et al., Phys. Rev. Lett. **87**, 274801 (2001).

[21] T. Schätz, et al., Applied Physics B **76**, 183 (2003).

[22] R.W. Hasse et al., , Annals of Phys. **203**, 419 (1990).

[23] G. Birkl, et al., Nature **357**, 310 (1992).

[24] M. Drewsen, et al., Phys. Rev. Lett. **81**, 2878 (1998).

[25] D.H.E. Dubin, T.M. O'Neil, Rev. Mod. Phys. **71**, 87 (1999).

[26] J.P. Schiffer, Phys. Rev. Lett. **88**, 205003 (2002).

[27] The amplitude of the rf driven micro-motion amounts to $\Delta r \approx \sqrt{2}\omega_{sec} r/\Omega \propto 1/\Omega^2$.

[28] J.P. Schiffer, et al., Proc. Natl. Acad. Sci. USA **97**, 10697 (2000).

[29] I. Hofmann, in [4], p. 3 (1996).

[30] S.Y. Lee and H. Okamoto, Phys. Rev. Lett. **80**, 5133 (1998).

[31] I. Lauer, et al., Phys. Rev. Lett. **81**, 2052 (1998).

COMPUTATIONAL STUDIES OF COLLECTIVE BEAM DYNAMICS IN HIGH INTENSITY RINGS

J.A. Holmes, S. Cousineau, V. Danilov, S. Henderson, A. Shishlo, ORNL, Oak Ridge, TN 37831, USA
A. Fedotov, BNL, Upton, NY 11793, USA

Abstract

Collective interactions of the beam with itself and with its periodic lattice surroundings in high intensity accelerator rings, such as PSR and SNS, can lead to beam growth, halo generation, and losses. These interactions also provide a rich source of dynamic phenomena for analytical, computational, and experimental study. With continuing increases in model development and computer power, a number of sophisticated codes are now capable of detailed realistic studies of collective beam dynamics in rings. We concentrate here on a computational examination of high intensity beam dynamics in SNS. These studies include the effects of the accelerator lattice, space charge, impedances, losses and collimation, and magnet errors.

OVERVIEW

High-intensity proton rings are characterized by low energy, high intensity beams, and by low loss requirements. Collective effects due to space charge and wakefields strongly affect the beam behavior, and single particle models do not suffice. Because of the complexity of collective phenomena for bunched beams in high-intensity rings, a computational approach is productive for theoretical studies and indispensable in solving detailed design and engineering problems. Recognizing this, accelerator physicists from ORNL, BNL, and Fermilab have been developing an object-oriented general-purpose code, ORBIT [1,2].

ORBIT is designed specifically for beam dynamics calculations in high-intensity rings. Its intended use is the detailed simulation of realistic accelerator problems, although it is equally applicable to idealized situations. ORBIT is a particle-in-cell tracking code in 6D phase space that transports bunches of interacting particles through a series of nodes representing elements, dynamic effects, or diagnostics that occur in the accelerator. ORBIT has been designed to simulate real machines: it has detailed models for strip-foil injection including painting, scattering, and nuclear processes; RF focusing and acceleration; symplectic transport through various magnetic elements with optional hard-edge fringe fields; alignment and field errors, closed obit calculation, and error correction; longitudinal and transverse impedances; longitudinal, transverse, and three-dimensional space charge forces; feedback stabilization of instabilities; beam-in-gap cleaning, collimation, and limiting apertures; and the calculation of many useful diagnostic quantities.

ORBIT has been applied to a variety of problems in high intensity rings. These include investigations in basic ring physics, diverse applications to the design and analysis of the SNS ring, analysis of emittance measurements in the CIS at Indiana University, extensive studies of the dynamics behind the beam broadening at high intensity in PSR at Los Alamos National Laboratory, and simulation of space charge effects at injection in the Fermilab Proton Driver Study II. Because of the understanding of PSR beam broadening gained using ORBIT, correction of the driving n=4 lattice harmonic is currently under study. Some of these applications are described in Refs. [3-8]. More recently, ORBIT is being applied to study space charge effects during injection into the Fermilab Booster Ring. This work is of importance because the Booster is the intensity bottleneck in the Fermilab accelerators, and because a significant fraction of the losses in the Booster occur during the first three milliseconds.

In addition to the PSR harmonic correction and Fermilab Booster calculations, present applications of ORBIT focus on the use of the new and computationally demanding physics models to study and reoptimize as realistically as possible injection scenarios in the SNS Ring. The product of these studies will be a total foil to target simulation picture of the injection, accumulation, and ring to target transport processes. This simulation picture will actually consist of a whole series of calculations to differentiate and understand the effects of foil scattering, single particle transport, fringe fields, errors and error correction, space charge, impedances, and collimation. Ultimately, the goal is to optimize the injection with respect to losses and beam-on-target, which requires varying the painting scheme, lattice tunes, chromaticities, and collimation scraper settings. We now present initial results of this study.

SNS FOIL TO TARGET SIMULATIONS

To begin the SNS foil to target studies, we consider the SNS lattice with the nominal bare tunes (Q_x, Q_y) = (6.23, 6.20), no chromaticity correction, and 1.44 MW beam power, which corresponds to a final bunch of $1.5*10^{14}$ protons. The calculations include the effects of the strip foil and painting, symplectic single particle transport with hard edge fringe fields, dual harmonic RF focusing, longitudinal and transverse impedances, space charge, apertures and collimation, and magnet errors and correction. The first task was to determine the computational requirements imposed by convergence of the space charge model. For the SNS Ring, with bunch length in excess of 160m and slow variation in longitudinal density, the 2.5D transverse and separate longitudinal space charge model are sufficiently accurate unless transverse impedance effects become important. The space charge convergence tests were conducted with

0-7803-7738-9/03/$17.00 © 2003 IEEE

the transverse impedance set to zero. For ORBIT's three space charge models, the grid resolution and the number of particles were varied until convergence was achieved. The resulting grid sizes and numbers of particles were 64x64 mesh and 159000 particles for the 2.5D direct force space charge solver, 256x256 mesh and 530000 particles for the 2.5D potential space charge solver, and 256x256x64 mesh and 1590000 particles for the 3D solver. The difference in requirements between the 2.5D direct force and potential solvers is a result of the necessity of taking a derivative to obtain the force when the potential solver is used. Figure 1 shows the horizontal emittance profiles of the final accumulated beam at the $1*10^{-3}$ level for the converged cases of the three space charge models, and it is clear that unless the transverse impedance generates instabilities that necessitate a 3D treatment, either of the 2.5D models is adequate.

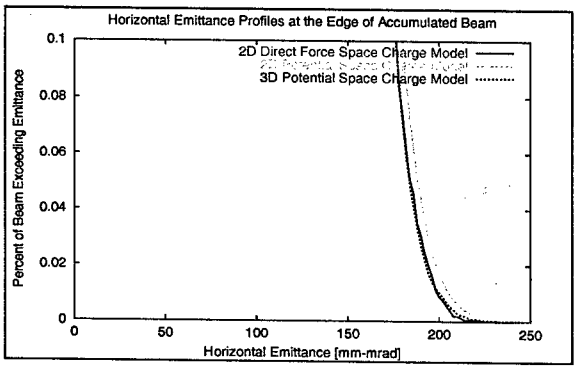

Figure 1. Percentage of beam with emittance exceeding the value indicated for the 2.5D direct force solver (red) with 159000 particles, the 2.5D potential solver (green) with 530000 particles, and the 3D solver (blue) with 1590000 particles.

In order to determine if the 3D space charge treatment is necessary, the transverse impedance was set to that of the ring extraction kicker, which is the dominant impedance in the ring, and a 3D space charge calculation was conducted. The results indicated transverse stability at 1.44 MW (the instability threshold is at about 2 MW), so the 2.5D direct force transverse space charge model is suitable for these studies.

The next step was optimization of the injection scheme and placement of the adjustable primary collimators. The injection painting was previously optimized for a 2 MW beam and correlated horizontal and vertical bumps. Because the present studies are carried out for 1.44 MW, a smaller transverse beam can be painted. In addition, by splitting the settings of two of the families of arc quadrupoles, which are nominally equal, the beta functions at critical locations can be varied while maintaining constant tunes and achromatic arcs. Studies were conducted varying both the size of the painted beam and the arc quadrupole settings, and a new reference case was determined. The result was a correlated painting scheme 86% the size of the optimized 2 MW case and equal arc quadrupole settings. Figure 2 shows the incoherent tune footprint at the end of injection.

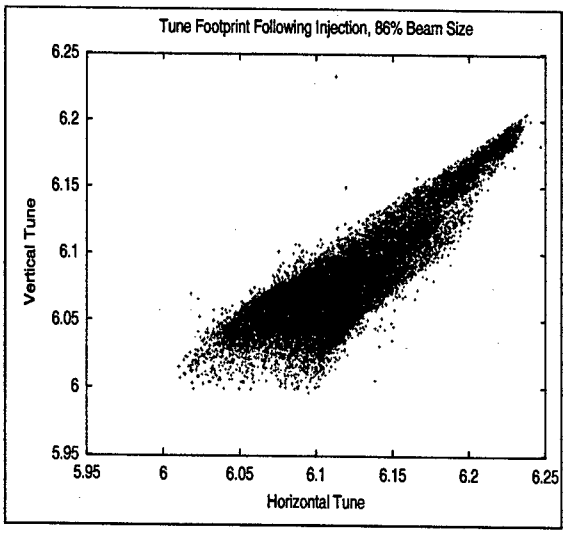

Figure 2. Incoherent tune footprint at the end of accumulation for 1.44 MW beam power.

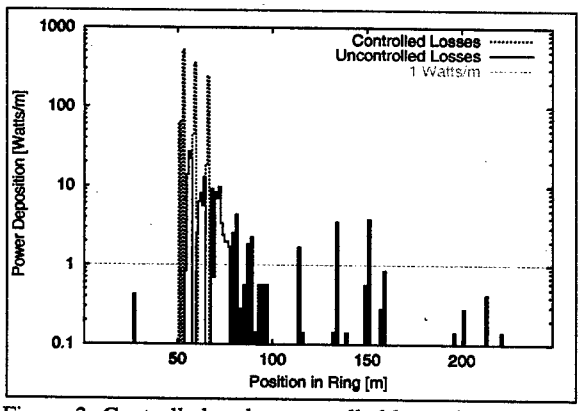

Figure 3. Controlled and uncontrolled beam losses in the SNS Ring, as calculated by the ORBIT collimation model.

We use this result to determine the placement of the adjustable collimation beam scrapers to collect at most $1.0*10^{-3}$ of the beam, thus preventing uncontrolled beam loss. With placement of the primary scrapers at 140-162 pi-mm-mrad, less than $1.0*10^{-4}$ of the beam is scraped in this case, and the collimation efficiency for the scraped beam is above 90%. Figure 3 shows the results of a power deposition calculation, using the ORBIT collimation package, for losses around the ring due to collimated beam. Because such a small portion of the beam was lost in the dynamic calculation, this collimation calculation was carried out by artificially forcing emittance growth to generate beam/scraper interaction. The power deposition scale is based on a normalization of $1.0*10^{-3}$ of the 1.44 MW beam impacting the scrapers. The results here show that the SNS collimation system collects about 90% of the scraped beam as controlled loss.

Another important consideration is the beam footprint on the target. Engineering considerations require at least 90% of the beam to land in a 20cm x 7cm rectangle on the target face with a maximum current density not exceeding 250mA/mm^2. We use ORBIT to transport the final accumulated beam through the Ring to Target Beam Transport line and through the target window, modeled as a solid 4mm steel collimator, and finally to the target. Figure 4 shows a contour plot of the beam current on target as calculated by ORBIT. For this case, 91% of the accumulated beam falls into the 20cm x 7 cm rectangle and the peak beam current is 179mA/mm^2.

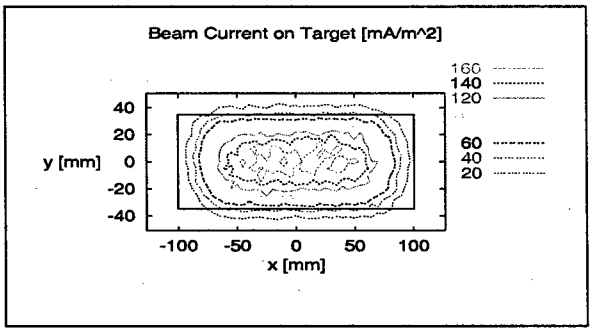

Figure 4. Beam current on target as calculated by ORBIT.

We are now extending this initial work to include a comprehensive study of alignment and field errors in bends and quadrupoles. In the first of these studies, we considered the effect of uniformly distributed random quadrupole alignment errors. At the anticipated level of ±0.25 mm random errors, beam losses remain below $1*10^{-4}$, but at twice that level beam losses increase rapidly. For the case of ±1.0 mm randomly distributed quadrupole alignment errors, 56% of the beam was lost during injection. After correcting these errors using the ORBIT error correction model on a pencil beam to set the dipole corrector strengths, the losses for injection again fell back to less than $1*10^{-4}$.

As a different application of ORBIT to SNS, we consider the possibility of painting round beams. We accomplish this by setting the bare tunes equal at (Q_x, Q_y) = (6.23, 6.23) and using the chromaticity sextupoles to correct to zero chromaticity. The injection scheme is also modified to simultaneously bump the coordinates and the perpendicular momenta with the time dependence chosen to give a uniform density distribution. The resulting distribution has essentially linear transverse space charge forces and will remain elliptical (circular if the tunes are equal) under transport. Figure 5 shows the particle distribution for a round beam at 1.44 MW intensity. As these studies progress, they will be expanded to a wide range of cases and issues, including other working points, higher beam intensities, and other injection schemes, such as round beams.

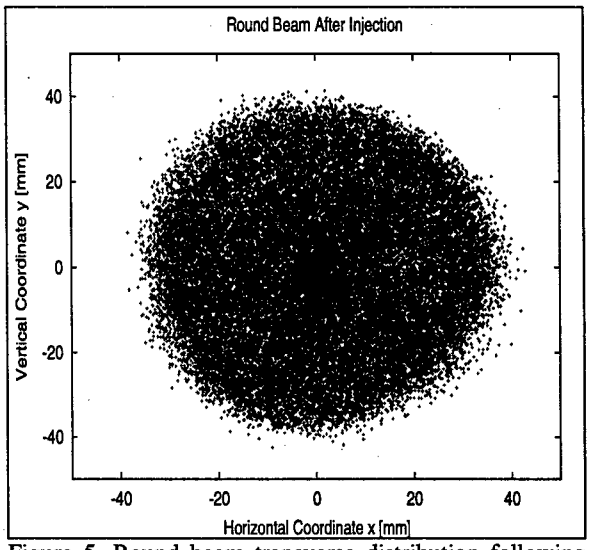

Figure 5. Round beam transverse distribution following injection.

ACKNOWLEDGMENT

SNS is managed by UT-Battelle, LLC, under contract DE-AC05-00OR22725 for the U.S. Department of Energy. SNS is a partnership of six national laboratories: Argonne, Brookhaven, Jefferson, Lawrence Berkeley, Los Alamos, and Oak Ridge.

REFERENCES

[1] J. Galambos, J. Holmes, D. Olsen, A. Luccio, and J. Beebe-Wang, ORBIT Users Manual, http://www.sns.gov//APGroup/Codes/Codes.htm

[2] J. Galambos, S. Danilov, D. Jeon, J. Holmes, D. Olsen, J. Beebe-Wang, and A. Luccio, in Proceedings of the 1999 Particle Accelerator Conference, (New York, 1999) 3143.

[3] J. A. Holmes, V. V. Danilov, J. D. Galambos, D. Jeon, and D. K. Olsen, *Phys. Rev. Special Topics – AB* **2**, (1999) 114202.

[4] A. V. Fedotov, J. A. Holmes, and R. L. Gluckstern, *Phys. Rev. Special Topics – AB* **4**, (2001) 084202.

[5] S. Cousineau, J. Holmes, J. Galambos, A. Fedotov, J. Wei, and R. Macek, submitted to *Phys. Rev. Special Topics – AB*.

[6] K. Woody, J. A. Holmes, V. Danilov, and J. D. Galambos, in *Proceedings of the 2001 Particle Accelerator Conference*, (Chicago, 2001).

[7] V.Danilov, J. Galambos, and J. Holmes, in *Proceedings of the 2001 Particle Accelerator Conference*, (Chicago, 2001).

[8] G.W. Foster, W. Chou, E. Malamud, "Proton Driver Study II (Part 1)," Fermilab-TM-2169, (2002).

EFFECT OF STIMULATED AND THERMAL DESORPTION IN DARHT-2

T. P. Hughes*, MRC, Albuquerque, NM, USA, H. Davis† LANL, Los Alamos, NM, USA

Abstract

The DARHT-2 accelerator generates a 2 kA, 18 MeV, 2 μsec flat-top electron beam. The beam risetime is about 700 ns, and a "beam cleanup zone" (BCUZ) has been designed to scrape off these mismatched electrons. Experiments on DARHT-1 (which has a 60 ns flat-top) have provided excellent quantitative data on stimulated and thermal desorption of neutral monolayers on various metal surfaces by multi-MeV electrons. We have used these data in the particle-in-cell code LSP to model the production of ions from the walls of the DARHT-2 BCUZ. The effect of these ions on the transport of the main beam pulse is discussed.

INTRODUCTION

The DARHT-2 linear induction accelerator [1] is designed to produce a 2 kA, 18 MV, 2 μs flat-top electron beam. The injector is driven directly by a Marx bank, and has a long voltage risetime: 1–99% in 700 ns. As a result, there is a considerable amount of beam charge which is mismatched to the solenoid transport channel. The design of a "beam cleanup zone" (BCUZ) to filter out this charge was previously described [2]. In this paper, we present a computational estimate of the ion charge produced by beam electrons striking the walls of the BCUZ. The computational model uses data from experiments carried out on DARHT-1 [3], a companion accelerator with a 60 ns beam pulse [1].

COMPUTATIONAL MODEL

Beam Generation

The DARHT-2 injector geometry is shown in Fig. 1. A 10 m sections of beam pipe is modeled in $2\frac{1}{2}$-D using the electromagnetic particle-in-cell (PIC) simulation code LSP[4]. The transmission line attached to the radial boundary at T_{AK} in Fig. 1 produces the voltage pulse shown in Fig. 2 [5]. The cathode is treated as a zero-work-function, space-charge-limited emitter. Emitted electrons are given a transverse temperature corresponding to the surface temperature ($\approx 1000°$ C). The beam electrons pass through the accelerating gaps and solenoidal fields of the first eight accelerating cells. As in the physical accelerator, each gap in the simulation is powered by a separate transmission line attached at the boundary (T_1–T_8 in Fig. 1). The accelerating voltage, also shown in Fig. 2, is based on the experimentally-measured voltage trace [5]. The magnetic tune, shown in Fig. 3 was chosen to avoid any beam-loss

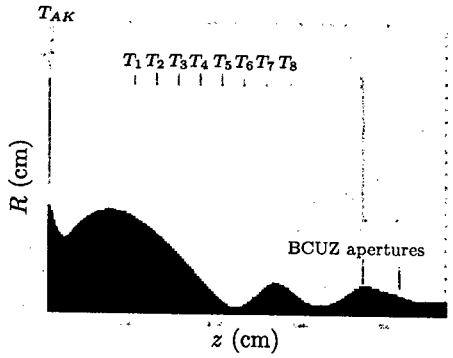

Figure 1: Geometry of desorption calculation, showing injector, 8 accelerating gaps, and BCUZ. The beam is shown at the flat-top energy and current.

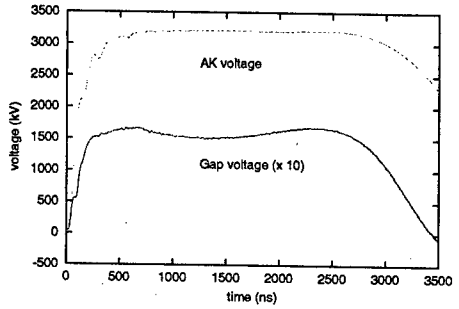

Figure 2: Voltage pulse applied to AK gap (green) and to accelelerating gaps (red). The latter has been multiplied by 10 for scaling purposes.

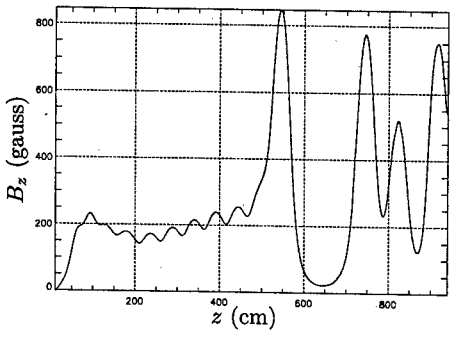

Figure 3: Axial magnetic field tune used in Fig. 1.

*tph@mrcabq.com
†davis@lanl.gov

0-7803-7738-9/03/$17.00 © 2003 IEEE

in the accelerating cells, and to scrape off the beam-head in the BCUZ[2]. In the simulation, we see no beam loss until the start of the BCUZ, about 6 meters from the cathode.

Ion Generation Model

When energetic electrons strike a solid surface, they can generate neutral molecules and ions. There are two mechanisms for generating neutrals: stimulated desorption (ESD) and thermal desorption. Ions can be generated directly by ESD and by a two-step process of neutral desorption followed by ionization. In LSP, these processes are modeled by the following equations:

$$\frac{dN_d^n}{dt} = \frac{j_e}{e}\sigma_d^n N_a + N_a \nu \exp\left(-\frac{Q_b}{T}\right) \quad (1)$$

$$\frac{dN_d^+}{dt} = \frac{j_e}{e}\sigma_d^+ N_a \quad (2)$$

$$\frac{d(N_d^n + N_d^+)}{dt} = -\frac{dN_a}{dt} \quad (3)$$

$$\frac{dN_i}{dt} = \frac{j_e}{e}\sigma_i N_d \quad (4)$$

where N_d^n is the area density of desorbed neutral particles, N_a is the area density of adsorbed particles, N_d^+ is the area density of desorbed ions, N_i is the area density of ions due to gas-phase ionization, σ_d^n, σ_d^+ and σ_i are the cross-sections for stimulated desorption of neutral species, stimulated desorption of ionized species, and gas-phase ionization of the neutral species, respectively, j_e is the electron current density striking the wall, ν is a thermal-desorption rate-constant (typically 10^{13} s^{-1}), Q_b is the binding energy of the adsorbed material in eV, and T is the surface temperature in eV.

In the calculation, we initialize the surfaces with one monolayer (10^{15} cm^{-2}) of neutral water. In the DARHT-1 experiments [3], the stimulated neutral desorption yield, $N_a\sigma_d^n$, was measured to be in the range 0.1–0.2, and the adsorbed inventory was estimated to be about 1 monolayer, mainly consisting of water. Thermal desorption became significant when the surface temperature increased by 300–400° C. Roughly, a desorption rate of one monolayer/ns occurs when the surface temperature reaches $Q_b/9$ eV, which corresponds to about 630 K ($\approx 330°$ C above room temperature) for $Q_b = 0.5$ eV, a typical value for water vapor [6]. At room temperature (300 K) the desorption rate is a factor of 2×10^4 smaller.

Neutrals produced by either stimulated or thermal desorption can be ionized by subsequent beam electrons. We use the gas-phase cross-section for water molecule ionization by relativistic electrons: $\sigma_i = 0.9 \times 10^{-18}$ cm^2 [7]. Water is known to "crack" under electron impact, producing significant fractions of OH^+ and H^+, in addition to H_2O^+ [8]. We have not included these species in the calculation.

Direct stimulated production of ions was not measured in the DARHT-1 experiments. Typically, the cross-section for producing ions is much less than that for neutrals [9].

Figure 4: Beam (blue) and H_2O^+ (orange) distributions at $t = 1000$ ns; cf. Fig. 1.

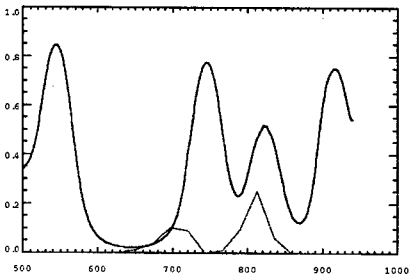

Figure 5: Ratio of ion (H_2O^+) charge to beam charge vs. z at $t = 1000$ ns, within a radius of 1.5 cm (red line). The axial solenoidal magnetic field in kilogauss is overplotted (black). Horizontal scale is in cm.

We have used a value $\sigma_d^+ = 0.01\sigma_d^n = 2 \times 10^{-18}$ cm^2 in the calculation.

EFFECT ON THE ELECTRON BEAM

Ions resulting from stimulated desorption or from ionization of desorbed neutrals can affect the tune and stability of the electron beam. A snapshot of the particle distribution at $t = 1000$ ns is shown in Fig. 4. By this time, about 1000 μC of beam electron charge has struck the wall, yielding about 2 μC of stimulated ion charge. Taking the line-ratio of stimulated ion charge to beam charge within a radius of 1.5 cm from the axis, we get the results shown by the red line in Fig. 5. The dominant contribution to the ion line-density is from stimulated ions. The number of ions generated from desorbed neutrals is much less: the surface temperature rises by at most 50° C, as shown in Fig.6. From Fig. 7 is clear that the ions have a large effect on the beam exiting the BCUZ. We can convert the line-charge ratio f to an equivalent magnetic field through the relation

$$B_{eff} \approx 3.4\sqrt{2\nu\gamma f}/r_b \quad \text{kG} \quad (5)$$

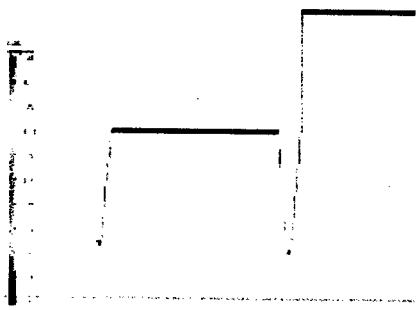

Figure 6: Surface temperature rise (K), in the BCUZ region at the end of the beam risetime.

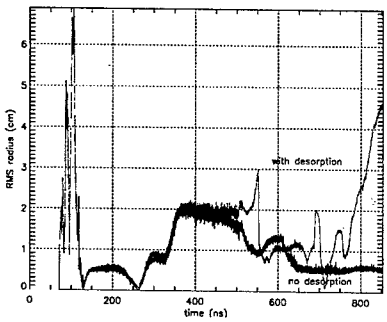

Figure 7: RMS beam radius at $z = 938$ cm with (red line) and without (black line) the effect of desorbed ions.

where ν is Budker's parameter for the beam current and r_b is the beam radius in cm. Thus, the first peak in f in Fig. 5 is roughly equivalent to a 1 kG field extending over 30-40 cm, comparable to the actual focusing solenoids in Fig. 5.

CONCLUSIONS

Beam deposition on the walls of the DARHT-2 beam cleanup zone generates ions through direct stimulated desorption and through neutral desorption followed by impact ionization. For lack of data, the stimulated ion yield used in the calculation is a free parameter. For a sample value equal to 1% of the measured neutral yield, there is a large disruption of the beam. Experimental data on the stimulated ion yield is needed to make a prediction for how large the effect will be in the actual machine.

ACKNOWLEDGMENTS

This work was supported by Los Alamos National Laboratory. The simulations were carried out on the Qsc parallel computer under an Institutional Computing grant from LANL.

REFERENCES

[1] M.J. Burns, B.E. Carlsten, H.A. Davis, C.A. Ekdahl, C.M. Fortgang, B.T. McCuistian, F.E. Merrill, K.E. Nielsen, C.A. Wilkenson, K.P. Chow, W.M. Fawley, H.L. Rutkowski, W.L. Waldron, S.S. Yu, G.J. Caporaso, Y.-J. Chen, E.G. Cook, S. Sampayan, J.A. Watson, G.A. Westenskow, and T.P. Hughes. Status of the DARHT phase 2 long-pulse accelerator. In *Proceedings of the 2001 Particle Accelerator Conference*, number 01CH37268C (http://accelConferenceweb.cern.ch/AccelConf/p01/-PAPERS/WOAA008.PDF).

[2] T.P. Hughes, D.P. Prono, W.M. Tuzel, and J.R. Vananne. Design of beam cleanup zone for DARHT-2. In *Proceedings of the 2001 Particle Accelerator Conference*, number 01CH37268C, (http://accelConferenceweb.cern.ch/AccelConf/p01/-PAPERS/RPPH038.PDF).

[3] H. Davis, D. Moir, and R. Olson. Measurements of thermally desorbed ions from beam-target interactions. In *Proceedings of the 2003 Particle Accelerator Conference*, 1993. Paper ROPB003.

[4] LSP is a software product of Mission Research Corporation (http://www.mrcabq.com).

[5] M. Kang and K. Nielsen, 2003. Private communication.

[6] M.E. Cuneo. The effect of electrode contamination, cleaning and conditioning on high-energy pulsed-power device performance. *IEEE Trans. Dielectr. Electr. Insul.*, 6:469, 1999.

[7] T. C. Genoni and T. P. Hughes. Ion-hose instability in a long-pulse linear induction accelerator. *Phys. Rev. ST Accel. Beams*, 6, 030401, 2003.

[8] M. V. V. S. Rao, I. Iga, and S.K. Srivastava. Ionization cross-sections for the production of positive ions from H2O by electron impact. *J. Geophys. Res.*, 100:26421, 1995.

[9] T. E. Madey and J. T. Yates, Jr. Electron-stimulated desorption as a tool for studies of chemisorption: A Review. *J. Vac. Sci. Technol.*, 8(4):525, 1971.

BEAM-BEAM INTERACTION, ELECTRON CLOUD, AND INTRABEAM SCATTERING FOR PROTON SUPER-BUNCHES

F. Ruggiero, F. Zimmermann, CERN, Geneva, Switzerland;
G. Rumolo, GSI Darmstadt,Germany; Y. Papaphilippou, ESRF Grenoble, France

Abstract

Super-bunches are long bunches with a flat longitudinal profile, which could potentially increase the LHC luminosity in a future upgrade. We present example parameters and discuss a variety of issues related to such super-bunches, including beam-beam tune shift, tune footprints, crossing schemes, luminosity, intrabeam scattering, and electron cloud. We highlight the benefits, disadvantages and open questions.

INTRODUCTION

About 20 years after the CERN ISR stopped colliding protons against protons, its luminosity has not yet been reached by any of the succeeding hadron colliders. The impressive performance of the ISR is illustrated in Table 1.

Table 1: Parameters of past and present hadron colliders.

collider	commiss. date	energy per p [GeV]	peak lum. $\hat{L}$ [10^{32} cm^{-2}s^{-1}]
ISR	1970	31	1.4
SppS	1980	315	0.06
Tevatron	1987	980	0.4
RHIC	2000	100	0.02 (pol.)

The Large Hadron Collider (LHC) at CERN is scheduled to come on line in 2007. With a design energy of 7 TeV, it aims at a luminosity of 10^{34} cm^{-2}s^{-1}, which is 70 times the ISR peak value. A recent feasibility study for an LHC upgrade [1] indicates various possibilities to further increase both luminosity and energy.

A characteristic feature of the ISR is that, unlike any of the later machines, it collided coasting (*i.e.*, unbunched) beams, at a high current. In a multi-TeV collider, like the LHC or its upgrade, this is not possible, since we must provide an abort gap without beam, for machine protection and beam removal, and the total current is limited by synchrotron radiation heat load. Nevertheless, there is a way to mimic the ISR. Namely, we can produce a quasi-coasting beam, if we confine one or several long bunches with a uniform ('flat') density profile by a barrier rf bucket. The collisions of such super-bunches was first proposed by K. Takayama for a VLHC [2]. It is made feasible by recent advances in rf technology [3].

From the beam dynamics perspective, super-bunches offer three distinct advantages: (i) A partial cancellation between central and long-range components of the beam-beam tune shift, which is realized by colliding the beams at two interaction points (IPs) with alternating (orthogonal) planes of crossing, so that the crossing planes are either horizontal and vertical, respectively, or, for example, tilted at 45° and 135°. The second arrangement is called 'inclined hybrid' crossing. (ii) Absence of PACMAN bunches at the head or tail of a bunch train, which, for conventional bunched beams, encounter an irregular number of long-range collisions and could suffer from a reduced beam lifetime or enhanced emittance growth. (iii) The possibility of avoiding beam-induced multipacting and electron-cloud build up. However, at the same time the particle-physics detectors face new challenges, *e.g.*, an increased number of pile-up events and an enhanced radiation damage, which is intrinsically linked to the higher luminosity.

Prospects and beam dynamics for super-bunches in an upgraded LHC have been discussed in detail in [4].

LUMINOSITY AND TUNE SHIFT

Hadron colliders are limited by the beam-beam tune shift. Based on the SPS experience, a maximum total tune shift $\Delta Q_{\rm tot}$ (sum over all IPs) of 0.01 appears to be a realistic and conservative upper value and has been the design criterion for the LHC. For a constant beam-beam tune shift, the LHC luminosity with alternating crossing at two IPs can be raised above the nominal value by increasing the product of bunch length and crossing angle roughly in proportion to the bunch population [5]. Figure 1 suggests that a factor 5–6 increase in luminosity may be attainable for Gaussian bunches.

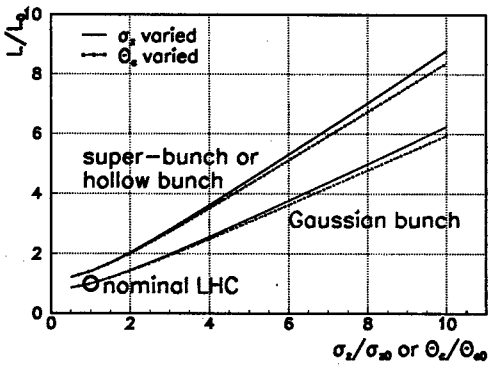

Figure 1: Relative increase in LHC luminosity vs. rms length (or crossing angle) for Gaussian or hollow bunches, maintaining a constant beam-beam tune shift with alternating crossing; axes are normalized to the nominal bunch length $\sigma_{z0} = 7.6$ cm and crossing angle $\theta_{c0} = 300$ μrad, and to the luminosity at the beam-beam limit ($L_0 \approx 2.3 \times 10^{34}$ cm^{-2}s^{-1}) [5].

0-7803-7738-9/03/$17.00 © 2003 IEEE

As also shown in Fig. 1, an additional factor of 1.4 can be gained by colliding bunches with a flat longitudinal profile, *e.g.*, super-bunches, instead of Gaussian bunches. In both cases, the parameter region of interest is (1) an rms bunch length σ_z much larger than the transverse beam size σ^*, *i.e.*, $\sigma^* \ll \sigma_z$, (2) a large Piwinski parameter $\theta\sigma_z/(2\sigma^*) \gg 1$, and (3) a full crossing angle θ which is small compared with 1 but larger than the rms IP beam divergence, or $\sqrt{\sigma^*/\beta^*} \ll \theta \ll 1$. In this regime, the luminosity for Gaussian bunches in [5] simplifies to [4]

$$L^{\text{Gaussian}} \approx \frac{f_{\text{coll}}\gamma\epsilon_N}{r_p^2\beta^*}\Delta Q_{\text{tot}}^2\frac{\pi\theta\sigma_z}{2\sigma^*}\,, \qquad (1)$$

where f_{coll} is the bunch collision frequency, and ϵ_N the normalized 1-σ emittance. The expression for a uniform bunch of length l_{flat} is identical, only that σ_z is replaced by $l_{\text{flat}}/\sqrt{\pi}$. The total tune shift for either profile is [4]:

$$\Delta Q_{\text{tot}} \approx \sqrt{\frac{2}{\pi}}\frac{r_p\beta^*}{\gamma\sigma^*\theta}\lambda\,, \qquad (2)$$

where λ denotes the (peak) line density. Combining (1), or its equivalent for a uniform bunch, with (2) confirms that the luminosity for a flat profile is $\sqrt{2}$ higher than for a Gaussian bunch of equal total tune shift and charge [4].

Super-bunches are only one way to create a flat profile; another possibility are shorter 'hollow bunches', already available from the PS booster [6].

Table 2 compares the nominal and ultimate LHC design parameters with three tentative options for a luminosity upgrade. All upgrades employ a reduced β^*, and promise luminosities a factor 7–9 above nominal. In the second rightmost column we consider a large 'Piwinski parameter', *i.e.*, $\sigma_z\theta/(2\sigma^*) \gg 1$, with enhanced crossing angle and bunch current, but still keep 2808 bunches. The two sets of numbers in this column refer to either Gaussian bunches (up) or to uniform bunches (down). The far right column contains parameters for a single super-bunch.

Figure 2 shows the transverse diffusion rate (increase of action variance per turn) on a logarithmic scale, obtained from a weak-strong beam-beam model as in [8], for super-bunches colliding at two different crossing angles in two orientations. For $\theta = 1$ mrad, the diffusion rate is much smaller than in the nominal LHC, and there is no threshold 'diffusive aperture' as for the latter (see, *e.g.*, [8]). Figure 3 displays tune footprints, calculated for amplitudes up to 10σ by a frequency-map analysis [9]. Gaussian and super-bunches are compared for two different crossing schemes. The maximum tune excursions are smaller for super-bunches and for inclined hybrid crossing.

ELECTRON CLOUD

A further important benefit of super-bunches is an almost complete suppression of the electron-cloud build up and the associated heat load. If the beam profile is uniform, only photo-electrons generated at the very end of the bunch passage can be accelerated and acquire energy in the beam field. All other electrons traverse a quasi-static beam potential without any net energy gain.

Table 2: Nominal and ultimate LHC parameters compared with those for three hypothetical LHC upgrades based on either large Piwinski parameter or super-bunches [1]. The normalized transverse emittance (1σ) is 3.75 μm, and the beam energy 7 TeV, for all the cases shown.

parameter	nom.	ult.	upgrades	
no. of bunches n_b	2808	2808	2808	1
rms bunch length σ_z [cm]	7.6	7.6	7.6, 4.2	7500
rms energy spread σ_δ [10^{-4}]	1.1	1.1	1.1, 3.7	5.8
beta at IP [m] β^*	0.5	0.5	0.25	0.25
crossing angle θ [μrad]	300	315	485	1000
beam current I_b [A]	0.56	0.86	1.3, 1.3	1.0
luminosity L [10^{34} cm^{-2}s^{-1}]	1	2.3	7.3, 9.7	9.0
σ_δ IBS growth time τ_{IBS} [h]	134	86	56, 674	1712

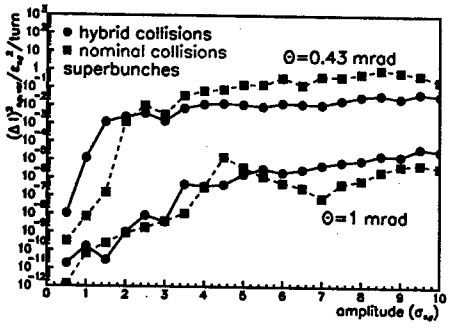

Figure 2: Simulated diffusion rate vs. amplitude for intense super-bunches of $\lambda = 8.8 \times 10^{11}$ m^{-1} [4].

As an illustration, Fig. 4 shows the heat load per meter, simulated assuming 10% linearly rising and falling bunch edges, as a function of the super-bunch length. The luminosity is held constant, equal to 6×10^{34} cm^{-2} s^{-1} at $\beta^* = 0.25$ m and $\theta = 300$ μrad, by decreasing the number of bunches (and increasing their spacing) in proportion

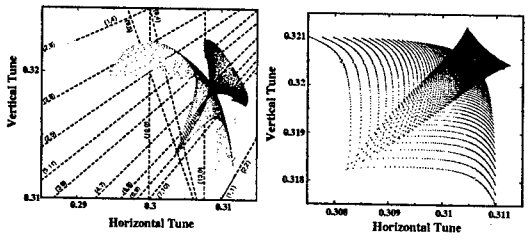

Figure 3: Tune footprints comparing $x - y$ (red) and inclined hybrid crossings (blue) for nominal Gaussian bunches at $\theta = 300$ μrad (left) and intense super-bunches of $\lambda = 8.8 \times 10^{11}$ m^{-1} with $\theta = 1$ mrad (right) [4].

to the bunch length. The maximum available cooling capacity in the LHC arcs is about 1 W/m. For total bunch lengths of 1 m or higher, the electron-cloud heat load becomes insignificant, even at a maximum secondary emission yield as large as $\delta_{\max} = 1.4$. This should be compared with the nominal LHC, where $\delta_{\max} < 1.2$ is required, or with alternative upgrade options entailing a larger number of bunches, where even for $\delta_{\max} = 1.1$ the cooling budget is exceeded [1].

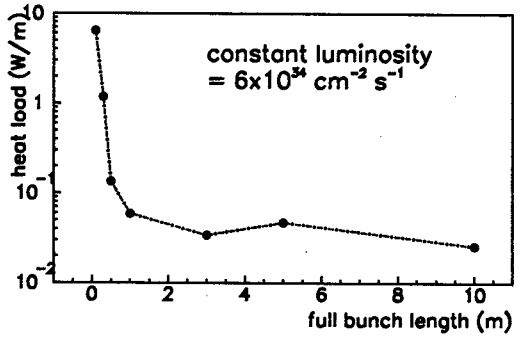

Figure 4: Simulated heat load in an LHC arc dipole due to the electron cloud vs. super-bunch length for $\delta_{\max} = 1.4$, and $\lambda = 8 \times 10^{11}$ m^{-1} [7].

We have simulated the emittance growth due to the interaction with an electron cloud for Gaussian and uniform bunches of identical rms length (75 mm) and bunch population [4]. The emittance growth of the uniform bunch is about 2 times smaller than for the Gaussian. The main difference, aside from the bunch profile, is the longitudinal dynamics. The regular Gaussian bunch is held in a sinusoidal rf bucket, where all particles oscillate at about the same synchrotron tune $Q_s = 0.0116$. The super-bunch is confined by steep rf barriers, so that its synchrotron tune, $Q_s = C\alpha_c\delta/(2l_{\rm flat})$, depends linearly on the particle momentum δ (where $l_{\rm flat}$ is the full bunch length, C the cirumference, α_c the momentum compaction). The larger synchrotron-tune spread has a stabilizing effect.

INTRABEAM SCATTERING

An important emittance-growth mechanism in hadron colliders is intrabeam scattering (IBS). The difference in IBS growth rates between a Gaussian bunch and a super-bunch arises solely from integrating the square of the longitudinal density $\lambda(s)$. The relation between the two IBS growth rates is

$$\frac{1}{\tau_{\rm IBS}^{\rm flat}} = \frac{2\sqrt{\pi}\sigma_z}{l_{\rm flat}} \frac{N_{b,\rm flat}}{N_{b,\rm Gaussian}} \frac{1}{\tau_{\rm IBS}^{\rm Gaussian}}, \qquad (3)$$

assuming that the momentum spread is the same. Then, for equal bunch population N_b and $l_{\rm flat} = \sqrt{2\pi}\sigma_z$, both luminosity and IBS growth rate of a uniform (super-)bunch are $\sqrt{2}$ times larger than for a Gaussian bunch. IBS growth rates can be calculated by MAD [10], which computes the Bjorken-Mtingwa expressions [11], or estimated by further approximating the simplified formula of [12] as

$$\frac{1}{\tau_{\rm IBS,\delta}^{\rm flat}} \equiv \frac{1}{\sigma_\delta}\frac{d\sigma_\delta}{dt} \approx \frac{\sqrt{\pi} r_p^2 c N_b (\log)}{8\gamma^3 \epsilon_\perp^{3/2} l_{\rm flat}\sigma_\delta^3} \frac{1}{\sqrt{\beta_\perp}\sqrt{\frac{1}{\sigma_\delta^2} + \frac{<\mathcal{H}_x>}{\epsilon_\perp}}}, \qquad (4)$$

and $1/\tau_{\rm IBS,x}^{\rm flat} \approx \sigma_{\delta^2} < \mathcal{H}_x > /(\epsilon_\perp \tau_{\rm IBS,\delta}^{\rm flat})$, where (log) denotes the Coulomb logarithm, and $< \mathcal{H}_x >$ the average dispersion invariant. In Fig. 5, these estimates are compared with the exact MAD computation as a function of the momentum spread. The agreement is extremely good for the transverse plane. Longitudinally, there is a discrepancy up to 30% for large values of σ_δ, which is due partly to our rough averaging and partly to the simplifications in [12]. Fig. 5 illustrates that the IBS rise times increase substantially for larger momentum spread, which amounts to another possible advantage of the super-bunches.

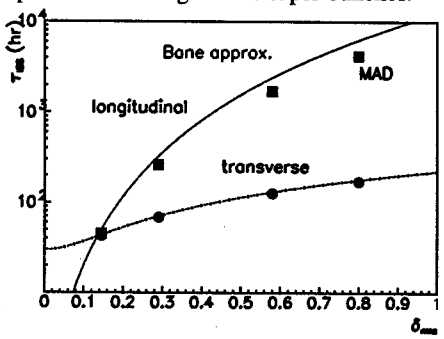

Figure 5: Intrabeam scattering growth times for super-bunches in the LHC vs. σ_δ, according to Eq. (4) (the lines) or calculated by MAD (the plotting symbols).

CONCLUSIONS

Super-bunch collisions in a future LHC upgrade promise a higher luminosity, that may reach ten times the nominal value, accompanied by an improved beam-beam dynamics, negligible heat load from electron cloud, and increased IBS rise times. The larger luminosity and IBS rise times may also be realized by hollow bunches. A number of open questions, such as PACMAN like forces acting on individual particles during part of their synchrotron motion and strong-strong beam-beam dynamics, remain to be explored.

REFERENCES

[1] O. Brüning et al., LHC-PROJECT-REPORT-626 (2002).
[2] K. Takayama et al., Phys. Rev. Lett. 88, 144801 (2002).
[3] RPIA2002, *http://conference.kek.jp/RPIA2002*.
[4] F. Ruggiero et al., LHC-PROJECT-REPORT-627 (2003).
[5] F. Ruggiero, F. Zimmermann, PRST-AB 5, 061001 (2002).
[6] C. Carli, M. Chanel, AIP Conf.Proc. 642, p. 313 (2003).
[7] F. Zimmermann, Proc. EPAC'02, Paris, p. 25 (2002).
[8] Y. Papaphilippou et al., PRST-AB 2, 104001 (1999).
[9] J. Laskar, Astron. Astrophys. 198, 341 (1988).
[10] H. Grote, F.C. Iselin, CERN/SL/90-13 (AP).
[11] J.D. Bjorken, S.K. Mtingwa, Part. Acc. 134, p. 115 (1983).
[12] K.L.F. Bane, Proc. EPAC 2002, Paris, p. 1443 (2002).

A NEW ANALYSIS OF INTRABEAM SCATTERING*

Boaz Nash†, Juhao Wu, Karl Bane, Alex Chao, SLAC, Menlo Park, CA, 94025

Abstract

Beginning with the Fokker-Planck equation we present a new analysis of intrabeam scattering (IBS) in electron storage rings. Our approach is distinguished by having no ill-defined Coulomb logarithm, a fundamental drawback of previous approaches. We treat the case of linear $x_\beta y_\beta$ coupling in detail, deriving explicit expressions for the second moment invariants and their time evolution in the presence of IBS. We compare our results with those of Bjorken-Mtingwa, as well as with measurements performed at KEK's ATF damping ring. More details of our derivations will be published elsewhere.

EVOLUTION EQUATIONS

We consider a smooth focusing approximation Hamiltonian representing the symplectic part of the dynamics in the storage ring given by $H = (1/2)S_{ij}z_iz_j$ with $\vec{z} = (x, x', y, y', z, \delta)$. If we consider damping and diffusion processes (both radiation and IBS) as well as the Hamiltonian evolution, the beam distribution function $f(\vec{z}, t)$ evolves via the Fokker-Planck equation:

$$\frac{\partial f}{\partial t} = \frac{\partial}{\partial z_i}\left(-B_i f + \frac{1}{2}\frac{\partial}{\partial z_j}D_{ij}f\right) \qquad (1)$$

with $B_i = C_{ij}z_j + \langle\langle \delta z_i\rangle_W/\delta t\rangle_{\rm IBS}$, $D_{ij} = d_{ij} + \langle\langle \delta z_i \delta z_j\rangle_W/\delta t\rangle_{\rm IBS}$. The various matrices are given by $C = JS - b$, b is the damping matrix, d is the diffusion matrix, and J is the symplectic inner product matrix $J = {\rm diag}(\{0\ 1\}, \{-1\ 0\})$. The IBS average $\langle\ \rangle_W$ is over the probability that a given particle with phase space position $\vec{z}$ will change by $\delta\vec{z}$ in a time δt. In a coordinate system where x, y, z are real positions, only $W(\delta p_a)$ $(a = 1 \ldots n)$ will be non-zero. For $2n$-D phase space, there exist n invariants of H: $g_a = \vec{z}^T G^a \vec{z}$ with $G^a = JU\tilde{G}^a U^T J$, where U is the symplectic matrix whose columns consist of pairs of eigenvectors of JS, $(v_a, -iv_a^*)$ normalized such that $v_a^T J v_b = -i\delta_{ab}$, and $\tilde{G}^a$ is given by having $-i\sigma_x = (\{0\ -i\}, \{-i\ 0\})$ in the $a^{\rm th}$ spot along the diagonal and the rest 0's. The RMS emittance is $\epsilon_a = \langle g_a\rangle/2$.

If the damping and diffusion are slow compared to the Hamiltonian evolution, the distribution will approximately be a Gaussian function of the invariants:

$$f(\vec{z},t) = \frac{N}{\Gamma}e^{-\frac{1}{2}z_iz_j\mathbb{M}_{ij}(t)} \approx \frac{N}{\Gamma}e^{-\frac{g_1}{\langle g_1\rangle(t)} - \frac{g_2}{\langle g_2\rangle(t)} - \frac{g_3}{\langle g_3\rangle(t)}} \qquad (2)$$

The distribution is normalized so that $\int d\vec{z} f(\vec{z}) = N$, and the phase space volume is given by $\Gamma = (\pi)^3\langle g_1\rangle\langle g_2\rangle\langle g_3\rangle$. IBS is most naturally analyzed in the beam frame which we notate by $\vec{Z} = (\vec{X}, \vec{P})$. With small x', y', and for large relativistic γ factor, the Lorentz transformation is simply $X = x, Y = y, Z = \gamma z, P_x = P_0 x', P_y = P_0 y', P_z = P_0\delta/\gamma, dt = \gamma d\bar{t}$ with P_0 the reference momentum. We introduce $\vec{z} = L\vec{Z}$. For the distribution matrices, we write

$$\bar{\mathbb{M}} = \sum_{a=1}^{3}\bar{\mathbb{M}}^{(a)} = \sum_{a=1}^{3}\begin{pmatrix}\mathbb{A}^{(a)} & \mathbb{B}^{(a)}\\ \mathbb{B}^{(a)T} & \mathbb{C}^{(a)}\end{pmatrix} \qquad (3)$$

where $\bar{\mathbb{M}} = L^T\mathbb{M}L$ is $\mathbb{M}$ expressed in the beam frame and $\bar{\mathbb{M}}^{(a)} = 2L^TG^{(a)}L/\langle g_a\rangle$.

From (1), the evolution of the moments $\Sigma_{ij} = \langle z_iz_j\rangle_f$ is

$$\frac{d\Sigma_{ij}}{dt} = \left(\langle B_iz_j\rangle_f + \frac{1}{2}\langle D_{ij}\rangle_f\right) + (i \leftrightarrow j) \qquad (4)$$

Note that $\Sigma^{-1} = \mathbb{M}$. We can also show that the evolution of the average values of the invariants is

$$\frac{d\langle g_a\rangle}{dt} = -2\alpha_a(\langle g_a\rangle - \langle g_a\rangle_0) + \left(\frac{d\langle g_a\rangle}{dt}\right)^{\rm IBS} \qquad (5)$$

where the equilibrium values of the invariants without IBS are $\langle g_a\rangle_0 = d_a/(2\alpha_a)$, or $\epsilon_{a0} = d_a/(4\alpha_a)$ with $2\alpha_a = {\rm Tr}(\tilde{b}_a)$ and $d_a = {\rm Tr}\,(G^a d)$ where $\tilde{b}_a$ is the $a^{\rm th}$ 2×2 block along the diagonal of $\tilde{b} = U^{-1}bU$. To first order, the α_a are the real parts of the eigenvalues of the matrix C.

We define the IBS growth rate as $T_a^{-1} = (d\langle g_a\rangle/dt)^{\rm IBS}/\langle g_a\rangle$. For Eq. (4) there are 2 types of terms in $(d\Sigma/dt)^{\rm IBS}$, one in the form of $\langle x_ap_b\rangle$ and the other $\langle p_ap_b\rangle$. Using Eq. (3), we get

$$\frac{1}{T_a} = \frac{1}{2}{\rm Tr}\left(M^a\frac{d\Sigma^{\rm IBS}}{dt}\right) = \frac{1}{2}\mathcal{A}{\rm Tr}\left(\mathbb{B}^{(a)}\mathbb{Q} + \mathbb{C}^{(a)}\mathbb{K}\right) \qquad (6)$$

where $\mathcal{A}\mathbb{K}_{ab} = d\langle P_aP_b\rangle/dt|_{\rm IBS}$, $\mathcal{A}\mathbb{Q}_{ab} = d\langle X_aP_b\rangle/dt|_{\rm IBS}$ and $\mathcal{A}$ contains overall constants. We've moved into the beam frame using ${\rm Tr}\,(M^a\Sigma) = {\rm Tr}(\bar{M}^a\bar{\Sigma})$ with $\Sigma = L\bar{\Sigma}L^T$.

IBS DAMPING AND DIFFUSION

IBS has been studied extensively [1-4,7], with Bjorken-Mtingwa (BM)[2] and Piwinski (P)[3] the main foundations of later derivations. We start from first principles, aiming for a clearer understanding of the subject. In addition to having no Coulomb log, our approach differs from [4] and [7] in that we follow invariants directly and give explicit expressions for them in the case of global coupling.

We compute $\bar{B}_a^{\rm IBS}(\vec{Z}) = \langle\delta P_a\rangle_W/\delta\bar{t}$ and $\bar{D}_{ab}^{\rm IBS}(\vec{Z}) = \langle\delta P_a\delta P_b\rangle_W/\delta\bar{t}$. Let the two particles have coordinates $\vec{Z}_1$ and $\vec{Z}_2$ and let $\vec{r} = \vec{X}_1 - \vec{X}_2$ and $\vec{\Delta} = \vec{P}_1 - \vec{P}_2$. If we consider them undergoing a scattering process, the impact parameter is $\vec{b} = \vec{r} - r(\hat{\Delta}\cdot\hat{r})\hat{\Delta}$, where hats designate unit vectors. In the small angle approximation, the scatter leads to a total momentum kick $\delta\vec{P}_1 \approx -4k^2/(\Delta^3b^2)\hat{\Delta} + 2k/(\Delta b)\hat{b}$ where $k = (mc)^2r_0$ with r_0 the classical particle radius. For δP_a, we discard the 2nd term which should rightfully be included in the space charge analysis, and then keep the term in $\delta P_a\delta P_b$ required for energy conservation. We then average these quantities over the portion of particle 2's phase space where the time to the distance of minimum approach

*This work was supported by the U.S. Department of Energy under Contract No. DE-AC03-76SF00515.

† bnash@slac.stanford.edu

$t_{\min} = -m(r/\Delta)\hat{\Delta}\cdot\hat{r}$ is less than $\delta\bar{t}$. Letting $\delta\bar{t}\to 0$ we arrive at

$$\frac{\langle\delta P_a\rangle_W}{\delta\bar{t}} = -\frac{4k^2}{m}\int d\vec{\Delta}\, d\vec{r}\;\frac{\hat{\Delta}_a}{\Delta^2 b^3}\bar{f}(\vec{X}_2,\vec{P}_2)\delta(\hat{\Delta}\cdot\hat{r}) \quad (7)$$

$$\frac{\langle\delta P_a\delta P_b\rangle_W}{\delta\bar{t}} = \frac{4k^2}{m}\int d\vec{\Delta}\, d\vec{r}\;\frac{\hat{b}_i\hat{b}_j}{\Delta b^3}\bar{f}(\vec{X}_2,\vec{P}_2)\delta(\hat{\Delta}\cdot\hat{r}) \quad (8)$$

After use of the delta function in the integral, b can be replaced by $r=|\vec{r}|$. $\bar{f}$ is f normalized so that $\int d\vec{Z}\bar{f}(\vec{Z})=1$. If we replace the spatial distribution with the local constant density, and absorb the spatial divergence into a Coulomb log, these reduce to the Rosenbluth Potentials[6].

REDUCE TO ANGULAR INTEGRALS

For the IBS contribution to the moment evolution equations, we can combine the damping and diffusion together using (4) [1]. For Gaussian distributions, the result is:

$$\mathbb{K}_{ab} = \int\frac{d^6\vec{\xi}}{\Delta r^3}\left[\hat{r}_a\hat{r}_b - \hat{\Delta}_a\hat{\Delta}_b\right]e^{-\frac{1}{2}\xi_i\xi_j\breve{\mathbb{M}}_{ij}}\delta(\hat{\Delta}\cdot\hat{r}) \quad (9)$$

where $\breve{\mathbb{M}}$ is the unitless $\mathbb{M}$ matrix expressed in the basis of $\vec{Z}$, i.e. we use[2] $\breve{\mathbb{A}} = r_m^2\mathbb{A}$, $\breve{\mathbb{B}} = (r_m P_0)\mathbb{B}$, $\breve{\mathbb{C}} = P_0^2\mathbb{C}$. Also, $\vec{\xi} = (\vec{r},\vec{\Delta})$. For the overall constant, $\mathcal{A} = Nk^2/(\gamma m\bar{\Gamma})$ with $\bar{\Gamma} = P_0^3\Gamma$. We also can compute:

$$\mathbb{Q}_{ab} = -\frac{1}{2}\int d^6\vec{\xi}\,\frac{\hat{r}_a\hat{\Delta}_b}{\Delta^2 r^2}e^{-\frac{1}{2}\xi_i\xi_j\breve{\mathbb{M}}_{ij}}\delta(\hat{\Delta}\cdot\hat{r}) \quad (10)$$

Ignore $\mathbb{Q}_{ab}$ for now (no "Coulomb log" behaviour). If we do the $|\vec{r}|$ and $|\vec{\Delta}|$ integrals and the integral from the δ function in $\mathbb{K}_{ab}$ we are left with

$$\mathbb{K}_{ab} = \frac{1}{2}\int d\Omega\,\frac{-h_{ab}}{h_3}[\log(\frac{h_1}{2}) + \gamma_E - q\tan^{-1}q] \quad (11)$$

with $h_{ab} = \hat{r}_a\hat{r}_b - \hat{\Delta}_a\hat{\Delta}_b$, $h_1 = \breve{\mathbb{A}}_{ab}\hat{r}_a\hat{r}_b$, $h_2 = \breve{\mathbb{B}}_{ab}\hat{r}_a\hat{\Delta}_b$, $h_3 = \breve{\mathbb{C}}_{ab}\hat{\Delta}_a\hat{\Delta}_b$, and $q = h_2/\sqrt{4h_1h_3 - h_2^2}$; $\gamma_E \approx 0.577$. The q term in (11) will often be small and we drop it here. Approximating the $\log() + \gamma_E$ term as a constant gives what we call the Coulomb log approximation. This can be shown to reduce exactly to the equivalent expression in BM. We denote it by $\mathbb{K}^{\rm BM}$. The quotient of these two expressions can be used to define the Coulomb log:

$$2\mathrm{Log}_{ab} = \frac{\int d\Omega\frac{h_{ab}}{h_3}(-\log(\frac{h_1}{2}) - \gamma_E)}{\int d\Omega\frac{h_{ab}}{h_3}} = \frac{\mathbb{K}_{ab}}{\mathbb{K}^{\rm BM}_{ab}} \quad (12)$$

This allows us to explore the range over which the usual approach of having a single Coulomb log makes sense.

THE CASE OF A COUPLED BEAM

With both x and y dispersion and $x_\beta y_\beta$ coupling parameter κ in the smooth approximation, we use the Hamiltonian $H = (\beta c/2)(k_x x_\beta^2 + x'^2 + 2\kappa x_\beta y_\beta + k_y y_\beta^2 + y'^2 - (k_z/\alpha_c)z_\beta^2 - \alpha_c\delta^2)$ where $x_\beta = x - \eta_x\delta$, $y_\beta = y - \eta_y\delta$, $z_\beta = z - \eta_x x' - \eta_y y'$ and $\alpha_c = k_x\eta_x^2 + k_y\eta_y^2$ is the momentum compaction factor. βc is the reference particle velocity. We use lab time as the independent variable. The smoothed frequencies are $k_x = 1/\beta_x^2 = (\nu_x/R)^2$, $k_y = 1/\beta_y^2 = (\nu_y/R)^2$, $k_z = (\nu_s/R)^2$, with $\nu_{x,y,s}$ the horizontal, vertical betatron and synchrotron tunes respectively. $R = \mathbf{C}/2\pi$ with $\mathbf{C}$ the storage ring circumference. We parametrize k_x, k_y and κ by $k_x = k_0 + \Lambda\cos\psi$, $k_y = k_0 - \Lambda\cos\psi$, $\kappa = \Lambda\sin\psi$. $\Lambda = \sqrt{(k_x - k_y)^2/4 + \kappa^2}$ and $\tan\psi = 2\kappa/(k_x - k_y)$. $\psi/2$ is the tilt angle in the x_β,y_β plane. The eigeninvariants are

$$\begin{aligned} g_{1,2} &= \frac{1}{2\sqrt{k_0\pm\Lambda}}([(k_0\pm\Lambda)x_\beta^2 + x'^2](1\pm\cos\psi) + \\ &\quad [(k_0\pm\Lambda)y_\beta^2 + y'^2](1\mp\cos\psi) \pm \\ &\quad 2[(k_0\pm\Lambda)x_\beta y_\beta + x'y']\sin\psi), \text{(1 upper sign,2 lower sign)} \\ g_3 &= (z_\beta^2/\beta_z) + \beta_z\delta^2 \end{aligned} \quad (13)$$

where $\beta_z = R\alpha_c/\nu_s$. Note that $H = \frac{\beta c}{2}(\sqrt{k_0+\Lambda}\,g_1 + \sqrt{k_0-\Lambda}\,g_2 - \sqrt{k_z}\,g_3)$. The IBS growth rates are

$$\begin{aligned} \frac{1}{T_{1,2}} &= \frac{\mathcal{A}}{4\epsilon_{1,2}\sqrt{k_0\pm\Lambda}}[(1\pm\cos\psi)\mathbb{K}_{11} \pm 2\sin\psi\mathbb{K}_{12} \\ &+ (1\mp\cos\psi)\mathbb{K}_{22} + \gamma^2(k_0\pm\Lambda)(\eta_x^2(1\pm\cos\psi) \\ &+ \eta_y^2(1\mp\cos\psi))\mathbb{K}_{33}] \\ \frac{1}{T_3} &= \frac{\mathcal{A}\gamma^2}{\sigma_\delta^2}\mathbb{K}_{33} \end{aligned} \quad (14)$$

The damping matrix has non-zero elements $b_{22} = 2\alpha_x$, $b_{44} = 2\alpha_y$, $b_{66} = 2\alpha_z$ and the rest of the elements are 0. The diffusion matrix d has just one non-zero element (ignoring intrinsic x', y' diffusion), $d_{66} = \mathcal{D}/E_0^2$, where $\mathcal{D} = 55r_0\hbar mc^4\gamma^7/(24\sqrt{3}\rho^3)$. These yield coupled damping constants $\alpha_{1,2} = \frac{1}{2}\alpha_x(1\pm\cos\psi) + \frac{1}{2}\alpha_y(1\mp\cos\psi)$, $\alpha_3 = \alpha_z$ and diffusion constants $d_{1,2} = \mathcal{D}\sqrt{k_0\pm\Lambda}(\eta_{x,y}\cos\frac{\psi}{2} \pm \eta_{y,x}\sin\frac{\psi}{2})^2$, $d_3 = \beta_z\mathcal{D}$ which yield equilibrium emittances without IBS of

$$\begin{aligned} \epsilon_{(1,2)0} &= \left\langle\frac{\mathcal{D}\sqrt{k_0\pm\Lambda}[\eta_{x,y}\cos\frac{\psi}{2} \pm \eta_{y,x}\sin\frac{\psi}{2}]^2}{2[\alpha_x + \alpha_y \pm (\alpha_x - \alpha_y)\cos\psi]}\right\rangle_b\frac{\rho}{R} \\ \epsilon_{30} &= \left\langle\frac{\mathcal{D}\beta_z}{4\alpha_z}\right\rangle_b\frac{\rho}{R}. \end{aligned} \quad (15)$$

We have assumed that the lattice is isomagnetic and hence the $1/\rho^3$ average in $\mathcal{D}$ causes the other parameters to be averaged only in the bends with an overall ρ/R normalization. In the zero coupling limit, we also replace $\langle\eta_{x,y}^2/\beta_{x,y}\rangle$ with $\langle\mathcal{H}_{x,y}\rangle$. The observable transverse beam sizes are related to the invariants by

$$\sigma_{x,y}^2 = \frac{\epsilon_{1,2}\cos^2\frac{\psi}{2}}{\sqrt{k_0\pm\Lambda}} + \frac{\epsilon_{2,1}(1-\cos\psi)}{\sqrt{k_0\mp\Lambda}} + \frac{\epsilon_3\sqrt{k_z}\eta_{x,y}^2}{\alpha_c} \quad (16)$$

When $\psi\to 0$, we recover $\sigma_{x,y}^2 = \beta_{x,y}\epsilon_{x,y} + \sigma_\delta^2\eta_{x,y}^2$.

APPLICATION TO THE ATF

As an application of our analysis, we compared with the data taken at the ATF in April 2000. Ref. [1] attempted this using a combination of the program SAD and IBS expressions based on BM with coupling added in a heuristic way. There was an apparent discrepancy between theory and experiment in the current dependence of the projected vertical emittance, $\epsilon_{y,\rm pr} = (\sigma_y^2\sigma_{y'}^2 - \sigma_{yy'}^2)^{\frac{1}{2}}$. Our analysis provides a solid base to explore this issue.

[1] This derivation of the BM results from the Rosenbluth potentials[6] was carried out by M. Venturini [5].

[2] The quantity r_m is the minimum impact parameter cut-off required because (9) diverges for small distances. We take it to be a typical distance of minimum approach, $r_m = r_0\beta_x/(\gamma^2\epsilon_x)$. This cut-off is also consistent with the small angle approximation used in the analysis.

We vary κ and compare equilibrium values for $\epsilon_x, \sigma_s, \sigma_\delta$, and $\epsilon_{y,\mathrm{pr}}$. We also (as in [1]) vary β_z with current computed from the σ_s, σ_δ data, as a linear model for bunch lengthening. We use $E_0 = 1.28$ GeV, $\eta_x = 0.052$ m, $\eta_y = 3$ mm, $\beta_x = 3.9$ m, $\beta_y = 4.5$ m, $\epsilon_{x0} = 1.05 \times 10^{-9}$ m, $\nu_s = .0049$, $\alpha_c = .0029$, $\mathbf{C} = 138.6$ m, $\rho/R = 0.260$. $\tau_a = 1/\alpha_a$ are $\tau_x = 18.2$ ms, $\tau_y = 29.2$ ms, and $\tau_p = 20.9$ ms.

Figure 1 shows the evolution of the invariants starting with injection values. We evolve the invariants using (5), (11), and (14). The parameters correspond to the 3.1 mA point on the middle curve of Figure 2. Note that $\epsilon_{y\,\mathrm{pr}}/\epsilon_x$ is not constant, and hence there is not an exact global coupling paameter κ' such that $\epsilon_{y,\,\mathrm{pr}}(t) = \kappa' \epsilon_x(t)$.

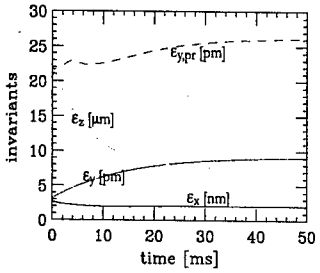

Figure 1: Time evolution of emittances.

Figure 2 shows a comparison of equilibrium projected vertical emittance (solid curves) to the data (diamonds). ϵ_x and σ_δ are not shown, but agreement is comparable to that in [1]. By adjusting the coupling, we can get the correct magnitude in $\epsilon_{y,pr}$, but the slope still does not agree. For $\eta_y = 3$mm, we need κ/k_0 between .02 and .03 which corresponds to a tilt angle between 4 and 6 degrees. ϵ_y (dashed curves) is smaller than $\epsilon_{y,\mathrm{pr}}$. This gives an indication of the effect coupling has had on the measurements. In the

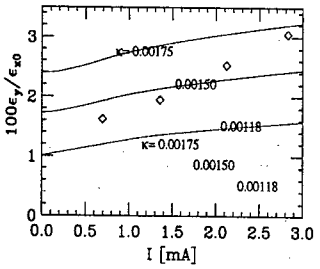

Figure 2: Comparison with ATF measurements. (κ in m^{-2})

ATF, the beam is coolest in δ and hottest in x. Thus, $\mathbb{K}_{33}$ is positive and $\mathbb{K}_{11}$ negative. $\mathbb{K}_{22}$ can be either positive or negative (energy conservation gives $\sum_a \mathbb{K}_{aa} = 0$.) We find the biggest difference between $\mathbb{K}_{ab}$ and $\mathbb{K}_{ab}^{\mathrm{BM}}$ for $\mathbb{K}_{22}$. In the small coupling limit, the $\mathbb{K}_{22}$ and the $\mathbb{K}_{33}$ contributions to $1/T_2$ have a relative coefficient of $\gamma^2\eta_y^2/\beta_y^2$. In the "High Energy Approximation", one keeps only the $\mathbb{K}_{33}$ term. However, for the ATF parameters, if $\eta_y < 1.8$ mm, $\mathbb{K}_{22}$ can become important. In Figure 3 we plot the ratio of the Coulomb logs defined in (12) to the conventional Coulomb log $L_c = \log(\sigma_y/r_m)$ ($L_c \approx 16$ for ATF) for varying vertical dispersion and zero coupling (since BM dealt only with the uncoupled case). Effectively, we are varying the beam aspect ratio, with the right side of the plot approaching a round beam. Near $\eta_y = 28$ mm, the intrinsic vertical growth rates $\mathbb{K}_{22}$ and $\mathbb{K}_{22}^{\mathrm{BM}}$ have opposite signs. Finally note that both Log_{11}/L_c and Log_{33}/L_c are close to 1 over a wide range of beam aspect ratios.

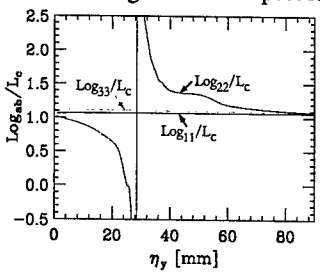

Figure 3: Ratios of computed to nominal Coulomb log.

CONCLUSIONS AND FUTURE WORK

We have given new expressions for the IBS damping and diffusion coefficients B_a and D_{ab} and the moment evolution quantities $\mathcal{A}\mathbb{K}_{ab}$. We include the position distribution in our approach (the matrix $\mathbb{A}$ for Gaussians), a necessary step in understanding the effect that the shape of the beam has on IBS. For Gaussian beams, we have reduced the expressions to 3-D angular integrals. In fact we can reduce them to 2-D integrals with some increase in complexity. We find that for flat beams with ATF parameters, Bjorken-Mtingwa with $b_{\max}$ equal to the vertical beam size gives excellent results for the horizontal and longitudinal growth rates, but can break down for the intrinsic vertical growth rate. We expect that for $\eta_y < 1.8$ mm, for some values of κ and $\nu_x - \nu_y$, there may be observable differences in the growth rates and/or equilibria in the ATF.

We have also included global $x_\beta y_\beta$ coupling explicitly for the first time and computed the evolution of the invariants for the case of the ATF damping ring. We find that the dependence of $\epsilon_{y,\mathrm{pr}}$ on beam current cannot be explained by our model which suggests that non-IBS physics and/or measurement error may be occurring. The offset can be explained, however, with a beam tilt angle of 4-6 degrees.

Future plans include exploration of full $\eta_y, \kappa, \nu_x - \nu_y$ parameter space in the ATF, application to protons or heavy ions, synchrobetatron coupling, non-Gaussian equilibria and extension beyond the smooth approximation.

BN would like to acknowledge Marco Venturini and Ben Freivogel for many useful discussions.

REFERENCES

[1] K. Bane et. al., Phys. Rev. STAB, **5**,084403, 2002.

[2] J.D. Bjorken, S.K. Mtingwa, Part. Accel. **13**, 115 (1983)

[3] A. Piwinski, *Handbook of Accelerator Physics and Engineering*, Ed. Chao, Tigner, World Sci., Singapore, (1999), p.126

[4] A. Piwinski, DESY 90-113, (1990)

[5] M. Venturini, Private Communication (2002)

[6] M. Rosenbluth et. al., Phys. Rev. **107**, 1 (1957)

[7] K. Kubo, K. Oide, Phys. Rev. STAB, **12**,124401, (2001)

NONLINEAR RESONANCE BENCH-MARKING EXPERIMENT AT THE CERN PROTON SYNCHROTRON

I. Hofmann*, G. Franchetti, GSI, 64291 Darmstadt, Germany
M. Giovannozzi, M. Martini and E. Metral, CERN, 1211 Geneva, Switzerland

Abstract

As a first step of a space charge - nonlinear resonance benchmarking experiment over a large number of turns, beam loss and emittance evolution were measured over 1 s on a 1.4 GeV kinetic energy flat-bottom in the presence of a single octupole. By lowering the working point towards the resonance a gradual transition from a loss-free core emittance blow-up to a regime dominated by continuous loss was found. Our 3D simulations with analytical space charge show that trapping on the resonance due to synchrotron oscillation causes the observed core emittance growth as well as halo formation, where the latter is explained as the source of the observed loss.

1 INTRODUCTION

The study of the combined effect of space charge and nonlinear resonances over as many as 10^5 - 10^6 turns is gaining importance with the need of optimizing the performance of synchrotrons employing high intensity or high phase space density. The latter is relevant for the PS as part of the injector for the LHC; furthermore for the SIS100 of the GSI future project [1], where it is necessary to hold the high-intensity bunches between injections over typically 1 s, and at a loss level not exceeding 1%. Up to now comparison of simulation with experimental work for second or higher order resonances has been successfully carried out in the millisecond time frame [2, 3]. In the realm of long-term behavior, instead, where self-consistent 3D simulation is beyond current computer capabilities, the question of adequate approximations in space charge calculation is a challenging one. Moreover, an explanation of the proper mechanisms describing the combined effect of nonlinearity, space charge and synchrotron oscillation - as suggested recently in a simplified model in Ref. [4] - is crucial.

2 MEASUREMENTS

The measurements where carried out as part of a high intensity machine development time at the PS in October 2002. The number of protons in the bunch was $1.1 \cdot 10^{12}$ – small enough to avoid overlap with other resonances. A vertical maximum space charge tune shift of 0.12, and a horizontal one of 0.075 (for minimum amplitude particles) were achieved with relatively small emittances of $\epsilon_x = 9$ mm mrad and $\epsilon_y = 4.5$ mm mrad (unnormalized at 2σ). The bunch profiles measured 10 ms after injection were found to be Gaussian in all directions in the absence of the octupole. The vertical machine tune was set to $Q_y = 6.12$, and the horizontal tune was varied in the interval $6.25 < Q_x < 6.32$. The chromaticity is close to the natural one, hence the small momentum spread of 10^{-3} allows ignoring chromatic effects. The kinetic energy was kept at the injection value of 1.4 GeV with a measurement window of 1 s ($4.4 \cdot 10^5$ turns) over which the bunch intensity was monitored with a current transformer. The calibrated octupole (here $k_3 = 1.215 \cdot I\ \mathrm{m}^{-3}$) was powered to 40 A at 110 ms after injection to excite the resonance $4Q_x = 25$. We used the transverse profiles measured with the flying wire (20 m/s), fitted a Gaussian profile to them, and determined their rms emittances. Initial and - in most cases - final profiles were actually found quite close to Gaussian.

In Fig. 1 results of final measurements 1 s after injection are plotted as a function of the machine working point. Our main finding is the existence of two regimes: an emittance growth dominated regime for Q_x sufficiently above the resonance - in our example $Q_x > 6.28$, and a loss dominated regime for $Q_x < 6.28$. It is noted that for the working point of maximum loss ($Q_x = 6.27$) the emittance also shrinks, since large amplitude particles are preferably extracted. The time evolution of the bunch intensity for $Q_x = 6.27$ is shown in Fig. 2. Note the continuous loss at a nearly constant rate after an initially enhanced loss (the intensity drop at 1200 ms is caused by the kicker event).

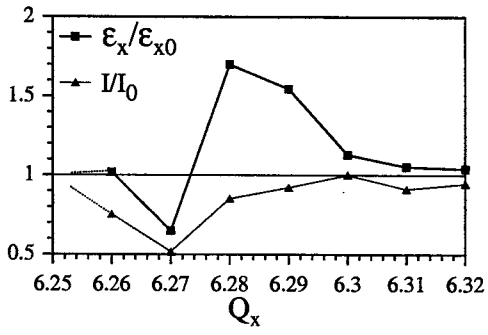

Figure 1: Experimental results on final rms emittance (of Gaussian fit) and beam current relative to initial values.

* i.hofmann@gsi.de

0-7803-7738-9/03/$17.00 © 2003 IEEE

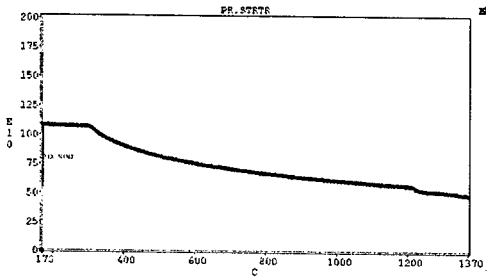

Figure 2: Measured bunch intensity as function of time at $Q_x = 6.27$ with octupole powered at 280 ms (110 ms after injection at time 170 ms).

3 SIMULATION

For an interpretation of these results we have carried out a series of simulation runs in 2D and 3D. We have replaced, for simplicity, the linear PS focusing lattice by constant focusing and ignored lattice nonlinearities besides the contribution from the well-defined octupole. We have also ignored the smaller vertical beam emittance of the experiment and assumed a circular cross section to match with the limitation in the analytical 3D space charge model, which is based on a rotational ellipsoid. The horizontal emittance has been chosen such as to reproduce accurately the maximum horizontal space charge tune shift extracted from the measurement, which we believe is the crucial issue since we are not dealing with a coupling resonance.

The loss observed in the experiment cannot be attributed to the shrinking of the dynamic aperture as a result of the octupole alone. To support this we have carried out a numerical study on the dynamic aperture by searching the maximum stable radius of test particles placed into 20 different directions in the upper half of the $x - y$ plane. We have found that the nominal octupole (40 A) leads to a dynamic aperture (10^5 turns) of about 5σ (with σ the horizontal rms beam size) near $Q_x = 6.25$, which may not be small enough to cause extraction of particles, and a more complete knowledge of machine nonlinearities may be required to explain the loss. Assuming 200 A octupole current we have calculated that the dynamic aperture shrinks to a radius of 2.5σ near $Q_x = 6.25$ for 10^3 turns, and about 2.2σ for 10^5 turns. Note that one expects a theoretical reduction proportional to the inverse square root of the octupole strength, which is roughly confirmed by our simulations.

We first attempt a comparison with the fully self-consistent 2D particle-in-cell (PIC) version of the MICROMAP code [5] with 10^5 simulation particles. We employ a Gaussian distribution function and a 64x64 grid filling a rectangular boundary of 70x70 mm size. We find no loss for 40 A: the rms emittance growth remains below 2%; for comparison, it is 15% - independent of octupole strenght - at $Q_x = 6.25$ in the absence of space charge (the time it takes is about inversely proportional to the octupole strength). We explain this strikingly low saturation level as a consequence of the large space charge de-tuning relative to the natural de-tuning effect of the octupole. A more pronounced effect, with a loss regime and an emittance growth regime analogous to the experiment, is obtained assuming a 5 times stronger octupole. This is shown in Fig. 3 after 100 turns, where the effect is practically saturated. The saturated maximum emittance growth is now about 8%, which reflects the reduced space charge de-tuning relative to the octupole strength. The loss regime confirms the shrinking of the dynamic aperture for $Q_x \rightarrow 6.25$.

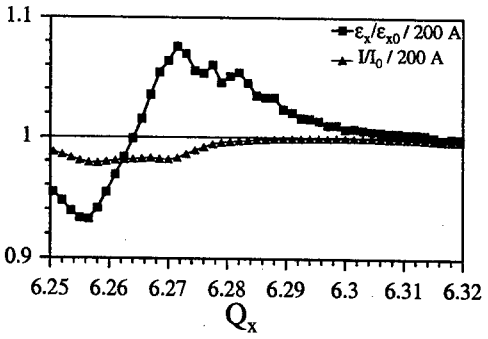

Figure 3: Result of fully self-consistent 2D simulation with 5x stronger octupole (200 A) after 1000 turns. Shown are rms emittances and total intensity in units of initial values.

In order to explore the evolution over significantly longer times we replace the fully self-consistent space charge calculation by an analytical approximation. While such analytical space charge models ignore the dynamically changing space charge force, they have the advantage of being much faster and avoiding the inherent noise of PIC-simulation. As a first example we extend the above 2D coasting beam study with the same transverse rms values, a Gaussian transverse distribution and an analytical space charge force consistent with the initial Gaussian distribution using a method generalized from Ref.[6]. The result after 10^3 turns is found to deviate by not more than $\pm 10\%$ from the self-consistent simulation, with practically no change between 10^3 and 10^5 turns. This suggests that self-consistency might not be an important factor as long as emittance growth or loss are small enough.

For the 3D simulation we employ a density distribution of the kind $(1-x^2/a^2)^3$ in all three directions. We can then perform an exact integration of Poisson's equation using a similar method as in 2D. Using 2000 test particles we generate a (initially) consistent distribution in 6D phase space with the same bunch length (200 ns at 4σ) and synchrotron period (645 turns) as in the experiment.

The dependence on the working point is shown in Fig. 4 to give a similar behavior as in the experiment for $Q_x > 6.28$, but no loss for smaller tunes. For better comparison with the experiment we apply a Gaussian fit to the simulation data and determine the rms emittance from it, which puts the emphasis on the core emittance. Note that the relatively large emittance growth without accompanying loss

reflects the large physical aperture in both experiment and simulation, if compared with the initial beam size. For an assumed 200 A octupole, instead, the simulation shows a continuous loss ($< 25\%$) due to the much reduced dynamical aperture.

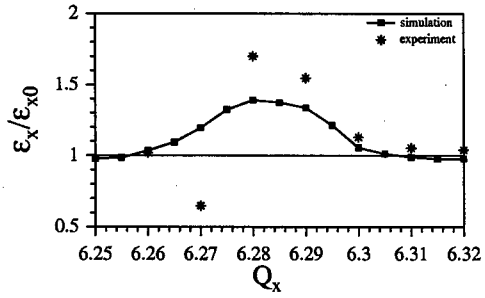

Figure 4: 3D simulation using analytical space charge (40 A octupole). Shown are simulated rms emittances (Gaussian fit) after $5 \cdot 10^5$ turns, and experimental values.

The rms emittance evolution of a typical case is shown in Fig. 5, which compares well with the measured data. The main difference is that the simulation rms emittance growth saturates, since particles with a small enough synchrotron amplitude (depending on Q_x) can never cross the resonance. We compare this result with a modification, where the growing emittance is used to update the horizontal rms size. As a result of this rms self-consistency space charge gets weaker, which allows more particles to cross the resonance. This enhances the growth and leads to even better agreement with the measurement.

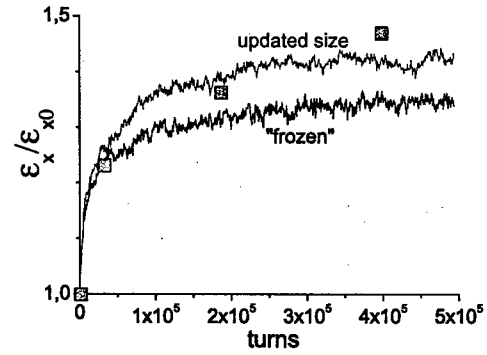

Figure 5: 3D simulation emittance evolution for $Q_x = 6.29$ comparing analytical "frozen" space charge with results obtained by using a continuously updated rms size (squares: measured values).

Our interpretation of the significant difference between 2D and 3D relies on synchrotron motion: in 2D particles can be on resonance for basically *one* value of the betatron amplitude, and if so they get easily de-tuned again with only small amplitude increase, due to the dominant space charge de-tuning; in 3D the synchrotron motion carries the particles from high to low space charge, thus a large number of particles is able to periodically cross the resonance at various betatron amplitudes. Eventually such particles are caught by the resonance, which implies that they are driven to larger transverse amplitude to compensate the enhanced space charge when moving back to the bunch center. As was shown in Ref. [4] such trapping may be followed by de-trapping after some time unless the particle hits the aperture. Therefore the resulting maximum halo increases for $Q_x \rightarrow 6.25$ (Fig. 6), which is the reason for the loss region in the experiment, where apparently further nonlinearities cause a smaller dynamic aperture than in the simulation and lead to extraction. Note that for $Q_x \rightarrow 6.32$, where the resonance loses its effect, the maximum halo size agrees with the initial beam edge of 3σ.

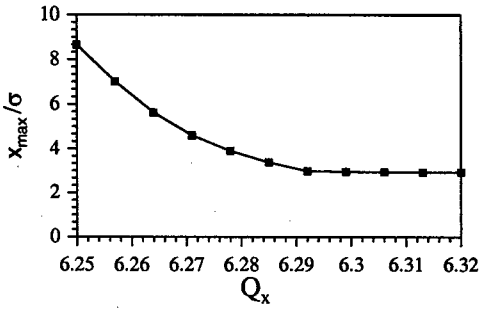

Figure 6: Halo radius (in units of initial σ).

4 CONCLUSION

The synchrotron oscillation has been shown to enhance significantly the response on the octupole. In the emittance growth regime quite good agreement is achieved with the measurements over half a million turns, which supports our 3D space charge model and interpretation. We predict the formation of a halo increasing in size for $Q_x \rightarrow 6.25$ and claim this is the source of the measured loss. Future measurements should consider weaker octupoles, where the predicted halo might be entirely inside the dynamic aperture. Cross-checks with fully self-consistent 3D simulation over some 10^4 turns are planned for the near future.

5 REFERENCES

[1] see http://www.gsi.de/GSI Future/cdr/ (Technical report); W. Henning, also P. Spiller et al., this conference.

[2] S. Cousineau *et al.*, Phys. Rev. ST Accel. Beams **6**, 034205 (2003).

[3] K. Takayama et al., EPAC02, p. 1413 (2002)

[4] G. Franchetti and I. Hofmann, AIP Conf. Proc. **642**, 260 (2002).

[5] G. Franchetti, I. Hofmann, and G. Turchetti, *AIP Conference Proceedings* **448**, 233 (1998).

[6] Q. Qian, R. C. Davidson, and C. Chen, Phys. Plasmas **2**, 2674 (1995).

STRAY-ELECTRON ACCUMULATION AND EFFECTS IN HIF ACCELERATORS

R.H. Cohen[1,2,*], A. Friedman[1,2], M.A. Furman[3], S.M. Lund[1,2], A.W. Molvik[1,2], P. Stoltz[4], J.-L. Vay[1,2]
[1] Virtual National Laboratory for Heavy Ion Fusion
[2] Lawrence Livermore National Laboratory, Livermore, CA 94550
[3] Lawrence Berkeley National Laboratory, Berkeley, CA 94720
[4] TechX Corp., Boulder, CO

Abstract

Stray electrons can be introduced in positive-charge accelerators for heavy ion fusion (or other applications) as a result of ionization of ambient gas or gas released from walls due to halo-ion impact, or as a result of secondary-electron emission. Electron accumulation is impacted by the ion beam potential, accelerating fields, multipole magnetic fields used for beam focus, and the pulse duration. We highlight the distinguishing features of heavy-ion accelerators as they relate to stray-electron issues, and present first results from a sequence of simulations to characterize the electron cloud that follows from realistic ion distributions. Also, we present ion simulations with prescribed random electron distributions, undertaken to begin to quantify the effects of electrons on ion beam quality.

INTRODUCTION

Stray electrons are becoming increasingly recognized as a serious concern for heavy-ion fusion (HIF) accelerators. Electron clouds have already been recognized as a serious issue for accelerator applications such as high-energy physics [1]. In addition to common concerns and physics issues, there are a number of aspects of HIF accelerators that distinguish stray-electron cloud accumulation, dynamics, and effects from those in accelerators for other applications. In this paper we survey the differentiating aspects, report on progress in developing a computational capability to predict electron cloud accumulation and effects, and present calculations illustrating the effect of prescribed electron cloud distributions on ion beam quality. We restrict attention here to magnetic quadrupole-based focusing systems in induction linacs. Electrostatic quadrupoles have a natural electron sweeping mechanism; solenoidal-magnetic-field-based systems have a different set of issues.

DISTINGUISHING ASPECTS OF ELECTRON ISSUES IN HIF ACCELERATORS

The relevant distinguishing features of (magnetic quadrupole-based) HIF accelerators are linear geometry with a high line-charge density, a long injected pulse (multi-μs in a driver), a relatively low energy (~ 1 MeV – a few GeV), an economic mandate to fill as large a fraction of the beamline cross section as possible, and a relatively large fraction of the accelerator length occupied by the quadrupole focusing magnets (can be > 50% at the injector end of the accelerator). Also conditioning of the beam pipe in such accelerators is difficult; hence the emission coefficients for neutral gas upon ion bombardment are large (> 10^3 per incident ion; see *e.g.* Ref. [2]). Finally, there is beam pipe only inside the quadrupole magnets.

For these reasons, the predominant source of stray electrons in the injector end of a HIF driver is expected to be ionization of neutrals released when halo ions strike the close-fitting beam pipe inside the quadrupoles. These electrons are born deeply trapped radially by the beam's electrostatic potential, and constrained to slow **E×B** and magnetic axial drift motions by the quadrupole magnetic fields until they reach a gap. In accelerating gaps they can acquire sufficient energy to escape the beam potential and will tend to do so in the fringe field of the next quadrupole; hence their lifetime is of order of the time to drift the length of a quadrupole, and their density is highest in the quadrupoles.

In the high-energy end of a driver, or in short-pulse ($\lesssim 1$ μs) experiments, where neutrals from walls cannot penetrate far into the beam, ion-produced secondary electrons can dominate. Nonadiabatic effects (collisionless pitch-angle scattering) [3] can cause secondary electrons that pass near the beam center to be magnetically trapped and so live longer than their nominal single-transverse-transit lifetime during beam flattop.

TOWARD A MODEL OF ELECTRON CLOUD DISTRIBUTION

We are assembling a set of computational tools to enable prediction of an electron cloud distribution in the WARP particle-in-cell code. The key ingredients are: wall electron and neutral-particle source modules, which take as input the distribution of halo ions striking walls; a neutral-transport module, to follow neutral particles emitted from surfaces into the beam interior; a bulk electron source module, which provide an electron birth distribution given the volumetric neutral gas and beam densities; and modules that describe at various levels of approximation (full orbit, gyro-averaged, bounce averaged) the subsequent electron dynamics. The ultimate goal is to have a self-consistent description of the

*rcohen@llnl.gov

0-7803-7738-9/03/$17.00 © 2003 IEEE

electron cloud, its dynamics, and its impact back on the beam-ion distribution.

We presently have operational a subset of these tools, specifically a wall electron source module [4] and a full-orbit electron dynamics calculation. A sample result is shown in Fig. 1, applicable to a (hypothetical) transport experiment that would consist of 100 quadrupoles of the type now in the High-Current Experiment (HCX) [5]. In this simulation, a wall ion beam distribution from a WARP simulation is input to the electron source module, which then provides information about the local emission of secondary electrons [4]. The full orbits of the emitted electrons are then followed (until lost or to a maximum of 4000 time steps). Fig. 1 is a contour plot of the resulting electron distribution, projected into a plane transverse to the beam propagation. Almost all of the incident ions impinged on the wall in a location where magnetic field lines are confined close to the pipe wall, as one would expect based on simple beam envelope considerations. Hence almost all of the electrons are concentrated there as well. The contours that extend into the interior are produced by electrons that drift into the magnetic-field-free gap before being lost. This calculation underscores the importance of folding into the secondary-electron production calculation the effects of ion scattering at the surface; such scattering can lead to an enhanced ion flux on the walls closer to the quadrupole principal axes (*i.e.*, the straight field lines that pass through the middle), and was not included in the results shown.

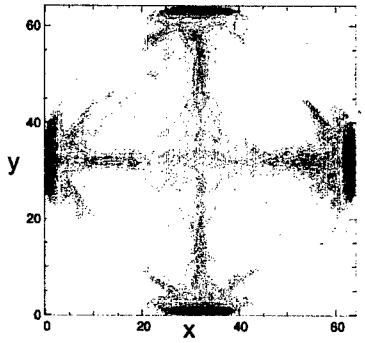

Fig. 1. Contour plot of accumulated electron density (logarithmically spaced contours span a factor of 10^4).

EFFECT OF SPECIFIED ELECTRON DISTRIBUTIONS ON BEAM QUALITY

To begin to assess the effect of electrons on the beam-ion distribution, we have run a series of WARP ion simulations (in a mode which follows a slice of a beam through a set of magnets) with specified negative charge distributions to mock up the electron cloud. Such simulations of course cannot address ion phenomena associated with mutually consistent electron and ion dynamics, such as electron-driven ion instabilities. But it provides an indication of the level of electron contamination required to produce significant levels of halo, emittance growth, etc., via uncompensated reduction of the beam space charge.

We consider three types of electron distributions: spatially uniform, random variations in density, and random displacements of the electron cloud centroid. For all cases we consider the electron density distribution to be uniform within the nominal ion beam envelope inside a quadrupole (but possibly displaced transversely). This is in recognition that the electrons live for of the order of the time to drift through a quadrupole in an accelerator, and that they random-walk with a step size of a quadrupole half-lattice period in a (focused) drift section. For the cases with displacements of beam centroid, the displacements are taken to be along one or the other of the lines 45° from the quadrupole principal axes, a restriction consistent with electron bounce motion. In all cases the ions are followed through 100 lattice periods (200 quadrupoles).

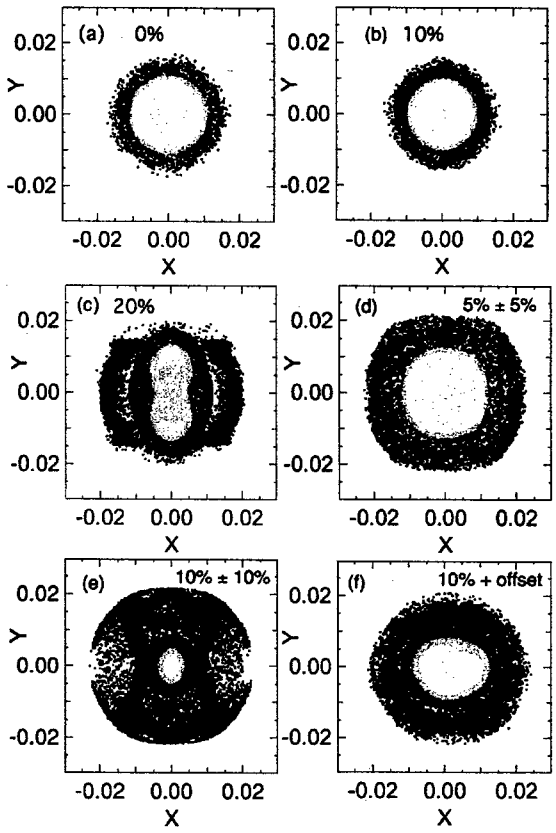

Fig. 2. x-y ion scatter plots for (a) no electrons; (b-c) constant density; (d-e) randomly modulated density; (e-f) random displacements. Percentages are mean electron density relative to peak beam density.

Shown in Fig. 2 are transverse-position ion scatter plots at the end of the run for following distributions of electron density n_e: no electrons; uniform 10% and 20% relative (to ions) density, random quad-to-quad n_e variations with mean densities 5% and 10% of the ion density (with 100% maximum modulation in both cases), and 10%

mean with random radial displacements (uniformly distributed out to a displacement equal to a beam radius).

Not shown are cases with random amplitude variations about a 2% mean and radial displacements of a 20% electron cloud; the former shows only small departures from the case with no electrons; the latter is similar to fig. 2e.. Also not shown is a 100% amplitude-modulated 10% density case, but with the mean subtracted out (that is, "electron" densities vary from –10% to +10%); the results are qualitatively indistinguishable from the case with the mean present. From these figures we conclude that, over the length considered, a uniform electron cloud has little effect through at least 10% relative density, while at 20% relative density significant beam degradation occurs. But the effects are stronger for random offsets, and stronger yet for random amplitude variations; in particular, with the random variations, significant spreading is observed with lower fractional electron densities.

We can also analyze the evolution of various statistical quantities as the beam propagates. For all cases with finite n_e, the beam emittance grows approximately linearly (or a bit faster) until the envelope becomes large enough that significant scrape-off on the pipe (r = 2.3 cm) occurs, and, for the highest-n_e cases, subsequently grows dramatically. During the same time interval, the beam envelope grows roughly linearly for the random amplitude and offset cases, and faster than linear for constant n_e. The beam current is nearly constant during this period (but decreases significantly after). As examples, we show the principal-direction emittances and and envelopes (twice the r.m.s. transverse coordinates) as functions of axial position for the 5% and 10% density-with-amplitude-modulation cases. These results illustrate that the change in statistical quantities varies more rapidly than the electron density; we will characterize this trend more quantitatively in the future.

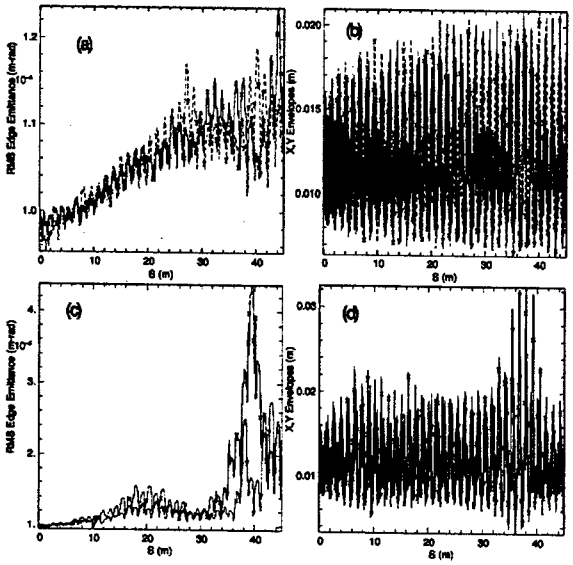

Fig. 3. x-y emittances (a,c) and envelopes (b,d) for randomly modulated density about 5% (a,b) and 10% (c,d) relative electron density

DISCUSSION

We have reported on first steps in a program to develop a self-consistent picture of electron clouds and their effects on ions in HIF accelerators. Our suite of simulation tools will be applicable to a broad range of accelerators, though our focus in this paper is on the unique aspects of the HIF application. The HIF application is distinguished by its geometry (linear), its long pulse length, high current, and high fraction of the radial cross section filled by beam.

The results on the electron clouds produced from secondary electrons associated with ion scrape-off show expected behavior: ions are scraped off predominantly in the interior of the quadrupole where the elliptical distortion of the beam envelope is greatest; most ion loss is then at azimuthal positions where field lines are short and nearly tangent to the walls. The results lack, and underscore the need to include, surface ion scattering, which will result in more electrons being released on field lines that penetrate significantly into the beam.

The simulations of frozen negative charge perturbations on ion beam quality provide a useful preview of effects that may be expected in fully self-consistent electron-ion simulations. In particular they indicate that random fluctuations, particularly of the electron density, are considerably more effective than a constant electron density in destroying the ion beam quality. They also indicate that the emittance and envelope grow gradually over the length of the beam until the beam envelope reaches the vicinity of the beam pipe, and that their growth scales faster than linear with the electron density.

ACKNOWLEDGEMENT

This work was performed for the U.S. Department of Energy under contracts W7405-ENG-48 at U.C. Lawrence Livermore National Laboratory and DE-AC03-76F00098 at U.C. Lawrence Berkeley National Laboratory.

REFERENCES

[1] See *e.g.*, ECLOUD 02 Workshop, CERN Report CERN-2002-001, http:// wwwslap.cern.ch/collective/ ecloud02/proceedings/

[2] A.W. Molvik, R.H. Cohen, A. Friedman, *et al.*, "Initial Experi-mental Studies of Electron Accumulation in a Heavy-Ion Beam", paper TOPC004, this meeting (2003).

[3] See, *e.g.*, R.H. Cohen, G. Rowlands and J. Foote, Phys. Fluids **21**, 14 (1978) and references therein.

[4] P.H. Stoltz, M.A. Furman, J.-L. Vay, A.W. Molvik and R.H. Cohen, Phys. Rev. ST Accel. Beams **6**, 054701 (2003).

[5] P.A. Seidl, D. Baca, F.M. Bieniosek *et al.*, "The High Current Transport Experiment for Heavy Ion Fusion", paper ROAC001, this meeting (2003).

OBSERVATION OF STRONG-STRONG AND OTHER BEAM-BEAM EFFECTS IN RHIC*

W. Fischer†, M. Blaskiewicz, J.M. Brennan, P. Cameron, R. Connolly, C. Montag, S. Peggs, F. Pilat, V. Ptitsyn, S. Tepikian, D. Trbojevic, J. van Zeijts, BNL, Upton, NY 11973, USA

Abstract

RHIC is currently the only hadron collider in which strong-strong beam-beam effects can be seen. For the first time, coherent beam-beam modes were observed in a bunched beam hadron collider. Other beam-beam effects in RHIC were observed in operation and in dedicated experiments with gold ions, deuterons and protons. Observations include measurements of beam-beam induced tune shifts, lifetime and emittance growth measurements with and without beam-beam interaction, and background rates as a function of tunes. During ramps unequal radio frequencies in the two rings cause the crossing points to move longitudinally. Thus bunches experience beam-beam interactions only in intervals and the tunes are modulated. In this article we summarize the most important beam-beam observations made so far.

1 INTRODUCTION

The beam-beam interaction is a major consideration in the operation of RHIC. It can lead to emittance growth and particle loss, and is a source for experimental background. Machine parameters, close to the maximum parameters achieved so far, are presented in Tab. 1. RHIC consists of two superconducting rings, Blue and Yellow, and has produced gold-gold, proton-proton and deuteron-gold collisions [1]. With RHIC's interaction region design (Fig. 1) and with 4 experiments beams experience 4 head-on, and 2 long-range collisions per turn. The long-range interactions are with at least 7 rms beams sizes separation. With 120 or less bunches per ring (the current limit), sets of 3 bunches in one ring and 3 bunches in the other ring are coupled through the beam-beam interaction.

Even small tune shifts due to the beam-beam interaction can be observed directly with a high precision tune measurement system [2]. In Fig. 2 a tune shift measurement is shown that was taken 3 hours into a gold-gold store.

Two beam splitting DX dipoles are the magnets closest to the interaction point (IP). They are each 10 m away from the IP (Fig. 1). Beams collide nominally without a crossing angle. With rf manipulations, the crossing point can be moved longitudinally. If the bunch spacing is large enough (with 60 or less bunches per ring), it is possible to separate the beams longitudinally and switch off all 6 beam-beam interactions. If the crossing point is moved within the DX magnets, an observed tune shift is a sign of crossing angles (Figs. 1 and 2). The sum of all residual crossing angles is typically about 0.5 mrad.

* Work supported by US DOE, contract No DE-AC02-98CH10886.

† Wolfram.Fischer@bnl.gov

Table 1: Machine parameters relevant to beam-beam interactions, for Au-Au and p-p collisions.

parameter	unit	Au-Au	p-p
relativistic γ, injection	...	10.5	25.9
relativistic γ, store	...	107.4	106.6
no of bunches n_b	...	55	55
ions per bunch N_b	10^9	1	100
emittance $\epsilon_{N\,x,y\,95\%}$	μm	10	20
chromaticities (ξ_x, ξ_y)	...	(+2,+2)	
harmonic no. h, store	...	7×360	360
synchrotron tune Q_s	10^{-3}	3.0	0.5
rms bunch length σ_z	m	0.3	0.7
rms momentum spread σ_p/p	10^{-3}	0.15	0.3
envelope function at IP β^*	m	1–10	
beam-beam ξ/IP	...	0.0023	0.0037
crossing angle θ	mrad	0.0	
head-on collisions	...	4	
parasitic collisions	...	2	

Beam-beam phenomena observed in other hadron colliders [3] can also be seen in RHIC. In addition, with bunches of equal intensity the beams are subject to strong-strong effects. To accommodate acceleration of different species, the two RHIC rings have independent rf systems. With different rf frequencies the beam-beam interaction is modulated and can have a visible impact on the beam lifetime.

The beam-beam tune shift depends on the bunch intensity and emittance. Since the bunch intensities can be measured with good precision, the beam-beam tune shift measurement also provides an emittance estimate.

2 LIFETIME AND EMITTANCE GROWTH

The beam-beam interaction is most pronounced for proton-proton collisions with larger β^* values (Tab. 1). In lattices with small β^* uncorrected nonlinear field errors in the triplets have a significant impact on the beam lifetime. Fig. 3 shows the distributions of the bunched beam lifetimes for polarized proton collisions during the 2001 run, with $\beta^* = 3$ m at all IPs. The distributions are relatively

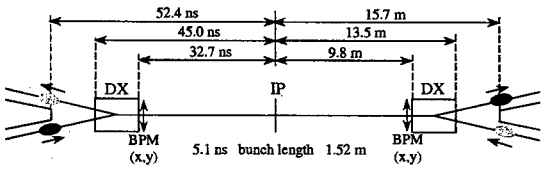

Figure 1: RHIC interaction region. Beams share a common beam pipe between the beam splitting DX dipoles. The bunch spacing shown corresponds to a fill pattern of 120 symmetrically distributed bunches.

0-7803-7738-9/03/$17.00 © 2003 IEEE

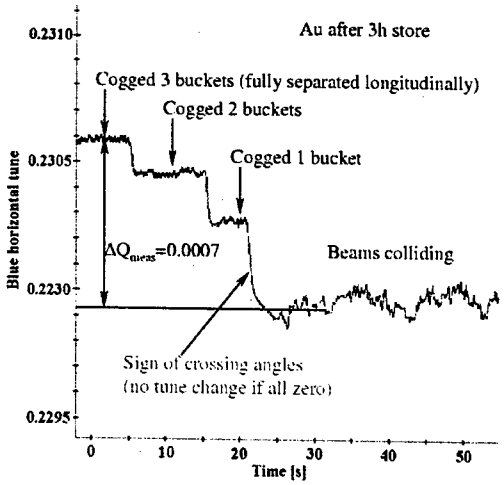

Figure 2: Tune as a function of longitudinal beam crossing position. Cogging by one acceleration bucket moves the crossing point by 5 m.

wide with a mean of about 15 hours. The average bunch intensity for all stores in the plot is $N_b = 0.4 \cdot 10^{11}$. Gold beam lifetimes are generally lower due to intra-beam scattering. A deuteron beam without collisions, in a lattice with $\beta^* = 2 - 10$ m, provides a good comparison to see the impact of the beam-beam interaction. Its lifetime is only marginally influenced by intra-beam scattering or nonlinear triplet errors. 55 bunches with $N_b = 0.5 \cdot 10^{11}$, stored for an hour, showed a lifetime of 830 h.

From the change in the beam intensity and the observed luminosity an estimate for the emittance growth can be obtained, assuming the same emittance in both beams. For proton-proton collisions we find $\Delta\epsilon/\epsilon = 4\%$ in the first store hour (with an rms value of 5%). For comparison, no emittance growth was observed with the ionization profile monitor in the deuteron beam measurement without beam-beam interaction.

3 WORKING POINT AND BACKGROUND

Both transverse RHIC fractional tunes (Q_x, Q_y) are kept between 0.2 and 0.25, and during stores close to the coupling resonance $Q_x = Q_y$. In this area the lowest order

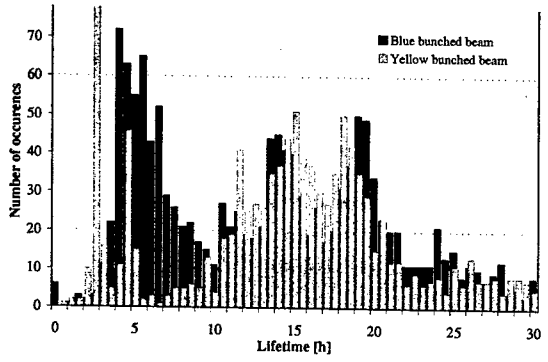

Figure 3: Blue and Yellow bunched beam lifetimes with proton-proton collision during one month of operation.

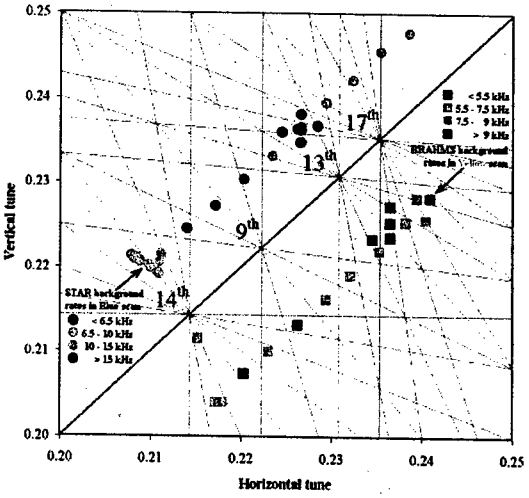

Figure 4: Experimental background rates as a function of fractional tunes. For these measurements deuterons in the Blue ring collide with gold ions in the Yellow ring. The total beam-beam tune spread due to the beam-beam interaction is about $\Delta Q_{tot} = 0.005$ in both measurements.

resonances are of order 9, 13, 14 and 17 (Fig. 4). If the nonlinear dynamics are dominated by the beam-beam interaction and the crossing angles are all zero, no odd-order resonances are driven.

Experimental background rates were observed as a function of the tunes with deuteron-gold collisions (Fig. 4). The tunes were moved parallel to the $Q_x = Q_y$ line, scanning the area considered for operation. With both beams, high background rates were found near 9^{th} order resonances, and low background rates near 13^{th} order resonances. The working points with low background rates are used in operation. High background rates near 9^{th} order resonances are another sign of residual crossing angles (cf. Fig. 2). Increased background rates were also found with a transverse offset [4].

4 STRONG-STRONG OBSERVATIONS

RHIC sees strong-strong beam-beam effects. In addition to the tune (σ-mode) a new transverse oscillation mode (π-mode) occurs. For a single collision per turn the π-mode is at a tune $Y\xi$ below the σ-mode, where $Y \approx 1.2$ for round beams [5]. If the beam-beam interaction is the dominant nonlinear effect, the π-mode can be outside the continuous spectrum and thus be undamped [6].

Coherent beam-beam modes were observed in an experiment with proton beams, with a beam-beam parameter $\xi = 0.003$ and a single collision per turn (Fig. 5). The measured difference between the σ- and π-modes is consistent with a Yokoya factor of $Y \approx 1.2$. The locations of the π-modes were reproduced in a strong-strong simulation [8]. π-modes were also observed in routine operation with a beam-beam parameter $\xi = 0.0015$, four collisions per turn and linear coupling (Fig. 6). The π-modes could be suppressed by small changes in one of the tunes.

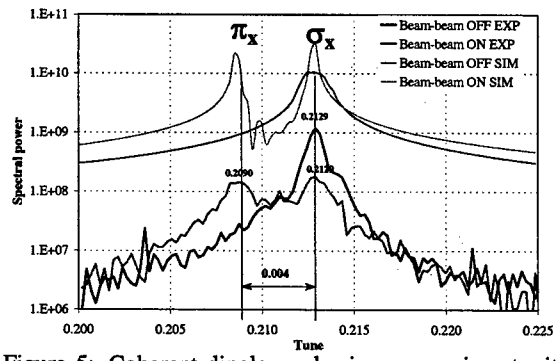

Figure 5: Coherent dipole modes in an experiment with a single proton bunch per beam, and in a corresponding simulation [8]. $\xi = 0.003$, spectra from 4096 turns.

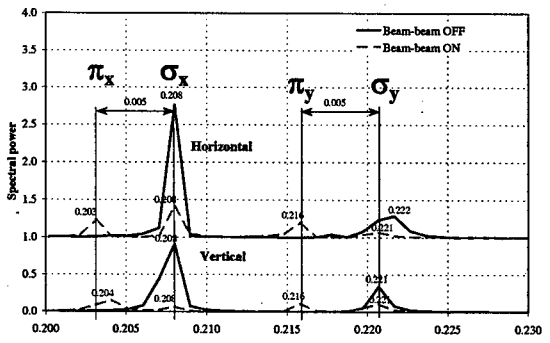

Figure 6: Coherent dipoles modes in operation with 4 collisions per turn. $\xi = 0.0015$/IP, spectra from 1024 turns.

5 UNEQUAL RF FREQUENCIES

When the two RHIC beams have different radio frequencies f_{rf} the beam crossing points move longitudinally with the speed

$$v_{CP} = \frac{c}{2}\frac{\Delta f_{rf}}{f_{rf}}, \qquad (1)$$

where c is the particle speed. Values of $\Delta f_{rf} = 5$ Hz and $v_{CP} = 27$ m/s are typical for gold beams in both rings. When deuteron and gold beams were injected with the same rigidity, $\Delta f_{rf} = 44$ kHz is needed and $v_{CP} = 3$ m/turn. Beams experience the beam-beam interaction only when the crossing point is between the DX magnets (Fig. 1). With slowly moving crossing points (gold-gold case) the beam-beam interaction is modulated, with fast moving crossing points (deuteron-gold case) beams experience pseudo random interactions in time.

Slowly moving crossing points and head-on collisions lead to tune modulation and to unacceptable beam lifetime [9]. The tune modulation depth is determined by the beam-beam parameter, the modulation waveform by the crossing angle, and the modulation frequency by the fill pattern and the difference in the rf frequencies Δf_{rf}. Fig. 7 shows a case typical for gold-gold operation. To avoid this unwanted effect, beams are transversely separated during ramps. For proton beams, which do not pass through transition, the frequencies were locked on the ramp [10].

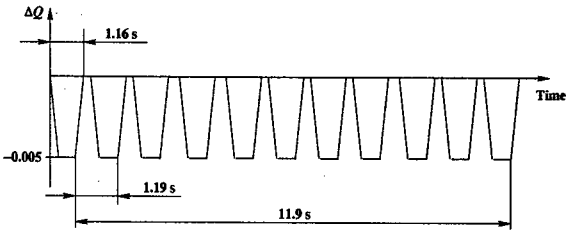

Figure 7: Tune modulation of particles in the center of a bunch due to moving collsion points, for $\Delta f_{rf} = 5$ Hz, no crossing angle, 60 bunches and a total beam-beam tune shift of $\Delta Q_{tot} = -0.005$.

The fast moving crossing points with deuteron and gold beams, injected at the same rigidity, lead to unacceptable beam lifetime even with large beam separation. Both beams experienced pseudo-random dipole kicks that lead to emittance growth. Beams had to be injected at the same relativistic γ, and therefore the same rf frequency, to avoid this effect.

6 SUMMARY

The beam-beam interaction has a significant impact on lifetime and emittance of the RHIC beams. In addition to beam-beam effects observed in other hadron colliders, coherent beam-beam modes were seen for the first time. With independent rf systems for both rings, differences in the rf frequencies can lead to tune modulation and emittance growth.

7 REFERENCES

[1] T. Roser, "RHIC status and plans", these proceedings.

[2] P. Cameron et al., "RHIC third generation PLL tune system", these proceedings.

[3] S. Saritepe, G. Goderre, and S. Peggs, "Observations of the beam-beam interaction in hadron colliders", in "Frontiers of particle beams: intensity limitations", Springer-Verlag, Lecture Notes in Physics (1991).

[4] A. Drees, Z. Xu, H. Huang, "Resutlts from vernier scans at RHIC during runs 2000-2003", these proceedings.

[5] K. Yokoya and H. Koiso, "Tune shift of coherent beam-beam oscillations", Part. Accel. Vol. 27, pp. 181-186 (1990).

[6] Y. Alexahin, "On the Landau Damping and Decoherence of Transverse Dipole Oscillations in Colliding Beams", *Part. Accel.*,**V59**, p. 43; CERN-SL-96-064 (AP) (1996).

[7] W. Fischer, L. Ahrens, M. Bai, M. Blaskiewicz, P. Cameron, R. Michnoff, F. Pilat, V. Ptitsyn, T. Sen, S. Tepikian, D. Trbojevic, M. Vogt, and J. van Zeijts, "Observation of coherent beam-beam modes in RHIC", BNL C-A/AP/75 (2002).

[8] M. Vogt, J.A. Ellison, W. Fischer, and T. Sen, "Simulations of coherent beam-beam modes at RHIC", proceedings of the 2002 European Particle Accelerator Conference, Paris (2002).

[9] W. Fischer, P. Cameron, S. Peggs, and T. Satogata, "Tune modulation from beam-beam interaction and unequal radio frequencies in RHIC", BNL C-A/AP/72 (2002).

[10] M. Brennan et al.,"Operation of the RHIC rf system", these proceedings.

Proceedings of the 2003 Particle Accelerator Conference

PROGRESS REPORT ON THE SMALL ISOCHRONOUS RING PROJECT AT NSCL *

E. Pozdeyev, R. Fontus, D. Lawton, F. Marti, J. Rodriguez,
D. Sanderson, R.C. York, A. Zeller, R. Zink
NSCL, MSU, East Lansing, MI 48824-1341, USA

Abstract

The small Isochronous Ring (SIR), whose main objectives are experimental studies of space charge effects in the isochronous regime and validation of space charge codes, is under development at the National Superconducting Cyclotron Laboratory (NSCL) at Michigan State University (MSU). The ring is a small-scale experiment that simulates the dynamics of intense beams in large-scale accelerators. It will store hydrogen and deuterium ions at energies of approximately 20-30 keV for a few tens of turns. The low beam energy and the small scale of the experiment provide a unique opportunity to perform accurate experiments on space charge dominated beams that are difficult to conduct in large-scale accelerators because of power and timing limitations imposed on beam diagnostics. The paper reports the status of the project and describes the progress in the development of ring subsystems.

INTRODUCTION

In recent years, there has been a increased interest in space charge effects in isochronous cyclotrons. Inspired by successful high-current operation of the Ring Cyclotron at PSI, several authors proposed to use an isochronous cyclotron as a driver for a number of applications [1],[2],[3] including radioactive waste transmutation, energy production with accelerator driven nuclear reactors, generation of neutrons and other secondary particles, etc. Tentative designs of such a machine have a maximum beam energy of 1 GeV and a beam current of 10 mA, yielding a total beam power of 10 MW.

Successful operation of a 10 MW cyclotron would be impossible without a deep understanding of space charge effects in the isochronous regime. There is a tremendous demand for experimental data that can be extrapolated to predict the evolution of beams of higher intensity. This experimental data can be also used to validate codes that are used for simulations of space charge effects in cyclotrons and other types of machines.

Detailed measurement of beam parameters in existing high current machines is difficult because of power and timing requirements on diagnostics. We developed the Small Isochronous Ring (SIR) project ([4],[5],[6]) at Michigan State University to study space charge effects in circular machines working in or close to the isochronous regime. The ring is a small-scale experiment that requires low beam intensities to simulate the dynamics of intense beams in large-scale accelerators. The important issues to be addressed by the ring are the space charge induced vortex motion specific to the isochronous regime, the longitudinal break-up of long bunches, formation of the self-consistent stable charge distribution by short bunches, and formation of weak beam tails and beam halo. The results of the experiments will have applications to high current isochronous cyclotrons and synchrotrons at the transition gamma. The possibility of accurate measurement of beam parameters will also allow SIR to be used as a convenient tool for validation of multi-particle codes used for space charge simulations.

* Work supported by NSF Grant PHY 0110253

DESIGN FEATURES

The SIR lattice consists of four 90° dipole magnets with edge focusing. The edge focusing provides both vertical focusing and isochronism in the ring. Because the ring is isochronous there is no need for an RF system to keep the beam bunched. However, an accelerating gap can later be installed in the ring for experiments with high intensity beams in a non-isochronous regime. In the operational ring, a pulsed electrostatic deflector will be used to send the beam to a fast Faraday Cup after a chosen number of turns. The longitudinal beam profile will be measured by the Faraday Cup with a time resolution of 1 ns that corresponds to a spatial resolution of 1-2 mm. Examination of the beam profile measured after a different number of turns can provide better insight into space charge effects in the isochronous regime.

Figure 1shows a photograph of the project taken in May, 2003. Table 1 lists main SIR parameters. More details on the SIR lattice and beam dynamics in the ring can be found in [7].

Ion source, injection line, and injection system

A multi-cusp ion source that can be biased up to 30 keV is used for production of hydrogen beams. The source generates three mass states: H^+, H_2^+, and H_3^+. A dipole magnet situated 70 cm below the ion source separates the species and sends a selected beam towards the ring. The dipole is identical to the four magnets that form the ring. The injection line also includes an Einzel lens, a beam diagnostics box, electrostatic deflector plates, a quadrupole triplet that matches the injection line with the ring, and a beam chopper.

The beam is injected into the ring by a pulsed electrostatic inflector. Voltage on the inflector plates is regulated

0-7803-7738-9/03/$17.00 © 2003 IEEE

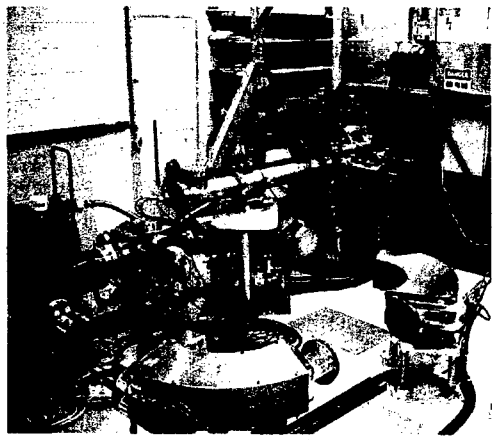

Figure 1: Photograph of the project taken in May, 2003. Four magnets seen in the foreground form the Small Isochronous Ring. Each magnet includes an aluminum C-shaped vacuum chamber with bi-metal flanges attached to the ends. C-shaped tubes of the two magnets closest to the injection point are connected to the vacuum chamber of the injection section. A piece of the injection line connects the injection section and the beam emittance measurement box seen in the background. The mass-state separator magnet with the ion source on top of it can be seen behind the box.

Table 1: Main SIR parameters

Beams	H_2^+, D
Max. Energy	30 keV
β (E=20 keV)	$5 \cdot 10^{-3}$
Bare tunes, ν_x, ν_y	1.15, 1.11
Compaction factor, α_p	1.0
Circumference	6.57 m
Lap time (E=20 keV)	5μs
Number of turns (limited by vacuum)	30
Repetition rate	100 Hz
Peak current	20 μA
Pulse Length (E=20 keV)	50 ns - 4 μs
Emittance	50 $\pi \cdot$ mm $\cdot$ mrad
Inj./Extr. energy spread	0.1% - 10%
SC tune shift	0.05-0.2

by two fast semiconductor switches manufactured by Directed Energy, Inc. The switches are designed to drive capacitive loads and capable of generating 3.5 kV, rectangular pulses with a rise/decay time of 25 ns.

The ion source, injection line, and injection section of the ring have been assembled and beam-tested. Paper [8] provides more details on a design and commissioning of the ions source, injection line, and injection system.

Dipole magnets, quadrupole correctors, and steering

Five identical dipole magnets are used for the project. Four magnets form the ring, and one is used as a mass-state separator in the injection line. Table 2 lists main parameters of the magnets.

Table 2: Magnet parameters

Gap	71.4 mm
Bending angle	90°
Bending radius	0.45 m
Magnetic field	800 Gauss
Pole face angle	26°
Magnet weight	210 kg
Power consumption	700 (x5=3500) W

All the dipole magnets have been assembled, installed on supports, and aligned. Because the magnets are all identical, we have mapped only one of the magnets in detail. To measure the field we used an NMR probe inside of the magnet and a Hall probe close to the edges. A normalized difference of the measured field from the field predicted by TOSCA did not exceed $3 \cdot 10^{-4}$ inside the magnet and 2% at the edges. The measured effective length of the magnet was larger than predicted by 2.54 mm or approximately 0.3%. Using the measured field we calculated the betatron tunes in SIR. The radial tune ν_x had the same value in the measured field and in the field generated by TOSCA. The vertical tune ν_y calculated in the measured field was lower than ν_y calculated in the TOSCA field by 0.01.

Each dipole magnet includes a gradient corrector coil and a dipole corrector coil. The final setup of the ring will also include four electrostatic quadrupoles and four vertical electrostatic deflectors.

Vacuum system

The vacuum chamber in all the dipoles is made of aluminum to avoid complications arising from variation of the μ. The injection line and parts of vacuum chamber between magnets are made of 304 stainless steel. Aluminum and stainless steel parts are joined by bi-metal flanges manufactured by Atlas Technologies.

Two main sources of residual gas in the ring are outgasing from the walls of the vacuum chamber and the gas flux from the ion source. We plan to use three or four 500 l/s turbo-pumps in the final setup with one or two pumps installed in the injection line and two pumps in the ring. Vacuum calculations show that pressure in the ring will be lower than 10^{-7} Torr if the ion source pressure is 1.0 mTorr. The expected beam life-time at this pressure, which is primarily determined by electron capture, is approximately 100 turns.

Diagnostics

Diagnostics in the injection line consist of the beam emittance measurement box and a Faraday cup installed at the end of the line. Currently we use a "slow", unmatched version of the Faraday cup, which will be later substituted with a "fast" coaxial Faraday cup.

A retractable phosphor screen is situated in the injection section of the ring. It can be moved in one of the three positions: in the way of the beam coming from the injection line, in the median plane to detect the beam after a single turn, and below the median plane completely out of the way. The rest of diagnostics in SIR will include two vertical and two horizontal scanning wire monitors, two capacitive BPMs, and a movable fast Faraday cup. This Faraday cup will be used for measurement of the 2D longitudinal-radial profiles of the beam with an accuracy of 1-2 mm.

INJECTION LINE TEST

The injection line and the injection section of the ring along with pieces of the vacuum chamber in two magnets closest to the injection point were assembled and pumped down to a vacuum of $5 \cdot 10^{-8}$ Torr after several days. The first attempt to run the beam through the injection line was successful. A 15 keV H_2^+ beam went through the injection line, was deflected into the median plane of the ring, and went through the first quarter of the ring. A Faraday cup situated after the first ring dipole registered a beam current of approximately 60 μA. The measured emittance of the beam was $15\ \pi \cdot mm \cdot mrad$.

The beam chopper was tested in the regime of long bunches. It cut the DC beam into 5-μsec-long pulses that were registered by the "slow", unmatched Faraday cup at the end of the injection line. A test of the capability of the chopper to generate short (50-ns-long) bunches requires a Fast Faraday cup with better time resolution.

FUTURE PLANS

Our future plans include:

- Construction
  Design and assembly of remaining pieces of the vacuum chamber of the ring. Development, test, and installation of diagnostics in the ring, including a fast Faraday cup. Development of a control system and control software for the project.

- Commissioning
  Injection in the ring, stable multi-turn operation, and measurement of beam parameters for low beam intensity, 1-5 μA. Use of deuterium instead of hydrogen if the beam life-time is too short.

- Experiments, Phase I
  Experiments on the longitudinal beam dynamics in the isochronous regime with tune shifts of 0.03-0.05. Comparison of experimental results to multi-particle simulations.

- Experiments, Phase II
  Experiments with high intensity beam in a non-isochronous regime. An expected tune shift at Phase II is 0.2 and larger. Operation of the ring with such a beam current may require installation of a simple RF system.

ACKNOWLEDGMENT

We would like to thanks J. Bierwagen for preparing drawings of SIR hardware. The authors would like also to express their gratitude to D. Pedtke for developing the ion source safety system. His expertise in electronics and helpful suggestions were crucial for a fast progress of the project. We are grateful to S. Hitchcock, D. Devereaux, and A. Mond for their assistance with assembling parts of the project.

REFERENCES

[1] Th. Stammbach et al., "The 0.9 MW Proton Beam at PSI and Studies on a 10 MW Cyclotron", Proc. 2nd Int. Conf. on Accelerator-Driven Transmutation Technologies, Kalmar 1996, p.1013

[2] Y. Alenitsky et al., "The High Current Cyclotron Complex for an Electro-nuclear Way of Production of Energy", Proc. 16th Int. Conf. on Cyclotrons and Their Applications, East Lansing 2001, p.434

[3] G.Kim, D. May, P. McIntyre, A. Sattarov, "A Superconducting Isochronous Cyclotron Stack as a Driver for a Thorium-Cycle Power Reactor", Proc. 16th Int. Conf. on Cyclotrons and Their Applications, East Lansing 2001, p.437

[4] E. Pozdeyev, "Small Isochronous Ring for Experimental Study of the Longitudinal Space Charge Effect in Isochronous Cyclotrons", Proc. of PAC 2001 (Chicago), p. 3549-3551.

[5] E. Pozdeyev, F. Marti, J. Rodriguez, R. York, "Small Isochronous Ring Project at NSCL", Proc. of EPAC 2002 (Paris), p. 1395-1397.

[6] J. Rodriguez, E. Pozdeyev, F. Marti, "Injection Line of the Small Isochronous Ring", Proc. of EPAC 2002 (Paris), p. 1401-1403.

[7] E. Pozdeyev, J. Rodriguez, "Computer Simulations of the Beam Dynamics in the Small Isochronous Ring", Proc. of EPAC 2002 (Paris), p. 1398-1400.

[8] J. Rodriguez, F. Marti, E. Pozdeyev, "Initial Experimental Results of the Small Isochronous Ring", these proceedings

THE LHC SUPERCONDUCTING MAGNETS

L. Rossi, Accelerator Technology Division, CERN, Geneva, Switzerland

Abstract

The Large Hadron Collider (LHC) is under construction at CERN. Most of its 27 km underground tunnel will be filled with superconducting magnets, mainly 15 m long dipoles and 3 m long quadrupoles. The 1232 main dipole and 392 main quadrupole magnets, are complemented by a number of insertion quadrupole magnets: including 86 MQM (matching), 26 MQY (wide aperture) and 32 low-beta quadrupoles (the latter built by KEK and Fermilab). The about 6000 superconducting corrector magnets, many of them individually powered, are also very critical for the functioning of the accelerator. Using copper stabilized NbTi Rutherford cables or single strands, these superconducting magnets will operate in superfluid helium at 1.9 K. The paper reviews the main characteristics of these magnets and addresses the critical points of the design with respect to their use in such a complicated accelerator like LHC. Then the status of the production of the superconducting cable and of the magnets is given, with particular emphasis given to the QA/QC procedures taken to ensure the industrial production according to the tight requirements, and the results on the first 30 main dipoles is presented. Finally, the plan put in place to meet the LHC schedule is discussed.

INTRODUCTION

The Large Hadron Collider [1] is designed to accelerate two counter rotating proton beams from injection energy of 0.45 TeV up to a flat top energy of 7 TeV, at which collisions take place for about 10 hours. The main dipole magnets (Main Bends, MBs), fill more than 2/3 of the ring, a 27 km ong underground tunnel. The remaining tunnel length is almost all dedicated to beam focusing (Main Quadrupole, MQ) to other beam optics functions (chromaticity control, dispersion suppression, matching sections, etc.) and to the Interaction Regions. This means that the 27 km tunnel, made available by the decommissioning of LEP in 2001, will be filled with about 19 km of cryodipoles and 2.5 km of short straight sections (SSS) that accommodate main sextupoles and corrector magnets in the same cold mass of the MQ. The dipoles are optical elements of the machine and they must be set to the same field level, or better still, to the same bending strength, BL, to within a few 10^{-4}. The poor performance of one dipole cannot be compensated by better performance of another one otherwise the weakest dipole will eventually determine the energy performance of the whole machine.

In total 1232 main dipoles (1104 in the lattice and 128 in the Dispersion Suppression -DS- sections) and 392 main quadrupoles (360 in the lattice and 32 in the DS) will be installed. The MB cross section is shown in Fig. 1.

The main magnets are complemented by 86 superconducting quadrupoles used in the matching/DS sections (MQM) and by 26 wide aperture quadrupoles (MQY) that play a fundamental role in the matching sections.

The interaction regions (IR) are equipped with 32 single bore, large aperture (70 mm), 5 m-long superconducting quadrupoles and with 20 special dipoles for beam separation. The low beta quadrupoles and the beam separation dipoles are being built by USA National laboratories and by KEK-J, and production is proceeding very satisfactorily. However they will not be discussed in this paper.

For the LHC more than 6000 superconducting corrector magnets are foreseen. All are powered in series by octant or in smaller series, with exception of the orbit correctors, to have the maximum flexibility. They also are a considerable challenge in the Project.

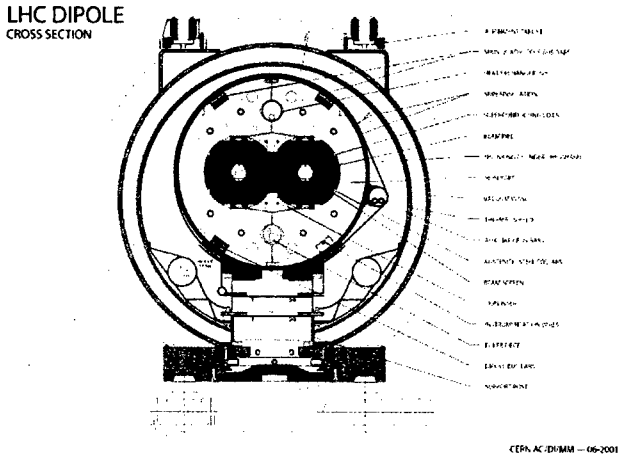

Fig. 1. Cross section of the LHC Main Dipole in its cryostat.

MAGNET DESIGN

Main Dipoles

The design of the LHC MBs has gone through about 10 years of evolution with three generations of design [2] [3]. All main magnets work in superfluid helium (a fundamental choice done as early as 1989 to allow to go beyond 8 T with a sufficient stability margin). The magnets are designed for a nominal operation current of about 11600 A for a central field of 8.33 T, with possibility to reach 9 T (ultimate field). The basic design characteristics of the present third and final generation are:

0-7803-7738-9/03/$17.00 © 2003 IEEE

1) Coil Layout

Coils are wound from NbTi Rutherford cables whose characteristics can be found in [4]. The layout is based on six-conductor blocks arranged in two nested layers. The six-block arrangement is more stable and leaves more room for minor optimizations.

2) Collars

They are of the twin type, i.e. unique collar for the two apertures. They are obtained by fine blanking according to a shape that results in the desired coil cavity geometry under stress and cold conditions. For this reason the collars are slightly elliptical (ε = 0.1 mm) when punched. The choice of stainless steel, introduced relatively late in the Project after a long period when an aluminum alloy was preferred, is not strictly necessary to reach the design field but allows a more comfortable margin in the construction and assembly tolerances. This partly compensates for the higher cost of austenitic steel with respect to aluminum alloy. Also, thanks to its higher rigidity, the use of austenitic steel helps to limit conductor movements, an important issue in magnets where field accuracy is required at 1 cm from the conductor. The severe tolerance on collars (±25 micron) are respected in production with a reasonable margin, although we have to check carefully that jumps due to tool sharpering or replacement are controlled.

3) Coils Characteristics

The coils are composed of poles of two layers each. The need to avoid sorting that would certainly slow the production, or make it more complicated, requires that each pole, and even each layer, be identical within 100 μm. Indeed a 100 μm variation in the azimuthal coil size corresponds to a variation of about 0.1% of the main field, 3.5 and –0.4 units (10^{-4}) of the main harmonics, sextupole and decapole respectively, and to about 12 MPa in azimuthal coil pre-stress. A coil with nominal size and compressive modulus (some 12 MPa at room temperature and 17 MPa at cold) will be submitted to 75 MPa pre-stress. Since the allowed range for coil pre-stress is 60-90 MPa, if the coils differ more than 125 μm from the target they will require a shim thickness different from the nominal size, to the detriment of the field quality. This reason together with necessity of top-bottom and left-right symmetry means that the coils must all be similar, within the quoted figures. The strategy is to avoid single coil shim adaptation for reasons of time and cost and to control components dimensions and process characteristics vs. time.

4) Cold Mass Assembly

The collared coil assembly is surrounded by the magnetic circuit contained by a shrinking cylinder, see Fig. 1, formed by welding two half-shells made out of 316 LN stainless steel. This provides the necessary rigidity for the whole magnet. The forces are transmitted by interference among very rigid pieces (collars and yoke). Therefore not only the precision of the single pieces is high but the assembly must also ensure this precision over the 15 m magnet length.

It is of some interest to note that near the magnet ends, for 370 mm, the laminations are composed of an outer shell of low carbon steel, like the magnet straight part, and with an inner shell, 20 mm thick, of special non magnetic stainless steel whose mechanical properties, namely the thermal contraction, have been selected in order to match exactly that of the iron. These nested laminations, are designed to lower the peak field on the coil end (always a quench risk region) while preserving the maximum magnetic length and improving the quadrupole due to aperture coupling at the end.

The magnet must be curved, with a sagitta of about 9 mm, corresponding to a radius of curvature of 2812.36 m. This curvature has a tolerance of ± 1 mm, with the exception of the extremities of the magnet where the tolerance is tighter: ±0.3 (systematic) and 0.5 mm r.m.s. in order to keep the corrector magnets centered with respect to the beam tube, to avoid harmonic feed down (detrimental to beam optics.)

Main Quadrupoles

In order to save money and complexity over the whole project, the coil is not graded, and the same cable, identical to the one used for the outer layer of the MBs, is employed to wind both layers of the quadrupoles. This means that the magnetic design is not fully optimized but allows the use of real double pancake techniques, avoiding the splice between layers in the high field region. Nominal gradient is 223 T/m, and 241 T/m at ultimate machine performance (9 T dipole field) when the peak field in the coils reaches 7.5 T. It is worth noticing that although the peak field is somehow reduced in the MQs with respect to the MBs, the field quality is not. Due to a decision to eliminate the dodecapole (first allowed harmonic in quadrupoles) corrector magnets in the machine, the field quality of all quadrupoles must be excellent.

Each coil aperture is independently collared in a four-fold symmetric vertical press, with strong non-magnetic austenitic steel single collars, 27 mm thick. The two apertures are then assembled in a laminated yoke with a central iron arm that decouples the two apertures. Each coil-collar assembly is not supported by the yoke (self supporting collars), that is coupled to the coils only by 3.5 m long centering and antitorsion keys. As it is well known for quadrupoles the alignment is a critical issue. It is obtained by fitting with dowels the yoke into a very precise (better than 100 μm straightness) 5.3 m long inertia tube. The same inertia tube is used also to ensure the proper alignment for other magnets, like sextupoles, octupoles and corrector magnets, forming the so called straight sections. Keeping the tolerances on this assembly will be one of the major challenges in the MQ construction.

A detailed review of the MQ design together with the results on the prototyping phase is reported in, [6]. The MQ is a collaboration among CERN and CEA-Saclay who took care of the design, prototyping and is involved in the follow-up.

Insertion Magnets

For dispersion suppression a certain number of standard MQ, will be inserted in special cold masses, and special quadrupoles, MQM, are employed. MQM has been specially designed to provide almost the same gradient, in the same aperture as the one of the MQ, with 5 kA only. Since each of them, and each aperture, is independently powered, high current would have implied too large power dissipation at 1.9 K. In addition they come in a variety of lengths, the longest being L_m =4.8 m. They have self-supporting collars and the yoke is enclosed by a shrinking cylinder to provide rigidity and a rather low pre-stress.

The MQY, whose design stems out from the first LHC design for an IR quadrupoles, has the difficult task to accommodate larger bore quadrupole (70 mm) while keeping the inter-beam distance of 194.3 mm. The necessity of independent powering and single cryogenic feed for each of them has been satisfied with a design that requires special grading of the cables and maximization of the overall current density (fully keystoned cable). Because of the advanced design they can deliver a nominal G = 160 T/m at about 3.6 kA at 4.5 K, such making possible individual cooling circuit.

A cross section of the MQY [7]. cold mass is shown in Fig.2.

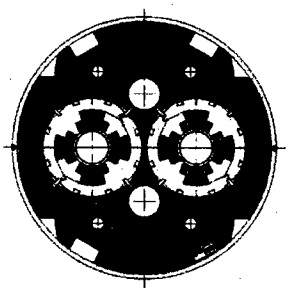

Fig. 2. Cross section of a MQY, with its very thin iron among the apertures

Correctors Magnets

Here the variety is such that a detailed description is left to a specialized paper.[8]. As spool pieces on all the main dipoles we have sextupole correctors (one per channel, electrically independent to allow different current) and octupole and decapole correctors on half of the dipoles, only. Most of the approximately 1000 orbit correctors, are put in the same assembly of the main sextupoles and mounted in the inertia tube of the MQ. The same accommodation has been found for the main octupoles and the tuning quadrupoles, all placed in the SSS together with MQ.

For most of these magnets the special counter winding technique has been applied, with formation of small cable in situ by joining a number of standard strands with wet winding technique, to have a relatively high current at low cost.

Among them, particularly challenging is the long tuning quadrupole, MQTL, that have to operate at 130 T/m, has fully impregnated coils, hot shrink fitted with a cyilinder, and whose coil length is almost 1.5 m.

PROCUREMENTS POLICY AND PRODUCTION STATUS

Main Dipoles and Main Quadrupoles

Three companies, involved since the beginning in the R&D, the French consortium Alstom MSA – Jeumont Industries, Ansaldo Superconduttori (Italy) and Babcok Noell Nuclear (Germany), were each assigned a pre-series contract for dipole cold masses (3×30 dipoles) in autumn 1999 and the final contract (series) for further 3×386 dipoles in spring 2002, for a total contract value exceeding M€ 300.

For the MQs the strategy was different. Given the size, full-length prototyping was developed in the laboratory (CEA-CERN). Then the tender among all European magnet manufacturers for the total quantity of 400 MQ was assigned in 1999 to Accel (Germany).

CERN Supplied Components

As part of a cost saving strategy and in order to keep under control the characteristics of the magnet components having some impact on the final quality and on the schedule, all main components are supplied by CERN to the magnet manufacturers.

This strategy implies that CERN becomes a supplier of its suppliers with an intricate share of responsibility that makes CERN fully responsible for the magnet performance, except in case of negligence or clear fault of the dipole manufacturer. This requires a complex strategy of component procurement and storage. Logistics is certainly one major challenge in this magnet production, together with handling of traceability and non-conformity, all done through an "ad hoc" system called MTF and suitable database.

CERN Supplied Large Tooling

Most of the large tooling, such as the machine for coil measuring and the large presses used for coil collaring and for cold mass welding were specified and procured directly by CERN. In particular the construction and the commissioning of the welding presses were very complicated, These presses have to assure the delivery of a compressive force, to align laminations and to stress the skin, while maintaining the alignment of the 15 m long cold mass according to a shape that, once the shells are welded, should ensure the right curvature. They are equipped with automatic synchronous (both sides) welding equipment, capable of carrying out the welds of the 10 mm thick 316 LN half-shells in a single working shift. The weld must guarantee good quality and a regular pre-stress of about 150 ± 30 MPa and, of course, be leak tight to about 10^{-11}mbar l s^{-1}. The root pass is welded by STT, a rather new process with speed of 70 mm/minute, that has the main advantage of being able to tolerate gap variation of almost ± 1 mm. The equipment for SST and MIG is the same, with an obvious advantage (MIG is a necessary choice for the filling passes.

Finally, as part of the large tooling it is worth mentioning among others the Laser Tracker that is fundamental to measure the curvature, planarity, twist, and inter-aperture distance of the magnets, all along the 15 m long narrow Cold Bore Tube (CBT), with the requested 0.1 mm precision. It is also essential to measure the position (and actually to facilitate in the positioning during their assembly), of the all "3-D" components, i.e. at the magnet extremities. As previously said there are elements that need to be positioned and welded at ± 0.3 mm distance from the ideal line that is defined by the center of the CBT. Although difficult to operate in an industrial environment that looks for quality but also time schedule, the Laser Tracker is proving to be essential, without which the required geometry and alignment of these magnets cannot be guaranteed.

For MB the companies have almost all tooling installed and qualified and they have 60-70% of the personnel required for full rate production, about 35 MB/months in total, to be reached in June 2004. One year of delay has been accumulated in the pre-series phase, and integrated in the main contract signature. To date all companies have almost finished the pre-series magnets and are already winding and collaring for the series. The main problem we are currently working on is the quality of the welding, since repair can be accepted for only a very limited number of magnets, in order to avoid cost and delays. Furthermore the non perfect operation of the welding is probably one of the sources of the too large variability of the magnet curvature: an attempt to cure it with a re-shaping did not give good results and the baseline to obtain good shape directly from the press is pursued. The contract calls for a termination in summer 2006 with very little margin over the installation schedule and today we have 2-3 months of delay.

For the MQ all the tooling is ready and personnel has been hired and trained. Some six months delays has been built up due to longer time to prepare the new workshop, to revamp the CEA tooling, to install and qualify properly the new tooling and to start production of some critical element (like end spacers). Then a major delay in the delivery of a CERN component, namely the MSCB magnet that is needed to complete all MQ cold masses, has impeded the ramp of the production as foreseen, although the company continued to advance in the bare MQ (i.e. up to yoking) productions. However the problem has now been solved, and production is foreseen to be completed well in 2005.

Insertion Magnets

For these magnets the design and then the tendering was finished somehow later than the main magnets. In 2000-2001 all contract were placed (Tesla engineering, GB, for MQM and Accel, D, for MQY) with a strategy that is more oriented to a turn-key product of the bare magnet (i.e. until yoke) with cables, insulation, shells and few other components supplied by CERN. Then the bare magnets will be completed as cold masses at CERN in the factory that was set up for dipole prototyping.

For the MQM the first two magnet prototypes have been delivered by Industry (and very successfully tested). The manufacturer has finished installing all necessary tooling for series production and to hire and train almost all the staff. As soon as the cable production becomes continuous, the company can increase its production to the rate of 4 MQM/month, that will allow the work to finish in 2005.

The situation of the MQY is different. Here the limited number and the fact that they are built in the same factory as the MQ, allow some synergy and movement of personnel among the projects according to needs and schedule requirements. The first prototype is expected at CERN by Summer 2003 and the whole production to be finished by Spring 2006.

Corrector Magnets

Given the large number of contracts, the production status varies very much. Some contracts, such as MCS, the sextupole spool pieces for the dipoles run very well, while others like the decapole-dodecapole spool piece was consistently delayed, although the need of this magnet on 50% of the dipoles only has reduced the impact on dipole production.

The critical one for the main magnets is the MSCB that is slowing down the production of MQ, as previously noted, but other correctors magnets, such as the tuning quadrupoles MQT are near to enter into the critical path.

However now all companies are in production and strategies to catch up (or to avoid further) delays are under discussion.

Production Steering: Magnetic Field

Magnetic field measurements have been introduced in all companies. Measurements are done both after coil collaring and after Cold Mass assembly, at room temperature and therefore reduced current, or as single modules in case of correctors. For corrector magnets, measurements are required at 4.2 K in the companies.

Through these measurements done on collared coils, and thanks to the fact that there is a very good correlation between warm and cold measurements, we can keep under controls the harmonics. Today for the dipoles, the delay between winding and collared measurements is less than 2 months, while the elapsed time from winding to cold test results at CERN is typically 8-10 months. Just recently two further corrective actions for MBs have been decided: i) A change in magnetic length, making it shorter in one company and longer in the other two, to compensate a difference in field strength ii) An increase of the mid-plane gap of about 100 microns, to lower the main harmonics (b_3, b_5 and b_7) by suitable amounts.

It is worth emphasising that magnetic measurements are a mean to intercept minor or serious assembly errors, as already happened two times [9].

PRE-SERIES DIPOLE RESULTS AND DELIVERY

Quench results are very encouraging. The dipole magnets, that were plagued for long time in the R&D phase by long training, are now well qualified for nominal operation and very few have difficulties reaching the ultimate field (9 T). Especially the memory (second thermal cycle) is excellent as shown by the graph of Fig. 3. The weak point of the cold test is the electrical robustness: so far we had approximately 10% of the pre-series magnets that had electrical non-conformities of various types, although only two fatal. Still this is certainly a point that calls for improvement of the cleaning and better QA in the manufacturers premises, since the test procedure foreseen by the QA plan is already as severe as possible.

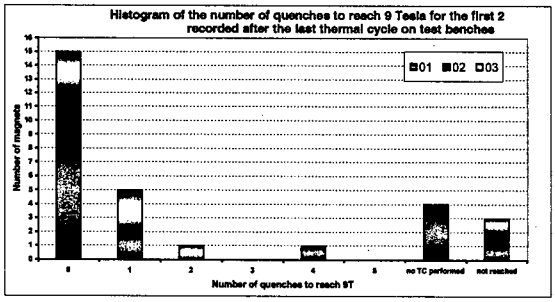

Fig. 3 Number of quench for each of the 29 dipoles tested so far, after first thermal cycles to reach ultimate field of 9 T.

As for delivery, the dipoles provide the 'clock' to the entire project, so their schedule is very critical. The end of all three contracts is foreseen today by June 2006. The actual situation is depicted in Fig. 4, where both the pre-series and series contracts (the sum of the three manufacturers), is compared with actual delivery. To day we are missing some 60 cold masses to be perfectly on time, i.e. approximately 2 months when the foreseen maximum rate of 30-35 CM/months will be attained, in second half of 2004. This is the critical point, indeed: if the extrapolation from the 8 CM/month we have got in March-April (a rate that suffers by the necessary intervention on the welding press) to a number which is four times is correct. All indications coming from the companies are positive, in all single area the stated rate has been actually obtained, although not contemporarily, except in the area of welding repair, that have to be near zero. In Fig. 4 the rate of collared coils (60% of the production time and more delicate than CM assembly, in principle), that shows good progress. Even better is pole production that recently has attained the very comfortable rate of 15 equivalent dipoles. Finally very encouraging is the production of cable for main dipoles and quadrupoles, including cabling, whose initial delays have been so much spoken about. Actually today we have produced already the largest quantity of Sc cable for a single project and have delivered one octant to dipole manufacturers. Thanks to the effort of the CERN team and the commitments of the companies, we have today at CERN more than one octant as strategic stock.

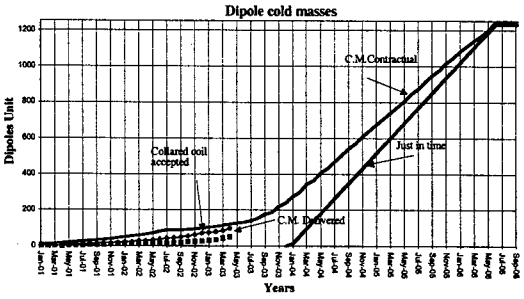

Fig. 4 Delivery of main dipoles (CM, squares), of Collared coils (CC, diamond), contract profiles and just-on-time curves

ACKNOWLEDGEMENT

The author is indebted to many colleagues of the CERN AT division and in particular to: A. Ijspeert, P. Lienard, R. Ostoijc, P. Pugnat, D. Richter.

REFERENCES

[1] R. Schmidt, "Status of the LHC", Presented at EPAC02.

[2] L. Rossi, "State-of-the-Art Accelerator Magnets", *IEEE Trans. On Applied Superconduct.*, Vol. 12, No. 1 March 2002, p .219-227.

[3] L. Rossi, "The LHC Main Dipoles and Quadrupoles towards series production", *IEEE Trans. On Applied Superconductivity* Applied Superconductivity Conference (ASC) 2002, Houston, USA.

[4] J. D. Adam et al., " Status of the LHC Superconducting Cable Mass Production", *IEEE Trans, on Applied Superconductivity,* Vol. 12, No. 1, March 2002, p. 1056-1062.

[5] P. Fessia, D. Perini, S. Russenschuck, C. Voellinger, R. Vuillermet and C. Wyss, "Selection of the Cross-Section Design for the LHC Main Dipole", *IEEE Trans. On Applied Superconductivity*, Vol.10, No.1, March 2000, p. 65-68

[6] J. Billan, V. Remondino, A. Siemko, N. Smirnov, T. Tortschanoff, M. Peyrot, J.M. Rifflet, F. Simon, "Performance of Prototypes and Start up of Series Fabrication of the LHC Arc Quadrupoles", Proc. PAC 2001 (Particle Accelerator Conference), Chicago, June 2001

[7] R. Ostojic, "The LHC Insertion Magnets", *IEEE Trans. On Applied Superconductivity*, Vol. 12, No. 1 March 2002,p. 196-201

[8] A. Ijspeert et al."Principles developed for the construction of the high performance, low-cost superconducting LHC corrector magnets", *IEEE Trans, on Applied Superconductivity,* Vol. 12, No. 1, March 2002, p.90-93

[9] E. Todesco et al. "Controlling field quality in magnet production" Proceedings of XII Chamonix Workshop, CERN-AB-2003-008 ADM (2003) 104-10.

HIGH-FIELD ACCELERATOR MAGNETS BEYOND LHC

A. Devred,* CEA/Saclay, DSM/DAPNIA/SACM, 91191 Gif-sur-Yvette, France
& CERN, Accelerator Technology Division, CH-1211 Geneva, 23, Switzerland

Abstract

The LHC magnet R&D Program has shown that the limit of NbTi technology at 1.8 K was in the range 10 to 10.5 T. Hence, to go beyond the 10-T threshold, it is necessary to change of superconducting material. Given the state of the art in HTS, the only serious candidate is Nb_3Sn. A series of dipole magnet models built at Twente University and LBNL and a vigorous program underway at FNAL have demonstrated the feasibility of Nb_3Sn magnet technology. The next step is to bring this technology to maturity, which requires further conductor and conductor insulation development and a simplification of manufacturing processes. After outlining a roadmap to address outstanding issues, we evoke the US proposal for a second generation of LHC Insertion Region (IR) magnets and the Next European Dipole (NED) initiative promoted by the European Steering Group on Accelerator R&D (ESGARD).

WHY DO WE NEED HIGHER-FIELD ACCELERATOR MAGNETS?

The Push Towards Higher Fields

For a given tunnel size, the energy of a circular machine is limited by the strength of bending magnets. Moreover, for both linear and circular colliders, the luminosity is determined (mainly) by the optics of Interaction Regions (IR's), which is itself limited by the strength and quality of IR magnets. Over the years, there has been a constant push from the High-Energy Physics (HEP) community to keep developing higher-field and higher-field gradient accelerator magnets.

Brief History

The push towards higher fields led naturally to the use of superconductors. Worthy of mention is the pioneer work carried out by W.B. Sampson at Brookhaven National Laboratory (BNL) in the mid 1960's, illustrated in Figure 1 by a 76-mm-aperture, 85-T/m quadrupole magnet model wound from Nb_3Sn ribbons and cold tested in January 1966 [1]. (Note that the aperture and field gradient of this model are similar to those of the HERA quadrupole magnets developed 15 years later [2].)

The first successful use of superconducting magnets in a machine took place at the Tevatron, at Fermi National Accelerator Laboratory (FNAL) [3]. The Tevatron, which relies on 774 6.1-m-long, 76.2-mm-aperture, 4-T arc dipole magnets, was commissioned in 1983 and has been running very reliably since then. It was instrumental in demonstrating the feasibility and reliability of superconducting magnet systems and has paved the way to their commercial applications (such as Magnetic Resonance Imaging or MRI systems).

* arnaud.devred@cea.fr

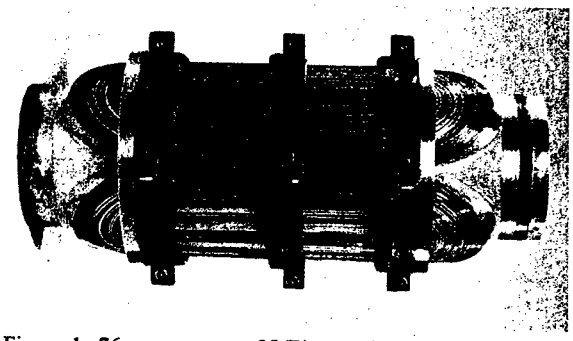

Figure 1: 76-mm-aperture, 85-T/m quadrupole model wound from Nb_3Sn ribbons by W.B. Sampson at BNL in 1965 [1].

Since the time of the Tevatron, significant progress has been made in the design and production of superconductors and accelerator magnets, leading to a gain of a factor ~2 in dipole field. The ongoing superconducting magnet productions for the Large Hadron Collider (LHC) at CERN, which, among others, call for 1232 14.2-m-long, 56-mm-twin-aperture, 8.33-T arc dipole magnets, is the culmination of 20 years of superconducting accelerator magnet development around the world [4]. The idea of building the LHC first emerged in 1982 [5], and the machine is expected to be turned on in the Spring of 2007, a mere 25 years later.

What's next?

In addition to arc dipole and quadrupole magnets, LHC also requires a number of superconducting IR magnets, including triplets of final-focusing quadrupole magnets, which are presently being built at FNAL and KEK [6]. Due to the high radiation doses to which they will be subjected, the life expectancy of these magnets is estimated around 7 years. Hence, it is likely that they will have to be replaced in 2015, thereby offering the opportunity of upgrading LHC IR optics to improve luminosity.

Several scenarios of LHC IR upgrades are already being considered [7], [8]. The most conservative ones keep the present optics layout but rely on stronger final-focusing quadrupole magnets. The most innovative ones call for a different optics layout, where the beam-separation dipole magnets are located in front of the final-focusing quadrupole magnets to reduce long-range, beam-beam interactions, as illustrated in Figure 2. In any case, these various scenarios require the development of large-aperture, high-field or high-field-gradient magnets.

Mid 2010's is also the earliest time frame when one can expect to need final-focusing quadrupole magnets for any of the proposed linear collider projects. In the case of linear colliders, the magnet requirements are very IR-design dependent.

0-7803-7738-9/03/$17.00 © 2003 IEEE

Figure 2: LHC-IR upgrade scenario where the beam-separation dipoles (D1 and D2) are located in front of the inner-triplet of final-focusing quadrupoles (Q1, Q2 and Q3) [7].

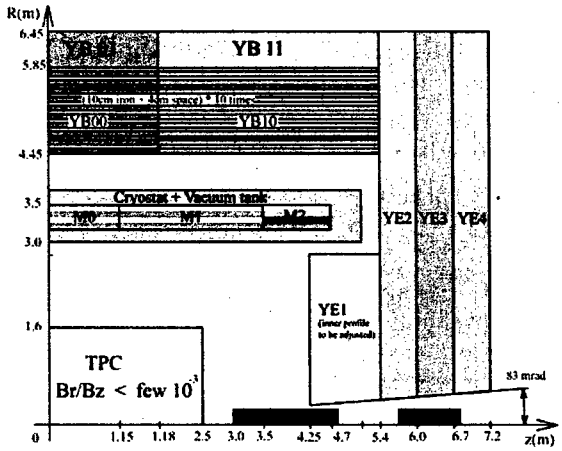

Figure 3: Layout of TESLA 1st IR where the final-focusing quadrupoles (Q3 & Q4) are located inside the detector solenoid (whose winding sections are labelled M0, M1 & M2) [9].

For the first IR of the Tera Electron volts Superconducting Linear Accelerator (TESLA), the layout proposed in the Technical Design Report (TDR) relies on final-focusing quadrupole magnets producing 250 T/m in a 56-mm-single-aperture. However, these magnets are positioned very close to the interaction point and must operate in the 4-T background field of the detector solenoid (see Figure 3) [9]. For the Next Linear Collider (NLC), or the second IR of TESLA, where it is foreseen that the two beams cross with a large angle, the final-focusing quadrupole magnets must be made very compact (*i.e.*, with a small overall outer radius) so as to clear the way for the crossing beam [10].

Roadmap for High-Field Magnet R&D

Given the prospects outlined above, a roadmap for high-field accelerator magnet development appears to be

- To get ready for LHC IR upgrade in 2015 (which calls for large-aperture, high-performance dipole or quadrupole magnets; note that here cost is not the primary issue),
- To develop final-focusing quadrupole magnets for implementation in a linear collider IR in the mid-2010's (which calls for LHC-type quadrupole magnets in a solenoidal background field or for compact quadrupole magnets; note that here also cost is not the primary issue),
- To promote generic magnet R&D aimed at LHC energy upgrade or a VLHC in the mid 2020's (which calls for high-performance, low-cost dipole and quadrupole magnets).

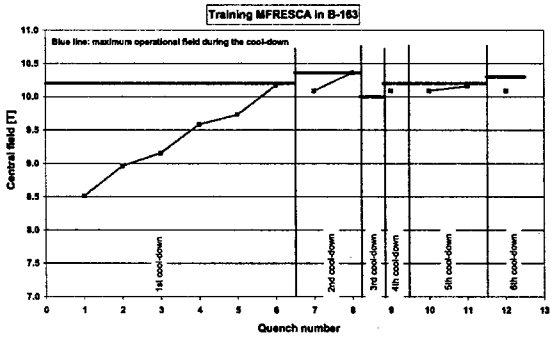

Figure 4: Quench performance of 88-mm-aperture (NbTi) MFRESCA dipole magnet model at CERN [13].

WHY IS IT SO HARD?

Twelve years may seem like a long time to develop a new dipole or quadrupole magnet design for LHC or linear collider IR applications. The issue, however, is that we cannot extrapolate existing designs and that we need to change of superconductor technology.

State of the Art in NbTi

Since the time of the Tevatron, the most widely used superconductor is a ductile alloy of niobium-titanium (NbTi) easy to co-process with copper by conventional extrusion and drawing techniques [11]. The world production of NbTi is estimated around 1500 metric tons per year, mainly under the form of multifilamentary composite wires for use in MRI magnets.

After several iterations, the CERN/LHC dipole magnet R&D program was successful in working out a design suitable for industrial production, but it demonstrated also that the limit of NbTi magnets (cooled down to superfluid helium at 1.8 K) lied in the 10-to-10.5-T range. This is illustrated in Figure 4, which shows the quench performance of the 88-mm-single-aperture MFRESCA dipole magnet, designed and built by a team led by D. Leroy and presently implemented in the superconducting cable test facility at CERN [12], [13]. Hence, to go beyond the present limitations and cross the 10-T threshold, it appears necessary to change of superconducting material.

Beyond NbTi: Nb_3Sn

High Temperature Superconductors (HTS) are not yet ready for large-scale applications requiring high current densities under high magnetic fields, and it is likely that it will take at least another decade before they become competitive. The limited gain that can be expected from ternary NbTiTa alloys does not seem worth the investment. The present upper critical field of MgB_2 wires is two low. Nb_3Al exhibits promising properties, but there are serious manufacturing issues that have yet to be resolved. It follows that the only serious candidate to succeed NbTi is the intermetallic compound Nb_3Sn, whose world production is estimated around 15 metric tons per year (also under the form of multifilamentary composite wires) [14].

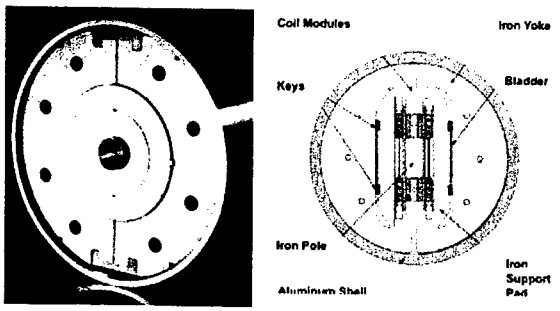

Figure 5: Record-breaking Nb_3Sn dipole magnet models; (a) 50-aperture, $\cos\theta$-type MSUT at Twente University (left) [19] and (b) 25-mm-gap, racetrack-type RD-3 at LBNL (right) [21].

Nb_3Sn has a critical temperature, T_C, and an upper critical field, B_{C2}, that are about twice those of NbTi. However, once formed, it becomes brittle and its critical parameters (T_C, B_{C2}, and the critical current density, J_C) are strain sensitive [15]. The brittleness and strain-sensitivity of Nb_3Sn require a different approach to all manufacturing processes and, so far, have limited its use to specific applications (such as insert coils for high-field Nuclear Magnetic Resonance or NMR spectrometers).

Progress on Nb_3Sn Technology

In spite of the aforementioned difficulties, significant progress has been made over the last decade thanks to

- The successful manufacturing and tests of the model coils for the International Thermonuclear Experimental Reactor (ITER) project, which, among other, have required the production of ~30 metric tons of Nb_3Sn wires [16], [17],
- A US National Program for the development of high-performance Nb_3Sn wires, supervised by R.M. Scanlan at Lawrence Berkeley National Laboratory (LBNL), which has led already to a three-to-four-fold increase in J_C with respect to ITER model coil specifications [18],
- A series of record-breaking dipole magnet models, opening the 10-to-15 T range, including the 50-mm-aperture, $\cos\theta$-type, MSUT model, built at Twente University and cold tested at CERN in 1995, which reached 11 T on its first quench at 4.4 K (Fig. 5(a)) [19], the 50-mm-aperture, $\cos\theta$-type, D20 model, built and cold tested at LBNL, which, after some training, reached 13.5 T at 1.8 K in 1997 [20], and the 25-mm-gap, racetrack-type, RD-3 model, also built and cold tested at LBNL, which, after some training reached 14.7 T at 4.2 K in 2001 (Fig. 5(b)) [21].

This progress shows that, although the Nb_3Sn technology is not yet mature, it could be at hand for the high-field and high-field-gradient accelerator magnets needed for LHC IR upgrade and for the IR's of future linear colliders. However, it is clear also that we need to keep working hard if we want to turn these few successful demonstrators into accelerator-class devices that can be implemented in a machine within 10 to 15 years.

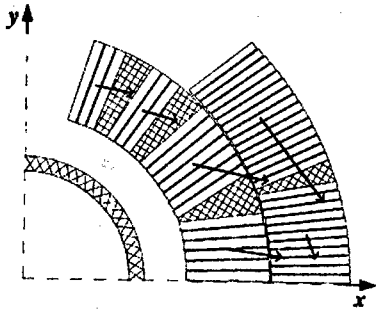

Figure 6: Lorentz force distribution in a quadrant of a $\cos\theta$ dipole magnet coil assembly (Courtesy R. Gupta).

WHAT DO WE HAVE TO DO?

Task List

Given the present state of the art on accelerator magnet technology and the requirements foreseen for LHC IR upgrade and for IR's of future linear colliders, we need

- To revisit magnetic and mechanical designs to achieve enhanced performances with magnet coils made from brittle materials,
- To address coil cooling issues under high beam losses,
- To keep promoting high-performance Nb_3Sn wire development (and to ensure the survival of multiple suppliers around the world),
- To improve robustness and assess radiation hardness of Nb_3Sn conductor insulation (see, for instance, the innovative insulation scheme developed by Composite Technology Development, Inc., or CEA/Saclay [22]),
- To put into practice all of the above in magnet models and prototypes.

Of course, a number of laboratories around the world are already actively tackling these issues, including BNL, FNAL and LBNL in the USA, and CEA/Saclay and Twente University in Europe. A detailed review of the ongoing programs can be found elsewhere [23]. Given the limited space at our disposal, let us single out the problem of magnetic design.

Revisiting Magnetic Design

Most superconducting accelerator magnets rely on so-called saddle-shape coils, which, in their long straight sections approximate $\cos\theta$ or $\cos2\theta$ conductor distributions. Such designs were first optimized at BNL in the mid 1960's using R.A. Beth's complex formalism [24]. They are very efficient in terms of superconductor use and to control field quality, but, as illustrated in Figure 6, they result in a transverse stress accumulation towards the coil assembly midplane that could become detrimental when dealing with brittle conductors. Nevertheless, and in spite of the very high Lorentz forces developed in the MSUT and D20 models (which were both of $\cos\theta$-type), the performance of these magnets did not appear to be limited by stress-induced degradation.

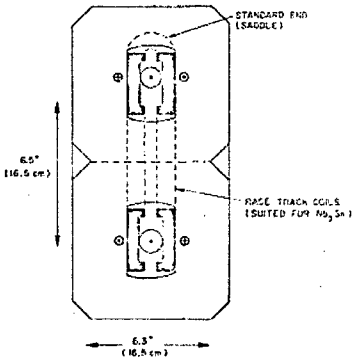

Figure 7: Original design of dual-bore dipole magnet relying on Racetrack-type coils first proposed by G.K. Danby (BNL) in 1983 [25].

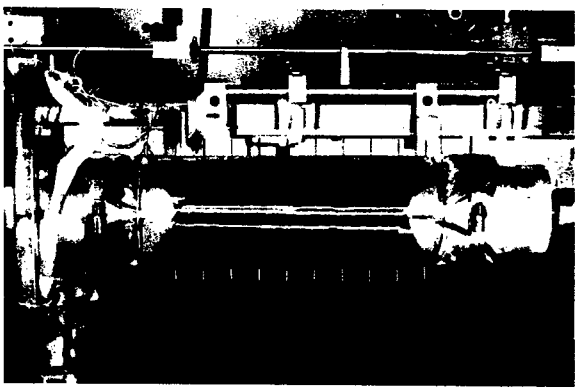

Figure 8: Dipole magnet model based on a double helix coil under manufacturing at CEA/Saclay in 1974 [27].

The good results of the MSUT and D20 models indicate that we have not yet reached a hard limit on the mechanical point of view. This implies that, for LHC IR upgrade and for the first IR of TESLA, we can still safely rely on "conventional" $\cos\theta$ or $\cos 2\theta$ designs.

However, in the longer run, and given the very open time-scale for a LHC energy upgrade or a VLHC, it is, of course, worthwhile to investigate other designs. Among possible candidates, let us mention the racetrack-type coil design, illustrated in Figure 7, which was first proposed by G. Danby at BNL in 1983 [25] and was subsequently resuscitated by R. Gupta in 1996 [26]. This design has become the workhorse of the LBNL high-field magnet program and was used for the RD-3 model.

As a curiosity, let us also mention the double-helix coil design, illustrated in Figure 8 [27], which was investigated in the early 1970's and which is also being brought back into actuality by several authors.

HOW TO GET ORGANIZED?

At present, most of the worldwide resources are (for good reasons) used up by LHC and very little is left for accelerator magnet R&D. Given the little resources that are available

- We cannot afford to do everything at once, and we need to target our activities towards a limited number of clearly identified goals,
- We should avoid unnecessary work duplication and try to coordinate efforts among interested partners.

Some attempts at developing integrated programs are presently being made both in the USA and in the EU.

US LARP

BNL, FNAL and LBNL are presently collaborating to the US-LHC Accelerator Project, which, among others, include the in-kind contribution of a number of superconducting (NbTi) LHC IR magnets. In parallel, all 3 laboratories are also pursuing independent high-field magnet programs that are well described in the literature.

The US-LHC Accelerator Project team, led by J. Strait, FNAL, is now proposing to extend the present collaboration beyond LHC construction and is developing a US-LHC Accelerator Research Program (LARP) aimed at LHC IR upgrade. The Program scope and details are still under discussion. It will include Nb_3Sn magnet R&D work on both dipole and quadrupole magnets, but will focus mainly on large-aperture (up to 110 mm), high-field-gradient (> 200 T/m) quadrupole magnets [28].

EU CARE/NED Proposal

In October 2002, the European Committee for Future Accelerators (ECFA) has set up the European Steering Group for Accelerator R&D (ESGARD), chaired by R. Aleksan, CEA/Saclay, with the mandate of preparing a coherent set of bids to apply for EU funding [29]. The first outcome of ESGARD is the Coordinated Accelerator Research in Europe (CARE) proposal of Integrated Activities (IA), which was submitted to the EU on April 15, 2003.

The CARE proposal is a first attempt at integrating all HEP-related accelerator R&D in Europe and is supported by more than 100 institutes. It includes 3 Network Activities (linear colliders, neutrino beams and hadrom colliders) and 6 Joint Research Activies (JRA's), to develop specific hardware pieces or systems. One of the JRA's, nicknamed NED (for Next European Dipole) focuses on high field magnets.

The main objective of the NED JRA is to develop a large-aperture (up to 88 mm), high-field (up to 15 T) dipole magnet model, relying on high performance Nb_3Sn conductors (non-Cu J_C up to 1500 A/mm^2 at 4.2 K and 15 T). Such magnet is aimed at demonstrating the feasibility of the LHC IR upgrade scenario illustrated in Figure 2 where the beam-separation dipole magnets are located in front of the final-focusing quadrupole magnets, and it complements the US LARP. In addition, the NED magnet could be used to replace the MFRESCA magnet and upgrade the CERN cable test facility.

The NED JRA involves 7 collaborators (CEA/Saclay, CERN, INFN Milan and Genoa, RAL, Twente University and Wroclaw University) plus several industrial partners. The EU decision is expected before the end of the year. If approved, the program will start on January 1st, 2004, and the magnet should be cold tested in the Fall of 2008.

CONCLUSION

The US LARP and the EU NED proposal offer unique opportunities to develop the next generation of high-field magnets that will be needed for LHC-IR upgrade and for the IR's of future linear colliders.

Beyond HEP applications, such programs will help superconducting wire manufacturers to keep improving the performance and quality of their commercial Nb_3Sn products (such as high-field NMR wires).

Furthermore, lessons learned from Nb_3Sn should also help future HTS applications.

Let us hope that these two programs will be funded at a suitable level and that the accelerator magnet community will be given the means of maintaining its level of Excellency and of preparing its future...

REFERENCES

[1] W.B. Sampson, "Superconducting Magnets for Beam Handling and Accelerators." In H. Hadley (ed.), *Proc. of 2nd Int. Conf. on Magnet Technology*, pp. 574–578, 1967.

[2] R. Auzolle, A. Patoux, *et al.*, "Construction and test of superconducting quadrupole prototypes for HERA," *Journal de Physique*, Vol. 45 (Colloque C1, supplément au No. 1), pp. 263–266, 1984.

[3] H.T. Edwards, "The Tevatron Energy Doubler: a Superconducting Accelerator," *Ann. Rev. Nucl. Part. Sci.*, Vol. 35, pp. 605–660, 1985.

[4] L. Rossi, "LHC Superconducting Magnets," in these Proceedings.

[5] H. Schopper, "LEP and Future Options" *Proc. of 12th Int. Conf. on High Energy Accel.*, pp. 658–663, 1983.

[6] J.S. Kirby, "Production Status of the LHC Inner Triplet Magnet System," to appear in the Proceedings of the Applied Superconductivity Conference, Houston, TX, August 4-9, 2002.

[7] O. Brüning, R. Cappi, *et al.*, "LHC Luminosity and Energy Upgrade: A Feasibility Study," CERN LHC-Project Report 626, December 1, 2002.

[8] J. Strait, M. Lamm, *et al.*, "Towards a New LHC Interaction Region Design for a Luminosity Upgrade," in these Proceedings.

[9] A. Devred, C. Gourdin, *et al.*, "Conceptual Design for the Final Focus Quadrupole Magnets for TESLA," DESY TESLA-2001-17, CEA/DSM DAPNIA-STCM-01-03, 2001.

[10] B. Parker, BNL, private communication, 2003.

[11] P.J. Lee, D.C. Larbalestier, *et al.*, "Chapter 5: Fabrications Methods." In K. Osamura (ed.), *Composite Superconductors*, New York, NY: Marcel Dekker, Inc., pp. 237–321, 1994.

[12] D. Leroy, G. Spigo, *et al.*, "Design and Manufacture of a Large-Bore 10 T Superconducting Dipole for the CERN Cable Test Facility," *IEEE Trans. Appl. Supercond.*, Vol. 10 No. 1, pp. 178–182, 2000.

[13] A.P. Verweij, CERN, private communication, 2003.

[14] P.J. Lee, "Advances in Superconducting Strands for Accelerator Magnet Application," in these Proceedings.

[15] J.W. Ekin, "Strain Effects in Superconducting Compounds" *Adv. Cryo. Eng. (Materials)*, Vol. 30, pp. 823–836, 1984.

[16] N. Martovetsky, P. Michael, *et al.*, "ITER CS Model Coil and CS Insert Test Results," *IEEE Trans. Appl. Supercond.*, Vol. 11 No. 1, pp. 2030–2033, 2001.

[17] R. Heller, D. Ciazynski, "Evaluation of the Current Sharing Temperature of the ITER Toroidal Field Model Coil," to appear in the Proceedings of the Applied Superconductivity Conference, Houston, TX, August 4-9, 2002.

[18] R.M. Scanlan and D.R. Dietderich, "Progress and Plans for the US HEP Conductor Development Program" to appear in the Proceedings of the Applied Superconductivity Conference, Houston, TX, August 4-9, 2002.

[19] A. den Ouden, H. ten Kate, *et al.*, "Quench characteristics of the 11 T Nb_3Sn model dipole magnet MSUT," *Proc. of 15th Int. Conf. on Magnet Technology*, Beijing, China: Science Press, pp. 339–342, 1998.

[20] A.D. McInturff, R. Benjegerdes, *et al.*, "Test Results for a High Field (13T) Nb_3Sn Dipole," *Proc. of 1997 Part. Accel. Conf.*, pp. 3212–3214, 1998.

[21] R. Benjegerdes, P.Bish, *et al.*, "Fabrication and Test Results of a High Field, Nb_3Sn Superconducting Racetrack Dipole Magnet," *Proc. of 2001 Part. Accel. Conf.*, pp. 208–210, 2001.

[22] A. Devred, "Insulation Systems for Nb_3Sn Accelerator Magnet Coils Manufactured by the Wind & React Technique," *IEEE Trans. Appl. Supercond.*, Vol. 12 No. 1, pp. 1232–1237, 2002.

[23] M.J. Lamm, "Nb_3Sn Accelerator Magnet Development Around the World," to appear in the Proceedings of the Applied Superconductivity Conference, Houston, TX, August 4-9, 2002.

[24] R.A. Beth, "Complex Representation and Computation of Two-Dimensional Magnetic Fields," *J. Appl. Phys.*, Vol. 37 No. 7, pp. 2568-2571, 1966.

[25] G. Danby, R. Palmer, *et al.*, "Panel Discussion of Magnets for a Big Machine," *Proc. of 12th Int. Conf. on High-Energy Accel.*, pp.52–62, 1983.

[26] R.C. Gupta, "A Common Coil Design for High Field 2-in-1 Accelerator Magnets," *Proc. of 1997 Part. Accel. Conf.*, pp. 3344–3346, 1998.

[27] J. LeBars, private communication, 1974.

[28] A.V. Zlobin, V.V. Kashikin, *et al.*, "Aperture Limitations for 2nd Generation Nb_3Sn LHC IR Quadrupoles," in these Proceedings.

[29] http://esgard.lal.in2p3.fr

ADVANCES IN SUPERCONDUCTING STRANDS FOR ACCELERATOR MAGNET APPLICATION

Peter J. Lee and David C. Larbalestier, Applied Superconductivity Center, University of Wisconsin-Madison, Madison, WI 53706-1609, USA

Abstract

Considerable advances have recently been obtained in the critical current densities J_c of Nb_3Sn based superconductors - the prime candidates for the next generation of superconducting accelerator magnets. The non-Cu critical current densities now approach 3000 A/mm² at 12 T and 4.2 K in engineering quality strand. The design of new strands minimizes the amount of Cu in the package from which the Nb_3Sn is formed and increases the Sn level beyond that required to simply achieve A15 stoichiometry. The result is an A15 layer that is significantly more uniform than earlier generations of wire, both chemically and microstructurally, and wires that significantly surpasses previous Nb_3Sn strands in layer critical current density and in the specific grain boundary pinning force. Remarkably, these developments have been achieved in internal Sn based strands manufactured using both the modified jelly-roll technique with Nb-Ti alloy and the rod-in-tube approach with Nb-Ta alloy. The rod-in-tube approach is particularly exciting because it offers greater manufacturing flexibility. Advances have also been made in strand designs that offer the potential to reduce the large effective filament diameters, which are an issue with these new high-J_c strands. We review the latest developments in Nb_3Sn superconductors and compare their performance and potential with other round-wire high-field superconductors.

INTRODUCTION

The LHC marks the end of a series of colliders that have capitalized on increasing current densities available in Nb-Ti alloy based superconducting strand. Nb-Ti has proven to be a remarkably durable superconductor, dominating superconducting magnet design from the FNAL Tevatron (on-line in 1983) to the LHC (expected completion 2006). Multifilamentary superconducting strands based on Nb-Ti alloys are strong, ductile, and relatively inexpensive but are limited in operation to fields below ~11 T (2 K). In Figure 1 we compare the critical current density variation with applied magnetic field for superconductors of interest to accelerator magnet designers. With the exception of the Bi2223 tapes and the MgB_2-SiC [1] data, the critical current densities shown are available in multifilamentary round-wire form suitable for magnet fabrication. Development of superconductors for accelerator magnets with fields greater than 11 T has focused on Nb_3Sn. Being brittle, the A15 structure of Nb_3Sn must be made from ductile components that can be drawn to wire, meaning that, unlike Nb-Ti, the materials package needed to make the superconductor contains more than just the A15 filament. Raising the J_c of Nb_3Sn is then both a question of maximizing the quantity of A15 within this package and of optimizing the A15 properties. The latest generation of Nb_3Sn strands can support non-stabilizer critical current densities in excess of 1000 A/mm² at fields up to 17 T at 4.2 K. Bi-2212, also a brittle material, can support ~1000 A/mm² out beyond 28 T. However, whereas Nb_3Sn conductors can be made with small Cu-stabilizer cross-sections, at present the engineering critical current density, J_e, of Bi-2212

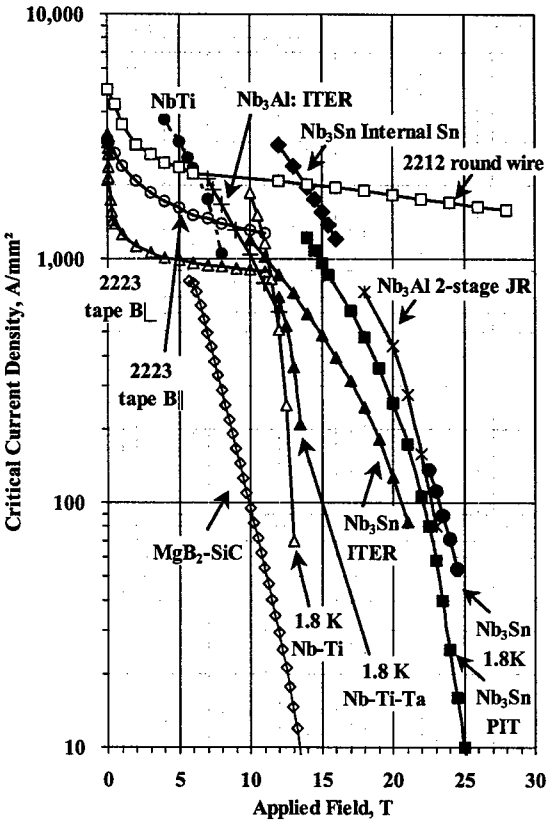

Figure 1: A comparison of critical current density with applied magnetic field for superconductors of actual or potential interest for accelerator magnets.

This work was supported in part by the U.S. Department of Energy under Grants DE-FG02-91ER40643 (High Energy Physics) and DE-FG02-86ER52131 (Office of Fusion Energy Sciences).

The authors may be contacted at the Applied Superconductivity Center at the University of Wisconsin-Madison, Madison WI 53706, USA (phone: 608-263-1760; fax: 608-263-1087; e-mail: peterlee@wisc.edu). D. C. Larbalestier is also with the Department of Materials Science and Engineering and Department of Physics.

0-7803-7738-9/03/$17.00 © 2003 IEEE

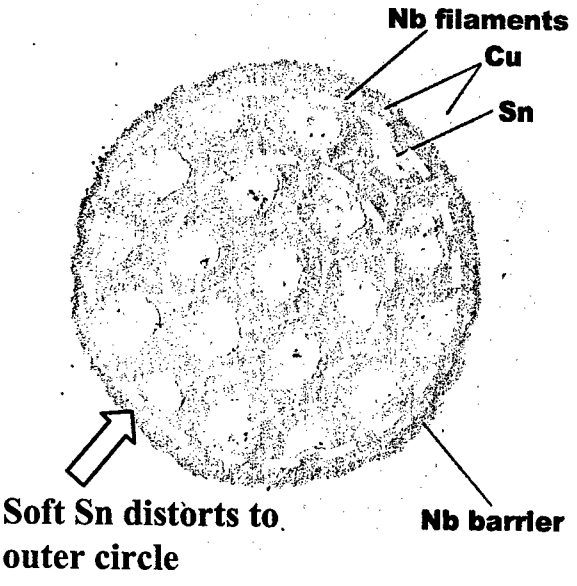

Figure 2: Cu-split sub-element high J_c strand produced by IGC-AS (now Outokumpu Advanced Superconductors).

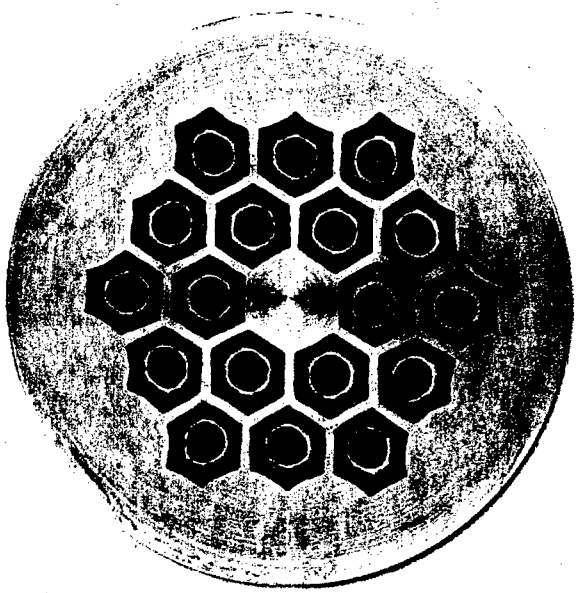

Figure 3: Hot Extruded Rod billet cross-section Image courtesy of Jeff Parrell, OI-ST.

conductors is still much reduced by the large Ag area in the strand. The latest generation of strand from OI-ST achieves J_e of 600 A/mm² at 12 T, 4.2 K with a 28 % Bi-2212 area [2]. Nb_3Al offers a high strength alternative but is much more expensive to manufacture than Nb_3Sn, which has not, so far, shown strength limitation in well designed high field accelerator magnets. MgB_2 has future long term potential for low cost and exhibits critical current densities that, although presently lagging behind Nb_3Sn, continue to show progress [e.g. 1]. A remarkable development in the past year has been the enhancement of the upper critical field by manipulation of the resistivity, with the upper critical field, H_{c2}, vs. temperature surface exceeding Nb_3Sn. [3]. In previous reviews we have examined the potential for High Temperature Superconductors [4] and MgB_2 [5] to high energy physics; in this paper we will focus on developments in Nb_3Sn.

PROGRESS IN NB_3SN

Of the available superconductors, Nb_3Sn is the closest to targets set for the next generation of accelerator magnets [6]. The critical current density, J_c, (non-Cu, 12 T, 4.2 K) is very close to the 3000 A/mm² target, although the residual resistance ratio, RRR, is very low (2-13) in recent billets, due to diffusion barrier through-reaction in most cases. The effective filament size is still 2-3 times the 40 μm target, except for strands fabricated by the powder-in-tube (PIT) process. Piece length is reasonable good, considering the (250-1500 m) small billet sizes and the developmental nature of the strand for which two billets are rarely identical in design. New, more scaleable designs are showing promising results, for instance the Rod Restack Process at OI-ST that has achieved 2900 A/mm² (12 T, 4.2 K). There has been little progress in reducing heat treatment times for internal Sn to less that 150 hrs but PIT can be optimized at the desired 50 hr reaction. PIT wire costs are still limited by the small production scale and technical difficulties in scale-up.

Nb_3Sn has a big advantage over competing superconductors with respect to large-scale strand, cable and magnet production experience, such as record-setting

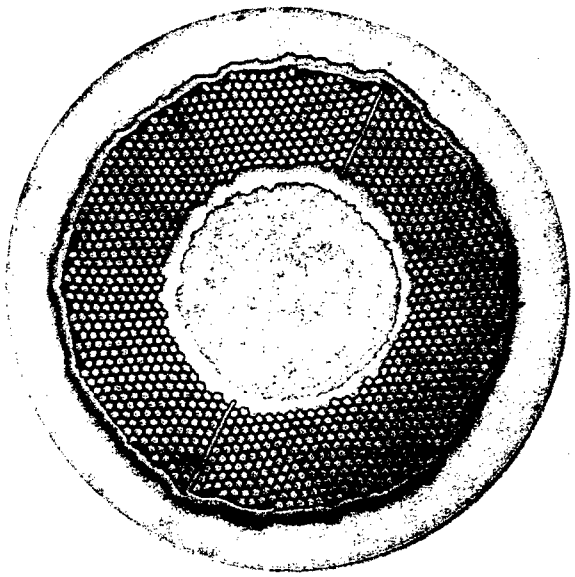

Figure 4: Single-stack, Internal Tin conductor "MEIT" manufactured by Supergenics LLC/Outokumpu Advanced Superconductors under a DOE-SBIR program. The single central Sn core reduces Sn distortion. It incorporates Nb-Ta fins to reduce the effective filament diameter. Image courtesy of Bruce Zeitlin of Supergenics, LLC.

dipole magnets at LBNL, the huge (150 ton, 13 T) ITER Central Solenoid Model Coil (ITER-CSMC)[7], It is also available from multiple vendors worldwide. Although the brittleness of Nb_3Sn dictates that it be used in the wind-and-react configuration for small-radius magnets, it can also be used in the react-and-wind approach for larger magnets [8].

Issues with Sn elements in Conductors

The use of elemental or weakly alloyed Sn has been crucial to the production of high critical current densities in internal Sn and even PIT strands. Higher Sn content pushes the Sn:Nb ratio in the A15, never always Nb_3Sn composition, closer to the stoichiometric ratio of highest H_{c2} and T_c [9]. Sn however is soft and not only becomes distorted itself during final wire drawing but also distorts the surrounding filament pack (see Figure 1), limiting the amount of post-billet-assembly processing that can be performed. Furthermore, in order to achieve useful piece length, the filament pack must be metallurgically bonded, which normally requires warm processing incompatible with the low melting point Sn (232 °C). One way around this problem is to assemble and warm-extrude the sub-element with Cu in the place of the Sn and then drill a hole in the Cu for the Sn after the other components are bonded. However, the smallest gun-drill diameter in a typical full-length 0.9 m billet is 4.7 mm. Taking account of the Sn distortion after assembly, this limits the number of sub-elements that can be stacked into a final billet without severe piece length problems.

One method to circumvent this problem being explored by OI-ST, uses salt in the place of the Sn, allowing hot extrusion of both the sub-element and final composite assemblies [10]. This process, termed HER for Hot Extruded Rod, is illustrated by the billet cross-section shown in Figure 3. After the first extrusion, the salt cores can be washed away and replaced with Sn at a late stage in the processing. With hot extrusion permitted for both sub-element and final composite assemblies, this process has excellent scalability.

The lack of Sn distortion in the center of the composite in Figure 2 suggests another alternative. The Mono Element Internal Tin conductor "MEIT" [11], uses a single central Sn core with a concentric extrusion-bonded

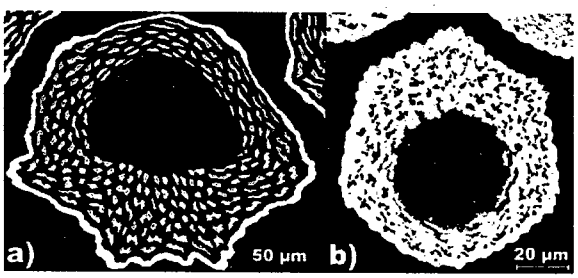

Figure 5: Comparison of Sub-element cross-sections in a) a high-Cu low hysteresis loss ITER-CSMC MJR strand fabricated by TWC, and b) a low-Cu, high J_c MJR strand fabricated by OI-ST.

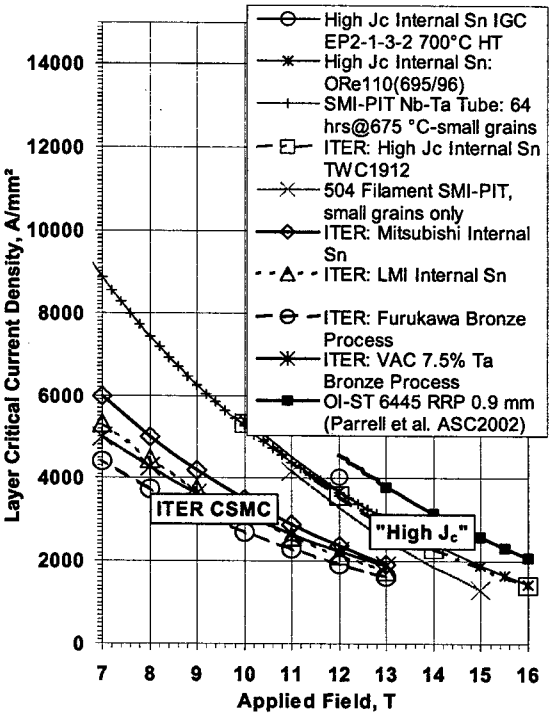

Figure 6: Comparison of the layer critical current densities for ITER-CSMC (low hysteresis loss) and recent "high J_c" Nb_3Sn composites. Note how different the intrinsic performance of the Nb_3Sn is.

Nb/Cu filament stack (gun-drilling of the solid Cu core is used to introduce the Sn after extrusion). Because there is now only one sub-element, the strand must be drawn to fine wire (< 0.2 mm diameter). Although such a fine wire may require a 2-level cable, the high symmetry means minimal Sn distortion (see Figure 4), high potential for good piece length, and low cost.

Issues with Sub-Element Size

To produce high overall J_c, the non-Cu sub-element must have a minimum of Cu filler and a high Sn concentration. This can enhance the A15 fraction to ~0.5 and dramatically enhances the layer critical current density. Figure 6 contrasts the high-Cu, low hysteresis loss ITER-CSMC strands with recent, low-Cu, "high-J_c" designs. Although some ITER-CSMC strands had high Sn:Nb ratios, the additional Cu required to isolate the individual filaments for low hysteresis loss (see Figure 5a) resulted in inferior Nb_3Sn-layer quality, even though the overall Nb_3Sn composition difference between the 2 designs was only ~1 at.% Sn [12]. Unfortunately the low-Cu requirement for highest J_c results in complete physical bonding of the individual Nb_3Sn filaments into a continuous ring of Nb_3Sn (see Figure 5b). Not only is the effective filament diameter, d_{eff}, increased by physical joining of the filaments but the core of the sub-element is

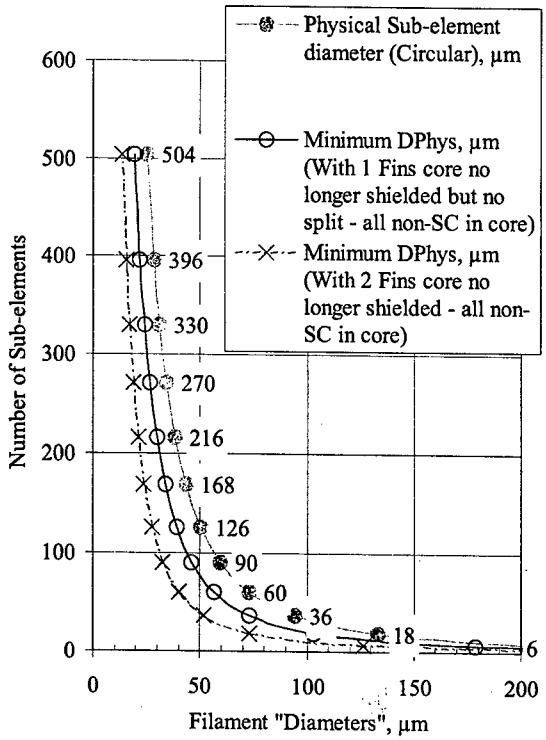

Figure 7: Calculated physical filament diameters based on simple circular geometries for a typical cable strand wire diameter (0.8 mm) and for a Cu:Non-Cu ratio of 1. The typical R&D high-J_c internal-Sn billets have 18-37 sub-elements in their restack, limiting them to sub-element diameters >100 μm. The Nb-Ta fins of Figure 4 can avoid shielding of the residual sub-element Sn-cores (open circles) by dividing the sub-element into two components, which do not shield their core (X). This plot was suggested by one made by R. Scanlan [13].

also shielded, making the entire sub-element cross-section behave as one and proportionately increasing the loss.

This small size of R&D billets and the problem of Sn distortion limits the restack numbers of sub-elements so far to 18-37. By using simple scaling arguments, we can see that this limits the sub-element diameters to >100 μm (Figure 7), well above that desired for low hysteresis loss for both HEP and fusion magnet use.

Supergenics LLC has developed a sub-element splitting technology using Nb-Ta dividers (patent pending) that should "un-shield" the sub-element core by subdividing the sub-element filament pack. In Figure 7 we model the effect of "un-shielding" the core with one Nb-Ta divider, as well as the added benefit of un-shielding the core and splitting the A15 volume with two dividers. Figure 7 shows that there must be at least 60 sub-elements to approach the desired 40 μm effective filament size target. Although 504-filament PIT conductors which exceed the 40 μm target have been made, this goal seems much more feasible for internal Sn than experience with internal Sn is much more widespread than with PIT.

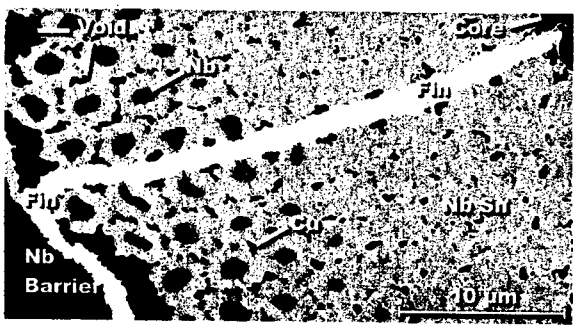

Figure 8: A false color atomic number sensitive electron backscatter image of a sub-element cross-section near a Nb-Ta fin after reaction. Composite fabricated by Outokumpu Advanced Superconductors/Supergenics and heat treated by E. Barzi at FNAL.

The first attempts by Supergenics LLC/Outokumpu Advanced Superconductors under a DOE-SBIR program at using such Nb-Ta dividers has been successful in producing composites of 18 and 36 sub-elements, although significant reaction of the Nb-Ta alloy fin with Sn has reduced its effectiveness. In Figure 8, we show a false-color, atomic-number-sensitive, electron-backscatter image near a Nb-Ta fin after reaction. The inside filaments (right, yellow) are evidently fully reacted while the outer filaments (left) furthest away from the original Sn core have unreacted Nb cores (blue). Near the original Sn core, the fin is full reacted by Sn, apparently robbing the outer filaments of needed Sn. The result is a significantly reduced J_c of the composite. The "fin", however, has been successful in stopping the reaction with the outside Nb diffusion barrier (blue, left), so that a continuous shielding external Nb_3Sn layer is not produced.

Closer examination of the Nb-Ta reaction region in Figure 9 reveals a complex reaction producing changes in composition and thickness of the grain boundaries in the

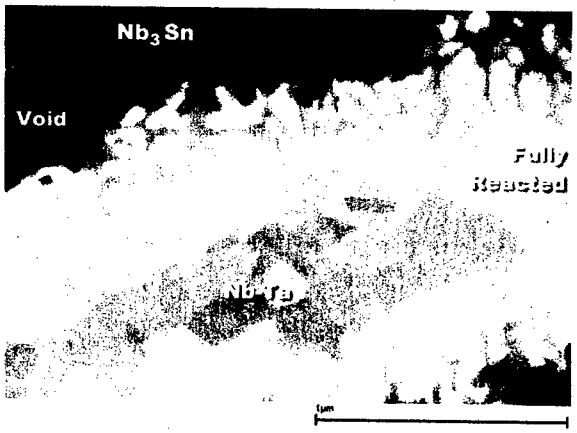

Figure 9: Atomic-number sensitive, electron-backscatter image of the Nb-Ta divider in Figure 8 in the fully reacted region. The grain boundaries in the reacted divider and the adjacent Nb_3Sn are clearly of variable composition.

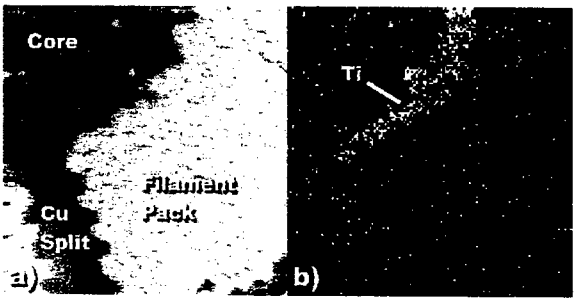

Figure 10: Detail of Core/Filament Pack region of OAS 0.4 mm dia. monocore strand after 150h/530°C heat treatment in the investigation of Suenaga [15] and Uhlrich [14]. In a) an atomic-number sensitive electron backscatter image and b) a spectral image (energy dispersive x-ray) show that Ti (white) segregates to the inner side of the Nb (blue) filament pack (Cu in red, Sn in green).

$Ta(Nb)_3Sn$ and the Nb_3Sn. This suggests that an alternative barrier, perhaps Ta, might be more effective in implementing this promising concept for reduced d_{eff}.

Issues with Ti

Alloying the Nb with Ti (or Ta) is required to raise H_{c2} and maximize high field J_c but increases the cost of the Nb alloy and can reduce piece length. Thus incorporating Ti into the Sn core has been investigated too.. With ever decreasing Cu content in the filament pack, however, this route has become less effective because Ti reduces the mobility of Sn through the filament pack [15]. Energy dispersive x-ray analysis has indicated that the Ti forms a Nb-Sn-Ti ternary phase at the core/filament-pack interface. The segregation of the Ti can be clearly seen in the EDS spectral image in Figure 10b.

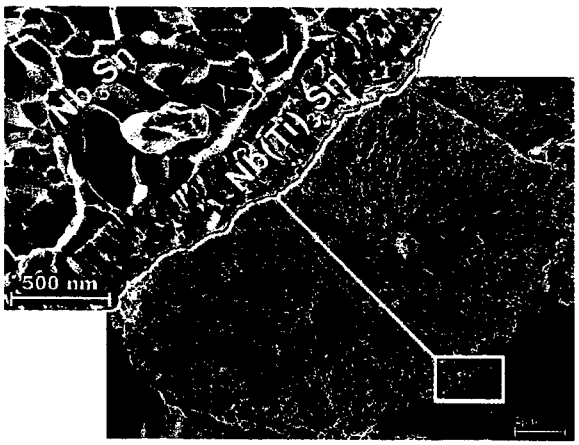

Figure 11: High resolution field emission scanning electron microscope image of an outer filament in a 1st generation OI-ST HER strand where the Ti has only partially penetrated the Nb filament. Fracture of the filaments reveals two sizes of A15 grains, The $Nb(Ti)_3Sn$ grains are much smaller than the pure Nb_3Sn grains.

An extreme case of non-uniform Ti distribution can be seen in Figure 11, where the Ti only partially penetrates the Nb filament – leading in this case to 2 distinct A15 layers. New methods of Ti alloying are now being investigated under the DOE-SBIR program.

ACCELERATOR CONDUCTOR ISSUES

Remarkable progress has been made towards a new generation of conductors that meet the goals of the high energy physics community. As the preceding sections indicate, however, there is still plenty to do. Among the key issues that still need to be resolved are:

1. How low can the effective filament size for "High J_c" Nb_3Sn strand be reduced?
2. Can the cost of PIT strand be reduced so that it competes with internal Sn?
3. Can the expected cost reduction in internal Sn conductors be achieved without sacrificing properties?
4. How close are we to the intrinsic performance limits for Nb_3Sn strand J_c?

REFERENCES

[1] S.X. Dou, et al., App. Phys. Lett. 81(18), pp. 3419-3421 (2002).
[2] Private communication from S. Hong and K. Marken.
[3] A. Gurevich, et al. "Anomalous enhancement of the upper critical field in the two-gap superconductor MgB_2 by selective tuning of impurity scattering" (submitted to Nature December 2002).
[4] D. C. Larbalestier and P. J. Lee, IEEE 1999 Particle Accelerator Conference, vol. 1, pp. 177-181, 1999
[5] L.D. Cooley, C.B. Eom, E.E. Hellstrom, and D.C. Larbalestier, 2001 Particle Accelerator Conference, Vol.1, pp: 203 –207, 2001.
[6] R. M. Scanlan, IEEE Transactions on Applied Superconductivity, 11(1), pp. 2150 –2155 (2001).
[7] N. Martovetsky et al., IEEE Trans. Applied Superconductivity, 12(1), pp. 600-5 (2002).
[8] R. McClusky, K.E. Robins and W.B. Sampson, IEEE trans. on Magnetics, 27, pp. 1991-1995 (1991).
[9] H. Devantay, et al., *J. Mat. Sci.*, 16, 2145 (1981).
[10] US Patent Number 5534219
[11] B. A.. Zeitlin, et al. Adv. in Cryo. Eng., 48, pp. 978-985, 2002.
[12] P. J. Lee et al., paper 2MK05 presented at ASC 2002, to be published in IEEE Trans. Applied Superconductivity.
[13] R. Scanlan, "J_c and $D_{effective}$: Where are we now, and what do we need to do?" presentation at the Low Temperature Superconductor Workshop, Napa, 2002.
[14] J. Uhlrich, University of Wisconsin REU project in collaboration with M Suenaga, LBNL, 2002.
[15] M. Suenaga, "Sn Diffusion Effects in High I_c Internal Tin Processed Wires," presentation at the Low Temperature Superconductor Workshop, Napa, 2002.

NOVEL INSERTION DEVICES*

E.R. Moog#, Advanced Photon Source, Argonne National Lab, Argonne IL 60439, USA

Abstract

Permanent magnet planar undulators are used at synchrotrons worldwide and serve as versatile radiation sources. For some experiments, however, photon characteristics other than what is achievable with planar devices are desired. Undulators can be tailored to adjust photon characteristics, such as brightness, tuning curves, polarization, harmonic content, and heat load, to suit them to a particular experiment. One specialized device is the electromagnetic circularly polarizing undulator at the Advanced Photon Source (APS). At a few facilities, plans are underway to build superconducting undulators with short period lengths to provide higher energy radiation. At APS, the possibility of building an undulator with a variable period is also being investigated. Some users, driven by a desire for lower on-axis heat load or for circular polarization, prefer other types of devices, such as Apple-style undulators or figure-eight devices. Characteristics of the radiation output and advantages of these various types of devices are presented.

INTRODUCTION

The designers of synchrotron radiation facility beamlines have choices to make in their selection of an insertion device (ID) for the beamline. The overall length of the device is typically a predetermined standard length based on the space available, and the minimum gap is determined by storage ring considerations and the vacuum chamber size (or, if there is no vacuum chamber in the ID gap, by the effect on beam lifetime [1]), but the period length and magnetic configuration (i.e., planar, helical, or other) can be selected. These will determine the polarization characteristics, tuning range, and power output.

PLANAR UNDULATORS

A sample set of tuning curves intended to guide a user in selecting the period length for a new planar device is shown in Fig. 1. The user expects to concentrate on energies near the Se and Br edges, but does not want to sacrifice tunability. For each of the period lengths shown, the number of periods has been changed to keep the overall device length constant at 2.1 m. As can be seen, the on-axis brilliance would be higher for the shorter period length undulators, but if the period length gets too short there will be a gap between the 1st and 3rd harmonics. Extending the 3rd harmonic to lower energy so it would overlap the 1st would require higher magnetic field strength than can be readily achieved by a planar undulator at the 10.5-mm minimum gap allowed by the standard APS ID vacuum chamber.

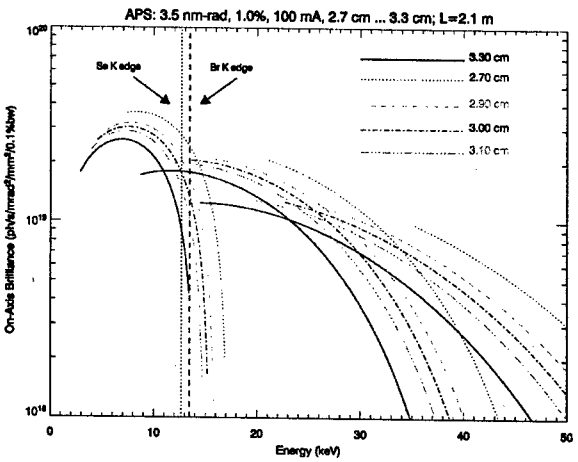

Figure 1: Tuning curves of on-axis brilliance vs. photon energy, showing the 1st, 3rd, and 5th harmonics for different period length undulators. Number of periods is adjusted to keep the overall undulator length constant at 2.1 m. A shorter period length gives higher brilliance but may result in a gap between harmonics.

Another important consideration for the user is the power output of the ID – either total power, power density or both. Figure 2 shows the total power and the ratio of the brilliance to the total power as a function of photon energy. (The trends for the power density look very similar.) The highest power comes at small gap, whether the energy to be selected is the 1st, 3rd, or 5th harmonic. There are differences in the details of the power load between the different period lengths, but clearly the biggest difference in power is determined by whether the desired energy can be reached in the 1st harmonic rather than requiring the 3rd and a closed gap.

In-Vacuum Undulator

The peak magnetic field can be increased by decreasing the gap. To overcome the limit imposed by the vacuum chamber, the entire undulator can be put in vacuum [1-3]. Shorter period lengths become reasonable because the device can be taken to magnetic gaps that are a few mm smaller – the limit comes when the beam lifetime begins to be affected. Additional precautions must be taken to ensure that the magnets and poles are vacuum-compatible and bakeable. The magnetic arrays must present a smooth conductive face to the beam so as to avoid resistive-wall instabilities; this can be accomplished with a Cu/Ni foil laid over the magnets. The Cu conductive face is toward the beam and the Ni is attracted to the magnets and holds the foil in place. The magnets will be closer to the beam where they are exposed to higher radiation levels, so radiation-induced demagnetization is a greater hazard and due consideration should be given to the choice of magnet material.

*Supported by the US D.O.E., BES-Materials Sciences, under contract W-31-109-ENG-38.
moog@aps.anl.gov

0-7803-7738-9/03/$17.00 © 2003 IEEE

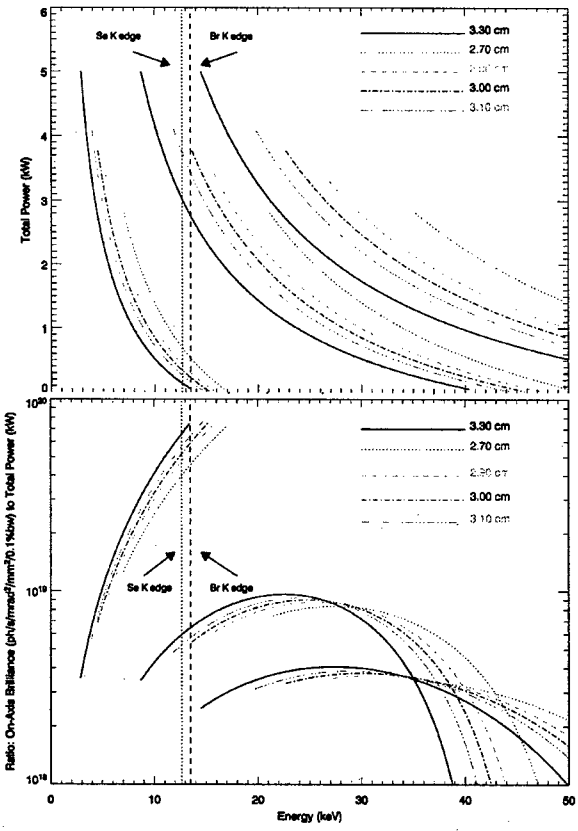

Figure 2: Total power (top) and brilliance/power (bottom) vs. energy for the same undulators as in Fig. 1. There are differences in the power levels for the different period lengths, but the most significant minimization in power (and maximizing of ratio) is when the desired energy can be reached in the first harmonic rather than the third.

Superconducting Undulator

Superconducting undulators have been proposed as a means of going beyond the field strengths that are achievable with in-vacuum undulators. Although superconducting wavelength shifters and wigglers have been built and used [3], meeting the magnetic field quality requirements of undulators has been a challenge. Recently, a test section of undulator was built [4]. A similar scheme that is under consideration at APS is shown in Fig. 3. An Fe mandrel has slots cut into it where the superconducting wire is wound. The Fe material between the slots acts as poles, and there are two mandrels, one above and one below the beam axis. Challenges anticipated in making such a device work include providing sufficient cooling such that beam heating effects do not cause quenching, and developing the techniques needed to measure the magnetic field and to attain the necessary field quality.

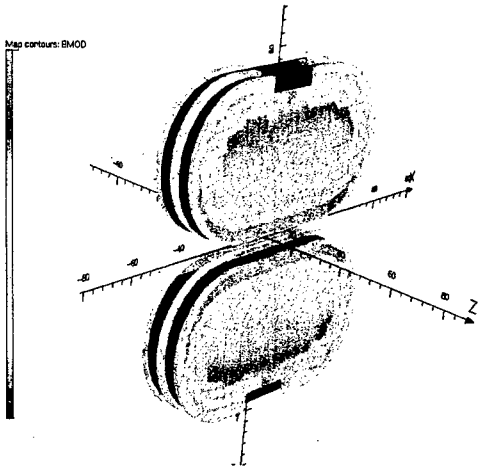

Figure 3: Model for a superconducting undulator. Slots for the superconductor windings are cut into the iron mandrels, one above the beam and the other below. The remaining part of the mandrel serves as pole pieces. Also shown is the result of a calculation of |B|.

Variable-Period Undulator

A variable-period undulator based on a staggered array undulator [5] has been proposed [6]. As with a staggered array, a solenoid with a strong axial field has vanadium permendur poles inserted in the bore, as shown in Fig. 4. The poles perturb the field as shown in Fig. 5, resulting in a periodic transverse or vertical field on axis. To make the period vary, the poles can be moved in position longitudinally. Although the magnetic field on axis of such a device is weaker than for a permanent-magnet undulator of the same period length and gap, the tunability range can still be quite wide. In addition, the period chosen to reach a particular energy photon can be the period where the peak in the tuning curve falls at that energy, making for a higher brilliance, as shown in Fig. 6. A further advantage of this type of device is that the high brilliance does not come with the penalty of a high power output. Instead, as shown in the lower panel of Fig. 6, the power remains low compared to a standard planar undulator.

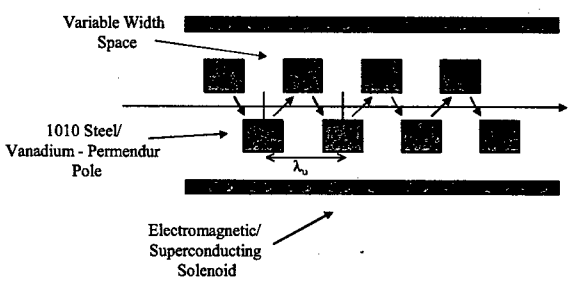

Figure 4: Schematic for a variable-period undulator.

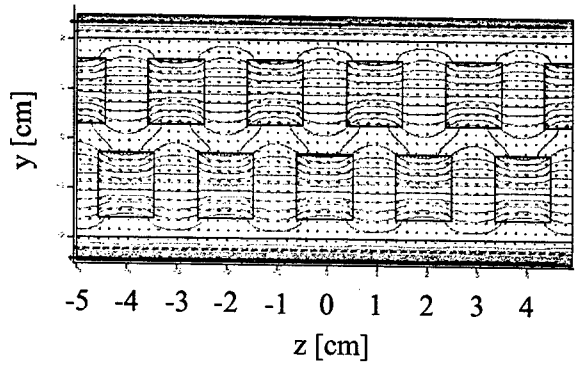

Figure 5: Magnetic flux lines show the effect of the steel poles on the solenoid field. A spatially oscillating undulator field results on axis.

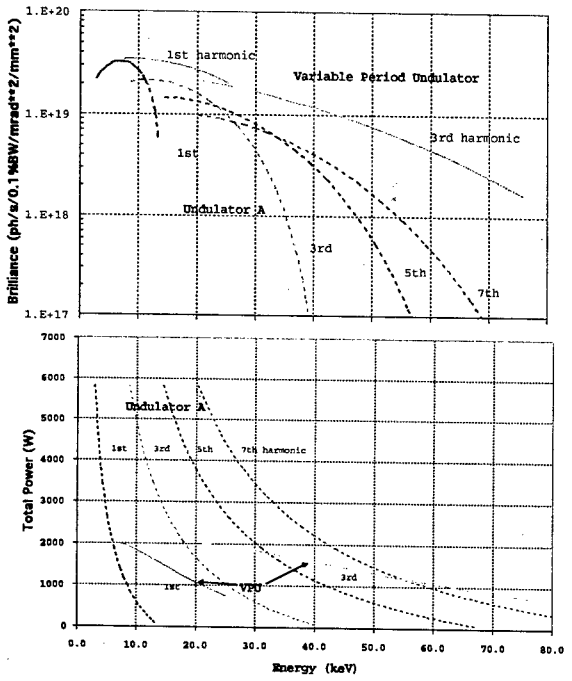

Figure 6: Brilliance and total power from a variable-period undulator, as compared to a standard APS planar Undulator A. The brilliance matches or exceeds that of Undulator A, while the power load is much lower.

VARIABLE POLARIZATION DEVICES

The radiation of a standard planar undulator is linearly polarized in the wiggle plane (usually horizontal). Some experiments, however, need circularly or elliptically polarized light, and some of those experiments are helped significantly if the polarization can be switched rapidly between left- and right-handed circular polarization.

Wigglers

Segments of the trajectory of the beam through the undulator, taken alone, will produce circular polarization–consider the lobe of the trajectory where the acceleration is constant in direction. If viewed from above or below the plane of the beam wiggles, that trajectory segment is a half circle and will produce circularly polarized light if its radiation can be separated from the radiation from the return lobe of trajectory. One scheme to accomplish this separation is the asymmetric wiggler [7], in which there is a strong field in one direction over a short distance followed by a weaker field over a longer distance. (The field integral still must be zero to avoid perturbing the beam in the rest of the storage ring.) Radiation from the weaker field is less intense and at a different energy than that from the strong field, so the net effect is quasicircular polarized radiation with one handedness above the wiggle plane and the other below.

Another scheme is an elliptical wiggler [8], where, instead of viewing the light from an off-axis angle, the beam trajectory is tilted up for one lobe and down for the other. This is accomplished by a magnetic field with a strong oscillating vertical field component and a weak oscillating horizontal field component that is shifted by a quarter period with respect to the vertical field. The elliptical trajectory gives circularly polarized light on axis and bright linearly polarized light above and below the axis. If the weaker horizontal magnetic field is provided by an electromagnet with a switchable power supply, the handedness of the circular polarization can be switched.

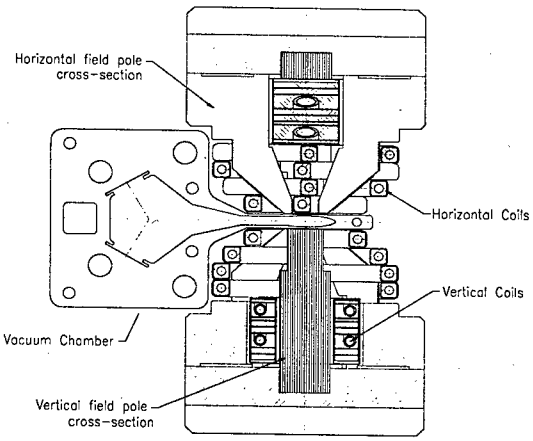

Figure 7: Cross section of an all-electromagnetic circular polarizing undulator. The top shows a cross section through horizontal-field poles, the bottom through a vertical field pole. The vertical poles are offset from the horizontal ones by a quarter period so the particle trajectory can be circular if the vertical and horizontal field strengths are equal. Depending on which coils are carrying current and the amount of current, the polarization can be circular, vertically linear, horizontally linear, or elliptical.

Undulators with a Variety of Polarizations

Switchable circular polarization can also be obtained from an undulator, and these undulators can be very flexible devices that allow a variety of different polarizations. An all-electromagnetic device in use at APS [9] is shown in Fig. 7. This undulator can deliver either-handedness of circular polarization and switch between them at up to 10 Hz. If only the vertical (or horizontal) field coils are powered, it will deliver horizontally (or vertically) linearly polarized light. Elliptical polarization is possible if both the vertical and horizontal fields are on, but delivering different field strengths.

This all-electromagnetic circularly polarizing undulator has a relatively long period of 12.8 cm and delivers light in the 0.5- to 3-keV range. To deliver higher energy light, the period length would have to be made shorter. A significantly shorter period is not feasible for a conventional electromagnetic device, however, because there would be no room for the coils. Instead, if a shorter period length is desired, a permanent magnet "Apple-style" undulator can be used.

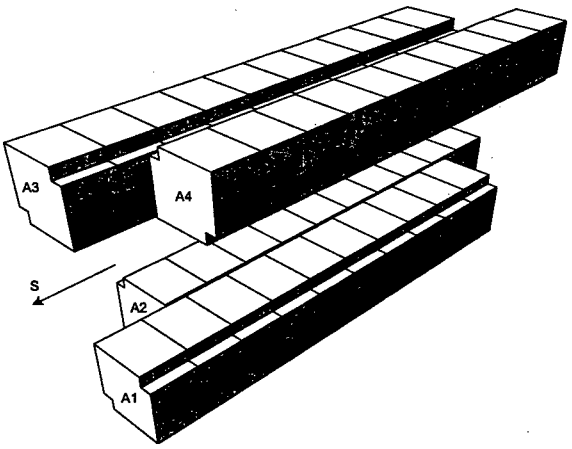

Figure 8: Apple-style undulator. Two arrays of magnets above the beam axis and two arrays below the beam create the undulator field. They can be shifted longitudinally with respect to one another in order to vary the polarization.

An Apple undulator [10], shown in Fig. 8, has four separate magnetic arrays, two above the beam and two below. In addition to opening and closing the gap to adjust the field strength, the arrays can be shifted lengthwise with respect to one another. Depending on the phase between the arrays, it can produce either vertical or horizontal linear polarization, either left- or right-handed circular polarization, or elliptical polarization. Switching between the different polarizations is possible, but involves a mechanical motion and so is not as fast as for the electromagnetic devices.

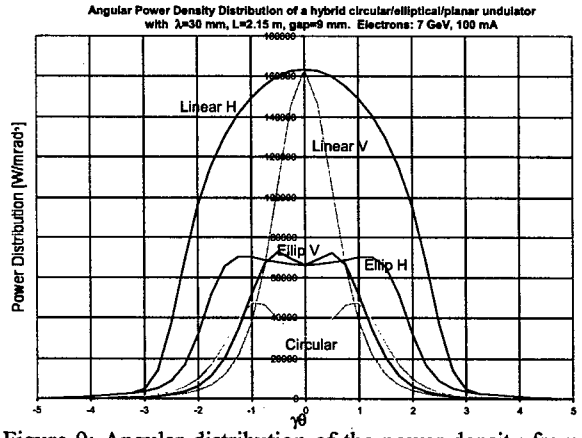

Figure 9: Angular distribution of the power density from an Apple-style undulator in different polarization modes. On-axis power density is lowest with circular polarization.

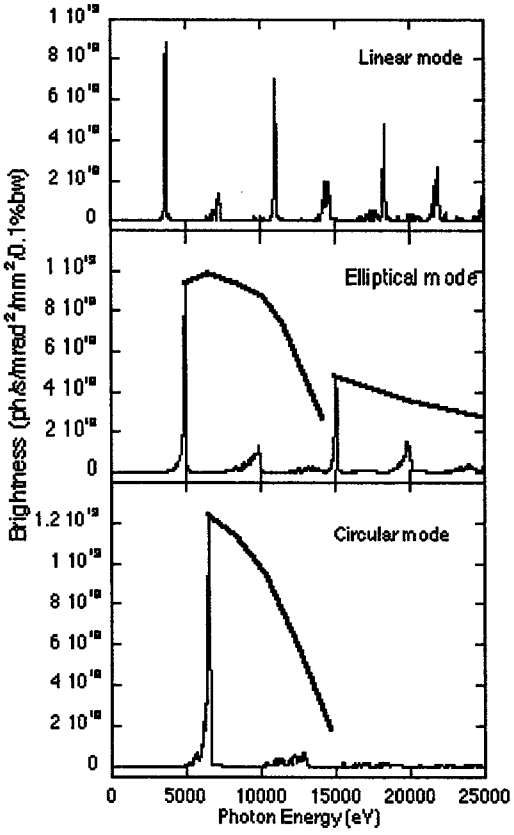

Figure 10: Brightness from an Apple-style undulator in various polarization modes. The brightness in the circular mode is high despite the reduced power.

Circular polarization that results from a helical trajectory of the particle beam has the advantage that there are no higher harmonics of the radiation on axis. This

reduces the problem of high-harmonic contamination. Another advantage comes in the spatial distribution of the power. Figure 9 shows the angular distribution of the power density from an Apple undulator in linear, circular, and elliptical polarization modes. The on-axis power is lowest in the circular mode, and the power continuing down the beamline can be reduced further with a mask that stops the ring of radiation at the angle $1/\gamma$. The lower power in circular polarization mode does not come at the cost of reduced useful brightness, though, as can be seen in Fig. 10. In circular mode the brightness is even higher than in the linear mode.

There are challenges involved with an Apple-style undulator, however. While the magnetic field of a planar undulator is very uniform through some transverse distance, the Apple magnetic field clearly is not. This results in beam focusing effects that are intrinsic to the device and that vary with gap and phase. Various schemes have been developed to correct the devices, but they don't work for all phases. As a result, much of the compensation for the device's effect on the beam orbit and tune has to be external to the device.

Figure-8 Undulators

The conventional way of producing lower-energy photons for a user is to increase the period length of the planar undulator. Particularly with the higher-energy, 6- to 8-GeV storage rings, this reaches the point where the power levels in the photon beam become excessive. Figure-8 undulators provide an alternative [2]. The magnetic array shown in Fig. 11 has an array of magnets at the center of each jaw to produce a vertical field with one period. Side magnet arrays produce a horizontal magnetic field with a period length that is twice as long. Viewed from the end, the particle beam trajectory will be a figure eight. As with a circular polarizing undulator, the particle trajectory never points directly down the nominal beam axis, so neither does most of the power. Instead, the distribution of the power resembles a < sign, as shown in Fig. 12. A mask or pinhole can block the intense power and allow only the on-axis radiation through. Although the power level is reduced compared to a conventional undulator, the flux in the fundamental harmonic remains as high as for the conventional undulator. The figure-8 undulator also produces half-integer harmonics in the radiation spectrum due to the longer period side magnet arrays. The linear polarization of the radiation can be vertical or horizontal, depending on whether it is an integer or half-integer harmonic.

ACKNOWLEDGMENTS

I thank my colleagues for the figures used here: R. Dejus for Figs. 1 and 2, S.H. Kim for Fig. 3, G. Shenoy and J. Lewellen for Figs. 4-6, J. Chavanne for Fig. 8, S. Sasaki for Figs. 9 and 10, and B. Diviacco for Figs. 11 and 12.

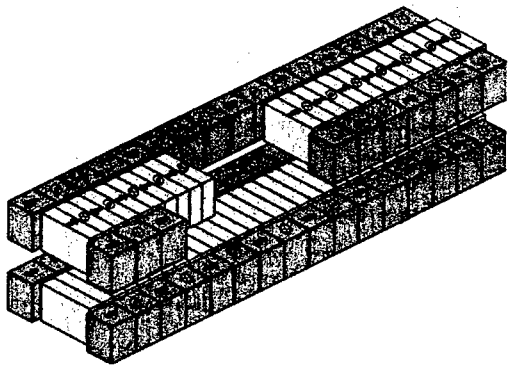

Figure 11: Magnetic structures of a figure-8 undulator. The side arrays produce a horizontal magnetic field with a period twice as long as that of the vertical field.

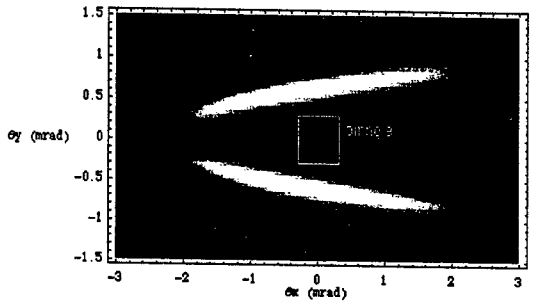

Figure 12: Spatial power distribution from a figure-8 undulator. The pinhole shown will block most of the power but still transmit as much first-harmonic flux as a conventional undulator.

REFERENCES

[1] J. Chavanne, C. Penel, B. Plan, and F. Revol, these proceedings.
[2] H. Kitamura, J. Synchr. Rad 5 (1998) 184.
[3] J. Chavanne and P. Elleaume, "Technology of Insertion Devices," in *Undulators, Wigglers and Their Applications*, H. Onuki and P. Elleaume, Eds. (Taylor & Francis, 2003), and references therein.
[4] R. Rossmanith and S. Chouhan, these proceedings.
[5] Y.C. Huang, H.C. Wang, R.H. Pantell, J. Feinstein, and J. Harris, Nucl. Instrum. Methods A341 (1994) 431.
[6] G.K. Shenoy, J. Lewellen, D. Shu, and N. Vinokurov, J. Synchr. Rad. 10 (2003) 205.
[7] H. Onuki, "Polarizing undulators and wigglers," in *Undulators, Wigglers and Their Applications*, H. Onuki and P. Elleaume, Eds. (Taylor & Francis, 2003) p. 233, and references therein.
[8] Ibid., p. 230, and references therein.
[9] E. Gluskin et al., AIP Conf. Proc.: Synchrotron Radiation Instrumentation 1999, Vol. 521, P. Pianetta, J. Arthur, and S. Brennan, Eds. (AIP 2000), pp. 344-347.
[10] S. Sasaki, Nucl. Instrum. Methods A347 (1994) 83.

RADIATION RESISTANT MAGNET R&D AT THE NSCL*

A. F. Zeller#, J. C. DeKamp, NSCL, Michigan State University, E. Lansing, MI 48824 USA

Abstract

Proposed high radiation environment projects like the Rare Isotope (RIA) and the Neutrino Factory (NF) require magnetic elements that are radiation resistant. Development of radiation resistant magnets at the National Superconducting Cyclotron Lab (NSCL) has been underway for several years. The focus has been on superconducting devices, as resistive solutions have been know for two decades, but have relatively small current densities. Higher current density options than can be commercially manufactured have been examined. Several solutions for superconducting versions use radiation resistant epoxies, for medium level hardness, and variations on Cable-in-Conduit-Conductor (CICC) for high-radiation areas. These allow engineering current densities of more than 100 A/mm^2.

INTRODUCTION

Proposed projects like RIA [1] and the NF [2] require strong magnets that must operate in high radiation environments. Because failures result in significant down time, due to the difficulties of working in a radioactive area, magnetic elements must be radiation resistant for the lifetime of the project. It is possible and likely that resistive magnets can be used in various places, but there is a strong desire to use superconducting coils because the engineering current density can be up to ten times higher. This is particularly important for quadrupoles where high gradients and large apertures are required for acceptance of secondary particles.

The most radiation-sensitive part of a magnet is the electrical insulation. Conductors like copper and aluminum are many orders of magnitude more radiation resistant than organic insulators. Even the superconductors, NbTi and Nb_3Sn, are at least twenty-five times more resistant than the common organic epoxies and ten times better than organic insulation [3]. Attempting to invent new radiation resistant organic materials is very expensive and very likely to fail; therefore, development of coils using present materials in new ways has been started.

RESISTIVE OPTIONS

The successful solution used at Los Alamos National Lab and the Paul Scherrer Institute for radiation resistant magnets is to surround standard copper conductor, either hollow or solid, with magnesium oxide (MgO) inside a copper sheath. The coils are then potted with solder [4]. Work at KEK duplicates this except the potting is done with an inorganic matrix [5].

Aluminum conductor that has an insulating anodized layer has been used since the 1950's [6], but the higher resistivity of aluminum and the brittleness of the anodized layer have limited its usefulness. A potentially more productive approach is to have a thin aluminum layer on the outside of a hollow copper conductor [7]. The single attempt at this met with limited success and was not attempted on a commercial scale. A manufacturer was located who tried unsuccessfully to co-extrude aluminum around the hollow copper conductor. Because of the thinness of the anodized layer (~0.01 mm), a more compact coil using hollow aluminum conductor can be fabricated. Unfortunately, for the same temperature rise in the cooling water, this gains about 10% over a copper conductor in the same coil cross section.

SUPERCONDUCTING COILS

Superconducting coil options can be divided up into two groups: low and high current density. High current density superconducting coils use some type of epoxy to constrain the conductor from moving due to the Lorenz Forces. Current densities in the coil (engineering current densities) range from 60 A/mm^2 to well over 500 A/mm^2, depending on the forces and the magnetic field. Low current density options are cryostable coils or those wound with CICC. The low current density solutions use intimate contact between the conductor and liquid helium for stability. It has the big advantage in that large amounts of nuclear heating can be removed without affecting magnet operation.

High current density options

Presently, a commercial company, Composite Technology Development, Inc. (CTD) is working on more radiation resistant epoxies. They have developed several systems that increase the radiation resistance by factors of two or three, relative to standard epoxies. Polyimids, like Kapton® provide excellent radiation resistance and would be used as primary wire insulation. Test windings with CTD-422 epoxy system are underway to determine whether the NSCL's standard wet winding method of coil fabrication is possible. This would lead to significant improvements in coil lifetimes in areas where the expected doses are ~10 MGy per year.

Lower current options

It should be pointed out that lower current is only with respect to potted superconducting technology and that it is 3-10 times higher than resistive technology when the magnets have to exhibit long-term reliability. The absolute need to construct magnets that require no maintenance for 10-20 years tends to lead to lower current density

*Supported in part under NSF grants PHY-0110253, -0104619, -9809799 and DOE grant DE-FG0200ER41144
#zeller@nscl.msu.edu

0-7803-7738-9/03/$17.00 © 2003 IEEE

solutions. Additionally, quench protection issues also go in the direction of lower current densities. Many cryostable coils have been constructed with G10 as the only insulation. Substituting an inorganic, such as alumna (Al_2O_3), should provide a way to produce a radiation resistant magnet with current densities of 40-60 A/mm^2. Alumna is, however, much more brittle than G10 or other composite materials, so it would require demonstration before using it in a deployed magnet. One possible problem with using a cryostable magnet in a high radiation environment is the coils are not self-protecting in case of a quench. They need some external energy absorption system with an active quench detection circuit. Making these radiation hard may be difficult. Figure 1 shows a test wind of an inorganic cryostable coil. Coil height is approximately 50 mm. A second coil that will be inserted in the bore of a solenoid for stability testing is presently being wound.

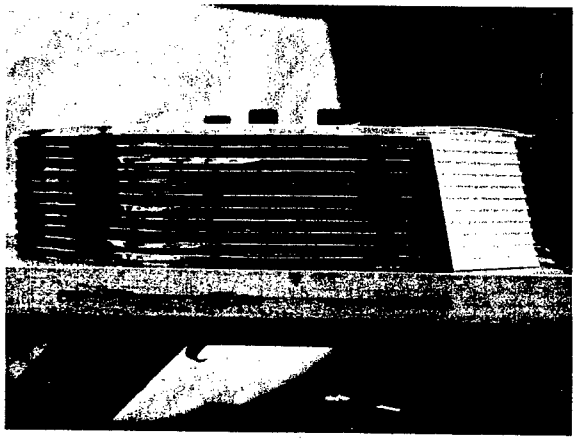

Figure 1: All-inorganic, cryostable test coil.

CICC Options

CICC has advantages over cryostable radiation hard magnets:

- Higher current densities are possible.
- Higher helium mass flow is possible for heat removal.
- Less complicated cryostats are required.
- Coil winding easier.

Disadvantages are more costly conductor and the very limited bending of the conductor due to the brittleness of the insulators.

Anodized CICC

Aluminum conduit can be anodized on the inside to leave the outside available for use as a welding surface, so the entire coil is a single, self-supporting structure [8]. Because of the difficulty in getting good conductor fill-fractions, a test loop was constructed for testing at the Plasma Science and Fusion Center at MIT, shown in figure 2. The conduit is first bent to the final shape and then anodized. The 325 strands of 0.25 mm are then forced through the conduit. Since this last step is difficult, a fill-factor of 40% was achieved. Normal CICC is typically 70-90%, so the stability had to be tested.

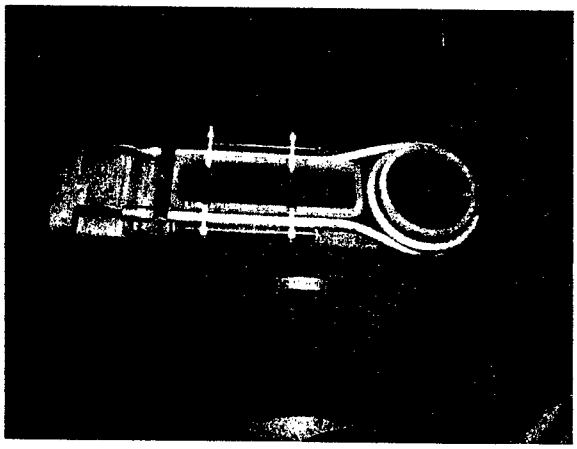

Figure 2: Test loop in testing support.

The individual wires in the conductor are made from material that is optimized for high-field operation, while the test magnets was intended for short on-times at fields less than 5 T. The results are shown in figure 3.

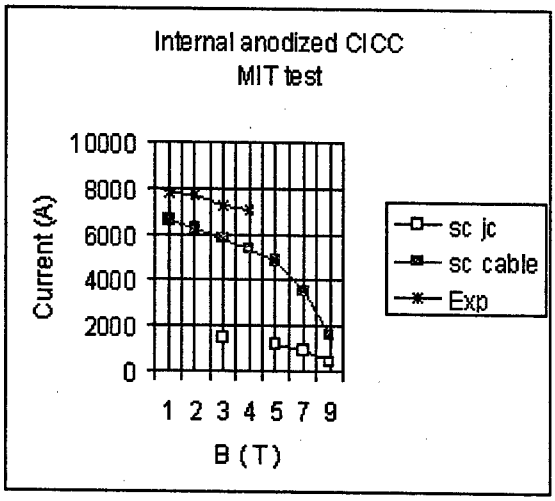

Figure 3: Test results. The curve labeled "sc jc" is the current density in the superconductor in A/mm

The experimental results appear higher than the short sample limit, but the cable short sample is derived by multiplying the individual guaranteed wire critical current by the number of wires. The actual short sample will be higher, and the background field is only accurate to within 10%. It would appear there isn't a problem with stability due to a low fill factor. Since the projected single turn cross section is 1 cm^2, the engineering current density is 70 A/mm^2. The conductor has a copper-to-superconductor

ratio of 3:1, so by decreasing it to 1.5:1, we can double the current density. In addition, if we use a conductor optimized for 2-4 T, a further factor of two increase can be obtained. The reduction in copper-to-superconductor may impact the stability, though, so further test are planned. Because the power supply used in the test is limited to 10 kA, smaller conduit is being used, as well as fewer individual conductors.

Even though the anodized layer is brittle, it is still possible to bend it over some radius before it fails. The sulfuric acid process used for the test pieces produce an ~ 18 μm thick layer. This will withstand a 500 V potential. Bending the 9.5 mm diameter conduit to a radius of 250 mm reduced the break down voltage to 100 V. Complete failure occurred at 200 mm.

High magnetic field operation (> 9 T) requires the use of Nb_3Sn as the superconducting material. Because this material is brittle, the coil must be formed first, anodized, the unreacted conductor inserted, then heat treatment to form the superconducting compound. Aluminum melts below the heat treatment temperature, so something like titanium would be needed. Considerable work would need to be done to make this practical.

Metal Oxide Insulated CICC

Magnesium oxide insulated conductor has been used successfully for at least two decades, so a superconducting version would be very desirable. One would simply fill the cooling passage with superconductor, as shown in figure 4.

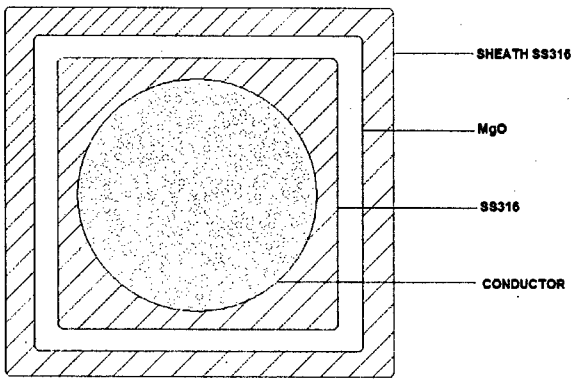

Figure 4: Metal oxide insulated CICC.

The difference between standard CICC is the addition of the sheath around the metal oxide. This reduces the available current density, although some of it can be recovered because the inner conduit can be made thinner because the outer conduit adds to the strength. Taking a nominal 15 mm^2 CICC and adding 1 mm each of metal oxide and stainless steel, reduces the current density by about 20%. There are several advantages to this type of conductor that outweigh any lost current density:

- The conductor is flexible.
- Magnesium oxide, aluminum oxide or spinel can be used for insulation.
- It is likely that Nb_3Sn with wind and react technology may be used.

One problem with the metal oxide insulated conductor when used in resistive magnets is the loss of resistance when the metal oxide absorbs water from the air. The conductor is sealed, but it is difficult to completely eliminate it. For operation at liquid helium temperatures, any trapped moisture or air is frozen out. The three possible metal oxides have different radiation resistances, with spinel (an aluminum and magnesium oxide) being the best. Unfortunately, it is more expensive and it's drawing properties not as good as MgO. All three of the oxides are used in high temperature applications, so they can readily withstand the 700 C heat treatment temperatures used in formation of Nb_3Sn, opening up operation at the high field needed in the NF.

A collaboration with the original manufacturer of the metal oxide insulated conductor, Pyrotenax (now Tyco Thermal Controls) has been started to examine these possibilities.

SUMMARY

Several lines of development are being pursued in the development of radiation resistant coils for use in future accelerators. The most promising are the use of anodization to produce the insulation and other metal oxides for insulation of CICC coils.

ACKNOWLEGMENTS

The assistance of D. Zdanowitz and J. Spencer at Great Lakes Metal Finishing for developing the anodizing process, P. Fabian and M. Tupper at CTD, R. Curran and P. Malone at Tyco and T. Antaya and M. Takayasu is greatly appreciated and acknowledged.

REFERENCES

[1] B. S. Sherrill, NIMB (2003), in press.
[2] http://www.fnal.gov/projects/muon_collider/nu-factory/
[3] M. E. Sawan and P. L. Walstrom, Fusion Technology 10 (1986) 741.
[4] A. Harvey and S. A. Walker, IEEE Trans. Nucl. Sci. NS-16 (1969) 611.
[5] K. H. Tanaka et al, IEEE Trans on Applied Superconductivity 10 (2000) 206.
[6] P. Smits, Modern Metals 14(#7) (1958) 30.
[7] W. J. Leonhardt, Proc. 1989 IEEE PAC (1989) 366.
[8] A. F. Zeller, Adv in Cryo Eng 48A (2002) 255.

PERFORMANCE SUMMARY OF THE HELICAL MAGNETS FOR RHIC*

E. Willen, M. Anerella, J. Escallier, G. Ganetis, A. Ghosh, R. Gupta, M. Harrison, A. Jain, W. MacKay, A. Marone, J. Muratore, S. Plate, R. Thomas, P. Wanderer and KC Wu, BNL, Upton, NY 11973, USA
M. Okamura, RIKEN, Japan

Abstract

A series of four Snake and eight Rotator superconducting helical magnet assemblies has been built and installed in RHIC to control the polarization of protons during acceleration and storage in that machine. Each of these assemblies consists of four 2.4 m long dipole magnets in each of which the field rotates through 360 degrees along the magnet's length. The magnets were made by winding one millimeter diameter superconducting 7-strand cable into slots milled into thick-walled aluminum tubes. The magnets produce 4 Tesla field at a current of 320 amperes and are quench-protected with 0.050 ohm resistors placed across the winding in each slot. A total of 48 of these 2.4 m magnets has been built, tested and installed. This paper summarizes their quench performance as well as their field uniformity, of which the integral field is the most critical. All magnets reached the required operating field level of 4 T, and the integral field of the magnets was generally about half of the maximum permissible level of 0.050 Tesla meters.

INTRODUCTION

Magnets to control proton spin were required in RHIC to enable a program of spin physics using polarized proton collisions [1]. These magnets precess the proton spin from up to down and back again on each orbit around the ring, thereby avoiding depolarizing resonances during acceleration. They also precess the proton spin at each of two experimental detectors from vertical to longitudinal for the study of such oriented collisions. The magnets were built over several years and are now completely installed and are operational beginning with the 2003 RHIC running period.

LAYOUT

To achieve the required spin rotations, helical magnets were developed in which the dipole field rotates through 360° in a distance of 2.4 m. Helical magnets offered a more compact and efficient design than could be achieved with a combination of rotated dipole magnets. Precessing the proton spin without a net deflection of the orbit was achieved by combining four of the helical magnets into one long cryostatted device with different field strength, helix direction, and helix orientation in each device, depending on its task. They are called "Snakes" because of the serpentine particle trajectory through the device. The available space in the RHIC lattice determined the overall length and therefore the required field of the magnets. The coil inner diameter is a large 100 mm to allow adequate space for the beam trajectory (the RHIC dipoles have a coil aperture of 80 mm). Four Snakes were required, two in each ring, to avoid depolarizing resonances, and eight Snakes, also called Rotators, were required to orient the spin at the detectors. Thus, a total of 48, 2.4 m long helical magnets was required. A low operating current was needed to ease the cryogenic load from the numerous power leads to these magnets, which are spread around the ring.

*Work supported in part by the U.S. Department of Energy.

DESIGN

The design has been described in previous papers [2-4]. Briefly, the coils are made by placing conductor, a Kapton-wrapped cable made of seven, twisted 0.33 mm NbTi superconducting wires, into slots milled into aluminum cylinders. These cylinders with their windings are later overwrapped with a wet layup of fiberglass/epoxy, then machined to a precise diameter. Each magnet has an inner coil with seven slots and an outer coil with nine slots. The two coils are assembled into a laminated yoke made of one piece laminations to make a single, 2.4 m long helical dipole. End plates are added and electrical connections including quench protection resistors across each winding are made. Four of these helical dipoles are assembled into a stainless steel shell to complete the helium enclosure and the support structure for the final cryostatted magnet, which operates with forced flow helium at 4.5 K. A few parameters of the dipole magnet are given in Table I.

Table I: Selected parameters of the helical dipole.

Parameter	Units	Value
Aperture	mm	100
Magnetic length	m	2.4
Field	T	4
Current	A	320
Number of turns		1680
Inductance	H	4.8
Stored energy @ 4 T	kJ	240
Diameter of yoke	mm	355.6
Num. of strands in cable		7
Strand diameter	mm	0.33
Cu to non-Cu ratio		2.5:1

CONSTRUCTION

The coils are constructed by manually placing the Kapton-wrapped cable into the slots in an orderly array. The sides of the slots have been previously insulated with Kapton for good electrical insulation. A layer of prepreg

0-7803-7738-9/03/$17.00 © 2003 IEEE

material (B-stage epoxy/fiberglass cloth) is placed between each layer. When all the turns are in place, press plates are placed on top of the windings and the coil is wrapped with tensioned Kevlar cord, then placed in an oven where the epoxy is cured while the coil rotates. The turns move radially inward as the epoxy softens and flows in this curing operation. The end result is a compact matrix of cable turns, Kapton, fiberglass and epoxy filling the slot. A photograph of a coil is shown in Fig. 1.

Figure 1: Photograph of a helical coil with conductors.

The thickness of the prepreg material, initially 0.25 mm but finally 0.075 mm after compression, at first keeps the turns at a larger radial position. As the turns are heated and moved radially inward by the tensioned Kevlar, extra cable length is generated because of the helix along the length and because of the crossover from side to side in the ends. This extra length is accommodated by providing greater slot width in the ends. The extra space, too large to be completely filled with the prepreg epoxy, is later filled with ceramic-loaded epoxy.

MEASUREMENTS

Numerous electrical tests during construction ensured that most construction faults were caught. An occasional turn-to-turn short or coil-to-ground fault occurred in the construction program caused by misplaced turns, generally from cable buckling while curing. Abbreviated warm measurements verified that all windings were connected in the proper sequence. All the 48 magnets were cryogenically tested for quench performance and field quality. Six magnets developed faults during or after cryogenic testing and required disassembly and rewinding of a particular winding in the coil. Detailed field measurements for each magnet are available in various formats at Brookhaven.

Training

Most of the 48 magnets required some training to reach the desired 4 T field (320 A). Fig. 2 shows the distribution of first quenches and Fig. 3 shows the number of quenches before the current exceeded 320 A. Nine magnets required no training, 28 required three or less, and 11 required more than three. The training is attributed to a paucity of epoxy in the windings, revealed as voids in those windings that were on occasion taken apart or replaced to correct faults. This was a problem particularly in the ends where slots were wider. Several of the early coils required excessive training (up to 18 quenches) but this problem improved as experience in placing and compressing the cable into the slots was gained by the technical staff. Virtually all the training occurred in the inner coils in one of the windings away from the midplane, the region of highest Lorentz forces and therefore as expected. In those magnets with thermal cycles, the magnets for the most part remembered their training, except for several of the early magnets where some retraining was necessary. This is shown in Fig. 4.

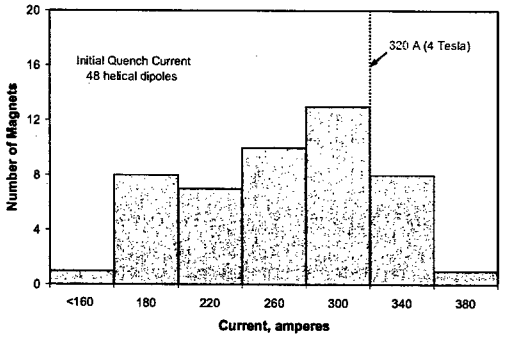

Figure 2: Distribution of initial quench currents.

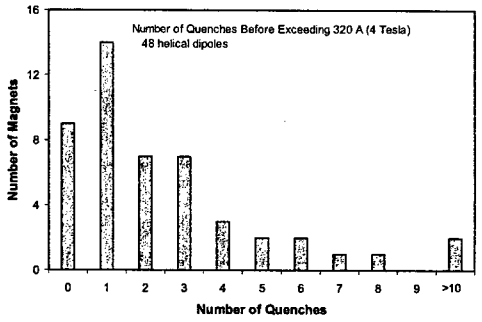

Figure 3: Number of required quenches.

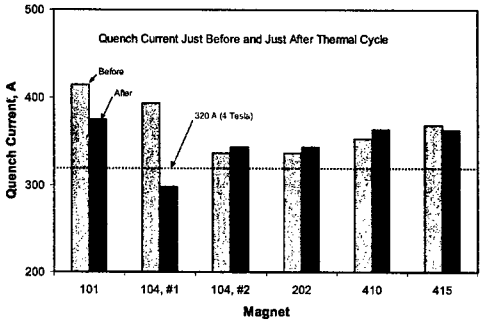

Figure 4: Retraining after thermal cycle.

Integral Field

An important requirement for the helical magnets was that the integral field be small or zero in order to avoid net deflections of the beam. The specification was that the field integral be less than 0.025 T·m. This was measured with a long, rotating coil with a radius of 25 mm that extended the full length of the magnet including any fringe field at the ends. A typical measurement is shown in Fig. 5 where the maximum of the residual is 0.018 T·m, well within the required limit. This was typical for all the magnets; none had a value greater than 50% of the limit.

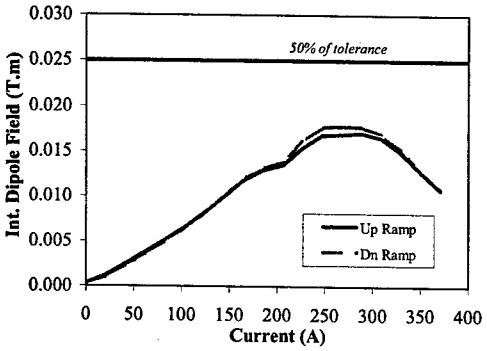

Figure 5: Example of measured integral field. The structure in the curves is due to limitations in the uniformity of the measuring coil.

Multipoles

In a helical magnet, all field multipoles (harmonics) oscillate with axial position. Over the length of the magnet, the effect of these multipoles on the particle trajectory tends to cancel, so the requirements on field quality are less stringent than for normal accelerator magnets: the local $\Delta|B|/|B|$ should be kept reasonably below 1%. A rotating coil to measure the harmonics should be as short as possible in order to avoid signal cancellation. The measuring coil used to measure these magnets was only 51 mm long, about 2% of the wavelength of the helix. It had a radius of 34.2 mm, and the reference radius used to express the harmonics is 31 mm. A total of 56 turns in the tangential winding of the coil ensured adequate signal strength for good measurements. Flux cancellation because of the helical field reduces the dipole field by 0.25% for the dipole term and by 2.7% for the 30-pole term, an effect corrected in the reported results.

Measurements at many currents were typically made at a single location in the center of the magnet and as a function of axial position at several currents [5]. The axial variations of the quadrupole and the sextupole components are shown in Fig. 6. The asymmetry in the quadrupole component along the length of the magnet varies magnet to magnet but the data shown are typical and are believed to result from a combination of coil asymmetries inside the iron yoke and the centering technique used. The variation of the sextupole amplitude with current results from iron saturation in the yoke.

The normal sextupole field as a function of current is shown in Fig. 7 (left) for most of the magnets on a single plot. The right side shows the same data normalized to zero at 102 A on the up ramp. The harmonics are expressed in a coordinate system where the y-axis coincides with the dipole field direction. This allowed harmonic is quite consistent over all the magnets.

The following conclusions can be drawn:

- There is considerable magnet-to-magnet variation in the harmonics resulting from geometric differences in the magnets.

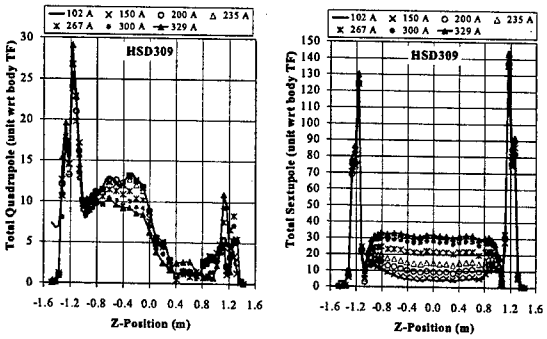

Figure 6: Example of measured quadrupole and sextupole fields in a typical magnet.

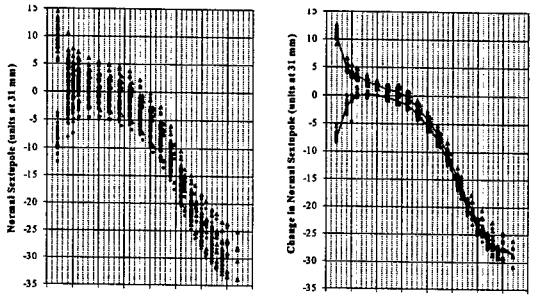

Figure 7: Unnormalized (left) and normalized sextupole harmonic for the magnets.

- The current dependence of the harmonics has small magnet-to-magnet variations.
- Z-scans in small axial increments show significant axial variation in the lower order harmonics.
- All harmonics are within safe limits for machine operation.

REFERENCES

Note: A number of these papers are available at the BNL web site.

[1] Design Manual: Polarized Proton Collider at RHIC, M. Syphers, Editor, BNL, July, 1998.

[2] E. Willen, R. Gupta, A. Jain, E. Kelly, G. Morgan, J. Muratore, R. Thomas, A Helical Magnet Design for RHIC, PAC97, Vancouver, May, 1997.

[3] E. Willen, E. Kelly, M. Anerella, J. Escallier, G. Ganetis, A. Ghosh, A. Jain, A. Marone, G. Morgan, J. Muratore, A. Prodell, P. Wanderer, Construction of Helical Magnets for RHIC, PAC99, New York, March/April, 1999.

[4] E. Willen, M. Anerella, J. Escallier, G. Ganetis, A. Ghosh, A. Jain, E. Kelly, G. Morgan, J. Muratore, A. Prodell, P. Wanderer, Performance of Helical Magnets for RHIC, MT16, Ponte Vedra, FL, September/October 1999.

[5] A. Jain, G. Ganetis, W. Louie, A. Marone, J, Muratore, R. Thomas, P. Wanderer, E. Willen, Measurements of Field Quality in Helical Dipoles for RHIC, Proc. 12th International Magnet Measurement Workshop, October, 2002.

PRODUCTION AND TESTING CONSIDERATIONS FOR CESR-C WIGGLER MAGNETS *

D. Rice†, S. Chapman, R. Gallagher, Y. He, J. Kandaswamy, V. Medjidzade, A. Mikhailichenko, N. Mistry, T. Moore, S. Richichi, K. Smolenski, A.B. Temnykh, W. Trask,
Laboratory for Elementary-Particle Physics, Cornell University, Ithaca, NY, USA
E. Smith, Laboratory of Atomic and Solid State Physics, Cornell University

Abstract

After construction of a prototype unit, five additional wiggler magnets for the CESR-c conversion have been completed at a rate exceeding one per month. These 2.1 T superferric magnets are built and assembled primarily in house with a minimal staff. We describe the general design and fabrication methods for these magnets. An additional 10 magnets will be constructed to complete the complement in the ring plus two spare units.

INTRODUCTION

The CESR-c conversion [1] at Cornell University's Laboratory for Elementary-Particle Physics will increase the world data set in the 3 to 5 GeV c.m. range by factors of 20 to 100 in the next 4 years. Achieving luminosities well above 10^{32} cm^{-2}-sec^{-1} in a machine optimized for 10.6 GeV c.m. energy however requires significant modifications. In addition to the lower beam rigidity, the loss of a factor of 20 in radiation damping at the lower energy affects injection, single beam stability, and luminosity performance.

Wiggler Design Requirements

Restoration of this radiation damping is the dominant hardware task in the CESR-c conversion program. Over 15 m of 2.1 Tesla wiggler magnets generate the radiation to accomplish the damping. Details of the magnetic design may be found in reference [2]. The peak field is chosen as high as possible given limits on acceptable energy spread in the beam, which scales as $\sqrt{B}$.

Field quality requirements are high because of their dominant role in the CESR guide field. In the CESR-c layout the wigglers produce 90% of the synchrotron radiation in the ring. Furthermore the different horizontal closed orbits (up to ±20 mm) of the electrons and positrons used to separate the beams at parasitic crossings causes them to pass through the wigglers far off the central axis with opposite displacements. Investigations with tracking codes have shown that the field at the (longitudinal) center of each wiggler pole must drop off no more than 0.3% at ±45 mm (the vacuum chamber aperture). [3,4] A ±25 mm vertical beam-stay-clear mandates an unusually large gap between poles.

The requirements above quickly led us to choose superferric technology over conventional copper-ferric (too much power) or permanent magnet (precluded by large pole spacing).

* Work supported by the U.S. National Science Foundation
† dhr1@cornell.edu

WIGGLER DESIGN

Principle Design Features

Having chosen the 2.1 T peak field as described above, the period of the wiggler was set at 40 cm as a compromise between the inherent vertical non-linearities (increasing as $1/\lambda^2$ where λ is the pole period) and the field roll-off induced non-linearities that increase as λ^2. The length was chosen as 1.725 m flange-to-flange (1.3 m active length) to optimize use of available space.

We spent considerable time deciding between odd and even pole configurations. While the arguments are too detailed to cover here, the greater flexibility in operating current (field quality) provided by the even pole arrangement carried the decision in the end (units 1 and 2 are 7-pole, units 3 and higher are 8-pole). Four full-length (20 cm long) inner poles are bordered by two 15 cm poles, followed in turn by end poles 10 cm long and with reduced strength to give ¼ bend angle relative to the central poles. This configuration gives zero net angle and displacement, and minimizes the asymmetry in trajectory through the wiggler.

The cold mass is enclosed in two separate volumes of liquid helium, joined by several jumper tubes with bellows. This cold mass is shielded from the warm beam pipe and cylindrical enclosure by liquid nitrogen cooled aluminum sheets. A companion paper [5] in this conference describes the cryostat in detail.

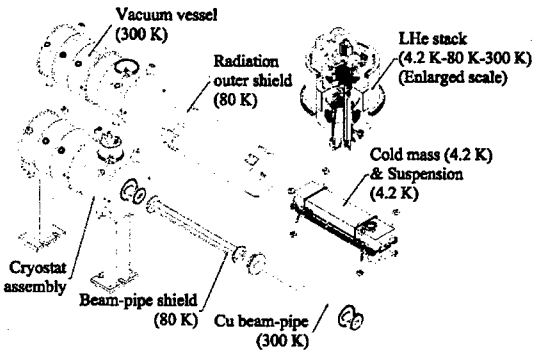

Figure 1: CESR-c wiggler components

Cryogens are provided from a 150 m long transfer line tapping into a preexisting system for the CESR superconducting RF cavities. Local PID controllers

0-7803-7738-9/03/$17.00 © 2003 IEEE

regulate cryostat He gas pressure and LHe and LN_2 liquid levels. Each wiggler has its own main and trim (end poles) power supplies.

MANUFACTURING PLAN

For both scheduling and cost considerations, most of the fabrication and all assembly and testing are done in house. Outside work included:

- Machining and plating (where appropriate) of pole pieces, large iron and stainless-steel pieces, and several small pieces required in large quantities.
- Fabrication and leak checking of the cryostat outer jacket with all flanges.
- Fabrication of rolled or formed Al 77k shields.
- Cu extrusions for the beam line vacuum chamber.

Manufacturing Components

The component tasks of manufacturing the wigglers are easily broken into several parts that can be performed in a pipelined manner. These are described individually.

1) Coil winding: Coils are wound directly on individual machined and plated low carbon iron pole pieces. The main poles require 660 turns of 0.75 mm Formvar insulated Nb-Ti wire with 80 μm filament diameter and 1.35:1 Cu:SC ratio. The wire is wet wound with Epotek T905™ epoxy, stopping every five layers and clamping with shim blocks to maintain uniform dimensions - one hour is sufficient to set the wires in place. After a couple of weeks training, one winder can complete one main pole per day, or a trim pole (two windings) in two days.

2a) Placement and preloading of poles: The finished poles are placed on a 70 mm thick "yoke plate" that serves as flux return and support. Since the windings of adjacent poles experience large magnetic forces under operation, the coil assembly must be preloaded with about 16 tons of force (~40 MPa pressure on coils) to prevent coil motion after cooldown and the accompanying shrinkage of material. Because of small variations in final coil package dimensions, the gaps between coils must be filled with custom fitted shims to assure uniform pressure.

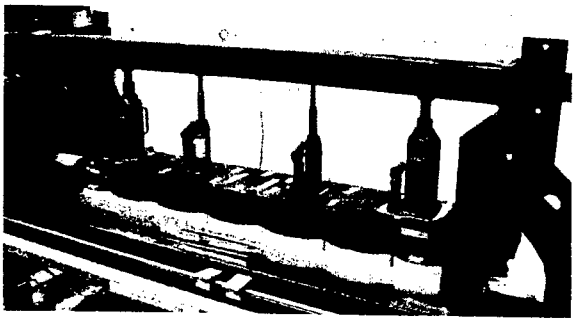

Figure 2: Magnet preload (yellow cylinder on the left)

Once the preload pressure is applied the pole pieces are pinned in place and endplates installed. After preload the wiring on the half-magnet is completed and checked.

2b) Cold mass enclosure: Next the assembly is placed on the stainless-steel (s-s) base plate and 6 mm s-s plates welded on the sides and ends. A preliminary leak-check of the half cold mass assembly is done at this time since the connecting tubes cannot be rewelded once the connecting wires are installed in them. Then the top and bottom s-s plates (also 6 mm) are welded in place. The two half cold masses are assembled around the beam pipe and inner heat shield, and leak checked.

3) Assembly in cryostat: Once assembled, the whole cold mass assembly is placed on rails ready for the cryostat and 77 K heat shield. A short section of the outer cryostat shell is first put in place to give access for installation of wiring and tubing. Once the stack (current lead and instrumentation feedthrough) and cryogen tubing connections are made up, the second shell section is installed and suspension adjusted to properly position the cold mass. Vacuum leak checks are performed before and after final welding of the end plates.

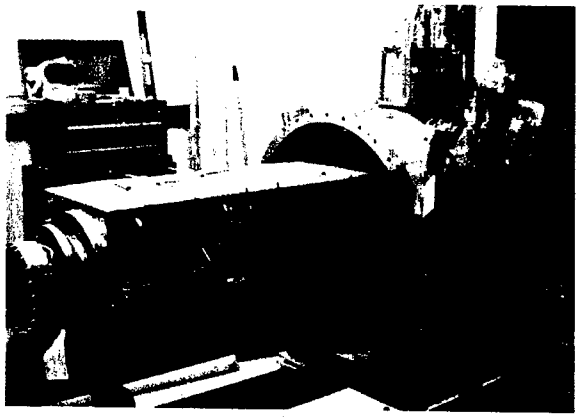

Figure 3: Cold mass in first cryostat section with stack

4) Training and field mapping: The finished wiggler is tested using LHe from a dewar (recovering the cold gas) and LN_2 from the lab distribution system. During cool down cryogen usage and temperatures vs. time are recorded to check for irregularities. Magnet current is increased to full design level with one to three training quenches encountered in the first six wigglers. Field mapping uses both precision Hall probes and a flip coil for integral measurements. After field mapping the current is increased to ~6% above maximum operating level. LHe use is recorded throughout the testing.

Alignment: During assembly the magnet iron is referenced to the cold mass enclosure, then the cold mass enclosure to survey fixtures on the end flanges of the cryostat using a total station (theodolite) instrument. The final uncertainty in positioning of the magnet in the accelerator reference system is estimated to be ± ½ mm in position and ± ½ mr roll.

Manufacturing Scheduling

In a continuous production mode, each of the tasks, 1-4, above can be done overlapping with the others, though in practice our limited resources are often shared between

two or more, reducing the pipelining efficiency. Figure 4 shows how these tasks are scheduled for several wigglers.

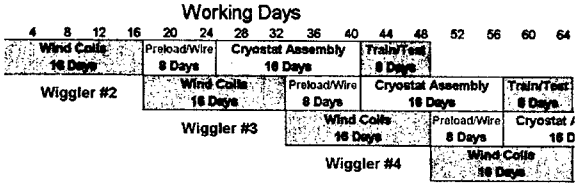

Figure 4: Pipelined manufacturing schedule

The schedule above is based on our experience with the last three wigglers (units 4-6) built for installation in the storage ring during Spring, 2003.

In addition, there are several asynchronous tasks such as beam line chamber fabrication and testing, assembling 77 K heat shields, constructing wiring harness, bending tubing, etc. Several other operations are hidden in the schedule above - for example, we have two coil winders who spend 2/3 time actually winding, and the balance doing preparation & cleanup work and occasional work on other projects.

During the production period (one wiggler every three weeks) internal resources averaged about five full time equivalent (FTE) senior technical and supervisory people and 13 FTE technical support people. The cost for parts and outside machining and fabrication was about $80k per wiggler unit.

TESTING PROGRAM

Evolution of the Testing Program

The testing program evolved significantly during the manufacture of the first six wiggler units. Initially we cold tested most of the individual pole windings before assembly on to the yoke plate. Before welding the LHe enclosure around the half-magnets, after which replacing a defective pole becomes much more difficult, we tested the entire magnet in a vertical dewar. Finally we tested the completed unit in its permanent cryostat.

The single pole cold tests, even when we made fixtures to test two at once, were labor intensive and required significant quantities of LHe. We quickly reduced this program to testing one or two poles per magnet, then only if the coil winders or warm test (see below) suggested some problem or change in technique. No poles failed this test once the winding technique was established.

The vertical test was abandoned after wigglers #2 and #3 showed no failures. (The prototype wiggler, #1, developed a ground fault in the final horizontal test; subsequently we improved the insulation around the coil.) Dropping this test not only saves a week in the schedule and about $3,000 of LHe, but not having the coils saturated with helium before assembly in the cold mass enclosure dramatically improves the sensitivity of the leak check process.

Final Testing Program

During coil production (before the individual cold tests were cut back) a warm test of individual poles was developed that proved effective in finding shorted turns and turn count errors. A pole is passed under a long, narrow pickup coil in 1 cm steps. The change in integrated voltage from the coil between zero and 1 amp current is compared with a reference pole. Differences equivalent to 0.2 turns are readily visible, as are displacements in winding location of 20-30 μm.

This warm test, combined with the vigilance of the coil winders, has resulted in 100% good poles being installed in the wigglers with no further tests. Insulation testing is of course done at several stages of assembly - starting with 1000 volt tests of individual coils, being reduced to 500 volts after final assembly of the wiggler. Wiring continuity checks are also performed at several points.

The last three wigglers produced were cooled to LHe temperatures only after complete assembly into the cryostat. The time to replace a pole at this stage is approximately two weeks (but an additional penalty is disruption of production). So far this procedure has been effective. The measurements during this final test were briefly described above. Other than a small skew quadrupole component in the first two (7 pole) wigglers [6], the measured field has met all specifications.

SUMMARY & ACKNOWLEDGEMENTS

The CESR-c wiggler design has proven to be robust and lends itself easily to moderate scale production. The field quality meets specifications and is very reproducible. We have developed an effective testing program that works well with the aggressive production schedule.

We gratefully acknowledge the talented technical support staff at LEPP. In particular we thank machine shop supervisors Chuck Firenze and John Kaminski for their suggestions to optimize the design for production and tireless work with outside machine shops.

REFERENCES

[1] D. Rice, "CESR-c - A Frontier Machine for QCD and Weak Decay Physics in the Charm Region," EPAC'02, Paris, June 2002, p. 428

[2] A. Mikhailichenko, "Optimized Wiggler Magnet for CESR," PAC'01, Chicago, June 2001, p. 3648

[3] J. Crittenden et al., "Design Considerations for the CESR-c Wiggler Magnets," PAC'03, Portland, May 2003, WPAE009

[4] D. Sagan, "A Symplectic Model for Wigglers," PAC'03, Portland, May 2003, MPPG006

[5] Y. He et al., "Design and Operation of the Cryostat for the CESR-c Superconducting Wiggler Magnets," PAC'03, Portland, May 2003, WPPE037

[6] A. Temnykh, "Vibrating Wire and Flipping Coil Magnetic Measurement of a CESR-c 7-pole Wiggler Magnet," PAC'03, Portland, May 2003, MPPG007

MAGNETIC FIELD MEASUREMENTS OF THE NB_3SN COMMON COIL DIPOLE RD3C

L. Chiesa#, S. Caspi, D.R. Dietderich, P. Ferracin, S.A. Gourlay, R.R. Hafalia, A.F. Lietzke, A.D. McInturff, G. Sabbi and R.M. Scanlan, LBNL, Berkeley, CA 94720, USA

Abstract

Goal of the LBNL Superconducting Magnet Program is to establish the technologies associated with very high field superconducting magnets, to provide cost-effective options for the next generation of high-energy colliders. Recent efforts have focused on the design, fabrication and test of Nb_3Sn common coil dipoles. The RD3b test has demonstrated operation at very high field and stress levels. RD3c is the first common coil prototype addressing field quality issues. A flat racetrack coil was wound on both sides of a central bore plate, using hard spacers to control the geometric field harmonics. The resulting coil module was inserted between the outer coil modules of RD3b, and pre-stressed using the reusable yoke and shell loading structure. In this paper, magnetic field measurements of RD3c are reported and compared with theoretical predictions.

INTRODUCTION

Magnet parameters

RD3c was conceived as a simple coil configuration that would test the capability to obtain geometric field quality in the range required for high energy accelerators. RD3c was composed of RD3b's outer coils, yoke and shell structure [1-3] and a new inner coil, clamped between the two outer coils [4]. In Table 1 the RD3c performance parameters are listed.

Table 1: RD3c Performance Parameters

$I^{(ss)}$ (kA)	11.9
$B_0^{(ss)}$ (T)	10.9
$J_{cu}^{(ss)}$ (inner) (kA/mm^2)	1.6
$J_{cu}^{(ss)}$ (outer) (kA/mm^2)	1.6

* Calculated values. Training was suspended before maximum current was achieved.

The new inner module was composed of two single-layer coils, with one spacer per layer. The two layers were wound on both sides of two central bore plates and connected by an S-bend ramp through the island-pole. The spacers near each borehole allowed enhancing the field quality by compensating the large positive sextupole generated by the outer coils. The design was not optimized to correct the end field and the iron saturation harmonics. As in RD3b, the inner coils were separated by an aluminum-bronze bore-plate. A thicker mid-plane bore-plate was designed to contain the 35 mm bore and allow the insertion of a 25 mm diameter, rotating-coil probe. Fig. 1 shows the cross section of RD3c.

* This work was supported under contract DE-AD03-76SF00098 by the Director, Office of Energy Research, Office of High Energy Physics, U.S. Department of Energy.

lchiesa@lbl.gov

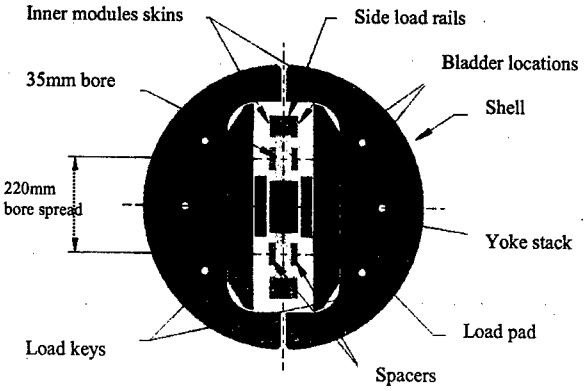

Figure 1: The magnet cross-section for RD3c.

The goal of this magnet was to measure field harmonic data after standard training, quench and ramp rate studies [3]. Training started at 77% of short sample and reached 92%. At this point it was decided to suspend training and perform magnetic measurements.

MAGNETIC MEASUREMENTS RESULTS

Test Set-Up

A rectangular coordinate system is defined by the z-axis at the center of the magnet aperture and pointing from the return end towards the leads end, the x-axis horizontal pointing to the right of an observer who faces the leads of the inner module and the y-axis defined by the right hand rule (Fig. 2).

The field is represented in terms of harmonic coefficients defined by the power series expansion shown in equation (1) with r_0 10 mm:

$$B_y + iB_x = B_{ref} \sum_{n=1}^{\infty} (b_n + ia_n) \left(\frac{x+iy}{r_0} \right)^{n-1} \qquad (1)$$

The rotating coil, 428 mm long, has 11.7 mm radius and 5 windings: 1 tangential, 2 dipole bucking, and 2 quadrupole bucking (not used in this test). The dual dipole correction coils were wired to provide a high-resolution harmonic signal by suppressing the fundamental dipole component. The probe rotated at constant speed of 1Hz. Both the tangential and bucked signals were amplified with an integrating amplifier, digitized at 1kHz with 24 bit HP3458A DMV's, and Fourier analyzed relative to the fundamental. The resulting harmonics were corrected for the appropriate amplifier gain and coil harmonic sensitivities, and normalized to a radius of 10 mm to compare them with the calculations.

0-7803-7738-9/03/$17.00 © 2003 IEEE

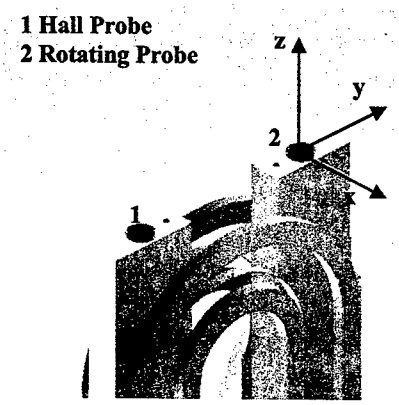

Figure 2: RD3c inner module and definition of coordinate system.

A Hall probe was inserted in the other bore for an independent measurement of the dipole field.

Magnet field quality

Four current cycles were applied to the magnet, in order to measure the hysteresis harmonics. The central 43 cm integral harmonics were measured on the fly during the cycles.

A first set of measurements (MM03) was obtained during the first and second cycles and a second set of measurements (MM04) was obtained during the third and fourth cycles. The ramp rate was 10 A/s for MM03 and for the first cycle of MM04 and 30A/s for the second cycle of MM04. All ramp cycles, with the exception of the second cycle, went to 10 kA and back, with several pauses to measure the superconductor magnetization. At 10 kA longitudinal scan data were collected. After these measurements were taken the magnet was ramped down to 500 A where the current was held prior to the start of the next cycle. During the cycle with 30 A/s ramp rate, no holds were performed and an entire loop up to 10 kA and down to 0 A was completed.

The normalized allowed central harmonic integrals at 90% of short sample are summarized in Table 2. In the same table the main dipole B1 calculated and measured with the rotating probe and with the Hall probe is shown.

A 5 units difference between the measured normal sextupole and the calculated values was recorded at 10 kA. A 15 units difference was observed for the skew quadrupole. The calculated values of the normal sextupole and skew quadrupole are a consequence of iron and end effects, features not specifically optimized for this test. Since the shift from the expected values is constant with the current (Fig. 5), geometric effects are probably the cause of this difference. Preliminary calculations of the effects of cooldown do not explain this difference. The discrepancy could be explained by effects such as position of supporting pads, displacement of the coils and fabrication tolerances (Table 3). Higher order harmonics are small and in agreement with the calculated values.

The normalized central sextupole for the 10A/s cycles is shown in Fig. 3. At 10 kA a significant hysteresis was still present mainly due to persistent currents effects. The residual hysteris was predicted from 2D calculations, also shown in Fig. 3, based on magnetization data of the strands (courtesy of Ohio State University). The calculated values and measurements were shifted in order to be symmetric around 0 unit at 10 kA. This allowed a better comparison between the 2D calculations and the measurements showing a reasonable agreement of the data with the predicted behavior.

Table 2: Calculated and Measured Main dipole B1 and allowed harmonics at 10kA

Normal	Calc	Meas	Skew	Calc	Meas
b_3	-5.44	-10.39	a_2	-31.2	-15.65
b_5	-0.24	-0.02	a_4	-1.56	-1.45
b_7	0.58	0.61	a_6	0.01	-0.20
B1(T) integrated	9.16	9.77	B1(T) central	9.23	9.26

Measured values: 1E-4 units, averaged between up-ramp and down-ramp to cancel the hysteresis (r_0= 10mm).

Table 3: Sensitivity to geometric effect

Normal sextupole	Value	Δb_3
Inner/outer cable thickness	+10 μm	+0.3/-1.15
Central spacer height	+100 μm	+0.5
Inner/outer coil horiz. position	+100 μm	+0.9/+0.4
Skew quadrupole	Value	Δa_2
Inner/outer coil vert. displac.	+100 μm	+3.0/-2.8

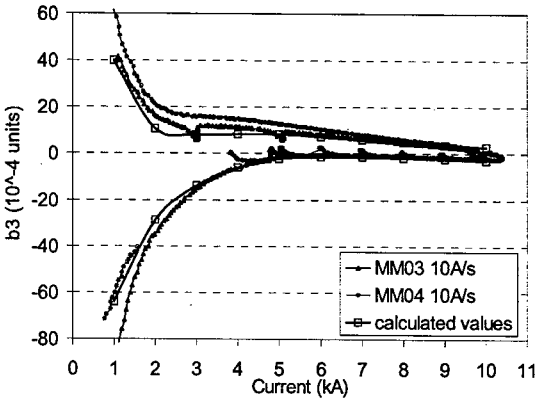

Figure 3: Normal sextupole, 10A/s measurements and 2D hysterisis calculation using magnetization data of strands.

The Hall probe measurements in one bore were compared with the peak central field calculations. For current above 3 kA the measurements agree with the calculated values within 0.5% (Fig. 4). Below 3 kA the discrepancy increases up to 2%. Persistent and eddy current effects are not included in the calculations. In the second bore the measurements of the dipole component performed with the rotating coil were compared with the 3D calculated integrals over the probe-coil length (slightly lower than the central value due to the ends effect). In this case there was a systematic deviation of 5% from the calculated values, which is still under investigation.

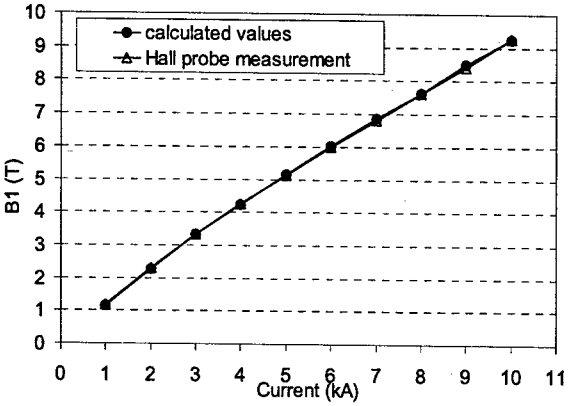

Figure 4: Main dipole component as a function of current.

The geometric normalized sextupole as a function of current is shown in Fig. 5. Up-ramp and down-ramp values were averaged to eliminate ramp rate and magnetization hysteresis. The average of the measurements with its error bars was compared with the calculation. The current dependence of the harmonic value is due to saturation of the iron. The measured normal sextupole well reproduces the expected saturation effect but had a relatively constant shift of 5 units from the absolute value as mentioned earlier.

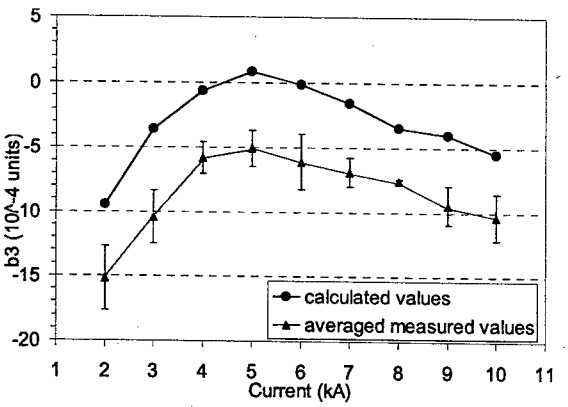

Figure 5: Normalized integrated sextupole as a function of magnet current (data averaged among up-down ramps).

Longitudinal scans were also performed. The measured values of the main dipole field B1 and normal sextupole component were compared with the calculated values. For the main component B1 a scaling factor was applied to account for the 5% B1 error previously discussed. The data also needed to be shifted longitudinally 18 mm relative to the center position, which was determined roughly by oscilloscope measurements. An 18 mm error was well within the uncertainty of this method of positioning. For the sextupole, the expected dependence from position was satisfactory but a negative 5 units shift from the calculated values was again observed Fig. 6.

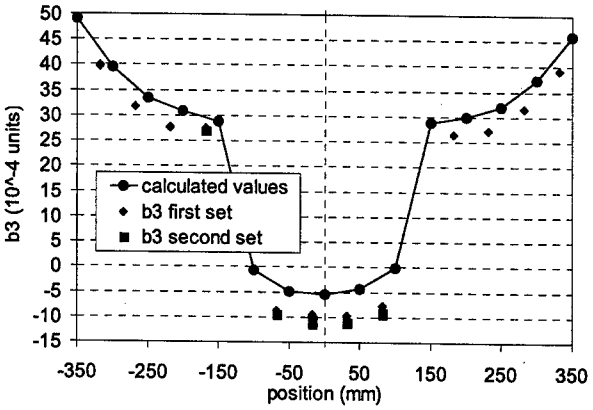

Figure 6: Axial dependence of the sextupole b3 relative to the center of the magnet.

CONCLUSIONS

RD3c was the first high field common coil with basic field quality features. The results obtained in this first attempt were very satisfactory considering the design constrains of the magnet. Several upgrades of the test facility were also implemented for this test (new header and vertical motion apparatus).

Further investigations will be addressed in order to explain the discrepancies between calculation and measurements. A careful analysis of fabrication tolerances and their effect on field quality is required. Possible sources of field error are also the mechanical effects due to deformation of the coil under Lorentz forces at cold compared to the room temperature unstressed geometry, and magnetization effects (visible at low currents). Samples of iron and aluminum-bronze bore plate are being measured at NIST to confirm the permeability values used in the model.

A second thermal cycle with more focused measurements is planned to improve the quality of data collected and increase the statistic of results. It will allow a better understanding of magnetization and eddy current effects and the investigation of snap back behavior in Nb_3Sn magnets.

Common coil designs optimized to address iron saturation and field quality have been developed and will be implemented in future prototypes [6].

REFERENCES

[1] S.A. Gourlay et al., *IEEE Trans. Appl. Superconduc.*, Vol. 11, No. 1, March 2001, p.2164.

[2] A.F. Lietzke et al., "Fabrication and Test Results of a High Field, Nb_3Sn Racetrack Dipole", *Proceedings: 2001 Particle Accelerator Conference*, Chicago, IL, June 2001, p.208.

[3] A.F. Lietzke et al., "Test Results of RD3c, a Nb_3Sn Common-Coil Racetrack Dipole Magnet", *Proceedings: IEEE Trans. Appl. Superconduc.*, Houston, TX, August 2001.

[4] S. Caspi et al., "A New Support Structure for High Field magnets", *IEEE Trans. Appl. Superconduc.*, Vol. 12, No. 1, March 2002, p. 47.

[5] G. Sabbi et al., "Design of Racetrack Coils for High-Field Dipole Magnets", *IEEE Trans. Appl. Superconduc.*, Vol. 11, No. 1, March 2001, p. 2280.

CONTROLLING FIELD QUALITY IN MAGNET PRODUCTION

L. Bottura, A. Devred, V. Remondino, S. Sanfilippo, W. Scandale, E. Todesco, C. Vollinger, E. Wildner, CERN, Geneva 1211, Switzerland

Abstract

The field quality measurements at room temperature of around 100 collared coils of the main LHC dipoles are analysed. Using correlations to field measurements at 1.9 K, comparison with beam dynamics limits are discussed. Both random and systematic components are analysed, allowing to pin out the most critical multipoles. Corrective actions that have been taken during the pre-series phase are presented; we focus on the low order systematic multipoles that are shown to be the most difficult components to steer. A preliminary analysis of the integrated main field and of its implications on the possible scenarios for the installation are also carried out.

INTRODUCTION

Magnetic measurements are carried out with a 75 mm long rotating coil on 20 consecutive positions in longitudinal direction to cover the 15 m-long LHC dipoles. For each position, the field harmonics up to order 15 are measured, in both apertures. Each harmonics averaged over the dipole axis is compared to beam dynamics requirements, whilst spikes in the longitudinal profile help in detecting local defects during assembly.

In this paper we will discuss our approach for quality control, identify targets for field shape, present limits to corrective actions during production and finally examine the status of field quality in the pre-series LHC dipoles. We will express units in 10^{-4}, at 17 mm reference radius.

QUALITY CONTROL

In order to fix field-shape ranges for quality control, for each manufacturer, we select a sufficiently large group of data and we separate them into three sets: straight part, connection and non-connection heads. We compute the average and the σ for each set, rejecting cases clearly out of statistics [1], and we set control limits at $\pm 3.5\ \sigma$ (warning) and at $\pm 7\ \sigma$ (alarm). For Gaussian distributions, we should expect a single warning during the production. We use the same approach both for collared coils and for the cold mass. In the latter case, for a more stringent test, we compute the difference from collared coil harmonics, since the contribution of the iron yoke is very stable [2].

Automatic checks of magnetic measurements allowed us to detect both faulty measurements (4 over 98) and assembly errors (2 over 98). We found the first error in collared coil 2002, having a big spike of 40 units in the main field, of 24 units in b_2, plus minor spikes in a_2, a_3 and b_3 along a length of 2 m in the central part. This was induced by the erroneous insertion of a second coil protection sheet, 0.5 mm thick, in the corresponding dipole section. We found the second error in collared coil 1027, showing a localized spike in b_2 of 5.5 units, with minor anomalies in b_3 and a_2. This was induced by a missing shim, 0.8 mm thick, along a length of 1.5 m, in the pole outer layer. We could predict its location by field simulations considering the sign of the faulty harmonics.

FIELD QUALITY TARGETS

Targets for field shape harmonics are given in terms of systematic (average along the ring), random (σ for one arc – a priori the same in each arc) and uncertainty (σ of the average per arc) [3]. Random and uncertainty targets result from a compromise between what is needed for beam stability and what can be reached with realistic mechanical tolerances. The final choice mostly relies on experience of previous machines [4,5]. Systematic targets and their acceptance ranges, instead, result from beam dynamics considerations only: any target is achievable by the design of the coil cross-section, whilst keeping it within the allowed range for the whole production is the true challenge. Ranges for systematic harmonics at injection and at high energy differ by an offset resulting from persistent currents, iron saturation and electro-magnetic forces [6]. Their intersection determines the effective range for field quality. Finally, targets and ranges for collared coil harmonics result from correlation of harmonics measured in warm and in cold conditions.

The criticality of each harmonic is proportional to the ratio between its measured spread during production and the allowed range for the systematic value. In Table 1, lower order harmonics are evaluated for already produced collared coils. With our criterion, b_5, a_2 and a_4 are the most critical, whilst b_3, b_4 and a_3 are the easiest to control.

Table I: Measured random component versus the allowed range for the systematic, given in Ref. [3].

	b_3	b_5	b_7	b_2	b_4	a_2	a_3	a_4
σ	1.50	0.45	0.17	0.70	0.11	1.30	0.40	0.30
range	7.00	0.70	0.48	2.20	0.74	2.00	1.40	0.28

LIMITS TO CORRECTIVE ACTIONS

The time sequence of the dipole production shows that we should take corrective actions already on collared coils in order to shorten the feedback delay. A correlation between measurements at 300 K in the industry and in cold operational conditions is needed for an effective steering of the field quality.

A predictive magnetic model is another key tool, since forecasting absolute values of field harmonics is essential in conceiving prototypes. With our numerical model which also evaluates iron contributions and coil deformations [6-9], we obtained an agreement between measured and expected values of 1 to 2 times the measured random component. Indeed, b_3 agrees within 3

0-7803-7738-9/03/$17.00 © 2003 IEEE

units, b_5 within 1 unit and b_7 within 0.4 units. If deformations are neglected, the agreement on b_5 becomes much worse (4 σ, i.e. 2 units) [8-9]. This is however insufficient for steering the field quality, and iterations on the coil design are needed. In this case, our model is used in differential, to enhance the precision. For the LHC dipoles we carried out a comparison between model and measurements in three different cases:

- In reshaping the iron insert to reduce the systematic values of b_2 and b_4 [10].
- In resizing the polar shims to optimize the systematic values of b_3, b_5 and b_7 [11, 12].
- In choosing the size of the mid-plane insulation to optimize the systematic values of b_3 b_5 and b_7 [13].

The agreement, always found within 20%, is considered excellent. Indeed, just to evaluate the effect of a coil deformation we may use a different realistic hypothesis, which may already lead to differences up to 10%.

In comparing the harmonics of the collared coils with cold measurements we observe a linear correlation with a slope close to the theoretical value of 1/1.18, induced by the iron yoke effect of 18% on the main field [14]. The spread around the linear fit is to be compared to the allowed ranges for systematic components [3]. This spread is large only for a_2, a_4 and b_5. On the other hand, the influence of persistent currents on b_3, b_5 and b_7 seems to be well understood and reproducible.

FIELD QUALITY STATUS

Systematic harmonics

All systematic skew and even normal harmonics are within targets. The corrective action taken at the end of the prototype phase on the insert shape to correct b_2 and b_4 [10] has been effective. The odd normal harmonics are shown in the right part of Fig. 1, and are still too large for the second cross-section.

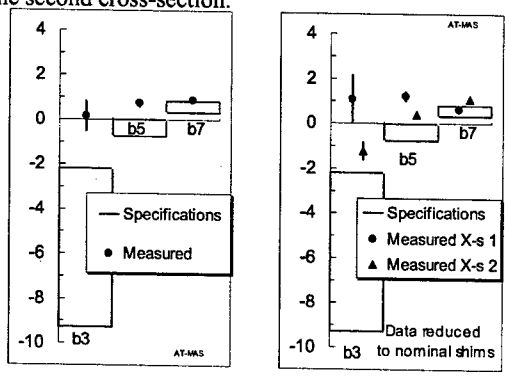

Figure 1: Systematic b_3, b_5 and b_7 (blue dots) versus beam dynamics targets (red), raw data (left) and data separated by cross-section, reduced to nominal shims (right).

In order to reduce b_3 and b_5, we decided on a reshaping of the internal copper wedges by less than 0.4 mm, keeping the same coil and collar shape [15]. Our aim was shifting b_3 by -3.5 units, b_5 by –1.35 units and b_7 by +0.18 units. The observed effect instead was -3 units for b_3, -0.80 units for b_5 and +0.45 for b_7. We decided to change the cross section after 9 collared coils. Afterwards we saw an unexpected trend of 7 units of b_3 in the first 15 collared coils. We could explain only a part of the trend (2 units) by out-of-tolerance copper wedges [16].

Random harmonics

In Fig. 2, we show random harmonics in collared coils, reduced to nominal shims. Data relative to the first cross-section shows larger spreads than in the second cross-section, due to a learning process during the production. The random imperfections are well within specifications or at the limit as for the integrated main field BdL, for b_2 and for b_5. Only b_3 is out-of-tolerance because of the trend in first cross-section. This makes the installation scenario of a full dipole mixing compatible with beam dynamics targets from the point of view of geometric harmonics.

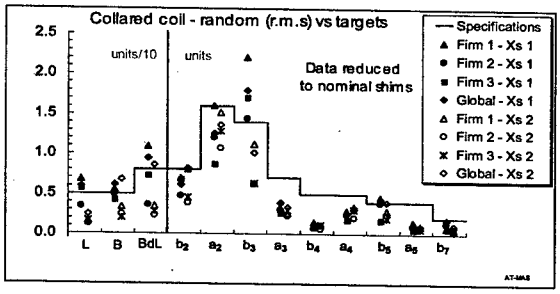

Figure 2: Random multipoles: targets versus measured values per manufacturer and for the full production, separated by cross-sections, reduced to nominal shims.

First estimates of uncertainty

We observe a non-negligible difference between manufacturers in the following quantities:

- Main field: approx. 20 units difference between Firm3 and the other Firms.
- b_2: 1.5 units smaller (larger) value in aperture 1 (aperture 2) for Firm3 than elsewhere, probably due to different collar manufacturers.
- b_5: 1 unit of differences between Firm1 and Firm2, Firm3 being in between.
- b_7: up to 0.4 units of difference between Firm1 and Firm2, Firm3 being in between.

Magnetic length, b_3, b_4 and skews show no systematic differences between manufacturers.

OPEN POINTS

Systematic odd normal multipoles

The present large values of systematic b_5 and b_7 seem to have a negligible impact on beam stability. However, in case of a drift, these multipoles can go out-of-tolerance. Moreover, at high field, b_3 should be corrected using chromatic sextupoles, thereby reducing operational flexibility. In order to reduce b_3 b_5 and b_7 a solution is to

increase the thickness of the insulation in the coil mid-plane [17]. An additional layer of 0.1 mm insulation would recover safer values for these multipoles, with a minimal cost. A test on a 1 m-long model is in progress, showing results in agreement with models [13].

Systematic differences in integrated main field

In collared coils 30 to 80, the integrated main field is systematically larger by about 20 units in Firm3, as shown in Fig. 3. This brings the random *BdL* at the limit of the target and stem in a variation of the main field in the straight part, whilst the magnetic length does not show relevant differences between manufacturers. A difference of 56 μm (0.2%) in the coil radius can explain it. Instead, nor copper wedge dimension errors, neither differences in collar manufacturers (contrary to the case of b_2) can explain this difference. We can correct the effect by acting on ferromagnetic laminations to compensate with a higher or lower magnetic length the offset in the main field. A decrease of magnetic length in Firm3 and an increase elsewhere according to the maximal values given in the dipole specification should allow to compensating half of this systematic offset. Data in operational conditions partially confirm this offset, but more statistics would be desirable before carrying out the corrective action.

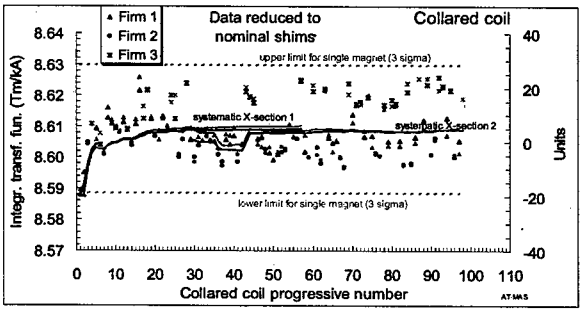

Figure 3: Integrated main field in the collared coil: measured data (markers) and ±3σ limit (dotted lines). Data reduced to nominal shims.

Field quality variation after re-collaring

Four magnets have been re-collared for electrical problems or assembly faults. Field quality measurements showed a non-negligible systematic variation of odd normal multipoles: the larger effect is a positive change of b_5 of around 0.5 units. This could be due to a plastic deformation of the coil or maybe of the collars. Indeed, this should not play a relevant role in the field quality control since we expect to collar more than once only a small fraction of collared coils.

CONCLUSIONS

The magnetic field of 98 collared coils, 56 cold masses and 24 cryomagnets has been measured. Magnetic measurements at room temperature are being successfully used as a tool to detect faulty components or assembly procedures. Two collared coils have been intercepted for anomalies in magnetic field, and in both cases assembly errors have been found. The automatic procedures to screen magnetic measurements are active. Measured random harmonics are within specifications for beam dynamics [3]. The hard part is steering systematic harmonics, like a_2 a_4 and b_5 where the allowed range is small compared to the random part.

Our capability of modelling field quality in the collared coil is rather good [10]. Sensitivities matrices can be estimated with 20% error. The absolute agreement between model and measurements is within two times the random component, coil deformations playing a strong role for the b_5 [8-9]. The steering of field quality should be based on collared coil data, due to the delay of months between coil assembly and final tests at 1.9 K. Correlations between collared coil data and measurements at 1.9 K are rather good since the contribution of persistent currents, saturation and Lorentz forces is well reproducible, but they should be carefully monitored during the whole production.

Systematic skew and even normal multipoles are within targets. For odd normal multipoles we applied corrective action on the coil cross-section [15], and the present values provide the required beam stability. However, we are at the limit of the targets for b_3, b_5 and b_7 hence an additional corrective action will be probably necessary.

A corrective action based on a change of the magnetic length is in preparation to compensate part of the 20 units difference in BdL between Firm3 and the other manufacturers.

ACKNOWLEDGEMENTS

We wish to thank L. Rossi and J. Billan for support, discussions and help given in this work. We acknowledge I. Vanenkov for providing data and analysis of coil size and impact on field quality. We thank D. Tommasini and his team and the project engineers of the AT-MAS group for the constant support in the analysis and for providing assembly data. Thanks to S. Fartoukh and O. Bruning for discussing the beam dynamics targets and for comments.

REFERENCES

[1] S. Pauletta, Master Thesis, Torino University (2002).
[2] E. Wildner, E. Todesco, priv. communication (2003).
[3] S. Fartoukh, O. Bruning, *LHC Pr. Rep.* **501** (2001).
[4] L. Walckiers, private communication (1999).
[5] L. Walckiers et al, EPAC (2002) 260-2.
[6] R. Gupta et al., EPAC (1994) 2298-300.
[7] S. Russenschuck, *LHC Project Report* **276** (1999).
[8] P. Ferracin et al, *IEEE Tr. Appl. Supercon.* **12** (2001)
[9] P. Ferracin, Ph.D. Thesis, Torino University (2001).
[10] P. Ferracin et al., *LHC Project Report* **467** (2001).
[11] Z. Ang et al, *IEEE Tr. Appl. Supercon.* **10** (1999).
[12] P. Ferracin et al, *Phys. Rev. STAB,* **5** (2002).
[13] cern.ch/lhc-div-mms/MMSPAGES/MA/mid_ins.html
[14] P. Tollestrup, Fermilab Report UPC-86 (1979).
[15] E. Todesco et al, EPAC (2002) 2439-41.
[16] B. Bellesia et al, *LHC Pr. Rep.* (2003) in press.
[17] L. Bottura, internal memorandum, March 2001.

ENERGY RECOVERY LINACS LIGHT SOURCES: AN OVERVIEW

J. B. Murphy, NSLS/BNL, Upton, NY 11973 USA

Abstract

Sparked by the highly successful operation of energy recovery linac (ERL) free electron lasers (FELs) at TJNAF [1] and JAERI [2] and also by the novel MARS light source (LS) proposal from BINP [3], numerous facilities worldwide are now considering ERL based light source projects. A survey of the various light sources and FELs based on ERL technology will be given. An overview of the critical R&D issues that must be addressed in future ERLs will also be presented.

INTRODUCTION

Motivation for an ERL Light Source

State of the art storage ring based synchrotron light sources are achieving horizontal emittances of a few nanometers & values of 10^2-10^3 less for the vertical plane yielding a brightness ~ 10^{21} ph/sec/0.1%BW/mm^2-mrad^2. Further reduction in the equilibrium emittance is becoming very challenging due to dynamic aperture limitations and short lifetimes. It is also unlikely that electron bunch lengths in rings will shrink much below 10 ps (RMS). ERL based light sources are being explored as the pathway to even higher brightness and sub picosecond pulses.

In contrast to an electron storage ring which stores the same electrons for hours in an equilibrium state, in an ERL it is only the energy of the electrons, not the electrons themselves, that is 'stored'. Individual electrons may spend as little as 1 μs in an ERL and as such never reach an equilibrium state. It is precisely the fact that the electrons are continually being refreshed, while the energy is recovered for use by succeeding electrons, that makes an ERL such an attractive concept.

Why Energy Recovery?

The power in an electron beam of current I and energy E can be written as:

$$P\,[GW] = E\,[GeV] \bullet I\,[Amp]. \qquad (1)$$

For a 6 GeV light source like the ESRF the power in the electron beam is 1.2 GW. This is possible because the same electrons are circulating in the machine generating the large average current (200 ma) and the RF system only has to replace a small fraction of this power, that which is radiated in the dipoles and insertion devices, ~ 1-2 MW. To generate a 200 ma CW average current in a 6 GeV linac without energy recovery would require paying the electric bill for the full 1.2 GW.

Brief Historical Perspective

As early as 1965 Tigner [4] proposed 'energy recovery' in opposing superconducting (SC) linacs to generate colliding beams for high energy physics. Recirculating linacs & racetrack microtrons have been part of the accelerator landscape for more than twenty years [5,6]; some of the early machines already included SC cavities: the Illinois racetrack microtron [7], the Stanford SC recyclotrons [8] and the S-DALINAC at Darmstadt [9].

However it wasn't until 1986 that 'energy recovery', in the sense now being considered, was successfully demonstrated on the SCA FEL machine at the Stanford HEPL [10]. This pioneering experiment, which included 1.3 GHz SC multicell cavities, succeeding in accelerating a beam in the linac in the first pass and by adjusting the path length in the return arc the beam was properly phased and decelerated in a second pass through the linac. In addition to recognizing the possible savings in RF power and shielding, and the increases in overall efficiency, the HEPL team also suggested the installation of an FEL wiggler in the return leg. This last suggestion for an ERL FEL was never realized on the SCA machine, it would take another dozen years for this novel idea to be brought to fruition at TJNAF and JAERI.

Stimulated by these innovative machines, numerous proposals to use ERL technology to construct novel light sources have appeared recently.

ERL Light Source Basics

In its most basic form an ERL light source (LS) consists of an electron source, a linear accelerator, a magnetic arc lattice to return the electron beam through the linac with a 180° phase shift for deceleration, a device to convert electron kinetic energy into photons (an undulator or FEL) and finally a beam dump (see Fig. 1).

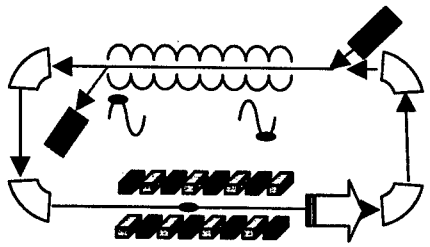

Figure 1: Generic 1.5 Turn ERL Light Source

Variations on this basic theme are also possible:

- N-passes through the same linac coupled with N-arcs can reduce the size of the linac and yield N different energy beams but this requires the linac to support N-times the current in one arc,
- linac sections can occur on opposite sides of the arc to generate two different energy beams, etc.

The objectives in an ERL LS are to:

- produce the highest quality electron beam in the injector with the "lowest possible energy as this energy is unrecoverable,

0-7803-7738-9/03/$17.00 © 2003 IEEE

- accelerate the electron beam to the final energy with high efficiency,
- transport the electrons to the photon generator (e.g. undulator, FEL) without corruption & with optimized transverse and longitudinal profiles,
- convert as much kinetic energy of the electrons to photons as possible,
- recover as much of the remaining electron energy in the linac to maximize the overall wall plug efficiency before dumping the beam with a minimum of activation in the dump.

KEY ELEMENTS OF AN ERL

Electron Injectors

In contrast to a storage ring where an injected electron beam of poor quality can be "cleaned up" with radiation damping, in an ERL one must produce the highest quality beam "at birth" as effects such as space charge, wakefields & dilution will only degrade the beam quality. However, this fact cuts both ways, and suggests a "natural upgrade path" for an ERL whereby improvements in the injector could enhance the overall system performance.

There are several possible injectors we shall only mention two, both of them photoinjectors: DC & RF. The first class of injector has produced the highest rep rate beams (~100 MHz), while the second class has produced the best normalized emittances ($\varepsilon_N \equiv \gamma\varepsilon \approx 1$ μm) for a charge per bunch Q ~ 0.1-1 nC.

The JLAB FEL is driven by a DC photoinjector operating at 350 kV and it produces an electron beam with ε_N ~ 15-25 μm for a charge per bunch of 60-135 pC at a rep rate of 37-75 MHz [11]. The gun has recently been upgraded to operate at 500 kV and it is undergoing commissioning.

An RF photoinjector makes use of extremely high accelerating gradients (~ 100 MV/m) to rapidly accelerate the electrons from the cathode and thereby reduce the emittance growth at low energy caused by space charge [12]. To date, the RF guns have produced the highest quality electron beams but typically at a rep rate of 10-100 Hz. The exception is the 433 MHz Boeing injector which operated with a 25% duty cycle [13]. The challenge for high rep rate RF photoinjectors is to balance the high gradient, which produces the low emittance, against thermal effects.

One way to bypass thermal problems is to make use of a SC photoinjector. In fact a SC RF gun is being explored but significant R&D will be required before this is the gun of choice [14].

Superconducting Linacs (SC RF)

In the last decade, superconducting RF technology has matured to the point that virtually all new and future accelerators, be they for light sources or otherwise, incorporate SC RF. This is true for rings, FELs and recirculating machines, e.g., CEBAF, LEP, SNS, SOLEIL, TESLA, XFEL, etc,

The JAERI FEL [2] makes use of two five cell 500 MHz SC cavities, but most of the other ERLs considered in this overview chose higher frequency cavity designs such as those in Table 1. Even though the TESLA design has benefited from extensive development in the last decade, it is slated for use in a "pulsed mode" for both the collider and the XFEL. Additional work will have to be done on any of the linac structures if average currents are to exceed 100 ma, as significant HOM power will have to removed from the cryostats.

Table 1: SC Linac Properties

Parameter	CEBAF (Original/New)	TESLA
f_{RF} [GHz	1.5	1.3
Cells per Cavity	5/7	9
Grad. [MeV/m]	5-8/12	15-20
Q	$2\text{-}5\times10^9/6.5\times10^9$	1×10^{10}

Arc Optics

The magnetic arcs in an ERL serve two purposes, 1) to return the electron beam to the linac entrance with a phase shift for deceleration and 2) to optimize the transverse and longitudinal profiles of the electron beam for both photon generation and recovery in the linac and dump.

The choice of arc optics is dictated by the energy of the ERL, its particular application and the quality of the electron beam required. Quantum fluctuations due to incoherent synchrotron radiation in 2π of bending magnets of the arcs gives rise to an energy spread and emittance increase [15]:

$$\Delta\sigma_\varepsilon^2 = \frac{55\pi r_e \lambda_c}{24\sqrt{3}}\frac{\gamma^5}{\rho^2}, \qquad (2)$$

$$\Delta\varepsilon_x = \frac{\sigma_\varepsilon^2}{2\pi\rho}\int_{BM} H\,ds, \qquad (3)$$

where $H(s) \equiv \gamma\eta^2 + 2\alpha\eta\eta' + \beta\eta'^2$ is the Courant-Snyder parameter.

To prevent excessive energy spread the dipole bending radius, ρ, must be chosen sufficiently large. To combat the rapid growth in emittance with energy, $\Delta\varepsilon \sim \gamma^5$, the Courant-Snyder parameter must be kept small by segmented the dipoles into many pieces as is done in storage ring LS lattices. For example the 180° Bates bends which are suitable for the 48 MeV TJNAF FEL are not acceptable for a 5 GeV low emittance ERL LS. This latter source might require a large number of triple bend achromat (TBA) cells for the arc which minimizes emittance growth and provides tuning of the momentum compaction of the arcs for bunch compression [16].

Combining an energy chirp from the linac with either a dedicated bunch compressor or using the dispersive nature of the arcs allows for manipulation of the longitudinal phase in an ERL, in particular compression of the electron bunches to the sub picosecond level. Nonlinearities in the linac and arcs will affect the minimum bunch length achievable: the long electron bunches from the injector

will sample the nonlinearities in the linac waveform and this can be compensated with a third harmonic cavity, while nonlinearities in the arcs can be compensated using sextupoles and higher order multipoles.

The focusing in the linac can present a challenge even for the simple ERL configuration of Figure 1 as the beam energy is increasing on the first pass and decreasing on the second pass so that the effective strength of the quadrupoles varies by the energy ratio E_{final} / $E_{injection}$. The limit on this ratio is not yet known. Simulation suggests that a ratio as large as 5 GeV / 10 MeV might be possible [17]. Recent experimental work has achieved ratios of 1 GeV / 20-50 MeV [18].

The overall optics of the ERL also plays a critical role in determining the threshold current for the multi turn beam breakup instability [6]. The characteristic behavior of the threshold current can be seen if one assumes a single HOM with frequency ω, initial electron momentum p_0, HOM shunt impedance & quality factor (R/Q) & Q, recirculation time τ_r, and TRANSPORT matrix element R_{12} [6,19,20],

$$I_{th} = \frac{2c^2 p_0}{e[R/Q]Q\omega\left|R_{12}\mathrm{Sin}(\omega\tau_r)\right|}. \quad (4)$$

For the more realistic case with many HOMs distributed in a long linac a numerical solution is required [19].

Wakefields

Longitudinal wakefields can modify the electron bunch phase space, increase the energy spread, lead to heating of machine components and result in emittance growth. For effects on a single bunch, such as the coherent synchrotron radiation wakefield (CSR), it is the peak current that is of concern, while in the case of component heating the average current also plays a role. The multicell linac wake and CSR are "unavoidable" as the beam must be accelerated and bent in the arcs to be returned for deceleration. The resistive wall and surface roughness wakes must be accounted for in insertion devices, particularly small gap devices.

FEL ERLS

Oscillator FELs

FELs operating in an oscillator configuration have long been the workhorses of FEL user facilities based on both linacs or storage rings. While the storage based FELs are limited by the quality of the "captive electron beam", the linac based devices have the advantage of replenishing the electron beam on each pulse. In either case, only a few percent of the electron energy is converted to photons.

The "ERL twist" allows for:

- an overall improvement in the wall plug efficiency,
- a tremendous increase in the average electron current and hence the FEL power,
- reduced activation in the beam dump.

At present there are two operating FEL oscillator ERLs based on SC linacs, one at TJNAF [1] and the other at JAERI [2]. There is also an FEL ERL at BINP which makes uses of room temperature RF cavities and has started operation in single pass mode but has plans for an 8 turn racetrack configuration [21]. The TJNAF machine is the most developed of the three, having achieved an average power of 2 kW at λ = 3 μm operating in ERL mode in 2000. A summary of the parameters of these ERLs, and their proposed upgrades, is given in Table 2.

Table 2: Operating Oscillator FELs (I) & Upgrades (II)

Parameter	TJNAF I	TJNAF II	JAERI I/II	BINP I/II
E [MeV]	48	160	17	14/100
I_{ave} [ma]	5	10	5/40	4/50
Q/bunch [pC]	65	130	500/ 1000	700
ε_N [μm]	15	10	30	20
Rep Rate [MHz]	75	75	10	5.6-22.5
Duty Cycle	100	100	1/100	100
P_{FEL} [KW]	2	10/4	2.3/10	-/100
λ_{FEL} [μm]	3-6	3/0.5	22	150

In addition to the operating oscillator FELs, the 4GLS proposal from the Daresbury Laboratory includes both IR and VUV oscillator FELs in a 600 MeV SC linac based ERL [22]. An R&D program leading up to the 4GLS received governmental approval in April 2003.

High Gain FELs

FELs operating in the IR or UV can make use of mirrors to provide feedback in a "low gain" oscillator configuration. For soft or hard x-ray FELs mirrors are not available necessitating a high gain FEL scenario, either a Self Amplified Spontaneous Emission (SASE) or a seeded scheme such as High Gain Harmonic Generation (HGHG). There are several ERL proposals which include high gain FELs:

- LANL has proposed a SASE FEL with a tapered wiggler and a room temperature linac [23],
- 4GLS proposes a SASE XUV FEL [22],
- LUX includes soft x-ray HGHG FELs with an option for energy recovery [24],
- an HGHG FEL was studied as part of a racetrack microtron injector for MAX IV [25],
- BESSY's soft x-ray FEL proposal mentions an option for energy recovery [26].

While the virtues of energy recovery for high average power oscillator FELs has already been proven, the need for energy recovery is less clear for high gain FELs, a notion supported by the fact that neither the LCLS nor the XFEL incorporates it. It remains to be seen what rep rate is optimal for these devices which will determine if energy recovery is worth the additional expense. If the

sample is destroyed on a single shot from the extreme peak power in a pulse, there's no need for a MHz rep rate!

SYNCHROTRON LIGHT ERLS

The Holy Grail in a synchrotron light source is to produce a high brightness photon beam using a diffraction limited electron beam. The on axis average brightness for an undulator source is given approximately as,

$$B_{ave} \approx \frac{1}{8\pi}\frac{I}{e}\frac{\alpha N_u}{\left(\varepsilon_x \oplus \lambda\!\!\!^{-}/2\right)\left(\varepsilon_y \oplus \lambda\!\!\!^{-}/2\right)}\frac{\Delta\omega}{\omega}, \qquad (5)$$

where the larger of ε or $\lambda\!\!\!^{-}/2$ is chosen in each bracket of the denominator. A diffraction limited source is defined as $\varepsilon \approx \lambda\!\!\!^{-}/2$; there is little gained by reducing the electron emittance beyond the light emittance ($\lambda\!\!\!^{-}/2$).

For 12 keV x-rays (1 Å), a diffraction limited electron beam should have $\varepsilon \sim 8$ pico-meter! This is more than 2 orders of magnitude smaller than the typical horizontal emittance in present day storage rings (1-5 nm); the vertical emittance in a third generation ring can be pushed to the diffraction limit at the expense of beam lifetime.

The potential promises of an ERL based light source are:

- diffraction limited round electron beams ($\varepsilon_x = \varepsilon_y$) from photoinjectors or nanotips,
- very long insertion devices in the return arcs,
- energy recovery will permit large circulating currents and hence high fluxes,
- "top-off" operation,
- bunch compression will provide sub picosecond electron bunches,
- reduced electron energy spread,
- variable pulse formats for timing experiments.

Attracted by the above possibilities, several facilities are developing conceptual designs for an ERL light source. The novel MARS concept introduced by the BINP team in 1998 has been followed by at least five other ERL based light source proposals which emphasize different subsets of the aforementioned ERL promises. Table 3 lists these ERL proposals & their anticipated brightness.

Table 3: Conceptual Synchrotron Light Source ERLs

Item	Cornell [27]	ERL SYN [28]	KEK [29]	LUX [24]	PERL [30]	MARS [3]
E [GeV]	5-6	3.5	2.5-5	2.5-3	3	5.4
I_{ave} [ma]	100	100	100	-	200	1
B_{ave} [10^{22}]	1	6	3	-	0.1	30

The machines in table 3 all emphasize the production of hard x-rays using multi GeV electron beams and they can roughly be group into three categories:

- MARS emphasizes diffraction limited electron beams with very long undulators to generate high brightness photon beams with a narrow line width, but at the expense of photon flux since I = 1 ma,
- Cornell, ERL SYN, KEK and PERL consider large circulating currents I ~ 100 ma to satisfy the flux users while preserving the option to trade off current to reduce the beam emittance and boost brightness,
- LUX as presently proposed is a recirculating machine which has energy recovery as an option; it includes both HGHG FELs and a novel scheme of "photon compression" to generate tunable, sub 100 fs pulses by spontaneous emission in undulators [31].

It should be noted that none of the machines under discussion here are actually in the construction phase as each faces R&D challenges before a full fledged multi GeV ERL based light source facility can be realized. True to form for an evolving technology, several paths forward are under consideration:

- the Cornell [32] & KEK teams have proposed low energy (100-300 MeV), high current (100 ma) prototype machines before embarking on a multi GeV facility,
- PERL [33] & ERL SYN [34] have suggested a staged approach whereby a multi GeV machine is initially operated as a storage ring, and later upgraded to an ERL as the technology matures,
- to reduce the duty cycle on the injector and the linac it has been suggested that electrons could circulate for a small fraction of a damping time (~ 100 turns) in an "circulator ring" before deceleration in the linac [35, 36].

An important first step toward the realization of a high energy ERL was taken recently at TJNAF when the CEBAF machine was operated in energy recovery mode with 85 μA. The 50 MeV injected beam was accelerated up to 1 GeV and back in two complete passes [18].

OTHER ERL PROPOSALS

For completeness it should be noted that ERLs are also being considered for purposes other than light sources; there are at least two proposals related to nuclear physics:

- Electron cooling of heavy ions in RHIC [37],
- Electron-Light Ion Collider [38].

In the first case a low energy (E = 54 MeV), high current electron beam (I = 300 ma = 10 nC x 28 MHz) in an ERL interacts with the heavy ions in the RHIC collider to "cool" the ions. The electron cooling combats the "heating" of the ions by intrabeam scattering and thereby increasing the integrated luminosity of RHIC by nearly an order of magnitude. An R&D program to develop the 704 MHz SC linac and the high precision cooling solenoid has recently begun at BNL.

In the second proposal, known as ELIC, a high energy electron beam (E = 5 GeV), obtained from operating the CEBAF recirculating linac in energy recovery mode, is made to collide with a new source of 50-100 GeV light ions for nuclear physics experiments.

Preliminary consideration has also been given to colliding 10 GeV polarized electrons in an ERL with the gold ions in RHIC [39].

SUMMARY & FUTURE OUTLOOK

The operating FEL oscillator ERLs stand as brilliant proof-of-principle experiments which demonstrate many important ERL fundamentals such as:

- CW average currents of 5 ma at 15-50 MeV,
- High rep rate photoinjectors: up to 75 MHz with normalized emittance $\varepsilon_N \sim$ 10-30 μm,
- High efficiency energy recovery ($\eta > 99\%$),
- Preservation of electron beam quality in the arcs,
- Longitudinal phase space manipulation for sub-picosecond electron bunch compression,
- High average power photons (P >2 kW).

These pioneering experiments have laid a firm foundation for ERL based technology and provide the impetus to pursue the R&D necessary to realize the next generation of proposed ERLs which will require:

- high brightness ($\varepsilon_N < 1$ μm) CW electron sources capable of high average currents (I ~ 100 ma),
- long lifetime cathode materials and robust laser sources for CW photoinjectors,
- optimization of SC RF frequency, number of cells per cavity, gradient and HOM extraction,
- control of the electron beam halo,
- shorter photon and electron pulses ($\tau < 100$ fs),
- beam stability and feedback systems to transform ERLs into state of the art user facilities.

The next decade should be an exciting one for ERL development as existing machines will be upgraded to yield even higher performance, critical R&D issues will be explored and some new proposals will likely begin construction.

ACKNOWLEDGEMENTS

The author would like to thank Drs. I. Bazarov, I. Ben-Zvi, J. Corlett, S. Gruner, R. Hajima, G. Hoffstaetter, G. Krafft, A. Magerl, L. Merminga, G. Neil, E. Seddon, C. Sinclair, T. Smith, T. Suwada, N. Vinokurov & S. Werin for graciously sharing information on their ERL projects. Fruitful discussions on ERLs with the NSLS staff are gratefully acknowledged. This work performed under DOE contract DE-AC02-76CH00016.

REFERENCES

[1] G.R. Neil, et. al., Phys. Rev. Lett. 84, (2000) 662.
[2] R. Hajima, et. al., to appear in Proc. FEL 2002.
[3] G.N. Kulipanov, A.N. Skrinsky and N.A. Vinokurov, J. Synchrotron Rad. 5 (1998) 176.
[4] M. Tigner, Nuovo Cimento 37 (1965) 1228.
[5] C.M. Lyneis, et. al., NIM 204 (1983) 269.
[6] R.E. Rand, "Recirculating Electron Accelerators", Harwood Academic, London (1984).
[7] P. Axel, et. al., IEEE Trans Nucl. Sci. NS-26 (3) (1979) 3143.
[8] C.M. Lyneis, et. al., IEEE Trans Nucl. Sci. NS-26 (3) (1979) 3246.
[9] V. Aab, et. al., Proc EPAC (1988) 335.
[10] T.I. Smith, et. al., NIM A 259, (1987) 1.
[11] T. Siggins, et. al., NIM A 475, (2001) 549.
[12] X.J. Wang, BNL Report 52624 (2001).
[13] D. Dowell, in BNL Report 52624 (2001).
[14] E. Barhels, et. al., NIM A 445 (2000) 408.
[15] M. Sands, SLAC-121, (1970).
[16] V. Yakimenko, et. al., Proc. PAC 2001 (2001) 3344.
[17] I. Bazarov, et. al., Proc. PAC 2001 (2001) 3347.
[18] A. Bogacz, et.al. this proceedings (2003).
[19] G.A. Krafft, et. al., JLAB TN-01-011 (1988).
[20] G.A. Kraft & J.J. Bisognano, Proc. PAC 1987 (1987) 1356.
[21] N. Vinokurov, et. al., Proc. 2nd APAC 2001 (2001), 257.
[22] M.W. Poole, J.A. Clarke & E.A. Seddon, Proc. EPAC 2002, (2002) 733.
[23] D. Nguyen & H. Freund, to appear in Proc. FEL 2002.
[24] J.N. Corlett, et. al., Proc. EPAC 2002 (2002) 668.
[25] M. Eriksson, et. al, Proc. FEL 2002.
[26] M. Abo-Bakr, et. al., NIM A 483 (2002) 470.
[27] S. Gruner, D. Bilderback & M. Tigner, Cornell ERL White Paper (2000).
[28] D.E. Berkaev, et. al., Proc. EPAC 2002 (2002) 724.
[29] T. Suwada, et. al., Proc. ICFA Future LS (2000).
[30] I. Ben-Zvi, et. al., Proc. PAC 2001 (2001) 350.
[31] A. Zholents, et. al., NIM A 425 (1999) 385.
[32] C. Sinclair, et. al., Proc. EPAC 2002 (2002) 644.
[33] J.B. Murphy, Proc. ICFA Future LS (2000).
[34] A. Magerl, et. al., Proc. ICFA Future LS (2000).
[35] Y. Derbenev, Proc. EPAC 2002 (2002) 314.
[36] B. Podobedov, private communication (2000).
[37] I. Ben-Zvi, et. al., this proceedings (2003).
[38] L. Merminga, et. al., Proc. EPAC 2002 (2002) 203.
[39] I. Ben-Zvi, J. Kewisch, J. Murphy & S. Peggs, NIM A 463 (2001) 94.

FEL OSCILLATORS

George R. Neil
Thomas Jefferson National Accelerator Facility, Newport News, Virginia, USA

Abstract

FEL Oscillators have been around since 1977 providing not only a test bed for the physics of Free Electron Lasers and electron/photon interactions but as a workhorse of scientific research. More than 30 FEL oscillators are presently operating around the world spanning a wavelength range from the mm region to the ultraviolet using DC and rf linear accelerators and storage rings as electron sources. The characteristics that have driven the development of these sources are the desire for high peak and average power, high micropulse energies, wavelength tunability, timing flexibility, and wavelengths that are unavailable from more conventional laser sources. Substantial user programs have been performed using such sources encompassing medicine, biology, solid state research, atomic and molecular physics, effects of non-linear fields, surface science, polymer science, pulsed laser vapor deposition, to name just a few. Recently the incorporation of energy recovery systems has permitted extension of the average power capabilities to the kW level and beyond. Moreover the use of collective radiation and Thompson/Compton scattering has produced substantial fluxes of THz radiation, X-rays, and gamma rays. This paper will discuss at a summary level the physics of such devices, survey existing and planned facilities, and touch on the applications that have driven the development of these popular light sources.

INTRODUCTION

Like other lasers, the FEL consists of a gain medium, a means to put energy into it, a means for dealing with the spent energy, and an optical system to appropriately direct the photons produced. The gain medium in the FEL is the electron beam produced by various types of accelerator. Electron accelerators are a relatively well-developed technology and the engineering involved is well known; however, the FEL puts extreme demands on the quality of the electron beam and care must be taken of the details of accelerator design. Indeed, the feasibility of FEL designs have always hinged on the beam brightness produced by the accelerator. The output of the FEL also mimics to a great extent the temporal characteristics of the electron source so that the desired radiation characteristics influence the choice of accelerator technology.

In wavelength regions where mirror technology is robust, FEL oscillators are the preferred approach because the lower gain required in such systems relaxes demands on peak current and electron beam quality. Figure 1 illustrates the components of such a FEL oscillator. Oscillators have been the primary approach for FELs operating in the mm wave to near UV range for 25 years. A large number are in operation around the world and they have been highly successful as scientific instruments

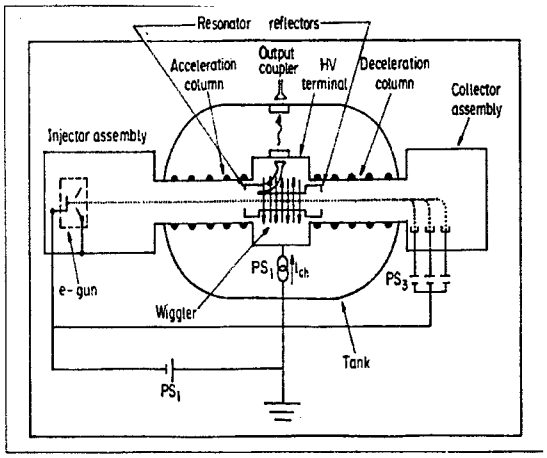

Figure 1: The mm wave FEL oscillator at Tel Aviv University utilizes a wiggler at high voltage with current recovery of the electron beam for CW operation at high power. Figure courtesy A. Gover.

for users. While much new effort in the FEL community is focused on pushing FEL performance to operation in the VUV and X-ray region where amplifiers are more appropriate, FEL oscillator user facilities are expected to remain a major factor in light source applications.

ATTRIBUTES OF FEL OSCILLATORS

If the small signal gain is greater than the round trip losses in the optical cavity then the signal will naturally grow to saturation. For stable operation and to extract significant fractions of the electron beam energy it is generally desirable to have the small signal gain exceed 3 times the cavity losses including outcoupling. This is not a severe restriction since mirrors can be fabricated with less than 1% loss from the IR down to around 250 nm in wavelength. Thus practical FEL designs can exist where the signal pass gain is only a few percent although more gain is certainly advisable. Since the gain can be so low, injector brightness requirements can be comparatively modest, the wiggler can be short, and its tolerances modest. Over most of its operating range the FEL output of such a system is stable and low noise. Most systems operate with a Fourier transform limited bandwidth. If desired, wavelength selectivity can be driven by the mirror optical coating reflectivity. Another advantage is that the optical mode produced is well-defined by the optical cavity and the spatial filtering provided by the small gain medium.

0-7803-7738-9/03/$17.00 © 2003 IEEE

These advantages come at a price though even beyond the requirement for reflective mirrors. For example, in an oscillator the FEL determines lasing wavelength, not you. It generally stabilizes at the point of maximum net gain in the system although there are exceptions to this if the maximum saturated gain exists in a frequency "island" inaccessible to the starting oscillation frequency. Another disadvantage is that the accelerator must produce a stable pulse train of electrons; one pulse isn't enough. The pulse train must continue long enough for the optical mode to grow to saturation.

There is also the requirement for getting useful optical power out of the cavity; either a partially transparent mirror, reflective window, or grating must be used, or some physical method to out-couple the power must be employed, e.g., a hole in the mirror or a scraper. And last, but not least, the optical resonator cavity length and transverse alignment must meet stringent stability requirements.

Since the wavelength range desired guides one toward a particular accelerator approach and such accelerator approach determines many of the macroscopic characteristics of the FEL output we will present below a set of examples of FEL oscillators arranged by wavelength starting with the longest wavelength output and moving toward the UV. A more complete listing of operational FELs can be found in the annual proceedings of the International Free Electron Laser Conference [1].

FIR FEL Oscillators

At wavelengths ranging from millimeter waves to the mid-infrared, DC accelerators such as pulse line accelerators and modulators can be used to accelerate the beam from a either a thermionic or field emission cathode. Induction linacs have been used at these wavelengths as well. At these longer wavelengths, the FEL gain can be very high and very high peak powers can be produced. Typically only electrostatic accelerators produce beam pulses long enough for oscillator to be practical. DC sources also have the potential of producing high average power at high efficiencies if some means of recovering the beam energy or current such as depressed collectors is used.

Electrostatic accelerators can, in principal, produce CW beams; however, in order to do so it is necessary to recycle the current in the spent beams to replenish the charging current. In practice, CW operation requires the recovery of better than 99% of the spent current. This has been done at high efficiency [2] and offers the promise of achieving CW operation [3]. An alternative is to produce the beam near ground potential and have the wiggler at high positive potential and then recover the beam at ground again (see Figure 1). Two systems are under test to utilize this approach to produce high average power at 130-250 GHz for heating of fusion research plasmas [4,5] Operation on the third harmonic has yielded 30 micron output with modest voltages [6].

Near IR Oscillators

Operation at wavelengths from the near infra-red IR through the visible requires beam energies in excess of 10 MeV. For these applications, the most commonly used accelerator is a conventional copper RF linac. Examples of this technology are the S-band (2856 MHz) system at Vanderbilt University, a large set of wigglers on the FELI facility at Osaka University, the FELIX facility at FOM in the Netherlands, and many others around the world using conventional pulsed linac technology with injectors that typically produce 10 μs macropulses with a pulse repetition frequencies (PRF) of up to 60 Hz.

These have limited duty factors due to ohmic heating in the cavities by the microwaves. A copper machine at Boeing Aerospace pushed this technology to its fullest with a 433 MHz accelerator that is capable of cw operation and has demonstrated a 25% duty factor. Nearly 130 ma of high quality macropulse current was produced at over 1 nanocoulomb per bunch [7].

Highly successful user facilities have been constructed at Osaka University (FELI)[8], FOM (FELIX)[9], Science University of Tokyo (FEL-SUT)[10], and Vanderbilt[11].

FELI

An example of the success that can be achieved with very high energy copper linacs is the lasing at 278 nm achieved from the 165 MeV linac at FELI in Japan [8]. Wigglers in this facility have operated at wavelengths from 80 to 0.28 microns. The laser produced 1.5 mJ/pulse in 24 μs macropulses at 20 Hz PRF. The lasing achieved here is the shortest oscillator wavelength to date on a linac-driven system. Among the extensive studies carried out at the FELI facility in Japan are resonant excitations of molecular vibrations [12], band discontinuities of semiconductor heterojunctions [13], and isotope separation [14]. The tunability, power, and pulse variability of the FEL has made it an efficient biophysical research tool [15].

FELIX

Arguably the most productive IR User facility in the world is the FELIX facility at FOM in the Netherlands. There are two lasers on the system which have been extensively used for studies in solid state dynamics, atomic clusters, and magnetic materials. Felix offers lasing from 16-250 um or 4-30 um from two FELs at 10 Hz with 100 mJ produced per macropulse. The machine is stable enough that the users typically operate the machine themselves. A particular success of the facility is in incorporating a number of enhancements to the use of photons such as synchronized pulse slicing of individual micropulses as well as other synchronized lasers. A substantial set of publications can be reviewed from their web site [16]. One particularly interesting result has been the identification of titanium carbide as a constituent of interstellar plasmas. An upgrade presently in construction will permit intracavity tests at an internal

focus. The high fields produced will permit the study of a number of non-linear phenomena.

Jefferson Lab FEL

An alternate to copper accelerator technology capable of CW or long macropulses is the superconducting RF linac structure (SRF) typified by the Continuous Electron Beam Accelerator (CEBA) at Thomas Jefferson National Accelerator Facility which produces 4 GeV electron beams for nuclear physics research using 1497 MHz cavities operated at 2K. Ohmic losses are reduced to negligible levels with the SRF structures (6 W/cavity at typical gradients) while maintaining high acceleration gradients (5 to 18 MV/m).

The IR Demo was completed in September 1998. The injector is the critical technology for operation of systems such as this; it must produce high average currents at high brightness. This system utilizes a DC photocathode operating at 320 kV to produce a 74.85 MHz pulse train of 60 pC. This gun produces the highest average brightness of any injector gun in the world and delivered in excess of 5.3 kilocoulombs from a single GaAs crystal at 1% quantum efficiency operating in the green from a doubled Nd:YLF laser beam. The IR Demo beam was accelerated to between 36 and 48 MeV and produced over 2 kW of CW average power[17]. In addition, the system produced 4 watts of power lasing on the fifth harmonic at 1 micron. Third harmonic operation at 1 micron achieved 300 W CW [18] and, even beyond this, conversion to > 60 W of green and > 10 W of UV at high efficiency in doubling, tripling and quadrupling crystals. Up to 10^9 photons/sec of Thompson scattered X-rays in the 5 to 15 keV range are produced when the FEL pulse scatters off subsequent electron bunches. The system also synchronously produces $>10^4$ more THz power (50 W) in sub-picosecond pulses than any other source [19].

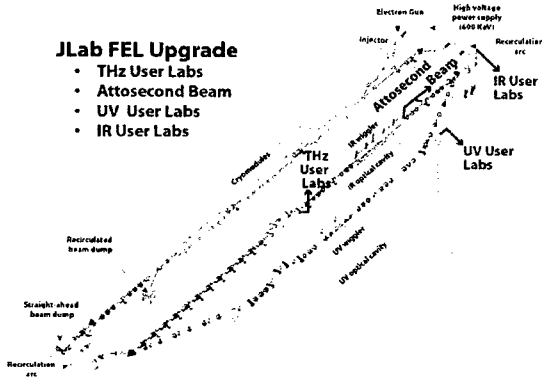

Figure 2: The Jefferson Lab IR Upgrade FEL oscillators utilize energy recovery of the spent electron beam for high efficiency and CW operation. Output ports will provide user light at a number of wavelengths ranging from X-rays down to terahertz. This is the highest average power tunable laser in the world.

An Upgrade of the system now in commissioning will produce continuously over 10 kW in the IR from 1 to 14 microns and over 1 kW in the 250 to 1000 nm range (Figure 2). The system uses energy recovery of the beam as demonstrated in the IR DEMO to reduce required rf power, virtually eliminate activation of components, and reduce power handling requirements on the dump. The machine will deliver beams of high power THz, IR, and UV to a set of User Labs for scientific and applied studies. Such studies on the IR Demo have already been extremely successful in exploring vibrational dynamics of interstitial hydrogen in crystalline silicon, carbon nanotubes, and pulsed laser deposition [20, 21]. Future applications will include those as well as microengineered structures, non-linear dynamics in atomic clusters, and metal amorphization. This machine is viewed as the first of a new category of high power, high brightness light sources called Energy Recovering Linacs (ERLs) with the potential to extend beyond the performance of third generation synchrotrons in both brilliances as well as offering the capability of femtosecond light pulses for dynamics studies. [22-24] (See Figure 3).

A similar energy recovery effort for high power generation is underway at the Japan Atomic Energy Research Institute (JAERI)[25,26].

Stanford Superconducting Accelerator FELs

The original FEL oscillator work was performed on the pioneering Stanford Superconducting Accelerator [27] and since that time the facility has been a center for research into FELs and their application [28,29]. The focus of the facility over the last decade has been the utilization of the FEL with a wide range of other laser sources to perform materials research with picosecond pulses. At present two FELs are installed on the linac which is undergoing an upgrade of the accelerator structures. The FIR FEL produces 1 W of 15 - 85 micron light from a tunable 25 period electromagnetic wiggler.

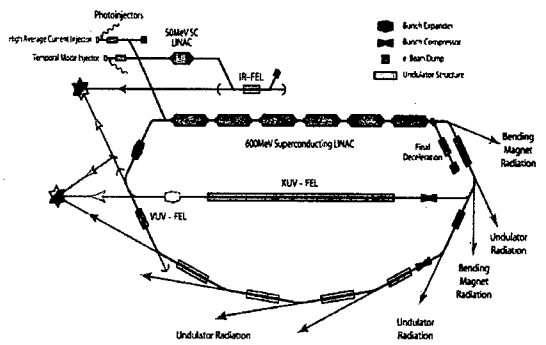

Figure 3: The Proposed 4GLS System at Daresbury Laboratory (for "Fourth Generation Light Source"). The Facility will consist of several FELs and an Energy Recovering Linac with a SASE FEL capability. Figure courtesy E. Seddon.

The MIR system produces 2 W in the 3 - 15 micron range from a 12.68m optical cavity around a 72 period hybrid wiggler of 31 mm wavelength. The FELs can be made to lase on alternating macropulses with essentially independent control of the optical output. Key studies at Stanford include second order nonlinear susceptibility of the conduction band and valence band quantum well (QW) structures extracted from the interference between second harmonic fields of QWs and GaAs substrate as determined by the azimuthal dependence of the second harmonic power. This was the first demonstration of difference frequency generation of mid-IR in any QW [30]. Groups at Stanford also studied vibrational dynamics in glass forming liquids. These were the first vibrational photon echo experiments and first comprehensive temperature dependent pump probe measurements on any condensed matter system [31].

In Dresden, construction of a superconducting FEL called ELBE is proceeding along the same lines[32].

UV FEL OSCILLATORS

In addition to UV oscillators on linac based systems such as FELI, the JLab Upgrade, and the proposed 4GLS, storage rings can be a cost effective alternative to producing the energies of up to a few GeV for operation at wavelengths in the ultraviolet spectrum [33]. The gain of the FEL drops inversely with the energy and mirror technology becomes increasingly difficult below 250 nm so that at some point oscillators become non-viable. The time to damp the energy spread introduced in the beam limits the average power that can be produced [34], although typically ring based FELs can operate in either a CW mode or as a high pulse power "Q-switched" mode where lasing undergoes a relaxation oscillation by damping between high power pulses.

Duke UV Ring

An example of such a storage ring system is at Duke University [35]. The ring has a circumference of 107.46m and provisions for two straight sections, and an energy range of 0.25 to 1.2 GeV. The machine can accommodate average currents of up to 115 mA. The OK4 wiggler system lased successfully at 345 nm beginning in December 1996 producing 150 mW and small signal gains of nearly 10%. This system has since lased at wavelengths as short as 193 nm. This system also demonstrated Compton scattering of the FEL light to produce gamma rays at up to 250 MeV which are used for fundamental nuclear physics research (Figure 4). While other lasers can be used for Compton scattering, the natural synchronism and physical overlap between the electron beam and light produced in the FEL is a major advantage for using the FEL light itself. Other FEL storage rings have also achieved notable success: VEPP3 [36], Super-ACO [37], UVSOR [38], and NIJI-IV [39] and ELETTRA [40].

SUMMARY

The discussion above illustrates the breadth of FEL oscillators' capabilities. These facilities continue to grow and produce increasing capabilities for basic and applied studies in biological, solid state, atomic and molecular physics. The wavelength ranges over which oscillators are the optimal approach include the rich area of vibrational and phonon activity of solids. Over much of the operational range of these devices no other system offers the pulse energy, or tuning bandwidth that FELs permit. It is expected that FEL oscillators will continue to be productive research tools for many years to come.

As shown especially in facilities such as FELIX and the Stanford FELs, manipulations of the optical beam such as noise eaters, cavity dumping, loss modulation, cavity length modulation, intensity mapping, mode selection, mode locking, spectral filtering etc., can provide substantial enhancements for user experiments and need further development. These are all pretty well established in conventional lasers but still largely undeveloped in FELs to the same level seen in conventional lasers.

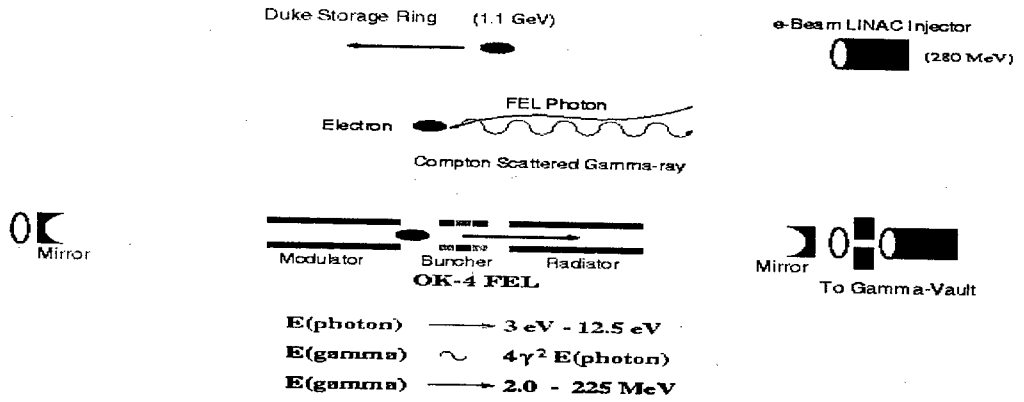

Figure 4: Setup of the DUKE OK-4 Compton gamma ray source. Figure courtesy V. Litvinenko

ACKNOWLEDGEMENTS

Work supported by the U.S. DOE Contract #DE-AC05-84ER40150, Office of Naval Research, Air Force Research Laboratory, Commonwealth of Virginia and the Laser Processing Consortium.

I have drawn on the support of a number of scientists at JLab and around the world in assembling this paper. At JLab I'd like to acknowledge the support of our entire FEL team for support and inspiration, especially Steve Benson, Gwyn Williams, and Fred Dylla who made numerous suggestions for improving this work. For freely sharing the details about their significant FEL oscillator facilities I'd like to thank Todd Smith, Bill Colson, Avi Gover, Vladimir Litvinenko, Elaine Seddon, Lex van der Meer, Kunio Awazu, and Esuke Minehara.

REFERENCES

[1] Colson, W. B., 2001, Nucl. Instr. and Meth. in Phys. Rsch. A**475**, 397.

[2] G. Ramian, Nucl. Instrum. Meth., **A318** (1992), pp. 225-229.

[3] B. C. Lee, S. K. Kim, Y. U. Jeong, S. O. Cho, B. H. Cha, and J. Lee, Nucl. Instrum. Meth., **A375** (1996), pp. 28-31.

[4] M. Caplan, M. Valentini, C. Van Der Geer, W. Urbanus, Nucl. Instrum. Meth., **A375** (1995) pp. 91-94.

[5] A. Abramovich, et al., Nucl. Instrum. Meth. **A373** (1997) pp. II-41-44.

[6] G. Ramian, J. Kaminski, S. J. Allen, Nucl. Instrum. Meth., **A393** (1997) pp. 220-224.

[7] D. H. Dowell, S. Z. Bethel, K. D. Friddell, Nucl. Instrum. Meth. **A356** (1995) pp. 167-176.

[8] T. Tomimasu, et al., Free Electron Laser and Its Applications in Asia, pp. 65-74, 1997.

[9] D. A. Jaroszynski, et al., Nucl. Instrum. Meth., **A375**, 647-650, 1996.

[10] Haruo Kuroda, Proc. Infrared Electron Laser and Its Application, Japan J. Apl. Phys. **41** (2002) Suppl. 41-1, 1-9.

[11] C. Brau, Nucl. Instr. and Meth. in Phys. Rsch. A **407**, (1998) 1.

[12] Yoshihito Maeda, et al., FEL and Its Applications in Asia, T. Tomimasu, E. Nishimika, T. Mitsuyu ed., Ionics Publishing, Tokyo. (1997) pp. 307-314

[13] T. Suzuki,. Et al., Appl. Phys. Lett., vol. 69, pp. 4136-4138, 1996.

[14] S. Kuribayashi, T. Tomimasu, S. Kawanishi, and S. Arai, FEL and Its Applications in Asia, T. Tomimasu, E. Nishimika, T. Mitsuyu ed., Ionics Publishing, Tokyo. (1997) pp. 263-270

[15] B. Jean, Nucl. Instrum. Meth., vol. A393, pp. 540-543, 1997.

[16] http://www.rijnh.nl/n4/n3/n5/f1234.htm

[17] G. R. Neil, et al., Phys. Rev. Let. **84**, 662 2000.

[18] Benson, S. et al, 1999, Nucl Instr and Meth in Phys Rsch A **409**, 27.

[19] G.L. Carr, M.C. Martin, W.R. McKinney, K. Jordan, G.R. Neil and G.P. Williams, Nature 420 153-156 2002.

[20] G. Lupke, X. Zhang, B. Sun, A. Fraser, N. H. Tolk, and L. C. Feldman, Phys. Rev. Lett. **88**, 135501, 2002.

[21] P. C. Eklund, et al., Nano Letters **2** 561 2002.

[22] George R. Neil and Lia Merminga, Reviews of Modern Physics **74**, 685 2002.

[23] Sol M. Gruner, et al., Rev. Sci. Instr. **73** 1402-1406, 2002.

[24] M.W. Poole, J. A. Clarke, and E. A. Seddon, Proc. EPAC 2002 Paris France(2002) 733-735.

[25] Minehara, E. J. et al., 2000, Nucl. Instr. and Meth. in Phys. Rsch. A **445**, 183.

[26] Minehara, E.J. et al., Proc. European Particle Accelerator Conference Vienna Austria August 2000, 758.

[27] Deacon, D. A. G., L. R. Elias, J. M. J. Madey, G. J. Ramian, H. A. Schwettman, and T. I. Smith, 1977 Phys. Rev. Lett. **38**, p. 892.

[28] Schwettman, H. A., T. I. Smith and R. L. Swent, 1996 Nucl. Instr. and Meth. A375, 662.

[29] Smith, Todd, 1999 Proceedings of the SPIE, Accelerator-Based Sources of Infrared and Spectroscopic Applications.

[30] H. C. Chui, G. L. Woods, M. M. Fejer, E. L. Martinet, and J. S. Harris, Jr., Appl. Phys. Lett. **66** (1995) 265-267.

[31] A. Tokmakoff and M. D. Fayer, J. Chem. Phys., vol. 103, pp. 2810-2817, 1995.

[32] Bucher, A. et al., presented at the 21st International Free Electron Laser Conference, Hamburg, August 1999 Paper II-49.

[33] M. E. Couprie, Nucl. Instrum. Meth., **A393** (1997) pp. 13-17.

[34] H. P. Freund and G. R. Neil, IEEE. **87**, No. 5, May 1999, pp. 782-803.

[35] V. Litvinenko, et al., Proceedings of SPIE Conference (FEL Challenges), February 13-14, 1997, San Jose, CA, 2988 (1997) pp.188-199.

[36] N. A. Vinokurov, et al., Rev. Sci. Instr., vol. 60, pp. 1435-1438, 1989.

[37] T. Hara, M. E. Couprie, A. Delboulbé, P. Troussel, D. Gontier, and M. Billardon, Nucl. Instrum. Meth., vol. A341, pp. 21-23, 1994.

[38] S. Takano, H. Hama, and G. Isoyama, Nucl. Instrum. Meth., vol. A331, pp. 20-26, 1993.

[39] T. Yamazaki, et al., Nucl. Instrum. Meth., vol. A331, pp. 27-33, 1993.

[40] G. De Ninno, et al., Proc European Particle Accelerator Conference, Paris, France 799-801, (2002).

A RECIRCULATING LINAC-BASED FACILITY FOR ULTRAFAST X-RAY SCIENCE*

J. N. Corlett, W. A. Barletta, S. DeSantis, L. Doolittle, W. M. Fawley, M.A. Green, P. Heimann, S. Leone, S. Lidia, D. Li, A. Ratti, K. Robinson, R. Schoenlein, J. Staples, W. Wan, R. Wells, A.Wolski, and A. Zholents, LBNL, Berkeley, California, USA; F. Parmigiani, UCSC, Brecia, Italy; M. Placidi, W. Pirkl, Geneva, Switzerland; R. A. Rimmer, Thomas Jefferson National Accelerator Facility, Virginia, U.S.A., S. Wang, Indiana University, U.S.A.

Abstract

We present an updated design for a proposed source of ultra-fast synchrotron radiation pulses based on a recirculating superconducting linac [1,2], in particular the incorporation of EUV and soft x-ray production. The project has been named LUX – Linac-based Ultrafast X-ray facility. The source produces intense x-ray pulses with duration of 10-100 fs at a 10 kHz repetition rate, with synchronization of 10's fs, optimized for the study of ultra-fast dynamics. The photon range covers the EUV to hard x-ray spectrum by use of seeded harmonic generation in undulators, and a specialized technique for ultra-short-pulse photon production in the 1-10 keV range. High-brightness rf photocathodes produce electron bunches which are optimized either for coherent emission in free-electron lasers, or to provide a large x/y emittance ration and small vertical emittance which allows for manipulation to produce short-pulse hard x-rays. An injector linac accelerates the beam to 120 MeV, and is followed by four passes through a 600-720 MeV recirculating linac. We outline the major technical components of the proposed facility.

OVERVIEW

A recirculating linac accelerates 2 ps electron bunches to 2.5-3 GeV, where the bunches radiate in multiple insertion devices. Intense soft x-rays are produced by cascaded harmonic generation scheme, similar to high-gain harmonic-generation (HGHG) - a laser-seeded process in a cascaded series of undulators, resulting in enhanced radiation at selected harmonics of the seed [3,4]. The coherent soft x-rays can be tuned over a range of tens of eV to 1 keV, and ultrashort seed laser pulses produce pulse durations of 10-200 fs. Hard x-rays are produced by spontaneous emission of the electrons in narrow-gap, short-period undulators. By use of a novel bunch tilting process followed by optical compression, hard x-ray pulse durations of 50-100 fs are obtained over a range of 1-10 keV [1,5]. Synchronization of the x-rays with lasers is critical for experiments, and optical pulses initiate both cascaded harmonic generation seed lasers and experimental end station amplifiers for precise timing [1,6]. The femtosecond x-rays are produced at a 10 kHz repetition rate, with variable polarization, and with peak fluxes comparable to third generation light sources. Thus, the proposed LUX facility would provide stable, synchronized, tunable, ultrafast x-ray pulses to multiple beamlines operating simultaneously over a broad range of x-ray wavelengths.

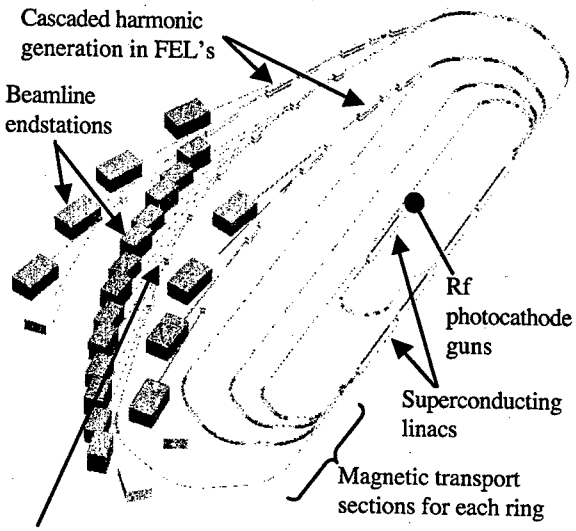

Figure 1. Machine layout. The beams generated at the rf photocathode guns travel through the injector linac, main linac, transport arcs, deflecting cavities, and either hard x-ray production section or a cascaded harmonic generation section, to the beam dump. Machine footprint is approximately 150x50 m.

ACCELERATOR DESIGN

Electron pulses are produced at a rate of 10 kHz in high-brightness rf photocathode guns [7,8]. Two sources are used - one with a conventional circular cross-section beam optimized for production of high-brightness EUV and soft x-ray radiation in the harmonic generation scheme, the other with a flattened cross-section beam for production of hard x-rays [8]. The beam quality requirements of the rf photocathode guns are already demonstrated, with normalized emittance of approximately 3 mm-mrad at 1 nC charge, although higher repetition rates have not been addressed to date. Conventionally, rf photocathode guns employ a simple right-circular geometry or "pillbox"

* This work supported by the U.S. Department of Energy under Contract No. DE-AC03-76SF00098

0-7803-7738-9/03/$17.00 © 2003 IEEE

shaped cavities, and operate over 10-100 Hz pulse repetition rate. The cathode is mounted on the cavity axis and electrons are rapidly accelerated by the rf electric fields, minimizing space-charge effects in the low-energy beam. For high duty cycle operation, thermal limitations prevent such designs from operating at an electric field sufficiently high to produce good beam emittance. For the LUX facility we have produced a conceptual design optimized for operation at high gradient and high repetition rate, and producing low-emittance bunches. This design incorporates features that increase cavity surface area to reduce deposited power density and enhance the accelerating electric field at the cathode (82 W/cm^2 maximum power density for 64 MV/m at the cathode) [7].

Application of a solenoidal magnetic field on the cathode of the flat-beam gun, followed by a specially configured skew-quadrupole channel located after the injector-linac, allows production of a "flat" beam with x/y emittance ratio 50/1 and small vertical normalized emittance of 0.4 mm-mrad [8,9]. This technique has been successfully demonstrated at Fermilab, with properties close to LUX design parameters [10].

Following the injector linac, a third-harmonic cavity is used to linearize the correlated energy spread introduced in the injector linac, and to manipulate the longitudinal phase-space in preparation for bunch compression. The beam is then transported to the entrance of the recirculating linear accelerator. In the transport line from injector linac to main linac, the bunches are compressed from 20 ps to 2 ps, with a final energy spread of ±200 keV. This transport line is carefully designed to compensate for the effects of coherent synchrotron radiation at the shorter bunch lengths [11].

In the recirculating linac the maximum energy of 3 GeV is achieved after four passes through the 720 MeV superconducting rf structure, or 2.5 GeV with the main linac operating at 600 MeV. Identical cryomodules containing multiple accelerating cavities are used for the main linac and the injector linac. The superconducting linacs have advantages in providing a compact and efficient accelerator, extremely stable rf fields, and inherently small perturbative effects on the beam. Significant advances have been made in superconducting rf technology in recent years, and the parameters of the proven TESLA superconducting rf systems developed at DESY have been used in LUX design studies [12]. Planned upgrades for the CEBAF facility at TJNAF also meet the requirements for the LUX linacs [13]. Our design is for an accelerating gradient of up to 20 MV/m in the main linac. The electron bunch repetition interval in LUX is less than the superconducting cavity filling time, and the linacs are more efficiently operated in cw mode. Engineering modifications to existing cryomodule designs required to accommodate significantly increased thermal load in the liquid helium are described in [1].

The flexibility of the LUX lattice design allows control and preservation of electron beam transverse and longitudinal emittances, minimizing the influence of collective effects [11,14]. Longitudinal and transverse dynamics have been modeled from the RF gun through the injector linac and all passes of the main linac. In the injector, a harmonic cavity will be used to control the longitudinal phase-space following the injector linac [11]. The bunch length and magnet bend angle in the lowest energy arcs of the machine result in a regime in which coherent synchrotron radiation emission could be expected, and the vacuum chamber geometry is designed to minimize this effect by shielding against lower-frequency radiation [15]. The recirculating ring arcs are achromatic and isochronous to preserve beam quality. Our studies include particle tracking with cavity wakefields, resistive wall impedance, magnet errors and misalignments, and show only modest emittance growth, with negligible impact on machine performance. The lattice is designed to allow manipulation of the bunch phase space on each pass if required, and also to accommodate bunch rates greater than the 10 kHz baseline design.

LUX will have the capacity for energy recovery in the linacs. However, for the baseline beam power of a few tens of kW, the beam will be taken directly to a shielded dump following the x-ray production sections.

At the exit of the final arc the flat-beam electron bunches receive a time-correlated vertical kick in a dipole-mode RF cavity. This imparts to the electron bunch a transverse momentum that is correlated in amplitude to longitudinal position within the bunch. The electrons then radiate x-rays in the downstream chain of undulators and dipole magnets, imprinting this correlation in the geometrical distribution of the x-ray pulse. The correlated x-ray pulse is then compressed to 10's fs duration by use of asymmetrically cut crystal optics. The bunch deflecting technique is identical to the "crab-cavity" schemes proposed for several electron-positron colliders. A total deflecting voltage of 8.5 MV is required, and we have developed a preliminary design for a 7-cell superconducting deflecting cavity [16].

Narrow-gap in-vacuo superconducting undulator designs provide tunable high-flux sources in the 1–12 keV range. The calculated flux of 10 keV photons from 1 nC bunches at 3 GeV and 10 kHz is 6×10^{10} photons/s/0.1%BW for a 4 mm gap, 14 mm period, 2 T peak magnetic field undulator. Similar insertion devices are currently being prototyped and designs are expected to mature in the near future.

A laser-seeded cascaded harmonic-generation scheme produces high-flux, short-pulse photons over an energy range of tens of eV to 1 keV. In this process the circular cross-section high-brightness electron beam is extracted from the recirculating linac, and passed through an undulator where a co-propagating seed laser modulates the charge distribution over a short length of the bunch. The scheme has been developed and demonstrated at the Brookhaven DUV FEL facility [4]. The imposed modulation results in enhanced radiation at specific

wavelengths and a selected wavelength is amplified in a following undulator, tuned to a higher harmonic of the seed laser. The electron pulse is then delayed in a short chicane, and the process repeated by modulating a fresh portion of the beam this time with the harmonic radiation produced in the previous undulator. Using a tunable optical parametric amplifier as the seed, and variable undulators, allows significant tunability in four stages of harmonic generation, variable flux up to 10^{13} photons per pulse, and variable pulse duration depending on the seed laser parameters [3]. Two chains of cascaded harmonic generation are proposed, providing exceptional flexibility in producing EUV and soft x-ray pulses. Circular polarization is attainable by use of elliptical undulators, and flux stability of 0.1% or better is obtained in seconds from random pulse-pulse flux variations of 10-20% at 10 kHz repetition-rate. The use of tapered undulators allows tailoring of flux to individual experiments, to avoid space-charge effects in, for example, photoemission processes.

Sophisticated laser systems will be an integral part of the LUX facility, providing experiment excitation pulses, and stable timing signals, as well as the electron source through the photocathode laser. Each endstation will have it's own dedicated laser system and optical manipulation and diagnostics, and optical tables and equipment will be contained within a stable and controlled environment. Multiple tuneable lasers covering a range of 267-3000 nm and pulse durations of $\leq$ 50 fs are required for experiment initiation, together with temporal and spatial filtering to optimize performance for specific experimental applications. Distribution systems using fibre-optic transmission lines will provide optical seed pulses to each beamline, with feedback based on interferometric measurements to stabilize the path lengths [6]. Developments in laser technology are expected to result in significant improvements in the coming years, which will be incorporated into our design with minimal impact on accelerator systems.

Synchronization and timing of the ultra-short x-ray pulses to the experimental excitation pulse is critical to studies of ultra-fast dynamics. For LUX we propose to generate inherently stable pulses by using seeded FEL systems and bunch manipulation. In the case of EUV and soft x-ray production, the cascaded harmonic generation seed laser oscillator also drives the sample excitation laser, resulting in timing stability of approximately 20 fs. For our scheme of hard x-ray production by bunch manipulation followed by x-ray pulse compression, we find that the phase jitter of the deflecting cavities with respect to the experimental laser pulse dominates timing issues [1]. Phase and amplitude feedback of the deflecting cavities is expected to provide x-ray pulse to laser pulse timing stability of 50 fs or better. To stabilize all timing and rf signals in the facility, we propose to use a phase-locked laser oscillator as the facility master oscillator. The RF gun, linacs, and deflecting cavities may thus be phase-locked to the experimental excitation lasers, and timing jitter between the optical laser and the x-ray pulse emitted by the beam minimized [6].

SUMMARY

A recirculating linac user facility is proposed to address the growing national and international need for ultrafast x-ray scientific research. The LUX facility is based on existing accelerator technology, coupled with an array of advanced tunable femtosecond lasers, and is capable of performing an enormous variety of pump-probe type experiments with soft and hard x-rays. The facility has been specifically designed with a view toward solving problems in ultrafast science, and it's impact will be across all fields of science.

REFERENCES

[1] J. N. Corlett et al, "Feasibility study for a recirculating linac-based facility for femtosecond dynamics", LBNL formal report LBNL-51766, December 2002.

[2] J. N. Corlett, et al, " A Recirculating Linac Based Synchrotron Light Source for Ultrafast X-ray Science", Proc. EPAC'02, Paris, France, June 2002.

[3] W. Fawley et al, "Simulation studies of an XUV/soft x-ray harmonic-cascade FEL for the proposed LBNL recirculating linac", this conference.

[4] L.-H. Yu et al, "High-Gain Harmonic-Generation Free-Electron Laser", Science **289** 932-934 (2000).

[5] A. Zholents et al "Generation of subpicosecond x-ray pulses using RF orbit deflection", NIM A 425 (1999) 385-389.

[6] J. Corlett et al, "Techniques for Synchronization of X-ray Pulses to the Pump Laser in an Ultrafast X-ray Facility", this conference.

[7] J. Staples et al, "The LBNL Femtosource 10 kHz Photoinjector", this conference.

[8] S. Lidia et al, "An Injector for the Proposed Berkeley Ultrafast X-Ray Light Source", this conference.

[9] S. Wang et al, "Flat beam production in low energy injectors", this conference

[10] D. Edwards et al, "The Flat Beam Experiment at the FNAL Photoinjector", Proc. XXth International Linac Conference, Monterey, 2000.

[11] A. Zholents et al, "Longitudinal phase-space control in the Berkeley Femtosecond X-ray light source", this conference.

[12] TESLA Technical Design Report, DESY 2001-011, March 2001.

[13] L. Harwood, C. Reece, "CEBAF at 12 and 25 GeV", Proc. SRF2001, Tsukuba, Japan, Sept. 2001.

[14] S. De Santis et al "Collective effects analysis for the Berkeley femtosource", this conference

[15] R. Wells et al, "Recirculating linac vacuum system", this conference

[16] D. Li et al, "Deflecting rf cavity design for a recirculating linac-based facility for ultrafast x-ray science", this conference.

4GLS: A NEW TYPE OF FOURTH GENERATION LIGHT SOURCE FACILITY

M W Poole, S L Bennett, M A Bowler, N Bliss, J A Clarke, D M Dykes, R C Farrow, C Gerth, D J Holder, M A MacDonald, B Muratori, H L Owen, F M Quinn, E. A. Seddon, S L Smith, V P Suller and N R Thompson, Daresbury Laboratory, Warrington, UK

I N Ross, Rutherford Appleton Laboratory, Didcot, UK

B McNeil, Strathclyde University, Glasgow, UK

Abstract

Consideration is now being given in the UK to the provision of an advanced facility at lower energy to complement the DIAMOND x-ray light source. The proposed solution, 4GLS, is a superconducting energy recovery linac (ERL) with an output energy around 600 MeV, delivering both CW beam currents up to 100 mA and alternatively high charge bunches for FEL applications. Production and manipulation of short electron bunches (fs) is a vital part of the source specification. In addition to beam lines from undulator sources in the ERL recovery path there will be three FELs: two will be oscillator types in the infrared and VUV respectively, and the third will be a high gain system for XUV output. The project is outlined, together with its status and the R&D challenges posed. A funded prototype based on a 50 MeV ERL is also described.

1 ERL LIGHT SOURCE CONCEPT

The origin of this project is the requirement in the UK to continue its investment in advanced radiation sources based on particle accelerators. A strategy has been developed to replace the existing national light source, the world's first dedicated 2nd generation X-ray source (the SRS), with more advanced facilities that are optimised for specific spectral regions [1]. As a first step the 3 GeV x-ray source DIAMOND has been funded and is now under construction [2].

For a low energy source complementary to DIAMOND it had initially been assumed that a 3rd generation storage ring would be built, but alternative ideas emerged during 2001 [3]. In order to overcome the well known limitations of low energy storage rings below 1 GeV, and also to exploit the sub-ps bunch regime, attention turned to linac-based sources that can combine exceptionally high transverse and longitudinal brightness. Linacs have already played a major role in the development of free electron lasers (FELs) but these have usually required high peak but modest average brightness whereas a national light source will also need to deliver high average fluxes. Achieving average linac currents as high as those in 3rd generation light source rings requires a combination of superconducting technology and energy recovery linac (ERL) principles. Such systems have now been successfully demonstrated at two laboratories [4,5], leading to a number of recent proposals to apply these results to higher energy projects generating x-rays [6,7]. As an intermediate step the Cornell team have proposed a demonstrator at 100 MeV and 100 mA [8]. A related series of novel light source proposals has a multi-pass configuration [9] but may omit energy recovery [10].

Once the ERL is adopted for such a spontaneous light source its superior properties also become attractive for advanced FEL development. For example the greatly enhanced peak beam currents in a linac can be exploited in a high gain FEL, by removing the mirror technology limitations of a more conventional optical cavity. Such a linac-based source then provides unique opportunities for the combination of spontaneous and stimulated (coherent) sources at a single centre: this is the unique feature of our 4GLS proposal.

2 PROJECT OUTLINE

The feasibility of this new light source philosophy has been studied and developed by a project team at Daresbury, together with strong strategic and scientific input from the potential user base in the UK academic community. The science case, which has emphasised the exploitation of ultra-short (fs) pulses and the extent to which multiple sources would be utilised (eg for pump-probe experiments), was reviewed and accepted by funding agencies early in 2002. The 4GLS project concept is illustrated schematically in Fig. 1 which contains the principal components although omitting many important practical details. It has been described in more detail elsewhere [11] and will therefore only be briefly repeated here.

The 600 MeV linac comprises a superconducting accelerating structure and one possible solution is to adapt the successful 1.3 GHz TESLA modules [12] to the demands of a CW operating mode. For the purposes of 4GLS feasibility studies, including outline costings and layout considerations, a modest accelerating gradient of only 15 MeV/m has been assumed, implying a total length of about 60 m and 350 kW RF power to drive five modules. Higher gradients have been achieved at DESY

0-7803-7738-9/03/$17.00 © 2003 IEEE

but at much lower duty cycles; de-rating also substantially reduces the 2 K cryogenic burden although this may still exceed 100 W per cryomodule. It will also be essential greatly to enhance HOM damping and out-coupling by modifications to these structures. To achieve the target 100 mA the BBU instability threshold must be raised by HOM damping and by optimised transport line optics [13]; active feedback systems will also be incorporated. Specifying a bunch length in the linac to exceed 1 ps allows the losses to be controlled but the cryogenic plant will be rated to at least 1 kW at 2 K (ie about 1 MW AC power installation).

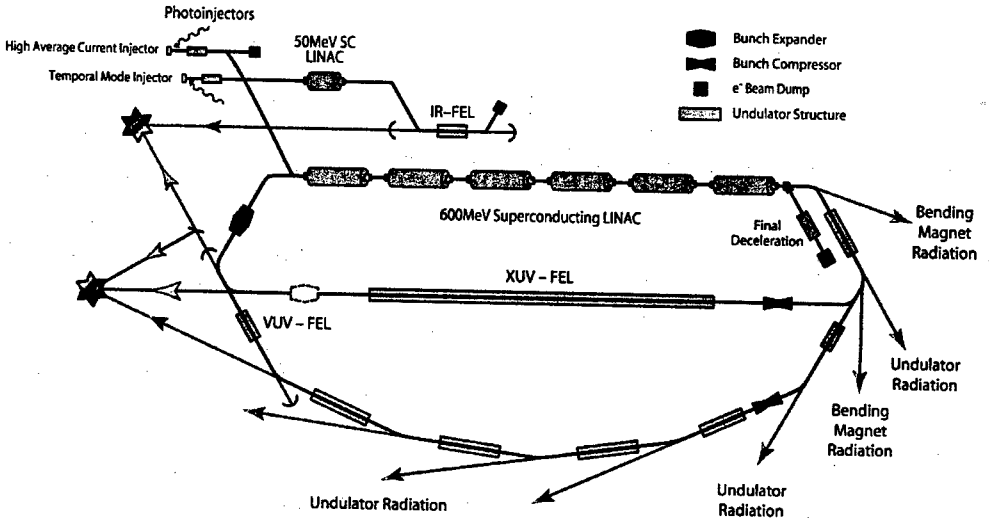

Figure 1: Schematic Layout of 4GLS Light Source Concept

Two photocathode guns are included to cover both high-average and high-peak current operating modes. A CW gun must be developed to deliver at least 100 mA in a reliable manner for a user facility. Selection of this gun will necessitate an R&D programme comparing various solutions, including DC or RF types and various cathode-laser combinations. The option of a superconducting gun will also be assessed but is unlikely to be adopted for initial stages of the project. The second gun generates the high charge per bunch needed for FEL operations: it will have a specification more similar to those being achieved in the latest linear collider and SASE FEL projects and can utilise their conclusions. This gun gives additional flexibility for production of bunch trains with a variety of pulse structures, whilst maintaining high average output for the spontaneous emission users.

Figure 1 does not detail the important electron beam transport system but it will be based on two arcs, employing tunable achromats to achieve isochronous transport over a broad energy acceptance. This is under study to determine their implications for variable R_{56} control, for beam dynamics, for overall layout footprint and for technical aspects in a 600 MeV solution. Bunch compression can be achieved both in arcs and in magnetic chicanes, but is shown schematically in Fig. 1 to indicate that fs bunch lengths will be controlled as required in local parts of the transport system. Design guidelines for arcs and chicanes are already known, in particular for minimisation of coherent synchrotron radiation (CSR) effects [14].

It should be noted that unlike other projects 4GLS needs good access to radiation from undulators (and perhaps even bends) within the arcs. Figure 1 indicates a series of beam lines feeding user stations, in some cases from fs source points, and the transport focusing optics will be locally optimised for beam dimensions at individual undulators. A cavity FEL operating in the VUV range (3-10 eV) is also included. The electron beam can be switched into a parallel return path to feed a long undulator for a high gain XUV-FEL system to deliver 10-100 eV output, with maximum compression immediately upstream of its entrance. Energy recovery is probably unnecessary in this low duty cycle mode having reduced average current. The infra-red FEL is supplied from an independent superconducting linac and will provide high quality, stable output over a range from perhaps 3-75 μm. A feature of the 4GLS proposal is the linking of the outputs from these various sources to permit a range of pump-probe experiments to be undertaken.

3 ERL PROTOTYPE PROJECT

The challenges of 4GLS are considerable and are in the areas of beam dynamics, accelerator technology, FEL physics and effective user exploitation. On 2 April 2003 it was announced that the next stage of the project evolution would be immediate funding of an Exploratory Phase. This will include construction of a smaller scale ERL Prototype (ERLP) intended to address these issues in such a test facility at Daresbury, to be completed by 2006.

The ERLP will demonstrate energy recovery with an electron beam generated by a photocathode injector and accelerated in a superconducting linac module to at least 50 MeV. It will also incorporate an FEL test facility based on a wiggler magnet previously used in the Jefferson Laboratory IRFEL and supplied on loan as part of an international collaboration. These important physics and technology aspects will allow all of the critical 4GLS challenges to be encountered in advance of the final project construction phase.

The layout of the ERLP is now being finalised, with particular emphasis on tailoring its footprint to match an available building and infrastructure. A comparative study of Bates [15] and triple-bend achromat (TBA) arcs is underway, covering issues ranging from flexible beam dynamics through to compactness. The transport line will also include magnetic compression chicanes, to generate fs electron bunches and radiation pulses and to study associated problems (eg CSR effects, pulse synchronisation). The TBA version is shown in Fig. 2 which includes a TESLA-type linac module and the J-Lab wiggler as a reference. Injection and extraction chicanes will be needed upstream and downstream from the linac cryomodule. Start-to-end beam simulations with integrated codes have commenced and will eventually be benchmarked by the experimental data from ERLP. In parallel FEL design studies are being undertaken and will include calculation of coherent emission from the ultra-short bunches that will be available.

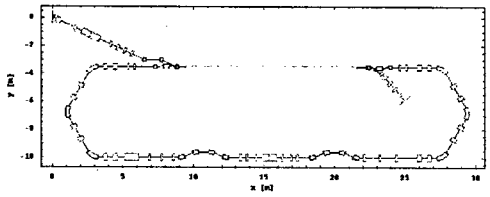

Figure 2: Preliminary ERLP Beam Transport

A photocathode gun test stand will be constructed to allow experiments to commence early in 2004 and it is likely that a DC gun based on established designs will be selected for initial experiments, in which case an RF buncher and booster will be added. It is hoped to install the linac itself and its cryogenics later that year. Attention will also be given to the advanced diagnostics necessary to make full use of the Prototype programme.

Figure 3 shows the planned layout in a converted building that already has extensive shielding and other services available. Again the TBA design is shown, but both the TBA and Bates footprints have similar dimensions and no decision has yet been made on the optimum choice.

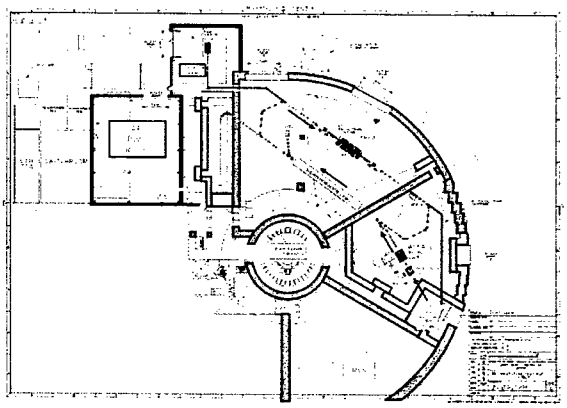

Figure 3: Possible ERLP Layout

4 REFERENCES

[1] M W Poole & V P Suller, "Proposals for New UK Light Sources", EPAC'94, London

[2] R P Walker, "Progress with the Diamond Light Source Project", these Proceedings

[3] J A Clarke et al, "Prospects for a 4th Generation Light Source for the UK", PAC'01, Chicago

[4] G R Neil et al, Phys Rev Lett 84(4), 662 (2000)

[5] N Nishimori et al, "Commissioning of JAERI Energy Recovery Linac", EPAC'02, Paris

[6] I Ben-Zvi et al, "Photoinjected Energy Recovery Linac Upgrade for the National Synchrotron Light Source", PAC'01, Chicago

[7] I V Bazarov et al, "The Energy Recovery Linac (ERL) as a Driver for X-ray Producing Insertion Devices", PAC'01, Chicago

[8] I Bazarov et al, "Phase 1 Energy Recovery Linac at Cornell University", EPAC'02, Paris

[9] D A Kayran et al, "MARS: A Project of a Diffraction Limited Fourth Generation X-ray Source",APAC'98

[10] J N Corlett et al, "A Dedicated Synchrotron Light Source for Ultrafast X-ray Science", PAC'01, Chicago

[11] M W Poole et al, "4GLS: an Advanced Multi-source Low Energy Photon Facility for the UK", EPAC'02, Paris

[12] TESLA Technical Design Report, DESY 2001-011

[13] I V Bazarov et al, "Linac Optics for Energy Recovery Linac", PAC'01, Chicago

[14] J H Wu et al, "CSR Analysis for the Photoinjected Energy Recovery Linac and UVFEL Projects at the NSLS", PAC'01, Chicago

[15] J Flanz et al, Nucl Instr Meth A241, 325 (1985)

THE CORNELL ERL PROTOTYPE PROJECT *

G.H. Hoffstaetter†, B. Barstow, I.V. Bazarov, S. Belomestnykh, D. Bilderback, S. Gruner, M. Liepe, H. Padamsee, D. Sagan, V. Shemelin, C. Sinclair, R. Talman, M. Tigner, V. Veshcherevich, Cornell University, Ithaca, NY and G.A. Krafft, L. Merminga, TJNAF, Newport News, VA

Abstract

Synchrotron light sources based on Energy Recovery Linacs (ERLs) show promise to deliver X-ray beams with both brilliance and X-ray pulse duration far superior to the values that can be achieved with storage ring technology. Cornell University, in collaboration with Jefferson Laboratory, has proposed the construction of a prototype ERL. This 100MeV, 100mA CW superconducting electron accelerator will be used to study and resolve the many accelerator physics and technology issues of this type of machine. These studies are essential before ERLs can be confidently proposed for large-scale applications such as synchrotron light sources. Key issues include the generation of high average current, high brightness electron beams; acceleration and transport of these beams while preserving their brightness; adequate damping of higher order modes (HOMs) to assure beam stability; removal of large amounts of HOM power from the cryogenic environment; stable RF control of cavities operating at very high external Q; reduction of beam losses to very low levels; and the development of precision non-intercepting diagnostics to allow beam setup, control and characterization. Our prototype design allows us to address these and other issues over a broad range of parameter space. This design, along with recent progress on understanding these issues, will be presented.

INTRODUCTION

To profit from the smaller transverse and longitudinal emittances that a linac can offer, compared to a circular high energy physics collider or synchrotron light source, it is necessary to be able to accelerate beams to the energies (several GeV) and with the currents (several 100mA) that are typical in these storage rings. This would require that the linac delivers a power of order 1GW to beam. Without somehow recovering this energy after the beam has been used, such a linac would be practically unfeasible.

Energy recovery can be achieved by decelerating high energy electrons to generate cavity fields which in turn accelerate new electrons to high energy. With this, large beam powers that are not accessible in a conventional linac can be produced. ERLs were proposed over 30 years ago. However, to continuously transfer field energy from electrons to the RF cavities and back to new electrons, it is essential that the cavities are continuously filled with field energy. This means that they have to be operated in continuous wave (CW) mode. Since CW normal conducting cavities with high accelerating fields require an unrealistic amount of cooling, and since SC cavities have only recently achieved sufficiently high fields, ERLs have not been technically feasabe for many years.

At TJNAF and at JAERI, SC cavities were used to demonstrate energy recovery for low energy (50 and 17MeV) and low current (5mA) beams. These laboratories made significant achievements and showed they could save most of the energy required for beam acceleration. While for the FEL at TJNAF, the beam power in energy recovery mode is about 4 times higher than that without the recovery, these ERLs never produced beam powers that could not have been produced with a conventional linac. However, since the TESLA collaboration has demonstrated the reliable operation of SC cavities with accelerating field well above 20MV/m, several laboratories have proposed high power ERLs for different purposes. Designs for light production with different parameter sets and various applications are being worked on by Cornell University, BNL, Daresbury, TJNAF, and JAERI (see PAC2003), the University of Erlangen, Novosibirsk (see EPAC2002) and KEK. TJNAF has incorporated an ERL in its design of an electron–ion collider (EIC) for medium energy physics while BNL is working on an ERL–based electron cooler for the ions in the relativistic ion collider (RHIC).

THE CORNELL ERL PROJECT

Since neither an electron source, nor an injector system, nor an ERL, has ever been built for the required large beam powers and small transverse and longitudinal emittances, it is essential to build a prototype facility [1] that can verify the functionality of all essential devices and physical processes before endeavoring onto a large user facility. The Wilson laboratory at Cornell University has proposed to the NSF to build such a prototype and to perform the required proof of principle. This proposal has been favorably reviewed by the NSF and is strongly supported by Cornell University. A decision by the NSF is expected soon.

While Cornell plans an ERL light source [2], knowledge obtained in the ERL prototype facility would profit a scientific community that is much larger than the already very large and diverse group of synchrotron radiation users, and includes medium and high energy physicists working on an EIC and at RHIC.

The Cornell CHESS laboratory currently uses the Cornell Electron Storage Ring (CESR) as a second generation synchrotron light source at 5GeV. As a future light source for this laboratory, an ERL seems ideal. It can enlarge the wide range of applications of third generation light sources by producing beams similar to the CW beams from these modern facilities, albeit with higher brilliance due to the

* Work supported by Cornell University and US DOE under contract DE-AC05-85ER40150

† Georg.Hoffstaetter@cornell.edu

0-7803-7738-9/03/$17.00 © 2003 IEEE

much smaller horizontal emittance and possibly smaller energy spread. At the same time, it can serve more specialized experiments that require ultra small emittances for high spacial resolution or ultra short bunches for high temporal resolution [2].

Since CESR is planning to phase down its high energy physics program in about 5 years, we have studied whether CESR components, its tunnel, and its infrastructure could be used to house an ERL facility [3].

A detailed set of parameters has not yet been fixed and can still be influenced by findings from the ERL prototype. The currently planned parameters together with those of the prototype are listed in Table 1.

THE CORNELL PROTOTYPE

Table 1: The Cornell ERL Prototype and light source

Parameter		Prototype	Light source
Energy	(GeV)	0.1	5
Current	(mA)	100	100
Inj. energy	(MeV)	5–15	5–15
Rep. Rate	(GHz)	1.3	1.3
Acc. gradient	(MV/m)	20	20
Q of cavities	(10^{10})	1	1
external Q	(10^7)	2.6	2.6
Charge/Bunch	(pC)	77	77
nominal σ_E	(10^{-3})	0.2	0.2
nominal σ_τ	(ps)	2	2
nominal ϵ_N	(μm)	2	2
short pulse σ_τ	(ps)	< 0.1	< 0.1
microbeam ϵ_N	(μm)	0.2	0.2
Main Linac Cavities		5	≈ 250
Refrigerator@2K	(kW)	0.2	≈ 17

The prototype ERL at Cornell, shown in Fig. 1, is planned to have very similar parameters to the light source facility. The differences are essentially that (a) the prototype injector is only capable of producing 5MeV beam at 100mA and the light source might require a higher energy and thus more injector cavities, (b) the main linac in the prototype has only one cryomodule with only 5 cavities while the full facility has 8 cavities per module and more than 30 cryomodules, and (c) the cost and power consumption of the prototype is significantly smaller. After completion, many parts of the prototype, especially the entire gun and injector, can be used for the ERL light source.

Issues that should be investigated by the ERL prototype before a full-scale ERL user facility is built include:

Gun: Achieving the small normalized emittance of 2μm in the undulators requires around 1μm at the high voltage DC gun, which has to deliver 100mA from its negative electron affinity GaAs photo cathode. Design parameters are 500 to 750kV in a pressurized SF_6 atmosphere, a Ti:sapphire laser operating at 780nm with several Watts at 1.3GHz repetition rate [4]. Such a gun relies heavily on space charge compensation [5] and has never been operated at the required high currents. Furthermore, microbeams with ultra-small emittances of 0.2μm in the undulators are envisioned for high resolution X-ray imaging. Such beams could only be produced with reduced currents.

Injector: The injector is designed to send bunches with 77pC and with emittances of less than 1.5μm into the linac. The injector allows the acceleration of 100mA beam current to 5MeV, with every bucket filled, and of 50 or 33mA beam current to 10MeV or 15MeV when every second or third bucket is filled. Testing will show which injector energy should be chosen for the Cornell ERL light source. Each of the 5 two-cell SC injector cavities couples about 100kW to the beam. The cavities are designed to be dipole-mode-free and are equipped with a symmetric input coupler to avoid a transverse kick. [6, 7, 8].

Halo formation: Space charge forces are most nonlinear for particles at the outside of the beam and can create a dilute halo. Collimating the beam, however, can cause activation and heat load in the cryogenic environment. Collimating at high energy additionally reduces the efficiency by wasting power for electrons that do not participate in the energy recovery. Study of halo formation and its removal will therefore be important.

CSR: Coherent synchrotron radiation (CSR) can significantly increase the transverse and longitudinal emittances, especially for short-bunch operation. CSR is such a complex process that it is essential to verify the accuracy of current CSR simulations.

Cavities and cryomodules: While much will be adopted from the successful TESLA cavities and cryomodules, some modifications are needed for CW operation. These modifications are mainly related to the large HOM power that has to be extracted and to the large heat load of about 40W that has to be cooled at 2K per cavity. For frequencies up to about 3GHz, 4 output HOM couplers of the TTF type are used per cavity. Between the cavities there will additionally be a ferrite beam pipe absorber of the CESR type for frequencies larger than about 3GHz [9].

Cavity control: Due to the high external Q, the width of the cavity resonance is very narrow (50Hz for $Q_{ext} = 2.6 \cdot 10^7$). Controlling the cavity under the presence of microphonic noise thus becomes a challenge [10]. Tests in the prototype will show what maximal Q_{ext} can be achieved.

Beam breakup: While the power required for acceleration limits the beam current in conventional linacs, the required power in an ERL is virtually independent of the beam current. However, the total current is limited by the beam breakup (BBU) instability, which arises when cavity modes that deflect the beam transversely are coherently excited by the recirculating beam and grow faster than they can be damped. The particle optics in the linac and in the return arc has been designed to raise the BBU limit to 100–200mA. However, the BBU limit depends on the detailed HOM damping and HOM spectrum, which cannot be simulated very well.

Short bunches: The ERL light source will have users that

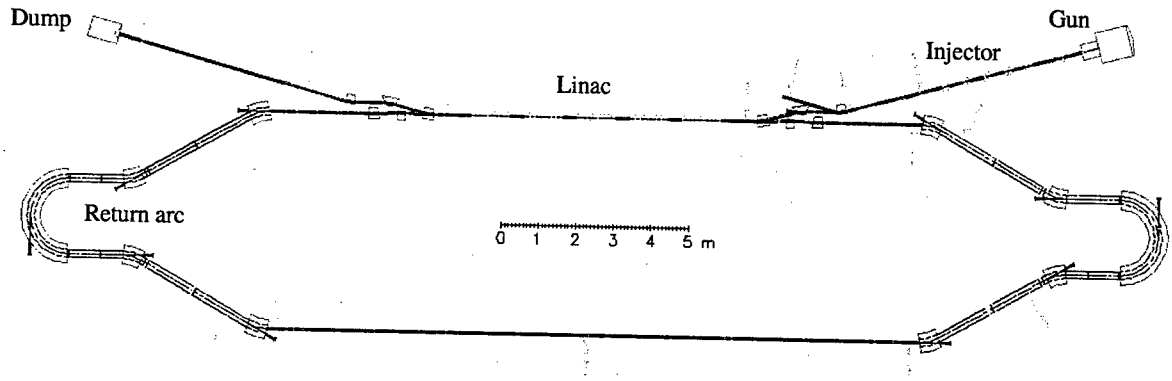

Figure 1: Layout of the Cornell ERL Prototype

require 100fs pulses and users for which a 2ps bunch length is sufficient. While 2ps pulses can be created in the injector by a 20ps laser pulse and subsequent bunching, a 100fs pulse requires additional pulse compression. In order to reduce HOMs, the bunch will be compressed at full energy. A flexible nonlinear bunch compression optics has been designed and will be tested [11].

Phase space: The relative energy spread at high energy of below $0.2 \cdot 10^{-3}$ can increase strongly when the beam is decelerated. If the longitudinal phase space distribution was uncorrelated, the rms energy spread would become at least 20% after deceleration from 5GeV to 5MeV, which may well result in beam loss in the last RF section. The longitudinal phase space therefore has to be manipulated by nonlinear optical elements so that the nonlinear phase space correlation is reduced by the waveform of the decelerating cavities [12].

Dump: To first approximation the energy at the dump is the same as the injector energy. A quadrupole optics will spread the 1MW beam power (that would result from 10MeV operation) over a cooled collector.

Beam diagnostics: In order to allow for the planned detailed beam dynamics studies in the prototype, a very precise knowledge of beam position, the three emittances, and the beam halo will be required along the accelerator. The following tools will be developed: high precision BPMs, beam–ionization profile monitors, transition radiation and synchrotron radiation beam size monitors for reduced and full average current operation, bunch length monitors that use infrared spectrometry of the coherent synchrotron and diffraction radiation, and moving wires for halo measurements. All of these will be very valuable for the ERL light source as well, since reliable diagnostics will be needed for controlling the high power beam and for stabilizing the beam-position to the requirements of the users.

CONCLUSION

There are strong reasons to believe that SC cavity technology is sufficiently advanced to allow for high fields, high average current, CW operation in an ERL. However, many components will have to be optimized and beam dynamics issues have to be investigated in a prototype accelerator. The risks of not building a prototype seems too high, and the financial burden of building one at Cornell seems relatively benign considering the benefit that it would have to all the ongoing ERL projects.

REFERENCES

[1] I.V. Bazarov, et al. *Phase I Energy Recovery Linac at Corell University*, proc. of EPAC02.

[2] S.M. Gruner, M. Tigner (eds.), *Phase I Energy Recovery Linac (ERL) Synchrotron Light Source at Cornell University*, Report CHESS-01-003 at http://erl.chess.cornell.edu/papers/ERL_Study.pdf (2001)

[3] G.H. Hoffstaetter, et al., *A Lattice for a 5GeV ERL in the CESR Tunnel*, proc. of PAC03.

[4] C. Sinclair, *Very High Voltage Photoemission Electron Guns*, proc. of PAC03.

[5] I.V. Bazarov, C.K. Sinclair, *High Brightness, High Current Injector Design for the Cornell ERL Prototype*, proc. of PAC03.

[6] V. Shemelin, et al., *Dipole-mode-free and kick-free 2-Cell Cavity for the SC ERL Injector*, proc. of PAC03.

[7] V. Veshecherevich, et al., *Input Coupler for ERL Injector Cavities*, proc. of PAC03.

[8] H. Padamsee , et al., *Overview of the Cornell ERL Injector Cryomodule*, proc. of PAC03.

[9] M. Liepe, S. Belomestnykh, *First Studies for a Low Temperature Higher-Order-Mode Absorber for the Cornell ERL Prototype*, proc. of PAC03.

[10] M. Liepe, et al., *RF Parameter and Field Stability Requirements for the Cornell ERL Prototype*, proc. of PAC03.

[11] P. Piot, D. Douglas, and G. A. Krafft, *Longitudinal phase space manipulation in energy recovering linac-driven free-electron lasers*, Phys Rev ST-AB, 6, 030702 (2003)

[12] I.V. Bazarov, G.H. Hoffstaetter, *Lattice options for a 5GeV Light Source at Cornell*, proc. of PAC03.

CEBAF ENERGY RECOVERY EXPERIMENT*

A. Bogacz#, K. Beard, J. Bengtsson, C. Butler, Y. Chao, S. Chattopadhyay, H. Dong, D. Douglas, A. Freyberger, A. Guerra, R. Hicks, A. Hofler, C. Hovater, A. Hutton, R. Kazimi, R. Lauze, L. Merminga, T. Plawski, Y. Roblin, M. Spata, C. Tennant, M. Tiefenback,
Jefferson Lab, Newport News, VA, 23606, USA
A. Bernhard, A. Magerl, Friedrich-Alexander University of Erlangen-Nürnberg, Germany
H. Toyokawa, National Institute of Advanced Industrial Science and Technology, Tsukuba, Japan

Abstract

A successful GeV scale energy recovery demonstration with high ratio of accelerated-to-recovered energies (50:1) was recently carried out on the CEBAF recirculating linear accelerator. Future high energy (multi-GeV), high current (hundreds of milli-Amperes) beams would require gigaWatt-class RF systems in conventional linacs - a prohibitively expensive proposition. However, invoking energy recovery [1] alleviates extreme RF power demands; required RF power becomes nearly independent of beam current, which improves linac efficiency and increases cost effectiveness. Furthermore, energy recovering linacs promise efficiencies of storage rings, while maintaining beam quality of linacs: superior emittance and energy spread and short bunches (sub-pico sec.). Finally, energy recovery alleviates shielding, if the beam is dumped below the neutron production threshold. Jefferson Lab has demonstrated its expertise in the field of Energy Recovery Linacs (ERLs) with the successful operation of the Infrared FEL, where 5 mA of average beam current have been accelerated up to 50 MeV and the energy stored in the beam was recovered via deceleration and given back to the RF power source. To date this has been the largest scale demonstration of energy recovery.

MOTIVATION

Presently there are designs for several ERL based accelerator systems world-wide. These include designs for FELs (KAERI, BINP Accelerator-Recuperator), synchrotron light sources (Cornell/J-Lab ERL, ERLSYN, 4GLS, BINP MARS), electron cooling devices (BNL-BINP) and electron-ion colliders (ELIC, eRHIC). Some of the ERL-based accelerator applications that are being proposed require beam currents of the order of 100 mA, while the beam energy for these applications ranges from the currently achieved 50 MeV up to 5 GeV. There are several important accelerator physics and technological issues that must be resolved before any of these applications can be realized. The J-Lab FEL Upgrade, presently under construction and designed to accelerate 10 mA up to 150-200 MeV and then subjected to energy recovery, and the proposed Cornell/J-Lab ERL Prototype, designed to accelerate 100 mA up to 100 MeV and then decelerated for energy recovery, will be ideal test beds for the understanding of high current phenomena in ERL devices. Last year, in an effort to address the issues of energy recovering high-energy beams, Jefferson Lab proposed a minimally invasive energy recovery experiment utilizing the CEBAF accelerator [2]. The experiment was successfully carried out at the end of March '03 by demonstrating energy recovery of a 1 GeV beam. Until this experiment, there were no plans aimed to address issues related to beam quality preservation in systems with large final beam energy (up to 1GeV) or a large energy ratio between final and injected beams (a factor of 50).

THE EXPERIMENT

General Layout

A schematic representation of the CEBAF with Energy Recovery experiment is illustrated in Figure 1. Beam is injected into the North Linac at 56 MeV where it is accelerated to 556 MeV. The beam traverses Arc1 and then begins acceleration through the South Linac where it reaches a maximum energy of 1056 MeV. Following the South Linac, the beam passes through a newly installed phase delay chicane. The chicane was designed to create a path length differential of exactly ½-RF wavelength so that upon re-entry into the North Linac, the beam is 180^0 out of phase with the cavities and will subsequently be decelerated to 556 MeV. After traversing Arc1 the beam enters the South Linac - still out of phase with the cavities - and is decelerated to 56 MeV at which point the spent electron beam is sent to a dump. In this way the beam gives energy back to the RF system, which may be used to accelerate subsequent beam.

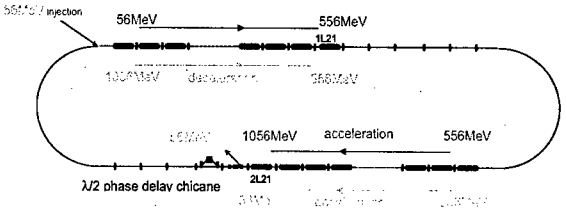

Figure 1: CEBAF Energy Recovery Experiment - layout

Beam Transport – Linac Optics

The linac optics were optimized for the two beams so that the lower energy beam in each linac had a tight, 120^0 betatron phase advance per cell lattice, as illustrated in Figures 2 and 3. Appropriate optics design for the spreader and recombiner of Arc2 (following South Linac) facilitates compensation of beta mismatches introduced by optimizing the linac optics for the lower energy beam.

*work supported by the US DoE under contract DE-AC05-84ER40150.
#bogacz@jlab.org

0-7803-7738-9/03/$17.00 © 2003 IEEE

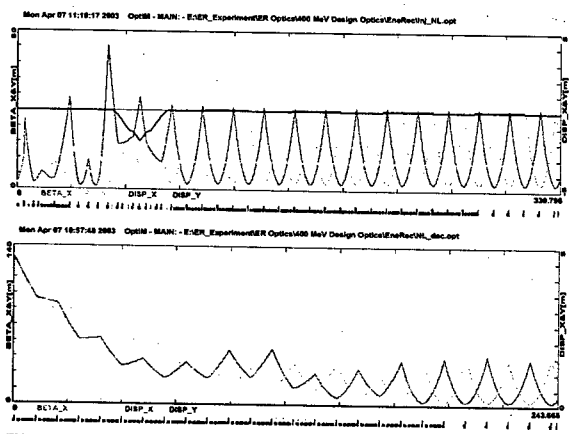

Figure 2: North Linac – top: 120° per cell lattice for the accelerating beam (56–556MeV) and bottom: mismatched optics for the decelerating beam (1056–556MeV)

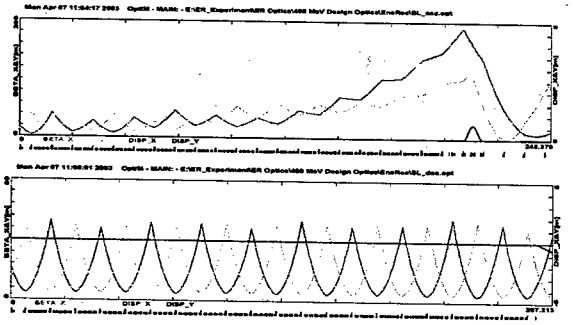

Figure 3: South Linac – top: mismatched optics for the accelerating beam (556–1056MeV) and bottom: 120° per cell lattice for the decelerating beam (556–56MeV)

MEASUREMENTS

To gain a quantitative understanding of the beam behavior through the machine, an intense effort has been made towards planning measurements for the experiment [2]. One of the most critical is measuring the beam emittance, which serves as a figure of merit by characterizing the extent to which beam quality is preserved during energy recovery. A scheme has been implemented to measure the emittance of the energy-recovered beam prior to being sent to the dump [3], as well as in the injector and in each arc. In this way one can understand how the emittance evolves through the machine. One of the performance limitations of high-energy beams is a beam halo or small regions of phase space outside the beam core. Furthermore, the halo was measured at several locatins: in the injector, in both arcs and in the extraction dump to ascertain what effects energy recovery has on halo formation and evolution. In addition to the beam-based measurements mentioned above, another important class of measurements deals with the RF system's response to energy recovery. It tested the RF system response by measuring the gradient and phase stability with and without energy recovery for selected cavities throughout the North and South Linac. Once satisfactory measurements have been obtained using the nominal 56 MeV injection energy, a parametric study exercising high final energy (1020 MeV) to injection (20 MeV) ratios was carried out with the measurements repeated

RESULTS

Initial evidence of energy recovery mode is illustrated in Figure 4 by a synchrotron light monitor view of two beams in Arc1: the accelerated and half-way-energy-recovered beams at 556 MeV.

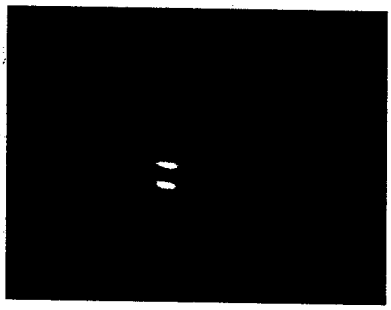

Figure 4: Arc1 synchrotron light monitor – two 'spots': accelerated/decelerated beams at 556 Me

Similarly, Figure 5 shows the two beams further downstream (end of South Linac): almost-fully-accelerated (~1GeV) and almost-fully-energy-recovered (~100MeV) beams as seen on a viewer.

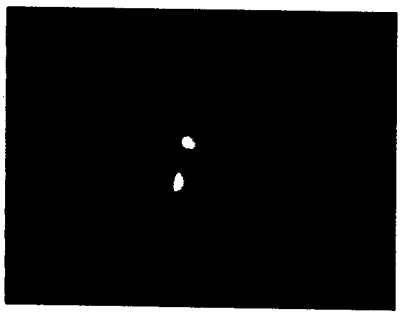

Figure 5: Two beams (~ 1 GeV and ~ 100 MeV) at the end of South Linac - SL16 beam viewer (E_{inj} = 20 MeV)

Finally, a fully energy recovered beam at 56 MeV, as seen on an optical transition radiation monitor in the extraction line is illustrated in Figure 6.

Emittance Measurements

Transverse emittance has been measured with wire scanners for altered optics (quads scan with 'closed beta bump') at several locations throughout the energy recovery cycle: at injection, in both arcs and right before extraction into the dump. A typical wire scan with two beams is illustrated in Figure 7.

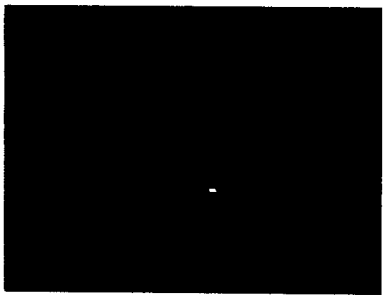

Figure 6: Energy recovered beam (56 MeV) at the dump (optical transition radiation monitor view)

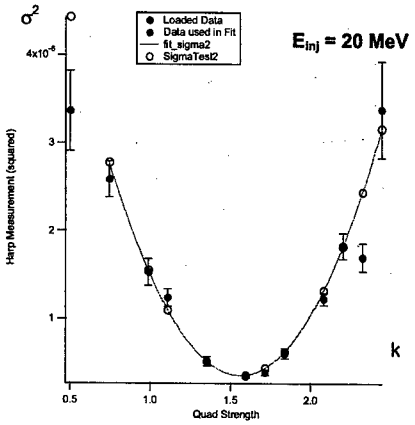

Figure 7: Wire scan with two beams – fully accelerated and energy-recovered beams

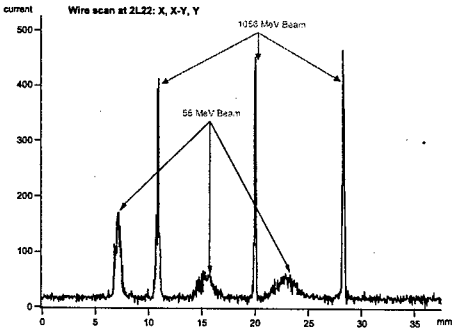

Figure 8: Emittance as extracted from least-squares quadratic fit

Emittance measurements in the quad-drift-wire configuration were carried out for varying quad strength (a quad directly upstream from the scanner). Parabolic dependence of measured beam profile (σ^2 vs quad strength k) is described in Figure 8.

Halo Measurement

Large dynamic range beam profile measurements of the energy recovered beam were carried out in front of the extraction dump. The measurements were made with a wire scanner and three photomultiplier tubes located 60cm downstream [4]. Figure 9 shows the measured beam profiles (X on right, Y on left) the Y profile is consistent with a Gaussian distribution through five decades of beam intensity.

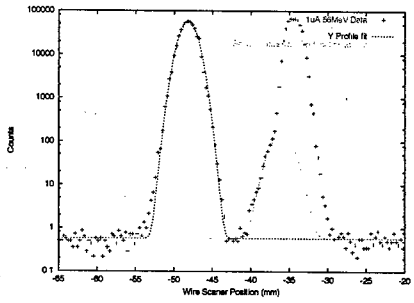

Figure 9: Beam halo (56 MeV, 1μA beam)

RF Transient Measurement

Finally, RF transients at full charge were measured for the last cavity in South Linac. Forward power required by the cavity with and without energy recovery is shown in Figure 10. One can see significant drop in forward power in the energy recovery mode.

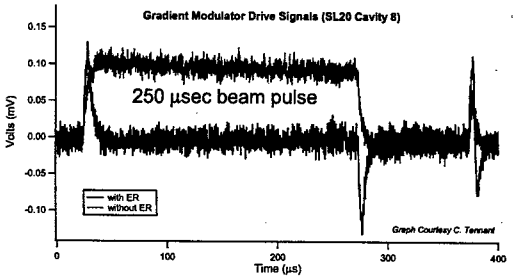

Figure 10: Forward power with/without energy recovery

SUMMARY

Measured beam quality characteristics show no degradation of the initial phase space during the energy recovery process. Beam profile is consistent with a Gaussian distribution. Analysis to obtain limits on the amount of beam halo is in progress. There is expectation for future R&D activities on Energy Recovery at CEBAF.

REFERENCES

[1] M. Tigner, Nuovo Cimento, "A Possible Apparatus for Electron Clashing-Beam Experiments", **37** (1965)

[2] A. Bogacz, et al., "CEBAF Energy Recovery Experiment", JLAB-TN-03-006, (2002).

[3] C. Tennant, "An Overview of Emittance Measurements for CEBAF-ER", JLAB-TN-03-004, (2003).

[4] A. Freyberger, "Large Dynamic Range Beam Profile Measurements with Low Current Electron Beams", this proceedings

Proceedings of the 2003 Particle Accelerator Conference

STEPS TOWARDS X-RAY SOURCES BASED ON LINAC-DRIVEN FREE-ELECTRON LASERS

P. Castro*, DESY, 22603 Hamburg, Germany

Abstract

X-rays play a crucial role in the study of structural and electronic properties of matter on an atomic scale. With high-brilliance x-ray sources high resolution imaging and the observation of very fast chemical processes become possible. A high-brilliance x-ray free-electron laser (FEL) based on linear accelerator technology using the principle of self-amplified spontaneous emission (SASE) appears to be the most promising approach. However, the high electron beam quality required by the SASE FEL process presents challenges to the linear accelerator community. Recent results obtained in several SASE FEL test facilities in the visible and ultra-violet ranges have demonstrated the viability of injector systems to deliver high brightness electron bunches and longitudinal compression schemes to obtain a few kA peak current while preserving beam brightness over a small slice of the bunch length. Challenges to new facilities reside in understanding the underlying physics to extend the technology to the x-ray region (about 0.1 nm) and in developing high-resolution phase space diagnostics. After a brief introduction to the SASE principle, we review the encouraging results of the recent experiments and present technical concepts to meet the requirements in the FEL facilities presently under construction.

INTRODUCTION

There is a large interest in both the particle accelerator community and the synchrotron radiation users community to construct FELs operating in the x-ray region (about 1 Å). A list of x-ray FEL facilities presently planned is given in Table 1. The scientific applications of x-ray FEL radiation are discussed in extensive detail in [1, 2, 3, 4].

Location	Facility	range [Å]	Referen.
DESY	TESLA X-FEL	0.85-64	[1]
SLAC	LCLS	1.5-15	[5]
MIT-Bates	X-ray FEL	3-1000	[6, 7]
FERMI	ELETTRA	12-15	[8]
BESSY	SASE-FEL	12-600	[3]
INFN Rome	SPARX	15-135	[9, 10]
Spring-8	SCSS	36	[11]
Daresbury	4GLS	124	[12, 4]

Table 1: Proposed/planned x-ray FEL facilities (ordered by minimum wavelength reach).

* pedro.castro@desy.de

X-ray FELs will deliver photon beams with a peak brilliance nearly ten order of magnitude larger than present x-ray sources. These FELs are driven by linear accelerators producing short bunches (in the order of 0.1 ps) with normalized transverse emittances of about 1 mm·mrad. High density electron bunches are accelerated to energies between 10 and 20 GeV and travel through undulator magnets with a length of about 100 m. A large part of the increase in photon brilliance with respect to present x-ray sources is due to the contribution of the undulator spontaneous radiation alone, since the peak current inside the bunch is large and the undulator is relatively long. The spontaneous synchrotron radiation emitted by the bunch in the first meters of the undulator is amplified under the principle of Self-Amplified Spontaneous Emission (SASE) [13, 14]. After a sufficient length, the radiation power saturates on a level about 5 to 6 orders of magnitude higher than spontaneous radiation.

This type of x-ray source presents also the property of being easily tunable. The radiation wavelength λ_r of the first harmonic of the FEL radiation [15] is related to the period length λ_u of a planar undulator by

$$\lambda_r = \frac{\lambda_u}{2\gamma^2}\left(1+\frac{K^2}{2}\right) \qquad (1)$$

where $\gamma = E/m_e c^2$ is the relativistic factor of the electrons, $K = eB_u\lambda_u/2\pi m_e c$ the 'undulator parameter' and B_u the peak magnetic field in the undulator. Thus, the FEL wavelength is tunable either by changing the electron energy in the linac or by changing the gap height of the undulator (and thus its magnetic field).

Another characteristic of the SASE FELs is the extreme short radiation pulse. In order to reach peak currents of a few keV, the bunches have to be compressed down to sub-picosecond lengths. The length of the radiation pulse generated by these short bunches is in the order of 0.1 ps, which allows the study of very fast chemical and physical processes.

The feasibility of SASE FELs have been proved at infrared, visible and ultraviolet wavelengths. Proof-of-principle experiments on SASE FEL have been successfully conducted in various laboratories. FEL saturation has been observed with 385 nm in LEUTL at ANL [16], with 840 nm in VISA at UCLA [17] and with 98 nm in TTF1 at DESY [18, 19]. Moreover, first user experiments at VUV wavelengths have been conducted [20, 21] at the TTF1 FEL.

0-7803-7738-9/03/$17.00 © 2003 IEEE

ELECTRON BEAM REQUIREMENTS

In a SASE FEL, lasing occurs in a single pass of a relativistic, high quality electron bunch through a long undulator magnet. The radiation power $P(z)$ grows exponentially with the distance z along the undulator

$$P(z) = P_o \cdot A \cdot \exp\left(\frac{2z}{L_g}\right)$$

where L_g is the field gain length, P_o the effective input power[1], and $A = 1/9$ in one-dimensional FEL theory with an ideal electron beam. This "high gain mode" requires an electron beam with transverse emittances of roughly

$$\epsilon_N \leq \gamma \frac{\lambda_r}{4\pi}$$

where ϵ_N is the normalized rms emittance and γ is the Lorentz relativistic factor of the electron. For a photon wavelength of 1 Å and typical undulator parameters the required beam energy is between 10 GeV and 20 GeV. At these energies, the emittance required is about 1 mm·mrad both in horizontal and vertical planes. This requirement is to be fulfilled by at least part of the beam or, rather to say, by a slice of the bunch. The so-called 'slice emittance' is therefore the relevant parameter.

At the same time, the energy spread and current of this slice has to fulfill that

$$\frac{\sigma_E}{E} < \rho \quad ,$$

which is the FEL parameter given by

$$\rho \approx \frac{1}{4\pi}\left(\frac{\mu_o e}{2m_e c}\frac{K^2 \hat{I}\lambda_u^2}{\gamma^2 \beta \varepsilon_N}\right)^{1/3}$$

where μ_o is the permeability of vacuum, $\hat{I}$ is the peak electron current and β is the mean value of the beta function in the undulator. Additionally, ρ determines the FEL gain length

$$L_g \sim \frac{\lambda_u}{4\pi\sqrt{3}\rho}$$

(as given in the one-dimensional FEL theory). For SASE saturation, the undulator length must be roughly 20 times the gain length. Maintaining a reasonable length for the undulator poses a restriction on the minimum value for ρ and therefore for the energy spread and peak current. Typical design values for x-ray FELs are $\sigma_E/E \sim 0.05\%$, $\hat{I} \sim 4$ kA and about 100 m undulator length. A significant deviation from these parameters can cause a dramatic decrease on the FEL gain and reduce the FEL power at the exit of the undulator. An example of the degrading effect on the FEL gain due to an increase of the transverse emittance in LCLS is shown in Fig. 1.

[1]The spontaneous undulator radiation is used as an input signal to the downstream part.

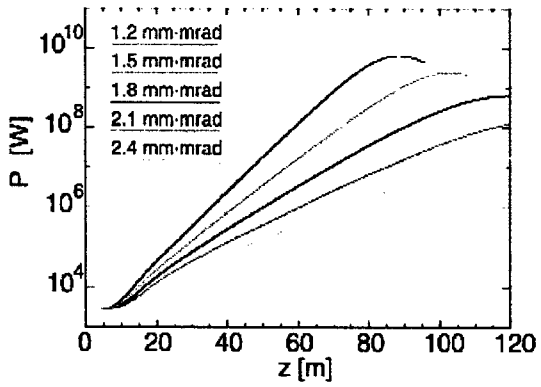

Figure 1: Development of the photon beam power as a function of the undulator length for various values of the transverse electron beam normalized emittance at LCLS. (Courtesy of S. Reiche)

The requirements on low emittance and high peak current electron beam are met with a high-brightness rf photocathode gun equipped with an emittance compensation solenoid, plus bunch length compression in stages at high energy, where space charge effects are reduced.

The research and progress in the technology and accelerator physics of linear colliders have produced the tools and knowledge necessary to control wakefields in order to achieve acceleration with minimal longitudinal and transverse emittance dilution.

Yet another requirement is the alignment of the electron beam trajectory in the undulator. The electron beam, focused in the undulator section to a transverse size of about 0.1 mm, has to be kept in essentially complete overlap with the photon beam during its passage through the undulator in order to maintain maximum amplification by intense electron-photon interactions. The straight trajectory inside the undulator can be achieved with beam-based alignment.

HIGH-BRIGHTNESS INJECTORS

RF photoinjectors have been developed as the most effective method of achieving very bright electron pulses. In a rf photocathode gun, electrons are emitted when a laser beam strikes the surface of the cathode. The cathode is placed at the middle plane of an rf cavity with very high accelerating field. The rf field boosts the electron bunch to relativistic energies in order to overcome the Coulomb forces that tend to blow up the emittance (so called space charge effect). As an example for rf gun, the side view of the LCLS design of a 1.6-cell S-band gun [22] is shown in Fig. 2.

The design goal of rf photocathode guns is a 3 ps-(rms)-long bunch of 1 nC charge with a normalized rms emittance of 1 mm·mrad. This corresponds to a peak current of about 100 A. These levels have not yet been simultaneously achieved to date, but most measurements reflect the

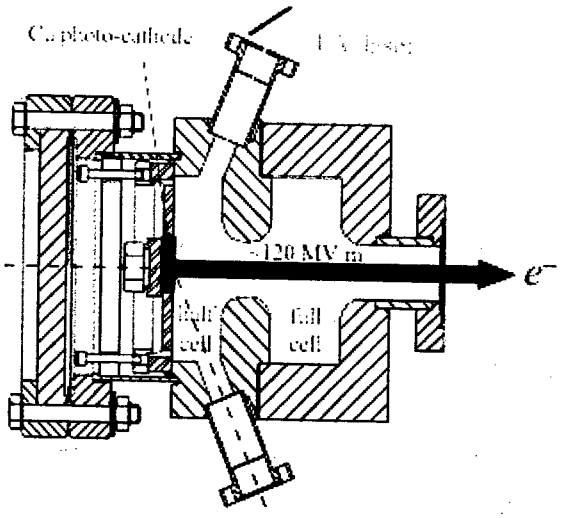

Figure 2: Side view of the RF photocathode design for LCLS

'projected' emittance. Some measurements have indicated sub-mm·mrad slice emittance levels [23, 24], but at a reduced charge of $0.1 - 0.3$ nC. A review of experimental results on high-brightness photoinjectors is given in [25]. A comparison of the brightness defined as

$$B = \frac{\hat{I}}{\varepsilon_N^2}$$

is shown in fig. 3.

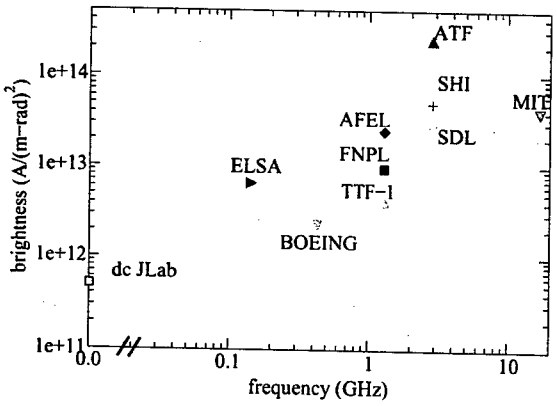

Figure 3: Comparison of the brightness of various photoinjectors (from ref. [25]).

LONGITUDINAL BUNCH COMPRESSION

The peak current produced by a low emittance gun is still not large enough in order to reach saturation within a reasonable undulator length. The bunch can be longitudinally compressed only at ultra-relativistic beam energies, where the space charge forces are reduced drastically.

Bunch compression is typically achieved by accelerating the bunch off-crest and using a magnetic chicane. The off-crest acceleration provides an energy chirp along the bunch length, so that the electrons in the head of the bunch gain less energy than the electrons in the tail. The magnetic chicane (for example, a series of four dipole magnets) introduces an energy dependent path length (see Fig. 4) so that the chirped bunch is compressed in length.

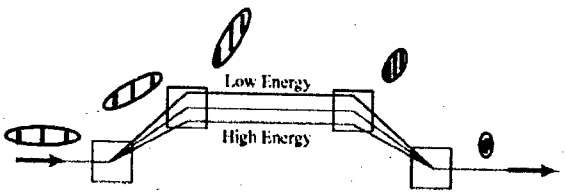

Figure 4: Schematic of a magnetic chicane for bunch compression.

The off-crest acceleration introduces, however, a non-linear energy correlation along the bunch train. For large incoming bunches the effect is non-negligible and can lead to the formation of a large spike at the head of the bunch as it is shown in Fig. 5. It is possible to compensate the non-linearities by including a higher harmonic rf accelerating section. This has been proposed for the first compressor in TESLA [27], in LCLS [28] in TTF2 FEL [29] and at Boeing [30].

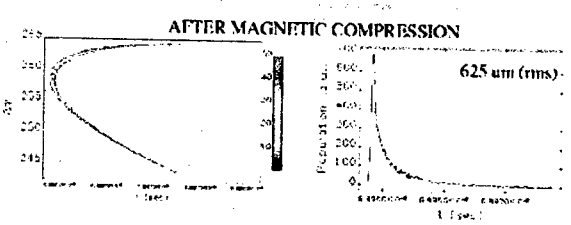

Figure 5: Simulation results of longitudinal compression of a long bunch including the non-linearities of the rf curvature. Longitudinal phase-space diagram (left plot) and profile (right plot) of the bunch after magnetic compression.

The off-crest acceleration in the linac can introduce timing jitter. The energy-phase correlation increases the sensitivity of the energy stability and the final bunch length to the phase jitter in the photocathode laser and rf timing. Energy jitter further increases the timing jitter due to the path length dependence of the magnetic chicane.

At very short bunch lengths, the Coherent Synchrotron Radiation (CSR) plays an relevant role in the beam dynamics inside the bunch compressor dipoles. The power dissipated increases with the square of the number of electrons and is, therefore, several orders of magnitude larger than the incoherent radiation (see Fig. 6). CSR effects in bunch compressors can have a tremendous impact on the beam (see for example [26]). Radiation from the tail of

the electron bunch can catch up to the head of the electron bunch due to the curved electron path. This radiation field interacts with the bunch while traveling through the bending magnet, potentially adding correlated energy spread and emittance to the electron bunch. The effect of CSR maybe shielded by choosing a small enough vacuum chamber height. CSR effects have been extensively studied in simulations and taken into account in the design of magnetic chicanes.

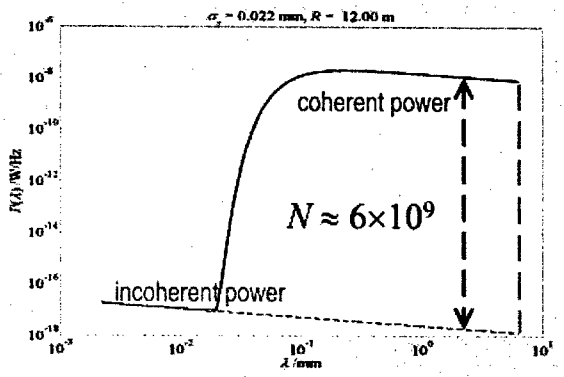

Figure 6: Radiation power spectra of the coherent and incoherent synchrotron radiation. The green dashed line indicates the cutoff of the vacuum chamber dimensions.

Due to all these phenomena described above, it is preferable to utilize two or three rather than one chicane and to compress in a multi-stage regime. A multi-stage bunch compressor presents the advantage of tuning the length of the FEL pulse. This ability of changing the radiation pulse length has been demonstrated at TTF1 [19]. Indirect measurements of the radiation pulse length (see Fig. 7) indicate the possibility to vary the width of the current spike between 30 fs and 100 fs by changing the compressor settings.

DIAGNOSTICS

A very important aspect for the operation of SASE FELs is electron beam diagnostics. Various techniques have been developed for the measurement of bunch lengths smaller than 1 mm, and for the measurement of the slice emittance and energy spread of compressed bunches.

A method streaking the bunch by a transverse mode rf structure has been successfully tested in SLAC [31]. The rf field deflects the bunch vertically and the beam is intercepted on a screen downstream the structure. The rf-phase is tuned so that the head and the tail of the bunch receive a different kick amplitude. Thus, the vertical profile of the spot at the screen corresponds to the longitudinal profile of the bunch. Scanning the strength of a quadrupole allows a measurement of the vertical slice emittance along the bunch length.

Several other methods to measure the bunch length have been investigated. The longitudinal bunch profile at TTF1

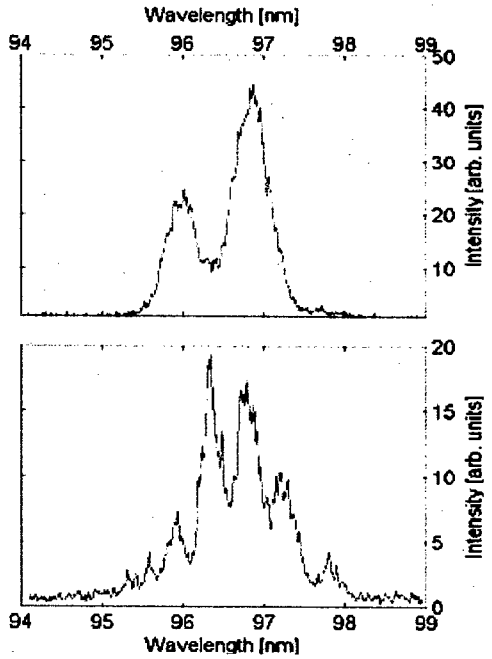

Figure 7: Spectra from $\sim$ 40 fs (top) and $\sim$ 100 fs(bottom) long FEL pulses. The number of longitudinal optical modes (spikes in the spectrum) depends on the electron bunch length.

has been measured using interferometry of coherent synchrotron radiation, longitudinal phase-space tomography [32] and by the means of a 300-fs-resolution streak camera looking at dipole synchrotron radiation [33]. Electro-optical sampling of the near field [34] and spectroscopy of coherent infrared radiation are planned for TTF2.

The diagnotic block placed between undulator modules requires a very compact design. Quadrupoles are placed on movable support and precise beam position monitors allows for beam-based alignment. A three dimensional picture of the diagnostic block (including wirescanners) mounted on a stable support for the TTF2 undulator section is shown in Fig. 8.

CONCLUSIONS

X-ray FELs will have between 8 to 10 orders of magnitude larger brilliance than present x-ray sources. Proof-of-principle experiments have demonstrated the capability of injectors and linac to deliver high quality electron beam that meet the requirements for FELs down to 80 nm wavelengths producing results in full agreement with theory. Although a gap of a factor 1000 in wavelength remains to be covered, a improvement on key electron beam parameters of a factor 2-3 is needed and is expected to be achieved. In the near future, TTF2 at DESY will test the feasibility for wavelengths down to 60 Å and will be the test-bed of a broad range of user experiments.

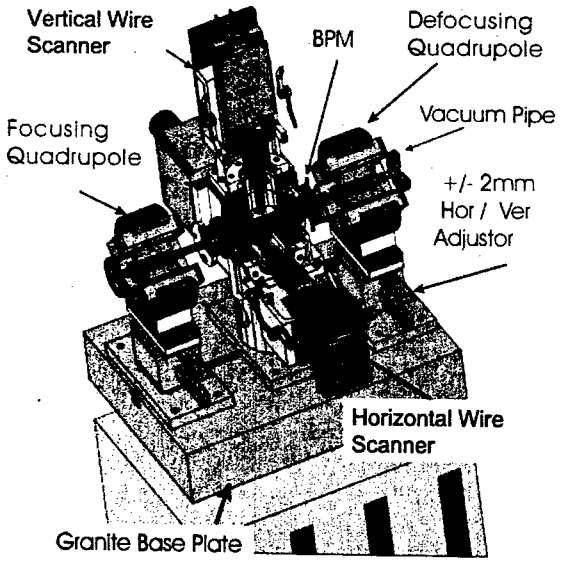

Figure 8: Diagnostic block and quadrupoles located between 4.5 m long undulator modules in TTF2.

REFERENCES

[1] R. Brinkmann, K. Flöttmann, J. Rossbach, P. Schmüser, N. Walker and H. Weise (eds.); "TESLA Technical Design Report, Part V The x-ray free-electron laser", DESY 2001-011, Hamburg, 2001.

[2] "LCLS The first experiments", http://www-ssrl.slac.stanford.edu/LCLS/papers/LCLS_Experiments_2.pdf

[3] "Visions of Science: The BESSY SASE-FEL"; *http://www.bessy.de/lab_profile/01.FEL/sc*

[4] 4GLS homepage *http://www.4gls.ac.uk*

[5] "LCLS CDR", SLAC-R-593, April 2002.

[6] "X-ray Laser User Facility at Bates Laboratory"; Proposal to the National Science Foundation, April 2003. *http://mitbates.mit.edu/xfel/fel_files/nsfproposal.pdf*

[7] T. Zwart et al., "The MIT Bates X-Ray Laser Project"; Proceedings of PAC'03, Portland (OR), May 2003.

[8] M. Altarelli, "The FERMI@ELETTRA Project"; *http://www.elettra.trieste.it/science/elettranews/volume44/en103.html*

[9] L. Palumbo, "Design Study of a Soft X-Rays SASE-FEL Source"; Proceedings of EPAC'02, Paris, June 2002.

[10] D. Alesini et al., "The SPARC Project: A High-Brightness Electron Beam Source at LNF to Drive a SASE-FEL Experiment"; Proceedings of FEL'02, Argonne (IL), Sept. 2002.

[11] SCSS homepage *http://www-xfel.spring8.or.jp/SCSS.htm*

[12] D.T. Clarke et al., "4GLS - A Fourth Generation Light Source that for the biomedical scientist is more than a laser and more than a storage ring"; SPIE Preprint, Feb. 2002.

[13] R. Bonifacio, C. Pellegrini, L.M. Narducci, Opt. Commun. **50,** 373 (1984)

[14] A.M. Kondratenko, E.L. Saldin, Part. Accelerators **10,** 207 (1980)

[15] J.M.J. Madey, J. Appl. Phys. **42,** 1906 (1971).

[16] S. Milton et al., "Exponential gain and saturation of a self-amplified spontaneous emission free-electron laser"; Science **292,** 2037 (2001).

[17] A. Tremaine et al., "Saturation measurements of a visible SASE FEL"; Proceedings of the PAC'01, Chicago (IL), May 2001.

[18] V. Ayvazyan et al., "Generation of GW Radiation Pulses from a VUV Free-Electron Laser Operating in the Femtosecond Regime"; Phys.Rev.Lett.**88,** 104802 (2002).

[19] V. Ayvazyan et al., "A new powerful source for coherent VUV radiation: Demonstration of exponential growth and saturation a the TTF free-electron laser"; Eur.Phys.J.D **20,** pp 149-156 (2003).

[20] H. Wabnitz et al., "Multiple ionization of atom clusters by intense soft X-rays from a free-electron laser"; Nature Vol. 420, pp 482-485, Dec.2002.

[21] L. Juha et al., "Ablation of various materials with intense XUV radiation"; Proc. of FEL'02, Argonne (IL), Sept. 2002.

[22] C. Limborg et al., "New optimization for the LCLS photoinjector", Proceedings of the EPAC'02, Paris, June 2002.

[23] W. Graves et al., "Experimental study of sub-ps slice electron beam parameters in a photoinjector"; submitted to FEL-2002, Argonne (IL), Sept. 2002.

[24] D.H. Dowell et al., "Slice emittance measurements at the SLAC gun test facility"; submitted to FEL-2002, Argonne (IL), Sept. 2002.

[25] P. Piot, "Review of experimental results on high-brightness photo-emission electron sources"; Submitted to World Scientific, DESY M 02-02, Dec. 2002.

[26] M. Hüning, Ph. Piot, H. Schlarb, "Observation of longitudinal phase space fragmentation at the TESLA test facility free-electron laser"; NIM A **475** Issues 1-2, pp 348-352, Dec. 2001.

[27] M. Ferrario et al., "Conceptual design of the XFEL photoinjector"; TESLA-FEL-2001-03, Feb. 2001.

[28] P. Emma, "X-band rf harmonic compensation for linear bunch compression in the LCLS"; LCLS-TN-01-1, Nov. 2001.

[29] K. Flöttmann, T. Limberg, P. Piot, "Generation of ultrashort electron bunches by cancellation of nonlinear distortions in the longitudinal phase space"; TESLA-FEL-2001-06, June 2001.

[30] D. Dowell et al., "Magnetic pulse compression using a third-order linearizer"; Proc. of PAC'95, Dallas (TX), May 1995.

[31] P. Krejcik et al., "A transverse rf deflecting structure for bunch length and phase space diagnostics"; Proc. of PAC'01, Chicago (IL), May 2001.

[32] M. Hüning, "Investigations of the longitudinal charge distribution in very short electron bunches"; Proc. of DIPAC'01, Grenoble, May 2001.

[33] Ch. Gerth et al., "Bunch length and phase stability measurements at the TESLA test facility"; Proc. of FEL'02, Argonne (IL), Sept. 2002.

[34] M. Brunken et al., "Electro-optic experiments at the TESLA test facility"; Proc. of FEL'01, Darmstadt, Sept. 2001.

COMPUTATION OF FEL PROCESSES

S. Reiche
UCLA Department of Physics & Astronomy, Los Angeles, CA 90095-1547, USA

Abstract

The Free-Electron Laser process is the interaction between an electron beam and a co-propagating radiation field, resulting in a collective instability with an exponential growth of the radiation field and the current modulation in the electron bunch. Although analytical models can describe the fundamental FEL amplification, the complexity of the FEL process with a multi-particle system and the evolution of a radiation field demands numerical calculation.

To achieve optimum performance the numerical solvers for FEL codes are highly specialized, using alternative methods than standard PIC codes. This presentation describes the basic algorithm for FEL simulations and addresses in particular the problems and limitations of simulating the FEL process.

INTRODUCTION

The FEL process is a collective instability [1] where an electron beam interacts with a co-propagating radiation field, coupled by the transverse deflection due to a periodic magnetic field of an undulator or wiggler. The output of the Free-Electron Laser depends on a large parameter space of input parameters ranging from the field of the undulator field, to the quality and pulse length of the driving electron beam, to the fluctuation in the initial position of each electron. The numerics have to be precise to several orders of magnitude in the Fourier components of the current modulation and the amplitude of the radiation field.

With several Free-Electron Lasers planned or under construction [2] it is essential to predict the performance as accurately as possible. In the design phase analytical formulae [3] are efficient to find the design parameters of the FEL, then numerical simulations can evaluate the choice of these parameters and predict any additional change in the performance with respect to the analytical model.

Modelling of the FEL process is challenging due to the different scales of the process. On the one hand, the radiation and the electron beam have to be tracked for the undulator length, which can range between one and a few hundred meters. On the other hand, the simulation has to resolve electron motion well below the radiation wavelength, which can range down to 1 Ångstrom. The scale of up to 12 orders of magnitude makes the Particle-in-Cell approach impractical.

With the ongoing research of high-gain single pass Free-Electron Lasers [4] over the last 20 years, numerical codes have been developed. Most of the time they were limited by the available computer resources of their time and the wavelength of interest. Long wavelength FELs are easier to model because the stronger diffraction tends to "wash-out" finer details in the electron distribution and motion. But, for VUV and X-ray FELs the performance is more sensitive to the beam quality, in particular the beam emittance or external effects such as undulator wakefields [20] or errors in the undulator field [21]. In addition, the start-up from noise (SASE FEL) and the extension of the wavelength range due to harmonics have a growing interest.

Table 1: Free-Electron Laser simulation codes, showing the number of dimensions, ability to do time-dependence, and harmonics.

Code	Beam	Dim.	Time	Harm.
Fast[5]	Particles	3D	Yes	No
Felex[6]	Particles	3D	Yes	No
Felos[7]	Particles	3D	Yes	Yes
Fels[8]	Particles	3D	No	No
Fred3D[9]	Particles	3D	No	No
FS1T[10]	Collective	1D	Yes	No
Genesis 1.3[11]	Particles	3D	Yes	No
Ginger[12]	Particles	2D	Yes	No
Medusa[13]	Particles	3D	No	Yes
Nutmeg[14]	Particles	2D	No	Yes
Perseo[15]	Particles	1D	Yes	Yes
Prometeo[16]	Particles	1D	No	Yes
Ron[17]	Collective	3D	Yes	No
Sarah[18]	Collective	1D	Yes	No
TDA3D[19]	Particle	3D	No	Yes

Table 1 lists the features of several Free-Electron Laser codes. A beam description by collective variables allows a faster calculation time but the validity of the output is limited to the start-up and linear regime of the FEL. Similar, a SASE FEL process can only be simulated when the codes covers time-dependent variation of the electron beam and radiation field.

In the following sections we describe the core algorithm of a FEL code and the additional problems of time-dependent simulation. With the ongoing effort to better predict the FEL output the simulations has been extended to cover the entire process from the generation of the electron bunch to the delivery of the FEL radiation to the experimental station, where the FEL process is only a part of the start-end simulation [22]. The last section covers this

0-7803-7738-9/03/$17.00 © 2003 IEEE

final topic.

CORE ALGORITHM

With a few exceptions, the fundamental assumption of all Free-Electron Laser simulation codes is that the interaction between the electrons and the radiation field is negligible over one undulator period. A significant effect has to be accumulated over many periods, restricting the interaction to a narrow frequency bandwidth around the resonant wavelength of the Free-Electron Laser. The electron motion is averaged over one undulator period, eliminating the requirement to resolve each period with multiple integration steps. In fact, the integration step size can be chosen to be a fraction of the gain length [23] of the Free-Electron Laser. This is beneficial for short wavelength FELs, where the number of undulator periods is large in comparison to a long wavelength FEL, but the number of gain lengths and, thus, the number of integration steps remains the same.

The natural selection of a narrow bandwidth due to the resonance approximation, allows to expand the radiation field around the dominant oscillation $\exp[ik(z-ct)]$, where k is the wave number of the resonance wavelength. The change in the field amplitude A is small compared to this oscillation and the field equation is simplified by the paraxial approximation to

$$\left[\vec{\nabla}^2 - 2ik\left(\frac{\partial}{c\partial t}+\frac{\partial}{\partial z}\right)\right]A = -\frac{e^2\mu_0}{m} f_c a_u \left\langle \frac{e^{-i\theta}}{\gamma}\right\rangle \quad , \tag{1}$$

where f_c is the coupling coefficient between the electron beam and the radiation field, a_u is the undulator parameter, γ is the electron energy and $\theta = (k+k_u)z - ct$ is the ponderomotive phase of the electron with k_u as the undulator wavenumber and μ_0 as the magnetic permeability.

Because the continuous amplitude A cannot be described numerically in full detail, the field is either represented by a finite set of grid points or a set of orthonormal functions. The first approach is the most common and the field equation is solved by standard Finite-Difference methods [24].

For SASE FELs, which starts from the spontaneous radiation at the beginning of the undulator, the source term in the right hand side of Eq. 1 has strong fluctuations in the transverse direction before the process of transverse coherence smooth out the transverse bunching profile. In this initial stage many higher modes couple with the beam with almost equal strength. Thus, the growth rate in the calculated power depends strongly on the number of available modes or grid points. This artifact arises from the fact that the integration step size and the grid size determines the frequency interval and solid angle in which the spontaneous radiation is emitted [25]. In the limit of infinitely small step sizes and grid spacing the full power of the spontaneous radiation would be included by the simulations. For X-ray FELs, the initial power level of the higher modes can mask the exponential growth of the spontaneous radiation emitted in the coherent solid angle of the FEL radiation. Fig. 1 shows the evolution of the radiation power in the near field for the 3D code Genesis 1.3 and the 2D code Ginger. The difference in the power level of these codes is apparent. The number of modes is about a factor of 200 higher in Genesis 1.3 than in Ginger. The amount of total power for the 3D case is in good agreement with the theory ([25]).

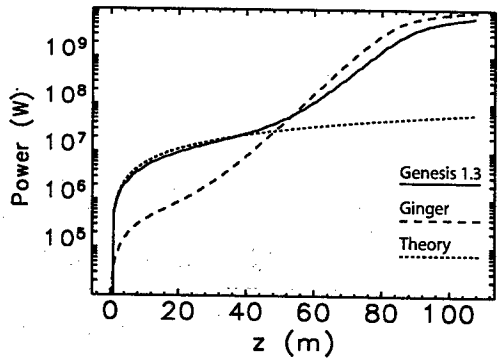

Figure 1: Radiation power in near field zone for the 3D code Genesis 1.3, the 2D code Ginger and the theoretically resolved power, using the grid dimension and integration step size as in the Genesis 1.3 run.

The integration of the equations of motion for the macro particles, resembling the phase space distribution of the electron beam, typically uses a simple and stable solver such as 4th order Runge-Kutta or Predictor-Corrector methods [26]. External effects such as wake fields [27] or the energy loss due to the emission of the spontaneous radiation [28] are applied by pre-calculated values or analytical formulae. A self-consistent description would render the calculation speed of the highly specialized case of the Free-Electron Laser interaction intractable.

For SASE simulations the codes must supply the correct statistics in the current fluctuation of the electron bunch. Averaging over many shots, the phase of the bunching factor $b =< \exp[i\theta] >$ should be a uniform distribution, while the absolute square follows a negative exponential distribution, with a mean value of the inverse of the number electrons [29]. The number of macro particles is typically much smaller than the number of electrons to be modelled. Pure random phases of the macro particles would yield too strong of fluctuation in the current and, thus, too high emission levels of the spontaneous radiation.

To avoid the noise statistics problem the loading of the phase space distribution is split into three steps. The first step fills all dimensions except for the ponderomotive phase, which is equivalent to the longitudinal position. Typically a quiet start method [30] is applied, based on the generalize bit-reverse technique of the Halton sequence [31].

In the second step the longitudinal phase is added, either by an equidistant distribution, a random number generator or a Halton sequence, but it fills only one out of n_b bins in the ponderomotive phase between 0 and 2π. Then

the entire 6D distribution is copied into the remaining bins. Each macro particle and its $n_b - 1$ mirror particles form a beamlet. The bunching factor of each beamlet is ensured to be zero due to the mirror procedure. The choice of n_b also determines the validity of the higher harmonics in the bunching factor. The calculated value is physically meaningful only for harmonics n_h up to $n_h < (n_b - 1)/2$ [33]. Therefore the minimal requirement is four bins if only the fundamental radiation ($n_h = 1$) is considered in the simulation.

The last step models the fluctuations in the particle positions. The Penman algorithm [32] adds a random offset from a uniform distribution to each macro particle. The width of the uniform distribution depends on the number of electrons to be simulated. A further improvement is the method of complex harmonic phasors [33], which also reproduces the correct statistic for the higher harmonics in the bunching factor.

Fig. 2 shows the basic flow diagram for the majority of FEL codes. Steady-state codes have the grey parts omitted.

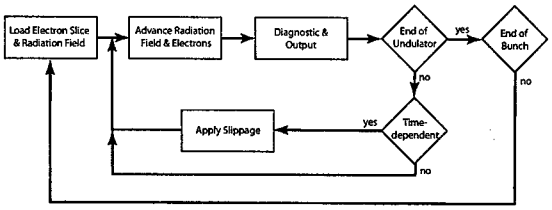

Figure 2: Algorithm for FEL simulations. Additions for time-dependent simulations are marked with grey boxes.

TIME-DEPENDENT SIMULATION

A computationally efficient method is the steady-state simulation, where any longitudinal variation in the electron beam parameter of radiation field is excluded. However, the efficiency comes at a price: less physics is included. The simulation covers only a single slice with a thickness of one radiation wavelength. The effect of slippage is not sufficiently covered because the periodic boundary condition in the longitudinal direction feeds the forward propagating radiation field back into the same slice.

Any simulation of longitudinal variation in the electron beam, including the initial fluctuation of the electron positions for the SASE operation of an FEL, require incorporating slippage effects in the simulation. For this purpose the electron bunch and the radiation field are sampled with multiple slices of constant spacing. A fully consistent description would keep all slices in the memory at once. Because each slice has about 10000 macro particles and the total number of slices can easily exceed 100000 for short wavelength FELs, the high memory demands could only be fulfilled by a massive parallel computer architecture.

The memory problem is solved by assuming a "quasi"-periodic situation of the radiation field and electron beam. The simulation is split into steady-state simulation over a short subsection of the undulator and advancing the radiation field to the next electron slice. For a giving spacing Δt the length of the steady-state integration is $\Delta z = (\lambda_u/\lambda)c\Delta t$. Because the information is propagated only in the forward direction, the simulation can start with the first electron slice at the tail of the electron bunch. After each integration length Δz the radiation field is temporary stored in memory or on the hard disk. After the slice is fully propagated through the undulator, the next electron slice is loaded and seeded with the radiation field in memory. The radiation field is again stored for the next slice after the integration distance Δz. Using this method the number of slices do not impose a limit on the memory. The maximum required information is the sampled radiation field with a spacing of Δt over the full slippage length of the FEL.

This sequential integration along the electron bunch from the tail to the head introduces several restrictions for the validity of the simulation:

First a strong impact of steady-state integrations has to be avoided by a frequent advance of the radiation field. Typically the occurring spikes in the radiation profile have to be resolved with enough slices, which is equivalent to the statement that Δz has to be much smaller than the FEL gain length or that the sampling of the radiation field can resolve the entire FEL bandwidth in the frequency domain.

Second, the seeding for the first slice is unknown if only a subsection of the electron bunch is simulated. This results in invalid field values over the first slippage length. Therefore the total time window – the product of the number of slices and the spacing Δt – must be larger than the slippage length.

Third, the gain is reduced if the mean energy of the electron slice deviates from the resonant energy of the central wavelength, as it is the case of an electron beam with an energy chirp [34]. The problem is solved by a smaller spacing of the slices, which is equivalent to a larger frequency bandwidth of the FEL simulation.

START-END SIMULATION

The initial conditions of the electron beam or radiation beam are often more complicated than are described by a few parameters such as mean and rms values of the 6D phase space distribution. In addition, X-ray Free-Electron Lasers have co-operation lengths [35] shorter than the bunch length. Different parts of the bunch amplify the radiation independently. Projected quantities such as the emittance of energy spread loose the merit of describing the beam. Instead sliced values are of relevance with a slice thickness given by the co-operation length. Fig. 3 shows the input phase space distribution for the LCLS X-ray FEL and the output radiation profile of the FEL from a start-end simulation. The shape of the distribution denies a parameterization of the beam profile with mean energy and energy spread values, because the FEL performance depends critically on the explicit shape of the distribution in energy.

To predict the performance of a Free-Electron Laser requires an effort to model the entire FEL process, starting from the electron bunch creation to the experimental station for the laser light. Because the entire process cannot be simulated by a single code, a chain of specialized codes are used. The interface between the codes is the exchange of entire particle or field distributions, or if the distribution is simple enough, a list of mean and rms values of the distribution.

The following is a list of the major components of the start-end simulation chain and the emphasize of the physical/numerical problems, addressed by the codes. The codes, listed here, have been used in context of modelling existing and future Free-Electron Lasers.

In the rf photo electron gun the electrons experience a strong acceleration from being at rest to a highly relativistic motion. The space charge forces of the generated electron beam determines the slice emittances. Point-point calculation scales with the square of the macro particle numbers, which imposes a limit for the acceptable number of particles. RF gun codes execute faster when the space charge field is evaluated on a grid. The grid filters out high frequency components, which would otherwise yield a stringent restriction on the integration step size. The particles are tracked to an energy, where the space charge field has a negligible impact. Codes, already successfully used in start-end simulations, are PARMELA [36] and ASTRA [37].

The propagation of the beam through the linac uses standard tracking methods such as matrix multiplication, including higher order effects. The support of wakefields are essential for a complete simulation of the beam transport. The overall execution time is fast compared to other codes in the start-end simulation, but due to the large set of input parameters such as field strength of each magnet or the phase and amplitude of each rf cavity, the optimization process is rather complex. Due to its scripting capability, ELEGANT [38] is useful tool for this task.

Although ELEGANT has an analytical model of the coherent synchrotron radiation [39] in a bend, the process of bunch compression in a magnetic chicane can be calculated in more detail with the specialized code Trafic4 [40]; the price is an execution time comparable to time-dependent FEL simulations.

Time-dependent simulations have been described in the previous chapter. For a complete picture of the beam dynamics within the undulator, the following processes should be included in the simulations: undulator wakefields, energy loss by the emission of spontaneous radiation, the increase of the energy spread due to the quantum fluctuation [41] in the emission of spontaneous radiation. The codes FAST, GINGER and GENESIS 1.3 are capable of modeling the above and are used in a start-end simulation.

The incorporation of the propagation of the FEL radiation through the beam line optics is currently under development [42]. Various programs exist, which can advance a single amplitude/phase front of the output radiation. However the output of time-dependent FEL codes is a lattice of these wavefronts, creating a 3D grid of the radiation field. Optical elements such as gratings or monochromators would require the Fourier transformation, the calculation of the Green's function for the optical element and then the inverse Fourier transformation to get back the field information in time domain. While the time-dependent FEL simulations sequentially calculate the radiation field without having the entire field in memory, it is essential for the Fourier transformations. To limit the memory demand a filter function might be necessary to reduce the amount of information in the field.

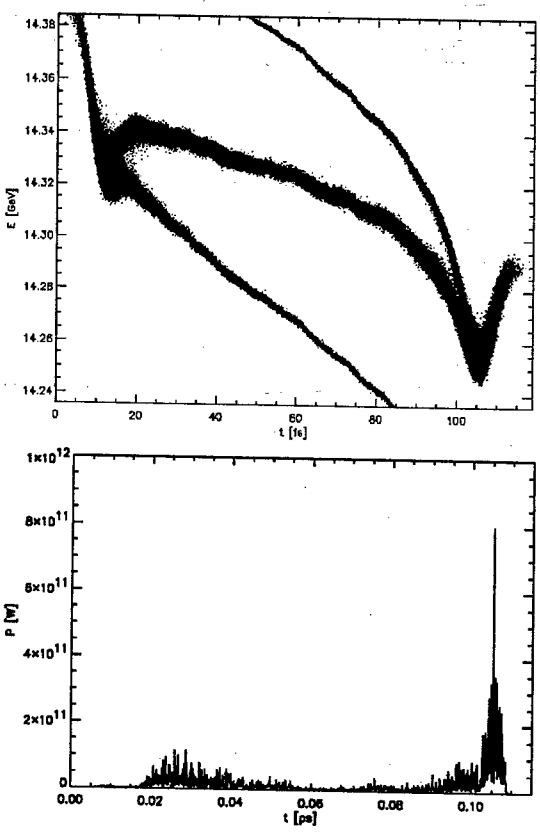

Figure 3: Initial phase space distribution at the entrance of the LCLS undulator (top graph) and radiation profile at the exit of the FEL (bottom graph), based on a start-end simulation for the LCLS X-ray FEL.

CONCLUSION

Numerical tools are invaluable for the modeling of high-gain Free-Electron Lasers, because they extend the capability to model realistic cases with many input parameters. The algorithm deviates from standard PIC codes due to the extreme scale of the FEL process. While the undulator

length is up to 100 m long, the field and electron distribution has to be resolved on a sub-Ångstrom level.

Various FEL codes exist, following similar approachs to model the FEL interaction. With the ongoing growth in computational speed and memory, the codes have become capable of handling more complex cases with a finer detail of description and more macro particles and grid points.

Besides the continuous improvement in the algorithm of the FEL codes, the interface with other accelerator/non-FEL codes has been improved. This allows to simulate the entire process, starting from the rf gun to experimental station, using the FEL light. However, these start-end simulations are complex and require an experienced user for each code in the simulation chain.

REFERENCES

[1] A.M. Kondradenko and E.L. Saldin, Part. Accel. **10** (1980) 207; R. Bonifacio, C. Pellegrini, and L.M. Narducci, Opt. Comm. **50** (1984) 373

[2] *Linac Coherent Light Source (LCLS)*, SLAC-R-521, UC-414 (1998) and *TESLA - Technical Design Report*, DESY 2001-011, ECFA 2001-209, TESLA Report 2001-23, TESLA-FEL 2001-05, Deutsches Elektronen Synchrotron, Hamburg, Germany (2001)

[3] L.-H. Yu *et al.*, Phys. Rev. Lett. **64** (1990) 3011

[4] e.g. R.L. Elias *et al.*, Phys. Rev. Lett. **36** (1976) 717; M. Hogan *al.*, Phys. Rev. Lett. **81** (1998) 4867; V. Ayvazyan *et al.*, Phys. Ref. Lett. **88** (2002) 104802

[5] E.L. Saldin, E.A. Schneidmiller, M.V. Yurkov, Nucl. Inst. & Meth. **A429** (1999) 233

[6] B.D. McVey, Nucl. Inst. & Meth. **A250** (1986) 449

[7] Private Communication with Z. Weng, Y. Shi

[8] D. Nölle, DELTA Int. Rep. 91-13, Dortmund, Germany, 1991

[9] E.T. Scharlemann, J. Appl. Phys. **58(6)** (1985) 2154

[10] Private Communication with E.L. Saldin, E.A. Schneidmiller, M.V. Yurkov

[11] S. Reiche, Nucl. Inst. & Meth. **A429** (1999) 243

[12] W.M. Fawley, *An Informal Manual for GINGER and its Post-processor XPLOTGIN*, LBID-2141, CBP Tech Note-104, UC-414, 1995

[13] H.P. Freund, T.M. Antonsen, Jr., *Principles of Free-electron Lasers*, 2nd Edition. Chapman & Hall, London, 1986, Phys. Rev. **E 52** (1995) 5401

[14] E.T. Scharlemann and W.M. Fawley, **SPIE 1045** (1989) 18

[15] L. Gianessi, Proc. of the 27th Advanced ICFA Beam Dynamics Workshop, Cagliari, Sardinia, Italy (2002)

[16] G. Dattoli, M. Galli, and P.L. Ottaviani, ENEA Internal Report No. RT/INN/93/09

[17] R.J. Dejus, O. Shevchenko, N. Vinokurov, Nucl. Inst. & Meth. **A429** (1999) 225

[18] Private Communication with P. Pierini

[19] T.M. Tran,J.S. Wurtel, Computer Physics Communicationd **54** (1989) 263

[20] C. Pellegrini *et al*, Nucl. Inst. & Meth. **A475** (2001) 328

[21] B.M. Kincaid, J. Opt. Soc. Am. **B2** (1985) 1294

[22] M. Borland *et al*, Nucl. Inst. & Meth. **A483** (2003) 268

[23] E.L. saldin, E.A. Schneidmiller, and M..V. yurkov, *the Physics of Free Electron Lasers* (Springer - Berlin - 2000)

[24] W.F. Ames, *Numerical Methods for Partial Differential Equations* (Academic Press - New York - 1969)

[25] Z. Huang, Proc. of the 24th Free-Electron Laser Conference, Argonne, USA, 2002

[26] W.H. Press *et al.*, *Numerical Recipes* (Cambridge University Press - Cambridge - 1986)

[27] S. Reiche and H. Schlarb, Nucl. Inst. & Meth. **A445** (2000) 155

[28] J.D. Jackson, *Classical Electrodynamics* (John Wiley and SOns - New York - 1975)

[29] J. Goodman, *Statistical Optics* (John Wiley and Sons - New York - 1985)

[30] T.M. Tran and J.S. Wurtele, Comp. Phys. Comm. **54** (1989) 263

[31] J.H. Halton, Numerische Mathematik **2** (1960) 84

[32] C. Penman and B.W.J. McNeil, Opt. Comm. **80** (1992) 82

[33] W.M. Fawley, Phys. Rev. STAB **5** (2002) 070701

[34] W.M. Fawley, Proc. of the 24th Free-Electron Laser Conference, Argonne, USA, 2002

[35] R. Bonifacio *et al.*, Phys. Rev. Lett. **73** (1994) 70

[36] J. Billen, PARMELA, Los Alamos National Laboratory report LA-UR-96-1835, 1996

[37] K. Flöttmann, Astra User Manual, *http://www.desy.de/ mpyflo/*

[38] M. Borland, Argonne National Laboratory Report LS-287, 2000

[39] Y.S. Derbenev, J. Rossbach, E.L. Saldin and V.D. Shiltsev, TESLA-FEL 95-05, Deutsches Elektronen Synchrotron, Hamburg, Germany

[40] A. Kabel, M. Dohlus and T. Limberg, Nucl. Inst. & Meth. **A445** (2000) 338

[41] E.L. Saldin *et al*, Nucl. Inst. & Meth. **A381** (1996) 545

[42] Private Communication with R. Bionta

APPLICATIONS OF THE CANCELLATION EFFECT IN CSR STUDIES

R. Li, Jefferson Lab, Newport News, Virginia, USA*

INTRODUCTION

The cancellation effect in the dynamics of relativistic beams on a curved trajectory is studied in Ref. [1] based on the canonical formulation of the dynamics equations and retarded potentials. In this paper, we first discuss in a coherent manner various applications of the cancellation effect, such as a coasting beam, a short bunch in steady-state interacting with off-orbit particles, transient self-interaction of a short bunch entering a circular orbit from a straight path, and a converging beam in a bunch compression chicane. Next, spectrometer measurement and Landau damping in microbunching process are discussed based on new dynamics equations which explicitly use the cancellation effect.

REVIEW OF THEORY

According to Ref. [1], for a relativistic charged bunch moving on a curved trajectory with curvature $\kappa(s)$, the first order equation for the particle's horizontal motion is ($r = R + x$ and $R(s) = 1/\kappa(s)$):

$$\frac{d^2x}{c^2dt^2} + \frac{x}{R^2} = \frac{1}{E_0}\left(\frac{\Delta E(t)}{r} + F_x^{\rm col}\right) \qquad (1)$$

where $\Delta E(t) = E(t) - E_0$ is the deviation of the kinetic energy E from the design energy E_0, and $F_x^{\rm col}$ is the horizontal Lorentz force (or Talman's force [2]) due to bunch collective interaction on the curved path:

$$F_x^{\rm col} = F^{\rm CSCF} + F_x^{\rm eff}, \quad F^{\rm CSCF} = \frac{e\beta_s A_s^{\rm col}}{r} \simeq e\frac{\Phi^{\rm col} + \Delta\Phi}{r} \qquad (2)$$

where $F^{\rm CSCF}$ is the "centrifugal space charge force" (using retarded potentials), and $\Delta\Phi = A_s^{\rm col} - \Phi^{\rm col}$. The change of E follows

$$\frac{dE}{cdt} = \mathbf{F}\cdot\mathbf{v}/c = -e\frac{d\Phi}{cdt} + F_v^{\rm eff} \qquad (3)$$

and thus after integration one gets $\Delta E/r$ in Eq. (1)

$$\frac{\Delta E}{r} = \frac{\Delta E^{\rm tot}(t_0)}{r} + \frac{1}{r}\int_{t_0}^{t} F_v^{\rm eff}(t')cdt' - e\frac{\Phi^{\rm col}}{r} \qquad (4)$$

with $\Delta E^{\rm tot}(t_0) = (E + e\Phi^{\rm col})|_{t_0} - E_0$. The effective forces in Eqs. (2) and (4) are

$$F_x^{\rm eff} = \frac{\partial \mathcal{L}_{\rm int}^{\rm col}}{\partial x} - e\frac{dA_x^{\rm col}}{cdt}, \quad F_v^{\rm eff} = -\frac{\partial \mathcal{L}_{\rm int}^{\rm col}}{c\partial t} \qquad (5)$$

where ∂_x and ∂_t only act on Φ and A_λ in the interaction Lagrangian

$$\mathcal{L}_{\rm int}^{\rm col} = -e(\Phi^{\rm col} - \sum_\lambda \beta_\lambda A_\lambda). \qquad (6)$$

Here $q_\lambda = \mathbf{e}_\lambda \cdot \mathbf{q}$ for $\mathbf{q}$ being $\boldsymbol{\beta}$ or $\mathbf{A}$, with $\mathbf{e}_\lambda$ the Frenet-Serret bases. Using retarded potentials, $\Phi^{\rm col}$ and $A_s^{\rm col}$ exhibit logarithmic dependence on the particles' transverse position in bunch due to local interaction singularities. However, since locally the nearby particles are nearly parallel in motion for ultra-relativistic bunches, there is relativistic cancellation bewteen the local interaction contributions to $A_s^{\rm col}$ in Eq. (2) and to $\Phi^{\rm col}$ in Eq. (4). Similar cancellation also occurs bewteen $\Phi^{\rm col}$ and $A_s^{\rm col}$ in $\mathcal{L}_{\rm int}^{\rm col}$ in Eq. (6). Thus the effective forces in Eq. (5) are dominated by contributions from the long-range interactions and are basically free from the logarithmic behavior. After inserting Eqs. (2) and (4) into Eq. (1), and letting $G_{\rm res} = e(A_s^{\rm col} - \Phi^{\rm col})/r$, one gets

$$\frac{d^2x}{c^2dt^2} + \frac{x}{R^2} \simeq \frac{1}{E_0}\left(\frac{\Delta E^{\rm tot}}{r} + \frac{1}{r}\int_{t_0}^{t} F_v^{\rm eff} + F_x^{\rm eff} + G_{\rm res}\right). \qquad (7)$$

For short bunches on a circular path, $\sigma_z/R \ll 1$, we have [1] $\mathcal{O}(G_{\rm res}) \ll \mathcal{O}(F_x^{\rm eff}) \ll \mathcal{O}(F_v^{\rm eff})$. Hence $G_{\rm res}$ in Eq. (7) is practically negligible.

CANCELLATION IN VARIOUS CASES

Note the horizontal dynamics is driven by *both* $\Delta E/r$ and $F_x^{\rm col}$ in Eq. (1), and the cancellation is between the logarithmic potentials in each of these two driving terms. Including one term without the other may lead to unrealistic results.

F_x^{col} in a Storage Ring

The importance of $F_x^{\rm col}$ in a storage ring, due to the collective contribution of the single particle generated radiation (or acceleration) fields on the curved path, was first pointed out by Talman [2]. If only $F_x^{\rm col}$ in Eq. (1) is included without the $\Delta E/r$ term, the drastic dependence of $F_x^{\rm col}$ (due to $A_s^{\rm col}$ in Eq. (2)) on the particles' transverse position—as shown in Fig. 1 of Ref. [2]—could lead to horizontal tune shift and chromaticity and contribute to the appearance of nonlinear resonances (Fig. 2 of Ref. [2]). However, this effect of $eA_s^{\rm col}/r$ in $F_x^{\rm col}$ of Eq. (2) is basically cancelled by the effect of $e\Phi^{\rm col}/r$ in $\Delta E/r$ of Eq. (4).

Cancellation for a Line Coasting Beam

The cancellation effect was first pointed out by Lee [3] for a coasting beam when both the two driving terms in Eq. (1) are included. For the line coasting beam example ($\beta_s = 1$) in Ref. [3], one gets for $x = r - R$ and $w = x/R$ (R: radius of equilibrium orbit)

$$\mathcal{L}_{\rm int}^{\rm col} = -e(\Phi^{\rm col} - A_s^{\rm col}) = e\Delta\Phi$$

*This work was supported by the U.S. DOE Contract No. DE-AC05-84ER40150.

0-7803-7738-9/03/$17.00 © 2003 IEEE

$$= -2\lambda e\left[2 - w + \frac{w^2}{8} + \frac{1}{4}w^2\ln\frac{w}{8} + \cdots\right], \quad (8)$$

$$F_x^{\rm eff} = -\frac{2\lambda e}{R}\left[-1 + \frac{w}{2} + \frac{1}{2}w\ln\frac{w}{8} + \cdots\right], \quad (9)$$

$$F_v^{\rm eff} = 0, \quad (10)$$

$$F_x^{\rm col} = \frac{2\lambda e}{R}\left[-\ln\frac{w}{8} - 1 + \frac{3}{2}w + w\ln\frac{w}{8} + \cdots\right], \quad (11)$$

$$\frac{-e\Phi^{\rm col}}{R} = -\frac{2\lambda e}{R}\left[-\ln\frac{w}{8} + \frac{w}{2} + \frac{w}{2}\ln\frac{w}{8} + \cdots\right] \quad (12)$$

which yields

$$\frac{\Delta E}{R} + F_x^{\rm col} = \frac{\Delta E^{\rm tot}}{R} + F_x^{\rm eff}. \quad (13)$$

Note that $F_x^{\rm col}$ is a centrifugal force with a divergent gradient $\partial F_x^{\rm col}/\partial x \simeq -2\lambda e/Rx$. In contrast, the effective radial force has negligible gradient compared to $\partial_x F_x^{\rm col}$

$$\frac{\partial F_x^{\rm eff}}{\partial x} = \frac{2\lambda e}{R}\left(\frac{1}{2R} + \frac{1}{2R}\ln\frac{w}{8} + \cdots\right). \quad (14)$$

Here the constant part of $F_x^{\rm eff}$ serves to readjust the equilibrium orbit for each particle

$$\frac{(E + e\Phi^{\rm col})|_R - E_0}{R} + F_x^{\rm eff}(R) = 0. \quad (15)$$

Non-inertial Space Charge Force

We now turn to short bunches. For a steady-state line bunch on a circular orbit with uniform charge distribution acting on off-orbit particles, the longitudinal electric field is given by Eq. (5) of Ref. [4], in which the second term gives the non-inertial space charge force $F^{\rm NSCF}$. If $F_x^{\rm col}$ is not included in Eq. (1), the kinetic energy change ΔE induced by $F^{\rm NSCF}$ could cause extra emittance growth in addition to that caused by the usual CSR forces, as shown in Figs. 7-13 of Ref. [4]. However, studies show [5] that $F^{\rm NSCF}$ is $-e\,d\Phi^{\rm col}/cdt$ term in Eq. (3). Thus once $F_x^{\rm col}$ is included on the equal footing as $\Delta E/r$ in Eq. (1), the integrated effect of $F^{\rm NSCF}$, or $-e\Phi^{\rm col}/r$ in Eq. (4), is actually cancelled by the $e\Phi^{\rm col}/r$ term in $F_x^{\rm col}$ of Eq. (2).

Transient Longitudinal Force

For a rigid-line-bunch entering a circular orbit from a straight path, the longitudinal collective force on the particles is given by Eq. (87) of Ref.[6]:

$$\frac{dE(z,\theta)}{cdt} = T_1(z,R,\theta) + T_2(z,R,\theta) \quad (16)$$

where for $K = -2e^2/(3R^2)^{1/3}$ and $z_\theta = R\theta^3/24$,

$$T_1 = K\left[\lambda(z - z_\theta) - \lambda(z - 4z_\theta)\right]/z_\theta^{1/3}, \quad (17)$$

$$T_2 = K\int_{z-z_\theta}^{z}\frac{dz'}{(z-z')^{1/3}}\frac{d\lambda(z')}{dz'} \quad (18)$$

with R the radius of the circular orbit, $z = s - \beta ct$ the longitudinal position of the particle in the bunch, λ the longitudinal charge density, and θ the angle of the bunch into the bend. Sometimes in CSR simulations, Eq. (16) is used to calculate ΔE in Eq. (1) and the consequent effect on the bunch horizontal dynamics without $F_x^{\rm col}$ as another driving term for Eq. (1). Comparing with Eq. (3), one finds a part of $dE(z,\phi)/cdt$ in Eq. (16) is related to the potential energy change. Thus the integrated effect of $-ed\Phi^{\rm col}/cdt$ in Eqs. (3) or (16)— which contributes to $-e\Phi^{\rm col}/r$ in Eq. (4)— is actually cancelled by $e\Phi^{\rm col}/r$ in Eq. (2) once $F_x^{\rm col}$ is included in these simulations. After the cancellation, the horizontal dynamics is governed by the effective forces as in Eq. (7). For example, compared to Eq. (16), the *effective* longitudinal force at entrance of a bend is

$$F_v^{\rm eff}(z,\theta) = T_1'(z,\theta) + T_2(z,\theta) \quad (19)$$

with T_2 in Eq. (18), and $T_1'(z,\theta)$ derived using Ref. [7]

$$T_1'(z,\theta) = e^2\int_{z_\theta}^{\infty}dz'\left[\frac{d\lambda(z-z')}{dz'}\right.$$
$$\left.\times\frac{2\sin^2(\theta/2)}{\sqrt{(z'-4z_\theta)^2 + [R(1-\cos\theta)/\gamma]^2}}\right]. \quad (20)$$

Converging Beams in Chicanes

For a 4-bend bunch compression chicane, the maximum compression often occurs during the drift before the last bend, where the hard compression could cause significant potential energy change $\Phi^{\rm col} - \Phi^{\rm col}(t_0)$ which further increases the kinetic energy spread σ_δ, as given in Eq. (4). If only $\Delta E/r$ is used in Eq. (1) without $F_x^{\rm col}$, one would conclude [8] that significant emittance growth could result from this $\Delta\sigma_\delta$ as the bunch passes the 4th bend. However, $\Phi^{\rm col}$ in Eq. (4) is actually cancelled by that in Eq. (2). Thus according to Eq. (7), the horizontal dynamics in the 4-th bend depends on the canonical energy offset $\Delta E^{\rm tot}$ at the entrance of the bend, in addition to the effective forces. This $\Delta E^{\rm tot}$ is only changed by $F_v^{\rm eff}$ generated from the previous bend, but not by the beam convergence in the drift.

NEW DYNAMICS EQUATIONS

Using (x, x', z, δ) as dynamical variables, and s as an independent variable, with $\delta = (E - E_0)/E_0$, the complete first order equations of motion for dynamics in the bending plane are ($k_\beta(s)$ is the focusing strength)

$$\begin{cases} \dfrac{dx}{ds} = x' \\ \dfrac{dx'}{ds} = -k_\beta^2 x + \dfrac{\delta}{R(s)} + \dfrac{F_x^{\rm col}}{E_0} \\ \dfrac{dz}{ds} = -\dfrac{x}{R(s)} \\ \dfrac{d\delta}{ds} = \dfrac{1}{E_0}(F_s^{\rm col} + x' F_x^{\rm col}) \end{cases} \quad (21)$$

Here the local (nearby particle) interaction contributions to the longitudinal and transverse collective Lorentz forces, $F_s^{\rm col}$ and $F_x^{\rm col}$, need to be computed carefully; and their effects on the bunch dynamics eventually get cancelled implicitly as Eq. (21) is integrated over time. Using equations

in Sec. 2, one can have the following new description of the dynamics with the cancellation effect explicitly expressed

$$\begin{cases} \dfrac{dx}{ds} = x' \\ \dfrac{dx'}{ds} = -k_\beta^2 x + \dfrac{\delta_H}{R(s)} + \dfrac{F_x^{\rm eff} + G_{\rm res}}{E_0} \\ \dfrac{dz}{ds} = -\dfrac{x}{R(s)} \\ \dfrac{d\delta_H}{ds} = \dfrac{F_v^{\rm eff}}{E_0} \end{cases} \tag{22}$$

where $G_{\rm res} = e(A_s^{\rm col} - \Phi^{\rm col})/R(s)$, and (x, x', z, δ_H) are the new dynamical variables with $\delta_H = [(E + e\Phi^{\rm col}) - E_0]/E_0$ ($H = E + e\Phi^{\rm col}$ is the Hamiltonian conjugate to t). For short bunches ($\sigma_z \ll R$), $G_{\rm res}$ is negligible; and $F_v^{\rm eff}$ and $F_x^{\rm eff}$ in Eq. (22) are mainly dominated by the long range interactions. For a coasting line beam [3], $G_{\rm res}$ is comparable to $F_x^{\rm eff}$. However, the logarithmic singularities in $A_s^{\rm col}$ and in $\Phi^{\rm col}$ are still cancelled.

To study the microbunching instability in a bunch compression chicane, we change the dynamical variables (x, x', z, δ_H) to $(J, \psi, \tilde{z}, \tilde{\delta}_H)$, with J, ψ the action-angle variables, $\tilde{z}$ the initial longitudinal position of a particle in the bunch and $\tilde{\delta}_H$ the initial uncorrelated canonical energy offset for zero effective forces

$$\begin{cases} x = \sqrt{2J\beta(s)}\cos[\psi + \psi_0(s)] + D_x\delta_H \\ x' = -\sqrt{\dfrac{2J}{\beta(s)}}\{\sin[\psi + \psi_0(s)] + \alpha(s)\cos[\psi + \psi_0(s)]\} \\ \qquad\qquad + D_x'\delta_H \\ z = -D_x'x + D_x x' + \tilde{z} + R_{56}\delta_H \\ \delta_H = \tilde{\delta}_H - u\tilde{z} \end{cases} \tag{23}$$

with $\beta(s)$ and $\alpha(s)$ the designed twiss parameters in the horizontal phase space, u the initial linear δ-z correlation imposed on the bunch by an RF cavity, and [9]

$$\psi_0(s) = \int_0^s \frac{ds'}{\beta(s')}, \quad R_{56}(s) = -\int_0^s \frac{D(s')}{R(s')}ds',$$
$$D_x(s) = \sqrt{\beta(s)}\int_0^s \frac{ds'}{R(s')}\sqrt{\beta(s')}\sin[\psi_0(s) - \psi_0(s')]. \tag{24}$$

Converting Eq. (22) to equations for the new variables, we have the Vlasov equation for the distribution function $\rho(J, \psi, \tilde{z}, \tilde{\delta}_H, s)$

$$\frac{\partial\rho}{\partial s} + \frac{F_v^{\rm eff}}{E_0}\cdot A + \frac{F_x^{\rm eff}}{E_0}\cdot B = 0 \tag{25}$$

with

$$A = \eta_1\frac{\partial\rho}{\partial J} + \eta_2\frac{\partial\rho}{\partial\psi} - R_{56}\frac{\partial\rho}{\partial\tilde{z}} + (1 - uR_{56})\frac{\partial\rho}{\partial\tilde{\delta}_H},$$
$$B = -\left[f_1\frac{\partial\rho}{\partial J} + f_2\frac{\partial\rho}{\partial\psi} + D_x\frac{\partial\rho}{\partial\tilde{z}} + uD_x\frac{\partial\rho}{\partial\tilde{\delta}_H}\right],$$

for

$$f_1(J, \psi, s) = \sqrt{2J\beta(s)}\sin[\psi + \psi_0(s)],$$
$$f_2(J, \psi, s) = \sqrt{\beta(s)/2J}\cos[\psi + \psi_0(s)], \tag{26}$$

$$\eta_1 = D_x'f_1 - D_xf_1', \qquad \eta_2 = D_x'f_2 - D_xf_2' \tag{27}$$

where $f_{1,2}' = \partial f_{1,2}/\partial s$ and $D_x' = dD_x/ds$. At steady-state, the effective forces yield impedances [9]

$$\frac{F_{v,x}^{\rm eff}(z)}{E_0} = \frac{Nr_e}{\gamma_0}\int_{-\infty}^{\infty}\lambda(k)Z_{v,x}^{\rm eff}(k)e^{ikz}dk \tag{28}$$

$$Z_v^{\rm eff} = \frac{ik^{1/3}}{R(s)^{2/3}}(-0.94 + 1.63i), \qquad Z_x^{\rm eff} = -\frac{2}{R(s)}.$$

For $(kR)^{1/3} \gg 1$, one has $\mathcal{O}(Z_x^{\rm eff}) \ll \mathcal{O}(Z_v^{\rm eff})$.

DISCUSSIONS

Eq. (22) shows that the dispersion effect is related to the canonical energy offset δ_H instead of the kinetic energy offset δ. This is because in Eq. (21), $F_x^{\rm col}$ contains $F^{\rm CSCF}$ (as in Eq. (2)) which represents the dispersion effect for the potential energy $e\Phi^{\rm col}/E_0$, just as $\delta/R(s)$ in Eq. (21) represents the dispersion effect for the kinetic energy δ. Consequently, for a single bend spectrometer, due to the existence of Talman's force $F_x^{\rm col}$, the horizontal particle distribution from the spectrometer measurement is actually related to the canonical energy spread instead of the kinetic energy spread. These measurements also include effects of $F_v^{\rm eff}$ and $F_x^{\rm eff}$. Therefore the spectrometer data needs to be carefully interpreted when the collective interactions are strong, especially when the potential energy spread is no less than that of the kinetic energy spread.

For an achromatic bending system, the initial $\delta_H(s_0)$ in Eq. (22) does not directly cause emittance growth. However, $\delta_H(s_0)$ could play a role of Landau damping in the microbunching process. Previous studies [9] of the microbunching in a chicane, based on Eq. (21) assuming $F_x^{\rm col} = 0$ and $\Phi^{\rm col} = 0$, show Landau damping due to $\rho(J, \psi, \tilde{z}, \tilde{\delta}, 0)$. However, with $F_x^{\rm col} \neq 0$ and $\Phi^{\rm col} \neq 0$, Eqs. (25)-(28) show that it is really $\rho(J, \psi, \tilde{z}, \tilde{\delta}_H, 0)$ which causes the decoherence for the microbunching process. Here the distribution over $\tilde{\delta}_H$ at s_0 needs to be carefully determined. The effect of transient $F_v^{\rm eff}$ and $F_x^{\rm eff}$ in Eq. (25) will be further studied.

The author thanks Ya. S. Derbenev for helpful discussions.

REFERENCES

[1] R. Li and Ya. S. Derbenev, JLAB-TN-02-054 (2002).

[2] R. Talman, Phys. Rev. Lett. **56**, p.1429 (1986).

[3] E. P. Lee, *Particle Accelerators*, **25**, p.241 (1990).

[4] B. E. Carlsten, Phys. Rev. E **54**, p.838 (1996).

[5] R. Li, *Proceedings of the 2nd ICFA Advanced Accelerator Workshop*, p.369 (1999).

[6] E. L. Saldin, E. A. Schneidmiller, and M. V. Yurkov, Nucl. Instrum. Methods Phys. Res. Sect. A **398**, 373 (1997).

[7] R. Li, C. L. Bohn, and J. J. Bisognano, Proc. SPIE **3154**, p.223, San Diego (1997).

[8] K. L. F. Bane and A. W. Chao, Phys. Rev. ST Accel. Beams **5**, 104401, (2002).

[9] S. Heifets, G. Stupakov and S. Krinsky, Phys. Rev. ST Accel. Beams **5**, 064401, (2002).

PULSE LENGTH CONTROL IN AN X-RAY FEL BY USING WAKEFIELDS

S. Reiche[1], P. Emma[2], C. Pellegrini[1]
[1]UCLA - Dept. of Physics & Astronomy, Los Angeles, CA 90095-1547, USA
[2]Stanford Linear Accelerator Laboratory, Stanford, CA 94309, USA

Abstract

For the users of the high-brightness radiation sources of free-electron lasers it is desirable to reduce the FEL pulse length to 10 fs and below for time-resolved pump and probe experiments. Although it can be achieved by conventional compression methods for the electron beam or the chirped FEL pulse, the technical realization is demanding. In this presentation we study the impact of longitudinal wakefields in the undulator and how their properties can be used to reduced the amplifying part of the bunch to the desired length. Methods of actively controlling the wakefields are presented.

INTRODUCTION

With the realization of the 4th generation light sources LCLS[1] and TESLA FEL[2] in the X-ray regimes, new experiments in various fields of science will become possible[3]. In particular, there is an interest in short x-ray pulses for femto-chemistry or imaging of single molecules. The design pulse lengths of the afore mentioned X-ray FELs are too long (e.g. 230 fs for LCLS) for these classes of experiments, which require a pulse length of around 10 fs.

In general, undulator wakefields degrade the FEL performance[7] by shifting parts of the bunch outside the FEL energy resonance condition. Because the cooperation length of an X-ray FEL is small, undulator wakefields have a 'local' effect on the electron bunch. As a consequence, spontaneous radiation is amplified only for those parts of the bunch where wakefield energy loss is compensated by undulator tapering. In this paper, we investigate the wakefield effects (Sec.) and how different current profiles or vacuum chamber materials can be used to achieved short FEL pulses (Sec.). The discussion is centered on the LCLS project ($\gamma_0 = 280774$, $I_p = 3.4$ kA, $e_n = 1.2$ mm·mrad and $\sigma_\gamma = 6 \cdot 10^{-5}$ %) [1].

WAKEFIELDS EFFECTS

Wakefields are generated by the electron bunch as it passes through the undulator vacuum chamber. The amplitude is determined by the dimensions and properties of the chamber. The electrons leave a trailing electric field, which influences the succeeding particles. The dominant wakefield is the resistive wall wakefield due to a finite electric conductivity σ of the chamber wall. Other types of wakefields arise from changes in the vacuum chamber geometry [5] or surface roughness [6]. For typical LCLS parameter their amplitudes are two orders of magnitude smaller than the resistive wall wakefields. Although these wakes have no impact on the FEL pulse length, they are included in the simulations for completeness.

The interaction strength of the resistive wall wakefields is expressed by the single particle wake potential[4]

$$W_s(z) = -\frac{4cZ_0}{3\pi R^2}\left(e^{\frac{z}{\zeta}}\cos\left[\sqrt{3}\frac{z}{\zeta}\right] - \frac{\sqrt{18}}{\pi}\int_0^\infty \frac{x^2 e^{\frac{z}{\zeta}x^2}}{x^6+8}dx\right) \tag{1}$$

where the bunch tail is in the direction $z < 0$, c is the speed of light, Z_0 is the vacuum impedance, R is the beam pipe radius and

$$\zeta = \left[\frac{2R^2}{Z_0\sigma}\right]^{\frac{1}{3}} \tag{2}$$

is the characteristic length of the resistive wall wake potential. In the ultra-relativistic approximation, preceeding electrons are not influenced by the electron and thus $W_s(z > 0) = 0$.

For the LCLS design case with a radius of $R = 2.5$ mm and a copper plated chamber $\sigma = 5.8 \cdot 10^7\ \Omega^{-1}\mathrm{m}^{-1}$, the characteristic length $\zeta = 8.3\ \mu$m is an order of magnitude smaller than the LCLS bunch length.

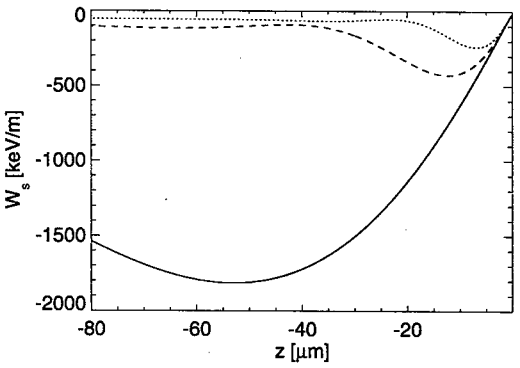

Figure 1: Wake potential for copper, steel and graphite vacuum chambers (dotted, dashed and solid line, respectively) and a 3.4 kA step profile.

The single particle wake potentials are convoluted with the current profile. If the profile exhibits any structure on a scale compared to or smaller than the characteristic size of the single particle potential, the total wake potential is strongly enhanced by this coherence effect. As an example, Fig. 1 shows the total wake potential for the LCLS

0-7803-7738-9/03/$17.00 © 2003 IEEE

uniform step profile and different conducting materials for the vacuum chamber, assuming the expected parameters for the geometric and surface roughness wake. The potential is dominated by the resistive wall wakefields and the location of the transition minimum is approximately the characteristic length ζ away from the head ($z = 0$). Within the transition region of the first 15 μm, the wake potential has a minimum value of -250 keV/m before it levels out at -30 keV/m for the main part of the bunch.

The undulator wakefields are distinguished from the wakefields in the main linac, because they effect the FEL processes dynamically by changing the electron energy during the FEL interaction. While these wakefields are similar to the incoherent emission of undulator radiation, the energy change varies along the bunch in the case of wakefields. A specific energy loss rate $d\hat{\gamma}/ds$ is compensated only by an undulator field taper given by, $da_u/ds = (a_u^2+1)/(\gamma a_u)d\hat{\gamma}/ds$ with s the position within the undulator and $a_u = eB_{rms}\lambda_u/2\pi mc$ the dimensionless undulator parameter, B_{rms} the rms magnetic field on axis, and λ_u the undulator period. Due to the variation in the wake potential only parts of the bunch remains in resonance with the field. The 'local' amplification is degraded if the electrons are shifted outside the acceptance of the FEL bandwidth before reaching saturation. The acceptance for any energy loss rate $d\gamma/ds$ is given by

$$\left|\frac{d\gamma}{ds} - \frac{\gamma a_u}{a_u^2+1}\frac{da_u}{ds}\right| < \frac{\rho^2\gamma}{\lambda_u} \qquad (3)$$

where ρ is the FEL parameter[8] and λ_u is the undulator period.

For LCLS, the bandwidth is 100 keV/m around the compensated energy gradient. In the standard case of the copper-plated vacuum chamber, the head of the bunch does not radiate because the local wake potential lies outside the acceptance of 100 keV/m.

On the other hand, if the acceptance bandwidth is centered around a unique value of the wake potential by a proper choice of the undulator taper, then only a short subsection of the bunch can be selected for lasing. In the following we discuss different conducting materials or bunch profiles and how they can be used to achieved short FEL pulses.

CURRENT PROFILES

In the following we analyse several current profiles and determine, how suitable they are for achieving short FEL pulses. We also consider steel or graphite as the vacuum chamber material, as the standard case of copper is not sufficient enough to achieve short FEL pulses.

The wake potential for copper, steel and graphite are shown in Fig. 1. For copper most of the wake potential lies within the acceptance of 100 keV/m, except for the large amplitude at the head of the bunch. By tapering for the maximum energy loss most of the bunch would not saturate. The minimum amplitude of about 250 keV/m corresponds to an overall taper of 0.2% of the magnetic field. The size of the pulse is about 16 μm for tapers between 0.16% and 0.2%. Weaker taper gradients gradually split the pulse into two. As for copper the taper for a steel vacuum chamber has to compensate the minimum of the wake potential (400 keV/m) to achieve a single, short FEL pulse. The pulse length is 20 μm or larger because the wake minimum is less curved ($\zeta = 29$ μm) than for copper: The area, which lies within the acceptance bandwidth, is longer. For copper and steel it is required to compensate the maximum of the wake potential. Otherwise the energy loss is compensated for more than one region of the electron bunch, resulting in multiple radiation pulses per electron bunch. A graphite vacuum chamber generates large wakes amplitudes and the wake potential is monotonic for amplitudes between 0 and 1.2 MeV/m. Because the slope of the wake potential is steep around the compensated gradient, it crosses the acceptance bandwidth over a short distance, which is in strong contrast to copper and steel, where a "wide" maximum lies in the acceptance bandwidth. The resulting FEL pulse length is below 5 fs FWHM and insensitive to the taper gradient (Fig. 2).

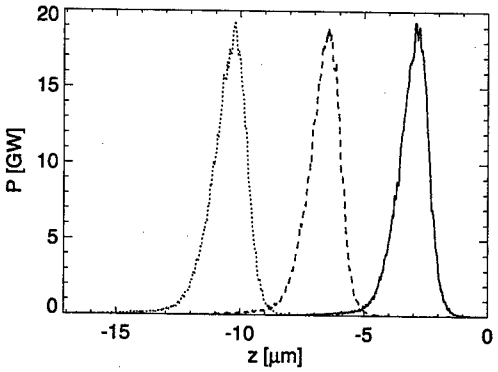

Figure 2: FEL pulse at undulator exit for different overall taper of 0.2%, 0.4% and 0.6% (solid, dashed and dotted line, respectively). The wake potential is based on a step profile and a graphite vacuum chamber.

Gaussian current profiles at LCLS are impractical for achieving short FEL pulses by using wakefields. Due to the smooth profile the wake potential has no large transient at the head of the bunch. In addition the wake potential for graphite is not as steep as for the step profile, limiting the minimum achievable pulse length to 25 fs for an rms electron bunch length of 15 μm.

Profiles with a steep rising edge and an exponential drop ($I(z) = I_0 \exp[z/\sigma_z]$) performs slightly better than the step profile. The width of the maximum for copper and steel is further reduced by the asymmetry in the current, where one side has a shorter gain length due to the higher current. Fig. 3 shows the results for two rms beam sizes of 10 μm and 20 μm. Although the 10 μm case does not reach saturation because the effective current was below 3

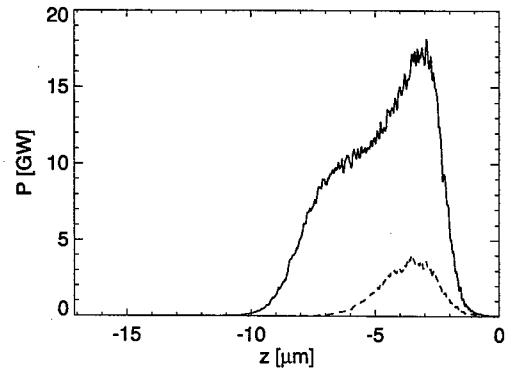

Figure 3: FEL pulse at undulator exit for different bunch lengths of the exponential current profile (20 μm rms size – solid line, 10 μm rms size – dashed line).

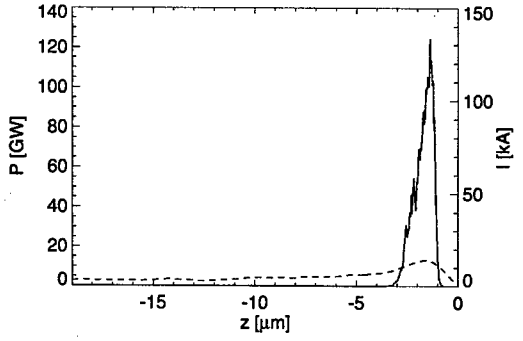

Figure 4: FEL pulse and current profile (solid and dashed line, respectively) at undulator exit, based on a start-end simulation.

kA the FEL pulse length is 10 fs FWHM without the need to change the vacuum chamber material for the LCLS design case to a poorer conducting material.

Simple profiles, as discussed in the previous paragraphs, are very unlikely to be generated, because space charge, rf curvature, wakefields, and coherent synchrotron radiation in the compressor affect the electron beam quality before the beam is injected into the undulator. To estimate a realistic profile a start-end simulation is employed, using PARMELA and ELEGANT, to generate a fully 6 dimensional phase space distribution, which is imported into GENESIS 1.3 and propagated through the undulator. In the LCLS standard case with rf curvature, wakefields and two stages of bunch compression, the simulation predicts large spikes in the current distribution at the head and tail of the bunch. While the tail spike has no impact for our discussion, the head spike has a width shorter than 10 microns while the peak current reaches almost 15 kA. This spike has less than 10% of the total charge but it doubles the wake amplitude for a copper-plated vacuum chamber as compared to a uniform distribution. The maximum resistive-wall wakefield amplitude is 500 keV/m. Although the beam current does not drop below 3.5 kA, the emittance and energy spread in this region is large enough to inhibit the FEL amplification. Choosing an overall taper of 0.4% results in a FEL pulse length of 5 fs FWHM as shown in Fig. 4. The pulse length is insensitive up to a 15% variation in the current or taper. In addition, the higher peak current allows a higher saturation power than for the step profile.

CONCLUSION

It has been shown that the combination of undulator wake potentials and undulator field taper can select a short subsection of the bunch to reach saturation. The use of a poor conductor (e.g. graphite) as the vacuum chamber material allows for a much more stable operation. The disadvantage is that the FEL cannot operate in short and long pulse mode without changing the vacuum chamber.

Another solution is to manipulate the current profile. If edges or spikes with a size smaller than the characteristic length of the wakefield are present, the wakefield amplitude is locally enhanced. The selection by the acceptance bandwidth of the field taper gets shorter. The pulse length can be further reduced if the beam properties such as current, energy spread or emittance varies over the selected part of the bunch.

Start-end simulation has shown for the LCLS, it is possible to achieve an x-ray pulse length of 10 fs or shorter. It requires a modest tapering of 0.5%.

REFERENCES

[1] *Linac Coherent Light Source (LCLS) Design Study Report*, SLAC-R-521, UC-414 (1998)

[2] *TESLA - Technical Design Report* DESY 2001-011, ECFA 2001-209, TESLA Report 2001-23, TESLA-FEL 2001-05, Deutsches Elektronen-Synchrotron, Hamburg, Germany (2001)

[3] G.K. Shenoy, J. Stoehr (eds.),*LCLS - The First Experiments*, Stanford (2000)

[4] K. Bane, SLAC Report AP-87 (1991)

[5] K. Bane. M. Sands, Part. Accel. **25** (1990) 73

[6] K. Bane,G.V. Stupakov, SLAC Report, SLAC-PUB-8599 (2000)

[7] S. Reiche *et al.* Nucl. Inst. & Meth. **A475** (2001) 328

[8] R. Bonifacio, C. Pellegrini, L.M. Narducci, Opt. Comm. **50** (1984) 373

FERMI@ELETTRA: THE SINGLE-PASS FREE-ELECTRON LASER FOR THE VUV AND SOFT X-RAY SPECTRAL RANGE AT ELETTRA

R.J. Bakker, C.J. Bocchetta, P. Craievich, M.B. Danailov, G. D'Auria, B. Diviacco, M. Ferianis, S. Di Mitri, G. De Ninno, V. Smaluk, L. Tosi, V. Verzilov,
Sincrotrone Trieste S.C.p.A., S.S.14 km 163,5 in Area Science Park, 34012 Trieste, Italy

Abstract

The FERMI proposal is an initiative from ELETTRA, INFM and other Italian institutes, to construct a single-pass FEL user-facility, to be located next to the third-generation synchrotron radiation facility ELETTRA in Trieste, Italy. For the initial phase, the project aims for lasing from 100 nm to 10 nm, with the use of the existing 1.2-GeV S-band linac. As a next step, the accelerator system should be extended to reach 1.2 nm. In all stages, reliability and flexibility are of importance. That is, seeding schemes are considered to improve the SASE output. In addition, users of this new source will have full control over both wavelength and polarization of the radiation.

The initiative is a response to the Italian government's call for proposals for a multi-purpose pulsed laser X-ray source. In anticipation of a positive decision, the Sincrotrone Trieste has initiated the ELETTRA Linac FEL project (ELF), i.e., an R&D project to facilitate a quick and effective implementation of the first step of FERMI. Here, we describe the main features of the project. Emphasis is given to the implementation and initial steps and the ELF project.

INTRODUCTION

FERMI@ELETTRA is a research and development proposal for the construction of a single-pass FEL user-facility for the Vacuum Ultra-Violet (VUV) to the X-ray spectral region, i.e., from 100 nm (12 eV) to 1.24 nm (1 keV). It is foreseen to build-up this machine in three successive stages, aiming for lasing from 100 nm to 40 nm, from 40 nm to 10 nm, and from 10 nm to 1.24 nm, respectively. The first two stages are based on use of the existing 1.2-GeV linac. For the latter stage, the energy of the linac will be extended up to 3.0 GeV. An artist impression of project is given in Fig. 1.

The FEL is intended to operate as a user-facility. Hence, the target capabilities and specifications have been defined in close collaboration with potential users [1]. The most important machine properties are:

- An S-band accelerator with advanced feedback and feed-forward systems to improve the stability
- High-power short optical pulses (~100 fs) with a high pulse-to-pulse reproducibility
- APPLE II type undulators to enable flexible tuning of both the wavelength and the polarization
- Implementation of seeding schemes for further stabilization of the FEL process

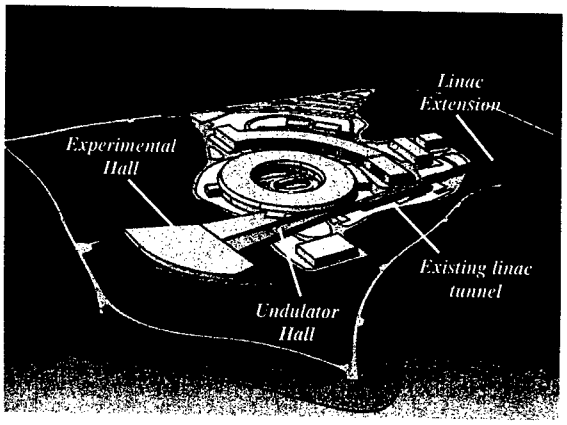

Figure 1: Overview of the ELETTRA laboratory-site after completion of the FERMI project. In the center and top are the buildings in place today. On the left, the undulator hall and the experimental hall are an extension of the existing linac tunnel. The linac extension on the right permits an extension of the spectral range from 10 to 1.2 nm.

Table 1: FERMI@ELETTRA machine parameters

	Stage 1+2	Stage 3
Wavelength (nm)	100/40/10	1.2
Peak brightness*	0.1/0.3/0.9	55
Peak power (GW)	2.3/1.8/0.75	3.0
Beam Energy (GeV)	1.2	3.0
Norm. emittance (mm-mrad)	2.0	2.0
Peak current (kA)	0.6	2.5
Rms e-beam pulse length (fs)	250	160
Charge per pulse (nC)	0.38	1
Energy spread (%)	0.05	0.05
Repetition frequency (Hz)	10	10 – 50
FEL parameter ρ (10^{-3})	4.8/3.2/1.6	1.2
Gain length (m)	0.7/0.8/1.3	2.6

* (ph/s/mm^2/mrad^2/0.1%BW)(×10^{30})

The key-parameters are summarized in Tab. 1. To ensure effective operation, the machine will be built using a progressive approach where users will gain access to the machine in an as early as possible stage. Feedback from this approach is then used to refine the design for the successive stages of the project.

While the project waits for funding the ELETTRA Linac FEL project (ELF) has been initiated. ELF is an R&D project to facilitate a quick and effective implementation of the first step of the FERMI proposal with the use of the existing 1.2-GeV linac. As a final goal, ELF aims to reach

0-7803-7738-9/03/$17.00 © 2003 IEEE

both lasing and initial user experiments in the wavelength range from 100 nm to 10 nm with a single undulator-line. For the longer wavelength-target, the electron beam energy will be reduced from 1.0 to 0.5 GeV as compared to the original proposal. The electron beam parameters for the shortest wavelength target remain identical to the ones quoted in Tab. 1.

Presently, the ELF project focuses on: (1) a more detailed implementation of the plans proposed for the FERMI project, (2) a further build-up of expertise in areas beneficial to FEL development and (3) steps for implementation of the FEL. There is special attention to steps, necessary to enhance the parameters of the ELETTRA linac to a regime necessary to facilitate FEL R&D.

ELF PROJECT

The existing 65.5-m long, 1.2-GeV linac [2] forms an ideal starting-point for a linac-based FEL. It is located in a 110-m long underground tunnel and consists of S-band structures, each individually controlled. An overview of the infrastructure is given in Fig. 2.

The normal operating mode of the linac is a 10-Hz repetition of 800 ns RF-pulses. The maximum achievable energy is 1.2 GeV. Presently the linac serves as injector for the ELETTRA storage ring. Typically, this service requires 1.5 hours of dedicated operation per day. The remaining time is available for FEL development and operation. In addition, a full energy booster is under construction [3]. The present time-schedule foresees completion of this project in 2005, after which the linac will be dedicated to FEL activities only.

For the ELF project, we aim for lasing in successive steps at 100, 40 and 10 nm. Specifications are summarized in Tab. 2. To transform the linac into a suitable FEL driver, several tasks need to be performed: (1) replacement of the existing electron beam source with a low-emittance injector, (2) modification of the electron beam optics, including bunch compressor systems, to increase the peak current and performance, (3) installation of an undulator line, and (4) installation of additional electron-beam and photon-beam diagnostics to monitor the machine performance in each stage. Additionally there is a special interest in a FEL seeding scheme for the initial phase of the project.

Table 2: ELF target parameters

Wavelength Target (nm)	100	40	10
Peak brightness *,#	0.1	0.7	7.7
Peak power (GW) #	0.7	1.3	3.8
Beam Energy (GeV)	0.5	0.7	1.0
Norm. emittance (mm-mrad)	2.0	2.0	1.5
Peak current (kA)	0.6	1.0	2.5
Rms e-beam pulse length (fs)	667	400	160
Charge per pulse (nC)	1	1	1
Energy spread (%)	0.1	0.1	0.1
Repetition frequency (Hz)	10	10	10
RMS Undulator Strength#	1.95	2.6	4.0
Undulator Gap (mm) #	12	14	21
Average β function (m)	7.6	7.6	7.6
FEL parameter ρ (10^{-3})#	2.0	1.8	1.6
Saturation Length (m) #	19	21	24

* (ph/s/mm^2/mrad^2/0.1%BW)(×10^{30}), # Planar undulator field

RF Photo Injector

The present injector utilizes a thermionic triode, which does not perform sufficiently for lasing at even the longest wavelength. Hence, a second injector with improved capabilities will be installed. The original gun must remain operational to guarantee injection into the storage ring. For the new electron beam source, three rf photocathode guns are under consideration: (1) a high brightness photo-injector of the BNL/SLAC/UCLA type [4], a 2.6 cell gun developed at the TUE [5], and a higher-order mode 1-cell cavity presently developed by Lewellen at the APS [6]. For any of the options, both the timing-structure and the driving laser, are close to the ones chosen for the LCLS project [4], i.e., 1 nC with a 10 ps flat-top profile. For an optimum performance, there is emphasis on transverse and longitudinal laser pulse-shaping techniques. The driving laser will be located adjacent to the linac tunnel in an existing shielded area, see Fig. 2.

A schematic overview of the injector is presented in Fig. 3. Initially it can be installed as a stand-alone test stand and connected to the main linac during one of the regular shutdown periods. The design of the diagnostic section (emittance and energy spread) is such that it provides sufficient resolution and can be fitted into the space required for the emittance compensation scheme. Slight modifications to the design are still necessary and depend on the final choice of the RF photo cathode gun.

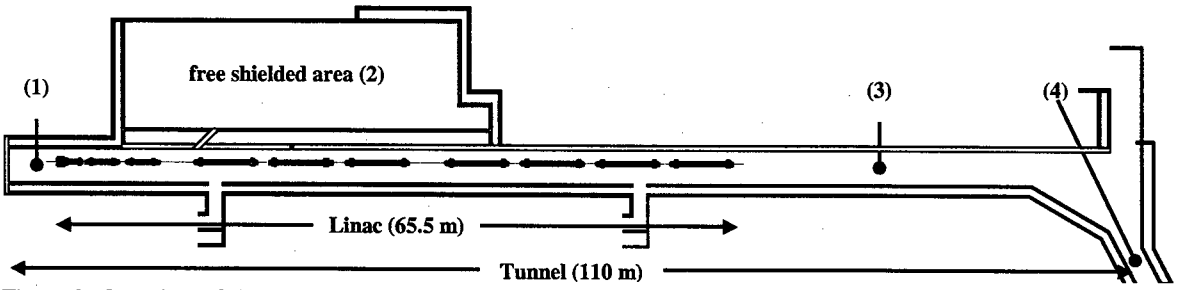

Figure 2: Overview of the existing linac tunnel. The marked areas are: location of a RF photo-injector test stand (1), a shielded area for the driving laser (2), and free area to facilitate the installation of an undulator and moving of accelerator modules (3). The area on the bottom right (4) leads to the injection point of the storage ring. The klystron area is located above the linac tunnel.

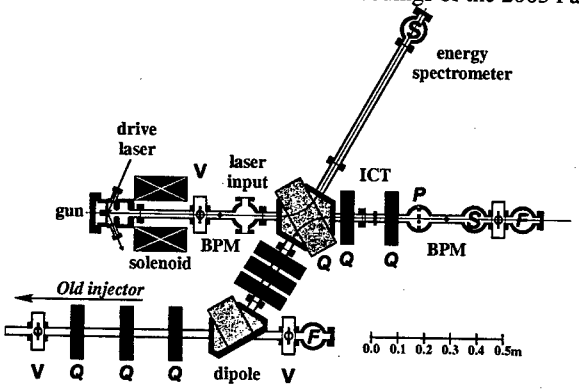

Figure 3: Schematic layout of the injector: (F) faraday cup, (P) pepper pot, (Q) quadrupoles, (S) screens, and (V) vacuum valves. The Faraday cup on the right indicates the position of the first accelerator cavity. The beam-line at the bottom enables use of the present thermionic gun.

Linear Accelerator Section

The only modifications to the structure of the linac are the relocation of one accelerating section to allow for the introduction of magnetic bunch-compressors and additional diagnostics. Similar to the photo-injector, all activities can be executed during normal shutdown periods without interfering with ELETTRA operations.

For initial lasing at 100 nm, it is foreseen to start with modest peak-currents. Hence, the demands for the magnetic bunch compression system are relaxed and a single compression-stage at an energy of 120 MeV is sufficient. In this phase, even a third harmonic cavity to enhance the compression efficiency is not strictly necessary though it would permit a more flexible manipulation of the electron beam. For lasing at shorter wavelengths, it will be necessary to install such a system. Especially for lasing at 10 nm the target peak current is more challenging and a 3rd harmonic cavity in combination with a second compression stage is mandatory.

Undulator Section and Seeding

The undulator section will consist of a 6.5-m period pure FODO lattice with 2.48-m long, 4-cm period undulators. The undulator period is chosen identical to the undulator designated for the second phase of the FERMI proposal. Consequently, the electron beam energy for the initial phase of the project will be reduced to allow lasing at 100 nm.

The final undulator design is still under consideration. For the downstream sections, APPLE II type of undulators will be used to allow a flexible tuning of both the wavelength and polarization. The period is a compromise between a compact design (shorter period) and the complexity of manufacturing (longer period). The choice of the upstream sections of the undulator depends on the desired operational mode of the FEL which is still under discussion: (1) a pure SASE mode of operation or seeding with a conventional low-power laser on a sub-harmonic, or (2) lasing with the aid of a HGHG seeding scheme [7].

For the former option, a variable gap planar undulator with identical period can be used. The latter requires the construction of a sub-harmonic undulator.

For both types of seeding schemes, conventional laser systems are available. Seeding on a sub-harmonic is compatible with a pure SASE mode of operation and, hence, more straightforward for the initial phase of the project. The HGHG scheme might prove to be more cost effective. Both seeding-schemes might suffer from the initially anticipated pulse-to-pulse jitter of the central energy of the electron beam that exceeds the gain bandwidth of the FEL and hence, the effectiveness of the seeding process. This effect can be counter-acted with the use of a sufficiently large energy-chirped beam. Studies indicate that such options are feasible within the parameter range of the ELF project. In such a case, the third harmonic RF cavity will also be mandatory for the initial phase of the project since it permits a sufficient flexible control of the electron beam.

FERMI PROJECT

Since the target parameters of the ELF project are compatible with the FERMI@ELETTRA proposal, the projects can be merged effectively without loss of capital. The space available in the present linac tunnel does not permit the ELF to develop to the status of user-facility. For this, it is necessary to construct a user-hall, such as depicted in Fig. 1. Construction of such a hall, as described in the FERMI proposal [1], would thus form the first natural transformation step. This would also permit a further development towards of a full-scale next-generation light-source user facility, e.g., by constructing parallel undulator beam-lines and implementing an increased repetition rate of the system.

REFERENCES

[1] FERMI@ELETTRA, Preliminary Conceptual Design Report, Sincrotrone Trieste, Feb., 2002

[2] G. D'auria, et al., "Operation and Status of the ELETTRA Injection Linac", Particle Accelerator Conference, Vancouver, Canada, May 1997

[3] F. Iazzourene, "Update on the Linear and Nonlinear Optics of the ELETTRA Full Energy Booster Synchrotron", European Particle Accelerator Conference, Paris, France, June 2002

[4] LCLS CDR, SLAC-R-593, 2002

[5] M.J. de Loos, S.B. van der Geer, F.B. Kiewiet, O.J. Luiten, M.J. van der Wiel, Proceedings of EPAC 2002, Paris, France

[6] J.W. Lewellen, "Higher-order mode RF guns," Phys. Rev. ST Accel. Beams 4, 040101 (Issue 4 – April 2001)

[7] L-H. Yu and J. Wu, "Simulations for the FERMI@ELETTRA Proposal to Generate 40-nm and 10-nm Coherent Radiation using the HGHG Scheme", Proc. of the FEL conference 2002.

SATURATION OF THE NSLS DUV-FEL AT BNL

A. Doyuran*, L. DiMauro, W. Graves#, R. Heese, E. D. Johnson, S. Krinsky, H. Loos, J.B. Murphy, G. Rakowsky, J. Rose, T. Shaftan, B. Sheehy, Y. Shen, J. Skaritka, X.J. Wang, Z. Wu, L.H. Yu,
BNL, UPTON, NY, USA

Abstract

The Deep Ultra Violet Free Electron Laser (DUV-FEL) experiment has reached a milestone by saturating the Free Electron Laser using High Gain Harmonic Generation (HGHG) method in the Source Development Laboratory (SDL) at NSLS. It utilizes the 10 m long, 3.9 cm period NISUS wiggler. The goal of the project is to produce radiation at a wavelength less than 100 nm, utilizing the HGHG method. HGHG at 266 nm has been accomplished by seeding with the 800 nm Ti:Sapphire laser and observed saturation. The third harmonic at 88 nm accompanying the 266 nm is being used in an ion pair imaging experiment in chemistry. We discuss the measurement of energy, gain, spectrum, and pulse length of the FEL output. We also describe the diagnostics used for operating the FEL.

INTRODUCTION

There is a substantial interest in producing coherent radiation using single pass FELs from Deep-UV down to the X-ray regime [1]. In this article, we present the first demonstration of HGHG FEL in the ultraviolet at 266 nm with the seed laser at 800 nm. Previously, a proof of principle experiment has been done in the IR regime at ATF BNL [2]. In many applications an FEL operates in Self Amplified Spontaneous Emission (SASE) mode [3-6]. In this case the radiation starts from shot noise, therefore the light is not temporally coherent and the pulse-to-pulse energy fluctuation is big. In HGHG case [2,7,8] the electron is seeded by a conventional laser, therefore the radiation inherits the properties of the seed laser, producing excellent temporal and spatial coherence. The energy and central wavelength stability is limited by the accelerator stability and the spectral bandwidth is much narrower than SASE. The pulse length of the radiation can be controlled by the seed laser, thus enabling to produce ultrashort pulses.

OVERVIEW OF THE FACILITY

The accelerator consists of a Ti:Sapphire laser system, a 1.6 cell RF photo-cathode gun, 4 SLAC-type linac tanks and a 4-dipole chicane (Fig 1). A photo-cathode RF gun is illuminated by the tripled Ti:Sapphire laser at 266 nm producing 300 pC charge, 4 ps FWHM bunch length, and a 4.5 MeV energy electron beam with normalized emittance of 4-5 μm. The first two linac tanks accelerate the electron bunch with the second tank off-crest by 26° to introduce an energy chirp. A 4-dipole chicane compresses the bunch to about 1 ps FWHM. The third linac tank is used to remove the remaining energy chirp with additional acceleration and the fourth tank accelerates the bunch to 177 MeV. This tank is also used for bunch length measurements using the zero-phasing method [9].

HGHG PROCESS

The three major components of the experiment are modulator, dispersive magnet, and radiator. The modulator is tuned to the wavelength of the seed laser. Its length is 0.8 m and has a period of 8 cm with $K = 1.67$. The 800 nm seed laser derived from the Ti:Sapphire laser with 9 ps FWHM pulse length interacts with the electron beam. This introduces an energy modulation in the electron bunch. A local bump is introduced by four trim magnets to bypass the seed laser insertion mirror. The Rayleigh range is estimated to be 2.4 m from the beam sizes measured at two pop-in monitor locations in the modulator. Then the dispersion magnet converts the energy modulation into a density modulation. The radiator is tuned to the 3rd harmonic of the seed laser at 266 nm. The NISUS wiggler (radiator) is 10 m long and has 3.89 cm period and 0.31 T peak field [10]. The synchronization between the electron beam and the seed laser is established by using a picosecond resolution streak camera at the end of the beam line. We obtain the temporal position of the SASE and seed laser pulse with the streak camera and adjust the delay stage for proper synchronization. The transverse alignment is established by overlapping the two beams on two pop-in monitors in the modulator. The HGHG output is optimized for maximum coherent radiation at the beginning of NISUS by varying the dispersion magnet current. Since the seed laser pulse is longitudinally chirped, only a small part of the bandwidth is seen by the electron beam with a bunch length of 1 ps. The wiggler is not long enough for SASE FEL to saturate because the typical gain length is about 0.8-1 m and SASE needs more than 20 gain length to reach saturation. Since HGHG starts from a pre-bunched electron beam, the radiation process begins coherently and saturates within the length of the wiggler.

DIAGNOSTICS AND MEASUREMENTS

The NISUS wiggler consists of 16 sections. Every section is equipped with a pop-in monitor, a four-wire system, and pancake magnets. Pop-in monitors utilizing Cerium doped YAG crystals are used to monitor the electron beam [11]. The four-wire system at each section can produce quadrupole fields providing additional focusing and a dipole field for trajectory corrections. Pancake shaped magnets located at the top and bottom of the wiggler provide a vertical magnetic field and can be used in horizontal trajectory correction [12,13]. A fiber coupled He-Ne laser is used for alignment through NISUS.

*Corresponding Author: doyuran@bnl.gov
MIT-Bates Linear Accelerator Center Middleton, MA 01949

0-7803-7738-9/03/$17.00 © 2003 IEEE

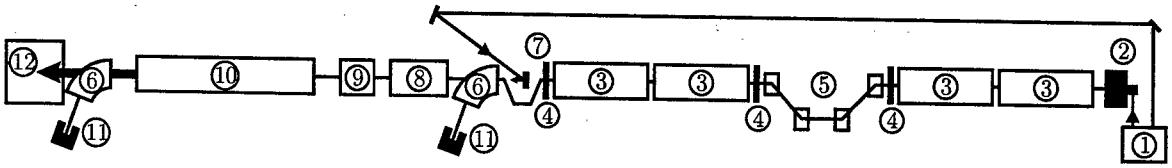

FIG.1: The NSLS DUV-FEL layout: 1-gun and seed laser system, 2-RF gun, 3-linac tanks, 4-focusing triplets, 5-magnetic chicane, 6-spectrometer dipoles, 7-seed laser mirror, 8-modulator, 9-dispersive section, 10-radiator (NISUS), 11-beam dumps, 12-FEL measurement area.

The position of the laser at each monitor is recorded and these positions are used as a reference for the electron beam trajectory. The position and the beam size of the electron beam at each pop-in monitor is measured and the trajectory of the beam is corrected using automated MATLAB and EPIC routines. This way we can easily calculate the emittance and the twiss parameters of the beam and adjust the upstream quadrupole currents to have a proper matching into the wiggler. A number of sections are also equipped with the detectors to measure the energy of the FEL. A calibrated joule meter is used to measure the total energy at the exit. A high-resolution spectrometer is used to measure the spectrum of the SASE and HGHG light.

Gain Measurement

We have two methods to measure the gain of the FEL. One is measuring the energy using the detectors along NISUS and the other is measuring the energy at the exit Joule meter by kicking the electron beam at different sections using the pancake magnets. Both methods are proven to be consistent with each other.

Fig 2 shows the energy of the HGHG outputs as a function of the distance in the wiggler using the kicking method and simulations of the gain with the TDA code [8] for two input seed powers. For the 1.8 MW input seed laser power the HGHG saturates near the end of the wiggler. For the 30 MW input seed laser power the HGHG saturates around the half of the wiggler. The TDA simulation predicts the power should go down after saturation but measurement shows the energy still grows very slowly. Since the electron beam has varying current and emittance along the bunch, different parts of the beam reach saturation at different times.

The HGHG output power stability is basically limited by the accelerator stability. The typical average output is approximately 100 μJ. Figure 3 shows the statistic of the pulse energy measurement which is 7 % over one minute. Since January 2003 the third harmonic at 88 nm which accompanies the 266 nm is being used for an ion pair imaging experiment [14], which has benefited from the stability of the HGHG output.

Spectrum Measurement

The spectrum of the FEL output was measured with a high-resolution spectrometer at the end of the beam line. Fig 4 shows the single shot HGHG and SASE spectra. The FWHM bandwidth of the HGHG pulse is 0.23 nm. Since the seed laser is 9 ps long and the electron beam is 1 ps long only 1/9th of the spectrum is seen by the electron beam.

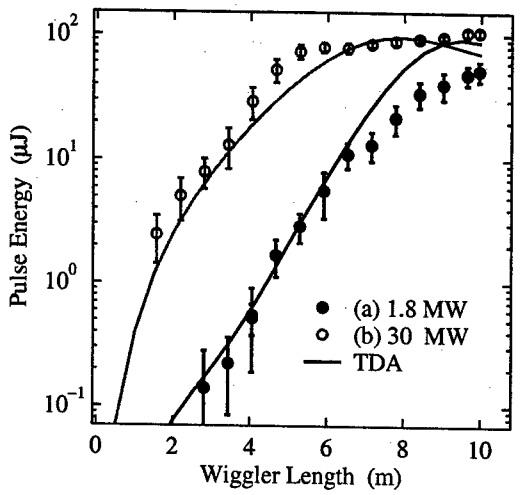

FIG. 2: Pulse energy vs. distance for two values of the input seed laser power: (a) 1.8 MW and (b) 30 MW. The solid curves are TDA simulation results.

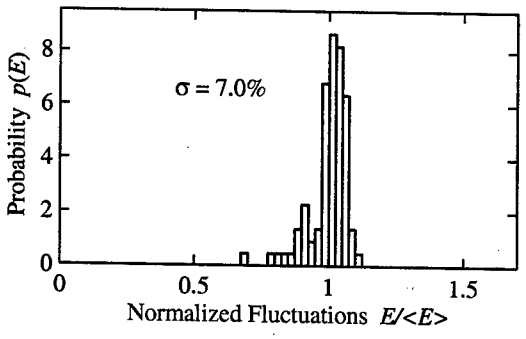

FIG. 3: Histogram of HGHG output pulse energy with 30MW seed power

The seed laser has ~ 6 nm bandwidth which 0.7 nm is seen by electron beam. At the third harmonic we expect 0.23 nm bandwidth which is precisely what was measured. The HGHG spectral brightness is 2×10^5 times larger than SASE because NISUS is not long enough to saturate.

To do a fair comparison we used the GENESIS 1.3 [15] code to calculate the spectrum of SASE after 20 m of NISUS structure (Fig 4). However, due to a larger bandwidth SASE has still an order of magnitude smaller spectral brightness.

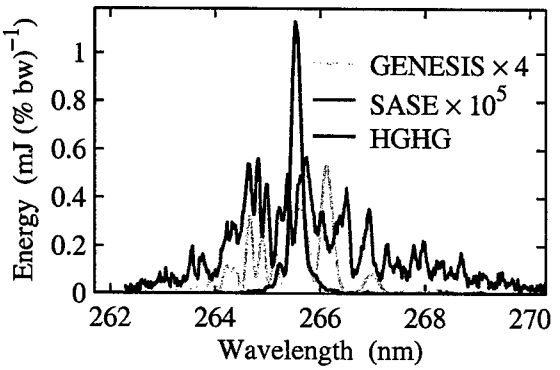

FIG. 4: Single shot HGHG spectrum for 30 MW seed (blue), single shot SASE spectrum measured by blocking the seed laser (red) and simulation the SASE spectrum after 20 m of NISUS structure (green). The average spacing between spikes in the SASE spectrum is used to estimate the pulse length.

Pulse Length Measurement

The average spacing between the spikes in the SASE spectrum gives an estimate the radiation pulse length according to

$$T_b = \frac{\lambda^2}{0.64 c \Delta\lambda} = 1 \text{ ps [16].}$$

The measured electron pulse length is 1 ps FWHM. We also used a multi-shot two-photon absorption pump-probe autocorrelator to measure the HGHG pulse length and obtained 0.63 ps FWHM (Fig 5).

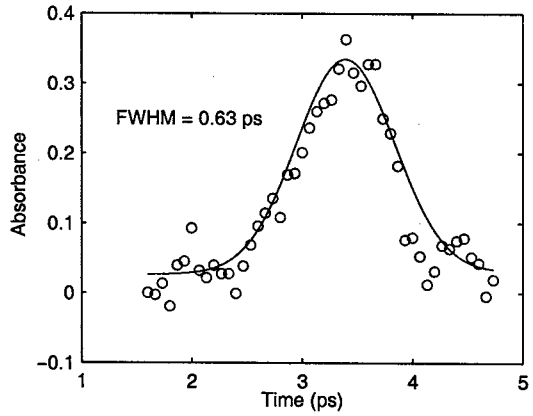

FIG. 5: Pulse length measurement of the HGHG output using two-photon absorption pump-probe autocorrelation for a seed power of 1.8 MW.

For a Gaussian Fourier transform limited beam, the pulse length should be $\tau = 0.44$ ps with the measured bandwidth of 0.23 nm, whereas for a square Fourier transform limited beam $\tau \cong 1$ ps. The measured 0.63 ps pulse length is near Fourier transform limited region.

CONCLUSION

The DUV-FEL experiment has successfully reached saturation. The output energy is measured to be 100 μJ corresponding to a power of 100 MW. The output is longitudinally nearly Fourier transform limited and the shot to shot stability is limited by the accelerator performance. The spectral bandwidth is very narrow and as expected. A first user experiment at DUV-FEL has started using the 88 nm third harmonic which accompanies the 266 nm HGHG.

ACKNOWLEDGEMENT

This work was supported by U.S. Department of Energy, Office of Basic Energy Sciences, under Contract No. DE-AC02-98CH10886 and by Office of Naval Research Grant No. N00014-97-1-0845.

REFERENCES

[1] S. Leone, *Report of the BESAC Panel on Novel Coherent Light Sources* (U.S. Department of Energy, Washington, D.C., 1999).
[2] L.-H. Yu et al., Science 289, 932 (2000).
[3] J. Galayda, ed., Linac Coherent Light Source Conceptual Design Report, SLAC-R-593 (2002).
[4] V. Ayvazyan et al., Phys. Rev. Lett. 88, 104802 (2002).
[5] S. V. Milton et al., Science 292, 2037 (2001).
[6] A. Tremaine et al., Phys. Rev. Lett. 88, 204801 (2002).
[7] I. Ben-Zvi, L. F. Di Mauro, S. Krinsky, M. White, and L. H. Yu, Nucl. Instr. Meth. A304, 181 (1991).
[8] L.-H. Yu, Phys. Rev. A 44, 5178 (1991).
[9] D. X. Wang, G. A. Kraft, and C. K. Sinclair, Phys. Rev. E 57, 2283 (1998).
[10] A. Doyuran, Diagnostic System for the NISUS Wiggler and FEL Observations at the BNL SDL, EPAC 2002 Conf. Proceedings
[11] K. E. Robinson et al., Nucl. Instr. Meth. A291, 394 (1990).
[12] T. Shaftan, Beam-Based Trajectory Alignment in the NISUS Wiggler, FEL 2002 Conf. Proceedings
[13] H. Loos, Beam-Based Trajectory Alignment in the NISUS Wiggler, EPAC 2002 Conf. Proceedings
[14] X. Liu, R. L. Gross, and A. G. Suits, Science 294, 2527 (2001).
[15] S. Reiche, Nucl. Inst. Meth A 429 (1999) 243
[16] S. Krinsky and R. L. Gluckstern, Nucl. Instrum. Meth. A483, 57 (2002).

THE CANADIAN LIGHT SOURCE

L. Dallin, I. Blomqvist, M. de Jong, D. Lowe and M. Silzer, Canadian Light Source, University of Saskatchewan, 101 Perimeter Road, Saskatoon, Saskatchewan, S7N 0X4, Canada

Abstract

The Canadian Light Source (CLS), at the University of Saskatchewan, was funded in April, 1999. It consists of an injection system (250 MeV linac and full energy booster) and a 12 cell DBA 2.9 GeV storage ring. The injection system is now fully operational and construction of the storage ring is well under way with commissioning expected to commence in the summer of 2003. The compact lattice (171 m) requires space saving technologies including strong focusing in the magnets, a superconducting RF cavity and "chicaning" of two insertion devices (IDs) in the 5 m straights. IDs have been designed at the CLS and most will be built on site. Magnets and power supplies have been designed to maintain tight control over machine functions, orbit and transverse coupling. The vacuum chamber and the girder system for the ring incorporate modular designs best suited for a compact lattice. Front ends have been designed for all source points including the chicaned IDs. Development of the CLS subsystems has proceeded with a strong emphasis on a "design-build" project management style. For this, CLS developed detailed preliminary designs and worked with industry to engineer the final products. The project remains on budget and the CLS is expected to be fully operational by the target date of January, 2004.

CLS DESIGN GOAL

The goal of the CLS[1] design is to produce brilliant light in a compact source. Brilliance, $\mathcal{B}$, is proportional to the electron beam energy, E, the current, I, and inversely proportional to the transverse beam sizes, σ, and angular divergences, σ', as:

$$\mathcal{B} \propto E\ I\ (\sigma_{Tx}\ \sigma_{Ty}\ \sigma'_{Tx}\ \sigma'_{Ty})^{-1/2}$$

where the source terms have both beam(e) and radiation(r) components:

$$\sigma_T^2 = \sigma_e^2 + \sigma_r^2 .$$

For medium energy sources such as the CLS the radiation dominates the angular terms so that the dependence of the brilliance of the electron beam is[2]:

$$\mathcal{B} \propto E\ I\ (\psi\ \varepsilon_x)^{-1}\ (\beta_x\ \beta_y)^{-1/2}$$

where $\sigma_e^2 = \beta\varepsilon$ and $\varepsilon_y = \sin^2\psi$. ψ, the coupling angle[3], is assumed to be small. The history of the CLS involves the optimization of the above factors with the constraint, early in CLS history, that the source circumference be about 100 m.

HISTORY

The early version of the present source, is described in the 1991 document: "A Proposal from the Canadian Institute for Synchrotron Radiation (CISR) to NSERC for a Collaborative Special Project and Program Grant for Study Funds for a Canadian Synchrotron". At this time the interest of the user community was with "soft" xrays and an electron energy of 1.5 GeV was chosen. To have control over the β-functions a racetrack design was contemplated. The design consisted of four to six I-cell bend regions surrounding straights with extra quadrupoles to allow for variable functions in the straights. The design contemplated the use of superconducting (SC) bends in some locations to boost the photon energies produced. Also proposed was the idea to replace one or more bends with an SC wiggle-bend. The drawback of this design is the limited number of straights in a compact lattice.

By 1994, a more conventional Triple Bend Achromat (TBA) lattice[4] was proposed. This design was a 1.5 GeV lattice with 8 cells. The emittance of this source was low at 6 nm-rad. The ring circumference was 104 m. At the same time, more hard X-ray users were interested. It was felt that 8 straights were too few and the beam energy too low.

By 1995 a Double Bend Achromat (DBA) lattice[5] was proposed. This lattice had twelve cells and a focussing configuration that remains to this day. The beam energy was increased to 2.5 GeV and the circumference to 127. The emittance increased to 14 nm-rad. Still, access to more straights and higher photon energies (20 keV undulator radiation) were requested.

The Present Machine

In 1999 funding for the CLS was secured. By this time the energy had increased to 2.9 GeV. Shortly, the straight sections were increased in length to 5.2 m and the circumference became 170.88 m. The lattice was 'frozen' and construction began. The increased straight length allows for doubling up (duplexing) of IDs in each straight. Furthermore, by using extra dipole magnets to "chicane" the beam through the straights the two IDs can delivery beam to separate beamlines. The chicanes[6] separate the photon beams by about 1.5 mrad. This allows the use of a single front end.

To achieve 20 keV undulator radiation it is necessary to exploit the higher undulator harmonics (up to n=15). To ensure quality control of the undulator construction, CLS will manufacture the undulators on site. Five insertion devices will be available for the first suite of CLS beamlines.

0-7803-7738-9/03/$17.00 © 2003 IEEE

COMPACT LATTICE

The compact DBA lattice is achieve by making the magnet lengths as short as possible. At the same time the focussing is strong to minimizing ε_x, Consequently, the lattice requires magnets[7] with high field strengths. A low β_y option requires running some quadrupoles near their design limit.

The dipoles have a bending field of 1.354 T and a field gradient of –38.7 T/m. An upright coil design is used to minimize the total overall length. A smooth distribution of gradient errors in the lattice reduces perturbation of the optics[8].

The lattice uses the minimum number (three) of quadrupole families. This allows for reasonable control of the optics. Maximum field gradients of 22 T/m are achieved. The use of separate power supplies for each quadrupole helps with compensating for the effects of IDs.

The minimum number (two) of sextupole families is used. Harmonic analysis indicated that little was to be gained by introducing extra sextupoles to cancel geometric effects. The maximum sextupole strengths are 270 T/m^2. The sextupoles include extra windings to produce horizontal and vertical correctors in one family and skew quadrupole fields in both families. Orbit correction also includes 24 XY corrector magnets that will be capable of corrections up to 100 Hz [9].

Views of the lattice are shown in figures 1 and 2.

Q C Q B S Q S Q S B Q C Q

Figure 1. Compact Lattice Interior: Q: quad.; B: bend; S: Sextupole; C: Corrector.

Figure 2. Lattice Exterior

BRILLIANCE

The development of the compact lattice has determined the machine functions and beam energy. Two beam factors remain to enhance the brilliance: the beam current, I, and the coupling angle, ψ. Of course, brilliance is ultimately served by the development of undulators. Selected lattice parameters are shown in Table 1.

Table 1: CLS Lattice Parameters

Circumference	170.88 m
Periodicity	12
Tunes: ν_x,ν_y	10.22, 3.26 (*4.26)
Momentum compaction	0.0038
Straights length β_x, β_y, η_x (at centre) β_x, β_y, η_x (* low β_y option)	 5.2 m 8.5, 4.6, 0.15 m 9.1, 2.7, 0.15 m
RF frequency voltage harmonic number energy acceptance	500 MHz 2.4 MV 285 1.54%
Energy loss per turn	0.876 MeV
Horizontal emittance	18.1(*17.8) nm-rad
Energy spread	0.111%
Full bunch length	65 ps

SuperConducting RF cavity:

The choice for the CLS RF system is a SC cavity based on the Cornell design[10]. Two advantages are low higher order modes (HOMs) and a large voltage (2.4 to 3.0 MV) in a single cell. Both these features will result in long beam lifetimes. With the presently installed power levels (300 kW), it should be possible to store currents up to 280 mA at 2.9 GeV and 500 mA at 2.5 GeV. Future development of the cavity technology may allow 500 mA at 2.9 GeV. The high performance of the SC cavity allows delivery of the required RF power in a single straight. The CLS SC cavity is shown in figure 3.

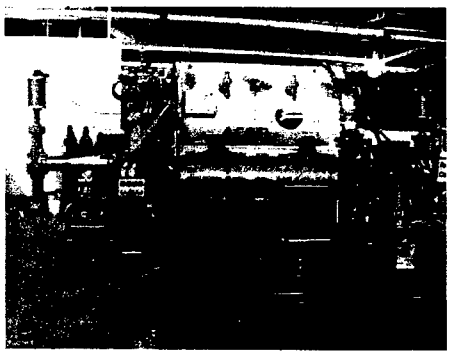

Figure 3. Superconducting Cavity

Coupling Control

Control of coupling studied earlier[11] has been investigated further. The simplest technique is to deduce the coupling from motion in the vertical plane when a horizontal "kink" is introduced into the orbit. This technique requires measurements of the closed orbit that allows time average measurements.

Using twelve of the skew quadrupoles and measuring the motion in each of the twelve straights, simulations show it is possible to reduce the vertical coupling to 0.02%. This may be lower than desirable for achieving reasonable beam lifetimes. However, if beam "top-up" is used, lifetime becomes less of an issue. It may also be possible to reduce the coupling locally. By using a coupling angle monitor[11] it is possible to reduce the beam size in one straight to almost half the average value. This may have some application when small gap undulators are used.

Results of coupling simulations are shown in figures 3 and 4. The beams shown are arrays of particles tracked over 1000 turns. The initial beam is generated in six dimensions using the nominal damped beam. The initial vertical beam emittance is $\varepsilon_x \times 10^{-5}$. Coupling, introduced by random misalignments of the lattice elements, results in growth of the vertical beam emittance.

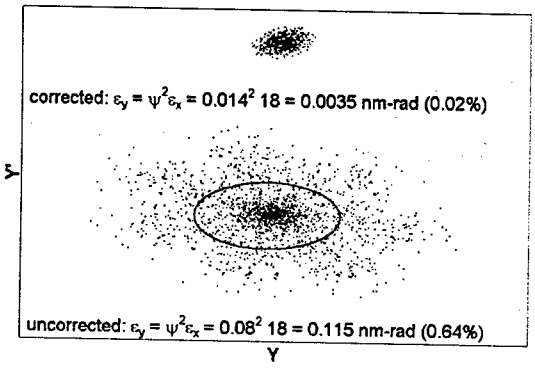

Figure 4. Coupling Correction Using Closed Orbit Measurements.

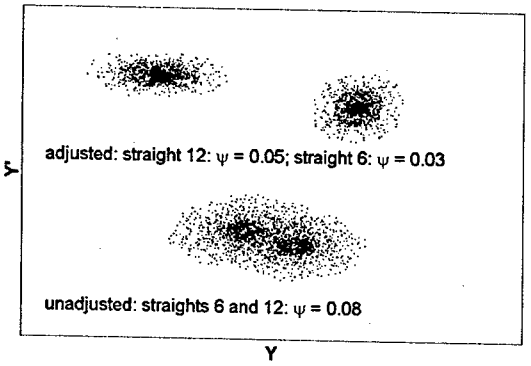

Figure 5. Coupling Adjustment Using Coupling Angle Monitor.

Insertion Devices

Five IDs are presently approved for the CLS. They are the four undulators and the SC wiggler shown in Table 2 and figure 6. As mentioned, the undulators will be built at the CLS. A high precision magnet mapping facility is now under development and the construction of the undulators will begin before the end of 2003. Specification of the SC wiggler has been completed. It is expected to be built, off site, by the end of 2004.,

Table 2: Approved CLS Insertion Devices

ID	Gap (min.)	Period	Poles	Photon energies
	mm	mm		eV
Undulators				
EPU	15	75	43	100 – 1000 (Circular) 100 – 3000 (Linear)
PPM	25	185	19	5.5 - 250
PPM	12.5	45	53	250 -1900
Hybrid	5	20	145	6k –18k
Wiggler				Critical energy
SC	15	35	60	10

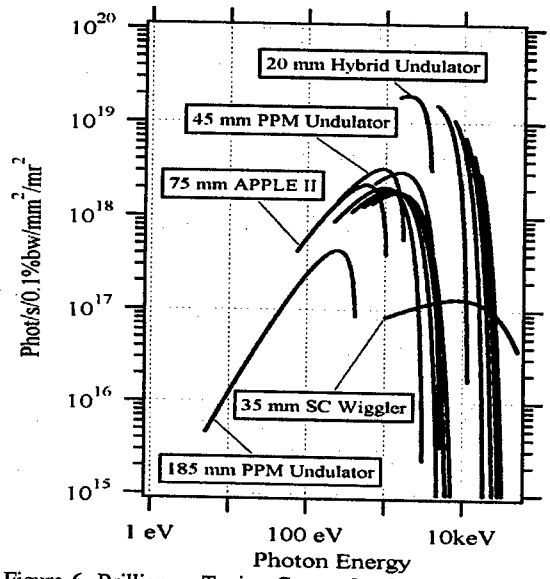

Figure 6. Brilliance: Tuning Curves for CLS Undulators and Photon Curve for the SC Wiggler.

With the duplexing of the straights it will be possible to install two Elliptically Polarizing Undulators (EPUs) in tandem. Under normal operations, the chicane magnets will separate the beam produced into two beamlines. With some extra chicanery (two more chicane magnets) it will be possible to direct both beams down the same line. In this way it should be possible to rapidly switch between polarization states using optical components in the beam line.

Beamlines

The layout of the initial CLS beamlines is shown in figure 7. The storage ring is located asymmetrically in a square building about 85x85 m^2. This allows for a variety of beamline lengths. For future expansion the north wall (top of figure) can be removed and beamlines developed in that direction.

As well as the beamlines associated with the IDs mentioned above, two Infrared (IR) beamlines are under development on bending magnet sources. Two beam diagnostic beamlines are also being built.

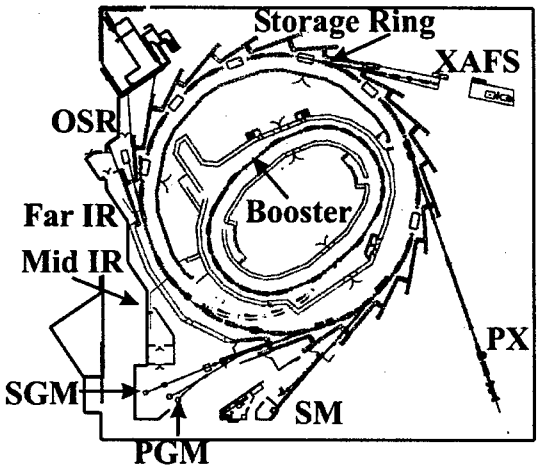

Figure 7. Initial CLS Beamlines. Also shown are the booster and the storage ring (SR1).

CLS STATUS

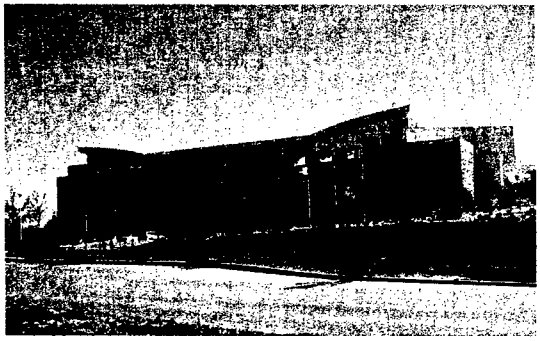

Figure 8. CLS Building.

The CLS building is shown in figure 8. Construction began in 1999 and was completed by the end of 2000. The full energy booster has been installed has was fully commissioned by September, 2002. Installation of the storage ring is expected to be complete by the summer of 2003 when storage ring commissioning will begin. At the same time, the beamlines will be installed for commissioning by the end of the year.

Booster Commissioning

A final result achieved during booster commissioning is shown in figure 9. Signals from the Fast Current Transformer (FCT), the Parametric Current Transformer (PCT) and a dipole field are shown. A 40 mA peak current was injected at 250 MeV and a 20 mA peak current was extracted at 2.9 GeV. Beam losses occur due to inefficient capture in the RF bucket at injection and reduction of relative RF overvoltage at extraction. This is shown by the average current measured by the PCT.

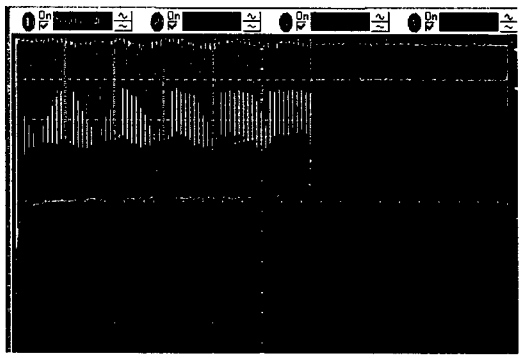

Figure 9. Booster Ramping. Upper: FCT; Lower: PCT (negative signal); Middle: Dipole Field.

REFERENCES

[1] L. O. Dallin, I. Blomqvist, M. de Jong, E. Hallin, D. S. Lowe and R. M. Silzer, "The Canadian Light Source: An Update", PAC2001, p. 2680.

[2] K. Kim, "Characteristics of Synchrotron Radiation", AIP Conference Proceedings 184, p. 565, 1989.

[3] L C. Teng, "Global and Local Horizontal-Vertical Decoupling", PAC'97, Vancouver, p. 1359.

[4] L. O. Dallin, SAL/TM/SYNCH/02 "Design for Synchrotron Light Source at SAL", March, 1994.

[5] L. O. Dallin, SAL/TM/SYNCH/08 "DBA Synchrotron Light Source", March, 1995.

[6] Ingvar Blomqvist, CLS Design Note 5.8.25.3 Rev. 0 " Specification for Chicane Magnets and External Correction Coils ", February, 2003.

[7] L. O. Dallin. D. Lowe and J. Swirsky, "Canadian Light Source Magnets", these proceedings.

[8] T. Y. Lee and L. O. Dallin, CLS Design Note 5.2.36.12 Rev 0 "Distribution of Dipole Gradient Errors in the CLS Storage Ring", January, 2003.

[9] L. Dallin, CLS Design Note 5.2.31.4 Rev A "XY Orbit Correctors", May, 2000.

[10] S. Bauer et al, "Fabrication, Test and First Operation of Superconducting Accelerator Modules for Storage Rings", these proceedings.

[11] L. O. Dallin, "Local Transverse Coupling Control", PAC2001, p. 2677.

[12] L. Praestegaard et al, "Status of the Canadian Light Source Booster Synchrotron", EPAC2002, p. 611.

More is available at the CLS website. See http://www.lightsource.ca/

SUPERBEND UPGRADE AT THE ADVANCED LIGHT SOURCE*

D. Robin† for the Superbend team, LBNL, Berkeley, CA, USA 94720

Abstract

At the ALS there had been an increasing demand for additional high brightness hard x-ray beamlines in the 7 to 40 keV range. In response to that demand, the ALS storage ring was modified in August 2001. Three 1.3 tesla normal conducting bending magnets were removed and replaced with three 5 Tesla superconducting magnets (Superbends). The radiation produced by these Superbends is an order of magnitude higher in photon brightness and flux at 12 keV than that of the 1.3 Tesla bends, making them excellent sources of hard x-rays for protein crystallography and other hard x-ray applications. At the same time the Superbends do not compromise the performance of the facility in the UV and soft x-ray regions of the spectrum. The Superbend will eventually feed 12 new beam lines greatly enhancing the facility's capacity in the hard x-ray region. The Superbend project is the biggest upgrade to the ALS storage ring since it was commissioned in 1993. In this paper we present a history of the project, as well as the installation, commissioning, and resulting performance of the ALS with Superbends.

INTRODUCTION

October 4, 2001 marked the completion of the Superbend Project — the biggest upgrade to Berkeley Laboratory's Advanced Light Source (ALS) since the synchrotron light source was first commissioned for users in 1993. On that day the ALS facility began user operation with three newly installed Superbends and first light generated from one of these Superbends reached the end station of the first Superbend beamline. With the successful completion of the Superbend project the ALS has transformed itself, greatly increasing its capability and capacity to deliver bright hard x-ray beams (up to 40 keV) to users [1, 2, 4, 3]. There has been a large demand for Superbend beamlines. At the time of this conference 7 of the 12 beamlines have been committed — 3 are in operation for protein crystallography and 2 more under construction, 1 beamline is under construction for tomography and 1 for high pressure diffraction. At the end of the year all 7 will be in operation for users. This still leaves 5 beamlines which have yet to be committed. The 3 protein crystallography beamlines which have been in operation for about one year have performed extremely well and have help to solve many protein structures. With the Superbend upgrade the ALS has greatly extended its capacity and capability in the hard x-ray regime.

The ALS was initially designed to be optimized for the generation of radiation from the UV to Soft x-ray range (10 to 1500 eV). Over the years it has developed a strong user community in this spectral region. At the same time, the ALS saw a large growth in a user community outside of this core region — in the hard x-ray region. Prior to the installation of the Superbends there were two sources of hard x-rays: the normal conducting 1.3 Tesla dipoles and a 2 Tesla wiggler. The wiggler beamline which uses 12 keV photons generated from the wiggler proved to be one of the most productive protein crystallography beamlines in the world demonstrating the capabilities of lower electron energy synchrotrons like the ALS to do hard x-ray science [5]. The success of beamline 5 together with the need for more protein crystallography beamlines worldwide [6] fueled the demand for more hard x-ray beamlines at the ALS. There was also a demand from the tomography and powder diffraction communities demanding even higher energy x-rays (up to 40 keV).

Superbends versus Wigglers

There are several types of synchrotron based sources for generating hard x-rays — bending magnets, wigglers, wavelength shifters, or undulators. Due to the relatively low electron beam energy, 1.9 GeV, of the ALS made the generation of 12 - 40 keV photons impractical with an undulator. Therefore the practical choices were bends or wigglers. At an electron beam energy of 1.9 GeV, the and a Superbend field of 5 Tesla, the Superbend beamlines and have a critical photon energy of 12 keV and are a good source of photons up to 40 keV. In principle the ALS could have chosen to use wigglers to generate hard x-rays. However there were many advantages of the Superbends. First, by replacing normal bends with Superbends, none of the few remaining empty insertion device straight sections were used. Second, the Superbends provided a high capacity— up to 12 new beamlines (four from each bend) versus a wiggler that only can support 3 beamlines. Third, it is possible to perform the powerful technique of multiple-wavelength anomalous diffraction (MAD) on 9 of the 12 Superbend beamlines versus only 1 of the 3 wiggler beamlines. Fourth, the Superbends were higher in flux density than the wiggler (due to the smaller electron beam size) making them a superior source of 12 keV photons for protein crystallography [4]. This meant that the experimental beam time is shorter. Fifth, the total radiation power in the Superbend beamlines is significantly smaller than that of the wiggler making the beamlines simpler. All totaled, the Superbend solution was a cost effective way to greatly increase the hard x-ray capability of the ALS facility.

* This work was supported by the Director, Office of Energy Research, Office of Basic Energy Sciences, Materials Sciences Division of the U.S. Department of Energy, under Contract No. DE-AC03-76SF00098.

† DSRobin@lbl.gov

0-7803-7738-9/03/$17.00 © 2003 IEEE

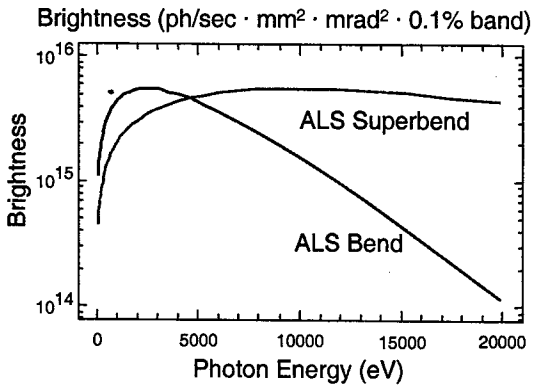

Figure 1: Brightness of a Superbend versus the normal conducting bend

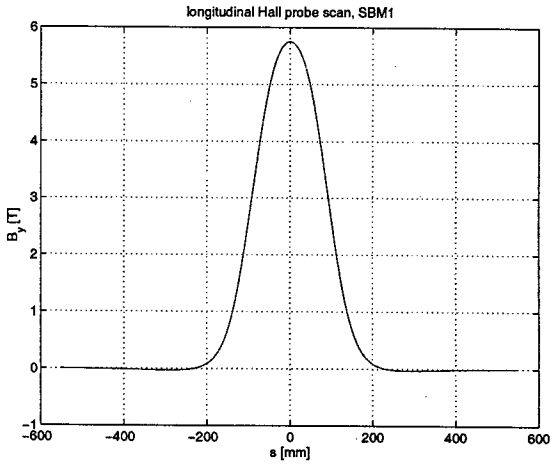

Figure 3: Magnetic field versus longitudinal position at 300 Amps (1.9GeV settings).

Goals and Challenges

The main goal of the project was to modify the storage ring lattice by replacing three of the thirtysix, 1.3 Tesla, normal conducting, 10 degree, bending magnets with three, 5 Tesla, superconducting, 10 degree, bending magnets (Superbends) [9, 10]. This was done by modifying three of the twelve ALS sectors. Fig. 2 shows how each of the 3 sectors was modified to include Superbends. A typical sector without Superbends can be seen in Fig. 2 (top) and one modified to include Superbends is shown in Fig. 2 (bottom). One sees that the central dipole, B2, in the sector is replaced by a Superbend. The Superbend magnetic field versus longitudinal position is plotted in Fig. 3 for the 1.9 GeV settings. The Superbend reaches a peak magnetic field of 5.7 Tesla and is about 5 Tesla at the locations of the four beamlines.

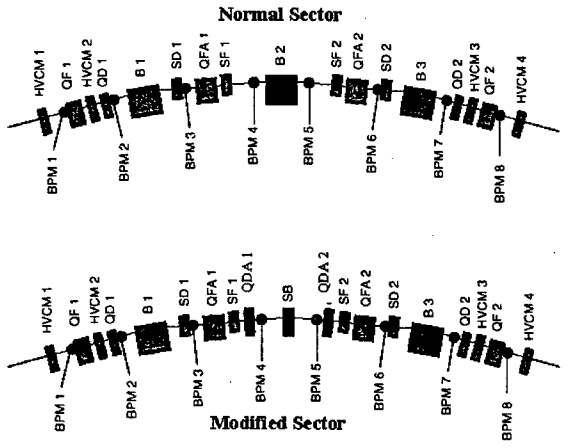

Figure 2: Magnetic layout of a normal (top) and modified (bottom) sector.

Unlike the normal dipoles, the Superbends do not have a quadrupole focusing component. Two new quadrupoles QDA1 and QDA2 are added to the lattice and the QFA quadrupoles in a Superbend sector are put on separate power supplies. It was necessary to make this change in the quadrupole configuration in order to better match the Superbend sectors to the non Superbend sectors to improve the particle beam dynamics.

Choosing Superbends versus wigglers as a source of hard x-rays let the ALS with some unique challenges. This was the first-ever retrofit of superconducting bend magnets into the storage ring of an operating synchrotron radiation source. The Superbends would be an essential part of the storage ring lattice and problems with them not only affect the users of the Superbends but all users at the ALS. Therefore it was necessary to ensure that the transition to Superbend operation was transparent. Superbends needed to be installed and commissioned in a short period and the resulting influence on the existing users should be small. There could be no significant impact on beam orbit stability, fill times, or reliability, brightness, and lifetime.

SUPERBEND PROJECT

The idea of retrofitting the ALS storage rings with high field superconducting magnets to produce hard x-rays was conceived in the early 1990s. In 1995 a project began to see if it was possible design a superconducting coil and core of a magnet that would meet the needs of the ALS [7]. In 1998, based upon the successful tests of a coil and core [8] combined with the increasing demand from the user community, the ALS decided to embark upon the Superbend project [2, 5].

The Superbend project officially began in September 1998 with the formation of the Superbend team. The goal of the team was to ensure a smooth transition to Superbend operation for the existing users. The requirement of a smooth transition drove many of the design choices, some of which are discussed in this paper. The reader is referred

to other publications for more details [9, 10, 11, 12, 13].

Beam orbit stabilty is on of the most critical performance parameters for the users. Before Superbends the ALS integrated rms orbit stability in the insertion device straights was about 3 μm horizontally and 2 μm vertically for a frequency range of 1 - 200 Hz. There were two concerns about Superbend operation effecting the orbit stability. They were that orbit jitter would be caused by fluctuations of the powersupply currents of the Superbend and normal conducting bend magnets causing orbit jitter as well as the vibration of the Superbend cryosystem causing the Superbends and neighboring magnets to vibrate also causing orbit jitter. Prior to installation of the Superbends all 36 normal conducting bends were powered by one power supply. In that case powersupply fluctuations resulted in energy changes but not orbit changes. After the installation of Superbends, power supply fluctuations could cause both energy and orbit changes. Therefore both the tolerances of the cryosystem and power supply were very tight and these systems were extensively tested.

Fill times is another important performance criteria for the users. The ALS does not have a full energy injector and therefore before filling the storage ring the electron energy needs to be ramped from 1.9 GeV down to 1.5 GeV where the ring is filled and the ramped back up to 1.9 GeV. Prior to the Superbend upgrade the ramping time was approximately 1 minute in each direction. The Superbend magnet and cryosystm were designed to ramp within that time without quenching. The power supply and control system for Superbends were designed to coordinated well with the other magnets to minimally distort the beam orbit during ramping.

Reliability is another important performance criteria for the users. The Superbends could not significantly impact the total unscheduled downtime of the accelerator. Reliability strongly influenced the choice of cryosystem. A two stage 1.5 Watt Sumitomo cryocooler was chosen for each magnet. Fig. 4 shows a drawing of the cyrosystem. At the high temperature stage there was a nitrogen reservoir and at the low temperature stage there was a helium reservoir. The magnet was conductively cooled with the cryocooler and high temperature Superconducting leads were used between the nitrogen and Helium stages to minimize the heat leak. In the event of a failure of the cryosystem, the magnets could run on external cryogens with a seemless transition between the two modes. In addition a full spare was constructed which could be exchanged in an emergency.

Precommissioning and Beam Dynamics Tests

In order to ensure that the transition to Superbend operation was transparent, the Superbend team adopted the strategy of precomissioning as many subsystems (with and without beam) as possible prior to the actual installation of the Superbends. Much of the work has been described in previous papers.

To minimize the impact on users, the Superbend installation was split into two medium length (6 week) shutdowns. In the first shutdown (which occurred in March 2000) all major components of the project, excluding the actual Superbend magnets were installed [10]. In the second shutdown (which began in August 2001) the Superbends were installed and commissioned [11].

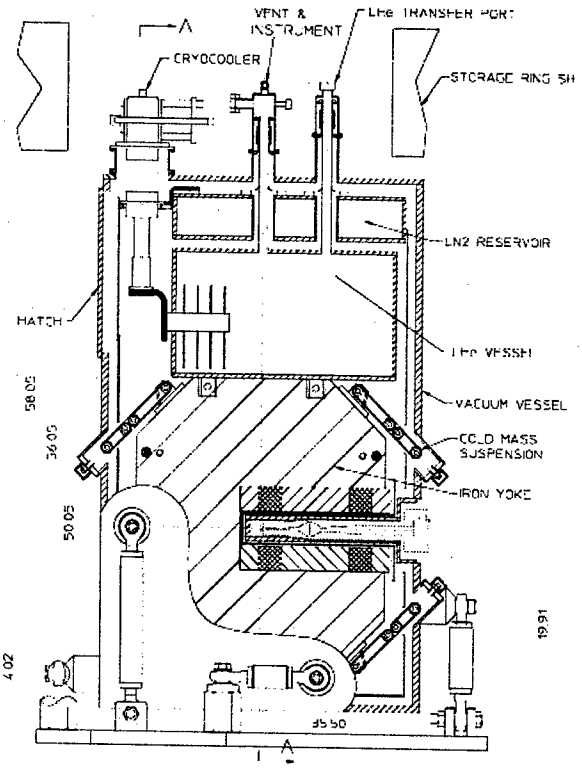

Figure 4: Drawing of the Superbend cryostat and cryocooler

Prior to the Superbend installation, the Superbend systems were extensively modeled and tested. The team performed thorough cryogenic testing [12, 13], magnet measurements [14], vibration testing, powersupply and controls testing [10]. The results of these tests showed that the system was very reliable. During these tests one of the four Superbends was put through the equivalent of 4 years of ramping and cycling with no measurable degradation in cryogenic and mechnical performance. The backup cryogenic system was tested to ensure that the Superbends could transition smoothly to external cryogenic operation in the event of a cryocooler failure [9].

Extensive modeling and measurements were done to ensure that the Superbend upgrade did not impact the lifetime and brightness of the non Superbend users. In terms of brightness, the higher Superbend field necessarily increases the horizontal emittance. Early lattice designs resulted in a doubling of the horizontal emittance. In order not too significantly increase the horizontal emittance, two modifications of the lattice were made. First, finite dispersion

(6 cm) was introduced in the 12 straight sections and second, the QFA and QDAs in the Superbend sectors were adjusted to further reduce the emittance. The result was a small (~20%) increase in horizontal emittance.

Finally the Superbends could not significantly impact the beam lifetime. The lifetime of the ALS is Touchek dominated and the main concern is that the Superbends would break the lattices 12-fold symmetry, to 3 greatly increasing the resonance excitation resulting in larger beam loss.

Extensive beam dynamics studies were performed primarily to accurately predict and minimize the impact of the Superbends on the lifetime and injection efficiency. We built upon experimental and theoretical studies using the technique of Frequency Map Analysis to study the dynamics of particles in the ALS [17, 18]. Fig. 5 shows the dynamic aperture and on-energy frequency map displayed in amplitude space. The diffusion rate of the particles are indicated by the color. Initial conditions of particles with high diffusion are plotted in red and those with low diffusion are plotted in blue. One can see that the dynamics is well behaved horizontally up to 12 mm which is more than sufficient for a 10 mm injection offset of the ALS.

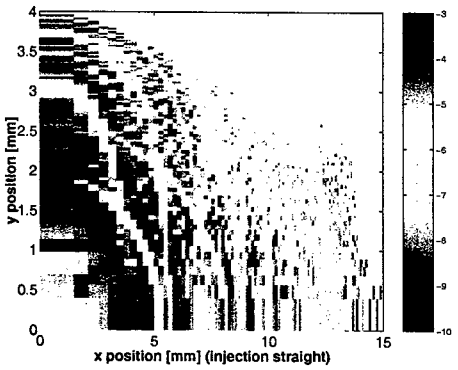

Figure 5: On-energy frequency map of the ALS plotted in amplitude space at the injection point.

The dynamics models were experimentally tested prior to the actual installation of the Superbends. Using the QDA magnets that were installed in the first shutdown, the symmentry of the ring was broken and off energy frequency maps and lifetimes were measured. With the symmetry breaking of the QDAs approximately equivalent to the symmetry breaking due to the Superbends, the dynamic momentum aperture remained close to the RF acceptance at 2.5%. These tests agreed well with our model predictions.

Installation and Commissioning

The installation and commissioning of the Superbends occurred in a 6 week period that began on August 20, 2001 and ended on October 3, 2001. A picture of the first Superbend being installed can be seen in Fig. 6. The installation period lasted for 11 days. During that time 3 normal magnets were removed, 3 Superbends installed, a portion of the injection line disassembled and reinstalled. In addition the new controls, powersupplies, diagnostics, and external cryogenics were installed and tested.

Figure 6: Installation of the first Superbend.

Commissioning began on August 31, 2001 and proceeded faster than expected. First beam was injected within 5 minutes of first attempt, 100 mA stored within 1 hour, first energy ramping with beam later that day, and the impact of the Superbends was evaluated within 2 weeks. The beam was delivered back to users on October 4, 2001 with first Superbend light in the first Superbend beamline. The results of the installation and commissioning are described in detail in another paper at this meeting [11]. During commissioning a lattice with 6 cm dispersion in the straights was adopted. This allowed us to minimize the change in emittance from the Superbends.

Impact of Superbends on the ALS

Looking back one can clearly say that the Superbend project met all, and in many cases exceeded, the project goals. They were installed with no significant impact on the non-Superbend users [11]. Immediately following the installation of Superbends, the lifetime was the same as before, fast orbit stability was the same, slow orbit stability was better, injection and ramping times were comparable and there was a small change in the beam sizes (see Table 1) and no noticable change in brightness. The hard x-ray community is currently making use of the new capabilities and have already achieved some very exciting results [19].

At the time of this meeting it has been nearly 20 months since the ALS Superbend upgrade. In those 20 months the Superbends have been extremely reliable. Superbend system failures have accounted for a small fraction of the total downtime of the ALS. In fact the largest portion of the downtime that was related to operating with Superbends were that the ALS experienced in increase in the failure rate of waterflow meters on photon stops — many of which

Table 1: Comparison of parameters before and after Superbends at the insertion device beamline (.0) and the bend magnet beamlines (.1, .2, .3, .4)

Parameter	Before Superbends	After Superbends
Natural emit.	5.5 rad nm	6.75 rad nm
Energy spread	0.08%	0.1%
Beamline	Hor. beam size	Hor. beam size
x.0	250 μm	310 μm
x.1	50 μm	57 μm
x.2 and x.3	100 μm	100 μm
x.4	60 μm	65 μm
Beamline	Ver. beam size	Ver. beam size
y.0	30 μm	23 μm
y.1	65 μm	54 μm
y.2 and y.3	20 μm	15 μm
y.4	60 μm	52 μm

were located downstream of the Superbends and were presumably failing due to the increased radiation exposure.

The cryosystem has also proven to be very reliable and there has only been one failure. This occurred in March 2003 two weeks prior to a four week scheduled shutdown of the ALS. On one of the Superbends the cryocooler stopped functioning. The Superbends ran with external cryogens for 2 weeks following that failure. The failure resulted in a total downtime of 6 hours. Part of that downtime was due to attempt to restart the cryocooler and part was due to modifications in some controls software to reduce the ramping rate. The operation of Superbends with the cryogens went smoothly with no further downtime. This experience demonstrated the feasibility of operation with cryogens and convinced us that in the case of future failures one should be able to transition between crocooler and cryogenic operation without any downtime.

The three Superbend beamlines have been in production mode for over one year. These initial beamlines were for protein crystallography and have solved more than 200 structures. The performance of the beamline compares favorably to the wiggler beamline. Two more protein crystallography beamlines, a tomography beamline and a high pressure diffraction beamline will be in operation before the end of this year. So this has greatly expanded the capability of the ALS in the hard x-ray regime.

ACKNOWLEDGEMENTS

The author would like to thank the members of the Superbend team for their outstanding effort in ensuring the success of the project. The author would also like to thank the management of the ALS and AFRD divisions for their support and encouragement.

REFERENCES

[1] B. G. Levi, "Gamble Pays Off at the Advanced Light Source", Physics Today (2002), January; 55, pp. 17

[2] D. Robin, A. Robinson, L. Tamura, "Superbends expand the scope of Berkeley's ALS", CERN Courier, (2002), March; Vol. 42, No. 2, pp. 28-31

[3] D. Robin et.al. "Successful Completion of the Superbend Project", Proceedings of the 2002 European Particle Accelerator Conference, (2002) pp. 215-217

[4] L. Tamura and A. Robinson, "Superbends Era Begins Swiftly at the ALS", Synchrotron Radiation News, (2002); Vol 15, No. 1, pp. 30-34

[5] R. Service, "Upgrade Brings Hope to Berkeley's Advanced Light Source", Science (1999) August 27; 285, pp. 1344

[6] R. Service, "Wiggling and Undulating Out of an X-ray Shortage", Science (1999) August 27; 285, pp. 1342-1346

[7] C. E. Taylor and S. Caspi, "A 6.3 T Bend Magnet for the Advanced Light Source", IEEE Trans. Magnetics 32, No. 4, (1996), pp. 2175-2178

[8] C. E. Taylor, et al., "Test of a High-Field Magnet for the ALS", Transactions on Applied Superconductivity 9, No. 2, (1999), pp. 479-482

[9] "Superbend Magnet System Conceptual Design Report", Lawrence Berkeley National Laboratory Publication, PUB-5457, Apr. (2000)

[10] D. Robin, et al., "Superbend Project at the Advanced Light Source", Proceedings of the 2001 IEEE Particle Accelerator Conference, Chicago, 2632 - 2634 (2001)

[11] C. Steier, et al., "Commissioning of the Advanced Light Source with Superbends", European Particle Accelerator Conference, 754 -756 (2002)

[12] J. Zbasnik, et al., "Test of a GM cryocooler and high Tc leads for use on the ALS Superbend magnets", Published in the proceedings of the (1999) CEC, Montreal, July 1999

[13] J. Zbasnik, et al., "ALS Superbend Magnet System", IEEE Trans. on Applied Superconductivity, Vol. 11, No. 1, March, (2001), pp. 2531-2534

[14] S. Marks, et al., "ALS Superbend Magnet Performance", Published in the proceedings of the 17th International Conference on Magnetic Technology, Geneva, (2001)

[15] S. Caspi, M. Helm, and L. J. Laslett, "The use of harmonics in 3-D Magnetic Fields", IEEE Trans. Magn. Vol. 30, No. 4, (1996)

[16] H. Nishimura and D. Robin, "Impact of Superbends at the ALS", Proceedings of the 1999 IEEE Particle Accelerator Conference, New York, (2001) pp. 203 - 205

[17] D. Robin et al., "Global dynamics of the Advanced Light Source revealed through experimental frequency map analysis"Phys. Rev. Lett., 85, pp. 558, (2000)

[18] C. Steier et al., "Measuring and Optimizing the Momentum Aperture in a Particle Storage Ring", Phys. Rev. E 65, 056506 (2002)

[19] See for example G. Rudenko et. al., Science **298**,2353 (2002) and E. Yu. Science **300**, 976 (2003)

PROGRESS REPORT ON THE CONSTRUCTION OF SOLEIL

M.P. Level, J.M. Filhol P. Brunelle, R. Chaput, A.Daël, J. C. Denard, C. Herbeaux, A. Loulergue, O. Marcouillé, L. Nadolski, R. Nagaoka, J.L. Marlats, P. Marchand, A. Nadji, M.A. Tordeux,
Synchrotron SOLEIL, L'Orme des Merisiers Bât. A, St Aubin, BP 48 – 91192 Gif-sur Yvette cedex (FRANCE)

Abstract

The construction phase of SOLEIL, the French third generation Synchrotron radiation Source has begun in January 2002 with the aim of starting Users operation in spring 2006. The machine now consists in a 354 m circumference ring, with 16 DB cells and 24 straight sections. The optics, with distributed dispersion, features a low 3.7 nmrad emittance at the 2.75 GeV operating energy, so as to provide high brilliance, from the VUV up to the hard X ray domain. In order to provide a long lifetime (18 hours), and beam position stabilities in the micron range, significant attention was paid at each design stage (optics, magnets, beam position monitors, vacuum and RF systems,..), including on the design of the building, the construction of which will start in summer 2003. All the magnets have been designed and are in the last stage to be ordered. The qualification of the 352 MHz super-conducting RF cavity prototype has been done on the ESRF ring. Insertion devices are being designed with the goal of serving a very large scientific community with high performances in an energy range as large as 5 eV to 18 keV with undulators. The contract was placed for the 100 MeV Linac for a delivery summer 2004.

1 INTRODUCTION

Since the beginning of 2001, a new SOLEIL team has being constituted and the detailed design has been finalised. The construction period (phase 1), has started in 2002 with the goal of completing the commissioning of the machine and of the 10 first beamlines beginning of 2006 followed by a gradual installation of 14 other beamlines in parallel to operation up to 2009 (phase 2). Due to the new scientific context as well as new developments and studies, improvements have been brought to several parts of the SOLEIL equipment.

2 LATTICE

The lattice consists of 16 DB cells and 4 super periods in which the 2 central cells are modified to create 2 additional straight sections (3.6m) by drifting apart the two quadrupole doublets located in-between the two bending magnets of the cell [1]. The machine provides now 24 straight sections (4x12m, 12x7m, 8x3.6m) among which 20 are dedicated to install insertion devices (one long straight is necessary to locate the injection equipments, two medium straights will be occupied by the super-conducting RF cavities and a short straight is reserved for diagnostics and feedbacks). Figure 1 shows the optical functions of one of the four super periods and the table 1 gives the main parameters.

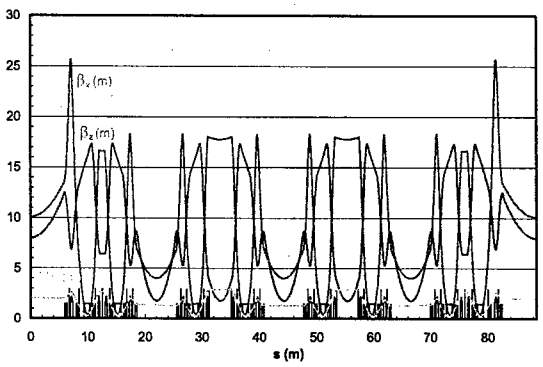

Fig. 1 Lattice and optical functions for one super period of the storage ring

Table 1 Main parameters of the storage ring

Energy	2.75 GeV
Circumference	354.097 m
Horizontal emittance (rms)	3.73 nmrad
N. of cells / N. of super periods	16 / 4
Straight sections	12 m x 4 ; 7 m x 12 ; 3.6 m x 8
Betatron tunes, ν_x / ν_z	18.2 / 10.3
Chromaticities ξ_x / ξ_z	- 2.84/- 2.23
Momentum compaction	4.38×10^{-4}
Energy dispersion	$1.016\ 10^{-3}$
Radio Frequency	352.202 MHz
Peak RF Voltage	4.8 MV
Max energy loss per turn (IDs)	1 300 keV
Design current (416 bunches)	500 mA

A good dynamic acceptance is achieved even for large energy deviation (up to 6%) thanks, among others, to a small variation of the tune with energy.

Beam dynamics was computed, using a full 6D tracking code (extension of TRACY II) which allows to take into account non linear betatron and synchrotron motions, synchrotron radiation and coupling from horizontal to vertical plane [2]. As predicted, due to the low value of the first order and the relatively high value of the second order of the momentum compaction the dynamics is dominated by the non linear synchrotron motion. Moreover it has been shown that the 1% coupling induces vertical betatron amplitudes from Touschek scattering which lead to losses in small vertical gaps undulators. In order to avoid this effect a new working point, a little more far away from the coupling resonance, has been chosen.

For 500 mA distributed in 416 bunches, the Touschek lifetime calculated with natural bunch length, 1%

0-7803-7738-9/03/$17.00 © 2003 IEEE

coupling and 5mm aperture in short straight section (undulator of 1.8 meter long) is $\tau_{T1/2}$ = 36 h. Combined with a vacuum lifetime of 27 h for a pressure of 10^{-9} mbar, this gives a total beam lifetime of approximately 18 h.

3 MAGNETS

All the magnets have been designed with 3D model on TOSCA code. For dipoles (1m magnetic length and 5.36m bending radius) the H structure has been preferred in order to reduce the effect of saturation due to the high 1.71T field value. The main parameters of the quadrupoles and sextupoles are:

	Quadrupoles	Sextupoles
Number	132 / 28	88* / 32**
Length (mm)	320 / 460	160 mm
Bore (mm)	66 mm	73 mm
Force	19 T/m / 23 T/m	320 T/m²
Useful Zone	35 mm	35 mm

For the quadrupoles (figure of 8 structure), the profile have been very well optimised leading to very small multipolar components: respectively 9 10^{-6} and –5 10^{-5} for the 12 poles and the 20 poles expressed in ΔB/B at 30 mm. The sextupoles include horizontal and vertical dipoles correctors (respectively 7 mTxm and 4.4 mTxm) as well as skew quadrupoles (51.2 mT). They are compacts (*) or with ears (**) following their position in the cell in order to allow Xray extraction lines.

Contracts have been placed for dipoles, quadrupoles and sextupoles.

4 ULTRA VACUUM SYSTEM

In the dipole vacuum chamber, the 12 kW power and the power density (~ 200 W/mm² at normal incidence) to be dissipated are relatively high due to the short bending radius. It requires a combination of two absorbers, a crotch absorber in the antechamber part followed by a longitudinal absorber. Based on the ANKA design, the cooling system of the crotch has been improved by spreading the power on 3 rows of teeth cooled by six water channels for each jaw.

Material will be stainless steel 316LN for dipole vessels, BPMs and bellows and aluminium 6061 for all straight part of the machine (quadrupoles, sextupoles and insertions). All Aluminium vacuum chambers will be coated with NEG (Ti, Zr, V). The main advantage is a very low photon stimulated desorption rate after activation of the NEG which leads to an estimated conditioning time of 23Ah to reach a 10^{-9} mbar average pressure instead of 730 Ah for uncoated stainless steel. The effect on the machine impedance has been evaluated. The resistive wall instability threshold (multibunch mode) would not be modified but the transverse mode coupling one (single bunch mode) might be lower specially for narrow gap insertions. Further investigation will be done.

5 RF SYSTEM

The superconducting HOM free RF prototype was tested in 2002 on the ESRF storage ring. It generated in stable and reliable conditions, a peak RF voltage of more than 3 MV, with a power of about 200 kW through each main coupler [3]. This level of performance corresponds to the SOLEIL requirements for the first year of operation starting in 2005, therefore, it was decided that this prototype will be the first RF cavity. It will be installed after some modifications to reduce some over heating of the dipole type HOM couplers and undue high static cryogenic losses. In parallel, the design of a second cryomodule integrating all the prototype experience has been launched.

For the 352 MHz power source, after an extensive study of the different technological options, solid state amplifier based on the technology developed at LURE and already chosen for the booster, have been adopted. Each cavity will be powered by a 200 kW (4x 50 kW) amplifier which is constituted by about 750 modules. Many advantages as reliability, easy maintenance, simple start-up procedures (no high voltage) etc. are expected. The booster transmitter is already under construction and the manufacture of the storage ring modules will be launched very soon.

6 INSERTION DEVICES

Among the proposed ID beamlines, six IDs of four different kinds have been identified to begin operating for the commissioning of SOLEIL (phase 1). Table 2 presents their principal characteristics and Figure 2 shows the expected brilliance performances.

Table 2: Principal characteristics of the IDs

	HU640	**HU256**	**HU80**	**U20**
Numb.	1	1	1	3
Energy	5 – 40 eV	10 – 1000* eV	80 –1500* eV	3 – 18 keV
Type	Electro.	Electro.	Apple II	Hybrid in vacuum
Polar.	Circ./Lin. variable	Circ./Lin.	Circ./Lin.	Linear
Min. gap	19 mm	15 mm	15 mm	5.5 mm
Period	640 mm	256 mm	80 mm	20 mm
N. per.	14	14	21	90
B_{xmax} B_{zmax}	0.09 T 0.11 T	0.275 T 0.400 T	0.76 T 0.85 T	- 1.03 T
S. Sect.	Long	Medium	Medium	Short

For these two beamlines, the large energy range to be covered requires one additional undulator (respectively HU60 and HU40) which will be built later.

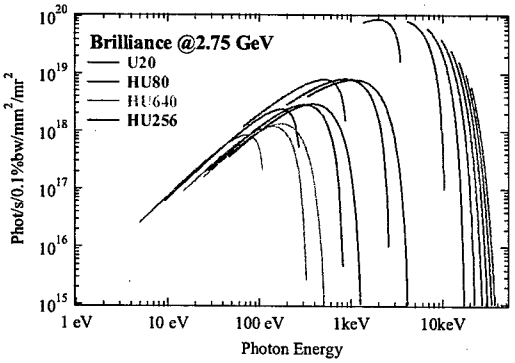

Fig 2: Brilliance phase 1.

The elliptical undulator HU640

HU640 is designed to produce any kind of polarization from linear to circular by tuning the values of the vertical and horizontal components of the field (resp. Bz and Bx) and by varying the phasing between both components. The magnetic structure is composed of three sets of coils (red, blue and green in the figure 1). Green coils produce the horizontal components Bx. Blue and red coils which are shifted each other by a quarter of period, produce Bz. HU640 can be switched rapidly (rising time of 0.2 s from -Bxmax to +Bxmax) at a repetition rate of 1 Hz

Both Bz and Bx are produced by air-coils in order to avoid cross talk between components. The operation of the ID is then completely linear with the currents injected in each set of coils.

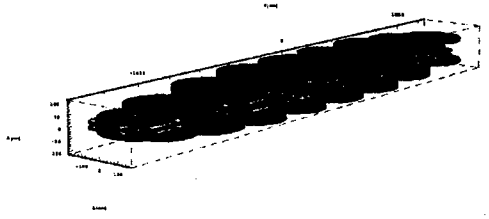

The elliptical undulator HU256

As the horizontal field required for vertical polarization is relatively high (0.275T), no existing model are available, so an original design has been proposed, taking into account that the design of the vacuum chamber (made in aluminium with NEG coating) does not need any opening in the medium plan. The magnet assembly is constituted by an alternated succession of 28 vertical dipoles and 28 horizontal dipoles, magnetically independent.

The call for tender for these 2 undulators will be launched in July 2003.

7 BEAM POSITION STABILITY

In order to avoid differential settlement between the experimental hall and the ring tunnel) the chosen solution consists in an unique slab (0.80 m thick) for storage ring and experimental hall, built on simple piles (548) anchored down to the sand layer at - 15 m. The stability specifications are satisfied: For example, when a new beamline is installed, the total static deformation of the neighbouring beamline and of the nearest point of the ring will be less than 40 μm.

The girders have been carefully designed both for static specifications and dynamic specifications (3 jacks with locking system) with its first resonance mode higher than 40 Hz in order to avoid any amplification of technical or cultural noise.

For both slow and fast orbit feedbacks we select a new type of BPMs (electronics DSP based) developed by I-Tech company. This system combines the advantages of 4 channels system (first turns and turn by turn measurements) and those of electrode multiplexing system (good intrinsic stability and low sensitivity to beam current and bunch pattern) thanks to a new automatic calibration scheme proposed by SOLEIL.

8 TOP UP INJECTION

The injector system, composed of a 100 MeV electron LINAC followed by a full energy (2.75 GeV) booster synchrotron has being designed in view of top-up injection:

- The LINAC specifications have been defined in order to be able to compensate a lifetime as bad as 4 hours by injecting one pulse every 2 min. The contract has been placed in October 2002, first tests are expected in December for a commissioning in summer 2004.
- The booster design (22 FODO cells with 36 dipoles) provides a 150 nmrad emittance . The power supplies (switching type with digital regulation loop following the SLS concept) work at 3 Hz frequency and can be operated on a single pulse basis.

The dipoles are under construction and the calls for tenders for multipoles have been launched beginning April. All injection/extraction elements designs are finalised.

9 REFERENCES

[1] M.P. Level et al., "Status of the SOLEIL Project," EPAC 2002, Paris, France, 212 (2002).

[2] M. Belgroune et al., "Refined tracking procedure for the SOLEIL energy acceptance calculation," this conference.

[3] J. Jacob et al., "Successful beam test of the SOLEIL SC HOM free cavity prototype at the ESRF ring," this conference.

PROGRESS WITH THE DIAMOND LIGHT SOURCE PROJECT

R.P. Walker, Diamond Light Source Ltd., Rutherford Appleton Laboratory, UK,
on behalf of the DLS and CCLRC Diamond Project Team staff

Abstract

The current status of the detailed design and construction of the UK's new 3rd generation light source, Diamond, is described.

INTRODUCTION

The Diamond Light Source is a new medium-energy high brightness synchrotron light facility which is under construction on the Rutherford Appleton Laboratory site in Oxfordshire, U.K. The evolution and progress of the Diamond project has been reported regularly at accelerator conferences [1,2,3]. The basic design is contained in the Design Specification Report which was published in June 2002 [4]. Table 1 lists the main parameters of Diamond. Injection of the storage ring is by means of a 100 MeV Linac and full energy booster synchrotron.

Table 1. Main parameters of the Diamond storage ring

Energy	3 GeV
Circumference	561.6 m
Lattice	24 cell DBA 6 fold symmetry
Current	300 mA
Lifetime	> 10 h
Emittance (H,V)	2.7, 0.03 nm
No. of straights available for insertion devices	22

At the end of March 2002 Diamond Light Source Ltd. was formed under a Joint Venture Agreement between the UK Government and the Wellcome Trust and the project moved into the construction phase, with an approved, fixed, budget for the facility which includes an initial complement of 7 insertion device beamlines. Significant progress has been made since then with detailed design, specification and procurement, in line with the agreed project plan which is based on starting user operation in January 2007. The first contract for the machine has been let (the Linac) and Calls for Tenders have been issued for the storage ring quadrupoles, superconducting cavities and amplifiers.

BUILDINGS AND FOUNDATIONS

The consultants for the design of the buildings and services, JacobsGIBB Ltd., were appointed in January 2002. Scheme design was completed in July 2002 and detailed design is now complete in some areas and close to overall completion. This has required a great deal of interaction with the machine team to define details of the layout of the machines and transfer lines, and in particular the radiation shielding, personnel labyrinths, control and instrumentation areas and service routes etc. Figure 1 shows the overall layout.

In January this year the Main Contractor, Costain Limited, was appointed under a two-stage contract. The first-stage covers the enabling works (and other services) which started on-schedule in March 2003. The main works are due to start in October 2003. A key date for the project as a whole is the start of machine installation which is scheduled for September 2004.

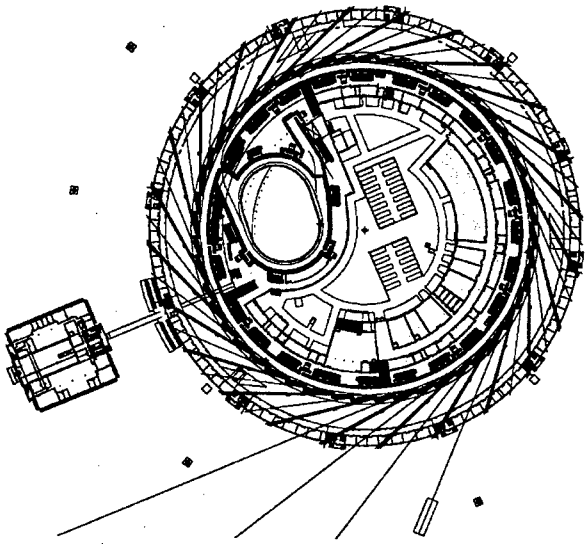

Figure 1. Layout of the Diamond Light Source

One of the design development areas that has involved a close interaction with both machine and beamline designers has been the issue of the foundations. It has been known for some time that extensive piling would be necessary to achieve the tight specification on differential settlement which was originally set at 0.1 mm/10m/year for the storage ring (0.25 mm for the experimental hall). During 2002 a detailed set of site investigations was carried out involving cone penetration tests, trial boreholes, test piles, analysis of soil samples etc. to gain further information about the nature and variability of the subsoil on the Diamond site. In addition, measurements of response to various dynamic excitations were made in order to calibrate a numerical model that was used to determine the relative merits of different foundation solutions in terms of vibration behaviour. In parallel with this, various simulations of the effect of settlement on the machine [5] and beamlines were made.

The results of this work confirm that even to achieve a settlement performance that is within an order of magnitude of that originally specified a piled solution is

0-7803-7738-9/03/$17.00 © 2003 IEEE

necessary. The next most significant factor in determining the performance of the foundation is whether a deliberate void is formed between the slab and the piles. A compromise is necessary between better static behaviour (favouring a void to isolate the slab from the shrink/swell movement of the ground) and dynamic behaviour (favouring direct contact between the slab and the ground to reduce vibrations). The final choice is to include a void, since contact with the ground can also lead to an unwanted localised upward heaving between the piles, the "pincushion" effect, introducing significant angles which could adversely affect both machine and beamline operation. A moderately thick slab (600 mm for the experimental hall) and close pile spacing (3 m) were then chosen, particularly to improve the dynamic behaviour, but which also serves to reduce differential settlement. Finally, to avoid the introduction of localised differential movements between source and experiment, the experimental hall and storage ring tunnel slabs will be joined.

LINAC

Table 2. Main parameters of the Diamond Linac

Energy	100 MeV
Multibunch charge	≥ 3 nC
Multibunch length	300 ns
Single bunch charge	≥ 1.5 nC
Normalised Emittance (1σ)	≤ 50 mm mrad
Energy spread (total)	≤ ± 1.5 %

The 100 MeV Linac pre-injector will be supplied by ACCEL Instruments GmbH under a turn-key contract. DLS will however supply vacuum, controls and diagnostic equipment in order to standardise components across the facility. The main parameters of the Linac are given in Table 2. Single- and multi-bunch modes of operation will be provided and both of these will be possible in top-up mode, with charges as low as 50 pC, and with flexible pulse formats, within the maximum repetition rate of 5 Hz.

BOOSTER

An outline booster lattice design was presented in [4,6] based on a two-fold symmetric 44-cell FODO structure with 8 missing magnets, producing zero dispersion regions for injection (single-turn on-axis), extraction (single-turn), RF and diagnostics. Since then the design has been refined in much greater detail, in particular to define aperture requirements and study non-linear dynamics including the effects of eddy-current induced sextupole fields. A small change has also been made in circumference to optimise synchronisation with the storage ring. The main parameters of the booster are given in Table 3.

The aperture calculations take into account beam size and residual closed orbit errors after correction of magnet alignment errors, and include further allowances for tune point variation, effects of ground motion and other effects. This results in a beam-stay-clear (BSC) aperture (total) in the dipoles of 44 mm (horizontal) x 16 mm (vertical). Dynamic aperture calculations including the effect of induced eddy currents show that a thin-walled vessel is not needed and that a 1 mm stainless steel vessel can be used even at the nominal cycling frequency of 5 Hz (see Fig. 2). Taking into account suitable shape and alignment tolerances leads to a nominal vacuum vessel internal dimensions of 46 x 17.2 mm and a final magnet gap, including a 0.3 mm thick layer of material for electrical isolation, of 21 mm.

Table 3. Main parameters of the Diamond Booster

Peak Energy	3 GeV
Circumference	158.4 m
Lattice	44 cell FODO 8 missing dipoles
Current (max)	6 mA
Tunes	7.16, 4.11
Chromaticity	-0.3, -6.2
Emittance (3 GeV)	135 nm rad

In the straight sections a constant aperture will be used defined by the maximum in the F and D quadrupoles. The resulting BSC is 50.4 x 17.8 mm. Internal vacuum vessel dimensions of 52 x 24 have been chosen to produce a more readily achievable vacuum vessel cross-section without affecting the magnet inscribed radius. Allowing for a 1 mm gap between vessel and poles leads to inscribed radii of 21 mm in the quadrupoles and 24 mm in the sextupoles. Dimensions in the injection and extraction regions have not yet been finalised.

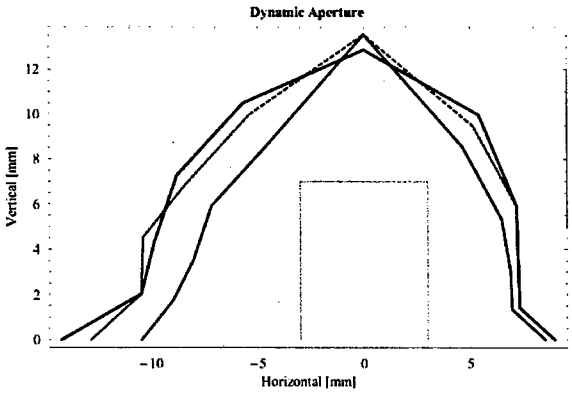

Figure 2. Dynamic aperture in the booster at injection energy and zero chromaticity, taking into account eddy current fields, for on-momentum (red) and off-momentum (-1.5 %, black, + 1.5 % blue) particles. The reference point is at the symmetry point in the region of zero dispersion. The box indicates the required aperture for beam size.

Outline magnet designs based on these apertures have now been produced and vacuum calculations performed to demonstrate feasibility of the proposed pumping scheme. An outline engineering layout of the magnets and vacuum system has also been produced, covering everything except the injection, extraction and RF cells. A Call for Tender for these magnet and UHV vacuum assemblies, mounted on ready-to-install girders which make up 137 m of the booster circumference, will soon be made. Figure 3 shows the outline design for one such assembly. This strategy was chosen in order to make best use of the limited in-house resources, while still allowing DLS to maintain control of the overall system and profit from specialised manufacture for the injection and extraction elements, power supplies, RF system, controls and diagnostics etc.

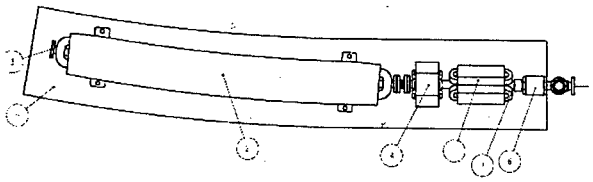

Figure 3. Booster magnet and vacuum assembly unit.

The outline magnet designs are sufficient to fix the power supply parameters and allow procurement to proceed in parallel. The power supplies will be of a switched-mode type to enable the flexibility needed for top-up injection. Since the resulting peak output voltage of the dipole supply of 2.05 kV is quite high (with the nominal peak current of 870 A for 3 GeV operation plus a 10 % working margin and assuming a biased-sine wave excitation at 5 Hz), cost and reliability issues become a concern and so a reduction of the repetition rate is presently under consideration.

STORAGE RING

A change in philosophy of the engineering layout has recently been agreed, namely to incorporate the dipole magnets on the girders whereas they were previously separate. This has several advantages such as allowing more pre-assembly work, minimising the number of handling operations in the ring building, improving relative alignment of the dipoles and crotch vessels with respect to the straights, and easing the design and operation of motorised girder positioning system. It also reduces the number of vacuum connections to be made between externally baked assemblies from 4 to 2 in each achromat. The design philosophy remains that there will be no in-situ bakeout (except of ID vessels), as discussed and reconfirmed at a recent international workshop [7]. Figure 4 shows the largest of the modified girders, 6 m long and weighing an estimated 16.7 T. Further work has also been carried out to refine the pumping scheme. Figure 5 shows the layout of the vacuum system for a complete achromat, with manual valves to allow future front-end installation without letting-up the ring.

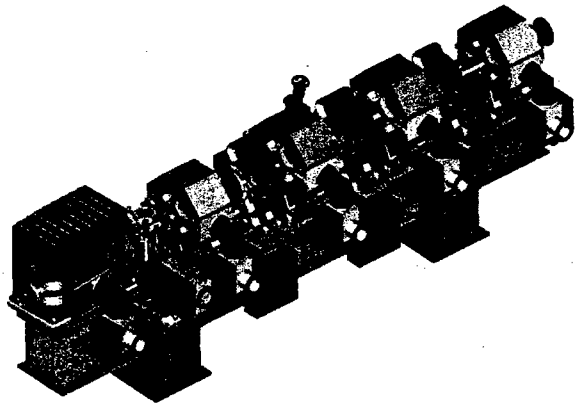

Figure 4. Extended storage ring girder assembly

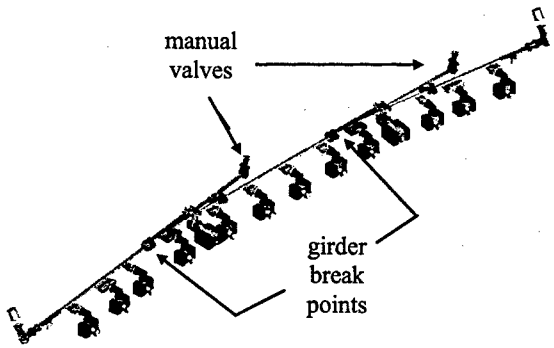

Figure 5. Vacuum system assembly for one achromat.

REFERENCES

[1] M.W. Poole et al., "Evolution of the Diamond Light Source", Proc. EPAC 2000, Vienna, p. 280.

[2] J.A. Clarke et al., "The Diamond Project: an Advanced Light Source for the UK", Proc. PAC 2001, Chicago, p. 227.

[3] V.P. Suller, "Status of the Diamond Light Source Project", Proc. EPAC 2002, Paris, p. 757.

[4] "Diamond Synchrotron Light Source: Report of the Design Specification", CCLRC, June 2002.

[5] J.K. Jones, "Slow Ground Motion Modelling of Diamond", this Conference.

[6] D.J. Scott et al., "A Revised Diamond Booster Design", Proc. EPAC 2002, Paris, p. 617.

[7] R.J.Reid et al., "Summary Report of the Diamond Vacuum Workshop", Sep. 2002, ASTeC Vacuum Science web site: http://www.astec.ac.uk/vacsi

SPEAR 3 UPGRADE PROJECT: THE FINAL YEAR[†]

R. Hettel, R. Akre, S. Allison, P. Bellomo, R. Boyce, L. Cadapan, R. Cassel, B. Choi, W. Corbett, D. Dell'Orco, T. Elioff, I. Evans, R. Fuller, A. Hill, D. Keeley, N. Kurita, J Langton, G. Leyh, C.Limborg, D. Macnair, D. Martin, P. Mcintosh, E. Medvedko, C. Ng, I. Nzeadibe, J. Olsen, M. Ortega, C. Pappas, S. Park, T. Rabedeau, H. Rarback, A, Ringwall, P. Rodriguez, J. Safranek, H. Schwarz, B. Scott, J. Sebek, S. Smith, T. Straumann, J. Tanabe, A. Terebilo, A. Trautwein, C. Wermelskirchen, M. Widmeyer, R. Yotam, K. Zuo
SSRL/SLAC, Stanford, CA 94309, USA

Abstract

During April, 2003, the SPEAR 2 storage ring, which served the high energy physics community from 1972 to 1987, and the synchrotron radiation community for an additional 15 years, was removed from its shielding tunnel in order to install the new 3-GeV, 500-mA SPEAR 3 light source. From May to November, SSRL will excavate the tunnel floor and pour a new concrete floor, and then install pre-assembled girders holding magnets, copper vacuum chambers, PEP-II-style rf cavities, and beam line front end components. At the same time, power supply, instrumentation and control, and other ancillary systems will be configured, leading to a commissioning period beginning in November 2003. The progress of accelerator component implementation and installation during the final year of the project will be reviewed.

1 OVERVIEW

The SPEAR 3 upgrade project [1,2] is in its final year with commissioning scheduled to begin in November 2003. The new ring, with basic parameters summarized in Table 1, will provide one to two orders of magnitude higher performance than SPEAR II and will benefit the materials science, molecular environmental science, structural molecular biology and macromolecular crystallography communities. The 4-year, 58 M$ SPEAR 3 upgrade project is administered by the DOE, with ~50% joint funding from NIH. Now >85% complete, the project will completely replace the tunnel floor, rafts, vacuum chamber, magnets, RF, power supplies and cable plant in a 7-month shutdown period that began March 31.

At this writing, the SPEAR 2 storage ring no longer exists. All SPEAR 2 magnet girders, vacuum chambers, power supplies, and most cables and controls have been removed from the SPEAR site (Fig 1). Shielding, utilities and other ancillary systems have already been modified, and a large fraction of the new cable plant has been installed in trays outside the tunnel. Modified transport line components and a new septum magnet are nearly complete and will enable 3-GeV injection. The 10-Hz booster synchrotron, which has been operating for 2.3-GeV injection since 1990, has been modestly upgraded for 3-GeV operation. The progress and difficulties of SPEAR 3 ring implementation are discussed below.

Table 1: Parameters for SPEAR 2 and SPEAR 3.

	SPEAR 2	SPEAR 3
Energy	3 GeV	3 GeV
Current	100 mA	500 mA
Emittance (w/ID)	160 nm-rad	18 nm-rad
RF frequency	358.5 MHz	476.3 MHz
RF gap voltage	1.6 MV	3.2 MV
Lifetime @ Imax	30 h	>17h
Critical energy	4.8 keV	7.6 keV
Tunes (x,y,s)	7.18,5.28,.019	14.19, 5.23, .007
e- σ (x,y,s) - ID	2.0,.05,23 mm	0.43,0.3,4.9 mm
e- σ (x,y,s)-dipole	.79,.20,23 mm	.16,.05,4.9 mm
Injection energy	2.3 GeV	3 GeV

Figure 1: Removal of SPEAR 2 magnet/chamber girders.

2 ACCELERATOR SYSTEM PROGRESS

All of the 36 gradient dipoles [3], 94 Collins-type quadruoles, 72 sextupoles and 108 H/V corrector magnets, plus spares for each, have been received from IHEP, Beijing, magnetically measured, fiducialized, and are presently being installed on support rafts (Fig. 2).

[†]Work supported in part by Department of Energy Contract DE-AC03-76SF00515 and Office of Basic Energy Sciences, Division of Chemical Sciences.

With a few modifications to fabrication methods, which included a small change to the quadrupole pole chamfer (Fig. 3), the magnets met or exceeded specification. Current-to-field transfer functions have been derived for each magnet family and fitted with 5th-order polynomials to be used for control. A ~2% reduction in the measured 15Q transfer function accounts for field truncation by nearby corrector field clamp shields. Magnetic measurement of the vertical Lambertson septum magnet is in progress; the end-field mirror plate is being modified to minimize field leakage (towards a goal of <10 G-m).

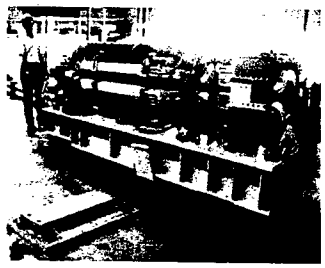

Figure 2: Magnet raft on installation rollers. Grouted mounting plate in foreground.

Figure 3: Sub-mm cut in quad chamfer reduced n =6 multipole to $<5x10^{-4}$.

Production and bake-out of 56 copper girder vacuum chambers was successfully completed in April. The height of the slot between beam duct and antechamber, which is critical to minimize the risk of damage from mis-steered ID synchrotron radiation (SR), was held to ±1.75 mm per horizontal surface, measured using a novel device that utilized optical tooling to scan the inside walls of the completed chamber. The orbit interlock trip level was modified for an effective slot height of ~8 mm to accommodate vacuum deflection, alignment tolerances and measurement uncertainties. Additional engineering analysis was required during the production of these chambers to reduce stresses in the welds. Unanticipated, large hard plane bows from the machining of the copper created a need to optimize the machining process, welding set-up and bulk material production. Late beam position monitor (BPM) design changes coupled with a change in manufacturing facility resulted in a less robust unit than its PEP-II predecessor. Extensive weld parameter development limited stresses in the BPMs. Fabrication of straight section chambers and components is in progress or complete, including 3 new copper-plated ID chambers, septum chamber, injection kickers, tune driver, PPS-beam stoppers, DCCT [4], low-Z drift, transition chambers and 6 styles of rf-shielded bellows modules.

Figure 4: BM1 chamber after bake-out.

The PEP-II LER titanium sublimation pump design was adapted for this machine. Due to space constraints a smaller 8"-diameter pump was designed and the filament was reoriented from vertical to horizontal to increase the pump fin surface area that was exposed to Ti deposition. Delivery of the 4 PEP-II-style rf cavities from Accel in Germany was delayed because of welding-induced leakage problems with the copper plating that covers the water cooling channels. The problem was resolved by replacing the "brightened" copper plating, which contains an additive to form very small grain size that produces a hard, easy-to-machine coating, with pure copper plating, as was done for the original PEP cavities (Fig. 5). Three cavities from have now been received at SLAC, and two have been tested at full voltage (850 kV) with HOM loads and waveguide windows. Other rf system components are being installed, including the HV power supply (which had problems with oil leaks in the optically triggered crowbar SCRs), 1.2 MW klystron (which required repair after operation at PEP-II), and digital low-level control system (which had to be redesigned by an "emergency" task force to overcome the unavailability obsolete parts after the original designers left SLAC).

Figure 5: RF cavity body plated with leaky "brightened" copper (left) and leak-tight pure copper (right).

All magnet power supplies (1- MW dipole supply, 6 large supplies (~100 kW) for magnet strings, 80 intermediate supplies (~10 kW) for individual magnets, and 150 bipolar supplies for correctors and ID trims) have been delivered and are being tested. These supplies use IGBT chopper technology and are digitally controlled. The 3 IGBT kicker magnet induction pulsers (Fig. 6) are also complete and tested. The pulsers, intermediate and bipolar supplies are being pre-assembled in racks to reduce installation time.

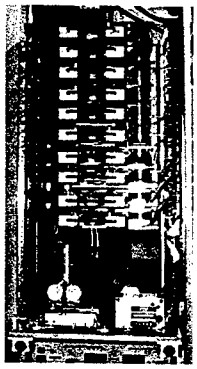

Figure 6: 15-kV IGBT kicker pulser.

Implementation of software and hardware interface components will continue up to the end of the project. Channel Access servers have been added to the existing VMS computers to enable EPICS compliance. Several EPICS IOCs have been configured on PowerPCs using the RTEMS real-time operating system [5], including those for power supply control, BPM data acquisition, and for interfacing to PLC protection systems. Machine modelling and control applications are being configured by the accelerator physics group using MATLAB™ with Channel Access [6]. Applications include SVD orbit correction and slow feedback, quadrupole modulation lattice calibration [7], LOCO [8], the Accelerator Toolbox [9], orbit interlock verification algorithm, and lattice parameter control. Hardware interface components are in production, including units to receive analog signals from commercial BPM processors, filter the signals, and distribute them to the digital orbit acquisition system and to the analog orbit interlock.

The majority of the BPM processing system (54 out 94 channels) consists of switched-button processors, which have been received from Bergoz, and are now being tested. The multiplexed down-converted button signals are digitized directly with 16-bit ADCs for precise orbit detection, bypassing the analog de-multiplexing and difference/sum circuitry in the processors. The analog-processed signals are used for the orbit interlock. Non-multiplexed, parallel-button RF-IF processors with externally coupled test tone are also being designed, which, in combination with Echotek ECDR814 digital receivers, will provide 1st-turn, turn-turn (with micron resolution), and high-resolution averaged orbit acquisition. Orbits will be acquired from the two types of processors at a 4 kHz rate over dedicated 100-Mb Ethernet LANs to a central CPU, which will perform an SVD orbit feedback algorithm at that rate and serve low-pass-filtered orbits to the control system. 24-bit orbit corrector setpoints will be transmitted to 54 vertical and 54 horizontal bipolar power supplies over digital control links at the 4 kHz rate [10], enabling a closed-loop feedback bandwidth of ~200 Hz.

Other I&C systems to be completed by October include PLC-based machine protection systems, the orbit interlock system (that prevents damage to the vacuum chamber and photon beam lines from mis-steered synchrotron radiation), a beam current interlock (that prevents over-filling the ring), and a UV synchrotron light monitor capable of resolving the 50-μm vertical beam size [11]. The rf and timing signal generating system and the 358 MHz I/Q phase shifting unit used to control injection timing in the booster are complete.

3 INSTALLATION AND OPERATION

With the removal of all SPEAR 2 components and the excavation of the tunnel and power supply room floors complete, the remainder of the SPEAR 3 installation can begin. The pouring of new concrete floors for the tunnel, which has been excavated ~18" to solid sandstone, and for the power supply room is about to commence. In a month, the low-shrinkage concrete will have stabilized enough to begin installing new alignment monuments. In July, raft mounting plates with alignment pins will be set precisely into the floor and hundreds of support mounting holes will be drilled. The pre-assembled magnet rafts and straight section assemblies will be rolled into the tunnel and secured over a 2-week period beginning in mid-August. Vacuum hardware will be installed and pumped down between mid-August and mid-October. The tunnel cable plant and IDs will be installed in this period as well. Final alignment will take place during the last half of October, with ring lock-up scheduled for October 30. System check-outs will take place in November, and commissioning with beam will begin in December. Photon beam lines will be commissioned as well, and will be used by local users as beam becomes available. A gradual transition from commissioning to user operation is expected during the first several months of operation, with monthly days-long ring accesses anticipated for continuing beam line component and shielding installation and accelerator maintenance.

The first SPEAR 3 operational run will be at 100 mA since most of the photon beam lines will not have been upgraded for 500 mA operation. To reduce the installation period, not all ring shielding and ID chamber masks needed for 500 mA will be in place at first; these components will be installed by the second run beginning Fall, 2004. Periodic 500-mA operation will then be possible, with un-upgraded beam lines locked shut. 500-mA operation for all beam lines is scheduled for 2007.

REFERENCES

[1] "SPEAR 3 Design Report", SLAC-R-069, 1999.
[2] J. Corbett et al., "The SPEAR 3 Light Source", EPAC '02, Paris, June 2002, 665.
[3] N. Li et al., "SPEAR 3 Gradient Dipole Core Fabrication", WPAB061, these proceedings
[4] N. Kurita et al., "SPEAR 3 DCCT", WPAG011, these proceedings.
[5] T. Straumann, "Experiences with RTEMS", 2002, http://www-csr.bessy.de/control/Epics02/.
[6] J. Corbett et al., "Accelerator Control Middleware", WPPE020, these proceedings.
[7] A. Terebilo, ""Global Beam-Based Alignment Algorithm", WPAB089, these proceedings.
[8] J. Safranek et al, "Linear Optic Correction Algorithm in MATLAB", FPAG037, these proceedings.
[9] A. Terebilo, "Accelerator Modeling with MATLAB Accelerator Toolbox", PAC01, Chicago, June, 3203.
[10] E. Medvedko et al., "High Resolution Analog/Digital PS Controller", MPPE012, these proceedings.
[11] C. Limborg et al., "An Ultrviolet Light Monitor for SPEAR3", EPAC 02, Paris, June 2002, 1824.

SESAME, A 2.5 GEV SYNCHROTRON LIGHT SOURCE FOR THE MIDDLE EAST REGION

D.Einfeld[1], R.H.Sarraf[2], M.Attal[3], K.Tavakoli[3], H.Hashemi[4], H.Hassanzadegan[4], E. Al-Dmour[1], B.Kalantari[5], A.Aladwan[5], H.Tarawneh[6], S.Varnasery[7]

Abstract

Developed under the auspices of UNESCO, SESAME (Synchrotron light for Experimental Science and Application in the Middle East) will be a major international research center in the Middle East and Mediterranean region where most of the applications require hard x-rays up to 20 KeV photons. At the 6th of January 2003 the official foundation of SESAME as well as the ground breaking for the building took place. The accelerator SESAME is based upon the synchrotron light source BESSY I, which was, with the operation of BESSY II, devoted to SESAME. The original plan was to upgrade BESSY I to an energy of 1 GeV and use super conducting wigglers to reach 20 keV photons. According to the present design SESAME will be a 2.5GeV 3rd Generation light source with an emittance of 24.6 nm.rad and up to 13 places for the installation of insertion devices with an average length of 3.1 meters. The circumference of the machine will be 124.8 m. As injector the 800 MeV Booster Synchrotron of BESSY I will be used with minor changes. At SESAME around 39.7% of the circumference can be used for the installation of insertion devices. At the beginning of operation 6 beam lines should be installed.

INTRODUCTION

According to the workshops held in the Middle East Region the scientific case for SESAME includes structural molecular biology, molecular environmental science, surface and interface science, micro mechanical devices, x-ray imaging, archaeological microanalysis, material characterization, and medical applications. Most of this applications require hard x-rays up to 20 KeV photons. Within the "Green Book"-design [1] this 20 KeV can be reached by upgrading BESSY I from 0.8 to 1 GeV and use 7.5 T super conducting wigglers. In order to increase the number of hard X-ray beam lines it was decided to upgrade the SESAME to 2.0 GeV and to optimize the design for a higher brilliance with a larger number of straight sections (White Book) [2]. According to the "1st User Workshop of SESAMA" in Amman, October 2002, it should be possible to reach the selenium K-edge with in-vacuum undulators. This is only possible by increasing the energy to 2.5 GeV. The proposed upgrade to this energy is presented in this paper.

[1] UNESCO office Amman, Jordan. [2] Al-Balqa Applied University, Alt-Salt, Jordan. [3] LURE, Orsay, France. [4] DESY Hamburg, Germany. [5] Swiss Light Source, Villingen, Switzerland. [6] MAX-Lab, University Lund, Lund, Sweden. [7] Daresbury Laboratory, Daresbury, United Kingdom.

NEW LATTICE

For the new lattice a so called "TME-Optic" [3] was chosen, which gives the smallest emittance and it should give the highest percentage of the circumference, dedicated to the installation of the insertion devices. The basic elements of the lattice are a combined function bending magnets, with a set of quadrupoles and sextupoles on each side. The combined bending magnets perform the deflection and the focusing in the vertical direction, the quadrupoles make only the horizontal focusing.

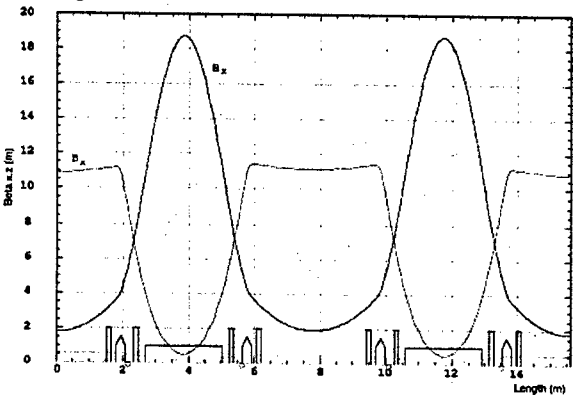

Figure 1: Optical functions of SESAME lattice, The green line represents dispersion, the pink circles represent the BPMs, while the correctors will be inside the sextupoles.

Table 1: Main parameters of the new SESAME upgrade

Parameters	Values
E (GeV), No. of BMs	2.5 , 16
C (m), Σ(Str.Sec.) / C	124.8 , 39.7%
ε_x (nm.rad)	24.6
Qx , Qz	7.217 , 5.192
ζx , ξz	- 13.1 , - 13.8
βx , βz , ηx (m)	11.12, 1.89, 0.453 (8 sec.) 10.9, 1.73, 0.534 (other 8 sec.)
B_0 (T) , n (strength)	1.4 , 12.9 (k = -0.3636 m^{-2})
No., Gr. of Quads	32 (2 families) 19 T/m
No., Gr. of Sext.	64 , 116 T/m2
No. of Str. Sec.	16 (8 x 3 m + 8 x 3.19 m)

0-7803-7738-9/03/$17.00 © 2003 IEEE

The machine functions of one unit cell are given in figure 1. and the main parameters of the ring are summarized in table 1. For operational purposes it must be possible to change the vertical tuning. For SESAME the gradient in the bending magnets must be varied by ±6% in order to change the tune by ±0.5. Using pole-face windings that will be introduced into the bending magnets will do this. To reach a sufficient dynamic aperture and an energy acceptance of 4%, chromatic and harmonic sextupoles have to be used. The arrangements of the magnets within one cell are given in figure 2 and the layout of the whole storage ring is given in figure 3. It should be noted here that the above optics is the original one from paper [2] and it could be changed a bit to get the optimum optics for high brilliance due to different insertion devices number and types according to the requirements of the users.

LAYOUT OF THE MACHINE

The layout of one cell is given in figure 2. The main elements are the 22.5 degrees vertical focusing bending

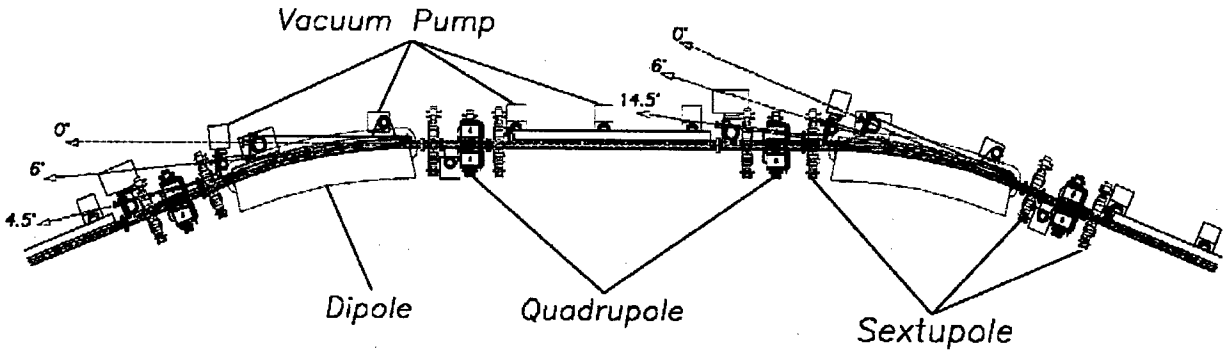

Figure 2: Arrangements of magnets within one unit cell of the storage ring SESAME.

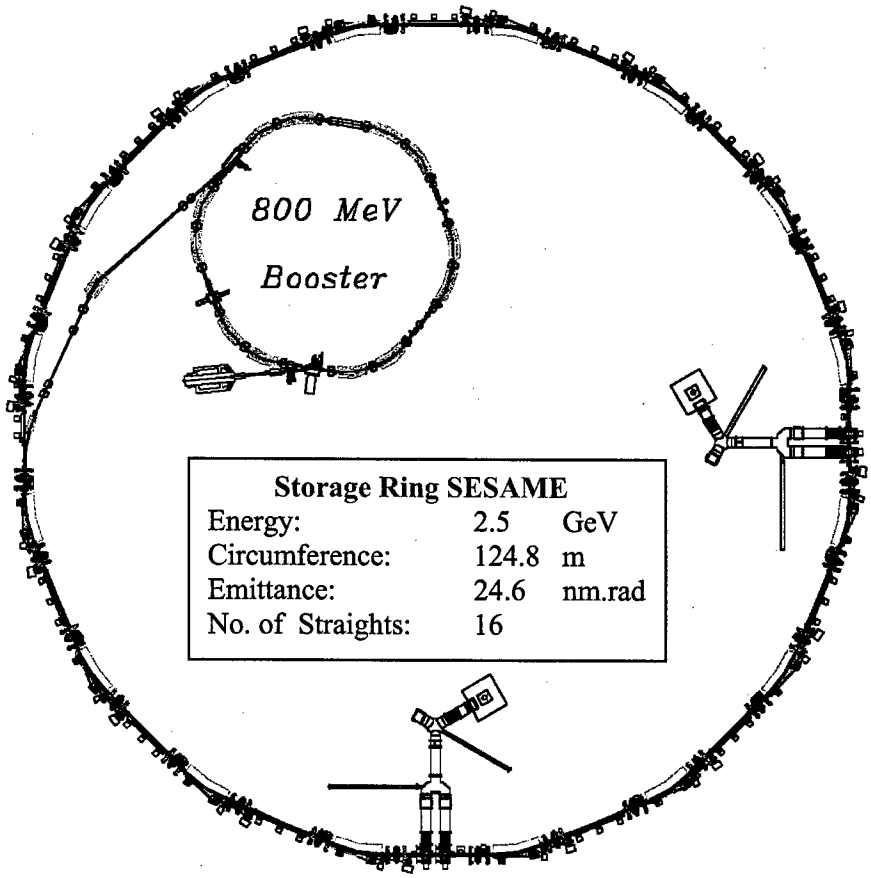

Figure 3: Layout of the 2.5 GeV storage ring of SESAME

magnets with the quadrupoles and sextupoles are located around it. The average length of the straight sections is 3.1 meters. It is foreseen to extract two beam lines (6° & 14.5°) from each bending magnet in addition to one zero-degree line which comes from upstream insertion device. The layout of the whole storage ring with the 800 MeV BESSY I booster synchrotron is shown in figure 3.

COMPONENTS OF THE MACHINE

The original BESSY I injector will be used with some modifications. Instead of the 10 Hz white circuits, 1 to 3 Hz fast power supplies will be used. Hence all power supplies have to be replaced. With this transaction the current for all power supplies will be increased in order to upgrade the energy of the injector from 0.8 to 1 GeV. At this energy the flux in the bendings is 1.25 T. Perhaps in a later stage the 20 MeV Microtron as pre-injector will be replaced by a 50 MeV linac or racetrack microtron.

According to the upgrading of 2.5 GeV, the bending magnets with a flux of 1.4 Tesla and a gradient of 3 T/m must be new. This is also true for the quadrupoles and sextupoles. With the changes of the circumference from 64 to 124.8 m the vacuum system must be new. It will be an antechamber system like SLS or the CLS. All photons will be stopped at lump absorbers. Overall a pumping speed of 32000 L/s will be installed in order to get after one year of operation an average pressure of 1 nTorr.

The RF-system will be build up in steps too, which are determined by the donations of other laboratories. DESY will donate to the project some 250 kW klystrons and ELETTRA a cavity and the low level electronics. The layout of the RF-system will be the same as for ANKA. All the power supplies for the project will be build in collaboration between SESAME and the Yerevan Physics Institute (Yerphi). The intention is to use the higher power parts of the old power supplies and replace the electronics. For the control system we expect some donations from the Swiss Light Source. The concept is based upon EPICS but for graphical user interface we take the ANKA approach. The same control system will be used for both, the machine and the beam lines. The whole diagnostics system for the SESAME storage ring will be new.

BRILLIANCE OF RADIATION

The brilliance of the emitted radiation of a 400 mA stored beam from the different sources are presented in figure 4. For the bending magnet it is given for the energies 1.0, 1.5, 2.0, and 2.50 GeV. For the wigglers with the maximum flux density of 2.0 T (W100), 2.5 T (W120) and 3.5 T(W80). For the undulators with the period length of 40 mm (U40), 25 mm (U25) and 14 mm (U14). U25 is an in-vacuum undulator and U14 is an super conducting mini undulator.

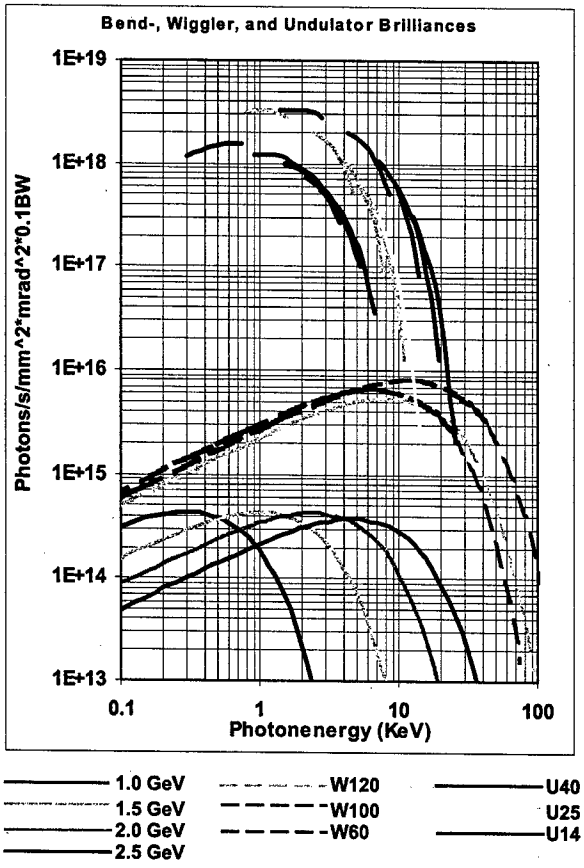

Figure 4: Brilliance of the synchrotron radiation emitted from the stored beam in the bending, wigglers and undulators.

ACKNOWLEDGEMENTS

The authors gratefully acknowledge the contribution of Gustav Adolf Voss (DESY), Mark Plesko (JSI), Amor Nadji (LURE), Lothar Schulz (SLS) and Ernst Weihreter (BESSY). Many thanks to all the colleagues at the different host laboratories [ANKA, DESY, MAXLAB, LURE, SLS, DARESBURY, ELLETRA].

REFERENCES

[1] Green Book, Conceptual Design Report for SESAME, OCT 99, BESSY, Berlin.

[2] White Book, Conceptual Design for the Upgrading of SESAME to 2 GeV, UNESCO-Office, Amman, July 2002

[3] A. ROPERT, Lattices and Emittances, CAS, 1996, CERN 98-04.

[4] First operation of the Swiss Light Source, EPAC02, 3-7 June 2002, Paris.

[5] Gradient Dipole Magnets for the Canadian light Source, EPAC02, 3-7 June 2002, Paris.

NSLS UPGRADE CONCEPT*

B. Podobedov#, J.M. Ablett, L. Berman, R. Biscardi, G.L. Carr, B. Casey, S. Dierker, A. Doyuran, R. Heese, S. Hulbert, E. Johnson, C.C. Kao, S.L. Kramer, H. Loos, J.B. Murphy, R. Pindak, S. Pjerov, J. Rose, T. Shaftan, B. Sheehy, P. Siddons, N. Towne, J.M. Wang, X.J. Wang, L.H. Yu,
National Synchrotron Light Source, BNL, Upton, NY 11973-5000, USA

Abstract

To address the growing needs of the NSLS user community we are aggressively pursuing R&D towards a facility upgrade. The present goals are a 3 GeV ultra-low emittance storage ring, tailored to the 5-20 keV photon energy range, that will triple the present NSLS ID capacity, and provide three orders of magnitude increase in brightness over the present brightest NSLS beamlines. To achieve these goals we propose a 24 period TBA lattice, with extensive use of super-conducting small gap undulators. This paper reviews our preliminary design and the key accelerator physics issues.

MOTIVATION, SCOPE AND GOALS

The NSLS facility was designed in the late 1970s and consists of two 2nd generation storage rings emphasizing the production of high flux synchrotron radiation (SR) from bending magnets. These rings were the first DBA (Double Bend Achromat) lattices in the world. The smaller 800 MeV VUV ring covers the photon energy range from far infrared to >0.6 keV. The X-ray ring now operates up to 2.8 GeV, providing photons up to 26 keV, with brightness several orders of magnitude higher than its design value. At this stage, however, there is no foreseeable way to decrease the horizontal emittance significantly below 60 nm which, once the SPEAR upgrade is complete, will leave the NSLS X-ray ring far behind the other three US DOE operated light sources. Additionally, the 8-fold periodicity of the lattice severely limits the number of insertion devices (ID). Today's most important and challenging scientific problems require x-rays with higher average brightness than can be produced by the NSLS.

A significant number of these problems, including a rapidly expanding field of structural biology, are primarily interested in the 5-20 keV energy range. While our user case is still refining we are now intending to provide the maximum average brightness in this energy range emphasizing a high average current multi-bunch operations.

While linac-based SR sources are being considered at this time, acting on the recent recommendations of the DOE Basic Energy Sciences Advisory Committee, that emphasized conservative approach to the NSLS upgrade, we are now concentrating on a 3rd generation storage ring.

The main design goals for the storage ring are:

1) Deliver an average brightness in the range of 10^{20}-10^{21} photons/second/0.1%bw/mm^2/mr^2 for 5-20 keV photons (x10^3 gain over the present NSLS brightest beamline X25).
2) Provide at least 20 undulator straight sections.
3) Meet the user requirements at minimum cost.

OVERVIEW AND BASIC PARAMETERS

By reducing vertical coupling, 3rd generation light sources can obtain diffraction-limited emittance in the vertical plane, making the brightness inversely proportional to the horizontal emittance. For a given number of straight sections, smaller horizontal emittance is achievable by going to a larger number of bending magnets per period. To meet the needs for more undulator beamlines, we did try to fit a higher periodicity lattice in the existing 170 m long tunnel but, found no solution to provide a competitive light source. It was also felt that a long shutdown for construction would have a severe impact on the present NSLS user program. Consequently the proposed upgrade has a larger circumference ring situated close to the present NSLS and the new Brookhaven Center for Functional Nanomaterials. The new storage ring (NSLS-II) will have a full-energy booster for top-off mode operation.

Based on extensive lattice design studies, providing a horizontal emittance in the 1-2 nm range with a 24 period lattice and 4 m long ID straight sections would require a circumference ~0.5 km. A diffraction limited vertical emittance for 1 Å then fixes the coupling at ~0.5%.

Beam current is usually limited by the SR heating of vacuum chamber components and often specifically by the heat load on the wall of the dipole chamber. With our choice of bending radius and 0.5 A beam current, the SR wall heating of 10 W/m is similar to what is routinely handled in the PEP-II B-factory. Limitations coming from collective effects are described below.

While the combination of increased beam current and reduced emittance will improve the brightness by more than a factor of 100 for the bending magnet users, it is not going to get us all the way to the 1st design goal. We believe, however, that extending the mini-gap undulator (MGU) technology, successfully used in the present NSLS, into a super-conducting regime will accomplish that goal. Assuming device parameters that we believe will be achievable after several years of aggressive R&D, the design ring of 3 GeV should produce continuous coverage up to 20 keV. Brightness curves for these and other IDs are shown in Fig. 1, where NSLS-II ID length is assumed to be 2 m for in-vacuum IDs and 2.5 m otherwise. The small gap super-conducting undulator

*Work supported by US DOE
#boris@bnl.gov

0-7803-7738-9/03/$17.00 © 2003 IEEE

(SCU) will be the workhorse of NSLS-II used in up to 18 ID straights. Other IDs may include soft x-ray undulators (SXU) and super-conducting wigglers (SCW, not shown).

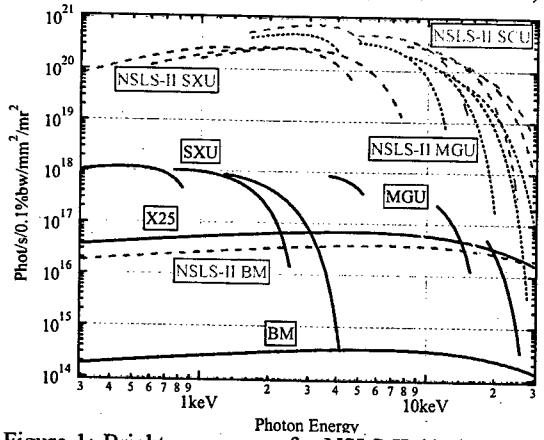

Figure 1: Brightness curves for NSLS-II (dash, color), and for present NSLS (solid black and grey).

Key machine parameters are summarized in Table 1 and are further described in the rest of the paper.

Table 1: Ring Parameters (preliminary)

Nominal Energy	3 GeV
Circumference	523 m
Number of periods	24 TBA
Max. ID Length	4 m
Natural Emittance	1.5 nm
Betatron Coupling	0.5%
Momentum Compaction	0.000187
Bend Radius	7.64 m
Tunes H/V	36.38/13.72
Energy Spread	0.095%
RF Frequency	500 MHz
RF Bucket Height	3%
Natural Bunch Length (rms)	13 ps
Maximum Current	500 mA

SMALL GAP UNDULATORS

Medium-energy rings must use short-period (~ 1 cm) undulators to generate tunable, multi-keV photon beams. Permanent magnet (PM) based, short-period, in-vacuum undulators, which the NSLS has pioneered in the past decade, suffer from low fields, low K values (~1), limited tuning range and incomplete spectral coverage (MGU in Fig. 1.) Due to the relatively high emittance in the present X-ray ring, the holes are partially filled by the even harmonics (shown in grey).

Full coverage of the 5-20 keV range in a 3 GeV ring can be attained with a longer period, in-vacuum MGU having K_{max}>1.32, with its fundamental tunable down to 1.67 keV. This would give the desired coverage using the 3rd, 5th and higher harmonics up to the 11th. An MGU with a 19 mm period, a minimum gap of 5 mm and a phase error of <2° rms (NSLS-II MGU in Fig. 1) could fill this requirement. Its fundamental also covers 1.67-4.0 keV.

SCU technology, under development at the NSLS, other light sources and in industry, promises even better performance in this energy range. For example, coverage from 1.67 to 20 keV with no skips and with higher brightness, could be achieved with an SCU having a 15 mm period, a 5 mm gap (NSLS-II SCU in Fig. 1) and an *average* current density in the windings, J_{avg} ~1200 A/mm^2. This level of J_{avg} is within the realm of NbTi super-conductors. If the gap must be increased, the increased J_{avg} may require more exotic super-conductors. This and other challenging R&D will be addressed by a newly formed 4-lab collaboration (NSLS, SLAC, ALS and APS).

LATTICE AND MAGNETS

The candidate lattice we are now considering to meet the design goals for the NSLS upgrade is a 24 period Three Bend Achromat (TBA). Although many light sources, including the X-ray ring at the NSLS, give up the achromatic condition to achieve lower emittance, this condition does minimize the impact of undulator field change between the users. The TBA lattice is quite flexible with higher emittance tunes yielding lower chromaticity, for the day one lattice. Finally, the TBA lattice is the lowest multiplicity of bend magnets designs that can achieve the isochronous condition without breaking the lattice periodicity. This preserves an option of a possible future upgrade to a linac-based technology.

The lattice assumes gradient dipoles used to reduce the length of a period. To provide additional flexibility, three dispersion quadrupoles are used to vary the lattice properties without giving up on the achromatic condition. By changing the outer two dipole magnets to half the bending angle and length, a lower emittance was achieved. This could be optimised further in later designs closer to the optimum ratio of $\sqrt[3]{3}$:1 [1], but a simple 2:1 split was used so far.

The low emittance TBA lattice shown in Fig. 2 has a natural emittance of 1.5 nm but with large chromaticity. Three families of chromaticity correcting sextupoles are shown to reduce the magnitude of the chromaticity or make it slightly positive. Two families of harmonic correction sextupoles are installed in the dispersion free region to reduce the impact of the chromatic correction sextupoles on the dynamic aperture. The dynamic aperture in the TBA lattice is limited by many competing higher order non-linear resonances coming from chromatic sextupoles. Several design codes [2-3] attempt to minimize these driving terms by phasing the sextupoles in the lattice. The five families provided in this design provide a dynamic aperture sufficient for injection into an ideal lattice. Future designs will break the 24-fold periodicity, providing additional harmonic sextupoles families for expansion of the dynamic aperture with errors, as was used in the Swiss Light Source [4] and proposed for the DIAMOND ring [5].

Space is provided in the straight section for correction magnets and injection bumps. Some correction magnets

are combined in the sextupole magnets to save space. The correction magnets in the straight section are capable of deflecting the closed orbit inward by ~1 cm, to avoid the SR of the upstream dipole magnet. Additional correctors in the dispersion region and dipole back-leg windings will provide closed orbit correction.

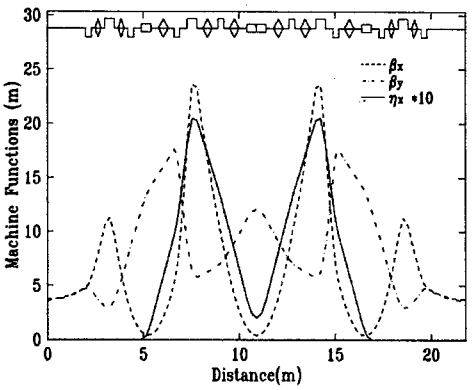

Figure 2: NSLS-II magnet layout and lattice functions.

RF SYSTEM

The RF system must deliver about 0.8 MW RF power for SR losses when the lattice is loaded with its full complement of insertion devices (18 SCUs and 2 SCW is assumed). Additional power is required to sustain the fields in the cavities, for RF losses, and for power lost to higher-order modes (HOMs), resistive-wall, etc. The cavities together must also be able to sustain approximately 2.8 MV voltage to provide 3% momentum acceptance, which we presently use as a baseline.

The choice of cavity technology, either normal-conducting or super-conducting, is determined by their ability to provide RF voltage, maximum power delivery, the spectrum of trapped higher-order modes and their damping, and other considerations. Super-conducting (SC) RF cavities are available that are capable of providing the full accelerating voltage from one cavity. They also have a very limited number of trapped HOMs, which are well damped. Proven operational input-coupler power figures [6] (e.g., CESR and KEK-B cavities) imply three cavities are required to meet the 0.8 MW RF power figure. With regard to available room-temperature cavities, a minimum of three are needed to meet the 2.8-MV requirement; three are more than adequate to deliver the RF power. So, while three cavities is a baseline requirement using either technology, further development and improved fabrication techniques of input couplers for SC cavities may obviate the need for a third cavity. For these and other reasons, SC cavities are proposed.

COLLECTIVE EFFECTS AND LIFETIME

Although self-stabilizing, the longitudinal microwave instability is important since the energy-spread reduces the brightness, especially for higher undulator harmonics. The Boussard criterion limits the broad-band impedance to $|Z/n|_{max}$~0.1 Ω (assuming 0.86 mA/bunch due to 1/3 of the ring ion clearing gap). This should be possible to achieve via careful impedance control. The threshold could be further raised using harmonic RF. Since up to 1 m is reserved for SCU/MGU tapers, they will not present significant impedance.

Due to multiple small-gap devices, transverse coherent single bunch instabilities, such as TMCI and microwave, are very important. While raising the chromaticity could circumvent them [7], this will ultimately limit the dynamic aperture and/or require strong sextupoles. We are currently planning an R&D program to spec and design an MGU chamber with acceptable transverse impedance. We are also trying to extrapolate from the experience with small gap devices at NSLS and other light sources.

Our preliminary estimates do not show significant coupled-bunch instability due to resistive wall. The effect of small ID gaps is partially compensated by small beta functions and, in case of SCU, reduced wall impedance. Instabilities due to HOM are less expected due to SC RF.

For the intra-beam scattering (IBS) we are probably within parameter range already probed by existing facilities, (ATF-KEK, ALS, etc) and we do not expect the IBS to affect the multi-bunch operation. ZAP and SAD show only a few % emittance blow-up at 1.5 mA/bunch.

The acceptance at the edge of a 2-m long MGU is 1.6 10^{-6} m-rad. For 1 nTorr N_2 equivalent pressure, this results in lifetime of ~40 hours. Similarly, bremstrahlung lifetime is about 50 hours. As a result, similar to other 3rd generation light sources, the lifetime is expected to be Touschek dominated. Calculations give a half-life of less than 2 hours. While this should not be a problem running in a top-off mode, it requires putting some thought into radiation shielding. Again, a harmonic RF system could alleviate this problem.

Detailed lifetime calculations are needed to carefully take into account physical and dynamic apertures, non-linear synchrotron motion, etc.

SUMMARY AND FUTURE WORK

We are at the very beginning of this project. The most pressing R&D issues are:

- Mini-gap super-conducting undulators.
- Lattice optimisation for dynamic aperture.
- Collective effects, and especially the microwave and transverse single bunch instabilities.
- Booster design and injection details.
- Orbit stability and feedbacks.

REFERENCES

[1] S.Y. Lee, Phys. Rev **E 54,** p. 1940, (1996).
[2] HARMON-M. Donald, D. Schofield LEP-420, (1982).
[3] OPA- A. Streun, http://slsbd.psi.ch/~streun/opa .
[4] A. Streun, et. al., PAC'2001, p. 224, (2001).
[5] DIAMOND Design Specification, (June 2002).
[6] S. Belomestnykh, CESR Report No. SRF 021105-09.
[7] P. Kernel et al., EPAC 2000, p. 1133, (2000).

SINGLE-PARTICLE BEAM DYNAMICS IN BOOMERANG*

Alan Jackson, LBNL and the Australian Synchrotron Project, Melbourne, Australia
Hiroshi Nishimura, LBNL, Berkeley, CA 94720 USA

Abstract

We describe simulations of the beam dynamics in the storage ring (Boomerang), a 3-GeV third-generation light source being designed for the Australian Synchrotron Project[1]. The simulations were performed with the code Goemon[2]. They form the basis for design specifications for storage ring components (apertures, alignment tolerances, magnet quality, etc.), and for determining performance characteristics such as coupling and beam lifetime.

INTRODUCTION

"Boomerang" is the 3-GeV storage ring at the heart of the Australian Synchrotron Project (ASP), a National facility being built by the Victorian Government at a site adjacent to Monash University, 20 km from the center of Melbourne. Like other modern intermediate energy facilities, Boomerang features auxiliary sextupoles in the dispersion-free region of the lattice (sometimes called harmonic sextupoles) in order to provide an acceptable dynamic aperture. In this case the dynamic aperture was found to lie well outside the anticipated physical aperture. This then gives us the opportunity to match various physical parameters (apertures, RF voltage, etc.), whilst maintaining overall performance requirements such as beam lifetime. In this paper we describe the lattice and basic beam dynamics of the storage ring, and the process through which the physical parameters of the accelerator components are defined.

THE MAGNET LATTICE AND BEAMDYNAMICS

The magnet lattice [3] has been optimized to emphasize a low beam emittance within a short achromatic section. One unit cell of the lattice is shown schematically in Fig. 1, and the lattice functions are plotted in Fig. 2 for the nominal, and Fig.3 for the low-emittance mode operations. Notable in the design are: (1) the chromatic sextupoles SV and SH are "embedded" in the compound achromat magnets - thereby minimizing the strengths of the sextupoles; and (2) there are no defocusing quadrupoles in the long straight section - giving more space for straight section elements. The periodicity of the lattice is 14 resulting in a circumference of 216 m. Beam parameters are summarized in Table 1.

- This work was supported by the Director, Office of Energy Research, Office of Basic Energy Sciences, Material Sciences Division, U. S. Department of Energy, under Contract No. DE-AC03-76SF00098;
- and by The Victorian Government's Department of Infrastructure, Major Projects Victoria. Nauru House. Melbourne 3000. Australia.

With this magnet configuration the auxiliary sextupoles were optimized to give adequate dynamic aperture. The resulting dynamic aperture (see Fig. 4 for the nominal mode) is insensitive to the absolute setting of the sextupoles to about 10% of their setting. I.e., these settings do not represent a narrow peak of the maximum aperture in auxiliary sextupole space. It has also been found that the dynamic aperture is not sensitive to magnet errors (in normal ranges), since the amplitude dependent tune variations are small until the test particles get close to the edges of the dynamic aperture. As an example, we show ν_x as a function of betatron amplitude in Fig. 5 for the nominal mode. Again this seems typical of lattices designed with auxiliary sextupoles.

Table 1. Main Beam parameters

Energy	3.00		GeV
Beam Current	200		mA
νx	13.3		
νy	5.2		
βx*	9.47	8.23	m
βy*	2.46	2.43	m
η*	0.00	0.247	m
Mom.Compaction	1.97E-3	2.09E-3	
Natural Chrom H	-30.8	-28.5	
Natural Chrom V	-23.9	-24.4	
Radiation Loss	931.6		keV/turn
Natural E Spread	1.02E-3	1.03E-3	
Natural Emittance	1.58E-8	6.97E-9	
Rad. Damping H	3.42	3.38	msec
Rad. Damping V	4.64	4.64	msec
Rad. Damping E	2.82	2.86	msec
k of Bend	-0.335		1/m^2
k of Q1	1.7617	1.7891	1/m^2
k of Q2	-0.9145	-0.9174	1/m^2
k of Q3	1.9244	1.9064	1/m^2
RF Frequency	499.654		MHz

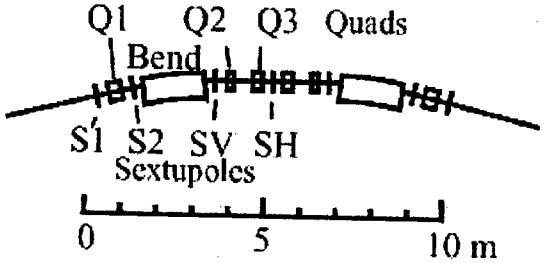

Figure 1. Unit Cell

0-7803-7738-9/03/$17.00 © 2003 IEEE

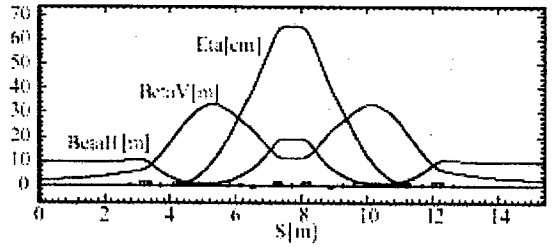

Figure 2. Nominal Mode Lattice Function

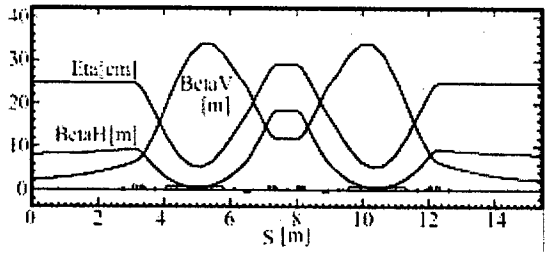

Figure 3. Low-Emittance Mode Lattice Function

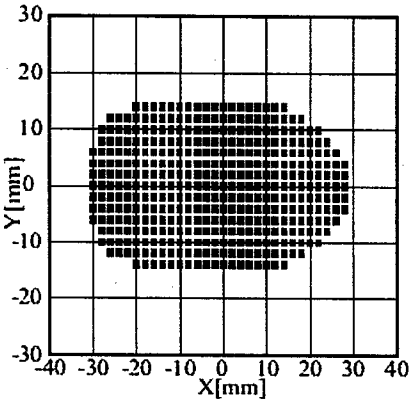

Figure 4. Dynamic Aperture for 400 Turns

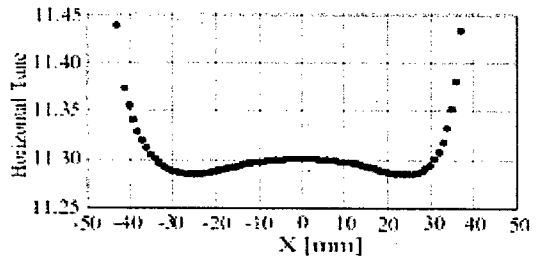

Figure 5. Amplitude-dependent Tune Shift Horizontal

APERTURE

Given that the storage ring has a dynamic aperture that is likely to be larger than the physical apertures in the storage ring, we are free to define accelerator apertures and magnet good-field regions through other constraints.

Vertical beam stay-clear

We choose to define the vertical stay-clear by a 4 m long vacuum chamber centered in the long straight section, with an aperture of +/- 5 mm. Under almost all reasonable scenarios for βy^* this defines the aperture to be constrained to a value of 5 mm at by = 4.0 m, or alternatively the vertical acceptance is defined to be Ay = 6.25 x 10^{-6} m-rad. The maximum vertical beam stay-clear occurs in the dipole magnets at a value of +/- 15 mm. The dipole magnets must be designed with an aperture consistent with this.

Horizontal stay-clear

The horizontal stay-clear in Boomerang turns out to be dominated by the apertures required to contain Touschek scattered electrons. We will show later that this aperture gives a horizontal acceptance that is much larger than the vertical acceptance. This in turn means that elastic gas scattering lifetimes are limited by just one plane – the vertical plane.

The bremsstrahlung lifetime in Boomerang is about 40 hours. In order to get a Touschek lifetime of ~ 40 hours we need an RF voltage of 3 MV. Such a voltage, at 500 MHz, can be achieved by four warm cavities, or possibly by a single superconducting cavity. This is equivalent to an energy acceptance of ~ 2.2%. Note that this is also well within the dynamic energy acceptance of the ring, which is in excess of 4%.

Tracking Touschek 2.2% scattered particles around the ring show that they paint an aperture that reaches 33 mm in the center of the achromat. Fig. 6 shows the trajectories around the ring of a -2% scattered particle over 100 turns.

We therefore choose the horizontal stay clear consistent with the above argument. In the straight sections it corresponds to a value of 14 mm, and the maximum quadrupole and sextupole apertures must be consistent with a good field region of +/- 33 mm in the center of the achromat. We note that the horizontal acceptance is Ax > 23 x 10^{-6} m-rad (defined by the position of the injection septum), and that this is significantly larger than the vertical acceptance.

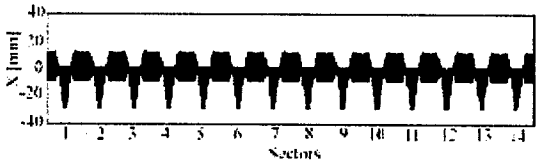

Fig.6 Overlapping Trajectories of a Particle Scattered with -2 % of Energy Deviation

BEAM LIFETIME

We are now in a position to estimate beam lifetimes.
We make the following assumptions:
(1) Use the apertures and RF voltages described above.
(2) Vacuum pressure of 1 nTorr, N_2 equivalent.
(3) Beam current of 200 mA in 300 bunches out of 360 buckets.
(4) Emittances per Table 1; i.e. 16 and 7 nm-rad.
We then get values of:

Table 2: Components of the Beam Lifetime

Emittance	16 nm	7 nm
Coulomb scattering	78 hours	77 hours
Bremsstrahlung	39 hours	39 hours
Touschek	102 hours	39 hours
Quantum	huge	huge
Combined	20.7 hours	15.6 hours

INSERSION DEVICE COMPENSATION SCHEME

The four families of sextupole magnets work very effectively to increase the dynamic aperture. Therefore, the ring is quite tolerant to the effect of insertion devices. An extreme scenario for simulation is to insert two ALS W16 wigglers ($\lambda w = 16$ cm, 19 periods, $B_{max} = 2.1$ T) in consecutive sectors. The resulting β-beat is ~ 15 %. Such beating can be corrected locally by using quadrupoles on each side of the wiggler. The global tunes are refitted. The loss of the dynamic aperture is up to 10% after re-optimizing the sextupoles. For undulators, compensation using 6 quadrupoles on both sides of each undulator is sufficient.

LATTICE ERRORS AND ORBIT CORRECTIONS

The closed orbit distortion (COD) is very sensitive to lattice errors, and precise COD correction is required to restore the machine performance. There are 70 horizontal correctors, 56 vertical correctors and 98 beam position monitors for the COD correction. The COD was simulated with the random magnet errors listed in Table 3 and corrected by using the singular-value decomposition (SVD) method based on the sensitivity matrices.

Table 3: Magnet Random Errors

Field Error $\Delta K/K$	1.0E-3
Tilt Error ΔT	0.5E-3 rad
Misalignment	0.15E-3 m

The residual COD rms average over tens of random seeds is 0.16~0.18 mm in both transverse planes with the BPM readout error of 0.15 mm. If the target values are given to the BPM readout, it goes down to ~ 0.05 mm by using the ideal sensitivity matrices.

In reality, once the beam is stored with reasonable beam time, it becomes possible to use beam-based alignment and analysis. Note that in Boomerang all quadrupoles are powered separately. We estimate that the residual COD with respect to these quadrupole centers will be 0.01~0.02 mm by taking advantage of measured sensitivity matrices.

The higher-order field errors of the magnets have also simulated to confirm that they do not hamper the COD correction or the resulting dynamic aperture. After correction, the loss of the dynamic aperture is estimated at 10 ~ 15 % of the ideal. The average corrector setting is around 0.1 mrad in both planes

DISCUSSION

The design of a light source is an iterative process in which one desired parameter can be traded off against others, including the cost of the facility. We have shown above that in the case of the ASP we have arrived at a reasonably self-consistent set of parameters. Given the lattice, which itself was the result of many iterations between circumference, number of achromats, emittance, and overall size, etc., we have a solution in which:

- the dynamic aperture in all three planes is outside the apertures defined by physical constraints;
- the cavity voltage is reasonable (more would require more cavities, larger-aperture multipole magnets, and less would reduce the beam lifetime);
- the beam stay-clear is reasonable (larger would require larger-aperture multipole magnets, and less would reduce the beam lifetime);
- the magnet apertures and vacuum requirements are consistent with recognized norms within the synchrotron community; and
- the beam lifetime is acceptable.

REFERENCES

[1] http://www.synchrotron.vic.gov.au/
[2] H. Nishimura, "Goemon, A C++ Library for Accelerator Modeling and Analysis," PAC 2001, Chicago, July 2001, p. 3066.
[3] J.W. Boldeman, "The Australian Synchrotron Light Source", EPAC 2002, Paris, June 2002, p. 650.

ADVANCED PHOTON SOURCE BOOSTER SYNCHROTRON LOW-EMITTANCE LATTICE COMMISSIONING RESULTS *

Nicholas S. Sereno, Michael Borland, Hairong Shang
Advanced Photon Source/ANL, Argonne, IL 60439, USA

Abstract

Recent efforts at the APS have focused on reducing beam loss during storage ring (SR) injection to minimize radiation damage to the APS undulators. Reducing beam loss at injection is particularly important during top-up operation where injection occurs once every two minutes. One way to potentially improve injection efficiency is to simply reduce the emittance of the beam from the APS booster, thereby allowing the beam to be brought closer to the injection septum. Recently several low-emittance operating modes for the APS booster have been studied. The emittance is lowered from the standard value by increasing the horizontal tune in stages. The vertical tune is simultaneously decreased to minimize the required defocusing sextupole strength for chromaticity correction. Calculations indicate that up to 29% reduction in emittance is possible—a result that has been achieved in studies. A lattice with emittance 17% lower than the standard lattice has been thoroughly commissioned and has been used for routine APS top-up operation since July 2002. Results of beam measurements and comparison to calculations for various low-emittance lattices are reported in this paper.

MOTIVATION

The APS injector machines are presently the focus of studies with the ultimate goals of improving overall injector system availability and reliability for storage ring (SR) top-up operation. Successful studies to lower the emittance of the APS booster synchrotron were completed in December 2002. These studies are part of an ongoing effort to improve injection efficiency into the SR for top-up operation using the SR low-emittance lattice (2.9 nm effective emittance [1]). Improved injection efficiency results in reduced losses and hence less radiation dose to the SR insertion devices. Lower booster emittance combined with ongoing booster-to-storage ring (BTS) transport line matching optimization are helping to improve SR injection efficiency toward the ultimate goal of 100% (present efficiency is 70 to 80%).

BOOSTER STANDARD AND LOW-EMITTANCE LATTICES

The APS booster is designed to linearly ramp the beam (at up to 6 nC) from 0.325 to 7 GeV in 225 ms at a 2-Hz cycle rate for full energy injection into the APS storage ring for top-up. The booster consists of four quadrants with ten FODO cells per quadrant. In each quadrant, one FODO cell is used to suppress the dispersion in the straight sections by removing a single dipole (missing magnet configuration). The booster magnets are arranged in families connected to a single supply in series: 68 dipoles (BM), 40 focusing quadrupoles (QF), 40 defocusing quadrupoles (QD), 32 focusing sextupoles (SF), and 32 defocusing sextupoles (SD). The beam is injected on-axis and extracted while the power supply families are ramping. The rf system consists of four 352-MHz 5-cell cavities located in the dispersion-free straight sections.

The current in the BM, QF, and QD families is linearly ramped from zero starting at the same point in time. This allows the tunes to be set to those required for the nominal 132 nm-radian standard lattice $\nu_x = 11.75$, $\nu_y = 9.80$. For this horizontal tune, the missing magnet in each quadrant results in zero dispersion in the straight sections.

Alternative APS booster lattices were studied using the accelerator design and tracking code **elegant** [2]. This is straightforward with **elegant** because it allows us to optimize the emittance directly. The main constraint on our ability to optimize booster parameters using **elegant** is that each magnet family is wired in series. Therefore, there are exactly four parameters (two quadrupole and two sextupole strengths) that can be varied to set the tunes and correct the chromaticity. In this way, a series of lattices with different quadrupole and sextupole family strengths were obtained with progressively lower emittance. The dynamic aperture was also simulated using **elegant** for the various lattices. Calculations show that dynamic aperture should be more than adequate for lattices with up to 30% lower emittance.

Table 1 shows the three booster lattices commissioned and used for operations. The first lattice listed is the original design lattice (standard lattice) with zero-dispersion straight sections. Increasing the horizontal tune in steps of an integer results in a great reduction in the total emittance. The lowest (92 nm) emittance lattice has a much smaller vertical tune, which has two advantages. First, the required QF focusing strength required to achieve a horizontal tune of 13.75 is minimized. Second, the required sextupole strength to correct chromaticity is also minimized. The booster is presently run with the 92-nm-radian lattice for normal operations. The 92-nm-radian lattice is near the practical lower limit for the booster emittance since for this lattice the QF family is powered nearly at its maximum strength.

* Work supported by U.S. Department of Energy, Office of Basic Energy Sciences, under Contract No. W-31-109-ENG-38.

0-7803-7738-9/03/$17.00 © 2003 IEEE

Table 1. Commissioned Lattice Tunes and Emittances

Horizontal Tune ν_x	Vertical Tune ν_y	Emittance (π nm-radians)
11.75	9.8	132
12.75	9.8	109
13.75	5.8	92

BOOSTER LOW-EMITTANCE LATTICE COMMISSIONING

The **elegant** calculations of new booster lattices described in the previous section indicate that there should be no problems in pushing the booster lattice to these lower emittances. Booster lattice commissioning was accomplished by starting with the booster operating in its well-characterized 132-nm-radian standard lattice. Tune measurements (both integer and fractional tunes) were used to determine quadrupole and sextupole family magnet slope parameters. We also made use of new orbit correction software and upgraded beam position monitors (BPMs) [3]. Iterating between orbit correction, tune measurement/correction, and chromaticity correction was necessary to make fine adjustments to the lattices.

Lattice commissioning followed a straightforward process starting with the 132-nm-radian standard lattice. First, the intermediate emittance 109-nm-radian lattice was commissioned by simply increasing the horizontal tune by one full integer while keeping the vertical tune constant. The chromaticity was corrected by simply using the sextupole strength values computed by **elegant**. The orbit was also corrected for the 109-nm-radian lattice and the tunes and chromaticity slightly adjusted as a final step. Next, several intermediate lattices were commissioned—a process that finally resulted in obtaining the 92-nm-radian lattice. Starting with the 109-nm-radian lattice, the horizontal tune was increased 1 full integer while the vertical tune was kept constant. Next, the vertical tune was successively decreased in single integer steps, until the 92-nm-radian lattice tunes were achieved. Finally, the orbit was corrected and the tunes and chromaticity were slightly adjusted for the 92-nm-radian lattice.

In order for the tunes to stay constant up the ramp, the BM, QF, and QD ramps must start at the same zero current point on the time axis [4]. If this is not the case, the tunes will slew with time, possibly resulting in beam loss from the tune crossing a lattice resonance. For a FODO lattice, the tunes are for the most part dependent only on the QF (horizontal tune) and QD (vertical tune) strengths. Therefore, increasing or decreasing the QF (QD) slope changes primarily the horizontal (vertical) tune. In these studies, a small change in the QF or QD slope was made and the corresponding tune change was observed. In this way, an experimental determination was made of the amount of QF or QD slope (dI/dt) change required to increase or decrease the tune by one integer. Typically after the increase or decrease of a given tune was made, small adjustments of the other tune using the complementary quadrupole family were required to precisely set the fractional tunes.

Fractional and Integer Tune Measurements

Measurement of the fractional tune was accomplished using a Hewlett Packard 89440A Vector Signal Analyzer (VSA) in spectrogram mode. Figure 1 shows a typical spectrogram where the horizontal axis is frequency, the vertical axis is time, and color is intensity. In the figure, time increases downward or in other words, the top of the figure represents the injection point. The difference signal obtained from striplines installed in the booster gives the tune signal. The tunes are excited by using the booster extraction kicker to "ping" the beam at a 40-Hz rate. The individual ping excitation of each tune is apparent in Figure 1 as tune lines every 25 ms (1/40 Hz).

The VSA spectrogram is used not only as a tool to set the fractional tune but also to tell on which side of the half integer resonance the tunes are located. One can do this by increasing the QF and QD ramp slope slightly and observing which way the tunes move. In Figure 1, the higher frequency pair of tunes should move higher in frequency if the tunes are above the half integer. The reverse is true of the lower frequency pair of tunes.

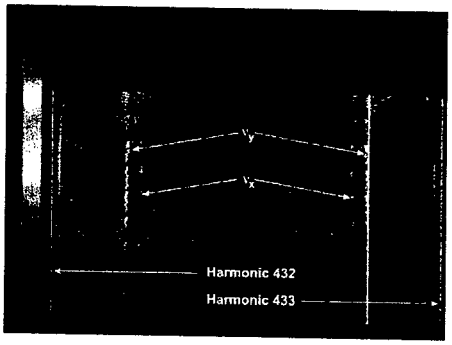

Figure 1: VSA spectrogram of booster tunes from injection to extraction for the 132-nm-radian lattice. The frequency span in the figure equals one revolution frequency (814 kHz) between revolution harmonics 432 and 433. The fractional tunes are set to their nominal ν_x = 0.75 and ν_y = 0.80 and show up as the upper sideband signal pair of harmonic 432 and the lower sideband signal pair of harmonic 433. A synchrotron sideband is also seen next to each revolution harmonic from injection to approximately halfway up the ramp.

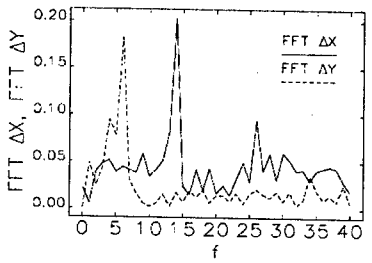

Figure 2: FFT of horizontal and vertical difference orbit showing the integer tunes of 14 (horizontal) and 6 (vertical) for the 92-nm-radian lattice.

The integer part of the tunes can be determined by exciting a difference orbit in each plane using a horizontal and vertical corrector and recording the betatron oscillation for a single turn using the BPMs. The single turn data is processed by normalizing the maximum BPM number index to 1 and taking the FFT. The result is shown in Figure 2. One can clearly see the integer tunes show up as peaks at tunes of 6 and 14, respectively (corresponding to $\nu_x = 13.75$ and $\nu_y = 5.80$ for the 92-nm-radian lattice). The sign of the difference orbit at the position of the exciting corrector can also be used to determine on which side of the half integer the fractional tunes exist.

Orbit Correction

A tool was developed to perform orbit correction in each plane at various points along the ramp. The method uses the standard SVD algorithm applied at selected points anywhere between injection and extraction. The software application allows the user to select BPM and corrector configurations and uses the computed **elegant** inverse response matrix for a given lattice to determine the new vector of corrector current changes from the BPM vector. The application also allows the user to select the number of ramp points to correct the orbit, feedback gain, and BPM averaging, and provides plotting diagnostics to analyze the orbit correction process. This tool was used after setting the fractional and integer tunes for a new lattice.

Chromaticity and Dispersion Measurements

Chromaticity and dispersion measurements were performed on each lattice listed in Table 1 for verification purposes. A convenient software tool was developed to measure both parameters simultaneously while varying the rf frequency. Each measurement can be performed at any given point between injection and extraction. The chromaticity measurement was performed using the VSA to measure the tunes as a function of rf frequency. The dispersion measurement was performed by varying the rf frequency and collecting both horizontal and vertical BPM readings.

The results are shown in Figures 3 and 4 for the 92-nm-radian lattice. Figure 3 shows good agreement between the dispersion measurement compared with the **elegant** calculation for the 92-nm-radian lattice. The chromaticity is shown as a function of time up the ramp. The sextupole settings used were slightly adjusted to zero the chromaticity. Figure 4 shows the chromaticity is slightly negative at parts of the ramp. This does not present a problem from head-tail instability for the 92-nm-radian lattice at up to 4 nC of charge per pulse.

CONCLUSION

Successful commissioning of booster low-emittance lattices is part of the ultimate goal of improving APS injector reliability and availability for SR top-up injection. The APS booster 92-nm-radian lattice has been used since January 2003 for routine SR top-up operation. This lattice used in combination with ongoing matching studies of the BTS transport line have as the ultimate goal improving SR top-up injection efficiency to 100%.

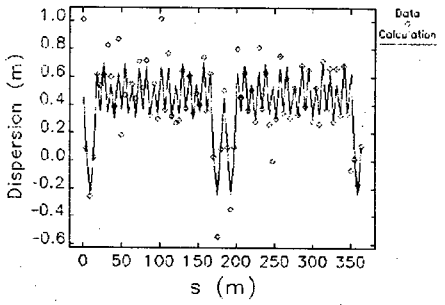

Figure 3: Measured horizontal dispersion at extraction compared to **elegant** calculation for the 92-nm-radian lattice. Agreement is generally good with differences attributable to BPM gain differences.

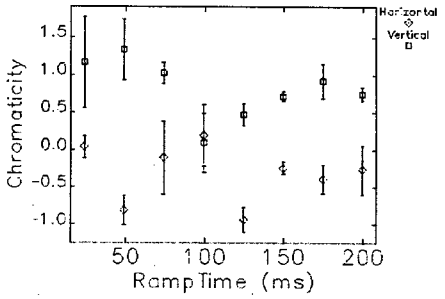

Figure 4: Measured chromaticity for the 92-nm-radian lattice where injection is at 0 ms and extraction is at 225 ms. Vertical data are seen to be biased slightly positive and horizontal slightly negative. The negative horizontal chromaticity at 125 ms may be the reason some loss is is observed at roughly this point above 4 nC/pulse.

ACKNOWLEDGEMENTS

The authors wish to acknowledge many valuable discussions with L. Emery regarding FODO lattices. The authors also thank the APS power supply group for modifying the quadrupole family current transductors, which enabled higher currents to be accurately measured for low-emittance lattice commissioning.

REFERENCES

[1] L. Emery, private communication.
[2] M. Borland, "elegant: A Flexible SDDS-Compliant Code for Accelerator Simulation," APS Light Source Note LS-287, September 2000.
[3] N. Sereno, F. Lenkszus, R. Lill, "APS Booster Synchrotron BPM Upgrade and Applications," these proceedings.
[4] S. V. Milton, "The APS Booster Synchrotron: Commissioning and Operational Experience," Proceedings of the 1995 PAC, 594-596 (1996).
[5] N. S. Sereno, "APS Booster Synchrotron RF Sub-harmonic Capture Design," these proceedings.

GENERATION OF HIGH-ENERGY SYNCHROTRON RADIATION WITH A 10-T SUPERCONDUCTING WIGGLER INSTALLED IN THE SPring-8 STORAGE RING

K. Soutome*, S. Daté, H. Ego, T. Fukui, M. Hara, N. Hosoda, Y. Kawashima, M. Kodera, N. Kumagai, T. Magome, M. Masaki, T. Masuda, S. Matsui, T. Nakamura, T. Noda, Y. Ohashi, T. Ohshima, M. Oishi, H. Saeki, S. Sasaki, M. Shoji, S. Takano, M. Takao, T. Takashima, H. Takebe, K. Tamura, H. Tanaka, Y. Taniuchi, K. Tsumaki, T. Yorita, C. Zhang, H. Yonehara
SPring-8, Hyogo 679-5198, Japan
J. Schimizu, The Japan Research Institute Ltd., Osaka 542-0081, Japan
A. Batrakov, G. Karpov, G. Kulipanov, M. Kuzin, V. Shkaruba, A. Skrinsky, N. Mezentsev
Budker Institute of Nuclear Physics, Novosibirsk 630090, Russia

Abstract

A three-pole 10-T superconducting wiggler was installed in the 8-GeV electron storage ring at SPring-8 for generating high-energy synchrotron radiation. Beam tests were carried out to check its performance and to investigate the effects on a stored beam. A beam was successfully stored at magnetic fields of the wiggler up to 9.7 T. The beam current was limited to 1 mA to avoid unnecessarily high heat-load on photon absorbers and radiation damage to accelerator components. Beam parameters such as a horizontal beam size, a bunch length, betatron tune shifts were measured. A spectrum of high-energy synchrotron radiation from the wiggler was also measured with the NaI scintillator at an extremely low beam current of about 8 pA.

INTRODUCTION

There are some demands of using high-energy gamma rays in the energy range from a few hundred keV to several or ten MeV. Intense low-energy positron beams can be produced via the electron-positron pair-production process by high-energy gamma rays. The low-energy positron beam is a powerful probe of Fermi surface and defects in materials science[1]. In nuclear astrophysics, it becomes probable to measure photonuclear reaction cross sections of some key elements such as ^{16}O and ^{180}Ta in the scenario of nucleosynthesis[2]. High-energy photons of about a few hundred keV to 500 keV can be used in, for example, Compton scattering experiments. Another possibility is the generation of neutrons via photodisintegration of ^{9}Be[3].

To generate high-energy gamma rays Csonka[4] proposed to use a micropole undulator. We proposed[5] to use a high-field superconducting wiggler (SCW) since necessary techniques are ready in Budker INP to develop SCW and an 8-GeV electron storage ring is available at SPring-8. We designed and fabricated a 10-T superconducting wiggler at Budker INP[6, 7] and installed it in the SPring-8 storage ring in August, 2002. Beam tests were then carried out and the results are reported in this paper.

* soutome@spring8.or.jp

THREE-POLE SUPERCONDUCTING WIGGLER

A design value of the maximum field of SCW is 10 T and the achieved maximum value is 10.3 T recorded in a test site at SPring-8[8]. A field distribution was measured on the median plane of the electron orbit by using a Hall sensor fixed on a carbon rod and calibrated with NMR probes. The measured dipole field distribution along the wiggler axis is shown in Fig. 1 by the solid line. The peak value is 10.136 T. A calculated distribution is also shown by the dashed line. Calculated and measured fields agree well. The maximum values of the position and angle of the electron orbit at 10 T are 7.3 mm and ±25 mrad, respectively.

The first integral of the measured magnetic field along the electron orbit was 0.011 Tm, which corresponds to a horizontal kick angle of 0.4 mrad for an 8-GeV electron beam. This kick can be compensated by tuning two independent power supplies connecting to central and side poles of SCW.

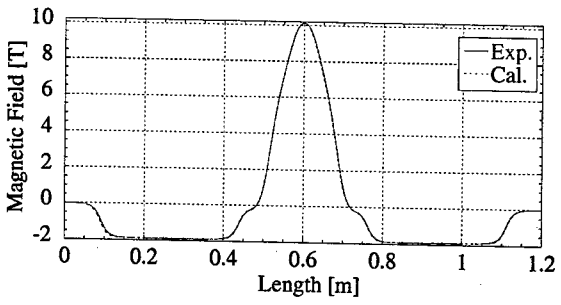

Figure 1: Dipole field distribution of SCW.

From the measured field distribution we evaluated quadrupole and sextupole components caused by non-uniformity of the fields. The integrated values of quadrupole and sextupole components are 0.50 T (defocusing) and 45 T/m (focusing), respectively, when the peak field is 10.136 T.

The details on SCW are described in Ref.[7].

0-7803-7738-9/03/$17.00 © 2003 IEEE

BEAM TEST

For the purpose of beam tests, a stored current of 1 mA is enough to check the performance of SCW and to investigate the effects on a stored beam. Due to this limit of the beam current, we can avoid unnecessarily high heat-load on photon absorbers and radiation damage to accelerator components.

To perform efficient orbit corrections in both horizontal and vertical directions, we installed two horizontal and two vertical correction magnets upstream and downstream by SCW. Furthermore, we introduced two independent power supplies for two quadrupole magnets adjacent to SCW to compensate optics distortion. Though this scheme was found to be efficient to recover tune shifts, we did not routinely use it during a beam test.

Effects of SCW

Since the defocusing force becomes stronger as the field of SCW becomes higher, we changed a working point from a nominal point $(\nu_x, \nu_y) = (40.15, 18.35)$ to (40.24, 18.35) at the beginning of the beam test, where ν_x and ν_y are the horizontal and vertical betatron tunes, respectively. The horizontal and vertical betatron functions at SCW are 25 m and 7 m, respectively.

In Fig. 2 we show the horizontal and vertical betatron tunes as a function of the peak field of SCW. Measured values are shown by solid circles (horizontal) and solid triangles (vertical). During excitation of SCW we changed the strength of the quadrupole magnets adjacent to it, and the betatron tunes were shifted by this change. The measured tunes in the figure are corrected by this amount. In Fig. 2 we show calculated tunes at 10.136 T by open symbols. The horizontal tune shifts can be explained by the quadrupole component of measured magnetic fields and the vertical ones can be explained by adding the effect of edge focusing.

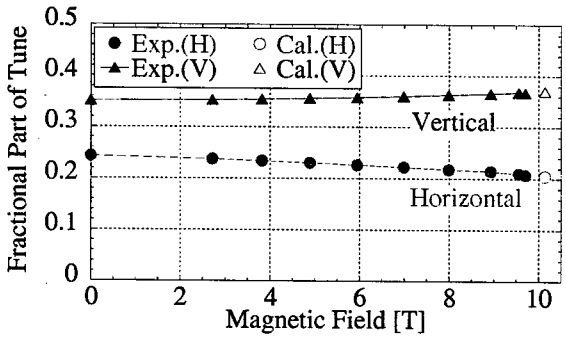

Figure 2: Betatron tunes as a function of the SCW peak field.

To study the effects on beam emittance, we measured the horizontal beam size at the point of beam injection in the following way[9]: we store a single-bunch beam, scrape it by firing bump magnets, measure a beam-loss rate and repeat this procedure by changing the height of a bump orbit. By assuming a gaussian density distribution for a circulating beam, we can obtain the root-mean-square beam size by fitting the data points of the beam-loss rate with the method of least squares. The results are shown in Fig. 3 by solid circles. Measured values are normalized by a value at 0 T to show relative change. The solid curve shows a calculation by using the field data shown in Fig. 1. We obtained good agreement between the experimental data and calculation results. An emittance is increased from 6.4 nmrad at 0 T to 13 nmrad at 10 T. This large increment is due to a large horizontal betatron function in a position of SCW.

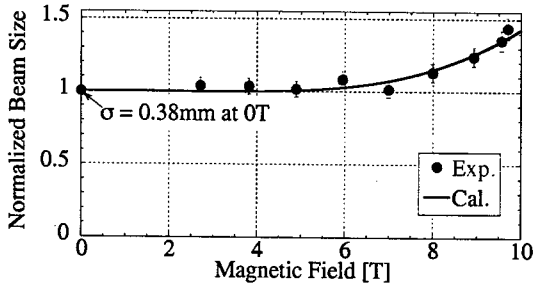

Figure 3: Horizontal beam size normalized by a value at 0 T.

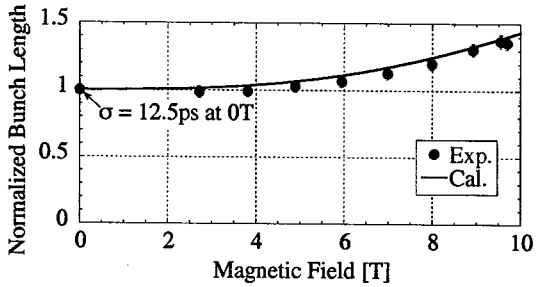

Figure 4: Bunch length normalized by a value at 0 T.

The normalized bunch length is shown in Fig. 4. An energy spread is increased from 0.11 % at 0 T to 0.15 % at 10 T due to emission of photons by SCW.

The sextupole field component of SCW mainly affects the dynamic aperture. (Though the sextupole as well as the quadrupole component changes chromaticities, a change in chromaticity is less than 0.1 and can be neglected.) The dynamic aperture was calculated by taking account of the sextupole components. The results show that the aperture is reduced in the horizontal direction. It is reduced typically from (-15 mm, +8 mm) to (-10 mm, +7 mm) at the point of beam injection. The injection efficiency was decreased by this reduction of the aperture.

Photon Energy Spectrum

We measured a spectrum of high-energy synchrotron radiation (SR) by using the NaI(Tl) scintillator and a photomultiplier (PM) when the SCW peak field was 9.5 T. A single-bunch electron beam of 0.11 mA was firstly stored and then scraped by firing bump magnets. The ratio of the number of electrons before and after scraping was estimated by the photon-counting method[10]. We then measured a photon spectrum at an extremely low beam current of 8 pA(±20 %).

A schematic drawing of a photon beamline is shown in Fig. 5. All equipments for the spectrum measurement were installed in the storage ring tunnel. No experimental hutch was constructed and the photon beam was not extracted from the tunnel.

To separate ultra-high vacuum and atmosphere we put two windows in the photon beamline. One is made of Be with a thickness of 0.25 mm and the other Al with a thickness of 3 mm. A block of Pb with a thickness of 50 mm was set downstream from the windows to cut low-energy gamma rays.

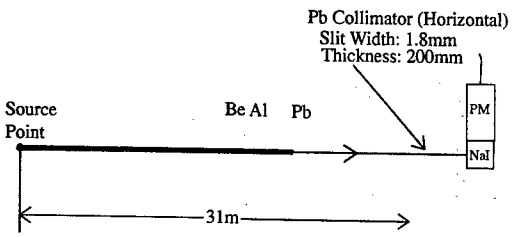

Figure 5: Experimental setup for spectrum measurement.

In Fig. 6 we show the measured photon-energy spectrum together with simulation results obtained by the GEANT3-code[11]. The energy calibration of the detector was done by using a radioactive source of ^{60}Co which emits gamma rays of 1.17 MeV and 1.33 MeV. The dashed lines in Fig.6 indicate the ambiguity of estimation of a total number of stored electrons. Reasonable agreement of the experimental data on the simulations was obtained. There is a possibiliy that a slight difference between the experimental data and the simulations comes from radiation damage of the detector during the spectrum measurement and/or from a systematic error of energy calibration. Alignment errors of a Pb collimator could also be a source of ambiguities in simulations.

SUMMARY

We installed a 10-T superconducting wiggler in the SPring-8 storage ring and carried out beam tests. Beam parameters and a photon spectrum were measured, and the results agreed well with calculations based on the measured field distribution.

The effects of SCW on the stored beam are not small. When the peak field of SCW is 10 T, the horizontal emittance becomes twice. The reason is that the SPring-8 storage ring is operated with a "high-beta" optics and the straight section where SCW was installed has a large horizontal betatron function.

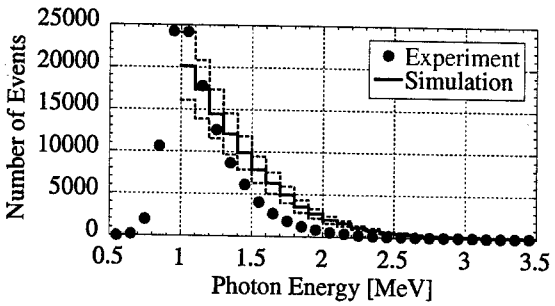

Figure 6: Photon spectrum at a magnetic field of 9.5 T.

When we consider the effects on the stored beam together with high heat-load, it is hard to use SCW in user-time since many SR users require highly brilliant and stable X-ray beams. Nevertheless, the applications of high-energy gamma rays generated by SCW are interesting and important, and we are now looking for a possible way of using SCW not for the beam test but for real applications.

ACKNOWLEDGMENTS

The authors would like to thank Prof. T. Hata in Osaka City University for valuable suggestions to improve cooling efficiencies of the cryostat for SCW. They also thank the staff of the facilities and utilities division and the safety office of SPring-8 for installation of SCW.

REFERENCES

[1] P.J. Schultz and K.G. Lynn, *Rev. Mod. Phys.* **60** (1988) 701.

[2] H.Utsunomiya, *et.al.*, *Phys. Rev.* **C67** (2003) 015807; H. Utsunomiya, in Proc. of Int. Workshop on Laser Photons at SPring-8 (2000) p.89.

[3] D.A.Gryaznykh, V.A. Lykov and V.V. Plokhoi, *Nucl. Instr. and Meth.* **A448** (2000) 106.

[4] P.L. Csonka, *Nucl. Instr. and Meth.* **A345** (1994) 1.

[5] A. Ando, *et.al.*, *J. Synchrotron Rad.* **3** (1996) 201.

[6] ISTC Project No.767C, Technical Report (1999).

[7] M. Fedurin, *et.al.*, *Nucl. Instr. and Meth.* **A448** (2000) 51; M. Fedurin, *et.al.*, *Nucl. Instr. and Meth.* **A470** (2001) 34.

[8] A. Batrakov, *et.al.*, *Nucl. Instr. and Meth.* **A467** (2001) 190.

[9] K. Soutome, *et.al.*, *SPring-8 Ann. Rep. 1999*, p.136. (http://www.spring8.or.jp/e/publication/ann_rep/AR99.html)

[10] K. Tamura, *SPring-8 Ann. Rep. 1998*, p.146. (http://www.spring8.or.jp/e/publication/ann_rep/AR98.html)

[11] GEANT Detector Description and Simulation Tool, CERN Program Library W5013 (1994).

IN-VACUUM UNDULATORS AT ESRF

J. Chavanne, C. Penel, B. Plan, F. Revol, ESRF, F38043, Grenoble France

Abstract

Five in-vacuum undulators are currently in routine operation at the ESRF with a minimum gap of 5 mm to 6 mm. The results of the magnetic measurements are presented. The measured interaction with the stored beam (closed orbit distortion, lifetime) are discussed. Three additional devices are at present being constructed including a magnetic structure of hybrid type. They are all dedicated to operation at high photon energy above 50 keV and require an optimum spectrum shimming. The magnet temperature is permanently monitored in all different time filling modes of the ring. An estimation of the heat load deposited by the beam in the flexible input/output transition as well as in the copper sheet covering the magnet blocks is given.

1 INTRODUCTION

Starting beginning of 1999 five in-vacuum undulators have been progressively installed on the ESRF storage ring. Three other devices are being measured in the laboratory and will be installed before the end of year 2003. Their main characteristics are summarized in Table 1. With the exception of the ID11 devices (a prototype), the nominal magnetic length of standards in-vacuum undulators is 2 meters (Figure 1).

Table 1: Status and main parameters of the ESRF in-vacuum undulators.

ID straight	Period [mm]	Magnetic length[m]	Min./Max gap [mm]	Install. date
11	23	1.6	5/30	Jan 99
22	23	2	6/30	Jul 01
29	21	2	6/30	Dec 01
9	17	2	6/30	Dec 01
13	18	2	6/30	Jul 02
30	23	2	6/30	Jul 03
30	23	2	6/30	Jul 03
11	22	2	6/30	Dec 03

Due to baking requirements (120 deg C) and possible radiation damages at small gaps, all devices are based on the Sm_2Co_{17} permanent magnet material. The magnetic structure is of pure permanent magnet type (p.p.m.) for 6 devices. Two devices are based on the hybrid technology (ID11 U23 and ID11 U22).

2 MAGNETIC MEASUREMENTS

The magnetic measurement and field correction methods are essentially derived from the techniques used for conventional undulators. Nevertheless these methods had to be refined when considering the very small gaps (5 mm) and the constraints connected to ultra high vacuum operations. One example is the design of new narrow 3D hall probe keepers allowing field mapping at gaps as small as 3 mm.

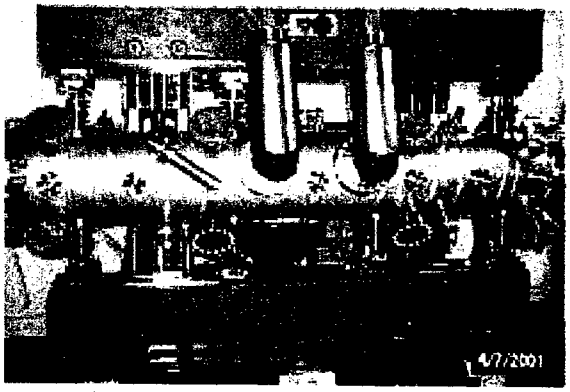

Figure 1: Standard 2 m long ESRF in-vacuum undulator ready for installation

2-1 Multipole shimming

The multipole shimming based on thin soft iron shims as used for conventional undulators is not advisable for in-vacuum device because the shims cannot be glued on the magnet faces. The control of the field integrals is made in two steps:

- Each module containing one or three magnets (two modules make a period) is characterized in field integral. A pairing is determined that minimizes the field integral after assembly. In addition, the field integrals are regularly measured during the undulator assembly and the selection of the next modules to assemble is selected based on the measured field integral.
- After assembly, the field integrals are further tuned using an array of small magnets located at each end of each magnet jaw.

This process is time consuming but allows a high efficiency of field integral corrections. Figure 2 shows the resulting field integral components (gaps of 5 mm and 30 mm) versus horizontal position for the latest undulator (ID30 U23). The associated variation of the on-axis first and second field integrals versus gap is represented in Figure 3.

2-2 Spectrum shimming

The three last devices of Table 1 are expected to operate at high photon energy on the high harmonics of the spectrum (7 to 11). The flux and brilliance of high harmonics are very sensitive to the optical phase errors and require special correction (spectrum shimming). Without any correction the r.m.s value of the phase error computed at each pole is usually in the range of 6 to 8 degrees. Spectrum shimming focuses essentially on the reduction of the r.m.s phase error around 2 degrees at the small gaps (5 or 6 mm). The method relies on the local

0-7803-7738-9/03/$17.00 © 2003 IEEE

vertical repositioning (± 100 μm maximum) of the magnet modules. The r.m.s. phase errors after correction as a function of gap is presented in Figure 4 for the first ID30 U23 in-vacuum undulator.

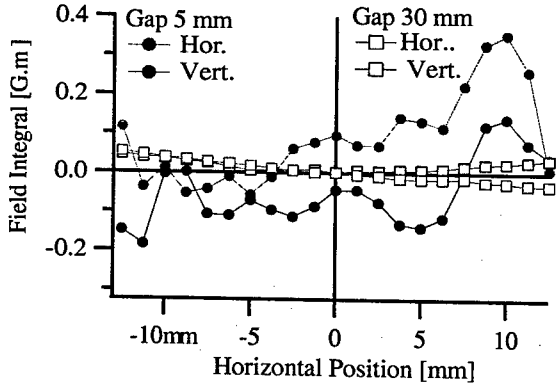

Figure 2: Field integral components versus horizontal position for the in-vacuum undulator ID30 U23 at gaps 5 mm (circular markers) and 30 mm (square markers).

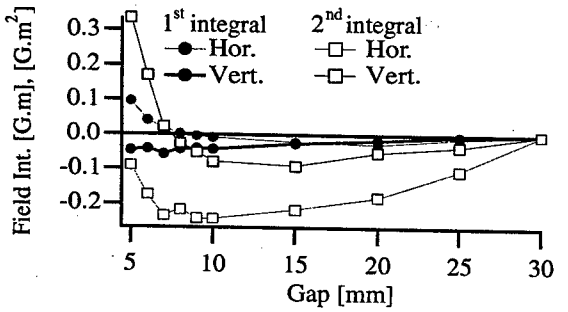

Figure 3:On-axis first and second field integrals component as functions of gap for the in-vacuum undulator ID30 U23.

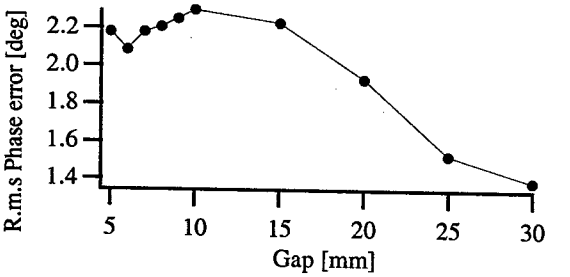

Figure 4: R.m.s phase error as a function of gap for the ID30 U23 device.

3 INTERACTION WITH THE STORED BEAM

3 -1 Closed Orbit Distortions

The most visible interaction of in-vacuum undulators with the stored beam is Closed Orbit Distortions (CODs) induced while varying the gaps. Such measurement is made for all installed IDs on a regular basis (every two months) using an automated procedure. The method involves the reading of all BPMs and adequate fits on data to derive the first and second field integral variations with gap with a reference taken at the opened gap. Table 2 compares the maximum variations of the first and second field integrals in both planes measured in the laboratory and derived from COD measurements for the last four in-vacuum undulators installed. The first integral components ΔIx (horizontal) and ΔIz (vertical) are expressed in G.m and for the second field integrals ΔJz (vertical) and ΔJx (horizontal) the data are in $G.m^2$. In all cases, the maximum gap is 30 mm (reference gap) and the minimum gap is 6 mm. The COD measurements are in good agreement with magnetic measurements. Such COD results are very similar to those observed for conventional out of vacuum IDs and no active correction needs to be implemented

3-2 Effect on beam lifetime

The effect of in-vacuum undulators on the beam lifetime is another important issue. Lifetime reduction is only visible in the multibunch electron filling modes (uniform and 2* 1/3 filling pattern I=200mA, lifetime 60-80 hours) for gaps higher than 5 mm [1]. For all installed in-vacuum undulators, no effect is visible when closing the ID gap down to 6mm. The reduction of the lifetime remains lower than 10 % when closing further the gap to 5 mm. This effect is very reproducible from one device to another. This is acceptable for future operation of our in-vacuum undulators at the minimum gap of 5 mm. The vertical beta function in the middle of the 5 m straight section is 2.5 m. A straight section can accommodate two in-vacuum undulators segments (ID11, ID30)

Table 2: Measurements of 1st and 2nd field integral variation versus gap for 4 in-vacuum undulators, left part: magnetic measurements, right part: derived from COD.

	Magnetic Measurements				From COD			
ID #	ΔIz	ΔJz	ΔIx	ΔJx	ΔIz	ΔJz	ΔIx	ΔJz
ID9 U17	0.05	0.1	0.09	0.2	0.1	0.1	0.12	0.3
ID13 U18	0.04	0.5	0.11	0.4	0.13	0.4	0.1	0.5
ID22 U23	0.1	0.75	0.1	0.5	0.3	0.9	0.25	0.3
ID29 U21	0.08	0.13	0.09	0.5	0.16	0.4	0.2	0.8

4 HEAT LOAD BUDGET

The ESRF in-vacuum undulators include a water cooling system, as shown in Figure 5. It consists of two separate circuits in thermal contact with the copper blocks ends and stainless steel girder (clamping). The temperature of the magnetic structure is permanently monitored versus time at different positions along the magnetic array (6 for each upper and lower array). The observation of the thermal variations of an in-vacuum undulator is a long time process. Indeed, the global thermal behaviour of the in-vacuum components is

governed by a typical time constant of 28 hours which prevents reliable measurements over a few hours.
The water cooling has been disconnected on two devices (ID22 U23 and ID29 U21) for a period of 6 months starting after the summer 2002 shutdown. This experiment had two main interests:

- Evaluation of the efficiency of water cooling
- Estimation of the heat load deposited by the electron beam in the flexible input/output transitions and in the copper sheet covering the magnetic assembly.

Several parameters such as temperatures of the magnet assemblies, ID gaps set by the beamlines, beam current and lifetime were stored in a database with a typical time period of 1 minute.

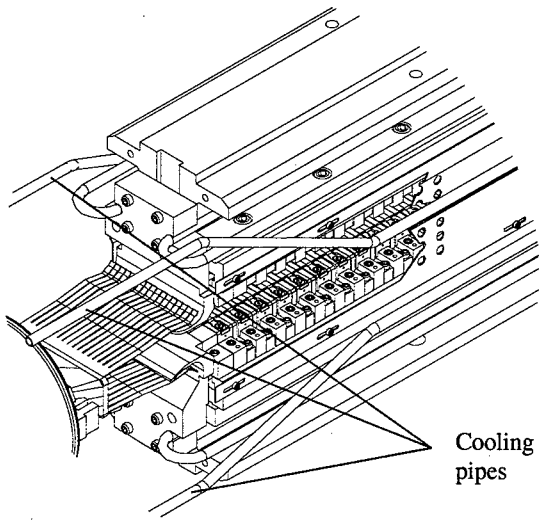

Figure 5: 3D view of the cooling circuit in the end section of an in-vacuum undulator.

Without any water cooling the heat is essentially transmitted to outside through the 16 stainless steel columns connecting the outside main girders and the in-vacuum magnetic assembly. The thermal resistance (≈ 16 deg C/Watt) of each column is the dominant parameter controlling the heat transfer.

4-1 Experimental results

The data extracted from the database concerns only constant gap operation over a period of time larger than four days. Two different electron beam filling modes have been analysed: 16 bunches and uniform filling pattern (992 bunches). Obviously, in these two modes, the beam current is not constant but decreases from 90 mA (200 mA) to 60 mA (170 mA) in the 16 bunches (uniform) filling mode with the periodicity of injections. The temperature of reference measured without current in this experiment was around 24.5 deg C.
The essential observation results are;

- The two undulators have almost the same behaviour
- For the same filling mode the average temperature of the magnet assembly is at its highest when the ID gap is open (30 mm).
- The maximum average temperature of 61 deg C is obtained in the 16 bunches mode (gap 30 mm)

The highest average temperature reached with cooling is 30 deg C in 16 bunches at a gap of 30 mm.

4-2 Empirical model

A very simple static thermal model of the in-vacuum undulator is presented in Figure 6.

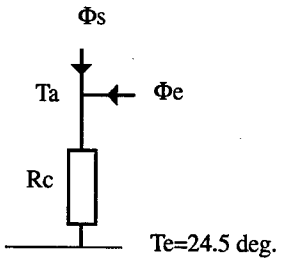

Figure 6: thermal model of the in-vacuum undulator

The purpose of this model is to determine the heat coming from the flexible input/output transitions (Φ_e) according to:

$$\Phi_e = \frac{(T_a - T_e)}{R_c} - \Phi s \qquad (1)$$

T_a is the average measured temperature of the magnet assembly, T_e is the temperature at the end of the columns out of vacuum (24.5 deg. C) and R_c is the thermal resistance of the 16 columns in parallel (R_c=1 deg/Watt). The heat deposited by the beam in the copper sheet (Φs) is evaluated analytically [2] [3] and averaged over beam current and bunch length variations during a beam decay.

Table 3: Empirical heat budget for in-vacuum undulators

ID gap [mm]	Filling mode	Ta [deg C]	Φs [W]	Φ_e [W]
6	16 b	45	6.5	14
6	Unif.	42	2	15.5
30	16 b	61	0.9	35.6
30	Unif.	44	0.6	18.9

The data in Table 3 suggest that the temperature of the magnet assembly is mostly dominated by the heat deposited in the flexible input/output transitions. The higher values for Φ_e at opened gap (30 mm) favour the geometrical wake field as the main source of heat.

5 REFERENCES

[1] J. Chavanne, P. Van Vaerenbergh , P. Elleaume, T. Gunzel ,EPAC 2000, Vienna, p. 2346-2348
[2] J.B. Murphy et al., PAC01, Chicago, p.465-467
[3] K. Bane S. Krinsky, PAC93, Washington, p.3375-3377

POSSIBLE LONG-TERM IMPROVEMENTS TO THE ADVANCED PHOTON SOURCE *

L. Emery†, M. Borland‡, Argonne National Laboratory, Argonne, IL 60439, USA

Abstract

Although third-generation light sources like the Advanced Photon Source (APS) already deliver very high performance, there are many user experiments that could benefit from further improvements. Improved brightness, improved beam stability, higher single-bunch current, more beamlines, and shorter bunches are all of interest to certain user groups. In this paper, we outline some possibilities to meet some of these needs.

Presently, the APS has an effective horizontal emittance of 3.0 nm-rad, achieved by allowing dispersion in the straight sections. Top-up allows us to go lower in spite of the poor lifetime, which we could do by adding pole-face windings to the dipoles to reduce the emittance to 1.8 nm-rad. A more dramatic effort would involve shortening the dipoles, which would have the added benefit of increasing the straight-section length from 5 m to 9 m.

Beyond this, several much more speculative ideas have been explored. One of these is to use the APS ring as part of an energy recovery linac facility, with single- or multi-turn circulation of a high-brightness linac beam in the existing ring. We present some preliminary simulations of the performance of this option. Another possibility is replacement of the APS storage ring with a next-generation ring capable of ultra-low emittance and making full use of top-up. We present a concept for a facility that promises 75 pm-rad horizontal emittance and 10m-long straight sections.

INTRODUCTION

Several ideas for improving the 7-GeV Advanced Photon Source (APS) are presented here. The main features and the identification of technological areas that needs further exploration are described.

POSSIBLE MODIFICATIONS OF THE APS STORAGE RING

The emittance can be reduced by increasing the horizontal damping partition number through a change in rf frequency. We have reduced the emittance during studies from 3.0 nm-rad to 2.5 nm-rad. While the rf frequency was changed in steps, the values of tunes and chromaticity were adjusted manually to keep them constant. Because of dispersion, the orbit at the straight section was steered horizontally by about -2 mm. When steering the beam back, the emittance returned close to the original value. Perhaps an angle steering while keeping the orbit at -2 mm would have sufficed to restore the photon beam steering, which we haven't tried. Clearly, changing rf frequency invites many operational difficulties.

An alternative to changing the rf frequency is to add a field gradient to the dipole by using pole face windings. The model emittance is significantly reduced (ϵ = 1.2 nm-rad, ϵ_{eff}=1.8 nm-rad, ν_x=46.2, ν_y=32.27). The lifetime will certainly decrease because of the higher nonlinearity. Figure 1 shows the lattice functions.

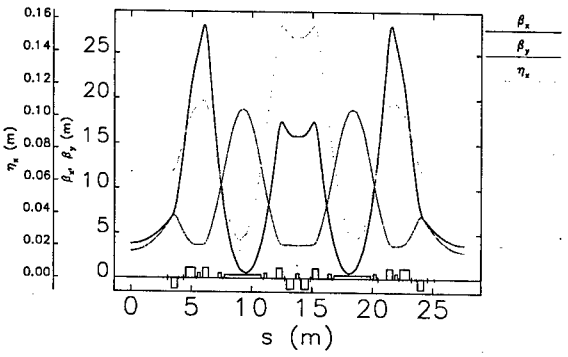

Figure 1: Machine functions of a much lower emittance lattice cell with gradients in the dipole.

The normalized gradient k for the dipole is optimized at -0.17 m^{-2}. The field in the dipole gap will vary from 0.2 T to 1.0 T, which is a large relative range. The pole winding could either cover the 10-cm width of the pole or cover only about +/- 3 cm of good field region to reduce the range in field, though one should be mindful of fringe fields. The current sheet value is given by $I = (k(B\rho)g_{1/2}w)/(4\pi \times 10^{-7})$. With k = -0.17 m^{-2}, $B\rho$ = 23.3 T-m, half-gap $g_{1/2}$ = 0.03 m, and width w = 0.105 m, the required I is 10 kA-turn. Since a maximum of 10 A/mm^2 for cooled conductors might be possible according to [1], the coil thickness could be as small as 10 mm. Cooling limits of conductors should be further explored to see if the coil thickness can be reduced.

The fact that all APS multipoles have individual power supplies allows gradual changes to the machine configuration, so we could implement such changes over a series of one-month shutdowns.

As previously reported in [2], lengthening the straight sections enables users to install three or possibly four undulators for greater flexibility of operation. This would not only increase the brightness for users who demand it, it would provide multiple beamlines from a single straight section for applications that are less demanding. Presently about L = 5.0 m is available for installation of undula-

* Work supported by U.S. Department of Energy, Office of Basic Energy Sciences under Contract No. W-31-109-ENG-38.

† emery@aps.anl.gov
‡ borland@aps.anl.gov

0-7803-7738-9/03/$17.00 © 2003 IEEE

tors in the 5.9-m straight section. Removing the nearest quadrupole magnet from the two adjacent girders, or replacing the dipoles with shorter ones, or both would allow space for an extra ID or two. One option is to replace the two closest 0.6-T, 3-m-long dipoles with 1.8-T, 1-m-long gradient dipoles. These special solutions have increased emittance, so we may only allow one or a few such straight section modifications. Various configurations are presently being pursued [3].

ENERGY RECOVERY LINAC

In addition to advanced storage rings and FELs, another concept for a next-generation light source is the Energy Recovery Linac (ERL) [4, 5]. In this concept, a superconducting linac is used to accelerate high-quality electron bunches to multi-GeV energies. The bunches are passed through one or more undulators in the course of being bent around a race-track transport line, which brings them back to the head of the linac. If the path length is such as to delay the bunch phase by 180 degrees, then the energy is extracted from the beam, which is then dumped at a relatively low energy. In this way, a high-duty-factor beam can be provided with relatively modest energy consumption.

A variation on the ERL concept involves injecting the beam from a superconducting linac into a storage ring, where it is allowed to circulate one or more turns. This has two potential advantages: First, the bunch rate from the linac injector can potentially be reduced without reducing the average flux delivered to users. Second, if this is done with an existing storage ring, then existing undulators and beamlines potentially benefit from higher beam quality and shorter bunches. In such a scenario, beam would be extracted from the ring after circulating one more more turns and then be sent back into the linac in the opposite direction.

We performed a preliminary evaluation of the possibility of such a facility at the APS, using the existing APS storage ring. Of particular concern were incoherent and coherent synchrotron radiation (ISR and CSR) effects. We used `elegant` to investigate three lattices: a lattice with zero-dispersion in the straight sections ("ZD" lattice), a lattice with low emittance ("LE" lattice), and an isochronous lattice with minimized emittance ("ISO" lattice). For each lattice, we injected a 50-pC bunch with 0.01% initial rms energy spread, 1-μm-rad initial normalized rms emittance, and 50-μm initial rms bunch length. The ZD lattice was the clear winner in terms of emittance, with less than 10% emittance growth in the first turn. This is because energy spread due to CSR does not result in effective emittance growth in the straight sections. In the longitudinal plane, the lattices are fairly close. Figure 2 shows simulation results for a single turn.

It must be noted that these simulations used a Gaussian input beam, which may be very misleading [6]. A more trustworthy simulation requires a complete simulation of the injector, including bunch compression. Any such problems can be mitigated by making the initial bunch longer and increasing the energy spread. Simply increasing the initial bunch length to 100 μm allows one to increase the charge to 100 pC while keeping the emittance growth under 10%. In addition, using a longer bunch opens the option of circulating for many turns. Figure 3 shows simulation results for a 100-pC bunch with initial rms bunch length of 300 μm (1 ps). The modest emittance growth suggests that a multiturn scenario would be feasible.

In addition to multiturn tracking and use of a realistic initial bunch distribution, these simulations should be extended to include wakefields. The recent development of an impedance database for the APS [7] will be useful in this regard.

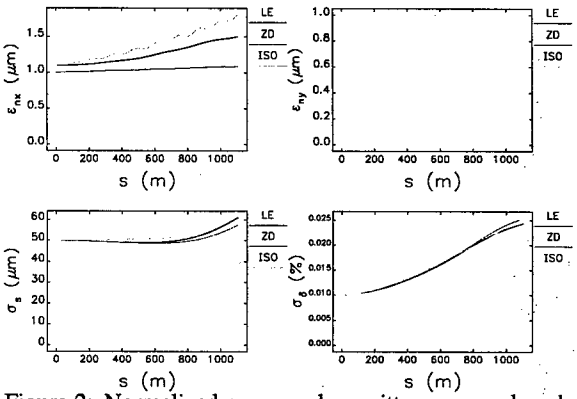

Figure 2: Normalized rms x and y emittances, rms bunch length, and rms momentum spread vs distance, for one turn in APS of a 50-pC bunch, for three trial lattices.

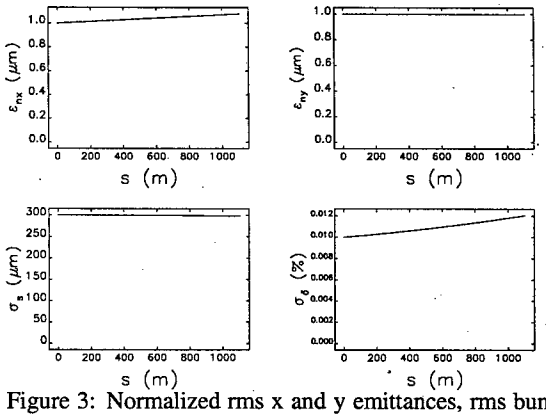

Figure 3: Normalized rms x and y emittances, rms bunch length, and rms momentum spread vs distance, for one turn in APS of a 100-pC bunch for the ZD lattice. The initial bunch length is 300 μm.

REPLACEMENT STORAGE RINGS

Another way to enhance the existing APS beamlines is to replace the APS ring with a new, lower-emittance ring. We investigated several possibilities for this. The most obvious

improvement is to double the number of cells in the lattice, which should reduce the emittance eightfold. In addition to this, we have investigated a more extreme concept that could reduce the emittance 100-fold.

For the 80-sector exercise, we started with the present APS design and then cut the length of all magnets and drift spaces in half, producing two subsectors in each present sector. We eliminated the straight section and triplets from the center, allowing us to lengthen the existing straight section to about 7.6 m from the present 4.8 m. `elegant` was used to minimize the effective emittance subject to various contraints on the beta functions. Figure 4 shows the lattice functions for this concept, which has a nominal effective emittance of 0.3 nm-rad.

The 80-sector ring is only about ten times better than the present-day APS, and may seem to offer too little improvement to justify the cost. To get truly low emittance, we developed a somewhat speculative concept called the eXtreme Photon Source (XPS). It features 40 sectors with three strong gradient dipoles per sector. Instead of separate quadrupoles and sextupoles, we assumed combined-function 12-pole magnets. Since there is dispersion everywhere, this promises to allow correction of the chromaticity from each quadrupole at the quadrupole itself. To improve stability and make the magnets feasible, we also suggest that all magnets be of a variable permanent magnet design. Figure 5 shows the lattice functions. The nominal effective emittance is 75 pm-rad, with a 20% increase expected from intrabeam scattering (assuming full coupling). The lattice allows approximately 10 m for insertion devices in each straight section.

Because of the strong sextupoles in this lattice, the dynamic aperture is too small to allow accumulation. In addition, the beam lifetime is estimated at about 45 minutes assuming 1 mA/bunch and 7.5 MV rf voltage. Hence, we would have to use on-axis injection and inject frequently, using a high-current, low-emittance injector. We propose using the existing APS ring (moved to the floor of the tunnel) as an accumulator ring for the XPS ring. In this proposal, both the APS and XPS would have approximately the same stored beam current at all times. When the beam in the XPS had decayed excessively, it would be swapped with the beam in the accumulator during a single turn. (This entails filling only half the circumference in each machine.) After swapping, the bunches in the former XPS beam would be replenished with the injector and then kept ready using top-up until the next "swap-up" was required. An advantage of using on-axis injection is that we can operate on the coupling resonance, thus providing round beams and smaller horizontal emitance.

The dynamic aperture for the bare lattice without errors is about ± 0.75 mm in both planes for energy offsets from -2% to 2%. Because of the small emittance, this corresponds to more than 20 times the rms beam size. Clearly, much more work is required on this concept, but it appears promising. Note that the normalized emittance of this 7-GeV ring is about 0.5 μm, comparable to proposed ERL and FEL linacs. Like ERL and (to a lesser extent) FEL proposals, the XPS is highly speculative and requires new technology. Our studies indicate that investigation of the requirements for such a ring could be very worthwhile.

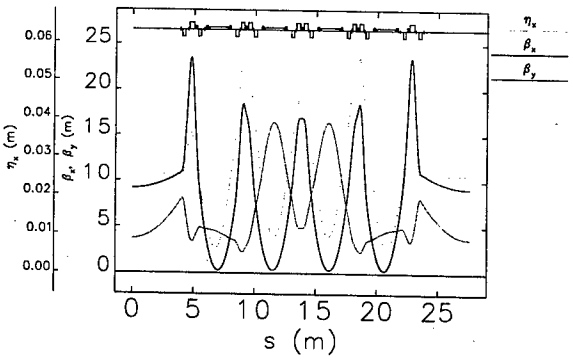

Figure 4: Lattice functions for the 80-sector concept replacement ring.

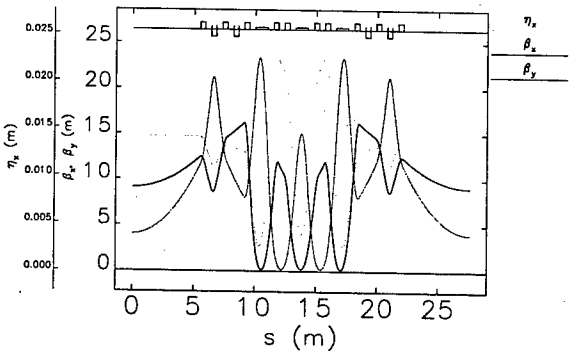

Figure 5: Lattice functions for the eXtreme Photon Source concept replacement ring.

REFERENCES

[1] G. E. Fischer, AIP Conference Proceedings 153, 1120 (1987).

[2] L. Emery et al. "Progress and Prospects Toward Brightness Improvements at the Advanced Photon Source," 2001 PAC, Chicago, 2602 (2002).

[3] V. Sajaev, private communication.

[4] S. Gruner, D. Bilderback, and M. Tigner, "Synchrotron Radiation Sources for the Future," white paper, http://erl.chess.cornell.edu/Papers/Papers.htm.

[5] I. Ben-Zvi et al., "Photoinjected Energy Recovery Linac Upgrade for the National Synchrotron Light Source," 2001 PAC, Chicago, 350 (2002).

[6] M. Borland et al., "Start-to-End Simulation of Self-Amplified Spontaneous Emission Free-Electron Lasers from the Gun through the Undulator," NIM A 483 (2002) 268-272.

[7] Y. Chae, "The Impedance Database and Its Application to the APS Storage Ring," these proceedings.

Proceedings of the 2003 Particle Accelerator Conference

SIMULATION TOOLS FOR HIGH INTENSITY RINGS

S. Cousineau* , ORNL, Oak Ridge, TN 37830, USA

Abstract

Several codes have been developed specifically to simulate beam dynamics in high intensity rings. These codes contain detailed algorithms for modeling the relevant physics in the beam, from single particle transport to important collective effects, including space charge and impedances. Among the various codes, a number of different methods have been adopted for the treatment of space charge. The codes have been applied to a variety of problems in existing machines, as well as for the study, design, and optimization of future machines. A review of existing ring simulation codes is presented, with specific emphasis on the space charge implementation. A more in-depth description of the features and application histories of a few specific codes is given, as well as a summary of code benchmarks with experimental data.

INTRODUCTION

The low loss requirements for future high intensity rings will require detailed knowledge of beam dynamics in the machine. Large scale computational models provide an invaluable tool for simulating the multitude of processes that can contribute to beam loss. In particular, in the regime of high beam intensities and low beam energies, collective effects such as space charge and impedances have a significant effect on the beam behavior. In order to predict beam loss at the levels required by future machines, i.e., tiny fractions of the beam intensity, the simulations must realistically account for the entire transport of the beam in the ring, from mapping through external magnetic fields to modeling of collective effects. Due to the complexity of this task, a computational framework is natural. Simulations of this type are productive in the analysis of instability thresholds, halo development, and emittance dilution in existing machines, and are equivalently useful in the design and optimization of future machines.

In the past few years, a wealth of simulation tools geared specifically for application to high intensity rings has been developed. The majority of these tools began as small, in-house codes written with a specific problem in mind, but have subsequently been upgraded into more general packages applicable across a broad range of problems. Each package, or code, typically contains models for a substantial subset of the relevant physical process: injection, strip foil effects, RF capture and acceleration, transport through linear and nonlinear magnetic fields, field errors, fringe fields, space charge, impedances, boundaries and image charges, electron-proton interactions, apertures and collimation, modeling of non-standard hardware, diagnostic capabilities, etc.

A realistic simulation of a high intensity beam would ideally algorithms for all the relevant physics together with a large number of macro-particles to reduce numerical noise. However, because of the computational expense of many of the algorithms, especially the collective algorithms, one usually must limit either the number of models included, or the number of macro-particles. Typically, the most dominant effects on the beam are known apriori, and the algorithms representing these effects are prioritized over algorithms which contribute only marginally to the beam behavior. Recently, this problem has been alleviated somewhat by the implementation of parallel computing into many of the codes. The parallel framework allows for fast processing of large jobs, which may include multiple collective processes, as well as large numbers of particles ($\geq 10^6$). Though there is still progress to be made, many simulations can now realistically portray beam behavior in a high intensity ring.

With the capability to simulate real machines comes the opportunity to benchmark the codes against experimental data. Successful benchmarks with experiment are critical to establishing credibility of the models in the codes. Additionally, since codes are often used for the design of future machines, a successful benchmark with a current machine lends confidence to the predictions for future machines. Experimental studies at several existing machines have recently been undertaken, and effort is underway to involve a larger number of codes in more ambitious benchmark tests.

This paper presents a review of the current state-of-the-art in in simulation tools for high intensity ring beams. Aspects of the various treatments of space charge are highlighted. A brief summary of code capabilities for a representative sampling of codes is presented, and a discussion of specific problems to which the code has been applied is given. Summary tables of each code availability, space charge implementation, and code benchmark versus experiment are also shown.

SUMMARY OF AVAILABLE CODES

Information on many of the available ring space charge codes was presented at the ICFA Beam Dynamics Mini-Workshop on Space Charge Simulation [1]. Table 1 lists the codes and gives the details of code accessibility and documentation, programming language, appropriate platform for installation, parallelization status, and any additional external libraries required.

*SNS is managed by UT-Battelle, LLC, under contract DE-AC05-00OR22725 for the U.S. Department of Energy. SNS is a partnership of six national laboratories: Argonne, Brookhaven, Jefferson, Lawrence Berkeley, Los Alamos, and Oak Ridge.

0-7803-7738-9/03/$17.00 © 2003 IEEE

Table 1: Summary of codes and portability.

CODE	Access Information	Language	Platform	Parallel Capability	External Libraries
ESME	www-ap.fnal.gov/ESME/	F77	Unix/Linux	Yes	None
LONG1D	www.triumf.ca/people/koscielniak/long1d.htm	F77	DEC/Linux	No	GPlot, CERN libs
Track 1D, 2D, 3D	c.prior@rl.ak.uk	F77	Any	No	None
SIMPSONS	shinji.machida@kek.jp	F77	Any	In progress	None
ACCSIM	www.triumf.ca/compserv/accsim.html	F77	Unix/Linux	No	CERN libs
ORBIT-ORNL	www.sns.gov/APGroup/Codes/orbit.htm	C++	Unix/Linux	Yes	MPI, SuperCode, MXYZTPLK, FFTW
ORBIT-BNL	luccio@bnl.gov	C++	Unix/Linux	Yes	MPI
ML/IMPACT	rdryne@lbl.gov	F90	Unix/Linux	Yes	MPI
GenTrackE	andreas.adelmann@psi.ch	C++	Unix/Linux	Yes	MPI
Best	hongqin@princeton.edu	F90	Unix/Linux	Yes	MPI, OpenMP
Synergia	spentz@fnal.gov	F90/C+	Unix/Linux	Yes	MPI

An important component of any code simulating high intensity ring beams is the space charge algorithm. Historically, space charge effects were considered important mainly in linear accelerators, where the peak density of particles is much greater than in rings. Several space charge codes exist for linacs, many of which have been extensively applied to space charge studies in current and future machines [2]. Recently, space charge has been recognized as an important phenomenon for rings as well. Even for very high intensity ring beams, the space charge force is small compared to that in linac beams. However, due to the periodic nature of rings and the long duration time spent there, the ring beam is sensitive to resonant excitations induced by space charge, and a relatively small space charge force can significantly alter the beam behavior. Implementation of space charge routines for rings began as early as 1980 [3]. The effort has increased dramatically in recent years, stimulated by projects such as the SNS machine [4] and the prospect of future high intensity proton drivers.

A variety of approaches to solving Poisson's equation for the ring beam have been developed, each with its own merits and drawbacks. One problem that all space charge algorithms must contend with is the computation expense of the problem, which normally occupies the largest single portion of CPU run time. This expense is rooted in the large number of macro-particles, the finely-spaced meshes, and the small integration lengths required by space charge solvers to provide accurate results with low numerical noise. To overcome this hurdle, many codes contain fast solvers which rely on a few approximations, or parallel processing capabilities, or both. Some of the more common approaches to solving Poisson's equation for the beam include various types of spectral methods (FFT convolutions in mode-space), finite element methods (FEM), or fast multipole method (FMM) techniques.

Table 2 gives a summary of routines and parameters relevant to the space charge implementation for the codes shown in Table 1 . For each code, the table lists the independent variable used for tracking, the dimension of the space charge model, the number of macro-particles that are typically tracked, the type of space charge algorithm, and whether any image or boundary charges can be included. Recall that the parallel capability of the codes is listed in Table 1.

DETAILS OF SOME SPECIFIC CODES

In this section, a brief discussion of some of the codes listed in Tables 1 and 2 is given. In addition to summarizing capabilities or highlighting key features, a few of the problems to which the codes have been applied are also presented. Unfortunately, due to space considerations, it is not possible to present separate reviews all of the codes listed in Tables 1 and 2. The discussion below is intended as representative sampling of codes and some of their applications, not a comprehensive survey.

ESME

The ESME code is designed for tracking in longitudinal phase space of a beam [5], and for other aspects of a proton synchrotron that are governed by RF. The code follows the beam distribution in energy and azimuth on a turn-by-turn basis, where the independent variable for tracking is the revolution time of the synchrotron. The code began development in the early 1980's, and has been extended considerably since this time, with implementation of the space charge algorithm in 1986. ESME now contains comprehensive capabilities for modeling the physics relevant to the longitudinal dynamics of the beam, including, but not limited to,

- Energy ramps: linear, parabolic, cubic, biased sinusoid, user defined
- Arbitrary phase and voltage curves, multiple RF sources, exact sinusoidal, non-sinusoidal
- Lattice nonlinearity via $\Delta p/p$ expansion

Table 2: Summary of routines and parameters relevant to space charge implementation.

CODE	Independent Variable	Dimension of SC Model	Number of Particles	Space Charge Model	Boundaries & Images
ESME	revolution time	1D long.	10^7	smoothed $\frac{d\lambda}{dz}$	Circular conducting wall
LONG1D	revolution time	1D long.	10^6	smoothed $\frac{d\lambda}{dz}$	Conducting wall
Track 1D, 2D, 3D	revolution time; s; s	1D; 2D; 3D	10^6	smoothed $\frac{d\lambda}{dz}$; FEM; FEM	Variable g-factor; Automatic treatment; Automatic treatment
SIMPSONS	t	2D, 3D	$\geq 10^4$	FFT in cylin. coords.	Circular conducting wall
ACCSIM	s	2.5D	$\geq 10^5$	Hybrid FMM	Conducting wall
ORBIT-ORNL	s	1D, 2.5D, 3D	$\geq 10^6$	FFT, force or potential	Conducting wall
ORBIT-BNL	s	1D, 2D, 3D	10^6	SU + LOR	Conducting wall, automatic images
ML/IMPACT	s	3D	$\geq 10^6$	Spectral	None
GenTrackE	t/s	3D	$\geq 10^9$	FEM, Multi-grid	Periodic, Dirichlet or Neumann, mixed
Best	t	3D	$\geq 10^6$	Spectral, FD	Circular conducting wall
Synergia	s	3D	$\geq 10^6$	Spectral	Open, periodic, rectangular, circular

- Momentum aperture checking
- Machine to machine transfers
- γ_t jump and RF phase reversal
- Imaginary γ_t lattices
- Voltage and phase feedback
- Space charge
- Wall impedances
- Graphics and diagnostics.

Having been in use for quite some time now, there is an exhaustive list of problems to which ESME has been applied. For example, it has been used at the Fermilab Main Ring and Injector to study bunch coalescing, phase lock, and slip stacking; at the Fermilab Booster for studies of transition crossing, γ_t jump, and beam instabilities; at the SNS in benchmark studies with the ORBIT code and for bunch shape manipulation in the SNS accumulator ring; and for a multitude of studies at other machines, including the CERN PS and SPS, the Pimms Medical Synchrotron, Petra (for protons), and a future proton driver machine.

TRACK 1D, 2D, and 3D

The Track codes consist of three separate codes for tracking in the longitudinal dimension (Track1D), in the transverse dimensions (Track2D), and in all three dimensions (Track3D) [6]. Like the ESME code, Track2D was developed in the early 1980's, and has a long history of additions, revisions, and applications. It was possibly the first particle-pushing code to perform multi-turn injection with full nonlinear space charge, this work having been performed for fusion studies in 1980 [3]. An essential feature of the space charge implementation is that it is based on a finite element approach, which allows for easy handling of complicated geometries. The algorithms also provides automatic treatment of image charges for open, periodic, elliptical, polygonal, and lossy boundaries.

As main in-house codes at the Rutherford-Appleton Laboratory, the Track codes have been extensively applied in upgrade and development studies of the ISIS machine. These studies have resulted in upgrade of the injection system and the design and installation of a new dual-harmonic RF system, due to come on line in the next year. Additionally, the Track codes have been used for studies of injection, funnel optimization, and chopper optimization in the ESS design, for studies at CERN machines (PS, PS Booster, and SPS), for simulations of a future proton driver at Fermilab, and for studies of a future neutrino factory.

ACCSIM

The ACCSIM code is unique from many of its predecessors in that it was specifically developed as a "ready-to-run" package for general use in the study, design, and optimization of accelerator rings and transport lines [7]. The code is comparably well-documented and a detailed User's Manual is available [8]. Not only is ACCSIM attractive from the standpoint of portability and user-friendliness, it also has a comprehensive suite of physics models. Some of these models are:

- Injection: internal distribution generators, painting,

foil effects
- First order tracking and thin element capabilities
- RF and acceleration, barrier RF
- Apertures for any element, collimators and targets
- Pick-up and damper systems
- Space charge: longitudinal, 2.5D transverse
- Image charges
- Many diagnostics, built in graphics.

The space charge routine is a hybrid FMM routine which yields computational times scaling with N_g, the number of grid points. This is a significant improvement over the scaling of the pure FMM routine, which depends on the number of particles, N_p [7]. The reference to 2.5D in the space charge routine refers to the fact that the transverse and longitudinal directions are quasi-independent, with coupling induced from length terms and longitudinal density factors. A new improvement to ACCSIM is the inclusion of a MAD parser into the program. This is currently available in the newest beta-release version, ACCSIM 4.

ACCSIM has been used at many laboratories for a variety of ring machine studies. Benchmarks with experimental data have been performed for the CERN PS Booster and the KEK 12 GeV PS, both of which yielded successful results. Additionally, ACCSIM has been used for studies of injection at the Tsukub Hitachi medical synchrotron, for studies of injection and space charge in the future SNS 1 GeV accumulator ring, and for studies of injection and collimation in the J-PARC 3 GeV ring, to name just a few.

ORBIT

Historically, ORBIT began as a C++ rewrite of the F77-based ACCSIM code [9]. The motivation for the rewrite was two-fold: to provide a modular structure for programming, and to incorporate a driver shell for "on-the-fly" scripting. SuperCode was the driver shell chosen at the time and is still in use in the Oak Ridge version of ORBIT, ORBIT-ORNL. However, an effort is underway to replace SuperCode with a more standard, well-documented Python interface; the completion of this work is imminent.

Owing mainly to the modular structure of the code, ORBIT-ORNL has been developed as a collaborative effort between many authors. The modularity allows for the easy addition of new source code (a module), which acts independently from other modules. This structure helps a developer isolate and identify errors, and allows a user to pick and choose among existing modules to formulate a combination appropriate to the problem at hand. Among the available models in the ORBIT-ORNL code are:

- Injection: internal distribution generators, painting, foil effects
- Single particle transport: First or second order tracking, symplectic TEAPOT-type maps, or Mxyzptlk library. library.
- RF and acceleration
- Magnet errors and fringe fields
- closed orbit calculation and correction
- Apertures and collimators
- Space charge: 1D longitudinal, 2.5D force or potential, or 3D potential
- Image charges
- Transverse and longitudinal impedances
- Feedback and stabilization
- Diagnostics

ORBIT-ORNL has been the main code in use for simulations of the future SNS accumulator ring beam. It has been used for injection optimization, for collimation system design and optimization, for studies of halo formation from space charge, impedances, and resonance crossing, for development of a feedback and stabilization system, and for studies of loss distributions around the ring. Outside of the SNS project, ORBIT-ORNL was the main tool applied in a comprehensive study of space charge effects in the PSR ring [10], and is now in use for space charge studies of the Fermilab Booster ring.

The ORBIT-ORNL version presented above is housed at Oak Ridge National Laboratory and is different than the version housed at Brookhaven National Laboratory, ORBIT-BNL [11]. Both versions originated from the first ORBIT rewrite of ACCSIM, but eventually two different codes emerged under separate developers. ORBIT-BNL incorporates many of the same capabilities as the ORBIT-ORNL, including full 3D space charge, parallel capabilities, and impedances, but it no longer makes use of the driver shell format. Additionally, the algorithms for many of the routines differ, as demonstrated by Table 2. Though ORBIT-BNL uses position (s) as the independent variable for tracking, the space charge algorithm is formulated to remove the resulting approximation in the time domain. ORBIT-BNL also been used for machine studies, including simulations of the SNS accumulator ring, of the AGS, the AGS Booster, and the RHIC machine at Brookhaven, and also for simulations of SIS at the GSI.

New Directions: IMPACT-MaryLie, GenTrackE, UAL

A few codes that are either new to space charge simulation in rings or will be entering the scene soon are IMPACT-MaryLie, GenTrackE, and UAL.

The linear accelerator code IMPACT has recently been merged with the MaryLie package to provide particle tracking in rings. The new code, IMPACT-MaryLie [12], contains relevant modules from the original IMPACT code, as well as two new space charge computation methods: a Hermite-Gaussian expansion model, and a cellular analytic convolution model. Both of these models are designed to minimize the field error induced when solving Poisson's equation for beams with extreme aspect ratios.

GenTrackE is a framework for particle tracking applications which aims to provide good scalability for very large parallel processing jobs. The code features either truncated

Table 3: Summary of code benchmarks with experimental data.

Code - Machine	Quantity Compared	Agreement Level
ESME - Fermilab Booster	Longitudinal parameters	Good
ESME - CERN PS	Longitudinal parameters	Good
Track1D - ISIS	Longitudinal parameters	Good
ACCSIM - CERN PS	Beam profiles	Good
ACCSIM - KEK PS	Beam profiles	Good
ORBIT-ORNL - PSR	Beam profiles	Good
SIMPSON - KEK Booster	Emittance exchange	Good
ORBIT-ORNL - Fermilab Booster	Emittance growth	Under study
Best - PSR	E-cloud effects	Fair

power series maps or time integration methods for tracking, and an finite-element approach to space charge with semi-unstructured griding. Currently, the code has be run with up to 7×10^9 grid points. One application making use the GenTrackE framework is a parallelized, self-consistent electron-cloud model [13], adapted from M. Furman and M. Pivi's probabilistic model [14].

The Unified Accelerator Libraries, or UAL, is not a particle-tracking code by itself, but is rather a collection of libraries that address diverse accelerator tasks [15]. Methods included in the libraries are derived from other codes, such as ACCSIM, TEAPOT, Zlib, etc. The official version of UAL does not currently contain a space charge implementation, but a non-official local version at BNL has been modified to provide the ORBIT-ORNL space charge routines. The modification has been successfully used for studies of the SNS beam, and future plans for UAL include adding this capability to the official version.

SUMMARY OF BENCHMARKS WITH EXPERIMENT

An important test of the validity of the models incorporated into any simulation tool is whether the model can be successfully benchmarked with experiment. Unfortunately, only a limited number of beam parameters can be evaluated through experimental measurement, and the experimental data is often complicated by effects that are not easily separated from the physical process under study. The task in any benchmark is to extract meaningful measurements where either a single physical phenomenon is isolated, or in which the effects of other phenomena can be easily identified. Many of these experiments have been performed and the data has been used for benchmarking of codes. Table 3 summarizes a number of these benchmarks.

Overall, the success rate for benchmark of simple quantities, such as beam profiles, is high. However, there is a distinct lack of benchmarks with more complicated quantities, such as emittances and coherent tunes. Toward this end, a plan was formulated at the ICFA Beam Dynamics Mini-Workshop on Space charge Simulation for a multiple code benchmark (ORBIT, ACCSIM, IMPACT-MaryLie, GenTrackE, and Best) with existing experimental data from the CERN PS [16, 17]. Two data sets have been identified for the study: 1) Emittance measurements while crossing the integer and half-integer resonances, and 2) measurement of emittance exchange while crossing the fourth-order Montague resonance, $2Q_x - 2Q_y = 0$.

REFERENCES

[1] http://www.isis.rl.ac.uk/AcceleratorTheory/workshop/workshop.htm

[2] R. Ryne *et al*, *Proceedings of the 2001 Particle Accelerator Conference*, (Chicago, 2001) 264.

[3] C. Prior, private communication.

[4] N. Holtkamp *et al*, *Proceedings of the 2002 European Particle Accelerator Conference*, (Paris, 2002) 164.

[5] http://www-ap.fnal.gov/ESME/

[6] C. Prior, RAL Technical Report, RAL-TR-1998-048.

[7] F.W. Jones, *AIP Conference Proceedings*, **448**, 359 (AIP, NY, 1998).

[8] F. Jones, Users' Guide to ACCSIM, TRI-UMF Design Notes, TRI-DN-90-17 (1990), http://www.triumf.ca/compserv/accsim.html.

[9] J. D. Galambos *et al*, The ORBIT User's Manual, http://www.sns.gov//APGroup/Codes/Codes.htm.

[10] S. Cousineau, *Understanding Space Charge and Controlling Beam Loss in High Intensity Synchrotrons*, PhD Thesis, Indiana University, 2003, unpublished; "Studies of Resonant Beam Behavior in the PSR," PRST-AB, submitted.

[11] A. Luccio *et al*, *AIP Conference Proceedings*, **448** 390 (Shelter Island, 1998).

[12] R. Ryne, "MaryLie/IMPACT: A Parallel 5th Order Beam Optics Code with Space Charge," *Proceedings of the 2003 Particle Accelerator Conference*, (Portland, 2003).

[13] M. A. Furman and A. Adelman, "Self-Consistent Parallel 3D Electron-Cloud Simulation in Arbitrary External Fields," *Proceedings of the 2003 Particle Accelerator Conference*, (Portland, 2003).

[14] M.A. Furman and M.T.F. Pivi, PRST-AB **5** 124404 (2002).

[15] www.ual.bnl.gov

[16] E. Metral, "Measurements of Transverse Space Charge Effects in the CERN Proton Synchrotron," *Proceedings of the 2003 Particle Accelerator Conference*, (Portland, 2003).

[17] I. Hofmann, "Nonlinear Resonance Benchmarking Experiment at the CERN Proton Synchrotron *Proceedings of the 2003 Particle Accelerator Conference*, (Portland, 2003)

MULTIPACTING SIMULATIONS FOR SUPERCONDUCTING CAVITIES AND RF COUPLER WAVEGUIDES*

R.L. Geng†, LEPP, Cornell University, Ithaca, NY 14853, USA

Abstract

Multipacting (MP) has recently received a renewed interest in the community of superconducting RF. In this paper, I will overview the developments of MP simulations for SRF cavities and RF couplers, summarize the simulation results, compare experiment results with simulation predictions and examine the algorithms. After identifying the discrepancy between the predictions and experiments, suggestions are given to further improve the simulations.

INTRODUCTION

MP is a phenomenon of resonant secondary emission multiplication, first described by Farnsworth in 1934 [1]. The operating mechanism of MP is that participating electrons, driven by RF fields, impact a surface and release secondary electrons, which in turn driven by RF fields, are made to impact again and release more secondary electrons. This process will go on resonantly (electrons are "synchronized" to RF fields) until the number of electrons are saturated due to some limiting mechanism. MP may occur in an array of evacuated RF devices and may involve one surface or two surfaces.

MP was intensively studied in the 40s and 50s for a specific case, namely two-sided MP in a parallel plate, in the context of high frequency gaseous discharge. Gill and von Engels [2] and others developed theoretical formulations for the parallel plate MP. Hatch and Williams [3] extended the work and generalized the formulation to allow construction of MP susceptible zones, including higher order MP. These formulations have now become known as "constant k theory" to reflect the adoption of a constant ratio between the electron velocity upon impact (v_i) to the velocity at emission (v_0). Theoretical treatments were also developed by Krebs and Meerbach [4] and by Tamagawa [5]. Instead of imposing a constant ratio to v_i/v_0, they adopted a constant v_0, typically equivalent to a few eV. In the 80s, the "constant v_0" theory was advanced by Shemelin [6] and by Vaughan [7] in which important effects like the phase stability and the MP saturation due to space charge are explicitly examined. In most MP simulation studies to be presented in this paper, a constant v_0 is adopted.

Simulation studies of MP in the superconducting RF (SRF) community can be traced back to the 70s, when MP was a major SRF cavity performance limitation [8]. With the aid of computer simulations, a new type of MP, one-point MP, was discovered in pill-box like cavities by Lyneis et al. [10] and in muffin-tin cavities by Padamsee et al. [11]. Klein and Proch showed through simulation studies that a spherical cavity shape is free of one-point MP [12]. This finding resulted a breakthrough in SRF cavity performance. MP then became less of a concern until 1984, when two-point MP was discovered in a 500 MHz spherical cavity by Weingarten [14] through a combined experimental and simulation study. Owing to its nature, two-point MP did not become a limiting mechanism.

MP has recently received a renewed interest in the SRF community. This is mainly due to the fact that this mechanism is found to cause harmful RF breakdown in today's multi-hundred kW couplers for SRF cavities. In addition, two-sided MP has been identified in elliptical cavities for a broad frequency range from 200 MHz to 3000 MHz. Numerical simulations have been advanced in the past decade, allowing systematic studies of MP characteristics of new RF structures [15]. Several simulation tools now exist to evaluate MP likely-hood and to predict MP suppression methods [16]. Important experimental verifications of the predictions made by these codes have been brought forward since last year. In this paper, I will overview the developments of MP simulations in SRF cavities and couplers, summarize the simulation results, compare experiment results with simulation predictions and examine the algorithms. Suggestions are given to improve the simulations.

MP SIMULATIONS FOR SRF CAVITIES

ONE-POINT MP

One-point MP was a major SRF cavity performance limitation in the 70s. It occurs in regions where RF magnetic field is nearly uniform and RF electric field has a non-zero normal component. MP electrons come back to the emission location after an integer (N, N being the order of MP) multiples of RF period. Fig. 1 illustrates trajectories of MP electrons in a muffin-tin cavity [11].

The MP field levels are determined by the magnetic field and scale like $B_N \sim f/N$, where f is RF frequency. The electron impact energy is determined by the normal component of the electric field E_n and has a frequency dependence of $B_N \sim E_n^2/f^2$. The synchronism between MP electrons and RF field is stable only for a narrow phase range near zero-cross of the electric field, as a result, MP bands are well separated and each has a narrow width.

Interim olutions to suppress one-point MP include sharpening the corner for pill-box cavities and grooving the surface of MP susceptible regions for muffin-tin cavities.

* Work supported by NSF
† rg58@cornell.edu

0-7803-7738-9/03/$17.00 © 2003 IEEE

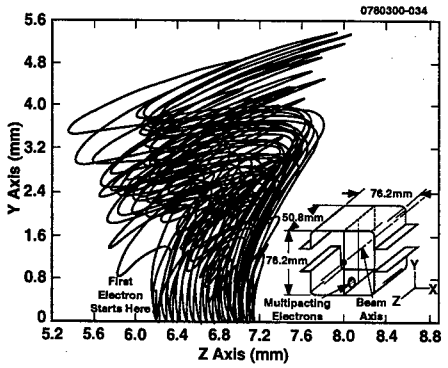

Figure 1: One-point MP in a muffin-tin cavity.

These solutions were both experimentally verified.

The most successful solution to one-point MP is to round the cavity wall to make a spherical cavity [12]. In this geometry, electrons are bent to the equator where energy gain is small. The same MP suppression effect is achieved in the elliptical cavity shape yet with added mechanical strength [13]. The spherical/elliptical cavity shapes have become the mainstream for $\beta = 1$ cavities.

TWO-POINT MP

Two-point MP [14] occurs in small regions near the equator of a spherical/elliptical cavity. Two points symmetric about the equator are involved. The flight time between impacts is an odd-integer (2N-1, N being the order of MP) multiples of half period. Fig. 2 shows the trajectory of two-point MP electrons in a 1.3 GHz TESLA cavity [17]. The synchronism is maintained by the magnetic field and MP levels scale linearly with frequency $B_N \sim f/(2N-1)$. The impact energy for the 1^{st} order two-point MP is in the range of 30 - 50 eV, irrespective of RF frequency. The synchronism between MP electrons and RF field is stable for a wide range (20° - 40°) of phase angle and hence the MP barriers are wider compared with that of one-point MP.

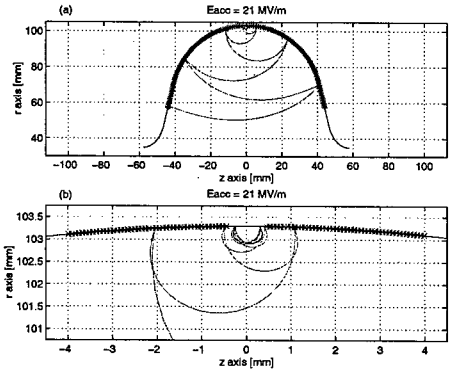

Figure 2: Two-point MP in a single-cell 1.3 GHz TESLA cavity. Note resonant trajectories in (b).

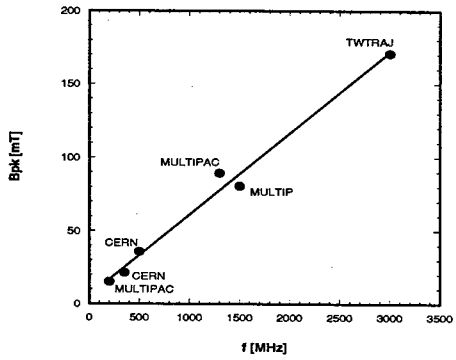

Figure 3: Calculated peak magnetic fields of two-point MP (1^{st} order) at various frequencies: 200 MHz [18], 350 MHz and 500 MHz [14], 1300 MHz [17], 1500 MHz [19], 3000 MHz [20]. Labels indicate names of the simulation code.

Two-point MP has been recognized in other $\beta = 1$ elliptical cavities for a wide frequency range from 200 MHz to 3000 GHz through numerical simulations supported by experimental evidence [18] [14] [15] [19] [20]. Fig. 3 summarizes the peak magnetic field levels of the 1^{st} order two-point MP at various frequencies. From Fig. 3, the following scaling law can be established for the 1^{st} order two-point MP in spherical/elliptical $\beta = 1$ cavities: $B[mT] = 5 + 55f[GHz]$.

Although two-point MP's are ubiquitous, they are not expected to limit the cavity performance owing to the fact that the impact energy is very close to the first cross-over of the secondary emission yield (SEY) curve, which shifts up after the surface is "cleaned up" by processing.

MP SIMULATIONS FOR COUPLER WAVEGUIDES

Gradient performance of SRF cavities has been steadily increasing. SRF cavities now demands higher and higher RF power to be delivered by couplers. Since the 90s, MP in RF couplers emerges to be an issue that needs to dealt with seriously.

COAX LINES

Simulation studies of MP in coax lines were attempted as early as 1968 [21] with a neglected RF magnetic field. Results presented below are mainly due to the recent work in [22] [23] and particularly in [24] [25]. The dominant MP mode in a coax line is one-sided MP on the surface of the outer conductor as illustrated in Fig. 4. For a narrow power range, two-sided MP across the inner and outer conductor also exists. In SW mode, MP sites are fixed near the maxima of the electric field. In TW mode, MP electrons travel along with the wave. The MP power levels obey the following scaling law: $P \sim (fd)^4 Z$ (one-sided MP); $P \sim (fd)^4 Z^2$ (two-sided MP), where f is frequency, d the radius of the outer conductor and Z the line impedance.

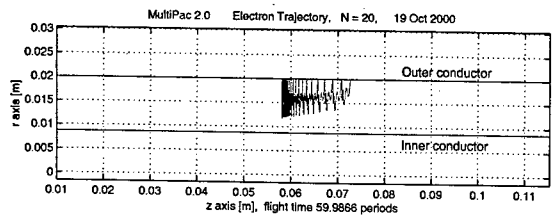

Figure 4: A one-sided MP (3^{rd} order) in a 1.3 GHz 50 Ω coax line with a standing wave.

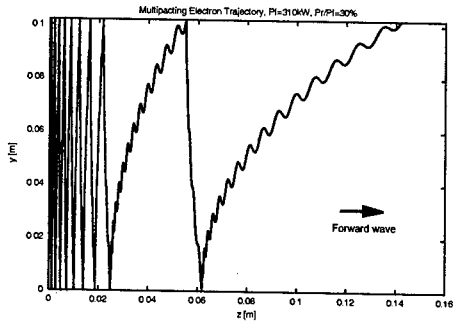

Figure 5: Two-sided MP (5^{th} order) in a 500 MHz rectangular waveguide with a partially reflected wave. The trajectory starts from the origin.

The impact energy for one-sided MP has a nearly linear dependence on the forward power and can reach 2000 eV for typical cases.

MP in coax lines can be suppressed by simply enlarging the gap between the inner and outer conductor so that a same MP barrier is shifted to a higher power level. Or it can be suppressed by the so called "DC biasing method" [22] [25], which calls for imposing a DC bias voltage on the inner conductor. Full MP suppression can be realized with either polarity of the bias voltage. Full suppression voltage scales like $|V_{bias}| \sim fdZ$ and has a typical value of 3 kV for most modern applications. At an intermediate negative bias voltage, the one-sided MP on the surface of the outer conductor can be intensified. This effect is sometimes used to process RF couplers before their operations [26]. It should be pointed out that at an intermediate positive bias voltage, one-sided MP on the *inner conductor* surface may occur.

RECTANGULAR WAVEGUIDES

The dominant MP mode in a rectangular waveguide is two-sided MP between broad walls in the high electric field region [27]. MP electrons traverse the gap in an odd-integer (2N-1, N being the order of MP) multiples of RF period. Most MP barriers encountered in modern rectangular coupler waveguides are higher order MP's. Fig. 5 illustrates the trajectory of MP electrons in the mid-plane of a 500 MHz rectangular waveguide with a partially reflected wave. It is shown that MP electrons travel along with the forward wave. The impact energy is linearly dependent on the forward power and can reach 1000 eV for the typical case. Not surprisingly, there is some similarity between rectangular waveguide MP and parallel plate MP. It is justified that MP power levels obey the following scaling law: $P \sim (fb)^4$, where f is RF frequency and b the narrow dimension of the waveguide.

MP in rectangular waveguide can be suppressed by opening cut-off slots on broad walls and can be suppressed by the "DC magnetic biasing" method [28]. The magnetic biasing method asks for imposing a weak longitudinal magnetic field (~ 20 Guass). Full suppression can be realized with either polarity of the bias field. The full suppression bias field for the TW mode scales like $B_{bias} \sim \sqrt{P/(fab^3)}$, where P is the forward power, a the wide dimension and b the narrow dimension of the waveguide [29]. MP in rectangular waveguide can be intensified at an intermediate bias field due to oblique incidence. This effect may be used to process waveguides.

CERAMIC WINDOWS

A full coverage of MP on a ceramic is out of the scope of this paper. However, this subject should not be neglected. Simulation studies show that classical resonant MP occurs on the single ceramic surface or between the ceramic surface and surrounding metal surfaces [30] [31]. Recent theoretical and numerical work by Kishek and Lau [32] point out that due to charge effect, MP occurs on a ceramic surface in a non-resonant fashion and hence for a much wider power range. Coating with a low SEY material is a remedy.

ALGORITHMS FOR MP SIMULATIONS

The algorithms of MP simulations are illustrated in Fig. 6. For a given geometry, a virtual electron is launched at a known field level from a known surface location with

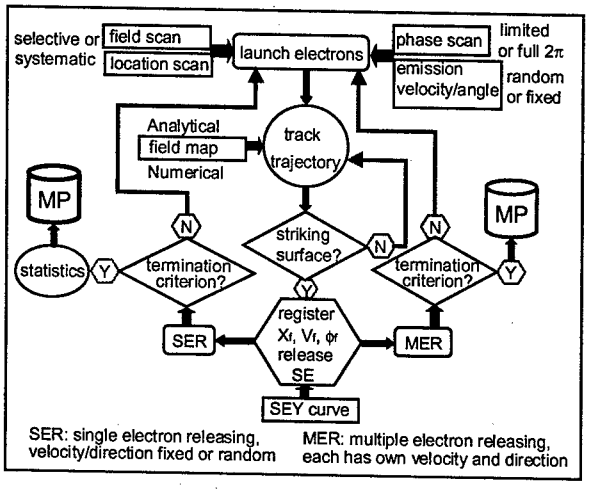

Figure 6: MP algorithm.

respect to a chosen phase of the RF field. The kinetic energy and direction of the electron at emission are also specified. The trajectory of the virtual electron is tracked by solving its equations of motion, which are coupled ODE's. Numerical integration are made by various methods such as leap-frog or Runge-Kutta. RF fields in the structure are obtained analytically or numerically (imported from an external field solver or supplied by the MP code itself).[1] At each integration step, judgment is made to check if the electron strikes a surface (this is the major difference from regular ray tracing). If the answer is no, the integration goes on to the next step. If the answer is yes, the impact location, the velocity of the electron and the phase angle of the RF field upon impact are registered. Then the virtual electron is re-emitted from the impact site and its tracking is continued until its next impact with a surface, and so on. After a certain number (usually 30 - 50) of impacts have been made, the tracking is stopped[2] and the following calculation is performed,

$$e_N = \prod_i^N \delta_i, \qquad (1)$$

where N is the total number of impacts, i is the index for each impact, and δ_i is the SEY, calculated for each impact according to the corresponding kinetic energy and direction of the electron upon impact. e_N is nothing but the important concept of enhanced counter function, introduced in [23]. For a virtual electron that can make N times of impact, $e_N > 0$.

The above described process is repeated for a large set of combined launching parameters: RF field, launching location, phase angle, launching energy and launching angle. After all the launching possibilities are exhausted, MP susceptible zone is constructed. For each field level, e_N's of all virtual electrons that can make N impacts are summarized and then normalized to the total number of launched electrons for this field level. MP is predicted for the field levels at which $e_N > 1$ (the physical significance of this criterion is apparent).

Once a MP field level is determined, the MP location(s) can also be pin-pointed by analyzing the impact locations that have been registered. With the MP field level and location both determined, calculations are repeated to trace out the trajectory of MP electrons and to find out the time of flight between impacts (the order of MP).

MP simulations in the past are performed with *selective* field levels and locations for which MP is already accurately observed by experiments. Today, MP simulations need to deal with untested RF structures, for which MP susceptible field levels and locations are not known. A *systematic scan* of field levels and locations is required for launching virtual electrons.

[1]For apparent reasons, it is essential to have high quality numerical fields near surfaces.

[2]Tracking of a virtual electron can be terminated before N times of impacts are made for various reasons. For example, if the virtual electron is re-emitted in a retarding field, it may be pulled back to the surface shortly after the emission and hit the surface with a rather low (a few eV) energy. In this case, tracking of this virtual electron should be aborted and another virtual electron is launched. For the aborted electron, $e_N = 0$.

SER AND MER

Most of today's MP codes adopt the single electron releasing (SER) scheme in modeling secondary electron emission. This means that there is only one virtual electron before and after impact (in fact, there is only ONE virtual electron at any instant). Upon re-emission, a fixed kinetic energy (typically 2 - 5 eV) and a fixed direction (usually normal to the surface) are assigned to the virtual electron. Assignment of these quantities are sometimes done in a random fashion according to the velocity and angular distribution function of secondary emission.

Multiple electron releasing (MER) scheme was adopted by Ben-Zvi et al. [9] in their MP studies of a pill-box SRF cavity in 1973. In this case, when a virtual electron impacts a surface with sufficient energy, multiple virtual electrons (number determined by SEY) are re-emitted. Each new virtual electron has its own initial energy and direction assigned by a Monte Carlo process which considers the velocity and angular distribution function of secondary emission. Ultimately, there is a large number of virtual electrons being tracked simultaneously. MP is predicted when a threshold number of electrons is reached.

EXTERNAL AND INTERNAL PARAMETERS

Scanned launching parameters can be divided into two groups: external and internal. External parameters include RF field, RF frequency, and dimensions of the RF structure (which determine launching locations). Internal parameters include phase angle, emission energy, and emission direction. MP codes differ mainly in the way of scanning internal parameters. Some codes limit the phase angle to $[\pi, 2\pi]$, which means launching is allowed only in an accelerating field. In fact, electrons emitted in a retarding field can also escape from the surface, because of the finite initial energy (2 - 5 eV). The importance of this effect on the bandwidth of MP barriers is explicitly examined theoretically in [6] and numerically in [28]. It is emphasized here that allowing launching, and re-emission, of virtual electrons for the full 2π phase angle range is essential.[3]

CODES AND VERIFICATIONS

There exist several codes (2D and 3D) for MP simulation (see Krawczyk [16]). When analytical RF fields are not available, an EM field solver is needed. Some codes use external field solvers such as MAFIA, OSCAR2D, SUPERFISH and SuperLANS and some use integrated internal solvers. Although most codes are not distributed, some codes are available for interested users [33] [34].

[3]Of course the electron will be pulled back to the surface if it experiences an extended period of deceleration. Such an electron will be aborted.

Verifications of code predictions have been brought about by recent experiments. There exists good agreement for two-point MP in elliptical $\beta = 1$ SRF cavities [17] [18] and low β cavities [35] when a pessimistic SEY is used. Simulation results on an array of low β cavities are consistent with test results [36]. However, some experimentally observed MP barriers can not be predicted, even by using an exaggerating SEY [35] [18].

Predictions on MP in coupler waveguides agree qualitatively with experiments. A better agreement is evident for a fresh waveguide than for a "processed" waveguide. [37] [38]. Measured MP bands are usually continuous, in contrast to well separated bands predicted by simulations. During recent measurements of RF couplers for SNS, only 2 harmless MP barriers were observed, despite 7 barriers being predicted by simulations [39].

RECOMMENDATIONS

Major reasons causing discrepancies between simulation predictions and measurement results are listed below,

- Lack of SEY data of actual surfaces (at RT and low temperatures) for impact energy range of 20 -60 eV.
- Truncated internal parameters. For example: forbidden emission in a retarding field.
- Negligence of angular and velocity distribution of secondary emssion.
- Negligence of MP dispersing effect such as space charge effect.

Corresponding recommendations for improving MP simulations are listed below,

- Need help from surface scientists to provide realistic SEY data for impact energy range of 20 -60 eV.
- Allow re-emission for 2π phase angle.
- Implement the angular and velocity distribution of secondary emission through a Monte Carlo process. An MER algorithm is a good candidate.
- Include space charge effect - may eventually ask for PIC simulations.
- Develop advanced 3D codes for MP simulations of complicated RF stuctures, like low β resonators.

CONCLUSION

Numerical simulations have played a critical role in understanding and suppression of MP in SRF cavities and RF coupler waveguides. MP simulation algorithms have advanced in the past decade and a comprehensive MP survey of RF structures is now possible. Simulation predictions are well supported by experiments in most cases. Reasons for the remaining discrepancies are identified. It is necessary to implement internal parameters like angular and velocity distributions of secondary emission and to implement space charge effect. This might be best achieved by using an MER algorithm.

REFERENCES

[1] P.T. Farnsworth, J. Franklin Institute, 218, 411 (1934).

[2] E.W.B. Gill and A. von Engel, Proc. R. Soc. London, A192, 446 (1948).

[3] A.J. Hatch and H.B. Williams, JAP, 25, 417 (1954); PR, 112, 681 (1958).

[4] K. Krebs and H. Meerbach, Ann. Physik, 15, 189 (1955).

[5] H. Tamagawa, E.T.J. of Japan, September 1957, 93 (1957).

[6] V.D. Shemelin, Sov. Phys. Tech. Phys., 31, 1029 (1986).

[7] J.R.M. Vaughan, IEEE Trans. Electron Devices, 35, 1172 (1988).

[8] MP is primarily perceived as a deleterious effect in the SRF community, despite its useful application in other areas.

[9] I. Ben-Zvi, J.F. Crawford, J.P. Turneaure, IEEE Trans. Nucl. Sci., NS-20, 54 (1973).

[10] C.M. Lyneis, H.A. Schwettman, J.P. Turneaure, APL., 31, 541 (1977).

[11] H. Padamsee, A. Joshi, JAP, 50, 1112 (1979).

[12] U. Klein, D. Proch, Proc. of the Conference on Future Possibilities for Electron Accelerators, N1-17 (1979).

[13] P. Kneisel et al., NIM, 188, 669 (1981).

[14] W. Weingarten, Proc. of the 2nd SRF Workshop, 551 (1984).

[15] E. Somersalo, P. Ylä-Oijala, D. Proch, J. Sarvas, Particle Accelerators, 59, 107 (1998).

[16] F.L. Krawczyk, Proc. of the 10th SRF Workshop, (2001).

[17] R. Ylä-Oijala, Particle Accelerators, 63, 105 (1999).

[18] R.L. Geng et al., these Proceedings, Paper TPAB049.

[19] J. Knobloch, W. Hartung, H. Padamsee, Proc. of the 8th SRF Workshop, 1017 (1997).

[20] P. Fabbricatore et al., Proc. of the 7th SRF Workshop, 385 (1995).

[21] J.P. Budlinger, A. Laisne, NIM, 61, 253 (1968).

[22] J. Tückmantel et al., PAC1995, p.1642.

[23] E. Somersalo, P. Ylä-Oijala, D. Proch, PAC1995, P. 1500.

[24] P. Ylä-Oijala, TESLA Report, TESLA 97-20, (1997).

[25] P. Ylä-Oijala, TESLA Report, TESLA 97-21, (1997).

[26] Y. Kijima et al., EPAC2000, p.2040.

[27] R.L. Geng, H. Padamsee, PAC1999, p.429.

[28] R.L. Geng, H. Padamsee, V. Shemelin, PAC2001, p.1228.

[29] R.L. Geng et. al, accepted for publication in NIM-A.

[30] S. Yamaguchi, Y. Saito, S. Anami, S. Michizono, IEEE Trans. Nucl. Sci., 39, 278 (1992).

[31] H. Matsumoto, PAC1999, p.536.

[32] R.A. Kishek and Y.Y. Lau, PRL, 80, 193 (1998).

[33] P. Ylä-Oijala, D. Proch, Proc. of the 10th SRF Workshop, (2001).

[34] http://www.fieldp.com/

[35] G. Devanz, EPAC2000, p.1366.

[36] W. Hartung et al., Proc. of the 10th SRF Workshop, (2001).

[37] G. Devanz, PRST-AB, 4, 012001 (2001).

[38] R.L. Geng et al., EPAC2002, p.2238.

[39] M. Stirbet, High Power Coupler Workshop, Jlab, (2002).

CASCADE – AN ADVANCED COMPUTATIONAL TOOL FOR WAVEGUIDE COMPONENTS AND WINDOW DESIGN

L. Ives, J. Neilson, W. Vogler, Calabazas Creek Research, Inc., Saratoga, USA

Abstract

CASCADE is an advanced design program for 2-port waveguide components, RF windows, and waveguide systems. It provides rapid and user-friendly analysis of waveguide components such as filters, nonlinear tapers, mode converters, microwave cavities, and RF windows. It calculates scattering parameters (transmission/reflection coefficients) for general waveguide structures composed of cylindrical, rectangular, or coaxial waveguides. Transistions between waveguide types are also allowed. The program includes dielectric properties of ceramic and finite conductivity of metal surfaces. A built-in optimizer dramatically reduces design time, and the program can import scattering matrices from other program, such as HFSS or measured data, for total system scattering matrix analysis. Statistical tolerance analsysis provides information for reducing manufacturing costs by identifying the impact of dimensional tolerances on performance. The basic theory is described, and a number of examples are presented.

INTRODUCTION

In order to transfer RF power from sources, such as klystrons or magnetrons, the power must pass through a series of components. Typically, the power passes through the vacuum window at the source and enters a waveguide. Between the source and the final destination, it may pass through transitions, bends, filters, mode converters or other structures required by the installation or the final load. These components must be designed such that the power is transmitted or converted efficiently without reflecting significant power back toward the source or converting it to parasitic modes or unusable RF or thermal power. CASCADE is an advanced program for designing such components or systems.

A key parameter in the design of any waveguide system is cost. First, the engineering time to design waveguide systems depends on the performance requirements and the device specifications, such as power level, bandwidth, loss/efficiency, reliability, and duty. Once the performance requirements are achieved, the engineer must consider production cost to manufacture and assemble the system. In many cases, hundreds of components must be built for large installations. The unit cost is an important consideration for the total system cost. CASCADE is a highly efficient and accurate tool for designing individual components or large systems consisting of a series of components. The program is very user-friendly and executes very rapidly on standard personal computers. Because of its rapid execution, it becomes possible to implement automated optimization routines that can iterate geometrical parameters to achieve performance goals specified by the user. Thus, the computer can design the component or system with little interaction by the user, once the optimization process is initiated. This results in a dramatic reduction in engineering time with achievement of performance goals not practical with manual execution.

The statistical tolerancing feature in CASCADE allows the engineer to determine the impact of dimensional tolerances on device performance. Tolerances can then be relaxed as much as possible while still achieving performance goals, significantly reducing machining costs, particularly for large quantity systems.

CASCADE is designed to model 2-port devices consisting of combinations of rectangular, cylindrical, or coaxial structures. The program can model dielectric materials and include the effects of finite conductivity. It can include the impact of 3D structures by importing calculated or measured scattering parameters. This allows performance optimization of complex waveguide systems.

THEORY OF OPERATION

Calculation of the scattering matrices in CASCADE is implemented by the mode-matching technique. Details of the derivation can be found in numerous papers[1-3], so only a brief outline of the development is presented here. The field in each waveguide section is represented by the expansion of the electric and magnetic eigenmodes $\vec{e}_i$ and $\vec{h}_i$ respectively:

$$\vec{E} = \sum_i (f_i + b_i)\,\vec{e}_i\,,\ \vec{H} = \sum_i \left(\frac{f_i - b_i}{Z_i}\right)\vec{h}_i$$

where f is the modal amplitude of the forward wave, b is the amplitude of the backward wave and Z is the characteristic impedance. Applying continuity of tangential E and H across the common aperture area of the waveguides and enforcing zero tangential electric field on the wall of the larger guide yields the scattering matrices:

$$S_{11} = [I + Z_1 P^T Y_2 P]^{-1}[I - Z_1 P^T Y_2 P]$$
$$S_{12} = 2[I + Z_1 P^T Y_2 P]^{-1} Z_1 P^T Y_2$$
$$S_{21} = 2[I + P Z_1 P^T Y_2]^{-1} P$$
$$S_{22} = -[I + P Z_1 P^T Y_2]^{-1}[I - Z_1 P^T Y_2 P]$$

0-7803-7738-9/03/$17.00 © 2003 IEEE

The coupling matrix P is defined as

$$P_{ji} = \int_{CA} \vec{e}_{j2} \bullet \vec{e}^{*}_{j1} dA$$

where the integration is performed over the common aperture area between the guides. The complete system scattering matrix is obtained by cascading[3] the scattering matrices of each section.

PROGRAM OPERATION

CASCADE includes a user-friendly, intuitive interface for geometrical input and specification of execution parameters. Each geometrical section is described by completing a GUI screen determined by the type of section. Figure 1 shows the input screen for a rectangular waveguide section.

The GUI allows input of the relevant geometry, the internal medium (vacuum, ceramic, etc.) and the wall conductivity. The waveguide system geometry is sequentially generated using a series of input screens for various waveguide types.

Several types of analysis are supported. These include:

- scattering matrix – used for determining transmission or reflection characteristics,
- resonant frequency calculation – determines frequency and Q of non-reentrant cavities,
- determinant sweep – searches structure for potential trapped of parasitic modes.

GUI screens are provided for determining the type of analysis, accuracy of the calculation, and frequency range of interest. Execution of a single simulation typically takes only a few seconds.

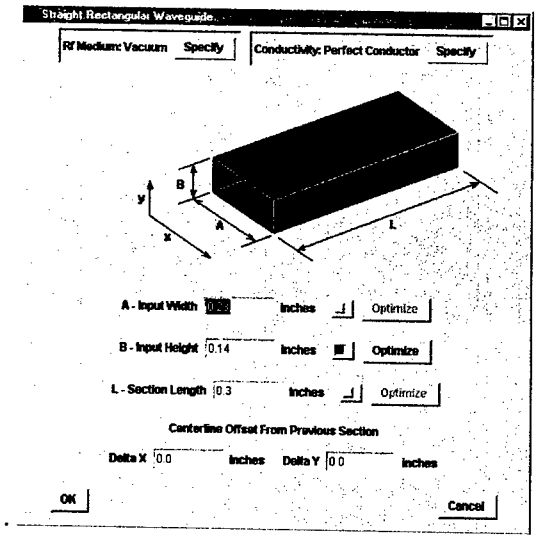

Figure 1. Input screen for rectangular waveguide section

To facilitate rapid component and system design, CASCADE includes three optimization algorithms. These are:

- Quasi-Newton
- Non-Smooth
- Least Squares

To perform an optimization analysis, the user specifies which geometrical parameters can be varied and the allowable variation. The user selects the optimization algorithm and the performance criteria. Once optimization is initiated, the program searches the available parameter space for the optimum solution until it is found or the maximum number or iterations is achieved. In this way, significantly more parameter space can be investigated much faster than practical with manual operation.

Once an acceptable performance is achieved, the user can determine the impact of dimensional tolerances on the performance. The user adds tolerance values to critical dimensions and specifies the number of cases to be investigated, typically 500-1000. The program then sequentially executes analysis of the geometry while varying the critical dimensions within the tolerance ranges specified. When, concluded, the program displays a histogram showing the number of cases falling within various performance ranges (Fig. 2).

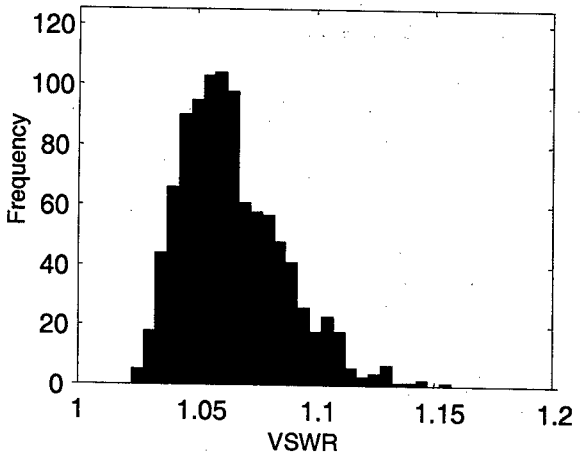

Figure 2. Histographic display of tolerance analysis results

There are many systems, however, where complex 3D waveguide components exist for which analysis by CASCADE is not applicable. In these cases, the complex 3D component can be modeled using other computer programs, such as MAFIA or HFSS. The scattering matrix for these components can by used as input to CASCADE to design the total system.

An example is the input cavity for a gyroklystron and consists of a rectangular waveguide wrapped around a cylindrical cavity. Power is coupled in using rectangular slots cut between the waveguide and the inner cylindrical cavity. The geometry is shown in Figure 3. Two scattering

matrix files are required from HFSS. One is generated with multiple frequency points across the band of operation. This will allow plotting of S11 across the frequency range of interest. Since coupling to the cavity is optimized at the center frequency of the cavity (45.7 GHz), another scattering matrix file is required from HFSS that includes only the scattering parameters at the center frequency.

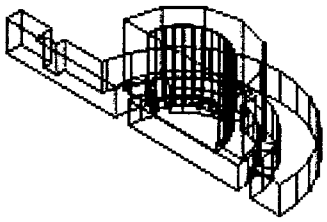

Figure 3. Gyroklystron input coupler

The matching section consists of three rectangular waveguide sections serving as input to the external scattering matrix file. The first section represents a standard rectangular waveguide. The second section represents an iris to provide the matching element. The width of this section and third section are set to match the width dimension of the input cavity. The height of the iris and the distance from the input cavity were initially obtained from rough, analytical calculations. The resulting performance is shown in Figure 4. Note that the match is higher than the operating frequency of the cavity.

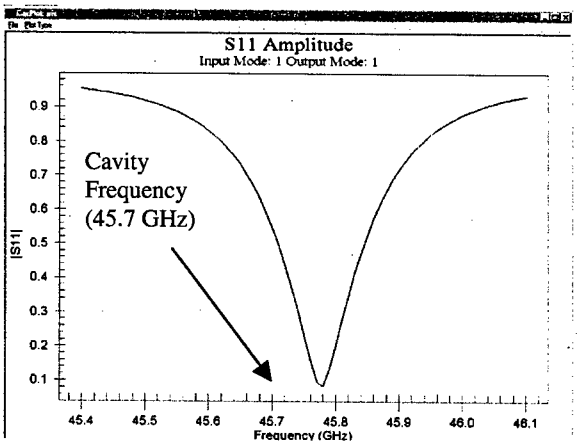

Figure 4. Initial performance of gyroklystron input coupler

The optimizer was then used to modify the geometry to shift the match to the center frequency of the circuit. The result, shown in Figure 5, required several minutes of computer time to obtain.

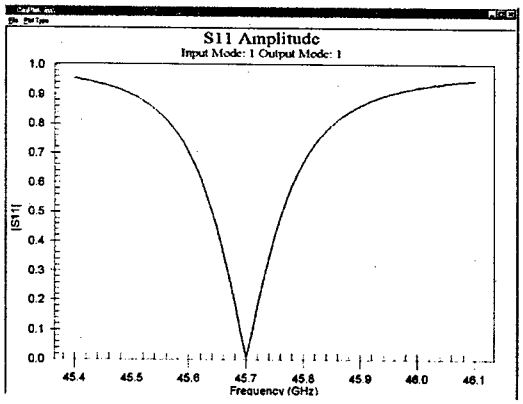

Figure 5. Final performance of gyroklystron coupler

CASCADE provides a variety of output plots, including scattering parameters, VSWR, mode sweeps, and Smith Charts. In addition, a number of tabular outputs are available. Custom plots and data can be displayed by post processing the output binary data file.

ACKNOWLEDGEMENTS

This development was funded by U.S. Navy contract number N00014-96-C-2107 and U.S. Department of Energy contract DE-FG03-97ER82343.

REFERENCES

[1] A. Wexler, "Solution of Waveguide Discontinuities by Modal Analysis," IEEE Trans. Microwave Theory Tech., vol. MTT-15, 1967, p. 508.

[2] R. Safavi-Naini and R. H. Macphie, "On Solving Waveguide Junction Scattering Problems by the Conservation of Complex Power Technique," IEEE Trans. Microwave Theory Tech., vol. MTT-29, 1981, p. 337.

[3] C. James, "Analysis and Design of TE11-to-HE11 Corrugate Cylindrical Waveguide Mode Converters," IEEE Trans. Microwave Theory Tech., vol. MTT-29, 1981, p. 1059.

Proceedings of the 2003 Particle Accelerator Conference

TOWARDS THE UAL OPEN SOURCE PROJECT

N. Malitsky, R. Talman, M. Blaskiewicz, R. Calaga, R. Fliller III,
A. Luccio, T. Satogata, J. Wei, BNL, Upton, NY 11973, USA

Abstract

Unified Accelerator Libraries (UAL[1]) software has been introduced as an open accelerator simulation environment providing support for many-to-many associations between diverse accelerator algorithms and diverse accelerator applications. Recently, UAL has been successfully applied to the development and study of the SNS Ring realistic beam dynamics modelincluding a complex combination of several physical effects and dynamic processes (such as injection painting, field errors, space charge effects, impedances, fringe fields, misalignments, etc.). The SNS and previous applications have confirmed the major UAL conceptual solutions and have encouraged us to transform this software into an Open Source project[2]. The major efforts have been releasing documentation and consolidation of UAL modules based on the Accelerator Propagator Framework (APF). At this time, the documentation encompasses User Guide, API specification of C++ classes, Perl User interface, and a collection of feature-illustrating examples. Also APF has been implemented to enhance the UAL infrastructure by providing a uniform mechanism for development and integration of accelerator algorithms. The key part of this approach is the Accelerator Propagator Description Format (APDF) that provides physicists a mechanism for switching among simulation models within their applications.

SNS RING APPLICATION

The need to reduce beam losses to parts per ten thousand in the SNS high intensity proton accelerator complex have introduced a new level of requirements and expectations for beam dynamics studies. Realistic predictions at this level of precision demand a close reproduction of a complex combination of effects and dynamic processes in the accelerator simulation model. To address these tasks, the SNS Ring Accelerator Physics Group developed the SNS Ring package based on the UAL simulation environment[3]. Topics to which the package has been applied include[4][5]:

- optimization of injection painting schemes;
- nonlinear effects arising from kinematics terms, magnet imperfections, and fringe fields;
- dynamic aperture and diffusion map studies;
- effect of space charge during transverse painting;
- tune spreads from space charge, chromaticity, and other nonlinearity in combination;
- intensity limitation and choice of working point dictated by imperfection resonance crossing in the presence of space charge;
- half-integer coherent resonance crossing;
- collective instability due to transverse coupling impedance;
- halo development and beam loss modeling.

These intensive studies required the deployment of the UAL software on parallel clusters. The original architecture was comfortably fitted to the Message-Passing Interface (MPI) parallel environment without any changes of existing modules. Then the time consuming algorithms were implemented as extensions (C++ shared libraries) and combined with other sequential and parallel components.

ACCELERATOR PROPAGATOR FRAMEWORK

The extensibility of the UAL environment is provided by its main architectural principle: separation of propagators from accelerator elements. This approach enables one to apply a variety of different simulation modules to the same accelerator lattice. Having initially rejected any implicit linkage between algorithm and element, the Accelerator Propagator Framework defines a mechanism for connecting accelerator elements with propagators tailored to each particular simulation model. In order to describe the structure of the simulation model, we have introduced the Accelerator Propagator Description Format (APDF). One can consider the APDF file to be a complement to the MAD lattice file. Its structure and relationship to elements and algorithms are indicated in Fig. 1.

Just as the initial lattice description unwinds into a (long) ordered list of all elements in the lattice, the propagator builder associates an appropriate propagator with every element in this list. But, as Fig.1 indicates, default associations permit the APDF file to be quite brief. Some of the possible algorithms are indicated in the figure. "MltTracker" and "DriftTracker" implement pure, element-by-element, kick tracking, for example through elements "qd1" and "sd1", by virtue of their element type being either "quadrupole" or "sextupole". "SectorTracker" implements concatenated, matrix or nonlinear mapping, for example from just before element "d1" to just before element "qf1". Tracking algorithm can also be associated with element based on the element name; for example the "BPM" algorithm is associated with element "bpm1" in Fig.1. This facilitates special processing at particular elements. Like

0-7803-7738-9/03/$17.00 © 2003 IEEE

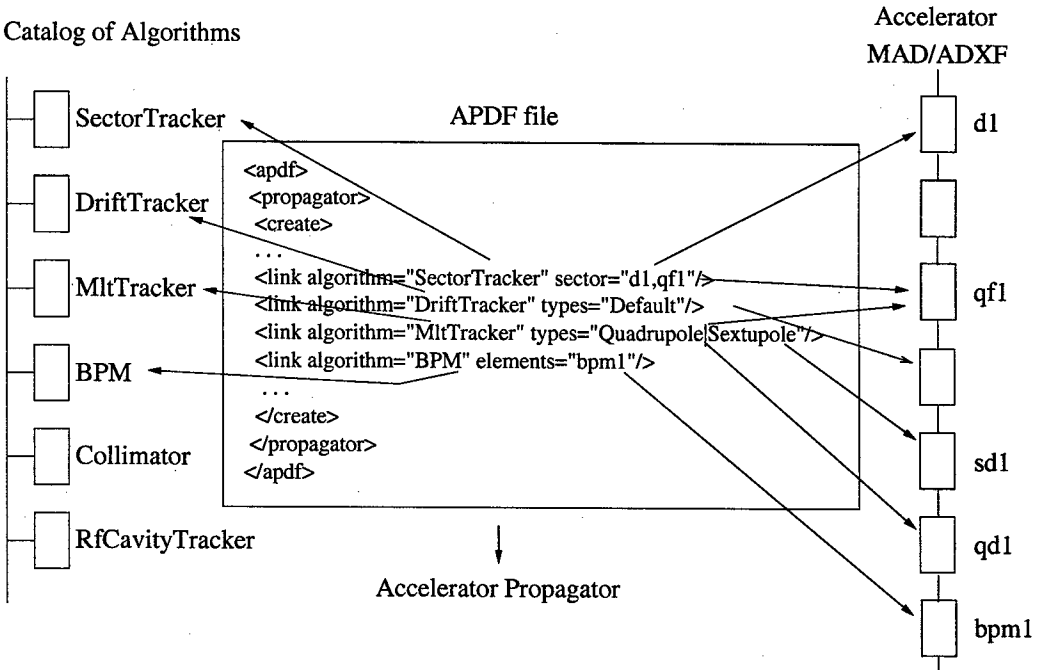

Figure 1: Figure illustrating the APDF-defined linkage between accelerator elements (or sectors) on the right to propagation elements on the left.

the MAD format, APDF addresses a spectrum of applications ranging from small special tasks to full-scale, realistic model encompassing heterogeneous algorithms and special effects. Some possible modeling scenarios are indicated in Table1, which is intended to be self-explanatory. Many of these scenarios have been applied within UAL in the past, but only as dedicated applications. The APDF provides these capabilities without any additional programming complication. Examples have been:

1 Longitudinal beam dynamics	2D matrices + RF tracker
2 Linear lattice functions	4D matrices
3 Fast tracking with chromatic effects (Fast Teapot)	6D matrices with chromatic extensions + selected quad, sext, RF trackers
4 Instumentation modeling, e.g. beam transfer function	#3 + propagators for active diagnostic devices, such as AC dipole
5 Dynamic aperture, halo, IR background investigation	element-type associations
6 Special localized effect, beam-beam, impedance, ions	#3 or #5 + propagator for special effect
7 Near-symplectic large amplitude modeling	octupole imperfection maps, plus kick tracking
8 Full-scale ''realistic''	all of the above

UAL ARCHITECTURE

The organization of the UAL components is indicated schematically in Fig. 2

At this time, the APF-based modules included in UAL are:

- ZLIB: numerical library for differential algebra[6]

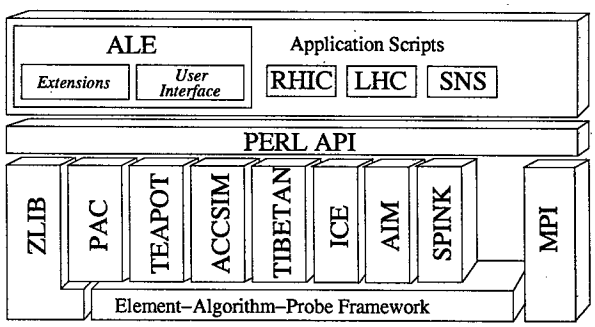

Figure 2: UAL architecture. The figure represents dependency metaphorically, by gravity; codes appearing higher up are supported by (that is, use) codes further down. The upper levels of the figure indicate control via scripting language (PERL).

- PAC: Platform for Accelerator Codes[7]
- TEAPOT: Thin Element Program for Optics and Tracking[8]
- ACCSIM : Accelerator Simulation Code[9]
- TIBETAN : longitudinal phase space tracking program[10]

Modules that are partially supported and are under active development are

- SPINK: tracking code for polarized particles in a circular accelerator[11]

- ICE: Incoherent and Coherent Effects[12]
- AIM: Accelerator Instrumentation Module

The Application Programming Interface (API), written in Perl, provides a universal shell for integrating and managing all project extensions. Consolidation of C++ interfaces has also created a basis for supporting Swig-based interfaces to other script languages (e.g. Python).

POST PROCESSING APPLICATIONS

Another potential benefit of an environment such as UAL is the feasability and economy of "infrastructure" (shared resources) such as postprocessors, plotting/histogramming/fitting for visualization, input and output translation, and parallel processing.

One example of this sort has been preliminary integration of the UAL environment with the ROOT environment[13]. ROOT is an open source project that has been used for many years by high energy nuclear and particle physics experiments for data and simulation analysis. It consists of a C/C++ interpreter CINT and a large number of C++ classes implementing fitting, graphing, GUI, mathematics and various programming functions. A C/C++ interpeter offers an alternative approach to traditional scripting languages, such as PERL or PYTHON, and allows physicists and developers to use a single programming language for an entire project. This environment is especially appropriate for detector background investigations conducted jointly by detector shielding groups and accelerator physicists because ROOT is so well established in the particle physics sector. In one such investigation a proposed RHIC collimator setup was investigated by processing UAL tracking results with the ROOT toolkit. The resulting particle flux distributions can then be passed to experimental physicists for their simulation of detector background.

Another post processing example involved the investigation of Model Independent Analysis (MIA[14]), starting from the following (complete) APDF file:

```
<apdf>
  <propagator>
    <link algorithm="TEAPOT::DriftTracker"
          types= "Default" />
    <link algorithm="TEAPOT::DipoleTracker"
          types="SBend" />
    <link algorithm="TEAPOT::MltTracker"
          types="Quadrupole|Sextupole|Multipole|
                 [VH]kicker|Kicker" />
    <link algorithm="TIBETAN::RfCavityTracker"
          types="RfCavity" />
    <link algorithm="MIA::BPM"
                types="Monitor" />
  </propagator>
</apdf>
```

To simulate MIA, multiturn output from T turns at each of B BPM's was recorded and the resulting TxB matrix was subsequently subjected to singular value decomposition analysis to extract the fundamental modes of the accelerator. When the lattice Twiss functions were reconstructed from the extracted phases at every BPM they were in excellent agreement with the lattice functions determined directly from the original lattice model.

Another post processing approach is to launch a graphing program from within the UAL PERL script. For nonlinear analysis a by-now standard approach is to subject turn-by-turn data to FFT analysis, to extract the tunes by peak location and then to identify accelerator resonances as sum or difference frequencies. The program GRACE[15] makes all these capabilities available and provides graphical output either file driven or via pipe. Zooming, panning, labeling and other prettification and output of the graphs can then be performed, completely independent of UAL, using routine GRACE capabilities. Phase space plots normalized by calculated Twiss parameters can be produced similarly.

REFERENCES

[1] N. Malitsky and R. Talman, *Unified Accelerator Libraries,* AIP 391, 1996.

[2] See `http://www.ual.bnl.gov`. References to original reports and publications are contained in the User Guide accessible from that source: N. Malitsky and R. Talman, UAL User Guide, BNL Formal Report 71010-2003, 2002

[3] N.Malitsky et al, *Application of UAL to High-Intensity Beam Dynamics Studies in the SNS Accumulator Ring,* EPAC 2002.

[4] A.V.Fedotov et al. *Effect of Nonlinearities on Beam Dynamics in the SNS Accumulator Ring,* EPAC00, p. 1492.

[5] A.V.Fedotov et al. *Excitation of Resonances Due to the Space Charge and Magnet Errors in the SNS Ring,* PQC01, p. 2878.

[6] Y. Yan and C-Y. Yan *Numerical Library for Differential Algebra,* SSCL-300, 1990.

[7] N. Malitsky, A. Reshetov, and G. Bourianoff, *Platform for Accelerator Codes,* SSCL-675, 1994.

[8] L. Schachinger and R. Talman, *TEAPOT: A Thin Element Program for Optics and Tracking,* Part. Accel. **22**, 35 (1987).

[9] F. Jones, `http://www.triumf.ca/compserv/accsim.html`, *User's Guide to ACCSIM,* 1990.

[10] J. Wei, *Longitudinal Dynamics of the Non-Adiabatic Regime on Alternating-Gradient Synchrotrons,* Ph.D thesis (1990).

[11] A. Luccio, *Spin Tracking in RHIC (Code Spink),* Proceedings of the Adriatico Research Conference, World Scientific, 1997, p.235.

[12] M. Blaskiewicz, PRSTAB, Volume 1, 044201, 1998.

[13] R. Brun et al., *An Object-Oriented Data Analysis Framework,* `http://root.cern.ch`

[14] J.Irwin et al., *Model-Independent Beam Dynamics Analysis,* Physical Review Letters, Vol 82(8), 1999.

[15] `http://plasma-gate.weizmann.ac.il/Grace/`

SIMULATION USING INITIAL 4D BEAM PARTICLE DISTRIBUTIONS SYNTHESIZED FROM EXPERIMENTAL DATA*

A. Friedman†[1,3], F. M. Bieniosek[2,3], C. M. Celata[2,3], D. P. Grote[1,3], L. R. Prost[2,3], P. A. Seidl[2,3]
[1]LLNL, Livermore, CA 94550 USA; [2]LBNL, Berkeley, CA 94720 USA
[3]Heavy Ion Fusion Virtual National Laboratory

Abstract

In experiments exploring the dynamics of intense beams for Heavy Ion Fusion, detailed 2D projections of the beam's 4D transverse particle distribution function $f(x, y, x' \equiv p_x/p_z, y' \equiv p_y/p_z)$ are obtained at a sequence of stations, using moving slits and Faraday cups. These projections do not uniquely specify the 4D distribution, so we use maximum-entropy Monte-Carlo techniques to complete the specification and tomographically "synthesize" an approximation to f. Our initial studies used simulated beam data from a self-consistent 2D simulation of the High Current Experiment (HCX) [1] at LBNL. Runs initiated using a simple "semi-Gaussian" model distribution failed to exhibit an emittance evolution similar to that of the reference case. Initial distributions synthesized from the (simulated) slit scan data yielded much better agreement. We have begun to launch simulations of HCX with initial conditions synthesized from slit-scan diagnostics. We present here the techniques, initial simulation results, initial analysis of new "optical slit" data yielding projections such as $f(x, y, x')$, and future plans.

SYNTHESIS OF 4D DISTRIBUTION FROM 2D PROJECTIONS

We have developed algorithms which reproduce, in the limit of many particles and fine data grids, the measured distribution in the (x, x') plane and the (y, y') plane, as well as the data from (x, y) when it is available [2]. The three-plane method we have used the most begins by assigning target "counts" $N(x, y)$ of the numbers of particles to be loaded into each spatial "bin" (area element), proportional to the measured f in the bin. The sum of the N's is equal to the desired total number of simulation particles; the use of bins reduces statistical noise relative to random spatial loading following a probability distribution. We may use a sampling region which fills the entire 4-box bounded by the extremes of the measured data, or, optionally, one with "rounded corners" in the unmeasured planes. In the latter case, it is necessary to compute a corrected probability $f^*(x, x')$ by dividing the original $f(x, x')$ by the area in (y, y') of the sampling region at that (x, x'). Similarly, we compute $f^*(y, y')$. The following steps are repeated until all "bin counts" have been decremented to zero: (1) Generate a random point (x_i, y_i, x_i', y_i') in the 4-box; (2) Accept the point as the coordinates of a particle only if it falls within the sampling region, the bin count $N(x_i, y_i) > 0$, $f^*(x_i, x_i') > \text{Random}(0, 1)$, and $f^*(y_i, y_i') > \text{Random}(0, 1)$; (3) If the point is accepted, decrement $N(x_i, y_i)$. Because the tomography problem is underdetermined, the sampling region is almost arbitrary and must be specified empirically. We have generally employed one [2] which consists of the intersection of the interiors of a 4-ellipsoid and four 4-cylinders, all with semi-axes of order the extent of the data along the principal axes. As is noted below, in our case it may be better to omit or modify the sampling-region constraint.

SIMULATION USING MODEL DATA FROM A REFERENCE SIMULATION

In order to to assess the potential utility of launching sinulations using experimental data, we began with a self-consistent "transverse slice" WARP [3] simulation of HCX beginning at the source, for which the true 4D distribution was known. Input to the syntheses consisted of projectional phase-space densities (obtained by nearest-grid-point weighting of the simulated particles from the reference run at the entrance to the HCX transport line) in the (x, x') and (y, y') planes, and, for the 3-plane synthesis, the (x, y) plane. Projections of the input distribution are shown in Fig. 1. Some results of one such synthesis are

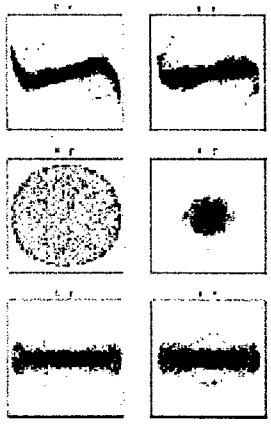

Figure 1: Projections of sampled particles onto principal planes at injector exit, for the reference simulation.

shown in Fig. 2; here the input planes (x, x') and (y, y') are not shown because they are faithfully reproduced, by design. Note that the synthesis fails to recreate the structures in the (x, y') and (y, x') planes.

*Work performed under the auspices of the U.S. DoE by the University of California, Lawrence Livermore and Lawrence Berkeley National Laboratories under Contract Nos. W-7405-Eng-48 and DE-AC03-76SF00098.

† af@llnl.gov

0-7803-7738-9/03/$17.00 © 2003 IEEE

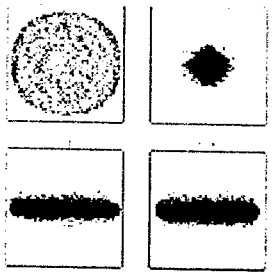

Figure 2: Projections of sampled particles onto principal planes at injector exit for 3-plane synthesized distribution.

Fig. 3 compares the emittance evolution in runs with various initial particle distributions [4]; all begin at the injector exit ($z = -3.11$m).

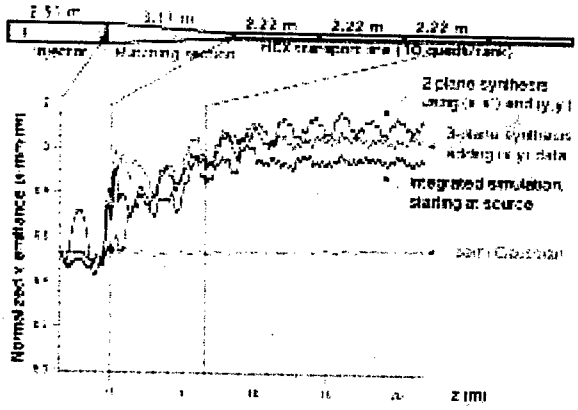

Figure 3: Simulation results: evolution of (x, x') emittance for self-consistent, 2-plane reconstruction, 3-plane reconstruction, and semi-Gaussian beams.

SIMULATION USING INITIAL DATA FROM HIGH CURRENT EXPERIMENT

Encouraged by the above results, we synthesized an initial particle distribution for the HCX using 2-plane initially, and then 3-plane data. Our original attempt at folding in spatial density information employed time-integrated data from kapton film; we soon discovered that the time-integrated distribution is significantly "smeared" due to variations in the beam properties over the pulse duration. Here we show results based on a single time-slice near mid-pulse, using crossed-slit measurements. The vertical-moving slit was downstream, so to obtain a consistent density at the position of the forward slit, the y coordinate was "rescaled" using the mean envelope expansion derived from the parallel-slit data. These data are shown in Fig. 4. Using the initial particle set so generated, we ran a WARP simulation through the (2.22 m, 10 quad) transport line; see also [5]. In Fig. 5 we show the measured beam at the

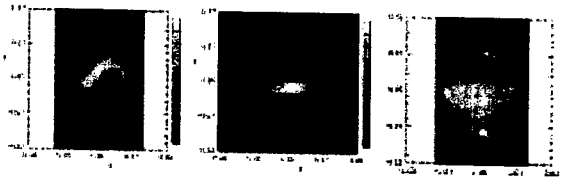

Figure 4: (x, x'), (y, y') and (x, y) views of beam at upstream station QD1 of HCX electrostatic transport line. White dots in first two views denote actual data points.

downstream station "D-end" and the corresponding simulation results. While the beam dimensions and some important features such as the "hollowing" in the spatial density show rough agreement, and the absence of some features in the simulated beam can be explained by the fact that it was loaded in the center of the pipe while the experimental beam had shifted off-center, the agreement between the simulated and measured beams is far from ideal. We conjectured that correlations in unmeasured planes, *e.g.* (y, x'), were not being captured by the synthesis process. This gave increased impetus to the development of the new diagnostic capabilities described below and in [6].

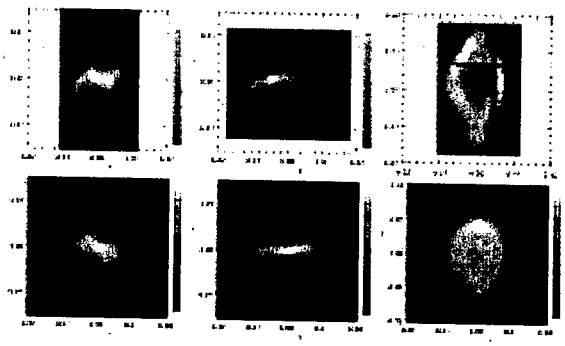

Figure 5: Top row: beam at downstream station D-end; bottom row: simulation result (same views).

ANALYSIS OF 3D "OPTICAL SLIT" DATA

We have started analyzing data from "optical slit" scans (two views, with slits moving in x and y respectively), recently carried out at the D-end station (2.22-m) of HCX. The apparatus is shown schematically in Fig. 6. We now describe the post-processing steps which are aimed at building up a self-consistent data set, and point out features of the derived data which support the view that nonzero correlations in the "other" planes are present.

For each pulse viewed using the horizontal scanner with the slit at some x, the raw image holds $f(u, v)$ at that x: $x' = (u - x)/dz_h$, so a pixel at (x, u, v) contributes to $f(x, x', v)$ at $(x, (u - x)/dz_h, v)$. The beam distribution in the slit plane is a function of a "derived" coordinate y, which is presently rescaled from v on the image plane using the mean beam envelope convergence in the vertical plane.

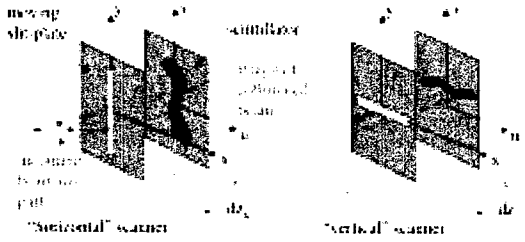

Figure 6: Schematics of "optical slit" scanners.

Thus, obtaining the y values associated with each pixel for the horizontal data set requires use of the vertical data set. The mean convergence in the vertical plane, α_y, is: $\alpha_y = \left\langle (y-\bar{y})(y'-\bar{y'}) \right\rangle / \left\langle (y-\bar{y})^2 \right\rangle$ (where the averages are f-weighted), and the transformation is: $y = v/(1+\alpha_y dz_h)$. The vertical scanner is handled similarly.

Fig. 7 contains views of the measured $f(x,y,x')$. In the first panel f is averaged over y, as in a parallel-slit scanner. However, the latter two panels, showing $f(x,-1.95\text{cm},x')$ and $f(x,,0.8\text{mm},x')$, show that $f(x,,y,x')$ is not independent of y. Note that this is the data set of [6] (Figs. 3-5 therein), and was taken using machine parameters differing from those of Figs. 4 and 5 of this paper.

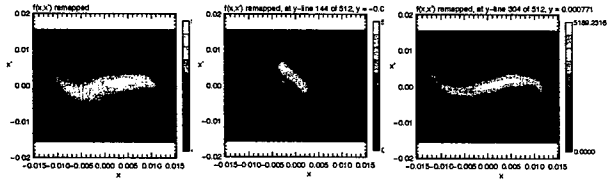

Figure 7: (x,x') phase space from optical slit at D-end: integrated over y, and at two particular y locations.

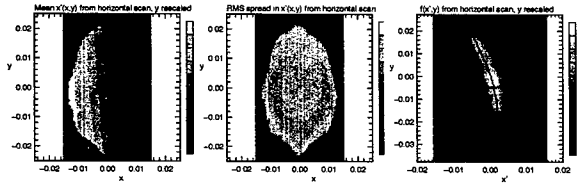

Figure 8: Optical slit data at D-end (see text).

The first two panels of Fig. 8 show moments of the distribution as functions of spatial position (at the slit plane): $\bar{x'}(x,y)$ and $x'_{rms}(x,y)$. Note that $\bar{x'}(x,y)$ is not truly linear in x and independent of y as it would be in a perfectly aligned system with no anharmonic forces. Note also the roughly factor-of-two variation in the transverse (x) thermal speed evident in the second panel. The third panel shows $f(x',y)$ from the horizontal scan; note the dependence of the mean x' upon y, shown as a black trace running from top to bottom of the plot. (The horizontal line is the image of a support in the diagnostic). From this last view it is evident that extreme values of x' are found at the extremes in y of the distribution. This feature contradicts the *ansatz* we had made in our syntheses, which employed a sampling region that disallowed exteme values of x' when y was at its extremes; this may explain some of the descrepancy between simulation and experiment.

PLANS

We plan to improve the remapping of the raw data from the scintillator plane to the slit plane. As a first step, we will employ an x-dependent mean vertical slope, $\bar{y'}(x)$, and a y-dependent mean horizontal slope, $\bar{x'}(y)$. As can be seen in the last panel of Fig. 8, $\bar{x'}$ is indeed not independent of y, and we expect that accounting for this will correct a distortion in the slit-plane spatial image obtained from the vertical scan. In general, we plan to retain centroid displacements and mean slopes, all of which are currently removed in the analysis, in future syntheses of f; this will require good fiducials in the experimental data. It may also be possible to use a spatially-dependent α to account for deviations from linear convergence or divergence.

The next step in our development of a benchmarked "local" simulation capability (as contrasted with a "source-to-end" capability, which is also being pursued) will be to employ projectional 3D data (two or more views) or 4D data (sampled and interpolated) as the basis of the distribution synthesis. It is planned that a compact version of the optical slit diagnostic will be fielded at the upstream QD1 station of HCX, and when that data is available we will carry out the synthesis and simulations.

To synthesize a distribution, we may use the optical slit data to specify spatial bin counts $N(x,y)$ and probability distributions $f(x')$ and $f(y')$ at each cell in (x,y), and load the particles in that cell with random x' values obeying those distributions. It would also be possible to employ a sampling region that excludes the "corners" in (x',y') for particles in a spatial cell. Correlations in that plane are not measured by the optical slits, but may in the future be inferred from hole-plate data.

Multi-hole plates directly yield 4D data, but that data is sparse. It is hoped that interpolations in the velocity distribution, combined with a direct measurement of the spatial density, will yield accurate estimates of $f(x,y,x',y')$.

REFERENCES

[1] Seidl, P. A., *et. al.*, these *Proceedings*.

[2] Friedman, A., Grote, D. P., Celata, C. M., and Staples, J. W., "Use of projectional phase space data to infer a 4D particle distribution," *Laser and Particle Beams*, in press.

[3] Grote, D. P., Friedman, A., Craig, G. D., Haber, I., and Sharp, W. M., Nucl. Instr. and Meth. **A. 464**, 563 (2001).

[4] Celata, C. M., Friedman, A., Grote, D. P., Haber, I., Henestroza, E., *et. al.*, "Particle-in-Cell Simulations of Beam Dynamics in the HCX," *Laser and Particle Beams*, in press.

[5] Celata, C. M., *et. al.*, these *Proceedings*.

[6] Bieniosek, F. M., *et. al.*, these *Proceedings*.

REMOTE OPERATIONS IN A GLOBAL ACCELERATOR NETWORK

S. Peggs, T. Satogata, BNL, USA, D. Agarwal, LBNL, USA, D. Rice, Cornell University, USA

Abstract

The INTRODUCTION to this paper summarizes the history of the Global Accelerator Network (GAN) concept and the recent workshops that discussed the relationship between GAN and Remote Operations. The REMOTE OPERATIONS SCENARIOS section brings out the organizational philosophy embodied in GAN-like and to non-GAN-like scenarios. The set of major TOPICS RAISED AT THE WORKSHOPS are only partially resolved. COLLABORATION TOOLS are described and discussed, followed by examples of REMOTE ACCELERATOR CONTROL PROJECTS around the world.

INTRODUCTION

Remote control of accelerators has been widespread for about 2 decades, in large accelerators such as LEP and HERA where the control room is of order 10 km from the farthest part of the ring. Accelerator engineers and physicists routinely "dial in" to lab computers to check on their equipment, or for general adjustments to equipment and databases, where security policies permit. Technically, most of these duties could be done just as well 1,000 km from the accelerator. The arrival of ever higher bandwidth connections, in the home, office, and in the lab, promises to greatly enhance such routine "single site" remote operations. Recently, much interest has been expressed in "multiple site" remote operations. Although it is not necessary to tightly link the two topics, "Remote Operations" and "GAN" are often considered together. While the original GAN inspiration was the goal of enabling construction of a Linear Collider as an international project, the same remote operations concepts can be applied to any accelerator, large or small, trans-national or intra-national, new or old. Multiple site remote operations are potentially relevant to the APS, CESR, LHC, and the VLHC, as well as to a Linear Collider.

Reports and workshops. Two ICFA working groups studied and reported on the GAN concept in 2001 [1]. The first report examines the *General Considerations and Implementation*, while the second reports on many *Technical Considerations* that are relevant to the topic at hand, Remote Operations. Three workshops were held in 2002, gathering together social scientists and members of the accelerator and experimental community, to consider "Enabling the Global Accelerator Network" (Cornell University), "Collaboration Tools for the Global Accelerator Network" (Lawrence Berkeley Laboratory), and "Remote Operations" (Shelter Island) [2, 3, 4].

REAP. Early in 2003 a working group on Remote Experiments in Accelerator Physics [5] (REAP) was formed under the Beam Dynamics Panel [6] of ICFA, to promote and facilitate communication between laboratories interested in accelerator remote operations. While the focus is on accelerator physics experiments, REAP activities share many of the technical and sociological challenges that a GAN would face. Lessons learned in carrying out remote accelerator physics experiments will be invaluable in setting up more extensive remote operations. REAP maintains a database of accelerator physics experiments employing remote operations, and is developing guidelines for easily accessible webcast seminars. Future work also includes maintaining a library of documentation on remote operations, distributing newsletters, further development of network communications, and workshop sponsorship.

Foundation technologies. The accelerator and experimental physics communities were crucial early implementers of the World Wide Web foundation technology, both because of our extreme performance requirements, and because of our willingness and ability to work at the bleeding edge. It is reasonable – although far from certain – to expect that we will again be involved in a profound paradigm shift, through the emerging technologies that will enable us to meet the rapidly expanding challenges of experimental data analysis, and Remote Operations. Even less certain is the timescale, the exact implementation, and, especially, the social impact of the next great leap forward. Consider, for example, the potential impact of Remote Operations in the context of pilot-less military airplanes.

The need to greatly enhance our ability to share resources in real time increases by orders of magnitude the demands that are placed on networks. Remote control rooms and video conferencing are examples of functions that place such demands – what will they look like with 3 or 6 more orders of magnitude of bandwidth?

REMOTE OPERATIONS SCENARIOS

Experience with multi-institution accelerator construction projects, and particle physics experiments, illuminates the challenges in balancing the need for partner institution autonomy against the need for successful and efficient integration. However, collaborative accelerator construction projects to date have employed the "build and forget" management model – responsibility and ownership is sooner or later handed off completely to the "host laboratory". (This is not the case for particle physics experiments, where the collaborations continue on a more or less equal footing well beyond the construction and data-taking phases.) In contrast, the central tenet of the GAN philosophy is that the partner laboratories remain involved in perpetuity, as equal partners. There is no "host laboratory" but rather a "site

0-7803-7738-9/03/$17.00 © 2003 IEEE

laboratory", and the Project Manager (for example) is probably not an employee of the site laboratory. That is, the site laboratory relinquishes centralized control, in order to secure the continued *distributed symmetric* participation of the partners who build the accelerator sub-systems.

The need for a distributed symmetric organization is probably the most important example of a high level external requirement in a GAN-like remote operations scenario. However, there are many other new issues – technical, social, and non-traditional – that are also vitally important to both GAN-like and non-GAN-like scenarios. Needs that must be addressed in any remote operations scenario include facility coordination and intimate day-to-day facility knowledge, emergency response, and procedural consistency. New challenges potentially include cross-cultural integration, language adoption, and the lack of casual, serendipitous interactions. These challenges are often organizational and social, rather than technical.

Many of these same issues are also relevant, although perhaps not so stressful, to the experimental physics community. For example, the CMS experiment in the LHC plans to install a Virtual Control Room at Fermilab. Some take the GAN philosophy one step further, in proposing the concept of a joint accelerator/experimental Virtual Control Room.

Symmetric and Asymmetric Control Rooms

Potential remote control room implementations cover a spectrum from a simple asymmetric scenario with occasional consultation of remote experts, to a symmetric scenario with functionally- and organizationally-equivalent control rooms at each partner laboratory. In the **symmetric sequential** model the executive privilege for operating the accelerator is passed off between multiple control rooms that are (close to) identical. Control of the accelerator complex rotates between the partner labs, perhaps as quickly as shift by shift. In the **symmetric simultaneous** model, multiple control rooms are simultaneously all more or less equally active, nonetheless with executive control clearly defined. A control room in an **asymmetric** scenario may be complete, or it may invoke collaborative tools to give just a virtual presence in a complete on-site control room. The functionality can then be adjusted to best serve the diverse needs of each remote operations user group.

The needs of many **operations user groups** must be considered during routine and non-routine operations. These groups include *operation crews and co-ordinators, accelerator physicists, experimental groups, subsystem hardware and software experts, application programmers, control system integration experts, and system administrators.* While there is no simple consensus on a best remote operations scenario for all these groups, there is a general consensus that any remote experts responsible for a subsystem must remain actively engaged, through continued accelerator operations. There is also a consensus that an off-site control room with full remote operations capability is now (or soon will be) a feasible alternative to routine travel to the site.

TOPICS RAISED AT THE WORKSHOPS

Details of the workshop discussions on the following topics can be found in the 3 workshop proceedings [2, 3, 4].

Controls Architecture. Remote operations, like large international detector construction, sets critical consistency constraints on controls language, training, and procedures. Comprehensive system simulations and early adoption of top- and middleware tools are essential, and standards must be followed to assure facility consistency and maintainability. This is particularly important in the project's system integration and commissioning phases. Security is a particularly important part of the controls architecture.

Standardization versus accommodation. Standards are organizationally required for language, software development and version control, documents, testing, quality assurance and operations procedures. Negotiation of the balance between a strong central authority responsible for integration, and diverse partner labs responsible for development, operations and support, is among the dominant challenges of large-scale remote operations. How far through the control engineering systems must uniformity be required? Uniformity leads to lower costs, better maintainability, and decreased confusion, but accommodation leads to design flexibility and a greater degree of "ownership". A standards committee should urge conformity, without rushing to establish standards prematurely.

Operational evolution. Installation and commissioning require a substantial on-site presence of participants, including future remote experts. This period is a primary opportunity for community and mutual interest building that will sustain interest through the transition from early commissioning to the continuous upgrade phase. The remote operations environment must be attractive to the operations user groups, in order to keep activity levels high.

Social communications. For long-term organizational viability, remote operations should allow nearly the same range of interpersonal interactions as co-located personnel. Easily used communication devices such as video walls should proliferate. Casual interactions and other low-level contacts are the most important channels for team-building – familiarity breeds content.

Training and procedures. Common operator training is required. Inter-lab participatory tutelage and "hands-on" training will also build community and encourage common practices, but early simulation training will potentially be quite difficult. All operations documentation and reviews must be freely-available from all control rooms, including playback of operations activities for training and review purposes. Routine mixing of operations member assignments between member labs will be useful to promote community.

Maintenance and spares. Remote maintenance scenarios include the need for detailed consultation between an

on-site repair crew and remote experts. Ownership and responsibility for failed components must be clearly defined, and there must be checks and balances for remote experts to verify repairs and proper system performance. It is not completely obvious that an increased spares inventory is necessary, especially if components are duplicated among multiple projects supported by an individual participant laboratory.

The 1% problem. Expert intervention on-site is expected about 20 times per year, or for about 1% of interventions, in a large remote operations facility. This typically implies an interruption of operations for approximately two days if extended air travel is required. Possible remedies include improved internal diagnostics, extensive logging, and enhanced remote diagnosis. None of these solutions are prohibitively expensive, and all of them are also "good practice" features for a locally-controlled accelerator.

An Example: KEK ATF. After careful consideration in 2000, KEK personnel decided not to retroactively implement a full remote operations capability for the ATF ring. The radiation safety reporting path was critical in this decision – an on-site control room shift leader is required for all shifts. Most of the appropriate documentation was in Japanese, providing a language barrier to foreign collaboration. The technical problems were surmountable, but inbuilt social and organizational issues demonstrated that remote operations as an afterthought is at best difficult.

COLLABORATION TOOLS

Many efforts to build and deploy collaboration environments in support of remote access have been launched in the past decade. As a result, many collaborative tools are now available, and several studies of collaborations have been conducted. Success depends on many factors including the technologies used, the social environment, the goals, the level of support, and the level of need. An important factor is time and place: users might work at the same or different times, and in the same or different places. Collaboration often involves a mixture of types of interactions, requiring an appropriate array of tools.

Technologies

Collaboration technologies facilitate several modes of interaction. One mode involves interpersonal communication including speech, video, text, and e-mail, while another enables access to stored data and information, including real time monitoring. Several tools support conversations. Text-based chats like Instant Messaging (IM), Multi-User Dungeons (MUD), and Internet Relay Chats (IRC) provide mostly synchronous interaction but can also allow intermittent interactions. Secure text messaging and presence capabilities are provided by the Berkeley Lab Secure Messaging Tool. Video conferencing tools include Polycom Video Conferencing, NetMeeting, Virtual Rooms Videoconferencing System (VRVS), and Access Grids. These tools provide varying degrees of visual and audio interaction capabilities and immersion. The Access Grid provides a very immersive experience with a large video wall to project all the participants, several camera views of participants, and naturalistic audio. Technologies like NetMeeting, Via Video, and the VRVS system provide limited immersion capabilities during workstation-based interactions, including meetings over high and low bandwidth. Capture and replay capabilities are currently emerging. Soon, data will be archived and annotated for continuing discussion.

Several tools augment synchronous interactions, allowing participants to talk about a shared display, data stream, or report. A number of technologies allow this: screen sharing, electronic whiteboards, presentation software, and remote control panels. Ideas currently under development include workstation "docking" and peer-to-peer file sharing capabilities, which allow users to share data on any computer or PDA in a relatively ad hoc fashion. Electronic notebooks that allow access to an organized stream of activity, comments, and data are in use in various communities. Most accelerators already use electronic log-books.

Some cutting edge technologies focus on the awareness that people have of others availability and current work. Presence information plays an important role in the perception that collaborators are working together. Collaborative workflow systems under development incorporate Grid technologies to provide security and to allow submission of compute jobs on Grid enabled machines. Shared editing of text and documents is an important collaborative activity that has not yet been adequately addressed.

Social factors

A number of issues – security, privacy, interruptions, ease of use and training – must all be addressed, before collaboration technologies are acceptable to end users. Participants need mechanisms for identifying themselves and having private interactions. A person on video wants to be able to see all the people viewing that video. Whatever technology is employed needs to be easy to use, and must be platform independent. Applications must be customizable to particular situations. Participants need to evolve interaction rules of conduct that are mutually acceptable and widely known.

Participants in collaborations across national and cultural boundaries (including between laboratories in the same country) may have to relinquish a substantial portion of their habits, to seek a common working mode. Conscious effort will have to be spent on finding best working practices, and ways to adapt to them. Semi-formal techniques such as "User-Centered Design" can be used to extract requirements for a collaborative environment by producing a preliminary view of the users goals, work practices, and likely interaction patterns and needs

Coordination functionalities

The coordination that takes place in all these settings is both asynchronous and synchronous, involving both scheduled meetings and informal communication. Required functionalities include:

Meeting support. Users want to be able to give and attend meetings and presentations remotely, with both audio and video of the presenter along with the slides or presentations of other things (like a data stream, simulation results, 3-D CAD tools, video, documents, visualization and electronic notebooks). All participants should be able to see all other participants, in order to capture their reactions. People should be able to connect from their offices as well as from special conferencing rooms, and should be able to participate when traveling. This raises the issue of whether and how to make solitary participants equal members of meetings. If passive participation and multi-tasking is appropriate – perhaps when connected at the desktop – it is desirable to have the stream running in the background.

Informal meetings. On occasion, such as when an unexpected result happens, people need immediate access to associates for consultation. For this, an awareness/presence system with appropriate rules about its use (a cultural issue) will support finding and contacting the right person. Once contacted, the kinds of technology that support formal meetings would support these less formal sessions.

Remote operations. In order to establish efficient two-way communication it is only necessary to duplicate what is on a subset of screens, and NOT the entire control room. Screens should "look" the same to everyone. A meeting room is needed for the development and discussion of run plans, analysis, information exchange at shift changes, et cetera. Also needed are electronic whiteboards visible at remote locations, and computers for logging data streams, and for analyzing and displaying summary data. Since the operators hands and eyes are busy, the primary communication will likely be a wireless headset. Video of the remote partner helps communication. The same kind of views and communication channels help during installation, testing, and commissioning, et cetera, for those who need never be on site.

Experience at BNL/RHIC. A VRVS video conferencing system was used to broadcast shift change and other daily meetings during the 2003 RHIC run. Experiment control rooms and personnel offices had non-interactive access to these broadcasts. This approach was abandoned after approximately two weeks of use – only one operations coordinator knew how to operate the video conferencing equipment, and interest quickly waned when equipment problems developed. This experience emphasizes an adoption expectation for communications utilities: they should be as convenient and reliable as a telephone. Simple video conferencing systems are just barely reaching this state. Advanced video conferencing software like the Access Grid are far from this ease of use.

ACCELERATOR REMOTE CONTROL PROJECTS

A total of 22 in-progress and planned experiments was presented at the Shelter Island workshop, and is tabulated in the proceedings [7]. Table 1 lists a representative sample of six of them. A brief description of three remote operations activities (two of them initiated after the Shelter Island workshop) illustrates the breadth of these endeavors.

Examples of current and planned experiments

Small scale (current): Remote controls enable both faculty and students at a small university to experience and carry out research at a large facility, without frequent or prolonged travel. A series of remote diagnostic and tuning experiments on the Cornell Electron Storage Ring (CESR) is being carried out by a faculty member at Alfred University, a small institution approximately 100 km from the lab [8]. The faculty member had been a member of the accelerator physics staff at CESR for several years, and thus did not need to make an initial on-site stay to become familiar with accelerator infrastructure, or to build the personal links necessary for close collaboration. Orbit and aperture measurements on the injector synchrotron have been made.

Since the CESR control programs use X-windows displays, remote operation is enabled simply by logging in to the CESR control computers. (Additional control for authorization must be put in place before using the system on a widespread scale.) In addition to conventional control and monitoring functions (including graphical history displays) a digitizing oscilloscope provides updates of screen data at roughly 5 Hz. Coordination with the accelerator operator is made by telephone.

Medium scale (current): An experiment to characterize and improve photoinjector performance has been in progress in the A0 hall at Fermilab for over 4 years [9]. The collaboration – between institutions in the US, Italy, and Germany – is working on development of an injector for the TESLA and TTF accelerators, and on the study of novel applications of high brightness, pulsed electron beams. For example, a recent study of the effect of the injectors bunch compression chicane on bunch properties has been carried out primarily by operation from DESY [10, 11]. The central energy, energy spread, bunch length, and transverse emittance were measured for several combinations of RF cavity phase and chicane magnet currents.

Because the photoinjector experiment was not originally designed with remote operation in mind, several functions – RF transmitter on/off, laser adjustments, and cryogenics control – are performed locally. These need only intermittent attention, mostly at the beginning and end of shifts. Other local functions are also available remotely using VNC, a cross platform program duplicating a local computer screen and keyboard at a remote site. A remotely controlled video switch allows any of a number of TV images to be sent to a web browser window faster than 1 Hz. The composite signal is captured by a frame grabber, then

Table 1: Representative Remote Operations Projects

Partners	Experiment	Goals	Site Lab	Software	Status
BNL, FNAL	IR Linear Corr.	Remote beam ops	BNL (RHIC)	Local, ACNET	Proposed
JLab, SNS, LANL	SNS SRF Commissioning	Evaluate RF cavity perf.	JLab	EPICS	Proposed
DESY, Cornell, Ohio State, U. Mich.	TTF DAQ	Database tools for accel. data, collaborative tools	DESY (TTF)	DOOCS, VRVS	Proposed
Cornell, Alfred U.	Accelerator diagnostics	Devel. remote tools, improve accel. perform.	Cornell (CESR)	Local, X-windows	Ongoing
FNAL, DESY	A0 Photoinjector	Develop high current injectors	FNAL	PC, MAC, SUN	Ongoing
KEK, SLAC	Beam based alignment and analysis - ATF	Damping ring development, remote control	KEK (ATF)	MATLAB, V-system	Ongoing

converted to jpeg format to reduce required bandwidth. Video conferencing and a mutually accessible electronic log book complete the remote control package.

Large scale (proposed): A recent proposal to the European Steering Group on Accelerator R&D (ESGARD) [12] includes a comprehensive program to use working examples of a Multipurpose Virtual Laboratory (MVL) to demonstrate "far remote operation" capabilities and the essential components envisaged in GAN [13]. Seven different accelerator technology projects will be used as development test beds. The GANMVL collaboration of 6 major European laboratories plans a 3 year time scale for the project, with an estimated effort of 80 person-years.

MVL works in a client-server configuration. The server will contain hardware and software to capture measured accelerator data, user controls and audio/video data. These real-time data will be distributed to the clients and projected into an interactive virtual environment. In order to approach the scientific and social interaction environment of a single laboratory, video and audio links will use 3-D audio and stereo video technology. Streaming transmissions will employ secure technologies to guarantee smooth and uninterrupted data flow. Standardization of vocabulary, comprehensive authorization procedures, plug and play hardware, and planning for remote coordination of operations planning, maintenance, troubleshooting and repair will be studied and developed.

CONCLUSIONS

Multiple site remote operations are necessary in the GAN management model of the distributed symmetric participation of equal partners in a future large scale accelerator project. Remote operations – whether in a symmetric sequential, symmetric simultaneous, or an asymmetric scenario – are also acquiring powerful potential advantages in non-GAN-like applications. Thanks to rapid communications advances, it is becoming possible to envisage tightly knit but broadly dispersed communities of accelerator operations user groups. The challenges to successful implementation are as much social as technical. Evolving technologies from the Access Grid to the Multipurpose Virtual Laboratory deserve close attention. However, new modes of communication must become as simple and reliable as a telephone before broad acceptance is assured. Contemporary video conferencing still leaves much to be desired. The broader societal impact of any such new foundation technology is as hard to predict as it was for the World Wide Web in its early evolutionary period.

ACKNOWLEDGEMENTS

We are very grateful for the contributions of K.Desler, F.Willeke, all the workshop participants, and the personnel of the CREW project at the University of Michigan.

REFERENCES

[1] http://www.fnal.gov/directorate/icfa/icfa_tforce_reports.html

[2] http://www.lns.cornell.edu/ganwkshp

[3] http://www-itg.lbl.gov/Collaboratories/GANMtg

[4] http://www.rhichome.bnl.gov/RemOp

[5] http://www.lepp.cornell.edu/icfa/reap

[6] http://wwwslap.cern.ch/icfa/

[7] http://www.rhichome.bnl.gov/RemOp/docs/WG1_ganprojects_020919.PDF

[8] R. Holtzapple, private communication

[9] J.-P. Carneiro, et al., "First Results of the Fermilab High-Brightness RF Photoinjector", PAC'99, New York, 1999, p. 2027

[10] J.-P. Carneiro, et al., "Study of a Magnetic Chicane at the FNAL/NICADD Photo-injector Using Remote Operation from DESY", EPAC'02, Paris, 2002, p. 1759

[11] N.Barov et al., "Remote Operation of the Fermilab/NICADD Photoinjector", FERMILAB-TM-2167, 2002

[12] http://esgard.lal.in2p3.fr

[13] F.Willeke, private communication

INTEGRATION OF ORBIT CONTROL WITH REAL-TIME FEEDBACK*

F. Lenkszus, L. Emery, R. Soliday, H. Shang, O. Singh, M. Borland†
Argonne National Laboratory, Argonne, Illinois 60439 USA

Abstract

The Advanced Photon Source uses two distinct control programs for orbit control and stability—a full-featured workstation-based program for orbit control (sddscontrollaw) and an EPICS-based system, the Real-Time Fast Feedback System (RTFS), to reduce orbit motion. The sddscontrollaw program has been ported to EPICS and moved from the UNIX environment to an EPICS IOC attached to the RTFS. This EPICS-based program uses the RTFS's reflective memory to gather beam position information and write corrector power supplies, thus avoiding variable network latencies. This allows the orbit control to run at a correction rate 50 times that of the workstation implementation, which virtually eliminates orbit motion caused by insertion device gap changes. Issues raised by the integration of orbit control into the real-time feedback system and performance improvements are discussed.

INTRODUCTION

The Advanced Photon Source uses two feedback systems operating in parallel to correct the transverse orbit. The "slow," DC orbit correction (OC) system performs orbit control and local steering [1,2], while the real-time orbit feedback system [3] reduces faster orbit motion. The real-time feedback (RTFS) system is AC coupled and operates at an iteration rate of 1534 Hz, while the DC system when operated on a UNIX workstation has operated at iteration intervals of 0.5 to 4.0 seconds.

The workstation-based control-law software has been ported to the real-time operating system, VxWorks, used by the APS control system EPICS IOCs. A new IOC, the datapool, has been added to the RTFS reflective memory network. The datapool IOC has access to all beam position monitor (BPM) position data and all corrector set points through the reflective memory connection. Thus the datapool provides a dedicated platform on which to run orbit correction without local area network involvement except to set up and monitor operation. The result is that DC orbit correction now runs 50 times faster with a very deterministic iteration interval.

EVOLUTION OF THE DATAPOOL

Prior to the addition of the datapool IOC, DC orbit correction ran at iteration intervals of 2.5 to 4 seconds. The sddscontrollaw program was required to fetch BPM position data from 43 BPM and RTFS IOCs and write corrector values to 20 power supply IOCs. The time required to fetch data, compute corrections, and write correctors for a single plane was measured to be 800 milliseconds with a variability of ±500 milliseconds [4]. Variable network latencies due to the large number of IOCs involved in the process and the uncertain process scheduling in the UNIX workstation environment were probably large contributors to the long iteration time with such a large variability.

Initially, while the port of sddscontrollaw to VxWorks was in process, the datapool IOC was used as a single point of focus for position data for the workstation-based OC; i.e, all BPM position data were transferred as vectors between the workstation and the datapool. Corrector set points were still sent as scalars to power supply IOCs. This permitted the OC iteration rate to be increased to 2 Hz, but a large variability in time to complete each iteration was still observed.

The VxWorks port of the control-law software allows both planes to be run on the datapool IOC simultaneously at 20 Hz. This is a 50-fold increase over the iteration rate in use prior to the datapool IOC.

THE HARDWARE

The datapool is an EPICS IOC based on a Motorola 366-MHz, MVME2700 processor. This IOC also contains a Pentek 50-MHz model 4284 DSP card [5]. A VMIC 5588 reflective memory card [6] provides the interface to the fast-feedback system's network and thus provides access to all BPM position vectors and corrector set-point vectors. Reflective memories are connected to a 29.5-MB/s fiber-optic ring. An in-house card, the feedback system interface card, receives the RTFS sample clock, which is currently set to 1534 Hz. A block diagram is shown in Fig. 1.

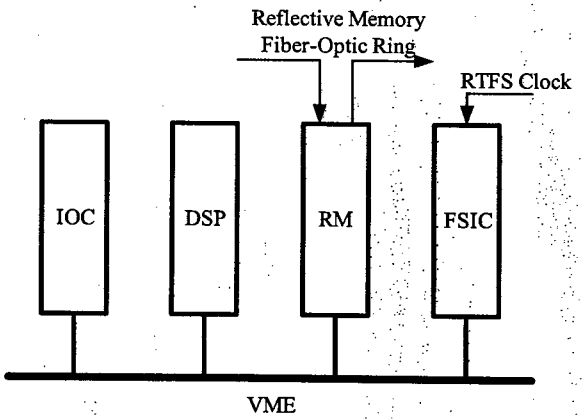

Figure 1: Datapool IOC block diagram showing the IOC and DSP processors, reflective memory (RM), and feedback system interface (FSIC).

*Work supported by U.S. Department of Energy, Office of Basic Energy Sciences, under Contract No. W-31-109-ENG-38.
†also at Lyncean Technologies, Palo Alto, CA 94300 USA

0-7803-7738-9/03/$17.00 © 2003 IEEE

DATA ACQUISITION

Figure 2 shows the data flow and processing in the datapool IOC. The RTFS deposits all BPM data into its reflective memory network at its iteration rate (1534 kHz). This data consists of x and y positions from 320 monopulse rf BPMs, 70 narrowband rf BPMs, and 70 insertion device x-ray BPMs; and y positions from 70 bending magnet (BM) x-ray BPMs. Not all values have underlying physical devices yet. These 990 position values are available to any IOC attached to the RTFS reflective memory network including the datapool IOC. The datapool IOC digital signal processor (DSP) reads these position vectors at one-half of the feedback system sample rate and applies a 2-pole digital filter to each value. All computations are vectorized. The processing is done at one-half of the feedback system sample rate because the DSP card currently in use cannot read the 990 values and compute the required 990 digital filters at the full sample rate. The digital filter cutoff frequency is specified by an EPICS process variable and thus is easily changed. The DSP generates an interrupt to the IOC processor at a decimated rate determined by another EPICS process variable.

Upon each interrupt from the DSP, the IOC reads the filtered position vectors from the DSP's dual-ported RAM and deposits them into EPICS waveform records. Polynomial linearization appropriate to chamber types is applied to each vector. Offset, set-point, and gain vectors are applied using EPICS subroutine records to implement the vector processing.

At this time the sddscontrollaw does not process synchronously at the decimated data rate, rather its iteration rate is derived from the real-time operating system's 60-Hz system clock.

The control-laws compute corrector delta vectors and deposit them into corrector delta waveform records. These vector deltas are accumulated in another EPICS waveform record. The resultant 317 element horizontal and vertical corrector vectors are deposited into the RTFS's reflective memory network along with an update flag. Each RTFS DSP (20 horizontal plane and 20 vertical plane) reads the portion of the corrector vector corresponding to its span of control and writes the values to the individual corrector power supply regulators.

The datapool IOC records the last 128 values written to each of the 634 correctors. Separate time stamps are recorded for each plane. Upon beam loss, the control-laws suspend iterations and thus, the corrector history buffers contain the last 128 values for each corrector. These temporal records are available as EPICS waveform records for postmortem analysis of beam-loss events.

The datapool IOC also provides BPM set-point vectors for the RTFS. These vectors are processed by each RTFS DSP in a manner similar to the corrector set-point vectors. This feature is a key component of the orbit control/RTFS overlap compensation discussed below.

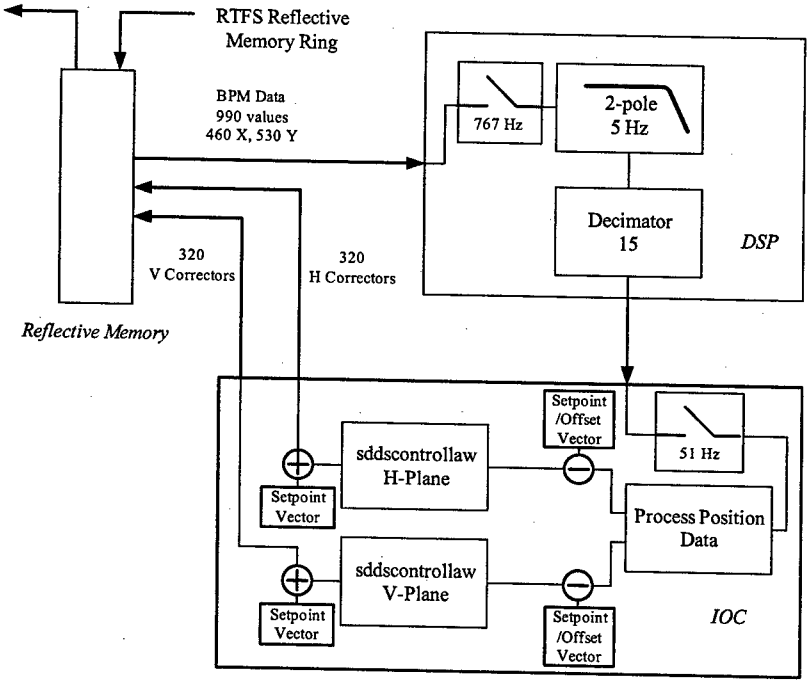

Figure 2: Data Acquisition and Processing Flow.

ORBIT CONTROL PROGRAM

Sddscontrollaw is part of the SDDS suite of tools [7]. The workstation version is used extensively at APS to do feedback with EPICS process variables. It offers configuration flexibility to accommodate various focusing lattices. It also provides "despiking" to automatically remove bad BPMs without operator intervention, limits on the maximum change per iteration, and testing of quantities for valid conditions [2]. Compensation for intensity-dependent BPM offsets is handled by a separate workstation program (sddsfeedforward). An input file containing measurement and control process variables defines a gain matrix for a simple control-law equation. By default, the sddscontrollaw tries to regulate the measurement values to zero. An additional file containing process variables to check for out-of-range conditions may also be defined.

The VxWorks version of sddscontrollaw provides most of the features of the workstation version. Testing for out-of-range conditions is handled by a separate workstation process (sddspvtest) that communicates out-of-range conditions via summary EPICS PVs. The use of an external process to test for out-of-range conditions significantly reduces the IOC load when the number of test PVs is large. The VxWorks version is controlled by a custom EPICS record type named sddsLaunch. This record includes an array field that is loaded with a text string containing sddscontrollaw configuration file names and options. One sddsLaunch record is required for each instance of sddscontrollaw. For the datapool orbit control case, two such records are required – one for each plane.

Porting sddscontrollaw to VxWorks required modifying not only the sddscontrollaw code, but also all the SDDS libraries. Several factors conspired to increase the difficulty of this port. The original sddscontrollaw made extensive use of the EPICS EZCA library, which is not available under VxWorks. Thus all SDDS channel access routines had to be rewritten in native EPICS channel access (CA) calls. Another major change to the code involved aggressively going after memory leaks, no matter how small, because VxWorks, unlike other operation systems, does not release memory after a task exits. The difficulty of this task was increased because the original code was written to exit without memory deallocation upon encountering an error. The code also contained many global variables that would confound running multiple instances of control-law. This problem was solved by placing the global variables in a large structure, which is accessible through a VxWorks task variable pointer, thus making the structure private to the task.

Additional problems arose because the original SDDS libraries were not written to be reentrant. Thus, if there was more than one instance of sddscontrollaw running on an IOC, odd problems would occasionally occur. This problem was overcome by loading a separate but identical instance of SDDS libraries for each sddscontrollaw.

Local steering is accomplished by aborting sddscontrollaw for the plane to be steered, suspending the other plane, loading a new configuration that combines both planes, and restarting sddscontrollaw. Upon completion of the steering, sddscontrollaw is again aborted and restarted with the original orbit control configuration. The suspended plane is also restarted.

We encountered random and severe problems with the initial port of sddscontrollaw to VxWorks following an abort. The IOC was left in a state that required reboot. The exact failures were not repeatable and occurred about 10% of the time. The exact cause was not identified, but we suspect it was associated with ancillary tasks spawned by channel access (CA). Since all the EPICS process variables are local to the datapool IOC, a second version of sddscontrollaw was created that used EPICS database access in place of CA. This version ran significantly faster and eliminated the failures we experienced when aborting sddscontrollaw. The datapool IOC now uses the database access version of sddscontrollaw.

The horizontal and vertical control-laws operate independently each using an instance of sddscontrollaw. Each plane uses 80 correctors (two per sector). This allows compensation for perturbations from individual insertion device gap changes. The vertical plane uses 80 rf BPMs, including all the narrowband BPMs, and all the available BM x-ray BPMs. Thus, those sectors with BM sources use four BPMs. Excluded are rf BPMs affected by a vacuum chamber higher-order mode [8] that gives a strong dependence on small bunch pattern changes.

All available rf and BM BPMs are used by the horizontal-plane sddscontrollaw. The vacuum chamber higher-order mode mentioned above doesn't affect the horizontal position readbacks.

We are in the process of including ID x-ray BPMs. These BPMs require offset feedforwarding to compensate for effects caused by ID gap changes. At the time of this writing, one pair of ID x-ray BPMs is included.

OPERATOR INTERFACE

The graphical user interfaces (GUIs) developed for orbit control used two fundamental principles that have governed all GUIs developed at APS, which are, sadly, not widely followed elsewhere but are worth repeating here: 1) Split up the work into smaller GUI applications, which may be usable for other applications. 2) Allow the GUI application to be configurable for different modes.

The operator interface for orbit control has been split into three GUIs: Modification of a database of "good" BPMs and correctors for OC, creation of corrector and BPM configuration files, and orbit control.

The GUI for maintaining a database of "good" BPMs and correctors is configurable for either "corrector" or "BPM" mode. This database also includes fields for whether or not a BPM or corrector exists, is valid for logging, is available for DC OC, is available for RTFB, etc. The database contains about 20 fields for BPMs and six fields for correctors, many of which are useful for applications other than OC.

The files related to corrector and BPM configurations for the DC OC and the RTFB are handled by a GUI configured by a base directory unique to the DC and RTFB correction systems. The datapool and workstation configurations saved for DC OC are distinguished by parameter data saved at the time of the creation of the configuration.

To simplify operations, the same GUI is used to operate DC OC in either datapool or workstation mode. A "START" button executes all the necessary setup commands and launches an sddscontrollaw process in either a workstation or datapool as determined from the parameter data read from the entered configuration name.

The setup commands that are common for both modes of OC consist of aborting any previous instance of sddscontrollaw, asserting the correct operation mode of the correctors, setting up BPM averaging, and writing status to several "In Use" corrector and BPM EPICS process variables.

In datapool mode, there are additional steps to initialize vector PVs for corrector set points, BPM offsets and set points, and RTFB BPM set points. Differences between the vector PVs and the scalar-equivalent PVs outside of the datapool IOC are calculated and significant differences are reported.

INTEGRATION WITH REAL-TIME FEEDBACK

Increasing the OC iteration rate from 0.4 Hz (2.5-second iteration interval) to 20 Hz increases its correction bandwidth from 0.025 Hz to 1.3 Hz. Since the AC coupled RTFS's correction bandwidth extends down to approximately 0.02 Hz, the range where the two systems overlap is significantly increased. If no precautions are taken, when OC and RTFS are run simultaneously they will tend to "fight" each other within their shared overlap band. The lower cutoff of RTFS could be increased to reduce the overlap. Thus one is faced with trading off overlap and the resulting "fighting" with no overlap and the resultant dead band where no correction occurs. This issue is of increased importance with the higher bandwidth OC, since insertion device gap changes near minimum gap contribute to significant beam perturbations below 1 Hz.

An overlap compensation scheme has been developed [9] and implemented that allows the two systems to overlap and operate with reduced fighting in the overlap band. The scheme is based on DC OC applying feed-forward to subtract its anticipated orbit perturbations from RTFS BPM set points. This effectively "blinds" RTFS to DC OC orbit changes, thus allowing the two systems to overlap without fighting and avoid a dead band where no orbit correction occurs.

RESULTS

The measured total IOC processor load running both orbit control planes was measured as 13%, 25%, 39%, 52%, and 91% at iteration rates of 0, 10, 20, 30, and 60 Hz. Currently both planes run at 20 Hz.

X-ray-beamline insertion device (ID) gap changes near minimum gap cause significant beam perturbations below 1 Hz. Increasing the bandwidth of the DC orbit correction combined with OC/RTFS overlap compensation reduces the perturbations from these moving ID gaps. Figure 3 shows the effect of ID gap changes for OC running on the datapool IOC at iteration intervals of 2.2, 0.8, and 0.1 seconds. It is expected that OC running at 20 Hz will reduce these perturbations further.

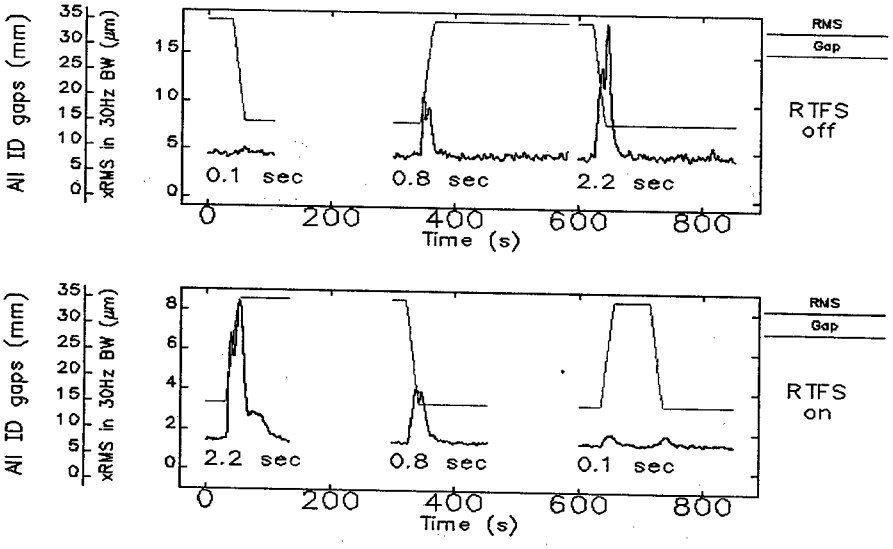

Figure 3: Reduction in orbit motion due to ID gap changes for orbit control iteration periods of 2.2, 0.8, and 0.1 seconds.

PLANNED IMPROVEMENTS

Presently the orbit control programs sample the BPM vectors asynchronously at a rate derived from the VxWorks 60-Hz system clock. We plan to add a mechanism to facilitate synchronizing sddscontrollaw iterations with the decimated BPM sample rate.

As mentioned previously, the IOC processor presently used is a 366-MHz Motorola MVME2700. We have in house a 450-MHz Motorola MVME5100 that we plan to install, and anticipate this will allow OC to run at even higher iteration rates.

CONCLUSION

The orbit control code used at APS on workstations has been ported to VxWorks and now runs on an IOC processor. This has allowed orbit control to run at 20 Hz, which is 50 times the rate used prior to addition of the datapool IOC. A primary benefit has been a significant reduction in orbit perturbations due to insertion device gap changes near minimum gap.

REFERENCES

[1] G. Decker, "Orbit Control at the Advanced Photon Source," DIPAC 2001 Proceedings, ESRF, pp. 177-179 (2001).

[2] L. Emery, M. Borland, "Advances in Orbit Drift Correction in the Advanced Photon Source Storage Ring," Proc. of the 1997 Particle Accelerator Conference, Vancouver, BC, pp. 742-744 (1998).

[3] J. Carwardine, F. Lenkszus, "Real-Time Orbit Feedback at the APS," AIP Conference Proceedings 451, pp. 125-144 (1998).

[4] Louis Emery, APS, private communication.

[5] Pentek, Inc., Upper Saddle River, NJ 07458, www.pentek.com.

[6] VMIC, Inc., Huntsville, AL 35803, www.vmic.com.

[7] M. Borland, "Applications Toolkit for Accelerator Control and Analysis," Proc. of the 1997 Particle Accelerator Conference, Vancouver, BC, pp. 2487-2489 (1998).

[8] X. Sun, G. Decker, "Eigenmodes in Two Simplified Chamber Structures Studied for Spurious Microwaves in the APS Storage Ring Beam Chamber," APS Light Source Note LS-299, April 30, 2003.

[9] C. Schwartz, L. Emery, "Compensating the Frequency Deadband of the APS Real-Time and DC Transverse Orbit Correction Systems," Proceedings of the 2001 Particle Accelerator Conference, Chicago, IL, pp. 1234-1236 (2001).

CONTROL SYSTEMS ON LOW COST COMPUTERS

Ernest L. Williams Jr., Greg S. Lawson, ORNL, Oak Ridge, TN 37830, USA

Abstract

Computing infrastructures for accelerator control systems can now be built using low cost, commodity-type computers. The commonly used EPICS control system toolkit has been adapted to facilitate its deployment on Pentium-based PCs running the Linux operating system, as well as on other inexpensive platforms.

Low-cost, reliable enterprise-class computers can be obtained from many commercial vendors for such control system network-based services as Domain Name Service (DNS), Network Information Services (NIS), and Dynamic Host Configuration Protocol (DHCP). Control system file servers can also be configured using inexpensive rack-mounted PCs and multiple monitor operator consoles can be built with Linux-based PCs or standard X-windows software with high performance video graphic adapters. At the front end of the control system, input-output controllers can be configured also as PCs running embedded Windows.

Several accelerator laboratories, including the Spallation Neutron Source (SNS) at the Oak Ridge National Laboratory are taking advantage of these possibilities. This paper will review the use of inexpensive computers in the accelerator community, with particular emphasis on the issues and applications at SNS.

1 INTRODUCTION

Commodity based personal computers (PCs) are starting to play a larger role in the accelerator community. PCs running the Linux operating system (OS) have already begun replacing the traditional SUN Solaris and HP-UX control system file servers. Many of the accelerator labs have introduced the PC to achieve the flexibility of choosing non-proprietary hardware and software. This flexibility allows a combination of both an "open source" and a commercial software mix at some labs. For example, the control system enterprise file servers, database servers, and network support servers can be run using Linux while smart embedded front-end processors can be based on Windows Embedded XP. The EPICS developer community has strived to make the control system software toolkit LINUX and WIN32 ready. The recent introduction of an operating system independent (OSI) version of EPICS (3.14.x) [1] facilitates its use on commodity-type PCs running the OS of your choice. The large base of PC vendors helps to optimize cost, reliability, and availability. We discuss below some of the control system integration issues, vendor support, reliability, and remote management. We also summarize how some accelerator labs deploy and use commodity-type PCs at their facility.

2 ARCHITECTURE

The low cost of PC-based servers allow the controls system infrastructure to use a de-centralized "black-box" appliance architecture (DBA). The DBA architecture allows each PC to perform one job and one job only. This reduces the load on each server and increases the reliability. Think of this is as "one box" - "one service". For example, one box for DHCP, one box for DNS, one box for NIS, one box for an EPICS archiver, one box for an EPICS alarm handler, one box for an EPICS front-end process boot server, etc... Figure 1 shown below illustrates the concept of DBA.

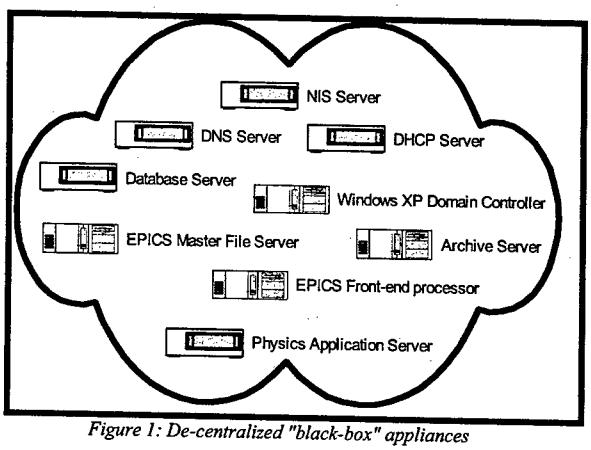

Figure 1: De-centralized "black-box" appliances

The DBA architecture also lends itself to taking advantage of external storage solutions such as network attached storage (NAS) appliances. The cost of external storage continues to go down. Having the option of using multiple PCs gives the control system designer freedom to choose the CPU architecture specific for the application. Taking a look at the various choices with Intel processors:

Intel Itanium 2 ---- High-end number crunching servers

Intel Xeon ---- High-end file server applications

Intel Pentium 4 --- Human machine interface (HMI) workstations.

Intel Pentium 4 Mobile --- Mobile HMI used for control system maintenance activity.

Since Moore's Law continues to hold even after 38 years; current PC bus architectures will have to change to keep up with the continued enhancements in the processor world. The next generation bus technology is needed due to the increased I/O demands for high-bandwidth and low latency control system applications. Applications such as real-time video over Gigabit Ethernet, fiber channel data storage applications, and high-performance graphics applications require better bus performance. PCI-64 boasts a transfer rate of 264 Mbytes/sec. What will be

0-7803-7738-9/03/$17.00 © 2003 IEEE

next after PCI bus? PCI-X offers a short term interim solution with a bus throughput of about one Gigabyte per second. PCI Express a serial I/O technology will provide bandwidth up to 16 Gigabytes per second and supports chip-to-chip level interfaces. Infiniband is another promising prospective bus technology. Infiniband is a serial switch-based architecture and specification for moving data between processors and I/O devices. This new bus technology offers a throughput of up to 10 Gigabytes per second. There are already products based on Infiniband on the market for external peripherals. The standard PC serial (i.e. RS232) interface is being taken over by Universal Serial Bus (USB) and FireWire (IEEE 1394). The next generation commodity-type PC will probably use PCI Express for chip level interfaces and graphics adapters while storage and other high-speed peripherals will use the Infiniband technology.

3 REMOTE MANAGEMENT AND MAINTENANCE

Most facilities deploy a combination of centralized and distributed computers across the control system enterprise and must deal with remote management and maintenance issues. Remote Health monitoring and PC hardware management can be subdivided into three categories:

1. Low-level system monitoring/management
2. Operating system monitoring/management
3. Network system monitoring/management

Remote Health monitoring and PC hardware management can be done effectively using industry standard approaches. Remote management is now a commodity since; most PC vendors now provide the Intelligent Platform Management Interface (IPMI) standard especially for their high-end servers. IPMI is a standardized, abstracted, message-based interface to intelligent platform management hardware [2]. Health monitoring hardware based on IPMI is used to track system parameters such as fan speed, temperature, voltages, processor statistics, etc... Facilities with heterogeneous server environments can take advantage of the interoperability of IPMI. Remote power-off/reset, firmware updates, and hardware inventory is also supported via IPMI. The promoters of IPMI include well-known manufactures such as Intel, Dell, Hewlett Packard, and NEC. All SNS control system servers are IPMI compliant. The SNS uses the DELL PowerEdge server line for many of the applications. DELL provides a third-party software tool called Dell OpenManage (see figure 2) that integrates with their IPMI compliant servers

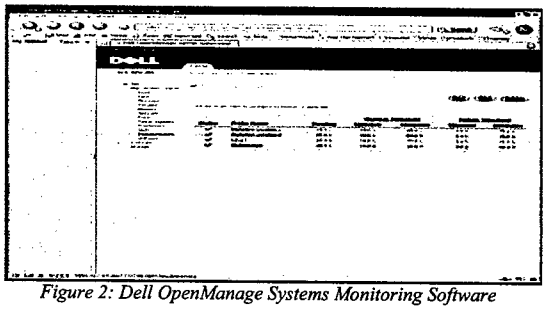

Figure 2: Dell OpenManage Systems Monitoring Software

In a heterogeneous environment the challenge of keeping tabs on the operating systems services and daemons can be difficult. There are many commercial and open-source solutions that will do the job. The idea is to select a software solution that is client/server based which queries monitored services across the network and displays system status on a "user friendly" interface. A software solution that uses the simple network management protocol (SNMP) will also help maintain interoperability across systems. Critical network services that may support the control system network such as DNS, NIS, and DHCP usually run on a server class PC and must be checked for availability. Automatic notification of the appropriate control system or information Technology (IT) personnel can be challenging if the enterprise is behind a firewall. The need to perform periodic software updates, bug fixes, and security patches remotely across many platforms warrants reliable and robust software distribution tools. The SNS control system will standardize on Microsoft System Management Software (SMS) for software distribution management on beam diagnostics Windows XP systems.

The SNS has also standardized on the Red Hat Linux OS and will use a combination of open source and commercial solutions for software management and system monitoring. In a client/server environment the network health is also critical and must be monitored as well. The open source community and commercial vendors provide many cost effective solutions for monitoring and managing networks. The SNS uses a combination of HP OpenVIEW and CISCO Works 2000 to monitor and manage the accelerator network. We are currently at work to integrate the health monitoring of the entire control system infrastructure into EPICS.

4 FRONT-END PROCESSORS

The days of the minicomputer and CAMAC I/O as a front-end processor (FEP) have long been over. We find that VMEbus/VXIbus is still the most popular FEP implementation. However, another player has been carving out its place as a FEP in the accelerator community. Well, now commodity-type PCs are consistently becoming the "first draft" pick. Rack mount PCs offer an amazing amount of processing power for the cost. The large quantity of I/O modules

available for PCs continues to increase allowing accelerator control systems engineers flexibility in design and implementation.

The SNS plans to use about four hundred rack-mount PCs as FEPs for the beam diagnostics control system. There are already beam diagnostic FEPs installed and running on the SNS front-End section of the LINAC. The FEPs for the beam diagnostics are thought of as network attached diagnostics (NADS) [3]. The Beam Diagnostics group has chosen the NAD approach to provide a stand-alone FEP for each beam diagnostic sensor. An example of the SNS Beam Position Monitor (BPM) NADS versus the traditional VME-based FEP is shown in figure 3.

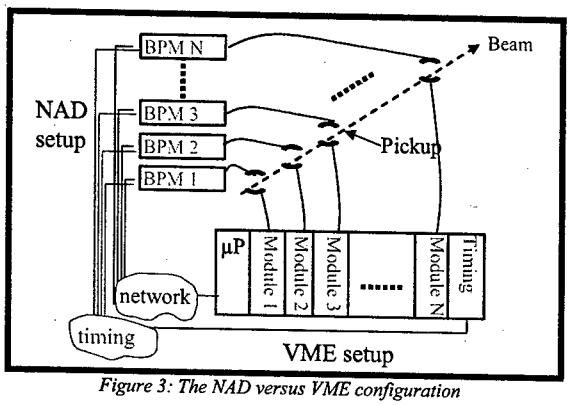

Figure 3: The NAD versus VME configuration

Currently the NADS are running on top of Windows XP Embedded OS. The NAD applications are developed and run in LabVIEW. Careful configuration of the OS and application programming with LabVIEW ensures the reliability and robustness of the system. LabVIEW was selected as the programming environment for the NADS because of its rapid software prototyping ability. The PC-based platform chosen for the NADS allows the selection of an OS and software toolkit to be application driven. For applications that require a hard real-time OS a commercial solution such as VxWorks or an open source solution like RTEMS can be used. Real-time performance can also be achieved by putting more of the processing burden in Field Programmable Gate Arrays (FPGA) s. Many of the PCI I/O cards used for the beam diagnostics sensors are built around FPGAs. The use of operating system independent software such as EPICS R3.14 gives the control system engineer the freedom to architect the combination of commodity-type PC and software for a sound FEP blueprint.

5 CONCLUSION

An outlook towards the future shows commodity-type PCs playing an ever-increasing role in the accelerator community. The continuing advances in PC processor, memory, peripherals, and bus technologies will keep performance high and costs low. Commercial software companies are embracing the open-source model and delivering high-end applications on PC platforms. Do low cost PCs imply a decrease in high availability? Many hardware and software vendors are evolving their technical support model to provide high-quality 24x7 support. Even the open source OS software vendors are evolving the software configuration and release cycle to provide better performance and stability. One example of this is the recent introduction of the "Linux Advanced Server and Workstation" from Red Hat Inc. A survey of other accelerator labs on the use of PCs for control systems showed that integration of PCs into new and existing facilities is still on the rise. The Swiss Light Source (PSI) has led the way in building their entire control system infrastructure on commodity-type PCs except for the use of VME-based FEPs. The SNS will also continue to deploy its control system on top of commodity-type PCs with a mix of both VME/VXI and PC front-end processors.

6 REFERENCES

[1] L. Dalesio, "EPICS: Recent Applications and Future Directions," PAC 2001, Chicago, Illinois., USA, May 5-7, 2003

[2] http://developer.intel.com/design/servers/ipmi

[3] W. Blokland, T. Shea and M. Stettler, "Network Attached Devices at SNS," to be published at DIPAC 2003, Mainz, Germany, May 5-7, 2003

Proceedings of the 2003 Particle Accelerator Conference

INTEGRATING CONTROL SYSTEMS TO BEAM DYNAMICS APPLICATIONS WITH CORBA

M. Böge, J. Chrin, PSI, Villigen, Switzerland

Abstract

High level beam dynamics applications typically require access to several distributed components, among which the hardware control system and an accelerator simulation model are crucial. A CORBA Application Program Interface (API) provides clients with the necessary objects with which to develop even the most complex of applications. This is exemplified by the global orbit feedback system at the SLS which is both a consumer to event generated data and a party to remote method invocations on a variety of servers. In particular, use is made of methods provided by the Portable Object Adapter (POA) to create and activate persistent objects, the Implementation Repository (IMR) for the automatic reactivation of servers and the Event Service for the propagation of controls and physics data.

INTRODUCTION

A considerable number of high-level beam dynamics (BD) applications have been developed for the operation and monitoring of the SLS accelerator facilities. Fig. 1 captures typical components required by BD applications. Their number and demand on computer resources motivated, in part, a desire for a distributed computing environment. To this end, the Common Object Request Broker (CORBA), an emerging standard for Distributed Object Computing (DOC), has been employed. Its use at the SLS has allowed to realize the potential benefits of distributed computing, and to simultaneously exploit features inherent to CORBA such as the interoperability between objects of different race (language) and creed (platform). Complex

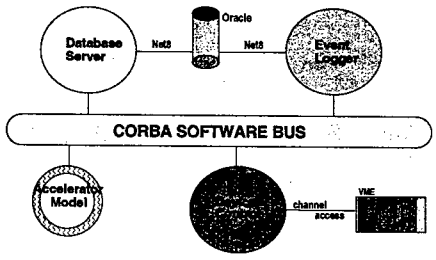

Figure 1: DOC components serving BD applications

tasks, such as the modeling of the SLS accelerators, can thus be handled by dedicated computers, and developed into reusable components that can be accessed through remote method invocations. Persevering with the notion of DOC and developing the entire suite of BD components as CORBA objects, further elevates the level at which applications are designed and implemented. Platforms hosting high-level software applications are no longer limited to the libraries and extensions available to the host operating system as the introduction of a CORBA middleware layer serves to *extend* the developers chosen programming language. BD application developers are, henceforth, able to focus on the specifics of the application at hand, such as determining user-friendly Graphical User Interfaces (GUIs), rather than struggle with the intricate internals of numerous Application Program Interfaces (APIs) and low-level communication protocols.

THE CORBA ARCHITECTURE

The most fundamental component of CORBA is the Object Request Broker (ORB) whose task is to facilitate communication between objects. Given an Interoperable Object Reference (IOR), the ORB is able to locate target objects and transmit data to and from remote method invocations. The interface to a CORBA object is specified using the CORBA Interface Definition Language (IDL). An IDL compiler translates the IDL definition into an application programming language, such as C++, Java or Tcl/Tk, generating IDL stubs and skeletons that respectively provide the framework for client-side and server-side proxy code. Compilation of applications incorporating IDL stubs provides a strongly-typed Static Invocation Interface (SII). Conversely, the Dynamic Invocation Interface (DII) and the Dynamic Skeleton Interface (DSI) allows objects to be created without *prior* knowledge of the IDL interface. Requests and responses between objects are delivered in a standard format defined by the Internet Inter-ORB Protocol (IIOP). Requests are marshaled in a platform independent format, by the client stub (or in the DII), and unmarshaled on the server-side into a platform specific format by the IDL skeleton (or in the DSI) and the object adapter, which serves as a mediator between an object's implementation, the servant, and its ORB, thereby decoupling user code from ORB processing. The Portable Object Adapter (POA) provides CORBA objects with a common set of methods for accessing ORB functions, ranging from user authentication to object activation and object persistence. It's most basic task, however, is to create object references and to dispatch ORB requests aimed at target objects to their respective servants. The characteristics of the POA are defined at creation time by a set of POA policies. A server can host any number of POAs, each with its own set of policies to govern the processing of requests. Among the more advanced features of the POA is the servant manager which assumes the role of reactivating server objects (servants) as they are required. It also provides a mechanism to save and restore an object's state. This, coupled with the use of the Implementation Repository (IMR), that handles

0-7803-7738-9/03/$17.00 © 2003 IEEE

the automated start and restart of servers, realizes object persistency. Requests for server reactivation can, alternatively, be delegated to a single default servant which provides implementations for many objects, thereby increasing the scalability for CORBA servers. Fig. 2 shows the

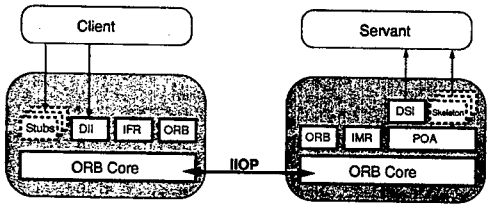

Figure 2: The CORBA client-server architecture

components of the CORBA architectural model. The ORB core is implemented as a runtime library linked into client-server applications.

Client and Server Perspectives

Despite the plethora of new terms and concepts introduced, CORBA, nevertheless, remains true to the DOC objective of providing developers with familiar object-oriented techniques with which to program distributed applications. Indeed, from the client perspective, once an IOR is obtained (typically from a Naming Service which maps names to object references) a remote method invocation essentially takes on the appearance of a local function call: `object->operation(arguments);` whilst the communication details of client-server programming are essentially hidden from the client, a more intimate involvement with the ORB is required when developing servers. In particular appropriate POA policies need to be chosen to configure object adapters that best fulfill the requirements of the server.

Exploiting the POA

Transient and persistent objects are two categories of objects that relate to the lifespan policies of the POA. A transient object is short-lived with a lifetime that is bounded by the POA in which it was created. A persistent object, on the other hand, is long-lived with a lifetime that is unbounded. It can consequently outlive the very server process wherein it was created. This has several advantages. A server may be shutdown whenever it is not needed to save resources. Server updates can be implemented transparently by restarting the server. In developing a DOC environment, the command to start a server may be replaced with a remote shell invocation and the next server instance run remotely, without the client being aware. Persistent objects also maintain their identify after a server crash. Whilst the POA supports and implements persistent objects, it does not handle the administrative aspects of server activations. This is managed by the IMR which stores an activation record for each server process; it is consulted automatically whenever a (re-)launch of a server is mandated. Thus, by virtue of the capabilities of the POA, and the activation techniques of the IMR, BD applications are never starved of the servers they require.

The Event Service

A reactive, event-based, form of programming is also supported by the CORBA Event Service which provides services for the creation and management of CORBA event channels. These may be used by CORBA supplier/consumer clients to propagate events asynchronously on a push or pull basis. Event channels are created and registered with the CORBA Naming Service allowing clients to obtain object references in the usual manner. Communication is anonymous in that the supplier does not require knowledge of the receiving consumers. The CORBA Event Service has been usefully employed in the monitoring of hardware devices and in the distribution of recalibrated data to client consumers.

THE SLS CORBA SERVERS

Server objects, typically of persistent type, have been developed using the CORBA 2.3 compliant product MICO [1]. The services which these objects provide are briefly reported here (for a more details see [2] and [3]):

Accelerator Model: A dedicated host ("Model Server" in Fig. 3) runs the servers ("TRACY Servers") that perform the modeling of transfer-lines, booster and storage ring. Procedures utilize selected routines from the TRACY accelerator physics library [4], enabling clients to employ accelerator optimization methods *online*.

Device Controls: The CDEV C++ class controls library provides the API to the EPICS-based accelerator device control system. The "CDEV Server" running on the host "CORBA Server" supplies functionality for both synchronous and asynchronous interactions with the control system. Monitored devices and recalibrated data are propagated to clients through CORBA event channels. Recently an interface to the EZCA C controls library ("EZCA Server") has been added for increased performance.

Database Access: A database server provides access to Oracle instances through the Oracle Template Library (OTL) and the Oracle Call Interface (OCI). Methods executing SQL statements that perform database retrieval and modification operations have been provided.

Logging Facility: A CORBA message server has been developed using the the UNIX syslog logging facility. Runtime messages are sent to the logger with various priority levels, the threshold for which can be adjusted dynamically for any given servant.

A COMPLEX CORBA APPLICATION

One of the most complex CORBA applications at the SLS is the implementation of a slow and the system integration of a fast global orbit feedback system. The system is based on 72 Beam Position Monitors (BPMs) and 72

correctors in the horizontal and vertical plane distributed around the storage ring. The corrector/BPM response matrix is "inverted" using SVD in case of a non quadratic response matrix taking into account *all* eigenvalues.

The realization of the global orbit feedback has been carried out in two steps. A Slow Orbit Feedback (SOFB) with relaxed requirements (< 3 Hz correction rate) is in operation since August 2001 [5]. The experience gained with the various subsystems served as a basis for the implementation of a Fast Orbit Feedback (FOFB) (4 KHz orbit sampling rate) which is presently under commissioning [6].

The Slow Orbit Feedback (SOFB)

Since the beginning of SLS operation global orbit corrections have been successfully applied manually by the operators with the help of the Tcl/Tk CORBA GUI "oco Client". Due to the inherent modularity of the CORBA environment, thoroughly tested underlying CORBA components like the "TRACY Server" and the "CDEV Server" could be combined to implement the SOFB. In this case the operator is "replaced" by a C++ CORBA client ("Feedback Client") which initiates an orbit correction at a given rate (see Fig. 3). For the SOFB the digital BPM system [7]

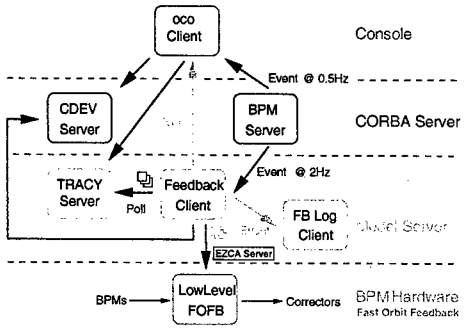

Figure 3: Schematic View of the SOFB: the "Feedback Client" on the "Model Server" level replaces the operator driven GUI "oco Client" on the "Console" level. It gets BPM data from the "BPM Server", asks the "TRACY Server" for the model predicted corrector pattern and applies the correction through the "CDEV Server".

is operated in an injection triggered mode which provides "stroboscopic" position readings averaged over 2 ms at a rate of 3 Hz with a resolution ≈ 0.3 μm. A "BPM Server" monitors, collects and sends the BPM data to the "Feedback Client" with 2 Hz. A low pass filter is applied to several successive BPM data sets. The data are then sent to the "TRACY Server" which predicts a corrector pattern to restore the "Golden Orbit" which is defined by the orbit centered in the quadrupoles. Additionally, local bumps at the location of the insertion devices are taken into account in order to steer the photon beam according to the demands of the experiments. Finally, the proposed correction is applied by toggling between the horizontal and the vertical plane resulting in a SOFB correction rate of ≈ 0.4 Hz.

The Fast Orbit Feedback (FOFB)

In the SLS storage ring a properly chosen BPM/corrector layout leads to an "inverted" response matrix where only the diagonal and their adjacent coefficients have non zero values. Thus, corrector settings are only determined by position readings from nearby BPMs [8]. This feature allows to run the FOFB decentralized, integrated in the 12 BPM stations of the storage ring where each of the stations handles 6 BPMs and correctors. The BPM data are transmitted over fiber optic links between adjacent stations. In order to provide well defined starting conditions for the FOFB the SOFB corrects the orbit to < 5 μm rms. The FOFB gets initialized and started through the SOFB which downloads the "Golden Orbit", 6×6 sub-matrices of the "inverted" 72×72 response matrix, 1×6 sub-matrices of the "inverted" 72×1 off-energy response matrix and the FOFB loop PID parameters to the BPM stations (see Fig. 3). The SOFB continues to run in a "watchdog" like passive mode without touching any corrector other than the RF frequency. But it keeps monitoring BPM and corrector values. Whenever a BPM is switched off, declared faulty or a corrector is close to saturation the FOFB is stopped and restarted with adapted settings. The off-energy content of the horizontal orbit is taken into account by the FOFB but corrected by the SOFB.

CONCLUSION

CORBA extends the capabilities of the programming languages used by BD application developers, thereby elevating the level at which complex applications exemplified by the orbit feedback system at the SLS are designed and implemented. The flexibility of the POA, coupled with the server activation records within the IMR, can be exploited to provide a robust and modular client-server framework.

REFERENCES

[1] A. Puder, K. Römer, "MICO, An Open Source CORBA Implementation", 3rd Edition, Pub: dpunkt.verlag, Heidelberg, December 1999.

[2] M. Böge et al., "Commissioning of the SLS using CORBA Based Beam Dynamics Applications", PAC'01, Chicago, June 2001.

[3] M. Böge, J. Chrin, "On the Use of CORBA in High Level Software Applications at the SLS", ICALEPCS 2001, San Jose, November 2001.

[4] J. Bengtsson, "TRACY-2 User's Manual", SLS Internal Document, February 1997; M. Böge, "Update on TRACY-2 Documentation", SLS-TME-TA-1999-0002, June 1999.

[5] M. Böge et al., "Orbit Control at the SLS Storage Ring", EPAC'02, Paris, June 2002.

[6] T. Schilcher et al., "Commissioning of the Fast Orbit Feedback at the SLS", Contribution to this Conference.

[7] V. Schlott et al., "Commissioning of the SLS Digital BPM System", PAC'01, Chicago, June 2001.

[8] M. Böge et al., "Fast Closed Orbit Control in the SLS Storage Ring", PAC'99, New York, March 1999.

MEASURING AND MATCHING TRANSPORT OPTICS AT JEFFERSON LAB

Yu-Chiu Chao, Thomas Jefferson National Accelerator Facility, Newport News, VA 23606

Abstract

Well-controlled optical transport over long range is important for many types of nuclear and high energy physics experiments. It is essential in achieving the desired beam parameters, minimizing optical sensitivity, and ensuring acceptable helicity correlated orbit differences for parity-type experiments. A precise and rigorous program for evaluating optical matching errors, and a deterministic algorithm for obtaining global matching solutions thus holds considerable promise for both accelerator design and operation, although the latter has defied attempts so far due to its almost intractable complexity. For the CEBAF accelerator at Jefferson Lab, this difficulty is further exacerbated by the extreme matching condition necessary for a 5 pass recirculating linac, elements that can introduce considerable optical error, and loss of long-range difference orbit orthogonality due to these effects, all of which impose a very tight demand on the accuracy of the measured transfer matrix as input to the matching algorithm. Research in methods for both measuring and matching optical transport has led to recent successful demonstration of deterministic matching of the optical transport of CEBAF. The global nature of the matching algorithm allows efficient exploration of solutions not easily accessible by traditional methods and serves to signal configuration flaws in the machine.

INTRODUCTION

The CEBAF accelerator at Jefferson Lab is a 6 GeV, recirculating linac where CW electron beam is recirculated 5 times through 2 linacs before being delivered to 3 nuclear physics experiment targets. Complex longitudinal and transverse beam manipulations take place during this 6-kilometer journey. The need to maintain good transport optics at CEBAF is mandated by the following reasons: 1). containment of beam envelope and orbit fluctuation; 2). minimal optical sensitivity due to intermediate betatron blowup, even if corrected at the end; 3). control of phase space damping and betatron mismatch to levels acceptable to parity experiments in eliminating undesirable helicity-correlated beam coordinates on target; 4). manageable beam profile on target.

To meet the ever more stringent demands for matching transport optics at CEBAF, a program has been developed and tested online. It is in the process of being turned into a standard operational tool. In this paper we will discuss the challenges encountered, the detail of the methods developed, and experience from online application.

CHALLENGES

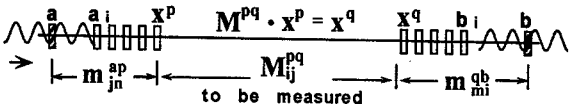

Figure 1: Concept of transfer matrix measurement.

1.1 Measuring Optical Transport

Figure 1 shows the concept of measuring transfer matrix across an unknown section of the beam line. Difference orbits are launched across a beam line section where optical model is known reliably at both end segments **p** and **q**, but not in between. The models of **p** and **q** are then used to interpret the transfer matrix **M** in between. This scheme has many advantages over similar methods relying on knowledge of kickers used to launch the difference orbits, and is capable of supporting rigorous analysis of errors in **M** [1]. The error covariance between elements of **M** obtained under this scheme is given in equation (1) for x-plane where indices i, j, k, m run from 1 to 2 for x & x'. The error in **M** depends on data parameters (red): the sample size **No**, the signal-to-noise ratio $\mathbf{S_B}$, a measure of the correlation among the difference orbits **Td**, and machine parameters (blue): numbers of BPM's $\mathbf{N_B}$, lattice-dependent form factors $\mathcal{M}$, and momentum ratio **Pp/Pq**. To minimize measurement error, one needs high statistics, high signal-to-noise ratio, and minimal correlation among the difference orbits used. Unfortunately this correlation, no matter how carefully one prepares the difference orbits, tends to increase as the orbit covers progressively more distance and optical errors while **Td** approaches 0 in extreme cases[1].

$$\left\langle \delta M_{ij}^{pq} \cdot \delta M_{km}^{pq} \right\rangle = 2 \cdot \frac{1}{N_O} \cdot S_B^{jm} \cdot \frac{1}{T_{(d)}^{jm}} \cdot \left[\frac{1}{N_{Bp}} \cdot \mathcal{M}_b^i \cdot \mathcal{M}_b^k + \frac{1}{N_{Bq}} \cdot \mathcal{M}_a^i \cdot \mathcal{M}_a^k \cdot \left(\frac{P_p}{P_q} \right) \right], \quad i,j,k,m=1,2.$$

$$S_B^{jm} = \frac{\sigma_B^2}{\sigma_O^{pj} \cdot \sigma_O^{pm}}, \quad T_{(d)}^{jm} = \begin{cases} (1-R_p^2), & j=m \\ (1-R_p^2), & j \neq m \end{cases}, \quad R_p^2 = \frac{\left\langle x_1^p \cdot x_2^p \right\rangle^2}{\left\langle x_1^p \cdot x_1^p \right\rangle \cdot \left\langle x_2^p \cdot x_2^p \right\rangle}. \tag{1}$$

* This work was supported by U.S. DOE Contract No DE-AC05-84-ER40150.

[1] This reflects the fact that symplectic maps are not unitary.

1.2 Matching Optical Transport

The challenge for effective transport matching is that the method needs to work in a control room on beam lines possibly far from a well-matched state. Open-ended search for initial conditions good enough for local-minimum type of algorithms to find a decent solution is highly undesirable. In addition, one needs to know when matching system configuration is defective or matching goal itself is unattainable for the given system, such that refinement of the system or goal should be considered rather than more futile attempts. This is impossible via local-minimum algorithms.

THE PROGRAM USED AT CEBAF

1.3 Measuring Optical Transport

At CEBAF an existing difference orbit program (FOPT) has been upgraded to meet the challenges outlined above for high precision transfer matrix measurement. Main features include: 1). ability to launch difference orbits at any location in order to ensure orbit orthogonality; 2). automatic scaling of amplitude to allowed maximum; 3). ability to form phase space coverage as specified by user; 4). ability to generate high statistics data. In addition post-processing programs perform data screening, further orthogonalization of difference orbits, and symplectification of the measured transfer matrix. Interface to the energy feedback system is being planned, which will further reduce data error caused by dispersion leak.

The recirculating arcs, with their well-calibrated model, serve as the sections where difference orbit data is interpreted and used in turn to calculate the transfer matrix and degree of mismatch across the region between the arcs. This region includes the linac, the beam separation and recombination systems, and the path length control "doglegs", where most of the transverse and longitudinal beam manipulations take place and betatron matching is performed more as a routine during machine setup and tuning. Future plan includes sub-dividing this structure even further to reduce optical sensitivity caused by intermediate betatron blowup at the Arc-Linac interface.

Difference orbits generated by this program has also been propagated over the entire 5 passes to study various aspects of the global transport, most notably the damping of phases space and overall betatron matching. Due to its ability to support high precision analysis, the global transport picture thus derived is very reliable and serves as a useful basis for evaluating overall accelerator performance.

To quantify mismatch and assess effectiveness of the matching program, Courant Snyder (CS) parameters are used. For a given design optics and a difference orbit, it is given by equation (2) where Σ represents the design twiss matrix and $\mathbf{X}$ the difference orbit vector. This parameter can be calculated for the 2 sections on either end of the region of interest, one for each orbit. The mismatch is quantified as the maximal possible ratio between these 2 CS parameters for any orbit. An equivalent picture is visualized via design beam envelopes on both ends of the section of interest brought to a common point by the measured transfer matrix of this section. In the normalized phase space of one beam the other is an ellipse, whose semi-major axis has the length equal to the maximal CS ratio described above.

$$C = X^T \cdot \Sigma^{-1} \cdot X,$$
$$\Sigma = \begin{pmatrix} \beta_D & -\alpha_D \\ -\alpha_D & \gamma_D \end{pmatrix}, \quad X = \begin{pmatrix} x \\ x' \end{pmatrix}. \qquad (2)$$

1.4 Matching Optical Transport

In the spirit of the previous section, the problem of transport matching is cast in the form of twiss parameter matching with the aim of turning arbitrary incoming $\alpha_{x/y}$ and $\beta_{x/y}$ into desired outgoing $\alpha_{x/y}$ and $\beta_{x/y}$ using 4 thick quadrupole lenses. This is not exactly the same as restoring the design transfer matrix, for which 6 quadrupoles would be required, but ensures proper transport of the design beam and, for all practical purposes, proper containment of betatron blowup.

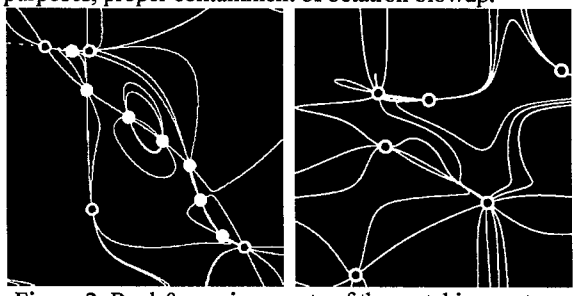

Figure 2: Real & spurious roots of the matching system.

The matching problem as posed processes considerable complexity. An algorithm capable of solving for global solutions of such systems has nonetheless been developed [2]. The advantage over local optimization algorithms is obvious: 1). single-path deterministic process requiring no open-ended tuning or "inspired human intervention"; 2). ability to explore solution space not possible with local methods; 3). elimination of need to "condition" the system before matching; 4). ability to reveal configuration or target problems when real solution is absent. Figure 2 shows the equivalent 2-dimensional solution space to the matching system in 2 examples. The lines represent zero contours of the quadruploe strengths satisfying partial matching conditions. Their intersections (cyan dots) represent real solutions., while red dots are spurious solutions arising from variable elimination. The system on the left has many solutions, while the one on the left has none due to unrealistic matching target. User has the option to choose among the global solutions the one with minimal quad strength, minimal quad change, or minimal intermediate blowup. A mechanism to allow partial matching is also available, where the mismatched

beam ellipse in the normalized phase space of the design beam is allowed to take on reduced semi-major axis while keeping the same orientation, corresponding to a reduced CS mismatch value. This is conjectured to be the most adiabatic path for partial matching targets. Option of different matching quads can also be invoked to yield preferable alternative solutions.

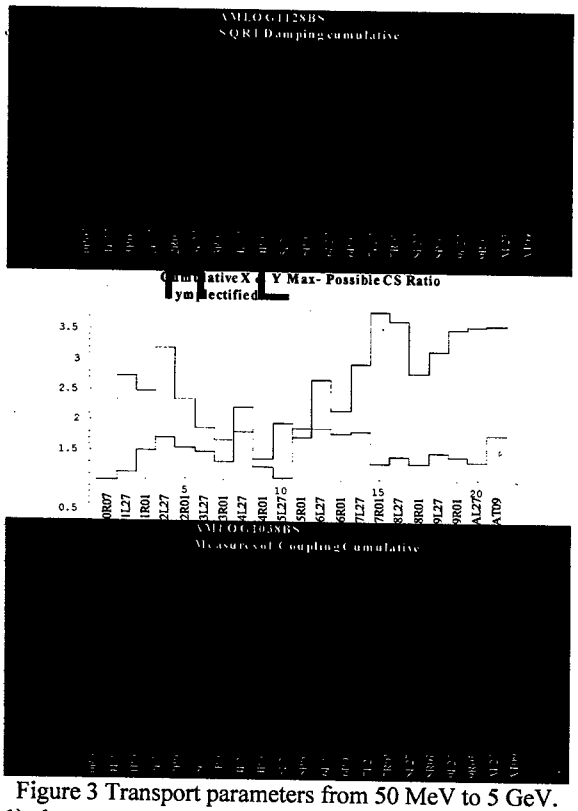

Figure 3 Transport parameters from 50 MeV to 5 GeV.
1) phase space area (sqrt), red: theory; yellow: measured.
2). CS parameter (squared), red: X; blue: Y.
3). 4 measures of coupling based on determinants of sub-matrices of the measured 4 by 4 transfer matrix.

OPERATIONAL EXPERIENCE

The transport measurement and matching programs have been demonstrated to work successfully at CEBAF. Figure 3 shows various transport properties over the entire 5 passes measured using difference orbits launched at 50 MeV and propagated to 5 GeV over 6 kms. The phase space damping closely follows theoretical values. Another measurement based on this technique demonstrated the damping of phase space to within a few 10^{-3} of the theoretical value.

Table 1 summarizes some of the online applications of the transport matching program. Although not necessarily among the most impressive of the tests, these are among tests where transport was measured after matching. Three cases are shown with blue and red ellipses representing design & measured X (left) & Y (right) phase space. The first shows the initial measurement, the predicted outcome, and the final measurement after applying partial matching. The second shows a solution involving non-local quad solutions. The third demonstrates, apart from the algorithm itself, the level of measurement resolution, machine reproducibility and settability that allows the ability to fine tune an already good match to 100%. All solutions were obtained with a single run of the matching algorithm.

ACKNOWLEDGEMENTS

The author would like to thank Leigh Harwood, Andrew Hutton, Valeri Lebedev, Yves Roblin and Chris Slominski for useful comments or help in this effort.

REFERENCES

[1] Y. Chao, "Optics-driven design criteria for BPMs", Proceedings of the Sixth Beam Instrumentation Workshop, Vancouver, B. C., Canada, 1994.
[2] Y. Chao, "A full-order, almost deterministic optical matching algorithm", Proceeding of the 2001 Particle Accelerator Conference, Chicago, 2001.

Table 1. Results of On-line Application of Transport Matching Program

	A partial solution	Solution with non-local root	100% fine tuning
Initial measured	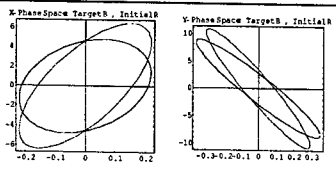	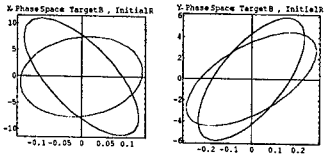	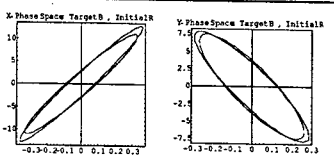
predicted	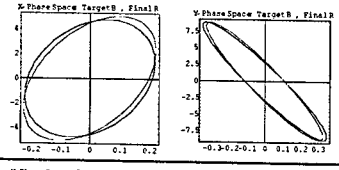	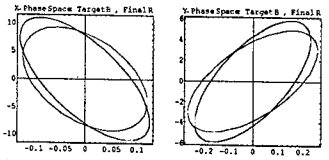	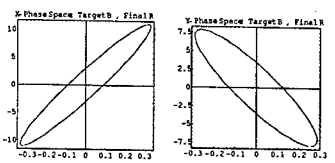
Final measured	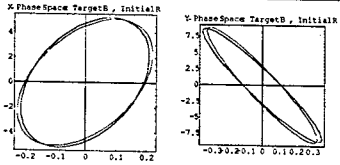	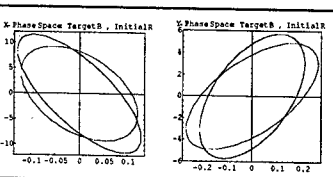	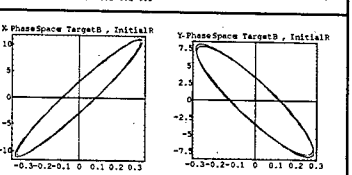

Proceedings of the 2003 Particle Accelerator Conference

FORMATION AND DISSIPATION OF THE ELECTRON CLOUD*

M. A. Furman†, LBNL, Berkeley, CA 94720, USA

Abstract

We present an understanding of the effect of various features of the secondary emission yield (SEY) and secondary emission spectrum on the formation and dissipation of the electron cloud (EC). This understanding is based on dedicated experimental studies at several storage rings and systematic benchmarks of simulations against these measurements.

INTRODUCTION

The electron-cloud effect (ECE) has been investigated experimentally, by simulations, and analytically at various storage rings for several years now [1]. Experimental investigations have made significant progress owing to the use of special-purposes devices such as retarding-field analyzers (RFA) installed at the APS, the PSR and BEPC [2], sweeping detectors at the PSR [3], and a strip detector at the SPS [4, 5]. These detectors allow the measurement of the electron flux and energy spectrum at the vacuum chamber wall, plus certain features of the EC distribution in the bulk. In addition, there is indirect evidence for the ECE at these and other storage rings from vacuum pressure measurements, tune spectra along the bunch train, bunch-by-bunch luminosity measurements, and BPM signals [4].

In this article we attempt to summarize our understanding of ECEs primarily at the APS, PSR and SPS based on the code POSINST [6], particularly the effects from features of the SEY and emission energy spectrum. The strength of the code is based on the embodiment of a detailed model for the secondary emission process [7]. We use as inputs to the simulation various laboratory measurements of the SEY and spectrum for various materials.

FORMATION

Primary mechanisms

Depending upon the type of machine, the EC is seeded by primary electrons from three main sources: photoelectrons, ionization of residual gas, and electrons produced by stray beam particles hitting the chamber wall. As these processes are essentially incoherent, it is customary to quantify them in terms of the number of primary electrons produced per beam particle per unit time, $\dot{n}_{pr}$, or per beam particle per unit length of beam traversal, n'_{pr}. These two are related by $\dot{n}_{pr} = n'_{pr} v_b$, where v_b is the speed of the beam.

*Work supported by the US DOE under contract DE-AC03-76SF00098.

† mafurman@lbl.gov

We can estimate the various contributions to n'_{pr} from various other quantities. Photoelectrons are generated when synchrotron radiation emitted by the beam strikes the vacuum chamber. This is typically the dominant source of primary electrons for high-energy beams. The contribution from photoelectrons is given by

$$n'_{e(\gamma)} = Y_{\text{eff}}\, n'_{\gamma} \tag{1}$$

where n'_{γ} is the number of photons striking the vacuum chamber wall that are emitted per beam particle per unit length of trajectory, and Y_{eff} is the effective quantum efficiency, which must take into account factors such as the photon reflectivity of the surface, the photon angle of incidence on the surface, the photon energy spectrum, and the possible existence of an antechamber through which most photons can escape. Typical values for Y_{eff} are estimated in the range 0.05–1.

The contribution to primary electrons from residual gas ionization can be estimated from the gas density. The inverse of the mean free path for an ionization event by a particle traveling in a gas is given by $\rho\sigma_i$, where σ_i is the ionization cross-section. Expressing the gas density ρ in terms of the pressure and temperature yields

$$n'_{e(ion)}\,[\mathrm{m}^{-1}] = 3.3\,\sigma_i\,[\text{Mbarn}] \times p_v\,[\text{Torr}] \times \frac{294}{T\,[\text{K}]} \tag{2}$$

where p_v is the vacuum pressure and T the temperature (implicit in this formula is the assumption that the ionization event yields a single electron). A typical value for σ_i is 2 Mbarns for a high-energy particle of unit charge [8]. Ionization of residual gas is typically the dominant source of primary electrons for relatively low-intensity hadron machines.

The contribution from stray beam particles striking the chamber walls is given by

$$n'_{e(bpl)} = \eta_{\text{eff}}\, n'_{bpl} \tag{3}$$

where n'_{bpl} is the number of lost beam particles per beam particle per unit length of beam traversal, and η_{eff} is the effective electron yield per particle-wall collision ("*bpl*" stands for "beam-particle loss"). Beam particle losses is typically the dominant source of primary electrons for intense, low-energy proton storage rings such as spallation neutron sources.

The three above-mentioned types of primary electrons are produced with different spectra, and in different parts of the chamber. These details need to be taken into account in simulations. As for the time distribution of the electron production, it is reasonable to assume the proportionally

$$n'_e \propto \lambda_b(t) \tag{4}$$

0-7803-7738-9/03/$17.00 © 2003 IEEE

where n'_e represents any of the n''s above, and $\lambda_b(t)$ is the beam line density at time t at a given azimuthal location in the ring. This proportionality is fairly obvious for the ionization electrons. As for photoelectrons, it is justified by noting that (a) only the incoherent photons radiated by the beam as it traverses a magnet are, in practice, significant, and (b) the photons, once radiated, remain substantially comoving with the beam until they hit the chamber wall. The same argument can be applied to the stray beam particles, regardless of the mechanism by which they are lost.

A basic quantity that is used to characterize the intensity of the EC is the electron line density as a function of time in a given section of the machine, $\lambda_e(t)$. Assuming that there is no antechamber, and that one can neglect the escape of the electrons at the endpoints of the given section, charge conservation implies that the rate of change in the number electrons in such a section is given by

$$\dot{N}_e = \underbrace{\dot{N}_{e(\gamma)} + \dot{N}_{e(ion)} + \dot{N}_{e(bpl)}}_{\text{primaries}} + \underbrace{\dot{N}_{sec} - \dot{N}_{col}}_{\text{net secondaries}} \qquad (5)$$

where $\dot{N}_{col}$ is the rate of electron-wall collisions, and $\dot{N}_{sec}$ is the rate of secondary electrons produced in such collisions. Defining $\delta_{\text{eff}} = \dot{N}_{sec}/\dot{N}_{col}$ and dividing by the length of the section and multiplying by the electronic charge yields

$$\dot{\lambda}_e(t) = v_b n'_{pr} \lambda_b(t)/Z + (\delta_{\text{eff}} - 1) p I_{ew} \qquad (6)$$

where Z is the beam-particle charge in units of e, p is the perimeter of the chamber cross section, $n'_{pr} = n'_{e(\gamma)} + n'_{e(ion)} + n'_{e(bpl)}$, and I_{ew} is the electron flux at the wall (units of current per unit area).[1] If electrons leave the chamber section through the antechamber or through the endpoints, these must be subtracted from the right-hand side of (6).This equation has not much predictive power, but its virtue lies in the fact that it relates several physical quantities that are either measured or simulated, and serves as a good check on calculations.

Secondary emission yield

In practice, it is often the case that the most important contribution to the EC is from secondary electron emission, embodied by δ_{eff} in Eq. (6). The secondary emission yield (SEY) function $\delta(E_0)$ is the average number of electrons emitted when an electron impinges on a surface at energy E_0. It reaches a peak $\delta_{\max}$ at an energy $E_0 = E_{\max}$. A fairly detailed microscopic description of the secondary emission process is presented in Ref. 7, upon which we base the simulated examples discussed below.

To illustrate the sensitivity of the ECE to the SEY, we consider two sample measurements of δ and $d\delta/dE$, one for copper, the other one for stainless steel, both of which have $\delta_{\max} \simeq 2.05$ and $E_{\max} \simeq 300$ eV, that are discussed in detail in Ref. 7. Fig.1 shows a simulated example of the sensitivity exhibited by the EC line density to $\delta_{\max}$ in a field-free region of the PSR. The two traces labeled $\delta_{\max} =$ 1.5 and 1.7 were obtained taking as basic input the stainless steel sample of Ref. 7 and scaling $\delta(E_0)$ down from its true peak value of 2.05 to either 1.5 or 1.7, respectively. It is apparent that the peak value of λ_e is almost an order of magnitude larger for $\delta_{\max} = 1.7$ than for 1.5, while the plateau value in between bunches is a factor ~ 2 larger. An equally strong sensitivity is observed in the simulated electron-wall flux I_{ew} (not shown).

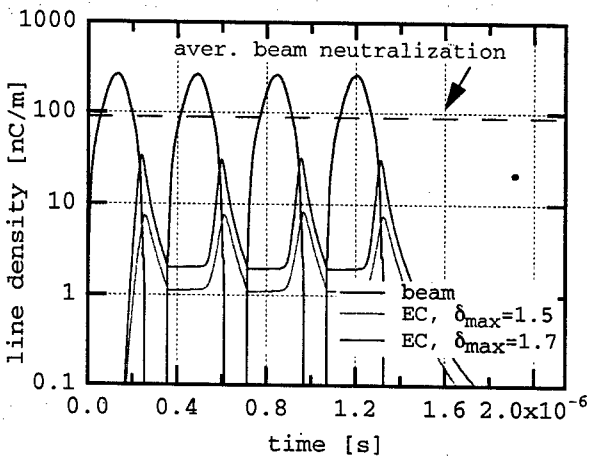

Figure 1: Simulated EC line density in a field-free region of the PSR for $\delta_{\max} = 1.5$ and 1.7. The beam, whose line density is also shown, has 5×10^{13} protons/bunch, and the primary electrons were assumed to be generated only from stray protons at a rate $n'_{e(bpl)} = 4.44 \times 10^{-6}$ e/m.

Secondary emission spectrum

A quantity closely related to δ is the emitted-energy spectrum of the secondary electrons, $d\delta/dE$ at given incident energy E_0, where E is the emitted electron energy. The spectrum covers the region $0 < E \lesssim E_0$. The spectrum exhibits three fairly distinct main components: elastically reflected electrons, rediffused, and true secondaries [7]. The SEY is given by

$$\delta(E_0) = \int_0^{E_0} dE \, \frac{d\delta}{dE} \qquad (7)$$

so that $\delta = \delta_e + \delta_r + \delta_{ts}$. The elastic electrons are emitted within a narrow peak (FWHM$\sim \pm 3$ eV) centered at $E \simeq E_0$. The rediffused electrons are emitted with a fairly uniform energy distribution in $\sim 50 < E < E_0$, and the true secondaries in a broad peak at $0 < E \lesssim 50$ eV. Depending upon various features of the storage ring considered, the three components can contribute differently to various aspects of the ECE. To illustrate this point,

[1] In Eq. (6) Z appears explicitly because n'_{pr} is the electron production rate *per beam particle*, not *per unit charge*. I am indebted to M. Blaskiewicz for bringing this equation to my attention.

we consider again the two above-mentioned sample measurements for copper and stainless steel. Even though $\delta_{\max}$ is almost the same for these two samples, the relative contributions of the three SEY components are quite different: for the stainless steel sample at $E_0 = 300$ eV, $(\delta_e, \delta_r, \delta_{ts}) \simeq (6\%, 37\%, 57\%)$ of δ, while for the copper sample, $(\delta_e, \delta_r, \delta_{ts}) \simeq (1\%, 9\%, 90\%)$ of δ. To illustrate the dependence of these relative ratios, we consider the simulated electron line density in an arc dipole in the LHC [6], shown in Fig. 2, and the power deposited by the electrons on the vacuum chamber walls, shown in Fig. 3.

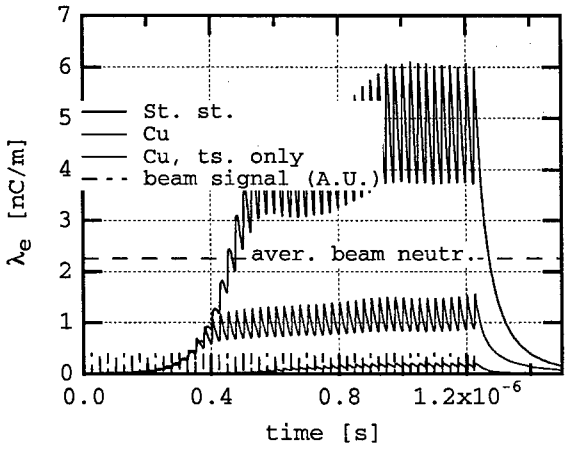

Figure 2: Simulated EC line density in an arc dipole magnet of the LHC assuming that the secondary emission off the chamber wall corresponds to a stainless steel sample, a copper sample, or a copper sample in which the elastic and rediffused electrons are artificially suppressed, ie., true secondaries only (see text for details). In all three cases, $\delta_{\max} \simeq 2.05$ at $E_{\max} \simeq 300$ eV. In the first two, $\delta(0) \simeq 0.5$, while in the third, $\delta(0) = 0$. The beam, whose signal in arbitrary units is indicated by a dashed line, has $N = 1.05 \times 10^{11}$ protons/bunch, and the primary electrons were assumed to be generated only from the photoelectric process at a rate $n'_{e(\gamma)} = 6.3 \times 10^{-4}$ e/m.

The sensitivity exhibited in Figs. 2 and 3 can be explained from other features of the EC in this particular case (not shown in this article), and can be attributed to features of $\delta(E_0)$ and $d\delta/dE$. As it can be seen in Fig. 3, the peak power deposition occurs ~ 5 ns after the passage of the bunch, since this is the time it takes for the electrons kicked by the bunch to reach the chamber wall. The electrons that remain in the chamber for the balance of the interbunch gap may bounce off the walls once or a few times, and their average energy degrades with successive bounces. This degradation occurs primarily from the "conversion" of an incident electron into true secondary electrons, which are emitted with energies below ~ 50 eV. For the stainless steel sample, this energy degradation is slower than for the other cases because the electron emission spectrum has a relatively smaller true secondary component. Therefore,

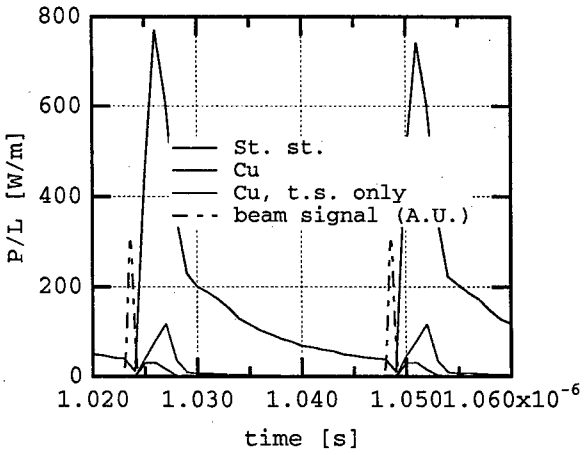

Figure 3: Simulated EC power deposition per unit length in an arc dipole magnet of the LHC for the same conditions as in Fig. 2. Only a short time interval (40 ns, with two bunch passages) is shown, chosen from the steady-state portion of the simulation.

since the energy of the slow electrons is relatively high, so is the corresponding SEY, hence these electrons also survive longer than in the other samples. Thus, when a new bunch comes along, it kicks a larger number of electrons into the wall for the stainless steel sample than for the others, leading to higher power deposition.

Beam-induced multipacting

An important mechanism for the EC formation is beam-induced multipacting (BIM) [9]. If a relativistic beam is composed of short, positively-charged bunches with N particles of charge Ze and bunch spacing s_b, a resonance condition occurs when the traversal time Δt of an electron across the chamber under the influence of one bunch equals s_b/c. If the impulse approximation is valid (bunch length $\ll s_b$), the resonance condition is $G = 1$, where G is defined by

$$G = \frac{ZNr_e s_b}{d^2} \tag{8}$$

where $r_e = e^2/mc^2 = 2.82 \times 10^{-15}$ m is the classical radius of the electron and d is the half-height of the vacuum chamber (or radius, if round). This definition of G is only pertinent to field-free regions and to dipole magnetic fields; in this latter case, $2d$ is the full size of the chamber along the magnetic field direction.

The condition $G = 1$ is necessary but not sufficient to lead to multipacting. The second necessary condition is $\delta_{\text{eff}} > 1$. When these two conditions are simultaneously valid, the EC density increases exponentially in time as successive bunches go by until a saturation is reached owing to space-charge forces. In addition to a rapid growth of the electron density, the electron-wall collision energy is typically high, leading to other phenomena such as rapid

and intense gas desorption and a possible catastrophic vacuum pressure increase.

BIM has been investigated in dedicated studies at the APS. Measurements have been obtained of I_{ew} and energy spectrum at the wall with RFAs, both for positron and electron beams [2, 10]. In these studies, a train of ten equally-spaced bunches of 2 mA/bunch were injected in the machine, and I_{ew} measured for various values of s_b in the range 1-128 RF buckets. Since the chamber cross-section is elliptical with semiaxes a, b and the measurements were done in a field-free region, the value of s_b for which $G = 1$, ie., $s_b = d^2/Nr_e$, is not unique because d ranges in $b < d < a$. Simulations and measurements are in good agreement, and a clear bump is seem in I_{ew} when d is in this range [11].

A form of BIM is also seen for the case of very long bunches, such as the PSR, even though the electron traversal time Δt is much shorter than the bunch length. The phenomenon, "trailing-edge multipacting," is observed in the trailing edge of the bunch [3]. In this case the resonance condition obtains when Δt equals the oscillation period of an electron in the potential well of the bunch. Simulations show that the multipacting ("prompt") electrons are generated at the wall during the passage of the leading edge of the bunch, are temporarily trapped by the increasing depth of the potential well, and are then released as the depth decreases during the trailing edge. The phenomenon can be seen in Fig. 1; the electron flux at the wall (not shown) exhibits similar features as the density.

If the trailing edge of the bunch is artificially truncated keeping the bunch population fixed, trailing edge multipacting is effectively suppressed owing to the effective breaking of the resonance condition [12].

A weak ($\sim 20-30$ G) solenoidal field has been shown to be an effective means of controlling the ECE in B factories [1] by forcing the electrons to remain close to the walls of the chamber. However, a BIM condition arises if the bunch spacing s_b/c equals the electron cyclotron period in the solenoidal field [13].

DISSIPATION

If the beam is extracted from the machine, the EC dissipates. The rate of dissipation can yield important information about $\delta(E_0)$ for $E_0 \simeq 0$. The dissipation process also operates in the gap between bunches if the spacing s_b is significantly long, as is the case of the LHC. We consider a "blob" of N electrons, crossing the chamber in a time interval Δt. By definition of δ_{eff}, after one collision there will remain $N' = \delta_{\text{eff}} N$ electrons. If the electrons keep bouncing back and forth, after n collisions there will remain $N_n = Ne^{-n\Delta t/\tau}$ electrons, where τ is the decay time of the EC, hence we conclude that $\delta_{\text{eff}} = \exp(-\Delta t/\tau)$ [3, 14].

In the simplest estimation of Δt we assume that the electrons are created at the wall with a given kinetic energy E and that they cross the chamber along a diameter (if the chamber is round). If the EC is sufficiently dilute, we can neglect the space-charge force hence the energy E is conserved, so that $\Delta t = (d/c) \times (2mc^2/E)^{1/2}$, hence

$$\delta_{\text{eff}} = \exp\left\{-\frac{d}{c\tau}\sqrt{\frac{2mc^2}{E}}\right\} \qquad (9)$$

where $2d$ is the full width of the chamber (or diameter if round), and m is the mass of the electron. In this analysis we have neglected the image forces, an approximation that simulations appear to support, as shown below. If one takes into account the energy-angle secondary emission spectrum, and the angular dependence of the SEY, an improved equation can be derived [14].

The development and deployment of a "sweeping electron detector" has allowed the measurement of the EC density in the bulk at the PSR [3]. These measurements show a fairly exponential decay of the EC with $\tau \simeq 200$ ns. Assuming a typical value $E = 4$ eV and $d = 5$ cm, one obtains $\delta_{\text{eff}} \simeq 0.5$.

In order to test the applicability of Eq. (9), we ran a simulation for the PSR using as input the above-mentioned model for stainless steel SEY, with $\delta(E_0)$ scaled so that $\delta_{\max} = 1.7$. Results are shown in Fig. 4 for the line density. A similar simulation for the SPS in a region with a dipole field $B = 0.2$ T and rectangular chamber of half-sizes $(a, b) = (7.7, 2.25)$ cm, shows a slope of 170 ns.

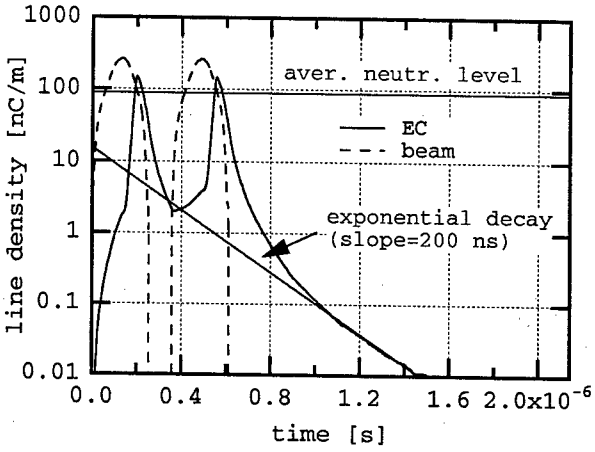

Figure 4: Line density for a field-free region of the PSR for $N = 5 \times 10^{13}$, $\delta_{\max} = 1.7$, $\delta(0) = 0.4$, and an artificially high primary electron production rate $n'_{e(bpl)} = 4 \times 10^{-4}$ e/m.

One sees that the EC density indeed reaches an approximately exponential decay regime after a while (~ 400 ns) following beam extraction, with a slope in good agreement with Eq. (9). These results, combined with the simulation results for the electron-wall collision energy as a function of time (not shown), imply that the value of δ_{eff} extracted from Eq. (9) can be sensibly interpreted as $\delta(0)$.

CONDITIONING

Since the ECE can lead, in practice, to various performance limitations for intense beams, it is desirable to have as low a SEY as possible. The SEY of a given surface can be reduced ("conditioned") by several mechanisms, including electron bombardment. Therefore, the ECE itself can lead to conditioning of the vacuum chamber (beam scrubbing).

Such conditioning has been observed at several storage rings including the SPS, where it is very effective, as evidenced by significant improvement of the vacuum pressure, *in situ* SEY measurements, and electron flux at the wall of a specialized detector [4] after ~a few days of running. In addition, tests with TiVZr coatings indicate a full suppression of BIM once activated.

At the PSR it is observed that the prompt electron signal (ie., BIM electrons) is subject to conditioning, decreasing by factors of ~ 5 in certain regions of the machine after ~a few weeks of running (albeit at low current). The conditioning effect is stronger for stainless steel than for TiN coatings, although it is location dependent. The prompt signal is also sensitive to the bunch population N; it does not show signs of saturation up to $N \simeq 8 \times 10^{13}$. On the other hand, the swept-electron signal saturates for N beyond $\sim 5 \times 10^{13}$ and, significantly, the decay constant τ is roughly independent of N, location, conditioning state and surface material (stainless steel or TiN) [3]. Combining these observations with the results discussed above, one concludes that beam scrubbing effectively reduces $\delta_{\max}$ but leaves $\delta(0)$ unchanged. Although the PSR is the only storage ring that has produced evidence for this conclusion, it does not appear to be contradicted by experience at other machines. Nor does it contradict basic surface physics, because $\delta_{\max}$ and $\delta(0)$ are dominated by different processes: the former is dominated by true secondary electron production, while the latter is dominated by electron backscattering. Furthermore, recent measurements obtained for laboratory-conditioned Cu samples also show this effect: $\delta_{\max}$ for a sample is reduced from ~ 2 in the "as-received" state to ~ 1 in the fully scrubbed state, while $\delta(0)$ remains unchanged [15].

CONCLUSIONS

A consistent picture of the ECE is clearly emerging, particularly concerning the effects from the secondary electron emission. The understanding achieved is the result of dedicated experimental studies at various machines, especially the APS, SPS and PSR, combined with methodical simulation benchmarks. Recent progress in this understanding is leading to the elucidation of the effects from the three main components of the electron emission spectrum on different parts of the EC phase space, and its corresponding effects on EC density, electron flux and energy deposition on the vacuum chamber walls. Recent measurements indicate a differential beam scrubbing effect on the SEY: while the peak SEY is clearly reduced with electron bombardment, it appears that the SEY below $\sim 5 - 10$ eV incident energy remains unchanged. If these measurements are confirmed, one can expect stronger ECEs than anticipated for beams with well-separated bunches.

ACKNOWLEDGMENTS

I am indebted to M. Blaskiewicz, M. Jiménez, R. Macek and F. Zimmermann for providing me important information relevant to the preparation of this talk. I am also grateful, for ongoing or past discussions and/or collaboration, to A. Adelmann, G. Arduini, M. Blaskiewicz, O. Brüning, Y. H. Cai, R. Cimino, I. Collins, O. Gröbner, K. Harkay, S. Heifets, N. Hilleret, J. M. Jiménez, R. Kirby, G. Lambertson, R. Macek, K. Ohmi, M. Pivi, G. Rumolo, and F. Zimmermann. I am grateful to NERSC for supercomputer support.

REFERENCES

[1] Mini-Workshop on Electron-Cloud Simulations for Proton and Positron Beams ECLOUD'02, CERN, Apr. 15-18 (CERN Yellow Report No. CERN-2002-001) 2002 http://slap.cern.ch/collective/ecloud02/

[2] R.A. Rosenberg, K.C. Harkay, NIMPR A **453** (2000), 507-513.

[3] R. Macek et al., these proceedings.

[4] J. M. Jim'enez, these proceedings.

[5] F. Zimmermann et. al., these proceedings.

[6] M. A. Furman and M. Pivi, Proc. EPAC02, Paris, June 3-7, 2002.

[7] M. A. Furman and M. Pivi, PRSTAB **5**, 124404 (2002).

[8] M. Reiser, *Theory and Design of Charged Particle Beams*, J. Wiley & Sons, 1994, Sec. 4.6.

[9] O. Gröbner, Proc. 10th Intl. Accel. Conf., Serpukhov, 1977, pp. 277–282.

[10] K. C. Harkay and R. A. Rosenberg, PRSTAB **6**, 034402 (2003).

[11] M. A. Furman, M. Pivi, K. C. Harkay and R. A. Rosenberg, Proc. PAC01, Chicago, June 18-22, 2001, 679.

[12] M. Pivi and M. A. Furman, these proceedings, paper RPPG024.

[13] Y. H. Cai, M. Pivi, and M. A. Furman, Proc. PAC03, Portland, OR, May 12-16, 2003.

[14] R. Macek, A. Browman, M. A. Furman and M. Pivi, to be published.

[15] R. Cimino and I. Collins, Proc. DR2003 Damping Ring Workshop, Daresbury, UK, Jan. 27-29, 2003. http://www.astec.ac.uk/conf/dampingring/

ELECTRON CLOUD EFFECTS IN PRESENT AND FUTURE HIGH INTENSITY HADRON MACHINES

M. Blaskiewicz*† BNL, Upton NY 11973, USA

1 INTRODUCTION

Electron cloud effects have manifested in several Hadron Machines. Table 1 lists basic machine parameters of past and present hadron machines where electron clouds have influenced operations. This instability has also been seen in the AGS Booster[15], but under extreme conditions. Table 2 lists high intensity proton machines that are under construction. The goal of the present work is to take what is known about electron cloud problems in current machines, mainly the LANL PSR, and attempt to extrapolate to the new machines.

2 FORMATION OF THE ELECTRON CLOUD

Electron clouds created by gas stripping [18, 19, 20, 21], foil scattering [6, 22, 7], or losses are present in all accelerators, to some extent. For problems to occur the initial seed distribution needs to be amplified [1]. For short bunches the process has been considered by many authors [18, 19, 20, 21]. For the LANL PSR, and the machines in Table 2, the bunches are long and an electron trapped within the beam performs many transverse oscillations during a single bunch passage [23]. Fig. 1 shws a simulation for typical PSR parameters. If the electron line charge density, λ_e (units of Coulombs/meter) is small compared with the proton line charge density, λ_p then a fairly accurate expression for the strike energy can found [16]

$$E_{\rm strike} = -\frac{\pi m_e c^2}{2}\left(\frac{b}{c}\right)^2 \frac{d\omega_e}{dt}, \qquad (1)$$

where b is the beam pipe radius, c is the speed of light, and the instantaneous electron oscillation frequency is

$$\omega_e(t) = \sqrt{\frac{e\lambda_p(t)}{2\pi\epsilon_0 m_e(\sigma^2 + 2b^2/\pi)}}, \qquad (2)$$

with σ the rms beam radius. The strike energy is positive on the trailing edge of the bunch ($\dot{\omega}_e < 0$) and equation (1) is valid only when the electron frequency does not have a large fractional change per period, $|\dot{\omega}_e| \ll \omega_e^2$. From the PSR simulation the electron has an energy of 45 eV for the first wall strike, while equation (1) predicts 55 eV. Typical numbers for ISIS give $E_{\rm strike} \lesssim 10$ eV.

When an electron strikes a surface it can be reflected, rediffused or stopped[2]. During this process another electron may gain enough energy to leave the surface. A useful experimental measure is the secondary emission yield: the ratio of the total number of electrons leaving the surface to the total number incident upon the surface. Figure 2 shows measurements of secondary yield for titanium nitride coated stainless steel with normally incident electrons.

	I_{peak}	$\frac{\sigma_f}{f}$	$\sigma_\perp$	KE	b	Q_β
	(A)	10^{-5}	(mm)	(GeV)	(mm)	
BINP PSR 1-3	0.5	1300	2.5	0.001	40	0.7
CERN ISR 4,5	20	14	2	30	35	8.9
LANL PSR 6-8	70	63	7.6	0.787	50	2.2
CERN SPS 9	7	0.26	2.5	26	23	26.6
CERN PS 10,11	7	1.9	6.3	26	35	6.2
BNL RHIC 12-14	2	0.4	2	11A	30	28.2

Table 1: Basic machine parameters for past and existing hadron machines with electron clouds. For RHIC the ion species is gold, with a kinetic energy of 11GeV/nucleon. All the others are proton machines.

	ORNL SNS[16]	J-PARC 3 GeV[17]	J-PARC 50 GeV[17]
I_{peak}(A)	80	20 - 38	38 - 196
$\frac{\sigma_f}{f}(10^{-5})$	55	590 - 32	41 - 0.33
$\sigma_\perp$ (mm)	14	19 - 12	11 - 5
KE (GeV)	1	0.375 - 3	3 - 50
b (mm)	100	125	65
Q_β	6.3	4.2	22.2

Table 2: Basic machine parameters for high intensity proton machines under construction. For the J-PARC machines parameters are labeled as injection - extraction .

* blaskiewicz@bnl.gov

† Work performed under contract number #DE-AC05-00OR2275 with the auspices of the U.S. Department of Energy

[1] The BINP PSR, which used high gas density, is a notable exception

[2] This is a phemonenolgical, classical picture

0-7803-7738-9/03/$17.00 © 2003 IEEE

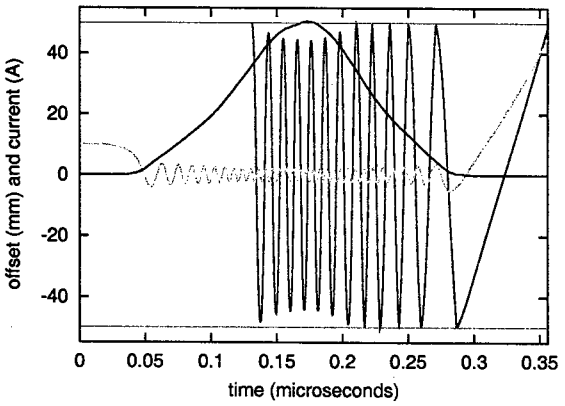

Figure 1: Proton beam current (blue) and positions for captured (green) and loss created (red) electrons. The beam pipe radius is 50 mm (violet).

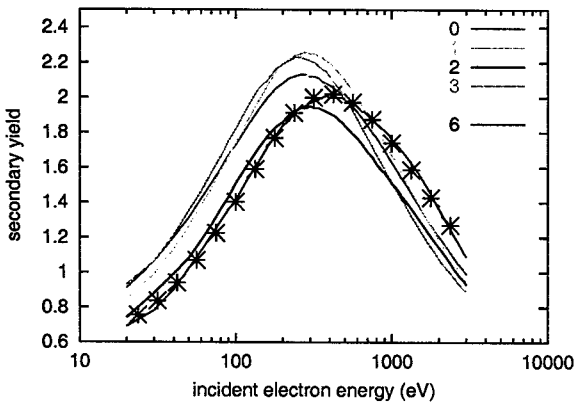

Figure 2: Secondary emission yield for titanium nitride coated stainless steel from similarly manufactured samples. The samples were manufactured by P.He and H.C. Hseuh of the BNL vacuum group. The measurements were performed by B. Henrist of the CERN vacuum group. The surfaces have not been baked or conditioned in any way. The solid lines are data and the markers are a fit of the CSEC model to the blue curve. Of all the fits, the one shown had the largest rms deviation from the data, 0.025.

The data in Figure 2 have been fitted using a phemoninological model and that model was subsequently used in a simulation of electron cloud formation for the SNS. This cylindrically symmetric electron cloud code (CSEC) and its benchmarking against M. Furman's positron instability code (POSINST [25]) are described in [16]. Figure 3 shows the proton line density and the electron line density within one σ of the beam axis. The primary electrons were estimated assuming 1% of the beam was lost over 1000 turns and that 20 electrons were generated by each lost proton [24]. The electrons create a focusing lens, which travels with the beam. For SNS with 15 nC/m of electrons in the beam the electrons give a tune shift $\approx +0.05$.

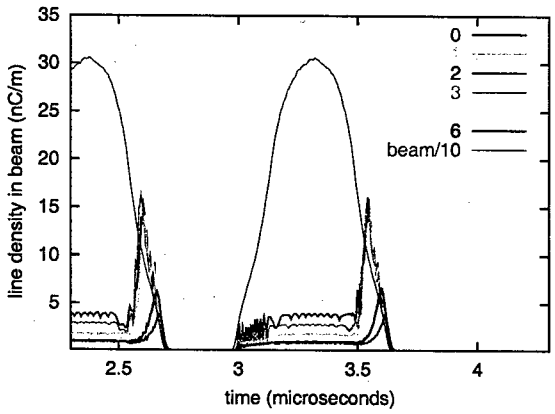

Figure 3: SNS line charge densities for the beam and electron cloud within $r = \sigma$ for each of the six secondary yield curves in Fig. 2.

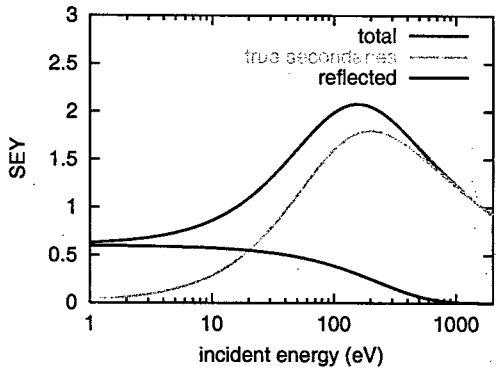

Figure 4: Secondary yield curve for stainless steel. Note the significant reflections at low energy.

Figure 4 shows a reasonable secondary yield curve for clean stainless steel. Taking this secondary yield, 20 electrons per lost proton, 0.1% beam loss over 2000 turns, and parameters for the J-PARC 3 GeV rapid cycling synchrotron [17] yields Figure 5. The peak electron line density from these CSEC simulations corresponds to an instantaneous neutralization of 1.2% at extraction. Increasing the electron generation rate by a factor of 10 changed the results by less than 10%. The electron clouds pictured in Figures 3 and 5 evolve as the beam passes and result in a considerable electron flux to the wall. For Figure 3 the net charge per turn varies between 40 and 700 $\mathrm{pC/cm^2/turn}$ with electrons in excess of 100 eV depositing between 10 and 50 $\mathrm{pC/cm^2/turn}$. For the J-PARC simulations the total charge per turn is 45 and 110 $\mathrm{pC/cm^2/turn}$ for injection and extraction, respectively. Only about 1% of these electrons have a strike energy greater than 100 eV.

These electrons striking the wall will desorb gas molecules and can cause the pressure to rise [20, 26, 27]. For machines with a large duty cycle a dramatic pressure rise can result from a very modest electron flux. Over time,

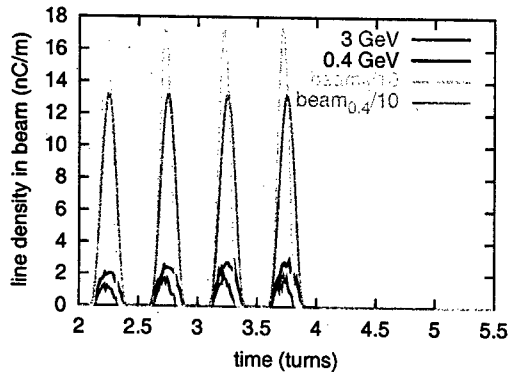

Figure 5: Line charge densities for the beam and electron cloud within $r = \sigma$ for the J-PARC 3 GeV RCS, using the secondary yield curve in Fig. 4.

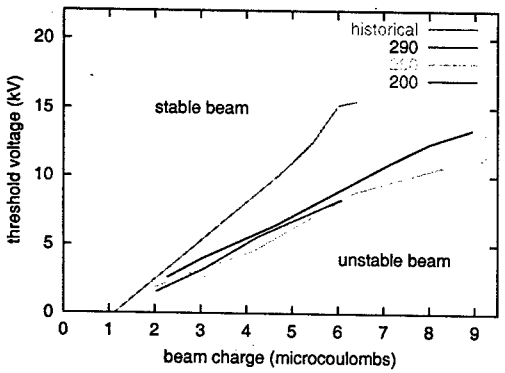

Figure 6: Threshold RF voltage versus beam intensity for PSR, courtesy R.J. Macek. The threshold RF voltage is the smallest RF voltage for which the beam is stable. The historical curve represents the situation before the direct H^- injection upgrade and the extended run during 2001. Threshold curves near the end of the 2001 run for injected bunch lengths of 200, 260, and 290 ns are shown for comparison.

the adsorbed gas will be exhausted. Also, the electrons striking the wall eventually reduce the secondary yield. The desorbed gas places requirements on the vacuum system. Significant reduction in the secondary yield requires a net electron dose of order 0.1 C/cm^2 [28, 29]. If the SNS beam is stable under the conditions shown in Figure 3, this conditioning will take about a week of running time. Scaling to J-PARC parameters, a few weeks of running time are needed for conditioning. The question at hand is whether the beam will be stable at sufficiently high intensity for conditioning to occur.

3 EC INSTABILITY

The electron cloud instability in the LANL PSR has been well documented [6, 8, 30, 31, 32, 33, 16]. Figure 6 shows the threshold RF voltage as a function of beam current for different epochs and bunch lengths. When the instability occurs, the observed oscillation frequency agrees with the calculated electron oscillation frequency [30]. The threshold is quite sharp [16], so one expects that a linearized calculation should provide adequate threshold estimates.

Bunched beam stability estimates based on the linearized Vlasov equation are a natural starting point. Early treatments considered positron bunches [34, 35], and techniques developed for the transverse mode coupling instability [36] yielded results which agreed with simulations [37, 38, 34]. For high intensity proton machines the bunches are long and electrons perform many oscillations as the bunch passes. Traditional techniques require matrices with millions of elements and are a significant computational challenge. An alternate technique, which models the RF system using a barrier bucket, yields much smaller matrices [16]. Since the bunch is square the electron oscillation frequency is constant within the bunch

$$\omega_e = \omega_0 Q_e = \sqrt{\frac{e\lambda_p}{2\pi\epsilon_0 m_e a^2}},$$

where ω_0 is the angular revolution frequency and a is the beam radius. The strength of the electron cloud interaction is determined by the parameter

$$Q_p^2 = \frac{e\lambda_e}{2\pi\epsilon_0\omega_0^2\gamma m_p a^2}, \tag{3}$$

where we assume that the cloud has the same radius as the beam[3]. Even though we take the radii to be equal, the proton beam radius varies with the lattice functions. To model this spread we assume the electron response function can be modeled as a parallel LRC resonator with quality factor Q_r.

Figure 7 compares the output of the bunched beam eigenvalue code with thresholds obtained using the coasting beam dispersion relation [40, 4, 5, 41, 42],

$$1 = \Delta Q_0 \int \frac{dv\rho(v)}{\Delta Q + \Delta Q_{sc} - vQ_e}, \tag{4}$$

where $v = (\omega - \omega_0)/\omega_0$ is the fractional frequency difference, $\rho(v)$ is the normalized density with $\int \rho(v)dv = 1$, ΔQ is the coherent tune when frequency spread is included, and ΔQ_{sc} is the space charge tune shift. The cold beam tune shift is

$$\Delta Q_0 = \Delta Q_{sc} + i\frac{Q_p^2 Q_r}{2Q_\beta}. \tag{5}$$

where Q_β is the betatron tune. The derivation of equation 4 assumes $\Delta Q \ll Q_\beta$ and $Q_r \ll Q_e$. Taking lattice functions for PSR and SNS, calculating the variation in ω_e for an elliptical (KV) beam, and equating equivalent widths of the resistive transfer function; one finds $Q_r \approx 3$.

[3]Notice that Q_p is the betatron tune the protons would have in the absence of other focussing forces.

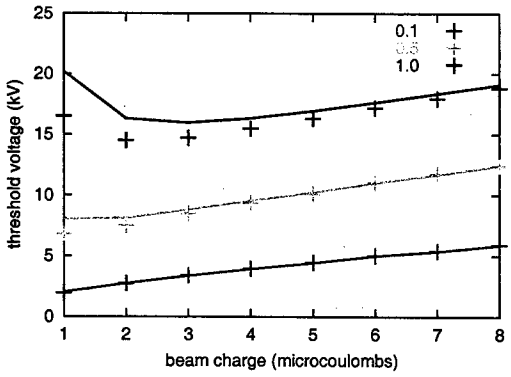

Figure 7: Threshold voltage versus bunch charge for the PSR parameter regime. The symbols are the thresholds for the bunched beam eigenvalue problem. The solid line is the estimate using the coasting beam dispersion relation, equation (4). The different colors correspond to $\lambda_e = 1$, 0.5, and 0.1 nC/m.

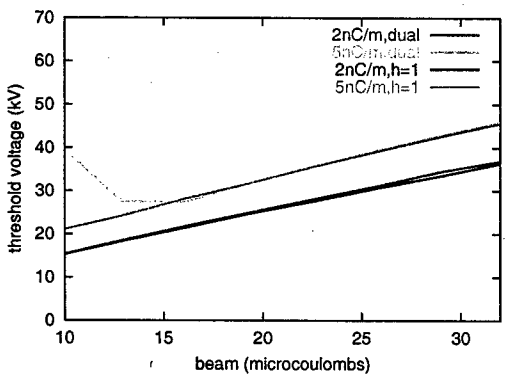

Figure 8: Threshold $h = 1$ voltage versus bunch charge for SNS. These were done for a dual harmonic RF system, as well as for $h = 1$ alone. The design $h = 1$ voltage for SNS is 40 kV.

In [16] threshold voltages were calculated for a variety of beam and cloud parameters. However, the various codes calculated values of Q_e and Q_p too large by a factor of $\sqrt{2}$. Additionally, the estimates now use the peak beam current, and momentum distributions calculated from a simulation of multi-turn injection. The PSR calculations still give values of threshold voltage that are 3 to 4 times larger than in Fig 6. Results for SNS are shown in Figure 8.

Other hand calculations include centroid models [43, 35], which are known as beam break-up models in the linac community. The basic idea here is to neglect synchrotron oscillations so that one can integrate out the dependence on $(\omega - \omega_0)/\omega_0$. The shape of the unstable modes look similar to those observed in PSR but threshold estimates are difficult.

Behavior of the instability well beyond threshold is discussed in [44]. Including the dependence of electron oscillation frequency with electron amplitude reduces the growth rate of the instability. This is in line with the growth rates observed in PSR, which are significantly slower than those from equation (5).

4 SIMULATIONS

Simulations of both coasting [47, 48, 49] and bunched [45, 46, 17, 16] beams have been done. The coasting beam simulations involve a fully 3-dimensional solution to the Vlasov equation, but do not yet include the effects of secondary emission. The bunched beam simulations use approximate equations of motion for the protons and electrons but some include secondary emission and synchrotron oscillations. One key question regards the effect of nonlinear forces. The coasting beam simulations [49, Figs 2 and 3] show that electron cloud instabilities do not exist for cold beams if the beam and cloud densities are low enough. This is well known when there is no spread in the electron bounce frequency, and this frequency is sufficiently far from the nearest, unstable, betatron sideband [40, 5, 15]. However, the simulations in [49] have electron frequency spread. In [16] the inclusion of nonlinear space charge effects led to estimates in better agreement with experimental PSR stability thresholds. In the meantime, the author has done some simulations of the equation

$$\frac{d^2\mathbf{x}_j}{d\theta^2} + Q_j^2\mathbf{x}_j = \frac{1}{N}\sum_{k=1}^{N}\left(\nu\mathbf{x}_k + \alpha\frac{d\mathbf{x}_k}{d\theta}\right) + \frac{C_{sc}}{N}\sum_{k=1}^{N}\frac{\mathbf{x}_j - \mathbf{x}_k}{|\mathbf{x}_j - \mathbf{x}_k|^2 + \epsilon^2},$$

where $\mathbf{x}_j$ is a two dimensional vector, Q_j^2, ν, and α are diagonal 2 by 2 matrices, ϵ is a smoothing parameter, and C_{sc} parameterizes the strength of the space charge force. Each Q_j^2 is different and chosen from a parabolic distribution.

Simulations were done by increasing N with a fixed integration time until results converged. For $C_{sc} = 0$, the simulations agree with the coasting beam dispersion relation within a few percent. Simulations with space charge are compared with the analytic theory in Fig. 9. With no spread in Q_j the tune shift is ΔQ_0. Stable simulations of a smooth beam are green crosses and the red are unstable. The red threshold curve is calculated using linear space charge. The blue threshold curve is a hand estimate based on the soft upper limit discussed in [50]. The simulations show a much smaller effect than the hand estimate and the difference corresponds to a factor ~ 4 in RF voltage. The resolution of this problem is a serious, practical matter. Accurate determinations of required momentum aperture and RF voltage could result in significant cost savings for future machines.

5 ACKNOWLEDGEMENTS

This work has benefited from conversations with P. Channell, V.A. Danilov, R. Davidson, W. Fischer, M. Furman,

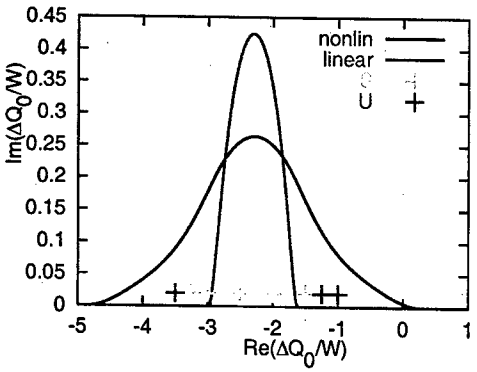

Figure 9: Various estimates of nonlinear space charge effects with $P(Q) = (3/4W)(1-(Q-Q_0)^2/W^2)$.

K. Harkay, G. Lambertson, Y.Y. Lee, R.J. Macek, M. Pivi, A.G. Ruggiero, H. Qin, T.S. Wang, J. Wei and S.Y. Zhang. Special thanks to the BNL vacuum group for preparing the titanium nitride coated samples and the CERN vacuum group for measuring the secondary yield.

6 REFERENCES

[1] G.I. Budker, G.I. Dimov, V.G. Dudnikov, *Proceedings of the International Symposium on Electron and Positron Storage Rings*, VIII-6-1, Saclay 1966.

[2] G.I. Budker, G.I. Dimov, V.G. Dudnikov, A.A. Sokolov, V.G. Shamovsky, *Sixth International Conference on High Energy Accelerators*, A-103, Cambridge Massachusetts, 1967.

[3] V. Dudnikov, 8th ICFA Beam Dynamics Mini-workshop, Santa Fe, (2000), available online at http://www.aps.anl.gov/conferences/icfa/two-stream.html

[4] H. G. Hereward, CERN 71-15 (1971).

[5] E. Keil, B. Zotter, CERN/ISR-TH/71-58, (1971).

[6] D. Neuffer, E. Colton, D. Fitzgerald, T. Hardek, R. Hutson, R. Macek, M. Plum, H. Thiessen, T.S. Wang *NIM* **A321** p1 (1992).

[7] M. A. Plum, D.H. Fitzgerald, D. Johnson, J. Langenbrunner, R.J. Macek, F. Merril, P. Morton, B. Prichard, O. Sander, M. Shulze, H.A. Thiessen, T.S. Wang, C.A. Wilkinson, PAC97 p 1611.

[8] R. Macek, AIP Conf. 448, p116, (1998)

[9] G. Arduini, V. Baglin, O. Bruning, R. Cappi, F. Caspers, P. Collier, I.R. Collins, K. Cornelis, R. Garoby, O. Gröbner, B. Henrist, N. Hilleret, W. Holfle, J.M. Jimenez, J.M. Laurent, T. Linnecar, E. Mercier, M. Pivi, F. Ruggiero, G. Rumolo, C. Scheuerlein, J. Tuckmantel, L. Vos, F. Zimmermann EPAC00, p259, (2000) *and references therein.*

[10] R. Cappi, M. Giovannozzi, E. Metral, G. Metral, F. Zimmermann, PAC01, p682 (2001).

[11] R. Cappi, M. Giovannozzi, E. Metral, G. Metral, G. Rumolo, F. Zimmermann, PRSTAB, **5**, 094401, (2002)

[12] W. Fischer *etal* EPAC02, 1485, (2002)

[13] H.C. Hseuh, L.A. Smart, S.Y. Zhang, EPAC02, 2559, (2002)

[14] W. Fischer, J.M. Brennan, M. Blaskiewicz, T. Satogata, PRSTAB **5**, 124401, (2002).

[15] M. Blaskiewicz, AIP Conf. 496, p321, (1999).

[16] M. Blaskiewicz, M.A. Furman, M. Pivi, R.J. Macek, PRSTAB, **6** 104203 2003

[17] K. Ohmi, T. Toyama, C. Ohmori, PRSTAB **5**, 114402, (2002).

[18] G.V. Stupakov, LHC Project Report 141 (1997).

[19] M.A. Furman and G. Lambertson, in Proceedings of the International Workshop on Multibunch Instabilities in Future Electron and Positron Colliders, Tsukuba, Japan, 1997.

[20] O. Gröbner, PAC97

[21] F. Zimmermann, PAC01, p666, (2001).

[22] M. Plum, PSR Tech Note PSR-94-001 (1994).

[23] V. Danilov, J. Galambos, D. Jeon, J. Holmes, D. Olsen, D. Fitzgerald, R. Macek, M. Plum, J. Griffin, A. Burov, PAC99, p1201 (1999).

[24] P. Thieberger, A.L. Hanson, D.B. Stetski, V. Zajic, S.Y. Zhang, H. Ludewig, PRA, **61**, 042901 (2000).

[25] M. Pivi, M.A. Furman *Phys Rev S.T Accel Beams*, **5** 124404

[26] U. Iriso-Ariz *etal*, these proceedings

[27] S.Y.Zhang *etal*, these proceedings

[28] B. Henrist, N. Hilleret, C. Scheuerlein, M. Taborelli, G. Vorlaufer, EPAC02, p2553 (2002).

[29] Y. Kijima, S. Mitsunobu, T. Furuya, R. Noer, The 10th Workshop on RF Superconductivity, contribution PT027, available online at http://conference.kek.jp/SRF2001/.

[30] R. Macek, 8th ICFA Beam Dynamics Mini-workshop, Santa Fe, (2000), available online at http://www.aps.anl.gov/conferences/icfa/two-stream.html

[31] R.J. Macek, PAC01 p688 (2001).

[32] R.J. Macek Proceedings ICANS XV, KEK Nov 2001, p229.

[33] A. Browman, 8th ICFA Beam Dynamics Mini-workshop, Santa Fe, (2000).

[34] K. Ohmi, F. Zimmermann, E. Perevedentsev, *Phys Rev E*, **65** 016502 (2001).

[35] E. Perevedentsev, CERN-2002-001, p 171. (2002).

[36] Y. Chin, CERN/LEP-TH/88-05 (1988), *and references therein.*

[37] K. Ohmi, PRL, **75**, 1526 (1995).

[38] K. Ohmi, F. Zimmermann, PRL, **85** 18, p3821, (2000).

[39] G. Rumolo, F. Zimmermann, H. Fukuma, K. Ohmi, PAC01, p1889, (2001).

[40] B.V. Chirikov, *Sov. Atomic Energy*, **19** p1149 (1965).

[41] L. J. Laslett, A. M. Sessler, D. Möhl, NIMA, **121**, p517, 1974.

[42] R. C. Davidson, H. Qin, P. H. Stoltz, Phys Rev ST Accel Beams, 054401, 1999.

[43] T.S.F. Wang, P.J. Channell, R.J. Macek, R. Davidson, *Phys Rev S.T Accel Beams*, **6** 014204 (2003).

[44] P.J. Channell, *Phys Rev S.T Accel Beams* **5** 114401 (2002).

[45] M. Blaskiewicz, 8th ICFA Beam Dynamics Mini-workshop, Santa Fe, (2000).

[46] T.S. Wang, P.J. Channell, R. Macek, R.C. Davidson, PAC01, 704, (2001)

[47] R.C. Davidson, H. Qin, P.J. Channell, PRSTAB, **2** 074401 (1999).

[48] H. Qin, R.C. Davidson, E. Startsev, W.W. Lee, PAC01, 693, (2001)

[49] H. Qin, E. Startsev, R.C. Davidson, PRSTAB **6** 014401 (2003)

[50] M. Blaskiewicz, *Phys Rev ST Accel Beams* **4**, 044202, (2001).

ELECTRON CLOUD STUDIES AND ANALYSES AT SPS FOR LHC-TYPE BEAMS

J.M. Jimenez, G. Arduini, V. Baglin, P. Collier, G. Ferioli, B. Henrist, N. Hilleret, L. Jensen, B. Jenninger, J.M. Laurent, A. Rossi, K. Weiss, F. Zimmermann
AT / AB Collaboration, CERN, Geneva, Switzerland

Abstract

A summary of the main results obtained so far from the electron cloud studies using strip detectors, pick-ups, COLDEX and a 100 MHz coaxial resonator will be presented. The spatial and energy distributions of the electrons in the cloud measured by the strip detectors will be detailed and compared to the results obtained with a conventional retarding field detector. The evidence of the scrubbing effect and of the NEG coatings as remedies to reduce the electron cloud activity will also be shown.

In a second part, the improved hardware of the experiments will be presented together with the program of measurements foreseen for the 2003 SPS run.

1 SET UP & MAIN RESULTS

1.1 Electron Cloud thresholds, build up

1.1.1 Set up description

Since 1998, the electron cloud activity is being studied in the SPS with LHC-type beams[1] using the pressure gauges and shielded pick-ups [1][2][3]. During the shutdown of 2001-02, three different versions of strip-detectors have been installed to study independently or simultaneously the spatial distribution and the energy distributions of the electrons in the cloud [4].

1.1.2 Electron Cloud thresholds, build up

The electron cloud multipacting is driven mainly by the beam parameters and by the secondary electron yield (δ_{max}, Energy of the maximum of the secondary electron yield) of the wall surface.

Immediately after the air venting during the 2001/02 shutdown, the threshold of the electron cloud, measured with a single batch-injection, was $3.0\text{x}10^{10}$ p/bunch in the dipole field regions and $5.5\text{x}10^{10}$ p/bunch for the field-free. In a dipole field, the appearance threshold of the two lateral strips was $5.5\text{x}10^{10}$ p/bunch and at $1.3\text{x}10^{11}$ p/bunch, a 3rd central strip appeared as predicted by the simulations [5][6]. The observations showed that the central strip tends to disappear after a few hours of scrubbing and an attempt of explanation will be given in §1.4. Fig.1 shows the electron cloud build up in a dipole field with 4 batches injected.

The electron cloud build up is strongly dependent on the beam potential (bunch intensity and length) which determines the kick to the electrons. As expected, the measurements showed an increase of the electron cloud intensity by a factor of 7 to 10 when the bunch intensity is doubled from $5.0\text{x}10^{10}$ to $1.1\text{x}10^{11}$ p/bunch.

Similarly, a decrease of the bunch length by 30% doubles the electron cloud intensity (Fig.2) and a 3rd central strip appears already at $1.1\text{x}10^{11}$ p/bunch instead of $1.3\text{x}10^{11}$ p/bunch for the nominal bunch length (4 ns). Conversely, if the bunch length is increased by 30%, the electron cloud disappeared (Fig.2).

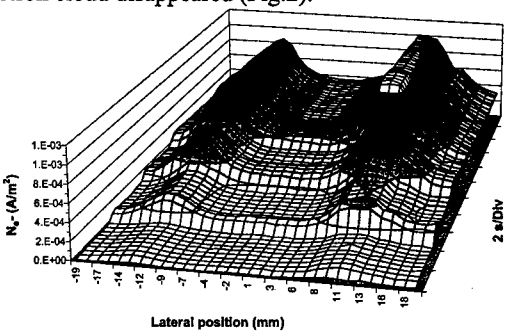

Fig.1: Electron cloud signal measured using the strip-detector in a dipole field with 4 batches injected.

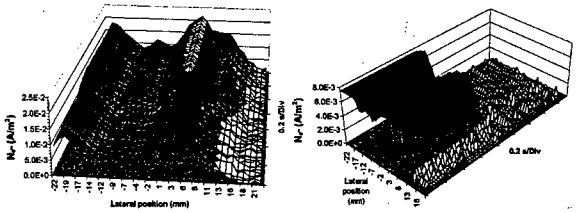

Fig.2: The electron cloud is enhanced by a bunch length decrease (left,-30%), and disappears with an increase of the bunch length (right, +30%).

1.1.3 Multi-batch – Surviving electrons

To optimise the injection of the LHC, 3 or 4 batches will be accumulated in the SPS before being injected into the LHC. The measurements made using the pick-ups confirmed that the electron cloud build up during the passage of the 2nd, the 3rd and 4th batch is enhanced by the passage of the preceding batches (Fig.3). If the lifetime of the electrons is higher than the 225 ns batch spacing, the surviving electrons created during the previous batch passage will enhance the build up during the passage of the following batches. But after the 4th batch passage and due to the revolution time in the SPS, i.e. 23 μs, the 1st batch will pass once again after 14.6 μs. This delay

[1] 1-4 batches of 72 bunches injected from the PS machine, 25 ns bunch spacing, 225 ns batch spacing, $1.3\text{x}10^{11}$ protons/bunch ($1.7\text{x}10^{11}$ ultimate) and 4ns bunch length (4σ) at injection energy (26 GeV).

0-7803-7738-9/03/$17.00 © 2003 IEEE

appears as long enough to loose all the surviving electrons.

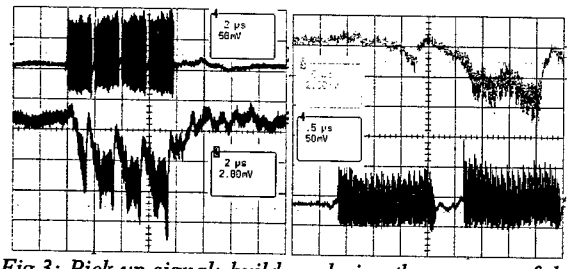

Fig.3: Pick-up signal: build up during the passage of the 2nd, 3rd and 4th batch enhanced by the passage of the preceding batches (left). A 550 ns batch spacing did not decouple the build up of two successive batches (right).

1.1.4 Scrubbing Effect

Two scrubbing periods, 15 days of beam in total, gave evidence of a "scrubbing effect". All around the SPS, both in the field-free and dipole field regions, the pressures decreased by 10^3 in 4 days, 10^4 in 10 days (Fig.4).

Meanwhile, the threshold in the dipole field increased from $3.0\text{x}10^{10}$ to $1.0\text{x}10^{11}$ p/bunch and from $5.0\text{x}10^{10}$ to more than $1.3\text{x}10^{11}$ p/bunch in the field-free regions. No signal could be detected in the field-free regions after 10 days of LHC-type beams with a 4 batches injected.

Similarly, the evolution of the electron cloud activity measured by the strip-detectors throughout the cleaning process showed a decrease of the electron flux by a factor 10^2 in 10 days in a field-free region.

Several parameters measured (pressures, electron cloud intensity, heat load measured by the calorimeters [7][8]) showed that the beam-induced multipacting and thus the scrubbing stopped after 4 days in the field-free regions which is consistent with the in situ measurement of the secondary electron yield (SEY), which remained constant after 4 days; the δ_{max} was between 1.5 and 1.6. After short periods without LHC-type beams, the SEY drifted up i.e. from 1.5 to 1.7 in two weeks time. However, the initial value was recovered after 4 hours with nominal intensity LHC-type beams with at least 3 batch-injections.

1.1.5 Effect of the ramp in energy

At the end of the scrubbing period, a small ramp in energy was introduced after the 4th batch-injection; the proton energy was increased up to 55 GeV to check whether or not the scrubbing run should be made at injection energy (costs of operation) or if unexpected enhancement effects will imply going to higher energies.

The effect of this small ramp was bigger than expected since it induced a small displacement of the orbit (Fig.5) producing pressure rises all around the SPS machine and an enhancement of the electron cloud intensity measured by the strip-detectors.

A squeezing of the bunch during the ramp, which implies an increase of the beam potential, and therefore an increase of the electron energies could easily explain the increase of the electron cloud activity. The pressure rises can be explained by the orbit displacement, which involved new "less scrubbed" surfaces. This hypothesis is consistent with the measurements made by introducing a small orbit displacement between 3 to 4 mm with respect to the nominal orbit, which produced an increase of the pressures $\Delta P/P$ by 3 to 5 depending on the chamber shape and position in the SPS ring. The pressure rises clearly indicate that the electrons are bombarding non-scrubbed surfaces; Consistently, the electron cloud activity measured by the strip-detectors increased by more than a factor 2.

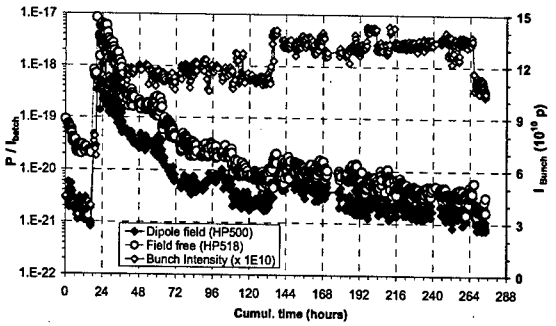

Fig.4: Pressure decreases both in dipole and field-free regions with the LHC-type beam exposure. The pressures are normalised to the batch intensity ($P/I_{bunch}\text{x}72\text{x}N_{bacthes}$).

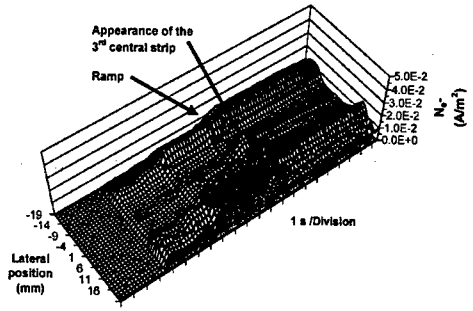

Fig.5: Small orbit displacement seen by the strip-detectors due to the ramp to 55 GeV.

1.2 Vacuum behaviour of cold surfaces COLDEX

The COLDEX experiments, which was previously installed in the EPA ring (PS Complex) to measure the photon stimulated desorption, has been installed in a field-free region of the SPS (HP417) in May 2002. The aim of this experiment was to study the dynamic pressure evolutions in presence of LHC-type beams at cold (5-20 K) with a beam screen design close to the LHC one.

The COLDEX beam screen was made out of OFE copper with a length of 2.2 m and with an elliptic shape (H = 84 mm, V = 66 mm). A 1 % of the total surface is composed of holes, which allow the transfer of gases from the beam screen to the cold bore. The cold bore is operated between 3 to 5 K while the beam screen could be operated from 5 to 100 K.

UHV pressure gauges, residual gas analyser and gas injection (Fig.6) allow following the partial and total

pressures. The heat load is measured on the cryogenic cooling circuit.

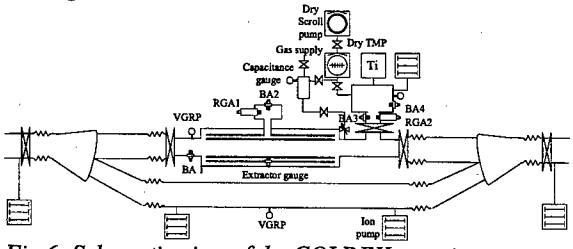

Fig.6: Schematic view of the COLDEX experiment

The pressure in COLDEX also suggests a scrubbing effect; the pressure decreased by 10^2 after 4 days (Fig.7) reaching the equivalent of 100 hours beam lifetime in the LHC. During all the evolution, the beam screen was kept around 8 K and the cold bore at 5 K. The increase during a few hours of the beam screen temperature to 120 K did not change the picture; the same result was obtained after the injection of one monolayer of hydrogen.

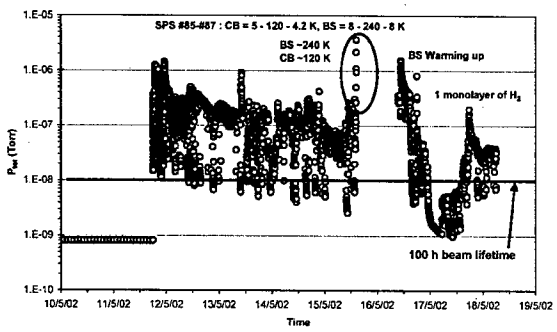

Fig.7: Pressure evolution in the COLDEX during the 1st scrubbing run.

The preliminary results obtained on the heat loads measured by COLDEX (95 % duty cycle, $1.1\text{x}10^{11}$ p/bunch) still need confirmation since the heat load measured is larger than the available cooling power in the LHC. The simulations made for a similar geometry and assuming a SEY of 1.4 gave similar results [6].

1.3 NEG: A remedy to the Electron Cloud

The use of NEG pumping coatings (TiZrV) [9] has been approved as the vacuum baseline for the vacuum chambers of the LHC room temperature long strait sections. It was expected that the low secondary electron yield of the NEG surface after activation (δ=1.1) [10] and even if saturated (δ=1.2 with a CO saturation) [11], should decrease the electron cloud.

To validate the NEG behaviour, a test bench was installed in the SPS with a symmetrical layout allowing a direct comparison between NEG coated chambers and stainless steel chambers with identical shapes [12].

Fig.8 shows the difference in behaviour between a non-activated NEG and an activated and saturated NEG. With the non-activated NEG, an electron current is measured by the shielded pick-ups and the NEG coated chamber behaves like the reference stainless steel chamber. After activation and even if fully saturated (water coming from the non-baked upstream and downstream vacuum chambers), the results confirmed that no electron cloud signal is visible at nominal bunch intensity with 4 batches injected. In presence of beam, the predominant gases are, as expected: H_2, CO, CO_2 and CH_4.

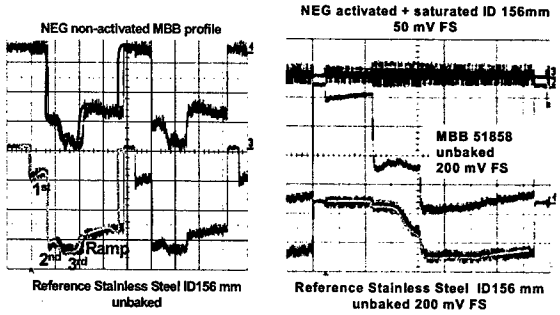

Fig.8: Electron cloud signals measured using pick-ups on a reference stainless steel chamber as compared to a non-activated NEG coated chamber (left) and to an activated and saturated NEG coated chamber (right).

1.4 Spatial and Energy distributions

The spatial distribution of the electrons in the cloud has been confirmed using a 36-channels strip-detector, which allowed twice the resolution, obtained in 2001 and recent simulations fit fairly well the measurements [13]. At $1.1\text{x}10^{11}$ and $1.3\text{x}10^{11}$ p/bunch, the two vertical lateral strips of the cloud will stand on top of the beam screen pumping slots (9 and 11.5 mm respectively from the center) inducing additional heat load to the cold bore. The decision to insert a pumping slot shielding to intercept the electrons passing through the slots was accepted and is now in the LHC baseline [14].

The energy distribution of the electrons in the cloud was measured using the strip-detectors in both the dipole field and field-free conditions and using a conventional retarding field detector in a field-free region. Due to hardware limitations, the electrons with energies below 20 eV could not be measured. However, the impact of this limitation is small both on the heat load budget and on the pressure rises induced by the electron stimulated desorption (ESD) mechanism since for both processes, the expected contribution of the low energy electrons (<20 eV) is small (< 20 %).

In the dipole field where most of the electrons are trapped in two vertical lateral strips by the magnetic field, the energy distribution showed a peak between 180 and 200 eV to be compared with the 80 eV measured in the field-free regions.

The simultaneous energy and spatial distributions studies showed that most of the high-energy electrons i.e. above 200 eV, are located in the central strip (Fig.9). The two lateral strips have electrons with energies below 180 eV. This last observation could explain why the central strip tends to disappear after several hours of LHC-type beam. In fact, the decrease of the secondary electron yield is enhanced by the amount of primary electrons. After a

given dose, the amount of electrons produced, i.e. δ_{SEY} above the multipacting threshold is reached earlier for the electrons with energies above 800 eV thus causing the extinction of the cloud in the central area.

1.5 Coaxial resonator 100 MHz

Multipacting measurements were also performed in the Laboratory without beam, using a 100 MHz coaxial resonator. The external conductor of the resonant cavity (Fig.10) is a 1500 mm in length (DN100) stainless steel vacuum chamber. A lateral cut-off tube (DN35) allows connecting an electron pick-up in the central part of the resonator, where the electric field is maximized in the l/2 mode [15]. A stainless steel grid, perforated by 2 mm holes, closes this port in order to maintain the chamber wall continuity and to shield the pickup from the RF signal. This grid is treated in the same way as the chamber.

The onset of multipactor is detected by the observation of several changes in the cavity behaviour, which happen when the input power reaches the multipactor threshold. Those following changes constitute the cavity multipactor signature: collection of electrons by the pick-up, a simultaneous increase of the vacuum pressure, a saturation of the output signal, an increase of the reflected signal, a detuning of the cavity and the generation of harmonics.

If baked below the activation threshold (150°C), the multipactor threshold of the NEG coated chamber is similar to the one of an unbaked stainless steel. After the activation of the NEG coating, the multipacting threshold increased and the amount of electrons collected by the pick-up decreased. Fig.11 shows how the output voltage trend is modified above a given input power threshold due to the adsorption of a fraction of the input power by the multipacting electrons. When activated, the output signal increases linearly with the input power indicating the absence of electrons. The same measurements were made at liquid nitrogen temperature (77 K) and with an activated NEG, no electron multipacting was measured (Fig.11). Even intentioned cryosorbtion of gases (CO, CO2 and air) onto the inner wall of the cavity did not change the picture.

2 OBJECTIVES FOR 2003

The vacuum studies at cryogenic temperature will be the priority of the new measurement campaign. The aim is to study the effect of surface coverage on the vacuum stability. The proof of existence of a scrubbing effect at cryogenic temperature is also a major issue since the scrubbing was only confirmed at room temperature. These experiments will be carried out using the COLDEX experiment equipped with a beam screen design closer to the LHC baseline. The higher order modes shielding has been improved to avoid any contribution to the heat load measured by COLDEX using a dedicated thermometry. An RT calorimeter with a similar aperture will allow comparing heat loads at cold and room temperature. The measurements at cryogenic temperature will also rely on the results given by a new cold strip-detector, which is a strip-detector operating between 20 and 30 K installed in a remotely controlled dipole corrector.

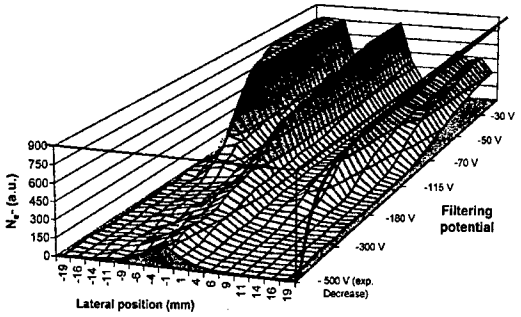

Fig.9: Spatial energy distribution ($d^2N/dxdE$) of the electrons measured in a single-cycle mode using the retarding field strip-detector.

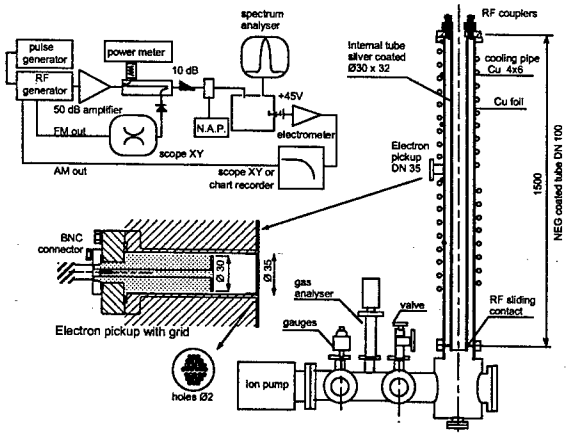

Fig.10: Schematic view of the 100 MHz coaxial resonator

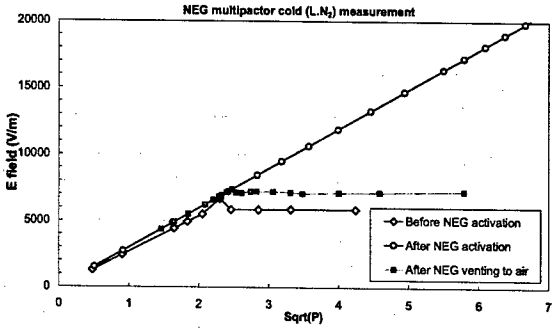

Fig.11: Multipacting measured on a NEG coated chamber at liquid nitrogen temperature.

For the LHC, heat loads will be an issue and the scaling from the SPS results to the LHC at room and cryogenic temperature, in dipole and field-free are essentials. Benchmarking the simulations is also necessary and the dependence of the electron cloud build up on the height of the vacuum chamber will be studied using a variable aperture strip-detector. This strip-detector operating at RT in a remotely controlled dipole corrector has two moving

plates and allows apertures between 50 and 85 mm in the vertical plane. The exchangeable plates will allow testing solutions to cure the electron cloud.

A remotely controlled dipole magnet installed on top of the SEY detector will allow studying the evolution of the SEY in a dipole field condition. Since the electron cloud threshold is lower in dipole field conditions, an additional decrease of the SEY is expected.

The NEG coatings used in the LHC LSS appear to be a remedy for the electron cloud. The SPS NEG test bench will be used again to validate the preliminary measurements obtained in 2002. A cycled and saturated NEG will also be studied and compared to a fresh NEG coating.

Finally, the parameters influencing the electron cloud build up will be studied, like the cloud intensity at ultimate bunch intensity, the effect of 6 homogeneously distributed batches in the SPS to verify if the electrons can survive a 3μs batch spacing, the effect of the 75 ns bunch spacing and the energy distributions measured with a new retarding field detector with an increased resolution.

3 CONCLUSIONS AND DISCUSSIONS

As being the LHC injector, the scrubbing runs confirmed that after 5 days of scrubbing, the SPS should be able to inject 3 or 4 batches at nominal intensity into the LHC.

However, the electron cloud is still "visible" after about 500 hours of LHC-type beams with 4 batch-injections at nominal intensity but only in the arcs (dipole field regions) both as pressure rises and on the electron signals collected by the strip-detectors. In the field-free regions, i.e. in the long straight sections, the electron cloud activity decreased below the detection level of the strip-detectors ($< 10^{-9}$ A/m). This observation is not in contradiction with the scrubbing efficiency since most of the LHC beam time used for the scrubbing was with 1 or 2 batches injected with bunch intensities close to the electron cloud threshold after 4 days of scrubbing. The scrubbing efficiency depends on the amount and energy of the impinging electrons (bunch intensity, bunch length, number of batches). Similarly to RF and HV devices, the scrubbing efficiency is limited by the parameters used during the scrubbing. The scrubbing will not be effective if running conditions are more favourable for the electron cloud build up.

The ultimate SEY value reached after 4 days in the field-free regions in the SPS (δ=1.5) shows the multipacting threshold under these conditions. Analytical calculations [16] made recently fit fairly well to the measurements. The upward drift of the SEY (δ) observed if the SPS is not operated with LHC-type beams is not an issue since measurements confirmed that the SEY recovered its initial value after 4 hours of operation with LHC-type beams above the electron cloud threshold. The detrimental effect of the ramp in energy (up to 450 GeV) on the electron cloud build up as a consequence of the bunch length shortening and of the beam orbit displacement during the ramp, need to be confirmed and quantified.

For the LHC, the major concern is the excessive heat load due to the electron cloud. Data have been collected and are being compared with the predictions from simulations. However, the LHC situation is expected to be more complicated since most of the machine is at a cryogenic temperature and therefore the gases cryosorbed on the inner surfaces of the vacuum chambers could modify the present picture obtained at room temperature. The scrubbing efficiency is not yet confirmed on cold surfaces on which the energy of the impinging electrons may be decreased by the cryosorbed gases.

The different filling schemes in the two machines also complicate the extrapolation from the SPS situation to the LHC. In the SPS and with 4 batches injected, the surviving electrons are thought to be lost in the 14.6 μs between the 4th batch passage and a new passage of the 1st batch. In the LHC [17], the situation could be less favourable since the ring will be full of batches and the maximum spacing between batches will not exceed 3μs, corresponding to the rise time of the LHC dump kickers. If the electrons from the cloud survive these gaps, the build up may be significantly enhanced.

REFERENCES

[1] J.M. Jimenez et al., Workshop Chamonix XI (2001)
[2] J.M. Jimenez et al., PAC01, CHICAGO (2001)
[3] J.M. Jimenez et al., LHC Project Report 632(2003)
[4] J.M. Jimenez et al., LHC Project Report (2003)
[5] F. Zimmermann et al., Workshop Chamonix X (2000)
[6] F. Zimmermann and al., Scrubbing days CERN 2002
[7] N. Hilleret and al, Scrubbing days CERN 2002
[8] V. Baglin, Scrubbing days CERN 2002
[9] C. Benvenuti et al., Vacuum 60 (2001) 57-65.
[10] C. Scheuerlein et al., CERN EST/2000-07 (SM).
[11] B. Henrist et al., CERN Vac. Tech. Note 98-08.
[12] A. Rossi, Scrubbing days CERN 2002
[13] F. Zimmermann, Workshop Chamonix XII (2002)
[14] N. Kos, EDMS 362883 (CERN)
[15] U. Iriso Ariz, Vacuum Technical Note 02-12
[16] L. Vos (private comm. to be published, CERN)
[17] O. Brunning, Minutes of the 59th PLC59 (CERN)

ACKNOWLEDGMENTS

K. Cornelis[1], D. Manglunki[1], SPS & PS Operators[1], T. Bohl[1], P. Baudrenghien[1], W. Hofle[1], N. Delruelle[2], O. Drouyer[2], D. Legrand[2], O. Pirrotte[2], J. Arnold[2], J-C. Billy[2], I. Collins[2], R. Gavaggio[2], G. Mathis[2], R. Wintzer[2], J. Hansen[2], P. Chiggiato[3], P. Costa-Pinto[3], C. Grünhagel[3], J. Ramillon[3], N. Munda[3], G. Favre[3], D. Valero[3], M. Blanc and peoples from the Main workshop[3], M. Doets[4], P. d. Groen[4], G. vd Heide[4], B. Kaan[4], S. Klous[4], J. Kuyt[4], Y. Lefèvre[4], E.V. Leeuwen[4], O. Postma[4], F. Schimmel[4], C. Zegers[4]. [1]AB, [2]AT and [3]EST Divisions, [4]NIKHEF for COLDEX

INITIAL EXPERIMENTAL STUDIES OF ELECTRON ACCUMULATION IN A HEAVY-ION BEAM*

A.W. Molvik[1,2,*], D. Baca[1,3], F.M. Bieniosek[1,3], R.H. Cohen[1,2,*], A. Friedman[1,2], M.A. Furman[3], E.P. Lee[1,3], S.M. Lund[1,2], L. Prost[1,3], A. Sakumi[4], P.A. Seidl[1,3], J.-L. Vay[1,3]

[1] Virtual National Laboratory for Heavy Ion Fusion
[2] Lawrence Livermore National Laboratory, Livermore, CA 94550
[3] Lawrence Berkeley National Laboratory, Berkeley, CA 94720
[4] RIKEN, (Now at CERN)

Abstract

Accelerators for heavy-ion inertial fusion energy (HIF) have an economic incentive to fit beam tubes tightly to beams, putting them at risk from electron clouds produced by emission of electrons and gas from walls. Theory and PIC simulations suggest that the electrons will be radially trapped in the ≥1 kV ion-beam potential. We are beginning studies on the High-Current Experiment (HCX) with unique capabilities to characterize electron production and trapping, the effects on ion beams, and mitigation techniques. We are measuring the flux of electrons and gas evolved from a target, whose angle to the beam can be varied between 78° and 88° from normal incidence. Quadrupole magnets are operating with a variety of internal charged particle diagnostics to measure the beam halo loss, net charge, electron ionization rate, and gas density.

INTRODUCTION

Electron cloud effects (ECEs) are increasingly recognized as important, but incompletely understood, dynamical phenomena, which can severely limit the performance of colliders, the next generation of high-intensity rings, or future high-intensity heavy ion accelerators such as envisioned in Heavy Ion Inertial Fusion (HIF) [1].

Accelerators for HIF have an economic incentive to fit beam tubes tightly to beams. This places them at risk from gas desorption runaway, and from electron clouds produced by secondary electrons and ionization of gas. We have initiated an experimental and theoretical program to measure, understand, and model these effects in heavy-ion accelerators [2].

HCX CAPABILITIES

Theory and PIC simulations suggest that the electrons will be radially trapped in the ≥1 kV ion-beam potential [2,3], and can be detrapped by drifting into an upstream acceleration gap [2]. We have installed four quadrupole magnets on the High-Current Experiment (HCX) [4] at LBNL with internal electron diagnostics.

On HCX we are studying the transport of a 1 MeV, 180 mA, K^+ ion beam. (HCX has also operated at 1.8 MeV, 500 mA.) It has a beam potential of ~1.5 kV, rise and fall times of 1 μs, and a flattop duration of 4 μs, repeated at 10 s intervals. Electron transit times between walls are in the range of 7 ns, almost 3 orders of magnitude shorter than the flattop duration. This enables exploration of unique electron trapping regimes: multipactor trapping will not occur during the flattop, however secondary electrons will be trapped during the rise time. Ionization of gas by the beam generates deeply trapped electrons, the ions from gas are expelled in ≤1 μs.

Trailing edge multipacting, if it occurs, will be at the end of the fall time when the bounce time of electrons between walls grows to ≥25 ns as the beam potential falls below 100 V. Then electrons gain ≥40 eV on each transit. But, all electrons should be lost before the next pulse, 10 s later in HCX, 0.2 s later in a future power plant driver. On PSR, electrons are observable for surprisingly long times, but still only until 1 μs after a pulse [5]

HCX provides an opportunity to search for subtle electron trapping mechanisms. To elaborate – an electron emitted from the beam tube with a few eV is accelerated by the beam potential to ~10^3 higher energy, then decelerates towards the opposite wall. An irreversible conversion of only ~10^{-3} of the peak radial energy to axial or azimuthal energy will trap the electron, preventing it from reaching the opposite wall.

We have used the Gas-Electron Source Diagnostic (GESD) on the HCX to measure the flux of electrons and gas evolved from a target, whose angle to the beam can be varied between 78° and 88° from normal incidence. The results will be discussed in subsequent sections.

We have installed a variety of charged particle diagnostics in quadrupole magnets to characterize electron production and trapping: (1) Electrodes, flush with the beam tube wall, are to measure the beam halo loss plus the resulting secondary electron emission. Using the electron-emission coefficient measured with the GESD, we can infer the beam-halo loss. (2) Capacitive probes measure the net beam charge from which we can infer electron densities if they exceed a few percent of the beam density. (3) Grids shield collectors from the 3-orders-of-magnitude larger capacitive signal, to enable measurement of the current of expelled ions from ionization of gas. This ion current will be calibrated against an ion gauge, varying the pressure by leaking in a known gas. Then, we can determine the time dependence of gas density in the beam. It also directly measures the production rate of electrons from gas (when corrected by the ratio of the ionization cross section to the sum of ionization and charge-exchange cross sections). Slit scanners and beam profile diagnostics

*molvik1@llnl.gov

0-7803-7738-9/03/$17.00 © 2003 IEEE

before and after the quadrupole magnets allow effects of electrons on the ion beam to be determined.

At present, the diagnostic bias power supplies, signal preamps, and data acquisition recorders and software produce reasonable signals. We are ready to commission the diagnostics to establish the validity of the information. Then we can proceed to experiments that study the two major sources of electrons: secondary emission from the beam tube and ionization of background and desorbed gas.

ION SCATTERING FROM SURFACE

We study ion scattering from surfaces with the TRIM (now SRIM) Monte Carlo code [6]. We found that large fractions of the incident beam ions "backscatter" near grazing incidence. Two consequences are:

(1) Halo ions in quadrupole magnets tend to be lost where the magnetic field is tangent to the beam tube, which confines secondary electrons to remain harmlessly near the wall [2]. But ion scattering allows energetic ions to impinge the beam tube at other azimuths where the field lines pass through the beam. Secondaries generated there could be trapped within the beam.

(2) Gridded collectors depend upon suppressing secondary electrons, generated at one electrode, from reaching another. The initial gridded collectors are located only at azimuths where the magnetic field is tangent to the electrode surfaces, resulting in magnetic insulation of collectors from grids. These can measure expelled ions, but not currents of detrapped electrons.

ELECTRON EMISSION

On HCX, we use the GESD to measure electron emission and gas desorption from 1 MeV K^+ ions incident on a stainless-steel target near grazing incidence (Fig. 2). These data allow us to calibrate electrodes in magnetic quadrupoles that are flush with the beam tube: by measuring the secondary emission current, we infer the beam loss and the gas desorption. We also anticipate using the GESD to study mitigation techniques for reducing electron emission and gas desorption.

The surface of the target has been ground, with grooves parallel to the beam direction to minimize the ploughed-field variations in ion angle of incidence on a microscopic scale. Each electrode can be biased independently. The electron suppressor ring is biased to –200 V to block electrons from entering or leaving the GESD.

To measure the beam current into the GESD, we raise the target to the upper position in Fig. 2, exposing a Faraday cup to the beam. We bias the grid to -150 V, and the target/Faraday cup to –40 V. The HCX beam is expanding over the 1.5 m drift to the GESD, so that the current into the GESD is ~0.14 mA, out of a total beam current of 180 mA at 1 MeV. Maintaining the ion-beam current at <<1 mA is necessary to avoid limiting the electron emission current by space charge (the target to grid gap is ~7 cm) rather than by electron emission.

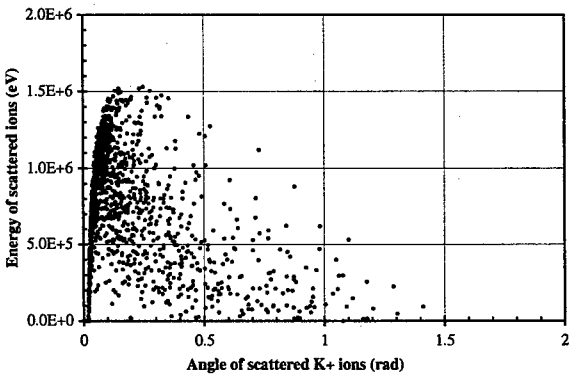

Figure 1. TRIM-98 results for 2000 1.8 MeV K^+ ions incident on stainless steel, 88° from normal. The energy is shown Vs. the angle for the backscattered 64% of ions.

To measure the electron emission current, we bias the grid to +150 V and the reflected ion catcher to –25V, leaving the target at –40 V. The catcher is designed to "catch" about 90% of ions reflected (back-scattered) from the target. The SRIM code [6] calculates that 60-70% of ions incident on the target near grazing incidence will be reflected. We minimize the catcher current by biasing it 15V positive relative to the target.

The electron emission coefficient is shown in Fig. 3(a). We apply models based on electron energy input from ion beam dE/dx in matter. These models predict the magnitude [7] and the angular dependence of the electron emission coefficient η_e [8], $\eta_e \propto d/\cos(\theta)$, where $d/\cos(\theta)$ is the ion path length through a thin $d \approx 2$ nm thick surface layer (where secondary electrons originate).

The electron emission falls below the $1/\cos(\theta)$ curve beyond 86° due to large-angle nuclear scattering of ions out of the 2 nm layer. [8]. We tested this model for saturation with the SRIM 2003 code [6] by varying the thickness d of a thin foil with 1 MeV K^+ incident on 88°, until the transmitted distance normalized to $d/\cos(\theta)$ was near 0.75 [we settled for 0.78 as shown in Fig. 3(a)], the

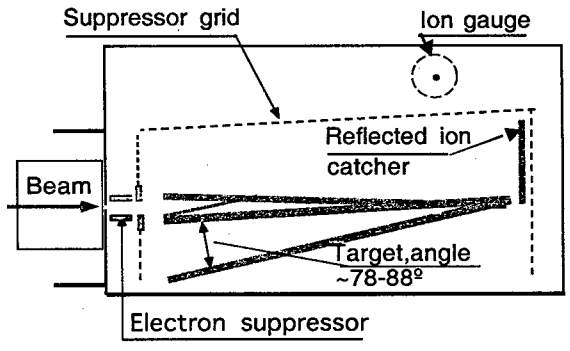

Figure 2. The Gas-Electron Source Diagnostic (GESD). Beam from the left is incident on a target whose angle of incidence can be varied between 78° and 88° relative to normal. The target is shown at 3 angles, the upper position centers a vee-shaped Faraday cup on the aperture.

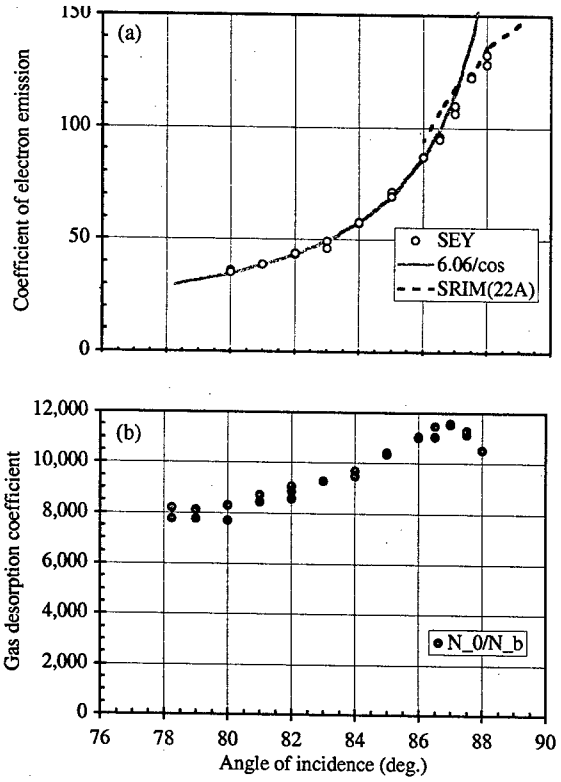

Figure 3. (a) Electron emission from 1 MeV K^+ incident on stainless steel surface varies as 1/cos(θ) with angle of incidence relative to normal. (b) Gas desorption varies more slowly with angle of incidence than 1/cos(θ).

amount by which the measured η_e fell below 1/cos(θ). We found that d = 2.2 nm satisfied this condition. Then using this thickness at other angles gave the dashed line curve in Fig. 3(a), which is a reasonable fit to the data at other angles near grazing incidence.

GAS DESORPTION

The gas desorption coefficient η_0, is measured from the pressure rise after a pulse. The GESD pumps out through the 0.3 by 2.5 cm entrance aperture, plus a 1 cm diameter hole, giving a pump-out time constant of 0.3 sec, long enough for an ion gauge to determine the peak pressure, but short compared with the 10 s before the next pulse. The less than 1/cos(θ) dependence of gas desorption indicates that it is not only from layers of gas adsorbed on the surface (Fig. 2(b)).

We calibrated the GESD Bayard-Alpert ion gauge, over a range of emission currents from 0.5-10 mA and at two pressures 0.7 and 2.5 × 10^{-6} Torr, against a Granville Phillips Stabil-Ion Gauge. The sensitivity varied with emission current over a range of 13%, from a low of 7.7 $Torr^{-1}$ at 2 mA to about 8.7 $Torr^{-1}$ approaching 10 mA. This compares with the nominal 10 $Torr^{-1}$ for the GESD gauge.

We compare two models for desorption: physical and electronic sputtering. Electronic sputtering is due to the electronic component of dE/dx [9,10], which is evaluated with the SRIM code [6]. Physical sputtering results from the nuclear scattering component of dE/dx, but is much less than the electronic component for K^+ ions with energy exceeding 250 keV.

The major difficulty with the electronic sputtering model for desorption from accelerator beam tubes is that it is not expected to be applicable to ions impinging on metals, because free electrons rapidly neutralize charge separation in the ion track, preventing a coulomb explosion. Ion gauges have an analogous difficulty, they can only measure volatile molecules that can impinge walls many times without sticking. Measurements at CERN found the dominant desorbed gases to be CO, CO_2, H_2, and CH_4 [11], all insulators in solid or liquid form.

The compelling motivation to use this model is that much more energy is available from electronic stopping than from nuclear stopping in the energy range for heavy-ion fusion, and even more so for high-energy physics. With physical sputtering from the nuclear scattering, it is difficult to get coefficients greater than a few tens, but electronic sputtering is energetically capable of producing desorption coefficients in the range of thousands as observed here and at CERN [11].

ACKNOWLEDGEMENT

We are grateful to R. Hipple, W. Strelo and their staff for excellent technical support. This work was performed for the U.S. Department of Energy under contracts W7405-ENG-48 at U.C. Lawrence Livermore National Laboratory and DE-AC03-76F00098 at U.C. Lawrence Berkeley National Laboratory.

REFERENCES

[1] http://wwwslap.cern.ch/collective/ecloud02/proceedings/index.html
[2] R. H. Cohen, et al., "Stray electron accumulation and effects in HIF accelerators", paper TOAA010 this conference.
[3] W.B. Herrmannsfeldt, Nuclear Instrum and Meth. in Phys. Res. A 464, 305 (2001).
[4] P.A. Seidl, D. Baca, F.M. Bieniosek *et al.*, "The High Current Transport Experiment for Heavy Ion Fusion", paper ROAC001, this meeting (2003).
[5] R.J. Macek, et al., "Observation of an Intense Electron Cloud at the LANSCE Proton Storage Ring," LANSCE Div. Tech. Rev. (2002).
[6] J.F. Ziegler, http://www.srim.org/.
[7] P. H. Stoltz, M. A. Furman, J.-L. Vay, A.W. Molvik and R.H. Cohen, "Numerical simulation of the generation of secondary electrons in the High Current Experiment", Phys. Rev. ST Accel. Beams **6**, 054701 (2003).
[8] P. Thieberger, et al., Phys. Rev. A61, 042901 (2000).
[9] W. L. Brown, et al., Phys. Rev. Lett. 45, 1632 (1980).
[10] W.L. Brown, R. E. Johnson, Nucl. Instrum. and Meth. B13, 295 (1986).
[11] E. Mahner, et al., Phys. Rev. Special Topics - Accelerators and Beams 6, 013201 (2003).

SIMULATION STUDY OF ELECTRON CLOUD MULTIPACTING IN STRAIGHT SECTIONS OF PEP-II*

A. Novokhatski** and J. Seeman, SLAC, Stanford, CA 94309, USA

Abstract

Simulation studies of electron cloud multipacting were performed for the SLAC B-factory vacuum chamber for different bunch trains and solenoidal magnetic field. Results show that increasing the number of positron bunches by a factor of two and keeping the same current per bunch means that the solenoidal field needs to be doubled in order to keep the same electron cloud density. Fortunately there are regions that are "free of multipacting" at smaller values of field where the electron cloud density can not get very high. To build the electron cloud, positron bunches have to lose some amount of their kinetic energy through the longitudinal electric field. When the cloud is already established, this longitudinal field acts as an oscillating force. This action is similar to the action of RF fields in a cavity. As a result the positron bunches will have different lengths throughout the train.

INTRODUCTION

The electron cloud at PEP-II in the low-energy positron ring is built up from multipacting electrons in the straight section vacuum chamber and secondary emission of electrons from the vacuum antechamber in the arcs. Placing solenoidal magnetic fields around the ring successfully reduced multipacting and damped the electron cloud instability [1]. PEP-II has an upgrade plan that is leading toward higher luminosity by doubling the number of bunches and halving the bunch spacing [2]. Here we present an attempt to understand the effect from this new bunch pattern on electron cloud multipacting.

THE MODEL OF ELECTRON CLOUD

The physical nature of the multipacting process leads us to use the phase distribution function for the best description of the electron cloud and for a precise modelling of secondary electron emission. It is worth noting that the usual approach of particle tracking cannot accurately describe the probability process of secondary electron emission. The energy distribution of the secondary electrons, which are emitted from a surface bombarded with primary electrons, has a narrow peak of order 5-6 eV. However, in order to have a secondary emission yield of more than one electron, the primary electrons must have energies of several tens of electron volts. This means the emitted electrons have to be accelerated by the field of positron bunches up to these energies in order to build up the multipacting process. The force vector of a positron bunch determines the vector of secondary electron momentum, so the initial angular distribution of emitted electrons does not play a significant role. Finally, without multipacting the number of primary electrons coming from photoemission is not enough to create a noticeable effect on the positrons.

In the straight sections of PEP-II the vacuum chamber is round and made from stainless steel. The electric field of a positron bunch moving along the axis of a round tube gives a radial kick to the cloud electrons. If the surface of the tube wall is azimuthally homogeneous (secondary emission yield is the same everywhere), then we can imagine that the electron cloud will also be azimuthally homogeneous. Therefore we only need a two-dimension phase distribution function of radius and radial momentum to get a complete description of the electron cloud in a straight section.

Vlasov equation and electromagnetic forces

The phase distribution function $\Psi(t,r,V)$ describes the electron cloud density on the phase plane of radius and radial momentum as illustrated in Fig. 1.

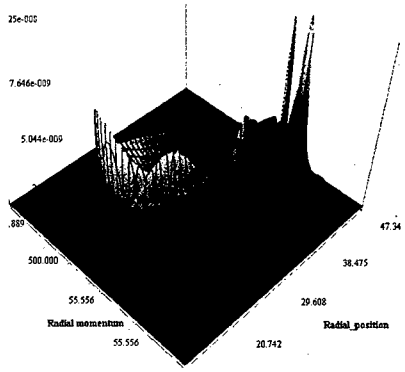

Figure 1: Phase distribution function with radial momentum on the left stand and radius on the right.

The phase distribution function obeys the Vlasov equation $\frac{\partial}{\partial t}\Psi + \frac{F}{m_e}\frac{\partial}{\partial V}\Psi + V\frac{\partial}{\partial r}\Psi = 0$

where m_e is the electron mass, F is the total force acting on the electrons from a positron bunch field, from space charge field and from the solenoid magnetic field. The electric field of a positron bunch with a Gaussian shape is

$$E_{bunch}(r,t) = \frac{c}{2\pi r} \times \frac{Z_0 I^+_{bunch}}{f_{rev}} \times \frac{1}{\sigma\sqrt{2\pi}} \exp\left(-\frac{(ct)^2}{2\sigma^2}\right)$$

The solenoidal radial force is

$$F_{sol}/m_e = r * \Omega^2 * \left(\left(\frac{a}{r}\right)^4 * \left(1 - \frac{\dot{\varphi}_0}{\Omega}\right)^2 - 1\right)$$

Work supported by Department of Energy contract DE-AC03-76SF00515.

**novo@slac.stanford.edu

0-7803-7738-9/03/$17.00 © 2003 IEEE

where I^+_{bunch} is the positron bunch current, σ is the bunch length, f_{rev} is the revolution ring frequency and $Z_0 = 120\pi$, $\Omega = \frac{e}{2m_e c} H$ is the Larmor frequency, a is the radius of the vacuum pipe and $a\varphi_0$ is the initial azimuth velocity. Azimuthal motion has this invariant $r^2(\dot{\varphi} - \Omega) = a^2(\dot{\varphi}_0 - \Omega)$. The space charge field has radial and longitudinal components. In the case of a periodical series of positron bunches i.e. $E(t,z,r) = E(t - z/c, 0, r)$), these components are:

$$E_r^{sc} = \frac{Z_0 c}{2} \bar{n}_e \frac{a^2}{r} \int_0^r (n + \frac{1}{Z_0 c^2} \frac{\partial}{\partial \tau} E_z) r' dr' \Big/ \int_0^a n r dr$$

$$E_z^{sc}(r,\tau) = Z_0 * \int_r^a j_r(r',\tau) dr'$$

j_r is the radial electron cloud current. These formulas give an estimation of the average electron cloud density

$$\bar{n}_e = \frac{2}{a^2} \int_0^a n_e r dr = 2 \frac{I^+_{bunch}}{\pi a^2 f_{rev} cT}$$

and the energy gain for cloud electrons at the chamber wall from the kick of a positron bunch

$$W = \frac{m_e c^2}{2} \left(\frac{Z_0 I^+_{bunch}}{m_e c f_{rev} 2\pi a} \right)^2$$

The spacing between positron bunches cT is equal to the RF wavelength multiplied by the spacing number N. For I^+_{bunch}=2mA, f_{rev}=136 kHz, a=47mm and cT=1260mm (N=2) we get W=31eV and $\bar{n} = 2 * 10^{13} m^{-3}$. This means that accelerated electrons that hit the wall can produce more than one secondary particle. The cloud density is of the order of the density of the residual gas in vacuum chamber (p~1nTorr).

Computer algorithm

A double-step semi-implicit finite-difference scheme with an artificial diffusion parameter is used to numerically solve the Vlasov equation. The scheme has a very good dispersion relation up to the mesh-size wavelength and a small enough diffusion is needed to compensate any oscillation effects at the mesh-size frequency. The wall conditions are described by the probability function

$$\Psi_{in}(r = a) * V_{in} = \Psi_{out}(r = a) * V_{out} \times P(\varepsilon_{in}, \varepsilon_{out})$$

The probability function $P(\varepsilon_{in}, \varepsilon_{out})$ is a combination of secondary emission yield and a spectrum of secondary electrons. We use the secondary emission yield as a function of the primary electron energy, which was measured by R.E. Kirby for stainless steel [3]. We choose zero yields for the zero energy of primary electrons. The energy spectrum of the secondary electrons includes inelastically backscattered and elastically reflected electrons. Detailed information about algorithm can be found in [4].

MULTIPACTING AT SMALL FIELDS

First simulations were carried out for small solenoidal fields to study the growth rates of cloud density due to multipacting. We start with the some initial distribution of photoelectrons then let positron bunches appear periodically in time and watch how the electron cloud density changes in time. Fig.2 shows the dynamics of the cloud density with a positron train that has bunch spacing of every other RF bucket (by 2) and bunch current of 2mA for different values of solenoidal field. At the beginning, the cloud density increases somewhat like an exponential, but then saturates due to the action of space charge forces.

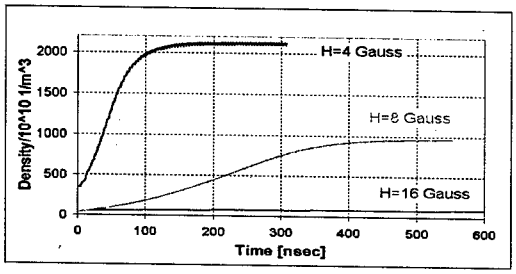

Figure 2: Dynamics of electron cloud density

MAIN RESONANCE

While studying the behaviour of the electron cloud for different solenoidal fields we found a strong resonance. This resonance happens when the time interval between the positron bunches is equal to the flight time of the secondary particles back to wall. The flight time is primarily determined by the solenoidal field H but there is a contribution from the cloud size and intensity. Naturally the resonance depends strongly upon the secondary emission function. The resonance is the boundary between completely different behaviours of the electron cloud. Multipacting happens when the flight time is a little bit smaller than the positron time interval, when the solenoidal field is a little bit higher than the resonance field $H > H_{res}$. There is no multipacting when $H < H_{res}$. Fig.3 illustrates this effect.

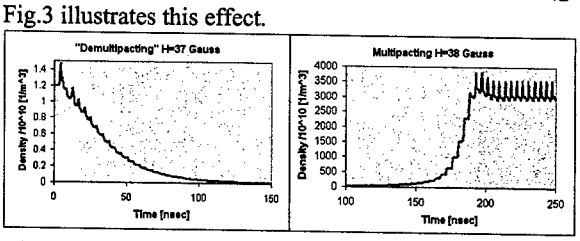

Figure 3: Cloud density behaviour in resonance region: in solenoidal field of 37 Gauss (left) and 38 Gauss (right).

A difference of only 1 Gauss in solenoidal field completely changes the behaviour of the cloud. Corresponding phase photos (high plots) of the clouds are shown at Fig.4. Clouds are "shot" just before the positron

bunch arrives. Secondary particles, produced by high-energy particles previous positron bunches are ready to be accelerated by the next positron bunch. After acceleration they will come back to the wall and produce more new particles.

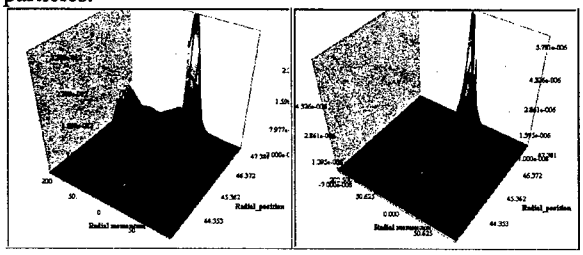

Figure 4: Electron clouds on the phase plane just before a positron bunch arrives. The left picture is for a solenoidal filed H= 37G and the right picture for H=38G.

It is possible to see that the "right" cloud mainly consists of secondary particles. However the "left" cloud has an additional high-energy peak, which will be decelerated by the positron bunch and will arrive at the wall with very little energy and hence will not produce new secondary particles. Therefore the density will go down and eventually the "left" cloud will decay away.

OTHER RESONANCES

We can assume that there can be some other resonances. A resonance can also happen if the flight time of the secondary particle is equal to an integer number of time intervals between positron bunches.

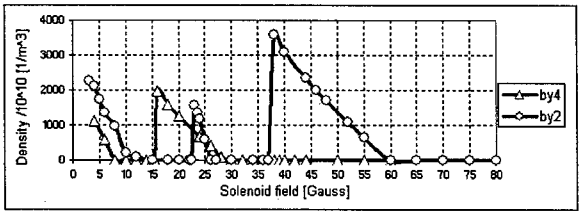

Figure 5: Electron cloud saturated density (N= 2, 4).

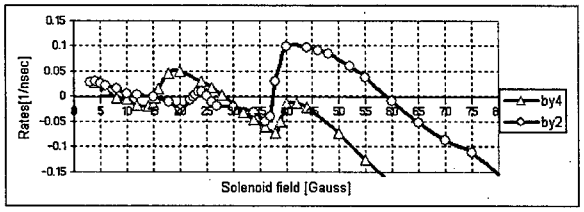

Figure 6: Growth/damping rates for (N=2, 4).

These resonances happen at smaller values of the solenoidal field. In our case we have a second resonance at solenoidal field strength of 23G. Other resonances are in the region below 10 G. Fig.5 and Fig. 6 show the saturated values of the electron cloud as a function of the solenoidal field and growth/damping rates. Negative values mean that the cloud decay away after some time. There is no multipacting when the solenoidal field is more than 60 G. Clear regions are also in the gap of 26-36 G and 14-22 G. For comparison we present analogue curves for the positron bunch spacing by 4. The main resonance is moved to 16 G, other resonances are in the region below 8 G. No multipacting after 30 G and in the gap 8-15 G. It is interesting to note that in the region of 39 G there is a jump in the damping rate. It suggests that there is a half integer resonance: the forced frequency from the field of positron bunches is two times smaller than the repetition rate of the secondary electron emission.

LONGITUDINAL ELECTRIC FIELD OF THE ELECTRON CLOUD

Positron bunches have to lose some of their kinetic energy in order to build the electron cloud. The field that is responsible for the energy transformation is the longitudinal electric field. When the cloud is already built, this longitudinal field acts as an oscillating force on the cloud electrons and gives, at the same time, an additional energy variation inside the positron bunches. The head of the positron bunch is accelerated and the tail is decelerated. This action of the longitudinal field is similar to the action of RF fields in a cavity and it has the same sign. As a result the positron bunches will have different lengths throughout the train. Figure 11 shows a longitudinal field together with the positron bunch shape. The energy gradient along a positron bunch is more than 2.5kV/m². The total length of all the straight sections in the positron storage ring is around 740 m, so the total effect of the electron cloud can be of the order of 1.85MV/m, which is equivalent to 185 kV of RF voltage at 476 MHz. It is easy to make an analytical estimation for this effect. The additional energy variation in a positron bunch can be easily estimated:

$$\Delta W / l = \frac{2}{\lambda_{RF} * N} m_e c^2 * \left(\frac{Z_0 I^+_{bunch}}{m_e c f_{rev} 2\pi a} \right)^2$$

This formula gives the same result we obtain from computer simulations.

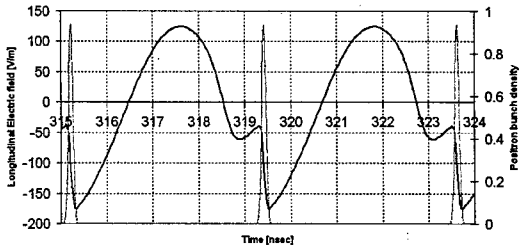

Figure 7: Longitudinal electric field in the electron cloud. Solenoidal field is 38 G and the bunch spacing N=2.

REFERENCES

[1] A. Kulikov et al., PAC'01, Chicago, June 2001, p. 1903.
[2] J. Seeman et al., EPAC'2, Paris, June 2002, p.434.
[3] R. E. Kirby and F. K. King, NIM A 469(2001) p.1.
[4] A. Novokhatski and J. Seeman, Proc. of the ICAP 2002, East Lansing, Michigan, 2002.

SURVEY OF DIGITAL FEEDBACK SYSTEMS IN HIGH CURRENT STORAGE RINGS *

D. Teytelman†, SLAC, Menlo Park, CA 94025, USA

Abstract

In the last decade demand for brightness in synchrotron light sources and luminosity in circular colliders led to construction of multiple high current storage rings. Many of these new machines require feedback systems to achieve design stored beam currents. In the same time frame the rapid advances in the technology of digital signal processing allowed the implementation of these complex feedback systems. In this paper I concentrate on three applications of feedback to storage rings: orbit control in light sources, coupled-bunch instability control, and low-level RF control. Each of these applications is challenging in areas of processing bandwidth, algorithm complexity, and control of time-varying beam and system dynamics. I will review existing implementations as well as comment on promising future directions.

INTRODUCTION

In the last 10-15 years digital feedback became not only an accepted tool in the accelerator community, but a critical tool necessary for success of a modern storage ring. There many applications of the digital feedback methods in different areas of machine operation including, but not limited to, coupled-bunch instability control, low-level RF control, orbit feedback, and luminosity optimization in colliders.

FEEDBACK FUNDAMENTALS

The objective in feedback control is to make some output of a dynamic system behave in a desired way by manipulating the input of that system. A general block-diagram of such a system is shown in Fig. 1. The system consists of the physical system (plant) the output of which we want to control. The output signal y is measured by the sensors and sent to the controller. The control objective might be to keep y small (or close to some constant value) - this is defined as a *regulator problem*. A different objective is to make plant output y follow some reference signal r - a *servomechanism problem*. Controller in Fig. 1 can be a regulator - then input r is omitted - or a servo. In any case controller determines the error between plant output and desired value and, based on the knowledge of plant dynamics, computes the control output u. The control signal is then applied to the plant via actuators.

Performance of a feedback system can be evaluated using many different approaches. For a servo problem time-domain response characteristics are popular. These include

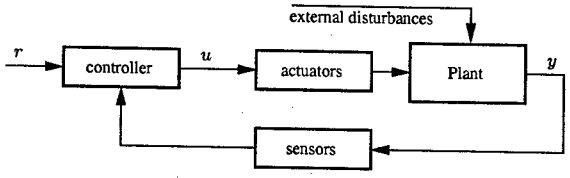

Figure 1: Generalized block diagram of a feedback system

step response parameters such as rise time, settling time, overshoot. Tracking errors in response to constant or linearly varying inputs are often used as well [1].

For a regulator application steady-state errors in response to known disturbance spectra provide an important performance measure. Such errors can be evaluated using the root-mean square (RMS) or peak approaches. Another important measure of feedback performance is the RMS or peak actuator effort, especially important due to the finite excursion ranges of physical actuators.

Multi-input multi-output systems

Many feedback control problems in storage rings involve multiple inputs and outputs. An example of a MIMO system is dynamic behavior of coupled-bunch instabilities. Here each bunch can be considered as a harmonic oscillator coupled to all other bunches. This results in a fully coupled MIMO system with individual bunch positions being plant outputs and bunch correction kicks as plant inputs. For a single beam position sensor and a single correction kicker the individual bunch signals are time multiplexed making the system seem to be single-input single-output (SISO).

Feedback control of MIMO systems is computationally intensive. In general, for an M-input N-output plant the feedback controller must perform $M \times N$ transfer matrix computation. Each element of such matrix has dynamic behavior and can be implemented as an analog or digital filter. In practice one tries to avoid full transfer matrix computation by using diagonal or sparse structures. Often the controller can be reduced to a constant-coefficient matrix multiplication combined with a diagonal dynamic controller.

Digital feedback control

A digital feedback controller usually consists of one or more analog-to-digital converters (ADCs) which digitize analog sensor signals. These digitized signals are processed by a linear or non-linear control algorithm to compute actuator signals. A reference input for the servomechanism applications can be introduced in either continuous or discrete-time domains. The output of the controller is

* Work supported by U.S. Department of Energy contract DE-AC03-76SF00515

† dim@slac.stanford.edu

0-7803-7738-9/03/$17.00 © 2003 IEEE

usually applied to actuators via the back-end digital-to-analog converters (DACs).

The feedback control algorithm is commonly implemented as a linear time-invariant system using finite or infinite impulse response (FIR or IIR) structures. Nonlinear control methods can sometimes offer better performance, but are more difficult to analyze and design than linear controllers. For certain applications, e.g. control of a double integrator plant, non-linear control structures have been well developed and analyzed [2, p. 581].

Control algorithm design methods can be separated into two main classes: emulation of continuous-time controllers and discrete-time design [2, p. 158]. The emulation approach is attractive since the design is done in the continuous domain. It is especially useful if proven continuous-time controllers already exist. However reliable discrete emulation of such controllers requires significant oversampling of the control bandwidth with suggested sampling rate to control bandwidth ratios of 20 to 30 [1, p. 601].

Design of digital feedback controllers in the discrete-time often uses proportional-integral-derivative (PID) structures. Tuning and optimization of PID control is straightforward, however PID designs are best suited to relatively simple plant dynamics.

A more sophisticated design method is the state-space control when the actuator signal is computed from the information on the internal states of the plant. Such an approach provides the designer with independent control of all closed-loop plant poles. Since internal states of the plant are rarely available in full, a parallel model of the plant dynamics (an estimator) is commonly used to estimate the internal state of the plant. The estimator is normally used in a closed loop configuration which adjusts the estimated states using the error between estimator and plant outputs. The next step in the control design is to use optimal control methods to design both the estimator and the state-to-actuator matrix. Commonly used approaches include linear quadratic regulator steady-state optimal control which minimizes the weighted quadratic sum of state and actuator excursions. Optimal estimator design is often based on a Kalman filter which optimizes state estimation using the knowledge of process and sensor noise [2, p. 444].

Robust control design extends the notion of optimality to include the sensitivity of the closed-loop system to variations in loop parameters and other uncertain terms.

Waterbed effect

The plant is subject to external disturbances which affect the output y. As one of the performance criteria of the control system one can consider the reduction of the transfer gain from external disturbance input to plant output.

Let $L(j\omega)$ to be the open-loop transfer function of a SISO system. Then the sensitivity function $S(j\omega) = (1 + L(j\omega))^{-1}$ determines transfer characteristics from an input to a summing junction to its output.

The Bode integral theorem states that if the open-loop transfer function has no poles in the right-hand plane (a stable system) and there two or more poles than zeros, the following equation holds

$$\int_0^\infty \log|S(j\omega)|d\omega = 0 \qquad (1)$$

According to this equation, if the sensitivity function is reduced in some band of frequencies it must necessarily increase elsewhere. For a system with a bandlimited loop transfer function it can be shown [3, p. 89] that Eq. 1 leads to a peaking phenomenon in the sensitivity function. Thus a comparison with a waterbed: when one pushes down $|S(j\omega)|$ in one place it pops up in another.

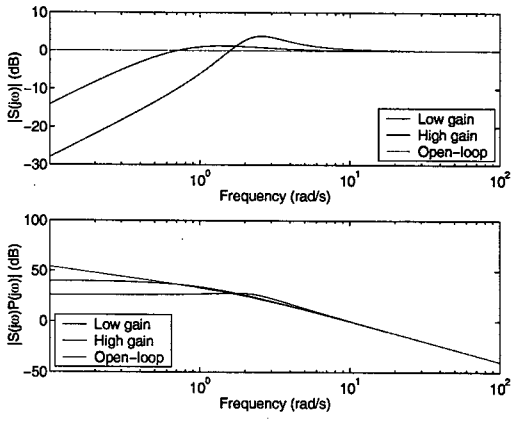

Figure 2: $|S(j\omega)|$ for two loop gain settings as well as open-loop is shown on the top plot, while the gain from the input to the output of the plant is illustrated on the bottom.

The waterbed effect is illustrated in Fig. 2 for proportional feedback around the plant $P(s) = \frac{100}{s(s+2)}$. Application of the feedback attenuates the unity open-loop sensitivity function at low frequencies with moderate peaking above 0.8 rad/s. When the feedback gain is raised, improvement of the low-frequency disturbance rejection is accompanied by increased peaking. Note, however, that the bottom plot shows much smaller disturbance amplification if the effect is measured at the plant's output.

In order to achieve improvement with feedback three techniques are traditionally used for waterbed effect mitigation. The first method is to consider not just the sensitivity function, but its product with the plant transfer function $P(j\omega)$. If sensitivity amplification occurs in a range of frequencies where plant response is small, the overall effect is attenuated. However one must remember that noise induced elsewhere in the feedback loop, e.g. additive sensor noise, will be amplified by $S(j\omega)$. Another method is to use the knowledge of external disturbance spectra to place sensitivity function peaks away from significant excitations. Finally, for rejection of periodic disturbances one can use the feedforward approach.

FEEDBACK CONTROL OF COUPLED-BUNCH INSTABILITIES

Control of transverse and longitudinal coupled-bunch instabilities is critical for successful operation of the high-current storage rings. Designers of the bunch-by-bunch feedback systems used digital technology quite early on due to two factors. They needed a way to implement one-turn bunch delay which for large rings is more feasible digitally. Also, bunch motion is sampled at the revolution frequency by a beam position monitor (BPM) making this problem a natural fit for discrete-time processing. Early feedback systems [4] only used digital delay while the next generations of bunch-by-bunch feedback [5] combined both digital delay and filtering.

It is convenient to model coupled-bunch instabilities as a MIMO system consisting of N coupled harmonic oscillators. Such a structure in combination with a bunch-by-bunch feedback controller is shown in Fig. 3. Longitudinal or transverse positions of bunches are the outputs of the plant while the voltage kicks are the inputs.

The goal of the feedback system is to stabilize the plant transfer $\mathbf{G}(s)$. A powerful control architecture in this case is diagonal, i.e. bunch-by-bunch feedback. The correction signal for a given bunch is computed based only on the motion of that bunch. It can be shown that a bunch-by-bunch feedback system that acts equally on every bunch also acts equally on every eigenmode. Since eigenmodes normally differ only parametrically, bunch-by-bunch feedback can provide simultaneous stabilization of all eigenmodes.

Three feedback designs capable of processing bunch signals at 2 ns intervals and controlling coupled-bunch instabilities in the machines with thousands of bunches and hundreds of unstable eigenmodes emerged in the 1990s. One of these is the longitudinal feedback system currently in use at ALS, BESSY-II, DAΦNE, PEP-II, and PLS, the second was developed for KEK-B, and the third was designed by the ELETTRA/SLS collaboration.

The SLAC/ALS/DAΦNE design is a longitudinal only feedback system due to its use of downsampling [6]. The system is very flexible and has been used to sample bunch

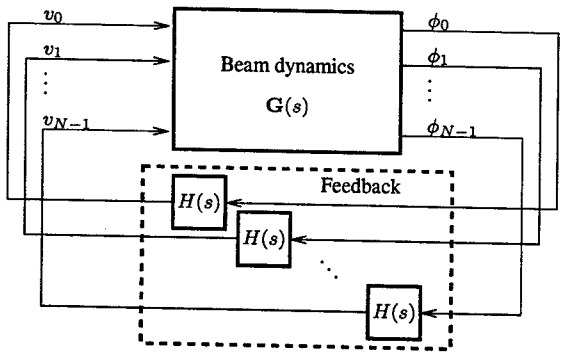

Figure 3: Block diagram of the beam and the bunch-by-bunch feedback system

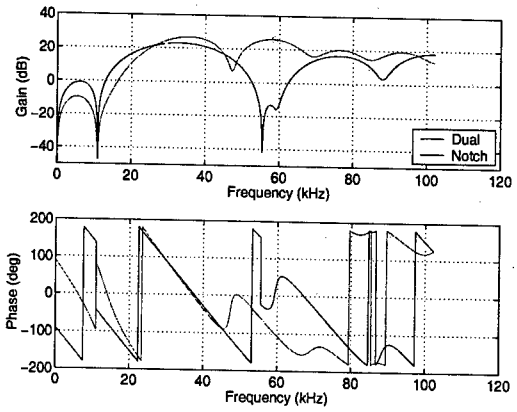

Figure 4: Magnitude (top) and phase (bottom) responses of a dual-peak and peak-notch filters used in control and study of quadrupole instabilities in DAΦNE e^- ring

motion at 238–500 MHz and to process 120–1746 bunches. The feedback correction signal is computed using either a 12-tap FIR algorithm or a 12^{th} order IIR filter.

The KEK-B feedback system processes every bunch on every turn and, therefore, can be used for either transverse or longitudinal feedback. The system parameters are matched to KEK-B RF frequency of 508 MHz and harmonic number of 5120. The control filter in this case is a much simpler two-tap FIR [7].

Finally, the ELETTRA/SLS design bridges the gap between the first two systems. It is capable of processing every bunch on every turn for transverse feedback using a 5-tap FIR filter to compute the correction signal. The system can also be reconfigured for downsampled longitudinal processing with longer, 10-tap FIR filters. Thus the ELETTRA/SLS design combines capabilities for transverse processing of the KEK-B system with the relatively complex control algorithms of the SLAC/ALS/DAΦNE system [8].

The value of digital feedback flexibility is seen in the longitudinal feedback system at DAΦNE configured to simultaneously control both dipole and quadrupole instabilities [9]. Due to large bunch length in this machine the dipole feedback system can affect the quadrupole dynamics of the beam. Frequency separation of dipole and quadrupole signals makes it possible to design feedback controllers for simultaneous stabilization of both instabilities. A filter design algorithm has been developed for this task and allows independent control of gain and phase responses at and around these two frequencies. In Fig. 4 frequency responses of two control filters are presented. The dual-peak filter has gain peaks centered at the synchrotron frequency and its first harmonic with nearly equal gains and $+90$ and -90 degrees phase shifts for dipole and quadrupole oscillations respectively. The second filter with a notch at the quadrupole frequency is used to allow growth of quadrupole instabilities while maintaining control of dipole motion. Such a filter was used first to verify the existence of quadrupole instabilities and rule out

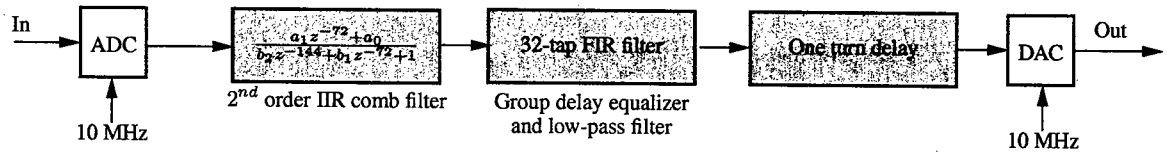

Figure 5: A block diagram of one channel of PEP-II double-peaked comb filter

excitation of quadrupole motion via the dipole feedback system. In addition, these filters have been used to conduct grow/damp measurements of the quadrupole coupled-bunch instabilities [10].

LOW-LEVEL RF CONTROL

In the PEP-II collider sophisticated low-level RF feedback loops are used to reduce the effective fundamental impedance of the RF cavities seen by the beam. This brings down the longitudinal coupled-bunch instability growth rates into the manageable range. Direct and comb feedback loops are the two main elements of low-level RF feedback providing impedance control over ± 1.3 MHz band around the RF frequency. These wideband loops are complemented by multiple slower hardware and software feedback loops used to maintain a consistent operating point of the klystron, eliminate loop gain and phase changes with the klystron output power shifts, reject periodic gap transients, etc. [11].

The achievable gain of the direct loop is determined by the total group delay in the system. In order to minimize the controller delay the direct loop processing is analog and has a total of 86 ns of delay. Compare this with a single sample delay of 100 ns if using digital processing at 10 MHz. To improve impedance reduction at the synchrotron sidebands of revolution harmonics a double-peaked comb filter loop is used. This comb filter applies significant additional loop gain in a narrowband manner thus avoiding the group-delay limitation of the direct loop. Such filter is adjusted for a full turn of delay to obtain proper (periodic) phasing at all revolution harmonics. One of the two channels of this filter is illustrated in Fig. 5. The filter samples cavity I and Q signals at 10 MHz resulting in 72 samples per turn. The second order IIR filter is used to generate peaks at the synchrotron sidebands as well as notches at the revolution harmonics. The IIR filter is followed by a 32-tap FIR filter which implements a group-delay equalizer as well as a low-pass filter. The system allows for 25 ns steps in DAC clock edge placement for improved one-turn delay matching.

GLOBAL ORBIT FEEDBACK

Application of feedback formalism to orbit feedback started with the pioneering work of R. Hettel on local orbit control in 1983 [12]. By 1989 a global orbit feedback system was implemented and tested at NSLS VUV ring [13]. This system used analog signal processing and was limited to 4 position sensors and 4 corrector magnets. Later systems used fast digital feedback capable of sampling at 1 kHz or faster and supporting tens and hundreds of BPMs and correctors. Such systems were implemented and commissioned at the APS [14], ESRF [15], and many other storage rings.

Global orbit feedback control algorithms utilize the information in response matrix $\mathbf{R}$ which relates small-signal corrector changes $\Delta\vec{c}$ and the resulting orbit shifts $\Delta\vec{x}$:

$$\Delta\vec{x} = \mathbf{R}\Delta\vec{c}$$

The BPM-to-corrector transformation matrix $\mathbf{R_{inv}}$ is computed to minimize the error term $|\mathbf{R}\mathbf{R_{inv}}\Delta\vec{x} - \Delta\vec{x}|$ using direct matrix inversion or singular value decomposition [16].

A general block diagram of a global orbit feedback system is shown in Fig. 6. Transverse position of the beam is measured at N BPMs distributed around the ring. The measured orbit is digitized and subtracted from a reference orbit. The error signal is processed by the compensation filter and transformed from the BPM space to the corrector space using $\mathbf{R_{inv}}$. Resulting correction terms are added to reference magnet settings and applied to the corrector magnets via DACs and power supplies.

Main technical challenges in fast global orbit feedback are due to the distributed nature of the sensors and the actuators. Correction computation generally requires the information from all of the BPMs leading to adoption of reflective memory [14] and fast networking [17] communication schemes. The choice of the control structure is by no means obvious. While static correction is addressed by the inverse response matrix, the compensation filter is very important for achieving good dynamic performance, e.g. external disturbance rejection. Most designs to date have used variants of PID control as a compensation filter, optimal and robust controller designs should be explored. Placement of

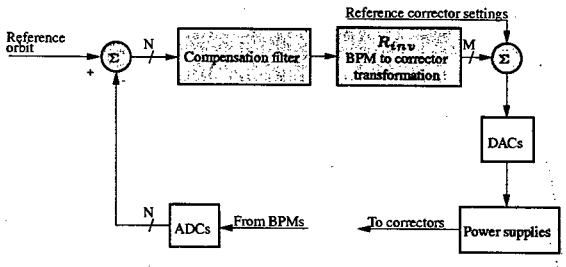

Figure 6: Block diagram of a global orbit feedback system

Table 1: Comparison of three digital feedback applications in storage rings

Parameter	Bunch-by-bunch feedback	Global orbit feedback	Low-level RF feedback
Processing domain	Digital	Digital	Hybrid analog/digital
Processing rate	23–500 MHz	1–5 kHz	10 MHz
Control inputs/outputs	12–5120	16–160	2×72
MIMO control	Diagonal	Inverse response matrix/diagonal	Diagonal
Control complexity	12^{th} order IIR	4^{th} order IIR	2^{nd} order IIR,32-tap FIR

the dynamic controller in the BPM, eigenvector, or corrector basis strongly affects the closed-loop behavior of the system. Control algorithm in the eigenvector basis would allow one to better filter small eigenvalues which are more sensitive to individual BPM errors. Finally, control filters in the corrector basis provide a way to equalize system response between fast and slow corrector magnets. Corrector saturation issues are important in a practical system and are partially addressed by the SVD algorithm.

SUMMARY

Table 1 summarizes the digital feedback applications in high-current storage rings that were considered in this paper. These applications cover a wide range of sampling rates and input-output dimensions as well as a wide range of control algorithm complexities. Diagonal control dominates the MIMO feedback architectures, mostly due to computational complexity limitations; even fully coupled implementations separate dynamic control into a diagonal structure. Analog feedback is still important, especially for ultra-low group delay medium-to-wideband applications. At the same time even analog feedback channels benefit from integrated digital diagnostics.

Promising future directions for digital feedback in storage rings involve higher sampling rates and ADC resolutions. Faster sampling, in turn, leads to wider use of digital receiver structures to detect beam signals. Explosive growth in commercial digital signal processing architectures in the last 10 years resulted in powerful off-the-shelf signal processing products which can be used to accelerate feedback development cycles. Application of optimal and robust control methods can help to improve both performance and reliability of feedback systems.

ACKNOWLEDGMENTS

I'd like to thank A. Drago for bringing to my attention the interaction of the longitudinal feedback system and the quadrupole coupled-bunch instabilities as well as for helping to set up and perform quadrupole instability studies. I would like to thank P. Corredoura, F. Pedersen, H, Schwarz, and R. Tighe for helping me better understand the complex dynamics of PEP-II LLRF. I am indebted to J. D. Fox for his enlightening comments on many technical issues.

REFERENCES

[1] G. F. Franklin, J. D. Powell, and A. Emami-Naeini, *Feedback Control of Dynamic Systems*. Reading, Massachusetts: Addison-Wesley, 1991.

[2] G. F. Franklin, J. D. Powell, and M. L. Workman, *Digital Control of Dynamic Systems*. Reading, Massachusetts: Addison-Wesley, 1992.

[3] J. C. Doyle, B. A. Francis, and A. R. Tannenbaum *Feedback control theory* New York: Macmillan Pub. Co., 1992

[4] M. A. Allen, M. Cornacchia and A. Millich, *IEEE Trans. Nucl. Sci.*, vol. 26, p. 3287, 1979.

[5] D. Heins *et al.* "Wide Band Multibunch Feedback Systems For Petra," DESY-89-157, 1989.

[6] H. A. Hindi *et al.* "Downsampled bunch by bunch feedback for PEP-II," in *B factories: the state of the art in accelerators, detectors and physics*, pp. 216–219, SLAC, 1992.

[7] M. Tobiyama and E. Kikutani, *Phys. Rev. ST Accel. Beams*, vol. 3, p. 012801, 2000.

[8] C. G. M. Lonza, D. Bulfone, "Digital processing electronics for the ELETTRA transverse multi-bunch feedback system," in *ICALEPCS* , (Trieste, Italy), pp. 255–257, Comitato Conferenze ELETTRA, 1999.

[9] A. Drago *et al.*, *Phys. Rev. ST Accel. Beams*, vol. 6, p. 052801, 2003.

[10] A. Drago, *et al.*, DAΦNE Technical Note No. BM-10, 2002

[11] P. Corredoura, "Architecture and performance of the PEP-II low-level RF system," in *Proceedings of the 1999 PAC*, (Piscataway, NJ, USA), pp. 435–439, IEEE, 1999.

[12] R. O. Hettel, *Trans. Nucl. Sci.* vol. 30, p. 2228, 1983.

[13] L. H. Yu, "Orbit Stability And Feedback Control In Synchrotron Radiation Rings," in *Proceedings of the 1989 PAC*, (Piscataway, NJ, USA), pp. 54–59, IEEE, 1989.

[14] J. A. Carwardine and F. R. Lenkszus, "Real-Time Orbit Feedback at the APS," in *Beam Instr. Workshop: Proceedings*, (Woodbury, NY, USA), pp. 125–144, AIP, 1998.

[15] E. Plouviez, J. M. Koch and F. Uberto, "A fast global feedback system to correct the beam position deviation in the ESRF storage ring," in *Proceedings of the* 6^{th} *EPAC*, (Bristol), pp. 1729–1731, IOP Publishing, 1998.

[16] Y. Chung, G. Decker and K. Evans, "Closed Orbit Correction Using Singular Value Decomposition Of The Response Matrix," in *1993 IEEE PAC: proceedings*, (Piscataway, NJ, USA), pp. 2263–2265, IEEE, 1994.

[17] A. Biocca *et al.*, "Design of a Fast Global Orbit Feedback System for the Advanced Light Source," in *Proceedings of the 2001 PAC*, pp. 1252–1254, IEEE, 2001.

BUNCH-BY-BUNCH DIGITAL DAMPERS FOR THE FERMILAB MAIN INJECTOR AND RECYCLER

G. William Foster#, Sten Hansen, Dennis Nicklaus, Warren Schappert, Alexei Seminov, Dave Wildman, FNAL, Batavia, IL 60510
W. Ashmanskas, University of Chicago / Argonne National Lab, Chicago, IL, USA

Abstract

A digital transverse and longitudinal bunch-by-bunch damper has been prototyped and tested. The damper is based on immediate 14-bit digitization at 212 MHz (4x the 53 MHz RF bunch frequency), digital pipelined processing in field-programmable gate array (FPGA) logic, and a digitally synthesized damping kick driven by a 212 MHz DAC. A single board performs all calculations for both transverse and longitudinal damping, as well as providing extensive diagnostic read out, and automatically switching between the variety of beam types present. Initial prototyping was carried out by customizing firmware on a commercial board, and has successfully demonstrated bunch-by-bunch transverse damping, antidamping, and pinging. Longitudinal damping uses identical firmware with different FIR coefficients, and will be beam tested when cavities and power amplifiers are installed in the Main Injector summer 2003. A second generation board, in which damping calculations for all 3 coordinates are performed in a single large FPGA is in fabrication. Several other applications are being considered for this board, including implementation of an entire Low-Level RF system on a single board.

INTRODUCTION AND MOTIVATION

Fermilab's Run II began without functioning beam dampers on any of its accelerators. Existing dampers had either been decommissioned or were inappropriate for collider mode operations. As a result, a crash program to develop general-purpose dampers using state-of-the art digital techniques was initiated for the Main Injector and Recycler, in addition to specialized dampers for the Tevatron[1-2] and Booster [3].

A main motivation for adopting a digital approach to beam dampers for the Main Injector and Recycler was its flexibility to deal with the wide variety of beam types and operating modes present. Longitudinal and transverse instability and injection dampers were required. Beam types include ramping and stored Antiproton and Proton beams. RF beam structures requiring damping include 53 MHz full batches (1-6 trains of 84 bunches in the h=588 RF system), 53 MHz short batches(5-15 bunches), 53 MHz coalesced bunch, 2.5 MHZ and 7.5 MHZ batches, and DC beam. These modes are interleaved arbitrarily on a cycle-by-cycle basis during Main Injector operations.

Additional operations such as bunch-by-bunch variable gain damping and anti-damping, pinging and noise injection, selective bunch ejection, variation of filter coefficients during the machine ramp, and longitudinal arbitrary RF waveform generation were desired. A "virtual oscilliscope" capability was desired to display signals at various stages of processing. These features can be provided without additional hardware in a system based on digital processing with large-scale programmable logic.

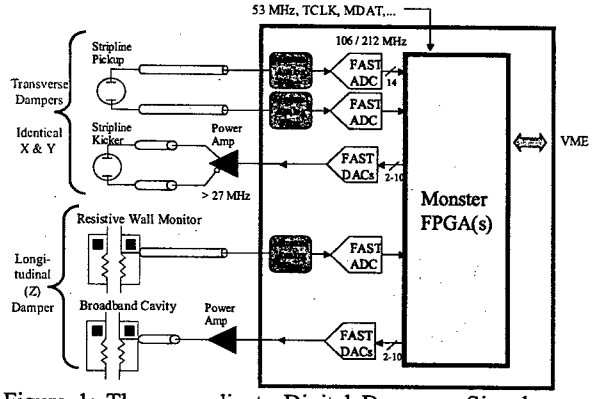

Figure 1: Three-coordinate Digital Damper. Signals on cables from the tunnel are immediately digitized, processed with bunch-by-bunch multi-turn digital filters in a large Field-Programmable Gate Array (FPGA), and the digitally calculated kick is sent through a DAC to the power amplifier and transverse or longitudinal kicker.

DIGITIZATION RATES

A fundamental design decision is the required ADC conversion rate. We have chosen 4x the RF bunch frequency. This represents the minimum digitization rate needed to capture a bunch-by-bunch amplitude and phase, while rejecting DC and closed-orbit offsets. In the frequency domain, this permits reconstruction of the In-phase and Quadrature (I&Q) components at the RF carrier frequency with simple 2-point sample differences. See figs. 2-4.

The minimum DAC update rate for a bunch-by-bunch damper is equal to the RF frequency. However, we have found it advantageous to have a DAC update rate 4x (and eventually 8x) the bunch frequency, driven by an up-sampling FIR. This permits digitally fine-tuning the kick timing, sculpting the drive waveform to correct for analog defects in the power amplifier and cables, and kicking the beam at frequencies above baseband [3].

#gwf@fnal.gov

0-7803-7738-9/03/$17.00 © 2003 IEEE

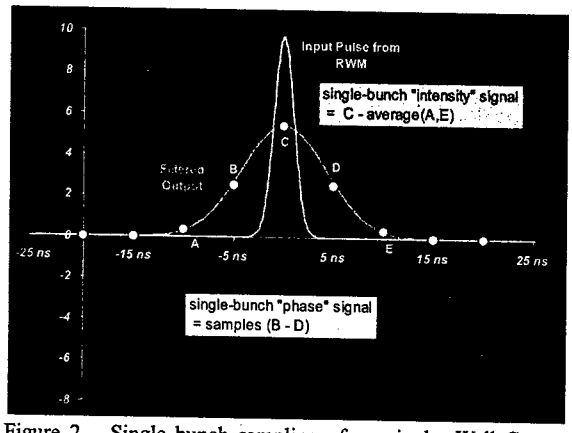

Figure 2 – Single bunch sampling of a unipolar Wall Current Monitor (WCM) signal with four 212 MHz samples per 53 MHz bunch. A 70 MHz low pass "anti-aliasing" filter spreads the pulse +/- 5 ns in time so the ADC will not miss the bunch signal. The filter's suppression of the sharp 1-2 ns peak from theWCM signal also reduces the dynamic range required from the ADC. The bunch amplitude is obtained from the 3-point difference of samples (C-average of (A,E)). The bunch phase is obtained from the 2-point difference (B-D).

b

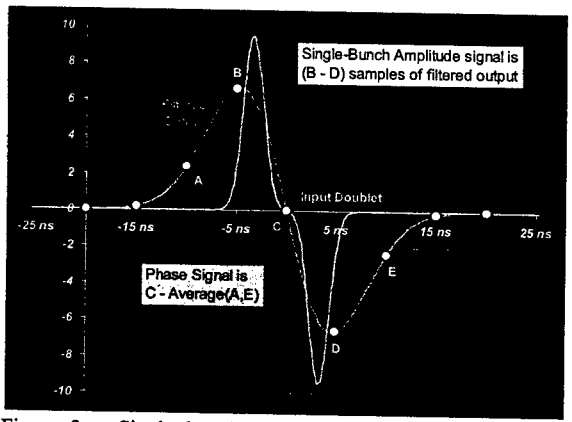

Figure 3 – Single bunch sampling of bipolar doublet at 4 samples/bunch. The situation is identical to unipolar sampling except that the roles of the Amplitude and Phase signals are reversed.

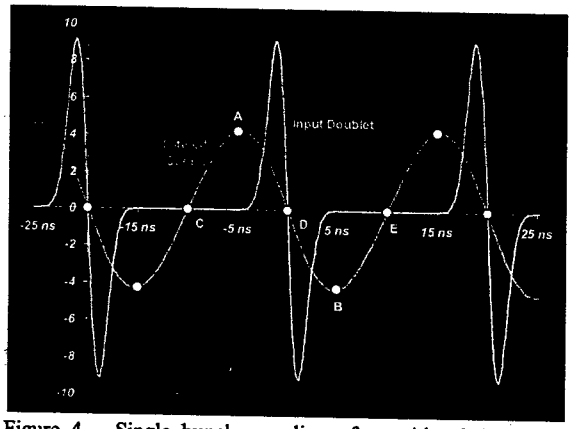

Figure 4 – Single bunch sampling of repetitive bunch train. Although the filtered signal resembles a sine wave, it actually contains bunch-by-bunch phase and amplitude information.

PROTOTYPE HARDWARE

The prototype hardware (figure 5) uses an Echotek ECDR-814X-AD card with 8 channels of 14-bit 106 MHz digitization (interleaved to provide four channels of 212 MHz sampling), a 212 MHz DAC daughtercard, a VME-64 crate with Power-PC readout processor, and an interface box containing filters, buffer amplifiers, signal splitters, and delay cables.

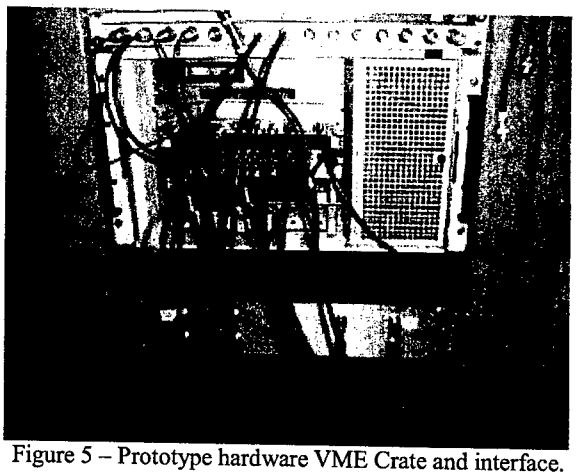

Figure 5 – Prototype hardware VME Crate and interface.

The longitudinal damper input signal is the phase signal from a wall current monitor, digitized as shown in fig. 2. The transverse damper signal is derived from the difference output of hybrid transformer connected to a stripline pickup. The position signal is a bipolar signal with amplitude proportional to the bunch position, digitized as in figures 3 & 4. One pickup is used in each coordinate. All signals go through a low-pass filter (Mini-Circuits BLP-70) and buffer amplifiers for overload protection and signal termination. They are then resistively split into two ADC channels, with one channel delayed by ~5ns to obtain 212 MHz interleaved sampling.

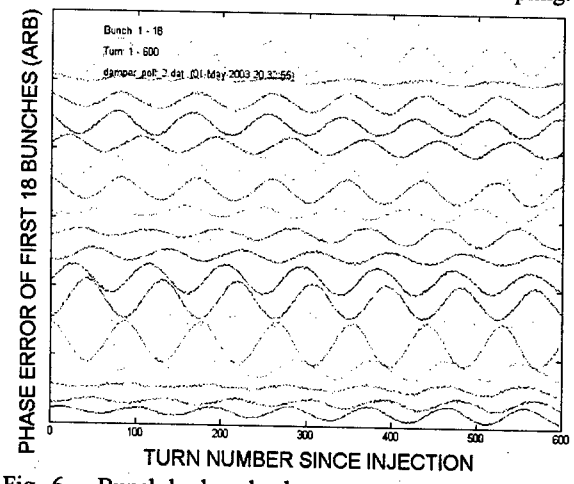

Fig. 6 – Bunch-by-bunch phase measurements with the Main Injector Damper, showing bunches executing synchrotron oscillations due to individual phase and energy errors present in beam delivered from the Booster.

An online display was generated by a MATLAB application which can display bunch-by-bunch amplitude, phase, tune, raw ADC or digitally filtered data or the applied kick. Data can be displayed for single bunches or as a function of bunch number or turn number.

Digital Filter Algorithms

Transverse and longitudinal filters use identical firmware with different FIR filter coefficients. The transverse damper is a digitally pipelined 3-turn filter similar to ref. [3]. The transverse kick for each bunch is calculated as the weighted sum of the transverse bunch positions measured on the previous turns (a 3-turn FIR filter). The three weights are uniquely determined by the system gain, the machine tune and the betatron phases at the pickups and kicker, and the fact that the weights must sum to zero in order to reject closed orbit distortion.

The longitudinal kick to each bunch is proportional to the rate of change of the phase of that bunch. This derivative is calculated by taking the weighted sum of the phase measurements made on the last 8 turns (an 8-turn FIR filter). The eight FIR weights are given by a linear ramp passing through zero between the 4^{th} and 5^{th} bunch. This choice of weights rejects DC phase offsets and is mathematically equivalent to a least-squares fit to the slope of the phase on the last 8 turns.

BEAM TEST RESULTS

The transverse damper took advantage of existing stripline pickups and kickers, and worked essentially as soon as the firmware was completed (see figure 7).

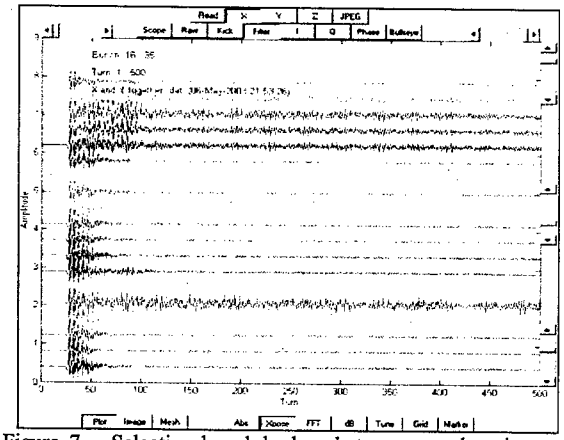

Figure 7 – Selective bunch-by-bunch transverse damping and anti-damping of 53 MHz bunches for the first 600 turns in the Main Injector. Each trace represents the turn-by-turn position of a single bunch. All bunches were damped except the group of four near the top (which were left alone), and the single bunch near the bottom (which was antidamped and eventually ejected).

The selective transverse antidamping or pinging of bunches (fig. 7,8) was straightforward to implement in the FPGA firmware. This opens up possibilities for tailoring the bunch structure and offers the amusing possibility of neutrino communications.

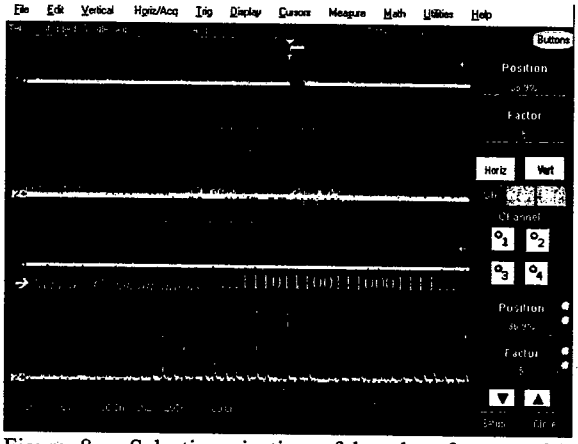

Figure 8 – Selective ejection of bunches from an 84-bunch batch during acceleration in the Main Injector.

Longitudinal damping digital filters have been tested with beam and perform as expected. Actual tests of longitudinal damping await the installation of broadband damping cavities and amplifiers currently scheduled for August 2003.

FUTURE PLANS

A second generation card has been built and will be tested soon. Damping calculations for all three coordinates are performed on a single large FPGA (Altera EP1S25F672C6) instead of the 5 smaller FPGAs on the prototype card. Four channels of 212 MHz ADCs avoids the need for interleaving 106 MHz digitizers. D/A conversion is performed by four 424 MHz DACs, which will allow "sculpting" the kicker output waveform to correct for analog defects in the power amps and cables. The system will be packaged as a standalone (NIM) module with an Ethernet interface, thereby eliminating the VME crate, backplane, and readout CPU.

It is clear that the general approach of immediate high speed digitization and FPGA processing has a number of other potential applications in accelerator instrumentation and LLRF control. The large number of high performance PLLs on modern FPGAs opens up additional possibilities. Some applications that we are considering are: beam loading compensation, beam position monitors, beam stacking manipulations using broadband RF systems, and possibly the complete replacement of the LLRF system for the FNAL Booster with the single card developed for dampers.

REFERENCES

[1] C. Y. Tan and J. Steimel, "The Tevatron Bunch-by-Bunch Longitudinal Dampers", PAC'03.

[2] W. A. Pellico and D. Wildman, "Booster's Coupled Bunch Damper Upgrade", PAC'03.

[3] Klute, Kohaupt et. al., "The Transverse Damping System with PLL Tune Measurement for HERA P", EPAC'96.

CALCULATIONS AND OBSERVATIONS OF THE LONGITUDINAL INSTABILITY CAUSED BY THE FERRITE INDUCTORS AT THE LOS ALAMOS PROTON STORAGE RING (PSR) *

C. Beltran†, Indiana University, Bloomington, IN, USA
A. A. Browman and R. J. Macek, LANL, Los Alamos, NM, USA

Abstract

The frequency dependence of the complex permeability of the ferrite (at room temperature and 125°C) used in the inductors at PSR has been determined by comparing the S_{11} parameters from a jig containing ferrite and a MAFIA [1] (a program package for the computation of electromagnetic fields) simulation of the jig. Both the frequency response and the longitudinal impedance of the inductive inserts were obtained by simulating the inductor cavity in MAFIA using the ferrite properties from the aforementioned fit. Experimental observations of the longitudinal instability caused by the ferrite inductors at room temperature in a bunched coasting beam have been made. Comparisons of observed and simulated growth times, resonant frequencies, and width of the instability will be discussed.

LONGITUDINAL INSTABILITY

Three inductive inserts [2], consisting of 30 "cores" each, were installed in the PSR in the late '90's to compensate the space charge effect in the beam. A core is a cylindrically shaped ferrite, with thickness of one inch, inner diameter of 5 inches, and an outer diameter of 8 inches. A large longitudinal instability was noticed at approximately 75 MHz, that was devastating to the beam (see Fig. 1).

It was proposed by Popovic [3] that heating the ferrite would eliminate the instability. The three inserts were removed, and replaced by two inserts that were capable of being heated. The heating proposal was then tested and verified in the PSR. How the properties of the ferrite change during heating to cure this instability is the focus of this paper.

COMPLEX PERMEABILITY

The complex permeability, denoted by $\mu = \mu' + i\mu''$ is a function of frequency. To uncover the frequency dependence, a comparison was made of the measured S_{11} parameters done by Browman [4] of a jig containing a sample core of the ferrite used in PSR to a MAFIA simulation. The jig was designed to maximize the sensitivity to the magnetic properties of the ferrite.

* Work conducted at the Los Alamos National Laboratory, which is operated by the University of California for the United States Department of Energy under contract w-7405-ENG-36.

† National Physical Science Consortium (NPSC) Fellow, Los Alamos National Laboratory, with support from DOE DE-FG02-92ER40747 and NSF PHY-0140251: cbeltran@lanl.gov

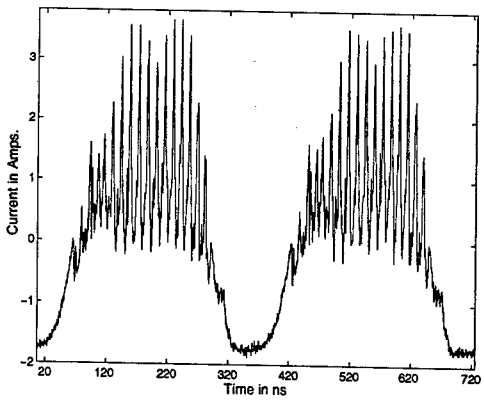

Figure 1: Longitudinal instability caused by the inductive inserts at room temperature.

To find the frequency dependence of the complex permeability of the ferrite, the jig was simulated in MAFIA. Values of μ' and μ'' were selected for the simulated ferrite at a particular frequency. The S_{11} parameters at that frequency were then calculated and compared to the experimental S_{11} parameters at that frequency. The μ's were then adjusted accordingly, until an agreement of better then 1% was achieved. The relative permittivity, ϵ_r, of the ferrite was assumed to be constant at 13.

This was done for data sets at both room temperature and 125°C. The frequency dependence of the complex permeability for the two temperatures is displayed in Fig. 2.

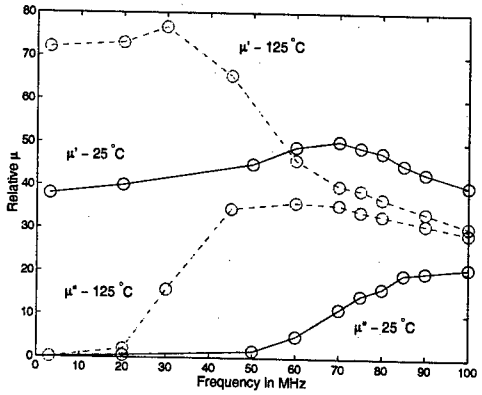

Figure 2: Complex permeability as a function of frequency for both room temperature and 125°C.

0-7803-7738-9/03/$17.00 © 2003 IEEE

IMPEDANCE

An inductor cavity was simulated in MAFIA using the aforementioned ferrite properties to calculate the impedance resulting from the ferrite inductors. This was done for both room temperature and $125°C$. Fig. 3 is a plot of the real part of the longitudinal impedance for one inductor cavity at room temperature and $125°C$.

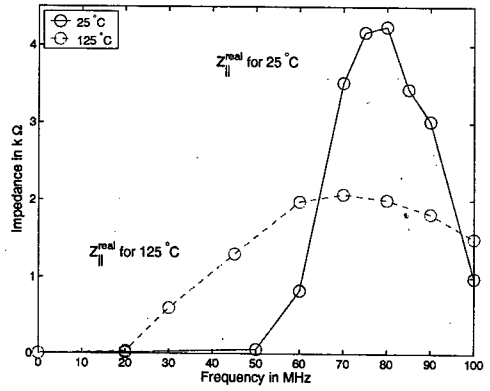

Figure 3: Real longitudinal impedance for one inductive insert at room temperature and $125°C$.

Notice the change in height and width of the impedance. Similarly, the imaginary part of the impedance also changes when the ferrite is heated (see Fig. 4).

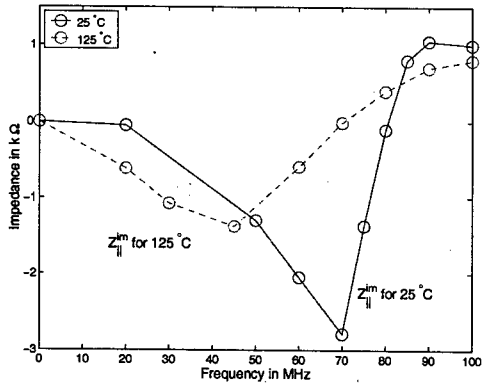

Figure 4: Imaginary longitudinal impedance for one inductive insert at room temperature and $125°C$.

ESME SIMULATION

A PSR bunched coasting beam with a bunch length of $250ns$, $650nC$ of charge, and the impedance of three inductive inserts at room temperature was simulated in ESME [5] (a longitudinal multiparticle tracking code). The momentum distribution used in the ESME simulation was the sum of two gaussians, with 66% in the $\frac{\Delta p}{p}|_{wide} = 6.9 \times 10^{-3}$ and 34% in the $\frac{\Delta p}{p}|_{narrow} = 2.8 \times 10^{-3}$. This momentum distribution was chosen to best fit the wire scanner measurements of the incoming linac beam.

Growth Time

The growth time of the longitudinal instability for the experimental data, as well as the ESME simulation were derived from the turn by turn growth of the amplitude of the summed powers of the harmonics around the resonance of the instability. Fig. 5 shows the evolution of the growth for the experiment and ESME simulation. For this simulation, a user routine was added to ESME which produced a continuous sequence of intensity vs. time histograms for each turn.

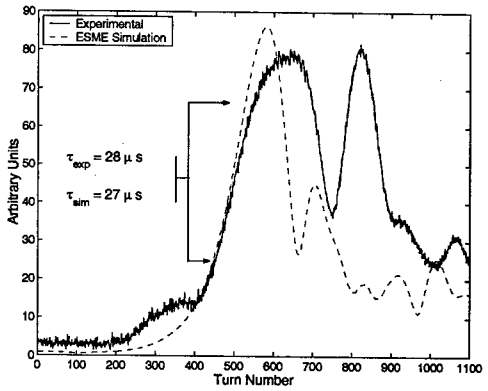

Figure 5: Experimental and ESME growth of the longitudinal instability at room temperature.

The experiment has a growth time of $28\mu s$, and the ESME simulation has a growth time of $27\mu s$.

Power Spectral Density (PSD)

The Q for both the experiment and ESME simulation is defined as the peak frequency (ω_p) of the PSD divided by the full width at half max (Γ) of the PSD.

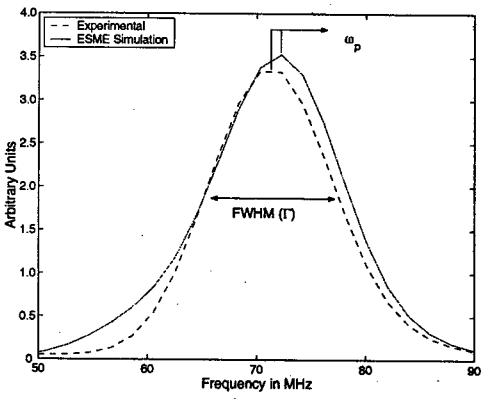

Figure 6: Experimental and ESME PSD for room temperature.

From Fig. 6, $Q_{exp} = \frac{\omega_p}{\Gamma}|_{exp} = \frac{71MHz}{14MHz} = 5.1$. The PSD for the ESME simulation is just slightly different, with $\omega_p = 72MHz$ and $\Gamma = 15MHz$, giving $Q_{sim} = 4.8$.

TIME MODE EVOLUTION

An interesting way to look at the data is with the time mode evolution plot. The x-coordinate represents the time within the bunch and the y-coordinate is the turn number. The color represents the amplitude of the current, with blue being low and red being high. Fig. 7 is the time mode evolution of the experimental data.

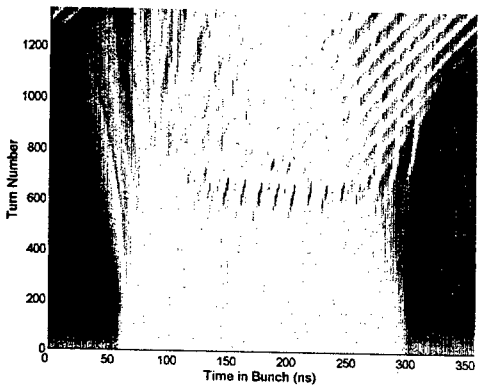

Figure 7: Experimental time mode evolution at room temperature (color).

From this type of a plot, one can see the microbunching and energy loss in the beam due to the impedance. The time mode evolution plot of the ESME simulation (Fig.8) is very similar to the experimental plot.

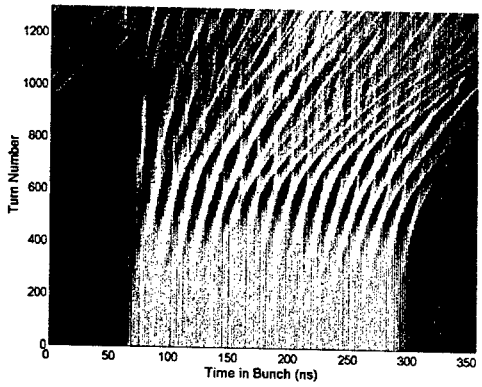

Figure 8: ESME time mode evolution at room temperature (color).

HEATING THE FERRITE

Because of the instability caused by the 3 inductive inserts, they were removed, and two inserts with heating capability were installed. When the ferrite was heated to $125°C$ the longitudinal instability was cured, while maintaining the desired space charge compensation.

As shown in Fig. 3, heating the ferrite to $125°C$ reduces the maximum height of the impedance by a factor of two, and also broadens the impedance by a factor of two. An ESME simulation with the impedance of two heated inductive inserts also shows an elimination of the longitudinal instability.

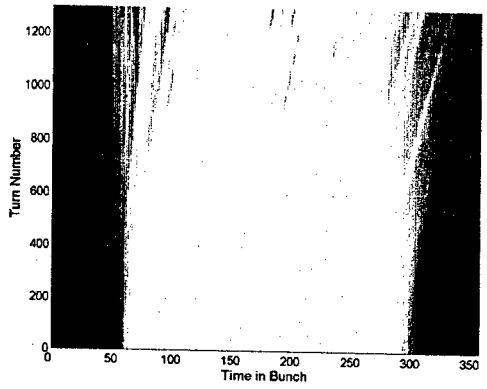

Figure 9: ESME time mode evolution for two inductors at $125°C$ (color).

ACKNOWLEDGMENTS

The authors acknowledge many useful discussions with Tai-Sen Wang, Larry Rybarcyk, Sergey Kurennoy, Frank Krawczyk, Pat Colestock, and S. Y. Lee and informative correspondence with Dave Wildman, Bill Ng, and James Griffin. We are especially grateful to James MacLachlan for the unrestricted use of his ESME code. One of us, Chris Beltran, would like to thank his thesis advisor S.Y. Lee for his support.

REFERENCES

[1] CST, "MAFIA Manual 4.00", http://www.cst.de, January 1997.

[2] M. Plum et al., "Experimental study of passive compensation of space charge at the Los Alamos National Laboratory Proton Storage Ring", PRST-AB V.2, 064201, June 1999.

[3] K. Y. Ng, "Physics of Collective Beam Instabilities", Fermilab-Conf-00/142-T, Ch 5.7.3, June 2000.

[4] A. Browman, Memo to R. Macek (macek57), April 2001 http://lansce2−serv.atdiv.lanl.gov/browman/CY2001/

[5] J. A. MacLachlan, J. Ostiguy, "User's Guide to ESME 2002", February 2002.

MICROBUNCHING AND BEAM BREAK-UP IN DUV-FEL ACCELERATOR

T. Shaftan#, H.Loos, B. Sheehy, L. Carr, BNL, Upton, USA
Z. Huang, C. Limborg, SLAC, Menlo Park, USA,
W.S. Graves, MIT-Bates, Boston, USA

Abstract

We present the results of electron beam longitudinal modulation studies in the DUV-FEL accelerator. For bunch length determination we used the "zero-phasing" method, based on a measurement of the chirped electron bunch energy spectra. The measurements revealed a spiky structure in the longitudinal phase space [1]. A model based on space charge effect is considered [2] to explain of the obtained phenomena.

The analysis of the energy spectra has shown a sensitivity of the structure to the electron beam peak current, energy and longitudinal non-uniformity of the RF gun drive laser. Analytical calculations have demonstrated a qualitative agreement with experimental observations. Several experiments have been made to compare with theory; measured results are reviewed in this paper. The obtained effect is briefly discussed in relation to high brightness accelerators.

INTRODUCTION AND MOTIVATION

A detailed description of the DUV-FEL accelerator can be found in our earlier publications [3]. The DUV-FEL includes a photocathode RF gun, illuminated by a short pulse Ti:Sa laser. The following two linac sections accelerate the beam up to an energy of 70 MeV. The second linac tank is dephased, producing a time-energy correlation, which a four-magnet chicane, located downstream, converts into longitudinal bunching. Since the bunch is "undercompressed", the third linac tank is used to remove residual chirp, and, in combination with the fourth tank, accelerates the bunch up to the nominal energy for FEL operations (177 MeV).

For a successful FEL performance a peak current of 300 A is needed, which requires an initial bunch length of 1.5 ps RMS for the 300 pC electron bunch to be reduced to 0.4 ps RMS (compression ratio of 3.75).

For the electron bunch length characterization we use the "zero-phasing" method [4], in which no further acceleration is done after the bunch compressor, but an energy chirp is imparted to the beam with the last linac section (with calibrated RF amplitude). A 72° spectrometer dipole transforms the correlated energy spread into a spatial distribution on a downstream monitor. The RMS size of the horizontal projection σ_x, due to a known amount of chirp $E_{RF} \cdot k_{RF}$, corresponds to the bunch length σ_z:

$$\sigma_z = \frac{E_0}{E_{RF}} \frac{1}{\eta \cdot k_{RF}} \sigma_x ,$$

where η is the dispersion and E_0 the energy at the monitor location.

First measurements of the compressed bunch length demonstrated a strong modulation of the energy spectra, obtained via "zero-phasing" [1]. In some cases the electron beam image became broken into several distinctive bunches with a separation of the order of 200 fs (Fig. 1). At the same time the uncompressed bunch spectra were smooth, witnessing the existence of a collective effect, which is driving the modulation during the compression process. For low charge (~20 pC) spikes are visible and sharp even for an uncompressed beam.

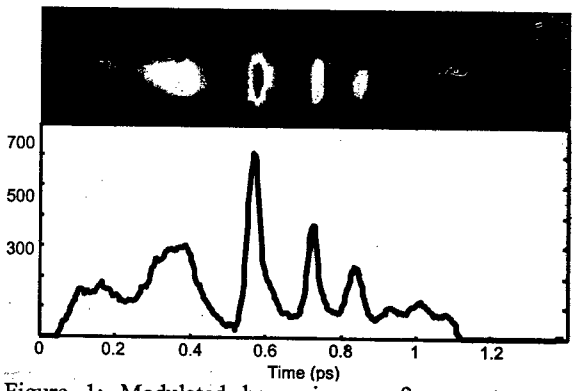

Figure 1: Modulated beam image after spectrometer (upper figure), vertical axes is y-coordinate; horizontal one is proportional to beam energy. Bottom figure: "zero-phasing" projection of the beam on upper plot, horizontal axis is scaled in picoseconds.

Since the chirping tank is running at zero-crossing, it does not introduce a nonlinearity into the longitudinal phase space. The spectrometer magnet aberrations are also small, so the assumption about a linear correspondence between the chirped bunch energy spectrum and the longitudinal bunch density seems to be valid if no collective effects are taken into account. Therefore the sharp spikes in the electron energy spectra could be treated as spikes in the longitudinal bunch density. Calculating the FEL slippage length as 70 um for lasing at 266 nm, it follows that the spike width was comparable or less than the slippage length, which had to cause a degradation of the FEL performance. Thus the role of the collective effect has to be studied, also considering that a similar effect has been obtained recently in the TESLA linac [5].

INITIAL EXPERIMENTS AND OBSERVATIONS

We observed strong modulations (as large as 100 %) in the "zero-phasing" projection for the uncompressed bunch at low charge (20 pC). The fundamental harmonic of the

0-7803-7738-9/03/$17.00 © 2003 IEEE

modulation frequency spectrum peaks at 1.6 THz (190 μm). This high frequency range can be associated only with the drive laser (266 nm, bandwidth 5% RMS), since the RF bandwidth in all other accelerator components is limited to several GHz. We measure the temporal profile of the laser by cross correlating it with the 120 fsec, 800 nm oscillator pulse in a nonlinear optical crystal. This measurement has a resolution of ~200 fs, due to velocity mismatch in the crystal. Some modulation is observed (Fig. 2). The magnitude of the modulation may be larger than indicated in the figure if its period is below the cross-correlator's resolution, or due to the fact that the cross-correlation is a multi-shot measurement.

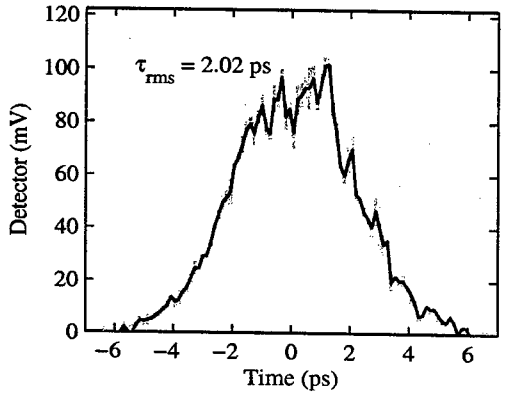

Figure 2: Laser cross-correlation profile.

For an explanation of the modulation dynamics for the uncompressed bunch we developed the following hypothesis. The initial laser modulation gets mapped into the electron bunch phase space at the low energy end of the accelerator (in the gun and first linac tank). At low charge the space charge forces transfer initial density non-uniformities into an energy modulation along the bunch. Since the uncorrelated energy spread is small ($\sigma_\gamma/\gamma \sim 10^{-5}$), an energy modulation (~10^{-4} for 20 pC) becomes visible in the energy spectrum of the chirped bunch.

For an uncompressed bunch with higher charge the space charge forces become stronger and smear out the energy modulation. This increases the projected beam energy spread and reduces the observed modulation in the chirped beam energy spectrum.

This hypothesis is currently being studied using the PARMELA code.

Since the modulation is sensitive to the peak current and appears in an initially smooth beam during the compression process, one should consider a collective effect, responsible for the development of structure. Earlier [1], we discussed CSR in the chicane as a possible mechanism for the instability. However, it has been shown [6] that the effect of CSR leads only to a small gain for microbunching. Another possible source of microbunching is the spectrometer dipole, which itself has a strong impact on the longitudinal beam dynamics of the electron beam. Calculations of CSR and space charge effects in the spectrometer dipole [2] exhibited very low gain for this case as well.

A CSR-mediated effect has to be sensitive to the bending radius in the chicane magnets. We compressed the beam for several different chicane strengths (R_{56}), keeping the final bunch length constant. Since the compression ratio is equal to 1 – h R_{56}, where h is the energy chirp, there is always a combination of h and R_{56} that will maintain a constant compression ratio and, therefore, a constant final peak current of the bunch. Thus the initial and final beam properties do not change* for different chicane strengths and we can distinguish whether the modulation is sensitive to the bending radius of the chicane or not. The result of this experiment is that, though there is some reduction of modulation for smaller R_{56} at low compression ratio, in general, the modulation is insensitive to chicane settings.

MODEL OF THE EFFECT AND COMPARISON WITH EXPERIMENT

It has been shown [2], that the space charge force for our experimental conditions can be strong enough to transform small longitudinal density non-uniformities into a modulation of the average energy along the bunch. The plasma oscillation wavelength of the compressed beam becomes comparable to the length of the drift between chicane and spectrometer (~15 m) for the wavelength range of the modulation. Chirping such an energy-modulated bunch (Fig. 3) one would see sharp spikes in the energy spectrum, corresponding to variations of the energy. At the same time this effect cannot enhance the density bunching in the electron beam, since the longitudinal space charge force is equivalent to a pure imaginary capacitive impedance.

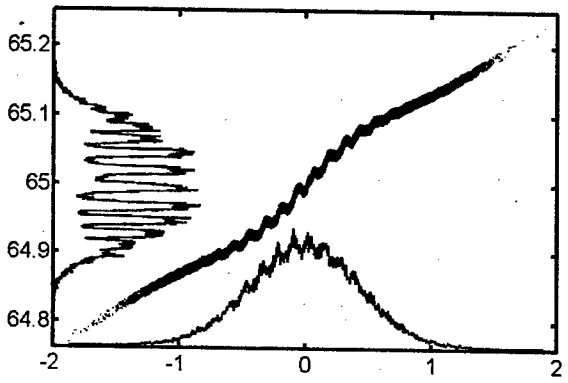

Figure 3: Illustration of electron bunch longitudinal phase space. Abscissa is time (ps), ordinate is energy (MeV). The space charge wake induces variations of the energy along the chirped bunch leading to deeply modulated energy spectra.

As the space charge impedance depends only on the beam energy and transverse size (assuming uniform

* Note, also, that the transverse beam envelope along the accelerator has been kept constant during measurements.

transverse distribution and no vacuum chamber), we performed experiments, varying these beam parameters and studying the modulation.

Accelerating or decelerating the compressed beam in the third linac tank we varied the energy of the electrons from 50 to 110 MeV. Zero-phasing projections of the electron beam for different energies show that the modulation reduces with increasing energy, as expected.

Using three lattices with different beam envelopes (0.5, 1.0, 1.5 mm RMS) we measured the dependence of the modulation versus beam size. It was explicitly shown, that the modulation, being present when the beam size is small, almost vanishes at a larger beam cross section.

Measuring the dependence of the modulation versus charge was an important stage in the experiments. Electron beams with different charge (40, 100, 200, 300 pC) were generated, compressed and transported to the spectrometer dipole. Special attention was paid to insure both the transverse and longitudinal particle transport along the accelerator to be approximately the same for different amounts of bunch charge. In this case only the peak current was scaled together with changing the beam charge.

The measurements done for the uncompressed beam revealed the dynamics of the structure at low charge, where the modulation is strong and visible, but only weakly depends on the particle transport at high energy. During the compression the modulation wavelength gets scaled down according to the compression ratio without a significant enhancement of the structure.

As the peak current in the uncompressed beam increases the structure vanishes, and the beam exhibits an almost smooth distribution for some 300 pC of charge. After compression the modulation reappears, but the period of modulation stays the same as for the case of low charge.

Finally we checked if the beam modulation is associated with bunching in the longitudinal particle density. Varying the electron beam size along the channel we generated "modulated" and "non-modulated" beams. Using an IR bolometer together with low-pass IR filters (cut-off at 40 μm, 100 μm, 160 μm) we measured CTR from a metallic mirror, installed inside the vacuum chamber. The characteristic modulation wavelength was estimated as 90 μm, using chirped bunch profiles. Measuring the CTR power with different filters we have not obtained any difference between "modulated" and "non-modulated" beam conditions. This proves that the modulation does not introduce any additional density bunching in the electron beam.

CONCLUSION

In this paper we discussed the peculiar effect of longitudinal beam dynamics in the DUV-FEL linear accelerator. A space charge model of the phenomenon is in qualitative agreement with experimental data. The experiments show a sensitivity of the effect to the electron beam energy, transverse size and peak current. It was also shown that the induced modulation does not enhance the density bunching in the electron beam. Since the drive laser is a likely source of this structure, high-resolution optical diagnostics are needed for more quantitative studies. Therefore a single-shot SPIDER apparatus [7] with high resolution is being developed.

One of the important questions is whether this structure can be dangerous for the accelerator performance. First, this effect is sensitive to the initial laser structure, so for a perfectly uniform longitudinal laser profile a modulation does not exist, unless it is created on latter stages in the accelerator. At the same time this structure, if present in the beam, can cause at least two problems. First, it increases the projected energy spread in the bunch. Second, the modulation, developed in the beam at low energy, becomes "frozen" at a higher energy. Then, any magnetic system (bending system, chicane-compressor) may convert this modulation into real spatial bunching for a modulation wavelength of $\lambda_{mod} = 2\ R_{56}\ \Delta\gamma_{mod}/\gamma$, where $\Delta\gamma_{mod}$ is the amplitude of the space charge induced energy spread. Now this effect can degrade the electron beam quality due to coherent radiation of the spikes during the compression process. So, for any specific configuration of the accelerator, the allowable amount of modulation must be calculated and the appropriate laser quality established.

ACKNOWLEDGEMENTS

We would like to thank D. Dowell, A. Doyuran, P. Emma, S. Krinsky, J.B. Murphy, J. Rose, X.J. Wang, J. Wu, Z. Wu, L.H. Yu for many useful discussions and comments. This work is performed under DOE contract DE-AC02-76CH00016.

REFERENCES

[1] "Ultrashort electron bunch length measurements at DUVFEL", W. Graves et al., PAC 2001, Chicago, p. 2224

[2] "Beam energy modulation and its impact on rf zero-phasing bunch profile measurement", Z. Huang, SLAC-PUB-9788

[3] "Electron Bunch Compression in the SDL linac", T.Shaftan et al., EPAC'02, Paris, June 2002,p. 834.

[4] "Measurements of femtosecond electron bunches using a rf zero-phasing method", D.X. Wang et. al., Phys. Rev., E, 57, 2283 (1998)

[5] "Observation of longitudinal phase space fragmentation at the TESLA test facility free-electron laser", Ph. Piot et al., NIM A 475 (2001), pp. 348-352

[6] "Experiments in Coherent Radiation at SDL", H. Loos et al., EPAC'02, Paris, June 2002,p. 814.

[7] "Spectral phase interferometry for Direct Electric-Field Reconstruction of Ultrashort Optical Pulses", C. Iaconis et al., Opt. Lett. 23, 792 (1998).

Corresponding author, e-mail: shaftan@bnl.gov

TOOLS TO PREDICT BEAM BREAKUP IN RECIRCULATING LINACS*

K.Beard, L.Merminga, B.Yunn, TJNAF, Newport News, VA 23606, USA

Abstract

An important limitation on the maximum beam current in a recirculating linac is due to beam breakup caused by higher order modes (HOM) excited in the RF cavities. A HOM delivers a transverse kick to a beam bunch, the bunch on the next pass can then drive the HOM and cause it to grow until the beam is lost. Two codes, MATBBU and TDBBU, have been written to estimate the threshold current for a set of HOMs and accelerator optics. The relative merits and limitations of each is discussed in detail.

INTRODUCTION

Often the greatest beam current limitation in a recirculating linac is imposed by beam breakup (BBU) caused by transverse higher order modes (HOMs) in the accelerating cavities. The basic idea, very briefly, is that a bunch passing through a cavity off axis excites a transverse electromagnetic mode in the cavity. When the same bunch later returns to that same cavity, it will again interact with the same mode; under the correct circumstances, that mode will grow until it deflects the beam sufficiently to cause the beam to be lost. The exact combination of HOM characteristics, beam transport, and recirculation time determine whether a given mode will lead to an instability.

For a single recirculation, a singe cavity, and a single mode, the expression for the beam break threshold current is approximately:[1]

$$I_t = \frac{-2\,p_r c}{e\,(R/Q)_m\,Q_m\,k_m\,M_{12}^{(r)}\,\sin(\omega_m t_r)\,e^{\frac{\omega_m t_r}{2Q_m}}}$$

where I_t is the threshold current, $p_r c$ is the momentum leaving the cavity, e is the charge of the electron, $(R/Q)_m$ is the shunt impedance, Q_m the quality factor of the mode, k_m is the wavenumber of the mode, ω_m is the frequency of the mode, $M_{12}^{(r)}$ is the component of the transport matrix, and t_r is the recirculation time.

TDBBU

Solving the problem for many modes in many cavities and multiple passes becomes more complicated.[2][3] The JLab CEBAF 12GeV upgrade has a design current of 100uA and about 2600 HOMs of interest; the Jlab 10 kW FEL has a design current of 10mA and about 200 HOMs of interest.

One approach is to use the TDBBU code written by G.Krafft, modified by B.Yunn, and then by K.Beard. It works in the time domain as a tracking code. Individual bunches are injected into the machine; a small amount of noise is added, the bunches stepped through the machine, and each HOM mode updated. The process is repeated for a time long (~10x) with respect to the growth time of a mode (~2 Q_m/ω_m), and the transverse positions of the bunches at a point in the machine are plotted. An instability appears as growth in the transverse position:

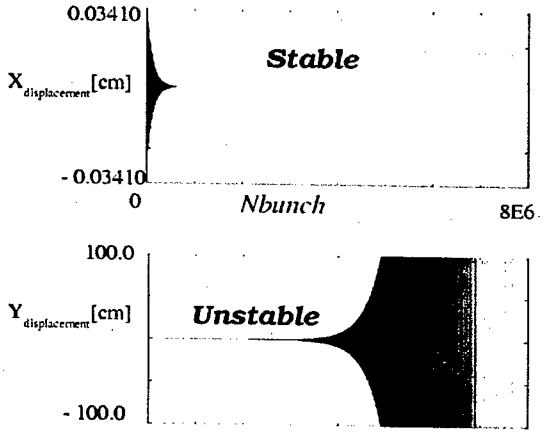

Figure 1: TDBBU output for stable ($I<I_t$) and unstable ($I>I_t$) examples.

To find the threshold current, the current used is turned up an down and the calculation repeated; an automatic algorithm to do this is included in the new version of TDBBU. It examines the output and decides whether the situation appears stable, unstable, or indeterminate, then adjusts the current appropriately and runs again.

As the required runtime goes ~N_{HOMs} * Q_m/ω_m, this approach is becomes cumbersome for very high Qs. Another approach is to solve the problem in the frequency domain. If one assumes a steady state solution, the problem can be reduced to solving for the complex eigenvalues of a matrix.[6]

MATBBU

The MATBBU[7] code reads in the same input file as TDBBU. It then sweeps through a frequency range, for each frequency it calculates a matrix and searches for

*This work was supported by US DOE Contract No. DE-AC05-84-ER40150

eigenvalues of the matrix. The lowest eigenvalue falling on the real positive axis correspond to the threshold current

In the initial case of the 10 kW FEL, there were 56 HOMs/axis, requiring that a complex 111x111 matrix's eigenvalues be found. This takes some significant time on any computer; in addition, the high Q's mean that the regions of interest are very narrow; only a few Hz wide. Typically, one would like to sweep a 2MHz wide space; doing that with just "brute force" by sweeping in 1Hz steps requires $2x10^6$ steps, or, very roughly for a 733MHz Pentium III, about that number of seconds (about 3 weeks) for each band (there were 11). In addition, this sweep should be repeated many times for a number of different HOM distributions representing manufacturing tolerances (typically 10). Putting that together, one would expect to use about **7 years** of CPU time.

That seemed too long a time to wait. To make matters worse, the time to solve a single matrix goes roughly as $N_{HOM}^{3.6}$, so solving the case of for the CEBAF 12 GeV upgrade with 800 HOMs/axis rather than the FEL upgrade's 56 would require roughly 14,000 times the CPU time.

Fortunately, there are several ways to speed up the process. First, the eigenvalues' behavior is smoothly varying; an infinitesimal change in the frequency should only change an eigenvalue slightly. This means that an active search can be used; the frequency is changed up or down slightly and the eigenvalues tracked to determine the frequency at which they cross the positive real axis. The minimum frequency step size is then only limited by the numeric noise. The actual algorithm is somewhat more complicated by the presence of multiple eigenvalues and is discussed in detail in the tech note [7]. Previous versions of the code required the user to attempt to extrapolate the threshold from relatively widely scattered points; the iterative search removes those ambiguities.

Next, the size of the problem can be greatly reduced by considering only those HOMs whose frequencies are near to that in question and excluding those which have frequencies far away. The new version can divide the frequency range up into regions of interest (ROIs) and treat each as a separate problem.

Lastly, ignoring eigenvalues with components larger than a preset cutoff current simplifies the tracking. Typically, the cutoff current is set to be at least 10 times the threshold current of interest.

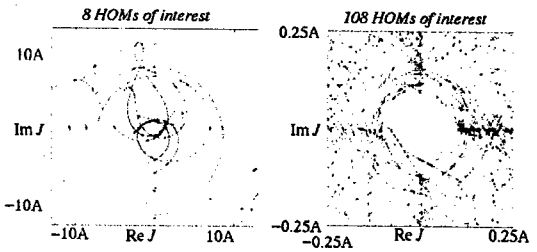

Figure 2. MATBBU output for 8 and 108 HOMs of interest in the 10 kW FEL with a proposed supercell module.

In many cases of interest the exact frequency of each HOM in each cavity isn't known, but predicted to be distributed about a central value. It is then necessary to run multiple cases representing "as built" accelerators. MATBBU can now automatically generate and run input files with the appropriate distributions, and the results can then be shown as a scatter plot.

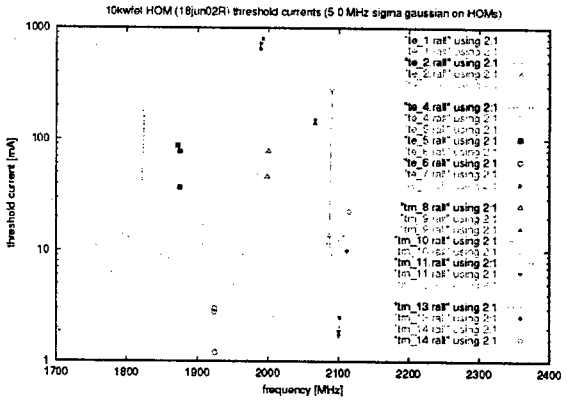

Figure 3. MATBBU predictions for 3 as-built FELs using a proposed module design and a 5 MHz sigma spread in cavity HOM frequencies.

Generally, for modes with high Qs ($>10^5$), the threshold current due to a given mode scales very nearly as 1/Q. This property has been used to set the specification for the maximum Q for each HOM to avoid BBU at the design current.

COMPARISON

Both TDBBU and MATBBU use the same input file and share much of their structure; both are written in FORTRAN77 with some ANSI C routines for portability and a command line interface. Both have been tested under a number of UNIX platforms, including GNU-Linux, HP-UX, SunOS, CrayOS, and IBM-AIX MATBBU may use either the IMSL[8] or LAPACK[9] math library.

From a practical standpoint, the biggest difference in the codes is that TDBBU "sees" all the modes, while MATBBU only "sees" modes near near the frequency its scanning. Unless the number of HOMs is very large (1000s), for Qs ~ 10^6, MATBBU runs much faster than TDBBU (minutes vs. hours).

Table 1. Calculations using various Q_{ext} for a single mode with a f_{HOM}=2114.8 MHz and R/Q= 5.6 W/cm^2 in the central cavities of the 10 kW FEL.

Qrun	Runtime [uS]	Cray [hr]	IX [mA] tdbbu (matbbu)	IY [mA] tdbbu (matbbu)	Linux [min]
1.0E+05	150	0.09	128 (120.7)	120 (147.2)	<1 min.
3.0E+05	450	0.3	44 (39.8)	48 (48.7)	
1.0E+06	1500	0.9	13 (11.9)	15 (14.6)	
2.0E+06	3000	1.8	(6.0)	(7.3)	
7.0E+06	11400	7	(1.7)	(2.1)	<1 min.

To compare the codes, various test cases of for the 10 kW FEL were run and were found to agree to ~10-20% when the only important HOMs were those within MATBBU's frequency range (Table 1).

SUMMARY

The MATBBU and TDBBU codes have been developed at Jlab and recently improved and used to predict the BBU thresholds for the CEBAF 12GeV upgrade and the 10 kW FEL upgrade. Both codes and their documentation will soon be available on the CASA [10] web site.

REFERENCES

[1] G.A.Krafft, J.J. Bisognano and S.Laubach, Jlab Tech Note JLAB-TN-01-011

[2] J.J. Bisognano and R.L. Gluckstern, Proc. of 1988 Linear Accelerator Conf., 388 (1988)

[3] G.A. Krafft and J.J. Bisognano, 1987 PAC Proceedings, 1356 (1987)

[4] K.B. Beard, L. Merminga, B.Yunn, Jlab Tech. Note JLAB-TN-02-043

[5]K .B. Beard, L. Merminga, B.Yunn, Jlab Tech. Note JLAB-TN-02-045

[6] J.J. Bisognano and R.L. Gluckstern, 1987 PAC Proceedings, 1078 (1987)

[7] K .B. Beard, L. Merminga, B.Yunn, Jlab Tech. Note JLAB-TN-02-044

[8] Visual Numerics, Inc., *http://www.vsi.com/products.imsl*

[9] LAPACK's User Guide, E.Anderson et al, *http://www.netlib.org/lapack/*

[10] *http://casa.jlab.org*

FUTURE PLANS FOR e^+e^- FACTORIES

C.Biscari, LNF-INFN, Frascati, Italy

Abstract

In the last decade luminosities of lepton colliders have greatly risen. There are several ingredients of the success: the progress in the handling of high currents and multibunch regimes, in the beam-beam interaction limits understanding, in particle dynamics simulation codes, in the diagnostic systems to control beam sizes and orbits, in the background shielding.

Now is time to go further in the high luminosity frontiers: experiments are asking for more precision measurements, and the accelerator community is facing projects where the increase of luminosity by orders of magnitude is conceivable. New ideas, main upgrades and plans in the factories presently in operation around the world are the subject of this paper.

INTRODUCTION

The frontier of high luminosity does not coincide with the high energy one. Non-search colliders dedicated to precision physics have in last decade advanced the luminosity by one order of magnitude. The great success of B-factories which in few years have reached their design goals has demonstrated to the physics community the possibility of reaching in their experiments unprecedented precisions approaching theory limits.

For sake of discussion, the diagram of the luminosity, L, versus energies, E, can be divided in three zones (see Fig.1): in the first zone the energy increase is privileged for new particles production, reaching the maximum with LEP; the corresponding luminosity is continuously improved, both for its dependence on energy and for the advances in technologies and collision physics. Beyond LEP linear colliders will supplant circular ones; VLLC should double LEP energy but at the price of one order of magnitude in ring size. In the second zone there are the present factories, with luminosities one order of magnitude larger than the previous ones at the same intermediate energies. The third zone represents the future, in which upgrades by a factor 10 seem reachable with present technologies, while higher upgrades are subjected to R&D progress.

The physics community asks for higher fluxes of particles at the intermediate energies[1-4]. The annihilation production cross section in e^+e^- collisions is proportional to the inverse square of the energy, and the necessary integrated luminosity scales accordingly:

$$\int L \propto \frac{1}{\sigma} \propto E^2 \qquad (1)$$

Table I shows the approximate integrated luminosities already collected by all experiments in the energy range between the Φ and the B, and the luminosities requested for competitive experiments in the LHC era. There is a long path before reaching the wanted specifications. A review of the plans of e^+e^- factories according to their energy is described in the paper.

Table 1 - Collected and requested integrated luminosities

	E_{cm} (GeV)	logged $\int L$	requested $\int L$
Beauty	10.6	~ 300fb^{-1}	10 ab^{-1}
τ-charm	3.9	< 1 fb^{-1}	>100 fb^{-1}
light quarks	1-2	< 100pb^{-1}	500 pb^{-1}
Φ	1	< 1 fb^{-1}	100 fb^{-1}

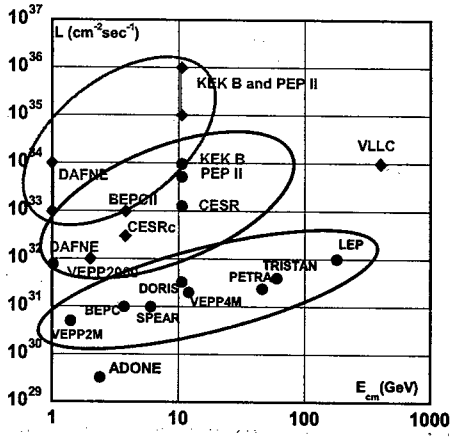

Figure 1: Luminosity versus energy in lepton circular colliders. Past and present results (blue dots), future projects and designs (red diamonds)

LUMINOSITY CONSIDERATIONS

Storing high currents in closely spaced bunches and squeezing as much as possible beam sizes translates in luminosity increase, according to:

$$L = \frac{f_{coll}}{4\pi} \frac{N^+ N^-}{\sigma_x^* \sigma_y^*} \qquad (2)$$

The collision frequency, f_{coll}, the bunch populations, $N^{+,-}$, the transverse beam sizes, $\sigma_{x,y}^*$, apparently independent, are strongly related by the beam-beam interaction and by collective effects. According to the collider regime, L can be written in terms of the characteristic beam-beam tune shift parameters, $\xi_{x,y}$, the emittances, $\varepsilon_{x,y}$, the betatron functions at the IP, $\beta_{x,y}^*$: when the reachable $\xi_{x,y}$ is the most severe luminosity limitation, L for flat beams is usually expressed as:

$$L = \frac{\pi f_{coll}}{r_o^2} \frac{\gamma^2 \varepsilon_x}{\beta_y^*} \xi_x \xi_y \qquad (3)$$

which compared with eq.1 shows the same dependence with the energy.

0-7803-7738-9/03/$17.00 © 2003 IEEE

High currents

All high current issues have been addressed by the collider physicists together with the synchrotron radiation community. The understanding and control of machine impedances has increased the threshold instabilities in all high brilliance rings. The present generation of bunch by bunch feedbacks for multibunch operation, first tested in synchrotron light sources[5], is operational in all factories and is also a powerful diagnostic tool.

Ion trapping in electron rings, already known when first generation factories were designed, is controlled by gaps in bunch trains and/or ion clearing electrodes. Electron cloud instability (ECI) in e^+ rings, which was first observed at the KEK Photon Factory in 1995, is one of the main limiting effects in increasing the currents in B-factories. The photoemission and multipacting creates additional loads to vacuum and cryogenic systems, and the emittance blow-up constitutes a serious limitation to luminosity. Solenoidal windings are the present cure of the instability; new vacuum chamber designs are being developed, in collaboration with the hadron collider community, also threatened by the ECI.

Besides instabilities induced by collective effects, high currents are responsible for intense photon fluxes on the vacuum chambers and high loads on rf system; vacuum, cooling and rf technology developments are always correlated with every achievement in the luminosity scale[6].

Beam-beam

Beam-beam effect limits the single bunch luminosity. All present factories, but VEPP2000, are based on the multibunch regime. Crossing angle is now better understood. The Piwinski factor relating the crossing angle θ with the characteristic dimensions of the bunch:

$$\phi = \theta \frac{\sigma_L}{\sigma_x} \qquad (4)$$

has reached values that 10 years ago were considered dangerous source of synchrobetatron resonances.

Small values of β_y* are obtained thanks to magnet technology, which has developed small dimension - high gradient quadrupoles to be placed near IPs.

Careful tuning of single ring working point, dynamic aperture optimisation, possibility of coupling corrections up to very small values (coupling of the order of 0.1% have been obtained), are all dowels of the puzzle for obtaining high beam-beam tune shifts.

Background

Background rejection from experiments is one of the key points of any collider. Continuous optimization of background is done routinely at all present factories, and adding masks, collimators, and cooling is envisaged in next future in all of them. In the lower energy factories, where background is dominated by Touschek losses, the lattice configuration of the whole ring is optimized for minimisation of losses in the detector areas.

Lifetime and injection

Average to peak luminosities ratios depend on lifetime and injection rates. Lifetimes decrease as currents are raised due to beam-gas scattering and Touschek effect, this last becoming predominant in low-energy rings. At extremely high luminosity the annihilation process becomes the predominant particle loss effect. Presently the beam lifetimes are of the order of hours, but will be shortened to few minutes in the super-factories regime. Only continuous injection will allow the operation of the colliders, and background at injection becomes one the key-point to be solved.

BEAUTY FACTORIES

The two B-factories, KEK-B and PEP II, on the opposite sides of the Pacific Ocean, have reached their design values in a very short time, compared to the scale of accelerator history, despite these values were considered challenging when in the 90's the projects were conceived. During the preparation of this manuscript I have corrected the luminosity records several times.

CESR has also operated in this range of energy; this collider has shown along the years an increase in performances able to compete with the newer collider generations, and is now going towards lower energies. It kept for some time the record of luminosity and it can cover all the physics from the J/Ψ to the Beauty.

Both KEKB and PEPII plan upgrades for next two-three years, optimizing the existing systems to reach luminosities of few $10^{34}cm^{-2}sec^{-1}$. Further steps on luminosity are being planned in a time scale of 10 years. Table 2 shows some of the main parameters for the future upgrades [7-8].

Table 2 - B factories from 10^{34} to 10^{36} $cm^{-2}sec^{-1}$

Collider	KEK-B		PEP-II		
	super	hyper	next	super	hyper
E + (GeV)	3.5	3.5	3.1	3.5	3.5
E - (GeV)	8.0	8.0	9.0	8.0	8.0
C (m)	3016	3016	2199	2199	2199
L $10^{34}cm^{-2}s^{-1}$	10	40-100	2.5 - 4	20	100
IPs	1	1	1	1	1
β (m) (h)*	0.30	0.15	0.5	0.3	0.15
β (m) (v)*	0.003	0.003	0.0065	0.0037	0.0015
ε (n rad) (h)	33	33	44	44	44
ε (n rad) (v)	2	0.33	0.44	0.44	0.44
θ (mrad)	±15	0	0 -± 4	±10	±15
ξ (h)	0.068	0.1	0.08	0.10	0.10
ξ (v)	0.05	0.2	0.08	0.10	0.10
N bunches	5018	5018	1700	3400	7000
I+ (A)	9.4	17.2	4.5	11.0	10.3
I - (A)	4.1	7.8	2.0	4.8	2.35
f_{RF} (MHz)	509	509	476	476	952

PEP-II upgrades

The goal of reaching L of the order of 10^{34} cm^{-2}sec^{-1} by 2005 is based on adding rf stations in order to increase currents and number of bunches. Shorter bunches, and therefore smaller β_y^* will be possible. An upgrade of the longitudinal feedback system with new electronics and DAFNE-like kicker[9] will increase the effectiveness of the system. Higher injection rate, correlated with added collimators to shield injection background will pay on the integrated luminosity. Solenoidal windings for ECI together with increased cooling should help in the current increase.

The same philosophy is foreseen up to 2008, but pushing parameters to more limiting values: β_y^* will be decreased by 50% by moving quadrupoles closer to IP, a small crossing angle in the new IR will be introduced, higher currents will be based on the feedback system upgrade to go to 2-bucket spacing. All these actions should push luminosities up to 2-4 10^{34} cm^{-2}sec^{-1}. $\xi_{x,y}$ of 0.08 are considered achievable.

Higher luminosity considerations will be of course related to the achievements obtained at that point; with the today know-how, the idea is to increase the collision frequency by filling all buckets, without increasing bunch currents, together with a larger crossing angle and smaller betas at IP. The total current will be doubled and to save wall power the energy asymmetry will be diminished. Tune shifts will be 0.1 and L of the order of 10^{35}cm^{-2}sec^{-1}.

The main upgrade for a further increase is again doubling the number of bunches by changing f_{rf} to 950 MHz, and still increasing the crossing angle. With the same b-b tune shift and slighly lower currents per bunch the total L could reach values of 10^{36} cm^{-2}sec^{-1}. R&D on the rf cavity and related systems is already in progress.

KEK-B upgrades

The Japanese B-factory has recently exceeded the 10^{34} cm^{-2}sec^{-1} goal, the maximum luminosity ever reached. The upgrades for a factor 10 are based on an increase of the bunch number by a factor 4, together with an increase of the bunch current, lowering β_y^* by a factor 2 and increasing the crossing angle. An increase of the emittance keeps the b-b tune shifts equal to the present ones. The main challenge are the high current effects; the rf system will be upgraded and SC rf cavities will be added. A beam-energy switch is envisaged, so that e^+ are stored in the HER with lower currents to weaken the ECI effect. An upgrade of the injector is thus being studied to accelerate positrons up to 8 GeV. Intensive R&D on vacuum chamber design, with antichambers and special rf shields is in progress, and prototypes are being constructed to be installed soon in the collider for first tests.

Crab crossing and head-on collisions are the key point to reach 10^{36} cm^{-2}sec^{-1}: higher b-b tune shifts by doubling the current per bunch and no reduction factor due to crossing angle are predicted by simulations. The very high ξ_y is obtained also by lowering the coupling.

TAU-CHARM FACTORIES

BEPCII, CESRc

CESR is moving toward lower energies. Wigglers are added to increase radiation damping, and this is the main feature for the new configuration. The first wiggler has just been installed and commissioned. Other 12-14 wigglers will be installed in one year and CESR will run until 2008 at three energies between 3.1 and 4.1 GeV.

In China BEPC will be upgraded to become the first completely dedicated tau-charm factory, still mantaining the synchotron radiation production. Its design is based on the double ring scheme, with energies ranging between 1.5 and 2.5GeV per beam, optimized at 1.89 GeV. An inner ring will be installed inside the old one, so that each beam will travel in half outer ring and half inner one. Superconducting cavities fitting the bunch length requirements will be installed. The production began in 2002 and commissioning is foreseen for 2006.

Table 3 shows the design values of the Chinese τ-charm factory[10] together with the CESR-c[11] parameters at the same energy.

Table 3 - Tau charm factories

Collider	CESRc	BEPC II
status	operating	in construction
E (GeV)	1.88	1.89
C (m)	768	237.5
L (10^{32} cm^{-2}s^{-1})	3	10
IPs	1	1
β* (m) (h / v)	0.7/ 0.011	1 / .015
ε (μ rad) (h / v)	0.22	0.17 / 0.002
θ (mrad)	± 2.8	± 11
φ (rad)	0.07	0.4
σ_z (cm)	1.0	1.5
N_b (10^{10})	6.4	4.8
ξ (h / v)	0.03 / 0.03	0.04 / 0.04
N bunches	45	93
I (A)	.18	0.91
f_{RF} (MHz)	500.0	499.8
V (MV)	10	1.5

LIGHT QUARKS FACTORIES

Physics at energies between the φ and τ have been covered during last years by VEPP-2M (shut down in 2000) and BEPC colliders. The interest for this energy range had produced the proposal for PEP-N[12]. Now a collider, innovative in its design and concepts, is in construction: VEPP2000. At this energy range the interesting physics needs moderate integrated luminosities, as shown in Table 1.

VEPP2000

A 2 GeV collider (from there the 2000 in the name), whose design is based on the concept of round colliding beams, is being constructed in Novosibirsk[13], after the shutdown of VEPP-2M three years ago. This is a very important step in the beam-beam interaction understanding. The expected b-b tune shift is twice smaller than the corresponding flat-beam one with the same particle density, thus predicting a single bunch luminosity of $10^{32}cm^{-2}sec^{-1}$[14].

The collider can be operated also with flat beams and at energies ranging from 500 Mev to 1 GeV per beam. Its compact design is based on very high field normal conducting dipoles (2.4T) and houses two experiments in the two simmetric Interaction Regions. Focusing in the two interaction regions is performed by SC solenoids, which also rotate by $\pi/2$ the planes of betatron oscillations, thus creating emittance in both transverse modes. Dynamic aperture is challenging due to the high chromaticity and beam sizes on both planes.

Dipoles are bein installed, solenoids are in the construction phase and first beam is foreseen in one year from now.

Fig. 2 - View of the VEPP-2000 collider

Table 4 - Light quarks factories

Collider	VEPP2000	DAFNE 2
status	in construction	design study
E (GeV)	1.	1.
C (m)	24	97
L (10^{32} $cm^{-2}s^{-1}$)	1	1
IPs	2	1
β^* (m) (h / v)	0.1 / 0.1	1.5 / 0.025
ε (μ rad) (h / v)	0.136 / 0.136	0.5 / 0.0025
θ (mrad)	0	±15
ϕ (rad)(Piw)	0	0.26
σ_z (cm)	3	1.1
N_b (10^{10})	10	3
ξ (h / v)	0.1 / 0.1	0.014 / 0.024
N bunches	1	30
I (A)	0.20	0.45
f_{RF} (MHz)	172	368.3
V (MV)	0.12	0.25

DAFNE2

DAΦNE has been constructed to operate at the Φ resonance. Some of the systems are dimensioned to operate also at higher energies. It is presently under discussion which will be the future of the collider. One of the possibilities is to increase the energy by a factor of two [15]. The project is named DAFNE2, where "F" stands for Frascati and "2" for the E_{cm}. No crucial issues from the accelerator physics point of view are envisaged. The main hardware modifications concern dipoles, splitter magnets, and low-beta quadrupoles, while rf and vacuum systems are already dimensioned for the high energy, with a lower beam current. The main parameters are given in table 4 together with those of VEPP2000 for comparison.

Φ-FACTORIES

DAΦNE is the only Φ-Factory presently in operation. VEPP2000 can be operated also at the Φ resonance, with of course a lower luminosity than the optimum one.

DAΦNE

By the end of 2005 all the current physics programs are expected to be almost completed, with an overall delivered integrated luminosity in excess of $3fb^{-1}$ and luminosities higher than $10^{32}cm^{-2}sec^{-1}$. Operation is done in time sharing between the two experiments, since simultaneous collisions at both IPs are critical. After the DEAR completion [16], during the 2003 shutdown the third experiment, FINUDA, is being installed, and will share the collider with KLOE during the next few years. Crossing angle will be increased with respect to design values, by changing the low beta configuration from FDF to DF. Both β_x^* and β_y^* will be lowered. Sextupole components are being added to a family of quadrupoles for dynamic aperture optimization. Damaged ion clearing electrodes are being replaced.

The interest for values of the luminosity larger by a factor 10[4] than the design ones has lead to the study of possible new designs of the factory.

Experience has shown that powerful radiation damping is needed; presently in DAΦNE natural damping is increased by a factor two by the wigglers, which on one hand increase achievable b-b tune shifts, but on the other one limit the dynamic aperture. Simulations [17] show that roughly a factor 10 on τ_d would allow an increase of the b-b tune shifts by a factor of two. A preliminary design of a ϕ-factory is being studied. The parameters are shown in Table 4, together with those which are foreseen for next future in the present configuration. The preliminary design, named DAΦNE-w[18], is based on cells where positive and negative normal conducting bendings alternate, with a net positive bending angle and an increase in radiation damping. The layout and the vacuum chamber design are different from the present one. Special care is dedicated to optimise the dynamic aperture, and is mainly dominated by the non linear terms arising from the wiggling bendings. Increase of the average luminosity is expected from continuous injection scheme, based on the separation of the now shared e^+ and e- injection transfer lines.

Table 4 - ϕ factories

Collider	DAΦNE	DAΦNE w
status	until 2005	design study
E (GeV)	.51	.51
C (m)	97	80
L (10^{32} cm^{-2}s^{-1})	> 1	> 10
IPs	1	1
β^* (m) (h / v)	1 / 0.025	0.5 / 0.01
ε (μ rad) (h / v)	0.6 / 0.006	0.2 / 0.001
θ (mrad)	± 16	± 15
ϕ (rad)	0.39	0.57
σ_z (cm)	2	1.2
N_b (10^{10})	3.6	3.5
ξ (h / v)	0.027 / 0.043	.079 / 0.070
N bunches	100	95
I (A)	1.8	2.0
f_{RF} (MHz)	368.3	369
V (MV)	0.2	0. 5

NEW IDEAS

New, original, sometimes daring ideas for increasing the particle production are arising. I will mention some of them.

Collision with four-beam scheme, which was tested in DORIS and DCI, with neutralization of the charge between e+ and e$^-$, and no b-b linear tune shift, has been revisited by the KEKB group[7] .

Collide beams of higher energies with large crossing angles, so that E_{cm} corresponds to the Φ, is being investigated for DAΦNE: two 1.5 GeV rings colliding at 140° (meaning that beams travel in the same direction), will produce Φ's with a boost such that K_s decays in length of 1m, while K_L can be detected at distances up to 10 m, simplifying the problem of detector background shielding. The main advantage is the less critical behaviour of a higher energy ring from the point of view of beam lifetime and radiation damping. Luminosity and ξ behaviour with large crossing angle have been investigated[19]. The main disadvantage is the need of very short bunch. Introduction of a "longitudinal low beta" at the IP, so that the beam changes its length along the ring and is minimum at the IP, by tuning the R_{56} term along the ring, is being investigated.

Collide ring against linac is another idea being taken into consideration.

CONCLUSIONS

The next steps of the lepton factories are straightforward and consist in optimizing all the techniques developed during last ten years, expecting in all cases an increase in peak and integrated luminosity by about a factor 10. New ideas to push the luminosity values by another order of magnitude are being investigated. Round beam collisions will soon be tested at VEPP2000, answering to the question whether b-b tune shift limits can be raised. Fig.3 summarizes the foreseen timetable for the present factories in next future.

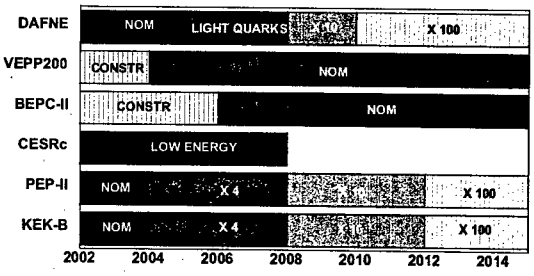

Fig. 3 - Timetable of foreseen factories future

ACKNOWLEDGMENTS

Colleagues from all the mentioned colliders have kindly provided informations about their projects. Without mentioning everybody, I thank them all, sure that the fruitful collaboration between laboratories will continue in the pursue for higher luminosities.

REFERENCES

[1] S. Olsen, "Search for New Physics at Super-B Factories", Report to the ICFA Seminar, CERN October 2002
[2] P.Roudeau, "Tau and Charm Physics Highlights", Proc. of Lepton-Photon 01,Rome, Italy, p.119,2001
[3] "e+e- Physics at Intermediate Energies Workshop, SLAC, 30April-2May 2001
[4] F.Bossi, G.Colangelo, G.Isidori, "Searching for KL-> πo ν ν at a Φ-factory", Eur.Phys.Jour. C6 (1999), 109-119
[5] D. Teytelman et al., "Operation and Performance of the PEPII Prototype Longitudinal Damping System at the ALS", IEEE PAC 1995:2420-2422 (QCD183:P3:1995)
[6] K.Akai, "High Intensity Issues for Super B-Factories", these proceedings (2003)
[7] Y. Ohnishi, private communication
[8] J.Seeman, private communication
[9] P. McIntosh et al. "An Over-damped Cavity Longitudinal Kicker for the PEP-II LER" these proceedings (2003)
[10] Zhang, Chuang, private communication
[11] D. Rice., for the CESR-c Working Group CESR-C*, "A Frontier Machine For QCD and Weak Decay Physics in the Charm Region", Proc. of EPAC02 Conference, Paris,2002
[12] Y.Cai et al. "PEP-N: a 0.8GeV x 3.1 GeV Collider at SLAC", Proc. of PAC2001, Chicago, p.3564
[13] Y.Shatunov et al. "Project of a New e-e+ Collider VEPP2000", Proc. of EPAC02 Conference, Paris,2002.
[14] A. Valishev, E. Perevedentsev , K. Ohmi, "Strong-Strong Simulation of Beam-Beam Interaction for Round Beams", these proceedings (2003).
[15] G. Benedetti et al., " Feasibility study of a 2 GeV lepton collider at DAFNE", these proceedings (2003).
[16] C. Curceanu, "Kaonic nitrogen and hydrogen", Proc.of "XLI International Winter Meeting on Nuclear Physics" Bormio, Italy, 2003
[17] M. Zobov, private communication
[18] Dafne team, "DAFNE-w design", LNF Technical Note, in preparation
[19] P.Raimondi, M.Zobov, "Tune Shift in b-b Collisions with a Crossing Angle", DAFNE Tech. Note, G58 April 2003

INTERACTION REGION UPGRADES OF E^+E^- B-FACTORIES*

M. Sullivan†, Stanford Linear Accelerator Center, P.O. Box 20450, Stanford, CA 94309
for the PEP-II team

Abstract

Both the PEP-II and KEKB B-Factories have plans to upgrade their Interaction Regions (IRs) in order to improve luminosity performance. Last summer PEP-II added cooling to the IR beam pipe in order to increase beam currents thereby raising the luminosity. In addition, PEP-II is working on a design that modifies the permanent magnets near the Interaction Point (IP) for an even higher luminosity increase. KEKB is also planning an improvement to their IR that will decrease the detector beam pipe radius. In addition, KEK has a design to increase the luminosity of KEKB to 1×10^{35} cm^{-2} sec^{-1} which includes changes to the IR. PEP-II is also investigating the feasibility of a 1×10^{36} cm^{-2} sec^{-1} luminosity design. I summarize these various upgrades and concentrate on issues common to the different designs.

1 INTRODUCTION

The two asymmetric-energy B-Factories, PEP-II and KEKB, have made and are in the process of making improvements in the IR. The IR plays an important role in any effort to improve luminosity performance. Table 1 lists several accelerator parameters that are important for more luminosity and that have an influence in the IR.

Table 1: Some accelerator parameters that are related to luminosity and are important to the IR.

	PEP-II		KEKB	
	Present	Design	Present	Design
E^- (GeV)	9.0	9.0	8.5	8.5
E^+ (GeV)	3.1	3.1	3.5	3.5
I^- (A)	1.1	0.75	1.0	1.1
I^+ (A)	1.7	2.1	1.4	2.6
n_b	939	1658	1284	5000
I_b^- (mA)	1.17	0.45	0.78	0.22
I_b^+ (mA)	1.81	1.29	1.09	0.52
β_x^* (cm)	35	50	60	33
β_y^* (mm)	11	15	6-7	10
L ($x10^{33}$)	6.1	3.0	10.0	10.0
Collision	Head-on		±11 mrad xing ang.	

*work supported by the Department of Energy under contract number DE-AC03-76SF00515.
†sullivan@slac.Stanford.edu

As we can see from the table, both accelerators have increased luminosity by increasing the bunch current in both beams. In fact, PEP-II has achieved twice the design luminosity with a little over half the number of design bunches and with significantly more design HER beam current, while KEKB has just reached design luminosity with only a little over 25% of the design number of bunches and with nearly the design HER current. These higher bunch currents have greatly increased the HOM power produced in these machines when compared to the original estimates. This, in turn, has led to heating issues for both accelerators. Both accelerators are also attempting to lower the β_y^* as much as possible to further increase the luminosity. In order to benefit from this decrease the bunch length must be shortened to a comparable size. Shortening the bunch length also increases HOM power.

2 PEP-II

The PEP-II accelerator [1] uses strong horizontal dipole permanent magnet (PM) magnets (B1) to bring the 9 GeV and 3.1 GeV beams into a head-on collision. These 0.5 m dipoles start at 0.21 m from the IP. The beams then travel through a 1.2 m shared PM vertically focusing quadrupole that starts at 0.9 m from the IP. This quadrupole (QD1) is centered on the high-energy beam (HEB) orbit in order to maximize the horizontal bending of the low-energy beam (LEB) and separate the beams enough to place QF2, a horizontally focusing septum magnet for the LEB, 2.8 m from the IP. Figure 1 shows a layout view of the PEP-II IR.

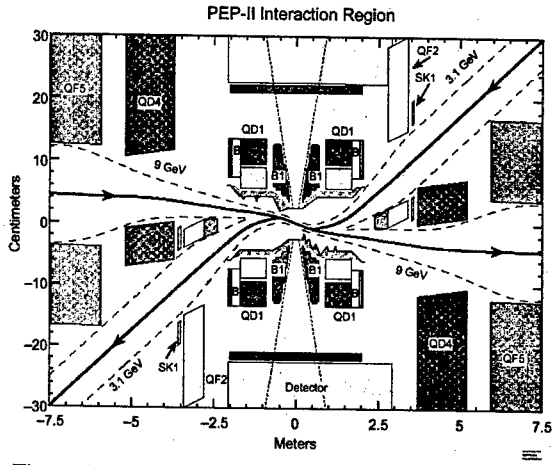

Figure 1. Layout of the PEP-II Interaction Region. Note the expanded vertical scale. The beams are brought into a head-on collision by the (~0.8T) dipole magnets (B1).

0-7803-7738-9/03/$17.00 © 2003 IEEE

Outboard of QF2 are the two final focus magnets for the HEB, QD4 and QF5. Both of these magnets are also septum magnets. The QD4 magnets are positioned such that the HEB travels through the magnet with a 14 mm offset. This offset horizontally steers the HEB so as to direct the produced quadrupole synchrotron radiation (SR) from the QF5 magnet away from the Be beam pipe located at the collision point.

SR masks under the B1 magnets shield the Be chamber from direct SR and all radiation from upstream sources as well as from backscattered downstream surfaces must bounce off of at least two surfaces before they can strike the Be chamber. Primary detector backgrounds for the silicon vertex tracker (SVT) come from off-energy beam particles (Beam-gas-Bremsstrahlung or BGB) that are swept out in the horizontal plane by the upstream Q4 magnet for the HER and the upstream Q1 and B1 magnets for the LEB.

The Be beam pipe consists of two thin walls (800μm and 400 μm) with a 1.2 mm water channel between the walls. The water absorbs the power deposited in the chamber from HOMs and resistive wall losses. At typical operating beam currents the Be chamber water absorbs about 1 kW of power. At each end of the Be is located a small 2 convolution bellows that is designed to minimize stresses in the chamber when nearby beam pipes move from thermal heating. The chambers on either side of the Be beam pipe are composed of mixtures of copper and dispersion strengthened copper (GlidCop). The GlidCop pieces absorb the significant amount of SR power that strikes the masking (~3 kW from the LEB and ~ 1 kW from the HEB).

The entire assembly of Q1 and B1 magnets with copper and Be beam pipes is rigidly held in a support tube that is positioned inside the BaBar detector. The ends of the support tube couple to the rafts on either side of the detector that hold the Q2, Q4 and Q5 magnets. The bellows at each end of the support tube connect to the Q2 vacuum chamber where the beams go into separate beam pipes. This junction of two beam pipes to the one beam pipe in the support tube generates significant HOM power (~5 kW) which is absorbed by silicon carbide tiles brazed into the two bellows sections at the ends of the support tube.

Last year, we discovered that the small bellows on either side of the Be beam pipe were getting hot through heating from HOM power penetrating the internal RF shields. The heating was observed by a thermocouple attached close to the bellows (see Fig. 2). The shields were designed to protect the bellows from longitudinal modes but the presence of the nearby SR masks can convert these modes into transverse modes. In particular, an H11 mode generated at an angle that couples to the longitudinal electric field [2]. (See Figs. 3 and 4.) These transverse modes can penetrate the longitudinal slits and deposit power in the stainless steel bellows convolutions.

The temperature rise was about 100°F at the thermocouple which, in itself, was not too alarming but the computer model for the heating of the bellows indicated that the actual bellows convolutions were significantly hotter (~300°C).

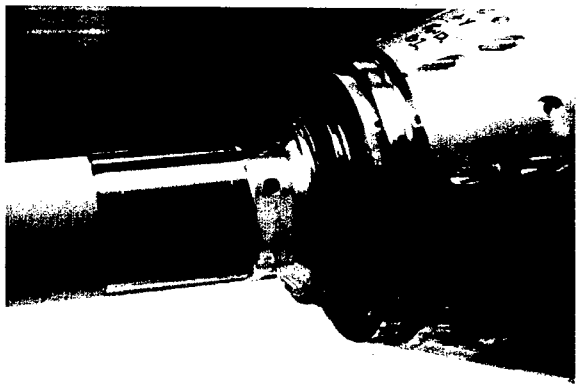

Figure 2. Picture of the small bellows convolutions near the Be beam pipe that heat up from HOM power. The thermocouple that registered the heat can be seen. The location of the thermocouple is between the bellows and the Be beam pipe which is covered with a sheet of Ta. The computer model of this area indicated that the bellows convolutions were much hotter than the readings from the thermocouple. The permanent magnet slices of the B1 magnet are shown to the right of the bellows.

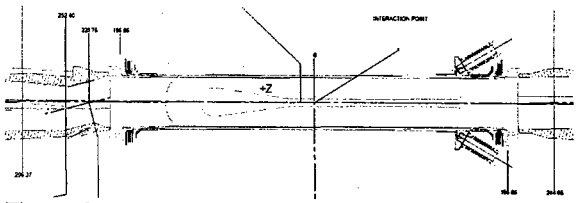

Figure 3. Drawing of the Be beam pipe and bellows sections at each end of the Be. The Be is brazed to stainless steel sleeves and the bellows sections are welded to the SS sleeves. The Be is cooled by water which enters and exits through the tubing on the right side of the drawing. The main SR mask for the LEB can be seen on the left and is 25 cm from the IP, the SR mask for the HEB is located on the right side but is farther away (50 cm from the IP) and is not seen.

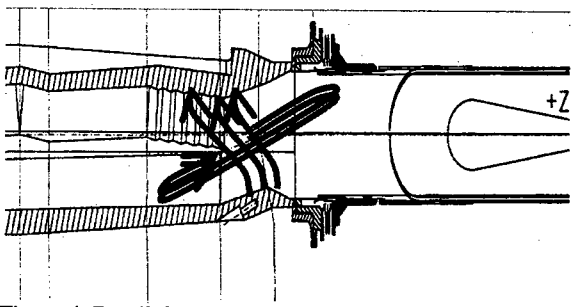

Figure 4. Detail drawing of the LEB SR mask and bellows section. The green arrows indicate the electric fields of the passing beam bunches and the subsequent magnetic field lines (in red) from H11 that can penetrate the slots in the RF shield of the bellows.

Last summer, we removed the support tube in order to add cooling to these small bellows near the Be beam pipe. In addition, we also rebuilt the Q2 chamber on the detector forward side and increased the number of HOM power absorbing tiles in the bellows sections at the ends of the support tube. So far, the results are very encouraging. The heating in the small bellows is very well controlled and should not become a problem until the heating increases by at least a factor of three. The temperature rise at the original thermocouple location is now 40°F for almost the same amount of beam current. Figs. 5 and 6 show further details about the cooling improvements.

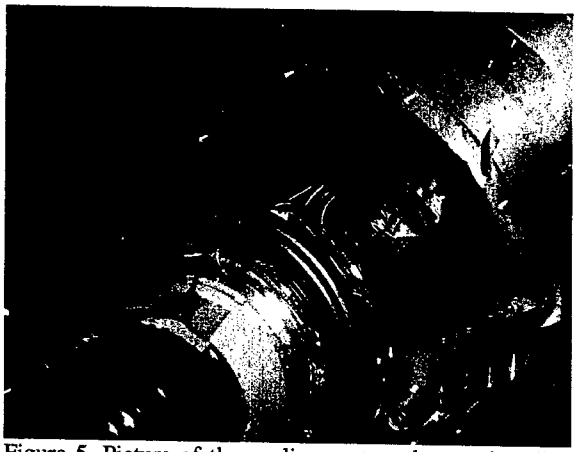

Figure 5. Picture of the cooling system that we installed last summer. The first 3 slices of B1 magnetic material were removed for access to the area. The small tubes (1/8 in. stainless steel) of air and water were threaded under the B1 magnet and can be seen between the bellows and the magnetic material. Three separate water circuits and two separate air circuits were installed for each bellows section. Each air circuit has two independent supply tubes.

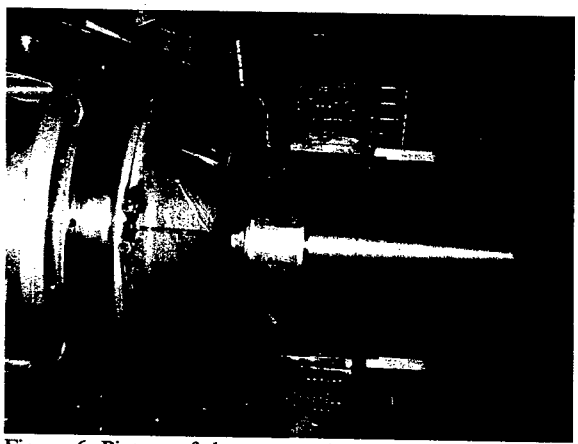

Figure 6. Picture of the new cooling covered by the final air shield to minimize the amount of air blowing at the SVT. One also sees one half of the SVT installed. The SVT is mounted on the small gimbal ring seen to the left in the photo. The bellows section on the other side of the Be beam pipe was also cooled with the new air and water circuits described above even though that side has better cooling from the Be water cooling system.

3 KEKB

The KEKB IR design has several distinct differences when compared to the PEP-II design. KEKB collides the two beams with a ±11 mrad crossing angle thereby eliminating the need for strong horizontal dipoles to separate the beams. In addition, the 3.5 GeV positron and 8 GeV electron beams enter the IR on-axis in all incoming quadrupoles. This eliminates any strong SR fans from bending magnets upstream of the IP and minimizes SR backgrounds in the detector. Figure 7 shows a layout of the KEKB IR.

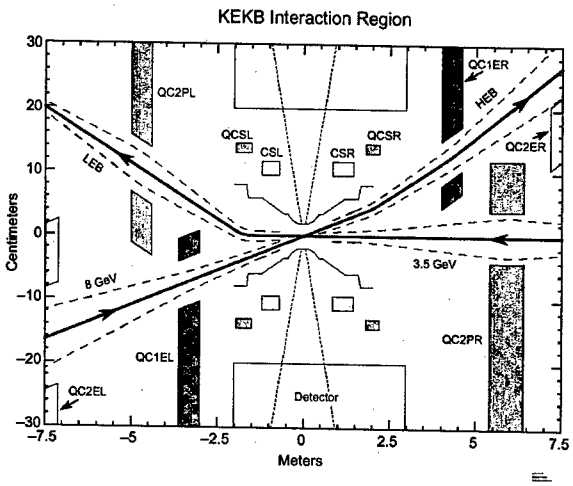

Figure 7. Layout of the KEKB IR. The incoming beams are on-axis and the outgoing beams are off-axis in the shared QCSL and QCSR superconducting quadrupoles. Note the expanded vertical scale. For comparison, the scales in this plot are the same as the scales used for the PEP-II layout in Figure 1.

SR from quadrupole magnets (focusing radiation) is still an issue and, in general, masks are still needed close to the IP to protect the detector Be beam pipe from this SR. The KEKB design has two small SR masks located near the Be beam pipe for just this purpose. See fig. 8 for more details.

The KEKB design, like PEP-II, has the quadrupole nearest to the IP shared by both beams. This means that the outgoing beams are far off-axis as they travel through these shared inner quads. The outgoing beams then generate SR fans of significant power, part of which can backscatter from surfaces relatively close to the detector and be seen as a background in the silicon vertex detector (SVD) located around the Be beam pipe.

KEKB has also experienced heating near the Be beam pipe from HOM power. They have replaced one Be chamber due to heating issues and have had one Be beam

pipe fail in a manner that has not been fully understood but was probably related to a heating issue.

4 NEAR TERM UPGRADES

Both B-Factories have plans for near-term upgrades in the IR that are designed to improve machine performance.

4.1 KEKB

This summer KEKB will replace the 2.0 cm radius Be beam pipe with a new smaller radius (1.5 cm) beam pipe in order to improve the detector vertex resolution by making room for another layer of tracking detectors and by getting radially closer to the IP [3]. The new design has no SR masks near the Be beam pipe in order to eliminate these "mode converters" and minimize the HOM power generated near the Be beam pipe. Figure 8 shows the difference between the present and new beam pipes. The new beam pipe will use a liquid coolant rather than the present design which employs He gas.

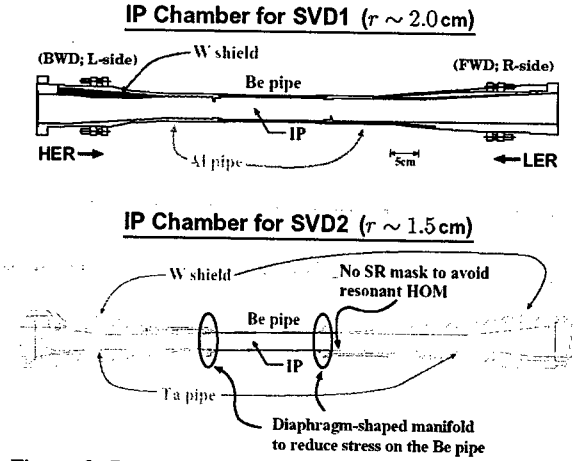

Figure 8. Drawings of the present KEKB Be beam pipe with some of the shielding and masking and of the new Be beam pipe to be installed this summer. Note that the two small SR masks in the present beam pipe are not preserved in the new beam pipe. The lost particle (BGB) shielding has also been improved. The smaller beam pipe radius is also evident.

4.2 PEP-II

PEP-II also plans to upgrade the IR in 2005. The strong dipole magnets will be modified with the last 20 cm of the dipole field being replaced by a strong focusing quadrupole field. This effectively moves the Q1 magnet closer to the IP allowing for lower β_y^* values at the collision point. This change reduces the B·dl of the dipole field from 0.329 T to 0.176 T and introduces a small (±3.25 mrad) crossing angle at the IP. The change also greatly reduces the total amount of SR generated by these dipoles. The crossing angle separates the beams more quickly which decreases the tune shift seen by the beams at the parasitic crossings on either side of the collision point and opens up the possibility of putting bunches in every RF bucket for a total number of 3400 bunches. This upgrade is being designed to allow the β_y^* values to go down to 5 mm. Lowering the β_y^* down to 5 mm of course means that PEP-II will also have to concentrate on making the bunch length shorter than the present values of 11-13 mm. The shorter bunches will then also increase the HOM power generated in the IR. Figure 9 shows a layout of the upgraded PEP-II IR.

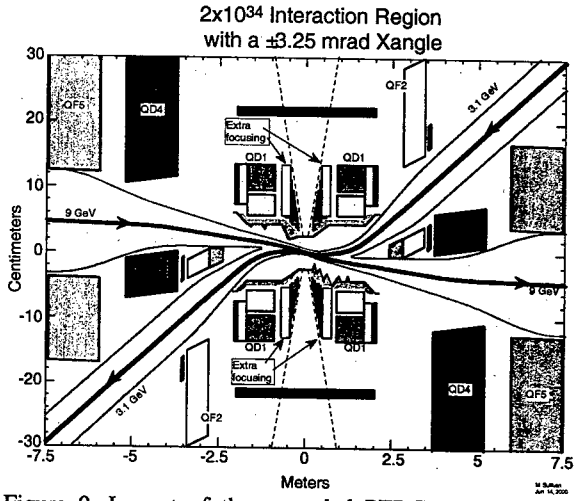

Figure 9. Layout of the upgraded PEP-II IR. Note the expanded vertical scale. The last four slices (20 cm) of the B1 magnets have been replaced with quadrupole field to increase the focusing and effectively move the QD1 magnet closer to the IP.

5 VERY HIGH LUMINOSITY IRS

Both B-Factories are also working on designs to greatly increase the luminosity. Both designs call for increased beam currents (10-25 A) and for still lower β_y^* values (1.5–3 mm). HOM power will be a major concern for these high-current machines.

5.1 SuperKEKB

KEK has a well-developed design to upgrade KEKB to a 1×10^{35} cm^{-2} sec^{-1} luminosity machine [4-5]. The beam currents are 9.4 A for the LEB and 4.1 A for the HEB. The β_y^* value is 3 mm and the bunch length is 3 mm. The design for the IR is very similar to the present KEKB (see Figure 10). The incoming beams are, again, on-axis and the outgoing beams are off-axis in the shared quadrupoles that are closest to the IP. The crossing angle has been increased to ±15 mrads in order to preserve beam separation and maintain the option of putting beam into every RF bucket (~5000). This increase in the crossing angle will tend to increase the amount of locally generated SR on top of the large current increases and controlling this SR power will have to be studied very carefully.

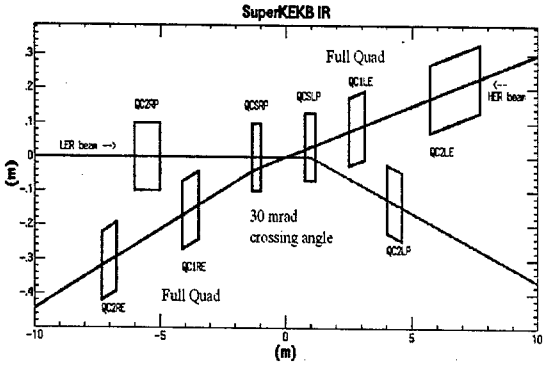

Figure 10. Layout of the superKEKB IR design. The superconducting quads are closer to the IP. In order to get a similar beam separation as the present KEKB, the crossing angle has been increased to ±15 mrads.

5.2 A 1×10^{36} Luminosity PEP-II

For PEP-II, the very preliminary IR design for a 1×10^{36} cm^{-2} sec^{-1} luminosity machine employs a crossing angle of ±12 mrads similar to the present KEKB machine [6]. The design has symmetric optics and orbits and that means that SR fans are generated in the upstream shared quadrupoles. The power from the fans is quite large due to the very high beam currents and care must be taken to properly absorb this power and to account for the backgrounds from these fans as well as the from the quadrupole focusing radiation. Figure 11 shows a layout of the IR for a 1×10^{36} luminosity design. The beam currents are 22 A for the LEB and 10 A for the HEB, but other designs are being considered with currents of 16 A and 7 A respectively. The β_y^* values go as low as 1.5 mm. The beam energies for this design are 8 GeV for the HEB and 3.5 GeV for the LEB.

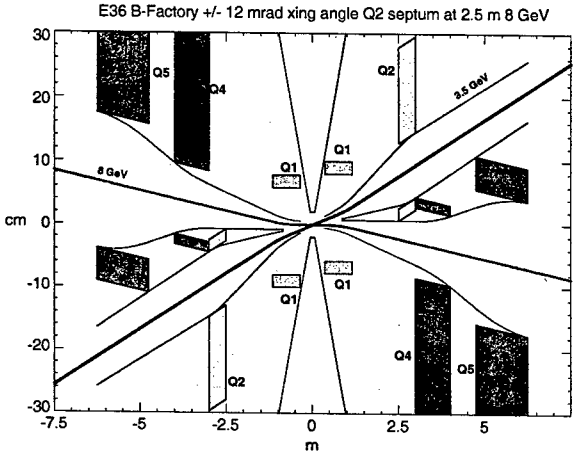

Figure 11. Layout of a preliminary design for the IR of a 1×10^{36} cm^{-2} sec^{-1} luminosity machine at SLAC. There are no dipole magnets to bring the beams into collision. Instead a crossing angle of ±12 mrads is used. The shared quadrupoles are superconducting and are symmetrically positioned to generate the same bending in the beam upstream as well as downstream of the IP. The SR fans generated by these beams are shown in the figure. The powerful HEB beams stay inside the beam envelope until at least more than 10 m from the IP thereby allowing the power to spread out and become more manageable. The SR fans from the LEB start to strike the beam pipe about 5 m from the IP.

6 SUMMARY

The present B-Factories have achieved very impressive luminosity peaks with far fewer bunches than was assumed in the original designs. The beam currents, however, are approaching and, in some cases, exceeding the design values. This combination has greatly increased the single bunch current and this has, in turn, increased the HOM power. The increase in HOM power has been seen in both B-Factory interaction regions and both factories have had to improve cooling near the Be beam pipe due to HOM power. Future upgrades to these IRs have to include HOM power implications.

Designs of even higher luminosity B-Factories entail large beam currents and short bunch lengths, both of which increase the total HOM power. In addition, the large beam currents generate intense synchrotron radiation fans in the IR of these designs that must be kept under control. Experience from the present B-Factories will be an invaluable benchmark for estimating the HOM power, SR backgrounds, beam-gas backgrounds and heating from these very high current machines.

7 ACKNOWLEDGEMENTS

We wish to thank the SLAC staff for their dedicated support of the PEP-II accelerator. We especially thank the operations group for their unfailing effort to keep this machine running and for tuning the machine to ever higher luminosities.

8 REFERENCES

[1] "PEP-II an Asymmetric *B* Factory", Conceptual Design Report, CALT-68-1869, LBL-PUB-5379, SLAC-418, UCRL-ID-114055, UC-IIRPA-93-01, June 1993.

[2] A. Novokhatski, "IR2 IP HOM Calculations and Measurements", PEPII Performance Wkshp, Jan 2002 http://www.slac.stanford.edu/~sullivan/PEPII_perf_wkshp_2002/IPhoms_Novo.pdf

[3] T. Abe, "IP Chamber for SVD2", KEKB Rev. Feb 10-12, 2003 http://www-kekb.kek.jp/review_2003/abe.pdf

[4] http://www-kekb.kek.jp/SuperKEKB/EoI.pdf

[5] N. Ohuchi, "Interaction Region Design for SuperKEKB", KEKB Review Feb 10-12, 2003 http://www-kekb.kek.jp/review_2003/ohuchi.pdf

[6] M. Sullivan, "IR Upgrades and Options", SLAC Long-Range Scenarios, Mar 20, 2003 http://www.slac.stanford.edu/~sullivan/IR_upgrades_Bday.pdf

Proceedings of the 2003 Particle Accelerator Conference

RECENT DEVELOPMENTS IN DESIGNS FOR e^+e^- COLLIDERS

K. Ohmi for the KEKB Commissioning Group
KEK, Oho, Tsukuba, 305-0801, Japan

Abstract

We discuss an design of future e^+e^- collider from the view point of the beam dynamics. The crossing angle permits short bunch spacing without complex design of the interaction region. In KEKB, the crossing angle did not degrade the collision performance. However we need to study how the crossing angle affects the beam-beam interaction for the future high luminosity colliders. The electron cloud instability, which limited the luminosity performance in positron ring, have been somehow recovered by using solenoid magnets. The ion instability, which have been observed in electron rings, may be serious for higher beam current. We have to study which particle should be stored in high or low energy rings to minimize the instability effects. The coherent synchrotron radiation becomes serious for short bunch length and high bunch current. We discuss these issues one by one.

INTRODUCTION

B factories in the world, PEP-II and KEKB, have been successfully operated with very high luminosities. The peak luminosities of PEP-II and KEKB are 0.61×10^{34} and 1.06×10^{34} cm^{-2}s^{-1}, respectively, at May, 2003. The operations are somewhat different from their original designs. In the both factories, the number of bunches is less than the design values, and bunch current is higher than the design values. They are operated in a regime where beam-beam parameter is saturated ~ 0.05.

We are challenging to get more luminosity everyday. The solenoid magnet coils to avoid the electron cloud effects were wound everywhere as possible as we could. The horizontal tune was controlled to keep closed to half integer. Vertical tune and chromaticity was scanned to get higher luminosity and useful beam life time every time. Geometrical condition of collision, offset of two beam, vertical crossing angle and RF phase were scanned and feed backed in every second. All of optics parameters at the collision point, $\beta_{x(y)}$ functions, dispersions ($\eta_{x(y)}$, $\eta'_{x(y)}$), x-y coupling parameters ($R_1 - R_4$) were scanned every time [1, 2].

In PEP-II, 945 bunches are stored with 6 ns spacing. In KEKB, 1000 bunches had been stored with 8 ns spacing, because increasing of the number of bunch did not contribute luminosity until last year (2002) perhaps due to electron cloud effects, not parasitic collision effects. As the result of addition of solenoid magnets in every long shutdown periods, the number of bunches can be made increase gradually. Attempt to increase the number of bunches has been continued in KEKB.

In the both of SLAC and KEK, upgrade plans toward the luminosity of $10^{35} - 10^{36}$ cm^{-2}s^{-1} are proposed. We discuss the design development of the upgrade plan of KEKB, named by super KEKB, in this report. The parameters for the present operation of KEKB and those for the design of Super KEKB are shown in Table 1.

We discuss three topics: beam-beam effects, instabilities and coherent synchrotron radiation. Collision with/without a crossing angle is reviewed in Sec.II. Electron cloud and ion instabilities are discussed in Sec.III. These studies inform which particle stored in low energy or high energy rings. Longitudinal single bunch instability due to the coherent synchrotron radiation is discussed in Sec.IV.

CROSSING ANGLE

In high luminosity e^+e^- factories, KEKB and DAΦNE adopt collision with finite crossing angle, and PEP-II adopts head-on collision. Crossing angle makes easy a design of the interaction region for the narrow bunch spacing. However the crossing collision scheme had been considered to be a taboo, since the unsuccessful experience of DORIS in DESY. In KEK and INFN, many studies were performed to decide the adoption of the crossing collision scheme [3, 4, 5]. KEKB and PEP-II have achieved luminosities of 1.06×10^{34} and 0.61×10^{34} cm^{-2}s^{-1}, respectively at May, 2003. The beam-beam parameters are 0.05 for KEKB, respectively. Consequently, the crossing angle does not affect the beam-beam performance in the region of the beam-beam parameter up to 0.05.

We now target higher luminosity, $L = 10^{35} \sim 10^{36}$ cm^{-2}s^{-1}. The beam-beam parameter should be higher to get the luminosity. We need to review the effect of crossing angle on the beam-beam interaction for a higher beam-beam parameter.

Collision with a half crossing angle of θ is equivalent to that between beams with z dependent dispersion ($\zeta_x = \theta$) at the interaction point [6]. Crab cavities generate the dispersion $\zeta_x(s)$. Matching the dispersion as $\zeta_x = -\theta$ at the interaction point, effects of the crossing angle are canceled [7].

We have studied the beam-beam effects using the weak-strong and strong-strong simulation methods [8]. In the weak-strong method, one beam is represented by macro-particles and another beam is represented by a fixed Gaussian charge distribution. In the strong-strong method, both beams are represented by many macro-particles, and their interactions are evaluated by the particle in cell method.

The weak-strong simulation is executed for 100 macro-particles and 10 or more longitudinal slices during 40,000

0-7803-7738-9/03/$17.00 © 2003 IEEE

Table 1: Basic parameters of present KEKB and Super KEKB

	KEKB		Super KEKB	
	HER	LER	HER	LER
particle	e^-	e^+	$e^\pm$	$e^\mp$
C	$3016m$		$3016m$	
E	8 GeV	3.5 GeV	8 GeV	3.5 GeV
$N_\pm$	5.4×10^{10}	7.3×10^{10}		
N_{bunch}	1280		5000	
β_x/β_y	60 cm / 7 mm		15 cm / 3 mm	
ε_x	24 nm	18 nm	18 nm	
σ_z	7 mm		3.5 mm	
$\nu_x/\nu_y/\nu_s$	0.515/0.565/0.02		0.515/0.565/0.02	
τ_{xy}/T_0	4,000	4,000	4,000	4,000-8,000
θ_c	11 mrad		$0 - 15$ mrad	
$L(\text{cm}^{-2}\text{s}^{-1})$	1.06×10^{34}		$1 \times 10^{35} - 10^{36}$	

revolutions. The strong-strong simulation is executed for 100,000 macro-particles and 5 longitudinal slices during 20,000 revolutions.

We calculated the luminosity for various current keeping the transparency condition. Figure 1 shows the beam-beam tune shift which is estimated by the luminosity for the positron current, I_+. Pictures (a) and (b) are given by the weak-strong, and (c) and (d) are by the strong-strong. The tune shift should linearly depends on I_+, if there is no dynamical effect of the beam-beam interaction. In the weak-strong simulation, the tune shift linearly increases up to 0.25 for head-on collision, while it saturates around less than 0.08 for crossing angle 11 mrad. The tune shift is extremely high beyond all belief. We use operating tune which is close to half integer in horizontal as is operated in KEKB.

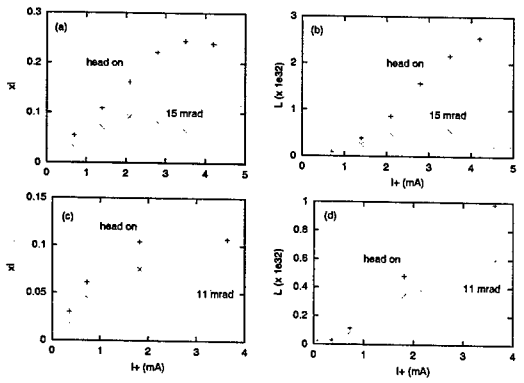

Figure 1: Beam-beam parameter (a)(c) and luminosity (b)(d) function of positron current for collisions with/without crossing angle. Pictures (a) and (b) are obtained by the weak-strong simulation, and (c) and (d) are by the strong-strong simulation.

Beam-beam halo is another limitation of the beam-beam effect [9]. The halo is evaluated by a very long term simulation using the weak-strong method. We used brute force simulation using 500 particle times 10^6 turn, though there is some technique to reduce the calculation time [9, 11]. The CPU time was a few 10 minute for 10 longitudinal slices. Figure 2 shows distribution of beam particles in $x - y$ plane. The particle times turn numbers, 5×10^8, corresponds to more than 1 hour. Concerning also beam-beam halo, the head-on collision is better than that with finite crossing angle. [10].

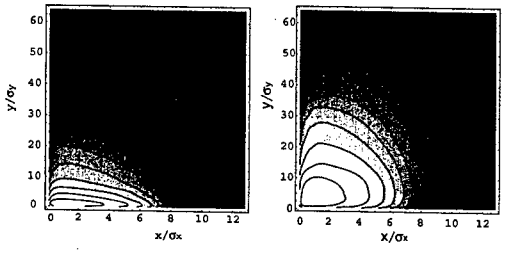

Figure 2: Beam-beam halo for collisions without (left) and with (right) crossing angle estimated by the weak-strong simulation.

PARTICLE AND ENERGY

In asymmetric B factories, PEP-II and KEKB, energies of electrons and positrons are chosen to be 8-9 GeV and 3-3.5 GeV. The choice is reasonable by considering an injector Linac, in which positrons are created as secondary particles by electrons accelerated to be several GeV. Electron beam can be accelerated to higher energy, while its intensity, which is primary, is stronger than that of positron beam.

From the viewpoint of the beam-beam interaction, the

number of particles with the low energy in a bunch is required to be more than those with the high energy. The so-called transparency condition is $N_H\gamma_H = N_L\gamma_L$, where $N_{H(L)}$ and $\gamma_{H(L)}$ are the number of particles and the relativistic factor of the high (low) energy, respectively. There is a merit to choose that electron beam has a lower energy.

In the B factories, ion and electron cloud instabilities are observed in electron and positron rings, respectively, and they affect the performances of the rings. We survey these instabilities and study which beam should have high or low energy.

Electron cloud effect

We first estimate build-up of an electron cloud for two case of the positron beam energies, $E = 3.5$ GeV and 8 GeV. The photoelectron instability model [12] is used for the estimation of the build-up. There are some codes to estimate the build-up [12, 13, 14]. We used the code PEI [12].

The primary electrons are created by synchrotron radiation with a production rate, $n_e = 0.0015/(\mathrm{m}\cdot\mathrm{e}^+)$, for a positron passage per a mater. This production rate corresponds that 100 photons create 1 photoelectron at the chamber surface. This is an empirical value for a test ante-chamber at KEKB. The photons are assumed to be created uniformly at the chamber.

The secondary yield is used a formula given by ref.[13],

$$Y_2(E) = Y_0 \exp(-5E/E_{max}) + Y_{max}\frac{E}{E_{max}}\frac{1.44}{0.44+(E/E_{max})^{1.44}}. \quad (1)$$

$E_{max} = 200$ eV, $Y_0 = 0.5$ and $Y_{max} = 1.2$ are used here.

Figure 3 shows the electron cloud density for the beam energy of the cases of 3.5 GeV and 8 GeV. The density for 8 GeV is higher than that for 3.5 GeV: ρ_e(8GeV)> ρ_e(3.5 GeV).

In a regime for a lower cloud density than neutralization, electrons are strongly overfocused by the beam, therefore cloud density is determined by dynamical balance of creation and absorption. In another regime for a high cloud density close to neutralization, the overfocusing force is weakened, therefore electrons tend to be accumulated up to the neutralization. If these two cases of 3.5 ad 8 GeV are in the first regime, the cloud density of 8 GeV case should be more than that of 3.5 GeV: ρ_e(8 GeV)> ρ_e(3.5 GeV). Because the transparency condition, $N_H\gamma_H = N_L\gamma_L$, gives an equal number of photoelectrons production due to the number of photon scaling to $N_+\gamma_+$, and the overfocusing force of low energy (high intensity) beam is stronger. If they are in the second regime, the electron line density is near the beam line density: that is, 3.5 GeV, which is higher line density, should be higher density, ρ_e(8 GeV)< ρ_e(3.5 GeV).

The simulation result in Figure 3, ρ_e(8 GeV)> ρ_e(3.5 GeV), shows that the both cases are in the first regime. The case of 8 GeV has so slow build-up time that it may be in the second regime. Since these behaviors depend on parameters as electron production and secondary rates etc., we need more study whether these results are always obtained.

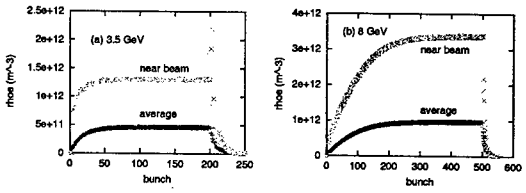

Figure 3: Electron cloud density for 3.5 GeV and 8 GeV cases.

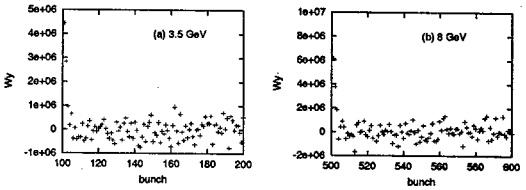

Figure 4: Wake field caused by the electron cloud for 3.5 GeV and 8 GeV cases.

We first estimate the coupled bunch instability caused by the electron cloud [12]. A bunch train which passes through the electron cloud experiences a wake force. Figure 4 shows the wake field for each case. The growth time can be estimated by the wake force induced by the electron cloud. The growth times were obtained as $\tau = 0.3T_0$ and $0.4T_0$ for the case of 8 GeV and 3.5 GeV, respectively. The growth time for 8 GeV was a little faster than that for 3.5 GeV. The strongest mode was around $m \approx 4500$, whose frequency was $\omega \approx (5120 - 4500)\omega_0 - \omega_\beta$ for either case. The growth rates are too fast to recover a bunch by bunch feedback system. Actually the electron cloud should be removed by solenoid magnets, ante-chamber, electrodes and other measures. We here focus the relative value of the growth: that is, 3.5 GeV is a little slower. This result may be due to that the cloud density for 3.5 GeV was further weaker, though the gamma factor is smaller.

We next study single bunch instability due to the electron cloud. The positron beam, which passes through the electron cloud, experiences a short range wake force. The wake force causes the strong head-tail instability. The instability can be simulated by some simulation codes [15, 16, 17, 18]. Figure 5 shows the growth of the vertical beam size for the cases of 3.5 and 8 GeV obtained by the code PEHTS [17].

The threshold of the strong head-tail instability due to the electron cloud is $\rho_{e,th} = 0.5 - 1 \times 10^{12}$ m^{-3} for 3 GeV and $1 - 2 \times 10^{12}$ m^{-3} for 8 GeV. The threshold densities for the cases of 3.5 and 8 GeV are about half of those estimated by the build up code in Figure 3. These results show that

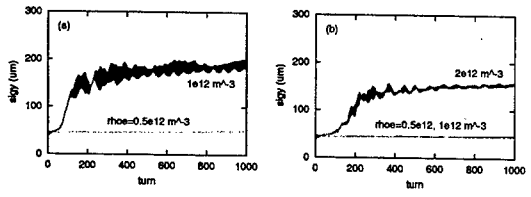

Figure 5: Growth of the single bunch instability caused by the electron cloud for (a) 3.5 GeV and (b) 8 GeV cases.

difficulties for the two cases are not big difference, because effect of γ is cancelled by the density difference.

Ion effect

We study which should choose 3.5 or 8 GeV for the electron beam energy. In an electron ring, ions, which produced by ionization of residual gas due to the beam, trapped in the bunch train, and causes a two-stream instability [19]. We studied this instability using a simulation model shown in Ref.[20, 21]. Electron bunch is assumed to be Gaussian distribution in the transverse plane and ions are represented by point-like macro-particles. In the simulation, the instability is caused by the oscillation of ions bounded in the bunch train. Ion species and yield are assumed as CO^+ and 4×10^{-9}/(m·e). This yield corresponds to the pressure of 1×10^{-7} Pa. Figure 6 shows growth of transverse amplitudes, $\sqrt{J_{y(x)}}$. Vertical growth is faster than horizontal

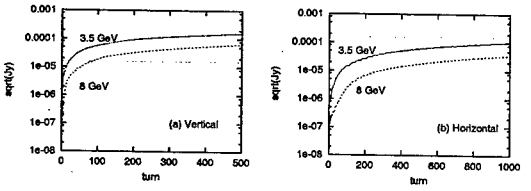

Figure 6: Growth of the fast ion instability. Blue and red lines are evolutions of $\sqrt{J_{y(x)}}\,\mathrm{m}^{1/2}$ for $E = 8$ GeV and 3.5 GeV, respectively. Pictures (a) and (b) depict the vertical and horizontal growth, respectively.

one. The growth time is ~ 50 and < 10 turns for 8 GeV and 3.5 GeV cases, respectively. The growth time of each energy case is reasonable for the consideration of the γ factor and the beam line density. Perhaps growth time of 50 turn is limit for bunch by bunch feedback system. Concerning ion issue, the option of 8 GeV is better.

COHERENT SYNCHROTRON RADIATION

Bunch lengthening is important issue for keeping the length with high population. The threshold of longitudinal single bunch instability is discussed using Keil-Schnell-Boussard relation [22]. The impedance threshold value is given by

$$|Z_\parallel/n| = 0.66 Z_0 \frac{\alpha\gamma}{N_e r_e} \sigma_\delta^2 \sigma_z. \tag{2}$$

where $n = \omega/\omega_0$ and α is the momentum compaction factor. The threshold of the impedance Z/n is $\sim$0.05 Ω for present KEKB.

Coherent synchrotron radiation affects the bunch lengthening [23, 24]. The wake force of the coherent radiation is given by [25, 26]

$$W_0(z) = \frac{2}{(3R^2)^{1/3}} \frac{\partial}{\partial z} z^{-1/3} \tag{3}$$

where R is the bending radius. The impedance integrated over the circumference is given as

$$Z_\parallel(\omega) = \frac{iAZ_0}{2} \left(\frac{\omega R}{c}\right)^{1/3} \tag{4}$$

where $A = 3^{-1/3}\Gamma(2/3)(\sqrt{3}i - 1) = 1.63i - 0.94$. Since the impedance scales as $Z/n \propto \omega^{-2/3}$, the Keil-Schnell-Boussard criteria gives threshold frequency (ω_{th}) of the instability,

$$\omega_{th} R/c = 2.0 \Lambda^{3/2}, \tag{5}$$

where [1]

$$\Lambda = \frac{N_e r_e}{\alpha\gamma\sigma_\delta^2 \sqrt{2\pi}\sigma_z} \frac{R}{\bar{R}} \tag{6}$$

and $\bar{R} = L/2\pi = c/\omega_0$.

We have to consider that lower frequency component of the impedance, which satisfies a condition of $\omega\sigma_z/c < 1$, does not contribute the instability. The frequency component, which satisfies $\omega R/c > (\pi R/2b)^{3/2}$, is shielded by the chamber wall, where b is the chamber radius [27]. This gives another necessary condition for the instability, $b\Lambda/R > 1$.

The length of the bending magnet should be remember to be short for LER, $L_{\mathrm{Bend}} = 0.76$ m [24]. If the correlation is determined by interaction in a bending magnet, the correlation length is estimated by the overtaking length for the radiation.

$$\ell_{\mathrm{cor}} = \frac{1}{3R^2} \left(\frac{L_{\mathrm{Bend}}}{2}\right)^3. \tag{7}$$

It is difficult to understand whether the synchrotron radiation emitted in a bending magnet affects the motion in another bending magnet. If it does not affect, the wake force should be truncated with the correlation length. Otherwise, a numerical simulation of motion, in which the correlation across bending magnets is included, should be performed [24].

These values for KEKB and super KEKB are summarized in Table 2.

[1] The coefficient of $\Lambda^{3/2}$ was followed by Ref.[23].

Table 2: Coherent synchrotron radiation effect for KEKB and Super KEKB

	KEKB		Super KEKB	
	LER	HER	LER	HER
N_e	7.3×10^{10}	5.4×10^{10}	1.2×10^{11}	5.4×10^{11}
σ_z	5 mm	5 mm	3.5 mm	3.5 mm
α	10^{-4}	10^{-4}	10^{-4}	10^{-4}
σ_δ	7×10^{-4}	7×10^{-4}	7×10^{-4}	7×10^{-4}
Λ	1674	2905	4087	4150
ω_{th}	2.5×10^{12} s^{-1}	1.1×10^{12} s^{-1}	8.9×10^{12} s^{-1}	2.2×10^{13} s^{-1}
$\omega_{th}\sigma_z/c$	42	17	104	21
$b\Lambda/R$	5.1	1.7	11.9	2.4
L_{bend}	0.76 m	5.8 m	0.76 m	5.8 m
$\ell_{\rm cor}$	69 μm	1 mm	69 μm	1 mm

SUMMARY

We discussed the design development of future B factories based on parameters of Super KEKB concerning the three issues (1) beam-beam effect with/without crossing angle, (2) energy choice, electron cloud and ion instabilities, and (3) coherent synchrotron radiation. The collision performance was improved for the head-on collision at high beam-beam parameter $\xi > 0.05$ in our simulations. Crab cavities make the condition of the head-on collision effectively for the finite crossing angle scheme of the beamline arrangement. The crab cavity is expected to boost up the luminosity. Studies of the electron cloud and ion instabilities gave information of energy choice, which particles e^+ or e^- should be accumulated in high/low energy ring. In the present simulation, LER-e^+ option was slightly better than HER-e^+ option. Since this result may be delicate for the electron production parameters, careful studies are needed. In either case, it is important to be cured by antechamber, solenoids, etc. Coherent synchrotron radiation affects the bunch lengthening in the B factories. We have to solve how to treat the correlation length.

The author thanks fruitful discussions with S. Heifets, Y. Ohnishi, K. Oide, E. Perevedentsev, G. Stupakov, M. Tawada, K. Yokoya and F. Zimmermann.

REFERENCES

[1] K. Akai et al., Nucl. Instrum. Meth. **A499**, 191 (2003).

[2] K. Ohmi, Proceedings of EPAC2000, 433 (2000).

[3] K. Hirata, Phys. Rev. Lett., **74**, 2228 (1995).

[4] "KEKB B-factory design report", KEK Report 95-7 (1995).

[5] K. Hirata, M. Zobiv, proceedings of EPAC96, 1158 (1996); M. Zobov et al., Frascati Phys. Ser. 10, 303 (1998).

[6] K. Ohmi, K. Hirata and K. Oide, Phys. Rev. **E49**, 751 (1994).

[7] K. Oide, K. Yokoya, Phys. Rev. **A40**, 315 (1989).

[8] K. Ohmi, Phys. Rev. **E62**, 7287 (2000).

[9] T. Chen, J. Irwin, R. Siemann, Phys. Rev. **E49**, 2323 (1994).

[10] J. Irwin, private communications.

[11] D. Shatilov, KEK-report, 96-14 (1994).

[12] K. Ohmi, Phys. Rev. Lett. **75**, 1526 (1995).

[13] M. Furman, G.R. Lambertson, Proceedings of MBI97 (KEK Report No. 97-17,1997), p. 170.

[14] F. Zimmermann, see CERN ECLOUD web page.

[15] K. Ohmi, F.Zimmermann, Phys. Rev. Lett., **85**, 3821 (2000).

[16] G. Rumolo, *et al.*, Proceedings of PAC2001,

[17] K. Ohmi, Proceedings of PAC2001,

[18] Y. Cai, Proceedings of ECLOUD2002.

[19] T.O. Raubenheimer, F. Zimmermann, Phys. Rev. **E52**, 5487 (1995).

[20] K. Ohmi, Phys. Rev. **E55**, 7550 (1997).

[21] S. Heifets, Proceedings of MBI97 (KEK Report No. 97-17,1997), p. 98.

[22] E. Keil and W. Schnell, CERN Report TH-RF/69-48 (1969); D. Boussard, CERN Lab II/RF/Int 75-2 (1975).

[23] G. Stupakov, S. Heifets, Phys. Rev. ST-AB., **5**, 054402, (2002).

[24] K. Yokoya, private communications.

[25] J.B. Murphy, S. Krinsky, R.L. Gluckstern, Part. Accel. **57**, 9 (1997).

[26] Y.S. Derbenev *et al.*, DESY Report No. TESLA-FEL 95-05, 1995.

[27] R.L. Warnock, SLAC Report No. SLAC-PUB-5375, 1990.

BUILDUP OF ELECTRON CLOUD WITH DIFFERENT BUNCH PATTERN IN THE PRESENCE OF SOLENOID FIELD*

Yunhai Cai, Mauro Pivi, SLAC, Menlo Park, CA 94025, USA
Miguel Furman, LBNL, Berkeley, CA 94720, USA

Abstract

We have augmented the code POSINST to include solenoid fields, and used it to simulate the build up of electron cloud due to electron multipacting in the PEP-II positron ring. We find that the distribution of electrons is strongly affected by the resonances associated with the cyclotron period and bunch spacing. In addition, we discover a threshold beyond which the electron density grows exponentially until it reaches the space charge limit. The threshold does not depend on the bunch spacing but does depend on the positron bunch population.

INTRODUCTION

It is well established by many experimental evidences [1, 2] at KEKB and PEP-II that the instabilities caused by electron impose a severe limitation upon the luminosity in e^+e^- storage rings. Based on the experiments [1] at KEKB, there exists a current threshold beyond which the vertical beam size at the interaction point starts to grow like $\sigma_y^* \propto N_p^2/S_b$, where N_p is the bunch population and S_b is the spacing between two sequential bunches. Since N_p is normally set at the limit allowed by the beam-beam interaction, this observation implies that S_b cannot be too small otherwise the vertical blow-up degrades the luminosity. As a result, both B-factories are currently operated $S_b \approx 2$m, which is larger than its design value.

Experimentally, the solenoid field raises the threshold of the blow-up and therefore allows the increase of luminosity. On the other hand, we know from the simulation performed by Zimmermann [3] that longitudinal solenoid field B_s confines the electrons near the wall of the vacuum chamber and therefore reduces the cloud density near the positron beam. All this indicates that both S_b and B_s play vital roles in the physics of electron cloud instability. In this paper, we will study the dynamics between the positron beam and electron cloud with different S_b and B_s to reveal the physics indicated from the simulations and experiments.

ELECTRON MOTION

Our work starts with implementing longitudinal solenoid field in the code POSINST [4]. For simplicity, we assume that $\vec{B}$ is a constant and ignore any end effects of the solenoid. For a relativistic electron, the equation of motion can be written

$$\dot{\vec{v}} = -\vec{v} \times \frac{e\vec{B}}{\gamma mc} = \vec{\omega} \times \vec{v}, \qquad (1)$$

where $\vec{\omega} = e\vec{B}/\gamma mc$ is the cyclotron frequency of the electron. The solution of Eq. (1) is a helical orbit with the axis of the helix parallel to the magnetic field and the Larmor radius $r = v_\perp/\omega$. Along the field, electron moves in a constant speed $v_\parallel$. This solution is programmed in the code to compute the motion of the electrons where the solenoid field is at presence.

Parameter	Description	Value
E(Gev)	beam energy	3.1
C(m)	circumference	2200
N_p	bunch population	1.0×10^{11}
$\bar{\beta}$(m)	average beta function	17.0
$\epsilon_{x,y}$(nm-rad)	emittance x,y	24.0, 3.0
σ_z(cm)	bunch length	1.3
S_{RF}(m)	RF bucket spacing	0.63
δ_{max}	max secondary yield	2.0
E_{max}(eV)	energy at yield max	300
$\delta(0)$	yield low energy el.	0.5
r_b(cm)	beam pipe radius	4.5

Table 1: Simulation parameters for the LER at PEP-II

The parameters used in the simulation is tabulated in Table 1. S_b has to be a multiple of the RF spacing S_{RF}. N_p corresponds to the value at the peak of a typical fill in the recent operation. The values of δ_{max}, E_{max}, and δ_0 are chosen for the beam pipe of stainless steel in the straight sections where we have seen most electrons in the ring.

BUNCH TRAIN

Our simulation focuses on the electrons accumulated through the secondary emission from the beam pipe in the straight sections where not many primary electrons should be generated because of lack of synchrotron radiation. In the simulation, we generate a large number of electrons only at the first bunch passage and let electron cloud develops by the secondary emission process until a saturation density is reached.

The bunch pattern used in the simulation consists of a short train, long abort gap, and a long train. The density of electron cloud is clearly building up along the long train after the gap as shown in Fig. 1. Without solenoid field,

*Work supported by the Department of Energy under Contract No. DE-AC03-76SF00515 and DE-AC03-76SF00098.

0-7803-7738-9/03/$17.00 © 2003 IEEE

the average density grows extremely fast along the train but saturates quickly near twice the neutralization density $\rho_e = N_p/\pi r_b^2 S_b$ due to the balance between the space charge and secondary yield. As the solenoid field increases, both the growth rate and the saturation level decrease. At $B_s =$ 15G, we see a very gradual growth of the density along the train of 600 bunches. Assuming that the cloud density is proportional to the vertical beam blow-up, this simulation may be used to explain the observation of the very slow blow-up along the train after the initial installation of the solenoids at KEKB [1]. As B_s reaches 25G, the average electron density does not grow and is kept below 5% of ρ_e. That is near the density at which the head-tail instability occurs in the LER [5]. Fortunately, the density near the beam drops even more since the solenoid field restraints the electrons near the wall.

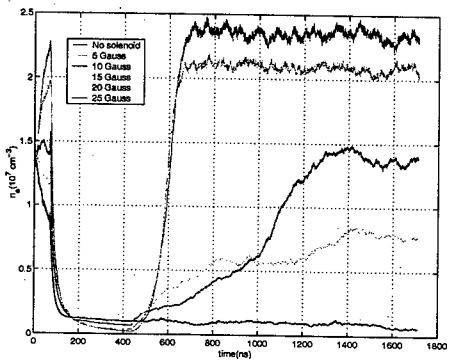

Figure 1: Density of electron cloud as a function of time when a bunch train passes through a stainless-steel beam pipe and longitudinal solenoid at different settings. The bunch spacing $S_b = 2S_{RF}$.

CYCLOTRON RESONANCE

As B_s increases further, we find at 40G that the saturation density along the bunch train actually become larger than the density without solenoid as shown in Fig. 2. However, with a close inspection of the distribution, we observed that nearly all electrons are confined in the vicinity of the wall. It is clearly seen from the figure that this phenomenon appears as a resonance.

Indeed, the result can be explained by a resonance associated with the cyclotron frequency ω and the bunch spacing S_b. Given the low-energy nature of the secondary electrons (100 eV), the radius of cyclotron motions is much smaller than the radius of beam pipe. The time for an electron coming out of the wall and then bending back by the magnetic filed and finally hitting the wall is nearly half of the cyclotron period $T_c = 2\pi/\omega$. The resonance occurs when this time coincides with the time interval between two consecutive bunches, namely

$$T_c/2 = S_b/c. \qquad (2)$$

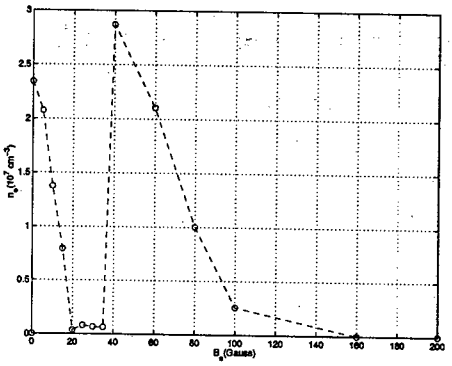

Figure 2: Saturation density along the bunch train as a function of solenoid field. The bunch spacing $S_b = 2S_{RF}$.

Since $\gamma \approx 1$ for typical secondary electrons, this resonance is almost independent of the velocities of electron and therefore much stronger than the resonance occurred in drift space. The condition of cyclotron resonance is given by

$$B_s^c = \frac{\pi mc^2}{eS_b}. \qquad (3)$$

Given $S_b = 1.26$m, we have $B_s^c = 40$G. That agrees with the simulation. In addition, we can see from Fig. 2 that minimum density occurs at $B_s = B_s^c/2$. If the bunch spacing is increased to $S_b = 3S_{RF}, 4S_{RF}$, B_s^c is reduced to 30G, 20G according to Eq. (3). Indeed, that is well confirmed by the simulation. Moreover, we find that the characters of dynamics are essentially the same if we keep the product of S_b and B_s as a constant.

THRESHOLD OF MULTIPACTING

A threshold of multipacting was observed[2] between 700mA to 900mA with 692 bunches spaced 4-RF buckets at PEP-II. The measurement was carried out without or with the solenoid field of 30G. To understand the threshold mechanism, we run simulations with the similar parameters as in the experiments.

The results of the simulation are shown in Fig 3. It is clearly seen from the figure that there exists a threshold beyond which the density of the electron cloud grows until it reaches the saturation. The threshold is independent of the bunch spacing S_b if one retains $S_b B_s$ as a constant. Above threshold, the saturated density is proportional to the line density of the beam N_p/S_b indicating it is limited by the space charge. Since the peak beam current at PEP-II is already operated well above the threshold, the simulation predicts that a two-fold increase of the electrons when the bunch spacing is shorten from $4S_{FR}$ to $2S_{RF}$ even if the solenoid field is doubled.

The threshold in the simulation is about 6.5×10^{10} compared with $(4.6 - 6.0) \times 10^{10}$ in the observation. Without solenoid, however, the simulation disagrees with the observation because the absence of the nearby threshold in the

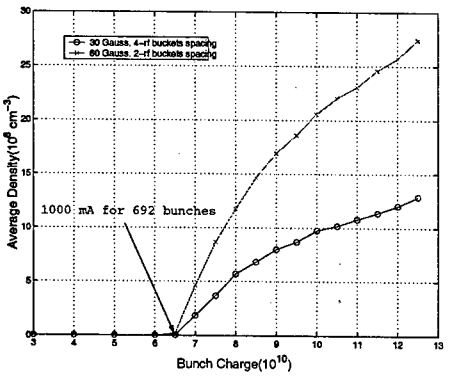

Figure 3: Saturated density as a function of the bunch population. The circles represent the case of 4-RF spacing and 30G solenoid field. The crosses represent 2-RF spacing and 60G field.

simulation.

For an electron near the wall, the momentum kick due to a bunch is given by [4]

$$\Delta p \simeq -\frac{e^2 N_p}{c}\frac{2}{r_b} \tag{4}$$

and thus the energy received from the bunch is

$$\Delta E \simeq \frac{2mc^2 N_p^2 r_e^2}{r_b^2}, \tag{5}$$

where r_e is the classic radius of electron. If the electron reaches the wall before the next bunch arrives ($B_s > B_s^c$), multipacting of electrons occurs if

$$\Delta E \geq E_{\delta=1}, \tag{6}$$

where $E_{\delta=1}$ (typically 20-100eV) is the energy above which the secondary yield δ larger than one. This yields the threshold of bunch population

$$N_p^{th} \simeq \frac{r_b}{r_e}\sqrt{\frac{E_{\delta=1}}{2E_0}}, \tag{7}$$

where $E_0 = mc^2$. In this simulation, we have $E_{\delta=1} \simeq 30$ eV. Using Eq. (7), we obtain $N_p^{th} \simeq 8.8 \times 10^{10}$ compared with 6.5×10^{10} found in the simulation. Besides reducing the secondary yield, enlarging the radius of beam pipe may be more effective way to increase the threshold as indicated in Eq. (7).

MULTI-BUNCH INSTABILITY

As the solenoid field increases, the electrons are gradually confined within the vicinity of the wall. However, under the condition of cyclotron resonance, there exist even more electrons than without solenoid. It was not clear if these electrons could cause any instability since they are so far away from the beam.

To answer this question, we compute the long-range wake as a function of the solenoid field and estimate the growth rate $1/\tau$. The wakes are shown in Fig 4. In this simulation, we have used a bunch spacing $S_b = 3S_{RF}$. Clearly from the figure, the peak values of wake are comparable at $B_s = 0$ and $B_s = 30$G (at the resonance). The growth time $\tau = 31, 9870, 145\mu s$ at $B_s = 0, 20, 30$G respectively.

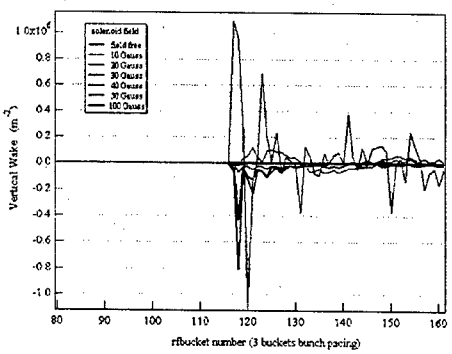

Figure 4: Long-range wake function due to electron cloud for bunch spacing $S_b = 3S_{RF}$.

DISCUSSION

Based on the simulation, we find that the cyclotron motion of electrons plays important role in generating and accumulating secondary electrons. When the resonance condition is satisfied, we see huge amount electrons near the wall. Although they are far away from the positron beam, they still create the long-range wake strong enough to cause multi-bunch instability.

In addition, if the solenoid field is strong enough $B_s > B_s^c$, we find that there exists a threshold for multipacting under which there is no accumulated electrons. This discovery may provide us a method to completely eliminate the electron cloud with larger enough beam pipe and lower enough secondary yield.

ACKNOWLEDGMENTS

We would like to thank Franz-Josef Decker, Stan Ecklund, Artem Kulikov, Sam Heifets, John Seeman, Mike Sullivan, and Uli Wienands for many helpful discussions. We are grateful to NERSC for supercomputer support.

REFERENCES

[1] H. Fukuma *et al*, Proc. EPAC, Vienna, Austria, 2000, p. 1124.

[2] A. Kulikov, *et al*, Proc. PAC, Chicago, 2001, p. 1903.

[3] F. Zimmermann, CERN SL-Note-2000-004 AP(2000).

[4] M.A. Furman and G.R. Lambertson, LBNL-41123/CBP Note-246, March 1998.

[5] Y. Cai, Proc. ECLOUD'02, CERN, Ganeva, Switzerland, 2002, p. 141.

Proceedings of the 2003 Particle Accelerator Conference

STUDY OF BEAM-BEAM INTERACTIONS WITH/WITHOUT CROSSING ANGLE

K. Ohmi, M. Tawada and K. Oide
KEK, Oho, Tsukuba, 305-0801, Japan

Abstract

In recent high luminosity colliders, the finite crossing angle scheme becomes popular to gain the multiplicity of luminosity with multi-bunch or long bunch operation. Success of KEKB showed that it was no problem to achieve the beam-beam parameter up to 0.05. We have studied the beam-beam interactions with/without crossing angle toward higher luminosity. We discuss how the crossing angle affects the beam-beam parameter and luminosity in the present KEK B factory (KEKB) using computer simulations.

INTRODUCTION

High luminosity B factories, KEKB and PEP-II are operated successfully at KEK and SLAC, respectively. The collision scheme in KEKB was designed so that two beams collide with a finite crossing angle, 2×11 mrad, by 2 ns repetition. While head-on collision scheme was adopted in PEP-II by 4 ns repetition. Crossing angle makes easy a design of interaction region for the narrow bunch spacing. However the crossing collision scheme had been considered to be a taboo, since the unsuccessful experience of DORIS in DESY. In KEK, many studies were performed to decide the adoption of the crossing collision scheme [1, 2, 3]. KEKB and PEP-II have achieved luminosities of 1.06×10^{34} and 0.61×10^{34} cm^{-2}s^{-1}, respectively at May of 2003. Such high luminosities were not believed to be realized when their design works had started. In recent high luminosity colliders, the crossing angle scheme becomes popular to gain the high repetition of the luminosity.

The luminosities are achieved by a high repetition frequency, which is $1/3 \sim 1/4$ of the design. The bunches spacing, which is inverse of the repetition frequency, is 8-6 ns and 6 ns for KEKB and PEP-II, respectively. Narrower bunch spacing does not contribute the luminosity perhaps due to the electron cloud effect in both of the machines. The operating tune is just slightly upper of half integer in horizontal, and is optimized around 0.54-0.56 in vertical.

We review the crossing collision scheme in the point of view of progress toward higher luminosity.

FORMALISM OF COLLISION WITH CROSSING ANGLE

We discuss the beam-beam effects with/without crossing angle using computer simulations. The collision with crossing angle is treated by Lorenz boost to a head-on frame from the laboratory frame [1, 2]: i.e., particles in the beam are transferred to the head on frame, experience the collision, and are transferred to laboratory frame by the inverse of the Lorenz boost. The transformation is given for a half crossing angle θ by

$$\begin{aligned} x^* &= \tan\theta z + \left(1 + \frac{p_x^*}{p_s^*}\sin\theta\right) x \\ y^* &= y + \sin\theta \frac{p_y^*}{p_s^*} x \\ z^* &= \frac{z}{\cos\theta} - \frac{H^*}{p_s^*}\sin\theta x \\ p_x^* &= \frac{p_x - \tan\theta H}{\cos\theta} \\ p_y^* &= \frac{p_y}{\cos\theta} \\ p_z^* &= p_z - \tan\theta p_x + \tan^2\theta H, \end{aligned} \tag{1}$$

where

$$H = (1+p_z) - \sqrt{(1+p_z)^2 - p_x^2 - p_y^2}$$

$$p_s = \sqrt{(1+p_z)^2 - p_x^2 - p_y^2}$$

A star designates a dynamical variable in the head-on frame. Note that the x^* and y^* axes are defined in the same direction for both beams, while the s^* axis is defined in opposite directions, since the two beams travel in opposite directions.

The linear part of the transformation is expressed by a matrix

$$M_{crs} = \begin{pmatrix} 1 & 0 & 0 & 0 & \tan\theta & 0 \\ 0 & 1/\cos\theta & 0 & 0 & 0 & 0 \\ 0 & 0 & 1 & 0 & 0 & 0 \\ 0 & 0 & 0 & 1/\cos\theta & 0 & 0 \\ 0 & 0 & 0 & 0 & 1/\cos\theta & 0 \\ 0 & \tan\theta & 0 & 0 & 0 & 1 \end{pmatrix}. \tag{2}$$

This transformation is not symplectic: the determinant of the Jacobian matrix of the transformation is not 1, but $\cos^{-3}\theta$. The fact is due to that Lorenz transformation is not symplectic for the accelerator coordinate, because the Hamiltonian is divided by a reference momentum.

The transformation and its inverse are performed before and after the beam-beam interaction, respectively. If we consider only linear part, the revolution matrix is expressed by

$$M_{crs} M_{arc} M_{crs}^{-1}. \tag{3}$$

where M_{arc} is the transfer matrix of arc section. For small θ, the revolution matrix is equivalent to that with z-dependent dispersion $\zeta_x = \theta$ [4] at the interaction point,

0-7803-7738-9/03/$17.00 © 2003 IEEE

$s = s^*$. The beam envelope has $\langle xz \rangle \propto \zeta_x(s)$ in the head-on frame.

Crab cavities create a z-dependent dispersion $\zeta_{x,crab}(s)$. Controlling $\zeta_{x,crab}(s^*)$ at the interaction point using the crab cavities, the effective crossing angle, which the beam experiences, can be chosen arbitrary. Head-on collision of the beams with $\langle xz \rangle = 0$ is realized by $\zeta_{x,crab} = -\theta$ effectively.

We use two simulation models, weak strong and strong-strong models, to study the beam-beam interactions. In the weak-strong model, one beam is fixed Gaussian distribution in the six dimensional phase space, while the other beam is represented by macro-particles. Macro-particles are transferred from the laboratory frame to the head-on one using Eq.(2). The beam envelope of the strong beam is transferred by

$$M_{crs}\langle \boldsymbol{x}\boldsymbol{x}^t \rangle M_{crs}^t. \tag{4}$$

In the strong-strong model, both of the beams are represented by macro-particles, which can have an arbitrary distribution. The beam-beam force is estimated by the particle in cell method [5]. Macro-particles of the both beams are transferred by Eq.(2).

We now consider collision of two beams in the head-on frame. The beam has longitudinal structure, bunch length, The simulation has to take into account of the longitudinal dynamics: bunch length and synchrotron motion. In the weak-strong simulation, we obeyed a method written in Ref. [6], so-called the synchro-beam map. The target bunch, which is 6-D fixed Gaussian distribution, is divided into several longitudinal slices, and collision between a slice and particle in the weak beam is calculated. The collision point of a slice (z_j) and the particle (z) is

$$s = z - z_j \tag{5}$$

Beam envelope of the slice is transferred to the collision point by

$$R(s(z)) = T(s(z), 0)R(0)T^t(s(z), 0). \tag{6}$$

Particles are translated

$$\boldsymbol{x}(s(z)) = \mathcal{T}(s(z))\boldsymbol{x}(0) = \exp\left[- : \frac{(p_x^2 + p_y^2)s(z)}{2} : \right] \boldsymbol{x}(0) \tag{7}$$

The beam envelope is a function of z, therefore the beam-beam force have a longitudinal kick.

In the strong-strong simulation, similar method is used [7]. If we estimate collision between slice by slice at $s = (z_i - z_j)/2$, 20-30 slices are needed depending on the beam intensity and the computation time is too long [8, 9, 10]. Two dimensional potential, which determines the beam-beam force, is estimated at a collision point front ($s_f = (z_{i,f} - z_j)/2$) and back ($s_b = (z_{i,b} - z_j)/2$) face of the (i-th) slice containing the particle. The potential of the target slice $\phi(s)$ is transferred to the collision point of the particle by a linear interpolation,

$$\phi_j(s) = \frac{\phi_j(s_f) - \phi_j(s_b)}{s_f - s_b}(s - s_b). \tag{8}$$

An energy change proportional to $\partial\phi/\partial z$, which is caused by the interaction depending on z, is included in the simulation.

We divided a bunch into 5 to 10 slices. The number of slice required depends on the beam-beam parameter: i.e., higher beam-beam parameter requires more number of slices. In our parameter region, the simulation results converged the number of slice.

SIMULATION RESULTS

We studied the effect of crossing angle on the beam-beam parameter and luminosity for the machine parameters as is shown in Table 1. In the weak-strong simulation, 100 macro-particles are tracked up to 40,000 turns (10τ), and the luminosity was calculated by averaging it during 20,000 through 40,000 turns. In the strong-strong simulation, 100,000 macro-particles are tracked up to 20,000 turns. The luminosity was given by that calculated at the last turn. The bunch population of electrons (N_-) in the high energy ring (HER) is scanned 1×10^{10} to 1.2×10^{11}. The transparency condition was kept as $N_+\gamma_+ = N_-\gamma_-$ to avoid complex behavior for unbalance of the beams. The beam-beam parameter was calculated by the luminosity,

$$\xi_y = \frac{2r_e\beta_y}{N_\pm\gamma_\pm}\frac{L}{f_{rep}}, \tag{9}$$

where the reduction factor of the luminosity and the beam-beam parameter is approximated to be the same.

Table 1: Basic parameters of KEKB

	HER	LER
C	$3016m$	
E	8 GeV	3.5 GeV
β_x/β_y	60 cm / 7 mm	
$\varepsilon_x/\varepsilon_y$	18 nm / 0.18 nm	
σ_z	7. mm	
$\nu_x/\nu_y/\nu_s$	0.515/0.565/0.02	
τ_{xy}/T_0	4,000 turn	4,000 turn
θ_c	$0 \sim 2 \times 11$ mrad	

Fig. 1 shows the relation of the beam-beam parameter ξ and the bunch population for head-on and crossing collision with a half crossing angle of 11 mrad. The result of the head-on collision is considered to be the same as that of the crossing collision with crab cavities set as $\zeta_{x,crs} = -\phi$. Pictures (a) and (b) were obtained by the weak-strong and strong-strong simulations, respectively. The beam-beam parameters for the head-on collision is remarkable higher than that for the crossing collision in both of the simulation. The beam-beam parameter ξ is linearly increase up to over 0.2 in the weak strong simulation, while ξ is saturated around 0.1-0.12 in the strong-strong simulation. The beam-beam limit is 0.1 or > 0.2 for the head-on collision. There is somewhat difference of the beam-beam limit

for the weak-strong and the strong-strong simulation. ξ at crossing collision is similar behavior for the both of two simulations: that is, ξ is saturated around 0.06.

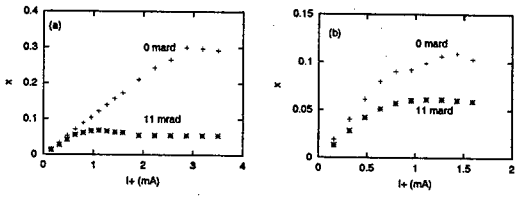

Figure 1: Beam-beam parameters obtained by weak-strong and strong-strong simulations.

Fig. 2 shows luminosity for various crossing angle. The geometrical luminosity, which is also plotted in the figure, has loose dependence for the crossing angle. The simulated luminosity is peak structure near zero-crossing angle for the simulations. The peak structure of the strong-strong simulation is narrower than that of the weak-strong simulation.

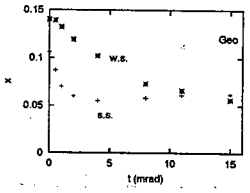

Figure 2: Beam-beam parameters v.s. crossing angle. Three points,

The horizontal tune is chosen to be slightly upper of a half integer in KEKB. The beam-beam behavior depends on the tune value. Fig. 3 shows beam-beam parameter for various horizontal tune given by the weak-strong simulation. The beam-beam parameter decreases for separating from the half integer. The figure shows that the extremely high beam-beam parameter ~ 0.2 is achieved at the tune closed to a half integer.

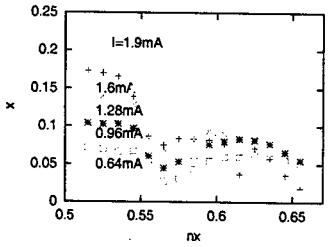

Figure 3: Beam-beam parameter v.s. horizontal tune for various positron current at $\nu_y = 0.565$.

CONCLUSION

We studied beam-beam effect with/without crossing angle using weak-strong and strong-strong simulations. The beam-beam parameter (ξ) linearly increased more than 0.2 for the current in the weak-strong simulation and was saturated at ~ 0.1 in the strong-strong simulation in the head-on collision. While ξ was saturated at around ~ 0.06 for a finite crossing angle in both of the simulations. In either case, the beam-beam parameter for the head-on collision is much better than that with the crossing angle. Crab cavities, which realize the head-on collision effectively, can be expected to upgrade the luminosity twice or four times.

The luminosity is degraded by various reasons, for example, orbit and optics errors [11]. The crossing angle is a kind of optics error, z dependent dispersion (ζ), at the collision point. When a source which degrades the luminosity exists, the two type of simulations, weak-strong and strong-strong, give similar results.

We have to know the beam-beam parameters for the case that all of sources of degradation are removed. There is difference for the beam-beam limit between the two type of simulations. We do not know whether the weak-strong model is reliable to estimate the beam-beam limit, while unphysical numerical noises, which are contained in the PIC algorithm or longitudinal slicing, may degrade for the strong-strong simulation at a high current. Tune operating point is essential for the high beam-beam parameter. We do not discard the possibility of the very high beam-beam parameter, ~ 0.2, obtained by the weak-strong simulation, though more studies are required.

The authors thank members of KEKB commissioning group for fruitful discussions.

REFERENCES

[1] K. Oide, K. Yokoya, Phys. Rev. **A40**, 315 (1989).

[2] K. Hirata, Phys. Rev. Lett., **74**, 2228 (1995).

[3] "KEKB B-factory design report", KEK Report 95-7 (1995).

[4] K. Ohmi, K. Hirata and K. Oide, Phys. Rev. **E49**, 751 (1994).

[5] K. Ohmi, Phys. Rev. E**62**, 7287 (2000).

[6] K. Hirata, H. Moshammer and F. Ruggiero, Particle Accelerators, **40**, 205 (1993).

[7] K. Ohmi and A. W. Chao, proceedings of the Mini-Workshop on Electron-Cloud Simulations for Proton and Positron Beams, CERN, 15-18 April, 2002, CERN-2002-001 (2002).

[8] M. Tawada et. al., Proceedings of a Workshop on beam-beam effects in circular colliders, Fermilab, June 25-27, 2001, FERMILAB-Conf-01/390-T, 17 (2001).

[9] E. B.Anderson and J. T.Rogers, Proceedings of a Workshop on beam-beam effects in circular colliders, Fermilab, June 25-27, 2001, FERMILAB-Conf-01/390-T, 136 (2001).

[10] Y. Cai, private communications.

[11] K. Ohmi, Proceedings of EPAC2000, 433 (2000).

Proceedings of the 2003 Particle Accelerator Conference

HIGH INTENSITY ISSUES FOR SUPER B-FACTORIES

K. Akai, KEK,Tsukuba, Japan

Abstract

The present B-factories, KEKB and PEP-II, have achieved or exceeded their design luminosities. A luminosity of 10^{34} cm^{-2} s^{-1} has become a reality. As upgrading of these machines to increase the luminosity further by ten times or more to extend the physics coverage, Super B-factories are being considered. Beam current should be about 10 A in the Low Energy Ring (LER) and 4 A in the High Energy Ring (HER), or even much higher, with a short bunch length of about 3 mm. It is very challenging for various hardware components, especially for RF system and beam-line vacuum components, to store such an extremely high beam current. Crab crossing is also considered to drastically increase the beam-beam tune shift limit, that results in a further increase of the luminosity. In this paper, high intensity issues for the Super B-factories are discussed.

INTRODUCTION

KEKB and PEP-II are asymmetric-energy, double-ring, electron-positron colliders aimed at producing B and anti-B mesons at high rate as in factories. They were commissioned in 1998 and have been operating for physics experiment. Their performances have been improving steadily and already achieved or exceeded their design luminosities: KEKB and PEP-II achieved remarkable luminosities of 1.03×10^{34} cm^{-2} s^{-1} [1] and 6.1×10^{33} cm^{-2} s^{-1} [2], respectively. Integrated luminosity of 1 fb^{-1} is obtained within only two or three days of operation. The accumulated physics data in KEKB and PEP-II had produced the discovery of CP violation in B and anti-B meson system.

Common features of the B-factories to realize the high luminosity include high beam current of about 2 A in LER and 1 A in HER, small β_y^* at the interaction point (IP) and a short bunch length. Major differences between them include crossing scheme at the IP and the type of RF cavities. KEKB has adopted a finite-angle crossing scheme at an angle of $\pm$ 11 mrad, whereas PEP-II adopted head-on collision using separation dipole magnets. The RF cavities will be discussed in detail later.

Recently, there is increasing physics motivation for upgrading the B-factories to increase the luminosity by one or two orders of magnitude to reach 10^{35} or even 10^{36} cm^{-2} s^{-1}. Design works for Super-KEKB and Super PEP-II are going on. The major upgrading to Super-KEKB is considered in 2006 to 2007 so as not to lose its competitiveness to LHC-B and BTeV. In order to realize such an extremely high luminosity, the beam current should be increased to about 10 A or even 20 A with a very short bunch length of 3 mm. In addition, according to recent beam-beam simulations, the crab crossing is expected to drastically increase the beam-beam tune shift limit, that results in a further increase of the luminosity.

In this paper, we discuss issues related to the extremely high beam current in the Super B-factories. In particular, requirements and possible solutions for the hardware components such as RF system and beam-line vacuum components are described. Some of the operating experiences of the present B-factories are also given. In addition, a possible crab crossing scheme is proposed.

HIGH CURRENT BEAM

Table 1 shows major beam parameters currently operating in KEKB and the design values of Super-KEKB for the luminosity of 10^{35} cm^{-2}s^{-1}. It is expected that the luminosity further increases by several times with the same beam current if the crab crossing scheme is adopted. A much higher luminosity of 10^{36} cm^{-2}s^{-1} is also considered with a beam current of about 20 A in LER and 8 A in HER together with the crab crossing.

Table 1: Major beam parameters currently operating in KEKB and the design values of Super-KEKB for 10^{35} cm^{-2}s^{-1}

	KEKB		Super-KEKB	
	LER	HER	LER	HER
Particles	e^+	e^-	e^-	e^+
Beam energy (GeV)	3.5	8.0	3.5	8.0
Beam current (A)	1.41	1.06	9.4	4.1
Circumference (m)	3016		3016	
No. of bunches	1284		5120	
Bunch spacing (m)	2.4		0.6	
Crossing angle (mrad)	$\pm$11		$\pm$15	
RF voltage (MV)	8.0	13.0	14.0	23.0
β_x at IP (cm)	59	58	30	30
β_y at IP (cm)	0.58	0.7	0.3	0.3
Bunch length (mm)	6$\sim$7	6$\sim$7	3	3
Beam power (MW)	2.5	3.7	18.3	16.0
(radiation loss)			(11.3)	(14.3)
(parasitic loss)			(7.0)†	(1.7)††
Luminosity (/cm^{2}s)	1.03×10^{34}		1×10^{35}	

Total loss factor is assumed 40† and 50 †† V/pC.

The high beam current immediately results in following considerations. Although they were also important in the B-factories, much more attentions and measures are needed for the Super B-factories.

0-7803-7738-9/03/$17.00 © 2003 IEEE

- Coupled-bunch instabilities: The growth rate is proportional to the beam current. Any higher-order mode (HOM) impedance in cavities or other beam-line components should be sufficiently reduced. Instabilities caused by other sources such as the resistive wall, fast-ion and photo-electron cloud also need to be suppressed. A powerful bunch-by-bunch feedback system is inevitable.
- Heating and other problems: Beam-line components are exposed to strong HOM, synchrotron radiation, and even the intense beam itself. They can be damaged by heating, discharge or even direct hit of the beams. They must be robust and low-impedance.
- Impedance budget: The total loss factor and the imaginary part of the impedance in the ring should be kept as low as possible, especially for the short bunch length.
- Large RF power and heavy beam-loading: A large amount of power lost by the beam should be compensated by the RF system. On the other hand, required RF voltage is relatively low, regardless of the high beam current. As a consequence, a large amount of power should be provided by each cavity. High-power RF components should be stably operated at about one MW. The heavy beam-loading also needs careful design of the control system for the accelerating mode.

RF SYSTEM

Two types of cavities are used in KEKB: Accelerator Resonantly coupled with Energy Storage (ARES) [3] and single-cell superconducting cavities (SCC) [4]. The ARES alone is used in LER and a combination of ARES and SCC is adopted in HER. The RF system has been operating stably. It is expected that it can be used with a beam current of up to about 10 A in LER and 4 A in HER of Super-KEKB, if following improvements and changes are made. This strategy helps greatly reduce the construction cost for the upgrading.

- The impedance at driving frequencies associated with the accelerating mode of cavities should be much more reduced by a strong feedback system, even with the ARES and SCC.
- The HOM dampers should be improved to absorb a large amount of HOM power of up to 100 kW/cavity generated in the cavity.
- The number of RF stations and the beam power provided by each cavity should be increased to meet the large amount of total beam power, four times as high as that of KEKB.
- Other small changes are reducing the loaded-Q values of the accelerating mode, eliminating tapers outside the cavity to reduce the loss factor, and so on.

The RF-related parameters are shown in Table 2. More details are discussed below.

Table 2: RF parameters for Super-KEKB

	Super-KEKB	
	LER	HER
Beam current (A)	9.4	4.1
Beam power (MW)	18.3	16.0
RF voltage (MV)	14.0	23.0
RF frequency (MHz)	508.887	
Revolution freq. (kHz)	99.4	
Type of cavities	ARES	ARES+SCC
No. of cavities	28	16+12
Voltage/cav. (MV)	0.5	0.5/1.3
Detuning (kHz)	71	31/74
No. of cav./klystron	1	1/1
No. of klystrons	28	16+12
Klystron power (kW)	850	850/480
AC power (MW)	40	23+10

Instability Driven by the Accelerating Mode

Growth rate and cures In storage rings, the resonant frequency of the cavities should be detuned toward the lower side in order to compensate for the reactive component of the beam loading. The detuning frequency (Δf) is given by

$$\Delta f = \frac{I \sin\phi_s}{2V_c} \times \left(\frac{R}{Q}\right) f = \frac{P_b \tan\phi_s}{4\pi U}, \qquad (1)$$

where f is the RF frequency, I the beam current, ϕ_s the synchronous phase, V_c the cavity voltage, P_b the power to the beam, and U the stored energy in the cavity. For the B-factories, Δf can be comparable to, or even exceed the revolution frequency, due to the large beam current and small revolution frequency (large circumference ring). The coupling impedance at the driving frequencies, the upper synchrotron sideband of revolution harmonic frequencies, becomes significantly high due to the high impedance of the accelerating mode. A key issue for the RF system of the B- and Super B-factories is how to avoid the longitudinal coupled-bunch instability caused by the large detuning of the cavities.

KEKB and PEP-II have taken different strategies to solve the problem. As seen in Eq. 1, Δf is reduced by increasing the stored energy U or the accelerating voltage V_c. The ARES used in KEKB is a normal-conducting three-cavity system where an energy-storage cavity operating in a high-Q mode is coupled with an accelerating cavity via a coupling cavity in between. And the SCC is operated at a high accelerating voltage. The stored energy in the ARES and SCC is about ten times as high as that in conventional normal-conducting cavities. Thus the detuning frequency is reduced by a factor of ten.

In PEP II, conventional normal-conducting cavities are used and the detuning frequency exceeds the revolution frequency. PEP-II relies on a combination of feedback loops to reduce the impedance at the driving frequencies: a direct

loop, a comb filter loop, and a bunch-by-bunch feedback system.

Operation in B-factories There is a sufficient margin for the stability threshold in HER of KEKB: no instability has been observed up to the design beam current of 1.1 A. In LER of KEKB, on the other hand, even with the ARES cavities, suppression of the instability is marginal at the design beam current of 2.6 A. The threshold current is even reduced due to the lower operating RF voltage than the design value to avoid excessive HOM heating at several vacuum components. Consequently, the -1 mode damper is needed to store a beam of more than 1 A, although the required reduction of the impedance is about 15 dB and it is sufficient to apply it to only one RF station among ten stations.

In PEP-II, it was observed that the growth rate is higher than expected and the margin for stable operation with various errors is relatively small with high beam current. One reason is deterioration of the feedback property due to saturation of klystron output power. The operating beam current is sometimes limited by RF trips caused by the unstable feedback loops [5].

Super B-factory case In the case of Super-KEKB, even with the ARES and/or SCC, the detuning frequency becomes close to the revolution frequency. The growth rate of the -1 mode will be much higher than the case of KEKB and much more impedance reduction is required. A powerful feedback system with comb filters is inevitable, although the number of modes that need to be cured is much less than the case of conventional cavities.

Bunch-Gap Transient

A part of the ring is reserved as an abort gap where no bunch is filled to allow for a rise time of the beam abort kicker. The abort gap also works as an ion-clearing or photo-electron clearing gap in the electron or positron ring, respectively. The gap length of KEKB is about 0.5 μsec, that is 5% of the ring circumference. The bunch gap, however, modulates the longitudinal position of the bunches, since the beam-loading effect is different between the bunch train and the gap. A large phase modulation can affect the RF system such as modulating the RF power and phase and deteriorating the performance of the feedback loops. In addition, the luminosity can be reduced by different phase modulation between the two rings.

In order to avoid the harmful effects, it is desired that the phase modulation is kept less than several degrees. The high stored energy of the ARES and SCC is also beneficial to reduce the phase modulation, since it is inversely proportional to the stored energy. Even so, the gap length should be reduced to less than 0.2 μsec. Otherwise, the phase modulation will be unacceptable. A faster rise time of the abort kicker is required.

HOM Damping

The accelerating cavity of the ARES in KEKB and the PEP-II cavity have waveguides to extract and damp the HOM's generated in the cavities. The SCC in KEKB adopted a beam-pipe damping scheme, where ferrite absorbers are attached inside the beam pipe on both sides of the cavity.

To use the ARES and SCC in Super-KEKB, followings should be taken into account. First, the HOM power per cavity is estimated to be about 100 kW and 50 kW in LER and HER, respectively, which is beyond the capacity of the present HOM absorbers. The HOM dampers must be improved to meet the requirement. Second, the growth rate of the instability is increased due to the higher beam current. A longitudinal bunch-by-bunch feedback is required, which is not necessary in KEKB. The growth time of transverse instability is about 3 ms and it can be cured by the present bunch-by-bunch feedback system.

BEAM-LINE COMPONENTS

In the operation of KEKB and PEP-II, several beam-line components have suffered from various kinds of troubles caused by the high current beam. A lot of efforts have been made to solve the problems: the improvements allow us now to store a beam of 1$\sim$2 A stably. This kind of efforts, however, would continue whenever the beam current is pushed to higher values. It provides us with useful information also for the Super B-factories to review the troubles and cures taken in the B-factories. Some of the experiences in KEKB are presented below.

Movable Masks

Movable masks are used to block particles out of normal orbit in order to reduce background noise on the physics detector and to avoid any damage on the detector and other hardware components caused by the abnormal beam.

Early versions of the movable masks in KEKB have mask-heads protruded inside the chamber. They had various kinds of troubles: vacuum leaks occurred several times due to heating or discharge. In addition, coupled-bunch instability was excited at several hundred mA. Most of them are caused by trapped HOM in the masks. Although they were improved to some extent by attaching HOM absorbers that reduces the Q-value of the trapped HOM, it is hardly expected to be able to be used with much higher beam current.

They have been replaced with a moving-chamber type of the masks similar as those used in PEP-II. The amount of HOM power is reduced and is not trapped. The masks of this type have been operating well. One problem encountered is heating of the bellows on both sides of the masks caused by TE-like HOM generated at the bending region around the mask-head. Two measures have been taken: one is to reduce the bending angle to have more smooth

transition, and the other is to install HOM dampers that selectively damp the TE mode propagating along the chamber. The improved mask is expected to withstand a beam of several amperes. More details are presented elsewhere [6].

Bellows and Other Components

Bellows had serious troubles several times. In most cases, finger contacts for RF shielding are damaged due to discharge caused by HOM or synchrotron radiation. In particular, the TE-like HOM generated near the masks or other non-symmetric structures is harmful, since the slits between the fingers are located longitudinally. It would be the best solution if a bellowsless system is possible, where all adjacent vacuum chambers are welded to each other. Alternatively, a new type of bellows is being considered. It has a comb structure connection for the RF shield, instead of the RF shield fingers [6]. It is expected to reduce the loss factor and to avoid multipactoring.

Some other problems related to the high current beam encountered in KEKB are listed below.

- Heating of chambers and radiation masks near the interaction region caused by radiation and/or HOM.
- Abnormal heating of Beryllium beam pipe of the Belle detector due to a resonant build-up of HOM trapped between two radiation masks.
- Troubles on strip line electrodes of feedback kickers caused by discharge and/or thermal stress.

Damage by Unstable Beam

In KEKB, an unstable beam sometimes caused a large effect on the beam-line hardware components. The most serious problem was damage of the head of movable masks. Grooves or protrusions were generated on the surface of the mask head, which prevented the beam injection and storage. Another problem was a large amount of radiation hitting the Silicon Vertex Detector of the Belle detector. The worst case was 5 kRad at one time. Since its performance can be degraded with an accumulated dose of about 500 kRad, this is also a serious problem for a long-term operation.

It was found that they were caused by an unstable beam due to RF trips. The longitudinal phase and energy of the beam drastically changes, that gives rise to a large deviation from normal orbit and optics. Although interlock signals in the RF system are connected to the beam abort system, it did not help all cases: the abnormal RF field sometimes resulted in unstable beam before any interlock is detected to trigger the abort system.

In order to solve the problem, the protection system was reinforced as follows. The beam abort is triggered when the longitudinal phase of the beam deviates from a nominal value by one degree. The beam abort is also triggered by an abnormal cavity voltage caused by discharge or quench in the SCC. After these protections were completed, the RF trips never caused any damage on the masks or other components [7]. In addition, beam-loss monitors using PIN diodes were implemented along the ring [8]. These fast abort systems work to protect the beam-line components against abnormal beam conditions.

CRAB CROSSING

Luminosity Boost

The finite-angle crossing scheme adopted in KEKB does not require any separation dipole magnets and makes the interaction region much simpler than in the head-on collision scheme. Another advantage is that bunches are separated quickly after the collision so that parasitic collision is not a concern, even when every bucket is filled by bunches. Geometrical luminosity reduction was estimated to be 10 — 20 %, depending on the bunch length. The crab crossing scheme [9] was considered to be a fall-back option in case some unexpected problems are encountered with the finite-angle crossing scheme. The success of KEKB encourages us to employ the finite-angle crossing also in Super-KEKB, even with a larger crossing angle of $\pm$ 15 mrad. It is considered that the luminosity of 10^{35} cm^{-2} s^{-1} can be reached with this scheme.

A recent beam-beam simulation showed, however, that the head-on collision can drastically increase the beam-beam tune shift limit that results in a significant luminosity increase by several times [10]. The effect is much more than what had been thought before. Consequently, the crab crossing scheme is attracting much more attention for Super-KEKB. Parameters for the crab crossing is shown in Table 3.

Table 3: Parameters for the crab crossing in Super-KEKB

	LER	HER
Beam energy (GeV)	3.5	8.0
Beam current (A)	9.4	4.1
RF frequency (MHz)	508.887	
Crossing angle (mrad)	$\pm$ 15	
β_x^* (m)	0.3	0.3
$\beta_{x,crab}$ (m)	100$\sim$200	200$\sim$400
Required kick (MV)	0.90$\sim$0.64	1.45$\sim$1.03

Crab Cavities

In order to generate a transverse kick needed for the crab crossing, crab cavities will be used. It must be a HOM-damped structure as the accelerating cavities. Since the crab cavity is operating in a dipole mode such as the TM110 mode, there is a lower frequency parasitic mode. It is the TM010 mode which corresponds to the accelerating mode in the accelerating cavities and has high longitudinal coupling impedance. It is difficult to damp this mode with the conventional damping scheme using waveguide dampers or beam pipe dampers.

Type-I cavity A superconducting crab cavity for the B-factories was proposed in 1992 [11]. It employs a coaxial beam pipe damper together with a notch filter attached to an extremely polarized cell ("squashed" cell). All monopole and dipole parasitic modes are damped, including the lowest frequency TM010 mode and the unwanted polarization of the TM110 mode, while the crabbing mode is kept high Q-value. The R&D efforts are being continued at KEK, aiming at fabricating full-scale niobium cavities [12].

This cavity was designed for a beam of 1~2 A and is expected to have sufficient properties for the B-factories. However, if it is used in Super-KEKB LER with a beam current of 10 A, following problems can arise. First, the HOM power of more than 200 kW should be absorbed by the HOM dampers. However, similar types of dampers used in the SCC of KEKB have been operated up to only about 10 kW. Second, much more reduction of the HOM impedance is required for the 10 A beam. It should be noted that the growth rate of transverse instability driven by one crab cavity can be comparable to that of about ten accelerating cavities, even if the HOM impedance is about the same. The reason is that a large beta-function at the crab cavity, $\beta_{x,crab}$, is chosen to reduce the required kick voltage, whereas the growth rate is proportional to $\beta_{x,crab}$.

Type-II cavity for 10 A Recently, a new design of crab cavity was proposed for much higher beam current [13]. It is equipped with several waveguide HOM dampers. Optimization of the cell and dampers has been carried out. All parasitic modes except the TM010 mode are sufficiently damped for a beam of 10 A. The highest HOM impedance is reduced by a factor of ten compared with the type-I cavity. In addition, the loss factor is reduced by half since relatively widely opened beam pipes are used compared with the coaxial beam pipe of the type-I cavity.

In order to avoid the instability driven by the TM010 mode, following measures are studied. The frequency of this mode is controlled at the middle of adjacent revolution harmonic frequencies. It can be done by implementing frequency monitoring system and two independent tuners. The coupling impedance at the driving frequencies is further reduced by a feedback system using parallel comb filters, which is similar as the -1 mode damper for the accelerating cavities. The required feedback gain is less than 20 dB, which is comparable to the existing -1 mode damper of KEKB.

OTHER ISSUES

Positron Blow-up by Photo-Electron Cloud

Blow-up of the positron beam caused by photo-electron cloud [14] was one of the most serious problems in KEKB. In order to cure it, solenoid coils were wound on the chambers of LER. As the covered length by the solenoid coils is increased, the threshold current has been increased. Most of the drift space is now covered by the solenoids and the serious blow-up disappeared up to the present operating beam current [15]. For the Super-KEKB it seems inevitable to adopt the ante-chambers similar as those used in PEP-II. In addition, to suppress further the electron cloud density, the charge of stored beams will be switched: the positron beam is stored in HER and the electron beam in LER.

Continuous Injection

Continuous injection is being tested at KEKB and PEP-II. In this scheme the lost particles of the stored beam are continuously compensated by injection while the detector is taking physics data. This scheme must be adopted in the Super B-factories to maximize the integrated luminosity because of a short beam life time. It also allows for pushing the beam-beam tune shift limit significantly higher that shortens the beam-beam interaction lifetime significantly.

FUTURE STUDIES

For realizing the Super B-factories, many studies and developments must be done. Key issues for the RF system are improvement of the HOM dampers and a powerful feedback for the accelerating mode-related instabilities. Beamline components must be robust and low-impedance. In particular, R&D of the ante-chambers, movable masks, and bellows (or bellowsless system) are crucial. It is planned that crab cavities will be installed in KEKB in 2005 to examine the effect of the crab crossing. Finally, we believe that continuous efforts to push the beam current of the present B-factories higher will give us important directions toward the Super B-factories.

REFERENCES

[1] H. Koiso et al. in these proceedings.

[2] http://www.slac.stanford.edu/accel/pepii/home.html.

[3] Y. Yamazaki and T. Kageyama, Part. Accel. 44, p. 107, 1994.

[4] T. Furuya et al. Proc. e+e- Factories, p. 55, KEK, 1999.

[5] J. Fox, talk presented at KEK on Mar. 17, 2003.

[6] Y. Suetsugu, in these proceedings.

[7] K. Akai et al. EPAC2002, p. 2112, Paris, 2002.

[8] M. Arinaga et al. Nuclear Instruments and Methods, 499, p. 100, 2003.

[9] K. Oide and K. Yokoya, Phy. Rev. A40, 315, 1989.

[10] K. Ohmi, in these proceedings.

[11] K. Akai et al. Proc. B factories, p. 181, SLAC-400, 1992.

[12] K. Hosoyama et al. Proc. 1st Asian Part. Accel. Conf., p. 828, 1998.

[13] K. Akai, KEKB memo No. 225, KEK, Mar. 2003.

[14] K. Ohmi and F. Zimmermann, Phys. Rev. Lett. 85, 3821, 2000.

[15] H. Fukuma, Proc. ECLOUD02, CERN-2002-001, 2002.

R&D TOWARD NEUTRINO FACTORIES AND MUON COLLIDERS*

Michael S. Zisman, Lawrence Berkeley National Laboratory, Berkeley, CA 94720, U.S.A.

Abstract

R&D aimed at the production, acceleration, and storage of intense muon beams is under way in the U.S., in Europe, and in Japan. Considerable progress has been made in the past few years toward the design of a "Neutrino Factory" in which a beam of 20–50 GeV μ^- or μ^+ is stored. Decay neutrinos from the beam illuminate a detector located roughly 3000 km from the ring. Here, we briefly describe the ingredients of a Neutrino Factory and then discuss the current R&D program and its results. A key concept in the design is "ionization cooling," a process whereby the muon emittance is reduced by repeated interactions with an absorber material followed by reacceleration with high-gradient rf cavities. Plans to test this concept in the Muon Ionization Cooling Experiment (MICE) are well along and are described briefly.

INTRODUCTION

Presently, there is intensive worldwide activity to design a Neutrino Factory, and ultimately to develop a Muon Collider. The former facility would provide an intense beam of electron neutrinos (or anti-neutrinos) to study neutrino oscillations and hopefully to observe, for the first time, charge-conjugation–parity (CP) violations in the lepton sector. Observation of this phenomenon would provide a window to very high energy neutrino effects, and possibly provide an explanation for the observed matter–antimatter asymmetry in the universe. The latter facility would initially facilitate the study of the Higgs boson and could ultimately provide an energy-frontier machine small enough to fit on an existing laboratory site.

In the U.S., the activities take place under the auspices of the Neutrino Factory and Muon Collider Collaboration (MC), a group of some 130 scientists and engineers drawn from national laboratories and universities. In Europe, there is a corresponding organization, the European Neutrino Group (ENG). There is also a Japanese Neutrino Factory Working Group, centered at KEK but having members from Japanese universities as well. These groups are attacking the problems of intense muon beam accelerators on a broad front, and considerable progress has been made. In this paper, the primary emphasis will be on the R&D activities of the MC, although some activities of the other groups will be mentioned.

NEUTRINO FACTORY INGREDIENTS

A schematic of a possible Neutrino Factory is shown in Fig. 1. A high-power proton beam (1–4 MW) impinges on a production target, producing pions. These are captured into a solenoidal decay channel where they decay into muons. The resulting muon beam then undergoes "phase rotation," converting a beam with a large energy spread and a small time spread into a beam with a smaller energy spread and a longer time spread. The beam is then bunched into a train of 201 MHz bunches and cooled in an ionization cooling channel. These activities all take place at low muon momentum, roughly 200 MeV/c. After cooling, the muon beam is accelerated to its final energy (20–50 GeV) and stored in a ring with one or more straight sections aimed at detectors located several thousand km from the ring. Two feasibility studies of complete systems have been done [1,2], with the conclusion that such a facility is possible, albeit challenging.

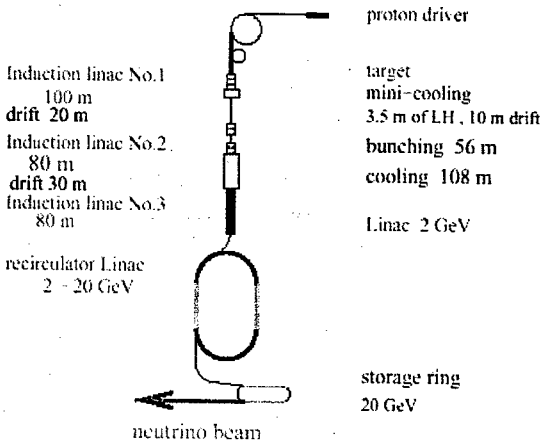

Figure 1: Schematic of Neutrino Factory layout, taken from Ref. [2].

Ionization Cooling

Ionization cooling is a key feature of intense muon beam facilities. This is because the production process described above results in a muon beam with very large emittance. (The short lifetime of the muon, 2.2 μs at rest, eliminates any alternative cooling schemes, such as stochastic or electron cooling.) The process, illustrated in Fig. 2, is analogous to synchrotron radiation damping. In

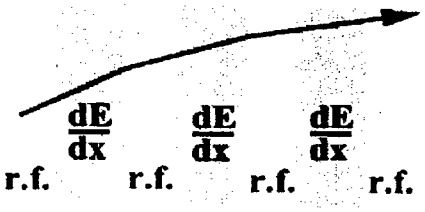

Figure 2: Schematic of ionization cooling process.

*Supported by U.S. Department of Energy, Division of High-Energy Physics under contract number DE-AC03-76SF00098.

0-7803-7738-9/03/$17.00 © 2003 IEEE

place of synchrotron radiation, ionization cooling makes use of energy loss in an absorber to decrease the particle's momentum in all dimensions; energy gain in the rf cavities restores only the longitudinal component. Repeating the process many times results in a decrease of p_x/p_z, and thus the transverse emittance.

There is also a heating term, analogous to the quantum excitation in the radiation damping case, resulting from multiple scattering in the absorber material. The balance between cooling and heating gives rise to an equilibrium emittance, given approximately by

$$\varepsilon_{x,N,equil.} = \frac{\beta_\perp (0.014\,\mathrm{GeV})^2}{2\beta m_\mu X_0 \left|\frac{dE_\mu}{ds}\right|} \qquad (1)$$

where $\beta_\perp$ is the Twiss parameter at the absorber location, $\beta(\equiv v/c)$ is the particle velocity, m_μ is the muon mass, X_0 is the radiation length and dE_μ/ds is the energy loss per unit length in the absorber material. To reach a low emittance, strong focusing (low $\beta_\perp$), large energy loss, and large radiation length are preferred. The latter features favor H_2 as the absorber material.

R&D PROGRAM PROGRESS

Targetry

In the past few years, the MC has carried out initial beam tests at the AGS of both solid (C rod) and liquid (Hg jet) targets [3]. Unfortunately, this program has no beam time scheduled at the AGS in FY2003 and we expect none in FY2004 either. This is clearly a major impediment to further progress. Tests of C sublimation are being carried out at ORNL. Earlier work [4] indicated a target lifetime of 1 month at a beam power of 1.2 MW. We plan He atmosphere tests to see if the sublimation rate can be reduced to the level where 4 MW beam power is practical.

With regard to the Hg jet tests, the open questions concern injection into a strong solenoidal field (≈20 T) and nonlinear behavior of the jet dynamics at full proton intensity. To explore these issues, we have designed a test magnet capable of providing up to 15 T, we are designing a Hg jet system capable of the required 20–30 m/s velocity, and we have continued our simulation effort to predict and interpret our results.

In our initial beam tests, we reached an intensity of about 4×10^{12} p/pulse, compared with our design value of 16×10^{12} p/pulse. Tests of bunch merging techniques are under way, as illustrated in Fig. 3. These have already reached 10×10^{12} p/pulse, showing that the approach is workable.

Europe also has a strong program in Targetry, focusing on development of magnetic horns [5], and, in collaboration with the MC, working on Hg jet issues, such as the jet behavior in a strong magnetic field [6]. They have put considerable emphasis on developing a Superconducting Proton Linac (SPL) to serve as a proton driver. The concept being considered [7] is shown in Fig. 4. The original idea was to reutilize surplus LEP 352 MHz rf equipment, but more recent thinking has favored using a 700 MHz linac implementation.

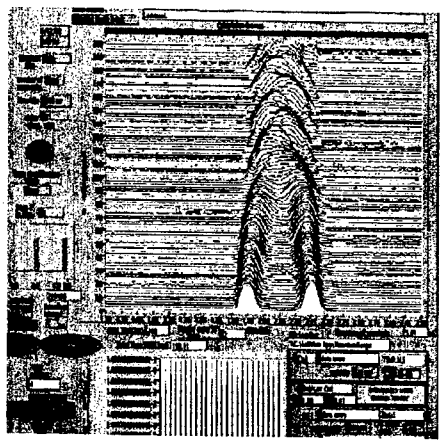

Figure 3: Demonstration of bunch merging at AGS. Two bunches on harmonic 12 are coalesced into one bunch on harmonic 6.

Cooling

This activity includes hardware R&D on cavities, absorbers, and solenoids, along with a significant simulation effort to design and optimize cooling channels.

Because the cooling channel rf system is immersed in a strong solenoidal field, the cavities must be normal conducting. To optimize the shunt impedance, we enclose the cavity ends with a conducting metal window. Our experimental rf work to date has been done at 805 MHz, that is, one-quarter scale with respect to the 201 MHz frequency intended for the cooling channel. The main issue to study is limits to the achievable gradient, i.e., breakdown and dark current phenomena.

The pillbox cavity [8] we employ for tests is shown in Fig. 5, along with its input waveguide. This cavity fits into the bore of our 5-T solenoid in Lab G at Fermilab. In the absence of a solenoidal field, and with copper windows, the cavity reached 34 MV/m, exceeding its 30 MV/m design goal. With the solenoidal field, the performance was poorer (18 MV/m) and the radiation levels from the cavity were much higher. We conclude from these tests that the presence of the magnetic field enhances physical damage to the cavity surfaces, though the detailed mechanism is uncertain. Some evidence for healing was found, in the sense that the cavity partially

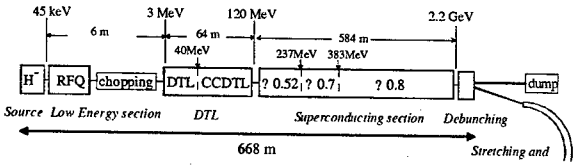

Figure 4: Diagram of proposed SPL configuration at CERN.

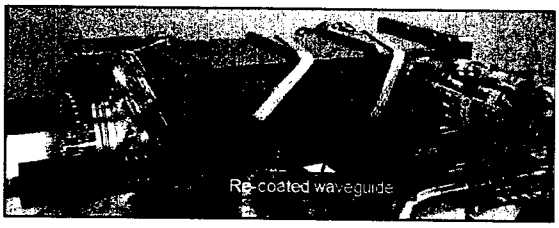

Figure 5: 805 MHz pillbox cavity used in high-power tests at Fermilab.

recovered to lower radiation levels when reprocessed without magnetic field. Inspection of the cavity after the tests showed pitting of the copper windows and copper "dust" at the bottom of the cavity.

We next replaced the copper windows with TiN-coated beryllium windows. Beryllium is the material of choice for a cooing channel because of its low Z (resulting in less multiple scattering). The conditioning went smoothly without a magnetic field, demonstrating that the parallel geometry of the windows does not result in inordinate multipactoring. After operation with magnetic fields, we again removed the windows for inspection. Figure 6 shows a section of the window and indicates that sputtered copper is present on its surface. No damage to the beryllium surface was observed, an encouraging result. This evidence suggests we need to focus more on the copper body than on the windows themselves to reach higher gradients. We plan to explore coatings of other materials that may mitigate these effects.

Even with the field present, beryllium windows produce lower backgrounds than copper windows under comparable conditions, as shown in Fig. 7.

As noted above, a crucial ingredient in the rf cavity design is the window that terminates the electric fields. Ideally, such a window would be perfectly conducting, transparent to the muon beam, and sufficiently rigid to have no effect on the cavity frequency. Our initial concept [9] was to use a thin flat window of pre-stressed beryllium foil. In practice, however, even at 805 MHz it is difficult to preserve the flatness as the window heats, and the thick frame required to support the pre-stress makes the windows expensive. For 201 MHz cavities, with correspondingly larger aperture, the approach was becoming impractical. Instead, we are now pursuing a

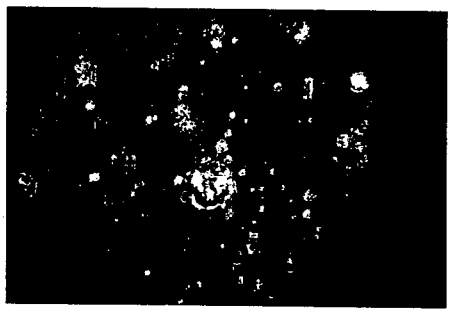

Figure 6: Be window surface showing sputtered copper.

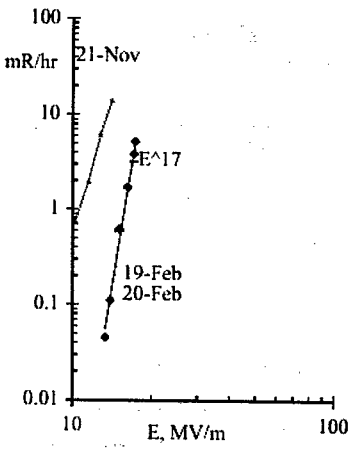

Figure 7: Background levels for copper windows (upper curve) and beryllium windows (lower curve) under identical magnetic field conditions.

pre-curved beryllium window that will bow predictably as it heats. The window is designed with a dual curvature, patterned after the absorber window design (see below) developed with University of Oxford.

As mentioned earlier, the cavity frequency envisioned for a cooling channel is 201 MHz. For the past year, we have worked on the engineering design [10] for such a cavity (see Fig. 8). Fabrication of a prototype cavity began this year and will be completed in about one year.

Thin, yet very strong, aluminum windows are needed for the liquid-hydrogen absorbers. A simple torispherical design has demonstrated the ability to support 8 atm pressure with a 340 μm window, sufficient for our needs [11]. An improved version with a double curvature (see Fig. 9) promises to be even thinner and stronger. Fabrication of the new windows is in progress, after which pressure tests will be performed to validate the predicted performance based on finite-element analysis.

An area to test absorbers and 201 MHz rf cavities is presently under construction at Fermilab. This area, which should be available in Fall 2003, is situated at the end of the 400 MeV proton linac and could ultimately be used for beam tests of cooling channel components.

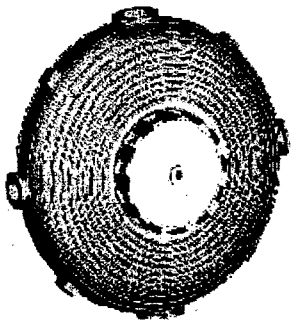

Figure 8: 201 MHz cavity for muon cooling channel.

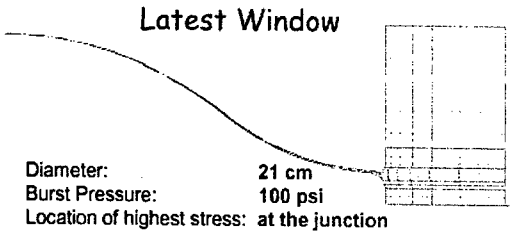

Figure 9: Improved absorber window design.

Acceleration

Although much of the R&D work for muon beams centers around cooling, there are other areas of focus. For muon acceleration, we need to develop 201 MHz superconducting cavities. While superconducting cavities at higher frequencies are by now relatively standard items, the cavity size required for 201 MHz (see Fig. 10) makes this a challenging component. The present focus [12] is to achieve high gradients, high Q, and acceptable mechanical stability. To date, the test cavity has operated at an accelerating gradient of 11 MV/m and has demonstrated a low-power Q of 10^{10}. Still needed are designs for the ancillary items required for a complete cavity module: input coupler, higher-order-mode coupler, and tuner.

In Japan, a substantial Fixed-Frequency Alternating Gradient (FFAG) accelerator development program is under way. In the Japanese Neutrino Factory scheme, a cascaded series of FFAG rings is used to capture the muon beam from the target area and bring it to its final energy of 20–50 GeV. An FFAG for 150 MeV protons has recently been completed, and is presently being commissioned. A series of FFAG workshops [13] is being held to better understand the features and potential promise of such devices.

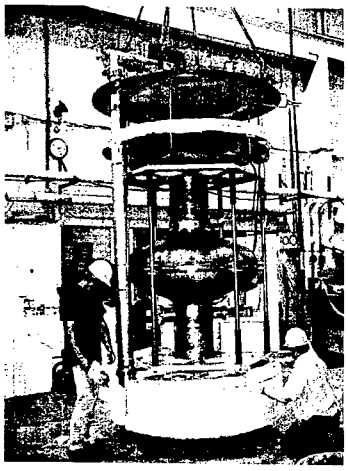

Figure 10: 201 MHz superconducting cavity under test at Cornell.

Simulations

The focus of the simulations group in the past year has been on "emittance exchange." In this process, dispersion is introduced into the cooling channel and a variable thickness ("wedge") absorber is used to reduce the longitudinal emittance of the beam. Though this approach increases the transverse emittance, the standard cooling technique described earlier reduces this, with the result that the cooling takes place in 6D phase space. The natural way to do this is to arrange the cooling channel into a cooling ring [14,15]. Simulations of one such ring are presented in Fig. 11. We see that after some 10 turns in the 33 m circumference ring the 6D emittance is reduced by a factor of 302. Practical realization of such a ring requires full aperture injection and extraction kickers that are fast and powerful. This remains a challenging problem.

MICE ACTIVITIES

Although ionization cooling of muons is expected to be straightforward from a physics viewpoint, it has not been experimentally demonstrated. Given that a Neutrino Factory facility based on this concept will be expensive, it is clearly prudent to invest in a demonstration of this key principle. An international group has been formed, the MICE Collaboration, to propose and then carry out an experiment to study ionization cooling of muons. The group submitted a formal proposal [16] to Rutherford Appleton Laboratory (RAL) in January, 2003 and underwent a formal international review in February, 2003. The review committee has recently recommended that the experiment be approved, and we anticipate a favorable response from RAL soon. With a motivated collaboration, an enthusiastic host laboratory, and a solid experiment design, the time to carry out the experiment is now. Among other things, MICE forces us to deal with operational and cost issues early.

The MICE Collaboration has members from Europe, Japan, and the U.S. Funding requests to their agencies

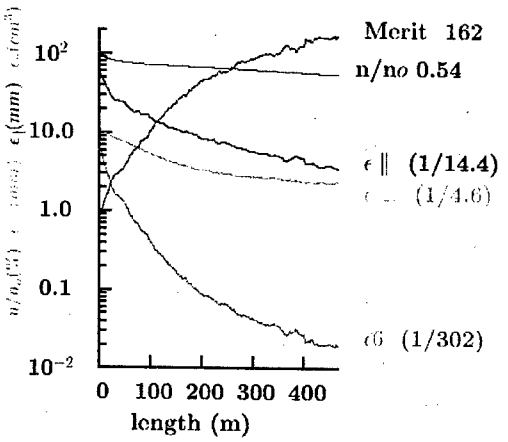

Figure 11: Simulations for RFOFO cooling ring [15].

have already been made by the UK and the U.S. groups. After formal approval by RAL, other groups will likewise make formal funding requests. It is anticipated that data taking will happen in 2007–2008.

Figure 12 illustrates the basic ingredients of MICE. The cooling channel components include liquid-hydrogen energy absorbers (capable of handling ≈100 W), 201 MHz rf cavities to restore the lost energy (capable of up to 17 MV/m), and solenoid magnets to contain the muons (capable of reaching about 5 T). In addition, the experiment provides a diffuser to create a large emittance sample, an upstream diagnostics section to define the initial emittance, and a downstream diagnostics section to measure the final emittance and provide particle identification.

R&D PLANS

In the next few years there are specific R&D plans in all technical areas.

For the Targetry program, the main item is to fabricate a 15 T test magnet and test it with beam from the AGS or elsewhere.

The Cooling program will complete fabrication of the 201 MHz high-gradient cavity and test it up to the required gradient of 17 MV/m. Liquid-hydrogen absorbers will be fabricated and tested, including all safety aspects. These tasks will be carried out in the MUCOOL Test Area at Fermilab.

Acceleration work will continue to concentrate on development of a 201 MHz superconducting rf cavity module, with the aim of reaching a gradient of 17 MV/m.

Simulation work will aim toward a well defined ring cooler concept that can be turned into a fully engineered ring design. They will also develop scenarios for incorporating a ring cooler into an end-to-end Neutrino Factory design. This may be done in the context of a "world" feasibility study of a Neutrino Factory that serves as a follow-on to the two U.S. studies done several years ago [1,2].

MICE activities will center on designing and fabricating the required beam line components and detectors. Accompanying this will be a strong software effort to develop the data acquisition, data analysis, and simulation tools needed to interpret the experimental results.

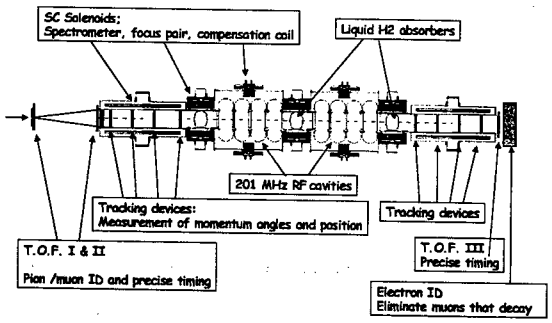

Figure 12: Schematic layout of MICE.

SUMMARY

The intense muon beam R&D program continues to make excellent progress on all fronts, due to the efforts of many dedicated scientists and engineers in Europe, Japan, and the U.S. Hardware development is continuing at a good pace and the simulation effort has made great strides in developing 6D cooling scenarios. The interaction of the R&D groups from the three regions is very positive, and serves as a model for working together on major international projects. The hardware components being developed will serve as prototypes for MICE. This key experiment, a grass-roots effort from all three regions, is expecting formal approval from RAL in the near future. If funding is made available in a timely way, this experiment could begin in a few years.

Despite the progress, it is clear that funding limitations are hampering the effort in all three regions. Restoring a healthy funding level for accelerator R&D is critical for maintaining the health of high-energy physics, and must be a priority to preserve the future of the field.

REFERENCES

[1] N. Holtkamp and D. Finley, eds. Fermilab Pub-00/108-E, May 2000; http://www.cap.bnl.gov/mumu/studyii/report/Feasibility-I/Feasibility-I-fnal.pdf

[2] S. Ozaki, R. Palmer, M. S. Zisman, and J. Gallardo, eds., BNL Report-52623; http://www.cap.bnl.gov/mumu/studyii/final_draft/The-Report.pdf

[3] A. Hassenein, *et al.*, Nucl. Instr. Meth. in Phys. Res. A 503, 70 (2003).

[4] J. R. Haines and C C Tsai, ORNL/TM-2002/27, report no. R02-113138, see http://www.ornl.gov/~webworks/cppr/y2002/rpt/ 113138.pdf

[5] H. L. Ravn, Nucl. Instr. Meth. in Phys. Res. A 503, 340 (2003).

[6] A. Fabich and J. Lettry, Nucl. Instr. Meth. in Phys. Res. A 503, 336 (2003).

[7] K. Bongardt *et al.*, in Proc. 2002 European Particle Accel. Conf., Paris, France, June 3–7, 2002, p. 969.

[8] D. Li *et al.*, in Proc. 2002 European Particle Accel. Conf., Paris, France, June 3–7, 2002, p. 2160.

[9] D. Li *et al.*, in Proc. 2002 European Particle Accel. Conf., Paris, France, June 3–7, 2002, p. 2163.

[10] R. Rimmer *et al.*, in Proc. 2002 European Particle Accel. Conf., Paris, France, June 3–7, 2002, p. 2190.

[11] D. M. Kaplan *et al.*, in Proc. 2001 Particle Accel. Conf., Chicago, June 18–22, 2001, p. 3888.

[12] H. Padamsee, in Proc. 2001 Particle Accel. Conf., Chicago, June 18–22, 2001, p. 468.

[13] See http://hadron.kek.jp/FFAG/FFAG03_HP/ and links contained therein.

[14] V. Balbekov, *et al.*, in Proc. 2001 Particle Accel. Conf., Chicago, June 18–22, 2001, p. 3867.

[15] R. B. Palmer, in Proc. 2002 Neutrino Factory Workshop, London, England, July 1–6, 2002; to be published in J. Phys. G.

[16] http://hep04.phys.iit.edu/cooldemo/micenotes/public/pdf/MICE0021/MICE0021.pdf

100 BUNCH DAΦNE OPERATION

A. Drago, D. Alesini, G. Benedetti, M. Biagini, C. Biscari, R. Boni, M. Boscolo, A. Clozza, G.Delle Monache, G. Di Pirro, A. Gallo, A. Ghigo, S. Guiducci, F. Marcellini, G. Mazzitelli, C. Milardi, L.Pellegrino, M. Preger, P. Raimondi, R. Ricci, C. Sanelli, M. Serio, F. Sgamma, A. Stecchi, A.Stella, C. Vaccarezza, M. Vescovi, M. Zobov, I.N.F.N.- L.N.F., Frascati, Italy.

Abstract

The DAΦNE collider has been operating by filling 100 consecutive buckets out of the available 120 with a gap to avoid ion trapping in the electron beam. To reduce the effect of the parasitic crossings the crossing angle has been increased up to 29 mrad and the horizontal beta function at the interaction point lowered down to 1.7 m. Moreover both transverse and longitudinal feedbacks have been optimized for this more demanding mode of operation. Comparison between 100 and 50 bunches operation in 2002 runs is presented.

INTRODUCTION

DAΦNE is a e^+/e^- collider, with center of mass energy 1.02 GeV (Φ-Factory). It has two symmetric main rings and two IP's: KLOE detector is in IP1, DEAR detector is in IP2. The harmonic number is 120 and this is the maximum number of storable bunches. The minimum bunch distance is 2.7 nsec, corresponding to ~80 cm, and the maximum single bunch design current is 44 mA (achieved > 200 mA).

The peak luminosity can be expressed as function of number of bunches (n_b) and single bunch currents (I^+ and I^-)

$$L = \frac{n_b I^+ I^-}{4\pi f_{rev} e^2 \sigma_x \sigma_y} \qquad (1)$$

where f_{rev} is the revolution frequency, e is the electron charge, σ_x and σ_y are the horizontal and vertical r.m.s. sizes of the bunch.

The peak luminosity is proportional to the number of colliding bunches and to the product of the single bunch currents. We want to increase the luminosity and this can be done also increasing the number of colliding bunches and the single bunch currents.

Since the tune shift (ξ) is proportional to the bunch current (I) and tends to saturate when the current increases (up to now $\xi < 0.03$), it is not effective to inject the single bunch current over a threshold, so we have increased the number of colliding bunches.

An ion clearing gap is necessary for the e^- beam: it can be between 15% and 25% of the ring. Usually a uniform train of bunches followed by one gap is stored: every bunch of the train can be separated from the following one by N empty buckets (N=0,1,2,...).

Different bunch patterns have been used for collision in the past. In the year 1999 the collision bunch pattern was composed by a train of 23 bunches separated by 3 empty buckets and followed by ¼ ring gap.

During the year 2000 the collision bunch pattern was 30 bunches separated by 2 empty buckets and followed by ¼ ring gap.

In the year 2001 and 2002 the collision bunch pattern was 50 bunches separated by 1 empty bucket and followed by 1/6 ring gap.

In the last 2 months of the year 2002, in the IP2, for DEAR detector, the bunch pattern used for collision was 100 contiguous bunches followed by 1/6 ring gap. In Fig.1 a sketch of the colliding pattern in the years 1999-2002 is presented.

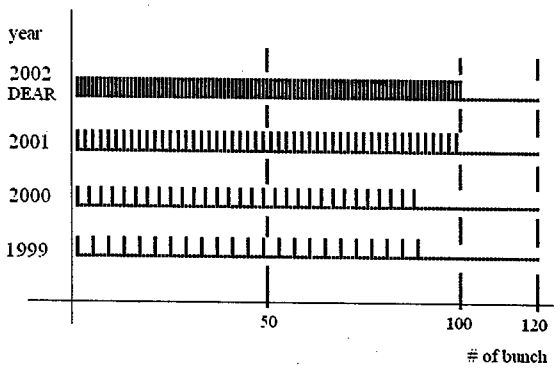

Fig. 1: – Colliding bunch patterns, years 1999-2002.

OPTICS DEVELOPMENTS

With the aim to bring into collision 100 contiguous bunches, some modifications to the optic layout have been implemented to minimize the effects of the parasitic crossings:

1) a lower horizontal beta in the Interaction Region (see Fig. 2);
2) a larger Crossing Angle at the IP, from 12.5*2 mrad to 14.5*2 mrad;
3) a smaller horizontal emittance.

With these modifications the first parasitic crossing horizontal separation (@40 cm from IP) has increased from 5 σ_x to 12 σ_x.

Minimizing of the horizontal size (see points 1 and 3 listed above) gave also a single bunch luminosity increase.

In order to reduce the non-linearities, three octupole magnets have been installed in each ring. Tuning correctly the machine non-linearities, it has been possible to reach better lifetimes, dynamic apertures and improve beam-beam performance. A machine model has been developed to study the linear and non-linear behaviour [1].

0-7803-7738-9/03/$17.00 © 2003 IEEE

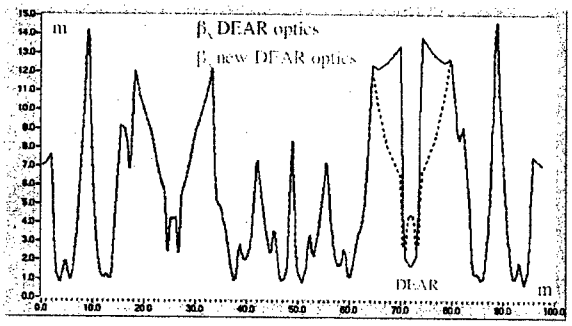

Figure 2: The horizontal beta at IP2 has been lowered: 4.4m at December 2001(blue), 1.7m after April 2002 (red).

The Piwinski's angle is evaluated as a "badness factor". It is given by the formula

$$\theta = \frac{\sigma_z \phi}{\sigma_x} < 1 \qquad (2)$$

where σ_z and σ_x are the longitudinal and horizontal r.m.s. sizes of the bunch and ϕ is the crossing angle.

Table 1: Piwinski's angle θ for different DAΦNE setup.

	σ_z cm	βx, m	β_y, m	ε_x, 10^{-6}	σ_x mm	σ_y μ	ϕ mrad	θ
Design	3	4.5	.045	1	2.12	20	12.5	.18
KLOE	2.5	2.7	.026	.74	1.41	20	11.5	.20
DEAR, Decemb. 2002	2	2.54	.040	.78	1.13	20	13.5	.24
DEAR, After April 2002	2	1.7	.030	.62	1.03	20	14.5	.28

In Table 1 are reported several machine parameters applied to four different machine setup: design, collision for Kloe, collision for DEAR before and after April 2002. β_x and β_y are the horizontal and vertical betatron functions, ε_x is the horizontal emittance, ϕ is the crossing angle at the IP, and θ is the Piwinski's angle.

As it can be seen, in order to bring into collision 100 bunches, the crossing angle and, as consequence, Piwinski's angle have been increased. However, this practically does not affect the single bunch luminosity.

BEAM DYNAMICS

The DAΦNE longitudinal dynamics is affected by strong coupled bunch synchrotron dipole oscillations well damped by the feedback developed with SLAC/LBL.

Besides in both rings, at high currents, harmful longitudinal quadrupole instabilities need to be cured.

In Fig. 3 a positron beam power spectrum measured by a powerful real time FFT analyzer HP3587s is shown. The beam spectrum, recorded with 100 bunches, 900mA, in collision, shows a large longitudinal quadrupole instability on the mode #76.

The Longitudinal feedback, built to damp the synchrotron dipole oscillations, is able, using a special setup, to damp the quadrupole motion [2].

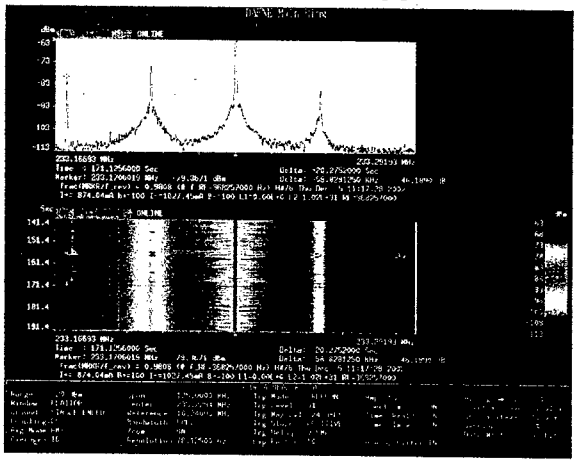

Fig.3: - e^+ beam power spectrum measured by a real time FFT analyzer HP3587. The beam spectrum, (100 bunches, 900mA, in collision) shows a large longitudinal quadrupole instability.

Vertical and horizontal instabilities require powerful feedback systems.

In the year 1999 the collision bunch pattern was 23 bunches each separated by 3 empty buckets. Only the longitudinal feedback was installed at full power (3x250W), without any transverse feedbacks.

During the year 2000 the collision bunch pattern was 30 bunches each separated by 2 empty buckets. The vertical feedbacks were added with reduced power (2x100W). In the year 2001 the collision bunch pattern was 50 bunches separated by 1 empty bucket. The vertical feedbacks were working at full power (2x250W) and the horizontal ones with reduced power (2x100W).

In the last 2 months of the year 2002 the bunch pattern was 100 contiguous bunches colliding in IP2 (DEAR) and the complete control of longitudinal quadrupole in both rings was successfully achieved.

With the new layout, it has been possible to store more than 1.8A with stable e^- beam in 90 contiguous bunches (single beam not colliding, >20mA per bunch), while in 50 bunches separated by 1 empty bucket, the maximum current achieved was smaller (~1.250A).

To achieve this, it has been necessary a very accurate transverse and longitudinal feedback setup and a complete separation of the signal of contiguous bunches in the feedbacks.

RESULTS

In this section we present the results obtained in the October–December 2002 shifts with 100 bunches colliding. In Fig.4 signals coming from two longitudinal pickups and showing the e^+ and e^- bunch train during collision, are monitored by an oscilloscope.

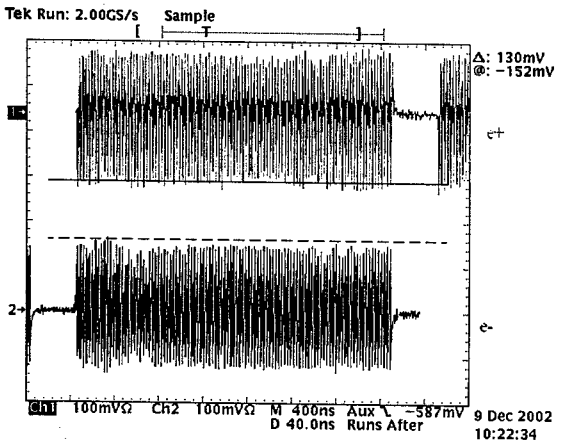

Fig.4: - Signals from two longitudinal pickups show the e^+ and e^- bunch train during collision monitored by an oscilloscope.

During the collision shifts more than 2 Ampere have been usually stored in two beams with acceptable background and lifetime.

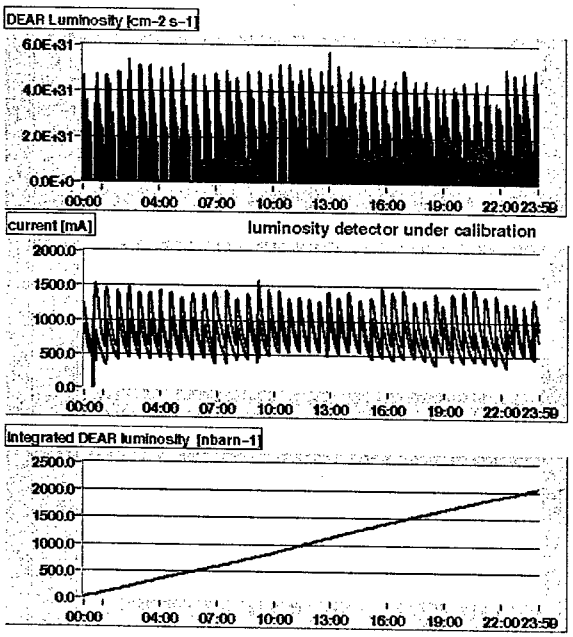

Fig.5: – Peak and integrated luminosity in 24h (12/8/02).

The collider has shown a very good reliability: in Fig. 5 the peak luminosity, currents and integrated luminosity are presented for one of the best 24 hours of data taking (12/8/2002, IP2). With 100 bunches a DEAR peak luminosity of $7*10^{31}$ cm-2 s-1 has been achieved while with 50 bunch it was $4.5*10^{31}$ cm-2 s-1. With 100 bunches a DEAR integrated luminosity of 2 $pbarn^{-1}$ per day has been reached while with 50 bunches the maximum value was 1.1 $pbarn^{-1}$. This has allowed completing the physics program for the DEAR experiment.

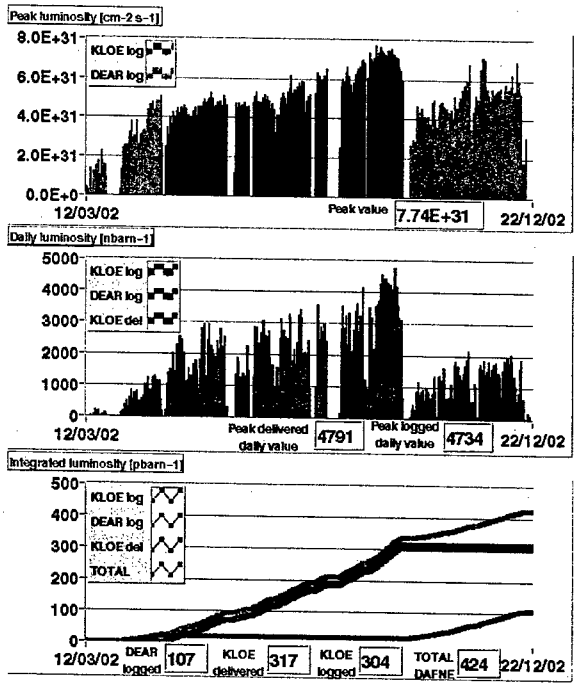

Fig. 6: – Year 2002 peak and integrated luminosity.

CONCLUSION

During 2002 it has been possible to collide with 100 contiguous bunches (out of 120) by implementing a new machine setup, lowering the horizontal beta at the IP, increasing the crossing angle and decreasing the horizontal emittance.

Storing high current in 100 bunches has become possible using powerful active feedback systems necessary to damp longitudinal dipole oscillations, longitudinal quadrupole, horizontal and vertical instabilities.

As result both peak and integrated luminosity have grown and there is still margin for further improvements increasing the currents up to 20mA per bunch; these results have been obtained in only two months.

With these shifts, DEAR experiment has completed the data taking. New IR's for KLOE and FINUDA detectors have been designed taking in mind this approach and are ready for the next shifts.

REFERENCES

[1] Milardi et al. "Developments in Linear and Non-Linear DAΦNE Lattice", RPAG025, these proceedings.

[2] A. Drago et al. "Longitudinal quadrupole instability and control in the Frascati DAΦNE electron ring", Phys. Rev. ST-AB, Vol.6, I5, 052801 (2003).

STUDY OF BEAM-BEAM EFFECTS IN HERA WITH SELF-CONSISTENT BEAM-BEAM SIMULATION

J. Shi* and L. Jin, University of Kansas, Lawrence, KS 66049
G.H. Hoffstaetter, Cornell University, Ithaca, NY 14850

Abstract

The beam-beam effect in HERA was studied with a self-consistent beam-beam simulation by using the particle-in-cell method. A remarkable agreement between the experimental measurement and the simulation result was observed on the emittance growth, luminosity reduction, and coherent tune shifts. The simulation study also showed that the chaotic coherent beam-beam instability could occur in HERA and this collective beam-beam instability could be avoided with a slightly different working point.

INTRODUCTION

In the current luminosity upgrade of HERA, the luminosity is expected to increase roughly by a factor of 4.5. To achieve this goal, the beam-beam parameter of the electron beam ($\xi_{e,x}$, $\xi_{e,y}$) will be increased to (0.034, 0.052). To examine any possible luminosity reduction due to beam-beam effects, several beam experiments were performed on HERA [2, 1, 3]. In order to have a better understanding of those experimental data and to evaluate the beam-beam effect in the HERA upgrade, the dynamics of beam-size growth and the stability of the coherent beam-beam oscillation in HERA were studied with a self-consistent beam-beam simulation. A remarkable agreement between the experimental measurement and the simulation result was observed on the emittance growth, luminosity reduction, and coherent tune shifts. The simulation study also showed that the chaotic coherent beam-beam instability [4] could occur in HERA. It was found that when the beam-beam parameter of the electron beam exceeds a threshold that corresponds to an overlap of the electron beam with a low-order single-particle beam-beam resonance, the onset of the collective beam-beam instability results in an enhanced growth of the proton-beam emittance. After the onset of this collective beam-beam instability, the phase-space area near the origin (closed orbit) becomes unstable for beam centroids and two initially centered beams could develop a spontaneous chaotic coherent oscillation due to beam-beam interactions. A study of the dynamics of beam particle distributions showed that after the onset of the beam-beam instability, the distributions significantly deviate from Gaussian distribution due to beam halo. The formation of the beam halo is a result of chaotic transport (chaotic diffusion) of particles from beam cores to beam tails. In the HERA Upgrade, the beam-beam parameter of the positron beam is over 20 and 100 times larger than that of the proton beam in the horizontal and vertical direction, respectively, and the two rings have a very different working point. Traditionally, the beam-beam effect in such situation is considered as a typical strong-weak or very unsymmetrical case. For the strong-weak beam-beam interactions, it is commonly believed that the coherent beam-beam effects is not important. This study showed that the traditional boundary between the strong-strong and strong-weak beam-beam interactions is no longer valid in the nonlinear regime of beam-beam interactions. For high-intensity beams, the nonlinear beam-beam perturbation could dominate the beam dynamics and the collective beam-beam instability could therefore occur in both cases of strong-strong (symmetrical or nearly symmetrical) and strong-weak (very unsymmetrical) beam-beam interactions.

In the simulation, the linear HERA lattice with one or two IPs was used. The beam-beam interaction at each IP was represented by a kick in transverse phase space and the beam-beam kick was calculated by using particle-in-cell method with 5×10^5 macro-particles in each beam. The code used in this study is an expanded version of [4] that is currently capable of studying beam-beam effects of proton or lepton beams with any aspect ratio. The motion of particles was tracked in 4-dimensional transverse phase space without synchrotron oscillation and momentum deviation. For lepton beams, the quantum excitation and synchrotron damping are treated as kicks in each turn during the tracking [5].

NON-COLLECTIVE BEAM-BEAM EFFECTS

The beam experiment in HERA Accelerator Study 2000 studied the beam-beam effect at a very large beam-beam tune shift of the electron beam [1]. In the experiment, the vertical beam-beam parameter of the e^+ beam was varied from 0.047 to 0.272 by changing the vertical beta-function $\beta^*_{e,y}$ of the e^+ beam at IPs from 0.7 m to 4.0 m. Detailed experimental parameters can be found in Ref. [1]. In the experiment, the emittance of the e^+ beam after collision and the luminosity were measured as functions of $\beta^*_{e,y}$ at both HERA IPs, H1 and ZEUS. To have a better understanding of those measured data, we have reconstructed the HERA beam experiment with the beam-beam simulation. This study also served a detailed benchmark of our beam-beam simulation code with the experimental measurement.

Figure 1 plots the emittance growth of the e^+ beam and the specific luminosity as a function of $\beta^*_{e,y}$ measured in the experiment and calculated by the beam-beam simulation. For each $\beta^*_{e,y}$ where the measurement was performed, two data points correspond to the measurement at H1 and

* Supported by the US DOE under Grant No. DE-FG03-00ER41153.

0-7803-7738-9/03/$17.00 © 2003 IEEE

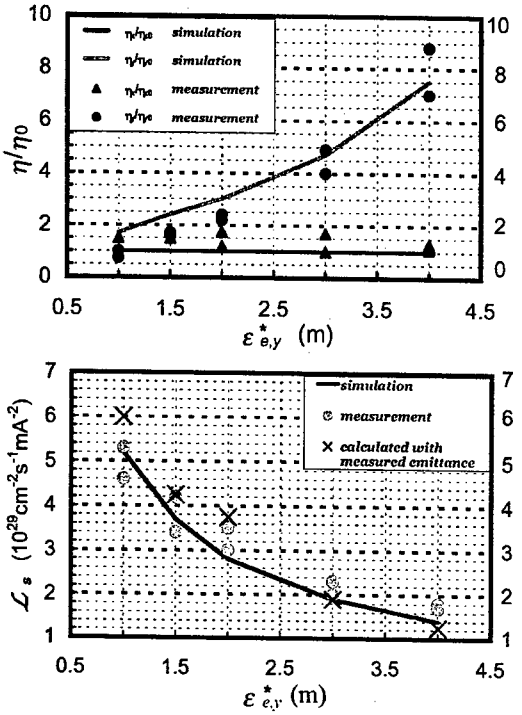

Figure 1: Emittance of the e^+ beam (upper figure) and specific luminosity (lower figure) v.s. $\beta^*_{e,y}$. ϵ_0 is the emittance without collision. Discrete points are from the experiment and continuous curves from the simulation. In the emittance plot, the upper (lower) curve is the vertical (horizontal) emittance.

ZEUS, respectively. Both the emittance and the luminosity plot show a remarkable agreement between the experiment and the simulation. In the experiment, the coherent tune was also measured at $\beta^*_{e,y} = 4.0$ m. Table 1 lists the coherent tune measured in the experiment and calculated by the simulation and it shows a very good agreement between the experiment and the simulation. In order to understand such the small coherent tune shifts, the eigen-frequencies of the coherent oscillation was derived for the un-symmetrical case of beam-beam interaction based on the assumption of rigid Gaussian beams [2]. With the enlarged e^+-beam emittance in Fig. 1, however, the coherent tune calculated from the derived formula does not agree well with the experimental or simulation result (see Table 1). The discrepancy here is due to a non-Gaussian distribution of the e^+ beam. A study of the dynamics of particle distributions during the beam-beam simulation showed that the distribution of the e^+ beam deviated from a Gaussian distribution with a significant drop at beam core and a growth of beam tails (see Fig. 2). Compared with the distribution of the e^+ beam, a Gaussian beam has more particles in the core. The coherent beam-beam tune shift calculated from the derived formula is therefore larger than the real tune shift of the e^+ beam.

Table 1: Coherent tune of the e^+ beam at $\beta^*_{e,y} = 4.0$ m. "Gaussian Beams" is the tune calculated with the measured e^+-beam emittances by using the derived formula for two non-symmetrical Gaussian beams

	ν_x	ν_y
Experiment	52.160	52.233
Simulation	52.162	52.232
Gaussian Beams	52.156	52.227

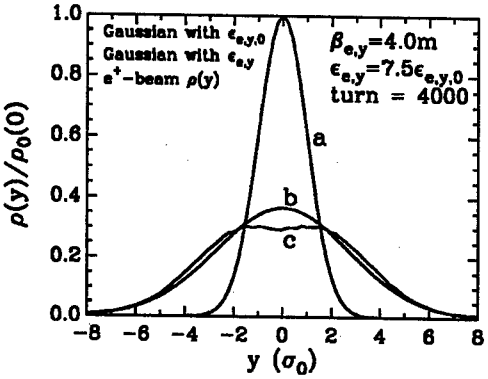

Figure 2: The vertical projection of the e^+-beam distribution at $\beta^*_{e,y} = 4.0$ m. (a) The initial beam distribution (Gaussian); (b) the Gaussian distribution with enlarged e^+-beam emittance; and (c) the e^+-beam distribution.

COLLECTIVE BEAM-BEAM INSTABILITY

Simulation has been conducted for the HERA Upgrade with two e-p collisions. When the working point of the e beam is at $\vec{\nu}_e = (54.14,\ 51.21)$, the onset of the chaotic coherent beam-beam instability results in an emittance blowup on the p beam and a significant luminosity reduction (see Fig. 3). Moreover, the two initially centered beams developed a spontaneous chaotic coherent oscillation (see Fig. 4). A study of the dynamics of beam-beam tune spread of the e beam showed that this collective beam-beam instability is due to an overlap of the e beam and the 4th-order resonance (see Fig. 5). It can be clear seen in Fig. 5 that many particles in the e beam are trapped inside the resonance. A simulation with a slightly different working point $\vec{\nu}_e = (54.072,\ 51.107)$ of the e beam was therefore performed. At this new working point, the e-beam is away from the 4th-order resonance. The beam centroid motion is stable and no significant emittance growth was observed on the p beam. Consequently, the luminosity is recovered to the design value (see Fig. 3). The collective beam-beam instability in this case can be therefore avoided by eliminating the crossings of major beam-beam resonance. To determine the threshold of the onset of the coherent beam-beam instability, the emittance growth of the p beam was studied as a function of bunch current of the p beam in the case

of one interaction point. It was found that the threshold is at 50% design p-beam current. This further confirms the effect of the 4th-order resonance on the collective beam-beam instability since at 50% design p-beam current the e beam avoids the crossing of the 4th-order resonance. To verify the effect of the 4th-order resonance, a beam experiment was performed on HERA recently [3]. In the experiment, the emittance of the p beam and luminosity were measured and compared at two different working points of the e^+ beam. When the working point of the e^+ beam is at $\vec{\nu}_e = (0.140,\ 0.210)$, the e^+ beam does not cross any major beam-beam resonance. In this case, no significant emittance growth of the p beam and the luminosity reduction were observed. When the working point of the e^+ beam was moved to $\vec{\nu}_e = (0.215,\ 0.296)$, on the other hand, the e^+ beam overlaps with the 4th-order resonance and a more than 30% emittance growth was observed in both horizontal and vertical emittance of the p beam. We were able to reconstruct this experiment with the beam-beam simulation. The phenomena observed in the experiment agree well with that of the beam-beam simulation.

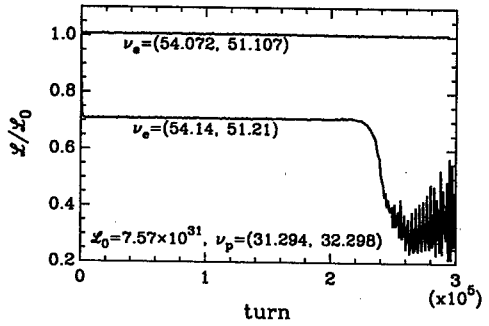

Figure 3: Luminosity in HERA Upgrade with two e-p collisions.

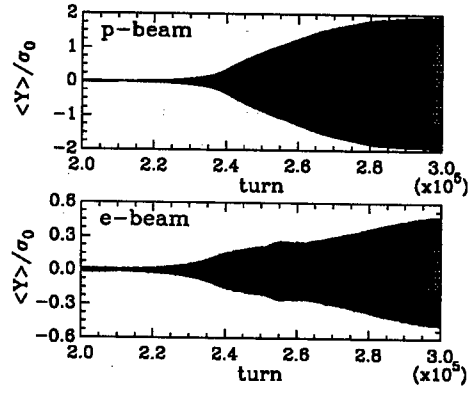

Figure 4: Chaotic coherent beam oscillation in HERA Upgrade with two e-p collisions at $\vec{\nu}_e = (54.14,\ 51.21)$.

Another aspect of the collective beam-beam instability is the importance of the beam-beam tune spread to the beam instability [6]. The simulation study suggested that having

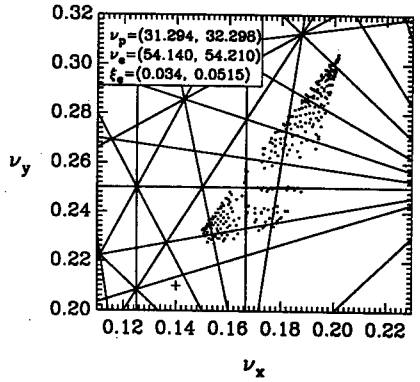

Figure 5: Tune spread of the e beam in HERA Upgrade with two e-p collisions when $\vec{\nu}_e = (54.14,\ 51.21)$.

a large beam-beam tune spread may benefit the stability of beams in certain situation. One such example is when the working point of the e^+ beam is such that the e^+ beam crosses only the 4th-order resonance of $2\nu_x + 2\nu_y = 1$ when there is one IP in the ring while crosses three 4th-order resonance lines including $2\nu_x + 2\nu_y = 1$ when there are two IPs in the ring. Note that the incoherent beam-beam tune shift as well as the beam-beam tune spread in the case of two IPs is about twice as large as that in the case of one IP. It was found in the simulation that the collective beam-beam instability occurs in the case of one IP but in the case of two IPs. Similar phenomenon has also been observed in the recent HERA experiment [3]. In the near-linear regime of beam-beam interactions, the beam-beam tune spread is the dominant beam-beam effect and a smaller beam-beam tune spread could benefit beams by reducing the possibility of resonance crossings. In the nonlinear regime of beam-beam interactions, however, the phase-dependent perturbation of beam-beam interactions could lead to the onset of the chaotic coherent beam-beam instability. In this situation, having a large tune spread could benefit the beam stability since the existence of a sizable tune spread is one of necessary conditions for the Landau damping that could suppress the coherent beam-beam instability and, moreover, the existence of a large tune spread reduces the possibility of trapping particles inside a bad resonances.

REFERENCES

[1] G.H. Hoffstaetter, *HERA Accelerator Studies 2000*, DESY HERA 00-07, (2000).

[2] G.H. Hoffstaetter, *HERA Accelerator Studies 1999*, DESY HERA 00-02, (2000).

[3] M. Minty, " Summary of Recent Beam-Beam Experiments After the Luminosity Upgrade", preprint, (2003).

[4] J. Shi and D. Yao, Phy. Rev. E62, 1258 (2000).

[5] K. Hirata and F. Ruggiero, CERN/LEP-TH/89-43 (1989).

[6] L. Jin and J. Shi, "Importance of Coherent Beam-Beam Effects to the Compensation of Beam-Beam Tune Spread in Hadron Colliders", submitted to Phys. Rev. E, (2003).

ELECTRON-ION COLLISIONS AT RHIC USING A HIGH INTENSITY SELF-POLARIZING ELECTRON RING*

V. Ptitsyn, J. Kewisch, B. Parker, S. Peggs, D. Trbojevic, BNL, Upton, NY, USA
D.E. Berkaev, I.A. Koop, A.V. Otboev, Yu.M. Shatunov, BINP, Novosibirsk, Russia
C. Tschalaer, J.B. van der Laan, F. Wang, MIT-Bates, Middleton, MA, USA
D.P. Barber, DESY, Hamburg, Germany

Abstract

We consider the design of an electron-ion collider realized by adding a self-polarizing electron ring to the existing RHIC collider. It would provide polarized electron-proton and unpolarized electron-ion beam collisions in the center of mass energy range of 30-100 Gev and at luminosities up to 10^{33} $cm^{-2}s^{-1}$ for e-p and 10^{31} $cm^{-2}s^{-1}$ for e-Au collisions. An electron storage ring lattice has been developed which provides a short polarization time for an electron beam in the 5-10 GeV energy range and which satisfies the luminosity goals. We describe the modifications to the RHIC interaction region layout required for both efficient beam separation and also for longitudinal electron and proton beam polarization at the collision point.

INTRODUCTION

In recent years a strong physics interest in an electron-ion collider has emerged. An electron-ion collider would probe QCD in a manner not previously possible through collisions between electrons and beams of atomic nuclei as well as collisions between polarized electron and proton beams. The availability of longitudinally polarized electron and proton beams at the collision point is a prerequisite for such an electron-ion collider.

The RHIC collider at Brookhaven National Laboratory (BNL) is currently providing beams of gold ions, deuterons and polarized protons for colliding beam physics experiments at the positions of four experimental detectors [1]. The possible scenarios and accelerator issues of the addition of an electron accelerator to the RHIC complex have been discussed in [2]. The addition should be done in a way which involves minimal reconstruction of RHIC itself and should be financially acceptable. Here we describe a design for the new "eRHIC " collider based on a self-polarizing electron storage ring and developed in collaboration between BNL, the Budker Institute for Nuclear Physics (BINP) and the MIT-BATES laboratory.

DESIGN LAYOUT

This design suggests construction of an electron ring with an energy, E, of 5-10 GeV which will have a circumference of 5/16 of that of RHIC and an intersection with RHIC in one of the existing experimental areas (see Fig.1). The electron beam from an unpolarized electron source is accelerated in the linac to 2GeV and injected into the ring. In the later stages of the project the linac energy can be increased to 5 GeV. After injection the electron beam is accelerated to collision energies of 5-10 GeV where it becomes spin polarized through the emission of synchrotron radiation (the Sokolov-Ternov effect). Thus it is important for the design to ensure a short enough polarization time. Stored positrons could be polarized in the same way.

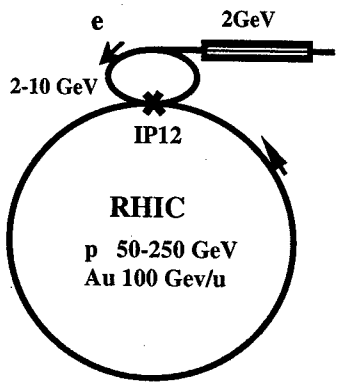

Figure 1: Design layout

The lattice of the electron ring consists of two arcs with regular FODO structures and two straight sections: one for the beam collisions and the other for accelerating cavities and other necessary equipment. For fixed bending radii the polarization time τ_p is proportional to E^{-5}. But a short polarization time over the whole energy range is achieved by a special design for the electron ring bending magnets. These so-called "superbend" magnets consist of three parts (see Fig.2). The magnetic fields, B, of the short central parts and of the longer outer parts are scaled differently with the beam energy, while keeping the total bending angle of the magnet the same. Such a field arrangement allows an optimal balance to be maintained between the quantities of the interest: τ_p , which at a chosen energy is proportional to B^{-3} and synchrotron radiation losses, proportional to B^2 at a chosen energy. At 5 GeV energy the relatively high field of 2T in the central part of the magnet is used to decrease polarization time, while at 10 GeV the field is reduced to decrease the synchrotron radiation power load. At 10 GeV the setup with a uniform field in the outer and central parts of the superbend at provides a polarization time of 8min and

* Work performed under Contract No. DE-AC02-76CH00016 with the U.S. Deparment of Energy

0-7803-7738-9/03/$17.00 © 2003 IEEE

7MW of synchrotron radiation. Ways to accommodate this power load are under consideration. The polarization time and beam emittance dependence on beam energy are shown in Figure 3.

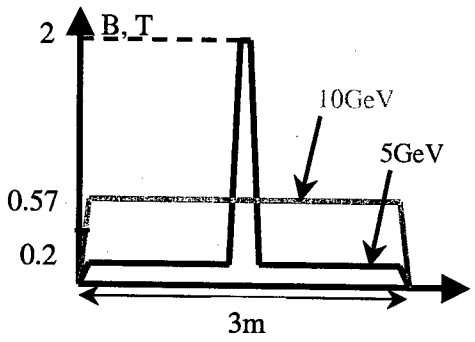

Figure 2: Field distribution (B) along the superbend magnet for 5 and 10 GeV beam energies.

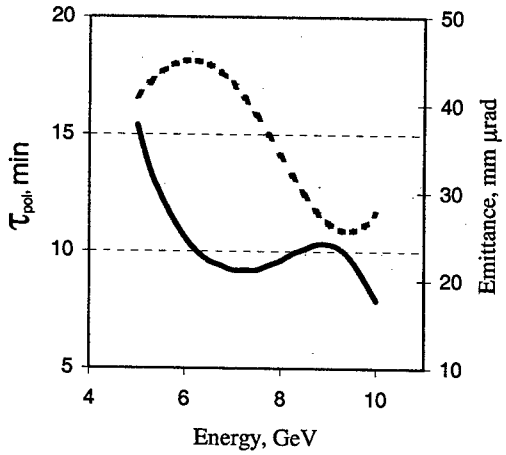

Figure 3: Electron beam polarization time (solid) and emittance (dashed) versus the beam energy for the superbend central field changing linearly from 0.57T (at 5GeV) to 2T (at 10 GeV).

Since the magnet fields in the superbend magnet do not scale linearly with the beam energy, the beam path inside the magnet depends on the energy. In order to control the change of path length with the energy and thus eliminate radial shift of the orbit, special dipole magnet insertions are being considered.

LUMINOSITY CONSIDERATIONS

The maximum luminosity of a collider depends, among other things, on the tolerable beam-beam parameters ξ. It has been predicted that the destructive effect of beam-beam forces can be minimized by using round beam collision geometry based on conservation of the angular momentum [3]. This involves 2 conditions: equal beam sizes and equal betatron tunes. Then the luminosity is

$$L=\left(\frac{4\pi\gamma_e\gamma_i}{r_e r_i}\right)\cdot\xi_e\cdot\xi_i\cdot\sqrt{\frac{\varepsilon_e\varepsilon_i}{\beta_e^*\beta_i^*}}\cdot F_c$$

Following world wide experience, we have assumed limiting values of 0.05 (electrons) and 0.005 (protons) for the beam-beam parameters. Since the origins of the formation of the beam emittances are quite different, as well as their dependences on energy, tools for emittance control in both the electron and the ion ring are needed for keeping the beam sizes matched at the collision point. For the electron ring the superbends provide the flexibility for emittance manipulations. In the ion ring the emittance control should be done by a beam cooling device.

Following experience (B-factories or LEP for electrons; RHIC, Tevatron for protons) we have accepted 10^{11} particles per bunch as a reasonably achievable number.

The main parameters of eRHIC for the current variants of the electron and ion ring lattices are listed in Table 1 for the cases of e-p and e-Au collisions.

Table 1:Basic beam parameters

Parameters	e-ring	ion ring	
		p	Au
C, m	1022	3833	
E, GeV	5–10	250	100/u
n_b	96	360	
N_b	$1\cdot10^{11}$	$1\cdot10^{11}$	$1\cdot10^{9}$
I, A	0.45	0.45	
ε_{rms}, mm μrad	45–25	17–9	
β^*, cm	10	27	
σ^*, mm	0.07–0.05	0.07–0.05	
ξ	≤0.05	≤0.005	
L, $cm^{-2}\ s^{-1}$		$(0.5\text{-}0.9)\cdot10^{33}$	$(0.5\text{-}0.9)\cdot10^{31}$

To achieve the required proton and ion beam parameters some parts of RHIC will have to be upgraded.

First, in order to achieve and maintain the required gold beam emittance during collisions, a cooling system should be developed and installed in the ion rings. Cooling would also be required for experiments involving proton beams with energy below 200 GeV. The development of an electron cooling system for RHIC is currently underway[4].

Also, the reduction of the proton (ion) β^* from the currently used 1m to the 27cm required by the eRHIC design, will possibly call for longitudinal cooling to prevent luminosity reduction by the hour-glass effect.

The upgrade to 360 bunches from the current 55 or 110 bunches was foreseen at the RHIC design stage and looks feasible. Some modifications in the injection system will be needed. Also, better theoretical and experimental understanding of the pressure rise and electron cloud effects observed during RHIC operation is needed in

order to improve the maximum achievable total current of the ion and proton beams[5].

IR DESIGN

The interaction region design should provide focusing to the low β^* and effective beam separation to avoid parasitic collisions (with the about 35ns between consecutive bunches). At the same time it would be preferable to minimize the reconstruction of the existing RHIC rings.

Two possible schemes for the interaction region layout have been proposed so far with horizontal and vertical beam separation (see Figure 4).

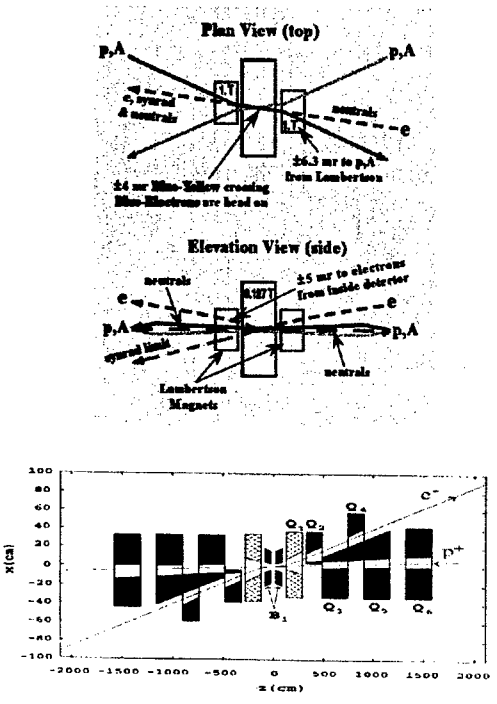

Figure 4: Two suggested schemes of the interaction regions: with vertical (top) and horizontal separation (bottom).

In both schemes the beam separation is initiated by the magnetic field inside the experimental detector itself. The focusing quadrupoles nearest to the collision point could also be put inside the detector. Thus the further development of the interaction region design should be coupled with the initial development of the experimental detector itself. During this work the important issues of minimizing detector background and the protection of the detector from synchrotron radiation should be resolved.

In order to transform the vertical polarization in the arcs of the electron and proton rings into longitudinal polarization, spin rotators will be installed around the interaction region. For the proton ring the rotators will be similar to the rotators, based on helical dipoles, already used at two RHIC interaction regions for proton-proton beam experiments. For the electron ring the use of a pair of solenoidal spin rotators has been suggested. They would produce exactly longitudinal polarization at an energy of 7.5 GeV. The spin-transparency conditions needed for obtaining sufficient electron polarization are well known [6].

POLARIZATION ISSUES

For an ideal machine without errors and beam-beam forces an electron polarization of about 90% is achieved after 8-15min of beam storage. But misalignments and beam-beam forces can lead to strong depolarization. The effect of the extra magnetic fields in and around the detector can also be significant. A first order calculation of the polarization shows that with a rms vertical closed orbit error of 0.5 mm the maximum equilibrium polarization might drop to the 50-60% level if no specific corrections are made. Fortunately, it has been demonstrated at HERA that depolarizing effects can be minimized with harmonic correction of the closed orbit [7]. Such schemes should be used at eRHIC. Together with feedback from a fast polarimeter, based on the Compton backscattering of a laser beam, it might be possible to optimize the polarization continuously on-line. Also, the storage ring design itself can be re-optimized to provide less sensitivity to depolarizing resonances.

CONCLUSIONS

The design of an electron-ion collider (eRHIC) presented here is based on the construction of a self-polarizing electron ring. The collider will provide polarized electron-proton and unpolarized electron-ion beam collisions in the center of mass energy range of 30-100 Gev and at luminosities up to 10^{33} $cm^{-2}s^{-1}$ for e-p and 10^{31} $cm^{-2}s^{-1}$ for e-Au collisions. The polarization time of 8-15min is achieved using superbend magnets in the electron ring. The collider design could be realized using the present level of the accelerator technology and could also be used to store and collide polarized positrons.

REFERENCES

[1] T. Satogata et al., "Commissioning of RHIC Deutron-Gold Collisions", these proceedings.
H. Huang et al., "Polarized Proton Operations in the AGS and RHIC", these proceedings.
[2] I. Ben-Zvi, J. Kewish, J. Murphy, S.Peggs, Nucl. Instr. Meth. **A463**, 2001, p.94.
[3] A.N. Filippov et al., Proc. of 15th Int. Conf. High Energy Accelerators, Hamburg , 1992, p.1145.
[4] I. Ben-Zvi et al., "R&D towards Cooling of the RHIC Collider", these proceedings.
[5] S.Y. Zhang et al., "RHIC Pressure Rise and Electron Cloud", these proceedings.
[6] Yu.M. Shatunov et al., "Status of e-ring design for EIC", presented at SPIN2002 , Upton, 2002.
[7] D.P. Barber et al., Physics Letters, **B343**, 1995, p.436.

Proceedings of the 2003 Particle Accelerator Conference

INVESTIGATION OF THE FLAT-BEAM MODEL OF THE BEAM-BEAM INTERACTION

Bjoern S. Schmekel, Georg Hoffstaetter and Joseph T. Rogers
Cornell University, Ithaca, New York 14853, USA

Abstract

At the interaction point of a storage ring collider each beam is subject to perturbations due to the electromagnetic field of the counter-rotating beam. For flat beams, a well known approximation models the beam by a current sheet which is uniform in the horizontal plane, restricting the particle motion to the vertical direction. In this classical model a water-bag beam distribution is used to find working points and beam-beam tune shift parameters which lead to a stable beam distribution. We try to find stability criteria for a more realistic Gaussian equilibrium distribution. In order to analyze the instabilities, a linearized Vlasov equation is solved computing radial and angular modes to first order in the displacement from the design trajectory.

BEAM EVOLUTION

We model the flat beam as a current sheet which is uniform in the horizontal direction, x, and consider only motion in the vertical direction, y. Consider one-dimensional phase space distributions ψ_1 and ψ_2 of the two beams which are normalized to unity. Then the impulse from the second (first) on the first (second) beam is

$$\Delta y'_{1,2} = -I_{\psi_{2,1}}(y,s) \tag{1}$$

where we define

$$I_\psi(y,s) \equiv \frac{4\pi N r_e}{\gamma} \int_{-\infty}^{\infty} d\overline{y}\,\mathrm{sgn}(y-\overline{y}) \int_{-\infty}^{\infty} d\overline{y}'\psi(\overline{y},\overline{y}',s) \tag{2}$$

and N is the number of particles per unit width in x and r_e the classical radius of the electron. The equations describing the motion of $\psi_{1,2}$ are given by the two Vlasov equations

$$\frac{\partial\psi_{1,2}}{\partial s} + y'\frac{\partial\psi_{1,2}}{\partial y} - K(s)y\frac{\partial\psi_{1,2}}{\partial y'} - \frac{\partial\psi_{1,2}}{\partial y'}\delta_p(s)I_{\psi_{2,1}}(y,s) = 0 \tag{3}$$

We want to determine whether the beam is stable. That is, we want to know if small perturbations of the phase space density grow. Thus, we choose a perturbative ansatz

$$\psi_{1,2} = \psi_0 \pm \Delta\psi_{1,2} \tag{4}$$

where ψ_0 is the equilibrium distribution, i.e. a solution of eqn. 3 with $\psi_1(y,y',s) = \psi_2(y,y',s) = \psi_0(y,y')$. Substituting eqn. 4 into eqn. 3, subtracting eqn. 3 written for the equilibrium distribution and neglecting the term which is a product of two perturbations we find

$$\frac{\partial\Delta\psi_{1,2}}{\partial s} + y'\frac{\partial\Delta\psi_{1,2}}{\partial y} - \frac{\partial\Delta\psi_{1,2}}{\partial y'}F(y,s) - \delta_p(s)\frac{\partial\psi_0}{\partial y'}I_{\Delta\psi_{2,1}} = 0 \tag{5}$$

where

$$F(y,s) = K(s)y + \delta_p(s)I_{\psi_0}(y) \tag{6}$$

If we approximate the beam-beam force as linear in y

$$F(y,s) \approx F(s)y \tag{7}$$

we can treat the perturbation as a part of the perturbed focusing function $F(s)$. In the next step we transform eqn. 5 to action-angle coordinates

$$y = \sqrt{2\beta J}\cos\phi \quad y' = -\sqrt{2\beta J}\frac{\sin\phi+\alpha\cos\phi}{\beta} \tag{8}$$

where β denotes the beta function perturbed by the beta beat due to the linearized beam-beam kick from ψ_0. We choose a smooth approximation in which $\alpha = 0$. Forming the linear combinations for the σ- and the π-mode $f_\pm = \Delta\psi_1 \pm \Delta\psi_2$, eqn. 5 can be decoupled and rewritten in action-angle coordinates as

$$\frac{\partial f_\pm}{\partial s} + \frac{1}{\beta}\frac{\partial f_\pm}{\partial\phi} \pm \sqrt{2\beta J}\sin\phi\,\delta_p(s)\frac{\partial\psi_0}{\partial J}I_{f_\pm} = 0 \tag{9}$$

assuming that $\psi_0 = \psi_0(J)$. In order to stay consistent with our approximations we still have to linearize the remaining integral. In the following discussion we omit the label $\pm$.

EQUILIBRIUM DISTRIBUTION

When the interaction term in eqn. 3 is not considered any differentiable distribution which depends solely on J is an equilibrium distribution. In general ψ_0 will be a function of both J and ϕ, though. Fortunately, an arbitrary differentiable function of J is an equilibrium distribution at least to linear order in y after introducing the perturbed betatron function. We choose a Gaussian equilibrium distribution

$$\psi_0(J) = \frac{1}{2\pi\epsilon}e^{-\frac{J}{\epsilon}} \tag{10}$$

since in the presence of damping and quantum excitation the beam distribution naturally tends to a Gaussian distribution.

0-7803-7738-9/03/$17.00 © 2003 IEEE

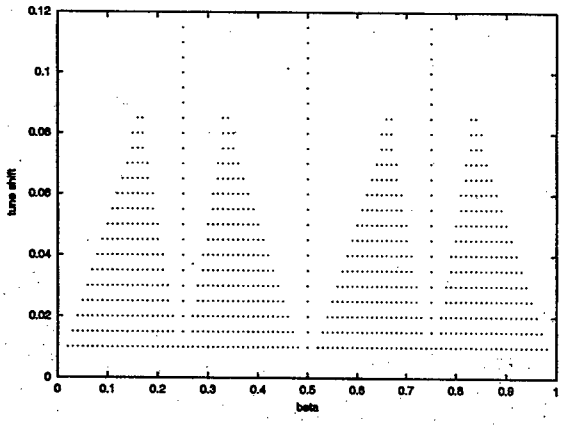

Figure 1: Stability diagram for $n = 0, l = -2 \ldots 2$

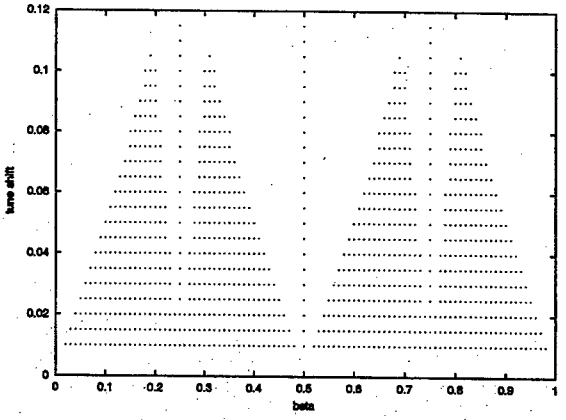

Figure 2: Stability diagram for $n = 0 \ldots 2, l = -2 \ldots 2$

SOLVING THE EQUATIONS OF MOTION

We expand the linearized version of eqn. 9 using the ansatz

$$f(J,\phi,s) = \sum_{n'l'} g_{n'l'}(s) e^{-\frac{J}{\epsilon}} L_{n'}\left(\frac{J}{\epsilon}\right) e^{il'\phi} \qquad (11)$$

where the n'-th Laguerre polynomial is denoted by $L_{n'}$ and the summation runs from 0 to ∞ for n' and from $-\infty$ to ∞ for l'. Substituting eqn. 10 and eqn. 11 into eqn. 9 we obtain eqn. 12

COHERENT BEAM-BEAM INSTABILITY

We solve the ODE 12 and rewrite the solution in matrix form such that the beam transport after one turn is described by a matrix T which acts on a column vector G that contains all g_{nl}, i.e. $G(C) = TG(0)$ and parametrize the beam-current by introducing the tune shift parameter

$$\Delta\nu \equiv \frac{N r_e}{\gamma}\sqrt{\frac{2\beta^*}{\pi\epsilon}}, \qquad (13)$$

where β^* denotes the beta function at the interaction point. In order to decide whether the system is stable or not we have to find out what happens to an arbitrary initial perturbation after a large number of turns, i.e. one needs to consider the limit T^N where $N \longrightarrow \infty$. Every matrix norm of the latter quantity tends to infinity if the absolute value of all eigenvalues of T are bigger than 1.

RESULTS AND DISCUSSION

In Fig. 1 and 2 we have drawn a point if the absolute value of all eigenvalues of T is smaller or equal 1 for both the σ- and the π-mode. The first and second order resonances can be recognized clearly. Resonances of orders higher than 2 cannot be expected in our linearized model. From the diagrams we conclude that the inclusion of radial modes tends to stabilize the beam. In Fig. 3 and 4 we determine which mode becomes unstable by selecting

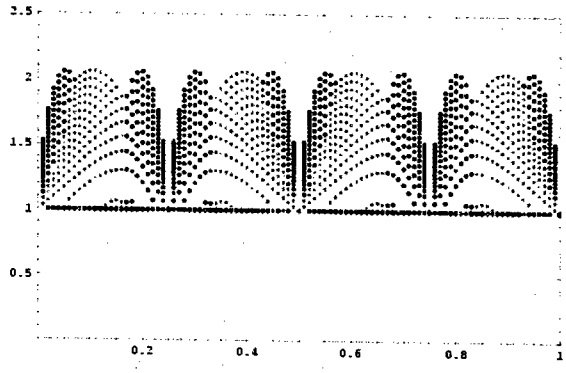

Figure 3: Absolute value of the largest eigenvalue vs. perturbed tune. Light grey points indicate unstable $l = \pm 1$ modes, medium grey and dark grey points indicate unstable $l = \pm 2$ modes. The following modes were included: $n = 0, l = -2 \ldots 2$

the biggest component of the eigenvector which is associated with the largest eigenvalue. The plot shows that in the absence of dynamics in the radial direction $l = \pm 1$ and $l = \pm 2$ modes become unstable in the vicinity of $\nu = 0.5$, but in Fig. 4 only $l = \pm 1$ modes are excited around $\nu = 0.5$. Furthermore, the unstable $l = \pm 2$ modes which accumulate in the vicinity of $\nu = 0.25$ and $\nu = 0.75$ are attenuated. Therefore, the radial motion leads to a damping of the $l = \pm 2$ modes.

In Fig. 5 we computed the phase of the largest eigenvalue of $l = \pm 2$ instabilities (σ-mode only) versus the perturbed tune for various $\Delta\nu$. The slope of the two lower lines is 2 which indicates that the collective oscillation frequency of the quadrupole mode is twice the single particle oscillation frequency. In Fig. 6 the spread is significantly lower. In an unstable region the imaginary part of the highest eigenvalue vanishes which causes those characteristic plateaus.

$$\frac{\partial g_{nl}}{\partial s} + \frac{il}{\beta} g_{nl} \pm \frac{(2n)!\sqrt{\pi}}{2(2n-1)(2^n n!)^2} \frac{4\pi N r_e}{\gamma\epsilon^2} \frac{\sqrt{2\beta\epsilon}}{2\pi} \frac{1}{2i} \left(\delta_{l,1} - \delta_{l,-1}\right) \delta_p(s) \left[-4\epsilon \sum_{l'} g_{0,2l'+1} \frac{(-1)^{l'}}{2l'+1}\right]$$
$$\pm \frac{2\beta(-1)}{2\pi} \frac{1}{4i} \frac{4\pi N r_e}{\gamma\epsilon} \left(\delta_{n,0} - \delta_{n,1}\right) \left(\delta_{l,2} - \delta_{l,-2}\right) \delta_p(s) \left[2\sqrt{\frac{2\epsilon}{\beta}} \sum_{n'l'} g_{n',2l'} (-1)^{l'} \frac{(2n')!\sqrt{\pi}}{(2^{n'} n'!)^2}\right] = 0 \qquad (12)$$

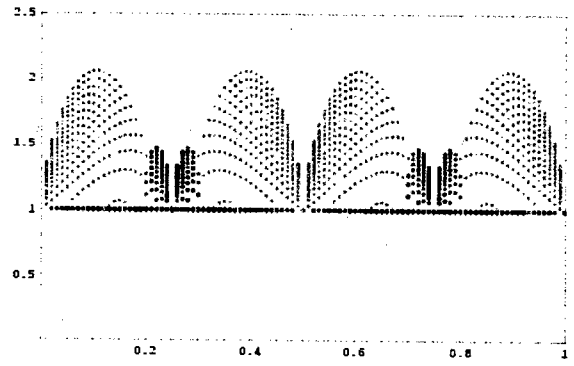

Figure 4: Same as Fig. 3, but for $n = 0 \ldots 1, l = -2 \ldots 2$

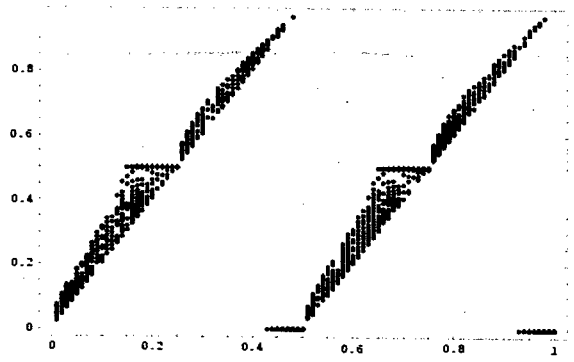

Figure 5: Phase vs. perturbed tune for $n = 0$, $l = \pm 2$ modes (σ-mode only).

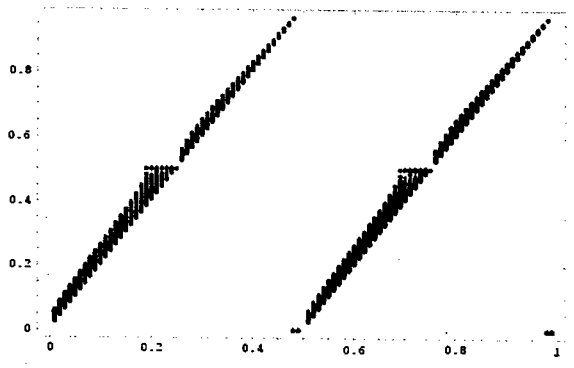

Figure 6: Phase vs. perturbed tune for $n = 0 \ldots 1, l = \pm 2$ modes.

POSSIBLE EXTENSIONS

We have extended our model to account for damping by synchrotron radiation. In order to obtain the equilibrium distribution 10 quantum excitation must be included as well. This turns eqn. 3 into a Fokker-Planck equation. In our preliminary computations we found that the graphs we presented above remain unchanged for realistic values of the damping and excitation coefficients. To simplify the Fokker-Planck equation we averaged over the phases in the damping and excitation terms but not in the beam-beam interaction term. This can be justified since the betatron phases in the terms for damping and quantum excitation change during one turn while the phase in the interaction term changes only once per turn.

Higher order resonances can be studied by not linearizing the integral in eqn. 9 and assuming that $f_\pm$ contains only one radial mode. However, this procedure is complicated by the fact that eqn. 10 is not an equilibrium anymore. Ignoring these problems one can obtain plots similar to Fig. 1 with higher order resonances. For accelerators with different tunes for the rotating and counter-rotating beam a bigger transfer matrix which describes the evolution of the g_{nl} for both beams can be derived easily.

ACKNOWLEDGMENTS

We would like to express our gratitude to Alex Chao from SLAC for his helpful criticism. This work was supported by the National Science Foundation.

REFERENCES

[1] A. W. Chao, R. D. Ruth, "Coherent Beam-Beam Instability in Colliding-Beam Storage Rings", Particle Accelerators, 1985, Vol. 16, pp. 201-216, Gordon and Breach

Proceedings of the 2003 Particle Accelerator Conference

FREQUENCY MAP ANALYSIS AND PARTICLE ACCELERATORS

J.Laskar
Astronomie et Systèmes Dynamiques, CNRS-UMR8028, IMCCE-Observatoire de Paris,
77 Av Denfert-Rochereau, 75014 Paris

Abstract

The development of frequency map analysis in particle accelerators is reviewed. In many examples, the frequency map is folded at large amplitudes. The fold is a singularity in the frequency map that induces a change of the signature of the torsion. When the torsion is non definite, the dynamical behavior of the beam needs to be studied very precisely, as directions of fast escape may occur.

INTRODUCTION

Frequency map analysis (FMA) was introduced for the demonstration and understanding of the chaotic behavior of the Solar System [1], that can be considered as a dynamical system with $3N$ degrees of freedom (DOF), where N is the number of the planets. The method applies more generally to any Hamiltonian system or symplectic map (eventually with some small dissipation) [2, 3, 4]. It is particularly interesting for systems of DOF larger than 2, when a simple surface of section fails to provided a global view of the dynamics of the system. FMA is now largely used, from studies on atomic physics [5] to galactic dynamics [6, 7, 8, 9, 10]. The application to particle accelerator dynamics was very natural [11], as the motion of a single particle in a storage ring is usually described in a surface of section of the beam by a symplectic map of dimension 4, or eventually of dimension 6 when the synchrotron oscillation is also taken into account. Since, FMA has been applied to many machines, providing in each case a picture ID of the dynamics of the beam [12, 13, 14, 15, 16, 17]. Reviews of the method with demonstrations of its convergence for regular trajectories can be found in [18, 19, 20]. Here, after a brief recall of the main aspects of FMA, we will focus on the implications of folds that appear in several examples of frequency maps.

FREQUENCY MAPS

Although FMA is not a perturbative theory, it is useful to describe its properties for a Hamiltonian close to integrable, where a rigorous setting can be derived. Let us thus consider a n–DOF Hamiltonian system in the form $H(I,\theta) = H_0(I) + \varepsilon H_1(I,\theta)$, where H is real analytic for canonical variables $(I,\theta) \in B^n \times \mathbb{T}^n$, B^n is a domain of $\mathbb{R}^n$ and $\mathbb{T}^n$ is the n-dimensional torus. For $\varepsilon = 0$, the Hamiltonian reduces to $H_0(I)$ and is integrable. The equations of motion are then for all $j = 1, \ldots, n$

$$\dot{I}_j = 0 \ , \quad \dot{\theta}_j = \frac{\partial H_0(I)}{\partial I_j} = \nu_j(I) \ ; \tag{1}$$

The motion in phase space takes place on tori, products of circles with radii I_j, which are described at constant velocity $\nu_j(I)$. If the system is nondegenerate, that is if

$$det\left(\frac{\partial \nu(I)}{\partial I}\right) = det\left(\frac{\partial^2 H_0(I)}{\partial I^2}\right) \neq 0 \tag{2}$$

the frequency map

$$\begin{array}{c} F : \mathbb{B}^n \longrightarrow \mathbb{R}^n \\ (I) \longrightarrow (\nu) \end{array} \tag{3}$$

is a diffeomorphism (one to one smooth map) on its image Ω, and the tori are as well described by the action variables $(I) \in B^n$ or by the frequency vector $(\nu) \in \Omega$. For a non-degenerate system, KAM theorem [21] still asserts that for sufficiently small values of ε , there exists a Cantor set Ω_ε of values of (ν), satisfying a Diophantine condition of the form

$$|< k, \nu >| = |k_1\nu_1 + \ldots + k_n\nu_n| > \kappa_\varepsilon/|k|^m \tag{4}$$

for which the perturbed system still possesses smooth invariant tori with linear flow (the KAM tori). Moreover, these tori that survive on a totally discontinuous set of initial conditions are still properly ordered in some sense as, according to Pöschel [22], there exists a diffeomorphism

$$\Psi : \mathbb{T}^n \times \Omega \longrightarrow \mathbb{T}^n \times B^n; \qquad (\varphi, \nu) \longrightarrow (\theta, I) \tag{5}$$

which is analytical with respect to φ, C^∞ in ν, and on $\mathbb{T}^n \times \Omega_\varepsilon$ transforms the Hamiltonian equations into the trivial system

$$\dot{\nu}_j = 0 \ , \quad \dot{\varphi}_j = \nu_j \ . \tag{6}$$

If we fix $\theta \in \mathbb{T}^n$ to some value $\theta = \theta_0$, we obtain a frequency map on B^n defined as

$$\begin{array}{c} F_{\theta_0} : B^n \longrightarrow \Omega \\ I \longrightarrow (\nu) = p_2(\Psi^{-1}(\theta_0, I)) \end{array} \tag{7}$$

where p_2 is the projection on Ω ($p_2(\phi, \nu) = \nu$). For sufficiently small ε, the torsion condition (2) ensures that the frequency map F_{θ_0} is still a smooth diffeomorphism.

0-7803-7738-9/03/$17.00 © 2003 IEEE

FREQUENCY MAP ANALYSIS

The FMA method relies heavily on the observation that when a quasiperiodic function $f(t)$ is given numerically over a finite time span $[-T,T]$, it is possible to recover its fundamental frequencies in a very precise way, several orders of magnitude more precisely than by simple Fourier analysis. Indeed, let

$$f(t) = e^{i\nu_1 t} + \sum_{k\in\mathbb{Z}^n-(1,0,\ldots,0)} a_k e^{i\langle k,\nu\rangle t} \quad , \quad a_k \in \mathbb{C} \quad (8)$$

be a KAM quasiperiodic solution of our Hamiltonian system, where the frequency vector (ν) satisfies a Diophantine condition (4). The frequency analysis algorithm NAFF will provide an approximation $f'(t) = \sum_{k=1}^{N} a_k e^{i\omega_k t}$ of $f(t)$ from its numerical knowledge over a finite time span $[-T,T]$. The frequencies ω_k and complex amplitudes a_k are computed through an iterative scheme. In order to determine the first frequency ω_1, one searches for the maximum amplitude of $\phi(\sigma) = \langle f(t), e^{i\sigma t}\rangle$ where the scalar product $\langle f(t), g(t)\rangle$ is defined by

$$\langle f(t), g(t)\rangle = \frac{1}{2T}\int_{-T}^{T} f(t)\bar{g}(t)\chi(t)dt \, , \quad (9)$$

and where $\chi(t)$ is a weight function. Once the first periodic term $e^{i\omega_1 t}$ is found, its complex amplitude a_1 is obtained by orthogonal projection, and the process is restarted on the remaining part of the function $f_1(t) = f(t) - a_1 e^{i\omega_1 t}$. For a KAM quasiperiodic solution (8), the computed frequency ν_1^T converges very rapidly towards the true frequency ν_1 as [19, 20]

$$\nu_1 - \nu_1^T = O(\frac{1}{T^{2p+2}}) \quad (10)$$

where p is the order of the cosine window $\chi_p(t) = 2^p(p!)^2(1+\cos\pi t)^p/(2p)!$ used in (9). To construct numerically a frequency map, we will fix all initial angles $\theta_i = \theta_{i0}$, and for each initial action values $(I) = (I_1,\ldots,I_n)$, integrate numerically the trajectories over a finite time interval of length T. The fundamental frequencies (ν) are computed by the previous (NAFF) algorithm, for all initial actions (I), and we thus construct a correspondence :

$$\begin{aligned} F_{\theta_0}^T : B^n &\longrightarrow \Omega \\ I &\longrightarrow (\nu) \end{aligned} \quad (11)$$

that converges towards F_{θ_0} as $T \longrightarrow +\infty$. This map will thus be regular on the set of regular trajectories, and whenever its appears to be non regular, it will reveal the existence of chaotic orbits (see [3, 18, 19] for more details). In practice, to study the dynamics of a beam, in a given surface of section corresponding to a starting location on the lattice, one can fix the two transverse momenta, and integrate the trajectories with a tracking code for a network of initial conditions spanning both horizontal and vertical directions (Fig.1).

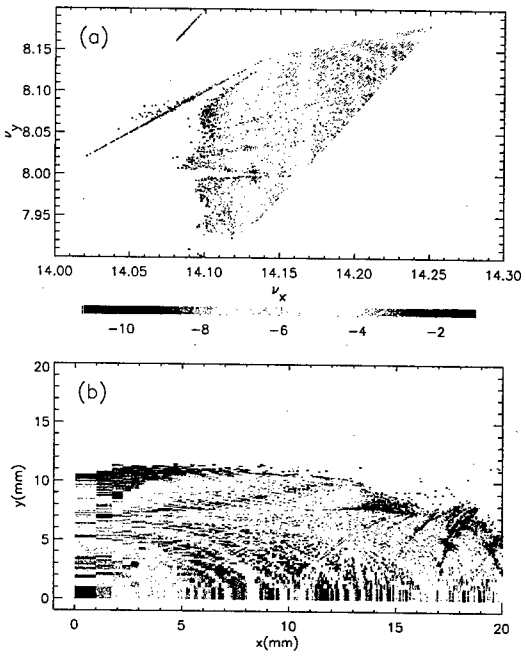

Figure 1: Frequency map for an ideal lattice of the ALS. The initial conditions are taken over a mesh in the horizontal (x) and vertical direction (y) (bottom), and the corresponding frequencies are plotted in the frequency plane (top). The color indicates the regularity of the orbits : from blue (very regular), to red (very chaotic), while the absence of a dot means that the particle escaped. This allows to easily relate the resonant features observed in the frequency space to regions of the physical space [11, 12, 16]

EXPERIMENTAL FREQUENCY MAPS

The first frequency maps that were made [11] used numerical models of an ideal lattice (Fig.1). But errors in the magnets, misalignments, and all breakings of the lattice symmetry will in general reduce considerably the stable part of the beam by increasing the strength of the nonlinearities and number of dangerous resonances. A large effort has been made at the ALS to measure precisely these defects [23] and the resulting frequency map provides a more realistic vision of the current machine [12, 13, 17]. Nevertheless, the most critical way to check the real dynamical behavior of a beam remains the construction of an experimental frequency map [24, 25, 13, 26].

In order to realize such a map, fast pinger magnets are used to kick the beam horizontally and vertically in order to span the phase space in both directions. The beam position is recorded using turn by turn beam position monitors, and the resulting data is analyzed using frequency analysis algorithms. The first complete experimental frequency map was realized at the ALS (Fig.2), probing the importance of coupling resonances of high order in the actual behavior of the beam, with an amazing agreement with the numerical model [13].

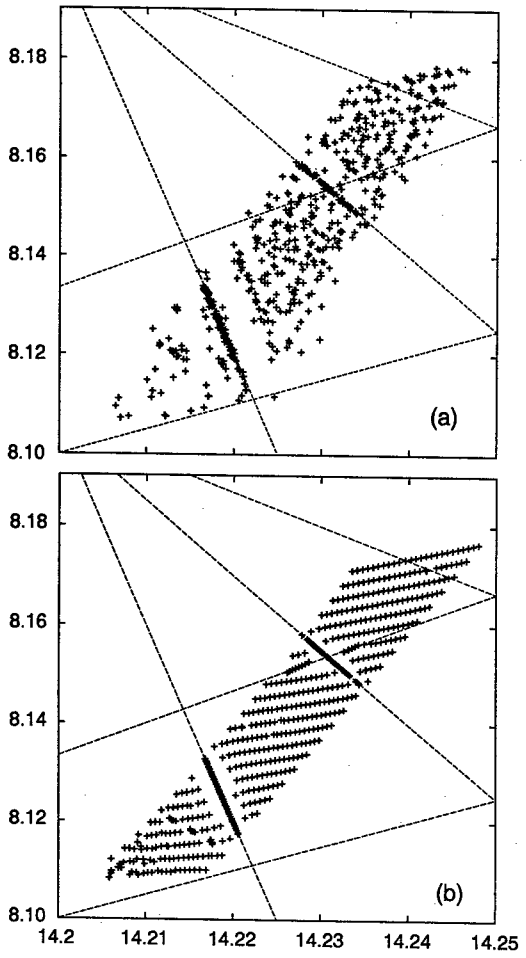

Figure 2: Experimental frequency map (a), and numerical simulation (b) for the ALS with its current settings. Resonances of order ≤ 5 are plotted with dotted lines [13] .

FOLDED FREQUENCY MAPS

In several examples, the frequency map appears to be folded. This occurs when the terms of higher degrees in the Hamiltonian become dominant over the quadratic terms as the amplitude increases [15, 27, 17]. Sometimes this occurs as the sextuploles strength have been adjusted in order to avoid some resonant lines that are thought to be dangerous, or merely as the result of beam-beam interactions [15] (Fig. 3). In order to better understand the implications of this folded map, we need to look more closely to the torsion.

The torsion matrix (a generalization of tune-shift with amplitude), is defined as the Jacobian matrix

$$M = \left(\frac{\partial \nu(I)}{\partial I} \right) \approx \left(\frac{\partial^2 H_0(I)}{\partial I^2} \right) \qquad (12)$$

If we remove the linear terms of the Hamiltonians by a proper change of variable, and limit its expansion to the

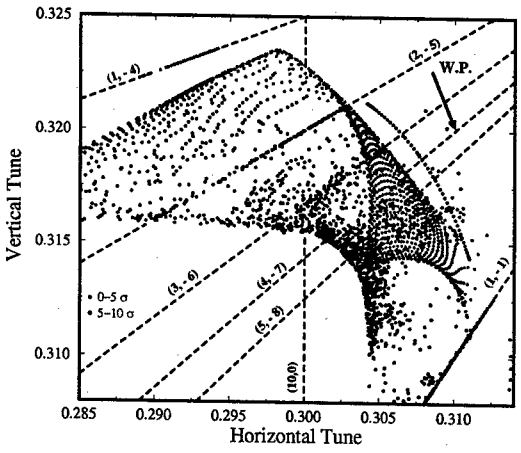

Figure 3: Frequency map of a beam-beam interaction simulation for the LHC [15].

lower orders, the Hamiltonian becomes

$$H = \frac{1}{2} I^\tau \, M \, I + o(I^2) + O(\varepsilon) \, , \qquad (13)$$

where I^τ is the transpose of I. For a fixed energy value h, even in presence of chaotic diffusion, the variations of the actions will thus be limited by $I^\tau \, M \, I \approx 2h = Cte$, and in an equivalent way, when considering the frequencies, $(\nu) \approx M \times (I)$, the diffusion of the frequencies will fulfill

$$\nu^\tau M^{-1} \nu \approx 2h = Cte \qquad (14)$$

where M^{-1} is a symmetric 2×2 matrix for a typical accelerator dynamics, when the synchrotron oscillation is neglected. It is known that when the torsion M is the matrix of a definite quadratic form, finite time stability results exist, that do not persist in case of non definite torsion [28]. This can be understood as in case of non-definite torsion, the isotropic directions of the quadratic form M will lead to directions of fast escape :

Let $M^{-1} = \begin{pmatrix} a & c \\ c & b \end{pmatrix}$. The vector $V = (x, y)$ is an isotropic direction if $V^\tau M^{-1} V = ax^2 + 2cxy + by^2 = 0$. The discriminant of this equation in x is $\Delta = y^2(c^2 - ab) = -y^2 \det(M^{-1})$. Thus, if $\det(M) > 0$, we have $\Delta < 0$: the quadratic form is definite and there are no isotropic directions. On the contrary, when $\det(M) < 0$, $\Delta > 0$ and there are 2 isotropic directions, that will act as asymptotes for the diffusion of the frequencies. The different behavior of the diffusion for definite or non definite torsion is illustrated in Figs. 4a,b. In both figures, the dynamical system is very similar but Fig.4a will correspond to a quadratic Hamiltonian of the form $H_+ \approx I_1^2 + I_2^2$, while Fig.4b has non definite torsion ($H_- \approx I_1^2 - I_2^2$). The chaotic zones are very similar, but for H_+, the trajectories remain bounded over 10^7 iterations while for H_- the resonance $1 : 1$ is a direction of fast escape, as the motion of the frequencies

tend to bring them closer to this resonance line while for H_+ the diffusion of the frequencies tends to make them escape the resonance.

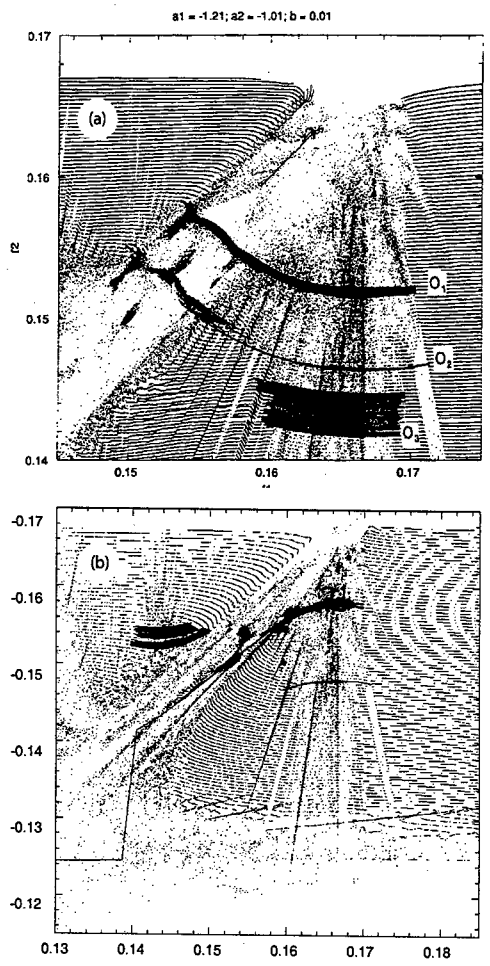

Figure 4: (a) Diffusion of the orbits in a symplectic map of dimension 4 with definite torsion. The background is the image by the frequency map of a regular mesh of initial conditions in the action plane, obtained with only 500 iterations, while the three trajectories O_1, O_2, O_3 are obtained by following the frequencies over 10^7 turns, and reveal the actual diffusion of the chaotic trajectories in the frequency plane. [3]. (b) Diffusion with non definite torsion. The dynamical system is similar as in figure 4a, but the system has now non definite torsion. The chaotic trajectories in the frequency plane now follows hyperbolic trajectories, with occasionally a fast direction of escape (here the resonance (1:1)) [19].

Folded maps

As the signature of the torsion is associated to the determinant of the Jacobian matrix, it becomes easy to understand the torsion behavior for a 2-dimensional frequency map. First let us recall that for a $\mathbb{R}^2 \longrightarrow \mathbb{R}^2$ map, the only singularities that generically occur are folds or cusps [29]. In all cases, the folds correspond to locations where the determinant of the Jacobian matrix M is null. If the torsion is definite in the center part of the beam, as required to ensure its maximum stability, the torsion will become non-definite after the fold which can lead to directions of fast diffusion (Fig.5). One should thus analyze very carefully the dynamical behavior after a fold. If the trajectories in the considered region are very regular, no significant diffusion will occur, and there may also be small chaotic regions where the diffusion is limited by the presence of neighboring regular regions, as in figure 4b, but one needs to check very carefully that no region of fast escape (as the 1:1 resonance in Fig. 4b) are present in the operating condition of the machine.

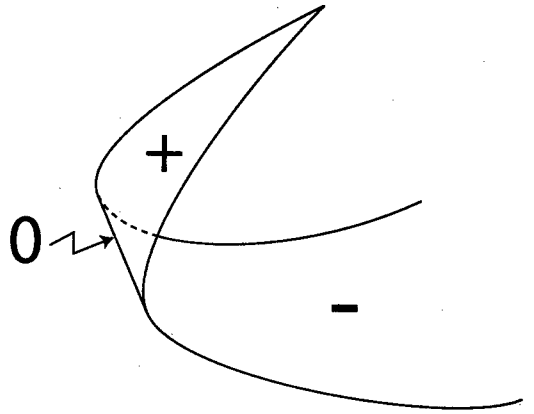

Figure 5: folded frequency map. The determinant of the torsion matrix is zero on the fold, and its sign changes on each side of the fold, as well as the signature of the torsion.

In fact, if there are directions of fast escape, these may be detected with traditional tracking of the particles, but in cases of a double folded frequency map (Fig.6), the tracking may not reveal any escape, as the possible unstable orbits resulting from non-definite torsion are still bounded by the region of definite torsion that lays after the second fold. One should be aware that these designs are potentially very unstable. Indeed, in a real machine, the existence of errors in the lattice will decrease significantly the stable zone of the beam. The outer part of the beam may thus be destroyed, leading to possibility of escape for the particles in the non-definite torsion region, and the only usable part of the beam will remain the inner region with definite torsion. It is clear that in this case, all the efforts made in the design to avoid some resonant lines by bending the frequency map become totally vain.

Additionally, some analytical computation of the torsion could also be useful for the determination of the possible isotropic directions and the design of a lattice for which they are not harmful.

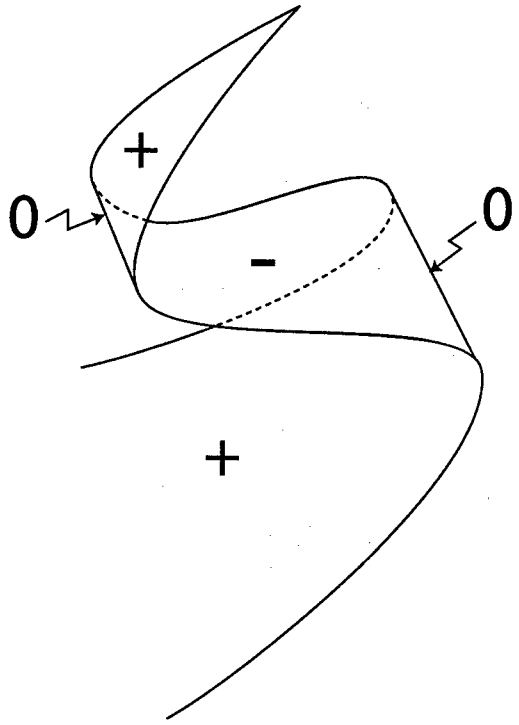

Figure 6: 2-folded frequency map.

REFERENCES

[1] Laskar, J., The chaotic motion of the solar system. A numerical estimate of the size of the chaotic zones, *Icarus*, **88**, (266-291) (1990)

[2] Laskar, J., Froeschlé, C., Celletti, A., The measure of chaos by the numerical analysis of the fundamental frequencies. Application to the standard mapping, *Physica D*, **56**, (253-269) (1992)

[3] Laskar, J., Frequency analysis for multi-dimensional systems. Global dynamics and diffusion, *Physica D*, **67**, (257-281) (1993)

[4] Laskar, J., Robutel, P., The chaotic obliquity of the planets, *Nature*, **361**, (608-612) (1993)

[5] Von Milczewski, J., Farrelly, D. Uzer, T., Frequency Analysis of 3D Electronic 1/r Dynamics: Tuning between Order and Chaos *Phys. Rev. Let.*, **78**, 1436–1439 (1997)

[6] Papaphilippou, Y., Laskar, J., Frequency map analysis and global dynamics in a two degrees of freedom galactic potential, *Astron. Astrophys.*, **307**, (427-449) (1996)

[7] Papaphilippou, Y., Laskar, J., Global dynamics of triaxial galactic models through frequency map analysis, *Astron. Astrophys.*, **329**, (451-481) (1998)

[8] Valluri, M., Merritt, D., Regular and Chaotic Dynamics of Triaxial Stellar Systems *Astrophys. J.*,**506**, 686–711 (1998)

[9] Merritt, D., Valluri, M., Resonant Orbits in Triaxial Galaxies *Astron. J.*,**118**, 1177–1189 (1999)

[10] Wachlin, F. C.; Ferraz-Mello, S., Frequency map analysis of the orbital structure in elliptical galaxies *M.N.R.A.S.* **298**, 1, 22–32 (1998)

[11] Dumas, S., Laskar, J., Global Dynamics and Long-Time Stability in Hamiltonian Systems via Numerical Frequency Analysis, *Phys. Rev. Lett.*, **70**, (2975-2979) (1993)

[12] Laskar, J., Robin, D., Application of frequency map analysis to the ALS, *Particle Accelerator*, **54**, (183-192) (1996)

[13] Robin, D., Steir, C., Laskar, J., Nadolski, L., Global dynamics of the ALS revealed through experimental Frequency Map Analysis, *Phys. Rev. Let.*, **85**, pp. 558-561 (2000)

[14] Comunian, M., Pisent, A., Bazzani, A., Turchetti, G., Rambaldi, S.:2001, Frequency map analysis of a three-dimensional particle in the core model of a high intensity linac, *Phys. Rev. ST Accel. Beams* **4**, 124201 (2001)

[15] Papahilippou, Y. Zimmermann, F., Weak-strong beam-beam simulations for the Large Hadron Collider, *Phys. Rev. ST Accel. Beams* **2**, 104001 (1999)

[16] Steier, C., Robin, D., Nadolski, L., Decking, W., Wu, Y., Laskar, J., Measuring and optimizing the momentum aperture in a particle accelerator, *Phys. Rev. E*, **65**, (056506) (2002)

[17] Nadolski, L., Laskar, J., Review of third generation light sources through frequency map analysis *Phys. Rev. E, submitted* (2003)

[18] Laskar, J., Frequency map analysis of an Hamiltonian system, Workshop on Nonlinear dynamics in particle accelerator, Arcidosso, 1994, AIP Conf. proc. **344**, *S. Chattopadhyay, M. Cornacchia, C. Pellegrini, Eds, AIP Press, New York*, pp 130–159 (1995)

[19] Laskar, J., Introduction to frequency map analysis, *in proc. of NATO ASI Hamiltonian Systems with Three or More Degrees of Freedom, C. Simò ed, Kluwer*, 134–150 (1999)

[20] Laskar, J., Frequency map analysis and quasiperiodic decompositions. *preprint (www.bdl.fr/Equipes/ASD-/preprints/prep.2003/laskar_porq1.pdf)* (2003)

[21] Arnold, V.I., Kozlov, V.V., Neishtadt, A.I., Mathematical aspects of classical and celestial mechanics, *Dyn. Systems III*, V.I. Arnold, ed., Springer, New York. (1988)

[22] J. Pöschel, Integrability of Hamiltonian systems on Cantor sets, *Comm. Pure Appl. Math.*, **25**, 653–695 (1982)

[23] Robin, D., Safranek, J., Decking, W., Realizing the Benefits of restored Periodicity in the Advanced Light Source, *Phys. Rev. ST Accel. Beams*, **2**, 044001 (1999)

[24] Terebilo, A., Pellegrini, C., Cornacchia, M., Corbett, J., Martin, D., "Experimental non-linear beam dynamics studies at SPEAR", 1997 Particle Accelerator Conference, Vancouver, Canada, 1457 – 1459 (1998)

[25] Bartolini, R., Leunissen, L.H.A., Papaphilippou, Y., Schmidt, F., Verdier, A., "Measurement of resonance driving terms from turn-by-turn data", Particle Accelerator Conference, New York, 1557 - 1559 (1999)

[26] Papaphilippou, Y., Farvacque, L., Ropert, A., Laskar, J., Probing the non-linear dynamics of the ESRF storage ring with experimental frequency maps, PAC'03, Portland (2003)

[27] Belgroune, M., Brunelle, P., Laskar, J., Nadji, A., Application of the frequency map analysis to the new lattice of the SOLEIL project, EPAC2002 (2002)

[28] Nekhoroshev, N.N.:1977,An exponential estimates for the time of stability of nearly integrable Hamiltonian Systems,*Russian Math. Surveys*, **32**, 1–65 (and Niedermann, 2003, *private communication*)

[29] Arnold, V.I., Goryumov, V.V., Lyashko, O.V., Vasil'ev, V.A., Singularity theory I, *Dyn. Systems VI*, V.I. Arnold, ed., Springer, New York (1993)

Proceedings of the 2003 Particle Accelerator Conference

RESONANCES AND BEAM LOSS IN HIGH INTENSITY RINGS*

A.V. Fedotov
BNL, Upton, NY 11973, USA

Abstract

Operation of high-intensity rings requires minimal beam loss. Among numerous effects which contribute to losses in rings, the interplay of excited resonances is typically an unavoidable source of halo and beam loss. Such resonances can be driven by space charge itself, magnet errors or a combined effect of both. In this paper we review several resonant effects which can limit beam intensity in a circular machine. The space-charge limit and selection of a working point in the ring are also discussed.

INTRODUCTION

In general, beam loss can be separated into a design (or technical) and a beam dynamics part. A control of the beam loss which falls under the design can be very challenging. In addition, various effects of beam dynamics give significant contribution to the beam loss. Typically, the maximum achievable intensity is limited by beam dynamics which dominates high-intensity operation, including various space-charge effects, collective instabilities, etc. As far as radioactivation at high intensity is concerned, if the collective instability occurs, then further operation is not possible. This requires finding a cure for the instability either by implementing some design changes or by damping the instability. In this paper, we discuss the beam loss due to another fundamental intensity-stopper in the AG rings - the resonances. An overview of the specifics for the resonant driven beam loss at high-intensity is given. Here, the term "high-intensity" is used in reference to conventional synchrotrons and storage rings. The intensity is described by a depression of the betatron tunes due to the space-charge forces. Such a tune depression is defined as $\eta = \nu/\nu_0$, where ν is the space-charge depressed tune, and ν_0 is the zero-current tune. The main focus of this paper is a conventional ring where achievable tune depression is relatively weak $\eta = 0.9 - 0.98$, so that one can treat the space-charge effect as a perturbation which leads to a small shift $\Delta\nu_{sc}$ of the betatron tunes ($\nu \approx \nu_0 - \Delta\nu_{sc}$, with $\Delta\nu_{sc} \ll \nu_0$). In linear accelerators, the words "high intensity" usually refer to $\eta < 0.8$. In another class of circular accelerators where special measures are undertaken to compensate emittance growth due to resonance crossing (such as cooler rings), the tune depression can be very strong, with the definition of the space-charge limit corresponding to an ultimately cold beam $\eta \to 0$.

* Work supported by the SNS through UT-Battelle, LLC, under contract DE-AC05-00OR22725 for the U.S. Department of Energy.

BEAM LOSS AND HALO MECHANISMS

An uncontrolled beam loss typically occurs due to a halo surrounding the beam core. Not surprisingly, there are many mechanisms which contribute to halo generation in both linear and circular accelerators [1]. The task is to identify the most important of them and come up with possible cures. Most of the effects which are important mechanisms for halo production in linear accelerators are also relevant to rings. However, due to a significant difference in the regimes of the tune depression, the time scale (growth rates) of the space-charge driven effects becomes very different. There are also some ring-specific mechanisms due to the possibility of accumulating some effects over successive turns, as well as due to a longer storage time.

SPACE-CHARGE RESONANCES

We refer to the space-charge resonances as those which are driven by the space-charge potential itself rather than the field potential of the magnets. Their importance was first shown by Montague for the coupling resonance [2]:

$$2\nu_x - 2\nu_y = 0, \tag{1}$$

where the factor of 2 in front of $\nu_{x,y}$ reflects the driving coupling term x^2y^2 in the space-charge potential, making it a fourth-order resonance. This resonance can occur even for a lattice without any perturbation since it requires only zero-th harmonic in the Fourier component of the perturbation. Due to the fact that this resonance is a difference symmetric resonance, such coupling can lead to significant halo only for a beam with unequal emittances. A detailed analytic analysis of this type of resonance was recently presented using collective beam dynamics in connection with high-current transport systems [3]. There, one can have a ratio of the transverse and longitudinal tunes which is very different from unity thus allowing the possibility of a nonlinear asymmetric ($n_x \neq n_y$) coupling resonance with significant energy exchange between the two planes:

$$n_x\nu_x - n_y\nu_y = 0, \tag{2}$$

in the single-particle approximation, or more generally [3]:

$$n_x\nu_x + n_y\nu_y + \Delta\omega = 0, \tag{3}$$

based on the approach of collective dynamics, where the $\Delta\omega$ represent an additional shift with respect to the depressed incoherent tunes, and the integers n_x, n_y can be positive or negative.

0-7803-7738-9/03/$17.00 © 2003 IEEE

Collective coupling resonances

Until recently, an analytic treatment of the space-charge coupling resonances in rings was limited to a single-particle approach, although computer simulations were able to provide a more accurate description [5],[4]. An assumption of constant beam size and frozen beam potential in a typical analysis does not accurately describe the resonant beam behavior. This was realized long ago [6], and an analytic approach of collective beam dynamics was used by Sacherer to describe beam response to the one-dimensional resonances [7]. An extension to the two-dimensional isotropic beams was formulated by Gluckstern [8] and for more realistic anisotropic beams by Hofmann [3]. The latter allowed a direct application to circular accelerators where the beams are typically non-round with different transverse emittances, and to linacs, where one can have significantly different focusing constants (tunes) in different planes. This made it possible to put the space-charge coupling resonances in 2-D into a more self-consistent framework of coherent resonances for collective beam modes [3]. In conjunction with particle simulation codes, these analyses allowed exploration of the parameter space of the focusing constants in linear accelerators with the finding that nonequipartitioned beams can avoid emittance exchange as long as they are not near the stopbands of the space-charge coupling resonances [9]. In fact, such a recommendation to avoid the space-charge coupling resonances is usual in rings. The difference is that in linacs one can have very different focusing constants, which requires consideration of many asymmetric space-charge coupling resonances with the zero-th harmonic of the perturbation. In AG rings, however, the betatron tunes are typically not very different from one another, thus leaving the symmetric Montague resonance as the resonance with the zero-th harmonic. Recently, the study of such a resonance in rings, using the theory of collective beam modes, was presented [10]. Other resonances are possible when the driving force comes from the space-charge potential while the resonant harmonic results from the lattice periodicity which makes the nonlinear asymmetric space-charge coupling resonances important in rings as well [4]. When these effects are studied for a weak tune depression, it is important to remember that the dynamic rates of these effects depend on the tune depression (this effect makes it a primary concern in high-intensity linear accelerators).

Intrinsic incoherent resonances

The oscillating space-charge force can also lead to another class of resonances where individual particles inside the beam can get into resonance with an oscillating beam mode. These resonances are referred to as intrinsic or incoherent resonances of the individual particles. Such a parametric resonance mechanism was suggested as one of the dominant effects for halo generation in linacs [11]. Some literature on this subject can be found, for example, in Ref. [12]. In recent years, existence of self-consistent three-dimensional computer codes allowed systematic studies of this mechanism for realistic beam distributions [13],[14],[9].

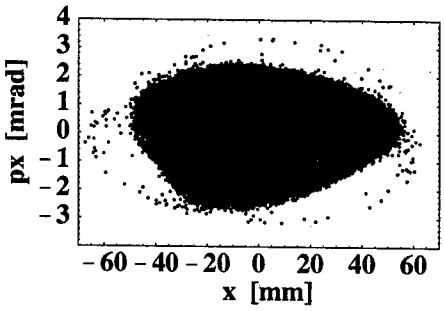

Figure 1: Incoherent resonance of individual particles with the 3rd order driven collective beam mode.

Such resonances between the motion of the individual particles and collective beam oscillations are governed by the rms beam mismatch. For example, in the case of a uniform density beam envelope, which is oscillating with the frequency Ω and the mismatch parameter μ, the equation of motion for the individual particle has the form

$$x'' + q^2 x = \mu \frac{2\kappa}{a_0^2} x \cos \Omega\theta, \qquad (4)$$

where κ is the space-charge parameter, and $q^2 = k^2 - \kappa/a_0^2$ is the depressed incoherent frequency without the approximation of small space charge. This equation has a primary parametric resonance at $q = \Omega/2$. When higher order terms are included, one also gets the non-linear parametric resonances [15]. The halo extent associated with the $1:2$ parametric resonance was extensively studied for the envelope modes in high-current linacs. It is straightforward to show analytically, that for a small μ, the halo extent (finite due to the nonlinearity omitted from Eq. 4) has a linear dependence on μ and a very weak dependence on the space-charge parameter. In fact, the halo extent associated with this resonance is large not only for a strong tune depression of the order of $\eta \sim 0.5$ (typical for linacs) but also for tune depression of only a few percent $\eta \sim 0.97$ (typical for rings). However, in the limit of zero space charge, the motion near the core is very regular, and the rate at which particles are driven into the 1:2 resonance becomes very small. As a result, for space charge with $\eta \sim 0.98$, it takes significantly more time for the particles to be trapped into the 1:2 resonance [16].

The rate of halo development (which is a function of both the mismatch parameter and tune depression) becomes the most important question when one tries to estimate an effect of such a parametric resonance on halo formation in rings. In addition, when applied to accumulator rings, one should take into account many other effects such as the fact that the beam intensity is not a constant during accumulation, the phase-mixing effect due to multi-turn injection, etc. [16]. Taking into account all these effects, simulations

for the SNS ring showed that this intrinsic resonance may not be a problem [17].

The incoherent resonances, which were discussed above, and, which are also known as the mechanism for the "parametric halo", did not require any resonances with the lattice since the collective oscillation was induced by a mismatch. In rings, however, such collective beam modes may have a fast excitation as a result of both the space charge and machine resonances. The resonances of the individual particles with such driven collective beam modes are called "driven incoherent resonances", since the collective modes are resonantly driven (Fig. 1). In such a situation, the incoherent resonances may play an important role in halo formation even in the limit of weak tune depression, as will be discussed in the following sections.

MACHINE RESONANCES AND SPACE CHARGE

The beam loss associated with lattice driven resonances is typically the dominant one in conventional high-intensity rings. When choosing the operating point in the tune space, one carefully avoids resonances driven by the lattice periodicity, which are referred to as structure resonances. However, the unavoidable presence of errors in the magnetic field imposes a restriction associated with the imperfection resonances. Although technically such resonances are not the space-charge induced resonances since they are driven by the lattice harmonics, space charge plays an important role here as well. First, it creates the problem since the tunes are depressed by the space charge towards the resonances. On the other hand, the space charge introduces an effective nonlinearity which changes the beam response to the resonances.

Collective beam response

A single-particle approach with a frozen beam potential was introduced to study effects of the space-charge tune depression in the tune space [18]. This approach was later generalized to include the effect of the wall images [19]. It was quickly noted that the space-charge potential can itself change in a response to the external time dependent perturbation [6]. To include this effect, the resonance response required a treatment of collective beam dynamics [7], which takes into account the fact that the space-charge force depresses not just the single-particle frequencies but also the collective modes of the beam oscillation. As a result, the response to an external perturbation occurs when the tune of the corresponding collective mode is depressed towards the resonance condition. An extensive study of these effects recently reemerged due to the increasing interest in high-power circular accelerators [20]-[21]. Although availability of powerful computer codes allowed one to study these effects self-consistently with the prediction of beam loss due to the space-charge and imperfection resonances for a specific accelerator [4], [22], the theory of collective resonant response provided a good tool in understanding the beam behavior observed in simulations.

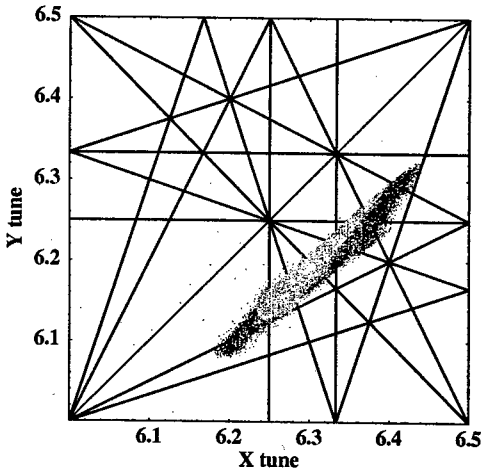

Figure 2: Tune spread of a 2MW SNS beam: only space-charge spread (green), space charge plus $dp/p = 1\%$ (pink). The tune-box is chosen free from the structure resonances. The imperfection resonances for the 2nd, 3rd and 4th orders are shown in red, black and blue, respectively.

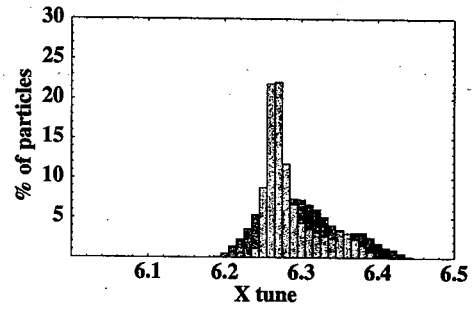

Figure 3: Horizontal distribution of the depressed tunes, corresponding to the tune-spread shown in Fig.1.

Integer and half-integer collective response

In general, in the case of non-linear imperfection errors one needs to consider the tune values near the corresponding non-linear resonances. The excited high-order modes respond to the imperfection harmonics according to

$$n = \Omega_m, \tag{5}$$

which is the coherent resonance condition for any order beam mode $\Omega_m = m\nu_0 - \Delta\Omega_{m,sc}$, derived by Sacherer [7]. To derive such condition for $m > 2$ modes, one needs to use either the high-order moment equations or the Vlasov equation. In addition, the effect of periodic focusing adds the possibility of the collective modes resonating at half-

integer values, which corresponds to the parametric (half-integer) resonance [23]:

$$n/2 = \Omega_m. \quad (6)$$

For completeness, we note that in the absence of non-linear imperfections, the periodic oscillation of the high-order modes are well defined so that the condition $n = \Omega_m$ no longer applies [23], and stability is determined solely by the parametric condition $n/2 = \Omega_m$ (see Ref. [26] for discussion). This effect becomes dominant in high-current transport channels or cooler rings, if the imperfections are not important. With the harmonic n now standing for the structure harmonic, the beam encounters a whole set of the instabilities of the corresponding collective modes in the process of the space-charge tune depression. Such instabilities were first numerically explored in connection with the transport channels [24], and recently were analytically described using the terminology of the resonances with an application to cooler rings [23].

Space-charge limit

A restriction imposed by the integer and half-integer single-particle tune values ("space-charge limit") can be written, using the self-consistent condition in Eq. 5 (for the case of linear perturbations), as

$$n = \Omega_2 = 2\nu_0 - \Delta\Omega_{2,sc}, \quad (7)$$

where Ω_2 is the frequency of the 2nd order coherent mode of beam oscillations (beam envelopes). The effect of the periodic focusing adds the possibility of a parametric resonance of the beam envelopes

$$n/2 = \Omega_2, \quad (8)$$

also known as the "envelope instability" [25]. According to Eq. 8, the envelope instability can limit the allowable tune space to only 0.25. This may have an impact on the performance of a high-intensity machine. The situations when such an envelope instability should be considered, and, whether it can alter the space-charge limit governed by the Eq. 7, are discussed in [26]. If such a parametric resonance is driven by the imperfection errors, the resonance is expected to be very narrow, and the envelope growth is detuned at a very low level due to the nonlinearity [21]. In fact, this is why the effect of the envelope instability was found to be negligible in rings, provided that the tune-box is chosen free of the structure resonances, and only the imperfection harmonics are of a concern [26].

Tune spread, resonance crossing and halo growth

The dependence of frequency on amplitude introduces an important asymmetric feature in resonance crossing. Depending on the sign of the nonlinearity, the frequency can grow or decay as the amplitude increases. In the case of the nonlinearity due to the space-charge, one gets a frequency increase with amplitude. As a result, when the resonance is crossed in the direction in which the peak intensity in the bunch is decreasing, the beam will experience a sudden large (but finite) jump in oscillation amplitude. If an error term, driving the resonance, is not very big, and there is sufficient aperture to accommodate such oscillations, one can cross the resonance in this direction with relatively low losses. On the other hand, when the resonance is crossed in the direction in which the peak intensity is increasing (for example, due to beam bunching or due to a multi-turn injection), this results in an adiabatic increase of the oscillation amplitude at resonance crossing. As a result, the high-intensity crossing of resonances in this direction without significant beam loss may be possible only with proper correction [27].

Another important feature of resonance crossing with space charge (when the peak intensity is increasing) is that small amplitude particles within the beam core experience the largest tune shifts. A typical tune spread of a 2MW beam in the SNS is shown in Fig. 2, where the tune spread in a bunched beam solely due to the space-charge is shown with a green color while the total tune spread with an additional $dp/p = 1\%$ is shown with a pink color. In Fig. 3, the corresponding single-particle tune distribution is shown, for example, in the horizontal direction. The resonances are first crossed with small-amplitude particles. Already the single-particle approximation shows that the current can be further increased until the resonance condition is reached by the large-amplitude particles. A more self-consistent description can be obtained via a collective approach for a beam with a non-linear distribution. In this case, the particles with small amplitudes are depressed below the resonance. At a critical intensity one gets a coherent resonant response. The frequency of the corresponding collective oscillation is increasing with amplitude so that the large-amplitude particles can be trapped into the resonance with the corresponding oscillating beam mode (Fig. 1). Some insights into the mechanisms of particle trapping into the islands and thus corresponding emittance growth, can be obtained analytically with an appropriate treatment of the nonlinear terms which provide bounded motion [28]. However, other important effects like the redistribution process due to resonance crossing, the dynamical redistribution as a result of multi-turn injection, the longitudinal effects of a bunched beam, etc, cannot be included analytically in a simple way. As a result, a more self-consistent description is obtained with realistic simulations. One of such important dynamic effects is shown, for example, in Fig. 4. Due to emittance increase, the effective space-charge depression becomes smaller, which allows a further increase in the intensity with a further subsequent growth of the emittance which can be seen as a saturation of the maximum tune shifts in the tune diagram.

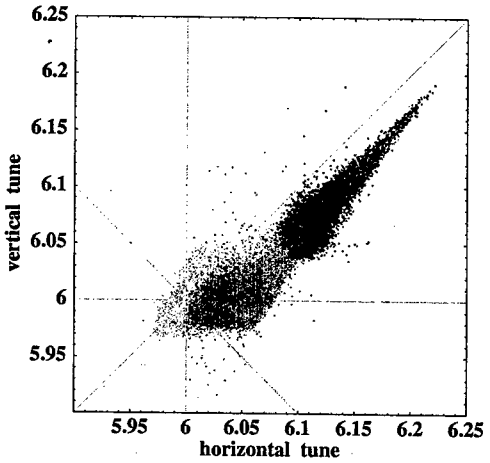

Figure 4: Space-charge tune spread of a bunched beam in the SNS for three beam intensities: $N = 2 \cdot 10^{14}$ (red), $3 \cdot 10^{14}$ (pink) and $4 \cdot 10^{14}$ (green) protons in the beam.

Selection of working point in high-intensity rings

Selection of a working point in a high-intensity ring requires careful consideration of both the space-charge and lattice driven resonances. First, tune-box which is free from structure resonances is selected. Then one considers whether the space-charge coupling resonances may give undesirable effects, which depends on the tune splitting and the ratio of the emittances in different planes. The best point is typically below the $1/4$ tunes which minimizes loss due to the high-order resonances. The harmonic $2n$ for an integer n below the fractional tune of 0.25 and the harmonic n for the half-integer $n/2$ tune below 0.75 preferably should be the imperfection harmonics, which may allow a space-charge shift in excess of the incoherent value of 0.25. If the working point is selected above the low-order nonlinear resonaces ($1/4$ and $1/3$ tune values), then all the required correctors should be available for an independent correction of these resonances. In the latter case, the exact level of loss will depend on the nature of the resonance, the beam intensity, the correction scheme, etc.

Resonance correction for high-intensity

The theory of imperfection resonances and their correction was developed based on the motion of single particles. As a result, it was successfully applied when space-charge effects are negligible. In the absence of a good physical picture of the space-charge effects in resonance crossing, any unsuccessful correction of a resonance for high-intensity operation, can be easily blamed on complicated space-charge effects. Now that we have some analytic understanding of the space-charge effects in resonance crossing and more importantly, the tools of the self-consistent computer simulations, we may attempt to resolve some of the questions related to the correction of the nonlinear resonances for high intensity [27]. Our conclusion is that one can provide good correction for the nonlinear imperfection resonances even for high-intensity operation.

ACKNOWLEDGMENTS

I am indebted to R.L. Gluckstern, I. Hofmann, G. Parzen, J. Holmes, S. Danilov, S. Cousineau, H. Okamoto, J. Wei, Y. Papaphilippou, N. Malitsky and V. Ptitsyn for numerous useful discussions on this subject. I am also grateful to the Accelerator Physics group of the SNS project for their useful comments, constant encouragement and support.

REFERENCES

[1] A.V. Fedotov, "Mechanisms of halo formation", HALO'03 Workshop (Montauk, New York, 2003).

[2] B.W. Montague, CERN Report 68-38 (1968).

[3] I. Hofmann, Phys. Rev E 57, p. 4713 (1998).

[4] S. Machida, Nucl. Inst. Meth. A309, p. 43 (1991); A384, p. 316 (1997).

[5] I. Hofmann, K. Beckert, Proc. PAC'85, p. 2264 (1985)

[6] L. Smith, Conf. on High Energy Acc. (Dubna, Russia) , p. 1232; P. Lapostolle, p. 1235 (1963).

[7] F. Sacherer, LNBL Report UCRL-18454 (1968).

[8] R.L. Gluckstern, Proc. of LINAC'70, p. 811 (1970).

[9] I. Hofmann et al., Proc. of EPAC'02 (Paris), p.74 (2002).

[10] A.V. Fedotov, J. Holmes and R.L. Gluckstern, Phys. Rev. STAB, 4, 084202 (2001).

[11] J.S. O'Connell et al., Proc. of PAC'03 (Washington D.C.), p. 3657; R.A. Jameson, p. 3926 (1993).

[12] A.V. Fedotov and R.L. Gluckstern, Proc. of PAC'99 (New York), p. 607, and ref. therein (1999).

[13] A.V. Fedotov et al., Phys. Rev. STAB, 2, 014201 (1999).

[14] J. Qiang and R.D. Ryne, Phys. Rev. STAB,3, 064201 (2000).

[15] J. M. Lagniel, N. Inst. Meth. A345, p. 46 and p. 405 (1994); A. Riabko et al. , Phys. Rev. E 51, p. 3529 (1995).

[16] A.V. Fedotov et al., Proc. of Workshop on beam halo and scraping (Wisconsin), p. 27 (1999).

[17] A.V. Fedotov et al., Proc. of EPAC'00, p. 1289 (2000).

[18] M.S. Livingston, MIT Report 60, p. 154 (1953).

[19] L.J. Laslett, BNL Report 7535, p. 324 (1963).

[20] R. Baartman, AIP Conf. Proc. 448, (New York), p. 56 ; S. Machida and M. Ikegami, p. 73 (1998).

[21] A.V. Fedotov and I. Hofmann, PR STAB, 5, 024202 (2002).

[22] A.V. Fedotov et al., Proc. of PAC'01, p.2848; N. Malitsky, A. Fedotov and J. Wei, Proc. of EPAC'02, p.1646 (2002).

[23] H. Okamoto, K. Yokoya, N. Inst. Meth., A482, p.51 (2002).

[24] I. Hofmann et al., Part. Accel., 13, p. 145 (1983).

[25] J. Struckmeier, M. Reiser, Part. Accel., 14, p.227 (1984).

[26] A.V. Fedotov, I.Hofmann, R.L.Gluckstern, H.Okamoto, "Application of envelope instability to rings" (these Proc.).

[27] A.V. Fedotov and G. Parzen, "Compensation of non-linear resonances in the presence of space charge", (these Proc.).

[28] A.V. Fedotov, "Analysis of parametric resonance in rings", Univ. of Maryland Report, unpublished (1998).

ADIABATIC BEAM TRAPPING IN STABLE ISLANDS OF TRANSVERSE PHASE SPACE: MEASUREMENT RESULTS AT CERN PROTON SYNCHROTRON

R. Cappi, M. Giovannozzi, M. Martini, E. Métral, G. Métral, R. Steerenberg
CERN, Geneva, Switzerland

A.-S. Müller, ISS, Forschungszentrum Karlsruhe, Germany

Abstract

Recently a novel approach to the problem of multi-turn extraction was proposed. It consists of splitting the beam by adiabatic capture inside stable islands created in the transverse phase space by sextupoles and octupoles. Numerical simulations indicate that such a technique should be feasible and potentially superior to the method presently used at the CERN Proton Synchrotron. During 2002, intense efforts were devoted to the experimental verification of this newly proposed extraction mode. Finally, beam capture into the islands was observed. In this paper, the extraction principle is briefly reviewed and the experimental results are presented and discussed in detail.

INTRODUCTION

With the approval of the CERN Neutrino to Gran Sasso Project [1], efforts were devoted to the feasibility study of an intensity upgrade of the Proton Synchrotron (PS) and Super Proton Synchrotron (SPS) complex [2]. A delicate point in the present scheme for the beam generation is the multi-turn extraction from PS to SPS, the so-called Continuous Transfer (CT) [3]. Due to the difference in circumference, $C_{\rm SPS} = 11 C_{\rm PS}$, and given the constraint of minimising the SPS filling time, the beam is extracted from the PS over five turns in two consecutive cycles. This is obtained by means of an electrostatic septum, used to slice the beam, and a proper choice of the horizontal tune (6.25) (see Refs. [3, 4] for more details). The main drawbacks of this technique are the intrinsic losses on the electrostatic septum and the poor betatron matching of the five slices [4], which in turn might transfer into injection losses into the SPS.

Recently, an alternative method was proposed, where the beam is split in the transverse phase space by means of adiabatic capture inside stable islands [5, 6] (see Fig. 1 for typical simulation results). The new technique would allow overcoming the bottlenecks of the present extraction mode. Not only, beam losses are reduced to almost zero, but also the phase space matching is highly improved (see Ref. [4] for a comparative analysis of the two approaches).

Following the positive results of the numerical simulations, further simulation studies were carried out to get more insight in the capture process [7], as well as experimental measurements to asses the feasibility of this new extraction mode.

MEASUREMENT CAMPAIGN

Machine and Instrumentation Modifications

To generate the stable islands used to capture the beam, nonlinear elements, such as sextupoles and octupoles, are needed. To this aim two sextupoles were installed in the ring, as well as two octupoles: elements of the same type are connected in series to provide the necessary strength and each pair is powered independently.

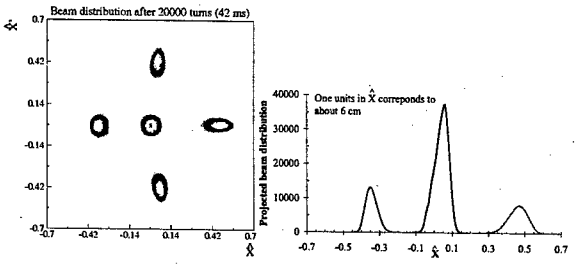

Figure 1: Results of the numerical simulations for the adiabatic capture inside stable islands (left: final pahse space distribution, right: projected beam distribution onto horizontal axis).

Two types of measurements are needed, namely phase space measurement and beam profile measurement during the various stages of the beam capture. The first one requires a multi-turn measurement of the beam position using two beam position monitors 90° apart in phase space [8]. A new acquisition system, based on a fast digitiser, was developed [9, 10]. The beam profile measurement was obtained with a flying wire scanner device [11] currently available in the PS ring. A schematic layout of the PS ring including the newly installed elements as well as other key devices for the adiabatic beam capture tests described in this paper is shown in Fig. 2.

Phase Space Measurement

The new extraction mode requires a precise control of the islands' position and size. Hence, a good knowledge of the phase space structure is of uttermost importance.

The technique used is the standard one, i.e. the beam trajectory is perturbed by means of a kicker magnet (notably the one normally used to fast extract the beam) and betatron oscillations are observed on two pickups 90° apart. To overcome some difficulties due to the islands' phase

0-7803-7738-9/03/$17.00 © 2003 IEEE

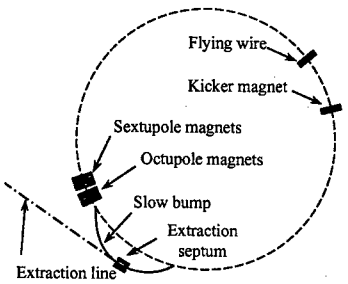

Figure 2: Layout of the PS machine including the key elements for the test of adiabatic capture. Other elements (not shown here) are involved in the final stage of the five-turn extraction.

at the kicker location, two kicks separated by three turns, which is the minimum delay due to hardware limitations, were used, thus allowing to scan along the diagonal in phase space. During the measurements the special sextupoles and octupoles were set to their computed values, i.e. $K_2 = 1.04\ \mathrm{m}^{-2}$ and $K_3 = 127.95\ \mathrm{m}^{-3}$, where $K_i = L/(B_0\,\rho)\,\partial^i B_y/\partial x^i$ are the sextupolar and octupolar integrated gradients. These measurements are strongly affected by beam de-coherence. In fact, as the beam position monitors measure the centre of gravity of the beam charge distribution, the detected signal fades out after some turns. Special care was taken to minimise such an effect. In particular, a low-intensity (about 6×10^{11} protons), single-bunch beam was chosen to have small emittances, defined as $\epsilon^*_{h/v} = \beta\gamma\sigma^2_{h,v}/\beta_{h,v}$, namely $\epsilon^*{}_h \approx 2\ \mu$m, $\epsilon^*{}_v \approx 1.5\ \mu$m and $\Delta p/p \approx 1.5 \times 10^{-3}$. This choice allows scanning better the phase space structures, also avoiding filamentation in the transverse plane, and hence signal de-coherence. Furthermore, due to the plain FOFDOD structure of the PS lattice, no location with zero dispersion exists, implying that the dedicated sextupoles and octupoles have a strong chromatic effect, leading to a measured value of $\xi_h = Q'_h/Q_h \approx 1.7$ and $\xi_v \approx 0.6$. After a careful tuning, the chromaticity was reduced to $\xi_h \approx 0.1$ and $\xi_v \approx 0.9$ (see Ref. [12] for more details on this point). Also, the rf-voltage was decreased to reduce $\Delta p/p$ to about 0.4×10^{-3}. The main results of the phase space measurement campaign are shown in Fig. 3. The various plots refer to different kick amplitudes. In the first portrait, regular motion represented by circular phase space trajectories is visible and signal de-coherence is also apparent. As the the kick amplitude is further increased, fourth-fold symmetrical trajectories appear: the beam is kicked inside the stable islands of the fourth-order resonance. A rather strong signal de-coherence is revealed by the curly-shaped beam trajectory, spiralling towards the origin. In principle, particles inside the islands should generate a coherent, albeit small, signal lasting over a long period. The strong de-coherence can be explained by assuming that time-dependent effects make the islands moving in phase space. This is the case when tune ripple is present or when considerable coupling between longitudinal and transverse degrees-of-freedom induce tune modulation via chromaticity. In fact, it turned out that the improvement of the quadrupoles power supplies made it possible to cure completely the problem. Finally, it is worthwhile pointing out that the results shown in Fig. 3 are in reasonable agreement with the model of the PS machine and with the phase space topology assumed in the numerical simulations [5, 6].

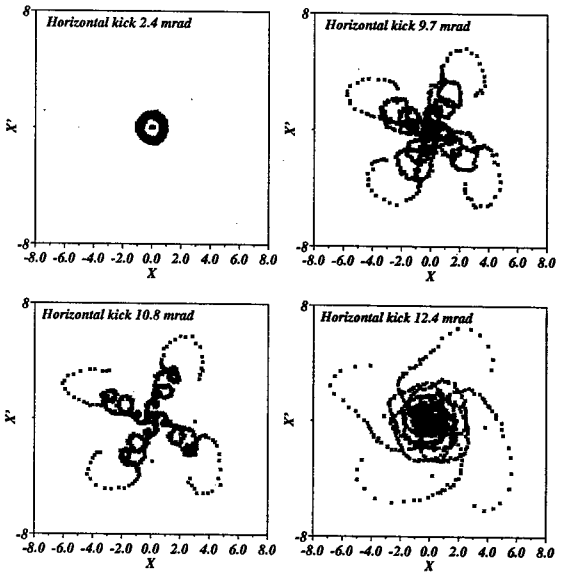

Figure 3: Horizontal normalised phase space measured with the multi-turn system (about 1.5×10^3 turns are plotted).

Adiabatic Capture

After having verified that the main ingredients, namely stable islands, were present in the phase space for the nominal parameters used in numerical simulations, the first tests of adiabatic capture were undertaken. To this aim, the horizontal tune was swept through the fourth-order resonance to induce and observe the trapping phenomenon. The horizontal emittance was increased ($\epsilon^*{}_h \approx 12\ \mu$m) to simulate a high-intensity beam, the other beam parameters being unchanged. The experimental conditions are shown in Fig. 4, where the horizontal tune, the strength of the nonlinear elements, and the beam intensity are plotted as a function of time. When the strength of the nonlinear elements levels out, the beam momentum is 14 GeV/c and the magnetic field is constant: the power supplies are rather slow, imposing to start ramping during acceleration. The initial value of the tune is chosen near the fourth-order resonance, then a linear change is applied, during which the capture of beam particles inside islands occurs. The final value of the tune is varied for different beam profile measurements to change the islands' separation. As far as the beam intensity is concerned, some minor losses are visible during the ramping of the nonlinear elements, while during the actual trapping no sign of losses is visible.

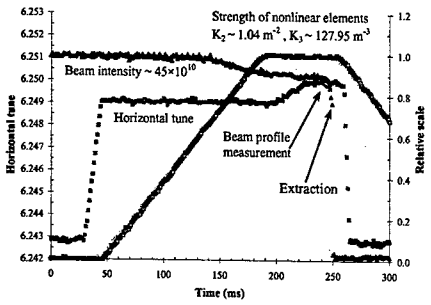

Figure 4: Experimental conditions during the tests for adiabatic capture inside stable islands.

The main results are shown in Fig. 5, where the beam profile measured by the flying wire scanner is shown for different values of the final tune.

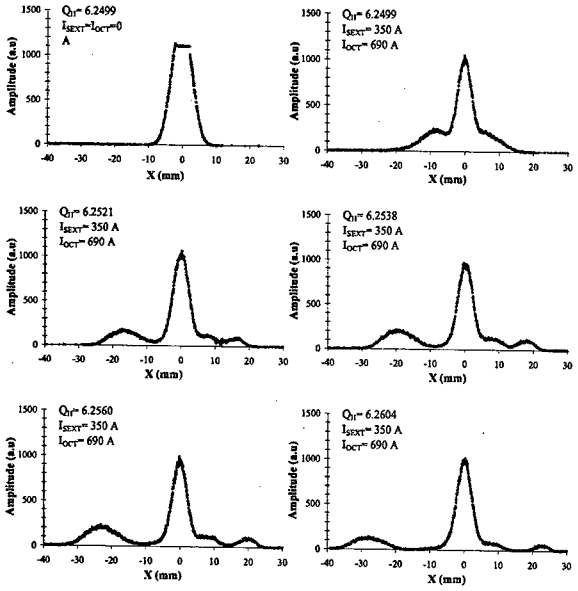

Figure 5: Horizontal beam profile measured by a flying wire scanner, for different final values of the tune. The first profile represents the initial beam distribution, when no capture occurs. The choice of the gain, optimised for the subsequent stages of adiabatic capture, explains the signal saturation.

The first profile is the reference picture: the tune is changed, but as the nonlinear elements are switched off no effect on the beam distribution is visible. The other pictures differ by the value of the final tune: the nonlinear elements are switched on and three additional peaks are clearly visible, whose separation increases as the tune is varied. One should keep in mind that, although the beam is split in five beamlets [5, 6], the wire scanner measures the projection onto the x-axis (see also Fig. 1), therefore, the central peak is higher than the others as it represents the superposition of three beamlets.

CONCLUSIONS AND OUTLOOK

The first tests of adiabatic beam trapping inside stable islands proved that the capture process, already observed in numerical simulations, occurs also in real machines. Beam splitting in five beamlets was detected and their separation measured as a function of the final value of the horizontal tune. Further tests are planned to study the dependence of the beam parameters on the speed of the tune variation (adiabaticity), and on sextupole and octupole strengths. Then it will be crucial testing this novel approach using higher-intensity bunches as well as multi-bunch beams. Of course, actual five-turn extraction will be also tested during the 2003 experimental campaign.

ACKNOWLEDGEMENTS

We would like to thank M. E. Angoletta, J. Belleman, J. L. Gonzalez for developing and supporting the multi-turn acquisition system, and M. Benedikt, M. Chanel for preparing the different beams in the PS-Booster.

REFERENCES

[1] K. Elsener (Ed.) et al., "The CERN Neutrino Beam to Gran Sasso (Conceptual Technical Design)", *CERN* **98-02** (1998).

[2] R. Cappi (Ed.) et al., "Increasing proton intensity of PS and SPS", *CERN-PS (AE)* **2001-041** (2001).

[3] C. Bovet et al., in *1973 Particle Accelerator Conference*, edited by D. W. Dupen (IEEE, New York, 1973) p. 438.

[4] R. Cappi, M. Giovannozzi, "Computation of Betatron Mismatch and Emittance Blow-up for Multi-Turn Extraction", *CERN PS (AE)* **2002-083** (2002).

[5] R. Cappi, M. Giovannozzi, *Phys. Rev. Lett.* **88**, (2002) 104801.

[6] R. Cappi, M.Giovannozzi, in *Eighth Particle European Accelerator Conference*, edited by J. Poole and C. Petit-Jean-Genaz (Institute of Physics, UK London, 2002) p. 1250.

[7] R. Cappi, M. Giovannozzi, "Adiabatic Capture of Charged Particles in Stable Islands: a Novel Approach to Multi-Turn Extraction", these proceedings.

[8] P.Morton et al., *IEEE Trans. on Nucl. Sci.* **32**, (1985) p. 2291.

[9] M. E. Angoletta et al., in *Eighth Particle European Accelerator Conference*, edited by J. Poole and C. Petit-Jean-Genaz (Institute of Physics, UK London, 2002) p. 1273.

[10] M. E. Angoletta, A.-S. Müller, in *Eighth Particle European Accelerator Conference*, edited by J. Poole and C. Petit-Jean-Genaz (Institute of Physics, UK London, 2002) p. 1948.

[11] C. Steinbach, M. Van Rooij, *IEEE Trans. Nucl. Sci.* **32**, (1985) p. 1920.

[12] R. Cappi et al., "Optics Studies for the CERN Proton Synchrotron Machine: Linear and Nonlinear Modelling Using Beam Based Measurements", these proceedings.

NONLINEAR DYNAMICS IN THE DUKE STORAGE RING WITH FEL WIGGLERS *

Y. K. Wu†, J. Li, S. F. Mikhailov, V. Litvinenko, FEL Lab, Duke University, NC 27708-0319, USA

Abstract

Single particle dynamics in the storage ring can be significantly influenced by strong nonlinearities from long and strong-field insertion devices. This paper reports our preliminary results on the dynamics impact of the 24 m long OK5 FEL in the Duke ring. Initial studies are performed using an intermediate lattice with two OK5 wigglers. The dynamic aperture is computed using a recently developed symplectic wiggler integrator and the frequency map technique, NAFF. We have observed significant dynamic aperture reduction due to OK5 wigglers at lower beam energies. We also report our preliminary findings on the means to improve beam dynamics with wigglers.

1 INTRODUCTION

The Duke storage ring is designed as a dedicated driver for Free Electron Lasers (FELs). The first operational FEL on the Duke ring is the 8-meter long OK4 FEL with two planar wigglers [1], originally designed for the VEPP-3 storage ring at Budker Institute of Nuclear Physics (BINP), Russia. Since 1998, the OK4 FEL has demonstrated broad tuneability from 2.1 μm to 194 nm. Operating in both continuous-wave (CW) and giant pulse modes, the OK4 FEL has been used in medical, biological, chemical, and surface science research. Operating in a two-bunch mode, the OK4 FEL, via Compton scattering, also serves as a driver for a linearly polarized monochromatic gamma source in a wide energy range from 0.7 MeV to 58 MeV.

The capabilities of the OK4 FEL are limited in two main areas: (1) the relatively small gain limits the shortest lasing wavelength; (2) the strong on-axis synchrotron radiation from the linearly polarized wigglers causes significant mirror damage. To overcome these limitations, a next generation FEL, a variably polarized 24-meter long OK5 FEL system, has been specially designed to increase the FEL gain, to reduce the on-axis radiation, and to match the high quality of the electron beam in the storage ring.

The OK5 FEL system [2] consists of four 4-meter long wigglers and three bunchers. Each wiggler is comprised of two electro-magnetic pole-tip arrays, one vertical and one horizontal, shifted for a quarter of the wiggler period with respect to each other. By controlling the horizontal and vertical magnetic fields independently via two power suppliers, the OK5 wigglers can be configured to produce radiation with various polarizations, from linear and elliptical polarizations to left and right circular polarizations.

The overall performance of the Duke storage ring depends critically on the dynamic aperture. A large momentum dynamic aperture helps increase the beam lifetime and extends the no-loss mode of gamma-ray operation to higher energies. A large transverse dynamic aperture is essential for injection, especially for the future top-off injection with a booster ring while operating the OK5 FEL. At a low beam energy, the dynamic aperture can be significantly altered by OK5 wigglers with strong nonlinearities. The dynamics impact of OK5 wigglers is the main focus of this paper.

2 OK5 FEL LATTICES

The Duke FEL storage ring is a race-track structure comprised of two compact 180-degree arcs and two 34.21 m long straight sections. One of the two straights is dedicated to driving FEL light sources. This straight section lattice is designed with bilateral symmetry to host the present OK4 FEL. To achieve the additional flexibility required for the OK5 FEL operation, the new straight section lattice [3] has been redesigned using a combination of quad doublets and triplets. Each triplet cell includes a quadrupole triplet (QF-QD-QF), a buncher, and an OK5 wiggler. The three triplet quads are individually powered to provide compensations for linear focusing changes due to varying OK5 settings. Two quad doublets are used to match the β-functions between the arc and OK5 lattice. A comparison of OK5 and OK4 wiggler parameters is shown in Table 1.

Table 1: Comparison of OK4 and OK5 wiggler parameters.

	OK4 FEL	OK5 FEL
Total wiggler length [m]	6.7	16.16
No. of wigglers	2	4
No. of periods per wiggler	33.5	33
Wiggler periods [cm]	10	12
Wiggler gap [mm]	22.6	40 × 40
Peak magnetic field [kGs]	5.3	3.0
Max. wiggler $K = \frac{e B_0}{k_w m_e c^2}$	4.9	3.4

The exact length of the triplet cell is chosen to be 6.71625 m, exactly a sixteenth of the ring circumference, in order to produce gamma-rays. When operated with 8 equally spaced bunches, the maximum number of collision points are five: three at the center of the defocusing quad in the triplet and two in the matching sections. Each triplet employs four sets of horizontal and vertical orbit correctors to individually control collision points in the quads.

With this triplet design, the OK5 lattice is very flexible to allow a wide range of β-functions at the center of wigglers. In fact, β_x and β_y can be tuned from 4 m to 10 m in arbitrary combinations. By adjusting quads in the FEL straight, the betatron beating due to changing OK5 settings can be fully compensated, resulting in small residual tune changes ($max(d\nu_{x,y}) < 0.007$). A typical OK5 triplet lat-

*Work Supported by DOE grant DE-FG05-91ER40665 and DoD MFEL Program as managed by the AFOSR, grant F49620-001-0370.

† wu@fel.duke.edu, 1-919-660-2654 (phone).

tice is shown in Fig. 1, resulting in a set of vertical OK5 wiggler arrays energized.

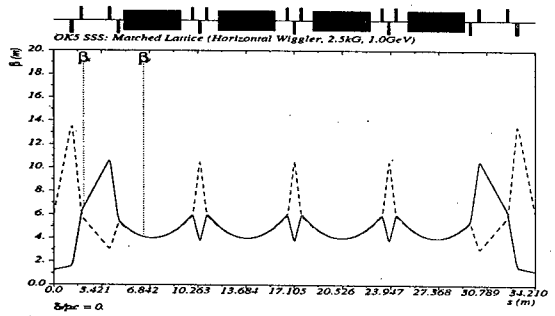

Figure 1: Dispersion-free OK5 FEL lattice at 1 GeV. Powered as horizontal wigglers, the maximum field in the OK5 is 2.5 KGs. The solid and dashed lines are β_x and β_y respectively. At the center of the wiggler, $\beta_x = \beta_y = 4$ m.

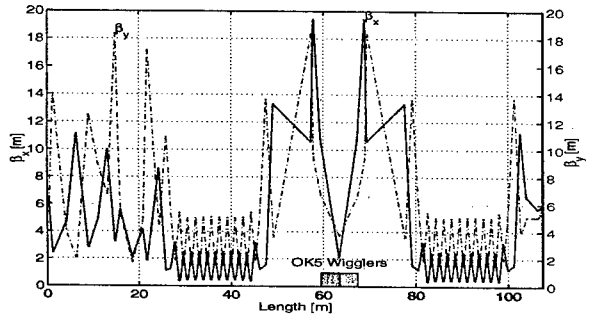

Figure 2: β-functions for the Duke ring with two OK5 wigglers located at the center of the FEL straight ($\beta_x = 2.14$, $\beta_y = 3.75$ m). The beam energy is 300 MeV and OK5 wigglers are circularly polarized with a peak field of 1.8 kG for each wiggler array. The solid and dashed lines are β_x and β_y respectively.

The long OK5 wigglers are expected to significantly alter the beam dynamics in the ring. To minimize dynamics risk associated with OK5 wigglers, an incremental upgrade plan has been developed with its first phase to test two OK5 wigglers. One of possible scenarios is to install two OK5 wigglers in the present location of OK4 wigglers in an intermediate lattice. To cover a range of gamma-ray energies and polarizations, three operation modes of this lattice have been investigated:

1. a 1 GeV lattice for the production of 100 MeV circularly polarized gamma beams;
2. a 300 MeV lattice for the production of 2 MeV circularly polarized gamma beams;
3. a 300 MeV lattice for the production of 2 MeV linearly polarized gamma beams;

The ring beta functions for the above mode 2 operation is shown in Fig. 2. The circularly polarized OK5 wigglers are described by a field model in the following section.

3 WIGGLER MODEL

The circularly polarized field of OK5 wigglers is expressed as the superposition of two sets of linearly polarized wiggler fields generated by two independent wiggler arrays. For example, the horizontally polarized light is generated by the vertical wiggle array. Its field is described by a set of wiggler harmonics with the mid-plane symmetry as follows:

$$
\begin{aligned}
B_y &= -\sum_{m,n} C_{mn} \cos(k_{xl}x)\cosh(k_{ym}y)\cos(k_{zn}z+\theta_{zn}),\\
B_x &= \sum_{m,n} C_{mn}\frac{k_{xl}}{k_{ym}} \sin(k_{xl}x)\sinh(k_{ym}y)\cos(k_{zn}z+\theta_{zn}),\\
B_z &= \sum_{m,n} C_{mn}\frac{k_{zn}}{k_{ym}} \cos(k_{xl}x)\sinh(k_{ym}y)\sin(k_{zn}z+\theta_{zn}),\\
\vec{B}_{\rm H} &= (B_x, B_y, B_z),
\end{aligned}
$$

where, C_{mn} are the amplitudes of wiggler harmonics, $k_{ym}^2 = k_{xl}^2 + k_{zn}^2$, $k_{zn} = n\,k_w$, $k_w = 2\pi/\lambda_w$, and θ_{zn} are the relative phases of wiggler harmonics. The magnetic field of a vertically polarized wiggler generated by the horizontal wiggler array, $\vec{B}_{\rm V}(x,y,z)$, can be expressed in the similar manner by interchanging the arguments x and y in the above expression. When the iron saturation is not significant, the general wiggler field in a variably polarized OK5 wiggler can be expressed as the sum of the two linearly polarized fields:

$$
\vec{B}(x,y,z) = a\,\vec{B}_{\rm H}(x,y,z) + b\,\vec{B}_{\rm V}(x,y,z+\frac{\lambda_u}{4}),
$$

where $-1 \le a \le 1$ and $-1 \le b \le 1$. For example, to produce circularly polarized radiation, $a = b = 1$.

Table 2: A set of normalized horizontal wiggler harmonics for dynamics simulation.

Modes	$C_{m,n}$	k_x/k_w	k_y/k_w	k_z/k_w
1	1.025	1.0592	1.4567	1
2	-0.0094	4.1272	4.2466	1
3	-0.0156	2.9555	4.2113	3

To compute the OK5 wiggler field, a 2D/3D magnet design code, Mermaid [4], has been used extensively. The numerically calculated 3D fields on a transverse grid are stored using 128 wiggler harmonics. An analytic wiggler model with three dominant harmonics are obtained by fitting the model with the calculated field on a cylindrical surface inside the wiggler (see Table 2).

4 DYNAMICS WITH TWO WIGGLERS

As found in the previous studies, long wigglers can have a significant influence on the single particle dynamics in the Duke ring [5]. The most significant dynamics impact is expected at the lowest e-beam energy with the strongest effective nonlinearity of wigglers. The dynamics studies are performed using a recently developed symplectic wiggler integrator [6] and the frequency map analysis method, NAFF, of J. Laskar [7]. Fig. 3 and Fig. 4 show the computed dynamic apertures for a bare lattice without OK5

wigglers and a 300 MeV lattice with circularly polarized OK5 wigglers to produce 2 MeV gamma beams. In Fig. 3, the large footprint of the bare lattice (the left plots) in both configuration and tune spaces is reduced to a much smaller footprint when two OK5 wigglers are turned on (the right plots). The reduction in the momentum aperture, from (-2.7%, 3.8%) to (-2.8%, 3.1%), will reduce the beam lifetime when OK5 wigglers are turned on. Significant transverse dynamic aperture reduction is observed in Fig. 4 for on-momentum particles. This can have significant impact on the injection efficiency, which is critical for our future top-off injection with a booster ring.

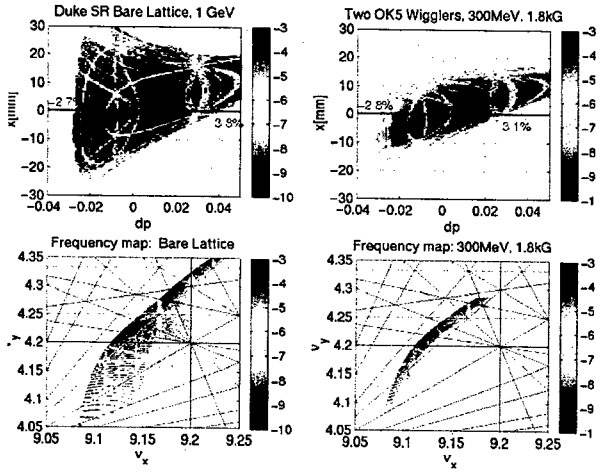

Figure 3: Horizontal and momentum aperture comparison at the center of the arc, $\beta_x = 2.48$, $\beta_y = 1.56$ m. On the left, a Duke ring lattice without wigglers; on the right, a Duke ring lattice with two OK5 wigglers energized.

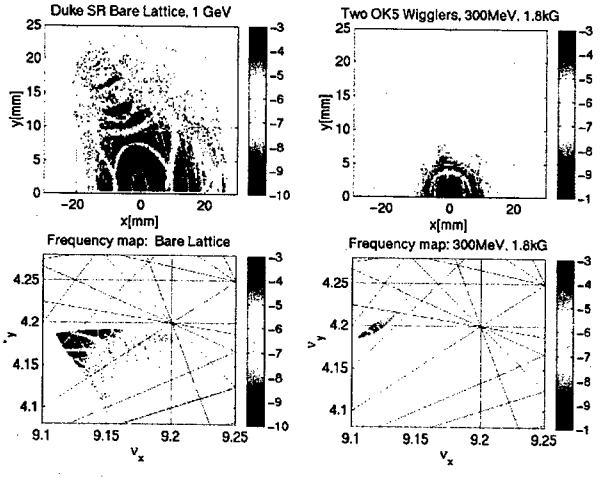

Figure 4: Horizontal and vertical aperture comparison for on-momentum particles at the center of the arc. On the left, a Duke ring lattice without wigglers; on the right, a Duke ring lattice with two OK5 wigglers energized.

The dynamics impact of two OK5 wigglers for three operational modes is summarized in Table 3. At 1 GeV, a small reduction in the transverse dynamic aperture is not expected to have any direct impact on the ring performance. However, at 300 MeV in both linearly and circularly polarized modes, momentum and transverse apertures are significantly reduced. Most notably, the vertical aperture is reduced by about a factor of four. Some preliminary studies have been performed in search of possible field compensation solutions. One study assumes that OK5 wigglers were comprised of two ideal wiggler arrays with infinite poles (no field roll-off). The computed dynamic aperture for this scenario is shown as the last row of Table 3. In this case, both the momentum aperture and vertical aperture are restored to the similar values as the bare lattice. Therefore, it seems possible to recover some of the lost aperture by certain field compensation schemes built into OK5 wigglers. Several wiggler pole-tip modifications have been designed and their impacts on dynamics will be carefully investigated.

Table 3: Computed dynamic apertures with or without OK5 wigglers.

Duke Ring Lattice	Energy Aper. [%]	Hori. Aper. [mm]	Vert. Aper. [mm]
Bare Lattice	(-2.7,3.8)	(-15, 24.9)	13.5
1 GeV, circular	(-2.7,3.8)	(-12.6,17.7)	8.86
0.3 GeV, circular	(-2.8, 3.1)	(-9.9, 13.5)	6.5
0.3 GeV, linear	(-2.7, 2.7)	(-11.7, 17.4)	7.25
0.3 GeV, ideal wig	(-2.8, 3.7)	(-10.5, 14.7)	13.75

5 SUMMARY

In this paper, we have reported our preliminary findings on the Duke ring dynamics with two OK5 wigglers. Significant dynamics aperture reduction has been observed due to the strong nonlinearities of the long wigglers. In the near future, we plan to study the dynamics impact of four OK5 wigglers in its final lattice configuration. In particular, we would like to investigate possible wiggler field compensation schemes and optimal lattice designs to improve the Duke ring dynamics with the OK5 FEL.

Finally, we would like to thank E. Forest at KEK, D. S. Robin and C. Steier at LBNL, and J. Laskar at BdL, Paris for their help on various parts of this work.

6 REFERENCES

[1] I. B. Drobyazko and *et al.*, Nucl. Instr. and Mech. A 282 (1989), 424–430.

[2] V. N. Litvinenko and *et al.*, Nucl. Instr. Methods, v. A475, pp. 407–416 (2001).

[3] Y. K. Wu and *et al.*, Nucl. Instr. Methods, v. A475, pp. 253–259 (2001).

[4] A. N. Dubrovin, "MERMAID, the 2D/3D code for magnetic design," Novosibirsk, Russia.

[5] Y. Wu and *et al.*, Nucl. Instr. and Mech. A 341 (1994), 363–366.

[6] Y. K. Wu and *et al.*, Proc. of PAC2001, Chicago, p. 459 (2001).

[7] J. Laskar, Physica (Amsterdam), 67D, p. 257–281 (1993).

STOCHASTIC COOLING STUDIES IN RHIC*

M. Blaskiewicz†, J.M. Brennan, P. Cameron, J. Wei
BNL, Upton NY 11973, USA

Abstract

Emittance growth due to Intra-Beam Scattering significantly reduces the heavy ion luminosity lifetime in RHIC. Stochastic cooling of the stored beam could improve things considerably by counteracting IBS and preventing particles from escaping the rf bucket [1]. High frequency bunched-beam stochastic cooling is especially challenging but observations of Schottky signals in the 4-8 GHz band indicate that conditions are favorable in RHIC [2] . We report here on measurements of the longitudinal beam transfer function carried out with a pickup/kicker pair on loan from FNAL TEVATRON. Results imply that for ions a coasting beam description is applicable and we outline some general features of a viable momentum cooling system for RHIC.

1 INTRODUCTION

When colliding gold (Au) ions in RHIC, the longitudinal emittance grows during the course of a store. The dominant mechanism is intrabeam scattering (IBS), which is the result of small angle Coulomb collisions between the ions in a single bunch. Figure 1 shows the evolution of the total and bunched intensities. The deuteron beam remains in the RF bucket with nearly constant intensity. For the gold beam both the bunched and total intensities decay with time. Figure 2 shows the evolution of the gold longitudinal profile. The traces have been scaled to a peak value of one. The initial peak current was 2.4 amperes and seven hours later it is 0.4 amperes. The net RF voltage per turn is given by[4]

$$V(\phi) = V_A \sin(\phi) + V_S \sin(7\phi) \qquad (1)$$

where ϕ is in units of RF phase for the accelerating cavities with $h = 360$, $V_A \approx 250$ kV is the voltage on the accelerating cavities, $V_S \approx 2.4$ MV is the voltage on the storage cavities, and the stable synchronous phase is $\phi = \pi$ since store is above transition ($\gamma > \gamma_T$). The FNAL pickup and kicker are installed in the yellow ring. During the gold-deuterium run we worked with the gold beam. During the polarized proton run we worked with protons.

2 COHERENT BEAM RESPONSE

Figure 3 compares the coherent response of gold to protons. The FNAL kicker [5] was driven with about 5 Watts of power at single frequencies, 5 GHz for gold, 4 GHz for protons. The longitudinal beam response was detected with the FNAL pickup. The difference in the noise floor is due

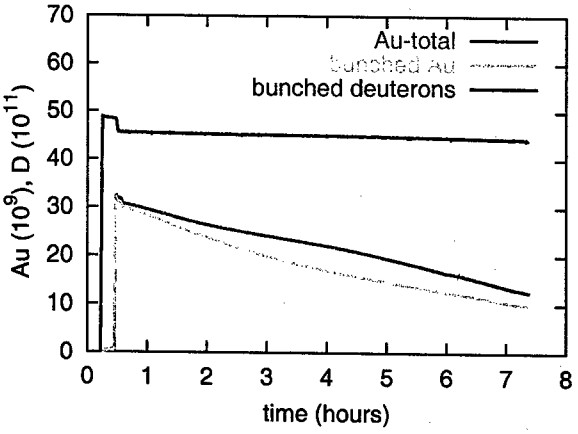

Figure 1: Evolution of the bunched and total intensity in gold (Au) and deuteron (D) beams. There are 55 bunches of each species and the bunched beam data have been smoothed to reduce noise.

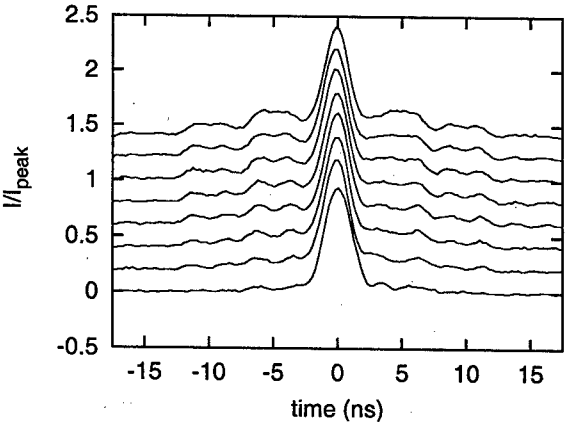

Figure 2: Evolution of the longitudinal profile for an Au bunch. The lowest trace was taken just after rebucketing and each trace above is an hour later.

to different gain in our experimental setups. In both cases the beam was driven at $f_{cent} - \Delta f$ with $\Delta f \approx 5$ kHz. The proton beam spectrum has two narrow lines that are absent in the gold signal. The proton beam shows a strong narrow band signal near the revolution line that was also observed in the Tevatron [3]. We suspect this signal is due to long lived coherent oscillations in the proton beam [6]. Since IBS rates for gold are about 10 times larger than those for protons, we expect gold coherence to diffuse away. The proton signal also shows a narrow line at $f_{cent} + \Delta f$, which is reminiscent of a bunched beam response. This feature

* Work performed under contract numbers #DE-AC02-98CH10886 and #DE-AC05-00OR2275 with the auspices of the United States Department of Energy.

† blaskiewicz@bnl.gov

0-7803-7738-9/03/$17.00 © 2003 IEEE

was not always present in the proton spectrum.

To analyze the data consider a coasting beam that has the same number of particles and the same momentum distribution as the bunched beam. The rms Schottky current for both cases satisfies

$$\left|\frac{I_s}{\bar{I}}\right|^2 = \frac{2P(f)\delta f}{N}, \qquad (2)$$

where I_s denotes the rms Schottky current, $\bar{I}$ is the DC beam current, δf is the resolution bandwidth of the spectrum analyzer, $P(f)$ is the normalized frequency distribution, and N is the number of particles in the beam.

Now take the same coasting beam and apply a longitudinal voltage kick $\hat{V}\cos(\Omega t)$. Model the beam's frequency distribution as a Lorentzian so that

$$P(f) = \frac{\Delta f}{\pi}\frac{1}{(f - f_{cent})^2 + \Delta f^2}.$$

For drive frequencies near the center of the distribution, and neglecting collective effects, the ratio of the rms beam current at the drive frequency to the coasting beam current is

$$\left|\frac{I_c}{\bar{I}}\right| = \frac{q\hat{V}}{E_T\hat{\epsilon}^2}\frac{1}{2\sqrt{2}\pi f_{cent}T_0|\eta|}, \qquad (3)$$

where $E_T = \gamma mc^2$ is the total energy per particle, q is the charge per particle, $T_0 \approx 12.8\mu$s is the revolution period, and $\hat{\epsilon} = \Delta f/|\eta|f_{cent}$ is the fractional energy spread.

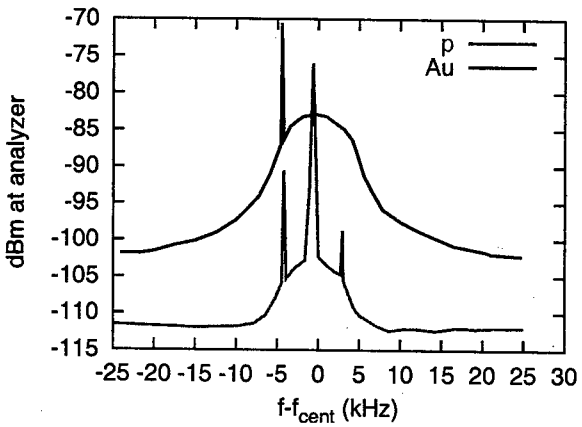

Figure 3: Power spectra of gold and proton beams driven by the FNAL kicker. The resolution bandwidth of the spectrum analyzer was 30 Hz.

Figure 4 shows the beam transfer function for protons taken with an HP8753 network analyzer using a 10 Hz intermediate frequency bandwidth. The curves are very similar to what one expects for coasting beams [8]. Fig 5 was taken during the same store with the same instrumental setup. When the coherent spike near the revolution line in Fig 5 is ignored, the calculated ratio of the coherent power

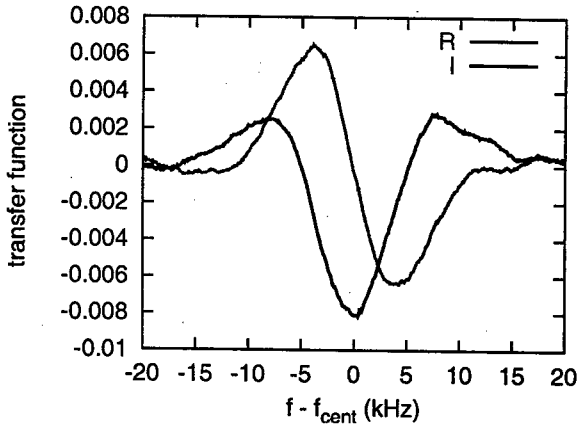

Figure 4: Transfer function measurements for protons at 4.8 GHz.

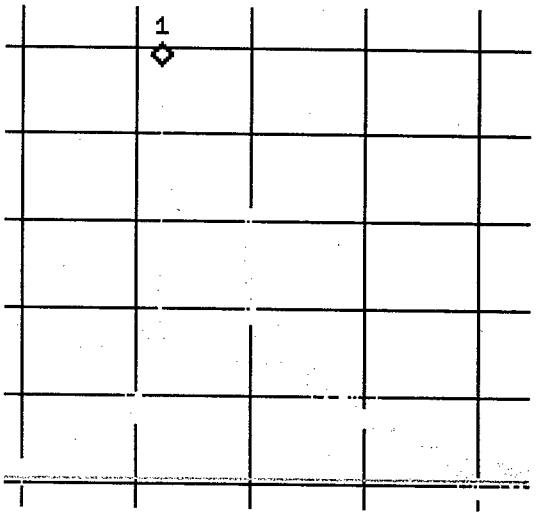

Figure 5: Proton power spectrum when transfer function measurements were made. The center frequency is 4.8 GHz, the horizontal scale is 5 kHz/div, and the vertical scale is 5 dBm/div. There were $N = 10^{12}$ protons and $\gamma = 107$. The noise floor, denoted by the green line, is -86 dBm.

to the Schottky power agrees with the measurement within 1 dB. With both qualitative and quantitative agreement, we have confidence that a coasting beam theory, modified via the bunching factor of the beam, is reasonable for specifying a cooling system.

3 COOLING SYSTEM

Consider a cooling system of bandwidth W. Let N_b be the number of particles per bunch and let τ_b be the bunch length. The number of particles per independent sample of the cooling system is $N_s = N_b/2\tau_b W$ [10]. Consider the

rms energy spread $\sigma_e = E_T\sigma_p/p$; the cooling time is

$$\frac{\sigma_E}{\dot{\sigma}_E} \equiv \tau_E = \frac{N_s M}{f_0}, \quad (4)$$

where M is the mixing factor. For RHIC gold parameters with a 4-8 GHz cooling system and 10^9 particles per bunch we get $N_s M = 2.8 \times 10^8$ which in turn implies $\tau_E \approx 1$ hour. Detailed calculations [7] have shown that this cooling time will significantly improve the integrated luminosity.

Stochastic cooling for RHIC might better be refered to as stochastic confinement. The main goal is to keep particles in the RF bucket, not to reduce the rms momentum spread. Consider a single particle with no RF voltage [8]. In the absence of a cooling system the revolution frequency is constant and the beam current is given by

$$I(\theta,t) = \frac{\omega q}{2\pi} \sum_{k=-\infty}^{\infty} e^{jk[\omega t - \theta]}, \quad (5)$$

where ω is the particle's angular revolution frequency and $\theta = s/R$ is the machine azimuth. Suppose the cooling pickup is at azimuth θ_P and the kicker is at azimuth θ_K. We assume that the change in revolution frequency per turn satisfies $\delta\omega \ll \omega_0/k_{\max}$ where $\omega_0 = 2\pi/T_0$ and $k_{\max}$ is the largest revolution harmonic for which the cooling system has a significant gain. Then, the average rate at which the particle gains or losses energy is given by

$$\frac{dE}{dt} = \left(\frac{\omega q}{2\pi}\right)^2 \sum_{k=-\infty}^{\infty} e^{jk(\theta_K - \theta_P)} Z_T(k\omega) e^{-jk\omega T_d}, \quad (6)$$

$$= \left(\frac{\omega q}{2\pi}\right)^2 \sum_{k=-\infty}^{\infty} S_k,$$

where Z_T is the transfer impedance between the pickup and kicker and T_d is the delay. We do not plan on cutting a chord across the RHIC ring so the kicker will be placed upstream of the pickup and T_d is chosen so that $\theta_K - \theta_P - \omega_0 T_d = -2\pi$. Then

$$S_k = Z_T(k\omega) e^{-jk\Delta\omega T_d}, \quad (7)$$

where $\Delta\omega = \omega - \omega_0$. For the cooling system to be effective the transfer impedance must cause particles with $\omega > \omega_0$ to be accelerated, and particles with $\omega < \omega_0$ to be decellerated. Therefore, the real part of the transfer impedance must change sign at revolution lines. A natural candidate is a one turn delay notch filter [9] which has a transfer function $T(\Omega) = 1 - \exp(-j\Omega T_0)$. This will be implemented using a fiber optic delay line so there is no loss associated with the delayed signal. We apply one or two such filters in series. Also, we model the net transfer function of the pickup, kicker, and any phase shifters to be $T(\Omega) = jR(\Omega)$ where $R(\Omega)$ is real in the center of the cooling band and has small imaginary parts. Then,

$$S_k = jR(k\omega)\left(1 - e^{-jk\Delta\omega T_0}\right)^n e^{-jk\Delta\omega T_d}. \quad (8)$$

Results for $n = 1, 2$, with $T_d = 2T_0/3$ and $R(\Omega)$ constant between 4 and 8 GHz are shown in Figure 6. The horizontal scale is for fractional moment shifts with $|dp/p| \leq 0.2\%$. The largest voltages available can confine particles with $|dp/p| \leq 0.17\%$, where the filter with $k = 2$ has good gain.

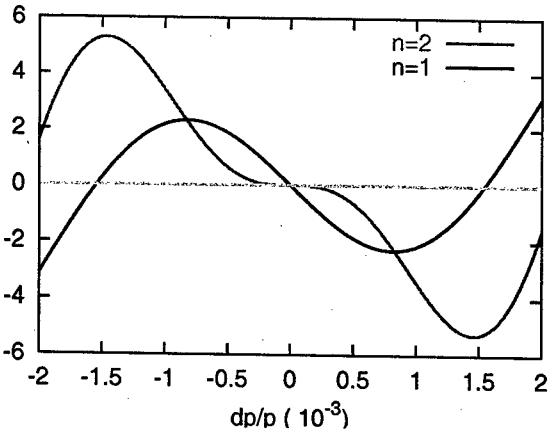

Figure 6: Plot of eq (6) with S_k from eq (8) for RHIC parameters. The vertical scale is in arbitrary units. For the horizontal scale $\Delta\omega/\omega_0 = -\eta dp/p$. For $n = 2$, the filter has good gain at the edge of the bucket.

4 ACKNOWLEDGEMENTS

Many thanks to Fritz Caspers of CERN for useful conversations and encouragement. This work would have been impossible without Dave Mcginnis and Ralph Pasquinelli of FNAL, who helped with both the hardware, and our understanding of how to use it. Finally, we acknowledge the dedication and expertise of the BNL instrumentation and RF groups.

5 REFERENCES

[1] J. Wei, A.G. Ruggiero, BNL/AD/RHIC-71 (1990).

[2] J.M. Brennan, M. Blaskiewicz, P. Cameron, J. Wei, 308, EPAC02

[3] G. Jackson, Workshop on Beam Cooling, Montreux, 1993, CERN 94-03, (1994).

[4] J.M. Brennan, Operation of the RHIC RF System, PAC03.

[5] D. McGinnis, J. Budlong, G. Jackson, J. Marriner, D. Poll, PAC01, p1389 (1991).

[6] M. Blaskiewicz, *et.al.* Longitudinal Solitons in RHIC, PAC03

[7] J. Wei, Workshop on Beam Cooling, Montreux, 1993, CERN 94-03, (1994).

[8] F. Sacherer CERN-ISR-TH/78-11 (1978).

[9] G. Carron, L. Thorndahl CERN-ISR-RF/78-12 (1978).

[10] D. Mohl, CERN 87-03, p 453 (1987).

ACCELERATOR PHYSICS CHALLENGES OF THE FS-SLICING UPGRADE AT THE ALS*

C. Steier†, E. Forest‡, L. Nadolski, H. Nishimura, D. Robin,
W. Wan, Y. Wu§, A. Zholents, LBNL, Berkeley, CA 94720, USA

Abstract

The goal of the Femtoslicing project at the ALS is to provide 100-200 fs long pulses of soft and hard x-rays with moderate flux and with a repetion rate of 10-40 kHz for experiments concerning ultrafast dynamics in solid state physics, chemistry and biology. The femtoslicing principle employs a femtosecond laser beam to interact resonantly (inverse FEL interaction) with the electron beam in the ALS. The induced energy spread over the femtosecond duration is converted to a transverse displacement by exploiting the dispersion of the storage ring. The displaced femtosecond electron pulse then radiates and produces femtosecond synchrotron radiation. To achieve the necessary spatial separation of the energy modulated slice from the rest of the bunch, a sizeable local vertical dispersion bump in the undulator used as radiator is required. This presents challenges in terms of the nonlinear dynamics and control of the vertical emittance.

INTRODUCTION

The ALS is a third generation synchrotron light source located at Lawrence Berkeley National Laboratory. It was originally designed to provide very bright VUV and soft x-ray beams and has been in operation since 1993. To generate short pulses of x-rays with durations of a few hundred femtoseconds, an innovative technique has been developed at the ALS [1]. This technique uses the interaction of an electron bunch with a femtosecond laser beam within a wiggler to energy-modulate (slice) a short section of that bunch. Using spatial or angular [2] dispersion downstream of the interaction with the laser one can then isolate fs x-ray pulses. Over the past years a science case has been developed to make use of this new source of x-rays. The proposed experiments make use of time resolved spectroscopic techniques (time resolved x-ray diffraction or time resolved x-ray absorption spectroscopy) and require higher average photon flux than can be delivered by the ALS bending magnet beamlines which were used for the demonstration experiments of the slicing technique. To increase the average flux of fs x-rays a plan for a new ultrafast x-ray undulator beamline has been developed. The beamline complex is now in its design and initial construction phase. A sketch of the main accelerator components of the new beamline is shown in Fig. 1.

The upgrade consists of several key components, including two new insertion devices (modulator and radiator), a new undulator beamline complex, a new laser system with significantly higher repetition rate and modifications to the storage ring to create the vertical dispersion bump used to spatially separate the sliced electrons/photons. One of the new insertion devices is a new wiggler which is simultaneously used for protein crystallography and as modulator for the slicing. It will have a shorter period (11.4 cm compared to 16 cm of the existing wiggler) to allow for optimized use both by the protein crystallographers and the slicing experiments by allowing slicing on its first instead of third harmonic at 1.9 GeV. The second insertion device will be an in-vacuum, permanent magnet undulator, similar to the ones used at Spring-8, ESRF and SLS. Since the photon energy range of the science covered by the new facility is very wide (about 200 eV to 10 keV), the new undulator will be used both as an undulator up to about 3-4 keV and as a wiggler up to 10 keV.

CHALLENGES

The accelerator physics efforts to support the new fs x-ray undulator beamline have been centered on three main areas: generating the vertical dispersion bump to provide the spatial separation to isolate the fs x-rays pulses, minimizing the vertical emittance and spurious dispersion [3], and studying insertion device related issues [4, 5]. Additional details about those studies can be found in the given references. This article summarizes all results.

The issues studied in connection with the insertion devices include - to just name some examples - their effect on the nonlinear dynamics, resistive wall heating effects, impedance issues and the effects caused by the field imperfections of the devices (coupling, focusing and orbit errors). Working together with the magnet group of the ALS, a set of specifications and a magnetic design for the new wiggler have been developed minimizing all detrimental impacts on the electron beam. For the in-vacuum undulator, the studies are in their final phase.

Beam Dynamics in Insertion Devices

One of the most dangerous effects insertion devices can have on the transverse single particle beam dynamics is the effect of the transverse field roll-off [6]. Since the particles follow undulating trajectories the nonlinear kick due to the transverse field roll-off can accumulate resulting in a potentially large reduction in dynamic aperture and dynamic

* This work was supported by the U.S. Department of Energy, under Contract No. DE-AC03-76SF00098.

† CSteier@lbl.gov

‡ Permanent Address: KEK, 1-1 Oho, Tsukuba, Ibaraki 305, Japan

§ Permanent Address: Duke University, Durham, NC27708, USA

0-7803-7738-9/03/$17.00 © 2003 IEEE

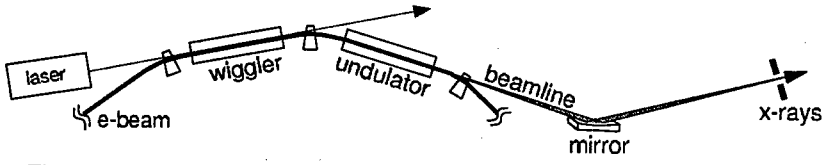

Figure 1: Sketch of fs-slicing layout for the new undulator beamline at the ALS.

momentum aperture. Since the (Touschek) lifetime at the ALS is already dominated by the transverse single particle dynamics (i.e. the dynamic momentum aperture [7]) this is a potentially very serious effect. Therefore it has been studied in extensive detail using 3 dimensional magnetic field models (TOSCA) of the chosen wiggler design, the fit of an analytical field model to this numerical field data and a new symplectic integrator [8]. Fig. 2 shows the results of one of the simulation runs. Shown are on-energy fequency maps in configuration space calculated by tracking particles with different initial conditions for 1000 turns. The color code indicates the diffusion rate on a logarithmic scale.

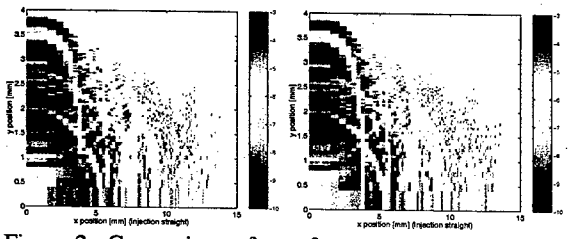

Figure 2: Comparison of two frequency maps in configuration space. W11 wiggler without any horizontal field roll-off (left) and with 125% of the nominal horizontal field roll-of (right).

The left plot shows the frequency map for a wiggler (11.4 cm period, 1.91 T field) without any horizontal field roll-off (i.e. the main effect in the tracking is the vertical tune shift from the wiggler). The right plot shows the case of a wiggler with mostly the same parameters but now a horizontal field roll-off is included (125% of the nominal field roll-off). As one can see, there is virtually no difference between the two frequency maps. The same was true in off-energy simulations. Therefore we are very confident that the field roll-off of the chosen design will not be an issue and the effects of the new wiggler on the beam dynamics will be completely dominated by its linear vertical tune shift (which is virtually identical to the one from the existing wiggler it replaces).

Separation

To separate the sliced beam from the main bunch, different techniques can be used. We decided to use vertical spatial separation with a closed vertical dispersion bump, since it allows the use of the radiator in wiggler mode and the use of dispersive spectroscopy in the beamline. Fig. 3 shows the vertical dispersion bump, which is generated as a closed bump with negligible coupling using four or eight skew quadrupole magnets. The main issue that has been studied in connection with the dispersion bump is the impact on the nonlinear dynamics of the ALS, particularly injection efficiency and lifetime.

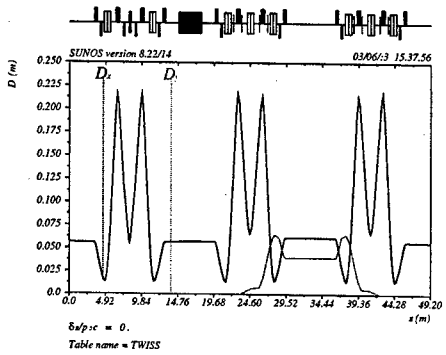

Figure 3: Layout of the closed vertical dispersion bump used to generate the necessary separation of the sliced bunch at the radiator. A total of four or eight skew quadrupoles is used.

A dispersion bump of sufficient amplitude has been demonstrated experimentally (see Fig. 4) and its impact on the momentum aperture was negligible. To generate the necessary skew quadrupole gradients, some magnets had to be modified and the effects of differential pole saturation was studied. No problems were found related to the about 1% reduction of the sextupole field of the combined sextupole/skew quadrupole magnets, caused by the strong skew quadrupole fields. The increase in vertical emittance caused by the dispersion bump was relatively modest (quantum excitation in the two bending magnets inside the bump) and agreed with calculations. However, in simulations we found one potential problem: the dispersion bump as we currently implement it generates a large local coupling inside the bump, which causes the (planned) small vertical aperture of the insertion device to be transformed into a moderate horizontal aperture, limiting the momentum aperture. This effect is currently under study and a solution using more (eight) skew quadrupoles to generate the dispersion bump while minimizing the local coupling angle looks very promising.

Coupling Correction

Minimizing the vertical emittance and spurious dispersion allows one to maximize the brightness of a synchrotron radiation source. Because the Touschek lifetime of a low emittance, low energy light source like the ALS is very short, reducing the vertical emittance below the op-

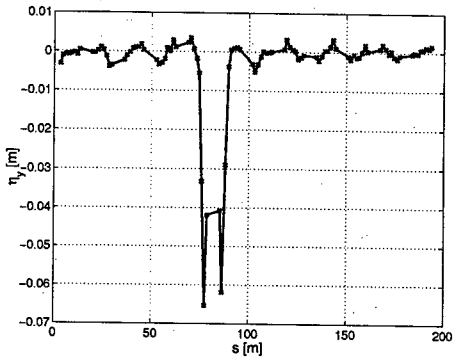

Figure 4: Measured vertical dispersion bump. The leakage of the bump was caused by a difference in saturation between the individual skew quadrupoles due to the additional orbit correction windings. Nevertheless, the leakage is already acceptable.

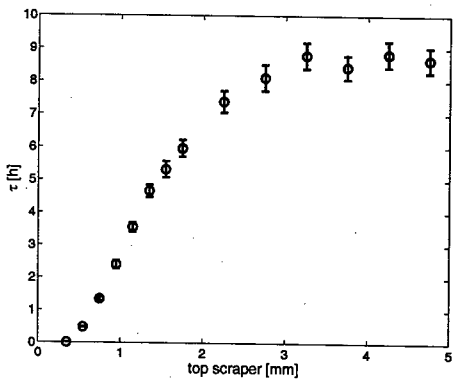

Figure 5: Lifetime of the ALS versus half aperture in one straight, measured using a scraper: The lifetime reduction for a lattice with corrected coupling and vertical dispersion wave to increase the vertical emittance is small down to a full vertical aperture of about 5 mm.

erational value of about 150 pm, which is used at the moment, would have reduced the lifetime to unacceptable values (below 8 hours at 400 mA). For the future, this situation will change with the use of top-up injection. The new fs beamline on the other hand will directly create vertical emittance because of the fairly strong insertion device inside the vertical dispersion bump. Therefore it will be important to minimize the baseline vertical emittance without the dispersion bump. Using 18 individual skew quadrupole magnets, whose power supplies have been installed last year, vertical emittances of about 5 pm have been demonstrated (an improvement of a factor of 30 compared to the current operating condition) [3]. This will allow the new beamline to operate with an optimized size of the vertical dispersion bump maximizing the femtosecond x-ray signal to noise ratio for a given brightness (vertical emittance) for all other beamlines.

Impact of Vertical Aperture on Lifetime

For permanent magnet as well as for superconducting insertion devices the possible performance depends strongly on the possible minimum gap of the magnetic structure. Therefore it is important to determine the minimum physical vertical aperture which can be tolerated with respect to beam lifetime and injection efficiency. At the ALS the limit used to be a full vertical aperture of about 8 mm. With an improved lattice, better correction of the lattice symmetry and especially better control of coupling it was possible to reduce this limit to a full aperture of about 5 mm [5]. This was verified by measurements using a scraper at the ALS. Fig. 5 shows a scraper measurement in the ALS with corrected coupling and the vertical emittance increased to its current nominal value of 150 pm by using a vertical dispersion wave. The lifetime reduction in those conditions is fairly small down to a full vertical aperture of about 5 mm.

SUMMARY

A new undulator beamline for femtosecond x-rays is under design and consruction at the ALS. It will start with beamline commissioning at the end of 2004 or early in 2005. The accelerator physics issues associated with the new facility have been successfully studied. The dynamics in the insertion devices (especially the effects of the transverse field roll-off of the wiggler) has been studied extensively and no problems were found. A vertical dispersion bump for spatial separation of the fs x-rays has been demonstrated with more than sufficient amplitude (4 cm) and minimal negative impact. Methods for vertical emittance and dispersion control have been established, achieving much better results than necessary. The impact of small gaps (5 mm full gap) on lifetime and injection efficiency have been studied with positive results. The main remaining issue is the interaction between the narrow vertical aperture in the radiator and the vertical dispersion bump. A solution using 8 instead of 4 skew quadrupoles to minimize the local coupling for a fixed vertical dispersion works in simulations. A measurement program to test this in detail will start in June.

REFERENCES

[1] Zholents and Zolotorev, Phys. Rev. Lett., 76, 916,1996.

[2] S. Khan et al., Layout of a Femtosecond X-Ray Source at BESSY II, these proceedings.

[3] C. Steier et al., Coupling correction and Beam Dynamics at Ultralow Vertical Emittance in the ALS, these proceedings.

[4] W. Wan et al., ID Modeling at the ALS, these proceedings.

[5] D. Robin et al., Impact of Narrow Gap Chambers on the Lifetime at the ALS, these proceedings.

[6] J. Safranek et al., Phys. Rev. STAB 5, 010701 (2002).

[7] C. Steier et al., Phys. Rev. E 65, 056506 (2002).

[8] Y. Wu et al., Proceedings of PAC 2001, Chicago, USA, 459 (2001).

HEAVY-ION BEAM DYNAMICS IN THE RARE ISOTOPE ACCELERATOR FACILITY *

P.N. Ostroumov#, Physics Division, Argonne National Laboratory, 9700 S. Cass Avenue, Argonne, IL, 60439, USA

Abstract

Recently the possibility of simulteniously accelerating particles with a range of charge-to-mass ratios (~20%) to the same energy was proposed and demonstrated for a superconducting (SC) linac [1]. This development has two immediate applications: 1) acceleration of heavy ions that are limited by ion-source intensities in a high-power medium energy linac such as the driver linac for the proposed Rare-Isotope Accelerator (RIA) Facility and 2) substantial intensity enhancement of secondary radioactive beams in post-accelerators.

ACCELERATION OF MULTIPLE-CHARGE STATE HEAVY-ION BEAMS

The concept of multiple charge state (multi-q) beam acceleration can enhance the utility of high-intensity linacs for heavy ions where the ions may have to be stripped repeatedly to make optimal use of the accelerating voltage. Such linacs are being considered for major facilities for nuclear physics research [2]. For example, accelerating ^{238}U to 400 MeV/u will require two or three stages of stripping. If only one charge state were accepted after each stripping, the intensity at each stage would be reduced by a factor of ~5 and the maximum beam power would be available ≈4.6 kW with present ion source performance. A scheme where essentially all the charge states can be accelerated delivers ~80% of the beam thus providing up 56 kW at the desired final energy. In addition, it was shown that the front end of a SC linac can be designed to accept two charge states of heavy-ion beam from the ECR ion source, doubling the available beam power [3].

A comprehensive study of multi-q beam dynamics in SC linacs has been reported in ref. [4]. The simultaneous acceleration of neighboring charge states becomes possible because the high charge-to-mass ratio makes the required phase offsets of the synchronous particles small:

$$\varphi_{s,q_i} = -\arccos\left[\frac{q_0}{q_i}\times\cos\varphi_{s,q_0}\right], \qquad (1)$$

where q_0 is the reference charge state with corresponding synchronous phase $\varphi_{s,q0}$, the sub-index i corresponds to the neighboring charge state with the same mass number A. For the best matching, bunches with different charge states must be injected into the linac at slightly different rf phases. The higher the charge state, the sooner it must arrive at the SC resonator to be matched. For most applications, relatively few charge states need to be accelerated simultaneously. Therefore the differences in the matched synchronous phases are just a few degrees and time matching system is not necessary. If all charge states are injected at the same time (at the same rf phase), then each charge state bunch will perform coherent synchrotron oscillations with respect to q_0. One can view this as an increase in the effective longitudinal emittance of the total beam, relative to the (partial) longitudinal emittance of the individual charge state bunches.

The spread in charge states that can be accepted for acceleration depends primarily on the extent that the focusing system can limit emittance growth in transverse phase space. In high intensity linacs, the tolerable emittance growth is set by the intensity of lost energetic ions that can produce residual activation of the accelerator components. Therefore, in heavy-ion linacs at low intensity or low energy, a wide range of Δq/q, about ±10%, can be accepted and accelerated. However in high intensity (~10^{13} ions/s) and medium energy (~400 MeV/u) machines, the tolerable spread of charge states is lower, ~±3 %. In radioactive linacs the limitation for the range of Δq/q is imposed by an acceptable beam quality.

Standard periodic focusing theory can be used to analyze the simultaneous acceleration of the several charge states. Our studies show that effective transverse emittance growth of multi-q beams is caused by slightly mismatched conditions for different charge states in the periodic focusing channel and misaligned focusing elements. This effect restricts the tolerable charge spread in the linac.

A test of this concept with uranium beams was performed at the 50 MV SC linear accelerator at Argonne National Laboratory (the ATLAS accelerator). Uranium ions, stripped in a foil, with 8 charge states (Δq/q ≈20%) have been accelerated through a portion of the ATLAS linac from 286 MeV to 690 MeV, with 94% of the injected uranium in the accelerated beam. Emittance of the resultant beam has been measured and the energy spread was 1.3% compared to 0.4% for a single charge state [1]. As is shown in this paper multi-q beam parameters can be significantly improved by careful design of the accelerator components.

THE RIA DRIVER LINAC

The RIA is being considered as a major nuclear science facility for the near future. A cw SC 1.4 GV driver linac and 120 MV post-accelerator are being designed for the RIA Facility. A conceptual design of the driver linac has been developed (see, for example, [5,6]), the major elements of which are shown in Fig. 1. Except for the injector radio frequency quadrupole (RFQ), the entire linac is based on SC accelerating structures. The "baseline" driver linac design consists of ~400 SC cavities

* Work supported by the U. S. Department of Energy under contract W-31-109-ENG-38.
#ostroumov@phy.anl.gov

0-7803-7738-9/03/$17.00 © 2003 IEEE

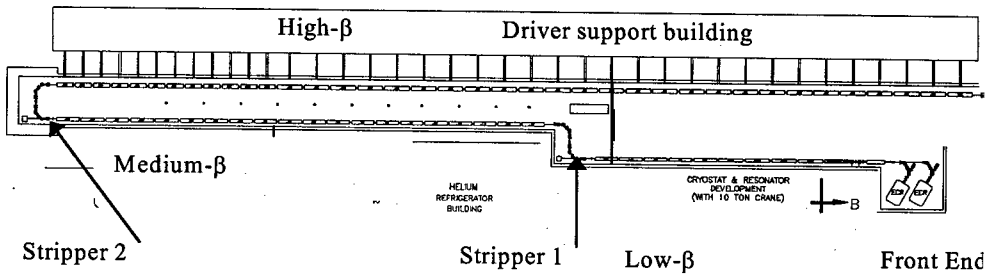

Figure 1: Elements of the proposed RIA driver linac.

of 9 different types. The majority of the cavities (98%) fall into 7 different types. Recently we have developed a variation of the driver linac based on triple-spoke SC resonators being designed at ANL [5]. This option reduces total number of cavities to ~350 with fewer types of the SC resonators.

The driver linac can be tuned to provide a uranium beam at an energy of 400 MeV/u and can be re-tuned to provide a proton beam at 900 MeV. To obtain 400 MeV/u uranium beams the driver linac uses two strippers. Three different sections of the linac are demarked by the charge-strippers. The low-β section of the linac is that portion prior to the first stripper, the medium-β section is between the two strippers, and the high-β section is that portion following the second stripper. The low-β section includes a front end with the possibility to accept for acceleration two charge states simultaneously and a SC linac up to ~10 MeV/u for uranium. The medium-β and high-β sections are designed for acceleration of multi-q beams. After each stripper, there is a magnetic transport system (MTS) [7] which provides six-dimensional matching of multiple-q beams into the following accelerating structure. In addition, the MTS is designed to separate and dump the low-intensity unwanted charge states in order to avoid beam losses in the high-energy section of the driver linac.

The driver linac is a high intensity machine and relative beam losses in the high-energy section must be kept below 10^{-4}. Acceleration of multi-q uranium beams places stringent requirements on the linac design. Any other lighter ion beam with much smaller emittances can be accelerated with no losses. End-to-end beam dynamics simulations in six-dimensional phase space have been applied to study all possible sources of beam halo formation and possible beam loss in the driver linac. Major contributors to the effective emittance growth were identified as: a) multiplicity of charge states; b) passage through the stripping foils and c) random errors of rf fields and misalignments of focusing elements. We have developed the concept of a "beam-loss-free" linac which implies beam halo collimation in designated areas.

Front End of the Driver Linac

The front end of the RIA driver linac is shown schematically in Fig. 2. It consists of two ECR ion sources, a low energy beam transport (LEBT), a multi-harmonic buncher, a 57.5 MHz RFQ, and, finally, a medium energy beam transport (MEBT) which matches beam into the superconducting linac.

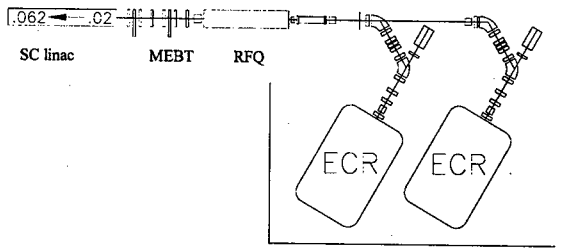

Figure 2: Front End of the RIA driver linac.

An ECR type of source is well matched to the requirement for cw, high-charge-state ion beams over the full mass range. The heaviest beam needed for the RIA driver is uranium, which is the most demanding in terms of ion source performance. The LEBT is designed to select and separate the required ion species and to bunch and match either one or two charge states of ions with masses above 180 into the following RFQ structure [8].

The primary design goal for the RFQ is to establish a low output emittance so that the acceleration of multiple-charge-state beams through the rest of the linac becomes straightforward. As was discussed in our previous work [3], a multi-harmonic buncher must be used upstream of the RFQ to produce the lowest possible longitudinal emittance of two-charge-state beams. The acceleration starts with a small separatrix whose length is kept constant along the RFQ. For the parameters of the RFQ given in ref. [9] the longitudinal emittance at the level 99.9% is less than 2 π·keV/u-nsec for the two-charge-state uranium beam.

Accelerating-Focusing Lattice of the SC linac

The baseline design of the driver linac was described in ref. [10]. Below we present the results of beam dynamics studies for the latest version of the driver linac design which includes the following main modifications: 1) peak surface electric field in all drift-tube SC resonators is assumed to be 20 MV/m except the first seven 4-gap quarter wave resonators; 2) the high-β section of the

driver linac contains two types of triple-spoke resonators [5] instead of three types of elliptical resonators operating at a peak electric field 27.5 MV/m.

The linac comprises 352 SC cavities distributed in 68 cryostat modules. Except for the first cryostat which contains seven 4-gap resonators and one 2-gap resonator, the linac consists of 6 different types of cryostats filled by five different types of resonators. Fundamental frequency is 57.5 MHz and the linac comprises SC resonators operating at the 1st, 2nd, 3rd and 6th harmonics. Transverse focussing is provided by SC solenoids contained in the same cryostat modules as the cavities. Such an array, with the cavities operated at a synchronous phase φ_S=-30°, provides strong focussing in both transverse and longitudinal phase space. Due to the strong damping of the bunch phase width as beam energy is increased, some sections of the linac can be set at a synchronous phase φ_S =-25°.

Beam Dynamics Simulations

Beam dynamics studies have been performed with the goal of optimizing the linac structure in order to reduce possible effective emittance growth of the multi-q uranium beam. The end-to-end simulation of beam dynamics is being performed by the TRACK code [11] which integrates the particle equations of motion through the electric and magnetic fields of the SC cavities, the 3D field components having been obtained from numerical solution of Maxwell's equations for each specified cavity geometry. The motion of the particles is traced in 6D phase space, and generally represents the dynamics of the multi-component heavy-ion beams with good spatial resolution. After recent modifications the TRACK code supports all elements of the driver linac such as RFQ, multi-harmonic buncher, bending magnets, magnetic and electrostatic focusing devices. All TRACK elements are represented with realistic three-dimensional field distributions which naturally include fringe fields.

Prior to numerical ray-tracing of mutli-q beam through the linac, the rms transverse and longitudinal beam parameters were matched carefully using fitting codes for a trial beam. A particularly critical aspect of fitting was to avoid beam mismatch at the transitions between focusing periods of differing length and between the cryostats. Note that the focusing lattice length is different for each of the four types of SC cavities. Final adjustment of the longitudinal matching is done by setting appropriate value of synchronous phase. The first-order design of the linac is done by the TRACE-3D code. Beam transport codes such as TRANSPORT, GIOS and COSY were used for the design of multi-q beam transitions and switchyard [3,7,8]. Comparative beam dynamics studies in the high-β section of the RIA driver linac have been performed for two types of accelerating structures: elliptical cavities as in the baseline proposal and triple-spoke cavities.

The simulation starts from the exit of the ECR HV platform. The multi-component heavy-ion beam is transported through the achromatic charge-selection system and accelerated by the RFQ (see Fig. 2). In these simulations, 10^6 particles remaining after the RFQ represent a two-charge state uranium beam in the low-β section, five charge states in the medium-β and four charge states in the high-β section. The envelope of a beam containing 10^6 particles along the SC section of the linac is shown in Fig. 3. The beam is axially-symmetric along the linac but not in the post-stripper MTS. The passage through the strippers was simulated by the SRIM code [12] and the calculated particle distribution was incorporated into TRACK.

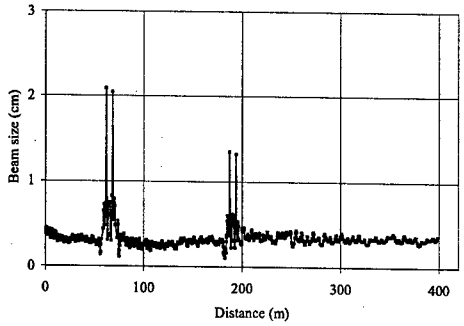

Figure 3: Maximum size of the beam presented by 10^6 particles in the horizontal plane along the driver linac.

For the safety margin, in simulations we have assumed that the standard deviation of the energy straggling is 5 times larger than the value predicted by the SRIM code. This large safety factor is appropriate due to the lack of trustable experimental data for the stripping energy ~85 MeV/u of uranium ions. Table 1 shows the rms and total normalized emittance growth in the driver linac.

Table 1. Rms and total (100% of particles) emittance growth factor in the driver linac.

No errors			
	Horizontal	Vertical	Longitudinal
Rms	1.5	1.5	4.9
Total	4.8	4.9	35
With errors			
Rms	1.8	1.9	9.5
Total	5.8	6.8	35

All errors are randomly generated as a uniform distribution with the rms values given in ref. [9]. The sensitivity of multi-q beam parameters to various types of random errors and misalignments were studied by the ray-tracing code TRACK. The most important errors affecting transverse beam motion are the misalignments of the transverse focusing elements. Due to the strong defocusing of low velocity particles by the SC cavities the misalignments of the SC cavities were also taken into account. Phase and amplitude errors of the rf field are fast fluctuations and produce effective longitudinal emittance growth of multi-q beams. Monte Carlo simulations of the dynamics of multi-q beams in the presence of both accelerating field and alignment errors have been performed. We introduced alignment errors by displacing

separately both ends of each solenoid and SC cavity in both X and Y directions. Then we tracked the multi-q beam represented by 10^4 particles through the whole linac and noted the increase in emittance resulting from all types of errors. As was discussed in ref. [4] a multi-q beam requires frequent corrective steering in order to avoid appreciable emittance growth. Therefore, our simulation was done in the presence of steering elements along the linac. This entire simulation was then repeated two hundred times, each time with a different, random set of errors. These studies show that in the worse case both transverse and longitudinal total emittances are well within the linac acceptance. No particle losses along the linac were observed.

Phase space plots obtained during 200 seeds are accumulated and shown in Fig. 4. As is seen the multi-q uranium beam can be accelerated up to 400 MeV/u within ±0.25% energy spread and remains within ±40 psec time width. A longitudinal emittance of 80 π·keV/u-nsec contains all particles shown in Fig. 4.

Recently independent beam dynamics studies of the driver linac for the RIA have been performed at MSU (see, for example, [13]). These studies confirmed all basic concepts for the design of high-intensity SC linacs with the capability to accelerate multi-q beams originally discussed in ref. [1-11].

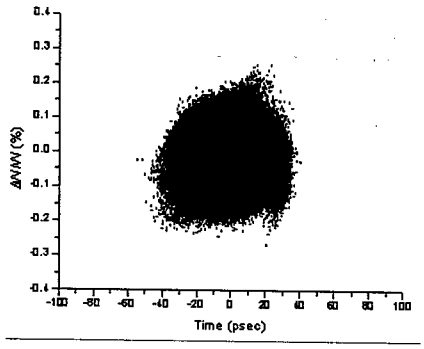

Figure 4: Phase space plots of a four charge state uranium beam at the exit of the driver linac.

POST-ACCELERATORS

The ability to accelerate multi-q radioactive beams (RIB) is especially valuable due to the extremely low intensities of secondary particles. In addition, the intensity of the RIB drops after the strippers which are necessary to reduce the total accelerating voltage. The post-stripper section of the RIA post-accelerator will be designed for the acceleration of multi-q beams to enhance the available beam intensities for experiments. As it was shown in [1] a wide range of the charge spread Δq/q, about 20%, can be accepted and accelerated in the ATLAS accelerator. In the design of the RIA post-accelerator we have restricted the possible range of Δq/q to ≤11% in order to avoid a phase space emittance halo. As a consequence of multi-q acceleration the total acceleration efficiency is significantly higher than for single charge-state beams, as shown in Fig. 5. The RIB linac of the RIA Facility [14] will produce beam intensities higher by a factor of ~20 as compared with post-accelerators based on an ECR charge breeder. As it follows from beam measurements in ATLAS, the transverse and longitudinal emittances of multi-q beams will be larger by a factor of ~3 for the charge spread Δq/q=20% [1]. The RIA post-accelerator based on ATLAS will provide better beam quality because the charge spread will be restricted to Δq/q <11%.

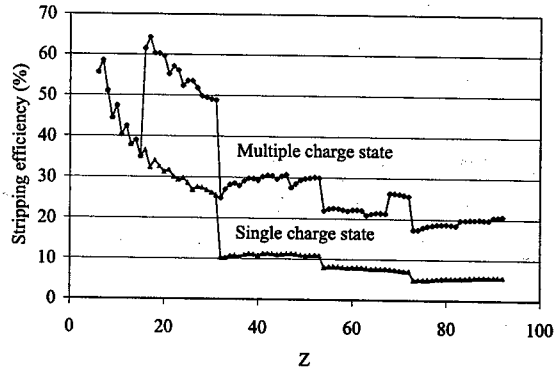

Figure 5: RIB linac overall stripping efficiency in the regime of single and multi-q beam acceleration.

The first RIB linac purposely designed for the multi-q heavy-ion beam acceleration will be commissioned soon at TRIUMF [15]. The project ISAC-II is well advanced and the first stage of the post-accelerator consisting of ~ 20 MV of accelerating voltage is planned for commissioning by April 2005.

The EUROSOL project has been discussed during last several years extensively (see, for example, [16]). The project calls for a 100 MeV/u post-accelerator with multi-q acceleration feature. The latter significantly reduces the required total voltage for acceleration of the heaviest ^{132}Sn ions and provides almost complete transmission after two stripping stages.

Multi-q beam acceptance from charge-breeder

There are wide discussions and proposals to use ECR charge-breeders to produce higher charge state RIBs at very low velocities before the injection into the RFQ or other resonant accelerating structures. For example, this configuration is accepted as a baseline design for the ISAC-II [15] and EUROSOL [16]. A technique to accept two charge states of stable ions from the ECR and accelerate them simultaneously in an RFQ has been reported in ref. [3]. Similar technique can be applied to accept two or three charge states from the charge-breeder of radioactive ions. Figure 6 shows an injector configuration which can accept three charge states from the charge-breeder and accelerate them in the RFQ. In this particular example the RFQ has similar parameters as the ISAC-I RFQ operating at 35 MHz and accelerating ions with minimum charge-to-mass ratio 1/30 from 2 keV/u to 150 keV/u [17]. Two bending magnets 2 and two electrostatic quadrupoles 3 are tuned to provide an

achromatic bend of three charge states. The multi-

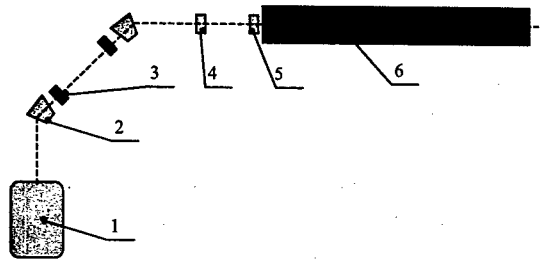

Figure 6: Schematic layout of the multi-q RIB injector. Legend: 1 – charge breeder; 2 – 45° bending magnet; 3 – electrostatic quadrupole; 4 – multi-harmonic buncher; 5 – resonator, 6 – 35 MHz RFQ.

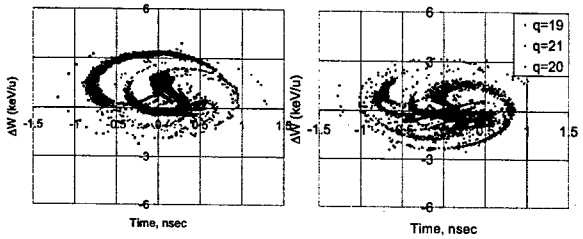

Figure 7: Phase space plots of three-charge-state gold beam at the exit of the RFQ.

harmonic buncher (MHB) 4 operating at fundamental frequency 35/3 MHz modulates ion velocities of three neighbouring charge states. Over the drift space from the MHB 4 and following resonator 5 the distance between the bunches of charge states q-1, q and q+1 becomes equal to 120° at the fundamental frequency. Therefore in the RFQ, each charge state occupies its own bucket. The resonator 5, operating at the fundamental frequency, serves as a velocity equalizer (VE). It does not change the velocity of the ion with central charge state q but equalizes velocities of ions with charge states q-1 and q+1. The straight section of the LEBT upstream of the RFQ is filled by the focusing elements which provide matching to the RFQ acceptance.

As an example, we have designed the injector and simulated a ^{200}Au ion beam with charge states 19,20,21 from the ECR source to the end of the RFQ. If beam matching is done carefully there is no transverse emittance growth of a three-charge-state beam.

Acceleration of a three-charge-state beam can be done with and without the VE. Using the VE one can get lower longitudinal emittance of multi-q beam. However the energy acceptance of the RFQ is large and three- charge-state beams can be accelerated without any VE with the same efficiency 89% as for the single-charge-state beam. Table 2 shows the longitudinal rms emittance for three regimes of the injector operation: acceleration of a single charge state and 3 charge state acceleration with and without the VE. Figure 7 shows phase space plots for a three-charge-state beam without the VE (the left plots) and with the VE (the right plots). As is clear the velocity equalizer helps to produce brighter beam in the longitudinal phase space and reduces rms emittance of the accelerated multi-q beam.

Table 2. Longitudinal rms emittance at the exit of the RFQ (π·keV/u-nsec)

Single q	3-q with VE	3-q without VE
0.16	0.35	0.63

CONCLUSION

The capabilities of SC linacs to accelerate intense heavy-ion beams can be substantially improved by the multiple-charge-state beam acceleration. These results have important implications for the proposed RIA facility for short-lived beams of nuclei. The technique is widely accepted by accelerator physicists worldwide and a number of heavy-ion linacs are being designed with multi-q beam accelerating capability.

REFERENCES

[1] P.N. Ostroumov, R.C. Pardo, G.P. Zinkann, K.W. Shepard and J.A. Nolen., Physical Review Letters, 86, N 13, 26 March 2001, p. 2798-2801 (2001).
[2] K. W. Shepard et al., in the Proc. of the 9th Inter. Workshop on RF Superconductivity, Santa Fe, New Mexico, p. 345.
[3] P.N. Ostroumov, K. W. Shepard, V.N. Aseev and A.A. Kolomiets, Proc of the 2000 Linac Conf., Monterey, August 2000, SLAC–R-561, p. 202.
[4] P.N. Ostroumov and K. W. Shepard, Phys. Rev. ST Accel. Beams **3**, 030101 (2000).
[5] K. W. Shepard, Paper ROPA003 at this conference.
[6] J.A. Nolen, Paper MO302 presented at LINAC 2002, Gyeongju, Korea, August 2002. http://linac2002.postech.ac.kr/db/proceeding.
[7] M. Portillo, V.N. Aseev, J.A. Nolen and P.N. Ostroumov, Proc. the 2001 PAC, June 2001, Chicago, IL, p. 3012.
[8] A.A. Kolomiets, P.N. Ostroumov, V.N. Aseev and R.C. Pardo. Paper RPAB068 at this conference.
[9] P.N. Ostroumov et al., Phys. Rev. ST Accel. Beams **5**, 060101 (2002).
[10] P. N. Ostroumov. Phys. Rev. ST. Accel. Beams **5**, 030101 (2002).
[11] P. N. Ostroumov and K. W. Shepard, Phys. Rev. ST. Accel. Beams **11**, 030101 (2001).
[12] J.F. Ziegler, J.P. Biersack and U. Littmark, The Stopping and Range of Ions and Solids, Pergamon Press, NY, 1996.
[13] D. Gorelov et al. Proc. Of the EPAC 2002, Paris, 2002, p. 900.
[14] R. Laxdal. Paper ROPA010 at this conference.
[15] P.N. Ostroumov, et al. NIM, Section B, **204**, (May 2003), p. 433.
[16] http://www.ganil.fr/eurisol/
[17] L. Root. TRIUMF Design Report TRI-DN-96-9, April 1996.

SPIN DYNAMICS IN AGS AND RHIC*

W. W. MacKay†, L. Ahrens, M. Bai, K. Brown, E. D. Courant, J. W. Glenn, H. Huang,
A. U. Luccio, V. Ptitsyn, T. Roser, T. Satogata, S. Tepikian, N. Tsoupas, and A. N. Zelenski
BNL, Upton, NY 11973, USA.

Abstract

A fundamental aspect of particle physics is the spin of the particles. With polarized beams, the internal structure of the proton may be probed in ways that are unattainable with unpolarized beams. The Relativistic Heavy Ion Collider (RHIC) has the unique capability of colliding protons with both transverse and longitudinal polarization at center-of-mass energies up to 500 GeV. In this paper we examine the methods used to accelerate and manipulate polarized proton beams in RHIC and its injectors. Special techniques include the use of a partial Siberian snake and an ac dipole in the AGS. In RHIC we use four superconducting helical Siberian snakes (two per ring) for acceleration, and eight superconducting helical rotators for independent control of polarization directions at two interaction regions.

INTRODUCTION

The RHIC collider has been described in detail elsewhere[1], but it is worth noting (see Fig.1) the particular components used for spin control.

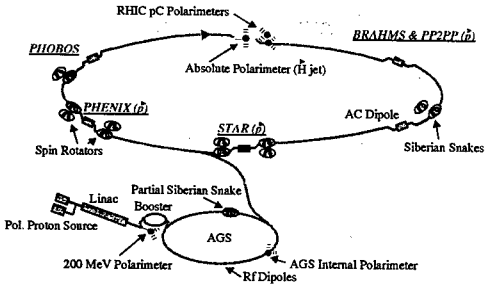

Figure 1: The accelerator complex for polarized protons. The beam in the RHIC Blue ring goes clockwise and in the Yellow ring counterclockwise.

An H^- beam with polarized protons is produced by the optically pumped polarized ion source (OPPIS). The H^- beam is accelerated in the RFQ and linac to 200 MeV ($\gamma = 1.21$). The beam is then stripped on injection to the Booster and accelerated to 2.46 GeV ($\gamma = 2.62$). Acceleration continues in the AGS up to 24.3 GeV ($\gamma = 25.94$) followed by transfer into either of the RHIC rings. There are several polarimeters to measure the polarization at various stages: one at the source, another at the end of the linac, a p+C CNI (Coulomb Nuclear Interference) polarimeters in the AGS and and each RHIC ring, as well as local polarimeters at the STAR and PHENIX detectors. There is a partial Siberian snake in the AGS and a pair of full Siberian snakes in each of the RHIC ring. Around each of the STAR and PHENIX detectors are four rotators as shown to manipulate the polarization direction through the experiment. There is an rf dipole magnet in the AGS to aid in spin resonance crossing. RHIC has an additional ac dipole which will be used for spin flipping. A hydrogen jet polarimeter is presently under construction and will provide in the future an absolute calibration of the CNI polarimeters in RHIC.

* Work performed under the auspices of the U. S. Department of Energy (contract # DE-ACO2-98CH10886) and RIKEN of Japan.

† waldo@bnl.gov

SPIN PRECESSION AND DYNAMICS

In the local rest frame of the proton, the spin precession of the proton obeys the Thomas-Frenkel equation:[2]

$$\frac{d\vec{S}^\diamond}{dt} = \frac{q}{\gamma m}\vec{S}^\diamond \times \left[(1+G\gamma)\vec{B}_\perp + (1+G)\vec{B}_\parallel + \left(G\gamma + \frac{\gamma}{\gamma+1}\right)\frac{\vec{E}\times\vec{v}}{c^2}\right]. \quad (1)$$

This is a mixed description with t, $\vec{B}$, and $\vec{E}$ in the lab frame, but having the spin $\vec{S}^\diamond$ in local rest frame of the proton where the spatial components of $\vec{S}^\diamond$ do not suffer the Lorentz lengthening of $S_\parallel$ when boosted to the lab frame. Here the anomalous g-factor of the magnetic moment for the proton is

$$G = \frac{g-2}{2} = 1.7928. \quad (2)$$

If we consider the simple case of an idealized particle with a flat closed orbit and spin-component in the horizontal plane and only vertical magnetic fields, Eq. 1 simplifies to

$$\frac{d\vec{S}^\diamond}{dt} = \frac{q}{\gamma m}\vec{S}^\diamond \times \left[(1+G\gamma)\vec{B}_\perp\right]. \quad (3)$$

$$\frac{d\vec{p}}{dt} = \frac{q}{\gamma m}\vec{p} \times \vec{B}_\perp. \quad (4)$$

is the Lorentz force for comparison. In this case the spin component precesses a factor of $1 + G\gamma$ times faster than particle's velocity. A spin tune ν_s can be defined the number of precessions of the spin in the particle's rest frame per turn (see Fig. 2a). In this case $\nu_s = G\gamma$. It should be noted that for a simple ring ν_s is proportional to energy.

A radial field component causing a vertical deflection of the particle by an angle α will cause the spin to precess about the radial direction by an angle $(1 + G\gamma)\alpha$. Since rotations about different axes do not commute, such vertical excursions can modify the amount of precession and the

0-7803-7738-9/03/$17.00 © 2003 IEEE

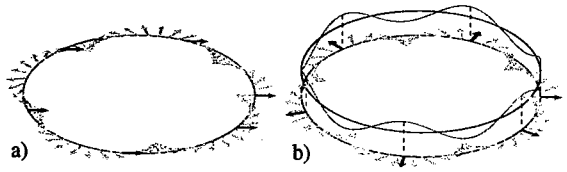

Figure 2: a) Conceptual plot of spin precession of the horizontal spin component for a spin tune of $\nu_s = 4.5$. b) Conceptual example of the intrinsic resonance $Q_v = \nu_s = 5.5$.

spin tune. In addition the local axis about which the spins precess may move away from the vertical.

Integer (imperfection) resonances which are caused by misalignments of magnets can be quite strong and may flip the direction of polarization as the energy is ramped. For protons the energy separation of the imperfection resonances is 523 MeV.

The deflections of the vertical betatron oscillation also cause vertical precessions which can build up when the spin tune matches the vertical betatron tune Q_v. (See Fig. 2b.) This type of resonance is called an intrinsic resonance. Clearly there can be coupling resonances where the horizontal tune comes into play, and in electron rings with large synchrotron oscillations, there are even synchrotron sidebands. For the most common resonances (intrinsic and imperfection) the resonance condition may be written as

$$\nu_s = N + N_v Q_v, \tag{5}$$

where N and N_v are integers.

Invariant spin field

For the usual six dimensional phase space we have a closed orbit with the periodicity condition $\vec{q}_0(s + L) = \vec{q}_0(s)$ where L is the circumference of the ring, and the subscript zero indicates the closed-orbit trajectory. For the closed orbit, we can calculate a stable spin direction $\hat{n}_0(s) = \hat{n}_0(s + L)$. Other particles which are not on the closed orbit see different fields on every turn so that the amount of spin precession and direction will vary from turn to turn. For reasonable conditions we can still find a periodic condition for different locations in phase space, if we treat stable spin direction $\hat{n}(\vec{q}, \vec{p}, s)$ as a field associated with a point in phase space rather than being attached to individual particles.[3] For a given ensemble of particles the maximum possible polarization can not be more than the ensemble average of the spin field, although it may be less than this value. The individual particles may have spins which are not pointing in the direction of the corresponding $\hat{n}$-vector. Away from spin resonances the spin field vectors will be pointing in roughly the same direction, but near a resonance they can deviate quite wildly. Even though the polarization average of the ensemble may drop to zero near a resonance, the average may recover a nonzero value later when moving away from the resonance. In contrast to protons, electrons will lose this memory of polarization very quickly due to radiation effects.

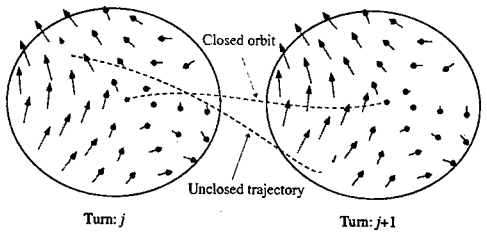

Figure 3: Illustration of the invariant spin field. For the closed orbit $\vec{n}_0(s) = \vec{n}_0(s + L)$, with coordinates $\vec{q}_0(s) = \vec{q}_0(s + L)$ and polarization direction $\vec{P}_0(s) = \vec{P}_0(s + L)$. For other locations in phase space: $\vec{n}(\vec{q}, \vec{p}, s) = \vec{n}(\vec{q}, \vec{p}, s + L)$, even though in general $q(s + L) \neq q(s)$ and $\vec{P}(s + L) \neq \vec{P}(s)$.

THE REAL MACHINES

The linac provides a beam with about 70% polarization. In the Booster ($G\gamma$ from 2.18 to 4.7), we cross two imperfection resonances by actually increasing the vertical closed orbit distortion to cause two total spin flips. We extract just below the first intrinsic resonance $\nu_s = Q_v = 4.9$.

In the AGS with a more complicated resonance structure; the acceleration goes from $G\gamma = 4.7$ up to 46.5. Here we use a partial solenoidal snake to cause a larger lattice disturbance with a rotation of the spin about the longitudinal axis (see Eq. 1) and enhance spin flipping at the imperfection resonances. A single partial snake in the ring will open up stop bands in the spin tune at the integer as shown in Fig. 4a. Since a partial snake will tilt the stable spin direction away from the vertical, in the AGS we inject with the snake essentially off and then ramp it up to about 5% (9° of rotation) for the ramp. At flattop, the snake is ramped down to about 0.3% (essentially off) for extraction to RHIC. With a single full snake in a ring the fractional part of ν_s will be $\frac{1}{2}$, and we could expect the imperfection resonances go away. With a single full snake, the stable spin direction is in the horizontal plane which makes it difficult to match polarization from one ring to the next. As we increase energy, more precessions happen in the space between snake crossings, and the deleterious effects still build up, so that at RHIC energies up to $G\gamma = 478$ (250 GeV) a single snake would not be enough to maintain a reasonable amount of polarization. Higher energies require more snakes.

In RHIC we typically inject and ramp with two full snakes on opposite sides of the rings (see Fig. 4b). Here the stable spin direction is vertical outside the snakes; a spin-up bunch in one half of the flips over at a snake to point down in the other half of the ring and flips back to up in the second snake.

The Froissart-Stora formula[4] gives the ratio of final to

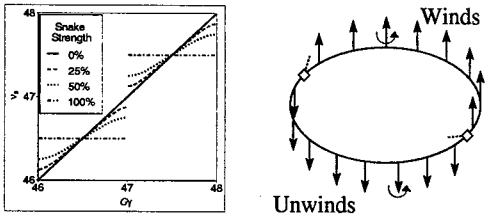

Figure 4: a) A single partial snake in a ring opens up stop bands for the spin tune. The percentage refers to the amount of spin rotation from the snake: 100% corresponds to 180° of rotation. b) With two full snakes on opposite sides of the ring that have rotation axes perpendicular to each other the stable direction spin will be vertically up in one half of the ring and down in the other half, and the spin tune will be 0.5.

initial polarization for an isolated resonance crossing:

$$\frac{P_f}{P_i} = 2\exp\left(-\frac{\pi|\epsilon|^2}{2\alpha}\right) - 1, \qquad (6)$$

where $\alpha = dG\gamma/d\theta$ is the ramp rate in units of $G\gamma$ per radian of bend around the ring, and ϵ is the resonance strength of the vertical oscillation or Fourier amplitude of the driving component. For a large resonance strength, the spin can essentially completely flip over. Relative intrinsic resonance strengths for the AGS are shown in Fig. 5.

Fig. 6 shows a simulation of an interesting region of the energy ramp with two imperfection crossings, an intrinsic crossing, and a small coupling resonance. An ac dipole can be made to vertically shake the beam near the betatron tune line, so that large amplitude oscillations will enhance the spin resonance thus inducing more spin flip at the intrinsic resonance. With the ac dipole pulsed at the $\nu_s = 0 + Q_v$ intrinsic resonance, a second simulation shows a almost complete spin flip at this intrinsic resonance.

Using the CNI polarimeter in the AGS we were able to measure the polarization flips up the ramp from just above

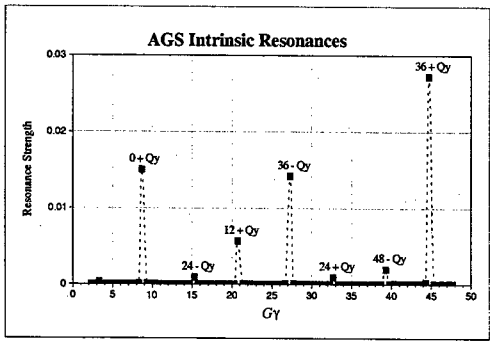

Figure 5: Calculated relative strengths of imperfection resonances in the AGS. It should be noted that there are 12 superperiods in the AGS, so the strongest intrinsic resonances occur with N being a multiple of 12 and $N_v = \pm 1$.

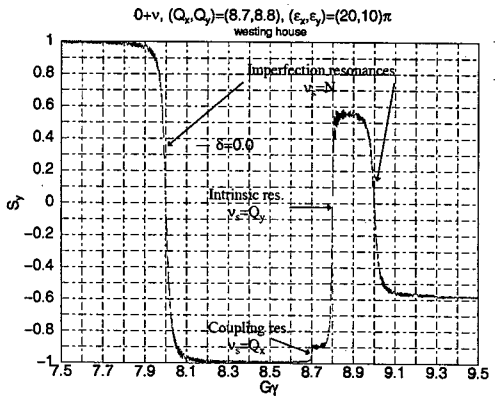

Figure 6: Simulation of resonance crossings near the first intrinsic resonance in the AGS. This shows two imperfection resonances, an intrinsic resonance and a hint of a coupling resonance.

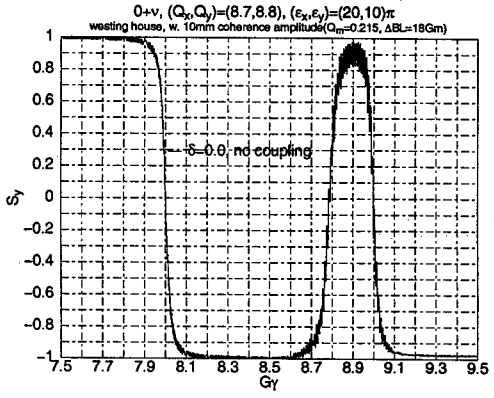

Figure 7: Simulation of the resonance crossing of Fig. 6 with an ac dipole pulse to enhance spin flipping at the intrinsic resonance. The polarization is almost completely preserved.

transition energy to the extraction energy by collecting data from many cycles over a few nights. Fig. 8 shows the raw asymmetry measurement with many flips at the integral $G\gamma$ values. We use the ac dipole to enhance spin flipping at four intrinsic resonances: $\nu_s = 0 + Q_v$, $12 + Q_v$, $36 - Q_v$, and $36 + Q_v$. Due to a lack of strength of the ac dipole we expect a loss of polarization at the $36 + Q_v$ with a decrease by a factor of about 0.85 at this resonance.

Fig. 9 shows a calculation of spin tracking by some large resonances in RHIC. A particle at a large amplitude oscillation sees a larger effect when crossing the resonances, and in this case does not recover the initial polarization direction. The core of the beam with smaller amplitudes shows a good retention of polarization. We have measured a decrease in polarization sometimes if the carbon filament target is placed in the tails of the beam away from the core. By severe scraping (to 1/6 intensity) of the beam in the Booster

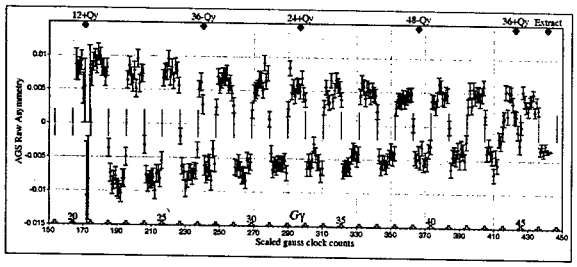

Figure 8: Measured raw asymmetry from the CNI polarimeter above transition in the AGS. Note the extra flips induced by ac dipole pulses at $12 + Q_v$, $36 - Q_v$, and $36 + Q_v$. Since we do not know the energy dependence of analyzing power for this polarimeter we have plotted this as raw asymmetry rather than absolute polarization. We estimate that here the final asymmetry at extraction corresponds to about 30% polarization.

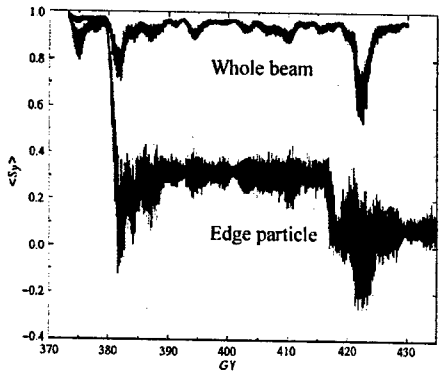

Figure 9: Calculation of spin in the region of a pair of strong resonances in RHIC. Particles with larger amplitude betatron oscillations may experience more precession away from the central stable spin direction $\vec{n}_0$ of the center of the beam.

in all three dimensions we can obtain a very small beam from the AGS with up to 45% or more polarization.

RHIC helical Siberian snakes and rotators

A snake is an insertion device which rotates the spin about an axis in the horizontal plane. The simplest type of snake is a solenoid which rotates the spin around the longitudinal axis. As can be seen from Eq. 1 the amount rotation from a longitudinal field decreases with energy, so a solenoid becomes less effective more higher energy machines. Another drawback of solenoids is orbital coupling. In order to maintain a spin tune of 0.5 with two snakes on opposite sides of the ring, the rotation axes of the two snakes must be kept perpendicular. If the axes were parallel, the spin tune would be zero – a bad situation for maintaining polarization.

The RHIC snakes are constructed of four helical superconducting dipoles with right-handed pitch and fields as indicated in Fig. 10. Fig. 11 shows the snake-like trajectory and spin rotation through a RHIC snake. In contrast with the solenoidal snake, in a helical snake spin rotation is primarily due to the transverse fields so that the rotation is essentially independent of energy. Each snake is powered by two power supplies: The outer pair of helices are connected in series with opposite polarity to one supply, and the inner pair are likewise connected in series with opposite polarity to the second supply. This orientation of fields guarantees that the snake will act as an insertion device with minimal impact on the orbit outside the snake.

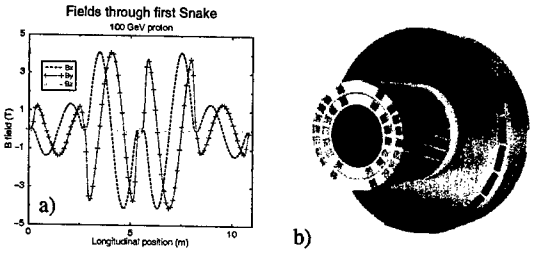

Figure 10: Superconducting helical Siberian snake. a) Magnetic fields along design orbit. The field at the end of each helix is vertical. b) Cross section of magnet showing the helical windings. The iron laminations are 14 inches in diameter.

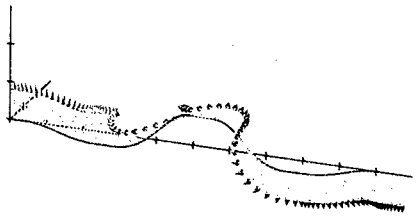

Figure 11: Trajectory and spin through a RHIC snake.

There is another type of spin resonance which is driven by snakes called a snake resonance.[4] Fig. 12 shows a simulation of snake resonances for RHIC with two snakes. We have actually seen indications of the 3/14 resonance showing up with decreased or zero polarization after a ramp when the horizontal tune Q_h has come close to and sometimes crossed 3/14 as shown in Fig. 13

The spin rotators for longitudinal polarization are made of four helical superconducting dipoles. In this case we alternate the handedness of the pitch rather than polarity. Moving clockwise around both rings the pattern at each rotator is: right-left-right-left. For a rotator the field at the end of each helix is horizontal. Each pair (inner and outer) of helices within a rotator is again connected in series to a different power supply. The rotation axis of this kind of rotator lies in the plane perpendicular to the beam and not necessarily in the horizontal plane as in a snake. The rotators are laid out around one of the experiments as indicated in Fig. 14

As with the snakes the amount of rotation is essentially

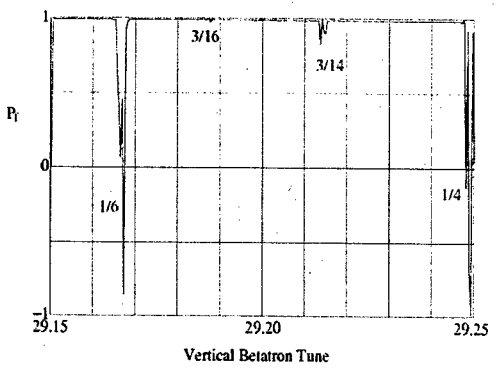

Figure 12: Simulation of hybrid snake resonances in RHIC. In RHIC we have observed depolarization with coupling when the horizontal betatron tune dips down to 3/14. There is also depolarization when the vertical tune nears 0.25.

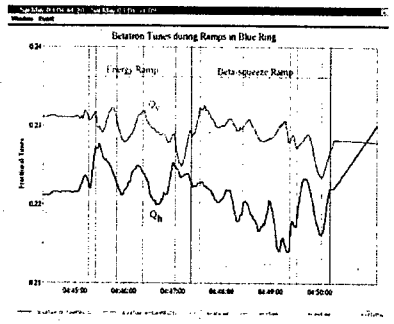

Figure 13: Measured betatron tunes in the Blue ring through the energy and and beta-squeeze ramps. The injection and energy-ramp lattice has $\beta^* = 10$ m at all six interaction regions in both planes. After reaching the operating energy we then squeeze the PHENIX and STAR IR's to 1 m and and the BRAHMS and PHOBOS IR's to 3 m leaving the two remaining IR's at 10 m.

independent of energy. However due to the net horizontal bend between the rotator and interaction region there is an energy dependent precession which must be compensated to achieve a longitudinal polarization at the collision point. Fig. 15 shows how the spin precession differs at the injection and top energies.

PRESENT RUN STATUS

One of the inner helical dipoles in a Yellow ring snake failed with an open conductor. We reconfigured the snake to run with a single pair of helices by reversing the power supply connections to the outer pair of helices; with this configuration the snake can provide a rotation of $\mu = 158°$ and the required rotation axis of $\phi = -45°$ to maintain $\nu_s = 0.5$. Rotators around PHENIX have been turned on and are providing longitudinal polarization after changing the polarity of the power supplies.[5] (With the wrong sign

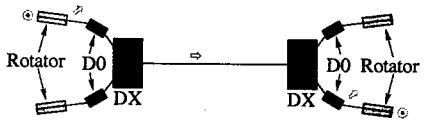

Figure 14: There are two rotators in each ring on either side of both the STAR and PHENIX detectors. Between the rotators and experiment are four dipoles (D0 and DX) to steer the beams into head-on collisions. The final-focus triplets (not indicated) are located between the rotators and and D0 magnets. For each ring the incoming rotator and outgoing rotator are parallel. There is a net bend angle of ± 3.675 mrad from the rotator to the collision point.

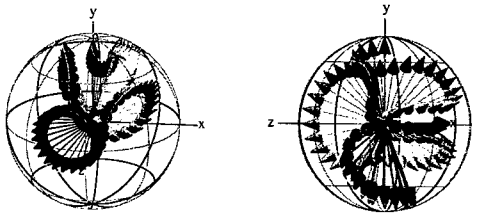

Figure 15: Spin precession through a rotator from vertical to horizontal for two energies: 24.3 GeV (left) and 250 GeV (right). At the lower energy the horizontal precession from the D0 and DX magnets is only about 10°, but at 250 GeV it is about 100°.

at 100 GeV the polarization is effectively radial. Oops.)

The injected polarization is frequently above 40% in RHIC, but we appear to be losing a quarter to a half of the polarization during the beta-squeeze ramp. Squeezing to 1 m at 100 GeV causes the beam to explore the edges of the triplet aperture with strong nonlinearities and coupling. In the previous run we saw evidence[6] of the 3/14 snake resonance with coupling depolarizing the beam with $\beta^* = 3$ m at all six IR's. With the weak snake in the Yellow ring, the polarization at storage is not quite as good as in the Blue ring. While we have accomplished a lot in the few weeks per year dedicated to polarized protons, there is still a lot of complicated work yet to reach the full potential of the world's first polarized hadron collider.

REFERENCES

[1] I. Alekseev et al., *Polarized proton collider at RHIC*, NIM A **499** (2003), 392.

[2] L. H. Thomas, *Phil. Mag.* S. 7, **3**, 1 (1927).

[3] D. P. Barber et al,, "Electrons are not Protons", in EICA Workshop, Upton NY, BNL-52663 (2002).

[4] S. Y. Lee, *Spin Dynamics and Snakes in Synchrotrons*, World Scientific, Singapore (1997).

[5] W. W. MacKay et al., "Commissioning Spin Rotators in RHIC", These Proceedings.

[6] Vahid H. Ranjbar, Thesis "Increasing Proton Polarization in AGS and RHIC", Indiana Univ. (2002).

Proceedings of the 2003 Particle Accelerator Conference

BEAM DYNAMICS IN A STORAGE RING FOR NEUTRAL (POLAR) MOLECULES*

Glen R. Lambertson, University of California, Lawrence Berkeley National Laboratory, MS 71-159, Berkeley, CA 94720 USA

Abstract

The force from a non-uniform electric field on the electric dipole moment of a molecule may be used to circulate and focus molecules in a storage ring. The nature of the forces from multipole electrodes for bending and focusing are described for strong-field-seeking and for weak-field-seeking molecules. Fringe-field forces are analyzed. Examples of storage ring designs are presented; these include long straight sections and provide bunching and acceleration.

INTRODUCTION

Molecules that have an electric dipole moment can be deflected, focused and accelerated by gradients of an electric field. We are studying the design of a storage ring for molecules that will have bunching and straight sections for experimental purposes. It will make available molecules in free space for scattering and spectroscopic measurements. In a circular ring constructed by Crompvoets et. al. [1], single bunches of molecules have been injected and observed to circulate for six turns. To provide a large current of molecules for injection at low velocity, these must be decelerated from a high-intensity source.

FORCES

The force on a molecule from a gradient in electric field magnitude is given by

$$\vec{F} = -\vec{\nabla} W(E) = -\frac{dW}{dE}\vec{\nabla}E = P\vec{\nabla}E \qquad (1)$$

where W is the potential of the polarized molecule in the field of magnitude E and P is its effective dipole moment in the field E. In contrast with a charged particle, here the force is a function of the magnitude of E without regard for the direction of E. The function W depends on the type of molecule and its rotational state and P may be either in the direction of the field, positive, or opposed, negative. This polarity of P makes the molecule either strong-field-seeking or weak-field-seeking. Examples of W are shown in Fig. 1.

*Work supported by the Office of Science, U.S. Department of Energy under Contract No. DE-AC03-76SF00098

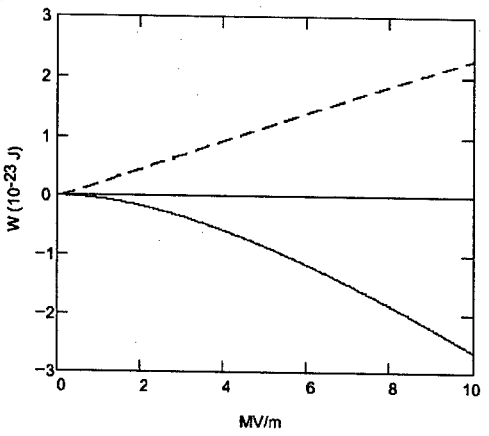

Figure 1: Potentials of methyl fluoride (CH3F) in the ground state (solid curve) and of deuterated ammonia (14N2H3) in the |J,K,M>=|1,1,-1> state (dashed curve).

In a 2-dimensional field that is the gradient of the potential

$$\Psi = Eo[y + a_2 xy + a_3(x^2 - \frac{y^2}{3})y] \qquad (2)$$

the forces on the x and y axes are

$$F_x(x,0) = P\,Eo(a_2 + a_3 x) \qquad (3a)$$

$$F_y(0,y) = P\,Eo\frac{[(a_2)^2 - 2a_3(1 - a_3 y^2)]y}{\sqrt{(a_2 y)^2 + (1 - a_3 y^2)^2}} \qquad (3b)$$

The strength Eo of the dipole component determines the polarization P. In the absence of a quadrupole term, i.e. a_2=0, this biased sextupole provides focusing and defocusing much like a quadrupole does for a charged particle. A biased quadrupole, a_2 only, will provide an x-deflecting force and a y-defocusing force for strong-field-seekers or y–focusing for weak-seekers. And with all three multipole components in the field, one may have focusing in both directions for weak-seekers but not this double-focusing for strong-seekers. While the forces for

0-7803-7738-9/03/$17.00 © 2003 IEEE

small excursions can be nearly linear on the axes, elsewhere they are not. This is shown in Fig. 2 where off-axis forces for CH_3F in a typical biased sextupole field are plotted. The addition of decapole and higher multipoles can alter the character of the nonlinearities. The advantages of this have not been fully explored.

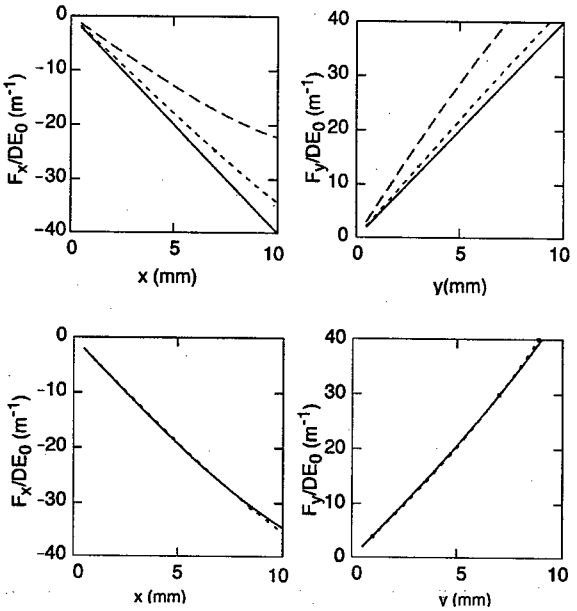

Figure 2: Force functions in a combined dipole and sextupole field. F_x at y = 0, 5, and 10 mm. F_y at x = 0, 5, and 10 mm. (upper) a_3 = 2000. (lower) As in upper but with added decapole, a_5 = 1350000; off-axis forces superpose those on axis but all are now nonlinear.

The fringing fields at entrance and exit of a field electrode have a focusing effect in the direction of the *E*-field. This is in the defocusing sense for strong-field-seekers and focusing for weak-field-seekers. If a molecule is moving in the *z* direction at distance *y* from the midplane in a known fringe field, one can numerically integrate $m\frac{d^2y}{dt^2} = \frac{-dW}{dE}$ to find the molecule's motion. A useful approximation for small *y* requiring only the field on the midplane uses

$$\frac{\partial E_y}{\partial y} \approx y\frac{\partial^2 E_y}{\partial y^2} = y\left[\frac{1}{E_y}\left(\frac{\partial E_y}{\partial z}\right)^2 - \frac{\partial^2 E_y}{\partial z^2}\right] \qquad (4)$$

The overall focusing from passage through a length of changing field can then be expressed as a lens of focal length *f* calculated as

$$\frac{1}{f} = \int\frac{-1}{y}\frac{d^2y}{dz^2} = \int\frac{1}{mv^2}\frac{dW}{dE}\left[\frac{1}{E_y}\left(\frac{\partial E_y}{\partial z}\right)^2 - \frac{\partial^2 E_y}{\partial z^2}\right] \qquad (5)$$

Here *W*, E_y, and the velocity *v* all vary with *z* but this is still the most compact nearly-analytical way to obtain the effect of a fringing field. We see that by reducing $\partial E/\partial z$ by making the fringing length longer one could reduce an undesired fringe-effect, but that often conflicts with the desire to reduce the overall length of a molecule guide field.

To accelerate the molecule, a gradient, or ΔE, in the direction of motion gives an energy change

$$\Delta\frac{1}{2}mv^2 = \Delta W(E) \qquad (6)$$

However, if a molecule is in a uniform field that changes with time, no acceleration results. Therefore if a molecule enters a field region and then the field is reduced, a strong-field-seeker will have gained velocity, or a weak-field-seeker will lose velocity. This process can be used repeatedly to make a large change in velocity or may be used with a ramped field pulse to act as a buncher.

RING FOR A WEAK-FIELD-SEEKER

As noted above, a bending field may be made to provide focusing simultaneously in the two transverse directions for a weak-field-seeking molecule. And the fringe fields are focusing. These actions aid greatly in designing a storage ring. But because the weak-seeker is not in the ground state, it is susceptible to transition to another state if in a weak and direction-changing field. Therefore the ring must have on the entire orbit a polarizing field of unchanging sign, but this is not difficult to provide.

The molecule in this example[2] is deuterated ammonia ($^{14}N^2H_3$) in the state |J,K,M>=|1,1,-1>. The velocity in field-free space is 90 m/s, about 10 kelvin energy. The ring is in racetrack configuration as seen in Fig. 3. Arc radius is 20 cm and ring circumference is 3.36 meter. Straight sections are each 1 meter with 32 cm free for injection and access to the beam of molecules. Taking advantage of the double-focusing, the 90° arc electrodes are continuous sextupoles in which the orbit is offset from zero field to provide the bending force; the gap is 12 mm. An alternating-gradient triplet of biased sextupole lenses matches the beam motion from the arc into the straight section. The horizontal betatron tune is 5.25 and vertical, 5.20. the betatron functions and the dispersion are shown in Fig. 4. The field strengths and multipole coefficients of the guide-field elements are given in Table I. Transverse acceptances of the ring are 35 mm-mrad horizontal and 71 mm-mrad vertical with ±1% momentum spread. At the bunchers, the dispersion should be zero to avoid synchro-betatron coupling; to facilitate this the betatron phase advance is 2π in each quadrant of arc.

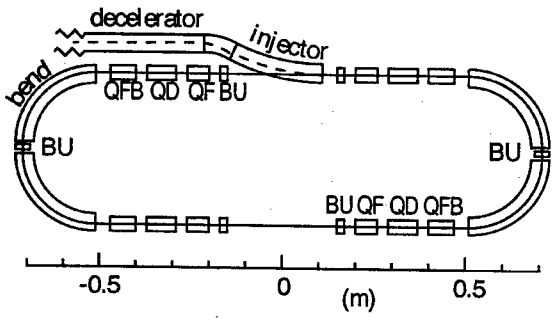

Figure 3: Layout of ring for deuterated ammonia at 90 m/s. Focusing lenses are labeled Q, and bunchers, BU.

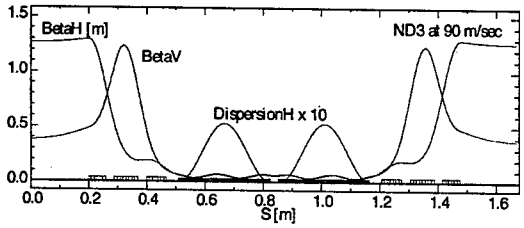

Figure 4: Betatron functions and dispersion of the $^{14}N^2H_3$ ring.

Table I: Field Strengths *Eo*, Multipole Coefficients, and Lengths *L* of the Guide Fields in the $^{14}N^2H_3$ Ring

	Eo [MV/m]	a_2 [m^{-1}]	a_3 [m^{-2}]	*L* [cm]
Bend	3.37	157	5667	31.4
QF	2.88	0	-2000	6.0
QD	3.55	0	-2000	8.0
QBF	4.30	0	-2000	3.0

Injection is from a decelerator that brings molecules from 310 m/s to 90 m/s in a length of 3.4 meter. Bunches from the decelerator are injected through a bending electrode similar to that used in the arcs of the ring but pulsed off in a time that is much less than the 38 msec circulation period to allow filling of a large fraction of the circumference.

The bunches are injected into 60 longitudinal buckets created by six parallel-plate bunching electrodes in the ring. The field in a buncher is pulsed at 1.6 KHz with a triangular waveform that, as required, accelerates late-arriving molecules and decelerates early ones. The field seen by an on-energy molecule is only 1 MV/m in a gap of 30 mm. Bunches with ±1% velocity spread that are captured in the ring are 7 mm long and spaced 56 mm. Using a pulsed jet source into the decelerator, a single bunch contains 6.8 x 10^8 molecules and if all 60 buckets are filled, the circulating intensity would be 1.1 x 10^{12} molecules per second. The bunchers may be used to decelerate the bunches by synchronously sweeping their frequency and the strengths of the ring guide fields. Without tune compensations, the velocity may be reduced to 60 m/s; with more controllable field parameters, this could be extended.

RING FOR A STRONG-FIELD-SEEKER

The molecule in this example[3] is methyl fluoride (CH^3F) in its ground state at 30 m/s. As seen in Fig. 1, the potential *W* is quite nonlinear and in beam trajectory calculations this must be used to find the velocity and force at each point as the molecule moves through fields of various strengths. This is a greater factor at low velocity. For example, the 30 m/s is the velocity in zero field; that rises to 33.2 m/s in the 4 MV/m field of the bend electrodes.

This example ring has eight superperiods, each with arc and straight sections as shown in Fig. 5. The circumference is 9.85 meter and tunes are 13.37 horizontal and 10.40 vertical. Acceptances are 11 mm-mrad horizontal and 21 vertical with ±1.2% velocity spread. An arc has four cells with D/2-F-D/2 lattice; a cell has $\pi/2$ phase advance in each plane. Each F and D sector in a cell has a dipole and a quadrupole component to provide the deflection and a sextupole term that reverses between F and D. Field strength across the 8 mm aperture varies only about 1%. The plate voltages of F and D are alike so that adjacent ends of successive sectors may be brought very close to reduce fringing fields in the transition region between them. A D-F-D triplet of lenses matches from arc to straight.

The force of gravity can displace by millimeters the vertical closed orbit if not compensated. A small vertical deflecting electrode in each triplet region reduces the displacement to about 0.1 mm at mid-straight as shown in Fig. 6. This correction may be adjusted when the velocity of the circulating molecules is changed.

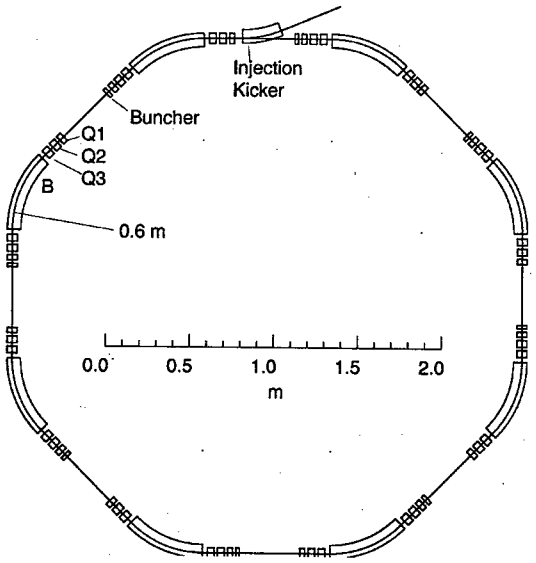

Figure 5: Layout of the storage ring for methyl fluoride.

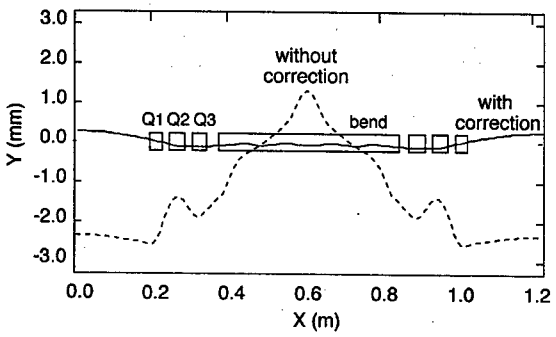

Figure 6: Displacement of the vertical closed orbit by gravity force, with and without compensation.

DECELERATOR DESIGN

A decelerator to provide low-velocity molecules for injection is a substantial part of a storage ring facility. It consists of a series of pulsed electrodes with uniform fields; in each of these, the field E reduces the molecule's energy as in Eq. 6[3]. Many such electrodes are required; for methyl fluoride, 120 electrodes with pulsed field of 9 MV/m are required to reduce 310 m/s to 30 m/s. Between the pulsed electrodes one needs focusing lenses; in the case of strong-seeking CH_3F, one lens for each pulsed decelerating electrode is required to confine the molecules transversely in the presence of the defocusing from fringe fields. Each electrode must have a length of uniform field for the bunch and this added to the lengths of fringing determines the bunch spacing and frequency at the exit end. A small slope on the top of the voltage pulse provides bunching action. If the same train of shaped pulses is applied to all electrodes, the bunch length varies as the square-root of velocity while bunch spacing is proportional to velocity. This allows the electrode lengths to be halved in an upstream portion of the array and greatly reduces its overall length. Some parameters of a 15.1-meter long decelerator for CH_3F are given in Table II. There are two electrodes per bunch spacing for velocity above 102 m/s.

Table II: Decelerator Parameters

Entering velocity [m/s]	310
Exit velocity [m/s]	30
Exit emittance [mm-mrad]	30
Exit bunch length [mm]	8
Electrode gap [mm]	6
Pulsed decelerating field [MV/m]	9
Lens dipole component [MV/m]	4.5
Entrance electrode length [mm]	124
Exit electrode length [mm]	24
Overall length [m]	15.1

CONCLUSIONS

For each manipulation with polar molecules there appears to be a method—different from that for charged particles and often with aggravating nonlinearities. But the low velocity brings the convenience of slow time scales for the components and small size. Electrodes for the guide fields are easy to fabricate and power. Storage ring concepts at this time are not highly developed. We need some experience as a preparation for more ambitious designs in response to the needs of users.

ACKNOWLEDGEMENTS

Designs and calculations reported here have been carried out in collaboration with Harvey Gould, Juris Kalnins, and Hiroshi Nishimura. Work on the synchrotron storage ring is supported by the Director, Office of Science, of the U.S. Department of Energy, and work on the linear decelerator is supported by the Director, Office of Science, Office of Basic Energy Sciences, of the U.S. Department of Energy, both under Contract No. DE-AC03-76SF00098.

REFERENCES

[1] F. Crompvoets, H. Bethlem, R. Jongma, and G. Meijer, "A prototype storage ring for neutral molecules", *Nature* 411, 174, (2001).

[2] H. Nishimura, G. Lambertson, J. Kalnins, and H. Gould, "Feasibility of a synchrotron storage ring for neutral polar molecules", to be published in RSI, LBNL-51597.

[3] H. Nishimura, G. Lambertson, J. Kalnins, and H. Gould, "Lattices for Milli-eV Neutral Molecules", in this proceedings, Portland, Oregon, May 2003.

MUON ACCELERATION IN FFAG RINGS

E. Keil*, Katharinenstr. 17, Berlin, Germany
A.M. Sessler†, Lawrence Berkeley National Laboratory, Berkeley, CA 94720, USA

Abstract

Compared to muon acceleration in re-circulating linear accelerators, considered earlier, muon acceleration in FFAG rings holds the promise of having one arc instead of several, and a smaller number of RF cavities; i.e., using more than a few turns for acceleration from about 6 to about 20 GeV/c. We consider non-scaling FFAG machines (but with limited tune variation) that are essentially strong-focusing rings with a dispersion small enough to keep muons over the full momentum range inside the same magnet aperture. We compare several scenarios: (i) Rings with straight sections, long enough - a few metres - to house super-conducting RF cavities at about 200 MHz (and with enough space for decay of the magnetic fields in neighbouring components to a level of about 10 mGauss; (ii) Rings with shorter straight sections, just long enough about a metre to house normal-conducting RF cavities also operating at about 200 MHz; (iii) Racetrack-shaped rings with compact arcs without RF cavities, joined to long straight sections with super-conducting RF cavities by adiabatic transition sections that match between them over the wide momentum range needed; (iv) Rings with a number of superperiods (about 10) so that there are only a number of sc RF sections. In all four scenarios we consider the travel time of the muons around the ring which depends on the muon momentum and, hence, produces variable phase at the RF cavities during the acceleration process.

INTRODUCTION

Neutrino factory studies [1, 2, 3], based on accelerating and storing muons, assumed that the muons are accelerated in a linear accelerator up to a few GeV, and in one or two recirculating linear accelerators RLA similar to CEBAF to the energy of the storage ring, 20 to 50 GeV. In an RLA, the muons travel through two linear accelerators several times, and through half-circular arcs, one for each recirculation, at either end. Between the linear accelerators and the arcs are spreaders, which distribute the muons of different energy from the linear accelerators into the arcs, and combiners, which do the opposite. Spreaders and combiners become rapidly more complicated and costly when the number of recirculations increases. It is 4 or 5 in [1, 2, 3].

Non-Scaling FFAG Rings

In FFAG rings, muons are accelerated by a factor ≈ 3 in a lattice with a single aperture. There are no spreaders and combiners. Such lattices hold the promise of a larger number of recirculations, and hence of reduced cost. We discuss how muons are accelerated in an FFAG ring, and present several designs of non-scaling FFAG rings. The phase advances μ_x and μ_y in a cell vary approximately in inverse proportion to the particle momentum. They should remain below the half-integral resonance at the lower edge of the operating range in $\delta p/p$. The tunes Q_x and Q_y in the whole ring cover many integral and half-integral values.

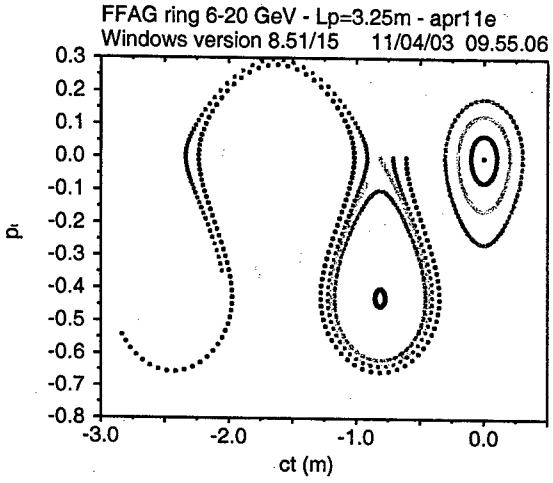

Figure 1: Longitudinal phase space trajectories of 13 particles, tracked for 30 turns, cf. Section .

FFAG Acceleration

Fig. 1 shows trajectories in longitudinal phase space $(ct, p_t = \Delta p/p_0)$ for the lattice in Section . Nine particles are launched at regular intervals between the fixed points at $ct = 0$ m and $p_t = 0$, and $ct = -3.25/4$ m and $p_t = 0$. Four of them execute synchrotron oscillations in buckets around the stable fixed point. Another four particles follow wavy open trajectories around the two stable fixed points. Acceleration happens close to these trajectories, which cover the whole operating range from $p_t \approx -0.6$ to $p_t \approx 0.2$. The green particle starts very close to the unstable fixed point and almost returns to it. Four particles are launched below the unstable fixed point at $ct = -3.25/4$ m with $p_t = -0.1, -0.2, -0.3, -0.4$. Their initial transverse coordinates coincide with their respective closed orbit. These particles execute stable synchrotron oscillations in buckets around a second stable fixed point at $ct = -3.25/4$ m and $p_t \approx -0.4$. This stable fixed point is related to the variation of the travel time $\Delta t(p_t)$ of second and higher order [4] in p_t which results in $\Delta t(p_t) \approx 0$ s at

* Eberhard.Keil@t-online.de

† Supported by the U.S. Department of Energy under Contract No. DE-AC03-76SF00098

0-7803-7738-9/03/$17.00 © 2003 IEEE

$p_t \approx -0.4$. Phase space trajectories with the shape shown in Fig. 1 only occur when V the maximum energy gain per turn of a muon that travels on the crest of the RF wave, exceeds the threshold in Tab. 1. To get the peak RF voltage divide by the transit time factor < 1. Our typical RF voltage is about twice the threshold value.

SCENARIO 1: S.C. RF

The lattice [5] has 3 m long straight sections, long enough to house a single-cell super-conducting RF cavity at about 200 MHz, including the distances needed to protect it from stray field of neighbouring magnetic elements. We have re-evaluated the parameters shown in Tab. 1.

SCENARIO 2: N.C. RF

Two lattice styles have straight sections long enough for a single-cell room-temperature RF cavity at $\approx$ 200 MHz.

Modified FODO Lattice

The modified FODO lattice is derived from [5] by halving the length of the lattice cell. Horizontal focusing happens in the quadrupole, while bending and vertical focusing happen in a combined-function dipole magnet. The 1.4 m long drift space is still long enough for normal-conducting RF cavities operating at about 200 MHz. Tab. 1 shows parameters, Fig. 2 layout and optical functions.

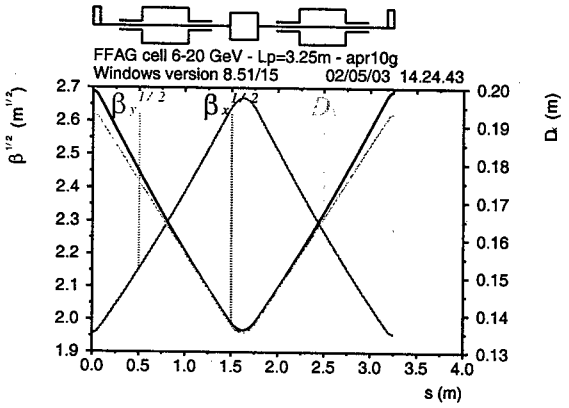

Figure 2: Layout and optical functions of cell apr10g

Modified Achromat

Achromats, used in the study of ELFE [6] and the RLA design at CERN, consist of 2 FODO cells for focusing, and have dipoles in the half cells surrounding every second F quadrupole. The horizontal dispersion D_x vanishes in every second F quadrupole. Our modified achromats for FFAG acceleration have the opposite quadrupole polarities, and $D_x > 0$ everywhere. The half cells without dipoles provide space for normal-conducting RF cavities. Fig. 3 shows layout and optical functions, Tab. 1 parameters. The second zero of ct is at $p_t \approx -0.55$. The half-integral stopband is at $p_t \approx -0.52$. Hence, the modified achromat accelerates from $p_t \approx -0.5$ to ≈ 0.2 inside buckets, when RF voltage and bucket height are large enough. Changing parameters should move the stopband below the second zero, and permit acceleration over a larger momentum range.

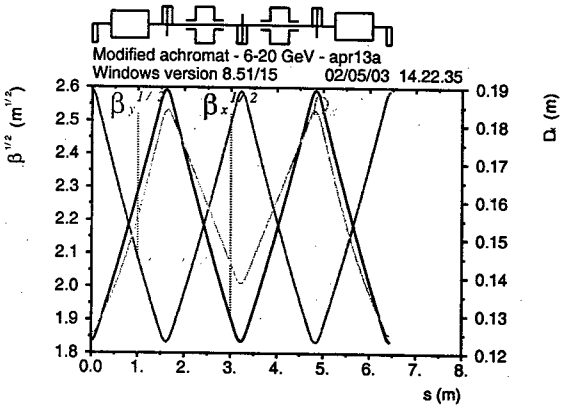

Figure 3: Layout and optical functions of period apr13a

SCENARIO 3: RACETRACK

Racetrack rings consist of closely-packed arcs that bend the muon, and transport it from one straight section, with ample space for accelerating RF cavities, to the other. Between arcs and straight sections are adiabatic transitions.

Adiabatic Transitions

Adiabatic transitions match the orbit functions between the arcs and straight sections over the whole energy range of the FFAG ring. This is achieved by smoothly varying the period length and the bending angle between the typical arc and straight section cells. We use the Fermi function $F(n,B,N) = [1+\exp(B(2n/N-1))]^{-1}$ with number of transition periods N, running index n, and parameter $B \approx 2\ldots5$ describing the smoothness. The factor 2 in F ensures that the transition happens near $n = N/2$. For $B > 1$ but not $B \gg 1$, we have $F(0,B,N) < 1$ and $F(N,B,N) > 0$. We overcome this problem by using

$$G(n,B,N) = \frac{F(n,B,N) - F(N,B,N)}{F(0,B,N) - F(N,B,N)} \quad (1)$$

with $G(0,B,N) = 1$ and $G(N,B,N) = 0$. In the n-th FODO cell, length L_n, dispersion D_n, and bending angle/period $\varphi_n = \varphi_1 D_n / L_n$ become, with indices 1 and 2 referring to arc and straight section cells:

$$L_n = L_2 + (L_1 - L_2)G(n,B_\beta,N) \quad (2)$$

$$D_n = D_1 G(n,B_D,N) \quad (3)$$

Racetrack Lattice

We study adiabatic transitions in a lattice that consists of drift spaces and thin elements. The FODO arc periods have

Table 1: Parameters of Johnstone-Koscielniak [5] lattice apr09r, modified Johnstone lattice apr10g, modified achromats apr13a and racetrack lattice apr29o. The phase advances are about 0.1 in apr09r, apr10g, and apr29o, and 0.2 in achr06.

	apr09r	apr10g	apr13a	apr29o	
Total reference energy E	16.5	16	16.5	16.5	GeV
Energy range	6...20	6...20	6...20	6...20	GeV
Range of $\delta p/p$	−.636...+.212	−.625...+.250	−.636...+.212	−.636...+.212	
Range of hor. offsets in F quads x	−76...79	−45...50	−54...46	−137/144	mm
Period length L_p	6.5	3.25	6.449	5...10	m
Number of periods N_p	314	280	140	264	
Circumference C	2041	910	902.8	1610	m
Magnetic gradients G_F/G_D	75/−32	141/−71	1.15/−1.15	–	T/m
Dipole field B	3.1	4.0	1.53	–	T
Path length spread	535	410	397	1685	mm
RF frequency	184.5	184.5	185.9	186.2	MHz
Threshold/typical circumf. RF accel. V	1036/1884	812/1680	–/1680	–/	MV
Typical number of turns	10	10	11		

super-imposed quadrupoles and dipoles, and $L_1 = 5$ m, $\varphi_1 = 31.4$ mr and phase advance $\mu/2\pi = 0.1$. The straight section cells have $L_2 = 10$ m and $\mu/2\pi = 0.1$. An arc surrounded by transitions bends the muon beam by about π. We use a 112.5 m long transition with $N = 16$ and $B = 3$. Four such transitions are in a racetrack machine. The number of cells in a straight section, 14, will be adjusted later to optimize number and voltage of the RF cavities.

Without acceleration, the residual non-adiabaticity causes oscillations of D_x, β_x and β_y, and stopbands. In the straight sections at $p_t = 0$, the amplitude of the D_x oscillations increases with decreasing N. For fixed N, it has minima near $B = 3$. At $N = 16$ and $B = 3$, $|D_x| < 0.1$ m. The β-beating is less than 7.5% for $N \geq 12$. Both $|D_x|$ and $|x| \to \infty$, and momentum compaction $\alpha_c \to \pm\infty$ at even horizontal tunes Q_x; β_x and $\beta_y \to \infty$ at integral Q_x.

The racetrack lattice has a much weaker second-order variation of ct than those in Sections and . Hence, $ct \neq 0$ for $-0.6 < p_t < 0$, the muons must be accelerated inside buckets with stable fixed point $ct = 0$ and $p_t = 0$, and not on trajectories similar to those in Fig. 1. We have studied acceleration over a large range of RF cavity voltages. We have not found a value with the bucket height needed. In addition, the synchrotron motion is chaotic, and the edges of the bucket are fuzzy. On might either attempt to increase the second-order variation of ct, or frequency modulate the RF cavities as in a synchrotron.

SCENARIO 4: SUPER-PERIODS

We studied a lattice with 10 superperiods, each consisting of 10 arc cells and 9 straight section cells from Section , i.e. without transitions. For $-0.6215 \leq p_t \leq +0.138$, the phase advances in the superperiod cover the ranges $5.911988 \geq \mu_x \geq 1.522851$ and $5.788112 \geq \mu_y \geq 1.605385$. In the absence of acceleration, we find wide stopbands at the 4 integral and the 4 half-integral phase advances within these ranges. The extreme absolute values of dispersion $|D_x|$ and orbit offset $|x|$ tend towards ∞ at the edges of the integral stopbands, while β_x and β_y reach ∞ at the edges of the integral and half-integral stopbands. We have not succeeded in accelerating muons through these stopbands. We have not studied super-periodic lattices with adiabatic transitions between arcs and straight sections.

CONCLUSIONS

Two styles of FODO lattices, suitable for superconducting and room-temperature RF systems, respectively, accelerate muons outside buckets from about 6 to about 20 GeV in about 10 turns with less than about 2 GeV circumferential acceleration V. This value of V is at most one half, and the number of arcs is 2/7, of those in an RLA with four turns, and there are no spreaders and combiners. The circumferences C are $\approx$ 2 km and $\approx$ 1 km, respectively. A modified achromat accelerates muon inside buckets from about 8.25 to about 19.8 GeV in 11 turns with a similar circumferential RF voltage, at $C \approx 1$ km, and can probably be improved to cover the whole momentum range. We have not succeeded in accelerating muons in a racetrack machine with adiabatic transitions between arcs and straight sections and a super-conducting RF system. We have not succeeded in accelerating in a super-periodic machine. We have presented FFAG rings with very interesting properties. We leave their optimization for the future, as well as further studies of scenarios 3 and 4.

REFERENCES

[1] N. Holtkamp et al., FERMILAB-PUB-00-108-E (2000)

[2] S. Ozaki et al., BNL-52623 (June 2001)

[3] P. Gruber et al., CERN-PS-2002-080-PP (16 Dec 2002)

[4] K.Y. Ng in Handbook of Accelerator Physics and Engineering, 2nd printing (World Scientific, Singapore 2002) 94.

[5] C. Johnstone and S. Koscielniak, FFAGS for Rapid Acceleration, submitted to Elsevier Science, 11 Sep 2002.

[6] K. Aulenbacher et al., ELFE at CERN, CERN 99-10 (1999)

TRANSVERSE IMPEDANCE DISTRIBUTION MEASUREMENTS USING THE RESPONSE MATRIX FIT METHOD AT APS*

V. Sajaev, Argonne National Laboratory, Argonne, IL 60439 USA

Abstract

The Advanced Photon Source storage ring has a number of narrow-gap insertion device vacuum chambers, and there is a plan to further increase their number. These vacuum chambers contribute to the impedance of the machine and to the impedance limits the single-bunch current threshold. In order to understand the contribution of the vacuum chambers and its dependence on the gap, the distribution of the vertical transverse impedance around the circumference of the APS storage ring has been determined using the response matrix fit method. This method allows us to find focusing errors around the storage ring and was originally used to determine and correct the linear model of the APS. The high accuracy of the method enables us to measure the variation of betatron phase advance around the ring with beam current. Results of these measurements are reported and the impedance of different parts of the storage ring is presented.

INTRODUCTION

The Advanced Photon Source (APS) is a third-generation synchrotron light source based on a 7-GeV electron storage ring. The synchrotron radiation is mainly produced by undulators. Optimization of beamlines calls for small undulator gaps. Therefore the undulators are installed on dedicated small gap insertion device (ID) vacuum chambers. APS has 35 5-m-long straight sections available for undulators; 27 of them are currently occupied. Most of the ID vacuum chambers have an 8-mm inner aperture, and two chambers have a 5-mm aperture. These vacuum chambers are believed to be the main source of the transverse impedance of the machine.

Our goal is to measure the vertical transverse impedance distribution around the machine and determine the contribution of the ID vacuum chambers. Although one can measure the combined effects of all chambers by measuring the transverse tune shift with single-bunch current [1], it is difficult to accurately measure the small change in this tune shift after only one or a few new ID chambers are installed.

In the past a number of attempts have been made to measure the impedance of separate parts of accelerators. Phase advance measurements from beam position monitor (BPM) turn-by-turn histories were used at LEP [2] to measure the impedance distribution around the ring. This method was tried at APS; however, the accuracy of the measurements was not sufficient to determine the impedance of a single ID vacuum chamber. Recently, the accuracy of turn-by-turn BPM measurements at APS was greatly improved using the Model Independent Analysis (MIA) [3]. It was demonstrated that with MIA the phase advance measurements similar to LEP provide enough accuracy to reveal the main impedance structure of the APS ring. However, this work was not pursued. There is also a different approach, which uses local orbit bumps to probe different parts of an accelerator [4-6]. All these methods employ the fact that the beam sees the impedance as a defocusing quadrupole whose strength depends on the beam current.

At APS we have implemented a method for precise measurement of beta functions along the ring [7]. The method employs an orbit response matrix fit to determine the distribution of focusing errors around the machine and then uses these errors to calculate beta functions (the details on the response matrix fit and more references can be found in [8]). Since the impedance can be represented as a current-dependent quadrupole, the measurement of the beta functions with different currents could be used to determine the impedance distribution around the machine.

We report on a sensitive method for measuring the transverse impedance distribution along the machine that uses the response matrix fit method to calculate local betatron phase advance changes due to different beam currents.

RESPONSE MATRIX FIT

The orbit response matrix is the change in the orbit at the BPMs as a function of the changes in steering magnets. The response matrix is defined by the linear lattice of the machine; therefore it can be used to calibrate the linear optics in a storage ring.

The main idea of the analysis is to adjust the quadrupole gradients of a computer model of the storage ring until the model response matrix best fits the measured response matrix. The problem of fitting the response matrix is solved in the following way. Let the response matrix M be a function of the vector of variables x. Then we need to solve the equation

$$M_{measured} - M_{model}(x) = 0$$

which can be solved by Newton's method:

$$\Delta x = \left(\frac{\partial M_{model}}{\partial x}\right)^{-1} \cdot \left(M_{measured} - M_{model}(x_0)\right),$$

where x_0 corresponds to the initial model. To solve this equation, we rewrite the response matrix as one vector consisting of $N_{corr} \times N_{bpm}$ values, where N_{corr} is the number of correctors used in the response matrix and N_{bpm} is the number of BPMs. Then the derivative of the response matrix would be a $(N_{corr} \times N_{bpm}) \times N_{var}$ matrix, where N_{var} is the number of variables upon which the response matrix depends. Finally, to fit the response matrix, we have to determine all variables upon which the response matrix depends, calculate the derivative of the response matrix

* This work is supported by U.S. Department of Energy, Office of Basic Energy Sciences under Contract No. W-31-109-ENG-38.

0-7803-7738-9/03/$17.00 © 2003 IEEE

with respect to these variables, and then invert it. After that, the solution can be found by iteration.

The most obvious and important variables are focusing errors (quadrupole calibration errors or orbit errors in sextupoles), corrector calibration errors, and BPM gain errors. Another obvious but less important variable is the energy shift associated with the changing of each steering magnet. The choice of what variables to use depends on details of the particular storage ring and how accurately the response matrix can be measured.

The APS storage ring is 40-fold periodic. Each sector consists of two dipoles, ten quadrupoles, and seven sextupoles. There are also eight horizontal and eight vertical steering magnets and nine to eleven BPMs per sector. Possible focusing errors could come from miscalibration of quadrupole power supplies (each quadrupole at APS has its own power supply) and from horizontal orbit errors in sextupoles, so that the total possible number of focusing errors per sector could be up to 17. Obviously, there are not enough BPMs to resolve all possible focusing errors; therefore we keep only quadrupoles in our model. Since the average betatron phase advance per quadrupole is only 0.09, we consider that the quadrupoles alone could accurately reproduce all possible focusing errors in the storage ring.

In order to limit the size of the derivative of the response matrix, we use only 40 horizontal and 40 vertical correctors and all available BPMs. In this case the two-dimensional uncoupled response matrix contains about 32,000 elements and depends on approximately 1400 variables. The overall size of the derivative in double precision is about 350 MB.

MEASUREMENTS

The APS storage ring vacuum chambers are made of aluminum and have an elliptic 85×42 mm size. When an undulator is installed in a sector, a 5-m-long section of the vacuum chamber is replaced with a narrow-gap ID chamber (total length of one sector is 27.6 m). Most of the APS insertion devices have 8-mm-gap vacuum chambers; two IDs in sectors 3 and 4 have 5-mm-gap vacuum chambers. Normal and ID vacuum chambers are connected with 20-cm-long tapers. Figure 1 represents locations of the small-gap vacuum chambers installed at the APS storage ring at this moment. We expect the vertical impedance to be dominated by these small-gap ID vacuum chambers.

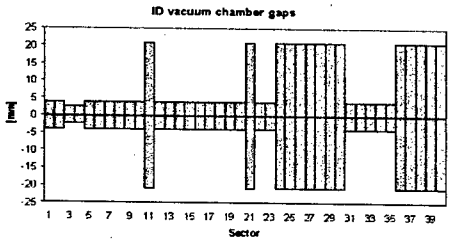

Figure 1: ID vacuum chamber gaps.

In order to obtain the change in focusing around the ring with the beam intensity, we measure the response matrices for different beam currents, analyze them to get beta functions, and then compare the local phase advances. Figure 2 shows the phase advance difference between the two response matrices measured with 10 mA and 1 mA in a single bunch. One can easily see a sharp change in phase caused by 5-mm chambers in sectors 3 and 4 and flat regions corresponding to no ID chambers in sectors 24 to 30 and 36 to 40. Fast oscillation of the phase advance difference is explained by beta function mismatch, caused by changes in focusing. Figure 2 confirms our expectations that the main contribution comes from ID vacuum chambers.

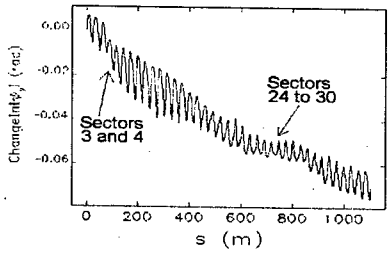

Figure 2: Betatron phase advance difference between 10-mA and 1-mA cases.

This measurement also yields the tune slope with current, which can be used to calculate the total transverse impedance. Figure 3 (left) shows vertical betatron tune dependence on the beam current defined by the following formula:

$$\frac{d\nu}{dI} = \frac{R}{2\pi\sigma_s E}\sum\langle\beta\rangle_i Z_{eff}^{(i)} .$$

The measurements are so accurate that one can see a deviation from linear dependence due to bunch length variation with the current. To keep the bunch length constant, the rf voltage was varied during measurements.

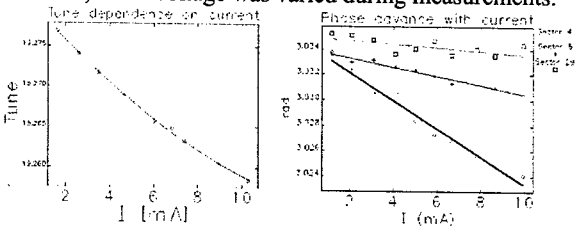

Figure 3: Left – vertical tune slope with current. Right – vertical phase advance slopes with current for different sectors.

In order to get the local distribution of the impedance around the ring, we analyze the phase-advance changes due to a change in the beam current sector by sector. Figure 3 (right) shows typical betatron phase-advance slopes for sectors 4, 5, and 29 (5-mm-, 8-mm- and 42-mm-gap ID vacuum chambers, respectively).

The APS storage ring operates in two different modes: 7.7-nm high-emittance lattice and 2.4-nm low-emittance lattice. The vertical beta functions of the two lattices are almost equal in the locations of the ID vacuum chambers, but have different average vertical beta functions. Phase

slope distribution measurements were conducted for both low-emittance and high-emittance lattices. Though the transverse impedance does not change with the lattice, the defocusing effect of the impedance depends on beta functions; therefore the phase-advance slope is expected to be similar for sectors with small-gap vacuum chambers. Figure 4 presents the distribution of phase slope with current along the APS storage ring for two lattices. As expected, the biggest phase advance change occurs in sectors 3 and 4, where 5-mm vacuum chambers are installed. Also, all sectors without small-gap chambers are clearly seen. It is important to note that the phase-advance changes for sectors 24 through 30 are larger for the low-emittance lattice. This is explained by the fact that for these sectors the impedance is approximately evenly distributed along the sector, and the scaling is due to average vertical beta function difference. Thus the measurements are reliable even for sectors without the small-gap ID vacuum chambers.

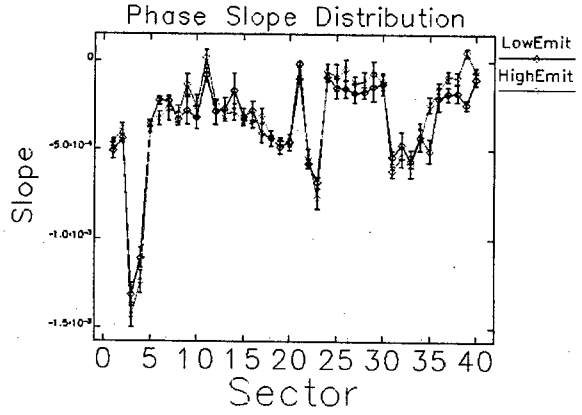

Figure 4: Phase advance slopes distribution.

The effective transverse impedance is the integral over the machine impedance, multiplied by the bunch spectrum squared. For a particular impedance component, it can be found from measured slopes of the phase advance

$$Z_{eff}^{i} = \frac{E\sigma_s}{R\beta_i}\frac{d\mu}{dI}.$$

The beta functions have to be taken at the location of the impedance elements. For the ID vacuum chamber we use the average over the 5-m-long ID straight section, otherwise we use the beta function averaged over the entire sector. The bunch length is 40 ps and is maintained approximately constant during measurements by varying the rf voltage. The resulting values for the various sectors as well as the total effective vertical impedances are shown in Table 1 for both high- and low-emittance lattices. The phase-advance slopes and impedances shown in the table are averaged over all similar sectors, i.e., all empty sectors, all sectors with 8-mm ID vacuum chambers, etc. For calculation of the impedance of the ID vacuum chambers Z_{8mm}^{eff} and Z_{5mm}^{eff}, the average phase slope of the empty sector was subtracted. These results compare well with the impedance model and with the measurements in [5].

Table 1: Phase Slopes and Impedances

		High Emittance	Low Emittance
$\langle\beta\rangle_{sector}$	m	12.2	16.3
$\langle\beta\rangle_{ID}$	m	4.7	3.7
$d\mu/dI_{no\ ID}$	rad/A	-0.09	-0.14
$d\mu/dI_{8mm}$	rad/A	-0.39	-0.40
$d\mu/dI_{5mm}$	rad/A	-1.33	-1.21
Z_{noID}^{eff}	kΩ/m	3.5	4.1
Z_{8mm}^{eff}	kΩ/m	31	34
Z_{5mm}^{eff}	kΩ/m	126	138
Z_{total}^{eff}	MΩ/m	1.06	1.17

CONCLUSION

Analysis of the measured orbit response matrix provides detailed information concerning storage ring optics. The optics measurements are so precise that one can see the phase-advance difference due to different beam currents. This was used to derive the distribution of the vertical impedance around the APS storage ring. It was found that the small-gap ID vacuum chambers contribute the most to the storage ring vertical impedance. The actual values of the vertical impedance of the chambers with different gaps were determined.

ACKNOWLEDGMENTS

The author would like to thank the staff at the APS, particularly Steve Milton for his encouragement and support of the work and Louis Emery for tremendous help with operational, software, and physics issues. Also, the author would like to thank K. Harkay, Y.-C. Chae, and E. Trakhtenberg for numerous useful discussions and H. Shang for helping with programming.

REFERENCES

[1] K. Harkay and N. Sereno, Proceedings of PAC 1997, Vancouver, Canada, p. 1700 (1998).
[2] D. Brandt et al, Proceedings of PAC 1995, Dallas, p. 570 (1996).
[3] C.-X. Wang, Proceedings of PAC 2001, Chicago, p. 1354 (2001).
[4] V. Kiselev, V. Smaluk, "A Method for Measurement of Transverse Impedance along Storage Ring," Proceedings of the 4th European Workshop on Diagnostics for Particle Accelerators, Chester, 1999.
[5] L. Emery, G. Decker and J. Galayda, Proceedings of PAC 2001, Chicago, p.1823 (2001).
[6] L. Farvacque, E. Plouviez, Proceedings of EPAC 2002, Paris, p.1550 (2002).
[7] V. Sajaev, L. Emery, Proceedings of EPAC 2002, Paris, p. 742 (2002).
[8] J. Safranek, Nucl. Instrum. Methods A 388, p. 27 (1997).

FEMTO-SECONDS ELECTRON BEAM DIFFRACTION USING PHOTOCATHODE RF GUN*

X.J. Wang#, and Z. Wu, NSLS, BNL, Upton, NY 11973, USA
Hyotcherl (Harry) Ihee, University of Chicago, USA and Korea Advanced Institute of Science and Technology, South Korea

Abstract

One of the 21st century scientific frontiers is to explore the molecule structure transition in the femto-second time scale. X-ray free electron laser (XFEL) is one of the tools now under development for investigating femto-second structure transition. We are proposing an alternative technique – femto-second electron diffraction based on the photocathode RF gun. We will present a design of a kHz femto-seconds electron diffraction system based on the photocathode RF gun. Our simulation shows that, photocathode RF gun can produce 100 fs (FWHM) electron bunch with millions electrons at about 2 MeV. This is at least one order of magnitude reduction in bunch length, and two orders of magnitude increase in number of electrons comparing to present DC electron diffraction system. We will also discuss various issues and limitations related to MeV electron diffraction.

INTRODUCTION

X-ray and electron are two most powerful tools for characterizing atomic and molecular structures. The recent development of electron storage ring based X-ray source and electron microscope made it possible to observe the ultra-small world with Å resolution [1,2]. On the other hand, development of the laser technologies, especially picosecond (10^{-12} s) and femtosecond (10^{-15}) lasers, made it possible of observing the ultra-fast process [3].

Directly observation of structure transition and molecular dynamics process, such as chemical bond breaking, is one of the fundamental issues in nano-science, chemistry, biology and many other scientific endeavours. Such capability demands the marriage of ultra-small technologies, such as X-ray and electron diffraction, and ultra-fast technolgies. X-ray free electron laser (FEL) now being developed in US and Germany [4,5] is one of the examples of such marriage. Ultra-fast electron diffraction (UED) [3, 6] has been developed to investigate the ultra-fast structure transition.

X-ray and Electron diffraction are two complementary technologies. For example, X-ray diffraction is better suit for large angle diffraction; while electron diffraction is the choice for small angle diffraction. The Thompson scattering cross section is dominating contributing factor for X-ray diffraction while it is the Rutherford scattering cross section for electron diffraction. The difference between x-ray and electron scattering arises from the scattering operator L:[7]

$$\text{X-ray diffraction:} \quad L_x = \sum_i e^{i\mathbf{s}\mathbf{r}_i}$$

$$\text{Electron diffraction:} \quad L_e = \sum_j Z_j e^{i\mathbf{s}\mathbf{R}_j} - \sum_i e^{i\mathbf{s}\mathbf{r}_i}$$

The sums in these formulas stretch over all particles of a molecule. Where s is the magnitude of the momentum transfer vector, Z_j is the nuclear charge of atom j, and the distances R_j and r_i are over the nuclei j and electrons i, respectively. It can be seen that the x-ray diffraction signal is the Fourier transform of the electron density distribution within a molecule. The electron diffraction signal is the Fourier transform of nuclear and electronic charge distributions. For gas molecule and charge density distribution characterization, electron diffraction is widely used because of large interaction cross section. Electron diffraction is also relative compact and less harmful to bio-molecules.

Using a streak camera tube, 100 ps time resolution was realized in the initial UED setup [6] (Fig.1). A single laser is used for both electron beam generation and pump the sample under investigation. Most advances in UED are due to the progress of the laser technologies in the last twenty years. The state of art UED has time resolution on the order of several ps with 10^4 electrons [8]. Since molecular structure transition and chemical bond breaking take place on the time scale of 100 fs or less [3], femtosecond electron diffraction is desired for femtochemistry and other ultra-fast studies. We propose to develop a femtosecond electron diffraction facility using photocathode RF gun technology [9].

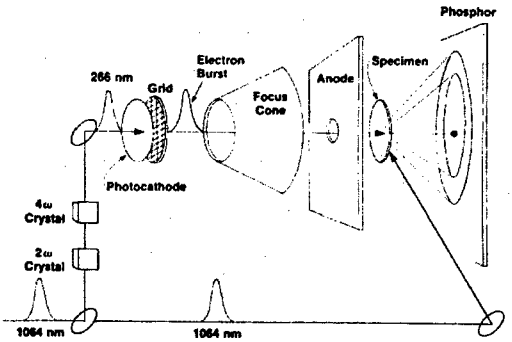

Figure 1: Schematic of UED setup from ref.[6].

The birth of photocathode RF gun can be traced to UED, it is a marriage of laser and high power RF technologies. Laser is used to generate electron beam, and control both the temporal and spatial distribution of

*Work supported by the US DOE.
#xwang@bnl.gov

electron beam. The photoelectron generated by the laser is rapidly accelerated to high energy. The higher electron beam energy, and flexibility of electron beam control made it possible to generate 100 fs electron in the photocathode RF gun. In the following section, a brief discussion on the time resolution of electron diffraction is presented. Then we will present the femtosecond electron beam generation using photocathode RF gun, and concluded with the discussion on the possible issues of femtosecond electron diffraction using photocathode RF gun.

CHALLENGES IN FEMTOSECONDS ELECTRON DIFFRACTION

For a typical electron diffraction based pump-probe experiment depicted in figure 1, the total time resolution can be expressed as following [10],

$$\Delta t^2 = \Delta t^2_{la} + \Delta t^2_{VM} + \Delta t^2_{eb} + \Delta t^2_{jit} \quad (1)$$

where is Δt_{la} is the laser pulse length, which is limited to 4.5 fs. Δt_{VM} is so called velocity mismatch between the laser and electron beam in the interaction region. It depends on the geometry of the interaction and dimension of the sample or molecule beam. It can be reduce with higher energy electron beam or geometric optimization. For the laser and electron beam parallel configuration and molecule beam size on the order of a couple hundred microns, Δt_{VM} will be less than 100 fs if electron beam energy more than one MeV. Δt_{jit} is the jitter between the pump laser and electron beam. For DC gun based electron diffraction system, it is negligible. To break the picosecond time barrier and reach 100 fs time resolution, femtosecond electron beam is the key.

Femtosecond electron beam generation for electron diffraction was studied extensively recently [11-12] for electron beam energy around 50 keV. The large energy spread and bunch lengthening due to space charge effect prevents it from reaching below ps. Space charge effects play a fundamental role in generation and preservation of femtosecond electron beam. To generate and preserve femtoseconds electron beam, longitudinal space charge effect must be carefully considered since it is much more sensitive to the beam energy than transverse space charge effect (fifth power vs third power). The bunch lengthening due to space charge effect can be estimated in a drift space by [13]:

$$\Delta \ell = \frac{2QcL}{I_a R \ell \gamma^4}^2 \quad (2)$$

where Q is the charge in the bunch, c is the speed of the light, L is the drift distance, Ia =17 kA, R is the bunch radius, ℓ is the bunch length and γ is the beam energy. The strong dependency of the bunch lengthening on the energy is the major barrier to produce and preserve femtosecond electron beam. As beam energy increases, it becomes more rigid and difficult to control (focusing) longitudinally. Balancing between space charge effects and bunching (focusing) demands that, bunching should be accompanied by the acceleration simultaneously. Photocathode RF gun is the technology capable of producing femtosecond electron beam with reasonable number of electrons [14].

FEMTOSECONDS ELECTRON BEAM GENERATION BY RF GUN

Higher electric field and beam energy from RF gun will lead to significant reduction in space charge effect. Another important advantage of using photocathode RF gun to produce femtoseconds electron beam is its capability of compressing the electron beam as it is being accelerated in the time dependent RF field [14]. This allows us to use longer laser pulse and reduce space charge effect further near the cathode region. Figure 2 shows photo-electron beam energy as function of the RF gun phase and field gradient on the cathode. By choosing proper field gradient and RF gun phase, the electron beam energy spread can be minimized. The photocathode RF gun considered here is 1.6 cell BNL S-band RF gun. The electron bunch length at both the RF gun exit and the target station (1 m down stream) is plotted as RF gun phase in figure 3 for the field gradient 50 MV/m. The number of electrons for this simulation is about 10^6, and laser pulse length is about 500 fs. If the number of electron is reduce to 10^5, simulation shows that, electron bunch length at the target station will be less than 100 fs. Table 1 summarize the expected performance of the photocathode RF gun at the field gradient 50 MV/m. For the purpose of comparison, typical DC gun is also listed there.

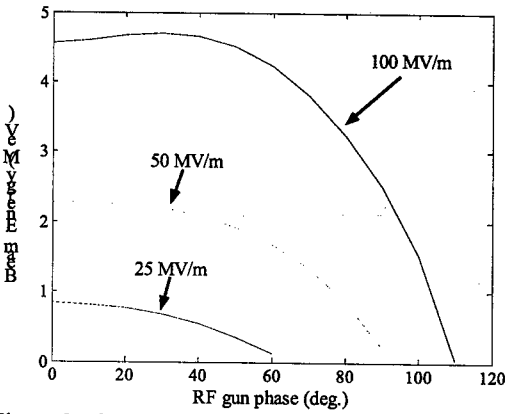

Figure 2: photo-electron beam energy vs. RF gun phase for three field gradients.

Several new issues arise from using photocathode RF gun, energy spread and timing jitter between the RF field and laser are two prominent examples. As we pointed out earlier, by proper selecting the field gradient (50 MV/m) and RF gun phase, energy spread as low as 0.01% can realized, which is comparable to DC gun.

Our studies show timing jitter can be easily controlled to below 100 fs even with couple hundreds fs jitter between

the laser and RF systems [15]. For pump-probe experiment, one laser system will be used for both pumping the sample and generating electron beam, so the jitter is the arrive time between the laser and electron beam. This jitter is dominated by the electron beam energy jitter because of the flatness of energy beam energy as function of the RF gun phase [15].

The success of femtoseconds electron diffraction depends on the electron beam quality. We propose to perform a proof of principle experiment at the BNL DUV-FEL facility to answer one of the key questions, that is, whether electron diffraction is measurable with MeV electron beam produced by the photocathode RF gun. We propose initial diffraction experiment will performed using thin metal film, such as Al. This can also be used to optimize electron beam for diffraction in the later stage. We will consider using gas sample, such as CCl4 or CF3I, or single crystal.

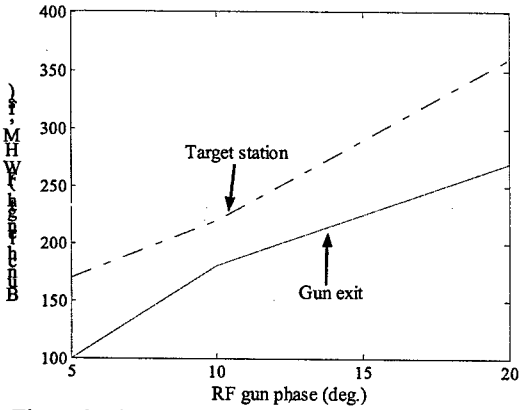

Figure 3: photo-electron beam bunch length vs. RF gun phase at gun exit and target station.

ACKNOWLEDGEMENT

We would like to thank the support from National Synchrotron Light Source (NSLS) and BNL director office. The encouragement and constructive suggestion from Drs C.C. Kao and J.B. Murphy is grateful acknowledged.

Table 1: Summary of femtoseconds electron beam properties for RF and DC guns.

	RF gun	DC Gun
Field on the cathode (MV/m)	50 – 100	10
Beam energy (MeV)	1.5 -4	0.03
No. of electrons	10^5 - 10^6	10^4
Bunch length (FWHM, fs)	100 - 200	4000
Energy spread (%)	0.01 – 0.005	0.01

REFERENCES

[1] Jianwei Miao *et al*, Phys. Rev. Lett., **89**, 088303-1 (2002).
[2] P. E. Batson *et al*, Nature, **418**, 617 (2002).
[3] A.H. Zewail, *Femtochemistry*, (World Scientific 1994).
[4] J. Galayda, ed., Linac Coherent Light Source (LCLS) Conceptual Design Report, SLAC-R-593 (2002).
[5] TESLA TECHNICAL DESIGN REPORT SUPPLEMENT, DESY 2002-167, TESLA-FEL-2002-9 (2002).
[6] G. Mourour and S. Williamson, Appl. Phys. Lett., **41**, 44 (1982).
[7] Time-resolved Electron and X-Ray Diffraction, edited by P.M. Rentzepis. (SPIE Publishing, Bellingham, WA, 1995).
[8] H. Ihee *et al*, Science, **Vol. 291**, 460 (2001).
[9] J. S. Fraser *et al*, PAC'87, p.1705 (1987).
[10] J. C. Williamson and A.H. Zewail, Chem. Phys. Lett., 209, 10 (1993).
[11] B.L Qian and H. E. Elsayed-Ali, Phys. Rev. E. **65** 046502-1 (2002).
[12] B. J. Siwick *et al*, J. Appl. Phys., **92**, 1643 (2002).
[13] C.E. Clayton *et al*, IEEE Trans. On Plasma Science, **24**, 400 (1996).
[14] X.J. Wang *et al*, Phys. Rev. E **54**, (1996) R3121-3124.
[15] X.J. Wang, "Timing Jitter Issues for Photocathode RF gun Based Linac System", to be presented at the FEL'03.

COMMISSIONING OF THE SPPS LINAC BUNCH COMPRESSOR

P. Krejcik, F.-J. Decker, P. Emma, K. Hacker, L. Hendrickson, C. L. O'Connell, H. Schlarb, H. Smith, M. Stanek, SLAC, Stanford, CA 94025, USA

Abstract

First results and beam measurements are presented for the recently installed linac bunch compressor chicane. The new bunch compressor produces ultra-short electron bunches for the Sub-Picosecond Photon Source (SPPS) and for test beams such as the E164 Plasma Wakefield experiment. This paper will give an overview of the first experiences with tuning and optimizing the compressor together with a description of the beam diagnostics and beam measurements. These measurements form the basis for further detailed study of emittance growth effects such as CSR and wakefields in a previously unmeasured regime of ultra-short bunch lengths.

INTRODUCTION

The SPPS project was conceived [1] to create extremely short bunches in the SLAC linac using a four-dipole bunch compressor chicane [2] located at the 1/3rd point along the linac. The chicane was installed in the linac in the summer of 2002 and beam commissioning began in November 2002. The short bunches are to be used in a number of experiments in the Final Focus Test Beam line (FFTB), and in addition provide a rich opportunity for machine studies in this new regime of accelerator physics [3]. The first experiments to utilize the high energy-density beam include the E164 Plasma Wakefield Experiment [4] in which the strength of the beam-plasma interaction is expected to scale approximately with the inverse of the bunch length squared. A 2.5 m long undulator has also been installed in the FFTB to generate short-pulse X-rays for SPPS experiments.

The short bunches are produced in the linac in a three stage bunch compression process beginning with electron beams extracted from the North Damping Ring (NDR), shown in figure 1. The 3 nC, 6 mm long bunch from the NDR is compressed to 1.16 mm in the Ring To Linac (RTL) beamline compressor. The wakefields in the linac combined with accelerating the beam off-crest by −19.5° give the beam an energy chirp, or correlated energy spread of $\sigma_E/E_0 = 1.6\%$ rms at the $E_0 = 9$ GeV entrance to the chicane in sector 10 of the linac. The momentum compaction, R_{56} = -76 mm, of the 14.3 m long chicane, made up of four 1.8 m long, 1.6 T dipole magnets, rotates the bunch in longitudinal phase space to give a final bunch length of 50 μm rms.

The short bunch generates strong wakefields in the linac downstream of the chicane which create a further correlated energy spread of $\sigma_E/E_0 = 1.5\%$ rms in the $E_0 =$ 28.5 GeV beam at the end of the linac. The transport optics of the FFTB will be tuned for a momentum compaction, R_{56} = 2 mm, for the forthcoming SPPS experiments to give a final compressed bunch length of 12 μm rms, resulting in a peak current of 30 kA. In this paper we focus on the operation of the new linac bunch compressor.

MODE OF OPERATION

Successful production of short bunches for multiple experimental programs necessitates sharing the beam pulses in the linac with PEP II operation. The linac is operated at 30 Hz to provide 9 GeV electrons and 3 GeV positrons, via the damping rings, for PEP II injection. A third electron bunch is accelerated to 23.5 GeV to produce positrons from a target located in sector 19 of the linac. A fourth bunch of electrons is available as a test beam and can be transported to the end of the linac to the FFTB line at 10 Hz, dropping down to 1 Hz during PEP II fills. The bulk of the klystrons in the final 1/3rd of the linac are not

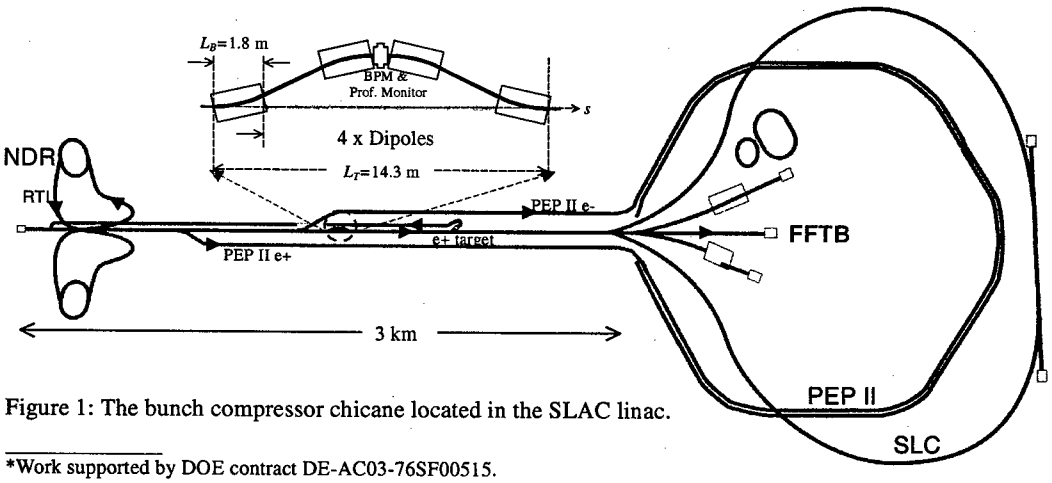

Figure 1: The bunch compressor chicane located in the SLAC linac.

*Work supported by DOE contract DE-AC03-76SF00515.

powered, except for a few tubes to provide energy control in a feedback system, so the 28.5 GeV test beam coasts through most of this section of the linac.

Only the test beam and the "scavenger" beam for positron production are transported through the sector 10 chicane. The two beam pulses can be individually controlled for bunch compression by pulsed control of both the RTL compressor RF amplitude and the RF phase at which the bunch is launched into the linac from the NDR. The linac can be set up to leave the scavenger beam uncompressed while the test beam is tuned to give the desired bunch length for experiments in the FFTB. The chicane does introduce a fixed path length difference relative to the straight ahead beams which requires a compensating change of 130° S-band in the downstream klystron phases and positron arrival time in the South Damping Ring (SDR).

The chicane magnets are powered by a 100 kW dc supply, which remains on for both the PEP II and Test Beam programs. An automated procedure was created for switching the linac state in the event that the chicane is turned off for straight ahead beam operation.

Although the chicane has a generous energy acceptance of $\Delta E/E_0 = \pm 17\%$, there is a Machine Protection System (MPS) to prevent pulses with large energy errors from damaging the vacuum chamber. The MPS comprises beam loss monitors and toroid beam current comparators at the chicane entrance and exit which lower the repetition rate of the scavenger and test beams until the fault is cleared.

BEAM TUNING

The minimum bunch length has been optimized for a charge of 2.1×10^{10} electrons per bunch, such that the wakefield contribution to the energy chirp produces the most linearly correlated energy spread in the bunch. The desired magnitude of the correlated energy spread is produced by accelerating the beam −19.5° from crest in sectors 2 through 6 in the linac. Sectors 7 and 8 are not powered during PEP II operation and the energy at the chicane is kept constant with a sector 9 energy feedback loop to hold the beam in the middle of the magnet aperture. A BPM placed at the peak dispersion location in the chicane where η_x = 45 cm allows the energy to be measured with a relative accuracy of 0.01% and is utilized in the energy feedback loop. The feedback loop [5] controls the phase of a pair of orthogonally phased klystrons to correct the energy without altering the average beam phase.

The beam energy measured by the feedback loop is a convenient way to calibrate the relative phase of the klystrons with respect to the RF crest, allowing the beam phase to be accurately set at the desired value of −19.5°.

A retractable profile monitor installed adjacent to the high-dispersion BPM in the chicane allows the energy spread of the beam to be measured by digitizing the video image of the beam on the screen and measuring the width of the spot. The energy spread at the end of the linac is measured on a profile monitor in the FFTB beam dump.

Two techniques are used for the tuning of the bunch length. One is a fast, relative measurement of bunch length changes for tuning purposes and the second uses a semi-invasive technique for an absolute determination of the bunch length.

Wake loss scans of bunch length

At the very short bunch lengths produced by the chicane the longitudinal wakes, or beam loading, over the remaining length of the linac, cause a significant energy loss that can be easily resolved at the energy dispersive locations at the end of the linac. The longitudinal wakes in the S-band accelerating structure have been extensively modeled and these measurements have provided a unique opportunity to validate the theory at such short bunch lengths [6].

The bunch length can be varied by scanning the phase of the klystrons upstream of the chicane (sectors 2–6). The energy feedback using the chicane BPM keeps the energy constant at the chicane during the phase scan so that any change in energy measured at the end of the linac will only be due to influences downstream of the chicane. The energy feedback at the end of the linac provides a convenient tool for measuring the energy change at a dispersive BPM. Figure 2 illustrates the measured energy change as a function of linac phase, showing a distinct minimum at a phase where the bunch length is minimized.

The exact phase at which the minimum occurs is dependant on the RTL compressor RF amplitude and on the bunch charge. The wake loss scan can also be used to find the optimum RTL compressor amplitude for a given setting of the linac phase. For a given compressor amplitude the predicted energy loss versus linac phase is compared to the measured energy loss in figure 2.

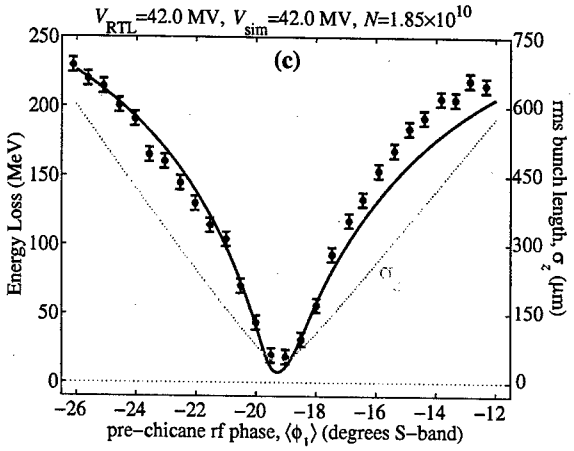

Figure 2: Energy measurement (points) and theory (solid) at end-of-linac shows maximum loss at the RF phase corresponding to minimum bunch length. Simulated rms bunch length (dashed) is also shown on right scale.

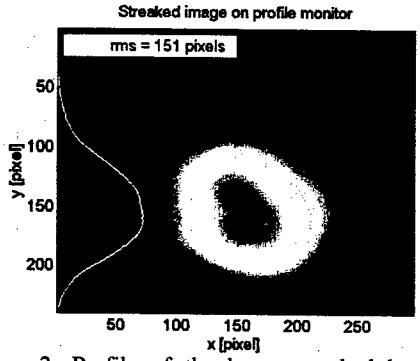

Figure 3: Profile of the beam streaked by the RF deflecting cavity.

RF transverse deflecting cavity measurement

The bunch length is measured with a 2.4 m long S-band RF transverse deflecting cavity [7] located near the end of the linac in sector 29. A deflection amplitude of 22 MV is achieved with an input power of 25 MW to the structure, which vertically streaks the beam across a profile monitor, shown in figure 3. The maximum resolving power of around 20 μm is obtained with the bunch at the zero-phase crossing of the RF, when there is no net deflection. The absolute calibration of the spot size on the screen to units of bunch length is obtained by offsetting the phase of the cavity and measuring the deflection of the beam centroid on the screen in pixels per degree S-band.

The bunch length is deduced from measuring the beam size at the screen for both settings of the zero-phase crossing and a third measurement with the cavity off. An automated procedure that relies on an orbit feedback to maintain the cavity phase accurately at the zero-crossing has been developed for measuring the bunch length. The rms width of the streaked beam profile is often biased by tails in the beam distribution so a Gaussian fit is used to give a bunch length for the core of the beam. The rms width calculated from a double-asymmetric Gaussian fit is better suited to the non-Gaussian profiles, but it is more sensitive to pulse-to-pulse variations in the beam distribution.

The vertical beam size squared measured at the three

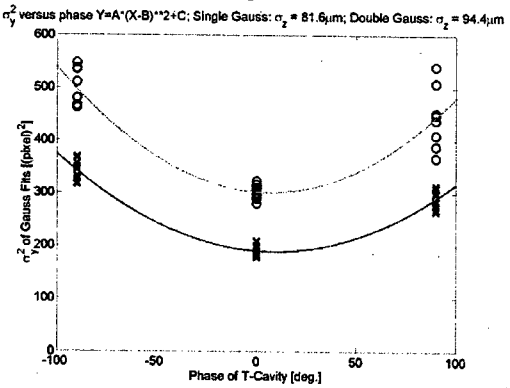

Figure 3 Vertical size squared of the streaked beam versus RF phase of the deflecting cavity using Gaussian fits (lower) and double-asymmetric Gaussian fits (upper).

cavity settings is fitted to a quadratic function,

$$\sigma_y^2 = A\phi_{rf}^2 + B$$

shown in figure 4, and together with the screen calibration C [pixels/deg. S-band] yields the bunch length

$$\sigma_z = \lambda_{rf}\sqrt{A}/4C$$

Bunch lengths in the range 50–100 μm rms have been measured in the linac with this technique for a bunch charge of 3 nC.

Transverse emittance

Emittances of $\gamma\varepsilon_x$ = 40 and $\gamma\varepsilon_y$ = 5 microns have been achieved for the compressed bunch at the end of the linac using the damping ring and linac diagnostic and tuning techniques developed for SLC. The small bunch length in the chicane, particularly in the final bend magnet can result in some emittance growth through coherent synchrotron radiation (CSR). A horizontal emittance growth of 22% has been measured with the chicane on relative to the chicane off. This is consistent with the predicted growth using theoretical models and particle tracking codes [8], where about half the growth is attributed to CSR and the other half to incoherent synchrotron radiation (ISR). These results help provide an upper limit for the expected, larger relative emittance growth in the LCLS and other short bunch machines.

REFERENCES

[1] M. Cornacchia et al., "A Subpicosecond Photon Pulse Facility for SLAC", SLAC-PUB-8950, LCLS-TN-01-7, Aug 2001. 28pp.

[2] L. Bentson, P. Emma, P. Krejcik *A New Bunch Compressor Chicane for the SLAC Linac*, EPAC'02, Paris, Fr., June 2002.

[3] L. Bentson, P. Bolton, E. Bong, P. Emma, J. Galayda, J. Hastings, P. Krejcik, C. Rago, J. Rifkin, C.M. Spencer *FEL Research & Development at the SLAC Sub-Picosecond Photon Source, SPPS*, FEL2002 24th Int. FEL Conf. To be publ. in NIM A.

[4] M. Hogan et al., *E-164 & E-164X: High Gradient Plasma Wakefield Acceleration Using Ultra-Short Bunches*, PAC'03, Portland, OR, USA, May 2003.

[5] L. Hendrickson et al, *Generalized Fast Feedback System in the SLC*, Int. Conf. on Accel. and Large Exp. Physics Control Systems, Tsukuba, Japan, Nov. 11-15, 1991. Publ. in ICALEPCS 1991:414-419

[6] K. Bane, et al., Measurement of the Longitudinal Wake in the SLAC Linac for Extremely Short Bunches, PAC'03, Portland, OR, USA, May 2003.

[7] R. Akre et al, *Bunch Length Measurements Using a Transverse Deflecting Structure in the SLAC linac*, EPAC'02, Paris, France, June 2002.

[8] P. Emma, F.-J. Decker, P. Krejcik, C. O'Connell, H. Schlarb, M. Woodley, *Measurements of Transverse Emittance Growth due to Coherent Synchrotron Radiation in the SLAC SPPS Bunch Compressor Chicane*, PAC'03, Portland, OR, USA, May 2003.

Proceedings of the 2003 Particle Accelerator Conference

BEAM TRANSPORT EXPERIMENTS OVER HALF-TURN AT THE UNIVERSITY OF MARYLAND ELECTRON RING (UMER)*

S. Bernal†, B. Beaudoin, Y. Cui, D. Feldman, R. Feldman, M. Glanzer, T. Godlove, I. Haber, J. Harris, M. Holloway, Y. Huo, R.A. Kishek, D. Lamb, W-T. Lee, H. Li, B. Quinn, M. Reiser, A. Valfells, M. Walter, M. Wilson, R. Yun, Y. Zou, and P.G. O'Shea,
Institute for Research in Electronics and Applied Physics,
University of Maryland, College Park, MD 20742

Abstract

The University of Maryland Electron Ring (UMER), designed for studies of space-charge dominated beam transport in a strong focusing lattice, is nearing completion. UMER models, for example, the recirculator machine envisioned as a possible driver for heavy-ion inertial fusion. The UMER lattice consists of 36 FODO periods distributed among 18, 20^0-bending sections containing two dipole magnets each. The main diagnostics are phosphor screens and capacitive beam position monitors placed at the center of each bending section. In addition, pepper-pot and slit-wire emittance meters, as well as an energy analyzer are in operation. We present here results of beam matching and characterization for a range of currents extending from about 1 mA to 100 mA, all at 10 keV and 100 ns pulse duration. With typical focusing given by σ_0=76^0, the zero-current betatron phase advance per period, the range of currents corresponds to tune depressions of 0.8 to 0.2. This range covers both the emittance dominated and extreme space-charge dominated regimes, which is unprecedented for a circular machine.

INTRODUCTION

The University of Maryland Electron Ring (UMER) is designed for *scaled* experiments employing low energy (up to 10 keV), high current (up to 100 mA) electron beams. A general description and motivation of the ring can be found in the UMER web page [1] and recent publications [2]. The development of individual components has been presented in papers at the 1999 and 2001 PACs, and updates appear in these Proceedings. Construction of a machine with a layout similar to UMER's was undertaken a few years ago at Lawrence Livermore National Laboratory. In the Livermore ring, a 80 keV (initial energy) potassium-ion beam was successfully transported and accelerated over one quarter turn [3]. In this paper, we report on results of electron beam transport experiments over one-half turn, i.e. 18 FODO periods. A detailed account of experiments over one-quarter turn was submitted for publication [4].

* Work supported by the U.S. Department of Energy.
† sabern@glue.umd.edu

LAYOUT AND DIAGNOSTICS

A photograph of the current UMER setup and the corresponding schematics are shown in Figure 1. The DC injector consists of a short solenoid, seven printed-circuit (PC) quadrupoles, a DC bending dipole, a number of elements for beam steering, and two sets of Helmholtz coils for balancing of the Earth's magnetic field. Results of rms envelope matching experiments with a former version of the injector were presented before [5]. The former DC injector employed six PC quadrupoles instead of seven, over a distance of one meter, approximately. The new DC injector not only provides a smoother transition into the periodic FODO lattice, but also fits the geometry of the pulsed, Y-shaped injector which is nearing completion (see M. Walter et al, TPPB025 paper in these proceedings.)

Nine bending sections (labeled RC1 through RC9 in Fig. 1) follow the matching/injection section. Each section contains two FODO periods, i.e. four PC quadrupoles and two PC bending dipoles, and a diagnostics chamber between the quadrupoles in the straight part. In addition, short PC steering dipoles for vertical steering are placed over the 4-1/2" flanges between sections. An important feature of UMER is that it takes advantage of the bending action of the Earth's magnetic field on the 10 keV electron beam. Thus, the required current on the PC bending dipoles is reduced from near 3.0 A to about 2.5 A.

The diagnostics in the straight section include a phosphor screen (chamber labeled IC1 in Fig. 1), a combination beam-position monitor (BPM)- Phosphor Screen (at IC2), and a fast Bergoz transformer between quadrupoles Q2 and Q3 for current measurements. The chambers in the ring sections also have a combination BPM-Phosphor Screen. The beam image is reflected at a mirror oriented at 45^0 and monitored through a window in each diagnostics chamber (Fig. 1). The phosphor screen/mirror housing is attached to the bottom plate of the BPM, so either one can be placed in line by means of an actuator. The BPMs are multiplexed and computer monitored (see B. Quinn et al, WPPB073 paper in these proceedings.) . End diagnostics include a second Bergoz coil near the entrance to the large diagnostics chamber and a magnetically-actuated phosphor screen system. The large diagnostic chamber houses a pepper-pot for integrated emittance measurements, as well as a slit-wire assembly for both horizontal and vertical, time-resolved

0-7803-7738-9/03/$17.00 © 2003 IEEE

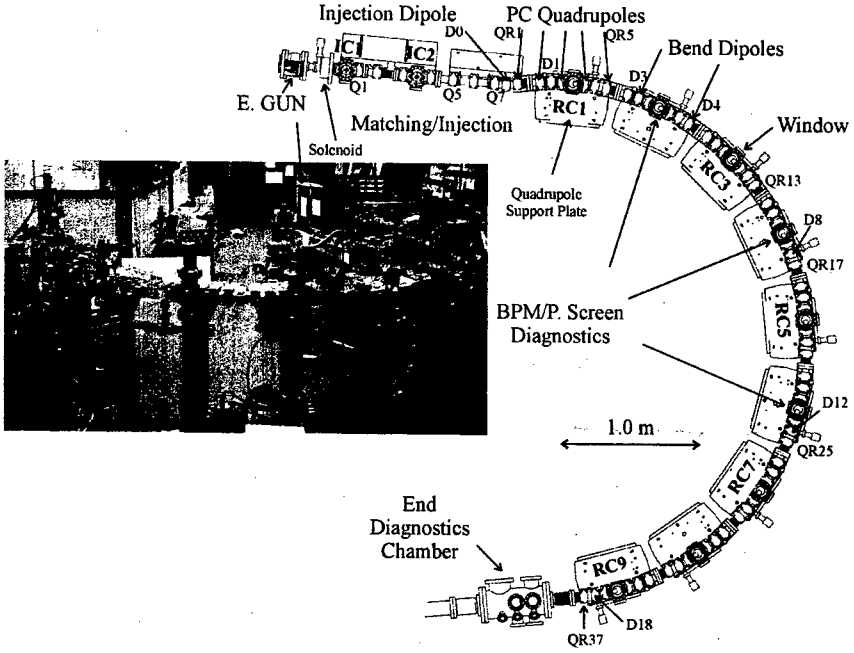

Figure 1: Photo and schematics of current UMER experiment. See text for explanation on labels.

emittance measurements (see M. Walter et al, TPPB074 paper in these proceedings.)

Lastly, we have installed a Nd:YAG laser near the exit of the UMER electron gun and demonstrated photoemission from the dispenser cathode. With pulse energies of 1-2 mJ in the 2nd and 3rd harmonics, we are able to obtain space-charge limited current pulses (100 mA) with pulse widths of 4.5ns. By adjusting the cathode temperature, we can produce combined thermionic and photoelectric pulses, and with suitable masks in the optical path, we have produced multiple beamlets from the UMER cathode. The new photoinjector has already proved to be a useful tool for initial studies of longitudinal beam dynamics (see A. Valfells et al, WPAG020 paper in these proceedings.)

Table 1: Beam Parameters (10keV, σ_0=76^0, ϵ=4$\times$rms, unnormalized emittance)

Current (mA)	Initial ϵ (μm)	Avg. Beam Radius (mm)	Tune Depression
0.55±5%	5±20%	1.3	0.8
24±2%	30	5.3	0.3
85±2%	55	9.5	0.16

BEAM ALIGNMENT AND RMS ENVELOPE MATCHING

Experiments were conducted with three different beam currents (see Table 1), the lowest one corresponding to an emittance-dominated beam and the other two in the region of extreme space-charge dominated transport. No current losses were measured for the 0.55 and 24 mA beams, but a <5% loss may occur for the 85 mA beam, which is attributable to halo particles from envelope mismatch. Beam-based alignment, on the other hand, varies from the lowest current cases to the 85 mA case, i.e. the steering dipoles have to be set differently for the highest current. This can be understood by the fact that beam- centroid drift from image forces, in addition to beam distortions from quadrupole rotation errors, plays a larger role for the highest current.

Beam-based alignment was done with the BPMs as follows: the "Left−Right" and "Top−Bottom" electrode signals from a BPM were minimized for different bending currents in the two bending dipoles upstream of the BPM chamber. The correct bending-currents pair was obtained by a scan of the quadrupole upstream of the BPM. As an example, the currents of dipoles D2 and D3 (Fig. 1) are varied and the BPM on RC1 monitored. The correct pair of currents, i.e. the one that gives both correct centroid and beam angle through the BPM, is chosen after current scans (±1.0 A) of QR3. The error in centroid location from this procedure is ±0.1 to ±0.4 mm, depending on beam current (see B. Quinn et al, WPPB073 paper in these proceedings.)

As mentioned above, another important factor in the experiments is the error in quadrupole rotation about the magnetic axis. Although the four quadrupoles in a given 20^0 bending section share a common support plate (see Fig. 1), there are small differences in roll angle among

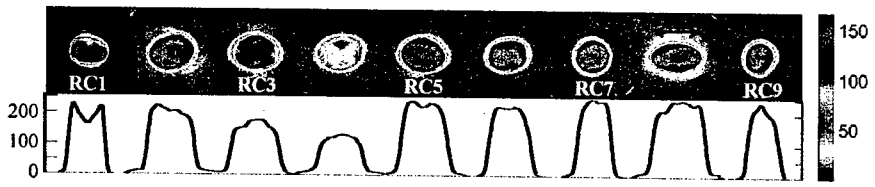

Figure 2: False-color rendering of fluorescent screen pictures of 24 mA beam (see Table 1) in the nine ring chambers, and horizontal straight-cut density profiles (8-bit grayscale, unnormalized).

the quadrupoles arising from assembly, mounting and other mechanical factors. Furthermore, the support plates in all ring chambers do not share exactly the same plane, despite an effort to adjust them with the help of an optical alignment system (see M. Walter et al, WPPB075 paper in these proceedings.) In order to alleviate the problem, the quadrupole mounts were individually leveled with an error of ± 1.0 mrad. Still, a residual effect of these errors is obvious in the beam cross section orientation, as seen in the picture montage of Figure 2 for the 24 mA beam. We should add that the CCD camera itself was leveled with the same accuracy as for the quadrupole mounts.

Initial rms envelope-matching calculations for the 24 mA beam (at 10 keV) are based on a straight FODO lattice (see [5]). The effective (2 rms) experimental beam radii in the two transverse directions are obtained from the fluorescent screen pictures. As can be seen in the picture montage of Fig. 2, the vertical dimension of the beam is essentially constant if one excludes the visible halo. However, the horizontal dimension shows a sudden increase, accompanied by an extended halo, from RC7 to RC8. Pepperpot emittance measurements, on the other hand, yield $\epsilon_{x,y}$=42,28 $\pm 5\mu$m at the end of the 180^0 system, compared with $\epsilon_{x,y}$=30,36 $\pm 5\mu$m from previous experiments over four ring chambers (i.e. a 90^0 bend). The value of initial emittance quoted in Table 1 is the number expected from linearly scaling the measured initial emittance of the full 100 $\pm$ 5mA beam. This scaling is based on the use of a 1.5 mm (radius) aperture to obtain the 24 mA beam. Finally, time-integrated measurements with the slit-wire system yield $\epsilon_{x,y}$=30,20μm, but a comparison between results from the two emittance meters is not straightforward.

The experiment with the 85 mA beam yields pictures with features similar to those of the 24 mA beam, except for generally larger cross section tilts. The first pepperpot emittance measurements, on the other hand, reveal an increase of 20-25% over the 90^0-system results, but additional tests that include the slit-wire meter are needed.

Other features under investigation are the possibility of transverse waves in the beam (see bottom of Fig. 2), associated anisotropy, dispersive and bunch-end effects, energy spread evolution and other studies of longitudinal dynamics. Concerning the latter, an accompanying paper presents results on the evolution of non-square current profiles in the ring (see A. Valfells et al, WPAG020 paper in these proceedings.)

CONCLUSION

We have demonstrated emittance as well as space-charge dominated beam transport in a 180^0 bend system. We are developing the "single-turn" beam physics in UMER as we build the machine. Foremost are beam-based alignment and envelope matching. They are increasingly more difficult for higher currents, despite better S/N in the signals from the capacitive BPMs. This is so because of the role of image forces and quadrupole rotation errors. The way bending couples with these effects is still under study, and its understanding should provide the means for transport with minimum emittance growth, a prerequisite for multi-turn operation in UMER.

REFERENCES

[1] http://www.ipr.umd.edu/ebte/ring/

[2] P.G. O'Shea et al., "Experiments with Space-Charge-Dominated Beams for Heavy-ion Fusion Applications", Laser and particle beams, 20, 599-602 (2002). P.G. O'Shea et al, Nucl. Instr. Phys. Res. A **464**, 646-652 (2001).

[3] L. Ahle et al., "Results from the Recirculator Project at LLNL", Nucl. Instr. Phys. Res. A **464**, 557-562 (2001).

[4] S. Bernal et al., submitted to Nucl. Instr. Phys. Res. A.

[5] S. Bernal et al., "Beam Tests of the 10 keV Injector for the University of Maryland Electron Ring (UMER)", Proc. PAC 2001, Chicago, Ill (2001).

NEUTRINO BEAM FACILITIES AND PROJECTS*

W.T. Weng#, M.V. Diwan, BNL, Upton, NY 11973, USA

Abstract

Neutrino oscillations have been firmly established by the experimental results on Atmospheric and Solar neutrinos. As impressive as the results from these experiments are, it is clear that we are just getting started on a long-term experimental program to understand neutrino masses, mixing, and possibly leptonic CP violation. Many new facilities and experiments are underway to explore the detailed oscillation mechanism for comparison with theoretical predictions. Also, further improvements on neutrino oscillations using a muon storage ring based on Neutrino Factory will be covered.

INTRODUCTION AND NEUTRINO OSCILLATION

Dr. Ray Davis of BNL and Prof. Masatoshi Koshiba of Japan shared the 2002 Nobel Prize in Physics for their path-breaking measurement of the terrestrial fluxes of Solar and atmospheric neutrinos. Their research established that neutrinos have mass and oscillate among three flavor states as they propagate through space and time. Neutrino oscillations can arise if the flavor and mass eigenstates are not the same. Assuming three flavors and mass eigenstates, a specific form of the mixing matrix for the three known active flavors has been developed by Maki, Nakagawa and Sakata and is known as the "MNS matrix" [1]:

$$U=\begin{pmatrix} c_{13}c_{12} & c_{13}c_{12} & s_{13}e^{-i\delta} \\ -c_{23}s_{12}-s_{13}s_{23}c_{12}e^{i\delta} & c_{23}c_{12}-s_{13}s_{23}s_{12}e^{i\delta} & c_{13}s_{23} \\ s_{23}s_{12}-s_{13}c_{23}c_{12}e^{i\delta} & -s_{23}c_{12}-s_{13}c_{23}s_{12}e^{i\delta} & c_{13}c_{23} \end{pmatrix}$$

Where $c_{ij} = \cos\theta_{ij}$ and $s_{ij} = \sin\theta_{ij}$. This is completely analogous to the CKM matrix for the quark sector. Of importance, we note that a CP-violating phase δ is possible. Interpretation of the experimental results is based on oscillations of one neutrino flavor state, ν_e, ν_μ, ν_τ, into the others, and described quantum mechanically in terms of neutrino mass eigenstates, ν_1, ν_2, and ν_3. For example, for a ν_μ-beam coming from a neutrino facility, the ν_e appearance probability to leading order is given by

$$P_{\nu_\mu\to\nu_e}=\sin^2(\theta_{23})\sin^2(2\theta_{13})\sin^2\left(\frac{1.27\Delta m^2_{32}(eV^2)L(km)}{E_\nu(GeV)}\right) \quad (1)$$

A detector must be placed at an appropriate distance from the neutrino source to allow the neutrino enough time to oscillate. The combined experimental results indicate that, the mass differences involved in the transitions are measured to be approximately $\Delta m^2_{21} = (5-10)\times10^{-5}eV^2$ for the solar neutrinos and $\Delta m^2_{32} \equiv m(\nu_3)^2 - m(\nu_2)^2 = \pm(1.6-4.0)\times10^{-3}eV^2$ for the atmospheric neutrinos, with large mixing strengths, $\sin^2 2\theta_{12} \sim 0.8$ and $\sin^2 2\theta_{23} \sim 1.0$ in both cases. These parameters will be measured with better accuracy in the experiments that are now either under construction or taking data. Nevertheless, the parameters are now sufficiently well-known that they open the possibility for accelerator based very long baseline experiments that can explore the complete set of neutrino oscillation parameters, perform precise measurements of the mixing parameters, and search for new physics.

SURVEY OF EXISTING AND APPROVED FACILITIES

For an effective experiment to study neutrino properties, one needs a good neutrino source and a reliable way of detection. For an accelerator-based system, a powerful proton accelerator and a well-designed target and beam focusing system are required. When the protons hit the target, copious number of pions are generated which quickly decay into muons and neutrinos. To increase the flux of neutrinos at a detector far away from the target, a pulsed horn is usually deployed to provide additional focusing of the pion beam. In table 1 we list the world-wide neutrino facilities and their design parameters. The first type of facilities are those already in use, or under construction. The second type are those in the planning, or proposal stage.

As shown in Eq. (1) the ν_μ oscillation probability is governing by the ratio of L/E_ν indicating that the distance from the target to the detector, L, and the neutrino beam energy, E_ν, are important parameters for a design of the neutrino beam facility. Therefore, in Table 1 those two parameters are listed in addition to that of the proton beam. Total flux per year for each facility is arrived at by assuming 10^7 seconds of operation per year. E_ν usually is chosen according to Eq. 1 to be around the first peak of oscillation, where $1.27\Delta m^2_{32}L/E = \pi/2$. However, for the proposal by BNL, all energies from about 1.0 GeV to 7.0 GeV are included in the analysis, since it aims at seeing the pattern of several oscillations. Another quantity included is the fiducial mass, FM, of the far detector which determines the event rate and resolution of the data.

*Work performed under the auspices of the U.S. Department of Energy.
#weng@bnl.gov

0-7803-7738-9/03/$17.00 © 2003 IEEE

Table 1. High Intensity Proton Sources for Neutrino Experiments

Machine	Flux (10^{13}/pulse)	Rep Rate (Hz)	Ep (GeV)	Power (MW)	Eν (GeV)	L (km)	Detector	FM (kT)
Existing and Approved								
KEK PS	0.8	0.5	12	0.005	1.3	250	SK	22.5
Fermilab Booster	0.5	7.5	8	0.05	0.7	0.5	Mini Boone	0.4
Fermilab Main Injector	3	0.54	120	0.4	3.5	735	MINOS	5.4
CERN SPS	4.8	0.17	400	0.5	17	732	ICARUS OPERA	2.35 1.65
J-PARC 50 GeV	32	0.3	50	0.75	0.8	295	SK	22.5
Proposed Facilities								
Fermilab MI Upgrade	15	0.65	120	1.9	3.5	735	MINOS	5.4
BNL AGS Upgrade	9	2.5	28	1	1.0-7.0	2540	UNO or 3M	500
J-PARC Upgrade	32	0.9	50	2.2	0.8	295	HK	540
CERN SPL	23	50	2.2	4	0.26	130		40

Since the location and distance of the detector are important aspects of neutrino oscillation experiments, we show in Fig. 1 maps of the three existing facilities.

K2K uses a "standard" neutrino beam configuration. The 12 GeV protons impinge on a target to produce pions. The pions are focused using a double-horn system in the direction (on-axis) of Super-Kamiokande and directed down a decay pipe which is ~150m long. The peak neutrino energy is about 1.3 GeV. To date, a total of 5.6×10^{19} protons have been delivered to the K2K neutrino beam target. This has resulted in a total of 29 single-ring muon-like events observed at Super-Kamiokande with the expected number being 42 ± 6 events with no oscillations. An oscillation analysis on these events shows that the resulting oscillation parameters are in good agreement with those measured from the atmospheric neutrinos [2], although the result is still statistically limited.

A new Japanese construction project, J-PARC, is in progress at JAERI-Tokai site aiming the completion by March 2007 [3]. Using the 50 GeV proton synchrotron in J-PARC, a long baseline neutrino oscillation experiment is being planned. In the first phase of the project, the power of the 50 GeV PS will be 0.75 MW, and SK will be used as the far detector. The intensity of the neutrino beam is expected to be about 2 orders of magnitudes higher than K2K. The baseline length between JAERI and SK is 295 km. The goals of the first phase are the precise measurements of oscillation parameters in ν_μ disappearance and the discovery of ν_e appearance. Also, $\nu_\mu \rightarrow \nu_\tau$ or $\nu_\mu \rightarrow \nu_s$ oscillation can be tested by measuring the number of NC interactions in SK.

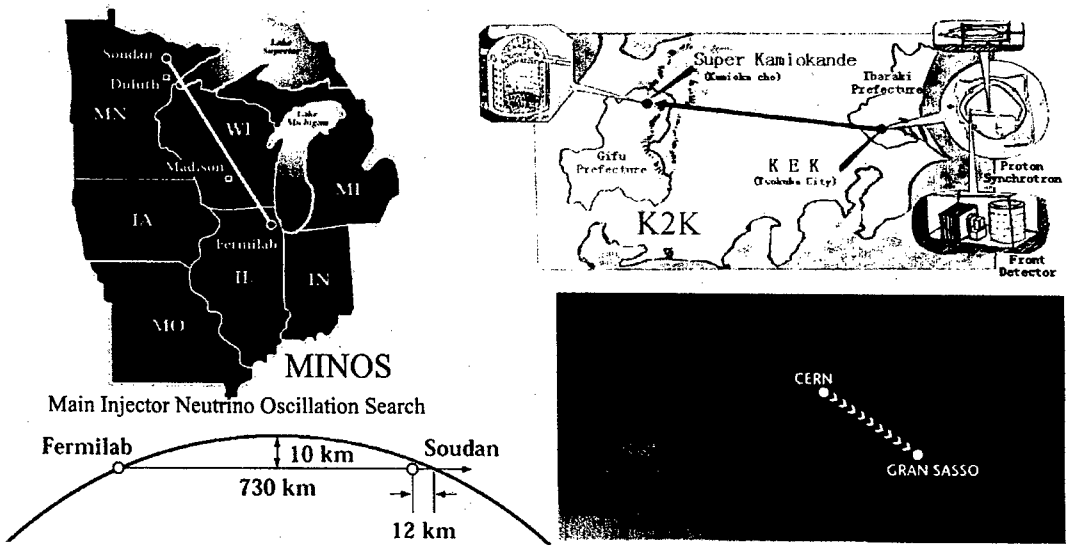

Figure 1: Map for K2K, NUMI, and CNGS Experiments

In the US, the current long-baseline project is the MINOS (Main Injector Neutrino Oscillation Search) experiment using the NuMI (Neutrinos at the Main Injector) beamline at Fermilab[4]. MINOS will make use of the intense neutrino beam afforded by the Main Injector to make precise measurements of neutrino oscillations associated with the "atmospheric" signal. By 2005, the Main Injector is expected to provide 120 GeV, 4×10^{13} protons per pulse every 1.9 sec to the NuMI target. This operation corresponds to 0.4 MW of proton power for ν-productoin.

The NuMI beamline is larger than that of the K2K beamline. It uses a graphite target because of higher beam power. It is also tunable to scan a wider ν energy spectrum.

The MINOS experiment utilizes a near and far detector of very similar construction in order to permit precise measurements of oscillation parameters, clear demonstration of the oscillation signature and precise determination of the flavor participation of all neutrino types involved in the oscillations. The MINOS detectors are sampling calorimeters with 2.54 cm thick iron absorbers interleaved with 1.0 cm thick plastic scintillator strips, which are 4 cm wide. The iron in the detectors is magnetized with typical field of 1.5 T.

The MINOS far detector has a total mass of 5.4 kT. Roughly 5000 ν_μ charged-current events are expected, in the absence of oscillations, in the far detector for two years of running. A picture of the MINOS detector assembly at the Soudan mine is shown in Fig. 2.

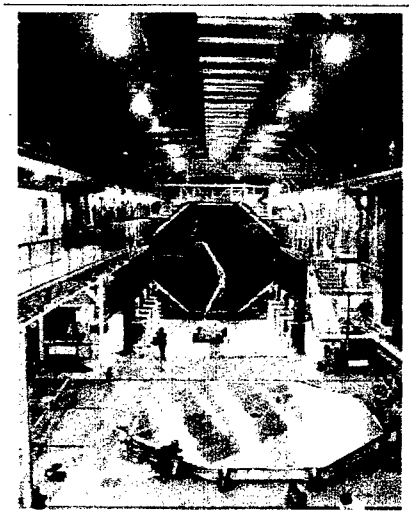

Figure 2: Installation of MINOS Detector

The third near-term long-baseline project which is also in construction is the CERN to Gran Sasso (CNGS) beamline and experiments [5]. The CNGS beamline will use 400 GeV protons from the SPS to create a high energy neutrino beam (E_{avg} = 17 GeV) aimed at the Gran Sasso. The primary goal of this beamline and the experiments at the Gran Sasso will be to demonstrate the direct appearance of ν_τ CC events from the ν_μ beam. This beam will be commissioned in 2006.

The two detectors which will initially utilize this beam at the Gran Sasso are Opera and Icarus. Opera will use plates of emulsion interleaved with thin lead plates to look for CC ν_τ events where the τ is produced in the lead and then subsequently decays in a gap downstream where a kinked track will be observed in the emulsion. Opera plans a total detector mass of about 2 kT, dominated by the mass of the lead. Icarus is a large liquid argon TPC that can identify CC ν_τ events on a statistical basis through the transverse momentum imbalance which results when a τ decays to a muon or electron.

SURVEY OF PROPOSED FACILITIES (SUPERBEAM)

The existing and approved projects were designed before the neutrino oscillations had been unequivocally confirmed and were also limited by proton beam power. Typical event rates are about few tens to a hundreds per year. With the advent of recent discoveries and interest, many more powerful facilities have been proposed. All of them aim to reach proton beam power in the range of 1.0 to 4.0 MW to substantially increase the event rate to several thousands. Recent progresse on the design of the high power proton drivers were reviewed in references [6] and [7]. Such facilities allow precision measurements of most of the mixing parameters and mass differences. The BNL proposal based on a 1 MW upgraded AGS and a 2540 km baseline intends to observe the oscillation pattern as a function of neutrino beam energy, covering three full oscillations yielding precise resolution of all interested parameters. An unique aspect of the BNL proposal is the ability to measure CP parameters with ν_μ beam alone.

When upgrade paths are discussed for various neutrino beam facilities, usually only the accelerator is presented. However, the most difficult part is the target and associated pion decay channel and radiation shielding. Much R&D effort needs to be expended on a reliable target system for more than 2 MW power, and the associated infrastructure is very difficult to revamp after operation due to the intense radiation environment.

As shown in Table 1, NuMI can be upgraded to about 2 MW by increasing the Main Injector intensity from 3×10^{13} ppp to 15×10^{13} ppp and increase the repetition rate by 20%. Similarly, J-PARC can upgrade the proton beam power to 2.2 MW by tripling the repetition rate of the 50 GeV synchrotron. Both the NuMI upgrade project and the J-PARC stage 2 project are designed to provide a "narrow band" off-axis ν beam [8]. Such a beam is

expected to reduce the neutral current interaction background to the ν_μ-ν_e appearance search.

In Europe, there is an idea of a superbeam LBL experiment in which the neutrino beam is produced by a superconducting Super Proton Linac (SPL) at CERN and detected by a detector at Modane laboratory in the Furejus tunnel, 130 km from CERN [9]. The proposed SPL is a 2.2 GeV LINAC with 4 MW beam power operated at 75-Hz repetition rate and 1.5×10^{14} protons/pulse. The neutrino beam is a conventional wide-band beam with the expected neutrino ranges < 500 MeV. This matches with the oscillation maximum of ~ 300 MeV at $\Delta m^2 = 3 \times 10^{-3}$ eV^2.

In BNL's superbeam proposal, the neutrino beam is produced by the 28 GeV proton beam from the Alternating Gradient Synchrotron (AGS) at BNL and is detected by a large detector of 500 kT, most likely of the water Cherenkov type, at a distance of 2540 km. For this discussion, the detector is assumed to be located at the Homestake mine in Lead, South Dakota. The primary purposes are precise determination of oscillation parameters, search for ν_e appearance and CP violation. The main ingredients of this new facility are (1) construction of a superconducting LINAC to raise the injection energy to 1.2 GeV, (2) increase the repetition rate of the AGS from 0.6 to 2.5 Hz, and (3) construction of a 1.0 MW target station and neutrino beam channel. [10,11]

The layout of the proposed addition of the 1.2 GeV SCL and the AGS is shown in Fig. 3. The target and horn system are designed in such a way that neutrinos with energy from about 1 GeV to 7 GeV are copiously produced.

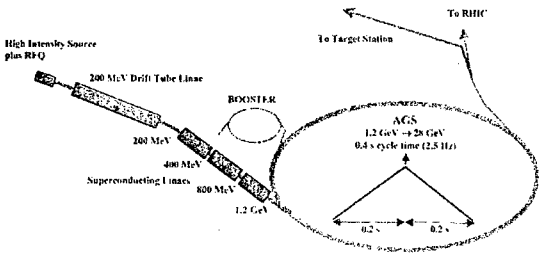

Figure 3: AGS Upgrade to 1 MW

To achieve the 1 MW upgrade option of the proton driver at BNL serious consideration has been given to both the target material and horn configuration. A solid target is a viable choice for a 1 MW beam. Low and high Z materials have been investigated both in terms of the material endurance as well as the feasibility of target/horn configuration. Results of the parametric studies on material choices regarding pion production are shown in Fig. 4.

A graphite-based carbon-carbon composite is selected as a target material both for its low-Z and thermo-mechanical properties. Various aluminum-based materials are being considered for horn conductors.

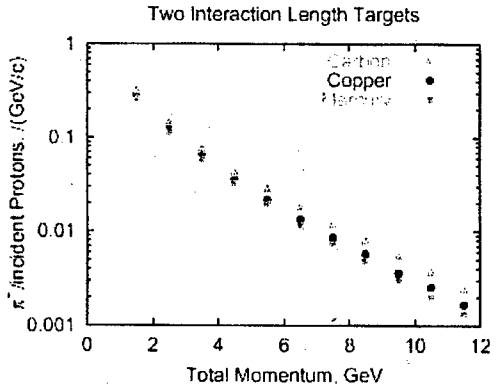

Figure 4: Pion production as function of proton momentum for different materials

The main source of ν_μ is the two body pion decay $\pi^+ \rightarrow \nu_\mu \mu^+$. The pions are produced in interactions of the proton beam with a target. Neutrino energy from the above decay is

$$E_\nu \cong \frac{0.43 E_\pi}{1+\gamma^2\theta^2}, \qquad (2)$$

where γ is the pion relativistic boost and θ is the neutrino emission angle at decay. It is seen from the above equation that in order to get a neutrino beam of the energy of 1.0 – 7.0 GeV in a detector placed on the facility axis, one would need to focus pions of 2.3 to 11.7 GeV energy. This wideband spectrum can be achieved by a careful design of a multiple horn system.

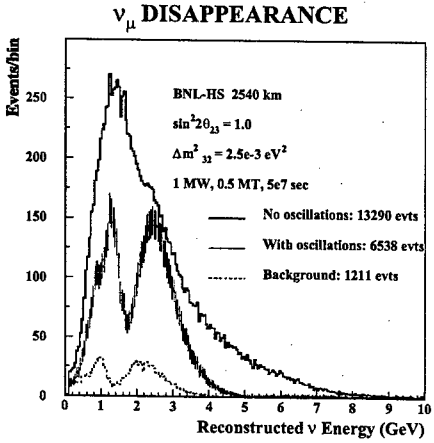

Figure 5: ν_μ Disappearance

With a target located at 2540 km away, more than two full neutrino oscillations can be detected to yield much better determination of mixing parameters and mass squared differences. Shown in Fig. 5 is the expected reconstructed neutrino energy spectrum of detected single muon track events in a 0.5 MT detector at 2540 km from BNL in which quasielastic events are expected to

dominate. 1.0 MW of beam power and 5 years of running are assumed. The top histogram is without oscillations; the middle error bars are with oscillations and the bottom histogram is the contribution of the background to the oscillated signal only. The oscillated plot is for $\Delta m^2_{32} = 0.0025\, eV^2$. The AGS neutrino facility can be upgraded to 4 MW by doubling both the intensity and the repetition rate of the AGS.

As shown in reference [10], if $\sin^2 2\theta_{13} \geq 0.01$ then the wide band BNL spectrum of ν_e events from the $\nu_\mu \rightarrow \nu_e$ oscillation contains sufficient information to determine both δ_{cp} and θ_{13} with good resolution and few ambiguities. One of the simulation results is shown in Fig. 6.

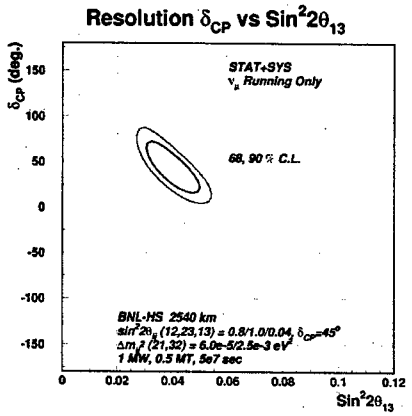

Figure 6: Mass-ordering and CP-violation parameter δ_{cp}

NEUTRINO FACTORY

Around 1998, it was realized that neutrino beams generated from muon storage rings could be very intense and pure. The muon storage ring designed to produce a large number of neutrinos for experiment is called a "Neutrino Factory" [12]. The design calls for a 4 MW proton driver to produce about 5×10^{20} μ/year at about 300 MeV. The muons are then quickly accelerated to about 10-20 GeV to be stored in a storage ring with long straight sections that produce the neutrino beam aiming at the detector. Depending on the size and distance of the detector, typically $10^5 \sim 10^6$ neutrino events can fall into the fiducial volume of the detector for experiment. Such beams will have unique properties:

- Very intense beams, on order tens to hundreds of times more intense than planned superbeams.
- Relatively clean narrow-band beams.
- Intense, high energy ν_e and $\overline{\nu}_e$ beams.

The comparison for the determination of the parameter θ_{13} for Superbeam and Neutrino Factory is given in Fig. 7 [13]. It is shown that the Neutrino Factory can give a reliable determination of $\sin^2 \theta_{13}$ down to about a few 10^{-5}.

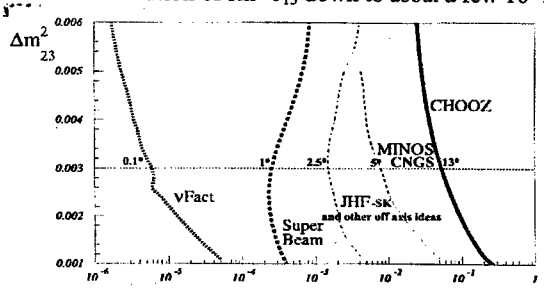

Figure 7: The reach of $\sin^2 \theta_{13}$ by various experiments

While the sensitivity of experiments with conventional horn focused ν_μ beams are limited by the intrinsic background of ν_e to about $\sin^2 2\theta_{13} > 0.005$, the ν factory approach is much more sensitive. Nevertheless, unlike the wide band approach promoted by the BNL group, the CP measurement with the ν factory must be done by comparing the probability of $\nu_\mu \rightarrow \nu_e$ versus $\overline{\nu}_\mu \rightarrow \overline{\nu}_e$. Such an approach naturally makes the running time much longer and the interpretation of the result is considered to have ambiguities unless the experiment is performed with many different baselines [14,15].

ACKNOWLEDGMENT

The authors would like to thank the information provided by NuMI and MINOS project of FNAL. The contribution by the BNL Neutrino Working Group is also appreciated.

REFERENCES

[1] Z. Maki, M. Hakagawa, and S. Sakata, Prog. Theor. Phys. 28:870, 1962.
[2] S. Fukuda, et al., Phys. Rev. Lett. 86:5656, 2001.
[3] Y. Mori, AIP Conf. Proc. 642, p. 23, 2002.
[4] J. Hylen, NBI-02, CERN, March 2002.
[5] K. Elsener, NBI-02, CERN, March 2002.
[6] W.T. Weng, Proc. PAC 1997, p. 42, May 1997.
[7] W. Chou, AIP Conf. Proc. 642, p. 29, 2002.
[8] D. Beavis, et al., E889 Physics Design Report, BNL 52459, April 1995.
[9] H. Haseroth, Nucl. Ins. And Meth. A472, p.376, 2001.
[10] M. Diwan, et al., "Very Long Baseline Neutrino Oscillation Experiments", submitted for Phys. Rev. D, March 2003, also hep-ph/0303081.
[11] M. Diwan, W. Marciano, and W.T. Weng, et al., "AGS Super Neutrino Beam Facility", BNL-71228-IR, April 2003.
[12] K. McDonald, "R&D Efforts for Neutrino Factories and Muon Colliders", these proceedings.
[13] A. Blondel, ICFA Seminar, CERN, October 2002.
[14] V.D. Barger, et al., PRD63 113011 (2001).
[15] P. Huber, et al., Nucl. Phys. B645, 3-48 (2002).

STORAGE RINGS FOR FAST COOLING OF ANTIPROTON AND RADIOACTIVE ION BEAMS

B. Franzke, P. Beller, K. Beckert, A. Dolinskii, P. Hülsmann, F. Nolden, C. Peschke, M. Steck,
GSI, Planckstrasse 1, D-64291 Darmstadt, Germany

Abstract

Production, fast cooling, and accumulation of intense secondary beams, antiprotons and rare isotopes, are key issues of the new accelerator facility proposed for GSI. Single primary bunches of 2×10^{13} protons at 29 GeV and 1×10^{12} U^{28+}-ions at 1 GeV/u shall be delivered from the new, fast-ramped 100 Tm-synchrotron SIS100. A large acceptance, reversible polarity collector ring CR is foreseen for fast RF debunching followed by fast stochastic pre-cooling in all phase planes. The envisaged total pre-cooling times are 4-5 s for 3 GeV antiprotons and 0.5-1 s for fully stripped RI at 740 MeV/u. Stochastic accumulation of antiprotons shall be made in a separate accumulator ring RESR. The RI beams are transferred to a New Experimental Storage Ring NESR, where electron cooling (EC) is applied simultaneously to internal target experiments. For experiments with antiprotons, a special 50 Tm storage ring HESR shall be equipped with internal target and EC up to 15 GeV, optionally also with stochastic cooling. The HESR design aims at a maximum luminosity of $2\times10^{32}cm^{-2}s^{-1}$ and at 100 keV energy resolution at lower luminosity. Basic design issues for the storage ring complex and results of numerical simulations of cooling rates and equilibrium beam properties are discussed.

1 OVERVIEW TO NEW FACILITY

The conceptual design report for an "International Accelerator Facility for Beams of Ions and Antiprotons" [1] on the GSI site was presented in autumn 2001. The proposal was evaluated in 2002 among other proposals for large-scale research instruments by the federal Research Council, which gave a fairly positive recommendation in favor of the GSI-proposal. In a press release of February 9, 2003, the federal research minister (BMBF) gave 'green light' for the preparation of the 675 M€ project a quarter of which has to be contributed by international partners.

The proposed accelerator complex (see fig. 1) may be characterized by following major scientific objectives:

- Nuclear structure physics with rare isotope beams (RI beams) at high mean intensities for external target experiments and high peak intensities for internal target experiments with cooled beams of short-lived nuclei.
- Nuclear collision experiments investigating compressed baryonic matter with heavy projectiles up to $^{238}U^{92+}$ at specific projectile energies up to 34 GeV/u.
- Internal target experiments with cooled antiproton beams at luminosities up to $2\times10^{32}\,cm^{-2}\,s^{-1}$ for investigations of exotic hadronic states with high resolution.
- Atomic physics experiments with high-Z ions in a wide energy range up to relativistic energies.
- Plasma physics experiments investigating evolution and properties of hot, dense plasmas generated by means of intense heavy ion beam pulses.

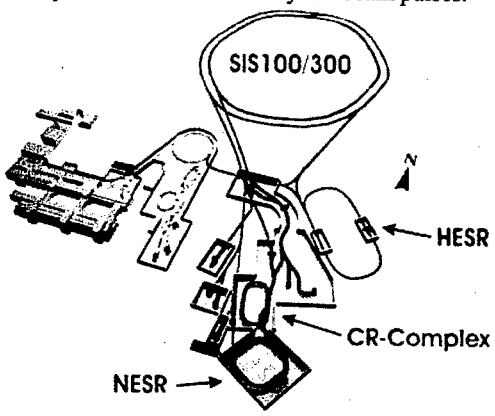

Figure 1: Preliminary layout of the proposed accelerator/storage ring facility at GSI (see text below).

The layout of the proposed accelerator/storage ring complex is shown in figure 1. The existing UNILAC-SIS18 accelerators (left side) shall serve as injectors, supplemented by a 50 MeV proton linac for antiproton production. The fast-cycling 100 Tm-synchrotron SIS100 [2], equipped with super-ferric 2 T-dipoles (ramp rate 4 T/s), will accelerate 1×10^{12} U^{28+}-ions per cycle for RI production at 1-2.7 GeV/u and 2×10^{13} protons per cycle for antiproton production at 29 GeV. The high beam intensities per SIS100 cycle are obtained by means of multi-turn filling the SIS18 up to the space charge limit at injection energy (11.5 MeV/u for heavy ions and 50 MeV for protons) and by accumulating 4 to 5 SIS18 cycles in the correspondingly larger SIS100 ring. The super-conducting 300 Tm-SIS300, installed in the same ring tunnel, will be used to accelerate about 1×10^{10} U^{92+}-ions up to 34 GeV/u for nuclear collision experiments, but alternatively also as stretcher for SIS100-beams.

This contribution describes the concept of collection, fast cooling and accumulation of RI and antiproton beams in the 13 Tm-CR complex consisting of a large acceptance Collector Ring CR and an accumulator ring RESR. The pre-cooled beams are led to Experimental Storage Rings (xESR) equipped with internal target experiments and electron coolers: RI beams to the 13 Tm-NESR and antiproton beams via SIS100 to the 50 Tm-HESR.

0-7803-7738-9/03/$17.00 © 2003 IEEE

2 SECONDARY BEAM PRODUCTION

2.1 *Rare Isotope Beams*

Experimental data measured at the existing fragments separator FRS behind SIS18 confirmed that optimal yields of neutron-rich, i.e. most exotic, nuclei are obtained by induced fission of ^{238}U-projectiles at energies up to 1.5 GeV/u. Therefore, ^{238}U may be considered as reference nucleus for the formation of rare isotope ion beams at the proposed facility. The acceleration of $^{238}U^{28+}$ ions in the proposed SIS18-SIS100 accelerator combination will allow not only to attain a high primary beam intensity of 1×10^{12} ions per cycle, but also to compress all projectiles into a single bunch of only 50 ns duration and 2% full momentum spread. The concept of time focusing minimizes the increase of the longitudinal emittance for the secondary beams and makes it possible to apply fast debunching (i.e. fast momentum spread reduction) after injection to the CR.

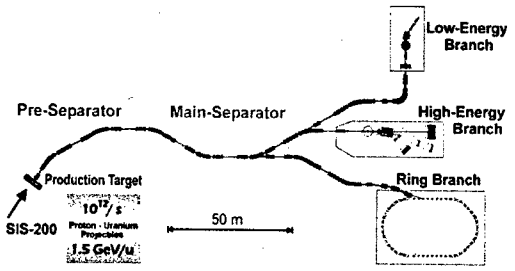

Figure 2: Layout of the Super-FRS [3], a magnetic separator equipped with super-ferric dipole and quadrupole magnets. The maximum bending power $B\times\rho_{max}$ is 20 Tm, the resolving power $M/\Delta M$ about 1500.

Table 1: A few examples of expected RI intensities per SIS100 cycle after Super-FRS and injection to the CR. The heavy species are produced by induced fission of 1×10^{12} uranium projectiles per cycle at 1.5 GeV/u, the lighter ones by fragmentation of lighter projectiles (e.g. ^{55}Ni from ^{58}Ni) at lower specific energies. Decay times are given for nuclei at rest [3].

Nucleus	Yield / cycle	Decay time $\tau_{1/2}$ [s]
$^{11}Be^{4+}$	6.0×10^{8}	13.8
$^{46}Ar^{18+}$	3.2×10^{8}	7.8
$^{55}Ni^{28+}$	3.9×10^{7}	0.2
$^{71}Ni^{28+}$	6.7×10^{6}	2.6
$^{91}Kr^{36+}$	4.2×10^{7}	8.6
$^{104}Sn^{50+}$	5.0×10^{5}	20.8
$^{132}Sn^{50+}$	4.0×10^{7}	39.7
$^{133}Sn^{50+}$	4.0×10^{6}	1.4
$^{187}Pb^{82+}$	1.0×10^{7}	15.0
$^{207}Fr^{87+}$	3.2×10^{7}	14.8
$^{227}U^{92+}$	1.6×10^{6}	66

It should be mentioned that, by each beam bunch, a rather large fraction (up to 30%) of the total beam energy of about 57 kJ at 1.5 GeV/u is deposited in a small volume of about 10 mm^3 in the (C, Al or Mg) production target of a few g cm^{-2} thickness. The power loss of 340 GW averaged over 50 ns will destroy every kind of conventional (solid) target by immediate melting and shock waves [4]. Therefore, the development of targets that can be renewed after each beam bunch (every second or even faster) is crucial.

2.2 *Antiproton Beam*

The bunching procedure described above is applied also to the proton beam for the antiproton production. The concept – kinetic energy of 29 GeV and intensity of 2×10^{13} primary protons, target and collection techniques, and acceptance of the CR (see Tab. 2) – is very similar to that of the former AAC-complex at CERN [5, 6]. However, because of the higher proton intensity and energy, we expect a somewhat higher antiproton yield of 5×10^{-6} per incident proton at the desired energy of 3 GeV, i.e. about 1×10^{8} per bunch.

3 FAST COOLING IN CR COMPLEX

The necessity of fast cooling and accumulation in the CR complex is determined by the consumption rates at the highest luminosities for the internal target experiments with the cooled secondary beams and, in the case of rare isotope beams, additionally by the decay time $\gamma\tau_{1/2}$ of the exotic nuclei in the laboratory system (see table 1).

Table 2: Selection of basic CR parameters.

Bending power	13 Tm		
Circumference	200.6 m		
Super periodicity	2		
Lattice type	FODO		
Operation modes	Pbar cooling	RIB cooling	Isochr. mode
Maximum energy [GeV/u]	3	0.79	0.79
Betatron tunes Q_h	4.62	3.42	2.36
Q_v	4.19	3.36	3.36
Transition energy, γ_{tr}	4.3	2.88	1.84
Horiz. acceptance [μm]	240	200	70
Vertical acceptance [μm]	240	200	50
Momentum acceptance	±3%	±1.75%	±0.7%
Stoch. cooling at [GeV/u]	3	0.74	-
at β=v/c	0.97	0.84	-
at γ	4.2	1.8	1.84
Revol. frequency [MHz]	1.5	1.3	1.3
Frequency slip factor η	≤0.07	0.17	0.0
Rf peak amplitude [kV]	400	400	-
$\delta p/p$ after de-bunching	±0.6%	±0.35%	-

3.1 *CR Lattice*

The large acceptance Collector Ring CR (see table 2 and figure 3) is the first stage of the storage ring branch of the proposed facility [7]. Its maximum bending power of 13 Tm allows for the injection of rare isotope beams at 740 MeV/u and, reversing the polarity of all magnets, of antiproton beams at 3 GeV. Mainly due to the different

particle velocities the ion optics has to be flexible in order to achieve optimal conditions for fast stochastic cooling for both species of beams (see table 2). In addition, the CR has to be operated in the isochronous mode ($\gamma=\gamma_t$) at a relatively low γ_t=1.84 for time-of-flight mass spectrometry of exotic nuclei.

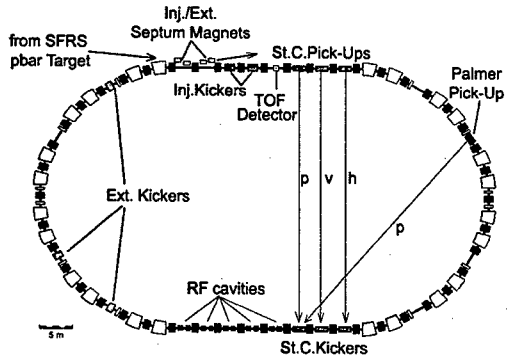

Figure 3: Layout of the Collector Ring CR. The ring will be equipped with superferric dipole magnets. The Palmer pickup is necessary only for rare isotope beams at the beginning of momentum cooling (too strong unwanted mixing).

So far, two different lattice structures have been studied carefully: a lattice with identical ion optical settings in 180^0-arcs and a so-called split ring lattice with strongly reduced frequency slip factor η in the arc between stochastic cooling pickups and kickers, which had been already proposed about 10 years ago for the Super-LEAR lattice [8]. The results of the studies for the split ring lattice in comparison with the symmetric lattice may be summarized as following:

- the number of quadrupole families is increased by nearly a factor of 2,
- chromaticity and higher order field corrections are much more complicated, and
- the dynamic apertures seem to be considerably smaller (if not too small) compared to the physical apertures.

Before the final decision about the choice of the CR lattice, numerical calculations of transverse cooling rates for all phases of the cooling process have to be completed.

3.2 *Bunch Rotation*

As explained above the injected secondary beam particles are concentrated in a single, 50 ns long beam bunch. This permits, immediately after injection, fast momentum spread reduction by a factor of approximately 5 by means of bunch rotation followed by adiabatic debunching. The first harmonic RF cavities have to be tuned to 1.3 MHz for RI beams and to 1.5 MHz for antiprotons. A rather high total RF voltage of 400 kV_{pp} is necessary in the case of RI bunches, for which a compromise between enough horizontal acceptance and sufficiently small frequency slip factor η=0.17 is much harder to find.

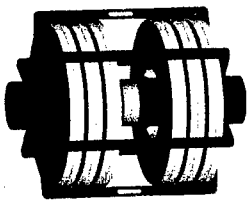

Load material	MA
Reson. RF for RI	1.3 MHz
Reson. RF for pbar	1.5 MHz
Voltage	40 kV_{pp}
Shunt impedance	929 Ω
Power	862 kW
Length	1 m

Figure 4: Preliminary layout and parameters of the CR bunch rotation cavity. 10 cavities are required.

3.3 *Stochastic Cooling*

The starting conditions for stochastic cooling are determined by large transverse emittances and by the momentum spread after bunch rotation and adiabatic debunching. Because of the stronger (unwanted) mixing the momentum cooling of rare isotope beams starts with the so-called Palmer method until the momentum spread is below the mixing limit for notch filter cooling ($\delta p/p \approx \pm 0.1\%$). The Palmer pickup is installed at a position, where the dispersion amplitude is large compared to the betatron amplitude. The momentum deviation is deduced from the difference between signals from inner and outer electrodes of the pickup system. As the Schottky power is proportional to the square of the ionic charge Z, the high charge states of rare isotopes ($Z \geq 25$) guarantee an excellent signal to (thermal) noise ratio.

Table 3: Parameters for stochastic cooling at CR

		Pbar cooling	RI cooling
After injection	Horiz. emittance [μm]	240	200
	Vertical emittance [μm]	240	200
	Momentum spread [%]	±3	±1.75
After debunching	Horiz. emittance [μm]	240	200
	Vertical emittance [μm]	240	200
	Momentum spread [%]	±0.5	±0.35
After cooling	Horiz. emittance [μm]	0.5	5
	Vertical emittance [μm]	0.5	5
	Momentum spread [%]	±0.1	±0.05
Total cooling time [s]		5.0	0.5-1

Transverse cooling of antiprotons and rare isotopes will be switched on when the unwanted mixing between pickups and kickers has reached tolerable values and the wanted mixing between kickers and pickups is still strong enough. This is the case at a momentum spread of approximately ±0.3%. This preliminary estimate has to be confirmed by numerical simulation of the cooling process. The corresponding computer code based on the Fokker-Planck approach is in preparation and should be available by the end of this year.

The preliminary technical layout of the stochastic cooling system at the CR is based on power-amplifiers for two or three bands in the frequency range 1 to 4 GHz. The 50 Ω-kickers will be equipped with a total power of about 8 kW. Mainly for the antiproton cooling it is crucial to aim at optimal signal to noise ratio at the pickup side. Cooling of pickup terminators with liquid-N_2 and applica-

tion of low noise head amplifiers are envisaged. In addition, the mechanical distance between pickup electrodes is planned to be reduced synchronously to the progress of transverse cooling, in order to yield an optimal Schottky signal.

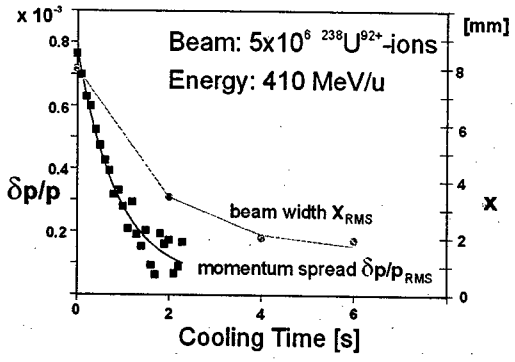

Figure 5: Results of stochastic cooling experiment at ESR (see text).

The requirement of a total cooling time of 5 s for antiprotons is considered to be feasible if the "state of the art" achieved at CERN and FNAL is applied adequately to the technical design of the CR cooling system. For rare isotope cooling, the total cooling time of 0.5 s seems to be rather challenging, though the signal to noise ratio for highly charged ions is excellent. Fortunately, the results of cooling experiments at the ESR with artificially heated fully stripped uranium ions at 410 MeV/u are quite promising (see fig. 5). Cooling time constants of less than 1 s for momentum cooling and 2 s for horizontal emittance cooling were obtained with about 500 W total power at 50 Ω-kickers in the frequency band 0.9-1.65 GHz.

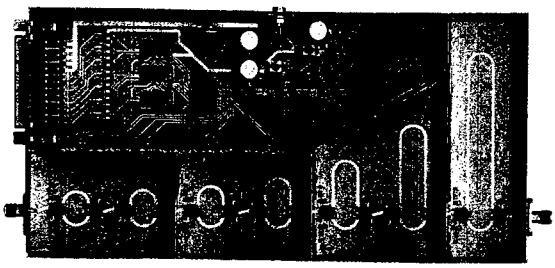

Figure 6: Prototype of a 1.27 ns-delay electronically switched in steps of 10 ps.

So far, we believe that the same pickup and kicker electrodes can be employed for both the RI and the antiproton stochastic cooling. Novel planar electrodes (slit couplers) suitable for the relativistic parameter γ of the beam particles, 1.8 for RI and 4.2 for antiprotons, are under development. The 15% difference in the particle velocities has to be taken into account for the signal combination as well for the electrical length adjustment of transmission lines and notch filters. Suitable electronically switched delay units are under development. A prototype is seen in Figure 6.

4 BEAM ACCUMULATION

4.1 *Rare Isotope Accumulation*

Pre-cooled rare isotope bunches can be transferred either directly or after deceleration in the RESR to a lower specific energy to the NESR. If allowed by the lifetime of nuclei, the rare isotope beams may be accumulated in the NESR by means of RF stacking and electron cooling. This method has been applied successfully for many years at the existing ESR. Achievable stacking factors are proportional to the beam lifetime divided by the time between two subsequent injections. If the latter is assumed to be about 1 s, we may expect stacking factors that are approximately equal to the nuclear decay time of the exotic ions in the laboratory system (see table 1). Hence, e.g. for ^{132}Sn, one could accumulate up to 2.4×10^9 nuclei within one minute. With an internal target of 4×10^{13} atoms/cm^2 and 1 MHz revolution frequency a luminosity of about 1×10^{29} cm^{-2}s^{-1} would be available for experiments.

4.2 *Antiproton Accumulation*

After pre-cooling in the CR, single bunches of up to 1×10^8 antiprotons are transferred every 5 s to the accumulator ring RESR, where RF stacking will be combined with stochastic accumulation. The injected bunch is captured into a first harmonic RF bucket, moved towards the tail of the stack and de-bunched there. The momentum cooling into the stack core is made by two or three separate pickup and kicker systems. In addition, the core of the stack has to be cooled all the time in all phase planes. About 7×10^{10} antiprotons per hour shall be accumulated this way. The accumulated antiproton beam is transferred to SIS100, where it is accelerated to the energy required for the internal target experiment at the HESR. The design of the RESR, recently added to the storage ring complex, is in a very early stage. The main motivation was, to have a ring especially optimized for the fast accumulation of antiprotons. The lattice is under investigation and the conceptual design of the stochastic accumulation system has just begun. We hope to get, at least, some advise from experts at FNAL and CERN, where similar requirements have been fulfilled many years ago.

5 ELECTRON COOLING CONCEPT

5.1 *RI beams in NESR*

Because of the short lifetime of exotic nuclei one has to optimize stochastic pre-cooling in the CR and final electron cooling in the NESR. Stochastic cooling rates decrease strongly when the beam temperatures approach a certain lower limit, where the (wanted) mixing is so slow and the signal to noise ratio so small that the cooling process is stopped. Electron cooling rates show the opposite behavior. They reach optimal values as soon as the longitudinal and transverse beam temperatures are small enough, i.e. the relative velocities between cooling electrons and ions are comparable to the mean electron velocity spread. The envisaged final beam parameters after precooling in the CR (see table 3) may be considered as op-

timal parameters for the subsequent electron cooling in the NESR, where electron cooling rates between 1 and 10 s^{-1} are required.

Main applications for electron cooling at the NESR are

- fast accumulation of RI beams,
- compensation for beam heating and mean energy loss in the internal target in proton scattering experiments, and
- formation of short ion bunches for the collision with electron bunches for electron scattering experiments, including the compensation for phase space dilution by beam-beam effects.

Main parameters of the NESR electron cooler are:

- 10-450 keV variable electron energy corresponding to electron cooling in the ion energy range 20 to 800 MeV/u,
- up to 2 A electron current at a beam diameter of 25 mm,
- ≤ 0.2 eV transverse electron temperature,
- about 0.2 T solenoid field in the cooling section with a straightness of $B_\perp/B_\parallel \leq 5\times10^{-5}$, and
- effective cooler length of 4 m.

The rather tight tolerance for the straightness of the magnetic field in the cooling section is absolutely necessary to attain the envisaged cooling rates ≥10 s^{-1}, especially at high cooling energies. Numerical simulations using different codes have confirmed this. Another result of the simulations is the necessity of sufficiently high magnetic field strength, in order to achieve the so-called magnetized cooling delivering much higher cooling rates compared to non-magnetized cooling at lower fields. The simulation results are in fairly good agreement with experimental cooling results at the ESR in a wide range of ion energy up to 450 MeV/u.

5.2 Antiprotons in HESR

Very similar to the situation in the NESR, beam quality and luminosity in the HESR will be determined by the capability to counteract beam heating caused by antiproton-target interactions and by intra-beam scattering. The realization of the technical requirements that can be derived from the experimental experience with electron cooling at lower energies is quite challenging. As mentioned above and confirmed by recently performed numerical simulations strong cooling can be achieved only by magnetized cooling requiring a strong longitudinal magnetic field ($B_\parallel \geq 0.5$ T) that guides the electron beam along the entire interaction region of up to 30 m length. It is evident that the requirements concerning the parallelism of the magnetic field ($B_\perp/B_\parallel \leq 1\times10^{-5}$) are even more stringent than for the NESR electron cooler and absolutely mandatory for reasonably high cooling rates (0.1 to 0.01 s^{-1}), especially at the highest antiproton energies between 10 and 14 GeV.

The generation of a cold electron beam at energies up to 8 MeV (corresponding to an antiproton energy of 14 GeV) with an electron current of up to 1 A is another technical challenge. If magnetized cooling with a maximum energy of 8 MeV is required, two possible solutions for the acceleration of the electrons are conceivable: electrostatic acceleration or linear RF accelerator. Electrostatic acceleration certainly has the advantage of small energy spread in the electron beam compared to the acceleration by an RF linac. Moreover, it provides a continuous electron beam without any time structure, which would be best suited for the cooling of a coasting antiproton beam in the HESR.

The acceleration of electron beams in commercially available electrostatic accelerators might be feasible if the electron beam current can be recuperated with high efficiency. An electron current loss below 100 μA seems to be acceptable in this type of accelerator. First experiments in the framework of a similar research program at FNAL/USA are promising [9], but, so far, the project is not focused to achieve the considerably higher cooling rates by means of magnetized cooling. The technical feasibility of magnetized cooling in the full energy range of the HESR is presently being studied in close cooperation with BINP in Novosibirsk.

REFERENCES

[1] "An International Accelerator Facility for Beams of Ions and Antiprotons", Conceptual Design Report, GSI, November 2001.

[2] P. Spiller et al., contribution to this conference, ROPA006.

[3] Information about Super-FRS and RI production rates taken from [1], p. 145 ff.

[4] N.A. Tahir et al., Phys. Rev. **E 60**, 4715 (1999).

[5] H. Koziol and S. Maury, CERN-PS 95-15 (AR/PD) (1995).

[6] D. Möhl, Hyperfine Interactions **109**, 33 (1997).

[7] A. Dolinskii et al., Proc. of 8th Europ. Part. Acc. Conf., Paris, 2002.

[8] R. Giannini, P. Lefèvre, D. Möhl, Nucl. Phys. **A 558**, 519c (1993)

[9] J. A. MacLachlan, editor, *"Prospectus for an Electron Cooling System for the Recycler"*, Fermilab-TM-2016 (1998).

HIGH POWER TARGETS FOR ISOL RADIOACTIVE ION BEAM FACILITY

P. G. Bricault, M. Dombsky, P. W. Schmor, TRIUMF, Vancouver, B.C., Canada
A. Dowling, U. of Victoria, Victoria, B.C., Canada

Abstract

The ISAC Radioactive Ion Beams (RIB) facility is operational since November 1998. The facility utilizes the Isotopic Separation On Line (ISOL) method to produce the RIB. The new ISAC facility at TRIUMF utilizes up to 100 μA of proton at 500 MeV from the existing H$^-$ cyclotron. In 2000 the laboratory was approved to extend the mass range from 60 to 150 and the energy range from 1.5 to 6.5 A*MeV.

At the beginning of ISAC operation the proton beam intensity was limited 1 to 40 μA on foil targets and to 1 to 15 μA on compound target. The development of new kind of target allows us to run routinely to 50 μA even on compound targets, such as Nb, Ta, SiC, TiC and ZrC.

INTRODUCTION

The ISAC facility is described elsewhere [1], it is a radioactive ion beam (RIB) facility that uses the isotope separation on line (ISOL) technique to produce radioactive ion beams (RIB). The ISOL system consists of a primary production beam, a target/ion source, a mass separator, and a separated beam transport system. These systems together act as the source of radioactive ion beams to be provided to the accelerator or the low-energy experimental areas. We utilize the 500 MeV - 100μA primary proton beam extracted from the H$^-$ cyclotron. A new beam line has been built to transport this beam to one of the two target stations followed immediately by a residual proton beam dump.

A novel approach for the target/ion source station allows us to bombard the thick target with unprecedent beam intensity without compromising the worker safety. The target/ion source assembly and heavy ion optics components are located in a shield canyon under 2 m of steel shielding allowing high proton beam intensity on thick target.

Existing foil targets can accommodate up to 40 μA beam intensities and the available intensities of many radionuclides can be expected to scale with the proton beam currents. But, production targets capable of withstanding proton beam intensities up to 100 μA without compromising the radionuclide yield and the lifetime of the target is a challenge. Several approaches to the dissipation of the power in such targets have been investigated and a realistic solution for the removal of the heat from the target container is proposed.

However, for composite target the heat transfer within the target material itself is highly target dependent. We start investigating the coating of target material with highly conductive carbon foil. First tests with SiC, TiC and ZrC show that we can operates up to 50 μA proton beam intensity for period greater than 10 weeks without compromising the yield significantly. A new target equipped with radial fins was built and tested off-line.

We recognize that target and ion source development is sometime a long process. It interferes with the science program since we use the same target station. It is propose for the next 5-year plan to built a dedicated target station for target/ ion source development.

ISOL METHOD

The ISOL method is well described in Ref. [1] and reference therein, we will just give the basic principles that guide the release of radioactive atoms from a thick target in order to understand the issues we are facing. In the ISOL method a light, energetic beam bombards a high Z target material. The radiogenic elements produced in the collisions are stop into the target material matrix. As we can see the resulting amount of radiogenic elements are in minute quantity with respect to the bulk of the target material. The yield of the wanted specie can be expressed as follow:

$$Yield(/s) = \sigma \Phi_p N_t \varepsilon_d \varepsilon_e \varepsilon_i \varepsilon_t \qquad (1)$$

Where σ is the reaction cross-section, Φ_p the proton flux, N_t the number of target nuclei. The maximum possible rate is attenuated by the efficiencies ε of product diffusion, effusion, ionization and transport respectively.

The release of the exotic atoms from the target to the ion source can be view as two different processes, 1) the diffusion inside the crystal to the surface of the grain or foil, 2) the effusion from place to place until the atom reaches the ion source opening. The two processes can be expressed fairly well using the Fick's laws and are well described by Kirchner [2]. The physics program interested in using radioactive ion beams is mainly interested by nucleus far from stability, where in general the half-life is quite short, few ms to s. To obtain an efficient release of those short-lived nuclei we usually operated the target at high temperature.

Diffusion Process

Solid state diffusion is driven by the concentration gradient of impurities or vacancies. Fick's equation describes well this mechanism.

$$\frac{\partial n}{\partial t} = D\nabla^2 n - n\lambda, \qquad (2)$$

where, D is the diffusion coefficient, which varies with the temperature and the activation energy. It can be expressed as follow,

$$D = D_0 e^{(-E_a/kT)}. \qquad (3)$$

0-7803-7738-9/03/$17.00 © 2003 IEEE

The activation energy is the energy that must be supplied to the atom through the lattice to enable the atom to move from site to site. The diffusion coefficient D_0 depends on the vibration frequency and lattice parameters.

The release efficiency can be found by solving equation 2,

$$\varepsilon_D = \frac{\tanh\sqrt{\lambda\pi^2/4\mu_0}}{\sqrt{\lambda\pi^2/4\mu_0}}, \qquad (4)$$

$$\lambda = \ln 2/T_{1/2}.$$

where, $\lambda = \ln 2/T_{1/2}$, $T_{1/2}$ is the half-live of the nuclei,

$\mu_0 = \pi^2 D/d$, d is related to the grain size or foil thickness.

Effusion process

Once the atom has diffused and reach the surface of the granule or foil the next step is governed by the effusion process, which is the equivalent of the evacuation of a volume through an orifice. This process depends on the following parameters:

1) the mean number of collision with the target material surface and container walls,

2) the mean sticking time per collision, which depends on the temperature and absorption enthalpy ΔH_a.

3) the mean flight time between collision, which depend on the mass, temperature and target geometry.

This process can be described using an exponential time dependence with a time constant ν.

$$1/\nu = \chi(\tau_a + \tau_f), \qquad (5)$$

where, τ_a is the mean sticking time and τ_f is the mean flight time between collision. The mean sticking time is given by the Frenkel equation

$$\tau_a = \tau_0 e^{(H_{ad}/kT)}, \qquad (6)$$

where H_{ad} is the absorption enthalpy, T the temperature and τ_0 is the lattice vibration period. H_{ad} depends on the chemistry between the atoms of interest and the target material.

The effusion efficiency is expressed by

$$\varepsilon_e = \upsilon/(\upsilon + \lambda). \qquad (7)$$

From equations 3 and 6 we can optimize the target in order to improve the release of a specific atom. We can select the target material with the minimal grain or foil size that can be made. Selection of a target material that can operate at ultra high temperature will increase the diffusion and the effusion release. The choice of the couple, target material-nuclei of interest can be extremely beneficial by selecting a material, which has the lowest absorption enthalpy. Keeping the volume and thus the surface as small as possible will improve the release of short-lived nuclei by reducing the number of collision.

HOW TO IMPROVE THE YIELD?

Once the target operates at it maximum temperature to increase RIB intensity we can play with the other two available parameters: target thickness, N_t and the incident proton flux, Φ_p. Unfortunately, there very little gain by increasing the target thickness. The effusion process, which depends mainly on the number of collision shows that an increase in volume will result in a larger number of collision. The short-lived nuclei produced far from the evacuation hole in the target container will decay before reaching the orifice. Furthermore, the one produced close to the evacuation hole can effuse away and never reach the orifice. There is a definite advantage to keep the target as short as possible for the short-lived nuclei of interest.

By increasing the flux of incident particle we can hope that the yield of a specific nuclei will increase linearly with the beam intensity. At ISAC we have observed that in fact the yield of ^{74}Rb and ^{11}Li increase faster than the linear proton beam increase. Figure 1 and 2 show the resulting RIB intensities as a function of proton intensity. The non-linear increase may due to radiation diffusion enhancement mechanisms.

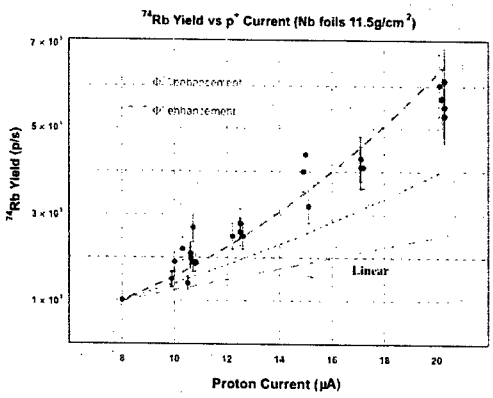

Figure 1: Yield of ^{74}Rb as a function of the incident proton beam. Curves show the projected yield expectations from proton flux dependences of Φ_p, $\Phi^{3/2}$ and Φ^2 applied to the 8 μA yield.

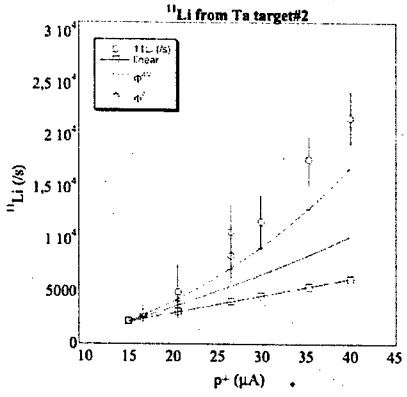

Figure 2: Yield of ^{11}Li as function of the incident proton beam. Curves show the projected yield expectations from proton flux dependences of Φ_p, $\Phi^{3/2}$ and Φ^2 applied to the 15 μA yield.

Radionuclide Yield Enhancements

Since the first ISAC target operated at the 10 μA level, nonlinear increases of both total extracted ion current and yields of specific radionuclides have been observed, [3]. Originally, the nonlinear enhancement was attributed to faster product diffusion resulting from a rising central target temperature; up to the 10 μA level, no power balancing was performed. With target irradiations above 10 μA levels, the Joule heating of targets was reduced to balance the beam power. Initial expectations were, that with a successful balance, the yields would begin to show the expected linear dependence on proton flux. Contrary to expectations, the observed yields continued to display nonlinear enhancements with increasing beam flux. Furthermore, yields of ^{74}Rb from the first niobium foil target operated with 20 μA of proton beam appeared to be essentially independent of applied resistive heating at the maximum proton beam current.

From equation 1) we can say that a nonlinear relation of yield to (Φ_p) likely results from effects buried in one of the efficiency terms. Increased diffusion resulting from radiation effects in materials is well known and the kinetics of radiation enhanced diffusion under steady state equilibrium bombardment conditions have been described in reviews by Dienes & Damask [4] and Sizeman [5]. Under steady irradiation conditions, lattice defects in the form of vacancies and interstitial atoms (Frenkel pairs) are continuously produced in the target matrix. Diffusion is enhanced by increased concentrations of such defects. The defects are mobile and can diffuse and anneal by different mechanisms, either by diffusing to "sinks" in the host lattice (such as dislocations or the matrix surface) or by direct recombination of vacancy and interstitial pairs.

At high temperatures, the diffusion enhancement has a $\Phi_p^{1/2}$ dependence for the recombinant annealing mechanism, while the "sink" annealing mechanism has a linear Φ_p dependence. Combined with the basic linear Φ_p dependence for production, the two cases should display overall correlations to $\Phi_p^{3/2}$ (recombination) and Φ_p^2 (sink). At ISAC, radiation enhanced diffusion effects have been observed with both metal foil and carbide targets.

Figure 1 and 2 show the yield of ^{74}Rb and ^{11}Li from Nb and Ta foil target, respectively. These plots show a clear indication of the non-linearity of the resulting yield as a function of the proton beam intensity.

HIGH POWER TARGETS

In the Isotope Separation On Line (ISOL) method the element of interest are created during the collision of the proton beam with a target nucleus. The products are stopped into the target material. The target material is normally kept at high temperature (~2000 °C) in order to speed the diffusion of the exotic atoms inside the target material to the surface from which they desorbed. Then the exotic atoms effuse to the transfer tube and the ion source.

Figure 3 shows a photograph of the actual ISAC target. The long cylinder is the oven and contains the target material. It is resistively heated by passing up to 800 Amperes in the leads that we see at both ends. The radioactive atoms are transferred to the ion source by the transfer tube that sticks up perpendicularly to the target tube.

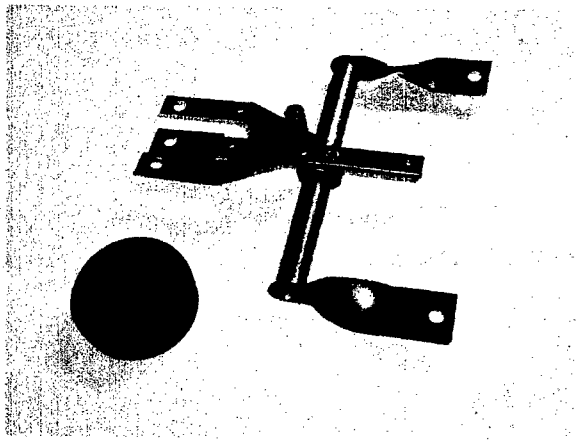

Figure 3 : The ISAC target is composed of a Ta target container and a reentrant transfer tube. The black disk is used as a scale; it is 3 inches in diameter by 1 inch thick.

The current passing though the target is adjusted depending to the target material vapor pressure, and the proton beam intensity. The idea is to keep the centre of the material at a safe temperature. When we are running at low proton intensity a power supply (10 V, 1000 A.) provides the thermal heating in order to speed the release of radioactive atoms to the ion source. In the current design we are limited to proton beam intensity lower than 40 to 50 μA. The main reason being that is the amount of power those targets can radiate at the operating temperature. In order to go beyond this limit we need to modify the target. Several groups had worked and are working on the subject. Even though, this is not a review we will look at the most significant achievements in the field.

High Power Target development

The ISOL target is quite different from any other high power target such as, neutron spallation or projectile fragmentation targets. To obtain the best release efficiency the target has to be uniformly heated to temperature around 1500° C to 2200° C.

The main issue is to provide enough cooling to operate the target at a safe limit. Too much heat will evaporate the target material. Too much cooling will impair the release of exotic atom of interest. They will condensate on the cold region and decay before they can reach the ion source. The trick will be to design a target that can withstand for long period of beam bombardment at high power and provide a quick release of short-lived exotic atoms.

In 1987 Eaton *et al.* [6] had proposed a concept for a high power ISOL target based on the 600 MeV-100 μA SC. The power deposition in the target varies from 3 kW for light Z target to 37 kW for Ta target. For actinide targets an extra 34 W/μA was added to take into account the energy deposition due to fission products. The cooling was done by enhanced radiation cooling using four longitudinal fins for the low power-target. For the high-power target it was done by enhanced radiation conducting cooling. The calculation shows that it will be difficult to take advantage of the full 100 μA using these schemes. For example, the Ta foil target using both enhanced radiation and conductive cooling will only support 84% of a full 100 μA. Such target was never tested on-line with intense proton beam.

In 1992 Talbert *et al.* [7] proposed a new approach based on the addition of an annular gap between the target container and a water-cooled jacket or a heat pipe.

In 1994 the RIST project [8,9] proposed the development of a Ta foil target that will take advantage of the 800 MeV-100 μA beam from the RAL, UK. The RIST target was developed and tested off-line and on-line [10]. The target is a tube 4 cm in diameter and 20 cm long. It is filled with 25 μm thick Ta foils. The target was designed for power dissipation of 25 kW. The radiative power is absorbed in a water-cooled copper jacket. The target is composed from about 6000 discs and washers. These discs and washers are diffusion bounded together to form a tube. They measured an emissivity between 0,7 and 0,8.

Unfortunately, the test with proton beam never took place, instead the target was move to ISOLDE where it was operated using the 2 μA proton beam from the PS booster [11].

The RIST approach can only be applicable to foil-target which, can be made by diffusion bounding. It limits severely the use of such target for specific beam. This approach eliminates most of the potential target material such as refractory oxides or carbides.

At ISAC we have developed a fin target [12] that can dissipated 25 kW of beam power. Instead of building a target using the diffusion bounded technique we then considered adding radial fins to a Ta tube. The fins are 55 by 55 mm cut out from a Ta foil sheet 380 μm thick. An undersized hole is punched in the centre and extruded using a conical shaped tool to the tube diameter. Then the fins are installed onto the tube from each side of the central block. Once the fins are installed we used a special tool to expand the Ta tube in order to improve the contact between the tube and the fins. We observed an improvement by a factor three in the resistance across the contact area. Contrary to the RIST target the fins are added onto the target container. This allows us to insert any type of target inside at the condition that the heat can be transferred from the target material to the target container wall.

Figure 4 shows a photograph of the fined target. The fins are 55 by 55 mm cut out from a Ta foil sheet 380 μm thick. An undersized hole is punched in the centre and extruded using a conical shaped tool to the tube diameter. Then the fins are installed onto the tube from each side of the central block. Once the fins are installed we used a special tool to expand the Ta tube in order to improve the contact between the tube and the fins. We observed an improvement by a factor three in the resistance across the contact area. The initial test shows that an emissivity of 0.92 is feasible [12].

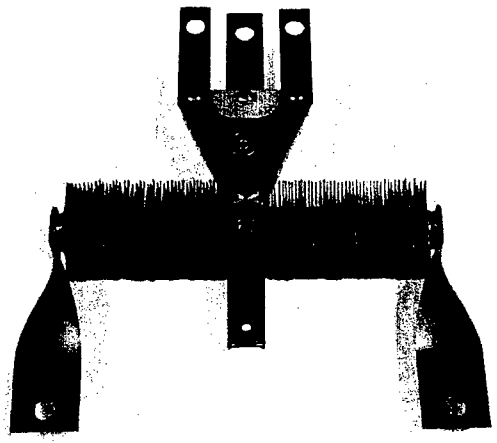

Figure 4 : ISAC fined target. It is the same target as shown in figure 2 onto which we have installed the fins.

TEST STATION FOR HIGH POWER TARGET

Before going on-line with such a target we need to test the concept off-line using the same amount of power. An electron beam heating system has been developed to test the target behavior under such conditions. A W filament running along the target axis is heated to several thousand degrees and produces the electrons, which are accelerated toward the target container. The filament is biased using a 1.5 kV- 40 Amperes power supply.

The present ISAC facility at TRIUMF is fed by one beam line, beamline 2A that can direct beam to one of the two target stations. One of these targets has been in use since ISAC was commissioned; the second one is currently being commissioned. The numbers of proposals for ISAC experiments are such that we feel the need to deliver more simultaneous RIB to experiments. A proposal has been made for another beamline to ISAC so as to make additional beams available. Through partial extraction by H- stripping, this proposed line would extract a 450-500 MeV beam from extraction port 4 of the TRIUMF cyclotron. A fast switching system would be used to feed an additional two target stations each of them equipped with its own mass separator system. These new target stations will allow target and ions sources development and also allow at least three simultaneous experiments at ISAC [13].

The actual ISAC facility comprises two target stations. They share the same proton and the same mass separator. We can swap from one to the other by reversing the magnetic field in the Y magnet in beam line 2A. This

mode of operation does not permit target and new ion beam development and deliver RIB to experiments at the same time.

Development of new RIB is crucial since each element can take up to 2 years before they can be delivered to experiments. On the other hand ion sources development in the harsh environment of the target is even more crucial.

In order to allow targets and ion sources development for the future program at ISAC we are planning to build new target stations on the new beam line 4. The actual target hall will be expanded to the west to include room for the two new target stations. The idea is to use as much the actual infrastructure we have developed over the last 10 years for the remote handling, nuclear ventilation, waste storage, etc. Furthermore, the new target station will use the same technology we have successfully developed for our actual RIB operation. Figure 5 shows a layout of the actual and proposed target stations. Each of the new stations will have its own mass separator in order to be able to switch from development work to RIB delivery in a very short delay.

Eventually, we will be able to deliver more beams by the addition of a new switchyard in the diagnostic box like the ISOLDE GPS design [14]. This design allows the selection of three ion beams within the mass range of ± 15% from the central ray. This setup will eventually allow us to serve three experiments at the same time.

DISCUSSION AND CONCLUSION

We have developed a fined target that can dissipate up to 25 kW of beam power. The production of a specific exotic nucleus depends greatly on the target nucleus. There is no universal target material that will produce intense beam of all elements. Contrary to the RIST target technology where the target is made from disk and washer of Ta foil we added the fins onto the target container tube. This allows us to use a large variety of different target material. Foil target materials are inserted into the tube and when the entire target material and container are at high temperature a bound is form between the foil and the wall of the container. For compound target we have developed a technique that allow us to back carbide targets material onto a carbon sheet. The carbon sheet has a high thermal conduction in the transverse plane. The high conductivity of the carbon allows the release of the heat to the target container.

ACKNOWLEDGEMENT

This work is supported by the National Research Council of Canada through TRIUMF.

We want to thank the ISAC operating crew for their help during the yield measurement shifts.

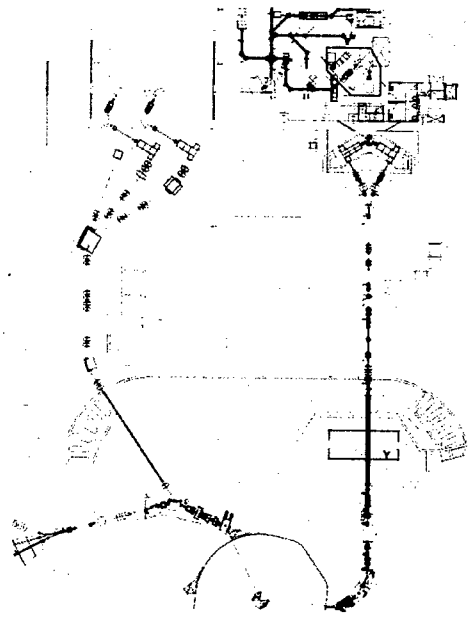

Figure 5: The ISAC new target station for target development.

REFERENCES

[1] P. G. Bricault, M. Dombsky, P. W. Schmor, and G. Stanford, Nuclear Instruments and Methods, B126 (1997) p. 213.
[2] R. Kirchner, NIM B70 (1992) 186.
[3] M. Dombsky, P. Bricault, T. Hodges, A. Hurst & P. Schmor, Nucl. Phys. A701 (2002) 486
[4] G. J. Dienes and A. C. Damask, J. Appl. Phys. 29 (1958) 1716
[5] R. Sizeman, J. Nucl. Mater. 69 & 70 (1978) 386
[6] T. W. Eaton, H. L. Ravn and ISOLDE col., NIM B26 (1987) 190.
[7] W. L. Talbert, H.-H. Hsu and F. C. Prenger, NIM B70 (1992) 175.
[8] J. R. J. Bennett et al., Proc. 4th European Particle Accelerator Conf., London, 1994, p. 1415.
[9] J. R. J. Bennett et al., NIM B126 (1997) 117.
[10] J. R. J Bennett, Nucl. Instr. and Meth. B126 (1997) 105.
[11] J.R.J. Bennett, "Experience with the RIST target, diffusion, effusion delays, etc.", EURISOL meeting, www.ganil.fr/eurisol/targetgroupmeetings
[12] P. Bricault, M. Dombsky, A. Dowling and M. Lane, NIM B204 (2003) 319.
[13] G. Stinson and P. Bricault, "A PROPOSAL FOR AN ADDITIONAL BEAMLINE TO THE TRIUMF ISAC FACILITY",this conference
[14] E. Kugler et al, Nucl. Instr. and Meth. B70 (1992) 41.

TRANSMISSION OF MUONS IN AN ALTERNATING GRADIENT FUNNELING SYSTEM

F. Lemuet and F. Méot, CEA/DAPNIA
B. Autin and A. Verdier, CERN

Abstract

One important issue in a neutrino factory is the target system for pion production. The A.G. funneling system addressed here consists of four horns, with 1 MW target per horn, followed by a recombination A.G. channel and a FODO decay channel. The transmission of this scheme is analyzed in detail. It is compared with that of a simple solenoid for several sets of optics parameters. This study makes it possible to gain in transmission efficiency in comparison with earlier proposals.

INTRODUCTION

This paper reports on optimization studies concerning a muon production channel based on alternating gradient focusing. The system has been proposed some years ago [1] and underwent several design changes to improve the collection efficiency.

The latter is defined for a given beam emittance as the ratio between the number of muons that make it to the end of the channel in that emittance and the number of protons on the target.

We first describe the channel which is an evolution of the scheme proposed in [1]. Then the efficiency optimisation is described and compared with standard schemes using high field solenoids.

AG CHANNEL OPTICS

The system features an ensemble of four horns placed close to each other and an alternating gradient matching section which steers the four beams into the FODO channel. The advantages of this system have been described in [2] : the life of the horn is lengthened and the power on the target is reduced by four, which makes the target feasible according to studies done for spallation sources.

The optics functions in the matching section, computed with MAD [3], are shown on fig. 1. The curve labelled x represents the trajectory of the beam centroid. At the exit of the horn (top left in fig. 1), this trajectory makes an angle of about 0.1 rad with the axis of the system. This axis is common both to the matching section and the decay channel. Consequently the primary beam with an energy much higher than that of the pions goes practically straight and can be extracted in a dump placed at the entrance of the FODO channel.

The optics functions in the latter are a periodic continuation of the last oscillations shown on the right of fig. 1.

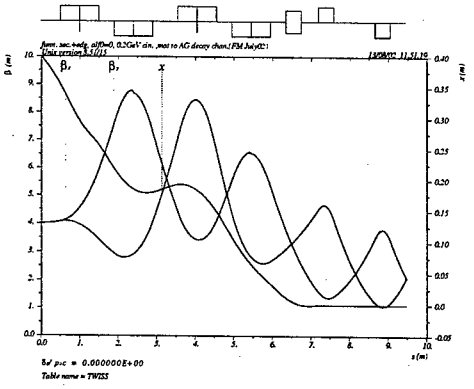

Figure 1: Optics functions of in the funneling section.

An important feature of the matching section is that the dispersion (not shown on fig. 1) is matched to zero at its end, i.e. it constitutes a first order achromat. The maximum amplitude of the dispersion is of the order of 10 cm.

The edge fields of the quadrupoles have been taken into account in the matching. The angle θ the beam centroid trajectory makes with the ends of the quadrupoles at position x in the horizontal plane introduces a thin quadrupole of focal length $\theta x k$ in the vertical plane, k being the normalised gradient of the quadrupole. Consequently the MAD matching procedure has to be iterative as a change of the gradients causes a change of the trajectory.

It has been checked with a numerical integration of the trajectory, using the code ZGOUBI [4], that this approach is accurate enough. The maximum residual amplitude of the centroid trajectory in the FODO channel obtained this way, is of the order of 1mm (instead of zero as on fig. 1), i.e. negligible compared with the apertures of the system.

The efficiency of muon transmission has been estimated by tracking trajectories also with ZGOUBI (detailed examples can be found in ref. [2]).

Aperture limitations along the FODO decay channel cause only weak pion losses if the aperture radius is larger than about 0.3 m. Muons losses concern predominantly low energy particles [5] ; because of the emittance induced by the pion decay, the aperture radius has to be at least 0.4 m in order to minimize the muon losses. In the matching section the aperture has to be 0.6 m at entrance and can be reduced at exit.

It is important to recall that these aperture radii are associated with an emittance of 0.01 π m. Should a larger emittance be transmitted, apertures would have to scale with the square root of the emittance. This shows clearly the limits of the system which cannot be used for a muon collider in its present status.

0-7803-7738-9/03/$17.00 © 2003 IEEE

PION DISTRIBUTION

The efficiency of the channel has been assessed by tracking the trajectories of 40000 pions pertaining to a realistic distribution [6]. The coordinates of these pions were obtained by tracking 10^6 protons on the target with the simulation program MARS [7].

The pion distribution in energy at the exit of the horn is shown on fig. 2. The pions are considered to start all at the same time as the time dilation of the muon beam is mainly due to the speed distribution and the length of the decay channel. The distribution in the transverse horizontal phase space (for the vertical plane it is similar) is shown on fig. 3. This beam has been tracked through both the AG

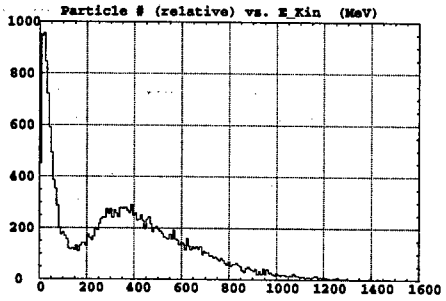

Figure 2: Energy distribution of the pions at the exit of the horn (beginning of the decay channel).

channel and a solenoid channel for the sake of comparison. Both systems have the same 0.4 m radius aperture restriction (apart from the AG channel matching section that must have a larger aperture as stressed earlier).

EFFICIENCY

The collection efficiency of the AG channel has to be defined for a given 6D emittance, because the muons have to be accelerated and stored in machines with a given acceptance. The efficiency is defined as the ratio between the number of muons counted at the exit of the channel and the total number of muons at its entrance, i.e. 40000 in our case. In fact this concept is less clear than it seems because of the large energy spread in the beam. For this reason it cannot be admitted that the optics of the subsequent machine vary little with the momentum deviation in the beam. Nevertheless the particles are counted in ellipses of a given

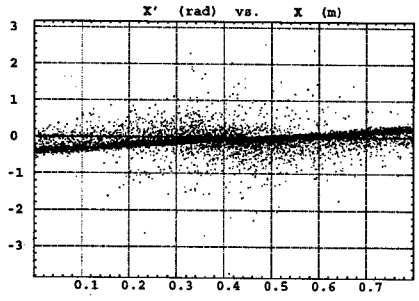

Figure 3: Distribution of the pions in the transverse phase space at the exit of the horn (beginning of the decay channel). The distribution is tilted ($\alpha \neq 0$).

surface, referred to as emittance, in each plane, which implies that there is a sort of "global matching" such that all particles in the ellipse will stay in its transforms when the beam continues downstream whatever their energy.

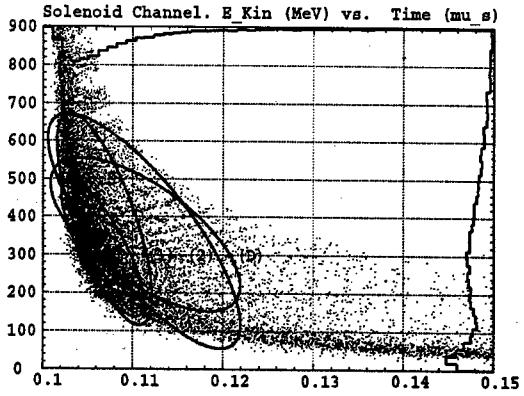

Figure 4: Matching optimum ellipses with surfaces 0.1, 0.5, 1 and 2 π eV.s for the case of the solenoid channel. (D) is the from the correlation matrix.

In the longitudinal plane there is some difficulty to find the optimum ellipse. If the optics functions are computed with the correlation matrix, it does not provide the optimum because of the shape of the longitudinal distribution which is far from elliptical. This is particularly true for the case of the solenoid where large distribution tails extend along each coordinate axis. Consequently the strategy consists of finding, for a given acceptance ϵ_l/π , the position and form that yield the largest number of particles within the frontier. This is performed with a matching procedure, with variables the ellipse parameters and its position, and with sole constraint the maximum counting within the ellipse. Depending on the surface, the so determined optimum ellipse will have a different shape, position and orientation as shown on fig. 4.

A similar procedure is applied to match the transverse admittance at channel exit, given a limit acceptance $\epsilon_{x,z}/\pi$.

The variation of the efficiencies of both the AG and the solenoid channel with the longitudinal acceptance are shown on fig. 5 for the case where the funneling section is matched for an upright ellipse (α =0 in both planes at the entrance of the section). Two ranges of field values are considered in the AG magnets : either regular values as available from conventional warm technology, or twice that field integral which has the merit of giving optimised transmission. The AG channel shows in a general manner better transmission than the solenoid (the field value in latter has also been optimised for maximum transmission). We notice that the efficiency varies only slowly with the longitudinal emittance when the latter is larger than 1 eV.s. This is a practical optimum longitudinal emittance which has to be considered for subsequent acceleration, whether there is cooling or not.

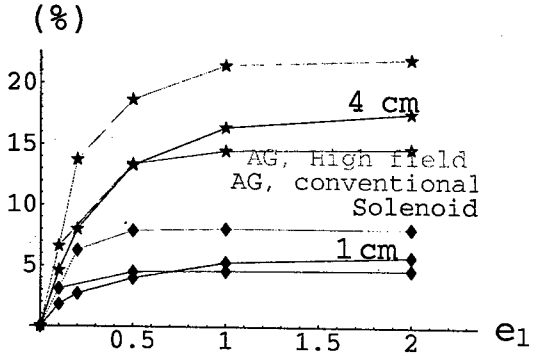

Figure 5: Efficiency of the AG channel versus longitudinal emittance ϵ_l/π (eV.s) for values of transverse emittance $\epsilon_{x,z}/\pi = 1$ cm and 4 cm. The solenoid case is also shown for comparison.

PARAMETRIC STUDIES

The variation of two parameters has been investigated, namely the value of α at the entrance of the funneling section and the value of the central energy of the particles.

It is clear on fig. 3 that the phase space ellipse is not upright. From an ellipse fit, we can infer that α is about -2. The funneling section has been re-matched accordingly for a value of α of -1. The transmission is then worse. Then it has been re-matched for a value of α of +0.5 and the transmission is better. In order to understand this it is important to keep in mind that the distribution shown on fig. 3 concerns particles with a large momentum spread. Therefore it is not obvious to know from this distribution to which value of α the section has to be matched.

A similar remark applies to the value of the reference momentum of the distribution for which the matching is done. The average momentum of the particles varies along the line as shown on fig. 6. There seems to be a tendency that the transmission efficiency is improved when the quadrupole gradients follow the average muon momentum, so that the beam experiences a constant focusing. This is the subject of studies being carried on presently.

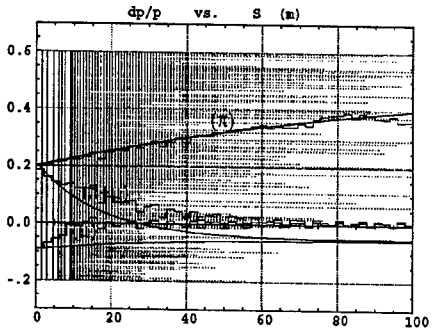

Figure 6: Average momentum of the π, μ and $\pi + \mu$ beams as a function of their position along the decay channel, from Monte Carlo. Solid lines are theoretical, in the loss-free case [5].

CONCLUSION

The transmission efficiency of the AG funneling system has been evaluated for a realistic pion distribution and their subsequent decay muons. For small transverse emittance of about 0.01πrad.m, the AG funneling channel is more efficient than the pure solenoid decay channel with a transmission of about 5% for a longitudinal emittance of about 1 eV.s. As there is about 0.04 pion per p.o.t., this system produces 2.2×10^{13} muons per second for 1 MW on each of the four targets (a total of 1.1×10^{16}p/s). This is below the nominal parameters of the neutrino factory only by a factor of four.

Maximised transmission in the AG is obtained with about twice higher magnet field integrals, which may raise such concern as larger betatron functions detrimental to decay induced transverse emittance increase, or as the feasibility of higher field magnets, issues still to be investigated further.

This system can then be considered as a doable proposal if the subsequent acceleration system can accommodate the emittances.

REFERENCES

[1] B. Autin, A. Verdier, Multiple beam collection. Procs. Neutrino Factory Workshop NuFact01, Tsukuba (May 2001). Also NuFact Note 100 (October 2001) CERN.

[2] B. Autin, F. Méot, A. Verdier, Muon collection in an alternating gradient channel, Proc. NuFact02 workshop, London, July 1-6 (2002), to be published by NIM A. Also NUFACT Note 123.

[3] H. Grote and F.C. Iselin, The MAD program (Methodical Accelerator Design) version 8.16, User's reference manual, CERN/SL/90-13(AP), (rev. 4) (March 27, 1995).

[4] F. Méot and S. Valéro, Zgoubi user's guide, Report CEA/DSM/DAPNIA/SEA-97-13, Saclay, October 1997.

[5] B. Autin, F. Méot, A. Verdier, Theoretical Studies Regarding Particle Densities In A π/μ Decay Channel, this conference.

[6] Provided by S. Gillardoni, J. Pasternak, CERN, 2002.

[7] MARS computer code, N. Mokhov, Fermilab.

[8] B. Autin, F. Méot, A. Verdier, Efficiency of an alternating gradient muon collection channel. CERN NUFACT Note 123. Also CEA DAPNIA-03-017.

RF SUPERCONDUCTIVITY: ENABLING TECHNOLOGY FOR THE FUTURE

H. Edwards#, FNAL, Batavia, IL 60510, USA, and DESY, Hamburg, Germany

Abstract

It has been my good fortune to work for two directors, Bob Wilson and Bjoern Wiik, who had vision on directions of future accelerator technology. In 1992, Bjoern Wiik, soon to become Director of DESY, organized an international effort dedicated to a dramatic improvement in performance and cost of accelerating structures based on RF superconductivity. In this paper I will discuss the degree to which this goal has been achieved and the accompanying technology advances. Today, RF superconductivity is the technology of choice for high duty factor, high beam brightness applications and a serious competitor for use in a linear collider.

INTRODUCTION

This paper is a review of superconducting cavity development and is divided into three sections:

- first a history of the development of superconducting rf systems prior to the start of the TESLA R&D program and through the 90's [1],
- then the evolution of the TESLA 1.3GHz cavity development [2],
- and finally an overview of other superconducting cavity R&D, and future applications that are being proposed.

This talk is dedicated to Robert Wilson and Bjoern Wiik, two leaders of outstanding talent and vision, for whom it has been my great fortune to work.

RF SUPERCONDUCTIVITY BRIEF HISTORY

Ideas for the possibility of using superconducting materials for RF cavity structures first blossomed in the 1960's. P. Wilson, Schwettman, and Fairbanks at Stanford proposed an electron linac of 20 GeV, 10% duty factor, with cavity gradients of 10 MV/m. At Harwell, Banford and Stafford proposed a proton linac. Montague at CERN proposed a superconducting cavity separated beamline, and Susini began surface studies at 300MHz on lead and Niobium. At Stanford studies began at S band.

It is interesting to note that the Stanford proposed electron linac parameters are not unlike those of the present TESLA FEL project, that a proton linac (SNS) is now being built, that CERN went on to build a Kaon separated beam and that Fermilab (CKM) plans such a beam. Stanford went on to build HEPL, one of the first superconducting RF (srf) accelerators, which has recently been upgraded with TESLA cavities.

#hedwards@fnal.gov

Work supported by URA,Inc under contract with the U.S. Department of Energy, contract DE-AC02-76CH03000

Twenty years later by the '80's prototype cavities were beginning to be built with gradients up to ~7MV/m. Active programs were underway at Cornell (which produced the CEBAF cavity design), KEK, CERN, and Wuppertal. At this time Padamsee at Cornell developed the 1400C Titanization process that led to better residual resistance ratio (RRR) and higher thermal conductivity in the niobium material and less sensitivity to quench.

By '92 before the start of the TESLA R&D program, a number of laboratories had significant superconducting RF installations with cavity gradients of 3 to 7 MV/m. These installations are listed in Fig 1. The TRISTAN ring at KEK was the largest installation. CEBAF construction was proceeding at 16 cavities per month, and LEP cavity production had started. By 2000 there would be over 5 GV and over one km of superconducting structures that had been installed for electron or heavy ion acceleration.

	Nbr. of cav.		MHz	m	MV/m	MV
MACSE	5	5-cell	1500	2.5	6.5	16
S-DALINAC	10	20-cell	3000	10.0	5.9	59
HERA	16	4-cell	500	19.2	3.6	69
HEPL				30.8	3.0	92
TRISTAN	32	5-cell	508	47.2	6.6	310
CEBAF	106	5-cell	1497	53.0	7.6	400
LEP	12	4-cell	352	20.4	3.7	75

Figure 1: Status of SRF installations in 1992 [1].

Two Projects of the '90's

Two major projects of the '90's were CEBAF recirculating linac at Jefferson Laboratory and the LEP electron positron collider energy upgrade to 200 GeV cm.

Both systems are (or were) operated well above design gradients. Achieved operational gradients are (were) limited by cavity trip rates that could be tolerated by the experimental program in a tradeoff with beam energy delivered. There has been a steady evolution of energy with time, and in both installations the superconducting systems have been very reliable.

CEBAF [3] was completed in 1993, and was designed for 4 GeV beam and 5 MV/m cavity gradient at 1.5 GHz frequency. There are 338 5 cell, 1/2 m cavities in 42 modules. Today it operates at 5.8 GeV with 5 passes, and an average gradient of 6.9 MV/m (45% above design). The active cavity length is 169 m and the total accelerating voltage is about 1160 MV. The major limitation to gradient is the RF cold window location close to the cavity. Field emission from the cavity leads to arcing of the cold window. This is a design limitation that can be addressed in any future design. In operation, gradient is set to limit RF trips to 100/day (with ~45 sec recovery). Thus trips are a major source of unavailability,

0-7803-7738-9/03/$17.00 © 2003 IEEE

typically of order 3.5%, whereas failures of the SRF installation is very low (~0.2% of operating time) and cryogenics is ~0.9%. An upgrade for CEBAF to 12 GeV is underway.

The LEP-2000 collider [4] achieved up to 209 GeV cm energy operation before decommissioning to make way for LHC. LEP had 288 1.7m 350 MHz superconducting cavities, for a total active length of 490 m. These cavities were driven by 36 1 MW cw klystrons. The design gradient was 6 MV/m, however 7.2 MV/m average gradient was achieved (20% above design) for a total accelerating voltage of 3600 MV. Because of the demands of the experimental program search for the Higgs, the gradient was pushed higher and higher, requiring considerable processing during maintenance times and a sophisticated operating strategy. By 2000, the last year of operation, this strategy included increasing the acceleration voltage during a beam store so that by the end of a store all klystron systems were required to hold the beams. At the beginning of a store one klystron system was held as margin (2.7%) in case of a trip, after reduction of lumonsity to some level the energy was increased and all systems were required. Mean time before trip was about 14 minutes, with RF recovery of 2 min. Trips were generally due to field emission leading to excessive helium usage and helium interlock trips. Fig. 2 illustrates the evolution of available RF voltage and beam energy at LEP over the 5 years of operation ending in 2000.

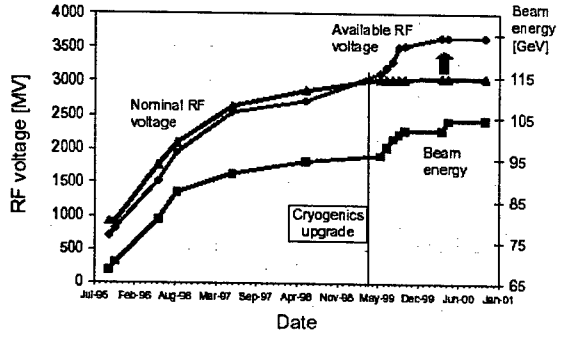

Figure 2: LEP operation showing the increase in available rf voltage over nominal design voltage, and resulting increased beam energy. [4]

These two examples of major accelerators that have used superconducting RF illustrate ability to push the cavities to levels where operation is limited by trips due to field emission at gradients well beyond design. System reliability exclusive of trip rates was excellent.

THE TESLA R&D PROGRAM

In 1992 Bjoern Wiik organized a collaboration to undertake SRF cavity R&D with focus toward its use for linear colliders (LC). The large aperture of the superconducting 1.3 GHz cavities leads to low wake fields, relaxed alignment tolerances, and less emittance dilution with the possibility of long bunch trains, bunch to bunch feedback and emergency turnoff within a fraction of a bunch train pulse. Potential benefits have been acknowledged since the beginning of LC R&D but projected costs were considered too high. The TESLA R&D program had the goal of a cost reduction of a factor of 20 per MV. This could be accomplished by an increase of a factor of 5 in gradient from the then typical 5 MV/m to 25 MV/m and a cost reduction per unit length over existing installations of a factor of 4. This cost reduction could be realized by long continuous module strings with many cavities without warm-cold transitions. The initial gradient goal set for realization in the TESLA Test Facility (TTF) was 15 MV/m with a clear path toward 25 MV/m for a LC. Now the goal for TESLA 800 (800 GeV cm) is 35 MV/m and cavity R&D is focused to that end.

The R&D for cavity improvement has concentrated on a number of areas with care toward careful, high quality manufacturing, processing, preparation, and testing. There has been no one specific most important improvement area but rather careful attention in many areas that has led to success. Many of these procedures had been developed through international R&D efforts prior to TESLA.

The cavity improvement efforts included [2, 5]:

- High RRR Niobium for better thermal conductivity.
- Scanning sheet Nb material for defects and inclusions of non-Niobium material using eddy current scanning devices (and more recently squid scanners as well).
- Care in preparation for e-beam welding and good vacuum during welding.
- High temperature heat treatment (HT) of the finished cavity at 800 C (to remove H and prevent Q disease), or the more effective treatment with Titanium at 1400 C to getter O2 and increase the thermal conductivity by about a factor of 2 above that of the high RRR sheet.
- Cavity tuning for field flatness.
- Buffered chemical polishing (BCP) followed by ultra pure water (UPW) rinsing.
- High pressure water rinse (HPR) to remove particles and eliminate field emission.
- Clean room assembly in class 10-100 cleanrooms.

The fabrication and preparation is followed by a series of tests of cavity gradient and Q performance:

- Vertical dewar test of the "bare" cavity (without helium vessel, tuner or input coupler).
- Horizontal dewar test of the "dressed" cavity (with helium vessel, tuner, input coupler).
- Module assemblies of 8 cavities per module.
- TTF installation and test of the 8 cavity module, and operation for beam acceleration.

Performance limitations can be caused by inclusions, dust particles, resistive regions, high surface resistance, or

bad thermal conductivity and ultimately by the theoretical Hc limit. The limitations are:

- Cavity quench or thermal breakdown
- Field emission
- Multipacting
- Q slope (drop in Q at high gradient)

Early in the program a very significant set of tests was carried out at Cornell. These tests performed on three 1.3 GHz 5 cell cavities fabricated at Cornell showed that greater than 25 MV/m at Q of $5x10^9$ was indeed achievable. A technique of high peak power processing (HPP) was used to achieve these results.

The Cavity Program with BCP

The TESLA program has involved fabrication of the 9 cell 1.3 GHz cavities by industry from the very beginning. Four different vendors have produced cavities. In time there have been 3 production runs. The fourth is underway presently. In total over 80 cavities have been produced. The processing, tuning, assembly, and testing is all done at DESY. Results of the first 3 production runs, and the modules assembled from these cavities are illustrated in Fig. 3 [2]. One sees the improvement in quality and reproducibility as the productions have proceeded. Much of this improvement has been due to improved welding, better niobium control, better overall quality control, and the learning curve associated with the production of a number of cavities. In Fig. 4 [2], a comparison of test results is given for those obtained in the vertical test dewar of bare cavities with cw RF, against those obtained in the horizontal test dewar of fully dressed cavities with pulsed RF (1.3ms). Though the scatter in correlation is large it is important that there is no obvious deterioration of gradient after the cavities are fully dressed. In fact some cavities perform better in the horizontal cryostat after being "dressed ", probably because of thermal heating differences between cw and pulsed operation. It is interesting to note that already in this data set some are achieving gradients of 33 to 35 MV/m.

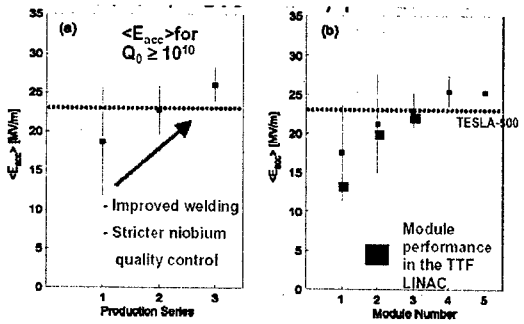

Figure 3: Cavity performance results from a) successive production runs, and b) when installed in TTF modules.

Fig. 5 shows the good reproducibility of vertical results (cw) from cavities of the 3rd production run prepared with BCP surface chemistry. However it is clear the there is a rapid drop in Q ("Q slope") above about 25MV/m. Some of these same cavities show higher gradient operation in the horizontal pulsed tests as illustrated in Fig. 6. Many are at or near the required 35MV/m @ Q of $5x10^9$. However the Q slope indicates that cavities prepared in this manner are reaching their performance limitations.

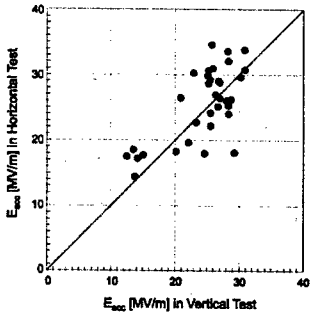

Figure 4: Reproducibility of results in the horizontal test of dressed cavities vs. in the vertical test of bare cavities.

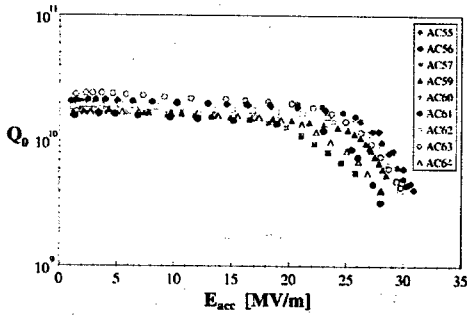

Figure 5: Vertical dewar results for cavities from the 3rd production processed with BCP [2].

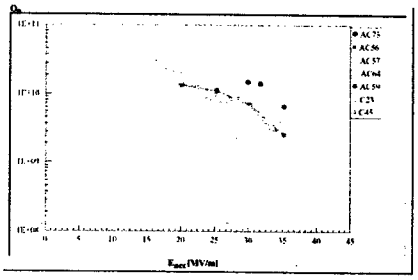

Figure 6: Horizontal pulsed test results of TESLA cavities. AC73 is electropolished, the rest have BCP treatment.

Electropolishing

The development and refinement of the electropolishing (EP) process has been successfully pursued by a broad international collaboration of laboratories working on srf R&D (CERN, DESY, JLab, KEK, Saclay). The effort is an excellent example of the power of international collaboration.

One cell cavities have been electropolished at CERN and measured at DESY as part of studies carried out in a CERN-DESY collaboration [5]. KEK (with Nomura

Plating) has developed the electropolishing process so that it can be used with good results on multicell cavities [6]. KEK has electropolished a number of multicell cavities for DESY and JLab. DESY and JLab are both bringing on their own EP facilities based on the KEK development.

The EP process is usually done after heat treatment (HT) at 1400 or 800C, and BCP etching as greater of 100 microns of niobium must be removed and the EP rate of removal is ~ 1/2 micron/min. Whereas the BCP process makes for differential etching of the different crystal grains and surface discontinuities at the grain boundaries, the EP process concentrates electric current on surface high points and removes them. The result is a very smooth surface. The rough surface produced by BCP can lead to local field enhancement that could be detrimental especially as local H fields approach the theoretical Hc limit [6,7].

Results from single cell cavities with EP preparation showed very interesting results [5]. The cavities did not show remarkably better results than BCP prepared cavities until a 120C bake was performed as a final step. Before the 120C bake a strong Q slope was observed at gradients above 25MV/m as with the BCP preparation. There was no field emission associated with the Q slope. (Emission is a usual explanation.) After the bake, the Q slope was much reduced and gradients in excess of 40 MV/m were observed.

Initial vertical dewar results from 4 TESLA 9 cell cavities (out of 9) electropolished at KEK then shipped to DESY for final HPR and 120 bake are shown in Fig. 7. Test results of one of these cavities in the horizontal dewar before and after being "dressed" is illustrated in Fig. 8. This cavity has achieved gradients of 37 MV/m in 10 Hz, 1.3 ms pulsed mode. [5]

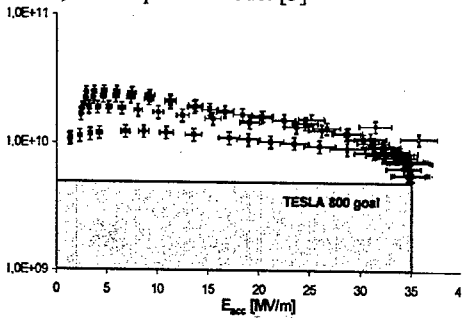

Figure 7: First results of EP processing on four cavities.

Clearly the 120C bake has some very important influence on the superconducting properties of the cavities. There is evidence that oxygen from the oxide surface layer diffuses into the first ~100 microns of material and effects the superconducting surface resistance by changing the electron mean free path. (Other changes to the superconducting properties may be going on as well.) [6]

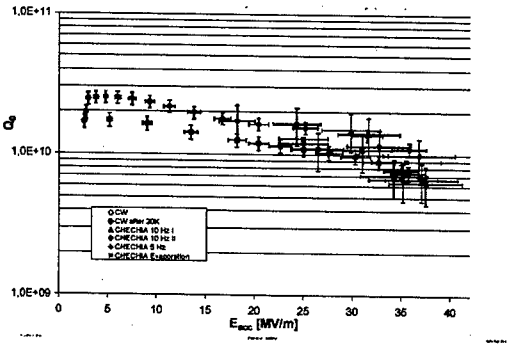

Figure 8: Horizontal pulsed test of EP cavity AC73.

It is still early to know just what the best preparation with EP will be and further understanding of the modification of the surface layer is needed. One outstanding question relevant to cavity production processing is whether heat treatment at 1400C will be required or if the easier 800C treatment will be adequate.

ACTIVITIES IN OTHER R&D AREAS & NEW APPLICATIONS OR POSSIBLE PROJECTS

Other SRF R&D

Superconducting cavity R&D efforts are going on in a number of other areas. Only some of these can be mentioned here [8]. In some cases the motivation is directed toward future potential projects, in other cases the motivation is driven by possible cost reduction through the use of less niobium material or simplified fabrication processes.

Sputtered cavity development (as was done for LEP) continues for low frequency applications where cavity size makes use of solid Nb prohibitive. LHC will use 16 400 Mhz single cell cavities with specification of 5 MV/m and Q $2x10^9$ at 4.5 K. These cavities have been produced by industry and operate above specification. They typically reach ~9MV/m and Q~$1x10^9$ at 4.5K, and up to 14MV/m at 2.5K. As with other sputtered cavities, the Q slope is large and continuous from low Eacc. Understanding and curing this is an important area of R&D that would make it possible to push the use of sputtered cavities to higher gradient.

Cornell and CERN have a collaboration to fabricate and test 200 MHz single cell cavities for muon acceleration [8]. First cavity tests have reached Eacc ~11 MV/m (goal is ~17 MV/m). Here again Q slope is very evident.

A different approach is being pursued at DESY in collaboration with Jlab. Nb/Cu clad single cell cavities are produced by hydroforming without an equator weld. Tests of one of these cavities have achieved 40 MV/m and Q ~ $9x10^9$, with almost no Q slope. Interestingly, preparation was BCP, 800C HT, HPR, and 140C bake.

A completely different area where there has been good success is the low beta spoke cavity effort at Argonne and

LANL. It shows great promise for application in RIA (Rare Isotope Accelerator) for β~0.3-0.4 structures [8].

Ongoing and Potential Projects

The prominent ongoing accelerator project using srf is SNS . The change to superconducting cavities took place relatively late in the planning. However this application of srf is natural because of the need to minimize beam loss, large aperture of the cavities and their potential to provide further beam energy increases. The ability to use the srf technology at SNS was a direct spinoff from the TESLA R&D. SNS linac uses 81 800 MHz srf cavities of 2 β types from 186 to 1000 MeV. Cavity production overseen by JLab is well underway. Fig. 9 shows first tests of high beta cavities with BCP and EP processing. Performance is well above specification (including the increased high β specification that was changed when EP was adapted for processing of the high β cavities) [8].

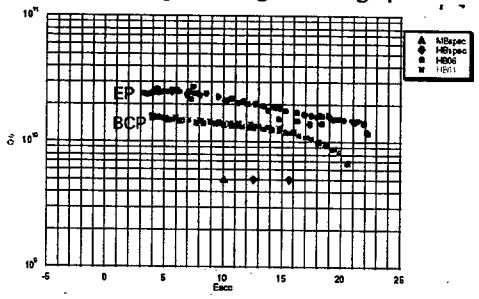

Figure 9: First results from Jlab on SNS high β structures prepared with BCP or the new EP setup [9].

JLab is also working on an upgrade of CEBAF to 12GeV, and work is underway on the ERL FEL Upgrade to 10kW. EP cavities have been tested to 19 MV/m [8].

TESLA TTF II linac is being assembled. It will have energy to 1 GeV and use cavities of more recent production series. It will produce SASE FEL radiation to 6 nm. The TESLA GeV XFEL project (10 to 20 GeV linac) has been approved by the German government at 50% funding support. The remaining support will come from collaborating countries. [8]

It is interesting to review the reports submitted to DoE for development of its 20 road map plan. Though many of the ideas, doubtless will not survive to the project level, it is striking to note just how many rely on srf technology. Listed by DoE Science Divisions, these include:

Basic Energy Sciences (BES)

- SNS- power upgrade to 3MW
- "Greenfield" XFEL (beyond LCLS)
- LUX- Linac based Ultra-fast Xrays (LBL srf recirculating linac)
- ACNS- Acc based Continuous Neutron Source (BNL 10MW)
- Crosscutting issues- investigation of Energy Recovery Linac (ERL) applications

Nuclear Physics (NP)

- RIA-Rare Isotope Accelerator (400MeV/nucleon)
- CEBAF 12 GeV Upgrade

High Energy Physics (HEP)

- Linear Collider- cold or warm
- CKM- Charged Kaons at Main Injector (FNAL separated beamline)
- Neutrino Super Beam- Proton Driver (warm or cold, BNL or FNAL)
- Neutrino Factory

There are also proposals to NSF:

- Cornell ERL
- MIT-Bates X-ray laser (4 GeV linac)

And finally BNL is discussing a high current electron linac for electron cooling at RHIC.

CONCLUSIONS

Superconducting RF systems of the 90's have demonstrated remarkable reliability, and operability at limits considerably in excess of design.

The TESLA R&D program has been a model of concerted R&D. It has been dramatically successful at pushing the gradient of superconducting cavities to a level required for Linear Collider application. The improvements in cavity performance have made it possible to use the superconducting technology in projects such as SNS.

There still remains more work, and more to understand in order to achieve high performance, reliable and cost effective cavities. But the TESLA R&D program clearly shows how well planned R&D with a major commitment can succeed in making real progress.

Superconducting RF has become a major enabling technology for accelerator projects of the future.

ACKNOWLEDGEMENT

This talk has been prepared with the help of, and information from many individuals. In particular I would like to thank Lutz Lilje for much of the information on the TESLA program. Others, who's help has been critical are: Kurt Hubner, Hasan Padamsee, Carlo Pagani, Charles Reece, Claus Rode, Steve Suhring, Hans Weise.

REFERENCES

[1] H. Weise, LINAC 98, p. 674, Aug. 1998, ANL-98/28.
[2] TESLA Technical Design Report, DESY 2001-011, ISBN: 3-935702-06-X, March 2001.
[3] C. Reece, et al, Proc. 2001 PAC, p. 1186, IEEE: 01CH37268C, ISBN: 0-7803-7193-3, 2001.
[4] P. Brown, et al, Proc. 2001 PAC, p. 1059, IEEE: 01CH37268C, ISBN: 0-7803-7193-3, 2001.
[5] L. Lilje, DESY-Thesis-2001-034, July 2001, ISSN 1435-8085; L. Lilje, private communication.
[6] K. Saito & P. Kneisel, TUP031, Proc. 9th SRF Workshop, LA-13782-C, LANL, 1999;
K. Saito, ROAA002, this conference.
[7] J. Knoblock et al, TUA005, Proc. 9th SRF Workshop, LA-13782-C, LANL, 1999.
[8] See a number of papers this conference.
[9] C. Rode, private communication.

MURA DAYS

Keith R. Symon, University of Wisconsin-Madison, Madison, WI 53706, USA

Abstract

The Midwestern Universities Research Association (MURA),incorporated in the mid nineteen-fifties, was a unique institution in that, although it never succeeded in its primary goal of building a multi-GeV particle accelerator, it remained in existence for more than ten years, during which the MURA group made many contributions to the science of particle accelerators. Included among these were the invention of fixed field alternating gradient (FFAG) accelerators and spiral sector cyclotrons, an extensive analysis of rf acceleration with particular attention to the consequences of Liouville's theorem, beam stacking, analytic and computational studies of nonlinear orbit theory, studies of collective instabilities, and the first demonstration of practical ways to achieve colliding beams, Although no large FFAG accelerators were ever built, model FFAG accelerators turned out to be excellent devices for the experimental study of accelerator problems because they separate the guide field from the acceleration process. Models were used to study nonlinear resonances, acceleration processes, space charge limits, and beam stacking. Among the last MURA projects was an electron storage ring that became the first machine dedicated exclusively to the production of synchrotron radiation for experiments, a facility which evolved into the highly successful Synchrotron Radiation Center at the University of Wisconsin-Madison.

MURA

The Midwestern Universities Research Association (MURA) was incorporated in 1954 with fifteen universities as members. Its purpose was to promote a large accelerator in the Midwest. In 1956 the MURA working group located in Madison, Wisconsin, the chosen site for a MURA accelerator. During the next thirteen years some 74 MURA employees, graduate students, and staff from MURA universities participated in the working group, making many important contributions to accelerator science. I'll discuss the technical and scientific contributions of MURA, not the political aspects which are also of interest.

FFAG

1954 saw the invention of the Fixed Field Alternating Gradient (FFAG) accelerator. In an FFAG accelerator the guide magnetic field is constant and accommodates all orbits from injection to output energy. Focusing is achieved by means of alternating gradients, a principle which had just been invented. The idea had also occurred to other people. We received a paper from Tihiro Ohkawa in Japan presenting the same idea. Ohkawa was invited to visit and joined the MURA working group.

The advantage of a fixed field machine is that it separates the guide field from the acceleration process. This allows a great variety of acceleration schemes and simplifies accelerator experiments.

Radial Sector Model

The first FFAG configuration proposed was a radial sector accelerator. Figure 1 shows a model which operated in 1956. The injection energy at the inner orbit was 20 keV; the energy at the outer orbit radius at 54 cm was 400 keV. You can see the betatron core which provided a very easy way to accelerate electrons. An experiment, for example an rf acceleration process, could be carried out, and the result observed by betatron accelerating the resulting beam onto a detector.

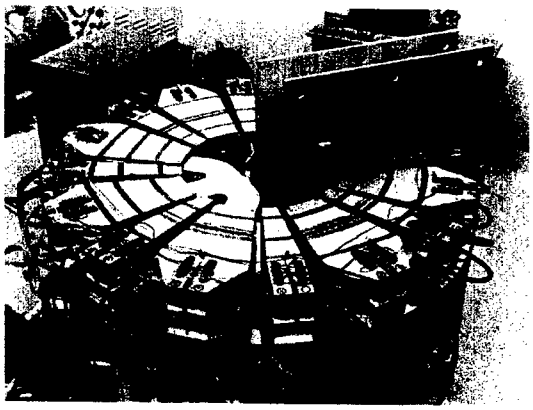

Figure 1: Radial Sector Model.

There are eight sectors, each consisting of a large and a small magnet. The magnetic field increases with radius as R^k, with k=3.36. The field in the smaller magnet is reversed, providing the alternating gradient. This of course makes the orbit circumference about 5 times larger than it would be for a uniform magnetic field.

Figure 2: Important Visitors

In order to make the orbits scale in proportion to the radius, it is desirable to have the magnetic field pattern scale in proportion to the radius. This is guaranteed if the magnet gap is proportional to the radius, a solution favored by

0-7803-7738-9/03/$17.00 © 2003 IEEE

theorists. The builders preferred to save iron, copper and power by keeping the gap constant and shaping the field by appropriate windings. After a decisionless debate in which we all agreed that either solution would work, we took a vote which came out in favor of geometric scaling of the magnets.

We had a few important visitors who were interested in the model. In Figure 2 you should be able to identify Niels Bohr and Subramanian Chandrasekhar.

Spiral Sector Model

Donald Kerst invented the spiral sector FFAG configuration. Figure 3 shows a spiral sector model which began operation in 1957. Each sector has just one magnet whose edges spiral out in radius. Particles crossing the edges at an angle experience alternating gradient focusing. Because there are no reverse fields, the circumference of the orbit is only about two times that for a uniform field.

Figure 3: Spiral Sector Model

Jackson Laslett and I worked on the theory of spiral sector orbits. At first we thought the chief advantage of this configuration was that it is sufficiently complicated that it is hard to show that it will not work. But indeed it does work very well.

In designing this model we made detailed analytical and digital computations of orbits and magnetic fields. As a result the machine operated when first turned on, perhaps a record for accelerator construction.

NONLINEAR ORBITS

In most accelerators, magnetic fields are made to vary as linearly as possible, so that nonlinear effects are small perturbations. In FFAG machines nonlinear effects are important and determine the stability limits which determine the maximum allowed oscillation amplitudes.

Experiments were done on both models to check theoretical predictions regarding orbit stability as a function of betatron oscillation frequencies. Figure 4 is a contour plot showing beam intensity in the radial sector model as a function of the number of radial oscillations per revolution plotted horizontally and the number of vertical oscillations per revolution plotted vertically. Theoretically predicted linear and nonlinear resonances lie along the straight lines shown. One can see the wide stop band along the linear resonance ν_x=3, as well as reductions in intensity along other linear and nonlinear resonances. Similar measurements made with the spiral sector model also confirm the predictions of orbit theory.

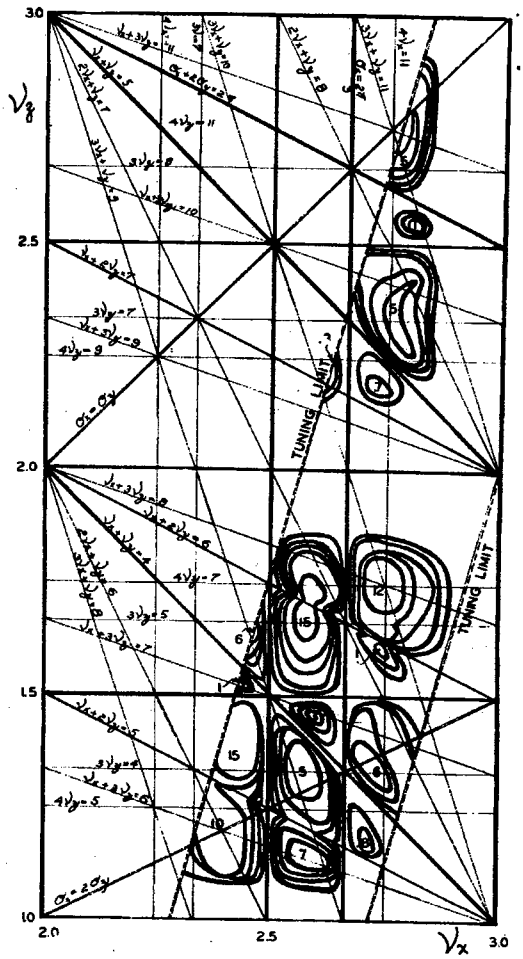

Figure 4: Resonance Survey, Radial Sector Model

Numerical calculations of FFAG orbits often showed apparently random behavior which we called "stochastic" behavior. Such behavior would now be called "chaotic". At first we were not sure whether these effects were real or artifacts of the numerical calculation. We devised exactly canonical numerical algorithms to eliminate the possibility of nonphysical features of the algorithm. We also made extensive checks to guard against round-off errors. We thus convinced ourselves that these stochastic effects are real.

RF ACCELERATION

Fixed field accelerators allow a great variety of rf acceleration schemes. One possibility is beam stacking, where we inject successive beams and accelerate each up to an intermediate energy. Donald Kerst mentioned this to Eugene Wigner who pointed out that Liouville's theorem

would be relevant. When he reported this to us, Andrew Sessler and I realized that this was a key to studying rf acceleration processes. We wrote a paper on rf acceleration[1] in which we discussed this and other topics.

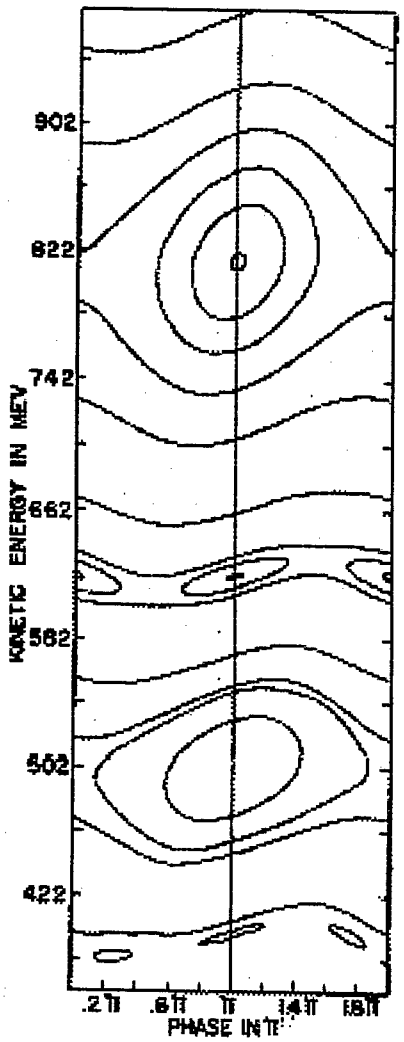

Figure 5: Numerical Simulation of rf Acceleration

Figure 5 shows the results of a numerical simulation of an rf acceleration process in which the radio frequency and voltage are fixed. Once per revolution we plot a point at the particle energy and the rf phase when the particle arrives at the accelerating gap. There is a fixed point at phase π, energy 500 MeV, where the radio frequency is 9 times the revolution frequency, and another at 814 MeV where the radio frequency is 10 times the revolution frequency. Both points are surrounded by trapping regions where the points lie on closed curves surrounding the fixed points. If we were to change the radio frequency slowly, the trapped phase points would be carried up or down in energy. This suggested to me using a high harmonic number so that there are a number of trapping regions between the injection and output energy. By modulating the frequency, these regions could be moved upward past the injector so as to carry injected particles to the output energy. I called this scheme a "bucket lift" in analogy with the devices used by farmers to load hay or grain into their barns. The trapping regions were then called "buckets", a name which is still in use, although no bucket lift accelerator was ever constructed.

Because of Liouville's theorem, the phase points in any rf acceleration process move like an incompressible (two-dimensional) fluid. This makes the name "bucket" even more appropriate. An interesting consequence is that if the buckets are moved upward, the surrounding untrapped phase space must on average move downward. We call this "phase displacement".

Beam stacking experiments were carried out on the FFAG models. Figure 6 shows the results for the radial sector model. These are oscillographs of beam intensity vs. energy. Because of the way the experiments were carried out, energy increases toward the left. The first trace shows an injected beam at an initial energy. The beam is captured in a bucket and accelerated up to a higher energy. The result is shown in the second trace where we also see a little untrapped beam remaining at the initial energy. In contrast to actual beam stacking, in this experiment we did not inject successive beams, but simply carried out successive rf cycles. The result after 4 cycles is shown in the third trace. We see that the result of four cycles is to accelerate most of the remaining beam and to displace the first beam down in energy.

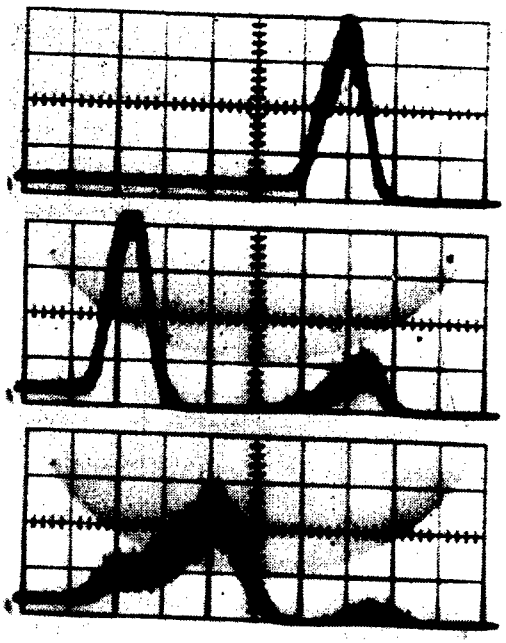

Figure 6: Beam Stacking Experiment

Among other topics studied theoretically and experimentally by the MURA group are acceleration of buckets, phase displacement, capture of a beam in an expanding bucket, and acceleration across the transition energy.

With high rf voltages, we observed stochastic phenomena near the boundaries of a bucket, as shown in Figure 7. On the hypothesis that stochastic phenomena occur when bucket boundaries overlap, we ran a case with two nearby rf frequencies with voltages such that the predicted buckets would overlap. The results in Figure 8 give totally chaotic orbits. The solid curves are the predicted bucket boundaries.

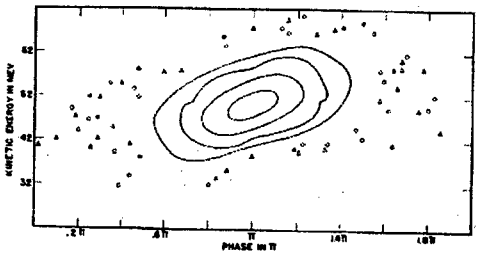

Figure 7: Stochastic behavior near bucket boundary

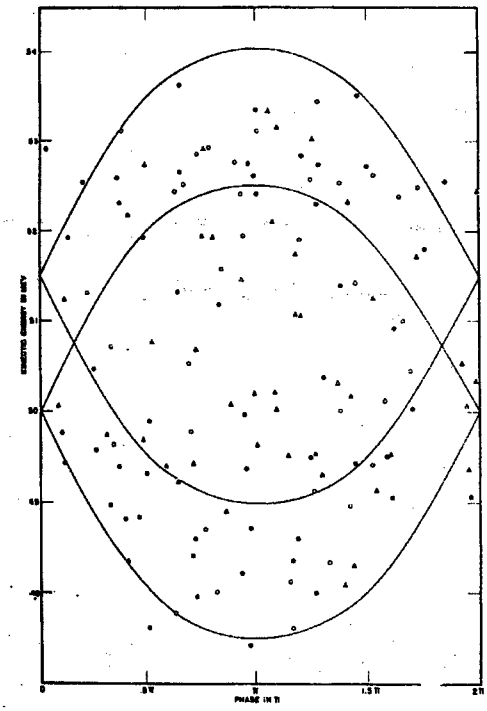

Figure 8: Scattered orbits in two overlapping buckets

COLLIDING BEAMS

The center-of-mass energy for a collision of a particle of relativistic energy E with a stationary particle is proportional to $E^{1/2}$. This suggests the energy advantage in letting two equal energy particles collide, in which case the center-of-mass energy is the sum of the energies of the colliding particles. For example, two 15 GeV protons colliding head-on produce a center-of-mass energy of 30 GeV. A single proton hitting a stationary proton would have to have an energy of 450 GeV to produce the same center-of-mass energy.

Unfortunately the cross sections are such that the event rate for accelerator beams achievable up to that time would be impractically low. It was Kerst who observed that with the intensity achievable with stacked beams, colliding beam experiments become practical.[2]

I remember being invited to give a colloquium on this subject at the University of Illinois. When I mentioned colliding beams, the audience burst out laughing. I was somewhat taken aback until I learned later that the week before professors Kerst and Kruger had shot pea shooters at each other from opposite sides of the stage.

50 MEV MODEL

A 50 MeV electron model was constructed which first operated in 1961. (See Figure 9.) It was a radial sector machine with two identical magnets in each sector, with oppositely directed magnetic fields. It was first pointed out by Ohkawa that particles in such a machine can circulate in either direction, and that the orbits are closed because they are at larger radii in the positive magnets. This configuration would allow colliding beams in a single machine. However the ratio of circumference to that for a uniform field is about 8.

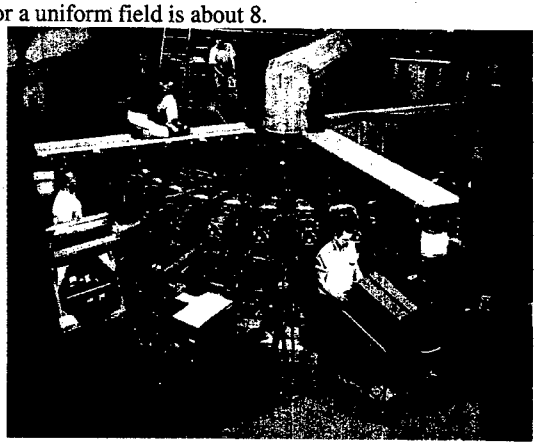

Figure 9: 50 MeV Model

The machine was successfully operated in the two-way mode. However most of the experiments were performed in a one-way mode with one of each pair of magnets excited to a higher field than the other. In case we had trouble crossing the transition energy at 1.13 MeV, betatron cores were installed; they can be seen in the figure. However we were able to accelerate over the transition energy with the rf cavity, so most experiments were carried out using rf buckets from the injection energy (100 keV). The green cavity on the right powers the rf accelerating gap. We had to make up for radiation loss of a few volts per turn in the stacked beam. Due to its energy spread, we would have had to use a high voltage on an accelerating gap in order to trap the stacked beam in a bucket. We therefore chose to make up the radiation loss by phase displacement, using a low voltage supplied by the red cavity on the left. Its frequency was modulated so as to

move an empty bucket down through the stacked beam from above.

After compensating for positive ions with clearing electrodes, and compensating for instabilities with feedback, and providing compensation for the effect of the stacked beam current on the magnets, we succeeded in stacking a beam of over 10 amperes!

OTHER MURA CONTRIBUTIONS

FFAG Cyclotrons

Conventional cyclotrons cannot accelerate protons much above 20 to 30MeV because of the decrease in revolution frequency caused by relativistic effects and by the field gradient required for vertical focusing. Using an FFAG field, one can let the magnetic field increase with energy at such a rate as to keep the revolution frequency constant up to a much higher energy. Many FFAG cyclotrons with spiral sector geometry have been constructed. Except for their use in accelerator experiments, this is the only practical application of the FFAG accelerators.

Instabilities

The MURA working group made analytical, numerical, and experimental studies of space charge limits and collective instabilities. Carl Nielson called our attention to the negative mass instability. A detailed theoretical analysis was given in a paper at the 1959 CERN Symposium.[3]

THE END

Proposals

During its thirteen year life, MURA submitted some half-dozen proposals to the AEC for FFAG accelerators in the 10 to 20 GeV range. Some emphasized colliding beams and high intensity single beams, and some proposed only high intensity single beams. None of these proposals was approved.

Why did MURA fail?

The end of high energy FFAG accelerators was a result of two developments, in both of which MURA played a role. The first was the invention of the storage ring by Lichtenberg, Newton, and Ross[4] at MURA and independently by G.K. O'Neill[5] at Princeton and SLAC. Using many of the techniques proposed by MURA, storage rings were a much cheaper way of achieving colliding beams.

The second development was he invention of the cascade synchrotron. In 1959 MURA conducted a summer workshop to which accelerator and high energy scientists were invited to study the design and utilization of FFAG accelerators. Mathew Sands, an invitee, chose instead to study the possibility of using a rapid cycling synchrotron to inject at an intermediate energy into a second synchrotron for further acceleration. He was able to show that this scheme could achieve high beam intensities not much less than those promised by FFAG, and at much lower cost.

FFAG accelerators would have worked as proposed, but that was not the way to build high energy machines.

After MURA

In 1967 MURA disbanded and sold its site and laboratory to the University of Wisconsin-Madison. The lab became the Physical Sciences Laboratory. Ednor Rowe built a small storage ring, Tantalus, initially for orbit studies, but later converted into a synchrotron radiation source, the first dedicated synchrotron radiation source. Tantalus began the Synchrotron Radiation Center. An 800 MeV storage ring, Aladdin was later added; it is still serving many users from around the country and the world.

Some MURA people remained at PSL and SRC, and some went to Fermilab, Berkeley and Brookhaven. The location of Fermilab in the Midwest is in part due to the activities of MURA.

Conclusion

Perhaps it is a good idea, if we want to maximize progress, not to give people what they propose.

REFERENCES

[1] K.R. Symon and A.M. Sessler, "Methods of radio frequency acceleration in fixed field accelerators with applications to high current and intersecting beam accelerators," CERN Symposium on High Energy Accelerators and Pion Physics, June, 1956, pp. 44-58.

[2] D.W. Kerst, "Properties of an intersecting beam accelerating system," CERN Symposium, 1956, pp. 36-39.

[3] C.E. Nielsen, A,M. Sessler and K.R. Symon, "Longitudinal instabilities in intense relativistic beams," International Conference on High-Energy Accelerators and Instrumentation - CERN 1959, pp. 239-252.

[4]D.B. Lichtenberg, R.G. Newton and M.H. Ross, "Intersecting Beam Accelerator with Storage Ring," MURA Report 110, April 26, 1956.

[5] G.K. O'Neill, Phys. Rev., **102**, 1418, 1956.

SNS CRYOMODULE PERFORMANCE*

J. Preble*, I. E. Campisi, E. Daly, G. K. Davis, J. R. Delayen, M. Drury, C. Grenoble, J. Hogan, L. King, P. Kneisel, J. Mammosser, T. Powers, M. Stirbet, H. Wang, T. Whitlatch, M. Wiseman.

Thomas Jefferson National Accelerator Facility Newport News, Va, 23606, USA

Abstract

Thomas Jefferson National Accelerating Facility, Jefferson Lab, is producing 24 Superconducting Radio Frequency (SRF) cryomodules for the Spallation Neutron Source (SNS) cold linac. This includes one medium-β (0.61) prototype, 11 medium-β production, and 12 high beta (0.81) production cryomodules. After testing [1], the medium-β prototype cryomodule was shipped to Oak Ridge National Laboratory (ORNL) and acceptance check out has been completed. All production orders for cavities and cryomodule components are being received at this time and the medium-β cryomodule production run has started. Each of the medium-β cryomodules is scheduled to undergo complete operational performance testing at Jefferson Laboratory before shipment to ORNL. The performance results of cryomodules to date will be discussed.

INTRODUCTION

Jefferson Lab has started production of the 24 Superconducting Radio Frequency (SRF) cryomodules for the Spallation Neutron Source that is being built at ORNL. To date three cryomodules have been completed and two more are in various stages of completion. Production schedule includes completion and testing of one medium beta cryomodule approximately every three weeks. Testing plans for subassemblies and completed assemblies are in place to support this schedule. The testing program is intended to support design, acceptance, and operational characterization of the cryomodules. Critical cryomodule components are tested at sub-assembly levels prior to cryomodule integration. Testing of the completed cryomodules follows. Currently, three cryomodules have been completed. One of these has completed integrated testing in the Jefferson Lab Cryomodule Test Facility (CMTF), and the second is being tested.

SUB-ASSEMBLIES

The cost of, and time required for, disassembly and rework of a completed cryomodule is prohibitive and therefore critical sub-assemblies must be qualified prior to integration into higher-level assemblies. Additionally, lifetime testing is required for some components to ensure they will continue to be operational over the 40-year life required for SNS accelerator systems. Included in these two categories are the Fundamental Power Couplers (FPC), cavity frequency tuners for lifetime requirements, and the SRF cavities themselves.

Fundamental Power Couplers

SNS cavities use a coaxial coupler design for 48 kW average power and driven by a 550 kW klystron with 1.3 ms pulses at 60 Hz[2]. All FPC's are processed on one of two warm test stands [3]. Processing includes a 24-hour vacuum bake resulting in vacuum levels ~ 5 E-10 mbar followed by RF processing to 1 MW traveling wave and 2.4 MW standing wave power levels [4]. To date 21 FPC's have been processed to levels required for SNS operations with no difficulties

Cavity Frequency Tuners

The SNS tuner design has been adapted from a Saclay design for the TESLA cavities. For SNS application the requirements are listed in table 1. To achieve these requirements a piezo element has been incorporated into the "dead leg" and provides the required fine-tuning adjustment. The tuner assembly is shown in figure 1 with the drive train on the top left and the piezo element on the bottom right.

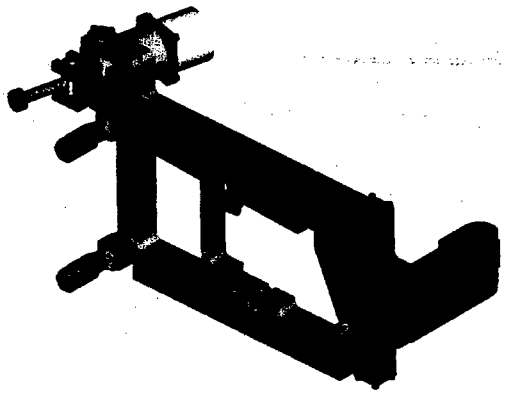

Figure 1. SNS Cavity Tuner Assembly

* Work supported by the U.S. Department of Energy under contract DE-AC05-00-OR22725
#preble@jlab.org

0-7803-7738-9/03/$17.00 © 2003 IEEE

Prototype tuners were fabricated and tested in the Vertical Test Area (VTA) where both prolonged test cycles and rapid turn around are possible. A complete tuner assembly was mounted to a mechanical spring representative of a cavity load at maximum tuning force. This assembly is place in an evacuated can to model the cryomodule insulating vacuum where the tuner operates. A linear position monitor was mounted on the tuner assembly and used to measure tuner travel during operation. Initial testing of the tuner included cycling over small ranges equivalent to 4 kHz and 16 kHz. Initially the tuner performed as expected but at the end of the first extended period of operation there was an increase in required torque from the motor to drive the tuner. This was thought to be a sign of wear on the lead screw. The tuner was then operated through its entire range of motion, equivalent to ~400 kHz, and the required motor torque returned to its initial value. Subsequent testing has included a full stroke cycle after each 6 months of equivalent life and the problem has not returned. A total of 30 years of equivalent life has been accumulated.

	Mechanical	Piezo
Travel (mm)	1.8	10^{-2}
Freq. Range (kHz)	200	2
Freq. Resolution (Hz)	60	NA
Load (N)	8900	15000

Table 1. SNS Tuner Requirements

Cavities

All cavities undergo a final assembly and testing at Jefferson Lab that includes warm tuning, installation into helium vessels, and qualification in the VTA prior to being assembled into a cavity string and then into a cryomodule. Warm tuning is performed at several stages of the assembly with a final check of the field flatness after the helium vessel installation process. The SNS requirement for cavity field flatness is <8%. A typical measurement is shown in figure 2 and the measurements to date are shown in figure 3.

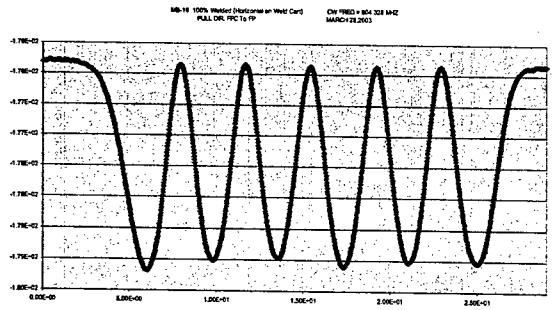

Figure 2. Typical Field Flatness Measurement

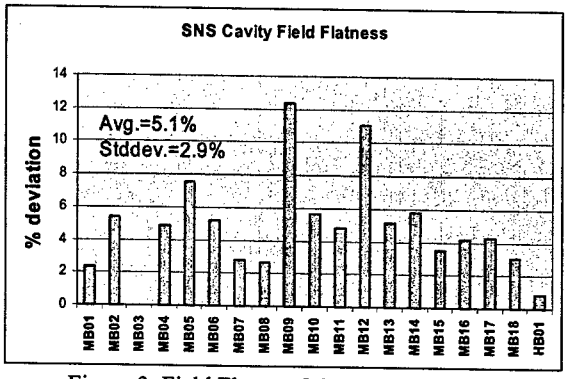

Figure 3. Field Flatness Measurements to Date

During VTA cold testing the cavities are qualified at 2 K. To date 16 cavities have been qualified which includes the measurement of cavity Q_0, figure 4, onset of field emission (FE) and the maximum E_{acc} and is interpreted as ???. Eacc limitations include cavity quench, field emission, and RF power limitations.

Eacc Limit	Q0 at 10 MV/m	FE Onset
15 MV/m	$1.2\ 10^{10}$	9 MV/m

Table 2. Average Values from VTA Testing

For cavities that have passed qualification testing, average values for limiting E_{acc}, Q_0 at nominal operating gradient, and onset of field emission, as evidenced by the start of measurable radiation, are listed in table 2. VTA testing is also monitored for trends as a feedback into the production process and process charts are maintained. Process charts are shown in figure 5 and 6.

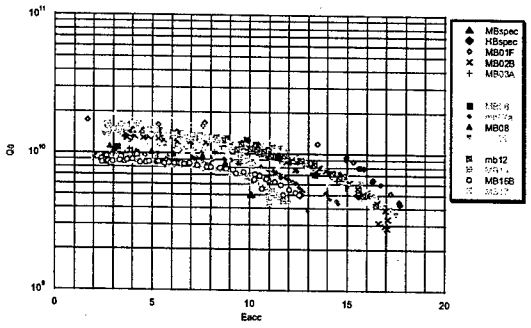

Figure 4. Q_0 vs E_{acc} for SNS Medium Beta Cavities

* Work supported by the U.S. Department of Energy under contract DE-AC05-00-OR22725
#preble@jlab.org

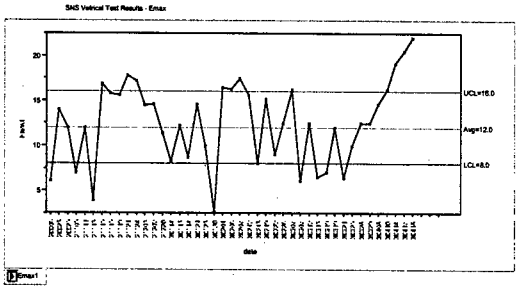

Figure 5. Cavity E_{acc} Limit Process Chart

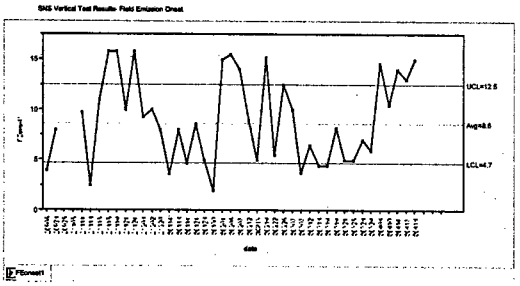

Figure 6. Cavity FE Onset Process Chart

INTEGRATED CRYOMODULE PERFORMANCE

During integrated cryomodule testing systems are in their final configuration and operated at 2 K using low power RF, a 20 kW CW RF source and 1 MW pulsed RF source. Testing of the first three or four cryomodules will include a larger set of tests to include design and operational characterization that will be eliminated on subsequent tests where acceptance testing is the goal. Additional tests will be required as issues of interest are identified throughout production.

Cryogenics

The SNS cryomodule incorporates a final counter-flow heat exchanger into the cryostat utilizing the sub-atmospheric return helium gas to cool the primary supply process stream before the J-T valve [5] and uses a bypass to circumvent this during cooldown. A typical cooldown is shown in figure 7. The cavities are cooled at a rate of ~200 K/Hr with the entire process taking ~8 hours from opening the J-T valve to the start of liquid collection. Heat loads for the primary and shield circuits, 12 ± 3 and 130 ± 10 watts respectively, are measured several days after cooldown to ensure all components are in thermal equilibrium.

Fundamental Power Coupler

After cooldown of the cryomodule the FPC's for all cavities require RF conditioning. Conditioning is

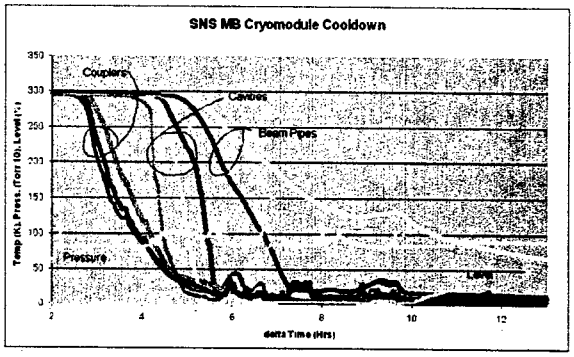

Figure 7. Cryomodule Cooldown

accomplished with the 1 MW RF source using 1.3 ms pulses at 60 Hz while maintain the coupler vacuum below 10^{-7} mbar. RF power is increased to 180-250 kW on all cavities with a typical process shown if figure 8. After initial conditioning the FPC's demonstrate a memory of the conditioning and do not require reconditioning during turn on after days of non-operation although some minor exceptions have been observed.

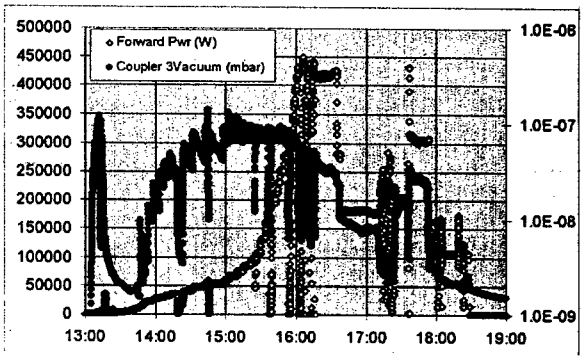

Figure 8. FPC Processing with Time in Hours

Cavity Frequency Tuner

Eight tuners have been tested after integration into cryomodule including three in the medium-β prototype and five in the first production cryomodule. During the testing of the prototype cryomodule the tuners performed as expected with the mechanical and piezo tuners providing in excess of 400 kHz and 3 kHz tuning range respectively. The mechanical tuner performance over an abbreviated range and the piezo tuner resolution measurement are shown in Figures 9 and 10. The piezo tuner was not part of the initial design and was included to allow for compensation for Lorentz force detuning during pulsed operations.

* Work supported by the U.S. Department of Energy under contract DE-AC05-00-OR22725
#preble@jlab.org

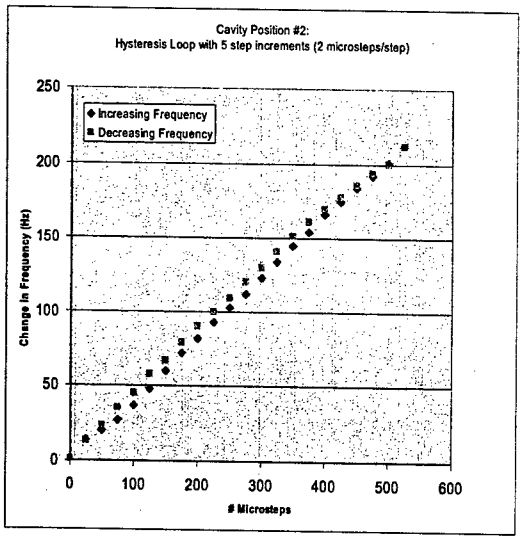

Figure 9. Mechanical Tuner

After initial fabrication and test of the prototype tuners a production run for the medium and high beta cryomodules followed. Identical components were procured and integrated into the production cryomodules without subassembly testing. During the testing of M01, the first medium-β production cryomodule, all tuners worked after cooldown but two mechanical tuners, position #1 and #2, started to operate

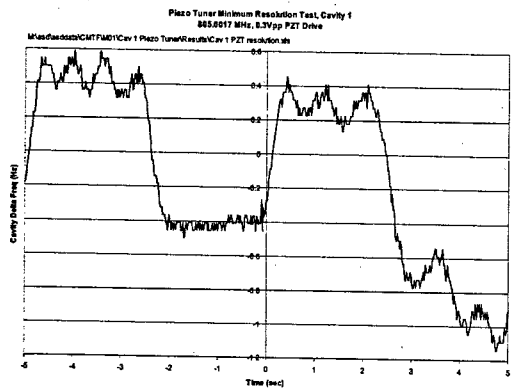

Figure 10. Piezo Tuner Resolution, ~ 1Hz

intermittently after a period of several days with no operation. The third tuner, position #3, continued to perform as expected. The two problematic tuner drive assemblies were removed and replaced with assemblies that had been qualified in the VTA using the life cycle test fixture. Qualification included operations over the full range of motion as well as periods of cold soaking to approximate conditions observed in the M01 cryomodule. After a second cool down and test cycle two tuners, position #2 and #3 operated intermittently. Cavity position #1 has operated continuously since replacement.

Investigation into the source of the tuner problems is underway. The suspect components are in the drive assembly and include the cold stepper motor, harmonic drive, lead screw, and lead screw nut. We are presently working with the designers and vendors to identify failure modes and solutions.

Cavity Performance

During testing in the CMTF cavity performance is characterized including Q_0 and FE as a function of E_{acc}, maximum E_{acc}, Q_{ext} of FPC's, HOM damping, HOM probe rejection of fundamental power, and identification of cavity mechanical modes using Lorentz force and the piezo tuner as drivers. The cavities have all performed above specification for Q_0, Figure 11, and maximum E_{acc}. Maximum gradient for all cavities has been in the range of 15-20 MV/m with the onset of FE above 10 MV/m for ½ of the cavities and no measurable radiation for the other ½ of the cavities at maximum gradient.

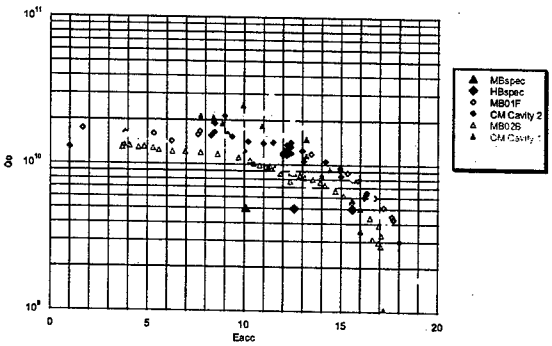

Figure 11. Cavity Q_0 in Final Assembly

Considerable attention has been focused on the mechanical modes of the cavities and the dynamic Lorentz force detuning of the cavities as there is a concern regarding control of the RF during pulsed operations [6]. Dynamic Lorentz force detuning is measured by the cavity frequency shift during a RF pulse while operating at the SNS design of a 6% duty factor at 60 Hz and operating gradient of 10.1 MV/m. The measured frequency shift of ~300 Hz is below the requirement of 470 Hz. The frequency shift resulting from background microphonics noise is also measured. Measurements of the first mode and amplitude for M01 are included in Table 3. These levels are well within requirements for SNS.

RMS Background, Hz	1.1	2.9	1.3
1st Mechanical Mode	69	60	69

Table 3. M01 Microphonics Amplitude and 1st modes

Measurements of the mechanical modes are done both by sweeping the modulation frequency of an amplitude modulated cavity gradient and piezo excitation voltage.

* Work supported by the U.S. Department of Energy under contract DE-AC05-00-OR22725
#preble@jlab.org

The transfer functions for these are shown in Figures 12 and 13 where the x-axis shows the frequency of the driving term and the y-axis is the cavity response amplitude.

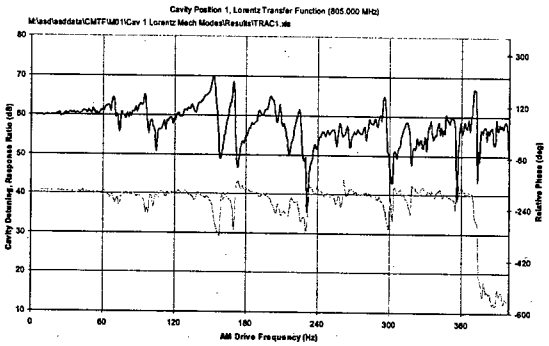

Figure 12. Gradient Modulated Mechanical Mode Mapping

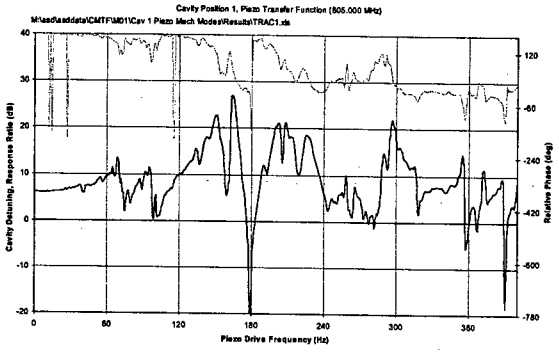

Figure 13. Piezo Modulated Mechanical Mode Mapping

HOM damping is measured for all significant modes as well as the rejection of the fundamental frequency by the pickup probe. HOM mode filters achieve Q's below 10^4 for all critical modes, meeting the SNS requirements. Initial Q specification for the HOM filter fundamental notch filter was 10^{12} but has been reduced to $3x10^{10}$ and measured values range from ~$5x10^{10}$ to ~$5x10^{14}$.

SUMMARY

The performance characterization of the SNS cryomodules has included testing of sub-assemblies for more than 4 cryomodules and 2 final assemblies, the prototype and first production medium-β cryomodule. Cavity performance has exceeded E_{acc} and Q_0 requirements for all qualified components and completed assemblies with no significant change in performance between VTA and cryomodule configurations. A focused testing program continues to characterize cryomodule performance for SNS operations. These tests will continue as required to support operations at SNS.

There are problems with the mechanical tuners resulting in intermittent operation. The suspect components are in the drive train that can be replaced with little effort. Replacement of the tuner drive assemblies is planned after rework and qualification of assemblies has been completed.

* Work supported by the U.S. Department of Energy under contract DE-AC05-00-OR22725
#preble@jlab.org

REFERENCES

[1]S. Smee, H. Wang, M. Stirbet, T. Powers, M. Drury, J.R. Delayen, E. Daly, G. Ciovati, C.E. Reece, P. Kneisel, K. Davis, K. Wilson, J. Preble, J. Mammosser, Isidoro Campisi, "Results of the Cryogenic Testing of the SNS Prototype Cryomodule" *2002 Linear Accelerator Conference*

[2]K.M. Wilson, Isidoro Campisi, Peter Kneisel, William Schneider, Edward Daly, Mircea Stirbet, "The Fundamental Power Coupler for the Spallation Neutron Source (SNS) Superconducting Cavities", *PAC 2001, 18-22 Jun 2001, Chicago, Illinois*

[3]K.M. Wilson, C. Grenoble, G.K. Davis, Tom Powers, Ganapati Myneni, Mike Drury, Isidoro Campisi, Mircea Stirbet, "Processing Test Stand for the Fundamental Power Couplers of the Spallation Neutron Source (SNS) Superconducting Cavities", *PAC 2001, 18-22 Jun 2001, Chicago, Illinois*

[4]M. Stirbet etal, "Testing Procedures and Results of the Prototype Fundamental Power Coupler for the Spallation Neutron Source", *PAC 2001, 18-22 Jun 2001, Chicago, Illinois*

[5]E. F. Daly, V. Ganni, C. H. Rode, W. J. Schneider, K. M. Wilson and M. A. Wiseman, "Spallation Neutron Source Cryomodule Heat Loads and Thermal Design", Advances in Cryogenics, Vol. 47A, p. 531.

[6]J.R. Delayen, "Piezolectric Tuner Compensation of Lorentz Detuning in Superconducting Cavities", These Proceedings

DEVELOPMENT OF ELECTROPOLISHING TECHNOLOGY FOR SUPERCONDUCTING CAVITIES

K.Saito#, KEK, 1-1 Oho, Tsukuba-shi, Ibaraki-ken, Japan

Abstract

In this paper, a brief review is given for electro-polishing (EP) of niobium superconducting (sc) cavities. KEK original EP method is introduced. This method can produce high gradient of 40MV/m, which will be the fundamental limit of high pure niobium sc cavities. A required surface smoothness is estimated to be less than 2μm in order to prevent field enhancement problem in sc cavity.

ELECTROPOLISHING OF NIOBIUM CAVITIES

Surface preparation is one of major issues for super-conducting (sc) RF cavities. Unloaded Q-value (Q_0) of sc cavities is in a range of 10^9 – 10^{11} and higher than 6 orders of magnitude than normal conducting cavities. Surface defects or surface contaminations make bad effect so sensitively on the RF sc performances: high Q and high gradient.

So far, chemical polishing (CP) or electropolishing (EP) has been used as the main preparation method for niobium cavities. As seen in Fig.1, EP produces a smoother surface than CP. Levelling mechanism in EP is illustrated in Fig.2. Electropolishing a metal as an anode, the electro-chemical reaction generates a liquid layer by the viscous complex salt near the surface. At peaks, anode current concentrates more than bottoms due to the smaller electric resistivity with the thin liquid layer and that results in levelling process. P.A.Jacquet [1] invented EP method in 1935. He found out that a plateau region appears in current density (see Fig.2 right) and plays an important role in EP process.

In the early feasibility study of sc cavities in 1960-1975th, people were of great interest in EP and many

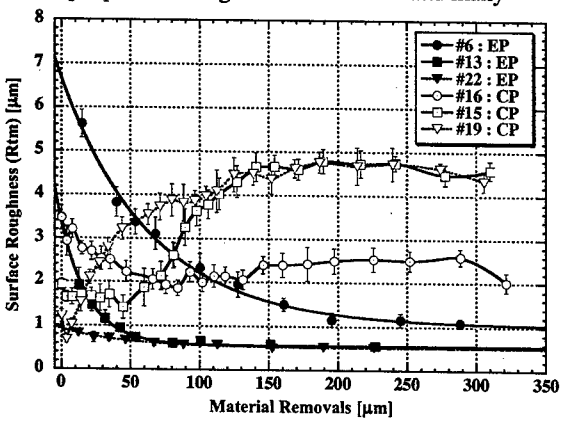

Figure 1: Surface roughness of niobium by EP or CP.

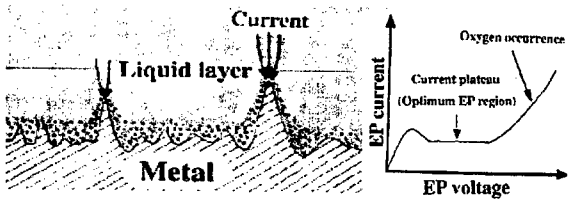

Figure 2: Principle of levelling process in electro-polishing (left) and plateau in current density in electropolishing (right).

efforts took place. A most famous work was done by H.Diepers et al. in Siemens Company using the EP acid consisted of sulfuric acid and hydrofluoric acid : H_2SO_4 (>93%) : HF (40%) = 10 : 85 V/V in collaboration with KfK Karlsruhe in 1971 [2]. They developed that the optimum EP condition of niobium is not in the plateau current density but current oscillation as shown in Fig.3. The current oscillation reflects building up and partial decrement of oxide film on niobium surface. It decays in a few minutes after switching on voltage. In order to recover the oscillation, one has to agitated EP acid or to move cavity in switch off. Thus, their method results in intermittent EP. Combining this method with heat treatment and oxypolishing (OP), B.Hillenbrand et al. achieved 1490 Gauss in RF surface peak magnetic field (Hp) with an x-band TM_{010} cylindrical niobium cavity [3]. This number corresponds to the accelerating field gradient (Eacc) of 34MV/m. Its reproducibility was poor but it should be emphasized the high gradient performance by EP was already demonstrated in the pioneer studies.

For multi-cell structures, A.Reuth and O.Schmidt in Siemens Company invented a rather realistic EP system based on the current oscillation control in 1977 [4]. In their method, a cavity is set horizontally in an acid bath. EP acid is filled up to a half level of the cavity through a cathode tube set in it. Voltage is applied to the cavity for several minutes resting it until the current oscillation decreases. Then, switching off the voltage, EP acid in the cavity is agitated by pump acid circulation to remove the

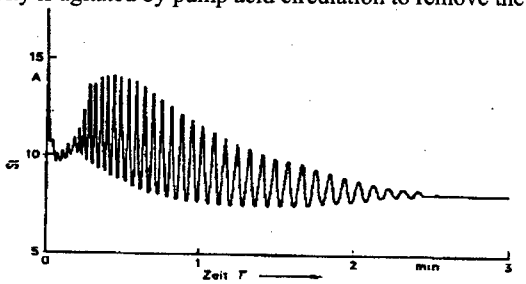

Figure 3: Current oscillation appeared in EP of niobium.

ksaito@post.kek.jp

0-7803-7738-9/03/$17.00 © 2003 IEEE

oxide film on the surface. Thereafter, the cavity is rotated slightly and the voltage is applied again. Such a process is repeated up to the required material removal. In this method, hydrogen gas generated during EP escapes out easily through openings at the beam tube ends. However, this method was never used in their further R&D. EP was very complicate than CP. In those days, CP was getting enough high cavity performance and many laboratories had preferred CP to EP except for KEK.

Hydrogen increases seriously surface resistance of sc niobium cavities. S.Isagawa in KEK investigated this problem in 1979 [5]. He pointed out that hydrogen is picked up niobium material during chemical process like CP or EP and degrades the sc RF property. Hydrogen degassing is crucial to get excellent cavity performance.

Y.Kojima and T.Furuya et al. in KEK followed the current oscillation control at 500 MHz single-cell cavities with a belief in a benefit of the smoother surface by EP. They developed a cathode bag made of porous Teflon cloth to prevent hydrogen bubble attacking the cavity surface during EP. They reconfirmed that the process combined EP, OP and heat treatment produces a good sc cavity performance in 1982 [6]. However, using this KEK standard method for a multi-cell structure, it did not produce such an expected performance due to poor electropolishing around equator section of the cavity and by the imperfect hydrogen cure [7].

K.Saito et al. developed the horizontally rotating continuous electropolishing method (HRC-EP) for multi-cell cavity in 1986 as described in next section. He took Reuth's horizontal EP method but the EP condition was not in the current oscillation. HRC-EP produced high performance very reliably in TRISTAN 508 MHz 5-cell cavities. To date using this method with L-band (1300MHz) single-cell cavities, KEK has reached Eacc~40MV/m with a high probability. Now HRC-EP is regarded as the breakthrough technology for TESLA-800.

DEVELOPMENT OF HRC-EP

In 1985, KEK was preparing sc cavity production for TRISTAN energy upgrade program. They needed a new EP method to guarantee high cavity performance, in addition, to be suitable for the mass production. Siemens's method seemed to be inconvenient because the quantitative control of current oscillation was hard. The resultant intermitted EP procedure was too complicate. K.Saito searched other EP parameters easy in quantitative control and found out that EP condition of niobium is not always in current oscillation but current density of 30~100mA/cm^2 as shown in Fig. 4 , and at the acid temperature between 20^{o}C and 35^{o}C. In addition, he considered about continuous EP method against hydrogen problem. If niobium on anode is continuously applied a voltage, hydrogen ions (H^+) will not be picked up niobium by the potential barrier. The following chemical reaction occurs in EP :

$$2Nb + 10HF + 2H_2O \rightarrow 2H_2NbOF_5 + 5H_2 \uparrow \quad (1).$$

As mentioned in Fig. 2 , the liquid layer (niobium-fluorine complex) generated near the cavity surface governs the EP finishing. A balance between its generation and dissolving into the acid would determine the EP condition. Making a continuous mild agitation, the balance might keep a good EP condition. This agitation can be supplied by a slow continuous cavity rotation. He combined this idea to Reuth's horizontal EP method and innovated the HRC-EP. KEK and Nomura Plating developed the HRC-EP method in a close collaboration. The details are seen in the reference [8].

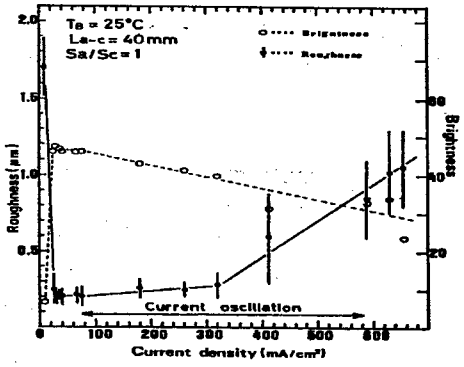

Figure 4: Optimum current density of niobium EP.

HRC-EP is presented in Fig.5. EP acid overflows from open mouths on the rotary sleeves, and retunes by gravity in a reservoir tank with a heat exchanger cooling the solution. Acid pumping speed into cavity depends on the cavity surface areas and is 60 l/min. for the TRISTAN 508 MHz 5-cell cavities. A porous Teflon bag cut open at the bottom side covers the cathode made of pure aluminium tube. This system has many advantages than Reuth's method. 1) EP acid is closed in the system, thus the system becomes very safe against the hazardous EP solution. 2) Only the inside surface is polished. It prolongs the life of EP solution. 3) Even the simple straight cathode structure can get enough current density because that only half of the cell surface immerses in EP solution increases the anode effective surface. Thus one can obtain a good polishing in all inner surfaces. 4) The control is much easy due to the continuous EP. 5) OP is no needed. That made the preparation very simple. Prevention of hydrogen problem by continuous potential control was just recently confirmed [9]. When niobium surface has a damage layer like by mechanical grinding, the potential control has no help against hydrogen [10]. In TRISTAN sc cavity production, we made buffing all half-cells and the potential control did not work. Therefore the

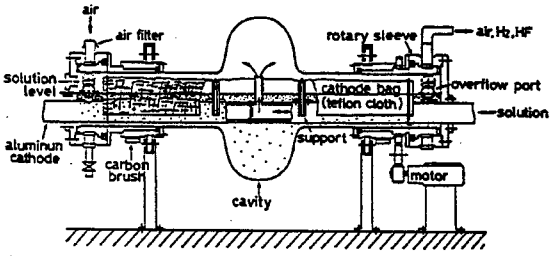

Figure 5: Horizontal rotated continuous electro-polishing.

all TRISTAN sc cavities (32 cavities) were heat treated to degas hydrogen. The average field gradient of 9.6 ± 1.4 MV/m and $Q_0 = 2.8 \pm 0.2$ at 5 MV/m @4.25 K were obtained in the vertical test. In that time, this performance was high comparing with other laboratory, for instance DESY-HERA.

SUPERIORITY OF EP WITH HIGH GRADIENT

After the TRISTAN, KEK L-band group started TESLA activity since 1990. One issue of this activity was to establish high gradient technology over 30MV/m based on TRISTAN sc cavity technique. Let's see the past 10 years history in Fig.6. This graph shows the achieved highest gradient in each year with L-band single-cell niobium cavities. Until 1994 a steady improvement is seen by several developments: high purity niobium material, 1400°C high temperature annealing (HT), high peak power processing (HPP). In 1995, high-pressure water-rinsing method (HPR) innovated by D.Bloess in CERN [11] was routinely used for L-band cavities by K.Saito [12] and P.Kniesel [13]. HPR can remove particle contamination on cavity surface very efficiently and results in elimination of field emission problem. Thus, HPR brought the jump in 1995. Since then gradient looks to be saturated around 40MV/m. Here it should be emphasized that 40 MV/m was achieved almost by EP except for two results by P.Kneisel in Fig. 6 (■ Nb bulk cavity, ■Nb/Cu clad cavity), which were obtained by CP. Today, we have 3 results with 40MV/m by CP including more recent result in Saclay [14]. CP can achieve 40MV/m but the probability is very low.

These results open several questions: 1) has EP superiority with high gradient, 2) why 40MV/m, and 3) is the saturation in high gradient by technology reason or fundamental field limitation, so on. The first question was answered by a hard work in KEK L-band group in 1997 [15]. The other questions will be answered later in this paper. Fig.7 shows a more recent clear result on the superiority of EP by E.Kako in KEK [16]. It was done using a cavity (S-3) from Saclay with RRR=230 and none annealing. The gradient upgraded to 38 MV/m by the second EP. Then switching to CP, field emission like

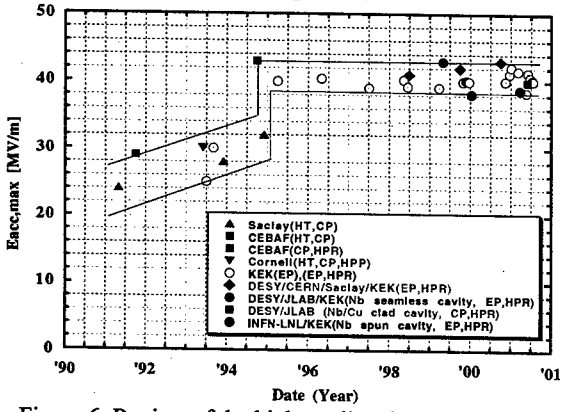

Figure 6: Review of the high gradient in last 10 years.

Q-degradation (called as Q-slope) appeared and the gradient degraded to 24 MV/m by the second CP. Taking successive EPs, the Q-slope has disappeared and the gradient improved to 40 MV/m. This fact shows a clear superiority of EP over CP with high gradient. Similar results were reported from Jlab/KEK [17] and DESY/CERN/Saclay collaboration [18]. Q-slope really appears in electropolished cavities too. It disappears by 120°C baking during vacuum evacuation [19] but in case of CP it still stays even taking bake.

J.Knobloch calculated the field enhancement at grain boundary step (~10 μm) on electron beam welded seam on cavity equator section in order to explain the Q-slope in chemically polished cavities [20]. His conclusion is that a field enhancement factor about 2 can easily happen on such a grain step, and the critical field reduces to the half of the smooth surface. The critical field with niobium sc cavity is 40MV/m as discussed later, therefore in chemical polished cavity, the superconductivity is locally broken around Eacc=20MV/m and resulting in Q-slope.

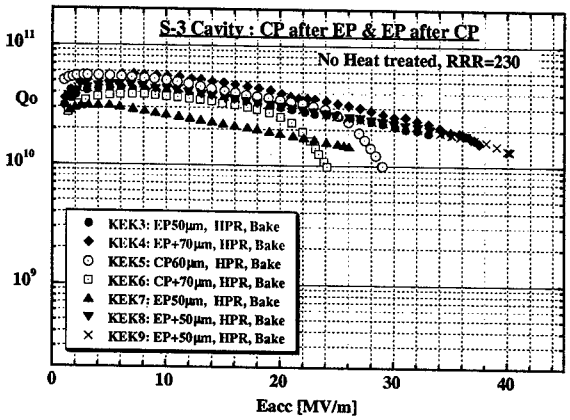

Figure 7: Evidence of the superiority of EP over CP with high gradient performance.

HIGH GRADIENT WITH MULTI-CELL CAVITIES

Next question is whether the superiority of EP can realize in multi-cell cavity. We have confirmed it by collaborations with Jlab and DESY. Fig.8 shows the recent result in DESY collaboration. High gradient performance is required for TESLA application. DESY current preparation is a combination of 1400°C hot annealing to purify niobium material by titanium getter, CP, and HPR. Their results by this process are shown in Fig.8 by hatched area [21]. The specification of TESLA-500: Eacc=23.5 MV/m @ $Q_0 = 1 \times 10^{10}$ is well satisfied. However, the TESLA-800 specification: Eacc=35 MV/m @ $Q_0 = 5 \times 10^9$ is in a far way.

New TTF 9-cell cavities were electropolished in KEK (Nomura Plating) and tested in DESY. First results are presented in Fig.8 (▲,●,■). 35MV/m was achieved in four cavities (one result is not presented in Fig.8) and the superiority of EP is clearly reconfirmed with TTF 9-cell cavities. Now, HRC-EP is the breakthrough technology

for TESLA-800. The technology transfer is under way from KEK to DESY or Jlab.

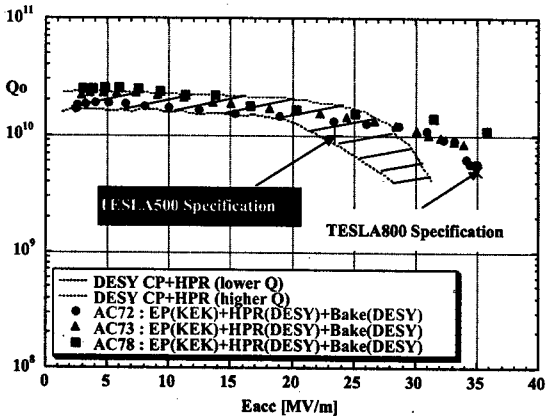

Figure 8: Results of electropolished TTF cavities.

CRITIAL FIELD OF NIOBIUM CAVITY

Here, let's discuss why the gradient is limited around 40MV/m with high pure niobium sc cavities. One candidate of the fundamental field limitation in sc RF application is superheating [22]. By this hypothesis critical field (Hsh) at a temperature T is given from an energy valance in a metastable state between a flux nucleation and sc condensation:

$$\frac{1}{2}\lambda_L(T)H_{sh}^2(T) = \xi(T)H_C^2(T) \qquad (2).$$

Here, λ_L is London penetration depth, ξ coherent length and H_C thermo-dynamical critical field. The factor 1/2 of the left hand in eq.(2) comes from the effective AC field ($Hsh/\sqrt{2}$). Superheating is based on G-L theory, which is available to the band-gap energy close to zero. Here, this condition will be satisfied because the considered magnetic field is close to H_C. Temperature dependences of λ_L, ξ were calculated from $H_{C2}(T)$ and $H_C(T)$ measurement results with Tokyo Denkai niobium material (RRR=400) using the relationships by G-L theory [23] :

$$H_{c2} = \frac{\phi_o}{4\pi\cdot\xi^2}\ ,\quad H_c = \frac{\phi_o}{4\pi\cdot\xi\cdot\lambda_L}\ ,\quad \phi_o = 2.07\cdot10^{-7}\ Gauss\,cm^2 \qquad (3).$$

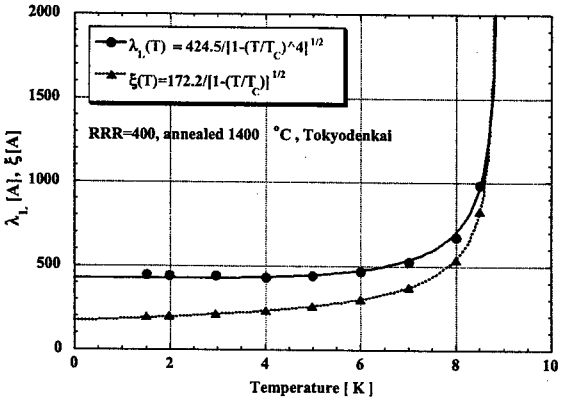

Figure 9: Temperature dependence of λ_L and ξ.

On the other hand, by the theory (high purity limit with ξ) temperature dependences of λ_L and ξ are expected as following: $\lambda_L(t) = \frac{\lambda_L(0)}{\sqrt{1-t^4}}$, $\xi(t) = \frac{\xi(0)}{\sqrt{1-t}}$, $t = \frac{T}{T_c}$ (4).

As seen in Fig.9, the calculated λ_L and ξ from experiment results are nicely fitted by eq.(4). As the theoretical temperature dependence of Hc is:

$$H_c(t) = H_c(0)\cdot(1-t^2) \qquad (5),$$

so the theoretical temperature dependence of H_{sh} is :

$$H_{sh}(t) = H_c(0)\cdot\sqrt{\frac{2\cdot\xi(0)}{\lambda_L(0)}}\cdot\sqrt{\frac{1-t^4}{1-t}}\cdot(1-t^2) \qquad (6).$$

On the other hand, for niobium sc cavities, Hsh(T) was directly calculated from the data in Fig.9 [24] and presented in Fig.10 by solid line. Critical fields (Hcf) at various temperatures of niobium sc cavity were nicely measured at Cornell University by short pulse measurement method (■) [25]. These data are presented in Fig.10 with KEK CW measurement results (○). Hsh(T) fits well all the date over the temperature range between 1.5K and 8.5K. It should be emphasized that only $H_C(T)$ or $H_{C1}(T)$ can not fit all the data satisfactorily [25]. Hsh is asymptotic to 1800 Gauss below 3K (t=0.32), which corresponds to Eacc = 41 MV/m. This value explains the saturation of the gradient around 40MV/m in high purity niobium sc cavities.

In order to reconfirm this analysis, Hcf(T) on Nb_3Sn (▲) or Pb (●) cavity [25] was parameter fitted by eq.(6) (dotted lines) in Fig.10. Good fittings were obtained. From this analysis, one will realize that high gradient of sc cavities has come to the fundamental limitation by superheating. As seen in eq.(6), Hsh depends on $\kappa_{GL}(\equiv 1/\sqrt{2}\cdot\lambda_L/\xi)$. For niobium cavity, beyond 40MV/m might be possible by κ_{GL} moderation [26] or new cavity design reduced Hp/Eacc ratio. If Hp/Eacc=40 Gauss/(MV/m), 45MV/m is possible.

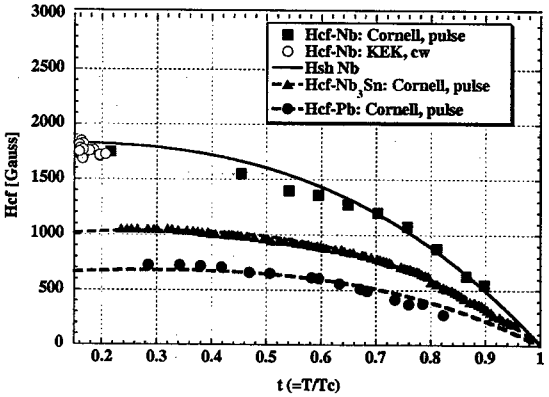

Figure 10: Critical RF fields (Hcf) of sc cavities and Hsh.

SURFACE ROUGHNESS

In the section 3 one would understand the importance of the cavity surface smoothness for high gradient performance. Here let's evaluate quantitatively the required surface smoothness analyzing Q-slope. In the presence of RF field, surface resistance (Rs) of our

niobium cavities with Hp/Eacc=43.8 Gauss/(MV/m) will be written as following [27]:

$$R_S(Eacc) = R_{BCS}(Eacc) + R_{res}$$

$$= \frac{A}{T + C \cdot Eacc} \cdot \exp\left[-\frac{B}{T + C \cdot Eacc} \cdot \sqrt{1 - \left(\frac{43.8 Eacc}{\sqrt{2} \cdot H_c} \right)^2} \right] + R_{res} \quad (7).$$

A factor $1/\sqrt{2}$ front of H_C in eq. (7) comes from the AC effective field. A, B and Rres are obtained by the temperature dependence measurement of Rs at low field. C · Eacc term in eq.(7) appears by heat stay effect on the RF surface due to the poor thermal conductivity in sc state. In our case these values are A=1.45E-4, B=18.6. Rres =2~10nΩ, and C = (3~5)E-3. When fixed A, B and Rs to the experimental values, eq.(7) includes two free parameters : C and Hc. Fig.11 shows the fitting results with a cavity performance by EP or CP. Eq.(7) nicely fits both results with reasonable H_C value: Hc=2230 Gauss for EP smooth surface. For the enough electropolished surface, the resultant Hc is the real thermo-dynamic critical magnetic field because no field enhancement happens. Remembering Knobloch's simulation, the resultant H_C value (954 Gauss) in CP will include a field enhancement effect. The ratio of 2230/954=2.34 is considered as a field enhancement factor due to the rough surface by CP finishing.

If one approves this analysis, one can obtain a relationship between surface roughness and the field enhancement factor. We have data with successive material removals and the Qo-Eacc excitation curves, for instance Fig.7. We can deduce the field enhancement fitting each Qo-Eacc excitation curve by eq.(7). In addition, we know the surface roughness from the relationship between the material removal and the surface roughness in Fig1. Thus, we obtained Fig.12. The detail will be presented somewhere else. This result is a preliminary one but suggests the surface roughness should be less than 2μm (Rz) to prevent RF field enhancement in sc cavities. The roughness of coarse will depend on the RF frequency.

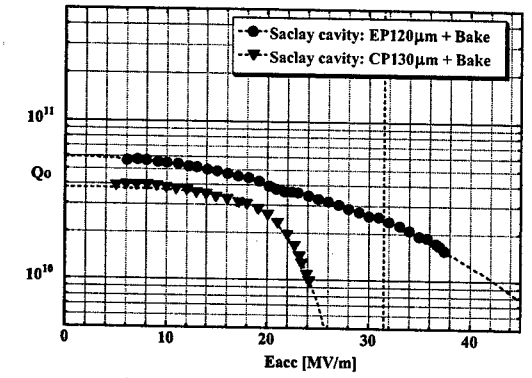

Figure 11: New Q-slope analysis.

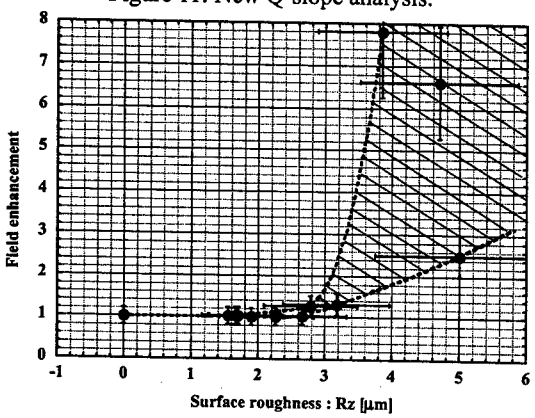

Figure12: Estimated surface roughness versus the field

SUMMARY

We have identified EP is an excellent technology for high gradient sc cavities by the smooth surface finishing. TESLA-800 is ready if one applies EP. High gradient of sc high purity niobium cavities is limited 40MV/m by fundamental limitation: superheating field. Still beyond 40 MV/m might be possible choosing new cavity shape or by the moderation of κ_{GL} of niobium material. The required surface smoothness will be less than 2μm in R_Z to prevent field enhancement with 1300MHz sc cavities.

REFERENCES

[1] P.A.Jacquet, Nature, 135, 1976(1935).
[2] H.Diepers et al., Phs. Lett. 37A, 139 (1971).
[3] B.Hillenbrand et al., Proc. of 9th Int. Conf High Energy Accelerator, Stanford, 143 (1974).
[4] A.Reuth and O.Schmidt, Japanese patent application Syowa 49 -122826
[5] S.Isagawa, Doctor thesis, Tokyo University (1979).
[6] Y.Kojima et al., Jpn.J.Appl. Phys. 21, 86 (1982).
[7] T.Furuya et al. Proc. of the 5th Sym. Accelerator Science and Technology, KEK, Sep. 1984, p.122
[8] K.Saito et al., Proc. of the 4th Workshop on RF Superconductivity, August 14-18, 1989, KEK, Tsukuba, pp.635-694.
[9] K.Saito et al., Proc. of the 9th Workshop on RF Superconductivity, November 1– 5, 1999, Santa Fe, NM USA, pp.283-287.
[10] T.Higuchi and K.Saito, Proc. of the Int. Workshop on Hydrogen in Metals & Vacuum Systems, November 11-13, 2002, Newport News, VA USA, to be published in the AIP Conference Proceedings Series Book.
[11] Ph. Bernard and D.Bloess et al., Proc. of 3rd EPAC, Berlin,Germany, 1992, p.1269.
[12] K.Saito et al., Proc. of the 6th Workshop on RF Superconductivity, Oct. 4-8,1993, Newport News, VA USA, pp.1151-1159.
[13] P.Kneisel et al., ibid. ref.[12], pp.628-636.
[14] B.Visentin, private communication.
[15] K.Saito et al., Proc. of the 8th Workshop on RF Superconductivity, Abano Terme, Italy, Oct. 6-10, 1997, pp.795-813.
[16] E.Kako et al., http://laacg1.lanl.gov/rfsc99/rfsc99.pdf,TUP011
[17] K.Saito and P.Kneisel, ibid. ref[16],TUP031
[18] L.Lilje et al., http://laacg1.lanl.gov/rfsc99/rfsc99.pdf, TUAoo1
[19] P.Kneisel, http://laacg1.lanl.gov/rfsc99/rfsc99.pdf,TUP044, B.Visentin et al., http://laacg1.lanl.gov/rfsc99/rfsc99.pdf, TUP015.
[20] J.Knobloch et al., http://laacg1.lanl.gov/rfsc99/rfsc99.pdf,TUA005.
[21] TESLA Technical Design Report (TDR) Part I (2001).
[22] G.Mueller, Proc. of the 3rd Workshop on RF Superconductivity, Sep.14-18, 1987, Argonne, IL. USA, pp.331-358.
[23] B.B.Goodmann, Rep. Prog. Phys.29, 445 (1966).
[24] K.Saito, http//www.kek.jp/conference/SRF2001.
[25] T.Hays and H.Padamsee, Proc of the 8th Workshop on Superconductivity. pp. 789 – 794.
[26] K.Saito, Niobium Workshop, http://www-bd.fnal.gor/niobium/
[27] K.Saito, to be published somewhere else.

COLD- AND BEAM TEST OF THE FIRST PROTOTYPES OF THE SUPERSTRUCTURE FOR THE TESLA COLLIDER

J. Sekutowicz, C. Albrecht, V. Ayvazyan, R. Bandelmann, T. Büttner, P. Castro, S. Choroba, J. Eschke, B. Faatz, A. Gössel, K. Honkavaara, B. Horst, J. Iversen, K. Jensch, H. Kaiser, R. Kammering, G. Kreps, D. Kostin, R. Lange, J. Lorkiewicz, A. Matheisen, W.-D. Möller, H.-B. Peters, D. Proch, K. Rehlich, D. Reschke, H. Schlarb, S. Schreiber, S. Simrock, W. Singer, X. Singer, K. Twarowski, G. Weichert, M. Wendt, G. Wojtkiewicz, K. Zapfe,
DESY, 22603 Hamburg, FRG
M. Liepe, Cornell University, Ithaca, NY 14853, USA
M. Huening, FNAL, Batavia, IL 60510, USA
M. Ferrario, INFN, 00044 Frascati, Italy
E. Pławski, INS, 05400 Otwock, Poland
C. Pagani, INFN, Milano, 20090 Segrate, Italy
N. Baboi, SLAC, Menlo Park, CA 94025, USA
H. Chen, H. Wenhui, C. Tang, S. Zheng, Tsinghua University, 100084 Beijing, China

Abstract

After three years of preparation, two superstructures, each made of two superconducting 7-cell weakly coupled subunits, have been installed in the TESLA Test Facility linac (TTF) for the cold- and beam test. The energy stability, the HOMs damping, the frequency and the field adjustment methods were tested. The measured results confirmed expectation on the superstructure performance and proved that alternative layout for the 800 GeV upgrade of the TESLA collider, as it was proposed in TDR [1], is feasible. We report on the test and give here an overview of its results which are commented in more detail elsewhere in these Proceedings.

INTRODUCTION

The superstructures (SSTs), chains of superconducting multi-cell cavities (subunits) connected by λ/2 long tube(s) have been proposed as an alternative layout for the TESLA main accelerator. This concept is discussed in more detail in [2, 3]. We re-call here two main advantages of the layout in comparison to the standard one, based on 9-cell cavities. The first economical advantage is that structures made of more cells will reduce the number of the Fundamental Power Couplers (FPC) in the linac. Consequently, the number of all auxiliaries needed to distribute the RF power, like: waveguides, bends, circulators, 3-stub transformers, loads etc., can be reduced too. In addition, the layout reduces the amount of electronics controlling phase and amplitude of cavities in the linac and simplifies the design of cryomodules due to less openings for the FPCs. The second advantage is the increased filling of the linac tunnel with accelerating structures, since the distance between subunits is λ/2 only. The space saving can be significant and in the case of here discussed versions of SSTs it amounts to ~1.8 km. The first superstructure (SST-I), as it has been proposed in [2], was meant to be made of four 7-cell cavities. We have built a Cu model of this version and six Nb 7-cell subunits.Meanwhile, a 2x9-cell version (SST-II) was studied and was found to be more attractive for the TESLA collider. This version keeps the same fill factor of the tunnel as the first one. SST-II is shorter and its production, cleaning and handling will be easier. Savings in the investment cost are of the same order for both superstructures. The RF parameters of both versions are listed in Table 1.

Table 1. RF parameters of both superstructures.

Parameter		SST-I	SST-II
Number of cells in subunit		7	9
Number of subunits		4	2
(R/Q) per subunit	[Ω]	732	985
E_{peak} / E_{acc}		2	2
B_{peak} / E_{acc}	[mT/(MV/m)]	4.2	4.2
L_{active}	[m]	3.23	2.08

PREPARATION OF THE TEST

2x7-cell prototype

We have "split" the 4x7-cell prototype in two 2x7-cell prototypes. The main argument to split the prototype of SST-I was similarity in the RF-properties of the 2x7-cell and the favorable 2x9-cell versions. The computed bunch-to-bunch energy variation for all bunches in the TESLA macro-pulse (HOMDYN [4]) was very similar, $\pm 5 \cdot 10^{-5}$ for 2x9-cell and $\pm 3 \cdot 10^{-5}$ for 2x7-cell version. The scheme of the Higher Order Modes (HOM) suppression in both versions is very similar also and is based on the HOM couplers of the same type as those used for standard 9-cell TTF cavities. The conclusion was that the beam test of already existing 7-cells subunits assembled in two 2x7-cell prototypes will tell us more about the favorable SST-II superstructure, will benchmark our computation and will give finally twice as much statistics for the measured results.

0-7803-7738-9/03/$17.00 © 2003 IEEE

TTF Linac

Both 2x7cell superstructures were assembled into a spare cryomodule and installed in the TTF linac next to the injector. The bunch-to-bunch energy measurement at the end of the linac, which was the main purpose of the experiment, was performed by means of the spectrometer dipole with two BPMs at its front and one BPM behind it. The highest estimated energy measurement accuracy was better than $2 \cdot 10^{-4}$. Due to a very intense experimental program at the TTF linac in the year 2002, a second cryomodule, housing eight 9-cell cavities, has been installed for a long-term performance test simultaneously with the superstructures. The presence of this cryomodule had consequences for the test as discussed below.

THE TEST

Balance of the stored energy in subunits

The field profiles of the accelerating mode of both superstructures have been measured with the help of the bead-pull (perturbation) technique before the final chemical treatment and the final high pressure water rinsing. Both prototypes (P1, P2) had a good field flatness, better than 92 % and 94 %, respectively. As usual, after final preparation and cool-down there is no more possibility to use a bead for the field measurement. Still, one can apply the perturbation method to balance the mean gradient in both subunits using the cold tuners instead of a bead to perturb the e-m fields. For this, the cold tuner of each subunit was moved by 1000, 2000 and 5000 steps and for each position the frequency change of the π-0 mode was measured. Then, the final positions of the tuners were chosen to maintain exactly f = 1.3 GHz of the π-0 mode and simultaneously to ensure that the change of frequency is the same, when the tuners are moved by the same number of steps. The final status of the prototypes was cross-checked in the following way. We compared, for each cold prototype, the fundamental passband frequencies with the frequencies measured at room temperature when the bead-pull method showed the best achievable field profile. The deviation from an ideal linear shift of frequencies is a very good indicator of any change in the profile. The measured deviation for both prototypes was very small, below $8 \cdot 10^{-6}$ and we concluded that profiles remained unchanged after the final preparation and after the cool-down.

Energy gain stability

This experiment was the "proof of principle" test. Our main concern was the energy flow via very weak coupling between subunits. The stability of the energy gain for all bunches in the train means that the cells' stored energy is refilled in time between two consecutive bunches. The test was performed in two parts. In the first one, we subjected the prototypes to a slow decay of the stored energy during the acceleration. In the second part we measured directly bunch-to-bunch energy modulation at the end of the linac. In this test both prototypes were operated very reliably at 15 MV/m. The operation of the injector, with the smallest charge fluctuation of 2.8 % within the macro-pulse, was possible, when the bunch charge did not exceeded 4 nC. We chose the bunch spacing of t_b = 1 μs to meet the highest sampling rate of the implemented BPMs' electronics. The rise time of e-m fields resulting from the matched Q_{load} value was 790 μs and the longest beam on time was limited to 530 μs by the klystron pulse length. Each prototype has been equipped with four field probes, placed one near each end-cell. They were used to monitor the field strength during the acceleration. An example of measured signals is shown in Fig. 1. Without the energy re-filling the beam would take almost 70% of the energy stored in the cells and the voltage would drop by 45 %. No such phenomenon was observed. All signals had noisy fluctuations. The strongest oscillation was at 250 kHz. It was caused by down-converters of the low level RF-system controlling the phase and the amplitude of accelerating fields. We found, in the second part of the experiment, six more oscillations caused by the feedback loops. The Fourier transformation of three signals (from the BPM behind the dipole), measured for three different gains in the feedback loop, is shown in Fig. 2. One can see in total 15 oscillations. Peaks No. 1, 2, 12 and 13 increased when the loop gain increased. Peaks No. 14 and 15 decreased vs. the gain. All other peaks remained unchanged. Seven peaks were due to the feedback loops, eight (No. 3÷10) were caused by the second cryomodule. All eight cavities of this cryomodule have been detuned from 1.3 GHz by roughly 200 kHz and no power was delivered to them during the entire energy gain test. Still, the beam induced voltage in these cavities has modulated the energy of bunches. Finally, the conclusion from the energy stability test was that, no slow gradient decay and

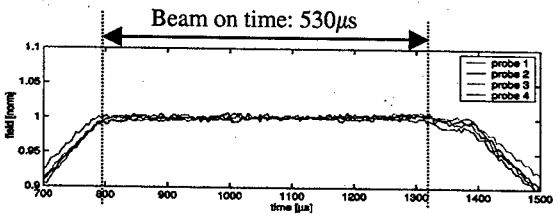

Figure 1: Signals from field probes of P2 measured during the acceleration of 530 bunches, q = 4 nC, t_b = 1 μs.

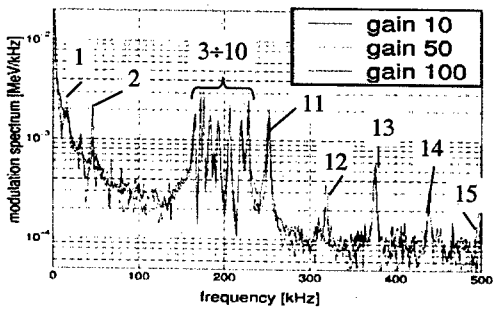

Figure 2: Spectrum of the energy modulation as measured at the end of the linac.

no modulation caused by superstructure prototypes was seen within the accuracy limit in the measurement [5]. This result proves that superstructures fulfill the TDR specification for the energy variation, which must be below $5 \cdot 10^{-4}$.

HOM damping

Each prototype had three HOM couplers, which had been attached to the end beam tubes and to the interconnection. The SST-II version will have four cells more and we plan to attach two HOM couplers at the interconnection to compensate for that. We will report on the results we measured for the transversal modes, since these modes are relevant for the quality of the TESLA beam. Three methods were applied to measure frequency and impedance, $Z = (R/Q) \cdot Q_{ext}$, of HOMs. At first, we measured the modes' frequency and Q_{ext} with a network analyzer. We measured modes up to 3.2 GHz. The method gives the mode impedance when one assumes that the actual (R/Q) is equal to its computed value. The method is limited to well "isolated" modes. The error in frequency measurement increases when Q_{ext} of a mode gets lower and when neighboring modes overlap.

The second method we applied was the active mode excitation [6]. Modes with high impedance were excited via one of the HOM couplers by means of a cw amplifier. By controlling the power coupled out by two other HOM couplers we estimated transversal kick (Z) and deflection of the on axis injected beam. It was compared to the value measured in the BPM, 15 m downstream from the cryomodule. The method can give all actual parameters of an excited mode: Z and the polarization if deflection is measured in x and y direction. It is sensitive to the setting of the beam line optics between cryomodule and the BPM. One can apply this method to modes, which couple well to HOM couplers. Forty-seven modes were measured with this method. The third method, applied to measure Z, was based on the HOM excitation by the accelerated beam when it passes the cavity off axis. The results are reported in [7]. All three methods verified a very good damping of HOMs. The suppression of dipoles with $(R/Q) > 1\ \Omega/cm^2$ is shown in Fig. 3. All modes relevant

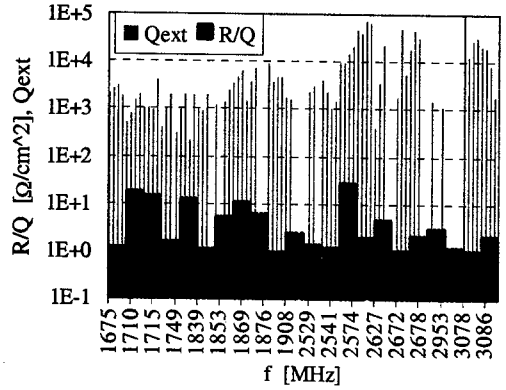

Figure 3: Damping of dipoles with $(R/Q) \geq 1\ \Omega/cm^2$.

for the TESLA collider, up to 2.58 GHz, were damped by a factor 5 to 100 better than the specification ($Q_{ext} \leq 10^5$). We have found a few modes only (in 5th passband, ~3.08 GHz), among 420 measured modes, with $Q_{ext}=10^7 \div 2 \cdot 10^8$. Their (R/Q)s are almost zero and thus they cannot degrade the quality of the TESLA beam.

FINAL REMARKS

The cold- and beam test of both prototypes has confirmed that one can use weakly coupled structures for the acceleration. Neither beam energy modulation, slow gradient decay nor insufficient HOM's damping resulting from the coupling of two subunits have been observed. The stability of the bunch-to-bunch energy gain was measured within the limit of the beam diagnostics in the TTF linac. Although, the accuracy of the energy gain measurement has not reached the level of the theoretical estimation, which was one order of magnitude smaller, the experiment showed that the TESLA specification already has been fulfilled. We have demonstrated two methods to balance the gradient in the weakly coupled subunits. The agreement of both methods was good and both confirmed that final chemical cleaning may be performed without additional degradation in the field flatness.

The experiment showed that the electronics for phase and amplitude control, used routinely to operate standard 9-cell cavities in the TTF linac, can be applied to operate the superstructures. Further improvement of the control system seems to be possible to provide better suppression of the modulations coming from the control system itself.

ACKNOWLEDGMENTS

We would like to express our gratitude to the TESLA collaboration group for many helpful discussions and to all operators of the TTF linac for their help.

REFERENCES

[1] R. Brinkmann et al., "TESLA Technical Design Report, Part II: The Accelerator", DESY 2001-01, Hamburg, March 2001.

[2] J. Sekutowicz et al., "Superconducting Superstructure", LC'97, Zvenigorod, October 1997.

[3] J. Sekutowicz et al., "Superconducting Superstructure for the TESLA Collider; A Concept", PR-ST AB, 1999.

[4] M. Ferrario et al., "Multi-Bunch Energy Spread Induced by Beam Loading in a Standing Wave Structure", Particle Accelerators, Vol. 52, 1996.

[5] H. Schlarb et al., "Bunch-to-Bunch Energy Stability Test of the Nb Prototypes of the TESLA Superstructure", PAC03, Portland, May 2003.

[6] J. Sekutowicz et al., "Active HOMs Excitation in the First Prototype of Superstructure", PAC03, Portland, May 2003.

[7] P. Castro et al., "Analysis of the HOM Damping with Modulated Beam in the First Prototype Superstructure", PAC03, Portland, May 2003.

FIRST DEMONSTRATION OF MICROPHONIC CONTROL OF A SUPERCONDUCTING CAVITY WITH A FAST PIEZOELECTRIC TUNER

Stefan Simrock, Gevorg Petrosyan, DESY; Alberto Facco, Vladimir Zviagintsev, INFN-LNL;
Stefano Andreoli, Rocco Paparella, INFN-Milano

Abstract

Superconducting cavities exhibit a high susceptibility to mechanical vibrations due to their narrow bandwidth of operation. The resulting modulation of the resonance frequency (typical amplitudes are, in the absence of mechanical dampers, a few tens of Hz at a modulation frequency of up to a few hundred Hz) can exceed the cavity bandwidth leading to a perturbation of the amplitude and phase of the accelerating field, which can be controlled only at the expense of rf power. It is therefore highly desirable to control the resonance frequency of the cavity with a fast controller. A fast mechanical tuner based on piezoelectric or magnetostrictive actuator appears very attractive, since its tuning is done simply by a micrometric deformation of the resonator geometry. In the past these tuners have been limited by mechanical resonances in the transfer function to a modulation bandwidth of about 1 Hz. With modern control theory and high speed DSPs and FPGAs it is now possible to design complex controllers which allow high gain up to several hundred Hz. In this paper we present first results of fast microphonics piezoelectric control for a superconducting quarter wave resonator. Microphonics at 42 Hz (inner conductor) are controlled despite a large mechanical resonance a 662 Hz in the actuator transfer function.

1 INTRODUCTION

The control of the resonance frequency of superconducting cavities is highly desirable particularly if frequency excursions induced by microphonics (or Lorentz force detuning in pulsed operation) exceed the bandwidth of the cavity. This is usually the case in accelerators with small beam loading such as heavy ion linacs, low current high energy electron linacs and energy recovery linacs.

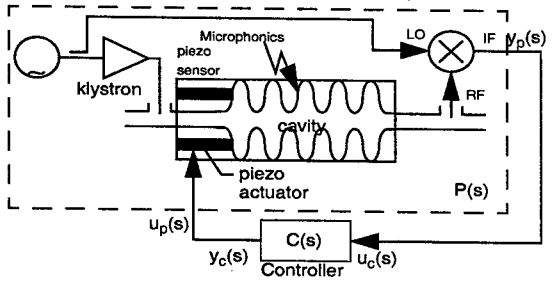

Fig.1: Schematic for feedback control of microphonics

Typical microphonic noise levels as measured in operational superconducting accelerators are of the order of several Hz to several tens of Hz with a frequency spectrum ranging up to a few hundred Hz. The observed spectrum is a result of a convolution of the spectrum of excitation and the coupling to the mechanical resonances of the cavities. Since microphonics are induced by mechanical vibrations a natural solution to the problems appears to be a fast mechanical actuator which is driven in such a way that the detuning caused by microphonics is perfectly compensated. Due to the partially statistical nature of the microphonic noise a negative feedback loop is necessary as shown in Figure 1.

The cavity resonance frequency is detected with a phase detector comparing the wave incident to the cavity (from the directional coupler for forward power) with the transmitted signal (field probe signal). Corrections for beam loading may be necessary and can be accomplished with digital signal processing. The fast mechanical frequency tuner can be realized with a piezoelectric or magnetostrictive actuator which are integrated with the motor driven mechanical tuner. The actuators typically allow for a length change of the cavity of a few micrometers resulting in frequency changes of some tens to some hundreds of Hz. Presently several labs are pursuing the control of microphonics and Lorentz force detuning with a piezoelectric actuator [1-5].

2 MICROPHONICS CONTROL ISSUES

Fast piezoelectric tuners are installed in several superconducting linacs but are usually used to control slow drifts (< 1 Hz) of the resonance frequency of the cavity. Attempts have been made to increase the bandwidth of the feedback loop to several hundred Hertz. The failure of these attempts can be explained by the mechanical resonances of the cavity which introduce several second order poles in the transferfunction between piezo actuator input and the cavity resonance frequency measured with a phase detector.

In practice the mechanical transfer functions of multicell cavities such as employed at the TESLA Test facility or at SNS are quite complicated because of the large number of resonances up to several kHz. For quarter wave cavities the resonances of the center conductor and the bottom plate are only few up to a several kHz and are well understood. While microphonics are usually coupled strongly to the low frequencies resonances of the center conductor, the piezo actuator couples to the higher frequency resonances of the bottom plate and only weakly to the center conductor. Therefore the QWR provides the ideal testbed for control of microphonics. In summary the issues related to the control of microphonics are:

- mechanical resonances in the transfer function of piezo tuner + delay from propagation of acoustic waves
- vibrations from the environment (microphonics) and piezo tuner couple differently to mechanical resonances
- different mechanical modes couple differently to the resonance frequency of the cavity. No linear superposition of detuning from individual mechanical modes possible i.e system is nonlinear.

0-7803-7738-9/03/$17.00 © 2003 IEEE

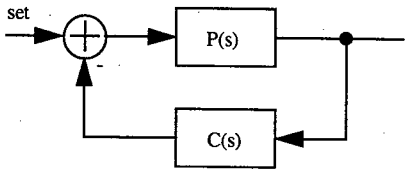

Fig.2: Feedback configuration with plant P(s) and Controller C(s)

- mechanical modes excited with large amplitude can potentially modulate the energy gain in multicell cavities significantly.

3 CONTROL OF MICROPHONICS

The goal is to find an acceptable controller C(s) for a given transferfunction P(s) of the piezo actuator in the control configuration shown in Figure 2.
The controller must fulfill several requirements

- Feedback loop must be stable i.e. the open loop transferfunction D(s)=P(s)C(s) must change the phase less than 180 deg. up to unity gain frequency.
- For fast reponse the phase margin should be at least 30-60 deg.
- Good error supression i.e. high gain of D(s) at frequencies which need to be controlled (up to several hundered Hz). The gain of D(s) should roll-off fast at higher frequencies to guarantee stability.
- Robust against small changes of the transfer function of the piezo actuator.

After choosing the desired open-loop frequency response D(s) the controller can be designed as

$$C(s) = \frac{D(s)}{P(s)}$$

A typical desired open loop transfer function would be a gain of 100 (= 40 dB) for frequencies from DC up to a few hundred Hz, then a steep roll-off (for example 3rd order low-pass with 60 dB/dec), a reduction of roll-off to 20 dB when unity gain is reached (this can be implemented with 2nd order high pass) followed by a fast roll-off above (2nd order low-pass) at a few kHz to prevent higher frequency resonances to cause instabilities.
With D(s) of 8-th order as described and assuming 10 mechanical resonances up to several kHz, the controller requires fairly high order polynomials (28-th order in the example) to be implemented. With the recent progress in digital signal processing hardware (DSPs and FPGAs) it is nowadays possible to implement such high order controllers with low latencies. For example a 20-th order transferfunction processed by a C67 DSP results in a latency of only 20 microseconds. Implementation on a VIRTEX II FPGA is expected to reduce latencies to below 1 microsecond and that very high order transferf unctions can be realized.

4 QWR AND PIEZO TUNER

The resonator [6,7] is a 80 MHz PIAVE type bulk niobium Quarter Wave Resonator (QWR) with mechanical damper. This type of QWRs has been operated in the linac at gradients of up to 6 MV/m. The operating bandwidth is only a few Hz and phaselock can be achieved without a fast frequency tuner. The resonator is ideally suited for the development of controllers for fast mechanical tuners for control of microphonics because it is a mechanically simple and well understood system.
For the experiment of controlling microphonics with a piezotuner the cavity was mounted in the cryostat after 8 months of storage while exposed to air without any rinsing done before installation. The tuning plate, a 1 mm thick copper disc with a 1 micrometer layer of sputtered niobium on the rf surface, has been mounted at the open end of the QWR.

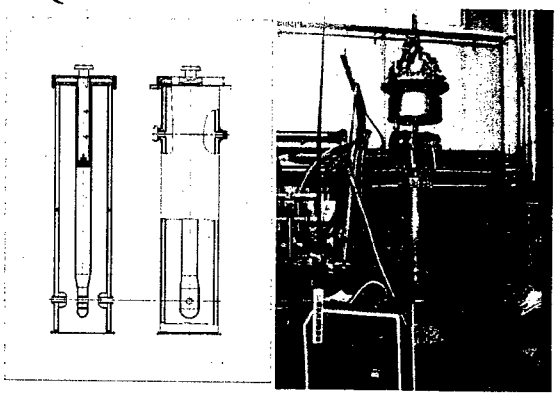

Fig.3: PIAVE type quarter wave resonator

The piezo, a EPCOS 8x8x30 mm crystal without internal preloading, was mounted in the center of the bottom plate along the resonator axis. The piezodriver was a 60 W, 400 mA, -10 to 15 V, model ENV 400 power supply from Piezojena. The measured tuning range generated by the piezo was 25Hz/100V at 4.2 K, corresponding to about 8 micrometer change in length of the piezo. The center conductor has the lowest resonance frequency at about 42 Hz while the tuning plate with the piezo had a lower mechanical mode at 672 Hz (calculated and measured). The resonator low power electrical Q measured during the test was 1.6e9.

Fig.4: Piezo tuner installed at bottom plate

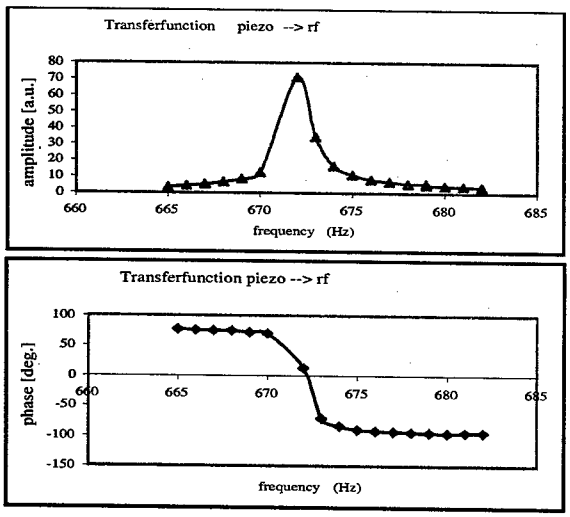

Fig.5: Transfer function of piezo tuner around 672 Hz

5 DIGITAL CONTROLLER

The digital controller made use of a C67 based DSP board (Model M67 from GBm) with an Omnibus module (A4D4) carrying 4 ADCs and 4 DACs with a maximum clock speed of 200 kHz. The DSP has been programmed in C++ to perform Matrix multiplications to realize transferfunction in state space form:

$$\hat{x}_{k+1} = A\hat{x}_k + B\hat{u}_k$$

$$\hat{y}_{k+1} = C\hat{x}_{k+1} + D\hat{u}_k$$

With the A matrix of size 20x20 transferfunction of to 20-th order could be realized. The computation time was of the order of 20 microseconds (including ADC and DAC conversion times) which is fully sufficient for feedback up to a few kHz.

Initially only a notch filter at 672 Hz and a low pass around 1 kHz have been implemented.

6 PERFORMANCE OF FEEDBACK

The feedback test has been performed at low fields to guarantee a linear response of the rf control system. During the test the cavity was locked at a gradient of about 1 MV/m. The resonator has been weakly locked in phase to allow a large residual phase error at 42 Hz. The forward power was 10 W, largely overcoupled resulting in a 3 dB bandwidth of about 50 Hz.The residual phase error in the rf control system, caused by resonator vibration due to environmental noise was reduced by one order of magnitude when activating the piezo control system. The resulting error suppression is shown in Figure 6.

7 CONCLUSION

Active suppression of microphonics in a superconducting quarter wave resonator has been demonstrated successfully. Besides reducing the microphonics by an order of magnitude, the standard controller could be turned off and the piezotuner was able to maintain the cavity in phase-lock.

Although the piezotuner did not couple to the dominating resonance of the center conductor which has been excited quite strongly by microphonics, a mechanical resonance of the bottom plate has been compensated with the digital controller. In the future it is expected that modern digital controllers allow for feedback control of microphonics in multicell cavities despite the complex mechanical mode structure.

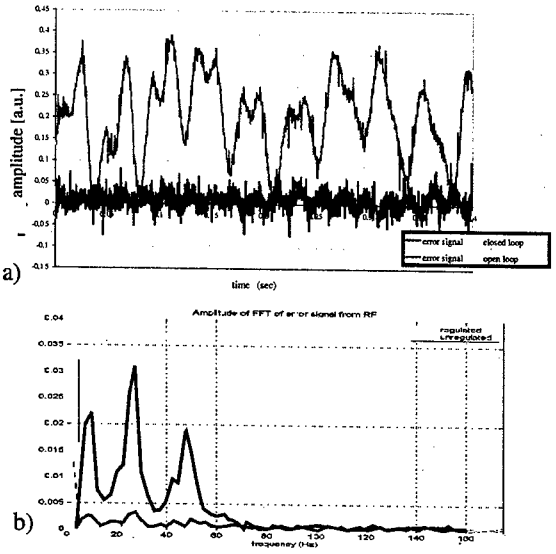

Fig.6: Active suppression of microphonic noise with feedback applied to fast piezo tuner. a) Time domain measurement. b) Frequency domain measurement

REFERENCES

[1] Matthias Liepe, Sergey Belomestnykh, "Microphonic Detuning in the 500 MHz Superconducting CESR Cavities", this conference

[2] Allan Rowe, Tim Berenc, Ruben Carcagno, Darryl Orris, "Microphonic Detuning Compensation in 3.9 GHz Superconducting RF Cavities", this conference

[3] Jean Delayen, G.K. Davis, "Piezolectric Tuner Compensation of Lorentz Detuning in Superconducting Cavities", this conference

[4] Marc Doleans, Sang-ho Kim, "Insights in the Physics of the Dynamic Detuning in SRF Cavities and Its Active Compensation", this conference

[5] Chad Joshi, Anil Mavanur, "Magnetostrictive Tuners for SRF Cavities", this conference

[6] A. Facco, V. Zviagintsev, S. Canella, A.M. Porcellato, F. Scarpa, "On-line performance of the mechanically damped superconducting low beta resonators", proc. of the European Particle Accelerator Conf., Stockholm , Sweden, 1998

[7] A. Facco, F. Scarpa and V. Zviagintsev, "Status of the non-RFQ resonators of the PIAVE heavy ion Linac", proc. of the European Particle Accelerator Conf., Wien, Austria, 2000.

RF POWER GENERATION IN LHC

O. Brunner, H. Frischholz, D. Valuch, CERN, Geneva, Switzerland

Abstract

The counter-rotating proton beams in the Large Hadron Collider (LHC) will be captured and then accelerated to their final energies of 2×7 TeV by two identical 400 MHz RF systems. The RF power source required for each beam comprises eight 300 kW klystrons. The output power of each klystron is fed via a circulator and a waveguide line to the input coupler of a single-cell superconducting (SC) cavity. Four klystrons are powered by a 100 kV, 40 A AC/DC power converter, previously used for the operation of the LEP klystrons. A five-gap thyratron crowbar protects the four klystrons in each of these units. The technical specification and measured performance of the various high-power elements are discussed. These include the 400 MHz/ 300 kW klystrons with emphasis on their group delay and the three-port circulators, which have to cope with peak reflected power levels up to twice the simultaneously applied incident power of 300 kW. In addition, a novel ferrite loaded waveguide absorber, used as termination for port 3 of the circulator is described, including its advantages with respect to a water-load. A system to measure the harmonic content in the klystron output signal is also presented.

INTRODUCTION

The European Laboratory for Particle Physics (CERN) is presently constructing the Large Hadron Collider in the existing 27 km circumference LEP tunnel. The two counter-rotating proton beams are captured and then accelerated by two identical 400 MHz RF systems. Superconducting cavities, operating at 4.5 K, provide the required accelerating field for ramping the beam energy up to 7 TeV. A maximum of 4800 kW of RF power is generated by sixteen 300kW/400 MHz klystrons. Each klystron feeds, via a Y-junction circulator and a WR2300 (half-height) waveguide line, a single-cell SC cavity. Eight of these cavities of are installed on each side of the former LEP intersection 'Point 4'. Four of them are housed in a common cryostat. The two beams are separated by 420 mm for about 45 m on each side of 'Point 4'. This allows the SC cavities to be installed without interfering with the vacuum pipe of the respective other beam. All klystrons with their circulators and loads, the HV interface bunkers, and the racks with the controls and interlock electronics are located on the ground floor of the former ALEPH experimental cavern, about 6 m below the beam lines. The average waveguide length between klystron and cavity is about 22 m.

Four klystrons are powered by one 100 kV/40 A power converter, previously used for the LEP klystrons. Their HV interface equipment, consisting of four modulators, a thyratron crowbar, a smoothing capacitor and an HV commutator, is housed in a fire-proof bunker. This forms, together with four cavities, an 'LHC/RF Module' (Fig.1).

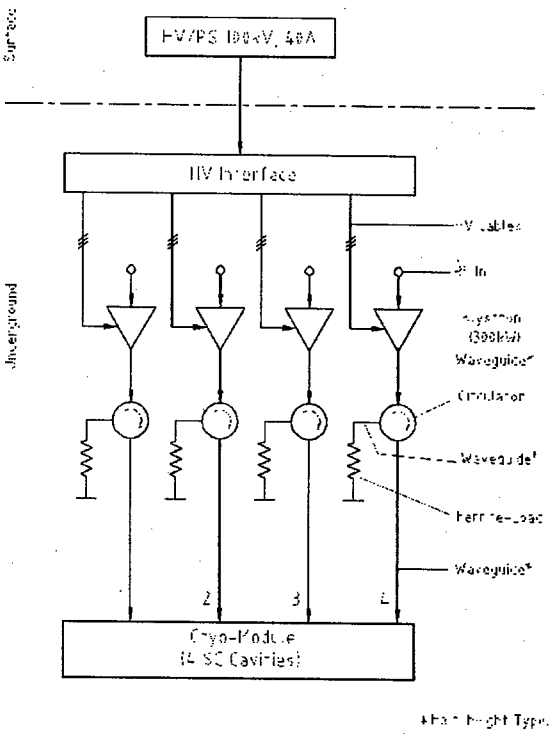

Figure 1: Schematic diagram of an LHC/RF module.

KLYSTRONS

The LHC klystrons were developed by a European company according to CERN specifications. By May 2003 (PAC 2003), five of the 20 klystrons ordered have been delivered and accepted by CERN. The main operating parameters at the rated output power (300 kW) are shown in Table 1.

An important parameter for the LHC klystrons is their group delay. CERN demands the group delay to be as short as possible since a fast vector feedback loop around each klystron/cavity assembly is required for beam stability. The total delay of this loop should not exceed 500 ns. At the acceptance test of the prototype a delay slightly over 100 ns was measured. For the series klystrons a value of ≤ 120 ns within the frequency range of $f_0 \pm 1$ MHz was then specified. Such a low group delay is obtained by tuning the five klystron cavities each either above or below the operating frequency. In particular the first two cavities are stagger-tuned. This increases the

0-7803-7738-9/03/$17.00 © 2003 IEEE

bandwidth of the klystron as required for low group delay. In addition, the loaded Q factor of the input cavity is well below 200 and that of the output cavity is 35. The penultimate cavity is tuned to more than 2% above the operating frequency, and therefore contributes little to the total group delay within the specified frequency range. The third cavity is tuned to a few MHz below the second harmonic of the operating frequency; it does not contribute to the group delay but enhances the klystron efficiency by about 4-5%. About 10% of the group delay is due to the electron transit time between input and output cavity.

The relatively low Q and the detuning of the input cavity causes, however, a low overall signal gain of only 37 dB; this is unusual for klystrons.

Table 1: Main Klystron Parameters at Rated Output Power

Rated Output Power	300 kW cw
Operating Frequency (f_0)	400.8 MHz
RF Input-to-Output Gain	≥ 37 dB
DC-to-RF Conversion Efficiency	≥ 62 %
-1dB Bandwidth (@1dB below rated output power)	≥ ±1 MHz
Group Delay at f_0±1MHz and 1dB below rated output power	≤ 120 ns
Load VSWR at any RF Phase	≤ 1.2
Harmonic Content in Output Signal at 2nd and 3rd Harmonic	≤ -30 dB
Beam Voltage (U_B)	54 kV
Beam Current (I_B)	≤ 9 A
Gun Perveance	1.5mA/V$^{3/2}$ -0/+10%
Modulation Anode Voltage (U_{MA})	≤ 35 kV
Modulation Anode Current (I_{MA})	≤ ±2.5 mA
Body Dissipation	≤ 10 kW
Collector Dissipation Capability	≥ 500 kW
Test Power at U_B ≤ 58kV and I_B ≤ 10A (for at least 1 hour)	330 kW cw

A special feature of the LHC klystron is the built-in modulation anode. It allows the cathode current to be controlled between 0 and 10 A. Unlike the LEP klystron, the LHC one does not require the cathode current to be ramped down in the absence of an RF drive signal, because the water-cooled collector of the LHC klystron can dissipate the full DC input power of 500 kW. The modulation anode is used only for optimizing the working point of the klystron.

The tube operation is stable up to the rated output power for a load mismatch of VSWR ≤ 1.2 which is assured by a three-port junction circulator in the output line of each klystron. In case of a higher VSWR (e.g. an arc in the output waveguide) a fast PIN-diode switch interrupts the RF drive signal to the klystron.

CIRCULATOR WITH TERMINATING LOAD

The LHC/RF three-port circulators must cope with high peak power levels, induced in the SC cavities by the proton beam. During injection they can be as high as twice the incident klystron power of 300 kW. These reflected signals are in the microsecond range and their contribution to the power dissipation in the circulator is negligible. However, the superposition of incident and reflected signals could cause arcing between the ferrite plates. This was simulated on the prototype circulator by short-circuiting the output port and applying the appropriate input power (P_{IN}), which is defined by:

$$P_{IN} = \frac{1}{4}\left(\sqrt{P_F} + \sqrt{P_R}\right)^2$$

For P_F = 300 kW and P_R = 600 kW the input power P_{IN} is 440 kW. No arcing was observed when 440 kW were applied with the short-circuit at port 2 being moved by steps of 5 cm over half a waveguide wavelength.

The saturation magnetization of the ferrites is temperature dependent. The external magnetization of the ferrites has therefore to be adjusted as a function of their temperatures, which depend on the incident and reflected power and cooling water temperature. The external field is generated by both a permanent and an electro magnet. The temperatures of the cooling water and the permanent magnet are measured, and the 'Temperature Control Unit' adjusts the current of the electro-magnet accordingly. At RF power levels up to 330kW and inlet water temperature variations of 25 ± 3°C the input match (S_{11}) and isolation (S_{12}) of the circulator can, thus, be kept at ≤ -28 dB within the specified bandwidth of f_0 ± 1 MHz .

For reasons of better performance and smaller size it was decided to use 330 kW ferrite-loaded waveguide absorbers instead of water-loads as port 3 terminations. In such a load small ferrite tiles are glued onto the inner walls of a waveguide, which is short-circuited at its far end. A crucial parameter is the power dissipated per unit surface of ferrite, which should not exceed 15 W/cm^2. It is achieved by choosing thin ferrite tiles at the input of the load and by gradually increasing their thickness towards the shortened end. The advantages of ferrite compared to water loads are the absence of water inside the waveguide or coaxial line, smaller size, higher bandwidth, and a nearly invariable phase angle of its reflected signal as a function of the absorbed power.

The total input reflection of the circulator is composed of S_{11}, S_{12}, and S_{13} (see Fig.2). The magnitudes of S_{12} (isolation) and S_{13} (reflection from ferrite load) are both about -28 dB. The phase angle between these two signals

is virtually constant and independent of input power and load mismatch at port 2. By adjusting the electrical length of the waveguide between circulator and ferrite load this angle can be made 180°. The input reflection can thus be reduced substantially and becomes nearly independent of the load conditions at port 2. An almost constant circulator input impedance is essential for stable klystron output power.

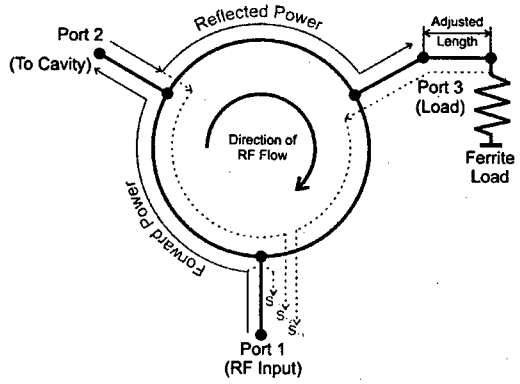

Figure 2: Schematic Diagram of Circulator with Termination Load

The standard 'Temperature Control Unit' (TCU) can cope with slow water temperature and load mismatch variations only. This is due to the time constant of the circulator's cooling circuit. If there are fast and large variations of one or both parameters the input VSWR of the circulator could briefly exceed the specified value. To avoid this, the TCU monitors the reflected RF signal between klystron and circulator. An additional built-in microprocessor controlled loop acts on the magnet current and minimizes rapidly the reflected signal as can be seen in Fig. 2. In this measurement the inlet water temperature was periodically varied by a few degrees.

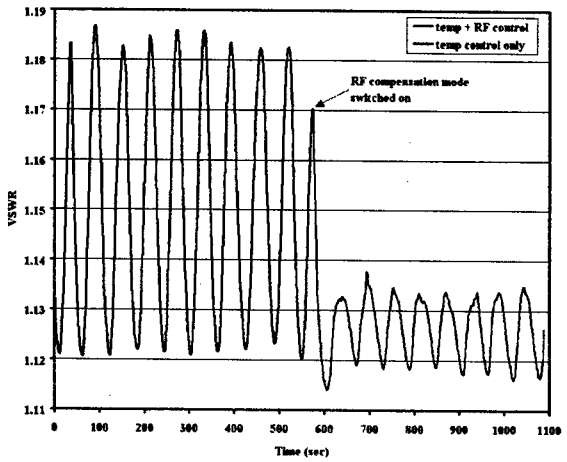

Figure 3: Input VSWR of the circulator with and without RF control at varying water temperatures

HARMONIC SIGNAL MEASUREMENTS

An advanced system for measuring the harmonic content in the klystron output signal based on [1] was developed. It consists of a piece of WR2300 half-height waveguide equipped with calibrated RF probes, an RF switching matrix, band filters, a vector voltmeter and a control computer. The system measures the power levels of all possible propagating modes at the fundamental (TE10), second (TE10, TE20, TE30), and third harmonic (TE10, TE20, TE30, TE40, TE11, TM11, TE21, TM21, TE01). Three probes are used at the narrow and nine probes (including a reference one) at the wide wall of the waveguide for measuring the electric field pattern. These data are inserted into a set of field equations, and the control computer calculates the power of each propagating mode. In its present state, measurements can only be performed using a wideband load, which is matched (VSWR≤1.12) in the frequency range from 400 to1200 MHz.

Measurements performed on the klystrons delivered so far indicate that the 2nd harmonic content is more than 50± 1 dB, and the 3rd harmonic more than 28±1 dB below the fundamental signal. The TE_{30} mode of the 3rd harmonic signal contains about 50% of the parasitic energy. These measurements will help to determine the type of HOM dampers, which may be required in the waveguide system to avoid arcing.

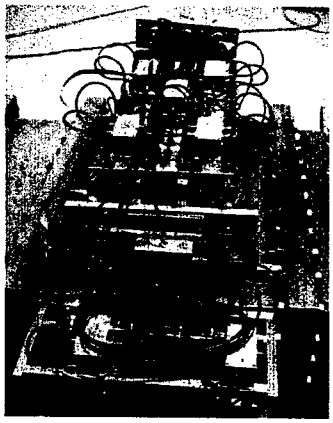

Figure 4: Harmonic measurement device

ACKNOWLEDGEMENTS

The authors would like to thank their colleagues in the AB/RF group for the development and construction of a new high-power test stand where the LHC klystrons, circulators, ferrite loads, and waveguide components are being tested prior to installation. Thanks are also due to representatives of the firms AFT and THALES for many useful discussions.

REFERENCES

[1] W.R. Fowkes and E.S. Wu, "Multimode Harmonic Power Output Measurement of SLAC High Power Klystrons". SLAC-PUB-3009, November 1982

OPERATION OF THE RHIC RF SYSTEMS*

J.M. Brennan#, M. Blaskiewicz, J. DeLong, W. Fischer, T. Hayes, K.S. Smith, A. Zaltsman,

Brookhaven National Laboratory
Upton, NY11973, USA

Abstract

Operational aspects of the RHIC rf system are described. To date three different beam combinations have been collided for physics production: gold-gold, deuteron-gold, and proton-proton(polarized).[1,2] To facilitate this flexibility the rf systems of the two rings are independent and self-sufficient.[3] Techniques to cope with problems such as, injection/capture, beam loading, bunch shortening, and rf noise have evolved and are explained.

INJECTION

The injector (AGS) holds the beam on a magnetic flattop (10 GeV/n for ions, 26 GeV for protons) for about 1 second while synchronization and bunch-by-bunch extraction to RHIC take place. Since single bunches are extracted any bunch filling pattern is possible. Typically 6,60, or 120 bunch patterns are used and a 1 μs gap is left for the abort kicker risetime.

Cogging in the AGS

The circumference ratio between the RHIC rings and the AGS is 19:4. This means that 19 times the RHIC revolution frequency equals the AGS bunch frequency when it has 4 bunches. Also every 4 turns of RHIC the same bunch aligns with a given bucket in RHIC. The hardware[4] that orchestrates the fill process is composed of four Direct Digital Synthesizers which share a common source clock and are synchronously started on an "cogging reset" event which precedes each fill. Table 1 list the clocks and gives their function. The phases of the kicker trigger and synchro reference clock advance appropriately between bunch transfers. Since the bunches are locked to the synchro reference clock they follow its phase change by making a radial (frequency) excursion. A Time Interval analyzer monitors and logs the time between the bunch and the kicker at each extraction.

clock	Frequency (RHIC)	function
RevTick	1 Frev*olution*	Marks bunch one
Kicker trig	¼ Frev	Fires the kickers
Synchro Ref	19Frev	Bunches lock to this
Beam Sync clock	360 Frev	Source for beam synch clock system

Table 1. Clocks of the injector synchronization system

* Work performed under contract DE-AC02-98CH10886 with US DOE.
# brennan@bnl.gov

Capture

Successful rf capture in founded in a precise measurement of the beam revolution frequency with the rf off. We inject a single bunch and measure the revolution frequency using data from a deep-memory oscilloscope. When the beam was injected the synchronization circuit in the AGS was responding to the RHIC clocks (Table 1) which were set to the best guess for the capture frequency. After the measurement the frequency of the clocks is corrected. In order not to change the beam energy, and hence revolution frequency, the AGS flattop field is adjusted according to, $\left(\frac{\Delta B}{B}\right)_{AGS} = \left(\gamma_{tr}^2\right)_{AGS}\left(\frac{\Delta f}{f}\right)_{RHIC}$, where Δf is the correction. The bunches of the two rings are separated longitudinally at injection to prevent beam-beam interaction. This requires that the two rings have exactly the same capture frequency and that the phase of RevTick clocks are preset. The exact frequency match can be achieved with no more than 1 mm difference in average orbit radius between the rings. The phase of the 19Frev synchro reference clock is adjusted to insure that the beam is injected into the center of the RHIC rf buckets.

RAMPS

The ramp rate to 100 GeV/nucleon is modest ($d\gamma/dt<1$) because the magnets are superconducting. A constant rf voltage of about 300 kV is supplied by two cavities which operate at a synchronous phase of less than 4 degrees. The voltage requirement follows from the necessary bucket area of > 1 eVs/n. The ion beams must cross the transition energy and the machine is equipped with fast transition-jump quadrupoles. The only special demand for the rf system is to provide a smooth phase reference to the beam control loops during the phase jump of the cavities.

Acceleration Cavities

The acceleration cavities are equipped with direct rf feedback with >38 dB gain. This feedback is essential for reducing the effective impedance below the threshold for instability. The practical gain is not limited by loop delay but by transients that occur when the cavity is, switched on/off, phase jump at transition, or multipactoring. The driver amplifiers have been upgraded to units that tolerate mismatch during transients. Cavities need to be conditioned against multipactoring for several days before the run starts. Gradual de-conditioning occurs over a time scale of months but the rf feedback helps break through multipactoring. To condition the cavities the rf feedback loop is opened via a remotely controlled transfer switch.

0-7803-7738-9/03/$17.00 © 2003 IEEE

Beam Control Feedback Loops

Ramping is normally performed with conventional phase and radial beam control loops.[5] For crossing the gamma transition the radial loop is a must. The phase loop damps coherent dipole oscillations and minimizes emittance growth during the ramp. The radial loop determines the precise value of frequency, which changes by 0.4 % for ions during the ramp.

The radial loop samples the beam position at two beam position monitors in an arc that are separated by approximately ½ betatron wavelength. To a first approximation this technique separates the effect of orbit distortion from average orbit changes. Experience has shown, however, that this is often not sufficient and the average of these two BPMs differs from the average of the entire orbit. In practice a dipole corrector between the two BPMs is "tweaked" to compensate.

The heart to the beam control system is a DSP (Texas Instruments C40) that reads the error signals and makes corrections to the rf frequency. The radius signal is sampled by a 16 bit ADC, clocked at the revolution frequency (78 kHz). The analog signal is generated in a homodyne detector with intensity normalization by implicit division in an AGC loop. A low-noise 1 kHz analog anti-aliasing filter precedes the ADC.

Phase data come from the bunch-by-bunch phase detector that measures every bunch on every turn. I and Q signals are obtained with 14 bit ADCs and converted to magnitude and phase using the "CORDIC" algorithm[6] in 100 ns. Phase data for each bunch are recorded in a deep memory for diagnostics while the average phase of all the bunches in one turn is reported to the DSP. The magnitude data are used in an automatic gain control circuit to maximize the dynamic range of the ADCs. The feedback equation is;

$$\begin{aligned}\delta\omega_{rf} &= k_{\varphi}(\varphi_{bunch} - \varphi_{s}) \\ &+ k_{R}(R_{Beam} - R_{steering}) \\ &+ k_{I}\int(R_{Beam} - R_{steering})dt\end{aligned} \qquad (1.1)$$

Where: k_{φ}=1600 Hz/radian, k_R= 330 Hz/mm, k_I=6400 Hz/mm/s. For the proton beam, which does not cross transition, the rings were locked in phase throughout the ramp by an additional term proportional the phase difference between the rings (measured at the revolution frequency). This prevents modulation of the beam-beam interaction during the ramp. The loops are open during the filling process and closed just before the ramp. When the loops close the averaged measured values of phase and radius are taken as the reference to the loops. Thereafter the reference values become the synchronous phase angle φ_s, and the radial steering command function $R_{steering}$ which updates at 720 Hz. The loops open at the end of the ramp.

Landau Cavities

High intensity bunches (~10^{11}charges) in RHIC are clearly unstable, exhibiting shape oscillations without damping for many millions of turns.[7] Proton bunches are stabilized by switching on one of the 197 MHz storage cavities at 100 kV to enhance synchrotron frequency spread and provide Landau damping. This Landau cavity is used throughout the ramp.

REBUCKETING

In local jargon "rebucketing" [8] refers to the process of compressing the bunch in length and transferring it from the 28 MHz system to the 197MHz storage system. A compression ratio of two or more is required. The technique of jumping to the unstable fixed point and back is most often used. The phase loop is active during the rebucketing to damp dipole oscillations (common cavities off). The precise set points for the relative phases of the storage cavities were obtained empirically by scanning the phases and measuring the synchrotron frequency to very high precision (0.1 %) from longitudinal Schottky signals at 2.7 GHz.[9]

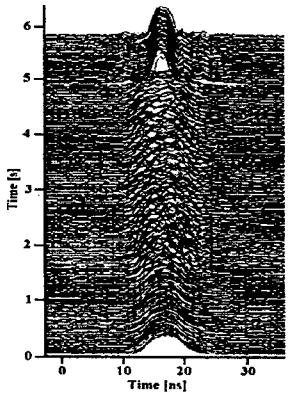

Figure 1. Evolution of the bunch shape during rebucketing. The bunch shape distortions begin 4 seconds before the gymnastic when the dampers are withdrawn.

Strategy to combat beam load/emittance growth

Beam loading is a major problem causing longitudinal emittance growth in the seconds just before rebucketing. When the storage cavities are at very low voltage while the tuning servo settles, a rapid onset of bunch shape distortions is seen (figure 1). The onset coincides with the withdrawal of the fundamental mode damper. Even though the cavity is equipped with high-gain rf feedback the beam induced voltage overwhelms the generator induced voltage and the system is unstable. The beam loading problem was overcome by shaping the Fourier spectrum of the bunch current such that second node in the envelope of the spectrum occurs near 197 MHz. (figure 2) Since this is the state where the bunch is stretched the compression gymnastic becomes just to snap up the 28 MHz voltage, and after ¼ synchrotron period switch on the 197 MHz voltage to approximately 3 MV.

Operationally this switch-on of the storage cavities (10 kV to ~ 1 MV in 1 ms) proved to be the most difficult. To address this a new technique of "frequency-shift" rebucketing was tested. In this technique the storage cavities are turned on slowly at an offset frequency of 2

kHz where they are de-coupled from the beam. At the rebucketing instant the frequency is jumped to the beam frequency. This is a minor transient for the cavities because it is only a fraction of their natural bandwidth.

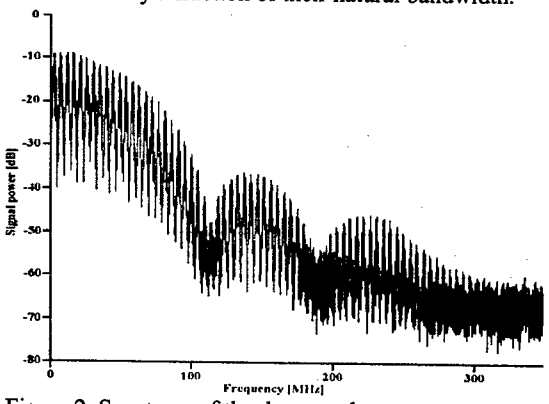

Figure 2. Spectrum of the deuteron beam current. The bunch has been stretched so that the second node is near the cavity frequency.

Hardware improvements

Luminosity lifetime improves with higher voltage in the storage cavities. The cavities of the storage system received a number of improvements before the latest run to allow for higher useable voltage. These included: water-cooling the ceramic windows of the power input coupler, rebuilding the solid state 2 kW driver amplifiers, installation of signal limiters to prevent overdrive at switch-on/off, and development of a software application to automate the high voltage conditioning of the cavities.

COGGING

Since the two rings of RHIC accelerate with independent rf systems they arrive at store with unequal frequencies. To bring the beam into collision, first the beam feedback loops are switched open without a transient. Then the frequency of each ring is ramped at 1 Hz/second (28 MHz system) to a set point for the collision frequency. This frequency is chosen to give the best-centered orbits in the arcs of both rings. The rings share a master 10 MHz clock for the Direct Digital Synthesizers and frequency control words are made exactly equal, thus locking the phase relationship between the bunches. The phase angle between the abort gaps is then measured automatically and a frequency excursion of 10 Hz is applied to one ring for a calculated time to align the abort gaps to within one bucket. Finally the rf phase between the vector sums of the acceleration cavities of the two rings is precisely measured with a LockIn amplifier (Standford Research, SR844) and a second frequency excursion aligns the collision spot to the Interaction Points. A longitudinal pickup at IP4 is used to calibrate the equipment. Since the same pickup measures both beams there is no systematic uncertainty in the collision point adjustment. The beams can be un-cogged and re-cogged at will (common cavities off) for machine experiments, such as beam-beam tune effects.

BUNCHED BEAM LIFETIME / RF NOISE

Intra-Beam Scattering is the fundamental limitation but rf noise can reduce bunched beam lifetime also. We are able to separate these effects in RHIC by comparing gold and deuterons upon which IBS has a negligible effect. An additional diagnostic tool is the fine structure of the longitudinal Schottky signals at high frequency. In the gold/deuteron run these techniques indicated a problem in the rf source.

Spectral purity of rf source

The Schottky spectrum from deuterons showed a sharp line at 120 Hz, which is within the band of the synchrotron frequencies. In fact, there was evidence of depopulation of the distribution in the neighborhood of the line. The strength of this line far exceeded the Schottky power, suggesting a coherent behavior for all bunches and thereby pointing to a problem with the spectral purity of the rf source. A high dynamic range measurement of the rf drive signal indeed revealed a line 120 Hz from the carrier (197 MHz) at – 72 dBc in a 10 Hz bandwidth. The generator of this signal was the HP8644B, phase locked to 28 MHz. A new source was built using the direct synthesis technique with better spectral purity (-90 dBc) and the bunched beam lifetime improved substantially. The master 10 MHz clock sets the ultimate noise floor. This is a Stanford Research FS725 Rubidium disciplined source with single sideband noise level less than –130 dBc/Hz at 10 Hz offset from the carrier. We find that in practice the noise floor is dominated by the power supply noise of the VME crates that house the synthesizers.

Power supply ripple in driver amplifier

Another possible source of rf noise is power supply ripple in the rf drive chain. At the highest rf voltage the 2 kW solid state driver amplifiers are close to their maximum output. We found that their dc regulators exhaust their compliance voltage and 180 Hz line frequency ripple modulates the rf output. This frequency is especially damaging to the beam since the band of synchrotron frequencies encompasses this value. The power supplies (120 A @ 60 V) were rebuilt with more compliance.

REFERENCES

[1] S. Ozaki, RHIC Commissioning, IEEE PAC2001, Chicago
[2] F. Pilat, RHIC Status and Plans, Proc. EPAC 2002, Paris, pp15-19
[3] J.M. Brennan, et al. RF Beam Control for RHIC, Proc. EPAC1998, Stockholm, pp. 1705-1707
[4] J. DeLong, et al. Synthesizer Controlled Beam Transfer from AGS to RHIC, IEEE PAC2001, Chicago, pp.1523-1525
[5] C. Schultheiss, J.M. Brennan, A State-Variale Description of the RHIC RF Control Loops, Proc. EPAC2002, Paris, pp.2097-2099
[6] R. Andraka, "A Survey of CORDIC Algorithms for FPGA based computers", FPGA 98, Monterey (1998). CA USA
[7] M. Blaskiewicz, et al., Longitudinal Solitions ... , these preceedings
[8] W.Pirkl, CERN, Private communication
[9] M. Blaskiewicz, et al. Longitudinal Impedance Measurements in RHIC, Proc. EPAC2002, Paris, pp.1488-1590

STATUS OF THE GLC X-BAND POWER SOURCE R&D

Y. H. Chin and GLC Development Group, KEK, Tsukuba, Ibaraki-ken, 305-0801, Japan

Abstract

In this paper, we summarize the R&D status of the X-band power source development for the GLC (Global Linear Collider, previously called JLC) project. Main emphases are on the latest achievements of the PPM klystrons and the development of the IGBT induction modulator. The pulse compression schemes and the optimisation of the tunnel layout for different configuration of the main linac are also discussed.

INTRODUCTION

The linear collider project in Japan, used to be called JLC (Japan Linear Collider), is now regarded as an Asian project promoted by the Asian Accelerator Community (ACFA). Addressing this major strategy change more clearly, the name of the project was recently changed to GLC (Global Linear Collider). The GLC/NLC design teams have been investigating the DLDS pulse compression system as a possible high efficiency option. However, the baseline pulse compression system was recently changed to the dual-moded SLED-II system to ensure a less expensive and faster demonstration of a full RF sub-unit [1]. In addition, the dual-moded SLED-II system is based on the single-moded SLED-II systems that have operated at the NLCTA for over five years, providing confidence in the design. The schematic configuration of the new RF power source unit together with accelerator structures is illustrated in Fig.1. A fundamental power source unit consists of one pair of periodic permanent magnet (PPM) focusing klystrons. The RF pulses from each klystron are 1.6 s in length and 75 MW in power. Then a time compression of the output pulses from klystrons is applied through a dual-moded SLED-II pulse compression system, which compresses the input RF pulse with a time compression factor of 1/4. This is accomplished by temporarily storing the RF power from klystrons within a pair of 29 m-long delay lines. A theoretical power gain is 3.3. With a 10% power loss in the waveguides, it results in a time-compressed pulse of 450 MW, 400 ns, as delivered to the entrance of accelerator structures. The output power from SLED-II feeds eight accelerator structures. Two dual tunnels, 14.1 km-long each, will accommodate the two main linacs. Figure 2 shows a conceptual view of the RF power source unit that is installed in the klystron tunnel, together with the accelerator structures in the accelerator tunnel.

The immediate goal of GLC/NLC is to satisfy the ILC-TRC requirements, which include tests of the RF power and energy handling capability of the dual-moded SLED-II pulse compression system at GLC/NLC design levels and the demonstration of the operation of PPM klystrons at the full repetition rate of 120Hz (NLC) or 150Hz (GLC). The GLC/NLC teams are currently working to fulfil these goals in 2003-2004.

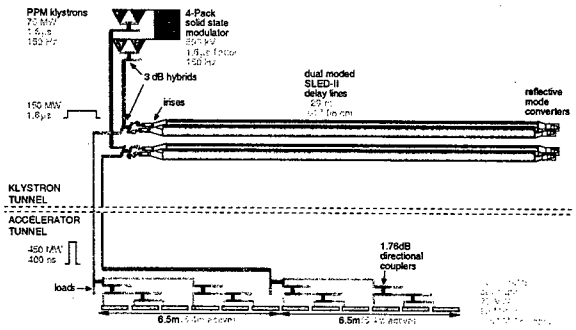

Figure 1: Schematic of GLC X-band linac RF unit.

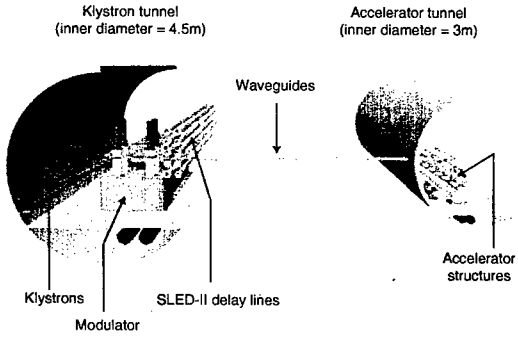

Figure 2: Main linac tunnels for GLC.

MODULATORS

The modulators for the main linacs of JLC are required to produce 1.6 s long, 500kV-260A pulses to each klystron with an efficiency of 80% at a repetition rate of 150 Hz. The line-type modulator, like those presently used for klystron testing at KEK, has some known deficiencies. The thyratron switch tube needs frequent tuning and has a limited lifetime of around 15,000 hours. The thyratron is a fast on switch, but is slow to back off. The overall efficiency of the modulator is 50-60% due to large losses in various components and relatively slow pulse rise and fall times as dictated by the pulse transformer with a high step-up ratio.

The solution to these problems adopted for GLC is to introduce semiconductor device as the switching device. The fast on-off Insulated Gate Bipolar Insulator (IGBT) solid-state switch is used as a power switch, and it is incorporated into an induction-linac type modulator design. The solid-state induction modulator [2] is basically a large stack of small pulse transformers. The primaries of the toroidal-cores are driven in parallel by a separate set (called cell) of IGBT switches and capacitors. While the individual primaries are operated at a relatively

0-7803-7738-9/03/$17.00 © 2003 IEEE

low voltage (3.2 kV), because of their parallel operation a very high voltage, adequate for driving klystrons without any step-up transformers, is induced on the secondary.

Previously, so called the linear induction modulator design was adopted as the most suitable for the 8-pack DLDS configuration, where the toroidal cores are lined up on a straight line, and the transformer secondary (made of a straight HV-cable) runs through their center for a simpler insulation design. Following the recent change in the pulse compression scheme from the DLDS to SLED-II that requires only a pair of klystron for operation, we went through re-optimisation process of our modulator design for the 2-pack configuration and concluded that the 4-turn secondary is the best configuration.

In the new design, the toroidal cores are stacked on two stories, and the 4-turn secondary (made of copper tubes) windings are threaded through them as illustrated in Fig.3. A driver cell, including an IGBT switch and two capacitors on a printed circuit board, is designed as a plug-in module. It can be easily accessed and replaced in the field for fast maintenance. NLC has already built a 4-pack prototype with a 3-turn secondary, and has demonstrated a high efficiency of more than 80% and a pulse shape with fast rise and fall times of 200-300 ns.

In the present prototype design, one modulator powers two klystrons. It consists of 42 FINEMET cores and 84 IGBT drivers, including 5% spears for the waveform compensation. It is designed to produce a 1.6 s-long output pulse of 500kV-1060A with 80% efficiency. The electrical and mechanical designs are nearing completion, and a 2-pack prototype will be operating in fall of 2003.

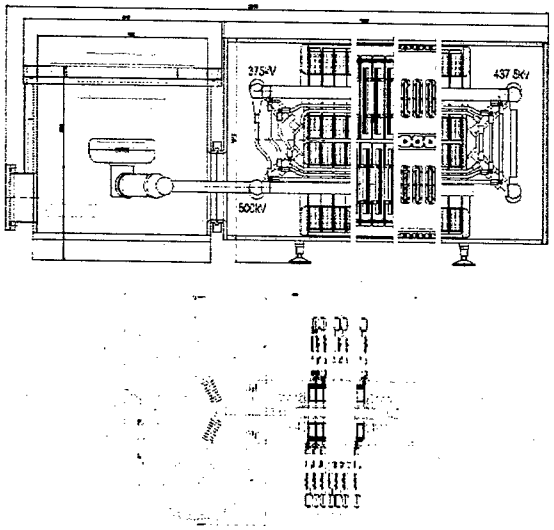

Figure 3: Side (top) and top (bottom) views of the IGBT induction modulator.

PPM KLYSTRONS

The X-band klystrons at GLC must produce 75 MW in 1.6 s pulses with 55% efficiency. The development of the X-band power sources has been one of the major goals for GLC/NLC R&D program. The actual R&D begun 15 years ago and has been much more difficult than initially anticipated. But now, the design is finally converging.

The power-consuming solenoid magnets cannot keep the operating cost manageable, and thus Periodic Permanent Magnet (PPM) klystrons are being developed which would consume no electric power for focusing, and would thus have a higher net efficiency. KEK carried out a two-year project with Toshiba to produce two PPM klystrons in two stages [3]. Figure 4 shows photos of the first two X-band PPM klystrons built in Japan, PPM-1 (left) and PPM-2 (right). The PPM-1 (later rebuilt as PPM-1.5) achieved 56 MW power with 50% efficiency at the standard 1.5 s pulse length. Neither oscillation of parasitic mode nor gun oscillation was observed. The electron beam transmission was found to be 100% when no RF signal was applied. However, since PPM-1 did not implement full features of body cooling, the repetition rate was limited at 25 Hz.

The second klystron (PPM-2) was also tested. The PPM introduced a full water-cooling system of the klystron body and the PPM stack. For a higher efficiency, some revisions of the resonant frequency of the penultimate cavity were made. The PPM-2 produced 73.2 MW at 500 kV for a 1.4 s pulse length. At 70 MW, the standard 1.5 s pulse was attained with an efficiency of 55%. The maximum efficiency reached 56%. The performance of the PPM-2 klystron is tabulated in Table 1. In respect of power, efficiency and pulse length, PPM-2 almost achieved the GLC specifications. The testing was terminated by the breakdown of the pulse transformer.

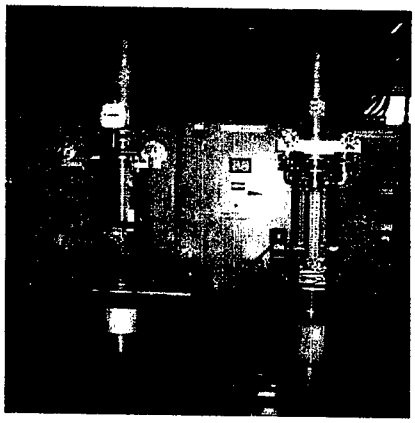

Figure 4: Photo of the first (PPM-1, right) and the second (PPM-2, left) PPM klystrons for GLC.

Table 1: Design parameters and actual performance of the PPM-2 klystron.

	Design	Achieved
Peak power (MW)	75	75.1
Efficiency (%)	55	56
Pulse length (s)	1.5	1.5 (at 70MW) 1.4 (at 73.2MW)
Repetition rate (pps)	150	25

Following the success of those two klystrons, the development plan was expanded for the next two years. In JFY 2001, the PPM-3 klystron was built and high power tested. The main goal of this klystron was to achieve the high repetition operation (limited to 50 Hz by the specification of the modulator) to prove that the PPM klystron is ready for use at GLC. To this end, refining and remodelling of the water-cooling system and the RF windows were made. Two 2nd-harmonic cavities were also installed to increase the efficiency. The output power of 65 MW was attained at a 1.5 s pulse length with 53% efficiency, as summarized in Table 2. The PPM-3 klystron successfully doubled the repetition rate to 50Hz (limited by the modulator). The TRC Report addressed that "the Working Group considers the JLC-X PPM-2 klystron a proof of existence (although tested only at half the repetition rate)". The testing was terminated by the failure of the one of the output windows, though the window outperformed the any of previously made windows.

Table 2: Design parameters and actual performance of the PPM-3 klystron.

	Design	Achieved
Peak power (MW)	75	65
Efficiency (%)	55	53
Pulse length (s)	1.5	1.5
Repetition rate (pps)	150	50

KEK is committed to trying its best to fulfil the TRC R2 requirement on PPM klystrons in 2003-2004. The remodelled PPM-2 with new windows was shipped to SLAC and its high power testing is under way. The aim is to satisfy the ILC-TRC requirement R2 that demands the demonstration of the operation at the full repetition rate of 120Hz (NLC) or 150Hz (GLC). The PPM-4 klystron, with an improved cooling system, is now under high power testing. The PPM-4 will be also shipped to SLAC for testing at 120Hz repetition rate after the conditioning at KEK is finished. The PPM-5 with further improved cooling system is being designed for completion in December 2003.

DUAL-MODED SLED-II

The SLED-II uses a pair of high-Q resonant delay lines as the temporary energy storage to produce flat output pulses. In the case of the single-moded SLED-II, when an output pulse length of 400 ns is required, as in the case of GLC, the natural length of the required delay lines would be 58m. This tends to result in a tunnel layout that is heavily crowded with many delay lines that are extending from neighboring klystron pairs. To address the space issue, a breakthrough concept of dual-moded SLED-II was invented for NLC at SLAC [4], and has been adopted for GLC as well. In this system, by using two modes in the delay lines, TE01 and TE02 modes, the delay lines, with a physical length of 29 m, can act as having an effective length of 58 m, adequate for producing 400 ns output pulses. The intrinsic efficiency of this dual-moded SLED-II pulse compression system is approximately 80%. In addition, by running the two pairs of delay lines, originating from two pairs of klystrons driven by a single modulator unit, into two opposite directions, a very nicely packed installation of the RF power sources can be realized. This is illustrated in Fig. 5. In this configuration, the number of parallel running delay lines will be limited to 10 at maximum, reduced from 18 in the nominal 8-pack configuration, and the delay lines are almost uniformly distributed through the linac. The working principle of the dual-moded SLED-II has been demonstrated in a low power testing by the US NLC group in 2002. Preparation work is under way for a high-power testing of the dual-moded SLED-II system in NLCTA at SLAC, as a joint (8-pack) project between the NLC and GLC groups, in order to fulfil the ILC-TRC requirements. In the first round of experiment in 2003, four 50 MW solenoid-focused klystrons, operating with 1.6 s pulse length, will be used. With this set-up a production of 600 MW in 400 ns pulses is expected. This will allow testing of many of the RF components at power levels higher by about 30% than what is needed for NLC/GLC. It is also planned, in late 2003 or early 2004, to use a pair of PPM klystrons as the power source for this SLED-II test station. KEK is participating in this 8-pack project by providing some SLED-II components. It was reported that the tapers used at the original dual-mode SLED-II delay lines may be a reason of measured degradation of the compression performance by a factor of 10%. KEK has designed alternate tapers for the dual-mode SLED-II delay lines to improve its performance and they are under fabrication. They will be shipped to SLAC to participate in the 8-pack project.

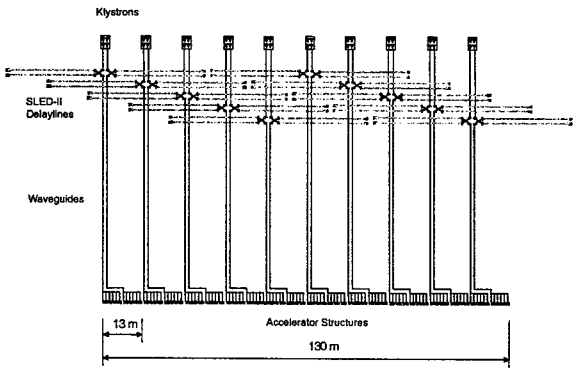

Figure 5: Optimised layout of SLED-II.

REFERENCES

[1] International Linear Collider Technical Review Committee Second Report 2003, SLAC-R-606, 2003.
[2] R. L. Cassel, et.al., PAC99, New York, 1999, p.1494.
[3] Y. H. Chin, et.al., PAC01, Chicago, 2001, p.3792.
[4] S. Tantawi, EPAC02, Paris, 2002, p.2334.

HIGH POWER TESTS OF A MULTIMODE X-BAND RF DISTRIBUTION SYSTEM*

S. Tantawi, and C. Nantista SLAC, Menlo Park, CA 94025, USA

Abstract

We present a multimode X-band rf pulse compression system suitable for the Next Linear Collider (NLC). The NLC main linacs operate at 11.424 GHz. A single NLC rf unit is required which produce 400 ns pulses with 600 MW of peak power. Each rf unit should power approximately 5 meters of accelerator structures. These rf units consist of two 75 MW klystrons and a dualmoded resonant delay line pulse compression system [1] that produce a flat output pulse. The pulse compression system components are all over moded and most components are design to operate with two modes at the same time. This approach allows increasing the power handling capabilities of the system while maintain a compact inexpensive system. We detail the design of this system and present experimental cold test results. The high power testing of the system is verified using four 50-MW solenoid focused klystrons. These Klystrons should be able to push the system beyond NLC requirements.

INTRODUCTION

Most proposed design for future linear colliders contains long runs of waveguides. In X-band room temperature designs these runs are in the order of 100 km or more. These waveguides are used for rf distribution and rf pulse compression. In particular, multi-bunch operation requires the rf pulse compression system to have flat output pulse for a relatively long duration. Producing, efficiently, such a flat pulse requires long waveguide delay sections. To reduce the losses and to enhance the power handling capabilities one must use overmoded waveguides. Manipulating rf signals in highly overmoded waveguide is not trivial. With even simple functions, such as bends, the designs are quit complicated in order to insure the propagation of a single mode without losses due to mode conversion to other modes.

To reduce the length of these waveguides we suggested multimoded systems [2]. In these systems the waveguide is utilized several times by carrying different modes at the same time. At first glance one might think that this would lead to extra complications in the design of most rf components. Indeed, one has to invent a whole new set of multimoded components. However, since simple manipulations such as bending an overmoded waveguide tends to couple the modes together; it turns out that multimoded components have simpler designs. This is also true from the mechanical design point of view; most of these components are compact.

Here, we will review the design of the dual-mode X-band rf system proposed for the Next Linear Collider (NLC). Recent experimental data are presented. A proof of principle experiment is being constructed at SLAC. The total output power is 600 MW for 400 nanoseconds.

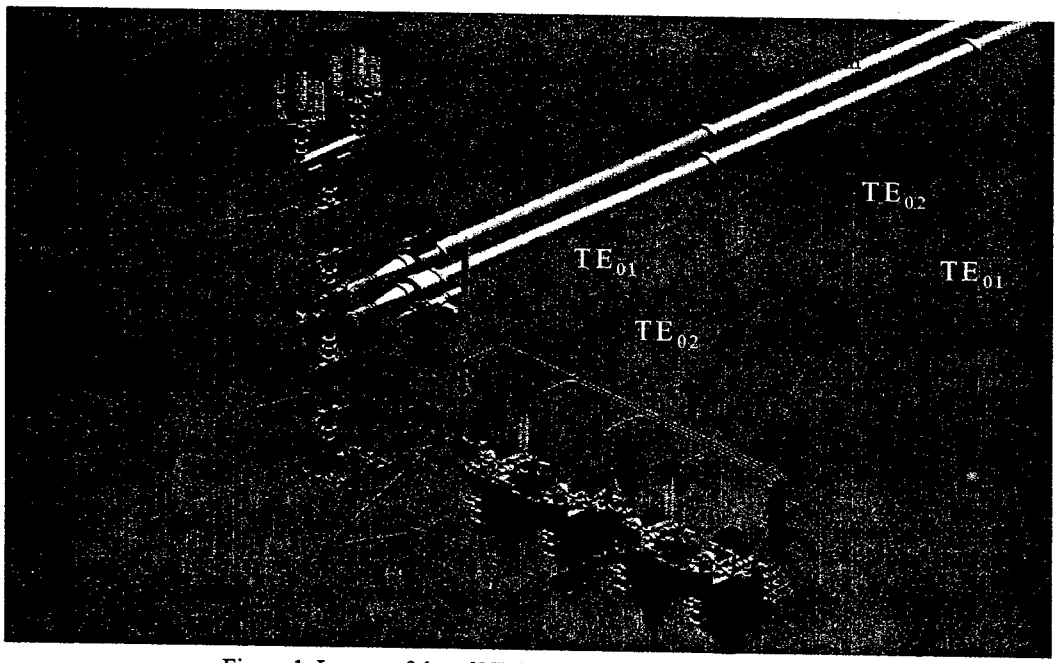

Figure 1. Layout of the of NLC proof of principle experiment.

0-7803-7738-9/03/$17.00 © 2003 IEEE

SYSTEM DESCRIPTION

The system is shown in Fig. 1. Four 50 MW klystrons will power a fully dual-moded resonance delay line pulse compression system. Both the transfer lines and the delay lines are dual-moded.

The modes carried by the transfer lines are controlled by the rf phases of the different klystrons The modes in the delay lines are controlled by a set of mode converters at the input and the end of each delay line. By manipulating the modes in both the transfer lines one could achieve, no pulse compression or a pulse compression ratio of 4. The total output power is 200 MW for 1.6 microseconds, and 600 MW for 400 nanoseconds.

We have adopted a general philosophy in our designs. Most of the manipulation of rf systems are made with planer components. These are rectangular waveguides with all manipulations are made in the H-plane. Two modes are allowed to propagate: the TE_{01} and the TE_{02} modes. Because manipulations are only two-dimensional the height of the waveguide is a free parameter, which is used to reduce the field and losses in the system. In this system we increased the height of most of the rectangular components to reduce the electric field level to approximately 45 MV/m. The waveguide cross-section is close to a square. We were careful not to increase the height more than necessary to avoided complications that results from increased level of overmoding.

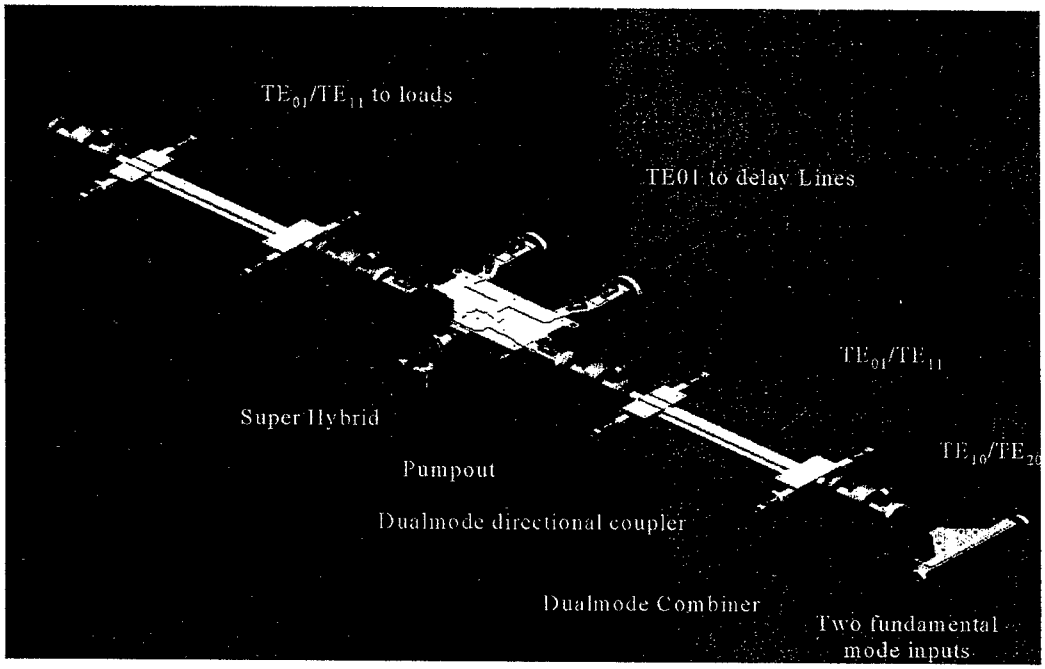

Figure 2. The dualmode transfer line.

To transport the rf signal we use circular waveguides. These carry the TE_{01} and the TE_{11} modes. We connect between circular and rectangular waveguides using a special types of tapers; mode preserving circular-to-rectangular tapers. These convert the TE_{10} rectangular mode into the TE_{11} circular mode and the TE_{20} rectangular mode into the TE_{01} circular mode. All vacuum functions, connection flanges and pumpout devices are implemented in circular waveguides. We also implemented the diagnostic devices, i.e.; mode selective directional coupler, in circular waveguides.

The highly overmoded delay lines carry both the TE_{01} and the TE_{02} modes. Because these two modes have no axial wall currents the design of the connection flanges is simplified.

TRANSFER LINE

The design of the transfer line and the pulse compression head is shown in Fig. 2. The four klystrons are divided into two banks each contain two klystrons. Each two klystrons are combined together to produce, essentially, a single rf source with an output power of 100 MW for a 1.6 μs. These two 100 MW rf source feeds the combiner (see Fig. 2). The combiner launches two modes in the system. The weight of each mode is dependent on the relative phase and amplitude between the two banks of klystrons. The system is designed such that if the launched mode is the TE_{20} rectangular (TE_{01} circular) then the power is directed to the delay line and the compressed pulse is launched at the output towards the load tree in the same mode. On the other hand if the launched mode is the

TE_{10} rectangular (TE_{11} circular) the power is directed to the loads at the same mode without pulse compression.

In the following we will present and describe each component in that line separately.

The Combiner

The combiner design together with an HFSS illustration to its functionality is shown in Fig. 3.

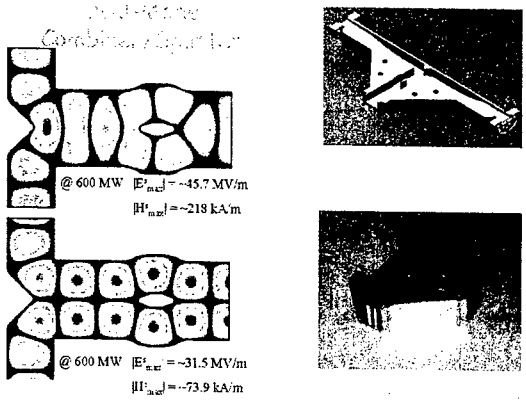

Figure 3. The dual moded combiner/splitter design.

Circular-to-Rectangular Taper

Figure 4. Shows the design of the circular-to-rectangular taper together with an HFSS simulation results.

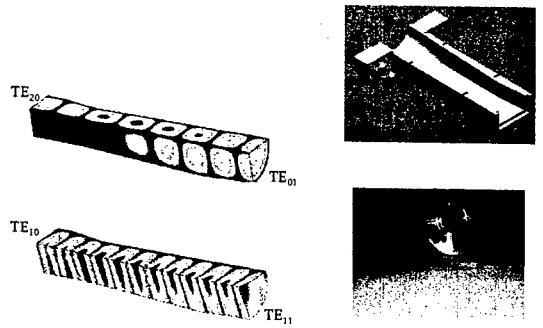

Figure 4. Dualmode Circular-to-Rectangular Taper.

To test the functionality of this taper together with the splitter we connected the two together as shown in Fig. 5. The TE_{01} mode is launched through the circular part of the taper using a wraparound mode converter. Then, the output of the taper launches the TE_{20} mode in the symmetry port of the combiner. The signal is split equally in the remaining two ports. We measured this signal through a specially designed set of instrumental height and width tapers, which reduces the waveguide cross-section to standard size and hence connectable to the network analyzer.

The results of these measurements are shown in Figs. 6a and 6b. From Fig. 6a one can estimate the total losses of the combiner, the circular to rectangular taper, the wraparound mode converter, and the instrumental tapers to be about 1.3%. Because of the asymmetry of the TE_{20} mode one should observe a π phase difference between the two ports. Within the measurment tolerances, this is verified in the experimental data shown in Fig. 6b.

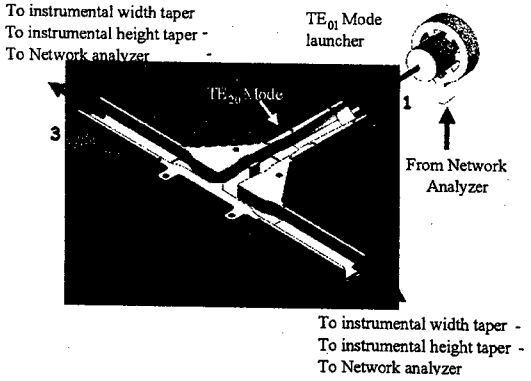

Figure 5. Cold Test Setup for the Combiner and Circular-to-Rectangular Taper.

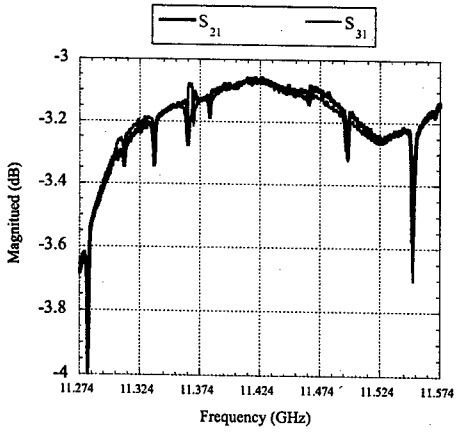

a)

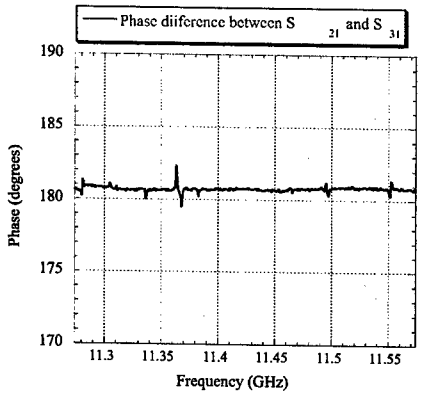

b)

Figure 6. Cold Test Results of: Splitter-Circular to rectangular taper-Wraparound mode converter-instrumental height taper-instrumental width taper. Total losses at 11.424 GHz =1.3%. a) Magnitude, b) Phase.

The Pumpout

Fig. 7 shows the structure of the circular pumpout. The number of holes around the azimuth is greater than the maximum azimuthal variation for any mode that can propagate in this waveguide. The distances between the rows of holes are adjusted to cancel any reflection for both propagating modes. Fig.8 shows the measured transmission for both modes.

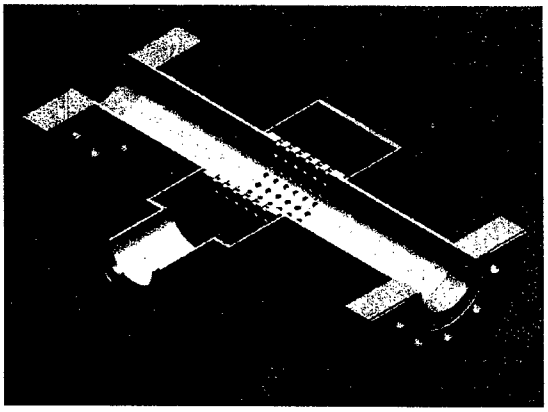

Figure 7. Pumpout design: the set of holes are designed to cancel any coupling or self-coupling for the TE_{01} and the TE_{11}

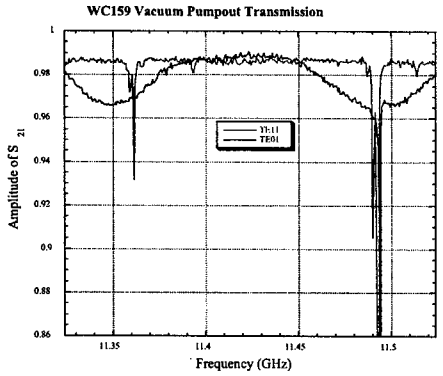

Figure 8. Cold Test Results of the dualmode pumpout

Dualmode Directional Coupler

The design is shown in Fig. 9. Two waveguides are coupled through a set of holes to the main circular waveguide. To couple the TE_{01} circular mode the width of the rectangular waveguide is adjusted to match the phase velocities. Because the circular waveguide is overmoded and the fundamental TE_{11} mode has a phase velocity close to the speed of light, one can not match this velocity in a single moded rectangular waveguide. To match the velocities we had to use a ridge waveguide.

To make the coupler directional and to discriminate coupling for unwanted modes the coupling hole pattern was chosen to represent a Hamming window. Finally, one has to bend the rectangular and ridge waveguide so that one can connect vacuum window and diagnostic devices. These bends also act as tapers to slandered size rectangular waveguides; WR90 in our case. The proper matching of these bends and the attached vacuum window is crucial for the marinating good directivity.

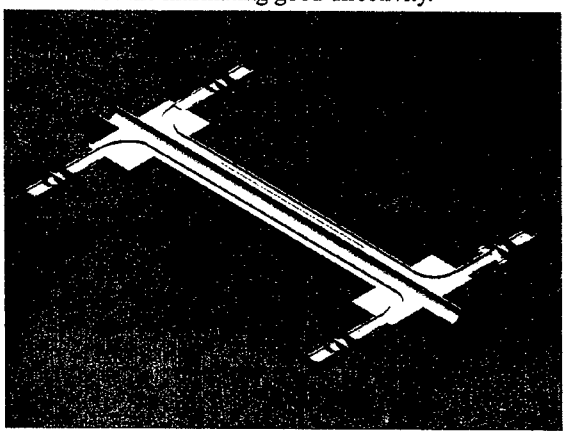

Figure 9. Dualmode directional coupler for system diagnostics.

In Fig. 10 we show the coupling to the TE11 arm due to an injected TE01 mode. Knowing that the coupling to the TE01 arm is –47 dB, one estimates a minimum isolation of –45 dB. The dynamic range of our equipment limited these measurements.

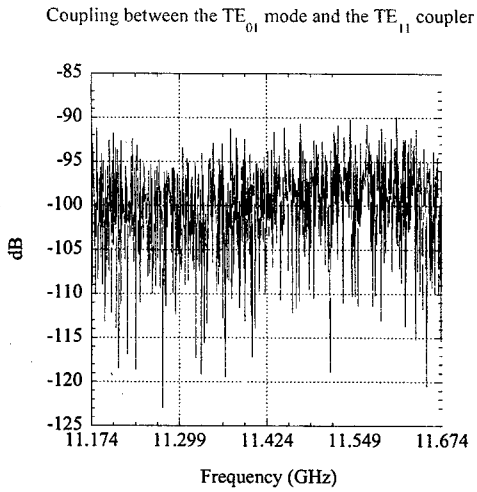

Figure 10. Coupling to the TE_{11} arm due to a TE_{01} mode. The dynamic range of the equipment limit.

The Sled Head

The heart of the pulse compression system is shown in Fig. 11. An illustration of its functionality is shown in Fig. 12. When the injected mode is the TE_{10} (TE_{11} circular) the signal passes through. When the injected mode id the TE_{20} (TE_{01} circular) the signal is sent to the delay line and the compressed pulse is sent to the output.

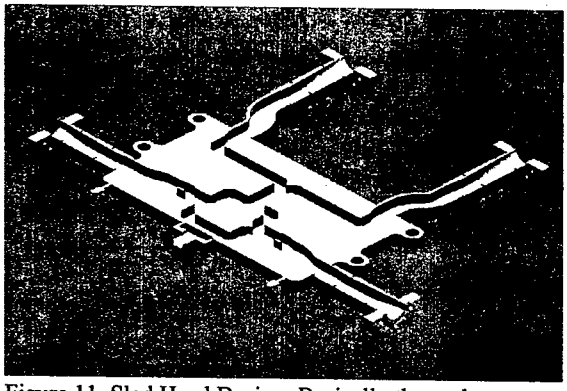

Figure 11. Sled Head Design: Basically three planer hybrids on one single substrate

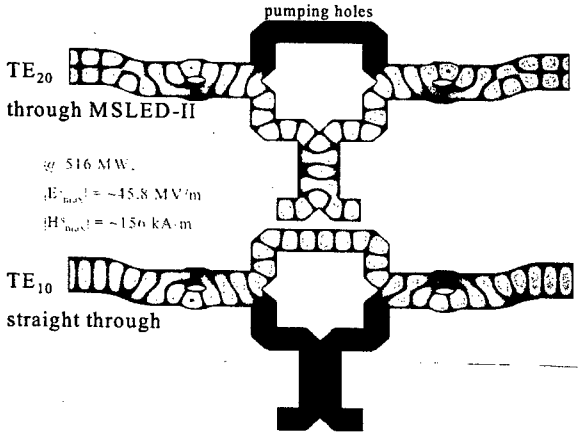

Figure 12 SLED Head Simulations

THE DUALMODE DELAY LINE

Consider the delay line shown in Fig. 1. The rf signal is injected into the delay line waveguide in the TE01 mode. This is the only azimuthally symmetric TE mode supported at the input port. The waveguide is then tapered up to a diameter that supports several TE0n modes. The TE01 mode travels all the way to the end of the delay line and then gets reflected and converted into the TE02 mode. The TE02 mode travels back to the beginning of this line and, since the input of the line cuts off this mode, gets reflected. If the input taper is designed carefully, TE02 can be reflected perfectly. Then, because of reciprocity, the TE02 wave gets converted back to TE01 at the end of the line. This mode then travels back and exits the line. The total delay in the delay line is twice that seen by a single moded line. Hence, one can cut the length of delay line by a factor of two.

The mode converter at the end of the delay line is shown in Figure 13. It is basically a step in the circular waveguide. If the big waveguide supports only the TE_{01} and the TE_{02} mode among all TE_{0n} modes and the small waveguide supports only the TE_{01} mode, then the device could be viewed as a three-port network. One can choose the diameter of the small guide such that the couplings between each mode in the large guide and the single mode in the small guide are equal. In this case, it is a symmetrical three-port network. A theory for such a device is presented in [3]. It shows that there exists a position for placing a short circuit in the middle arm of this three-port network (the small guide in this case) that makes it possible to transfer the power perfectly between the remaining two arms, or in this case between the TE_{01} and the TE_{02} modes in the large guide.

The only step left in the design of this end mode converter is a careful taper design that reduces the diameter of the delay line into the diameter of a waveguide that can support only TE_{01} and TE_{02} modes. The taper needs to transfer both modes perfectly. We made the compact taper by a computer-optimized series of steps as shown in Fig. 13. Similar design have been implemented for the input taper which Transfer the TE01 mode perfectely and reflects the TE02 mode without any mode convesion to any other TE0n modes.

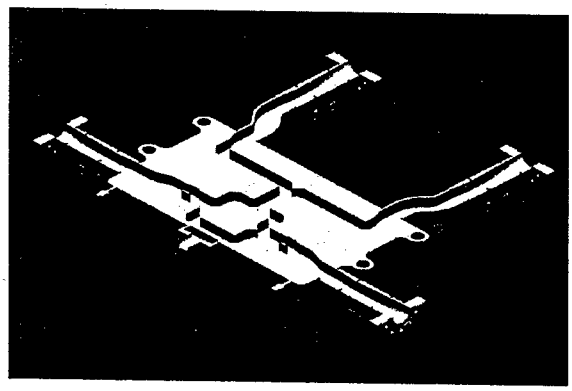

Figure 13. End Taper and Mode converter. The movable cup at the end of the taper reflects the TE01 mode into the TE02 mode.

ACKNOWLEDGEMENT

This work is a result of a continuous effort by many researches and engineers over many years. In particular, The efforts of N. Kroll, R. Miller, P. Wilson, V. Dolgashev, K. Fant, C. Pearson, and R. Ruth were instrumental to the results achieved to date. We wish also to thank Jose Chan for his persistence efforts during the manufacturing and testing of components

REFERENCES

[1] S.G. Tantawi, *et al.*, "The Generation of 400-MW RF Pulses at X Band Using Resonant Delay Lines," *IEEE Trans. Microwave Theory Tech.*, vol. 47, no. 12, pp. 2539-2546, Dec. 1999; SLAC-PUB-8074.

[2] S.G. Tantawi, et al., "A Multimoded RF Delay Line Distribution System for the Next Linear Collider," Phys.Rev.ST Accel.Beams, vol. 5, March 2002.

[3] Sami G. Tantawi, Ronald D. Ruth, Arnold E. Vlieks, and Max Zolotorev, "Active high-power RF pulse compression using optically switched resonant delay lines," IEEE Transactions on Microwave Theory and Techniques, MTT-45(8), August 1997, p. 1486–1492.

PROGRESS ON THE C-BAND ACCELERATOR FOR THE SPRING-8 COMPACT SASE SOURCE*

T. Shintake, T. Inagaki, K. Togawa, Y. H. Baba, K. Onoe, T. Tanaka, T. Hara, T. Bizen, T. Seike, X. Marechal, Y. Kawashima, T. Takashima, T. Kudo, S. Matsui, Z. Chao, H. Ego, K. Tamasaku, K. Sezaki, K. Saino, S. Takahashi, K. Takeshita, T. Ishikawa, H. Kitamura,
SPring-8/RIKEN, Harima Institute, Hyogo 679-5148, Japan
H. Matsumoto, Shigeru Takeda, M. Yoshida, Y. Takasu, KEK, Tsukuba, Ibaraki 305-0801, Japan

Abstract

SCSS: SPring-8 Compact SASE Source (Soft X-ray FEL project) was started in 2002 in order to establish the technology required for the X-ray Free Electron Laser at 1 Angstrom region [1]. Three key technologies: the short-period in-vacuum undulator, the high-gradient C-band accelerator and the low emittance electron source using CeB_6 single crystal thermionic-cathode enable to design the SCSS machine size within100 m facility. The C-band RF system R&D was originally started at KEK to establish linear-accelerator technology for the e^+e^- Linear Collider project [2], and transferred to SCSS project at SPring-8/RIKEN. In SCSS, 8 klystrons and modulators, 16 accelerating structures will be used to accelerate the beam up to 1 GeV. Construction and operation of SCSS machine will provide realistic information on reliability, maintainability and cost of the C-band RF system, which will be very useful to judge the reality of Linear Collider project based on C-band technology.

INTRODUCTION

An X-ray FEL based on the SASE concept requires a large-scale accelerator and a long undulator. It can provide X-ray beam into a few beam lines only, therefore the construction cost per one beam line becomes quite higher than that in the conventional SR machines.

Since the X-ray FEL will open a wide range of new science, many FEL-machines will be required all over the world in the future, similar to the today's SR source facilities. To realize this dream, the machine cost should be minimized. Reasonable cost would be the construction cost of a few X-ray beam lines in the existing SR facilities. To do this, first of all, we have to make the machine size compact, because the building as well as the machine itself becomes inexpensive. This is one of the important target in SCSS project, thus we put the word "Compact" in the project name.

In the SCSS project, we achieve this target by the following three key technologies, and they are illustrated in Fig. 1.

(1) Low emittance beam injector based on thermionic single crystal CeB_6 cathode, which makes the FEL gain higher, and saturation length shorter.

(2) High gradient C-band accelerator. The accelerating gradient is as high as 40 MV/m for single bunch, which enables the main linac length being only 30 m long to reach 1 GeV.

(3) In-vacuum undulator provide high field at short undulator period, thus the beam energy becomes lowered, resulting in smaller the accelerator size.

This paper describes the basic machine design, and current status of hardware R&D on SCSS.

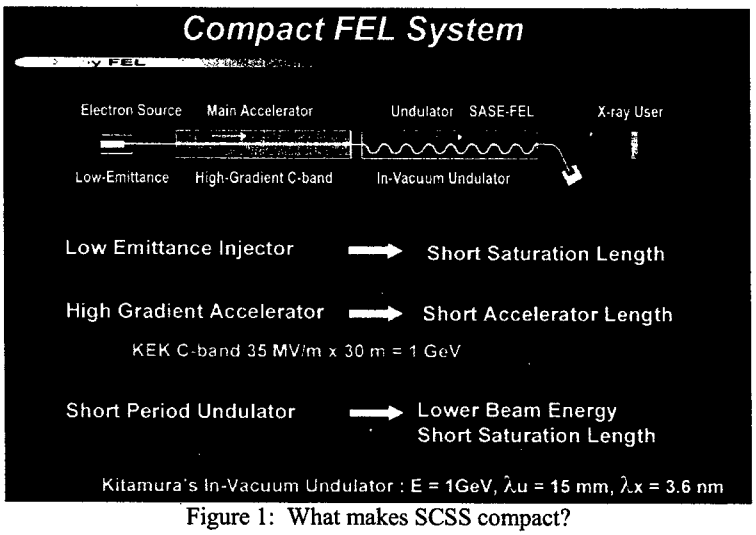

Figure 1: What makes SCSS compact?

SCSS MACHINE

Machine Layout

Figure 2 shows the machine layout at the final stage of SCSS project, whose parameter is summarized in Table-1. SCSS consists of the low emittance electron injector, the C-band high-gradient accelerator, the bunch compressors and the undulator section for FEL interaction.

In order to saturate FEL at shortest wavelength in SCSS: λ_x =3.6 nm within 20 m, we need electron beam with low transverse emittance below 2 π-mm.mrad, and short bunch-length of 0.5 $psec._{FWHM}$, the peak current of 2 kA, and 1 nC charge. The key issue in design is how to generate such a high quality beam. We decided to use high-voltage electron gun using single crystal CeB_6 cathode, followed by sub-harmonic buncher,

*Tsumoru Shintake: shintake@spring8.or.jp

0-7803-7738-9/03/$17.00 © 2003 IEEE

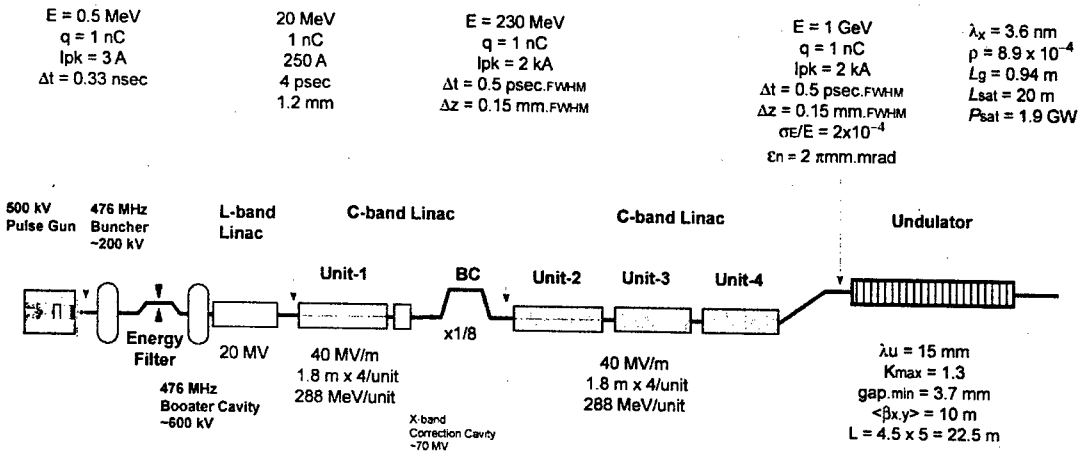

Figure 2: Four unit of the C-band RF-system will be used in the main linear accelerator of SCSS project.

booster and L-band buncher accelerator. This is the commonly used injector configuration in traditional electron accelerator. Using small size cathode, and high voltage gun, the low emittance beam can be generated. The design detail of the electron gun is reported by K. Togawa at this conference [3].

To make short bunch, the beam is chopped by a beam deflector, then velocity modulated in sub-harmonic buncher, and the bunch length is compressed with velocity bunching in drift section. Booster cavity raises the beam voltage to 1 MeV to avoid space-charge break, and the first section of the L-band accelerator compresses the bunch further. The beam energy reaches to 20 MeV after the L-band accelerator. Numerical simulation predicted the r.m.s. emittance around 1 π.mm.mrad, at 5 psec FWHM bunch length, and 0.5 nC charge.

Table-1 SCSS design parameter at final stage: 1 GeV. Note that the bunch length is denoted by FWHM value.

bunch charge	Q	1	nC
Normalized emittance	$\varepsilon_{nx,y}$	2	πmm.mrad
final electron energy	E	1	GeV
final r.m.s. energy spread	σ_δ	0.02	%
final FWHM bunch length	Δz	0.15	mm
	Δt	0.5	psec
peak current	I_{pk}	2	kA
undulator period	λ_u	15	mm
radiation wavelength	λ_x	3.6	nm
minimum gap	g	3.7	mm
maximum K-parameter	K	1.3	
undulator unit length	L_1	4.5	m
total undulator length		22.5	m
beta function	β	10	m
FEL parameter	ρ	8.9	x 10^{-4}
gain length	L_g	0.94	m
saturation length	L_{sat}	20	M
saturation power	P_{sat}	2.0	GW

As the undulator section, we use 5 segments of the in-vacuum undulator [4]. The permanent magnet sits inside vacuum, it can come close to the beam, thus it has advantage to generate high field at short period. SPring-8/RIEKN has enough experience on this design of undulator, at present, 19 in-vacuum undulator based on this scheme have been installed at SPring-8. This type has a great flexibility for beam operation of FEL. For example, for initial beam commissioning or machine tuning of upstream, the gap can opened widely. For the FEL operation we can close down to small gap. The first model for SCSS project has been developed in 2002, and its field quality met the requirement.

C-BAND MAIN ACCELERATOR

System Configuration

We use four units of C-band RF-system in 1 GeV machine as shown in Fig. 2. In each unit, two 50 MW klystron will be used in a pair, and those output power will be combined as shown in Fig 3. Through the rf-pulse compressor, the peak power is raised 3.5 times higher and

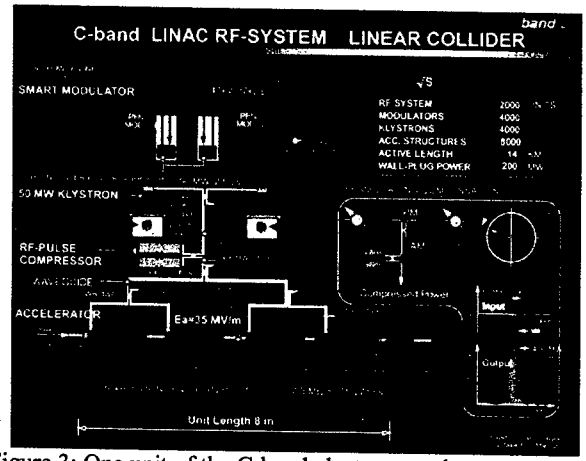

Figure 3: One unit of the C-band electron accelerator system.

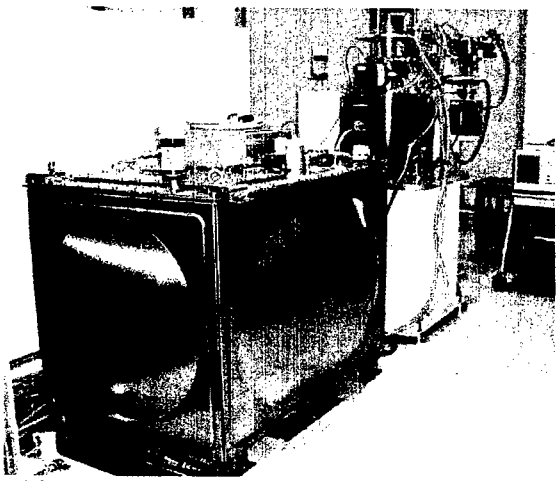

Figure 4: Klystron modulator (front) and 50 MW C-band klystron with pulse transformer tank (back).

fed into four accelerating structure. The nominal accelerating gradient is 35 MV/m for multi-bunch mode, and 40 MV/m for single bunch. While the multi-bunch operation is essential in e+e- linear collider to achieve higher luminosity, it is an optional mode in X-FEL project.

Klystron Modulator Power Supply[5]

To make the hardware system simple and maintenance easier, we decided to use the same model of the modulator power supply to feed pulsed HV power to the electron gun, the L-band accelerator and C-band accelerator. Not only the hardware itself, but also the control system, its software and manpower can be shared.

Figure 5: All of the high voltage components are immersed in the insulation oil inside a tank. The oil tank is made by standard panels commonly used in the water supply.

We use the PFN line type modulator. As the HV switching device, we chose the thyratron tube. With careful design on triggering circuitry and assembly method, the thyratron has long enough life-time, and quite reliable. We use twin-pulse trigger, which ensures to form uniform plasma density during hydrogen gas-discharge process. The thyratron tube is housed in a chimney, immersed in forced flow of insulation oil, thus the temperature is kept constant, which is important to preserve optimum gas pressure for the switching.

In SCSS project, we do not have R&D program for solid-state switch to replace the thyratron tube. In the future Linear Collider project, it is certainly necessary to use solid-state switching devices for maintenance reason of large scale machine. SCSS is a still small machine.

Fig. 4 shows the newly developed klystron modulator. All of the HV circuit components are mounted in a shielding tank as Fig. 5, and immersed with insulation oil. Merits of this closed design are

(1) Compact. W 1.7 m x D 1.2 m x H 1m.
(2) Good EMI shield.
(3) Better cooling for HV component.
(4) Eliminating cooling air fan.
(5) No dust accumulation due to high voltage in air.
(6) No environmental effects: moisture and temperature variation.

Inverter Power Supply for HV Capacitor Charging

IGBT switching power supply as Fig. 6 was developed to charge the HV capacitors in PFN circuit. The maximum rating is 50 kV, 30 kJ/sec. One technical issue in inverter switching scheme is the voltage fluctuation due to the finite size of charging step, it is usually 0.5 % level. To make this fluctuation lower, new control technique has been introduced, that is, the charging speed is lowered right before the voltage reaching to the target value. With this method, the voltage regulation level of 0.12% was achieved. Features in this power supply are

(1) Compact. W 480 mm x D 670 mm x H 530 mm.
(2) Maximum rating: 50 kV, 30 kJ/sec.
(3) Voltage regulation: 0.12 %.
(4) Efficiency: 87%

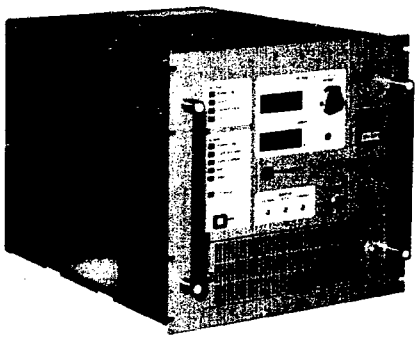

Figure 6: Inverter switching HV power supply. Courtesy of TOSHIBA Logistic Support Co.

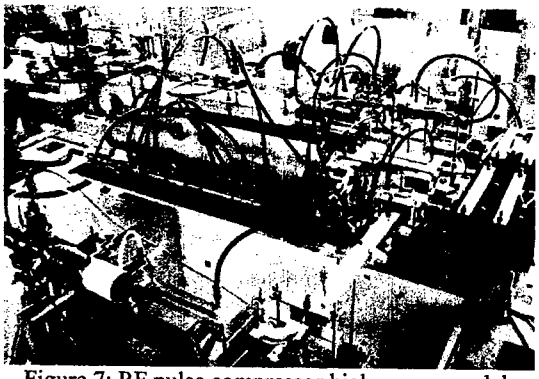

Figure 7: RF pulse compressor high-power model.

This power supply will be commonly used in the electron gun system, the L-band RF and the C-band RF-system.

50 MW C-band Klystron

Two 50 MW klystrons were fabricated in the year of 2002 for SCSS project.

(1) TOSHIBA E3746, C-band pulse klystron.
- Three cell travelling wave output structure.
- Solenoid focus.
- Tested 50 MW, 60 pps, 47%.

(2) TOSHIBA E3758A, C-band PPM klystron.
- Three cell travelling wave output structure.
- Permanent magnet focusing.
- 15 GHz parasitic oscillation was found.
- PPM klystron is 2nd option in SCSS.

RF Pulse Compressor

The high power model of rf pulse compressor has been developed and mounted in test bench as shown in Fig. 7. It is based on the three cell coupled-resonator cavity scheme to generate flat-top pulse [6]. In order to improve temperature sensitivity, the invar metal is used in the cavity cylinder, whose surface is covered by the OFC copper [7]. The temperature sensitivity is 13 kHz/deg.C, which is much lower than 96 kHz/deg.C of the copper, thus the water cooling system becomes simpler. High power test will be performed soon.

Accelerating Structure

In the SCSS project, the nominal operation mode is the single bunch. But we also design the multi-bunch operation mode as an option to obtain higher average X-ray flux. In order to cure the beam break up phenomena due to long-rage wakefield in the accelerating structure, we decide to use the choke-mode cavity [8]. In the C-band R&D at KEK, we developed the C-band accelerator structure using the choke-mode cavity, and tested its electrical performance in the ASSET beam line at SLAC in 1998. From the experiment, we confirmed that the basic wakefield damping performance was acceptable for the multi-bunch beam operation in the Linear Collider. At the same time, we found high-frequency parasitic oscillations in the measured wakefield, whose amplitude

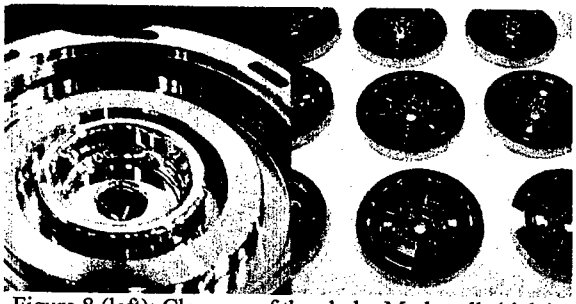

Figure 8 (left): Close-up of the choke-Mode cell. (right): SiC-rings were inserted in each cell for wakefield damping, it acts as a microwave absorber.

was the just on the border level for the beam emittance growth.

In SCSS project, we use the same accelerator structure as the KEK C-band design. Improvements were made on:

(1) By changing cell dimensions, the high frequency trapped mode was eliminated.

(2) For the metal bonding, instead of electro-forming, the brazing was used, because of the fabrication cost.

Fig. 8 shows the machined choke-mode cell, the central par forms the accelerating cavity, the groove is the choke resonator. The SiC ring is inserted in the outer groove, which is captured with wire-spring made of the tungsten wire. The race-track shaped holes are the water cooling channel. Fig. 9 shows, the accelerating structure in the brazing furnace. Total 91 cells are stack up, and active length is 1.8 m long.

Fig. 10 shows the field distribution along the structure measured by the bead-pull method. There are four lobes in phase plot, since the accelerating mode is $3\pi/4$, not the $2\pi/3$, widely used in the traditional travelling-wave

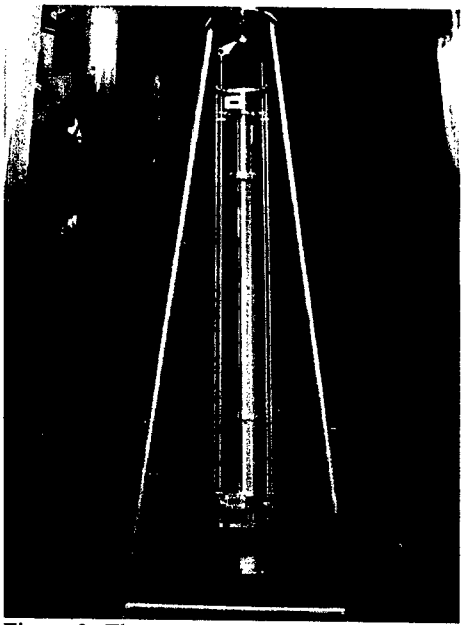

Figure 9: The 1.8 m long C-band accelerator in the brazing furnace.

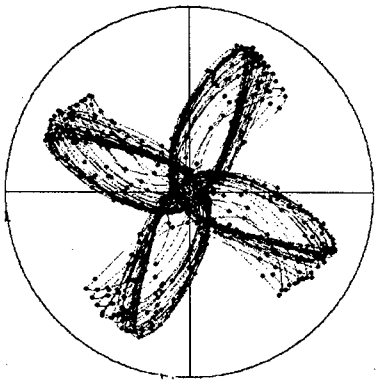

Figure 10: Bead-pull field measurement result. Four lobes correspond to $3\pi/4$ mode.

structure. The $3\pi/4$ mode was chosen to make the cell-length longer to fit the choke-groove in each cell. Each lobes are not overlapping well each other, it corresponds to $\pm$ 5 degree phase error, and energy gain loss due to this error is only 0.4 %.

Since the higher-order modes are damped by SiC rings, and those damping oscillation is independent by cell-to-cell, thus the dimension error, and its associated frequency error does not deteriorate the wakefield damping effect in the choke mode cavity. This is a big advantage superior to the other damping schemes, such as the field-cancelling techniques.

RF-BPM

RF-BPM utilises TM110-mode [9], in which the induced voltage has linear dependence to the beam position. The coupling to the signal is relatively large, thus this type of RF-BPM has a very high sensitivity.

In 1996 at FFTB facility of SLAC, using simple pill-box cavities, and comparing BPM signals from three RF-BPM's of series connection, the position resolution around 25 nm was recorded [10].

Using RF-BPM at high resolution and high accuracy, a special care has to be taken on signal filtering. The small BPM signal comes with a large amplitude common-mode signal, mostly TM01-mode, thus we need to eliminate this first, otherwise the head amplifier can be saturated or it causes position offset error.

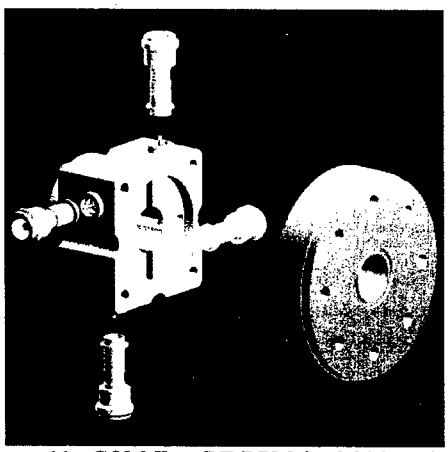

Figure 11: COM-Free RF-BPM for SCSS project.

In order to overcome this difficulty, the COM-Free RF-BPM concept was developed by the author. Using low level RF-signal, and a thin wire simulating beam in a cold model, it was experimentally confirmed that the electrical centre meets with the mechanical centre within 8 μm. The first model was mounted to the C-band accelerator and used for the ASSET beam test in 1998.

Figure 11 shows the newly developed RF-BPM for SCSS project. Four vane shaped grooves form the hybrid circuit, which eliminate the common mode power, and only the BPM signal is send to the detection circuit. The same RF-BPM will be used in the beam alignment station between undulators.

SUMMARY

The high power test and debugging of RF components will be performed in 2003-2004, machine construction in 2005-2006, and the first FEL operation is scheduled in 2007.

REFERENCES

[1] http://www-xfel.spring8.or.jp, T. Shintake, "SPring-8 Compact SASE Source", SPIE2001, San Diego, CA, USA, June 2001,

[2] T. Shintake et al., "C-band Linac RF-System for e+e- Linear Collider", PAC95, May 1995, Dallas Texas, USA

[3] K. Togawa et al., "Pulsed HV Electron Gun with Thermionic Cathode for the Soft X-ray FEL Project at SPring-8", this conference.

[4] T. Hara et al., J. Synchrotron Rad, 5, 403 (1998)

[5] H. Matsumoto et al., "A Closed Compact Modulator for 50 MW C-band (5712 MHz) Klystrons", Proc. 25th International Power Modulator Symposium and 2002 High Voltage Workshop, June 2002, ISBN 0-7803-7540-8; IEEE, Hollywood, California, 2002.

[6] T. Shintake and N. Akasaka, "A New RF Pulse-Compressor Using Multi-Cell Coupled-Cavity System", EPAC96, Sitges, Barcelona, Spain, June 1996

[7] M. Yoshida et al, "RF Pulse Compressor using Low Thermal Expansion Invar Material", 26th Linear Accelerator Meeting in Japan, Tsukuba, 2001.

[8] T. Shintake ,"The Choke Mode Cavity", Jpn. J. Appl. Phys. Vol. 31 (1992)

[9] T. Shintake, "Development of Nanometer Resolution RF-BPMs", Proc. HEAC99'

[10] T. Slaton, "Development of Nanometer Resolution C-band Radio Frequency Beam Position Monitor in The Final Focus Test Beam", SLAC-PUB-7921, August 1998

HIGH POWER TESTING OF X-BAND DIELECTRIC-LOADED ACCELERATING STRUCTURES*

J. G. Power, W. Gai, R. Konecny, C. Jing, W. Liu, ANL, Argonne, IL 60439, USA
S. H. Gold, Plasma Physics Division, NRL, Washington, DC 20375, USA
A. K. Kinkead, LET Corporation, Washington, DC 20007, USA

Abstract

A program is under way at Argonne National Laboratory, in collaboration with the Naval Research Laboratory (NRL), to develop RF-driven dielectric-loaded accelerating (DLA) structures, with the ultimate goal of demonstrating a compact, high-gradient linear accelerator based on this technology. In this paper, we report on the most recent results from a series of high power tests that are under way at NRL's X-band Magnicon facility. The design of the latest DLA structure has been fundamentally changed from the previous generation; it now has a modular construction that separates the RF coupler from the dielectric section. In this paper we present a detailed description of the design of the new structure and of the experimental setup used during the high power tests. In addition, we will report on experimental results of high power tests carried out on an alumina-based (ε=9.4) DLA structure.

INTRODUCTION

In recent years, much research has been done to develop new types of high gradient accelerating structures [1]. One of the most promising of these technologies is the dielectric loaded accelerating (DLA) structure, where a cylindrical copper tube is lined with a dielectric sleeve, driven by an external RF source. Although the proposed use of a dielectric-based structure for acceleration dates back to the 1950's, the first high power testing of these devices has taken place only recently [2-4].

Argonne National Laboratory, in collaboration with the Naval Research Laboratory, is carrying out high-power tests of DLA structures to investigate their suitability for use in high-gradient RF linear accelerators. In an experiment carried out at the NRL in 2002 [4], one X-band traveling-wave (TW-DLA) and one X-band standing-wave (SW-DLA) structure, both made of a MCT20-ceramic, underwent high power testing at the NRL 11.424-GHz Magnicon Facility [5]. During the tests approximately 10 MW of power was available, and the incident, reflected, and transmitted (TW only) powers were* monitored. In the TW-DLA test, the incident power that the structure could accept was limited to 600 kW, corresponding to a transmitted power of 170 kW, while in the SW-DLA test the limit was 100 kW. In both cases, when the incident power was raised above the stated limits, the reflected power and the vacuum pressure near the input coupler increased dramatically. Examination of the structures after the experiment revealed evidence of arcing in the input coupler. This result is similar to what was observed during a high power test of an S-band TW-DLA structure carried out at Yale [3]. In that case, the power that could be delivered into the tube was limited to 200 kW. This limit was caused by arcing in the input coupler, as evidenced by a blackened alumina surface.

The failure of the input couplers in both cases is thought to be due to the presence of dielectric at the coupling slot. This creates two problems: (1) the triple-point of vacuum-to-metal-to-dielectric in a region of high electric field that is expected to cause breakdown problems; and (2) high power density in the dielectric, since all the power passes through a small area of dielectric. In this paper, we report on high power tests carried out on a new DLA structure.

THE NEXT GENERATION DESIGN

Based on our analysis of the failures of the input couplers in both of the previous structures, we have designed a new DLA structure [6]. This structure has a modular construction that separates the coupling sections from the acceleration section and is based on the most recent NLC structure designs by Tantawi and Nantista [7]. Moving from left to right in Fig. 1, the new TW-DLA device consists of an all-metal TE_{10}-TM_{01} input coupler, a dielectric-lined, tapered input matching section, a dielectric-lined accelerating section, a dielectric-lined, tapered output matching section, and an all-metal TM_{01}-TE_{10} output coupler. This modular construction is expected to have good high power handling capabilities for two reasons: (1) the all-metal couplers have no triple-points; and (2) the power in the bulk dielectric is now distributed over the entire cross-section rather than just in the small area of the coupler slot.

In order to test the new structure design as quickly as possible, we chose to use Al_2O_3 in the matching sections and Al_2O_3 doped with Mg in the accelerating section for the dielectric material, since an alumina-based DLA structure is relatively easy to fabricate. In approximately six months, we designed, constructed, characterized, and UHV vacuum tested this structure. The TW-DLA structure parameters are: (1) the accelerating section dielectric is *200 mm* long, *I.D. = 10 mm*, *O.D. = 14.36 mm* and $\varepsilon_r = 9.4$; and (2) the matching section's dielectric is *I.D. = 24.16 mm* at the wide end and tapers to *I.D. = 10 mm* at the narrow end over a distance of *54.24 mm* with $\varepsilon_r = 9.7$. In bench-top tests, we measured S_{21} = *-0.1 dB* in coupler-to-coupler configuration and measured S_{21} = *-2 dB* for the complete structure. For this TM_{01} mode structure, the field in the vacuum is of the form

* Work funded by DoE and ONR

0-7803-7738-9/03/$17.00 © 2003 IEEE

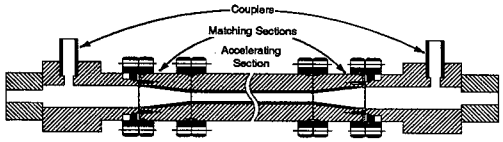

Figure 1: Cross section of the new modular DLA structure

$E_z(r,z,t) = E_0 I_0(k_r r)\cos(\omega t - k_z z)$ with normalization such that *80 kW* of power produces an axial accelerating gradient of E_0 = *1 MV/m*.

SETUP & PROCEDURE

The configuration used during the high power tests is shown in Figure 2. The magnicon (not shown) output is delivered through WR-90 vacuum waveguide, equipped with a 55.5 dB bi-directional coupler connected to calibrated crystal detectors, and into the input coupler of our device under test (D.U.T.). The output of the D.U.T. is delivered through short section of WR-90, equipped with an identical bi-directional coupler, and into a SLAC-type high-power load. The diagnostics available to monitor the D.U.T. during high power conditioning included (1) bi-directional couplers on both the input and output waveguide to monitor the incident, reflected, and transmitted power; (2) four ion pumps to provide vacuum and monitor pressure; (3) a Faraday cup downstream of the structure to monitor dark current; and (4) cameras to look for visible light along the axis of the structure in the event of a breakdown.

RESULTS & DISSCUSION

The testing of each D.U.T. was conducted by slowly increasing the output power of the magnicon, beginning from a low power level, while monitoring all the diagnostics to look for signs of breakdown. Typically, after an increase in the power level, the voltage signals from the bi-directional couplers were acquired with an oscilloscope and the vacuum pressure was recorded in the log. If either a visible light flash on the monitor or a non-zero reading on the Faraday cup ammeter were observed, the event was to be noted in the log.

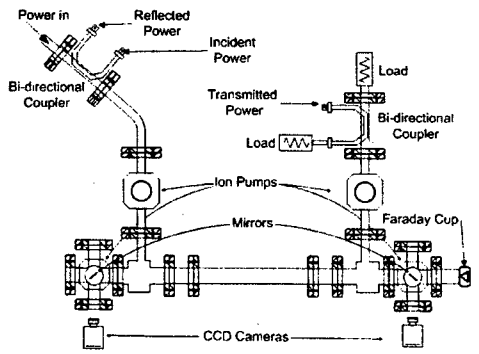

Figure 2: Diagram of the DLA structure installed at NRL's Magnicon Facility.

Coupler to Coupler Test

In this test, the D.U.T. was the two coupling sections connected directly to one another. The couplers were easily conditioned to the maximum available output power of the magnicon (10 MW) at an RF pulse length of 150 ns (FWHM) with no arcing observed. The transmission (S_{21}) through the coupler-to-coupler device was approximately *90 %* during the entire test. In short, the high power test of the couplers was a total success.

DLA Structure Test

In this test, we installed the complete DLA structure (Fig. 1), with its input coupler connected to the magnicon and its output coupler connected to the load. After a short conditioning period, we were able to increase the incident power to 5 MW ($E_z \approx$ *8 MV/m*) at an RF pulse length of 150 ns (FWHM) with no signs of breakdown observed at any time. This is the first time that over a MW of RF power was coupled into a DLA structure.

Measurement of the transmission coefficient (S_{21}, Fig. 3) and the reflection coefficient (S_{11}, Fig. 3) was as expected as long as the incident power remained below 0.1 MW, with $S_{21} \approx$ *75 %* and $S_{11} \approx$ *0.5 %*. (The other *25%* of the power is lost due to a combination of resistive losses and manufacturing imperfections of the structure.) However, when the incident power was increased above *0.1 MW* the transmission coefficient decreased, without a corresponding increase in the reflection coefficient. This means that some of the incident power was unaccounted for, or missing. For the remainder of this paper, we refer to this as the *missing power*. For example, at the highest incident power point (4.7 MW), the transmitted power was measured to be 1.2 MW and the reflected power was negligible. Estimating the power lost to attenuation in the DLA structure to be *1.2 MW* implies that the missing power is about *2.4 MW*. This calculation was repeated for all points and the result is shown in Figure 5.

Over the same range of incident power that the missing power appeared, we also observed light emission (Fig. 4) that appeared to be coming from the surface of the dielectric. By measuring the RS-170 analog video output from the CCD camera with an oscilloscope, triggered at the same rate as the magnicon, we were able to measure the light intensity as a function of incident power (Fig. 5). The lowest incident power for which the light intensity was observed was *0.6 MW*. The reason the light intensity seems to turn-on later than the missing power (*0.1 MW*) is most likely due to the fact that we can measure power with greater sensitivity.

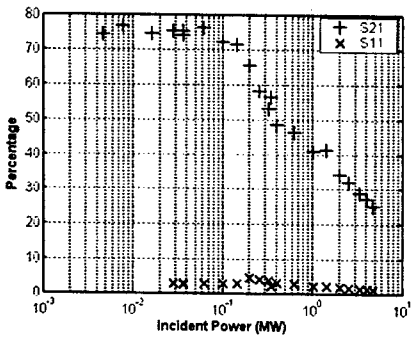

Figure 3: The measured values of the S parameters (in percentage) as a function of incident power made during the high-power test of the DLA Structure.

Secondary Electron Emission

Our preliminary investigation into this phenomenon leads us to believe that missing power and the light emission were caused by secondary electron emission (*SEE*) from the dielectric — similar to what others have observed on dielectric RF windows. To test this hypothesis during the high power test, we placed a horseshoe-shaped, permanent magnet (PM) of about 100 Gauss near the structure, since magnetic fields are often used to suppress *SEE*. The PM caused a slight decrease in the light intensity and a change in the transmitted power signal. At the minimum, this means that low energy electrons (< few keV) are involved in the missing power process, which is most likely due to *SEE*.

FUTURE WORK

We are currently developing a model of the secondary emission process in a cylindrical DLA structure that will be the subject of a future publication. Our preliminary investigation indicates that the *SEE* is causing single-surface multipactoring, since a resonant process does not appear to be involved, and the light emission is seen to be originating from the surface. In this case, a secondary electron migrates to the surface with initial kinetic energy of only a few eV, is accelerated by the RF fields, and then re-impacts the surface with enough kinetic energy to make more secondaries. We think that the SEE electrons

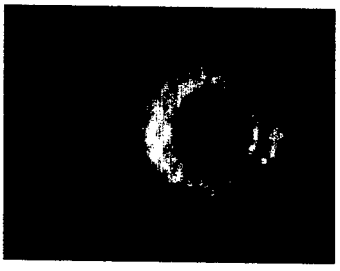

Figure 4: Image of light observed during the high power test. The dark region in the center of the ring is the vacuum hole inside the dielectric tube.

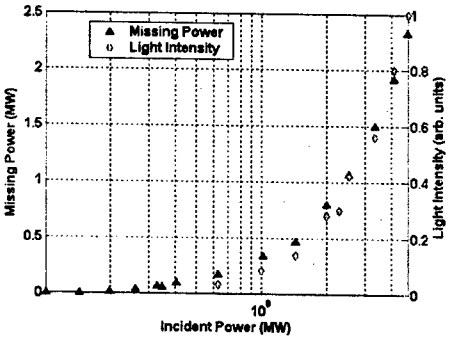

Figure 5: The missing power and light intensity as functions of the incident power.

continue to multiply in this manner until the electron cloud produces a large enough DC electric field to suppress additional secondaries. The electron cloud, thus produced, is what actually drains the energy from the RF field.

We are taking a two-pronged approach to suppress the secondary electron emission: (1) we are developing the expertise to coat the inside of the dielectrics with *TiN*, well known for its ability to suppress secondary emission by lowering δ; and (2) we will use other dielectric materials with lower δ — since alumina can be as high as 9. We suspect that if the secondary emission coefficient, δ, of the dielectric were reduced below 2, the single-surface multipactor could be suppressed.

CONCLUSION

A high power test has demonstrated for the first time that a DLA structure is capable of withstanding *5 MW* of incident power with no signs of dielectric breakdown. In addition, a new DLA structure design has solved the problem of arcing inside the coupler. The new design achieved S_{21} = -1.2 dB when the incident power was below *100 kW*, but power transmission decreased rapidly above that level. It is believed that SEE is responsible for this missing power. Future experiments will address this issue.

REFERENCES

[1] J.G. Power et al. in Advanced Accelerator Concepts, AIP Conference Proceedings 647, pp. 156-164 (2002).
[2] J.-M. Fang et al., Proc. PAC 2001, pp. 4020-4022.
[3] S.H. Gold et al., Proc. PAC 2001, pp. 3984-3986.
[4] J.G. Power et al., in Advanced Accelerator Concepts, AIP Conference Proceedings 647, pp. 556-564 (2002).
[5] S.H. Gold et al., in Advanced Accelerator Concepts, AIP Conference Proceedings 647, pp. 439–447 (2002).
[6] W. Liu et al., these proceedings.
[7] Private communication.

A DEMONSTRATION OF HIGH-GRADIENT ACCELERATION

W. Wuensch, C. Achard, S. Döbert*, H. H. Braun, I. Syratchev, M. Taborelli, I. Wilson,
CERN, Geneva, Switzerland

Abstract

One priority of the CLIC (Compact Linear Collider) accelerating-structure development program has been to investigate ways to achieve accelerating gradients above 150 MV/m. Two main concepts to achieve such high gradients have emerged: reduced surface field geometries and the use of alternative materials. An experimental demonstration of these two concepts has been made in CTFII (CLIC Test Facility) using three 30 GHz accelerating structures: one made entirely from copper, one with copper cavity walls and tungsten irises and one with copper cavity walls and molybdenum irises. A peak accelerating gradient of over 190 MV/m was achieved using the molybdenum-iris structure. The effect of pulse length on achievable gradient was investigated using a novel 'pulse stretcher'.

INTRODUCTION

The CLIC linear-collider design envisages the use of the rather high accelerating gradient of 150 MV/m, resulting in an input power of 130 MW to the 30 GHz accelerating structures [1]. Such an accelerating gradient, with the nominal 130 ns CLIC pulse length, has already been demonstrated with two small aperture copper X-band structures [2,3]. However the limiting breakdown gradients achieved in subsequent tests of X-band and 30 GHz structures [4,5] have been much lower. Although the exact reason for the higher performance of the early test structures is not yet clear [6,7], it seems to be related to their very low a/λ ratio of 0.11. One aspect of low a/λ geometries, a low ratio of peak surface field to accelerating gradient, has been used as a design criteria for CLIC accelerating structures [1]. The reduction of a/λ is however limited by short range wakefields, which grow cubically as the beam aperture becomes smaller, leading to unacceptable beam emittance growth.

The use of alternative materials to copper is consequently under investigation by the CLIC study as an additional way of obtaining very high accelerating gradients. Desirable characteristics of a candidate material include the ability to support a high surface electric field before breaking down, to resist damage from the arc that occurs once the breakdown has begun, and high electrical conductivity. Three refractory metals, tungsten, molybdenum and rhodium, are clear potential candidates and are used in low frequency (DC-50/60 Hz), high power and high voltage applications. Initial high gradient 30 GHz rf tests with tungsten yielded extremely encouraging results [8].

This report describes recent results of a systematic investigation of the relative high-gradient rf performances of copper, tungsten and molybdenum obtained from tests of structures with a common rf design that were tested using a standardized conditioning procedure. The structures are shown in Fig. 1.

The materials investigation was carried out in CTFII using 15 ns pulses, which are produced using the longest possible drive bunch train. In order to also investigate pulse length dependence a special rf pulse stretcher was designed and fabricated. This allowed the test of the copper structure with a 30 ns pulse and to address the issue of pulse length dependence of rf breakdown

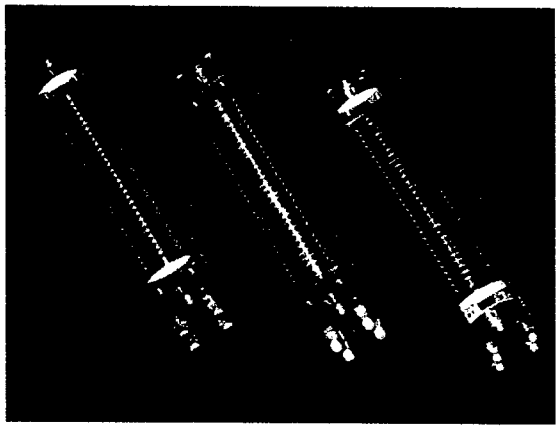

Figure 1: The copper, tungsten iris and molybdenum iris accelerating structures (10 cm active length).

THE STRUCTURES

The structure characteristics and fabrication techniques were chosen to provide, within the final year of CTFII operation, as direct a comparison between the high-gradient properties of copper, tungsten and molybdenum as possible. Structure parameters are summarized in Table 1. All the structures had identical clamped-on 'mode launcher' couplers [9] which have a peak surface field at least 20% lower than anywhere in the disk-loaded-waveguide part of the structure. In this way couplers are expected neither to limit nor complicate the tests.

The body of the copper structure was vacuum brazed while the tungsten and molybdenum structures were entirely clamped. The configuration of the clamping can be found in [8]. The copper structure was cleaned before brazing using the CERN standard chemical procedure. The tungsten irises were only degreased. The molybdenum irises where also vacuum fired at 800 °C before assembly. This was motivated by the observation of substantial degassing of the tungsten structure during conditioning. All three structures were tested in a vacuum can for best vacuum and minimum experimental turn-

*current address, SLAC, USA.

0-7803-7738-9/03/$17.00 © 2003 IEEE

around time. None of structures where in-situ baked, due to lack of time.

Table 1: Structure parameters. The bottom two values are for the cell geometry, i.e. are local values.

Frequency	29.984 GHz
Number of cells	30+2 matching cells
Phase advance	$2\pi/3$
Beam aperture	3.5 mm (constant)
Group velocity, v_g/c	4.6 %
Fill time	8.3 ns
$E_{surface}/E_{accelerating}$	2.2
Power for $E_{accelerating}$=150 MV/m	56 MW

MATERIAL INVESTIGATION

The structures were conditioned with 15 ns rf pulses and a repetition rate of 5 Hz by maintaining a nearly continuous, but controlled, level of breakdown. Breakdowns were identified using emitted current bursts, vacuum activity and missing rf energy. Periodically a measurement was made of the operating gradient and the results obtained are plotted in Fig. 2. These results show a clear influence of material on achievable accelerating gradient, with a substantial gain in gradient for the refractory metals. The final field values are summarized in Table 2. It should be noted that the tungsten-iris and molybdenum-iris tests were both stopped due to lack of testing time.

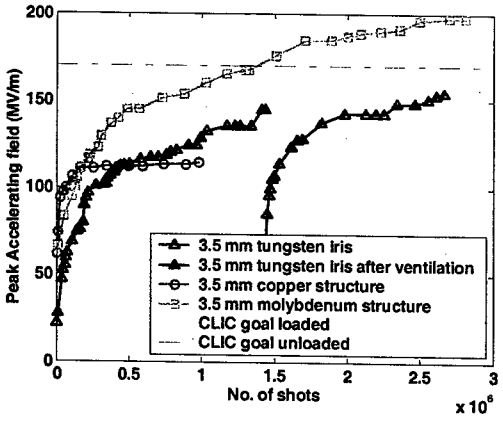

Figure 2: Conditioning history of the three structures.

Table 2: Final gradient values in MV/m.

Structure	Peak accelerating	Average accelerating	Peak surface
Copper	110	100	260
Tungsten	150	125	340
Molybdenum	193	153	426

A roughened surface and a slight erosion of material was observed, using an endoscope, in the copper structure on the surfaces with the highest electric field, which are located on the first irises of the copper structure. The tungsten and molybdenum structures were unbolted after the tests and were inspected by eye and electron microscope (SEM). SEM images show surface melting in the iris tips in the first few cells in both structures. Sub-micron cracks can be distinguished in the junction between melting regions, which are themselves about 10 microns in size. However, no erosion has taken place to a level that affects the rf characteristics of the structure. This has been confirmed by a comparison of rf measurements made before and after the tests. Further inspections are underway.

Evidence of arcing in some of the clamped cell to iris contacts was observed in the tungsten structure. This appeared as spots of roughened surface on the copper disk and corresponding plated copper spots on the tungsten iris. More care was taken to ensure an adequate contact pressure when assembling the molybdenum structure, and no traces of contact arcing was observed in it after testing.

It should be stressed that the ultimate and relative high gradient performances of tungsten and molybdenum may not have been determined yet because: neither the tungsten nor the molybdenum tests were taken to the point where the conditioning curves showed a clear saturation, there is evidence of contact arcing in the tungsten structure and only the molybdenum irises where vacuum fired.

The transition from stable to unstable operation was also investigated during the tests. Breakdown rate has been clearly identified as an important issue for a linear collider with many thousands of accelerating structures [10]. The transition from stable to unstable operation is remarkably smooth as illustrated in Fig. 3. For the conditioning curves shown in Fig. 2, a gradient of 130 MV/m would be quoted for this data. A gradient stable enough for a linear collider would need to be distinctly lower.

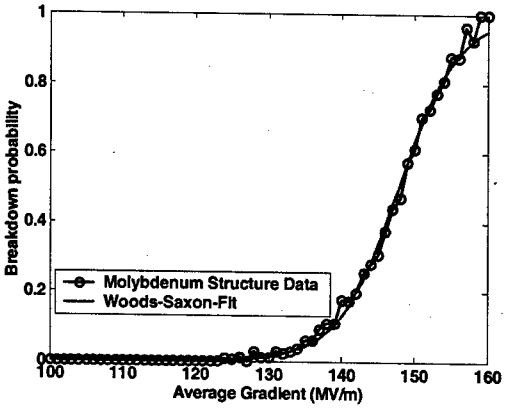

Figure 3: Breakdown probability as a function of gradient for the partially conditioned molybdenum structure.

PULSE-LENGTH DEPENDANCE

Although the high-gradient values described in the previous section are very encouraging, it should be stressed that the gradients were achieved with 15 ns pulses, while the CLIC nominal pulse length is 130 ns. The pulse length dependence of rf breakdown, and its origin, remains an open question. Achievable gradient is generally assumed to decrease with increasing pulse length. The 15 ns pulse length is fixed by the maximum electron bunch train length that CTFII can produce. In order to investigate pulse length, a novel rf 'pulse stretcher', which doubles the pulse length, was built [11]. The rf pulse produced by the stretcher in CTFII is shown in Fig. 4.

The stretcher was only used to condition the copper structure because the tungsten and molybdenum structures would have required more power than CTFII could deliver. The structure was conditioned with an additional one million 30 ns pulses after the initial one million 15 ns pulses. The encouraging result was that the same 120 MV/m gradient was achieved with both pulse lengths. The achievable gradient was also measured for 4 and 8 ns, to probe the turn-on time of an rf arc. The pulse length results are summarized in Fig. 5

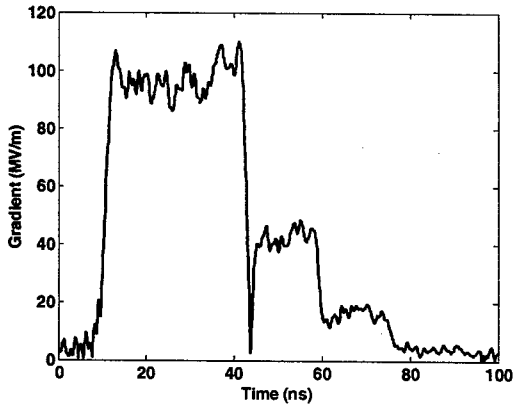

Figure 4: Rf pulse from stretcher.

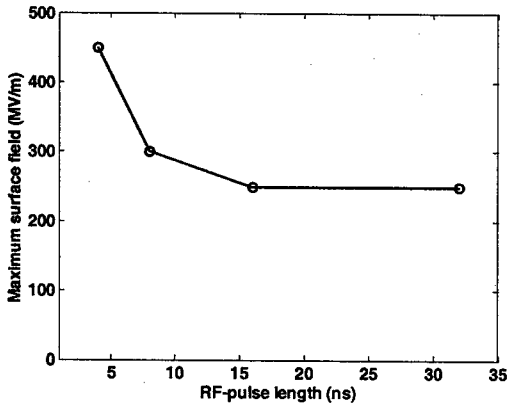

Figure 5: Pulse length dependence of the copper structure.

CONCLUSIONS

These tests have established that refractory metals can substantially increase the rf-breakdown limit in accelerating structures. Of course a consequence is that new structure fabrication techniques are required, but these test structures already represent a first step towards development of these techniques. Judging from the state of surfaces after conditioning, only the tips of the irises, where the surface electric field is highest, need to be made from new materials. In this case, composite accelerating structures would only be slightly less efficient than all-copper structures. The need to fabricate composite structure may also be motivated by pulsed surface heating, which may also require new materials. Although the highest gradient at which 30 GHz structures can run reliably at the full CLIC 130 ns pulse length has not yet been determined, a path with substantial potential has been identified.

ACKNOWLEDGEMENTS

The authors wish to acknowledge the essential theoretical and technical contributions of many colleagues, D. Allard, G. Arnaud-Izquerdo, C. Benvenuti, P. Gu, S. Heikkinen, E. Jensen, S. Leblanc, S. Mathot, and W. Schnell.

REFERENCES

[1] J.Y. Raguin, I. Wilson, W. Wuensch, "Progress in the Design of a Damped and Tapered Accelerating Structure for CLIC", these proceedings.

[2] T. Higo, T. Taniuchi, M. Yamamoto, J. Odagiri, S. Tokumoto, H. Mizuno, K. Takata, I. Wilson, W. Wuensch, "High Gradient Performance of X-Band Accelerating Sections for Linear Colliders", Particle Acclerators, 1994, Vol.48 pp. 43-59.

[3] J.W. Wang, G.A. Loew, R.J. Loewen, R.S. Ruth, A.E. Vlieks, I. Wilson, W. Wuensch, "SLAC/CERN High Gradient Tests of an X-Band Accelerating Section", CERN/SL 95-27, Proc. PAC95.

[4] H. H. Braun, S. Döbert, L. Groening, I. Wilson, W. Wuensch, "Status of CLIC High Gradient Studies", CERN/PS 2001-045 (RF), Proc. PAC2001.

[5] C. Adolphsen, these proceedings.

[6] W. Wuensch, "High-Gradient Breakdown in Normal-Conducting Cavities", CERN/PS 2002-28, Proc. EPAC2002.

[7] S. Döbert, "Status of Very High-Gradient Cavity Tests", CERN/PS 2002-60, Proc. LINAC2002.

[8] H.H. Braun, S. Döbert, I. Syratchev, M. Taborelli, I. Wilson, W. Wuensch, "CLIC High Gradient Test Results", CERN/PS2002-62, Proc. LINAC2002.

[9] S. Döbert, J-Y. Raguin, I. Syratchev, W. Wuensch, "Coupler Studies for CLIC Accelerating Structures", CERN/PS 2002-036, Proc. EPAC2002.

[10] TRC-Report 2003, SLAC-R-606, p.282.

[11] H.H. Braun, S. Döbert, P. Gu, I. Syratchev, I. Wilson, W. Wuensch,"30 GHz Rf Pulse Stretcher for CTF2", CLIC note 556.

The Spallation Neutron Source Diagnostics: Initial Integration and Commissioning Progress Report*

Saeed Assadi for the SNS diagnostic collaboration. Oak Ridge National Laboratory

Abstract

The Spallation Neutron Source (SNS) Project, a collaboration of six national laboratories, is constructing an accelerator based neutron facility at ORNL. The SNS accelerator systems will deliver a 1 GeV, 1.44 MW proton beam to a liquid mercury target. The high-beam power and desired high availability of the accelerator complex have had important consequences for the design and implementation of diagnostics at the SNS. Namely, diagnostic systems have been designed with high reliability, the ability for hands-on maintenance, redundancy in critical diagnostics, and commonality of subsystems in mind. The multi-laboratory diagnostics group has successfully implemented and commissioned a number of systems at LBNL during initial commissioning of the SNS Front-End systems. This talk reports on the team's progress in diagnostics commissioning and performance for the SNS, summarizes the approach that has been used in this multi-laboratory effort, describes the lessons learned and presents the technical and organizational challenges that lie ahead.

INTRODUCTION

Most of the beam diagnostics [1] at the Spallation Neutron Source (SNS) are similar to other accelerators: beam position monitors, beam loss monitors, wire scanners, beam current monitors, slit and collector emittance stations, Faraday Cups, etc. Each accelerator section, Figure (1) lists the suite of diagnostic systems and their channel counts[3,4]. As described below, additional systems will be provided for early commissioning of the Front End and the DTL. Systems are being designed and constructed by the multi-lab diagnostics team. The team is comprised of groups from BNL, LANL, LBNL, and ORNL. The ORNL group also coordinates the team's activities. A Diagnostics Advisory Committee provides external guidance. This committee reviews all major system designs at the conceptual and detailed design.

The low loss requirement (average loss of no more than 1 Watt/meter) has added challenges in the diagnostic design and implementation. For example, we added modified the BLM design to accommodate the machine protection system fast turn-off requirements. The other example is the diagnostics being implemented in the supper conducting LINAC (SCL). The high beam power and the superconducting rf cavity challenges have led to the development of a laser profile monitor system that replaces the wire scanner system in the superconducting linac (SCL). The challenges associated with the e-p instability and the expected beam loss in the ring also have led to improvements in the gas ionization profile monitor design. We have also taken advantage of

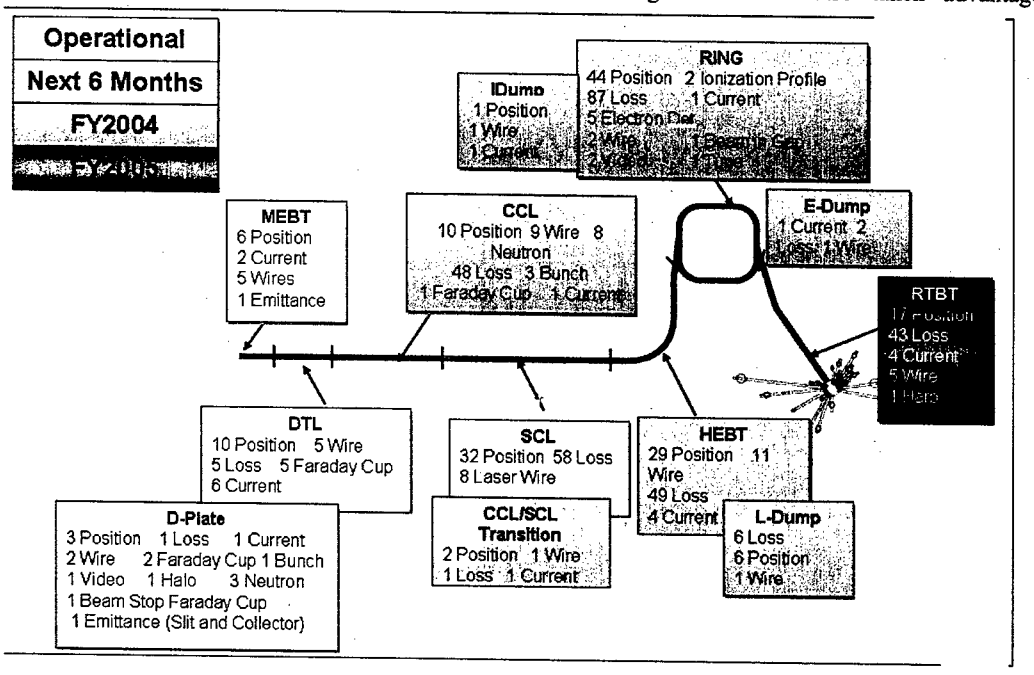

Fig. 1. Layout of the diagnostics in the SNS facility, color-coded to indicate the staged installation dates.

*Work supported by the Office of Science of the US Department of Energy.

0-7803-7738-9/03/$17.00 © 2003 IEEE

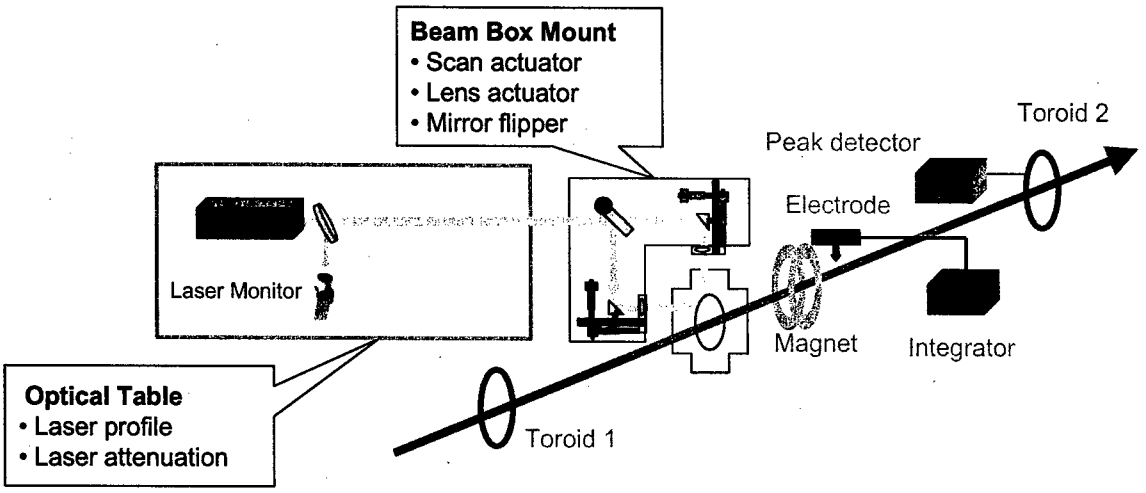

Fig. 2. Schematic layout of the SCL laser beam profile monitor.

technology developments by basing many of our diagnostics instrumentation designs on the personal computer (PC) platform. A layout of the various diagnostics systems is shown in Fig. 1.

LASER PROFILE MONITOR SYSTEM

The profile monitor system for the SCL was originally envisioned to be a carbon wire scanner system. However, linac designers were concerned about the possibility that carbon wire ablation, or broken wire fragments, could find their way into the superconducting cavities and cause them to fail. Carbon wire scanner actuator was developed [2] at Los Alamos National Laboratory (LANL) in tandem with experiments [3,4] using a laser to measure profiles of H^- beams at Brookhaven National Laboratory (BNL).

Once the laser profile monitor concept was proven by experiments at BNL 750 keV, 200 MeV LINAC, and subsequently on the SNS MEBT at Lawrence Berkeley National Laboratory, the decision was made to replace the carbon wire scanner system with the laser profile measurement system in the SCL. The advantages that the laser profile monitor system has over the wire scanner system are: 1) profiles can be measured during normal operations, as opposed to the 100 μs, 10 Hz duty factor restriction needed to prevent damage to carbon wires; and 2) there are no moving parts inside the vacuum system, thus reducing the possibility of a vacuum system failure. A disadvantage is that the laser is not as rad hard as a wire scanner actuator, but we have overcome this issue by placing the laser far away from the beam line.

The laser profile monitor concept is straightforward: a tightly focused laser beam is directed transversely through the H^- beam, causing photo-neutralization. It only take about .755eV to detach the electron. The released electrons are either swept away by magnetic fields normally present in the linac lattice, or directed by a special dipole magnet to an electron collector that may or may not be part of the laser profile monitor system. The beam profile is measured by scanning the laser beam across the H^- beam and measuring the resultant deficit in the H^- beam current and/or, if the released electrons are collected, by measuring their current. A simple schematic of the concept is shown in Fig. 2.

The advantage of collecting electrons vs. measuring the deficit in beam current are: 1) the signal to noise ratio is better because of the large numbers of released electrons; and 2) the simplicity of the electron collector, since the electron energy is well defined and the electrons are well collimated. The disadvantages are: 1) an external magnetic field is required, 2) an in-vacuum electron collector is required, and 3) the electron collector signal may suffer from interference caused by beam loss. At the SNS linac we will use both methods. Every laser station will have an electron collector, and there will be beam current measurements at the entrance and exit of the superconducting linac.

However, concerns about long-term radiation damage have led us to install a single laser in a room above the SNS linac, and to transport the laser beam to the profile monitor stations using a system of mirrors.

The laser chosen for the SNS system is the Continuum Powerlite Precision II, 600 mJ, 10 nsec, 1064 nm, 30 Hz ND-YAG laser. The laser beam is transported down through a hole in the ceiling of the beam tunnel at the downstream end of the linac, and then along the length of the linac to the various beam profile measurement stations. Each of the 32 warm inter-segment regions will contain a beam box with fused-silica view ports and an electron collector. However, to contain costs, only the first four inter-segment regions in the medium-beta portion of the SCL and the first four inter-segment regions in the high-beta portion of the SCL will be instrumented with the actuators, the electron deflection magnet, and the electronics needed to make a profile measurement. With this setup, a laser station can be moved or added in an 8-hour shift.

Proof of principle tests were conducted at BNL and on the SNS MEBT at LBNL. The most recent and most complete tests were conducted last January on the SNS MEBT at ORNL [5]. Shown in Figure 3 is an example of this latest test, where the SCL prototype system was installed at the end of the MEBT using the final-design beam box, dipole magnet, lenses and mirror actuators.

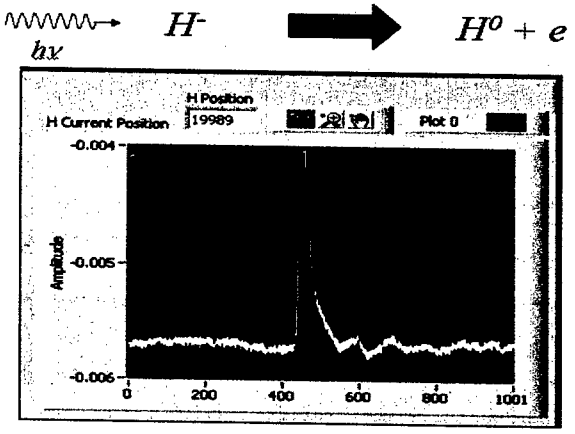

Figure 4. Photo-neutralization via laser beam observed on (BCM) beam current monitor.

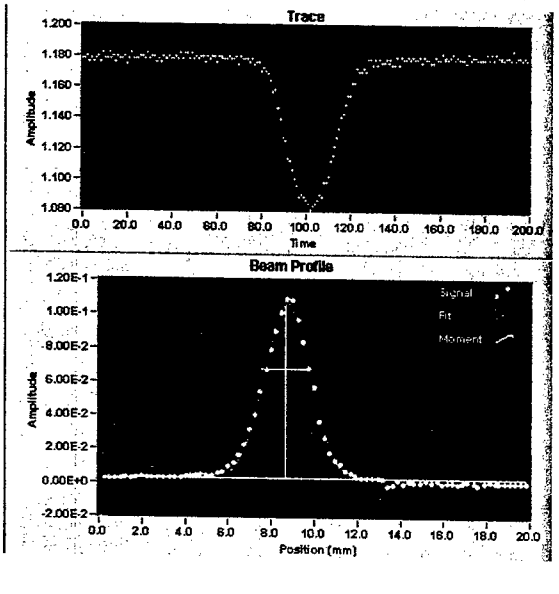

Figure 3. Horizontal beam profile in the SNS MEBT, measured January 2003. Top: an example of the electron collector signal. Bottom: the results of the measurement, with a Gaussian fit plotted out to 2.5 σ.

BEAM LOSS MONITORS

SNS will use 295 argon-filled ion chambers as the primary detectors for monitoring beam losses. Argon has the advantage of fast electron transit time compared to slower air filled detectors [6] The initial choice was an ion chamber designed for the Tevatron, but concerns about saturation at high dose rate and long ion transit time (~ 700 μsec at 2 kV bias) led to the development of a new ion chamber designed to overcome these limitations [7]. It utilizes a larger inner diameter electrode to significantly decrease the ion transit time and raise the collection efficiency for a 1% local loss.

The new design tested at BNL has proven to be superior to the original Tevatron BLM system. The smaller gap required careful high voltage design. Guard electrodes were used to divert leakage from the HV electrode to ground and define the active region. Voltage gradients have been reduced by rounding the electrode ends. Figure 5 shows the new design. Two prototypes tested at BNL.

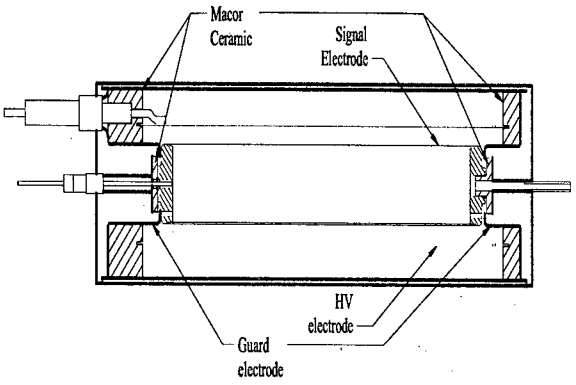

Figure 5. The new SNS ion chamber design.

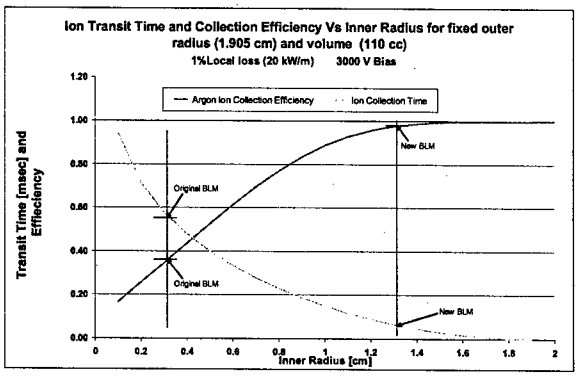

Figure 6. The collection efficiency and ion transit time are shown in Figure 1 as a function of inner cylinder radius

The first was filled with Nitrogen at 1 ATM. A second prototype with ahigher voltage feedthrough and improved ceramic and guard rings was able to hold 4.5 kV with 1 ATM Argon. Detailed description is presented in these proceedings [8].

IONIZATION PROFILE MONITOR

The SNS ionization profile monitor (IPM) being developed by the BNL team, to be installed in two (one horizontal, one vertical) locations in the ring. These are based on an improved version of the IPMs installed [9] in the RHIC ring. In fact, some of the improvements have already been tested on the RHIC IPMs.

The SNS (and RHIC) IPMs are based on electron collection in parallel electric and magnetic fields. The electrons are amplified by a micro-channel plate and collected on a 64-channel gold-plated printed circuit board. The simplified schematic is shown in Figure (7).

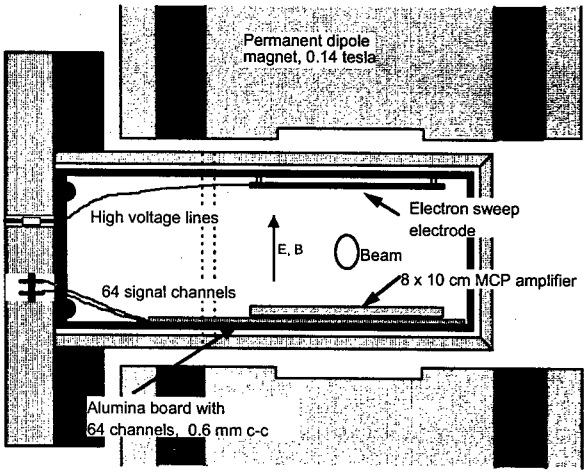

Figure 7. The original design of the SNS and RHIC IPM.

The detector components were inserted inside the beam-line. This restricted the aperture and made Detector components vulnerable to stray beam. The modifications to the RHIC IPM were necessary due to rf coupling to the beam, susceptibility to beam loss, and possible interference from the e-p beam instability. Beam loss in the vicinity of the IPM can cause the primary beam and secondary particle showers to pass through the micro-channel plate and the collector board, thus causing large background signals. Also, as demonstrated in the LANL Proton Storage Ring, the e-p instability can create huge amounts of electrons that could be collected by the IPM and possibly swamp the beam profile signal.

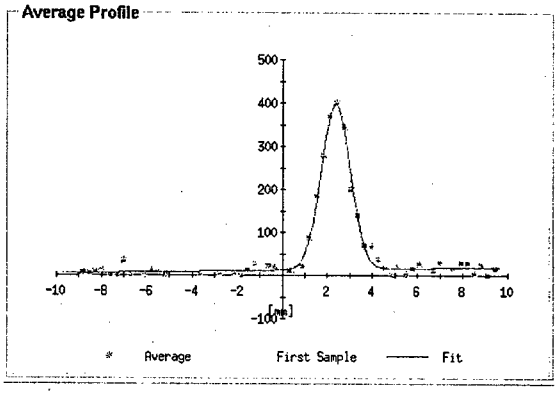

Figure 8. The modified SNS/RHIC ionization profile monitor measurement has lower background from e-p instabilities.

NETWORK ATTACHED DEVICES

At the SNS we have chosen to base many of our diagnostics on the rack-mounted personal computer (PC) platform, rather than the more typical VXI, VME, or

CAMAC platforms. The basic idea behind a Network Attached Device (NAD) is to implement an instrument as a single networked device with its own resources [1]. Our reasons include 1) lower costs; 2) an industry standard processor (PC) and internal bus (PCI); 3) each instrument can be a node on the network, thus reducing common failure points like a VME crate; and 4) the availability of a wide variety of low-cost, commercial off the shelf PCI cards. We also chose embedded Windows 2000 or Windows XP for the operating system, and LabVIEW for the signal acquisition and signal processing software. To round out the standard software suite [6], each PC runs Input-Output Controller (IOC) core software to make it appear to be an IOC to the EPICS control system. Bench tests on a prototype network attached device demonstrated a 100 element (with 4 bytes /element) waveform update rate of 1000 Hz from LabVIEW to EPICS.

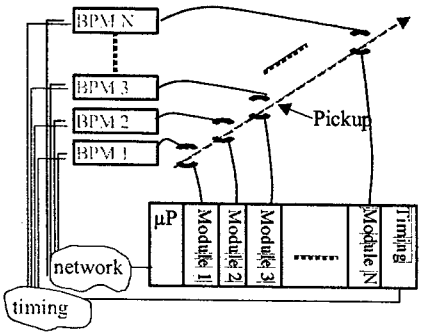

Figure 9. Concept of NAD vs. traditional VWE/VXI system.

With the prototype BPM, BCM, and wire scanner systems on the SNS MEBT at LBNL in February 2002 were based on the NAD model. .All these systems were brought on line in less than one week, and performed well during this initial commissioning period.

TEMPORARY DIAGNOSTICS

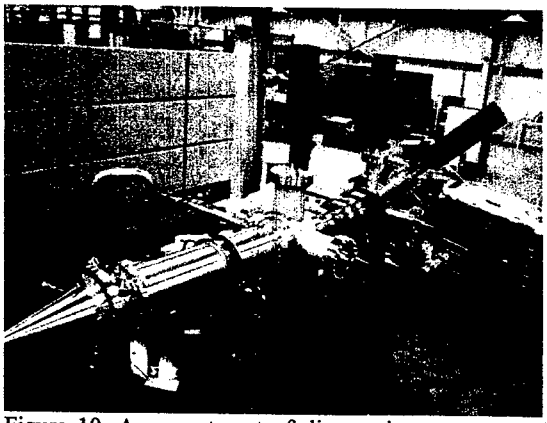

Figure 10. An assortment of diagnostics are prepared for the DTL tank one commissioning.

SUMMARY

An array of instrumentations have been designed to meet the challenges offered by the SNS project. These include the laser profile monitor for H^- beams, ultra fast Faraday cup proved to be useful to measure pico-second bunch length, the improvements to the RHIC ionization profile monitor, and the network attached devices based on the PC platform.

To date the SNS facility has been commissioned up through the end of the MEBT at 2.5 MeV using prototype BPM, BCM, wire scanner, and slit and collector emittance systems. All of these systems have performed well. The laser profile monitor concept was successfully tested on the MEBT, as well as LBNL and BNL.

The next phase of diagnostics installation is now in progress to prepare for DTL commissioning later this summer, followed by CCL commissioning in 2004. The SNS is expected to be fully commissioned by early 2006.

REFERENCES

[1] T.J. Shea et al., "SNS Accelerator Diagnostics: Progress and Challenges," proceedings of the 2001 Particle Accelerator Conference, Chicago, Ill, USA, June 18 – 22, 2001.

[2] R. Hardekopf et al, "Wire Scanner Design for the SNS Superconducting-RF Linac," proceedings of the 2001 Particle Accelerator Conference, Chicago, Ill, USA, June 18 – 22, 2001.

[3] R. Connolly et al., "Laser Profile Measurements of an H- Beam," proceedings of the 2001 Particle Accelerator Conference, Chicago, Ill, USA, June 18 – 22, 2001.

[4] R. Connolly et al., "Laser Beam-Profile Monitor Development at BNL for SNS," proceedings of the 2002 Beam Instrumentation Workshop, Upton, NY, USA, 6 – 9 May 2002.

[5] S. Assadi, et. al. "The SNS Laser Profile Monitor design and implementation", These proceedings.

[6] M. Plum, and D. Brown, "Response of Air- Filled Ion Chambers to High Intensity Radiation Pulses", Proceeding of the 1993 PAC, p2181

[7] R.L. Witkover, and D. Gassner "Design and Testing of the New Ion Chamber Loss Monitor for SNS", These proceedings

[8] R.L. Witkover, and D. Gassner "Design and Testing of the New Ion Chamber Loss Monitor for SNS", These proceedings.

[9] R. Connolly et al., "Performance of the RHIC IPM," proceedings of the 2001 Particle Accelerator Conference, Chicago, Ill, USA, June 18 – 22, 2001.

[10] W. Blokland et al., "Network Attached Devices at SNS," proceedings DIPAC 2003 conference.

[11] J. Power et al., "Beam Position Monitors for the SNS Linac," proceedings of the 2001 Particle Accelerator Conference, Chicago, Ill, USA, June 18 – 22, 2001.

LASER-BASED PROFILE MONITOR FOR ELECTRON BEAMS*

Marc Ross#, SLAC, Stanford, CA 94025, USA

Abstract

High performance TeV energy electron / positron colliders (LC) are the first machines to require online, non-invasive beam size monitors for micron and sub-micron for beam phase space optimization. Typical beam densities in the LC are well beyond the threshold density for single pulse melting and vaporization of any material, making conventional wire scanners ineffective. Using a finely focused, diffraction limited high power laser, it is possible to devise a sampling profile monitor that, in operation, resembles a wire scanner. Very high resolution laser-based profile monitors have been developed and tested, first at FFTB (SLAC) and later at SLC and ATF. The monitor has broad applicability and we review here the technology, application and status of ongoing research programs.

INTRODUCTION

Particle beam brightness and power have increased rapidly in the last decade with the advent of precision control and improved implementation of accelerator designs. Precision beam diagnostics for position and profile have proved vital. Present machines, such as the FFTB at SLAC [1], the ATF at KEK [2] and the SNS [3] have beams that require the use of new types of profile monitors because of their small size or power. Carbon wire scanners, perfected for use with the extremely small beams at SLC and FFTB [4], have been shown to have limited performance for high brightness beams. The debris resulting from wire failure in a superconducting linac, such as SNS, could harm the delicate niobium cavities. A laser-based profile monitor, in contrast, uses a transient pulse of photons that does not pose a real threat to the cavities. In addition, and more importantly for the linear collider, the laser beam can be focused to a size that is smaller than the smallest practical wire diameter, providing a minimum beam size measurement capability well beyond the wire scanner.

Interacting lasers and particle beams have long been used as experimental tools, notably for the production of neutral beams or in the measurement of electron / positron polarization [5,6]. Recent advances in laser and optical technology have made it effective to use very finely focused lasers to accurately probe, using a 90 degree collision angle, within particle beams in order to measure beam size and beam halo. In the last few years, several such probes have been constructed and operated successfully. In this paper we will review the design, operation and results from these devices, and outline issues for future work.

* Work supported by US Department of Energy under contract DE-AC03-76SF00515

#mcrec@slac.stanford.edu

Scattering of e+ / e- particles by laser photons is described by the Compton theory. While the Compton scattering amplitude for protons is much smaller, the photo-neutralization cross section for H^- beams is not, and a laser-based monitor is similarly effective for use with those beams.

In the laser monitor, a low energy optical photon collides with a high energy electron resulting in a high energy gamma ray and lower energy electron. The boosted photon energy is characterized by a sharp endpoint, $y_m=\omega_m/E_b$, (ω_m and E_b are the maximum gamma ray energy and the beam energy, respectively) corresponding to back scattering in the rest frame of the system, and a relatively flat cross section for lower energies. The total cross section, is large and this provides ample signal for the profile monitor, even when compared with conventional wire scanners.

As with conventional wire scanners, it is important to devise an efficient, low background method of detecting the scattered particles, either the degraded electrons or gamma rays, since this usually determines the system accuracy. The fraction of transferred energy at the kinematic endpoint, y_m, grows as a function of beam energy, making clean detection much easier at high energies. Figure 1 shows y_m as a function of E_b for two different laser frequencies, with the values typical of three laserwires indicated.

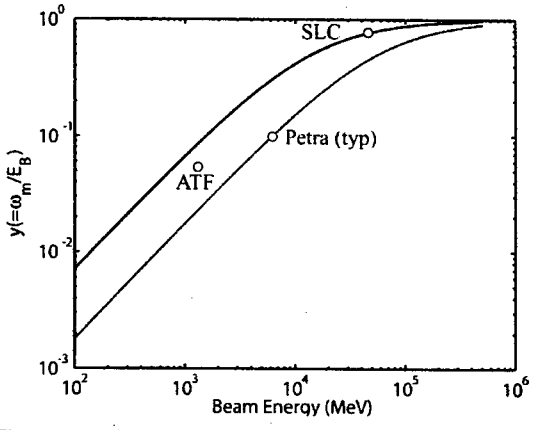

Figure 1: Relative Compton boosted gamma ray energy endpoint (y_m) as a function of electron beam energy for λ=1050nm (lower curve) and λ=350 nm (upper curve) lasers.

Whereas the fundamental physics of a laser-based monitor is straightforward, the implementation can be challenging and requires a detailed understanding of the technology. In this paper we examine the design and operation of five laser-based monitors, at 1) the SLC/SLD IP[7], 2) the KEK ATF[8,9], 3) DESY PETRA[10], the CERN CLIC Test Facility[11] and 4) the SNS (H-

0-7803-7738-9/03/$17.00 © 2003 IEEE

beam)[12]. In addition, since it was a pioneering device, we also include a reference to the FFTB nanometer interferometer monitor[13].

DESIGN

The profile monitor consists of 4 subsystems, 1) the laser, 2) an optical transport to bring the light to the beamline vacuum chamber, 3) the interaction region, with its optics, and 4) a scattered radiation detector. Since its operation and design resemble that of a wire scanner, we will refer to the laser-based profile monitor as a 'laserwire'.

As with conventional wire scanners, the properties of the 'scattering object', used to sample the electron beam charge density, must match the beam parameters. Tightly focused laser waists have limited length, known as the Rayleigh range. For a linear collider, with flat $\varepsilon_y/\varepsilon_x<1\%$, beams, this can smear the overlap region and may force, for example, the use of a very short wavelength laser. Table 1 lists the laser wavelength, intensity, spot size, 'spot length' (Rayleigh range), detector types, and pulse structure of several laserwires. Figure 2 shows a laser 'waist' scan, showing the Rayleigh range of the ATF laserwire.

The monitor resolution depends on the relative size of the two beams and, if they are similar in size, on the accuracy with which the focused laser spot is known. It is important to note that, if the laser spot size is accurately known, it is subtracted in quadrature from the measured profile giving a monitor resolution lower than the laser size. This is the case with the ATF laserwire, where the properties of the CW laser focus are well measured and stable.

An interesting feature of the laserwire is the ability to control the effective density of the beam sampler. Taken together with a high dynamic range detector, this may be used to significantly extend the dynamic range of the monitor, allowing the extremes of the beam to be sampled. Prototype measurements with the SNS injector H- beam, where beam halo information is very important, have shown sensitivity to less than 0.1% of the core beam density.

Table 1: Laserwire IP, laser, signal and beam energy.

	Laser			IP (σ in μm)				Nγ/e	E_beam (GeV)
	λ (nm)	P (MW)	σ_t (ns)	$\sigma_{L_\perp}$	$\sigma_{L_\parallel}$	$\sigma_{b\ x}$	$\sigma_{b\ y}$		
SLC/SLD	350	10	0.1	.4	12	3	0.8	1e4	46
ATF	532	.0002	CW	5.7	760	50	7	0.005	1.3
PETRA	1064	25	2	20	2000	200	20	1000	4-12
CTF	1047	300	0.004	30	5000	150	150	100	0.05
SNS (H^-)	1050	.03	2	100					0.000025

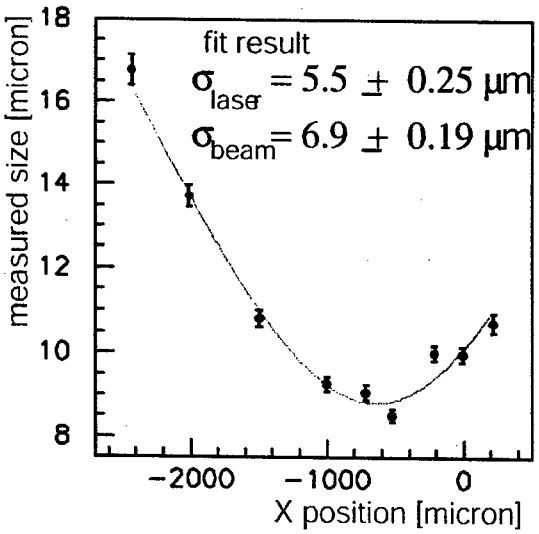

Figure 2: Laser waist scan (ATF damping ring) showing the laser Rayleigh range. The data are fit to the laser size (related to the Rayleigh range), the electron beam size (vertical in this case) and the centroid offset.

Laser

Recent advances in commercially available laser components have enabled laserwires. Affordable, reliable, high peak power components that allow billions of excellent quality pulses consistent with several years laserwire operation are available. However, reflective and transmissive component damage thresholds can vary widely and must be understood before use. A simple rule of thumb damage threshold is $1J/cm^2$. When the laser photon energy is increased, for example with the λ=350 nm SLC/SLD laserwire, bulk transmissive damage caused by non-linear optical harmonic generation is also possible. Most damage effects are self-degenerating, i.e. when they start, the damage site becomes partly opaque and the threshold drops rapidly. These and related topics are annually reviewed at the 'Boulder Damage Symposium' [14] and the best reference is [15].

High power short pulse lasers, which are readily available and provide a great deal more power than CW lasers, are the best for low repetition rate, high background linac environments. Of the laserwires listed in table 1, only the ATF damping ring laserwire works with a non-pulsed, CW, laser. While providing much more

power, pulsed lasers have two important drawbacks, 1) the details of the pulse structure may cause large fluctuations [16] and 2) adjustment of the time difference between the laser and the beam can greatly complicate the basic task of finding collisions, depending on the collision angle and pulse length.

A number of transverse laser modes are have been planned or tested. The simplest, lowest order mode of a laser is the monopole ('00mode') or gaussian mode. The laser energy is most tightly confined in this mode and it is relatively easy to generate in the laser itself by choosing an appropriate laser medium and using a limiting pinhole aperture. In this case the laser is diffraction limited and has the minimum possible emittance. The next highest mode is the dipole mode that has a central null. The characteristic size of the null is smaller than the minimum of the monopole mode, allowing measurement of smaller beams. The extreme case is the interferometer used at FFTB, where the laser beam was split and recombined so that a regular static fixed pitch interference pattern was formed. By adjusting the recombination angle, it was possible to vary the pitch of the pattern and allow measurement of beam sizes as low as 50 nm.

Optics

Optics are needed to match from the laser, (in an accessible part of the machine complex), to a transport line and to receive the beam from the transport and focus it to the IP. Additional low power optics may be needed for monitoring the laser transport and focus. Figure 6 shows the IP optics of the SLC/SLD laserwire.

The smallest possible '00 mode' laser spot is generated using very low f number optics. A rule of thumb, where we assume that the incoming beam optic is sized to match the input beam (+/- $3\sigma_{in}$), is $\sigma_0 \sim 1/2\, f^{\#}\, \lambda$. Consequently great care must be taken to make sure the optical system is aberration-free and constructed to the proper tolerances. The mechanical tolerances of the SLC/SLD IP are around 2 microns. It is not possible to directly measure the dimensions of the high power beam spot. Low power tests were done and a re-imaging system, capable of operation at full power, was used to monitor the performance of the optics and verify the incoming beam conditions.

Laser linear polarization, together with a Brewster angle plate, can be used as a 'switch' that directs the light either to the vertical IP or the horizontal IP.

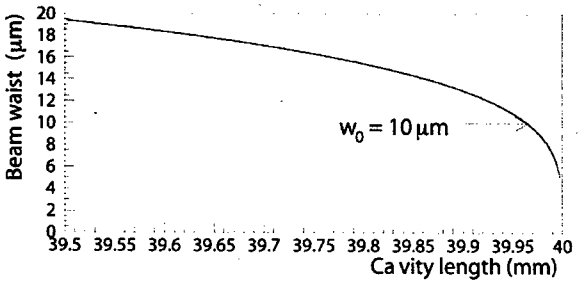

Figure 3: Laser spot size σ_0 as a function of D for spherical mirrors with radius D/2. The operating point for the ATF laserwire is indicated.

ATF Damping Ring Laserwire

The optical system used at ATF is quite different since it relies on a high gain, strongly focused resonant Fabry-Perot cavity. The cavity gain, x600, and requirement for a small waist (5um) determine the cavity design. Very high (99.9%) reflectivity spherical mirrors are used in an active, position feedback-controlled, mount to maintain high average power. The precision with which the cavity length (D) must be controlled is illustrated in figure 3 and 4, which shows the laser spot size at the waist minimum as a function of D.

The stiff flexure-based mirror mounts are shown in figure 5. The entire system is inside the ring vacuum system. A beam sleeve with two small holes for the optical resonator is used to control the ring vacuum chamber impedance.

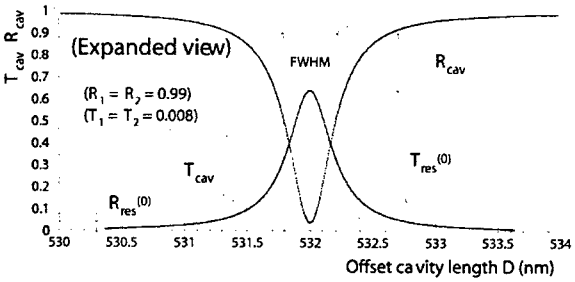

Figure 4: The Airy function for the ATF laserwire resonant cavity, showing the reflection and transmission of the cavity system.

Mechanical

It is well known that environmental contaminants, such as dust or organic residue, are often involved in the initiation of optical component damage. For this reason, high power lasers are often housed in expensive, cumbersome, clean rooms. This is more important for short wave lasers and is critical if high reliability for a large number of pulses is required.

The most fragile part of an optic is its surface. Two different types of anti-reflective (AR) coatings were considered, a conventional narrow-band multi-layer sputtered dielectric and a 'Sol-gel' wide-band (AR) coating. Sol-gel is an active getter for organic vapors and must be protected from them in a clean ultra-high vacuum quality environment.

For all laserwires, bringing diffraction limited d high quality wavefronts into the vacuum enclosure requires innovative engineering. The surface figure required for the SLC/SLD vacuum chamber windows ($\lambda/10$) forced a repolishing and coating of the windows after the attachment of the vacuum system weld eyelet.

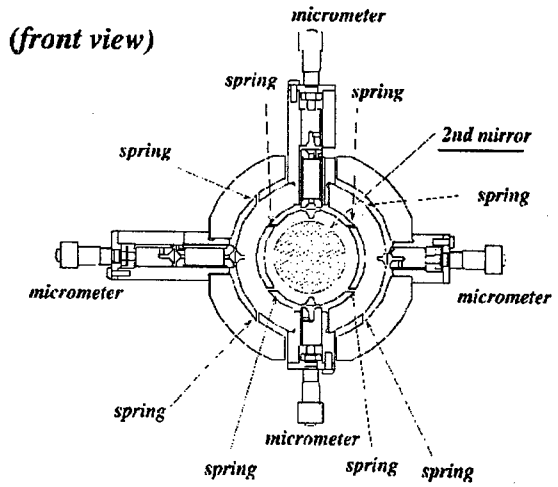

Figure 5: Intra-cavity view, facing one of the two spherical mirrors, of the Fabry-Perot resonator installed in the ATF damping ring. The electron beam passes from right to left and the opposing mirror, through which the light is injected, is mounted on a feedback-controlled drumhead flexure. The springs noted in the figure denote flexure couplings.

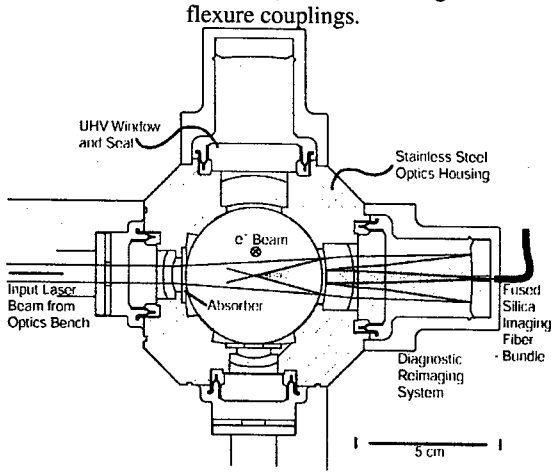

Figure 6: SLC/SLD Laserwire interaction point [17]. The laser beam enters from the right of the figure.

Data Acquisition

In high repetition rate environments, such as the ATF storage ring, counting rate based acquisition systems are possible. At ATF, where the average number of gamma-rays per bunch crossing is much less than one, single photon techniques allow precision timing so that multi-bunch profiles can be quickly collected. In the ATF storage ring, where the beam repetition rate is 2.2MHz, an average number of 200 revolutions occurs between counts. However, since the probability of multiple events in a single crossing is very small, it is possible to set an energy threshold. Since energy and emission angle are correlated in the 2-body Compton process, this is a very powerful way to control backgrounds.

OPERATION

For pulsed laser operation, a three-parameter (time, x and y) search must be done in order to begin scanning. This is in sharp contrast to the effort required to 'find' the carbon or tungsten wire. Several diagnostics are required in order to aid scanning set up. At SLC, a pair of matched length cables carried a signal from a monitor diode and a capacitive pickup (figure 7) to a sampling scope for monitoring. Once the residual 0.3 ns offset was found, this provided an important timing reference (the SLC laser pulse length σ_t=0.1ns and the beam bunch length σ_z=3ps).

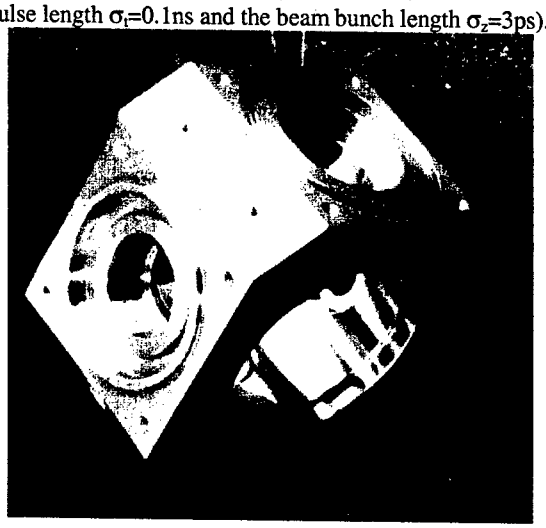

Figure 7: SLC/SLD Laserwire IP vacuum chamber. There are 8 faces that house 5 ports (input for vertical and horizontal, output for monitoring horizontal and a timing capacitive pickup (barely visible in the lower left of the figure).

The search procedure for starting laser collisions, once the timing is set correctly, uses the asymmetry of the focused laser waist. Given enough power, the collision signal can be measured far from the waist (in SLC ~ 0.5mm), along laser the direction. Once that dimension has been determined, only one parameter remains to be found and this is readily done using a laser 'waist' scan. After collisions have been established, a laser imager diagnostic can be used to prove that the laser is in the same position as it was for earlier measurements. This diagnostic is shown in figure 7.

RESULTS

Laserwire systems have proven very important for the studies at two linear collider test facilities, FFTB and ATF. At SLC/SLD, the laser scanner was more of a demonstration than a tool for machine operation. It was used to prove that the single beam sizes were as anticipated by the use of the beam-beam deflection scan. The scanner was commissioned relatively late in the life of the linear collider. Figure 8 shows a sample vertical

scan. Since the laser beam size is estimated to be σ_l =400 nm, we infer that the beam size σ_y=1.0um.

At the ATF, the laserwire has undergone several tests for systematic errors, including steering, detector acceptance and laser beam size tests. When compared with the other monitors developed for the low emittance beam, the laserwire seems the most accurate and repeatable and has proven a vital tool for understanding the ring.

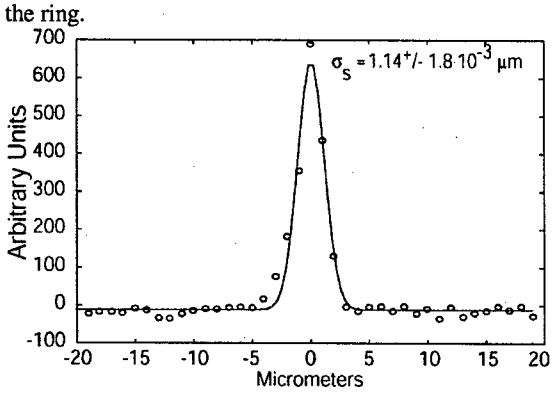

Figure 8: Sample scan from the SLC/SLD laserwire. The laser beam size and particle beam size, combined in quadrature, σ_s=1.14um.

DEVELOPMENT PROGRAMS

One of the most serious challenges facing laserwire developers is to control the cost and complexity of the installation. Both the CW laserwire, with complex feedback and the pulsed laserwire with synchronization and amplification stages, often require specialists to facilitate operation.

Laser technology, however, is quite advanced and a number of attractive features can be included in a lasewire design: 1) matching of the laser time structure with that of the beam, 2) 'fast scanning' of a multi-bunch beam such that a profile is developed in a single pulse, 3) scanning in time as well as position, 4) varying the laser pulse amplitude during the scan in a manner correlated with the expected signal in order to extend the dynamic range and make the process less invasive, 5) measuring bunch length using a mixture of two laser signals with almost the same wavelength and 6) adaptation of the interferometer or '01' mode.

REFERENCES

[1] V.A.Alexandrov *et al.*, "Results of Final Focus Test Beam," *16th IEEE Particle Accelerator Conference (PAC 95) and International Conference on High Energy Accelerators.*

[2] K. Kubo *et al.* [ATF Collaboration], "Extremely low vertical emittance beam in accelerator test facility at KEK," Phys. Rev. Lett. **88**, 194801 (2002)

[3] R. L. Kustom, "An overview of the Spallation Neutron Source project," *Proc. of the 20th Intl. Linac Conference LINAC 2000* TU101 (2000)

[4] C. Field, "The Wire scanner system of the final focus test beam," Nucl. Instrum. Meth. A **360**, 467 (1995)

[5] K. Abe *et al.* [SLAC Hybrid Facility Photon Collaboration], "Charm Photoproduction At 20-Gev", Phys. Rev. D **30**, 1 (1984).

[6] D. Neyret *et al.*, "A photon calorimeter using lead tungstate crystals for the CEBAF Hall A Compton polarimeter", Nucl. Instrum. Meth. A **443**, 231 (2000)

[7] R. Alley *et al.*, "A Laser-Based Beam Profile Monitor For The Slc/Sld Interaction Region", Nucl. Instrum. Meth. A **379**, 363 (1996) and M. C. Ross *et al.*, "A High Performance Spot Size Monitor" http://linac96.web.cern.ch/Linac96/Proceedings/Tuesday/TU206/Paper.html

[8] H. Sakai *et al.* "Measurement of a small vertical emittance with a laser wire beam profile monitor," Phys. Rev. ST Accel. Beams **5**, 122801 (2002).

[9] H. Sakai, *et al.*, "Performance Studies of a Laser Wire Beam Profile Monitor", Jpn. J. Appl. Phys., **41**, 6398-6408 (2002).

[10] G. A. Blair *et al.*, "R&D towards a laser based beam size monitor for the future linear collider," *8th European Particle Accelerator Conference (EPAC 2002)* and http://icfa-nanobeam.web.cern.ch/icfa-nanobeam/slides/kamps_LaserWirePetra.pdf

[11] J. Bosser *et al.*, "Laser wire scanner development on CTF II," *21st International Linac Conference (LINAC 2002.*

[12] S. Assadi et al., "The SNS Laser Profile Monitor Design and Implementation", these proceedings (WPPG054).

[13] T.Shintake, "Proposal of Nanometer beam size monitor for e+ e- linear colliders," Nucl. Instrum. Meth. A **311**, 453 (1992). and T. Shintake *et al.*, "Experiments of nanometer spot size monitor at FFTB using laser interferometry," 1995 *Particle Accelerator Conference and International Conference on High-Energy Accelerators, May 1 - 5, 1995,Dallas, Texas, U.S.A.*

[14] Boulder Damage Symposium / Annual Symposium on Optical Materials for High Power Lasers, SPIE/NIST.

[15] Koechner, W *Solid-state laser engineering*, 3rd edition, Springer Verlag, 1992.

[16] T. Kotseroglou *et al.*, "A laser heterodyne bunch length monitor for the SLC Interaction Point", *17th IEEE Particle Accelerator Conference (PAC 97): Accelerator Science, Technology and Applications*

[17] Bouwers, A., *Achievements in Optics*, New York, Elsevier, 1946; and Matsukov, D.D., J. Opt. Soc. Am., **34**, 270-284 (1944).

ELECTRON CLOUD DIAGNOSTICS IN USE AT THE LOS ALAMOS PSR *

R.J. Macek#, A. Browman, M. Borden, D. Fitzgerald, T.S. Wang, T. Zaugg, LANL, Los Alamos, NM 87545, USA
K. Harkay, R. Rosenberg, ANL, Argonne, IL, 60439, USA

Abstract

A variety of electron cloud diagnostics have been deployed at the Los Alamos Proton Storage Ring (PSR) to detect, measure, and characterize the electron cloud generated in this high intensity, long bunch accumulator ring. These include a version of the ANL-developed retarding field analyzers (RFA) augmented with LANL-developed electronics, a variant of the RFA denoted as the electron sweeping diagnostic (ESD), biased collection plates, and gas pulse measuring devices. The designs and experience with the performance and applicability to PSR are discussed.

INTRODUCTION

To thoroughly understand the electron cloud (EC) at PSR we seek as much information as possible on the sources of electrons, their relative strengths, the electron phase space density distribution as a function of time, and the interactions of the cloud with the proton beam and the accelerator hardware. In practice much less information is attainable. Historically, the first information on the electron cloud at PSR came in the early 1990's from various biased electrodes in the ring. The results were rather confusing and not understood but they did provide evidence of a large number of electrons at high beam intensities and even more electrons associated with unstable beam. A big step forward was the introduction in 1999 of the RFA augmented with fast electronics which showed clear evidence of many electrons striking the wall at the end of each beam bunch passage. The data including the energy spectra were consistent with trailing edge multipactor as a main contributor to the signal. In 2001 we implemented the electron sweeping diagnostic, a variant of the RFA, to measure the cold electrons remaining in the pipe during the beam-free gap between bunch passages.

RETARDING FIELD ANALYZER

The planar RFA, developed at ANL for application to the APS, is described in more detail in the literature [1]. This simple device, which measures the electrons striking the beam chamber wall, consists of two grids and a graphite-coated collector in a housing which is mounted on the beam pipe wall. Electrons enter the device through small slots (total area ~ 1cm^2) in the beam pipe and pass through a grounded grid, through a repeller grid that can be biased for electron energy selection, and finally reach the collector which is biased positive (+45 V) to insure electron collection and to suppress secondary emission.

Fast electronics [2] connected to the collector are used to obtain information on the time structure of the electrons. A block diagram of the present version of the electronics is shown in Figure 1. The chassis is placed about 1 meter below the beam line to reduce radiation damage to solid state components. The collector signal is connected to the electronics input by 1.2 m of 93 Ω cable. It has provision for gain changing attenuators (1, 0.1, and 0.01) and over-voltage clamps to protect sensitive components. The output amplifier drives a 50 Ω cable to a digital oscilloscope for data collection.

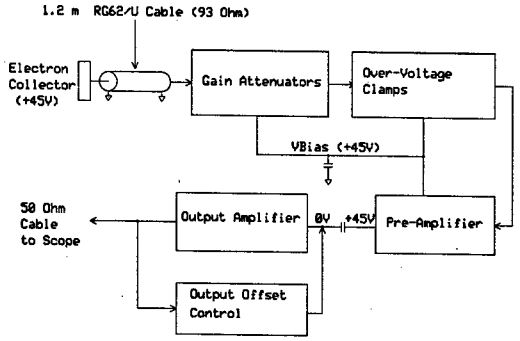

Figure 1. RFA Electronics Block Diagram.

Representative samples of the signals for various values of the repeller voltage are plotted in Figure 2 in time reference to the beam signal (wall current monitor). The data shown are for an earlier version with a transimpedance of 3.5 kΩ. Multiply the signal amplitude by 250 to convert to current density (μA/cm^2) striking the wall.

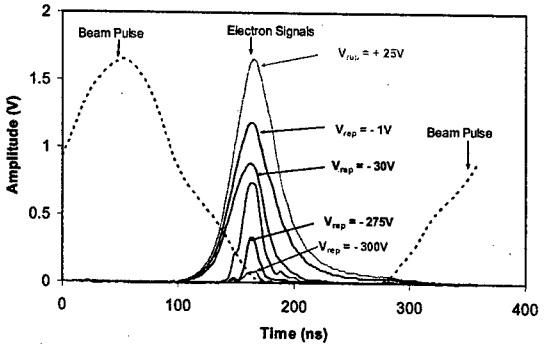

Figure 2. RFA signals in time reference to the circulating beam pulse. Data collected in section 4 of the ring for ~8 μC/pulse beam 7/2000.

* Work conducted at the Los Alamos National Laboratory, operated by the University of California for the U.S. Department of Energy under Contract No. W-7405-ENG-36.
#macek@lanl.gov

ELECTRON SWEEPING DIAGNOSTIC

The low energy electrons remaining at the end of the beam-free gap between bunch passages are of special interest since these will be captured by the next bunch passage and contribute most heavily to the average neutralization of the beam. They oscillate against the beam for the duration of the bunch passage and are therefore the ones most likely to drive the two-stream instability. To measure the low energy electrons lingering in the pipe we developed the electron sweeping diagnostic (ESD) [3]. It consists of a curved electrode ~40 cm long subtending a half-angle, α, of 75° placed opposite a large-aperture RFA (~10 cm^2) as shown in Figure 3.

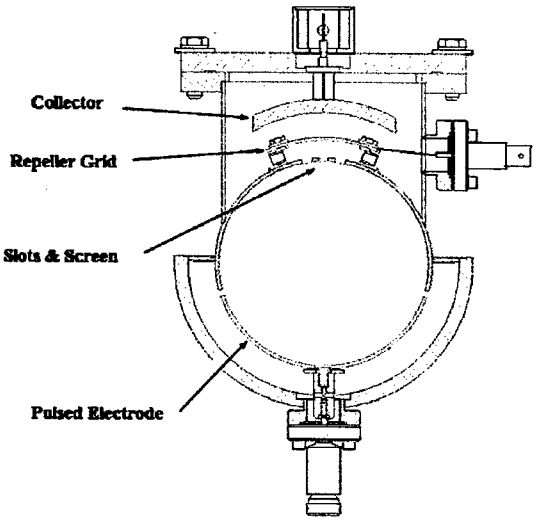

Figure 3. Cross-section of the electron sweeping diagnostic.

A short, fast (~15-20 ns rise time) pulse of ~-500V amplitude (can be up to ~ 1kV) applied to the electrode sweeps electrons into the RFA and thus selects the sampling time in the gap. The curved electrode is terminated with a suitable network of diodes (Phillips BYC8-600) and resistors to prevent charging the electrode by the beam yet allow application of the fast negative pulse. Calculations [4] of the various electron trajectories have been made to map out the detector acceptance assuming zero initial electron energy. The resulting acceptance region is shown in Figure 4 and corresponds to ~30% of the cross-sectional area of the beam chamber.

A sample of the data collected by the ESD is shown in Figure 5 for a 7.7 μC beam pulse. A typical prompt electron signal is seen at the end of the beam bunch since the ESD functions as large area RFA until the HV pulse is applied to the sweeping electrode. The "swept" electron signal at the end of the gap has a very fast rise time (~5ns) and a narrow width (~10 ns) as expected from design calculations but with a longer tail that is not completely understood. The ESD has also been used to measure the electron survival after the last bunch passage in the ring (after single turn extraction) with the interesting result that these electrons can linger for ~1 μs with an exponential decay time of ~ 170 ns [5].

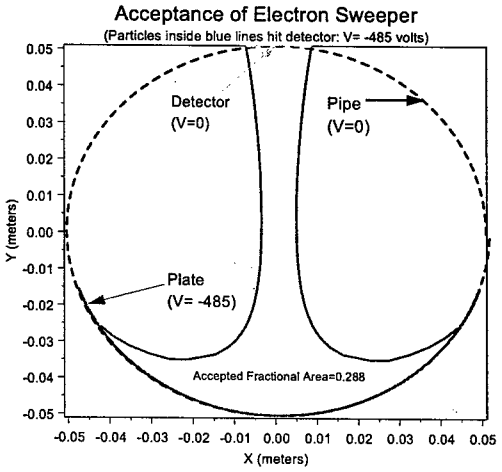

Figure 4. Acceptance region for the ESD. Low energy electrons inside the "trumpet" shaped region will strike the slotted area of the RFA.

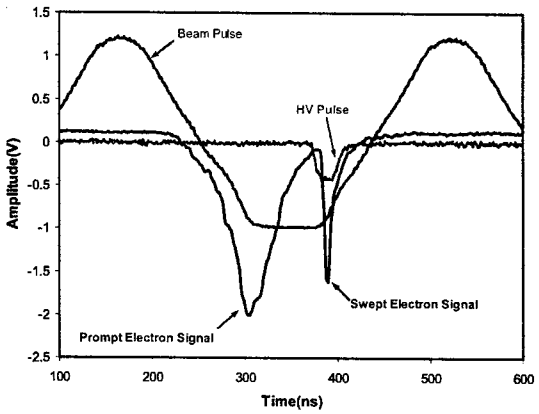

Figure 5. Representative signal from the ESD in time relation to the beam pulse and the -500V pulse applied to the sweeping electrode.

BIASED COLLECTION ELECTRODES

In our first efforts to measure electrons, we tried a variety of biased collection electrodes including parallel and curved plates, BPM striplines, split cylinders and the like in drift regions and in quadrupoles and finally using thin striplines in a ring dipole. Because of the large induced AC signals (100-200 V) from coupling to the beam it was necessary to heavily filter the signal with the result that the time resolution within a turn was lost.

Many puzzling features emerged during their use at moderate to higher intensities such as rather unusual bias curves that were difficult to understand and interpret. An example is shown in Figure 6 for biased strips (2.5 cm wide and ~ 20 cm along the beam axis) in a ring dipole (1.2 T field). The strips in the vertical (top and bottom) were connected together and separately the horizontal

strips (right and left) were connected together. For a given curve one pair was biased and the other grounded. The curves are labeled for the pair that was biased. The most puzzling feature is the fact that for positive bias both horizontal and vertical strips give nearly the same result. The electrons are constrained to follow the magnetic fields lines in the vertical (modified slightly by **ExB** drift) and it is a real mystery how the horizontal signal can be comparable to the vertical.

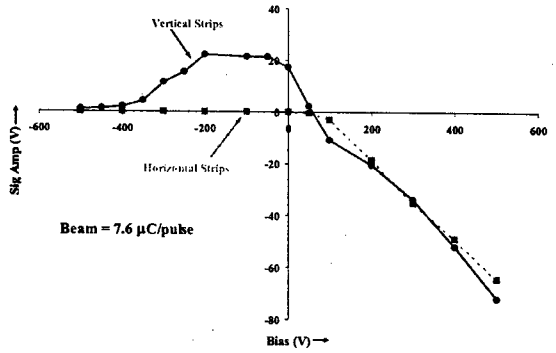

Figure 6. Signal amplitude from pairs of biased strips plotted as a function of applied bias voltage.

The biased electrode is a difficult situation to interpret. Its signal relates to the net charge or current collected i.e., electrons striking the electrode minus those leaving (e.g. secondary emission) rather than just the flux striking the wall as with the RFA. The degree of cancellation depends on a number of factors. During passage of the gap the bias field dominates electron motion and can collect electrons or sweep them to the wall depending on polarity. However, the space charge field of the beam dominates during much of the bunch passage. On the leading edge this pulls electrons into the beam away from the electrodes. On the trailing edge beam-induced multipacting can occur especially for electrons born near the wall. These effects tend to cancel one another and the average over a resolving time of tens of turns is sensitive to the degree of cancellation. In addition, the electrodes and the bias fields change the beam-wall environment and can significantly alter the multipacting process. Clearly the RFA and the ESD are more understandable devices.

ION PUMP GAS PULSE

Historically, a vacuum pressure rise was one of the first indications of the beam induced multipactor. A high flux of electrons on the wall desorbs gases which causes the pressure increase. In a machine, such as PSR, where the beam is accumulated for ~ 1ms then is off for 50 ms or more the average pressure increase is not so noticeable. However, for high peak intensity we can observe a pulse of the ion pump current that correlates well with the prompt electron signals in PSR. The diagnostic is very simple. We use a HV probe (1000:1 attenuation) to look at the voltage developed across a 100 kΩ resistor (in series with the pump) during beam accumulation. A sample signal is shown in Figure 7. The rise time of ~1 ms is consistent with the spread in velocity for light gases (H_2O, N_2) desorbed at room temperature at a location 30-40 cm from the active elements of the ion pump. The ion pump pulse tracks the RFA signal as it varies with beam intensity and as the EC diminishes over time from beam scrubbing.

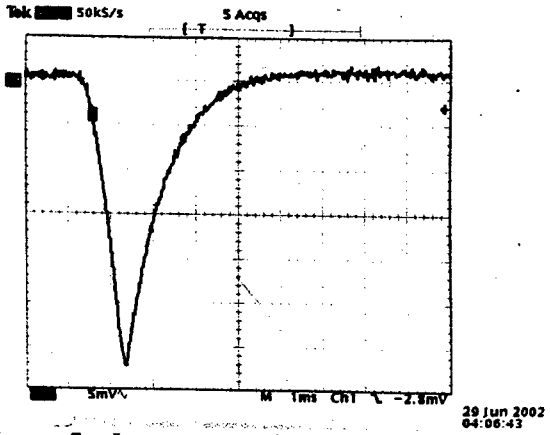

Figure 7. Ion pump pulse obtained during the accumulation and extraction of an 8 μC beam pulse.

SUMMARY AND CONCLUSIONS

Of the various EC diagnostics used at PSR, the RFA and ESD have provided the most detailed and valuable information. Furthermore, they have the advantage of not perturbing the EC or the processes of its formation. Biased electrodes do perturb the beam-wall environment, are complicated to interpret, and produce a number of puzzling features that are not understood. However, they have provided the only information we have for the EC in magnets. The ion pump pulse is a simple diagnostic to implement and, since there are many spread around the ring, they provide a more global sampling of the EC throughout the ring.

REFERENCES

[1] R.A. Rosenberg and K.C. Harkay, Nucl. Instrum. Methods **A453**, 507(2000).

[2] A. Browman, memo report on electronics design to R. Macek, 10/22/2001 (macek79). Available at http://lansce2-serv.atdiv.lanl.gov/browman/CY2001/.

[3] A. Browman, memo report on ESD design to R. Macek, 3/23/2001 (macek69 LANSCE-2 website).

[4] A. Browman ibid., also T. S. Wang etal, "the Static Electric Field of a Curved Electrode in a Beam Pipe," PSR Technical Note 01-003 (May 2001), Available at http://lansce2-serv.atdiv.lanl.gov/technotes/.

[5] R. Macek, ECLOUD'02 Proceedings, CERN-2002-001, 259(2002).

[6] M. Plum etal, PSR Technical Note 94-003, Available at http://lansce2-serv.atdiv.lanl.gov/technotes/.

LONGITUDINAL SPACE-CHARGE EFFECTS IN A RETARDING FIELD ENERGY ANALYZER

Y. Zou*, Y. Cui, I. Haber, M. Reiser and P.G. O'Shea, Institute for Research in Electronics and Applied Physics, University of Maryland, College Park, MD 20742, USA

Abstract

Experimental and theoretical work has been carried out to study the longitudinal space-charge effects in a retarding field energy analyzer. A one-dimensional model for both a mono-energetic beam and a thermal beam has been developed for this purpose. The study shows that, if the current density inside the device were higher than a critical value, the longitudinal space-charge effects would distort the measured energy spectrum. The measured mean energy will be shifted toward the low-energy side and the resulting spectrum will have a tail at the high-energy side. The measured FWHM and rms energy spread may also be affected.

INTRODUCTION

In order to characterize the energy spread in UMER [1], a retarding field energy analyzer has been developed and tested. The design and testing results of the device have been reported elsewhere [2, 3]. During the experiment, it was found that, when the current density in the analyzer is higher than a certain value, the measured energy spectrum is shifted towards the low-energy side compared to the one measured with low injected current. Fig. 1 depicts such a case, where Curve I is for a low-current case and Curve II is for a high-current case. At the same time, the energy spectrum measured with high current density has a tail at high-energy side. This is believed to be due to the longitudinal space-charge force in the device. The mean energy shift due to the space-charge effect was observed before in studies of the energy spread in a beam from an ion source, for example see Refs. [4, 5]. Ref. [6] gave an approximate analytical solution to explain the space-charge effect in the ion source, the result of which is similar to the Langmuir-Child equation. In this paper, we will, via analytical analysis and simulations, present new results for the longitudinal space-charge effect in this kind of devices.

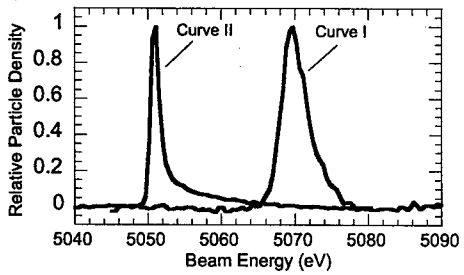

Fig. 1. Experimental result of energy spectrum. Injected current for Curve I is 0.2 mA, for Curve II is 2.2 mA.

*Email: yunzou@glue.umd.edu

FIELD SOLUTIONS FOR A MONO-ENERGETIC BEAM

The potential distribution in such a system is described by a one-dimensional Poisson equation:

$$\frac{d^2V}{dz^2}=-\frac{\rho}{\varepsilon_0}=-\frac{J}{\varepsilon_0\sqrt{\frac{2q(V+V_0)}{m}}}=CJ(V+V_0)^{-1/2} \tag{1}$$

Here, C is a constant defined as $C=-1/\left(\varepsilon_0(2q/m)^{1/2}\right)$. J is the current density and ε_0 is free space permittivity. V is the potential relative to the lab ground and V_0 is the voltage equivalent of the injected beam energy. The general solutions to this differential equation can be solved under three different regimes. The first regime is that V_r is a small negative voltage relative to the lab ground, in which case the potential distribution has a minimum with magnitude smaller than V_0. In the second regime, V_r is moderately large such that the potential decreases monotonically from ground to V_r. The third regime is that V_r is large enough such that the magnitude of the potential minimum is equal to V_0. This is equivalent to the virtual cathode formation in the electron gun and the beam particles start to be reflected back by this potential bump [7].

The solution to the first regime is given by

$$-\frac{3c_1}{4}(z-X_m)= \left((V(z)+V_0)^{1/2}+c_2\right)^{3/2}-3c_2\left((V(z)+V_0)^{1/2}+c_2\right)^{1/2} \tag{2}$$

for $0<z<X_m$, and

$$\frac{3c_1}{4}(z-X_m)= \left((V(z)+V_0)^{1/2}+c_2\right)^{3/2}-3c_2\left((V(z)+V_0)^{1/2}+c_2\right)^{1/2} \tag{3}$$

for $X_m<z<d_r$.

Here $c_1=\sqrt{4CJ_0}$, where J_0 is the injected current density. X_m is the location of the potential minimum; c_2 is an unknown constant. d_r is the total length of the device. X_m and c_2 are determined by the boundary condition:

$$\begin{cases}V(z)=0, & z=0\\ V(z)=V_r, & z=d_r\end{cases} \tag{4}$$

In the second regime, the potential decreases monotonically from zero to V_r and the solution is given by:

0-7803-7738-9/03/$17.00 © 2003 IEEE

$$-\frac{3c_1}{4}z = \left[\left((V(z)+V_0)^{1/2}+c_2\right)^{3/2}-\left((V(0)+V_0)^{1/2}+c_2\right)^{3/2}\right] - 3c_2\left[\left((V(z)+V_0)^{1/2}+c_2\right)^{1/2}-\left((V(0)+V_0)^{1/2}+c_2\right)^{1/2}\right], \quad (5)$$

where c_1 is the same constant as in the first regime and c_2 is an unknown constant determined by the boundary conditions.

In the third regime, the virtual cathode forms. The potential distribution is given by

$$V(z)+V_0 = \left(\frac{3}{4}\right)^{4/3}(4CJ_1)^{2/3}(X_m-z)^{4/3} \qquad 0<z<X_m \quad (6)$$

and

$$V(z)+V_0 = \left(\frac{3}{4}\right)^{4/3}(4CJ_2)^{2/3}(z-X_m)^{4/3} \qquad X_m<z<d_r \quad (7)$$

Here J_1 and J_2 are given by

$$J_1=(2-p)J_0 \quad 0<z<X_m \qquad J_2=pJ_0 \quad X_m<z<d_r \quad (8)$$

In Eqs.(6) and (7), the unknown constants are X_m and p, which are determined by the boundary conditions. The formation of the virtual cathode only happens when the beam current density inside the energy analyzer is larger than a limiting current. The magnitude of the limiting current is given by

$$J_{\lim}=\left(\frac{3}{4}\right)^2\frac{1}{4Cd_r^2}V_0^{3/2}, \quad (9)$$

which has the same format as Child's law. For convenience, we introduce a concept of normalized current density $\lambda=J_0/J_{lim}$, the ratio of the injected beam current density to the limiting current density J_{lim}. Fig. 2 shows the energy analyzer response to a monoenergetic beam with beam energy of 5 keV and normalized input current density of 0.8 and 1.4 respectively. For λ=0.8, the spectrum reveals the real beam spectrum, while for higher current, λ=1.4, the energy spectrum is shifted towards the low-energy side due to the space charge.

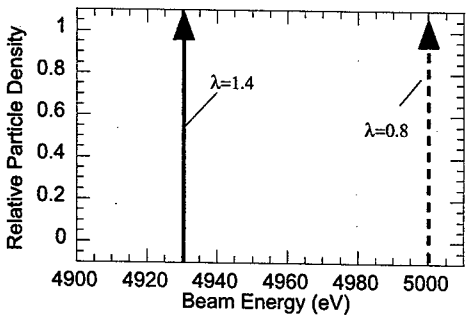

Fig. 2. Spectrum at different current densities.

FIELD SOLUTIONS FOR A THERMAL BEAM

At the entrance of the energy analyzer, the thermal beam has the following initial phase-space distribution

$$f_i(z=0,v_i)=f_0\exp\left(-\alpha^2(v_i-v_0)^2\right), \quad (10)$$

where $\alpha=\sqrt{m/(2k_BT_i)}$ is related to the beam energy spread. v_0 is the mean beam velocity. f_0 is the normalization factor. After particles enter the energy analyzer, the distribution becomes:

$$f_z(v_z)=f_0\exp\left(-\alpha^2\left(\sqrt{v_z^2-2\eta V(z)}-v_0\right)^2\right). \quad (11)$$

The Poisson equation for the system is written as:

$$V_1''(z)=-\frac{q}{\varepsilon_0}\left(\int_0^\infty f_z(v_z)dv_z+\int_0^{\sqrt{2\eta(V(z)-V_m)}}f_z(v_z)dv_z\right) \quad (12)$$

for $0<z<X_m$, and

$$V_2''(z)=-\frac{q}{\varepsilon_0}\int_{\sqrt{2\eta(V(z)-V_m)}}^\infty f_z(v_z)dv_z \quad (13)$$

for $X_m<z<d_r$.

Here, V_m is the magnitude of the potential minimum. In Eq. (12), the contribution of particle density comes from both forward particles and backward particles reflected back from the potential minimum at X_m. In Eq.(13), there are only forward particles.

Eqs. (12) and (13) can be numerically solved with appropriate boundary conditions. One example of the simulation results is shown in Fig. 3, where the input beam has mean energy of 5.070 keV and rms energy spread of 2.2 eV. The normalized current density λ is 0.062 and 1.2 respectively. Fig. 3(a) depicts the potential distribution for retarding voltage Vr= -5070 V. For small current (λ=0.062), The potential monotonically decreases from ground to V_r. For large space charge (λ=1.2), the potential distribution has a potential minimum, which is about 7 V below the retarding voltage. Fig. 3(b) shows the calculated spectrum for λ=0.062 and λ=1.2 respectively. At small current density, the device can reveal true beam spectrum, which has the rms energy spread of 2.2 eV. At high current density case, the spectrum is shifted towards the low energy side by 20 eV and becomes a delta function with zero energy width. In this case, the information of the rms energy spread and FWHM is totally lost. This is due to the abrupt formation of the potential minimum in the one-dimensional theory. In the real device, the potential at the beam edge will not be depressed as deeply as predicted by the one-dimensional theory. To illustrate this two-dimensional consideration without putting the effort to have a full 2D simulation, we build a simple model to have a 2D correction. At the center of the beam, we use the calculated value based on the 1D theory. At the edge of the beam, we set the value as $V=w*V_m+(1-w)*V_r$, which is the weighted average of the potential minimum, V_m and the retarding potential V_r.

In between, the potential increases quadratically from the center value to the edge value. This implies that we assume the particle density is uniform inside the beam. Fig. 3(c) depicts the result of this correction, which has a wider spectrum, and with a tail at the high-energy side. In this calculation, w is chosen as 0.685. This simple analysis shows the difference between the two-dimensional situation and the 1D theory. It indicates the necessity to have a full two-dimensional simulation. Another limitation of the theory is that this is a steady state solution. In reality, both magnitude and position of the potential minimum oscillate [8]. This will also make the energy spectrum wider than a delta function in the real situation.

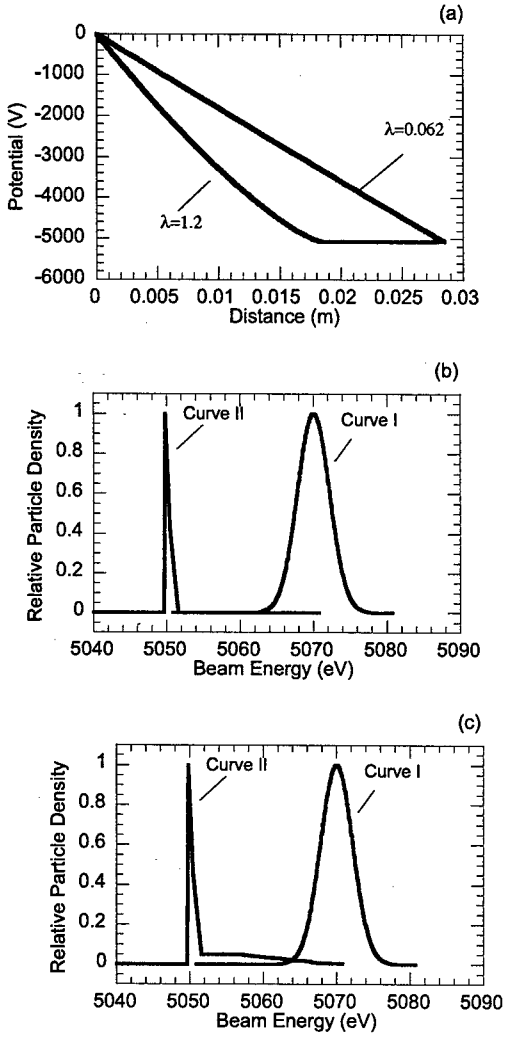

Fig. 3. (a) Potential distribution. (b) Energy spectrum. Curve I for λ=0.062, curve II for λ=1.2 (c) Energy spectrum with 2D correction. Curve I for λ=0.062, curve II for λ=1.2

CONCLUSION

The experimental and theoretical study shows that, if the current density inside the device is high enough, the space-charge effect could impact the performance of the energy analyzer. Specifically, the longitudinal space charge has three effects on the measurement. First, it will make the measured mean energy shifted toward the low-energy side. Second, it will cause a tail at the high-energy side. Third, it will affect the accuracy of FWHM and rms energy spread measurement. These effects are the artifacts of the device and we should avoid them in the experiment. According to the theory, if the normalized current density is below a critical value (λ=0.5), the longitudinal space-charge force does not affect the measurement any more. Therefore, we should keep the current density inside the device low for reducing the space-charge effect. The limitation of the theory lies in that this is a one-dimensional theory and we only solved the steady-state solution. A two-dimensional simulation with a PIC code is under way to study this problem in more detail.

ACKNOWLEDGEMENT

This research is supported by the U. S. Department of Energy.

REFERENCES

[1] P.G. O'Shea, M. Reiser, R.A. Kishek, S. Bernal, H. Li, M. Pruessner, V. Yun, Y. Cui, W. Zhang, Y. Zou, T. Godlove, D. Kehne, P. Haldemann, and I. Haber, "*The University of Maryland Electron Ring*", Nucl. Instr. and Meth. A **464**, 2001, p. 646-652.

[2] Y. Zou, Y. Cui, V. Yun, A. Valfells, R.A. Kishek, S. Bernal, I. Haber, M. Reiser, P.G. O'Shea, and J.G. Wang, "*Compact high-resolution retarding field energy analyzer for space-charge-dominated electron beams*", Phys. Rev. ST Accel. Beams **5**(7), 2002, p. 011502.

[3] Y. Cui, Y. Zou, I. Haber, R. Kishek, P.G. O'Shea, M. Reiser, and A. Valfells, "*Experimental Study of Beam Energy Spread in the Space-Charge Dominated Beams*", in *this proceeding*, 2003.

[4] T. Honzawa, T. Sekizawa, Y. Miyauchi, and T. Nagasawa, "*Effects of Space Charges in Gridded Energy Analyzer*", Jpn. J. Appl. Phys. **32**(12A), 1993, p. 5748.

[5] G. Donoso and P. Martin, "*Space-charge effects in a velocity analyzer of variable geometry*", Rev. Sci. Instrum. **61**(11), 1990, p. 3381.

[6] P. Martin and G. Donoso, "*A new Langmuir-Child equation including temperature effects*", Phys. Fluids B **1**(1), 1988, p. 247.

[7] Y. Zou, H. Li, M. Reiser and P.G. O'Shea, "*Theoretical Study of Transverse Emittance Growth in a Gridded Electron Gun*", submitted to NIM.

[8] I. Haber, private communication.

LONGITUDINAL EMITTANCE MEASUREMENTS IN THE FERMILAB RECYCLER RING *

C.M. Bhat and John P. Marriner
FNAL, Batavia, IL 60510, USA

Abstract

The Recycler Ring (RR) is a new 8GeV antiproton storage ring at Fermilab. Presently, this machine is being commissioned using protons from the Booster. It uses barrier buckets for stacking, un-stacking and storing the beam. At any given time, the RR is capable of storing proton or antiproton beams in multiple segments azimuthally. These segments of the beam may have widely differing longitudinal emittance and beam intensities and bunch lengths. It is highly essential to be able to measure the longitudinal emittance and keep track of the longitudinal dynamics at various stages of the operation of the RR. In this paper, we discuss a few methods of longitudinal emittance measurements in barrier buckets and discuss their merits and demerits.

INTRODUCTION

The Recycler Ring at Fermilab[1] is the world's largest antiproton storage ring built mainly using permanent magnets. For stacking the antiprotons in the RR, the beam will be transferred either from the Fermilab Accumulator Ring (cold beam) or from the Tevatron (un-used hot beam) via the Main Injector (MI). The hot and cold beams are stored in the RR in separate regions and cooled further. When beam is needed for the Tevatron collider operation, the cold beam from the RR will be extracted in the form of small bunches and transferred to the MI and accelerated to 150 GeV before injection into the Tevatron. All of these rf manipulations in RR are carried out using barrier buckets.

During the last year we had several antiproton stores in RR to understand the transverse and longitudinal dynamics, effectiveness of stochastic cooling system, beam life-time etc. We have also transferred the antiproton beam from the Recycler into the Main Injector and accelerated to 150 GeV.

The RR and the MI share the same underground tunnel. The MI acceleration cycles have significant effects on the longitudinal and transverse beam emittance of the stacked beam in the RR. After identification of this problem we have taken several measures to mitigate these effects and to minimize the emittance growth.

Over the past three years we have used different methods of emittance measurement to learn about the longitudinal dynamics at various stages of operation of the Recycler. In this paper, we review the methods used for longitudinal emittance measurements in barrier buckets and discuss their merits and demerits. We also illustrate the use of Monte Carlo methods to estimate the longitudinal emittance in case of a complex beam distribution.

* Work supported by the Universities Research Association, Inc., under contract DE-AC02-76CH03000 with the U.S. Department of Energy.

BARRIER BUCKETS AND LONGITUDINAL EMITTANCE

Use of rf barrier buckets is not new at the Fermilab accelerators. Sinusoidal rf barriers were invented[2] to be used in the antiproton Debuncher and Accumulator rings to produce longitudinal gaps in the stored beam.

A barrier bucket is characterized by barrier pulse shape V(t), pulse duration T_1 and gap between +ve and -ve pulses T_2. The general Hamiltonian for an arbitrary barrier rf bucket can be written as [3],

$$H = -\frac{\eta}{2\beta^2 E_o}(\Delta E)^2 - \frac{\int^{\tau} eV(\tau)d\tau}{T_0} \qquad (1)$$

where η is the slip-factor of the synchrotron, ΔE is energy deviation from synchronous energy E_0, T_0 is the revolution period of the charged particle, e is the electronic charge. The half bucket height is given by,

$$\Delta E_b = \sqrt{\frac{2\beta^2 E_0}{|\eta|}\frac{\left|\int_{T_2/2}^{T_2/2+T_1} eV(\tau)d\tau\right|}{T_0}} \qquad (2)$$

Here, we assume that the +ve and –ve pulses are symmetric about the center of the bucket. It is important to note that all physical quantities depend basically on $\int eV(\tau)d\tau$ not on the exact shape of the wave form if it had some symmetry about the bucket center.

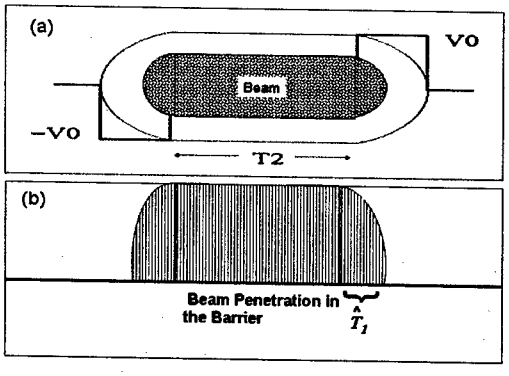

Figure 1: A schematic of RR beam phase-space distribution (a) in a rectangular barrier bucket and, (b) its projection along the time axis.

0-7803-7738-9/03/$17.00 © 2003 IEEE

The Recycler uses a wide-band (10kHz-100MHz) RF system capable of generating many barrier buckets of any shape[4] . The maximum height of a barrier pulse is set to about +/-2kV each. The width of a pulse can be varied. The pbar beam from the antiproton Accumulator will have 2.5 MHz rf structure and that from the Recycler to MI can have 2.5 MHz or 7.5 MHz rf structure. The rf system can also produce 2.5 MHz/7.5 MHz rf buckets in between barrier buckets. For a given peak rf voltage a wave form of rectangular shape gives maximum value of $\int V(\tau)d\tau$. Hence, we adopted a rectangular barrier bucket. The pulse width is selected to be ≈908 nsec.

A schematic view of RR barrier waveform with its bucket boundary (an equal Hamiltonian contour defining the bucket) and beam in it is shown in Figure 1. For the beam penetrating in the barrier the beam half height is given by

$$\Delta \hat{E}_b = \sqrt{\frac{2\beta^2 E_0}{|\eta|}\frac{eV_b \hat{T}_1}{T_0}} \qquad (3)$$

The longitudinal emittance ε_l is given by,

$$\varepsilon_l = 2T_2\Delta \hat{E} + \frac{8\pi|\eta|}{3\omega_o\beta^2 E_o eV_o}(\Delta \hat{E})^3 \qquad (4)$$

where $\omega_0=2\pi/T_0$ and β is ratio of velocity of the beam to velocity of the light. η = -0.0087, E_0=8.938GeV, T_0 = 11.12μsec for the Recycler.

TECHNIQUES FOR MEASUREMENT OF ε_l and ΔE

An accurate measurement of longitudinal emittance of particle beams in any synchrotron is not a trivial task. The knowledge of correct longitudinal emittance is key to the understanding the longitudinal beam dynamics. This in-turn helps to improve the proton-antiproton luminosity in the Tevatron. So far, we have used four different measurement techniques in the Recycler. They can be broadly classified into two categories: beam destructive techniques and non-destructive techniques. The destructive techniques are mainly one-time measurements. Their use in a storage ring like the Recycler is very limited. On the other hand, the non-destructive techniques are used as the major beam diagnostics in daily operations. Here, we describe both of these approaches for completeness.

Destructive Techniques

Two different methods of this type are illustrated here. The first method is based on matching the bucket area to bunch area. After the beam is captured in a barrier bucket the height of the rf pulse is adiabatically reduced while the width is held constant until the beam area fills the bucket. To determine the rf voltage, V_b, where the beam just fills the bucket a gated current integrator (GCI) [5] is used to measure the beam captured between the barriers. A schematic view of this method is shown in Figure 2 (left). Knowing the V_b and T_1 in equations 3 and 4, the beam energy spread and the beam area are measured. This technique was used in the early detection of the longitudinal emittance growth in the Recycler arising from the MI high energy cycles. Similar measurements can be made if we change the width of the barrier pulse keeping the pulse height constant. For barrier buckets with non-rectangular barrier pulses this method would be less useful.

The second method requires an ability to turn-off the barrier pulses much faster than the synchrotron period of the beam in the barrier bucket. Then the beam energy spread ΔE, the fractional change in orbiting time ΔT and total de-bunching time T are related according to

$$\frac{\Delta E}{E} = \frac{\beta^2}{\eta}\frac{\Delta T}{T} \qquad (5)$$

In the RR, the synchrotron oscillation period is about of 0.6 sec for a barrier bucket with T_2=1.6μsec and the beam rf voltage can be turned-off in <1msec. Figure 2 (right inset) illustrates an example of measuring ΔE by fast de-bunching method. The de-bunching time (from bottom to the top) and fractional increase in orbiting time is measured using digitized wall-current monitor data.

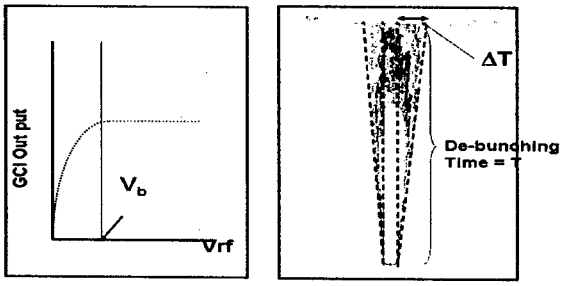

Figure 2: A schematic of the method which adopts varying rf voltage at a fixed pulse width in RR (left). Typical data from the fast de-bunching method in the RR (right).

Non-destructive Techniques

We are using two different methods of non-destructive type in the Recycler beam longitudinal emittance studies. The first of these is a variation on the traditional method of measuring the beam profile using a wall current monitor (WCM). A detailed account of use of WCM in longitudinal emittance measurement is given in ref.6. The second method is based on Schottky signal detection.

A. Resistive Wall Current Monitor

A WCM is a device which measures the image charge that flows along the vacuum chamber following the beam and hence reproduces the longitudinal profile of the beam.

We have a 4 GHz bandwidth pickup WCM[7] in the Recycler Ring. By knowing the exact location of the barrier pulse and their shapes one measures the beam penetration into the barrier pulse to measure the ΔE. For a beam confined in a rectangular barrier bucket the beam penetration is symmetric with respect to the center of the bunch. However, any asymmetry in the shape of the pulse or non-zero rf voltage in the gap between +ve and –ve barrier pulse (which might arise due to rf hardware or software systems) will result in an asymmetric beam penetration in the barrier. The WCM then measures different amounts of penetration in the barrier (later we illustrate an example of this type). The WCM data is very sensitive to small distortions in the barrier pulse. In particular, when the longitudinal emittance of the beam is small the WCM allows detection of distortion of the baseline between the barrier pulses.

The Recycler WCM signals are sent to a digitizing scope RDT720. The rf fan-out signals are also processed along with the WCM signals to measure the relative position of the barrier pulse in the ring. A special trigger module is developed to trigger the scope at different times of rf manipulation. Then the data is collected using a software program[8].

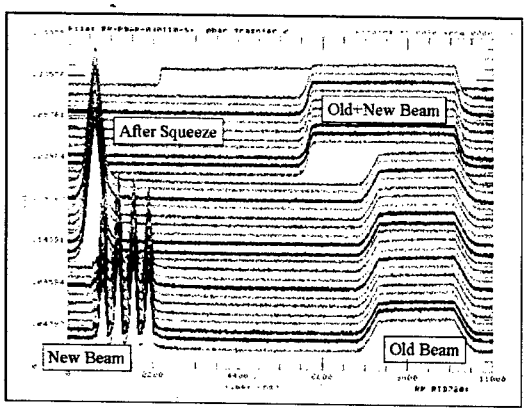

Figure 3: WCM data for antiproton stacking.

Figure 3 illustrates a case of pbar beam stacking in the Recycler. "New Beam" in this figure has 2.5MHz bunch structure. Knowing the bunch length and the peak rf voltage one can measure the longitudinal emittance of the beam at injection. Measuring the penetration of the beam into the barrier pulses and using equations (3) and (4) the longitudinal emittance of the beam in barrier buckets at various stages are estimated. The errors in the measured emittance mainly come from detector response, estimating the beam penetration into the barrier and the measured rf voltage.

B. Schottky Signals

Using Schottky signals for beam emittance measurements in a storage ring is an excellent method[9]. For a coasting beam, the energy spread ΔE and the frequency spread of the Schottky spectrum Δf are related according to

$$\frac{\Delta E}{E} = \frac{\beta^2}{\eta}\frac{\Delta f}{f} \tag{6}$$

where $f = nf_0$, f_0 is the revolution frequency of the synchronous particles and n is the harmonic number. Measuring the maximum energy spread using a Schottky detector resonating at a reasonable harmonic number (n~100) and a spectrum analyzer is straight forward.

In case of a sinusoidal bunched beam, the beam particles execute synchrotron oscillations. The time of passage of a particle in front of the detector is modulated according to synchrotron oscillation amplitude. Thus, the time coordinate $t \rightarrow t + \tau\sin(\Omega t + \phi)$ as compared to a coasting beam. The quantities τ, Ω, and ϕ are synchrotron amplitude, frequency and phase, respectively. Then the beam current for a single particle in frequency domain will take the form

$$i(t) = ef_0 + 2ef_0\sum_{n=1}^{\infty}\sum_{k=-\infty}^{k=\infty} J_k(n\omega_0\tau)\cos[(n\omega_0 + k\Omega)t + k\phi] \tag{7}$$

where J_k is the Bessel function of order k. Hence, in the case of bunched beam with some energy spread, each revolution frequency band at frequency nf_0 (as seen in the coasting beam) is replaced by a central line with an infinite number of satellites. Further, the satellites of order k with different values of n are correlated which gives rise to coherence. This feature of the bunched beam Schottky spectrum makes it more complicated to interpret for longitudinal emittance measurements. Fortunately, for sufficiently large n,(at high frequency), the equation (6) is an excellent approximation for all types of beams.

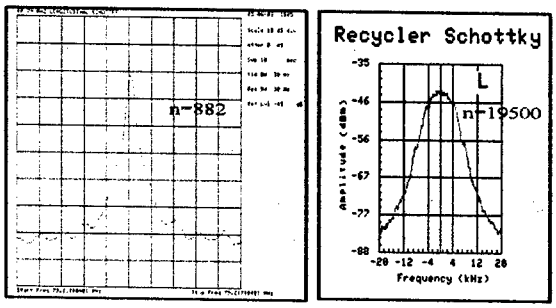

Figure 4: Typical Schottky spectra taken with two detectors. Left (n=882) and right (n=19500).

The beam bunched in barrier buckets can be described in terms of a sum over harmonics of the synchrotron frequency, but the synchrotron frequency spread is so big that the signal from a beam bunched in barrier is very similar to a truly coasting beam.

At the Recycler, we have used three Schottky detectors with frequencies 79MHz, 1.5GHz and 1.75GHz. They have n = 882, 16700, 19500, respectively. In Figure 4, we illustrate a typical longitudinal Schottky spectrum from two detectors with widely different harmonic

numbers. The data are taken for the same beam in a barrier bucket. The data shown on left are obtained with 79MHz Schottky detector and show in addition to the Schottky signal a prominent coherent peak at revolution harmonic. Hence, unambiguous determination of ΔE is difficult. The figure on the right hand side shows data with the 1.75GHz Schottky detector and does not show coherent peak. We find that the maximum energy spread is about 5.6MeV for the case illustrated here.

It is important to note that the measured ΔE using Schottky spectrum is independent of rf voltage wave form if spectrum does not show any coherent peak. However, the Schottky technique does not distinguish between captured beam or an un-captured beam. It can be gated to measure different parts of the beam.

C. Comparison between WCM and Schottky Methods

We have carried out a number of experiments to measure longitudinal emittance of the beam in Recycler Ring using Schottky signals and by using WCM. Here we illustrate two examples from these measurements

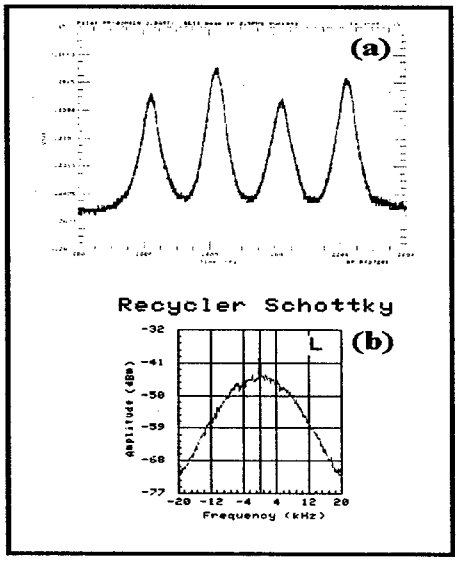

Figure 5: (a) WCM data for bunched beam in the Recycler, (b) 1.75GHz Schottky spectrum for the same beam.

Fig. 5 shows data from WCM and 1.75GHz Schottky detector for beam in four 2.5MHz buckets. The 2.5MHz rf voltage was about 2kV and average bunch length (90% by area) is about 260 nsec. We find that the measured emittance for assumed elliptical distribution to be 20eVs and $2\Delta E \approx 12$MeV (<20%). For the same beam the Schottky spectrum gives about $2\Delta E \approx 9$ MeV.

Data taken for the beam in a typical barrier bucket are shown in Figure 6. In this case T_2 =1.6 μsec. The measured $\varepsilon_l \approx 14$eVs and $\Delta E \approx 8$MeV from the WCM measurements can be compared to $\varepsilon_l \approx 9$eVs and $\Delta E \approx 5.6$MeV from Schottky measurements.

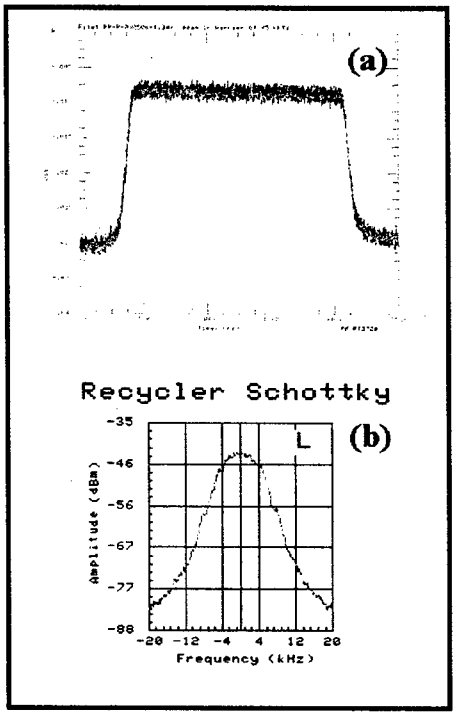

Figure 6: (a) WCM data for the beam in a rectangular barrier bucket, (b) 1.75GHz Schottky spectrum for the same beam. T_1=908nsec, T_2=1.6msec and V_0=2kV.

D. Some Special Cases

The perfect rectangular barrier pulse discussed above is not reality in the Recycler. Typically, a rectangular barrier pulse in the Recycler will be have rounded edges. In between barrier pulses there may be a small slope of a few percent of the total pulse amplitude. Besides, as one adds a number of barrier pulses around the accelerator ring the adjacent barrier pulses are found to be distorted at a few percent level. This phenomenon makes the measurement of longitudinal emittance more difficult.

Figure 7 illustrates a case with non-symmetric Vrf between barrier pulses. Figure 7(a) shows a WCM data for cooled pbar beam. We have made an attempt to simulate the WCM data using a multi-particle beam dynamics code (a Monte Carlo program), ESME[10]. In our model we have assumed a damping oscillating rf wave with a Vrf (max)=2.5% of 2kV between the barrier pulses which starts at the negative barrier pulse. This method predicts the longitudinal emittance to be about 51eVs and $\Delta E_{max} \approx 8$MeV. The energy spread estimated here can be compared with the Schottky signal method of 6.4MeV (at -10dB).

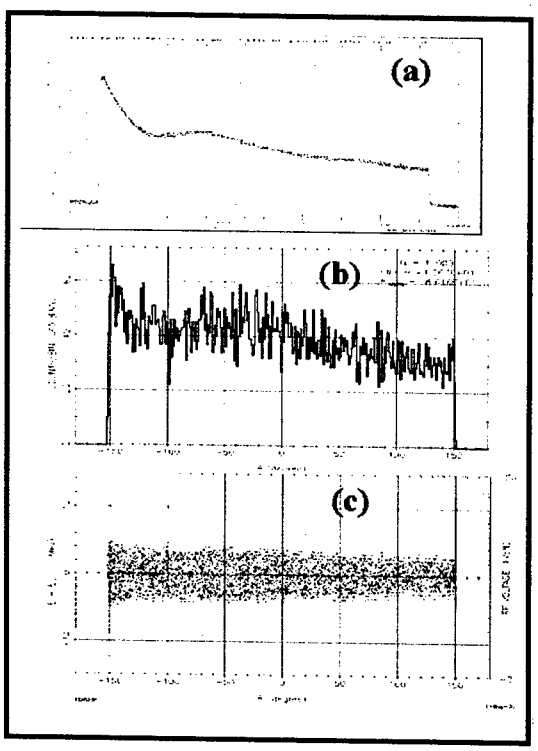

Figure 7: (a) WCM data for the cooled pbar beam in a rectangular barrier bucket with non-zero and non-symmetric Vrf in between the barrier pulses. (b) ESME multiparticle beam dynamics simulation for the distribution shown in (a). The (ΔE,$\Delta\theta$)–phase space distribution of beam particles as predicted from the simulation.

In summary we have measured the longitudinal emittance of the beam in the Recycler Ring by using four different techniques, two destructive and two non-destructive techniques. The WCM and Schottky spectrum methods are very promising, and are suitable for future applications in Recycler during routine operation. A more detailed understanding of the measurement errors is the subject of future effort.

The authors would like to thank D. Wildman and J. MacLachlan for many useful discussions, A. Cadorna, B. Fellenz (gated current integrator), Brian Chase (for LLRF settings), Ming-Jen Yang (for console application program to extract the digitized WCM data), Joe Dey and J. Reid (for their help in HLRF), M. Hu and D. Broemmelsiek (Schottky Detector settings) and Craig McClure (trigger circuit for RTD720 scope), and Operation group for their help during the course of this work.

REFERENCES

[1] G. Jackson, "The Fermilab Recycler Ring Technical Design Report" FERMILAB-TM-1991 (1996).
[2] G.E. Griffin et. al, IEEE, Trans. Nucl. Sci., NS-30, 3502 (1983).
[3] S.Y. Lee and K. Y. Ng, Phys. Rev. E, Vol. 55, 5992 (1997).
[4] J.E. Dey and D.W. Wildman, IEEE, Proc. the 1999 Part. Accel. Conf. New York, NY, 869, 1999).
[5] A. Cadorna et. al., "Gated Current Integrator for the Beam in the RR Barrier Buckets," this proceedings.
[6] R.C. Webber, AIP Conference Proceedings No. 212, page 85-126, edited by E.R Beadle and V.J. Castillo, Accelerator Instrumentation Upton, NY, 1989.
[7] Brian Fellenz and J. Crisp (private communications).
[8] Ming-Jen Yang, A console applications program (unpublished).
[9] D. Boussard, CERN SPS/86-11(ARF), Geneva 1986.
[10] J. MacLachlan, ESME modified to handle beam dynamics in barrier buckets (1996), (private communications 2001).

Proceedings of the 2003 Particle Accelerator Conference

CHIRPED-LASER BASED ELECTRON BUNCH LENGTH MONITOR

G. Berden*, G. Knippels†, D. Oepts, A.F.G. van der Meer,
FOM Institute Rijnhuizen / FELIX, Nieuwegein, The Netherlands

S.P. Jamison‡, X. Yan, A.M. MacLeod, W.A. Gillespie,
School of Computing and Advanced Technologies, University of Abertay Dundee, Dundee, UK

J.L. Shen§, Dept. of Physics, Capital Normal University, Beijing, China

I. Wilke, Rensselaer Polytechnic Institute, Troy, NY, USA

Abstract

An electron bunch length monitor will be discussed which is based on the birefringence induced by the Coulomb field of the bunch in an electro-optically active crystal that is placed in close proximity of the beam. This birefringence is used to change the polarization of an external laser probe pulse. Measurements, performed at the FELIX facility, both in sampling mode (where the 1 GHz micropulse repetition rate of the accelerator was used) and in single-shot mode, will be described. In the latter case, the laser pulse is stretched and chirped, which allows the longitudinal bunch profile to be encoded on its spectral content. Issues related to the (sub-picosecond) time resolution will be discussed.

INTRODUCTION

The electro-optic detection method makes use of the fact that the local electric field of a highly relativistic electron bunch moving in a straight line is almost entirely concentrated perpendicular to its direction of motion. This electric field makes an electro-optic crystal placed in the vicinity of the beam birefringent. The amount of birefringence depends on the strength of the electric field and is probed by monitoring the change of polarization of the light from a short pulse laser system.

At the Free Electron Laser for Infrared eXperiments (FELIX) [1] the electro-optic detection technique has been used to measure the electron bunch shape inside the accelerator beam pipe at the entrance of the undulator of the FEL [2, 3]. In this paper we describe two methods, which differ in the way the electric field induced birefringence is detected.

In the first method, the "delay-scan method" [2], a short laser pulse (shorter than the duration of the electron bunch) is used to sample the amount of birefringence. The delay between probe laser pulse and electron bunch is swept, and the intensity of the light transmitted through a crossed polarizer (analyzer) is measured as a function of delay.

In the second method, the "chirped-pulse spectrometer method" [3], a short probe pulsed is stretched into a pulse with a linear chirp and with a length longer than that of the electron bunch. In a linearly chirped pulse the instantaneous wavelength is proportional to time. When the electric field of an electron bunch and the chirped optical pulse copropagate in the electro-optic crystal, the various wavelength components of the chirped pulse passing through the crystal obtain different phase retardations, corresponding to different portions of the local electric field. By placing the crystal between crossed polarizers, the phase retardation in the wavelength spectrum is converted into an intensity modulation of this spectrum. Thus, the time profile of the local electric field of the electron bunch is linearly encoded on the wavelength spectrum of the optical probe beam. This wavelength spectrum is recorded single-shot with a linear diode array or a CCD camera after dispersing the optical pulse by a grating.

The electro-optic detection technique has been used in other laboratories as well. For example, Fitch et al. [4] have used the delay-scan method to measure the wake fields in the Fermilab high-brightness photo-injector (charge per bunch: 12 nC, bunch length 4.2 ps). They used a $LiTaO_3$ crystal as sensor which was oriented in such a way that they were able to probe longitudinal and radial components of the electric field. The measurements were related to the wall impedance.

Srinivasan-Rao et al. [5] proposed a method to encode the electron bunch profile on the *spatial* intensity distribution of the probe laser pulse. In this method the probe laser pulse is focused to form a line focus which is parallel to the direction of the electron beam. A thin electro-optic crystal is positioned at the waist of the laser beam which is directly below the electron beam. The intensity of the light trans-

* berden@rijnh.nl
† present address: Picarro, Sunnyvale, CA, USA
‡ also at: University of Strathclyde, Glasgow, UK
§ also at: University of Strathclyde, Glasgow, UK

0-7803-7738-9/03/$17.00 © 2003 IEEE

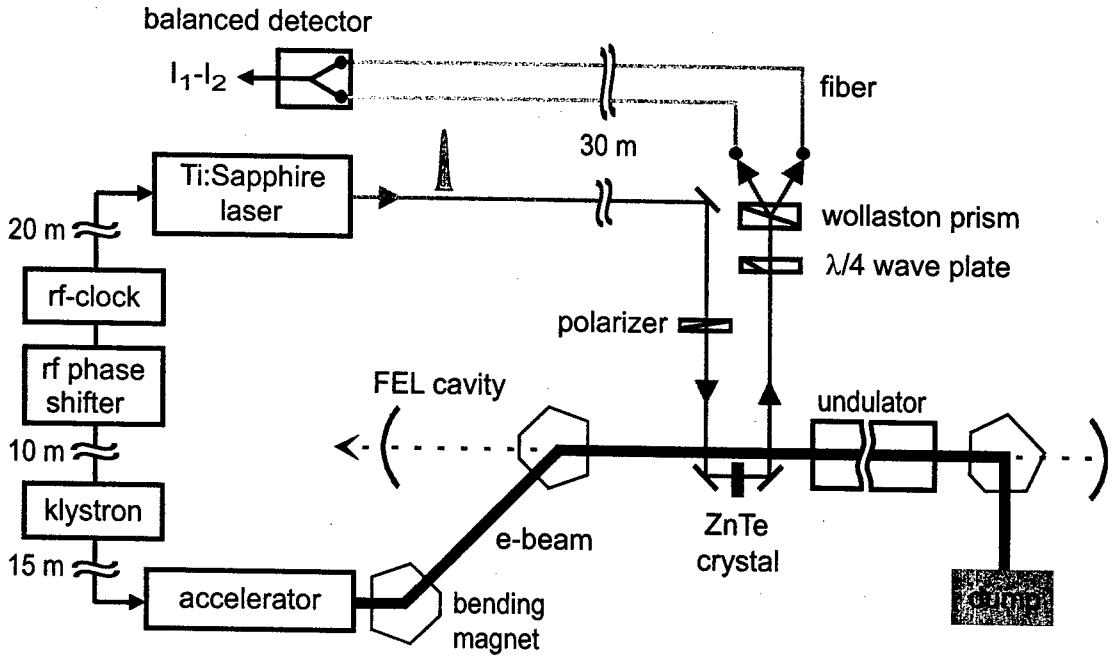

Figure 1: Experimental setup of the electro-optic "delay-scan method".

mitted by the crystal and a crossed analyzer is detected by a linear array. This spatially resolved intensity distribution is a measure of the temporal distribution of the charge in the electron beam. Measurements have not yet been reported.

THE ELECTRO-OPTIC CRYSTAL IN THE FELIX BEAMLINE

At FELIX, the electron bunch shape is measured inside the accelerator beam pipe at the entrance of the undulator. A 0.5 mm thick <110> ZnTe crystal is used as an electro-optic sensor and is placed with is 4×4 mm^2 front face perpendicular to the propagation direction of the electron beam (Figure 1). The probe laser beam is linearly polarized and passes through the ZnTe crystal parallel to the electron beam. A photograph of the part of the beamline containing the ZnTe crystal is shown in Figure 2. A small optical table is attached to the wall of the accelerator hall. It contains the last steering mirror to bring the laser beam from the laser room to the ZnTe crystal, a polarizer, the mirror which picks up the laser beam comming back from the crystal, the analyzer (in Fig. 1 this is a $\lambda/4$ waveplate / Wollaston prism combination), and fibers which bring the laser pulse back to laser room where the detection system is located. The laser beam enters and leaves the vacuum pipe through the same window. On the other side of the electron beam, the ZnTe crystal and two small mirrors are mounted on a translation stage.

The choice of the material and size of the crystal depends on many things. The phase retardation experienced by the probe laser passing through an electro-optic crystal is proportional to the length of the crystal, the electro-optic coefficient (of the order of pm/V) and the local electric field. The actual expression for the phase retardation depends on the orientation of the crystal with respect to the direction of the electric field and the polarization of the probe laser, and can be found in literature (see e.g. [6]). At a first glance the ideal crystal would be a long crystal with a high electro-optic coefficient. There are however a few limitations due to absorption and dispersion of the various frequency components of the electric field and probe

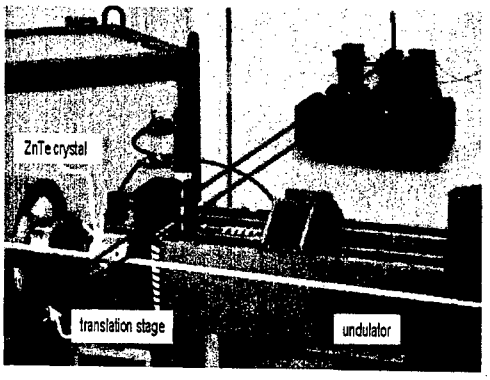

Figure 2: Photograph of the section of the electron beampipe containing the electro-optic crystal ZnTe. A small optical table is attached to the wall. The yellow and red lines indicate the electron beam and laser beam, respectively. The ZnTe crystal (in green) is mounted on a translation stage.

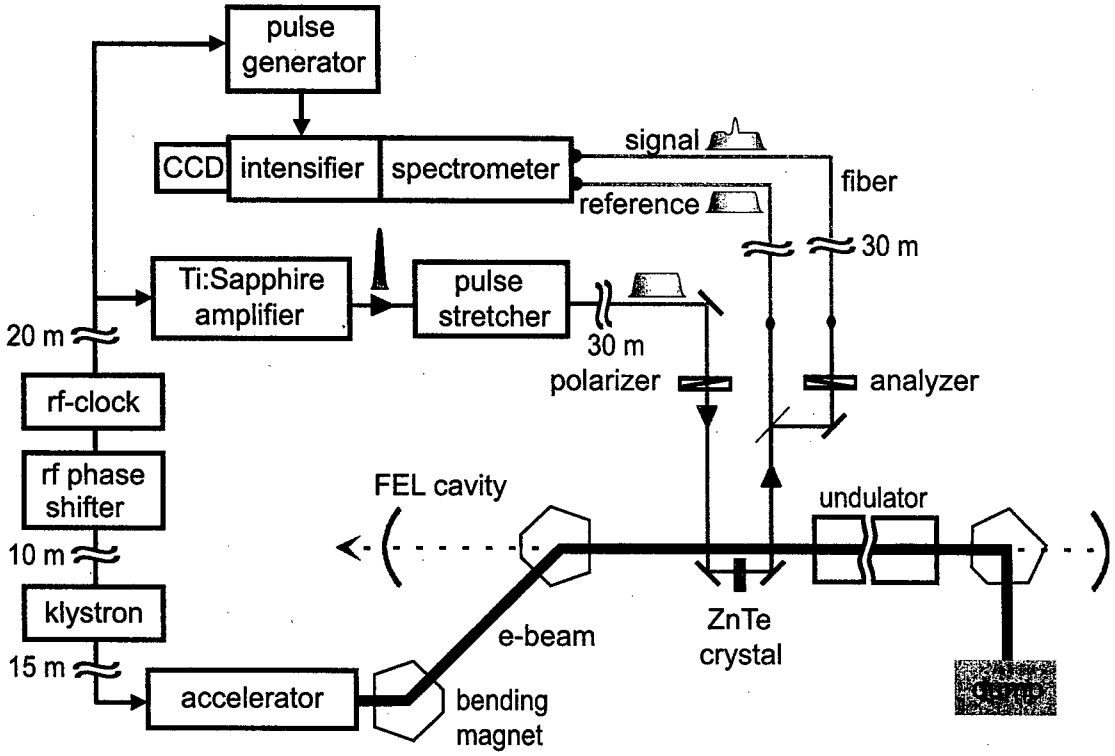

Figure 3: Experimental setup of the electro-optic "chirped pulse spectrometer method" for measuring single-shot images of the electric field profiles of individual electron bunches.

laser in the crystal (see also [7]). In ZnTe the velocity of a 800 nm probe pulse is identical to that of the 2.3 THz frequency component of the electric field; other frequency components of the electric field have different velocities, which means that the measured electric field profile will be distorted if the crystal is too long. Absorptions in the crystal lead to a distortion of the measured beam profile as well; ZnTe, for example, has a strong phonon absorption at 5.3 THz, limiting the temporal resolution to about 200 fs. These absorptions can be modeled and it has been shown that ZnTe crystals can be used to measure frequencies up to 37 THz [8]. Electro-optic sampling is a technique which originates from THz-science, and many details of this technique (crystal choice, measurement techniques, modeling, etc.) can be found in the literature.

DELAY-SCAN METHOD

The probe laser for the "delay-scan method" is a femtosecond Ti:Sapphire laser (wavelength 800 nm, pulse energy 5 nJ, repetition rate 100 MHz, pulse length 15 fs) which is actively synchronized to the accelerator rf clock [9] (see Figure 1). The delay between optical pulses and the electron bunches (beam energy 46 MeV, bunch charge 200 pC, micropulse repetition rate 25 MHz or 1 GHz, bunch length ~1.5 ps) can be varied with a phase shifter. This rf-phase shifter can sweep the probe laser pulses over the electron bunches with a rate of a few picoseconds per microsecond. Since there is an electron bunch every 1 or 40 ns and a probe pulse every 10 ns, this means that the complete electric field profile is measured in a few microseconds. This delay-scan method can therefore be used for real-time monitoring, although the measured profile is sampled from a few hundred individual electron bunches. A balanced detection arrangement was used instead of a crossed-polarizer detection setup in order to increase the signal-to-noise ratio. Electric field profiles of electron bunches with a FWHM of 1.7 ps have been measured by limiting the delay-scan to about 10 ps [2]. Longer

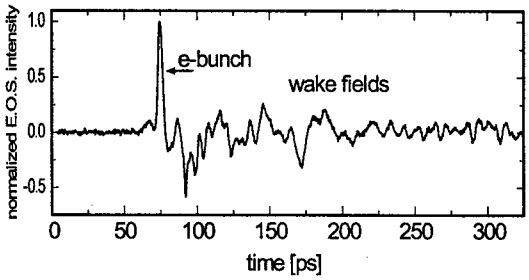

Figure 4: The electric field profile of the electron bunch measured at the entrance of the undulator. The leading edge is on the left.

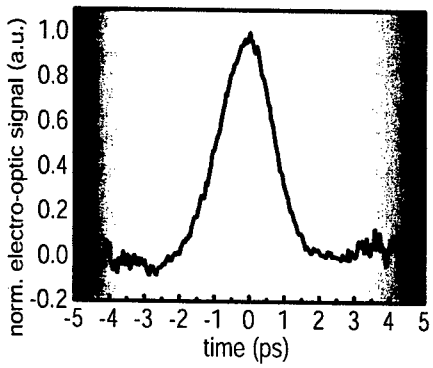

Figure 5: Single-shot measurement of the electric field profile of an individual electron bunch. The leading edge is on the right. The pulse length is about 1.7 ps FWHM. The shaded areas indicate the regions of increased noise introduced by the correction for the wavelength dependent variations in the intensity of the spectrum.

delay scans, of a few hundred picoseconds, have been made as well; these electric profiles show the effects of wake fields after the electron bunch. Figure 4 shows a typical measurement.

CHIRPED PULSE SPECTROMETER METHOD

The probe laser for the "chirped-pulse spectrometer method" is a femtosecond Ti:Sapphire amplifier (wavelength 800 nm, pulse energy 1 mJ, repetition rate 1 kHz, pulse length 30 fs) which is actively synchronized to the accelerator rf clock [10]. Laser pulses are linearly chirped in an optical stretcher [3]. The length of the pulse can easily be varied over a range of 30 fs to 20 ps with a single translation stage. The chirped beam leaving the beampipe is split into a signal beam and a reference beam that is used to monitor possible laser fluctuations (see Figure 3). The signal beam passes through an analyzer (a second polarizer) which is (nearly) crossed with respect to the first polarizer. Subsequently, the spectra of the chirped laser pulses are dispersed with a grating spectrometer and the line spectra are focussed onto a CCD camera. The intensifier in front of the CCD camera acts as a shutter (minimum gate 10 ns).

Figure 5 shows a single shot image of the electric field profile of an individual electron bunch after on-line data processing (details on the data processing can be found in Ref. [3]). By increasing the chirp, a larger time window is obtained, which allows monitoring of the electron bunch and wake fields (see [3]).

TEMPORAL RESOLUTION

The time resolution of the two electro-optic methods is determined by:

- the material and the length of the electro-optic crystal. The cut off for our 0.5 mm crystal is around 350 fs [11]; thus electron bunches shorter than 350 fs are broadened and/or distorted. Higher resolution can be obtained with a thinner crystal.

- the distance R from the electron beam to the electro-optic crystal, $\Delta t_d \approx 2R/\gamma c$ [12]. For our "delay-scan method" this is $\Delta t_d \approx 400$ fs for R=6 mm and γ=90, and for our "chirped-pulse spectrometer method" this is $\Delta t_d \approx 70$ fs for R=1 mm and γ=90.

- the length of the probe laser pulse, τ_0. In our "delay-scan method" τ_0=15 fs. For the "chirped-pulse spectrometer method" the length of the chirp τ_c plays a role as well. For bunch lengths shorter than $(\tau_0\tau_c)^{1/2}$ the measured profile will be broadened and/or distorted [13, 14]. In our case τ_0=30 fs and τ_c=4.48 ps, which gives $(\tau_0\tau_c)^{1/2} \approx$370 fs while the bunch length is $\approx$1.5 ps. The broadening is expected to be less than 100 fs.

- time jitter in the synchronization of the probe pulse to the electron bunch. In our case 50 fs in a few microseconds, on longer time scales 400 fs. In the single-shot measurement in Figure 5 time-jitter can be neglected since the profile has been recorded in about 10 ps (more about the synchronization can be found below).

- resolution of the spectrometer and diode array in the case of the "chirped-pulse spectrometer method". In our case this was about 300 fs. This can easily be improved by using a better spectrometer with a larger diode array.

SYNCHRONIZATION

For the study of very short electron bunches, the synchronization between the electron bunches and the probe laser pulses becomes more important. For the "delay-scan method" this is obvious, since time-jitter gives a broadening of the observed electric field profile. But also for the single-shot "chirped-pulse spectrometer method" the time-jitter is of great concern, although it does not give rise to a broadening of the profile. Let us consider an example: suppose we have an electron bunch of 100 fs, a very high resolution-spectrometer/diode array combination, a very thin ZnTe crystal and a short distance between electron beam and crystal. With a 15 fs laser, a time-window of about 170 fs is needed (thus $(\tau_0\tau_c)^{1/2} \approx$50 fs). If the jitter in the synchronization is on the order of 100 fs, the electric field profile would frequently lie partially outside the time window.

In our case the jitter is about 50 fs on a microsecond time scale, but 400 fs on a longer time scale. This jitter has been measured by cross correlating the FEL output with the optical pulse (see Ref. [9]; and qualitatively confirmed by our electron bunch experiments). An interesting question is where the dominant part of the jitter is originating from,

since both the laser and the electron bunches (and thus the FEL radiation) are locked to same the rf-clock. Most probably, the jitter is caused by fluctuations in the voltage of the power supply feeding the klystron.

Synchronization of a modelocked Ti:Sapphire laser, which is used to drive a photocathode, to a 3 GHz RF oscillator with a jitter of less than 29 fs has been reported [15]. But how well do the electron bunches remain synchronized to the laser after they have passed devices such as bunchers and accelerators?

FUTURE

It has been shown experimentally, by Jamison et al. [14], in the "chirped pulse spectrometer" detection of so-called optical half cycle pulses, that the measured profile is distorted and broadened when the duration of the electric field is larger than $(\tau_0\tau_c)^{1/2}$. This effect is caused by interference between spectral components of the modulation (induced by the electric field) and the spectral components of the chirped pulse [13, 14]. A way to circumvent these problems is to measure the chirped pulse in the time-domain, which can be done with a (single-shot) cross-correlator.

At the moment of writing this contribution, the first test measurements have been performed with a "chirped pulse cross-correlator" set-up at FELIX although we have not yet obtained a single shot cross-correlation measurement of the electron bunch. It is clear that the optical alignment of a cross-correlator is more complex than the alignment of a spectrometer. Other related methods have been proposed such as auto-correlation and Frequency Resolved Optical Gating (FROG) measurements [16].

CONCLUSION

Electro-optic sampling of the Coulomb field of the electron bunch is a promising method for real-time monitoring of the electron bunches. The method is non-destructive (it does not intercept the electron beam) and non-intrusive (although it is expected that the modification of the beamline will slightly influence beam properties, this has not yet been investigated in detail). At FELIX we have measured the length and shape of individual relativistic electron bunches with a subpicosond time resolution.

REFERENCES

[1] http://www.rijnh.nl/felix

[2] X. Yan, A.M. MacLeod, W.A. Gillespie, G.M.H. Knippels, D. Oepts, A.F.G. van der Meer, and W. Seidel, Phys. Rev. Lett. **85**, 3404 (2000)

[3] I. Wilke, A.M. MacLeod, W.A. Gillespie, G. Berden, G.M.H. Knippels, and A.F.G. van der Meer, Phys. Rev. Lett. **88**, 124801 (2002)

[4] M.J. Fitch, A.C. Melissinos, P.L. Colestock, J.-P. Carneiro, H.T. Edwards, and W.H. Hartung, Phys. Rev. Lett. **87**, 034801 (2001)

[5] T. Srinivasan-Rao, M. Amin, V. Castillo, D.M. Lazarus, D. Nikas, C. Ozben, Y.K. Semertzidis, A. Stillman, T. Tsang, and L. Kowalski, Phys. Rev. ST Accel. Beams **5**, 042801 (2002)

[6] L. Duvillaret, S. Rialland, and J.-L. Coutaz, J. Opt. Soc. Am. B **19**, 2692 and 2704 (2002)

[7] G. Berden, G.M.H. Knippels, D. Oepts, A.F.G. van der Meer, S.P. Jamison, A.M. MacLeod, W.A. Gillespie, J.L. Shen, and I. Wilke, DIPAC 2003, Mainz, Germany, May 2003.

[8] H.J. Bakker, G.C. Cho, H. Kurz, Q. Wu, and X.-C. Zhang, J. Opt. Soc. Am. B **15**, 1795 (1998)

[9] G.M.H. Knippels, M.J. van de Pol, H.P.M. Pellemans, P.C.M. Planken, and A.F.G. van der Meer, Opt. Lett. **23**, 1754 (1998)

[10] Actually, this laser system used for the "delay scan method" is the oscillator of the Ti:Sapphire amplifier used for the chirped pulse experiment. In principle, the oscillator system alone would give a better resolution in the chirped experiment. Unfortunately, the minimum integration time of our intensified CCD camera is 10 ns (determined by the minimum gate of the intensifier) which makes it impossible to select a single optical pulse out of the 100 MHz pulse train of the oscillator. A way to circumvent this problem without buying a faster intensifier is the use of a pulse slicer.

[11] G. Gallot, J. Zhang, R.W. McGowan, T.-I. Jeon, and D. Grischkowsky, Appl. Phys. Lett. **74**, 3450 (1999)

[12] D. Oepts and G.M.H. Knippels, Proc. 20th International FEL conference, Williamsburg, 1998 (Elsevier North Holland, Amsterdam, 1999), p. II-45.

[13] J.R. Fletcher, Opt. Express **10**, 1425 (2002)

[14] S.P. Jamison, J. Shen, A.M. MacLeod, and W.A. Gillespie, Opt. Lett. (2003) in press.

[15] F.B. Kiewiet, A.H. Kemper, O.J. Luiten, G.J.H. Brussaard, and M.J. van der Wiel, Nucl. Instr. and Meth. A **484**, 619 (2002).

[16] P. Bolton, D. Dowell, P. Krejcik, and J. Rifkin, AIP Conf. Proc. **648**, 491 (2002).

RHIC THIRD GENERATION PLL TUNE SYSTEM*

P. Cameron, J. Cupolo, W. Dawson, C. Degen, A. DellaPenna, M. Kesselman, A. Marusic, J. Mead, C. Schultheiss, R. Sikora, K. Vetter, J. Van Zeijts, BNL, Upton, NY 11973, USA

Abstract

During the RHIC 2000 run a prototype PLL tune measurement system was implemented using commercial off-the-shelf hardware. To meet the requirements for tune feedback during RHIC 2001/2002, this system was migrated into RHIC BPM modules, whose flexible DSP/FPGA architecture permitted the specialized processing needed for tune tracking and feedback during acceleration, and whose existing firewire interface provided communication with the Control System. For RHIC 2003 this system has migrated yet again, to state-of-the-art DSPs in VME. We report here on various improvements, extending from the pickup through the analog electronics and digital processing into the Controls interface, and on the performance gains that resulted from these improvements.

SYSTEM OVERVIEW

Our approach to PLL tune measurement has been described in some detail in earlier papers[1,2]. Here the focus is on giving a brief overview of the present system, with some discussion of improvements, followed by a presentation of measurement results. Finally we discuss outstanding problems with this system and their possible solutions.

Description

A block diagram of the system is shown in figure 1. The system is driven by a 28MHz low-level RF signal piped in on heliax from the RF to the Instrumentation control rooms. This signal clocks a custom numerically controlled oscillator, which together with the Pentek DSPs sits in VME. All frequencies in the tune system are thus synchronous with the beam. The NCO output goes thru a chain of multipliers and dividers to provide the local oscillator for the mixers, the 455KHz IF, and the 4x455KHz I/Q demodulation clock for the digitizer. The mixers are suppressed carrier single sideband modulators. The 245MHz output on the excitation side is highpass filtered before entering a 10W class A amplifier, which drives the 25cm long 50 ohm kicker striplines through a difference hybrid and about 100m of heliax into the tunnel. During normal operation kicker power is typically in the milliwatt range. The kicker excitation travels with the beam through the betatron-tune-dependent phase shift between the kicker and the resonant pickup[3]. The output from the pickup is passed thru hi-Q cavity bandpass filters, boosted by 30dB, and again transported via 100m of heliax to the mixer, whose output is again at 455KHz. By including the betatron frequency in the local oscillator for up and down conversion, the tune signal is always at this 455KHz frequency and the need for a tracking filter at the input to the digitizer is eliminated. A 3KHz bandwidth ceramic filter removes the dominant difference signal at the revolution line before the 120dB variable gain amplifier chain that precedes the digitizer.

After digitizing the amplitude and phase streams of the I/Q demodulated data are low-pass decimated, first by 890Hz averaging filters, then by 40Hz IIR filters. The phase information is used by a PID algorithm to control the NCO frequency and track the tune. The amplitude

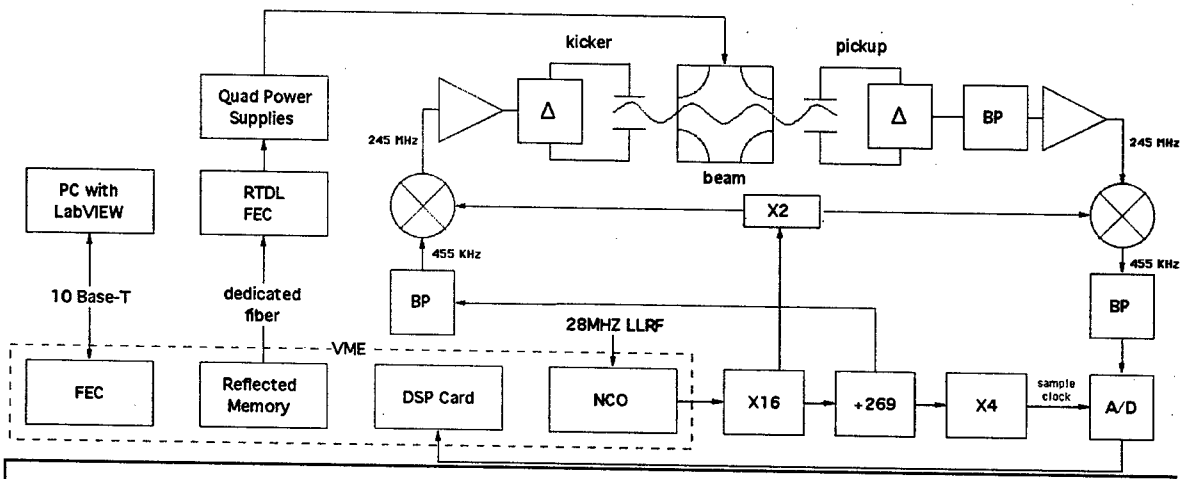

Figure 1 Block Diagram of the PLL/Tune Feedback System

0-7803-7738-9/03/$17.00 © 2003 IEEE

information is used to adjust the kicker power, compensating for variations in the beam transfer function portion of the loop gain. Overall system control is accomplished via a LabVIEW user interface.

Improvements

Several improvements have been incorporated into the present tune measurement system:

- the kicker and pickup were moved to locations with larger beta, resulting in ~6dB of improvement in S/N
- the 1m long kicker was replaced with a 25cm long kicker, resulting in significantly improved beam excitation at 245MHz
- digitizer frequency has been increased, resulting in ~7dB of processing gain
- the 455KHz ceramic filter diminished amplifier saturation problems and increased the number of effective digitizer bits
- the 40Hz digital lowpass filter reduced noise bandwidth, giving ~20dB improvement in S/N
- horizontal and vertical planes were driven at different revolution line harmonics, diminishig the effects of coupling and tune crossing

With these improvements performance was significantly enhanced in comparison with the previously described system.

MEASUREMENT RESULTS

Tune Tracking during Ramping

Figure 2 shows data from a six bunch Deuteron acceleration ramp during the commissioning phase of the RHIC2003 run. The ramp starts at the left side of the figure. The right vertical scale is beam current, and applies to the trace that begins in the upper left corner of the figure. The left vertical scale is fractional tune. The continuous traces are PLL data, and the dots are kicked tune measurements. The tunes have large excursions and cross at transition, as a result of the beam being off center in the fast transition quadrupoles. Agreement between PLL and kicked tunes is reasonably good, although the kicked tune measurement often has difficulty in discriminating between horizontal and vertical planes, probably due to a combination of coupling and beta functions at the pickup. Coupling also introduces error in the PLL tune measurement due to spurious phase leaking from the opposite plane. There was a 1Hz 200μ radius modulation during this ramp to permit chromaticity measurement. The large width of the PLL line at various times during the ramp is from large chromaticity.

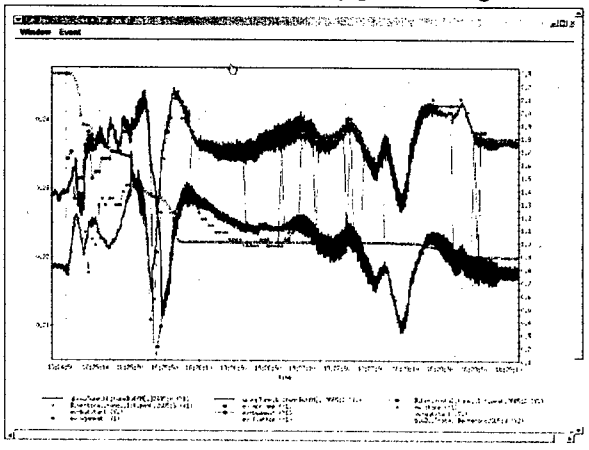

Fig. 2(color): Ramp Tunes

Tune Feedback

Figure 3 shows data from a six bunch Deuteron ramp with tune feedback[4]. Beam loss early in the ramp coincided with large tune fluctuation in the vertical plane, at a frequency of ~4Hz. Smaller fluctuations are visible late in the ramp in both planes, and in the horizontal plane after transition, and suggest that the tune feedback loop was close to the stability limit. Amplitude feedback on kicker power was not enabled for this ramp. Kicked tune data indicates that tunes were regulated at the level of .001 for a good portion of the ramp.

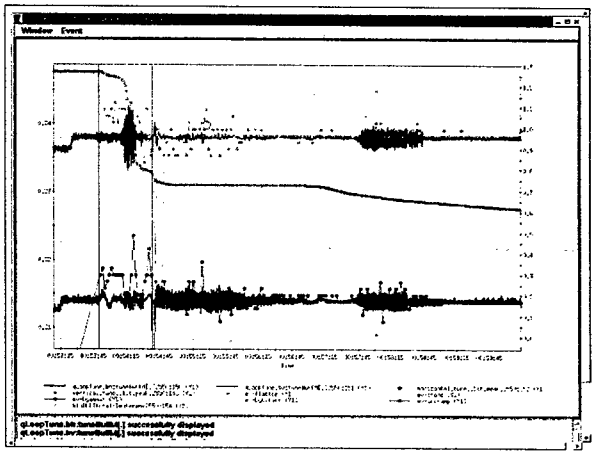

Fig. 3(color): Tune feedback

Figure 4 shows amplitude and phase data from the same ramp. The vertical scale is digitizer counts, which range between +/- 8192 with our 14 bit digitizers. The effects of transition and beam steering are clearly visible in this

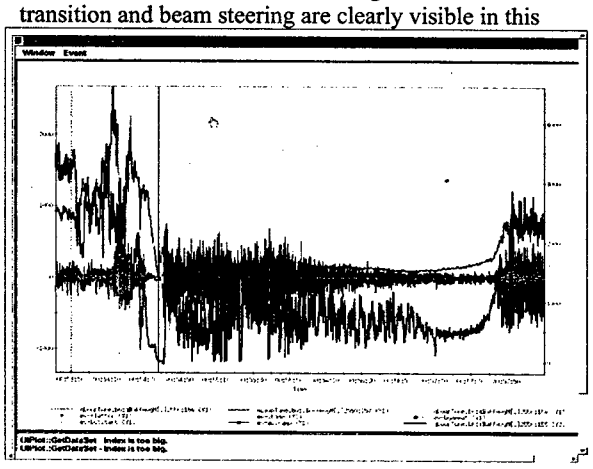

Fig. 4(color): Amplitude and Phase

figure, and will be discussed in more detail in the following section. It is interesting to note that shortly before transition the phase of the horizontal PLL jumped 180 degrees, and from that time on the loop would have been unstable if the gain approached unity.

Other Applications

The PLL has been employed in a variety of accelerator physics applications, including measurement and correction of non-linearities[5], chromaticity[6], and coupling[7], and measurement of beam-beam effects[8] and cryostat vibrations. A new technique[9] of coupling measurement was also investigated. Figure 5 shows data

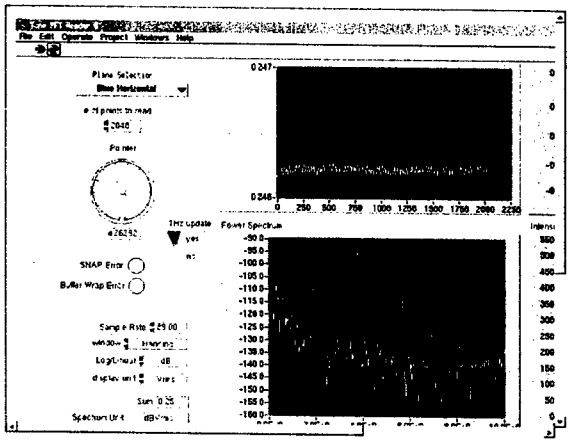

Fig. 5 Coupling Measurement

taken when two skew quad families were modulated at 2Hz and 180 degrees of relative phase. The upper right panel shows a brief time history of order 10^{-4} tune fluctuations. The lower right panel shows the FFT of the tune history. The energy at 4Hz appears as a result of coupling, and the amount of coupling can be calculated from the relative magnitudes of the 2Hz and 4Hz lines.

OUTSTANDING PROBLEMS

Preamp Saturation

Beam offset in the pickup drives the difference mode at the revolution harmonics, with amplitudes that can exceed the signal by ~60dB for offsets of a few mm. The problem is severe near transition, where bunch shortening extends the coherent spectrum of the 28MHz bunched beam up to the 245MHz pickup frequency, and where there are sudden large position and tune shifts due to firing of the transition quadrupoles. In addition, vertical IR bumps to minimize beam-beam effects during ramping are often not closed, and result in changing beam position at the PLL pickup. As the preamps saturate the noise floor comes up and the tune signal amplitude is diminished. These effects are visible in fig. 4 in both planes near transition, and in the vertical from transition to flattop. A servo on pickup position helps with slow position changes, but further measures are required for fast changes at transition. We continue to study methods of fast electronic compensation.

Coupling

While separating horizontal and vertical excitations in either or both time and frequency domains offers some relief, inevitably spurious phase from coupling comes through the beam, and can probably only be dealt with by minimizing coupling and maximizing tune separation.

Chromaticity Variations

Beam studies of the effect of chromaticity on PLL tune measurement were performed. Chromaticity was varied over a large range (from ~3 to ~19) while observing the effect on PLL amplitude and phase signals. The effect was surprisingly small, for reasons that are not yet understood. The conclusion has been that chromaticity control is probably not an issue for PLL operation.

Phase Compensation during Ramps

Several hundred meters of heliax carry 245MHz signals to and from the PLL pickups. During ramping the resulting phase shifts can be as great as ~700 degrees, and must be digitally compensated to within ~10 degrees. In theory this should be straightforward, but in practice anomalous phase shifts are observed and have not been understood. This causes phase compensation to be an often painful trail-and-error process. The planned solution is to move the mixers into the tunnel.

Emittance Growth

Measurable emittance growth results from kicker power of ~1W. At kicker powers below ~20mW there is no measurable emittance growth during ramping or store.

PID Loop Tuning

Loop gain is constrained by the fact that tune dither must be less than ~.001 to minimize beam loss during tune feedback, rendering typical PID tuning algorithms inapplicable. We are exploring alternative tuning algorithms, and alternatives to the PID control algorithm.

CONCLUSION

Tune feedback has been repeatedly demonstrated. Evolution to a true operational system continues.

REFERENCES

[1] P. Cameron et al, "Tune Feedback at RHIC", PAC2001, NY.

[2] P. Cameron et al, "Tune Measurement at RHIC", BIW02, Brookhaven.

[3] M. Kesselman et al, "Resonant BPM for Continuous Tune Measurement in RHIC", PAC2001, NY.

[4] C. Schultheiss et al, "Real-Time Betatron Tune Control in RHIC", EPAC2002, Paris.

[5] F. Pilat et al, "Nonlinear Effects in the RHIC Interaction Regions", these proceedings.

[6] S. Tepekian et al, "Chromaticity Correction Along the Ramp During the RHIC2003 run", these proc.

[7] J. Beebe-Wang and F. Pilat, "Fast Automated Decoupling at RHIC", these proceedings.

[8] W. Fischer et al, "Observation of Strong-Strong and Other Beam-Beam Effects in RHIC", these proc.

[9] T. Roser, private communication.

SELF-CONSISTENT, UNBIASED EXCLUSION METHODS OF EMITTANCE ANALYSIS

Martin P. Stockli, R. F. Welton, SNS, ORNL, Oak Ridge, TN 37830, USA*
R. Keller, SNS, LBNL, Berkeley, CA 94720, USA*

Abstract

We present a self-consistent method for analyzing measured emittance data that yields unbiased estimates for the rms emittance as well as its associated uncertainty. The self-consistent, unbiased elliptical exclusion analysis, SCUBEEx, uses an exclusion ellipse to determine the bias from the data outside the ellipse, before calculating the emittance from the bias-subtracted data within the ellipse. Variations of the ellipse size, shape, and orientation allow for objectively estimating the bias and the rms emittance.

INTRODUCTION

The emittance of a particle beam is the six-dimensional distribution of all position coordinates along the three configuration space directions and their associated velocity coordinates. Projecting it into the two-dimensional planes, {x-x'}, {y-y'}, and {z-z'}, respectively, reduces the emittance into three subsets. The description can be further reduced to the fractional area emittance, describing the area in either two-dimensional subset occupied by a fraction of the particle beam, which obviously is a function of the fraction value.

The description of the typical spread of the distribution with one single value was accomplished with the introduction of the root-mean-square emittance [1]. Based on the quantity of particles c(x,x') passing through the position coordinate x with a velocity component x', the rms emittance is defined as

$$\varepsilon = \sqrt{\langle x'^2 \rangle \langle x^2 \rangle - \langle xx' \rangle^2} \qquad \text{with}$$

$$\langle x^2 \rangle = \frac{\sum_{all} x^2 c(x,x')}{\sum_{all} c(x,x')}, \quad \langle x'^2 \rangle = \frac{\sum_{all} x'^2 c(x,x')}{\sum_{all} c(x,x')},$$

$$\text{and} \quad \langle xx' \rangle = \frac{\sum_{all} xx' c(x,x')}{\sum_{all} c(x,x')}.$$

The emittance often is given normalized to the particle velocity v and the speed of light c: $\varepsilon_{norm}=\varepsilon \cdot v \cdot (c^2-v^2)^{-1/2}$, a factor of 0.0118 for our 65 kV H^- beam.

Usually all coordinates are measured from the center of the particle distribution, which is accomplished by translating x and x' so that their first moments become zero. These translations minimize the rms emittance. The orientation and aspect ratio of the rms emittance ellipse are described by the Twiss parameters, namely,

$$\alpha = -\frac{\langle xx' \rangle}{\varepsilon}, \quad \beta = \frac{\langle x^2 \rangle}{\varepsilon}, \text{ and } \quad \gamma = \frac{\langle x'^2 \rangle}{\varepsilon}.$$

All these terms are well defined and can be evaluated without any problems as long as c(x,x') is well defined, for example in simulation data. Problems can arise when evaluating measured emittance data, because they contain noise and typically a small bias. These problems are normally avoided by excluding most of the background data through a threshold or through exclusion boundaries, although those methods can bias the results [2]. We present a method that systematically minimizes the net contributions from the background and self-consistently estimates the rms emittance and its uncertainty [3].

EMITTANCE MEASUREMENTS

Emittance measurements are in most cases double-slit experiments where the first slit samples a small fraction of the particle beam. The sampled beam spreads out before it is intercepted by the second slit to determine the associated transverse velocity distributions. When both slits are centered on the beam they record only a small fraction of the total particle flux, typically 1%. This fraction can drop to the 10^{-4} range when measuring the beam wings outside the beam core. Going further away from the beam core, one may find even smaller particle fluxes, the halo, until the flux gradually fades away and one measures pure background.

We describe the pure background with two components: the noise and the bias. The noise describes the local, quasi-random variations with a zero average. The bias describes the mean value, which is constant, at least locally. In principle the bias might vary gradually as a function of the position and velocity coordinates. However, we restrict this paper to uniform biases, as the presented background data do not exhibit any significant position or velocity dependence.

In the absence of an actual particle flux and a bias, one observes pure background noise, characterized by about the same number of small positive and small negative signals. We define positive as having the same polarity as the output when measuring the beam core, while negative refers to the opposite polarity. A positive bias can be recognized by a dominance of positive signals, whereas a negative bias by a dominance of negative signals.

Figure 1 shows measured emittance data as a density plot versus position x and velocity component x'. The large signals measured from the beam core occupy an

* SNS is a collaboration of six US National Laboratories: Argonne National Laboratory (ANL), Brookhaven National Laboratory (BNL), Thomas Jefferson National Accelerator Facility (TJNAF), Los Alamos National Laboratory (LANL), Lawrence Berkeley National Laboratory (LBNL), and Oak Ridge National Laboratory (ORNL). SNS is managed by UT-Battelle, LLC, under contract DE-AC05-00OR22725 for the U.S. Department of Energy.

0-7803-7738-9/03/$17.00 © 2003 IEEE

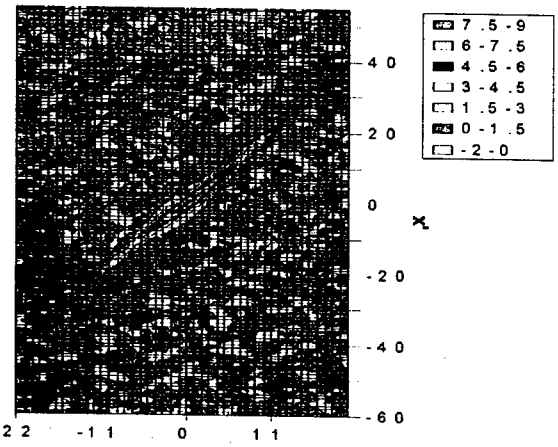

Figure 1: Emittance data from an expanding beam.

ellipse-like area with a diagonal orientation indicating an expanding beam. This colored structure is surrounded by a narrow zone of small, exclusively positive signals indicated in purple. Only further away from the beam core appear negative signals indicated in blue. Roughly 2/3 of the plotted area is consistent with pure background noise.

Applying the previously given formulas to all data yields α=-4.11, β=2.27, and γ= 7.88. For the rms emittance, one obtains ε=17.2 mm·mrad, which is the product of the two half axes of the rms emittance ellipse. Use of the half-axis product (HAP) with the dimension of mm·mrad is consistent with the emittance definition. We avoid the confusing π written as a part of the unit when it is supposed to be the multiplier for calculating the area.

THRESHOLD ANALYSIS

Applying a threshold commonly means that all values of a distribution above the threshold remain unchanged while all values below the threshold are set to zero before summing over all data.

Figure 2 shows the rms emittance estimated by applying a threshold to the data shown in figure 1 as a function of the threshold value. These thresholds, like all other values related to the measured signals, are quoted in percent of the maximum measured particle flux.

Some analysis codes exclude the negative signals from the emittance evaluations because they try to avoid having to deal with the "unphysical" reversed polarity. This is equivalent to setting a threshold at 0%, which overestimates the rms emittance as 203.4 mm·mrad. This grossly inflated value is caused by large contributions from the positive noise signals found at large x and x' values.

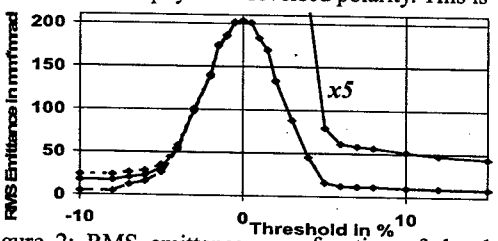

Figure 2: RMS emittance as a function of threshold applied to the data from figure 1 (solid line). The dotted and dashed lines show the emittance of the same data after adding to (dotted line) or subtracting from (dashed line) all data a bias of 0.005%.

To reduce such inflated values, most involved analysts increase the threshold to exclude all background data, often to a point where the emittance estimate no longer changes with small threshold changes. Figure 2, for example, shows the slope to change sevenfold at +6%, resulting in an rms emittance estimate of 12.2 mm·mrad.

There is, however, no absolute need to exclude the negative signals. On the contrary, their contributions compensate the contributions from the positive noise signals as one can see in Figure 2. When the threshold is set to –8%, which includes all data, the rms emittance is estimated at 17.2 mm·mrad, as previously found.

However, adding only a 0.005% bias to the data shown in Figure 1 increases the unthresholded rms emittance estimate to 23.9 mm·mrad, while subtracting a 0.005% bias reduces it to 4.6 mm·mrad, a factor of 5 difference caused by a small bias change of 0.01%. This severe sensitivity is caused by the large amount of background data in our example, especially those with large x and x' values. It causes rms emittance estimates from unthresholded data to be unreliable because small biases are not uncommon, and often unnoticed.

ELLIPTICAL EXCLUSION ANALYSIS

The reliability of rms emittance estimates can be improved by excluding pure background data, especially those located far from the core of the beam. The most reliable estimates are obtained when the exclusion boundary surrounds the data tightly without excluding any real signal. This task is difficult because some of the real signals are normally hidden in the noise. However, the absence of any significant net signal can be ascertained if one can vary the size of the exclusion area over a significant range without significantly changing the rms emittance estimate. Ellipses are best suited to conform tightly to typical emittance data. To demonstrate the elliptical exclusion analysis, we select as ellipse parameters the Twiss parameters α and β calculated from the data in Figure 1 after thresholding them at 10% to exclude all background signals.

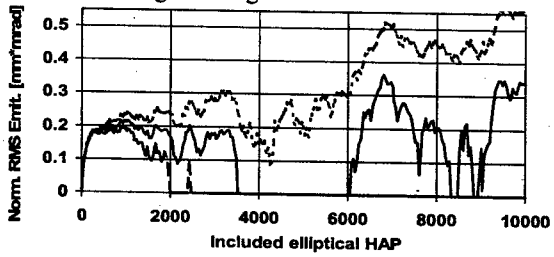

Figure 3: Normalized rms emittance estimates as a function of the exclusion ellipse HAP for the data of figure 1 (solid line), and after adding to (dotted line) or subtracting from (dashed line) all data a 0.05% bias.

The rms emittance estimates in Figure 3 vary wildly for large exclusion ellipses due to the same reasons why unthresholded estimates are unreliable. Shrinking the exclusion ellipse reduces these fluctuations until the solid line in Figure 3 forms a plateau below 2000 mm·mrad. Below 250 mm·mrad, the estimates start to fall off because one starts excluding data from real particle flux. The estimates, however, are sensitive to small biases as one can see from the two curves representing a +0.05% bias (dotted) and a –0.05% bias (dashed), indicating the need for a thorough bias analysis.

SELF-CONSISTENT BIAS ESTIMATION

Figure 4 shows the average of the signals measured outside the exclusion ellipse. Large ellipses yield large fluctuations because of the granularity of the few data found outside, e.g., only 11% of the data are outside 10,000 mm·mrad. More reliable bias estimates can be obtained for ellipses smaller than 3000 mm·mrad excluding more than 2/3 of the data.

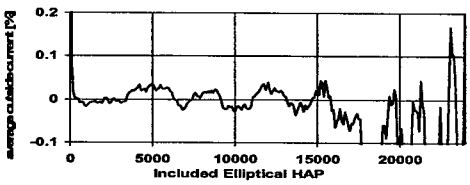

Figure 4: Average current signal outside the exclusion ellipse as a function of its HAP.

SELF-CONSISTENT UNBIASED ELLIPTICAL EXCLUSION ANALYSIS

The self-consistently determined bias needs to be subtracted from the raw data to counteract the sensitivity observed in the elliptical exclusion analysis. The top of Figure 5 shows the average of the current signals outside exclusion ellipses. The averages are fairly constant between 250 and 3000 mm·mrad, consistent with a bias of -0.008% ±0.01%.

The bottom of Figure 5 shows the rms emittance evaluated from the data within the ellipse after subtracting

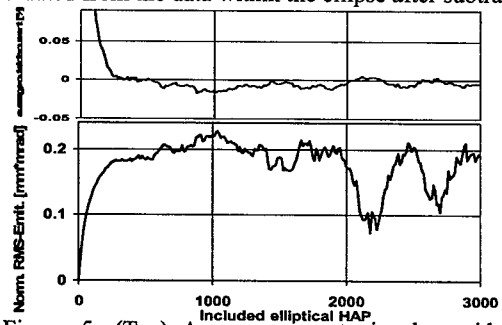

Figure 5: (Top) Average current signal outside and (bottom) normalized rms emittance estimated from the data inside the exclusion ellipse after subtracting the corresponding average outside current as a function of the exclusion ellipse HAP.

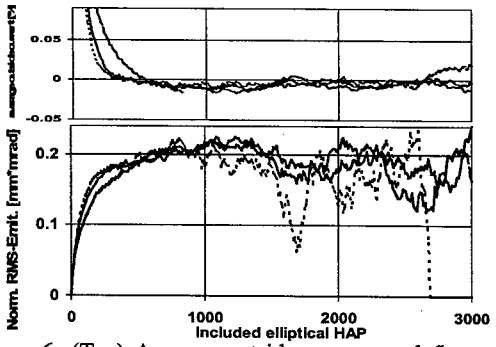

Figure 6: (Top) Average outside current and (bottom) normalized rms emittance of the bias subtracted data within the ellipse for three different exclusion ellipse sets.

the average current signal found outside the ellipse. The fluctuations caused by the noise clearly penetrate into the plateau. Even so, between 250 and 1400 mm·mrad the normalized rms emittance stays within 0.20 ±0.02 mm·mrad, consistent with a plateau.

Figure 6 is identical to Figure 5 except that the aspect ratio and orientation of the exclusion ellipse was determined from the data in Figure 1 after thresholding them at 5% (dotted), 20% (solid), and 90% (dashed). The figure shows that the dashed line requires a larger ellipse before the estimates reach the plateau, caused by a slightly different orientation of the ellipse determined from the 10% most intense measured signals. A threshold of 5% includes some noise leading to a less excentric ellipse and thus compresses the scale of Figure 5. However, Figure 6 shows that all evaluations are consistent with a bias of 0.008 ±0.01 and a normalized rms emittance of 0.20 ±0.02 mm·mrad.

CONCLUSIONS

With the robustness demonstrated we estimate with confidence the normalized rms emittance in our example at 0.20 ±0.02 mm·mrad. By chance, this is very close to the unnormalized 17 mm·mrad found earlier as the unthresholded estimate. It is, however, significantly larger than the estimate established through thresholding, which shows that thresholding is likely to exclude real signals from the wings and halo of the particle flux distribution.

REFERENCES

[1] C. LeJeune and J. Aubert, in "Applied Charged Particle Optics", edited by A. Septier (Academic Press, New York, 1980) p. 159.

[2] M.P. Stockli, R.F. Welton, R. Keller, A.P. Letchford, R.W. Thomae, and J.W.G. Thomason, in "Production and Neutralization of Negative Ions and Beams", edited by M.P. Stockli (AIP, New York, 2002) p 135.

[3] R.F. Welton, M.P. Stockli, R. Keller, R.W. Thomae, J.W.G. Thomason, J. Sherman, and J. Alessi, in "Production and Neutralization of Negative Ions and Beams", edited by M.P. Stockli (AIP, New York, 2002) p 160.

ELECTRON-BEAM SIZE MEASUREMENT WITH A BEAM PROFILE MONITOR USING FRESNEL ZONE PLATES

N. Nakamura, H. Sakai, K. Iida, K. Shinoe, H. Takaki
Institute for Solid State Physics, University of Tokyo, Kashiwa, Japan
H. Hayano, M. Nomura, Y. Kamiya, KEK, Tsukuba, Japan
T. Koseki, RIKEN, Wako, Japan
Y. Amemiya, Graduate School of Frontier Sciences, University of Tokyo, Kashiwa, Japan
N. Aoki, K. Nakayama, Toshiba corporation, Yokohama, Japan

Abstract

We have designed and constructed a non-destructive and real-time beam profile monitor in the KEK-ATF damping ring to measure the extremely small electron-beam size. The monitor has a microscopic structure where two Fresnel zone plates (FZPs) constitute an x-ray imaging optics. In the monitor system, synchrotron radiation from an electron beam is monochromatized by a silicon crystal and the transverse electron-beam image is twenty-times magnified by the two FZP and detected on the x-ray CCD camera. With this monitor, we have succeeded in obtaining a clear electron-beam image and measuring the electron-beam size less than 10 μm. The measured magnification of the imaging optics was in good agreement with the design value.

INTRODUCTION

A beam profile monitor with an x-ray imaging optics for synchrotron radiation (SR) is expected to measure the electron-beam size with a high spatial resolution in a non-destructive manner. Fresnel zone plates (FZPs) begin to be used as x-ray imaging lenses with advance of x-ray mask fabrication technologies. The spatial resolution, which depends on the outermost-zone width of FZPs, is capable of being less than 100 nm. A real-time beam profile monitor based on FZPs was already proposed and designed for the Super-SOR light source [1]. We have recently constructed the same type of beam profile monitor in the KEK-ATF damping ring [2] with a natural emittance of about 1 nm to study the feasibility of the monitor. In this paper, the new beam profile monitor using FZPs and the results of the beam size measurement will be presented.

IMAGING OPTICS

The x-ray imaging optics of the beam profile monitor consists of two FZPs, the condenser zone plate (CZP) and the micro zone plate (MZP), and it has a microscopic structure, as shown in Fig. 1. The magnification M of the imaging optics is given by $M = M_{CZP}\, M_{MZP}$, where M_{CZP} and M_{MZP} are the magnifications of the CZP and MZP.

The spatial resolution of the CZP, δ_{CZP}, is given by

$$\delta_{CZP} = 1.22\,\Delta r_{N,C} = 0.61\,\lambda f_C / r_{N,C} \,. \qquad (1)$$

Here, f_C is the focal length of the CZP for the wavelength λ and $r_{N,C}$ and $\Delta r_{N,C}$ are the radius and the width of the outermost zone of the CZP. The spatial resolution of the MZP, δ_{MZP}, is similarly expressed. The spatial resolution of each FZP corresponds to the distance between the center and first-zero positions of the diffraction pattern. The spatial resolution at the SR source point, δ_0, is given by

$$\delta_0 = \delta_{CZP} / M_{CZP} = 0.61 \frac{\lambda f_C}{r_{N,C} M_{CZP}} \,. \qquad (2)$$

This is equal to the spatial resolution of the imaging optics if the condition of $\delta_{CZP} > \delta_{MZP} / M_{MZP}$ is satisfied.

The radius of the CZP, $r_{N,C}$, should be $L_{C1}\sigma_{SR}$ or less so that the SR uniformly irradiates the CZP. Here L_{C1} and σ_{SR} are the distance from the source point to the CZP and the SR angular divergence. On the condition of $r_{N,C} = L_{C1}\sigma_{SR}$, the spatial resolution δ_0 [μm] is approximately expressed by the following equation:

$$\delta_0 = \frac{2.62\,\varepsilon_{ph}^{-0.575}\varepsilon_c^{-0.425} E_e}{1 + M_{CZP}} \,, \qquad (3)$$

where E_e [GeV], ε_c [keV] and ε_{ph} [keV] are the electron beam energy, the critical photon energy and the photon energy corresponding to the wavelength λ. The critical photon energy ε_c [keV] and the SR angular divergence σ_{SR} [rad] from a bending magnet (BM) is given by

$$\varepsilon_c = 0.665\, E_e^{\,2} B \qquad (4)$$

$$\sigma_{SR} = 0.289 \times 10^{-3} \left(\varepsilon_{ph}/\varepsilon_c\right)^{0.425} / E_e \,, \qquad (5)$$

where B[T] is the magnetic field at the BM. Here the angular divergence of the electron beam is assumed to be negligibly small as compared with that of the photon.

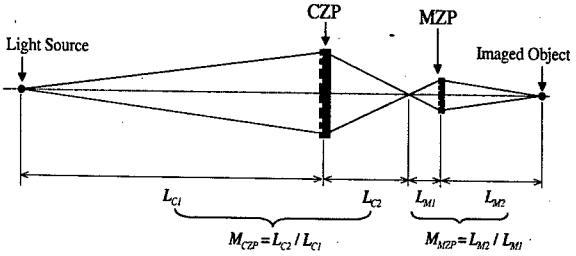

Figure 1: Imaging optics of the beam profile monitor.

MONITOR SYSTEM

Figure 2 shows the layout of the beam profile monitor system, which extracts the SR from the BM in the KEK-

0-7803-7738-9/03/$17.00 © 2003 IEEE

ATF damping ring. The magnetic field of the BM is 0.748 T for E_e = 1.28 GeV and the critical photon energy is 0.816 keV. This system mainly consists of a Si crystal monochromator, two FZPs (CZP and MZP) and an x-ray CCD camera. The specifications of the optical elements are summarized in Table 1.

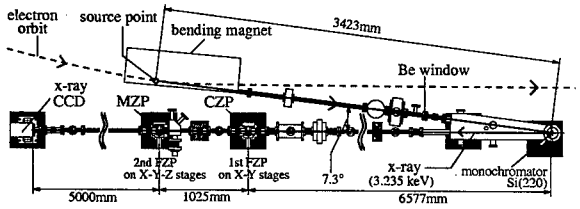

Figure 2: Layout of the beam profile monitor system.

Table 1. Specifications of optical elements

Fresnel zone plate	CZP	MZP
Total number of zones	6444	146
Radius	1.5 (1.26[a]) mm	37.3 μm
Outermost zone width	116 (138[b]) nm	128 nm
Focal length	0.91 m	24.9 mm
Magnification	M_{CZP}=0.1	M_{MZP}=200
Monochromator		
Spectral resolution	5.6×10^{-5}	
Crystal lattice plane	Si(220)	
Lattice spacing	0.192 nm	
Bragg angle θ_B	86.35°	
X-ray CCD camera		
Quantum efficiency	> 90 % @ 3.235keV	
Effective area	12.29 × 12.29 mm	
No. of pixels	512 × 512	
Pixel size	24 μm × 24 μm	

[a] The effective radius of the CZP defined by $L_{CI}\sigma_{SR}$.
[b] The zone width at the effective radius of the CZP.

The FZPs are formed by 0.8-μm-thick Ta absorber on 0.2-μm-thick SiN membrane. The magnifications of the FZPs, M_{CZP} and M_{MZP}, are 1/10 and 200 and hence the 20-times magnified image of the electron-beam can be obtained on the x-ray CCD camera. We selected the x-ray energy of 3.235 keV, considering the spatial resolution of the monitor, the energy dependence of the photon flux and some spatial restrictions of the ring facility. For the selected energy, the spatial resolution of the monitor calculated from Eq. (3) is 1.7 μm. Each FZP is mounted on the holder inserted between two bellow ducts. In order to align the two FZPs, both holders can be moved in the horizontal (x) and vertical (y) directions by motorized linear stages. The MZP holder can also be moved in the longitudinal (z) direction to match the focal plane to the CCD screen.

In order to avoid the effect of the energy aberration, the SR should be monochromatized before it arrives at the CZP. The required energy bandwidth $\Delta E/E$ is given by

$$\Delta E/E \le 2\sigma_{eb} M_{CZP}/r_{N,C}\ , \qquad (6)$$

where σ_{eb} is the size of the electron beam [3]. For the minimum size of the electron beam in the ATF damping ring (> 5 μm), the spectral resolution of less than 8.0×10^{-4} is needed. In the system, a Si(220) crystal is used to deflect the extracted x-ray beam from the bending magnet with the Bragg angle θ_B=86.35°. The spectral resolution of this monochromator is 5.6×10^{-5} and it fully satisfies the required condition of (6). The Si crystal can be rotated around the x- and y-axis for adjustment of the horizontal and vertical angles of the x-ray beam.

The x-ray CCD camera (HAMAMATSU C4880-21) is a direct incident type with a back-thinned illuminated CCD, which offers high quantum efficiency, more than 90 % for the x-ray energy of 3.235 keV. The pixel size is 24 μm and less than twenty times the spatial resolution of the imaging optics δ_0. The minimum exposure time is 20 ms and the maximum frame rate is 7 frames/s. The CCD is a full-frame transfer type and an x-ray shutter made of 50-μm-thick beryllium copper is installed before the CCD camera to cut off the x-ray irradiation during the readout.

MEASUREMENT

After adjusting the angles of the Si crystal and the horizontal and vertical positions of the FZPs, an electron-beam image was clearly observed on the CCD. The background mainly consisted of the readout noise and the x-rays transmitted through the FZPs and their count rates were much lower than that of the peak signal. However we subtracted these background components from the CCD data as possible. The position of the electron-beam image is more sensitive to the position change of the MZP by a factor of 200 than those of the transmitted x-rays. By changing the MZP position by few tens microns, which corresponds to only the size of one or two CCD pixels, the electron-beam image was moved out of the CCD frame while the background components were almost unchanged in position and intensity. The CCD data without the electron-beam image was used as the background data. Figure 3 shows an electron-beam image on the x-ray CCD after the background subtraction.

The horizontal and vertical profiles of the beam image were obtained by projecting the 2-dimensional intensity distribution on the horizontal and vertical axes and the horizontal and vertical image sizes by fitting the horizontal and vertical image profiles to gaussian curves. The longitudinal position of the MZP was scanned for searching the minimum image sizes, which suggested that the focal point of the MZP was on the x-ray CCD. The real beam sizes at the source point were obtained by dividing the minimum image sizes by the magnification of the imaging optics, which was measured by the method described later. The horizontal and vertical beam profiles and their fitted curves are shown in Fig. 4, where the axes of abscissas reflect the dimension at the source point. The beam sizes were measured on five different days with different beam currents and tuning conditions of the ring. The measurement results were summarized in Table 2. The measured horizontal and vertical beam sizes were 36 – 44 μm and 9.4 – 9.7 μm in 2002/05/30-06/07 and 37.6 μm and 6.9 – 7.5 μm in 2002/12/06-07.

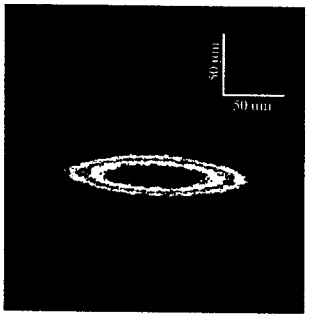

Figure 3: Electron beam image obtained by the beam profile monitor. The length of the horizontal and vertical white bars corresponds to 50 μm at the SR source point.

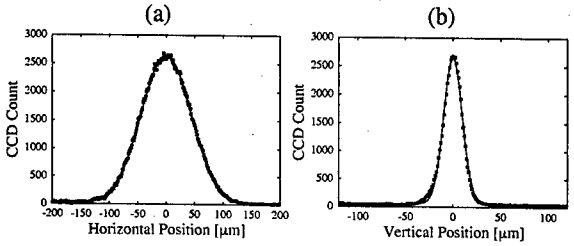

Figure 4: (a) horizontal and (b) vertical beam profiles with their fitted gaussian curves. Data from 2002/06/06.

Table 2: Summary of beam-size measurements

Date[a]	Beam size σ_x[μm], σ_y[μm]	Magnification
2002/05/30	38.1 ± 1.4, 9.52 ± 0.35	M=20.53 ± 0.76
2002/06/06	44.2 ± 1.6, 9.70 ± 0.36	M_{MZP}=204.8 ± 1.5
2002/06/07	36.3 ± 1.3, 9.38 ± 0.35	M_{CZP}=0.1002 ± 0.0038
2002/12/06	37.6 ± 2.0, 6.93 ± 0.37	M=21.08 ± 1.26[b]
2002/12/07	37.6 ± 2.0, 7.45 ± 0.39	

[a] The total beam currents were and 0.27, 2.5 and 0.5 mA in single-bunch mode for 2002/05/30, 2002/06/06 and 2002/06/07 and 3 mA in three-bunch mode for the two dates of 2002/12/06-07.
[b] The magnification of M_{MZP} was not measured for 2002/12/06-07.

The magnification of the imaging optics, $M=M_{CZP}M_{MZP}$, was obtained by measuring the horizontal beam position at the source point, x, and the horizontal position of the beam image on the CCD, X, at the same time. The variation of the beam image position ΔX is related to the variations of the horizontal beam position Δx by

$$\Delta X = M\Delta x = -M\frac{\eta_x}{\alpha}\frac{\Delta f_{rf}}{f_{rf}}, \qquad (7)$$

where η_x, α, f_{rf} and Δf_{rf} are the dispersion function at the SR source point, the momentum compaction factor, the rf frequency and its variation. The beam image position X was measured as function of Δf_{rf} and fitted to a straight line. The magnification was obtained from the slope of the fitted line and the ring parameters f_{rf}, η_x and α. Figure 5 shows the relation between the beam image position X and the horizontal beam position x. As shown in Table 2, the obtained magnification values of the imaging optics were almost equal to the design value of 20.

The magnification of the MZP was also evaluated by utilizing the fact that the ratio of the position change of the beam image to the position change of the MZP is equal to the magnification plus one. The center position of the beam image was measured with changing the MZP position. The obtained data were well fitted by a straight line and the magnification of the MZP was obtained. The magnification of the CZP was determined by the measured values of M and M_{MZP}. The measurement result agrees well with the design values of M_{MZP} and M_{CZP}, as shown in Table 2.

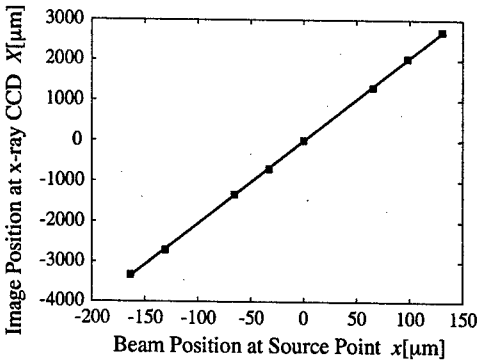

Figure 5: Relation between the horizontal beam position at the SR source point and the horizontal position of the beam image on the x-ray CCD. Data from 2002/05/30 - 06/07.

CONCLUSIONS

The FZP-based beam profile monitor was developed for measuring the extremely small size of the electron beam in the KEK-ATF damping ring. It is a real-time and non-destructive monitor with a high spatial resolution and consists of a silicon crystal monochromator, two FZPs (CZP and MZP) and an x-ray CCD camera. With this monitor, we directly obtained the transverse image of the electron beam and then measured the horizontal and vertical beam sizes. The horizontal beam sizes were about 40 μm and the vertical beam sizes 7 – 10 μm for five different days. The magnification was also measured and was in good agreement with the design value. The good performance and prospects of the monitor were confirmed in the experiments. Further measurements of the beam sizes will be carried out more systematically.

REFERENCES

[1] N. Nakamura, et al., Proceedings of the 2001 Particle Accelerator Conference, Chicago, 2001, pp. 1628-1630.
[2] F. Hinode, et al., KEK Internal Report No. 95-4, 1995.
[3] B. Niemann, D. Rudolph and G. Schmahl, Opt. Commun. 12 (1974) 160.

DEVELOPMENT OF A NEW BEAM-ENERGY-SPREAD MONITOR USING MULTI-STRIPLINE ELECTRODES

T. Suwada*, M. Satoh and K. Furukawa, KEK, Tsukuba, Ibaraki 305-0801, Japan

Abstract

A nondestructive beam-energy-spread monitor (BESM) using multi-stripline electrodes has been newly developed in order to measure and control the energy spread of a single-bunch electron beam at the 180-degree arc with a beam energy of 1.7 GeV in the KEKB injector linac. A proof-of-principle experiment was performed to verify the function of the BESM. The result shows that taking into account the second-order moment derived from the multipole-moment analysis, the energy spreads are estimated to be 0.150±0.007% and 0.264±0.004% for the electron beams with charges of 0.9 and 8 nC/bunch at the rf phase of the energy-spread minimum, respectively.

1 INTRODUCTION

The KEK B-Factory (KEKB) project [1] is in progress for testing CP violation in the decay of B mesons. KEKB is an asymmetric electron-positron collider comprising 3.5-GeV positron and 8-GeV electron rings. Since KEKB is a factory machine, well-controlled operation of the KEKB injector linac [2] is required for keeping the injection rate as high as possible and for maintaining stable operation. For this purpose, beam diagnostic and monitoring tools are essential. The energy spread of the primary electron beam for positron generation is often increased due to a long-term phase drift of high-power and booster klystrons. Thus, beam diagnostic and monitoring tools are required to cure the beam energy spread; furthermore, those are expected to control the longitudinal wakefields of the high-current primary electron beam pulse-by-pulse, especially at large energy dispersion sections.

The BESM with multi-stripline electrodes is one of very useful monitoring tools for satisfying such requirements, since it can measure the energy spread derived from a quadrupole moment of an electron beam. This monitor was designed based on a numerical analysis by applying the multipole moments of the electromagnetic field generated by a charged beam [3]. The BESM detects the spread of transverse beam widths at a large energy dispersion section by measuring any variation of the electromagnetic field distribution induced on the multi-stripline electrodes of the monitor. In this report the authors not only present a clear experimental verification of this analyis based on the previous works [4, 5], but also demonstrate that the second-order moment of an electron beam can be nondestructively measured by the BESM, depending on the variation of the energy spread. The BESM will enable to acquire beam characteristics of two beam bunches in an rf pulse in which scheme they are injected to the rings simultaneously.

* e-mail:tsuyoshi.suwada@kek.jp

2 MULTIPOLE-MOMENT ANALYSIS OF A CHARGED BEAM

For a conducting round duct, the image charges induced by a line charge can be solved as a boundary problem in which the electrostatic potential is equal on the duct [6] (also see Ref. [7]). The formula for the image charge density j is given by

$$j(r,\phi,R,\theta) = \frac{I(r,\phi)}{2\pi R}\frac{R^2-r^2}{R^2+r^2-2rR\cos(\theta-\phi)}, \quad (1)$$

where I is the line charge, (r,ϕ) and (R,θ) are the polar coordinates of the line charge and the pickup point on the duct, respectively, and R is the duct radius. Assuming the transverse r-distribution $\rho(r)$ of a traveling charged beam, the total image charge J is formulated by integrating the image charge density with a weight of the transverse distribution inside the duct area,

$$J(R,\theta) = \int_0^R \int_0^{2\pi} j(r,\phi,R,\theta)\rho(r) r dr d\phi. \quad (2)$$

It is easily expanded by a power series,

$$\begin{aligned} J(R,\theta) &= \frac{I_b}{2\pi R}\{1+\frac{2}{R}(\langle x\rangle\cos\theta+\langle y\rangle\sin\theta) \\ &\quad +\frac{2}{R^2}\left[\left(\langle x^2\rangle-\langle y^2\rangle+\langle x\rangle^2-\langle y\rangle^2\right)\cos 2\theta\right. \\ &\quad \left.+2\left(\langle xy\rangle+\langle x\rangle\langle y\rangle\right)\sin 2\theta\right] \\ &\quad +\text{higher orders}\}, \end{aligned} \quad (3)$$

where I_b is the beam charge, $\langle x\rangle$ and $\langle y\rangle$ are the charge center of gravity of the beam, $\langle x^2\rangle$ and $\langle y^2\rangle$ are the horizontal and vertical mean square half widths of the beam in the x and y directions, and $\langle xy\rangle$ is the x-y coupling in the transverse plane, respectively. A transverse beam-width measurement is performed to detect the second-order (quadrupole) moment J_q at the least orders. The quadrupole moment is described by using the following eight-pickup amplitudes [V_i (i=1-8)] of the BESM:

$$\begin{aligned} J_q &\equiv \int_0^{2\pi} J(R,\theta)\cos 2\theta d\theta \Big/ \int_0^{2\pi} J(R,\theta) d\theta, \\ &= \frac{1}{R^2}(\langle x^2\rangle-\langle y^2\rangle+\langle x\rangle^2-\langle y\rangle^2), \\ &\simeq \frac{\sum_{i=1}^{8} V_i\cos 2\theta}{\sum_{i=1}^{8} V_i}, \end{aligned} \quad (4)$$

0-7803-7738-9/03/$17.00 © 2003 IEEE

Normalization by summing the eight-pickup amplitudes needs to cancel out the beam charge fluctuations due to any beam measurement jitter. It is understood that the quadrupole moment is related to the transverse beam widths, while it also depends on the beam positions.

3 BEAM ENERGY-SPREAD MONITOR

Figure 1 show schematic cross-sectional drawings of the BESM. The mechanical design parameters are summarized in Table 1. The BESM is a conventional monitor with eight-stripline electrodes fabricated from stainless steel (SUS304) with $\pi/8$ rotational symmetry. The stripline length L was determined to be as long as could possibly be installed into the limited spaces in the beam line so as to increase the signal-to-noise ratio. The inner and outer radii, R_1 and R_2, and the angular width α of the electrode were chosen so as to comprise a 50-Ω-transmission line. The eight pickups with a relatively narrow angular width of 15 degree are mounted with a tilt of $\pi/8$ rad at the symmetrical polar coordinates in order to avoid any direct impinging of synchrotron radiation and off-energy electrons to the electrode surfaces at a large energy dispersion section.

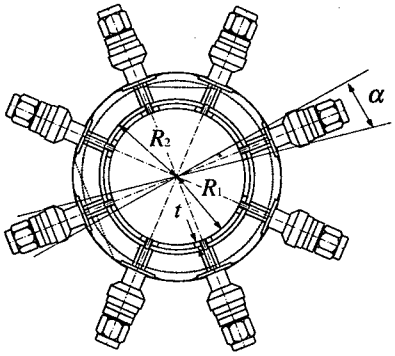

Figure 1: Schematic cross-sectional drawing of the beam energy-spread monitor.

Table 1: Mechanical design parameters of the BESM.

Mechanical parameter	
Innner radius R_1 (mm)	20.6
Outer raidus R_2 (mm)	23.4
Electrode angular width α (deg)	15
Electrode thickness t (mm)	1.5
Electrode length l (mm)	132.5
Total length L (mm)	283

4 BEAM TEST

Beam experiments using single-bunch electron beams of 0.9 and 8 nC/bunch were carried out under the nominal operation condition at the 180-degree arc after sector B where the beam energy is 1.7 GeV. The layout of the beam line is described elsewhere [2]. The multipole moments of the electron beam were measured by the BESM while the transverse spatial profiles of the beam were directly measured by a fluorescent screen monitor (SC) installed behind the BESM with a beam-synchronous CCD camera and a video-image frame grabber in order to calibrate the BESM results at a rate of 1 Hz.

The transverse beam widths at the locations of these monitors were controlled by changing the rf phase of the booster klystron at sector B. The BPMs located at sectors A, B and the arc monitored the beam positions and charges of the beam in order to control the beam positions and energy stably through the feedback systems without any beam loss during the experiment.

The beam experiments with the BESM were performed by measuring the quadrupole moment of the 0.9-nC electron beam, as a function of the horizontal (x) and vertical (y) beam positions. In this measurement the rf phase of the booster klystron at sector B was fixed to reduce the energy spread to its minimum with the beam-orbit and energy feedbacks at sector B off. The beam positions at the BESM were controlled by the field strength of upstream x and y steering magnets. The quadrupole moments of the 0.9-nC and 8-nC electron beam depending on the rf phase of the booster klystron were also measured while the beam positions of the electron beam were fixed at the center of the BESM with the beam-orbit and energy feedbacks on. One data point of the BESM was obtained by averaging 200 successive data with the statistical errors after the position dependence was corrected.

5 EXPERIMENTAL RESULTS

Figure 2 shows the variations of the quadrupole moment depending on the field strength of the upstream x steering magnet for the 0.9-nC electron beam with and without the beam-position corrections. It is clearly shown that after the corrections of the beam position, the quadrupole moment is constant over the measured range of the field strength of the steering magnet within the estimated errors. Figure 3 shows the variations of the quadrupole moment for the 0.9-nC and 8-nC electron beam depending on the rf phase of the booster klystron after the beam-position correction. For the 0.9-nC electron beam the beam-width data directly measured by the screen monitor are also added in order to compare the BESM data after the beam-profile correction on the transverse distributions.

The BESM data are related to the SC data by,

$$\langle x^2 \rangle - \langle y^2 \rangle = f\left(X^2 - Y^2\right) + g, \qquad (5)$$

where X and Y are the transverse beam widths measured by the screen monitor in HWHM, g is a fitting parameter caused by the gain imvalance and the geometrical errors of the eight pickups of the BESM, and the parameter f is the beam-profile correction factor depending upon the transverse distributions of the electron beam (see Ref. [7]). The

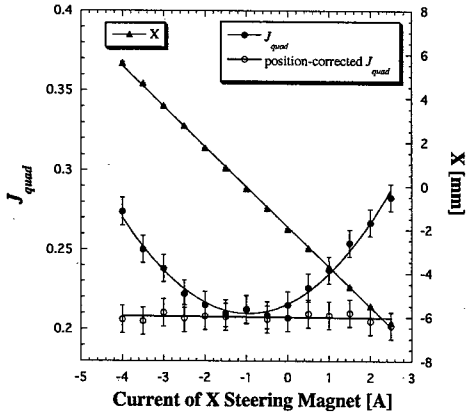

Figure 2: Variations of the quadrupole moment depending on the field strength of the horizontal upstream steering magnet for the 0.9-nC electron beam.

result shows that the transverse beam profile is approximately well described not by a Gaussian function, but by a parabolic function. The BESM data agree well with the corrected SC data within the estimated errors over the measured region of the rf phase.

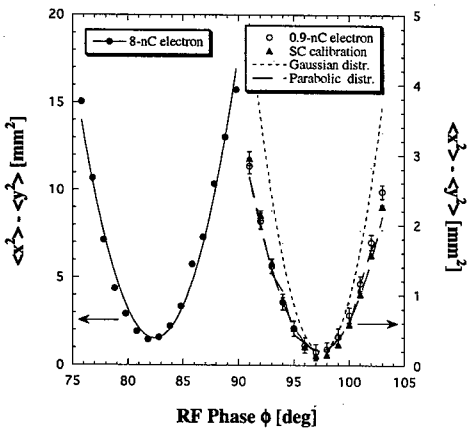

Figure 3: Variations of the quadrupole moment depending on the rf phase of the booster klystron.

Assuming that the vertical dispersion η_y is zero at the BESM, the energy spread ΔE of the electron beam can be estimated from the transverse beam widths along with the optics parameters (β functions and horizontal dispersion η_x) and the transverse emittances as follows:

$$\langle x^2\rangle - \langle y^2\rangle \simeq \beta_x\epsilon_x + (\eta_x\Delta E/E)^2 - \beta_y\epsilon_y + g, \quad (6)$$

where g is the same parameter as defined in Eq.(5), and the transverse emittances, ϵ_x and ϵ_y, were measured by wire scanners at the end of sector B (see Ref. [7]). The result shows that the obtained energy spreads are 0.150±0.007% and 0.264±0.004% for the electron beams with charges of 0.9 and 8 nC/bunch at the rf phase of the energy-spread minimum, respectively. The resolution for the energy-spread measurement is on the order of 10^{-3}, depending on the beam charge. Figure 4 shows the time trend of the measured quadrupole moment and the rf phase of the booster klystron during six hours, where the BESM data were obtained pulse-by-pulse and the rf phase data were taken every 1.5 minute. The good agreement between these two data is a clear demonstration of the principal function of the BESM.

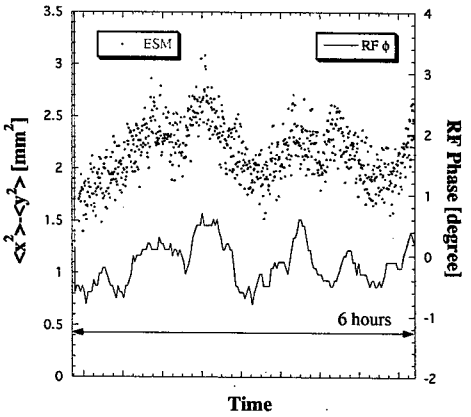

Figure 4: Time trend of the quadrupole moment and the rf phase of the booster klystron.

6 CONCLUSIONS

The second-order moments of single-bunch electron beams were accurately measured by the nondestructive beam-energy-spread monitor with multi-stripline electrodes at the injector linac. The result shows that the analyzed energy spreads were 0.150±0.007% and 0.264±0.004% for electron beams with charges of 0.9 and 8 nC/bunch at the rf phase of the energy-spread minimum, respectively. The authors have a plan to investigate beam characteristics of two beam bunches in the two beam bunch injection scheme in the nominal operation mode.

7 REFERENCES

[1] S. Kurokawa and E. Kikutani, Nucl. Instrum. Methods Phys. Res. A499 (2003) pp.1-7.

[2] I. Abe *et al.*, Nucl. Instrum. Methods Phys. Res. A499 (2003) pp.167-190.

[3] T. Suwada, *LINAC2000, Monterey, California, U.S.A., 2000*, pp.199-201.

[4] R. H. Miller, J. E. Clendenin, M. B. James and J. C. Sheppard, *HEAC'83, Fermilab, U.S.A., 1983*, pp.602-605.

[5] T. Suwada, Jpn. J. Appl. Phys. 40 (2001) pp.890-897.

[6] J. D. Jackson, *Classical Electrodynamics* (John Wiley & Sons, New York, 1975) 2nd ed., p.54.

[7] T. Suwada, M. Satoh and K Furukawa, Phys. Rev. ST Accel. Beams **6** 032801 (2003).

THE HIGH CURRENT TRANSPORT EXPERIMENT FOR HEAVY ION INERTIAL FUSION*

P.A. Seidl, D. Baca, F. M. Bieniosek, C.M. Celata, A. Faltens, L. R. Prost, G. Sabbi, W. L. Waldron,
Lawrence Berkeley National Laboratory, Berkeley, CA 94720 USA
R. Cohen, A. Friedman, S.M. Lund, A.W. Molvik
Lawrence Livermore National Laboratory, Livermore, CA 94550 USA
I. Haber
University of Maryland, College Park, MD 20742 USA

Abstract

The High Current Experiment (HCX) at Lawrence Berkeley National Laboratory is part of the US program to explore heavy-ion beam transport at a scale representative of the low-energy end of an induction linac driver for fusion energy production. The primary mission of this experiment is to investigate aperture fill factors acceptable for the transport of space-charge-dominated heavy-ion beams at high space-charge intensity (line-charge density ~ 0.2 μC/m) over long pulse durations (>4 μs) in alternating gradient electrostatic and magnetic quadrupoles. This experiment is testing -- at driver-relevant scale -- transport issues resulting from nonlinear space-charge effects and collective modes, beam centroid alignment and beam steering, matching, image charges, halo, electron cloud effects, and longitudinal bunch control. We present the results for a coasting 1 MeV K^+ ion beam transported through the first ten electrostatic transport quadrupoles, measured with beam-imaging and phase-space diagnostics. The latest additions to the experiment include measurements of the secondary ion, electron and atom coefficients due to halo ions scraping the wall, and four magnetic quadrupoles to explore similar issues in magnetic channels.

INTRODUCTION

The High Current Experiment (HCX) [1] located at Lawrence Berkeley National Lab and carried out by the HIF-VNL (Heavy-Ion Fusion Virtual National Laboratory: a collaboration between groups at LBNL, LLNL and Princeton Plasma Physics Laboratory, which has the goal of developing heavy-ion accelerators capable of igniting inertial-fusion targets for electric power production) is designed to explore the physics of intense beams with line-charge density of about 0.2 μC/m and pulse duration $4<\tau<10$ μs, close to the values of interest for a fusion driver. Experiments are performed near driver injection energy (1-1.8 MeV). HCX beam transport is at present mainly based on electrostatic quadrupole focusing, which provides efficient transport at low energy and provides clearing fields which sweep out unwanted electrons. However, magnetic transport experiments have commenced, to gain operational experience and to explore special limitations associated with magnetic focusing, in particular the onset of transport-limiting effects due to electrons trapped in the potential well of the ion beam.

* Supported by the Office of Energy Research, US DOE, at LBNL & LLNL, contract numbers DE-AC03-76SF00098 and W-7405-Eng-48.

EXPERIMENTAL CONFIGURATION

The present configuration begins with the K^+ ion source and injector, an electrostatic quadrupole matching section (six quadrupoles), and the first 10 electrostatic transport quadrupoles.

A multi-purpose diagnostic station (D-end) is at the end of the beam line (Fig. 1). Beam diagnostics are also located at the interface of the matching section and the ten transport quadrupoles (QD1) and after the last (D2) transport quadrupole in the periodic lattice. They include transverse slit scanners, Faraday cups and current transformers. The Gas and Electron Source Diagnostic (GESD) is located at the end of D-end.

Most measurements so far have been made at 1.0 MeV, to avoid any high voltage insulation issues in the injector. Though much of the beam physics should scale predictably between 1 and 2 MeV, future measurements will verify this, and also establish operating experience at higher injection energy. The beam energy at present is limited to 1.5 MeV until the water resistor that distributes the voltage along the injector column is modified. The column has operated at 1.8 MV during checks of the injector optics modifications.

To date, contact-ionization and alumino-silicate ion sources have been used. The injector beam characterization measurements and the first measurements through the HCX were made using the contact ionization source, before switching to the alumino-silicate source (100 mm diameter) in April 2002. Earlier versions of alumino-silicate sources suffered from poor current-density uniformity. There was a considerable alumino-silicate large-source R&D effort during 2001-2 aimed at improving the uniformity. As a consequence of improvements to the diode optics and the improvements to the ion source [2], the hollowness of the beam has decreased from 20% to 10%. The emittance has decreased from $\varepsilon_n = 10 \times 10^{-7}$ to 6×10^{-7} m compared to the theoretical minimum, $\varepsilon_n = 2R\sqrt{kT/m} = 1.7 \times 10^{-7}$ m where T is the source temperature and R is the radius. The experimental current is within 2% of the expected value based on 3D PIC simulations.

0-7803-7738-9/03/$17.00 © 2003 IEEE

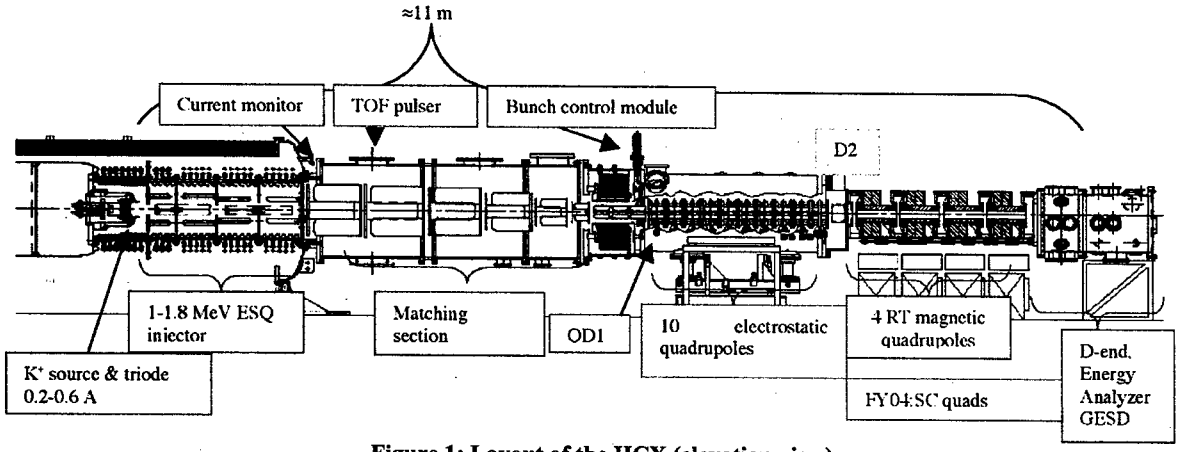

Figure 1: Layout of the HCX (elevation view).

In the operating range from 1.0 to 1.8 MeV the beam brightness ($B_n = I/\varepsilon_n^2$) is $0.7 < B_n < 2$ A/mm^2, and the number of ions per pulse is $6x10^{12} < N < 1.7 \times 10^{13}$.
First beam was transported in the HCX in January 2002, less that one month after the assembly of the initial configuration.

MATCHING AND TRANSPORT THROUGH ELECTROSTATIC QUADRUPOLES

The six-quadrupole matching section is designed to compress the beam area transversely by a factor ≈25 and produce the matched beam parameters for periodic transport in the electrostatic lattice. In this significant beam manipulation the radii of the first (QM1) and last (QM6) matching quadrupole bores are r_p=100 mm and 31 mm respectively, and the maximum envelope excursions occur in the first and second quadrupoles, with the beam filling radii up to 0.8• r_p. The beam centroid exiting the injector is offset from the beam line axis by a few millimeters and milliradians, and the centroid undergoes betatron oscillations through the first three (QM1-3) quadrupoles of the matching section until being corrected in QM4-6. QM4-6 may each be displaced in the horizontal and vertical directions by ±15mm to correct the beam centroid offset. Matching (QM1-6) and transport quadrupole (Q1-10) voltages range up to ±43 kV, and focusing gradients up to 10kV/cm^2. (Experiments at higher injection energy will require proportional increase in the quadrupole potentials to achieve a nearly identical envelope solution.)

Although the beam fills a relatively large fraction of the aperture in the early part of the matching section, pickup signals capacitively coupled to the quadrupole electrodes indicate that beam loss is less than 0.5% through the middle, or "flattop" of the beam pulse. Beam loss at the head and tail of the current pulse may be greater, and is presently being studied. The pickup signal due to lost ions is effectively amplified by the large secondary electron coefficient [3], making this diagnostic more sensitive to beam loss than comparisons of the total beam current data at the injector exit to that at QD1. The Faraday cup-current transformer ratio is >95(±2)%.

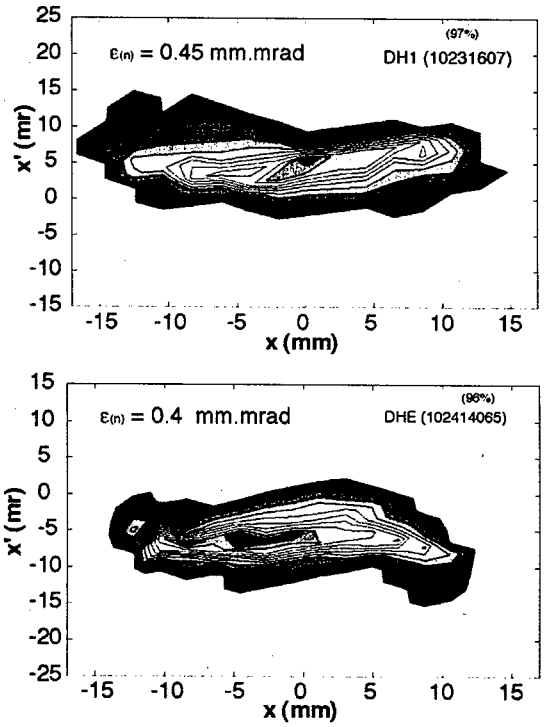

Figure 2: Horizontal phase space (a) before and (b) after the 10 quadrupole periodic transport lattice, for the 80% fill factor case, for a time slice near mid-pulse.

The steering quadrupole displacements (±1-4 mm typical) are determined by calculating the (single particle) trajectory through QM4-6 for a misaligned beam, and then solving for the required displacements. Three steering quadrupoles QM4-6) are used to align the beam centroid at QD1 (instead of the minimum of two displacements) subject to the additional constraint of minimizing the sum of displacements of the lenses. Following such a procedure, the beam centroid positions

(<x>, <y>) and angles (<x'>, <y'>) are routinely within 0.5 mm and 2 mrad of the central axis of the channel.

The horizontal phase space at QD1 is shown in Fig. 2a. The stability and reproducibility of the envelope measurements have been characterized by a standard deviation of ≈0.3 mm and ≈1 mrad among five repeated measurements. The achievable beam envelope and centroid control are key ingredients in determining the allowable filling factor as determined by beam loss and emittance growth. Integrating the envelope equation through the ten-quadrupole lattice to D2 (initialized with QD1 measures of envelope radii, convergence angles, current, and D-end measurements of beam energy) gives a calculated envelope in agreement with the experiment at the D2 location to within 0.4 mm and 3 mrad, (<10%). Early calculations of the envelope showed a larger discrepancy, which led to an analysis of several effects, which resolved most of the disagreement. The effects are: (1) Realistic fringe field model based on 3D field calculations; (2) quadrupole E_z and corresponding radial focusing force; (3) corrections for the grounded slit plates of the intercepting diagnostics that short out the self-field of the beam near the diagnostic; and (4) more accurate determination of the beam current and energy.

We have made two fill-factor measurements, for the envelope filling ≈60% and 80% of the available bore diameter in the transport channel. Each case requires a different matching solution in the matching section, and the fill factor (ratio of the beam major radius to aperture radius) is increased by tuning the upstream beam to the matched beam conditions in the transport section for a lower focusing gradient, rather than by changing the current.

PIC simulations [4] predict that matched beam excursions filling 80% of the quadrupole bore would result in negligible emittance growth, if perfect alignment and envelope control were maintained. Within the experimental sensitivity there is no evidence of emittance growth at the end of the electrostatic lattice for both 60% and 80% fill factor cases. Systematic biases such as those due to finite slit widths and rotational misalignments are still being analyzed, and may contribute an uncertainty of 10-20% to the emittance. Figure 2(b) show the horizontal beam phase space in the converging plane for the more aggressive 80%-filling factor of the 46mm-diameter aperture. Since the transportable current scales as the square of the fill factor, determining its maximum will have a large impact on the cost of multi-beam induction accelerators for HIF.

In the entire distance, and for both fill factor cases, currents collected on quadrupole electrodes indicate particle losses of <0.5%, while Faraday cup current monitors indicate ≈1% losses. Halo measurements indicate that the beam profile intensity ≈5 mm from the hard-edge of the beam distribution falls to the order of 10^{-4} of the peak density in the core of the beam, the sensitivity limit with present slit-cup diagnostics.

In the context of multiple beam arrays for heavy-ion fusion, electrostatic quadrupoles composed of cylindrical electrodes make a compact unit cell. For the beam measurements to date, the current density averaged over a unit cell is <J>≈40 A/m^2 (denominator includes the area occupied by the beam focusing electrodes between adjacent channels of an array), and future measurements at 1.8 MeV will increase this by 2-3x. Furthermore, it appears from these measurements that higher <J> might be possible. Compiling data to determine the optimum filling factor is a principal goal of the experiment.

BEAM CHARGE DISTRIBUTION

We observe a diamond-shaped beam pattern at QD1 (Fig. 3) and at D-end, which is attributed to nonlinear fields (that is, anharmonic field components not varying in direct proportion to the transverse coordinates) in the ESQ injector and electrostatic image forces in the matching and transport section. All the J(x,y) data will be used with the phase space data at QD1 to construct a consistent particle distribution for simulation studies [5].

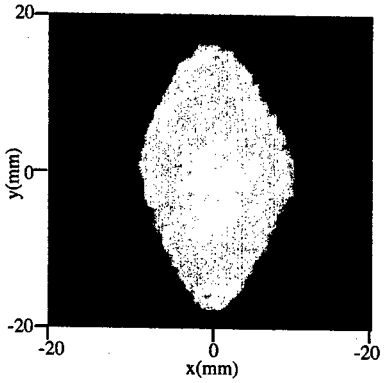

Figure 3: Beam current density profile J(x,y, t≈midpulse) measured with crossed slits at QD1.

The time-resolved crossed-slit data show that at QD1 the profile of the beam during the rise and fall of the beam current pulse is larger than during the flattop. Ballooning of the beam head was predicted for the beam exiting the injector from 3D particle-in-cell simulations and is attributed to a voltage risetime in the diode which is presently too slow to match the space-charge evolution of the current. Calculations of the head-tail dynamics through the rest of the HCX are underway.

TRANSVERSE PHASE SPACE DIAGNOSTIC DEVELOPMENT

In prototype tests, we have confirmed the utility of optical diagnostics for rapid and highly detailed measurements of beam phase space distributions [6].

Figure 4 shows an image from a typical slit scan from a prototype optical emittance scanner. The beam is imaged through the existing slits, already utilized in the conventional emittance scanner (Fig. 2), onto a thin alumina ceramic wafer, where charge buildup is prevented from secondary electron emission by a grounded wire grid placed directly on the screen. The response time of the

alumina is shorter than the rise (200 ns) and fall time of the beam current pulse. The images are viewed behind the wafer with a gated, image-intensified CCD camera. The slit is oriented vertically and is moved horizontally by a step motor. The images can be integrated to provide a simulated slit scan for comparison with conventional slit scanner data. A large amount of new phase space correlation information is available from the shapes of the images. Detailed analysis of the data is underway [5]. The technique will be used in the more crowded diagnostic gap at D1, and slits will be replaced with a pepper-pot hole arrangement, which will provide fully-correlated four-dimensional transverse phase space data.

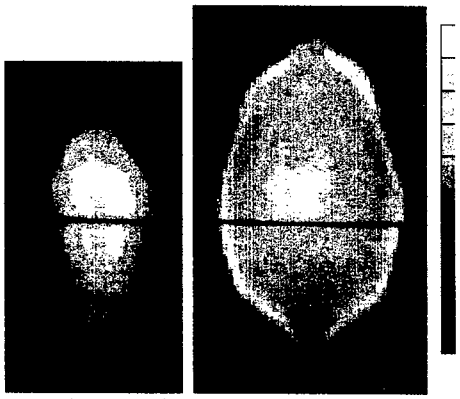

Figure 4: Beam intensity profile for 60% (left) and 80% (right) fill factor at the D2 location based on measured optical slit scan, referred to the horizontal slit plane. The scale for the images are 2.28 x 4.26 cm and 3.11x5.15 cm.

MEASUREMENT OF SECONDARY ELECTRONS AND ATOMS

The Gas-Electron Source Diagnostic (GESD) is designed to measure the gas desorption and secondary electron and ion emission due to heavy-ion beams impacting a surface [3]. Approximately 0.1% of the beam current passes through a small aperture and strikes a target, adjustable between angles of incidence from 75° to 88° relative to normal.

We observed a significant variation in secondary electron emission with the angle of the target (yield varies from 30-130 between 78° and 88°). Beam ions lost to the walls will be near grazing incidence, and therefore will have the higher values of secondary emission coefficient.

We find the gas desorption yield varies from 8-12 x 10^3/ion, with the angular dependence and magnitude similar to CERN data [7] with different beam parameters.

A beam line of four pulsed magnetic quadrupoles, instrumented with diagnostics to measure the production and energy of trapped electrons, secondary atoms and ions was installed [3,8] downstream of the first group of 10 electrostatic quads in April 2003, and will be a principal area of activity in the next year.

DIAGNOSTICS FOR ABSOLUTE BEAM ENERGY MEASUREMENTS

Two new diagnostics, an electrostatic energy analyzer (EA) and a time-of-flight pulser (TOF) were installed to more precisely determine the beam energy and to make longitudinal phase-space measurements.

The EA, a 90°-spectrometer with a radius of 46 cm, and a gap of 2.5 cm was operated up to ΔV = 110 kV. The relative accuracy is ± 0.2%, allowing us to follow variations in the beam energy as a function of time during the beam pulse. The calibration depends on the geometry and fringe fields of the analyzer. By changing the beam energy by a known absolute amount, we were able to provide an independent calibration: The beam passed through a 28%-transparent hole-plate, and the gas cloud created at the hole-plate stripped singly charged K^+ beam ions to doubly charged K^{2+}. The absolute calibration was determined by varying the electric potential at the plate, and thus the energy of the K^{2+} ions entering the EA.

For the TOF measurements, a fast pulser in the matching section (0.3 μs FWHM) induced 1% energy perturbations. These energy pulses manifest as 5-10% current perturbations measured 5.4 m downstream. Figure 5 shows the perturbation on the beam current waveform measured downstream along with a theoretical calculation of the expected perturbation based on a 1-D cold-fluid model. Comparing the measured and expected delay time of the perturbation determines the absolute energy of the beam.

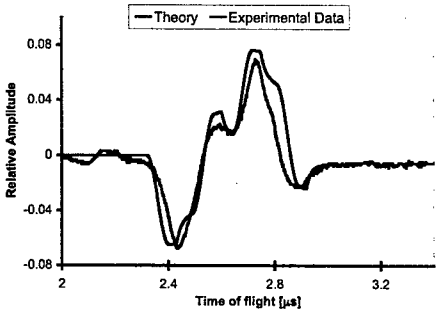

Figure 5: Cold fluid model vs. perturbation on the beam current waveform. Initial perturbation applied @ t = 0.

Both the TOF and EA diagnostics determine the absolute beam energy to ± 2%, with both measurements agreeing within these uncertainties. The precise determination of the energy is essential for the agreement between envelope simulations and experimental data.

Fig. 6 shows the longitudinal energy distribution obtained with the EA. The 10%-higher energy head and low-energy tail are understood to be from the beam longitudinal space charge, which accelerates particles at the front end of the bunch and decelerates particles at the rear of the pulse. These data also shows that in the middle of the pulse, the mean beam energy is constant to within 0.5 % for 3.1 μs.

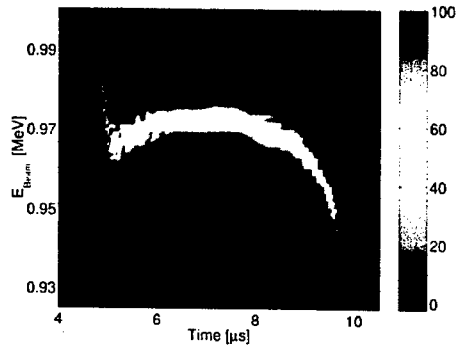

Figure 6: Longitudinal Energy Distribution measured with the electrostatic energy analyzer. K^+ ions were detected at the beam head with 1.1 MeV (not visible on this scale).

This information (particularly the head and tail energy variations with respect to the core of the beam pulse) will be used to help complete the design of a bunch end control module [10] to be installed next year between the matching section and the periodic transport lattice. This represents a first step towards conducting more longitudinal physics experiments.

SUPERCONDUCTING QUADRUPOLE DEVELOPMENT

Superconducting magnets will be installed in HCX. While pulsed magnets provide a more flexible alternative for initial experiments, superconducting technology is the most attractive in view of the ultimate fusion driver application. Superconducting magnets based on flat coils have received considerable attention in recent years, due to their simplicity and cost-effectiveness. The HCX design uses double-pancake coils wound around iron cores, and was derived from an earlier design of a multiple beam quadrupole array for heavy ion fusion.

A prototype cryostat housing two quadrupole magnets (an FD doublet) is completed. The unit includes a shielded straight chimney, needed to maximize the space available for induction acceleration cores surrounding the transport line of an induction linac.

The measurement of the field quality of an optimized prototype quadrupole is commencing [9].

CONCLUSIONS

The transport results through the first ten electrostatic quadrupoles show good beam control, agreement with an improved envelope model, and indicate that transport at 80% beam filling factors at the front end of a heavy-ion induction linac might be possible with acceptable emittance growth and beam loss. Other fill factors will be measured. Details of the measured phase space distribution are being used to initialize particle-in-cell simulations for comparison of data with theoretical models. Prototype diagnostic tests show that higher data acquisition rates and sensitivity to more correlations between the transverse phase space measurements will enhance future experimental output.

Future measurements of secondary electrons, ions and atoms in magnetic quadrupoles will also have a direct impact on future heavy ion induction accelerators.

Because the injected beam is non-uniform, and inevitably mismatched to a small extent, the first few quadrupoles in the HCX lattice as well as the quads in the matching section provide a region where the beam distribution can relax. While 10 or 20 quads are too few for settling questions of emittance evolution in a long transport system, they are of the correct length for the rapid evolution of the emittance and beam profile, which is expected in the front end of an accelerator. An additional 20-30 quadrupoles would increase the transport length to $4.5\text{-}6\bullet(2\pi v/\omega_p)$ plasma periods. Theoretical models predict that this would be just enough to observe the relaxation of phase space and distribution inhomogeneities [4, 5]. This leads to setting the bore diameter and choosing the optimum current.

ACKNOWLEDGEMENTS

We are grateful to R. Hipple, W. Strelo and their staff for excellent technical support.

REFERENCES

[1] P.A. Seidl, et al. Overview of the Scientific "Objectives of the High Current Experiment for Heavy-Ion Fusion" Proc. 2001 Part. Accel. Conf. pp. 2932-2934, IEEE #01CH37268C. Piscataway, NJ 08855. S.S. Yu et al., "An updated point design for heavy ion fusion", to be published in Fusion Sci. Tech.

[2] J.W. Kwan et al, LASER AND PARTICLE BEAMS 20 (4), 2002. LBNL-50221.

[3] A.W. Molvik et al., "Initial experimental studies of electron accumulation in a heavy-ion beam", these proceedings.

[4] C.M. Celata et al., LASER AND PARTICLE BEAMS 20 (4) p.577 (2002). C.M. Celata et al., "Particle-in-cell simulations of the high current experiment", these proceedings.

[5] A.Friedman et al., "Simulation using initial 4D beam particle distributions synthesized from experimental data", these proceedings.

[6] F.M. Bieniosek et al., these proceedings.

[7] E. Mahner, et al., Phys. Rev. ST-AB, 013201, (2003).

[8] A.W. Molvik et al., LASER AND PARTICLE BEAMS 20 (4), 2002. LBNL-51009.

[9] G.L. Sabbi et al., these proceedings.

[10] C. Burkhart, "The Closed-loop Amplifier Regulated Driver, a High Accuracy, Low Cost Modulator for HIF Accelerators," US Dept. of Energy SBIR final Report, DE-FG03-00ER83010, May 2001.

EMITTANCE MEASUREMENTS WITH A PULSED POWER PHOTO-INJECTOR

J. Smedley, T. Srinivasan-Rao and T. Tsang, Brookhaven National Laboratory, Upton, NY
J. P. Farrell and K. Batchelor, Brookhaven Technology Group, Setauket, NY

Abstract

This paper describes measurements of beam spot size and emittance of electron beams from a pulsed power photo-injector operating at 150keV output energy. In these measurements, electron bunches with charge up to 20 pC were created by a 300 fs pulse duration Ti: Sapphire laser system illuminating a polished copper cathode. Images of the electron beam were captured at two locations downstream from a solenoid focusing magnet. The focal spot size was studied as a function of bunch charge and accelerating gradient. Beam waists down to 85 microns were obtained. The focal spot size was found to be dominated by spherical aberration at low beam charges, however the beam trajectory is in good agreement with simulation.

INTRODUCTION

Photo-injector based electron sources represent the current state-of-the-art in the production of low emittance, high brightness electron beams. Pulsed power devices are capable of producing and maintaining a significantly higher accelerating gradient than other accelerating schemes, such as DC and RF guns. The benefit of larger accelerating gradient is investigated in section one, which presents simulations done with MAFIA and PARMELA of the electron trajectories, expected beam waist size and beam emittance. Section two describes the measurements of emittance made with the pulse power photo-injector.

SIMULATION

The electron emission from the pulsed gun as been modeled with numerous beam simulation packages [1]. The simulations presented here were performed in two stages. MAFIA was used to simulate the electron emission and initial acceleration. In the interest of computational efficiency, PARMELA was then used to transport the beam through the solenoid and calculate the expected waist size.

The geometry used for simulation in MAFIA is shown in fig. 1. It consists of two parallel electrodes, an anode and a cathode, with cylindrical symmetry. The spacing between the electrodes is adjustable (a 2mm gap is shown). The anode contains a 2mm diameter aperture to allow electron emission. The cathode is biased at –150 kV DC. A static voltage is assumed, as the real voltage pulse duration is 3000 times the duration of the photo-cathode laser. The electron bunch has a Gaussian temporal and spatial profile, with a FWHM of 300 fs and 0.43 mm, respectively. Thermal emittance has been neglected in these simulations, however previous simulations [1] for similar conditions have suggested that the typical thermal contributions to the emittance for this geometry is 0.17 mm-mrad.

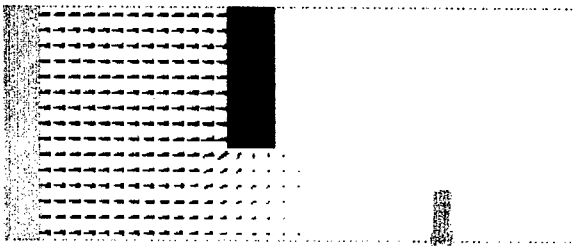

Figure 1 Geometry used in MAFIA (2mm electrode spacing). Field plot and electron bunch also shown.

After the beam has passed 2mm beyond the anode, the 4D phase space and charge of all of macro particles is recorded. The beam properties are calculated by MAFIA at this point. This information is used to generate an input file for PARMEL with a suitable charge distribution. PARMELA is used to transport the beam through the solenoid and predict the RMS spot size at the location of the 2nd BPM. The solenoid field was adjusted to produce a waist at this location.

This combination of MAFIA and PARMELA was used to simulate the beam for a variety bunch charges. The electrode spacing was varied in MAFIA as well. Shortening the electrode spacing has two effects: It increases the accelerating gradient, and it increases the lensing effect caused by the aperture in the anode. This lensing effect was found to play a critical role in determining the predicted focal spot size, due to spherical aberration in the solenoid lens. For low charge (under 1pC), this effect is the dominant factor in determining the beam spot size, and therefore limits the sensitivity of the emittance measurement. Figure 2 shows PARMELA calculated trajectories for the 0.5 pC beam emitted from electrode spacings (gaps) of 1 and 2 mm.

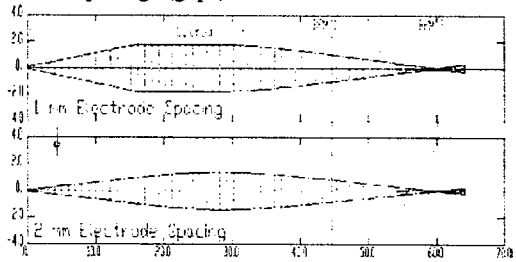

Figure 2 PARMELA simulations of beam trajectory.

The simulation results are shown in Table 1. Note that smaller emittance does not translate to smaller focal dimension, due to spherical aberration. The bias voltage on the cathode is 150 keV. Also shown is a case where

0-7803-7738-9/03/$17.00 © 2003 IEEE

the anode aperture replaced by a conductor that is beam-transparent (e.g. a foil or screen). In this case the beam divergence arises solely from space charge, and the focal spot size is not limited by spherical aberration.

Parameters		Mafia Results			PARMELA
Gap (mm)	Charge (pC)	Norm. Emit. (mm-mrad)	RMS Div. (mrad)	RMS Duration (ps)	Size @ waist (μm)
1	0.5	0.12	48	0.13	100
1	3	0.48	53	0.18	180
1	10	0.98	66	0.32	510
2	0.5	0.15	26	0.14	60
2	3	0.51	34	0.25	170
2	10	0.90	51	0.53	490
1	0.5	0.12	2	0.12	30

Table 1 Simulation results.

MEASUREMENT

Pulse Generator

The device used to generate the voltage pulse used for acceleration has been described in detail elsewhere [1]. The generator can deliver pulses from 150kV to 1 MV at the cathode, with a pulse duration of 1 ns and a rise and fall of 100 ps. The pulse-to-pulse amplitude stability of the generator is about 5%. The cathode consists of a flat, polished copper surface, with the edges beveled to reduce field enhancement. The anode is a stainless steel plate with a 2 mm diameter hole in the center. Micrometers external to the vacuum system control the position of this plate, allowing the inter-electrode spacing to be adjusted in-situ.

The laser used to extract electrons from the cathode was a frequency tripled, regeneratively amplified Ti: Sapphire system. The parameters of this system are: up to 80 μJ of 266 nm light, with a pulse duration of 300fs. The laser spot on the cathode had a FWHM of 0.43mm. The quantum efficiency (QE) of the cathode was measured to be $7x10^{-6}$ for an applied field of ~100 MV/m. The QE and it's dependence on the applied field has been studied previously [1]. Synchronization between the voltage and the photo-cathode laser is accomplished by using a 250mJ KrF Excimer laser to trigger a high pressure SF_6 spark gap in the pulser transmission line.

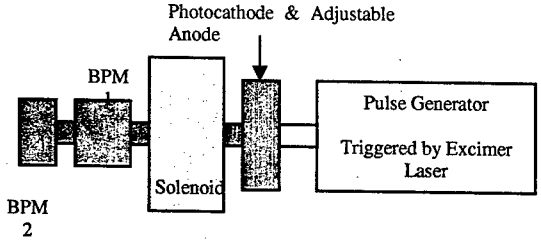

Figure 3 System Schematic

Emittance Measurement

To measure the emittance, a solenoid-focusing magnet has been placed at the output of the HV diode (fig. 3). The current to the solenoid is changed to vary its focusing strength. Two beam profile monitors (BPM) with a drift distance of 15.4 cm between them, are located down stream from the solenoid. Each BPM consists of a ~30μm thick layer of phosphor (Gd_2O_2S:Tb) deposited on a 37μm thick Al foil mounted perpendicular to the beam axis. A metal mirror behind the foil allows the phosphor to be imaged onto a camera outside the vacuum system. This mirror is electrically isolated and connected to a charge sensitive preamplifier, allowing it to act as a Faraday Cup.

For these measurements, the pulse generator was configured for a maximum voltage of 150 kV. Electrode spacings of 1, 1.5 and 2 mm were investigated, resulting in accelerating gradients of 75-150 MV/m. No field emission current was observed at these gradients; previous measurements[1] have observed the onset of significant dark current only at fields greater than 600 MV/m for a well-conditioned cathode.

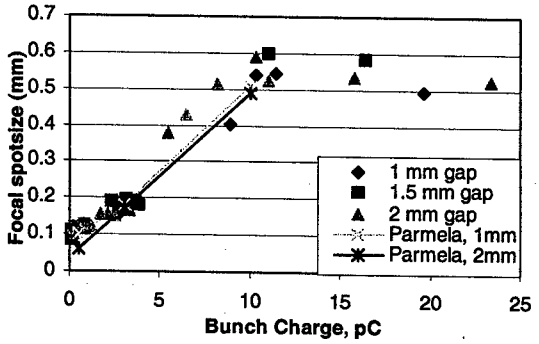

Figure 4 Waist size vs bunch charge

Figure 4 shows the measured rms beam radius at BPM 2 as a function of bunch charge. The minimum beam radius measured was 85 μm. Figure 5 shows several images from BPM 2, including cross sectional profiles. Both the experiment and the PARMELA simulations indicate, as the beam charge is increased from 0.3 pC to 11 pC, the spot size progresses from a spherical aberration dominated regime to a space charge dominated regime. The cross sectional profiles in the space charge dominated regime deviate significantly from the Gaussian distribution in both the simulations and experiments. The images at BPM 1 could only be obtained for high charge values (greater than 5 pC), as sufficient charge was required to cause observable illumination from the phosphor. For these shots, the measured spot varied from 2.3mm to 3.5mm RMS. Images in BPM 1 and BPM 2 with similar experimental parameters were paired for the emittance calculation. Similar charge values could not always be obtained, as a minimum of 5 pC was required to obtain an observable image on the 1st BPM.

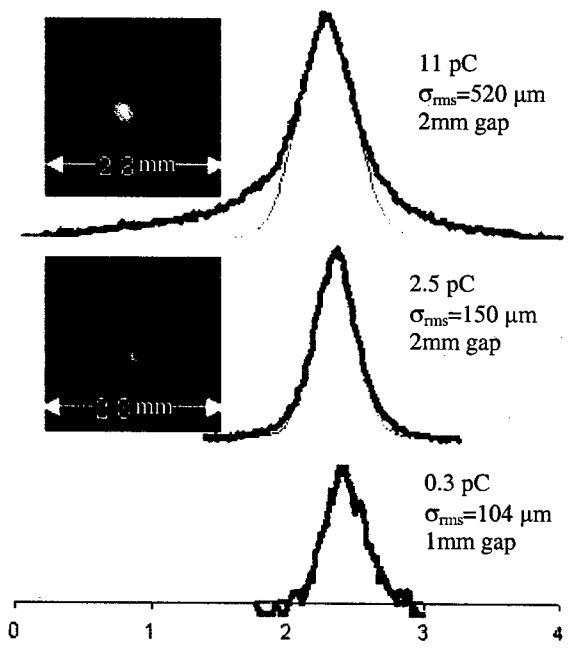

Figure 5 Images obtained with 2nd BPM. Gaussian fit to cross section above half max is displayed. The image for the 0.3 pC case is too faint to show in print. PARMELA simulation (not shown) agrees with the measured profiles.

Emittance Estimate

Due to the limitations imposed by the presence of spherical aberration, this measurement is not very sensitve to the beam emittance. To make a measurement of emittance using a two position technique, it is necessary that the beam spot approaching the focus be dominated by the beam emittance [2]. In this case, for charges above 1-2pC the beam waists shown in figure 3 are space charge dominated. Below this value in our experimental arrangement, the spherical aberration, rather than the emittance or charge, is the dominant factor. However, for cases where the space charge is not dominant, we can assume that the measured waist size is a sum in quadrature of aberration and emittance terms. The emittance can then be estimated by:

$$\varepsilon_n \approx \beta\gamma\left(\frac{\sigma_1\sigma_{2,\varepsilon}}{L}\right)$$

Here $\sigma_{2,\varepsilon}$ represents the beam radius at the beam waist (BPM 2) with the aberration removed, σ_1 represents the beam radius at the BPM 1 and L is the drift distance between the two BPMs. Using the smallest spot obtained (85 μm), the normalized emittance for a low charge (~ .1 pC) is 0.6±0.4 mm-mrad. The 0.3 pC spot shown in figure 5 (104 μm) yields an emittance of 0.5±0.5 mm-mrad. For a charge of 1 pC, the emittance is 1.2±0.7 mm-mrad. Here the assumption that space charge can be ignored is probably not valid, so this case is likely an upper bound. The current density at the cathode in this case is 2.3 kA/cm^2, comparable to that in RF guns. For these parameters, the simulations predict the beam at emission to be limited by thermal emittance to ~0.2 mm-mrad.

In addition to spherical aberration, other factors tend to increase the spot size at BPM 2. The shot-to-shot fluctuation of the beam energy shifts the focus around the location of BPM 2, introducing uncertainty in the location of the waist. In addition, the larger spot measured on BPM 1 must contain a charge of at least 5 pC for the image to be visible. The measured σ_1 is thus larger than that expected for low charges. Both of these effects will tend to cause overestimation of the beam emittance.

CONCLUSION & FUTURE PLANS

Photoemission from a copper cathode has been observed with a 300 fs laser. The resulting electron bunch has been accelerated using a pulsed high voltage to an energy of 150 keV. This beam has been focused by a solenoid, and beam profiles have been acquired at two BPMs. The waist size is dominated by spherical aberration in these cases, reducing the resolution of the emittance measurement. An emittance value of 0.5 mm-mrad for a current density at emission of 0.7 kA/cm^2 was obtained.

Simulations have demonstrated that the spherical aberration is caused by the anode aperture and resulting large beam divergence. Increasing the electrode gap will reduce this effect, while covering the anode aperture with a foil or conducting screen will remove it.

We plan to increase the voltage to ~900kV and measure emittance for higher gradients. We will also improve the diagnostic system to reduce or remove the spherical aberration; this will improve the resolution of our emittance measurement.

ACKNOWLEDGMENTS

The authors would like to thank M. Montemagno and J. Walsh for their expert technical assistance and V. Radeka for his support. J. Smedley would like to thank Q. Zhao for assistance with PARMELA. This work was supported by DOE contracts DE-AC02-98CH10886, DE-AC03-76SF00515 and DE-FG02-97ER82336.

REFERENCES

[1] T. Srinivasan-Rao, et al., "Simulation, Generation, and Characterization of High Brightness Electron Source at 1 GV/m Gradient"; BNL 66464; pres. PAC'99 Conf., New York, NY, 3/29-4/2/99; Proc. 1999 Particle Accelerator Conf., Eds. A. Luccio & W. Mackay, p. 75 (1999), also J. Smedley, *The Physics of the Pulsed Power Electron Gun*, Phd Thesis.

[2] S.G. Anderson, et al., Phys. Rev. ST Accel. Beams **5**, 014201 (2002)

A 50 kV SOLID STATE MULTIPULSE KICKER MODULATOR*

E. G. Cook, Lawrence Livermore National Laboratory, Livermore, CA 94550, USA

P. L. Walstrom, Los Alamos National Laboratory, Los Alamos, NM 87545, USA

Abstract

Performance requirements, design concepts, and test results for a prototype multipulse kicker modulator based on solid-state switches and a voltage-adding transformer topology are described. Tape-wound cores are stacked to form the transformer primary windings and a cylindrical pipe that passes through the circular inner diameters of the cores serves as the secondary winding of the step-up transformer. Boards containing MOSFET switches, trigger circuitry, and energy-storage capacitors plug into the core housings. A 50 kV prototype modulator that meets most of the facility requirements has been designed, fabricated, and tested at LLNL. More recent work has been concerned with designing and testing cores and boards with the full volt-second capability needed for 24-pulse operation. Results of the 50 kV prototype tests, preliminary tests of the full-volt-second cores and boards, and future development needs are described.

INTRODUCTION

In the Advanced Hydrotest Facility (AHF) proposed by Los Alamos National Laboratory, individual proton bunches will be extracted from a 50-GeV synchrotron by bunches will be extracted from a 50-GeV synchrotron by two 50-ohm parallel-plate transmission-line kickers that each produce an arbitrary time sequence of up to 24 kicks. In order to maximize the kick while minimizing the pulser voltage, the kickers are operated in a push-pull mode, a positive voltage pulse being applied one side and a negative pulse with equal magnitude to the other. The vertical plane between the two plates is a virtual ground when the pulses on the two sides are identical except for sign. Each side of the kicker separately represents a 50-ohm load and is separately terminated with a 50-ohm resistor. A kicker modulator capable of generating a string of approximately 25 pulses at arbitrary times within a total time of 100 microseconds or more is needed. Pulses with a 50 kV flattop of ±1% flatness and 75 ns duration, together with rise and fall times of 65 ns or shorter are required. Allowable after-pulse ringing and modulator output baseline changes are defined by the requirement that the circulating beam bunches remaining in the ring after a bunch pair has been kicked out not be disturbed; the maximum allowable baseline shift in AHF is 300 V, 300 ns after the trailing edge of the pulse, although less baseline shift would be desirable. The requirements cannot be met with the commonly used pulse-forming cables or networks (PFNs) switched with thyratrons. Accordingly, an ED&D program to build and test a solid-state modulator using a voltage-adding transformer was started at LLNL in the year 2001.

* Research supported by US Dept. of Energy under contracts W-7405-Eng-36 (LANL) and W-7405-Eng-48 (LLNL).

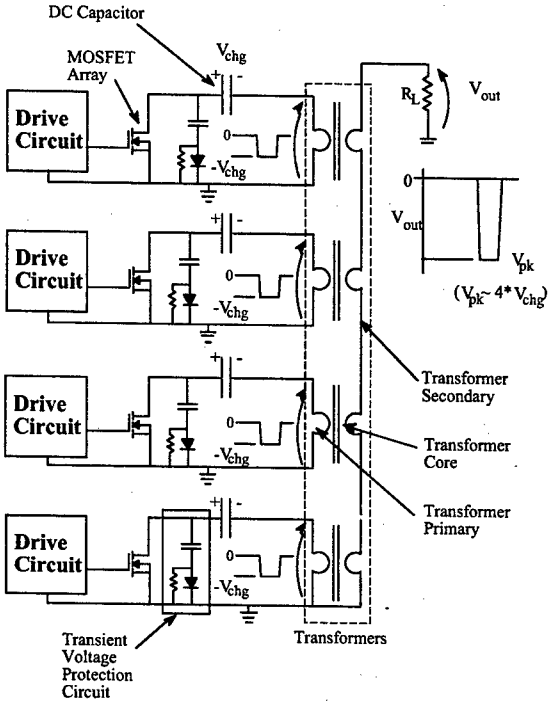

Fig. 1: Simplified circuit schematic for the voltage-adder concept.

THE VOLTAGE-ADDER CONCEPT

The present voltage-adder kicker modulator concept (see Fig. 1) is an outgrowth of solid-state pulsed-modulator development for induction accelerators at Livermore and is based on that of an existing 20 kV modulator built by the Lawrence Livermore National Laboratory for the DAHRT facility at LANL[1]. The voltage adder is basically a step-up transformer with many separately powered parallel single-turn primary windings and a series-connected secondary winding that couples to all of the cores. The transformer is formed from a stack of annular magnetic cores wound from Metglas or other high-permeability magnetic tape material. The output circuit is formed by a center cylinder that passes through the center of the core stack. Pulses of either positive or negative polarity are produced depending upon which end of the stack is grounded, a feature that is useful in powering push-pull kickers. Circuit boards with 12 parallel MOSFET switches plug into the spaces between the core housings. Energy for the pulses is stored in capacitors on the boards. Intrinsic switching times for the MOSFETS are approximately 15

0-7803-7738-9/03/$17.00 © 2003 IEEE

ns. Rise times for output pulse of the entire stack are considerably longer than 15 ns, due to a combination of various effects, including the MOSFET switching time, circuit inductances, and the finite length of the modulator. For a 50-kV pulser that is 10 feet tall, the two-way transit time of a TEM pulse from the top of the stack to the bottom and back to the top is approximately 20 ns. The actual 0-100% rise time for a 50-kV prototype pulser turned out to be approximately 40 ns, not including some overshoot at the front of the pulse. Each core provides approximately 700 V to the output pulse; for 50 kV output, cores are sized to provide the required volt-seconds for the output pulse train, which for AHF is 0.35 V-s for the entire stack. Additional circuits can be switched in to compensate for capacitor voltage droop in a long pulse train.

THE 50 KV PROTOTYPE MODULATOR

Fig. 2: Single-stack 50 kV modulator

A staged hardware development plan for the modulator was described in a paper given at the 2001 Particle Accelerator Conference [2]. The objective of the 2001 Stage 1 effort was a proof-of-principle demonstration of a 50 kV solid-state modulator that could meet most of the pulse requirements for the AHF extraction kicker except the full volt-seconds of the 24-pulse burst. To minimize cost and expedite the demonstration, the modulator used many parts designed to meet DARHT requirements. The modulator was fabricated and tested with a dummy 50-ohm load in 2001. The prototype kicker modulator consisted of 70 toroidal transformer modules with drive circuits. Initially, the cells were arranged in two columns with a crossover conductor connecting the center rods of the two stacks together. In initial tests of the prototype, a peak voltage of ~ 43kV into a 50Ω load was achieved. This was the maximum output voltage that could be achieved without over stressing the MOSFETs with regard to their drain-to-source voltage (the devices used have a maximum drain-source rating of 1000V and ~ 970 volts was measured during the turn-off of the devices). The voltage stress was due to the inductive voltage spike generated as a result of the very fast turn-off of the MOSFETs (< 10ns) and the subsequent dI/dt (~86kA/μs). The circuit boards were therefore modified to slow down the fall time of the gate drive pulse and the turn-off time of the power MOSFETs. After the making the above and other modifications to circuit boards, the modulator stack was rebuilt. In the rebuilding, changes were made to the output cable connections and the double-stack configuration was changed to a single-stack configuration to reduce impedance mismatch effects on the output pulse. The reconfigured modulator, shown in Fig. 2, is a structure approximately 10 feet tall. The reconfigured modulator was tested at 50 kV into a 50-ohm load at a 5 MHz burst frequency. A five-pulse burst is shown in Fig. 3.

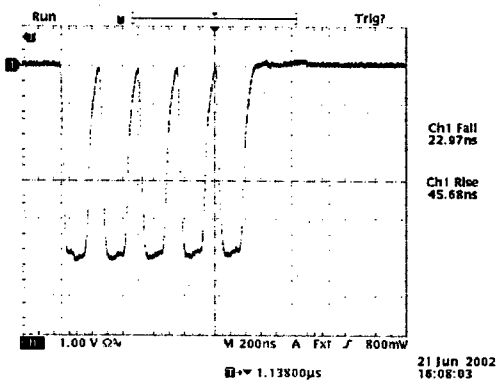

Fig. 3: 50 kV five-pulse burst from the prototype modulator

The ripple/droop over the entire flattop of the pulse of Fig. 3 is ~ ±1.2%. The pulse rise time is well within AHF requirements (measured at ~23ns at 10%-90%) and the pulse fall time is close to the maximum allowed (~46ns at 10-90% but closer to 70ns at 0%-100%). The pulse fall time was observed to increase substantially (from ~20ns to ~ 50ns) as the output voltage increased from 40kV to 50 kV. Measurements indicated that some of the MOSFETs were turning back on during turn-off due to energy coupled through the Miller capacitance into the gate drive circuit. Discussions with the MOSFET vendor indicated that newer devices are now available that have a smaller Miller capacitance. Slight changes to the gate drive circuit would also reduce the susceptibility to turn-on. Eliminating device turn-on by either of these options could reduce the output pulse fall time to the range of 20-30ns and easily exceed AHF pulse requirements. The inter-pulse voltage drops to less than 250 volts within approximately 300ns and meets requirements. Most of

the voltage that appears on the output after the main pulse is due to the transformer magnetization current, which increases with each pulse of the burst and reaches maximum value after the last pulse of the burst. The voltage that is generated in the primary circuit by the magnetization current decay is coupled into the secondary circuit and appears as a voltage (opposite polarity to main pulses) on the output. The duration of the voltage is determined by the L/R time-constant where L is the transformer's primary inductance and R is the resistance in the path of the magnetization current. Another contributor to the intra-pulse voltage is the very slight impedance mismatch between the adder stalk and the cable. The prototype modulator has demonstrated the capability of meeting most of the AHF pulse parameters. Two parameters that cannot be met due to hardware limitations are the full 24-pulse burst and voltage droop over the entire burst. The transformer therefore needed to be redesigned to have more volt-seconds to satisfy the burst requirement and the drive boards redesigned to have a much larger storage capacitance to satisfy the droop requirement.

DEVELOPMENT OF IMPROVED CORES AND DRIVE BOARDS

As the number of pulses in a burst increases, it becomes more difficult to meet the intra-pulse voltage requirement because magnetization current increases with each pulse of the burst. Therefore, in addition to increasing pulse number and quality, one of the goals of the drive board design and transformer design is to better dampen the magnetization current and/or reduce the magnetization current.

Core Development for the 24-pulse modulator

The objective of the core development effort of 2002 was to increase the magnetic core cross-sectional area to handle 24-pulse burst requirement and to reduce the magnetization current. The baseline design approach was to use for the core material Metglas™ SA1. With a mean pulse width of 150ns, 24 pulses in the burst, and a charge voltage of 750 volts, each core must provide a minimum of 2.70×10^{-3} V-s. Empirical data indicate that the useable ΔB for SA1 is ~ 1.46 T. Adding a 20 % safety factor gives a minimum core area of 4 in^2. However, As the magnetic core is not the major cost driver (~25% of total modulator costs), there is little incentive to minimize the core volume other than to keep the modulator reasonable in size. On the other hand, there is a strong motivation to have more core volume than required; the transformer should never saturate under any reasonable/normal operating condition and any extra core material serves to reduce the peak magnetization current. Metglas™ SA1, and annealed nanocrystalline and transverse annealed nanocrystalline cores of the same geometry as the new SA1 cores were procured and tested. The measurements showed that due to its higher permeability, the nanocrystalline material has substantially lower magnetization current (~40% of SA1 for the same core geometry), but has approximately 70% of the available volt-seconds. In view of these results, some type of nanocrystalline core is the preferred approach for future work.

Improved Drive Board Design

The most efficient approach to meeting the full AHF V-s requirement is to incorporate as much capacitance as possible on a board layout that is reasonable in size and cost and to incorporate extra adder cells into the final pulser design. Using boards with a new high energy-density 12 μF capacitor, the load voltage will have drooped 1% (500 volts) by the 13^{th} pulse. To compensate for this droop, additional adder cells charged to can be brought on line at various times through the pulse train. A new drive board incorporating the new capacitors, improved MOSFETS, and some other improvements was designed and successfully tested together with the new cores in a four-cell stack. Based on these results, a modulator with four extra compensation drive circuits/cells is expected to meet the AHF requirements.

SUMMARY AND PLANS FOR FUTURE DEVELOPMENT

A 50 KV, 1000 A pulsed kicker modulator meeting the objectives of Stages 1 and 2 the original development plan [2] has been designed and successfully tested. At present, due to lack of funding, execution of Stage3 (a full-scale modulator capable of producing the entire pulse train for AHF) has been postponed indefinitely. Nevertheless, a highly promising new modulator technology has been demonstrated. It is likely that the demonstrated voltage-adder approach will find use in accelerator technology and will eventually displace PFNs switched by gas-filled thyratron tubes in many applications.

REFERENCES

[1] J. A. Watson et al., "A Solid-State Modulator for High-Speed Kickers", Proc. PAC 2001, Chicago, IL, p. 3738.

[2] P. L. Walstrom and E. G. Cook, "Extraction Kickers and Modulators for the Advanced Hydrotest Facility", Proc. PAC 2001, Chicago, IL, p. 3735.

SOLID-STATE PULSED POWER SYSTEMS FOR THE NEXT LINEAR COLLIDER

Marcel P.J. Gaudreau, Jeffrey A. Casey, Ian Roth, Timothy Hawkey, Michael Kempkes, J. Michael Mulvaney; Diversified Technologies Inc. 35 Wiggins Ave. Bedford, MA USA

Abstract

Diversified Technologies, Inc. has received Phase II SBIR grants from the DOE for the application of solid-state switching to the Next Generation Linear Collider. Under the first of these, DTI delivered a hybrid modulator to SLAC in October 2002 for assessment. The modulator uses a solid-state series IGBT switch and a conventional pulse transformer to cathode pulse two klystrons at 500 kV, 530 A, with tight voltage regulation and pulse flattop.

During this effort, the pulse transformer was determined to be an obstacle to increased modulator performance. A second grant was received to develop a low impedance toroidal pulse transformer, to operate efficiently in the hybrid modulator. Under a third grant, DTI investigated transformerless options for solid state switching, and tested a scale prototype of a 500 kV Marx switch for improved efficiency.

This paper describes results from the hybrid modulator and Marx switch development efforts.

1 INTRODUCTION

Diversified Technologies, Inc. (DTI) has over a decade of experience in developing high voltage pulsed power systems using solid-state technology. DTI has obtained multiple SBIR grants from the Department of Energy to support the modulator development efforts for the Next Linear Collider (NLC). The NLC will require ~1600 klystrons, with a power load of over 120 MW. The goal of these efforts is to develop modulator technology capable of reducing the operating costs associated with the NLC and other large RF systems.

DTI's solid-state modulators are built from series stacks of IGBTs, configured for very high voltage standoff, and operated as single ideal SPST switches. These switches can open quickly (< 1 μs) under normal or even fault load currents, eliminating crowbar circuits and providing a high degree of load protection.

The near-ideal properties of solid-state switches make them well suited to remedy the inefficiencies of conventional line modulators. The challenging specifications of NLC klystron operation have required additional switch development through these programs.

2 HYBRID MODULATOR

A "hybrid modulator" uses a storage capacitor, a solid-state switch and a pulse transformer (Figure 1). The switch provides a high current pulse (~ 3500 A) into the pulse transformer at approximately 80 kV. The load on the secondary of the transformer is two parallel NLC klystrons, operating at 500 kV with a combined load of 1.5 μP (530 A), for 3 μs flattops of +/- 3%.

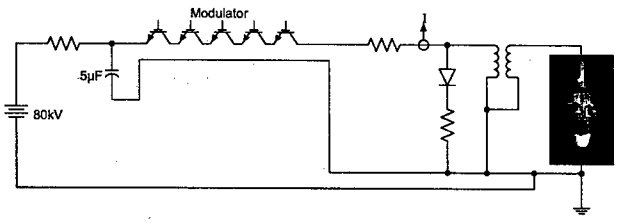

Figure 1: NLC Hybrid modulator schematic. The solid state switch pulses 3500 A at 80 kV to drive two 500 kV 265 A klystrons.

The resulting system is shown in Figure 2. The pulse transformer is in the foreground, and the solid state switch in the background. Controls are above the switch. The entire assembly is constructed to drop into a dual oil tank for cooling and insulation. Auxiliary systems are included for core bias and dual filament control. The full system was tested at DTI, and shipped to SLAC for further testing and for support of the klystron development efforts (Figure 3) in Fall 2002.

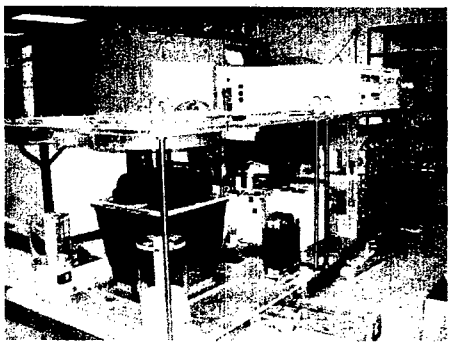

Figure 2: Hybrid modulator assembly, ready for immersion in oil.

0-7803-7738-9/03/$17.00 © 2003 IEEE

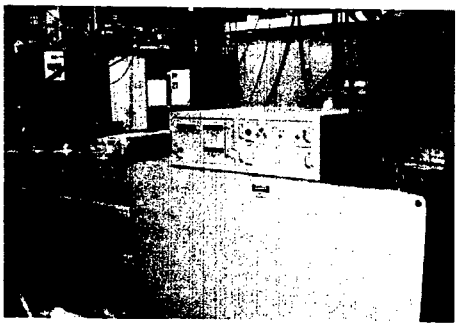

Figure 3: Hybrid Modulator in tank at SLAC, with a SLAC 5045 klystron in a load socket.

The critical performance constraint on the hybrid modulator is primary circuit inductance, to meet the high primary current and fast risetime desired, at the relatively low primary voltage. The switch accounted for this problem by assembly on a distributed transmission line. These transmission line characteristics, together with the product of the transformer primary leakage inductance and secondary parasitic capacitance, determine the pulse risetime.

Preliminary tests at DTI show that fast risetime has been achieved. Figure 4 shows the voltage waveform of a test pulse into a 990 Ω load at DTI. Note the overshoot and the ripple – both effects of the difference between the test (resistive) load and the design (perveance) load.

Initial tests at SLAC were performed using a single 5045 klystron, but with the cathode operated in temperature limited mode to mimic the effective 1.5 μP of the NLC design load. Figure 5 shows a nominal pulse at 421 kV cathode voltage. Additional inductance was added to the primary circuit for initial operation, as a safety factor for load-arcs. Note the slower risetime than in Figure 4. The full assembly also includes a small two stage tuned *LC* circuit, with about 10 kV of authority, which flattens out the capacitor droop during the pulse. The resulting flattop is better than +/- 0.5%, well within the +/- 3.0% specification.

The most challenging aspect of the hybrid modulator is arc protection. DTI's solid-state switches sense

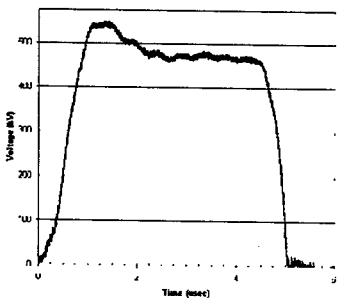

Figure 4: Fast pulse data at 500 kV, into a 990Ω load.

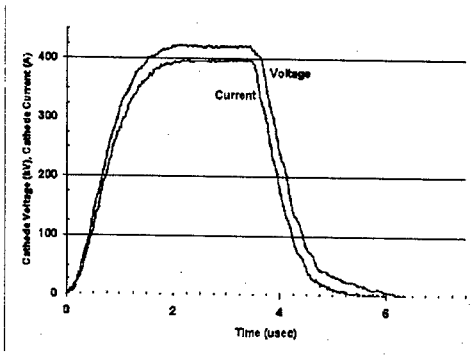

Figure 5: Hybrid modulator operation at SLAC. Load is 5045 klystron, with the cathode operated in temperature limited mode for an effective 1.5 μP load.

overcurrent conditions, which then command all the series switches to shut off. The response time of this event is approximately 750 ns. For the hybrid modulator, high current and high speed operation place a very large demand on the capability of the solid-state switch to open under large fault loads. The NLC hybrid switch is rated for 10 kA opening. Figure 6 shows a typical arc of the overdriven 5045 klystron during testing at SLAC. The upper trace shows the cathode voltage, which collapses

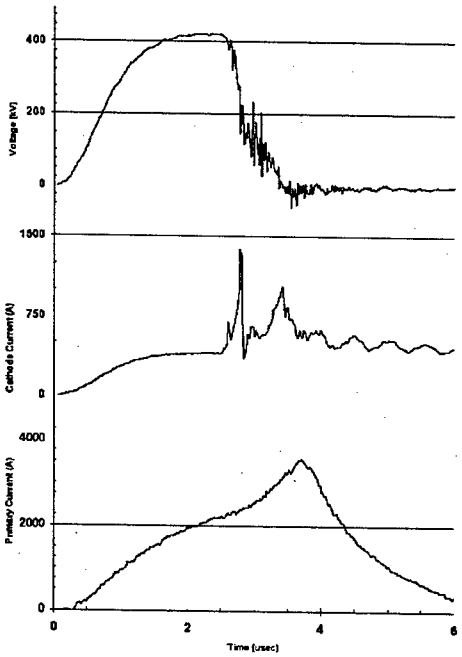

Figure 6: Hybrid modulator with a load arc at 420 kV. The load (5045 klystron) arcs at about 2.5 μs. The switch safely opens under full *fault* primary currents. The lag time is about 1 μs between arc occurrence and switch opening. (Primary current shown at reduced bandwidth.)

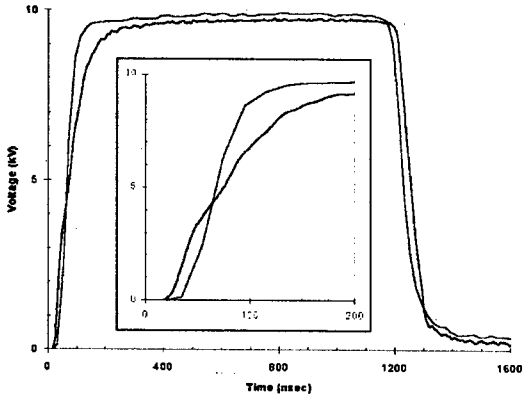

Figure 7: Single cell Marx switch risetime tests show very high speed. Both shots at 10 kV. Faster one into 59 ohms, slower one into 21 ohms.

from 421 kV at the arc. The middle trace shows the cathode current. There is a sharp spike of current as the parasitic capacitance of the pulse transformer discharges into the cathode, followed by a slower current rise as the primary circuit begins to deliver additional current. The lowest trace shows the primary current, which opens at a bit under 4 kA, about 1 μs after the arc is detected (this signal is processed through a reduced bandwidth amplifier).

A large part of the speed limitation in the primary circuit, aside from the inserted "safety inductance" (which will be reduced as testing continues), is due to the pulse transformer. Presently, this is a conventional Stangenes transformer (quadrifilar, slanted basket, with a Lord winding). Under a separate SBIR, we are developing an improved pulse transformer of toroidal geometry (based on work originally proposed by Kazarezov, [1]) for integration into the hybrid modulator at a later date.

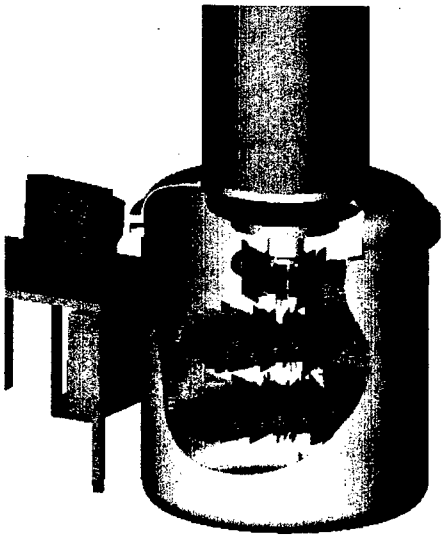

Figure 8: Proposed 500 kV "desk size" 250 A modulator.

3 TRANSFORMERLESS ARCHITECTURE

In parallel SBIR efforts, DTI is improving the overall power efficiency and performance by eliminating the pulse transformer altogether – motivated by a 5-10% net energy savings. Originally, two topologies were examined: a hard switch with a 500 kVDC supply, and a Marx switch [2]. Design studies and scale experiments have led us to concentrate on the Marx for further development.

A solid state Marx switch is somewhat different than conventional Marx switches fired by thyristors or spark gaps because the capacitors do *not* fully discharge during a pulse. Instead, the opening capabilities of the IGBT series switches are used, so that the intra-stage capacitors act as filters, and are only shallowly discharged. A very fast risetime and very high quality flattop can be delivered this way. The critical cost & performance requirement for the Marx switch is parasitic capacitance – analogous to the role of primary inductance in the hybrid modulator.

A scaled (50 kV, full current) Marx switch of five stages was built, and is presently undergoing final assessment at DTI. Figure 7 shows a single stage pulse, demonstrating the very fast risetime of the configuration. Design studies suggest that a full specification Marx switch for a single klystron (500 kV 265 A) will be "desktop" size as shown in Figure 8.

4 SUMMARY

We have a continuing advanced solid-state modulator development program to support the NLC efforts. These pulse power systems will improve performance and reduce operating costs of the NLC when built, and are presently aiding in the klystron development efforts as well. Several advanced technologies are under development, and one system – the hybrid modulator – has been delivered to SLAC for further assessment and use in klystron development and testing.

5 REFERENCES

[1] Kazarezov, et.al., "Pulse Transformer for the NLC Klystron".

[2] A. Krasnykh, R. Akre, S. Gold, and R. Koontz, "A Solid-state Marx Type Modulator for Driving a TWT," 24th International Power Modulator Symposium, 2000, Norfolk VA, USA. "Analyses for Klystron Modulator Approaches for NLC", International Linac Conference, Monterey CA, USA

This work has been supported by DOE SBIR grants (DE-FG02-99ER82775 and DE-FG02-99ER82776). We appreciate the assistance of our colleagues at the Stanford Linear Accelerator Center.

DESIGN, DEVELOPMENT, AND CONSTRUCTION OF SNS EXTRACTION FAST KICKER SYSTEM *

W. Zhang, J. Sandberg, R. Lambiase, Y.Y. Lee, R. Lockey, J. Mi, T. Nehring, C. Pai, N. Tsoupas, J. Tuozzolo, D. Warburton, and J. Wei
Brookhaven National Laboratory, Upton, NY 11973, USA

K. Rust, and R. Cutler
Oak Ridge National Laboratory, Oak Ridge, TN 37831

Abstract

The SNS accumulator ring extraction fast-kicker system was design, developed, and prototype tested at the Brookhaven National Laboratory. Its construction has just begun. The system is for one-turn fast extraction ejecting proton beam from the ring into the extraction septum gap and further deflecting into the ring-to-target beam transport line. The system consists of fourteen high-voltage modulators, their local control and auxiliary systems, and fourteen window frame magnet sections. High-voltage transmission cables will be used for pulse transmission from modulators to their corresponding magnet sections. The high-voltage and high-current pulse has a rise time about 200 ns, a pulse duration about 700 ns, and a current amplitude above 2500 Amp per modulator. The modulator design features a Blumlein Pulse-Forming-Network with ultra-low inductance high energy storage pulsed capacitors, an ultra-fast high-power hollow anode thyratron, a parallel resistor stack for low beam-impedance termination, and a saturable inductor stack for beam current isolation and pulse rise time sharpening. This design is driven by the considerations of low beam loss, high maintainability and reliability. All high voltage modulators will be placed outside the ring tunnel and the system is immune to one-kicker failure. In addition, the enlarged magnet aperture can accept all four working points. The design concept has been successfully proven by the prototype test. The techniques, considerations, and other related issues of the system design, development and construction are discussed in this paper.

INTRODUCTION

The SNS beam extraction will be a single turn, two-step process. The fast extraction kicker will eject beam into a Lambertson septum and deflecting further into the Ring to Target Beam Transport (RTBT) line.

A set of fourteen full aperture kickers will be used to eject 1 GeV proton beam vertically from the Accumulator Ring. It will take place at one of the four dispersion free straight sections, as shown in Figure 1. Seven kicker magnets are to be located upstream of the narrow quadrupole doublet and seven downstream of it.

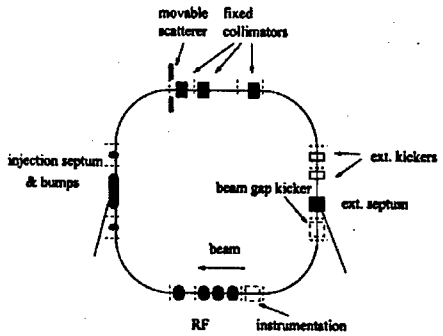

Figure 1: SNS Accumulator Ring Layout

A crucial part in this design is the high power pulse modulator system [1] [2] [3]. It is one of the largest fast kicker systems in its class. The combined maximum system output power will reach to several GVA. It will consist of fourteen high voltage modulators located outside of the tunnel in a dedicated service building, and their auxiliary power and control system. Pulse transmission will be carried out by high voltage pulsed cables from modulators to kicker magnets. The basic system layout is shown in Figure 2.

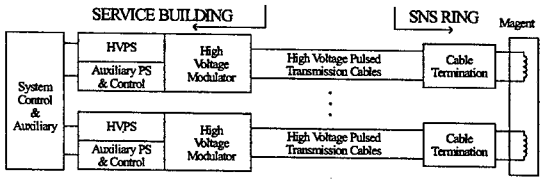

Figure 2: SNS extraction fast kicker system layout

The updated main parameter specifications [4] are listed in Table 1.

Table 1 Revised Main Parameter Specifications

Beam Rigidity	5.6575 T-M
Extraction Energy	1.0 GeV
Extraction type	Single-turn
Magnet window	Full aperture
Beam revolution period	945.4 ns (at 1.0 GeV)

* SNS is managed by UT-Battelle, LLC, under contract DE-AC05-00OR22725 for the U.S. Department of Energy. SNS is a partnership of six national laboratories: Argonne, Brookhaven, Jefferson, Lawrence Berkeley, Los Alamos, and Oak Ridge.

	911.1 ns (at 1.3 GeV)
Beam gap during extraction	250 ns
Bunch length (full)	645 ns
Maximum extraction rate	60 Hz
Pulse flat-top length	> 700 ns
Pulse Flat-top tolerance	+/- 3%
Pulse rise time	200 nS (1% - 95%)
Pulse fall time	< 16.6 ms
Kicker strength	1.276 to 1.775 mrad per section
Total deflection strength	20.344 mrad
Kicker horizontal aperture	120 mm to 211.3 mm
Kicker vertical aperture	166 mm to 243 mm
Kicker length	390 mm to 505 mm per section
Kicker magnet inductance	695 nH to 789 nH per section
Operating voltage	< 35 kV per section
Operating current	< 2.5 kA per section

This updated specification reflects the enlarged magnet apertures and increased output power to serve all working points of (ν_x, ν_y) at (6.23, 6.2), (6.4, 6.3), (6.23, 5.24), and (6.3, 5.8). These four working points are the nominal tune near coupling resonance $\nu_x = \nu_y$, an alternative working point away from the structure lines, a split-tune working point for decoupling, and an old working point, respectively [5].

Sufficient space is reserved to add two more magnets and modulators for future 1.3 GeV upgrade.

DESIGN AND DEVELOPMENT

To achieve maximum operability, maintainability, and lower beam impedance to minimize beam loss, as requested by SNS project, a new conceptual design was proposed in year 2000. This design features a Blumlein voltage doubler, a 25-ohm parallel resistor for beam impedance termination, two 50-ohm impedance cable in parallel for pulse transmission, and full reflection at magnet doubling the current magnitude. The saturable inductor will provide impedance isolation for beam current, and become saturated during output current rising edge for dark current suppression. All high maintenance devices will be located in service building; no active or dissipative components will be used in the radiation area. In Figure 3, the main schematic is illustrated.

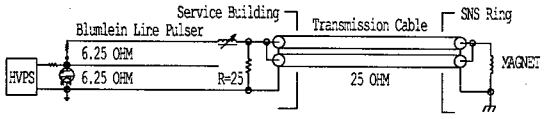

Figure 3: Simplified main schematic of SNS extraction kicker

Among many advantages offered by this design, the margin of the design parameter to operation is largely increased. Our physicists immediately recognized this feature and they seized the opportunity to improve physics performance of the main accumulator ring. The kicker magnet apertures have been enlarged to accommodate all four working points, further reduced beam impedance, and increased beam acceptance at kicker magnets. Compare with the year 2001 parameters, the required total output power of the kicker modulators have to be increased by 86%, and the margin of designed voltage over operating voltage shrink to 42% per modulator from 88% - 173% per modulator.

Although the maximum charging voltage is 50 kV, we set the operation voltage limit of the modulator at below 35 kV for the concerns of device lifetime, system reliability, fault tolerance, and system sustainability.

The Blumlein pulser can be implemented by two sets of high voltage cable pulse-forming lines or double deck of lumped L-C pulse forming networks. The later option was chosen for the compactness.

As constrained by the budget and very tied project schedule, the research and development efforts shall be limited only to the necessities to meet the minimum performance requirements. However, the criticality of the fast extraction kicker performance demands full and detailed verification on each stage of the system design and development. Therefore, we conducted design analysis, parameter optimization, and computer simulations to verify the design principle. Then, a proof-of-principle model circuit was build and tested. Its output current waveform nicely matched computer simulation. Further, a full-scale prototype modulator has been designed, constructed, and tested at Brookhaven National Laboratory. Its test results successfully demonstrate the design concept.

Mechanical design of the high voltage pulse modulator provides many features for easy maintenance, such as, the modulator internal structure can be lifted out from its fluid container for device change and pulse shaping. Figure 4 shows the prototype modulator.

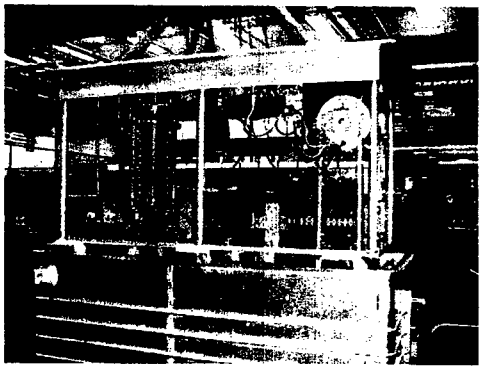

Figure 4: SNS extraction fast kicker modulator prototype

Varies tests have been conducted on the prototype modulator.

- For pulse shape verification and construction check, the unit was tested up to 40 kV in air, in single shot mode.

- At 35 kV full rated operation voltage, the prototype unit has been tested in silicon fluid at 60 Hz repetition rate for over 200 hours at August 2002.
- A 40 KV, 60 Hz repetition rate, 12 hours continuous accelerated lifetime test has been completed at August 2002.
- A 45 kV, 30 Hz repetition rate, 8 hours continuous accelerated lifetime test has been completed at August 2002.
- A 50 kV single shot mode test on going.

Figure 5 and Figure 6 show the magnet current waveforms at 50 kV.

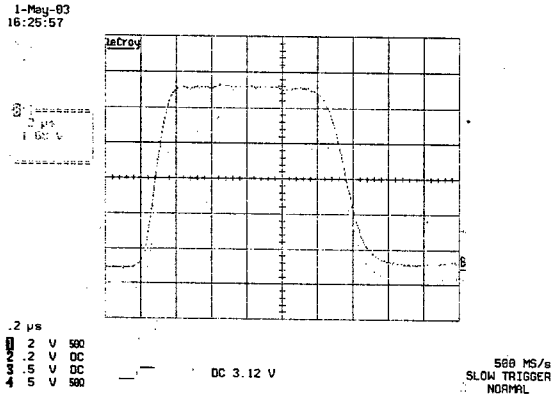

Figure 5: Magnet current waveform at 50 kV

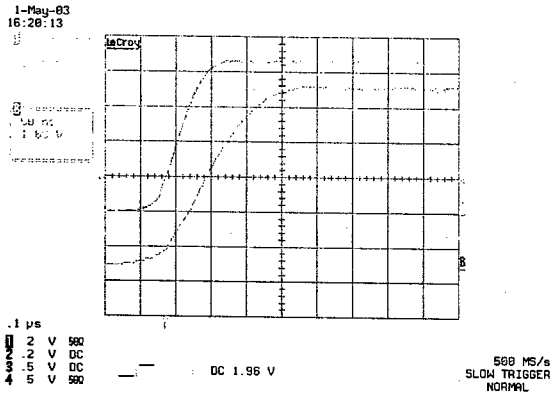

Figure 6: Magnet current rise time at 50 kV

In this design, all critical components are commercially available, which makes the design very cost effective. The main switch is an E2V CX1925X hollow anode thyratron rated for 80 kV and 15 kA. Its high voltage hold-off rating, high conduction speed, and reverse conduction capability make it a top choice for this application. The DOW Corning 561 silicon fluid is used for insulation. General Atomic Energy Product is the supplier of the ultra low inductance, 15 nH, silicon fluid filled high-energy pulse capacitors for PFN. Twelve Eupec's 6kV fast recovery diodes are used in reversing diode stack. Tri-axial high voltage pulse cables from Times Microwave will be used for pulse transmission. The 50 kV ALE high voltage capacitor charging power supply will be used one for each modulator system.

High voltage components specifications, testing methods, and technical standards are critical to ensure the system reliability. For example, the coaxial high voltage cables used in the prototype test were hi-potted to 100 kV during acceptance test; the high voltage pulse capacitors were also hi-potted to 100 kV in factory test; and the thyratron is rated and tested at a level more than twice of the operation voltage. So far, the performance and reliability of the high voltage components has been satisfactory, and no critical device failures have been observed.

CONSTRUCTION STATUS

The design and development stage of the SNS extraction fast kicker project has been concluded last year. Applied Power systems, a commercial company, has been awarded the contract to construct all fourteen high voltage modulators and corresponding auxiliary systems as specified and designed by Brookhaven National Laboratory.

Traditionally, all our high voltage, high current, and high-speed fast kicker modulators were designed, developed, and constructed at Brookhaven. This is the first time, we use commercial vendor to construct production units of the high voltage pulse modulators. The final design review has been completed; two meetings for progress check have been conducted at vendor's facility. The production is in progress.

ACKNOWLEDGEMENT

We would like to express our appreciations to Mr. W.A. Morris of ISIS, Dr. R. Sheldrake of E2V, Mr. R. Cooper and Mr. R. Hartsock of General Atomics for their expert advice and technical support.

REFERENCES

[1] W. Zhang, et al., "High Power Fast Kicker system for SNS Beam Extraction", Conference Record of the Twenty-Fifth International Power Modulator Symposium and 2002 High Voltage Workshop, June 30-July 3, 2002, pp 262-265.

[2] W. Zhang, et al., "A New Conceptual Design of the SNS Full Turn Fast Extraction Kicker Power Supply System", Proceedings, 2001 Particle Accelerator Conference, June 2001, pp. 3714-3716.

[3] W. Zhang, et al., "SNS full Turn Fast Extraction Kicker System", BNL Internal Technical Proposal Presentation, July 2000.

[4] N. Tsoupas, et al., "Beam Extraction from the SNS Ring", draft paper for SNS Design Manual, internal communication, Nov. 2002.

[5] J.Wei, et al., "Evolution of the Spallation Neutron Source Ring Lattice", 20TH ICFA Advanced Beam Dynamics Workshop, Chicago, IL, April 2002.

DESIGN, STATUS, AND FIRST OPERATIONS OF THE SPALLATION NEUTRON SOURCE POLYPHASE RESONANT CONVERTER MODULATOR SYSTEM*

W. A. Reass, S. E. Apgar, D. M. Baca, D. L. Borovina, J. T. Bradley III, J. D. Doss, J. M. Gonzales, R. F. Gribble, T. W. Hardek, M. T. Lynch, D. E. Rees, P. J. Tallerico, and P. G. Trujillo
Los Alamos National Laboratory, P.O. Box 1663, Los Alamos, NM 87545, USA
And
D. E. Anderson, D. A. Heidenreich, J. D. Hicks, and V. N. Leontiev
Oak Ridge National Laboratory, P.O. Box 2001, Oak Ridge, TN 37831, USA

Abstract

The Spallation Neutron Source (SNS) is a new 1.4 MW average power beam, 1 GeV accelerator being built at Oak Ridge National Laboratory. The accelerator requires 15 converter-modulator stations each providing between 9 and 11 MW pulses with up to a 1.1 MW average power. The converter-modulator can be described as a resonant 20 kHz polyphase boost inverter. Each converter modulator derives its buss voltage from a standard substation cast-core transformer. Each substation is followed by an SCR pre-regulator to accommodate voltage changes from no load to full load, in addition to providing a soft-start function. Energy storage is provided by self-clearing metallized hazy polypropylene traction capacitors. These capacitors do not fail short, but clear any internal anomaly. Three "H-Bridge" IGBT transistor networks are used to generate the polyphase 20 kHz transformer primary drive waveforms. The 20 kHz drive waveforms are time-gated to generate the desired klystron pulse width. Pulse width modulation of the individual 20 kHz pulses is utilized to provide regulated output waveforms with DSP based adaptive feedforward and feedback techniques. The boost transformer design utilizes nanocrystalline alloy that provides low core loss at design flux levels and switching frequencies. Capacitors are used on the transformer secondary networks to resonate the leakage inductance. The transformers are wound for a specific leakage inductance, not turns ratio. This design technique generates multiple secondary volts per turn as compared to the primary. With the appropriate tuning conditions, switching losses are minimized. The resonant topology has the added benefit of being deQed in a klystron fault condition, with little energy deposited in the arc. This obviates the need of crowbars or other related networks. A review of these design parameters, operational performance, production status, and ORNL installation and performance to date will be presented.

HARDWARE DESIGN

The system block diagram of the SNS converter-modulator is shown in Figure 1. This depicts a standard vacuum cast-core transformer substation followed by an SCR controller for DC voltage regulation. The converter-modulator follows with the self-healing capacitor energy storage bank. The fabrication of the converter-modulator systems is accomplished through industrial fabrication contracts for the four major subsystems, consisting of: A) the utility substation, B) the SCR phase controller, C) the converter-modulator assembly, and D) the equipment control rack. The converter-modulator assembly is a "build-to-print" contract, the others, a "build-to-specification", all awarded to the lowest cost qualifying bidder.

60 HZ UTILITY SYSTEMS

The individual converter-modulator substations contain harmonic traps and filters to maintain IEEE 519 and 141 standards within the local distribution network. To maximize substation efficiency (~99%), a standard "traction" style vacuum cast core transformer is used along with vacuum cast coils for the traps and filters. Since the unit contains no oil, secondary oil containment,

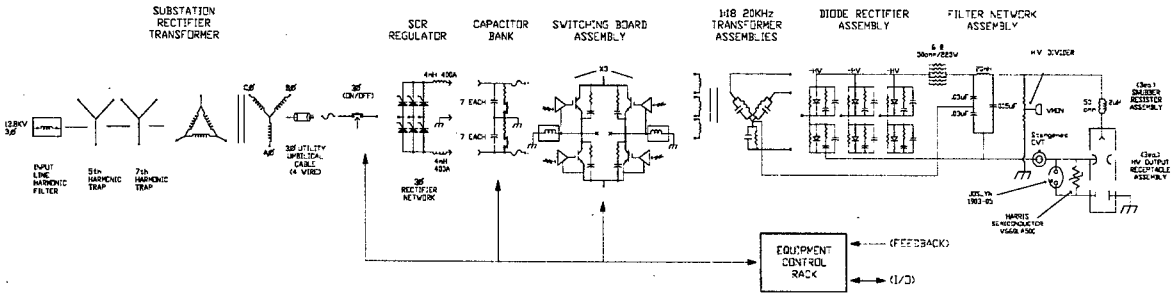

Figure 1: System Block Diagram

*Work supported by the Office of Basic Energy Science, Office of Science of the US Department of Energy, and by Oak Ridge National Laboratory

0-7803-7738-9/03/$17.00 © 2003 IEEE

fire suppression equipment, and environmental impact statements are not required. The overall design topology further simplifies installation, a single utility cable pull for the input and output with a lightweight, two-piece, design that can be "forked" into position onto the outdoor pad. To maintain balanced line currents and core flux, the neutral is not grounded. With the repetitive pulsed loading of the transformer, there are no engineering (e.g. harmonic mitigation) or cost advantages to utilize a 6 phase, 12 pulse rectification system. A standard 3 phase system is less expensive and easier to filter. The substations for the SNS Accelerator have been manufactured by *Dynapower Corporation* located in Burlington, Vermont.

SCR PHASE CONTROLLER

Each converter-modulator substation is followed by an SCR phase controller, located indoors, in the klystron gallery. A single utility pull using armored triplex between the substation and SCR regulator simplifies the interconnect between the pad and the indoor equipment. The SCR phase controller accommodates incoming line voltage variations resulting from network, transformer, and trap impedances, from no-load to full load. The SCR phase controller also provides the soft-start function and operates at a nominal +/- 1250 Volt output with a 400 Amp rating. This unit is 99.5% efficient and has also been manufactured by *Dynapower Corporation.*

CONVERTER MODULATOR ASSEMBLY

A view of the completed converter modulator assembly is shown in Figure 2. The oil tank, safety enclosure, and water distribution panel are the prominent features that can be noted in this figure. *Dynapower Corporation* located in Burlington, Vermont won the contract for the build-to-print converter modulator assembly. The first 4 production converter modulator assemblies have been delivered to ORNL in the 2nd quarter of fiscal year 2003.

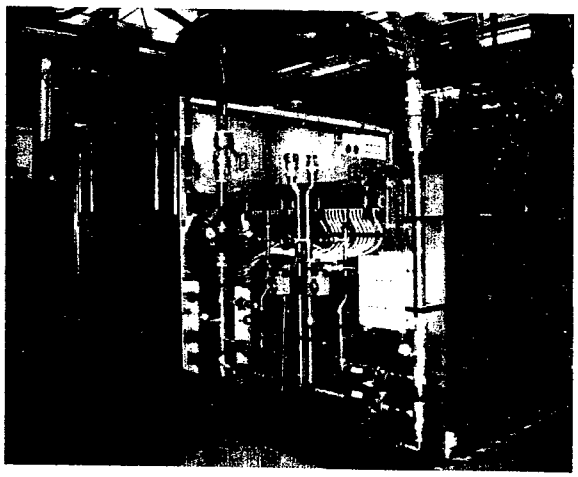

Figure 2: Converter Modulator Assembly

Self-Healing Capacitors

The energy storage capacitors used for the converter modulator are units similar to those used in traction application. *Thomson Passive Components* (AVX), located in Saint-Appollinaire, France worked with us to develop a lower inductance capacitor for our high power, 20 kHz, switching application. Internal fabrication methodology is optimized to provide enhanced current distribution within the capacitor and also minimize internal interconnect inductance. The all film design provides for excellent energy density and the use of high-ohm metal electrode deposition ensures good current balance through all the internal foil packs. As in traction applications, our capacitors use the technology of metallized hazy polypropylene dielectrics that do not fail short, but fuse or "clear" any internal anomaly. Also, at our capacitor voltage rating (1.5 kV), there has not been a recorded internal capacitor buss failure. With the converter modulator operation at full output with a maximum bank voltage of 1.2 kV, the capacitor lifetime is calculated to be over 300,000 hours, including derating factors. A view of the capacitor racks is shown in Figure 3. Bank fusing does not seem to reduce physical IGBT failure damage and fusing is not used in the present production design. However, it appears that the fusing can limit "action" in other failure modes and possibly reduce busswork or cabling damage. This is one area we will again examine in future designs.

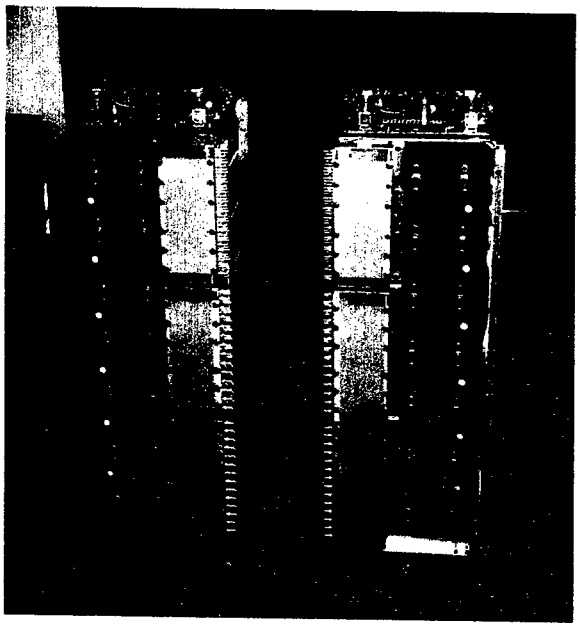

Figure 3: Capacitor Rack Assemblies

IGBT Switch Plate Assembly

The IGBT switch plate assemblies are designed to be easily removed like a large printed circuit card, such that maintenance and repair can be accommodated off-line. Sliding high-current contacts of multilam louvers interface to the transformer primary busswork, which

terminate on the modulator tank lid. Each switch plate contains four IGBT's in an "H-bridge" configuration. The IGBT device family is the 3300 Volt, 1200 Ampere devices. The *Eupec* FZ1200R33KL2 device is being utilized that have an improved "FIT" rate for higher voltage reliability. The mechanical design of the switch plate assembly has the IGBT's terminals directly opposite one-another (face-to-face), to provide a low inductance interconnection methodology. This results in a buss-work rail-to-rail inductance (V+ to V-) of ~4 NH. This low inductance is necessary for "snubberless" IGBT switching. Low inductance (~9 nH), high frequency IGBT bypass capacitors for this assembly have been developed by *General Atomics Energy Products* (formerly Maxwell) and are shown in Figure 4. The resulting inductance of the IGBT switch plate network of ~7 nH is desirable to minimize overshoot and ringing from the multi-kA 20 kHz switching that can have dI/dT's of ~10 kA/uS. The IGBT switch plate assemblies also must switch the peak power of the system, 11 MW, not just the average power. With the high peak powers involved, additional "on board" energy storage is provided by 8 each 10 uF, 2 kV capacitors, also manufactured by *General Atomics Energy Products.*

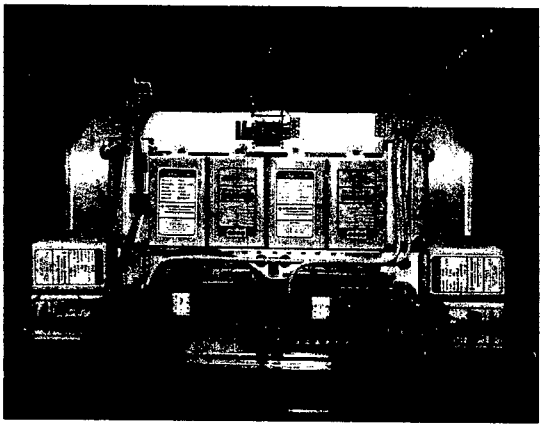

Figure 4: IGBT Switch Plate Assembly

Amorphous Nanocrystalline Boost Transformers

The development of the amorphous nanocrystalline transformer core was another long lead development for this project. The characteristics of the nano material are given in the following table:

Mu	50,000
Lamination Thickness	.0008"
Lamination Insulation	1 μM Namlite
Stacking Factor	~90%
Bsat	12.3 kG
Core Loss (our use)	~300 W
Core Weight (our use)	~95 lbs
Power (each core)	330 kW

Table 1: Nano Material Characteristics

The amorphous nanocrystalline material has exceptional performance as a function of frequency and flux density with the added benefit of having 'zero-magnetostriction". It does not vibrate or make significant noise with excitation. The windings on the core are wound as two single layer solenoids. A view of the nanocrystalline boost transformer is shown in Figure 5. The overall height is about 24" tall with a total assembly weight of ~150 lbs. The secondary windings are resonated with tuning capacitors which provide two important functions, (1) an optimized value provides "zero-voltage-switching" for the IGBT's, and (2), the multiple transformer resonant circuits create "polyphase resonant voltage multiplication". The transformers are wound with a ratio of 1:19, but the output is about 1:60. Unlike previous power transformers with the same "volts-per-turn" for both the primary and secondary, this design generates multiple volts-per-turn on the secondary. In addition, the core flux expended is that of the primary. It would seem that the secondary leakage inductance isolates the core from the voltage swing generated on the secondary. The zero-voltage-switching characteristic minimizes the IGBT switching loss, turn on is soft without forced commutation (and losses) of the opposite IGBT free-wheeling diode. The transformers are resonated with special capacitors developed by *General Atomics Energy Products* and circulate many MVAR at 20 kHz with 100% reversal to ~160 kV p-p.

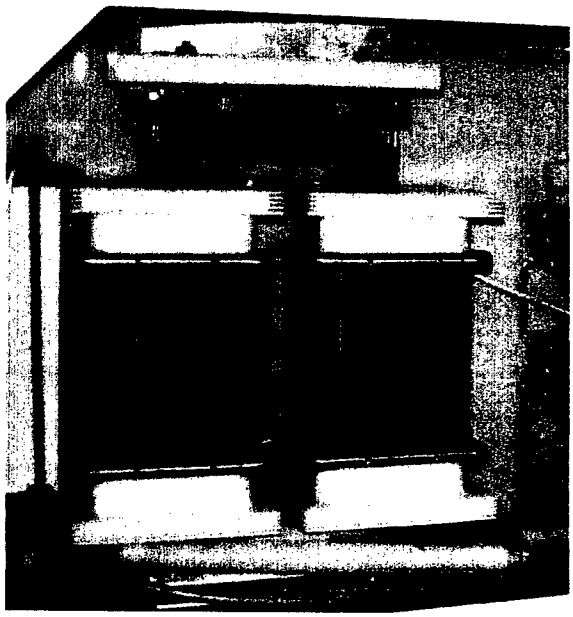

Figure 5: 330 kW Nanocrystalline Boost Transformer

Resonant Rectification System

To provide six pulse rectification of the 20 kHz, ~140 kV line-line voltages, resonant rectification techniques are used. Capacitors are placed in parallel with groups of rectification diodes. However, low loss; fast recovery diodes are still necessary for this design. 1,600 volt, 70 Amp ion implanted diodes manufactured by *IXYS* are

used in the 140 kV modulator assemblies. The circuit effect of the added rectification capacitance is that it acts like the transformer shunt peaking capacitors and must be considered in the analysis of the transformer tuning. The resonant rectification capacitors have the desirous effect to remove switching transients and "Miller" (ground) capacitance from the diodes. The Miller capacitance (to ground) can cause significant over-voltage of diodes high in the stack. The resonant rectification capacitors effectively swamp this failure mode. The resonant rectification capacitors are manufactured by *General Atomics Energy Products* and must have good tolerances, small size, and low equivalent series resistance and dissipation factor.

Output Filtering

Output filtering is provided by a standard "Pi-R" network. The input resistance helps mitigate ringing of the rectifier circuits. Filter capacitance values are chosen to provide adequate filtering yet minimize stored energy. The stored energy is wasted power that is lost at the end of the klystron pulse. With 120 kHz ripple frequency, high efficiency with good filtering can be attained.

EQUIPMENT CONTROL RACK

The operator and control room interface for the converter-modulator is via the equipment control rack. This rack controls and monitors all the power conditioning functions of the converter-modulator system such as the SCR controller, capacitor banks, IGBT switching network, oil tank assembly, and output load parameters. The rack includes functions for (Ethernet) "EPICS" based control I/O, Allen-Bradley PLC with local I/O and station keeping, fast electronic monitors, and controls. This includes personnel protection interlocks as well as all electronic fault protection systems. The fault protection systems have the appropriate thru-put delays and latching functions to minimize the probability of equipment damage. The Digital Signal Processor (DSP) based control system has adaptive feedforward and feedback networks with learning algorithms to generate regulated modulator output pulses. With Pulse Width Modulation (PWM) of the individual IGBT pulses, the output waveforms can be compensated for capacitor bank droop and network overshoot. Figure 6 shows the modulator output at 80 kV without adaptive controls and Figure 7 shows the 80 kV output with adaptive controls. The complete equipment control rack is manufactured by *Z-TEC Inc.* located in Albuquerque, NM. We have not operated at full average power with the DSP controls. Although we have had scheduling conflicts, recent modeling has shown dramatic increases in IGBT switching losses with PWM. We need to further examine these results and carefully proceed with PWM testing at high average power. Slight changes in programming and circuit values may be necessary to maintain efficient switching.

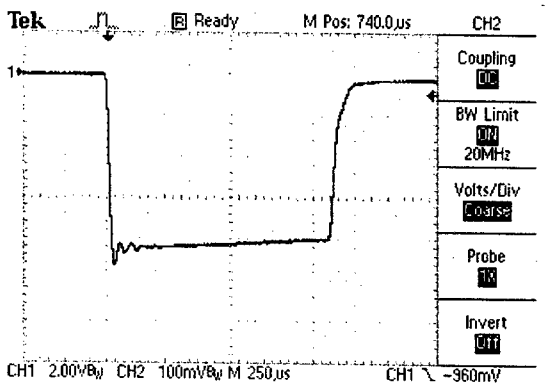

Figure 6: 80kV Output Pulse, 20kV/Division

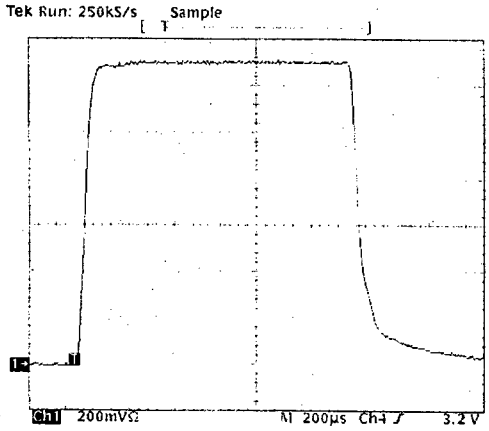

Figure 7: 80kV Output with Adaptive Feedforward/Feedback

OPERATIONAL RESULTS AND EFFICIENCY

Operations at full average power were achieved within a week of the installation of the high-power 5MW, 805 MHz Thales klystron. Figure 8 shows the output with 136 kV at the end of the pulse. We have operated the system to the limit of all our present loads, 130 kV at ~450 kW average power with the Marconi 2.5 MW, 402 MHz klystron and ~800 kW average power at 136 kV with the 5MW Thales 805 MHz klystron. With the single 2.5 MW tube, tests interestingly had an electrical efficiency of only ~88%, with ~ 3.7 kW loss per IGBT. Testing to the full ~136 kV output with the large 5 MW, 805 MHz Thales klystron (~800kW) gave IGBT losses of ~1.7 kW each, with an overall efficiency of 94%. Operation at higher power provides a better match to the resonant converter and affords "zero-voltage-switching" of the IGBTs. Operations continue at the ORNL SNS accelerator. Oak Ridge has operated 24/7 during accelerator RFQ commissioning as well as the recent Drift Tube (DTL) structure commissioning to full power. Start-up problems have been related to vendor Q/A issues and are being worked as the converter-modulator production unfolds.

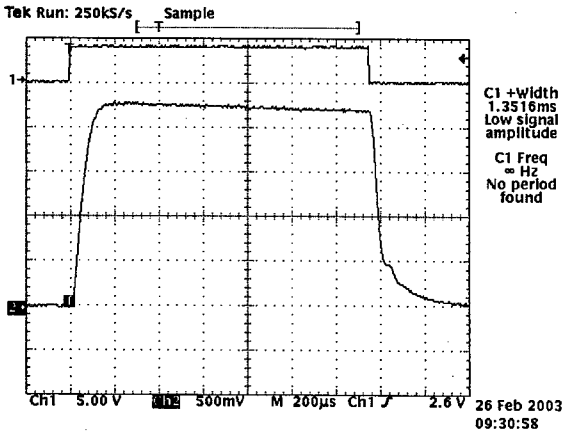

Figure 8: 136kV Output Pulse

Crowbar Tests

Extensive fault testing has also been performed with three times the anticipated SNS high-voltage cable length. These tests have been performed at voltages higher (~145 kV) than anticipated in our operation. Figure 9 shows a 130 kV crowbar test into a 5 joule wire. This test shows the result when the IGBT switching is disabled. Protection of the klystron is not dependant on the inhibit of IGBT switching and IGBT reliability is not dependant on interruption of gate drive during a klystron arc down.

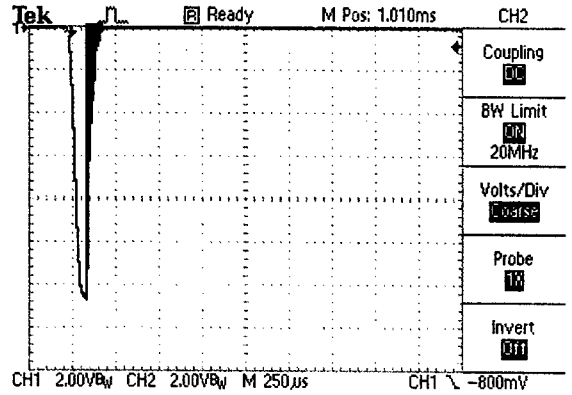

Figure 9: 130kV Self-Break Crowbar Test

Figure 10 shows an arc-down event with the IGBT's continuing to switch, which did not fuse the test wire. In the shorted condition, the resonance of the converter-modulator is deQed, and little power transfer results. The low primary drive voltage coupled into the relatively high leakage inductance of the transformer does not even create an over-current situation for the IGBT's. This provides for a design that has fault ride-through capabilities. These results match our modeling.

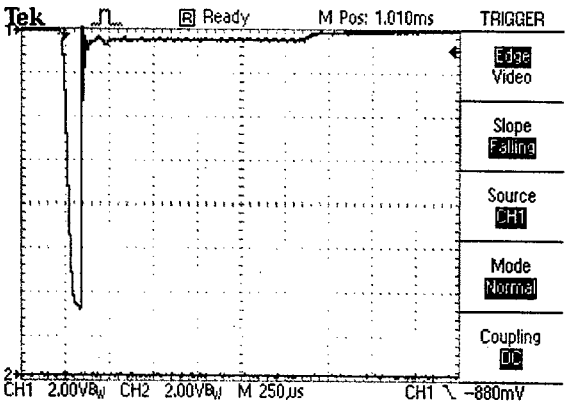

Figure 10: 130kV Run-On Fault Test

CONCLUSION

The polyphase resonant converter-modulator has demonstrated several new design methodologies that are expected to revolutionize long-pulse and "CW" modulator designs. These new technologies include special low inductance self-clearing capacitors, large amorphous nanocrystalline cut-core transformers, polyphase resonant voltage multiplication, resonant rectification, snubberless IGBT switching, and adaptive power supply control techniques. Design economies are achieved by the use of industrial traction components such as cast power transformers, IGBT's, and self-clearing capacitors. The compact and modular design minimizes on-site construction and a simplified utility interconnection scheme further reduces installation costs. The design does not require HV capacitor rooms and related crowbars. By generating high-voltage when needed, reliability and personnel safety is greatly enhanced. The system development to date has been completely successful and results indicate that operation to the full system average power (1.1 megawatts) should be achieved as required, within specification, when loads become available.

ACKNOWLEDGEMENTS

The authors appreciate the hard work and dedicated efforts of the mechanical and electrical fabrication technicians: Diego C. Jaramillo, Adam R. Martinez, Timothy A. Martinez, and John J. Sullard.

FIRST BEAM AT DARHT-II

Carl Ekdahl, E. O. Abeyta, L. Caudill, K. C. D. Chan, D. Dalmas, S. Eversole, R. Gallegos, J. Harrison, M. Holzscheiter, J. Johnson, E. Jacquez, B. Trent McCuistian, N. Montoya, K. Nielsen, D. Oro, L. Rodriguez, P. Rodriguez, M. Sanchez, M. Schauer, D. Simmons, H. V. Smith, J. Studebaker, G. Sullivan, C. Swinney, and R. Temple, LANL, Los Alamos, NM 87545, USA
Y. J. Chen, and T. Houck, LLNL, Livermore, CA 94551, USA
E. Henestroza, S. Eylon, W. Fawley, and S. S. Yu, LBNL, Berkeley, CA 94720, USA
H. Bender, W. Broste, C. Carlson, G. Durtschi, D. Frayer, D. Johnson, K. Jones, A. Meidinger, K. Moy, R. Sturgess, and C. Y. Tom, Bechtel Nevada, Los Alamos, NM 87544, USA
T. Hughes, and C. Mostrom, Mission Research, Albuquerque, NM 87110

Abstract

The second axis of the Dual Axis Radiographic Hydro-Test (DARHT) facility will provide up to four short (< 150 ns) radiation pulses for flash radiography of high-explosive driven implosion experiments[1]. To accomplish this the DARHT-II linear induction accelerator (LIA) will produce a 2-kA electron beam with 18-MeV kinetic energy, constant to within ± 0.5% for 2-μs. A fast kicker will cleave four short pulses out of the 2-μs flattop, with the bulk of the beam diverted into a dump. The short pulses will then be transported to the final-focus magnet, and focused onto a tantalum target for conversion to bremsstrahlung pulses for radiography. DARHT-II is a collaborative effort between the Los Alamos, Lawrence Livermore, and Lawrence Berkeley National Laboratories of the University of California.

INTRODUCTION

Commissioning of DARHT-II is proceeding in four phases. The first phase was a demonstration that the DARHT II technology could produce and accelerate a beam of electrons. Optimization of the injector and accelerator to produce a beam with the required final parameters and quality is the objective of the upcoming second phase of commissioning. The third phase will demonstrate the ability to produce multiple electron-beam pulses, and the final phase will demonstrate production of multiple-pulse radiographic-quality bremsstrahlung pulses.

DARHT-II was first turned on in early summer, 2002, and the first phase of commissioning is now complete. These tests were accomplished at reduced parameters to minimize risk of damage to this new accelerator. Table 1 shows the parameters for these experiments compared with the final parameters expected when all phases of commissioning are completed. We will detail some of the results from the first phase in this article.

ACCELERATOR

An 88-stage Marx generator that will produce a 3.2-MV output pulse that is flat for 2-μs powers the injector diode for DARHT-II. Because of the Marx risetime and the stray capacitances of injector structure, the risetime of this pulse at the diode is ~ 500 ns. To minimize risk of damage in the experiments reported here, the Marx generator was configured to produce a shorter, 1.2-μs FWHM pulse, which was even further shortened by using a crowbar switch on most shots.

A 16.5-cm diameter hot dispenser cathode in a shrouded Pierce-like diode produced a 1.2 –1.3-kA beam for the experiments reported here. The solenoidal magnetic-transport field is cancelled at the surface of the emitter with a bucking coil so that the (conserved) beam canonical angular momentum will be zero at the field-free bremsstrahlung converter, when installed.

After leaving the diode, the 3.0-MeV beam was accelerated by eight large-bore (36-cm diameter beam tube) induction cells to 4.2 MeV. The magnetic transport through these induction cells was tuned so that none of the off-energy electrons present in the ~500-ns beam head (produced by the diode-pulse risetime) executed betatron oscillations with amplitude greater than ¾ of the beam tube radius, thus keeping them well away from the accelerating gaps and insulators.

The beam next enters a special transport zone with a narrow energy bandpass to scrape off the long risetime, off-energy beam head. For these first experiments, this beam-head clean-up zone (BCUZ) was configured to pass the entire beam head during these initial tests, and the timing of the accelerator was set to accelerate the entire beam, including the rising portion of the pulse. The magnetic tune through the BCUZ compressed the beam to the smaller radius needed to match into the main accelerator.

After the BCUZ the beam enters the main accelerator, which consisted of 64 smaller-bore (25.4-cm diameter beam tube) "standard" induction cells for phase 1 experiments. Of these, two or three were inactive due to problems. The magnetic tune through the main accelerator gradually increased to a field of more than 1 kG on axis to suppress the beam-break-up (BBU) instability.

The magnetic tune for these experiments (Fig. 1) was designed using two beam dynamics codes [2]. First, the TRAK electron-gun design code [3] was used to establish initial conditions at the anode (initial radius, divergence, emittance) for the XTR envelope code [4] at the operating A-K potential of the diode. Then the tune was developed for the energy flattop of the beam using the accelerating voltages expected to be applied to the gaps. Finally, the

0-7803-7738-9/03/$17.00 © 2003 IEEE

transport of the off-energy beam head was checked using XTR simulations in steps of 100-kV A-K potential, with initial conditions from individual TRAK simulations.

Table 1: DARHT-II Parameters

	These Experiments	Final Parameters
Beam Current	1.2-1.3 kA	2.0 kA
Pulse Length	0.5-1.2 μs (FWHM)	2.0 μs (FlatTop)
Diode	3.0 MeV	3.2 MeV
8 Injector Cells	1.2 MeV	1.4 MeV
Installed Standard Cells	64	70
Active Standard Cells	61-62	70
Exit Energy	12.5-12.7 MeV	18 MeV

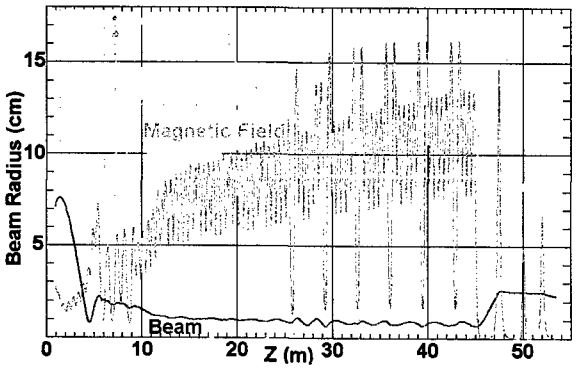

Figure 1. DARHT-II tune for commissioning experiments.

DIAGNOSTICS

DARHT-II is heavily instrumented with beam and pulsed-power diagnostics. In addition to diagnostics that monitor the Marx generator performance, there are capacitive dividers in the diode vacuum to measure the actual diode voltage waveform. Each induction cell has a resistive divider to measure the voltage waveform delivered by the PFN. There are beam position monitors (BPMs) at the entrance to each block of cells, as well as three more in the diode anode region, one at the exit of the injector cells, two in the BCUZ, and one just before the imaging target. For these experiments streak and framing cameras produced images of beam generated Cerenkov and optical transition radiation (OTR) light from targets inserted in the beam line. Finally, a magnetic spectrometer is used to measure the beam kinetic energy.

Diode Voltage Monitors

The A-K gap potential was measured using capacitive dividers. These monitors were 19-cm diameter plates positioned flush with the vacuum tank wall facing the diode cathode structure. Each monitor plate is integrated into a standard 45.7-cm vacuum port nipple. One of the monitors is recorded directly giving a signal proportional to dV/dt. This signal was integrated with software, and was calibrated against the beam energy measured with the magnetic spectrometer.

Beam Position Monitors

Each BPM consisted of an array of four B_θ-field detectors spaced 90° apart. Differencing the opposing detectors and normalizing to the sum of all four gave the position of the beam centroid with negligibly small errors [5]. Each detector was a (double-loop) balanced design with a Moebius crossover to minimize common mode signals arising from ground loops, radiation driven Compton currents, direct beam spill pickup, electric field pickup, and/or other interfering noise, EMP, or backgrounds. The loops were formed from SiO_2 insulated coax to maintain vacuum integrity and long term immunity to radiation backgrounds. Signals proportional to dB_θ/dt, were integrated and further processed in software to give beam current and centroid position. Calibration was accomplished in a "coaxial" test stand with an inner conductor that could be accurately offset from center. In addition to rigorous calibration, these BPMs have been checked against independently calibrated position monitors at the ETA, Thor, and DARHT-I accelerators.

Beam Imaging

Streak and framing cameras recorded images of beam generated Cerenkov and OTR light from targets inserted in the beam line at 45° to the axis. The targets were 0.3-mm thick SiO_2 wafers that were polished and aluminized on the front surface to produce OTR, and frosted on the back surface to scatter Cerenkov radiation into the line of sight orthogonal to the beamline. Target manipulation was accomplished by remote control from the control room.

The Bechtel/Nevada streak camera used a unique, anamorphic optical system that compressed the light in one dimension into a line that was imaged onto a coherent, linear fiber-optic array cemented to the remotely located camera. Two such arrangements provided simultaneous projections in the horizontal (X) and vertical (Y) directions, which were recorded on a 1024x1024 CCD readout camera. The anamorphic optical system simplified alignment, eliminated ambiguity resulting from beam motion, and eased analysis. Time-resolved moments and maximum-entropy reconstructions of the beam profile were obtained with analysis software (subject to the constraints of only two views) immediately after each shot.

The OTR angular distributions were recorded with a Bechtel/Nevada four-frame camera focused at infinity

through a large collection angle lens system. Another 1024x1024 CCD readout camera enabled immediate viewing and analysis of the data.

Spectrometer

A 45° sector magnet powered by a highly regulated supply is used to measure the energy of beam electrons passing through a 1-mm input collimator. The position of this beamlet in the momentum dispersion plane was registered with yet another Bechtel/Nevada streak camera with CCD readout. Light from a fast fluor in the momentum dispersion plane was focused onto a coherent fiber bundle that relayed it to the remotely located streak camera. This spectrometer system has been calibrated against an ion source, and has also been used to measure the energy of the DARHT-I and FXR (LLNL) beams.

RESULTS

A striking feature of this diode is the 7.8-MHz oscillation on the main pulse (Fig. 2 and Fig. 3), which is about ±1.5% of the voltage at the peak. This is an LC oscillation caused by the capacitances and inductances of the injector structure. This LC oscillation damps out with a time constant of ~780 ns with no beam loading the diode. The decay time decreases as beam current loads the circuit. We varied the diode current by operating the cathode at temperatures below that required for space-charge limited emission. Oscillation damping-rate data acquired in those experiments imply that the decay time should be less than 250 ns when we operate at 2 kA. If so, the oscillation amplitude should decay to less than 0.3% by the time the voltage reaches its flattop value. In any case, a resistive damping circuit to further quench this oscillation is now being tested, and could be installed if necessary.

As shown in Fig. 4, the beam is accelerated by the eight injector cells without loss of current within the ~2% uncertainty of the measurement. Some of the beam head is then lost in the 15.2-cm diameter BCUZ throat (Fig. 5). Very little further loss occurs as the beam is accelerated through the remaining 64 accelerator cells (Fig. 6). These results verify that the magnetic tune indeed realized the design goal of negligible off-energy beam-head loss in the cells.

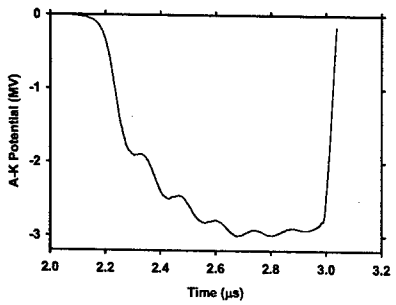

Figure 2. A-K gap potential.

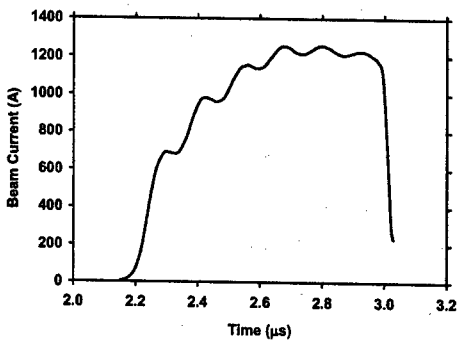

Figure 3. Electron beam current at diode exit.

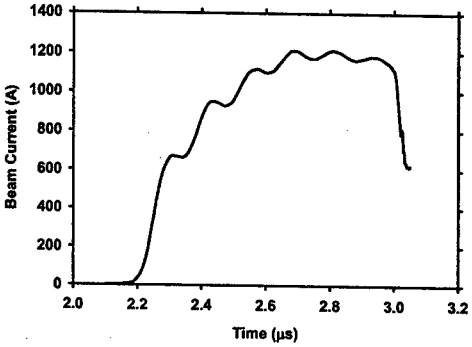

Figure 4. Electron beam current at exit of injector cells.

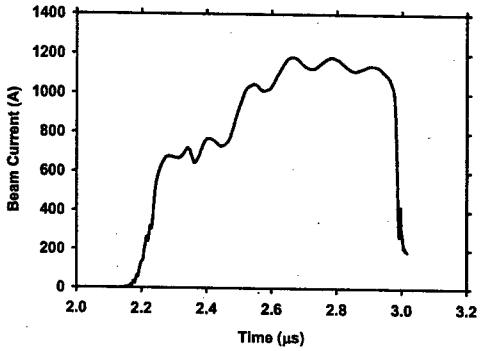

Figure 5. Electron beam current at BCUZ exit.

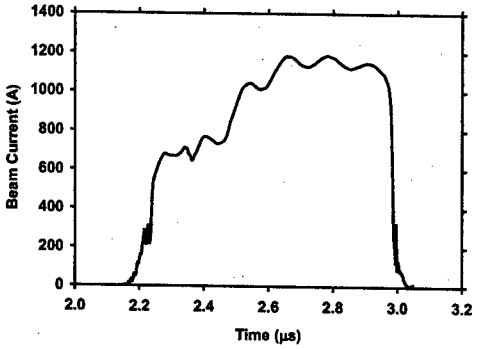

Figure 6. Electron beam current at accelerator exit.

The ±1.5% beam energy oscillation in the diode causes an oscillation of the beam position as a result of an accidental magnetic dipole in the diode region. This is clearly evident at the first BPM, located at the diode exit (Fig. 7). This initial motion is modified by the magnetic transport, but does not grow in amplitude through the accelerator (Fig. 8). Although DARHT-II is equipped with steering dipoles throughout, they were neither needed nor used for these experiments.

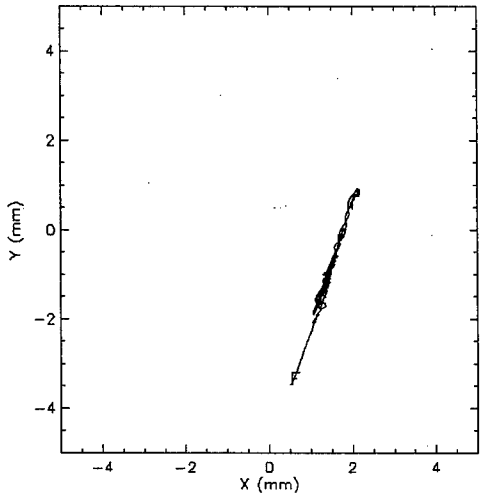

Figure 7. Beam position at diode exit during a 400-ns window around peak current. (S and F signify start and finish times).

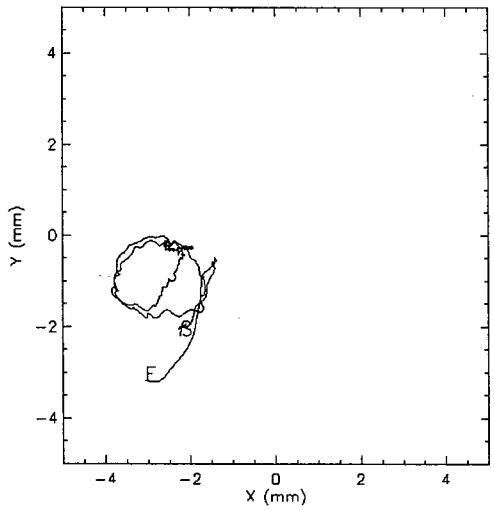

Figure 8. Beam position at accelerator exit during a 400-ns window around peak current. (S and F signify start and finish times).

The fully accelerated beam kinetic energy was measured with the magnetic spectrometer to be >12.2 MeV for 500 ns, with a peak energy >12.5 MeV (Fig. 9). The 7.8-MHz oscillations are clearly evident on this sensitive scale, although they amount to only ±0.4% of the accelerated beam energy.

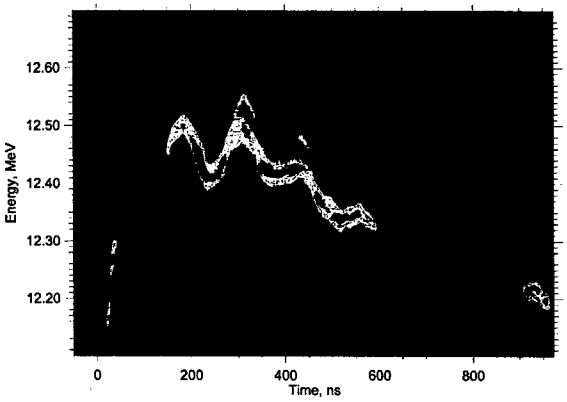

Figure 9. Streak camera readout of electron energy during an un-crowbarred pulse.

Spectrometer measurements of beam energy after the eight injector cells gave a peak of 4.2 MeV. The diode A-K potential was 3.0 MV, so these measurements indicate an average beam-loaded accelerating potential of 150 kV/cell for the injector and 136 kV/cell for the 61 active standard cells.

Anamorphic streak images (Fig. 10) of the beam after the accelerator exit showed that the elliptical beam profile had a Gaussian-like core surrounded by a halo.(Fig. 11) that includes <20% of the total current. The beam centroid motion seen in the streak images has excellent correlation with the beam position measured with a BPM 40 cm upstream of the imaging target.

Figure 10. 1.0-μs anamorphic streak images of ~1.5-cm diameter beam. Top: Projection in vertical plane (anamorphically compressed in horizontal direction). Bottom: Projection in horizontal plane(anamorphically compressed in vertical direction). Time runs left to right.

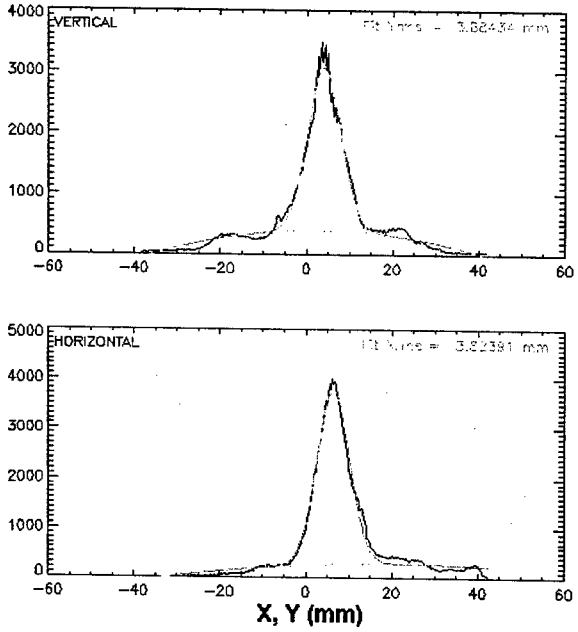

Figure 11. Projections at lineout time shown in Fig. 10. A fitted model consisting of a Gaussian core plus quadratic halo is over-plotted. Amplitude units are raw CCD counts.

Target heating is an issue for long-pulse beam imaging. If the imaging target gets too hot, evolved gas is ionized by electron impact, and ions are accelerated into the beam by the beam space charge, partially neutralizing it. This causes ion focusing of the beam, or even disruption [6], either of which invalidates the imaging data. The threshold for these effects is over 300C [7]. We estimated the temperature of the target by time-integrating movies of maximum-entropy reconstructions of the beam current density profile to get maps of charge deposition, and then temperature using stopping power and specific heat. We concluded that imaging data near the peak current, but shortly after the risetime, were likely free of confusing ion effects.

To estimate the beam emittance we changed the focal point on several consecutive shots using one of the solenoids after the accelerator exit. We then found the most likely emittance at the accelerator exit by fitting the profile size as a function of focus magnet strength with the XTR envelope code predictions [4,8]. The normalized Lapostolle emittance (4rms) was > 4000 π-mm-mr because of the halo (Fig. 11). On the other hand, had we scraped off the halo with an aperture, the emittance of the remaining beam core (~80% of total current) would have been < 1000 π-mm-mr.

We concluded this first round of commissioning with tests of resistance to BBU. No evidence of BBU growth was seen until the magnetic field strength was reduced by a factor of 5 throughout the 64 standard cells. Figure 12 shows a wavelet frequency analysis of the motion of the beam centroid, dX/dt, derived from un-integrated BPM signals near the end of the accelerator. On this shot with 20% field motion in the BBU frequency band is seen to grow at late times. This result verifies the robustness of this tune to BBU and implies BBU will be suppressed when we begin operations with the final 2-kA beam current.

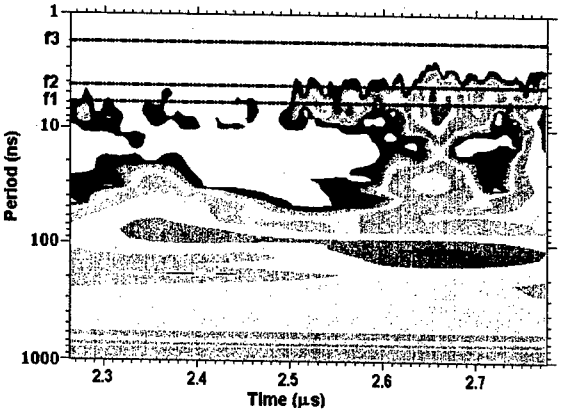

Figure 12. Frequency analysis of motion of the beam centroid with magnetic field reduced by factor of 5. BBU frequencies for the accelerator cells are f1=169 MHz, f2=236 MHz, and f3=572 MHz [9].

ACKNOWLEDGEMENTS

This work was supported by the US National Nuclear Security Agency and the US Department of Energy under contract W-7405-ENG-36.

REFERENCES

[1] "Status of the DARHT Phase 2 Long-Pulse Accelerator," M. J. Burns, et. al., PAC2001, Chicago, IL, June 2001, p. 325
[2] "Beamline tunes for DARHT-II phase-1 commissioning," Carl Ekdahl, Los Alamos National Laboratory report LAUR-02-3921, June 27, 2002
[3] "Finite-element Methods for Electron Gun Design," Stanley Humphries Jr., ICOPS'96, and www.fieldp.com
[4] "Beam injector and transport calculations for ITS," Thomas P. Hughes, David C. Moir and Paul W. Allison, PAC'95
[5] "Fourier-analyzing coil arrays for pulsed relativistic electron beam experiments," C. A. Ekdahl, Rev. Sci. Instrum. 55, 1221 (1984)
[6] "Effect of target-emitted ions on the focal spot of an intense electron beam," Dale R. Welch and Thomas P. Hughes, Lasers and Charged Particle Beams 16, 285 (1998)
[7] "Ion emission from solid surfaces induced by intense electron beam impact ." C. Vermare, H. A Davis, D. C. Moir, and T. P. Hughes, Phys. Plasmas 10, 277 (2003)
[8] "Reconstruction of initial beam conditions at the exit of the DARHT II accelerator," A.C. Paul, LINAC2000, Monterey, CA, August 2000, p. 455
[9] "BBU and Corkscrew Growth Predictions for the DARHT Second Axis Accelerator," Y. J. Chen and W. M. Fawley, PAC2001, Chicago, IL, June 2001, p. 3490

ELECTRON BEAM/CONVERTER TARGET INTERACTIONS IN RADIOGRAPHIC ACCELERATORS*

J. McCarrick, G. Caporaso, F. Chambers, Y.-J. Chen, S. Falabella, F. Goldin, G. Guethlein, D. Ho, R. Richardson, J. Weir, LLNL, Livermore, CA 94551, USA

Abstract

Linear induction accelerators used in X-ray radiography have single-pulse parameters of the order 20 MeV of electron beam energy, 2 kA of beam current, pulse lengths of 50-100 ns, and spot sizes of 1-2 mm. The thermal energy deposited in a bremsstrahlung converter target made of tantalum from such a pulse is ~80 kJ/cc, more than enough to bring the target material to a partially ionized state. The tail end of a single beam pulse, or any subsequent pulse in a multi-pulse train, undergoes a number of interactions with the target that can affect beam transport and radiographic performance. Positive ions extracted from the target plasma by the electron beam space charge can affect the beam focus and centroid stability. As the target expands on the inter-pulse time scale, the integrated line density of material decreases, eventually affecting the X-ray output of the system. If the target plume becomes sufficiently large, beam transport through it is affected by macroscopic charge and current neutralization effects and microscopic beam/plasma instability mechanisms. We will present a survey of some of these interactions, as well as some results of an extensive experimental and theoretical campaign to understand the practical amelioration of these effects, carried out at the ETA-II accelerator facility at the Lawrence Livermore National Laboratory.

INTRODUCTION

The purpose of a beam/target system in a radiographic accelerator facility is to produce X-rays from the incoming beam electrons via bremsstrahlung in the target material. Some typical requirements for a single X-ray pulse in an industrial radiography or explosives hydrotesting setting are shown in Table 1. In addition, there are now facilities capable of generating a series of X-ray pulses during a single event, allowing the recording of time-dependent data. The typical time scales of such events are microseconds, so that the pulse spacing in a multi-pulse train is perhaps 500 ns. Examples of such systems are the DARHT-II accelerator, a four pulse hydrotest facility now being commissioned at Los Alamos National Laboratory [1], and the ETA/Snowtron facility at Lawrence Livermore National Laboratory, a lower-energy two-pulse system dedicated to accelerator and converter target research and development [2].

If bremsstrahlung conversion were a completely efficient process, the landscape of beam/target interactions would already be well-explored territory. However, for every useful X-ray photon produced, a significant amount of waste heat is deposited in the target material. For the systems under consideration, the amount of heat deposited is roughly independent of beam energy and works out to about 80 kJ/cc in a target material such as tantalum (Ta), for a single beam pulse with the parameters given in the table. This is equivalent to 9 eV per target atom. Since most solids are bonded with energies of the order of a few eV, this means that a single beam pulse will turn at least some portion of the target material into a plasma with temperatures in the eV range.

Table 1: System parameters

System Requirement	E-beam Requirement	X-ray Requirement
High photon energy	20 MeV endpoint	1-10 MeV
High dose; Short exposure	~2 kA ~50 ns pulse	100s of rads 50 ns pulse
High resolution	~1 mm focus	1 mm source size

Since target material in a vapor or plasma state can undergo significant motion on an inter-pulse time scale, the nature of interactions between a beam and target will acquire an explicit dependence on time as well as energy deposited. As the target evolves, a low-density plume of material will develop ahead of the bulk remainder of material. This low-density region can support significant beam/target interactions that can change the beam characteristics before there has been significant X-ray production.

A beam/target interaction is considered "bad" if it affects either of the key radiographic parameters, source size and dose (in this context, there are no interactions that will have a serious impact on beam energy). This translates into interactions that have a significant impact on electron positions or angles, and thus on the positions and angles of the generated X-rays. X-rays from the wrong position will typically increase the effective source size. X-rays emitted at the wrong angle interact with the surrounding environs of the system and ultimately become a source of background noise, rather than useful dose.

SURVEY OF INTERACTIONS

Let us consider a brief survey of the various beam/target interactions. The primary interactions are, of

*This work was performed under the auspices of the U.S. Department of Energy by the University of California, Lawrence Livermore National Laboratory, under Contract No. W-7405-Eng-48.

0-7803-7738-9/03/$17.00 © 2003 IEEE

course, bremsstrahlung and small-angle scatter of electrons. The physics of these interactions need not be repeated here [3]; however, a detail worth noting is that in radiographic systems the "useful" photons are generally those emitted within a small angular cone of some preferred direction, hereafter referred to as "forward dose." Small-angle scatter puts a limit on the thickness of target material that will produce forward dose. Additional material may be present, and may have electrons transporting through it, but very few of those electrons will have their radiation cones aimed in the preferred direction.

The most dangerous beam/target interaction in the present context is the creation and extraction of light ions from contaminants in the target material. By disturbing the delicate balance between beam-generated electric and magnetic forces, ions change the beam transport in the target vicinity and are capable of disrupting source size and lowering forward dose. A typical target is a prompt source of ions, since just a few ns of heating brings the target to a temperature ~600 K, which is enough to desorb contaminants on the target surface. The desorbed neutrals are then ionized by the beam. After tens of ns, the bulk target material is heated into the eV range, and thermal ionization becomes the dominant ion source. Much work has been done recently to investigate the low-temperature mechanisms of ion production; details can be found in [4] and [5].

The hydrodynamic evolution of the vapor- or plasma-state target material is not a direct beam/target interaction, but nevertheless has significant impact on dose and source size. Radial motion of the target moves material out of the electron beam, lowering the integrated line density of material and therefore the dose. Axial motion of the target changes the geometric aspect ratio between small-angle scatter and X-ray production, so that the effective source size increases at fixed incoming beam size. Thus, target motion places a fundamental limit on the multi-pulse performance of a passive target.

There are a host of other interactions, but in the present application they are "benign" in the sense that they do not affect dose or source size. Typically they either make a change to the system that is steady-state relative to the beam flattop, or the interaction length is too small to have a deleterious effect. Backscattered electrons [6] are an example of the former. Secondary electrons that escape from the target are trapped in the negative potential produced by the beam space charge in front of the grounded target; the system reaches steady circulation in a few transit times, r_{beam}/c ~ a few ps. This low-energy electron "fog" changes the beam transport as a function of target thickness, but is compensated via static changes to the transport system for a given target.

The low-density plasma plume ahead of the bulk target material can interact with the beam as the target expands. At densities much lower than those which generate significant X-rays, the plasma will still support macroscopic image charges and currents in response to the beam charge and current. In any beam-plasma system, one must also worry about exciting a broad family of microscopic instabilities. However, the neutral plasma plume is moving at a velocity of order the thermal speed. For Ta at 5 eV this is ~2.3 mm/μs, so that even after several μs the plume size is ~1 cm. This is too short an interaction length to affect beam transport, even for a beam experiencing either extreme of complete charge or complete current neutralization via macroscopic mechanisms. Any microscopic modes that could be excited would be strongly convective and insignificant over such a short length. This has been verified experimentally, as detailed below.

BACKSTREAMING ION BEHAVIOR

The extraction of ions by the electron beam space charge from a source close to the target surface has been considered in numerous prior studies [e.g. 7]. However, it will be useful to review some of the basic behavior.

By disrupting the delicate balance between beam space charge and current normally present in beam transport, positive ions produce a strong focusing effect on the electron beam. Ions generated in the region where the beam is focused on a target pinch the beam to a smaller size, and move the location of the new focus upstream, away from the target. The beam size on the target, and the resulting X-ray source size, eventually grow monotonically. In addition, the oscillatory radial motion of the ions within the beam produces a nonuniform charge distribution and therefore nonlinear focusing forces, resulting in beam emittance growth and a corresponding reduction in forward dose.

The strength of the interaction can be characterized by a quantity called the *disruption length*, L_d [8].

$$L_d = r_{beam}\sqrt{\frac{\pi\gamma\beta^2 I_{Alfven}}{f I_{beam}}}, f \equiv \frac{\rho_{ion}}{\rho_{beam}}$$

The disruption length represents the size of an ion column that brings a beam to the threshold of monotonic spot growth. The envelope of the beam has been overfocused ahead of the target and expanded back to its original spot size at the targe plane. At full neutralization, L_d in the systems of interest is ~4 cm.

Light ions can exceed L_d very quickly. For a typical accelerating potential of 300 kV, protons reach 0.76 cm/ns, so that at the end of a 50 ns beam pulse the ion column would be 38 cm in length. Species with charge-to-mass ratios up to that of O+ are dangerous in 50 ns.

The number of ions to fill the disruption channel is quite small. At full neutralization, the number required is

$$N_{ion} = \frac{r_{beam}}{qc}\sqrt{\pi\gamma\beta^2 I_{Alfven} I_{beam} f} \approx 10^{12}$$

or what would be produced by ionizing one-tenth of a monolayer of surface contaminants. The number required is less at lower neutralizations because of the longer interaction length involved.

The effect can be observed experimentally. Figure 1 shows two sets of gated X-ray camera data from the ETA-II accelerator. The four frames from left to right shows data at different times within a single pulse, with gates of 10 ns each, spanning the 40 ns flattop of the beam. The first row shows a large incoming beam, which has a slower heating rate and lower accelerating potential, moving into the pinch phase of the ion effect by the end of the pulse. The second row shows a tightly focused incoming beam whose fast pinch phase is not captured in these frames, showing only the monotonic growth phase starting very early in time. The ions are beam-generated within a single pulse due to desorption and ionization of surface contaminants.

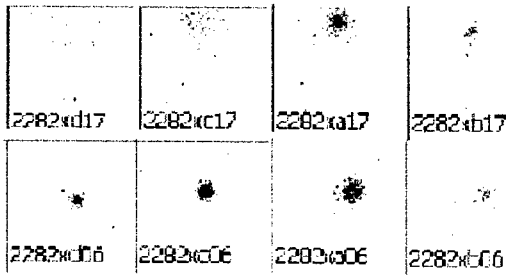

Figure 1: Time evolution of ETA-II X-ray spot with ions, for large (top row) and small (bottom) initial beam sizes.

Figure 2 shows a different form of data. The first plot is a continuous record of beam size versus time taken from a streak camera. Two sets of data are shown, for two different beam sizes. In these experiments, there was a strong ion source present at very early times, arising from a plasma generated very promptly by flashing over the surface of a quartz dielectric in the strong radial electric field of the electron beam. The second plot shows an extremely good match to the data produced via PIC modeling. The time axis of the simulation is shifted relative to the camera data so that the simulation starts at the beginning of the current flattop. It should be noted that the only fitting parameter in the simulation is the choice of ion species, namely H+. While there is much new data that shows H+ does not make up a significant fraction ions in the case of desorption, the quartz flashover data would not be matched by any heavier species.

Given the reality of ion disruption, it is vital to consider various means to combat the effect. The two obvious approaches are cleaning and blocking. In the case of cleaning, one seeks to remove all light contaminants from the target material, generally by some method of heating: resistive, laser ablation, e-beam heating. Such approaches are attractive since they do not interfere with the beam itself, but have undesirable features as well. Since only a small number of ions can cause problems, the cleaning must be very thorough. Furthermore, most approaches require that significant amounts of additional hardware be incorporated into the target system; cleaning must be in-situ since the redeposition times for contaminants present in the vacuum system are short relative to the operational times of the experiments.

Blocking means preventing the ions from forming the long interaction channel. This approach, too, has its pros and cons. An approach such as a mechanical barrier can be very simple to implement; however, it interacts with the beam. Both mechanical and electrical approaches (see [9] for examples of the latter) tend to result in trapping rather than absorption of ions, and an ion column too short to disrupt the beam focus can still cause emittance growth.

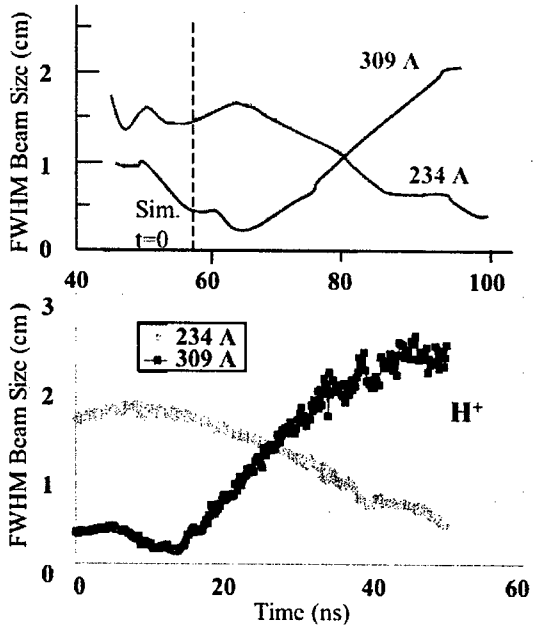

Figure 2: Data (top) and simulation (bottom) of beam disruption by prompt flashover ion source.

TRAPPING IONS WITH A FOIL BARRIER

The simplest technique for blocking ions is to insert a mechanical barrier, in the form of a thin foil, upstream of the target [10]. In order for the barrier to not be simply another contaminated surface that generates ions, a number of constraints must be met, some of them conflicting:

- The foil must be a grounded conductor. A dielectric will quickly flash over in the radial field of the electron beam.
- The foil must be thick and strong enough for self-support, but at the same time thin and light enough that the foil material is not strongly heated by the beam, and does not scatter the beam much in passage. A beam such as DARHT-II can have its emittance doubled by less than 40 μ of graphite.
- The foil must be close enough to the target so that the spacing is less than L_d, but at the same time far enough that the beam envelope is large enough to avoid significant heating.

- Radiographic requirements set the beam size on the target, and the previous requirements set the beam size at the foil and the space between them. This defines a beam envelope, and that envelope must be consistent with the transport system.

Once these requirements are met, the resulting volume defined by the grounded target, grounded barrier, and grounded beam pipe forms a trap rather than an ion absorber. Consider the motion of an individual ion as a function of the z coordinate between the target and the barrier. If the potential were one-dimensional, this would be a classical turning-point problem where an ion injected at one end with zero energy would reach the opposite end also with zero energy, and reflect. Any finite injection energy would kick the ion from the far end of the trap. In two or three dimensions, however, the problem is completely different. Consider a potential ϕ_0 in (r,z) space that is 1-D in z; a trough of infinite radial extent. Superimpose on this a small 2-D "bump" of localized extent, ϕ_1, as in Figure 3.

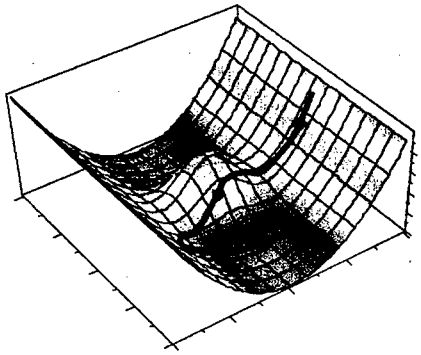

Figure 3: Particle motion in 1-D trough with 2-D bump.

A particle passing over this bump off-center will pick up a "kick" in radial velocity, which for small perturbations is

$$\Delta v_r \approx \frac{-q}{m}\int_{z_{\min}}^{z_{\max}} \frac{\frac{\partial \varphi_1}{\partial r}\,dz}{\sqrt{\frac{-2q}{m}\varphi_0}}$$

As the particle rises up the far end of the trough, there cannot be any radial forces near the grounded surface that can bring the radial velocity back to zero. There is no path the particle can take back to zero energy, and it will reflect in z at a critical point defined by

$$\left|\varphi(z_{crit})\right| = \tfrac{1}{2} m \Delta v_r^2$$

This result can be generalized to arbitrarily shaped grounded surfaces, where it can be shown that the bounce near the surface is essentially a specular reflection of the particle.

In the case of an ion in an electron beam, instead of a localized bump there is a long trench, but the mechanism is identical. For an ion oscillating in a uniform, parallel beam, the average kinetic energy tied up in radial velocity near the barrier is

$$\frac{\int_0^{<r_{emission}>} \varphi_{edge}\frac{r^2}{a^2} r dr}{\int_0^{<r_{emission}>} r dr} = \frac{2}{9}\varphi_{edge} \approx 13kV$$

where ϕ_{edge} is the drop from the beam edge to the center, ~60 kV. This represents the average injection energy it would take to kick an ion into the barrier, and is clearly greater than any reasonable thermal energy. The trapping effect is robust. This has been verified by fully self-consistent PIC simulations [11].

The notion of a grounded surface as specular reflector leads to conceptual (not necessarily practical) surfaces that can "bounce" ions completely out of the electron beam. The ions are not energetically trapped within the beam, although they tend to remain so geometrically. Thus, one can modify the geometry to change this behavior. Figure 4 shows one such conceptual surface, along with the beam envelope and tracks of ions that reach considerable radii outside the beam. Such a system could use a dielectric absorber to catch the ions, or simply take advantage of a much slower increase in f(t), since the volume to be filled becomes the pipe volume and not the beam volume.

Flat barrier systems have been tested successfully in ETA/Snowtron double-pulse experiments [3]. In addition to validating the barrier concept, the experiments also demonstrated safe transport of the electron beam through plasma plumes of various sizes, as the experiment was repeated for various delay times between the Snowtron pulse which generated the plasma and the ETA-II pulse which probed it. Longer times allowed the target/barrier region to fill with larger amounts of plasma; a tight focused was maintained in all cases.

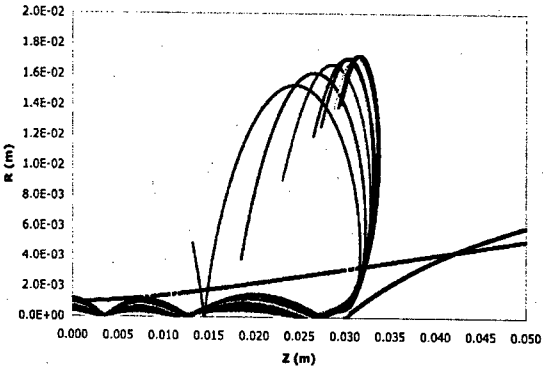

Figure 3: Surface which "bounces" ions out of beam

TARGET HYDRODYNAMICS

Target motion is the result of beam/target interactions rather than an interaction unto itself, but it is a critical phenomenon. It can be easily shown that, at long times relative to the initial acoustic transit time across the target, the decay of on-axis line density has the form

$$\frac{\int \rho(t)dz}{2\rho_o d} \rightarrow \frac{t_{decay}^2}{t^2}$$

where d is the target half-thickness and ρ_0 the initial density. The time dependence is independent of the material properties of the target, which enter only through the scale time, t_{decay}. Let us consider the case of a beam with scale radial dimension σ in the limit of $\varepsilon = d/\sigma << 1$. One can then show that t_{decay} has the form

$$t_{decay} \approx \frac{\sigma}{\varepsilon C_o} EOS(1)$$

where EOS(1) is an equation of state-dependent factor of order unity, and C_o is the initial sound speed of the target material just after heating by a beam pulse.

The geometric contribution to t_{decay} is set by the radiographic requirements and cannot be changed. The initial sound speed is a function of the energy deposition, which is also constrained by the radiographic requirements, and a lumped parameter we will call E_{bond}. E_{bond} is a measure of the energy required per target atom to bring it from the initial solid state to complete vapor, at essentially fixed volume. This is a possible knob to improve target performance.

One approach to using the E_{bond} knob is the composite target concept, described in [12]. The basic idea is build a designer mixture of high-Z material, for X-ray production, and low-Z material, that serves as a heat sink. By building the material with sufficiently small scale size of the high-Z material, one achieves fast heat transfer from high-Z to low-Z on the time scale of a single beam pulse. The material is designed such that the areal number density of low-Z material is much higher than the high-Z; the result is to add many more bonds that must be broken before the material can be vaporized, faster than one adds additional beam heating or scatter due to the presence of the additional low-Z material.

Composite targets have been successfully fabricated and tested at the ETA-II facility. Figure 5 compares measurements of t_{decay} for solid Ta and a Ta/B4C composite; the measurements were made with a low-energy X-ray backlighter after targets were struck with the ETA-II beam. The composite material has decay times three times greater than solid Ta at the tightest beam sizes, increasing to six times greater at more moderate sizes, a significant improvement.

CONCLUSIONS

Electron beam/converter target interactions in the context of radiography are judged by their effect on the two key radiographic parameters, dose and source size. In general, short interaction lengths protect against all but two interactions: backstreaming ions, and the thermally driven expansion of the target material. While very small amounts of ions can disrupt the beam very quickly, the foil barrier technique has proven to be a simple and effective remedy. Similarly, dramatic decreases in the rate at which line density depletes due to target expansion have been achieved in successful tests of composite target materials.

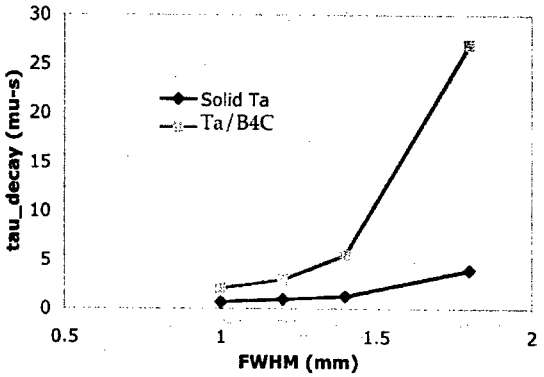

Figure 4: Decay time for composite vs. solid Ta.

ACKNOWLEDGEMENTS

The authors would like to thank the ETA-II experimental program at LLNL for providing the data shown in this paper.

REFERENCES

[1] C. Ekdahl, et al. "DARHT-II Commissioning Results," PAC 2003.

[2] S. Sampayan, et. al., "Beam-Target Interaction Experiments for Multipulse Bremsstrahlung Converters Applications", PAC 2001.

[3] J. D. Jackson. Classical Electrodynamics, Wiley, 1962.

[4] T. Hughes, H. Davis. "Effect of Stimulated and Thermal Desorption in DARHT 2," PAC 2003.

[5] H. Davis, et al. "Measurements of Thermally Desorbed Ions from Beam-Target Interactions," PAC 2003.

[6] S. Falabella, et al. "Effect of Backscattered Electrons on Electron Beam Focus," LINAC 2000.

[7] D. R. Welch and T. P. Hughes, Laser Part. Beams **16**, 285-294 (1998).

[8] G. Caporaso, Y.-J. Chen. "Analytic Model of Ion Emission from the Focus of an Intense Relativistic Beam on a Target," LINAC 1998.

[9] J. McCarrick, T. Houck. "The Effect of Trapped Backstreaming Ions on Beam Focus in Radiographic Accelerators," PAC 1999.

[10] T. P. Hughes, "Target Calculations for ITS Short-Focus Experiment", MRC/ABQ-N-589, Sept. 1997.

[11] Y.-J. Chen, et al. "High Intensity Beam and X-Ray Converter Target Interaction and Mitigation," AAC 2002.

[12] J. McCarrick. "A Composite Target Concept for Multi-Pulse Radiography," BEAMS 2002.

R&D WORKS ON 1MHZ POWER MODULATOR FOR INDUCTION SYNCHROTRON

Kunio KOSEKI*, Graduate University for Advanced Studies, 1-1 Oho, Tsukuba 305, JP
K.Takayama, J.Kishiro, K.Torikai, E.Nakamura, T.Toyama, Y.Arakida, S.Inagaki, M.Wake, H.Sato, M.Shirakata, S.Igarashi, and Y.Shimosaki KEK, 1-1 Oho, Tsukuba 305, JP

Abstract

A proof of principle experiment of an Induction Synchrotron [1,2] is scheduled in 2003 at the KEK 12GeV-PS. Proton bunches are accelerated with a 10kV of rectangular shaped induction voltage. An accelerating system consists of four induction cavities capable of individually generating a 2.5kV of output voltage. Each cavity is driven by a solid-state power modulator, which is operated at a revolution frequency of 600-800 kHz. The modulator circuit consists of MOS-FETs as switching element.

Uniformity in the voltage waveform is crucial for the stable acceleration. Ringing in the voltage waveform caused by coupling of self-inductance of circuit and output capacitance of MOS-FETs deteriorates the uniformity. With the help of circuit analysis and simulation, method of minimizing the self-inductance has been developed. Ratio of numbers of MOS-FETs in series and in parallel which defines the total output capacitance is also important to design the power modulator circuit.

Power loss in MOS-FET is also important for stable operation of the power modulator. By the circuit analysis, it is also found that the output capacitance contributes to the power loss.

1 INTRODUCTION

A novel concept of a proton synchrotron [1], referred to as an Induction Synchrotron, was proposed by K.Takayama and J.Kishiro. The Induction Synchrotron employs two types of induction cavities and power modulators [2]; one is for acceleration and the other is for the confinement of proton beams. This functional separation between beam handling and acceleration enables us to increase the beam intensity by utilizing the longitudinal phase space efficiently with an induction barrier voltage and an induction acceleration voltage.

One of the key devices of the Induction Synchrotron is a power modulator which generates a rectangular shaped voltage at a magnetic core loaded induction cavity with the same repetition rate as the revolution frequency of proton beams of up to 1 MHz.

The induction power modulator consists of four switches by MOS-FETs and composing a full bridge circuit as in DC-AC converter. The circuit of the induction power modulator and its trigger sequence is shown in Fig.1. In sequence 1) and 3) the voltage is induced at the magnetic core with non-zero value of dI/dt. In sequence 2) and 4) the primary current with dI/dt nearly equal to zero flows to the magnetic core without inducing a secondly voltage. Following those sequences from 1) to 4), a bipolar pulse voltage with the same amplitude is generated at the magnetic core.

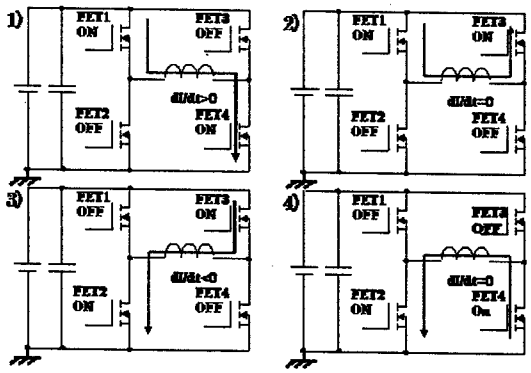

Fig. 1 : Circuit of the Induction Power Modulator and its trigger sequence

This report describes recent progress in the development of induction power modulator.

2 SPICE CIRCUIT MODEL

In a Spice model of the induction power modulator, drain current dependence on drain to source voltage of MOS-FET is characterized by Shichman-Hodges model. In this model, drain current is characterized by following two equations.

$$Id = \frac{kW}{L}\{(Vgs - Vt)Vds - \frac{Vds^2}{2}\} \quad (1)$$

for linear region in which drain current has almost linear dependence on drain to source voltage. And

$$Id = \frac{kW}{2L}(Vgs - Vt)^2(1 + \lambda Vds) \quad (2)$$

for saturation region in which drain current is square dependence on gate voltage. Here L is the channel length. W is the channel width. Vt is the gate threshold voltage. K is transconductance parameter. Lambda is channel length modulation. Parasitic capacitance, caused by P-N junction between p-substrate and n+ drain, is modelled by

0-7803-7738-9/03/$17.00 © 2003 IEEE

capacitance inserted between drain and source. Spice calculation result for drain current characterization is plotted in Fig. 2. Although an error between measured and calculated results was up to 46% for lower gate voltage of around threshold voltage, we had good agreement of the order of few % with higher gate voltage of up to 15 [V]. Here the threshold voltage for modelled MOS-FET was 3.85V.

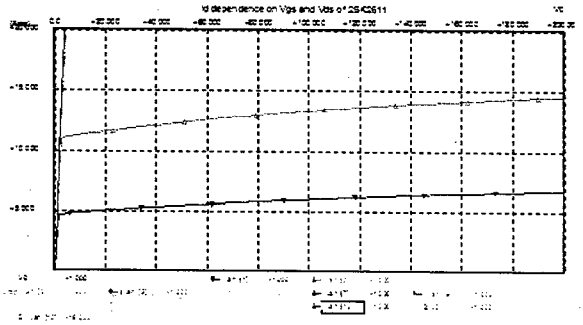

Fig. 2 : Calculated drain current dependence of modelled MOS-FET

Self-inductance of power modulator circuit should exist. For simplicity, it was inserted at typical four points as in Fig. 3.

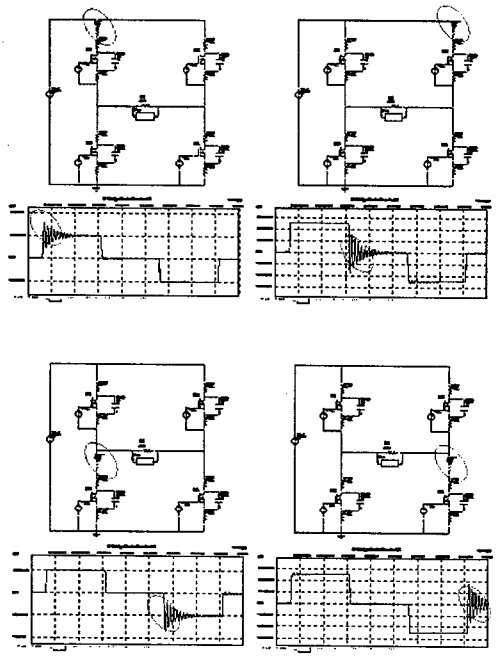

Fig. 3 : Spice model of the induction power modulator

From this calculation, it was found that the resonant coupling occurred by the output capacitance of MOS-FET and by the self-inductance of modulator circuit. As the resonant frequency is expressed by following equation, both output capacitance and self-inductance should be minimized.

$$f = \frac{1}{2\pi\sqrt{LC}} \tag{3}$$

Total amount of output capacitance is determined by number of MOS-FETs in series and in parallel. So, to design the induction power modulator, proper choice of number of MOS-FETs in series and in parallel should be made to avoid output voltage deterioration by resonant coupling. Total amount of output capacitance is calculated as low as 25 [pF] with 7 series and 1 parallel MOS-FETs.

Numerical treatment of self-inductance is also important to design the induction power modulator. To do this, we modelled a wiring pattern of circuit as rectangular shaped wiring with its height of a [m], width of b [m] and radii of wire of r [m]. The self-inductance of this rectangular wiring is calculated as in the following equation.

$$L = \frac{\mu}{\pi}\{-a\log(a+\sqrt{a^2+b^2}) - b\log(b+\sqrt{a^2+b^2}) + (a+b)\log(\frac{2ab}{r}) + 2\sqrt{a^2+b^2} - \frac{7}{4}(a+b)\} \tag{4}$$

It is found that, by proper choice of those parameters, self-inductance of the power modulator is minimized. For a=1 [mm], b=1 [m] and r=3 [mm], calculated self-inductance is as low as 92 [nH].

With above numerically calculated parasitic elements, output voltage was simulated as in Fig. 4.

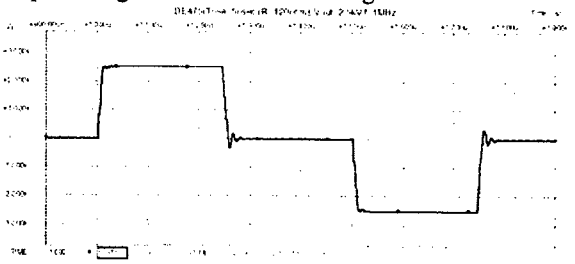

Fig. 4 : Simulated output wave form of the induction power modulator

3 THERMAL DESIGN

Stable operation of semiconductor devices requires accurate estimation of power loss and proper cooling system. By the help of Spice simulation, power loss at each of the MOS-FET was calculated as in Fig. 5.

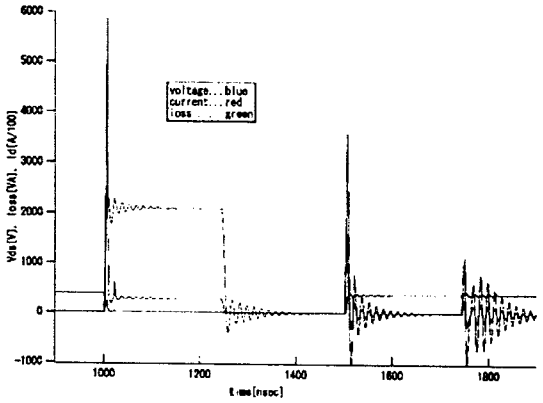

Fig. 5 : Calculated power loss at MOS-FET

As power loss is defined by following equation, it is calculated as 55 [W] for each MOS-FET.

$$P[W] = \frac{1}{T}\int_0^T V(t) \times I(t) dt \qquad (5)$$

Calculation is done with resistor load of 120 [Ω] which corresponds to an impedance of an induction cavity. We have decided to employ the indirect water cooling system for the induction power modulator after above calculation. Characteristic values of the induction power modulator are listed in table 1.

Table 1:Design values and characteristics of the Induction Power Modulator

DC Power Supply	50[kW]
Output Voltage	2.5 [kV]
Peak Output Current	821[A]
Duty of Pulse	50 [%]
Power Loss at MOS-FET	55[W]
Cooling of MOS-FET	Indirect water cooling
# of MOS-FETs in Series	7
# of MOS-FETs in Parallel	1

4 OPERATION RESULTS

The induction power modulator loaded with induction cavity was successfully operated in burst mode operation for test purpose. Repetition frequency was 500 [KHz]. Output voltage measured as gap voltage was 2.0 [kV] as in Fig. 6.

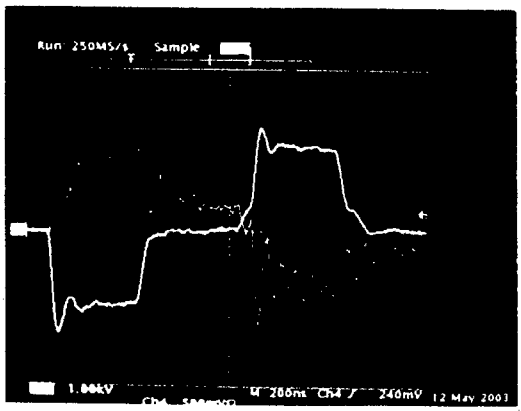

Fig. 6 : 500kHz burst-mode operation loaded with induction cavity.

5 CONCLUSIONS

An induction power modulator has been developed and successfully operated with induction cavity load in burst mode. A repetition rate of 500 [kHz] with 500 [nsec] of bipolar pulses was achieved. The output voltage measured at cavity gap was 2.0 [kV].

6 ACKNOWLEDGEMENTS

Sincere appreciation is given to Mr. Tokuchi of Nichicon Corp. for his great help during the assembly and operation of the Induction Power Modulator. The authors would also like to thank members of the 12GeV Proton Synchrotron at KEK for their advice and supports.

7 REFERENCES

[1]K. Takayama and J. Kishiro, "Induction synchrotron", Nucl. Inst. and Meth. A451/1, 304-317(2000)

[2]J.Kishiro, K.Takayama, E.Nakamura, K.Horioka, M.Watanabe, A.Tokuchi, and S.Naitoh, "Rappidly switched accelerating devices for Induction synchrotrons", in Proceedings of EPAC2000, 1966-1968(2000).

Proceedings of the 2003 Particle Accelerator Conference

SPALLATION NEUTRON SOURCE RING – STATUS, CHALLENGES, ISSUES, AND PERSPECTIVES*

Jie Wei†
for the Spallation Neutron Source Collaboration, USA

Abstract

The Spallation Neutron Source (SNS) ring is designed to accumulate beam pulses of 1.5×10^{14} protons of 1 GeV kinetic energy at a repetition rate of 60 Hz [1]. At such beam intensity and power, key design challenges include control of beam loss and radio-activation, construction of high-quality large-aperture magnets and power supplies, design of robust injection and extraction systems, minimization of beam-coupling impedances, and mitigation of electron-cloud effects. This paper discusses the status of the ring systems with emphasis on technical challenges and issues, and presents future perspectives towards a next-generation high-intensity facility.

INTRODUCTION

The SNS project is presently in the 5th year of a 7-year construction cycle [2]. The SNS ring, designed and constructed mainly by the Brookhaven National Laboratory, will accumulate pulses of 1.5×10^{14} protons of 1 GeV kinetic energy at a repetition rate of 60 Hz (Table 1) [1].

The primary concern is beam-loss induced radioactivation that can limit the ring's availability and maintainability. With a dedicated beam collimation in the ring at an efficiency above 90%, the tolerable fractional beam loss is about 10^{-3} [3].

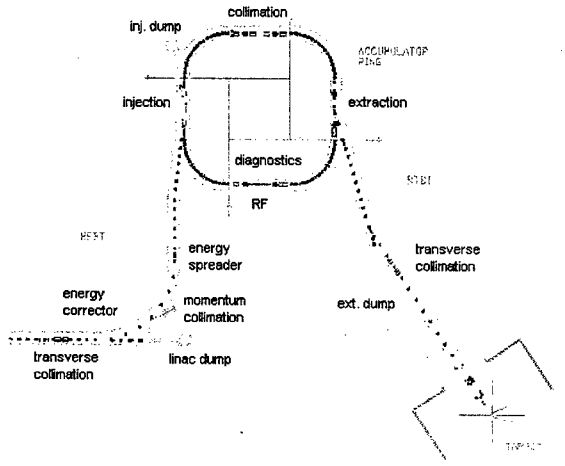

Figure 1: Layout of the SNS accumulator ring, the high-energy beam transport (HEBT), and the ring-to-target transport (RTBT).

Table 1: Major parameters of the SNS accumulator ring and its transport lines (HEBT and RTBT).

Quantity	Value
Circumference	248.0 m
HEBT, RTBT length	169, 151 m
Beam energy	1 GeV
Magnetic rigidity, $B\rho$	5.657 Tm
Average beam power	1.5 MW
Repetition rate	60 Hz
Number of protons per pulse	1.6×10^{14}
Revolution frequency	1.058 MHz
Peak RF voltage ($h = 1, 2$)	(40, 20) kV
No. of RF station (ring, HEBT, RTBT)	4, 2, 0
Unnorm. emittance ($\epsilon_x + \epsilon_y$, 99%)	240 $\pi\mu$m
Betatron acceptance	480 $\pi\mu$m
RF momentum acceptance	$\pm$ 1 %
Transverse tunes (ν_x, ν_y)	6.23, 6.20
Transition energy, γ_T	5.23
Natural chromaticities (ξ_x, ξ_y)	-7.9, -6.9
No. of super-periods	4
No. of dipole (ring, HEBT, RTBT)	39, 9, 1
Ring dipole field	0.7406 T
Ring dipole gap height	170 mm
No. of quad (ring, HEBT, RTBT)	53, 40, 32
Ring quad inner diameter	210-300 mm
No. of sextupole (ring, HEBT, RTBT)	20, 0, 0
Sextupole inner diameter	210-260 mm
No. of corrector (ring, HEBT, RTBT)	61, 18, 17
No. of kicker (injection, extraction)	8, 14
No. of scraper (ring, HEBT, RTBT)	4, 5, 0
No. of absorber (ring, HEBT, RTBT)	3, 3, 2
No. of vacuum pumps (ring, HEBT, RTBT)	50, 18, 12
No. of power supply (ring, HEBT, RTBT)	156, 48, 47
No. of BPM (ring, HEBT, RTBT)	44, 37, 17
No. of loss monitor (ring, HEBT, RTBT)	82, 62, 43
No. of current monitor (ring, HEBT, RTBT)	2, 5, 5
No. of profile monitor (ring, HEBT, RTBT)	4, 13, 8
Vacuum pressure, ring	10^{-8} Torr

ACCELERATOR DESIGN CHOICES

Accumulator ring

During the first year of construction, a study was performed comparing the present structure of full-energy linac plus accumulator ring to a rapid-cycling-synchrotron (RCS) design: a 60 Hz, 400 MeV linac feeds two, vertically stacked RCSs accelerating the proton beam to 2 GeV energy. The biggest challenge to the RCS design is from the stringent (1 W/m) beam-loss criterion: although relaxed by

*SNS is managed by UT-Battelle, LLC, under contract DE-AC05-00OR22725 for the U.S. Department of Energy. SNS is a partnership of six national laboratories: Argonne, Brookhaven, Jefferson, Lawrence Berkeley, Los Alamos, and Oak Ridge.

†jwei@bnl.gov

0-7803-7738-9/03/$17.00 © 2003 IEEE

a factor of 5, still only 0.4% uncontrolled loss is allowed for a 2 MW beam power assuming 90% collimation efficiency. On the other hand, among existing rings the lowest loss of about 0.3% is achieved at LANL's PSR, a 800 MeV accumulator, as opposed to typical losses of a few to tens of percent in RCSs (e.g. ISIS, FNAL and AGS Boosters).

As opposed to the accumulator, the RCSs operating at 30 Hz require a high RF voltage (about 400 kV per ring at 1.4 - 1.9 MHz) for fast acceleration, a large magnet aperture to accommodate the space charge at a lower energy, ceramic vacuum pipes with detailed RF shielding, and high-performance power supplies. Minimization of magnetic errors due to eddy current, ramping, saturation, and power-supply tracking is non-trivial. The study concluded that the required RCS design is technically more demanding and less cost effective [4].

Permanent magnets were considered as an option for the accumulator ring magnets. Electromagnetic magnets were chosen instead, given the uncertainty in the linac energy. This choice is especially appropriate to accommodate later-adopted superconducting-RF linac.

Ring FODO-doublet lattice

The four-fold symmetric ring lattice contains four dispersion-free straights, each housing injection, collimation, RF, and extraction (Fig. 1). Each achromatic arc consists of 4 FODO cells with 90° horizontal phase advance.

After optimization, the ring lattice has doublet straights [1]. The lattice combines the FODO structure's simplicity and ease of correction with the doublet structure's flexibility for injection and collimation. Injection at a dispersion-free region allows independently adjustable painting in the transverse (with orbit bumps in the ring) and longitudinal (with an energy-spreading phase-modulated RF cavity in the HEBT) directions for a robust operation. The 12.5 m-long uninterrupted straight section with a flexible phase advance further improves collimation efficiency. Comparing with the original all-FODO lattice, matching between the arcs and the straights increases the arc acceptance by 50% with the same magnet aperture (Fig. 2).

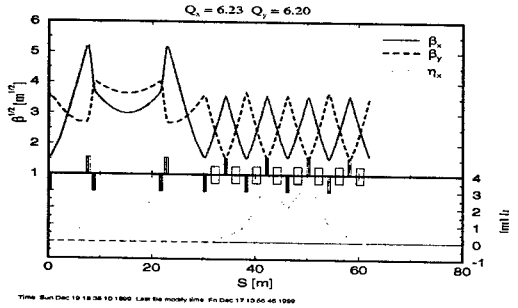

Figure 2: SNS ring FODO/doublet lattice.

Lessons learned

Solid-steel, as opposed to laminated-steel, was selected for most ring and transport magnet cores for cost savings.

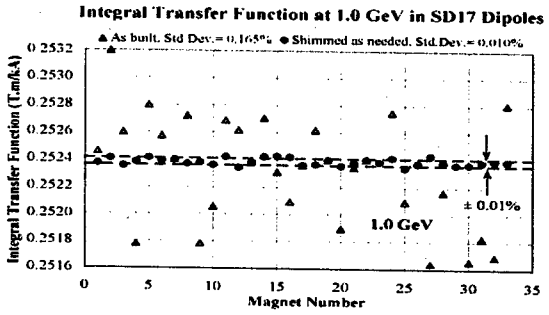

Figure 3: ITF Variation of the dipole magnets before and after shimming (courtesy P. Wanderer and A. Jain).

Individually, good field quality ($\sim 10^{-4}$ relative error at full acceptance) is achieved. However, excessive (up to 0.25%) magnet-to-magnet variation is found in the dipole integral transfer function (ITF) and its current dependence (Fig. 3) [5]. These dipoles are shimmed with iron sheets to achieve below 10^{-4} variation for 1 GeV operation, and sorted according to 1.3 GeV measurement data to minimize orbit corrector strength. Ring quadrupoles are partly sorted according to the power-supply family, and partly shimmed to achieve below 10^{-4} variation among each family.

The design does not allow in-situ baking of vacuum chambers that is needed for alternative NEG film coating.

PHYSICAL CHALLENGES

Main ring challenges include meeting the target requirements on the peak current density, minimizing uncontrolled beam loss, and controlling collective effects (space charge, instabilities, electron cloud [1].

Beam loss

Tables 2 and 3 list the expected controlled and uncontrolled beam loss. Beam collimation is performed at multiple locations (Fig. 1) to minimize the uncontrolled loss.

Space charge

The dominant collective effects are expected to be beam halo and beam loss generated by space-charge related res-

Table 2: Estimated controlled loss for a 2 MW beam.

Mechanism	Location	Fraction
HEBT:		
H^0 from linac	linac dump	10^{-5}
linac transverse tail	H/V-collimator	10^{-3}
linac energy jitter/spread	L-collimator	10^{-3}
Ring:		
beam-in-gap	BIG kicker	10^{-4}
excited H^0 at foil	collimator	1.3×10^{-5}
partial ionization at foil	injection dump	10^{-2}
foil miss	injection dump	10^{-2}
ring beam halo	collimator	1.9×10^{-3}
energy straggling at foil	collimator	3×10^{-6}
RTBT:		
kicker misfiring	collimator	10^{-5}

Table 3: Estimated uncontrolled loss of a 2 MW beam.

Mechanism	Location	Fraction	Power [W/m]
HEBT:			
H^- magnetic strip.	all HEBT	1.7×10^{-6}	0.02
collimator out-scatt.	achromat	7.5×10^{-6}	0.1
Ring:			
H^- magnetic strip.	inj. dipole	1.3×10^{-7}	0.3
nucl. scatt. at foil	foil	3.7×10^{-5}	2.5
collimation ineff.	all ring	10^{-4}	0.9
RTBT:			
nucl. scatt. at window	target window	4×10^{-2}	

onance crossing [6]. Other intensity-limiting mechanisms include electron-cloud effects and instabilities due to the extraction-kicker coupling impedance (Table 4).

The maximum incoherent space-charge tune spread is chosen to be 0.15 to avoid resonance-induced beam loss (Fig. 4). Transversely, the beam is painted to a full, unnormalized total emittance of 240 $\pi\mu$m. Longitudinally, a dual-harmonic RF system is used to achieve a bunching factor ~ 0.45, and HEBT energy spreader is used to paint a full momentum spread of $\pm0.7\%$ without enhancing tails.

Impedance and instabilities

Efforts are made to reduce the coupling impedance in a frequency range from about 200 Hz to above 50 MHz. 14 extraction kickers residing inside the vacuum chamber are major sources of transverse impedance. The impedance associated with the high-μ ferrite was reduced by terminating the pulse-forming network (PFN) circuit to 25 Ω, and by maximizing the width of the kicker module (Fig. 5).

Electron-cloud effects

Electron cloud remains to be an unresolved issue. Computer simulation indicates a trailing-edge electron concentration of peak value near 15 nC/m, much higher than the value simulated for the PSR ring [8].

Mitigation measures involve suppressing electron generation and enhancing Landau damping [9]. Magnetron (dc) sputtering is used to coat the surfaces with 0.1 μm TiN to reduce electron multipacting (Fig. 6). Electrons

Table 4: Collective effects and estimated thresholds for a 2 MW beam.

Mechanism	Threshold
Trans. space charge	$\Delta\nu_{sc} \approx -0.2$
Long. space charge	15 kV induced RF voltage
Trans. microwave instab.	$Z_\perp \approx 60$ kΩ/m
Long. microwave instab.	$\lvert Z_\parallel/n\rvert \approx 100\ \Omega$
Resistive wall	
($\xi = 0$)	$Z_\perp \approx 1.3$ kΩ/m at 200 kHz
($\xi = -3$)	$Z_\perp \approx 100$ kΩ/m at 200 kHz
Electron-cloud	above 2 nC/m

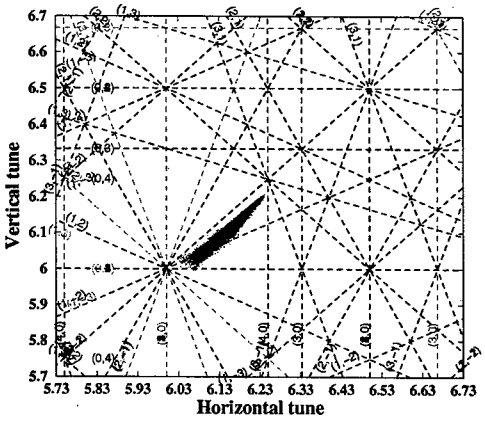

Figure 4: Transverse tune spread at the end of injection. Computer simulation is performed with UAL/ORBIT package [7]. Effects of space charge, transverse painting, chromaticity, kinematic non-linearity, fringe field, and magnetic manufacturing impections are included.

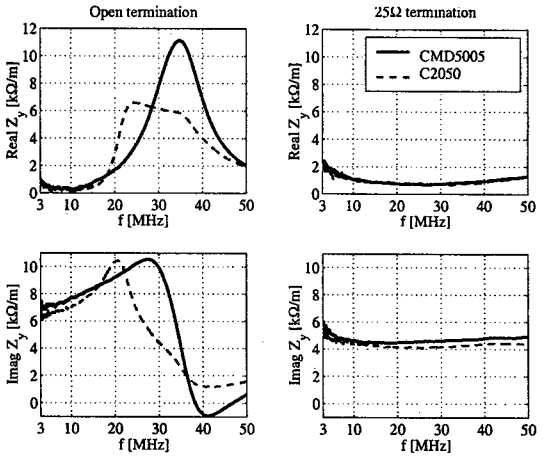

Figure 5: Comparison of measured coupling impedance for open and 25 Ω PFN termination, and high (1600) and medium (100) permeability ferrite of the extraction kicker (courtesy D. Davino and H. Hahn).

in the injection region are guided to the collectors with a low backscattering yield. A beam-in-gap kicker ensures a clean beam-gap. Vacuum ports are screened, and steps in the vacuum pipe are tapered to reduce peaked electric fields causing electron emission. A good vacuum reduces electrons from gas ionization. Solenoids are wound in the collimation sections to reduce multipacting. Electrodes are installed in the injection region (10 kV) and around the ring at BPM's (±1 kV) to clear the electron cloud. Electron detectors are installed at susceptible locations.

Enhancement of Landau damping includes a large vacuum chamber at locations of high dispersion and a large RF voltage to provide sufficient momentum acceptance, longitudinal painting to expand the momentum spread of the injecting beam, and lattice sextupole families for chromatic adjustments. Finally, a fast, wideband feedback system is

planned to damp instabilities.

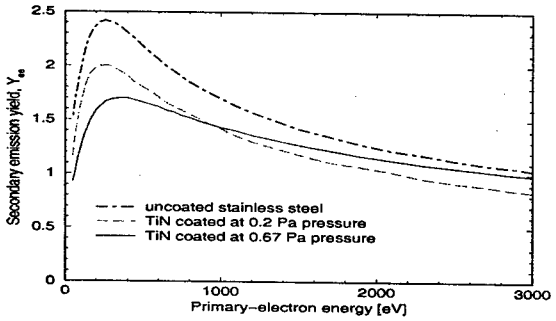

Figure 6: Measured secondary-electron yield for various coating conditions (courtesy P. He, H. Hseuh et al).

TECHNICAL ISSUES & STATUS

Injection

For charge-exchange injection of an intense H^- beam, free-hanging carbon and diamond foils are both developed to be mounted on a quick-exchange mechanism [10]. Stripped electrons are guided by the fringe field of tapered magnets and collected by heat-resistant C-C material attached to a water-cooled copper plate (Fig. 7). Both stripping foils and the electron catcher are monitored by video systems.

The transverse painting is achieved by 4 horizontal and 4 vertical dipoles with programmable power supplies. The measured minimum rise time (about 175 μs) is below the design value. The longitudinal painting is achieved by using a RF cavity located in the HEBT that is phase modulated with respect to the linac frequency.

Collimation

The H^- beam in the HEBT is cleaned with stripping foils, and then a magnetic field separates the stripped beam from the original H^- beam. The transverse collimation is located at the end of the linac upstream of the energy corrector, and the longitudinal collimation is located in the 90° bend achromat.

The proton beam in the ring is cleaned transversely with a two-stage system, wherein the primary scraper scatters the beam and enhances its impact distance in the secondary collector, so achieving a cleaning efficiency above 90%. The primary scraper consists of four tantalum blades, each 5 mm thick. They are spaced in 45 degree angles, adjustable to the varying needs of collimation aperture, and shielded for containing radioactivity. Due to reliability considerations, the secondary collectors are non-adjustable. Their vacuum chambers are made of double-layered stainless-steel filled with helium gas between the layers to detect leaks [11]. Longitudinally, the proton halo moved into the beam gap is cleaned by the beam-in-gap kicker and collected by the two-stage collimation system during the last 100 turns before extraction.

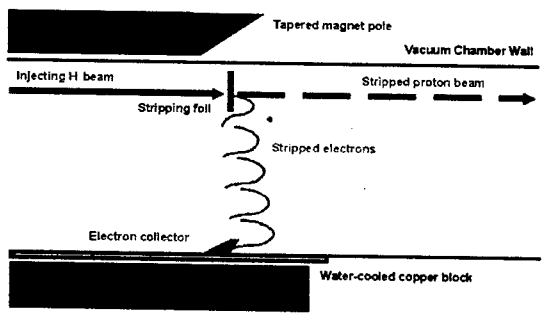

Figure 7: Injection area schematic layout.

Extraction

The beam is extracted during a single turn by being kicked vertically into the extraction channel of septum magnet. The septum bends the beam horizontally, and is also rotated to correct the vertical kicks. The kicker system consists of 14 individually powered modules, so that beam loss is negligible when one module fails. The PFNs are installed outside the ring tunnel for easy maintenance. The phase advance between the extraction kicker and the target is chosen so that the beam's position on target does not change if errors develop with the kickers.

To avoid complications due to rapid variations of the magnetic field, kicker magnets are made with a single-turn coil-winding and are placed inside the vacuum chamber. Good field quality is achieved with a high-permeability ferrite material. Saturable inductors isolate the influence of the PFN, shorten the rise time, and improve the flatness of the kicker-pulse's waveform. Beam density dependent closed-orbit deviation induced by the extraction kicker coupling-impedance at the given beam offset ("banana-closed orbit") is about 1 mm.

Vacuum and chamber coating

The design vacuum pressure is $(0.5 \sim 1)\times10^{-7}$ Torr in HEBT to minimize H^- stripping, 10^{-8} in the ring to minimize gas scattering and ion- and electron-induced desorptions, and $(0.5 \sim 1)\times10^{-7}$ Torr in RTBT.

The entire inner surface of ring vacuum chamber and extraction kicker ferrite is coated with TiN [9]. Two layers of coating are applied to the ceramic chamber for injection kickers: a 1μm-thick copper layer for by-passing the image charge, and a 0.1μm-thick TiN layer for a low secondary-electron yield, along with an exterior metal enclosure for dc current by-pass. This design allows the image-current passage above the lowest betatron sideband (~200 kHz) without degrading the magnetic-field penetration, eddy-current heating, and beam-induced heating.

Magnet, correction, power supply

Iterations are made on almost all kinds of magnets towards design expectation of magnetic accuracy at 10^{-4} for main dipoles and quadrupoles, 10^{-3} for sextupoles, chicane and transport magnets, and 10^{-2} for correctors. Some exceptions include a large (0.19×10^{-2}) systematic 20th

Table 5: Measured integral multipoles of the ring dipole magnet at a reference radius of 80 mm. The systematic b_1 is due to tapered dipole ends.

n	b_n		a_n	
	mean	S.D.	mean	S.D.
0	10000	0.0	0.0	0.0
1	-105.041	0.275	-0.262	0.951
2	0.163	0.433	-0.020	0.494
3	2.051	0.149	-0.050	0.316
4	1.143	0.200	0.000	0.113
5	0.064	0.095	0.001	0.158
6	-0.300	0.120	-0.017	0.105
8	-0.077	0.107	0.005	0.056
10	-0.176	0.129	0.003	0.028
12	0.094	0.143	-0.006	0.047

Table 6: Measured multipoles of the ring quadrupole magnet at a reference radius of 80 mm.

n	b_n		a_n	
	mean	S.D.	mean	S.D.
1	10000	0.00	–	–
2	-0.30	1.11	0.41	1.20
3	-0.06	0.58	0.05	0.32
4	-0.01	0.20	-0.04	0.23
5	1.20	0.25	-0.11	0.15
9	-0.73	0.02	0.00	0.06
13	-0.06	0.01	-0.01	0.02

pole on narrow-width quadrupoles used in the straights whose effects are negligible during the 1 ms accumulation, and large (6%) decapole in multi-coil skew-sextupole correctors [12].

Four-family sextupoles are arranged in 4-fold ring lattice symmetry for chromaticity adjustment without compromising the dynamic aperture. The ring correction elements consist of horizontal and vertical dipoles, normal and skew quadrupoles, normal and skew sextupoles, and octupoles for orbit correction and decoupling, amplitude detuning, and resonance corrections. Octupoles can be rotated to act as skew-octupoles if needed. The reduction in quadrupole transfer function ($\sim -0.2\%$) caused by the interference from nearby sextupole/corrector is easily adjusted. Resonance correction strategy is developed in the presence of space charge [6].

There is 1 power supply for the main dipoles, 6 for the quadrupoles, 4 for the sextupoles, 115 for the correctors and chicane dipoles, 8 for the injection kickers, and 14 for the extraction kickers. Good rise/fall time and matching have been achieved on pulsed supplies (programmable injection and extraction) [13].

RF system

The HEBT has two RF cavities operating around linac frequency of 805 MHz, one for energy correction and the other for longitudinal painting. The ring dual-harmonic RF system maintains a gap for the rise time of the extraction kicker while maintaining low peak beam current and large momentum spread, reducing space charge stopband related losses and coherent instabilities [14].

Diagnostics

The ring and transport diagnostics consists of beam position monitor, loss monitor, current monitor, wire scanner, beam-in-gap monitor, foil/catcher video monitor, ionization profile monitor (IPM, Fig. 8), coherent/incoherent tune measurement system, and electron detector [15].

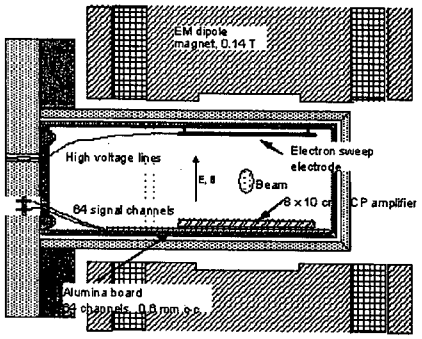

Figure 8: Ring IPM with sweeping electrodes, and with the multi-channel plates for electron collection recessed from the vacuum-chamber wall to avoid superfluous signals (courtesy R. Connolly).

Reliability and availability

Engineering design considers redundancy, radiation resistance, "active maintenance" capability (all-around cranes, quick-release flanges, quick-release water fittings, moveable shielding), and spares for areas of high radiation and activation.

FUTURE PERSPECTIVES

The ring and transport facility is designed with the potential to reach a beam energy up to 1.3 GeV and a beam power beyond 2 MW, capable of supplying a second neutron target [1]. Space is reserved for two additional extraction kickers, and for the replacement of 2 injection-chicane dipoles to satisfy H^0 stripping conditions.

We are indebted to the SNS teams and our collaborators for their devotion and contributions.

REFERENCES

[1] J. Wei et al, PRST-AB, **3** (1999) 080101; J. Wei, Rev. Mod. Phys. (Oct. 2003)
[2] N. Holtkamp, these proceedings
[3] N. Catalan-Lasheras et al PRST-AB **4** (2001) 010101
[4] J. Wei et al, EPAC00 (2000) 981
[5] P. Wanderer et al, these proceedings
[6] A. Fedotov, these proceedings
[7] N. Malitsky, these proceedings; J. Holmes, these proceedings
[8] M. Pivi, M. Furman, PRST-AB, **6** (2003) 034201
[9] M. Blaskiewicz; S.Y. Zhang et al; J. Wei et al, these proceedings; P. He et al, submitted to J. Vac. Sci. Tech. (2003)
[10] R. Shaw et al, these proceedings
[11] H. Ludewig et al; N. Simos et al, these proceedings
[12] J. Tuozzolo et al; N. Tsoupas et al; S. Badea et al; C. Pai, et al; J. Rank, et al, these proceedings
[13] J. Sandberg et al; W. Zhang et al, these proceedings
[14] A. Zaltsman et al; K. Smith et al, these proceedings.
[15] P. Cameron et al; M. Kesselman et al; D. Gassner et al; R. Connolly et al; R. Witkover et al, these proceedings.

THE JAERI-KEK JOINT PROJECT FOR THE HIGH-INTENSITY PROTON ACCELERATOR, J-PARC

Y. Yamazaki
JAERI, Tokai-mura, Naka-gun, Ibaraki-ken, 319-1195, Japan

Abstract

The J-PARC project comprises a 400-MeV linac, a 3-GeV, 1-MW rapid-cycling synchrotron (RCS), a 50-GeV main ring (MR), and experimental facilities using the 3- and 50-GeV beams. The J-PARC facility is under construction to be completed by March 2007. The J-PARC accelerators are based upon many newly developed technologies, including the RF system using the cavities loaded with the magnetic alloy (MA) and the linac components such as the RFQ linac with π-mode stabilizing loops (PISL's), the RF choppers, and others in order to realize their high beam powers. The recent results of the developments of these new technologies and the present status of the construction are reported.

INTRODUCTION

The High Intensity Proton Accelerator Facility Project in Japan [1-7] is now referred to as "J-PARC Project", which stands for Japan Proton Accelerator Research Complex. The facility is under construction as a joint project between Japan Atomic Energy Research Institute (JAERI) and High Energy Accelerator Research Organization (KEK) at the JAERI Tokai site. The construction started from April 2001 to be completed by the end of March 2007. The facility, which was so far funded, comprises a 400-MeV linac, a 3-GeV Rapid-Cycling Synchrotron (RCS), and a 50-GeV Synchrotron (Main Ring, MR) as shown in Fig. 1.

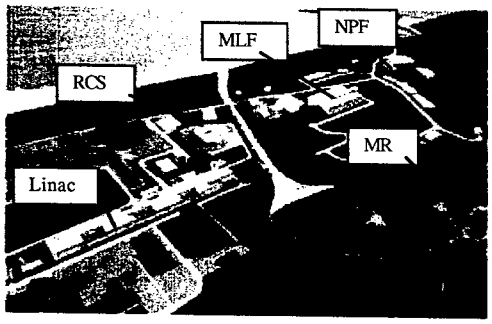

Figure 1: The expected view of the facility

The H^- beam with a peak current of 50 mA and a pulse width of 500 μs is accelerated up to 400 MeV by the linac, and then injected to the RCS with a repetition rate of 25 Hz. The beam is chopped with a chopping rate of 56 % in order to avoid the beam loss during the adiabatic capture, which would have been necessary without any chopper. The linac can be operated with a repetition rate of 50 Hz, the remaining half of which will be used for the basic study of the accelerator-driven nuclear waste transmutation system (ADS) in future.

The beam accelerated by the RCS with an average current of 333 μA and a beam power of 1 MW is fast extracted and transported to the Materials and Life Science Experimental Facility (MLF) most of the time. In this experimental area, the muon and the neutron production targets are located in a series. The 10 % of the beam is used for the muon production. Every 3.5 second, the beam is four times transported to the MR and injected to it. The 50-GeV beam accelerated there is slowly extracted to the Nuclear and Fundamental Particle Experimental Facility (NPF) with a duration of 1.6 s. The Kaon rare decay experiments, the hyper nucleus experiments, and others will be conducted there. Sometimes the beam is fast extracted to the neutrino production target. The produced neutrinos are sent to the SUPER KAMIOKANDE detector located 300-km west in order to conduct the long base line experiment.

The budget for the neutrino experiment facility will be submitted to the funding agency with a top priority this year. The operational energy of the MR will be limited to 40 GeV, until the fly-wheel power supply system is afforded in the Phase II.

The features of the accelerator design are presented in Ref. [6], while the design detail is described in the Technical Design Report (TDR) [7]. The distinctive features of the J-PARC accelerator are briefly summarized in Sec. 2. Then, the results of the developments after the last EPAC [6] and the construction status are reported in this paper.

The funding so far is almost as scheduled (see Fig. 2). As a result all the contracts have been done on schedule except for the high-energy linac (190-400 MeV) for the reason presented in Sec. 3. The construction is also on schedule, although several-month delay is expected for the MR. The ancient salt-pan remains were discovered in the location for the MR and NPF. The archaeological excavation of the remains will take nearly one year. On the other hand, this will have no influence on the schedule of the linac, RCS and MLF constructions.

The civil engineering for the linac was contracted by the end of JFY (Japanese Fiscal Year starting from April) 2001, and will be completed by mid JFY2004. That for the RCS was contracted mid JFY2002, and will be completed by the end of JFY2004. That for the MR was divided to the four sections, which will be contracted year by year, being completed by the end of JFY2005, if it were as planned. The full view of the J-PARC site now is shown in Fig. 3.

0-7803-7738-9/03/$17.00 © 2003 IEEE

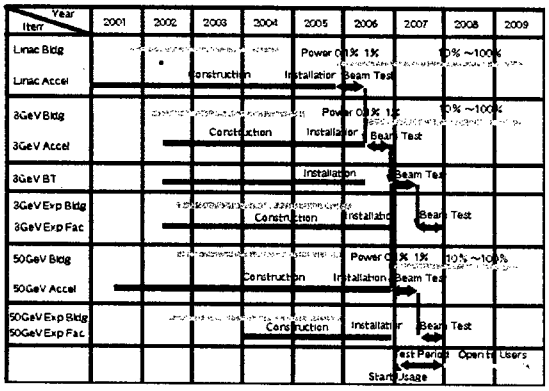

Figure 2: The schedule for the J-PARC project. The year shows Japanese Fiscal Year starting from April.

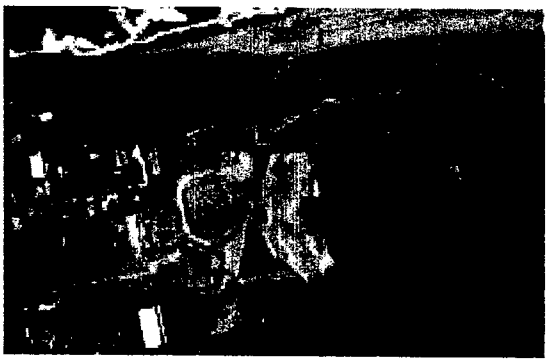

Figure 3: The present view of the facility

DISTINCTIVE FEATURES OF J-PARC ACCELERATOR

The distinctive features of the J-PARC accelerator are arising from its multi-purpose concept: the realization of the high beam powers of MW class in both the GeV and the several 10 GeV region. The 3-GeV RCS, which plays a role of the injector to the 50-GeV MR, also provides the 1-MW pulsed beam to the MLF. Since the Spallation Neutron Source Project in US (SNS) is a single-purpose one, it can utilize the full-energy linac and the accumulator ring (AR). The RCS scheme, which the J-PARC project makes use of, has the following advantages over the AR scheme.

First, the beam current is lower for the same beam power. Second, the more beam loss is allowed during the injection process, since the radioactivity and the radiation itself are reduced in proportion to its lower injection energy and further.

On the other hand, the choice of the high-power, high-energy RCS scheme requires many problems to solve. Among them, the following items are outstanding. First of all, the fast acceleration requires a number of the RF accelerating cavities with high field gradients. This requirement has never been fulfilled until the cavity loaded with the magnetic alloy (MA) is devised [8]. Second, the magnets [9] and vacuum chambers should be immune against the eddy current effect arising from the fast changing magnetic fields. Third, the injection scheme is hard to design for the large beam aperture. Fourth, the precise tracking of several families of magnets is required.

In addition to the challenges in the RCS itself, the linac is also required to provide the beam with accurate momenta ($\Delta p/p$ less than 0.1 % for J-PARC) and with low transverse emittances (typically 4π mm mrad for J-PARC). These are typically 99 % emittances rather than that of root mean square (rms), since many parameters are required for eliminating the beam loss, which should be of an order of 1 % at most. These values are necessary for the efficient painting on the beam apertures. In order to produce these high-quality beams, we devised the π-mode stabilizing loop (PISL) [10, 11] for the RFQ linac. Also, we decided to use electro-quadrupole magnets contained in the drift tubes of the DTL in order to keep the flexible knobs for the transverse tunes. The technologies were newly developed for minimizing the size of the coils with water-cooling channels by fully using the electroforming method and wire cutting [12].

Both the RCS and the MR are designed on the base of the lattices with the low and negative momentum compaction factors, respectively, which implies no transition crossing during acceleration [13]. The beam loss inherent to the transition crossing will be thus avoided. The slow extraction with the low beam loss (less than 1 %) from the MR is the most difficult issue to solve [14].

LINAC

The linac comprises a volume-production type of H^- ion source, a 50-keV low-energy beam transport (LEBT), a 3-MeV, 324-MHz Radio-Frequency Quadrupole (RFQ) linac, a 50-MeV, 324-MHz Drift-Tube Linac (DTL), a 190-MeV, 324-MHz Separated DTL (SDTL), and a 400-MeV, 972-MHz high-energy linac . The SDTL is the DTL with the quadrupole magnets outside the tank [15]. The Annular Ring Coupled Structure (ACS) [16, 17] has been developed for the high-energy linac. Most of the accelerator components were ordered by the end of JFY2002, except for the high-energy linac. We decided to increase the beam aperture of the RCS in order to keep the sufficient margin for the space charge effect (the Lasslette tune shift is –0.16). We also lengthen the RCS circumference by a factor of 10/9. Since some budget overflow is expected for these, we decided to take the following process. Taking the results of the bidding for all the accelerator components except for the high-energy part of the linac, we will determine how much we can afford for this. The linac beam with the energy lower than 400 MeV can be injected to the RCS, while most of the components for both the RCS and MR are necessary for the experiments. The lowering of the linac energy will have the influence on the beam power. The

budget request to recover the full linac energy will be submitted to the funding agency this year.

The components for all the three DTL tanks and four of the thirty two SDTL tanks in total have been completed. The four SDTL tanks and the 5-cell prototype of the DTL were already powered over their design values. The first DTL tank was assembled and the tuner positions and post coupler positions were adjusted until the uniform field distribution was realized with one percent accuracy (design value) [18, 19].

The beam test of the RFQ linac and the medium energy beam transport (MEBT) was continued in the KEK site until last March. The detail is presented in Sec. 6. The first DTL tank was then installed for the beam test to be started this summer as shown in Fig. 4.

Figure 4: The first tank of DTL installed in the tunnel at KEK site for the beam study

3-GEV RCS

A half of the RCS components were ordered by the end of JFY2002, including all the bending magnets (BM's), all the quadrupole magnets (QM's), two thirds of the magnet power supplies for them, all the ceramics vacuum chambers for the BM's and QM's, and all the kickers and their power supplies. The remaining components for the magnet power supplies, the injection system including bump magnets and their power supplies, the vacuum chambers for these, the remaining RF sources, the RF cavities and others will be contracted during this fiscal year.

The aluminum stranded conductors are used for both the BM's and QM's, in order to avoid the temperature rise and the Q deterioration arising from the eddy current effect. The use of laminated silicon steel sheets with a thickness of 0.5 mm and the slit cuts of the end plates and/or the core ends are all to ease the eddy current effect. The approximate Rogowsky Cut is utilized in order to avoid the concentration and the saturation of the fields. The prototype of the BM's and QM's are used for these test together with computational analysis. The decrease in the AC loss by these means are vital also for the stable operation of the magnet system for the following reason. The magnet system comprises eight resonant networks, including one BM system and seven families of QM's. In order to keep the eight networks operate stably, the Q values of the networks should be as high as possible.

The aluminum stranded conductors are, however, difficult to impregnate by polyimide resin, which is immune against radiation damage, but is hard to flow. Figure 5 shows how the stranded conductors are impregnated by the resin in vacuum and pressurized later. We are now confident of the procurements of these coils.

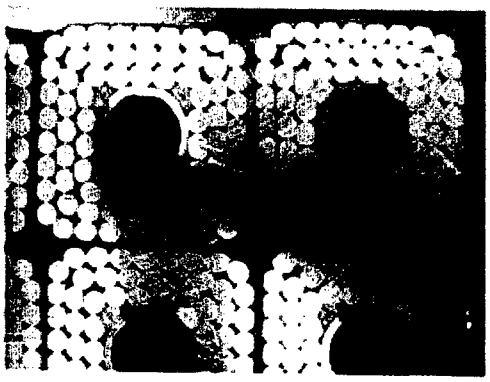

Figure 5: The stranded conductors impregnated by the polyimid resin to form the coil

50-GEV SYNCHROTRON

Most of the accelerator components were ordered except for the RF system and the injection and extraction systems. The first BM among ninety six 5.85-m BM's was shipped to KEK, where its field measurement and excitation test are under way (see Fig. 6).

As mentioned in Sec. 2, the RF system makes use of the cavities loaded with magnetic alloy (MA) in both RCS and MR, since the MA-loaded cavities have many advantages over the conventional ferrite-loaded ones, including the field gradient by almost one order of magnitude higher. Also, its low Q-value (a value of less than one is possible) drastically simplifies the RF system by eliminating any tuning system. On the other hand, its high R/Q (low stored energy) with the low Q value requires the wide-band beam loading compensation via feed-forward control. As a result, even the high power system should be wide-band. In order to minimize the band width necessary for the compensation, the Q-value is optimized by adjusting the gap between the MA cores radially cut under the condition of no tuning system necessary. The Q values thus optimized are 2.9 (1.5-mm gap) and 10 (10-mm gap) for the RCS and the MR, respectively.

A prototype of the RF system, comprising an RF cavity, a high-power amplifier and others, was completed for the 50-GeV MR as shown in Fig. 7. The system was successfully tested for 49 hours with a full peak power of

500 kW and a full duty factor of 50 %. The MA is directly water-cooled.

Figure 6: The first mass-produced BM for the MR

Figure 7: The RF cavity for the MR

The direct water cooling of the MA for the 3-GeV RCS gives rise to some problem during the high power test. The magnetic fields between the gap were locally concentrated and distorted, in particular for the small-gap case, since some magnetic imperfections at the gap surfaces arose from cutting the MA cores. The local heat-up damaged the polyimide resin, which are used to form the MA tapes into the cores. The indirect cooling is now under development, by sandwitching the MA core layers and the water-cooled copper layers with the polyimide resin in between. The resin includes aluminum nitride powder which is a good thermal conductor. The high-power test of this system will be started soon.

BEAM TEST OF FRONT-END LINAC

The beam test of the low-energy front is under way in KEK site [20, 21]. The present system comprises the H^- ion source, the LEBT, the 3-MeV RFQ linac, and the MEBT. At present, the first tank of DTL (20 MeV) is installed, and is under preparation for the high-power test and the beam test.

The RFQ linac used here was designed for the Japan Hadron Facility (JHF) project [22] which would produce the 0.6 MW beams with a linac peak current of 30 mA (the 50-mA RFQ linac for the J-PARC is now under development). The peak current of 29 mA was obtained with this system. The measured horizontal and vertical emittances of the beam at the end of the MEBT were 0.252 π mm mrad and 0.214 π mm mrad (r. m. s. normalized), respectively, at the peak current of 28.5 mA.

The chopper at the MEBT shown in Fig. 8 were tested with the beam. The measured rise and falling times of the beam are 10 ns, being sufficiently fast for eliminating the beam loss as designed (see Ref. [20]).

Figure 8: The RF chopper installed at the MEBT. The left figure shows the whole view of the two deflecting chopper cavities. The right figure shows the close view of the deflecting electrodes. The beam passes from left to right.

The stopper installed at the MEBT cannot stand all the 3-MeV chopped beams. The prechopper [7], which makes use of the induction decelerator made of the MA, was installed at the LEBT. The RFQ linac is designed to filter the beams, the energy of which is by 9 keV lower than the designed injection energy of 50 keV. The prechopper system was also tested with the beam. The combined test of the prechopper and the RF chopper will be done later, where the proper timing is necessary.

SUMMARY

The J-PARC accelerator, comprising the 400-MeV linac, the 3-GeV RCS, and the 50-GeV MR, is based upon many newly developed technologies. The developments have been successful, and the orderings of the accelerator components are on schedule so far. The first beam from the RCS will be transported to the MLF in March 2007. The beam injection to the MR, which is planned at the same time, will be delayed by several months, since the ancient salt-pan remains at the MR and NPF sites will be archaeologically investigated by excavation.

REFERENCES

[1] "The Joint Project for High-Intensity Proton Accelerators", KEK Report 99-4, JHF-99-3 and JAERI-Tech 99-056 (1999).

[2] Y. Yamazaki et al., "Accelerator Complex for the Joint Project of KEK/JHF and JAERI/NSP", Proc. 1999 Part. Acceler. Conf., THDL1 (1999).

[3] Y. Yamazaki et al., "High Intensity Proton Accelerators for the JAERI/KEK Joint Project", Proc. 2000 European Acceler. Conf., THOAF201(2000).

[4] Y. Yamazaki et al., "The Construction of the Low-Energy Front 60-MeV Linac for the JAERI/KEK Joint Project", Proc. 2000 Linac Conf., TUD07 (2000).

[5] Y. Yamazaki, "The Present Status of the JAERI/KEK Joint Project for High-Intensity Proton Accelerators, " Proc. 2001 Part. Acceler. Conf., WOAA007 (2001).

[6] Y. Yamazaki, "The JAERI/KEK Joint Project for High-Intensity Proton Accelerators," Proc. 2002 European Part. Acceler. Conf., TUZGB003, pp. 163 (2002).

[7] "Accelerator Technical Design Report for High-Intensity Proton Accelerator Project, J-PARC," KEK Report 2002-13 and JAERI-Tech 2003-44.

[8] C. Ohmori et al., "High-Field Gradient Cavity for JAERI-KEK Joint Project," Proc. 2002 European Part. Acceler. Conf., WEALA001, pp. 257 (2002).

[9] N. Tani et al., "Design of a Dipole Magnet for the 3 GeV Synchrotron of the JAERI/KEK Joint Project," Proc. 2002 European Part. Acceler. Conf., TUPD0028, pp. 2376 (2002).

[10] A. Ueno and Y. Yamazaki, Nucl. Instr. Meth. A300, 15 (1990).

[11] A. Ueno et al., Proc. 2002 Linac Conf., TU423 (2002).

[12] F. Yoshino et al., Proc. 2000 Linac Conf., TUD10 (2000).

[13] S. Machida et al., Proc. 1997 Part. Accel. Conf., pp. 1962 (1997).

[14] M. Tomizawa et al., "Design of Slow Extraction from 50 GeV Proton Synchrotron," Proc. 2002 European Part. Acceler. Conf., THPLE009, pp. 1058 (2002).

[15] T. Kato, KEK Report 92-10 (1992).

[16] T. Kageyama et al., Proc. 1994 Linac Conf., 248 (1994).

[17] H. Ao et al., "Cold-Model Tests of an Annular Coupled Structure for Upgrade of a J-PARC Linac", Proc. 2003 Part. Accel. Conf., RPAB046 (2003).

[18] F. Naito et al., Proc. 2002 Linac Conf., TH102 (2002).

[19] F. Naito et al., "Tuning of the RF field of the DTL for J-PARC," Proc. 2003 Part. Accel. Conf., RPAB049 (2003).

[20] T. Kato et al., "Beam Study with RF Choppers in the MEBT of the J-PARC Proton Linac," Proc. 2003 Part. Accel. Conf., TPAG014 (2003).

[21] M. Ikegami et al., "Beam Commissioning of the J-PARC Linac Medium Energy Beam Transport at KEK," Proc. 2003 Part. Accel. Conf., TPAG035 (2003).

[22] "JHF Accelerator Design Study Report", KEK Report 97-16 (1998).

STATUS OF LOW AND INTERMEDIATE VELOCITY SUPERCONDUCTING ACCELERATING STRUCTURES

K. W. Shepard, ANL, Argonne, IL 60439, USA

Abstract

Several types of reduced velocity (0.1 - 0.6c) superconducting accelerating structures are being developed for ion linacs to be used for spallation sources, exotic beam facilities, and other applications. This paper briefly reviews the characteristics and development status of some of the cavity types currently under development. Two different structure choices for the high-energy section of the proposed RIA driver linac are discussed.

INTRODUCTION

Historically, superconducting RF development has divided into two major classes of resonant cavity [1]. One class is cavities based on various forms and combinations of right circular cylindrical cells operating in the TM010 mode, or TM-class cavities. These have been developed primarily for velocity-of-light, electron beams. The other class is based on various forms and combinations of linear element or transmission line operating in a TEM mode, or TEM-class cavities. The latter class is exemplified by the numerous types of quarter-wave-line cavities developed for heavy-ion linacs. TM cavities have generally been relatively high-frequency, ~ 1 GHz, and have operated at 2K. TEM cavities have generally been developed at low frequencies, ~ 100 MHz, for low velocities, < 0.2c, and have operated at 4K.

Over the past several years, the velocity range of both TM and TEM class structures has been expanded, as cavities have been developed for high-energy and high-intensity proton and ion linacs. This has been exemplified for the TM-class in the development of 805 MHz, elliptical-cell cavities for velocities as low as 0.62c for the SNS project [2]. As is discussed below, much current work is developing a variety of TEM-class cavities for particle velocities up to 0.62c, at frequencies of 175-352 MHz.

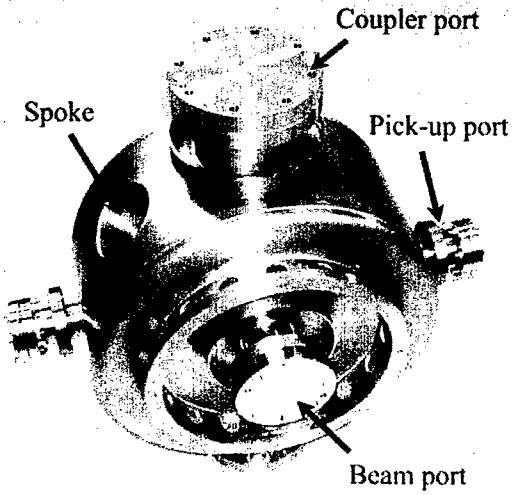

Figure 1: Los Alamos-built 350 MHz, β=0.175, single-spoke niobium cavity

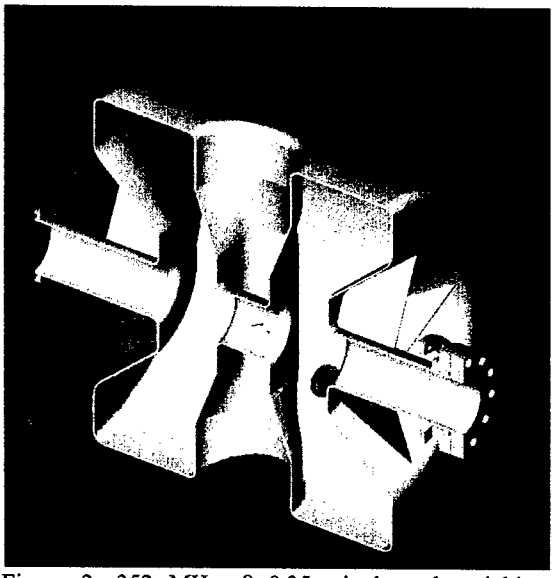

Figure 2: 352 MHz, β=0.35, single-spoke niobium cavity tested at IPN Orsay

These relatively high-velocity TEM-class cavities are based on two types of half-wave line structure, the coaxial half-wave line, which is similar to existing QWR structures, and spoke-loaded cavities, in which the transmission-line element is at right-angles to a cylindrical housing, a geometry similar to a spoke of a wheel. The spoke-loaded structure differs from the coaxial line in that it can be stacked into multi-cell combinations.

Several multiple-gap, low-velocity (<0.15c) half-wave TEM structures are being developed to provide relatively high-frequency structures to accept beam from high-intensity RFQ injectors systems.

Another thrust of recent development has been the application to TEM-class cavities of high-pressure-water rinse techniques, similar to those developed for TESLA and other TM cavities, to reduce surface particulates and increasing accelerating gradients.

In what follows, we will first summarize tests of recently completed prototype cavities, then list several cavities under development, but not yet tested, and finally, discuss application of TEM-class cavities to the high-energy section of the proposed RIA driver linac [3].

0-7803-7738-9/03/$17.00 © 2003 IEEE

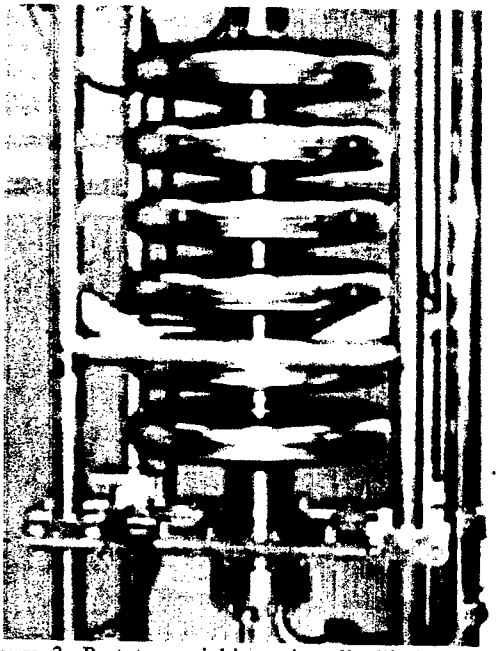

Figure 3: Prototype niobium six-cell elliptical-cell, 805 MHz, β=.47 cavity built by JLAB/MSU

RECENTLY TESTED CAVITIES

Los Alamos

At Los Alamos National Laboratory, two prototype single-spoke cavities designed to be injected with a high-intensity beam from the LEDA RFQ have been built and tested [4]. The 350 MHz, β=0.175 cavities, shown in Figure 1, have operated at 4K at peak surface electric fields as high as 37 MV/m.

IPN Orsay

At the Institute for Nuclear Physics at Orsay, spoke cavities are being developed for high-power proton linacs to support two European projects, XADS and EURISOL. A single-spoke, 352 MHz, β=0.35 cavity, shown in Figure 2, has been built and tested [5] and has operated at 4K with peak surface electric fields as high as 37 MV/m.

MSU-NSCL

At the National Cyclotron Laboratory at Michigan State University, a 322 MHz, β=0.29 coaxial half-wave cavity is being developed for the RIA driver linac [6]. A prototype has been built and tested and has operated at 4K with peak surface electric fields as high as 27 MV/m and at 2K as high as 33 MV/m.

JLAB/MSU

In a collaborative effort between JLAB and the National Cyclotron Laboratory, a TM-class, six-cell elliptical-cell cavity is being developed for the RIA driver linac [7]. A prototype 805 MHz, β=0.47 cavity, shown in Figure 3, has been completed and operated at 2K at peak surface electric fields above 50 MV/m.

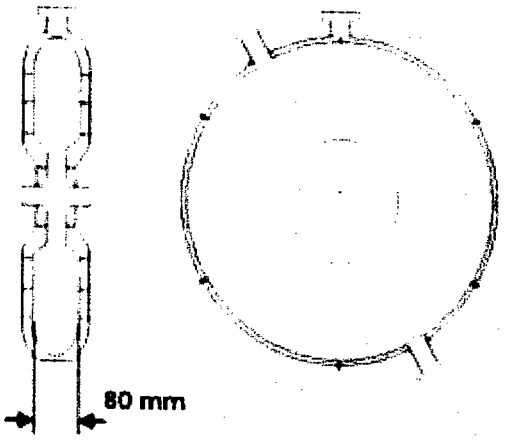

Figure 4: 352 MHz low-beta TM-class re-entrant cavity developed at INFN-Legnaro

INFN Legnaro

At INFN Legnaro, a TM-class re-entrant cavity is being developed to provide a high-frequency, low-beta structure for injection with a high-intensity proton beam from a 352 MHz RFQ [8]. The single-gap cavity, shown in Figure 4, has very broad velocity acceptance and is useful for particle velocities as low as 0.1c. In tests to date the cavity has operated at 4K at peak surface electric fields as high as 26 MV/m, and can provide 600 kV of acceleration with 7.5 watts of rf input.

Argonne

At Argonne National Laboratory a 345 MHz, two-spoke cavity is being developed for the RIA driver linac [9]. A prototype unit, shown in Figure 5, has been completed, and in initial tests at 4K has operated at peak surface electric fields as high as 40 MV/m. The prototype cavity can provide 3 MV of acceleration with 20 watts of rf input into 4K.

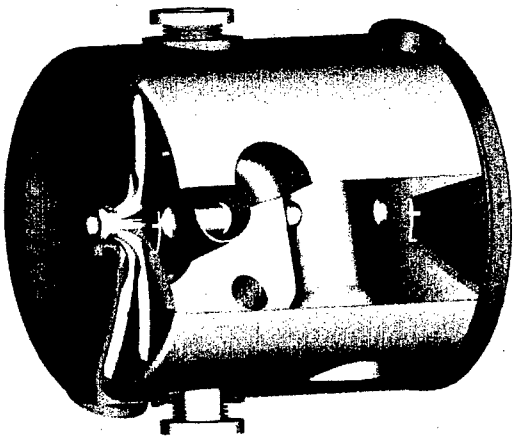

Figure 5: A 345 MHz, double-spoke, three-gap cavity for β=0.4. A niobium prototype has been built and tested at Argonne National Laboratory

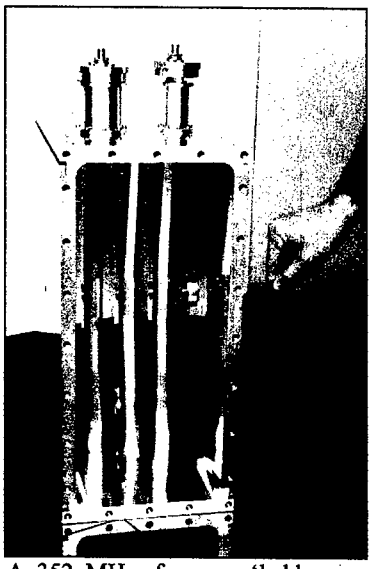

Figure 6: A 352 MHz, four-gap 'ladder resonator' for β=0.12 is being developed at INFN-Legnaro

UNDER DEVELOPMENT

Two different groups are developing low-velocity, multiple-gap structures to accelerate high-intensity beams from RFQ injectors. At INFN-Legnaro, a variant of the spoke structure, termed the "ladder resonator" is being developed [10]. A model of the 352 MHz, four-gap, β=0.12 structure is shown in Figure 6. At Frankfurt, a design for a 19-gap CH-structure has been developed, and a niobium prototype cavity is being constructed [11].

At Argonne National Laboratory, several types of cavity are being developed for use in the U.S RIA driver linac. Figure 7 shows two of these cavities [12]. One is a 115 MHz quarter-wave-line (QWR) structure for β=0.15, which has a drift tube shaped to correct rf magnetic dipole terms which cause beam steering in QWR structures. The other is a 172 MHz coaxial half-wave cavity for β=0.28. Niobium prototypes of both cavities are under construction with initial tests scheduled for late 2003.

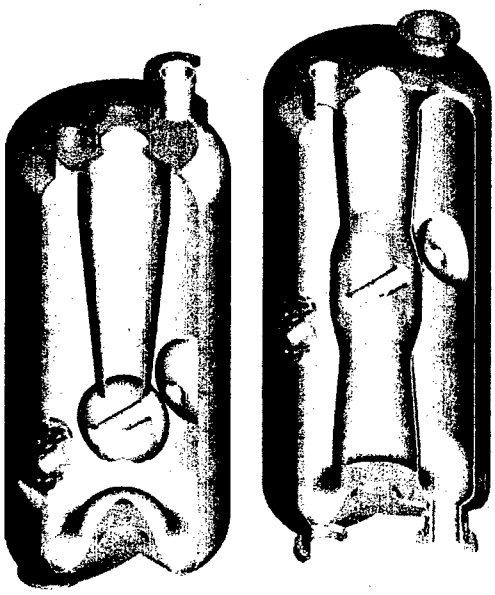

Figure 7: A 115 MHz, β=0.15 QWR cavity and a 172 MHz, β=0.27 coaxial half-wave cavity being prototyped at Argonne National Laboratory for the RIA driver linac.

SPOKE-CAVITY BASED HIGH-ENERGY ION LINAC

At Argonne National Laboratory, designs for two superconducting niobium, 345 MHz, three-spoke-loaded cavities for the velocity range $0.4<\beta<0.75$ have been developed [13]. Figure 8 shows a sectioned view of one of the two cavity types. The mechanical elements and overall design are similar to those of a recently tested 345 MHz two-spoke niobium cavity [9]. The cavities are being developed as an alternative to 805 MHz, elliptical-cell cavities in forming the high-energy section of the proposed RIA driver linac [3,13].

The RIA driver linac is required to operate cw, and to deliver at least 100 kW of uranium beam at an energy of 400 MeV/nucleon, and lighter ions at as high an energy as possible. For this application, TEM-class spoke-loaded structures offer a number of advantages with respect to TM elliptical-cell structures

For a given transverse diameter, elliptical-cell TM cavities operate at roughly twice the frequency of TEM spoke-loaded cavities. This simple fact has several important ramifications [1].

For multi-cell cavities, each cell is of length $\beta\lambda/2$ so that at lower frequency fewer cells are required, for a given overall length, which broadens the velocity acceptance of the structure. Conversely, for the same number of cells, a lower frequency cavity will be longer and produce more accelerating voltage than a higher frequency cavity, while maintaining the same velocity acceptance.

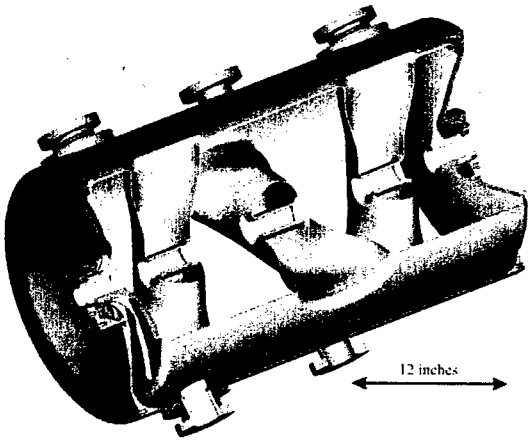

Figure 8: A 345 MHz, β=0.5 triple-spoke-loaded, four gap accelerating structure. A niobium prototype is under construction at Argonne National Laboratory.

Table 1: Electromagnetic parameters for the two triple-spoke cavities compared with two elliptical-cell six-cell cavities of similar β_{GEOM} = v/c developed for the SNS linac and for the RIA driver linac [13].

Cavity Type	Triple-Spoke	Elliptical Six-Cell	Triple-Spoke	Elliptical Six-Cell
β_{GEOM}	0.50	0.47	0.62	0.61
Frequency	345 MHz	805	345	805
Length	65.2 cm	52.55	80.87	68.2
$G = Q \cdot R_S$	85.7	136.7	93.0	179.0
R/Q	494	160	520	279
at an accelerating gradient of 1 MV/m:				
E_{PEAK}	2.88 MV/m	3.41	2.97	2.71
B_{PEAK}	86.5 G	69	88.6	57.2

Table 1 compares the electromagnetic parameters for two 805 MHz elliptical-cell and two 345 MHz spoke-loaded cavity geometries for the particle velocities β_{GEOM} = 0.5 and 0.62. We note that a critical parameter, the peak surface electric field, is comparable for the two classes of structure, even for particle velocities above 0.5c. Also, note that the shunt impedance R/Q is appreciably higher for the spoke-loaded cavities.

Figure 9 compares the voltage gain as a function of particle velocity for the two types of cavity, assuming operation of all cavities at a peak surface electric field of 27.5 MV/m. Figure 9 shows the advantage of the lower frequency for the TEM-class spoke-loaded cavities in providing both broader velocity acceptance and higher voltage per cavity. For the RIA driver linac, this means the linac can be built not only with fewer types of cavity, but also with fewer cavities. Further, because of the broader velocity acceptance, the linac provides appreciably higher output energy for proton beams.

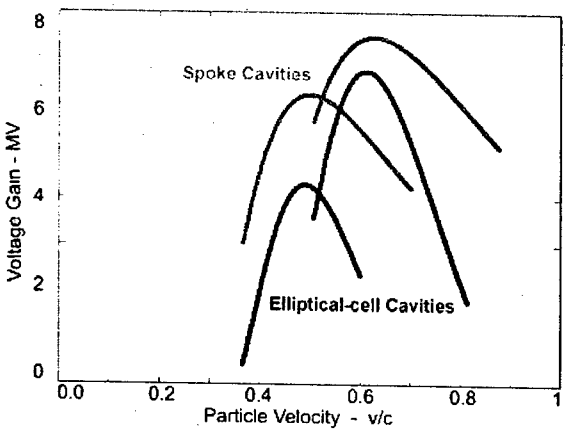

Figure 9: Velocity acceptance for two 345 MHz triple-spoke cavities compared with two 805 MHz elliptical 6-cell cavities, all operating at a peak surface electric field of 27.5 MV/m.

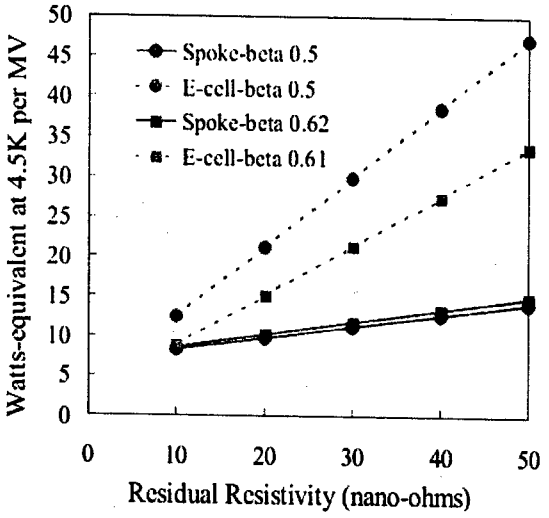

Figure 10: RF load into helium refrigeration as a function of cavity performance.

A major advantage of the lower frequency TEM structures is that the superconducting surface resistance is quadratic with frequency, so that using spoke loaded cavities will substantially reduce the rf losses and the refrigeration load, which is particularly important for cw operation. Also, at 345 MHz, the possibility of operation at 4K is opened, eliminating the need for sub-atmospheric cryrogenic system. Figure 10 compares the rf heat load required to maintain 1 MV of accelerating potential for the different cavities. In figure 10, all cavities are assumed to operate cw at a peak surface electric field of 27.5 MV/m. The spoke cavities are assumed to operate at 4.5K, and the elliptical-cell cavities at 2K. The 2K refrigeration system is assumed to operate at an efficiency such that 1 watt into 2K is equivalent to 4.5 watts at 4.5K.

Table 2: Summary of the parameters for the two design options for the high-energy section of the RIA driver linac (from reference [13])

Parameter	Triple-spoke	Elliptical-cell
Frequency (MHz)	345	805
Peak E field (MV/m)	27.5	27.5
No. of cavity types	2	3
Total no. of cavities	140	180
Temperature (K)	4.5	2.1
Aperture (mm)	40	80
Synchronous phase	-25°	-30°
Normalized Acceptance		
Trans. (π·mm·mrad)	35	70
Long. (π·keV/u-nsec)	280	60

The heat load is plotted as a function of cavity performance or quality in terms of an effective residual resistance, ranging from excellent performance (10 nΩ) to poor (50 nΩ). Recent cavity design goals, prototype results, and production results range from 15 – 30 nΩ. For this range of performance, the triple spoke cavities would reduce the refrigeration load by roughly a factor of two relative to the elliptical-cell design option.

Table 2 compares several major parameters for the two design options for the RIA driver linac. We simply note that the use of TEM-class, spoke loaded cavities offer a number of advantages in terms of cost, simplicity, and performance for this particular application.

CONCLUSIONS

The past several years have seen vigorous development of TEM-class low- and intermediate-velocity superconducting accelerating structures for a variety of applications. The development of half-wave loaded structures has greatly extended the velocity range covered by TEM-class cavities. The cross-over velocity at which elliptical-cell TM-class cavities become the structure of choice seems to be in the neighborhood of 0.5c, but requires detailed study for a given particular application because of the variety of choices of structure that are becoming available.

The use of new cleaning techniques has demonstrated a capability for substantially increasing the accelerating gradients at which TEM-class superconducting cavities are operated.

ACKNOWLEDGEMENTS

The author gratefully acknowledges the support and generosity of numerous colleagues in providing details of their ongoing development work. We also acknowledge the support of the U. S. Department of Energy, Nuclear Physics Division, under contract W-31-109-ENG-38.

REFERENCES

[1] J. R. Delayen, "Medium-β Superconducting Accelerating Structures", *Proc. 10th Workshop on RF Superconductivity*, Tsukuba, Japan, September 2001.

[2] M. White, "The Spallation Neutron Source (SNS)", *Proc. 2002 Linear Accelerator Conference*, Gyeongju, South Korea, August 2002.

[3] Kenneth W. Shepard, "The RIA Driver Linac", *Proc. 2002 Linear Accelerator Conference,* Gyeongju, South Korea, August 2002.

[4] Tsuyoshi Tajima, et al., "Test Results of Two LANL Beta = 0.175, 350-MHz, 2-Gap Spoke Cavities", in *Proc. 2003 Particle Accelerator Conference.*, Portland, Oregon, May 12-16, 2003.

[5] Guillaume Olre, "Status Report on Superconducting Spoke Cavities at IPN", in *Proc. 2003 Particle Accelerator Conference.*, Portland, Oregon, May 12-16, 2003

[6] Terry Grimm, et al., "Experimental Study of a 322 MHz v/c=0.28 Niobium Spoke", *Proc. 2003 Particle Accelerator Conference*, Portland, OR, May 2003.

[7] W. Hartung, et al., "Status Report on Multi-Cell Superconducting Cavity Development for Medium-Velocity Beams", in *Proc. 2003 Particle Accelerator Conference.*, Portland, Oregon, May 12-16, 2003

[8] A. Facco, et al., "RF Testing of the TRASCO Superconducting Reentrant Cavity for High Intensity Proton Beams", *Proc. Eighth European Particle Accelerator Conference*, Paris, France, June 3-7, 2002.

[9] J. Fuerst, et al., "Superconducting 345 MHz Two-Spoke Cavity for RIA", *Proc. 2003 Particle Accelerator Conference*, Portland, OR, May 2003.

[10] V. Andreev, et al., "The Ladder Resonator", *Phys. Rev. ST Accel. Beams 6*, 040101 (2003)

[11] Holger Podlech, et al., "HOM and Mechanical Analysis of a Superconducting CH-Cavity Prototype", *Proc. 2003 Particle Accelerator Conference*, Portland, OR, May 2003.

[12] Kenneth Shepard, et al., "Superconducting Intermediate-Velocity Cavity Development for RIA", *Proc. 2003 Particle Accelerator Conference*, Portland, OR, May 2003.

[13] K. W. Shepard, P. N. Ostroumov, and J.R. Delayen, "High-energy Ion Linacs based on Superconducting Spoke Cavities", submitted to *Phys. Rev. S.T. Accel. Beams*, June 2003.

UPGRADING CEBAF TO 12 GEV*

Leigh Harwood [1] (for the JLab 12 GeV developmental team)
TJNAF, Newport News, VA 23606 USA

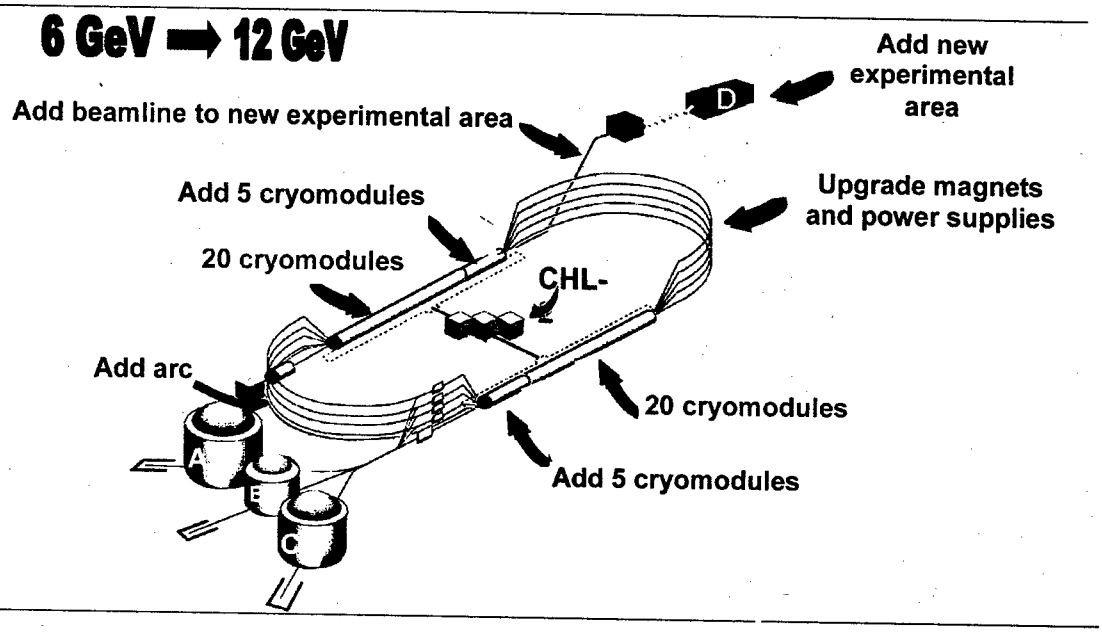

Abstract

As originally constructed, the Continuous Electron Beam Accelerator Facility (CEBAF) was a 4 GeV cw 5-pass recirculating linac. It has subsequently been enhanced to 5.7 GeV. Developments in lattice QCD have indicated that an extending CEBAF to 12 GeV would provide a unique opportunity to understand quark confinement. Jefferson Lab plans to reach 12 GeV by adding ten new 100 MV cryomodules and supporting rf systems to the present machine configuration. The 2K helium plant will be doubled. The beam transport system's capability will be doubled to 12 GeV with minimal replacement of components and with minimal saturation in the magnets. A new experimental hall, devoted to the quark confinement investigation, will be placed so that the beam transits one of the linacs 6 times (vs 5 times for the other linac). Beam emittances are degraded by synchrotron radiation such that the horizontal emittance of 1 nm-rad at 6 GeV increases to 7 nm-rad at 12 GeV. This paper discusses the issues listed above plus requirements for all systems and developmental opportunities presented by the project.

1 OVERVIEW

1.1 Motivation

The US National Academy of Science has identified understanding quark confinement as one of the ten most significant questions to be answered in physics in the 21st century. Lattice QCD calculations indicate that the explanation for confinement may lie in flux-tubes of gluons between quark pairs and also show that the flux-tubes' degrees of freedom yield exotic meson states. It appears possible to excite these exotic states with a beam of polarized 9 GeV photons and, most importantly, distinguish them from the other states. A high-quality, cw beam of 12 GeV electrons is the ideal way to produce the photons [1]. CEBAF presently has a high-quality cw beam of ~6 GeV and is thus an ideal platform upon which to base a facility.

1.2 Base requirements

6 MV of acceleration must be added. A new experimental area (for the exotic meson program) must be added to the present three. It will be on the opposite end of the accelerator from the existing ones; thus the beam that reaches the new end-station will transit one linac one more time than for any of the other end-stations.

12 GeV can be achieved by increasing the linac capabilities or increasing the number of passes. An analysis determined that it would be more cost effective to increase the linac capabilities than to reconfigure (rebuild) the beam transport system for additional passes. Therefore, the present 0.6 GV linacs will be upgraded to

*This work was supported by the U.S. Department of Energy Contract NumberDE-AC05-84-ER40150
[1] harwood@jlab.org

0-7803-7738-9/03/$17.00 © 2003 IEEE

1.1 GV. The exotic meson studies need < 5 μA; the other programs need much larger beam currents. It was decided to retain the present beam power limit of 1 MW.

The present beam transport system supports 5-pass beam at 6 GeV to each of the existing end-stations. It must be modified to deliver 11 GeV beam to those halls and have added the requisite beam transport to deliver the full 12 GeV beam to the photon radiator target for the new end-station, including an additional recirculation arc.

2 BEAM PHYSICS

2.1 Beam breakup

Beam breakup (BBU) driven by high-order modes (HOM's) in the cavities must always be addressed when using srf cavities even if the beam current in the cavities, < 1 mA in this case, is not exceptional on the scale of storage rings. As was done for 4 GeV CEBAF, the code TDBBU [2] was used to evaluate the situation. A specification of $Q < 2x10^6$ (versus $1x10^5$ for 4 GeV CEBAF) for the HOM's came out of the study. Initial tests of the new cavities indicate that there should be no problem with BBU for the upgrade.

2.2 Emittance, energy spread, and depolarizaion

Emittance growth from synchrotron radiation of the electrons in dispersive sections of the beam transport did not present a limitation to meeting the 1 nm-rad specification for CEBAF at 4 GeV. For the Upgrade, cost containment drove a desire to forego extensive modifications to the existing optics. Retaining those optics leads to emittances at 11 GeV in the existing end-stations of ε_x=7 nm-rad and ε_y=1 nm-rad. The projected energy spread at 12 GeV is 0.02%, as compared to 0.01% at 6 GeV. The CEBAF User's Group Board of Directors reviewed these values and found they did not limit the proposed research programs. Estimates for modifying the beam transport in order to reduce the dilution of the emittance by synchrotron radiation effects were ~$5M; it was decided to retain the present optics. Potential depolarization of the beam was checked and found to be inconsequential.

3 ACCELERATION

Note: The details of the acceleration systems (cryomodules, rf, and cryogenics) are described in detail in ref. [3]. The following is a summary of that information. It should be remembered that the existing systems will be used without modification.

3.1 SRF

The additional 0.5 GV/linac will be achieved by adding 5 new cryomodules (total of 10 needed for both linacs) each providing 100 MV. Each cryomodule will have eight 7-cell cavities. The cavities have a performance specification of $Q_0 = 8x10^9$ at 19.2 MV/m. While only 17.5 MV/m is required for the cryomodule to reach 100 MV, the specification was set at 19.2 MV/m to overcome the likelihood that some cavities might be off-line. The Q_0 specification was set by the requirement to fit within the projected cryogenics plant's capacity (see below). Key to meeting this performance is elimination of field emission. To accomplish this several steps will be taken: 1) changes in cryomodule design details aimed at excluding particulate-producing components [4,5], 2) changes in assembly procedures in order to better preclude contamination of cavities [6], and 3) utilization of in situ cavity processing to deal with any particulates. Electropolishing may be used. In addition a new cavity shape [7] will be used which has higher R/Q than the original CEBAF shape.

In addition, the tuner resolution has been improved versus that of the existing cryomodules, this being motivated by a desire to minimize the rf power required for keeping detuned cavities on-phase.

Prototype 7-cell cavities have exceeded the performance specification both with and without electropolishing. The first cryomodule with 7-cell cavities has been completed using many of the new procedures and design details; it achieved 82 MV. A second will be completed in 2003. New cell-shape options will be prototyped in 2003. The prototype 100 MV cryomodule is expected to completed in 2004.

3.2 Cryogenics

The present 2K helium plant is now operating at its full capacity. In anticipation of the Upgrade project, JLab acquired the former MFTF-B helium plant from LLNL, which has a capacity of >10 kW at 4K. We also have a redundant ("hot spare") 2K coldbox. With a reconditioned MFTF-B plant, the potential addition of an 80K exchanger, and utilization of the "spare" 2K coldbox, we will have a 2K plant with maximum capacity of ~5 kW at 2K. After allowance for system control headroom, there would be ~300W available for each of the new cryomodules, 250W of which would be available for dynamic load. At 19.2 MV/m, 250W translates to the $Q_0 = 8x10^9$ mentioned earlier.

3.3 RF

Each cavity will be energized by its own klystron. The required saturated output power for the klystrons is based on the following criteria: 1) ≤450 μA of beam transiting the cavity (limited by 1MW total beam power limit), 2) Q_{ext} is off-optimum by ≤ 30%, 3) maximum detuning ≤ 25 Hz of which 4 Hz is 2x the tuner resolution and 21 Hz is 6x the σ of the measured microphonics spectrum on existing cavities [8], 4) some cavities will be able to operate at 21 MV/m (10% above the mean of the population) and stay within the cryogenic limits, and 5) add 10% so that the klystron will still have gain. The result of the calculation was 12.5 kW. 13 kW has been chosen as the design specification to add headroom.

A new rf control module must also be developed. We anticipate using digital technology [9]. Preconceptual work is presently underway in collaboration with Cornell,

and DESY. Important control issues that must be addressed are:

- The cavities' will have multi-valued resonance detuning curves resulting from the high field and its accompanying large optimum external Q. A self-excited loop may be used to alleviate the problem.
- ~1/3 of the rf power is reserved for the effects of microphonics-induced detuning of the cavity. A potential solution is a new control algorithm [10] that uses a field modulation to damp the microphonics. The algorithm must be validated with a real cavity.

4 BEAM TRANSPORT

4.1 Upgrading existing beamlines

The existing beam transport system consists of ~400 dipoles (B*L≥0.2T-m) and ~700 quads. Simply replacing their power supplies is not viable because saturation in the return iron would require excessively large power supplies and installation of a large refrigerated cooling-water system. Replacing the magnets is also cost prohibitive. Another alternative was has been indentified.

For the majority of the dipoles, i.e. those in the nine 180° arcs and in the beamlines to the existing end-stations, the present "C" shape will be changed to "H" profiles by augmenting the magnets with bolted-on iron. Modeling and prototyping have shown that the saturation is only a few percent with the additional iron, while it would exceed 50% if the iron were not added.

The dipoles in the spreaders and recombiners (S/R), i.e. the sections of the beam transport system which separate the co-linear beams after they exit the linacs or combine them before re-injection into the linacs, are so closely spaced that the bolt-on iron option is often not viable. A combination of three approaches will be used: 1) reshape the poles to reduce the flux, and thus the saturation, 2) add coil packs and accept the saturation, and 3) add iron, but in lesser amounts than in the 180° arcs. For some magnets, no combination of the three options will work; those magnets will be replaced.

The quadrupole fields required for the Upgrade exceed the original design specifications of the present magnets for only ~10% of the population. Tests were performed that showed satisfactory field quality if the units were pushed to the required field levels. The plan now is to replace the power supplies on that 10% and run them well in excess of their original design specification; the remainder will be left "as is".

The dipole strings are energized by 32 power supplies varying in size up to 750 kW. All but nine will be reused for the upgrade. Those nine will be replaced with larger units that are anticipated to use one or more of a common power unit feeding a current regulating unit.

4.2 New beamlines

A new recirculation arc is needed so that the beam re-enters the north linac for its final acceleration before going to Hall D. Both Arc 10 and the beamline to Hall D must be built using new components. Thirty-two 4 m "H-style" dipoles will be used for Arc 10 and four of the same magnets will be used for the Hall D beamline. ~40 new quadrupoles will be built using a new design that is matched to the needs of these two beamlines.

4.3 Diagnostics

We presently anticipate no need to develop any new beam diagnostic instrumentation for this project. For the existing beamlines, no changes whatsoever are planned. New units of existing designs will be used for Arc 10 and for the beamline to Hall D. We need not add electronics for the beam position monitors in Arc 10 since they can be multiplexed onto the same electronics that presently monitor the existing arcs on that end of the accelerator.

5 PROJECT STATUS

The 12 GeV Upgrade received the endorsement of the US Nuclear Science Advisory Committee (NSAC) in its 2002 Long Range Plan. More recently, NSAC rated it's science as "absolutely central" and the project as "ready to start construction". With this endorsement, JLab is confident that the 12 GeV Upgrade will be a near-term priority project in the soon-to-be-released US Department of Energy Office of Science's 20-year Strategic Facilities Plan and will shortly thereafter receive approval from the US Department of Energy to proceed with the project.

6 SUMMARY

Lattice QCD calculations have indicated that the nature of quark confinement can be investigated with the availability of a 12 GeV cw electron beam. JLab has developed a cost-effective plan that builds on its existing infrastructure to deliver the 12 GeV beam and, furthermore, extend srf and rf control technologies. The project is under review by the US Department of Energy.

7 REFERENCES

[1] http://www.jlab.org/div_dept/physics_division/GeV.html
[2] B. Yunn, JLab internal report TN-01-028
[3] L. Harwood and C. Reece, "CEBAF at 12 and 25 GeV," SRF2001, Tsukuba, October 2001.
[4] Wilson, et al, RPAB064, this conference.
[5] Daly, et al, TPAB077, this conference.
[6] Mammosser, et al, RPAB062, this conference.
[7] Sekutowicz, et al, TPAB085, this conference.
[8] Delayen, et al, MPPB081, this conference.
[9] Hovater, et al, FPAB047, this conference.
[10] Delayen, "Electronic Damping of Microphonics in Superconducting Cavities", PAC-2001,

THE GSI SYNCHROTRON FACILITY PROPOSAL FOR ACCELERATION OF HIGH INTENSITY ION AND PROTON BEAMS

P. Spiller, K. Blasche, O. Boine-Frankenheim, G.. Franchetti, B. Franczak, I. Hofmann, P. Hülsmann, K. Kaspar, A. Krämer, G.. Moritz, E. Mustafin, H. Reich-Sprenger, P. Schütt, GSI, Darmstadt, Germany

Abstract

The two-stage synchrotron complex SIS100/SIS300 is the central part of the proposed "International Accelerator Facility for Ions and Antiprotons" at GSI [1]. The design concept of the synchrotrons will be described with emphasis on the status of R&D work, especially on the novel rapid cycling super-conducting magnets and on the required powerful, low-frequency RF-systems [2]. Furthermore studies are discussed, which refer to the life time of intermediate charged heavy ions and the dynamic vacuum pressure instability induced by ion beam desorption.

DESIGN CONCEPT

For the first synchrotron stage superconducting magnets of superferric type were proposed to provide a moderate pulse power at a rather large aperture of 130 x 65 mm and an operation with one cycle per second. A cold beam tube is foreseen to obtain a sufficiently high pumping speed for a stable operation with intermediate charge-state heavy ion beams.

The bending magnets are arranged in six arcs. The six long straight sections in between provide space for injection and extraction, the transfer line from SIS100 to SIS300 and also for the RF-systems required for acceleration (300 kV) and fast bunch compression (1000 kV). As in the SIS18 triplet focusing will be used to achieve a large acceptance at injection with dynamic change-over to doublet focusing during acceleration.

Four SIS18 booster cycles will be used to fill the SIS100 with up to 2.5×10^{13} protons or 1×10^{12} U^{28+} ions.

For the production of radioactive ion- and antiproton beams, the accelerated beam will be transformed into one single, short bunch (about 50ns for heavy ions). Thereby the produced secondary beams will have an appropriate time structure for injection, fast debunching and cooling in the planned array of storage rings. The SIS100 will be also used to accelerate antiproton beams from 500 MeV to 15 GeV for experiments in the high energy storage ring HESR.

The second synchrotron stage SIS300 was planned with superconducting cosθ-magnets for operation up to a flux density of 4 T. Meanwhile it is discussed to raise the flux density to 6 T by making use of double layer coils. The SIS300 ring will be mainly used for acceleration of U^{92+}-beams to high energies up to 34 GeV/u. In addition the SIS300 can be used as a stretcher ring to obtain a 100 % duty cycle, linac-like beam in operation with slow extraction

SUPERCONDUCTING MAGNETS

SIS100

Superconducting window-frame magnets shall be used in the SIS100 [3]. One major design goal was to achieve a low amount of stored energy, i.e. 45 kJ in a 2.62 m long dipole magnet with a beam tube aperture of 130 x 65 mm compared to 112 kJ in a conventional magnet as the one used in the SPS (CERN) or the SIS18 (GSI). Such a design reduces the total peak power of 120 magnets in fast pulse operation with a ramp rate of 4 T/s, a repetition rate of 1 Hz and a peak field of B=2 T to the moderate value of +22/-22 MVA compared to +62/-50 MVA in a conventional design.

In addition, the magnet weight will be strongly reduced to about 2 t per magnet compared to 20 t for a conventional magnet. The magnet design is based on the superferric cold iron magnet, which has been used in the Nuclotron at the JINR Dubna since 1993. In close cooperation with the JINR the dynamic losses of the existing magnets could be reduced to a value of 18 W/m. This translates into total power losses of 5.4 kW at 4 K for 120 dipole magnets using a standard triangular cycle (2 T, 1 Hz). In parallel an improvement of the field quality and the mechanical long-term stability was achieved. Figure 1 shows that the original losses of about 40 W/m have been reduced to 18 W/m.

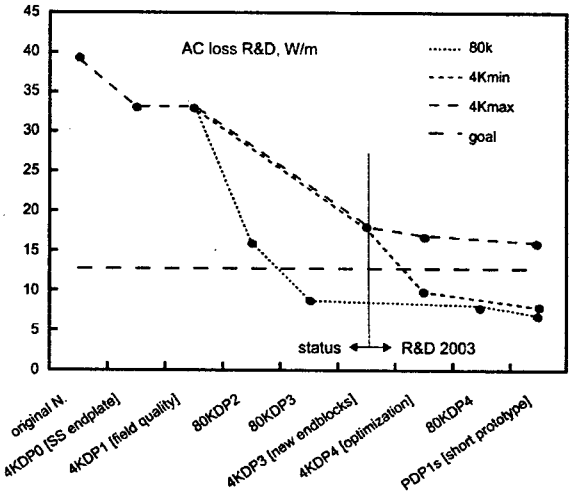

Figure 1 : A significant reduction of the dynamic losses of the Nuclotron magnet has been achieved.

To determine the sources of the losses, a detailed test program was launched. The 3D field configuration at the magnet ends was found to be one of the most important

0-7803-7738-9/03/$17.00 © 2003 IEEE

sources for eddy current losses in the iron yoke. 3D calculations confirmed the measured data [4].
In parallel, an alternative magnet design with an iron yoke at 80 K was developed and tested. The remaining AC loss in the coil amounts to 9 W/m (Figure 1) [5]. As an additional design option, the replacement of the Nuclotron cable by a CICC cable was studied [6].
The model magnet development for SIS100 shall be completed by the end of 2004.

SIS300

The SIS300 will be equipped with superconducting magnets similar to the RHIC arc dipole (BNL) with a one-layer cosθ-coil or the UNK dipole (IHEP), with a two-layer coil. In cooperation with BNL, a RHIC dipole was modified to reduce the dynamic losses for a standard triangular cycle (4 T, 1/8 Hz). Tests of a first model dipole started at the end of 2002. With the main emphasis on the development of a cored Rutherford cable dynamic losses of 9 W/m were achieved [7]. This translates into a total power loss of 2.8 kW at 4 K for 120 dipole magnets.
There is a strong user interest in raising the maximum beam energy of the second synchrotron stage by using 6 T dipole magnets for an operation of up to Bρ=300 Tm. In cooperation with IHEP the design of the 6T UNK dipole magnet, constructed with a two-layer cosθ-coil has been modified for operation at a fast ramp rate of 1 T/s [8]. Planned R&D to achieve this goal will include a large coil inner radius of 100 mm, an increase of the temperature margin and tests of model magnets.

RF SYSTEMS

The planned SIS100 operation requires powerful, low-frequency RF systems for stacking, acceleration and bunch compression. A low bunching factor is required in order to restrict the space charge tune shift during the long injection time of 1s to $\Delta Q<0.2$. Bunching factors of 0.45 and 0.85 can be achieved in a multi-harmonic and a barrier bucket potential. Both options are presently under investigation. An injection into a barrier bucket in SIS100 requires a time consuming preparation of the bunch before extraction in SIS18. Therefore the barrier bucket injection is not an appropriate scheme for the generation of maximum number of particles per second (gen. of secondary beams), but is considered for the generation of maximum number of particles per pulse (plasma physics exp.). For the generation of high average beam intensities a transfer into a two-harmonic potential in SIS100 is being considered as a sufficiently fast standard scheme.

Acceleration in SIS100 at h=10 requires a total RF voltage of 290 kV in a frequency range of 1.1-2.8 MHz. Furthermore 1 MW of compression voltage at the extremely low frequency of 465 kHz needs to be provided for the planned generation of short, single bunches after acceleration.

We investigate two alternative concepts for the technical layout of the RF systems. The first option is to install two separate RF systems for acceleration and compression, while the second option is to combine both functions in the same RF system [9]. Detailed design studies and optimisations with respect to costs, peak power requirements, shunt impedance and maintainability are in progress.

Table 1 : Comparison between separated and combined RF systems for acceleration and compression. $V_{0,a}$ and $V_{0,c}$ are the gap voltages of the acceleration and compression systems, $N_{a,c}$ the total number of cavities, $L_{a,c}$ the total RF system length and P_c the peak power of the compression system.

	$V_{0,a}$	$V_{0,c}$	$N_{a,c}$	$L_{a,c}$	P_c
Separate RF Systems	16 kV	40 kV	18+25	57 m +21 m	20 MW
Combined RF System	3 kV	10 kV	100	90 m	10 MW

The SIS300 RF system consists only of acceleration cavities which provide a total voltage of 80 kV.

DYNAMIC VACUUM AND LIFE TIME

Measurements in the SIS showed that the stripping cross section σ for U^{28+} at 8.6 MeV/u is of the order of 10^{-16} cm^{-2}. With increasing energy the observed beam lifetime does not improve, from this we conclude that the product σI (current I) remains constant under the present SIS UHV conditions [10]. In order to limit the beam losses due to stripping in the residual gas to values below a few percent a pressure in the 10^{-12} mbar region must be ensured in all (warm and cold) section of SIS 100/300. Recent experiments at CERN, BNL and GSI showed that lost heavy ions in the energy range between 1 and 10 MeV/u lead to large outgassing rates of heavy gas components from stainless steel chambers.
The measured desorption coefficients η varys between 10^3 and 10^5 molecules per incident beam ion. Assuming homogenously distributed stripping losses and pumping, the equilibrium dynamic pressure is

$$P = \frac{P_0}{1 - \frac{L}{S}\eta\sigma\frac{I}{q}}$$

with the pumping speed S, the base pressure $P_0 = Q/S$ (thermal outgassing rate Q), the circumference L and the beam current divided by the charge I/q. Using the existing pumping speeds in SIS ($S/L \approx 70$ l $m^{-1}s^{-1}$) together with the measured parameters we obtain a negative denominator, meaning a pressure instability, for the SIS 100 design current at injection energy. The pressure instability was observed in the SIS at relatively low ($N \approx 10^9$) uranium intensity confirming the desorption coefficients which were found at CERN. In order to maintain the required pressure of 10^{-12} mbar in the warm sections of SIS 100/300 ongoing efforts focus on low-η materials for collimators, on combined collimator/ pumping posts and on increased linear pumping in NEG coated chambers. All these measures should reduce the overall factor η/S

by a factor 1/1000 compared with the existing SIS. In the cold sections the cold wall pumping ($S/L \approx 10000\ l\ m^{-1}s^{-1}$) needs to be confirmed for the SIS 100/300 environment [11]. Such efficient pumping is hoped to limit the dynamic pressure increase in the cold sections.

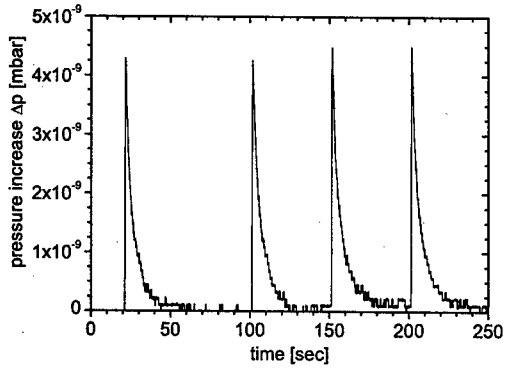

Figure 2 : Measured beam desorption induced total pressure increase in the test-stand. Shown is the pressure rise by the irradiation of a Cu sample with a 1.4 MeV/u C^{2+}-beam.

In order to measure the scaling of the desorption coefficient with projectile energy, mass and charge a desorption test-stand was recently set up at GSI. These experiments should also lead to low-η materials suitable for collimators or for vacuum chambers. First results with low energy (1.4 MeV/u) C^{2+}-ions irradiating a Cu target are shown in Figure 2.

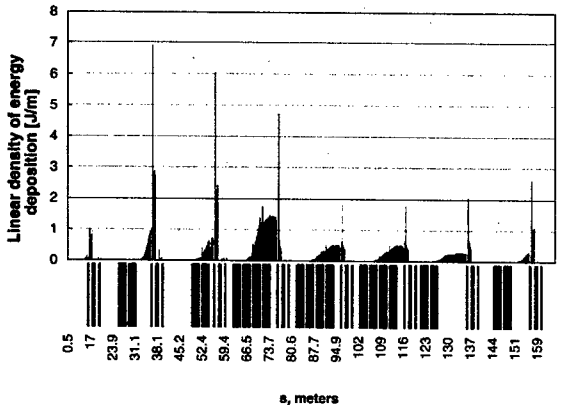

Figure 3 : Calculated distribution of beam loss induced energy deposition in one arc of SIS100, assuming 5% losses of the initially 10^{12} U^{28+} -ions.

The distribution of losses due to ionisation of U^{28+} to U^{29+} and the thereby deposited energy per meter have been determined for the SIS100 lattice. The losses occur mainly after charge separation in the arc dipoles. Figure 3 shows the calculated energy distribution assuming a fraction of 5 % lost ions. The plot shows the strongly peaked energy deposition along the beam pipe with a maximum after the first pair of dipoles following the straight sections.

One option to act against the vacuum instability is to control as many as possible of the lost ions by installing new types of collimators in the hot spots. Basis for this counter measure is the assumption that the threshold for vacuum instability can be enhanced if the loss-created desorption gases are to a large fraction prevented from reaching the optical axis. Therefore, a prototype of desorption collimator was developed for the U^{28+}-operation and will be tested in SIS18[12]. The concept of the proposed collimator is to localize beam losses and to capture the created desorption gases in a secondary vacuum chamber (Figure 4). A wedge shaped block acts as a collimator and is installed such that the surfaces points to contrary direction of the optical axis. In order to eliminate the desorption gases produced on the wedge surface, the secondary chamber was equipped with two high conductivity pumping ports and with a powerful cryo pumping system. First tests of the prototype desorption collimator are planned for August 2003.

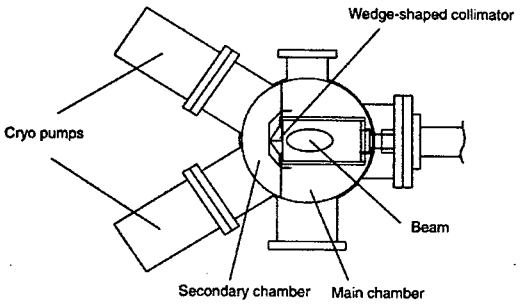

Figure 4 : Layout of a dedicated collimator for the control of ionisation beam losses and desorption gases.

ACKNOWLEDGMENT

We thank all internal and external colleagues who have contributed to the design and R&D work for SIS100/300.

REFERENCES

[1] Conceptual Design Report GSI(2001)
[2] P.Spiller et.al., Proc. of the EPAC02, Paris, (2002)626
[3] A.D.Kovalenko et al., Proc. of European Particle Accelerator Conference, Paris, France (2002), 2406
[4] A.D.Kovalenko et al., IEEE Transactions on Applied Superconductivity, 12 (2002) 161
[5] A.D. Kovalenko et al., Proceedings of Appl. Supercond. Conference, Houston, Texas (2002), to be published
[6] I. Koop, V.E.Keilin et al., Internal GSI Report (2003)
[7] M.N. Wilson et al., Proc. of Applied Superconductivity Conference, Houston, Texas (2002), to be published
[8] V.E.Keilin and S.S.Kozub, Internal GSI Report (2002)
[9] P.Hülsmann et.al., GSI internal Report
[10] A.Krämer et.al., Proc. of EPAC02, Paris,(2002)2547
[11] O.Gröbner, CAS, Snekersten (1999)127-138
[12] P.Spiller, GSI Internal Report, GSI-SIS-02-02

OBSERVATIONS OF ELECTRONS IN THE INTENSE PULSE NEUTRON SOURCE (IPNS) RAPID CYCLING SYNCHROTRON (RCS)*

J. C. Dooling†, F. R. Brumwell, W. S. Czyz, K.C. Harkay, M. K. Lien, and G. E. McMichael
Argonne National Laboratory, Argonne, IL 60439, USA

Abstract

In the process of accelerating protons from 50 to 450 MeV at 30 Hz, low-energy electrons are generated within the IPNS RCS vacuum chamber. Electrons from background gas stripping are detected using an Ionization Profile Monitor (IPM) to generate integrated, horizontal charge distributions of the single-harmonic bunch during acceleration. Recently, a Retarding Field Analyzer (RFA) was installed in the RCS to look for evidence of beam-induced multipacting by measuring the electrons ejected by the space charge of the beam. A wide-band, high-gain transimpedance amplifier has been built to observe time structure in the electron signal detected with the RFA. Though a noisy power supply prevented full I-V characteristics from being obtained, interesting features are observed; especially, after the period of phase modulation between the rf cavities that is deliberately introduced during the cycle. The phase modulation generates a longitudinal quadrupole oscillation in the bunch, which is believed to enhance beam stability. Preliminary results indicate that electron multipacting is not significant in the RCS. The effects of background gas neutralization are considered and details of the RFA measurements are presented.

INTRODUCTION

Space-charge neutralization can play an important roll in the transport properties of an ion beam, especially if the fractional neutralization becomes substantial. For example, in the IPNS accelerator, nitrogen gas is introduced between the H^- ion source and 750-kV, Cockcroft-Walton pre-accelerator, to mitigate space-charge blow-up of the beam[1]. Neutralization allows efficient transport of ions between the source and linac. In this case, the effect is primarily electric neutralization. In the RCS, the effects of neutralization are again present; due to the ionization of background gas; however, in this case, the magnetic field of the beam may also be involved.

ANALYSIS

The beam space-charge generates an electric field which drives positive background ions out of the beam channel, while attracting and trapping electrons. A uniform beam density is assumed across an average radius, r_b, and zero density outside to the wall radius r_w. The radial electric field may be expressed as, $E_r(r)=\rho(t)r/2\varepsilon_0$, for $r<r_b$, and $E_r(r)=\rho(t)r_b^2/2r\varepsilon_0$, for $r_b<r<r_w$, where $\rho(t)=e(n_i(t)-n_e(t))$ and $n_i(t)=Z(t)n_{bk}(t)+n_b(t)$. The background ion density, $n_{bk}(0)$ is initially assumed to be zero. Though this is a simple model, it is useful in examining the dynamics of the background ions. The average electric field, E_{av} across the inner radius can be used to compare non-relativistic transit times, $\tau_{tt}=(2mr_w/eE_{av})^{1/2}$ for the ions and electrons. For $3x10^{12}$ protons uniformly distributed within r_b=1.5 cm and occupying half of the 43 m RCS circumference (B_f=0.5), E_{av}=154 V/cm, assuming r_w=3.8 cm. The one way transit times for an electron and a singly-charged nitrogen ion, both starting with zero initial velocities are 1.7 ns and 270 ns. This can be compared with a bunch length of 225 ns near injection (h=1).

Analysis shows that beam space-charge can trap and release electrons[2]; in addition, secondary electron yield (SEY) from the wall may exceed unity leading to a build-up in the electron density and the development of an e-p instability[3,4]. The process of SE is distinct from background gas neutralization; in the former case, the creation of low-energy (free) background ions does not occur, and any positive background ions are quickly ejected by the beam space charge playing no roll in the process. However, if the electron density builds up quickly during the period of coasting beam injection and capture, the space-charge of the beam may be neutralized, preventing the ejection of background ions.

Determination of the neutralization time, τ_n, requires that the ionization cross section, σ be known. Following the discussion from Reiser[5], the calculated values of σ are presented in Figure 1 along with the neutralization folding times for background gas pressures of 1 μTorr and 2 μTorr N_2. The average background gas pressure in the RCS falls within this range. The neutralization folding time is given by, $\tau_n=(n_g\sigma v)^{-1}$, where n_g is the neutral background gas density. As shown in Figure 1, for 1 μTorr, τ_n varies from 0.5 ms to 1.0 ms during the acceleration period. For purpose of comparison, in the PSR at Los Alamos, τ_n = 20 ms.

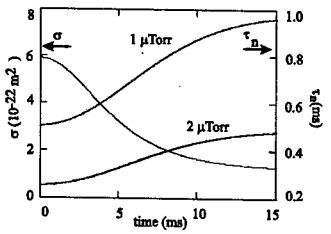

Figure 1: Ionization cross section and neutralization times in the RCS for 1 and 2 μTorr, N_2.

* This work is supported by the USDOE, contract W-31-109-ENG-38.
† jcdooling@anl.gov

0-7803-7738-9/03/$17.00 © 2003 IEEE

Given the ionization cross section and the background gas and beam densities, the average incremental ion and electron density created per cycle (Z=1) is $n_g n_b \sigma \beta c \Delta t$, where Δt is the revolution period. Assuming a round beam of radius r_b=1.5 cm, the average beam density is $n_b=2.0\times10^{14}$ m^{-3} (BF=0.5). At 1 μTorr, the background gas density exceeds that of the initial beam by more than 2 orders of magnitude.

Self-focusing may occur if the background plasma traps a portion of the beam's magnetic field. As the beam travels around the synchrotron, its current creates a magnetic field. A stationary plasma in the vicinity of the beam will have a tendency to maintain some of the impressed field for a period, τ_m. the magnetic decay time. The beam will experience the trapped magnetic field and respond to it. It is assumed that the trapped field, $\mathbf{B}_t$ is maintained by a current that travels in the same channel as the beam[6]. From the Lorentz force expression, $\mathbf{F}=q(\mathbf{E}+v\times\mathbf{B})$, it can be seen that the primary force on the beam protons is in the radial direction ($v_z=\beta c$, $\mathbf{B}\sim B a_\phi$). The radial force may be expressed as,

$$F_r(r) = q\beta c \frac{\mu_o I_m(r)}{2\pi r} \qquad (1)$$

where $I_m(r)=f_n I_b(r)$ and f_n is the fractional neutralization. Assuming a uniform current density, $I_m(r)\propto r^2$ and the focusing length is independent of radius within the beam. The focal length of the plasma lens is $f_{pl}=r/r'$ where $r'=v_r/v_s$ and $v_r=a_r\Delta t+v_{ro}$. Letting $v_{ro}=0$, and again writing Δt as the cycle time, $2\pi R/\beta c$, the focal length becomes,

$$f_{pl} = \frac{\beta\gamma mc}{q\mu_o I_m R} r_b^2 \qquad (2)$$

where I_m now represents the total magnetic current and R=6.83 m. Assuming the background plasma traps the average current (~2 A, B_f~0.2), the focal length of the plasma lens is 45 m, approximately the circumference of the ring. This is a relatively weak lens. In this simple model, though the lens is linear, its strength varies as r_b^{-2} (current density). In reality, the beam density is more like a Gaussian distribution and the trapped field likely will not vary linearly with r. In this case, the nonlinearity of the lens acts to couple longitudinal beam energy into the transverse planes.

Most treatments of electron cloud instability ignore the presence of background ions [7,8]. When the background gas pressure is low or the beam cycle time is short compared to the neutralization folding time, τ_n, this assumption may be acceptable. In the case of the RCS, the acceleration period is significantly longer than τ_n. The presence of a background plasma can alter the beam self-field and applied fields within the vacuum chamber.

EXPERIMENTAL ARRANGEMENT

The phase controller for the RCS rf includes a "scrambler" that causes a phase modulation in the rf accelerating voltage near the second harmonic of the synchronous frequency (~10 kHz). The scrambler is typically switched on between 8.5 ms and 9.5 ms into the acceleration period. Scrambler excitation couples longitudinal energy into transverse bunch motion and may help to disrupt the plasma channel growing with the beam. Without the scrambler, the beam sustains a substantial loss near the end of the cycle[9].

The Profile and Position System (PAPS)

The PAPS consists of two arrays of stainless steel grids, one on the bottom and the other on the side of the S6 straight section, detecting integrated horizontal and vertical electron currents, respectively[10]. The PAPS is a form of ionization profile monitor (IPM) and depends on the ionization of the background gas in an applied electric field to provide profile information. The horizontal PAPS is presented schematically in Figure 2.

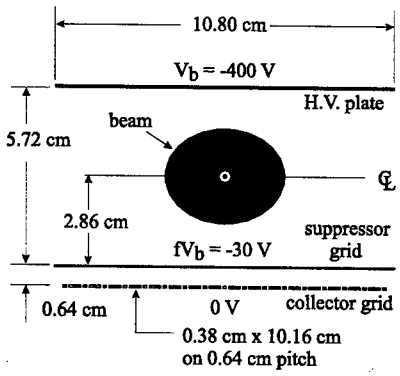

Fig. 2. Horizontal Profile and Position System (PAPS).

Typically, the PAPS bias plate voltage is set at -400 V. The horizontal PAPS device has a more desirable aspect ratio (plate width/beam gap) relative to its vertical partner, so here we will discuss only horizontal PAPS data. The horizontal device is made up of 16 stainless steel collector strips arrayed across the bottom of the diagnostic with a 0.25-in. (.64 cm) spacing from center to center as shown in Figure 2. Between each collector strip is a grounded guard strip. The PAPS bandwidth is 5 kHz. The amplitude of the PAPS profile is sensitive both to bias voltage and background pressure as shown in Figure 3. The PAPS data show processes associated with injection and the phase-modulating scrambler period. The profiles become multi-peaked and noisy after the scrambler burst around 10 ms; in addition, the peak amplitude is substantially reduced. The suppressor bias is maintained at a small fraction of the main bias. It is interesting to note that with zero bias, the profile inverts slightly, indicating a positive current, perhaps due to SE.

The Retarding Field Analyzer (RFA).

The RFA is an electron energy analyzer which has been described elsewhere[11]. The RFA assembly is mounted onto a 2.75 in. (7.0 cm) diameter stainless steel flange between the L5 cavity and triplet magnet 6 on the outboard side of the beam pipe at beam elevation.

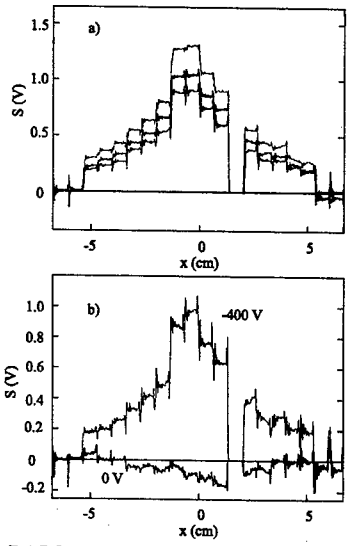

Figure 3. PAPS profiles with a) three background pressures increasing in ascending order from 0.4 μTorr to 1.2 μTorr 1 ms after injection, and b) -400 V and 0 V on the H.V. plate, 2 ms after injection. Ch. 11 is inactive.

Based on background gas ionization alone, the output signal from the RFA is expected to be small. An amplifier has been constructed with a transimpedance gain of 300 kΩ.; the voltage gain of the circuit into 50 Ω is 6000 (76 dB). Using the ionization cross section for nitrogen given above, the electron current per unit length, I_{el} is 46 μA/m at injection. The output amplifier voltage is calculated to be 2.4 mV. It is difficult to definitively say that electrons have been observed using the RFA. "Electron-like" signals are seen sporadically, for example the data in Figure 4 strongly suggests a burst of electrons during beam bunching early in the RCS cycle; however, such data are rarely repeated. This is under investigation.

Pie Electrodes

Another indication that electrons are present in the RCS come from broadband noise observed on split-can or "Pie" electrodes located in the short straight sections of the ring. The Pie electrodes are short striplines and therefore provide a differentiated current signal with respect to time. Beam position data is generated from this diagnostic using analog summing and differencing circuits. A sample of the broadband noise spectrum detected with the Pie electrodes is presented in Fig. 5. In the figure, the two spectra shown are obtained from an 80 μs slice of time data (20 kS at 250 MS/s) starting 10.88 ms after injection and approximately 2.5 ms after the scrambler period begins. The primary shape harmonics are visible in both spectra; however, in the scrambler spectrum, broad sidebands are in evidence. The sidebands move to higher frequency with time. It is the cycle without the large sidebands (and scrambler) that exhibit a 70 percent loss of beam prior to extraction.

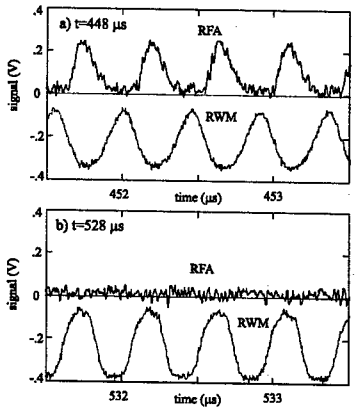

Figure 4: RFA and RWM data recorded just after injection, V_{ret}= 0 V, V_{col}=30 V (1 MΩ), a) t_{start}=448 μs, b) t_{start}=528 μs. The signals are temporally aligned.

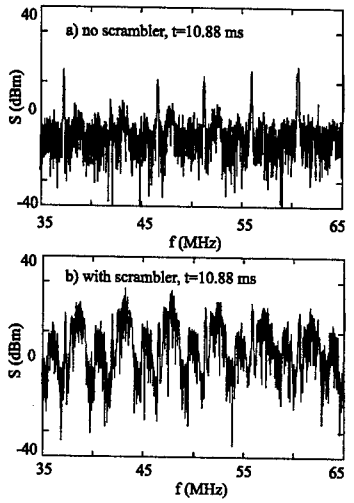

Figure 5: Pie spectra for an 80 μs slice of time data starting at 10.88 ms; a) no P and b) with PM.

REFERENCES

[1] V. Stipp and A. DeWitt, IEEE Trans. Nuc. Sci, NS-**32**(5), 1754(1985).
[2] D. V. Neuffer, Proc. PAC1991, p. 1077
[3] D.V. Neuffer, et al., NIM A **321**, 1(1992)
[4] R. Macek, et al., Proc. PAC2001, p 688.
[5] M. Reiser, *Theory and Design of Charged Particle Beams*, Wiley, New York, 1994, p. 274
[6] H. S. Uhm, R. C. Davidson, PRST-AB, **6**, 2003(034204)
[7] M. Blakiewicz, et al., PRST-AB, **6**, 014203(2003)
[8] G. Rumolo and F. Zimmermann, PRST-AB, **5**, 121002(2002).
[9] J. C. Dooling, et al., AIP Proc. **642**, Batavia, 77(2002)
[10] J. M. Bogarty, IEEE Trans. Nuc. Sci., **26**(3), 1979(3349).
[11] R. A. Rosenberg, and K. C. Harkay, NIM-A, **453**, 2000(507)

SPIRAL 2 : A HIGH INTENSITY DEUTERON AND ION LINEAR ACCELERATOR FOR EXOTIC BEAM PRODUCTION

Alban Mosnier, CEA-DAPNIA, Gif-sur-Yvette, France
for the SPIRAL 2 project team

Abstract

Based on the "LINAG Phase 1" conceptual design [1], a two years detailed study on a ISOL-type facility for the production of high intensity exotic beams, named SPIRAL2, has been launched. The rare isotope beams are produced via the fission process, with the aim of 10^{13} fissions/s at least, induced either by fast neutrons from a C converter in a UCx target or by direct bombardment of fissile material. The driver, with an acceleration potential of 40 MV, has to be upgradeable and versatile: it will accelerate deuterons (5 mA) and A/q=3 ions (1 mA) and even heavier ions in a later stage. It consists in high-performance ECR sources, an RFQ cavity and independent phase superconducting resonators.

The primary beam is transferred towards the production system, including converter, target and ion source. The exotic beam can be directly used in a low energy experimental area or is accelerated by the existing CIME cyclotron after increase of its charge-state by means of an ECR charge booster. The selection of the parameters as well as the technology result from an optimisation of the linac. Systematic beam dynamics calculations with space charge forces, 3-D field maps and alignment errors to check the robustness of the design and the very low loss rate all along the linac are in progress.

INTRODUCTION

In order to extend the study of the structure of nuclei far from stability to medium-mass nuclei at GANIL, a two-year detailed design study on an ISOL-type facility, named SPIRAL 2, has been launched. As the final intensities of RIB's will define the areas of the nuclear chart that will be accessible to experiments, high intensity primary beams as well as various production methods are needed. The production method of the rare isotope beams is based on a variation of the ISOL method by resorting to the fission process induced either by fast neutrons from a C converter in a UCx target, with the aim of producing more than 10^{13} fissions/s, or by direct bombardment of fissile material. Different types of ion source will be coupled to the target depending on their ionisation efficiency for the selected radioactive element. The isotopes will be bred to higher charge state for proper post-acceleration up to 6 MeV/u in the existing CIME cyclotron. In addition, the acceleration of heavy ion beams of high intensity, thanks to the forthcoming generation of ECR ion sources, will allow users to do fusion-evaporation physics. The driver, with an acceleration potential of 40 MV will accelerate 5 mA deuterons, 1 mA ions of mass-to-charge ratio A/q=3 and even higher A/q ions in a later stage (up to 6).

DRIVER LAYOUT

Due to the high beam power (200 kW) and to its modularity, the linac solution was chosen. As it must accelerate light ions (deuteron) and heavier ions of A/q=6, the linac was optimised in energy for A/q=3 ions. Moreover, the energy range of the driver for the heavy ions must be very flexible and extend from ~ 15 MeV/u to very low energies, as low as ~1 MeV/u. The main linac parameters are given in Table 1.

Table 1 : Main linac parameters

	A/q = 2	A/q =3
E_{in} [keV/u]	20	20
E_{out} [MeV/u]	20	14.5
$\varepsilon_{\perp}$ rms [π.mm.mrad]	0.2	0.4
ε_z rms [π.deg.MeV]	0.05	0.12
Intensity [mA]	5	1

Figure 1 shows the schematic layout of the driver. A first injector includes two ECR sources for deuterons and A/q = 3 ions, the associated Low-Energy Beam Transfers (LEBT) followed by a common RFQ cavity. A second injector for injecting the higher A/q ions beam is planned to run into the Medium-Energy Beam Transfer (MEBT). The beam is then accelerated up to a total energy larger than 40 MeV by an Independently Phased Superconducting Linac, providing a safe cw operation and high flexibility in the acceleration of different ion species and charge-to-mass ratios.

Ion sources

In order to avoid severe reduction of the beam intensity by using stripping foils at intermediate energies, one takes advantage of the continuous progress of high charge state ECR sources. The 5 mA deuteron beam will be produced either from a downgraded version of the high intensity SILHI source [2] (replacement of e.m. magnets by permanent magnets and modification of the extraction system) or from an improved version of the micro-phoenix source [3]. For the A/q=3 ions, the state-of-the-art in ECR sources gives 1 mA $_{18}O^{6+}$ and 0.2 mA $_{36}Ar.^{12+}$. High confinement fields (B_r ~ 2-3 T) and high frequency (f > 28 GHz) are required to increase the ion beam currents. Two options, based respectively on a fully superconducting ECR source and on a combination of permanent and high temperature superconducting magnets, are expected to start in 2004 in the framework of an european research program, named "Ion Sources for Intense Beams of Heavy Ions" (ISIBHI).

0-7803-7738-9/03/$17.00 © 2003 IEEE

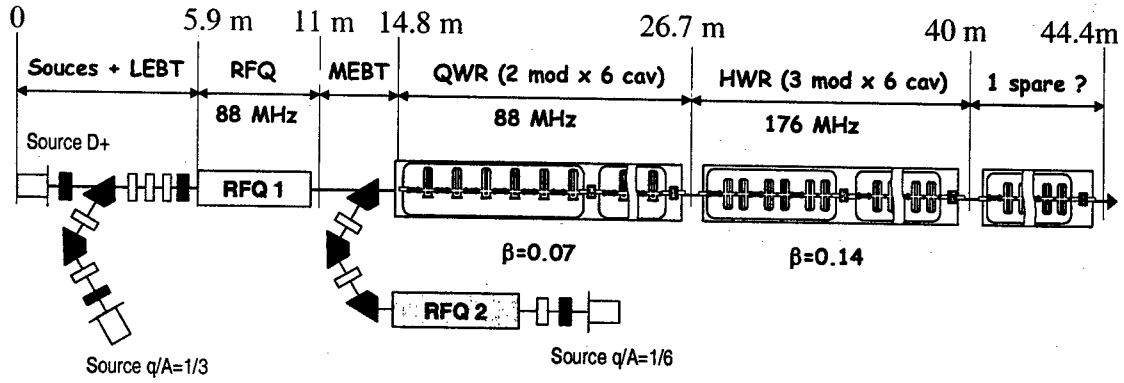

Figure 1 : Architecture of the SPIRAL 2 Linac

Frequency choice

On the one hand a low rf frequency at the linac front end offers a suitable longitudinal acceptance for the slow heavy ion beam, on the other hand a high rf frequency is preferred because of the more compact and consequently cheaper accelerating structures. As a tradeoff, a frequency jump at intermediate energy is generally chosen. Different frequency scenarii have then been studied:

- 88 MHz for the whole linac
- 88/176 MHz for the low/high energy part
- 176 MHz for the whole linac

Two types of superconducting cavities have been considered: Quarter-Wave Resonators (QWR) and Half-Wave Resonators (HWR). The former is quite convenient at low frequency whereas the latter is too bulky at low frequency but avoids the "steering effect" that can be detrimental for light particles [4]. The two-frequency scheme was finally chosen: the whole linac at 176 MHz leads to the highest number of resonators and the highest power consumption in the RFQ and jeopardizes the acceleration of heavy ions; the whole linac at 88 MHz gives the largest cavity aperture over beam size ratio but the too big diameters make the fabrication of resonators and cryostats tricky.

RFQ cavity

A high RFQ transmission is required (lower than 3% beam loss with all combined errors) to allow for hands on maintenance. Different technologies at 88 MHz were studied: the 4-vane type gives a safe cw operation even for a high electrode voltage (greater than 100 kV) and the highest transmission but a simplified mechanical design has to be found to compete with usually cheaper 4-rod or IH type RFQs. An only mechanically assembled cavity without brazing or welding and made from a simple copper tube is proposed. RF joints can be used because of the low power density (< 6 W/cm^2) and of the moderate magnetic fields (< 2500 A/m). Figure 2 shows the main parameters of the RFQ. The construction takes into account the non constant voltage and R_0 profile, the tolerances of 1% on the voltage law and of one tenth of mm on the vane tips displacement. One variant that introduces coupling windows in the vanes, also called "split-coaxial RFQ", thus reducing up to two times the external diameter, has not been retained because the peak power density is larger and the added complexity of the assembling makes the cost very similar.

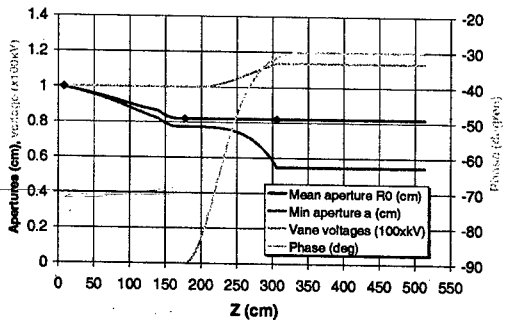

Figure 2 : Main RFQ parameters

The length of the RFQ is between 5 and 6.5 m, corresponding respectively to 0.75 and 1.0 MeV/u and will be determined by the results of start-to-end multi-particle simulations including all realistic errors.

Resonators and cryostats

Two resonator families that differ in geometric β and frequency are used. The β-values were optimised to give the shortest linac with a minimum number of resonators. The assumed accelerating field is 8 MV/m. The resulting linac comprises a total of 30 resonators and is composed of 2 modules of six β=0.07 resonators at 88 MHz and 3 modules of six β=0.14 resonators at 176 MHz. A slot is left at the end of the linac to allow for the installation of an additional 6-cavity module if the field of 8 MV/m could not be reached but decreased as low as 6.5 MV/m.

The shape of the resonators was first optimised to achieve the lowest peak fields. For example, the lowest electric and magnetic fields for the QWR type are obtained by enlarging the curvature radius of the drift tube and the stem diameter, respectively. The final geometry gives peak fields over accelerating field ratios of $E_{pk}/E_{acc} \sim 5$ and $B_{pk}/E_{acc} \sim 10$ mT/MV/m. An

accelerating field of 8 MV/m leads to $E_{pk} \approx 40$ MV/m and Bpk ≈ 80 mT, which should be achieved without too much effort by using the well-tried methods developed in the last ten years (high pressure rinsing, high purity niobium, clean conditions...). Besides, a conical shape of the stem and a rounded shape at the top improve the stiffening of the cavity. Figure 3 shows the geometries of both QWR and HWR types. Last, a slight modification of the wall at the beam ports location of the QWR will cancel the "steering effect" if beam dynamics calculations show that this effect is too strong.

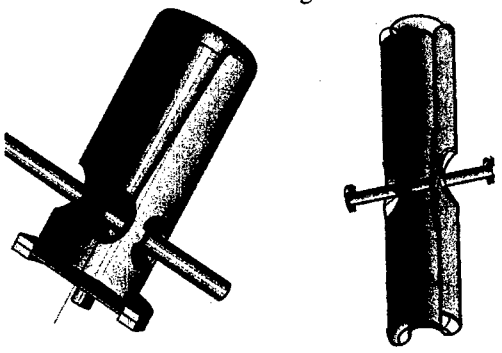

Figure 3 : QWR and HWR geometries

Up to now conservative values of spacing between the different components (bellows, flanges, cold-warm transition, etc) have been assumed. More attention will be paid to the reduction of these distances if the present cryostat length (~5 m) and inter-tank spacing are too large from the beam dynamics point of view.

LOW LEVEL RF

As a Low Level RF (LLRF) system is required for different types of accelerating structures (RFQ, QWR and HWR) fed by tube or solid-state amplifiers, the flexibility offered by digital systems makes them ideal candidates.

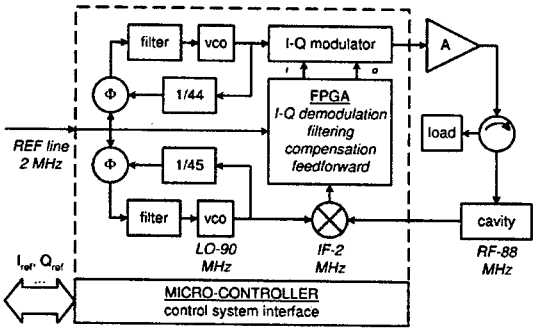

Figure 4 : Block diagram of the LLRF system.

A common hardware design (Figure 4) with a high integration level in a fast programmable logic chip (FPGA) will provide high performances in terms of noise and reliability and at a lower cost for manufacturing and maintenance. The reference signal of 2 MHz is sampled with the IF signal to provide a 4-quadrant I-Q demodulation. The dynamic compensation of the feedback loops, as well as an eventual feedforward, are implemented as IR filters in the same FPGA.

BEAM DYNAMICS

Two essential rules must be respected to avoid dilution and beam loss: the phase advance per lattice period must be lower than 90° and the beam must be carefully matched in all planes (longitudinal and transverse) between tanks. This statement favours a large number of cavities per tank and led to choose 6 cavities per cryostat. The focussing is ensured by solenoids instead of quadrupoles because the sensitivity to misalignments and the cost are lower but care must be paid to the tilt of the solenoids. The axial field is kept low enough (lower than 8 T) in order to use a classical technology of NbTi for the superconducting coils. Figure 5 shows for example the phase advance per cell and the beam power per cavity for a 5 mA deuteron beam and a maximum accelerating field of 8 MV/m. Detailed calculations are presented in [5,6]. The next step will be devoted to systematic start-to-end simulations including 3-D field maps and correction of beam steering induced by QWRs and alignment errors.

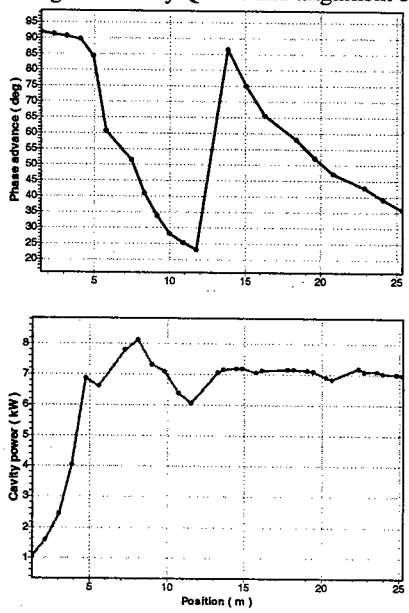

Figure 5 : Phase advance / cell (top) and beam power / cavity (bottom) along the SC linac for the D^+ beam.

REFERENCES

[1] http://www.ganil.fr/research/sp/reports/
[2] R. Gobin et al; "Saclay high intensity light ion source status", EPAC 2002, Paris, France
[3] P. Sortais et al, private communication
[4] A. Facco and V. Zviagintsev, Proc. of the PAC 2001, Chicago, p.1095.
[5] R. Duperrier et al., "Beam Dynamics Studies in SPIRAL 2 Linac", these proceedings, RPAB034
[6] P. Bertrand., "LIONS_LINAC : a new particle in cell code for linacs", these proceedings, FPAG011.

COSY-SCL, THE SUPERCONDUCTING INJECTOR LINAC FOR COSY

R.Toelle*, U.Bechstedt, N.Bongers, J.Dietrich, R.Eichhorn, F.M.Esser, O.Felden, R.Gebel, K.Henn, H.Jungwirth#, A.Lehrach, R.Maier, U.Pfister, D.Prasuhn, P.v.Rossen, A.Schnase, H.Schneider, Y.Senichev, R.Stassen, H.Stockhorst, E.Zaplatin, Forschungszentrum Juelich GmbH, Postfach 1913, D-52425 Juelich, Germany;
A.Schempp , IAP, Johann Wolfgang Goethe-Universitaet, Frankfurt am Main, Germany

Abstract

The superconducting injector linac COSY-SCL is being designed and constructed at the Forschungszentrum Juelich. The main goal of the new injector is to fill the cooler synchrotron COSY with polarized protons as well as with polarized deuterons up to the space-charge limit at injection energy. COSY-SCL is characterized by a base frequency of 160 MHz, 25 kV ion-source extraction voltage, a pulse length of up to 500 μs, a maximum repetition rate of 2 Hz, injection into the linac at β=0.073 and injection into COSY at kinetic energies of 52 MeV for protons and 56 MeV for deuterons, respectively. The injector configuration is presented, and its main subsystems -ion source (CIPIOS from IUCF for polarized H^- and D^-), RFQ (built in co-operation with the University of Frankfurt), linac (based on half-wave resonators operating at 160 and 320 MHz)- are described and discussed. The present status of the project is reported.

INTRODUCTION

Several independent review committees have identified a much enhanced future scientific potential for the COSY accelerator facility if intensities for polarized ions could be raised to about $2*10^{11}$, which roughly corresponds to the limitation by space charge. The evaluations also showed that a different injector is needed for this purpose because the present injector, the 30 years old isochronous cyclotron JULIC, is constituting a bottle neck that would foil any attempt to reach that goal. The most suitable new injector for COSY turned out to be a superconducting (sc) linac with independently phased single-cell cavities [1].

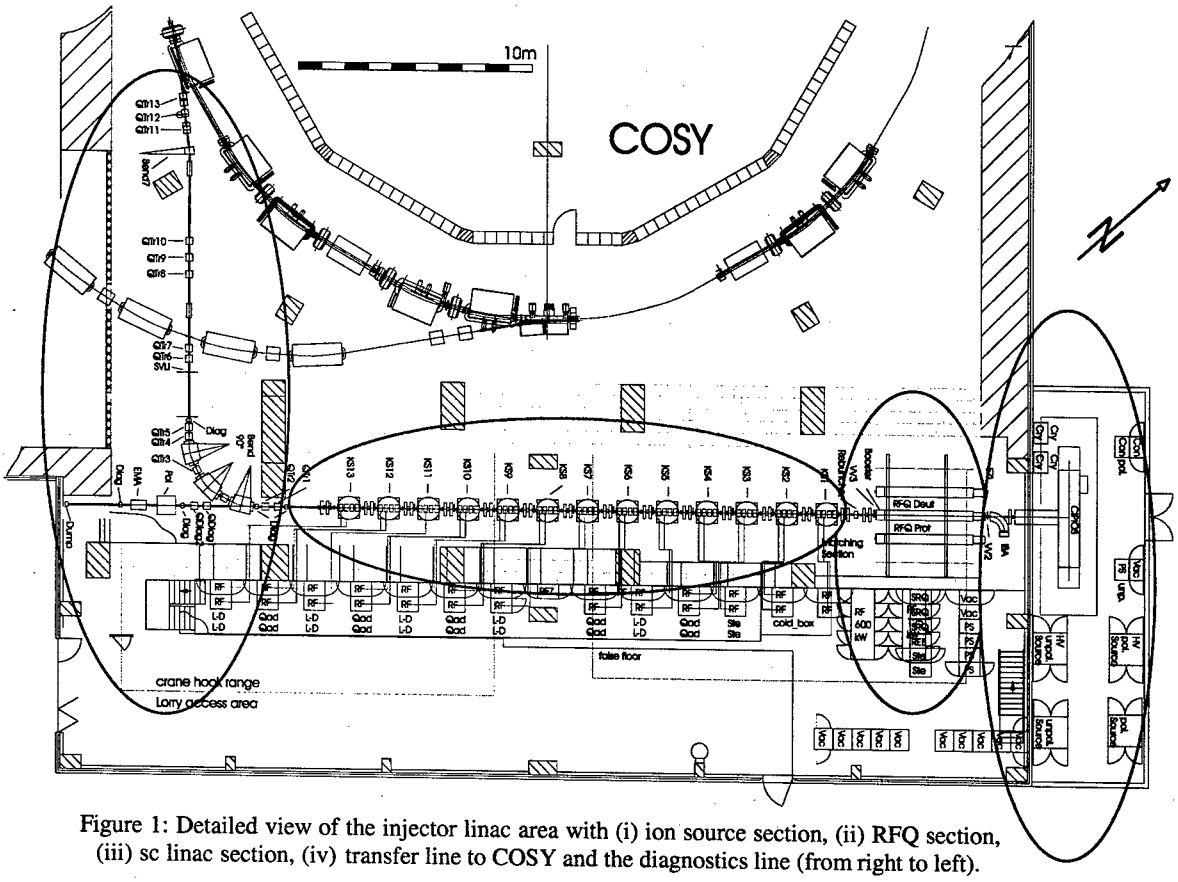

Figure 1: Detailed view of the injector linac area with (i) ion source section, (ii) RFQ section, (iii) sc linac section, (iv) transfer line to COSY and the diagnostics line (from right to left).

* r.toelle@fz-juelich.de
# present address: Accel Instruments, Bergisch Gladbach, Germany

LINAC CONCEPT

The new injector should be able to deliver polarized proton and deuteron beams with sufficient intensities to fill COSY to the space-charge limit at the chosen injection energy of about 50 MeV. In addition, the new injector should fit into the existing building of COSY to keep civil engineering costs low. Furthermore, construction should not interfere with the ongoing experimental program and allow a fast switching from the cyclotron to the new injector once it has been completed.

A normal conducting linac, due to its excessive length, turned out to be incompatible with the existing space limitations. In addition, a beam dynamics analysis showed that superconducting quarter-wave resonators such as in use at other facilities to accelerate heavy ions are not suitable in our energy range for light ions. Hence, a new design in form of superconducting half-wave resonator (HWR) structures was worked out.

For establishing this design, a large number of obstacles had to be overcome and new solutions for many crucial details had to be found. An international review committee scrutinized the proposed design and found that this project could make significant contributions to the development in this field of accelerator technology. Their encouragement and recommendations paved the way from design to construction.

Figure 1 shows the injector area and gives a detailed layout of the injector linac components. The cryogenic plant is not included in this picture, because the compressors will be located outside the building to sufficiently suppress mechanical vibrations.

ION SOURCES

The ion source complex located in the small annex will be able to deliver polarized and unpolarized H^- or D^- with an energy of 25 keV and pulses of up to 500 μs width at a repetition rate up to 2 Hz. Two ion sources are foreseen, a commercial multi-cusp source that is already delivered and the adapted CIPIOS source of Indiana University (IUCF). The contract for delivery has already been signed and also includes the electrostatic low energy beam-transport system. In addition, a collaboration with the INR-institute (Troitzk) was established to further improve the performance of this source. First results of this work, still obtained at IUCF, succeeded in significantly reducing the electron current emission and reached a much higher peak current as well as an increased pulse width. The product of these values will determine the number of ions that can be injected into COSY.

RFQS

The subsequent radio-frequency quadrupole (RFQ) section will be used to bunch the beam, accelerate the ions to 2.5 MeV/nucleon, and shape the phase space according to the requirements of the superconducting linac. As the velocity profiles are different, each ion species needs its own RFQ. The RFQs will be mounted alongside each other on a mechanical rail system to allow switching the ion species in less than one working day. Phase-space matching is achieved using 2 quadrupole doublets in combination with an rf-cavity, acting as a rebuncher [2]. The RFQs and the rebuncher cavity have been designed in collaboration with the University of Frankfurt/Main [3].

HALF-WAVE RESONATORS

The superconducting linac section comprises 11 unit cells plus an option for two further ones. Each cell is 1.7 m long. It contains at the outgoing end a quadrupole doublet for transverse focussing and a diagnostic box in between. The quadrupoles are designed for a maximum gradient of 45 T/m and will be operated in a pulsed mode to save electric power as well as space.

Although quarter-wave resonators have a proven record for the acceleration of heavy ions, the sensitivity of lighter ions to magnetic fields mandated the use of half-wave resonators. Four HWRs, made of ultra pure niobium and cooled close to 4 K, are grouped inside one cryostat without focusing elements. The resonators are arranged in two families. The first 20 resonators (β_{str}=0.11) operate at 160 MHz, and the following 24 resonators (β_{str}=0.2) operate at 320 MHz.

	160MHz	320MHz
β_{str}	0.11	0.2
R/Q	249	244
B_{peak}/E_{acc}	10.4	9.4
E_{peak}/E_{acc}	4.5	4

$$E_{acc} = \frac{\int_{-\infty}^{\infty} E(z)dz}{\beta\lambda}$$

Table 1: Characteristic data of the two HWR types with definition of E_{acc}.

The resonators have to provide very high acceleration gradients (6-8 MV/m) that are limited by the maximum magnetic fields tolerable inside the structure without quenching. To ensure reliable operation a design was chosen that limits the magnetic field to 80 mT in normal operation. The given acceleration gradient corresponds to 8 MV/m and will result in an average energy gain per resonator of slightly more than 1 MeV. The calculated distribution of the magnetic field in the resonator is shown in figure 2.

In close co-operation with industry, concepts for the manufacturing of such resonators have been developed. As no precedent for this type of rf-resonator exists, two companies have been selected to manufacture one prototype each. They use different manufacturing techniques for the critical 80 mT region, which ultimately will determine the performance. The final decision for the type of resonator to be used depends on the outcome of performance tests.

One of the cleaning ports at the resonator is used for rf-coupling. The coupler design has been developed in our

institute and the manufacturing of a prototype is in progress. The design takes into account the pulsed operation of the linac and tries to minimize cryogenic losses for this operational mode. The coupling strength can be adjusted for the acceleration of ions or rf-conditioning of the resonators. Each resonator will be driven individually in amplitude and phase by a commercial pulsed 4 kW solid state amplifier. A prototype of this amplifier has been successfully tested.

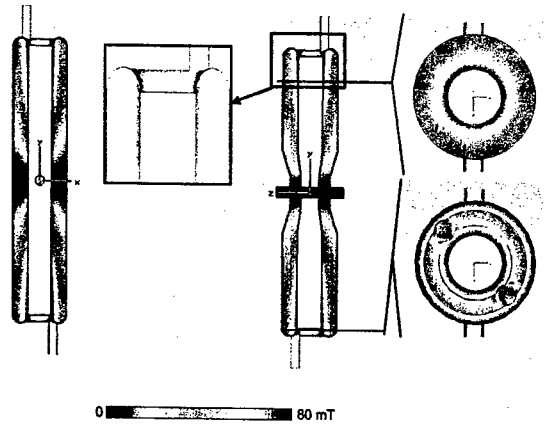

Figure 2: The magnetic field distributuion computed inside the cavity of the half-wave resonator. Sections perpendicular to (left) and in beam direction are shown with details of the most critical regions as indicated.

It is well known that superconducting resonators are very susceptible to microphonics due to their extremely narrow resonance curve. The mechanical vibration modes of the resonator have been studied with extensive simulations to arrive at a design with the necessary rf-stability for acceleration.

Another great concern in high performance super-conducting acceleration resonators for pulsed operation is the Lorentz force detuning. This effect becomes relevant as a result of the extremely high gradients reached inside such cavities, leading to a sizeable mechanical wall deformation and hence to a change of the resonance frequency well outside the allowed bandwidth. This change is proportional to the square of the peak rf-amplitude and has to be minimized by a careful choice of the structure. An extensive analysis has been carried out to establish the magnitude of this effect for the chosen design and for making appropriate design optimizations. The remaining detuning effect will be dealt with by a sophisticated adaptive feed-forward control system that employs piezo-actuators counteracting the deformation.

Also the development of an optimized cryostat is an issue of great concern as it affects to a high degree the operating costs of a superconducting injector. For a pulsed machine static losses and dynamic losses have to be carefully balanced. A further limitation exists in terms of the cryostat size, as the unit cell length may not exceed 1.7 m. This constraint is a consequence of the beam behaviour that can be expected from extensive beam dynamics simulation results. Protons and deuterons must move on stable trajectories in the required phase space during the entire acceleration process.

To conform to space requirements and at the same time keep thermal losses low, a design was developed for the cold-warm junctions of the beam ports of the cryostat, which had only a length of 60 mm. The calculated cryogenic loss of such a junction is only around 0.1 W. Figure 3 shows the results of the calculated thermal energy flow for such a cold-warm junction.

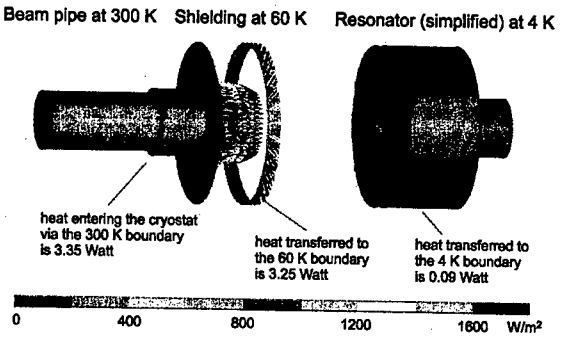

Figure 3: Calculated thermal energy flow for a cold-warm junction of the cryostat taking into account heat radiation and thermal conduction [4].

OUTLOOK

At the very end of the year 2002, due to unprecedented budget cuts imposed by the Federal Government, the Board of Directors of the Forschungszentrum Jülich has been left with no other choice but suspending the COSY-SCL project for at least two years. However, prototype work may proceed and first results can be expected during 2003/2004. The conviction that this new injector linac will be an important scientific gain for the COSY accelerator facility has not been diminished by this decision.

ACKNOWLEDGEMENT

The authors would like to thank especially A. Facco (INFN-LNL), A. Schempp (Univ. Frankfurt), K. W. Shepard (ANL) and S. O. Schriber (MSU) for fruitful discussions.

REFERENCES

[1] COSY-SCL Design Update, Internal Report, Forschungszentrum Juelich, March 2002 (http://www.fz-juelich.de/ikp/linac-public/)

[2] A. Lehrach, H. Jungwirth, R. Maier, R. Toelle, "Beam dynamic Calculations for the Superconducting Injector Linac", this conference

[3] K.-U. Kuehnel, A. Schempp, A. Schnase, R. Toelle, C. Welsch, "The RFQ-Injector for COSY-SCL", this conference

[4] H. Cords, "Berechnung der bereitzustellenden Kuehlleistung für den Kryostaten des geplanten LINAC zum Cooler Synchrotron COSY", Internal Report, FZJ-ZAT-378

THE ISAC-II UPGRADE AT TRIUMF - PROGRESS AND DEVELOPMENTS

R.E. Laxdal, G. Clark, G. Dutto, K. Fong, A. Mitra, Z.H. Peng, R. Poirier, W. Rawnsley, T. Ries, I. Sekachev, G. Stanford, TRIUMF*, 4004 Wesbrook Mall, Vancouver, Canada, V6T2A3

Abstract

TRIUMF is proceeding with a major upgrade to the ISAC project, ISAC-II, that includes the addition of 43 MV of heavy ion superconducting linear accelerator and an ECR charge state booster. An initial installation of 18 MV of mid beta cavities (β = 5.8%, 7.1%) is due for commissioning in 2005. The paper will describe the superconducting linac program at TRIUMF including the status of the production cavities, the design of the medium beta cryomodule and a summary of the activities of the SCRF laboratory.

1 INTRODUCTION

TRIUMF is now constructing an extension to the ISAC facility, ISAC-II, [1], to permit acceleration of radioactive ion beams up to energies of at least 6.5 MeV/u for masses up to 150. In brief the proposed acceleration scheme would use the existing ISAC RFQ (E = 150 keV/u) with the addition of an ECR charge state booster to achieve the required mass to charge ratio ($A/q \leq 30$) for masses up to 150. A new room temperature IH-DTL would accelerate the beam from the RFQ to 400 keV/u followed by a post-stripper heavy ion superconducting linac designed to accelerate ions of $A/q \leq 7$ to the final energy.

The superconducting linac is composed of two-gap, bulk niobium, quarter wave rf cavities, for acceleration, and superconducting solenoids, for periodic transverse focussing, housed in several cryomodules. The linac is grouped into low, medium and high beta sections corresponding to cavities with design velocities of β_o = 4.2%, β_o = 5.7, 7.1% and β_o = 10.4% respectively. The eight low beta cavities are housed in one long cryomodule with three solenoids interspersed between cavities. The twenty medium beta cavities are installed four per cryomodule in a total of five modules. Twenty high beta cavities are divided into two modules of six cavities and one module of eight cavities. Each of the medium and high beta cryomodules are equiped with one solenoid each.

Due to experimental pressure and budget limitations the installation of the linac has been grouped into three stages highlighted in Fig. 1. The initial Stage 0 to be completed in 2005 includes the installation of a transfer line from the ISAC DTL (E = 1.5 MeV/u) and the medium beta section to produce 18 MV of accelerating voltage for initial experiments. Stage 1 to be completed two years later includes the installation of the three high beta modules for a further 18 MV. The ISAC-II accelerator final Stage 2 is foreseen for 2010. The final energies expected for each stage are summarized in Fig. 2 with and without the inclusion of a secondary stripper before the medium beta section.

*TRIUMF receives funding via a contribution agreement through the National Research Council of Canada

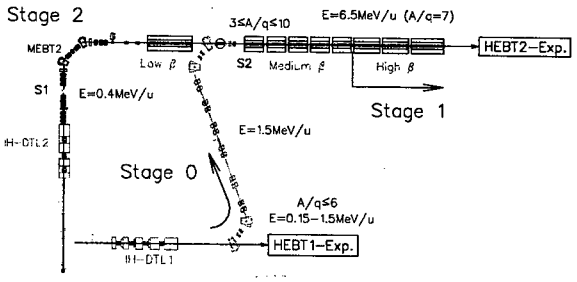

Figure 1: Stages 0, 1 and 2 for the ISAC-II upgrade.

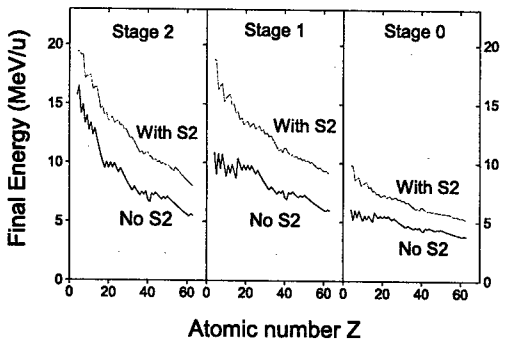

Figure 2: Final ion energy for Stages 0, 1 and 2.

A new building complete with linac vault, experimental areas, office and laboratory is now complete. Present studies are concentrating on design and development for the first stage installation.

2 BEAM DYNAMICS

Beam dynamics studies with realistic fields were done to optimize the high beta cavity design. Two cavity variants are considered.. One variant has identical transverse dimensions to the medium beta cavity but is designed as a 141 MHz cavity by shortening the overall length. In the other variant the cavity frequency is kept at 106 MHz but the cavity transverse dimensions are scaled to increase the beta from 7.1% to 10.4%. The quadrupole asymmetry in the accelerating fields [2] is somewhat larger in the high frequency case by virtue of the smaller inner conductor. A summary of the beam dynamics calculations is given in Fig. 3. The reduced quadrupole asymmetry in the low

0-7803-7738-9/03/$17.00 © 2003 IEEE

frequency cavity results in less asymmetry in the transverse envelope. However the transverse emittance is only marginally better.

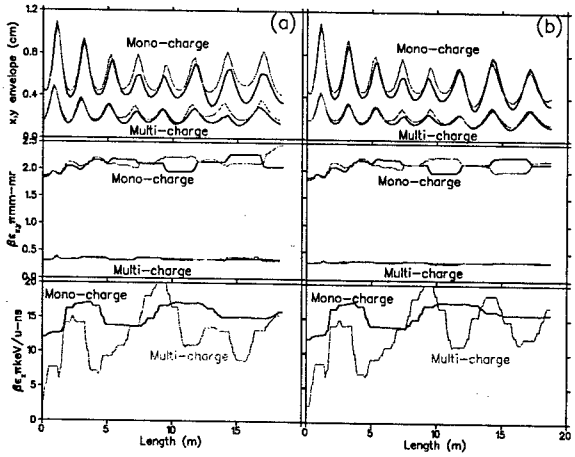

Figure 3: The transverse beam envelopes and the transverse and longitudinal emittances as a function of longitudinal position along the medium and high beta sections for (a) the 140MHz high beta variant and (b) the 106 MHz variant. In each case a single charge state beam with initial emittance of 1.8πmm-mr and 12πkeV/u-ns (ten times the expected emittances) is simulated. The large beam is used to characterize differences in the effective dynamic aperture of the two variants. Also shown is a multi-charge beam ($\Delta Q/Q = \pm 5\%$) with initial emittances of 0.3πmm-mr and $2.\pi$keV/u-ns.

3 HARDWARE AND DEVELOPMENT

Work is ongoing on several fronts with the goal of realizing beam delivery in 2005. The first major milestone is the cold test of a completed medium beta cryomodule in late 2003. An SCRF lab is set up in a neighbouring facility where cold tests are on-going at the rate of one per month. A summary of the present developments are given below.

3.1 Superconducting RF Systems

The ISAC-II medium beta design gradient is 6 MV/m giving a stored energy of $U_o = 3.2$ J. The natural bandwidth of ± 0.1 Hz is broadened by overcoupling. The required forward power on resonance is given by $P_f(W) \simeq \pi U_o \Delta f_{\frac{1}{2}}$ for overcoupled systems. The goal for the ISAC-II cavity tuner is to achieve fine (1 Hz) tuning capability with a response time to control fast helium pressure fluctuations allowing stable operation within a bandwidth of $\Delta f_{\frac{1}{2}} = 20$ Hz. This requires an rf system capable of delivering $P_f = 200$ W at the cavity. A set of four rack mounted 1 kW amplifiers with built in circulator and common driver supply have been acquired for the prototype cryomodule test for evaluation.

Rf Controls The RF Control system [3] for the superconducting cavities is a hybrid analogue/digital system. Each system consists of a self-excited feedback loop with phase-locked loops for phase and frequency stabilization. Amplitude and phase regulations, as well as tuning control, are performed using digital signal processors. Special pulsing circuitry is incorporated into the system to facilitate 'punching' through multipactoring. We have demonstrated fixed amplitude and phase regulation at the design gradient with the phase error used to drive the mechanical tuner to maintain cavity frequency.

LN2 Cooled Coupling Loop Initial cavity studies at TRIUMF were done with a coupling loop designed at INFN-Legnaro suitable for operation with lower gradients and lower forward power. Tests at higher power indicate an unacceptably large amount of power is deposited at 4 °K. A new coupler is being developed with the goal to reduce the helium load to no more than 1 W at the design gradient of 6 MV/m with $P_f = 200$ W. The coupler has a stainless steel body for thermal isolation and a copper outer conductor and rf feed line cooled with LN2.

Tuning Plate The tuning plate consists of 1 mm thick RRR Niobium sheet of 240 mm diameter fixed to the bottom Niobium flange. To increase flexibility the plate is spun with a single 'oil-can' convolution and milled with eight radial 1 mm slots. The performance of the slotted plate compares well to flat plate performance in rf cold tests (see Fig. 4). The plate is capable of allowing ± 20kHz (± 3 mm) of tuning range.

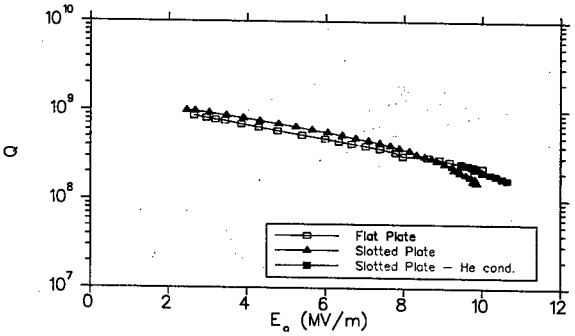

Figure 4: RF cold test results comparing cavity performance with a flat tuner plate and the new slotted plate.

Mechanical Tuner A prototype mechanical tuner[4] is now being tested. The tuning plate is actuated by a vertically mounted permanent magnet linear servo motor, at the top of the cryostat, using a 'zero backlash' lever and push rod configuration through a bellows feed-through. The system resolution at the tuner plate center is $\sim 0.055\mu$m (0.3 Hz). The demonstrated dynamic and coarse range of the tuner are ± 4 kHz and 33 kHz respectively. The tuner on-line performance is measured by altering the cavity frequency by forced variations of the helium pressure. The

tuner responds accurately to the pressure variation with a resolution better than 0.1μm (0.6 Hz)[4]. The demonstrated response bandwidth is presently limited to 20 Hz by a mechanical resonance.

Cavities A prototype of the $\beta_o = 7.1\%$ cavity designed in a collaboration with INFN-LNL, is routinely used for SCRF development tests. The niobium sub-assemblies of the twenty cavities of the medium beta section composed of eight $\beta_o = 5.7\%$ and twelve $\beta_o = 7.1\%$ cavities, are being fabricated in industry for completion in Aug. 2003. We have taken receipt of an initial series of four of the 7.1% cavities after chemical polishing at CERN. The cavities are being outfitted with stainless steel damper assemblies and pre-cool tubes in preparation for rf tests to begin later this month.

3.2 *Medium Beta Cryomodule*

A prototype of the medium beta cryomodule Fig. 5, is now in the detail design and fabrication phase. The vacuum tank consists of a stainless steel rectangular box and lid. All services and feedthroughs are located on the lid. Copper sheet cooled with $\simeq$ 36 m of LN2 piping serve as a heat shield. Cavities and solenoids are suspended from a common support frame itself suspended from the tank lid. Pre-cool of components is done by delivering cold helium vapour to the bottom of each major component through a supply manifold and 3/16" OD stainless steel tubing internal to the helium reservoir. Magnetic shielding in the form of high μ sheet is suspended between the warm wall and the cold shield. Thin diagnostic boxes are positioned at waists in the transverse envelopes between cryomodules.

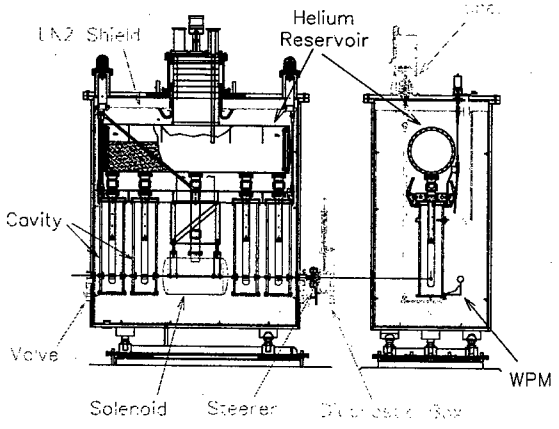

Figure 5: The ISAC-II prototype medium beta cryomodule.

Solenoids Focusing in the SC LINAC is provided by 9 Tesla 26 mm diameter bore SC solenoids of lengths 16, 34 and 45 cm corresponding to the low, medium and high beta cryomodules respectively. The solenoids are equiped with bucking coils to actively limit the fringe field in adjacent cavities to less than 0.1 T to prevent reduction in cavity performance. The magnets are mounted in a liquid Helium vessel fed from the common Helium header. An order for five medium beta and two high beta solenoids placed in industry has been delayed as the company has gone into receivership. The prototype magnet was obtained from the company and will be completed and tested at TRIUMF. A contract for the remaining seven magnets has just been let with another supplier.

Alignment The cavities must be aligned to within 0.4 mm and the solenoid to 0.2 mm. TRIUMF is developing a stretched wire alignment system based on the TESLA design[5]. Wire position monitors (WPM), each consisting of four striplines are attached to the cavities and solenoid by off-center alignment jigs. A wire running parallel to the beam axis and through the monitors carries an rf signal at 215 MHz. A Bergoz BPM card converts the rf signals from one monitor into DC X and Y signals while a multiplexer with GaAs switches scans through the monitors. A National Instruments ADC and I/O card controls the multiplexer and reads the DC signals.

3.3 *Charge State Booster*

A 14 GHz Phoenix source charge state booster is being assembled on a test stand at TRIUMF. The test stand includes an existing 1^+ ion source, beam-line optics, diagnostics for measuring conversion efficiency and emittance and an analyzing magnet. Development will begin in Sept. and last for one year before the CSB will be installed in the low energy beam line upstream of the RFQ for commissioning and production.

3.4 *Refrigeration*

The ISAC-II refrigeration system is now specified for tender. An order for the first phase will be awarded in June 2003 for commissioning by the end of 2004. A second equivalent order to cover the staged installation of ISAC-II is expected in about three years. Each phase calls for a 500 W class machine. Assuming an active rf load of 8 W/cavity (7 W rf surfaces, 1 W coupling loop) the expected linac load at 4.5 K exclusive of transfer lines is 290 W. The peak liquification required for a cryomodule cool down and fill of duration six hours is $\sim$ 5.2 gm/sec.

4 REFERENCES

[1] R.E. Laxdal, *ISAC-I and ISAC-II at TRIUMF: Achieved Performance and New Construction*, LINAC2002, Korea.

[2] M. Pasini, *et al*, *Beam Dynamics Studies on the ISAC-II Post Accelerator at TRIUMF*, EPAC2002, Paris.

[3] K. Fong, *et al*, *RF Control System for ISAC II Superconducting Cavities*, this conference.

[4] T. Ries, *et al*, *A Mechanical Tuner for the ISAC-II Quarter Wave Superconducting Cavities*, this conference.

[5] D. Giove, *et al*, *A Wire Position Monitor (WPM) System to Control the Cold Mass Movements Inside the TRF Cryomodule*, PAC 1997, pp. 3657-3659.

2 MW UPGRADE OF THE FERMILAB MAIN INJECTOR*

W. Chou# for the Proton Driver Study II Group, FNAL, Batavia, IL 60510, USA

Abstract

In January 2002, the Fermilab Director initiated a design study for a high average power, modest energy proton facility. An intensity upgrade to Fermilab's 120-GeV Main Injector (MI) represents an attractive concept for such a facility, which would leverage existing beam lines and experimental areas and would greatly enhance physics opportunities at Fermilab and in the U.S. With a Proton Driver replacing the present Booster, the beam intensity of the MI is expected to be increased by a factor of five. Accompanied by a shorter cycle, the beam power would reach 2 MW. This would make the MI a more powerful machine than the SNS or the J-PARC. Moreover, the high beam energy (120 GeV) and tunable energy range (8 - 120 GeV) would make it a unique high power proton facility. The upgrade study has been completed and published [1]. This paper gives a summary report.

INTRODUCTION

On January 10, 2002, the Fermilab Director issued a charge requesting a design report that would consist of three parts:

- An 8 GeV linac based Proton Driver;
- An 8 GeV synchrotron based Proton Driver;
- A 2 MW upgrade of the Main Injector.

About 2/3 of the report has been completed and published [1]. This paper is a summary of the MI upgrade part. For details the readers are referred to Part B of Ref. [1].

In the present Fermilab accelerator complex, which consists of two straight machines, six rings and a number of beam lines, the bottleneck that limits the beam intensity is the Booster. It is a 30-year-old machine and has never been upgraded. The machines on both sides of the Booster – the Linac in the upstream and the Main Injector in the downstream – can deliver or receive more particles than they do now. However, the number of protons per cycle from the Booster is limited to about 5×10^{12}. Otherwise the beam loss would become prohibitive. When the Booster is replaced by a new machine, dubbed the Proton Driver, this bottleneck would be eliminated. Consequently the beam intensity in the Main Injector would be greatly increased.

UPGRADE GOALS

The goals of this upgrade study are as follows:

- Increase beam intensity by a factor of 5;
- Reduce cycle time by 20%;
- Increase beam power by a factor of 6.

The main parameters are listed in Table 1. As a comparison, the present parameters are also listed. The extraction energy is tunable in the range from 8 to 120 GeV. At lower energy, the cycle time will be shorter. Therefore, the beam power would remain about the same and only be slightly reduced due to the constant "overhead" part of the cycle (e.g., injection front porch, parabola at the beginning of the acceleration, flat top, and magnet reset at the end of the cycle, see Fig. 4 below). The MI cycle time is a multiple of the Booster cycle, which is 66.7 ms (15 Hz). To accelerate 6 Booster batches to 120 GeV presently takes 28 Booster cycles. This would be shortened to 23 Booster cycles in the upgrade.

Table 1: Main Injector Parameters

	Present	Upgrade
Injection energy (GeV)	8	8
Extraction energy (GeV)	120	8-120
Protons per MI cycle (10^{13})	3	15
Cycle time at 120 GeV (s)	1.867	1.533
Beam power (MW)	0.3	1.9

BEAM DYNAMICS ISSUES

Transition Crossing

One main concern is possible particle loss and emittance dilution when an intense proton beam crosses the transition, which occurs at $\gamma = \gamma_T = 21.6$. A series of simulations using the code ESME were carried out. It seemed that with a γ_T-jump system, which will be described below, this problem can be resolved. Figure 1 shows two cases of a proton bunch after the transition, one without and another with γ_T-jump. The latter fit well in the RF bucket and has no losses.

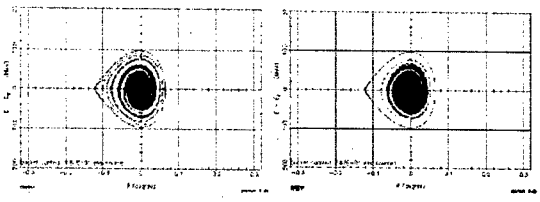

Figure 1: ESME simulation of a proton bunch in the longitudinal phase space after the transition. Left: without γ_T-jump. Right: with γ_T-jump.

Space Charge and Beam Stability

The coherent and incoherent betatron tune shift from space charge and image charge forces throughout the cycle were computed. The single bunch longitudinal microwave instability was also calculated using the Keil-Schnell criterion. The results are shown in Fig. 2. The tune shift (maximum < -0.2) is tolerable. The MI impedance budget $Z_{||}/n$ is 1.6 ohm [2], which is below the instability threshold except during the transition crossing, which will be taken care of by γ_T-jump. Therefore, they should not be major concerns.

0-7803-7738-9/03/$17.00 © 2003 IEEE

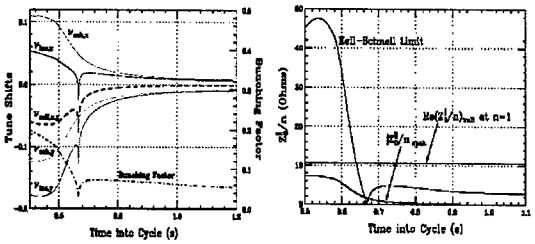

Figure 2: Left: Betatron tune shift during the cycle. Right: Instability limit during the cycle; the lowest point is at transition crossing.

TECHNICAL SYSTEMS UPGRADE

In order for the Main Injector to operate at 2 MW, most of the technical systems need to be upgraded. Some of these upgrades are major, some moderate. Here is an overview.

RF System

To accelerate 5 times more particles in a shorter period, the RF system requires a major upgrade. The number of cavities needs to be increased from 18 to 22. The number of power amplifier of each cavity also needs to be doubled from one to two, each capable of supplying approximately 400 kW of peak RF power. The second power amplifier will be installed in place of the existing cavity balancing top hat capacitor, as shown in Fig. 3.

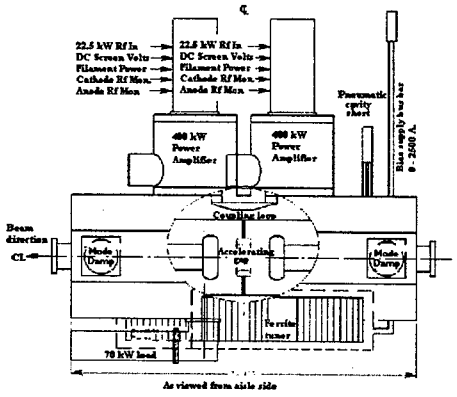

Figure 3: Twin power amplifiers on an RF cavity.

Magnet

The MI magnets will function adequately in the upgrade and modifications are unnecessary.

Power Supplies

A shorter cycle requires an increase of the maximum ramp rate from 240 GeV/s to 305 GeV/s. A modest upgrade is needed. Fig. 4 shows the voltage and current for a 1.5 sec cycle.

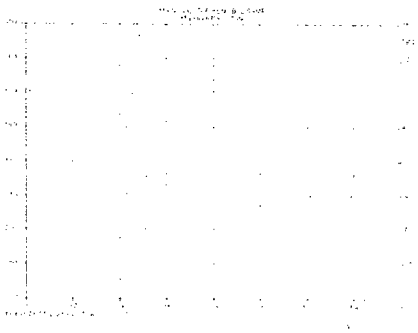

Figure 4: Magnet power supply voltage (green) and current (red).

Large Aperture Quadrupoles

In the Main Injector, a physical aperture bottleneck is at the quadrupoles upstream of the Lambertson magnets in several straight sections: MI 10, 30, 40, 52, 60 and 62. In order to reduce beam loss at these locations, large aperture quads need to be installed replacing the regular quads. The aperture will be increased from 83.48 mm to 102.24 mm, i.e., 4 inches.

Gamma-t Jump System

Presently there is no γ_T-jump system in the machine. But this system will be necessary in the upgrade. A description of this system can be found in Ref. [3]. It is a so-called first order jump system, making use of the zero-dispersion straight sections. Its main advantage is small and localized perturbation to the lattice when the γ_T-jump quads are activated. The system consists of 8 sets of pulsed quadrupole triplets. Each triplet has two quads in the arc and one of twice integrated strength in the straight section, with a phase advance of π between each quadrupole. The power supply uses a GTO as the fast switch and a resonant circuit with a 1 kHz resonant frequency. The beam pipe is made of Inconel 718.

This system can provide a $\Delta\gamma_T$ from +1 to -1 within 0.5 ms. It gives a jump rate of 4000 1/s, about 17 times faster than the normal ramp rate. Fig. 5 shows the quad current during the jump. The amplitude is adjustable. Fig. 6 shows the layout of the 8 triplets around the ring.

Figure 5: Magnet current of the pulsed γ_T-jump quads.

*Work supported by the Universities Research Association, Inc. under contract No. DE-AC02-76CH03000 with the U.S. Dept. of Energy.
#chou@fnal.gov

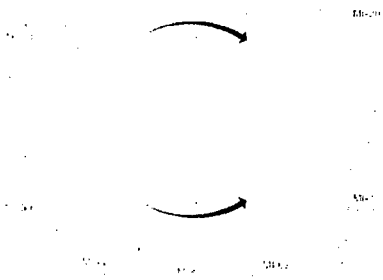

Figure 6: Layout of 8 γ_T-jump triplets. Green indicates the arcs, white the straight sections.

Radiation Shielding and Collimation

The shielding of the MI appears to be adequate for the upgrade. However, a collimation system is required in order to minimize the uncontrolled beam loss in the machine for reducing residual radioactivity so that hands-on maintenance can be performed. This system will be installed in MI 30. Fig. 7 illustrates a collimator.

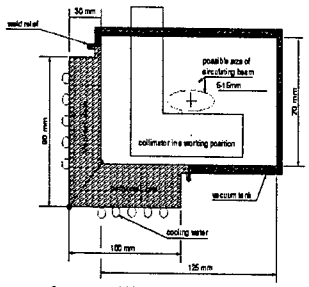

Figure 7: Secondary collimator cross-section.

Kickers

The MI beam pipe has a vertical aperture of 2-inch everywhere except at the kickers, which is 1.3-inch. In order to eliminate this bottleneck, the kicker aperture will be enlarged. Some kicker magnets also need to be rebuilt.

Abort System

With a modest upgrade, the present beam dump at MI 40 can absorb five times more protons. Fig. 8 shows the temperature rise of the abort dump.

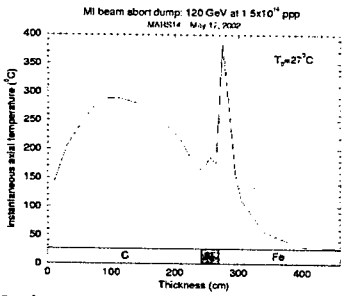

Figure 8: Maximum instantaneous temperature on the beam axis in the abort dump simulated by MARS.

Passive damper and active feedback

To suppress coupled bunch instabilities, both a passive damper and active feedback are needed. The former places nonlinear lossy materials (e.g., a special ferrite of which the loss parameter μ" is frequency dependent) in the RF cavity to damp the higher order modes (HOMs) while leaving the fundamental mode unaffected. The present longitudinal and transverse feedback systems can be used but need improvement.

Mechanical and Utility

The cooling capacity for magnets and power supplies appears to be sufficient in this upgrade. But the cooling system capacity for the RF system and cavities need to be doubled.

NuMI Beam Line

A $110M beam line for the neutrino experiment NuMI is under construction at Fermilab. It will use the protons from the MI. An upgraded MI would greatly enhance the physics potential of NuMI. To cope with 2 MW beam power, the shielding and cooling in the target hall, decay pipe and hadron absorber need to be upgraded. The ground water problem is a concern but there is a reasonable solution (see Ch. 21 of Ref. [1]).

COST ESTIMATE

The cost estimate was done using a bottom-up method. Namely, the cost of each system upgrade was estimated by the engineers in the corresponding departments. The total upgrade cost is about $36 M, including EDIA.

There are two possible ways to implement the MI upgrade. It can be done as a single "all-included" Fermilab project. Or the upgrade can be accomplished through a series of accelerator improvement projects (AIPs).

ACKNOWLEDGEMENT

A group of accelerator physicists and engineers from Fermilab's Beams Division, Technical Division, and FESS and ES&H sections contributed to this study. This paper is a report on behalf of this study group. The author expresses his thanks to them for their commitment and contributions to this study.

REFERENCES

[1] "Proton Driver Study II, Part 1," edited by G.W. Foster, W. Chou and E. Malamud, FERMILAB-TM-2169 (May 2002). Also on the web: http://www-bd.fnal.gov/pdriver/8GEV/

[2] W. Chou, "Intensity limitations in Fermilab Main Injector," PAC 1997 Proceedings, pp. 991-993.

[3] W. Chou et al., "Design of a gamma-t jump system for Fermilab Main Injector," PAC 1997 Proceedings, pp. 994-996.

MACHINE PROTECTION STRATEGIES FOR HIGH POWER ACCELERATORS*

C. Sibley, SNS - ORNL, Oak Ridge, TN 37830, USA

Abstract

The Machine Protection System Requirements for a number of accelerators have been reviewed. The specific requirements vary depending on the type of machine, beam power, pulse length, etc. Some system concepts are common to a number of accelerators and these systems will be discussed. The Machine Protection System (MPS) must protect beam apertures and insertable devices from damage, minimize radiation produced by the beam (ALARA) for hands on maintenance, and shut down the beam when beam-on-target parameters drift outside specifications. MPS systems should be used as an Accelerator diagnostic. MPS can trigger data acquisition when a fault occurs, and start post mortem applications automatically. Tight integration with timing and other systems allows automatic recovery from beam faults.

* SNS is managed by UT-Battelle, LLC, under contract DE-AC05-00OR22725 for the U.S. Department of Energy

INTRODUCTION

Machine protection systems have evolved from simple interlock systems to complex systems combining slow interlocks, fast interlocks to inhibit beam or trigger abort sequences, and sequences for automatically returning the accelerator to normal operation. MPS has to be fully integrated with global timing systems, adjacent MPS systems, beam diagnostics systems, RF systems, Control Systems, and others. Additionally, most new systems involve post mortem analysis to help sift through Gigabytes of data and pinpoint the cause of a failure or cause of drifting beam optics. High availability requirements, over 95% for SNS, dictate automation of recovery processes after an MPS fault.

In this paper we will discuss the role of MPS in:

1. Protecting the Machine
2. Protecting the Beam
3. Providing the Evidence
4. High Power Target protection; and
5. Assisting operations

PROTECT THE MACHINE

New accelerator facilities will have unprecedented beam power and beam power densities. The challenges presented depend on accelerator type, particle type, peak currents, maximum beam energy, etc. Spallation sources run loss-limited with high peak and average current on target. Linear colliders have very high current densities where a single errant pulse can cause considerable damage. Large hadron colliders have large stored energies in both beam and superconducting systems, both of which can damage beamline components and superconducting magnets. X-ray machines can damage the vacuum system by slight misalignments in wigglers, etc.

SNS will run in a loss-limited mode. Uncontrolled beam loss specifications are less than 1 W/m, or 10^{-4}. Collimation systems are designed to intercept beam in the linac where high losses are expected, or for halo cleaning. The total uncontrolled beam loss [2] in the SNS accumulator ring is compared with several other high current rings in Table 1. Some rings show large losses, but the injection rates are slow so the losses are allowable. At PSR the 0.3 % becomes significant due to the high-energy injection and 20 Hz operation. The beam loss goal for the SNS ring is very low at 0.01% but this is required for hands-on maintenance and availability reasons.

Table 1. Comparison of several rings, energies, peak currents, and beam loss.
(1) Accumulator rings, others are Rapid Cycling Synchrotrons
(2) Septum injection. Others are foil.

Machine	Einj	Eext	# Turns	Typ Ppp	Loss (%)
ISIS	70	800	300	1.6e13	10
PSR (1)	800	800	2300	3.1e13	0.3
KEK-PSB	40	500	50	2.0e12	10
FNAL-B	400	8000	15	2.0e12	30
AGS-B	200	1900	200	1.5e13	28
IPNS	50	450	140	3.0e12	17
CERN-PSB (2)	50	1400	15per ring	1.0e13	50
SNS (1)	1000	1000	1060	1.5e14	0.01

Neutron sources such as SNS, ISIS, and LANSCE use H^- sources to produce high-accumulated beam currents to strike a target in a short amount of time. SNS for instance accelerates 1060 turns at peak currents up to 38 ma. The H^- ions are stripped as they are injected into the accumulator ring, building up to 50 Amps peak. Extraction kickers are fired in the beam gap to steer the proton beam down the extraction line to a liquid mercury target to produce neutrons through spallation.

Linear colliders require very small beam size and high peak current to meet luminosity requirements. A single errant pulse will cause component damage if extracted from the damping ring. Recovery from faults requires the system to drop back in state and use pilot pulses. The systems have to measure pilot beams with sufficient accuracy, stability, and resolution for feedback systems to work properly. Pulse-to-pulse monitoring of beam parameters requires control system latencies much less than the beam repetition rate. Collimator design is critical

0-7803-7738-9/03/$17.00 © 2003 IEEE

to intercept the high power pulsed beam [3]. Use of the control system to monitor the properties of the beam pulse-to-pulse implies the control system is a "pulsed" control system.

Hadron colliders have very high stored energy in the beam and the superconducting magnets, 13 GJ per sector for the LHC [4]. Beam losses can cause damage due to radiation and thermal effects. The stored energy in the beam is high enough to damage any component in the ring if the beam is not cleanly aborted. Beam abort systems must dump the beam before the beam trajectory changes and inhibit beam until the quench completes and the magnetic field is restored. Recovery from beam dumps can take a couple of hours. Recovery from magnet system quenches can take several times longer. Light sources also have high currents and small beams. Besides damage from the beam, upwards of 10 kW in the x-ray beam can damage the vacuum chambers. Beam diagnostics are thus required to monitor the e+/- beam position and X-ray beam. At the APS for instance, beam position monitors average 32 turns of beam position data on a turn-by-turn basis and will abort the beam in 300 usec by disabling ring RF if measurements indicate beam position errors.

Fast Machine Protection Inputs

Beam Diagnostics are the main input to fast MPS systems. Beam loss monitors detect beam loss that can cause radiation and thermal damage to equipment in the beam line tunnels. Component damage depends on the beam energy, beam current, and current density.

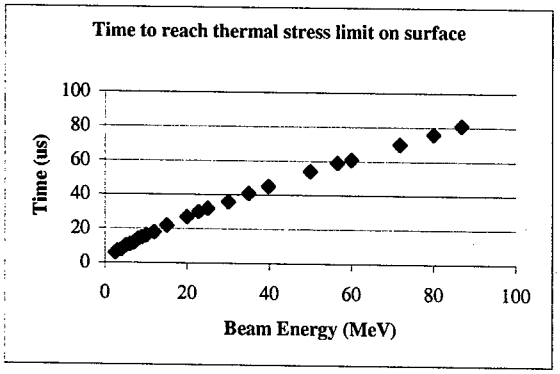

Figure 2. Time to reach the thermal stress limit in copper verses beam energy.

For SNS, damage will occur faster at lower energies [5]. Figure 2 shows the time to reach the thermal stress limit for copper assuming $\sigma_x = \sigma_y = 0.2$ cm, I = 36 ma, J = 62 J/gm (energy density). The time to reach the thermal stress limit at the bragg peak is quicker, however the peak energy deposition depth is dependant on beam energy and quickly goes beyond the thickness of the copper walls.

For low energy beams, differential current measurements are desired for fast beam loss detection [6]. A system using toroidal transformers was designed for the Tesla Test facility to provide a fast beam shutoff when the average loss exceeds 0.8 μa over the nominal 64 μa nominal machine current.

CW accelerators such as CEBAF [7] use beam current monitors for beam loss detection and beam current limits. The current monitoring system provides three functions:

1. Fault if beam loss exceeds loss limit.
2. Fault if current exceeds limit for an experimental hall.
3. Fault if current exceeds beam off threshold for multi end station operation.

The 2nd generation machine protection Beam Current Monitor / Accounting system was designed specifically for machine protection.

At higher beam energies, beam loss monitors are preferred. There are many publications available [8] on the topic of beam loss monitors. MPS systems typically receive faults from peak loss (within a pulse), integrated loss for a pulse, or integrated loss over many injection cycles or turns. Machines such as SNS, ISIS and TTF run loss-limited and need to keep losses below 10^{-4} for hands on maintenance. Superconducting accelerators such as the LHC will be affected by beam loss at a fraction of 10^{-8} of the beam [9]. Systems like the LHC use loss monitors for protection of the beam as well as protection of the machine. A beam dump due to a quench takes much longer to recover from than a beam abort due to increased losses.

Beam Position Monitors (BPM) are crucial for MPS systems in storage rings and linear colliders. Storage rings average beam position over a number of turns to determine if the closed orbit is exceeding some threshold. Beam abort is initiated to protect ring components from damage, or vacuum systems from damage due to mis-steered X-ray beams. In new collider designs, a pilot beam is used to verify beam optics for full power beam. The beam position monitors must have sufficient sensitivity to monitor these low intensity beams to accurately predict if the high power beam will be accelerated without damaging beam line components.

Machine operation and commissioning can continue without beam diagnostics however MPS function could be compromised. Systems that will be used for MPS should be designed with those goals from the beginning. Beam diagnostics for machine protection should be designed with some or all of the following system requirements, dependant on machine:

- Fail Safe Design, detects internal faults, cable connection status, power supply faults, etc.
- Remote self test and calibration capability, interpulse test functions (Force a fault between pulses)
- Controlled access to threshold settings
- Heartbeat from timing system
- Machine / beam mode aware
- Circular buffers, waveforms on demand
- Pulse-to-pulse or turn-by-turn (Deterministic)

As stated before, SNS will accumulate 1060 turns in the ring before extraction. There is a 250 nsec gap in the beam to allow the kicker system to ramp to full power. Any beam in the gap will be uncontrolled loss in the ring and extraction line. The goal is to keep the gap clean to

less than $1x10^{-4}$ of the injected current. With up to 50 amps circulating, this is a measurement range of greater than $1x10^{6}$. Several methods are being investigated. A beam-in-gap kicker will kick beam onto a collimator monitored by a fast loss monitor. A new technique used to monitor low currents for beam-in-gap measurements is the laser profile monitor, Figure 3 [10]. Electrons are measured on a collector after being deflected by a small dipole magnet.

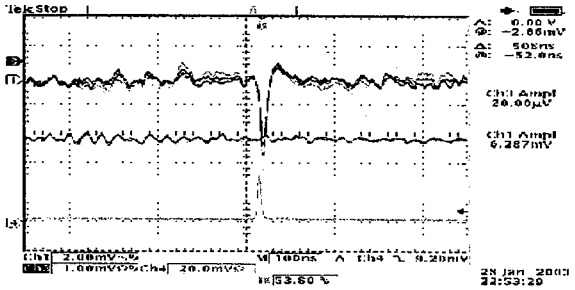

Figure 3. Beam-in-Gap measurement made by a fast laser pulse. The measurement above show about 60 ua of beam measured in the beam tail. Improvements in the amplifier design should bring the resolution below the 10^{-4} level.

Types of Machine Protection

A survey of several accelerators of different types show the following types of Machine Protection Systems (not all accelerators have all the systems) are implemented or are being designed. The names vary depending on the facility. Larger accelerators have several MPS systems, one per machine section. These need to be integrated with each other and other systems at a high level.

1. Average Machine Protection
2. Fast Protect
3. Beam Accounting
4. Maximum Allowable Intrapulse Difference (MAID) (and prepulse)

Average Machine Protection

The Average Machine Protection uses slow inputs from vacuum systems, power supply systems, etc for slow interlock inputs. Faults due to these inputs will cause damage due to mis-steering, defocusing, or intercepting the beam and the beam is inhibited until the fault is cleared. Systems will either mask these types of inputs from beam lines not in use using a Machine Mode indication, or the various beam lines are a subsystem in themselves, and are summed in a master MPS system. Some facilities allow masking of these under special circumstances, such as machine commissioning, BPM studies, beam-based alignment, etc. Other facilities hard code these inputs into PLC logic, FPGA logic or software and require repairs before the machine can be brought on line.

Fast Protect Systems

Fast Protect systems fall into three categories, turning off the beam as soon as possible, prohibiting beam from being injected to the next part of the accelerator or aborting the beam from a storage / accumulator ring. For long pulse accelerators, the mechanism is turning off the source. Electron storage rings may turn off the ring RF, allowing the beam to coast inward to collimators in the ring as the beam loses energy due to synchrotron radiation. Large hadron accelerators use fast, high reliable kicker systems to kick the beam out of the ring to a beam dump designed to handle the high power in the beam. Linear colliders must prevent an errant pulse from being launched into the accelerator, as an errant beam will cause damage and there is no way to prevent damage once the pulse is injected, because the monitoring signal can not catch up to the beam and abort systems.

SNS has two fast protect systems, Fast Protect Latched (FPL) and Fast Protect Auto Reset (FPAR). The hardware is the same; the FPGA logic is slightly different. Both have a maximum shutdown time of 20 usec, although it is faster closer to the source due to fewer IC propagation delays and shorter cable distances. There are two bypass mechanisms for the MPS hardware: software masks initiated by an operator (if enabled using hardware jumpers) and beam/machine mode masking through the timing system. Beam/machine modes are broadcast on the Real Time Data Link (RTDL) and will automatically bypass certain MPS inputs for diagnostic pulses to allow intrusive diagnostics to operate without operator intervention. The mode masks are downloaded during initialization, and verified periodically during operation. The beam/machine mode is encoded three ways in a 24-bit frame. There is an 8 bit CRC check of each frame. In addition, there is a 24-bit CRC frame for all RTDL frames broadcast in a cycle. The MPS hardware also uses the CYCLE_START event and the RTDL_VALID events for heartbeats indicating the timing system is healthy and stale modes are not used. The probability of detecting an erroneous mode broadcast on the RTDL using the two CRC checks, and encoding the data in three ways is better than 99.999994% [11].

Fast protect systems for linear colliders prevent errant beams from being launched into the accelerator. Once a pulse is launched, there is little to be done to protect the machine, except to design collimation systems to handle the beam. This is very difficult to impossible so some engineering is under way to design "sacrificial" collimator systems.

Beam Loss monitors at HERA often have the last chance to recognize a doomed beam and abort it safely before uncontrolled and possibly damaging losses occur.

Beam Accounting

Beam Current Accounting and Beam Loss Accounting are required for monitoring integrated losses and warning operations when loss limits are approached. Some systems will shut down the machine as the limits are reached. Beam loss and accounting are used to stop beam-induced radiation damage before it occurs. Some machines like CEBAF at JLAB have beam loss accounting to limit power to the various experimental halls. These limits are set by power limit requirements for

the experimental devices (spectrometers) and the beam dumps in each experimental hall.

Beam Loss monitors and beam current monitors are used in these systems. Beam loss monitors can pinpoint the beam loss better than current monitors, but calibration for absolute losses is harder due to the particle types, equipment shielding the detector, etc. Beam current monitors can be calibrated to a high degree of accuracy [CEBAF, TTF], but they can also be "fooled" by opposite charged particles or beam spray after beam loss.

Maximum Allowable Interpulse Difference (MAID)

MAID was originally designed to monitor orbit stability using BPM's and abort the beam if the orbit starts drifting outside allowable limits. In this case it is a turn-by-turn difference rather than an interpulse difference. It was planned for the Tevatron [12] but not really used. Complexes such as PEPII are using the MAID principle.

MAID requires previous pulsed data to be verified from the accelerator physics point of view-- that is the data fits within an ellipse defined by the beam envelope in the accelerator. This applies to beam position monitors, beam loss monitors and device control monitors [13]. Just prior to injection all systems that can change the beam trajectory or beam energy are verified to be operational. This prepulse system gives a final beam permit signal to allow beam. Beam is also monitored in damping rings or injection systems that will abort errant beams before being injected.

For accelerators depending on MAID, any intermittent faults require the injected beam to be brought to a low power state in the injection sequence. In order for full beam to proceed, an automated sequence to bring the beam back on line should be initiated. These procedures require integration of a number of systems, MPS between injectors, damping rings and accelerators, timing system sequences, control system feedback loops, feed forward algorithms, and timing systems. The complexity speaks for itself.

PROTECT THE BEAM (AVAILABILITY)

Protecting the beam is a goal for all accelerators desiring high beam availability. SNS goals are >95% availability at full power for production beam. Beam down time is increased unnecessarily when MPS provides false trips, or input devices provide nuisance trips. The MTBF decreases as the number of MPS inputs increases. For instance, the MTBF for inputs to the LHC have to exceed 200 years to meet the goal of less than 1 trip per 2 weeks.

Experience at LANSCE and the PSR have determined that losses of 1 W/m will allow hands-on accelerator maintenance (~100mR/hr at 1 foot), with transverse losses primarily at quadrupoles where the beta-max occurs [14]. Meeting the ALARA limits for hands-on maintenance will increase machine availability by reducing the time to repair.

Software masking of inputs allows components in the down slope of a bathtub curve to be identified during the commissioning process and masked out to increase beam time. If the component or device is not deemed critical for steering and focusing, it can be masked during operation until a suitable time for repair occurs.

PROVIDE THE EVIDENCE

MPS Faults should post Abort or Fault events locally or globally through the timing system. Control system devices, beam diagnostics, and pulse systems use these triggers to freeze circular buffers and provide waveforms of the interrupted pulse. Post mortem analysis will identify first faults using timestamps from MPS input faults.

Using a correlator tool, such as the XAL Correlator package developed by the AP group at SNS, faults can easily be captured and sorted by time (figure 4). Using the hierarchy provided, these faults can trigger capture of waveforms and slow data buffers depending on the location and type of the machine fault. This will help reduce data sorting from Gigabytes to Megabytes.

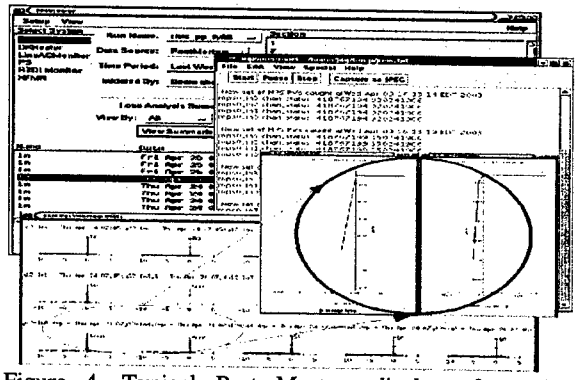

Figure 4. Typical Post Mortem displays for quick identification of MPS faults and root analysis. (RHIC Example)

The application will bring up the data post processed by:

Event	User Pulse	Sub System
Time Stamp	MPS Fault	Peak Loss
Timing Event	System	Data Excursion

Standard displays built into XAL include waterfall, XY correlator, 2d and 3d, Strip charts, phase space parameters, and difference from model, yesterdays beam, etc.

HIGH POWER TARGET PROTECTION

At SNS, the target requirements for errant pulses is less than 2 full power pulses for beam power within the nominal spot size (50% beam power outside of 200 mm x 70 mm) and for peak single pulse current density < 3.2×10^{16} protons/m^2.

Accelerator Physics fault studies have determined which quadrupoles could cause target parameters to be exceeded. In the majority of cases, large beam losses are predicted when the target parameters are exceeded [15]. Standard monitoring of RTBT beam line elements (On-Off), and loss monitor inputs provide a first level of defense. Redundant inputs are chosen from the AP studies where beam loss monitors and power supply status cannot monitor losses. These magnets are chosen for redundant input using current window monitoring for the power supply.

Accelerator physics models and commissioning results using wire scanners, harps, beam loss monitors, and beam position monitors define acceptable pulse-to-pulse windows for MAID. Control system performance needs to be verified for latency and Quality of Service (QoS). A single control system network should be sufficient but a second high QoS network can be added in the future if required.

OPERATIONS

The operator interface for MPS should make faults easy to locate, reset, and startup reset routines. During initial commissioning, faults are located manually or (preferably) using post mortem tools. As commissioning proceeds into operations, the fault discovery process is automated and operators note the number and type of fault in the logbooks.

Three types of interface screens are being implemented at SNS. A system overview screen shows the status of all MPS Machine Mode chains. An interlock view shows the MPS system where the chain is broken. Clicking down this screen path shown each MPS input and MPS chassis status from an MPS engineers point of view.

A machine-oriented view allows operations to link the fault to a location on the beam line. This allows device specific screens to pop up device status, cause of device fault, device reset functions, and MPS reset functions. Input masking is available at this level as well as the setting of chatter fault (N faults in M pulses) limits. A system status view is also offered showing MPS inputs by system and subsystem.

Each of these displays is highlighted in a fault condition. The operations group will eventually develop high-level screens to their taste. Other EPICS tools like the Alarm Handler also show MPS faults in a hierarchical manner.

CONCLUSIONS

Machine Protection is not just a system to shut off beam like an interlock chain. MPS needs to be tightly integrated with local MPS, global timing systems, global controls, beam diagnostics, and fast abort systems. Startup sequences can be very complex to automate bringing the beam online after an MPS fault Control systems used to provide pulse-to-pulse beam permit signals become a pulsed control system. Network infrastructures need to be provided to allow this functionality. Post mortem systems triggered by MPS will help operations recover from faults. Automatic recovery will further increase the availability of the machine. MPS should become a machine diagnostic tool, integrated with other systems to maximize availability and pinpoint failures for operations.

REFERENCES

[1] SNS Parameter List, SNS 100000000-PL0001 R08

[2] J. Alonso, "Beam Loss Working Group Report", LBNL, Berkeley CA 94720

[3] M. Ross, "Single Pulse Damage In Copper", SLAC, Stanford, CA94309, USA

[4] K. H. Meßl, "Architecture of the Machine Protection System", Chamonix XI, CERN, Geneva, Switzerland

[5] How Long a SNS Beam Pulse would Damage a Copper Accelerating Structure? R. E. Shafer, rev. 4/20/01.

[6] Jean Fusellier, "Beam Intensity Monitoring and Machine Protection By Toroidal Transformers On The TESLA Test Facility", EPAC96, CE-Saclay, F-91191 Gif-sur-Yvette

[7] R. Uric, "CEBAF Beam Loss Accounting", Proceedings if the 1995 Particle Accelerator Conference, pp.2652-4

[8] http://www.JACoW.org/

[9] F.Bordry, "Machine Protection for the LHC: Architecture of the Beam and Powering Interlock Systems", LHC Project Report 521, CERN, CH - 1211 Geneva 23, Switzerland

[10] Saeed Assadi, "Beam in Gap Measurements at the SNS Front-End", TPAG041 ,These proceedings

[11] E. Bjorklund "A Proposal to Remove the Run-Permit Mode from the SNS Event Link", SNS-NOTE-CNTRL-71

[12] M. Ross, private communication

[13] C.Adolphsen, "The Next Linear Collider Machine Protection System," Proceedings if the 1999 Particle Accelerator Conference , 1999 IEEE, p. 253.

[14] R. Hardekopf, "Beam Loss and Activation at LANSCE and SNS", Proceedings of the 7th Mini-Workshop on High-Brightness Beams, Sept. 1999

[15] Stuart Henderson,"Exploration of Beam Fault Scenarios for the Spallation Neutron Source Target", PAC2003, These proceedings, TPPE012

VACUUM SYSTEM FOR HIGH POWER LEPTON RINGS

Y.Suetsugu#, KEK, Tsukuba, Japan

Abstract

The vacuum system for a future high luminosity lepton rings are discussed citing the upgrade plans of KEKB and PEP-II as examples. The high luminosity means firstly the large beam currents as well as the short bunch length. The vacuum system has to cope with the resultant intense synchrotron radiation power and the high photon flux. Deliberate care should be paid for the beam impedance issues. The design will proceed based on the various experiences at present rings introducing novel ideas.

INTRODUCTION

The next generation of B-factories (Super B-factory, SBF) will have a luminosity of 10^{35} – 10^{36} cm^{-2} sec^{-1} to quest a new physics, SUSY related B-physics, for an example. Table 1 presents parameters of three high luminosity rings planed in KEK and SLAC [1,2]. Super KEKB is an upgrade plan of the present KEKB and Super PEP-II is that of PEP-II. The high luminosity firstly means the large beam currents, ten amperes typically, in addition to the small beam sizes at collision points. The vacuum system for such a high luminosity lepton collider has to cope with the resultant intense synchrotron radiation power and the high photon flux [2-4]. The material and the structure of beam chamber should be examined carefully to deal with the high power density. Photoelectron emission has to be cared for the positron ring to suppress the electron cloud instability [5]. Furthermore, since the bunch length should be short to relieve the hourglass effect at the collision point, the beam impedance issues will become much more important. A cautious attention should be paid for the smoothness of the beam chambers and the reduction of impedance. Here described is a strategy of vacuum system design for future high-luminosity rings, together with some conceptual designs of main vacuum components and their R&D status of Super KEKB and Super PEP-II.

ISSUES COMMING FROM HIGH CURRENTS

First of all, several basic issues are reviewed.

Heat and Gas Load by Synchrotron Radiation

As is well known, the total power, P, and the total photon number, N, of the synchrotron radiation (SR) are given by

$$P\,[\mathrm{W}] = 88.4\times10^{3}\,E\,[\mathrm{GeV}]^{4}\,I\,[\mathrm{A}]/\rho\,[\mathrm{m}],$$

$$N\,[\mathrm{photons\,s^{-1}}] = 8.08\times10^{20}\,E\,[\mathrm{GeV}]\,I\,[\mathrm{A}],$$

where E [GeV], I [A] and ρ [m] are the energy, the beam current and the bending radius of normal bending, respectively. The values are also summarized in Table 1. For the LER of Super KEKB, for an example, if the present single beam chamber (ϕ 94 mm, copper) is used, the maximum linear power density just downstream of a bending is 53.5 kW m^{-1} and the estimated temperature reaches up to 293 °C. The thermal stress is so high that the present beam chamber cannot be used as it is.

The average linear photon density along the ring is about 10^{19} photons s^{-1} m^{-1}. The gas load is, therefore, on the order of 10^{-8} Pa m^3 m^{-1} s^{-1} even for the photon stimulated gas desorption rate, η, of 1×10^{-6} molecules $photon^{-1}$. If the goal pressure is on the order of 10^{-7} Pa, the linear pumping speed of about 0.1 m^3 s^{-1} m^{-1} is necessary.

Tables 1: Vacuum related parameters of three future Super B-factories [1,2].

	Super KEKB (Phase I)		Super KEKB (Phase II)		Super PEP-II	
	LER (e^-)	HER (e^+)	LER (e^-)	HER (e^+)	LER (e^-)	HER (e^+)
Goal Luminosity [$cm^{-2}s^{-1}$]	1×10^{35}		$4\text{-}10\times10^{35}$		1×10^{36}	
Energy [GeV]	3.5	8.0	3.5	8.0	3.5	8
Circumference [m]	3016 (arc 2200)		3016 (arc 2200)		2200	
Beam current [A]	9.4	4.1	17.2	7.8	15.5	6.8
Bunch number	5018		5018		6900	
Bunch current [mA]	1.87	0.82	3.43	1.55	2.25	0.99
Bunch Length [mm]	3		3.5		1.75	
Beam Life Time [min]	~150					
Bending Radius (ρ) [m]	16.31	104.46	16.31	104.46	13.75	165
Critical Energy of SR [keV]	5.84	10.88	5.84	10.88	6.92	6.89
Total SR Power [MW]	7.64*	14.21	13.99*	27.03	14.95	14.92
Total Photons [photons s^{-1}]	2.66×10^{22}	2.65×10^{22}	4.86×10^{22}	5.04×10^{22}	4.38×10^{22}	4.40×10^{22}

*without wigglers

yusuke.suetsugu@kek.jp

0-7803-7738-9/03/$17.00 © 2003 IEEE

Heating by Excited HOM

Since the bunch length is short and, furthermore, the bunch current is large, the power of excited higher order modes (HOM) should be intense. The HOM power generated by an impedance source can be written by

$$W = k(\sigma)[\mathrm{VC}^{-1}]I[\mathrm{A}]^2\tau_b[\mathrm{s}],$$

where k is the loss factor of the impedance source and a function of the bunch length, σ. In most case, the k is almost in proportion to σ^{-1}. The τ_b is the bunch interval. The total loss increases in proportion to the square of beam current for the same τ_b, i.e. the same bunch numbers. For an example, even the impedance source with a loss factor of 0.01 V pC^{-1}, it induces the HOM of about 2 kW (I = 10 A and τ_b = 2 ns). The excited HOM results in the heating of vacuum components around the source. The trapped modes are likely to induce the beam instability. The impedance sources should be removed as much as possible to suppress the unnecessary HOM excitation.

Heating and Discharge by Wall Current

For a Gaussian bunch, the wall current, $I_w(t)$, and the mean square of that, $\langle I_w(t)^2\rangle$, can be expressed by

$$I_w(t) = \frac{I\tau_b c}{\sqrt{2\pi}\sigma} e^{-\frac{c^2t^2}{2\sigma^2}}, \left\langle I_w(t)^2 \right\rangle \approx \frac{I^2\tau_b c}{2\sqrt{\pi}\sigma},$$

where c is the velocity of light. For a bunch with σ = 3 mm, the peak wall current is about 800 A (I = 10 A and τ_b = 2 ns). The high impulse wall current could cause a discharge at a gap of beam chamber. The high mean square of current leads to the joule loss, which will be a problem for the coating in the ceramics chambers and for the surface with low electric conductivity.

Direct Damage by Beam

The circulating high current beam has a huge energy in itself. When the beam is steered accidentally or the beam has to be aborted, the beam hit the chamber material and the energy is dissipated there. When all of circulating particle hit a material, the total dissipated energy is about 350 kJ For 10 A beam for LER of Super KEKB. The energy concentrates to the transverse beam size on the material within a time of revolution time (~10 μs). The relativistic beam, of course, interacts with material through various processes and all of the energy does not always dissipated in the small volume [6]. The energy, however, will be enough to melt the metal when the beam injected to that with a thickness of several radiation length (see Fig.6).

DESIGN STRATEGY

The designs of the vacuum system for SBF in KEK (Super KEKB) and PEP-II (Super PEP-II) are undergoing taking account above issues. Followings are the design strategy and conceptual designs of several main vacuum components. Some R&Ds performed or undergoing are also touched briefly.

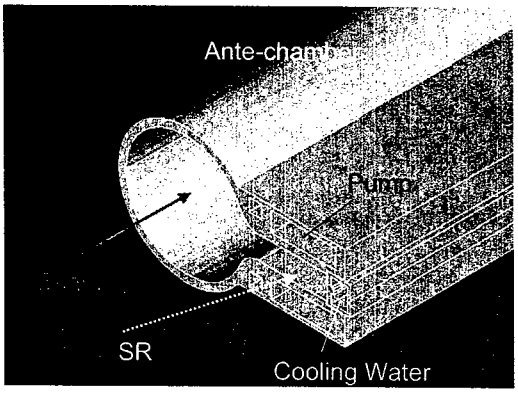

Figure 1: Typical structure of ante-chamber for the LER of Super-KEKB.

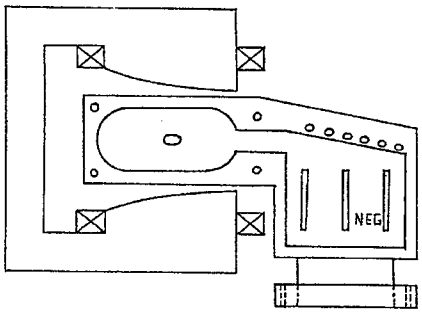

Figure 2: Cross section of beam chamber for Super PEP-II [2].

Beam Chamber

An ante-chamber scheme as adopted in the LER of PEP-II [7], where the SR goes through an adjacent channel, is a promising structure for a beam chamber in high current machine. A typical structure of the ante-chamber is shown in Fig.1 [3]. The ante-chamber consists of two channels, one is for the beam and another is for the SR. A narrow long slot connects those channels each other. The SR hit the sidewall at far side of the ante chamber, not the photon stop. The photon stop scheme cannot be realized due to the high concentrated power. Since the irradiated point of SR at the chamber wall goes far from the emitting point, the input SR power is diluted. For the LER of Super KEKB, the maximum power density at the sidewall of the ante-chamber will be about 40 W mm^{-2}, which is about 30 % of that for the single beam chamber and almost same as that of the present one. The maximum temperature and the thermal stress expected are about 150 °C and 260 MPa, respectively. The stress is well below the yield strength of a drawn copper (~350 MPa).

For the Super KEKB (Phase II) or Super PEP-II, however, the simple ante chamber as Fig.1 is not enough. A cross section of the beam chamber for the Super PEP-II is shown in Fig.2 [4]. The side wall of the antechamber

is tilted to dilute further the power density. In this case, the bore of the beam chamber is also enlarged to reduce the resistive wall effect.

The ante-chamber scheme will be especially preferable for positron ring from the point of photoelectron emission since the irradiation of SR is at the side wall far from beam channel. The beam field is also small and, therefore, the multipactoring will be hard to occur in the SR channel. In 2002, a test model of ante-chamber was installed in the LER of KEKB. The measured electron number in the beam channel reduced to about 1/7 of that for the usual single beam chamber [3]. The effectiveness reducing electrons in the beam channel by adopting ante-chamber scheme was demonstrated.

Pumping Scheme

The ultra-high vacuum in the high luminosity rings is necessary to reduce the background noise in the particle detector and to avoid ion-related instability rather than ensure the long lifetime (see Table 1). The linear pumping speed of about 0.1 $m^3\ s^{-1}\ m^{-1}$ is required as estimated above to get the average pressure on the order of 10^{-7} Pa during the operation. The pumping scheme is the distributed one to get high linear pumping speed. The pump will be a combination of the strip type NEG pumps and the ion pumps as the present KEKB [8,9]. The pump ports are equipped at SR channel to remove the impedance of pumping ports in the beam channel and to evacuate effectively the desorbed gas as shown in Fig.1 and 2.

Material of Chamber

At present, copper is the most suitable material for the beam chamber for its high thermal strength, the high electrical conductivity, the low thermal gas desorption (after proper chemical cleaning) and the relatively low photoelectron yield [7-9]. The copper beam chambers have been used in DESY (HERA), SLAC and KEK and their manufacturing technique, such as the welding (brazing) method and the cleaning procedure, has been well established.

Aluminium is another candidate of material [4]. The manufacturing and welding is actually easier than copper. Extrusion with a complex cross section is also possible. But the thermal strength and the melting point are inferior to copper. The application of aluminium may be limited.

Surface Treatment

Whether it is copper or aluminium, the recent technique to clean the surface and the η of less than 1×10^{-6} molecules $photon^{-1}$ will be achieved within the integrated linear photon density of about 10^{25} photons m^{-1} [8].

More important issue for the positron ring is to form a surface with low electron emission rate to suppress the electron cloud instability (ECI) [5]. The electron cloud consists of photoelectrons and secondary electrons. The secondary electrons are emitted from the surface by bombardment of high energy electrons accelerated by the beam induced field. Solenoid field seems successful in the present KEKB and PEP-II [10,11] and the ante-chamber structure described above will release the problem. To form a surface with a low photoelectron and secondary emission rate, however, will be a fundamental measure.

The present beam chamber of LER of PEP-II has TiN coating inside [7]. Recently it was reported that the NEG (Non-Evaporable Getter) coated surface has a low photoelectron and secondary electron yield [12,13]. The coated chamber was used in ESRF [14] and will be applied for LHC [15]. The NEG coated surface seems promising but the further R&Ds for the surface with low electron emission rate should be continued.

Connection of Chambers

Usually the number of connections sums up to about one thousands to construct a ring. Connection of chambers will raise a serious impedance problem in high luminosity machine. The present KEKB used a helico-flex seal between flanges, which matches the cross section of beam chamber [9]. The helicon-flex gasket has also a role of tight RF-shield and has been working successfully. However, even for the helico-flex seal, the loss factor of a flange connection goes up to about 1 V nC^{-1} for the short bunch length (σ_z = 3 mm). In the design of Super-PEP-II or Super-KEKB, the flange less connection is considered, where the adjacent ducts are connected by welding in situ [3,4].

The bellows chamber, which is usually inserted between adjacent beam chambers, raises another impedance problem and heating problem. In the Super-PEP II and Super-KEKB, the bellows less design was proposed [3,4]. The adjacent chambers will be connected directory by welding in situ. If the temperature of beam chambers during the beam operation is well controlled (less than 10 °C, for an example), the deformation of beam chamber may be tolerable. Remaining crucial problems are how to absorb the manufacture and alignment errors, and how to fit the welding surface. The further practical considerations should be necessary.

In the Super-KEKB, the connection using a bellows

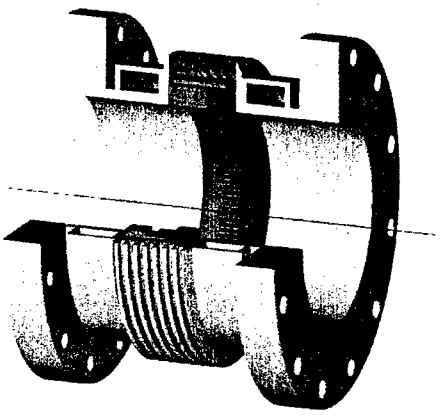

Figure 3: Conceptual drawing of bellows chamber with a new RF-shield structure.

chamber is also considered using a new RF-shield structure as described below [16].

RF-Shield in Bellows and Gate Valves

Usual RF-shield in bellows or gate valves are lots of thin fingers aligned azimuthally around the inner surface of beam chambers [17,18]. However, for the high current ring, the heating of those due to the HOM, especially the TE modes, will become a serious problem. The troubles have been reported at KEKB and PEP-II near the movable masks or the interaction region [8]. The impedance of a step (~1 mm) at RF shield structure ($k \sim 10$ V nC^{-1} at $\sigma =$ 3 mm) will be also a problem for the beam stability due to the large amount of it. The discharge at the sliding point will be another source of trouble due to a high wall current as described above.

Recently a new structure of RF-shield is proposed [19]. The shield is no more than fingers but nested comb teeth, aligned azimuthally with a pitch of 3 mm typically [16]. Since each tooth (copper) has a width and a radial thickness of 1 mm and 10 mm, respectively, the thermal strength is much better than a usual finger. The calculated loss factor is smaller than that of usual one by a factor of $3 \sim 4$. The R&D to apply the RF shield to the bellows or gate valves has just started. A conceptual drawing of the new RF-shield bellows chamber is shown in Fig.3 A trial model of bellows chamber with the new RF-shield will be installed in this summer in the KEKB and studied.

HOM Absorber

In the high current machine, the intense HOM can be generated at various kinds of vacuum components. The interaction region is also a big source of HOM where the cross section changes drastically and the beam passes at the off-centre of beam pipe. The intense HOM leads to the extra heating of vacuum components or the discharges inside those. The HOM absorbers will be indispensable to avoid these troubles caused by the HOM.

A winged HOM damper as shown in Fig.4 was newly designed base on that for KEKB ARES cavity system [20,21] and the trial model was installed near the movable masks of the KEKB in 2002, where the heating of bellows chambers has been observed [22]. The long narrow slots in the beam direction connect the beam chamber and two SiC HOM absorbers, and the damper can absorb effectively the TE mode. The loss factor is less than 10 V nC^{-1} at the bunch length of 10 mm. The capacity of a SiC rod is about 10 kW.

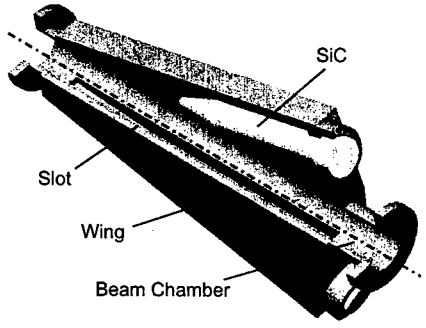

Figure 4: Structure of winged HOM damper developed in KEK.

Movable Mask (Collimator)

To protect the particle detector from damages by spent particles, the movable mask (collimator) system will be equipped. The trapped HOM free masks have been installed in the PEP-II and KEKB [23,24]. Even if the masks do not trap the HOM, however, they excite the HOM in any way. The HOM propagates along the beam chamber and heats up the components nearby [8]. Future masks should be combined with HOM absorbers. The reduced HOM design will be adopted at the same time [25].

Another problem expected is the damage of mask head, which have been already experienced in the KEKB [24]. The damages at the mask head resulted from the attack of beam steered abnormally. The same problem will arise at the beam abort window. An effective way to avoid the damage is to use the light material with a minimal length as a mask head. The temperatures along the beam path in copper, titanium, carbon and beryllium calculated by EGS4 as a function of the radiation length are shown in Fig.5 [26]. New ideas are to use spoiler scheme (Fig.6) and to use a rotating or a liquid metal as a spoiler [27,28].

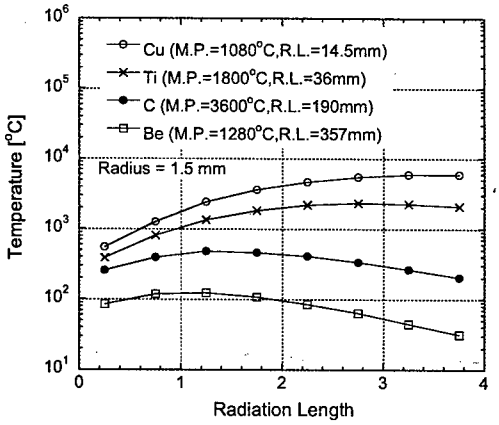

Figure 5: Estimated temperatures along the beam path when an 8 GeV electron beam with a radius of 1.5 mm is incident on copper, titanium, carbon and beryllium.

Figure 6: Spoiler type collimator [27].

The safe and rapid beam abort system using the beam orbit or the beam loss monitor will also help the damage of mask head.

OTHER ISSUES

The following are other key issues to be carefully considered.

(1) Design of the beam chambers at the interaction region. The design should take into account the aperture (the beta function should be large near the collision point), the impedance, the SR mask and the effective pumping scheme.

(2) Radiation shielding. Lead shielding around the beam chamber may be necessary.

(3) Alignment. An accurate alignment of the beam chamber will be a great importance for the accelerator dealing with an intense beam.

(4) Abort system. Once an accident occurs, such as a malfunction of machine components or a wrong operation, the steered beam easily damages the vacuum chamber or the movable masks as described above. A rapid and safe beam abort system is required.

(5) Alarm system. Many components, such as the photon stops, the bellows chambers, gate valves and so on, can be easily heated up by the intense synchrotron radiation or HOM if the cooling system failed. The flow rate of cooling waters and the temperatures of these components should be kept watching any time. A highly reliable alarm and interlock system should be prepared.

ACKNOWLEDGEMENTS

The authors would like to thank Dr. K.Oide, Dr. K.Kanazawa and many other staff of the Accelerator Laboratory in KEK for their continuous encouragement.

REFERENCES

[1] http://www-kekb.kek.jp/SuperKEKB/home.html; Y.Ohnishi, KEK Proceedings 2002-17 (2002) 1.

[2] http://www-user.slac.stanford.edu/seeman/index.html, "B- Factory Upgrade Scenarios".

[3] Y.Suetsugu, KEK Proceedings 2002-17 (2002) 7.

[4] J.T.Seeman, "HIGHER LUMINOSITY B-FACTORIES", PAC'01, Chicago, June 2001, p.305.

[5] For example, K.Ohmi and F.Zimmermann, P.R.L. 85 (2000) 3821.

[6] For example, "Review of Particle Physics", The European Physical Journal 15 (2000) 163.

[7] J.Dorfan, "PEP-II STATUS REPORT", EPAC'98, Stockholm, June 1998, p.33.

[8] K.Kanazawa et al., N.I.M. A 499 (2003) 66.

[9] K.Kanazawa et al., Appl. Surface Sci., 169-170 (2001) 715.

[10] K.Akai et al., N.I.M. A 499 (2003) 191.

[11] J.Seeman et al., "PEP-II STATUS AND FUTURE PLANS", EPAC'00, Paris, June 2002, p.434.

[12] B.Henrist et al., Appl. Surface Sci. 172 (2001) 95.

[13] J.M.Jimenez et al., "ELECTRON CLOUDS – RESULTS FROM SPS AND EXPERIMENTS FOR 2003", Proc. Chamonix XII (CERN-AB-2003-008 ADM), Chamonix, March 2003, p.327.

[14] R.Kersevan, "NEG-COATED VACUUM CHAMBERS AT THE ESRF: PRESENT STATUS AND FUTURE PLAN", EPAC'02, Paris, June 2002, p.2565.

[15] I.Collins et al., "VACUUM CALCULATIONS FOR THE LHC EXPERIMENTAL BEAM CHAMBERS", PAC'01, Chicago, June 2001, p.3153.

[16] Y.Suetsugu, et al., "CONCEPTUAL DESIGN OF VACUUM SYSTEM FOR SUPER KEKB", in these proceedings.

[17] Y.Suetsugu et al., Rev. Sci. Instrum (1996) 2796.

[18] J.T.Seeman, "PEP II STATUS AND PLANS", PAC'95, Dallas, May 1995, p.486.

[19] Y.Suetsugu, KEKB Machine Advisory Committee, March 2003.

[20] T.Kageyama et al., "THE ARES CAVITY FOR THE KEK B-FACTORY", EPAC'96, Sitges, November 1996, p.2008.

[21] Y.Takeuchi et al., "THE SiC ABSORBER FOR THE KEKB ARES CAVITY", EPAC'96, Sitges, November 1996, p.2020.

[22] Y.Suetsugu et al., "DEVELOPMENT OF WINGED HOM DAMPER FOR MOVABLE MASK IN KEKB", in these proceedings.

[23] J.Seeman etal., "PEP-II HIGH POWER LOW IMPEDNCE MOVABLE COLLIMATOR", EPAC'00, Vienna, June 2000, p.2298.

[24] Y.Suetsugu et al., "DEVELOPMENT OF THE MOVABLE MASK FREE FROM TRAPPED MODE FOR THE KEKB", PAC'01, Chicago, June 2001, p2186.

[25] K.Shibata et al., "DEVELOPMENT OF MOVABLE MASK WITH REDUCED-HOM DESIGN FOR KEKB", in theses proceedings.

[26] W.R.Nelson et al., KEK Proceedings 2000-20 (2000) 182.

[27] K.Bane et al., "Collimator Design and R&D", Machine Advisory Committee, SLAC, May 2001.

[28] J.Frisch et al., "ADVANCED COLLIMATOR ENGINEERING FOR THE NLC", PAC'01, Chicago, June 2001, p.1258.

THIN DIAMOND FILMS FOR SNS H⁻ INJECTION STRIPPING

R. W. Shaw, A. D. Herr, Chemical Sciences Division, Oak Ridge National Laboratory
C. S. Feigerle, Department of Chemistry, University of Tennessee/Knoxville
R. I. Cutler, SNS Project, Oak Ridge National Laboratory
C. J. Liaw, Y. Y. Lee, Brookhaven National Laboratory

Abstract

We have investigated the preparation and testing of thin diamond foils for use in stripping the SNS H⁻ Linac beam. A long useful lifetime for these foils is desirable to improve operational efficiency. Preliminary data presented at PAC 2001 indicated that diamond foils were superior to conventional evaporated carbon foils, exhibiting lifetimes approximately five-fold longer[1]. That work employed a fully supported diamond foil, a format that is not acceptable for the SNS application; at least two edges of the approximately 1x1 cm foils must be free standing to allow for beam rastering. Residual stress in a chemical vapor deposited (CVD) diamond foil results in film distortion (scrolling) when the film is released from its silicon growth substrate. We have attacked this problem by initially patterning the surface of CVD growth substrates with a 50 or 100 line/inch trapezoidal grating, followed by conformal diamond film growth on the patterned substrate. Then removal of the substrate by chemical etching produced a foil that possessed improved mechanical integrity due to its corrugation. The high nucleation density required to grow continuous, pinhole free diamond foils of the desired thickness (1 μm, 350 μg/cm²) was achieved by a combination of substrate surface scratching and seeding. A variety of diamond foils have been tested using the BNL 750 keV Radio Frequency Quadrupole H⁻ beam to simulate energy loss in the SNS. Those include flat, corrugated, microcrystalline, and nanocrystalline foils. Foil lifetimes are reported.

INTRODUCTION

Diamond thin films can be grown from the vapor phase by decomposition of methane in low pressure hydrogen. While the resulting films are polycrystalline, they exhibit many of the superb physical properties of natural diamond. We have prepared and tested diamond foils for use as the stripping foil for removing two electrons from the H⁻ ions in the 1 GeV Linac beam at the Spallation Neutron Source (SNS).

Preliminary BNL data presented at PAC 2001 indicated that a diamond foil was superior to conventional evaporated carbon foils, exhibiting a lifetime approximately five-fold longer[1]. Any improvement in foil lifetime before failure will be an operational advantage for the SNS, which will be operated nearly continuously for users.

The SNS will require a foil size approximately 1 x 2 cm, with a thickness of about 1 μm (350 μg/cm²). An optimum design goal requires that an individual foil will function for no less than about 200 hours. Multiple foils will be mounted on a 30-unit cassette changer to increase the overall facility operating time before new foils must be mounted. These foils can be supported mechanically by at most two edges, as the proton beam will be painted on and off the foil in both transverse directions. This latter criterion is particularly demanding because thin, polycrystalline diamond foils grown by chemical vapor deposition (CVD) are mechanically stable when affixed to their growth substrate, but curl dramatically when released due to stress in the foil. This stress is both intrinsic and thermal (stress produced by the large thermal expansion mismatch between diamond and the silicon growth substrate). We have attempted to overcome this mechanical instability problem by using two approaches: growth of nano-textured diamond and corrugation of diamond foils.

FILM STRESS AND NANO-TEXTURED DIAMOND

Residual film stress for materials grown at elevated temperature is a well known and studied topic. Windischmann and co-workers [2] have determined the stress in microwave plasma CVD diamond films as a function of the methane concentration in the reagent gas and as a function of the deposition temperature. Both tensile and compressive stress was observed, depending on the growth conditions.

We feel that an approach that holds promise for stress averaging and film strengthening is the preparation of nanostructured diamond. Such films have the potential to provide adequate strength at the ca. 1 μm thickness required. Several reports concerning nanocrystalline diamond, particularly from microwave-excited growth reactors, have appeared. Zhou and co-workers [3,4] discovered that the argon content of $CH_4/H_2/Ar$ microwave discharges leading to CVD diamond films exerts a substantial effect on the particle size of these polycrystalline films. Nanocrystalline textured films, with grain sizes ranging from 3 to 50 nm, can result. More recently, similar results were obtained using a hot filament growth chamber [5].

FOIL PREPARATION

Diamond films were grown using either a hot filament or a microwave reactor. The typical reagent gas mixture was 1 or 2% methane in hydrogen; the reactor pressure was maintained at 50 Torr, and the gas flow rate was 100 sccm. For nano-textured films, the input gas mixture was diluted with argon to create a 1/49/50 by volume

0-7803-7738-9/03/$17.00 © 2003 IEEE

$CH_4/H_2/Ar$ mixture. The substrate temperature was set either by adjusting the microwave power or the substrate heater current in the microwave and hot filament reactors, respectively. The growth rate was about 0.5 to 1 μm/hr. Greater thickness uniformity was achieved using the microwave reactor. The film thickness reported here is an estimate derived from the substrate mass change during growth, so is an average over the entire wafer surface. Films were characterized using SEM, TEM, surface profilometry, and micro-Raman spectroscopy. TEM analysis of our nano-textured diamond indicated that the typical particle size was 50 nm. A window was chemically etched in the substrate for accelerator beam foil lifetime testing using a mixture of 10:6:9 concentrated nitric: hydrofluoric:acetic acids.

Single crystal silicon wafers (100 orientation) were abraded using 0.1 μm diamond paste before film growth to create nucleation sites. Diamond films prepared using the CVD method are polycrystalline with grain dimensions ranging from less than one to about ten micrometers. To a large degree, the grain size is determined by the substrate surface nucleation density, as diamond grows by development of crystalline nuclei (seeds) that enlarge with further growth until they merge. Thus the seeding process is critical for our application, as the nucleation density must be sufficient to result in a pinhole-free film even though the growth is terminated at a 1 μm film thickness. Mechanical scratching of the substrate is commonly employed before growth in order to produce a high diamond nucleation density. We have extended that approach by first scratching with paste and then following with an ultrasonic bath wafer treatment in "Liquid Diamond", a concentrated slurry of 0.1 μm diamond particles (GE Micron Products, Deerfield Beach, FL). The latter treatment loaded the surface scratches with diamond seeds. After the ultrasonic treatment, the wafer was rinsed, but not thoroughly cleaned, so as to leave behind surface seeds.

Corrugated diamond foils were prepared through the use of a photolithographic technique. A 100 silicon wafer was oxidized to produce a 400-500 nm oxide layer. That surface was spin-coated with a polymer photoresist. The resist was exposed to ultraviolet light through a metal-on-glass mask (50 or 100 lines per inch at 50% duty factor) at contact. The resist was developed and rinsed to leave protective resist lines on the oxide surface. The exposed oxide was removed in a brief buffered oxide etch (BOE; 10:1, NH_4F:HF). The remaining resist was then stripped, and the wafer was etched in 25% tetramethyl ammonium hydroxide at 75 °C to produce surface trenches with approximately 45° walls in the exposed silicon. The protective oxide lines were then stripped using BOE. This process resulted in a trapezoidal pattern on the silicon surface with trench depths of approximately 20 μm. A conformal CVD diamond film was grown on this surface, and subsequently the silicon substrate was etched away to leave a corrugated foil. The sloping trench walls present a thickness to a normal incidence ion beam that is ca. 50% greater than the nominal foil thickness, but the portion of the foil that corresponds to the walls is only 7% of the entire foil area (at 50 lines/inch corrugation). A schematic view of an L-bracket supported sample is shown in Figure 1; the foil corrugations are arranged in a diagonal orientation to pin the free foil corner. An image of an actual sample is also shown; the corrugation period is 50 lines/inch for this sample.

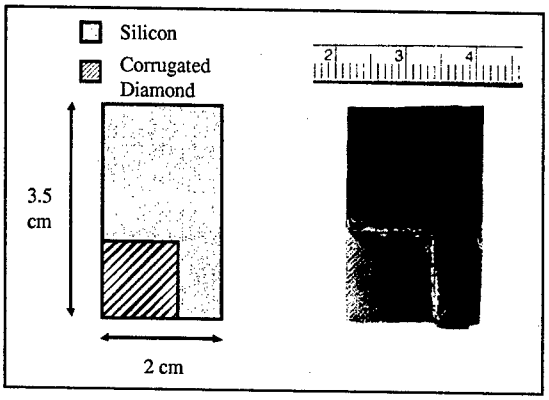

Figure 1. Schematic drawing and image of a corrugated foil test sample (50 Lines/inch). A cm scale is shown.

FOIL TESTS IN THE BNL LINAC BEAM

The wafers were beam tested at Brookhaven National Laboratory, using the 750 keV H^- Linac (6.7 Hz, 0.5 ms pulse). The beam was approximately circular, with a 3 mm diameter. A peak beam current of 2 mA was used for these tests so as to achieve the same energy loss in the foil as from the 50 mA, 1000-MeV SNS beam. Note that the SNS repetition rate is nine-fold higher than for the BNL Linac, and the foil lifetime in the SNS will be shorter. The test samples were 2 x 3.5 cm silicon coupons with a variety of window sizes: 7 mm round, 12x12 mm square ("window frame"), and 12x12 mm windows with L-bracket (two-edged) support. The total current was monitored behind the foil, and the lifetime was gauged by the time required for the current to drop to 90% of its initial value. However, tests were halted at about 130 hours, if the 90% current criterion had not been reached.

The test results are summarized in Table 1. Unfortunately our beam time for testing is limited, so the data are sparse at this time. However it can be seen that the lifetime for several of the foils exceeded 80 hours. The foils represented in Table 1 range from 1.0 to 1.9 μm average thickness. Two foils (#4 and 5) were nanocrystalline (i.e., grown in the hot filament chamber with $CH_4/H_2/Ar$ gas); the tests for both of these foils were terminated before the 90% criterion was reached. For comparison, foil #6 was microcrystalline; however, #6 was prepared with a smaller, round window and different

Table 1. Diamond foil lifetime test results for a 750 keV H^- beam for a variety of diamond foils. The lifetime is defined as the time at which the downstream current decreased to 90% of the initial value. Foil # 1 was grown at a substrate temperature (ca. 900 °C) approximately 200 °C hotter than #2.

Foil Number	Growth Technique	Foil Structure	Reagent Gas Methane Content	Average Foil Thickness (μm)	Window	Measured Lifetime (Hr)
1	Microwave	Micro-	1%	1.9	12x12 mm	85.4
2	Microwave	Micro-	2%	NA	12x12 mm	16.4
3	Hot Filament	Corrugated, Nano-	1%	1.8	12x12 mm L-Bracket	60.0
4	Hot Filament	Nano-	1%	0.96	12x12 mm	>133
5	Hot Filament	Nano-	1%	1.1	12x12 mm	>120
6	Hot Filament	Micro-	1%	0.81	7 mm, Round	3.6

temperature maxima may have resulted for these foils. Foils #1 and 2 were grown in the microwave-powered chamber and were microcrystalline; the longer lived foil was grown at a substrate temperature (ca. 900 °C) approximately 200 °C hotter than the comparison foil. Foil #3 was nanocrystalline, corrugated at 100 lines/inch, and supported on only two edges; its observed lifetime was 60 hours.

The tested foils were characterized using SEM and Raman spectroscopy to ascertain beam-induced material alteration. A round, dark foil spot of the same size as the H^- beam was observed. This region was typically wrinkled and damaged. Raman spectroscopic analysis showed clear evidence that a diamond-to-graphite conversion had occurred at the beam spot for both the nanocrystalline and microcrystalline foils. The sharp 1332 cm^{-1} diamond phonon line disappeared, and new broad lines appeared at the positions of the D and G bands of graphite [6].

CONCLUSIONS

To a large degree, corrugation of thin diamond films solves the curling problem for free standing foils. Flat foils scroll dramatically, while corrugated foils as large as 12 x12 mm only cup slightly. Our preliminary foil test results indicate that diamond foils with lifetimes greater than 100 hours can be prepared. It appears that nanocrystalline diamond exhibits a longer useful life than microcrystalline diamond for this beam stripping application. An L-bracket supported corrugated foil performed for 60 hours.

Future efforts will be focused on development of more reproducible diamond nucleation techniques, improvements in corrugation geometry, and on further foil testing in the Linac beam.

ACKNOWLEDGEMENTS

SNS is managed by UT-Battelle, LLC, under contract DE-AC05-00OR22725 for the U.S. Department of Energy. SNS is a collaboration of six US National Laboratories: Argonne National Laboratory (ANL), Brookhaven National Laboratory (BNL), Thomas Jefferson National Accelerator Facility (TJNAF), Los Alamos National Laboratory (LANL), Lawrence Berkeley National Laboratory (LBNL), and Oak Ridge National Laboratory (ORNL). ADH acknowledges an appointment to the U.S. Department of Energy's Energy Research Undergraduate Laboratory Fellowships (ERULF) Program at the Oak Ridge National Laboratory.

REFERENCES

[1] C.J. Liaw, Y.Y. Lee, and J. Tuozzolo, "Lifetime of carbon stripping foils for the spallation neutron source", PAC2001, Chicago, IL, p. 1538.

[2] H. Windischmann, G. F. Epps, Y. Cong, and R. W. Collins, J. Appl. Phys. 69 (1991) 2231.

[3] D. Zhou, D. M. Gruen, L. C. Qin, T. G. McCauley, and A. R. Krauss, J. Appl. Phys. 84 (1998) 1981.

[4] D. Zhou, T. G. McCauley, L. C. Qin, A. R. Krauss, and D. M. Gruen, J. Appl. Phys. 83 (1998) 540.

[5] T. Lin, G. Y. Yu, T. S. Lee, Z. X. Shen, and K. P. Loh, Appl. Phys. Let. 77 (2000) 2692.

[6] D. S. Knight and W. B. White, J. Mater. Res. 4 (1989) 385.

VACUUM PUMPING STUDY OF TITANIUM-ZIRCONIUM-VANADIUM THIN FILMS*

Yulin Li# and Simon Ho, LEPP, Cornell University, Ithaca, NY 14853, USA

*Abstract**

Vacuum pumping via non-evaporable getter (NEG) thin film deposited directly onto the interior of a vacuum chamber is a novel way to achieve extreme high vacuum. As part of R&D efforts for the proposed Energy Recovery Linac at Cornell, the pumping performance of Titanium-Zirconium-Vanadium (TiZrV) NEG thin films was investigated to provide 'engineering' data for designing vacuum systems using such NEG thin films. The compositions and growth rates of the NEG thin films, deposited on stainless steel tubes using DC Magnetron sputtering, were investigated using Rutherfield Back-scattering Spectrometry. The pumping speeds and capacities of the thin films for CO and H_2 were measured as functions of activation temperatures and durations, and film thickness. Though pumping of CO and H_2 by the NEG films is observed with activation temperatures as low as 150°C, the pumping performance of the NEG films improves significantly with activation temperatures above 250°C.

INTRODUCTION

An Energy Recovery Linac (ERL) prototype machine was proposed at Cornell University to study ERL-related accelerator physics and technology [1]. The knowledge and experience gained from the prototype ERL machine will pave the way for the development of a full scale ERL-based new generation synchrotron light sources.

Adequate vacuum performance is essential to the operation of many sub-systems of the proposed ERL prototype and the future ERL synchrotron light sources (such as the photo-cathode injector, beam pipes adjacent to the superconduting cryo-modules, and the insertion devices). The challenge to the vacuum system design arises from the need to achieve and maintain ultra-high and extreme-high vacuum conditions within a very limited space allowable for traditional pumping.

The use of non-evaporable getter (NEG) thin film [2] directly deposited onto the inside of a vacuum chamber has revolutionized the design of accelerator vacuum systems. The NEG film brings pumping to sources of gas-loads; it provides distributed pumping in a space-limited environment and has a very low outgassing rate and a low secondary electron emission yield [3]. The NEG thin films have been employed in many accelerator systems [4] with very successful vacuum performances.

As part of the R&D efforts for the ERL project, we studied the pumping performance of the Titanium-Zirconium-Vanadium (TiZrV) NEG thin films, deposited on the interior of stainless steel (SST) pipes. The TiZrV coating has the attractive feature [2] of a low activation temperature. One of the aims of the study is to provide vacuum 'engineering' data for designing vacuum systems using such NEG thin films.

NEG THIN FILM DEPOSITION

The TiZrV NEG films are deposited onto the interior wall of SST tubes, using a DC Magnetron Sputtering technique. The deposition system is shown in Figure 1. The SST tube (with an outer diameter of 4-in, welded between two 6-inch Con-Flat flanges) to be coated is mounted onto a 6-inch six-way cross. The deposition system is pumped by an 80 l/s turbo-molecular pump (TMP). The sputtering cathode, formed by twisting together 1-mm-diameter titanium, zirconium and vanadium wires, is connected to an SHV-type vacuum feedthrough at the top, and to a ceramic standoff at the bottom via a SST spring. UHP argon gas is introduced into the sputtering system through an adjustable leak valve. The Ar flow rate and pressure in the sputtering chamber are adjusted using the leak valve and a gate valve located between the sputtering chamber and the TMP. The Argon discharge is ignited and sustained by a DC voltage applied to the cathode and a magnetic field generated by a coaxial solenoid coil. The typical sputtering parameters are: 600-V cathode voltage, 200-G solenoid field, 2×10^{-3} torr Ar pressure and 30-mA sputtering current.

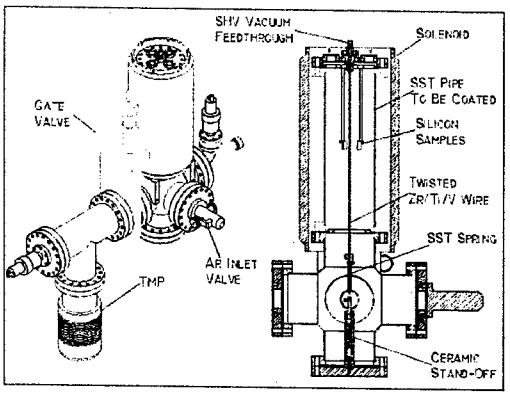

Figure 1. NEG Film Deposition System

The NEG film composition and deposition rates are measured using Rutherfield Backscattering Spectrometry (RBS). In the RBS measurements, the NEG thin film is deposited on 12 silicon samples, at various distances from the cathode for various sputtering durations, as shown in Fig.1. The RBS results from these silicon samples showed a NEG film relative composition of $Ti_{1.05}V_{1.85}Zr$ and a film deposition rate of 0.10-μm/hr on the inner wall of the 4-inch SST tube. After the RBS calibration runs, two flanged SST tubes were coated with NEG film with a thickness of 0.6μm and 2.0μm respectively.

* Work supported by the National Science Foundation
# YL67@cornell.edu

NEG FILM PUMPING PERFORMANCE

The vacuum pumping performance of the NEG thin films on the two SST tubes was measured using a setup depicted in Figure 2. The NEG-coated tube is connected to a TMP through a 0.25" diameter orifice. Calibrated leaks are used to introduce test gases into the system. The pressures above (P_1) and below (P_2) the orifice are measured using inverted magnetron cold cathode gauges. A residual gas analyzer (RGA) is also installed to the system. After an initial pump-down, the apparatus was baked out at 150°C for 48 hours.

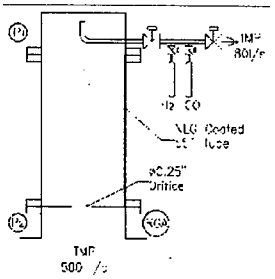

Figure 2. Apparatus for NEG Film Pumping Tests

The pumping speed and pumping capacity of the two NEG films are measured for the two test gases: hydrogen and carbon monoxide. The coated SST tube is heated to various activation temperatures (T_{act}) for durations (t_{act}) of 24-, 48- or 72-hours. The test gas is introduced into the system after the NEG-coated tube has cooled down to ambient temperature and the pressures (P_1 and P_2) are subsequently recorded until the NEG film is fully saturated. The pumping speed of the NEG film, S_{NEG}, can be calculated from the measured P_1 and P_2 using:

$$S_{NEG} = [\dot{Q}_{leak} - C(P_1 - P_2)]/P_1 , \qquad (1)$$

where $\dot{Q}_{leak}$ is the leak rate of the testing gas (2.37×10^{-4} for H_2 and 1.73×10^{-5} *torr•liter/sec* for CO), and C is the gas conductance of the orifice.

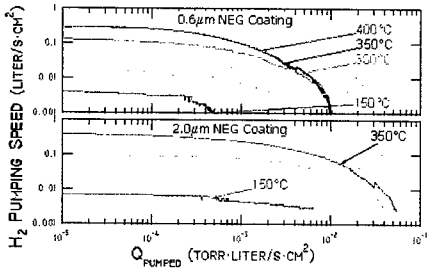

Figure 3. H_2 pumping speed vs. pumped H_2 at various activation temperatures, T_{act}, (48-hour duration).

The pumping speed measured (normalized by NEG-coated area, ~989 cm^2) for H_2 and CO are plotted as a function of the pumped gas load, Q_{pumped}, in Figures 3 and 4, at various T_{act} for the 48-hour duration. Q_{pumped} was calculated using:

$$Q_{pumped}^{CO,H_2} = \int (S_{NEG}^{CO,H_2} \cdot P_1) dt . \qquad (2)$$

The effect of activation duration on the pumping speed and capacity for the 0.6μm NEG film activated at 350°C is shown in Figure 5. A similar trend is observed for the 2μm NEG film.

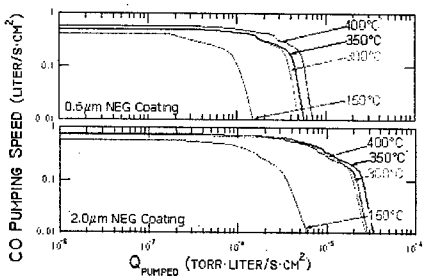

Figure 4. CO pumping speed vs. pumped CO at various activation temperatures, T_{act}, (48-hour duration).

The effect of t_{act} on the pumping is also shown in Figure 5. The pumping of CO is relatively insensitive to t_{act}. The results in Figs 3, 4 and 5 indicate that the NEG films can be fully activated at $T_{act}\geq350°C$ with $t_{act}\geq48$ hr.

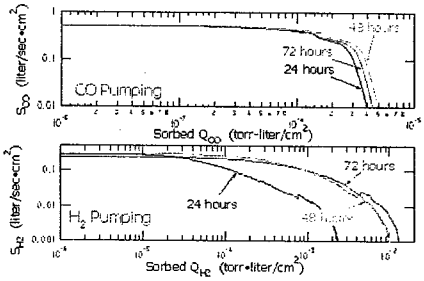

Figure 5. NEG film pumping speed at three activation durations, t_{act}, (T_{act}=350°) for the 0.6μm thick NEG film

DISCUSSION

The vacuum pumping performance of the NEG thin films can be evaluated from the initial pumping speed, S_0, (after each activation) and its pumping capacity.

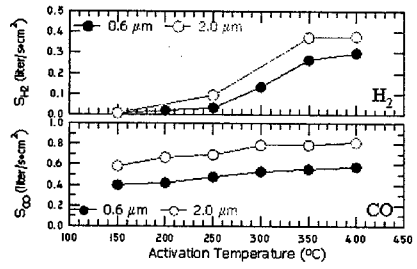

Figure 6 S_0 of CO and H_2 vs. T_{act} for both NEG films.

Using data shown in Figures 3 and 4, the dependence of S_0 of CO and H_2 on the T_{act} is plotted (Figure 6) for both the 0.6 and 2.0 μm NEG films. The S_0 of a gas depends on the reactivity of the NEG surface to the gas, and on the effective surface area (or surface roughness). This dependence is less important for CO than for H_2.

While S_0^{CO} increases slowly with increasing T_{act}, a significantly higher $S_0^{H_2}$ can be achieved with T_{act}>250°C. Higher S_0 is observed on the 2μm NEG film than on the 0.6μm NEG film for both CO and H_2 at tested T_{act}. This increase in S_0 on the thicker NEG film is most likely due to a corresponding increase in surface roughness. This is indicated by $S_0^{2\mu m} / S_0^{0.6\mu m}$ being nearly a constant at all T_{act} for both test gases.

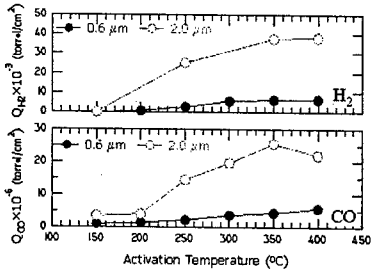

Figure 7. Pumping capacity (see test) of CO and H_2 vs. T_{act} for both NEG films.

Pumping capacity of the NEG film may be defined as the total amount of gas adsorbed (or pumped) by the film, Q_{total}, for the pumping speed to drop from S_0 to a lower value, S_f. Data in Figs. 3 and 4, and (arbitrarily) defining S_f^{CO}=0.1 l/s•cm^2 and $S_f^{H_2}$=0.01 l/s•cm^2, gave the dependence of Q_{total} on T_{act} in Fig. 7 for CO and H_2. The results show that (1) a significant gain in pumping capacity for CO and H_2 is obtained with T_{act}>250°C; and (2) a much higher pumping capacity is measured on the thicker NEG film for both CO and H_2. The pumping capacity for H_2 is orders of magnitude larger than that for CO, due to different pumping mechanism for CO and H_2 [5]. CO molecules are only chemically adsorbed onto the NEG surface and this is irreversible. But the pumping of H_2 is completely reversible [5]. At RT, hydrogen molecules dissociate on the NEG surface and the atomic hydrogen then diffuses into the NEG film. The dissolved hydrogen atoms recombine on the surface and desorb as gas molecules when the NEG is heated during activation.

While the CO pumping capacity depends on surface condition of the NEG film, the H_2 pumping capacity depends on the NEG film's bulk properties, such as hydrogen solubility of the NEG film and the residual hydrogen content in the NEG film after activation.

The hydrogen solubility of the NEG films is estimated by calculating the ratio $R_{H_2} = Q_{H_2}^{max} / n_{NEG}$, in which $Q_{H_2}^{max}$ is the total H_2 pumped by a fully activated NEG film and n_{NEG} is the NEG atomic density measured by RBS. The measured maximum R_{H_2} is ~14.2% and ~15.1% for the 0.6μm and 2.0μm NEG films respectively.

To demonstrate the effect of residual H content on hydrogen pumping capacity, we measured the amount of hydrogen desorbed during activation from a NEG film fully saturated with hydrogen, at a given T_{act}, and compared that to the amount of H_2 pumped subsequently. The results (Figure 8) clearly indicate the correlation between the H_2 desorbed from the NEG film during the activation and the H_2 pumping capacity.

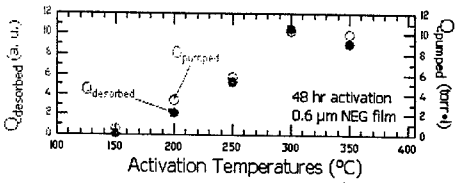

Figure 8. Amount of desorbed H_2 during activation and amount of pumped H_2 as function of T_{act}.

To illustrate the depletion of hydrogen from a saturated NEG film, deuterium was used to saturate a fully activated (72 hr at 400°C) NEG film. The measured D_2 pumping speed curve is very similar to that for H_2 shown in Fig.3. The D_2-saturated NEG film is then activated and traces of major RGA peaks during the activation are shown in Figure 9. The depletion of sorbed D_2 is evident. The observed steady H_2 desorption most likely originates from hydrogen in the substrate SST, which diffused into the NEG film and then desorbed from NEG surface at the activation temperatures.

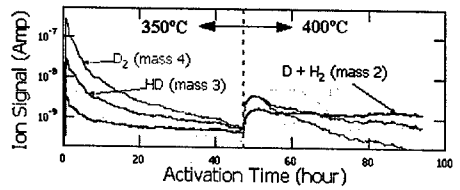

Figure 9. D_2 Desorption from NEG film during activation

CONCLUSION

TiZrV NEG thin films were deposited onto SST pipe via DC magnetron sputtering. The NEG films were characterized using RBS. Factors that affect the vacuum pumping performance of the thin films were investigated to provide 'engineering' data for vacuum system design. Vacuum pumping is observed at activation temperature as low as 150°C. Activation above 250°C will significantly enhance the pumping performance of the NEG thin films.

The authors would like to thank Dr. Revesz of Cornell High Energy Synchrotron Source for helping RBS measure-ments, and to thank Mr. Tim Giles of LEEP Vacuum Group for assistances in setting up vacuum pumping tests.

REFERENCES

[1] http://erl.chess.cornell.edu/papers/WhitePaper_v41.pdf
[2] C.Benvenuti, et al., Vacuum 60 (2001) p.57-65
[3] B.Henrist, et al, CERN Vac Tech. Notes 98-08, 98-20, and 00-32
[4] R.Kersevan, Proc. EPAC 2002, Paris, France, p.2565
[5] K.M.Welch, "Capture Pumping Technology", 2nd Ed. North-Holland, 2001 p.229

A NEW KIND OF BEAM PIPE FOR RAPID CYCLING PROTON SYNCHROTRONS

Zhijing Tang*, Weiren Chou*, Alex Chen*, FNAL, Batavia, IL 60510, USA

Abstract

A thin metallic beam pipe reinforced by multi-layer spiral metallic ribs is proposed for rapid cycling proton synchrotrons. The pipe is made of Inconel 718 with thickness of a few tenths of mm. Each spiral rib has a cross section of about 0.3 mm^2 and can be bonded to the pipe by using laser deposition technique (e.g., precision metal deposition, or PMD). Compared with other designs (e.g.., ceramic beam pipe with a metallic cage used in the ISIS at the RAL), this new pipe will reduce the magnet aperture significantly, which, in turn, reduces the construction and operating cost of a synchrotron. Numerical simulations and analytical modeling are used to investigate the structural strength and deformation, and the eddy current effects, including heating, magnetic field distortion and the electro-magnetic force on the beam pipe. The results show that this new beam pipe will work. It can be employed to high intensity rapid cycling proton synchrotrons, such as the proton driver at FERMILAB and the JHF at JAERI/KEK. Effort to build a prototype is under way.

THE BEAM PIPE

The cross section of the proposed beam pipe is 6 inch by 4 inch oval with thickness of 0.008 inch. The material is Inconel 718. The laser precision metal deposition (PMD) method will be used to put a spiral rib (same material with 18 mils height and 28 mils width can be applied repeatedly) around the tube to increase its strength against buckling. We select 10 layers of reinforcement (hence the total height of the rib is 0.18 inch) and the pitch of the rib is set to 1 inch. Some relevant material properties of Inconel 718 are: tension modules E = 29e6 psi, yield strength σ_y = 171e3 psi, ultimate strength σ_u = 196e3 psi, electric resistivity λ = 125e-8 ohm-m.

The beam pipe is subject to some loads. Mechanically there is a vacuum pressure, and electro-magnetically there is a time varying magnetic field:

$$B^{ext} = 0.85 - 0.632\cos(\omega t) + 0.079\sin(2\omega t),$$

where $\omega = 2\pi f$, and f = 15 Hz. This magnetic field is perpendicular to the major axis of the beam pipe cross section.

* Work supported by the US Department of Energy under contract No. DE-AC02-76CH03000.

Vacuum pressure is simple to analyze, but the effects of the time vary magnetic field is complex. We have to consider the eddy current, eddy current induced magnetic field and power loss, and electro-magnetic force.

STRUCTURAL MODEL

For structural analysis, we made a six inch finite element model. The only load considered here is the vacuum pressure of 14.5 psi. Electro-magnetic force will be discussed later. The boundary conditions are: $u_z = 0$ at $z = 0$; $u_x = 0$ at $x = 0$ and $z = 0$; $u_y = 0$ at $y = 0$ and $z = 0$.

Fig. 1 shows the maximum equivalent stress of 144 ksi. This maximum occurs near the end. If we look at the middle section of the model, which is more typical, we have maximum stress of 130 ksi. So we take 130 ksi as the maximum stress in the vacuum tube. Check the maximum stress against the ASME pressure vessel code [1], which gives the limiting stress about 170 ksi, we found out that this number is OK.

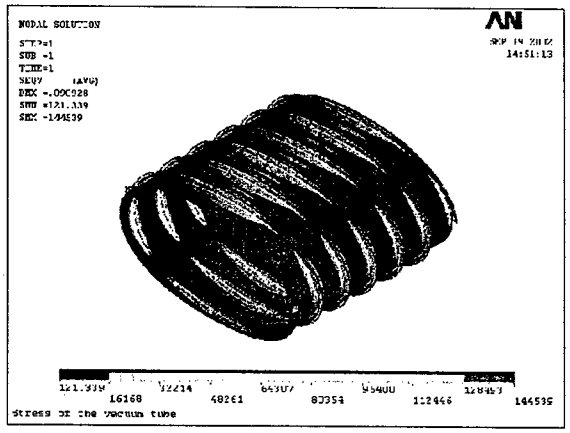

Figure 1. FEA structural model, stress plot

Fig. 2 shows the deformation of the beam pipe under vacuum pressure. For clarity, reinforce rib is not plotted. The major radius extends 0.055 inch (1.40 mm), and the minor radius shrink 0.089 inch (2.26 mm).

From these results, we see that the proposed beam pipe will survive the vacuum pressure. The only thing not so perfect is that the deformation is a little too big. To achieve required tube shape under vacuum condition, the

0-7803-7738-9/03/$17.00 © 2003 IEEE

beam pipe initially can be made with smaller major radius and larger minor radius.

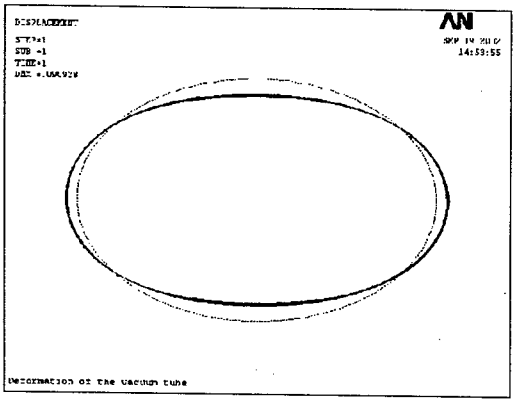

Figure 2. Deformation of Beam Pipe

ELECTRO-MAGNETIC EFFECTS

Since the beam pipe is made of metal, time varying external magnetic field will induce eddy current. This eddy current will have two effects: distort the external field and cause power loss.

For a single spiral rib, an argument based on symmetry will lead to the conclusion that the eddy current caused by the spiral rib is negligible compared with the beam pipe itself [2]. Once we have this conclusion, the analysis of the eddy current effects is easy. For oval beam pipe of infinite length, analytic solution can be found [2]. However, for completeness, we made a finite element model, and did some harmonic analysis. The results are compared with the analytic results.

For electro-magnetic analysis, we model only the beam pipe without the reinforce rib. Use 3-d element, we made a quarter model. The model length is 1 inch. The inside and outside are filled with vacuum and air elements. Since the effect is linear, we can analyze the 15 Hz field and 30 Hz field separately. The constant field has no eddy current effect.

For 15 Hz field, B_1 = 0.632 T, calculated power loss is 1.957 w, for 30 Hz field, B_2 = 0.632/8 T, power loss is 0.122 w. Add together, we have 2.079 w power loss for our model. Remember our model is a quarter model, so the total power loss should be 8.316 w/in, or 327 w/m. This number compare well with the analytical result, which is 323 w/m.

Now consider the magnetic field inside the vacuum tube on $y = 0$ plane. The results show that the magnitudes are almost exactly the same as that of the applied external fields, and the lag angles are extremely small. That is to say, that the magnetic field distortion due to eddy current is extremely small. Therefore, no correction will be needed. The analytic results are: The ratio of magnetic field induced by the eddy current to the external field is 0.613e-3 for 15 Hz field and 1.227e-3 for 30 Hz field.

The electro-magnetic force is calculated analytically. It is a time changing quantity. We integrate the total force acting on $x > 0$ half beam pipe

$$F = 1.462\, B\dot{B}$$

The Maximum value of this function is 110 N/m. Compare this with the total force caused by the vacuum pressure, which is 10157 N/m. We have the result that the former is about 1% of the later. Therefore when we did the structural analysis by neglecting the magnetic force, the error will be about 1%.

CONCLUSIONS

In summary, we restate the main results of the analysis in following: 1) The maximum stress in beam pipe under vacuum pressure is 144 ksi. 2) The deformation extends major radius 1.40 mm, and shrinks the minor radius 2.26 mm. 3) The power loss under considered magnetic field is 327 w/m. 4) The eddy current induced magnetic field can be neglected compared with the external field. 5) The electro-magnetic force can be neglected compared with the vacuum pressure.

From this study, we know that the proposed beam pipe should work, at least in theory. The problems will occur during manufacturing process, there the imperfections will be introduced. Some degree of damage to the tube material will be unavoidable. Since this tube is so thin, the final strength of the beam pipe will completely depend on the perfection of the manufacture techniques, therefore prototype study is needed.

REFERENCES

[1] ASME, *Pressure Vessel Code* (1995), Section VIII, Division 2.

[2] Z. Tang, *A New Kind of Vacuum Tube for Proton Driver* (2002), FERMILAB-TM-2118

ACCELERATOR AVAILABILITY AND RELIABILITY ISSUES*

S. Suhring, Jefferson Lab, Newport News, VA 23606, USA

Abstract

Maintaining reliable machine operations for existing machines as well as planning for future machines' operability present significant challenges to those responsible for system performance and improvement. Changes to machine requirements and beam specifications often reduce overall machine availability in an effort to meet user needs. Accelerator reliability issues from around the world will be presented, followed by a discussion of the major factors influencing machine availability.

INTRODUCTION

"The people at the other end of the machine must be happy." This quote by Hamid Aït Abderrahim [1] of the Centre d'Etude de l'Energie Nucléaire is both broad and true. No matter which large accelerator one considers—from synchrotron light sources, which have many dozens of simultaneous, short-run users, to high energy machines like Fermi's Tevatron with experiments that run for years, to recirculating CW superconducting machines like Jefferson Lab's electron accelerator, to machines presently under construction like the Spallation Neutron Source—happy people are the result of machine performance at a level that satisfies all of the affiliated parties.

Machines are built with a number of specific goals in mind, of which availability is just one. Other goals such as energy, luminosity, number of users, and throughput of research are just as likely to be sacrificed once the reality of operation settles in. For an experimentalist, beam energy might be sacrificed in order to keep the integrated beam delivery time / luminosity high. For a lab manager with a limited budget, beam time might be sacrificed to reduce power bills, maintenance deferred to lengthen machine run time, or spare parts inventories depleted. For the technical staff, documentation and system performance may never reach the intended level of excellence.

This paper will look at some of the common issues that affect the availability of existing large machines, and it may serve to help future projects in their planning, design, construction, and commissioning.

RECORD KEEPING

"A major difference between a 'well developed' science such as physics and some of the less 'well developed' sciences such as psychology or sociology is the degree to which things are measured." Fred S. Roberts [2]

Accurate record keeping of problems that interfere with beam delivery is central to keeping a machine operating well and making improvements to performance. These records should be started at the beginning of the commissioning stage and should be made available to anyone interested in the information. The machine operations group is the logical choice for record keeping and high-level analysis of lost time events. Recording a problem should be easy, and each event description should include actual times, duration, system, component, cause, and additional comments describing the event in detail.

Of course, some of this information may be incorrect as initially recorded, so a filtering of the information should take place. Such filtering should be done by a knowledgeable staff member who is familiar with all aspects of the machine and who has reasonable negotiating skills so that allocation of lost time can be fairly attributed. System owners should also be able to check regularly on their own system's lost time so that if corrections to the records are needed, they can be made.

The approach taken at Jefferson Lab is to record any and all system failures. This method is not universally used at other labs. JLab's philosophy is to keep 'luck' from entering into the discussion. If a system is down and another component fails, then both items have lost time recorded. This approach to lost time bookkeeping should not be confused with the Department of Energy contract metrics for beam delivery. The first identifies breakdowns or unacceptable performance; the second revolves around beam delivery time accounting. By recording all failures, honest assessments of overall system performance can be made and used for resource allocation decisions.

Early efforts to combine downtime information from laboratories around the world took place in the mid 1990s. [3] This attempt at data compilation was done to improve information exchange and to aid in the design effort of proposed machines. RAM (Reliability, Availability, Maintainability) studies were commonly discussed and to a lesser level still are. [4] However, projected performance of future machines based on an extrapolation of existing machine reliability has certain inherent flaws. Most importantly, the amount of data available is insufficient to make availability estimates. [5] Also, the generalization of system performance doesn't often overlay with the exotic nature and size of new machines. The revitalization of a worldwide reliability database is recognized as an important activity, and efforts are underway at the European Synchrotron Radiation Facility (ESRF) to develop just such a resource. [6]

Reliability theory relies on sound mathematical processes where Mean Time Between Failure (MTBF) and other terms can be measured, manipulated, plotted, and studied. [7] A typical visual representation of reliability theory is the bathtub curve, wherein a

*Supported by DOE Contract #DE-AC05-84ER40150

0-7803-7738-9/03/$17.00 © 2003 IEEE

component will have a high number of failures early in its life (startup problems or infant mortality), settle into a much lower failure rate during its useful lifetime, and then, near the end of its useful life, the component group will begin to degrade (see Figure 1).

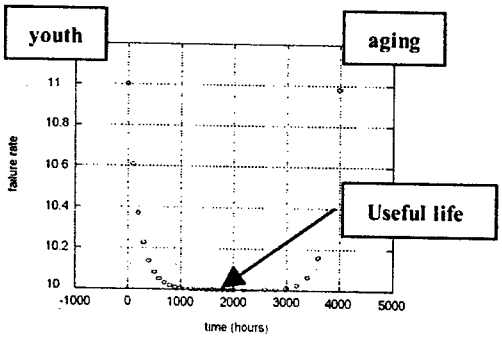

Figure 1: Bathtub curve.

The complexity of modern machines with hundreds of klystrons, thousands of magnets, tens of thousands of cable connections, and hundreds of thousands of control points does not easily allow for in-depth mathematical analysis for improving machine performance.

PRACTICAL RELIABILITY

"In a linear collider, all systems from injectors to beam dumps must be fully operational on every pulse."
ILC-TRC [8]

Who in our field would wait for a large enough statistical sample of failures before deciding on a course of action to improve the system in question? One failure is a point event. Two points imply a trend. By the time a problem occurs for a third time, the trend is well established and will not go away. The RF system engineers at Paul Scherrer Institut (PSI) analyze each and every failure. [9] This requires a significant investment, both in people's time and in data acquisition tools, but it has allowed PSI to quickly respond to problems and raise the reliability of their RF system to extraordinary levels.

Another means for improving reliability is to build enough redundancy into the system so that a certain number of failures do not interfere with machine performance. Experience has shown that when additional RF overhead is available, experimentalists will lobby for higher energy. This puts machine availability in jeopardy. It also highlights the difficult decisions that are made when trying to meet the needs of a user community.

There is no equation that can be used to calculate the risk/benefit ratio for the institutional decision to push a machine to higher performance goals. Often the opposite is true: performance goals are relaxed in order to allow for more stable machine operation. [10]

COMMON PROBLEMS

"There are a large number of things that can go wrong."
Roger Erickson [11]

If we begin to look at common problems among machines worldwide, a number of similarities emerge, not all of which can be discussed in this publication.

Water

Whether it be frozen pipes [12, 13], blocked flow [14, 15], failed hoses [16], erosion of fittings [17], or the interaction of dissimilar metals [18], water and its handling rank high among 'simple' systems that are a major source of lost time. Low Conductivity Water (LCW) and Deionized Water (DI) are often used interchangeably, and for this paper the distinction is unimportant.

If a perfect water system were to be designed, it would meet the specifications needed to provide adequate cooling, have redundancy in its pumps, and have the necessary monitoring to anticipate failures. And it would work from the start. The diabolical aspect of LCW problems is that they are often unseen until too late.

As an example, the original LCW plant at Jefferson Lab was constructed with iron body pumps and steel feed tanks. It operated without conductivity controls, relying on a 10% side stream through DI bottles. It operated for ~1 year before magnets began to overheat due to clogged coils. Samples were taken, and large concentrations of iron oxides were found. Conductivity monitoring and controls were installed and the iron/steel components replaced with stainless steel. Set points of 2 MΩ, 95°F ±0.5°F were established for the two 2000 gpm systems.

Eight years later, the magnets again began to overheat due to clogged coils. The sample analysis indicated copper oxides. The source? Oxygen levels within the water system were at their worst possible levels (~200 ppb) and were reacting with the copper cooling coils (see Figure 2). [19]

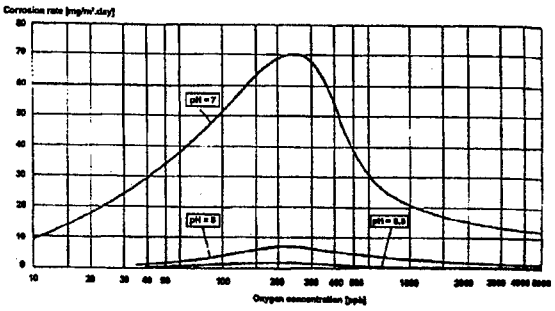

Fig. 2: Influence of dissolved oxygen on copper release rate. [20]

The solution? Installation of a de-oxygenation system to bring the concentration down to <10 ppb, full flow 0.5 micron filters, and hot citric acid etching and water flushing of the magnet coils to remove any built up material. Additionally, LCW system entry procedures were revised to require significant flushing and purging of all air prior to returning to normal flow circulation.

Buildings

"Infrastructure, although of minor importance in scientific minds, plays a non-negligible role . . ." Managing Science [21]

In machine enclosures and their service buildings, the lighting should be of high quality to promote good quality work. Furthermore, buildings should be equipped with air conditioning. This might be considered an extravagance, but when viewed as a reliable method of controlling the largest sources of premature electronics failure—heat, humidity, and dust—air conditioning becomes a necessity. Also, improved work conditions foster better quality technician performance, especially during the installation and commissioning stage of projects. Retrofitting buildings for air conditioning can be difficult. Conduit, cable trays, fire headers, and cooling water lines may limit air distribution options.

Electricity

Budget considerations and machine performance goals figure prominently when considering site power. The ~6 M€ capital outlay at ESRF resulted in an increase in availability from 95% to 98% with the installation of 10 1 MVA diesel engines and their associated controls, switches, and conditioners. [22] In addition to providing a more regular source of electricity, damage to equipment from power interruptions was greatly reduced.

If a real time backup power system isn't part of a power plan, then multiple power feeds onto a site will provide a quick means of restoring necessary services in the event of a supply problem. Finally, a robust site power distribution plan is incomplete unless the electrical substations are on loops that allow for "make before break" switching of feeds.

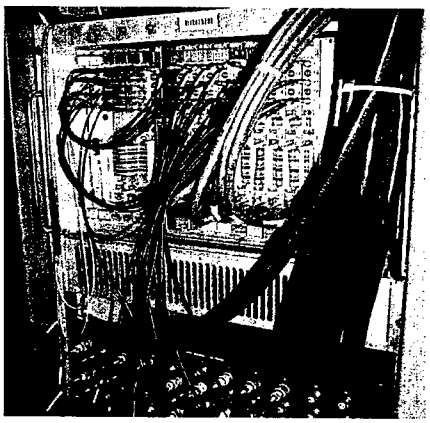

Figure 3: Filter and fan trays obstructed by cables.

Fans, Filters, and Cables

On a smaller scale, other seemingly simple items that have caused significant lost time are fans, filters and cables. Crate filters require periodic cleaning and small fans fail after 3–4 years. Problems arise when components are not easily serviced. With real estate in electronics racks at a premium, the tendency is to make designs as compact as possible, sometimes to the detriment of serviceability. Poor cable runs or the need to otherwise disassemble equipment may impede routine maintenance. There is the potential to create new problems by simply disturbing the equipment. [23] Sufficient rack space and selection of maintainable equipment is important to being able to keep systems operational (see Figure 3).

Electronics

At the board level, consideration should be given to the use of chip, trim, and low temperature coefficient precision resistors [24] where small magnet power supply regulation is crucial. Board standardization and interchangeability can significantly improve machine reproducibility and reduce set up time. JLab corrector magnet power supplies all regulate to ±2 mA (see Figure 4).

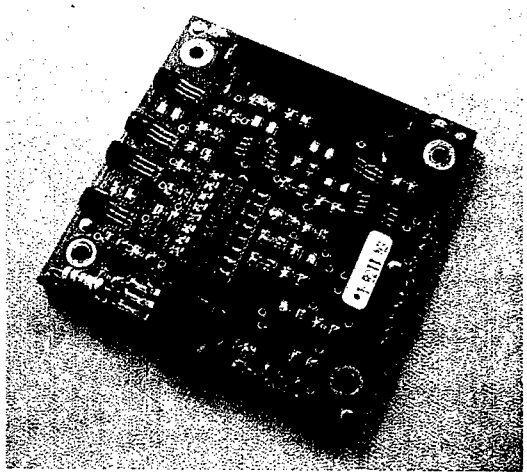

Figure 4: Analog block layout.

Software

Though component selection plays a large role in machine performance, understanding and controlling the devices may be even more critical. Picture a magnet mapping test area. Early in a project, detailed measurements of magnet performance are made. Were the measurements made using the machine's power supplies and control software? Was the hysteresis protocol even known when the mapping took place? Will the control system used to run the mapping test stand have the same timing and sequencing as the operational machine? Will the magnetic field in the test stand be the same as that seen by the beam? The answers to these questions will in

large part determine the time it takes to set up machines that require frequent energy changes.

Other software issues such as file management, speed (control system response time), and channel access security seem to be so integrally meshed with hardware that they are especially difficult to assess when problems arise. If the focus of machine availability were solely on hardware, then components could be designed toward perfection. Software has interdependencies between programs, applications, signals, and displays and is of such importance to operations that well regulated version controls are essential to machine availability. Test plan implementation should include roll back or back out procedures that are quick, clean, and well documented. High Level Applications involving energy, phase, and beam position are so closely interconnected that it can be difficult to assess problems in beam stability that result from the interaction of feedback loops.

Commissioning

Long-term machine performance can be enhanced with early beam commissioning tests. These studies can help identify design flaws and weed out component problems. Furthermore, the startup period can be used to develop procedures for safe, efficient operations. [25] A staged commissioning plan may require temporary radiation shielding walls and access control equipment. It may also need to address life safety issues of egress. But early beam-based tests provide an opportunity to develop a conduct-of-operations protocol, train operators and support staff, get documentation in order, and test software applications.

Machine Tuning

Machine setup and tuning is scheduled following planned shutdowns and maintenance periods. But when equipment or software is underperforming, lost time from tuning can be significant. Diagnostic tools to check equipment, control system performance, and beam quality will play prominently in identification of system degradation. Monitoring tools are often integrally linked to the beam—identifying a problem might rely on the components causing the problem. Tune time, like other interruptions to beam delivery, should be tracked, analyzed, and acted upon, leading to improved availability.

CONCLUSION

"It is a true wonder that they run at all."
Sture Hultqvist [26]

Our machines run quite well, considering the complexity of the systems and the demands placed upon them by the user community. Hardware availabilities of 70%–90% have been reached at large energy frontier machines and as high as >98% at synchrotron light sources. [27]

The lost time that is more difficult to address is the single, large, unrelated, unexpected event. The stories are the stuff of legends—bizarre vacuum events, animals in transformers, flashlights inadvertently left in beam lines. These problems are rarely repeat offenders, and if they had been anticipated, would not have happened. Probability trees and system failure predictions rarely take the inconceivable into account, but these events often cause significant interruption to a program. It is at just such times that the focus of a laboratory and its creative and talented staff come together to solve the problem and return to more normal availability issues.

With constant attention to detail and dedicated staff, the sources of lost time are avoided by a rigorous design effort, or identified during commissioning and operation. Solutions are implemented as quickly and efficiently as possible.

The major sources of lost time are constantly changing. Today's worst offender can be identified, corrected, and no longer be a significant source of trouble, making way for the next improvement.

ACKNOWLEDGMENTS

The author would like to recognize the scientists, engineers, operators, and technicians whose passion for excellence is demonstrated daily in their quest to improve machine performance.

REFERENCES

[1] Hamid Aiit Abderrahim, Centre d'Etude de l'Energie Nucléaire, private conversation, Accelerator Reliability Workshop, Grenoble France, Feb 2002 http://www.esrf.fr/conferences/ARW/index.htm

[2] F.S. Roberts, Measurement Theory. Addison-Wesley, Reading, MA, 1979.

[3] C. Piaszczyk, "Developing a Reliability Database Using Records from Existing Accelerator Facilities". World of Accelerator Operations. Canada 1998. http://ops5.triumf.ca/wao98/070-086.pdf

[4] G.Dodson, "Accelerator Systems RAM Analysis" http://216.239.53.100/search?q=cache:Vhq5Dfx2XasC:www.sns.gov/projectinfo/operations/ARR/ASD_RAM_Analysis.ppt+George+Dodson,+RAM&hl=en&ie=UTF-8

[5] International Linac Collider Technical Review Committee, Second Report, 2003. p.429 http://www.slac.stanford.edu/xorg/ilc-trc/2002/2002/report/03rephome.htm

[6] L. Hardy. "Accelerator Reliability-Availability" EPAC'02. http://accelconf.web.cern.ch/AccelConf/e02/PAPERS/WEXLA001.pdf

[7] E.Karantzoulis. "Reliability Aspects and Synchrotron Light Sources". WAO, Japan 2003 http://conference.kek.jp/wao2003/

[8] ILC-TRC op cit. p.459

[9] P.K.Sigg. "Improving the Reliability of the PSI Proton Accelerator RF Systems". ARW'02. http://www.esrf.fr/conferences/ARW/proceedings/TUEAM/Sigg.pdf
[10] C.Y.Yao. et.al. "Spare Parts at APS". ARW'02. http://www.esrf.fr/conferences/ARW/proceedings/TUEPM/Yao.pdf
[11] R.Erickson. SLAC, personal communication. 2003
[12] C.L.Hodgkinson, "Reliability Experience at the SRS: Fault Analysis and Related Actions". ARW'02 http://www.esrf.fr/conferences/ARW/proceedings/TUEAM/Hodgkinson_paper.pdf
[13] Erickson, op cit.
[14] E. Lampo, LBL, personal communication. 2003
[15] P. Ingrassia, BNL, personal communication. 2003
[16] T. Ohshima, "Machine Troubles During User Time at the SPring-8." http://www.esrf.fr/conferences/ARW/proceedings/TUEAM/ohshima-doc.pdf
[17] H. Sato, et al. "Experience of the Erosion – Corrosion Problems in the Main Ring Cooling Water System at the KEK-PS". http://accelconf.web.cern.ch/AccelConf/p01/PAPERS/TPAH093.PDF
[18] G.Decker, ANL, personal communication. 2003
[19] W.Rust, "Accelerator Magnet Plugging by Metal Oxides: A Theoretical Investigation, Remediation and Preliminary Results". PAC'03.
[20] E.Maughan, "Case Study – Copper Based Cooling Water Systems," 2nd International Workshop on Mechanical Engineering Design of Synchrotron Radiation and Instrumentation. http://www.aps.anl.gov/asd/me/medsi02/presentation/case_study.pdf
[21] C.Geles, et al. Managing Science. John Wiley & Sons, Inc. 2000.
[22] J.F. Bouteille, "The 'HQPS' a system to increase the ESRF mean time between failures". ARW'02
[23] A.Hillman, et al. "Magnet Power Supply Reliability at the Advanced Photon Source". PAC'01. http://accelconf.web.cern.ch/AccelConf/p01/PAPERS/FPAH002.PDF
[24] S. Wood. Jefferson Lab, personal communication. 2002.
[25] Lampo, op cit.
[26] S.Hultqvist, The Svedberg Lab, personal communication. 1998.
[27] ILC-TRC op cit. p. 430

LOW-CONDUCTIVITY WATER SYSTEMS FOR ACCELERATORS*

R. Dortwegt†
Advanced Photon Source, Argonne National Laboratory, Argonne, IL 60439, USA

Abstract

The performance of low-conductivity water (LCW) systems is of critical importance at accelerator facilities. An imbalance of water chemistry, supply temperature, or component availability can have a direct impact on machine performance. Downtime of the LCW system for any reason can result in downtime of the entire accelerator. LCW systems for copper components are similar to stator cooling systems for electric power generating equipment with respect to the chemistry of soluble copper and resultant corrosion. The basics of copper corrosion and agglomeration mechanisms, impact of dissolved oxygen concentration and pH, copper solubility data and its relationship with temperature, and relative corrosion rates for various possible operating regimes are available from existing literature and will be reviewed. Water treatment for aluminum LCW systems is different than for copper systems and will be outlined. Fundamental features of control systems capable of controlling LCW temperatures within a fraction of a degree will also be discussed. Operational reliability is very much related to system design, component selection, and operating practices, and some anecdotal information will be offered based on the author's experience.

INTRODUCTION

Accelerator components made of copper are routinely cooled by deionized (DI), low-conductivity water (LCW). Release of copper oxides from parent surfaces is common. Releases comprise reddish-brown residue (Cu_2O) and, depending on the concentration of dissolved oxygen (DO), black residue (CuO). Copper oxide scale can be released and can agglomerate such that flow through system components is significantly restricted or blocked altogether [1].

Water treatment considerations for aluminum systems are quite different than for copper systems. This discussion will be based on the experience at the Advanced Photon Source (APS) where aluminum LCW systems are segregated from copper LCW systems.

Components such as accelerating structures and radio frequency (rf) cavities routinely require temperature conditioning to tolerances in the neighborhood of ±0.05-0.1°C [2]. Conditioning is commonly performed with the LCW system. Such tolerances can be maintained using commercially available fluid-handling equipment and instrumentation, provided certain design parameters and techniques are employed.

Operational reliability is a strong function of system design and component selection. Certain design and implementation practices result in tangible benefits to the accelerator operator in the form of reduced downtime and reduced durations of repairs if downtime occurs.

*Work supported by U.S. Department of Energy, Office of Basic Energy Sciences, under Contract No. W-31-109-ENG-38.
†dortwegt@aps.anl.gov

COPPER CHEMISTRY

From the point of view of copper chemistry, accelerator LCW systems can be compared to stator cooling systems in electric power plants. Like copper accelerator components, copper stators in power generation equipment are cooled using LCW and are subject to the effects of copper corrosion and subsequent agglomeration and plugging. Plugging is exacerbated by high heat flux across copper surfaces since copper solubility is reduced as water temperature rises. The information presented here is assembled from the existing literature in the power industry and from conversations with experts [3-10].

Corrosion Mechanism [11]

Oxygen (O_2) and carbon dioxide (CO_2) are present in water due to interactions with the atmosphere. An oxide forms at the metal surface, which, in the absence of other influences, is stable. The presence of CO_2 in the water results in the formation of carbonic acid (H_2CO_3), which dissociates into HCO_3^- and hydrogen ions (H^+). H^+, which has an affinity for the oxygen atoms of the oxide, readily reacts to form water. The copper at the surface is now left in its ionic form and readily dissolves. The metal surface, now unprotected by the oxide, is again exposed to water, DO, and H^+, allowing the process to recur.

Dissolved Oxygen Concentration

The corrosion rate of copper in water (at neutral pH) as a function of DO is indicted in Fig. 1 [12]. The maximum rate occurs in the range of 200-300 ppb. "Low oxygen" and "high oxygen" operating regimes are defined relative to this maximum. Corrosion in low-oxygen regimes

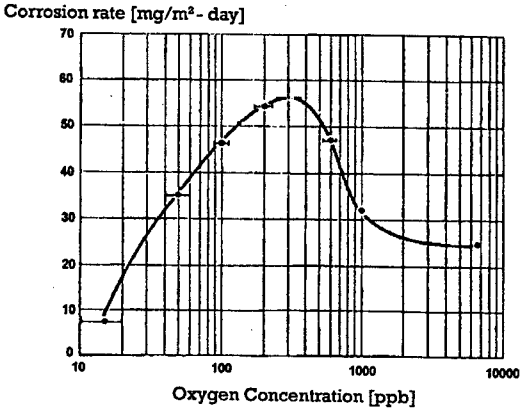

Figure 1: Corrosion rate vs. DO.

occurs mostly as Cu_2O. Corrosion in high-oxygen regimes occurs mostly as CuO. Copper cooling systems can be operated successfully in either regime. For high-oxygen systems, oxygen content must be actively maintained as, without the deliberate introduction of oxygen, DO will fall naturally as a result of the corrosion process. In the case of stator cooling systems, the choice is usually specified by the manufacturer but is sometimes changed by the owner if operating experience indicates a benefit [10,13].

Influence of pH

H^+ concentration influences the corrosion rate, as indicated in Fig. 2 [12]. The rate is minimized at pH values approaching 8.5 and greater. The Pourbaix diagram in Fig. 3 [14] indicates stable forms of copper in aqueous solution as a function of pH and metal potential. For pH values below 7.0, the copper ion is stable in solution. Formation of the ion occurs from the oxide state when pH is just below 7.0. Reaction of H^+ with the oxygen of the oxide occurs readily under these conditions.

For pH values above 7.0, the preferred form of the metal is the oxide. Replacement of the oxygen in the oxide does not occur as easily and slows the corrosion mechanism. This is consistent with Fig. 2 and provides an understanding of reduced corrosion rates when the solution is alkaline.

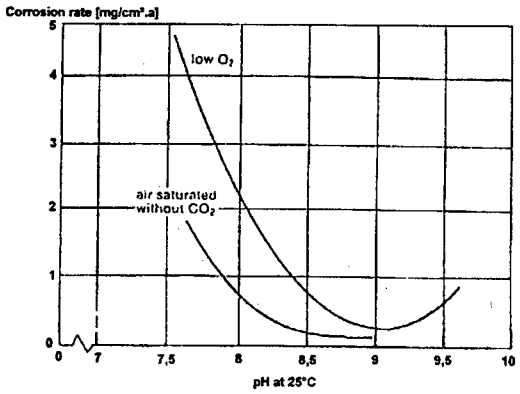

Figure 2: Corrosion rate vs. pH.

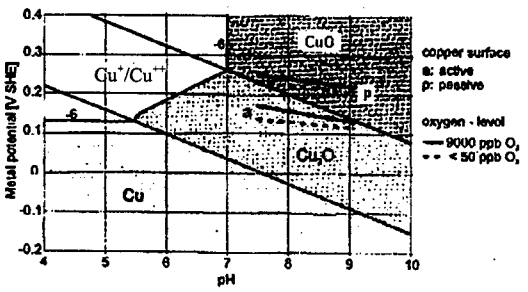

Figure 3: Pourbaix diagram for copper.

Influence of Temperature

Temperature plays a significant role in the solubility of copper in water, particularly at neutral to acidic pH. Figure 4 [13,15] indicates the relationship of copper solubility as a function of temperature for various values of pH. Figure 5 [13,15] indicates the relationship of solubility in terms of pH for various temperatures. When pH is lower than 7.0, the influence of temperature is more noticeable and provides an explanation for water flow restrictions that occur at the outlet ends of copper components where heat transfer takes place along the length of the component. It is logical to assume that most accelerator LCW systems operate under these constraints.

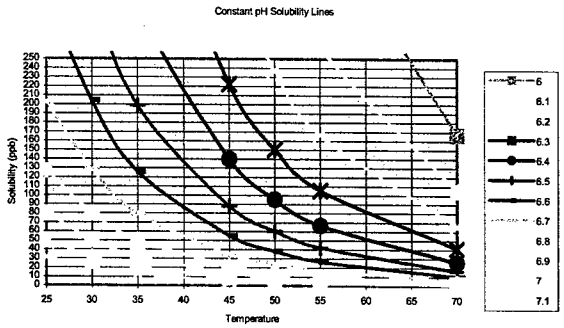

Figure 4: Copper solubility vs. temperature.

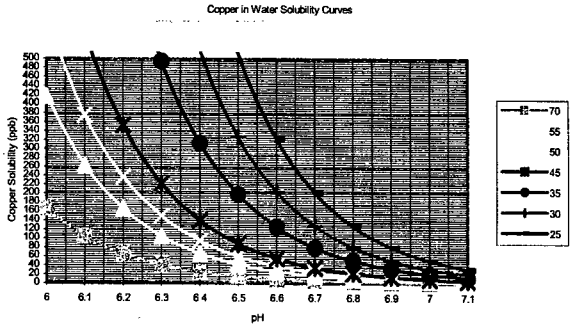

Figure 5: Copper solubility vs. pH.

Operating Regimes

Several options exist for choosing an operating regime for a copper-water system. These are:

- Neutral pH, low oxygen,
- Neutral pH, high oxygen,
- Elevated pH, low oxygen, and
- Elevated pH, high oxygen.

Figure 6 shows corrosion rate data for various operating regimes [13].

Limitations on Operating Regimes

The relationship between pH and resistivity of DI water is shown in Fig. 7. Most resins have a cation component in the hydrogen form and produce DI water to the left side of the curve (pH<7). If cation is in the sodium form, DI water is produced to the right side of the curve (pH>7).

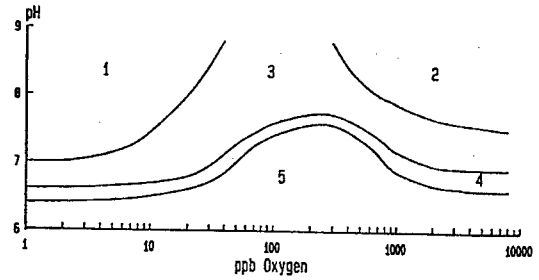

1&2: Corr. rate <0.1 µg/a 3: 0.1-0.4 µg/a 4: 0.4-1.0 µg/a
5: >1.0 µg/a

Figure 6: Corrosion data at various operating regimes.

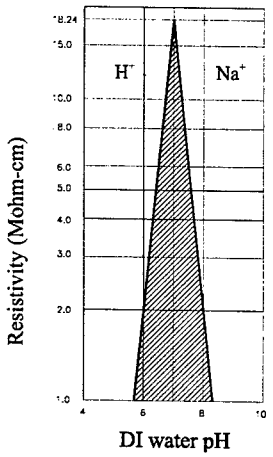

Figure 7: Resistivity limits of DI water.

Operation of a water system at a pH of 8.5 would require a resistivity of 1 Mohm-cm or lower. For many accelerators, this is not acceptable [1]. For example, at the APS, a resistivity value below 3.0 is not acceptable from the point of view of leakage currents. A more realistic minimum for resistivity is around 5.0. The corresponding maximum pH that is feasible is about 7.5.

With the maximum pH of an accelerator LCW system limited to 7.5 (essentially neutral), it is clear that the low-oxygen operating regime is more desirable since corrosion rates can be reduced to a lower value than for high oxygen (see Fig. 6).

Means of Controlling pH

It is common for resistivity to be maintained in LCW systems by the use of ion exchange resins. Positively charged ions are typically removed from the system by the cation resin and replaced with hydrogen ions. When this process occurs, the hydrogen ion content of the water system is increased (i.e., pH decreases). If the cation resin is processed in the sodium form, however, positively charged ions are replaced with a sodium ion, and the pH value increases.

Such a means is being employed in a stator cooling system at an Eskom generating facility in South Africa [13]. The treatment stream can be passed through either of two mixed-bed resin tanks as indicated in Fig. 8. When pH falls to a low limit, the mixed-bed tank with cation resin in the sodium form is brought online while the mixed bed in the hydrogen form is isolated (pH will rise). When pH again rises to a high limit, the mixed-bed tank with cation resin in the hydrogen form is brought online while the mixed bed in the sodium form is isolated (pH will fall).

Although pH control is achieved, the sampled process variable is resistivity (or conductivity) because of the direct relationship between resistivity and pH (see Fig. 7). It is important to verify periodically by direct pH measurement that the system exists on the positively sloped portion of the pH-resistivity curve (Fig. 7).

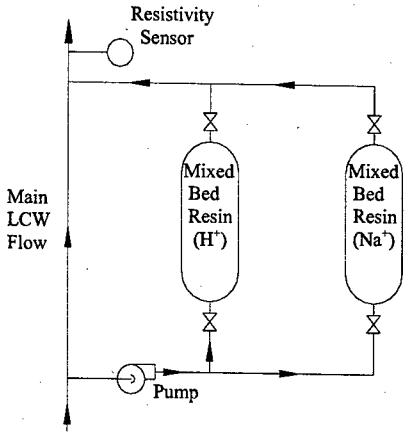

Figure 8: pH control method with mixed-bed resins.

Dealing with Copper Corrosion

Since copper corrosion can be minimized but not prevented altogether, it is necessary to be aware of techniques that will prevent or reduce the possibility of plugging. Experience at the APS indicates there are benefits to employing some of the following practices [1].

The use of small (<1/8" diam.) orifices for regulation of water flowrate should be avoided. This includes the use of passive flow-control devices having small, variable-area openings. Experience indicates that such orifices eventually experience build-up of copper oxide scale that reduces (or even stops) flow. At APS, such orifices and flow regulators are being replaced successfully with lengths of small-diameter tubing (e.g., 1/4" and 5/16" diam.). Such tubing is usually coiled for convenience.

Point-of-use filtration to around 0.5 micron nominal (2 micron absolute) has been successful. Filters are replaced only when differential pressure indicates a build-up. Changing filters on a routine schedule is avoided because it allows the ingress of oxygen and promotes higher corrosion rates.

All LCW that is treated in the central treatment loop is filtered to 0.05 micron. The treatment rate is approximately 5% of the total system throughput.

All make-up water is introduced to the LCW system at a vacuum deaerator to remove all but trace DO.

Branch lines that are not used regularly are maintained with a continuous minimum flow. A branch line with no flow can be a place where DO accumulates when the system is opened for maintenance. If not flushed with low-oxygen water, the branch will be a continuous source of DO contamination where it connects to rest of the LCW system.

Pump seals are flushed from the stuffing box out to the pump suction to avoid direct impingement of copper particles on seal faces. This avoids the build-up of copper oxides on seal faces, which was observed after numerous failures.

The use of flow-measuring equipment with moving parts is avoided. These moving parts are eventually coated with copper oxide. Moving parts are likely to fail in time.

It is imperative that the source of water for the initial system fill and for make-up be free of biological contamination. Once the system is filled, water must be kept circulating continuously to avoid stagnation and the possible growth of bacteria, as microbiologically influenced corrosion (MIC) can occur. A further precaution that may be taken is the use of ultraviolet (UV) radiation treatment of the polishing stream. The UV radiation interferes with the reproductive process of any microbes. Operation at trace DO levels further gives aerobic biological constituents (the first bacteria to collect in a colony) little oxygen to survive.

ALUMINUM LCW SYSTEMS

The information presented in this section is based on the implementation of aluminum LCW systems at the APS where aluminum accelerator components are conditioned by independent water loops operating at approximately 25°C containing no copper. This decision was taken to avoid a conflict in the needs between aluminum LCW treatment and treatment for copper LCW. As a result, electrochemical exchange of ions between copper and aluminum components is prevented.

Aluminum surfaces in LCW systems benefit from the very stable oxide layer that forms naturally, especially during initial operation. It is desirable to clean inside surfaces by a mild acid flush (such as an environmentally friendly, citric-based detergent) or by electropolishing. Upon initial fill with DI water containing naturally occurring levels of oxygen, heating the water to as high as 130-150°C will cause the deposition of a protective oxide layer to passivate inside surfaces.

Water treatment needs include only the polishing of the system with mixed-bed resins in the standard hydrogen form. Systems at APS operate between 13-16 Mohm-cm.

These systems are occasionally used to condition the APS vacuum chambers at 130-150 °C ("bakeout") prior to operation at ultrahigh vacuum. During this process, the water in the system is maintained in a low-conductivity condition by purging DI water (13-15 Mohm-cm) from a cooling loop into the heated bakeout loop at a rate of around 10% of the total bakeout flowrate. Water is simultaneously removed from the bakeout loop at an equivalent rate with the use of a heat recovery exchanger to minimize the heat load on the clean water purge. In this manner, mixed-bed resins are not exposed to bakeout system temperatures

TEMPERATURE REGULATION

Regardless of the tolerance of a temperature control system, traditional regulation systems employ feedback loops known as proportional-integral-derivative (PID) systems to control temperature. These systems have a sensor to detect the temperature and a controller to compare the actual temperature to a desired set point. The controller computes and delivers an output signal to a valve that throttles LCW flow through a heat exchanger. A system that has been successful at the APS is shown in Figure 9.

The detection of the actual LCW temperature is critical to maintaining regulation within tolerance. It is imperative that the resolution of the temperature-detection system be at least an order of magnitude better than the desired temperature tolerance. For example, if a tolerance of ±0.1°C is desired, it is necessary to detect changes in temperature on the order of 0.01°C or smaller.

The resolution of the temperature detection portion of the loop is determined by the incremental steps corresponding to the output of the analog-digital (A-D) converter in the processor. For example, if a temperature transmitter with a range of 50 °C is employed with a 16-bit A-D converter, the resolution will be $50/2^{15} = 0.0015$ °C (one bit is used for the sign of the number).

Throttle control valves must be matched to the application such that the smallest incremental change of valve position results in a temperature change less than the desired tolerance. Valves with actuators/positioners having a resolution of 0.25 to 0.5% have been used successfully.

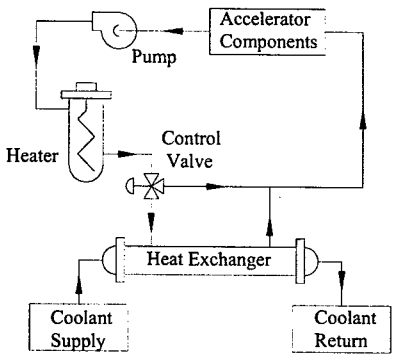

Figure 9: Temperature control loop employing mixing.

The choice of valve style is equally critical. The valve must have a dynamic range that is useful over a wide range of valve positions. One choice that has been employed successfully is a characterized three-way rotating plug valve. If a single valve or combination of two valves is used, a V-ball or characterized seat ball valve is recommended. Such valves can have a dynamic range on the order of 100:1.

It is essential that operating personnel responsible for system performance understand the process of control valve tuning to provide for the proper response of the valve to process upsets. For steady-state temperature control systems, the derivative term is usually not employed. Classes and texts to learn methods for control valve tuning are available from a range of sources [16].

Successful implementation of temperature control systems requires that time delays between temperature detection and valve actuation be minimized. It is imperative that the temperature sensor itself have a short time constant (e.g., 4 s) and be immersed directly in the water stream. The sensor should be located as near to the control valve as possible, and the valve should be located as near to the heat exchanger as possible.

Response times can also be reduced by implementing a system that employs mixing of relatively warm and cool streams to affect the delivery temperature as shown in Figure 9. If the mixing type system is replaced by a system that throttles coolant flow, changes in delivered water temperature require changes of the entire exchanger temperature rather than that of the delivered water only. This results in greater thermal inertia.

Accelerator components may not provide sufficient heating of LCW to allow for mixing of streams that are matched to the control valve and heat exchanger. In this case, it may be necessary to provide an additional heat source.

RELIABILITY

Operational reliability can be improved by following practices that have proven their value:

- Combine elements having similar flow rates into common series flow circuits to reduce the number of flow elements and related instrumentation,
- Remove flow-related instruments from all secured enclosures to reduce the time required to make repairs and exposure to radiation.
- Avoid flow elements with moving parts. Obstruction-type flow elements are an excellent alternative.

ACKNOWLEDGEMENTS

The author would like to acknowledge Mr. E. V. Maughn of The College of Knowledge, Duisburg, Germany and Mr. J.D. Aspden of Eskom, South Africa, who have directed the author to the literature in the field of copper corrosion and whose expertise and collegiality have been key factors in making this information available to those in the accelerator community.

REFERENCES

[1] R. Dortwegt, C. Putnam, and E. Swetin, "Mitigation of Copper Corrosion and Agglomeration in APS Process Water Systems," 2nd Int'l Workshop on Mechanical Engineering Design of Synchrotron Radiation Equipment and Instrumentation (MEDSI2002), Sept. 5-6, 2002, Argonne, IL, pp. 462-468 (2003).

[2] R. Dortwegt, S. Pasky, and M. White, "Improved Temperature Regulation of APS Linac Rf Components," Proc. of the XIX Int'l Linac Conf., Chicago, IL, 23-28 August, 1998, pp. 1001-1003 (1999).

[3] Electric Power Research Institute, *Primer on Maintaining the Integrity of Water-Cooled Generator Stator Windings*, prepared by Ontario Hydro, Toronto, Ontario, Canada, EPRI-TR-105504, Project 2577, Final Report (September 1995).

[4] P.H. Effertz, and W. Fichte, "Beeinflussung der Kupferkorrosion in hochreinem Wasser," *Yearbook of "vom Wasser Journal,"* pp. 433-441 (1974).

[5] H.G. Seipp, "Das Betriebsverhalten von Kupfer in wassergekuhlten Generatorwicklungen," VGB Kraftswerktechnik 59, **3**, pp. 72-75 (1979).

[6] H.G. Seipp, "Das Korrosionverhalten von Kupfer in wassergekuhlten Generatorwicklungen," VGB Kraftswerktechnik 59, **3**, pp. 245-248 (1979).

[7] H.G. Seipp, "Betriebsfahrungen mit wassergekuhlten Generatorwicklungen," VGB Kraftswerktechnik 63, **5**, pp. 408-413 (1983).

[8] K. Schleithoff and H.W Emshoff, "Optimization of the Conditioning of Generator Cooling Water," VGB Kraftswerktechnik 70, **9**, pp. 677-681 (1990).

[9] R. Svoboda, H. Sandmann, H. Seipp, and C. Liehr, "Water Chemistry in Generator Water Cooling Systems," Proceedings of the Interaction of Non-iron Based Materials with Water and Steam, Piacenza, Italy (June 1996).

[10] Eskom Standard GGS 0323, "Chemistry Standards for Water Cooled Generator Windings (Stator Coolant)," Rev. 5 (October 1998).

[11] H. Scholer and H. Euteneuer, "Corrosion of Copper by Deionized Cooling Water," European Accelerator Conference (EPAC), Rome (June 7-11, 1988), pp. 1067-1068 (1989).

[12] E.V. Maughan, "The Basics of Stator Coolant Water Chemistry," pre-seminar workshop presented at the 2000 International Chemistry On-Line Process Instrumentation Workshops in Clearwater, Florida (Nov. 14-17, 2000).

[13] Work performed by Eskom (J.D. Aspden), private communication.

[14] Work performed by Alstom, Switzerland (R. Svoboda), private communication.

[15] Work performed by Electricite de France, private communication.

[16] P.W. Murrill, Fundamentals of Process Control Theory, Instrument Society of America, research Triangle Park, North Carolina, USA, 1991.

ACCELERATOR MAGNET PLUGGING BY METAL OXIDES: A THEORETICAL INVESTIGATION, REMEDIATION AND PRELIMINARY RESULTS*

W.W. Rust, Ph.D., P.E., TJNAF, Newport News, VA 23606, USA

Abstract

The Thomas Jefferson National Accelerator Facility has experienced magnet overheating at high power. Overheating is caused by cooling water passages becoming plugged and is a direct result of the Dean Effect deposition of corrosion products suspended in the water. Solving simplified dynamic model equations of the flow in the magnet tubing bends yielded a relationship for plugging rate as a function of particle size, concentration, velocity, channel width and bend radius. Calculated deposition rates using data from a previous study are promising. Remediation has consisted of submicron filtration, magnet cleaning, and dissolved oxygen removal. Preliminary results are good: no accelerator outages have been attributed to magnet plugging since the remediation has been completed.

BACKGROUND

The Thomas Jefferson National Accelerator Facility (Jefferson Lab) Continuous Electron Beam Accelerator (CEBA) is a race track configured, multi-pass superconducting linear electron accelerator with magnets in the arc sections that recirculate the beam. The magnets, klystrons and power supplies are cooled with low conductivity water (LCW), which is supplied by four LCW systems.

All of the LCW systems are similar in design and construction. Circulating pumps move cooling water through headers and cooling passages associated with each system. The water returns to heat exchangers equipped with PID controllers that actuate three-way valves to maintain the desired temperature. Side stream mixed bed resin systems are used to polish the water. Each system is protected by pre and post filter arrays, sized for the appropriate flow through the resin bottles. All of the systems are equipped with combination head and make-up feed tanks that are maintained under positive nitrogen pressure.

The piping system is made of stainless steel, fibre cast pipe, copper pipe and tubing, plastic or rubber connection hoses, and brass hardware. Some magnets have capillary-like, sub-millimeter cooling passages.

Near pure water flowing through metallic piping tends to accumulate oxide particles. Over time, the particles will form a residue on the conductor walls. The residue is less thermally conductive than copper and interferes with heat transfer. Moreover, the residue noticeably affects the small passages by gradually blocking the flow of water, which further reduces heat transfer. Eventually, these magnets shut down due to overheating.

System improvements have been ongoing since the construction was completed. Nevertheless, corrosion related plugging problems emerged as beam energy increased and maintenance intervals decreased. A literature search revealed that the Fermi National Accelerator Laboratory (FNAL) had experienced similar problems and had solved them using mechanical oxygen removal and full flow filtration [1]. The Jefferson Lab began a trial program that emulated the equipment installed at FNAL, and hopefully will achieve comparable results.

ANALYTICAL ANALYSIS

Fluid flowing through a curved tube has a dynamically induced, secondary circulation that is normal to the main stream [2]. This effect was first investigated by Dean. [3]. Knowledge of the behavior of the induced flow field in terms of relevant fluid properties and design parameters could be used to predict the plugging rate. It can be shown that the average deposition rate for film of particles on a tube wall is:

$$\frac{dh}{dt} = c\Delta R\left[\frac{1}{A}\int\frac{\partial V_r}{\partial r}dA\right] \qquad (1)$$

Where h is the film thickness, c is the particle concentration, ΔR is the particle diameter, A is the deposition area along the radius of curvature, and V_r the radial component of the flow. Determining the value of the integral, even for a simplified case, could serve as guide for experimental verification and as a point of departure for future work.

Sandeep and Palazoglu [4] present an overview of the current work in secondary flow in coiled tubes, particularly with respect to heat transfer. The Dean number is defined as the product of the Reynolds' Number and the square root of the ratio of the tube diameter to the radius of curvature. The Dean number is modified by using the hydraulic radius non-circular channels. Although square and round passages are used in magnets, only square channels are analyzed here. To further minimize complications, the modelling for this problem will neglect second order effects to the extent necessary as discussed below.

The continuity equation, Eq. (2), and the momentum equation, Eq. (3), for incompressible flow are shown below.

$$\nabla \cdot V = 0 \qquad (2)$$

$$\rho\frac{\mathbf{DV}}{\mathbf{D}t} = \rho\mathbf{g} - \nabla\mathbf{p} + \mu\nabla^2\mathbf{V} \qquad (3)$$

*Work done under US DOE Contract DE-AC05-84ER0150

0-7803-7738-9/03/$17.00 © 2003 IEEE

A rectangular cylindrical co-ordinate system (r, θ, z) best describes a square passage flow channel. The inside radius (r_0) is measured from the origin. The dimension of the channel is w by w, and the inside lower corner is located at (r_0, 0, -w/2).

The momentum equation can be modified for pipe flow by realizing that gradients along the flow direction are small. [5] For a magnet flow passage, the tubing is usually wound with 90-degree bends with a section of straight tube between bends. The flow is assumed to be fully developed, and the velocity profile across the channel does not change appreciably in the time needed to pass through the bend. Also, the cross channel pressure gradient and flow velocity is small compared to its second derivatives. Applying these assumptions to continuity and momentum equation, one obtains the following set of equations governing the flow field, Ω:

$$\frac{\partial V_r}{\partial r}+\frac{\partial V_z}{\partial z}=0$$

$$-\frac{\rho}{\mu}\frac{V_\theta^2}{r}=\frac{1}{r}\left(\frac{\partial}{\partial r}\left(r\frac{\partial V_r}{\partial r}\right)\right)+\frac{\partial^2 V_r}{\partial z^2}$$

$$0=\frac{1}{r}\left(\frac{\partial}{\partial r}\left(r\frac{\partial V_z}{\partial r}\right)\right)+\frac{\partial^2 V_z}{\partial z^2}$$

And on the boundary walls, Γ:

$$V_r=0$$

$$V_z=0$$

Where the subscripts indicate the coordinate directions.

These assumptions have basically turned the problem into a two dimensional one. By doing so, a function can be defined that will identically satisfy the continuity equation. Namely:

$$\frac{\partial \phi}{\partial z}=V_r$$

$$\frac{\partial \phi}{\partial r}=-V_z$$

The procedure used to solve the momentum equation was to first normalize the dependent and independent variables. The resulting Poisson equation was solved iteratively using the method of lines for a second order accurate, centered difference scheme over 2500 points. The velocities were then back calculated from the solution set. A parametric study of the integral in equation (1) was performed for various ratios of width (w) to inside radius of curvature (r_0). The result is:

$$\frac{dh}{dt}=0.0277\left(\frac{w}{r_0}\right)\frac{c\Delta R V^2}{\nu} \qquad (4)$$

Where w is the width of the square channel, ν is the kinematic viscosity, and V is average fluid velocity. It should be noted that the integral term had both positive and negative deposition rates at various points across the deposition surface. Only the positive rate was considered because the negative rate would remove material. This could not occur because there would be no material to remove from a clean surface. This approximation should work well provided the deposition surface does not significantly disturb the flow. The long-term growth of the deposits will require more computational research.

SYSTEM IMPROVEMENT CHRONOLOGY

Plugging of LCW from iron oxide in cooling circuits first became a problem in 1993, soon after power supplies and magnets were installed. Unfortunately, iron body pumps with brass impellers were selected to circulate LCW. For ordinary treated system water, this is not a problem; however, the LCW system was designed to operate at full purity, 18 MΩ-cm. LCW with dissolved oxygen aggressively attacked the iron pumps, thus becoming a corrosion particle source. The pumps were replaced with stainless steel.

The aggressive nature of high purity water on metal was a concern for our aluminum beam dump. In 1995 and 1996, a conductivity control system was developed to reduce the water purity. The system worked so well it was installed in all LCW systems at the Jefferson Laboratory. The accelerator operating point was selected to be 2.0 MΩ-cm.

Also during the 1996 period, plugging of magnets had again become problematic. Henkel [6] found that plugging was caused by iron oxide (magnetite), which is caused by a "single electrode corrosion of iron particulates immersed in oxygenated water." Tubing bends were analysed and the inside radius surfaces were found generally to be coated with deposits. The amount varied from light and streaked to uniform and heavy. A fifteen-micron thickness (or about 3μ/yr) was typical of the average layer of magnetite deposits. Free stream header concentrations were found to be 10 ppb for iron and a diameter of 5 - 10 μ. To lower the dissolved oxygen concentration, oxygen scavenging resin bottles were added to the mixed bed array. A year before the study, filter porosity was decreased from 5μ to 0.5μ in the side stream to help clean the water. Local filtration was also installed near the most critical magnets. Improvements made to the system seemed to ameliorate the plugging problems.

In late 1999 and 2000, however, magnet trips due to heat excursions again manifested themselves. Additional testing showed a new character to the composition: particles were now mostly copper oxide with a ratio of 9 parts copper to 1 part iron.

Seeking other expert opinion, contact was made with other National Laboratories in the LCW production facility departments. Chris Ader of FNAL [7] sent us information on FNAL's solution to the problem. We immediately began work on a prototype system to emulate the FNAL system. Further knowledge on general process of copper corrosion was found [8,9].

DISSOLVED OXYGEN REMOVAL

Following FNAL, a dissolved oxygen removal system was installed. The primary element is a device called a contactor, which was placed in the side stream purification and feed system.

A contactor is basically a molecular sieve. System water with dissolved oxygen at a given partial pressure flows past one side of the sieve. The other side of the sieve is maintained at a lower oxygen partial pressure by using a vacuum pump, sweep gas, or both. The dissolved oxygen, carbon dioxide and other gasses diffuse through the sieve membrane and are carried away by the vacuum pump.

Also, full flow filters with 0.5 μ media were placed in the return side of the magnet LCW loop. This is in addition to the other filters already in place.

The pH is a key factor in the corrosion process. In general, pH over 7.0 minimizes both copper and iron corrosion, while a pH below 7.0 increases corrosion and adversely reduces the solubility of the copper oxides in hot wall passages. The contactor system removes dissolved carbon dioxide and increases LCW pH, while chemical removal of oxygen with scavenging resin lowers LCW pH. Since lower LCW pH is undesirable, the scavenging resin has been removed from the polishing system.

There are several general principles that should be observed when using an oxygen contactor:

1. No sub-atmospheric system pressure should be allowed to develop anywhere in the piping system.
2. The feed water must be degassed before being injected into the system.
3. Contactors are sensitive to excess temperature and pressure. Excessive pressure will destroy the contactor.
4. The system should be isolated from the atmosphere by using nitrogen to pressurize head tanks.
5. Magnet passages must eventually be chemically cleaned to remove oxide film. Film build-up is a natural consequence of flow dynamics. It is also directly related to thermal effects on copper oxide solubility.

CALCULATED DEPOSITION RATE COMPARED WITH MEASURED DATA

Although Eq. (4) was derived for a square channel, it could be tested by using the available data for circular specimens above. The inside radius of the analyzed bends is not stated, but judging from the magnet plans, the inside radius is probably between 25 and 35 mm. Moreover, the particle diameter is important to the rate of deposition. Henkel [6] observes that the size composition of the deposits varies greatly, even after local filtering. He notes that the "coating is being formed by mechanical adhesion of thousands of these particulates." This is very likely since magnetite particles will bond together magnetically. The main flow stream was filtered to 0.5 μ; one would expect the larger particles to form from an aggregate of smaller particles. This will result in two cases: Case I is a homogeneous fluid with 0.5μ particles suspended therein, and Case II is non-homogeneous fluid with 5μ particles formed from the smaller particles with the same total particle mass as Case I. One could surmise that the numerical concentration will vary accordingly, but there is not enough data available to show this. The tube forms a 90 degree bend with a 35 mm radius. Water flows through the channel with an average velocity of 0.06 m/s, a particle concentration of 10 parts per billion (ppb) for 0.5μ for Case I and 5μ for Case II. The kinematic viscosity of 300K water is 8.57E-7 m^2/s. For a circular channel, the diameter is substituted for the width of the square channel.

For Case I, the deposition rate is 3.1 μ/year and 31 μ/year for Case II with the same concentration. Case I agrees with the 3 μ/year mentioned above.

CONCLUSIONS

The plausibility of the deposition rate analysis presented here seems to agree with previous experience. The deposition rates for square and circular channels, which were not analyzed, are expected to be approximately the same.

Although our oxygen removal system has not been in service long enough to draw ironclad conclusions, we have not had any plugging problems as of this writing. We are optimistic that the system will improve the accelerator reliability.

REFERENCES

[1] Christine R. Ader, Elvin R. Harms, and James P. Morgan, "Experience with Copper Oxide Production in Antiproton Source Components at Fermi National Accelerator Laboratory," FERMILAB-Conf-00/086, Proceeding of the *American Society of Mechanical Engineer's Pressure Vessels and Piping*, Seattle, WA, July 2327,2000, pp. 6-7.

[2] Robert H. Perry, Dow W. Green and James O. Maloney, *Perry's Chemical Engineers' Handbook*, McGraw-Hill Companies, 1997, p. 6-18.

[3] W.R. Dean, "The Streamline Motion of Fluid in A Curved Pipe (Second Paper)," *Philosophical Magazine and Journal of Science*, April 1928, p. 673.

[4] K.P. Sandeep and T.K. Palazoglu, "Secondary Flow in Coiled Tubes," 1999 ASAE Annual International Meeting, Paper No.996148, Toronto, Canada, July 1999, p.1-5.

[5] Frank M. White, *Viscous Fluid Flow*, McGraw-Hill Book Company, New York, 1978, p.82.

[6] Daniel P. Henkel, "Continued Analysis of Low Conductivity Water System Copper Tubing," Report for SURA/TJNAF by Henkel Metallurgical Technologies, October 3, 1996, p.1, 3, 4, 24.

[7] Christine Ader, Personal Communication, Aug. 2001.

[8] R. Dortwegt and E.V. Maughan, "The Chemistry of Copper in Water and Related Studies Planned at the Advanced Photon Source," offprint, PAC 2001.

[9] Eric Maughan, "The Basics of Copper Cooling Water Chemistry," MEDSI 2002 workshop at the Advanced Proton Source, Argonne National Laboratory, Sept 5-6 2002.

Proceedings of the 2003 Particle Accelerator Conference

SAFETY CRITICAL MONITORING FOR PROMPT RADIATION HAZARDS

L. Moritz, J. Drozdoff, G. Dutto, F. Mammarella, M. Mouat, R. Ruegg, TRIUMF, B.C., Canada

Abstract

At TRIUMF we have used both passive and active methods to protect against potential prompt radiation hazards produced by accidental beam losses in high-intensity proton beam lines. These methods consist of shielding, exclusion areas, and the use of fast acting radiation monitors. The latter are located within the shielded areas and are set to terminate beam production on the detection of abnormal beam loss. A recent risk analysis has suggested a need for higher reliability in the protection against potential prompt radiation hazards where the shielding is relatively thin. To address this requirement TRIUMF has developed a new approach using two systems of independent and redundant monitoring devices located outside the shielding to protect against safety critical events with the required level of reliability. Verification of the system reliability is achieved by weekly testing of the safety critical monitors as well as the trip devices. When used in conjunction with the traditional beam loss monitors we are able to distinguish between safety critical events and non-safety critical beam trips.

INTRODUCTION

One of the dilemmas of shielding high-intensity accelerators is whether to everywhere install shielding that is sufficient to reduce radiation fields to low levels under conditions of maximum possible beam loss or whether to shield low beam-loss areas only for expected operational losses and rely on active protection systems to terminate beam operation in case of total or high accidental beam losses. Generally the reliability or integrity of shielding is assumed to be very high (although this may not be justified in all cases), but the reliability of active protection systems needs to be demonstrated for each particular design. At TRIUMF we have used active protection systems for some time, but their reliability had not been formally demonstrated. At the request of the Canadian regulatory authority we re-examined this issue and found a solution for achieving the required level of reliability without performing a detailed fault tree analysis.

INITIAL SYSTEM

The radiation protection system that had been installed for many years at TRIUMF consisted of a series of detectors deployed *inside* the shielding. The detectors had no local electronics so that they were reasonably resistant to radiation damage. Analogue signals from these detectors were conditioned and then sent to a central processing unit where the signals were converted into digital values and read 10 times per second by a microprocessor. These values were compared to a set point and any reading above the set point generated a 'warn' signal to alert the operators to a beam loss. If a reading exceeded twice this 'warn' level, a 'trip' was generated that turned off the 500 MeV accelerator using several redundant and diverse devices. The system had a number of features built into it to enhance reliability, such as a watchdog timer, power monitoring, temperature monitoring, run time checksum check etc., and was powered by an uninterruptible power supply. The response time of this system to turn off the accelerator was measured to be between 150 to 200 ms, sufficient to prevent a significant radiation dose to anyone outside the shielding even under the highest expected dose rates.

ANALYSIS

System Configuration

The close examination of this system in response to the request to demonstrate its reliability concluded the following:

- The system had the dual purpose of personnel and machine protection. As a result the warn and trip levels were set very close to the operating beam loss levels and had no relation to the radiation fields outside the shielding.
- Many of the radiation detectors were located in high-radiation areas making them difficult to service and calibrate.
- The detectors were not fail-safe and subsets were powered by the same power supply.
- There was redundancy in the system only in that detectors were reasonably closely spaced and that several devices were used to trip the accelerator.

The conclusion was that it would be difficult to modify the system so that it would have the required demonstrable reliability.

Historical Data

An examination of the historical record showed that the number of failures of this system had however been very low. During a period of approximately 20 years there had been no instance where the system had failed to respond correctly to a beam loss that would have resulted in a high radiation field outside the shielding.

The system had in fact been exercised frequently (often several times per week) because of the machine protect function that resulted in accelerator trips whenever the beam loss anywhere exceeded four times the normal operational losses, even when these were very low. The

0-7803-7738-9/03/$17.00 © 2003 IEEE

large number of accelerator trips made it difficult to separate out those beam loss events that might have led to very high, sustained radiation fields outside the shielding if the protection system had failed.

NEW APPROACH

In view of the above difficulties it was decided to use a new approach. This approach involved

- Creating a policy that defined the maximum tolerable radiation fields outside shielding under worst-case beam loss.
- Develop two completely independent systems for personnel protection with detectors located outside the shielding.
- Define a reliability goal for the remaining risk

Policy

A policy was defined that limits the maximum prompt radiation fields outside the accelerator and beam line shielding to 1 Sv h^{-1} for a point loss of the total beam intensity for which the accelerator or beam line is *licensed*. The rationale for this is that it is deemed not credible that a beam loss of this intensity could go undetected for more than 1 hour or could even persist without self-extinguishing itself via some catastrophic failure of the vacuum envelope. The maximum dose that could therefore be incurred would be 1 Sv, the threshold for immediate deterministic effects of a radiation exposure. This policy required that wherever a total beam loss could result in radiation fields greater than 1 Sv h^{-1}, the shielding would have to be upgraded or the area would have to be defined as an exclusion area that was interlocked so as to be inaccessible during operation.

New Protection Systems

Rather than attempting to improve the existing protection system it was decided that another system of similar design that was already used to measure neutron field levels outside the shielding and that used similar system architecture could be reconfigured to become a high-reliability system. This 'neutron monitoring system' had been used to generate alarms at relatively low ambient field levels, but had not been used to trip off the accelerator because of the slow response time of the neutron moderated BF_3 monitors. However, by incorporating a 'trip' function for these monitors at the relatively high level of 1 mSv h^{-1}, it was possible to have a response time as short as 200 ms.

To provide redundancy and therefore also to lower the reliability requirements for the neutron monitoring system, a second system with identical architecture but different detector technology was created. This second system uses plastic scintillators mounted on photomultiplier tubes and measures the current from these tubes as an analogue signal. These detectors are sensitive to both gamma and neutron fields and also differ in the way the signals are processed (analogue rather than pulse-counting for the neutron detectors).

Pairs of detectors, one from each system, were designated 'safety-critical' and were deployed outside the shielding in tamper-resistant metal locked cabinets with all wiring in accessible areas enclosed within metal conduit. The cabinets are provided with a port that allows insertion of an ^{241}Am-Be source for quick operational check.

Reliability Goal

As a goal for the level of reliability required, the value of 10^{-5} incidents per year was used, a figure that defines so-called 'safe' industries when applied to fatalities in the workplace [1].

An estimate of the number of events (such as magnets tripping off or vacuum valves being accidentally inserted into the beam path) that might initiate a total beam loss yielded a probability of approximately 10^{-1} per year. Therefore the requirement for the likelihood of occurrence of a failure of both systems to respond to such an event would be

$$10^{-1} \times 10^{-2} \times 10^{-2} = 10^{-5}, \qquad (1)$$

in other words each of the two independent systems must have a demonstrated failure rate of less than 10^{-2} per year.

In order to demonstrate that the systems in fact meet these levels of reliability, each of the detectors is tested on average once per week using the ^{241}Am-Be source and verifying that the correct level of signal is sent to the logic controller and then testing that the logic controller correctly trips the accelerator using all redundant devices. After two years of testing, the program will have established the required reliability of these systems.

In order to verify the estimate of the frequency of initiating events it is important to have a clear definition of what is meant by an 'initiating event'. The following definition was adopted: "a degradation or failure resulting in a sustained beam loss that, in the absence of the safety critical monitors, would lead to a dose rate outside the shielding greater than 50 $mSvh^{-1}$". Dose rates greater than 50 $mSvh^{-1}$ if sustained for the postulated maximum credible duration of one hour would lead to doses in excess of the Canadian one-year regulatory limit on dose for Nuclear Energy Workers [2]. Although a dose in excess of 50 mSv may not necessarily have serious health consequences for the exposed individual such an exposure would have severe consequences for TRIUMF.

The definition then gives an operational way to decide whether a beam excursion that trips the protection systems should be classified as an 'initiating event': it must result in a trip of the 'safety-critical' monitors and be capable of generating a sustained radiation field outside the shielding greater than 50 mSv h^{-1}. Since the deployment of these monitors more than one year ago, only one trip has occurred. This was due to a dipole magnet located some considerable distance upstream of the thin shielding monitored by the 'safety-critical' monitors. A problem with the dipole magnet power

supply resulted in a 15% change in the magnetic filed that steered the high-power proton beam into the beam pipe. An investigation that involved intentionally steering a lower power beam through the full range of magnet settings demonstrated that although the radiation field during the incident exceeded the monitor trip level, it could not have exceeded 50 $mSvh^{-1}$ and therefore should not be counted as one of the initiating events. By keeping a record of all such events we hope to demonstrate the estimates of the frequency of such events.

CONCLUSION

TRIUMF has developed a new approach to demonstrate the required high reliability for active radiation protection systems by implementing two systems of independent and redundant monitoring devices located outside the shielding to protect against safety critical events. Verification of the system reliability is achieved by weekly testing of the safety critical monitors as well as the trip devices. When used in conjunction with the traditional beam loss monitors we are able to distinguish between safety critical events and non-safety critical beam trips.

REFERENCES

[1] U.S. Department of Labor Bureau of Labor Statistics, *Fatal Workplace Injuries in 1995: A Collection of Data and Analysis*, Report 913, April 1997.

[2] Canadian Nuclear Safety Commission, *Radiation Protection Regulations*, SOR/2000-203, May 2000.

COMPREHENSIVE ELECTRO-MAGNETIC, THERMAL, AND STRUCTURAL FINITE ELEMENT ANALYSIS OF THE LITHIUM COLLECTION LENS AT THE FNAL ANTIPROTON SOURCE*

P. Hurh#, J. Morgan, S.Tariq, FNAL, Batavia, IL 60510, USA

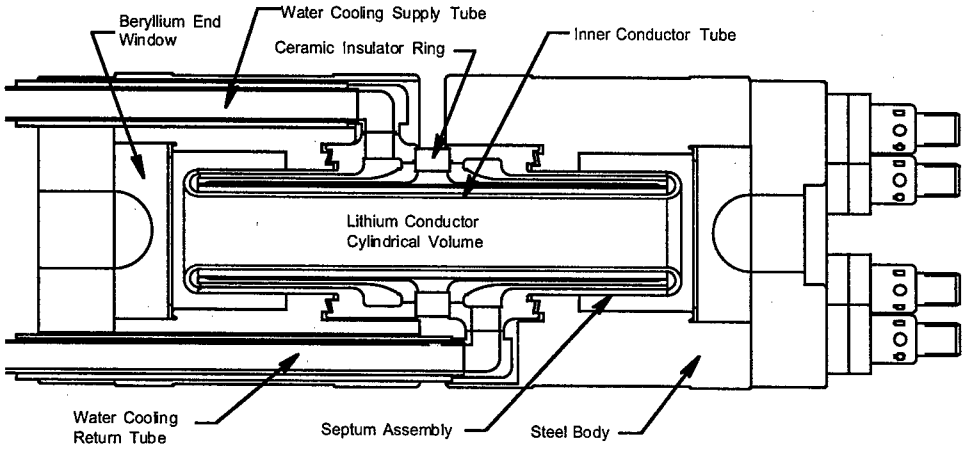

Figure 1: Cross-section diagram of Collection Lens Device. Septum conductor tube is shown in blue.

Abstract

A history of lithium Collection Lens failures at lower than designed focusing strengths has led to extensive efforts to quantify the Lens loading environment and structural behavior. A comprehensive finite element analysis (FEA) model of the lithium Lens has been developed as part of these efforts and as a tool to aid in future lithium lens design improvements. The FEA model includes complete device geometry, the excitement current pulse (damped sine wave), temperature dependent electrical, thermal and structural (including strain rate dependent) material properties. Latest results, including transient electro-magnetic, thermal and structural solutions, for the currently operational lithium Lens design are presented.

INTRODUCTION

The FNAL Antiproton Source incorporates a lithium Collection Lens to greatly improve the transmission efficiency of antiprotons into the Debuncher ring. The Lens has a large axial current passing through a solid lithium cylinder that produces a strong magnet field proportional to the radius. The design gradient of the 1 cm radius Lens was 1,000 T/m (10 Tesla surface field). However, operational lenses have not been able to sustain the design gradient for enough pulses to be practical, usually failing within days or weeks due to mechanical failures of the titanium tube that contains the lithium, historically called the septum [1]. Running Lenses at reduced gradient has allowed them to survive for an acceptable length of time, millions of pulses. The penalty for lowering the gradient is less antiproton yield due to reduced focusing strength. The operational gradient of the Collection Lens is 745 T/m..

The cross-section of the Lens device is shown in Figure 1. The most stressed part of the septum is the conductor tube. Stresses arise from several loading sources such as thermal expansion from ohmic and beam heating, magnetic forces from the current pulse, and structural loading from clamping bolts and lithium filling pre-load. In order to gain insight into the loading environment and structural behavior of the Lens, a comprehensive FEA model has been created.

MODEL DESCRIPTION

Using ANSYS® [2] FEA software a 10 degree wedge-shaped half model of the functional elements of the Lens was created to simulate the magnetic response of the Lens to a damped sine wave current pulse (angular freq. of 8622 Hz and damping coefficient of 1500 Hz). Joule heating results from this model were then applied to a matching thermal model of the Lens along with beam heating loads (estimated from MARS target simulations), transformer heating loads (estimated from empirical measurements), and cooling loads (estimated from ANSYS® FLOTRAN analysis). Temperature results from the thermal model were then read back into the magnetic model in order to re-evaluate material properties at the new temperature distribution. Each current pulse was broken into 10 steps (37 μsec each) with a cooling period of 2 seconds between pulses.

*Work supported by the US Department of Energy under contract No. DE-AC02-76CH03000.
#hurh@fnal.gov

0-7803-7738-9/03/$17.00 © 2003 IEEE

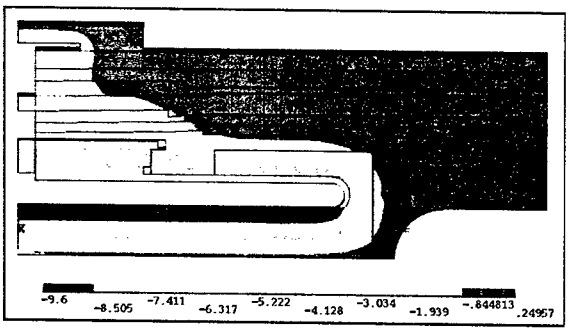

Fig. 2: Bθ (Tesla) for H.G. pulse at time of beam passage.

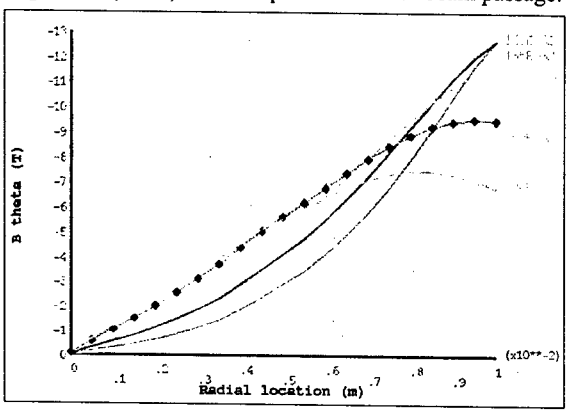

Fig. 3: Bθ vs Radius for various times. Dots denote time of beam passage.

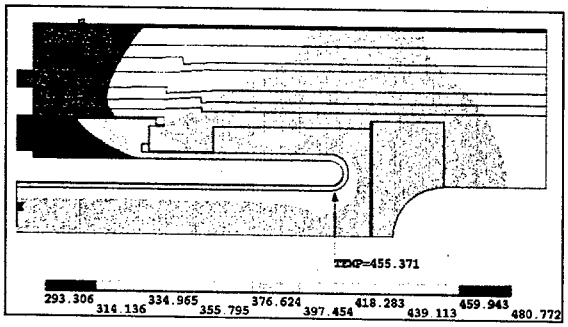

Fig. 4: Temp distribution. just after 400th H.G. pulse (K).

Nodal forces and temperature distributions were then applied to a matching structural model along with additional structural loads from the lithium pre-load and the tie-rod clamping forces.

As can be seen from the following results, the behavior of the lithium is essential to understanding the load environment. Lithium is a structurally soft material that exhibits viscoplastic hardening as well as creep softening. Results from viscoplastic tensile testing [3] were incorporated in this analysis, but as of this writing, creep effects have not yet been incorporated.

Three loading scenarios were simulated. First, a benchmark simulation was run to compare calculated temperature results with measured results. Second, a simulation was run with low gradient (L.G.) parameters (745 T/m, 500 kA peak current, 5E12 protons on target, 2 sec pulse repetition period). Finally a third simulation was run with the same parameters as the second, but with a high gradient (H.G.) pulse (1,000 T/m, 670 kA).

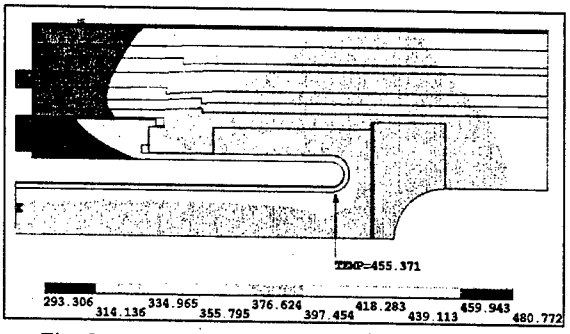

Fig. 5: Temp dist. just before 401st H.G. pulse (K).

RESULTS

For the sake of brevity most of the results pictured in the figures will be for the H.G. simulation. Comparisons to the lower gradient simulations will be made in the text.

Magnetic results of the model are as expected. The magnetic flux density in the theta direction is shown in Figure 2 for the time of beam passage. Figure 3 shows how the magnetic flux density changes with radius and time.

Figure 4 shows the temperature distribution in the Lens just after the 400th high gradient pulse. The hottest spot in the lithium is 182.4 °C. This is significant since the melting point of lithium is 180.6 °C. In comparison the lithium hot spot at the lower gradient is 120.6 °C. Figure 5 shows the temperature distribution just before the 401st high gradient pulse. Note that the hottest temperatures in the Lens are in the steel body half which is not directly cooled by water.

Although not pictured here, it is worth noting that the benchmark simulation results indicated temperatures in an instrumented area of the body half of 80 to 85 °C. This agrees with measured temperatures of 77 to 82 °C.

Figure 6 shows a vector plot of the displacement of the lithium during the peak magnetic forces of a high gradient pulse. It shows how the radially inward forces push the lithium out of the ends of the septum conductor tube. In addition, a small amount of lithium near the opening of the tube is shown to be moving back into the void created by the inwardly moving lithium. This indicates separation of the lithium from the septum tube wall is probable.

This possibility is further confirmed by looking at the hoop stress in the conductor tube versus time in Figure 7. The dip into negative stress when magnetic forces are the highest indicates that the tube is going into compression. Ideally, if the lithium pre-load is adequate, the tube wall should only be exposed to tensile stresses to avoid stress reversals. After the Lens warms up to quasi-static conditions, this lithium/titanium separation effect decreases in severity since the effective pre-load is increased by thermal expansion of the lithium. Figure 8 shows the hoop stress in the conductor tube for later high

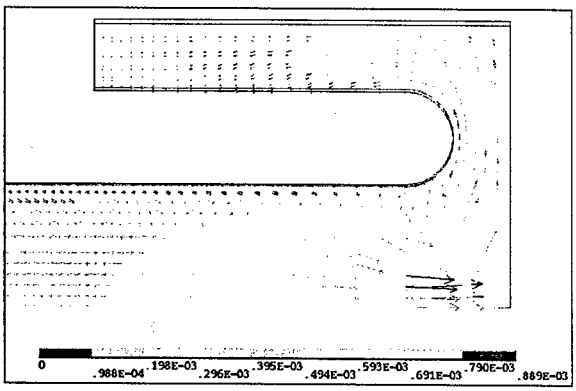

Fig. 6: Lithium displacement (m) at peak of H.G. pulse.

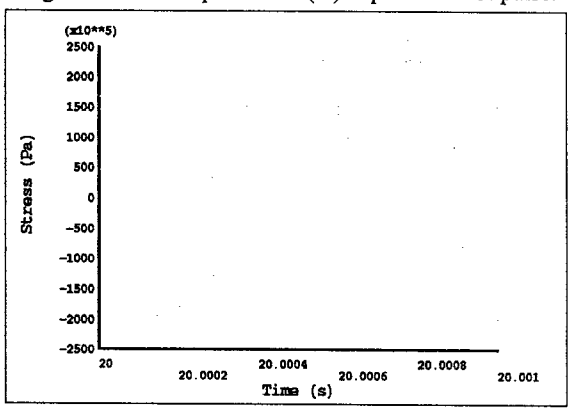

Fig. 7: Conductor tube hoop stress (Pa) in 1st H.G. pulse.

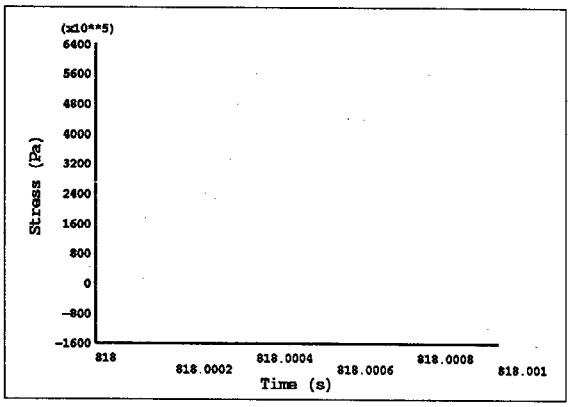

Fig. 8: Cond. tube hoop stress (Pa) in 400th H.G. pulse.

gradient pulses and can be compared to the curve in Figure 9 for the low gradient simulation.

Figure 10 shows the hoop stress in the conductor tube at points of maximum extremes during a quasi-static high gradient pulse. Displacements have been exaggerated by a factor of 20.

CONCLUSION

Although far from complete, this analysis has already yielded some significant results. There are obvious signs that at higher gradient, portions of the lithium may become liquid. Adding cooling to the body could help since a significant amount of heat is originating there.

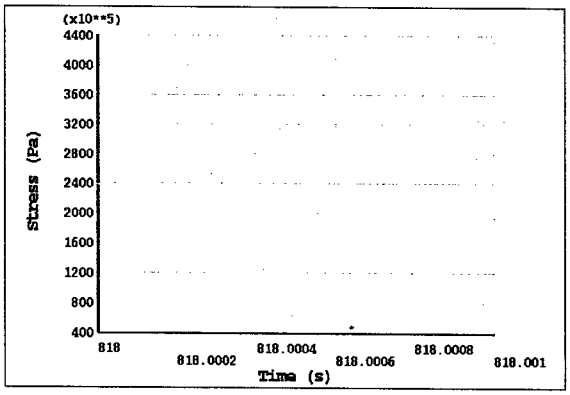

Fig. 9: Cond. tube hoop stress (Pa) in 400th L.G. pulse.

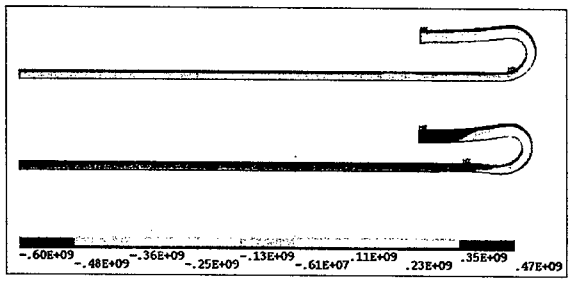

Fig. 10: Conductor tube hoop stress extremes (Pa) for 400th H.G. pulse at peak magnetic forces (top) and peak lithium temperature (bottom).

There are indications that at higher gradient the lithium may be separating from the septum conductor tube and causing detrimental stress reversals in the tube wall. Elimination of the buffer regions and/or higher lithium pre-loads may help avoid this effect. At higher gradient the estimated loading cycle (470 MPa, R=-.2) is nearing or surpassing fatigue thresholds for the Ti 6Al-4V alloy (462 MPa, R=.1, gentle surface grind [4]).

Future work should incorporate creep effects since significant recovery of plastic deformation between pulses could significantly alter the stress distribution in the septum tube. In addition, the high strains in the lithium suggest that lithium failure may be occurring. The behavior of failed lithium in compression is a complicated and probably unquantifiable phenomena. Future studies should be undertaken to ensure that the lithium failure limit in compression is not being surpassed.

REFERENCES

[1] P. Hurh, "Examination Results of Failed Collection Lens Septa 20 and 21", Fermilab MSDNote #MSDN-ME-000022 (2002).

[2] ANSYS® is a registered trademark of SAS IP Inc.

[3] S. Tariq, K. Ammigan, P. Hurh, R. Schultz, P. Liu, &J. K. Shang, "Li Material Testing- Fermilab Antiproton Source Lithium Collection Lens", TPAG013, PAC 2003, Portland (2003).

[4] Titanium and Titanium Alloys: Source Book, M. J. Donachie, Jr. Ed., American Society for Metals, Metals Park, p. 355 (1982).

INERTIAL SENSOR DEVELOPMENT FOR ACTIVE VIBRATION STABILIZATION

Josef Frisch, Eric Doyle, Leif Eriksson, Linda Hendrickson, Thomas Himel, Thomas Markiewicz, Richard Partridge, SLAC

Abstract

Future Linear Colliders require nanometer stability of the beams at the interaction point. One approach to stabilising the beams is to use feedback based on inertial sensors (accelerometers / seismometers) to control the positions of the final focus magnets. Commercial seismometers developed for geo-science applications have sufficient noise performance (nanometer noise down to a fraction of a hertz), but due to their large size and magnetic sensitivity are unsuitable for use in a linear collider detector. We report on the development of a high sensitivity, compact, non-magnetic inertial sensor for this application. In addition to its use in linear colliders, the sensor is also expected to have application in vibration measurement and control in synchrotron light sources

LINEAR COLLIDER STABILIZATION

The vertical beam spot sizes at the IP of linear colliders are on the order of a few nanometers, and in order to maintain luminosity the relative beam positions must be stabilised to a fraction of the beam size. Various technologies have been proposed for beam stabilization [1], [2]. Here we focus on mechanical stabilization based on inertial sensors for the final focus magnets for the NLC.

One of the largest contributions to beam motion is ground motion coupling to the final focus magnets. The differential motion of the ground at the frequencies of interest (0.1-100Hz), and at typical final focus magnet separations varies substantially between sites [3]. At a quiet site no additional mechanical stabilization is required; however technologies are being developed to allow operation at noisy sites.

Stabilization of the beams at low frequencies (typically below a few Hz) is provided by feedback based on the beam / beam deflection at the IP. At higher frequencies mechanical stabilization based on inertial sensors as described here, or on interferometers [4] is used. High frequency beam motion will be corrected with a fast intra-train feedback system [5].

INERTIAL SENSOR REQUIREMENTS

Feedback from inertial sensors has been used at SLAC to stabilise the 6 solid body degrees of freedom of a 40Kg aluminium block [6]. The performance of this system was limited by the noise of the compact geophones used for feedback.

Due to uncertainties in the expected ground motion levels, and in the amount of amplification of high frequency beam noise allowed from the beam-beam feedback, it is not possible to give a specific requirement for the inertial sensor noise For reasonable parameters, however, a noise level of $\sim 3\times10^{-9} M/s^2/Hz^{1/2}$ at frequencies above 0.1 Hz is sufficient.

The NLC final focus magnets are located within the detector solenoid, and must therefore be physically small, and able to operate in a ~ 1 Tesla magnetic field.

Commercial accelerometers designed for machinery vibration are compact, and those based on piezoelectric sensors are not sensitive to magnetic fields, but their noise floors are typically $\sim 10^{-6} M/s^2/Hz^{1/2}$. Commercial geophysics sensors (eg. Streckheisen STS-2) have noise floors $< 10^{-9} M/s^2/Hz^{1/2}$ but are physically large and are sensitive to magnetic fields.

We were unable to find commercial sensors which met our requirements, and began a project to develop a new inertial sensor, referred to here as the "NLC inertial sensor".

INERTIAL SENSOR THEORY

All inertial sensors consist of a mass suspended from a frame, with a measurement of their relative positions. Position sensor technologies can have very low noise, and the theoretical limit on the sensor sensitivity is the thermal noise of the mass and suspension. This thermal noise limit is due to thermal excitation of the fundamental mode of the mass, which due to the finite mechanical Q, has frequency components off of the resonance frequency. The acceleration noise due to thermal noise of the suspension and mass is given by $A=(4K_bTw_0/mQ)^{1/2}$ [7].

For linear collider applications it is the beam - beam separation, not acceleration which is of interest, so the low frequency noise is typically the most critical issue. In addition, various sources of 1/f noise contribute to low frequency noise.

High frequency performance is typically limited by the second mechanical resonance of the suspension system. The suspension is designed to maximise the lowest frequencies of higher order modes.

Sensors for vertical motion have an additional difficulty that they must measure accelerations which are (for our parameters) 10^9 smaller than the background gravitational acceleration. This manifests in the form of spring creep, and in temperature sensitivity due to changes in spring elastic modulus.

INERTIAL SENSOR DESIGN

For a simple mass on a spring suspension, the resonant frequency f is related to the change in spring length under

*Work Supported by Department of Energy Contract DE-AC03-76SF00515

0-7803-7738-9/03/$17.00 © 2003 IEEE

gravity $L=g/(2\pi f)^2$. A variety of "astatic" suspension designs are used in seismometers to obtain low resonance frequencies in a compact volume. [8].

The NLC inertial sensor uses a (non-astatic) leaf spring design with the unconventional feature that the spring is pre-bent to be flat under gravity load. The flat spring results in a high transverse mode frequency for a low fundamental frequency.

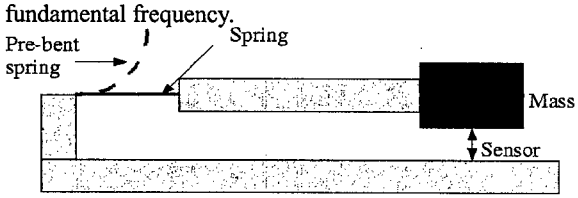

Figure 1: Pre-bent suspension spring

The fundamental resonance of the suspended mass has a relatively high Q (to reduce thermal noise) resulting in an enhancement in motion at resonance relative to low frequency motion. Rather than design a position sensor with high dynamic range, most high sensitivity seismic sensors use feedback to control the position of the suspended mass.

In most commercial feedback seismometers, the feedback element is magnetic. For the NLC inertial sensor, which must operate in a strong external field, an electrostatic pusher is used for feedback. Approximately 70V applied over a 300 micron gap provides sufficient force to control the mass position.

A variety of feedback algorithms can be used in the NLC inertial sensor DSP based feedback system. A conceptually simple one which will be used for initial sensor testing is to use feedback to maintain the mass position fixed relative to the sensor frame, and use the applied force as the acceleration signal.

SENSOR MECHANICAL / ELECTRICAL

The 40 gram Tungsten test mass is mounted on a 15cm long aluminium cantilever. The suspension spring is BeCu, pre-bent by 90 degrees to be flat under gravity load. The spring is operated at high stress (~75% of yield) to maximise the higher mode frequencies (as a result of ANSYS simulations).

The high stress in the spring results in creep which is compensated by a non-magnetic "picomotor" [9] that moves the spring support on a flexure mount. Creep measurements at SLAC indicate that the adjustment range will provide a ~20 year creep lifetime

The sensor is expected to be extremely sensitive to temperature changes in the suspension spring, with a 10^{-8}C change corresponding to the theoretical thermal noise at 0.1Hz. The change in spring stiffness due to temperature is common to all mechanical suspension designs, and in most low high sensitivity seismometers is mitigated by the use of springs with a small variation of K with temperature. Unfortunately these compensated materials are ferromagnetic, and unsuitable for our application. [10].

The NLC inertial sensor design includes a series of "thermal low pass filters" to reduce short timescale temperature variations of the support spring. The housing and spring are gold plated to reduce temperature changes due to thermal radiation. Thermal effects are expected to be the ultimate limit to low frequency performance of the sensor.

Table 1: Sensor Specifications

Test mass	40 grams	Design
Resonant f	1.46 Hz	Measured
Resonant Q	~50	Measured
Thermal Noise	2.5×10^{-10}M/s^2/Hz$^{1/2}$	Theory
Electrical noise	10^{-10}M/s^2/Hz$^{1/2}$	Calculated

The calculated electrical noise, assuming 100mW RF drive power, the estimated coupling, and a 10dB amplifier noise figure is less than the mechanical thermal noise. It is believed that 1/f noise in the mechanical system, rather than electrical noise will dominate the low frequency noise.

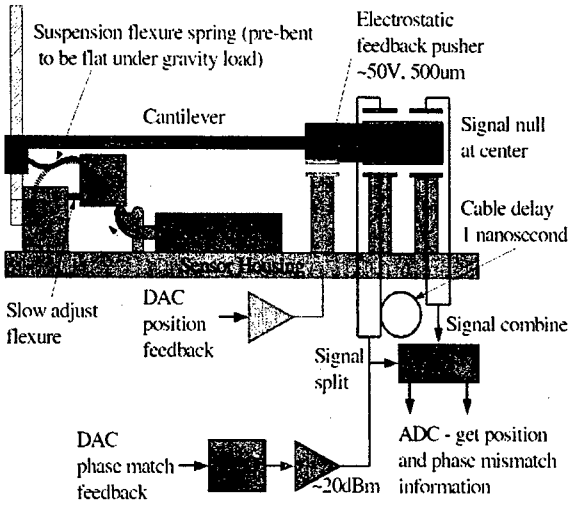

Figure 2: NLC inertial sensor block diagram

A capacitive sensor is used to measure the position of the test mass. An RF signal at ~450MHz is applied out of phase to two capacitive gaps on opposite sides of the test mass. When the mass is centered in the gap, the net voltage induced in the mass is zero. The induced voltage is capacitively coupled to the detection electronics.

Any mismatch in the drive gap capacitances results in a stable offset in the mass position for null signal. Any mismatch in the 180 degree phase shift between the two drive signals is corrected by changing the frequency of the oscillator.

The detection electronics amplifies the signals in low noise RF amplifiers, then uses an I/Q mixer to detect the vector components of the induced signal. DSP based feedback is used to null the I signal by adjusting the mass position, and the Q signal by adjusting the frequency.

The sensor components are mounted in a 18cm x 11cm x 6cm stainless vacuum chamber. Under atmospheric pressure, the mechanical Q is reduced from 50 to

approximately 4 due to air viscosity in the narrow gaps. In addition, the vacuum provides thermal insulation, and prevents noise due to convection currents.

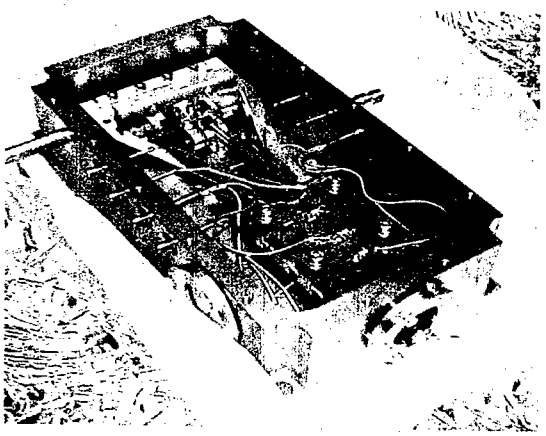

Figure 3: Sensor mechanics installed in vacuum chamber

PERFORMANCE TESTS

Mechanical construction of the first sensor is complete and testing has begun. The feedback system has not yet been commissioned for this sensor.

The NLC sensor is mounted on a 30 Ton shielding block, isolated from the ground by elastomeric supports. Two Streckheisen STS2 seismometers are also mounted on the block to provide reference and calibration signals. The raw output from the sensor is shown in figure 4.

The correlation function between the two STS-2 seismometers, and between a STS-2 and the NLC sensor is shown in figure 5.

The data does not yet indicate the noise floor of the NLC sensor; however the correlation between the sensor and a STS2 is good down to 0.2Hz, indicating that it is able to measure motion in the test lab down to this frequency.

PLANS

After the feedback is activated, the sensor response will be compared to a STS-2 seismometer in a seismically quiet location at SLAC. If the noise floor meets the NLC requirements, production of additional sensors will begin in late 2003.

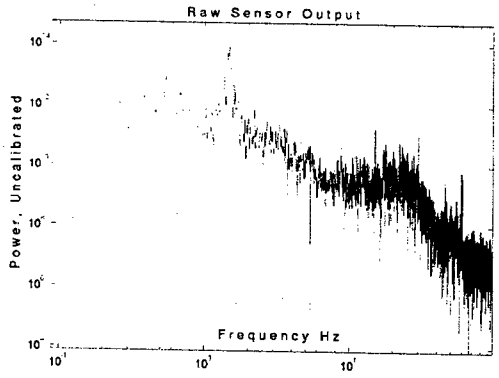

Figure 4: Sensor power spectrum

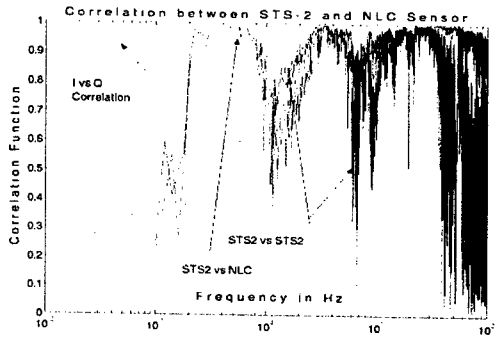

Figure 5: Correlation between STS-2 seismometers, STS2 vs NLC sensor, NLC I vs Q output

REFERENCES

[1] F. Richard et. al., "TESLA Technical Design Report"
[2] N. Phiney ed. 2001 Report on the Next Linear Collider, 2001, SLAC-R-571,
[3] A. Seryi, "Ground Motion and Vibration Issues for Accelerators", SLAC PUB 8893, 2001
[4] T. Mattison, "Vibration Suppression R&D at University of British Columbia", Snowmass 2001
[5] P. Burrows et al., "Feedback on Nanosecond Timescales for Linear Colliders", PAC2003
[6] J. Frisch et al., "Active Vibration Suppression R+D for the Next Linear Collider" SLAC-PUB-9419
[7] Bernstein et al. "Low -noise MEMS vibration sensor for geophysical aplicaitons" Proc. Solid-state Sensor and Actuator Workshop 1998 p55-58.
[8] LaCoste, L, "A new long period seismograph", Physics 5, 1934
[9] http://www.newfocus.com
[10] Collin Perry, Private communication.

REPORT FROM THE INTERNATIONAL LINEAR COLLIDER TECHNICAL REVIEW COMMITTEE

G. A. Loew, SLAC, Menlo Park, CA 94025, USA

Abstract

The International Linear Collider Technical Review Committee (ILC-TRC), formed in 1994, was reconvened in February 2001 by the International Committee for Future Accelerators (ICFA) to assess the current technical status of all electron-positron linear collider designs at hand in the world: TESLA, JLC-C, JLC-X/NLC and CLIC. The ILC-TRC worked for exactly two years and submitted its report to ICFA in February 2003.

This paper presents the motivation behind the study, the charge to the committee and its organization, a table of machine parameters for 500 GeV c.m. energy and later upgrades to higher energies, the methodology used to assess the designs, and a ranked list of R&D tasks still deemed necessary between now and the time any one of the projects is selected by the HEP community and begins construction. Possible future developments are briefly discussed.

MOTIVATION, CHARGE AND ORGANIZATION

The international high energy physics (HEP) community at the present time finds itself confronting a set of fascinating discoveries and new questions regarding the nature of matter and its fundamental particles and forces. The observation of neutrino oscillations that indicates that neutrinos have mass, measurements of the accelerating expansion of the universe that may be due to dark energy, and evidence for a period of rapid inflation at the beginning of the Big Bang are stimulating the entire field. Looming on the horizon are the potential discoveries of a Higgs particle that may reveal the origin of mass and of a whole family of supersymmetric particles that may be part of the cosmic dark matter. For the HEP community to elucidate these mysteries, new accelerators are indispensable.

During the past year, after careful deliberations, all three regional organizations of the HEP community (ACFA in Asia, HEPAP in North America, and ECFA in Europe) have reached the common conclusion that the next accelerator should be an electron-positron linear collider with an initial center-of-mass energy of 500 Giga-electronvolts (GeV), later upgradable to higher energies, and that it should be built and operated in parallel with the Large Hadron Collider under construction at CERN. Hence, this second report of the International Linear Collider Technical Review Committee (ILC-TRC) came at a very timely moment. The report was requested by the International Committee on Future Accelerators (ICFA) in February 2001 to assess the current technical status of electron-positron linear collider designs in the various regions. Note that the ILC-TRC was not asked to concern itself with either cost studies or the ultimate selection process of a machine. The study and production of the report took exactly two years. The report was submitted and accepted by ICFA at its February 14, 2003 meeting in Tsukuba, Japan.

The four e^+e^- colliders under consideration were TESLA (1.3 GHz), JLC(C) (5.7 GHz), JLC(X)/NLC (11.4 GHz), and CLIC (30 GHz).

The charge for the second ILC-TRC study is given below:

SECOND ILC-TRC CHARGE

- To assess the present technical status of the four LC designs at hand, and their potential for meeting the advertised parameters at 500 GeV c.m. Use common criteria, definitions, computer codes, *etc.*, for the assessments
- To assess the potential of each design for reaching higher energies above 500 GeV c.m.
- To establish, for each design, the R&D work that remains to be done in the next few years
- To suggest future areas of collaboration

The organization of the ILC-TRC showing the Steering Committee and the Working Groups is given below in Table 1.

Table 1

Chair	Gregory Loew (SLAC)
Steering Committee	Reinhard Brinkmann (DESY)
	Kaoru Yokoya (KEK)
	Tor Raubenheimer (SLAC)
	Gilbert Guignard (CERN)
Working Groups	
Technology, RF Power and Energy Performance Assessments	Daniel Boussard (CERN, Retired), Chair
Luminosity Performance Assessments	Gerry Dugan (Cornell), Chair
Reliability, Availability and Operability	Nan Phinney (SLAC) Ralph Pasquinelli (FNAL), Co-chairs

The members of the Steering Committee each contributed a complete description of their respective designs and upgrades (see full report [1] and Table 2 for a summary of the principal machine parameters). While all linear collider designs have undergone remarkable progress in the past 15 years, the machines reviewed here are not all in the same state of readiness. TESLA is most advanced in terms of the rf system feasibility tests mainly conducted at TTF (DESY). JLC-C consists only of a 400 GeV c.m. rf design based on technology being developed

0-7803-7738-9/03/$17.00 © 2003 IEEE

for a linac-based FEL at SPring-8 in Japan. JLC-X/NLC have an rf design based on ongoing tests at NLCTA and ASSET (SLAC). Both TESLA and JLC-X/NLC have fairly mature conceptual designs. CLIC follows a more novel approach based on a two-beam system studied at CTF (CERN), but it needs more time to be developed. If successful, CLIC could eventually reach 3 TeV c.m. within a footprint similar to the other schemes. Aside from the rf systems, all of the machines have benefited from advanced tests at FFTB (SLAC) and at ATF (KEK), and from experience with the first linear collider, the SLC, which operated at SLAC from 1988 through 1998. The SLC experience has been essential in understanding the luminosity potential of these four designs.

METHODOLOGY USED BY THE WORKING GROUPS

The assessments of the four linear colliders were carried out by the three Working Groups in Table 1, which in turn subdivided their tasks as follows:

Technology, RF Power and Energy Performance

Injectors, Damping Rings and Beam Delivery
Power Sources (Klystrons, Power Supplies, Modulators and Low Level RF)
Power Distribution (RF Pulse Compression, Waveguides, Two-beam)
Accelerator Structures

Luminosity Performance

Electron and Positron Sources (up to Damping Rings)
Damping Rings
Low Emittance Transport (from Damping Rings to IP)
Machine Detector Interface

Reliability, Availability and Operability

Compilation of data from existing machines
Component reliability issues
Machine Protection Systems
Commissioning, tuning, and maintenance

The groups assessed their respective systems and topics for all the machines. They then summarized their positive reactions as well as their concerns about all relevant design details, and translated their concerns into R&D topics and milestones required to mitigate these concerns. About 120 R&D issues were addressed. The ILC-TRC as a whole then ranked the R&D issues according to the following four criteria:

Ranking 1: R&D needed for feasibility demonstration of the machine:

The objective of these R&D items is to show that the key machine parameters are not unrealistic. In particular, a proof of existence of the basic critical constituents of the machines should be available upon completion of the Ranking 1 R&D items.

Ranking 2: R&D needed to finalize design choices and ensure reliability of the machine

These R&D items should validate the design of the machine, in a broad sense. They address the anticipated difficulties in areas such as the architecture of the subsystems, beam physics and instabilities, and tolerances. A very important objective is also to examine the reliability and operability of the machine, given the very large number of components and their complexity.

Ranking 3: R&D needed before starting production of systems and components

These R&D items describe detailed studies needed to specify machine components before construction and to verify their adequacy with respect to beam parameters and operating procedures.

Ranking 4: R&D desirable for technical or cost optimization

In parallel to the main stream of R&D needed to build a linear collider, there should be other studies aimed at exploring alternative solutions or improving our understanding of the problems encountered. The results of the Ranking 4 R&D items are likely to be exploited for improved technical performance, energy upgrades, or cost reduction.

GENERAL CONCLUSIONS

- The Steering Committee and the three Working Groups reached the following general conclusions:
- LC designs and technologies have made remarkable progress in the last 15 years
- Beam dynamics computer simulations have also made remarkable progress
- The Committee did not find insurmountable showstoppers to build TESLA, JLC-X/NLC or JLC-C in the next few years, and CLIC in a more distant future, given enough resources
- However, significant R&D, which is described below, remains to be done for all designs
- Reliability, availability and operability need much greater attention than given so far (see section on peak and integrated luminosity below).

RANKING OF RECOMMENDED R&D ISSUES

Specific concerns and assessments are described in great detail in the report [1]. All the R1 tasks and some of the R2 tasks (common to all machines) are reproduced here. The reader who is interested in more details should refer to the full report.

Ranking 1 Items
TESLA Upgrade to 800 GeV c.m.

- The committee considered that a feasibility demonstration of the machine requires the proof of existence of the basic building blocks of the linacs. In the case of TESLA at 500 GeV c.m., such

demonstration requires in particular that s.c. cavities installed in a cryomodule be running at the design gradient of 23.8 MV/m. This has been practically demonstrated at TTF1 with cavities treated by chemical processing. The other critical elements of a linac unit (multibeam klystron, modulator and power distribution) already exist.

- The feasibility demonstration of the TESLA energy upgrade to about 800 GeV c.m. requires that a cryomodule be assembled and tested at the design gradient of 35 MV/m. The test should prove that quench rates and breakdowns, including couplers, are commensurate with the operational expectations. It should also show that dark currents at the design gradient are manageable, which means that several cavities should be assembled together in the cryomodule. Tests with electropolished cavities assembled in a cryomodule were foreseen in 2003.

JLC-C

- The proposed choke-mode structures have not been tested at high power yet. High power testing of structures and pulse compressors at the design parameters are needed for JLC-C. Tests are foreseen at KEK and at the SPring-8 facility in the next years.

JLC-X/NLC

- For JLC-X/NLC, the validation of the presently achieved performance (gradient and trip rates) of low group velocity structures – but with an acceptable average iris radius, dipole mode detuning and manifolds for damping – constitutes the most critical Ranking 1 R&D issue. Tests of structures with these features are foreseen in 2003.
- The other critical element of the rf system is the dual-moded SLED-II pulse compression system. Tests of its rf power and energy handling capability at JLC-X/NLC design levels are planned in 2003. As far as the 75 MW X-band klystron is concerned, the Working Group considers the JLC-X PPM-2 klystron a proof of existence (although tested only at half the repetition rate). A similar comment can be made regarding the solid-state modulator tested at SLAC.

CLIC

- The presently tested CLIC structures have only been exposed to very short pulses (30 ns maximum) and were not equipped with wakefield damping. The first Ranking 1 R&D issue is to test the complete CLIC structures at the design gradient and with the design pulse length (130 ns). Tests with the design pulse length and with undamped structures are foreseen when CTF3 is available (April 2004).
- The validation of the drive beam generation with a fully loaded linac is foreseen in CTF3. Beam dynamics issues and achieving the overall efficiency look challenging.
- In the present CLIC design, an entire drive beam section must be turned off on any fault (in particular on any cavity fault). CLIC needs to develop a mechanism to turn off only a few structures in the event of a fault. At the time of writing this report, there is no specific R&D program aimed at that objective but possible schemes are being studied.

Ranking 2 Items Common To All Machines

Damping Rings

- Simulations and experiments to study electron cloud and fast ion instabilities
- Extraction kicker stability $<10^{-3}$ level
- Emittance correction algorithms

Low Emittance Transport

- Static and dynamic tuning studies using beam-based alignment techniques
- Development of critical beam instrumentation, including luminosity monitors
- Main linac module and quadrupole vibration studies

Overall Reliability Studies

- A detailed evaluation of critical subsystems reliability is needed to demonstrate that adequate redundancy is provided and that the assumed failure rate of individual components has been achieved.
- The performance of beam based tuning procedures to align magnets and structures must be demonstrated by complete simulations, in the presence of a wide variety of errors, both in the beam and in the components.

OVERALL IMPACT OF RELIABILITY ON PEAK AND INTEGRATED LUMINOSITY

The ILC-TRC spent considerable time and effort discussing the problem of reliability, availability, and operability, and their impact on peak and integrated luminosity which are equally important when one designs a collider. Much work has been done but much more is needed, regardless of which machine is selected. Unlike for storage rings, every pulse for a linear collider is a complete cycle from beginning to end. Experience with the SLC at SLAC from 1988 to 1998 showed that such a machine cannot reach its peak luminosity unless the hardware is reliable and machine tuning algorithms are highly automated. Without these conditions, the process of improving the luminosity does not converge. Furthermore, the major obstacles in running the SLC efficiently turned out to arise not from the linac rf system (which can be tested with prototypes), but from the damping rings, the positron source, the arcs, and the final focus. The future LC will not contain arcs but it will have long beam delivery systems with many collimators. None of these systems will be testable ahead of time in their entirety. Extrapolations to a linear collider that will be ten times as long and complex make these considerations even more stringent and difficult.

Even so, experience with existing accelerators can guide us by focusing on certain factors which are helpful in realistically estimating integrated luminosity. Four

relevant quantities, ST, HA, BE, and NL, are defined below.

- *ST* is the total scheduled calendar time for the machine in a year.
- *HA* is the fraction of time the machine hardware is available to produce beam. Hardware downtime includes both unscheduled repairs (when something critical breaks), scheduled repairs (either at regular intervals or when enough problems have accumulated), and all associated cooldown, warmup, and recovery times. For an accelerator, one must consider not only how long it takes to repair a failed component, but also the total time the beam is off because of the fault, including time lost due to access and the time taken to retune the beam.
- *BE* is the effective fraction of beam time actually delivering luminosity. Beam inefficiencies include Machine Development (time spent studying and improving the accelerator), the impact of tuning procedures, injection, and the luminosity decay during a store (for storage rings), Machine Protection trips and recovery (for linacs), and last but not least, the simple fact that accelerators do not manage to deliver the same luminosity on every pulse or for every store.
- NL is the nominal luminosity during a particular run. It may be greater or less than the design luminosity, but it usually increases steadily with time. For a storage ring, it is the typical luminosity at the beginning of a store. For a linear collider, it is the luminosity when the beams are colliding well.

Multiplying these four quantities together yields the integrated luminosity. The reader may perform such a calculation by making his or her own guesses based on other machines. If, for example, one takes an ST of 6500 hours, an HA of 80% (perhaps somewhat optimistic), a BE of 80% (which includes 10% for Machine Development and 10% for all other inefficiencies), and a hypothetical NL of, say $10x10^{33}cm^{-2}s^{-1}$, then one gets an integrated luminosity of 150 inverse femtobarns for that year.

The reader is cautioned not to take the above numbers as predictions, but rather to see this example as a reminder to the designers and builders of a linear collider of the importance of reliability, operability, and tunability.

A POSSIBLE ROADMAP FOR THE FUTURE

During the past year, the respective HEP communities in Asia, Europe and North America have constituted regional steering committees to organize the process that could eventually lead to the construction of an international linear collider. To coordinate their work, an International Linear Collider Steering Committee (ILCSC) has also been formed. A possible roadmap to achieve these goals is briefly outlined below.

- By 2004, the R1 tasks for TESLA and JLC-X/NLC will hopefully be accomplished.
- The ILCSC has already set up international accelerator and detector sub-committees to continue relevant studies. A "wise-persons" committee yet to be formed will recommend the selection of a single accelerator technology on the basis of physics reach, technical and cost comparisons, as the R1 tasks are completed.
- An International LC Design and Management Group will then be created to prepare a unified Technical Design Report and cost estimate in 2-3 years.
- Meanwhile, the three regional steering committees are engaging their respective government agencies to form the necessary international oversight, management and financial institutions to launch the LC.
- Once design and cost estimate are completed, an international decision to proceed can be made: host region(s) will come forward, and an ultimate site will be selected.
- Construction could then begin.

ACKNOWLEDGEMENT

The material presented in this paper was to a large extent extracted from the Executive Summary of the ILC-TRC Report [1]. In addition to the people called out in Table 1, the author wishes to thank all the other members of the committee who contributed to the study and to the report:

Chris Adolphsen (SLAC), Ralph Assmann (CERN), Hans H. Braun (CERN), YongHo Chin (KEK), Winfried Decking (DESY), Helen Edwards (FNAL), Jacques Gareyte (CERN), Kurt Hübner (CERN), Witold Kozanecki (CEA Saclay), Kiyoshi Kubo (KEK), Lutz Lilje (DESY), Pavel Logatchov (BINP), Ralph Pasquinelli (FNAL), Nan Phinney (SLAC), Joe Rogers (Cornell), Marc Ross (SLAC), Daniel Schulte (CERN), Andrei Seryi (SLAC), Ronald Settles (MPI), Tsumoru Shintake (KEK), Peter Tenenbaum (SLAC), Nobu Toge (KEK), Nick Walker (DESY), Hans Weise (DESY), Perry Wilson (SLAC), and Andy Wolski (LBNL)

REFERENCES

[1] The report may be found on the Web at: http://www.slac.stanford.edu/pubs/slacreports/slac-r-606.html

Copies of the entire report may be obtained by requesting SLAC-R-606 from the following address:
Stanford Linear Accelerator
2575 Sand Hill Road, MS-68
Menlo Park, CA 94025
E-mail address: epubs-l@slac.stanford.edu

Table 2: Summary of Machine Parameters

	TESLA		JLC-C		JLC-X/NLC*		CLIC	
Center of mass energy [GeV]	500	800	500	1000	500	1000	500	3000
RF frequency of main linac [GHz]	1.3		5.7	5.7 / 11.4†	11.4		30	
Design luminosity [10^{33} $cm^{-2}s^{-1}$]	34.0	58.0	14.1	25.0	25.0 (20.0)	25.0 (30.0)	21.0	80.0
Linac repetition rate [Hz]	5	4	100		150 (120)	100 (120)	200	100
Number of particles/bunch at IP [10^{10}]	2	1.4	0.75		0.75		0.4	
$\gamma\varepsilon^*_x$ / $\gamma\varepsilon^*_y$ emit. at IP [m·rad × 10^{-6}]	10 / 0.03	8 / 0.015	3.6 / 0.04		3.6 / 0.04		2.0 / 0.01	0.68 / 0.01
β^*_x / β^*_y at IP [mm]	15 / 0.40	15 / 0.40	8 / 0.20	13 / 0.11	8 / 0.11	13 / 0.11	10 / 0.05	16 / 0.07
σ^*_x / σ^*_y at IP before pinch‡ [nm]	554 / 5.0	392 / 2.8	243 / 4.0	219 / 2.1	243 / 3.0	219 / 2.1	202 / 1.2	60 / 0.7
σ^*_z at IP [μm]	300		200	110	110		35	
Number of bunches/pulse	2820	4886	192		192		154	
Bunch separation [nsec]	337	176	1.4		1.4		0.67	
Bunch train length [μsec]	950	860	0.267		0.267		0.102	
Beam power/beam [MW]	11.3	17.5	5.8	11.5	8.7 (6.9)	11.5 (13.8)	4.9	14.8
Unloaded/loaded gradient§ [MV/m]	23.8 / 23.8**	35 / 35	41.8 / 31.5	41.8 / 31.5 / 70 / 55	65 / 50		172 / 150	
Total number of klystrons	572	1212	4276	3392 / 4640	4064	8256	448	
Number of sections	20592	21816	8552	6784 / 13920	12192	24768	7272	44000
Total two-linac length [km]	30	30	17.1	29.2	13.8	27.6	5.0	28.0
Total beam delivery length [km]	3		3.7		3.7		5.2	
Proposed site length [km]	33		33		32		10.2	33.2
Total site AC power†† [MW]	140	200	233	300	243 (195)	292 (350)	175	410
Tunnel configuration‡‡	Single		Double		Double		Single	

* Numbers in ( ) in the JLC-X/NLC column correspond to the NLC design with 120 Hz repetition rate.

† The 1 TeV JLC-C collider uses a C-band rf system for the first 200 GeV of each linac followed by an X-band rf system for the remaining 300 GeV of acceleration--the X-band rf system would be identical to that described for the JLC-X band collider.

‡ For all designs except CLIC, the IP spot sizes are calculated as usual from the emittances and beta functions. With the design emittances in CLIC, nonlinear aberrations in the final focus system increase the final spot size by 20 to 40%.

§ The main linac loaded gradient includes the effect of single-bunch (all modes) and multibunch beam loading, assuming that the bunches ride on crest. Beam loading is based on bunch charges in the linacs, which are slightly higher than at the IP.

** With the present site layout for TESLA, 23.4 MV/m was the required energy gain per meter of accelerator structure. A detailed analysis by the ILC-TRC revealed that the gradient has to be increased to 23.8 MV/m when rf phasing, especially for BNS damping, is taken into account.

†† Total site power includes AC for linac rf and cooling systems as well as power for all other beam lines and site facilities.

‡‡ The single tunnel layout has both the klystrons and accelerator structures in the main linac tunnel while the double tunnel layout places the klystrons and modulators in a separate enclosure. In the CLIC scheme, the main linac uses a single tunnel since there are no klystrons or modulators associated with it. The 300 m-long CLIC drive beam accelerator is located in a tunnel with a separate klystron gallery on the surface.

DAMPING RING DESIGNS AND ISSUES*

A. Wolski#, LBNL, Berkeley, CA 94720, USA
W. Decking, DESY, Hamburg, Germany

Abstract

The luminosity performance of a future linear collider (LC) will depend critically on the performance of the damping rings. The design luminosities of the current LC proposals require rings with very short damping times, large acceptance, low equilibrium emittance and high beam intensity. We discuss the design strategies for lattices achieving the goals of dynamical stability, examine the challenges for alignment and coupling correction, and consider a variety of collective effects that threaten to limit beam quality. We put the design goals in context by referring to the experience of operating facilities, and outline the further research and development that is needed.

PERFORMANCE SPECIFICATIONS

The critical parameters for a linear collider damping ring are the injected and extracted emittances, repetition rate, bunch train structure, and bunch charge. Although they do not determine the damping ring design completely, these quantities place strong constraints on choices of the main design parameters, including the circumference and energy. An optimization process for a number of features of the lattice design for a linear collider damping ring has been suggested by Emma and Raubenheimer [1]. The final design is often a compromise between competing requirements. For example, a higher ring energy is favored by the need for a short damping time; however, the normalized natural emittance of a storage ring scales with the cube of the energy, so the need for a low emittance favors lower energies. The final choice of energy has to take into account collective effects, that are often more severe at low energy. There is rarely a clear-cut optimum value for any free design parameter.

The different technologies adopted for the main linacs strongly affect the damping ring design, principally through the train structure. TESLA, with a superconducting linac, has a long bunch train, consisting of 2820 bunches with 337 ns bunch spacing, and a relatively low repetition rate of 5 Hz. By contrast NLC, using a warm linac, has a train of 192 bunches with 1.4 ns spacing, and a higher repetition rate of 120 Hz. To store the TESLA bunch train in a single damping ring would require a ring with a 280 km circumference: the present design [2] brings the ring down to a practical length by injecting and extracting individual bunches so that their spacing in the ring is only 20 ns.

The warm machines (NLC, JLC and CLIC) have the opposite problem: the bunch trains are only approximately 80 m long, and to design a ring with sufficient cells in this circumference to meet the emittance specification is not practical. These machines therefore store several bunch trains at once, with each bunch trains remaining in the ring for as many machine cycles as there are trains in the ring.

The critical parameters specifying the performance of the damping rings are given in Table 1. As usual in the context of linear colliders, the normalized emittance is quoted.

Table 1: Damping Ring Design Specifications

	TESLA	NLC/JLC	CLIC
e^+ emittance in [μm]	14,000	45,000	-
e^- emittance in [μm]	40	150	10
Horiz. emit. out [μm]	8	3	1.6
Vert. emit. out [μm]	0.02	0.02	0.005
Repetition rate [Hz]	5	120/150	200
Bunches/train	2820	192	154
Bunch spacing [ns]	20	1.4	0.66
Bunch charge [10^{10}]	2	0.75	0.4

The positron beam arriving at the damping rings typically has a large six-dimensional emittance. For TESLA, the positron beam is produced from an undulator source, and is compact enough that it is feasible to design a ring that has a sufficiently large acceptance and that meets the specifications for the extracted emittance. The only difference between the electron and positron damping rings for TESLA, is that the positron ring has significantly more damping wiggler. In the case of NLC/JLC, the positron beam comes from a conventional tungsten-rhenium target source, and has significantly larger transverse and longitudinal emittances. To allow for this, the NLC/JLC designs include a positron pre-damping ring, that has a large acceptance and is required only to damp the beam to the point that it can be accepted by a positron main damping ring that is identical to the electron main damping ring.

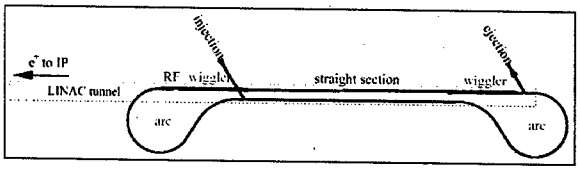

Figure 1: Conceptual Layout of the TESLA Damping Rings

The conceptual layout of one of the TESLA damping rings is shown in Figure 1. In the present design, each arc is approximately 1 km in circumference, and the straight sections are 7.5 km long and located in the main linac tunnel. The layout of the positron damping ring complex for the NLC is shown in Figure 2. The present design [3] includes a Main Damping Ring (MDR) of 300 m storing 3 bunch trains, and a Pre-Damping Ring (PDR) of 231 m,

*Work supported by the US DOE under contract DE-AC03-76SF00098
#awolski@lbl.gov

storing 2 bunch trains. The additional circumference of the NLC rings over the lengths of the bunch trains is necessary to allow for the rise/fall times of the injection and extraction kickers. We discuss injection and extraction schemes below.

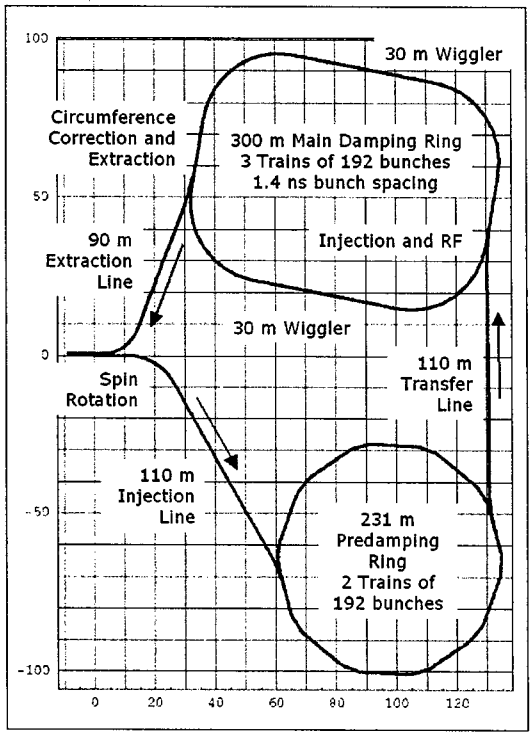

Figure 2: Layout of NLC Positron Damping Rings and Transport Lines

LATTICE DESIGN

Damping rings are similar in many respects to third generation synchrotron light sources, although the relationship is probably somewhat closer in the case of the warm machines. However, damping rings require lower natural emittances than are generally specified for light sources, and do not have the same requirement for many separate dispersion-free straight sections for insertion devices. This makes the Theoretical Minimum Emittance (TME) cell an appropriate choice for the arcs, since it allows a low natural emittance to be achieved with relatively few cells. The lattice functions in one TME arc cell in the NLC MDR are shown in Figure 3. TME cells are also used in the arcs in the CLIC and TESLA damping rings. The NLC PDR is actually a ten-fold Double Bend Achromat (DBA). A comparison between some of the parameters in the NLC MDR, the TESLA Damping Rings, the ALS, and a 5 GeV lattice for the ESRF [4] is given in Table 2.

There are a number of considerations that need to be addressed when designing the lattice. These include:

- The natural emittance is ideally a little below the specified extracted horizontal emittance, to allow some margin for collective effects.
- With an appropriate design, the damping wigglers can significantly reduce the natural emittance.
- A large momentum compaction is needed to give a reasonably long bunch, thus reducing the charge density and reducing the impact of collective effects.
- The natural chromaticity of the lattice must be kept small, and locations provided with large dispersion and good separation of the beta functions, to minimize the chromatic sextupole strengths and give a good dynamic aperture.
- The vertical tune should be sufficiently far from an integer value, so that the closed orbit and vertical dispersion are not highly sensitive to magnet misalignments.

Table 2: Comparison of some parameters of the TESLA Positron Damping Ring, the NLC MDR, ESRF and ALS

	TESLA	NLC	ESRF	ALS
Circumference [m]	17,000	300	845	197
Energy [GeV]	5	1.98	5	1.9
Emittance [μm]	8	2.4	25	25
Bunch length [mm]	6	5.5	6	7
Energy spread [%]	0.13	0.1	0.09	0.1
Energy loss [keV]	21,000	970	2700	280
Damping time [ms]	28	4.1	12	8.9

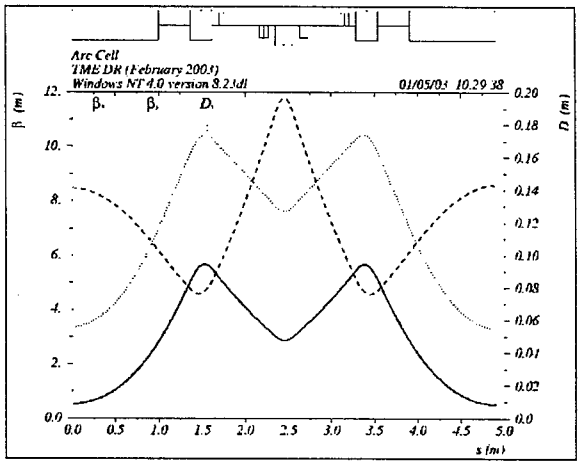

Figure 3: Lattice Functions in One TME Arc Cell in the NLC Main Damping Rings

INJECTION AND EXTRACTION

Injection schemes for synchrotron light sources generally rely on the radiation damping to merge injected off-axis bunches with stored bunches. This approach is not possible in a damping ring, since the bunch trains are stored for only a few damping times before being extracted. Instead, bunches are injected into the ring on-axis: a fast kicker is used to deflect the incoming bunches so that they have zero offset and angle with respect to the closed orbit at the exit of the kicker. Since the kicker ejects any stored charge that reaches it while it is turned on, the full bunch charge must be injected into the ring in

a single shot. The challenges in the kicker technology are somewhat different between the different machines. The TESLA kickers must have a rise/fall time of 20 ns, but the flat top only needs to be as long as a single bunch (some tens of picoseconds). For NLC and JLC, the rise and fall times are 65 ns, but a flat top of around 270 ns is needed. Achieving the desired stability on the flat top (a fractional variation of less than 5×10^{-4}) can be difficult, though some success has been demonstrated with the use of double-kicker schemes to relax the tolerances [5]. The CLIC Damping Rings require kickers with a rise/fall time of 30 ns, and a flat top of a little over 100 ns.

ACCEPTANCE

The large average injected beam power into a damping ring (48-68 kW for the warm machines, and 226 kW for TESLA) means that an injection efficiency close to 100% is needed to avoid intolerable radiation loads on components in the ring. The dynamic aperture is therefore an important issue (as is the physical aperture), and is limited by the sextupoles, nonlinear field components in the damping wigglers, systematic and random multipole error components in all magnets, and tuning errors. The bare lattice (with the only significant nonlinearities coming from the sextupoles) initially needs to be carefully designed to give a large dynamic aperture. As is clear from Table 2, the damping rings include much more wiggler than is usual in a light source (430 m in TESLA, 61 m in NLC, and 160 m in CLIC). The effects of the nonlinear components of the wiggler field therefore need to be carefully considered [6]. A detailed study for the NLC suggests that the wiggler effects, while visible in simulations, should not reduce the dynamic aperture to unacceptable values.

VERTICAL EMITTANCE

The specification for the extracted vertical emittance is demanding, and will require careful alignment of the magnets and rigorous coupling correction. The fundamental lower limit on the vertical emittance is placed by the opening angle of the synchrotron radiation, which excites vertical betatron oscillations even in a perfectly aligned lattice [7]. For the TESLA Damping Ring, this lower limit is approximately 1 nm (normalized) and for the NLC Main Damping Rings, it is approximately 0.8 nm. In practice, much larger vertical emittance is generated both by vertical dispersion and by betatron coupling. The sensitivity of a lattice to various misalignments can be estimated from knowledge of the lattice design [8], and may be quantified by giving the rms misalignment that, on its own, will generate a specified vertical emittance. Sensitivity values for the TESLA Damping Rings, the NLC Main Damping Rings, and the ALS are compared in Table 3. A vertical emittance of 0.02 μm has recently been achieved in the ALS [9]. Note that the values in Table 3 **should not be interpreted as tolerances**, and make no reference to skew correction of the coupling. The values quoted do, however, give an indication of the response of the vertical emittance to different misalignments for different lattices. The quadrupole jitter sensitivity quoted in Table 3 is the rms quadrupole misalignment that generates a vertical closed orbit distortion equal to the vertical beam size, which is the specified stability on the beam extracted from the damping rings. A potentially significant effect leading to emittance growth is the effect of stray fields [10].

Table 3: Sensitivity Estimates

	TESLA	NLC	ALS
Vertical emittance [μm]	0.014	0.019	0.02
Sextupole vertical alignment rms [μm]	11	53	30
Quadrupole roll rms [μrad]	38	511	200
Quadrupole jitter rms [μm]	76	264	230

COLLECTIVE EFFECTS

The relatively high beam intensity in the damping rings makes them vulnerable to a variety of collective instabilities that threaten to limit the operational performance. These effects range from the familiar "classical" instabilities such as those driven by the vacuum chamber impedance, to others that are less well understood, or only become significant in the new regimes in which the damping rings will operate.

Microwave Instability

The energy spread in the beam extracted from the damping rings is rotated into bunch length in the bunch compressors ahead of the main linac. It is necessary to avoid effects that increase the energy spread, that would lead directly into an increased bunch length in the linac. One such effect is the microwave instability, driven by the broad-band impedance of the vacuum chamber. Using the Boussard criterion, it is possible to estimate the threshold impedance at which the instability is expected to occur. It is usually desirable to aim for a vacuum chamber design that leaves a generous safety margin. For the TESLA DR, the impedance threshold is $Z/n = 100$ mΩ for the nominal bunch charge of 2×10^{10} particles. For the NLC MDRs, the impedance threshold is 630 mΩ for the nominal bunch charge of 0.75×10^{10}. The vacuum chamber design in each case will need to be given careful consideration.

Coherent Synchrotron Radiation

The synchrotron radiation has an effect on the beam that can be described by an impedance. Heifets and Stupakov have carried out an analysis of a potential instability driven by this impedance [11], which is analogous to the microwave instability. Effects consistent with the Heifets and Stupakov theory have been observed at BESSY II and at the ALS [12]. Calculations suggested that the design of the NLC MDRs developed in 2001 would operate close to this threshold, and this motivated a redesign of the lattice to raise the threshold by increasing the momentum compaction [3]. Studies are continuing. It is possible that interference effects of the radiation in the

wiggler can modify the form of the impedance, and this could be significant for a wiggler-dominated ring [13]. However, present indications are that in the present NLC MDR design, the threshold bunch charge for the CSR instability will be roughly an order of magnitude larger than the nominal bunch charge. The impedance scales inversely with the circumference of the ring, so for the TESLA Damping Rings, despite the long wiggler and large amount of radiation, CSR should be a small effect.

Space Charge Tune Shift

The relatively low energy of the TESLA Damping Rings for their large circumference means that there will be a large incoherent tune shift from space charge forces. A detailed analysis of the effect [14] indicated that the tune shift could result in emittance growth from particles crossing resonance lines in tune space. The proposed solution is to use combinations of skew quadrupoles to couple the beam locally in the straight sections. Tracking studies suggest that this solution would be effective in eliminating the effects of the space charge forces, and that the tolerances on tuning the "coupling bumps" are reasonable, so that it would still be possible to extract a beam with the specified vertical emittance.

Intrabeam Scattering

Intrabeam Scattering (IBS) is a familiar effect from proton machines, where the small angle scattering of particles within a bunch leads to growth of the six dimensional emittance. In electron machines, the relatively slow growth rates from IBS are usually overwhelmed by the radiation damping, but in very low emittance regimes, the bunch density can be high enough that IBS leads to an observable increase in the equilibrium emittance. Observations have been made at the KEK ATF [15] and at the ALS [16].

The IBS growth rates decrease with increasing bunch volume, and also depend strongly on the beam energy. The higher beam energy in the TESLA Damping Rings, as well as the larger beam sizes that come from the high beta functions in the long straights (apart from the coupling bumps designed to mitigate the space charge effects) mean that IBS is a comparatively small effect in the these rings. However, for the lower energy damping rings for the warm machines, IBS can potentially increase the extracted emittance above the specified values. Figure 4 shows the effect on the horizontal emittance in the NLC MDR calculated using the Bjorken-Mtingwa formalism [17]. The broken line shows the horizontal emittance decreasing from radiation damping to its equilibrium value. If IBS effects are included, as the vertical emittance approaches its equilibrium value, the IBS growth rates increase, leading to an increase in the horizontal emittance. With the nominal parameters, the extracted horizontal emittance is 3.23 μm, a little above the specified value of 3 μm.

There are a number of possible solutions that may be explored, including the use of harmonic cavities for bunch lengthening [18]. We also note that observations at the ATF are not in full agreement with the theory, and an experimental program is continuing with the aim of resolving the discrepancy.

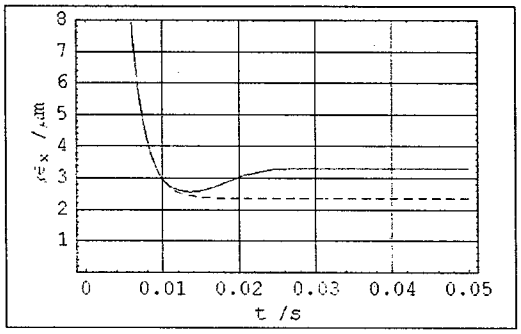

Figure 4: Effect of IBS on Horizontal Emittance in the NLC Main Damping Rings

IBS is a very strong effect in the CLIC Damping Rings, and presents significant challenges for their design [19].

Electron Cloud

Free electrons are generated in the vacuum chamber of an accelerator by a variety of processes, including photoemission, gas ionization, and secondary emission. Under certain circumstances, in positron storage rings the cloud density can reach very high levels (often saturating around the point where the electron charge in the chamber is equal to the proton or positron charge). The electron cloud can then drive single bunch or multibunch oscillations, effectively destabilizing the beam.

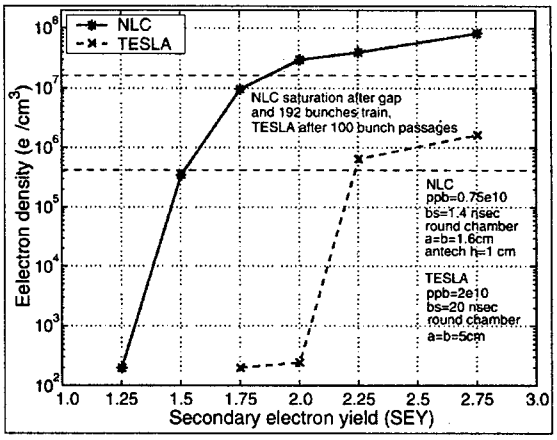

Figure 5: Mean Electron Cloud Density in the Damping Rings as a Function of Secondary Yield

Effects ascribed to electron cloud have been observed in a number of machines, notably in the low energy rings of the B Factories [20]. Estimates suggest that without taking action to prevent the build-up of the electron cloud, the impact on the operation of the TESLA and NLC/JLC Damping Rings could be severe [21]. Solenoids have provided an effective solution at the B Factories [22] by trapping secondary electrons near the vacuum chamber wall, and may be a possible solution for the TESLA Damping Rings. However, the rings for the warm

machines are densely packed with components, and the length that may be covered by solenoids is relatively small. Instead, it is proposed to use a low secondary electron yield (SEY) coating, such as titanium nitride, to suppress the production of electrons. Figure 5 shows the mean cloud density in field-free regions of the NLC positron MDR and TESLA positron DR as a function of the peak SEY of the chamber surface [23]. It should be noted that there is still considerable uncertainty in these results, but it seems clear that the larger bunch separation in TESLA greatly reduces the build-up by allowing time for the cloud to disperse between bunches. Bare aluminum typically has a peak SEY of 2.7. Experimental studies are underway to investigate the possibility of achieving peak SEY close to 1.

Fast Ion Instability

Ions generated during the passage of a single bunch train can couple the bunch motion, leading to increasing amplitude oscillations of bunches along the train. Although a theoretical model exists for this Fast Ion Instability [24], it has been difficult to study because of the lack of existing storage rings operating in an appropriate (very low emittance) regime. Qualitative observations have been made at the PLS, and at the ALS [25]. It is possible that the need to stay below the FII threshold will place demanding requirements on the vacuum systems, with pressures below 1 nTorr possibly needed. It is hoped that with the low coupling in the ALS achieved recently, quantitative studies may be performed to confirm the models.

OUTLOOK

Damping rings for any future linear collider will need to operate in parameter regimes not commonly achieved by existing storage rings. The designs are beginning to mature and solutions have been proposed for all the major technical challenges, although some of the suggested solutions (for example, low SEY coatings for the electron cloud) still need considerable work to be proven sufficiently effective. Experience at operating machines, for example the light sources and the KEK ATF prototype damping ring, will be crucial in developing the designs into real machines. Such experience will include optimizing the acceptance, tuning for low coupling, verifying the models for a range of collective effects, and operating the advanced diagnostics that operation of the damping rings will require.

REFERENCES

[1] P. Emma and T. Raubenheimer, "A Systematic Approach to Damping Ring Design", Phys. Rev. STAB, Volume 4, 021001, 2001.

[2] TESLA Technical Design Report, DESY 2001-011, 2001.

[3] A. Wolski et al, "A Lattice with Larger Momentum Compaction for the NLC Main Damping Rings", these proceedings.

[4] L. Hardy et al, "Recent Developments for an Improved Operation at the ESRF", PAC'01, 2001.

[5] T. Imai et al, "Highly Stable Beam Extraction by Double Kicker System", KEK Preprint 2002-16.

[6] M. Venturini, "Wigglers and Single Particle Dynamics in the NLC Damping Rings", these proceedings.

[7] T. Raubenheimer, "The Generation and Acceleration of Low Emittance Flat Beams for Future Linear Colliders", SLAC report 387, 1991.

[8] T. Raubenheimer and A. Wolski, "Comparison of Alignment Tolerances in Linear Collider Damping Rings with Operating Rings", Nanobeams'02.

[9] C. Steier et al, "Coupling Correction and Beam Dynamics at Ultralow Vertical Emittance in the ALS", these proceedings.

[10] W. Decking, "Influence of Klystron Stray Fields on TESLA Damping Ring", talk given at the TESLA Collaboration Meeting in Hamburg, January 2003, http://tesla.desy.de/tesla-apdg/mtgs/tesla-collab-22.01.03.htm

[11] S. Heifets and G. Stupakov, "Beam Instability and Microbunching due to Coherent Synchrotron Radiation", PAC'01, p.1856.

[12] J. Byrd et al, "Observation of Broadband Self-Amplified Spontaneous Coherent Terahertz Synchrotron Radiation in a Storage Ring", Phys. Rev. Lett. 89, 224801 (2002).

[13] J. Wu et al, "Calculation of the Coherent Synchrotron Radiation Impedance from a Wiggler", these proceedings.

[14] W. Decking and R. Brinkmann, "Space Charge Problems in the TESLA Damping Ring", EPAC'00, p.1024.

[15] K. Bane et al, "Intrabeam Scattering Analysis of ATF Beam Measurements", SLAC-PUB-8875, 2001.

[16] J. Corlett et al, "Measurements of Intrabeam Scattering at Low Emittance in the Advance Light Source", HEACC'01, 2001.

[17] J.D. Bjorken and S.K. Mtingwa, "Intrabeam Scattering", Particle Accelerators 13 p.115, 1983.

[18] S. de Santis and A. Wolski, "Harmonic Cavities for the NLC Damping Rings", these proceedings.

[19] M. Korostelev and F. Zimmermann, "A Lattice Design for the CLIC Damping Rings", DR'03, http://www.astec.ac.uk/conf/dampingring/

[20] H. Fukuma, "Electron Cloud Effects at KEK-B", Ecloud'02, CERN-2002-001. 2002.

[21] A. Wolski, "Electron Cloud in Linear Collider Damping Rings", Ecloud'02, CERN-2002-001. 2002.

[22] S.S. Win et al, "Study of Coupled Bunch Instability Caused by Electron Cloud in the KEKB Positron Ring", EPAC'02, p.1592.

[23] Thanks to Mauro Pivi (SLAC) for these results.

[24] T. Raubenheimer and F. Zimmermann, "Fast Beam-Ion Instability", Phys. Rev. E 52, p.5487, 1995.

[25] J. Byrd et al, "First Observations of a Fast Beam-Ion Instability at the ALS", EPAC'98, 1998.

DAMPING RING TO INTERACTION POINT BEAM TRANSPORT ISSUES

N. Walker, DESY, Hamburg, Germany,
D. Schulte, CERN, Geneva, Switzerland,
A. Wolski, LBNL, Berkeley, CA 94720, USA
P. Tenenbaum, A. Seryi, M. Woodley, SLAC, Stanford, CA 94309, USA

Abstract

One of the major challenges facing the proposed high-energy linear e^+e^- colliders is the preservation of the extremely small vertical emittance from the damping rings to the interaction point (IP). This emittance must be transported through bunch compression sections, the main linac and finally through the beam delivery system to the IP. Historically, the beam dynamics issues of each sub-system have been studied quasi-independently, with the beam conditions and tolerances being specified at the boundaries. As part of the recent International Linear Collider Technical Review Committee [1], new simulation tools have been developed to simulate the beam transport through the integrated system, including static and dynamic errors, stabilization systems, and tuning algorithms.

INTRODUCTION

Two major factors in achieving the ambitious luminosity goal of a few 10^{34} $cm^{-2}s^{-1}$ in a future e^+e^- linear collider are maintaining the small vertical normalised emittance, and keeping the nanometer-sized beams in collision at the IP. While the damping rings are responsible for producing these unprecedented normalised vertical emittances (~10^{-8} m), the beam transport from the damping ring to the IP – which includes the main linac – must preserve them to within tolerable levels.

The low emittance transport (LET) system generically refers to:

- the damping ring to main linac transport line, including bunch compression (BC) and pre-acceleration;
- the main linac;
- the beam delivery system (BDS).

Table 1 summarises the relevant parameters for the LET systems of the TESLA, JLC/NLC and CLIC designs. The beam parameters are specified at the main sub-system boundaries. To some extent, the BC and BDS sub-systems of the LET systems are interchangeable between the machines. The primary performance differences are driven by the choice of linac technology.

Table 1: Important design parameters for the LET sub-systems for TESLA, JLC/NLC and CLIC (taken from [1]).

			TESLA		JLC/NLC		CLIC		*Comments*
c.o.m. energy		GeV	500	800	500	1000	500	3000	*important for (all sections):*
particles / bunch		$\times 10^{10}$	2	1.4	0.75		0.4		*wakefields, beam-beam*
bunches / train			2820	4886	192		154		*long-range wakefields, intra-train feedback*
bunch separation		ns	337	176	1.4		0.67		
repetition rate		Hz	5	4	120[i]		200	100	*vibration suppression (orbit feedback)*
initial conditions (damping ring)	E_{beam}	GeV	5		1.98		2.42		
	$\gamma\varepsilon_y$	nm	20	10	20		5		*important for (all sections):*
	σ_δ	%	0.13		0.09		0.13		*chromatic effects*
	σ_z	mm	6		4		1.3		*wakefield effects, beam-beam*
after bunch compressor	E_{beam}	GeV	4.6		8		9		*TESLA uses single-stage compression. CLIC and NLC/JLC use two stage compression.*
	$\gamma\varepsilon_y$	nm	20	10	22		5		
	σ_δ	%	3		1.5		1.36		
	σ_z	mm	0.3		0.11		0.035		
IP (linac exit)	E_{beam}	GeV	250	400	250	500	250	1500	
	$\gamma\varepsilon_y$[ii]	nm	30	15	40		10		
	σ_δ	%	0.08[iii]		0.25		0.25		
	σ_z	mm	0.3		0.11		0.035		
	σ^*_y	nm	5	2.8	3	2.1	1.5	0.7	*drives vibration tolerances*
	L	$\times 10^{34}$ $cm^{-2}s^{-1}$	3	5	2	3	2	8	*including beam-beam enhancement*

i) NLC/JLC also has options for 150 Hz and 100 Hz operation at 500 GeV and 1 TeV respectively.
ii) Includes emittance dilution budget
iii) Represents the energy spread at the exit of the main linac. At the IP, the electrons have an additional contribution from the positron source undulator which increases the energy spread to ~0.15% at E_{beam} = 250 GeV.

0-7803-7738-9/03/$17.00 © 2003 IEEE

The International Linear Collider Technical Review Committee (ILC-TRC) published its findings earlier this year [1]. As part of that process, new simulations of the performance of the LET systems were performed. Several codes were developed and bench marked against each other. As a by-product of the review, the available simulation tools have become more sophisticated. In this report, we will first briefly overview the important issues pertaining to LET system performance, and then discuss the status of the simulation tools that are used to study them.

BEAM DYNAMICS ISSUES

One of the major challenges facing the LET system is achieving and maintaining the tight alignment tolerances. Although there are certainly other concerns in the LET systems*, we will concentrate on the alignment issues.

Before specifically discussing component alignment and beam-based tuning, we will first briefly discuss each LET sub-system in turn and highlight the main beam dynamics mechanisms that are important.

Bunch Compression

The bunch length must be compressed from the several millimetre lengths in the damping rings to the sub-millimetre lengths required at the IP, before injection into the main linac. Bunch compression is achieved by an effective $\pi/2$ rotation of the longitudinal phase space. In JLC/NLC this is achieved in two stages using an L-band compressor at 1.98 GeV and a X-band compressor at 8 GeV. The current TESLA design has a single-stage L-band compressor at 5 GeV. One direct consequence of bunch compression is the relatively large energy spread at the exit of the compressor, which can cause substantial emittance growth from dispersive effects arising from component misalignment. This is particularly true for the single stage TESLA system, where the ~3% energy spread after compression is responsible for a large fraction of the emittance growth budget over the first sections of the linac (~50% of the total linac emittance growth is over the first ~8% of the linac). The two-stage JLC/NLC design mitigates these effects to a large extent since the energy spread from the initial compression is first adiabatically reduced by accelerating the beam up to 8 GeV before the second stage is applied†.

Other important beam dynamics issues in the bunch compressors are:

- nonlinear optical effects – especially the nonlinear path-length terms – must be included in the simulations;
- wakefield effects and cavity misalignments (particularly tilts) for the longer bunches need to be considered.;
- the tolerances on both amplitude and phase of the RF tend to be very tight.

For the ILC-TRC the bunch compressor systems were only marginally included during the LET simulation studies, but this is being addressed in the current ongoing effort.

Main Linac

The dynamics of the main linac are generally divided into multi-bunch and single-bunch effects; the former is the study of long-range wakefields (higher-order modes, or HOMs), which can lead to multi-bunch beam break up (MBBU). Singe-bunch dynamics are concerned with the effects of short-range wakefields. Much engineering effort has been invested on mitigating the HOM effects by the use of detuned structures and HOM couplers. Assuming that these measures successfully damp the HOMs to the required levels, it is the single-bunch effects (short range wakes) that require the most attention: nearly all of the studies for the ILC-TRC were concerned with single-bunch dynamics.

Emittance dilution mechanisms can be loosely categorised into transverse wakefield effects and chromatic (dispersive) effects, although the two are related via beam loading and its compensation. Both effects are driven by the alignment of the components and the bunch trajectory (orbit). All of the linac beam-based tuning algorithms are ultimately concerned with achieving a 'gold orbit' which minimises the emittance dilution. The tolerances on both RF structure and quadrupole alignment are governed by several factors:

- structure alignment is dominated by the strength of the transverse wakefields which scale roughly as the 3rd power of the RF frequency, and are therefore much stronger in the X-band machines than in TESLA;
- the X-band designs compensate the stronger wakefields by use of shorter bunches, stronger focusing and longitudinally correlated energy spread (so-called BNS damping [2]), all of which lead to tighter (but still achievable) alignment tolerances;
- the intense beam-beam interaction in TESLA significantly increases the luminosity loss for a given (longitudinally correlated) emittance growth‡;
- the quadrupole alignment tolerance is a function of the energy spread in the beam, and the strength of the focusing, both of which change along the linac (especially in the presence of strong BNS damping);

Beam Delivery System (BDS)

The BDS is responsible for providing:

- the required strong demagnification of the beam to produce nanometre spot sizes at the IP;

* The reader is referred to (for example) the ILC-TRC report [1] for a more comprehensive discussion of all the issues pertaining to the beam dynamics of the LET systems.

† The final energy spread for JLC/NLC is comparable to the coherent energy spread introduced in the linac for BNS damping.

‡ See section on Beam-Beam effects.

- post-linac beam-halo collimation to shield the physics detector from background.

The strong demagnification is primarily achieved by the short focal length quadrupole doublet close to the IP. The resulting high chromaticity of this 'final lens' must be compensated using strong sextupole magnets in dispersive regions. The design of such optical systems requires a careful balance of nonlinear optical terms, and this ultimately leads to very tight tolerances on both field strength and alignment of the magnets. The worst case is the final doublet itself, where vibration stabilisation[§] to the ~nanometer RMS level is required.

All BDS designs contain a dedicated collimation section. The wakefields induced by the collimator gaps are a significant source of emittance dilution [3]. The collimator wakefields amplify the transverse beam jitter and increase the transverse emittance. The ILC-TRC has identified collimator wakefields as a concern for all the current proposed designs.

Beam-Beam Effects

The dynamics of the beam-beam interaction can be loosely characterised by the *disruption parameter*:

$$D_y \propto \frac{N_e \sigma_z}{\sigma_x \sigma_y}; \qquad \sigma_x >> \sigma_y \tag{1}$$

where N_e is the charge per bunch, and $\sigma_{x,y}$ are the RMS horizontal, vertical beam extents and σ_z is the RMS bunch length (all at the IP). TESLA has the highest value of disruption parameter at ~25 (for E_{cm} = 500 GeV), while JLC/NLC and CLIC have values of 13 and 8 respectively.

The large value for TESLA has a marked impact on the luminosity performance due to the so-called kink instability, where the collision effectively becomes unstable [4]. The luminosity becomes very sensitive to relatively small variations in the bunch charge distribution, particularly in terms of beam-beam offset: for TESLA, a $1\sigma_y$ vertical offset (5 nm) causes ~60% reduction in luminosity, compared to typically less than 10% for the lower disruption machines [1].

The sensitivity to beam-beam offset can for the most part be mitigated by the use of the fast intra-train beam-beam feedback system [5]. Unfortunately the high disruption parameter also makes the collision sensitive to the so-called 'banana' effect [4], or longitudinally correlated emittance growth of the type driven by wakefield effects. Up to 30% reduction in nominal luminosity has been simulated for TESLA due to this effect. Simulations have also shown that the loss can be regained by scanning the collision angle and offset at the IP, an optimisation that can potentially be performed during a single bunch-train [6].

Figures of Merit for Performance

In past studies, the RMS emittance has generally been adopted as the figure of merit for performance for linac studies, while the RMS transverse beam sizes at the IP were used for the BDS. While both of these quantities are certainly useful and important, care must be taken in interpreting such results when considering luminosity. For TESLA, it would be misleading to quote only RMS emittance and beam size performance due to the strong disruption effects. Conversely, RMS values can in some cases overestimate the impact on luminosity degradation: RMS values are sensitive to long tails on distributions which are often driven by nonlinear optics effects and wakefields, while the core of the distribution – responsible for the luminosity – remains unperturbed. In both cases, it is desirable to use the luminosity as simulated by a beam-beam code such as GUINEAPIG [7] to give a better estimate of performance. Many of the LET studies for the TRC (and since) have used simulation in which GUINEAPIG forms an integrated part.

STATIC AND DYNAMIC ALIGNMENT ERRORS

Table 2 lists the goal alignment tolerances for design luminosity, and the modelled installation accuracies. Irrespective of which technology is being discussed, the required tolerances needed to achieve the luminosity performance are not attainable with current state-of-the-art mechanical alignment and survey techniques, and beam-based tuning and alignment methods are required. At this point the beam diagnostics – and particularly beam position monitors (BPMs) – begin to play a very significant role. In general the achievable performance of these machines is limited by the resolution of the BPMs.

Static Alignment Errors

For the main linacs, two related methods of beam-based alignment have been considered in detail:

Dispersion Free Steering (DFS): as its name implies, the goal of this method is to find an orbit (trajectory) which does not generate dispersion. The beam-lattice energy match is varied (through a combination of beam energy and magnet optics changes[**]) and the resulting difference orbit recorded. From these measurements and knowledge of the optics an orbit is found which minimises the difference when the energy is changed. DFS suffers from several problems, not least that in the presence of BPM errors the orbit solutions tend to have very large amplitudes, and this tendency must be compensated by applying an additional constraint on the absolute orbit. The method is also sensitive to upstream beam jitter, which must be fitted out or averaged away to avoid confusing the algorithm. DFS has been extensively simulated for all linac designs with varying degrees of success, and has been experimentally demonstrated at the SLC [9] and at LEP [10].

[§] Both in terms of mechanical stabilisation and beam-based feedback systems.

[**] For TESLA it is important to change the initial beam energy to correctly measure the dispersive kicks from tilted cavities [8].

Table 2: Component tolerances for the main linacs. The Luminosity Tolerances are those random RMS values which result on average in the budgeted emittance growth after a 1-to-1 linac steering. The numbers should be taken as an *indication* of the alignment which the various beam-based methods must achieve. Units are μm and μrad.

		TESLA	JLC/NLC	CLIC
Luminosity Tolerances				
BPM offsets		25	5	0.7
structure	offsets	500	13	8
	tilts	300	100	8
Modelled Installation Accuracy				
quadrupole offsets		300	50	100
structure	offsets	300	25	20
	tilts	300	33	20
BPM	offsets	200	100	10
	res.	10	0.4	0.1
struct. BPM	res.	n/a	5	10
girder	offsets	200	50	-
	tilts	-	15	-

Notes: quadrupole, structure and BPM offsets are defined with respect to the girder alignment, with the exception of the BPM CLIC number, which is relative to a stretched wire system. The girder alignment is with respect to the accelerator reference line. A dash indicates an unknown (or not modelled) number.

Ballistic Alignment (BA): with this method, a reference line is established by turning all the magnets and RF[††] off and allowing the beam to coast through the section. The BPM readings are then used to define a straight reference line[‡‡], to which the orbit is steered when the nominal settings for the section are restored. Because a single ballistic shot is all that is required to establish the 'straight line' (to within the BPM resolution), the method is not so sensitive to beam jitter. The main disadvantage with BA is controlling the beam during the ballistic measurement, given that it will have a large β-beat and large coherent amplitude in the downstream linac sections.

Both of these methods address the quadrupole alignment and the related emittance dilution due to dispersive effects (they also implicitly address the issue of BPM offsets). The achievable results are ultimately given by the resolution of the BPMs.

The methods do not address the control of the structure alignment and the associated transverse wakefield effects. Here there is a clear difference between TESLA and the X-band machines, since the strength of the wakefields are much larger in the latter. For TESLA no additional alignment over that achieved during construction of the cryomodule and installation is foreseen. For both JLC/NLC and CLIC, the significantly tighter tolerance must again be achieved using beam-based techniques. Each structure will have a 'structure BPM' which will effectively measure the transverse dipole mode excited by an off-axis beam. Several adjacent structures will be mounted on a single remotely translatable girder allowing the average offset and tilt of the structures to be corrected to the μm- and μrad-level respectively.

[††] It is particularly important to turn off the RF for TESLA due to the transverse kicks from the tilted cavities [11]. For JLC/NLC and CLIC this is less of a problem since the cavity tilts are expected to be compensated during the structure girder alignment process.

[‡‡] The effects of transverse wakefields and other external fields will define how straight the ballistic line is.

Dynamic Alignment Errors (vibration)

Unfortunately dealing with the static errors is not the end of the story. Due to ground motion and other vibration sources, the accelerator components move away from their beam-based aligned positions over time. The most sensitive elements are the magnets in the Final Focus System, where vibration tolerances are in the ~1 to 100 nm range (the strong final doublet being the worst case). Fast quadrupole vibration leads to beam jitter which will:

- cause the beams to move out of collision at the IP; and
- increase the beam size at the IP due to emittance dilution.

Of these two mechanisms the first is generally the more critical. To compensate the effects of component vibration, three approaches are generally adopted (with varying degrees of emphasis):

- use of beam-based orbit feedback, particularly at the IP to maintain the beams in collision;
- mechanical stabilisation of components using either passive damping or active feedback;
- prudent choice of a 'quiet' site.

In all cases – and particularly when considering beam-based feedback – the frequency spectrum of the 'noise' and the spatial correlation must be considered. Three ground motion models have been developed [12] corresponding to measured quiet, medium and noisy sites. The models are now extensively used to simulate ground motion effects in the LET systems, examples of which can be found in [13].

For beam-based feedback, the beam repetition rate is critical. The high rates of the X-band machines allow suppression of beam motion (jitter) below ~10Hz; typical ground motion spectra above this frequency show motion at the nanometer level. For TESLA, the collisions at the IP are maintained within the long bunch train, which effectively removes all train-to-train jitter [5]. The effect on the emittance of the upstream jitter can be significant however, where the cut-off for the rep. rate limited orbit correction is typically 0.1 Hz. Orbit-based feedbacks at this rate are however sufficient for dealing with slow diffusive ground motion as described by the so-called *ATL* law [14].

SIMULATION TOOLS

The tools used to simulate the performance of the LET must support the necessary (important) beam dynamics and in addition allow the correct modelling of the various tuning algorithms outlined in the previous sections. Specifically they should:

- Correctly model the beam transport (i.e. transverse optics); for the BC and BDS sections this must also include nonlinear geometric and chromatic effects.
- Include acceleration (including the RF curvature).
- Include transverse and longitudinal wakefield effects.
- Support general three-dimensional component alignment errors (transverse offsets, tilts and rolls etc.).
- Allow several grouped components to move together simulating the action of girders and mechanical movers.
- Provide quasi-realistic models of diagnostics and corrector magnets.
- Allow modelling of the various tuning algorithms (DFS, BA, feedback systems etc.)
- Support ground motion models, specifically the frequency spectrum and the spatial correlation (particularly across the IP).

Several tools now exist for performing extensive and complex simulations of all aspects of the LET, although there is still room for improvement. For the more recent studies (specifically the TRC), the following tools were used, either separately, or *chained* together:

LIAR [15]: developed at SLAC to model both the SLC and NLC linacs; extensively used for NLC simulations.

PLACET [16]: developed to study both the CLIC main linac and drive beam dynamics. One particular noteworthy aspect of PLACET is its speed.

MERLIN [17]: developed at DESY for tuning and ground motion studies for the TESLA BDS, and extended to include the main linac and bunch compressor dynamics.

GUINEAPIG [7]: used extensively for modelling the beam-beam interaction.

DIMAD [18]: ray tracing optics code which includes synchrotron radiation effects, used for BDS and BC studies.

MADacc [19]: A SLAC version of the MAD code which includes acceleration and wakefields.

ELEGANT [20]: ray tracing code which includes acceleration, wakefields and both incoherent and coherent synchrotron radiation.

Each of these codes can be used with various degrees of successes for specific sub-systems of the LET, and several of them have been successfully benchmarked against each other [21].

SIMULATION AND THE REAL WORLD

The expected luminosity performance of all the linear collider designs is essentially based on simulation. The types of simulations briefly reviewed in this report have shown that the LET systems can for the most part perform to the design goals *providing* the initial conditions and hardware performance of the systems simulated are achieved. Specifically:

- the component installation alignment tolerances (table 2) are achieved;
- the BPMs and other diagnostics perform to the desired resolution and do not excessively drift;
- the mechanical magnet and girder movers (several hundreds for JLC/NLC and CLIC) perform to specification;
- fast feedback kickers and other corrector magnets perform within tolerances;
- the time required for static tuning is short compared to the characteristic time for the natural component drift.

The simulations are only as good as the information that goes into them. The next step is to include the impact of ground motion (vibration) on the static tuning algorithms[§§], a task that has already begun [22]. The effects of component failures and 'flyers' (*i.e.* a few % of components whose alignment are at several standard deviations of the distribution) also need to be quantified. Modelling of the alignment and survey techniques rather than just using random uncorrelated errors is another potential topic of study.

REFERENCES

[1] http://www.slac.stanford.edu/xorg/ilc-trc/2002/2002/report/03rep.htm (2003)
[2] V. E. Balakin, A. V. Novokhatsky, V. P. Smirnov (1983)
[3] P. Tenenbaum, LCC-Note-0101 (2002)
[4] R. Brinkmann, O. Napoly, D. Schulte, TESLA-01-16 (2001)
[5] I. Reyzl, Proc. EPAC 2000, p. 315-317 (2000).
[6] D. Schulte, Proc. Nanobeams 2002 Workshop, Lausanne (2002)
[7] D. Schulte, CERN-PS-99-14 (1999)
[8] T. Raubenheimer, R. Ruth, Nucl. Instrum. Meth. A302: 191-208 (1991)
[9] P. Tenenbaum, R. Brinkmann, V. Tsakanov, Proc. EPAC 2002, Paris (2002)
[10] R. Assmann *et al*, Phys. Rev. ST Accel. Beams 3: 121001 (2000)
[11] N. Walker, D. Schulte, these proceedings (RPAB007) (2003).
[12] *see for example* A. Seryi, SLAC-PUB-9647 (2003).
[13] A. Seryi et al, these proceedings (ROPC004) (2003); also L. Hendrickson et al, these proceedings (RPAB014) (2003).
[14] N. Walker, A. Wolski, TESLA-00-22 (2000).
[15] R. Assmann et al, SLAC/AP-103 (1997)
[16] http://dschulte.home.cern.ch/dschulte/placet.html
[17] http://www.desy.de/~merlin
[18] R. Servranckx *et al*, SLAC-0285 (1995)
[19] H. Grote et al, SLAC-PUB-8491, CERN-SL-2000-063-AP, (2000)
[20] M. Borland, Advanced Photon Source LS-287, September (2000)
[21] D. Schulte *et al*, SLAC-TN-03-002, LCC-0091, TESLA-2002-08, CLIC-513, (2002)
[22] P. Tenenbaum, these proceedings (RPAB021) (2003)

[§§] as identified by the TRC

EFFECTS OF DYNAMIC MISALIGNMENTS AND FEEDBACK PERFORMANCE ON LUMINOSITY STABILITY IN LINEAR COLLIDERS

A. Seryi, L. Hendrickson, T. O. Raubenheimer, P. Tenenbaum, M. Woodley SLAC, Stanford, USA*
D. Schulte CERN, Geneva, Switzerland

Abstract

The performance of high energy linear colliders depends critically on the stability with which they can maintain the collisions of nanometer-size beams. Ground motion and vibration, among other effects, will produce dynamic misalignments which can offset the beams at the collision point. A system of train-to-train and intra-train beam-beam feedbacks, possibly combined with additional beam-independent active systems, is planned to compensate for these effects. Extensive simulation studies of ground motion and luminosity stabilization have been performed as part of the work of the International Linear Collider Technical Review Committee [1]. This paper presents a comparison of the expected performance for TESLA, JLC/NLC and CLIC under various assumptions about feedbacks and the level of ground motion.

INTRODUCTION

Small emittances and nanometer-size beams at the interaction point of a linear collider lead to tight stability tolerances on the collider components. Ground motion and vibration can disturb alignment and degrade the luminosity via separation of the beams at the IP or beam emittance growth. A train-to-train beam-beam deflection feedback (or intra-train, as planned for TESLA) is necessary to keep the beams colliding. Below, we will investigate performance of such beam-beam feedback, in the presence of ground motion. Alignment tolerances for beam offset at the IP are much tighter than those for emittance growth, and therefore beam separation can occurs on a faster time scale than beam emittance growth. We therefore can ignore other orbit feedbacks (in the linac or beam delivery) which act on much slower time scales and the concentrate discussion only on the IP feedback and its performance.

ASSUMPTIONS AND METHODS

Ground motion amplitudes and correlation properties vary significantly from site to site and depend on many factors. To span the possible range of site conditions, three models of ground motion were considered: (**A** – "Low", **B** – "Intermediate", and **C** – "High" noise). These models are based on measurements on the tunnel floor of LEP and at California representative sites for **A**, at the SLAC tunnel and the Aurora mine near FNAL for **B**, and on the tunnel floor of HERA for **C**. The models are represented by a parameterized 2-D power spectrum $P(\omega, k)$, to properly describe both the spatial and temporal correlations of ground motion. The models include a contribution from diffusive ATL motion that dominates at low frequencies and vanishes for high frequencies, contribution from isotropically-distributed plane waves propagating in the ground representing fast motion including cultural noise, and systematic motion (occurring in month-year time scale). Each model is described by a couple dozens of parameters. The traditional spectra can be obtained from the 2-D spectrum, see an example in Fig.1. Details of the models and relevant parameters can be found in [2]. The models have been implemented in the codes Matlab-LIAR [3] and PLACET [4].

In addition to "on the tunnel floor" ground motion, it is important to consider any noises generated on the girders, inside and near of a cryostat, or amplification by imperfect girders (see more discussion in [1] and [5]). The specific case of vibration of an experimental detector that affects the stability of the final doublet (FD, which has the tightest jitter tolerances) is considered separately. The detector noise model is based on measurements made at SLD in 1995 [6] shown in Fig.2. These measurements would indicate about 30 nanometers of final doublets relative motion due to detector vibration. This should be considered a pessimistic upper limit as vibration control was not a design criteria for the SLD and the measurements were made under less than optimal conditions (e.g. the cooling water was on, but the magnetic field was off, which would otherwise stiffen the detector). Therefore, it is important to stress that the assumed model for detector vibration is pessimistic.

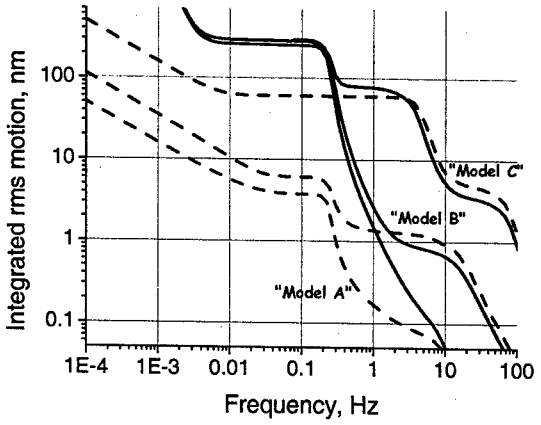

Figure 1: Example of ground motion modeling spectra. The integrated absolute spectra (solid lines) and the integrated relative (for dL=50m) spectra (dashed lines).

* Work supported in part by US DOE, Contract DE-AC03-76SF00515.

0-7803-7738-9/03/$17.00 © 2003 IEEE

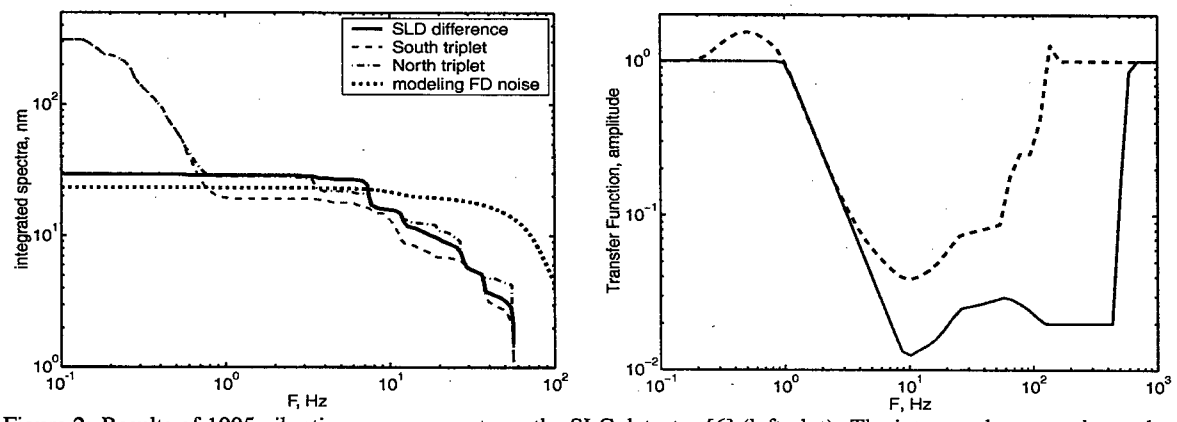

Figure 2: Results of 1995 vibration measurements on the SLC detector [6] (left plot). The integrated spectra shows that the difference of the motion (blue solid line) of the South triplet (red dashed curve) and the North triplet (green dash-dot curve) is about 30 nm, as measured by two STS-2 seismometers installed on the triplets. Black dotted line shows an approximation for the FD noise used in the integrated simulations. The right plot shows the modeling transfer functions used in simulations to represent FD stabilization.

In such conditions the final doublet in warm machines would require active stabilization. Both JLC/NLC and CLIC propose to use a combination of laser interferometers and/or inertial sensors to drive piezoelectric or electrostatic mechanical actuators or dipole correctors to adjust the position of the FD magnetic center, and such methods are being developed. The doublet stabilization was modeled by the idealized transfer function shown in Fig.2 (solid) or, for some cases, with a less idealized curve (dashed).

The train-by-train IP beam-beam feedback based on the NLC design [7] was reoptimized for each vibration assumption. The intra-train feedback was simulated in a "simple" way where the average position and angle offset was simply zeroed, and latency was ignored. For TESLA, a "full optimization" version was also studied which varied the offsets during the train to find maximum luminosity [8].

In simulations, first, the machines were misaligned and then a simple one-to-one trajectory correction applied to mimic a 'tuned' collider. In addition to quad and structure offsets, structure tilts were included. The rms magnitudes of the misalignments were chosen to produce nominal luminosity on average and to reproduce approximately the expected amount of yz and $y'z$ correlation along the bunch to realistically account for the banana effect. The beam-beam collisions were realistically simulated using the GUINEAPIG program [9]. In all cases, the luminosity was calculated for 256 pulses at the collider repetition rate, corresponding to an elapsed time of 51 seconds for TESLA, 2.1 seconds for NLC/JLC and 1.3 seconds for CLIC. For TESLA, this time is long enough to see a slow degradation in luminosity from orbit errors in the BDS, and consequently requires the inclusion of an upstream orbit feedback, not needed on a 1-2 second time scale. Simulations were made with Mat-LIAR and PLACET and represent in total over half a year of CPU time. For the cases cross-checked, good agreement between the codes was found. For these studies, only one bunch was tracked, and bunch-to-bunch effects were ignored.

SIMULATION RESULTS

Figure 3 is an example of results with only the train-to-train IP feedback, showing luminosity as a function of train number for each project (beam-beam parameters and train repetition rate affect strongly this performance, see more in [7]). All the simulation results are summarized in Figure 4 showing the percentage of luminosity obtained for each linear collider under GM models **A** through **C**, with and without additional final doublet vibration induced by the detector, and with different combinations of IP feedbacks and FD stabilization. Each point represents nine different seeds of Mat-LIAR run – three for the machine and three for the ground motion (PLACET simulations typically involved 25 seeds). The results are averaged over 256 trains (50 for TESLA, to ignore absence of BDS orbit feedback).

From these studies, one can see that for ground motion models **A** and **B** with no additional detector noise, all designs maintained nominal luminosity with the specified beam-based IP feedback alone (intra-train for TESLA, inter-train for the others).

For pessimistic estimate of detector noise the luminosity drops significantly (to ~35% for NLC/JLC and to ~12% for CLIC) independent of ground motion model. For models **A** & **B** the FD stabilization recovers full luminosity. For more pessimistic assumptions on FD stabilization, less FD vibration can be accommodated without degrading the luminosity – e.g. for NLC with model **B** the recovered luminosity is about 75%. For TESLA, the intra-train feedback is expected to compensate for detector noise.

For ground motion **C**, there was a significant deterioration of the luminosity. Even without detector noise, the luminosity dropped to below 30% for CLIC and below 60% for NLC/JLC. Doublet stabilization only improved this to 50-70%, independent of whether detector noise was included. For TESLA, the luminosity was 85% assuming a perfect intra-train angle and offset feedback. This could be raised to 95% with perfect luminosity maximization.

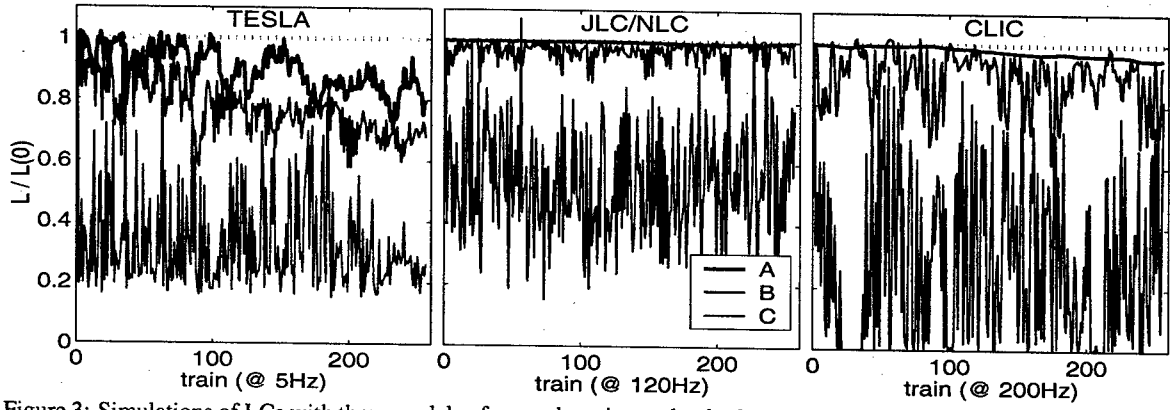

Figure 3: Simulations of LCs with three models of ground motion and only the train-to-train IP feedback. The FD follows the ground. The slow decline of luminosity in TESLA is due to the absence in simulations of the orbit correction in BDS.

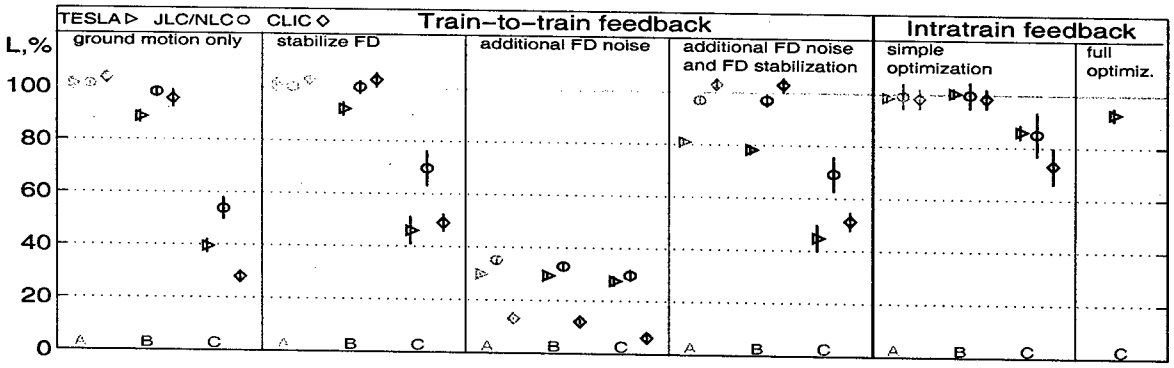

Figure 4: Percentage of luminosity obtained for each LC with ground motion models **A** ,**B**, **C**, with and without additional vibration of FD, and with different combinations of IP feedbacks and FD stabilization.

DISCUSSION AND SUMMARY

Many important effects were either not included or too idealized: multibunch effects; realistic effects of the intra-train position and angle kickers; intra-train IP feedback latency; jitter amplification due either to wakefields in the post-linac collimation system or due to multibunch parasitic beam-beam effects; interplay of different feedback systems with different time scales; hardware imperfections, e.g. beam losses affecting position monitors or finite resolution of the fast luminosity monitors; non-vibrational sources of beam jitter (train-to-train and intra-train), such as damping ring extraction kickers.

One of the challenges is not the luminosity loss itself, but its jitter. The results presented are based on the assumption of a machine tuned to the nominal luminosity at time zero – convergence of such tuning may be hampered by jitter of luminosity and orbits. High repetition rate of warm machines with possibility of averaging for more accurate measurements of luminosity, and possibility of luminosity maximization within the train for the cold machine, are the corresponding hopes of each design. The importance of jitter for tuning convergence is currently being studied.

Choice of a site for a linear collider which is sufficiently quiet now, will remain quiet in the future, would be also compatible with multi-TeV upgrade (which would further tighten the tolerances), is a challenge, especially because the choice cannot be made only on technical reasons. The TRC report [1] discuss the types of sites and expected noise level, and states that a shallow tunnel in unfavorable geology and/or in an urbanized area represents the greatest uncertainty and risk in estimating noise levels, and requires extremely careful study.

Technology-generated in-tunnel, on-girder and in-cryostat noise, for example currently being studied cooling water induced noises, vibration of quadrupoles inside cryostats, vibrations coming from klystron modulators [10], vibration transfer along and between the parallel tunnels, is another challenge which requires vigilant study and careful counter-engineering.

The authors appreciate productive collaboration with all the ILC-TRC group during these studies.

REFERENCES

[1] Second ILC-TRC Report, SLAC-R-606, 2003.
[2] A. Seryi, http://www.slac.stanford.edu/~seryi/gm/model/
[3] P. Tenenbaum, et al., SLAC-PUB-9263; EPAC 2002.
[4] D. Schulte, CERN-PS-2000-028-AE, CLIC-NOTE-437.
[5] A. Seryi, SLAC-PUB-9647, 2003.
[6] G. Bowden, private communication.
[7] L. Hendrickson, et al., in these proceedings.
[8] D. Schulte, CLIC-Note 560, 2003.
[9] D. Schulte, CERN-PS-99-14, 1999.
[10] F. Asiri, et al., in these proceedings.

COLLIDING NANOBEAMS IN CLIC WITH MAGNETS STABILIZED TO THE SUB-nm LEVEL

S. Redaelli*, R. Aßmann, W. Coosemans, G. Guignard,
D. Schulte, I. Wilson, F. Zimmermann, CERN, Geneva, Switzerland

Abstract

The Compact LInear Collider (CLIC) aims at colliding e^+e^- beams at 1.5 TeV with effective transverse spot sizes of 60 nm (horizontal) times 0.7 nm (vertical). Strict stability tolerances must be respected in order to achieve a sufficient overlap of the two colliding beams. A stability test stand has been set up at CERN, bringing latest stabilization technology to the accelerator field. Using this technology, a CLIC prototype magnet was stabilized in a normal CERN working environment to less than 1-nm vertical RMS motion above 4 Hz. Detailed simulations of the time-dependent luminosity performance of CLIC are discussed. They include the beam-beam interaction, the beam-based feedbacks and the measured data on magnet stability.

1 INTRODUCTION

The Compact LInear Collider (CLIC) Study at CERN [1] aims at colliding e^+e^- beams at 1.5 TeV with a luminosity of about $10^{35}\,cm^{-1}\,s^{-1}$. In order to achieve this luminosity performance the transverse beam size at the interaction point must be as small as 60 nm (horizontal) times 0.7 nm (vertical). CLIC will rely on a beam based feedback system for the correction of magnet motion below few Hz, but the faster motion of the quadrupole magnetic center must be mechanically stabilized to a fraction of the beam size. The vertical uncorrelated motion above 4 Hz for the CLIC quadrupoles must be smaller than 1.3 nm (linac) and 0.2 nm (final doublets) [2]. The final goal for the CLIC Stability Study is to demonstrate that such tolerances can actually be met. The approach that has been followed is to bring modern stabilization technologies to the accelerator field. The goals of the first phase of the CLIC Stability Study, as defined in January 2002, are: (1) Establish vibration measurements with sub-nanometer accuracy; (2) Investigate modern techniques for the stabilization of accelerator magnets; (3) Predict the time-dependent luminosity performance of CLIC with the achieved magnet stability. These items are addressed in the Sections 2, 3 and 4, respectively. In Section 5 some conclusions are drawn.

2 MEASUREMENT SETUP

A detailed summary on the sensors used for vibration measurements in the framework of the CLIC Stability Study is given in [2]. Here, the main characteristics of the sensors and the basic notation are briefly reviewed. The vibration measurements are performed with tri-axial geophones that measure velocities in the 4 Hz-315 Hz frequency range. In Fig. 1 two geophones installed on CLIC prototype quadrupoless are shown. These sensors have a sub-nanometer accuracy in the frequency range of interest. An upper limit for the resolution is given by the difference signal from two sensors placed side-by-side. At 4 Hz a 0.28 nm resolution was measured. The confidence in the absolute calibration of the geophones was assessed by comparing different vibration sensors. Two geophones from other manufacturers available at CERN and at ESRF [3] and a capacitive distance meter (relying on a different physical phenomenon for the vibration measurements) have been compared with the geophones of Fig. 1. These comparisons have demonstrated a good agreement between the different sensors. In a wide range of frequencies (5 Hz-50 Hz) and vibration amplitudes (0.1 nm-80 nm) the various measurements show a spread of a few percent. On the basis of these results, the absolute error of the vibration measurements is believed to be smaller than 10 %.

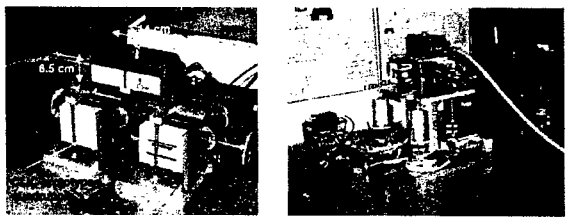

Figure 1: Installation of a CLIC prototype quadrupole on the stabilized honeycomb support structure. A doublet without (left) and with (right) a non vibration-optimized alignment support was used.

A geophone provides a measure of the vibration velocity $v(n)$ at the discrete times $n\Delta t$, where $\Delta t = 0.001$ s is the sampling time and $n = 1, 2, ..., N$. N is the total number of measurement points. The power spectral density of the displacement, $P(f_k)$ is defined for the discrete frequency $f_k = \frac{k}{N\Delta t}$ as:

$$P(f_k) = \frac{N\Delta t^3}{2\pi^2 k^2}\left|\sum_{n=1}^{N} v(n)e^{-2\pi i\frac{kn}{N}}\right|^2. \qquad (1)$$

The integrated RMS displacement induced by vibrations above $f_{min} = \frac{k_{min}}{N\Delta t}$ is given by:

$$I(f_{min}) = \sqrt{\frac{1}{N\Delta t}\sum_{k'=k_{min}}^{k_{max}} P(f_{k'})}, \qquad (2)$$

* PhD student at the University of Lausanne, CH, High Energy Physics Institute (UNIL-IPHE).

0-7803-7738-9/03/$17.00 © 2003 IEEE

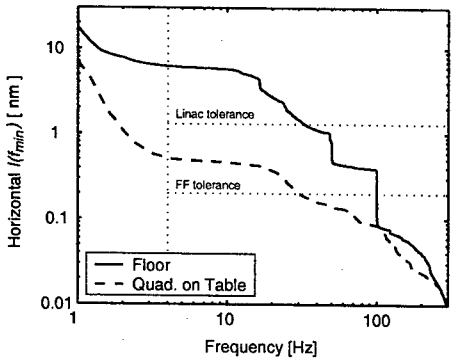

Figure 2: Integrated RMS vertical motion on the floor and on a stabilized CLIC prototype quadrupole(see Fig. 1, left part). Relevant CLIC tolerances are also indicated.

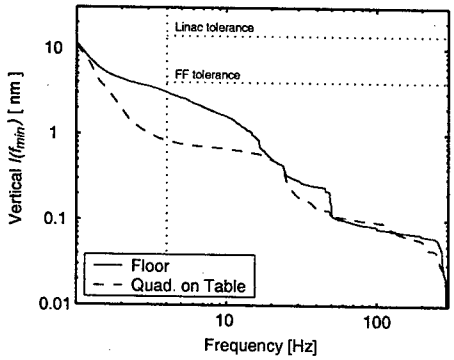

Figure 3: Integrated RMS horizontal motion on the floor and on a stabilized CLIC prototype quadrupole (see Fig. 1, left part). Relevant CLIC tolerances are also indicated.

where k_{max} corresponds to the largest measurable frequency. In order to reduce the statistical uncertainty on the measurement results, $P(f_k)$ is calculated as the average of several consecutive data sets.

3 QUADRUPOLE STABILIZATION TO THE SUB-NM LEVEL

The stabilization of the CLIC prototype quadrupoles is performed with state-of-the-art stabilization devices. The magnets are fixed on top of an honeycomb support structure (table) that sits on a stabilizing system. The quadrupole doublets can either be directly screwed onto the table top or be installed on the table via an alignment support structure, which is a non vibration-optimized support used in CLIC Test Facility II (CTF2) for the micrometric alignment of the quadrupoles (see Fig.1). This setup has also been used for detailed studies of water induced vibrations [4], support structure resonances [2] and effects of acoustical waves. A soft pneumatic system and a piezo-based stiff system have been used for the stabilization of the doublet. Here, only the results achieved with the stiff system are considered. A more complete overview of both systems is given in [2].

The vertical and the horizontal RMS motion, as measured on the floor and on a quadrupole doublet, are shown in Figs. 2 and 3. These results were obtained with the experimental setup of Fig. 1, left part. Above 4 Hz the doublet was stabilized vertically to (0.52 ± 0.01) nm with a ground motion of (6.20 ± 0.22) nm. The quadrupole vibration is within the CLIC linac tolerance (1.3 nm) and is only a factor 2.5 larger than the Final Focus tolerance (0.2 nm). The horizontal motion above 4 Hz was (0.84 ± 0.04) nm for the quadrupole instead of (3.05 ± 0.07) nm on the floor, both within the CLIC tolerances. The longitudinal motion on the quadrupole was (4.33 ± 0.28) nm instead of (4.30 ± 0.08) nm on the floor. This direction is not critical for luminosity considerations. It is important to point out that this magnet stability was achieved in a normal working environment of the CERN Meyrin site. The impact of measured quadrupole motion on the CLIC luminosity is discussed in the next section.

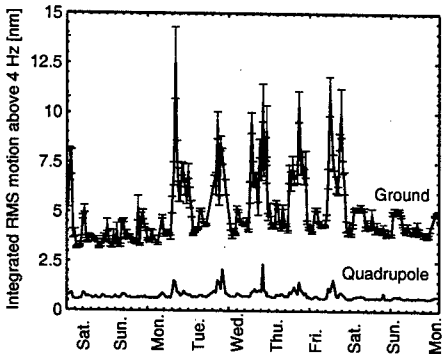

Figure 4: Vertical motion above 4 Hz versus time as measured on the floor and on a doublet, which was mounted on a CTF2-like alignment support. The error bars give the statistical uncertainty ($1\,\sigma$) and are omitted in the quadrupole lines because they are too small.

The quadrupole stability was continuously monitored for several days. On the table top, two doublets and one triplet were mounted on three independent alignment structures (see Fig. 1), like on a girder. The vertical motion above 4 Hz as measured on the floor and on one doublet is shown in Fig. 4 versus time. The cultural noise, which increases the ground motion up to 12 nm in the working days, is greatly reduced by the stabilization device: a stability below the 1 nm level is ensured almost independently of the cultural noise. Some residual perturbations are induced by people walking by the experimental setup or working close to it.

4 CLIC LUMINOSITY PERFORMANCE

The simulations of the time-dependent luminosity performance of CLIC have been performed for the beam delivery system (BDS) of [5], which provides a design luminosity of $0.8 \times 10^{35}\,\mathrm{cm}^{-2}\mathrm{s}^{-1}$. The validity of the tracking results has been assessed in [6, 7]. The available codes agree within a few percent for simulations without synchrotron radiation, like the ones considered in the following. On the basis of quoted results, `Merlin` [8] was used for the

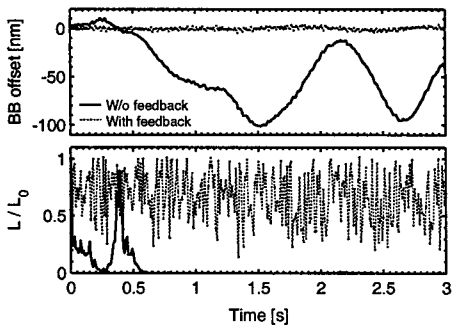

Figure 5: Time-dependent offset and luminosity for three seconds of CLIC operation with vibrating final doublets.

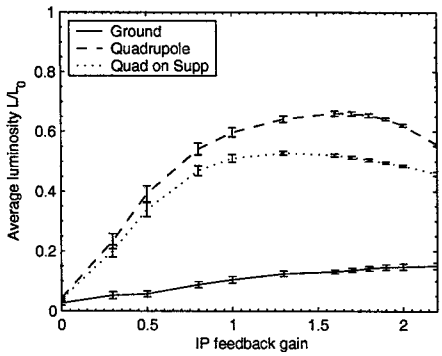

Figure 6: Average luminosity versus feedback gain when the doublets are moved according to the spectra of floor, quadrupole and quadrupole on an alignment support.

particle tracking. Full beam-beam (BB) simulations at the interaction point (IP) were performed with `GuineaPig` [9] and provided the luminosity and the BB deflection angle.

Two-beam simulations are carried out with the measured vibrational spectra of the CLIC prototype quadrupoles. The spectra are used to generate time-dependent misalignments of the quadrupoles at either side of the IP. Only the final doublets are moved because they induce the main impact on the luminosity (an additional 10 % luminosity reduction is found if all other quadrupoles of the BDS are moved according to the same vibrational spectrum). A pulse-to-pulse feedback system for correcting the IP beam offset has been implemented in `Merlin`. The relative BB offset at the IP (to be minimized by the feedback) is calculated from the BB deflection angle provided by the `GuineaPig` simulations. Beam scans in the horizontal and vertical plane are used to calibrate the deflection angle versus beam offset. This curve is fitted and inverted to provide the offset from the beam angle, as was done for instance for SLC [10].

A result of a time-dependent simulation with vibrating quadrupoles is shown in Fig. 5. The BB offset (top) and the luminosity (bottom) versus time are given. This simulation uses the measurements of Fig. 2 to generate the quadrupole offsets (aligned machines at time zero). The motion of the two final doublets is taken to be uncorrelated. Without an IP feedback the BB offset would increase by several tens of nanometer and the luminosity would be completely lost within a few bunches. The feedback correction compensates the low frequency component of the motion and allows recovering a large fraction of the nominal luminosity.

A scan of the feedback gain has been done to find the set point that gives the best luminosity. Fig. 6 shows the average luminosity over three seconds of CLIC operation, i.e. 300 consecutive pulses. The quadrupole stability achieved with only the table as support allows recovering 66 % of the CLIC design luminosity, to be compared with the 15 % obtained if the quadrupoled move like the ground. If the motion of a stabilized doublet with its non vibrational-optimized alignment support is considered, then 53 % of the design luminosity is obtained. The horizontal motion has shown not to be critical for CLIC. Both with the horizontal vibrations measured on the floor and on the CLIC prototype quadrupoles (with or without alignment support) more than 95 % of the design luminosity can be recovered with the IP feedback (for zero vertical motion).

5 CONCLUSIONS

For the first time a CLIC prototype quadrupole was stabilized vertically to the 0.5 nm level. This was achieved in a normal working area at CERN. This sub-nanometer stability allows ensuring that almost 70 % of the CLIC design luminosity can be achieved. The horizontal and longitudinal vibrations of the stabilized quadrupole have proven not to be a critical issue for CLIC. Even though some further improvements are still required, these results demonstrate the basic feasibility of colliding nanobeams for CLIC.

The authors would like to acknowledge the help from the colleagues at DESY, SLAC and ESRF, all the members of the CERN CLIC team (in particular W. Schnell), F. Ruggiero, M. Mayoud.

6 REFERENCES

[1] G. Guignard *et al.*, "A 3 TeV e^+e^- Linear Collider Based on the CLIC Technology," *CERN-2000-008.*

[2] R. Aßmann *et al.*, "The CLIC Stability Study on the Feasibility of Colliding High Energy Nanobeams," Proc. *Nanobeam2002*, September 2-6, Lausanne, CH (2002).

[3] S. Redaelli, L. Zhang *et al.*, to be published.

[4] S. Redaelli *et al.*, "Status of the CLIC Studies on Water Induced Quadrupole Vibrations", Proc. *Nanobeam2002*, September 2-6, Lausanne, CH (2002).

[5] F. Zimmermann *et al.*, "CLIC Beam Delivery System," Proc. *Nanobeam2002*, September 2-6, Lausanne, CH (2002).

[6] S. Redaelli *et al.*, "Comparison of Simulation Tools for Beam Delivery Systems of Linear Colliders", *EPAC2002*, Paris, FR (2002).

[7] S. Redaelli *et al.*, "Comparative Assessment of Simulation Tools for Beam Delivery Systems of Linear Colliders", Proc. *Nanobeam2002*, September 2-6, Lausanne, CH (2002).

[8] `http://www.desy.de/~merlin/`

[9] D. Schulte, "Beam-Beam Simulations with GUINEA-PIG," *ICAP98*, Monterey, CA., USA (1998).

[10] P. Bambade *et al.*, Phys. Rev. Lett. **62**, 2949 (1989).

NORMAL-CONDUCTING RF STRUCTURE TEST FACILITIES AND RESULTS *

C. Adolphsen
Stanford Linear Accelerator Center, Stanford University, Stanford CA 94309 USA

Abstract

The designs for a next-generation linear collider based on normal-conducting rf structures require operation at gradients much higher than those in existing linacs. For the NLC/JLC 11.4-GHz structures, the design unloaded gradient is 65 MV/m, which is about four times that of the 2.9-GHz SLAC Linac. The CLIC proposal using 30-GHz structures requires an even higher gradient, 170 MV/m. Both the CLIC and NLC/JLC groups are aggressively pursuing programs to develop structures that operate reliably at these gradients and also have acceptable efficiencies and transverse wakefields. Much progress has been made in the past few years, and this paper reviews the programs, test facilities and results from this research.

INTRODUCTION

During the past six years, the major R&D on normal-conducting accelerator structures has been in support of two linear collider initiatives [1]. The SLAC, FNAL and KEK based NLC/JLC design proposes 11.4-GHz rf technology as a 'modest' extrapolation of that of the 2.9 GHz SLAC Linac. The CERN-based CLIC design aims at multi-TeV operation, proposing a higher rf frequency, 30 GHz, at the limit to which conventional copper fabrication techniques can still be used. The desire for a higher operating frequency results from the associated cost benefits of having lower rf energy per pulse (hence fewer rf sources) and a higher operating gradient with reasonable structure efficiency (hence a shorter linac).

Higher frequencies have several drawbacks including the large transverse wakefields generated in the structures by the beam. The structure designs are strongly influenced by the need to limit emittance growth caused by short-range wakefields. In particular, it tightly constrains the allowed minimum average structure iris radius (a), which would otherwise be reduced to improve efficiency. The average radii currently being considered by both groups are about 17% of the rf wavelength (λ). This constraint has had implications for the structure high-gradient performance, as will become evident below.

The long-range transverse wakefields also need to be suppressed, and both designs use a combination of dipole-mode detuning and damping for this purpose. For the NLC/JLC structures, moderate damping is achieved by coupling the cells to four circular waveguides (manifolds) that run parallel to the structure. The CLIC design achieves stronger damping with four terminated, transverse waveguides attached to each cell. In each approach, there is enhanced pulsed heating near the openings in the cells that is a concern for high gradient operation.

The greatest challenge related to the choice of high rf frequency has been in achieving the design gradients. Both groups propose constant-gradient, traveling-wave structures where the upstream ends of the structures operate near the unloaded gradient. The design unloaded gradient for NLC/JLC is 65 MV/m (52 MV/m loaded), and for CLIC, it is 170 MV/m (150 MV/m loaded). The rf pulse length is tied to the frequency choice through the Q's of the structure cells. For efficiency, the pulse length is several times the structure fill time, and the fill time is roughly equal to the attenuation time, $Q/\omega \sim \omega^{-3/2}$. For NLC/JLC (CLIC) the rf pulse length is 400 ns (130 ns) and the structure fill time is 110 ns (30 ns).

Both groups had similar initial experiences in developing structures to meet these goals. In the mid-to-late 1990s, each group built and commissioned a test facility aimed at demonstrating rf system performance (for CLIC, the CLIC Test Facility II, or CTF II, at CERN, and for NLC, the NLC Test Accelerator, or NLCTA, at SLAC). During this time, high-gradient operation was not a major concern since earlier results showed >100 MV/m gradients were achievable at X-band, and that higher gradients seemed possible at higher frequencies [2]. However, when the test facilities came into full operation in 1999-2000, it became clear that the structures tested at that time, which required higher input powers and longer pulse lengths than in the earlier tests, would not meet performance requirements due to breakdown-related damage.

In the following sections, the NLC/JLC and CLIC high-gradient programs, facilities and test results are reviewed with the emphasis on the past year's findings [3].

NLCTA STRUCTURE TESTING

The first structures installed in the NLCTA linac were NLC prototypes built in part to test wakefield detuning and damping. They are 1.8-m long (206 cells), traveling wave ($2\pi/3$ phase advance per cell), nearly constant gradient (the group velocity varies from 12% to 3% c), and have an a/λ = 18% aperture. At the completion of NLCTA commissioning in 1997, four such structures had operated concurrently at unloaded gradients of 40-45 MV/m, close to the 50 MV/m requirement for the 0.5 TeV NLC design at that time. During 1997-99, the two linac power sources were upgraded to allow 70 MV/m operation, which had become the 0.5 TeV and 1 TeV NLC/JLC

* Work Supported by DOE Contract DE-AC03-76F00515.

0-7803-7738-9/03/$17.00 © 2003 IEEE

design unloaded gradient. It was during this period that performance limitations due to breakdown were fully realized, which initiated the high-gradient structure design program that is ongoing today. Since 2001, power from the two linac rf stations has been used to test 21 structures (up to four at a time), with over 10,000 hours of operation logged at 60 Hz [4].

The important structure performance metrics are (1) the time it takes to process to an unloaded gradient about 10% higher than nominal, (2) the breakdown rate at the nominal unloaded gradient and (3) the damage incurred during normal operation. With the large number of NLC/JLC structures, the processing time per structure should be less than a few hundred hours so they can be realistically conditioned during the five-year production period envisioned for a linear collider. Structure damage is characterized by the change in net phase advance through the structure and a few-degree shift per year would likely be acceptable, although much less is expected with stable operation.

An acceptable trip rate has been defined as one that would rarely (once a year) deplete the planned 2% reserve of NLC/JLC power sources assuming a 10-second recovery period after a trip (such periods have been shown feasible). For the 60-Hz operation at NLCTA, this requirement translates to < 0.1 trip per hour for a 60-cm structure. To be conservative, the structures are qualified at the 65 MV/m unloaded gradient with 400-ns square rf pulses. The corresponding NLC/JLC trip rate would likely be lower since the pulse length is effectively shorter (due to the 100-ns ramp for beam loading compensation) and the gradient lower (20% on average due to beam loading).

NLC/JLC TEST RESULTS

The past year saw the transition from testing experimental structures (so called T-Series structures) to testing those designed for use in the NLC/JLC (so called H-Series structures). The former had been built to examine how performance depends on structure length and group velocity. This study was motivated by the pattern of damage observed in the 1.8-m structures: the high group velocity (> 5% c) portions incurred extensive pitting and phase change with operation above about 50 MV/m, while the low group velocity portions remained relatively unscathed.

Seven T-Series structures were built with different lengths (20, 53 and 105 cm) and initial group velocities (5% c and 3% c). By mid-2002, six structures had been tested and showed that breakdown-related damage decreased significantly at lower group velocity and that structure length had little effect on performance. However, the breakdown rates in the input and output coupler cells were noticeably high. At 70 MV/m in the 3% c structures, the coupler rates were generally > 0.3 per hour while for the other 59 cells combined, they ranged from < 0.1 per hour to 0.3 per hour.

An autopsy of the input couplers revealed melting on the edges of the waveguide openings to the cell and extensive pitting near these edges and on the coupler iris. It was subsequently realized that the waveguide edges see large rf currents and the associated pulse heating can be significant if the edges are sharp. By design, the edges in the T-Series structures were much sharper (76-μm radius) than those in the 1.8-m structures (500-μm radius) where this problem was not seen. Simulations showed that the pulse heating for the T-Series structures was in the 130-270 °C range, well below the copper melting temperature, but high enough to produce stress-induced cracking, which can enhance the heating.

To see whether reducing the pulse heating would help, a structure was built using an input coupler design with lower peak currents (a 'mode-converter' type [5]) and an output coupler with larger radius (3 mm) edges. For the regular cells, a previously tested T-Series design (53 cm, 3% c) was used. This structure performed very well, with no enhancement of the coupler breakdown rates relative to the other cells. For the full structure, the breakdown rate at 90 MV/m with 400-ns pulses was about 1 per 25 hours. All structures have since been made using similar couplers.

Although the T-Series structure results were encouraging, their average cell iris radii (a/λ = 13%) are too small in that the resulting wakefield is unacceptably large. Thus, the next step was to develop NLC/JLC-compatible versions. The first task was to increase the iris size while keeping the low group velocity and maintaining a reasonable shunt impedance. This required both thickening the irises (from about 2 mm to 4 mm) and increasing the phase advance per cell (from 120° to 150°). The structures were also detuned and their lengths were optimized for efficiency. The resulting designs (H-Series) require higher input power relative to comparable T-Series structures (about 50% more at 3% c). This increase is more than expected from just the larger iris diameter because the thicker irises also reduced the shunt impedance. To date, six such structures have been tested at high gradients.

The first test was of a pair of structures, one 60 cm, 3% c (designated H60VG3), and the other 90 cm, 5% c (designated H90VG5). These structures were built before the coupler problem was remedied and have the sharp-edged design. Also, the pulse heating is higher for the H-Series structures due to the larger stored energy. During processing, coupler breakdowns did indeed limit the gradients to values below those achieved with the T-Series structures. In addition, at short pulse lengths where the coupler events did not dominate, the processing rate was much slower than that for the T-Series structures. The thicker H-Series irises may be a contributing factor since the high-field surface area is about twice as large. Nonetheless, the H60VG3 structure did eventually process to 72 MV/m, and excluding the input coupler, the breakdown rate was < 1 in 10 hours at 65 MV/m.

The next four structures processed to 70 MV/m much faster than the first two, and in one case, faster than most of the T-Series structures. None of these structures showed an enhanced coupler breakdown rate. However, at gradients > 70 MV/m with 400-ns pulses, the processing was slowed considerably by what are aptly called 'spitfests.' These are a series of breakdowns close to each other in location and in time (in many cases, they occur during the ramp-up sequence in power and pulse width that follows a breakdown). The damage caused by the initial breakdown in these sequences is likely creating additional breakdown sites. Such events were observed in the 1.8-m structures at lower gradients, and in the T-Series structures at higher gradients. In all cases, they become noticeable at roughly the same structure input power level (60-80 MW).

Two of the four structures are H60VG3 designs built by the FNAL structures group, which are the first ones they produced for testing [6]. Problems with the brazing furnace used for assembly caused a slight oxidation to the copper, which was removed from the second structure using a hydrogen bake. At NLCTA, the first structure would not process above 70 MV/m due to the large number of spitfests. The second structure performed much better, with a breakdown rate of about 1 per hour at 65 MV/m during a relatively short run. Future structures will be brazed in a custom-designed vacuum furnace at FNAL.

Another of the four structures is a 90-cm, 3% c design (H90VG3), which was built to test the feasibility of longer structures. It requires 30% more power for the same average gradient as H60VG3. When processed, it reached 75 MV/m with 400-ns pulses before being limited by spitfests. At 65 MV/m, the breakdown rate was about 1 per hour, but the spitfest nature of the events was still apparent. About 70% of the breakdowns occurred within 5 minutes of the previous one, although there were periods of up to 25 hours without any breakdown. Fig. 1 shows the dependence of the trip rate on gradient and pulse width after processing. At a fixed breakdown rate, the gradient scales as the -1/6 power of pulse width. By the end of the run, the breakdown rate had decreased to about 1 in 10 hours at 61 MV/m (less than 1 in 6 hours is required for this longer structure).

Roughly half of the breakdowns at 65 MV/m occurred in a few cells (three near the front and one in the middle). After the run, these 'hot' cells were examined using a boroscope. In the interior cell, a 100-μm piece of material that was pitted by breakdown was seen on the outer wall (a similar-looking contaminant in an earlier structure turned out to be aluminum). No obvious foreign material was seen in the upstream cells and a more thorough autopsy is underway.

The last of the four structures is a H60VG3 design whose middle six cells have manifold slots for wakefield damping. They were included to test whether pulse heating near the slot openings leads to breakdowns such as those in the sharp-edged couplers. To reduce this possibility, the slot openings were rounded to minimize the heating. A 43 °C temperature rise is expected at 65 MV/m with 400-ns pulses, which is believed to be safe based on the sharp-edged coupler operation experience.

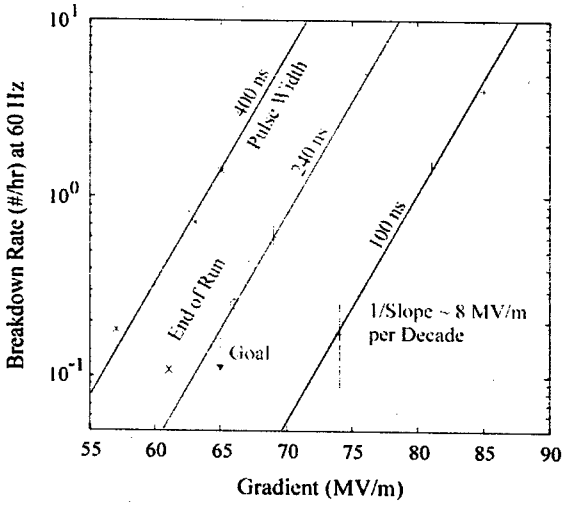

Fig. 1: Breakdown rate versus gradient and pulse width for the H90VG3 structure.

This structure processed fairly quickly (≈ 50 hours) and achieved 80 MV/m with 400-ns pulses before spitfests began to limit further gains. During this period, there was no obvious breakdown rate difference between the slotted and non-slotted cells. At lower gradients, a few hot cells became apparent, including a slotted one. These cells accounted for a sizeable fraction of breakdowns, as shown in Fig. 2. Since only one of the six slotted cells was hot and hot cells occur elsewhere, the breakdown enhancement in the slotted cell is probably not slot related.

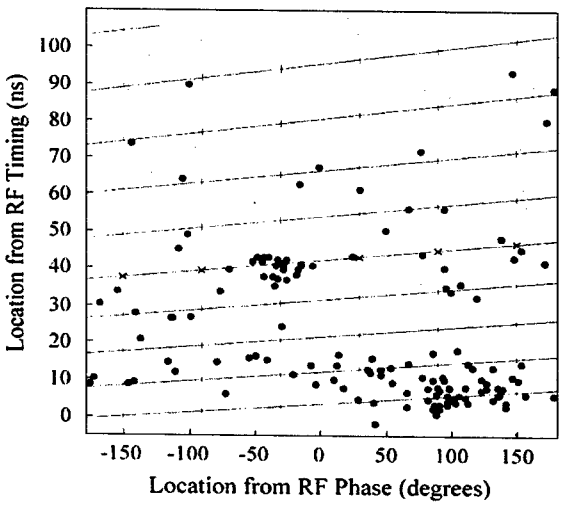

Fig. 2: H60VG3 breakdown locations (dots) at 65 MV/m inferred from reflected and transmitted RF. The cross hatches along the lines are cell locations (crosses are slotted cells) with the first upstream cell at the lower left.

During a 32-day run at 65 MV/m, the average trip rate was 0.21 per hour. Large day-to-day fluctuations occurred (up to 0.7 per hour) from 'flare-ups' in the hot cells. The spitfests were much reduced at this gradient, with 25% of breakdowns occurring within 5 minutes of the previous one. At 60 MV/m, the breakdown rate was well below 1 in 10 hours. This structure will be autopsied as well.

NLC/JLC SUMMARY AND OUTLOOK

The H-series results show that in structures with essential NLC/JLC features, reasonable processing times are possible and that breakdown rates close to those required can be achieved (damage rates also appear acceptable). Nonetheless, more operating overhead is desired, and a new version of the 60-cm structure design was recently adopted that has a smaller average iris radius ($a/\lambda = 17\%$) than the present structures ($a/\lambda = 18\%$). Decreasing the radius increases efficiency and will likely improve high-gradient performance due to the lower (7%) input power required. The transverse wakefield is about 20% larger, which is not expected to impact significantly the control of emittance growth in the NLC/JLC linacs.

The main goal within the next year is to operate eight such structures at 65 MV/m in the NLCTA. Tests of experimental structures will also continue, including ones aimed at achieving significantly higher gradients. One test will be of CERN-built, X-band structures with molybdenum and tungsten irises (part of the CLIC program described below). Another test will be of standing-wave structures with rounded-edged couplers. Earlier versions were limited to about 60 MV/m gradients, which may have been the result of their sharp-edged couplers [7].

At a more fundamental level, many questions remain such as the origin of breakdown and the large (×10) variation in processing rates. Surface analyses such as SEM, EDS, and AES have not found contaminants linked to breakdown sites, and residual gas analyses have not revealed any unexpected impurities. Also, the link between field emission and breakdown is unclear since the size of emitters would have to be very small (« micron) to explain the low dark currents (≈ 1 mA) that have been measured. Finally, the relationships among pulse heating, surface melting and breakdown are poorly understood. Not all couplers with high pulsed heating broke down so other conditions may be required, such as some minimum surface electric field. These and other questions will continue to be explored in future structure, waveguide and single-cell tests.

CLIC STRUCTURE DEVELOPMENT

The CLIC Test Facility II (CTF II) basically consists of two parallel beam lines (drive and probe) separated by about a meter [8]. It was designed when the CLIC linac required shorter rf pulses (12-18 ns) and lower gradients (80 MV/m). The drive-beam injector produces 16-ns long trains of 48 bunches with several nC per bunch, and the probe-beam injector generates single, 0.6-nC bunches. Both beams are first accelerated to about 45 MeV in individual S-band linacs. The drive beam is then decelerated in transfer structures to generate 15 ns, 30-GHz rf pulses. This power is fed locally to 30-GHz structures in the probe linac to accelerate the probe bunch.

When CTF II commissioning concluded in 1999, the probe linac contained five CLIC Accelerator Structures (CAS), each constant impedance, 28-cm long (86 cells) with a $2\pi/3$ phase advance, 8.6 % c group velocity, and an $a/\lambda = 0.2$ iris aperture. A constant-impedance design was used to simplify cell fabrication, but has the disadvantage that only the upstream cells 'see' the highest gradient (the gradient decreases by 20% along the structure). Moreover, the single-feed power coupler used in the CAS design enhances the surface fields on the coupler irises across from the waveguide opening by about 40%.

The basic results from the CAS testing were that processing plateaued after a 250-MV/m peak surface field was attained on the input coupler irises, and that rf breakdown severely eroded (≈ 100-μm deep) the high field surfaces, independent of how the irises were prepared. The corresponding first cell gradient was about 60 MV/m with the 15 pulses, far from the 170 MV/m required with 130-ns pulses.

These results led to the consideration of iris materials with melting temperatures higher than copper (1100 °C). For the structure to be practical, a reasonable conductivity (> 1/3 of copper) was required. Tungsten (W) was the first material tested due to its very high (3400 °C) melting temperature (its use in high-voltage switching applications also made it a plausible choice). In the initial tests, only the CAS input coupler iris material was changed (a clamped-on coupler was used for this purpose). The tungsten irises sustained higher surface fields (320 MV/m), limited by breakdowns elsewhere (mainly on the copper output coupler irises after a 250 MV/m surface field was reached). This success prompted a new structure design to exploit the higher possible surface fields.

For the couplers, a mode-converter design was used that has a 15% lower peak surface field than in the neighboring cells [9]. For the regular cells, the surface to on-axis field ratio was reduced from 2.8 to 2.2 by making the irises thicker and their radii smaller ($a/\lambda = 0.175$). The smaller radius is acceptable for CLIC, but it cannot be reduced much further because of wakefield problems. The success of the clamped-on couplers led to the adoption of a fully 'clampable' design where four bolts run through the structure to hold it together. The cells are made of copper and include a 10-mm OD slot to accommodate snugly fitting, interchangeable irises. With the smaller structure group velocity (4.6% c), the structure was shortened to 30 regular cells (10 cm) to keep the gradient attenuation at about 20% with all-copper cells.

Three such structures have been tested to date, one with ground tungsten irises, one with ground molybdenum (Mo) irises, and for comparison, one with standard, brazed copper cells [10]. When processed, the all-copper structure performed as expected, with little gain after a 250 MV/m surface field was reached on the first cell iris (later visual examination showed some erosion at the highest field regions of this cell). With the lower surface to on-axis field ratio, the first cell gradient was 110 MV/m at this limit, almost twice the CAS result.

The gradients achieved in the other structures were limited by the allowed processing time. After about three million pulses, the gradient reached in the first cell of the W structure was 150 MV/m (340 MV/m surface), and in the Mo structure, it was 193 MV/m (426 MV/m surface). As a candidate iris material, molybdenum was chosen because it is relatively easy to machine and has good HV hold-off properties at DC. Its melting temperature (2600 °C) is midway between copper and tungsten, so its faster processing is somewhat surprising. However, this may be a consequence of the Mo iris heat treatment (900 °C vacuum firing), which was done to prevent the high out-gassing experienced with the non-heat-treated W irises. When disassembled, the high-field regions on both the W and Mo first cell irises showed surface-layer melting but no obvious erosion; a more thorough examination is underway.

While the Mo structure results showed that CLIC-like gradients are possible, many challenges remain to achieve a 'CLIC-ready' structure. First, an acceptable breakdown rate at 170 MV/m needs to be shown at the 130-ns design pulse width in longer ($\approx$ 80 cell), constant-gradient structures. Also, if Mo or W irises are ultimately used, their surface area must be made smaller or else the Q loss would be prohibitive. If only the high field regions (> 50% of maximum) of the irises are made with these materials, a modest Q loss could be achieved (5%), although the fabrication of such tipped irises may be difficult. Finally, four radial waveguides need to be added to the outer region of each cell for wakefield damping. Pulse heating near the waveguide openings to the cells is of particular concern, given the high rf frequency and required field levels. In the latest design aimed at minimizing the heating, a 120 °C pulse temperature rise would occur under CLIC operating conditions, while a temperature rise below 60 °C is desired.

As for future testing, CTF II was decommissioned in October, 2002, and its components are being used for CTF 3. This facility will produce longer (130 ns), higher current (35 A), higher frequency (30 GHz) drive beams using the type of combiner rings envisioned for CLIC. High-power testing should resume in spring 2004 using the 5-A, 3-GHz injection beam for CTF 3. In the meantime, versions of the clamped structure scaled to X-band will be tested at NLCTA with Mo and W irises.

SUMMARY

The results from three generations of NLC/JLC structure tests show the need to operate at power levels (60-80 MW at 400 ns) below the regime where damage occurs. At this limit, the peak iris surface fields vary significantly: about 110 MV/m in the 1.8-m structures, 140 MV/m in the H-Series structures and up to 195 MV/m in the T-Series structures. In contrast, operation of the copper CLIC structures with 15-ns pulses appears to be surface-field limited (at about 250 MV/m). At this limit, the input power differs significantly for the two structure designs tested (23 MW and 35 MW). This insensitivity to power compared to the NLC/JLC structures may be due to the higher surface fields, shorter pulses and the much higher breakdown rates at which they were operated.

In regard to demonstrating a feasible design, the NLC/JLC group has operated structures with essential linear-collider features that basically meet the 65 MV/m performance requirements (at 60 MV/m, breakdown rates well within spec have been achieved). A lower-power structure design has been recently adopted that should prove more robust. The CLIC group has attained over 300 MV/m surface fields on W and Mo irises with 15-ns pulses. Although CLIC-level gradients were achieved in a Mo iris structure, significant challenges remain to demonstrate acceptable performance with 130-ns pulses in longer, damped, efficient structures.

REFERENCES

[1] International Linear Collider Technical Review Committee Second Report, SLAC-R-606, 2003.

[2] J. Wang and G. Loew, "RF Breakdown Studies in Copper Electron Linac Structures," SLAC-PUB-4866, March 1989.

[3] For an expanded version of this paper, see SLAC-PUB-9906.

[4] For earlier results, see C. Adolphsen, et al., SLAC-PUB-8573 and SLAC-PUB-8901, and J. Wang et al., TH464, LINAC 2002, August 2002.

[5] C Nantista et al., "Novel Accelerator Structure Couplers," these proceedings and Ivan Gonin et al., "Coupler Design for NLC/JLC Accelerating Structures," these proceedings.

[6] N. Solyak et al., "Development of X-Band Accelerating Structures at Fermilab," these proceedings.

[7] V. Dolgashev et al., "Status of X-band SW Structure Studies at SLAC," these proceedings.

[8] H. Braun, "Experimental Results and Technical R&D at CTF II", EPAC2000, June 2000.

[9] I. Syratchev, "Mode Launcher as an Alternative Approach to the Cavity-Based RF Coupler of Periodic Structures," CERN PS/RF/Note 2002-013.

[10] W. Wuensch et al., "A Demonstration of High-Gradient Acceleration," these proceedings.

Proceedings of the 2003 Particle Accelerator Conference

SUPERCONDUCTING RF STRUCTURES – TEST FACILITIES AND RESULTS

H. Weise, Deutsches Elektronen-Synchrotron, Hamburg, Germany
for the TESLA Collaboration

Abstract

The design of the TESLA superconducting electron-positron linear collider with an integrated X-ray laser laboratory was presented to several international committees including the German Science Council, advising the German government in matters of science. In preparation of this large facility, the TESLA Test Facility was set up at DESY. More than 40 institutes from nine countries have designed, constructed, commissioned and operated accelerator components. In close collaboration, superconducting accelerator cavities with gradients between 25 and more than 40 MV/m were developed. The TESLA Test Facility includes the preparation and testing of superconducting cavities as well as a 260 m long linac installation. The cavity performance with beam has been investigated while operating the linac as a driver for a SASE free-electron laser as well as during dedicated high gradient tests. More than 16 thousand hours of operation demonstrated this technology. Results of single cavity tests as well as of module tests without and with beam are presented.

INTRODUCTION

Superconducting cavity R&D of the TESLA collaboration has demonstrated the reliable production of 9-cell structures achieving gradients of 25 MV/m and higher at quality factors $Q_0 \geq 10^{10}$. Since a number of years there is broad consensus that the TESLA 9-cell cavity is a good choice for linear colliders as well as for FEL linear accelerators. The agreement is based on the results achieved at the TESLA Test Facility (TTF). Gradients of 35 MV/m and above were reached by applying a new preparation technique, i.e. electrolytic polishing. The gradient of prototype single-cell cavities exceeded 40 MV/m. At present a module equipped with electro-polished 9-cell TESLA cavities is under construction.

TTF Linac at DESY was constructed to show that high gradients achieved in individual 9-cell TESLA cavities could be maintained after assembly in an operating linac.

SUPERCONDUCTING RF STRUCTURES IN VERTICAL AND HORIZONTAL TESTS

Cavity tests in vertical as well as in horizontal cryostats were done to investigate accelerating gradient, quality factor, quench behaviour, Lorentz-force detuning, and last but not least to demonstrate the success of the cavity surface preparation and assembly procedure. The needed infrastructure for the test of RF structures was set up by the TESLA collaboration and is located at DESY.

Standard TESLA Nine-cell RF Structures

The TESLA 9-cell cavity is a standing wave structure of about 1 m length whose fundamental π-mode has a frequency of 1.3 GHz. The cavity is made from solid niobium and is bath-cooled by superfluid helium at 2 K. Each cavity is equipped with its own helium vessel; a tuning system driven by a stepping motor; a coaxial RF power coupler; a pickup probe; and two higher-order mode (HOM) couplers. A detailed parameter list including the niobium specification is given in [1].

Cavity fabrication is a delicate but nowadays established procedure. The TTF cavity production was done at several companies. According to industrial studies, the developed procedures are suitable for large-scale series production. Nevertheless, a careful design review was started in preparation of the TESLA XFEL (see below), which requires almost 1000 cavities.

The standard cavity treatment used for the last years includes a first approx. 100 μm removal from the inner surface. Buffered Chemical Polishing (BCP), i.e. etching, is the used method. Next is a first rinsing with ultra-pure water followed by drying in a class 100 clean room; annealing at 800°C in an Ultra High Vacuum oven to relieve mechanical stress as well as to out-gas dissolved hydrogen; heat treatment at 1400°C for further removal of other dissolved gases in presence of a thin titanium layer being evaporated on the inner and outer surface. This so-called post-purification increases the thermal conduction and the residual resistivity ratio (RRR) by about a factor of two. The titanium layer is finally removed again using BCP. Before the acceptance test in vertical dewars the cavities are mechanically tuned to adjust the resonance frequency to 1.3 GHz and to obtain equal field amplitudes in all 9 cells. This is followed by a light BCP, three steps of high-pressure water rinsing (100 bar), and drying in a class 10 clean room.

Performance of RF Structures

The excitation curve (unloaded quality factor Q_0 as a function of the on-axis accelerating field E_{acc}) of a high-performance 9-cell TESLA cavity shows an almost constant quality factor Q_0 of more than 10^{10} up to 25 MV/m, before the drop of Q_0 at higher gradients indicates that even such excellent multi-cell cavities are still far from reaching the theoretical limit of about 50 MV/m. In order to study this in detail, about 75 cavities, fabricated in three production series between 1993 and 2000, were subjected to the standard treatment mentioned above. Table 1 lists the achieved gradients at Q_0 above 10^{10}. Production series 3 has an average gradient of 26.1

0-7803-7738-9/03/$17.00 © 2003 IEEE

MV/m. At the TESLA-500 design gradient of 23.4 MV/m the measured Q_0 is $(1.39 \pm 0.35) \times 10^{10}$.

Table 1: Average acceleration gradients measured in the vertical test cryostat of the cavities in the three production series; for comparison the TESLA specification are listed as well.

Production Series	Gradient (MV/m) ($Q_0 \geq 10^{10}$)	σ (MV/m)
1	18.7	7.0
2	23.1	2.4
3	26.1	2.3
TESLA-500	23.4	
TESLA-XFEL	10...**17**...23.5	
TESLA-800	35 at 5×10^9	

Figure 1 shows the excitation curves of all 3rd production cavities. One cavity (AC67) had a cold Helium leak which could not be located so far. All remaining 3rd production cavities (AC70 to AC78) were used for the electro-polishing program (see below).

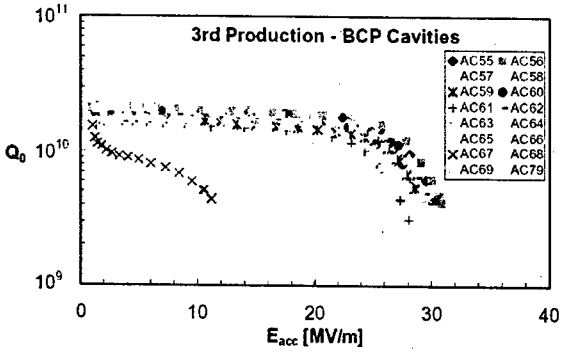

Figure 1: Excitation curves of cavities of the third production series. The measurement was done in a vertical test cryostat in 2 K superfluid helium. Systematic rms errors in the determination of the accelerating field and the quality factor are indicated in Fig.3.

Electro-polished RF Structures

The above mentioned BCP removal of niobium from the inner cavity surface produces a rough niobium surface with strong grain boundary etching. The achieved typical surface roughness is of the order of 1 μm rms. As an alternative method electro-polishing (EP) can be used in which a different acid mixture is used together with an additional electric current flow. Sharp edges and burrs are smoothed out and a very glossy surface can be obtained [2]. Since 1998 a joint R&D program of CERN, DESY, KEK and Saclay has been performed with this polishing method for single cell TESLA structures. Together with a succeeding 100 to 150°C baking of the evacuated cavity, accelerating gradients of 35 to 43 MV/m have been achieved in more than a dozen single-cell resonators [3]. This includes electron-beam welded as well as hydro-formed and spun cavities. The baking seems to be an essential prerequisite for reaching highest gradients without a strong degradation in quality factor.

The transfer of the electro-polishing method to multi-cell cavities has been studied at KEK for some years. Electro-polishing has been used by Nomura Plating for KEK's cavities for many years (e.g. Tristan, KEK-B). In a collaboration of KEK and DESY the electro-polishing of TESLA nine-cell cavities is being studied [4]. After some first tests with older 9-cell resonators, three electro-polished cavities from the last production achieved in a cw measurement the performance needed for TESLA-800: 35 MV/m at a Q_0 larger than 5×10^9. The cavities were tested for several hours at cw. A fourth cavity of this batch achieved 34 MV/m. Figure 2 shows the results. To further study the EP technique of multi-cell cavities, an electro-polishing facility for 9-cell resonators has been set up at DESY. First tests with single cell cavities already qualified the facility.

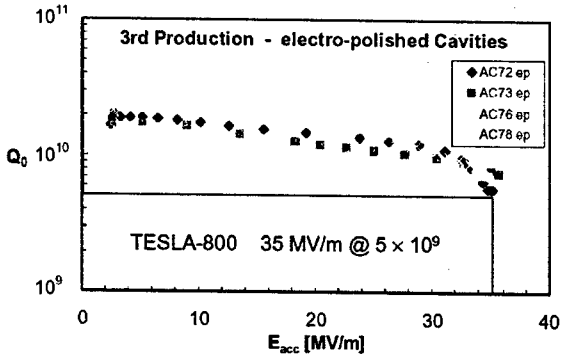

Figure 2: Excitation curve of a high-performance 9-cell TESLA cavity. The cavities are cooled by superfluid helium at 2 K.

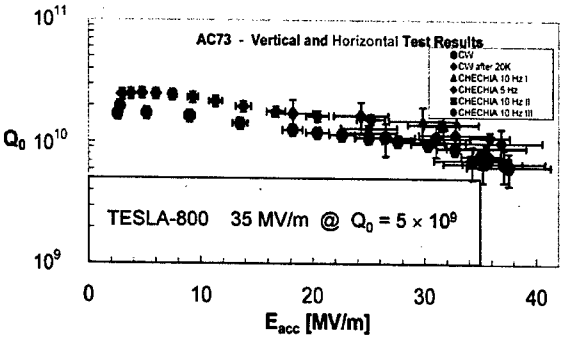

Figure 3: Excitation curves of the electro-polished high-performance 9-cell TESLA cavity AC73. Measurements in vertical as well as horizontal tests (CHECHIA) are shown. The systematic rms errors in the determination of the accelerating field and the quality factor are indicated.

Recently cavity AC73 has been measured in the horizontal test cryostat CHECHIA. For this purpose the helium vessel was welded onto the cavity and the RF power coupler was attached as well as the frequency

tuner. In this horizontal test one eighth of the standard TESLA module's string can be installed. Figure 3 summarizes the results of AC73. The CW curves were measured in the vertical test dewar. The horizontal measurements in CHECHIA confirm the previous results within the indicated error bars.

ACCELERATOR MODULES AND TESTS WITH BEAM

In the frame of the TESLA R&D work a number of accelerator modules housing eight 9-cell cavities each were built and tested. The design of these so-called cryomodules has been primarily driven by the need to reduce static losses and costs compared to existing superconducting cavity systems. At present the 3rd cryomodule generation is used for the 1 GeV extension of the TTF linac. The TESLA Design Report includes the description of a 17 m long module which is, except for the length, basically identical.

TTF Accelerator Modules

The TTF cryomodules use a 300 mm diameter helium gas return pipe (GRP) as the main support structure for the string of eight cavities, the quadrupoles as well as steering magnets, and the beam position monitor. The GRP is supported from above by three posts. Via these posts the common axis of the cavities and quadrupoles can be aligned with respect to the linac coordinate system since the cavities and quadrupoles themselves are aligned relative to the GRP. Figure 4 shows a cross section of the last module generation. The cavity position, the RF main input coupler, and the different radiation shields are visible.

Altogether eight cryomodules were assembled so far. The used 55 cavities belong to the three fabrication series mentioned above, the first ones dating back to 1993. Some cavities have been used for a second assembly. Table 2 gives the achieved accelerating gradients.

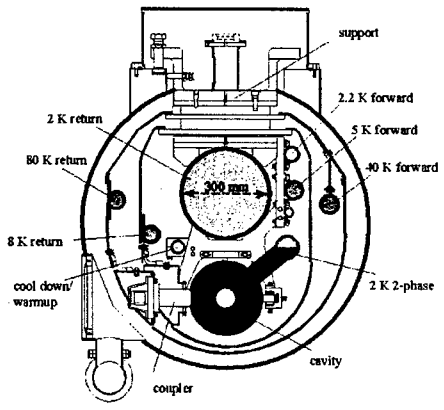

Figure 4: Cross section of the TTF Linac module (3rd generation).

Table 2: Accelerating gradients in MV/m achieved in the TTF Linac accelerator modules. Modules #3*, #4 and #5 are to be tested in late spring 2003, module 2* in fall 2003. The increased gradient spread for the recently assembled module 2* is caused by the fact that older cavities are re-used: The TTF2 injector requires only 15 MV/m for the first four cavities.

Module no.	RF test ($Q_0 \geq 10^{10}$)	σ MV/m	Beam operation	Assem. Date
#1	17.5	6.2	14 MV/m	10/97
#2	21.2	6.3	19 MV/m	09/98
#3	23.6	2.2	22.7 MV/m	04/99
#1*	25.3	2.0	20.3 MV/m	02/00
#4	25.4	2.7	spring 2003	10/01
#5	26.5	1.4	spring 2003	01/02
#3*	23.6	2.4	spring 2003	03/03
#2*	22.6	3.5	fall 2003	05/03

The column 'RF test' shows the average gradient per module at a quality factor $Q_0 \geq 10^{10}$, while 'beam operation' refers to the gradient determined by measuring the energy gain of accelerated electron bunches. The module number actually refers to the cryostat vessel, a '*' hints to a replacement of one or more cavities either following the ongoing cavity test program or due to a required repair. The inter-cavity connection was modified using a new flange design. Some other auxiliaries like the RF main input coupler are now used in a revised version.

Modules #2 and #3 were used for approximately 10,000 hours at a gradient of about 14 MV/m providing a 240 MeV beam for different experiments including stable FEL operation [5]. The achieved relative amplitude stability of 2×10^{-3} and absolute phase stability of 0.5 deg was within the requirements. In this standard TTF Linac configuration 16 cavities were driven by one klystron.

Module 1*, assembled in 02/2000, was tested with beam in fall 2002. The gradient, obtained in vertical and horizontal tests, promised an average module gradient close to 25 MV/m. The actually achieved gradient was 20.3 MV/m, a result being dominated by cavities 2 and 6 of this module. Both cavities have an extremely low onset for X-rays: approx. 12 MV/m. In both cases the maximum gradient was reduced from above 25 MV/m down to 18 MV/m. As a consequence the average gradient was determined using a modified power distribution scheme with additional 3 dB attenuators in front of the RF main input couplers of cavities 2 and 6. Under these conditions the average gradient for stable beam operation was measured to be 20.3 MV/m. A detailed cryogenic load measurement was not performed. Figure 5 summarizes the single cavity tests.

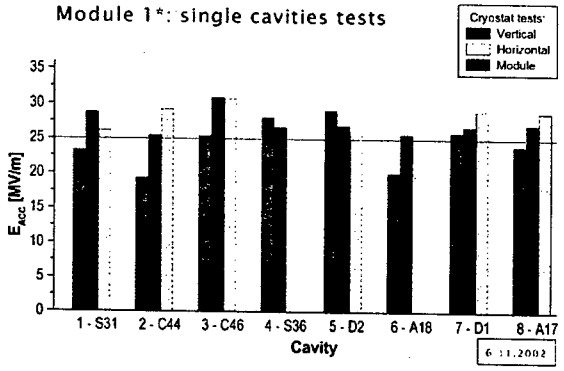

Figure 5: Comparison of gradient measurements in the vertical and horizontal test, and the TTF linac installation.

Careful analysis of the module 1* preparation and of assembly protocols especially in comparison to previous and succeeding modules could not completely explain the gradient reduction of both cavities 2 and 6. However, some problems during the string assembly were identified.

In parallel to the module 1* test, the repair of a leak between the helium system and the insulating vacuum in module 3 was started. The required disassembly of the outer RF main input coupler parts taught us that due to unfortunate handling the inner conductor might touch the niobium surface of the coupler port. The latest coupler generation uses an electrically isolated inner conductor (dc bias to suppress multipacting). Therefore the electrical resistance between the inner and outer conductor can be measured. For module 1* X-ray photographies were taken since an older type of RF input coupler is assembled. Indeed, some of the couplers have touched and may still touch the niobium. Better assembly procedures are required and under study.

Input and HOM Coupler

For TTF several coaxial power input couplers have been developed, consisting of a cold section which is mounted on the cavity in the clean room and closed by a ceramic window, and a warm section which contains the transition from the coaxial line to the waveguide. For TESLA a pulse power of 230 kW has to be transmitted to provide a gradient of 23.4 MV/m for a 950 μs long beam pulse of 9.5 mA. The external quality factor of the coupler can be adjusted by varying the penetration depth of the inner conductor. All couplers needed some conditioning, but then performed according to the specification. The conditioning time depends on the design of the coupler vacuum system which was clearly improved for the most recent coupler type. The maximum transmitted power was 1.5 MW in travelling mode operation

The intense electron bunches can excite eigenmodes of higher frequency in the resonator which must be damped to avoid multibunch instabilities and beam breakup. This is accomplished by extracting the stored energy via higher-order mode (HOM) couplers mounted on the beam pipe sections of the nine-cell resonators, the so-called cut-off tubes. At TTF the excitation of HOMs was studied in detail by accelerating the electron beam off-axis and modulating either the electron beam current or position. Main focus were the so-called trapped modes whose energy is concentrated in the central cells of the cavity. As a consequence of the measurement one of the two HOM couplers per cavity had to be rotated. With this new geometry the HOM quality factors will not exceed 10^5.

TTF Linac Layout

Until early summer 2002 the TTF Linac was operated with up to two accelerator modules as well as one capture cavity. Different modules, including the so-called superstructure were tested with electron beam. Two of the accelerator modules were operated for approximately 10,000 hours at a gradient of about 14 MV/m providing a 240 MeV beam for different experiments including stable FEL operation.

The TTF Linac in its final set-up will consist of the following sections: injector area including the RF gun and a first accelerator module, 150 MeV bunch compressor section, two standard accelerator sections, a second bunch compression section at 450 MeV, another two standard accelerator modules, collimator, undulator, and high energy beam analysis area in parallel to a photon diagnostic and transport section. A sixth accelerator module using electro-polished cavities can be installed between the end of the TTF linac and the collimator. A schematic of this layout is given in figure 6.

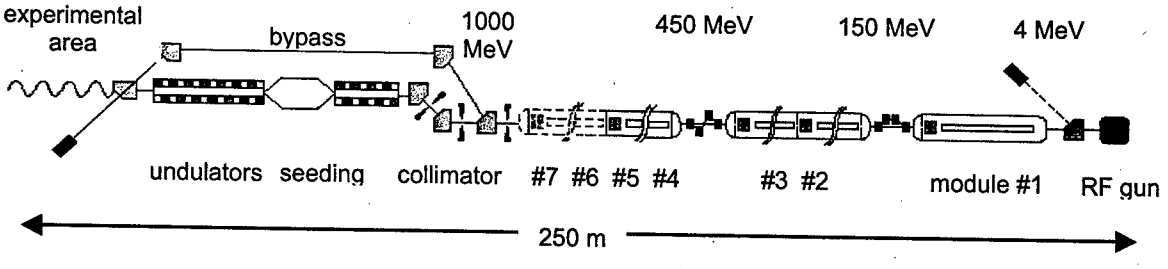

Figure 6: The extension of the TTF Linac to 1 GeV electron beam energy. The electron beam direction in this picture is from right to left.

TTF Linac Operation

Between its first commissioning in 1997 and the modifications in spring 2002, the TTF Linac was operated for approximately 13,000 hours, since 1999 for 7 days a week, 24 hours per day. Approximately 50% of the time was allocated to FEL operation including a large percentage of user time. Figure 7 gives the beam uptime and the operational uptime for a long run between summer 2001 and spring 2002. The percentage is given with respect to the scheduled operation time per week. The difference between beam and operational uptime is due to the time needed for tuning.

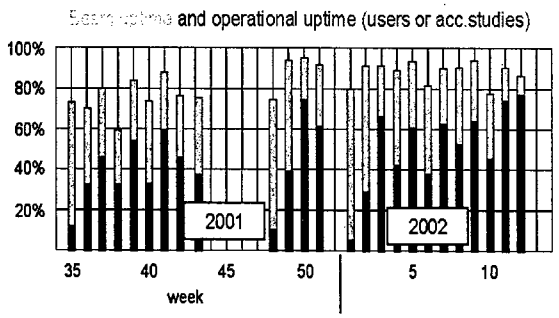

Figure 7: Beam uptime and operational uptime in the 2001/2002 run. The operational uptime was used for either FEL user operation or accelerator studies.

In a dedicated beam time period the high gradient performance of module #3 was studied. The main goals of this run were to operate the module near its maximum gradient, and to accelerate 800 μs long macro pulses comprising 1800 bunches with more than 3 nC bunch charge each. At an average gradient of 21.5 MV/m (5% below the quench limit) a macro pulse current of 7 mA with a bunch charge variation of 10% was accelerated, The achieved energy stability was $\sigma_E / E = 0.07\%$.

The run was carried out under dynamic conditions with beam tuning going on and various levels of operator expertise. The machine interlock system had to check for dangerous beam losses along the TTF Linac. Seven of the eight cavities in the module were operated at gradients between 19 and 22 MV/m. The overall average gradient was between 19.5 and 21.5 MV/m as measured with the beam. Typical module on time was ~ 90%. Trips have been counted but their source has not been investigated.

Over a total of 42 days, 291 trip events were recorded, an average of 8.4 events/day @ 5Hz for the 8 cavity module. This trip rate includes amongst other things both cavity and coupler trips. Partway through the run time a software RF inhibit was implemented so that potential quenches could be detected without tripping the interlock system. The recovery time after a trip depends on the trip reason and is of the order of one minute.

Though this run was not a test for extrapolation to the TESLA linac operational reliability of the superconducting cavities we believe these experiences are positive and point out some of the basic differences between superconducting and normal conducting cavity operation. We also believe that a sophisticated but flexible low-level RF system will be needed to handle a variety of exceptions. We note as well that the cavities in this test have been in operation for over 10,000 hours and that for this run they were operated very close to their limit, a situation that, assuming the high gradients of electro-polished cavities, will not occur for the 500 GeV TESLA collider.

OUTLOOK - CONCLUSION

The TTF Linac at DESY was used to demonstrate the viability of a superconducting linear collider. Based on the above mentioned and referenced results the TESLA Technical Design Report has been published in 2001. The proposal was evaluated by the German Science Council, advising the German government in matters of science [6].

Together with partners of the TESLA collaboration, DESY is extending the actual TTF set-up to 1 GeV. A FEL user facility with wavelengths down to 6 nm will be offered after the commissioning in 2004.

Based on the evaluation of the German Science Council and based on the successful operation of the TTF Free-Electron Laser, the German Federal Research Minister approved the XFEL and included half of the costs into its long-term investment program. The ministry announced negotiations on European cooperation to prepare a decision on construction within about two years, i.e. early 2005.

In view of this support for the XFEL, the TESLA Collaboration has started a careful design review of basically all components which were tested at the TTF. This includes the RF structures itself but is not limited to the accelerating sections; injectors, beam diagnostics, undulators have to be studied as well. Most of this work has large overlap with the continuing international research towards the TESLA Linear Collider. The need for industrial manufacturing of all accelerator components will push the superconducting technology in industry.

ACKNOWLEDGEMENT

Thanks to the TESLA collaboration. And special thanks to Lutz Lilje for analysing most of the above mentioned results.

REFERENCES

[1] TESLA TDR, TESLA-01-23,2001, page II-23.
[2] TESLA TDR, TESLA-01-23,2001, page II-35.
[3] L. Lilje et al., "Electropolishing and in-situ Baking of 1.3 GHz Niobium Cavities," RF Superconductivity Workshop, Santa Fe, 1999, pp. 74-76.
[4] K. Saito, ROAA0002, this conference.
[5] H. Weise, "Operational Experience with the Test Facilities for TESLA," Linac 2002, Gyeongju, Korea, 2000, to be published.
[6] http://www.wissenschaftsrat.de/presse/pm_2002.htm

RELIABILITY ISSUES FOR LINEAR COLLIDERS*

N. Phinney#, C. Adolphsen, M.C. Ross, SLAC, Stanford, CA 94309, USA

Abstract

To deliver a high integrated luminosity over several years of operation, a linear collider must not only meet its energy and luminosity performance goals, but also have a very high hardware availability and operating efficiency. The first challenge is the size and complexity of the facility. If the typical reliability of existing High Energy Physics accelerators is simply scaled to the size of a 500 GeV linear collider, the overall system availability will be too low. The final design must incorporate a more rigorous failure analysis as well as built-in overheads and redundancy. An additional challenge is the complexity of the tuning procedures required to preserve a very small beam emittance. These include beam-based alignment of magnets and rf structures, automated trajectory correction, feedback, emittance and luminosity optimization, and more. Another issue is the inherently large power densities in the beams, which can damage any beamline components they intercept. An extensive machine protection system is necessary to inhibit beam in case of a fault and automatically execute a recovery sequence. This paper will present the important issues in the context of the proposed linear collider designs.

HISTORICAL PERSPECTIVE

The early generations of accelerators were high energy physics machines which were technically innovative. Their primary emphasis was on achieving breakthroughs in energy and luminosity, usually under tight cost constraints. Given the overhead of fills and ramping for storage rings, the luminosity uptimes achieved were in the range of 50%.

The relative importance placed on reliability has evolved with the advent of accelerator user facilities such as the synchrotron light sources, and with the new generation of high energy physics 'factories'. The large energy-frontier colliders such as the Tevatron at FNAL, HERA at DESY, LEP at CERN, and SLC at SLAC have achieved hardware availabilities in the range of 70-90%. In contrast, the B-factories at SLAC and KEK have closer to 95% availability for the colliders themselves. Synchrotron light or spallation sources have invested significant effort into improving reliability and now reach 98-99.5% [1].

While it is true that these facilities are often smaller than the energy-frontier machines, and in some respects less demanding as to performance, the reliability achieved does not appear to scale with the size of the complex. Rather, it appears that the user facilities and factories have higher standards for acceptable availability and therefore allocate the necessary resources to reach that target level.

*Work supported by the U.S. Dept. of Energy under contract DE-AC03-76SF00515.

#nan@slac.stanford.edu

AVAILABILITY GOALS

A reasonable goal for a future linear collider would be to have a hardware availability of 80-85%. Hardware downtime should include unscheduled repairs (something critical breaks), scheduled repairs (either at regular intervals or when enough problems have accumulated), and all associated cooldown, warmup and recovery times. Typically in the past, only the light sources have included maintenance periods in their downtime accounting, but this is really appropriate for all facilities. Modern accelerators do not require routine 'preventative' maintenance and interventions are only 'scheduled' when there is broken hardware. Hence, they take away from the overall beam time that might otherwise be delivered. Note that each maintenance intervention takes on the order of 3 shifts, including edge effects and recovery. A 'day' every 3 weeks represents already a 5% hit.

The overall operating efficiency or beam availability is typically significantly smaller than the hardware uptime. The integrated luminosity delivered is closer to half of what might be expected from the peak rate, even for the high performance 'factories'. Beam inefficiencies include Machine Development (time spent studying and improving the accelerator), the impact of tuning procedures, injection and the luminosity decay during a store (for storage rings), Machine Protection trips and recovery (for linacs), and last but not least, the simple fact that accelerators do not manage to deliver the same luminosity every pulse or every store. A reasonable goal for a linear collider would be a beam efficiency of 75-80%, which would produce a delivered luminosity equal to ~65% of peak performance.

Achieving this availability goal will be a challenging task for a facility the size of a linear collider, but it is necessary in order to integrate significant luminosity. Experience with the SLC and more recently with recommissioning the upgraded Tevatron and HERA has shown that poor reliability can impact the peak luminosity achievable as well as the integrated performance. If the hardware interruptions are too frequent, the machine is not up long enough to effectively make progress on the luminosity issues. It was only after the SLC achieved reasonable reliability that the many beam tuning challenges for a linear collider could be addressed. The more complex next generation of colliders must be designed from the start for high availability so that the inevitable new problems can be overcome rapidly and effectively.

SIGNIFICANT ISSUES

Several aspects of a linear collider make achieving high reliability particularly challenging. First is the sheer size of the facility and the number of components which must

0-7803-7738-9/03/$17.00 © 2003 IEEE

be functional if the machine is to operate. If the typical reliability of existing HEP accelerators is simply scaled to the size of a 500 GeV linear collider, then the resulting uptime will be unacceptably low. Fortunately, this is amenable to engineering solutions. Reliability with large numbers of components was studied extensively for the Superconducting Super Collider project in Texas and more recently for projects such as the Large Hadron Collider in Switzerland and the Spallation Neutron Source in Tennessee. Reliability must be addressed up front by failure analysis, and appropriate remedies must be implemented. Adequate engineering margins are essential if components are to perform reliably in the long term. The key issue is whether sufficient engineering and financial resources are actually allocated during development and construction to produce a reliable system.

Linac rf systems

The main linac rf system demands particular care because of the large number of components with relatively short lifetimes. Table 1 lists the component counts as given in the 2003 Technical Review Committee Report [2]. The klystrons (and some modulator components) must be replaced frequently and are considered a consumable expense. In addition, the modulators, klystrons, distribution system, and structures or cavities will experience brief faults or breakdown events where the hardware can be reset and continue operation after an appropriate timeout. Because each unit contributes only a small fraction of the total energy, a fault will typically not interrupt operation, but simply cause that pulse to be slightly low in energy. All linear collider designs plan to include spare rf units which can be switched in when a unit faults or needs repair. Critical issues are the frequency and impact of faults, the adequacy of the spares overhead, and the accessibility and duration of repairs.

	TESLA	**JLC-C**	**JLC-X/NLC**
Modulators	572	2138	508
Klystrons	572	4276	4064
Rf Distribution	n/a	2138	2032
Structures/ Cavities	20592	6784	12192
Spare rf units	2%	5%	5%

Table 1: Main linac rf components required for 500 GeV center-of-mass (both linacs)

In the linear collider designs based on warm rf technology, the klystrons and modulators are installed in a separate support housing where they are accessible for repair while the collider is delivering luminosity. Since they can be replaced more or less continuously, the number of spares required is determined by estimated fluctuations in the failure rate. In the present JLC-X/NLC designs, 5% overhead has been allocated to cover both faults and failures. The design based on superconducting rf technology described in the TESLA Design Report [3] has a single tunnel. The modulators are installed in support housings but the klystrons, transformers, and high-power pulsed cables are in the tunnel with the accelerator and can only be repaired during a shutdown. The stated goal is to have a maintenance intervention no more often than every three weeks. This would be difficult to achieve without substantially more overhead than the allocated 2% spares.

Tuning procedures

Another aspect which makes a linear collider particularly challenging is in the complexity of the tuning procedures required to preserve a very small beam emittance. In all areas of the collider from the damping rings to the interaction point, the component alignment tolerances are extremely tight (micron-scale) and cannot be achieved by traditional survey techniques. All of the designs foresee extensive use of beam-based alignment. In addition, the tight tolerances make the machines very sensitive to vibration (nanometer-scale) and to slow drifts due to temperature and ground motion effects. As a result, beam-based feedback systems are mandatory, and both invasive and non-invasive retuning will be required at intervals.

Regardless of the main linac rf technology, no linear collider can be considered a static machine and tuning is required on a variety of timescales. Feedback is essential to keep the beams in collision. Without it, they would drift apart between pulses of the machine by as much as tens of nanometers at a noisy site, such as Hamburg, to a fraction of a nanometer at a quiet site, such as the LEP tunnel. TESLA plans to bring the beams into collision and optimize the positions within a single long bunch train. NLC/JLC-X use pulse-to-pulse feedback at 100-120 Hz to damp motion at frequencies below about 10 Hz. Trajectory feedback is required to keep the beams centered in the strong final focus sextupoles or the luminosity degrades within minutes. Trajectory feedback is required elsewhere to damp transients and correct slow drifts. Energy feedback must compensate for fluctuations in the total linac energy due to rf faults as well as to a variety of rf phase or amplitude errors. Re-steering of the main linacs and damping rings will be needed on the time scale of hours and dispersion correction of the rings on the time scale of days.

Alignment tolerances

The alignment tolerances differ for the two technologies, as do the methods forseen to correct errors. The quadrupole and cavity tolerances are 10 and 100 times looser for the superconducting main linacs, but the X-band linac will have high precision position monitors on both structures and magnets, and movable stages on each magnet or girder to effect the required alignment. In the damping rings, the situation is reversed. The X-band damping rings are similar to third generation light sources and have tolerances which are no more than a factor of 3

tighter than what has already been achieved [4]. The damping rings for TESLA will have tolerances which are another 3-10 times tighter, and these must be maintained over a 17 km circumference. Meeting these tolerances may require movable stages for precision alignment and/or more rigid supports than presently foreseen. Table 2 compares the tolerances for the TESLA and NLC damping ring designs with those for the recently completed Swiss Light Source (SLS) as given in Ref. 4. In the final focus, the alignment tolerances are similar for both designs but the superconducting collider is more sensitive to vibration because the low repetition rate limits the frequency to which feedback can be effective.

	SLS	NLC	TESLA
Energy [GeV]	2.4	2	5
Circumference [m]	288	300	17,000
Sext vert align [μm]	71	31	11
Quad roll align [μrad]	374	322	38
Quad vert jitter [nm]	230	75	76

Table 2: Alignment tolerances for the TESLA and NLC damping rings compared with tolerances at the Swiss Light Source (SLS)

MACHINE PROTECTION

The small, very intense, beams in a linear collider require a new approach to machine protection (MPS) untested at any existing or soon to be completed machine. The pulsed time structure of the beam, as opposed to the CW nature of storage rings like the Tevatron or LHC is an additional difficulty. A single, nominal intensity, bunch will damage almost any accelerator hardware it happens to strike downstream of the damping rings. Since it is not possible to stop a given beam bunch once extracted from the damping ring, there is little fundamental difference in the MPS exposure or design strategy for the different machines. The long inter-bunch interval in TESLA allows the beam to be switched off somewhat more quickly than in JLC/NLC. The minimum time required to turn off the beam is one full interpulse period for the JLC/NLC short train and about 1/10 of the train length (~100 μs or 300 bunches) for TESLA.

Protection system schemes have been proposed for both TESLA and JLC/NLC which appear feasible [5]. They must automatically control changes in beam power, both by halting operation when a fault is detected and by restoring operation when the fault is cleared. They rely heavily on the use of a pilot bunch and a fast permit system. The permit signal is derived from beam data taken on the previous pulse and from a system that monitors fast devices. Before operation can be resumed after a fault, the MPS must provide for the production of a sequence of pilot and low power pulses that prove the fitness of the downstream systems for high power operation.

TUNNEL CONFIGURATION

The TESLA Design Report [3] proposed a collider built within a single tunnel. This tunnel would contain the beam lines for the superconducting main linacs, damping rings, injectors, injector linacs, positron production, and beam delivery systems. The linac klystrons with pulse transformers, rf controls and high power pulsed cables, as well as many power supplies and electronics, would also be installed in the same tunnel. In contrast, the X-band rf machine would have separate tunnels for the injectors and damping rings and separate accessible support housings for klystrons, power supplies, electronics, etc. to facilitate repair during operation.

A single tunnel would require interrupting operation at frequent intervals to access the tunnel to replace failed klystrons and repair other components. Great care would be needed to ensure that all in-tunnel components had extremely high reliability. Because a single tunnel would house almost all beamlines, linac access would also impact the rings and injectors. The single tunnel also limits flexibility in initial commissioning. All of these issues would need to be carefully assessed with regard to reliability and efficiency. The single tunnel choice was driven by cost considerations and constraints of the DESY site, but could well be reconsidered for a superconducting linear collider built elsewhere.

CONCLUSIONS

To deliver the integrated luminosity demanded by the physics goals, a linear collider will need to be designed for very high hardware availability and beam efficiency. Nominal goals of 80-85% for hardware availability and 75-80% for beam efficiency will not be achieved without considerably more effort than has often been devoted in the past. A robust design requires rigorous failure analysis, generous built-in overheads and redundancy for critical components. Complex tuning procedures will demand an unprecendented level of automation. Overall these goals should be achievable, but only if sufficient attention and resources are allocated from the earliest design stage through commissioning and operation.

REFERENCES

[1] L. Hardy, "Accelerator Reliability - Availability", Proc. of EPAC02 (Paris, France, June 3-7 2002)

[2] International Linear Collider Technical Review Committee Second Report 2003, SLAC-R-606, January 2003.

[3] R. Brinkmann, et al., (eds.), TESLA Technical Design Report Part-II, DESY-2001-011, March 2001.

[4] T. Raubenheimer, A. Wolski, "Comparison of Alignment Tolerances in the Linear Collider Damping Rings with those in Operating Rings," LCC-112, January 2003.

[5] C. Adolphsen, et al., "The Next Linear Collider Machine Protection System," SLAC-PUB-8130, Proc. of PAC99, new York, NY, 29 Mar-2 Apr 1999.

THE JLC/NLC BASELINE DESIGN

P. Tenenbaum, SLAC, Stanford, CA USA *

Abstract

The JLC/NLC is a normal conducting linear collider based on X-band RF technology. The collider is designed to cover the center-of-mass energy range from 90 GeV to 1.3 TeV with a luminosity of 2 to 3 $\times 10^{34}$ cm^{-2}s^{-1} between 500 GeV and 1 TeV. The X-band RF system, which is based on the operating NLC Test Accelerator X-band RF system, was recently modified in a way that will ensure a less expensive and faster demonstration of a full RF subunit. In this paper, the baseline beam parameters and RF system design for the JLC/NLC will be described, along with the demonstration schedule.

1 THE JLC/NLC PROJECT

The concept of a linear collider for TeV-scale particle physics research is now well-established in the high energy physics community. The broad outlines of such a facility – initial operation at 0.5 TeV in the center-of-mass, ultimate energy reach of at least 1.0 TeV, and luminosity in excess of 10^{34}cm^{-2}s^{-1} over this range – have been endorsed by Asian, European, and U.S. advisory panels [1, 2, 3].

Over the last 10 years, a number of design proposals for linear colliders have been presented. The primary variable in the proposals is the design of the main linear accelerators, which in turn drives design variations in other systems (damping rings, etc.). At this time, two main linac technologies are in competition for use in the next generation linear collider: a low-frequency, long-pulse, superconducting RF system [4], and a high-frequency, short-pulse, normal conducting RF system. The latter is the basis for the Japan Linear Collider/Next Linear Collider (JLC/NLC), which is being advanced by Japan and the United States in concert.

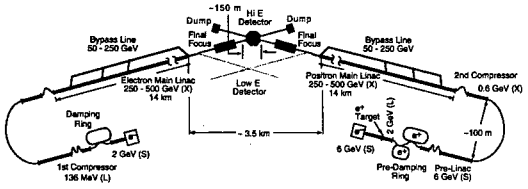

Figure 1: Schematic of the JLC/NLC design.

Figure 1 shows a schematic of the JLC/NLC design. Features of interest include:

- Conventional electron source (polarized DC gun) and positron source (thick production target with electron drive beam), based on SLC designs with appropriate improvements.
- Damping rings similar in design and parameters to third generation synchrotron light sources and the KEK-ATF prototype damping ring.
- Bypass lines parallel to each linac to transport lower-energy beams to the final focus without unwanted emittance dilution in unused portions of the linac.
- Two interaction regions capable of operation from 90 GeV to 1.3 TeV CM.

Figure 2 shows the layout of the JLC/NLC main linac: the accelerator and its support systems (klystrons, etc.) are in separate tunnels, so that the latter may be maintained without human access to the accelerator tunnel.

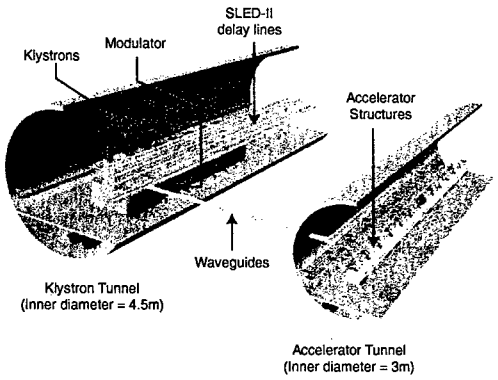

Figure 2: Two-tunnel layout of the JLC/NLC design.

2 ADVANTAGES OF X-BAND

Any proposed technology for a future linear collider must satisfy a number of competing demands: it must achieve an acceptably high gradient and an acceptably high efficiency of conversion from AC power to beam power to minimize construction and operating costs; it must achieve a high reliability; it must transport the beam with minimal dilution of the emittance, especially the very small vertical emittance; and it must be amenable to engineering and mass production, and may not place unacceptable demands upon the design or performance of any other subsystem.

The principal advantages of today's superconducting RF technology are very efficient acceleration, low input power (which eases the design of the RF power sources), and, because of the low frequency and weak wakefields of such

* Work supported by the US. Department of Energy, contract DE-AC03-76SF00515

0-7803-7738-9/03/$17.00 © 2003 IEEE

structures, loose alignment tolerances for emittance preservation. The most obvious advantage of higher-frequency, normal conducting RF structures is its relatively high accelerating gradient, which permits a high-frequency linac to be built on a smaller site than a comparable superconducting linac. In addition, there are a number of other, more subtle, advantages to the high-frequency system:

- High frequency structures are amenable to much shorter filling times than superconducting ones (on the order of 100 *nanoseconds* compared to 1 *millisecond.*
- Since the filling time of a high-frequency structure is so short, it can be pulsed many more times per second than a superconducting linac, which makes beam-based feedback on a linac-pulse to linac-pulse timescale more effective.
- Normal conducting structures have cleanliness requirements which are more compatible with industrial mass production than those of superconducting structures.
- Because normal conducting structures are not sealed up in a cryostat, optical and contact alignment techniques can be used and thus the tighter tolerances of such structures are not much harder to achieve than the tolerances on superconducting structures.
- As a result of the shorter fill time, high frequency structures are compatible with relatively short bunch trains, thus the beam sources and damping rings for such a complex are much more like existing systems than what would be needed for a superconducting linac.

The short bunch trains and small damping rings required for an X-band linear collider have also permitted test facilities for these portions of the complex to be constructed in a reasonable manner, although full testing of the emittance preservation and luminosity generation remains beyond the capability of any conceivable test facility.

3 OPERATING RANGE AND PARAMETERS

The JLC/NLC accelerating gradient is based on the requirements of cost optimization: higher gradients imply lower civil construction and accelerator costs but incur a penalty in RF power source costs. For X-band RF technology a shallow minimum in capital costs is found at an unloaded gradient of about 70 MeV/meter [5]; the JLC/NLC baseline has been chosen at 65 MeV/meter for this reason.

The physics mission of the linear collider requires operational capability at center-of-mass energies from 90 GeV to 1 TeV, and a luminosity in excess of $10^{34}\mathrm{cm}^{-2}\mathrm{s}^{-1}$ from 0.5 TeV to 1 TeV CM. The JLC/NLC parameters have been selected to achieve luminosity of 2 to 3 $\times 10^{34}\mathrm{cm}^{-2}\mathrm{s}^{-1}$ over the 0.5 to 1.0 TeV CM range. The relevant parameters are shown in Table 1. At lower CM energies the luminosity will be somewhat reduced due to the larger geometric emittance of the beam in the final focus and the increased impact of collimator wakefields at lower energies.

Table 1: JLC/NLC Parameters for 120 Hz repetition rate at a site with 60 Hz AC power. If constructed at a 50 Hz site, repetition rate becomes 150 Hz at 0.5 TeV CM and 100 Hz at 1.0 TeV CM, yielding 2.5×10^{34} luminosity for both energies.

Parameter	0.5 TeV CM	1.0 TeV CM
Luminosity (10^{34})	20	30
Bunch Charge (10^{10})	0.75	
Bunches/Train	192	
Bunch Spacing (nsec)	1.4	
σ_z (μm)	110	
$\gamma\epsilon_{x,y}$ at DR exit (μm)	3×0.02	
$\gamma\epsilon_{x,y}$ at IP (μm)	3.6×0.04	
$\beta^*_{x,y}$ (mm)	8×0.11	13×0.11
$\sigma^*_{x,y}$ (nm)	243×3.0	219×2.3
Pinch Enhancement	1.51	1.47

In order to achieve maximum luminosity, the JLC/NLC design assumes a substantial beam current (0.86 amperes), which results in a reduction of the accelerating gradient from 65 MeV/meter to 50 MeV/meter. Since the JLC/NLC accelerating structures are conditioned up to the full unloaded gradient of 65 MeV/meter, operation at higher CM energy is possible if the beam current is reduced, thus trading off luminosity for CM energy. At negligible loading, 1.3 TeV CM can be achieved in the baseline design at a luminosity of about $0.5 \times 10^{34}\mathrm{cm}^{-2}\mathrm{s}^{-1}$.

4 RF SYSTEM

Figure 3 shows the evolution of the JLC and NLC RF systems from 1996 to the present, unified JLC/NLC configuration. In 1999, the baseline RF system for the JLC/NLC consisted of the following: One solid-state modulator driving eight klystrons, each of which produced 75 MW peak power over a 1.5 μsec pulse length; the power from the klystrons was combined and distributed in a dual-mode Delay Line Distribution System (DLDS) pulse compression system; the resulting 375 nsec, 600 MW RF pulses were distributed to four RF girders, each of which included three 1.8 m X-band structures. The unloaded gradient reached 70 MeV/meter [10].

The principal disadvantage of the 1999 baseline system is that a minimum of 600 MW of klystron peak power is required for any system-level demonstration. In addition, high-power tests of accelerating structures have indicated that a 60 cm structure has superior performance to the longer structures favored in earlier configurations.

In order to demonstrate a "JLC/NLC-ready" RF system in a timely manner, the baseline design of the system

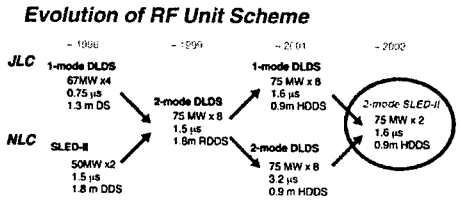

Figure 3: Evolution of the JLC and NLC main linac designs, from 1996 to the present.

was substantially modified. In the present baseline, one solid state modulator drives two klystrons, with 75 MW peak power and 1.6 μsec pulse length; the power from the klystrons is combined and compressed in one dual-moded SLED-II unit, with a pair of 31 meter long cylindrical waveguides; the resulting 400 nsec RF pulse is sent to one RF girder, which contains eight 0.6 m X-band structures; the latter reach 65 MeV/meter unloaded gradient.

The efficiency of the 2003 baseline is mildly reduced from that of the 1999 design because SLED-II is inherently less efficient than DLDS. As a result the unloaded gradient is lower, as noted above, and thus the linac length has been increased to compensate.

5 ACCELERATING STRUCTURE

The invariant requirements of the JLC/NLC structures are the frequency of the fundamental mode (11.424 GHz), and the attenuation parameter τ (0.55-0.60). The combination of these requirements in turn fixes the structure fill time at about 110 nanoseconds.

The 1999 baseline design envisioned use of structures with a 1.8 meter length, implying an average group velocity of about $0.06c$. During high-power RF testing, it was shown that such structures have unacceptable gradient limitations due to frequent, high-energy breakdown events damaging the upstream (high group-velocity) end of the structure [6]. Extensive testing has shown that structures with lower group velocity are less susceptible to damage.

The present JLC/NLC structure baseline design is 60 cm in length, implying an average group velocity of $0.02c$, tapering from $0.03c$ at the input coupler to $0.01c$ at the output coupler. The ratio of the average iris radius to the RF wavelength, a/λ, has been reduced from 0.18 to 0.17, which increases the shunt impedance of the structure at the expense of a moderate increase in the severity of the wakefields. In order to achieve the low group velocity while maintaining a large iris radius, the phase advance per cell has been increased to 150°, and in addition the thickness of the irises has been increased [7]. As in previous designs, a combination of dipole-mode detuning and weak damping will be used to control the long-range transverse wakefield; in the present design, use of "four-fold interleaving" (4 families of 60 cm structures with slight variations in dipole-mode frequencies between families) will reduce the long-range wakefield to negligible levels [8].

6 RF SYSTEM DEVELOPMENT AND TESTING

A prototype of the JLC/NLC baseline RF system is under construction at SLAC. The system will ultimately provide the design RF power level and pulse length to a baseline girder of eight (8) 0.6 meter RF structures. Testing milestones include:

- Demonstration of 450 MW power, 400 nsec pulse length out of a dual-moded SLED-II system with all associated support hardware and software (TRC R1 goal) [9] – Summer 2003.
- Acceptance testing of 0.6 meter RF structure with $a/\lambda = 0.17$ (TRC R1 goal) – Autumn 2003.
- Integrated system test: 1 modulator, 2 klystrons, 1 SLED-II system, eight (8) "JLC/NLC Ready" RF structures, and beam (TRC R2 goal) – mid-2004.

The first two milestones in the list above will be achieved using 50 MW, solenoid-focused klystrons. The "JLC/NLC-ready" klystron requires 75 MW peak power, 1.6 microsecond pulse length, 120 or 150 Hz repetition rate, and permanent magnet focusing. This klystron is being developed in a separate U.S./Japan program; a number of prototypes are already in testing, and additional units will become available over the next few months. It is expected, therefore, that all TRC R1 and R2 goals related to beam acceleration will be achieved within 1 year of this writing.

7 ACKNOWLEDGEMENTS

The JLC/NLC design is the result of the tireless efforts of collaboration members in the United States and Japan. Their excellent work is gratefully acknowledged.

8 REFERENCES

[1] *The Second ACFA Statement on the e^+e^- Linear Collider* (2001).

[2] *Report on the Working Group on the Future of Accelerator-Based Particle Physics in Europe* (2001).

[3] *DOE/NSF High Energy Physics Advisory Panel Subpanel on Long-Range Planning for High-Energy Physics* (2002).

[4] *TESLA Technical Design Report* (2001).

[5] C. Adolphsen, private communication.

[6] C. Adolphsen, these proceedings.

[7] Z. Li, these proceedings.

[8] R.M. Jones, these proceedings.

[9] *International Linear Collider Technical Review Committee Second Report* (2003).

[10] *International Study Group Progress Report on Linear Collider Development* (2000).

[11] *JLC Design Study* (1997).

[12] *2001 Report on the Next Linear Collider* (2001).

[13] *JLC Project: Linear Collider for TeV Physics* (2003).

BUNCH FREQUENCY MULTIPLICATION IN THE CLIC TEST FACILITY CTF3

F. Tecker*, R. Corsini, L. Rinolfi, CERN, Geneva, Switzerland
C. Biscari, A. Ghigo, M. Preger, LNF-INFN, Frascati, Italy
P. Royer, Institut de Physique des Hautes Energies, Université de Lausanne, Switzerland
A. Ferrari†, Department of Radiation Sciences, Uppsala University, Sweden

Abstract

The aim of the CLIC Test Facility CTF3 at CERN is to prove the feasibility of key issues of the two-beam based Compact Linear Collider (CLIC) study. In particular, it addresses the generation of a drive beam with the appropriate time structure to produce high power RF pulses at a frequency of 30 GHz.

The first major goal of CTF3 was to demonstrate, at low charge, the combination of successive bunch trains by RF deflectors in an isochronous ring. This bunch frequency multiplication has been successfully performed for various combination factors up to five and will be presented.

INTRODUCTION

The Compact Linear Collider (CLIC) study [1] aims at a multi-TeV (0.5 – 5 TeV centre-of-mass), high-luminosity ($8 \cdot 10^{34}\,\mathrm{cm}^{-2}\,\mathrm{s}^{-1}$) electron-positron collider for particle physics. The CLIC scheme is based on the Two-Beam Acceleration concept where a low-energy, high-intensity drive beam powers the main beam of a high-frequency (30 GHz) linear accelerator with a gradient of 150 MV/m.

One main challenge of this scheme is to generate the drive beam in a low-frequency accelerator and to obtain the required high-frequency bunch structure needed for 30 GHz RF production. This bunch structure is obtained by sending the beam through an isochronous combiner ring using RF deflectors to inject and combine electron bunches, thus increasing the bunch repetition frequency.

The aim of the CLIC Test Facility 3 (CTF3) project is to demonstrate the technical feasibility of the key concepts of CLIC. In a first stage (CTF3 Preliminary Phase) [2], a low current test of the bunch train combination was performed, where the injection into the ring by RF deflectors and the multiplication of the bunch repetition frequency were demonstrated.

THE PRELIMINARY PHASE OF CTF3

The Preliminary Phase of CTF3 made maximum use of the existing hardware of the former LEP Pre-Injector (LPI) complex at CERN. Some major modifications had to be performed to adapt the installation to the new requirements of CTF3. The general layout of the facility is shown in Fig. 1 and a detailed description can be found in [3]. The machine was commissioned and operated between September 2001 and October 2002.

The CTF3 Preliminary Phase installation consists of a 3 GHz linear accelerator with a matching section, an injection line, and a combiner ring. The thermionic gun [4] of the linac produces up to seven electron pulses of 6.6 ns FWHM spaced by 420 ns, equivalent to the revolution period of the ring. The 3 GHz bunching system subdivides these pulses into trains of approximately 20 bunches each, spaced by 333 ps. The charge per bunch is about 0.1 nC, limited for the combination process by the beam-loading in the linac accelerating structures. The linac accelerates the bunches to an energy of about 350 MeV before entering a matching section to adapt the transverse Twiss parameters of the beam to the injection line optics. The following injection line is achromatic and isochronous at first order to avoid bunch lengthening.

The ring has a design circumference of 125.647 m, optimized for the combination where the condition

$$C = n\lambda_0 \pm \frac{\lambda_0}{N} \qquad (1)$$

has to be met between the ring circumference C and the bunch frequency multiplication factor N. λ_0 is the RF wave length in the linac and the deflectors, and n an integer. The frequency can be slightly detuned in order to switch between different combination factors from three to five.

BUNCH TRAIN COMBINATION BY RF DEFLECTORS

The injection into the ring is done using two horizontally deflecting RF structures. They are located in the ring with a horizontal betatron phase advance of π between them to create a time-dependent local closed bump of the reference orbit. The kick strength and direction vary rapidly with time, allowing the interleaving of the bunches in the ring.

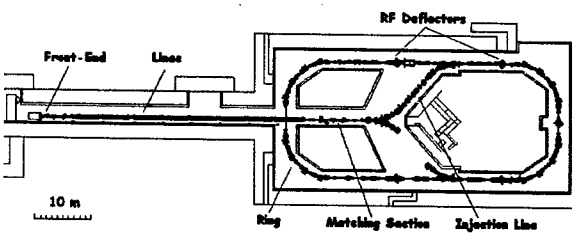

Figure 1: General layout of the CTF3 Preliminary Phase.

* tecker@cern.ch

† The research of A. Ferrari has been supported by a Marie Curie Fellowship of the European Community Programme "Improving Human Research Potential and the Socio-economic Knowledge Base" under contract number HPMF-CT-2000-00865.

0-7803-7738-9/03/$17.00 © 2003 IEEE

Fig. 2 shows the principle of the injection with RF deflectors for a frequency multiplication factor four:

1. The bunches of the incoming train always receive the maximum kick from the RF deflector and are deviated onto the closed orbit in the ring.
2. With Eq. 1 fulfilled (for combination factor $N = 4$), the bunches arrive after one turn in the deflectors at the zero-crossing of the RF field, and stay on the equilibrium orbit. The second train is injected into the ring.
3. After a second turn, the first train bunches are deflected towards the opposite direction, the second train bunches arrive at the zero-crossing, and the third train is injected.
4. At the injection of the fourth train, the first and third train bunches arrive at the zero-crossing, and the second train bunches are kicked away from the septum. The four trains are now combined in one single train. The initial bunch spacing is reduced by a factor four and the current multiplied by the same factor.

For combination factors other than four, the phase of the deflecting field at the passage of the bunches and hence the trajectories between the two deflectors change accordingly.

The RF deflectors are short resonant, travelling-wave, iris-loaded structures with a negative group velocity. In order to obtain the nominal deflecting angle of 4.5 mrad for injection at 350 MeV, a power of about 7 MW is needed in each of the deflectors. They are powered by a common klystron with a phase shifter and variable attenuator in one of the RF network branches to allow relative phase and amplitude adjustments. Two different types of RF deflectors (built by CERN and INFN Frascati [5]) were used in two running periods of CTF3.

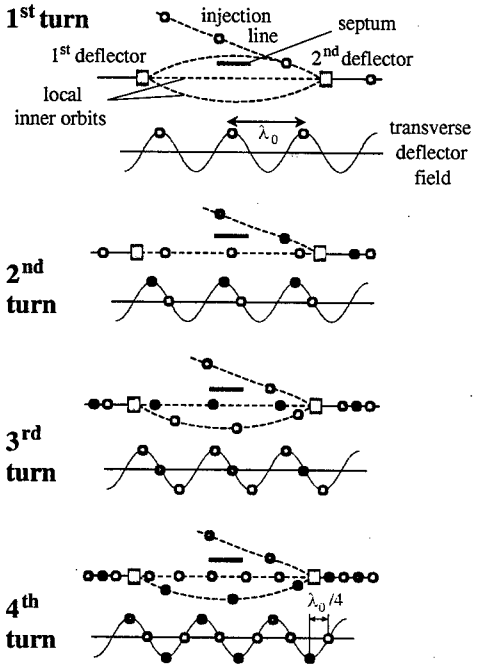

Figure 2: Bunch combination by RF deflector injection for a multiplication factor four.

EXPERIMENTAL RESULTS

The linac and the combiner ring had been commissioned in 2001 [6]. The RF deflectors had been installed in the beginning of 2002. Several measurements were performed in order to prepare the bunch train combination [7]. The energy was measured after the bunching system and at the end of the linac. The beam optics was measured in the linac and found in good agreement with the design. The dispersion of the injection line was determined and one difference from the design was corrected empirically to render the line isochronous. The betatron tunes of the ring were determined for different operating conditions and were in excellent agreement with the MAD machine model. The dispersion of the ring was measured for a non-isochronous optics and showed to be very close to the model.

The bunch length is a very important issue for the combination process. The bunches must be kept short to limit the variation of the injection kick strength and the transverse extension in the injection region. Simulations have shown that about 6.5 ps rms is the maximum acceptable bunch length. The bunch length measured at the end of the linac was of the order of 3 ps rms. This imposes that both the injection line and the combiner ring have to be isochronous to avoid significant bunch lengthening. For the ring, this means that the momentum compaction factor α must smaller than 10^{-4}. A non-zero α also leads to a changing bunch distance over a number of turns in the ring due to the energy variation between the different bunches within a train created by beam loading in the linac.

The isochronicity of the ring optics was carefully tuned by changing the current in one quadrupole family while observing with a streak camera the time structure of the synchrotron light emitted in a bending magnet. Finally, the bunch distance did not change over 60 turns within the measurement error. The bunch length measured on the streak camera profiles was of the order of 4 ps rms, not changing over several turns and comparable with the one obtained at the end of the linac. Thus, within the resolution limit of the streak camera, no bunch lengthening was observed either in the injection line or the ring, proving the isochronicity as required for the combination.

The RF frequency has to be adapted for each combination factor since the path length in the isochronous ring is constant (see Eq. 1). A procedure was developed to optimize the RF frequency and both amplitudes and phases of the two RF deflectors. This procedure minimizes the injection error with respect to the closed orbit of the ring and is described in detail in [8]. A combination factor four was obtained with a frequency of $f_4 = 2.998\,585$ GHz. After the optimization, the bunch train combination showed a 100% combination efficiency. The charge multiplication could be observed on the intensity signal of beam position monitors

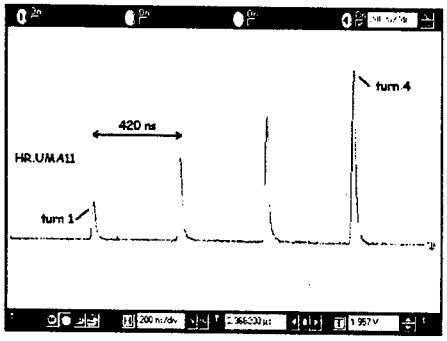

Figure 3: Intensity signal of a beam position monitor in the ring for a bunch combination by factor four.

in the ring. Fig. 3 shows that the charge increases each time a new train of bunches is combined with those circulating in the ring. The increase is not exactly linear due to pulse-to-pulse variations of the gun current.

The evolution of the time structure of the electron pulse was observed with the streak camera. Fig. 4 and 5 show typical images and corresponding intensity profiles.

For a combination factor five, the frequency was changed according to Eq. 1 and further optimized experimentally to $f_5 = 2.998\,715$ GHz. Again, a 100% combination efficiency could be obtained.

The combination performance was further studied by observing the bunch-to-bunch variations in transverse and longitudinal position [8]. Both could be minimised by the optimization procedure. Initially observed bunch spacing variations are due to the non-achromatic lattice at the observation point and could be reproduced by a linear optics model. These variations are compensated in the ejection region where the optics is achromatic.

An alternative method, based on beam frequency spectrum analysis, was also tested to monitor the frequency multiplication. A coaxial pick-up and its read-out electronics were designed and mounted in the ring to allow comparison of the amplitudes of five harmonics of the fundamental beam frequency (3 GHz) while combining the bunch trains. The commissioning of the monitor was a successful proof of principle for this new method [9].

CONCLUSIONS

The bunch frequency multiplication has been successfully demonstrated at low charge in the Preliminary Phase of CTF3. Up to five bunch trains were combined without any measurable losses.

This proof of principle is a crucial step in the CLIC study. In the next stage of CTF3 [10], the bunch train combination will have to be shown at higher bunch charge (2.3 nC) and with longer pulses (140 ns). The CTF3 Preliminary Phase has been dismantled to allow the installation of a new linac in the building for the next stage.

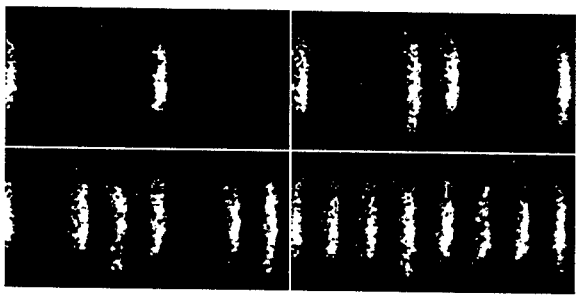

Figure 4: Bunch train combination of factor four, as observed with a streak camera. The horizontal axis represents time, the vertical corresponds to the horizontal position. The images are taken for one to four bunch trains injected.

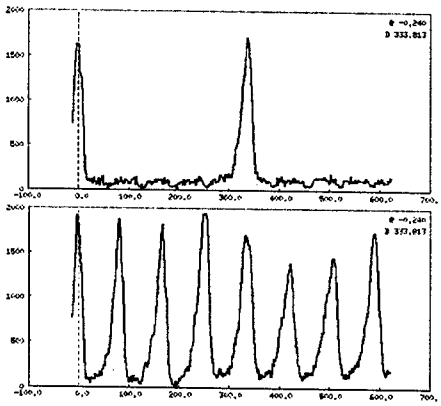

Figure 5: Longitudinal intensity profiles for a multiplication factor four. The horizontal axis is in ps. The two images correspond to injections of one and four bunch trains. Amplitude variations are again due to bunch current variations already present in the linac.

REFERENCES

[1] G. Guignard (ed.) *et al.*, "A 3-TeV e+ e- linear collider based on CLIC technology", CERN 2000-008.

[2] D. Allard *et al.*, "CTF3 Design Report. Preliminary Phase", CERN-PS-2001-072-RF.

[3] P. Royer, "Bunch frequency multiplication by RF injection into an isochronous ring", Ph.D. thesis, Université de Lausanne, Switzerland.

[4] G. Bienvenu *et al.*, "A Thermionic Electron Gun for the Preliminary Phase of CTF3", EPAC 2002, Paris, France.

[5] D. Alesini *et al.*, "RF beam deflectors for CTF3 combiner ring", EPAC 2002, Paris, France.

[6] R. Corsini *et al.*, "Status of the CTF3 commissioning", EPAC 2002, Paris, France, CLIC Note 522.

[7] R. Corsini *et al.*, "Report on the operation of the CTF3 Preliminary Phase, 8 Apr.-24 May 2002", PS/AE Note 2002-141.

[8] C. Biscari *et al.*, "Report on the third operation period of the CTF3 Preliminary Phase in 2002, 16 September - 25 October", PS/AE Note 2003-023.

[9] A. Ferrari *et al.*, "Development of a bunch frequency monitor for the Preliminary Phase of the CLIC Test Facility CTF3", DIPAC 2003, Mainz, Germany.

[10] G. Geschonke and A. Ghigo (ed.) *et al.*, "CTF3 design report", CERN/PS 2002-008 (RF).

FEEDBACK ON NANOSECOND TIMESCALES (FONT): RESULTS FROM FIRST BEAM TESTS AT THE NLCTA AT SLAC

P.N. Burrows (Queen Mary, University of London)

Abstract

We report on the first beam tests of the Feedback on Nanosecond Timescales (FONT) project to develop beam-based intra-train feedback for the Linear Collider.

INTRODUCTION

In order to achieve the design luminosity, in excess of $10^{34}/\mathrm{cm}^2/\mathrm{s}$, the vertical beam size in the next generation electron-positron Linear Collider must be of order a nanometre: 3 nm (J/NLC), 5 nm (TESLA), 0.7 nm, (CLIC). Any source of beam motion which results in relative vertical offsets of the two beams at the interaction point (IP) at the nanometre level will clearly reduce the luminosity from the design value. Maintaining vertical beam overlap is hence a particularly challenging goal for all these designs.

In order to keep the luminosity LOSS below 80% the beam-beam miss distance must be kept below 40, 30 and 5 nanometres for TESLA, J/NLC and CLIC, respectively. In order to keep the loss below 10% the beam overlap must be maintained to better than $1\sigma_y$, i.e. below 5 nanometres in all cases.

The many kinds of potential beam motion may be characterised in two classes: (i) slow drifts resulting from, for example, thermal excursions or component settling, with characteristic timescales varying from seconds to months; (ii) ground motion on a timescale comparable with the machine repetition time. Both kinds of motion were experienced in the decade-long experience at the SLAC Linear Collider (SLC), and were dealt with by employing slow- and fast-feedback systems, respectively. Cultural 'noise' is expected to dominate the ground motion spectrum at frequencies above 1 Hz and, depending on the site, could be at the level of tens of nanometres (r.m.s.). If uncorrected this would cause an a priori large and unknown vertical offset between the electron and positron beams that is DIFFERENT on each successive machine cycle.

Stabilisation of the effects of ground motion will hence be key to successful operation of the future Linear Collider; without it the luminosity may be 1-2 orders of magnitude below the design value, and the physics potential will not be realised.

LUMINOSITY RECOVERY

We are addressing the design of an intra-bunch-train fast-feedback (FB) system for the next-generation Linear Collider (LC). Other essential feedback systems that operate on longer timescales are discussed in [1]. A schematic of our system is shown in Figure 1. It comprises a fast beam position monitor (BPM) to detect the relative misalignment of the leading electron (or positron) bunches just downstream of the IP, a feedback loop, and a fast kicker for kicking later positron (or electron) bunches into collision. The latency of the system should be small enough so that it is able to make several iterative corrections to the beam position within the duration of the bunchtrain, i.e. the latency should be significantly less than 100 nanoseconds for J/NLC and CLIC. For TESLA the situation is more relaxed since there are 2820 bunches separated by 337 ns; a system with a sub-100-nanosecond latency would therefore be capable of bunch-to-bunch feedback.

We have written a simulation package for the feedback system, based on MATLAB/Simulink, that incorporates the beam-beam dynamics (based on GUINEAPIG) and the responses of the hardware components [2]. This allows us to study the feedback operation in 'closed loop' mode. We can also include arbitrary ground-motion model inputs, and multi-bunch wakefield effects, via simulation of the linac and beam delivery system using PLACET/MERLIN (TESLA) or a modified version of LIAR (J/NLC). We have used this simulation infrastructure to show that an intra-train FB system is capable of recovering more than 80% of the design luminosity, which would otherwise be lost due to ground motion.

FONT1: FIRST PROTOTYPE INTRA-TRAIN FEEDBACK SYSTEM

System components and beamline installation

We chose to develop our first prototype FONT experiment at the Next Linear Collider Test Accelerator (NLCTA) at SLAC since the length of the bunch train there can be made as long as 170 ns, which is close to the 270 ns in the J/NLC design and the 100 ns for CLIC, and the train charge of up to 10^{11} electrons is also close to the respective specifications. The time structure of the beam at NLCTA is such that bunches are spaced at X-band frequency, 11.424 GHz, corresponding to 0.08 ns between bunches. This is an order of magnitude shorter than the bunch spacing at J/NLC (1.4 ns) or CLIC (0.7 ns), which makes the test somewhat more difficult.

The layout of the FONT1 components in the NLCTA beamline is shown in Figure 2. The beam enters from the left and is first steered vertically using a dipole magnet (not shown). The beam position is measured roughly 4m downstream at the BPM. The position signal is processed and fed to a kicker that sits within the same assembly as the dipole. The kicker to BPM distance was chosen to match the separation between the IP and the FONT components

0-7803-7738-9/03/$17.00 © 2003 IEEE

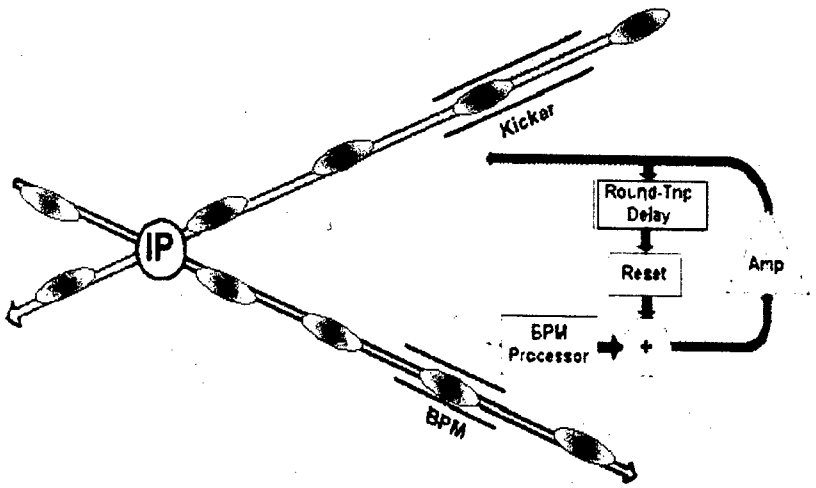

Figure 1: Schematic of the FONT system, showing the position of the BPM and kicker and the function of the FB loop, for an interaction region with a crossing angle.

in the real IR (Figure 1), so as to make the round-trip signal propagation time roughly the same.

We measured the signal propagation delays through our components and estimated the latency of the hardware to be 33 ns, comprising: 5 ns (BPM processor), 5ns (variable-gain preamplifier), 11 ns (Normalisation/FB circuit), 10 ns (kicker amplifier) and 2 ns (kicker fill time). We estimated the beam flight time between the kicker and BPM to be 14 ns, and the return signal cable propagation time to be 18 ns. Thus we estimated a total latency of 65 ns for the FONT1 test.

Results

We summarise the results in Figure 3. The top plot shows the vertical position of the NLCTA bunchtrain as recorded in the FONT BPM for 5 different initial positions that were set using the dipole. For these top plots the FB system was off, and these represent the starting positions of the deliberately offset beam.

The middle plot of Figure 3 represents the effect of the feed-forward part of the system, with the delay loop switched off. After one latency period the effect of the kicker on the beam is registered at the BPM. With a high gain choice the beam is steered almost perfectly to nominal position, independent of the starting position. After a further latency period the BPM registers a modified beam position that corresponds to the fact that the kicker was supplied with a reduced drive signal: the dispersion among the 5 corrected beam positions hence increases. This is precisely as designed, since the result of the first kicker correction reduces the position offset and hence also the second drive signal. After a further half latency period the entire bunchtrain has passed and the BPM signal falls to zero.

The bottom plot illustrates in addition the action of the delay loop. In the last half latency period before the bunchtrain has passed the effect of the delay loop can be seen: the correction applied after the first latency period is preserved and the beam remains steered close to nominal position. Note that we made no attempt to optimise in detail the kicker gain; also, the gain of the delay loop was set to unity and was not tuned.

From these results we conclude that we have made a correction to an electron beam that corresponds to 1.5 passes through a feed-forward, and a half-pass through a delay-loop feedback, system. The measured latency is 66 ns, which compares well with the a priori expected value of 65 ns. This represents a first proof of principle that such a system can operate on a timescale of relevance to the J/NLC or CLIC LC designs.

Plans

We propose to make a number of substantial improvements to the FONT setup at NLCTA, and to take further data in 2003. These include: the addition of two witness BPMs; optimised electronics with reduced latency; reconfiguration of beamline components in order to shorten the latency by about 16ns, thereby allowing a second pass around the delay loop and a more rigorous test of the full FB concept; building a new, solid-state amplifier; and correction of high-frequency position structure within the bunchtrain.

REFERENCES

[1] A. Seryi, these proceedings.

[2] G. White: these proceedings.

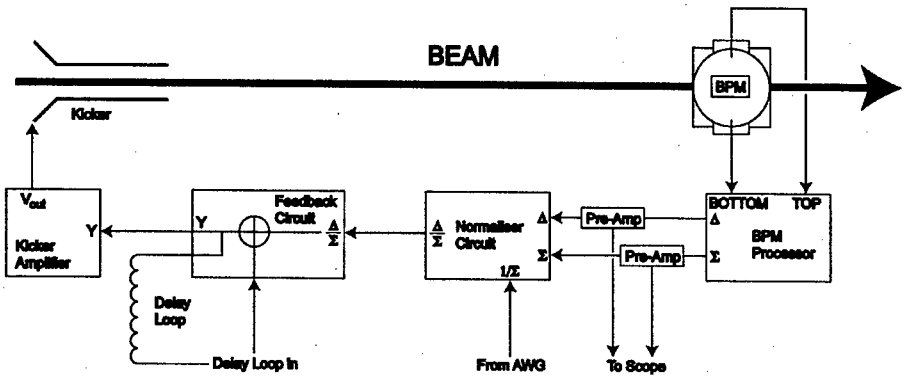

Figure 2: Schematic of FONT1 system in the NLCTA beamline.

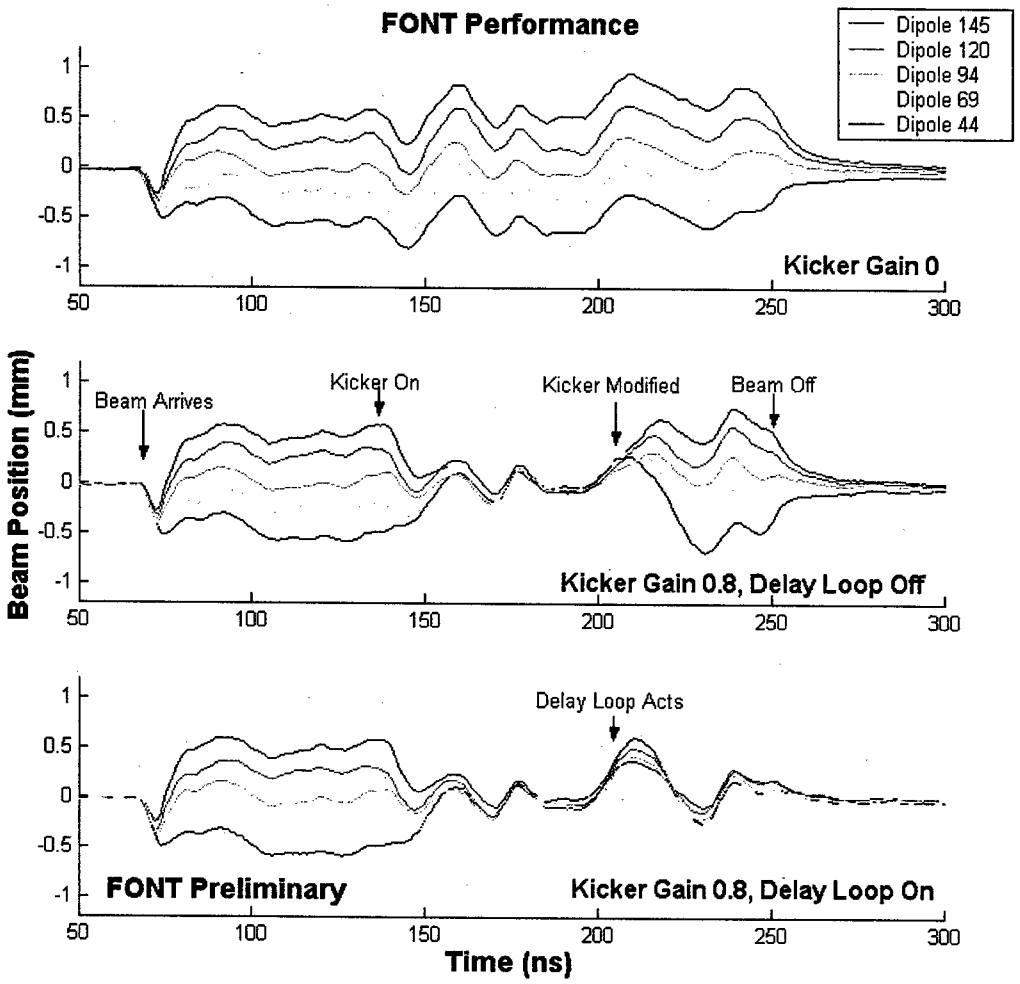

Figure 3: Operation of FONT1. Top: initial beam offsets; middle: with the delay-loop off; bottom: with the delay loop on.

TREATING PATIENTS WITH THE NPTC ACCELERATOR BASED PROTON TREATMENT FACILITY

J. Flanz, T. Delaney, H. Kooy, S. Rosenthal, U. Titt, MGH-NPTC, Boston, MA 02114

Abstract

The Northeast Proton Therapy Center (NPTC) at Massachusetts General Hospital has been treating patients with proton beams since November 2001. Over 200 patients were treated in the first year of operation. This facility has replaced the program at the Harvard Cyclotron Laboratory (HCL) where proton treatments had been underway for over three decades. Features such has rotating Gantries and deeper proton penetration allow a wider range of clinical applications at this new facility. The requirements of accelerator reproducibility and availability are perhaps at a higher level than those required at an accelerator based physics facility. These requirements and the system performance will be highlighted in this paper. Operation of a proton cyclotron produced by industry (Ion Beam Applications) and the four operating beam lines along with the Gantries and patient-positioning systems will be discussed. Of particular interest in addition to the required availability is the systematic approach to safety and accuracy in the design and implementation.

INTRODUCTION

Proton Therapy has been described and used for decades due to the dose localizing ability of the proton Bragg peak. A spread out Bragg peak is generated by combining Bragg peaks of different proton energies resulting in a flat dose distribution along the depth of the target as shown in the figure below.

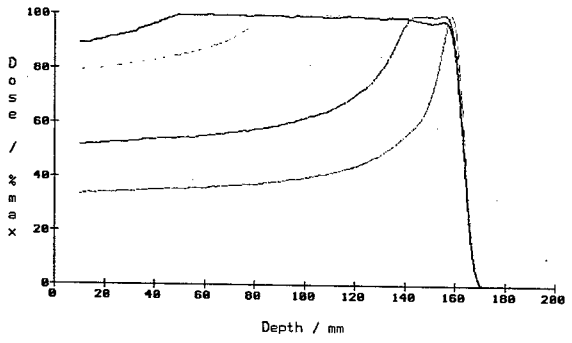

Figure 1: Spread Out Bragg Peak Depth Dose

After more than 30 years of treatment at HCL with good clinical results, but limited by the proton beam energy and the lack of rotating Gantries, the NPTC carries on this work expanding to other treatment sites. Some examples of the HCL successes include:

- Ocular Melanomas – 96% 10 yr. Success
- Chordoma – 98% 10yr success
- Paranasal Sinus - >80% success

In addition to the above head and neck sites, the NPTC includes clinical trials of body sites:

- Prostate
- Hepatocellular Carcinoma
- Lung Cancer
- Rectal Carcinoma
- Pediatric Tumors

The importance of dose sparing to healthy tissue in preventing side effects is shown in the xray vs. proton dose distributions for pediatric meduloblastoma below:

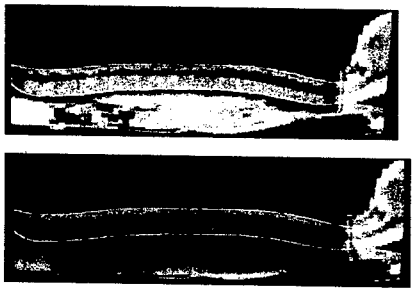

Figure 2: Proton (above) vs. Photon (below) dose distributions for spinal treatment.

The ultimate in conformal dose distribution is achieved in Intensity Modulated Radiotherapy. Photon IMRT dose distributions, in some cases rival conventional Proton dose distributions. However, the physics of the proton dose deposition ensures that IMPT (Proton) dose distributions will produce less collateral damage.

PROTON BEAM DELIVERY TECHNIQUES

The goal of proton beam delivery is to spread out the beam in such a way as to deliver the appropriate dose distribution to the tumor. This can be done in a variety of ways. The Passive technique is so named due to the lack of modifying the proton accelerator parameters, or any direct modification of the beam parameters. The Active technique directly modifies the beam.

Passive Scattering

The passive scattering method uses material to scatter and spread out the beam transversely. Various techniques can produce an optimized uniform distribution. The

0-7803-7738-9/03/$17.00 © 2003 IEEE

transverse target shape is achieved by using a collimator of the appropriate projection.

A range modulation system is used for longitudinal dose distribution. A wheel of varying thickness of material is spinning, in the path of the beam. As the beam passes through this wheel it loses energy, the relative intensities of the Bragg peaks is determined by the angular extent of this constant speed spinning wheel. This intensity can be adjusted by varying the beam intensity as a function of the wheel position. Distal Edge conformation can also be accomplished.

Active Scanning

The active beam scanning technique spreads out the beam transversely by manipulating the transverse position of the beam spot, usually with magnets, either by a continuous raster scan, or by a spot by spot delivery. In both methods, the beam intensity can be varied as a function of transverse position, thus achieving Intensity Modulated Proton Therapy (IMPT).

The range is adjusted by varying the beam energy directly, with no material in the beam.

THE NPTC EQUIPMENT

The NPTC equipment has been previously described. The 230 MeV cyclotron was manufactured by Ion Beam Applications s.a. (IBA). The isocentric rotating gantry was designed by General Atomics and IBA. The treatment equipment was built and installed in the Gantry, by IBA, as shown in figure 3.

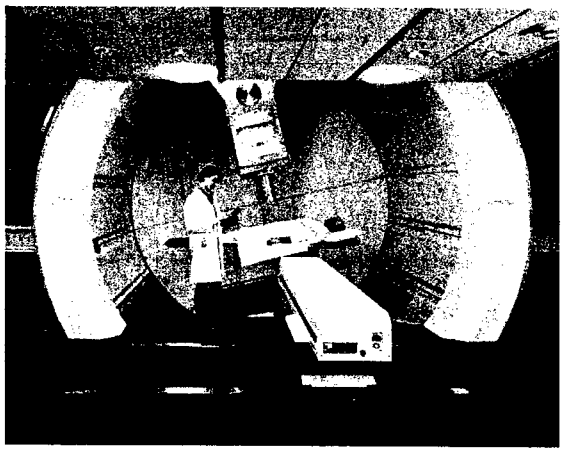

Figure 3: The NPTC Treatment Room Equipment in the Rotating Gantry

The Gantry rotates 360 degrees. The Patient Positioning System (PPS) is a couch with six motion axes, which allows a wide range of Gantry/PPS angular combinations.

Presently, the passive scattering technique is used for patient treatment. However the depth dose distribution is fine tuned with cyclotron intensity modulation. Figure 4 below shows the desired beam time distribution for an example compared with the actual extracted beam current from the cyclotron.

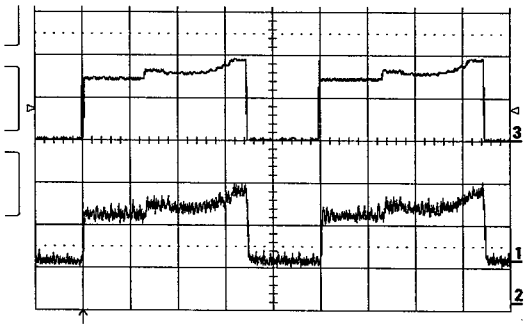

Figure 4: Upper trace is the desired beam current time distribution. Lower trace is the achieved distribution. The period between pulses it the range modulator wheel rotation period.

The modulation width of the SOBP is entered as a prescription parameter, and the system determines the appropriate equipment values. The treatment parameters are continuous over a large range. Figure 5 below shows the algorithmic function for the determination of the beam stop time, and the measured mod width determined over a period of months. The results show millimeter precision. The data for beam range shows sub-millimeter reproducibility.

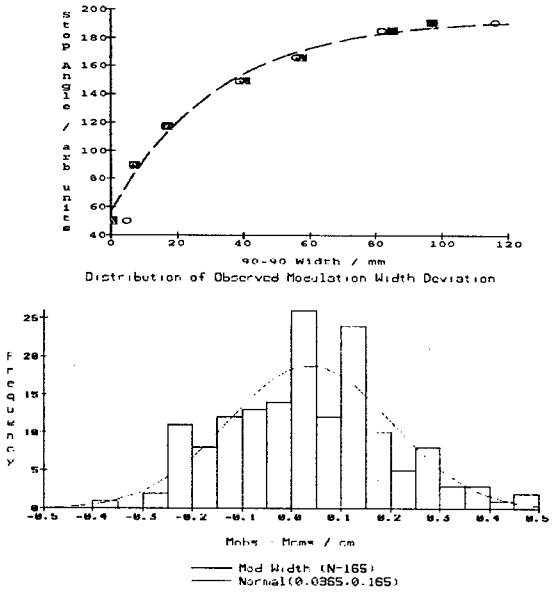

Figure 5: Predicted and Measured Modulation Widths

Tests have been made using the IMPT methodology. Transverse beam distributions are shown in the figure

below. This test was done with the present NPTC system, although it is not ready for patient treatment yet.

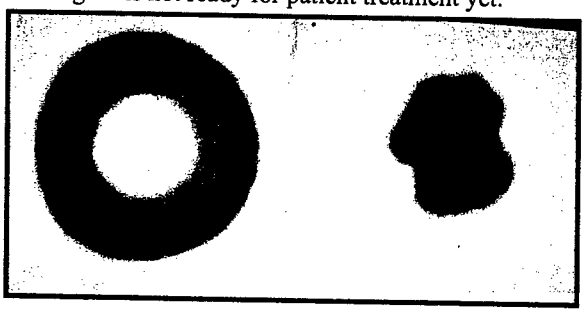

Figure 6: Radiographic film showing beam scanning. The left image is a raster scanned beam using intensity modulation to achieve the varying intensities. The right image only uses beam on and off states.

Positioning

The relative positioning among the beam, the PPS and other patient alignment devices (cross hairs, lasers) must be as precise as possible to minimize the time necessary for patient positioning. The PPS has a load cell which is used to compensate for PPS deflections under load. In addition, the Gantry Nozzle deflections are compensated for by appropriate positioning of the PPS.

Figure 7a shows a polaroid superposition of a beam spot, an xray cross hair and a fiducial attached to the PPS, marking the location of isocenter. Figure 7b is a polaroid film with a superposition of 8 beams from different Gantry angles demonstrating the coincidence of isocenter.

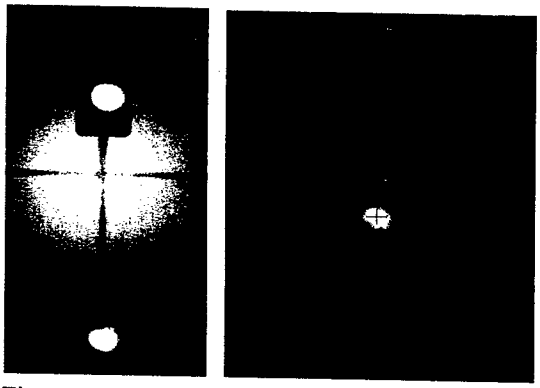

Figure 7: 7a (left) shows beam spot and cross hair; 7b right shows beam from different Gantry angles.

The NPTC equipment has a high level of automation including:

- Automated Conversion of Prescription to Equipment Parameters
- Prototype Automated Cyclotron Beam Tuning
- Automated Rf spark detection and short term processing
- Automated Energy Setup
- Automated Beam Steering
- Automated Positioning Accuracy Corrections

On the one hand, this allows for speed in treatment delivery, while requiring careful planning and implementation of safety checks.

SYSTEM SAFETY

The safety design is done system wide. The safety system protects against mechanical and dose errors. It is a design constraint to ensure that the software is not safety critical, therefore a hardwired interlock system with a redundant PLC deal with safety critical functions. The software is a tertiary redundancy not allowing anything to happen, that the Safety System would react to. In addition the software ensures the accuracy of the treatment delivery. In addition to redundant sensors ensuring that automated settings are correct, the system makes use of functionally redundant sensors. In this way, the final beam parameters are continuously monitored independently of the devices used to control the beam properties.

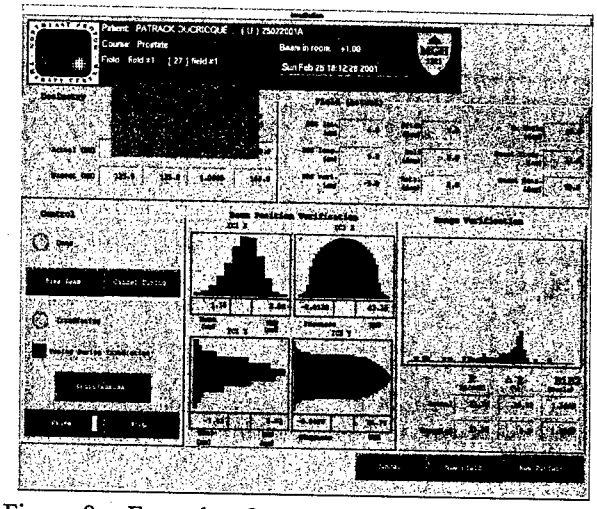

Figure 8: Example of a screen used during treatment showing beam parameters monitored in real time.

Figure 8 is an example of a screen displaying beam properties during treatment. The rightmost plot diplays the beam range. The leftmost plots are the horizontal and vertical beam profiles entering the Nozzle. There are limits placed on the beam position and size at that location. The middle plots are the horizontal and vertical scattered beams upstream of the isocenter. The profiles are not yet uniform at that location, however calculation of the skewness and kurtosis allow the system to determine if the beam profile is appropriate to that which will produce a flat beam at isocenter. These parameters are monitored at 100 msec intervals with warning and error tolerances.

SYSTEM AVAILABILITY

Figure 9 is a plot of the number of fields delivered per day for the first year of operation. The ramp up of patient treatments is evident. Aside from the one gradual dip

resulting from a drop in patient load, the other major dips indicate downtime.

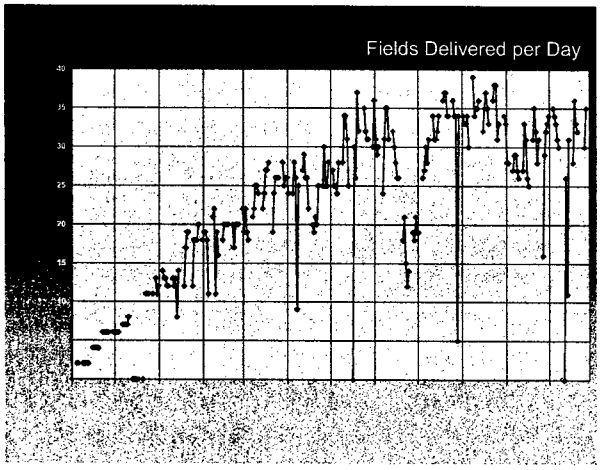

Figure 9: Plot of fields per day for the first year.

The original specification for availability of the facility was 95%. However with 20 treatment slots scheduled per Gantry this allows only ½ hour per day, or 1.5 minutes per treatment. It is desired to reduce the time for the treatment slot from 30 minutes to 20 minutes. In this case it will be necessary for less than 1 minute of delay per treatment.

In addition it is the case, due to the nature of fractionated radiotherapy, and the statistics of patient accrual, that any downtime of more than 2 days, in addition to a weekend, will require a patient to go off protocol. Therefore, it is very difficult, and would require a sharp reduction in patient treatments for a period of weeks, to schedule an extended shutdown for maintenance or other activities.

Figure 10 shows the availability for the first year of patient treatments. This availability is calculated by dividing the accrued downtime in the day by the time scheduled for the treatments. Even if all treatments are completed in the original scheduled time, there may still be downtime. The tolerance in a Hospital environment for downtime is extremely low. Linac based radiotherapy machines have less than 2% downtime

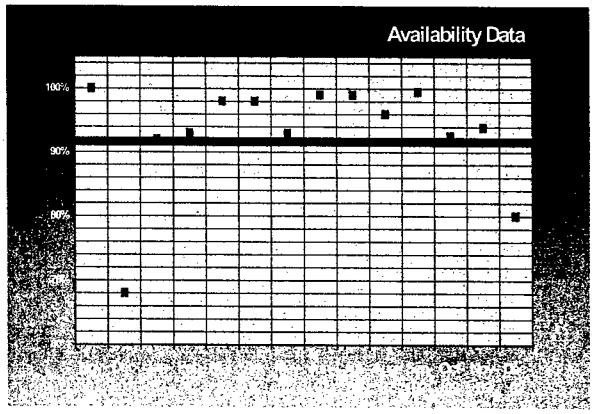

Figure 10: Availability; the black line at 94%

CONCLUSIONS

Patient treatment has been underway for about 1 ½ years. Patients are being treated safely and accurately. Developments are continuing to increase patient numbers and develop more advanced beam delivery techniques. For the most part the system performs well.

The real challenge of this endeavor was not the development of the equipment needed to produce and deliver an appropriate beam; but to produce this beam on demand 24 hours a day, 7 days a week with few personnel. A Hospital environment is used to the operation of an MRI machine or a LINAC, the closest relatives to the technology involved in Proton Therapy.

This facility is the result of over 30 years of the work of Medicine, Industry and Physics Laboratories. While the technology exists to build the accelerators, and beamlines and patient devices, the experience to provide the ultimate automation and extremely high availability is not yet mature. For a variety of reasons, it is not in the mission a laboratory to develop a completely automated system. Each system is different and constantly changing. Industry is good at developing production methods, and making it possible to build more than one machine and assemble the paperwork needed for qualifying and validating the equipment. However, without a clear direction from experience, the idea of fully instrumenting and fully optimizing the system equates to increasing expense. There is a low incentive on the part of industry to build this capability into a machine with the complexity of a proton therapy machine.

High availability, extensive diagnostics and full automation is required for widespread use. The lack of this capability may eventually limit the number of such facilities that will be operating. However, the motivation to continue to build these facilities can easily be seen in just the treatment of one patient.

HICAT- THE GERMAN HOSPITAL-BASED LIGHT ION CANCER THERAPY PROJECT

H. Eickhoff, R. Bär, A. Dolinskii, Th. Haberer, B. Schlitt, P. Spiller, U. Weinrich
and the GSI Therapy Project Group, GSI, Darmstadt; Germany

. *Abstract*

Starting in 1997 about 170 patients have been successfully treated by means of the intensity controlled rasterscan-method within the GSI experimental cancer treatment program. The developments and experiences of this program accompanied by intensive discussions with the medical community led to a proposal for a hospital based light ion accelerator facility for the clinic in Heidelberg, capable to treat about 1000 patients per year. [1]

Major aspects of the design are influenced from the experiences of the GSI cancer treatment program; the requirements of this facility, however, exceed in many fields those of this pilot project.

The main characteristics of this facility are the application of the rasterscan method with active intensity-, energy-, and beamsize- variation both at two treatment places after horizontal beam lines and in combination with the usage of an isocentric light ion gantry. The accelerator is designed to accelerate low LET ions (p, He) and high LET ions (C, O) to cover the specific medical requirements.

The project has been approved and contracts with industrial firms are in preparation; first patient treatments at this new facility are foreseen in 2006.

INTRODUCTION

Preparations for the realization of a dedicated cancer therapy facility at the University clinics of Heidelberg have started. The facility is designed to treat more than 1000 patients per year with the intensity controlled rasterscan method [2], successfully applied with carbon ions to about 170 patients treated since more than 5 years within the GSI therapy pilot project [3].

The GSI Pilot Therapy Project

The basis of the accelerator concept for a dedicated facility has to satisfy the demands of the medical community for the treatment procedures. One of the key aspects of the proposed facility is the application of the intensity controlled rasterscan treatment modality (Fig. 1), which is a novel treatment concept, developed at GSI and applied with excellent clinical results during patient treatments of the GSI pilot therapy program.

The basis of this treatment is, that the tumor volume can be composed of slices of different depths. These slices are irradiated with ions of specific energies, correlated to the requested penetration depth. As the applied dose is maximal near the maximal range of these ions ('Bragg-peak') a large dose can be applied to the tumor, while the surrounding tissue is affected with much lower dose rates. By a sequential treatment of such slices with adequate intensities the requested dose profile for the tumor volume is achieved. (Fig. 1).

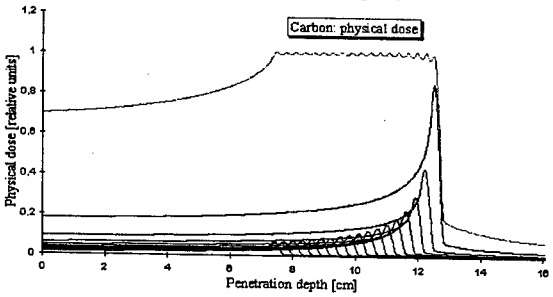

Fig. 1: Depth dose profile

To cover the lateral dimensions of the tumor the ion beam passes 2 fast scanner magnets (Fig. 2) that deflect the ions both in horizontal and vertical direction after being accelerated to the requested energy in a synchrotron and slowly extracted.

The rasterscan control system determines the excitation of the scanning magnets to achieve the requested dose profile, measuring the number of ions at a specific irradiation point by means of ionization chambers and the position and beam width at each scanning point by means of fast multiwire proportional counters in front of the patient. When a required dose limit has been reached the beam extraction is interrupted very fast (< 0.5 ms).

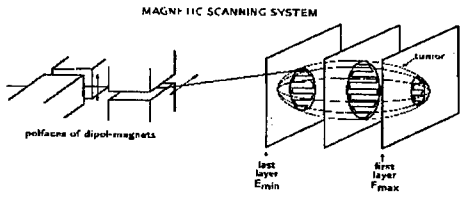

Fig. 2: Rasterscan-Method

This method demands fast, active energy-variation to achieve different penetration depths and intensity-variation to minimize the treatment time. Within the therapy pilot project at the existing GSI accelerator complex a system was developed, that for carbon ions between 90 and 430 MeV/u allows the reliable request of 255 energy-steps for sequential synchrotron cycles. Beside this energy variation also intensity- and beam spot

0-7803-7738-9/03/$17.00 © 2003 IEEE

variations at the treatment location on a pulse to pulse basis can be requested.

During the treatment periods of the last years several improvements of the treatment procedure have been achieved. The demanded tolerances for the beam-position accuracy, delivered from the accelerator, could be slightly reduced to about 2 mm by means of the position control loop installed in the treatment operating system, keeping the position stability at the treatment place in the sub-millimeter range.

THE DESIGN OF THE HEIDELBERG FACILITY

The main requirements of the proposed facility were intensively discussed with radiotherapists and biophysicists and can be summarized as follows:

- treatment both with low and high LET-ions
- relatively fast change of ion species
- 3 treatment areas to treat a large number of patients
- integration of an isocentric gantry
- ion-species : p, He, C, O
- ion-range (in water) : 20 - 300 mm
- ion-energy : 50 - 430 MeV/u
- extraction-time : 1 - 10 s
- beam-diameter : 4 - 10 mm (hor., vert.)
- intens. (ions/spill) : $1*10^6$ to $4*10^{10}$ (dependent upon ion species)

These requests are similar to those, already established at the GSI-pilot project, but extended by additional ion species.

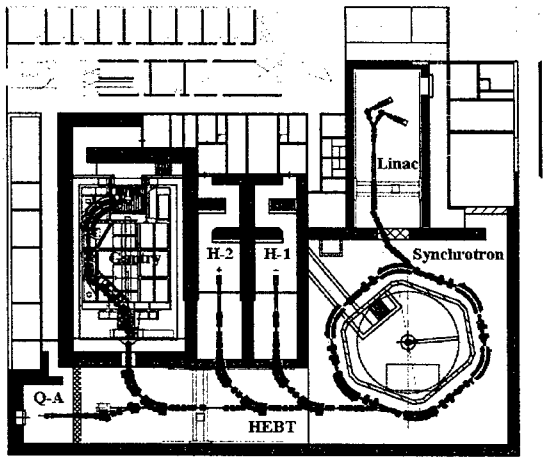

Fig. 3: Layout of the first underground floor, housing the accelerator complex

Fig. 3 shows the layout of the first underground floor of this facility with the accelerator sections and treatment places.

The building consists of 3 floors; the accelerator complex is located on the first and a major part of the additional technical installations on the second underground level. On ground level offices are located as well as the upper part of the gantry cave, that extends over all 3 floors.

The accelerator and beam transport sections consist of the following subsections:

a) Injector and Low Energy Beamline

For the ion generation two parallel ECR-sources are foreseen, giving the possibility to switch from proton to carbon treatment within a short time.

The ECR source is chosen, as this type provides a very stable intensity over a long time without adjustment of the source parameters.

The required particle currents between 80 μA (for $16O^{6+}$ and 1.2 mA for p) are rather conservative; beam tests of this commercially available source indicate, that both the current and the requested beam emittance can easily be achieved. The extraction energy of the ECR-source is 8 keV/u.

Within the low energy beam line the requested intensity reduction down to 0.1% of the maximal ion intensity will be performed by means of appropriate beam defocusing.

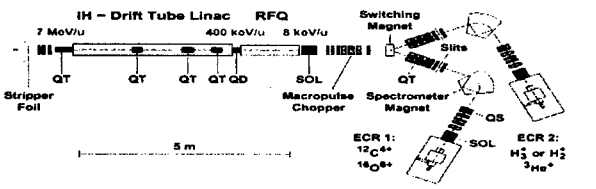

Fig. 4: Layout of the injector-linac

b) Linac, Medium Energy Beam Transport

A combination of RFQ and IH-linac structure with a total length of about 6 m is proposed to accelerate the ions up to 7 MeV/u [4]. The RF-frequency of these structures is 216 MHz. The designed pulse length is 200 μs, the maximal repetition frequency is 5 Hz. The normalized beam emittance is about 0.8 πmm mrad, the momentum spread ± 0.15%.

The medium energy beam transport consists of a stripping and a matching section to the synchrotron. In addition, for multiturn injection a chopper system is provided to match the pulse from the linac. A rf debuncher cavity is foreseen to reduce the momentum spread for the synchrotron injection in order to maximize the multiturn injection efficiency.

c) Synchrotron [5]

For the synchrotron with a circumference of about 64 meters 6 bending magnets with a maximum flux density of 1.53 T are provided. Four long and two short drift

spaces are available for the installation of injection and extraction elements and the RF-cavity. After a 15 to 20 turn injection, corresponding to an injection time of about 30 μs, the acceleration to the maximal extraction energy takes place within 1.0 s.

The synchrotron has a doublet focusing structure with a slightly different ion optical setting for beam injection and extraction.

For slow extraction the 'transverse knock out' method is proposed with variable extraction time between 1 and 10 s and multiple beam extraction at the same flat top. The easy realisation of multiple beam extraction in the same cycle with this method gives great advantages both for respiration gated treatments and for the minimization of the treatment duration using the rasterscan method.

d) High Energy Beam Transport (HEBT)

The high energy beam transport system delivers the slowly extracted beam to three treatment places. Just after the synchrotron extraction section a fast deflecting magnet will prohibit the beam delivery in case of interlocks.

At the end of the high energy transport line a 'Quality-Assurance' (QA)-place is foreseen for beam diagnosis purposes, further developments of the treatment technique and biophysical research activities.

e) Treatment Areas

In order to meet the demand for a patient flow of 1000 patients/year three treatment areas are foreseen. For the first and second area the beam will be delivered from a horizontal beam line, similar to that used at the GSI pilot project. The beam for the third treatment places will be delivered by a rotating beam transport system ('isocentric gantry'). All beam lines are equipped with horizontal and vertical scanning magnets and beam dignostic devices for the intensity controlled rasterscan. The integration of a PET monitoring system in the gantry beam line is proposed as well.

f) The Gantry

As up to now no heavy ion gantry system has been built design studies of the mechanical structure were performed by the firms ACCEL (in collaboration with SEAG) and MAN. By ACCEL/SEAG a frame of box girders between two support wheels is proposed, similar to that realized at the PSI proton gantry, that had been constructed by SEAG (see Fig. 5).

The diameter of the gantry is about 13 m; its total weight including all magnets and supports is estimated to be near 600 tons. FEM calculations for this structure result in a maximum angle dependent deformation of about 0.3 mm , which leads to a beam position variation at the isocenter of about 1.5 mm, mainly due to a steering of the last focusing quadrupole. Although reproducable positioning errors can be handled by means of appopriate steerer settings a fast on-line position correction with the scanner magnets, that is successfully in operation at the GSI pilot project, will probably be used in addition.

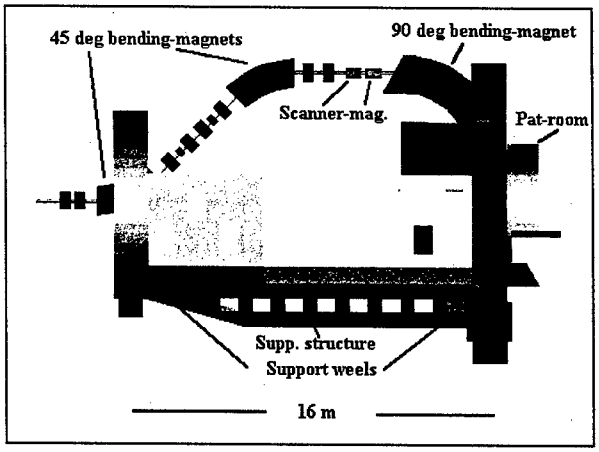

Fig. 5: View of a gantry structure concept (the upper structure elements are excluded to show the magnet elements)

In addition to construction aspects of the gantry structure beam tests of the last gantry section, including the scanner magnets and the 90 degrees bending magnet in a horizontal setup have been performed within the HGF-strategy funds for investigations on ‚Multifield irradiation techniques'.

SPECIAL INVESTIGATIONS

Linac-Developments

At the linac several developments and investigations took place [6].

For the rf tuning of the IH structure a 1:2 scaled cold model have been fabricated (see Fig. 6) and tunig activities are performed at the IAP of the University Frankfurt [7]. Different tuning methods were applied to achieve the correct resonant frequency of the structure and the requested field distribution. The tuning methods comprise 'volume'- and 'plunger'-tuning to reach the requested fundamental resonant frequency in all cavity sections, and variations of the lengths and distances of the 56 small drifttubes to optimize the field distribution. As a result of these optimization procedures the detailed geometry of the tank insertions could be defined.

Three long drift tubes inside the IH-structure are equipped with high gradient quadrupole triplet lenses, that have to operate at yoke flux densities close to 2 T. Due to the high flux densities and the pulsed operation of these lenses their yokes have to be made of stacked laminates of a CoFe-alloy (VX50) with a thickness of 0.3 mm. At GSI prototypes of these very compact magnets were produced in order to determine optimized fabrication possibilities and to verify the high packing density, requested due to the compact dimensions. Within

magnetic measurements the effective lengths and the influence of the field overlap was measured as well as the homogeneity of the gradient and the requested current to achieve the designed field gradients.

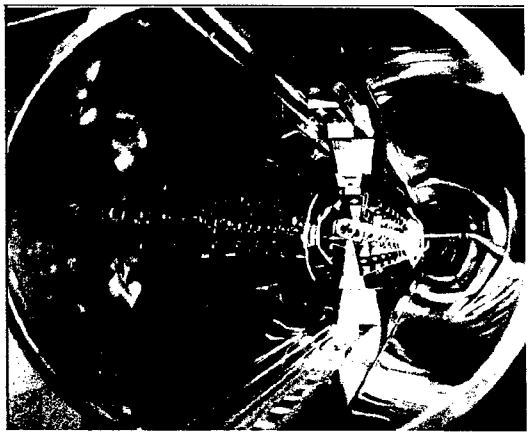

Fig. 6: IH-Model

The development and fabrication of the final amplifier stage of the 1.4 MW power amplifier had been started; this amplifier stage will be tested within the next 6 monthes at GSI and afterwards integrated into the RF power supply system.

The development and construction of the RFQ is finished; alignment- and rf-tests are under way at the IAP; beam tests with a proton beam are foreseen during the second half of 2003.

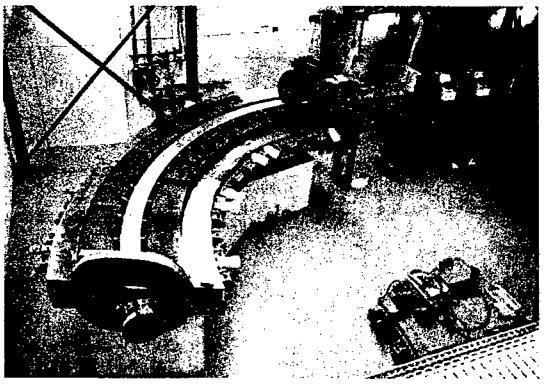

Fig. 7: Gantry segment (the upper yoke of the 90^0 dipole and its mirror plates not yet installed)

Gantry-Test-Segment

As a part of the HGF-strategy funds for investigations on "Multifield irradiation techniques" the components of the last gantry beam line section have been constructed. Beam-tests with this section, including a quadrupole doublet, the scanner magnets and the 90^0 bending magnet in a horizontal setup have started in 2002. [8]

Fig. 7 shows the gantry segment during the installation phase in a GSI experimental cave with the 90^0 dipole magnet in front and the scanner magnets and quadrupoles close to its entrance, seen from the isocenter position.

Before the installation of the segment took place intensive field measurements of the 90^0 dipole were performed, covering both the field homogeneity and its dynamic behaviour, that have also been subject of previous theoretical investigations. [9], [10]

The beam properties of the gantry segment have been tested during several, short test periods. These measurements included investigations of the beam-position and beam width behaviour over the requested maximum irradiation area of 200 * 200 mm at different ion energies. In addition a therapy-like operation mode was established to check the quality of 2D- and 3D-scanning at the isocenter, located about 1.8 m behind the 90^0 bending magnet.

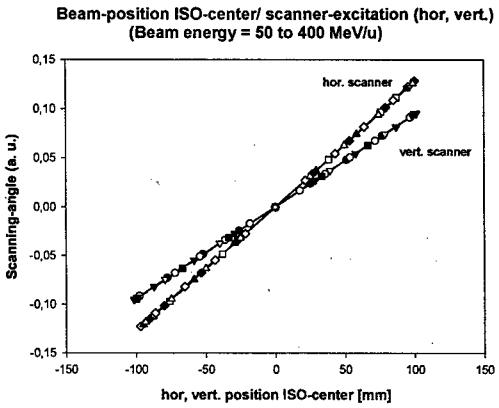

Fig. 8: Measurements of the beam position at the isocenter as a function of scanner excitations.

The measurement results are very close to the predictions and may be summarized as follows:

- the complete irradiation field can be reached,
- no field coupling between the scanner magnets and the dipole occured,
- due to the edge-angle of the dipole a stronger deflection of the horizontal than for the vertical scanner is requested (see Fig. 7),
- for constant settings the stability of the beam positions is better than 1 mm,
- the beam position at constant scanner angles varies over the treatment field in a range of about 3 mm (this can be compensated by adequate corrections of the scanner set values),
- due to the edge angle the beam diameter varies linerarly over the treatment field in a range of about ±15 % , which is tolerable,
- the scanning tests could be performed successfully for small and large treatment areas.

After having finished the tests of the gantry segment the components will be dismounted and stored until the assembly at Heidelberg.

ORGANIZATION, STATUS

After completion of the feasibility study, a technical description of the accelerator complex of this facility [11] and various preplanning activities, in May 2001 the scientific council of the federal republic approved the project with total costs of 70 M€ . These total costs will be covered to 50 % by public support and to 50% by credit financing of the Heidelberg clinics. At the end of 2001 detailed project preparations started and after the positive decision of the 'Großgeräte-Ausschuß' in May 2002 the tender process for the accelerator sections was started and a few months later also that for the building. The final approval of the supervisory board of the clinics took place in April 2003 on the basis of the offers from industrial firms.

The Therapy facility will be constructed and operated under the overall project leadership of the University Clinics of Heidelberg.

During the planning and construction phases the various activities for the facility are coordinated by the 'planning group medicine' of the Clinics institution and performed by:

- the Heidelberg building office for the design and construction of the building and the primary technical installations,
- the GSI for the layout and construction of the accelerator and beam transport sections including the gantry and the installations of the rasterscan-treatment; the latter in cooperation with the DKFZ (German cancer reserach centre) and the FZR (research center Rossendorf),
- The Radiological Clinics for the preparation of the medical installations

For the construction and assembly phase GSI will supervise the industrial firms, that will deliver the systems for the accelerator facility.

Parallel to the construction phase the employment and training of operating-personel is planned mainly at the GSI facility as a preparation of the operation phase. For the final operation a total staff of about 85 persons is estimated, including both the technical and the medical personel.

A rough schedule for the main steps of the project realization is given in the following table:

Table 1: Planned Schedule

Time (Year)	**activities**
2003	Contracts with suppliers for the accelerator-systems and building
2005	assembly of the accel.-systems
2006	overall commissioning
2006	patient treatments (hor. places)
2007	patient treatments (gantry)

REFERENCES

[1] J. Debus et al., 'Proposal for a dedicated ion beam facility for cancer therapy', 1998

[2] Th. Haberer et al., Nucl. Instr. Meth. A330, 296, (1993)

[3]: H. Eickhoff et al., 'The GSI Cancer Therapy Project', PAC 1997

[4] B. Schlitt, 'Design of a Carbon Injector for a Medical Accelerator Complex', EPAC 1998

[5] A. Dolinskii, 'The Synchrotron of the dedicated Ion beam Facility for Cancer Therapy, proposed for the clinic in Heidelberg', EPAC 2000

[6]: B. Schlitt at al, 'Development of a 7 MeV/u, 217 MHz Carbon Injector Linac for Therapy Facilities', Linac-Conf. 2002

[7] Y.Lu et al., 'RF Tuning of the IH Model Cavity for the Heidelberg Cancer Therapy Project', IAP internal note: IAP-ACCC-270103

[8]: H.Eickhoff et al.: 'Tests of a Light-ion Gantry Section as an example of preparations for the therapy facility in Heidelberg', EPAC 2002

[9] A. Kalimov, '3D-properties of the last gantry bending magnet', GSI-report, 1999

[10] A. Kalimov, 'Theoretical investigations of the Eddy Current Effects in the 90° Gantry Magnet', GSI-report, 1999

[11]: H. Eickhoff et al.: 'HICAT-The Heavy Ion Cancer Therapy accelerator facility for the Clinic in Heidelberg, Technical description', GSI, 2000

STATUS OF THE MIDWEST PROTON RADIOTHERAPY INSTITUTE

V. Anferov, J. Collins, D.L. Friesel, W. P. Jones, J. Katuin, S.B. Klein, & A.N. Schreuder
Indiana University Cyclotron Facility, Bloomington, IN 47408, USA

Abstract

Phase I construction of the Indiana University Midwest Proton Radiotherapy Institute (MPRI), including many reliability upgrades to the IUCF k220 cyclotron, construction of a variable energy proton Beam Delivery System (BDS), a horizontal beam Treatment Room with a Large Field Nozzle, and a Medical Clinic, is now complete. Commissioning of the BDS and the Large Field Nozzle is underway. Patient Treatment with this nozzle is scheduled to begin in late July 2003. This contribution discusses the unique features of the MPRI Cancer Treatment facility and the present Phase I commissioning results. In addition, two 360^0 rotating gantry systems were purchased from IBA in December 2002 for Phase II construction. The first gantry is scheduled for delivery in July 2003. The Phase II construction and installation schedule will also be briefly presented.

MPRI FACILITY DESCRIPTION

The MPRI Beam Production and Delivery Systems consist of the IUCF K220 separated sector cyclotrons [1], a 57m, 235 MeV proton beam "Trunk Line" to a Beam Dump, and three doubly achromatic Energy Selection beam lines (ES_n) to three Proton Beam Treatment Rooms (TR_n), as shown in Fig.1 [2][3]. A constant 206.5 MeV proton beam from the cyclotrons is delivered to the Beam Dump via the Trunk Line utilizing solid pole magnets. A Multi-Layer Faraday Cup (MLFC) in the Dump is used to monitor and maintain the beam energy and intensity from the cyclotron [4]. The proton energy in the Trunk Line is maintained at 206.5 ± 0.3 MeV as measured on the Dump MLFC, where the measured energy spread is ± 200 keV.

Fast ferrite magnets (3ms rise/fall time) in the Trunk Line are used to kick 206.5 MeV beam into the ES lines on demand. The ES line optics is designed as a double spectrometer to optimize momentum selection and beam transmission and to minimize neutron background in TR1 from the degrader. Proton beam energy, energy spread and intensity delivered to the Treatment Rooms are independently adjusted and verified in the ES lines using continuously variable double wedge Beryllium energy degraders, momentum band selection slits, MLFCs and non-destructive beam diagnostics. The ES line magnets are laminated to facilitate rapid beam energy changes. Figure 2 shows a detailed layout of the ES1 beam line.

The ES lines transmit 65 to 206.5 MeV protons (3.5 to 26 cm range in water) to the three Treatment Rooms. TR1 has two fixed horizontal treatment Nozzle systems, a Large Field Nozzle (up to 30 cm diameter, beam right) and an Eye Line Nozzle (beam Left). The nozzles are accessed by a ±10° switch magnet located at the end of ES1. The Large Field general purpose Nozzle is complete. An Eye Line Nozzle previously used at IUCF will be installed when patient needs require later in 2003 [5].

The ES2 and ES3 beam lines deliver similar beam to Treatment Rooms TR2 and TR3, each containing an IBA 360°-rotating Gantry. All ES lines are identical in design, except that ES2 and ES3 do not require the switch magnet. The MPRI BDS is designed to deliver dedicated beam to one Treatment Room at a time for patient treatment. A fourth Ferrite magnet, located down stream of ES3, is used to deliver beam to two general-purpose research rooms (not show in Fig. 1) when beam is not needed for patient treatment.

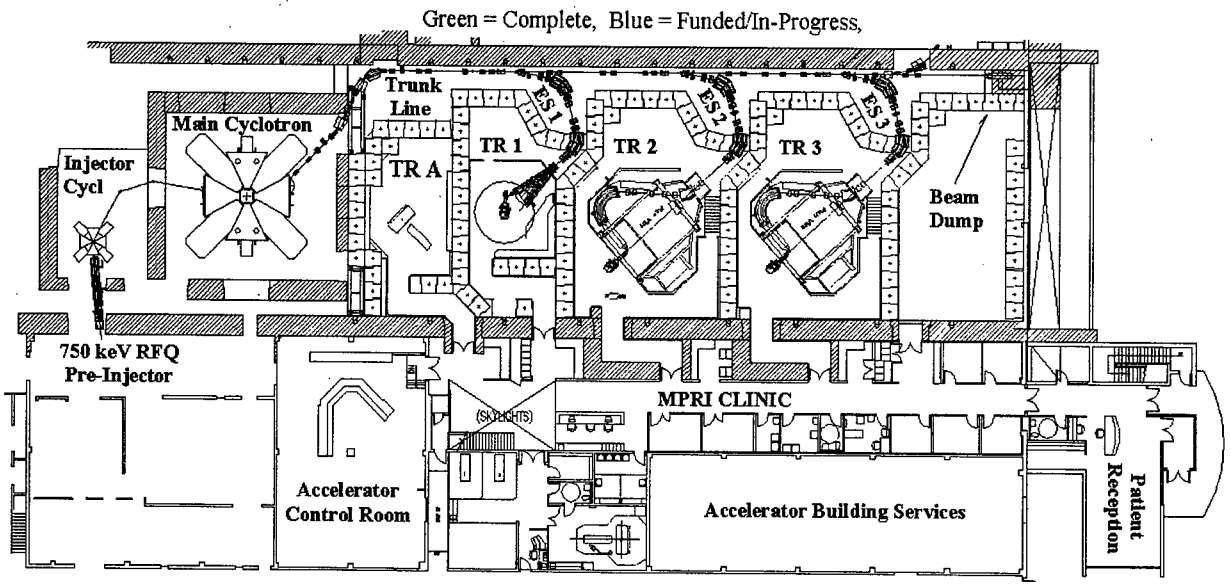

Figure 1. The MPRI Facility showing the IUCF cyclotrons, Trunk and ES lines, Treatment Rooms and Clinical Facilties.

0-7803-7738-9/03/$17.00 © 2003 IEEE

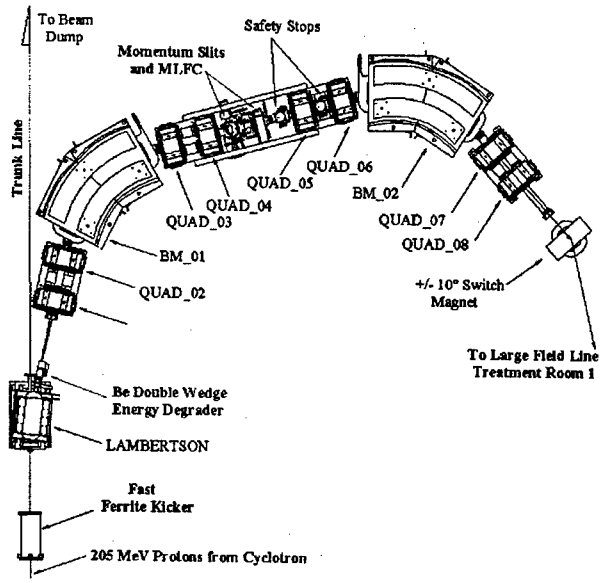

Figure 2. Layout of Energy Selection Beam line (ES1)

PHASE I CONSTRUCTION STATUS

Some MPRI Phase I beam commissioning and system validation results are described below.

Beam Production System Upgrades

Upgrades to the venerable IUCF cyclotrons (new water, vacuum, and computer control systems, ac and dc power upgrades, etc) needed to achieve the 95% operational reliability specified by MPRI [2] have been completed. A historically major source of breakdown, the 600 kV Cockroft-Walton pre-accelerator, is now being replaced by a 1 mA ECR proton ion source, a 750 keV RFQ pre-injector and a new cyclotron injection system designed to accept the higher injection energy [6]. The RFQ, built by AccSys Technology, Inc [7], and the in-house designed ECR source and 750 keV transport line were tested off-line at IUCF. Stable operation with 0.6 mA peak intensity proton beam at 750 keV was demonstrated, as reported elsewhere in these proceedings [8]. Installation of the pre-injector on the cyclotron began in April 2003 and final beam commissioning begins in May. Even without the upgrades, recent cyclotron operations at 206.5 MeV for ES1 and TR1 commissioning were reliable enough to meet MPRI performance requirements.

Trunk and ES Line Beam Commissioning

The doubly achromatic, focusing and transmission properties of the Trunk and ES1 lines are performing as designed [9]. Transmission through the ES1 line for ranges in water from 3.5 to 26 cm is shown in Fig 3. The transmission of protons degraded to 4 cm of range in water is 6.4%, as predicted, due in part to ES1's short length (11m), large acceptance (30π mm-mrad geom.), and the use of Beryllium as the degrader material. Calibration of the ES1 line tune, slits and MLFC using a water phantom at the isocenter of the Large Field Nozzle is complete and was used for Nozzle hardware, dose

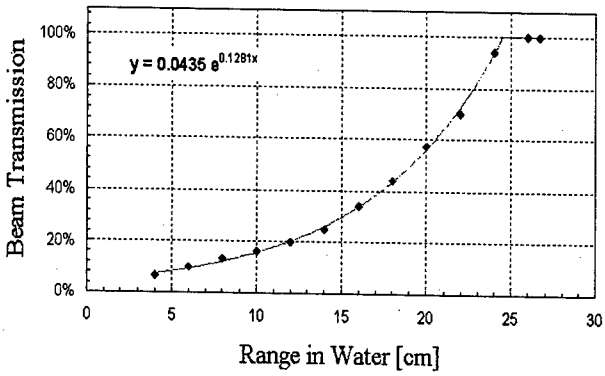

Figure 3. Transmission through ES1 vs. range in water.

delivery and treatment control system tests and validation. Water Phantom measurements of the momentum band slit effects on the width of pristine peaks for various proton energies are shown in Fig. 4.

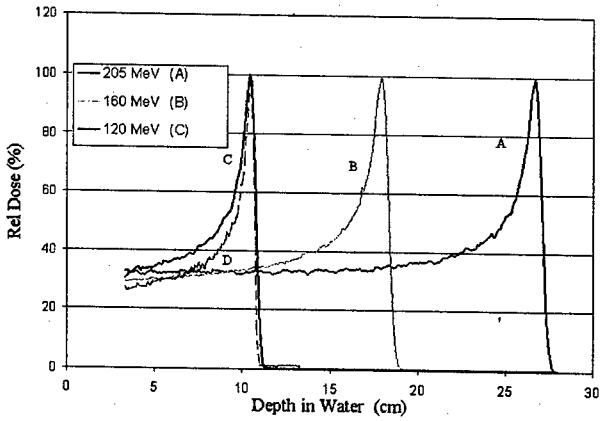

Figure 4. Pristine peak width vs. incident beam energy. Curve D shows the effect of the Momentum band slits.

Treatment Room 1 Commissioning

The MPRI fixed beam treatment room (TR1), shown in figure 5, contains two horizontal beam-line Nozzles: one for larger fields (2.5–30cm diameter) and high energy (Large Field Line) and another for small fields (1–3.5cm diameter) and lower energy treatments (Eye Line). Beam is delivered to only one Nozzle system at a time via the ±10° switch magnet. Active components of the Large Field Nozzle, shown in red, are both passive and active (wobbler magnet) beam spreading systems, collimators, four segmented and parallel plate ion chambers, and an IBA Snout system. Two industrial robots are used in TR1. A Motoman UP200 robot is used for precise patient positioning and a UP20 robot is use to position digital X-ray radiography panels for patient alignment [10].

Examples of proton beam Penumbra vs. energy and a full energy Spread Out Bragg Peak using the passive scattering system for a 12 cm field are shown in Fig. 6 and 7 respectively. Both measurements are well within the precision prescribed for the Large Field Nozzle in the MPRI Clinical Performance Requirements.

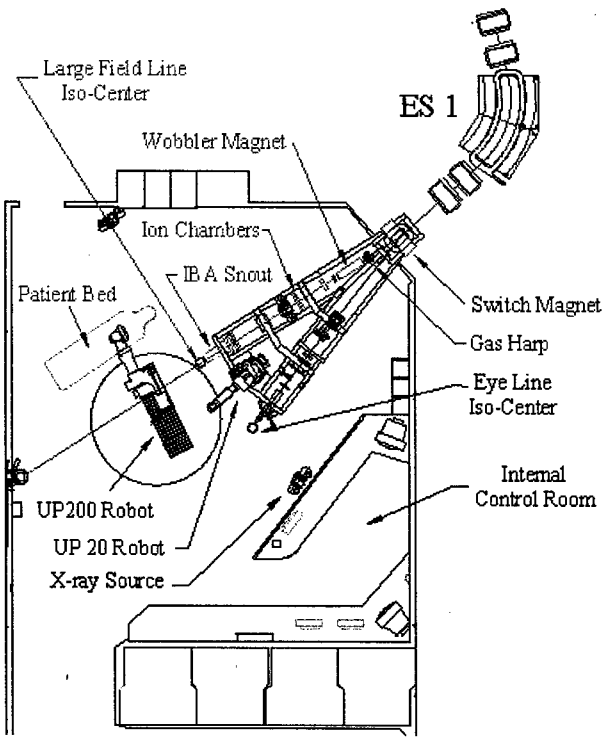

Figure 5. Layout of the fixed horizontal Treatment Room.

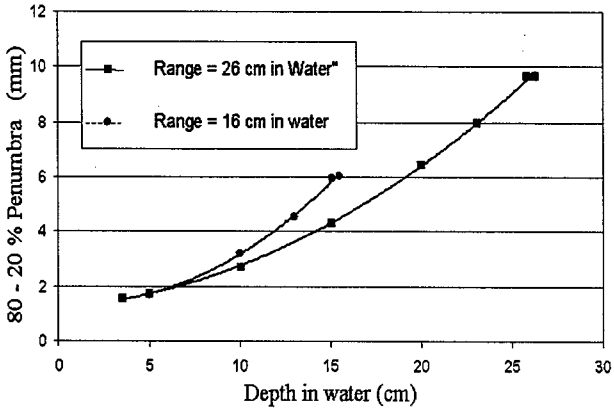

Figure 6, The effect of a lower incident beam energy on the proton beam penumbra.

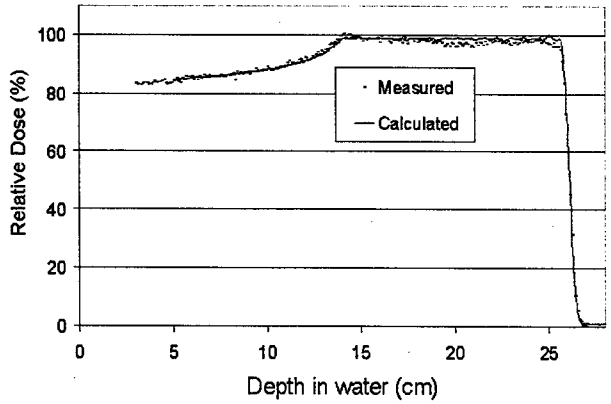

Figure 7, A typical Spread Out Bragg Peak (SOBP)

PHASE II CONSTRUCTION

MPRI Phase II construction, which includes installation of the ES2 and ES3 transport lines to Treatment Rooms TR2 and TR3 (Fig. 1), is underway. Two IBA gantries, purchased in December 2002, were selected for the Treatment Rooms on the combined basis of cost, operational efficiency and compatibility with the MPRI BDS. The ES lines were designed to provide a doubly achromatic round beam at the entrance of the gantry transport line that is well matched to the IBA gantry beam transport design. The gantries were purchased without the IBA nozzle or patient positioning and control systems. MPRI will use nozzle and patient positioning systems similar to those designed at IUCF and installed on the Large Field line in TR1. The IBA Gantry motion and beam transport elements will be interface to our in-house Treatment control system. Delivery of the TR2 and TR3 Gantries is scheduled for July 2003 and July 2004 respectively.

The 40'x29'x12' deep gantry pits were completed in 2001. Detailed pit modifications specific to the IBA gantries are underway and installation of gantry utility systems (water, power, etc) for both TR2 and TR3 will begin in June. Installation of the TR2 gantry rotating structure by IUCF personnel will start in July with guidance from IBA consulting engineers. Patient treatment is scheduled to begin in TR2 and TR3 in July 2004 and September 2005 respectively.

CONCLUSIONS

MPRI Phase I and II construction are proceeding on a fast track nearly as scheduled. Final patient treatment beam delivery, nozzle, dose monitoring and treatment control system test and validation will commence in June. Request for FDA 510k approval of the MPRI clinical facilities is also being actively pursued. Support for this work is provided by the State of Indiana, Indiana University, Clarion Health, the DOE (Grant No. DE-FG-02000ER62966) and the NIH (Grant No. C06 RR17407-01)

REFERENCES

[1] R.E. Pollock, PAC'77, IEEE Trans. Nucl. Sci, Vol. NS-24, No.3, (1977) p. 1505
[2] D.L. Friesel *et al,* PAC'01, IEEE 01CH37268BC, (2001) p. 645.
[3] D.L. Friesel. AIP Conf. Proc 600, (2001) p. 27.
[4] A.N. Schreuder *et al,* PTCOG XXXII, Uppsala, SE, (2000) p 8.
[5] C. Block *et al,* PTCOG XXX, Capetown, SA, Particles 24 (1999).
[6] D.L. Friesel *et al,* AIP Conf. 576, (2000) p. 651
[7] AccSys Technology, Inc, Rhamm@Linacs.com
[8] V. Derenchuk *et al,* TPPE009, these proc, (2003)
[9] V. Anferov *et al,* PAC'01, IEEE 01CH37268BC, (2001) p.2488.
[10] J. Katuin & A.N. Schreuder, Proc. CAARI 2002, Denton, TX (2002) to be Published.

DESIGN AND OPERATION OF A PROTON MICROSCOPE FOR RADIOGRAPHY AT 800 MEV

T. Mottershead, D. Barlow, B. Blind, G. Hogan, A. Jason, F. Merrill, K. Morley,
C. Morris, A. Saunders, R. Valdiviez
Los Alamos National Laboratory, Los Alamos, NM 87545

Abstract

A high-magnification high-resolution option is desirable for the study of small-scale dynamic experiments at the LANSCE 800-MeV Proton Radiography Facility. Magnification is achievable by either repowering the existing imaging-lens quadrupoles, using new high-gradient quadrupoles, or some hybrid combination of the two. The large and complex parameter space of magnetic optics solutions was studied extensively with the 3rd order optics code MARYLIE. Some of the hybrid solutions achieve magnifications up to 150, but at the price of high chromatic aberrations. In the end, a design using only new high-gradient permanent-magnet quadrupoles was selected and built at the design parameters that minimized chromatic aberration per unit magnification. The design has a moderate magnification of 7.1 and 15.8 at the two existing image stations. First-beam commissioning results exceeded expectations. Image contrast is produced by multiple Coulomb scattering in the thin objects. Early experimental objectives are to optimize this contrast by collimator design and by adjusting the correlation in the illuminating beam, as well as to characterize the (quite high) resolution limits of the system.

THE PROTON RADIOGRAPHY MICROSCOPE

Proton radiography is a new technology for imaging the interior of objects that can be penetrated by high-energy protons. A broad beam of high-energy protons shines through the object, and suffers path-dependent attenuation by collisions with the nuclei. It also suffers path-dependent spread in angle by multiple Coulomb scattering (MCS). The protons exit the object with an assortment of energies due to the losses on the varying paths through the object. The net effect is that an image is imprinted in the exit beam by its passage through the object. A magnetic lens after the object extracts the implicit image by refocusing the varied scattering angles onto a detector plane, where it is recorded by a set of gated TV cameras.

The pRAD System at LANSCE

The operational proton radiography facility at LANSCE contains a diffuser to spread the incident beam, an illuminator matching section to tailor its phase space distribution, and a monitor lens to copy this distribution onto the object. There are two consecutive magnetic imaging lenses after the object, each with its own image plane, called IL1 and IL2. Each lens is made of two identical cells containing a symmetric doublet of 12Q24 quadrupoles. The magnification is unity. All eight quads (named A through H in Fig. 1) have the same 5.7 T/m gradient, with alternating signs. The proton-microscope project was aimed at improving the resolution of the images for small objects, with the goal of studying phenomena on a scale of some tens of microns. The new equipment was to fit smoothly into the operations at LANSCE, and use as much of the existing equipment (e.g. the camera systems) as possible.

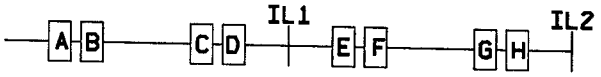

Figure 1 LANSCE pRAD Identity Lens Configuration

Image Resolution

The overall resolution of the system is determined by the performance of the digital TV readout cameras, by the scattering of light in the detector fluor, and by the performance of the magnetic lens. Magnetic magnification can spread the image over enough pixels to overcome the limitations of the optical system. The magnetic lens maps the phase space coordinates (x_0, θ_0) of the proton exiting the object to final position $x_f = R_{11}x_o + R_{12}\theta_0$ on the detector plane. Focus means the final position is independent of the initial angle θ_0. This occurs at the momentum where $R_{12} = 0$. Protons with other momenta are out of focus. To first order in Δ, their position on the detector plane is

$$x_f = Mx_0 + \Delta(R_{11}'\, x_0 + R_{12}'\, \theta_0)$$

where $M = R_{11}$ is the magnification, $\Delta = \delta p / p$ is the deviation from the focus momentum, and the primes indicate derivatives with respect to Δ. The first thing to note is that rays with the correlation $\theta_0 = wx_0$, where $w = -R_{11}' / R_{12}'$ are achromatic in that their final position is independent of their energy. An upstream matching section imposes this achromatic correlation on the illuminating beam, so a ray exiting the object with MCS angle φ has an initial trajectory angle $\theta_0 = wx_0 + \varphi$. Its final position is therefore $x_f = Mx_0 + C\varphi\Delta$, where $C \equiv R_{12}'$ is called the chromatic aberration coefficient of the lens. The position error in object coordinates for an off-energy proton is therefore $-C\varphi\Delta / M$. An appropriate average over the distribution of scattering angles and energy shifts gives the resolution spot size associated with a given path through the object. This makes chromatic aberration per unit magnification the proper measure of microscope resolution. The goal is to improve on the C/M = 12 meters chromatic aberration coefficient of the Identity lens.

0-7803-7738-9/03/$17.00 © 2003 IEEE

Fourier Points

The position at longitudinal location z of the general scattered ray with initial coordinates $(x_0, wx_0 + \varphi)$ is $x_0[C(z) + wS(z)] + \varphi S(z)$, where *S(z)* and *C(z)* are the usual sinelike and cosinelike basis rays of magnetic optics. The term in square brackets is the achromatic basis ray. The Fourier point is its zero crossing, where the trajectory position depends only on the MCS angle φ, independent of the initial position. A collimator at this location can attenuate the scattered rays, providing image contrast by darkening the final image pixels in the locations containing the material causing the scattering. The location and strength of the Fourier point is an important design consideration. It depends on the correlation coefficient *w* imposed by the matching section, and is not necessarily the same in both planes. Collimators can be optimized for the range of objcct areal densities to be studied.

Field-of-View

The expected mean scattering angle and energy shift depend on the size and composition of the object. The size of possible objects is limited by the field-of-view (FoV) of the lens, which is in turn limited by either the size of the beam pipe or the size of the detector. A square detector of dimension L x L can record an FoV of dimension L/M. The thickness of the possible object is presumably about the same. We may estimate the nuclear attenuation in pathlength z through an object as $\exp-(z\rho/\lambda_I)$, where ρ is the density, and λ_I is the nuclear interaction length in g/cm^2. The standard detector at LANSCE is a 5 glass fluor, so L=12.7 cm. With a magnification of 12.7, the FoV would be 1 cm. Higher magnification leads to a smaller FOV, suited for studying smaller objects. Note that nuclear attenuation in 1 cm of Cu, for example, is only 1%. The RMS polar MCS angle is 13 mrad, and the energy loss is 12.6 MeV. The MCS angle scales as the square root of the path length divided by the radiation length.

DESIGN OPTIONS

We seek to modify the operational system to achieve higher magnification and lower specific chromatics. The three basic alternatives are to repower the existing big quadrupoles, to build a new high-gradient small lens with permanent-magnet quadrupoles (PMQs), or to build a hybrid system using both. In all cases, the three design constraints are focus $(R_{12} = R_{34} = 0)$, and equal magnification $(R_{11} = \pm R_{33})$ in both planes.

Repowered Big Quadrupoles

Three constraints for eight quadrupoles allows a large space of allowed solutions. A methodical survey of this parameter space was undertaken, including analytic studies in the thin-lens approximation. The simplest example would be searching for a magnifier solution for a single four-quad lens. One of the quads could be set arbitrarily, and the other three varied to fit the design constraints. The scanning-the-fit procedure in the 3rd order design code MARYLIE was used to compute the relative chromatic aberration for all possible values of the fourth quad. The result was a peak magnification of M=2.265 on IL1, with relative chromatics of 3 m in the x-plane, and 19 m in the y-plane. A compound lens with two of these in succession results in squaring the magnification to M=5.131 on IL2, with chromatics of 3.5 and 22.7. Another four quad solution in the pattern AB00E00H (0 marks a quad that is turned off) results in peak magnification of M=5.82 and chromatics of 2.6 and 15.5. A pattern of the form ABCBAGH0, with B=-A, went to a magnification of M=33, with chromatics of 7.07 and 32.25. Here quad H was scanned, and quads A,C,and G adjusted to fit the 3 design constraints. Fig. 2 shows the relative chromatic aberration in both planes as a function of magnification for the later two designs. In all cases the relative chromatics are worse in at least one plane than the original Identity lens .

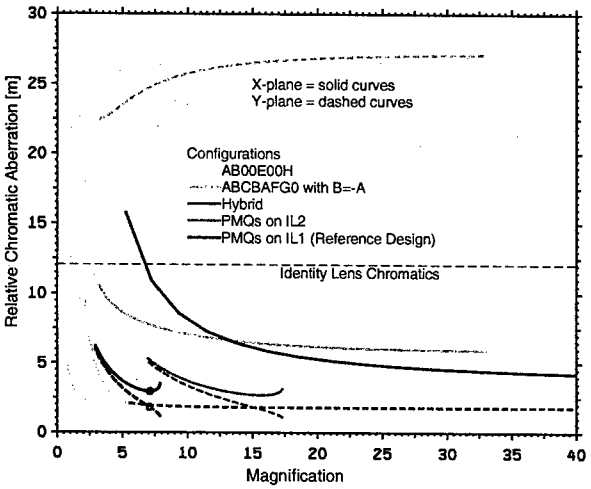

Figure 2. Parametric curves of relative chromatic aberration vs. magnification for 5 cases

High-Gradient PMQs

A Russian quadruplet has an inner doublet inside an outer doublet of opposite sign and half the strength. This type of lens made with high gradient PMQs works very well. The other big quadrupoles are turned off, and merely serve as a drift space. The proton trajectories from the object to the first image plane are shown in Fig 3.

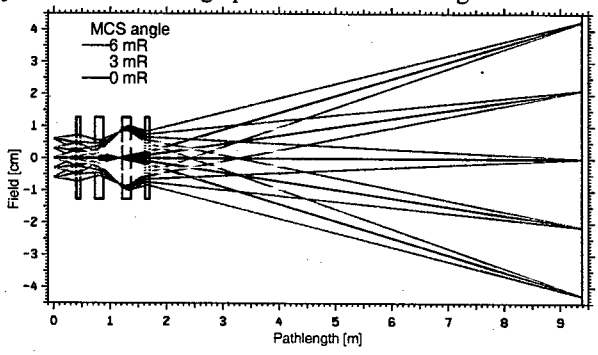

Figure 3: Rays in the PMQ microscope

The magnification depends on the distance from the object to the first quadrupole. The performance curves in Fig. 2 show an optimum at a focal standoff of 40 cm, which was chosen for the actual device. Since the strength of the quadrupoles is fixed, the lens must be focused by moving them. The rays in fig 3 are color coded by scattering angle in 3 milliradian increments, showing the Fourier point between the second and third quadrupoles.

Hybrid Systems

The PMQ lens was designed to operate with the 6 big downstream quads turned off. Solutions with the downstream quads turned on, however, can produce very high magnifications of over 100. The FOV is correspondingly small, while the relative aberrations are somewhat worse than with the PMQ lens alone. This may be a useful configuration for some experiments.

CONSTRUCTION AND OPERATION

The design iterations led to the final choice of 1.5 inch thick PMQ segments, with an inner diameter of 1.375 inches and an outer diameter of 4.0 inches. With the 1.2 T remnant field of NeFeB, the gradient is 71.6 T/m. The inner of quadrupoles are assembled from 4 segments each, so are 6 inches long. The outer half-strength pair are 3 inches long, and made of 2 segments each. The multipole error tolerances were determined in a study of their effect on image quality.

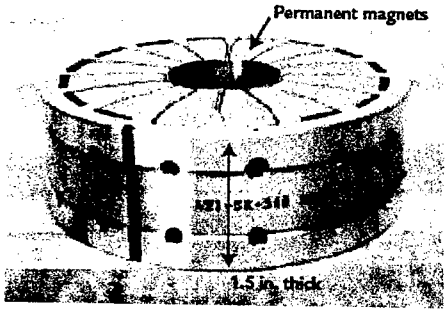

Figure 4. A PMQ segment.

The PMQs were made by Aster Corporation in 1.5 inch thick segments shown in fig 3. The segments were measured when received, and were well within design specifications. The measured gradient averaged 72.83 T/m. The microscope is mounted in the area C beamline in the location normally occupied by the first two large quadrupoles, which have been mounted on rails to facilitate the configuation change (fig 5). The quads slide over the 1.25" stainless steel beam pipe. Their position may be adjusted from the control room by actuators to focus the lens on either IL1 with a magnification of 7.2, or IL2 with a magnification of 15.8. The matching section was set to illuminate the object with the achromatic rays demanded by the lens. This placed the Fourier points about 12 mm apart and 6 cm before the entrance of the third quad. A tungsten collimator with a simple 5/32" aperture was placed in the pipe at this location.

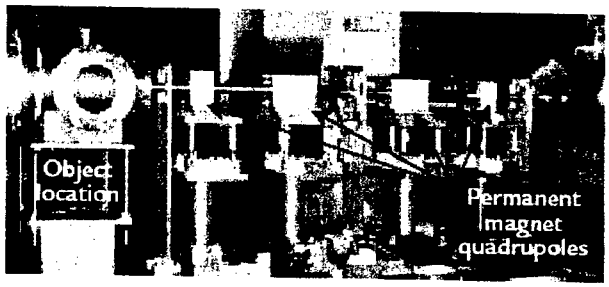

Figure 5. The microscope in the beamline. Large red objects in background are big quads A and B.

First Beam Test

The first test object used was a small stainless steel plate with the word LANL milled in it in 7 mm high letters.

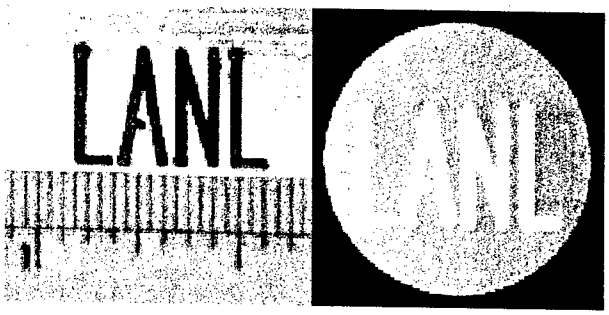

Figure. 6. First test object. Finest tick marks on ruler are 1/32 inch. Proton radiograph on right

At first beam a good picture was obtained with the nominal design settings. After some tuning, fig 6 was obtained.

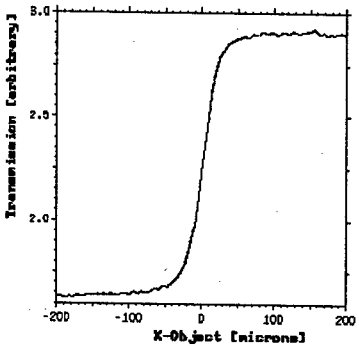

Figure. 7 Profile through edge of a letter

Fig. 7 shows a profile through the edge of a letter. Analysis of this profile indicates an overall resolution of about 17 microns, including the optical system. A finer test object is needed to fully characterize the magnetic resolution of the system, which is expected to be somewhat better.

REFERENCES

[1] C. T. Mottershead and J. D. Zumbro, "Magnetic Optics for Proton Radiography", Proc. 1997 Particle Accelerator Conf, Vancouver 1397 (1997)

[2] G. E. Hogan et al. "Proton Radiography", Proc. 1999 Particle Accelerator Conf, New York 579 (1999)

ANTIMATTER DRIVEN SAIL FOR DEEP SPACE MISSIONS

Gerald P. Jackson, Steven D. Howe
Hbar Technologies LLC, 1275 Roosevelt Road, Suite 103, West Chicago IL 60185-4815, USA

Abstract

The ultimate goal of this project is to identify and investigate an exploration architecture that would allow a light-weight instrument package to be sent to another stellar system. Due to the difficulty inherent in an interstellar mission, we have examined an architecture for a less demanding mission; sending a probe to the Kuiper Belt in a transit time of 10 years. Missions to deep space will require specific impulses greater than 6000 seconds in order to accomplish the mission within the career lifetime of an individual. Only two technologies available to mankind offer such performance; fusion and antimatter. Fusion has proven unattainable despite forty years of research and billion of dollars. Antimatter, alternatively, reacts with uranium 98% of the time in a well-described manner. However, development of a suitable propulsion system based on antimatter has not been shown until now. Our system analysis indicates that a 10 kg instrument payload could be sent to 250 AU in 10 years using 30 milligrams of antihydrogen. In addition, preliminary calculations also show that 17 grams of antihydrogen could send a similar probe to the next star, Alpha Centauri, in 40 years. We have designed a very straightforward system that will produce a variable specific impulse with a maximum of near one million seconds. The concept is one that can be throttled, that can be steered, and that can be demonstrated within the next two years. In this paper we identify the components of the system architecture that will be needed to perform a mission to the Kuiper Belt.

VISION

Sometime around 20 years in the future, humanity will want to send unmanned scientific spacecraft outside of the solar system to the hydrogen wall at the interface between the heliosphere and interstellar medium [1]. At approximately the same distance from the sun are the gravitation lens focal point of the sun and the low-density Kuiper comet belt. Approximately 10-100x further out is the Oort cloud, and yet another 10-100x further away is our nearest stellar neighbor, Alpha Centauri, that is 4.3 light-years away. Figure 1 contains a NASA/JPL slide showing these features on a logarithmic axis.

Based on current trends, the scientific instrumentation for such an unmanned probe is estimated to have a mass of approximately 10 kg. This leaves the spacecraft designers with a goal of creating propulsion and power systems that have masses comparable to the instrumentation. Based on this study, a roadmap toward the design and implementation of low mass systems is conceivable and, given 20 years, practical. In fact, the first stage of funding required to develop this idea has started.

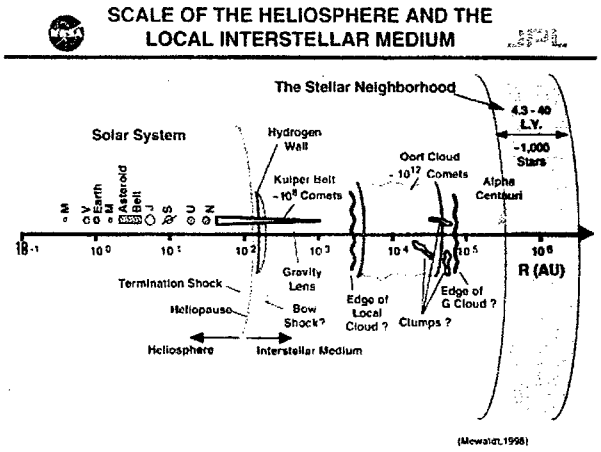

Figure 1: Solar system and interstellar features of intense interest for future scientific unmanned space missions.

SPACECRAFT OVERVIEW

Figure 1 contains a schematic representation of the proposed antimatter driven spacecraft [2]. There are four basic sections of the spacecraft, with the 10 kg instrumentation package at the rear, either attached rigidly to the body of the spacecraft or towed via tether a few kilometers behind and away from the pion and neutron flux from annihilations and fissions occurring at the sail in the front of the spacecraft.

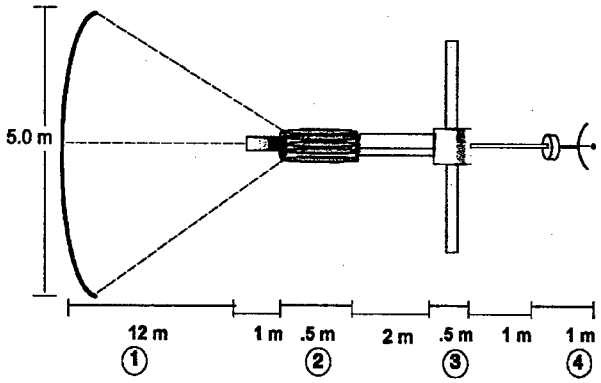

Figure 2: Proposed antimatter driven spacecraft. The primary subsystems are (1) a uranium coated carbon sail, (2) solid H2bar crystal storage units, (3) an antiproton driven electrical power supply, and (4) a 10 kg instrument package.

The basic nuclear physics behind this concept is the fact that antimatter incident on the surface of an uranium foil has a 98% probability of inducing a fission event [3].

0-7803-7738-9/03/$17.00 © 2003 IEEE

In undergoing fission it is found that two fragments of approximately palladium-111 are emitted back-to-back with a total energy of approximately 190 MeV. The velocity of the fission products is 1.39×10^7 m/s and the mass is 1.85×10^{-25} kg/atom. This velocity would equate to a specific impulse of 1.4 million seconds. In addition, there are numerous penetrating particles emitted such as high energy neutrons, gamma rays, and pions.

Imagine a cloud of antihydrogen drifting onto a thin uranium foil. On average, half of the fission fragments will have trajectories outside of the foil. These fragments do nothing other than carry away kinetic energy and reduce the overall energy efficiency of the concept. On the other hand, the other fission fragment enters the foil and is stopped via dE/dx. Because the incoming fission fragment can have any angle within 2π steradians, the forward momentum transfer is on average half of the per-fragment momentum. To stop a fission fragment propagating normal to the foil surface, the surface would have to be approximately 5.5 microns thick. In principle any material can be used as a backing layer to the uranium foil to provide this stopping power. Note that toward the end of life of the foil, its thickness will be much reduced and a high-strength, high melting point material is desired. We have chosen carbon for these reasons (fig. 3). A minimum thickness of 15 microns is required for dE/dx.

One possible enhancement might be to accelerate the incident antiprotons toward the uranium surface such that the stopping range of the antiprotons is well within the surface. It has been hypothesized that an annihilation event below the surface may create a cloud of ejecta which would increase the momentum transfer into the sail. An antiproton kinetic energy of 100 keV, easily created by electrostatically biasing the sail with respect to the antihydrogen container, would stop the antiprotons approximately 355 nm below the surface. The disadvantage of this concept is that more of the uranium in the sail is consumed, forcing the thickness for a mission to the Kuiper belt of 293 microns. Assuming a 5 m diameter sail, this gives the sail a mass of slightly

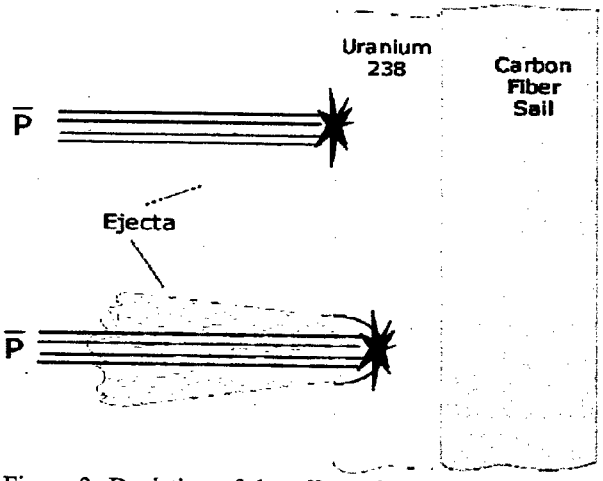

Figure 3: Depiction of the effect of annihilations on the sail as a function of incident antiproton kinetic energy.

over 100 kg. Though significantly heavier than the mass of the instrumentation, this is much lower than traditional ideas.

The advantage of this scenario is that it reduces the specific impulse of the drive, increasing the energy efficiency of the concept and reducing the number of antiprotons required. Figure 4 contains the results of a calculation showing the change in antiproton consumption as a function of the number of un-fissioned uranium atoms ejected per antiproton annihilation (N_{at}). The experimental characterization of this mass ejecta effect, if existent, is the focus of the next phase of the experimental development effort for this technology.

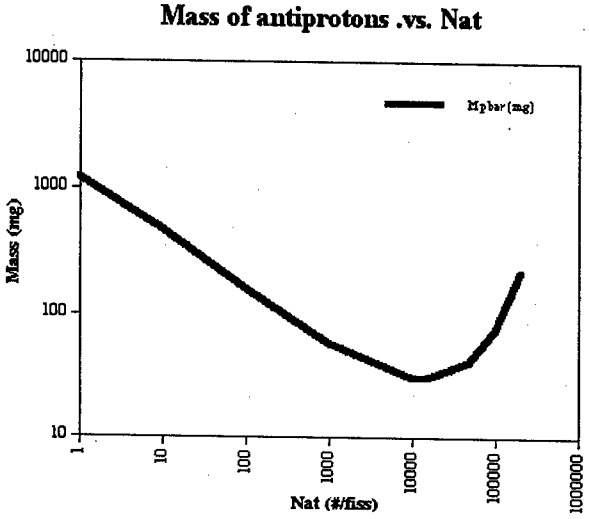

Figure 4: Calculation of the effect of the stored antimatter mass required for this mission scenario as a function of the number of uranium atoms ejected per annihilation.

Because the number of antiprotons required for this mission is roughly 2×10^{22}, space charge forces prevent their storage in that form. At a minimum, antihydrogen molecules must be formed. Because of the vapor pressure of solid hydrogen, very low cryogenic temperatures must be preserved.

The antihydrogen storage system is held 12 m away from the sail via four tethers. The storage system is envisioned to be an array of small chips resembling integrated circuit chips. Each chip, however, is not an electronic unit but contains a series of tunnels etched in a silicon substrate. Each tunnel is a sequence of electrodes. Each electrode pair forms a cell that contains a single pellet of solid antihydrogen. The operational scenario is similar to that of CCD chips, wherein charge is transported from one well to the next in a bucket-brigade manner. Each pellet holds approximately 10^{15} antihydrogen atoms and a charge of roughly 10^{-11} coulombs. Each tunnel holds 67 cells. There are 100 tunnels per 4 cm long chip. Thus, each chip holds 1.6×10^{19} antihydrogen atoms. There are roughly 2000 chips in the storage assembly. Total number of antihydrogen atoms is 1.8×10^{22} or 30.45 milligrams. The entire mass of the storage unit is about 9 kg.

The generation of onboard power is also accomplished using antiprotons. The industry-standard radioisotope thermoelectric generator used in the Voyager through Cassini missions has a specific mass at 194 kg/kw. We assumed a power requirement of 400 W based on the specifications for the Voyager spacecraft [4]. Again using antiproton annihilation on uranium nuclei, we now use the trajectory of fission fragments through a scintillator material, wavelength matched to photovoltaics, to generate power. The overall efficiency of such a unit is estimated to be 4.4%. Thus, around $2x10^{14}$ antiprotons per second are needed for the 400 W of electrical power. Dominated by the demands of signal transmissions to Earth, the power is generated on demand when communications back to Earth are desired. A waste-heat radiator is composed of two sheets, diametrically opposed, with the edges facing the sail. The sheets, designed as fins with a roughly triangular cross section, have a total surface area of 3.5 m^2. The radiator temperature is 620 C. The power unit mass is around 6.4 kg. Thus, the specific mass of the unit is 16 kg/kw.

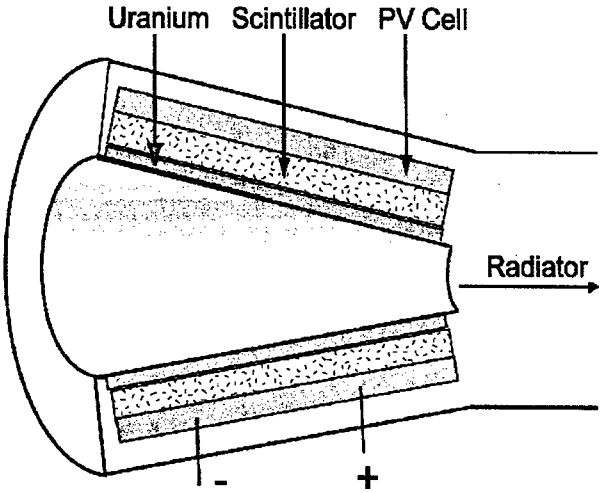

Figure 5: Schematic representation of the antiproton-based power generation system envisioned for anticipated missions. Instead of generating thrust, the fission fragments excite photons in the scintillator wavelength matched to the photovoltaic cells.

ANTIPROTON PRODUCTION

At present the Fermi National Accelerator Laboratory is capable of producing 10^{11} antiprotons per hour for a traditional total of 4450 hours per year. If every antiproton generated in a year was formed into antihydrogen and stored on board such an unmanned spacecraft, roughly $4.5x10^{14}$ antihydrogen atoms would be stored. This is enough to generate 400 W for two seconds, or 1 part in 40 million of the total antihydrogen inventory. At the present time, enough antiprotons are generated to perform millisecond type thrust tests. In order to reach the inventories of antiprotons needed for missions such as the one envisioned in this paper, it will be necessary to greatly increase the rate of antiproton production.

Basically, there are two ways to increase the antiproton production rate. The first is to put more protons on the antiproton production target. The limitations to this method are heating of the target and the cost of accelerating antiprotons. The second way is to increase the efficiency of antiproton production. At present, the Fermi production efficiency is 15 antiprotons for every million protons on target. An internal memo [5] suggests that an efficiency of even 1% is possible if a thin target is used and protons pass through the target repeatedly.

The present method of antiproton capture and cooling is optimized for the production of low emittance beams for use in colliding particle beam physics. Removing the resultant longitudinal and transverse emittance limitation imposed by this usage, a modified accelerator complex that decelerates and captures antiprotons without intermediate cooling can be readily envisioned. The design of such an accelerator complex is presently underway. In all, an increase in antiproton production rate of approximately 10,000x is envisioned in 10 years.

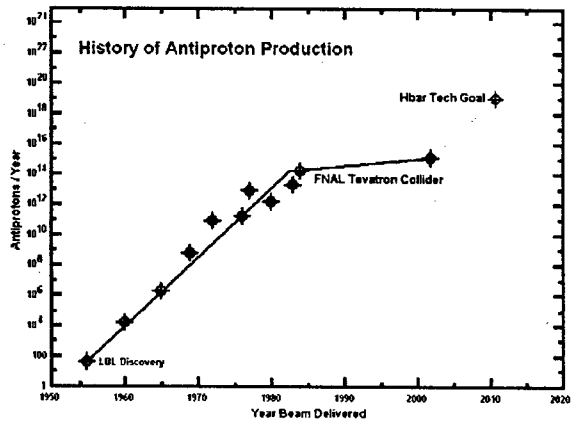

Figure 6: History and projection of record global antiproton production rates. The blue line in the center of the graph represents the recent Fermi National Accelerator Laboratory (FNAL) increases in production over the course of almost 20 years. The green line to the right indicates the goal of Hbar Technologies, LLC.

ACKNOWLEDGEMENTS

This work was supported by the NASA institute for Advanced Concepts (NIAC) [www.niac.usra.edu].

REFERENCES

[1] Astrophys. J. **591**, L61 (2003).
[2] S.Howe and G.Jackson, "NIAC Phase I Final Progress Report: Antimatter Driven Sail for Deep Space Missions", http://niac.usra.edu/files/library/fellows_mtg/oct02_mtg/pdf/740Howe.pdf.
[3] J.P.Bocquet, et.al., "Prompt Fission Induced by Antiproton Annihilation at Rest on Heavy Nuclei", Hadrons and Nuclei **342**, 183-189 (1992).
[4] http://nssdc.gsfc.nasa.gov/planetary/voyager.html.
[5] N. Mokhov and A.VanGinneken, "Increasing Antiproton Yields Via Recirculating Beam Targeting", Internal Fermilab technical memo FN-621, 1994.

FACILITIES FOR INDUSTRIAL CUSTOMERS AT THE DARESBURY SYNCHROTRON RADIATION SOURCE (SRS)

E. Towns-Andrews, E.J. MacLean*, CCLRC Daresbury Laboratory, Warrington, Cheshire, UK

Abstract

The Daresbury Synchrotron Radiation Source (SRS) [1] provides state-of-the-art analytical techniques from infrared to hard X-ray wavelengths. The unique characteristics of synchrotron radiation are ideal for analytical problems that require high spatial or temporal resolution or problems that are simply intractable using conventional instruments.

Here we outline the approach taken at the SRS towards industrial customers. We provide practical examples and case histories of how industrial processes have been improved in a diverse range of business sectors.

INTRODUCTION

An increasing number of large scale facilities exists worldwide, which have been traditionally used by universities and higher education institutions for pure research and development. In recognition of the needs of commercial customers, Daresbury Laboratory established *DARTS* (Daresbury Analytical Research and Technology Service) [2]. *DARTS* offers unique services which can be tailored to the needs of the customer, allowing access to synchrotron analytical facilities and also the significant expertise and knowledge of staff on site. The analytical portfolio offered by the facility encompasses imaging, spectroscopic and structural characterisation techniques. *DARTS* also has links to conventional analytical houses for standard analyses should these be required prior to use of the synchrotron. The nature of problems and issues solved by *DARTS* is varied and includes: investigations of product failure and non-conformance, manufacturing issues, basic R&D and information used in expert witness legal cases.

MARKETING STRATEGY

As a means of focusing the marketing activity of *DARTS*, the UK Department of Trade & Industry R&D Scoreboard [3] was used to identify those key sectors with large spend in research and development. The areas identified were: pharmaceuticals and healthcare, consumer products and food, chemicals and specialities, oils and polymers and aerospace and defence. It should be noted that this does not preclude the option of doing work for organisations based in other market sectors.

DARTS has also ensured that all intellectual property rights arising out of a data collection on behalf of a customer belong to the customer. If a pharmaceutical company, for example, is developing a new drug it is vital for them that their intellectual property rights are irrefutable.

Our final strategy has been to appoint dedicated customer relations staff to ensure that the process of accessing the beamtime for industry is as straightforward as possible. By creating the one-stop shop there is no longer any need for customers to be dealing with several different departments at Daresbury for contracts, experimental risk assessments, accommodation *etc.*

TECHNICAL APPLICATIONS

As described above, *DARTS* is actively marketing to five key market sectors. Examples of the types of experiment done in each of these are now given.

Pharmaceuticals & Healthcare

Pharmaceutical companies traditionally take a multidisciplinary approach to their research and hence use a variety of the techniques available on the SRS. Synchrotron X-ray diffraction has been used extensively in the structural studies of small molecules, which are potential drug candidates, and in their complexes with biological macromolecules. By using a combination of high-resolution powder diffraction, single crystal diffraction and protein crystallography, researchers from these companies have the potential for studying systems in depth at the same location.

A common technique used is single crystal X-ray diffraction for determining the molecular structure of drug molecules. Generally, single crystals can be grown that are large enough to use readily available laboratory-based X-ray instruments. However, in some cases this is not possible and Station 9.8 on the SRS has opened up a new route to obtaining crystal structures [4]. By harnessing the power of the X-rays produced by the synchrotron, researchers can look at increasingly smaller crystals. The smallest crystal currently used for a successful structure determination is 5 x 5 x 5 μm^3 [5].

A recent example of a complex drug structure solved by *DARTS* was in work for Organon Laboratories [6]. The drug in question is a steroid, rocuronium bromide, which is used as a neuromuscular blocker during surgery under anaesthetic. The action of the drug is reversed by subsequent injection of a cyclodextrin that encapsulates the steroid molecule, thus reversing its blocking effect. Conventional analytical techniques had shown that a complex was formed but not the exact nature of it.

Due to the complexity of the structure involved and the small size of the crystals, the structure of the complex

*darts@dl.ac.uk

0-7803-7738-9/03/$17.00 © 2003 IEEE

could not be solved from data obtained using conventional lab equipment because the diffraction was too weak. Station 9.8 allowed sufficient data to be collected to solve the structure but, even once the data were collected, the structure solution was less than routine. However, by using the wide knowledge base at Daresbury, techniques from protein crystallography were used to solve the structure. The structure shown in Figure 1 illustrates how the cyclodextrin binds the rocuronium as predicted.

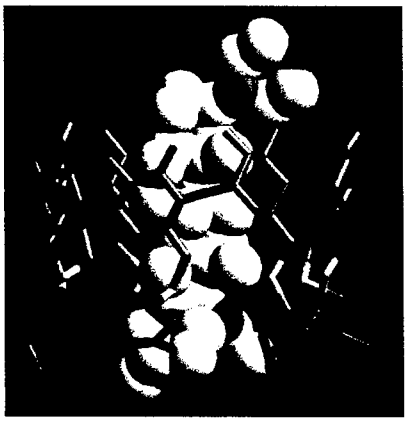

Figure 1: The complex of rocuronium bromide and a cyclodextrin

Preliminary trials have shown the cyclodextrin to reverse the effects of the neuromuscular blocker twice as fast as conventional treatments with none of the usual side effects. Human clinical trials are now taking place.

The second main area of interest for the pharmaceutical industry is determination of protein structure. Since many proteins are intrinsically associated with human health and disease, their structure can be key in developing new pharmaceuticals and drug therapies. The most common technique for obtaining precise information about the arrangement of atoms within a protein is X-ray crystallography. In many cases, conventional laboratory facilities cannot produce data of sufficient quality to resolve the structure of proteins. This is due to their complex characteristics such as low scattering power, poor ordering, crystal lifetime and susceptibility to radiation damage. Examples of non-proprietary work carried out at the SRS include, the anthrax lethal factor [7] and the structure of F1-ATPase [8] which was a key contributor to the Nobel Prize for Chemistry in 1997.

Where it is not possible to crystallise a particular protein, synchrotron UV circular dichroism (CD) can be used to determine secondary structure content. It has significant advantages over laboratory-based instruments including reduced data collection times, higher signal to noise ratios and extended wavelength resolution. Perhaps more importantly, CD can be used to study dynamic processes such as protein folding [9, 10] and misfolding – the basis of diseases such as Alzheimer's and bovine spongiform encephalitis (BSE). For pharmaceutical companies the opportunity to study drug binding in real time and effects on protein secondary structure offers deeper understanding of potential drug candidates.

Chemicals & Specialities

The use of pigments is widespread and includes coating technology, paints, inks and plastic coloration as well as more sophisticated technologies such as new information storage systems.

An important contributor to the colour of a pigment is the arrangement of the molecules within the pigment itself and, hence, to fully understand the colour properties of a pigment it is vital to know the crystal structure. Since a necessary property of a useful pigment is its small particle size, traditional approaches to obtaining crystal structures are not always possible. This is where the properties of synchrotron radiation can be exploited.

Solution of complex structures from powder diffraction data is a relatively new technique compared with single crystal structure solution. While it is possible to solve structures from powder diffraction methods using data collected on standard laboratory based diffractometers, the low symmetry of many organic materials can make analysis of the patterns troublesome due to severe peak overlap. The high resolution data obtainable using the SRS can sometimes overcome this problem.

One example of a pigment material studied using powder diffraction is DPP-Boc, a derivative of a class of pigments known as DPPs [11]. These are a relatively new class of organic pigments developed in the 1980s and 1990s by Ciba Specialty Chemicals. DPP pigments have found wide-ranging commercial use because of the range of colours possible by simply varying different substituent groups within the molecule. The structure of DPP-Boc was intractable from laboratory data, as the powder diffraction pattern could not be indexed. However, the higher resolution data from the synchrotron allowed successful indexing and subsequent structure solution from powder data using the Monte Carlo method [12].

Whilst powder diffraction is an important technique for investigating long range order in systems such as the pigments described above, other customers in this sector are more interested in the ability to study local order in development of their products. Understanding the near neighbour environment of active sites in catalytic systems is important and X-ray absorption spectroscopy is routinely used to study systems such as zeolites and electrode surfaces.

The use of *in situ* combined techniques for observing development of long range and short range order in real time has proved very attractive for understanding catalyst preparation. For example, non-proprietary research into iron phosphate catalysts has successfully used combined X-ray diffraction and quick scanning X-ray absorption spectroscopy at the SRS [13].

Aerospace & Defence

Non-destructive testing of materials is an area of huge importance to industries such as automotive and aerospace. The non-conformance of materials to required quality and/or safety specifications can lead to large scale manufacturing production lines being brought to a halt while the problem is resolved. Representatives from these industries have employed the rapid turn-round service *via DARTS* to investigate component failures using a variety of specialist techniques. Novel X-ray imaging, surface and diffraction methods allow non-destructive testing of specimens which ensure that any observed effects have not been introduced during sample preparation. The versatility of these methods can be extended to many types of materials including metals, synthetic polymers and natural products.

Recent work at the SRS [14] has shown that fast residual stress mapping can be achieved in deformed plate materials using energy-dispersive transmission X-ray diffraction. Discrimination by energy rather than angle allows *in situ* measurements to be made without having to consider complications inherent in angle scanning such as low penetration, variable sample path lengths and awkward sample shapes. By using orthogonal scanning, the results have shown that a spatial resolution may be achieved of 100 μm perpendicular to and of 1 mm along the beam for a number of different materials including a 6 x 3 x 100 mm two-phase Ti/Al/V aerospace alloy.

Having demonstrated the ability to optimise the SRS facility for this type of study, *DARTS* now offers fast residual stress mapping as a service for suitable materials.

Consumer Products & Food

Companies in this sector manufacture products as diverse as food, cosmetics, detergents and healthcare products which must perform consistently to consumer expectations. Understanding product behaviour at the most basic level, for example the phase behaviour of products with regard to storage and processing conditions, is a crucial requirement for manufacturers. Some systems studied by *DARTS* include oils, detergents, foodstuffs, personal hygiene products and dermatological creams.

Crystallisation is one of the dominant techniques used by the chemical and food industries for particle separation and purification. However, there is still a limited understanding of the detailed mechanisms associated with the formation of crystalline and amorphous solids from liquid mother phases, be they melts or solutions. In chocolate production the solidification process requires careful control because it significantly influences both the rheological properties of chocolate such as viscosity and adhesion and the physical properties of the end product, which are vital in determining the acceptability of a product in the marketplace.

Collaborative work between Heriot-Watt University and the research and manufacturing arms of Cadbury Ltd. [15] has used the SRS for small angle X-ray scattering measurements using an environmental shear stress cell for *in situ* studies.

Results indicate that the effect of shearing on the crystallisation of cocoa butter is significant in determining which of six possible polymorphs develops. Shearing induces form V formation from the very outset, and this is the form needed to produce good quality chocolate with the desired rheological and physical properties. In the case of a stagnant run, form V is never present. Thus the production of good quality chocolate under these conditions would be virtually impossible.

This methodology could have many other applications well beyond confectionery, not merely in the food industry but throughout chemical industry generally, including pharmaceuticals, where the final physical form and properties of a product are governed by processing and production conditions.

Whilst synchrotron IR microspectroscopy is emerging as a powerful analytical tool for many industrial customers, the high spatial resolution and significantly improved signal to noise ratios achievable over conventional globar systems is being exploited by a number of *DARTS* customers in this particular sector. The chemical mapping of hair cross sections [16] clearly demonstrates the power of this technique for evaluating the effects of hair care products which are under development and also for forensic science. In addition, non-proprietary work into the study of extruded amylopectin-gelatin blends [17] and oil distribution in fried foods [18] has demonstrated the potential of this technique in the food industry

Oils & Polymers

Work conducted in this sector covers a wide range of applications from development of novel catalysts to formulation of motor oils and production of packaging materials.

Polymer film manufacturer, UCB Films, requested evaluation of a coated polypropylene film used in food packaging, which degraded over a period of time resulting in increased opacity of the material when stored. The problem appeared to be related to the processing conditions under which the films had been manufactured.

DARTS utilised a multitechnique approach to this problem and employed grazing incidence X-ray diffraction (GIXD) and SAXS to investigate a number of polymer films from different processing batches. Figure 2 shows the GIXD data obtained from three samples.

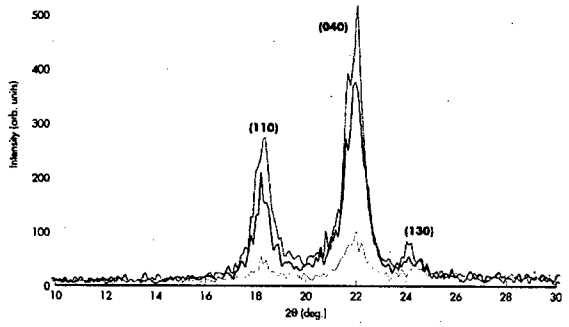

Figure 2 GIXD data of a series of polypropylene films

GIXD provided data from the 0.6 μm co-polymer coating. Peaks observed corresponded exactly to those expected for polypropylene. Therefore, despite the presence of up to 10 % ethylene in the copolymer, the molecular arrangement of polypropylene is being adopted in the crystallites of the coating layers. The peaks are sharper in the case of the clear films, implying a higher level of molecular order within the crystallites. SAXS data from the films indicated that the average particle size in the bulk material was approximately 200 Å in each case. On-line processing facilities at the SRS have enabled other *DARTS* customers to study in real time the effects of varying processing conditions on the properties of polymer products [19, 20]

In the manufacture of efficient and reliable engine oils it is important to understand and be able to control a multitude of complex chemical and physical processes. Examples of these processes include the interactions between different components of the engine oil and the effects of oil viscosity.

The role of the detergent in crank case lubricants is to provide a soluble base within the formulated engine oil and to neutralise acidic products which are introduced into the lubricant. Acidic products may originate from the blow-by gases produced during fuel combustion. Organic acids are also formed *in situ* in the crankcase through oxidation and degradation of the lubricant. If these acids are not rapidly neutralised, it may lead to corrosion within the crankcase.

Characterising the nature of the detergent additive, and hence its role in acid neutralisation, has proved difficult using standard analytical techniques. However, SAXS is ideally suited to this task since it provides a direct means of probing the structure of the detergent additive for different compositions of the oil base. Typically the calcium and magnesium detergent particles are 2050 Å in size, a range that is easily accommodated by the SAXS method. In addition to providing information about particle size, SAXS also enables the particle shape and size distributions to be determined.

Infineum (a joint venture between Shell and Exxon) has used *DARTS* to access SAXS facilities at the SRS [21] to characterise detergent additives in motor oil samples. This has allowed quantification of process changes, control of rheological properties and performance characteristics of the finished product and prediction of the various interactions that can occur between detergent molecules and other additives in the finished oil.

CONCLUSIONS

The uniqueness of the *DARTS* service as a customer-facing support team is achieved by a dedicated, trained team of staff drawn from all areas of the Synchrotron Radiation Department. This has enabled the expansion of the portfolio of techniques and target sectors as described above. This approach allows UK and international industry to access the expertise available at Daresbury in a cost-effective manner – they do not all need to have synchrotron experts in their own labs. Of course, should industrial scientists wish to do their own experiments, this access mechanism is also available through *DARTS*. We offer a range of access levels from beamtime only to "you send the sample, we send the results". A combination of these levels has sometimes been the most convenient way for a company to use the service.

REFERENCES

[1] http://srs.ac.uk/srs
[2] http://www.darts.ac.uk
[3] http://www.innovation.gov.uk/projects/rd_scoreboard/introfr.html
[4] R.J. Cernik, W. Clegg, C.R.A. Catlow, G. Bushnell-Wye, J.V. Flaherty, G.N. Greaves, I. Burrows, D.J. Taylor, S.J. Teat and M. Hamichi, J. Synch. Rad. 4 (1997) 279; W. Clegg, M.R.J. Elsegood, S.J. Teat, C. Redshaw and V.C. Gibson, J. Chem. Soc., Dalton Trans. (1998) 3037
[5] M. Wang, A. Mar and E.J. MacLean, J. Solid State Chem. in press (2003)
[6] A. Bom, M. Bradley, K. Cameron, J.K. Clark, J. van Egmond, H. Feilden, E.J. MacLean, A.W. Muir, R. Palin, D.C. Rees and M.-Q. Zhang, Angew. Chemie, Intl. Ed. Engl. 41 (2002) 266.
[7] A.D. Pannifer, T.Y. Wong, R. Schwarzenbacher, M. Renatus, C. Petosa, J. Bienkowska, D.B. Lacy, R.J. Collier, S. Park, S.H. Leppla, P. Hanna, and R.C. Liddington, Nature, 414 (2001) 229
[8] J-P. Abrahams, A.G.W. Leslie, R. Lutter and J.E. Walker Nature 370 (1994) 621
[9] B.A. Wallace, J. Synch. Rad. 7 (2000) 289
[10] D.T. Clarke, A.J. Doig, B.J. Stapeley and G.R. Jones, Proc. Natl. Acad. Sci. USA 96 (1999) 7232
[11] E.J. MacLean, M. Tremayne, B.M. Kariuki, K.D.M. Harris, A.F.M. Iqbal and Z. Hao, J. Chem. Soc., Perkin Trans. 2 (2000) 1513
[12] K.D.M. Harris, M. Tremayne, P. Lightfoot and P.G. Bruce J. Am. Chem. Soc. 116 (1994) 3543
[13] A.M. Beale and G. Sankar, J. Mater. Chem. 12 (2002) 3064
[14] A.M. Korsunsky, S.P. Collins, R.A. Owen, M.R. Daymond, S. Achtioui and K.E. James, J. Synch. Rad. 9 (2002) 77

[15] S.D. MacMillan, K.J. Roberts, A. Rossi, M.A. Wells, M.C. Polgreen and I.H. Smith, Cryst. Growth Design 2 (2002) 221

[16] F. Briki, B. Busson, L. Kreplak, P. Dumas and J. Doucet, Cell. Mol. Biol 46 (2000) 1005

[17] Z. Mousia, I.A. Farhat, M. Pearson, M.A. Chesters and J.R. Mitchell, Biopolymers (Biospectroscopy) 62 (2001) 208

[18] P. Bouchon, P. Hollins, M. Pearson, D.L. Pyle and M.J. Tobin, Journal of Food Science 66 (2001) 918

[19] D.J. Blundell, G. Eeckhaut, W. Fuller, A. Mahendrasingam and C. Martin, Polymer 43 (2002) 5197

[20] N.J. Terrill, P.A. Fairclough, E. Towns-Andrews, B.U. Komanschek, R.J. Young and A.J. Ryan, Polymer 39 (1998) 238

[21] J. Galsworthy, S. Hammond and D. Hone, Current Opinion in Colloid and Interface Science 5 (2000) 27

GAMMA-RAY COMPUTERIZED TOMOGRAPHY USING 10 MEV LASER-COMPTON PHOTON BEAM

#Hiroyuki Toyokawa, Tomohisa Mikado, Hiroshi Ogawa, Norihiro Sei, Kawakatsu Yamada, Masato Yasumoto, AIST, Tsukuba, Ibaraki 3058568, Japan
Hideaki Ohgaki, IAE, Kyoto University, Uji, Kyoto 6110011, Japan
Nobutada Aoki, Noriyasu Kobayashi, TOSHIBA PIC, Yokohama, Kanagawa 2300045, Japan

Abstract

We have developed a prototype high energy gamma-ray CT system for nondestructive inspection of heavy industrial products using laser-Compton photon beam, which was generated with an 800 MeV electron storage ring, TERAS, of AIST-Tsukuba and with an intense laser light source. A description of the prototype system and experimental results of CT imaging are presented.

INTRODUCTION

X-ray radiography is not only used as medical diagnosis tools, but also for industrial purposes, such as nondestructive inspection of industrial products. X-ray Computed Tomography (CT) is one of the most common and powerful tools for these applications. If the X-ray energy is sufficiently high, as high as that of the gamma-ray energy (typically, higher than a few MeV), the X-ray penetrates concretes and metals. High energy photon radiography is, then, a useful tool for a nondestructive inspection of bulk materials and metal die-casts. It is especially useful for an engineering process, so called the reverse engineering, which is one of the methods to improve the efficiency for a development of the industrial products, reducing the time to make various computer-aided design models.

Photons with the energies about a few MeV are useful for the inspection of materials with high atomic numbers (hereafter, high-Z materials), such as iron, copper and lead, because the total attenuation coefficient [1] is minimum around these energies. The attenuation coefficients for lighter materials, or low-Z materials, such as water, tissues and concrete, decrease with increasing photon energy, and are almost constant above 10 MeV. Radiography using photons over a few MeV is, then, almost free from the spectrum hardening effect and the metal artifact, and is useful for the inspection of various industrial products.

Laser Compton scattering (LCS) is one of the techniques to produce high energy intense photon beam [2]. Because the angular spread of the LCS photons is so small, on the order of a few mrad, that high resolution imaging of high-Z materials can be possible. One can obtain photons with good directionality and with narrow spectrum width, at the same time, by putting a collimator along the photon beam line, because the energy of the scattered-off photons via Compton scattering depends on the scattered angle, θ_2, as follows:

$$E_\gamma = \frac{E_L(1-\beta Cos[\theta_1])}{1-\beta Cos[\theta_2]+\frac{E_L(1-\beta Cos[\theta_2-\theta_1])}{E_e}}$$

$$where \qquad \beta=\sqrt{1-\gamma^2},\ \ \gamma=\frac{E_e}{0.511}$$

where E_γ, E_L and E_e stand for the energies of a LCS photon, a laser quantum and an electron, respectively, in MeV. θ_1 and θ_2 are the angles of the laser quantum before and after the Compton scattering, measured with respect to the motion of direction of the electron, where θ_1 becomes π in the head-on configuration.

Figure 1 shows the energy of a scattered photon as a function of the scattering angle, θ_2, assuming the head-on collision ($\theta_1 = \pi$) of a 760 MeV electron and a 1064 nm laser quantum, calculated from the Klein-Nishina formula. It is understood that energy spread of a few % can be obtained by confining the angular divergence in a few part of 10 mrad.

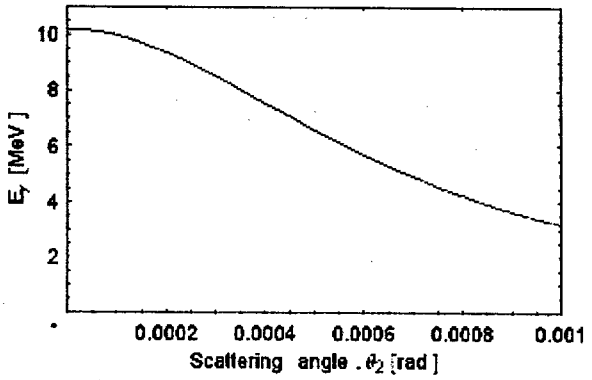

Figure 1: Energy of the 1064 nm laser quantum scattered via the Compton scattering with the 760 MeV electrons.

EXPERIMENT

Description of the experimental setup

We have been developing the LCS photon radiography and CT systems [3, 4] at the LCS photon facility of National Institute of Advanced Industrial Science and Technology (AIST) at Tsukuba [5, 6], and installed a prototype CT system, recently. The photon facility serves 1 - 40 MeV quasi-monochromatic and energy-tunable photon beams of up to 10^6 photons cm^{-2} s^{-1} using the 300 - 800 MeV electron storage ring, TERAS [7]. Recent experiment showed that the spatial resolution of the high

h.toyokawa@aist.go.jp; visiting researcher from AIST. Current contact, TJNAF, Newport News, VA 23606, USA.

0-7803-7738-9/03/$17.00 © 2003 IEEE

energy radiography system using 10 MeV LCS photon beam was better than 1 mm [4].

The CT experiments were done at the LCS-3 beam line of AIST-LCS photon facility. We used 10 MeV LCS photon beam in the experiment using the commercially-available Nd:YVO_4 laser (SPECTRA-PHYSICS, Millennia IR, TEM00 CW 10W).

Figure 2 shows a schematic view of the LCS-3 beam line of TERAS. The photon beam is generated via the Compton scattering at the center of one of the straight sections of TERAS. The photons go along with the electrons that are swept away at one of the bending magnets of TERAS downstream of the collision point, and go straight through the laser mirror and penetrate it losing negligible numbers of photons. The photon beam is transported about 12 m in the air to the experimental room. There is a lead collimator of inner diameter of 2.8 mm and thickness of 100 mm along the photon beam line. The role of this collimator is to roughly shape the energy spectrum and the beam profile of the LCS photons, and also to suppress the low-energy background photons, which are mainly produced from the bremsstrahlung of the relativistic electrons colliding with the residual gas molecules in the vacuum chamber. The beam divergence and the spot size at the sample, in this configuration, are approximately 0.2 mrad in half angle and 4.5 mm in diameter, respectively.

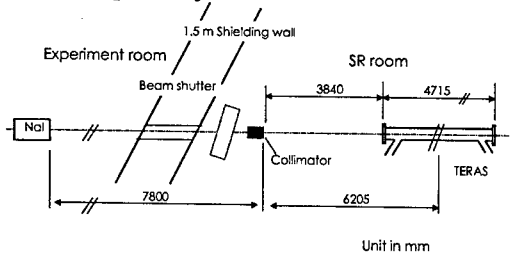

Figure 2: Schematic drawing of the LCS-3 beam line of AIST-LCS facility.

Figure 3 shows a schematic drawing of the hardware components for the prototype CT system installed in the LCS-3 beam line. Because the diameter and the divergence of the photon beam were very small, we designed the CT system as the 1st generation style. The distance of the sample object from the photon source (laser-electron collision point) is about 12 m. The sample object was put on a PC-controlled CT stage, which had three axes of motion; rotation, horizontal and vertical with respect to the photon beam. A large NaI(Tl) scintillation detector (8in x 12in) measures the energy and the intensity of the photons. It almost fully absorbs the photons with the energies up to 40 MeV. The 2nd collimator, which was placed behind the sample object not only defined the spectrum width and spatial resolution, but also reduced the background photons that were scattered-off from the sample object with small angles via the Compton scattering. We used a collimator of 2 mm inner diameter. The resulting beam diameter and the divergence are considered to be 1.8 mm and 80 μrad, respectively, at the sample position.

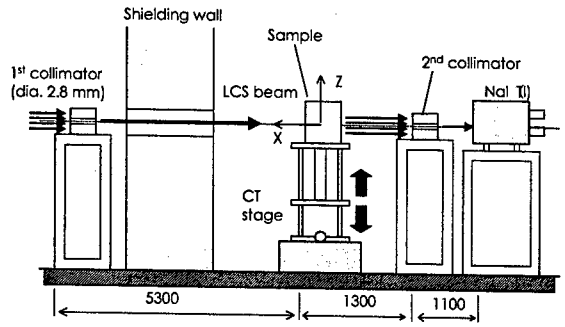

Figure 3: Schematic drawing of the prototype CT system.

Sample object

We chose the RF tetrode tube "TH571A" (THOMSON TUBES ELECTRONIQUES) as a sample object for the CT experiment, because it consisted of high-Z and low-Z materials and its inside structures were invisible from outside. The anode was put inside the iron vessel, and the cathode and grid structures were inside the ceramics insulator. This tube is usually used as a main amplifier for the RF power source of TERAS.

Figure 4 shows the radiograph of the sample object around the electrodes [4]. The metal grids and cathode are clearly seen through the ceramic insulator. Because we were interested in the structure of the electrode, we decided to take the CT images around these regions. The solid lines indicate the slice positions (1 ~ 8), which were numbered sequentially from bottom to top. The slice thickness and the scanned area were 1 mm and 100 x 100 mm^2, respectively.

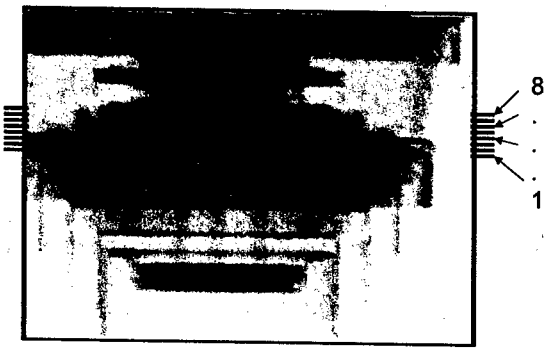

Figure 4: Radiograph around the electrode of the TH571A tetrode tube.

Measurement results

It took about 1 hour to scan each of the slices. The measurements were done as follows:

1. Rotating the sample object and counting the number of photons within each of the preset angle (3.6 degree, for example) until the object turns 360 degree (which results in 100 angular projection points, for 3.6 degrees increment).
2. Moving horizontally a preset step (1 mm, for example).
3. Repeating the process 1 and 2, until the total travel distance reaches the preset value (100 mm, for example).

4. Completion of a measurement for one slice. Then, moving vertically, and repeating the process 1 – 3 for another slice.

Figures 5 show the reconstructed CT images. We can see the cross-sectional views of inside the sample object. The numbers on the top of the images show the vertical positions, or the slice numbers shown in fig. 4. The CT images were reconstructed with the filtered back-projection method, off-line. The count-rate data were Fourier transformed using the Fast Fourier Transformation (FFT) algorithm, and convoluted with the filtering function. We used a step function with the highest cutoff frequency at the Nyquist frequency as the filtering function. The data in the Fourier regime were, then, inversely FFT followed by the coordinate exchange according to the standard tomography method.

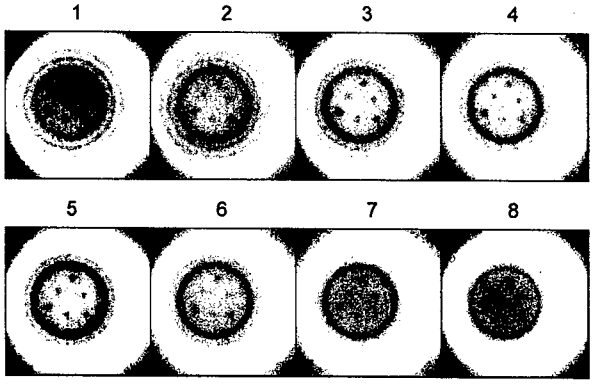

Figure 5: Cross-sectional images of the sample object obtained with the CT using the 10 MeV LCS photon beam.

DISCUSSION

The present results obtained with the prototype CT system showed that we were able to build the high energy photon CT system for the inspection of bulky industrial products. However, we should improve the present CT system in accordance with the following points to meet with the criteria for a practical use:

1. Reduction of the data acquisition time
2. Optimization of the spatial resolution

The first point is critical, because the current CT system requires 1 hour to obtain an image data for 100 mm x 100 mm area. Several ideas to reduce the measurement time have been discussed. Some of them are to increase the photon intensity, and the other ones are to upgrade the system to the second-generation CT system with fan-beam configuration, using multiple detector system. We are interested in how to make the LCS photon beam in a fan-beam configuration, and are preparing for the feasibility study. The second point is also important. Because the space for the CT system installation is limited, some of the optimal geometric conditions to give the best spatial resolution may not be achieved. So, we should evaluate the spatial resolution of the present CT system in the current configuration, first, and, then, try to optimize the system to give the best performance.

SUMMARY

The high energy photon radiography and CT systems using the 10 MeV laser Compton photon beam of AIST-LCS facility has been developed, and the first CT experiment was done. The sample object was the RF tetrode tube made of iron, copper, ceramics, and so on. We were able to obtain the cross-sectional images of the sample object.

ACKNOWLEGEMENTS

We would like to thank Nikolitsa Merminga of Jefferson Lab for her discussions and encouragement on this work. This study was financially supported by the Budget for Nuclear Research of the Ministry of Education, Culture, Sports, Science and Technology of Japan, based on the screening and counseling by the Atomic Energy Commission of Japan.

REFERENCES

[1] J. H. Hubbell, "Photon Cross Sections, Attenuation Coefficients, and Energy Absorption Coefficients from 10 keV to 100 GeV", NSRDS-NBS 29 (1969).
[2] R. H. Milburn, Phys. Rev. Lett. 10(3), 75-77 (1963).
[3] H. Toyokawa, H. Ohgaki, and T. Shima, IEEE Trans. Nucl. Sci. 49(1), 182-187 (2002).
[4] H. Toyokawa, H. Ohgaki, T. Mikado, K.Yamada, Rev. Sci. Instr. 73(9), 3358-3362 (2002).
[5] H. Ohgaki, H. Toyokawa, K. Kudo, N. Takeda, and T. Yamazaki, Nucl. Instr. and Meth. in Phys. Res. A455, 54-59 (2000).
[6] T. Yamazaki, T. Noguchi, S. Sugiyama, T. Mikado, M. Chiwaki, and T. Tomimasu, IEEE Trans. Nucl. Sci. 32(5), 3406-3409 (1985).
[7] T. Tomimasu, T. Noguchi, S. Sugiyama, T. Yamazaki, T. Mikado, and M. Chiwaki, IEEE Trans. Nucl. Sci.30(4), 3133-3135 (1983)

SIMULATION OF ACCELERATED ELECTRON SPECTRA IN LASER WAKEFIELD ACCELERATORS*

R.F. Hubbard,# D.F. Gordon, T.G. Jones, J.R. Peñano, P. Sprangle, A. Ting
Plasma Physics Division, Naval Research Laboratory, Washington, DC 20375, USA
B. Hafizi, A. Zigler, Icarus Research, Inc., Bethesda, MD 20824-0780, USA
D. Kaganovich, LET Corp., Washington, DC 20007,USA

Abstract

The generation of high quality electron beams in a laser wakefield accelerator (LWFA) is generally thought to require phased injection of an ultrashort electron bunch. However, simulations have shown that longer bunch, unphased injection may also produce high quality, short electron bunches if the injection energy is properly chosen. The process involves pruning of electrons that move into defocusing portions of the wakefield, along with strong phase bunching and rapid acceleration. Simulation results are consistent with a simple Hamiltonian model that numerically integrates particle orbits in an idealized wake potential. Simulations are also presented for a channel-guided LWFA system using optical injection

INTRODUCTION

A laser wakefield accelerator (LWFA) uses a high power (>TW), short laser pulse to produce a large amplitude plasma wave that can accelerate electrons to high energies over extraordinarily short distances [1-3]. The plasma wave has a phase velocity that is approximately equal to the group velocity of the laser pulse in the plasma.

A general strategy for producing high quality electron beams is being pursued at a number of institutions. This strategy involves three basic components. First, laser and plasma parameters are chosen to be in the "standard" LWFA regime, where the laser pulse length $c\tau_p$ is less than the plasma wavelength $\lambda_p = 2\pi c/\omega_p$. In this regime, the laser produces a strong, well-defined wakefield while limiting the growth of dangerous instabilities. The second part of the strategy is to use a plasma channel to provide optical guiding and thus increase the acceleration length. The acceleration length is usually limited by dephasing that arises from the difference in speed between the beam electrons and the group velocity of the laser pulse. The third part of strategy is to use an external electron beam source that provides precisely-timed ultrashort bunches injected into the optimal phase of the wake. The short period of the wakefield places difficult limitations on the bunch length and timing jitter of the injected electrons.

This precisely timed or phased electron injection is expected to result in high quality electron beams with small energy spread. It is inherently difficult for conventional RF injectors to achieve femtosecond precision, so most conceptual LWFA designs have employed some form of all-optical injection [4-6]. Integrated experiments demonstrating all-optical injection and LWFA acceleration are planned at several laboratories, but this milestone has not yet been achieved.

However, simulations and theoretical models presented in this paper will show that phased injection of precisely-timed ultrashort bunches may not be necessary. If the electron injection energy is properly chosen, a high quality accelerated electron beam is possible even if electrons are injected over a broad range of phases. This strategy involves matching the injection energy to the strength of the wakefield so that most injected electrons experience a defocusing radial electric field at some point and are lost or "pruned". Those electrons that survive experience strong phase bunching and can be accelerated to high energies with small energy spread.

UNPHASED INJECTION SIMULATONS

TurboWAVE is highly a parallelized particle-in-cell simulation code that has been used extensively to model intense laser propagation in plasmas [7]. For long range propagation in regimes where the plasma frequency is much less than the optical frequency, it has an option to use a ponderomotive guiding center (PGC) model that averages over the fast (optical) time scale. The simulations are fully relativistic and fully electromagnetic and include the transverse structure of the plasma wave, nonzero emittance and energy spread of injected electrons, and the nonlinear evolution of the driving laser pulse in the plasma channel. The channel-guided LWFA simulations described here have been run in a 2-D Cartesian geometry.

An example of a channel-guided LWFA TurboWAVE simulation with monoenergetic, unphased injection is shown below. The laser has $\lambda = 0.8$ μm, $\tau_p = 80$ fsec, peak power $P_0 = 8$ TW, and initial Gaussian radius $r_0 = 30$ μm. The channel on-axis density $n_0 = 5\text{x}10^{17}$ cm^{-3}, and the density doubling radius of the parabolic channel profile [3] is chosen to have a matched guiding spot size $r_M = r_0$. The injected electrons had an initial energy $W_0 = 1.6$ MeV and were loaded uniformly in phase behind the primary laser pulse. The normalized emittance ε_n for this bunch was 1 π mm-mrad.

*Supported by Department of Energy and Office of Naval Research.
#hubb@ppd.nrl.navy.mil

0-7803-7738-9/03/$17.00 © 2003 IEEE

Figure 1 shows the location of the laser pulse in the simulation box at injection (z = 0) and after 3.62 cm of propagation. The axial coordinate $z - ct$ defines position within the laser frame. Since the channel parameters were chosen to provide guiding at the initial spot size, the laser intensity contours at z = 3.46 cm show little change except for the usual group-velocity-driven phase slippage. However, there is a dramatic change in the injected electrons, which form very short, highly focused bunches.

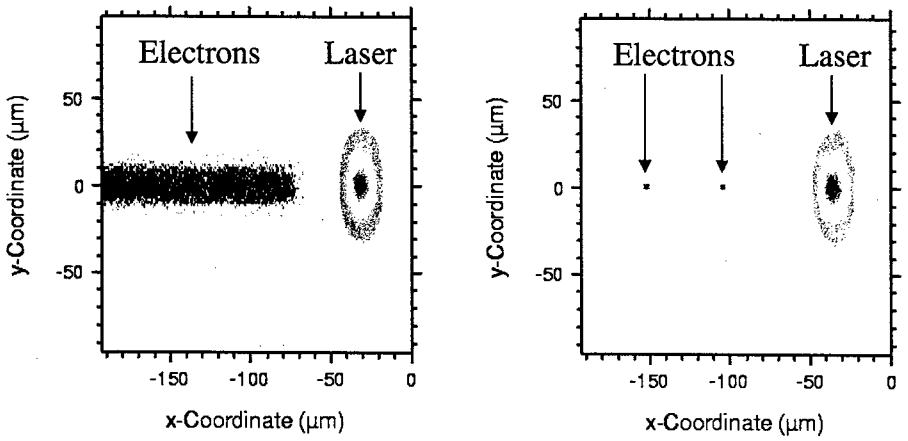

Figure 1: Contours of laser intensity and injected particle positions at injection (z = 0, left frame) and after 3.46 cm of propagation (right frame).

Figure 2 shows the energy distribution of the injected electrons at two different locations from this simulation. At z = 3,46 cm, the average energy <W> of the electrons is 230 MeV, with a small energy spread. At z = 6.62 cm, the average energy has increased to 400 MeV, and the energy spread has increased. Most of the original injected electrons have been lost due to expulsion by the strong radial electric fields in the defocusing portions of the wake. However, those that survive form short, well-defined beam bunches with modest energy spread.

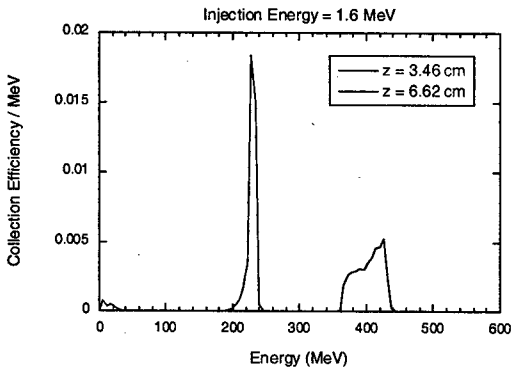

Figure 2: LWFA particle energy spectra at two locations

HAMILTONIAN ANALYSIS OF UNPHASED INJECTION

Trapping and acceleration of injected electrons are often analyzed by plotting particle phase space trajectories in a frame moving at the group velocity of an ideal guided laser pulse [2]. The Hamiltonian in this frame is given by $H(\gamma,\psi) = \gamma(1 - \beta_g\beta)mc^2 + e\phi_0\sin\psi$, where β and β_g are the particle velocity and wave group velocity, normalized to c, ϕ_0 is the peak wake potential, and $\psi = \omega_p(z/\beta_g c - t)$ is the particle phase. Although the analysis is one-dimensional, it is assumed that any particle that enters the defocusing portion of the wake ($\pi < \psi < 2\pi$ in the first wake bucket) is immediately lost.

The largest phase space closed orbit in the first bucket that satisfies $0 < \psi < \pi$ contains all orbits of particles that never cross into the defocusing region. This orbit is defined by $H(\gamma,\psi) = H(\gamma_g,0)$, where $\gamma_g = (1 - \beta_g^2)^{-1/2}$. The lowest point on this retaining orbit defines the minimum injection energy γ_{min} for trapping. For $\gamma_{min} < \gamma_0 < \gamma_g$, where γ_0 defines the injection energy, one can define a range of phases $\psi_{min} < \psi < \psi_{max}$ for particles that remain focused. The collection efficiency for particles loaded uniformly in phase is given by $\eta = (\psi_{max} - \psi_{min})/2\pi$. With an appropriate change of variables, the equations of particle momentum $p(z)$ and phase $\psi(\zeta)$ can be solved numerically for an idealized wake to give final output energy and phase as a function of input energy and phase. The final average energy <γ>, relative energy spread $\delta\gamma/\langle\gamma\rangle$, mean output phase <$\psi$>, and rms pulse width $\delta\psi^2$ can be obtained as functions of γ_0 and ϕ_0.

COMPARISON WITH SIMULATONS

For the parameters used in the previous simulation the normalized potential $e\phi_0/mc^2$ = 0.1. Figure 3 plots the collection frequency and normalized energy spread as functions of the unphased injection energy. The plot compares the Hamiltonian model with the TurboWAVE results at z = 6.62 cm for the parameters used in that simulation.

The Hamiltonian model shows that the collection efficiency rises much faster than the relative energy spread for injection energies slightly above the minimum trapping energy, which is 1.72 MeV in the theoretical model. The simulation collection efficiency follows the basic trend of the Hamiltonian model but is consistently higher. For W_0 = 1.6 MeV, which is slightly below the theoretical trapping threshold energy, η actually exceeds 0.2. The energy spread in the simulations also agrees well with the Hamiltonian model for injection energies near the trapping threshold.

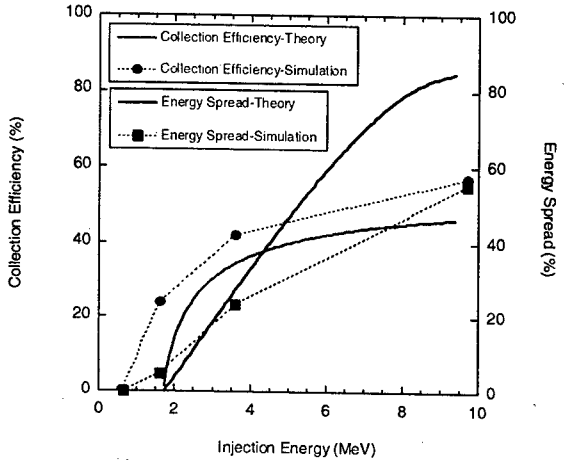

Figure 3: Collection efficiency (red) and energy spread (blue) as functions of the injection energy for the laser and plasma channel parameters used in Figs. 1 and 2. The curves are from the Hamiltonian analysis, and the symbols are from the TurboWAVE simulation.

MULTI-STAGE LWFA SIMULATIONS

This Section describes simulation of a channel-guided LWFA that would employ phased injection from an all-optical injector. This "end-to-end" simulation uses the 3-D version of TurboWAVE to generate an injection spectrum for a LIPA (Laser Ionization and Ponderomotive Acceleration) injector [5]. The LIPA simulation employs a 2 TW, 50 fsec Ti-sapphire pulse tightly focused onto a nitrogen gas jet and produces a 2 MeV, 20 fsec long, phased electron bunch with a modest energy spread. The output particles from this simulation are used to initialize a 2-D TurboWAVE simulation of the main LWFA acceleration stage. The 8 TW, 50 fsec, 30 μm radius LWFA pulse is guided in a three stage, ablative-wall capillary discharge plasma channel [8]. The on-axis channel density is $8x10^{17}$ cm^{-3} in the first stage and is slightly higher in the other stages in order to extend the dephasing length. Laser ionization of inner shell carbon electrons from the capillary discharge is included.

Figure 4 shows the simulation output spectrum at the end of each stage. The simulations predict average energies of almost 300 MeV after the first stage and 800 MeV after the third stage. The energy spread remains small throughout the acceleration process.

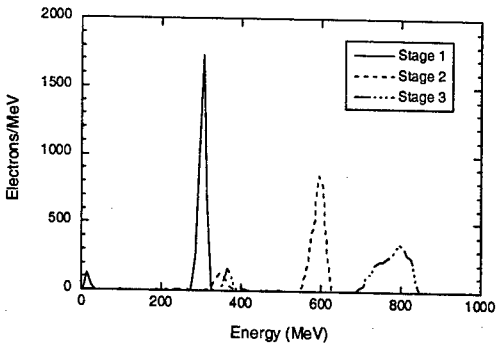

Figure 4: Energy spectra after each stage for a three-stage, channel-guided LWFA with LIPA injection.

SUMMARY

The TurboWAVE simulation code has been used to model acceleration of injected electrons in a channel-guided laser wakefield accelerator. It is often assumed that phased injection of precisely-timed, ultrashort electron bunches will be required to produce high quality accelerated electron beams with low emittance and energy spread. However, simulations show that high quality, ultrashort bunches can be produced during LWFA acceleration if the injection energy is slightly above the minimum energy for trapping. The process involves removal or pruning of electrons that move into defocusing portions of the wakefield, combined with strong phase bunching. The results suggest that extremely precise timing may not be necessary, making conventional RF injectors a more viable alternative to all-optical injection. "End-to-end" simulations of a three-stage LWFA with all-optical LIPA injection predicts almost 300 MeV gain after the first stage and 800 MeV after the third stage, with modest energy spread.

REFERENCES

[1] P. Sprangle, et al., Phys. Rev. E 63 (2001) 056405.
[2] E. Esarey, et al, IEEE Trans. Plasma Sci. 24 (1996) 252.
[3] R.F. Hubbard, et al., Phys. Rev. E 63 (2001) 036502.
[4] D. Umstadter, et al., Phys. Rev. Lett. 76 (1997) 2073.
[5] C. Moore, et al., Phys. Plasmas 8 (2001) 2481.
[6] E. Esarey, et al., Phys. Rev. Lett. 29 (1997) 2682.
[7] D. Gordon, et al., IEEE Trans. Plasma Sci. 28 (2000) 1224.
[8] D. Kaganovich, et al., Appl. Phys. Lett. 78 (2001) 3175.

ALL-OPTICAL BEAMLET TRAIN GENERATION*

John Cary,# Rodolfo Giacone, Chet Nieter, University of Colorado, Boulder CO 80309, USA
David Bruhwiler, Tech-X Corporation, Boulder, CO 80301, USA
Eric Esarey, Gwenael Fubiani, Wim Leemans, LBNL, Berkeley, CA 94720, USA

Abstract

One of the critical issues for the development of Laser Wake Field Acceleration (LWFA), which has the promise of creating table-top, GeV accelerators, is the loading of beamlets into the accelerating buckets. All optical injection schemes, which include LILAC [D. Umstadter *et al*, Phys. Rev. Lett. **76**, 2073 (1996)], beat-wave colliding pulse injection [E. Esarey *et al*, Phys. Rev. Lett. **14**, 2682 (1997)], wave breaking injection, and phase-kick injection, provide a technique for doing so. Although a single bunch can have desirable properties such as energy spread of the order of a few percent, femtosecond duration, and low emittance (<1 mm-mrad), recent simulations show that such methods lead to efficiencies of transfer of plasma wave energy to beam energy that are low compared with conventional RF accelerators when only a single pulse is generated. Our latest simulations show that one can improve on this situation through the generation of a beamlet train. This can occur naturally through phase-kick injection at the front of the train and transverse wave breaking for the trailing pulses. The result is an efficiency improvement of the order of the number of beamlets in the train.

INTRODUCTION

Plasma-based accelerators [1,2] can excite and sustain very high longitudinal electric fields that may overcome many of the limitations found in conventional RF accelerators. More precisely, the longitudinal electric fields can be as large or larger than the nonrelativistic wavebreaking field $E_0 = cm_e\omega_p/e$, where ω_p is the electron plasma frequency, and n_e is the electron plasma density. For $n_e = 10^{18}$ cm^{-3}, the electric field is $E_0 = 100$ GV/m, which is approximately three orders of magnitude greater that obtained in conventional RF linacs.

One widely investigated and very promising concept is the Laser Wake Field Accelerator (LWFA) [3], in which a laser drives a wake field in the plasma, and the wake field then accelerates electrons. Self-trapping and acceleration of electrons have been demonstrated though many experiments in the self-modulated (long-pulse) LWFA [4], with recent results [5] showing acceleration to 200 MeV over a distance of 3mm (66 GV/m). In this case the wake field grows through the modulational instability to the point where wave breaking occurs. The resulting electron beams typically have 100% energy spreads. In the short-pulse regime, where the length of the laser pulse is of the order of the plasma wavelength, $\lambda_p \equiv 2\pi c/\omega_p$, one can create clean wake fields, but then one has the problem of injecting electron bunches into those accelerating fields. Such bunches would have to be extremely short, with length of the order of the laser pulse length, i.e., multiple femtoseconds. These requirements are beyond current technology including that of photocathode radio-frequency electron guns.

For this reason, all-optical injection schemes have been proposed. Pulse propagation down a density ramp leads [6,7] to wave breaking, which then causes beams to form. In the *LILAC* scheme [8] a second, transversely propagating laser beam crosses the wake field, and the ponderomotive kick of the second beam injects particles up into the accelerating region of phase space. In the *beat-wave scheme* [9,10] three colliding pulses are used. Two pulses propagate in the forward (acceleration) direction. The pump (lead) pulse generates a fast (phase velocity near the speed of light) wake field. A trailing pulse follows the pump. The third, backward pulse passes through the lead pulse transparently, as it has orthogonal polarization, but then interacts strongly with the trailing pulse, which has the same polarization. In the phase-kick scheme (discussed below), there are only two collinear and oppositely propagating pulses. This scheme works when the pump pulse has large amplitude, which makes the generated wake-field have more favorable beam confinement properties. In this case, the backward pulse, of orthogonal polarization, causes a small change in the phase of some electrons, displacing them into the accelerating region of phase space.

In our simulations of phase-kick injection we observed that multiple beamlets could be formed. Through a series of longer simulations we further determined that these beamlets extended back over as many as eight trailing buckets, the total length that we simulated. Ultimately we have concluded that transverse wave breaking is the source of this additional injection. This has been confirmed by simulations with only a single pump pulse. In this case, plasma electrons spontaneously load the wake field. Hence, it may be possible to produce a long train of beamlets, with such perhaps a method for increasing the efficiency of transfer of plasma wave energy to energy of accelerated electrons.

PLASMA TO BEAM TRANSFER EFFICIENCY

Production of only a single beamlet has efficiency disadvantages. The efficiency η of just the conversion from wake field energy to plasma energy is optimistically estimated by the ratio of the energy, $N_b e E_p \lambda p$, extracted by the N_b particles in the beam by the peak electric field $E_p = k_p \Phi_p$ ($k_p = \omega_p/c$) in one plasma wavelength divided by the plasma wave energy, which is given in linear theory by

0-7803-7738-9/03/$17.00 © 2003 IEEE

$$W = \varepsilon_0 \int_z^{z+\lambda_p} dz \int_{-\infty}^{\infty} dx dy E^2 .$$

For a wake field with transverse dependence $\exp(-r^2/w^2)$, one obtains the estimate $\eta = f_{tr}(mc^2/\pi e\Phi_p)/(1+4/k_p^2 w^2)$, where $f_{tr} = N_b/n_p\lambda_p\pi w^2$ is the trapping fraction, which is the ratio of the number of beam particles in an accelerating bucket to the number involved in creating one wavelength of the wake field. This is what dominantly determines the efficiency, as the remaining factors are of order unity.

The trapping fraction f_{tr} has been calculated in a number of test-particle and self-consistent simulations. One-dimensional, test-particle calculations [9] find that the trapping fraction can be as high as 19%. However, in two-dimensional calculations, both test-particle [10] and self-consistent [11], it is generally observed that the trapping fraction has a maximum value beyond which the parameters of the beam (emittance, energy spread, etc.) are poor. This trapping fraction is much smaller, more like $f_{tr} = 5\text{x}10^{-4}$, thus implying an efficiency that is orders of magnitude below that of conventional accelerators.

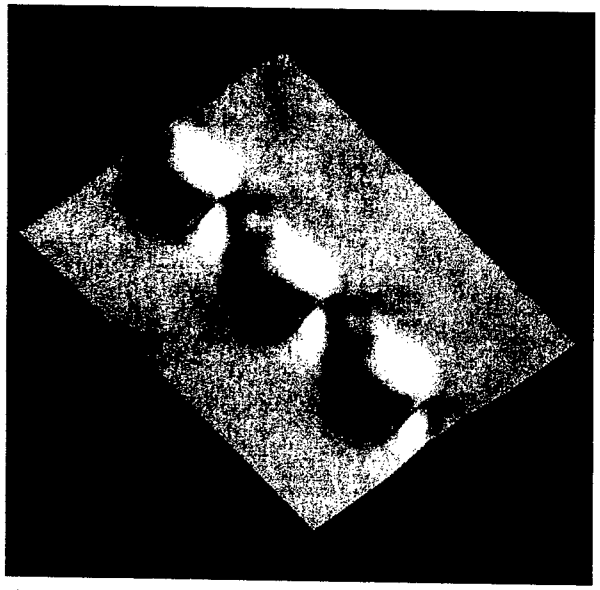

Fig. 1. The potential energy for a pulse with normalized amplitude a=1.7.

PHASE-KICK INJECTION

Phase-kick injection can occur at large pump amplitudes, where the nature of the wake field becomes more favorable to particle capture and confinement. Figure 1 shows the potential energy $e\Phi$ wake field from a 2D simulation where the incoming pulse has a peak amplitude of $a_p \equiv eE_p/m\omega c = 1.7$. (The negative electron charge is denoted by e.) As this figure shows, the region of negative potential expands dramatically. In addition, even the faces of the accelerating phase for positive potential acquire the curvature required for focusing. The result is that a small phase kick applied to the plasma electrons can put them on an invariant curve that is both accelerating and focused.

This has been verified through two-pulse simulations with the VORPAL code [12]. The pump pulse peak pulse amplitude was given by $a_p = 1.7$ and the backward pulse had $a_b = 0.8$. The plasma wavelength was 40 μm, the laser pulses were 20 μm long and 40 μm wide. The beamlet propagated for of the order of a mm. A full illustration of the dynamics is not possible within this space-limited proceedings, so we show only the final result for the longitudinal phase space in Fig. 2.

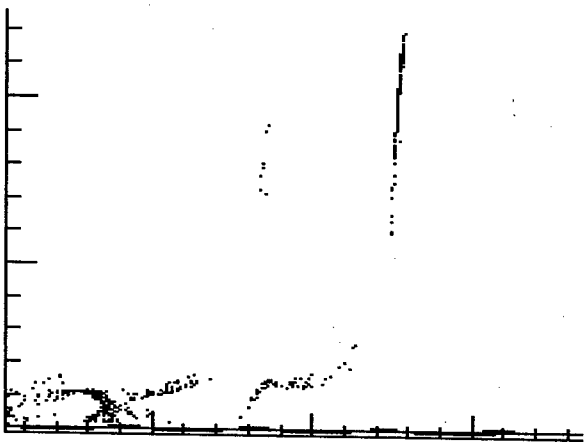

Fig. 2. Longitudinal phase space for a beamlet produced through phase-kick injection. The abscissa shows roughly five plasma wavelengths or 200 μm. The average relativistic factor γ of the particles is about 55.

SPONTANEOUS BEAMLET TRAIN GENERATION

Just behind the first beamlet in Fig. 2 one can see traces of a second beamlet. This seems somewhat reasonable, as phase-kick injection could possibly work for each of the accelerating buckets of the wake field. To test this, we carried out much longer simulations. As a result we found that we were generating beamlets in each of the buckets back through the length of the simulation. At first we thought that each of the trailing beamlets was generated by phase-kick injection interaction with the plasma particles at their oscillation peaks. This, along with a knowledge of the accelerating gradient, allows one to predict the energies of the successive beamlets. As the prediction did not agree with our observations, we began examining new mechanisms. Ultimately we found that the far trailing beamlets were generated with no backward pulse and arbitrarily slow density ramp.

An example of the beamlet train generation by a single pulse is shown in Fig. 3. In this case, the pump pulse has $a_p = 1.7$, with the simulation region being 10 plasma wavelengths long. Other parameters are as mentioned above. After roughly 1 mm of propagation, the spontaneously formed beams found in the 5th to 6th

buckets back are seen to have been accelerated to relativistic factors of the order of 30.

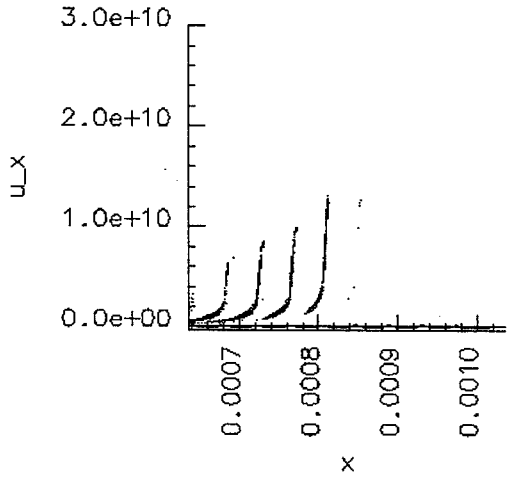

Fig. 3. Spontaneous injection by a single pump pulse.

We believe that the cause of this is transverse wave breaking [13]. The plasma oscillations have a smaller frequency in the center of the wake field, as average the relativistic factor and, hence, the effective mass is larger. This difference in frequency ultimately causes wavelength shortening to the point of wave breaking, which then injects the particles into the accelerating and focusing region of phase space.

Further work shows that we can combine the spontaneous particle injection with one of the other mechanisms, such as phase-kick or beat-wave injection, to obtain a continuous sequence of pulses.

SUMMARY AND CONCLUSIONS

Our simulations show that one can generate beamlet trains through combining injection due to transverse wave breaking with another form of injection. This has the potential for increasing the efficiency of LWFA systems, as each beamlet then reuses the plasma wave energy. For a case of N generated beamlets, one would then have an efficiency increase by a factor of N. Of course, this would require some method for continuing to energize the plasma wake field so that the trailing beamlets gain the same energy as the leading beamlets. A possibility is to have trailing, smaller laser pulses that re-energize the plasma wake field.

On the other hand, for early experiments our results might indicate that observation of well formed beams will be difficult due to the required temporal discrimination. This can be seen in Fig. 3, in which the beams are separated by 130 fs. Eventually each of the bunches does form a beam through naturally occurring focusing collimation. However, with each successive beamlet of lower energy, the collection after a modest acceleration distance continues to have 100% energy spread.

To improve upon this situation, we have now come up with two methods for obtaining single beamlets. These methods involve modifying the wake field so that it exists over only one or a few plasma wavelengths. In the first method, propagation in an appropriately chosen channel leads to wake field damping in just a few plasma wavelengths. As a result, only the first bucket has sufficient potential energy such that the separatrix extends far enough down that particles can be captured. Giacone *et al* [14] have now observed this process via simulations with VORPAL. In the second method, we follow the pump pulse with a second pulse that absorbs the wake field generated by the pump pulse, in accordance with the theory of [15]. Again only a single beamlet is produced. We believe that approaches like these may lead to the observation of optically injected, well-formed beams.

ACKNOWLEDGMENTS

This work supported by DoE under Contracts DE-FG03-99ER82903, DE-FG03-95ER40926 and DE-AC03-76SF00098, the SciDAC project DE-FG02-01ER41178, and NSF grant No. 0113907.

REFERENCES

1. T. Tajima and J. Dawson, Phys. Rev. Lett. **43**, 267 (1979).
2. P. Sprangle, E. Esarey, A. Ting, and G. Joyce, Appl. Phys. Lett. **53**, 2146 (1988).
3. P. Sprangle *et al.*, Phys. Rev. Lett. **69**, 2200 (1992); E. Esarey *et al.*, Phys. Fluids B **5**, 2690 (1993); J. Krall *et al.*, Phys. Rev. E **48**, 2157 (1993).
4. K. Nakajima *et al.*, Phys. Rev. Lett. **74**, 4428 (1995), A. Ting *et al.*, Phys. Plasmas **4**, 1889 (1997); W.P. Leemans et al., PRL **89**, 174802 (2002).
5. V. Malka et al., Science **298**, 1596-1600(2002).
6. S. Bulanov et al., PRE **58**, R5257--R5260 (1998).
7. R. G. Hemker, N. M. Hafz, M. Uesaka, Phys. Rev. STAB **5**, 041301 (2002).
8. D. Umstadter, J. K. Kim, E. Dodd, Phys. Rev. Lett. **76**, 2073 (1996).
9. E. Esarey *et al.*, Phys. Rev. Lett. **79**, 2682 (1997).
10. C. B. Schroeder *et al.*, Phys. Rev. Lett. E **59**, 6037 (1999).
11. R. Giacone et al., Proc. 2001 Particle Acceleration Conf., Edited by P. Lucas and S. Webber (IEEE, Piscataway, NJ, 2001), p. 4023.
12. C. Nieter and J. R. Cary, submitted to J. Comp. Phys. (2003), available at http://www-beams.colorado.edu/vorpal.
13. S. V. Bulanov, F. Pegoraro, A. M. Pukhov, and A. S. Sakharov, Phys. Rev. Lett. **78**, 4205 (1997).
14. R. Giacone *et al*, this conference, paper TPPG039.
15. V. I. Berezhiani and I. G. Murusidze, Physica Scripta **45**, 87 (1991).

SCALING LAWS OF A DIELECTRIC OPTICAL ACCELERATOR

L. Schächter[(1)], S. Banna[(1)], R. L. Byer[(2)], E. Colby[(3)], B. Cowan[(2)], M. Javanmard[(3)], A. Mizrahi[(1)], R. Noble[(3)], T. Plettner[(2)] and R. H. Siemann[(3)]

[(1)]Electrical Engineering Department, Technion – IIT, Haifa 32000, ISRAEL
[(2)]Department of Applied Physics, Stanford University- MC4085, Stanford CA 94305, USA
[(3)]SLAC, MS-7, Stanford University, P.O. Box 4349, Stanford, CA 94309, USA

Abstract

Some of the basic scaling laws of future dielectric optical accelerator are re-examined.

1 INTRODUCTION

Indications that solid-state lasers will reach wall-plug to light efficiencies of 30% or more make a laser-driven vacuum-accelerator [1-2] increasingly appealing. Since at the wavelength of relevant lasers, dielectrics may sustain significantly higher electric field and transmit power with reduced loss comparing to metals, the basic assumption is that laser accelerator structures will be dielectrics. For structures that have typical dimensions of a few microns, present manufacturing constraints entail either planar structures or acceleration structures with a higher degree of symmetry, similar to optical fibers. The former require re-evaluation of many of the scaling laws [3] that were developed for azimuthally symmetric structures whereas the latter have some inherent advantages, but thermal gradients as well as heat dissipation may become critical impediments. Efficiency, emittance and heat flow scaling laws that have been developed recently will be presented.

2 EFFICIENCY

One of the major questions that will determine the fate of any future accelerator is the efficiency since it is natural to require acceleration of the largest number of electrons at the minimal input power i.e., maximum efficiency. Denoting the laser power injected in the structure by P_L and the resulting gradient at the location of the electrons by E_{acc}, it is possible to define the interaction impedance as $Z_{int} \equiv |E_{acc}\lambda|^2 / P_L$ which characterizes any acceleration structure; in this expression λ is the wavelength in the vacuum. This laser pulse accelerates a bunch (Q) that as it moves in an arbitrary acceleration structure generates an electromagnetic wake. Associated with this wake there is a decelerating electric field component (E_{dec}) which by virtue of the linearity of Maxwell's equations, must be proportional to Q. Therefore, without loss of generality it is possible to assume that there is an effective transverse dimension denoted by R_{eff}, determined by the details of the structure and the bunch, such that $E_{dec} = 2Q / 4\pi\varepsilon_0 R_{eff}^2$.

Since it is possible to establish the power associated with the wake-field, $P_{wake} = Q v E_{dec}$, then the impedance definition as previously implies $Z_{wake} \equiv |E_{dec}\lambda|^2 / P_{wake} = Z_0 / 2\pi (R_{eff}/\lambda)^2$ wherein Z_0 is the vacuum impedance. For example, the interaction impedance of the photonic band-gap structure analyzed in Ref. 2, has an interaction impedance of $Z_{int} = 19.5\Omega$ at $1\mu m$ and for an accelerating gradient of 1GV/m the total power required is about 50kW. Furthermore, since the radius of the vacuum tunnel is $R = 0.678\lambda$ and it may be demonstrated [3-5] that $R_{eff} \simeq 1.23R$, then $Z_{wake} \simeq 86\Omega$.

With these two impedances, it is possible to determine the effective (loaded) gradient as

$$E_{eff} \equiv E_{acc} - E_{dec} = \frac{1}{\lambda}\sqrt{P_L Z_{int}} - \frac{QcZ_{wake}}{\lambda^2} \qquad (1)$$

therefore, the gain in the kinetic energy of the bunch in structure of length L is $\Delta U_{kin} \equiv QE_{eff}L$ whereas the total electromagnetic energy stored in the structure is $U_{em} \equiv P_L \tau_f = P_L (L/c)(1-\beta_{gr})/\beta_{gr}$ where τ_f is the fill-up time and $c\beta_{gr}$ is the group velocity. Based on these two energy definitions, the efficiency of the acceleration process is

$$\eta \equiv \frac{\Delta U_{kin}}{U_{em}} = \frac{Q(Q_0 - Q)}{Q_n^2} \qquad (2)$$

wherein $Q_n \equiv \sqrt{\frac{P_{laser}}{Z_{wake}} \frac{\lambda^2}{c^2} \frac{1-\beta_{gr}}{\beta_{gr}}}, Q_0 \equiv \frac{\lambda\sqrt{P_{laser} Z_{int}}}{cZ_{wake}}$.

Clearly, maximum efficiency occurs for an optimal value of the charge given by $Q_{opt} \equiv Q_0/2$ in which case the value of this efficiency is

$$\eta_{max} = \left(\frac{1}{2}\frac{Q_0}{Q_n}\right)^2 = \frac{1}{4}\frac{\beta_{gr}}{1-\beta_{gr}}\frac{Z_{int}}{Z_{wake}} \qquad (3)$$

implying that the maximum efficiency is determined by the ratio of the impedances and the group velocity. For the PBG structure mentioned above [2], the group velocity is 0.58c therefore the maximum possible efficiency is 7.86%. It is likely that considerations of energy spread will lead to charges and efficiencies below the optimum values.

0-7803-7738-9/03/$17.00 © 2003 IEEE

3 EMITTANCE

In an azimuthally symmetric structure, the ratio of the transverse force to the longitudinal force is virtually negligible since it is proportional to $|F_\perp / F_z| \approx \gamma^{-2}$. On the other hand, in a non-symmetric structure of a typical transverse dimension a, the ratio of the two forces is $|F_\perp / F_z| \approx \lambda / a$. 3D numerical simulations [3] of a bunch of 30GeV electrons indicate that the relative change in the emittance is drastically affected by the transverse dimension specifically, the relative change in the emittance across 10cm long acceleration structure when the wavelength is $\lambda = 1\mu$m scales like

$$\delta\varepsilon \equiv \frac{\varepsilon^{(\text{out})} - \varepsilon^{(\text{in})}}{\varepsilon^{(\text{in})}} \simeq \left(\frac{b}{a}\right)^{\nu} ; \qquad (4)$$

here E_{acc}=1 [GV/m] and the initial bunch length was 90°. The parameters b and ν depend on the radius of the beam (R_b) and in case $R_b = 3\mu$m the coefficients are b=15.4 and $\nu = 4.4$. The bunch length ($\Delta\chi$) also affects the emittance. A similar analysis shows that if $|\Delta\chi| < 90^o$, the emittance change is quadratic in $\Delta\chi$ namely,

$$\delta\varepsilon \simeq 1.1\times\left(\Delta\chi/180^o\right)^2 ; \qquad (5)$$

here R_b=3μm and a=20μm. In order to maintain low emittance change in a single acceleration module it is necessary to "symmetrise" the structure by constructing each module by sets of four non-symmetric segments each one rotated by 90°. For a typical transverse separation of (a=) 20μm, an initial bunch radius R_b=2μm, an average energy 30GeV with energy spread of 1% and bunch length of 3.6°

$$\delta\varepsilon \simeq 4.14\left[1+\left(N_{st}/15\right)^2\right]^{-1} \qquad (6)$$

where N_{st} is the number segments. For 400 segments the emittance increase in a 1m long acceleration structure is 0.6%, entailing a maximum segment length of 2.5mm.

4 THERMAL CONSIDERATIONS

Although dielectric materials are known to have low ohm loss there still is an important aspect of temperature gradients and heat dissipation. For investigating this phenomenon consider a hollow dielectric (ε) fiber of internal radius $R_{int}\left(\simeq 1[\mu\text{m}]\right)$ and external radius $R_{ext}\left(\simeq 30[\mu\text{m}]\right)$ An electromagnetic pulse propagates along this fiber and due to the Ohmic loss, represented here by $\tan\delta$, it is assumed that the thermal energy generated within the fiber volume is extracted from the outer surface where it is in contact with a perfect thermal conductor thus its temperature change vanishes hence $\Delta T(r = R_{ext}) = 0$. At the inner wall there is no thermal power-flow towards the vacuum thus $\left[\partial\Delta T/\partial r\right](r = R_{int}) = 0$. Both thermal characteristics of the structure, heat conductivity σ_T[J/sec m°K] and diffusion coefficient D[sec/m^2] are assumed to be uniform across the structure. Subject to the boundary conditions mentioned above, the variation in temperature (ΔT) across the structure may be determined using the diffusion equation driven by the electromagnetic power *loss density*. Since on the scale of one period of the wave ($2\pi/\omega_0 \equiv \lambda/c \simeq 3$fsec) there are no temperature variations, the electromagnetic power loss density is *averaged* over one period of the radiation field. The solution is further simplified by the following assumptions:

(i) $\left(v_{gr}\tau_p\right)^{-1} \ll p_s / R_{ext} \ll D v_{gr}$ wherein v_{gr} is the group velocity and p_s / R_{ext} represents the typical transverse variation of the temperature,

(ii) the diffusion time is much longer than the pulse duration (τ_p) $\tau_D \equiv DR_{ext}^2 \gg \tau_p$.

For convenience, the temperature change can be normalized with $T_N \equiv \frac{\tau_p}{\sigma_T D}\varepsilon\tan\delta\left[\frac{P_L}{\pi R_{int}^2}\frac{\omega_0}{c}\right]$ and the heat flow with $Q_N \equiv \frac{\tau_p}{DR_{ext}}\varepsilon\tan\delta\left[\frac{P_L}{\pi R_{int}^2}\frac{\omega_0}{c}\right]$. Figures 1 and 2 illustrate these two normalized quantities for the power distribution shown in Figure 3 representing the energy flux distribution in a Bragg structure acceleration structure [6].

For Zirconia (ZrO_2): $\tan\delta = 10^{-4}$, $\varepsilon = 2$ a total laser power of $P_L = 10[\text{kW}]$, $Z_{int} = 100[\Omega]$, $R_{ext} = 30[\mu\text{m}]$, $R_{int} = 0.5[\mu\text{m}]$, $\tau_p = 1[\text{psec}]$, $\sigma_T = 2[\text{W/m°K}]$ and $D = 1.15\times10^6[\text{sec/m}^2]$. The normalizing heat flux is $Q_N \simeq 46$ [W/cm^2] whereas the normalizing temperature is $T_N \simeq 7°$K. Zirconium has been chosen since it is a good thermal insulator thus the typical diffusion time $\tau_D\left(\equiv DR_{ext}^2 \simeq 1[\text{msec}]\right)$ is nine orders of magnitude larger than the pulse duration $\tau_p\left(\sim 1[\text{psec}]\right)$.

Figure 1 reveals a rapid increase in temperature (at $r = R_{int}$) from zero to a maximum and then exponential decay on a time-scale significantly shorter than the diffusion time (τ_D). Investigating the behavior on the scale of the laser pulse duration τ_p we find a linear increase from zero to the maximum value occurring at the end of the pulse. Using the estimate of T_N we conclude that the peak change in temperature is $\Delta T_{max} \simeq 0.1°$K.

While the temperature variation at $r = R_{int}$ occurs virtually instantaneously with the laser pulse, the heat reaches the output radius with a delay of the order of the diffusion time - see Figure 2; accordingly, the maximum heat flow to be dissipated is $Q_{max} \simeq 0.01[\text{W/cm}^2]$.

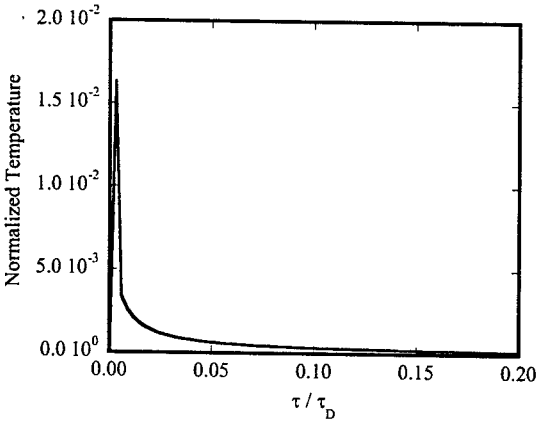

Figure 1: Variation in time of the normalized temperature at $r = R_{int}$.

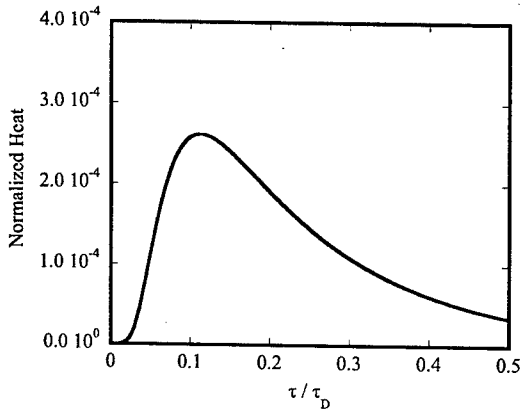

Figure 2: The variation in time of the normalized heat flow at $r = R_{ext}$.

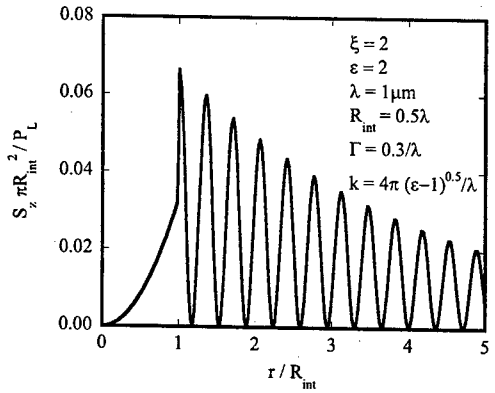

Figure 3: Transverse variation of the energy flux.

These two estimates account for a *single* pulse. In practice, a repetition rate of about 50 MHz will be required in order to satisfy the luminosity requirements on the one hand and heat dissipation on the other hand. As already indicated, the heat is deposited on the time scale of the pulse duration ($\tau_p \sim 1\text{psec}$) but it is dissipated along a diffusion time ($\tau_D \sim 0.1\text{msec}$). Consequently, heat from many laser pulses may accumulate before the dissipation affects the heat balance therefore, rather than considering the instantaneous power-loss (p_{loss}) averaged over one radiation period, we consider the density power loss averaged over one period of the repetition rate (T_{rr}) of the system. With this approach in mind, it is convenient to define the thermal trans-conductance as the ratio of the heat flow to the temperature increase at the two relevant locations thus in normalized terms it reads

$$\bar{G} \equiv \frac{R_{\text{ext}} Q_{\max}^{(\text{av})}}{\sigma \Delta T_{\max}^{(\text{av})}}. \qquad (7)$$

Simulations indicate that it is weakly dependent on the internal radius – less than 5% when $0.3 \le R_{\text{int}}/\lambda \le 0.8$ - but quite significantly dependent on the confinement parameter (Γ) $\bar{G} \simeq 0.26 + 0.05/\Gamma\lambda$ for $0.2 \le \Gamma\lambda \le 0.8$. Specifically, for $\Gamma = 0.3/\lambda$ and $R_{\text{int}} = 0.5\lambda$ it was found that $\bar{G} \simeq 0.42$.

Maximum average temperature was found to be $\Delta T_{\max}^{(\text{av})} = 59^{\circ}[\text{K}]$ whereas the energy flux is $Q_{\max}^{(\text{av})} = 160\,[\text{W/cm}^2]$. This energy flux represents a *passive* dissipation process but by virtue of the linearity of the system, if a fraction of these 160 [W/cm^2] are extracted *actively* with a thermo-coupler, we may actually cause the temperature change at the vacuum-dielectric interface to be significantly reduced.

5 ACKNOWLEDGEMENTS

This study was supported by the United States Department of Energy and the Israel Science Foundation.

6 REFERENCES

[1] Y. C. Huang et .al., Appl. Phys. Lett. **68**, 753 (1996).
[2] X.E. Lin; Phys. Rev. STAB, 4, 051301 1-7 (2001).
[3] L. Schächter et.al., Proc. AAC – 2002.
[4] L. Schächter et. al., NIM A, **388**, 8-16 (1997).
[5] D. Schieber et. al. Phys. Rev. E, **57**, 6008-15 (1998); **64**, 056503 1-8 (2001).
[6] A. Mizrahi et. al. see this Proceedings.

SELECTED ADVANCED ACCELERATION CONCEPTS*

J. L. Hirshfield**
Department of Physics, Yale University, New Haven, CT 06511, and
Omega-P, Inc., New Haven, CT 06511

Abstract

A précis is given of a critical review of a few advanced acceleration concepts that involve neither plasma nor periodic metallic slow-wave structures. These so-called "vacuum accelerators" are either externally driven using powerful rf or laser sources, or internally driven using strong wake fields set up by a train of drive bunches. Merits and limitations of each concept are given, and speculations are advanced on the potential of each to mature into a practical accelerator for use as a tool in high-energy physics or other scientific applications.

INTRODUCTION

Recent Particle Accelerator Conferences and Advanced Accelerator Concepts Workshops have included a category of ideas under the rubric *Electromagnetic Structure-Based Acceleration*—a catchall for concepts not involving plasma or traditional disk-loaded metallic structures [1]. Division of such concepts into slow-wave and fast-wave interactions is not uncommon.

Slow-wave concepts can involve dielectric-loaded waveguides excited at either microwave or optical wavelengths. Early experiments with dielectric-lined metallic-wall cylindrical microwave structures [2] showed that design and fabrication issues at the input coupler and the dielectric-wall interface demanded serious attention if the anticipated accelerating gradient was to be achieved. The nature of the limitations to achievement of accelerating gradients competitive with those for disk-loaded metallic structures is a topic of continuing research [3]. Other slow-wave concepts include planar dielectric structures (see below) and photonic band gap structures [4]. Any of these guided wave structures can be driven externally, using rf or laser pulses, or internally using wake fields from one or more driving bunches. Fast-wave concepts include the inverse free electron laser IFEL [5], and the laser autoresonance cyclotron accelerator LACARA [6].

The selected acceleration concepts discussed in this paper include a multi-cavity proton accelerator MCPC and LACARA, as examples of externally-driven fast-wave interactions, and wake field acceleration in a planar dielectric-lined structure—a beam-driven slow-wave interaction. Speculations are advanced on the potential of each to mature into practical accelerators for use as tools in high-energy physics or other scientific applications.

*Sponsored by US Department of Energy.
**jay.hirshfield@yale.edu Collaborators include Changbiao Wang, J.-Y. Fang, T. C. Marshall, S. Shchelkunov, V. P. Yakovlev, and M. A. LaPointe.

MULTI-CAVITY PROTON CYCLOTRON

The currently-favored choice for a high intensity 1-GeV class proton accelerator for a high-power neutron spallation source is a superconducting linac (SCL). For example, a 700 MHz SCL with an average acceleration gradient of 8.6 MV/m has been described for proton acceleration from 0.20 to 1.2 GeV in a 10 MW source [7]. In paper TPPG056 in these Proceedings, Wang *et al* give parameters for a >100 MW, 1 GeV proton accelerator that uses a cascade of TE_{111} cavities in a nearly-uniform 8-T magnetic field [8]. This multi-cavity proton cyclotron MCPC has the virtues of a relatively high effective acceleration gradient (~40 MV/m), modest surface fields on the walls of the room-temperature cavities (<7 MV/m), high efficiency (~70% at 122 mA), large beam apertures, intrinsic beam stability, wide injection phase window (2 rf cycles in the first cavity), and intrinsic beam scanning over a target. Against these appealing attributes one must weigh the need for a large superconducting solenoid—25 m long and ~4 m in diameter in the example given by Wang—in contrast to 120 m of superconducting rf cavities in the SCL mentioned above. MCPC is not likely to be practical for acceleration beyond several GeV, on account of the required very strong magnetic field. Nevertheless, this new concept for a fast-wave proton accelerator could be a viable candidate to drive a very high power neutron spallation source or, at lower current, for a compact GeV class versatile proton source. Testing of a four-cavity electron counterpart has been proposed.

LASER CYCLOTRON AUTORESONANCE ACCELERATOR

The Woodward-Lawson-Palmer (WLS) theorem states that no net acceleration is afforded a charged particle interacting linearly with, and passing without interruption along, an unbounded plane electromagnetic wave. Thus authentic vacuum acceleration requires a proximate medium to slow and/or refract the wave, a mirror or prism to deflect the wave, or the presence of another field such as a static magnetic field B. The B-field WLS theorem-breaker is the key to LACARA—laser cyclotron auto-resonance accelerator, an experimental test version of which is to be installed at ATF-BNL as soon as a long-delayed 6-T solenoid magnet is built and installed. For a two-meter interaction length, corresponding to five Rayleigh lengths for an 0.8 TW, 10.6 μm CO_2 laser focused to a waist radius of 1.2 mm, acceleration from 50 to 100 MeV is predicted for all electrons in an injected nC bunch [6]. This vacuum laser-acceleration scheme differs

0-7803-7738-9/03/$17.00 © 2003 IEEE

in several important respects from most other laser-based accelerators: in LACARA all electrons receive nearly the same energy gain; energy gain is possible over many Rayleigh lengths; no material medium or gas is close to the beam path; and slippage between laser pulse and a typical beam bunch is tolerably small. Acceleration gradient scales roughly with the square root of laser power, but falls as beam energy grows. Curiously, the required resonance B-field strength falls as the energy increases, in conformity with the autoresonance condition. In practice, the precise resonant B-field profile is not necessary, since the interaction typically occurs over only a small number of orbit gyrations—of the order of the number of Rayleigh lengths. On account of falling acceleration gradient with increased energy, LACARA is not likely a candidate for electron acceleration to energies above a few 100 MeV but, as will be discussed below, it has a unique property that enables generation of fs bunches which themselves could drive a high-gradient, high-energy accelerator.

FORMING FEMTOSECOND PLANAR BUNCHES FROM A LACARA BEAM

After exiting LACARA, as the strong solenoidal B-field tapers smoothly towards zero, individual electron orbits follow diverging linear paths that are sequentially displaced in azimuth at the optical frequency. When a 10.6 μm CO_2 laser is used, these paths recycle every 35.3 fs. For a LACARA as described above with an injected 50 MeV beam having rms emittance of 1.5 nm, the orbits trace a donut with a diameter of about 3 mm and a thickness of about 0.5 mm on a beam stop 150 cm from the LACARA center. If a hole is cut in the beam stop to pass 10% of the beam, then a sequence of 3.5 fs bunches emerges through it [6]. (The beam stop must of course be thick enough to stop the other 90% of the beam.) If several such holes are cut into the beam stop, then several trains of 3.5 fs (~ 1 μm) bunches emerge, following paths that diverge from one another. These separate trains can be reunited using quadrupole lenses. For a 1 ps, 1 nC bunch accelerated in LACARA, each train would contain 28 3.5 fs bunches, each with a charge of 3.5 pC. This scheme is the optical counterpart of the microwave "choppertron" [9]. Obviously, the size of the hole in the beam stop can be altered to form bunch widths larger or smaller than 3.5 fs, and the number of reunited trains of such bunches can be selected as well. Such variations can be effected merely by changing a single element in the arrangement—the beam stop.

Formation of a roundish beam chopped as described above into a beam with planar transverse profile has been shown possible by use of a single quadrupole lens [10]. For the 3.5 fs bunch example above, a quad of strength 3.5 kG-cm^{-1} is able to form a profile of width 3400 μm and height 68 μm (a 50:1 aspect ratio) at a distance of 21.5 cm from the beam stop. A train of 28 or more such 1-μm long planar bunches would thus be generated for subsequent use, for example as discussed next.

MICRON-SCALE HIGH GRADIENT WAKE FIELD ACCELERATOR DRIVEN BY FS PLANAR ELECTRON BUNCHES

In paper TPPG038 of these *Proceedings*, Fang *et al* show calculations and simulations for the wake fields set up by a train of fs planar bunches prepared using a LACARA beam, as described above, that pass through the vacuum channel between two parallel planar dielectric-lined metal plates [11]. The structure analyzed in [11] employed two 1.9 μm thick, 300 μm high slabs with relative dielectric constant $\varepsilon = 3.0$ deposited on copper, with a vacuum gap of 15.0 μm. Such a configuration is appealing for generation of intense wake fields for acceleration because it can be fabricated using microelectronics technology, it is fixed and rigid and thus suitable for assembly in a manifold staged array, it supports intense wake fields from pC planar bunches, and it supports relatively weak higher-order modes that can even provide transverse focusing.

A single 1 pC, 3.3 fs bunch with height 150 μm and width 10 μm can be shown to generate a wake field with a peak accelerating gradient of 70 MV/m, mainly in the lowest TM-like mode of the structure; constructive superposition of the wake fields of ten such bunches, each spaced by the wake field period, can be shown to generate a peak accelerating gradient of 618 MV/m for a test bunch at a distance of 1.14 mm behind the drive train. At this location, higher-order transverse wake forces can be shown to be focusing, yielding a 5×10 μm^2 beam spot about 6 cm along the structure, with stable betatron oscillations in transverse beam profile that persist for at least 50 cm along the structure. This result suggests that acceleration to the GeV level could be possible in a single module of such a structure, without need for external focusing.

Simulations using the PIC code KARAT for the same structure show that superposition of longitudinal wake fields occur much as in the computed results, but only in a • erenkov radiation zone that trails each drive bunch; close to the structure entrance a transition radiation zone exists with fields much weaker than those nearer the bunch; in an intermediate zone • erenkov and transition radiation overlap and interfere with one another. A theoretical model yielding comparable results for a single wake field mode in a solid cylindrical dielectric waveguide has been recently published [12]. These complicated effects near the structure entrance are not fully understood but, in any case, should not be of undue influence for structures whose lengths far exceed their largest transverse dimension. One can still conclude that stable ~GV/m accelerating wake fields can be excited by a periodic train of planar bunches in a dielectric-lined micron-scale planar structure.

OPINIONS AND SPECULATIONS

Exploration of novel advanced accelerator concepts is a fascinating and rewarding pastime. However, if utility to the scientific community and benefit to society at large

are to be taken into account, it is—in the author's opinion—incumbent upon researchers to occasionally take stock of their work and speculate as to whether a practical accelerator might emerge after maturation of any of the new concepts that they study. In particular, for use as a tool in future high energy physics research, an accelerator must not face insurmountable basic obstacles preventing it from reaching the TeV energy range for electrons and positrons, and tens-of-TeV energies for protons. In addition, the beam luminosity must not be prevented by insurmountable obstacles from reaching the range 10^{34} cm^{-2} sec^{-1}. On the other hand, if the accelerator is to be used in other areas of research or applications, different practical criteria will apply. For example, a proton driver for a high-power neutron spallation source or sub-critical nuclear reactor would require GeV-level energy and 10-100 MW beam power; while an electron beam source with femtosecond or attosecond bunches for direct excitation and study of atomic, chemical, biological, or nuclear transients (or for indirect excitation using x-rays generated by the bunches) would need be of moderate energy (probably 100's of MeV at most), moderate charge/bunch (sub-nC), but with good energy resolution, low emittance, and good bunch length definition. Considerations for industrial or medical accelerators invoke additional questions of size, cost, efficiency, and shielding.

In view of what is stated above for the several vacuum acceleration concepts discussed in this paper, it appears to be beyond present understanding for either MCPC or LACARA to reach TeV energies; the former because of the unrealizable magnetic field strength required, the latter because of the inverse relationship between acceleration gradient and beam energy. However, it seems that each concept might be developed for other applications; MCPC for a high-power proton driver, and LACARA to prepare a beam for chopping into fs or sub-fs bunches. The planar wake field accelerator concept is perhaps capable of staging, and thus could conceivably be operated with many stages each providing GeV-level energy gains. This would require a mechanical design capable of maintaining stable micron-scale tolerances over meter-long structures.

Achievement of high luminosity for MCPC translates to the issues of beam extraction and emittance, since high average current appears to pose no limitation. But for LACARA and a planar wake field accelerator driven by a beam prepared in LACARA, achievement of high luminosity translates into need for a TW-level CO_2 laser with a pulse repetition rate of 100's of kHz. The author is unqualified to speculate on the likelihood for realization of such a laser, not to mention its cost.

These evident limitations notwithstanding, it is the author's opinion that continued study of these and other advanced accelerator concepts is definitely warranted, not only to deepen basic physical understanding, but also to guard against missing out on any unforeseen discovery that might significantly alter the prospects.

REFERENCES

[1] See, for example, J. G. Power and W. D. Kimura, "Summary Report on Working Group 5: Electromagnetic Structure-Based Acceleration," in *Advanced Accelerator Concepts Tenth Workshop, Mandalay Beach, CA.* AIP Conf. Proc. **647** (AIP, New York, 2002), p. 156.

[2] J.-M. Fang, T.C. Marshall, J.L. Hirshfield, M.A. LaPointe, "An Experimental Test of a Microwave Inverse Cerenkov Accelerator (MICA)," in *Proc. PAC2001*, (IEEE, NJ, 2001), p. 4020.

[3] W. Gai and W. Liu, "RF Coupling Design for Dielectric Loaded Accelerating Structures," in this Proceedings.

[4] M. A. Shapiro, E. I. Smirnova, C. Chen, and R. J. Temkin, "Theoretical Analysis of Overmoded Dielectric Photonic Band Gap Structures for Accelerator Applications," in this Proceedings.

[5] R. B. Yoder, T. C. Marshall, and J. L. Hirshfield, "Energy Gain Measurements from a Microwave Inverse Free-Electron-Laser Accelerator," *Phys. Rev. Lett.* **86**, (2001) 1765.

[6] J. L. Hirshfield and C. Wang, "Laser-Driven Cyclotron Autoresonance Accelerator with Production of an Optically-Chopped Electron Beam," *Phys. Rev.* E **61**, 7252 (2000).

[7] A. G. Ruggiero, H. Ludewig, and S. Shapiro, "Study of a 10-MW Continuous Spallation Neutron Source," in this Proceedings.

[8] J. L. Hirshfield, C. Wang, and V. P. Yakovlev, "Multi-Cavity Proton Cyclotron Accelerator," *Phys. Rev. ST Accel. Beams* **5**, 081301 (2002).

[9] J. Haimson and B. Mecklenburg, "Design and Construction of a Chopper Driven 11.4 GHz Traveling Wave rf Generator," in *Proc. PAC1989*, (IEEE, New York, 1989), p. 243.

[10] T. C. Marshall, C. Wang, and J. L. Hirshfield, "Femtosecond Planar Electron Beam Source for Micron-Scale Dielectric Wake Field Accelerator," *Phys. Rev. ST AB* **4**, 121301 (2001).

[11] J.-M. Fang, T. C. Marshall, and V. Tarakanov, "Numerical Study of Interference between Transition Radiation and Cerenkov Wake Field Radiation in Dielectric Structures," in this Proceedings.

[12] I. N. Onishchenko, D. Yu. Sidorenko, and G. V. Sotnikov, "Structure of Electromagnetic Field Excited by an Electron Bunch in a Semi-Infinite Dielectric-Filled Waveguide," *Phys. Rev.* E **65**, 066501 (2002).

DIELECTRIC BRAGG ACCELERATOR

A. Mizrahi, L. Schächter, Electrical Engineering Department, Technion, Haifa 32000, Israel
R. L. Byer, Department of Applied Physics, Stanford University – MC4085, Stanford, CA 94305, USA
R. H. Siemann, SLAC, MS-7, Stanford University, P.O. Box 4349, Stanford, CA 94309, USA

Abstract

It is demonstrated that a planar Bragg reflection waveguide consisting of a series of dielectric layers may form an acceleration structure. It is shown that an interaction impedance per wavelength of over 100Ω is feasible with existing materials, Silica ($\varepsilon = 2.1$) and Zirconia ($\varepsilon = 4$), and if materials of high dielectric coefficient become available in the future, they may facilitate an interaction impedance per wavelength closer to 500Ω.

1 INTRODUCTION

Indications that solid-state lasers will reach wall-plug to light efficiencies of 30% or more make a laser-driven vacuum-accelerator increasingly appealing. Since at the wavelength of relevant lasers, dielectrics may sustain a significantly higher electric field and transmit power with reduced loss comparing to metals, the basic assumption is that laser accelerator structures will be made of dielectrics. Closed optical structures and near-field accelerators with dimensions comparable to the wavelength are both being considered. Examples of these two are: a) the LEAP [1] crossed laser beam accelerator where the interaction between the crossed laser beams and the particles is limited by slits to satisfy the Lawson-Woodward theorem [2, 3], and b) the *photonic band-gap* (PBG) concept where a laser pulse is guided in a dielectric structure with a vacuum tunnel bored in its center [4]. Lithography, which would result in planar structures, and optical fiber drawing are manufacturing techniques that seem well suited for laser driven structures that have typical dimensions of a few microns.

Motivated by the low-loss Bragg dielectric *planar* mirrors used in high-power lasers, it is suggested to harness this concept in order to confine the laser-field in an optical acceleration structure. Its essence is to form a hollow dielectric waveguide consisting of an almost perfect reflector made of a planar array of quarter-wavelength dielectric layers. In the transverse direction the geometry is similar to that of a dielectric mirror, however, its characteristics are slightly different since the wave number has a significant component ($k = \omega/c$) *parallel* to the dielectric surfaces, whereas in the case of a high-power laser mirror, the wave impinges *perpendicularly*.

2 DESCRIPTION OF THE SYSTEM

Consider a planar symmetric dielectric waveguide ($\partial/\partial y = 0$), as illustrated in Fig. 1, which has a vacuum inner layer of width $2D_{\rm int}$ and surrounding periodic layers made of two lossless materials $\varepsilon^{\rm I}, \varepsilon^{\rm II}$, the first layer

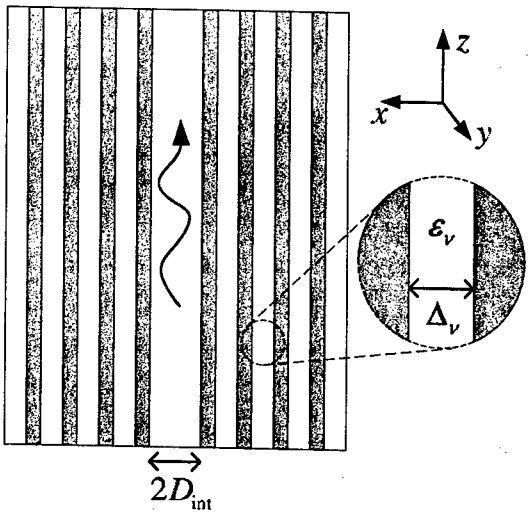

Figure 1: Planar dielectric waveguide.

having a relative dielectric coefficient $\varepsilon^{\rm I}$. Each layer has a thickness Δ_ν and a dielectric coefficient ε_ν. Assuming a steady-state regime ($e^{j\omega t}$) we focus on a mode having a phase velocity equal to the speed of light, or explicitly in the vacuum layer the electromagnetic field reads,

$$\begin{aligned} E_z &= E_0 e^{-j\frac{\omega}{c}z} \\ E_x &= j\frac{\omega}{c} x E_0 e^{-j\frac{\omega}{c}z} \\ H_y &= \frac{j}{\eta_0}\frac{\omega}{c} x E_0 e^{-j\frac{\omega}{c}z} \end{aligned} \tag{1}$$

and the field components within some dielectric layer ν are

$$\begin{aligned} E_z &= \left[A_\nu e^{-jk_\nu x} + B_\nu e^{+jk_\nu x}\right] e^{-j\frac{\omega}{c}z} \\ E_x &= \frac{-1}{\sqrt{\varepsilon_\nu - 1}}\left[A_\nu e^{-jk_\nu x} - B_\nu e^{+jk_\nu x}\right] e^{-j\frac{\omega}{c}z} \\ H_y &= \frac{-1}{Z_\nu}\left[A_\nu e^{-jk_\nu x} - B_\nu e^{+jk_\nu x}\right] e^{-j\frac{\omega}{c}z} \end{aligned} \tag{2}$$

wherein

$$Z_\nu \triangleq \eta_0\sqrt{\varepsilon_\nu - 1}/\varepsilon_\nu \tag{3}$$

is the transverse wave impedance and

$$k_\nu \triangleq \frac{\omega}{c}\sqrt{\varepsilon_\nu - 1} \tag{4}$$

is the transverse wavenumber. Imposing the continuity of E_z and H_y at the interfaces between the dielectric layers, a plane-wave matrix formulation is obtained. Given the geometry and the dielectric coefficients of a waveguide that

0-7803-7738-9/03/$17.00 © 2003 IEEE

supports the mode (1), the amplitudes in the second layer are dependent only on the vacuum fields. Imposing the continuity of the fields at the second boundary, we get that the amplitudes in the second layer depend only on the first and so forth, so that the amplitudes are determined from inside out.

3 FIELD CONFINEMENT

Analysis of the transverse propagation in the x direction is performed similarly to [5]. Assuming an infinite periodic structure, Floquet theorem leads to an eigen-value problem for the possible modes, and maximum attenuation per unit cell is seen to be achieved for the case of quarter-wavelength width layers. According to (4), each layer width should be $\lambda/(4\sqrt{\varepsilon-1})$, and an exponential decay is obtained. The attenuation in one period is given by the ratio of the lower to higher wave impedances of the two dielectric layers. In case of a plane wave impinging perpendicularly upon a planar interface, the impedance is $Z = \eta_0/\sqrt{\varepsilon}$, whereas if the wave has a phase velocity c in the z direction then the wave impedance is (3), which clearly has a maximum for $\varepsilon = 2$.

The above description of the confinement process, is of an *infinite* and ideal Bragg reflector. In case of a *finite* structure imposed by the vacuum tunnel, the design constraints on the first layer are different. The first layer, whose amplitudes are completely determined by $D_{\rm int}/\lambda$ and $\varepsilon^{\rm I}$, should be of such width that at the interface with the next layer, the perfect reflection condition is met. It may be conceived as a matching layer between the vacuum region to the subsequent periodic structure, as it rotates the amplitude vector dictated by the vacuum mode, to overlap the eigen-vector of the periodic structure. Confinement entails vanishing *real* part of the transverse component of the complex Poynting vector, meaning that in each dielectric layer there is a standing wave. Taking E_0 to be real without loss of generality, we get $A_\nu = B_\nu^*$. It is therefore evident that for the structure to truly support the mode, there must be an infinite number of layers, otherwise energy would "escape" and there would be no confinement. In a practical structure, the number of layers should be sufficient so that the outward power flow is negligible.

Fig. 2 illustrates a typical spatial distribution of the longitudinal electric field as well as the total electric field for a structure made of Silica ($\varepsilon^{\rm I} = 2.1$) and Zirconia ($\varepsilon^{\rm II} = 4$), and $D_{\rm int} = 0.3\lambda$. It shows that E_z is uniform in the vacuum layer while oscillating and decaying exponentially in the Bragg layers. Another feature is that E_z vanishes and achieves a maximum alternately at the discontinuities, which can be proved to be mathematically equivalent to the quarter- wavelength condition. Accordingly, the transverse electric field E_x, derived from E_z with respect to x, is maximal and discontinuous whenever E_z is zero, and zero whenever E_z peaks. The total electric field in turn undergoes a discontinuity every second interface.

Since our goal is to keep the energy as confined as possible in the vacuum inner layer, i.e., maximal interaction impedance, we may choose one of the dielectric materials to have $\varepsilon = 2$, and the other dielectric as large as possible. This will indeed create maximum attenuation per unit cell, however the interaction impedance depends on the total flowing power outside the vacuum layer, which tends to grow when low dielectric coefficient materials are used and the layers become thicker. Consequently, there exists a tradeoff between creating high contrast between the two materials, and using low dielectric coefficient materials. For instance, choosing one dielectric material to have $\varepsilon = 2$ and the the other as small as possible would result in high attenuation per period, but very low interaction impedance.

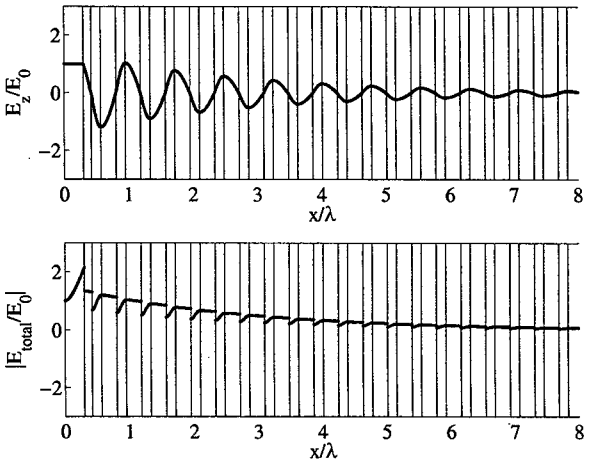

Figure 2: A typical distribution of the longitudinal electric field and the total electric field($D_{\rm int} = 0.3\lambda$, $\varepsilon^{\rm I} = 2.1$, $\varepsilon^{\rm II} = 4$).

4 ACCELERATOR PARAMETERS

4.1 Interaction Impedance

The interaction impedance is a measure of the accelerating gradient experienced by the electrons for a given amount of power injected into the system. Denoting by P the flowing power per unit length of y, the interaction impedance per unit length is defined by $Z_{\rm int}[\Omega m] \triangleq |\lambda E_0|^2/P$. Assuming that the materials' characteristics are known ($\varepsilon^{\rm I} = 2.1, \varepsilon^{\rm II} = 4$) and so is the laser wavelength (λ), the only free parameter left is the width of the internal vacuum layer $2D_{\rm int}$. Based on simulations, it was found that for $0.3 \le D_{\rm int}/\lambda \le 0.8$, the best fit for the interaction impedance is given by

$$\frac{Z_{\rm int}}{\eta_0\lambda}(\varepsilon^{\rm I}=2.1,\varepsilon^{\rm II}=4) \simeq 1.124 - 3.561\frac{D_{\rm int}}{\lambda} + 4.258\left(\frac{D_{\rm int}}{\lambda}\right)^2 - 1.823\left(\frac{D_{\rm int}}{\lambda}\right)^3 \quad (5)$$

which means $Z_{\rm int}/\lambda$ decreases monotonically from about 147Ω to about 26Ω.

Holding the vacuum region width to a constant value ($D_{\rm int} = 0.3\lambda$), Fig. 3 shows the contours of constant interaction impedance as a function of $(\varepsilon^{\rm I}, \varepsilon^{\rm II})$. Since no confinement is expected when the medium is uniform ($\varepsilon^{\rm I} = \varepsilon^{\rm II}$), the interaction impedance is virtually zero on the diagonal. Similarly, when either one of the dielectric coefficients is close to unity, the thickness of the layer being proportional to $1/\sqrt{\varepsilon - 1}$ implies large confinement space and therefore, low interaction impedance. In between these three minima regions there are two *asymmetric* regions of maximum interaction impedance. The asymmetry is dictated by the choice of the dielectric consisting the first layer ($\varepsilon^{\rm I}$). For the vacuum layer width chosen here, a larger impedance is obtained when the first layer is of lower value, but this trend may change for a different value of $D_{\rm int}$. Clearly, a *high dielectric coefficient* can significantly increase the interaction impedance. For example, taking Silica for the first layer and a material with $\varepsilon = 25$ for the second layer, leads to an interaction impedance per wavelength of 471Ω.

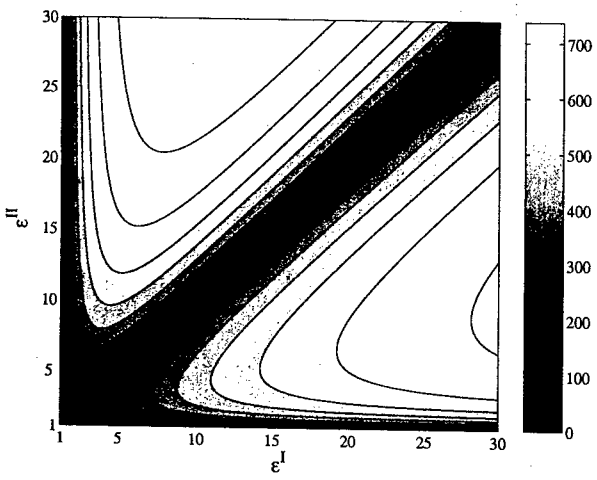

Figure 3: Contours of constant interaction impedance $Z_{\rm int}/\lambda[\Omega]$ as a function of $(\varepsilon^{\rm I}, \varepsilon^{\rm II})$, with $D_{\rm int} = 0.3\lambda$.

4.2 *Energy Velocity*

Denoting the energy density by $w_{\rm EN}$, we define the average energy per unit length as $W \triangleq \int_{-\infty}^{\infty} dx\, w_{\rm EN}(x)$ and the energy velocity is defined by $v_{\rm EN}/c \triangleq P/(cW)$. According to our simulations, for $0.3 \le D_{\rm int}/\lambda \le 0.8$, the energy velocity increases monotonically from about $0.42c$ to about $0.53c$. As before, the best fit of the simulation results is given by

$$\frac{v_{\rm EN}}{c}(\varepsilon^{\rm I} = 2.1, \varepsilon^{\rm II} = 4) \simeq 0.342 + 0.290\left(\frac{D_{\rm int}}{\lambda}\right) - 0.061\left(\frac{D_{\rm int}}{\lambda}\right)^2 \quad (6)$$

4.3 *Maximum Electric Field*

The last parameter of interest is the maximum electric field sustained by the structure before breakdown. According to (1) the magnitude of the electric field vector increases from a local minimum on axis, to a larger value

$$\frac{E_{\rm max}}{E_0} = \sqrt{1 + \left(\frac{2\pi D_{\rm int}}{\lambda}\right)^2} \quad (7)$$

at the vacuum-dielectric discontinuity; for most practical purposes this may also be considered the maximum electric field – fact revealed also by the bottom frame of Fig. 2. For avoiding breakdown it is assumed that the fluence threshold of the material limits the maximum field to about 2GV/m. Therefore, bearing in mind that the gradient of interest is of the order 1GV/m, then Eq. (7) entails the inner layer half-width should be

$$\frac{E_{\rm max}}{E_0} = 2 \Rightarrow D_{\rm int} \simeq 0.28\lambda \quad (8)$$

5 CONCLUSION

In the present study we have designed and analyzed an accelerator based on a Bragg reflection waveguide, where the layers have a width of a quarter of the transverse propagation wavelength $\lambda/(4\sqrt{\varepsilon - 1})$. An interaction impedance per wavelength of over 100Ω is feasible with existing materials. Materials of high dielectric coefficient can significantly improve the interaction impedance per wavelength to hundreds of Ohms.

The planar structure provides a good analogy, especially asymptotically, to a hollow *cylindrical* Bragg fiber accelerator. A cylindrical structure would have a higher interaction impedance than a planar structure for an internal radius $R_{\rm int} = D_{\rm int}$ for two reasons. For a given gradient the *maximum* field would be smaller as the radial electric field $E_r = \frac{j}{2}\frac{\omega}{c} r E_0 e^{-j\frac{\omega}{c}z}$ would be smaller by a factor of 2. The second reason is that in addition to the radial exponential decay, in the cylindrical case there would be a $1/r$ decay due to the cylindrical wave functions.

6 REFERENCES

[1] Y. C. Huang, D. Zheng, W. M. Tulloch, and R. L. Byer, "Proposed structure for a crossed-laser beam, GeV per meter gradient, vacuum electron linear accelerator," *Applied Physics Letters*, vol. 68, pp. 753–755, February 1996.

[2] J. D. Lawson, "Lasers and accelerators," *IEEE Transactions on Nuclear Science*, vol. 26, pp. 4217–19, June 1979.

[3] P. M. Woodward, *J. IEE*, vol. 93, p. 1554, 1947.

[4] X. E. Lin, "Photonic band gap fiber accelerator," *Physical Review Special Topics – Accelerators and Beams*, vol. 4, pp. 051301 1–7, May 2001.

[5] P. Yeh and A. Yariv, "Bragg reflection waveguides," *Optics Communications*, vol. 19, pp. 427–430, December 1976.

POSITRON BEAM PROPAGATION IN A METER LONG PLASMA CHANNEL

K. A. Marsh, B. E. Blue, C. E. Clayton, C. Joshi, W. B. Mori, UCLA, Los Angeles, CA, F.-J. Decker, M. J. Hogan, R. Iverson, C. O'Connell, P. Raimondi, R. Siemann, D. Walz, SLAC, Stanford, CA, T. C. Katsouleas, P. Muggli, USC, Los Angeles, CA

Abstract

Recent experiments and simulations have shown that positron beams propagating in plasmas can be focused and also create wakes with large accelerating gradients. For similar parameters, the wakes driven by positron beams are somewhat smaller compared to the case of an electron beam. Simulations have shown that the wake amplitude can be increased if the positron beam is propagated in a hollow plasma channel (Ref. 1). This paper, compares experimentally, the propagation and beam dynamics of a positron beam in a meter scale homogeneous plasma, to a positron beam hollow channel plasma. The results show that positron beams in hollow channels are less prone to distortions and deflections. Hollow channels were observed to guide the positron beam onto the channel axis. Beam energy loss was also observed implying the formation of a large wake amplitude. The experiments were carried out as part of the E-162 plasma wakefield experiments at SLAC.

INTRODUCTION

In the "blow out" regime of the plasma wakefield accelerator (PWFA) a high density electron beam exerts a large radial force on the plasma electrons, creating a nearly uniform ion column. As the beam passes through, plasma electrons rush back to neutralize the ions creating a large amplitude wake following the drive beam. The wake can be used to accelerate electrons in a trailing beam, or electrons in the tail of the drive beam can be used to probe the wake.

The ion column acts as a thick, underdense, plasma lens, with a large focusing strength thus producing multiple betatron oscillations as shown in reference 2. For a uniform ion column the force on the beam is linear with radius. In this case, the beam can propagate without distortion or emittance growth.

In the case of a positron beam, plasma electrons flow in to neutralize the beam in a very dynamic way. As the beam passes through, these plasma electrons rapidly exit leaving a large amplitude wake behind. Due to the large reservoir of plasma electrons surrounding the beam, electrons can be pulled in continuously. Some overshoot and pass through the beam or oscillate about the beam axis. The resulting focusing forces are nonlinear and vary with r and z along the beam as shown in Ref. 3. At best, nonlinear but symmetric forces, result in emittance growth and beam halo formation.

A radially inhomogeneous plasma can create a deflection or distortion of an electron beam due to the creation of an asymmetric ion column. Similarly, positron beams can be deflected or distorted due to a radially asymmetric flow of plasma electrons to one part of the positron beam or another. Also, electron or positron beams with head to tail tilts can be deflected and distorted. This is because forces on axially misaligned beam slices will have a focusing component plus a transverse deflecting component. These distortions and deflections are experimentally unwanted and have often been observed during E-162 runs.

Hollow channel plasmas can guide a positron beam. Ions on the channel wall repel the beam and confine it on axis. The physical mechanism and results are discussed further below.

EXPERIMENTAL SET UP

The experiment was conducted at SLAC as part of the PWFA work known as E-162. The experiment was located at the Final Focus Test Beam Facility (FFTB). The set up and measurement details are described in many other papers (See references). Here we give only a brief description. The 28.5 GeV positron beam was focused to the entrance of a uv photoionized lithium plasma. Typical beam parameters were, 2×10^{10} positrons per bunch, 600 μm rms bunch length, with a 25 μm beam size at the plasma entrance. The SLAC beam emittance was increased due to scattering from foils and from a thin uv coupling mirror placed in the beam line. The beam emittance at the plasma entrance was about 2×10^{-9} m-r.

A column of lithium vapor, 140 cm, long was produced in a heat pipe oven (Ref. 4). A uv ArF laser was used to single photon ionize the lithium vapor. For these experiments, the plasma density was proportional to uv fluence (J/cm^2). The plasma density ranged from (0 - 2)$\times10^{14}$ cm^{-3}. An axially uniform plasma can be produced by focusing the laser to compensate for uv absorption. Axial variations in plasma density do not significantly alter the resulting transverse dynamics of the beam as long as the scale of the density variation is larger than the betatron wavelength. When absorption is taken into account, the radial plasma profile mimics the laser profile.

0-7803-7738-9/03/$17.00 © 2003 IEEE

The plasma channel was produced by placing a mask in the center of the uv laser beam. The mask diameters used were 1 mm and .6 mm. An ideal plasma channel with rigid walls like that described in Ref. 1, would be difficult to produce due diffusion of the plasma. Since the laser fires ~ 200 ns before the positron beam arrives, this allows some time for diffusion to take place. We believe the beam is propagating in something more like a density depression than an ideal rigid channel. In any case this will be referred to as a hollow channel as well. Comparison to the case without a channel was performed for the same conditions by removing the mask.

The beam spot size and location was monitored by optical transition radiators (OTR) located upstream (US) and downstream (DS) of the plasma. Focusing and transverse dynamics were observed on the DSOTR verses a uv count which is proportional to the plasma density. Monitoring of the incoming beam parameters was a simple matter of toggling the uv laser so that no plasma was produced.

An imaging spectrometer was set up to monitor the changes in beam energy after traversing the plasma. A permanent dipole bending magnet was used to disperse the beam and quadrupole lenses were used to image the beam from the plasma exit to an aerogel Cherenkov radiator (CR). Imaging assures that the observed beam energy is true and not due to transverse effects. The magnetic dispersion is about 10 cm or 300 MeV /mm. The CR was imaged onto a CCD camera where changes of the beam energy were observed. CR light was also imaged on to a streak camera (SC) where changes in the beam energy along the pulse were monitored.

The incoming beam has a correlated energy spread of about 350 MeV with the higher energy in the head. Observation of energy gain of tail electrons is difficult unless they gain enough energy to be clearly seen above the energy of the head. By streaking the beam energy in time, we can look at the change in energy along the beam, particularly the energy loss of the middle of the beam and energy gain of the tail electrons.

RESULTS

Figure 1 compares the beam images at the DSOTR with no plasma, to plasma with and without a channel. With the channel the beam propagated and focused without distortion. Without a channel the beam was focused, but has an unwanted distortion. Figure 2 shows the average beam deflection verses uv counts, without the hollow channel. All the points are for the same input beam parameters. The beam was deflected without the channel indicating the plasma profile was radially inhomogeneous and or the beam was tilted. In contrast the beam was not deflected but rather guided with the hollow channel. Guiding occurs when the positron beam is misaligned or at a small angle to the hollow channel axis. The build up of ions on the channel wall, confine the beam by repelling the beam toward the channel axis.

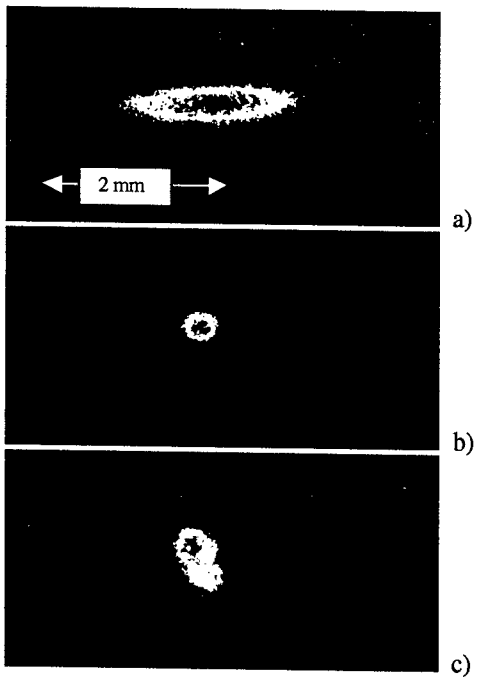

Figure 1. Comparison of positron beam images at the DSOTR for a) no plasma b) plasma with a hollow channel c) plasma without a channel .

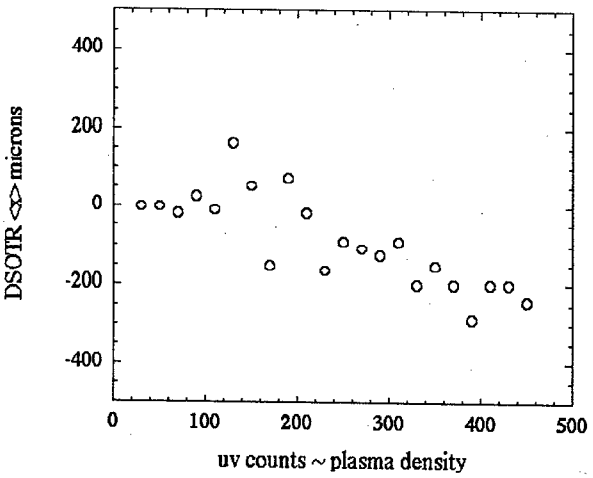

Figure 2. Average beam deflection verses uv counts (proportional to plasm density) for a plasma without a hollow channel.

Random shot to shot misaligment of the beam to the hollow channel axis occurred due to small energy variations of the beam. This resulted in steering from the slightly misaligned final focusing quads. Figure 3 shows the beam trajectory at the US and DS OTR's for 200 shots. The open circles show the correlation between beam location on the OTR's without plasma. The crosses

show the beam guiding with the hollow channel. The beam moves toward the center location in x, which demonstrates hollow channel guiding. Similarly the beam was also guided in y.

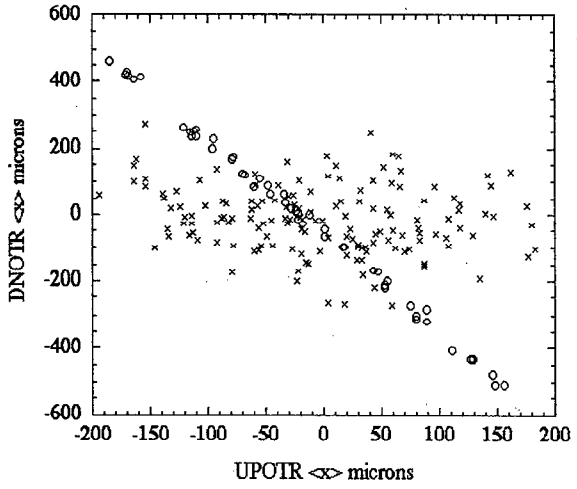

Figure 3. Beam guiding trajectory on DS vs. US OTR. The open circles show the correlation between beam location on the OTR's without plasma. Crosses show when the plasma is on the beam moves toward the center location of the channel in x.

As noted above, the homogeneous plasma actually has a radial profile peaked on axis like the uv laser. Beams not on axis with the plasma were deflected. A beam on a trajectory moving across the plasma axis would appear to steer toward the axis. This is not guiding as evidenced by the fact that the beam is deflected further as the plasma density was increased.

The plasma dynamics of a positron beam propagating in a hollow channel are illustrated in Fig. 4a. An annulus of plasma electrons are pulled toward the beam as the beam moves through the channel. Most of the plasma electrons reach the beam axis as it passes by. Therefore very few plasma electrons cross the beam allowing for propagation with low distortion and deflection. Figure 4b, shows the flow in of plasma electrons for the homogeneous case. Plasma electrons cross the beam and some oscillate about the axis leading to nonlinear focusing forces along the beam.

The central portion of the beam looses energy as it propagates through the plasma channel. Figure 5, compares CR images of the energy spectra for no plasma, a low density hollow channel and a high density hollow channel plasma. At low density we see the beam is focused, but no significant energy change. At high density the beam looses significant energy of about 200 MeV. To observe energy gain of the beam tail requires further analysis of the streak camera images.

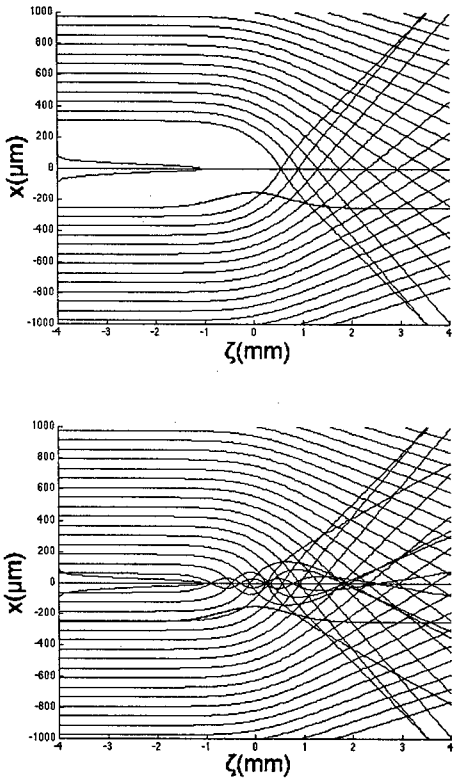

Figure 4. Illustration of plasma dynamics, a) with and b) without a hollow plasma channel. Beam moves to the left.

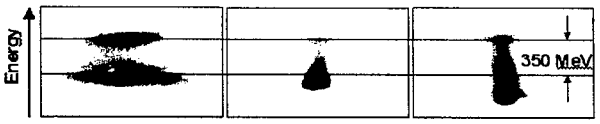

Figure 5. Energy spectrum of positron beam a) with no plasma compared to b) low density and c) high density hollow plasma channels.

REFERENCES

[1] S. Lee et al., Phys. Rev. E 64, 045501(R) (2001)
[2] C. E. Clayton et al., Phys. Rev. Lett. 88, 154801 (2002); C. O'Connell et al., PRST-AB 5, 121301 (2002)
[3] M. J. Hogan et al., Phys. Rev. Lett. accepted for publication; P. Muggli et al., these proceedings
[4] P. Muggli et al., IEEE Trans. Plasma Sci. 27, 791, (1999); K. A. Marsh et al., Advanced Accelerator Concepts, 10th Workshop, Mandalay Beach, CA, Ed. C. E. Clayton, P. Muggli, AIP Conf. Proc. #647, 2002, pp. 614-619.

We gratefully acknowledge our collaborators past and present, Brian "Photoshop" Flores and our DOE support. Work supported by DOE grants DE-FG03-92ER40727 andDE-FG03-92ER40745.

SIMULATION OF IONIZATION EFFECTS FOR HIGH-DENSITY POSITRON DRIVERS IN FUTURE PLASMA WAKEFIELD EXPERIMENTS*

D.L. Bruhwiler, D.A. Dimitrov and J.R. Cary#, Tech-X Corp., Boulder, CO 80301, USA
E. Esarey, W.P. Leemans, LBNL, Berkeley, CA 94720, USA

Abstract

The plasma wakefield accelerator (PWFA) concept has been proposed [1] as a potential energy doubler for present or future electron-positron colliders. Recent particle-in-cell (PIC) simulations have shown [2] that the self-fields of the required electron beam driver can tunnel ionize neutral Li, leading to plasma wake dynamics differing significantly from that of a preionized plasma. It has also been shown [3], for the case of a preionized plasma, that the plasma wake of a positron driver differs strongly from that of an electron driver. We will present new PIC simulations, using the OOPIC [4] code, showing the effects of tunneling ionization on the plasma wake generated by high-density positron drivers. The results will be compared to previous work on electron drivers with tunneling ionization and positron drivers without ionization. Parameters relevant to the energy doubler and the upcoming E-164x experiment [5] at the Stanford Linear Accelerator Center will be considered.

INTRODUCTION

Plasma-based accelerators have demonstrated accelerating fields in excess of 100 GV/m (for a review, see Ref. [6]), which is two to three orders beyond that of conventional technology. The acceleration field in a PWFA [7,8] is generated by a relativistic electron or positron beam. The self-fields of the drive bunch excite a wakefield that propagates close to the speed of light, *c*.

We present 2-D OOPIC simulations of PWFA configurations for both e+ and e- drive beams. Field-induced tunneling ionization is an important effect that has to be considered when designing advanced accelerators. The electric field magnitudes that are reached can be sufficient to tunnel ionize certain neutral gases. The released electrons contribute to the plasma density and affect the physics of the propagating beam and the formed wake.

Initially, we show results that demonstrate agreement with results previously published by Lee *et al.* [3]. Then we show new simulations for positron and electron beams with expected E-164x parameters. We studied both e+ and e- beams propagating in preionized plasma and in Cs neutral gas with the same density as in the preionized plasma case. The plasma is created completely by tunnelling ionization for the runs with Cs. The results for the positron beams with tunnelling ionization are the first such PIC simulations. Our parameter studies from these simulations are summarized for both beams and are relevant to the design of the E164x experiments.

*Funded by US DoE under grant no.'s DE-FG03-02ER83557, DE-FG02-01ER41178, DE-FG03-95ER40926 & DE-AC03-76SF00098.
#also University of Colorado, Boulder, CO 80309, USA

COMPARISON WITH PREVIOUS WORK

Recently, Lee *et al.* [3] published results from 3-D PIC simulations on plasma wakefield acceleration of a positron beam. We repeated these simulations, using 2-D cylindrical geometry, for both the electron and positron beams. Some of the relevant parameters for these benchmarking simulations are summarized in Table 1.

Table 1: Simulation Parameters

Quantity	Benchmarking	E-164x
dt [s]	$1\text{-}2 \times 10^{-14}$	1.5×10^{-15}
dz [μm]	12.75 - 25	1
dr [μm]	6.35 - 12.7	1
n_e [cm^{-3}]	4.3×10^{14}	10^{16} - 10^{17}
n_{Cs} [cm^{-3}]	--	10^{16} - 10^{17}
σ_r [μm]	75	20
σ_z [μm]	400	20
N_{ptcls}	2×10^{10}	1×10^{10}
E_{beam} [GeV]	30	30

In our OOPIC simulations, a positron or an electron beam with Gaussian distributions along the longitudinal and transverse directions is propagated in preionized plasma for 2 cm. Figure 1 shows a surface plot of the longitudinal electric field E_z from the positron run and a lineout (r = 0) in Fig. 2. The peak accelerating field of 210 MV/m is in excellent agreement with results in Ref. [3].

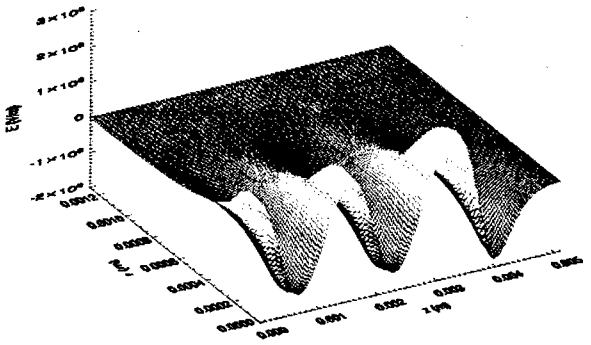

Figure 1: Surface plot of Ez for a positron driver, using parameters on the left side of Table 1.

0-7803-7738-9/03/$17.00 © 2003 IEEE

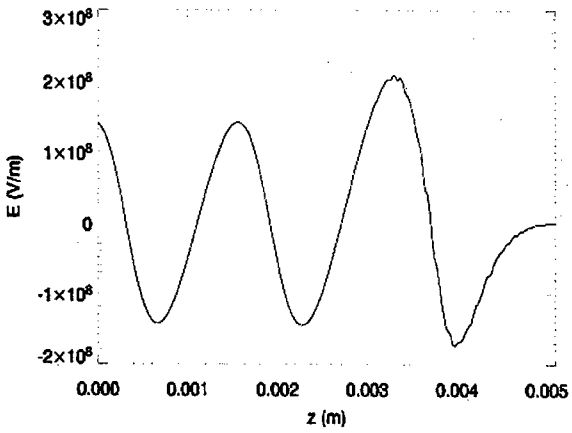

Figure 2: Line-out of E_z from Fig. 1, along r=0, for a positron driver.

The corresponding results for the electron simulations are shown in Fig.'s 3 and 4, again showing excellent agreement with Ref. [3] in all aspects, except for the details of the narrow field spike, which is an under-resolved feature and is not useful for accelerating particles.

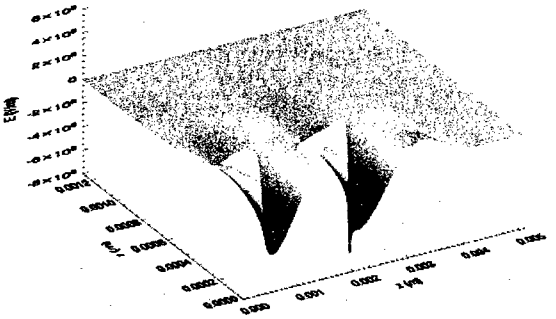

Figure 3: Surface plot of E_z for an electron driver, using parameters on the left side of Table 1.

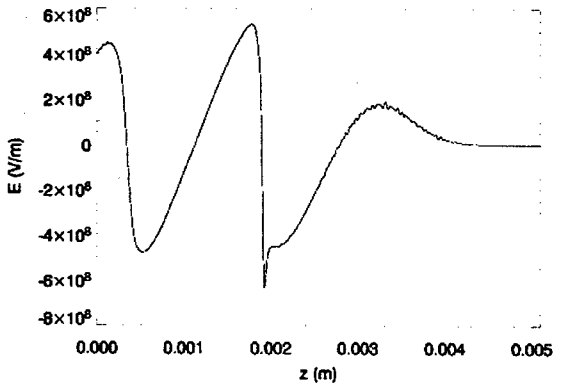

Figure 4: Line-out of E_z from Fig. 3, along r=0.

E-164x PARAMETERS

We now consider a new parameter regime, described by the right-hand column of Table 1, which is relevant to the planned E-164x experiment at SLAC – a follow-on to the presently running E-164 experiment. In choosing the range of densities to simulate, we considered Eq. (1) of Ref. [3] --

$$E_z \sim \frac{n_b\sqrt{2\pi}\left(k_p^2\sigma_r^2\right)k_p\sigma_z\exp\left(-k_p^2\sigma_z^2/2\right)}{\sqrt{n_o}\left(1+k_p^2\sigma_r^2\right)}\sin\left(k_p\left(z-ct\right)\right)$$

which is an approximate expression for the peak electric field in an electron-driven PWFA, derived from linear theory. If σ_r and σ_z are held fixed, then one can choose an optimal density by maximizing E_z.

In the limit that $k_p\,\sigma_r << 1$, one finds the optimal density can be expressed by the equation $k_p\,\sigma_z$ = sqrt(2). For the special case $k_p\,\sigma_r = k_p\,\sigma_z$, the optimal density is determined by $k_p\,\sigma_z = 1$. In general, the requirement is

$$k_p^2 = \left(1/2\sigma_r^2\right)\left[\sqrt{1+8\sigma_r^2/\sigma_z^2}-1\right].$$

For our parameters, the optimal plasma density is $7\text{x}10^{16}$ cm^{-3}, which is comparable to the beam density – putting us into a regime where linear theory is marginally valid.

Figure 5 shows the surface plot of E_z for a positron driver and a 100% pre-ionized plasma. The peak value just exceeds 10 GV/m, which is less than the cold wave-breaking field E_0~25 GV/m, consistent with a linear plasma response. Figure 6 shows a color contour plot of the electron number density in the wake.

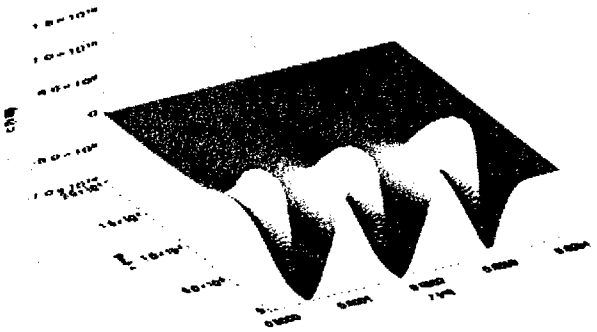

Figure 5: Surface plot of E_z for a positron driver in a pre-ionized plasma, using parameters on right side of Table 1.

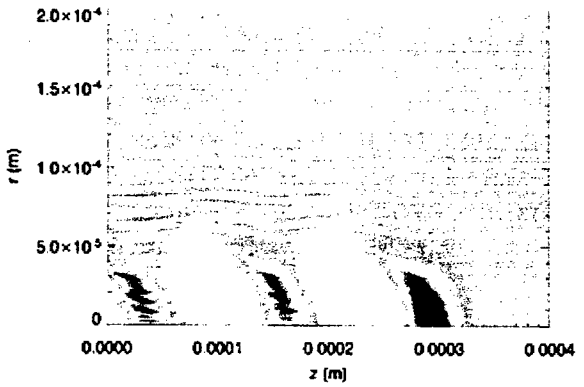

Figure 6: Contour plot of n_e for same case as in Fig. 5; the high densities create the large wake fields.

Figure 7 shows the surface plot of E_z for a positron driver in a neutral Cs gas. The wakefield is remarkably similar to that of the pre-ionized case, shown above in Fig. 5. Figure 8 shows a color contour plot of the electron number density in the wake – this image differs significantly from Fig. 6, because here the wake electrons are created locally by high electric fields.

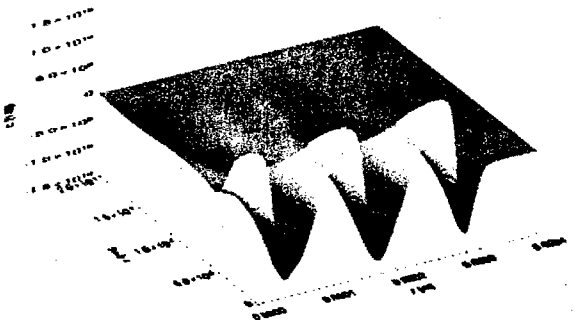

Figure 7: Surface plot of E_z for a positron driver in neutral Cs, using parameters on right side of Table 1.

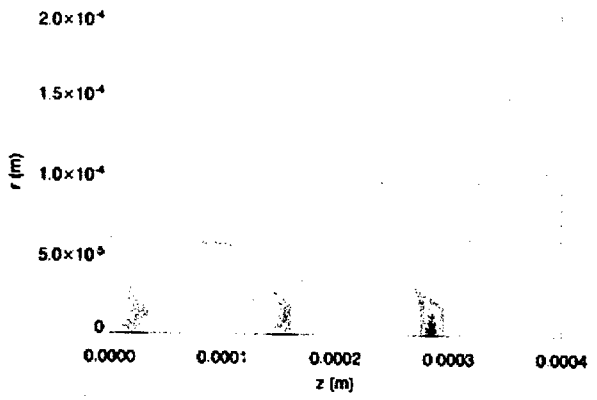

Figure 8: Contour plot of n_e for same case as in Fig. 7; all wake electrons are generated via tunneling ionization.

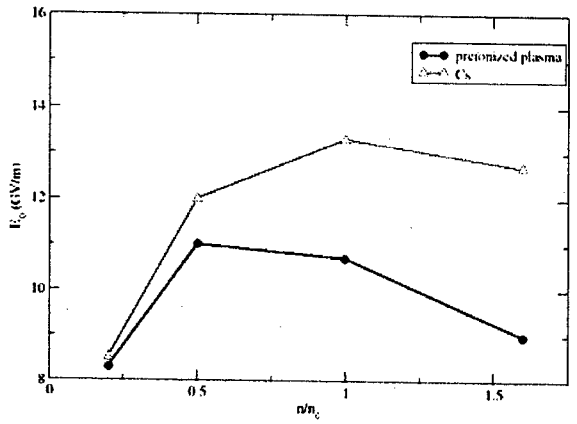

Figure 9: Variation of peak accelerating field with density for positron drivers in pre-ionized plasma & neutral Cs.

The density of the pre-ionized plasma, and alternatively of the neutral Cs gas, was scanned over a range centered on the prediction from linear theory. Figure 9 presents the peak E_z as a function of density, showing that for the neutral Cs case it peaks at slightly higher density and at slightly higher values than for the pre-ionized case.

These results strongly suggest that a high-density positron driver, such as one would find in a "plasma afterburner" scenario, does not require the Cs gas to be pre-ionized. Because it is practically impossible to 100% pre-ionize a gas, the effects of tunneling ionization would likely disrupt the idealized wake by ionizing much of the background gas. For these reasons, positron-driven PWFA's using a neutral gas like Cs show significant promise.

CONCLUSIONS

We have presented the first PIC simulations of e+ drivers for a PWFA, including the effects of tunneling ionization. Agreement with previous work for a pre-ionized plasma was shown. For new work, parameters relevant to E-164x were chosen.

For E-164x parameters, the results with TI of neutral Cs are very close to the ideal case of a pre-ionized plasma. In fact, the peak fields in the TI case are slightly higher. Thus, one could likely use neutral Cs gas for a full-scale "plasma afterburner" facility, which would save the expense and complexity of a UV laser system for pre-ionization.

ACKNOWLEDGEMENTS

The authors thank Richard Busby for his excellent Python scripts, which enable batch mode parameter sweeps and automatic image rendering with OOPIC. We also thank M. Hogan, C. Joshi, T. Katsouleas, K. Marsh, W. Mori and P. Muggli for many helpful discussions.

This work is supported in part by the SciDAC project -- Advanced Computing for 21st Century Accelerator Science & Technology, an initiative of the U.S. Department of Energy, under Contract No. DE-FG02-01ER41178. This work is further supported by the U.S. Department of Energy, under Contract No.'s DE-FG03-99ER82903, DE-FG03-95ER40926 and DE-AC03-76SF00098, and by Tech-X Corporation. This work used resources of the National Energy Research Scientific Computing Center.

REFERENCES

[1] S. Lee *et al.*, Phys. Rev. S.T. AB **5**, 011001 (2002).
[2] D.L. Bruhwiler *et al.*, Phys. Plasmas **10**, 2022 (2003).
[3] S. Lee et al., Phys. Rev. E **64**, 045501(R) (2001).
[4] D.L. Bruhwiler *et al.*, Phys. Rev. S.T. AB **4**, 101302 (2001); J.P. Verboncoeur *et al.*, Comp. Phys. Comm. **87**, 199 (1995).
[5] W. Lu *et al.*, Bull. Am. Phys. Soc. 47 (9), 316 (2002).
[6] Esarey *et al.*, IEEE Trans. Plasma Sci. **24**, 252 (1996).
[7] P. Chen *et al.*, Phys. Rev. Lett. **54**, 693 (1985).
[8] R. Ruth *et al.*, Part. Accel. **17**, 171 (1985).

Proceedings of the 2003 Particle Accelerator Conference

TECHNOLOGY OPTIONS FOR LINEAR COLLIDERS

G. Dugan
Laboratory for Elementary Particle Physics*, Cornell University, Ithaca, NY 14853

Abstract

A worldwide consensus has developed in the international high-energy physics community that an electron-positron linear collider, with an initial center-of-mass energy of around 500 GeV, should be the next energy frontier accelerator. This paper will review the technical highlights of options for the machine's realization, and discuss the advantages and disadvantages of each.

LINEAR COLLIDER MOTIVATIONS AND REQUIREMENTS

The international high-energy physics community has concluded that a high-energy, high-luminosity, electron-positron linear collider, operating concurrently with the Large Hadron Collider, is necessary to explore and understand electroweak unification and related physics at the TeV energy scale. The underlying science indicates the need for initial operation at a center-of-mass energy of 500 GeV, with capability for upgrade to roughly 1 TeV. An average luminosity of roughly 100-150 fb^{-1}/yr is required, corresponding to a peak luminosity of at least $2\times10^{34}\mathrm{cm}^{-2}\mathrm{s}^{-1}$.

To achieve the required luminosity, beams with very high transverse density must be brought into collision. The strong electromagnetic fields of these dense beams cause them to radiate copiously (producing "beamstralung") during the collision. To limit this radiation, which increases the effective energy spread of the beams and produces background, "flat" beams, with a small vertical-to-horizontal aspect ratio, are used. For flat beams, the peak luminosity of the linear collider is given by

$$\mathcal{L}\left[10^{34}\mathrm{cm}^{-2}\mathrm{s}^{-1}\right] \cong 121 N_\gamma H_D \frac{P_b\,[\mathrm{MW}]}{E_b\,[\mathrm{GeV}]\,\sigma_y\,[\mathrm{nm}]}$$

in which E_b is the beam energy, P_b is the beam power, σ_y is the vertical beam size at the collision point, N_γ is the number of beamstralung photons per electron, and H_D is the luminosity enhancement due to beam-beam focusing at the collision point. To limit beamstralung, N_γ must be kept in the range <2, for which $H_D \sim 1.5$.

This relation illustrates the need to collide beams with the highest feasible beam power, and the smallest feasible vertical spot size. These criteria drive much of the design of the linear collider.

*supported by the National Science Foundation under award NSF PHY-9809799

LINEAR COLLIDER ACCELERATOR SYSTEMS

The accelerator systems required for a linear collider include electron and positron sources in which the beams are created, damping rings[1] in which the beams are cooled to low emittance, main linacs in which the acceleration takes place, and beam delivery systems which bring the beams into collision. In the following sections, the options being considered for these accelerator systems will be described, the advantages and disadvantages noted, and the outstanding technical challenges outlined. A detailed presentation of the leading issues can be found in the recent report of the International Linear Collider Technical Review Committee[1].

MAIN LINACS

The dominant technical systems in the linear collider are the main linacs, and the choice of technology for the main linac accelerating structures is the fundamental design decision for the machine.

Options

Over the past two decades, an enormous amount of accelerator R&D has been done to develop technologies for the main linacs which can realize the demanding requirements at an affordable cost. The fruits of this R&D are the following options for the main linac accelerating structures:

- superconducting standing-wave cavities, operating at L-band (1.3 GHz), developed by the TESLA collaboration[2] at DESY;
- normal-conducting traveling-wave cavities, operating at X-band (11.4 GHz), developed by the JLC/NLC collaboration[3, 4] at SLAC and KEK[2];
- very high gradient normal-conducting traveling-wave cavities, operating at 30 GHz, potentially capable of reaching beam energies up to 1.5 TeV, being developed by the CLIC collaboration[5] at CERN.

The basic features of the three options are displayed in Table 1, for the baseline beam energy of 250 GeV, and for the upgrade energy.

TESLA utilizes 104 cm long 9-cell pure niobium standing-wave cavities, operating at 24 MV/m, in a static bath of 2 K liquid helium. The choice of a long RF pulse

[1]Bunch compressors are also required, but these systems will not be covered here due to space limitations.

[2]A C-band option, operating at 5.7 GHz, is also under consideration at KEK[4].

0-7803-7738-9/03/$17.00 © 2003 IEEE

Table 1: Linear Collider Options

Feature	TESLA		JLC/NLC		CLIC	
RF frequency [GHz]	1.3		11.4		30	
Beam energy [GeV]	250	400	250	500	250	1500
Luminosity [$\times 10^{34}$cm^{-2}s^{-1}]	3.4	5.3	2.5/2.0	2.5/3.0	2.1	8.0
Bunch population [$\times 10^{10}$]	2	1.4	0.75		0.4	
Rms vertical beam spot size at IP [nm]	5.0	2.8	3.0	2.1	1.2	0.7
Loaded accelerating gradient [MV/m]	24	35	50		150	
Two-linac length [km]	30		13.8	27.6	5.0	28.0
Number of accelerating structures	20592	21816	18288	37152	7272	44000
Number of klystrons	572	1212	4572	9288	448	
Linac cycle frequency [Hz]	5	4	150/120	100/120	200	100
Total AC power for linac [MW]	95	160	188/150	254/305	105	319
Total beam power [MW]	22.6	35	17.4/13.8	23/27.6	9.8	29.6
Efficiency (beam power/AC power) [%]	23.8	21.9	9.3/9.2	9.1/9.1	9.3	9.3

(1370 μs) is made possible by the ability of superconducting cavities to store energy with minimal losses. Because of the long RF pulse, the required peak RF power is relatively modest (240 kW), despite the substantial average beam power required to achieve high luminosity. Although small, the cavity losses are deposited at 2 K, and a large cryogenic plant is required to accommodate these losses.

JLC/NLC utilizes 60 cm long copper traveling-wave cavities, operating at a loaded gradient of 50 MV/m. The losses in the copper structure are limited by the use of a short RF pulse (0.4 μs). During the short RF pulse, the required peak power is quite high (56 MW), necessitating the use of high peak power X-band klystrons, together with a pulse compression scheme.

CLIC uses 50 cm long 30 GHz copper structures, operating at a loaded gradient of 150 MV/m and with a very short RF pulse (0.13 μs). Very high peak power (>200 MW) is required. As there is no available RF power source at this frequency and power, CLIC uses two-beam technology to transfer power from a low-energy, high current counter-propagating electron beam.

In addition to accelerating the beam, the main linacs are required to preserve the ultra-low emittance generated in the damping rings, which must be delivered to the interaction point. The principal emittance dilution mechanisms for an off-axis beam are dispersive growth, driven by energy spread in the linac quadrupoles; and wakefield-induced growth, driven by the transverse wakefields of the accelerating structures. To control long-range wakefields, the copper structures incorporate damping and detuning features in each cell, which require precise fabrication tolerances. The TESLA cavities use higher-order mode dampers at the cavity ends.

In practice, wakefield and dispersive emittance growth are controlled by alignment of the centers of the quadrupoles and the structures to the beam. Since the micron-level required precision cannot be attained in the *ab initio* survey, elaborate beam-based alignment schemes are required to determine the "gold orbit", together with feedback systems to maintain the beam on this orbit in the presence of natural and cultural ground motion. The beam-based alignment performance is limited by the features of the beam instrumentation, such as the resolution of the beam position monitor (BPM) system, and the precision of the emittance measurement system.

Advantages and disadvantages

The principal advantage of the warm linacs is the high accelerating gradient, which allows a shorter linac than TESLA, for the same final energy. Depending on the unit costs, this can translate into a cost advantage. The TESLA linac has two principal advantages: higher efficiency and reduced wakefields.

The higher efficiency of TESLA (see Table 1) implies that less average RF power, and hence less capital investment in RF hardware, is required for a given luminosity. This is offset to some extent by the need for a cryogenic plant to provide the ultralow cavity temperature. Nonetheless, even including this, TESLA is more than twice as efficient as the warm linacs.

The peak RF power is much lower in TESLA than in the warm linacs. The absence of the need for pulse compression and high peak-power klystrons makes the high-level RF system in TESLA much less elaborate. The bulk of the more compact TESLA RF system can be housed in the same tunnel as the linac beamline, while, for JLC/NLC, the RF systems must be housed in a separate tunnel parallel to the linac beamline tunnel. The single tunnel arrangement is less costly than the dual tunnel scheme, but has open questions related to reliability and maintainability of the RF components in the beamline tunnel.

TESLA's low frequency superconducting cavities have lower wakefields than the high frequency copper structures, leading to less stringent requirements on alignment tolerances and on the performance of beam position measure-

ment instrumentation. Special structure BPM's in the warm structures provide information on the position of the beam relative to the structure. Since this information is not directly available for the TESLA cavities, *ab initio* cavity positioning is more critical in this case. Cavity alignment in TESLA is complicated by the presence of the cryostat.

Natural ground motion, and motion induced by technical systems in the tunnel, will cause the linacs to become misaligned with time. Feedback systems are required to combat this motion. Pulse to pulse feedbacks are generally only effective up frequencies of roughly a tenth of the linac cycle rate, which is much lower in TESLA than in the warm linacs.

Outstanding technical challenges

The most important R&D challenge facing both options is a convincing demonstration of the design gradient in the accelerating structures, at the design efficiency and reliability.

For JLC/NLC, the original 1.8 m long structures have operated reliably at 40-45 MV/m, but when pushed to higher gradients, they exhibited excessive breakdown rates, erosion at the irises, and evidence of pulsed heating at the input couplers. Redesigns have focused on shorter (60 cm) structures, with lower group velocity and improved coupler design. A structure of this type has recently reached the design unloaded gradient of 65 MV/m, with an acceptable breakdown rate[6]. Several such structures are being fabricated and will be tested at SLAC later in 2003 and early 2004.

For TESLA, a number of 9-cell cavities have operated at gradients in excess of 24 MV/m, the requirement for operation at 250 GeV/beam. Using the newly developed electropolishing procedure for cavity fabrication, a 9-cell cavity, with input coupler, has exceeded the 35 MV/m goal[7], required for operation at 400 GeV/beam. There are plans to test more such electropolished 9-cell cavities at 35 MV/m later in 2003 and 2004.

The high power RF system required for JLC/NLC offers a number of challenges. High efficiency 75 MW X-band klystrons, with permanent magnet focusing and operating at 120 Hz, are needed. Prototypes have been built at SLAC and KEK, and the KEK prototypes have been successfully tested at full peak power and half the design repetition rate. The high power RF pulses from a pair of klystrons must be further boosted by a factor of 3.3 for delivery to a series of 8 accelerating structures. The required dual-mode SLED II pulse compression system has yet to be demonstrated at full power; this demonstration is slated for later this year. The RF system for TESLA is less demanding. Several prototypes of the required 10 MW multibeam L-band klystrons have met design specifications, but the tube lifetime remains to be determined.

The extremely high gradients required for CLIC, together with the novel character of the two-beam power source, constitute severe challenges. Gradients required for the CLIC structures have been achieved using irises made from refractory metals[6], but only with short ($\sim$15-30 ns) pulses. The elaborate two-beam pulse compression and frequency multiplication scheme requires extensive prototyping, planned for execution at CERN's test facilities between now and 2008.

There also remain open questions on the ability of any of the linacs to preserve the beam emittance to the degree required. The complexity of the required beam-based alignment means that the demonstration of emittance preservation requires extensive simulations. The simulations done to date have included in only an approximate way such effects as dynamic ground motion and instrumentation failures during the determination of the "gold orbit". The instrumentation requirements for beam-based alignment have been realized to date only in individual prototypes, and will be challenging to achieve in a large scale system. Component vibration at the level of natural ground motion is tolerable with the use of feedback, but very little additional vibration can be allowed from cultural sources, either external to the tunnel or arising from equipment within the machine.

ELECTRON AND POSITRON SOURCES

The electron and positron sources must produce beams with the proper time structure and intensity, for injection into the damping rings. The electron beam is required to have >80% polarization. The positron beam may be unpolarized, but an option for an upgrade to a polarized beam is highly desireable.

Options

A suitable technology for the electron source is a laser-driven DC polarized electron gun, utilizing a strained GaAs photocathode, followed by bunching and acceleration systems. This technology, which was utilized at the Stanford Linear Collider (SLC), is adaptable to the needs of any design.

The conventional technology for positron production involves creation of unpolarized positrons in a thick, heavy metal target, under bombardment by a few GeV electron beam. An alternate technology for positron production utilizes a few hundred GeV electron beam to produce 10-20 MeV photons in an undulator. Positrons are produced when the photons generate electromagnetic showers in a thin target. This method can produce more positrons per second than the conventional technology, and if a helical undulator is used, a polarized positron beam can be produced.

The baseline for JLC/NLC and CLIC uses the conventional technology positron source, although three parallel targets must be used because of target shock wave damage limits. With its long bunch train, TESLA requires twice as many positrons per second, and the baseline design achieves this using a planar undulator-based source. An upgrade to a helical undulator would provide polarized positrons.

Advantages and disadvantages

The conventional positron source has the advantage of having an existence proof in the SLC source. However, the need for three parallel target and collection systems introduces additional complexity and cost. Moreover, the positron emittance from the source is sufficiently large that a positron pre-damping ring is required. In addition, there is no possibility of positron polarization with this option.

The undulator-based positron source is capable of producing a high positron flux, with a smaller emittance than the conventional source, and can be upgraded to produce polarized positrons. However, such a source has never been built. In addition, a high energy electron beam is required for its operation. This adds significant complexity to the commissioning and operation of the collider.

Outstanding technical challenges

For the electron source, the major technical challenge is the development of the laser which illuminates the photocathode, with the required bunch time structure and bunch-to-bunch intensity variation ($\sim$1% for JLC/NLC and CLIC, $\sim$5% for TESLA).

The conventional positron source should be a straightforward extrapolation from the SLC source. For the TESLA undulator source, a 135 m long permanent magnet undulator is planned. For both options, the production target must rotate at high speed in a vacuum and radiation environment, which presents an engineering challenge.

DAMPING RINGS

The electron and positron beams from the sources are radiation cooled in the damping rings to produce ultralow transverse emittance flat beams, suitable for acceleration in the main linacs and high luminosity collisions at the interaction point. Most of the radiation damping in these rings is provided by wigglers.

Options

The length of the bunch train required by the linac is a major determining factor in the design of the damping rings.

For JLC/NLC and CLIC, the bunch train is sufficiently short that a 2 GeV damping ring of a few hundred meters in circumference is sufficient to store three trains. TESLA has a bunch train which is roughly 290 km in length. A ring of this size would be expensive, so the bunch train is stored in the ring in a compressed format, with about 20 ns between the bunches. The minimum bunch spacing is set by the pulse length of the injection and extraction kickers. Even in this compressed format, the bunch train still requires a ring of 17 km in circumference. To limit space charge effects in this large ring, the design energy is chosen to be 5 GeV. This energy still allows arcs of circumference about 2 km, so much of the ring can be straight. To reduce cost, this portion is placed in the same tunnel as the main linac.

Advantages and disadvantages

The small circumference of the damping ring for JLC/NLC and CLIC is its principal advantage. This translates directly into a cost benefit, as the technical components in the two ring options are similar, at least in the arcs.

The small ring has alignment tolerances similar to those of conventional synchrotron radiation rings of comparable size. The larger size of the TESLA ring makes it more sensitive to alignment tolerances, a situation which is the reverse of that obtaining for the linacs of the two options. In the TESLA ring, the beam must be coupled to generate a round cross section in the straight sections, to reduce space charge tune spread, while remaining flat to high precision in the arcs. This procedure appears feasible but is certainly an additional complexity.

The use of an undulator source for TESLA removes the necessity for a positron pre-damping ring. However, the positron damping ring must then have a large acceptance.

Outstanding technical challenges

Collective effects are currently thought to be the principal technical challenge for the damping rings. The electron cloud and fast ion effects may generate unacceptably large single and multi-bunch instabilities and tune spreads. To suppress the electron cloud effect, the vacuum chamber may be coated with materials which limit the secondary emission yield. Suppression of the fast ion instability may require a ringwide vacuum specification as low as 10^{-10} Torr. Elimination of classical instabilities, such as the microwave instability, requires a very low broadband impedance, roughly one-third of what has been achieved in existing machines.

Another major technical challenge for the damping rings is meeting the tight vertical emittance requirement. This is particularly challenging for CLIC. It requires very precise control of vertical dispersion and coupling in the rings, at the level which can only be realized through beam-based alignment, as in the main linacs. Simulations indicate that this is achievable, but there is not much margin. Experiments at the ATF[4] have demonstrated vertical emittances close to that required. To preserve the emittance after extraction, variations in the extraction kicker relative field strength must be limited to $< 10^{-3}$.

Particle loss is an issue because of the large beam power in the damping rings. The dynamic aperture is limited by nonlinear effects associated with the strong wigglers in the rings. Careful design of the wigglers and the machine lattice is needed to obtain the required aperture. This is particularly challenging in the TESLA positron damping ring.

BEAM DELIVERY SYSTEMS

The beam delivery systems transport the high energy electron and positron beams from the ends of the main linacs to the interaction point (IP). They must also transport the post-collision spent beam and the beamstralung

cleanly to beam dumps. Essential elements include collimation systems, machine protection, the final focus, spent beam transport lines, and beam dumps.

Options

JLC/NLC and CLIC, with their small bunch separation, are required to have a crossing angle at the IP, to avoid the multibunch kink effect. Crab cavities are used to prevent luminosity loss. The crossing angle geometry allows the spent beam and the beamstralung to be transported in a separate channel to the beam dumps. Because of the extremely small vertical beam size at the IP, jitter in the final focus quadrupoles must be limited with an active stabilization system.

TESLA has a large bunch separation and does not require a crossing angle. The current design uses head-on collisions, although a crossing angle solution is under consideration. The spent beam and beamstralung are transported out of the interaction region through the incoming beam final focus magnets. Separation into a spent beam channel is accomplished using electrostatic separators and a magnetic septum.

The final focus optics for JLC/NLC and CLIC has a nonzero dispersion function through the final doublet. This allows a local chromatic correction system for the final focus. TESLA uses a more conventional optics, without local chromatic control, but could easily adopt the other design. Both options make use of beam-beam focusing to enhance the luminosity.

Advantages and disadvantages

A beam delivery system with a crossing angle design can deal cleanly with the high power spent beam. In addition, a locally corrected final focus system has a number of advantages: stronger dipoles may be used, and collimation of off-energy particles is easier.

The TESLA design, with its head-on collisions, is simpler and requires no crab cavities. On the other hand, it is considerably more difficult to handle the spent beam and the beamstralung, as they must share the beamline with the incoming beam in the interaction region.

Although the vertical beam size in TESLA is comparable to that in JLC/NLC, the long bunch train allows bunch-by-bunch feedback, based on beam-beam deflection measurements, to correct for jitter, so that active stabilization of the final focus system should not be needed.

TESLA has a longer bunch length than JLC/NLC or CLIC. This makes the luminosity falloff with collision offset more severe, and also increases the sensitivity of the luminosity to emittance correlations. This problem can be partially controlled by the use of luminosity optimization feedback during the long bunch train, but this requires accurate and rapid luminosity monitoring.

Outstanding technical challenges

For all options, a major challenge is the development of a robust collimation system, which can adequately suppress background sources such as muons and synchrotron radiation, in the presence of complications such as collimator-induced wakefields. Since it constitutes the limiting aperture, the collimation system must also be integrated into the overall machine protection system.

For JLC/NLC, and particularly for CLIC, vibration stabilization of the final focus doublet is a key issue. Clean delivery of the spent beam and the beamstralung to the appropriate dumps is an issue for all options, but is more difficult for a head-on crossing design.

CONCLUSIONS

Designing, building and operating a linear collider is envisioned to be a fully international effort from the outset. Proponents in the three major regions with interest in the project (Asia, Europe, and North America) have formed steering groups to develop requirements and technology options for their bid to host the project. An International Linear Collider Steering Committee has been formed under the auspices of the International Committee for Future Accelerators. This committee will promote the construction of the linear collider as an international project by developing a global consensus on the requirements and helping to facilitate the technology choice for the machine. The resolution of critical R&D issues in 2004 would open the way for this technology choice. Subsequently, a technically limited schedule for a collider built in the US would include a project design and engineering phase from 2006-2008, followed by 6-7 years of construction, with operation starting in 2015-16.

REFERENCES

[1] G. Loew, ed., "International Linear Collider Technical Review Committee (ILC-TRC) Second Report", SLAC-R-606 (February, 2003).

[2] R. Brinkmann *et. al.*, eds., "TESLA Technical Design Report", DESY-2001-011 (March, 2001).

[3] T. O. Raubenheimer *et. al.*, eds., "Zeroth Order Design Report for the Next Linear Collider", SLAC-R-474 (1996); N. Phinney, ed., "2001 report on the Next Linear Collider: A report submitted to Snowmass '01", SLAC-R-571 (2001).

[4] K. Abe *et. al.*, "JLC Project Report, Draft", `http://lcdev.kek.jp/RMdraft/` (February, 2003).

[5] G. Guignard, ed., "A 3 TeV e^+e^- Linear Collider Based on CLIC Technology", CERN 2000-008 (July, 2000).

[6] C. Adolphsen, "Normal-Conducting RF Structures-Test Facilities and Results", paper ROPC006, contribution to this conference.

[7] H. Weise, "Superconducting RF Structures-Test Facilities and Results", paper ROPC007, contribution to this conference.

Abbott, S.R. 86
Abell, D. 1059
Aberle, O. 45, 878
Abeyta, E.O. 558
Ablett, J.M. 241
Abo-Bakr, M. 3020, 3023
Abrahamyan, K. 2114
Achard, C. 495
Ackermann, W. 3551, 3566
Adachi, T. 1679
Adams, D.J. 1527
Adelmann, A. 3524
Adolphsen, C. 668, 678, 1264, 2664, 2763
af Ugglas, M. 1590
Agarwal, D. 278
Agustsson, R. 944
Ahle, L. 989
Ahrens, L. 51, 405, 1542, 1545, 1640, 1685, 1697, 1706, 1715, 2441
Aiba, M. 1679, 3413, 3452
Aizatsky, N.I. 1107, 3303
Ajima, Y. 1978
Akai, K. 356
Akiyama, A. 2351
Akre, R. 235, 2107, 2285, 3141
Aladwan, A. 238
Alber, R. 983
Albrecht, C. 467
Al-Dmour, E. 238
Alduino, J. 2138, 2156
Aleksandrov, A. 65, 1524, 2598, 2706, 3536
Alekseev, I. 51
Alesini, D. 366, 2080, 2279, 2500, 2742, 3285
Alessandria, F. 2080, 3285
Alessi, J. 51, 89, 1637, 1715, 2793, 3282
Alexahin, Y. 1757
Alexandrov, V. 3536
Al-Khateeb, A. 2607
Allen, C.K. 2360, 3527
Allison, S. 235
Allison, T. 1485, 2379
Alsharo'a, M. 1792
Altmark, A. 1891, 1894, 1897
Alton, G.D. 995, 998, 1001
Ambrosio, G. 1966
Amemiya, Y. 530
Ames, F. 2869
Ammigan, K. 1452
Amundson, J. 2939, 3195
Anami, S. 1509
Anderberg, B. 2318, 2321
Anders, A. 98, 2622
Anders, W. 1186, 3020
Anderson, D. 3141
Anderson, D.E. 553
Anderson Jr., J. 1652
Anderson, R. 2390
Anderson, S.G. 95, 2957
Anderson, T.G. 1649, 3437
Andersson, A. 2318, 2321
Andler, G. 1590
Ando, L. 81
Andonian, G. 944, 947, 2110, 2112, 3321
Andreev, N. 1966
Andreoli, S. 470
Andresen, N. 869
Anerella, M. 164, 1939, 2162
Anferov, V. 699, 1563
Ang, Z. 1285
Anghel, A. 878
Angoletta, M.E. 2461
Ankenbrandt, C. 1792, 2936
Annala, G. 1730, 1972, 3062, 3359
Antokhin, E. 2198
Anzalone, E. 2382
Ao, H. 2826
Aoki, M. 1993, 2198
Aoki, N. 530, 713
Aoki, T. 2551
Apgar, S.E. 553
Arai, S. 1509
Arakida, Y. 568, 1512, 1784, 1807
Arduini, G. 307, 1718, 1727, 2240, 3038
Arkan, T. 1210
Arnold, N.D. 2327
Artoos, K. 1434
Aryshev, A.S. 2709
Asano, H. 1338
Asano, Y. 782
Aseev, V.N. 2875
Ashmanskas, W. 323
Asiri, F. 2748
Aspart, A. 1303
Assadi, S. 498, 1524, 1569, 2444, 2706
Assmann, R. 45, 665, 3494
Attal, M. 238
Autin, B. 444
Averboukh, I.I. 1074
Avilov, A. 1619
Ayvazyan, V. 467, 2342, 2730
Ayzatsky, M.I. 1605, 2098, 2878, 2969
Baartman, R. 1578, 1584
Baba, H. 3332
Baba, Y.H. 487
Baboi, N. 467, 1086, 1261, 1270
Babzien, M. 944, 1909
Baca, D. 312, 536, 553, 3294
Bacci, A. 2080, 3285, 3512
Bäcker, H.-J. 836
Badea, S.V. 2138, 2156
Bae, Y.S. 2539
Bagge, L. 1590
Baggett, K. 2183, 2186, 2189
Baglin, V. 307, 1727
Bähr, J. 2114
Bahrdt, J. 836
Bai, M. 51, 54, 405, 1697, 1706, 2204, 2207
Baichev, I. 3494
Bailey, C.P. 1527
Baishev, I. 45
Bajko, M. 1942
Bak, P. 3318
Bakker, R.J. 214

Balbekov, V. 1751, 2014, 2017
Balkcum, A. 1144
Ball, M.J. 1996
Balleyguier, P. 2053, 2458, 2601, 2799
Bandelmann, R. 467
Bandura, L. 1999
Bane, K. 126, 3126, 3252
Banna, S. 722, 1879
Bao, X. 2357
Baptiste, K. 869, 1240, 1252
Bär, R. 694
Barber, D.P. 372
Barletta, W.A. 186, 923
Barlow, D. 702, 1664
Barnard, J.J. 1521, 1990, 2658
Barnes, B. 1736
Barnes, C.D. 1530, 1933, 2101
Barnes, M.J. 1162
Barnes, P. 1309, 1323
Barni, D. 1341, 1506
Barov, N. 1870, 2682
Barr, D. 2512
Barr, G. 1987
Barstow, B. 192, 1317, 1320
Barsz, T. 2029
Bartolini, R. 914, 2077, 3285
Barton, D. 1637
Barty, C.P.J. 95
Baskiewicz, M. 302
Batchelor, K. 541
Batrakov, A. 250
Batygin, Y.K. 2751, 3548
Baudrenghien, P. 1718, 3050
Bauer, P. 1730, 1972, 3359
Bauer, S. 1410, 2887
Baum, D. 2527
Baynham, D.E. 1987
Bazarov, I. 192, 842, 848, 1201, 1317, 1323, 2062
Beard, K. 195, 332, 1104, 1575
Beaudoin, B. 426, 2312, 2571
Beche, J.-F. 2530
Bechstedt, U. 598, 3428
Bechtold, A. 1062
Beck, M. 2189
Beckert, K. 434
Beckman, L. 3389
Beczek, K. 2038
Beebe, E. 89
Beebe-Wang, J. 51, 1706
Beinhauer, W. 3551
Belgroune, M. 896
Bellavia, S. 1542
Bellenger, D.W.J. 1527
Beller, P. 434
Bellodi, G. 1527
Bellomo, P. 235
Bellucci, S. 917, 986
Beloglasov, V.I. 2878
Belohrad, D. 2461
Belomestnykh, S. 192, 1198, 1201, 1306, 1317, 1323, 1326, 1329, 1410, 1437, 2059, 3347
Beltran, C. 326, 3086
Bender, H. 558
Benedetti, G. 366, 2279, 2945
Benedetto, E. 1727, 3053
Benedikt, M. 1548
Bengtsson, J. 195
Benjamin, J. 1715
Bennett, J.R.J. 1527
Bennett, S.L. 189
Ben-Zvi, I. 39, 92, 944, 1300, 1909, 2005, 3186
Berden, G. 519
Berenc, T. 1736, 3362
Berg, J.S. 1804, 1816, 2002, 2210, 2213, 2216, 2219, 3413, 3485
Berg, S. 1416, 1422, 2029, 2038
Berg, W.J. 2417, 2420
Bergqvist, M. 2321
Berio, R. 989
Berkaev, D.E. 372
Berkvens, P. 854
Berman, L. 241
Bernal, S. 426, 1673, 1676, 2312, 2571, 2574, 2577, 2673
Bernard, A. 195
Bernardin, J. 1461
Bernaudin, P.-E. 2799
Bernstein, L. 989
Bertolucci, S. 3285
Bertrand, P. 2802, 3488
Bessonov, E. 1963
Bhashyam, S. 1966
Bhat, C.M. 514, 1769, 2345, 2348, 3180
Bhatt, R. 2643
Biagini, M. 366, 914, 2077, 2279, 2297, 2300, 2945, 3285
Biallas, G. 2123, 2135, 2183, 2186, 2189
Biarrotte, J.L. 1303, 2802
Biasci, J.C. 854
Bieler, T.R. 1359
Bieniosek, F.M. 98, 275, 312, 536, 1518, 2524, 2619, 3297
Bierwagen, J. 1353
Bilderback, D. 192
Bilheux, H. 998
Billen, J. 1461, 1515, 2844, 3518, 3521
Biller, E.Z. 1605, 2878
Billing, M. 3059
Binello, S. 1542, 1703
Bini, S. 917
Binkley, M.E. 2497
Biocca, A. 3374
Birkel, I. 893, 3273, 3276
Biryukov, V.M. 917, 986, 1655, 1691
Biscardi, R. 241
Biscari, C. 335, 366, 684, 2279, 2742, 2945, 3285
Bishofberger, K. 57, 1778, 1781
Bisognano, J.J. 3147
Bizen, T. 487
Björkhage, M. 1590

Bjorklund, E. 2354
Black, E. 983, 1792, 1834, 1999
Blair, G. 2739
Blanco-Vinuela, E. 1945
Blasche, K. 589
Blaskiewicz, M. 54, 135, 272, 394, 476, 797, 1195, 1569, 1706, 1715, 1816, 2595, 2598, 3026, 3029, 3035, 3344, 3419
Blind, B. 702, 1664, 2948
Bliss, N. 189, 1029
Blivet, S. 1303
Blokland, W. 1524, 2444, 2491, 2706
Blom, M. 1590
Blomqvist, I. 220
Blue, B.E. 731, 1530, 1864
Bluem, H. 92, 977
Bocchetta, C.J. 214
Boege, M. 3386
Boffo, C. 1210
Bogacz, A. 195
Böge, M. 291
Boggia, A. 3318
Bohl, T. 1718, 3050
Bohlen, H. 1144
Bohn, C.L. 2676
Bohnet, I. 2114
Boilot, D. 1332
Boimelshtein, Y. 3318
Boine-Frankenheim, O. 589, 2607
Bojtar, L. 2461
Boller, K.-J. 1900, 1903
Bolton, P.R. 2104, 2709, 3216
Bondarenco, N. 3329
Bondarev, B.I. 2679, 3002, 3530
Bongers, H. 2872
Bongers, N. 598
Boni, R. 366, 2279, 2742, 3285
Bookwalter, V. 1494
Borburgh, J. 1643
Borchard, P. 1113, 1116
Borden, M. 508, 2521, 3089, 3455
Bordry, F. 1945
Boriskin, V.N. 1107, 2878, 3303
Borissov, E. 1210
Borland, M. 247, 256, 283, 2330, 2417, 2420, 3138, 3461, 3470, 3473, 3476
Borovina, D.L. 553, 1168
Borrion, H. 2458
Bosch, R.A. 887, 929, 932, 935, 2373, 3147
Boscolo, I. 3285
Boscolo, M. 366, 914, 2077, 2279, 2945, 3285, 3548
Bosland, P. 878, 1332
Bosotti, A. 1341
Bossert, R. 1969
Bottura, L. 173, 1730, 1945
Bourcey, N. 1434
Bousson, S. 1303
Bowden, G. 1261, 1264
Bowler, M.A. 189
Boyce, J.R. 938, 941
Boyce, R. 235, 2174
Bozzini, D. 1945
Bradley III, J. 553, 1095, 1168, 1458
Brajuskovic, B. 830, 1017
Brarvar, S. 51
Braud, D. 1303
Braun, H. 495, 1156, 2721
Brautti, G. 3318
Bravin, E. 2464
Bredy, P. 878, 1332
Brelsford, B. 1542
Brenger, A. 2476
Brennan, J.M. 39, 51, 135, 394, 476, 1195, 1545, 1706, 1715, 3026, 3029, 3338, 3341, 3344
Bricault, P. 439, 1584, 1670
Bricker, S. 1353
Briddick, D. 2029, 2038
Bridges, F. 1092
Briggs, R. 3098
Brinkmann, A. 1374, 1395
Briscoe, B. 3282
Britvich, G.I. 917
Brodowski, J. 1195, 2156, 2444, 2598
Broemmelsiek, D. 3431
Broggi, F. 3285
Bromberek, D. 1416
Bross, A. 983, 1183
Broste, W. 558
Browdowski, J. 1428
Browman, A. 326, 508, 2521, 3086, 3089, 3455
Brown, B.C. 2165
Brown, C. 1446
Brown, K.A. 51, 405, 746, 1542, 1545, 1706, 1715, 2441, 2595, 3422
Brown, W. 95, 938, 2192, 2957
Browne, M. 2297
Bru, B. 2802
Brugger, M. 45, 3494
Bruhwiler, D.L. 719, 734
Brumwell, F.R. 592
Brunelle, P. 229, 896
Brunner, O. 473
Bruno, D. 743, 1700, 1706
Bruno, L. 45
Brüning, O.S. 42, 1748
Bui, T. 3560
Bukh, B. 2631, 2634
Bulfone, D. 3395
Bullard, D. 2183
Bultman, N. 1461, 2844
Bunce, G. 51
Burgazzi, L. 1506
Burgmer, R. 1948
Burke, D.L. 1264
Burkhardt, H. 45, 1721, 3041, 3044
Burns, M. 2354
Burov, A. 2020, 3062
Burrill, A. 39, 92
Burrows, P.N. 687
Busch, M. 2273
Bussmann, M. 112
Butler, C. 195

Butler, J. 1195
Büttner, T. 467
Byer, R. 722, 728, 1858
Bylinsky, I. 1285, 1584
Byrd, J. 863, 869, 1240, 2530
Cacciotti, L. 2476
Cadapan, L. 235
Cadorna, A. 2348
Cai, Y. 350, 2288, 2291, 2297, 2300, 3542
Calaga, R. 39, 272, 2207
Calatroni, S. 1309
Callahan, D.A. 2637
Calvet, O. 1434
Calzas-Rodriguez, C. 1945
Cameron, P. 54, 135, 394, 524, 1703, 1706, 2444, 2447, 2598, 2691, 2697, 3026, 3029
Campbell, L.P. 1909
Campisi, I. 457, 977, 1104, 1377
Cao, L. 2852
Capatina, O. 1434
Capista, D.P. 2165
Caporaso, G. 563
Cappi, R. 388, 2910, 2913
Carcagno, R. 1969, 1972
Cardona, J. 1059, 1706, 2901
Carey, D. 1446
Carli, W. 2872
Carlier, E. 1945
Carlson, C. (Bechtel) 558
Carlson, C. (BNL) 1715
Carlson, K. 2020
Carneiro, J.-P. 2065, 2068, 2114, 3548
Carr, G. 2354
Carr, G.L. 241, 1497
Carr, L. 329
Carroll, A. 1709, 3255
Carron, G. 1156
Carson, J. 1969
Carter, H. 1210, 1813
Cary, J.R. 719, 734, 1536, 1885, 1918, 2026
Casarin, K. 2309
Casey, B. 241
Casey, J.A. 547, 1500
Caspers, F. 1801, 2470, 2700, 3479
Caspi, S. 42, 170, 1984
Cassel, R. 235
Castellano, M. 2476, 3285
Castro, P. 198, 467, 1086, 2730
Catalan-Lasheras, N. 1428, 2144, 2225, 2598, 3026
Catani, L. 2476, 3285
Cattelino, M. 1144
Caudill, L. 558
Cederk€ll, J. 2869
Cee, R. 2114
Celata, C.M. 275, 536, 1518, 1521
Celona, L. 81
Cerniglia, P. 2444, 2697
Chacon-Golcher, E. 73, 3291, 3294
Chae, Y.-C. 3008, 3011, 3014, 3017
Chambers, F. 563, 2960
Champion, M. 1464, 3371, 3377
Chan, K.C.D. 558, 3210
Chang, C.H. 1041, 1044, 1047
Chang, C.K. 2376
Chang, H.P. 890, 1044
Chang, J.C. 1476, 1479, 1482, 2402, 2405
Chang, L.H. 1371, 2670
Chang, S.H. 2402, 2405
Chang, X. 39, 1300, 2005, 3186
Chao, A. 126
Chao, Y. 195, 294, 3243
Chao, Z. 487
Chapman, S. 167
Chaput, R. 229
Charrier, J.P. 1303
Chase, B. 1736, 1769
Chattopadhyay, S. 195
Chavanne, J. 253, 854
Chazot, G. 851
Cheever, D. 2324
Chel, S. 878, 1332
Chen, A. (FNAL) 623
Chen, A. (YY Labs) 2586
Chen, C. 1255, 1258, 2643, 2646, 2966
Chen, C.I. 3234
Chen, D. 1560, 3506, 3509
Chen, G. 2586
Chen, H. 467
Chen, J. 1044, 2376, 2554, 2557, 2580, 3237, 3392
Chen, J.R. 821, 1476, 1479, 1482, 2402, 2405
Chen, L. 2357
Chen, S. 1921
Chen, Y.-J. 558, 563, 2960, 3210
Chen, Z. 2844
Chen-Yao, L. 764
Cherbak, E. 1177
Chesnokov, Y. 917, 986, 1655, 1691
Cheung, H.W.K. 2488
Chevtsov, P. 2560
Chiadroni, E. 914, 3285
Chiaveri, E. 45, 878, 1309, 1332
Chiba, J. 1509
Chichili, D. 1969
Chien, Y.-C. 764, 767
Chiesa, L. 170, 1984
Chin, M. 869
Chin, Y.H. 479
Chiou, J. 764
Chishiro, E. 1338
Cho, Y.S. 1219, 1222, 2539, 2832, 2857, 2884
Choi, B. 235
Choi, B.H. 1219, 1222, 1602, 2539, 2832
Choi, J. 875, 3383
Choroba, S. 467
Chou, P.J. 1368, 3150
Chou, W. 604, 623, 1551, 1554, 1557, 2922, 2925, 2936

Chouhan, S. 899
Chrin, J. 291
Christensen, W. 2485
Christina, V. 920, 977, 2186
Christoph, M. 39
Chu, C. 2360, 2363, 3527
Chu, P. 2366
Chun, M.H. 1470, 2857
Chung, Y.C. 1479
Chupyra, A. 2769
Cialdi, S. 3285
Cianchi, A. 2476, 3285
Ciavola, G. 81
Cimino, R. 1727
Ciocci, F. 3285
Ciovati, G. 1362, 1374, 1395
Citver, G. 39, 92
Clark, G. 601
Clarke, D.G. 1029
Clarke, J.A. 189, 1029
Clarke-Gayther, M.A. 1473
Clauser, T. 3318
Clayton, C. 731, 1530, 1864, 1873, 1933
Clendenin, J. 2104, 2126, 2129, 3216
Clifft, B.E. 2426
Cline, D. 1787, 1876, 1909, 2008, 2709
Clozza, A. 366, 2279, 2742, 3285
Cobb, J.H. 1834
Codner, G. 2399
Cohen, R. 132, 312, 536
Colby, E. 722, 1858, 2101
Cole, J.M. 998
Cole, M. 92, 977, 2047, 2050
Coleman, J. 1485
Colestock, P. 977, 3086
Collier, M. 2844
Collier, P. 307, 1718, 1727
Collins, I. 1727
Collins, J. 699
Collins, S. 1661
Colocho, W. 2297
Compton, C. 1353, 1359, 1362
Conde, M.E. 2032
Coney, L. 1587
Congretel, G. 2799
Connolly, R. 135, 1706, 2444
Cook, E.G. 544
Coosemans, W. 665
Corbett, J. 2369, 2372
Corbett, W. 235
Corlett, J. 186, 812, 866, 923, 1246, 1249, 2086, 2408, 3198
Cornelis, K. 1718, 1727, 3038
Cornelis, M. 1942
Corniani, G. 1341
Corsini, R. 684, 2742
Courant, E.D. 405, 1697, 1816, 3485
Cousineau, S. 117, 259, 1428, 1569, 1572, 2598
Cowan, B. 722, 1855
Cox, L. 1144
Craddock, M.K. 1581
Craft, B. 1053, 2382
Craievich, P. 214, 878
Crandall, K. 1515, 2855
Crandall, K.R. 2889
Crane, J.K. 95
Crappell, A. 2382
Crawford, A. 1312
Crisp, J. 1781, 2348, 2491
Crittenden, J. 1023, 1954, 3425
Crofford, M. 3377
Cross, R.R. 95
Cui, Y. 426, 511, 3156
Cullerton, E. 3068
Cummings, K. 1095, 1237
Cummings, M.A. 1834
Cummings, M.A.C. 983, 1798, 1999
Cupolo, J. 524, 2444, 2697
Cusick, M. 1144
Cutler, R. 550, 617
Czyz, W.S. 592
Da¯l, A. 229
Dail, J. 2183
D'Alessio, C. 2500
Dallin, L. 220, 2195
Dalmas, D. 558
Daly, E. 457, 977, 1377, 2866
Danailov, M. 214, 2306
Danared, H. 1590
D'Angelo, A. 3285
Danilov, V. 117, 1569, 1572, 2598, 3032
Danilova, E. 2363
Daté, S. 250, 881
Datta, D. 3560
Datte, P. 2530
Dattoli, G. 914, 3285
D'Auria, G. 214
Davidson, R.C. 1667, 2655, 2658, 2661, 2975, 2978, 3117, 3120, 3123
Davino, D. 1428, 2147, 2598, 3035
Davis, G.K. 457, 1383
Davis, H. 120
Dawson, C. 2444, 2453, 2697, 3026
Dawson, W. 524
Day, L. 2429
De Baca, J.M. 1237
DeBarger, S. 3141
DeCarlo, A. 1467, 2706
De Conto, J.-M. 2802
Decker, F.-J. 423, 731, 1530, 1864, 1933, 2282, 2285, 2297, 2300, 2754, 3126, 3129
Decker, G. 833, 2688
Decking, W. 652
Decyk, V. 3174
DeFord, J.F. 3554
Degen, C. 524, 2444, 2697, 3026
Dehler, M. 3395
Dehning, B. 45, 2470
Deibele, C. 1524, 2706
Deitinghoff, H. 1335, 2942
de Jong, M. 220

Dejus, R.J. 1020
DeKamp, J.C. 161
Delaney, T. 690
Delayen, J. 92, 457, 992, 1098, 1291, 1380, 1383, 2379, 2860
DellaPenna, A. 524, 2444
Delle Monache, G. 366, 2279, 2742
Dell'Orco, D. 235, 2174
DeLong, J. 476, 1715, 3338, 3341, 3344
De Martinis, C. 2080, 3285
Demidov, N.V. 2878
Demirkan, M. 2318
Demma, Th. 2993, 2996, 2999
Demske, D. 1497
Denard, J.-C. 229, 2560
Denes, P. 2530
Deng, S. 1530, 1933
Den Hartog, P. 824, 830, 833, 1017
De Ninno, G. 214, 2306, 2309
Denz, R. 1945
Derbenev, Y. 941
Derenchuk, V.P. 1563
De Rijk, G. 1942
Deriy, B. 2261
Deryuga, V. 1619
De Santis, S. 186, 866, 2530, 2745, 3377
Deslandes, D. 2458
Desler, K. 2682
Devanz, G. 878, 1086
DeVoy, J. 2934
Devred, A. 42, 146, 173
Dewan, S. 770
Dey, J. 1204, 1769, 3353, 3356
Diao, C.Z. 968
Dickson, R. 2563
Diebele, C. 2444
Diep, A. 2312, 2571, 2577
Dierker, S. 241
Dietderich, D.R. 170, 1032, 1984
Dietrich, J. 598, 3428
Dilley, C.E. 1909
DiMarco, J. 1730, 1969, 1972
DiMauro, L. 217
Di Mitri, S. 214, 1050
Dimitrov, D.A. 734
Ding, Y. 2580
Di Pirro, G. 366, 2279, 2476, 3285
Di Salvo, R. 3285
Diviacco, B. 214, 1050, 2306
Diwan, M. 429, 1709, 3255
Dobbins, J. 2473, 3347
DÅbert, S. 495, 1156
Dodson, G. 1569
Doelling, D. 899
Dohan, D.A. 2327
Doleans, M. 1599
Dolgashev, V.A. 1264, 1267, 1276, 2763
Dolinskii, A. 434, 694
Dombsky, M. 439, 1584
Domning, E. 3374
Donald, M. 2288, 2297
Dong, H. 195
Dong, S. 758
Donley, L.I. 1159
Dooling, J.C. 592, 1159
Doolittle, L. 186, 1464, 2408, 3371, 3377
Doose, C. 1020
Doria, A. 3285
Dormiani, M. 3141
Dortwegt, R. 630, 2038
Doss, J.D. 553
D'Ottavio, T. 1715
Douglas, D. 195, 938, 977, 2183, 2186, 2189, 3243
Dovbnya, A.N. 1107, 2878, 3303
Dowell, D. 2104, 3216
Dowling, A. 439
Doyle, E. 644
Doyuran, A. 217, 241, 1192, 2455
Drago, A. 366, 2279, 2742, 3285
Dragt, A. 2772
Drees, A. 51, 54, 794, 797, 1685, 1688, 1691, 1706, 2691, 2904
Drees, K. 3026
Dris, S. 1204
Drozdoff, J. 638
Drozhdin, A. 1503, 1557, 1733, 1742, 2739, 2925, 2936
Drury, M. 457
Ducar, R. 1652
Ducimetiere, L. 1162
Dugan, G. 737
Duke, J.P. 2542
Du Mont, D. 1542
Dunkel, K. 2887
Duperrier, R. 2802, 2805
Durante, M. 1948
Durkin, A.P. 2679, 3002, 3530
DËrr, H.A. 836
DËrr, V. 836
Durtschi, G. 558
Duru, P. 854
Dutto, G. 601, 638, 1584
Dwinell, R.D. 86
Dykes, D.M. 189
Eberhardt, W. 836
Ebihara, K. 860, 1228
Ecklund, S. 2297, 2300
Edwards, D. 2068, 2682
Edwards, H. 447, 1213, 2682
Edwards, R.L. 1341, 1344
Efthimion, P. 98, 2622, 2655, 2661
Egawa, K. 1071, 1074
Ego, H. 250, 487
Ehrlich, R.D. 2399
Eichhorn, R. 598
Eickhoff, H. 694
Einfeld, D. 238
Eisen, E. 1122
Eisert, D.E. 887, 2373
Ekdahl, C. 558, 3210

Elioff, T. 235
Elleaume, P. 854
Ellis, S. 2841
Emamian, M. 2273
Emery, L. 256, 283, 833, 2261, 2330, 2423, 2438, 3461, 3464, 3470, 3473, 3476
Emhofer, S. 2869, 2872
Emma, P. 211, 423, 914, 926, 965, 1530, 1933, 3126, 3129, 3138
Endo, K. 1071, 1074
Eng, W. 743, 770, 1542, 2144
England, R.J. 3258
Enomoto, A. 2838
Erdelyi, B. 1760, 1772, 3542
Erdem, O. 1933
Eremeev, G. 1312
Erickson, R. 2297
Eriksson, L. 644
Eriksson, M. 2318, 2321
Ernst, D. 2174
Erokhin, A. 2769
Errede, D. 983, 1999
Esarey, E. 719, 734, 1885
Escallier, J. 164
Eschke, J. 467
Espinoza, C. 1664
Esposito, A. 3285
Esser, F.M. 598
Estrada, J. 1763
Evangelakis, G. 1709
Evans, I. 235
Evans, L.R. 19
Evans, R. 1485
Eversole, S. 558
Eylon, S. 98, 558, 1171, 2533, 2616, 2619, 2622, 2625, 2628, 2646, 3098
Ezura, E. 860, 1228
Faatz, B. 467
Fabbricatore, P. 1987
Fabris, A. 878
Facco, A. 470
Falabella, S. 563
Falce, L. 1113, 1116
Faltens, A. 536, 1990
Fan, L. 815
Fan, M. 1560, 3506, 3509
Fan, T.C. 1041, 1047
Fang, J.-M. 1882, 1924
Fang, S. 1285, 1404
Fang, Z. 1071, 1074
Fann, C.-S. 767
Fantini, A. 3285
Farinon, S. 1987
Farkhondeh, M. 956, 959, 980, 2324
Farrell, J.P. 541
Farrow, R.C. 189
Fartoukh, S. 2225
Farvacque, L. 854, 3189
Faucett, J. 2354
Faure, J. 1840
Faus-Golfe, A. 2240
Favale, A. 92
Fawley, W. 186, 558, 923, 959, 3098
Fedotov, A. 39, 117, 383, 1572, 2589, 2592, 2598, 3032
Fedurin, M. 1053, 2382, 2892
Feher, S. 1969
Feigerle, C.S. 617
Feikes, J. 845, 3023
Felden, O. 598
Feldman, D. 426, 3323
Feldman, R. 426
Fellenz, B. 2348, 2491
Ferguson, P. 1110
Ferianis, M. 214
Ferioli, G. 307
Fernow, R.C. 2002
Ferracin, P. 170, 1984
Ferrari, A. 45, 684
Ferrario, M. 467, 914, 2077, 2080, 2730, 3285, 3548
Fessenden, T.J. 2533
Fessia, P. 1942
Filhol, J.-M. 229, 1332
Filip, C.V. 1873
Findlay, A. 2461
Findlay, D.J.S. 2542
Finley, D. 1207, 1210, 1813
Fiorito, R. 1497, 2712
Fischer, R. 2476
Fischer, W. 51, 54, 135, 476, 794, 797, 1625, 1697, 1706, 1754, 2222, 2228, 3026, 3029
Fisher, A. 2285, 2297, 2300
Fisher, M. 887, 2303
Fittinghoff, D.N. 95
Fitzgerald, D. 508, 2521, 3089, 3455
Fitzgerald, J. 1781
Flanagan, J.W. 2503
Flanz, J. 690
Fliflet, A.W. 1128
Fliller III, R. 272, 1685, 1691, 1706, 2904
Floettmann, K. 965, 2114, 3500, 3548
Flora, F. 3285
Flora, R. 2491
Foley, M. 983, 1213
Folwell, N. 2664
Fong, K. 601, 1285, 1404, 1488
Fontenille, A. 2799
Fontus, R. 138
Forchi', V. 3395
Ford, R. 1652
Forest, E. 397, 1023, 2249
Foster, G.W. 323, 1649, 1766
Fox, B. 1688
Fox, J. 2297, 2300, 3141, 3389
Fox, W. 1461, 2841
Frak, B. 1715
Franchetti, G. 129, 589
Francis, V. 1029
Franczak, B. 589
Franklin, W.A. 2324
Franzke, B. 434
Frawczyk, F.L. 2083
Frayer, D. 558

Freyberger, A. 195, 2560, 2565, 3243
Friedlander, F. 1144
Friedman, A. 132, 275, 312, 536, 1518, 2673
Friesel, D.L. 699, 1065, 1563
Frigola, P. 947, 2110, 2112, 2192, 3321
Frisch, J. 644, 1279, 2545, 2548
Frischholz, H. 473
Froidefond, E. 2799, 2802
Fruneau, M. 2799
Fu, S. 1455, 1509
Fu, W. 1685
Fubiani, G. 719, 1885
Fuerst, J.D. 1291, 1294, 1297
Fujii, T. 1978
Fujita, T. 860, 3077, 3080, 3261
Fukami, K. 2551
Fukuda, S. 1509
Fukui, T. 250
Fukui, Y. (KEK) 1509
Fukui, Y. (UCLA) 1787, 1790, 2008, 2709
Fukuma, H. 860, 3056
Fuller, R. 235
Furman, M. 132, 297, 312, 350, 2598, 3219, 3222, 3524
Furukawa, K. (KEK) 533, 3368
Furukawa, K. (Osaka U) 755
Fusco, V. 914, 2077, 3285, 3548
Gagliano, J. 1416
Gai, W. 492, 1156, 1810, 1813, 1819, 1888, 1894, 2032
Galambos, J. 1569, 2360, 2363, 2366, 3527
Gallagher, R. 167
Gallardo, J.C. 1909, 2002, 3255
Gallegos, F. 2515, 2518
Gallegos, R. 558
Gallerano, G.P. 3285
Gallo, A. 366, 2080, 2279, 2742, 3285
Gamma, F.S. 3285
Gammino, S. 81
Ganetis, G. 164, 743, 1431, 1637, 1700, 1706, 2162
Gao, J. 3264, 3267
Gardner, C. 51, 1542, 1706, 1715
Gardner, I.S.K. 1527
Garnett, R.W. 2613
Garoby, R. 1724, 2336
Garrel, N. 1162
Garren, A.A. 1557, 1787, 1804, 1816, 2008, 2213, 2219, 3485
Gasser, Y. 1303
Gassner, D. 54, 794, 1425, 1542, 1691, 2444, 2447, 2450, 2694, 2904
Gattuso, C. 1649, 1766, 2931
Gaudreau, M.P.J. 547, 1500
Gaupp, A. 836
Gavrilov, N. 2273
Ge, L. 2664
Gebel, R. 598, 3428
Geddes, C.G.R. 1840
Geer, S. 983, 1183
Geisler, A. 899
Gelfand, N. 1557
Geng, R. 2580
Geng, R.L. 264, 1309, 1312, 1314, 1317, 1323, 2059
Genoni, T.C. 3165
Gensch, U. 2114
Genser, K. 1763
Gentzlinger, R. 1341, 2841
Gerigk, F. 1527
Geros, E. 73
Gerth, C. 189
Gerth, Ch. 911
Ghalam, A.Z. 3174
Ghigo, A. 366, 684, 1658, 2279, 2742, 3285
Ghiorso, W. 2524
Ghosh, A. 164, 2162
Giacone, R. 719, 1885
Giannessi, L. 914, 2077, 3285, 3548
Giannini, G. 917
Gibson, D.J. 95
Gibson, P. 2706
Gierman, S. 2104, 2667, 3216
Gillespie, W.A. 519
Gilpatrick, J.D. 2512, 3086
Gilson, E. 98, 2622, 2655, 2661
Giovannozzi, M. 129, 388, 2910, 2913, 2916
Giove, D. 2080, 3285
Giovenale, E. 3285
Girard, A. 81
Givens, M. 2029, 2038
Gjonaj, E. 3563
Glanzer, M. 426, 2571, 2577
Glass, H. 1766, 1969, 1972, 2168
Gl€Ùner, C. 1622
Glenn, J. 51, 405, 746, 1542, 1545, 1706, 1715, 2595, 3422
Gloor, W. 878
Gluckstern, R.L. 2592
Goddard, B. 45, 1646, 1721
Godlove, T. 426, 1673, 1676
Goeppner, G. 1416, 2029
Gold, S.H. 492, 1128, 1147
Goldin, F. 563
Golovko, N.G. 1605
Golub, Yu.Ya. 3101, 3103
Gomez, J. 1664
Gonin, I. 48, 1207, 1210, 1213, 2068
Gonzales, J.M. 553
Gonzalez, R. 2444
Goodzeit, C.L. 1996
Gopych, M. 3569
Gorbachev, A.M. 1147
Gordon, D.F. 716, 1846
Gordon, J. 2860

Gorelov, D. 2805, 2849, 2972
Gössel, A. 467, 1086, 1392
Gottschalk, S.C. 1909
Gould, H. 1837
Gould, O. 794, 3282
Gounder, K. 2928, 3434, 3437
Gourlay, S.A. 42, 170, 1032, 1984
Grabosch, H.J. 2114
Graef, H.-D. 3551, 3569
Graham, D. 89
Granata, V. 1945
Granatstein, V. 1140
Grau, M. 2444
Graves, W.S. 217, 329, 956, 959, 980, 1192
Gray, J.W. 1527
Green, M.A. (LBNL) 186, 1834, 1987
Green, M.A. (SRC) 887, 929
Greenwald, Z. 2056
Greenway, W. 1171
Grelick, A. 1416, 1422, 2029, 2038
Grenoble, C. 457
Gribble, R.F. 553
Grice, W. 1524, 2706
Griep, B. 2887
Grier, D. 1724
Griffin, J. 1554, 2922
Grimm, T. 1350, 1353, 1356, 1359, 1362, 1407, 2849, 2972
Grippo, A. 1485
Grisham, L. 2661, 3309
Grishin, V. 1007, 1010
Grote, D.P. 70, 275, 1518, 2637, 2673
Grote, H. 3497
Gruber, P. 1183, 1413
Gruner, S. 192
Gu, A. 2580
Guan, C.Y. 815
Guenzel, T. 854
Guerra, A. 195
Guethlein, G. 563
Guetz, A. 2664
Guidi, V. 917, 986, 1655
Guiducci, S. 366, 914, 2077, 2279, 2945, 3285
Guignard, G. 665
Guilhem, D. 2601
Guimbal, Ph. 2053, 2458
Gullotta, J. 54, 794, 1425, 2444, 2694
Gung, C. 1990
Gunther, K. 1113, 1116
Gupta, R. 42, 164, 1748, 1936, 1939
Guy, F.W. 2889
Gyr, M. 1646
Ha, K.M. 2857
Ha, W. 1861
Haase, M. 1724
Haber, I. 426, 511, 536, 1673, 2312, 2574, 2577, 2673, 3156, 3297
Haberer, Th. 694
Habs, D. 112, 2869, 2872
Hacker, K. 423
Hafalia, R.R. 170, 1984
Hafizi, B. 716, 1846
Hafz, N. 1849
Haga, K. 860
Hahn, A. 2488, 2491
Hahn, H. 39, 1625, 1706, 2147, 3035
Hahto, S.K. 3309
Hahto, S.T. 3309
Haimson, J. 2095
Hajima, R. 3443, 3446, 3449
Halaxa, E. 3297, 3300
Halbritter, J. 1374
Hall, R.P. 3300
Hamatsu, R. 2709
Hamm, R.W. 1563
Hammons, L. 1542, 1691
Han, J.H. 2114
Han, J.M. 1222, 2539, 2832, 2857, 2884
Han, S.H. 2539, 2832
Han, Y.J. 1470, 2857, 3114, 3383
Hanaki, H. 2838
Hanft, R. 1730, 1972
Hanna, B.M. 2497
Hanna, S.M. 1077
Hannink, R. 2625
Hannon, F.E. 1029
Hansen, R.W.C. 929
Hansen, S. 323
Hara, M. 250
Hara, T. 487
Harada, K. 857, 860, 3201
Hardek, T. 553, 1095, 1168, 1458, 1461
Hardekopf, R. 1461, 1661
Harding, D. 1730, 2168
Hardy, L. 854
Harkay, K. 508, 592, 2438, 3008, 3011, 3014, 3183
Harris, J. 426, 2312, 2571, 2577
Harrison, J. 558, 1237
Harrison, M. 39, 42, 164, 1748
Hartemann, F. 95, 938
Hartill, D. 1309, 2339
Hartline, R.E. 1792
Hartman, S. 752, 2270, 2273, 2482
Hartouni, E. 1446
Hartrott, M.v. 2114
Hartung, W. 1350, 1353, 1356, 1362, 1395, 2849, 2972
Harvey, M. 1715
Harwood, L. 586, 992, 1098
Hasegawa, K. 1509
Hashemi, H. 238
Hashiguchi, E. 1978
Hashiguchi, Y. 902, 3270
Hassanein, A. 1180
Hassanpour, N. 3389
Hassanzadegan, H. 238
Hassenzahl, W. 2162
Hatano, T. 1165
Hauviller, C. 1434
Hawkey, T. 547, 1500

Hawkins, S. 2533
Hayano, H. 530, 2545, 2548
Hayashizaki, N. 2826
Hayden, D. 2354
Hayes, M. 2231, 3494
Hayes, T. 476, 1706, 1715, 3338, 3341
He, D.H. 968
He, P. 54, 785, 788, 791, 1425, 2598
He, Y. 167, 2399
Hechler, M. 2706
Heese, R. 217, 241
Heidenreich, D.A. 553
Heifets, S. 2297, 2300, 3132, 3135
Heimann, P. 186, 1032
Heistermann, F. 3344
Held, B. 3554
Hemmer, M. 2390
Henderson, S. 117, 1467, 1569, 1572, 2598, 3416
Hendrickson, L. 423, 644, 662, 2545, 2757, 3126
Henestroza, E. 98, 558, 1171, 2616, 2619, 2622, 2625, 2628, 2637, 2646
Henn, K. 598, 3428
Henning, W. 16
Henrist, B. 1727
Henrist, H. 307
Henry, J. 1377, 2866
Heo, H. 3108
Heppner, G. 1685
Herbeaux, C. 229
Herr, A.D. 617
Herr, W. 3404
Hershcovitch, A. 39, 92
Hertel, I. 836
Herzog, R. 1945
Hess, M. 2643
Hettel, R. 235, 761
Hiatt, T. 2183, 2186, 2189
Hicks, J.D. 553
Hicks, R. 195, 2560
Hicks, W.R. 1377
Higashi, N. 1978
Higashi, Y. 2393, 2838
Hill, A. 235, 1273
Hill, C. 1029
Hilleret, N. 307, 788, 1727
Himel, T. 644, 2757
Hiramatsu, S. 2503
Hirashima, T. 1074
Hirata, K. 2996
Hirshfield, J.L. 725, 1128, 1131, 1147, 1150, 1882, 1924, 1927, 1930, 2881
Hitz, D. 81
Ho, D. 563
Ho, H.K. 1876
Ho, S. 620
Hobl, A. 899
Hock, J. 1542, 3422
Hoff, L. 1542, 2444
Hoffstaetter, G.H. 192, 369, 375, 842, 848
Höfle, W. 1718, 3038
Hofler, A. 195
Hofmann, I. 129, 589, 2592, 2607, 2954
Hogan, B. 1119
Hogan, G. 702
Hogan, J. 457, 1377, 2866
Hogan, M.J. 731, 1530, 1864, 1933
Holder, D.J. 189
Holldack, K. 836, 839, 2527, 3023
Holloway, M. 426, 2571
Holmes, J. 117, 1569, 1572, 3503
Holmes, R. 770
Holtkamp, N. 11
Holzscheiter, M. 558
Honkavaara, K. 467, 911, 2476
Hopkins, S. 1461
Horan, D. 1177
Hori, Y. 809, 860
Horioka, K. 1807
Horst, B. 467
Hosoda, N. 250, 2551
Hosokai, T. 2258
Houck, T. 558, 2628
Hourican, M. 1643
Hovater, C. 195, 1098, 2379
Howe, S. 705
Hseuh, H. 54, 785, 788, 791, 1425, 1715, 2144, 2147, 2390, 2598, 3419
Hsiao, F.Z. 2402, 2405
Hsiung, G.Y. 821
Hsu, K.T. 890, 1044, 2376, 2554, 2557, 3237, 3392
Hsu, S.-Y. 2376
Hsu, S.N. 821
Hu, K.H. 2376, 2554, 2557, 3237, 3392
Hu, M. 1649
Huang, C. 1530, 1864, 1933, 3174
Huang, H. (BNL) 51, 54, 405, 1697, 1706, 1712
Huang, H. (Yale U) 1688
Huang, J.Y. 875, 2539
Huang, M.H. 1047
Huang, Z. (ANL) 905
Huang, Z. (SLAC) 329, 3138, 3231
Hubbard, R.F. 716, 1846
Hubers, H.-W. 839
Huelsmann, P. 589
Huening, M. 467, 2074, 2682, 2730
Hughes, T. 120, 558, 3210
Huhn, A. 2444
Hulbert, S. 241
Hülsmann, P. 434
Humphries, S. 3557
Hung, D.S. 3234
Hunter, T. 2706
Huo, Y. 426, 2312
Hurh, P. 641, 1440, 1443, 1449, 1452
Hutchinson, E. 1542
Huttel, E. 893, 3273, 3276
Hutton, A. 195
Hwang, C.S. 821, 1041, 1044, 1047, 2376
Hwang, W.H. 2539, 2857
Iarocci, M. 1631
Iazzourene, F. 2306, 2309
Ieiri, T. 860, 3077, 3080

Igarashi, S. 568, 755, 1165, 1807, 2610
Igarashi, Y. 2838
Igarashi, Z. 1509
Igo, G. 51
Ihee, H. 420
Ihloff, E. 2324
Iida, K. 530
Iida, M. 1978
Iida, N. 2240
Ikeda, H. 2503
Ikeda, M. 3326
Ikegami, K. 1509
Ikegami, M. 1455, 1509, 2393, 2835
Ilg, T. 2841
Imai, T. 2829
Inagaki, S. 568, 1784
Inagaki, T. 487
Incurvati, M. 2279, 3285
Ingrassia, P. 1715
Irie, Y. 1512, 2509
Iriso-Ariz, U. 54, 794, 797, 1706, 1801, 3479
Isaev, V.A. 1147
Isagawa, S. 860, 1228
Ise, T. 755
Ishi, Y. 1512
Ishibashi, K. 1784
Ishikawa, T. 487
Ishimoto, S. 1834
Ishizuka, T. 3332
Ito, T. 1509, 2835
Ivanov, O. A. 1147
Ivanov, P.M. 3062
Ivanov, V. 1137, 2664, 3312, 3315
Ivanov, Yu.D. 3530
Ivanov, Yu.M. 917
Iversen, J. 467
Iverson, P. 1530
Iverson, R. 731, 1864, 1933, 2285, 2297
Ives, L. 269, 1110, 1113, 1116, 1119, 1125, 1127, 1137, 1140, 1142, 3312, 3560
Iwasaki, Y. 902, 2387, 3270
Iwashita, D. 1807
Iwashita, Y. 1993, 2198
Izawa, M. 3201
Jackson, A. 244
Jackson, G. 705, 3159, 3162
Jackson, J. 2153, 2159, 2390
Jacob, J. 854, 1332, 3192
Jacobs, K.D. 887, 929, 2303, 2373
Jacobson, E.G. 73
Jacobson, S. 3374
Jacques, E. 1303
Jacquez, E. 558
Jaeschke, E. 836, 2114
Jain, A. 39, 164, 1637, 2159, 2390
Jamilkowski, J. 1542
Jamison, S.P. 519
Jang, J.H. 1219, 2832, 2884
Jansma, W. 2029
Jansson, A. 1751, 1763
Jason, A. 702, 1664, 1966, 2948
Javanmard, M. 722, 1855
Jeanneret, J.-B. 45, 1682, 3494
Jenninger, B. 307, 1727
Jensch, K. 467
Jensen, A. 3315
Jensen, E. 2467, 2470
Jensen, J.-P. 749
Jensen, K.L. 3323
Jensen, L. 307
Jeon, D. 107, 1515, 2652, 2855
Jeong, K.K. 1222, 2832, 2884
Jeong, S.-H. 3114
Jia, L. 1431
Jia, Q.K. 968
Jian, X. 3506, 3509
Jiang, D. 2852
Jiang, H. 1359
Jimenez, J.M. 45, 307, 1727
Jin, L. 369
Jines, P. 2382, 2892
Jing, C. 492, 1810, 2032
Jing, D.M. 815
Jinnochi, O. 51
Jobe, K. 1279, 3141
Johnson, D. (Bechtel) 558
Johnson, D. (FNAL) 1649, 1766, 2931
Johnson, D. (UCLA) 1530, 1933
Johnson, E. 217, 241
Johnson, G. 2841
Johnson, J. 558
Johnson, M. 1350
Johnson, R.P. 1792
Johnstone, C. 983, 1446, 1557, 1649, 1831, 2216, 2931, 3413
Jones, F.W. 3404
Jones, J.K. 2243
Jones, K. 558
Jones, R.M. 1261, 1264, 1270, 2760, 2763
Jones, T. 716, 1846
Jones, W.P. 699, 1065, 1563
Jordan, K. 1485
Joshi, C. 731, 1530, 1858, 1864, 1873, 1933
Joshi, C.H. 1407
Joshi, P. 2162
Jowett, J.M. 1682
Julian, J. 1240
Julian, R.L. 929
Jung, J.Y. 3458
Jungwirth, H. 598, 2811
Junquera, T. 1303
Kabel, A.C. 2252, 3539, 3542, 3545
Kadokura, E. 1509
Kaertner, F.X. 959, 980
Kaganovich, D. 716
Kaganovich, I.D. 1667, 2975
Kageyama, T. 800, 803
Kahn, S.A. 1709, 3255, 3413
Kain, V. 45, 1685
Kaiser, H. 467
Kakihara, K. 2838
Kako, E. 1338

Kalantari, B. 238
Kalinichenko, A.I. 1080
Källberg, A. 1590
Kalnins, J.G. 1837, 2951
Kaltchev, D. 45, 1581, 3494
Kamikubota, N. 1509
Kamitani, T. 1225, 3288
Kamiya, Y. 530
Kammering, R. 467, 2730
Kanahara, T. 1978
Kanareykin, A. 1888, 1891, 1894, 1897
Kanazawa, K. 806, 2503
Kandaswamy, J. 167
Kaneko, N. 3326
Kang, H. 3180
Kang, H.S. 1470, 2857, 3383
Kao, C.C. 241
Kaplan, D.M. 1183, 1792, 1798, 1834
Kaplan, R. 1306, 1437, 3347
Karantzoulis, E. 2306, 2309
Karataev, P.V. 2709
Karl, F. 2390
Karmanenko, S. 1888
Karpov, G. 250
Kasemir, K. 3371, 3377
Kashikhin, V.S. 1966
Kashikhin, V.V. 1748, 1966, 1969, 1975
Kashiwagi, S. 3288
Kashtanov, E. 1781
Kaspar, K. 589
Kasper, P.H. 1503, 2936
Kasuga, T. 860, 1228, 3077, 3080, 3261
Kato, T. 1455, 1509, 2393, 2835
Katoh, T. 860, 2351
Katsouleas, T.C. 731, 1530, 1858, 1864, 1933, 3174
Katuin, J. 699, 1068
Kaugerts, J. 2162
Kawakubo, T. 1165, 1512
Kawamoto, T. 2351
Kawamura, M. 1509
Kawashima, Y. 250, 487
Kawata, H. 860
Kedzie, M. 1291, 1294, 1297
Keeley, D. 235, 2372
Keil, B. 3386
Keil, E. 414, 3413
Keil, R.G. 887
Kelez, N. 2527
Keller, L. 2739
Keller, R. 527, 3306
Kelley, J.P. 977, 1966
Kelly, J. 2706
Kelly, M.P. 1291, 1294, 1297
Kempkes, M.A. 547, 1500
Kephart, R. 1972
Kerby, J.S. 1745, 1969
Kersevan, R. 854
Kesar, A.S. 2095, 2536
Kesselman, M. 524, 2444, 2453
Kester, O. 2869, 2872
Kewisch, J. 39, 372, 1300, 1694, 1700, 2005, 2011, 3186
Khabiboulline, T. 48, 1207, 1210, 1213
Khachatryan, A.G. 1900, 1903
Khan, S. 836
Khodak, I.V. 2098
Kikuchi, M. 860, 3368
Kikuzawa, N. 3443, 3446, 3449
Kim, C. 1849, 1852, 1906, 1912, 2987
Kim, D.T. 1470, 2857
Kim, E.-S. 3105, 3108, 3111, 3114
Kim, G.H. 1849, 1852, 1906, 1912, 2987
Kim, J.B. 2984, 2987
Kim, J.U. 1849, 1852, 1906, 1912, 2987
Kim, K.-J. 905, 1813, 2682, 3138
Kim, K.R. 1602
Kim, M.G. 875, 3114
Kim, S.C. 2857, 3114
Kim, S.H. (ANL) 1020
Kim, S.-H. (ORNL) 1365, 1467, 1599
Kim, T.H. 1539
Kim, Y. (CHEP) 962, 965
Kim, Y. (DESY) 962, 965
Kim, Y.J. 2832, 2884
Kimura, N. 1978
Kimura, W.D. 1909
King, L. 457
King, Q. 1945
King, T.C. 2402, 2405
Kinkead, A.K. 492, 1128, 1147
Kinoshita, K. 2258
Kirchgessner, J. 1314
Kirk, H. 1628, 1631, 1634, 1709, 1787, 2008, 2213, 2219, 3255
Kishek, R.A. 426, 1673, 1676, 2574, 2577, 2673, 3156
Kishiro, J. 568, 1509, 1784, 1807
Kitamura, H. 487, 962, 965
Kitsuka, T. 902, 3270
Klein, H. 1335, 2942
Klein, H.-U. 1948
Klein, S.B. 699
Kleman, K.J. 887, 929, 2373, 3147
Klenov, V. 3282
Kling, N. 1542
Klotz, W.-D. 2360, 2363, 3527
Knapic, C. 1050
Kneisel, P. 92, 457, 1350, 1362, 1374, 1377, 1395, 1575, 2863
Knippels, G. 519
Knobloch, J. 1323
Ko, I.S. 1852, 2984
Ko, K. 2664
Koba, K. 1679, 1736
Kobayashi, H. 1509
Kobayashi, M. 860
Kobayashi, N. 713

Kobayashi, T. 1509
Kobayashi, Y. 857, 860, 2171, 3201, 3204
Kobilarcik, T. 1652, 2934
Koch, J.M. 851
Koda, S. 902, 2387, 3270
Kodera, M. 250
Koiso, H. 3368
Kokhanovski, S. 3282
Kolomiets, A.A. 2875
Komada, I. 2351
Kondaurov, M. 2769
Kondo, Y. 1509
Konecny, R. 492, 1156, 1810, 2032
Konkashbaev, I. 1180
Koop, I.A. 372, 2898
Koopman, J. 2470
Kooy, H. 690
Korbly, S. 2095, 2536
Korenev, I. 1013, 1611
Korenev, S. 1013, 1015, 1608, 1611, 1614
Koropsak, E. 3026
Korostelev, M. 2315
Koschik, A. 3044
Koscielniak, S. 1488, 1831, 3413
Koseki, K. 568, 1784, 1807
Koseki, T. 530, 857
Kostin, D. 467
Kostin, M. 1446
Kotlyar, Y. 1542
Kotov, V.I. 917, 1655
Kou, C.H. 1044
Kourbanis, I. 1736, 3353, 3356
Koutchouk, J.P. 2225
Kovach, P. 1939
Kozanecki, W. (CE Saclay) 2739
Kozanecki, W. (SLAC) 2297
Kozub, S. 1781
Kozyrev, E.V. 1128
Kponou, A. 89, 3282
Kraft, G.A. 192
Kramarenko, K. 1605, 2969
Krämer, A. 589
Krämer, D. 836, 1083, 2114
Kramer, S.L. 241
Kramper, B. 2020
Krasilnikov, M. 2114, 3551, 3566
Krasnogolovets, M.A. 1107, 3303
Krasnykh, A. 1137, 3312, 3315
Krause, S. 2324
Krawczyk, F.L. 1341, 1344
Krejcik, P. 423, 1530, 1933, 2297, 3126, 3129
Kreps, G. 467, 1392
Krinsky, S. 217, 3225
Krischel, D. 1948
Krishock, A. 1542
Kroc, T. 2020
Kroll, N.M. 1270
Kroyer, T. 2700
Krusche, A. 1724
Kuan, K.C. 821
Kuba, J. 95
Kubicki, T. 1204
Kubota, C. 1509
Kubota, T. 3335
Kubsky, S. 899
Kucharczyk, A. 2787
Kuchnir, M. 1792
Kudo, K. (AIST) 2387
Kudo, K. (KEK) 860, 2351
Kudo, T. 487
Kuehnel, K.-U. 1622, 2817
Kulikov, A. 2282, 2297
Kulinski, S. 2787
Kulipanov, G. 250
Kumada, M. 1993, 2198
Kumagai, N. 250, 782, 881, 884
Kumaran, R. 1285
Kuo, C.C. 890, 1044
Kuo, C.H. 764, 2376, 2554, 2557, 3234, 3237, 3392
Kuo, K.C. 1476
Kurennoy, S. 920, 977, 1661, 2083, 3515
Kurita, N. 235
Kusche, K.P. 1909
Kushnir, V.A. 1107, 1605, 2098, 2878, 3303
Kuske, P. 839, 1186, 3020, 3023
Kustom, R.L. 1020
Kuzikov, S. V. 1147
Kuzin, M. 250
Kuznetsov, A. 2769
Kuznetsov, G. 57, 1781
Kwan, J. 70, 3291, 3294, 3297, 3300, 3309
Kwiatkowski, S. 1240
Kwon, H.J. 1219, 1222, 2832, 2857, 2884
Kwon, S. 3371, 3377
Lach, J. 2769
Lackey, J.R. 1503, 2168, 2936
Ladd, P. 2706
Ladran, A. 1243, 2023
Lagniel, J.-M. 2601
Lai, S. 1763
Laier, U. 3569
Lamb, D. 426, 2571, 2574, 2577
Lambertson, G.R. 410, 1837
Lambiase, R.F. 550, 743, 770, 2144
Lamm, M. 42, 1730, 1969, 1972
Lamont, M. 45
Lange, R. 467
Langton, J. 235
LaPointe, M.A. 1131
Larbalestier, David C. 151
Larsson, JÅrgen 2321
Laskar, J. 378, 3189
Lau, T. 3563
Lau, W. 1243, 1834
Laurent, J.M. 307
Lauze, R. 195
Laverty, M. 1404
Lawson, Greg S. 288

Lawson, W. 1119, 1140
Lawton, D. 138
Laxdal, R.E. 601, 1488, 1584
Lazurik, V.M. 1616
Lazurik, V.T. 1080, 1616
Le, Tuong N. 3338, 3341
Lebedev, V.A. 29, 48, 1733, 1739, 1751, 2497, 3062
LeBlanc, G. 2318, 2321
Lebrun, P. 1739, 1754, 1763, 2703
Ledford, J.E. 1341
Lee, Demi 2376, 2554
Lee, E.P. 312, 1521, 2658, 2975
Lee, H.H. 2832
Lee, H.J. 1849, 1852, 1906, 1912, 2984, 2987
Lee, H.R. 1602
Lee, Jinhyung 2026
Lee, Peter J. 151
Lee, R.C. 54, 785, 794
Lee, S.Y. 1065, 3150, 3240
Lee, Soon-Hong 824
Lee, W.-T. 426, 2571, 2577
Lee, Y.-Y. 550, 571, 617, 1569, 1572, 1637, 2144, 2147, 2150, 2153, 2159, 2390, 2598, 3416
Leemans, W.P. 719, 734, 1840, 1885
Lefevre, T. 2464
Legg, R.A. 887
Lehrach, A. 598, 2811, 3428
Lei, S.C. 1476
Leibfritz, J. 2020
Leitner, D. 86
Leitner, M.A. 86, 1521, 1990
Lemaire, J.-L. 2601
Lemuet, F. 444
Lenci, S. 1122
Lenkszus, F. 283, 2435
Leone, S. 186
Leontiev, V.N. 553
Le Pimpec, F. 1279, 2748
LeSage, G.P. 95
Lessner, Eliane S. 3467
Letchford, A.P. 2542
Leung, K.N. 3309
Level, M.-P. 229, 1332
Leveling, A. 1440
Levi, D. 3285
Lewandowski, J.R. 1261, 1264
Lewellen, J.W. 905, 1813, 2029, 2035, 2038, 2132, 2333, 2417, 2420
Leyh, G.E. 235, 761, 1174
Li, C. 2357
Li, D. 186, 1183, 1243, 1246, 1249, 1389, 2023
Li, G. 968
Li, H. 426, 1673, 1676, 2574, 2577
Li, H.C. 2402, 2405
Li, J. 391, 2270, 2357, 2479
Li, Juexin 2715
Li, N. 2174
Li, R. 208, 941
Li, Shaoqing 2852
Li, Shiqui 1560
Li, W. 2357, 2715
Li, Xiaoguang 2852
Li, Y. (ANL) 905
Li, Y. (Cornell) 620, 2264, 2399
Li, Yuxiong 2715
Li, Z. 1264, 2664, 2760
Liaw, C.J. 617, 2444
Lidia, S.M. 186, 2086, 2089, 2092, 2682, 3198, 3500
Liebermann, H. 1335, 2820, 2942
Lien, M.K. 592
Liepe, M. 192, 467, 1201, 1317, 1320, 1323, 1326, 1329, 2059, 3347
Lietzke, A.F. 170, 1984, 1990
Ligi, C. 2279, 3285
Likhachev, S. 1010
Lill, Robert M. 2435
Lim, J. 2192
Lima, R.R. 2201
Limborg, C.G. 235, 329, 2077, 2104, 2667, 3216, 3548
Limon, P. 42
Lin, F.Y. 1047
Lin, M.C. 1371, 2402, 2670
Lin, Y.C. 1476
Lindgren, L.-J. 2318, 2321
Linnecar, T. 1718, 3050
Lipka, D. 2114
Litvinenko, V. 391, 752, 2273, 2479
Liu, C.Y. 1479, 1482
Liu, G. 2357
Liu, J.-F. 1341, 1344, 2083
Liu, J.Y. 968
Liu, Kuo-Bin 767
Liu, P. 1452
Liu, W. 492, 1156, 1810, 2032
Liu, Y. 998, 2607
Liu, Zuping 2715
Lo, Y.C. 3234
Lockey, R. 550, 1542
LoDestro, Vincent 3282
Loew, G.A. 647
Loewen, R. 1264
LÅfgren, P. 1590
Loftsdottir, A. 863
Logan, B.G. 1521, 2661
Logatchov, P. 3318
Loiacono, L. 3183
Longcoy, L. 2324
Longo, C. 1428
Lonza, M. 3395
Loos, H. 217, 241, 329, 908, 1192, 1497, 2455
Lopes, M.L. 1596, 2201
Lopez, A. 2029
Lorentz, B. 3428
Lorkiewicz, J. 467
Lorman, E. 2494, 3062
Losito, R. 878, 1309, 1332
Lou, G.H. 1044
Louie, W. 743, 1431, 1700
Loulergue, A. 229

Low, R. 1240
Lowe, D. 220, 2195
Lowenstein, D. 1715
Lu, J. 1285
Lu, W. 1870, 1933
Lucas, P. 2925
Luccio, A.U. 51, 272, 405, 1697, 1936
Ludewig, H. 1428, 1628, 1709, 2598, 2796
Ludvig, J. 2625
Ludwig, M. 2461
Lumpkin, A.H. 2411, 2414, 2417, 2420, 2423
Lund, S.M. 132, 312, 536, 1990, 2631, 2634
Luo, G.H. 890, 1041, 1371, 2670
Luo, Y. 2123, 2126, 2129, 2132, 2135, 2186
Luque, A. 3029
Lusk, M. 2354
Lyles, J.T.M. 1092
Lyn, L. 1240
Lynch, M.T. 553, 1095, 1168, 1458
Lyneis, C.M. 86
Lysenko, W.P. 2613
Ma, H. 1464, 3377
MacDonald, M.A. 189
Macek, R.J. 326, 508, 2521, 2598, 3086, 3089, 3419, 3455
MacGill, R. 1246
Machida, S. 1512, 1679, 3413, 3452
Machie, D. 1377, 2866
Macina, D. 1742
MacKay, W.W. 39, 51, 54, 164, 405, 1697, 1706, 1712, 1715, 1936
MacLachlan, J.A. 1554, 1736, 1769, 3180
MacLean, E.J. 708
MacLeod, A.M. 519
MacNair, D. 235
Madre, B. 1494
Maebara, S. 2829
Maesen, P. 1724
Magome, T. 250, 782
Mahler, G. 2156
Maier, R. 598, 2811, 2814, 3428
Maisheev, V.A. 917
Majeski, R. 2655
Makarov, O. 2261
Makita, Y. 1539
Malafronte, A.A. 2201
Malagu, C. 917, 1655
Malitsky, N. 272, 2919, 3482
Malm, K. 2150
Malmgren, L. 2321
Malo, J.F. 2470
Mammarella, F. 638
Mammosser, J. 457, 1104, 1386, 2860
Mansell, J. 1861
Mao, S. 779
Mapes, M. 785, 788, 1542, 2141
Marcellini, F. 366, 2080, 2279, 2742, 3141, 3285
Marchand, D. 2799
Marchand, P. 229, 878, 1332
Marchionni, A. 1649, 3440
Marcouill_, O. 229
Marechal, X. 487
Marhauser, F. 1189
Markiewicz, T. 644, 2739
Marks, S. 1032, 3458
Marlats, J.L. 229
Marneris, I. 746, 1542, 1637
Maroli, C. 3285, 3512
Marone, A. 164, 1939, 2162
Marque, S. 878
Marques, S.R. 2583, 3279
Marqversen, O. 2461
Marr, G. 1542, 1715
Marriner, J.P. 514, 2928, 3180, 3434, 3437
Marsden, D. 1110, 1119
Marsh, K.A. 731, 1530, 1864, 1873, 1933
Marshall, T.C. 1882, 1924, 1930
Marsi, M. 2306
Martens, M. (ANL) 2029
Martens, M. (FNAL) 1730, 1972, 3359
Marti, F. 138, 1353, 2649, 2849, 2972
Martin, D. 235
Martin, M.C. 863, 869
Martineau, R. 2841
Martinelli, G. 917, 1655
Martinez, D. 2512
Martini, M. 129, 388, 2913, 2916
Martins, M.N. 1593, 1596, 2201
Martovetsky, N. 1990
Marusic, A. 524, 1706
Maruyama, A. 1539
Maruyama, T. 2739
Masaki, M. 250, 881
Mastovsky, I. 2095
Masuda, T. 250
Masunov, E.S. 2640, 2963
Matheisen, A. 467
Matoba, M. 1679, 3452
Matsui, S. 250, 487, 884
Matsumoto, H. 487
Matsuoka, M. 1338
Mattioli, M. 3285
Matveev, Yu. 2273
Mauri, M. 2080
Mausner, L. 1628
Mavanur, A. 1407
Mazzitelli, G. 366, 1658, 2279
McCarrick, J. 563, 2533, 3557
McChesney, C.A. 2360, 3527
McCormick, D. 1279, 2545, 2548
McCrady, R. 2521, 3086, 3089, 3455
McCrea, M. 2183
McCuistian, B.T. 558
McDonald, J.L. 2385

McDonald, K.T. 1628, 1631, 1634, 1709
McGahern, W. 2390
McGee, M. 2020
McIntosh, P. 235, 1273, 3141
McInturff, A.D. 170, 1984
McIntyre, G. 39, 1691, 2904
McKinney, W. 869
McManamy, T. 1572
McMichael, G.E. 592, 1159
McNeil, B.W.J. 189, 950, 953
Mc Nerney, A. 746, 1542
Mead, J. 524, 2444, 2697
Mecklenburg, B. 2095
Medici, G. 3285
Medjidzade, V. 167, 2399
Medvedko, A. 2769
Medvedko, E. 235, 761
Meidinger, A. 558
Meinke, R.B. 1990, 1996
Meisner, K. 1736, 1769
Melin, G. 81
Meller, R.E. 2339
Meng, W. 1637, 2144, 2147, 2159, 2598
Meot, F. 444
Merl, R. 2354, 2515, 2518
Merminga, L. 192, 195, 332
Merrill, F. 702
Mertens, V. 1721
Mertins, H.-C. 836
Merz, W. 749
Messina, G. 3285
Meth, M. 1195
Métral, E. 129, 388, 2913, 2916, 3047
Métral, G. 388, 2913, 2916
Meyer, A. 1542
Meyer, B.J. 73
Meyer, F.W. 998
Meyer, T.S. 2491
Meyer Sr., R.E. 2485
Mezentsev, N. 250
Mezi, L. 914, 3285
Mi, C. 2447
Mi, J. 550, 1640, 2147
Michalek, W. 2029
Michelato, P. 1506, 2071, 2114
Michelotti, L. 1557
Michnoff, R. 1706, 2691, 3026
Miglionico, G. 2150
Migliorati, M. 2077, 3285
Mihalcea, D. 2682
Mihara, T. 2198
Mikado, T. 713, 971, 974
Mikhailichenko, A. 167, 1822, 1825, 1828, 1954, 1957, 1960, 1963, 2399, 2781, 2784, 3350
Mikhailov, S.F. 391, 752, 2273, 2276, 2482
Milani, D. 1945
Milardi, C. 366, 2279, 2742, 2945, 3285
Miles, J. 1942
Miller, R.H. 1264, 2760, 2763
Miller, T. 2382, 2892
Mills, G.D. 998
Milner, R. 956, 959, 980
Miltchev, V. 2114
Milton, S.V. 905, 1813
Minagawa, Y. 860, 3077, 3080, 3261
Minehara, E.J. 3443, 3446, 3449
Minervini, J. 1990
Miram, G. 1110, 1113, 1116, 1137, 1140, 1142, 3312
Mishra, C.S. 1, 1649, 1766, 2928, 3434, 3437, 3440
Mistry, N.B. 167, 2399
Mitchell, D. 1213
Mitra, A. 601
Mitrochenko, V.A. 1107, 3303
Mitrochenko, V.V. 1605, 2098, 2878
Mitsuhashi, T. 860, 2503, 2506, 3204, 3207
Miura, T. 2509, 2610
Miyajima, T. 860, 2171
Mizobata, M. 1071
Mizrahi, A. 722, 728
Mizuhara, A. 1142
Mizuhara, M. 1110, 1113, 1116, 1119
Modena, M. 1942
Moffitt, J.R. 2473
Mokhov, N.V. 42, 983, 1503, 1733, 1742, 1745, 1748, 2739, 2936
Möller, W.-D. 467
Molvik, A.W. 132, 312, 536
Monaco, L. 1506, 2071
Moncton, D.E. 959, 980
Monroe, J. 1587, 1652
Monroy, M. 1464, 3377
Montag, C. 51, 135, 1300, 1431, 1694, 1697, 1700, 1706, 2005, 2011, 2691, 2907, 3026, 3186
Montoya, D.I. 1341
Montoya, N. 558
Moog, E.R. 156, 1020
Moore, C. 1652, 2934
Moore, R. 1751, 1754, 2497
Moore, T. 167
Moraes, J.S. 2990
Morcombe, P. 752
Moretti, A. 1183, 1246, 1792, 2023
Morgan, G. 1936
Morgan, J. 641, 1443
Mori, W.B. 731, 1530, 1858, 1864, 1870, 1933, 3174
Mori, Y. 1231, 1234, 1679, 3413, 3452
Moricciani, D. 3285
Morishita, T. 2829
Moritz, G. 589, 2162
Moritz, L. 638
Morley, K. 702
Morris, C. 702
Morris, J. 746, 1542, 1715
Morris, W.A. 1527
Morse, E.C. 3291

Morvillo, M. 1724
Mosnier, A. 595
Mostacci, A. 1801, 2500, 3479
Mostrom, C. 558
Mottershead, T. 702, 1664
Mouat, M. 638
Moy, K. 558
Mueller, I. 2823
Mueller, N. 2823
Mueller, P.E. 1004
Muggli, P. 731, 1530, 1864, 1915, 1933
Muir, A.A. 1029
Mulholland, G. 1631
Mullany, B. 1428
Müller, A.-S. 388, 893, 2913, 3273, 3276
Mulvaney, J.M. 547, 1500
Murai, S. 1978
Murasugi, S. 1165
Muratore, J. 164, 2162
Muratori, B. 189
Murdoch, G. 1467, 2706
Murokh, A. 944, 2568
Murphy, B.F. 2104, 3216
Murphy, J.B. 176, 217, 241, 2455, 2808
Murray, S.N. 3306
Musser, S.E. 1356
Mustafin, E. 589
Musumeci, P. 1867, 1873, 2117, 2957, 3258
Muto, A. 1679, 3452
Muto, M. 755
Muto, T. 2709
Myakushko, L.K. 2878
Myneni, G. 1374
Na, J.H. 2832
Nadji, A. 229, 896
Nadolski, L. 229, 397, 896
Nagahashi, S. 860, 2171, 2351
Nagai, R. 3443, 3446, 3449
Nagaitsev, S. 2020
Nagaoka, R. 229
Naito, F. 1509, 2835
Nakai, H. 3326
Nakamoto, T. 1978
Nakamura, E. 568, 1165, 1784, 1807, 2610
Nakamura, N. 530, 857
Nakamura, S. 1539
Nakamura, T. 250, 881
Nakamura, T.T. 860, 2351
Nakanishi, H. 860, 1228
Nakanishi, T. 1539
Nakano, J. 1231, 1679, 3452
Nakashizu, T. 3326
Nakayama, K. 530
Nam, K.Y. 1602
Nam, S.H. 1470, 2539, 2857, 3108
Nantista, C.D. 482, 1276
Napoly, O. 2718, 2739
Narang, R. 1873
Nash, B. 126
Nassiri, A. 1416, 2038
Nath, S. 1461, 1515
Naumenko, G.A. 2709
Naylor, C. 1542
Naylor, G. 854
Nehring, T. 550
Neil, G.R. 181, 977
Neilson, J. 269, 1119, 1125, 1127
Nelson, J. 1279
Nelson, R. 1098
Nemesure, S. 1542
Nenasheva, E. 1888, 1894
Neri, F. 3086
Neumann, J. 1497
Newsham, D. 1153, 1156, 2123, 2126, 2129, 2132, 2135, 2186
Nexsen, W. 2533
Nezhevenko, O.A. 1128, 1131, 1147, 1150, 2881
Ng, C.-K. 235, 1264, 2664
Ng, K.Y. 1751, 2922, 3065
Nguyen, D. 977
Nicklaus, D. 323
Nicol, T. 1969
Nicolas, L.Y. 1733
Nielsen, K. 558
Nieter, C. 719, 1885, 1918
Nigorikawa, K. 1509
Nikitina, T.F. 2878
Nishimori, N. 3443, 3446, 3449
Nishimura, H. 244, 397, 1837, 2249, 2385
Noack, F. 836
Noble, R.J. 722, 1858
Noda, F. 1512
Noda, T. 250
Nogami, T. 809, 860
Noguchi, S. 1338, 1509
Nolden, F. 434
NÅlle, D. 2476
Nomura, M. 530
Norbrega, A. 1969
Nordberg, E. 2399
Norem, J. 1180, 1183, 1246, 1999
Norris, B. 983
Nosochkov, Y. 2288, 2291, 2300
Novati, M. 1506
Novokhatski, A. 315, 2294, 2297, 2300, 2981
Nusinovich, G. 1140
Nzeadibe, I. 235
Oakeley, O. 752
Obina, T. 860, 2351, 3077, 3080, 3201, 3207, 3261, 3365
Ochiai, Y. 902, 3270
O'Connell, C.L. 423, 731, 1530, 1864, 1933, 3126, 3129
Odagiri, J. 2351
Odajima, W. 1978
Oepts, D. 519
Oerter, B. 54, 1640
Ogata, A. 3335
Ogawa, H. 713, 971, 974
Ogawa, Y. 3368
Ogitsu, T. 1978, 3413
O'Hara, J.F. 2512
Ohashi, Y. 250

Ohgaki, H. 713, 902, 2387, 3270
Ohhata, H. 1978
Ohishi, M. 884
Ohkuma, H. 881
Ohmi, K. 345, 353, 3053, 3056, 3083, 3398
Ohmori, C. 1216, 1234, 1679, 3413, 3452
Ohnishi, Y. 3056, 3288
Ohnuma, S. 1557
Ohsawa, S. 2838, 3326
Ohsawa, Y. 860
Ohshima, T. 250, 782, 881, 2551
Ohuchi, N. 1978
Oide, K. 353, 2604
Oishi, M. 250, 782
Okada, M. 1509
Okamoto, H. 2592
Okamura, M. 164, 1936
Oleck, A.R. 1649
Olsen, J. 235, 761
Olson, C.L. 2685, 3165
Olson, M. 1781
Onishi, Y. 860
Onisto, H.J. 2583, 3279
Ono, M. 860, 1228
Onoe, K. 487, 3332
Oogoe, T. 2838
Oothoudt, M. 2354
Oppelt, A. 2114
Orikasa, T. 1978
Oro, D. 558
O'Rourke, S. 2975
Orris, D. 1969
Ortega, M. 235
Orzechowski, T. 3557
O'Shea, P.G. 426, 511, 1497, 1673, 1676, 2312, 2571, 2574, 2577, 2673, 2712, 3156, 3323
Österdahl, F. 1590
Ostiguy, J.-F. 2168, 2925, 3503
Ostojic, R. 42
Ostroumov, P.N. 400, 2426, 2790, 2875, 2963, 3467
Otboev, A.V. 372, 2898
Ott, K. 773, 776
Ottaviani, P.L. 3285
Ottavio, D. 2360
Owen, H.L. 189
Owens, T.L. 3344, 3380
Oz, E. 1530
Ozaki, T. 860
Ozelis, J.P. 1491, 1494
Paál, A. 1590
Padamsee, H. 192, 1201, 1309, 1312, 1314, 1317, 1320, 1323, 1410, 2059
Pagani, C. 467, 1300, 1341, 1506, 2114
Page, T. 1969
Pai, C. 550, 2144, 2147
Pakter, R. 1134, 2990
Palmer, D.T. 1858, 2107
Palmer, M.A. 2267, 2473
Palmer, R. 1816
Palmer, R.B. 1804, 1834, 1987, 2002, 3413
Palumbo, L. 944, 2500, 3285
Pantell, R.H. 1909
Paoluzzi, M. 1724
Papaphilippou, Y. 123, 851, 854, 1569, 2159, 3053, 3189
Paparella, R. 470
Pappas, C. 235
Paramonov, V. 2826
Pardo, R.C. 2426, 2875
Park, B.R. 1470
Park, B.S. 1602
Park, E.S. 875
Park, H.J. 3383
Park, J.H. 2539
Park, M.Y. 1219, 2832, 2884
Park, S. 235
Park, S.-S. 3114
Park, S.J. 2539
Parker, B. 372
Parkhomchuk, V. 2769
Parmigiani, F. 186
Parodi, R. 1395
Parsa, Z. 3005
Partridge, R. 644
Parzen, G. 2589
Pasky, S. 1419, 2038, 2333
Pasotti, C. 878
Pasquinelli, R.J. 3068, 3431
Pate, D. 39, 92
Pattengale, N. 2360
Pattengale, N.D. 3527
Patton, J. 2363
Paul, A.C. 2533, 2960
Paul, K. 2931
Paulon, R. 1506
Payet, J. 2718
Pearson, C. 1264
Peatman, W.B 836
Pedersen, F. 2461
Pedrozzi, M. 878
Peggs, S. 39, 42, 135, 278, 372, 797, 1059, 1691, 2204, 2901, 2904
Pei, Y.J. 818, 2852
Peiniger, M. 1410
Pekeler, M. 1410, 2887
Pelaia, T.A. 2360, 2363, 2366, 3527
Pellegrini, C. 211, 944, 1867, 1873
Pellegrino, L. 366, 2279, 3285
Pellico, W.A. 1587, 2936, 3177
Peñano, J.R. 716
Penco, G. 878
Penel, C. 253
Peng, Z.H. 601
Perevedentsev, E.A. 2898, 3398
Perez, F. 893, 3273, 3276
Perezhogin, S.A. 1605
Peschke, C. 434
Peters, H.-B. 467
Peterson, D. 3068
Peterson, E. 1294
Peterson, P.F. 2637
Peterson, T. 1966, 1969
Petra, M. 1020

Petracca, S. 2993, 2996, 2999
Petrillo, V. 3285, 3512
Petrossyan, B. 2114
Petrosyan, G. 470
Petrunin, A.A. 917
Petry, J.E. 1500
Peyrot, M. 1948
Pfeffer, H. 1781
Pfister, U. 598
Phillips, D. 1542
Phillips, L. 1401, 2860
Phinney, N. 678
Picardi, L. 3285
Pichoff, N. 2601, 2802, 3491
Pieck, M. 1168
Piekarz, H. 1649, 1981
Piel, C. 2887
Pierini, P. 1300, 1506
Pikalov, V.A. 917
Pikin, A. 89
Pilat, F. 42, 51, 1697, 1703, 1706, 1712, 2207
Pillai, C. 2515, 2518
Piller, M. 3377
Pinayev, I. 752, 2273
Pindak, R. 241
Piot, P. 911, 2682, 3500
Pirkl, W. 186
Pivi, M. 350, 2598, 3219, 3222
Pjerov, S. 241
Placidi, M. 186, 2530
Plan, B. 253
Planet, M. 2799
Plant, D. 2769
Plate, D. 1240
Plate, S. 164, 1939
Platz, M. 3569
Plawski, E. 467, 2787
Plawski, T. 195, 2379
Plettner, T. 722, 1861
Plouviez, E. 851, 854
Plum, M.A. 2429, 2444, 2485
Podlech, H. 1335, 2820, 2942
Podobedov, B. 241, 2808
Pogge, J. 1524, 2706
Pogorelsky, I.V. 1909
Poirier, R. 601, 1285, 1584
Polozov, S.M. 2963
Ponnaiyan, V. 54, 794
Pont, M. 893, 3273, 3276
Poole, M.W. 189, 950, 953
Popenko, V.A. 2878
Popov, G.F. 1080, 1616, 1619
Popov, V.G. 752, 2273
Popova, N. 1619
Popovic, M. 983, 1792
Pordes, S. 2491
Portmann, G. 890, 2369, 2372, 3213, 3374
Potter, J. 2354
Potter, K. 1467, 2706
Potylitsyn, A.P. 2709
Poupeau, J.P. 1303
Power, J. 1661, 2429, 3371, 3377
Power, J.G. 492, 1810, 1813, 1888, 1894, 2032, 2432, 2667
Power, K. 1936, 1939
Powers, T. 457, 2379
Pozdeyev, E. 138, 2649
Prasuhn, D. 598, 3428
Preble, J. 457, 977, 1104
Prebys, E.J. 1503, 1587, 1652, 2936
Preger, M.A. 366, 684, 1658, 2279, 2945, 3285
Preis, H. 1309
Prelec, K. 89
Prestemon, S. 1032
Prichard Jr., B.A. 73
Prior, C.R. 1527
Proch, D. 467
Prochnow, J. 2467
Prokop, M. 3371, 3377
Prom_, M. 2601
Prost, A. 1643
Prost, L.R. 275, 312, 536, 1518, 2524
Przeklasa, R.S. 1168
Ptitsyn, V. 51, 54, 135, 372, 405, 1697, 1703, 1706, 1712
Pu, Y. 1539
Puccio, B. 1945
Pugachev, G.D. 2878
Pugnat, P. 1942
Purcell, D. 2444, 2706
Pusina, J. 2086
Qian, B.L. 2646, 2966
Qian, Z. 1183, 1246
Qiang, J. 1509, 2613, 2954, 3401
Qin, B. 3506, 3509
Qin, H. 2655, 2658, 3117, 3120, 3123
Quan, S. 2580
Quast, T. 836
Quattromini, M. 914, 2077, 3285, 3548
Quigley, P. 1410, 1437
Quimby, D.C. 1909
Quinn, B. 426, 1673, 2312, 2571, 2574, 2577, 2673
Quinn, F.M. 189
Quirus, M. 2571, 2577
Rabedeau, T. 235
Rabehl, R. 1969
Radovinsky, A. 1990
Raguin, J.-Y. 2724
Raimondi, P. 366, 731, 2279, 2766, 2945, 3285
Raino, A. 3318
Raja, R. 1446
Raka, E. 2595
Rakhno, I.L. 983, 1742, 1745, 1748
Rakowsky, G. 217
Ranjbar, V. 3062
Rank, J. 39, 1467, 2150
Rao, Y.-N. 1578, 1584
Raparelli, M. 2476
Raparia, D. 571, 1428, 1467, 1569, 1572, 1637, 1709, 2150, 2153, 2156,

2390, 2598, 2793, 3282, 3416
Rarback, H. 235
Rathke, J.W. 92, 920, 977, 2186, 2790
Ratti, A. 186, 1464, 2530, 3371, 3377
Ratzinger, U. 1062, 1335, 2820, 2942
Raubenheimer, T.O. 662, 1038, 2739, 2754, 2757, 2760, 2775, 3219, 3231
Ravel, J.-C. 2799
Rawnsley, W. 601
Read, M.E. 1113, 1116, 1119, 1137, 1140, 1142
Reass, W.A. 553, 1168
Redaelli, S. 665
Redlin, H. 2114
Reece, C. 1377, 1398, 1494
Reece, K. 1569
Reed, C.A. 998
Rees, D.E. 553, 1095, 1168, 1458
Rees, G.H. 1527, 1557
Regan, A. 3371, 3377
Rehlich, K. 467, 2342, 2476
Reichardt, G. 836
Reiche, S. 211, 944, 947, 2110, 2112, 3153, 3321
Reich-Sprenger, H. 589
Reid, J. 48, 1204, 1213, 1769, 3353
Reilly, J. 1306
Reiser, M. 426, 511, 1673, 1676, 2312, 2571, 2574, 2577, 2673, 3156
Rej, D. 1461
Remondino, V. 173
Renieri, A. 3285
Rensfelt, K.-G. 1590
Repikhov, G.D. 2878
Reprintzev, L.V. 2878
Reschke, D. 467
Resende, X.R. 1056
Reshetnyak, N.G. 1107, 3303
Reuter, A. 92
Revol, F. 253
Revol, J.L. 851, 854
Rey, J.M. 1987
Reynolds, J. 2354
Rhee, S.J. 2177
Ricci, R. 366, 2279, 3285
Rice, D. 167, 278, 2399, 3425
Richards, D. 2844
Richardson, R. 563
Reiche, S. 203
Richichi, S. 167
Richter, A. 3551, 3569
Ries, T. 601, 1488
Rifflet, J.-M. 1948
Rimmer, R.A. 186, 977, 1104, 1183, 1243, 1246, 1389, 2023, 2092
Ringwall, A. 235
Rinn, J. 1942
Rinolfi, L. 684, 2742
Rios, P.B. 1593, 1596
Riot, V. 2530
Ritson, D. 1557
Ritter, J. 89, 3282
Rivetta, C. 3362
Rizzato, F.B. 2990
Robb, G.R.M. 950, 953
Robin, D. 224, 397, 2246, 2249, 3213
Robinson, K. 186
Robinson, T. 1119
Roblin, Y. 195
Robothom, W. 2168
Rock, B.Y. 2473
Rockford, J.H. 1987
Rode, C.H. 977, 2863
Rodrigiuez, M. 1237
Rodriguez, J. 138, 2649
Rodriguez, L. 558
Rodriguez, P. (LANL) 558
Rodriguez, P. (SLAC) 235
Rodriguez-Mateos, F. 1945
Rogers, G. 2303
Rogers, J.T. 375
Rogov, Yu.V. 1616
Rohlev, A. 2336
Rom, M. 3285
Romanov, G. 48, 1210
Romas'ko, V.G. 1107
Romè, M. 3285
Romero, D. 2354
Roncarolo, F. 2470
Ronsivalle, C. 914, 2077, 3285, 3548
Root, L. 1584
Ropert, A. 851, 854, 3189
Rose, C.R. 2485
Rose, D.V. 98, 2622, 2637, 2685, 3165
Rose, J. 217, 241, 1192, 2455, 2808
Roseberry, T. 1467
Rosenberg, R.A. 508, 3183
Rosenthal, S. 690
Rosenzweig, J.B. 95, 914, 944, 947, 1533, 1858, 1867, 1870, 1873, 2110, 2112, 2117, 2192, 2957, 3153, 3258, 3285, 3321
Roser, R. 1706
Roser, T. 24, 39, 51, 54, 405, 1545, 1637, 1697, 1715, 1936, 2204, 2793, 3026
Ross, I.N. 189
Ross, M.C. 503, 678, 1279, 2494, 2545, 2548, 2709
Rossbach, J. 2114
Rossen, P.v. 598
Rossi, A. 307, 1727
Rossi, C. 1724
Rossi, L. 42, 141
Rossmanith, R. 899, 3273
Rotela, E. 2790
Roth, I.S. 547, 1500
Rothgeb, T. 1377, 1386
Roudier, D. 1303
Rouleau, G. 73
Rowley, L. 2303
Rowton, L. 2841
Roy, P.K. 98, 2616, 2619, 2622, 2625, 2628
Roybal, R.J. 1341, 1661
Roybal, W. 1095, 1458
Royer, P. 684

Rubin, D.L. 1023, 2056, 2267, 3425
Rudolph, K. 2869, 2872
Rudychev, V. 1619
Ruegg, R. 638, 1584
Ruggiero, A.G. 1637, 2793, 2796
Ruggiero, F. 42, 45, 123, 1727
Ruggiero, R. 1748
Ruggles, S.C. 1168
Ruland, R. 2769
Rumolo, G. 123, 1727, 2234, 2607, 3038, 3041, 3044, 3053
Rusek, A. 1542
Rusnak, B. 989, 1347
Russell, A. 1652
Russell, S. 977
Russo, T. 1545, 3422
Rust, K. 550, 770
Rust, W.W. 635
Ruth, R.D. 1264
Ryan, J. 1542, 2595
Rybarcyk, L.J. 1092, 1566, 3086
Ryne, R.D. 1509, 2954, 3401
Saban, R. 1945
Sabbi, G. 42, 170, 536, 1032, 1521, 1984, 1990
Sabol, D. 2399
Saeki, H. 250
Saewert, G. 1781, 2020
Safranek, J. 235, 890, 3213
Sagan, D. 192, 848, 1023, 2267
Sahuquet, P. 1303
Saigusa, M. 2829
Saino, K. 487
Saito, K. 462
Sajaev, V. 417, 905
Sakai, H.R. 530, 857
Sakai, I. 1512, 1679, 3452
Sakamoto, Y. 860
Sakanaka, S. 860, 1228, 3207, 3365
Sakuda, M. 1807
Sakumi, A. 312
Saleh, N. 1921
Sanchez, B.J. 2515
Sanchez, M. 558
Sandberg, J. 550, 571, 743, 746, 770, 1640, 2144, 2147
Sanderson, D. 138
Sandner, W. 836, 2114
Sanelli, C. 366, 2279, 2742, 3285
Sanfilippo, S. 173
Sannibale, F. 863, 1658, 2527
Santucci, J. 2682
Sapozhnikov, L. 3389
Sarraf, R.H. 238
Sasaki, S. (ANL) 2261
Sasaki, S. (SPring-8) 250, 782
Sato, H. 568, 755, 1165, 1807, 1981
Sato, M. 860
Sato, Y. (IU) 3240
Sato, Y. (KEK) 1679, 2509, 3452
Satogata, T. 51, 54, 272, 278, 405, 1697, 1706, 1712, 1715, 2204, 2207, 2697, 2901, 3026, 3482
Satoh, M. 533, 860, 3368
Sauer, A. 1335, 2820, 2942
Saugnac, H. 1303
Saunders, A. 702
Saunders, J. 2860
Savage, R. 2390
Savalle, A. 2802
Savary, F. 1942
Savatteri, S. 746
Sawamura, M. 3443, 3446, 3449
Sazawa, S. 2829
Scaduto, J. 39, 92, 1631
Scandale, W. 173, 986, 1655
Scanlan, R.M. 170, 1032, 1984
Scarlett, C. 3255
Scarpine, V. 2414, 2494, 3062
Scarvie. T. 869, 2527, 3374
Schächter, L. 722, 728, 1879
Schaerf, C. 3285
Schaetz, T. 112
Schaller, S. 2354
Schamel, H. 3029
Schappert, W. 323, 2494
Schauer, M. 558
Scheer, M. 836
Scheidt, K. 854
Scheitrum, G. 3312, 3315
Schellong, B. 1948
Schempp, A. 598, 1062, 1622, 2817, 2823
Schilcher, T. 3386
Schimizu, J. 250
Schindl, K. 1682
Schirm, K.-M. 1948
Schlabach, P. 1730, 1969, 1972
Schlarb, H. 423, 467, 2074, 2730, 3126, 3129
Schlitt, B. 694, 1062
Schlott, V. 3386
Schlueter, R. 1032, 3458
Schmalzle, J. 1939, 2162
Schmekel, B.S. 375
Schmerge, J.F. 2104, 3216
Schmidt, C.W. 2020
Schmidt, F. 1754, 1757, 2207, 2228, 2231, 3494, 3497
Schmidt, P. 1948
Schmidt, R. 45, 1945
Schmidt-BÅcking, H. 1622
Schmidts, F. 1775
Schmor, P. 6, 439, 1584
Schnase, A. 598, 1216, 1234, 2817, 3428
Schneider, H. 598, 3428
Schneider, W.J. 2863
Schnitter, U. 2201
Schoenlein, R. 186, 2408, 2530
Schrage, D.L. 920, 977, 1341, 1344, 1661, 2083, 2790

Schramm, U. 112
Schreiber, S. 467, 911, 1086, 2068, 2071, 2114, 2730
Schreuder, A.N. 699
Schroeder, C.B. 1885
Schuett, P. 589
Schuh, P. 2297
Schulte, D. 657, 662, 665, 1727, 2721, 2727, 2733, 2736, 2739, 2757, 3053
Schultheiss, C. 524, 743
Schultheiss, T.J. 92, 920, 977, 2186, 2790
Schultz, D. 2129
Schultz, J. 1990
Schultz, R. 1443, 1449, 1452
Schulze, M. 3086
Schumann, R. 2114
Schussmann, G. 2664
Schwartz, H. 235
Schwarz, H. 1273, 2297, 3141
Scott, B. 235
Scott, D.J. 1029
Sears, C.M. 2101
Sears, J. 1309, 1312, 1314, 1323, 1410
Sebek, J. 235, 2494
Seberg, S. 2156
Seddon, E.A. 189
Seeman, J. 315, 2294, 2297, 2300
Sei, N. 713, 971, 974
Seidl, P.A. 275, 312, 536, 1518, 1990
Seifrid, P. 3068
Seike, T. 487
Sekachev, I. 601
Sekutowicz, J. 467, 977, 1086, 1300, 1374, 1377, 1392, 1395, 1575, 2730, 2866
Seletsky, S. 2020
Semenov, A. 323, 1781
Semertzidis, Y.K. 1625
Sen, T. 34, 42, 1754, 1757, 1760, 1772, 1775, 3401, 3542
Senf, F. 836
Senichev, Y. 598, 2814
Seo, J.-H. 3114
Seol, K.T. 2832, 2857
Serafini, L. 914, 2077, 2080, 3285, 3512
Serdobintsev, G.V. 2881
Sereno, N.S. 247, 827, 2420, 2435
Serio, L. 1945
Serio, M. 366, 2279, 2742, 3285
Serrano, J. 2336
Serriere, V. 3192
Sertore, D. 1506, 2071, 2114
Seryi, A. 657, 662, 2739, 2748, 2754, 2757, 2766, 2769
Sessler, A.M. 414, 3413
Setzer, S. 2114, 3566, 3569
Severino, F. 1195, 2441
Sezaki, K. 487
Sgamma, F. 366, 2279, 2742
Shaftan, T. 217, 241, 329, 908, 1192, 1497, 2455, 2808
Shang, H. 247, 283, 2330, 3461, 3470, 3473, 3476
Shang, J. 1452
Shao, L. 1876
Shapiro, A.H. 1341, 1344, 2083
Shapiro, M.A. 1255, 1258, 2536
Shapiro, S. 2796
Shaposhnikova, E. 1718, 3050
Sharamentov, S.I. 1291, 2426, 2790
Sharma, S. 2790
Sharp, W. 2622
Sharp, W.M. 98, 2637
Shatunov, P.Yu. 2898
Shatunov, Yu.M. 372, 2898
Shaw, R.W. 617
Shchelkunov, S.V. 1924
Shea, T.J. 1569, 2444, 2706
Sheehy, B. 217, 241, 329, 1192, 1497, 1819, 2455, 2808
Sheinman, I. 1888, 1891, 1897
Shelley, F. 2515, 2518
Shelley, Jr., F. 2354
Shemelin, V. 192, 1201, 1314, 1317, 2059
Shemyakin, A. 2020
Shen, J.L. 519
Shen, L. 2852
Shen, S. 1347
Shen, Y. 217, 2455
Shendrik, V.A. 2878
Shepard, K.W. 581, 1291, 1294, 1297
Shephard, M. 3560
Sheppard, J.C. 2751
Sherman, J. 73
Sherwood, R. 1661
Shi, J. 369
Shibata, K. 800, 803, 806
Shigaki, K. 1512
Shiho, M. 1807
Shiltsev, V. 48, 57, 1739, 1751, 1754, 1757, 1778, 1781, 2497, 2769, 3062
Shimada, T. 1512
Shimizu, N. 1165
Shimosaki, Y. 568, 1807, 2610
Shinoe, K. 530
Shintake, T. 487, 962, 965, 3332
Shintomi, T. 755, 1978
Shioya, T. 860
Shirakata, M. 568, 1807, 2610
Shishido, T. 1338
Shishlo, A. 117, 2360, 2363, 2366, 3527
Shkaruba, V. 250
Shkvarunets, A.G. 2712
Shoaee, H. 3371, 3377

Shoji, M. 250, 782, 2551
Shrey, T. 1542
Shubin, E. 2769
Shul'ga, N. 3329
Shumakov, I.V. 3530
Shuman, D. 98, 2625, 2628
Shurter, R.B. 2512
Shvedov, D. 2273
Shvets, G. 3117
Sibley, C. 607
Siddons, P. 241
Sideris, I.V. 2676
Sieber, T. 2869, 2872
Siemann, R.H. 722, 728, 731, 1530, 1855, 1858, 1864, 1879, 1933
Siemko, A. 1942
Sievers, P. 45
Sigler, F. 1664
Sikora, J. 1306, 3059
Sikora, R. 524, 2444
Silzer, M. 220
Simmons, D. 558
Simmons, L. 1213
Simoens, F. 1303
Simon, F. 1948
Simonsson, A. 1590
Simos, N. 1428, 1628, 1709, 3255
Simpson, J. 1813
Simrock, S. 467, 470, 2342, 2730
Sims, J. 2841
Sinclair, C.K. 76, 192, 1317, 2062
Singatulin, S. 2769
Singer, W. 467, 1374
Singer, X. 467
Singh, O. 283
Skarbo, B. 3318
Skaritka, J. 217, 1909, 2455
Skorobogatov, V.V. 917
Skrinsky, A. 250
Slaughter, D.R. 95
Slaughter, J. 1739, 1763
Smaluk, V. 214
Smart, L. 54, 785
Smedley, J. 541, 2132
Smirnov, A.V. 1153, 1156, 2123, 2129, 2132, 2135, 2186, 2640, 3171
Smirnova, E.I. 1255, 1258
Smith, B. 1210
Smith, E.N. 2399
Smith, G. 1715, 2444, 2453
Smith, H. 423
Smith, H.V. 558
Smith, J.C. 2267
Smith, K. 1377
Smith, K.S. 476, 1195, 1545, 1706, 1715, 2441, 3338, 3341, 3344, 3380
Smith, M. 2382
Smith, S. 235, 761
Smith, S.L. 189
Smith, T. 1279
Smith, T.L. 1416, 1422, 2038
Smolenski, K. 167, 1317, 2399
Snowel, M. 2574
Snydstrup, L. 1542
Soika, R. 2162
Soliday, R. 283, 1419, 2261, 3461, 3470, 3473, 3476
Solyak, N. 1207, 1210, 1213, 1781
Someya, H. 2509
Son, D. 962, 965
Song, L. 1110, 1142
Sonnad, K.G. 1536
Sorchetti, R. 2476
Soutome, K. 250, 782, 881
Spata, M. 195
Spataro, B. 914, 2500, 3285
Spataro, C. 2159
Spencer, C.M. 779, 2177
Spencer, J. 779, 1861, 2180
Spentzouris, P. 2939, 3195
Spickermann, T. 2521, 3086, 3089, 3455
Spiller, P. 589, 694
Spinka, H. 51
Spitz, R. 1195
Sprangle, P. 716, 1846
Sprehn, D. 3312
Springer, P.T. 95
Srinivasan-Rao, T. 39, 92, 541, 2047, 2132
Stanek, M. 423, 2297
Stanford, G. 601, 1488
Staples, J. 186, 1243, 1563, 2023, 2086, 2092, 2408, 3198
Starling, W.J. 2889
Startsev, E.A. 1667, 2975, 2978, 3120, 3123
Stascheck, A. 3569
Stassen, R. 598, 2814, 3428
Stecchi, A. 366, 2279, 2742, 3285
Steck, A. 2515
Steck, M. 434
Steerenberg, R. 388, 2913, 2916
Stefancich, M. 917, 1655
Stefanski, R. 1652
Steier, C. 397, 869, 2246, 2249, 3213, 3374
Steimel, J. 48, 1736, 3068, 3071, 3074, 3353, 3356, 3362
Stein, H.J. 3428
Stein, W. 2847
Steinhauer, L.C. 1909
Stella, A. 366, 2279, 2742, 3285
Stelzer, J.E. 73
Stenning, M. 1584
Stephan, F. 2114
Stephani, T. 1948
Stepin, D.L. 2878
Steski, D. 1715
Stettler, M. 2429, 2512, 3371, 3377
Stevens Jr., R.R. 73
Still, D. 1730
Stinson, G. 1584, 1670
Stirbet, M. 457
Stockhorst, H. 598, 3428
Stockli, M.P. 527, 3306
Stockwell, B. 1122, 1144
Stoltz, P. 132

Stott, J.P. 887, 2373
Stout, D. 2706
Stovall, J. 1515, 2652, 2855
Strait, J.B. 42, 1745, 1748, 1969, 1975
Straumann, T. 235, 761, 2494
Striganov, S.I. 1733
Strohman, C.R. 2473, 3347
Strohmer, S. 899
Studebaker, J. 558
Stulle, F. 3129
Stupakov, G.V. 102, 926, 1038, 3132, 3135, 3225, 3231
Sturgess, R. 558
Suetake, M. 860, 1228
Suetsugu, Y. 612, 800, 803, 806
Sugahara, R. 860
Sugai, I. 1512
Sugawara, S. 1978
Sugaya, M. 1231, 1679, 3452
Sugimoto, M. 2829
Sugimura, T. 3326
Sugita, K. 1978
Sugiyama, E. 1993
Suhring, S. 625
Suk, H. 1849, 1852, 1906, 1912, 2984, 2987
Suller, V.P. 189
Sullivan, G. 558
Sullivan, J. 2533
Sullivan, K. 2189
Sullivan, M. 340, 2282, 2294, 2297, 2300
Summers, D.J. 1804
Sun, D. 3068
Sun, X. 2688, 3008, 3011, 3014
Sun, Y. 2682
Sundelin, R. 1398, 1401
Suwada, T. 533, 1225, 3368
Suzuki, H. 1338
Svandrlik, M. 878
Svirida, D. 51
Swanson, C. 3371
Swenson, D.A. 2889
Swift, G. 2273
Swinney, C. 558
Swirsky, J. 2195
Sylvester, C. 1969
Symon, K.R. 452
Syphers, M. 1649, 1754, 2931
Syratchev, I. 495
Sytnik, V. 1781
Szott, Ph. 1303
Tabak, M. 2637
Taborelli, M. 495
Tada, J. 782
Tadano, M. 860, 2506
Tai, C.-Y. 1407
Tajima, T. 1341, 1344, 2083
Takagi, A. 1216, 1231, 1234, 1679, 2922, 3452
Takagi, T. 782
Takahashi, J. 1593, 1596, 2201
Takahashi, S. 487
Takahashi, T. 860, 1228
Takaki, H. 530, 857
Takala, B.E. 1168
Takano, S. 250, 881
Takao, M. 250, 782, 881
Takasaki, E. 1509, 2835
Takasaki, S. 860
Takashima, T. 250, 487
Takasu, Y. 487
Takayama, K. 568, 1784, 1807, 1981, 2610
Takayanagi, T. 1512
Takebe, H. 250
Takeda, H. 1515, 2855, 3518
Takeda, S. 487
Takeda, Y. 1512
Takeshita, K. 487
Takeuchi, H. 2829
Takeuchi, Y. 803, 860, 2351
Tallerico, P.J. 553, 1095, 1168, 1458, 1461
Talman, R. 192, 272, 848, 2919, 3482, 3485
Tamasaku, K. 487
Tamura, F. 1216, 1234
Tamura, K. 250, 881, 2551
Tan, C.Y. 1751, 2703, 3071, 3074
Tanabe, J. 2174
Tanabe, T. 235
Tanaka, H. (KEK) 1509, 2393, 2835
Tanaka, H. (Mitsubishi) 1539
Tanaka, H. (SPring-8) 250, 881
Tanaka, K. 1978
Tanaka, T. 487
Tang, C. 467
Tang, Z. 623
Tanimoto, Y. 809, 860
Taniuchi, T. 2838
Taniuchi, Y. 250
Tantawi, S.G. 482, 1125, 1127, 1261, 1264, 1270, 1276
Tarakanov, V.P. 1882
Tarasov, G.E. 2878
Tarawneh, H. 238, 2318, 2321
Tariq, S. 641, 1452
Tartaglia, M. 1730, 1969, 1972
Tateishi, T. 884
Tatum, B.A. 995
Tavakoli, K. 238
Tavares, P.F. 2583, 3279
Tawada, M. 353
Taylor, C. 86
Taylor, T. 42
Tazzari, S. 3285
Tazzioli, F. 3285
Tecker, F. 684
Tegenfeldt, F. 1945
Tejima, M. 860
Telfer, S. 947, 2110, 2112, 2120, 2192, 3321
Temkin, R.J. 1255, 1258, 2095, 2536
Temnykh, A. 167, 1026, 1954, 3425

Temple, R. 558
Tenenbaum, P. 657, 662, 681, 2739, 2757
Teng, L.C. 2895
ten Kate, H. 42
Tennant, C. 195, 2189, 3243
Tepikian, S. 51, 135, 405, 1706, 1712, 2144, 2159, 2390
Teramoto, A. 1071
Terashima, A. 1978
Terebilo, A. 235, 2255, 2369, 2372
Terekov, V. 1691
Terremoto, L.A.A. 1593
Tesarek, R. 2497
Teytelman, D. 318, 2297, 2300, 3141, 3389
Theobald, W. 1921
Thibus, J. 2823
Thieberger, P. 1628, 1634, 1715
Thiesen, H. 1945
Thikim, M. 2303
Thomas, C. 1575
Thomas, R. 164, 2162
Thomas-Madec, C. 1104, 1332
Thomason, J. 2542
Thompson, K.M. 1020
Thompson, M.C. 1870
Thompson, N.R. 189
Thomson, D. 3377
Thorndahl, L. 1156
Tiede, R. 2942
Tiefenback, M. 195, 3243
Tigner, M. 192, 1317
Tikhoplav, R. 2682
Timossi, C. 2385
Ting, A. 716, 1819, 1846
Tinsley, D. 3068
Titt, U. 690
Titus, P. 1631
Tiunov, M. 1781, 3318
Tkachenko, L. 1781
Tobiyama, M. 2709, 3141
Tochitsky, S.Ya. 1873
Todd, A. 977
Todd, R. 788, 791
Todesco, E. 173, 1942
Toelle, R. 598, 2811, 2814, 2817, 3428
Toellner, T. 2411
Togawa, K. 487, 3332
Tokuchi, A. 1165
Tollestrup, A.V. 48, 1733, 2491, 2497
Tolmachev, S. 1867
Tom, C.Y. 558
Tomàs, R. 2207, 2228, 2231, 2234, 2240, 2901
Tombolini, F. 917
Tomimasu, T. 902, 2387, 3270
Tomizawa, H. 2838
Tomizawa, M. 3083
Tomlin, R. 2936
Tompkins, J. 1730, 1966, 1969, 1972
Tordeux, M.A. 229
Torii, Y. 884
Torikai, K. 568, 1784, 1807
Torrez, P.A. 1237
Tortschanoff, T. 1948
Torun, Y. 1183, 1246, 1413, 1795
Tosi, L. 214, 1050, 2306, 2309
Totchisky, S. 1867
Toth, C. 1840
Touzzolo, J. 1428
Tovstiak, V.V. 1080
Towne, N. 241, 3168
Towns-Andrews, E. 708
Toyama, T. 568, 1784, 1807, 2610, 3083
Toyokawa, H. 195, 713, 902, 938, 974, 2387, 3270
Trakhtenberg, E. 824, 830, 1017
Trask, W. 167
Trautwein, A. 235
Travish, G. 944, 947, 1867, 1870, 2110, 2112, 2192, 3321
Trbojevic, D. 39, 51, 54, 135, 372, 794, 797, 1425, 1691, 1697, 1706, 1712, 1816, 2204, 2694, 2904, 3413, 3485
Tremaine, A.M. 95, 2192, 2957
Tromba, G. 2309
Trotman, J.V. 1527
Trovò, M. 2306
Trujillo, P.G. 553
Trzeciak, W. 887, 2303
Tsai, H.J. 890
Tsai, Z.D. 1479
Tsakov, I. 2114
Tsang, T. 541
Tschalaer, C. 372, 956, 959, 980, 2324
Tsentalovich, E. 2324
Tsoupas, N. 51, 405, 550, 1542, 1545, 1637, 1706, 1715, 2138, 2141, 2147, 2150, 2153, 2159
Tsuchiya, K. 860, 1978
Tsukishima, C. 1539
Tsumaki, K. 250, 782, 884
Tuckmantel, J. 1718, 3050
Tuozzolo, J. 550, 571, 1637, 2138, 2144, 2147, 2150, 2156, 2390, 2598
Tupikov, V. 2020
Tur, Yu.D. 2878
Turlington, L. 1350
Turner, J.L. 2297, 2754
Turner, W. 2530
Twarowski, K. 467
Uchiyama, T. 809, 860
Ueda, A. 860, 3201, 3204
Ueng, T.S. 3237
Ueno, A. 1509
Ueno, R. 1679
Uesaka, M. 2258
Uesugi, T. 1216, 1231, 1234, 1679, 3452
Ullrich, J. 1622
Umemori, K. 860, 1228
Umstadter, D. 1921
Underwood, D. 51
Urakawa, J. 2545, 2709

Uriot, D. 2802, 3491
Uvarov, V.L. 2878
Uythoven, J. 45, 1646
Vaccarezza, C. 366, 914, 2077, 2279, 2500, 2945, 3285
Valdiviez, R. 702, 1664
Valente, A.-M. 1401, 2860
Valente, P. 1658
Valentino, V. 3318
Valfells, A. 426, 1673, 2312, 2571, 2574, 2577, 3156
Valishev, A. 3398
Valuch, D. 473, 1089
van der Laan, J.B. 372, 956, 959, 980, 2324
van der Meer, A.F.G. 519
Vanenkov, I. 1951
van Goor, F.A. 1900, 1903
VanKuik, B. 1542
van Tilborg, J. 1840
van Weelderen, R. 1945
van Zeijts, J. 51, 135, 524, 1697, 1706, 1712
Varenne, F. 2802
Varfolomeev, A. 1867
Varfolomeev, Jr., A. 1867
Variale, V. 3318
Varnasery, S. 238
Vascotto, A. 2309
Vasserman, I. 2261
Vasyukhin, N. 2814
Vay, J.-L. 132, 312, 2673, 3297
Vaziri, K. 983
Velev, G. 1730, 1969, 1972
Veness, R. 1646
Venturini, M. 863, 2772, 3144
Venturini-Delsolaro, W. 1948
Verdier, A. 444, 2237
Vermare, C. 2464
Verzilov, V. 214
Vescovi, M. 366, 2279, 3285
Veshcherevich, V. 192, 1198, 1201, 1306, 1317
Vetter, K. 524, 2444, 2697
Vicario, C. 944, 3285
Vidal, R. 2497
Vignola, G. 1053, 1658
Vikharev, A.L. 1147
Vincenzi, D. 917, 1655
Vinogradov, N.E. 2790, 2963
Vinogradov, S.V. 3530
Vinokurov, N. 2273
Viren, B. 3255
Virgo, M. 3323
Virostek, S. 1243, 2023, 2092
Visentin, B. 1303
Vlachoudis, V. 45
Vlogaert, J. 1942
Vobly, P. 2273
Vogel, H. 1410, 2887
Vogel, V. 2545
Vogler, W. 269, 3560
Volk, J.T. 1766, 2180
Volkolupov, Yu.Ya. 1107, 3303
Volkov, V.N. 2041, 2044
Vollinger, C. 173, 1951
vom Stein, P. 1410, 2887
Vorobiev, L.G. 3533
Vos, L. 45, 1801
Wada, Y. 3335
Wahrer, B. 1032
Wait, G.D. 1162
Wake, M. 568, 1784, 1807, 1981
Waldron, W. 98, 536, 1171, 1521, 2628
Waldschmidt, G. 1422
Walker, N. 657, 2396, 2733, 2736, 2739
Walker, R.P. 232
Wallace, D.J. 2303
Wallace, P. 752, 2273
Wall_n, E. 2321
Wallig, J. 1246
Walstrom, P. 544, 1966
Walter, M. 426, 1673, 1676, 2312, 2571, 2574, 2577
Walz, D. 731, 1530, 1858, 1864, 1933
Wan, W. 186, 397, 2246, 2249
Wanderer, P. 164, 1637, 2159, 2162, 2390
Wang, B. 1032
Wang, C. 1927, 1930
Wang, C.J. 2554
Wang, C.X. 3407, 3410
Wang, Ch. 1041, 1371, 2402, 2670
Wang, D. 39, 1300, 2005, 3186, 3228
Wang, D.J. 890
Wang, F. 372, 956, 959, 980, 2324
Wang, H. (ANL) 1813, 2032
Wang, H. (TJNAF) 457, 1098, 1101, 1104, 1389
Wang, J.M. 241
Wang, J.P. 815, 2357
Wang, J.W. 1264, 2664, 2763
Wang, M.H. 890, 3150, 3240
Wang, P. 752, 2479
Wang, S. 1455, 1509
Wang, S.-H. 186, 2682, 3198
Wang, T. 1386, 1398, 2860
Wang, T.S. 508, 3092, 3095
Wang, X. 2174
Wang, X.J. 217, 241, 420, 1819, 2455, 2808
Wang, X.Z. 2586
Wang, Y. (CAMD) 2382, 2892
Wang, Y. (NSRL) 815
Wangler, T.P. 2613
Warburton, D. 550, 1625, 1640, 2147
Warner, A. 2020
Warner, D.K. 1237
Warnock, R. 3144
Warsop, C.M. 1527
Watanabe, Y. 1512
Watson, J.A. 2533, 2960
Wazlawik, S. 3569
Weathersby, S. 2981

Weaver, M. 2285
Webber, R.C. 1503, 2936
Weber, C. 1189
Weggel, R.J. 1628, 1631, 1634
Wei, J. 272, 394, 550, 571, 1569, 1572, 2153, 2159, 2390, 2598, 3029, 3032, 3416, 3419
Wei, W. 815
Weichert, G. 467
Weihreter, E. 1189
Weiland, T. 2114, 3249, 3252, 3551, 3563, 3566, 3569
Weiner, M. 2664
Weinrich, U. 694
Weir, J. 563, 2960
Weise, H. 673
Weiss, D. 785
Weiss, K. 307
Welch, D.R. 98, 2622, 2637, 2685, 3165
Welch, J. 3126
Wells, R.P. 186, 812
Welsch, C.P. 1622, 2817
Welton, R.F. 527, 3306
Wender, S.A. 1168
Wendt, M. 467, 1086, 2730
Weng, W.T. 429, 571, 1637, 1709, 2793
Wenhui, H. 467
Wenninger, J. 45, 1718
Werin, S. 2318, 2321
Werkema, S. 1554
Wermelskirchen, C. 235, 761
Wesling, S. 2029
Westenskow, G. 2533, 3297, 3300
Weterings, W. 1646
White, G.R. 2733, 2778
Whitlatch, T. 457, 977, 1377, 2866
Widger, D. 2399
Widjaja, C. 1921
Widmeyer, M. 235
Wiemerslage, G. 830
Wienands, U. 2297, 2300, 3141
Wilcox, R. 2408
Wildman, D. 323, 1781, 2922, 3177
Wildner, E. 173
Wilinski, M. 2441, 2444, 2691
Wilke, I. 519
Will, I. 836, 2114
Willen, E. 164, 1936, 1939
Williams, C.L. 998
Williams, E. 3374
Williams Jr., E.L. 288
Wilson, I. 495, 665, 1156, 2724
Wilson, K.M. 1377, 2866
Wilson, M. 426
Wilson, M.N. 2162
Wilson, P. 1264, 1282
Win, S.S. 3056
Wines, R. 2135, 2186
Wisdom, J. 1861
Wiseman, M. 457, 977, 1377
Witkover, R.L. 2444, 2447, 2450
Wittmer, W. 2237
Wojtkiewicz, G. 467
Wolf, M. 2664
Wolski, A. 186, 652, 657, 866, 2246, 2396, 2745, 2772, 2775, 3213
Wood, J. 51
Wood, R.L. 920, 977, 2083
Woodley, M. 657, 662, 2739, 2757, 2766, 2775, 3126, 3129
Woods, M. 2754
Wright, E. 1144
Wu, A.T. 1386, 2860
Wu, G. (NSRL) 815
Wu, G. (TJNAF) 1389, 1395, 1401, 1575
Wu, J. 126, 1035, 1038, 2775, 3228, 3231
Wu, J.K. 3294
Wu, K.C. 164
Wu, V. 1246, 1769
Wu, X. 2849, 2972
Wu, Y. 397
Wu, Y.K. 391, 752, 2249, 2270, 2273, 2479, 2482
Wu, Z. 217, 420, 1192, 1497, 1819, 2455
Wuensch, W. 495, 1156, 2467, 2724
WËstefeld, G. 836, 839, 845, 3020, 3023
Xiao, A. 2488
Xiao, M. 1730, 1757, 1760, 1772, 1775, 3401, 3542
Xie, M. 1843
Xiong, Y. 1560, 3506, 3509
Xu, H.L. 968
Xu, N. 2174
Xu, Z. (BNL) 1688
Xu, Z. (IMP) 1288
Yadav, S. 1748, 1969
Yakimenko, V. 944, 1909
Yakovlev, V.P. 1128, 1131, 1150, 1927, 2881
Yamada, K. 713, 971, 974
Yamada, R. 1981
Yamaguchi, S. 1509, 2838
Yamamoto, A. (IHI) 3326
Yamamoto, A. (KEK) 1978
Yamamoto, K. 1512
Yamamoto, M. 1216, 1234
Yamamoto, N. 860, 2351
Yamamoto, S. (KEK) 860
Yamamoto, S. (Mitsubishi) 1539
Yamanaka, S. 1165
Yamatsu, Y. 902, 3270
Yamazaki, A. 1679, 3452
Yamazaki, M. 1338
Yamazaki, Y. 576, 1509
Yan, X. (IAP) 1335
Yan, X. (UAD) 519
Yan, Y. 2297, 2300
Yang, B.X. 2411, 2423
Yang, J.S. 1470, 2857
Yang, M.J. 1649, 1766, 3440
Yang, S. 1243, 1834
Yang, X. 1288

Yanovsky, V. 1921
Yao, C. 758
Yao, C.Y. 2411, 2423, 2438
Yao, J. 2852
Yarovoi, T. 1867
Yasumoto, M. 713, 902, 971, 974, 3270
Yeh, M.K. 1371
Yin, Y. 2586
Yocky, J. 2297, 2754
Yoder, R. 1533, 1867, 1873, 2117, 3258
Yokoi, T. 1679, 3452
Yonehara, H. 250, 782, 884, 2551
Yonemura, Y. 1679, 3452
Yorita, T. 250, 782
York, R. 138, 1350, 1353, 1362, 2849, 2972, 3533
Yoshida, M. 487
Yoshii, M. 1216, 1234, 3452
Yoshikawa, H. 1509
Yoshimoto, M. 1679, 3452
Yoshimoto, S. 860, 1228
Yoshino, K. 1509, 2393
Yoshioka, M. 860
Yotam, R. 235
Young, A. 3141
Young, L.M. 60, 920, 977, 1461, 1515, 2844, 3515, 3521
Yu, D. 1153, 1156, 2123, 2126, 2129, 2132, 2135, 2186, 3171
Yu, I.H. 2857
Yu, J. 2132
Yu, L.H. 217, 241, 2455, 2808
Yu, S.S. 98, 558, 1171, 2616, 2619, 2622, 2625, 2628, 2637, 2646, 2661, 2685
Yu, T. 1560, 3506, 3509
Yuasa, Y. 1679, 3452
Yun, J.C. 1763
Yun, R. 426, 2571
Yunn, B. 332, 3246
Yusof, Z. 2032
Zadorozhny, V. 3005
Zagorodnov, I. 3249, 3252
Zahariou-Cohen, S. 1542
Zajic, V. 89
Zakutin, V.V. 1107, 3303
Zaltsman, A. 39, 476, 1195, 3344, 3380
Zambon, L. 3395
Zangrando, D. 1050
Zapfe, K. 467
Zaplatin, E. 598
Zaugg, T. 508, 2521, 3089, 3455
Zelenski, A. 51, 405, 3282
Zeller, A. 138, 161
Zeng, J. 770
Zeno, K. 51, 54, 794, 1542, 1545, 1715
Zhan, W. 1288
Zhang, B. 2580
Zhang, C. 250
Zhang, H. 818
Zhang, P. 1921
Zhang, P.F. 968
Zhang, S.C. 968
Zhang, S.Y. 51, 54, 785, 794, 1425, 1706, 1715, 2598, 2694, 3419
Zhang, W. (BNL) 550, 1640, 2147, 3255
Zhang, W. (IMP) 1288
Zhang, W. (YY Labs) 2586
Zhang, X.L. 57, 1754, 1757, 1778, 1781, 2703
Zhang, Y. (NSRL) 758
Zhang, Y. (ORNL) 995, 1001, 1004
Zhang, Y. (TJNAF) 941
Zhao, F.Y. 815
Zhao, H. 1288
Zhao, K. 2580
Zhao, Q. 92, 2047
Zhao, T. 2382, 2892
Zhao, Y. 39, 92, 1300, 2050
Zhavoronkov, N. 836
Zheng, H. 2922
Zheng, Q. 1404
Zheng, S. 467, 1392, 1395, 1575
Zhidkov, A. 2258
Zhiglo, V.F. 2098
Zholents, A. 186, 397, 812, 866, 872, 923, 2086, 2132, 2408, 3198
Zhou, F. 1876, 1909, 2709, 3186, 3228
Zhou, J. 2646, 2966
Zigler, A. 716
Zimmermann, F. 123, 307, 665, 1727, 1730, 1754, 1757, 1778, 2237, 2240, 2315, 2604, 2739, 3038, 3041, 3044, 3053, 3056
Zimmermann, H. 2823
Zink, R. 138
Zinkann, G.P. 2426, 2790
Zisman, M. 361, 1183, 1243, 1246, 2023, 2297
Zitelli, L. 1144
Zlobin, A.V. 42, 1748, 1966, 1969, 1975
Zobov, M. 366, 914, 2279, 2742, 2945, 3285
Zolfaghari, A. 956, 959, 980, 2324
Zolotorev, M. 2530
Zotter, B. 3044
Zou, Y. 426, 511, 1673, 2673, 3156
Zubets, V. 3282
Zuo, K. 235
Zviagintsev, V. 470
Zwart, T. 956, 959, 980, 2324